

64th Annual Conference on Magnetism and Magnetic Materials

ABSTRACTS

AIP Publishing

IEEE MAGNETICS

Jointly sponsored by AIP Publishing, LLC and the IEEE Magnetics Society

Session TU
TUTORIAL: NON-VON NEUMANN COMPUTING

Pallavi Dhagat, Chair
Oregon State University, Corvallis, OR, United States

INVITED PAPERS

2:30

TU-01. Neuromorphic Computing with Spintronic Devices.
D. Querlioz[1] *1. Centre de Nanosciences et de Nanotechnologies, Univ Paris-Sud, Palaiseau, France*

In recent years, Artificial Intelligence (AI) has progressed to an astonishing level through the development of algorithms known as deep neural networks. Nevertheless, AI has to face a challenge: its considerable energy consumption, order of magnitudes higher than brains on similar tasks. Neuromorphic computing aims at designing systems whose operating principles are to some extent inspired by brains, to reduce the energy consumption of AI. In this tutorial, we will try to understand why brains are more energy efficient than current AI, and how spintronic devices and materials can help close this energy gap. Looking at the organization of the brain will teach us fundamental lessons on the design of neuromorphic systems, which should closely associate computational units (artificial neurons) and memory units (artificial synapses). We will see that one of the biggest challenges, however, is the inadequacy of current memory technologies. We will then study how spin torque and other spintronic memories, which naturally resemble synapses, can by contrast provide a solution. Second, we will study recent developments that use the physics of spintronic devices, such as spin torque nanooscillators, directly for implementing artificial neurons. We will see the benefits and the challenges of this approach to computing, which mimics very closely the way that brains use their own basic devices. The specificities of spintronics, which can be tuned and engineered finely, are particularly exciting for this vision and open different perspectives in terms of scaling. We will also see that neuromorphic systems are sometimes less demanding in terms of device properties than conventional systems, which can allow using devices in a more optimal fashion. We will study the two main applications of neuromorphic hardware (inference and learning hardware), and show that they have very different device requirements. We will finally compare two visions for neuromorphic computing: the AI approach, which can bring immediate applications, and the longer term neuroscience-inspired approach. All these approaches do not call for the same device work.

J. Grollier, D. Querlioz and M. D. Stiles, "Spintronic nanodevices for bioinspired computing". *Proceedings of the IEEE*, *104*(10), 2024-2039 (2016). M. Romera, et al. "Vowel recognition with four coupled spin-torque nano-oscillators." *Nature* 563.7730 (2018): 230.

3:20

TU-02. Quantum Computing. *K. Itoh*[1] *1. Applied Physics and CSRN, Keio University, Yokohama, Japan*

This tutorial talk consists of the following three parts. 1) General introduction of quantum computing; from its basic concept to descriptions of a variety of quantum computing device schemes. 2) Introduction of the state-of-the-art in the silicon-based, spin qubit quantum computer development. 3) Introduction of quantum software developments for application in chemical engineering, financial engineering, and artificial intelligence fields. A priority is placed on the intuitive understanding for non-experts. Please come and enjoy.

4:10

TU-03. Benchmarking Quantum Computers and Future Directions for Superconducting Quantum Hardware. *H. Paik*[1] *1. IBM Q, IBM T J Watson Research Center, Yorktown Heights, NY, United States*

While the fully fault-tolerant universal quantum computing system is still many years ahead, building an early quantum computer with quantum advantage becomes a feasible near-term milestone that we can realistically plan. Increasing number of near-term applications has been accelerating the development of quantum hardware in the industries, and as quantum system size grows, we need a whole system metric to evaluate the level of hardware performance. I would like to introduce the quantum volume (arXiv:1811.12926) as a system-level metric that quantifies quantum computational power of early quantum computing processors, and will present an example of performance comparison among IBM Q public quantum processors in the cloud. The quantum volume depends on various individual component metrics such as gate fidelity and crosstalk. I will discuss some of the challenges in building superconducting quantum hardware and suggest few directions to improve the quantum volume.

Session AA
MAGNETS IN FLATLAND: 2D MAGNETIC MATERIALS
Wei Han, Chair
Peking University, Beijing, China

INVITED PAPERS

8:30

AA-01. Fundamental Spin Interactions Underlying the Magnetic Anisotropy in the Kitaev Ferromagnet CrI_3. *I. Lee*[1], F.G. Utermohlen[1], K. Hwang[1,2], D. Weber[1], C. Zhang[1], J.v. Tol[3], J.E. Goldberger[1], N. Trivedi[1] and P.C. Hammel[1] *1. The Ohio State University, Columbus, OH, United States; 2. Korea Institute for Advanced Study, Seoul, The Republic of Korea; 3. National High Magnetic Field Laboratory, Tallahassee, FL, United States*

In the two dimensional (2D) limit, magnetic anisotropy is known to be a key element in stabilizing the ferromagnetism.[1-3] However, the comprehensive Hamilitonian of the fundamental spin models explaining the experimental data such as magnetic anisotropy field, Curie temperature T_c and Dirac gap[4], has yet to be established. In this talk, we present the detailed magnetic anisotropy of a CrI_3 single crystal obtained through the measurement of angle dependence of ferromagnetic resonance (FMR). Also, we present a Hamiltonian describing the anisotropic spin interactions in 2D in terms of the experimentally measured Heisenberg, Kitaev, off-diagonal symmetric exchange and quadrupole interactions that incorporate the material's crystal symmetries. Calculation of T_c using spin wave theory and comparison with the experimentally known values reveal that CrI_3 is a Kitaev-dominant ferromagnet rather than Heisenberg. We also find that the off-diagonal symmetric exchange interaction stabilizes the long range of 2D ferromagnetic order by opening the magnon gap ~ 0.4 meV at the center of the Brillouin zone and we predict a Kitaev-interaction-induced ~ 5 meV magnon gap opening at the Dirac point. This work clarifies the complex anisotropic behaviour of spins in CrI_3, opening a route towards 2D ferromagnets with higher T_c and magnetically frustrated quantum spin liquids based on Kitaev physics.

[1] C. Gong et al., Nature, Vol. 546, p.265 (2017). [2] B. Huang et al., Nature, Vol. 546, p.270 (2017). [3] M. McGuire, Crystals, Vol. 7, p.121 (2017). [4] L. Chen et al. Phys. Rev. X, Vol. 8, 041028 (2018).

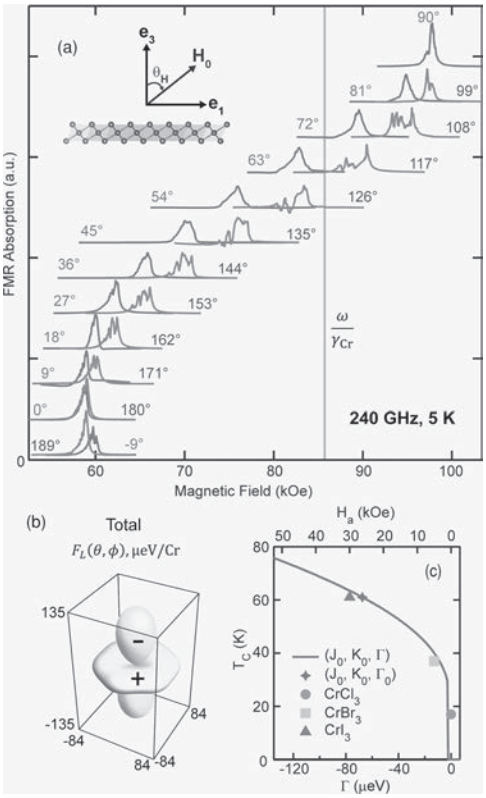


Fig. 1. (a) Evolution of the FMR spectrum as θ_H is varied, measured at 240 GHz and 5 K. Each spectrum is offset and scaled moderately for clarity. The same offset is applied for θ_H and 180°- θ_H. ω/γ_{Cr} denotes the corresponding resonance field for a free ion spin, where γ_{Cr} is the gyromagnetic ratio of the Cr^{3+} ions. (b) Total free energy density functional F_L of magnetic anisotropy for 240 GHz and 5 K. (c) Universal relationship between T_c and anisotropy field H_a (or off-diagonal symmetric exchange interaction energy Γ) known for CrX_3 (X = Cl, Br, I) bulk crystals [3], which shows a good agreement with our calculation (red line).

9:06

AA-02. Optical and electrical control of 2D magnets. *C. Jin*[1], Z. Tao[2], K.F. Mak[1,2] and J. Shan[1,2] *1. Kavli Institute at Cornell for Nanoscale Science, Cornell University, Ithaca, NY, United States; 2. School of Applied and Engineering Physics, Cornell University, Ithaca, NY, United States*

Two-dimensional (2D) van der Waals magnets have attracted much recent interest [1-8]. The 2D nature of these materials is expected to give rise to distinct physics from their bulk counterparts [1-2]. In addition, as atomically-thin layers, they can be easily incorporated into device architectures and van der Waals heterostructures to enable novel functionalities such as

gate-controllable magnetism and spin-filter tunneling [3-8]. In this talk, I will describe our recent magneto-optical spectroscopy studies to investigate the unique physical properties, such as modified magnetic coupling and enhanced spin fluctuations, in 2D magnetic insulators. I will also discuss our efforts on controlling these properties with optical and electrical methods, and the potential implications on the emerging spin phenomena as well as novel magnetic devices.

[1] M. Gibertini, M. Koperski, A. F. Morpurgo, K. S. Novoselov, *Nat Nanotechnol* 14, 408-419 (2019). [2]K. S. Burch, D. Mandrus, J. G. Park, *Nature* 563, 47-52 (2018). [3] T. C. Song *et al.*, *Science* 360, 1214-1218 (2018). [4] D. R. Klein *et al.*, *Science* 360, 1218-1222 (2018). [5] B. Huang *et al.*, *Nat Nanotechnol* 13, 544-548 (2018). [6] S. W. Jiang, L. Z. Li, Z. F. Wang, K. F. Mak, J. Shan, *Nat Nanotechnol* 13, 549-553 (2018). [7] S. W. Jiang, J. Shan, K. F. Mak, *Nat Mater* 17, 410 (2018). [8] S. W. Jiang, L. Z. Li, Z. F. Wang, J. Shan, and K. F. Mak, *Nature Electron*. 2, 159-163 (2019).

9:42

AA-03. Magnon Transport in Quasi-Two-Dimensional Van Der Waals Antiferromagnets. *W. Xing*[1] *1. Peking University, Beijing, China*

Recently, the emergence of 2D van der Waals magnets down to atomic layer thickness provides exciting platforms for exploring quantum magnetism and spintronics applications. To explore 2D magnets towards the future magnonics applications, we have investigated the magnon transport properties in quasi-2D van der Waals $MnPS_3$. In this talk, I will present the experimental observation of long distance magnon transport over several micrometers in quasi-2D van der Waals antiferromagnetic insulating $MnPS_3$. The transport of magnons could be described using magnon-dependent chemical potential and magnon relaxation length. As the quasi-2D $MnPS_3$ thickness decreases, a shorter magnon relaxation length is observed, which could be attributed to the surface-impurity-induced magnon scattering. Furthermore, I will introduce the electric field effect on the metal-insulator transition in multilayer ferromagnetic semiconducting $Cr_2Ge_2Te_6$, and the anomalous Hall effect mechanisms in ferromagnetic metallic $Fe_{0.29}TaS_2$.

[1] Wenyu Xing, et al, "Magnon transport in quasi-two-dimensional van der Waals antiferromagnets", Physical Review X, 9, 011026 (2019). [2] Wenyu Xing, et al, "Electric field effect in multilayer $Cr_2Ge_2Te_6$: a ferromagnetic 2D material", 2D Materials, 4, 024009 (2017).

10:18

AA-04. Epitaxial Growth and Magnetic Properties of Room Temperature 2D van der Waals Ferromagnets. *R. Kawakami*[1] *1. Dept. of Physics, The Ohio State University, Columbus, OH, United States*

Monolayer van der Waals (vdW) magnets provide an exciting opportunity for exploring two-dimensional (2D) magnetism for scientific and technological advances. One of the important direction is the epitaxial growth of 2D magnets with high ordering temperatures and large areas, which complement the work on smaller exfoliated materials. In this talk, I will discuss the development of room temperature ferromagnetism in the monolayer limit for epitaxial $MnSe_2$ vdW layers [1]. Since bulk Mn-Se compounds are not ferromagnetic and bulk van der Waals crystals of $MnSe_2$ do not exist, we rely on molecular beam epitaxy to grow far from equilibrium and epitaxially stabilize $MnSe_2$ layers on GaSe(0001) and $SnSe_2$(0001) epilayers. Magnetization measurements of monolayer $MnSe_2$ films on GaSe and $SnSe_2$ epilayers show ferromagnetic ordering with a large saturation magnetization of ~ 4 Bohr magnetons per Mn, which is consistent with density functional theory calculations predicting ferromagnetism in monolayer 1T-$MnSe_2$. Growing manganese selenide films on GaSe up to high thickness (~ 40 nm) produces α-MnSe(111), and an enhanced magnetic moment (~ 2x) compared to the monolayer $MnSe_2$ samples. Detailed structural characterization by scanning transmission electron microscopy (STEM), scanning tunneling microscopy (STM), and reflection high energy electron diffraction (RHEED) reveal an abrupt and clean interface between GaSe(0001) and α-MnSe(111). In particular, the structure measured by STEM is consistent with the presence of a $MnSe_2$ monolayer at the interface. These results hold promise for potential applications in energy efficient information storage and processing. Beyond these initial studies, we have investigated the growth of room temperature ferromagnets $MnSe_2$ and VSe_2 [2] on a variety of substrates including topological insulator Bi_2Se_3, III-V semiconductor GaAs(111), and highly-oriented pyrolytic graphite (HOPG). Among these studies, the heterostructures of magnetic layers with topological insulators are particularly interesting for current induced magnetic switching via spin-orbit torque. Further, these investigations have led to the synthesis of $MnBi_2Se_4$ a layered antiferromagnetic topological insulator, which integrates a $MnSe_2$ layer within a Bi_2Se_3 quintuple layer (i.e. septuple layer with a sequence of Se-Bi-Se-Mn-Se-Bi-Se). We report the growth, structural characterization, and magnetic and electronic properties of such materials.

1. O'Hara, D. J., Zhu, T., Trout, A. H., Ahmed, A. S., Luo, Y. K., Lee, C. H., Brenner, M. R., Rajan, S., Gupta, J. A., McComb, D. W. & Kawakami, R. K. Room Temperature Intrinsic Ferromagnetism in Epitaxial Manganese Selenide Films in the Monolayer Limit. *Nano Letters* 18, 3125 (2018). 2. Bonilla, M., Kolekar, S., Ma, Y., Diaz, H. C., Kalappattil, V., Das, R., Eggers, T., Gutierrez, H. R., Phan, M.-H. & Batzill, M. Strong Room-Temperature Ferromagnetism in VSe_2 Monolayers on van der Waals Substrates. *Nature Nanotechnology* 13, 289 (2018).

10:54

AA-05. Magnetic Order Near Room Temperature in Fe_5GeTe_2. *A. May*[1] *1. Oak Ridge National Lab, Oak Ridge, TN, United States*

$Fe_{5-x}GeTe_2$ is a van der Waals layered compound with Curie temperatures of 260-310K.[1,2] It is metallic and easily cleaved into thin flakes.[2] This material has similarities with the heavily-studied compound $Fe_{3-x}GeTe_2$,[3-6] but the compounds possess different crystal structures and physical properties. This talk will focus on the magnetic properties of $Fe_{5-x}GeTe_2$ single crystals, which possess a Curie temperature that depends on processing conditions. One of the magnetic sublattices remains dynamic down to approximately 120K, and these fluctuating moments greatly impact the transport properties. Exfoliation of bulk single crystals has produced 10nm thick flakes, which appear to have the high Curie temperature of the bulk based on Hall effect measurements.

[1] J. Stahl, E. Shlaen, and D. Johrendt, Z. Anorg. Allg.Chem., Vol. 644, p. 1923 (2018). [2] A.F. May, D. Ovchinnikov, Q. Zheng et al., ACS Nano, Vol. 13, p. 4436 (2019). [3] H.-J. Deiseroth, K. Aleksandrov, C. Reiner et al., Eur. J. Inorg. Chem., Vol. 2006, p. 1561 (2006). [4] A. F. May, S. Calder, C. Cantoni et al., Phys. Rev. B., Vol. 93, p. 014411 (2016). [5] Z. Fei, B. Huang, P. Malinowski et al., Nat. Mater., Vol. 17, p. 778 (2018). [6] Y. Deng, Y. Yu, Y. Song et al., Nature, Vol. 563, p. 94 (2018).

Session AB
ANTIFERROMAGNETIC SPINTRONICS I

Lorenzo Baldrati, Chair
Johannes Gutenberg-Universität Mainz, Mainz, Germany

CONTRIBUTED PAPERS

8:30

AB-01. Resonant Raman Spectroscopy of the Chiral Antiferromagnet $CoNb_3S_6$. *N. Hassan*[3,1], A. McCreary[1], N. Ghimire[2] and A.R. Hight Walker[1]
1. The National Institute of Standards and Technology, Gaithersburg, MD, United States; 2. Department of Physics & Astronomy, George Mason University, Fairfax, VA, United States; 3. Department of Physics and Astronomy, Johns Hopkins University, Baltimore, MD, United States

A new class of topological materials are made by inserting transition metal atoms into the atomic lattice of a well-known two-dimensional material. We report here the first full Raman characterization of the chiral antiferromagnet $CoNb_3S_6$; i.e. cobalt-doped NbS_2. $CoNb_3S_6$ exhibits a large c-axis anomalous Hall effect (AHE) not entirely attributable to the small intrinsic ferromagnetic component (Co) along the c-axis [1]. This interesting behavior suggests that the enhancement in AHE may be a combination of magnetic field in the presence of the near-Fermi energy Weyl nodes. Theory claims that interacting Weyl fermions could give rise to spin density waves [2]. Neutron scattering experiments of $CoNb_3S_6$ [3] showed incommensurate peaks; however, it was not clear whether the peaks are due to a spin spiral or a spin density wave. Magneto-Raman spectroscopy represents an optimal method to differentiate these structures. Wavelength- and polarized-dependent Raman spectra collected at room temperature from $CoNb_3S_6$ flakes are analyzed specifically in relation to the vibrational modes seen in NbS_2. Experiments of temperature- and magnetic field-dependent Raman spectroscopy to seek magnon (spin wave) signatures will be detailed.

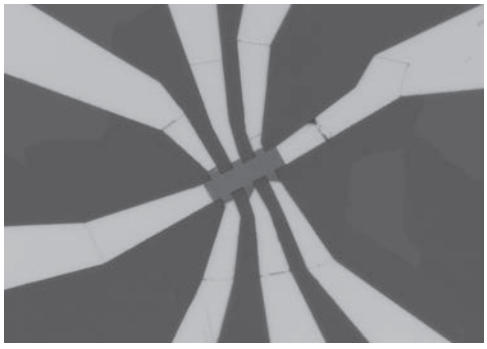
(1) Nirmal J. Ghimire, A. S. Botana, J. S. Jiang, Junjie Zhang, Y.-S. Chen and J. F. Mitchell, Nature Communications Vol. 9, Article number 3280 (2018) (2) Zachary M. Raines and Victor M. Galitski, Phys. Rev. B Vol. 96, p. 161115(R) (2017) (3) Private communication with N. Ghimire

8:42

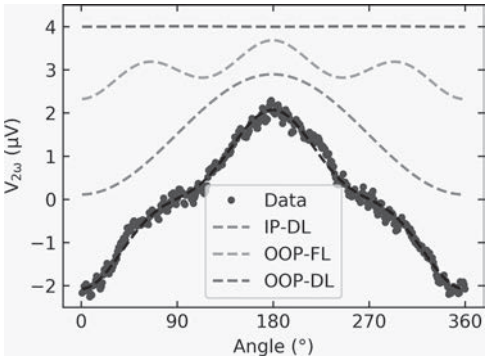
AB-02. Large Interfacial Spin-Orbit Torques in Permalloy/$NiPS_3$ Bilayers. *C. Schippers*[1], H. Swagten[1], B. Koopmans[1] and M. Guimarães[2]
1. Department of Applied Physics, Eindhoven University of Technology, Eindhoven, Netherlands; 2. Zernike Institute for Advanced Materials, University of Groningen, Groningen, Netherlands

With the emergence of spin-orbit torque based magnetic random-access memories, novel and more efficient ways of generating spin-orbit torques (SOTs) for switching the magnetization of a ferromagnetic layer have gained a lot of interest. Most methods use a heavy-metal layer to generate these torques, e.g. the spin-Hall effect in platinum. However, it has been theoretically demonstrated that interfacing the ferromagnet with an insulator with spin-orbit coupling can generate a variety of SOTs [1]. However, as heavy metals also generate SOTs in the bulk, it can be difficult to distinguish between the bulk and interfacial contribution. To investigate the generation of interfacial SOTs, we use nickel-thiophosphate ($NiPS_3$), a two-dimensional Van der Waals antiferromagnet, for generating interfacial SOTs on its interface with a ferromagnetic permalloy (Py, $Fe_{0.2}Ni_{0.8}$) layer. As $NiPS_3$ is an insulating material, any measured torque at the ferromagnet must be interfacial of nature. Moreover, $NiPS_3$ has a reduced symmetry in its antiferromagnetic phase. This can allow for the presence of an out-of-plane damping-like SOT, a type of torque that is often limited by symmetries in a material. Although this torque has been observed in the low-symmetry Van der Waals material WTe_2 [2], using $NiPS_3$ would provide a way of controlling this torque with the antiferromagnetic phase-transition. In this contribution we have used Hall-bar devices (Fig. 1) to perform harmonic Hall measurements (Fig. 2) to quantify the SOTs in our structures. We observe large interfacial out-of-plane field-like and in-plane damping-like torques the $NiPS_3$/Py bilayers, comparable to values of bulk heavy-metal-based SOT devices, such as Pt/Py bilayers. However, while it is allowed by symmetry, the out-of-plane damping-like SOT has not been observed. Our current efforts are focused at understanding our findings. We envision that this research adds to the understanding of the nature of interfacial spin-orbit torques and contributes to designing and optimizing future spintronics applications.

[1] V. P. Amin, M. D. Stiles, PRB, 94, 104420 (2016) [2] D. MacNeill, G.M. Stiehl, M. H. D. Guimarães, Nat. Phys. 13, 300–305 (2017)



One of the devices used for second harmonic Hall-measurements.



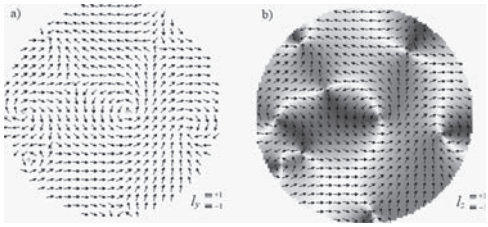
Typical second harmonic Hall measurement at T = 50 K where the different torque contributions can be quantified.

8:54

AB-03. Vortex-antivortex dynamics in easy plane antiferromagnetic materials. *G. Finocchio*[1], R. Tomasello[2], F. Garesci[1], M. Carpentieri[3], P. Khalili Amiri[4] and V. Lopez[4] *1. University of Messina, Messina, Italy; 2. FORTH, Heraklion, Greece; 3. Politecnico di Bari, Bari, Italy; 4. Northwestern University, Evanston, IL, United States*

It has been shown that AFM order, i.e. the Néel vector, can be manipulated optically, with strain, and electrical current. The latter is of particular relevance for the design of antiferromagnetic memories [1,2] and oscillators[3,4]. In addition, images of antiferromagnetic order in micrometer size devices show the presence of multiple domains [5], and in some materials also vortex and antivortex states can be stabilized[6]. Up to now, studies of domain wall statics and dynamics driven by spin-hall have been performed in perpendicular materials[7], while a systematic numerical study on vortex and antivortex pair dynamics is still missing. Here, we performed micromagnetic simulations to study static and dynamical properties of vortex antivortex pair stabilized in antiferromagnetic materials with easy plane anisotropy with circular shape on top an extended heavy metal with large spin-orbit coupling. The antiferromagnetic state is modeled by means of two vectors m1 and m2. These represent the normalized (with respect to the saturation magnetization) magnetizations of the two sub-lattices, whose dynamical manipulation is described by two coupled Landau-Lifshitz-Gilbert (LLG) equations[4]. We created a stability phase diagram dot diameter vs. anisotropy constant comparing the energy of vortex-antivortex, vortex and uniform state. Our results shows that in dot with diameter above 400nm the ground state of the Néel order can be strongly nonuniform. Figure 1(a) and (b) show an example of ground state having multi vortex and antivortex and antivortex pair ((a) z-component and (b) y-component of the Néel vector) calculated in a device with a diameter of 4000nm, as can be observed a very complex pattern is observed. We then consider the dynamics driven by spin-hall effect in vortex-antivortex pair with same and opposite polarity.

[1] Jungwirth, T., Marti, X., Wadley, P. & Wunderlich, J. *Nat. Nanotechnol.* 11, 231-241, (2016). [2] Moriyama, T., Oda, K., Ohkochi, T., Kimata, M. & Ono, T. *Sci. Rep.* 8, 14167, (2018). [3] Khymyn R., Lisenkov I., Tiberkevich V., Ivanov B. A. and Slavin A., *Sci. Rep*. 7, 43705 (2017). [4] Puliafito, V. *et al*. *Phys. Rev. B* 99, 024405, doi:10.1103/PhysRevB.99.024405, (2019). [5] Grzybowski, M. J. *et al. Phys. Rev. Lett.* 118, 057701, (2017). [6] Chmiel, F. P. *et al. Nat. Mater.* 17, 581-585, (2018). [7] Gomonay O., Jungwirth T., and Sinova J., *Phys. Rev. Lett*, 117, 017202 (2016).



Example of a micromagnetic state in an easy plane antiferromagnets. The state is characterized by a complex vortex-antivortex pattern of the magnetization. In (a) and (b) are displayed the z and the y component of the Néel vector (blue negative, red positive). The arrows indicate the in-plane component of the magnetization.

9:06

AB-04. Anomalous transport properties of hexagonal Mn_3Sn thin films. *P. Zilske*[1], S. Kurdi[2], G. Reiss[1] and J. Koo[1] *1. Center for Spinelectronic Materials and Devices, Bielefeld University, Bielefeld, Germany; 2. Department of Materials Science and Metallurgy, University of Cambridge, Cambridge, United Kingdom*

In the last decade, antiferromagnetic spintronics has been recognized as a very important field for future magnetic memory or logic applications [1]. Recently, the $D0_{19}$ ε-Mn_3X (X = Ga, Ge, Sn) system has emerged as a new candidate for active elements in spintronic devices. Theoretical calculations and first experimental results have shown large anomalous Hall and anomalous Nernst effects for those non-collinear antiferromagnets. However, these properties are only studied in detail in single crystal bulk samples, and achieving high quality thin films is required for their realization in devices [2-4]. Here, we report on structural, magnetic and transport properties of Mn_3Sn thin films. Epitaxial Ru/Mn_3Sn thin films were grown on c-Al_2O_3 single crystal substrates via magnetron co-sputtering. For detailed structural analysis, we performed high-resolution X-ray diffraction (XRD) measurements and transmission electron microscopy (TEM). The X-ray study reveals highly epitaxial films and single phase growth of the Mn_3Sn. Furthermore, TEM images show smooth interfaces and no inter-diffusion of any elements. In addition to the structural characterization, magnetic as well as transport properties has been measured. The in-plane M-H curve reveals clear hysteresis loop with remanence close to the bulk value. The hysteresis shows both small coercivity (15 mT) and saturation field (100 mT), cf. Fig.1. In addition, clear magnetic field dependent anomalous transport properties (anomalous Hall effect (AHE) and anomalous Nernst effect (ANE)) were obtained. The corresponding room temperature AHE, ρ_{zx}, and ANE, α_{xz}, data are also shown in Fig.1. Along those crystallographic directions, AHE and ANE have not yet been reported in thin film systems. In addition, temperature dependent AHE measurements will be discussed.

[1] T. Jungwirth, X. Marti, P. Wadley and J. Wunderlich, Nature Nanotech. 11, 231 (2016) [2] Y. Zhang, Y. Sun, H. Yang, J. Zelezny, S. P. P. Parkin, C. Felser and B. Yan, Phys. Rev. B 95, 075128 (2017) [3] S. Nakatsuji, N. Kiyohara, and T. Higo Nature 527, 212 (2015) [4] N. Kiyohara, T. Tomita and S. Nakatsuji, Phys. Rev. Appl. 5, 064009 (2016)

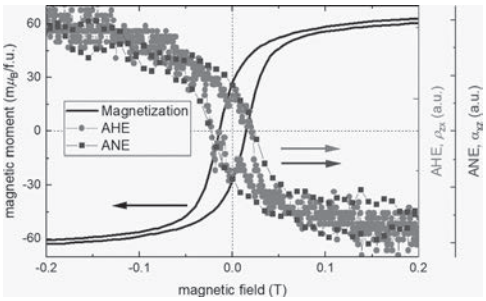


Fig.1 (left axis) Magnetization curve of a 60 nm Mn_3Sn sample. (right axis) Corresponding AHE and ANE measurements along specific crystallographic directions.

9:18

AB-05. Direct Probe of Uncompensated Magnetization at the Surface of an Antiferromagnetic FeF Layer. *P.N. Lapa*[1], I.V. Roshchin[2] and I.K. Schuller[1] *1. Department of Physics, University of California San Diego, La Jolla, CA, United States; 2. Department of Materials Science and Engineering, Texas A&M University, College Station, CA, United States*

Using a novel transport technique, we discovered a peculiar behavior of the uncompensated magnetization (UM) formed at the surface of an antiferromagnetic FeF layer. The key to this is the fabrication of an epitaxial antiferromagnet-conductor-ferromagnet spin valve [1], specifically, FeF (30nm)/Cu(10nm)/Co(5nm)/Ti(5nm). When the valve is cooled down to 10 K in in-plane magnetic field, the angular dependence of resistance can be represented as a superposition of two harmonics with 180° and 360° periodicity (Fig. 1). The 180° harmonic is present in the entire studied temperature range and it is caused by the anisotropic magnetoresistance of the Co layer. The 360° harmonic appears only at temperatures below Neel temperature of FeF (78 K). This is interpreted as due to a giant magnetoresistance caused by the scattering of charge carriers polarized by the Co layer on the UM at the FeF /Cu interface. The minimum of this harmonic occurs at the pinning direction of the UM. When the valve is cooled down in a magnetic field

applied along the easy axis of the FeF layer, the UM is pinned in the direction opposite to the cooling field. This discovery unambiguously confirms the earlier hypothesis for the mechanism of the positive exchange-bias effect observed in the FeF/ferromagnet bilayers [2] and the direction of the pinned UM in FeF [3-4]. Furthermore, the observation that the uni-directional anisotropy (180° asymmetry of the magnetoresistance) is preserved even in the field as high as 9 T, indicates that even such a field cannot break the UM pinning. For all cooling field orientations, even when it is perpendicular to the easy axis, the UM is pinned along the easy axis. This fact, combined with the pinning persisting in a high magnetic field clearly indicates that UM is rigidly coupled to the antiferromagnetic staggered order in FeF2. This discovery may be essential for applications in the area of antiferromagnetic spintronics. This research was supported by the Office of Basic Energy Science, U.S. Department of Energy, BES-DMS funded by the Department of Energy's Office of Basic Energy Science, DMR under grant DE FG02 87ER-45332.

[1] P.N. Lapa, et al., Phys. Rev. B 95 020409 (2017). [2] J. Nogués, et al., Phys. Rev. Lett. 76 4624 (1996). [3] S. Roy, et al., Phys. Rev. Lett. 95, 047201 (2005). [4] M.R. Fitzsimmons, et al., Phys Rev. B 75, 214412 (2007).

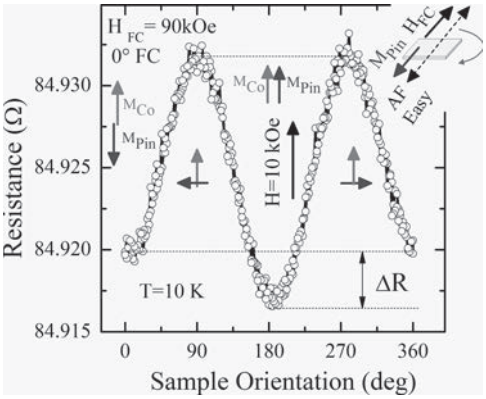


Fig. 1 Angular dependence of resistance measured after field cooling.

9:30

AB-06. Coherent Magnetic Small Angle Soft X-Ray Scattering for Structural and Dynamic Characterization of a Free-Standing B2-Ordered FeRh Thin Film. *J. Massey*[1], R.C. Temple[1], T. Almeida[2], R. Lamb[2], N. Peters[1], R. Campion[3], R. Fan[4], D. McGrouther[2], P. Steadman[4] and C.H. Marrows[1] *1. University of Leeds, Leeds, United Kingdom; 2. University of Glasgow, Glasgow, United Kingdom; 3. University of Nottingham, Nottingham, United Kingdom; 4. Diamond Light Source, Didcot, United Kingdom*

B2-ordered FeRh undergoes a first order phase transition from an antiferromagnet (AF) to a ferromagnet (FM) upon heating through the transition temperature ~ 380 K [1]. The FM phase through has been studied extensively through the phase transition using magnetic imaging techniques [2, 3, 4]. However, only one study exists that attempts to characterize the development of the AF phase through the transition and little is known about the properties of this phase [4]. Here, by combining both X-Ray Magnetic Circular Dichroism (XMCD) and X-Ray Magnetic Linear Dichroism (XMLD) with Small Angle X-Ray Scattering, it is possible to track the structural behaviour of both magnetic phases through the transition of a free-standing B2-ordered FeRh thin film. These studies reveal a change in the measured scatterer through the transition within the available Q range from FM domain walls to FM domains using XMCD and between FM domain walls and AF domains using XMLD. It is also seen to be possible to measure the dynamic behaviour of both magnetic phases by performing X-Ray Photon Correlation Spectroscopy (XPCS) studies throughout the transition. Fitting to stretched exponential relaxation model, characterised by the stretching exponent, β, the investigations performed using XMCD demonstrate a change in the dynamics behaviour across the transition consistent with the change in scatterer seen in the structural analysis. The investigations using XMLD, however, show a contrasting behaviour and reveals that various relaxation processes are introduced into the system alongside the AF material. By combining the two investigations it is possible to build up a comprehensive picture of how the dynamic behaviour changes through the transition. These investigations show that direct measurements of the structural and dynamic behaviour of the fully AF state are possible using this technique.

[1] G. Shirane *et al*., Phys. Rev. 134, 1964. [2] R. C. Temple *et al*. Phys. Rev. Mat. 2 104406, 2018. [3] T. P. Almeida *et al*. Sci. Rep. 7 17835, 2017. [4] C. Baldasseroni *et al*. J. Phys: Cond. Mat. 27 256001, 2015.

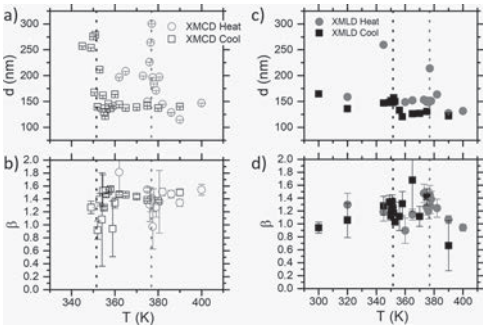


Figure 1: (a) shows the length scale, *d*, corresponding to a peak in the structure factor seen in the SAXS analysis when measured using XMCD. (b) shows the stretching exponent, β, extracted from the temporal correlation analysis for XPCS measurements taken using XMCD. (c) and (d) show the same quantities extracted for measurements performed using XMLD.

9:42

AB-07. Long-range chiral interlayer exchange coupling in synthetic antiferromagnets for 3D spin structures. *D. Han*[1,2], K. Lee[1], J. Hanke[1,3], Y. Mokrousov[1,3], K. Kim[2], W. Yoo[4], Y. van Hees[5], T. Kim[6], R. Lavrijsen[5], C. You[7], H. Swagten[5], M. Jung[4] and M. Kläui[1] *1. Institute of Physics, Johannes Gutenberg-Universität Mainz, Mainz, Germany; 2. Center for Spintronics, Korea Institute for Science and Technology, Seoul, The Republic of Korea; 3. Peter Grünberg Institut and Institute for Advanced Simulation, Forschungszentrum Jülich and JARA, Jülich, Germany; 4. Department of Physics, Sogang University, Seoul, The Republic of Korea; 5. Department of Applied Physics, Institute for Photonic Integration, Eindhoven University of Technology, Eindhoven, Netherlands; 6. Department of Advanced Materials Engineering, Sejong University, Seoul, The Republic of Korea; 7. Department of Emerging Materials Science, DGIST, Daegu, The Republic of Korea*

The exchange interaction is key for ferroic magnetic coupling and responsible for major phenomena in magnetic materials. This fundamental interaction combined with spin-orbit coupling leads to two components: symmetric and antisymmetric. While the symmetric term, generally referred to as a Heisenberg exchange coupling, gives rise to ferro- and antiferro-magnetism, the antisymmetric exchange coupling – Dzyaloshinskii-Moriya interaction [1,2] has recently attracted particular interest owing to its significant role in stabilizing topologically non-trivial spin textures [3-8] in a ferromagnetic layer. Beyond the *intra-layer* exchange coupling limited to a single ferromagnetic layer, the *interlayer* exchange coupling can also lead to ferro- or antiferromagnetic alignments of magnetic multilayers. This has served as a crucial element for modern devices and recently attracted renewed interests in the community in line with an emerging field of antiferromagnetic spintronics [9-11]. Most of the relevant studies, however, have so far focused only on its symmetric component, although its antisymmetric counterpart can arise, particularly, in systems with an inversion symmetry breaking

and spin-orbit coupling [12-14]. Here, we present experimental demonstrations of the antisymmetric interlayer exchange coupling in perpendicularly magnetized synthetic antiferromagnets [14]. Asymmetric hysteresis loops under an in-plane field unambiguously reveal a unidirectional and chiral nature of this novel interaction, which cannot be explained by any existing coupling mechanisms but by chiral interlayer exchange coupling, resulting in canted magnetizations. Theoretical studies by *ab initio* methods also suggest that such chiral interlayer exchange coupling is ultimately related to the spin-orbit coupling in multilayers and a reduced symmetry in the plane of multilayers. Our observation of chiral interlayer exchange coupling paves the way for engineering magnetic structures in particular in three-dimensions, which would enable novel unconventional logic devices.

[1] I. Dzyaloshinsky, *J. Phys. Chem. Solids* 4, 241–255 (1958). [2] T. Moriya, *Phys. Rev*. 120, 91 (1960). [3] S. Emori, U. Bauer, S.-M. Ahn, E. Martinez, and G. S. D. Beach, *Nat. Mater.* 12, 611 (2013). [4] K.-S. Ryu, L. Thomas, S.-H. Yang, and S. Parkin, *Nat. Nanotechnol*. 8, 527 (2013). [5] S. Woo *et al.*, *Nat. Mater.* 15, 501 (2016). [6] C. Moreau-Luchaire *et al.*, *Nat. Nanotechnol.* 11, 444 (2016). [7] K. Litzius *et al.*, *Nat. Phys.* 13, 170 (2016). [8] X. Z. Yu *et al, Nat. Commun.* 3, 988 (2012) [9] S.-H. Yang, K.-S. Ryu, and S. Parkin, Nat. Nanotechnol. 10, 221 (2015). [10] K.-J. Kim *et al.*, Nat. Mater. 16, 1187 (2017). [11] R. A. Duine, K.-J. Lee, S. Parkin, and M. D. Stiles, Nat. Phys. 14, 217 (2018). [12] E. Y. Vedmedenko, J. A. Arregri, P. Riego, and A. Berger, arXiv:1803.10570. [13] A. Fernández-Pacheco *et al.*, *Nat. Mater.* 18, 679 (2019). [14] D.-S. Han *et al.*, *Nat. Mater.* 18, 703 (2019).

9:54

AB-08. Signal-to-Noise Ratio and Maximum Detected Frequency of Terahertz-Frequency Spectrum Analyzer Based on an Antiferromagnetic Tunnel Junction. P. Artemchuk[1], S. Louis[2], O. Prokopenko[1], *V. Tiberkevich*[3] and A.N. Slavin[3] *1. Faculty of Radio Physics, Electronics and Computer Systems, Taras Shevchenko National University of Kyiv, Kyiv, Ukraine; 2. Department of Electrical and Computer Engineering, Oakland University, Rochester, MI, United States; 3. Department of Physics, Oakland University, Rochester, MI, United States*

An antiferromagnetic (AFM) tunnel junction (ATJ) is an ultra-fast spintronic device which seems to be promising for THz-frequency signal generation, detection and processing [1-3]. Here we calculate the signal-to-noise ratio (SNR) and maximum detected frequency of the previously proposed [3] spectrum analyzer based on a current driven Pt/IrMn/MgO/Pt ATJ as a function of two geometrical parameters: thickness d of the MgO tunneling barrier and the device lateral size a. The output voltage U_{dc} of the ATJ-based spectrum analyzer is reduced when the input signal frequency f increases, mainly due to the spurious influence of the ATJ capacitance [3]. When the input frequency reaches a certain value f_{max}, the detected voltage U_{dc} drops below the Johnson-Nyquist (JN) noise voltage U_{JN} making the signal detection impossible. We analyzed the dependences of the SNR = U_{dc}/U_{JN} and maximum frequency f_{max} of an ATJ spectrum analyzer on the MgO barrier thickness d and ATJ lateral size a. These results are calculated for the input signal power of 1 μW and temperature T = 293 K and are presented in Figs. 1, 2. As seen from Fig. 1, the SNR strongly decreases with the increase of the signal frequency f, while its dependence on the junction's lateral size a is relatively weak. The optimum size a of the ATJ junction is around 300 nm, where the maximum detected frequency f_{max} reaches 0.38 THz (see dashed line in Fig.2). The maximum frequency f_{max} strongly decreases with the increase of the barrier thickness d (see solid line in Fig.2), which is caused, mainly, by the exponential increase of the ATJ resistance and impedance mismatch between the ATJ and the 50 Ω input transmission line. Thus, an ATJ-based spectrum analyzer with optimum parameters (d ~ 1 nm, a ~ 300 nm) can be used for room-temperature detection of low-power (~ 1 μW) input signals with frequencies of up to ~ 0.38 THz.

[1] B.G. Park *et al*., Nature Mater., Vol. 10, p. 347 (2011). [2] O.R. Sulymenko *et al*., IEEE Magn. Lett., Vol. 9, p. 3104605 (2018). [3] P. Artemchuk *et al.*, Joint MMM-Intermag Conference, FC-02, p. 544.

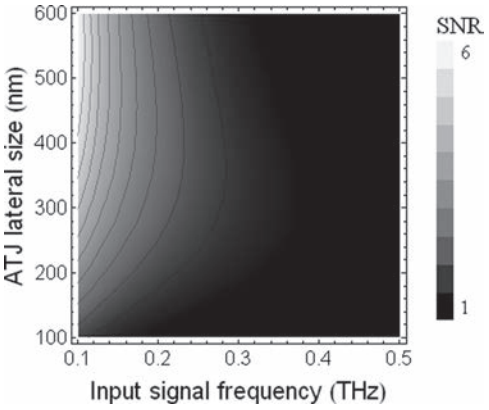


Fig. 1. SNR of an ATJ-based spectrum analyzer as a function of the signal frequency f and the junction's lateral size a. MgO barrier thickness d = 1 nm, signal power 1 μW.

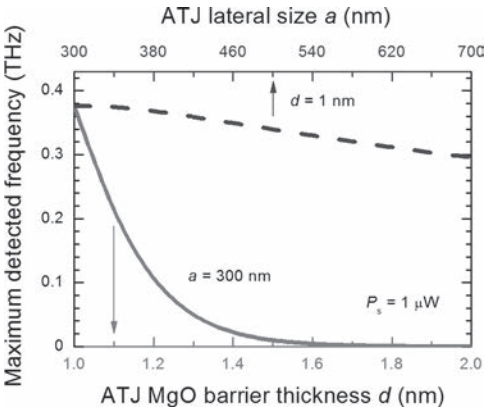


Fig. 2. Maximum frequency of an ATJ-based spectrum analyzer as a function of the MgO barrier thickness d (solid curve, bottom axis) and the junction's lateral size a (dashed curve, top axis).

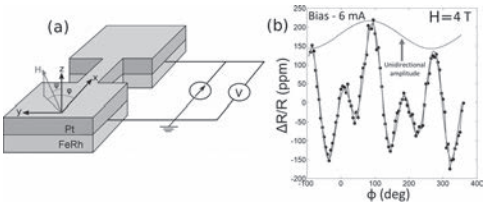
10:06

AB-09. Anisotropic Magnetoresistance and Unidirectional Magnetoresistance in Pt/FeRh Bilayers. *J. Sklenar*[1], H. Saglam[2], J. Oh[1], G. Hamilton[1], Y. Li[2], W. Zhang[3], S. Zhang[2], M. Gilbert[1], A. Hoffmann[2] and N. Mason[1] *1. University of Illinois at Urbana-Champaign, Urbana, IL, United States; 2. Argonne National Laboratory, Lemont, IL, United States; 3. Oakland University, Rochester, MI, United States*

In this work, we demonstrate a unidirectional magnetoresistance (UMR) effect in the antiferromagnetic phase of a Pt/FeRh bilayer. To date, UMR effects have now been established within a plethora of thin film heterostructures containing a ferromagnet and a non-magnetic layer capable of generating spin-currents. Two examples are found in ferromagnets adjacent to spin Hall metals or topological insulators [1, 2]. The origin of UMR is sometimes attributed to magnetization dynamics in the magnetic layer from the adjacent material producing the spin current. Importantly, these high frequency dynamics are generated and detected (via UMR) without the need for more specialized high-frequency electronics [2, 3, 4]. The UMR we observe appears after a large enough "threshold" current density is reached in the Pt. This suggests that the UMR is arising at the onset of antiferromagnetic magnetization dynamics being induced in the FeRh. Along with the UMR, we will present a detailed study on the related anisotropic magnetoresistance

(AMR) effect in both the ferromagnetic and antiferromagnetic phase of Pt/FeRh, upon which the UMR signal is superimposed. Work at The University of Illinois at Urbana-Champaign was supported by the National Science Foundation MRSEC program under NSF award number DMR-1720633. Work at Argonne was supported by the U.S. Department of Energy, Office of Science, Materials Sciences and Engineering Division.

[1] C. O. Avci, K. Garello, A. Ghosh, M. Gabureac, S. F. Alvarado and P. Gambardella, "Unidirectional spin Hall magnetoresistance in ferromagnet/normal metal bilayers," Nature Physics 11, 570-575 (2015). [2] K. Yasuda, A. Tsukazaki, R. Yoshimi, K. S. Takahashi, M. Kawasaki and Y. Tokura, "Large Unidiretional Magnetoresistance in a Magnetic Topological Insulator," Phys. Rev. Lett. 117, 127202 (2016). [3] S. Langenfeld, V. Tshitoyan, Z. Fang, A. Wells, T. A. Moore and A. J. Ferguson, "Exchange magnon induced resistance asymmetry in permalloy spin-Hall oscillators," Appl. Phys. Lett. 108, 192402 (2016). [4] K. -J. Kim, T. Li, S. Kim, T. Moriyama, T. Koyama, D. Chiba, K. -J. Lee, H. -W. Lee and T. Ono, "Possible contribution of high-energy magnons to unidirectional magnetoresistance in metallic bilayers," Appl. Phys. Exp. 12, 6 (2019).



(a) An illustration of our devices which are Pt/FeRh films patterned into a constricted geometry. The width of the Pt/FeRh wire is 500 nm and the Pt layer is 5 nm thick. We have studied FeRh layers having thicknesses between 7.5 -30 nm. A current bias can be applied across the device while a longitudinal resistance measurement is made. The resistance is measured as a field is rotated in the *xy*, *zx*, and *yz* plane. (b) The angular dependence of the Pt/FeRh bilayer is shown as a 4 T field is rotated in the *xy* plane with a 6 mA current bias present. The angular lineshape is a combination of a two- and four-fold AMR which we can identify as non-crystalline and crystalline magnetoresistance effects in the FeRh. Additionally, a UMR signal is identified which is not present at lower current densities.

10:18

AB-10. Topological Hall effect in weakly canted antiferromagnets.
J.J. Nakane[1], K. Nakazawa[2] and H. Kohno[1,3] *1. Physics, Nagoya University, Nagoya, Japan; 2. Earth and Space Science, Osaka University, Osaka, Japan; 3. Center for Spintronics Research Network (CSRN), Osaka University, Osaka, Japan*

The topological Hall effect (THE) is a Hall effect caused by a noncoplanar spin texture, or its spin chirality, in ferromagnetic conductors. This effect is absent in antiferromagnets due to the cancellation of the two sublattice chiralities [1,2]. If the moments are canted, however, the overall spin chirality, hence the THE, can be finite. Motivated by a recent experiment [3], we studied the THE in a weakly canted antiferromagnet with textured Néel (n) and uniform (l) components of magnetization. Treating the textured Néel component by a spin gauge field and the uniform component perturbatively, we derived an analytical expression for the topological Hall conductivity (THC). The result is first order in uniform moment, and is proportional to an emergent magnetic field, $\nabla\times A_{AF}$, where $A_{AF} = l.\partial_i n\times n$ is an emergent vector potential in antiferromagnets, which consists of the spin-chirality density (triple scalar product), $l.\partial_x l\times\partial_y l$, and a term $\sim(A_{AF}\times\nabla|l|)_z$ that arises from the spatial variation of the magnitude of the uniform moment. In the limit of small s-d exchange coupling $J_{sd}<<|\mu|$, where μ is the chemical potential measured from the antiferromagnetic gap center, the THC is linearly proportional to J_{sd} (a result analogous to the behavior of the THE in the weak-coupling region in ferromagnets [4,5]).

[1]P. M. Buhl, F. Freimuth, S. Blügel, et al., Phys. Status Solidi - Rapid Res. Lett., Vol. 11, 1700007 (2017) [2]B. Göbel, A. Mook, J. Henk, et al., Phys. Rev. B, Vol. 96, 060406(R) (2017) [3]L. Vistoli, W. Wang, A. Sander, et al., Nature Physics, Vol. 15, 67 (2019) [4]K. Nakazawa, M. Bibes and H. Kohno, J. Phys. Soc. Jpn., Vol. 87, 033705 (2018) [5]K. Nakazawa and H. Kohno, Phys. Rev. B, Vol. 99, 174425 (2019)

10:30

AB-11. Extraordinary magnetic anisotropy and relaxation dynamics in the non-collinear antiferromagnet $IrMn_3$.
S. Jenkins[1], R.W. Chantrell[1] and R.F. Evans[1] *1. Physics, University of York, York, United Kingdom*

Antiferromagnets have gained significant interest in recent years due to their potential application in antiferromagnetic spintronic devices and neuromorphic computing where the antiferromagnet is the active element. In non-collinear antiferromagnets such as IrMn the symmetry and temperature dependence of the effective anisotropy are poorly understood due to the difficulty in experimental measurements and the complexity of the materials. Iridium Manganese (IrMn) is the material of choice for most spintronic devices due to its high thermal stability and large exchange bias. Theoretical and experimental calculations of the effective anisotropy constant for IrMn differ by two orders of magnitude. Both theoretical[1] and experimental measurements[2] agree that the anisotropy has a uniaxial form but this contradicts the usually assumed relationship between crystallographic symmetry and the temperature dependence of the anisotropy from the Callen-Callen law. Here we calculate the effective anisotropy energy surface of $IrMn_3$ using an atomistic spin model with the VAMPIRE code[3] as shown in Fig. 1. We find a unique cubic-like symmetry of the anisotropy not seen in ferromagnets and that meta-stable spin structures lower the overall energy barrier to a tenth of that estimated from simple geometrical considerations, removing the discrepancy between experiment and theory. Fig. 2 shows the temperature scaling of the anisotropy energy barrier this has an exponent of 3.92, close to a uniaxial exponent of 3[4]. Our results demonstrate the importance of non-collinear spin states on the thermal stability of antiferromagnets with consequences for the practical application of antiferromagnets in devices operating at elevated temperatures.

[1] L. Szunyogh, et al, Phys Rev B, 79, (2009) [2] G. Vallejo-Fernandez, et al, App Phys Letters, 91, (2007) [3] R. F.L. Evans, et al, J Phys Cond. Matter, 26, (2014) [4] arXiv:1905.05069 [cond-mat.mtrl-sci]

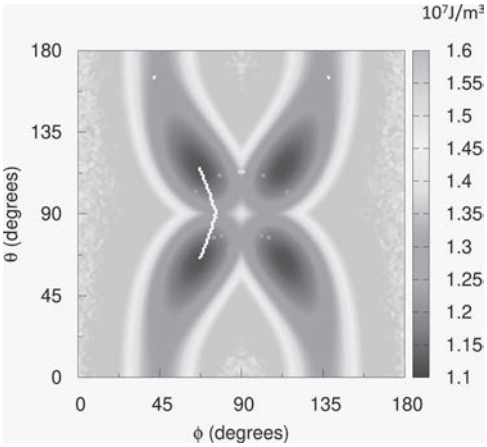


Fig. 1. Calculated anisotropy energy surface for L12 IrMn3 showing four ground state energy minima. The white line shows the minimum energy surface for rotation between two ground states.

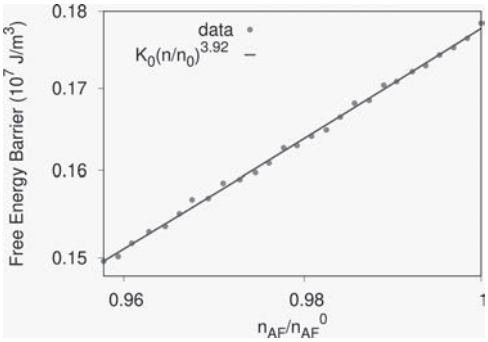


Fig. 2. The scaling of the effective energy barrier with sublattice magnetisation length n_{AF} fitted using $EB(n_{AF}) = E_0 n^l_{AF}$. l is calculated to be 3.92 ± 12 suggesting a scaling much slower than cubic anisotropy where l = 10 and more similar to uniaxial anisotropy l = 3.

10:42

AB-12. Magnetic and Electrical Transport Properties in Epitaxial Thin Films of the Non-Collinear Antiferromagnet Mn_3Sn. *J.M. Taylor*[1], A. Markou[2], E. Lesne[1], C. Felser[2] and S.S.P. Parkin[1] *1. NISE, Max Planck Institute of Microstructure Physics, Halle (Saale), Germany; 2. Solid State Chemistry, Max Planck Institute for Chemical Physics of Solids, Dresden, Germany*

A promising candidate for topological antiferromagnetic (AF) spintronic applications is the non-collinear AF Mn_3Sn [1]. Here, symmetry breaking inverse triangular AF order generates Berry curvature around Weyl points [2], in turn inducing novel electrical transport properties [3-5], as well as an anomalous magneto-optical Kerr effect (MOKE) [6]. This is enabled by a DMI mediated canting of Mn moments, which produces a small magnetization in the basal planes of the material and thus allows external manipulation of domain structure via external magnetic field [7]. In this work, the deposition of thin films of hexagonal Mn_3Sn down to thicknesses as low as 10 nm is reported [8]. X-ray diffractometry and transmission electron microscopy are used to demonstrate high-quality crystal structure, as well as to determine epitaxial growth relationships. Using lattice engineering on either $SrTiO_3$ or MgO substrates, films with both c-axis (0001) orientation and a novel (40-43) orientation are prepared. In the latter case, where a component of the uncompensated magnetic moment lies out of plane, a large anomalous Hall effect (AHE) is measured at room temperature with $\mu_0 H_c$ = 1.3 T. The angular dependence of ρ_{xy} is consistent with the crystallographic orientation of the hexagonal basal planes, indicating the intrinsic relationship between epitaxial thin film structure and the unique magnetotransport properties observed. These are accompanied by a large MOKE signal measured in polar geometry, which we observe in thin films of Mn_3Sn for the first time. However, SQUID magnetometry and X-ray magnetic circular dichroism measurements indicate a tiny uncompensated Mn magnetization, suggesting these phenomena have their origin in Berry curvature driven by the chiral spin texture. Finally, temperature dependent magnetotransport measurements demonstrate the onset of a large topological Hall effect, corresponding to an expected magnetic phase transition close to 50 K. Not previously reported for films of Mn_3Sn, this suggests further interesting applications of this material in its helical magnetic state. These results indicate the potential of Mn_3Sn thin films for use in AF *chiralitronic* devices.

[1] S. Nakatsuji, N. Kiyohara and T. Higo, *Nature*, 527, 212 (2015) [2] K. Kuroda *et al*, *Nature Materials*, 16, 1090 (2017) [3] N. H. Sung *et al*, *Appl. Phys. Lett*, 112, 132406 (2018) [4] X. Li *et al*, *SciPost Phys*, 5, 063 (2018) [5] M. Ikhlas *et al*, *Nature Physics*, 13, 1085 (2017) [6] A. L. Balk *et al*, *Appl. Phys. Lett*, 114, 032401 (2019) [7] T. Higo *et al*, *Nature Photonics*, 12, 73 (2018) [8] A. Markou, J. M. Taylor *et al*, *Phys. Rev. Mater*, 2, 051001(R) (2018)

10:54

AB-13. Magneto-optical Spectra of a Strained Non-collinear Antiferromagnet: Ab Initio Theory. *J. Zemen*[1,2], H.K. Singh[3], H. Zhang[3], F. Johnson[2], D. Boldrin[2], A. Mihai[4], B. Zou[4], L. Beran[5], J. Zázvorka[5], M. Veis[5], O. Heczko[1,6] and L. Cohen[2] *1. Faculty of Electrical Engineering, Czech Technical University in Prague, Prague, Czechia; 2. Department of Physics, Imperial College London, London, United Kingdom; 3. TU Darmstadt, Darmstadt, Germany; 4. Department of Materials, Imperial College London, London, United Kingdom; 5. Faculty of Mathematics and Physics, Charles University, Prague, Czechia; 6. Institute of Physics, Prague, Czechia*

We present magneto-optical spectra in an antiferromagnetic (AF) structure of metallic Mn_3AN (A = Ga, Sn, Ni, Ir). Magneto-optical Kerr Effect (MOKE) was measured in a closely related triangular AF structure of Mn_3Sn last year [1], which was the first observation of MOKE in an AF metal. The related Anomalous Hall Effect (AHE) has been measured in the same non-collinear AF system recently [2]. The family of Mn-based antiperovskite nitrides with general formula Mn_3AN shows promise for a wide range of applications in spintronics [3,4] and solid-state cooling [5,6]. The functionality is mainly derived from the frustrated exchange interactions in the triangular AF structure and its response to strain [4]. The intrinsic contribution to MOKE has been simulated for the cubic ground state of compounds with A = Ga, Zn, Ag, Ni recently [7]. Here we focus on the MOKE spectra of strained systems where the lower symmetry allows for novel magnetic phases that we predicted earlier [8]. We employ the Projector-Augmented Wave method (PAW) and linear response theory as implemented in the VASP code to derive the Kerr angle and ellipticity. Figure 1 shows simulated spectra for Mn_3GaN: the solid line corresponds to unstrained lattice with triangular AF order (the so-called G^{5g} representation) where MOKE vanishes due to the high symmetry; the dashed line is obtained for the same structure subjected to 1% compressive biaxial strain which results in canting of the local moments and finite MOKE; the dash-dotted line describes a collinear ferrimagnetic phase (local Mn moments aligned with the [110] axis, $FIM_{[110]}$) which we expect to form at 1% biaxial strain and elevated temperatures [8]. We compare our results for canted triangular and FIM phases to the corresponding MOKE spectra measured above and below the Néel temperature in Mn_3NiN and Mn_3GaN thin films deposited on different perovskite oxide substrates. We observe a qualitative agreement of the data below Néel temperature which can be interpreted as a confirmation of the desirable triangular AF structure of the thin film.

[1] T. Higo et al.: *Nature photonics*, 12.2, 73 (2018). [2] S. Nakatsuji et al.: *Nature* 527.7577, 212 (2015). [3] D. Boldrin, J. Zemen, L. F. Cohen et al.: *arXiv*:1902.04357 (2019). [4] D. Boldrin, J. Zemen, L. F. Cohen et al.: *ACS Appl. Mater. Interfaces*, 10, 18863 (2018). [5] D. Matsunami et al.: *Nature Materials*, 14, 73–78 (2015). [6] D. Boldrin, J. Zemen, L. F. Cohen et al.: *Phys. Rev. X*, 8, 041035 (2018). [7] X. Zhou, S. Blügel, Y. Mokousov et al.: *Phys. Rev. B*, 99, 104428 (2019). [8] J. Zemen, E. Mendive-Tapia et al.: *Phys. Rev. B*, 95, 184438 (2017).

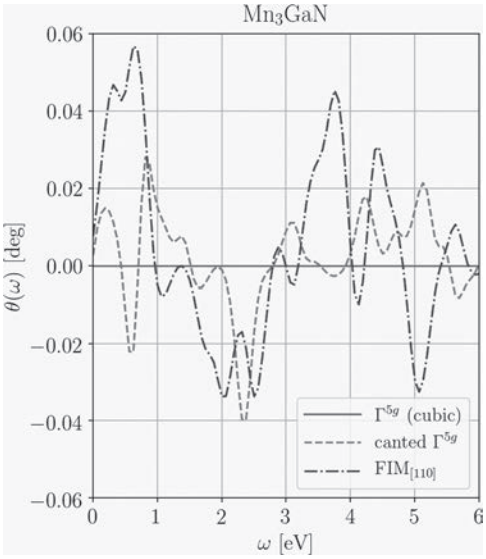


Figure 1: Kerr angle simulated for Mn_3GaN assuming the incident light at an angle of 10 degrees with respect to the [001] axis, the surface normal.

11:06

AB-14. Antiferromagnetic Skyrmion Crystals in Frustrated Triangular Lattices. *A.S. Raeliarijaona*[1], W. Fang[1], P. Chang[1,2], K. Belashchenko[1] and A. Kovalev[1] *1. Physics and Astronomy, University of Nebraska-Lincoln, Lincoln, NE, United States; 2. Computational and Data Sciences, George Mason University, Fairfax, VA, United States*

We investigate the existence of skyrmion crystal in antiferromagnetic triangular lattice in the presence of Dzyaloshinskii-Moriya interaction and magnetic anisotropy. As a possible realization, we studied transition metal dichalcogenides (TMDs) MoS2, decorated with magnetic atoms, such as Co, Cr, Mn, Fe, using first-principles density functional calculations. We further performed Monte Carlo simulations to calculate the zero-temperature phase diagram, as well as the finite temperature phases. We demonstrate that in these triangular systems we can realize antiferromagnetic skyrmion crystals, which reside on three sublattices, whose onset is facilitated by the magnetic anisotropy. The characteristics of the phases and the phase transition are obtained by computing the spin structure factor and the specific heat.

11:18

AB-15. Magneto-transport properties in the chiral antiferromagnet Mn_3X(*X*=Sn, Ge) thin films. *A. Kobayashi*[1], D. Qu[1,2], T. Higo[1,3], S. Nakatsuji[1,3] and Y. Otani[1,3] *1. ISSP, University of Tokyo, Kashiwa, Japan; 2. Institute of Physics, Academia Sinica, Taipei, Taiwan; 3. JST-CREST, Kawaguchi, Japan*

Antiferromagnets have recently attracted considerable attention as a key material for next generation devices owing to their advantages such as negligible stray field and high-frequency spin dynamics [1]. However, because of the absence of magnetization, neither electrical detection nor externally manipulation of the Néel state is possible although these functions are essential for the spintronic devices. Surprisingly large spontaneous transverse responses have recently been found in the noncollinear kagome-lattice antiferromagnets hexagonal Mn_3X (*X*=Sn, Ge). It exhibits large anomalous Hall [2-5], anomalous Nernst [6], and magneto optical Kerr effects [7] at room temperature. All these phenomena are characterized by the cluster magnetic octupole moment[8]. It also has been found that the spin Hall effect has an anomalous sign change when its triangularly ordered spins switch orientation in Mn_3Sn, because of the momentum-dependent spin splitting [9]. In noncollinear antiferromagnets, novel types of spin currents have been demonstrated to occur by symmetry arguments and calculations [10]. These spin currents have a longitudinal component of spin polarization and are analogous to spin-polarized currents in ferromagnets. This suggests the novel transport properties related to the spin-polarized currents such as magnetoresistance effect can be expected in Mn_3X. In this work we tried the synthesis of hexagonal Mn_3X (*X* = Sn, Ge) thin films by DC-magnetron sputtering. We obtained high quality hexagonal Mn_3Sn single phase [11], in addition to hexagonal, tetragonal and cubic phases of Mn_3Ge. The ferrimagnetic tetragonal Mn_3Ge has been known to have the large perpendicular magnetic anisotropy, the high spin polarization and the low Gilbert damping effect [12]. These features indicate the tetragonal Mn_3Ge is a good candidate material for spin-transfer-torque random access memory. For Mn_3Ge cubic system, only ferromagnetic $L1_2$ [13], and ferrimagnetic α-Mn structure [14] have been reported so far, however, our cubic structured Mn_3Ge showed pure antiferromagnetic behavior suggesting to take γ-Mn like disordered structure. The various magneto-transport properties for Mn_3X (*X*=Sn, Ge) will be reported.

[1] T. Jungwirth *et al*., Nat. Nanotech. 5, 231 (2016). [2] H. Chen *et al*., Phys. Rev. Lett. 112, 017205 (2014).[3] S. Nakatsuji *et al.*, Nature 527, 212 (2015).[4] N. Kiyohara, *et al.*, Phys. Rev. Appl. 5, 064009 (2016). [5] A.K. Nayak *et al*., Sci.Adv. 2, 1501870 (2016).[6] M. Ikhlas, *et al*., Nat. Phys. 13, 1085 (2017).[7] T. Higo *et al*., Nat. Photon. 12, 73 (2018). [8] M.-T. Suzuki *et al*., Phys. Rev. B 95, 094406 (2017).[9] M. Kimata *et al*., Nature 565, 627 (2019).[10] J. Zelezny *et al*., Phys. Rev. Lett. 119, 187204 (2017).[11] T. Higo, D. Qu, Y. Otani and S. Nakatsuji, *et al.,* Appl. Phys. Lett. 113, 202402 (2018).[12] S. Mizukami *et al*., Appl. Phys. Ex. 6, 123002 (2013).[13] H. Takizawa *et al*., J. Phys.: Con. Mat. 14, 1147 (2002). [14] D. D. Dung *et al.,* J. Appl. Phys. 109, 07C310 (2011).

Session AC
MAGNETIC LOGIC
Joseph S. Friedman, Chair
The University of Texas at Dallas, Richardson, TX, United States

INVITED PAPERS

8:30

AC-01. Spintronics Based RF Systems for Wireless Communication and Signal Processing. *A. Litvinenko*[1], P. Sethi[1], V. Iurchuk[1], S. Louis[2], C. Murapaka[1], V. Cros[3], P. Bortolotti[4], V. Tiberkevich[2], A.N. Slavin[2], A. Jenkins[5], R. Ferreira[5], B. Dieny[1] and U. Ebels[1] *1. Univ. Grenoble Alpes, CEA, CNRS, SPINTEC, Grenoble, France; 2. Oakland Univ., Rochester, MI, United States; 3. Unité Mixte de Physique CNRS, Thales, Univ. Paris-Sud, Univ. Paris-Saclay, Paris, France; 4. Thales TRT, Palaiseau, France; 5. International Iberian Nanotechnology Laboratory (INL), Braga, Portugal*

Since the first demonstration by Kiselev et al. [1], the technology of spin torque nano-oscillators (STNO) has made important progress improving device characteristics, such as the output power and generation linewidth, and demonstrating a large range of novel functionalities, such as DC-to-RF conversion for microwave signal generation, RF-to-DC conversion for microwave signal detection, and, also, different operational regimes, such as injection locking and frequency or amplitude modulation. Proof-of-concept systems based on STNOs have emerged imitating a neural network for vowel recognition [2], demonstrating wireless data transmission using OOK protocols [3], frequency synthesis based on a phase-locked loop [4], and microwave power harvesting to provide DC drive for nanoelectronics components [5]. The defining feature of STNOs is their nonlinear amplitude-frequency dependence that allows one to control the generated frequency via applied current on a nanosecond time scale. This fast tuning of an STNO is exploited here to demonstrate two RF systems making use of vortex-state STNO devices generating about 1 μW of output power. The first one is a communication system which is using a robust wireless protocol that overcomes problems of STNO phase stability by combining modulation with injection locking. The potential of this system is demonstrated through wireless voice transmission over 10 m distance, using conventional radio receivers [6]. The second system is an ultrafast spectrum analysis predicted in [7] that outperforms existing analogs based on VCO and YIG oscillators. A fully-functional nano-sized spectrum analyzer implementing FPGA was developed to demonstrate spectrum analysis on μs timescales for complex time-varying signals. The developed RF systems based on the state-of-the-art STNO devices demonstrate the characteristics that are sufficient to propose an alternative, nano-scale solutions for IoT and microwave signal processing applications. Financial support is acknowledged from ERC MAGICAL N° 669204, the French space agency CNES, the enhanced EUROTALENT program, as well as from the NSF of the USA Grants Nos. EFMA-1641989 and ECCS-1708982.

[1] I. S. Kiselev, J. C. Sankey, I. N. Krivorotov et al., Nature. Vol. 425, p.6956 (2003) [2] M. Romera, P Talatchian, S Tsunegi et al., Nature. Vol. 563, p.230–234 (2018) [3] H. S. Choi, S. Y. Kang, S. J. Cho et al., Sci. Rep. Vol. 4, p.5486 (2014) [4] M. Kreißig, R. Lebrun, F. Protze et al., AIP Advances, Vol. 7, p.056653 (2017) [5] B. Fang, M. Carpentieri, S. Louis et al., Phys. Rev. Appl. Vol. 11, p.014022 (2019) [6] A. Litvinenko, P. Sethi, C. Murapaka et al., arXiv:1905.02443 (2019) [7] S. Louis, O. Sulymenko, V. Tiberkevich et al., Appl. Phys. Lett. Vol. 113, p.112401 (2018)

9:06

AC-02. Computational Random Access Memory and Applications for Artificial Intelligence (AI). *J. Wang*[1] *1. Electrical and Computer Engineering, University of Minnesota, Minneapolis, MN, United States*

To enable local or edge AI like family-based robots and self-driving cars without using cloud computing, the power consumption for any available computing system is still four to six orders of magnitude higher than needed. This is largely because in modern computing architecture, also named as von Newman architecture, data is fetched from memory, travels through interconnects, is processed in a logic circuit, and is stored back into memory. We proposed a complete new architecture to realize the computation without data transfer between the memory and logic circuit [1,2]. Our idea is to directly use the memory cells to carry out the computation [1-3], e.g. compute at the data just mimicking the way our brain operation. We name this new computing architecture as computational random access memory (CRAM) [2]. We proposed and demonstrated a basic concept, voltage controlled logic (VCL). Fig. 1 shows the design illustration of voltage controlled logic performing a NAND operation with '1' and '0' inputs. We use MTJs as the basic units. Two parallel connected MTJs with high and low resistance states represent logic '1' and '0' respectively and serve as the two inputs of the NAND operation. The third MTJ at the bottom will act as a detector to detect if the parallel resistance of the two input MTJs is below a certain value and serve as the output of the NAND operation. In the case shown in this figure, the output MTJ is pushed beyond its own critical current and switched to logic '1' as expected for a NAND operation with '1' and '0' input. In this case, the state variable (resistance) is converted to current, which is quasi-linearly combined, and analyzed using the output MTJ as the threshold detector. In [1] we showed that there can be sufficient write margin between the input states. This new architecture can be implemented using a variety of available and proposed devices [2]. To implement a STT-RAM based CRAM, we introduce a 2T1M cell architecture shown in Fig. 2a. When the wordline for memory (WLM) is logic high, the cell behaves identically to the 1T1M MRAM cell, and the MTJ is accessible for read/write operations across bitline (BL) and bitline bar (BLB). However, when bitline for logic (BLL) is high, the access transistor to the shared logic line (LL) is enabled and the cell can be accessed for VCL operations using BL. Figure 2b shows a 2-input CRAM gate that is functionally equivalent to the 2-input VCL gates [1,2]. For a logic operation, the first two cells are loaded with the input data, either from a previous CRAM operation or by writing the data to RAM using the memory mode. BLL is enabled for these cells, which connects all of them to the LL. This allows for the function of CRAM to be entirely reprogrammable. Modeling and benchmarking for STT-RAM based CRAM vs other near and in memory computing has been carried out for different applications including bioinformatics computing [4], pattern recognition [5], binary-neural-net-based image classification [6]. Using digit recognition as an example, the energy efficiency could be improved by 40 times and the execution time was improved by 1400 times compared to the latest near memory computing scheme [5].

[1] A. Lyle, et al, "Direct communication between magnetic tunnel junctions for nonvolatile logic fanout architecture," Appl. Phys. Lett., 97 (2010) 152504. [2]J.-P. Wang and J. Harms, "General structure for computational random access memory (CRAM)," U.S. Patent 9224447 B2, 2015.

[3]H. Meng, J.G. Wang and J-P Wang, "A spintronics full adder for magnetic CPU", IEEE Electron Dev. Lett., 26 (2005) 360 [4]Z. Chowdhury, *et al*., "Efficient in-memory processing using spintronics", Computer Architecture Letters, 17, 1 (2018) 42 [5]M. Zabihi, et al, "In-memory processing on the spintronic CRAM: From hardware design to application mapping", IEEE Transactions on Computers, pp. 1-1. 10.1109/TC.2018.2858251 (2018); [6]M. Resch, et al, "Exploiting processing in non-volatile memory for binary neural network accelerators." arXiv:1812.03989 (2018)

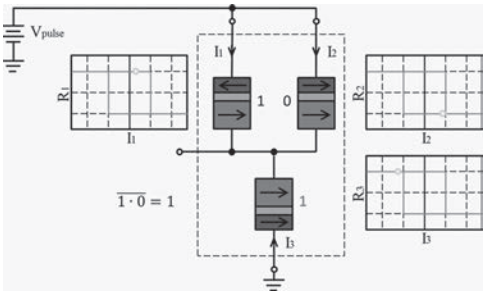


Fig. 1. VCL performing a NAND operation with '1' and '0' inputs. Two parallel connected MTJs with high and low resistance states represent logic '1' and '0' respectively and serve as the two inputs of the NAND operation. The third MTJ at the bottom will act as a detector to detect if the parallel resistance of the two input MTJs is below a certain value and serve as the output of the NAND operation.

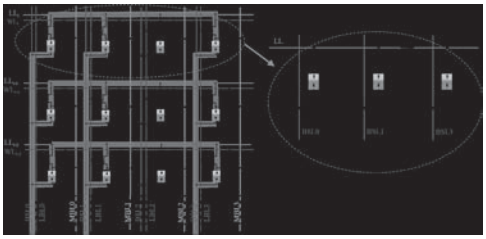


Fig. 2. Basic cell and gate in CRAM. (A) The 2T1M cell. BLB, BL, and WLM are the bitlines and wordlines of a standard SRAM cell. However, in the 2T1M cell there is an additional transistor that provides access to the logic line (LL). (B) Three cells connected together create a 2-input VCL gate.

CONTRIBUTED PAPERS

9:42

AC-03. Perpendicular Magnetic Anisotropy Tunnel Rectification Magnetoresistance Effect for In-Memory Computation. *K. Zhang*[1,2], K. Cao[1,2], Y. Zhang[1,2], J. Nan[1,2], Z. Zheng[1,2], L. Chen[1,2] and W. Zhao[1,2]
1. Fert Beijing Institute, Beihang University, Beijing, China; 2. School of Microelectronics, Beihang University, Beijing, China

In-memory computation (IMC) based on Spintronic devices shows promise to meet high-speed and low-power demands for information processing [1-4]. Recently, the discovery of tunnel rectification magnetoresistance (TRMR) [5] effect blazes a new path towards realizing efficient and multi-dimensional regulation capabilities. Here, an IMC scheme based on TRMR effect in perpendicular-magnetic-anisotropy (PMA) magnetic tunnel junction (MTJ) and diode hybrid structure (Fig. 1(a)) is demonstrated. The current-voltage (I-V) curves for parallel (P) and antiparallel (AP) states indicate the coexistence of rectification behavior and tunnel magnetoresistance (TMR) effect (Fig. 1(b)). We further perform TRMR measurement, in which alternating current (AC) is applied to generate direct-current (DC) voltage. High up to 275% TRMR ratio is observed at AC=150 μA (Fig. 1(c)). The TRMR is defined as TRMR = $(V_{AP}-V_P)/(V_P)\times100\%$, V_{AP} (V_P) representing the rectification voltage under AP (P) state. The MR value of the hybrid structure could be widely tuned with the varied DC offsets at AC=400 μA (Fig. 1(d)). Leveraging the AC/DC-regulated capability of the TRMR effect, we propose a scheme to implement IMC. Two MTJs in series are combined with a diode in parallel to construct a logic unit (Fig. 2(a)). The AP (P) state of MTJs is regarded as logic input '1' ('0'). The measured rectification voltage is the logic output and positive (negative) voltage represents logic output '1' ('0'). Using our established model, the I-V curves with AC = 500 μA for different states of the two MTJs could be figured out (Fig. 2(b)). By tuning the DC offset and setting different configurations, reconfigurable logic operations, including AND, OR, NOR and NAND could be realized (Fig. 2(c)). NOR logic operation is experimentally carried out to further validate the proposed scheme.

[1] A. Ney et al., Nature, Vol. 425, pp. 485-487 (2003). [2] S. Joo et al., Nature, Vol. 494, pp. 72-76 (2013). [3] Z. Luo et al., Adv. Mater., Vol. 29, 1605027 (2017). [4] X. Wang et al., Adv. Mater., Vol. 30, 1801318 (2018). [5] J. Wang et al., Nanoscale, Vol. 9, pp. 16073-16078 (2017).

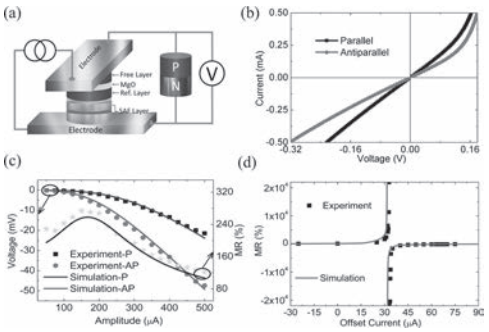


Fig. 1 (a) Schematic of the hybrid structure. (b) I-V curves for AP and P states. (c) AC amplitude dependent rectification voltage and MR ratio. (d) DC offsets dependent MR ratio.

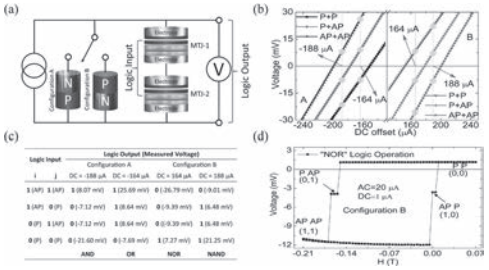


Fig. 2 (a) Schematic of the logic unit. (b) I-V curves mixed with AC = 500 μA under configuration A and B. (c) Truth table of the logic operations. (d) Experimental verification of NOR logic operation.

9:54

AC-04. Spin-Orbit-Torque Field Effect Transistor (SOTFET). *X. Li*[1], P. Dang[2], J. Casamento[3], Z. Zhang[1], A. Mei[3], D. Schlom[3], D. Jena[1,2], D. Ralph[4,5] and H.G. Xing[1,3] *1. School of Electrical and Computer Engineering, Cornell University, Ithaca, NY, United States; 2. School of Applied and Engineering Physics, Cornell University, Ithaca, NY, United States; 3. Department of Materials Science and Engineering, Cornell University, Ithaca, NY, United States; 4. Kavli Institute at Cornell for Nanoscale Science, Cornell University, Ithaca, NY, United States; 5. Department of Physics, Cornell University, Ithaca, NY, United States*

Magnetic memories have received boosted interest due to their nonvolatility, infinite endurance and fast read/write rates. However, existing magnetic memories confront challenges of relatively large write energy and limited on-off-ratio. To address the challenges, we propose a new memory device, the *spin-orbit-torque field effect transistor* (SOTFET), which has

potential for a large reduction in energy dissipation and significant increase in on-off-ratio, while retaining the virtues of magnetic memories. The basic structure of a SOTFET is shown in Fig. 1. The SOTFET gate stack is on top of a semiconductor channel and comprises three layers: a topological insulator (TI), a ferromagnet (FM), and a multiferroic insulator (MF) from the top to bottom. The working principle of a SOTFET is described as follows. When a charge current flows through the TI layer, transverse spin currents with different spin polarization separate and spins accumulate at the surfaces of the TI layer due to spin-momentum coupling[1]. Through spin-orbit-torque (SOT), the spin accumulated at the TI/FM interface switches the magnetization (M) of the FM that has a perpendicular magnetic anisotropy. Due to the exchange coupling between the FM and the MF[2], the magnetic dipole of the MF is also switched together with the M in the FM. Since the M and electric polarization (P) are strongly coupled in the MF material due to the Dzyaloshinskii-Moriya interaction (DMI)[2], the electric dipole in the MF switches in tandem. The resulting switching of P in the MF gates the semiconductor channel, which resembles FeFETs and NCFETs[3]. Therefore, the semiconductor channel acts as the read-out component, offering a high on-off-ratio. Here, we present a preliminary model of the SOTFET. The switching dynamics of M is modeled by the Landau-Lifshitz-Gilbert (LLG) equation[4]. The interaction between M and P is captured by DMI. And the P dynamics is modeled by Landau-Khalatnikov (LK) equation[5]. Our modeling results (Fig. 2) show that with FM and MF strongly coupled, the P in MF can be switched by applying current in the TI layer.

* This work was supported by the Semiconductor Research Corporation as nCORE task 2758 and under the NSF E2CDA program ECCS 1740286. [1] M. Z. Hasan and C. L. Kane, Rev. Mod. Phys. 82, 3045 (2010) [2] J. T. Heron et al, Nature 516, 370–373 (2014) [3] G. Pahwa et al, IEEE Transactions on Electron Devices, vol. 63, no. 12, pp. 4981-498 (2016) [4] D. C. Ralph and M.D. Stiles, Journal of Magnetism and Magnetic Materials, vol. 321, Issue 16, pp. 2508 (2009) [5] J. X. Zhang et al, J. Appl. Phys. 101, 114105 (2007)

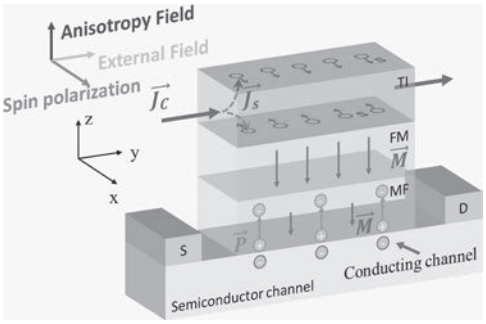


Fig. 1. Device structure of SOTFET

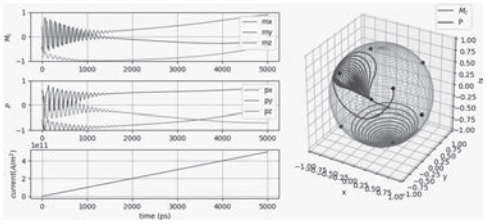


Fig. 2. Modeling results show passing current in the TI layer can switch the polarization P in the MF layer

10:06

AC-05. Reconfigurable Spin-Orbit Torque Driven Logic Device. *G.J. Lim*[1], D. Chua[1], W. Gan[1], C. Murapaka[2] and W. Lew[1] *1. Physics and Applied Physics, Nanyang Technological University, Singapore; 2. Indian Institute of Technology Hyderabad, Hyderabad, India*

Spintronic memory devices not only complement or displace conventional CMOS memory device due to their lower power consumption and faster operating speed, they are also promising candidates for logic devices [1]. Here, we present a stateful in-memory current-driven reconfigurable logic device based on the spin Hall effect. Using a double Hall cross structure sharing a common Hall bar, we show that the anomalous Hall voltage due to magnetization states across device channels can be interpreted as logical outputs. With appropriate thresholds and rectification, the logic device is demonstrated to operate as AND, NOR, XNOR, XOR, NIMP and Converse NIMP logic gates. By integrating a field line on each device, it is also possible to generate sufficient local Oersted field to break the switching symmetry typically required for deterministic spin-orbit torque switching in type-z devices. This allows on-the-fly reconfigurability of the individual double Hall cross devices. The device design also eliminates the need for reset pulses. Furthermore, the device can be operated in two modes: In Mode (I), the device logic gate is determined by the read currents, and the logic states are represented by the device magnetization. Mode (II) operates conversely, where the device logic gate is determined by the magnetization, and the logic states are represented by the read current. Finally, we simulate through compact modelling a half-adder based on the double Hall cross logic device.

[1] Zhang, H., et al., *Spintronic Processing Unit in Spin Transfer Torque Magnetic Random Access Memory*. IEEE Transactions on Electron Devices, 66(4): p. 2017-2022 (2019)

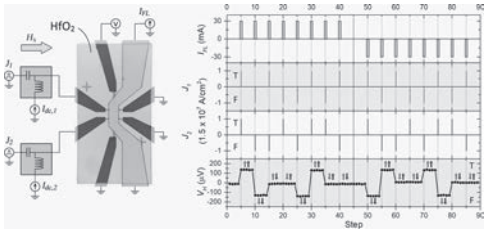


Fig. 1 – (Left) Optical microscopy image of device with integrated field line, accompanied with measurement set-up. (Right) Logical input and output for one device, demonstrating AND and NOR gates.

INVITED PAPER

10:18

AC-06. Proposal of Nonvolatile Logic-gates using Voltage-Control Spintronics Memory cell for AI application. *H. Yoda*[1], Y. Ohsawa[1] and Y. Kato[1] *1. Spin-Orbitronics Technologies, Inc., Kawasaki, Japan*

Recently, Artificial-Intelligence (AI), Machin-Learning (ML), and IOT have become hot topics and edge-computing should play a crucial role. Since the number of the edge-devices is estimated to exceed that of cellar phones by a factor of 10 and the edge-devices employ AI technologies, the edge-devices require both inexpensive micro-processors and ultra-low energy-consumption memories. However conventional technologies such as SRAM-based technologies and conventional nonvolatile memory technologies are thought to be unable to satisfy such requirements. Voltage-control spintronics memory (VoCSM) were proposed for a high-speed nonvolatile memory, a high-density nonvolatile memory, and a nonvolatile logic-gate applications [1], [2], [3]. This paper focuses on VoCSM-cell based logic-gates for the edge-devices. First half of this talk reviews the VoCSM developments

and the features of VoCSM-cells and the latter half focuses on VoCSM-cell based logic-gates for AI applications, including Voltage-Control Spintronics Logic (VoCSL). First, the VoCSM concept and the cell performances such as its small critical switching current, its low writing energy-consumption per bit, good write-error rate (WER), and unlimited endurance are reviewed. Second, the ultimate ultra-low energy-consumption of VoCSM-cell is estimated [4]. Third, VoCSM-cell-based logic-gates are reviewed [5], [6]. Fig.1 shows a straight-forward VoCSM-cell based logic-gate. The VoCSM-cell has 3 terminals and can be used as logic-gates. The terminal-1 & -2 are connected to the spin-hall electrode and the terminal-3 is connected to the MTJ. The terminal-1 is to supply write-current (I_w) as an input-1 and the terminal-2 is to apply voltage as an input-2. The terminal-3 is to sense the resistance of the MTJ to output the signal. Since the available magnetoresistance ratio (MR) is not large enough to read the data directly, the sense amplifier must be added as shown in the figure. Fig.2 shows another type of VoCSM-cell based logic-gate. In this case, the input-1 is a stored data in the MTJ and the input-2 is the voltage applied by the terminal-2. AND and OR logic-gates can be easily realized just by changing the write-current directions. Forth, binary-neural-network is reviewed. Since logic-gates should work frequently, unlimited endurance is one of must requirements. Because of this, most of nonvolatile memories cannot be used as a working memory for the logic-gates. Therefore, SRAM-based circuitries were proposed for AI [7]. The demerit of SRAM-based circuitries is large cell-size in addition to large leakage-current. It typically requires 6 transistors for the memory cell and additional circuitries for convolution of data. Fifth, after the importance of an XNOR-gate in AI applications especially for binary neural network is reviewed, several types of exclusive nor (XNOR) gates using VoCSM-cells including a new one are introduced in detail and explained their operations by which they work. These VoCSM-cell based XNOR gates have very simple structures because they do not requires additional circuitries [8]. The demerits of conventional MTJ based logic-gates are energy consumptions in writing data and reading data. However, in the case of VoCSM-cell based logic-gates writing voltage is very low and if the amplifiers are located in the peripheral circuits as shown in Figs.1 & 2, there is not a severe issue [6], [8]. The latter is an in-memory logic concept [6]. Finally, the benchmarking against existing volatile logic-gates and conventional MTJ based logic-gates. The issues and the possible solutions are addressed at the conference.

[1] H. Yoda, H. Sugiyama, T. Inokuchi, *et. al.*, IMW 2017 [2] H. Yoda, N. Shimomura, Y. Ohsawa, *et. al.*, IEDM 2016 [3] H. Yoda, Y. Ohsawa, Y. Kato, *et. al.*, The final reports of ImPACT Sahashi-program, https://www.jst.go.jp/impact/sahashi/results-briefing/generalization/jp_report.html [4] H. Yoda, Y. Ohsawa, Y. Kato, *et. al.*, Journal of Magnetics 24(1) 107-111, March 2019 [5] S. Inokuchi, K. Koi, N. Shimomura, *et. al.*, JP2018-053007(Applying) [6] H. Zhang, W. Kang, L. Wang, *et. al.*, IEEE Trans. Electron Devices, Vol.64, No. 10, Oct. 2017 [7] H. Valavi, P. Ramadge, E. Nestler, *et. al.*, VLSI Symp. on Circuits (VLSIC), June 2018 [8] K. Ikegami, T. Inokuchi, S. Fujita, *et. al.*, Proceedings of 2019 EDTN, DOI: 10.1109/EDTM.2019.8731182

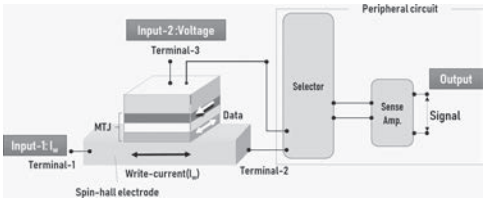


Fig. 1 Straight-forward VoCSM-cell based logic-gate application

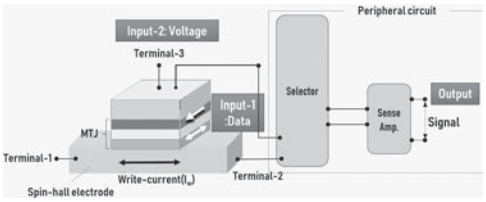


Fig.2 Another example of VoCSM-cell based logic-gate applications

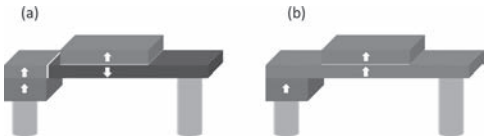
CONTRIBUTED PAPERS

10:54

AC-07. Development of Domain Wall Type Spin Memristor with Magnetic Fixed Layer. *T. Ashida*[1], T. Shibata[1], M. Ohta[1], S. Yamada[1], T. Shinohara[1], Y. Terasaki[1] and T. Sasaki[1] *1. Technology & Intellectual Property HQ, TDK Corporation, Ichikawa, Japan*

In recent years, various memristors have been studied for use as analogue neuromorphic computing devices [1,2]. Magnetic domain wall (DW) type spin memristor is one of those memristors and has been expected to show typical conductance change behavior. Recently, we experimentally demonstrated linear and symmetric conductance change of the spin memristor [3]. In the past report, we utilized a current induced DW injecting method to verify the concept. This method is suitable for operating a single element, but not preferable for evaluating a multiple element array. Thus, we paid attention to a magnetic fixed layer method, which can initialize multiple elements at once just by applying an external magnetic field. In this study, we developed a three-terminal MTJ element with the magnetic fixed layer and evaluated its conductance change behavior. Top-pinned type three-terminal MTJs were fabricated on a Si substrate. The film design was Si wafer /buffer /DW layer /CoFeB Free layer /tunnel barrier /CoFeB Reference layer /SAF-pinned layer. A DW fixed layer was fabricated on one side of DW layer. The typical junction size was 225 nm in width and 1000 nm in length, respectively. Fig. 1 shows magnetization configurations of the element. First, the element was totally reset by a strong magnetic field (+5kOe). Subsequently, a weak opposite field (-1.5kOe) was applied to reverse only the DW layer. Then, a single DW was introduced by the fixed layer, and conductance change was enabled by utilizing DW propagation driven by spin transfer torque (STT). On the other hand, the change was not observed when the element was applied after positive filed of +1.5kOe. The result indicated successful DW creation by the simple magnetic field operation which is important to realize the memristor array system. More details will be discussed in the conference.

[1]nature communication 9 2514 (2018) [2] ADVANCES IN PHYSICS:X 2 89 (2017) [3]14th 14th Joint MMM-Intermag Conference BD-01 Domain Wall Type Spin Memristor for Analogue Neuromorphic Computing



The magnetization configurations (a) after applying a weak negative magnetic field (-1.5kOe), or (b) a positive field (+1.5kOe). Prior to the DW creation, the element was reset by applying a strong positive field (+5kOe)

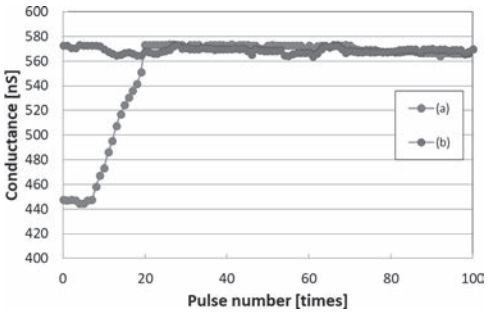


Fig. 2 Conductance response of the two magnetic configurations as a function of a driving current pulse number (J=-1.4×10^8 A/cm^2@5ns)

11:06

AC-08. Physical unclonable function based on reconfigurable nanoscale spin-orbit torque. *M. Carpentieri*[1], G. Siracusano[2], S. Chiappini[3], V. Puliafito[4], T. Moriyama[5], T. Ono[5], R. De Rose[6], M. Lanuzza[6], F. Crupi[6], Z. Zeng[7] and G. Finocchio[2] *1. Electrical and Information Engineering, Politecnico di Bari, Bari, Italy; 2. Mathematical and Computer Sciences, Physical Sciences and Earth Sciences, University of Messina, Messina, Italy; 3. INGV, Roma, Italy; 4. Engineering, University of Messina, Messina, Italy; 5. Kyoto University, Kyoto, Japan; 6. Informatics, Modeling, Electronics and System Engineering, University of Calabria, Rende, Italy; 7. Suzhou Institute of Nano-Tech and Nano-Bionics, Suzhou University, Suzhou, China*

Authentication based on magnetoresistive RAM would represent a real breakthrough, since it offers several advantages with respect to the True Random Number generator (TRNG) state-of-art [1]. We report on the proof-of-concept of spintronic TRNGs. They are realized by a bilayer W/CoFeB having a perpendicular easy axis, a current flow in the W gives rise to a spin-orbit torque (SOT) that drive the CoFeB state in a non-uniform configuration that evolves randomly to one of the two equilibrium states once the current is switched-off. Our findings show that TRNG can be activated by SOT opening exciting directions for novel applications of spintronics in security and, in particular, as a building block for reconfigurable Physical Unclonable Functions (PUFs) [2]. MTJs have been proposed for PUF development where the secret is derived thanks to magnetic textures such as domain wall or in spin-transfer torque MRAM (STT-MRAM) by applying current pulses near the value of 50% of switching probability. The idea developed in this work is to use the SOT-MRAMs as a building block for the PUF (see Fig.1). The main difference with STT-MRAM is the use of three terminals to separate the read and write operations. The information is written with the SOT originated by a current flowing in a heavy metal while the information is read via the resistance of the MTJ built on top of the heavy metal. Micromagnetic simulations of the magnetization dynamics in devices with perpendicular ferromagnets show that the switching occurs via nucleation process and that a stochastic switching is possible [3]. We experimentally considered a single circular dot (diameter 1 μm) with stable perpendicular magnetization as initial state, we applied a current pulse of 4 mA (voltage 8 V) for a duration of 15 ns. The current is able to drive the magnetization out of the equilibrium. When removing the current pulse, the magnetization goes back to the perpendicular direction, upward or downward, with a probability of about 50%. More numerical and experimental details and the proposed general architecture will be presented in the full paper.

[1] C. Herder, et al., Proc. IEEE 102, 1126–1141 (2014). [2] T. Marukame, et al., IEEE Trans. Magn. 50, 1–4 (2014). [3] G. Finocchio, et al., Appl. Phys. Lett. 102, (2013).

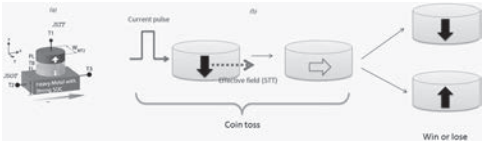


Fig. 1. (*a*) A schematic of the STO-MRAM. (*b*) Process of the magnetization reversal when is applied a current pulse of 4 mA.

Session AD
SPIN-ORBIT TORQUES I

Sergey Dushenko, Chair
University of Maryland, College Park/ National Institute of Standards and Technology, Gaithersburg, MD, United States

CONTRIBUTED PAPERS

8:30

AD-01. Spin-Orbit Torque in Graphene/Co Hetero-system. *K. Song*[1], A. Manchon[1] and u. Schwingenschlögl[1] *1. King Abdullah University of Science and Technology, Thuwal, Saudi Arabia*

Due to the growing demand of low-power, fast data processing, non-volatile magnetic random access memories are being considered as powerful alternative to current semiconducting technology [1]. In this context, the spin-orbit torque (SOT) technique has opened new development of innovative magnetic devices beyond memories and data storage [2]. The emblematic mechanism underlying the SOT technique is the interfacial Rashba effect that emerges at interfaces in the presence of strong spin-orbit coupling. This effect is particularly efficient at the interface between transition metal ferromagnets and topological insulators [3,4]. In conventional SOT devices, a heavy metal (Pt or W) adjacent to the magnetic layer is used to provide large spin-orbit coupling. Alternatively, it is also possible to exploit the spin-orbit coupling of the magnetic material itself by interfacing it with, e.g., a non-magnetic insulator [5]. We investigate interfacial spin texture and SOT at the interface between Co (001) and a graphene monolayer, a system that has recenlty been predicted to display large Rashba effect [6, 7], see Fig. a. When graphene is attached to the surface of Co (001), the inversion symmetry is broken, which results in the onset of a built-in perpendicular electric field. As a result, in the presence of the large SOC of Co, Rashba effect emerges at the interface. Therefore, *a spin density* driven by a net current can be achieved at the interface, bringing SOT into such a heterostructure [8]. Using first-principles calculations, we compute the band structure and project it onto Wannier orbitals to obtain the tight-binding Hamiltonian. Non-equilibrium properties then are derived by the Kubo formula. We show that Co atoms at the interface exhibit spin-momentum locking, which is line with the phenomenological picture presented above. Close to the Fermi level, the graphene Dirac cones couple with the Co 3*d* states around the K and K′ points (Fig. c), resulting in a spin texture odd in momentum k (Fig. *d*). This special spin texture promotes current-driven SOT. Our results show that the SOT can be used to electrically control the magnetization of the Co layer, and to realize fast non-volatile data reading and writing.

[1] A. D. Kent and D. C. Worledge, Nature Nanotechnology, Vol. 10, p. 187-191 (2015) [2] A. Manchon, *et al*., arXiv:1801.09636, 1-72 (2018) [3] D. C. Mahendra, *et al*., Nature Materials, Vol. 17, p. 800-807 (2018) [4] S. Ghosh and A. Manchon, Phys. Rev. B, Vol. 97, p. 134402 (2018) [5] S. Emori, *et al*. Phys. Rev. B, Vol. 93, p. 180402 (2016) [6] D. Eom, *et al*., Nano Lett., Vol. 9, p. 2844-2848 (2009) [7] H. Yang, *et al*., Nano Lett., Vol. 16, p. 145-151 (2016) [8] X. Qiu, *et al*., Phys. Rev. Lett., Vol. 117, p. 217206 (2016)

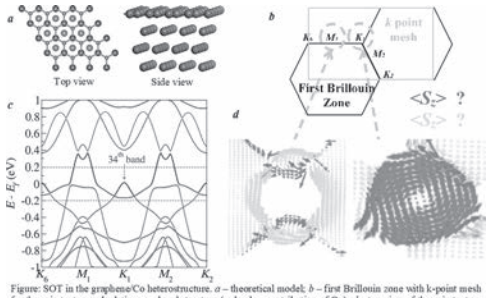


Figure: SOT in the graphene/Co heterostructure. *a* – theoretical model; *b* – first Brillouin zone with k-point mesh for the spin texture calculation; *c* – band structure (red color: contribution of Co); *d* – top view of the spin texture of the 34th band

8:42

AD-02. First-principles calculation of spin-orbit torque in TMD/ ferromagnet bilayers. *F. Xue*[1,2], J. Li[3] and P. Haney[2] *1. Institute for Research in Electronics and Applied Physics & Maryland Nanocenter, University of Maryland College Park, College Park, MD, United States; 2. Physical Measurement Laboratory, National Institute of Standards and Technology, Gaithersburg, MD, United States; 3. Joint Institute for Computational Sciences, University of Tennessee, Knoxville, TN, United States*

Motivated by recent discoveries of unconventional out-of-plane antidamping torque in WTe2/Permalloy system, we calculate the spin-orbit torque generated in two-dimensional transition metal dichalcogenide(TMD)/ferromagnet heterostructures using first-principles methods and linear response theory. Because of the strong spin-orbit coupling and the reduced crystal symmetry in these TMD materials, an unconventional form of the out-of-plane antidamping spin-orbit torque exists even when magnetization is in-plane, which is not allowed in the more common Pt/ferromagnet systems. Our numerical calculation of spin-orbit torques in heterostructures such as WTe_2/Co and MoTe_2/Co shows both out-of-plane and conventional anti-damping torques with comparable magnitude, around a few thousands \hbar/2e (\Omega m)^{-1}, when electric-field is applied perpendicular to the mirror plane of TMDs, which is consistent with the experimental observations. We find that the computed value of the unconventional out-of-plane antidamping torque is more sensitive to the details of the atomic structure of the Co layer and spin-orbit coupling strength of transition metal atoms than the conventional antidamping-like torque. Our numerical work confirms the existence of novel forms of spin-orbit torque in low crystal symmetry system, where the new out-of-plane spin-orbit torque could be useful in switching nanomagnets with perpendicular magnetic anisotropy for high-density applications.

8:54

AD-03. Spin-torque control of the anomalous Hall conductivity in non-collinear antiferromagnets. G. Gurung[1], *D. Shao*[1] and E.Y. Tsymbal[1]
1. Department of Physics and Astronomy, University of Nebraska Lincoln, Lincoln, NE, United States

Non-collinear antiferromagnetic materials have recently aroused significant interest due to the non-vanishing Berry curvature and the associated anomalous Hall effect sensitive to magnetic ordering. Especially interesting are antiperovskite compounds $ANMn_3$ (A = Ga, Cu, Ni) and their alloys, where the Néel vector can be reversed by the spin transfer torque. In this work, we explore series of antiperovskite compounds $Ga_{1-x}Ni_xNMn_3$ with competing Γ_{4g} and Γ_{5g} phases, where the magnetic moments of Mn atoms are aligned non-collinearly in the (111) plane. A spin-polarized electric current flowing the [111] direction produces a spin-transfer torque rotating the magnetic moments in the (111) plane. Based on the Landau-Lifshitz-Gilbert-Slonczewski equation, we model spin dynamics in these non-collinear antiferromagnets and obtain conditions at which a pulse of the spin-polarized current reverses the Néel vector and thus changes sign of the anomalous Hall conductivity. We find that the required current density largely depends on the magnetocrystalline anisotropy energy controlling the stability of the Γ_{4g} and Γ_{5g} phases. Using density functional theory methods, we calculate the magnetocrystalline anisotropy energy and the anomalous Hall conductivity in these antiperovskite compounds and find the optimum conditions for the current-induced reversal of the Néel vector. Our results demonstrate that the non-collinear antiperovskite antiferromagnets can be efficiently employed in spintronic devices.

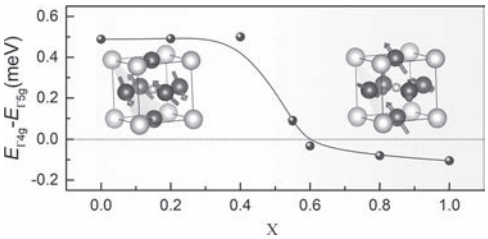


Fig. 1: Calculated magnetocrystalline anisotropy energy of antiperovskite $Ga_{1-x}Ni_xNMn_3$ indicating transition from the non-collinear antiferromagnetic Γ_{4g} to Γ_{5g} phase.

9:06

AD-04. Sub-terahertz magnetization dynamics in ferrimagnets driven by spin-transfer torques. *I. Lisenkov*[1], R. Khymyn[2], J. Åkerman[2], N. Sun[3] and B.A. Ivanov[4] *1. Winchester Technologies LLC, Burlington, MA, United States; 2. Department of Physics, University of Gothenburg, Gothenburg, Sweden; 3. ECE, Northeastern University, Boston, MA, United States; 4. Institute of Magnetism, Kiev, Ukraine*

The magnetic oscillations under spin transfer torque (STT) in antiferromagnetic (AFM) materials may reach up to THz frequencies due to a strong exchange interaction [1,2]. However, AFMs, such as NiO, possess a fundamental symmetry: their magnetic sublattices are identical and compensate each other. Therefore, experimental detection of Neel's order oscillations [3] is much harder than then detection of ferromagnetic resonance. Like AFMs, ferrimagnets (FiMs) have two counter-parallel magnetic sublattices bounded by the exchange interaction, but different magnetic atoms form these sublattices. Therefore the angular moment of each sublattice is different. The difference in the spin-angular moment enclosed on the sublattices is termed as a "spin-uncompensation." Here we develop a theory of spin-transfer torque induced dynamics in slightly uncompensated FiM materials [4]. We demonstrate that the difference in the angular momentum in each sublattice principally affects FiM magnetization behavior. As an example, we consider a bi-layer Pt/GdFeCo spin-Hall oscillator, see Fig. 1. DC electrical current runs in the Pt layer inducing STT acting on FiM. The trajectory of Neel's vector precession, driven by pure spin current, is conical, in contrast to a flat circle in the case of AFMs. At the same time, due to the exchange interaction, the frequency of these oscillations can reach sub-THz frequencies. The conical type of precession is essential, as it allows for a non-zero AC spin-pumping from FiM back into the Pt layer. The AC spin-current induces a non-zero THz electrical voltage via the inverse spin-Hall effect. In Fig. 2, we plot a dependence of the DC to AC spin-Hall resistance in a case of different spin-uncompensation of the magnetic sublattices. The dependence of the Hall resistance on the spin-uncompensation is non-trivial: a small spin-uncompensation creates a detectable spin-Hall voltage in a broad range of frequencies. At the same time, a relatively large uncompensation leads to smaller bandwidth of sub-THz generation.

[1] H. V. Gomonay and V. M. Loktev, Phys. Rev. B 81 144427 (2010) [2] R. Cheng, D. Xiao, and A. Brataas, Phys. Rev. Lett. 116 207603 (2016) [3] R. Khymyn, I. Lisenkov, V. Tiberkevich, B. A. Ivanov, and A. Slavin, Scientific Reports 7 43705 (2017) [4] Ivan Lisenkov, Roman Khymyn, Johan Akerman et al arXiv:1904.09341

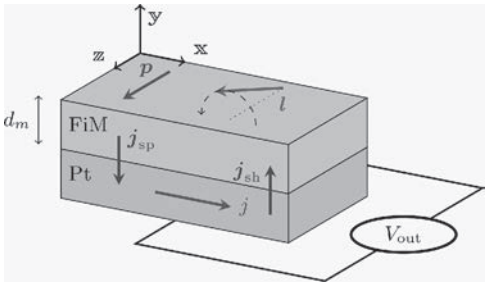
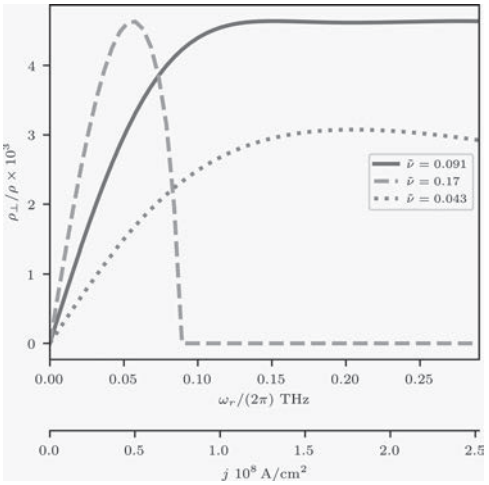


FIG. 1. Sketch showing the geometry of a ferrimagnetic spin-Hall oscillator



DC to AC Hall resistance as a function of the electric current density in the Pt layer and the oscilations frequency

9:18

AD-05. Anomalous Spin-Orbit Torques in Magnetic Single-Layer Films. W. Wang[1], T. Wang[2], V. Amin[3,4], Y. Wang[2], A. Radhakrishnan[1], A. Davidson[5], S.R. Allen[5], T.J. Silva[6], H. Ohldag[7], D. Balzar[5], B.L. Zink[5], P. Haney[4], J. Xiao[2], V. Lorenz[1] and *X. Fan*[5] *1. Physics, University of Illinois at Urbana-Champaign, Urbana, IL, United States; 2. Physics and Astronomy, University of Delaware, Newark, DE, United States; 3. Maryland Nanocenter, University of Maryland, College Park, MD, United States; 4. Center for Nanoscale Science and Technology, National Institute of Standards and Technology, Gaithersburg, MD, United States; 5. Physics and Astronomy, University of Denver, Denver, CO, United States; 6. Quantum Electromagnetics Division, National Institute of Standards and Technology, Boulder, CO, United States; 7. 7. Stanford Synchrotron Radiation Lightsource, SLAC National Accelerator Laboratory, Menlo Park, CA, United States*

The spin Hall effect couples charge and spin transport, enabling electrical control of magnetization. A quintessential example of spin-Hall-related transport is the anomalous Hall effect (AHE), first observed in 1880, in which an electric current perpendicular to the magnetization in a magnetic film generates charge accumulation on the surfaces. Illustrated in Fig.1, we report the observation of a counterpart of the AHE that we term the anomalous spin-orbit torque (ASOT) [1], wherein an electric current parallel to the magnetization generates opposite spin-orbit torques on the surfaces of the magnetic film. We interpret the ASOT as due to a spin-Hall-like current generated with an efficiency of in $Ni_{80}Fe_{20}$, comparable to the spin Hall angle of Pt [2]. Similar effects are also observed in other common ferromagnetic metals, including Co, Ni, and Fe. First principles calculations corroborate the order of magnitude of the measured values. This work suggests that a strong spin current with spin polarization transverse to the magnetization can be generated within a ferromagnet, despite spin dephasing. The large magnitude of the ASOT should be taken into consideration when investigating spin-orbit torques in ferromagnetic/nonmagnetic bilayers.

[1] Wang, W. *et al*. Anomalous Spin-Orbit Torque in Magnetic Single-Layer Films. arXiv: 1902.05490 (2019) [2] Liu, L., Moriyama, T., Ralph, D. C. & Buhrman, R. A. Spin-Torque Ferromagnetic Resonance Induced by the Spin Hall Effect. *Phys. Rev. Lett.* 106, 036601 (2011).

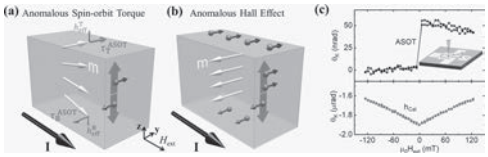


Figure 1 (a) Illustration of the anomalous spin-orbit torque when current is applied parallel with magnetization. The anomalous spin-orbit torques τ_T^{ASOT} and τ_B^{ASOT} are equivalent to effective fields h_{eff}^T and h_{eff}^B in the z direction. (b) Illustration of the anomalous Hall effect when current is applied perpendicular with magnetization. Due to the imbalance of majority and minority electrons, a net voltage accumulation is between the top and bottom surfaces. (c) Exemplary data of the MOKE signals due to the anomalous spin-orbit torque and an out-of-plane calibration field (h_{Cal}). The inset shows the experimental structure.

9:30

AD-06. Cr-induced Perpendicular Magnetic Anisotropy and Field-Free Spin-Orbit-Torque Switching. *T. Chuang*[1], C. Pai[2] and S. Huang[1] *1. Department of Physics, National Taiwan University, Taipei, Taiwan; 2. Department of Materials Science and Engineering, National Taiwan University, Taipei, Taiwan*

Current-induced spin-orbit torque (SOT) switching in a heterostructure with perpendicular magnetic anisotropy (PMA) has attracted great attention as a new writing method for spintronic devices. However, this highly attractive switching scheme is often accompanied by an unfavorable external magnetic field. In this work, we demonstrate polarity-controlled *field-free* SOT switching in 3d Cr, as shown in Fig. 1. Moreover, we find that Cr metal can induce strong interfacial PMA, without either heavy metal or MgO layer. Most importantly, field-free SOT switching could be achieved without introducing asymmetrical geometrical pattern, heavy metal, additional ferromagnetic or antiferromagnetic layers. We show that the underlying cause for the deterministic field-free switching lies in the slanted columnar microstructure, whose tilting angle is only around 5°, for the otherwise uniform thin films. The direction of oblique columnar structure dictates the up and down orientations of the PMA layer [1]. Our results uncover the significant role of 3d materials and shed light on field-free SOT magnetization switching.

[1] T. C. Chuang, C.F. Pai, and S.Y. Huang*, Physical Review Applied, in press (2019).

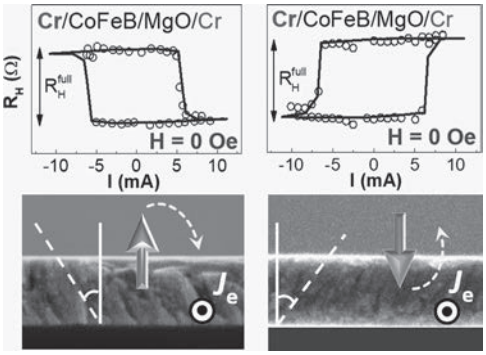


Fig. 1 The field-free spin-orbit torque switching in Cr/CoFeB/MgO/Cr heterostructures with different directions of oblique columnar structure. The R_H represents the anomalous Hall resistance.

9:42

AD-07. Enhanced Spin-Orbit Torque in Co/Pt System with Interfacial Oxidation Layer. *K. Hasegawa*[1], T. Koyama[2,3] and D. Chiba[2,3] *1. Applied Physics, The University of Tokyo, Bunkyo, Japan; 2. Osaka University, Ibaraki, Japan; 3. Center for Spintronics Research Network, Ibaraki, Japan*

In-plane current-induced spin-orbit torque (SOT) in ferromagnet (FM)/heavy metal (HM) heterostructures has attracted much interest as a new method for writing information in magnetic memories. Recent experiments have shown that the oxidation of entire FM or HM layer can significantly affect the SOT efficiency [1,2]. Since the FM/HM interface condition is assumed to be more essential for the SOT, control of the interface oxidation is crucial to examine the oxidation effect. Here we show the SOT efficiency is enhanced by inserting a thin CoO layer into Co/Pt interface [3]. Ta/Pd/Co layers were first deposited on thermally oxidized Si substrate. Then, the surface of the top Co layer was exposed to air to form surface oxidation layer (CoO). Finally, the CoO surface was covered by a Pt layer (an interface-oxidized (IO) sample). We also prepared an unoxidized (UO) sample with similar areal magnetic moment as a reference. Even though the insulating CoO is expected to reduce the spin-Hall-effect-induced vertical spin current injection from the Pt to Co, the damping-like (DL) and field-like (FL) SOT effective fields for the IO sample are several-fold and nearly an order of magnitude larger than those for the UO sample, respectively, at any current densities flowing in the Pt (see Fig.). The increase in the SOT is most likely attributed to the enhancement of the Rashba-Edelstein effect which originates from the oxygen-induced modulation of the electron distribution near the Co/Pt interface. The significant enhancement of FL torque is consistent with the above speculation because the Rashba-Edelstein effect mainly contributes to the FL torque. Since the enhancement of SOT is crucial for the efficient SOT-driven magnetization switching, the interface oxidation becomes one of important keys for developing the future magnetic memory devices. This work was supported by JSPS KAKENHI and Spintronics Research Network of Japan.

[1] X. Qiu et al., *Nat. Nanotech*., Vol. 10, p.333 (2015) [2] K.-U. Demasius et al., *Nat. Commun*., Vol. 7, p.10604 (2016) [3] K. Hasegawa et al., *Phys. Rev. B* Vol. 98, p.020405(R) (2018)

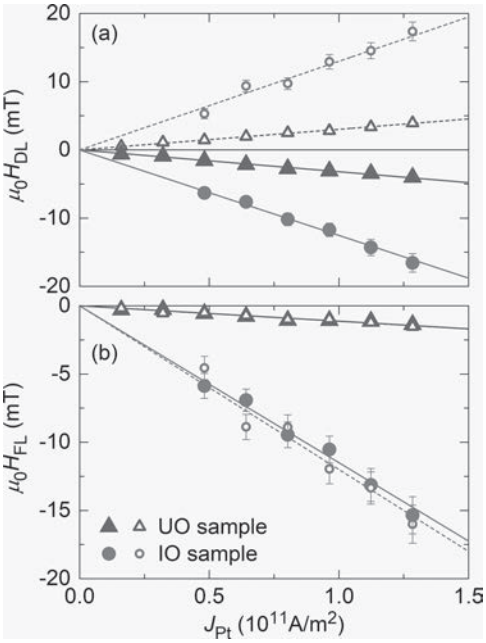


Fig. (a) The DL and (b) FL effective fields as a function of current density in the Pt layer for the IO and UO samples.

9:54

AD-08. Anatomy of Intrinsic Spin-Orbit Torque in Pt/Co Bilayer: Effect of Interfacial Co Oxidation. *F. Mahfouzi*[1] and N. Kioussis[1]
1. Physics and Astronomy, California State University, Northridge, CA, United States

Spin-Orbit torque (SOT) has recently attracted a lot of attention as a method to switch nano-scale magnetic bits, due to its promising features in terms of high efficiency and scalability. SOT is a relativistic phenomena that has its origin in the atomic spin-orbit couplings (SOC) in systems with broken inversion symmetry and is often separated into damping (Slonczewski)-like (DL) and field-like (FL) components. Despite the experimental successes in achieving magnetic switching using SOT, its microscopic origin in terms of the chemical environmental properties of the interface, thus far remains elusive [1]. In this work, we present a novel theoretical approach within the framework of the Green's function approach and first principles electronic structure calculations which allows to elucidate the microscopic origin of the spin-orbit torque (SOT) in heavy metal (HM/ferromagnet (FM) bilayers. We show that the SOT can be decomposed into spin-pumping and spin-orbital components and demonstrate that, (*i*), the FL-SOT is dominated by the spin-orbital component which can be expressed in terms of the difference of current-induced spin-resolved orbital moment accumulation at the interfacial HM atoms adjacent to the FM and (*ii*), the spin-orbital component cancels out the spin-memory loss contribution to the spin-Hall conductivity resulting in an enhancement of the total DL-SOT. We apply this approach to the Pt/Co bilayer to study the Pt-thickness dependence of both components of the SOT and the effect of interfacial Co oxidation on the SOTs. The theoretical results for the SOT versus Pt thickness are in excellent agreement with experiment [2]. The calculations reveal that in the presence of oxygen atoms adjacent to the interfacial Pt layer, the hybridization of the spin majority p-derived orbitals of oxygen atoms with the d-orbitals of interface Pt layer results in a significant reduction of the current-induced spin-majority orbital moment accumulation on the Pt layer, while the spin-minority contribution remains intact. This, in turn results in a sign reversal of the FL-SOT as observed in recent experiments [3]. Supported by NSF Grant No. ERC TANMS-1160504.

1. Frances Hellman *et al*., *Interface-induced phenomena in magnetism*, Rev. Mod. Phys. 89, 025006 (2017). 2. Minh-Hai Nguyen *et al*., *Spin Torque Study of the Spin Hall Conductivity and Spin Diffusion Length in Platinum Thin Films with Varying Resistivity*, Phys. Rev. Lett. 116, 126601 (2016). 3. Rahul Mishra *et al*., *Electric-field control of spin accumulation direction for spin-orbit torques*, Nat. Comm. 10, 248 (2019).

10:06

AD-09. Deterministic Spin-Orbit Torque Switching by a Light Metal Insertion. *A. Razavi*[1], H. Wu[1], Q. Shao[1], C. Fang[2], K. Wong[1], X. Han[2], G. Yu[2] and K. Wang[1] *1. Electrical and Computer Engineering, University of California, Los Angeles, Los Angeles, CA, United States; 2. Institute of Physics, Chinese Academy of Sciences, Beijing, China*

Spin-orbit torque (SOT) switching of magnetization is a promising emerging technology for non-volatile spintronic memory and logic applications [1, 2]. However, deterministic switching of perpendicular magnetization with SOTs requires an additional symmetry breaking [3], which is typically provided by an external magnetic field, making it impractical for applications. In this work, we present that by inserting a slightly asymmetric light-metal at the heavy-metal/ferromagnet interface of SOT heterostructures, current-induced out-of-plane effective magnetic fields are introduced that enable deterministic switching without the external magnetic fields. The creation of out-of-plane fields in such a structure (W/Ti/CoFeB) is explained by the Rashba-Edelstein effect and is a consequence of the in-plane structural symmetry breaking. The obtained out-of-plane effective fields enable deterministic SOT switching (Fig. 1). In contrast to previous reports [3], the innovation of this work is the use of a light metal insertion (Ti) with a long spin diffusion length and a negligible spin-orbit coupling, which results in uniform perpendicular magnetic anisotropy, coercive field, spin-orbit torque, and switching current density throughout the sample, despite the asymmetry of the Ti layer (Fig. 2). Furthermore, we show the scalability of our approach for field-free deterministic switching down to nanometer devices by fabricating a series of Hall bars with different sizes. Our work provides a physical understanding of field-free switching mechanism in asymmetric structures and provides a practical route for the implementation of spintronic memory and logic devices based on SOTs.

1. L. Liu, C.-F. Pai, Y. Li et al., Science, 336(6081): p. 555-558 (2012) 2. I.M. Miron, K. Garello, G. Gaudin et al., Nature, 476(7359): p. 189 (2011) 3. G. Yu, P. Upadhyaya, Y. Fan et al., Nature Nanotechnology, 9: p. 548 (2014)

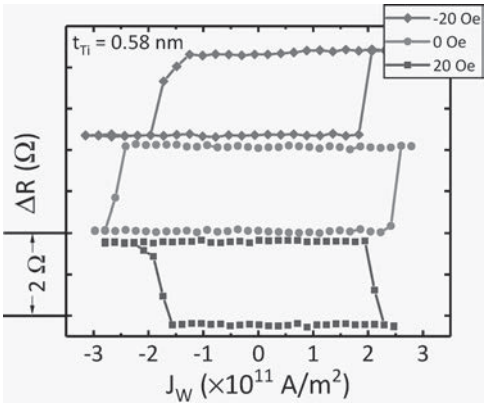


Figure 1. SOT switching in W/Ti/CoFeB/MgO structure under different in-plane external fields. 0 Oe plot corresponds to a field-free deterministic SOT switching.

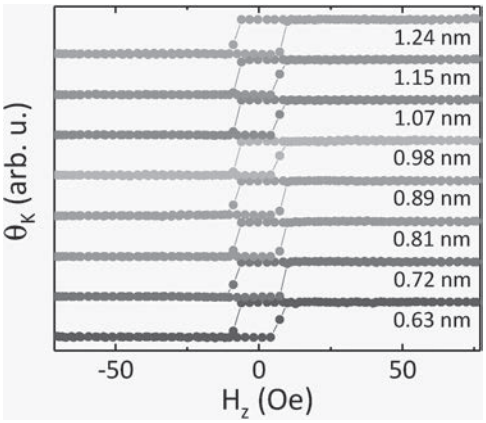


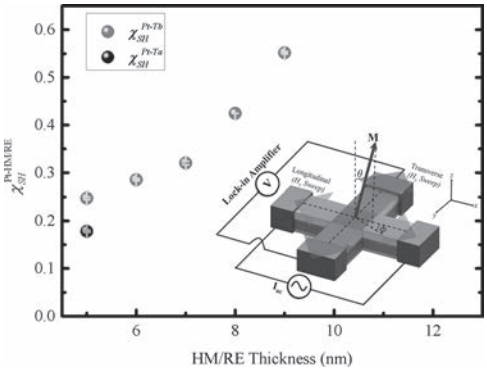
Figure 2. Perpendicular magnetic anisotropy studied by MOKE measurement in W/Ti/CoFeB/MgO system. A uniform coercive field is observed at all studied thicknesses.

10:18

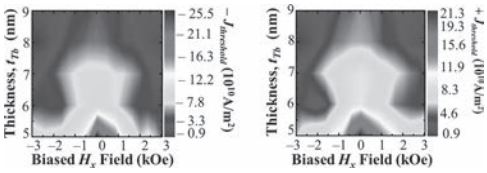
AD-10. Enhanced Spin Orbit Torques in Rare Earth Pt/[Co/Ni]$_2$/Co/Tb Systems. *Q. Wong*[2], C. Murapaka[2,1], W. Law[2], W. Gan[2], G.J. Lim[2] and W. Lew[2] *1. Indian Institute of Technology(Hyderabad), Hyderabad, India; 2. Nanyang Technological University, Singapore*

Substantial spin Hall contributions from rare earth (R) metals have been theoretically predicted due to the their partially filled *f*-orbitals, however, determination of spin Hall efficiency with R metal being a heavy metal replacement remains lacking. We report the enhanced effect of the R metal, Tb on the spin-orbit torque (SOT)-induced switching in Pt/[CoNi]$_2$/Co/Tb with perpendicular magnetic anisotropy (PMA). In this study, SOT efficiency was characterised using a H_z-biased harmonic measurement based on analytical solutions, as well as current induced magnetisation switching. Through the systematic variation of Tb thickness from 5nm to 9nm, the harmonic analyses reveal substantial enhancement of the SOT damping-like and field like terms. A relatively large spin Hall angle of Tb, was determined to be–0.18 to –0.480 for the thickness range. The increase of magnetisation switching efficiency with increasing Tb thickness affirms the sizeable anti-damping torque that was responsible for the deterministic switching. The negative sign of the spin Hall angle could also be observed by the sign change in the resistance-current hysteresis loop. These results affirm that Tb plays a significant role in contributing to the SOTs in these structures as the increased Tb concentration leads to an enhancement of the effective spin Hall angle and switching efficiency. Furthermore, angular dependence of the field-like term suggests the enhanced presence of the interfacial spin-orbit coupling. As such, rare earth Tb proves to be a potential alternative for spin Hall based switching.

[1] T. Tanaka and H. Kontani, "Intrinsic spin and orbital Hall effects in heavy-fermion systems," *Physical Review B - Condensed Matter and Materials Physics*, vol. 81, no. 22, p. 224401, 2010. [2] K. Ueda, C. F. Pai, A. J. Tan, M. Mann, and G. S. D. Beach, "Effect of rare earth metal on the spin-orbit torque in magnetic heterostructures," *Applied Physics Letters*, vol. 108, no. 23, p. 232405, 2016. [3] N. Reynolds *et al.*, "Spin Hall torques generated by rare-earth thin films," *Physical Review B*, vol. 95, no. 6, p. 64412, 2017. [4] Q. Y. Wong, C. Murapaka, W. C. Law, W. L. Gan, G. J. Lim, and W. S. Lew, "Enhanced Spin-Orbit Torques in Rare-Earth Pt/[Co/Ni]$_2$/Co/Tb," *Physical Review Applied*, vol. 11, no. 2, p. 024057, 2019.



Spin Hall efficiency, χ_{SH} for the Pt/[Co/Ni]$_2$/Co/Tb samples with variation of Tb thicknesses contrasted with reference Ta capped sample. Inset shows the schematic of the harmonic Hall measurement.



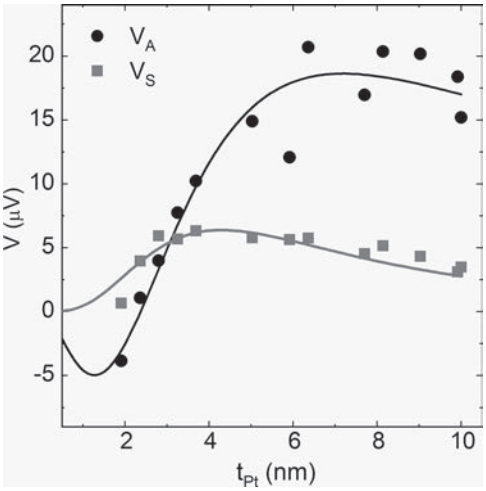
Current-induced magnetisation switching phase diagram for the film stacks variations from thickness of Tb from 5 nm to 9 nm, where $J_{threshold}$ is the minimum current density required for magnetisation switching to occur.

10:30

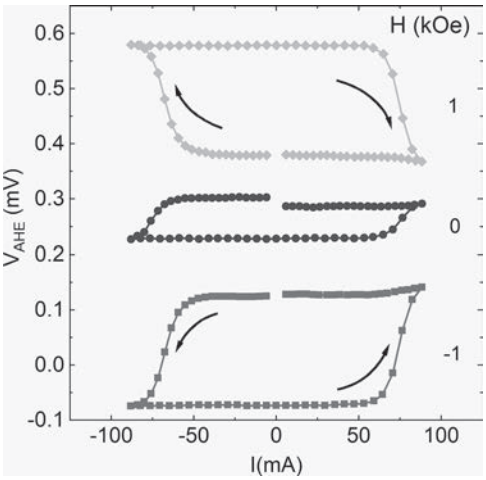
AD-11. Spin-orbit-torque induced dynamics and field-free switching in ferromagnet/heavy metal multilayers. *W. Skowronski*[1], S. Lazarski[1], K. Grochot[1], S. Zietek[1], J. Kanak[1], L. Karwacki[1,2], T. Stobiecki[1], P. Kuswik[2], F. Stobiecki[2] and J. Barnas[2] *1. Department of Electronics, AGH University of Science and Technology, Krakow, Poland; 2. Institute of Molecular Physics, Polish Academy of Sciences, Poznan, Poland*

Materials exhibiting high spin-orbit coupling such as heavy metals (HM) and topological insulators have been recently intensively studied due to their potential application in spintronics devices [1]. Driving charge current through such elements results in spin current generation that may be used for both magnetization switching and magnetization dynamics induction in a neighbouring ferromagnetic (FM) layer using spin orbit torque (SOT). We present studies on various combination of multilayers including HM: W, Ta, Ir, Pt and FM: Co, CoFeB. In FM/HM bilayers, based on the thickness dependent resistance and SOT-induced ferromagnetic resonance, the amplitude of the damping-like and field-like SOT components, as well as the interface contribution is extracted using an analytical model [2]. In addition, in FM/HM/FM systems, the HM can be used both as a source of the spin current and as a tunable coupler between two FM layers. Figure 1 presents the mixing voltage dependence from the SOT-induced dynamics in Co(5)/Pt(0-10) (thickness in nm) bilayers enabling determination of the spin Hall angle based on the model. In the optimized structure Co(5)/Pt(3-4)/Co(1) a field-free SOT-switching of perpendicuarly magnetized Co(1) coupled to the in-plane magnetized Co(5) was measured by applying different current to the Hall bar, while measuring anomalous Hall voltage - Fig. 2. [3]. In the discussed paper different material systems will be presented. Acknowledgements The project is supported by National Science Center, Poland, Grant No. 2015/17/D/ST3/00500. SL, KG, LK and TS acknowledge National Science Centre grant Spinorbitronics 2016/23/B/ST3/01430.

[1] – A. Manchon et al. arXiv:1801.09636 (2018) [2] – W. Skowronski et al. Phys. Rev. Applied 11, 024039 (2019) [3] – S. Lazarski et al. arXiv:1903.03368 (2019), accepted for Phys. Rev. Applied



Amplitudes of the symmetric and asymmetric component of SOT-FMR as a function of Pt thickness in Co(5)/Pt(0-10) bilayer.



Anomalous Hall voltage as a function of current measured in a different in-plane magnetic field.

10:42

AD-12. Influences of interfacial oxidization on surface magnetic energy, magnetic damping and spin-orbit-torques in Pt /ferromagnet /capping structures. *D. Lee*[1,2], W. Jeong[1,2], D. Yun[1,2], S. Park[3], B. Ju[1], H. Koo[2], B. Min[2], K. Lee[1] and O. Lee[2] *1. Korea University, Seoul, The Republic of Korea; 2. Korea Insutitute of Science and Technology, Seoul, The Republic of Korea; 3. Korea Basic Science Institute, Daejeon, The Republic of Korea*

Recently, spin-orbit torques (SOTs) have attracted much attention because the mechanism can efficiently reverse the magnetization in multilayers of heavy metal(HM)/ferromagnet(FM)/insulator with strong spin-orbit coupling (SOC). Although most of the research to date has focused on the HM/FM interface at which the generation of spin-current (J_S) and the enhancement in magnetic damping (α), several recent works have suggested that the physical and chemical properties of the capping (CAP) can also change the characteristics of SOTs. In addition, our previous work [1] demonstrated that the insertion of an ultrathin magnetic dusting layer between FM and MgO layers can play an important role in the determination of magnetic damping. Nevertheless, there is still a dearth of experimental work studying how the FM/CAP interface contributes to surface magnetic energy (K_S), α, SOT efficiencies (θ_{DL} and θ_{FL}) in HM/FM/CAP heterostructures. In this presentation, we present our experimental results [2] that investigate how a naturally formed magnetic oxide at the interface influences the magnetic properties. We examined six different series of layer stacks consisting of Pt / FM(Co or Py) / CAP (MgO, HfO and TaN). We illuminate, by utilizing X-ray photoelectron spectroscopy (XPS) and spin-torque ferromagnetic resonance (ST-FMR) measurements, an additional relaxation pathway of spin current in Pt/FM/CAP systems, namely the FM-oxide at the FM/CAP interface. The XPS showed the presence of interfacial FM-oxide, and ST-FMR demonstrated the deterioration of PMA associated with a formation of interfacial FM-oxides for both Co and Py samples. The interfacial oxide significantly influences α indicating an extra magnetic damping. This implies that the interfacial FM-oxide is a decent spin-current conductor, for instance, by incoherent magnon generation at the interfacial CoO, even above its magnetic ordering temperature (T_N). Our results facilitate a better understanding of the interfacial oxide contributions on the PMA, magnetic damping, and SOTs in Pt/FM/CAP systems.

[1] D. J. Lee, J. H. Kim, H. G. Park, K.-J. Lee, B.-K. Ju, H. C. Koo, B.-C. Min, and O. J. Lee*, "Spin-Orbit Torque and Magnetic Damping in Tailored Ferromagnetic Bilayers", Phys. Rev. Applied 10, 024029 (2018). [2] D. J. Lee, W. M. Jeong, D. H. Yun, S. Y. Park, B.-K. Ju, K.-J. Lee, H. C. Koo, B.-C. Min, and O. J. Lee*, Influences of interfacial oxidization on surface magnetic energy, magnetic damping and spin-orbit-torques in Pt / ferromagnet / capping structures, arXiv:1901.05777 (2019).

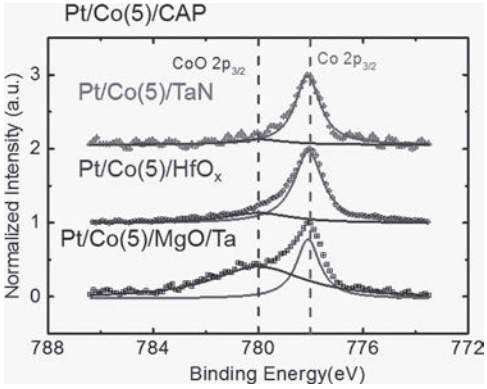


Fig.1 Co 2p3/2 and CoO 2p3/2 XPS spectral region from Pt/Co/CAP multilayers.

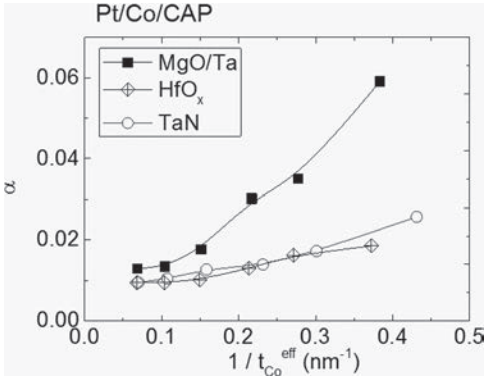


Fig.2 Obtained α as functions of $1/t_{Co}^{eff}$ from ST-FMR devices with Pt/Co/CAP multilayers.

10:54

AD-13. Disentanglement of Spin Orbit Torques in Platinum/Colbalt Bilayers with the Presence of Spin Hall Effect and Rashba-Edelstein Effect. *Y. Du*[1], H. Gamou[1], S. Takahashi[2], S. Karube[1,3], M. Kohda[1,3] and J. Nitta[1,3] *1. Department of Materials Science, Tohoku University, Sendai, Japan; 2. Advanced Institute for Materials Research, Tohoku University, Sendai, Japan; 3. Center for Spintronics Research Network, Tohoku University, Sendai, Japan*

We present a quantitative disentanglement of the current-induced spin orbit torques (SOTs) from the spin Hall effect (SHE) [1] and Rashba-Edelstein effect (REE) by performing a detailed harmonic Hall measurement in epitaxial Pt/Co bilayers. In-plane magnetized thin films of Pt(t_{Pt})/Co(1.95)/AlO_x(2) (thickness in nm) are fabricated into Hall bars for SOT measurement. Considering that both SHE and REE contribute to the DL-SOT, the data in Fig. 1(b) with t_{Pt} = 1.3-4.0 nm is fitted with $H_{DL} \approx H_{DL0}[1\text{-sech}(t_{Pt}/\lambda_{Pt})] + H_{DL2}$, where H_{DL0} and λ_{Pt} are the saturated DL-SOT from bulk Pt and the effective spin diffusion length (SDL) in Pt in this region, H_{DL2} is the saturated REE-induced DL-SOT at Pt/Co interface. The analysis above at different T yields an intrinsic contribution to the SHE and the Elliot-Yafet (EY) spin relaxation in *bulk* Pt, which agrees with previous studies [2,3]. A comparison of T-dependent DL-SOT and FL-SOT in thicker Pt region (*e.g.* t_{Pt} = 6.0 nm) shows that the SHE-induced FL-SOT is negligible in our samples. The t_{Pt} dependence of FL-SOT is thus fitted with $H_{FL} \approx H_{FL1}[1\text{-sech}(t_{Pt}/d_{REE1})]\text{sech}(t_{Pt}/\lambda_{Pt'}) + H_{FL2}[1\text{-sech}(t_{Pt}/d_{REE2})]$, where H_{FL1} and H_{FL2}, d_{REE1} and d_{REE2} are the saturated FL-SOT, effective REE thickness at sub./Pt and Pt/Co interfaces, respectively. Note that $\lambda_{Pt'}$, the SDL with t_{Pt} = 0.2-1.1 nm, is estimated from the λ_{Pt}-conductivity plot. The corresponding ξ_{FL1} and ξ_{FL2} [Fig. 2(a)] show comparable magnitude but opposite sign, consistent with the REE. Finally, the REE-induced DL-SOT from sub./Pt (ξ_{DL1}) interface is obtained with $H_{DL} \approx H_{DL1}[1\text{-sech}(t_{Pt}/d_{REE1})]$ $\text{sech}(t_{Pt}/\lambda_{Pt'}) + H_{DL2}[1\text{-sech}(t_{Pt}/d_{REE2})] + H_{DL0'}[1\text{-sech}(t_{Pt}/\lambda_{Pt'})]$, where H_{DL1} is the REE-induced DL-SOT from sub./Pt interface, $H_{DL0'}$ is the saturated SHE-induced DL-SOT with t_{Pt} = 0.2-1.1 nm, estimated based on the H_{DL0}-resistivity plot. The obtained ξ_{DL1} and ξ_{DL2} [Fig. 2(c)] show opposite sign and agree with the sign of ξ_{FL1} and ξ_{FL2}. This work provides a unified picture of the SOT in SH systems with both SHE and REE.

[1] L. Liu et al., Science 336, 555 (2012). [2] E. Sagasta et al., Physical Review B 94, 060412(R) (2016). [3] M.-H. Nguyen et al., Physical Review Letters 116, 126601 (2016).

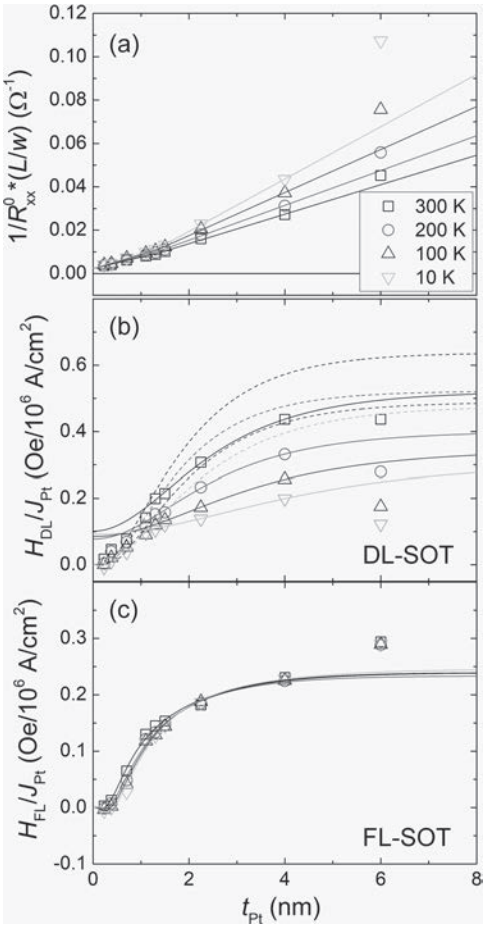


Fig. 1 (a) Inverse of the sheet resistance, (b) DL-SOT and (c) FL-SOT as a function of t_{Pt} at 10-300 K.

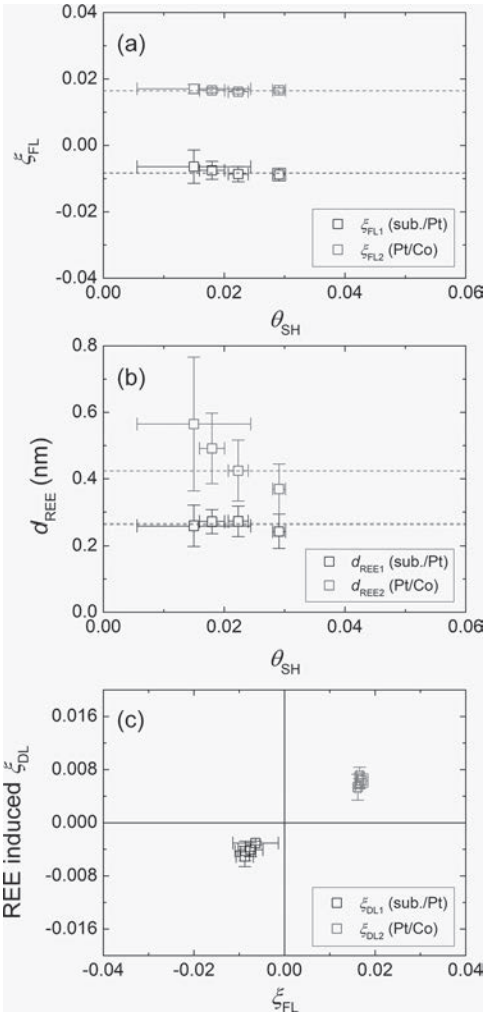


Fig. 2 (a) FL-SOT efficiency, (b) effective REE thickness and (c) REE-induced DL-SOT from sub./Pt and Pt/Co interfaces.

11:06

AD-14. First-principles calculation of the thickness dependence of spin-orbit torque in Co/Pt and Co/Au bilayers. *K. Belashchenko*[1], A. Kovalev[1] and M. van Schilfgaarde[2] *1. Department of Physics and Astronomy, University of Nebraska-Lincoln, Lincoln, NE, United States; 2. Department of Physics, King's College London, London, United Kingdom*

The dependence of spin-orbit torque on the thickness of the heavy-metal layer in Co/Pt and Co/Au bilayers is studied using the first-principles non-equilibrium Green's function formalism [1] combined with the Anderson disorder model. For Co/Pt, the torque is well described by a combination of damping-like, field-like, and planar-Hall-like terms, while in Co/Au only damping-like and field-like terms are important. The damping-like torque has the same sign in Co/Pt and Co/Au and behaves as a sum of the spin-Hall contribution, which increases with thickness in agreement the spin-diffusion model, and an interfacial contribution that is particularly large in Co/Pt. Variation of the disorder strength reveals a relatively small contribution of skew scattering compared to the dominant intrinsic contribution. The field-like torque has opposite signs in Co/Pt and Co/Au, and its variation with thickness is nonmonotonic. The planar-Hall-like term in Co/Pt increases with thickness, suggesting it is related to spin-Hall effect.

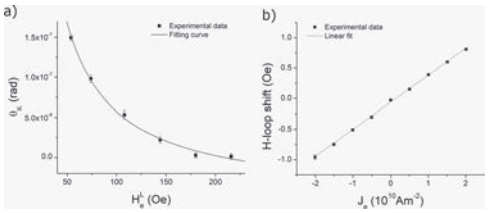
[1] K. D. Belashchenko, A. A. Kovalev, and M. van Schilfgaarde, Phys. Rev. Materials 3, 011401(R) (2019).

11:18

AD-15. Magneto-optical detection of spin-orbit torques with oblique incidence angle. *C.A. Gonzalez-Fuentes*[1] and C. Garcia[1] *1. Physics, UTFSM, Valparaiso, Chile*

Experimental techniques for the accurate quantification of spin-orbit orbit torques (SOTs) are crucial for the progress of applied spintronics. Up to date the detection of SOTs have been largely dominated by electrical detection methods, like Second Harmonic Generation [1] and Spin-Torque Ferromagnetic Resonance [2]. However, the interpretation of the data in these cases is difficult since requires the consideration of a variety of potential artifacts originated from magneto-transport, thermo-electric and spin-to-charge conversion effects [1]. Magneto-Optical Kerr Effect (MOKE) detection of SOTs [3], on the other side, has arisen as an alternative strategy to solve the above mentioned problems, since it can probe the magnetization reorientation directly, decoupled from the above mentioned artifacts. In this work we demonstrate the magneto-optical detection of the spin-current generated by the Spin Hall Effect in a Pt layer, injected into adjacent layer of NiFe. The damping-like component (DL) of SOT acts as an effective field on NiFe magnetization, inducing a tilting whose magnitude let us to deduce the spin hall angle of Pt (θ_{SH}). With this method we obtained a value of θ_{SH}=0.088 ± 0.006, falling inside the range of previously reported values measured with non magneto-optical methods. Respect to previously published similar works [3,4], our method employs oblique incidence angle, which allow us also to quantify the in-plane component of the Oersted by hysteresis loop shift measurements in longitudinal MOKE, without modifying the optical set-up. This, in turn, was employed for accurate calibration of the current density in Pt, without the need of assuming an equivalent electrical circuit for the NiFe/Pt bilayer [3].

[1] M. Hayashi, J. Kim, M. Yamanouchi, and H. Ohno, Phys. Rev. B 89, 144425 (2014). [2] L. Liu, T. Moriyama, D. C. Ralph, and R. A. Buhrman, Phys. Rev. Lett. 106, 036601 (2012). [3] X. Fan et al., Appl. Phys. Lett. 109, 122406 (2016). [4] A. M. Humphries et al., Nat. Commun. 8, 911 (2017).



(a) Measured Kerr rotation (θ_K) vs magnitude of longitudinal magnetic field (He^L) on a NeFe (10nm)/Pt(7nm) bilayer stripe subjected to a current density $J_e = 2.5\times10^{10}$ Am^{-2}. The fitting model is based on reference [3]. (b) Hystereis loop shift vs current density for the same stripe.

Session AE
TOPOLOGICAL SPIN TRANSPORT

Luqiao Liu, Chair
MIT, Cambridge, MA, United States

CONTRIBUTED PAPERS

8:30

AE-01. Spin-to-charge conversion in magnetic Weyl semimetals.
S. Zhang[1], A. Burkov[2], I. Martin[1] and O. Heinonen[1] *1. Materials Science Division, Argonne National Laboratory, Lemont, IL, United States; 2. Department of Physics and Astronomy, University of Waterloo, Waterloo, ON, Canada*

Weyl semimetals (WSM) are a newly discovered class of quantum materials which can host a number of exotic bulk transport properties, such as the chiral magnetic effect, negative magnetoresistance, and a novel anomalous Hall effect [1,2]. In this work [3], we theoretically investigated spin-to-charge conversion in magnetic WSMs with a single pair of Weyl nodes and broken time-reversal symmetry. We found that a charge current can be induced by injecting a pure spin current into a magnetic WSM layer from an adjacent nonmagnetic metal layer. Formally, the induced charge current was calculated by solving for the scattering wave functions and the nonequilibrium distribution functions in each layer in the ballistic regime. Interestingly, we found the spin-to-charge conversion in magnetic WSMs exhibits remarkable features that are distinctly differently from that arising from either the Rashba or Dirac surface state in various magnetic heterostructures studied previously [4]. For one thing, the induced charge current depends on spin and flowing directions of the injected spin current with respect to the crystallographic axes of the magnetic WSM; in particular, it vanishes along the direction parallel to the line connecting the two Weyl nodes, regardless of the direction of the injected spin. In addition, we showed that there exists a strong dependence of the induced charge current on the position of the Fermi level as well as on the separation between the two Weyl nodes. Therefore, spin-to-charge conversion may not only serve as experimental probes of magnetic WSMs but may also provide extra knobs for controlling the spin-charge conversion in these topological materials. Work by S.S.-L.Z., A.A.B. and O.G.H. was supported as part of the Center for the Advancement of Topological Materials, an Energy Frontier Research Center funded by the U.S. Department of Energy (DOE), Office of Science. I.M. acknowledges support from the US Department of Energy, Office of Science, Basic Energy Sciences, Division of Materials Science and Engineering.

[1] A. A. Burkov, Nat. Mater. Vol. 15, p. 1145 (2016). [2] N. P. Armitage, E. J. Mele and A. Vishwanath, Rev. Mod. Phys. Vol. 90, p. 015001(2018). [3] S. S-.L Zhang, A. A. Burkov, I. Martin and O. G. Heinonen, arXiv:1904.07181. [4] W. Han, Y. Otani, S. Maekawa, npj Quantum Materials Vol. 3, p. 27 (2018).

8:42

AE-02. Light–spin conversion through interfacial spin–momentum locked states in semimetal heterostructures.
H. Hirose[1], M. Kawaguchi[1] and M. Hayashi[1] *1. Physics, The University of Tokyo, Tokyo, Japan*

Irradiation of circularly polarized light with angular momentum of +1 or -1 causes spin selective excitation. This allows the generation of anisotropic spin polarized photocurrent under illumination of circular polarized light if the sample has spin–momentum locked states. This phenomenon, known as circular photogalvanic effect (CPGE), has been studied in semiconductor heterostructures[1] and topological insulators[2]. We have studied the helicity dependent photocurrent in semimetal heterostructures. We measure the photocurrent under illuminating a continuous wave laser in the visible range. We find the photocurrent in Cu/Bi heterostructure strongly depends on the helicity of the light as shown in Fig.1. The helicity dependent photocurrent is significantly reduced for a Bi single layer film, and the effect is nearly absent for a Cu single layer film. Conventional interpretation of the CPGE suggests that this photocurrent may be generated due to the existence of spin–momentum locked states of Rashba type at the Cu/Bi interface. However, the light energy of the visible light to excite carriers is about a hundred times larger than the bandgap of semi-metallic Bi. We therefore consider that the CPGE of the Cu/Bi heterostructure may have a different origin compared to conventional systems[3]. We discuss the origin of the helicity dependent photocurrent in the semimetal/metal bilayer systems.

[1] W. Weber, H.-I. Cho et al., Appl. Phys. Lett., Vol. 87, pp. 262106 (2005). [2] J. W. McIver, N. Gedik et al., Nat. Nanotechnol., Vol. 7, pp. 96-100 (2012). [3] H. Hirose, M. Hayashi et al, Appl. Phys. Lett., Vol. 113, pp. 222404 (2018).

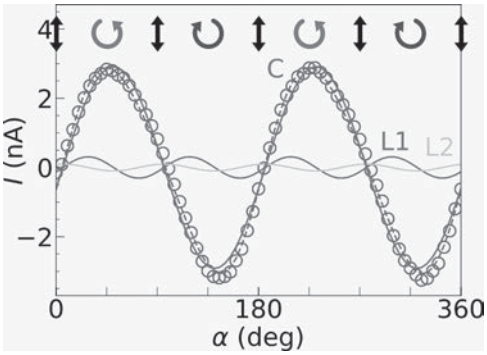


Figure1. The photocurrent measured in Cu/Bi heterostructure. The photocurrent is measured as a function of the angle (α) of the quarter-wave plate, which varies the light polarization. The device contacts lie perpendicular to the light incidence plane.

8:54

AE-03. Enhanced Gilbert Damping in Sputter Deposited Topological Insulator/Ferromagnet Heterostructures.
N. Bhattacharjee[1], I. Lisenkov[2], J. Wang[1] and N. Sun[1,2] *1. Electrical and Computer Engineering, Northeastern University, Boston, MA, United States; 2. Winchester Technologies LLC., Burlington, MA, United States*

Topological insulators (TI) have been known to possess topologically protected surface conducting states [1]. A TI placed in contact with a ferromagnetic (FM) generates spin-orbit torques (SOT) on the magnetization in FM [2,3]. A signature of SOT in FM/TI bilayers is an enchantment of Gilbert damping in FM. SOT in TI/FM heterostructures have been reported previously with TI films epitaxially grown with molecular beam epitaxy [2, 3]. Here we report enhanced Gilbert damping in sputter deposited

TI/FM $Bi_xTe_{(1-x)}$/CoFeB (BT/CFB) films. Samples of 20nm BT film were grown on a Si/SiO_2 substrate at 250°C and at 30°C followed by 20nm CFB deposition at 30°C (room temperature) using RF and DC magnetron sputtering respectively. X-ray diffraction (XRD) measurements reveal a crystalline 250°C BT film compared to an amorphous 30°C BT film (Fig. 1). Room temperature broadband ferromagnetic resonance (FMR) measurements were conducted for 250°C and 30°C heterostructures and a control sample where the TI was substituted with 3nm Al. A FWHM resonance linewidth was extracted and is shown in Fig. 2 as a function of frequency. The control and 30°C samples show almost identical linewidth, but the 250°C sample linewidth is much broader. The Gilbert damping coefficient, α, for the 250°C sample is 0.3, compared to 0.03 for 30°C and 0.02 for control. The calculated spin-mixing conductance, $g_{\uparrow\downarrow}$ for the 250°C sample is ~ $4x10^{21}m^{-2}$ which is in an order of magnitude higher than reported value for CFB/Pt films [4]. Moreover, the presence the crystalline TI on FM induces static effects on the magnetization. M-H loop measurements reveal a dramatic increase in the coercive field for the 250°C sample in contrast to the control and 30°C samples. This suggests a change in the surface magnetic anisotropy in the heterostructure due to spin-orbit coupling [5] at the interface, which occurs only for the crystalline phase of BT. Further, spin-torque FMR studies on our samples is being carried out to characterize the effects on magnetization dynamics due to TI/FM interfaces.

1.Y. L. Chen, J. G Anaytis and J. -H. Chu et al., Science Vol. 325, p. 5937 (2009). 2. A. R. Mellnik, J. S. Lee and A. Richardella et al., Nature Vol. 511, p. 449 (2014). 3. J. Han, A. Richardella and S. A. Siddiqui et al., Phys. Rev. Lett. Vol. 119, p. 077702 (2017). 4. M Belmeguenai, M. S. Gabor and F. Xigheim et al., J. Phys. D: Appl. Phys. Vol. 51 p. 045002 (2018). 5. A. Manchon, H. C. Koo and J. Nitta et al., Nature Materials Vol. 14, p. 871 (2015).

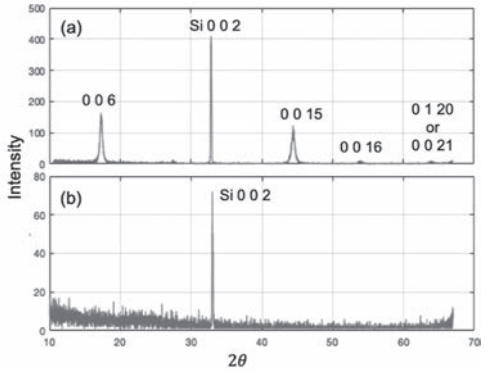


Figure 1. XRD spectra for: (a) 250°C, (b) 30°C samples

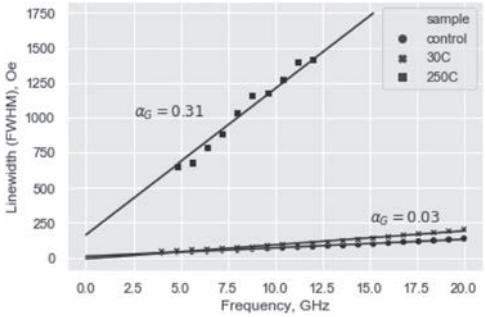


Figure 2. FMR linewidth vs frequency for 250°C (square), 30°C (cross) and control (circle) samples with linear fit.

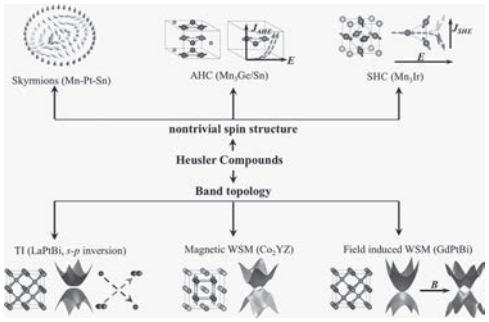
INVITED PAPER

9:06

AE-04. Topology and the consequences for spintronics and beyond.
C. Felser[1,2] and K. Manna[1] *1. Max Planck Institute, Dresden, Germany; 2. SEAS, Harvard University, Cambridge, MA, United States*

Topological insulators, Weyl and Dirac semimetals and new Fermions are new quantum states of matter, which have attracted considerable interest from the condensed matter community. Heusler compounds are a remarkable class of materials which exhibit a wide range of extraordinary multi-functionalities including tunable topological insulators, half metallic ferromagnets and non collinear topological spin structures [1]. The required band inversion has already been unambiguously identified by angle-resolved photoemission (ARPES) and transport [2, 3]. Weyl and Dirac semimetals open up new research directions and applications that result from the large Berry phases that they exhibit: these lead to giant anomalous Hall effect (AHE), giant anomalous Nernst and spin Hall effects (SHE) and topological spin structures [4]. Examples discussed in the talk are Mn_3Sn, $Co_3Sn_2S_2$ and Co_2MnGa. In the 2D limited we propose a Quantum anomalous Hall effect for $Co_3Sn_2S_2$ [5, 6].

[1] Graf, et al., Progress in Solid State Chemistry 39 1 (2011) [2] Liu, et al., Nature Communication 7, 12924 (2016) [3] Belopolski, Manna, et al., Science accepted (2019) preprint arXiv:1712.09992 [4] Manna, et al., Nature Reviews Materials 3, 244 (2018) preprint arXiv:1802.02838v1 [5] Xu, et al., Physical Review B 97, 235416 (2018) preprint arXiv:1801.0013 [6] Liu, et al., Nature Physics 14, 1125, (2018) preprint arXiv:1712.06722



Heusler compounds exhibiting typical s–p band inversion (Topological insulator). By breaking time-reversal symmetry, Weyl semimetals can exist in various magnetic Heusler materials, such as Co2MnAl (magnetic Weyl semimetal), Heusler compounds also host real-space topological states because of the existence of non-collinear magnetic structures and an anomalous Hall effect in zero moment compounds (Anomalous Hall effect), owing to spin-rotation symmetry breaking, a spin Hall effect (Spin Hall effect). A strong Dzyaloshinskii–moriya interaction leads to the observation of antiskyrmion structures in the tetragonal Heusler alloy (Antiskyrmion).

CONTRIBUTED PAPERS

9:42

AE-05. Spin-mixing conductance of ferromagnet/topological-insulator and ferromagnet/heavy-metal heterostructure: A first-principles Floquet-nonequilibrium Green function approach. *K. Dolui*[1], U. Bajpai[1] and B.K. Nikolić[1] *1. Department of Physics and Astronomy, University of Delaware, Newark, DE, United States*

The magnitude of experimentally observed spin pumping in ferromagnet/topological-insulator and ferromagnet/heavy-metal heterostructures is routinely interpreted in terms of standard spin-mixing conductance (SMC). However, this quantity is not well-defined when strong spin-orbit coupling (SOC) is present directly at the interface. Nevertheless, an effective SMC can be extracted as the pre-factor in pumped spin current I^S_z vs. precession cone angle θ dependence, as long as such dependence remains $I^S_z \propto \sin^2\theta$. Here we compute directly the pumped spin current, using noncollinear density functional theory Hamiltonian combined with charge conserving Floquet-nonequilibrium Green function formalism, flowing into semi-ininite Cu electrodes of two-terminal multilayers Cu/X/Co/Cu, where X = Bi_2Se_3, Pt and W and Cu. We show that pumped spin current gets reduced in the presence of interfacial SOC. However, stacking sequence and materials selection for constituting the heterostructure can eventually modulate the effective SMC [1].

[1] Kapildeb Dolui, Utkarsh Bajpai, Branislav K. Nikolic; arXiv:1905.01299

9:54

AE-06. Orthogonality-tuned superconducting spin pumping via perpendicularly magnetized Pt/Co/Pt spin sinks. *K. Jeon*[1,3], X. Montiel[2], C. Ciccarelli[3], H. Kurebayashi[5], L. Cohen[4], M. Blamire[1] and J. Robinson[1] *1. Department of Materials Science and Metallurgy, University of Cambridge, Cambridge, United Kingdom; 2. Royal Holloway, University of London, London, United Kingdom; 3. Cavendish Laboratory, University of Cambridge, Cambridge, United Kingdom; 4. The Blackett Laboratory, Imperial College London, London, United Kingdom; 5. London Centre for Nanotechnology and Department of Electronic and Electrical Engineering, University of College London, London, United Kingdom*

Superconducting spin currents - the flow/transfer of spin angular momentum through proximity-induced equal-spin triplet states into singlet superconductors (SCs) – are a key to practical superconducting spintronics1. Recent theoretical[2-4] and experimental efforts[5-7] have been devoted to showing that spin-orbit coupling (SOC) in conjunction with a magnetic exchange field hex generates the spinpolarized triplet supercurrents. Here we demonstrate that when perpendicularly magnetized Pt/Co/Pt spin sinks are proximity-coupled to Nb (singlet SC), spin-pumping efficiency in the superconducting state can be tuned by controlling the tilt angle θCo of the Co layer because it alters the degree of orthogonality between SOC and hex at the Nb/Pt/(Co/Pt) interface[2,3]. We also disentangle the contribution of interfacial SOC to the θCo-dependent superconducting spin-pumping efficiency from the other contributions by inserting a thin Cu spacer with weak SOC at the Nb/Pt/(Co/Pt) interface and find a sinusoidal maximum at θCo = 450, reflecting characteristic features of Rashba SOCinduced triplet pairing[2,3].

1. Linder, J. & Robinson, J. Nat. Phys. 11, 307–315 (2015). 2. Bergeret, F. S. & Tokatly, I. V. Phys. Rev. B 89, 134517 (2014). 3. Jacobsen, Sol H., Ouassou, Jabir A. & Linder, J. Phys. Rev. B 92, 024510 (2015). 4. Montiel, X. & Eschrig, M. Phys. Rev. B 98, 104513 (2018). 5. Jeon, K.-R. et al. Nat. Mater. 17, 499–503 (2018). 6. Banerjee, N. et al. Phys. Rev. B 97, 184521 (2018). 7. Satchell, N. & Birge, N. O. Phys. Rev. B 97, 214509 (2018).

10:06

AE-07. Unidirectional Spin Hall Magnetoresistance in Pt/Co and Ta/Co Bi- and Tri-layer Systems. *A. Moskaltsova*[1], J. Krieft[1], D. Graulich[1], T. Pohlmann[2,3], S. Francoual[3], J. Schmalhorst[1], T. Kuschel[1] and G. Reiss[1] *1. Center for Spinelectronic Materials and Devices, Department of Physics, Bielefeld University, Bielefeld, Germany; 2. Center of Physics and Chemistry of New Materials, University of Osnabrück, Osnabrück, Germany; 3. Deutsches Elektronen-Synchrotron DESY, Hamburg, Germany*

Lately, the unidirectional spin Hall magnetoresistance (USMR) has been observed in ferromagnetic (FM)/heavy metal (HM) bilayer systems [1, 2]. The USMR effect, being different from the spin Hall magnetoresistance (SMR), leads to the resistance change when either current direction or magnetization are reversed. This effect is explained by a drift-diffusion theory [3], where a spin Hall effect (SHE) induced spin accumulation can control electron mobility dependence on spin-polarization. The USMR can be used for reading memory devices, which can distinguish between in-plane states [4]. In addition, it was shown that in FM/HM systems with large spin-orbit coupling, a charge current flowing through the system generates spin-orbit torques (SOTs) that can switch the magnetization of the FM layer [5]. This effect is of large interest as a tool to control the magnetic state of a spintronic device, e.g. in SOT based magnetic random access memories. We report in this work USMR investigations of Pt/Co, Ta/Co and their trilayer systems. With variation of the HM position relatively to the FM, we are able to control interfacial spin accumulation and thus tune USMR strength. We found that additionally to the USMR there are other effects in both longitudinal and transverse geometries with sin 2φ symmetry. We identify these effects as anisotropic magnetothermopower (AMTP) and planar Nernst effect (PNE). For the bilayer systems, we found that R_{AMTP}/R_{USMR} is 4% and 30% for Pt and Ta cases respectively. For the samples containing Pt, a magnetic proximity effect occurs, which is responsible for the creation of a thin spin-polarized Pt layer in the vicinity of the FM [6, 7]. In this case, one has to take into account the additional Pt magnetic layer for the evaluation of a sample magnetic moment as well as of the magnetotransport properties. X-ray resonant magnetic reflectometry (XRMR) is a powerful method to characterize spin-depth profile as well as to extract Pt magnetic moment via ab-initio calculations. In this work, we use a combination of vibrating sample magnetometry (VSM) and XRMR as an effective tool to separate the Co magnetic moment from the additional induced moment in Pt.

[1] C. O. Avci et al., Nature Physics, Vol. 11, p. 570 (2015) [2] K. Olejnik et al., Physical Review B., Vol. 91, p. 180402 (2015) [3] S. Zhang and G. Vignale, Physical Review B, Vol. 94, p. 140411 (R) (2016) [4] C. O. Avci et al., Applied Physics Letters, Vol. 110, p. 203506 (2017) [5] A. Manchon et al., arXiv:1801.09636v2 [6] T. Kuschel et al., Physical Review Letters, Vol. 115, p. 097401 (2015) [7] C. Klewe et al., Physical Review B, Vol. 93, p. 214440 (2016)

10:18

AE-08. Observation of Large Unidirectional Rashba Magnetoresistance in Ge(111). *T. Guillet*[1], C. Zucchetti[2], Q. Barbedienne[3], A. Marty[1], G. Isella[2], C. Vergnaud[1], N. Reyren[3], J. George[3], A. Fert[3] and M. Jamet[1] *1. Univ. Grenoble Alpes, CEA, CNRS, Grenoble INP, IRIG-SPINTEC, Grenoble, France; 2. LNESS-Dipartimento di Fisica, Politecnico di Milano, Milan, Italy; 3. Unité Mixte de Physique, CNRS, Thales, Univ. Paris-Sud, Université Paris-Saclay, Palaiseau, France*

Tuning spin-orbit coupling (SOC) in semiconductors is of high interest as it could open a door towards spin manipulation with electric fields in an all-semiconductor technology platform. The existence of Rashba states at the subsurface of Ge(111) has been demonstrated by photoemission measurements and ab initio calculations [1]. Here we investigated the variation of the electrical resistance of Ge(111) grown epitaxially on semi-insulating Si(111) under the application of an external magnetic field. We report the observation of a unidirectional magnetoresistance (UMR) that scales linearly with

both the applied current density j and the magnetic field B. At low temperature, the UMR dominates all other MR contributions and can reach several percent for a magnetic field of 1 T and a low current density of 0.3A.m^{-1}. A similar MR behavior was reported in the literature in the topological insulator Bi_2Se_3 and two-dimensional electron gases, though orders of magnitude smaller than in Ge(111). Within a simple model based on spin –dependent scattering, we provide a new interpretation of UMR. We ascribe the origin of this magnetoresistance to the interplay between the externally applied magnetic field and the current-induced pseudo-magnetic field applied in the spin-splitted subsurface states of Ge(111). It progressively vanishes, either using a negative gate voltage due to carrier activation into the bulk (without spin-splitted bands), or by increasing the temperature due to the Rashba energy splitting of the subsurface states lower than ~58 kB. The highly developed technologies on semiconductor platforms point toward a ready optimization of the phenomenon.

[1] Y. Ohtsubo *et al.,* Phys. Rev. B 88, 245310 (2013) [2] T. Guillet *et al.,* arXiv:1906.04457

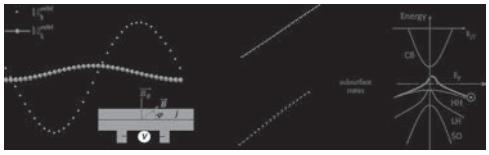


Fig. 1 – a) Experimental evidence of the UMR, the inset represents the measurement geometry, is the odd part of the longitudinal resistance defined as. Magnetic field b) and current c) dependence of the UMR signal, taken at φ=270° where the signal intensity is maximum, normalized by the zero field resistance. d) Scheme of the electronic band structure of Ge. The subsurface states splitted by Rashba spin-orbit coupling are highlighted and lie in the bandgap above the valence band.

10:30

AE-09. Spin transport measurements in metallic Bi/Ni nanowires.
M. Tokuda[1], N. Kabeya[1], K. Iwashita[1], H. Taniguchi[1], T. Arakawa[1,2], D. Yue[3], X. Gong[3], X. Jin[3], K. Kobayashi[1,4] and Y. Niimi[1,2] *1. Graduate School of Science, Osaka University, Toyonaka, Japan; 2. Center for Spintronics Research Network, Osaka University, Toyonaka, Japan; 3. Department of Physics, Fudan University, Shanghai, China; 4. Graduate School of Science, University of Tokyo, Bunkyo-ku, Japan*

Bismuth (Bi) is known as a material with strong spin-orbit interaction because of its large atomic number. Thus, Bi-related materials have been extensively studied in the field of spintronics. In terms of electrical conductivity, Bi thin film exhibits semiconducting behaviour in the temperature dependence of resistivity. However, when a few nanomator thick ferromagnetic nickel (Ni) film is put under Bi, the Bi/Ni bilayer thin films have a metallic transport property and even become superconductors below $T_C \approx 4$ K [1]. According to magnetization measurements with Bi/Ni thin films, the Ni layer keeps ferromagnetism even below T_C [2]. These results indicate that the Bi/Ni bilayer is a fascinating platform to study spin transport in nomal and superconducting state. The purpose of the present study is to investigate the spin transport properties in metallic Bi/Ni nanowires using the spin absorption method. Our spin transport device consists of ferromagnetic Py ($Ni_{81}Fe_{19}$) and metallic Bi (35 nm)/Ni (2 nm) nanowires bridged by a Cu stripe which enables us to transport spin accumulation generated at the Py/Cu junction to the metallic Bi/Ni nanowire (see the inset of Fig. 1). As shown in Fig. 1, the Bi/Ni nanowire shows a typical metallic temperature dependence in the resistivity and the superconducting transition at 4 K, which is similar to those in Bi/Ni thin films. Next we measured the inverse spin Hall effect (ISHE) in the Bi/Ni nanowire above T_C (see Fig. 2). The detected ISHE signal is small and positive (at 10 K), in contrast to that of Bi-doped Cu [3]. We also performed nonlocal spin valve measurements above T_C. The estimated spin diffusion length (≈3 nm) is much smaller than that of Bi alone (≈20 nm) [4]. In the presentation, we will mention some of our preliminary results below T_C.

[1] X. X. Gong *et al*., Chin. Phys. Lett. 32, 067402 (2015). [2] H. Zhou *et al*., J. Mag. Mag. Mater. 422, 73 (2017). [3] Y. Niimi *et al*., Phys. Rev. Lett. 109, 156602 (2012). [4] M. Tokuda *et al*., Appl. Phys. Express 12, 053005 (2019).

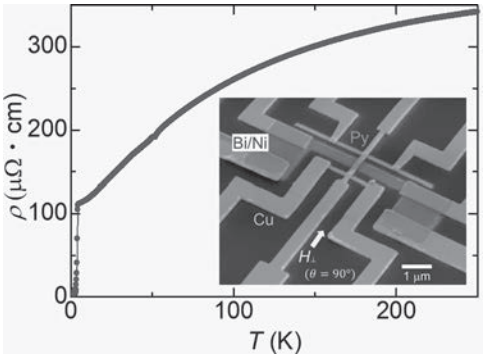


Fig. 1: Temperature dependence of the resistivity of the Bi/Ni wire. Inset: Scanning electron microscopy image of our spin transport device.

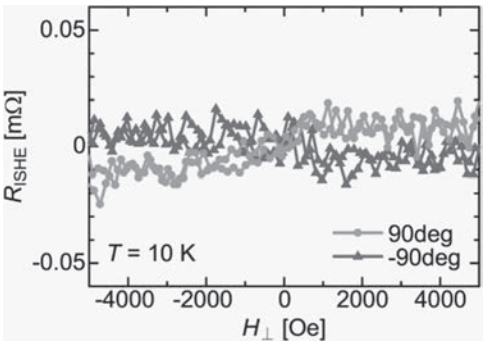


Fig. 2: Inverse spin Hall signals of Bi/Ni at 10 K.

10:42

AE-10. Electrical detection of diffusive spin current absorbed at Ag/Bi Rashba interface. *D. Ito*[1] and T. Kimura[1] *1. Physics, Kyushu university, Hukuoka, Japan*

Ag/Bi bilayer is well known as a representative interface for producing a strong Rashba spin-orbit interaction.[1] Owing to the strong spin-orbit coupling, an efficient spin-charge conversion, so-called inverse Rashba-Edelstein effect (IREE), is expected at the interface. Indeed, several groups have reported the observation of the IREE by mean of the spin pumping technique in the stacking multi-layered structures. However, such a spectroscopy measurement based on the ferromagnetic resonance gives rise to other undesired effects such as anisotropic magnetoresistance and anomalous Nernst effect, which make it difficult to analyze the IREE accurately. On the other hand, a nonlocal spin injection in a lateral spin valve structure enables us to provide an ideal platform for characterizing the diffusive spin current. Here, we develop a novel lateral structure for quantitative evaluation of IREE. Figure 1 shows the scanning electron microscope image of the fabricated device used for the present study. The nonlocally injected spin current from the CoFeAl strip is significantly absorbed in the Bi/Ag interface, resulting in the spin-charge conversion through IREE. The converted charge current can be detected as the electric voltage along the Bi/Ag wire. Although the spin diffusion in the Bi/Ag bilayer is strongly suppressed by the strong spin absorption, the highly spin-polarized CoFeAl electrode enables to induce the detectable spin current over several tens of nanometers. Figure 2 shows a representative electric signal measured at room temperature. A magnetic hysteresis loop consistent with IREE was clearly observed with the magnitude of 40 micro-Ohm. In the presentation, we will report the temperature dependence and the distance dependence of the IREE signal.

[1]C. R. Ast, J Henk, A Ernst, *et al.* : Phys. Rev. Lett. 98(2007)186807 [2]J. C. Rojas Sánchez, L. Vila, G. Desfonds, et al.: Nature Communications vol.4, Article number: 2944 (2013) [3]T. Kimura, Y. Otani : Phys. Rev. Lett.99, 196604 (2007) [4]S. Hu, H. Itoh, and T. Kimura. : NPG Asia Mater. 6, e127 (2014) [5]T. Kimura, J. Hamrle and Y. Otani : Phys. Rev. B 72, 014461 (2005). [6]T. Kimura, Y. Otani ad L. Vila : J. Appl. Phys. 103, 07F310 (2008).

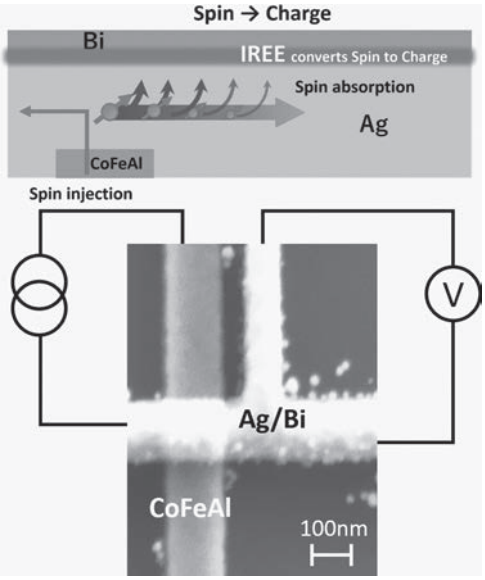


Fig.1: Conceptual image of electrical detection of IREE together with the SEM image of the fabricated device.

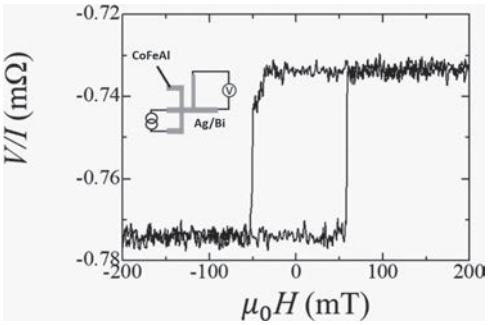


Fig.2 : Room temperature IREE signal in the Bi/Ag interface

10:54

AE-11. Tunable Spin-charge Conversion Across The Metal-insulator Transition in Vanadium Dioxide. *T.S. Safi*[1] and L. Liu[1] *1. EECS, Massachusetts Institute of Technology, Cambridge, MA, United States*

The charge-to-spin conversion efficiency is a crucial parameter in determining the performance of many useful spintronic materials. Usually, this conversion efficiency is an intrinsic material property, which cannot be easily modified without invoking chemical or structural changes in the underlying system. Here we demonstrate successful tuning of charge-spin conversion efficiency via the metal-insulator transition in a prototypical metal-insulator transition material. Vanadium dioxide (VO2), a quintessential strongly correlated electron compound, undergoes a temperature-driven structural phase transition near room temperature. This abrupt change in its electrical, optical, and thermal properties at transition has generated great interest from both technological and fundamental research perspectives; however, the spin related phenomenon remains largely unexplored. By employing ferromagnetic-resonance-driven spin pumping and the inverse spin Hall effect measurement, we find a swift, dramatic change in the spin pumping signal (decrease by >80%) and charge-spin conversion efficiency (increase by five times) upon transition. The large enhancement in the spin pumping signal across the metal-insulator transition provides the first evidence of variable spin-charge conversions of this material. The dramatic change in spin-charge conversion efficiency concomitant with the phase transition provides additional knobs to modulate the spin-charge conversion efficiency, leading to extra flexibilities in spintronic device design as well as providing new functionalities for spintronic devices, such as tunable spin-based memory and energy-harvesting devices.

11:06

AE-12. Spin transport in thermally-evaporated polyacene films and the derivative films induced by the spin-pumping. Y. Tanaka[1], T. Kono[1], M. Yamamoto[1], H. Tsujimoto[1], Y. Teki[2] and *E. Shikoh*[1] *1. Engineering, Osaka City University, Osaka, Japan; 2. Science, Osaka City University, Osaka, Japan*

Molecular materials are promising on the viewpoint of the spin transport because of their weak spin-orbit interaction. The spin transport in thermally-evaporated pentacene films at room temperature (RT) was achieved with the spin-pumping driven by the ferromagnetic resonance (FMR) [1, 2] although the spin transport mechanism was unclear. In this study, to clarify the mechanism, the spin transport in evaporated tetracene films and TIPS-pentacene films were tried by the spin-pumping. Since a tetracene molecule has less π-electrons per molecule than pentacene, the spin transport mechanism can be considered on a viewpoint of the π-electron number difference. A TIPS-pentacene, which is a pentacene-derivative molecule, was focused to investigate the spin transport mechanism from another viewpoint of the film crystallinity difference. Pd(10)/molecules (0 to 100)/$Ni_{80}Fe_{20}$(25 nm in thick) tri-layer samples were formed on SiO_2 substrates by using EB deposition or thermal evaporation. To avoid breaking the samples during $Ni_{80}Fe_{20}$ depositions, the substrate temperature was kept under 270 K. When the FMR of the $Ni_{80}Fe_{20}$ is excited with an ESR system, a pure spin current is injected from the $Ni_{80}Fe_{20}$ layer into the Pd layer via the molecular film. Then, the spin current is converted to a charge current due to the inverse spin-Hall effect (ISHE) in the Pd layer and detected as an electromotive force. For a control experiment, samples with a Cu layer instead of the Pd layer were formed since Cu has weaker spin-orbit interaction than Pd. The spin transport in a tetracene film has not been achieved yet because it was hard to form continuous tetracene films by thermal evaporation due to the high saturated vapor pressure. On TIPS-pentacene samples with a Pd layer, output voltages were observed under the FMR of the $Ni_{80}Fe_{20}$ and the voltage sign was inverted at the magnetization reversal of the $Ni_{80}Fe_{20}$. Meanwhile, no output voltages from the TIPS-samples with a Cu layer were observed under the FMR of the $Ni_{80}Fe_{20}$. These indicate that the output voltage observed from the TIPS-samples with a Pd is due to the ISHE. That is, the spin transport in evaporated TIPS-pentacene films by the spin-pumping was achieved at RT [3].

[1] Y. Tani, Y. Teki, E. Shikoh, *Appl. Phys. Lett.*, 107, 242406 (2015). [2] Y. Tani, T. Kondo, Y. Teki, E. Shikoh, *Appl. Phys. Lett.*, 110, 032403 (2017). [3] Y. Tanaka, T. Kono, Y. Teki, E. Shikoh, *IEEE Transaction on Magnetics*, 55, 1400304 (2019).

11:18

AE-13. Pure spin current manipulation in antiferromagnetically exchange coupled heterostructures. *L. Avilés Félix*[3], A. Butera[1], D. González Chávez[4], R. Sommer[4] and J.E. Gómez[2] *1. Centro Atómico Bariloche and Instituto Balseiro - Comisión Nacional de Energía Atómica (CNEA) & Consejo Nacional de Investigaciones Científicas y Técnicas (CONICET) Universidad Nacional de Cuyo (UNCUYO), San Carlos de Bariloche, Argentina; 2. Centro Atómico Bariloche - Comisión Nacional de Energía Atómica (CNEA) Consejo Nacional de Investigaciones Científicas y Técnicas (CONICET), San Carlos de Bariloche, Argentina; 3. Université Grenoble Alpes, CNRS, CEA, Grenoble INP, IRIG-SPINTEC, Grenoble, France; 4. Centro Brasileiro de Pesquisas Físicas, Rio de Janeiro, Brazil*

The adaptability of crystal antiferromagnets (AF) and synthetic antiferromagnets (SAF) in spintronic devices based on spin Hall effects has emerged during the last years. Recent works, both theoretical and experimental, highlight the role of AF not only as spin current injectors but also as angular momentum propagators in ferromagnetic/heavy metal layer (FM/ML) structures. The use of AF as spin current injectors into adjacent normal metals with strong spin orbit coupling (SOC) could lead to an enhancement of the spin Hall signal near the spin-flop transition in uniaxial antiferromagnets. In this work we report the use of a SAF (antiferromagnetically exchange coupled Co/Ru/Co) as a spin current injector and the observation of spin pumping and inverse spin Hall effect in [SAF]/Pt heterostructures [1,2]. By exploiting the interlayer exchange coupling strength (oscillatory RKKY-like coupling) and the spin-flop transition in the magnetization process of the SAF it is possible to rotate the magnetization of the Co layers at given angles away from the external magnetic field direction in resonance condition. The misalignment due to the spin-flop magnetization process combined with the spin pumping and the inverse spin Hall effect, allow to control and detect the polarization direction of the spin current pumped into the Pt. The control of the polarization direction of the spin current was also achieved by controlling the interlayer exchange coupling (IEC) via variations in the Ru spacer in the SAF-Pt system. By controlling the IEC strength and the spin flop transition in the magnetization process, it is also possible to produce spin currents polarized in different directions. Our results can lead to important advances in hybrid spintronic devices with improved functionalities, particularly the ability to control the polarization direction of spin currents and also the change of the sign of the ISHE signal induced in a metallic layer with the strong spin-orbit interaction.

[1] L. Avilés-Félix, A. Butera, and J. E. Gómez, Applied Physics Letters Vol. 110, p.052402 (2017). [2] L. Avilés-Félix, A. Butera, D. E. González-Chávez, R. L. Sommer and J. E. Gómez, Applied Physics Letters Vol. 123, p.123904 (2018)

Session AF
MAGNETIC CHARACTERIZATION I: BULK, SURFACES, AND INTERFACES

Chunhui Du, Chair
University of California, San Diego, La Jolla, CA, United States

CONTRIBUTED PAPERS

8:30

AF-01. Impact of Surface Laser Treatment on Magnetostriction and Magnetoelastic Properties of the GO FeSi Electrical Single Sheet.
E. Salloum[1], M. Nesser[1], O. Maloberti[4], S. Panier[1], P. Klimczyk[2] and J. Dupuy[3] *1. Laboratoire des Technologies Innovantes, Université de Picardie Jules Verne, Amiens, France; 2. Dr. Brockhaus Messstechnik GmbH and Co. KG, Lüdenscheid, Germany; 3. Multitel a.s.b.l, Mons, Belgium; 4. ESIEE, Amiens, France*

Grain-oriented elctrical steel is generally used in electrical machines like transformers. Laser surface treatment of such materials mainly used for iron losses reduction may also reduce noise and vibration due to magnetostrictive loads reduction. Surface laser treatment supplies additional stresses that changes the domain structure's configuration and modifies the magnetic and mechanical behavior. Laser treatment effect on magnetoelastic properties that characterize the magnetostrictive behavior is proposed. Experimentations are established in a single sheet tester (SST) where mechanical and magnetic macroscopic transient signals, as such the acceleration, the average induction and the applied magnetic field are synchronously measured. Mesoscopic magnetostrictive strain is identified with the measurements using a simple finite element mechanical approach. Next, magnetomechanical coupling between the magnetization process sensitive to laser treatment and the induced magnetostriction is considered for characterizing magnetoelastic properties. The latter are correlated with the static and dynamic mesocopic properties derived from the identification of the measured magnetic signals and the 1-D Maxwell diffusion model. We finally propose a parametric study that helps to understand the effect of different laser treatments on the magnetostrictive strain and the identified magnetoelastic properties. This strategy is the key for the reduction and eventually the optimization of noise and vibration in electrical machines next to iron losses reduction.

○ O. Maloberti, G. Meunier and A. Kedous Lebouc, IEEE T Magn, Vol. 44, p. 1-4 (2008) ○ S. Somkun, A. Moses and P. Anderson, IEEE T. Magn, Vol. 48, p. 711-714 (2012) ○ L. lahn, C. Wang, A. Allwardt, T. Belgrand and J. Blaszkowski, IEEE T Magn, Vol. 48, p. 1453-1456 (2012) ○ T. kajiwara and M. Enokizono, IEEE T. Magn, Vol. 50, p. 2002404 (2014) ○ P. Rasilo, D. Singh, A. Belahcen and A. Arkkio, IEEE T. Magn, Vol. 49, p. 2041-2044 (2013)

8:42

AF-02. Measurement of Demagnetization Factors and their Distribution in Assemblies of Magnetic Nanoparticles.
S.M. McCann[1] and *T. Mercer*[1,2] *1. Jeremiah Horrocks Institute for Mathematics, Physics & Astronomy, University of Central Lancashire, Preston, United Kingdom; 2. Department of Physics, University of liverpool, Liverpool, United Kingdom*

Continuiing interest in assemblies of magnetic nanoparticles is an important area of study, including superparamagnetic nanoparticles (SPNs) that offer potential biomedical applications such as drug delivery [1] and hyperthermia treatment [2]. Measuring the intrinsic magnetic properties of a sample requires determination of its dimensionless demagnetization factors, N_d, and thereby the *effective* applied field. Existing techniques are *unsutiable* for SPNs as they either require closure points of hysteresis loops or distinct anisotropy field, H_k, peaks found in transverse susceptibility, χ_t, curves of textured samples [3]; where a small AC field is applied transverse to a DC field, H_{DC}. Herein a new method is described for χ_t curves of randomly packed (untextured) SPN powders typically used; as shown in Fig. 1 for a magnetite sample of particle size ~ 10 nm packed in glass microslides of internal thickness, t, of 0.40 mm. Two χ_t curves as a function of H_{DC} are given for orientation (i) in-plane with the sample width, w, and (ii) out-of-plane (across t) for a w:t aspect ratio of 10:1. Widening of the peak across t in comparison to w is due to the increase by ΔN_d in this direction. From our development of established theory [4], we show that $\chi_t \propto 1/H_{DC}$ at saturation and hence the onset of approximately linear behaviour is expected at high field values beyond this point. This is indicated in Fig. 1 at around 500 and 550 kAm^{-1} across w and t respectively, resulting in a ΔN_d value of (0.21 ± 0.03). Confidence in the result was given by a computational model we developed based on interaction of poles at particle surfaces, yielding ΔN_d of (0.16 ± 0.02), (0.17 ± 0.02) and (0.19 ± 0.02) for the mean, median and mode respectively. A typical *number distribution* obtained from the model is shown in Fig. 2, where most particles have N_d values either below (across w) or above (across t) the factor of ⅓ expected for a uniform sphere. The resultant *spatial distribution* of N_d will also be given and discussed.

[1] M. Eizadi Sharifabad, et al., Nanomedicine (Lond.)., Vol. 11, p.2757 (2016). [2] S. Hatamie, B. Parseh and M.M. Ahadian, J Magn Magn Mater., Vol. 462, p.185 (2018). [3] P.R. Bissell, M. Vopsaroiu and R.D. Cookson, J Magn Magn Mater., Vol. 242, p.331 (2002). [4] A. Aharoni, E.H. Frei and S.Shtrikman, Bull, Res. Conc. of Israel., Vol. 6A, p.215 (1957).

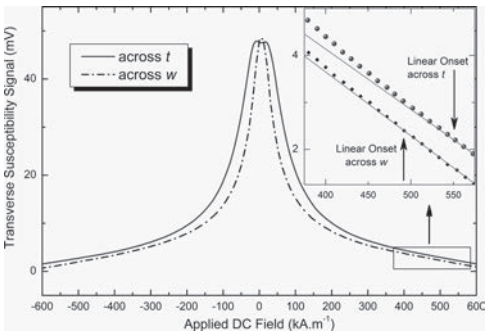


Fig. 1: Transverse susceptibility curves. The inset shows the linear onset used for SPN measurements.

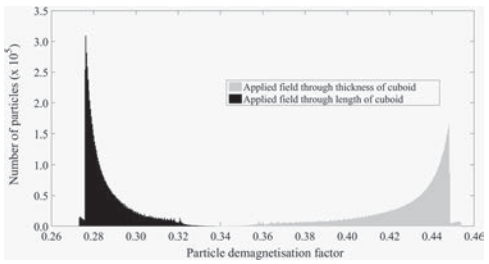


Fig 2: No. distribution across thickness and length of a cuboid sample. A uniform sphere would have N_d of ⅓ in each direction.

8:54

AF-03. A geometry-independent moment correction method for the MPMS3 SQUID-VSM magnetometer. *C. Amorim*[1], F. Mohseni[1], V. Amaral[1] and J.S. Amaral[1] *1. Physics and CICECO, Universidade de Aveiro, Aveiro, Portugal*

The sensitivity and automation capabilities of modern superconducting quantum interference device magnetometers are currently unmatched [1]. The measured moment values are, however, prone to deviations from their actual value due to geometric effects, namely sample size, shape, and radial offset [2,3]. A knowledgeable operator will correct measured moment values taking these effects into account. The current procedure for the MPMS3 magnetometer is based on an available simulation tool, valid for both VSM and DC methods [4]. Still, determining the correction factor requires samples with well-defined geometric shapes together with accurate sample dimensions and the usually difficult to determine radial offset [5]. There is no current solution to correct geometry effects of irregular shaped samples. Via an extensive use of the available Sample Geometry Simulator tool [4], in all available geometries, with sample dimensions and radial offset values limited only by the sample chamber volume, we find a systematic relation between the difference of VSM and DC measurements and the corresponding geometric correction factors of the MPMS3 SQUID-VSM device. This relation follows a clear trend, independent of sample size, shape or radial offset, for a given pair of DC scan length and VSM amplitude values. Exploiting this trend, a geometry-independent correction method is here presented and validated in worst-case scenario measurements of metallic Fe powder. In this data set, we observed a maximum deviation to the expected result of 32.5%, which was reduced to just 1.1%, by following the proposed correction method. While the presented methodology requires both DC and VSM data, its ease of use on irregular shaped samples and unknown radial offset values, can be of wide application by the magnetism/magnetometry community.

[1] M. Buchner, K. Höfler, B. Henne, V. Ney, A. Ney, J. Appl. Phys. Vol. 124, p. 161101 (2018) [2] P. Stamenov, and J. M. D. Coey, Rev. Sci. Instrum. Vol. 77, p. 015106 (2006) [3] Quantum Design MPMS Application Note 1500-015 (2010) [4] Quantum Design MPMS Application Note 1500-020 (2014) [5] G. Morrison, and H-C zur Loye, J. Solid State Chem. Vol. 221, p. 334 (2015)

9:06

AF-04. Broadband (kHz-GHz) visible light imaging of magnetic field with a combination of magnetic losses films and thermofluorescent coatings. H. Ragazzo[1], S. Faure[2], F. Issac[1], D. Prost[1], J. Carrey[2] and *J. Bobo*[3] *1. DEMR, ONERA, Toulouse, France; 2. INSA, LPCNO, Toulouse, France; 3. CEMES, CNRS, Toulouse, France*

Characterization of the electromagnetic field emitted by various sources (antenna, radar, coils...) is an important issue, either for civil or defense applications. The measurement of the electromagnetic field may be performed by a local probe, but infrared thermography imaging is a competitive alternative way. The latter method, called EMIR [1] (ElectroMagnetic InfraRed) has been used for years in particular at ONERA where it had been developed. We have subsequently improved EMIR method in order to probe microwave magnetic fields by using high permeability films composed of ferromagnetic microparticles in an insulating matrix or patterned ferromagnetic films [3]. More recently, we have successfully implemented this technique in the domain of visible light, named as EMVI [3] (Electro Magnetic Visible Light Imaging). As in the EMIR method, a thin film (sensitive to either electric field or magnetic field) is heated by the emitted field. This sensing film is coated with a polymer doped with fluorescent molecules (rhodamine B in our case). As the fluorescent emission of rhodamine depends on the temperature of the film, we get a thermofluorescent sensor. We will review several applications of EMVI method applied to various systems including induction flatcoils (operating in the 100-300 kHz range), metamaterial patch antenna [4,5] and HIS (High Impedance Surface) used in space applications (devices operating in the 1-5 GHz range). With the latest optimized version of our EMVI setup, using an array of green LEDs (40 W total light power, wavelength 535 nm) and a SCMOS camera, we could detect temperature changes down to 20 mK, magnetic field sensitivity lower than 1 A/m and a spatial resolution related to our camera and optics (typically 10 to 100 micrometers). We will also review the perspectives of development of EMVI for microscopy applications.

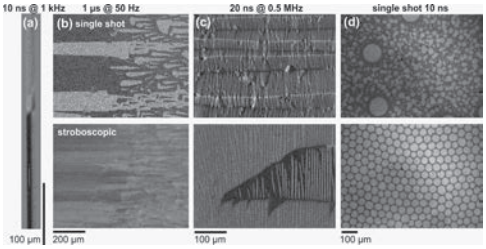
[1] P. Levesque, L. Leylekian, French Patent n°9816079 (1998) [2] J. Vernieres, J.F. Bobo, D. Prost, F. Issac, F. Boust, J. of Appl. Phys. 109, 07A323 (2011) [3] S. Faure, J.F. Bobo, J. Carrey, F. Issac and D. Prost, French Patent, n° 1758907 (2017) [4] H. Ragazzo, D.Prost, JF. Bobo, S. Faure, J. Carrey, F. Issac, IEEE Trans. Mag. 55 (2019) [5] S. Faure, J.F. Bobo, D. Prost, F. Issac and J. Carrey, Phys. Rev. Appl. 11, 054084 (2019)

9:18

AF-05. Dynamic magneto-optical imaging of magnetic materials – bridging the gap from microseconds to nanoseconds. M.J. Klug[1] and *J. McCord*[1] *1. Institute for Materials Science, Kiel University, Kiel, Germany*

Magnetic domain imaging provides direct access to the effective magnetic properties of materials from the macroscale down to the nanoscale. The analysis of the magnetic domain behavior by quasi-static magnetic domain imaging [1] has become an essential part for the characterization of magnetic materials. Using pulsed LED illumination sources, magnetic imaging with millisecond time resolution is possible. The stroboscopic wide-field imaging of magnetization dynamics with picosecond and faster time resolutions is achievable [2,3]. Yet, single shot magnetic imaging in the range from microseconds to nanoseconds, or in the MHz regime is nearly unexplored. Here, we introduce an imaging setup allowing for the imaging of magnetization responses with a highly flexible adjustable time resolution. Using a high-power solid-state laser with variable exposure, stroboscopic and especially single shot imaging with laser pulses down to 10 nanoseconds is demonstrated. Examples, displaying the feasibility of the various magnetic imaging modes, are the imaging of current induced domain wall propagation in magnetic nanowires (Fig. 1a) and domain repeatability in the magnetic reversal in electrical steel samples (Fig. 1b). Results of single shot and stroboscopic imaging with down to one microsecond time-resolution are directly compared. Imaging of electrically induced magnetization reversal in magnetoelectric composite samples at 0.5 MHz with 20 nanoseconds exposure reveals modulated magnetization reversal modes due to magneto-elastic self-energy effects (Fig. 1c and 1d). Single shot imaging of nucleation modes of magnetic bubbles with 10 nanoseconds time resolution display different stages of bubble generation (Fig. 1e). Other examples of the relevance of dynamic magnetic domain imaging in the MHz regime will be shown. Magnetic domain observations of magnetization dynamics dominated by domain wall nucleation and movement dominated processes, also on a single shot level, are now accessible directly from DC to the nanosecond regime with continuously variable illumination exposure. This work was supported through the Collaborative Research Centre CRC 1261 Magnetoelectric Sensors: From Composite Materials to Biomagnetic Diagnostic.

[1] J. McCord, Journal of Physics D: Applied Physics 48, 333001 (2015) [2] R.B. Holländer, C. Müller, M. Lohmann, B. Mozooni, J. McCord, Journal of Magnetism and Magnetic Materials 432, 283–290 (2017) [3] B. Mozooni, T. von Hofe, J. McCord, Physical Review B 90, 054410 (2014)

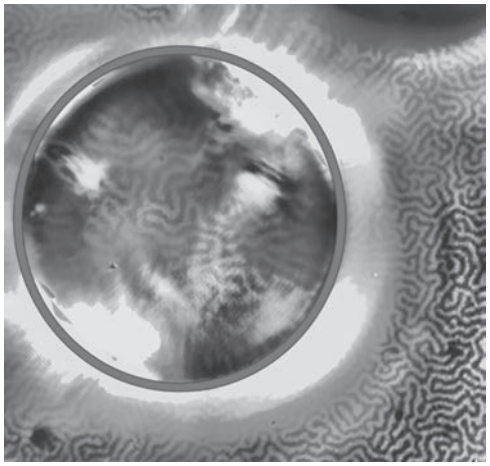


9:30

AF-06. Microsphere-assisted super-resolution magneto-optic imaging.
M. Vogel[1], A. Hendriks[2,1], J. Pearson[1], A. Hoffmann[1] and S.G. te Velthuis[1]
1. Materials Science Division, Argonne National Laboratory, Lemont, IL, United States; 2. Department of Applied Physics, Eindhoven University of Technology, Eindhoven, Netherlands

The diffraction limit [1] is a fundamental barrier in optical imaging, restricting the resolution for optical microscopy. The diffraction limit can be surpassed by the photonic nanojet phenomenon, generated by a lens-like dielectric micro-object [2]. Microspheres have been demonstrated as a powerful platform to challenge the diffraction limit by creating a virtual image with enhanced resolution and magnification [3,4]. Here we report on wide-field MOKE (Magneto-Optical Kerr effect) measurements harnessing the resolution enhancement of microspheres in an oil-immersion environment with white light illumination. In-plane and perpendicular magnetized domain configurations are imaged with and without the additional optical element. An increase of the spatial resolution is demonstrated for longitudinal and polar Kerr configuration. Our findings may serve as a way to optically study magnetization dynamics at smaller length scales. *Work at Argonne was supported by the US-DOE, Office of Science, MSED. Use of the Center for Nanoscale Materials was supported by the US-DOE, Office of Science, BES, under contract no. DE-AC02-06CH11357.*

[1] Lord Rayleigh,*Philosophical Magazine Series 5*, 8(49):261– 274 (1879) [2] Z. Chen, A. Taflove & V. Backman *Optics Express*, *12*(7), 1214 (2004) [3] Z. Wang, W. Guo, L. Li et al., *Nature Communications*, *2*(1), 218 (2008) [4] G. Huszka & M. A. M. Gijs, (2018) *Scientific Reports*, *8*(1), 601 (2018)



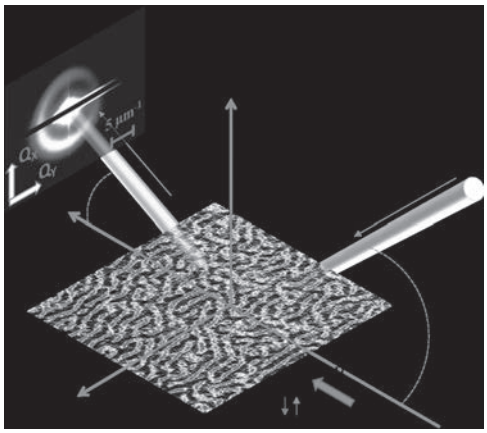
Polar magneto-optic Kerr image of domains in ferrimagnetic multilayers: Ta (4 nm)/Pt (5 nm)/[Co (0.5 nm)/Gd (1 nm)/Pt (1 m)]$_{10}$/Al (2 nm). The picture is stitched together from 2 images taken, focused on the sample surface and focused on the virtual image created by the microsphere (marked by the red ring).

9:42

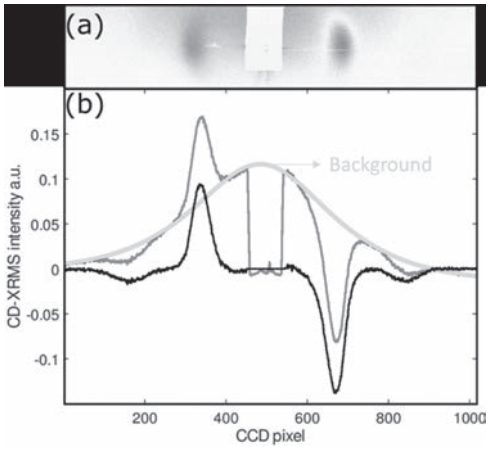
AF-07. Field dependence chirality in ferromagnetic multilayers probed by dichroism in x-ray resonant magnetic scattering.
E.O. Burgos Parra[1,2], J. Chauleau[1,2], W. Legrand[1], N. Reyren[1], F. Ajejas[1], D. Maccariello[1], S. Collin[1], H. Popescu[2], K. Bouzehouane[1], V. Cros[1], A. Fert[1] and N. Jaouen[2] *1. Unité mixte de physique CNRS/Thales, CNRS, Paris, France; 2. Synchrotron SOLEIL, Saint-Aubin, France*

Chiral magnetic structures induced by Dzyaloshinskii-Moriya interaction (DMI) [1] have been proposed as the cornerstone of new technology applications such as high-density data storage devices or neuromorphic computing [2], due their room temperature stability and efficient current induced motion. Recent studies of the amplitude of magnetic satellites of a crystal Bragg peak by Zhang *et al*. [3] showed that x-ray resonant magnetic scattering (XRMS) is a powerful tool to access to the relevant topological parameters of these magnetic structures. In this work, we use small angle reflectivity XRMS to reveal directly the chiral properties of FM multilayers with tailored magnetic chiralities driven by spin-orbit-related effects at interfaces [4,5]. We show that it can straightforwardly and unambiguously determine the main characteristics of chiral magnetic distributions in perpendicularly magnetized multilayers [4]: its chiral nature, the quantitative winding sense (clockwise or counterclockwise), and its type, *i.e.* Néel or Bloch. Moreover we prove that this approach combined with micromagnetic simulations reveals hybrid chiral spin texture in multilayers [5]. Finally, we studied the in plane field dependence intensity of the dichroism and the appearance of second order diffraction peaks, usually forbidden on these systems. An asymmetric change of the intensity of the magnetic asymmetry lobes and a hysteretic behavior of these ones with the external field suggest a complex interplay between the hybrid domain wall state existing in these systems and DMI fields. Projects ANR-15-GRFL-0005, ANR-17-CE24-0025, MIPR#HR0011831554 and H2020 F FET Proactive 824123 are acknowledged for their financial support.

[1] I. Dzyaloshinskii, J. of Phys. and Chem. of Solids 4, 241 (1958), T. Moriya, Phys. Rev. 120, 91 (1960) [2] A. Fert, N. Reyren and V. Cros, Nat. Rev. Mat. 2, 17031 (2017) [3] S. L. Zhang, G. van der Laan, and T. Hesjedal, Nat. Commun. 8, 14619 (2017) [4] J.-Y. Chauleau *et al.*, Phys. Rev. Lett. 120, 037202 (2018) [5] W. Legrand *et al.*, Sci. Adv. 4, eaat45 (2018)



Schematic of the experimental setup. Magnetic domains shown in the image corespond an a MFM image of the studied sample. The specular reflection of circular polarised x-rays is captured by a CCD camera.



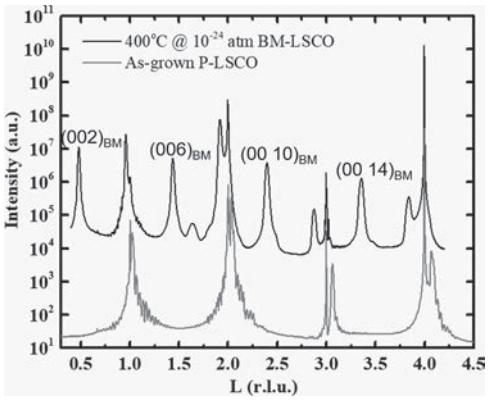
a) Circular dichroism (CD) of XRMS for a fixed in plane external field. (b) Each column of the CD camera is averaged and plotted (pink). A background subtraction (green) is performed to obtain a clean CD-XMRS image (black) to calculate the first and second order peak value of the dichroism for each external field.

9:54

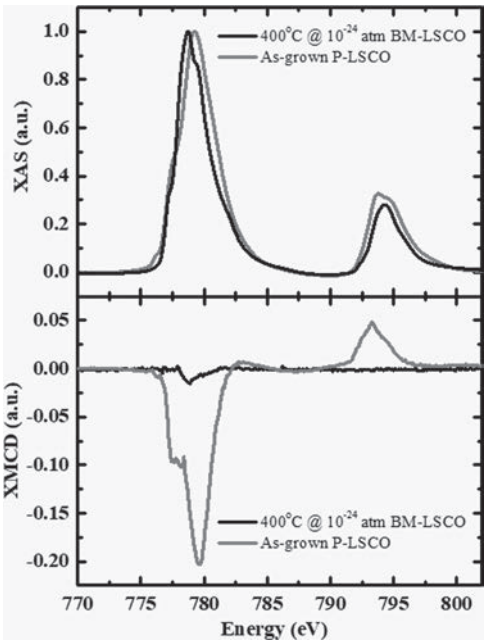
AF-08. Topotactic Transformations in Cobaltite Thin Films.
I. Chiu[1], Z. Zhang[2], M. Lee[3,6], P. Shafer[4], A. Mehta[5], S. Ramanathan[2], I.K. Schuller[3,6] and Y. Takamura[1] *1. University of California, Davis, Davis, CA, United States; 2. Purdue University, West Lafayette, IL, United States; 3. Materials Science and Engineering Program, University of California San Diego, La Jolla, CA, United States; 4. Lawrence Berkeley National Laboratory, Berkeley, CA, United States; 5. SLAC National Accelerator Laboratory, Menlo Park, CA, United States; 6. Department of Physics and Center for Advanced Nanoscience, University of California San Diego, La Jolla, CA, United States*

For transition metal oxides (TMOs), a change in oxygen stoichiometry can drastically modify their physical characteristics, such as electronic and ionic conductivity, ferroelectricity and magnetism. Varying the oxygen content in TMOs results in a transformation between structures such as perovskites (P) ABO_3, brownmillerites (BM) $ABO_{2.5}$, and square planar ABO_2 structures [1]. In this work, we study the evolution of physical properties by modifying the oxygen stoichiometry of $La_{0.7}Sr_{0.3}CoO_3$ (LSCO) thin films by exposing them to highly reducing environments. Under optimized annealing conditions (temperature > 400 ºC and oxygen partial pressure < 10^{-12} atm), the equilibrium P-LSCO phase undergoes a drastic topotactic transformation into the highly metastable oxygen-deficient BM-LSCO phase. The x-ray diffraction spectra indicate that a complete transformation of the entire film volume to the BM-LSCO phase has occurred with a 5.27% change in the out-of-plane lattice parameter compared to the parent P-LSCO phase. Despite this enormous lattice distortion, the BM-LSCO phase remains fully coherent with the underlying $(LaAlO_3)_{0.3}(Sr_2TaAlO_6)_{0.7}$ substrate. Resistivity and soft x-ray magnetic spectroscopy measurements demonstrate that the BM-LSCO phase is an antiferromagnetic insulator with Néel temperature above 300 K, in contrast to the P-LSCO phase which is a ferromagnetic metal below its Curie temperature ~ 220 K. These distinct changes in functional properties suggest that topotactic transformations are a promising route towards next generation memory and neuromorphic devices based on electric-field-driven movement of oxygen anions. The work was supported as part of the Quantum Materials for Energy Efficient Neuromorphic Computing, an Energy Frontier Research Center funded by the U.S. Department of Energy, Office of Science. This research used resources of the Advanced Light Source, which is a DOE Office of Science User Facility under Contract No. DE-AC02-05CH1123.

[1] T. G. Parsons, H. D'Hondt and M. A. Hayward, *Chem. Mater.*, 21, p. 5527 (2009)



The BM-LSCO film peaks shift to a lower two-theta values compared to those of the P-LSCO and the half-order peaks are observable due to quadrupling the unit cell parameter.



The ferromagnetic behaviors of P-LSCO were highly supressed after the annealing.

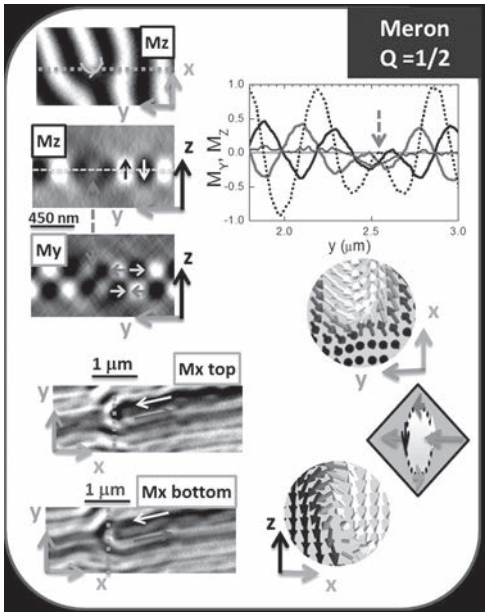
10:06

AF-09. Magnetic singularities in 3D by x-ray magnetic tomography.
A. Hierro-Rodriguez[1], *J. Martín*[2,3], C. Quiros[2,3], A. Sorrentino[4], L. Alvarez-Prado[2,3], J. Alameda[2,3], S. McVitie[1], E. Pereiro[4], M. Velez[2,3] and S. Ferrer[4] *1. SUPA, School of Physics and Astronomy, University of Glasgow, Glasgow, United Kingdom; 2. Física, Universidad de Oviedo, Oviedo, Spain; 3. CINN (CSIC-Universidad de Oviedo), El Entrego, Spain; 4. Alba Synchrotron, Cerdanyola del Valles, Spain*

Magnetic singularities such as vortices, antivortices, Bloch points and merons drive magnetization reversal in magnetic nanostructures and in perpendicular magnetic anisotropy thin films and multilayers [1,2]. For film thickness above a few nm, magnetostatic and surface effects create 3D magnetic patterns that are not easy to resolve with standard microscopy techniques. We have recently developed 3D magnetic reconstruction tomography [3] with a combination of soft X-ray transmission microscopy and magnetic dichroism. This method allows us to reconstruct the magnetization vector at ~ 25 nm lateral resolution and to localize magnetic singularities in thin films (thickness up to ~300 nm). In this work, we present the

tomographic reconstruction of the 3D magnetization configuration in a 240 nm thick NiFe/NdCo/NiFe multilayer as shown in the figure. We observe a periodic Mx-Mz domain pattern that coexist with a My-Mz closure structure across the multilayer thickness. We also identify different magnetic singularities (merons and Bloch points) at stripe bifurcations and characterize their topological configuration from the reconstructed vector magnetization maps. Work supported by Spanish MINECO (FIS2016-76058 (AEI/FEDER,EU))) and European Union's Horizon 2020 research and innovation program under Marie Sklodowska-Curie grant ref. H2020-MSCA-IF-2016-746958.

[1] C. Blanco-Roldán *et al.*, Nanoscale imaging of buried topological defects with quantitative X-ray magnetic microscopy. *Nat. Comm.* 6, 8196 (2015). [3] A. Hierro-Rodriguez *et al.*, Deterministic propagation of vortex-antivortex pairs in magnetic trilayers. *Appl. Phys. Lett.* 110, 262402 (2017). [2] A. Hierro-Rodriguez *et al.*, 3D reconstruction of magnetization from dichroic soft X-ray transmission tomography. *J. Synchrotron Rad.* 25, 1144 (2018).



Tomographic reconstruction of 3D magnetic configuration around a meron singularity located at the core of a bifurcation within the stripe pattern. Different cross sections are displayed to illustrate the spatial dependence of Mx, My, Mz magnetization components. 3D vectorial reconstrution shows a meron singularity with skyrmionic charge Q =1/2, that can be viewed either as a Mx-Mz vortex with My polarity in the vertical y-z plane or a half Mx-My vortex with Mz polarity change in the horizontal x-y plane.

10:18

AF-10. Determination of fine magnetic structure of magnetic multilayer with quasi antiferromagnetic layer by using polarized neutron reflectivity analysis. *Y. Zhong*[1], Y. Kurokawa[1], G. Nagashima[1], S. Horiike[1], T. Hanashima[2], D. Schönke[3], P. Krautscheid[3], R.M. Reeve[3], M. Kläui[3] and H. Yuasa[1] *1. Kyushu University, Fukuoka, Japan; 2. Neutron Science and Technology Center, CROSS, Naka, Japan; 3. Institute of Physics, Johannes Gutenberg-University Mainz, Mainz, Germany*

Recently antiferromagnetic (AFM) spintronics are drawing attention owing to the high resonance frequencies and zero stray fields [1,2]. In particular spin torque oscillation (STO) in AFM is attractive from the viewpoint high frequency generation. However, it is hard to directly observe STO. Therefore, we fabricated the novel quasi-AFM layer which has multiple domains with alternatively anti-parallel magnetization by using biquadratic magnetic coupling between two FM layers through an Fe-O layer [3-7]. The magnetic property of the quasi-AFM layer is expected to have properties that are intermediate between AFM and FM, which is useful to understand AFM dynamics. Since the fine magnetic structure of quasi-AFM is important to control STO frequency, we carried out polarized neutron reflectivity (PNR) analysis by BL17 SHARAKU in MLF, J-PARC. The Ta/Ru/IrMn/CoFe(A)/Fe-O/CoFe(B)/Cu/CoFe(C)/Cu/Ta films were sputtered on thermal oxidized Si wafers and annealed in a field to fix the magnetization of CoFe(A) in x direction by IrMn. If magnetizations of CoFe(A) and CoFe(B) are coupled with angles of about ±90 deg through Fe-O, the CoFe(B) would become the quasi-AFM, and it was roughly confirmed by M-H curves in Fig.1(a). Next, CoFe(B) magnetization was directly observed by SEM with polarization analyzer (SEMPA) in Fig.1(b). In low field, we expected the CoFe(B) to be quasi-AFM and in that case the x component of magnetization should be zero. However, scanning electron microscopy with polarization analysis images indicated that the CoFe(B) does not have perfect 90 deg magnetization with respect to CoFe (A) but various magnetic directions were observed in CoFe (B). The more accurate magnetizations were estimated by PNR analysis shown in Fig.1(c), indicating the CoFe(B) has magnetization of $1.35m_B$ in x direction. The average angle between the magnetization of CoFe(A) and CoFe(B) was estimated as ±42 degrees from $\cos^{-1}(1.35m_B / 1.82m_B)$. Such a microscopic magnetic configuration cannot be obtained unless we use SEMPA and PNR analysis, and provide an important insight to control magnetic structure of quasi-AFM.

[1] A. H. MacDonald et al., Phil. Trans., R. Soc. A 369, 3098 (2011). [2] R. Duine et al. Nature Mater. 10, 344 (2011). [3] T. Jungwirth et al., Nature Nanotechnology., 11, 231 (2016). [4] J. C. Slonczewski, Phys. Rev. Lett. 67, 3172 (1991) [5] H. Fukuzawa, et al., J. Appl. Phys. 91, 6684 (2002). [6] C. H. Lai et al., J. Appl. Phys. 93, 8412 (2003). [7] S. Maat and B. Gurney, J. Appl. Phys. 93, 7229(2003).

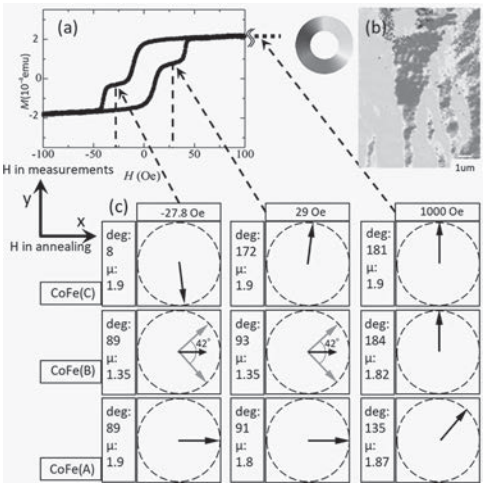


Fig.1 (a) M-H curve, (b) SEMPA images, (c) schematic magnetization images in field of -27.8 Oe, 29 Oe and 1000 Oe.

10:30

AF-11. Soft X-ray Induced Changes at the Exchange Biased NiO/Fe_3O_4 Interface. *P. Steadman*[1], J. Wollschlager[2], R. Fan[1], T. Pohlmann[2], K. Kuepper[2], P. Bencok[1] and M. Sussmuth[1] *1. Diamond Light Source, Didcot, United Kingdom; 2. University of Osnabrueck, Osnabrueck, Germany*

Magnetite (Fe_3O_4) is predicted to be half-metallic making it an ideal candidate for many spintronics applications. As one of the magnetic layers in a tunnel junction a half metallic will give a huge magnetoresistance and therefore a very sensitive device. Soft X-ray reflectivity has been used to study the magnetic depth profile in the exchange biased system Ni0/Fe_3O_4.[1,2] By tuning the X-ray energy to the L_3 absorption edge the scattered X-ray intensity is sensitive to the Fe magnetic moment.[3] The current study found that the incident beam causes irreversible changes to the Fe_3O_4 film

(see Fig. 1). By performing spectroscopy across the L_3 edge growth of the Fe^{2+} peak occurred with a decay of the Fe^{3+} peak indicative of reduction of the film (see Fig. 2). Rather surprisingly, these changes occur only in the Fe_3O_4 film near the interface whilst the majority of the film, including the surface, remains intact. This could be the result of strain or other structural differences near the interface that cause the Fe_3O_4 to be insulating even though the rest of the film is conducting. Strong production of secondary electrons could cause damage confined to the interface. The damage was strongest at the Fe *L* and O *K* resonances. No changes were detected in the NiO film. It is important to note that this damage could be minimised to an acceptable level by reducing the beam intensity.

[1] C. R. Hu, J. Zhu, G. Chen, J. X. Li, Y. Z. Wu Physics Letters A Vol. 376 p 3317 (2012) [2] P. Li, W. Y. Cui, H. L. Bai Solid State Communications Vol. 220 p 1 (2015) [3] J. P. Hannon, G. T. Trammell, M. Blume and D. Gibbs Phys. Rev. Lett.Vol. 61 p 1245 (1988)

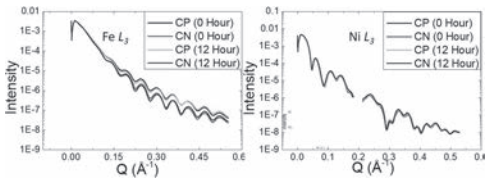


Fig. 1. Soft X-ray reflectivity results from the NiO/Fe_3O_4 bilayer. On the left the reflectivity is shown measured at the Fe L_3 edge (sensitive to Fe moments) and on the right reflectivity at the Ni L_3 edge (sensitive to Ni moments). CP and CN refer to opposite helicities of circular polarisation. The first and last measurements taken over twelve hours are shown for both reflectivities.

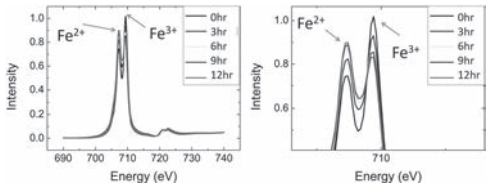


Fig. 2. The energy dependence of the reflectivity over a period of several hours. The right hand plot is a close up view of the top of the L_3 resonance. The Fe L_3 resonance shows two clearly resolved peaks which are separately due to Fe^{2+} and Fe^{3+} ions. The times for a sequence of measurements taken over twelve hours are shown. It is clear that the Fe^{2+} peak is increasing whilst the Fe^{3+} peak is decreasing.

10:42

AF-12. Exploring magnetic materials at beamline P09 at PETRA III.
J. Mardegan[1], S. Francoual[1], J. Sears[1] and P. Bereciartua-Perez[1] *1. Petra III, DESY, Hamburg, Germany*

P09 at PETRA III facility is a dedicated beamline to perform mainly resonant X-ray scattering and diffraction with several sample environment, such as cryostats, electromagnets and magnets enabling to investigate strongly correlated and magnetic materials. Using an in vacuum double phase retarder system, P09 is a unique beamline able to perform full polarization analysis between 2.7 and 15 keV [1,2]. This covered energy-range allows the scientific community to explore a wide range of materials, such as the 3-5d transition metals, besides the lanthanide and actinide series. In order to expand the investigated scientific cases, further developments have taken place allowing the users to perform: (a) magnetic scattering in the tender X-ray range; (b) magnetic scattering at high pressure and low temperatures (pressure of tens of GPa and temperature below 50 K); (c) magnetic circular dichroism [3]; magnetic reflectivity [4] and (d) full magnetic structure determination [5]. Hereby I will present the new experimental set-ups available at beamline P09 along with some of the recent scientific results obtained mainly with magnetic circular dichroism and magnetic reflectivity techniques, in which powder, single crystals and thin films have been investigated.

[1] Strempfer, J., Francoual, S., Reuther, D.; *et al. Resonant scattering and diffraction beamline P09 at PETRA III;* J. Synchrotron Rad.; vol. 20, pp. 541–549 (2013) [2] Francoual, S., Strempfer, J., Warren, J. ; *et al. Single-crystal X-ray diffraction and resonant X-ray magnetic scattering at helium-3 temperatures in high magnetic fields at beamline P09 at PETRA III,* J. Synchrotron Rad. 22(5), 1207 - 1214 (2015) [3] Mardegan J. R. L., Francoual S., Fabbris G.; *et al.*; *Magnetic properties of GdT_2Zn_{20} (T=Fe, Co) investigated by x-ray diffraction and spectroscopy;* Phys. Rev. B 93, 024421 (2016) [4] Kuschel T., Klewe C., Schmalhorst J.-M., *et al.*, *Static Magnetic Proximity Effect in Pt/NiFe2O4 and Pt/Fe Bilayers Investigated by X-Ray Resonant Magnetic Reflectivity;*Phys. Rev. Lett. 115, 097401 (2015). [5] Mardegan J. R. L, Bereciartua, P.; Francoual S., *et al.*, *Low temperature magnetic structure of $EuPtIn_4$*, to be submitted

10:54

AF-13. Imaging uncompensated moments and exchange-biased emergent ferromagnetism in FeRh thin films.
I. Gray[5], G. Stiehl[1], J. Heron[2], A. Mei[3], D. Schlom[3], R. Ramesh[4], D. Ralph[1] and G. Fuchs[5]
1. Department of Physics, Cornell University, Ithaca, NY, United States; 2. Department of Materials Science and Engineering, University of Michigan, Ann Arbor, Ann Arbor, MI, United States; 3. Department of Materials Science and Engineering, Cornell University, Ithaca, NY, United States; 4. Department of Materials Science and Engineering, University of California, Berkeley, Berkeley, CA, United States; 5. School of Applied and Engineering Physics, Cornell University, Ithaca, NY, United States

In an ideal Néel antiferromagnet (AF), each lattice-site spin is adjacent to an oppositely-pointing spin such that all spins are compensated [1]. In real AFs some spins are uncompensated [2], resulting in local magnetic moments within the AF. These uncompensated moments (UMs) are responsible for exchange bias [3], the most important current application of antiferromagnets. UMs are difficult to detect directly because any signal they produce is typically overwhelmed by the ferromagnetic (FM) layer in exchange-biased AF/FM bilayers. In this work [4] we use magneto-thermal microscopy [5,6] to image the uncompensated moments in FeRh, a room-temperature AF which undergoes a 1st-order phase transition from AF to FM at T_C near 100 °C [7]. In the AF phase below in Fig. 1, we image MgO(001)/20 nm FeRh/10 nm Pt as a function of magnetic field H_{app}. By taking the average and half-difference between positive and negative fields, we resolve both *pinned* UMs [8], which are strongly coupled to the AF bulk and are unaffected by applied magnetic field, and *unpinned* UMs, which are weakly coupled and can be reoriented by a 1 kOe applied field. In Fig. 2 we image as a function of temperature and magnetic field near T_C, where FM domains first nucleate and then percolate through the sample. Within the transition region, we observe some FM domains nucleating with an orientation that is not parallel to H_{app}, even when H_{app} is much greater than the coercivity field of the FM moments. This indicates that the emergent FM domains are exchange-coupled to the AF bulk. Our results provide new insight into the role of UMs in the magnetic phase transition in FeRh and suggest a general method for spatially resolving UMs in AF metals with magneto-thermal microscopy.

[1] L. Néel, Science 174, 985 (1971). [2] Y. Imry and S.-K. Ma, *Phys. Rev. Lett.* 35, 1399-1401 (1975). [3] J. Nogués and I. K. Schuller, *Journal of Magnetism and Magnetic Materials* 192, 203-232 (1999). [4] I. Gray et al, arXiv 1906.07243 (2019). [5] J. M. Bartell et al, *Nature Communications* 6, 8460 (2015). [6] J. M. Bartell et al, *Phys. Rev. Appl.* 7, 044004 (2017). [7] J. B. McKinnon, D. Melville, and E. W. Lee, *Journal of Physics C: Solid State Physics* 3, S46 (1970). [8] U. Nowak et al, *Phys. Rev. B* 66, 014430 (2002).

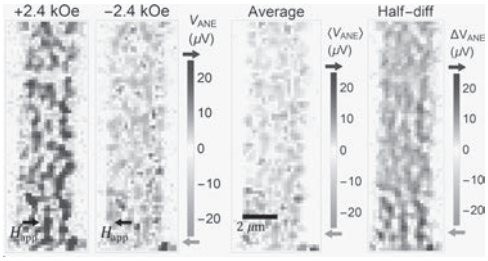


Fig. 1. Magneto-thermal imaging of FeRh at 25 °C in the AF phase as a function of magnetic field. The average between images at +2.4 kOe and -2.4 kOe shows *pinned* UMs, while the half-difference shows *unpinned* UMs.

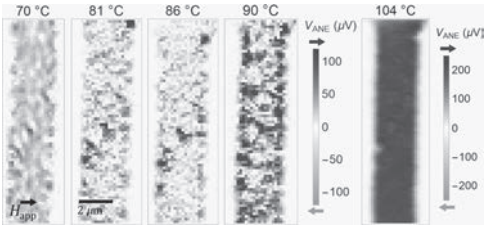
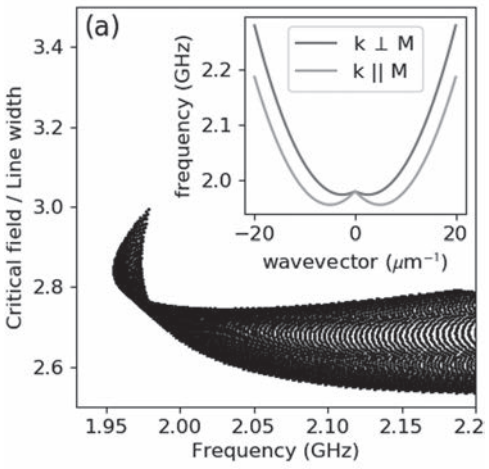


Fig. 2. Imaging as a function of temperature near T_C. Some FM moments nucleate antiparallel to the nominally saturating applied magnetic field, indicating that they are exchange-biased by the AF bulk.

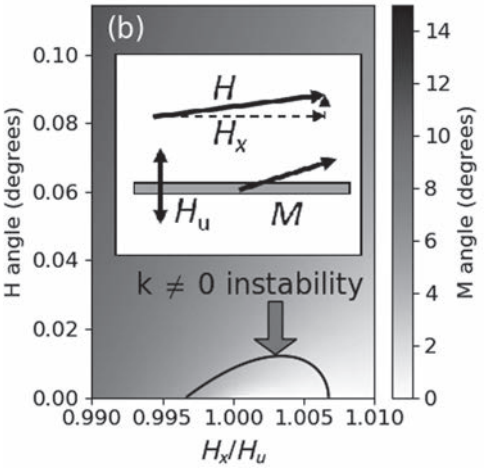
11:06

AF-14. Options for Exchange Stiffness Measurement in Thin Films.
R.D. McMichael[1] *1. Physical Measurement Laboratory, National Institute of Standards and Technology, Gaithersburg, MD, United States*

Exchange stiffness is difficult to measure accurately, and it is also an essential parameter for predicting device behavior. The need for exchange stiffness data, especially for ultrathin films, has grown with materials development for a variety of novel magnetic device applications. Here, we compare ideas for exchange stiffness measurement with emphasis on methods that avoid patterning. Without a lithographic length scale, the film thickness is used to gauge the exchange length, essentially by comparing thickness-dependent magnetostatic fields with wavevector-dependent exchange fields. The competition between these terms leads to features in the spin wave dispersion relation and in low frequency behavior. Results include models of parallel-pumped spin wave excitation and of low-frequency instabilities, both in films with perpendicular magnetic anisotropy and thickness less than 5 nm. Parallel pumping provides a probe of the spin wave dispersion relation, which includes a minimum spin wave frequency at $k \neq 0$, a saddle point, and a local maximum at $k = 0$. The calculated pumping instability threshold reveals the exchange-dependent minimum frequency, but is otherwise relatively featureless, so additional data would be needed to determine the exchange stiffness. The static magnetization configuration also has an exchange-dependent instability. With applied field in plane, there is an instability to finite k fluctuations at $H_{crit} \approx H_u + M_s\, t^2 / (4\, l_{ex})^2$ where H_u is the in-plane saturation field, M_s is the magnetization, t is the thickness and l_{ex} is the exchange length. Due to the sensitivity near the critical field, this instability exists only for applied fields that are very precisely aligned with the anisotropy hard axis, within 0.01° in our example ($\mu_0 M_s$ = 0.5 T, H_u = 0.05 T, t = 2 nm, l_{ex} = 5.8 nm).



(a) Critical pumping fields for parallel-pumped excitation of spin waves. Below the frequency minimum, the critical field diverges. Inset: spin wave dispersion for *k* parallel to and perpendicular to the in-plane magnetization.



(b) Stability analysis of a film with perpendicular magnetic anisotropy. The color scale indicates the equilibrium magnetization angle. Within the outlined region, k ≠ 0 ripple becomes unstable.

11:18

AF-15. Withdrawn

Session AG
DZYALOSHINSKII-MORIYA INTERACTION AND INTERFACIAL PHENOMENA

Simone Finizio, Chair
Paul Scherrer Institut, Villigen PSI, Switzerland

INVITED PAPER

8:30

AG-01. Controlling the Dzyaloshinskii-Moriya Interaction through interface modifications. *H. Nembach[1,2] 1. Quantum Electromagnetics, National Institute of Standards and Technology, Boulder, CO, United States; 2. JILA, University of Colorado, Boulder, CO, United States*

The Dzyaloshinskii-Moriya Interaction (DMI) gives rise to chiral magnetic structures, which include chiral spin-chains and skyrmions. The latter have recently received much attention, especially for their potential application for magnetic data storage. Each skyrmion would represent a bit and would be moved along a racetrack. DMI requires broken inversion symmetry and can exist in the bulk as well as at interfaces, for example at interfaces between a ferromagnet and a material with large spin-orbit coupling like heavy metals. More recently it has been shown that interfacial DMI can also exist at interfaces with graphene and oxides. We use Brillouin Light Scattering spectroscopy (BLS) to determine the DMI from the non-reciprocal frequency-shift Damon-Eshbach spin-waves [1]. In order to gain deeper insight into the underlying physics of DMI and explore ways, on how to tune the DMI through interface modifications, we prepared several sample series to study different aspects of the DMI. First, we prepared a Cu/$Co_{90}Fe_{10}$ and a Pt/$Co_{90}Fe_{10}$ sample series, which were in-situ oxidized for different times and subsequently capped to prevent any further oxidation. Density functional theory calculations have demonstrated that the hybridization and the associated charge transfer is important for the DMI and that interfaces with an oxide can have DMI. Our BLS measurements showed that oxide interfaces have DMI. Moreover, the spectroscopic splitting factor *g*, which we determined with ferromagnetic resonance spectroscopy, is correlated to the DMI. This is an indirect confirmation of the theory predictions regarding the role of hybridization and charge transfer [2], [3]. Next, we prepared a sample series, where we introduce a Cu dusting layer at the interface between a CoFeB and Pt to disrupt the Heisenberg exchange directly at the interface. SQUID magnetomety shows that the Cu dusting layer reduces the proximity magnetization in the Pt. The proximity magnetization is a direct result of the exchange coupling and can be seen as a measure for its strength. The DMI has the same Cu thickness dependence, see Fig.2, and we can conclude that the Heisenberg exchange and the DMI are correlated. We measured a similar correlation before for a $Ni_{80}Fe_{20}$ thickness series on Pt [1]. In another study, we investigated the impact of interface disorder on DMI. We irradiated Ta/CoFeB/Pt samples with 40 keV He+ ions. We find that the DMI first increase for lower ion fluences, before it is reduced for the highest fluence. This shows that an increase of disorder at the interface is beneficial to achieve high DMI. In contrast, ferromagnetic resonance measurements showed, that the perpendicular anisotropy monotonically decreases with ion irradiation. This shows that both phenomena have different underlying physics even though both involve spin-orbit coupling. Finally, we studied the role of interface symmetry on DMI. So far, most work on DMI has been carried out for highly symmetric interfaces. Low symmetry systems can have anisotropic DMI and can potentially support anti-skyrmions. We prepared a Pt/Fe(110) sample and found that the DMI is anisotropic with the strongest DMI along the [001] direction, which coincides with the magnetic easy axis, Fig.2.

[1] H.T. Nembach et al., Nature Physics 11, 825 (2015) [2] H. T. Nembach et al., arXiv:1906.08395 [3] A. Belabbes et al., Scientific Reports 6, 24634 (2016)

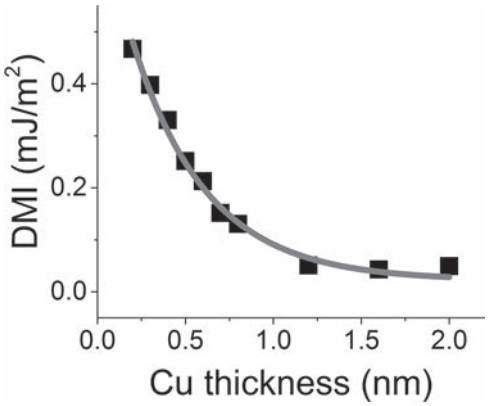


Fig. 1: DMI for the CoFeB/Cu(x)/Pt system.

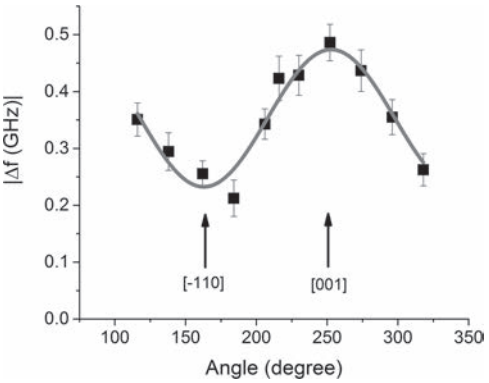


Fig. 2: Anisotropic DMI for Pt/Fe(110).

CONTRIBUTED PAPERS

9:06

AG-02. Significant Dzyaloshinskii–Moriya interaction induced by chemisorbed oxygen on ferromagnets. *G. Chen*[1], A. Mascaraque[2], M. Robertson[1], R. Lo Conte[3,4], M. Angel González Barrio[2], H. Ding[5], R. Wiesendanger[4], E.G. Michel[6], A.K. Schmid[7] and K. Liu[1,8] *1. University of California, Davis, Davis, CA, United States; 2. Depto. Física de Materiales, Universidad Complutense de Madrid, Madrid, Spain; 3. Department of Materials Science and Engineering, University of California, Berkeley, Berkeley, CA, United States; 4. Department of Physics, University of Hamburg, Hamburg, Germany; 5. Department of Physics, Nanjing University, Nanjing, China; 6. Depto. de Física de la Materia Condensada, Universidad Autónoma de Madrid, Madrid, Spain; 7. MSD, Lawrence Berkeley National Laboratory, Berkeley, CA, United States; 8. Physics Department, Georgetown University, Washington, DC, United States*

The Dzyaloshinskii–Moriya interaction (DMI) is an asymmetric exchange interaction that stabilizes chiral spin textures. It is induced by inversion symmetry breaking in chiral lattices or at interfaces [1,2]. Recently the interfacial DMI has been found in magnetic layers adjacent to the transition metals due to strong spin-orbit coupling [3], and at interfaces with graphene due to the Rashba effect [4]. In this work, we report the observation of significant DMI induced by chemisorption of oxygen on a ferromagnetic layer. The sign of this DMI and its large magnitude – despite the low atomic number of oxygen – are derived by examining the oxygen coverage dependent evolution of domain wall chirality. We find that the oxygen-induced DMI is comparable to the DMI induced at interfaces with most transition metals. This result extends the understanding of the DMI and supports oxygen-related design of spin-orbitronics devices. Support by the NSF (DMR-1610060 and DMR- 1905468), UCOP (MRP-17-454963), and DOE (DE-AC02-05CH11231) is gratefully acknowledged.

[1] M. Bode, et al. Nature 447, 190 (2007). [2] X. Yu, et al. Nature 465, 901 (2010). [3] W. Jiang, et al. Phys. Rep. 704, 1 (2017). [4] H. Yang, et al, Nat. Mater. 17, 605 (2018); F. Ajejas, et al. Nano Lett. 18, 5364 (2018).

9:18

AG-03. Tuning the properties of zero-field room temperature magnetic skyrmions by interlayer exchange coupling. *R. Lo Conte*[1,2], A.K. Nandy[3], G. Chen[4,5], A. Fernandes Cauduro[6], C. Ophus[6], K. Liu[5], A.K. Schmid[6] and R. Wiesendanger[2] *1. Materials Science and Engineering, University of California, Berkeley, Berkeley, CA, United States; 2. Institute of Applied Physics, University of Hamburg, Hamburg, Germany; 3. School of Physical Sciences, National Institute of Science Education and Research Bhubaneswar, Jatni, India; 4. Department of Physics, University of California, Davis, Davis, CA, United States; 5. Physics Department, Georgetown University, Washington, DC, United States; 6. NCEM - Molecular Foundry, Lawrence Berkeley National Laboratory, Berkeley, CA, United States*

Magnetic skyrmions [1,2], topologically protected magnetic quasi-particles, are at the core of many of the recently proposed spintronic devices. Many different materials systems have been shown hosting magnetic skyrmions at room temperature [3-6]. However, usually an external magnetic field is required to stabilize skyrmions in un-patterned magnetic thin-films, and this is not desirable for real applications due to scalability issues. Accordingly, it is highly desirable to have a robust and tunable protocol to build materials systems hosting magnetic skyrmions in zero external magnetic fields. Here we report the observation of isolated magnetic skyrmions at room temperature and zero magnetic field, stabilized through interlayer exchange coupling [7,8] between a *reference* magnet and a *free* magnet (Fig. 1). By carefully choosing the material and the thickness of the non-magnetic interlayer in between the two magnets, we are able to tune the chirality and the size of the observed skyrmions, whose 3D spin-texture is directly imaged by spin-polarized low energy electron microscopy. Our findings open up possibilities to the development of skyrmion-based spintronic devices suitable for general-use applications which go beyond modern nanoelectronics.

[1] A. Bogdanov and A. Hubert, J. Magn. Magn. Mater. 138, 255 (1994). [2] N. Romming et *al.*, Science 341, 636 (2013). [3] W. Jiang et al., Science 349, 283 (2015). [4] C. Moreau-Luchaire et *al.*, Nat. Nanotechnol. 11, 444 (2016). [5] S. Woo et *al.*, Nat. Mater. 15, 501 (2016). [6] A. Soumyanarayanan et *al.*, Nat. Mater. 16, 898 (2017). [7] A. K. Nandy et *al.*, *Phys. Rev. Lett.* 116, 177202 (2016). [8] G. Chen et *al.*, *Appl. Phys. Lett.* 106, 242404 (2015).

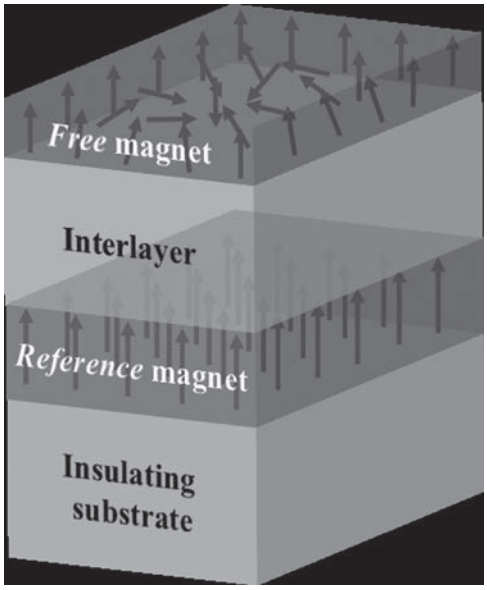


Fig. 1: Schematic of the studied multilayers, consisting of two magnetic layers with a non-magnetic interlayer in between, deposited on top of an insulating single crystal substrate. The *reference* magnetic layer is used to generate an effective field acting on the *free* magnet, allowing us to tune its magnetic properties. For specific thicknesses of the interlayer, room-temperature skyrmions are stabilized in the *free* magnet, without the application of any external magnetic field.

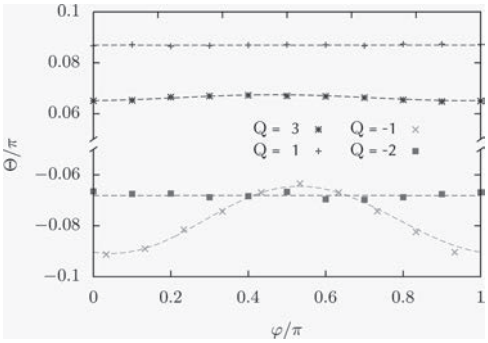
9:30

AG-04. Orientation dependent Current-induced Motion of Skyrmions with various Topologies. *M. Weissenhofer*[1] and U. Nowak[1] *1. University of Konstanz, Konstanz, Germany*

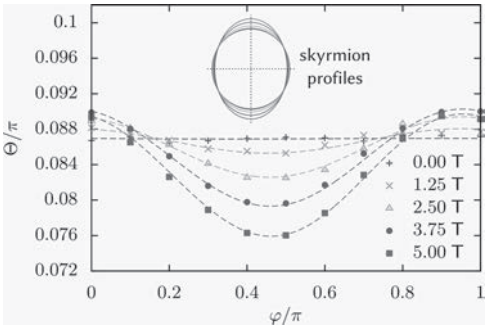
As they are small in size and easily movable by electric current, Skyrmions are promising candidates for next generation magnetic logic and memory devices. However, due to their non-trivial topological properties Skyrmions propagate along trajectories which deviate from the current direction, according to the so-called Skyrmion Hall effect (SHE) [1]. We study the current-driven motion of metastable localized spin structures with various topological charges in a $(Pt_{0.95}Ir_{0.05})$/Fe bilayer on a Pd(111) surface. We perform atomistic spin model simulations based on the Landau-Lifshitz-Gilbert equation with additional spin torque terms using a model hamiltonian parametrized by ab initio calculations [2,3] which are well supported by an approach based on the generalized Thiele equation. While the Dzyaloshinsky-Moriya interaction (DMI) in this system renders Skyrmions with $Q = 1$ energetically favorable, those with other topological charges are stabilized by the frustration of the exchange interaction, although being deformed by the DMI [4]. We demonstrate that besides a distinct dependence on the topological charge itself the dynamic response of Skyrmionic structures with topological charges $Q = -1$ and $Q = 3$ to a spin-polarized current exhibits

an orientation dependence due to the aforementioned deformation leading to a different SHE along different axis of the respective Skyrmion profiles (Fig. 1) [5]. This orientation dependence was found to increase with decreasing external field strength and consequently with increasing size of the skyrmions. We further show that such an orientation dependence can be induced by applying an in-plane external field which leads to an elongation of the Skyrmion profile along the field direction (Fig. 2). This possibly opens up a new promising pathway to the manipulation of skyrmion dynamics as it allows for the decrease of the Skyrmion Hall angle.

[1] N. Nagaosa and Y. Tokura, Nat. Nanotech., Vol. 8, p. 899-911 (2013). [2] Rózsa et al., Phys. Rev. Lett., Vol. 117, 157205 (2016). [3] Zázvorka et al, Nat. Nanotech., (2019) [4] Rózsa et al., Phys. Rev. B, Vol. 95, 094423 (2017). [5] Weißenhofer et al., Phys. Rev. B, in Press.



Simulation results (dots) and theoretical prediction (dashed lines) for the Skyrmion Hall angle Θ versus angle of applied current φ for skyrmions with topological charges Q as labeled.



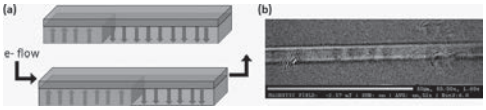
Skyrmion Hall angle Θ versus direction of applied current φ for skyrmions with Q = 1 for different strengths of the in-plane field.

9:42

AG-05. Insulator Spin-orbitronics: spin-orbit torque switching and skyrmions stabilized by chiral exchange interactions in thin film garnet heterostructures. *S. Ding*[1,2], A. Ross[1], R. Lebrun[1], S. Becker[1], K. Lee[1], I. Boventer[1], S. Das[1], J. Yang[2], G. Jakob[1] and M. Kläui[1] *1. Physics, Johannes Gutenberg University Mainz, Mainz, Germany; 2. Physics, Peking University, Beijing, Germany*

Insulating rare earth iron garnets (RIG) have drawn great interest in recent years due to their excellent performance in the field of spintronics, with low damping, soft ferromagnetic behavior and, magnetic and angular momentum compensation points. However for device applications, one would need a combination of stable spin structures and efficient electrical manipulation and both can be achieved by spin-orbit effects so that the combination is often termed spin-orbitronics. To obtain stable spin structures, chiral exchange interactions, such as the Dzyaloshinskii-Moriya interaction (DMI) can be employed. We use ultra-thin RIG films with perpendicular magnetic anisotropy (PMA) where efficient electrical switching [1] was observed. In our work, we grow high quality TmIG and GdIG [2] films by pulsed laser deposition. We first study the chiral DMI induced in thin film GGG/TmIG/Pt heterostructures [3]. We find for the first time a clear scaling of the DMI with the inverse of the TmIG layer thickness, which demonstrates the interfacial origin of the DMI [3]. We find a surprisingly long decay length so that we can obtain sizeable DMI in insulating TmIG even in >10 nm thick films, which is an order of magnitude larger than found for metallic systems. By direct imaging we find skyrmions and chiral domain walls and we identify the GGG/TmIG interface as the main source of the DMI. As the second step we then manipulate the magnetization and in particular the chiral spin structures by spin-orbit torques. We find that we can move the spin structures all synchronously confirming their chiral nature. Furthermore, switching of single domain particles is achieved for low current densities, down to $2.8*10^{10}$ A/m^2. So overall, we demonstrate that in insulating ferrimagnet based devices the key spin-orbit effects, namely chiral exchange interactions stabilizing skyrmions and efficient spin-orbit torques can be realized thus opening the field of Insulator Spin-Orbitronics.

[1] Can Onur Avci, et al., Nature Mater. 16, 309 (2017). [2] S. Geprägs et al., Nature Commun. 7, 10452 (2016) [3] S. Ding et al., arxiv:1906.07142 (2019)



Current induced motion of chiral domain walls in 8 nm TIG with 7 nm Pt (a) Sketch of device (b) Images of the TIG domains after ns current pulses. A reference imaged was taken before the pulses thus the black and white areas indicate the distance that DWs have moved.

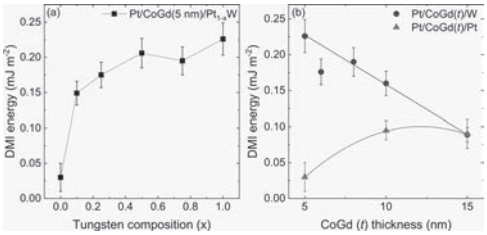
9:54

AG-06. Tuning Dzyaloshinskii-Moriya Interaction In Thin Ferrimagnetic CoGd Films to Create Magnetic Skyrmions. *Y. Quessab*[1], J. Xu[1], C.T. Ma[2], W. Zhou[2], G.A. Riley[3], J.M. Shaw[3], H. Nembach[3], J. Poon[2] and A.D. Kent[1] *1. Center for Quantum Phenomena, New York University, New York, NY, United States; 2. Department of Physics, University of Virginia, Charlottesville, VA, United States; 3. Quantum Electromagnetics Division, National Institute of Standards and Technology, Boulder, CO, United States*

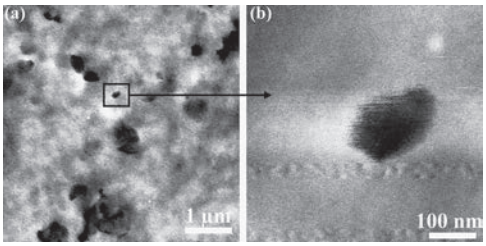
Magnetic skyrmions are attractive for spintronic applications, such as racetrack memories, to achieve very high density data storage. A magnetic skyrmion designates a local whirling of the spin configuration with a non-trivial topology. Skyrmions can be stabilized by Dyzaloshinkii-Moriya interactions (DMI) induced by strong spin-orbit coupling in the absence of inversion symmetry. Nearly compensated ferrimagnets with DMI are interesting materials due to their low stray fields and fast spin dynamics that can lead to ultrasmall and ultrafast skyrmions [1, 2]. Yet few studies have investigated *interfacial* (*i*-DMI) in ferrimagnets, which can be tuned to create skyrmions. Here we report a systematic study of the DMI in CoGd thin films as a function of the capping layer and magnetic thickness. We are able to tune the DMI in a range that stabilizes sub-100 nm skyrmions at room temperature in zero field. The *i*-DMI results from the breaking of the inversion symmetry by having different bottom and top interfaces. We studied the interfacial dependence of the DMI by Brillouin light scattering (BLS) as a function of the capping layer composition in Pt/CoGd(5 nm)/$Pt_{1-x}W_x$ (Fig. 1(a)). The samples were prepared by DC magnetron co-sputtering from Co and Gd sources. We found that 10% of W is enough to induce a DMI of about 0.15 mJ m^{-2}. Then we investigated the thickness *(t)* dependence of the DMI in Pt/CoGd(*t*)/(W or Pt) (Fig. 1(b)). The DMI decreases with the CoGd thickness in the asymmetric Pt/CoGd/W stack which confirms the interfacial nature of the DMI. Conversely, the DMI is non-zero even for the symmetric Pt/CoGd/Pt stack, likely due the difference in the nature of top and bottom interfaces, as seen in cross-sectional transmission electron microscopy. Finally, we show that films can have DMI in a range that allows skyrmion nucleation as shown by magnetic force microscopy (Fig. 2).

Our results provide insight into the key parameters to control the DMI in ferrimagnetic films toward achieving ultrasmall and ultrafast skyrmion motion. This research was supported by DARPA awards No. D18AP00009 and R186870004.

[1] L. Caretta *et al.*, Nature Nanotech 13, (2018) [2] S. Woo *et al.*, Nature Commun. 9, (2018)



Interfacial (a) and thickness (b) dependence of the DMI measured by BLS.



Skyrmion nucleation imaged in Pt/CoGd(10 nm)/W by MFM.

INVITED PAPER

10:06

AG-07. Strain-induced reversible manipulation of orbital magnetic moments in Ni/Cu multilayers on ferroelectric $BaTiO_3$. *J. Okabayashi*[1], Y. Miura[2] and T. Taniyama[3] *1. Research Center for Spectrochemistry, The University of Tokyo, Tokyo, Japan; 2. National Institute of Material Science, Tsukuba, Japan; 3. Nagoya University, Nagoya, Japan*

The coupling between ferromagnetic and ferroelectric properties has recently attracted considerable attention toward the creation of novel devices using multiferroic controlling of their properties. In particular, the hetero-interfaces in thin films comprising both ferromagnets and electrically polarized materials produce a rich variety of possibilities for creating multifunctional properties. Modulation of interfacial lattice constants by an electric field (*E*) induces interfacial changes in magnetism. The interfacial lattice distortion produces variations in magnetic properties, which are recognized as inverse magneto-striction effects. Moreover, magnetic anisotropy is also tuned by lattice distortions. Recent attempts have been focused on the modulation of the number of charge carriers at the interface between an ultrathin ferromagnetic layer and an oxide-barrier insulator in magnetic tunnel junctions. Other approaches, which are our focus in this study, are based on the interfacial mechanical strain coupling between ferromagnetic and ferroelectric layers using multiferroic hybrid structures. In this study, we focus on thin Ni layers sandwiched by Cu layers exhibit perpendicular magnetic anisotropy (PMA) because of the interfacial tensile strain in the Ni layers. Recently, *E*-control of the magnetic properties of Ni/Cu multilayers on $BaTiO_3$ was achieved; the magnetization was switched from the perpendicular axis to the in-plane easy axis by tuning the lattice distortion through the application of *E* [1]. To understand this relationship and the elastic phenomena from the view point of orbital magnetic moments, we developed a technique by applying an electric field in x-ray magnetic circular dichroism measurements (EXMCD) to clarify the mechanism of the electric-field-induced changes in the magnetic anisotropy of Ni/Cu multilayers on $BaTiO_3$ hetero-structures through lattice distortions. The samples were grown by using ultra-high vacuum molecular beam epitaxy on [100]-oriented $BaTiO_3$ single crystal substrates. The stacked structures are shown in Fig. 1a. The XAS and XMCD measurements for the Ni and Cu *L*-edges were performed at the KEK-PF BL-7A beamline, at room temperature. The EXMCD measurements were performed using the partial fluorescence yield mode. Figure 1b shows the Ni *L*-edge XAS and XMCD spectra by applying an electric field, *E*, of positive bias of 8 kV/cm. Sample surfaces are connected to ground and *E* is applied to the back side of the $BaTiO_3$ substrates. The spectral line shapes of the XAS and XMCD are modulated by *E* in normal incident (NI) case in spite of fixed sample measurement position. By comparing the results with and without *E*, we observed a slight variation in the peak asymmetries between the L_3 and L_2 edges. These results reveal that the orbital moments are modulated by applying *E*, thereby resulting in changes of magnetic anisotropy. The values of spin and orbital moments are estimated to be 0.56 and 0.055 μ_B, respectively, for an electric field of 0 kV/cm, and 0.56 and 0.045 μ_B, respectively, for an electric field of 8 kV/cm. The modulation of the orbital magnetic moments by 0.01 μ_B upon applying *E* is related to the induced lattice distortion of 2% from the $BaTiO_3$ substrates. Moreover, after releasing *E* to zero, spectral line shapes also revert to the pristine state [2]. Therefore, we conclude the reversible changes of orbital magnetic moments is induced by lattice distortion, which is the demonstration of novel orbital-elastic effect.

[1] Y. Shirahata *et al. NPG Asia Materials* 7, e198 (2015). [2] J. Okabayashi *et al., NPJ Quantum Mater. 4, 21 (2019)*.

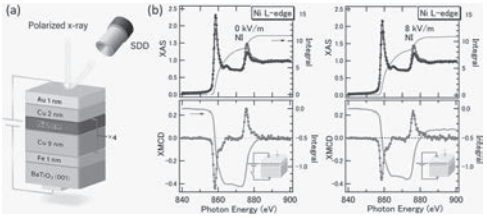


Fig. 1, (a) Schematic structure of the sample. The electrodes for applying the electric field are mounted at the top (Ni/Cu layer) and the bottom ($BaTiO_3$ substrate) of the films. (b) XAS and XMCD spectra obtained at Ni *L*-edges in partial-fluorescence-yield mode with and without an applied electric field.

CONTRIBUTED PAPERS

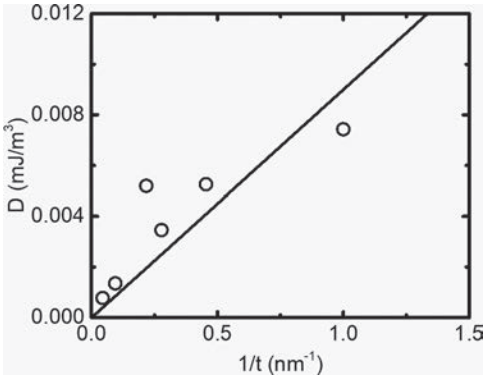
10:42

AG-08. Origins of Chiral Exchange Interactions in Centro-Symmetric Magnetic Insulators Arising from Rare-Earth Ions. *L.M. Caretta*[1], E.R. Rosenberg[1], F. Buettner[1], T. Fakhrul[1], P. Gargiani[2], M. Valvidares[2], P. Reddy[1], C. Avci[1], C. Ross[1] and G. Beach[1] *1. MIT, Cambridge, CA, United States; 2. ALBA Synchrotron, Barcelona, Spain*

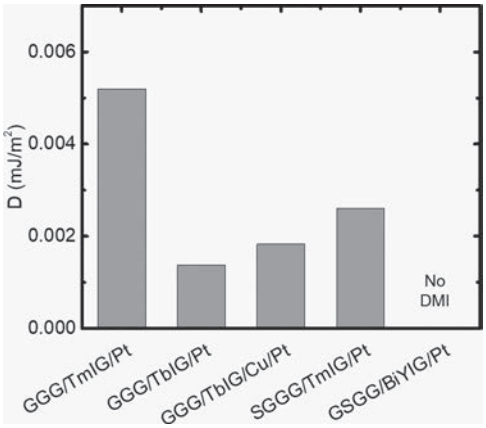
Chirality plays an essential role in physics and materials science. In magnetic materials, a chiral exchange interaction called the Dzyaloshinskii-Moriya interaction (DMI) can manifest from broken spatial inversion symmetry[1,2]. This discovery has led to the observation of chiral and topological spin textures, such as magnetic skyrmions and chiral domain walls[3–5]. Research has primarily focused on the study of chiral spin textures in metallic ferromagnet thin films with stacking asymmetry, where spin-orbit coupling at a heavy-metal/ferromagnet interface produces an interfacial DMI[4,5]. A broader class of materials, magnetic insulating garnets, have been extensively studied for their technologically desired spintronic properties, such as long magnon diffusion lengths and numerous magneto-optical effects[6,7]. Their low damping and ferrimagnetic properties also make them ripe candidates for high spin texture mobilities and fast spin texture velocities[6,7]. However, the DMI has only recently been observed in rare-earth iron garnet films, and the origins of the DMI are still not clear[8]. Here, we use current-induced domain

wall dynamics to systematically study the origins of the DMI in magnetic insulating garnets. We show that the DMI originates from broken symmetry at the substrate oxide/magnetic oxide and the heavy-metal/magnetic oxide interface. Additionally, we demonstrate a method to control the strength of the DMI by tuning the strain state of the garnet film. Moreover, by studying the rare-earth- and temperature-dependence of the DMI, we find that the DMI necessitates the presence of a rare-earth element in the magnetic insulator, suggesting new means to engineer chirality and ultimately new material and magnetic properties in this ubiquitous class of materials.

1 Dzyaloshinsky, I. *et al. J. Phys. Chem. Solids* 4, 241–255 (1958) 2 Moriya, T. *Phys. Rev.* 120, 91–98 (1960) 3 Emori, S. *et al. Nat. Mater.* 12, 611–6 (2013) 4 Ryu, K.-S. *et al. Nat. Nanotechnol.* 8, 527–533 (2013) 5 Woo, S. *et al. Nat. Mater.* 15, 501–506 (2016) 6 Kajiwara, Y. *et al. Nature* 464, 262–266 (2010) 7 Chumak, A. V *et al. Nat. Phys.* 11, 453 (2015) 8 Avci, C. O. *et al. Nat. Nanotechnol.* 14, 561–566 (2019)



DMI (D) as a function of TmIG thickness (t) in GGG/TmIG/Pt(4 nm)



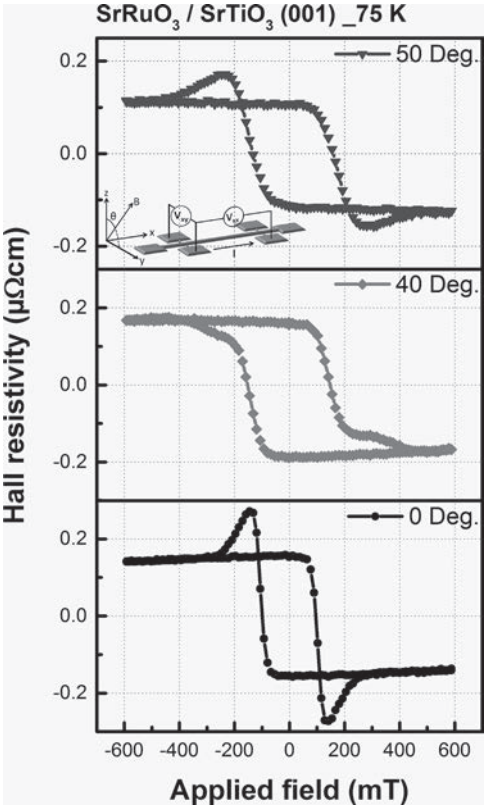
Comparison of DMI strength (D) in several magnetic insulating systems

10:54

AG-09. Robust skyrmion-bubble textures in single $SrRuO_3$ thin films stabilized by magnetic anisotropy. P. Zhang[1], A. Das[1], E. Barts[1], L. Si[2], M. Azhar[1], K. Held[2], M. Mostovoy[1] and *T. Banerjee*[1] *1. University of Groningen, Groningen, Netherlands; 2. Institut für Festkörperphysik, TU Wien, Wien, Austria*

We report on unconventional features in Hall transport in single $SrRuO_3$ thin films, akin to recent reports on topological Hall effect in $SrIrO_3/SrRuO_3$ bilayers [1,2] and ascribed to skyrmions. Unique to our findings are the i) robustness of these features (Fig.1) to the tilting magnetic field vector, manifested in their re-appearance with increasing angle of tilt, for temperatures below the magnetic phase transition and ii) the absence of a heavy metal layer. A systematic study of the magnetic anisotropy in strained $SrRuO_3$ (SRO) thin films grown epitaxially on a mixed surface terminated $SrTiO_3$ (100) (STO) was done using temperature dependence of the magnetization. Our density-functional theory calculation of a SRO/STO superlattice shows that the interface with intermixed RuO_2-TiO_2 lead to an exotic antiferromagnetic coupling, which flips to a high-spin ferromagnetic state under an external magnetic field. A careful analysis of the anomalous Hall resistivity with temperature shows a crossover from intrinsic to extrinsic mechanism and has distinct correlation with the observed unconventional features, ascribed to the topological Hall effect. To understand the mechanism leading to the stabilization of magnetic textures at our tailored interface, with sizeable spin-orbit coupling and in the absence of a strong interfacial Dzyaloshinskii-Moriya interaction, we modelled the magnetic energy incorporating anisotropy and dipolar interactions. We explain the experimental findings by the formation of magnetic bubble domains with skyrmion topology and relatively thick domain walls, using the model in Ref [3]. Further the robustness of the bubble arrays against the rotation of the magnetic field vector, as well as the relatively high critical magnetic fields are found to originate from the complex angular dependence of the magnetic anisotropy energy in $SrRuO_3$ films. [4] Such non-trivial competition between different local and non-local magnetic energies, leading to robust magnetic textures, at our engineered interfaces opens new opportunities for their manipulation with electric fields. Fig.1 : Magnetic field dependence of the Hall resistivity with increasing angle of the magnetic field (inset top panel).

[1] J. Matsuno, N. Ogawa, K. Yasuda, F. Kagawa, W. Koshibae, N. Nagaosa, Y. Tokura, and M. Kawasaki, Sci. Adv. 2, e1600304 (2016). [2] Y. Ohuchi, J. Matsuno, N. Ogawa, Y. Kozuka, M. Uchida, Y. Tokura, and M. Kawasaki, Nat. Commun. 9, 213 (2018). [3] X. Yu, M. Mostovoy, Y. Tokunaga, W. Zhang, K. Kimoto, Y. Matsui, Y. Kaneko, N. Nagaosa, and Y. Tokura, PNAS 109 (23) 8856-8860 (2012). [4] P. Zhang et al., submitted (2019).



11:06

AG-10. Effect of Spatially Modulated Dzyaloshinskii-Moriya Interaction Confinement on the Néel Skyrmions. *S. Bhatti*[1] and S. Piramanayagam[1] *1. School of Physical and Mathematical Sciences, Nanyang Technological University, Singapore*

Magnetic skyrmions have gained intense interest recently due to their abilities of circumventing the defects, small size and required low current for motion[1]. However, skyrmions in a racetrack move in transverse direction towards the edge of the track (due to skyrmion Hall effect). To avoid this detrimental effect, several methods have been proposed[2]. Here, we have proposed a new scheme based on the use of modulated Dzyaloshinskii-Moriya Interaction (DMI) energy by spatially modifying the DMI, which restrict the skyrmion's transverse motion[3]. DMI value was modulated on the edges, which reduces the total skyrmion energy as shown in the fig. 1. In our proposed approach, DMI of the track edges can be tuned locally, by practical approaches such as ion-implantation or compositional modifications that can be easily adapted in a CMOS-friendly manner. By using micromagnetic simulations, we have demonstrated the restriction of skyrmion's transverse motion to avoid the annihilation of the skyrmion. Moreover, the velocity and path of skyrmion can be manoeuvred by varying the current and DMI energy (fig. 2 (a)). Furthermore, we have demonstrated that the size of the skyrmions can be reduced, to some extent, by DMI energy wells' positions (fig. 2(b)). In addition, we have investigated the effect of magnetostatic interaction between the skyrmions in closely spaced neighbouring tracks for high density storage application (fig. 2(c)). Experiments are being carried out at the moment on CoFeB multi-stack, whose results will be presented during the conference.

1. A. Fert, V. Cros and J. Sampaio, Nature Nanotechnology., Vol. 8, p.152 (2013). 2. G. Finocchio, F. Büttner, R. Tomasello, et. al, Journal of Physics D: Applied Physics, Vol. 49, p.423001 (2016) 3. S. Bhatti and S. Piramanayagam, physica status solidi (RRL)–Rapid Research Letters.

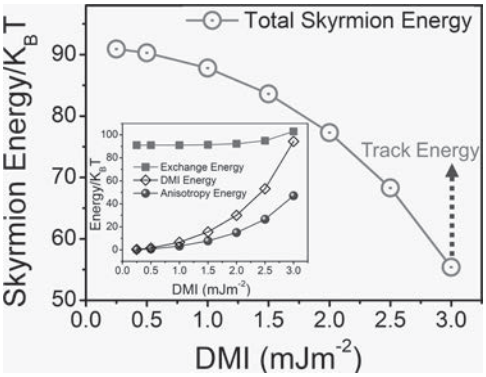


Fig. 1 Variation of total skyrmion energy as a function of varying DMI. Inset shows the modulation of different energies associated with skyrmion as function of DMI.

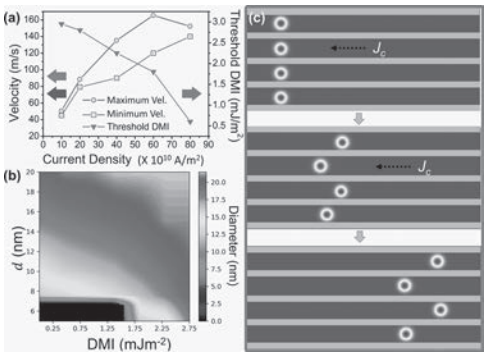


Fig. 2 (a) Dependence of skyrmion velocity and minimum DMI energy (threshold DMI) required to confine skyrmion on the current density simulated for damping constant α = 0.3. (b) Phase diagram of the skyrmion's diameter depicting the change in diameter of skyrmion as function of distance between the energy wells and DMI. (c) Magnetostatic interaction between multiple skyrmions.

11:18

AG-11. Robustness of Skyrmions in Amorphous GdCo with Interfacial Mixings. *C.T. Ma*[1], B.J. Kirby[2], W. Zhou[1] and J. Poon[1] *1. Physics, University of Virginia, Charlottesville, VA, United States; 2. NIST Center for Neutron Research, National Institute of Standards and Technology, Gaithersburg, MD, United States*

Magnetic skyrmions have been studied extensively for their applications in high-density energy efficient spintronics devices. Recently, ultrathin GdCo films on Pt have been shown to host Néel skyrmions as small as 10 nm [1]. In these materials, skyrmions are stabilized through the interfacial Dzyaloshinskii-Moriya interaction (DMI), which originates from a heavy metal interface. Thus, the interface quality is crucial in stabilizing and transporting skyrmions for device applications. We employed polarized neutron reflectometry (PNR) to investigate the interfacial properties of a W/Pt/GdCo(5 nm)/W/Pt heterostructure deposited on an Si/SiO_2 substrate. Fig. 1 shows temperature-dependent depth profiles determined from measurements taken in an in-plane 3 T field. The GdCo layer exhibits an inhomogeneous magnetization profile at all temperatures. Near the Pt/GdCo interface, a 2 nm region shows a compensation temperature (T_{comp}) of below 50 K. In contrast, away from the interface, T_{comp} of the rest of GdCo is found to be near 250 K. The reduction of T_{comp} likely arises from the intermixing of Pt and GdCo at the interface. With this mixing layer, the robustness of skyrmion in these heterostructures may be compromised. Based on results from PNR, we have simulated a heterostructure of $(GdCo)_{75}Pt_{25}$(2 nm)/GdCo(3 nm) to investigate the effect of the mixing layer on skyrmions in GdCo. We find that skyrmions, as small as 10 nm, remain stable in such magnetic heterostructure. To verify the robustness of these simulated skyrmions, we have utilized tomography as shown in Fig. 2. Columnar distributions of skyrmions are found across the structure. While the robustness and the stability of skyrmions persist with the presence of a mixing layer, further study is needed to investigate the effect on skyrmion's mobility. This work was supported by the DARPA Topological Excitations in Electronics (TEE) program (grant D18AP00009).

[1] L. Caretta *et al*. *Nat. Nanotechnol*. 13, 1154-1160 (2018).

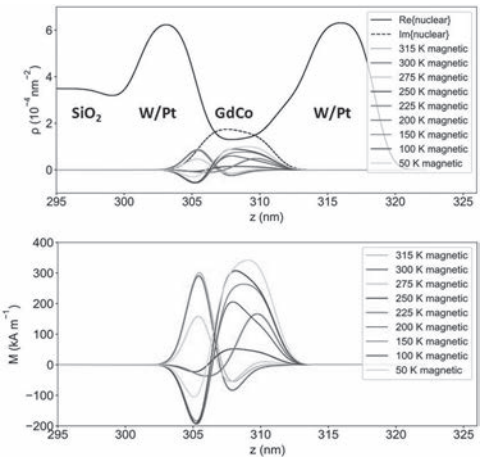


Fig. 1 Temperature-dependent scattering length density profiles (top) and in-plane magnetization profiles (bottom) of W/Pt/GdCo(5 nm)/W/Pt on Si/SiO_2 substrate.

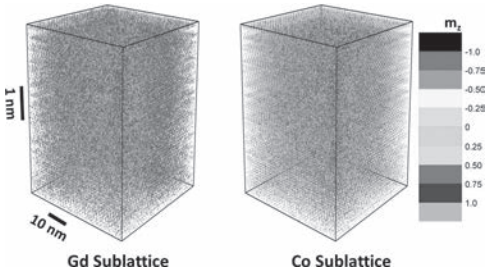


Fig. 2 Tomograph of a simulated skyrmion in 5 nm GdCo with 2 nm mixing layer. Color is mapped based on out-of-plane reduced magnetization (m_z) of each spin.

Session AH
MAGNETOELECTRIC DEVICES AND MAGNETO-IONICS

Rajesh Vilas Chopdekar, Chair
Lawrence Berkeley National Laboratory, Berkeley, CA, United States

CONTRIBUTED PAPERS

8:30

AH-01. Epitaxial Integration of Multiferroic $LuFeO_3$ onto a Semiconductor Device Platform. *J. Casamento*[1], P. Dang[3], X. Li[2], H. Lee[2], D. Schlom[1], H.G. Xing[2,1] and D. Jena[2,1] *1. Materials Science Engineering, Cornell University, Ithaca, NY, United States; 2. Electrical and Computer Engineering, Cornell University, Ithaca, NY, United States; 3. Applied Engineering Physics, Cornell University, Ithaca, NY, United States*

The integration of magnetic materials in semiconductor devices is an appealing prospect due to the potential for combining logic and nonvolatile memory. This can be achieved using multiferroic materials with coupled ferromagnetism and ferroelectricity to control electrical polarization with magnetization and vice versa. $LuFeO_3$ (LFO) is an attractive material for this purpose, being a multiferroic material that is ferroelectric below ~1050 K and weakly ferromagnetic below ~150 K[1,2]. Also, room temperature multiferroic behavior has been previously demonstrated in $LuFeO_3$-$LuFe_2O_4$ thin film superlattices[3]. High quality epitaxial growths of LFO by ozone molecular beam epitaxy on GaN (0001) have been achieved, as confirmed by X-ray diffraction (XRD), atomic force microscopy (AFM), and in-situ electron diffraction. XRD shows fringes relating to film thickness and AFM shows LFO surface roughness is less than 0.5 nm on a 2x2 μm scale. Piezoresponse force microscopy suggests that the epitaxial LFO on GaN is ferroelectric at room temperature, with a permanently poled pattern appearing from electrical bias. Hysteresis in seen in vibrating sample magnetometry measurements, indicating that it is ferromagnetic at low temperatures. These results indicate the feasibility of future integration of LFO-based ferroelectric and multiferroic phenomena into III-nitride optoelectronics. This work was supported by the National Science Foundation under Grant Nos. E2CDA ECCS-1740286, and EFMA-1741694 and the Semiconductor Research Corporation as nCORE task 2758. This work was performed in part at user facilities supported by NSF grants MRI-1338010, ECCS-1542081(CNF) and DMR-1719875 (CCMR).

[1] S. M. Disseler *et al*., Phys. Rev. Lett. 114(21), 217602 (2015) [2] J. A. Moyer *et al*., APL Mater., *2*(1), 012106 (2014) [3] J.A. Mundy *et al*., Nature., 537, 7621(2016)

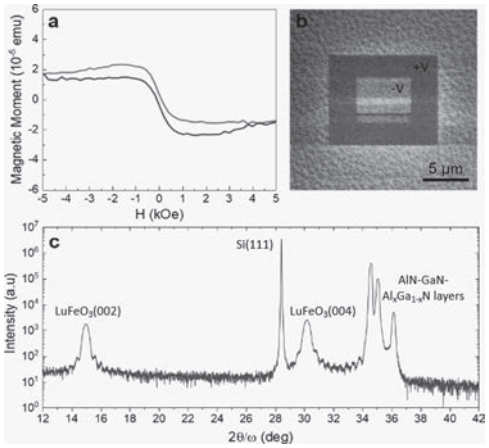
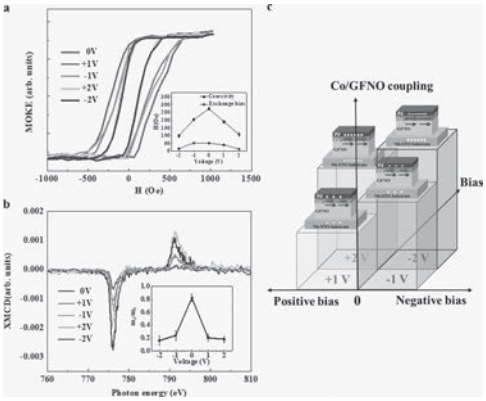


Fig. 1. Properties of epitaxial LFO grown on GaN. (a) Vibrating sample magnetometry measurement of LFO, showing a magnetic hysteresis at 50 K. (b) Piezoresponse force microscopy image of LFO on GaN at room temperature, showing that it can be electrically polled. (c) X-ray diffraction of high-quality LFO grown on GaN-based heterostructures.

8:42

AH-02. $GdFe_{0.8}Ni_{0.2}O_3$ as a new multiferroic compound for low-voltage-driven spintronic devices. K. Chen[1], Y. Huang[1], *S. Chang*[1] and Y. Tseng[1] *1. Materials Science & Engineering, National Chiao Tung University, HSINCHU, Taiwan*

At the forefront of spintronics, electrical (voltage) control of magnetic devices will require novel materials to increase drive current capability, as well as lowering power consumption and promoting operating speed. Multiferroic devices are potential for application of electrical (voltage) controlled devices, owing to coexisting ferroelectric (FE) and magnetic orders in a single phase. Therefore, the idea of making spintronic devices based on multiferroic materials comes very naturally. Unfortunately, development in the field of multiferroics is stagnating due to slow progress in the development of new multiferroic compounds. In this study, we demonstrated the use of sputtering to grow a new multiferroic thin film that features coupled FE and antiferromagnetic (AFM) orders at room temperature. The FE and magnetic orders of the film are very responsive to low applied voltages (+/- 1 volt) and the multiferroic behavior is sensitive to bias polarity. Combining this film with a Co ferromagnetic layer resulted in a heterostructure capable of generating discrete magnetic orders simply by altering the bias magnitude and bias sign. Thus, this material could double the number of available magnetic read-out states within a low voltage regime, which satisfies the requirements for low-power and high-storage technology. Theoretical analysis and experiment results indicate the importance of Ni-dopant in regulating the polarity-dependent multiferroicity of this Gadolinium ferrite system. We believe that the development of such materials could open the door to new spintronic architectures that exploit the local gating of magnetic properties, thereby reducing the energy required for switching while increasing storage capacities.



(a) MOKE hysteresis loop and (b) XMCD results of Co $L_{2,3}$-edges with bias-dependence for Pt/Co/GFNO/STO device; inset of (a) shows H_c (black) and H_{eb} (blue) as a function of applied bias; inset of (b) shows orbital/spin moment ratio (m_L/m_S) as a function of applied bias; m_L and m_S were obtained from XMCD spectral using sum-rule principles; (c) illustration showing control over multiple magnetic states (relying on Co/GFNO interface magnetic coupling) via cross-tuning of bias and polarity.

8:54

AH-03. Multilevel Nonvolatile Memory Effect in amorphous SmCo/(011) PMN-PT Heterostructure. *W. Liang*[1,3], J. Liu[1,3], F. Hu[1,3], J. Zhang[2,3], J. Wang[1,3], J. Sun[1,3] and B. Shen[1,3] *1. Institute of Physics, Chinese Academy of Sciences, Beijing, China; 2. Ningbo Institute of Materials Technology and Engineering, Chinese Academy of Sciences, Ningbo, China; 3. University of Chinese Academy of Sciences, Beijing, China*

Electric field control of magnetism is promising for developing dense, fast, nonvolatile magnetic random access memory with very low energy consumption. A feasible and effective method is using multiferroic materials, especially multiferroic heterostructures, and much progress has been made.[1,2] Among them, soft magnetic and ferrimagnetic materials are often chosen as ferromagnetic layers, while hard magnetic materials, which can bring higher recording density and signal-to-noise ratio, have got little attention. Our recent research indicated that two-state storage can be realized in amorphous hard magnetic SmCo/(011)PMN-PT heterostructure by utilizing the magnetostrictive properties of amorphous SmCo thin film and the polarization switching in PMN-PT substrate.[3] As known, the implementation of multilevel storage is conducive to further improving storage density. From this viewpoint, multilevel storage in amorphous SmCo/(011)PMN-PT heterostructure has been further demonstrated by controlling the polarization switching in PMN-PT substrate. One way is to apply unipolar electric field *E*, another is to apply minor-loop electric field *E*. When unipolar electric fields were cyclically applied, the polarization directions keep rotating on one side of out-plane (011), and will not flip to the other. Even the turning electric field reaches coercive field, the polarization directions lie in-plane of (011), i.e. the 4 possible in-plane <111> directions. As a result, turning electric field makes it possible to realize the multilevel switching of remnant magnetization Mr in amorphous SmCo/(011)PMN-PT heterostructure (Fig. 1a-b). Moreover, minor-loop cyclic electric fields can also produce similar multilevel switching, as shown in Fig. 1c-d. Relative mechanism has been comparably discussed for the both cases. The observed multilevel nonvolatile memory effect in amorphous SmCo/(011) PMN-PT heterostructure promotes the hard magnetic materials to be used in multifunctional information storage and novel spintronic devices.

[1] W. Eerenstein, M. Wiora and J. L. Prieto, Nat. Mater., 6, 348 (2007).
[2] S. Zhang, Y. G. Zhao and P. S. Li, Phys. Rev. Lett., 108, 137203 (2012).
[3] W. H. Liang, F. X. Hu and J. Zhang, Nanoscale, 11, 246 (2019).

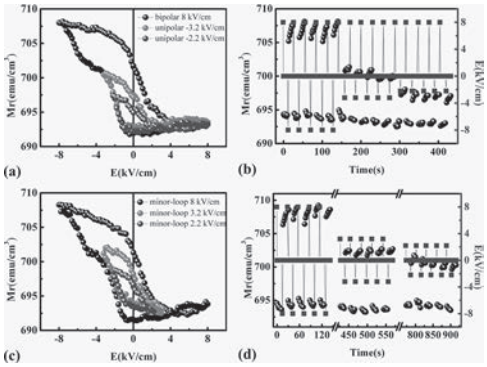


Fig. 1 Mr–E curves upon applying unipolar electric fields and the corresponding Mr multilevel switching (a-b). Mr–E curves under minor-loop electric fields and the corresponding Mr multilevel switching (c-d).

9:06

AH-04. Voltage-Controlled Superconducting Magnetic Quantum Memory. *A. Kenawy*[1,2], M. Milosevic[3], W. Magnus[3] and B. Soree[2] *1. Physics Department, KU Leuven, Leuven, Belgium; 2. imec, Leuven, Belgium; 3. University of Antwerp, Antwerp, Belgium*

Over the past few decades, superconducting circuits have been used to realize various novel electronic devices such as quantum bits, SQUIDs, parametric amplifiers, etc. One domain, however, where superconducting circuits fall short is information storage. Superconducting memories hinge on the quantization of magnetic flux in superconducting loops. Standard implementations store information as magnetic flux quanta in a superconducting loop interrupted by two Josephson junctions (i.e., a SQUID) [1]. However, due to the large inductance required, the size of the SQUID loop is limited to several micrometers, resulting in low-density memory chips. Here, we propose a scalable magnetic memory device consisting of a voltage-biased superconducting loop (e.g., a ring) threaded by a half-quantum flux bias. By numerically solving the time-dependent Ginzburg-Landau equations, we show that, by forming two weak links in the ring, the bias voltage modulates the free-energy barrier between neighboring flux states. Accordingly, by applying a time-dependent bias voltage in the microwave range, one can temporarily reduce the free-energy barrier and harness deterministic phase slips as a writing mechanism to change the number of stored flux quanta. We demonstrate writing speeds in the order of few picoseconds for aluminum nanorings. Since the proposed device does not require a large loop inductance, it can be scaled down, enabling a high-density memory technology.

[1] A. F. Kirichenko, S. Sarwana, D. K. Brock and M. Radpavar, "Pipelined DC-powered SFQ RAM," in *IEEE Transactions on Applied Superconductivity*, vol. 11, no. 1, pp. 537-540, March 2001

9:18

AH-05. Epitaxial Spin-Orbit Torque Materials on Multiferroic $LuFeO_3$ Coupled to a GaN HEMT. *P. Dang*[1], J. Casamento[2], X. Li[3], H. Lee[3], Z. Zhang[3], J. Singhal[3], Y. Tang[4], D. Ralph[4], D. Schlom[2], H.G. Xing[3,2] and D. Jena[3,2] *1. Applied and Engineering Physics, Cornell University, Ithaca, NY, United States; 2. Materials Science and Engineering, Cornell University, Ithaca, NY, United States; 3. Electrical and Computer Engineering, Cornell University, Ithaca, NY, United States; 4. Physics, Cornell University, Ithaca, NY, United States*

Multiferroic materials with strong magnetoelectric coupling present the possibility of controlling electrical polarization via magnetization switching. This can be applied to semiconductor transistors, where the polarization

switching of the multiferroic can gate the semiconducting channel. Such structures hold promise for combining magnetic memory and digital logic through integrating magnetic materials with semiconductor transistors. $LuFeO_3$ (LFO) is a magnetoelectric multiferroic with ferroelectric ordering below ~1050 K and canted antiferromagnetic ordering below ~150 K [1-3]. After high quality epitaxial growths of LFO onto GaN two-dimensional electron gases (2DEGs) by ozone molecular beam epitaxy, electrical measurements show that the nitride 2DEG survives the growth and is able to couple with LFO's ferroelectric polarization. Furthermore, low-temperature magnetoresistance measurements of the LFO/2DEG stack show a spontaneous change in resistance at certain magnetic fields, alluding to the possibility of changing the LFO's electrical polarization with a magnetic field. Magnetic $Mn_{1-x}Ga_x$ is then grown on top of the LFO to enhance the exchange bias of the structure and improve the possibility of switching electric dipoles with magnetic field. $Bi_{1-x}Sb_x$ / $Mn_{1-x}Ga_x$ spin-orbit torque (SOT) bilayers were recently shown to be a very efficient structure for magnetization switching [4], so combining the SOT bilayers with the LFO/2DEG structure holds promise for creating a field-effect transistor that is controlled by SOT. This work was supported by the Semiconductor Research Corporation as nCORE task 2758 and the National Science Foundation under Grant Nos. GRFP DGE-1650441, E2CDA ECCS-1740286, and NewLAW EFMA-1741694. This work was performed in part at the user facilities supported by NSF MRI-1338010, NSF ECCS-1542081 (CNF) and NSF DMR-1719875 (CCMR).

[1] W. Wang *et al*., Phys. Rev. Lett., 110(23), 237601 (2013) [2] J. A. Moyer *et al*., APL Mater., *2*(1), 012106 (2014) [3] S. M. Disseler *et al*., Phys. Rev. Lett., 114(21), 217602 (2015) [4] N. H. D. Khang *et al*., Nat. Mater., 17(9), 808–813 (2018)

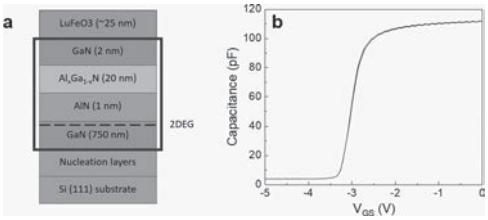


Fig. 1: Properties of the LFO/2DEG stack. (a) Layer structure of LFO grown on the GaN 2DEG. (b) Capacitance versus gate voltage measurement, showing depletion of carriers within the 2DEG via the LFO.

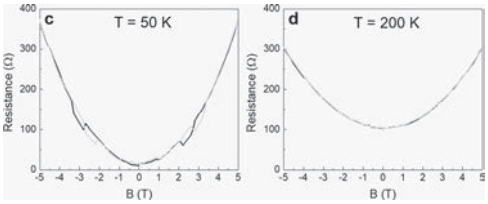


Fig. 2: Magnetoresistance of the LFO / 2DEG stack, showing potential switching behavior at (a) 50 K when LFO is magnetic, that does not appear at (b) 200 K when LFO is not.

9:30

AH-06. Smart Magnetoelectric Antennas for Magnetic Sensing and Energy Harvesting. *M. Zaeimbashi*[1], M. Nasrollahpour[1], X. Liang[1], H. Chen[1], A. Romano[1], Z. Xu[1], A. Mittal[1], N. Mirchandani[1], G. Jha[1], I. Martos-Repath[1], A. Khalifa[2], M. Onabajo[1], A. Shrivastava[1], S. Cash[2] and N.X. Sun[1] *1. ECE, Northeastern University, Boston, MA, United States; 2. Neurology, Massachusetts General Hospital, Boston, MA, United States*

Recent progress in the field of magnetoelectric (ME) materials have led to ultra-compact ME antennas with size of 2-3 order of magnitude smaller than that of conventional state-of-the-art compact antennas [1]. These miniaturized antennas could be suitable for Medical Implant Communications Service (MICS), in particular for wireless brain monitoring. A wireless implantable device should be able to perform multiple tasks in order to effectively monitor an individual's condition. For instance, a wireless implantable device should harvest their required energy in order to power their circuitry systems. In addition, the implant needs to record the body's information such as magnetic or electric fields in order to successfully track the changes the body. Finally, the implant should transmit the recorded data to the external antenna or device. In this work we're presenting an ultra-compact and smart magnetoelectric antenna that can single-handedly perform all three above-mentioned tasks: energy harvesting, magnetic field sensing, and data communication. This complimentary combination makes ME antennas suitable for brain implantation where magnetic field recording is required to monitor the brain functionality. Fig. 1 shows the optical microscope image of fabricated ME antenna with AlN/FeGaB thin-film structure. AlN acts as a piezo-material and FeGaB as a magneostrictive material. Proposed antenna has three parallel ME element, each with the size of 50×250 μm^2. Fig. 2a shows the architecture of energy harvesting setup. Fig. 2b shows the ME antenna concept and its functionality in receiving (energy harvesting) mode. Fig. 2c shows the S11 of ME antenna showing the resonant frequency of 2.25GHz. Fig. 2d shows the harvesting voltage from ME antenna, showing an induced voltage of 2.13mV when ME antenna is in presence of a 4.5nT RF magnetic field. Fig. 3a shows the ME antenna's phase response in magnetic sensing mode. Here, ME antenna is in presence of a 1kHz magnetic field with 6.6μT strength. Fig. 3b is the zoomed-in version of Fig. 3a and shows the 1kHz phase peak which corresponds to the 6.6μT magnetic field under measurement. The limit of detection of this antenna is 917pT.

[1] T. Nan, H. Lin, Y. Gao, A. Matyushov, G. Yu, H. Chen*, et al.*, "Acoustically actuated ultra-compact NEMS magnetoelectric antennas," *Nature communications,* vol. 8, p. 296, 2017.

INVITED PAPER

9:42

AH-07. Novel Magnetoelectric Nano-Plate Resonators for Sensors. H. Lin[2], X. Liang[1], N. Sun[1], N. Sun[1], M. Zaeimbashi[1] and *N. Sun*[1,2] *1. Electrical and Computer Engineering Department, Northeastern University, Boston, MA, United States; 2. Winchester Technologies, LLC, Burlington, MA, United States*

Integrated magnetoelectrics have been demonstrated to enable voltage control of magnetism, or vice versa, and have great potential for magnetic field sensors, antennas and magnetoelectric random access memories. Dr. Nian Sun has been playing a pioneering role in integrated magnetoelectrics. In this talk, he will cover the most recent progress on new integrated magnetoelectric NEMS (nanoelectromechanical system) based sensors and antennas. He will cover magnetoelectric materials, and their applications in different devices, including: novel ultra-compact RF NEMS acoustic magnetoelectric antennas immune from ground plane effect with $< l_0/100$ in size, self-biased operation and ground plane immunity; and ultra-sensitive RF NEMS magnetoelectric magnetometers with ultra-low noise for DC and AC magnetic fields sensing. These novel magnetoelectric sensors show great promise in compact, lightweight and power efficient sensors, radars, communication systems, biomedical devices, IoT, etc.

1. N.X. Sun and G. Srinivasan, *SPIN*, 02, 1240004 (2012); 2. J. Lou, et al., *Advanced Materials*, 21, 4711 (2009); 3. M. Liu, et al. *Advanced Functional Materials*, 21, 2593 (2011); 4. T. Nan, et al. *Scientific Reports*, 3, 1985 (2013); 5. M. Liu, et al. *Advanced Materials*, 25, 1435 (2013); 6. M. Liu, et al. *Advanced Functional Materials*, 19, 1826 (2009); 7. Ziyao Zhou, et al. *Nature Communications*, 6, 6082 (2015). 8. T. Nan, et al. *Nature Comm*. 8, 296 (2017).

CONTRIBUTED PAPERS

10:18

AH-08. Room-Temperature Voltage Control of Magnetism in Sr(Co,Fe)Ox Thin Films. *S. Ning*[1] and C. Ross[1] *1. Department of Materials Science and Engineering, MIT, Cambridge, MA, United States*

Although remarkable advances have been made in current-induced magnetic switching, the voltage control of the magnetic properties is drawing considerable attention as it can further reduce the switching power by using an electric field instead of a current. Several strategies have been developed for voltage control of magnetism, but are impeded by challenges such as the weak magnetoelectric (ME) coupling in single-phase multiferroic materials or ferroelectric/magnetic composites, and the thickness limitation and low Curie temperature of electrically gated ferromagnetic metals or semiconductors. Recently, magneto-ionic effects (voltage-driven ionic migration) has been used to manipulate the coercivity, exchange bias and magnetic anisotropy, but easy on-off switching of magnetism at room-temperature (RT) is still elusive. We demonstrate RT voltage-controlled magnetism switching in Sr(Co,Fe)Ox, (SCFO, $2.5<x<3$) thin films of thickness 50-150 nm produced by PLD on $SrTiO_3$. Via ionic liquid (IL) gating, oxygen ions can be inserted into or extracted from the films, leading to a reversible change of oxygen stoichiometry and valence states of Co and Fe ions, as well as a structural change between an oxygen-deficient phase (brownmillerite, BM) and a fully oxidized phase (perovskite, P) evident from in situ XRD analysis. The oxygen-deficient BM-SCFO is a G-type antiferromagnet with negligible net magnetization. A robust RT ferromagnetism is observed in the fully oxidized P-SCFO produced by the intercalation of oxygen ions through IL gating with a bias of -2 V. This behavior is absent in both parent materials ($SrCoO_x$ and $SrFeO_x$). The RT magnetization varies with Co/Fe ratio and is maximum (~100 emu/cm^3) at a ratio of Co/Fe = 1/1. When gating with a bias of +2 V, the magnetism rapidly vanishes in a few minutes with the structure gradually back to the BM phase due to the deintercalation of oxygen ions. The magnetic changes upon IL gating are reversible over multiple cycles. Our work makes it possible to utilize the oxygen migration driven by IL gating in SCFO thin films to realize reversible non-volatile switching of magnetism at RT, and provides a new direction for the RT electrical manipulation of magnetic properties.

10:30

AH-09. Magneto-Ionic Control of Exchange Bias in Gd/NiCoO. P. Murray[1], *C.J. Jensen*[2], A. Quintana[2], J. Zhang[3], X. Zhang[3] and K. Liu[2,1] *1. Physics Department, University of California, Davis, Davis, CA, United States; 2. Physics Department, Georgetown University, Washington, DC, United States; 3. King Abdullah University of Science & Technology, Thuwal, Saudi Arabia*

The presence of the interface-sensitive exchange bias effect in getter-metal / antiferromagnet (AF) oxide systems offers an ideal platform to probe the nature of the interfaces and to electrically control the exchange bias itself. As exchange bias is prominently featured in spin-valve type of spintronic devices that enables the control of magnetic configurations, magneto-ionic control of exchange bias may lead to substantially more energy-efficient switching using an electric field. We have investigated magneto-ionic control of exchange bias in Gd/NiCoO films. As a result of the O^{2-} ion migration at the interface, the multilayer structure is transformed into Gd/NiCo/NiCoO. Since the bulk Gd Curie temperature is at 292K, thus at room temperature the ferromagnetic (FM) signal observed in the as-grown sample is due to the redox-reduced NiCo at the Gd/NiCoO interface, similar to that seen in earlier studies of the GdFe/NiCoO system utilizing a ferrimagnet GdFe [1]. Upon field cooling, the hysteresis loop becomes shifted, with a significant exchange bias of ~ 280 Oe. The magnitude of the exchange bias depends on the thickness of the interfacial layer and of the AF layer. Interestingly, the exchange bias is enhanced by up to 15% in a bias electric field. Scanning transmission electron microscopy (STEM) directly reveals ion-migration-induced chemical segregation and microstructural disorder. Electron energy loss spectroscopy (EELS) shows that upon field cooling, the interfacial region become Ni-rich; this chemical segregation becomes more dramatic after voltage biasing. The observed enhancement of exchange bias under voltage gating may be related to the disorder-induced changes to the effective FM thickness at the interface, and the reduction of the FM NiCo moment, consistent with Malozemoff's random field model. This work has been supported by the NSF (DMR-1610060 and ECCS-1611424) and the nCORE-SMART Center.

[1]. D. A. Gilbert, et al, Nat. Commun., 7, 11050 (2016).

10:42

AH-10. Magneto-Ionic Control of Coercivity and Exchange Bias using Voltage-Tunable FeO_x/Fe Surface Layers. *J. Zehner*[1], R. Huhnstock[2], S. Oswald[1], S. Schneider[1], I. Soldatov[1], R. Schäfer[1], A. Ehresmann[2], K. Nielsch[1], D. Holzinger[2] and K. Leistner[1] *1. IFW Dresden, Dresden, Germany; 2. Institute of Physics, University of Kassel, Kassel, Germany*

Voltage-triggered ionic motion and redox reactions achieved by electrolytic gating of metal nanostructures enable large and non-volatile magnetic changes at room temperature.[1-3] This magneto-ionic control is highly interesting for novel energy efficient spintronic, actuation, and neuromorphic computing devices. So far, magneto-ionic mechanism are mainly used to control anisotropy and magnetization in magnetic layers with a thickness of a few monolayers or nanometers. In the present study, magneto-ionic effects on coercivity and exchange bias are demonstrated for sputtered and natively oxidized FeOx/Fe films with a thickness of up to 13 nm. Two systems are studied: (I) FeOx/Fe films with a uniaxial in-plane magnetic anisotropy on a Au layer (Figure 1) and (II) exchange bias FeOx/Fe films on an antiferromagnetic IrMn layer. In these systems, reversible oxidation and reduction reactions occur in the FeOx/Fe films at a low voltage of < 1 V in a liquid electrolyte. In the FeOx/Fe/Au films, this change in oxidation state induces large changes in coercivity, remanence, and magnetic domain size, and it makes voltage-induced 180° switching of magnetization possible at a small bias field. For the FeOx/Fe/IrMn systems, large changes in the exchange bias field are achieved (Figure 2).[4] The magnetic changes are revealed by in situ Kerr microscopy. The change of oxidation state and an associated thickness change of the iron oxide and Fe layers are proposed as the underlying mechanisms. This mechanism is proven by X-ray Photoelectron spectroscopy and transmission electron microscopy and it is consistent with a model for the exchange bias. Nonvolatility is achieved as the reduction proceeds at the buried FeOx/Fe interface, leaving the remaining oxide as a protective layer. In addition, a lateral voltage-controlled patterning of the exchange bias fields and magnetic domain state is demonstrated.[4] This versatile magneto-ionic control paves a new route for the development of future electrically controlled magnetic devices and for the design of exchange bias systems in general.

[1] K. Leistner, J. Wunderwald, N. Lange et al., Phys. Rev. B, 87, p. 224411 (2013) [2] C. Navarro-Senent, A. Quintana, E. Menendez et al., APL Mater. p. 030701 (2019) [3] A. Molinari, H. Hahn, R. Kruk, Adv. Mater. p. 1806662 (2019) [4] J. Zehner, R. Huhnstock, S. Oswald et al., Adv. Electr. Mater. 5, p. 1900296 (2019)

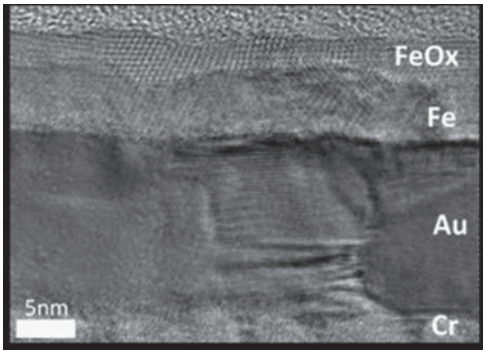


Fig. 1: HR-TEM cross-sectional image of the voltage-tunable FeOx/Fe/Au films

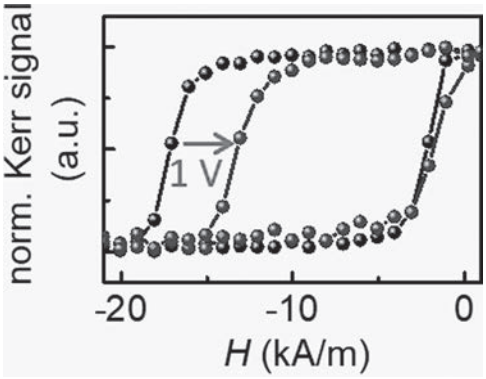


Fig. 2: Voltage-controlled exchange bias in FeOx/Fe/IrMn systems

10:54

AH-11. Boosting Magneto-Ionic Effects in Magnetic Mesoporous Films through Conformal Oxygen Getter/donor Nanocoatings. *C. Navarro Senent*[1], A. Quintana[1,2], E. Isarain Chávez[1], E. Weschke[3], P. Yu[4], M. Coll[4], E. Pellicer[1], E. Menéndez[1] and J. Sort[1,5] *1. Physics, Universitat Autonoma de Barcelona, Cerdanyola del Valles, Spain; 2. Physics, Georgetown University, Washington, WA, United States; 3. Helmholtz-Zentrum Berlin für Materialien und Energie, Berlin, Germany; 4. Institut de Ciència de Materials de Barcelona (ICMAB-CSIC), Bellaterra, Spain; 5. Institució Catalana de Recerca i Estudis Avançats (ICREA), Barcelona, Spain*

Over the last decades, a flurry of research has focused on the electrical control of magnetism. Magnetoelectric effects can be accomplished by different mechanisms,[1] for example magneto-ionics, which relies on the migration of ions (e.g. oxygen) driven by an electric field, as an effective approach for controlling the oxidation-reduction processes of a ferromagnetic material.[2,3] In this manner, magnetic properties can be easily manipulated by voltage taking advantage of ion diffusion through the ferromagnetic material. Large magneto-ionic effects in heterostructured films consisting of mesoporous Co–Pt films conformally coated with insulating oxide nanolayers are demonstrated. Mesoporous Co–Pt films, prepared by electrodeposition, are coated with Al_2O_3 and HfO_2 by atomic layer deposition (ALD) with the aim to promote voltage-driven ion migration during electrolyte-gating. Magnetic moment at saturation (m_S) and the coercivity (H_C) of Co–Pt are significantly manipulated after biasing either with negative or positive voltages. The application of a negative voltage decreases H_C and increases m_S, whereas positive voltage causes the reverse effect (increase in H_C and decrease in m_S). The same trends were observed in all heterostructures, i.e., uncoated Co–Pt, Co–Pt/Al_2O_3 and Co–Pt/HfO_2 films. Interestingly, the largest magneto-electric effects were obtained for Co–Pt/HfO_2 heterostructured films at negative voltages with an increase of m_S up to 76% and a decrease of H_C by 58%. The observed magnetoelectric changes arise from a reversible oxygen ion migration across the Co–Pt/oxide layer interface, resulting in variations of the Co oxidation state in the nanoporous Co–Pt film. The variations markedly depend on the nature of the ALD nanocoating deposited onto the underlying Co–Pt film, where HfO_2 acts as an oxygen getter layer, thereby triggering magneto-ionic effects at negative voltages, and Al_2O_3 works as oxygen donor layer, thus promoting effects at positive voltages. Hence, our work shows that the combination of a mesoporous magnetic alloy and a skin-like insulating oxide nanocoating is an appealing approach to enhance magneto-ionic effects and decrease power consumption in electrolyte-gated magneto-ionic devices.

[1] C. Navarro-Senent et al., *APL Materials* 7, 030701 (2019) [2] C. Navarro-Senent et al., *ACS Appl. Mater. Interfaces* 10, 44897 (2018) [3] A. Quintana et al., *ACS Nano* 12, 10291 (2018)

11:06

AH-12. Ionic chain size dependence of the low-field magneto-ionic response of ionic liquid/polymer composites. L. Fernandes[1], *E. Fernandez-Martin*[1], D.M. Correia[2,3] and S. Lanceros[1] *1. BCMaterials - Basque Center for Materials, Applications and Nanostructures, Leioa, Spain; 2. Departamento de Química, Universidade de Trás-os-Montes e Alto Douro, Vila Real, Portugal; 3. Departamento de Física, Faculdade de Ciências, Universidade do Minho, Braga, Portugal*

Magnetoelectric (ME) materials provide coupling between ferroelectric and magnetic orders, the coexistence of magnetization and electric polarization in the same material allowing an additional degree of freedom in the design of novel devices such as sensors, actuators, and multistate memory components. This work focus in obtaining a new type of ME response induced when magnetic ionic liquids (MILs) are introduced into a porous polymer matrix. This response is related to the ionic movement rather than to dipole variations, which we will denote it as magneto-ionic (MI) response. MILs are typically produced by the incorporation of a paramagnetic component into either the cation or anion in the IL structure, avoiding the need to include magnetic nanoparticles within the composite [1]. MILs combined with piezoelectric polymers, such as, poly(vinylidene fluoride) (PVDF) [2], represent thus a new class of electroactive smart materials with suitable magnetic, electric, mechanical and electromechanical properties for various applications [3]. These materials possess high response and therefore are suitable for low magnetic field sensing devices [4]. This work presents the effect of the ionic liquid chain size on the magnetic and MI response of the composites. The responsive composites based in imidazolium tetrachloroferrate ILs with different chain lengths ([$C_x$mim][$FeCl_4$])/PVDF x=2,4,8 and 14) were prepared by solvent casting with a concentration of MIL of 20 % wt. Figure 1 shows the magnetic hysteresis loops of the different ionic liquids displaying an increase of the paramagnetic response as the chain length increases. The electric response to ac magnetic fields with no dc magnetic has been obtained up to 100 kHz with a maximum ac field of 0.6 Oe (Figure 2) showing that the electrical response for a given frequency to the ac field is linear and decreases with increasing chain length.

[1] Daniela M. Correia et al., Low-field giant magneto-ionic response in polymer-based nanocomposites *Nanoscale*, 2018,10, 15747-15754 [2] C. Ribeiro et al, Electroactive poly(vinylidene fluoride)-based structures for advanced applications, *Nature Protocols*, vol. 13, pp. 681-704, March. 2018. [3] R. Mejri, et al., Effect of anion type in the performance of ionic liquid/poly (vinylidene fluoride) electrochemical actuators, *Journal of Non-Crystalline Solids,* vol. 453, pp. 8-15, December. 2016. [4] D.M. Correia, et al., Low-field magneto-ionic response in polymer-based nanocomposites, *Nanoscale*, vol. 10, pp. 15747-15754, July 2018.

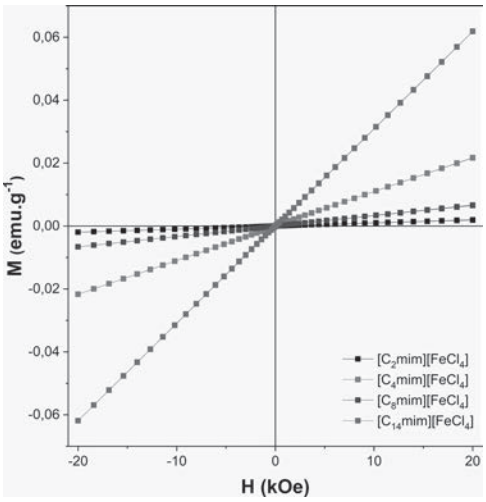


Fig1. Magnetic hysteresis loops of the [$C_x$mim][$FeCl_4$]/PVDF composite films at room temperature.

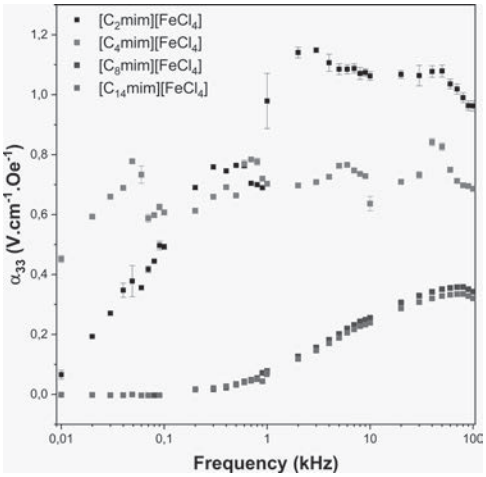


Fig2: MI effect of the [$C_x$mim][$FeCl_4$]/PVDF composite films. MI coefficient as a function of the frequency.

11:18

AH-13. Large Magnetoelectric Effect in Nanoporous Iron Oxide Thin Films Driven by Magneto-Ionics. S. Robbennolt[1], *A. Nicolenco*[1], P.M. Fernandez[1], S. Aufftet[2], V. Baltz[2], E. Pellicer[1], E. Menéndez[1] and J. Sort[1,3] *1. Physics, Autonomous University of Barcelona, Bellaterra, Spain; 2. SPINTEC, Univ. Grenoble Alpes/CNRS/INAC-CEA, Grenoble, France; 3. Institució Catalana de Recerca i Estudis Avançats (ICREA), Barcelona, Spain*

Voltage control of the magnetic properties of oxide thin films is highly appealing to enhance energy efficiency in miniaturized spintronic and magnetoelectric devices [1]. The Iron oxide system is of particular interest because Iron is cheap and environmentally-friendly and there are multiple Iron oxide phases that are stable at room temperature which all have distinct magnetic properties [2,3]. Herein, magnetoelectric effects in electrolyte-gated nanoporous iron oxide films (FeO_x) are investigated. Highly porous films were prepared by the evaporation-induced self-assembly of sol-gel precursors with a sacrificial block copolymer template. For comparison, films with less porosity but analogous crystallographic structure were also prepared using an identical procedure without the polymer template. The magnetoelectric properties of the films were investigated by recording magnetic moment *vs.* applied magnetic field loops as a function of applied voltage. An electrochemical cell is used to apply electric fields *in situ*, i.e., while the magnetic properties of the films are being measured. The templated (highly porous) films showed a very large magnetoelectric response with a maximum increase in magnetic moment at saturation by a factor of 13 and a noticeable two-fold increase of coercivity after applying –50 V [4]. The non-templated films also exhibited a pronounced increase of magnetic moment at saturation by a factor of 4, although the coercivity remained unaffected over the same voltage range. Magnetoelectric effects in these latter films were found to be fully reversible in the voltage window ±10 V. The observed changes in magnetic properties are concluded to be magneto-ionically driven with oxygen ion exchange between the iron oxide and the liquid electrolyte, as evidenced from Raman and X-ray photoelectron spectroscopy experiments.

[1] C. Navarro-Senent et al., *APL Materials* 7, 030701 (2019) [2] S. Dasgupta et al., *Adv. Mater. 26*, 4639–4644 (2014) [3] Q. Zhang et al., *Nano Lett.* 16, 583-587 (2016) [4] S. Robbennolt et al., *submitted to ACS Appl. Mater. Interfaces* (2019)

Session AI
DAMPING, INTERFACES, AND ANISOTROPY I
Eric Arturo Montoya, Chair
University of California, Irvine, Irvine, CA, United States

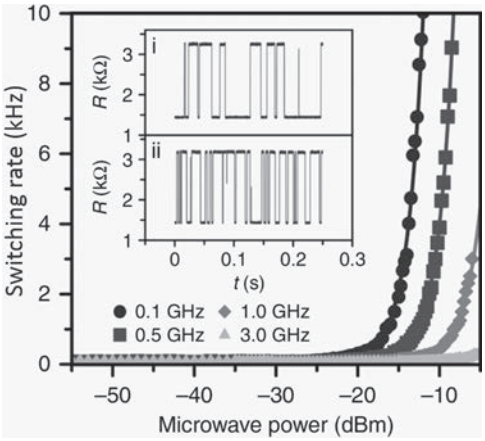
INVITED PAPER

8:30

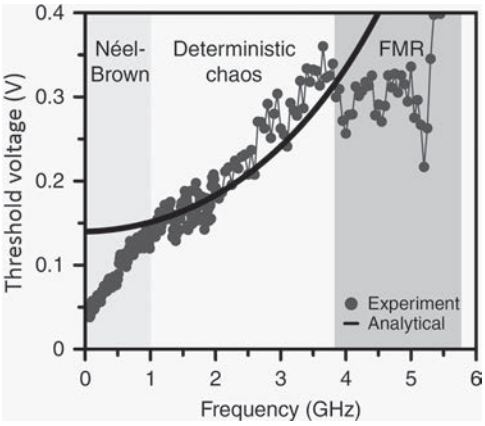
AI-01. Magnetization Reversal Driven by Low Dimensional Chaos in a Nanoscale Ferromagnet. *I. Krivorotov*[1], E.A. Montoya[1], S. Perna[2], J. Katine[3], Y. Chen[1], M. d'Aquino[4] and C. Serpico[2] *1. Department of Physics and Astronomy, University of California, Irvine, Irvine, CA, United States; 2. Department of Electrical Engineering and Information Technology, University of Naples Federico II, Naples, Italy; 3. Western Digital, San Jose, CA, United States; 4. Engineering Department, University of Naples "Parthenope", Naples, Italy*

Energy-efficient switching of magnetization is a central problem in nonvolatile magnetic storage and magnetic neuromorphic computing. In the past two decades, several efficient methods of magnetic switching were demonstrated including spin torque, magneto-electric, and microwave-assisted switching mechanisms. Here we experimentally show that alternating spin torque can strongly increase the rate of thermally-activated magnetic switching of the free layer in a nanoscale magnetic tunnel junction [1]. We present analytical and numerical calculations that explain these experimental findings and reveal the crucial role played by low dimensional magnetic chaos near saddle equilibria in enhancement of the switching rate. We study the effect of ac spin torque on magnetization reversal in a nanoscale ferromagnet with biaxial magnetic anisotropy (predominant easy plane with a weaker in-plane uniaxial anisotropy). The nanomagnet is a 1.8 nm thick $Co_{60}Fe_{20}B_{20}$ ellipse with lateral dimensions of 50 x 75 nm^2 that is the free layer in a magnetic tunnel junction (MTJ). The nanomagnet is sufficiently small to support a single-domain ground state and is superparamagnetic at room temperature. Switching of the free layer magnetization results in change of the MTJ resistance via tunneling magneto-resistance (TMR) [2]. We monitor stochastic switching of the nanomagnet via random telegraph noise (RTN) resistance measurements as a function of ac spin torque amplitude, as illustrated in Fig. 1. The RTN switchign rate as a function of microwave power applied to the MTJ is shown in Fig. 1 for several ac spin torque frequencies. All these frequencies lie below the ferromagnetic resonance (FMR) frequency of the free layer (5.1 GHz). This figure reveals a well-pronounced threshold character of the switching rate in spin torque amplitude proportional to the applied ac voltage. Fig. 2 shows the threshold ac drive voltage as a function of the drive frequency. The points are experimental data and the solid line is the zero-temperature theoretical prediction for the onset of chaotic dynamics [1]. The ac-driven chaotic dynamics having a threshold character is predicted to arise in this system when magnetization is near the top of the energy barrier separating the two energy wells of uniaxial anisotropy [3], [4]. In a band of energies near the top of the barrier, chaotic trajectories bring magnetization across the barrier and thereby induce magnetization switching. Fig. 2 reveals that the analytic theory of chaotic dynamics is in good agreement with experiment in the frequency range from 1 to 4 GHz. In the 4-6 GHz regime, the resonant absorption of energy due to FMR leads to an additional reduction in the energy barrier [5]. In the sub-1 GHz regime, the increase in Neel-Brown switching rate arises from adiabatic enhancement of the amplitude of thermal fluctuations of magnetization by spin torque. This work shows that ac spin torque driven chaos can facilitate thermally-assisted switching of magnetization in an MTJ, which provides a new path towards energy-efficient magnetic memory based on thermally stable MTJs. Additionally, MTJs with superparamagnetic free layers are employed in neuromorphic and reservoir computing schemes. Our results show that low-dimensional chaos provides tunability of switching rates in such systems, and therefore, may lead to computing schemes that use both stochasticity and deterministic chaos.

[1] E. A. Montoya *et al.*, *Nat. Commun.*, Vol. 10, p. 543, (2019) [2] S. Ikeda *et al.*, *IEEE Trans. Electron Devices*, Vol. 54, p. 991, (2007) [3] C. Serpico *et al.*, *J. Appl. Phys.*, Vol. 117, p. 17B719, (2015) [4] M. D'Aquino *et al.*, *Physica B: Condens. Matter*, Vol. 486, p. 121, (2016) [5] J.-G. Zhu, X. Zhu, and Y. Tang, *IEEE Trans. Magn.*, Vol. 44, p. 125, (2008)



Dependence of the free layer switching rate on microwave power and frequency. Insets show MTJ resistance as a function of time measured at 0.5 GHz and two ac power levels: (i) –55 dBm and (ii) –18.5 dBm.



Threshold ac drive voltage for onset of enhanced switching rate as a function of the ac drive frequency. The black solid line is a zero-temperature analytical prediction for the onset of ac-driven chaotic dynamics.

CONTRIBUTED PAPERS

9:06

AI-02. Narrow Total Linewidths in Low-Damping Epitaxial $Fe_{1-x}V_x$ Thin Films. *D.A. Smith*[1], Y. Lim[1], M. Clavel[2], M. Hudait[2] and S. Emori[1] *1. Physics, Virginia Tech, Blacksburg, VA, United States; 2. Electrical Engineering, Virginia Tech, Blacksburg, VA, United States*

To induce spin-torque precession of the magnetization with low threshold current densities, it is desirable to have ferromagnetic metals that possess low damping (narrow resonance linewidths) and low saturation magnetization. A commonly used material in spintronic devices, Fe, already has low Gilbert damping but high saturation magnetization. Alloying Fe with Co [1] allows the damping to decrease to record low values in metallic films but further increases the saturation magnetization. Previous theoretical [2] and experimental studies [3-5] have suggested that alloying Fe with V decreases both damping and saturation magnetization although realization of narrow total linewidths has remained elusive. In this study, we have grown high-quality epitaxial $Fe_{1-x}V_x$ thin films with narrow linewidths by cosputtering on MgO and $MgAl_2O_4$ substrates. The Gilbert damping parameter α and saturation magnetization M_{sat} for each sample are quantified using broadband ferromagnetic resonance (FMR) and vibrating sample magnometry, respectively. In contrast to prior experiments [5] that showed broad FMR linewidths (e.g. $\Delta H_{pp} \approx 40$ Oe at f = 17 GHz), our samples show significantly narrower total linewidths (e.g. $\Delta H_{pp} \approx 22$ Oe at f = 17 GHz, see Fig. 1). This reduction in linewidth is achieved by annealing the substrates at elevated temperatures prior to deposition, allowing for higher quality films and enabling the combination of low Gilbert damping and low inhomogeneous linewidth broadening ΔH_0, as shown in Fig. 2. Compared to epitaxial Fe samples deposited under similar conditions, we see a reduction in both the Gilbert damping and saturation magnetization by as much as ≈20% for $Fe_{80}V_{20}$. Our findings point to FeV as an attractive ferromagnetic alloy for energy-efficient spintronic devices.

1. M. Schoen, D. Thonig, M. Schneider, et al, Nature Physics, Vol. 12, p. 839 (2016) 2. S. Mankovsky, D. Kodderitzsch, G. Woltersdorf, et al, Phys. Rev. B., Vol. 87, p. 014430 (2013) 3. J.-M.L. Beaujour, A. D. Kent, D.W. Abraham, et al, J. Appl. Phys., Vol. 103, p. 07B519 (2008) 4. T. Devolder, T. Tahmasebi, S. Eimer, et al, Appl. Phys. Lett., Vol. 103, p. 242410 (2013) 5. C. Scheck, L. Cheng, I. Barsukov, et al, Phys. Rev. Lett., Vol. 98, p. 117601 (2007)

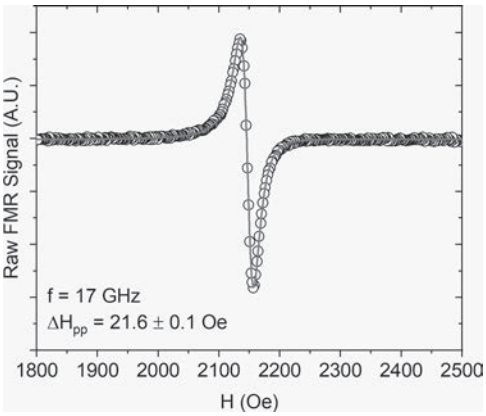


Figure 1: Exemplary FMR signal of $MgO/Fe_{90}V_{10}$ thin film at f = 17 GHz.

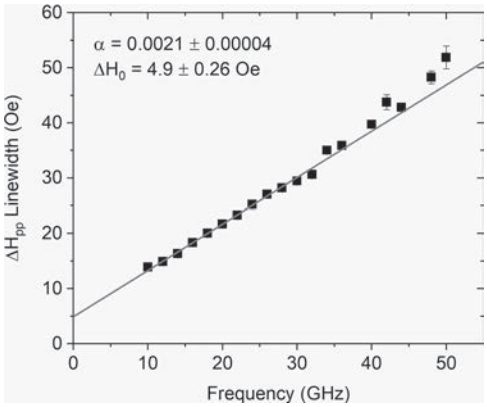


Figure 2: Linewidth vs. frequency plot for $MgO/Fe_{90}V_{10}$. The values of the Gilbert damping parameter and zero frequency linewidth are extracted from the linear fit.

9:18

AI-03. Anisotropic Damping in Multilayer Spintronic Devices. *A. Sapkota*[1,2], A. Farrar[3], T. Mewes[1,2] and C.K. Mewes[1,2] *1. Physics and Astronomy, The University of Alabama, Tuscaloosa, AL, United States; 2. Center for Materials for Information Technology (MINT), The University of Alabama, Tuscaloosa, AL, United States; 3. Harvard Medical School, Boston, MA, United States*

The reduced symmetry originating at the interface of ultra-thin films has a profound influence on the magnetization dynamics. Instead of a scalar damping parameter it leads to a damping tensor, which reflects the symmetry of the confined device, also known as anisotropic damping [1]. Our M^3 code [2] incorporates a damping tensor instead of a scalar damping parameter in the Landau-Lifshitz-Gilbert (LLG) equation [3, 4]. In our study, the damping tensor reflects the symmetry of a thin film structure with exchange bias. The rotational anisotropy contribution to the damping tensor reflects the crystal symmetry of the thin film whereas the orientational anisotropy contribution implies that components of the damping tensor depend on the direction of the magnetization. To understand the observed angular dependence of the damping in previous experimental paper [5, 6], we carried out micromagnetic calculations to simulate ferromagnetic resonance experiments. In micromagnetic simulations an external magnetic field is applied along various angles with respect to the exchange bias direction and in addition a small perpendicular field pulse is utilized to probe the magnetization dynamics. The frequency linewidth at various fields for different in-plane angles are determined by Fast Fourier Transform (FFT) of the recorded magnetizations. As shown in Fig. 1, fully micromagnetic linewidth data is fitted to determine the effective damping parameter α_{FMR}. These α_{FMR} reflect the symmetry of the damping tensor as demonstrated in Fig. 2. Our simulations explain the uniaxial and unidirectional anisotropy observed in experimental results [5, 6].[7]

1) K. Gilmore et al., Physical Review B 81(17), 174414 (2010). 2) http://magneticslab.ua.edu/micromagnetics-code.html. 3) V.G. Bar'yakhtar, and A. G. Danilevich, Low Temperature Physics 36(4), 303-309 (2010). 4) M. Dvornik et al., Physical Review B 88(5), 054427 (2013). 5) J. B Mohammadi et al., Physical Review B 95(6), 064414(2017). 6) A. Rai et al., Journal of Magnetism and Magnetic Materials 485, 374-380(2019). 7) I would like to acknowledge DARPA TEE: D18AP00011, NSF-CAREER: 1452670 and UAHPC.

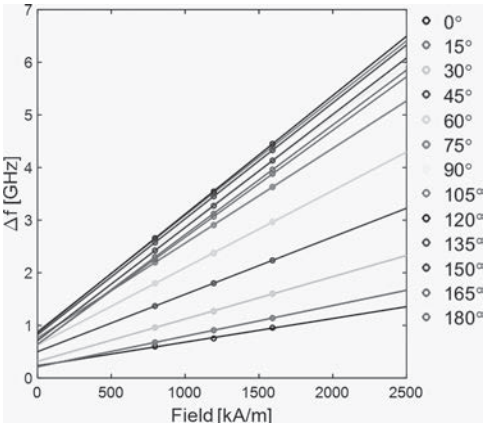


Fig. 1 Frequency linewidth Δf as a function of the applied field H. The symbols are obtained with fully micromagnetic simulations. Each set of linewidth data for a particular angle of applied field with respect to bias direction (different colors) are fitted (lines) to extract effective damping parameter α_{FMR} for each angle.

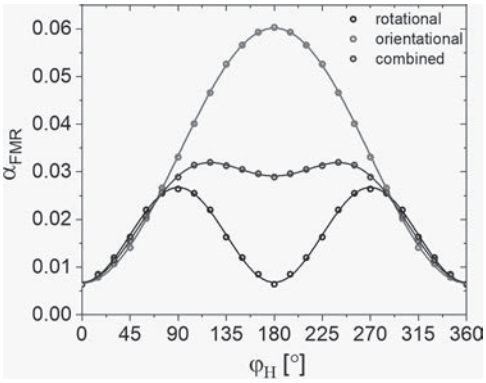


Fig. 2 Effective damping parameters determined from micromagnetic simulations for damping tensors with various anisotropies as indicated in the legends. Fitted lines demonstrate that the effective damping parameter also follows the same anisotropy as the damping tensor.

9:30

AI-04. Gilbert damping constant of NiMnSb half-Heusler alloy film with varying annealing temperature. *R. Mandal*[1], Z. Wen[1], T. Kubota[2,3], K. Takanashi[2,3] and Y. Takahashi[1] *1. Research Center for Spintronics and Magnetics Materials, National Institute for Materials Science, Tsukuba, Japan; 2. Institute for Materials Research, Tohoku University, Sendai, Japan; 3. Center for Spintronics Research Network, Tohoku University, Sendai, Japan*

Half-metallic Heusler alloys are primitive candidates for application in spintronic devices, such as magnetoresistive random access memory[1], current-perpendicular-to-plane giant magnetoresistance read heads for hard disk drives[2] for their high spin polarization and large magnetoresistance ratio. Compared to full Heusler alloys, half-Heusler alloys show large bandgap which helps to suppress thermal activation of electrons that could be advantageous for high-performance magnetoresistive devices. Epitaxially grown NiMnSb (NMS)[3] is a well-known candidate with all-potential properties for such applications. To further investigate the possibilities of this material for application in spintronic devices, the estimation of Gilbert damping (α) is necessary. Herein we report the estimation of α as a function of annealing temperature (T_{annl}) and structural ordering using time-resolved magneto-optical kerr effect (TRMOKE) microscope[4]. MgO-substrate/Cr(30 nm)/Ag(40 nm)/NMS(30 nm)/Al(1.5 nm) films were annealed from room temperature to 673 K. Out-of-plane X-ray diffraction patterns were measured for all the samples and NMS (002) and (004) superlattice peaks were clearly observed in all cases. With enhancement of T_{annl} the NMS (111) peak appears which ensures the formation of $C1_b$ type ordering. Figures 1 (a) and (b) show the maxima in degrees of order at T_{annl} = 573 K for both $B2$- and $C1_b$-type structures respectively and then drop again. To evaluate the α as a function of T_{annl}, the resonance frequency (f_r) was measured using TRMOKE microscope. Using the linearized LLG equation[5] α was estimated. The value of α (Fig. 1 (c)) decreases with T_{annl} and reaches a minimum value of 0.008 at T_{annl} = 573K where the degrees of order show maxima and then again increases, indicating that the degrees of order of samples have strong correlation with Gilbert damping. Therefore, we conclude the 30 nm thick NiMnSb thin film with T_{annl} =573K exhibited highly ordered structure and low magnetic damping showing favorable criteria for application in spintronic devices.

1) A. Hirohata *et al*., *Appl. Phys. A*, 111, 423 (2013). 2) Y. Sakuraba *et al., Appl. Phys. Lett.,* 101, 252408 (2012). 3) Z. Wen *et al*., *Sci. Rep.*, 5, 18387 (2015). 4) R. Mandal *et al*., *Appl. Phys. Lett.*, 113, 232406 (2018). 5) Y. K. Takahashi *et al*., *Appl. Phys. Lett.*, 110, 252409 (2017).

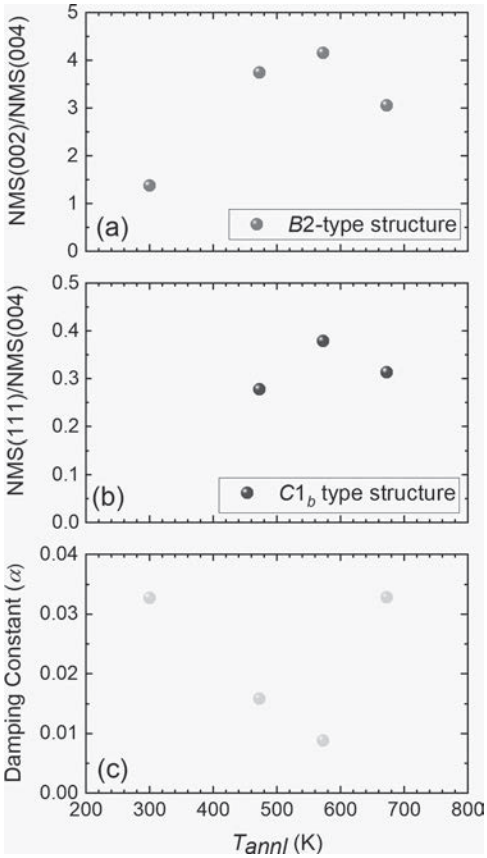


Fig.1: The degrees of order considering (a)$B2$-type structure, (b)$C1_b$ type structure and (c)damping constant plotted as a function of annealing temperature (T_{annl}) of NiMnSb thin film.

9:42

AI-05. Time-retarded damping and magnetic inertia in the Landau-Lifshitz-Gilbert equation self-consistently coupled to electronic time-dependent nonequilibrium Green functions. *U. Bajpai*[1] and B.K. Nikolić[1] *1. Physics and Astronomy, University of Delaware, Newark, DE, United States*

The conventional Landau-Lifshitz-Gilbert (LLG) equation is a widely used tool to describe the dynamics of local magnetic moments, viewed as classical vectors of fixed length, with their change assumed to take place

simultaneously with the cause. Here we demonstrate that recently developed [M. D. Petrović *et al.*, Phys. Rev. Appl. 10, 054038 (2018)] self-consistent coupling of the LLG equation to a time-dependent quantum-mechanical description of electrons—where nonequilibrium spin density from time-dependent nonequilibrium Green function (TDNEGF) calculations is inserted within a torque term into the LLG equation while local magnetic moments evolved by the LLG equation introduce time-dependent potential in the quantum Hamiltonian of electrons—microscopically generates time-retarded damping in the LLG equation described by a memory kernel that is also spatially dependent. For sufficiently slow dynamics of local magnetic moments on the memory time scale, the kernel can be expanded into power series to extract the Gilbert damping (proportional to the first time derivative of magnetization) and magnetic inertia (proportional to the second time derivative of magnetization) terms whose parameters, however, are *time-dependent* in contrast to time-independent parameters used in the conventional LLG equation. We use examples of single or multiple local magnetic moments precessing in an external magnetic field, as well as field-driven motion of a magnetic domain wall (DW), to quantify the difference in their time evolution computed from the conventional LLG equation versus the TDNEGF+LLG quantum-classical hybrid approach. The faster DW motion predicted by the TDNEGF+LLG approach reveals that important quantum effects, stemming essentially from a finite amount of time that it takes for a conduction electron spin to react to the motion of classical local magnetic moments, are missing from conventional classical micromagnetics simulations. We also demonstrate a large discrepancy between the TDNEGF+LLG-computed numerically exact and, therefore, nonperturbative result for charge current pumped by a moving DW and the same quantity computed by a perturbative spin motive force formula combined with the conventional LLG equation.

M. D. Petrović *et al.*, Phys. Rev. Appl. 10, 054038 (2018)

9:54

AI-06. Conductivity-Like Gilbert Damping due to Intraband Scattering in Epitaxial Iron. B. Khodadadi[1], A. Rai[2], A. Sapkota[2], A. Srivastava[2], B. Nepal[2], Y. Lim[1], D.A. Smith[1], C.K. Mewes[2], S. Budhathoki[2], A.J. Hauser[2], M. Gao[1], J. Li[1], D. Viehland[1], Z. Jiang[1], J.J. Heremans[1], P. Balachandran[3], T. Mewes[2] and *S. Emori*[1] *1. Virginia Tech, Blacksburg, VA, United States; 2. University of Alabama, Tuscaloosa, AL, United States; 3. University of Virginia, Charlottesville, VA, United States*

Confirming the origin of Gilbert damping by experiment has remained a challenge for many decades. This is the case even for some of the simplest ferromagnetic metals, such as pure Fe. Here, we experimentally identify Gilbert damping that increases with decreasing electronic scattering in thin films of BCC Fe. We directly compare the temperature dependence of Gilbert damping and electronic transport in pristine epitaxial films (Figure 1). Our observation of conductivity-like damping, which cannot be accounted for by classical eddy current loss, is in excellent quantitative agreement with theoretical predictions of Gilbert damping due to intraband scattering [1,2], as shown in Figure 2. These results resolve the longstanding question since the 1970s [3,4] about the role of intraband scattering in Gilbert damping in pure ferromagnetic metals. Furthermore, our experimental confirmation that clean ferromagnetic metals exhibit higher intrinsic damping (spin decoherence) at low temperatures may have important implications for designing magnetic media in quantum information applications. Acknowledgements: 4-VA, a collaborative partnership for advancing the Commonwealth of Virginia; NSF-CAREER 1452670; NASA CAN80NSSC18M0023.

1. K. Gilmore, Y. U. Idzerda, and M.D. Stiles, Phys. Rev. Lett., Vol. 99, p. 027204 (2007); K. Gilmore, Ph.D. Thesis (2007). 2. S. Mankovsky, D. Kodderitzsch, G. Woltersdorf, et al. Phys. Rev. B, Vol. 87, p. 014430 (2013). 3. S. M. Bhagat and P. Lubitz, Phys. Rev. B, Vol. 10, p. 179 (1974). 4. D. M. Edwards, J. Phys. Cond. Matter, Vol. 28, p. 086004 (2016).

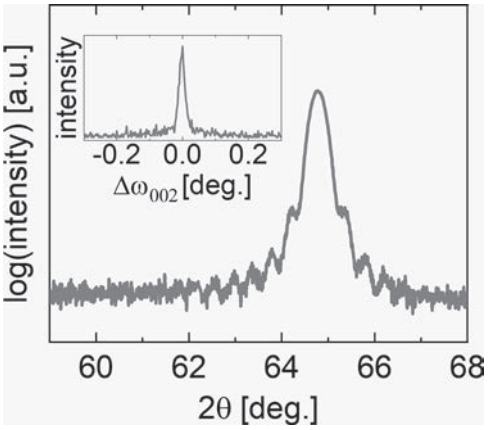


Figure 1. X-ray diffraction scan near the BCC (002) film peak of 25-nm-thick epitaxial Fe grown on a $MgAl_2O_4$ (001) substrate. Laue oscillations indicate smooth film interfaces. Inset: film-peak rocking curve with FWHM of only ~0.02 degrees, indicating minimal mosaic spread.

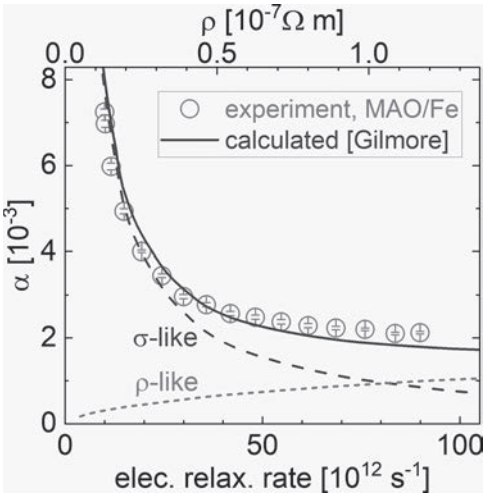


Figure 2. Comparison of the experimentally derived intrinsic Gilbert damping parameter (eddy current contribution subtracted) and the theoretically predicted Gilbert damping parameter (adapted from Ref. 1) plotted against the electronic relaxation time.

10:06

AI-07. Intrinsic damping of FeRh thin films. *G.A. Riley*[1,2], M.L. Schneider[1], H. Nembach[1], J.M. Shaw[1], J. Lauzier[3], J. de la Venta[3] and O. Eriksson[4] *1. Quantum Electromagnetics Division, National Institute of Standards and Technology, Boulder, CO, United States; 2. Center for Memory and Recording Research, University of California-San Diego, La Jolla, CA, United States; 3. Physics, Colorado State University, Fort Collins, CO, United States; 4. Department of Physics and Astronomy, Uppsala University, Uppsala, Sweden*

Thin film alloys of FeRh exhibit a large magnetoresistance (MR) effect due to a first order structural phase transition at temperatures near room temperature [1]. During the transition, the magnetization changes from an antiferromagnetic (AF) to a ferromagnetic (F) state and is accompanied by up to 50% change in electrical resistivity [2]. However, the physical mechanism for this transition driven MR is still being explored. A recent model based on density functional theory (DFT) calculations indicate that the large changes in resistivity result from a difference in electronic structure between the F

and AF states as well as increase in amplitude of spin fluctuations [2]. DFT calculations also predict a low damping for FeRh. Vector-network-analyzer ferromagnetic resonance (VNA-FMR) measurements in the perpendicular geometry were performed on FeRh thin films of two thicknesses: t=15 nm and 20 nm. The FeRh films were grown by dc magnetron sputtering on MgO (001) single crystal substrates and were capped with 3 nm of Al. The AF-F transition temperature was determined from magnetometry measurements. Prior to the FMR measurements the samples were heated to 390 K to ensure that the samples are in the ferromagnetic state. Damping was then determined from the slope of the measured linewidth for a range of temperatures above the transition temperature. The temperature-dependent magnetization was used to determine the radiative damping which was subtracted to determine the intrinsic damping following Ref. [3]. Figure 1 shows that the intrinsic damping is higher for the thin film, $\alpha = 3.26 \pm 0.14$, compared with $\alpha = 1.99 \pm 0.11$ for the thick film. The out-of-plane anisotropy, shown in Fig. 2, is considerably larger for the thin film as expected. These results offer a more comprehensive experimental picture of dissipative processes that occur in FeRh thin films to compare with forthcoming theoretical models. This work was supported by DOE award DE-SC0018237.

[1] V. L. Moruzzi and P. M. Marcus, Physical Review B 46, 14198 (1992) [2] S. Mankovsky*et al.*, Physical Review B 95, 155139 (2017) [3] M. A. W. Schoen *et al.*, Physical Review B 92, 184417 (2015)

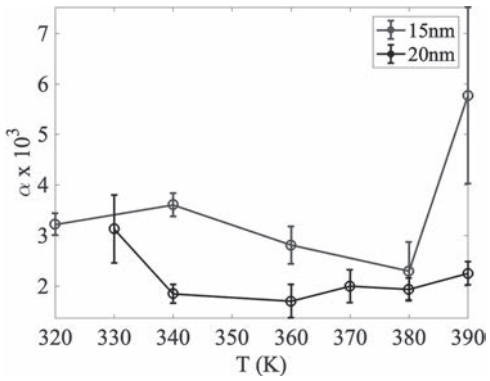


Fig. 1.Gilbert damping as a function of temperature of FeRh thin films of two thicknesses measured while cooling toward the FM to AFM transition.

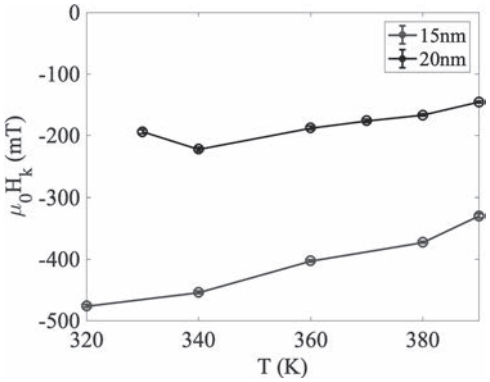


Fig. 2. Out-of-plane anisotropy for the two films as a function of temperature.

10:18

AI-08. Anisotropic Gilbert Damping in Sputtered $Fe_{0.7}Ga_{0.3}$ Films and Correlation with Crystal Structure. *W. Peria*[1], H. Yu[2], S. Lee[2], J.G. Barriocanal[3], I. Takeuchi[2] and P.A. Crowell[1] *1. School of Physics and Astronomy, University of Minnesota, Minneapolis, MN, United States; 2. Department of Materials Science and Engineering, University of Maryland, College Park, MD, United States; 3. Characterization Facility, University of Minnesota, Minneapolis, MN, United States*

The ability to engineer Gilbert damping is important for spintronics because it governs the switching efficiency in current-induced switching applications as well as the rate of spin relaxation, which plays an important role in magnetic storage applications. Certain compositions of FeGa alloys are known to have large magnetostriction coefficients, which is a valuable property for applications which rely on magnetomechanical transducers. We have measured ferromagnetic resonance linewidths of 30 nm $Fe_{0.7}Ga_{0.3}$/SiO_2/Si(001) (room temperature deposition) with field applied in-plane and out-of-plane (see figure). The in-plane linewidths show a nonlinear frequency dependence which is characteristic of two-magnon scattering. We fit the in-plane data using the model of McMichael and Krivosik [1] and obtain a Gilbert damping of 0.014, which agrees with a linear fit to the data above 20 GHz. We measure the Gilbert damping to be 0.0038 with the field applied out-of-plane, and therefore observe a Gilbert damping anisotropy of approximately a factor of 4. Furthermore, the anisotropy is reduced when the deposition temperature is increased to 200°C, which suggests a straightforward way of tuning the Gilbert damping. The defect correlation length obtained from the two-magnon fitting is in excellent agreement with the grain diameter measured from atomic force microscopy and the coherence length obtained from wide-angle x-ray diffraction (XRD). We show the existence of nanoprecipitates of epitaxial Fe_3Ga, which are known to enhance the magnetostriction in Galfenol ($Fe_{0.81}Ga_{0.19}$) [2]. These nanoprecipitates also show tetragonal distortion in XRD, which has recently been reported to cause anisotropic Gilbert damping in $Co_{0.5}Fe_{0.5}$ [3]. We conclude by positing structural distortions as the cause of the anisotropic damping.

[1] R. D. McMichael and P. Krivosik, IEEE Trans. Mag. 40, 2 (2004). [2] H. Cao *et al.,* Phys. Rev. Lett. 102, 127201 (2009). [3] Y. Li *et al.,* Phys. Rev. Lett. 122, 117203 (2019).

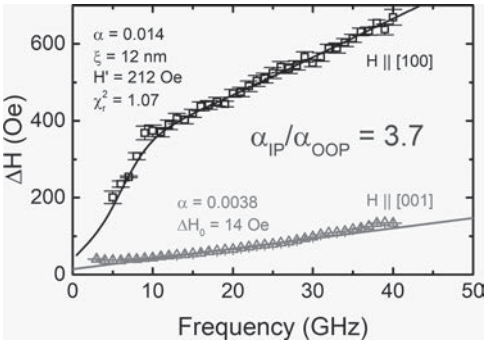


Fig. 1: Ferromagnetic resonance linewidths of 30 nm $Fe_{0.7}Ga_{0.3}$ for field applied in-plane (black) and out-of-plane (red).

10:30

AI-09. Choking nonlocal magnetic damping in exchange-biased ferromagnets. *T. Moriyama*[1], K. Oda[1] and T. Ono[1] *1. Kyoto University, Uji, Japan*

The Gilbert damping constant, α, is one of the important parameters characterizing the magnetization dynamics. It influences the switching speed of the magnetization and also determines the threshold current for various spin-torque-related phenomena [1]. It is, however, one of the least experimentally controllable magnetic parameters. Recently, we have revisited

the mechanism of the non-local damping with the exchange biased ferromagnet (FM)/antiferromagnet (AFM) multilayers and showed that the non-local damping was influenced by the Néel order in the AFM [2]. These results indeed offer a control of the magnetic damping by the magnetic order in the adjacent AFM. In this work, we particularly investigated the temperature dependence of the non-local damping in the exchange biased AFM/FM multilayer. α was characterized for the magnetization pointing along the exchange bias (EB) direction and against the EB direction by ferromagnetic resonance at elevated temperatures. Figure 1 (a) shows the temperature dependence of α in Pt (5nm)/FeMn (t_{FeMn} = 0 and 20nm)/FeNi (4nm). While α for t_{FeMn} = 0 nm slightly increases with the temperature, α for t_{FeMn} = 20 nm drastically decreases with increasing temperature. We also found that α measured against the EB is always greater than that measured along the EB. As shown in Fig. 1 (b), the difference (Δα) is linearly correlated with the strength of the EB, which is consistent with our previous observation [2]. The results essentially indicate that the non-local damping can be controlled by the adjacent antiferromagnet and its temperature dependent exchange bias. We also point out that such a strong temperature dependent damping may be very beneficial for spintronic applications involving a Joule heating upon the operation [3].

[1] Y. Tserkovnyak, *et al.*, *Rev. Mod. Phys.* 77, 1375 (2005). [2] T. Moriyama, *et al.*, *Phys. Rev. Lett.* 119, 267204 (2017). [3] T. Moriyama, *et al.*, *Phys. Rev. Appl.* 11, 011001 (2019).

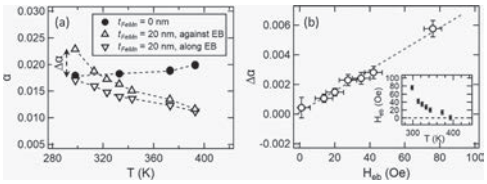


Figure 1: (a) The Gilbert damping, α, as a function of temperature for t_{FeMn} = 0 and 20 nm. (b) Δα as a function of the strength of EB (H_{eb}). The inset shows H_{eb} as a function of temperature.

10:42

AI-10. Effect of Temperature on the Magnetization Dynamics of Amorphous Co-Fe-B Thin Films with Various Thicknesses. *Y. Endo*[1,2], H. Tanaka[1], T. Nguyen[2,3], H. Sato[2,3], S. Ikeda[2,4] and T. Endoh[2,3]
1. Electrical Engineering, Tohoku University, Sendai, Japan; 2. CSIS, Tohoku University, Sendai, Japan; 3. CIES, Tohoku University, Sendai, Japan; 4. CSRN, Tohoku University, Sendai, Japan

The magnetization dynamics in amorphous Co-Fe-B thin films has been studied intensively for the rapid development of spintronics devices such as MRAM, spin-torque oscillator, spin-logic and so on. In particular, a Gilbert damping constant (α), which describes the strength of damping torque, is one of the key parameters to understand the dynamics. However, details about the effect of temperature on α in these thin films are not understood fully. Herein we evaluate α at various temperatures of amorphous Co-Fe-B thin films with the thicknesses of 5, 10, and 15 nm by a broadband ferromagnetic resonance (FMR) measurement technique, and discuss the effect of temperature on α in these films in detail. The effective saturation magnetization ($4\pi M_{s,eff}$), the inhomogeneous field ($\Delta H(0)$) and α were estimated by analyzing FMR spectra of each film at various temperature, and were plotted in Fig. 1 as a function of temperature. For each film thickness, $4\pi M_{s,eff}$ slightly increases as the temperature decreases, while its value for the thickness of 5 nm becomes lower than those for the thickness of 10 and 15 nm. The reason for this difference might be due to the enhancement of the surface anisotropy with the decreases of film thickness. In contrast, regardless of the film thickness, $\Delta H(0)$ and α slightly increase as the temperature decreases and markedly increase at the temperature below 150 K, which might be proportional to the wave number dependent electrical conductivity[1]. Additionally, in case of the film thickness of 5 nm, the increment of α for the temperature becomes larger, which might be ascribed to the magnetic inhomogeneity such as the anisotropy dispersion. Therefore, these results suggest that the tendency of damping in each Co-Fe-B film for temperature is mainly consistent with the behavior of damping expected by intra-band transition. The authors acknowledge the Core Research Cluster program of Tohoku Univ., Japan. This work was supported in part by JSPS KAKENHI Grant No. JP17H03226. This work was supported in part by CIES collaborative research from CIES, Tohoku University. This work was also supported in part by ASRC in Japan.

[1] B. Heinrich et al., J. Appl. Phys. 50, 7726 (1979).

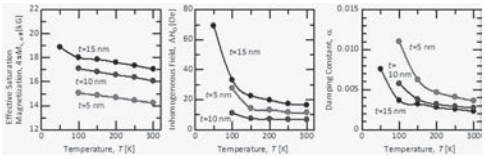


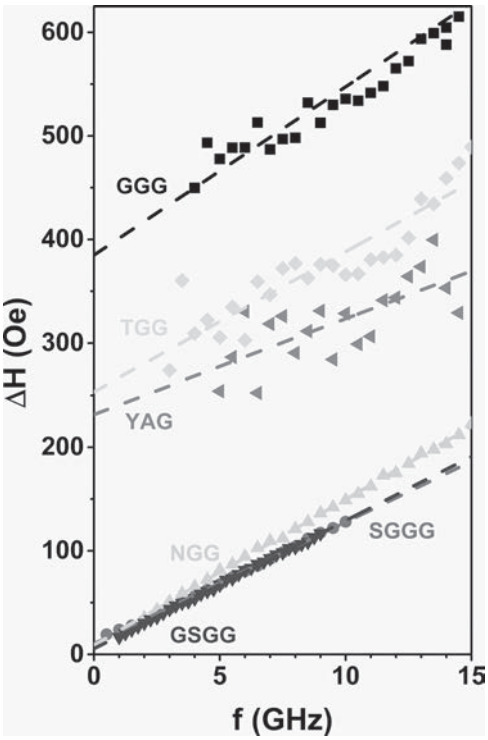
Fig. 1. Temperature dependence of $4\pi M_{s,eff}$, $\Delta H(0)$ and α for various thick Co-Fe-B films.

10:54

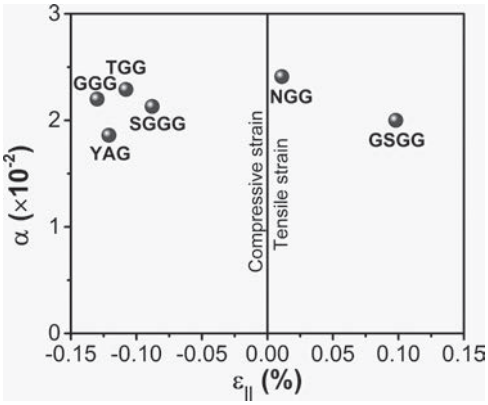
AI-11. Engineering Magnetic Properties via Strain in Europium Iron Garnet Thin Films. V.H. Ortiz[1], B. Arkook[1], J. Li[1], W. Yuan[1], *I. Barsukov*[1] and J. Shi[1] *1. Physics and Astronomy, University of California, Riverside, Riverside, CA, United States*

Ferrimagnetic insulators play an important role in spintronics research. Among ferrimagnetic insulators, rare earth iron garnets (REIGs) have a plethora of attributes desirable for practical applications. Controlled growth of epitaxial REIG thin films offers a unique opportunity to control their magnetic properties such as magnetic anisotropy and Gilbert damping [1][2][3]. In this work, we grow atomically flat europium iron garnet (EuIG) thin films by pulsed laser deposition. Employing various (111) garnet substrates and by varying film thickness from 10 to 50 nm, we control the strain from compressive to tensile regime, which is characterized using X-ray diffraction. We carry out angle- and frequency-dependent ferromagnetic resonance measurements and find a significant second-order perpendicular magnetic anisotropy in films with large compressive strain. While inhomogeneous linewidth increases with increasing strain, we find the Gilbert damping to be nearly constant (~ 10^{-2}). The results advance our understanding of spin dynamics in ferrimagnetic insulators and provide insights for material synthesis and engineering for various spintronics applications This work was supported as part of SHINES, an Energy Frontier Research Center funded by the U.S. Department of Energy, Office of Science, Basic Energy Sciences under Award SC0012670.

[1] Kubota, M., Shibuya, K., Tokunaga, Y., Kagawa, F., Tsukazaki, A., Tokura, Y., & Kawasaki, M. (2013). Systematic control of stress-induced anisotropy in pseudomorphic iron garnet thin films. *Journal of Magnetism and Magnetic Materials*, *339*, 63–70. https://doi.org/10.1016/j.jmmm.2013.02.045 [2] Wang, H., Du, C., Hammel, P. C., & Yang, F. (2014). Strain-tunable magnetocrystalline anisotropy in epitaxial $Y_3Fe_5O_{12}$ thin films. *Physical Review B*, *89*(13), 134404. https://doi.org/10.1103/PhysRevB.89.134404 [3] Ortiz, V. H., Aldosary, M., Li, J., Xu, Y., Lohmann, M. I., Sellappan, P., … Shi, J. (2018). Systematic control of strain-induced perpendicular magnetic anisotropy in epitaxial europium and terbium iron garnet thin films. *APL Materials*, *6*(12), 121113. https://doi.org/10.1063/1.5078645



Frequency dependent FMR. FWHM linewidth vs. frequency for 50 nm EuIG films grown on different garnet substrates.



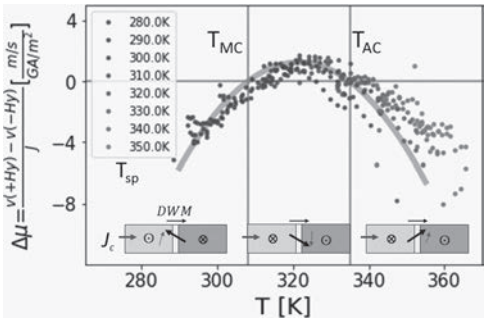
Gilbert damping α vs in-plane strain ε_I on EuIG films grown on different garnet substrates.

11:06

AI-12. Ferrimagnetic domain wall dynamics driven by Spin Orbit Torques revealed by in-plane fields through the compensation points in GdFeCo. *E. Haltz*[1*], J. Sampaio[1], R. Weil[1], S. Krishnia[1], L. Berges[1] and A. Mougin[1] *1. Laboratoire de Physique des Solides, Orsay, France*

To improve the efficiency of the manipulation of magnetic textures using spin torques, materials such as rare earth-transition metal ferrimagnetic alloys [1] are promising due to their tuneable magnetic properties (via temperature or chemical composition) [2]. At so-called compensation points (CPs), either magnetisation (at T_{MC}) or angular momentum (at T_{AC}) vanishes modifying the classic behaviour [3]. However, a full understanding of the magnetic dynamics at these CPs, including the determination of T_{AC}, still lacks. Domain wall motion (DWM) induced by current pulses (25ns) is studied in a 10μm wire made from co-evaporated $GdFeCo_{(5nm)}$ amorphous thin-film with perpendicular magnetic anisotropy and Pt covered[2]. Combining in-plane field and current J, the dynamics of the DW crossing CPs are probed within two approaches by Kerr microscopy. In a zero-field approach, the DW moves along J revealing a Spin Orbit Torque (SOT) process [4]. The velocity is very high (up to 700 m/s) [3]. However, the non-monotonous behaviour indicates Joule heating revealed by peaks of the domain wall mobility and assigned to TAC. We propose a second approach measuring the DWM driven by current under transverse in-plane field Hy. Moving a DW is related to tilting its internal magnetization [4] which is disclosed under Hy: Hy affects the magnetization angle, bringing it closer or farther to the Néel configuration, changing the SOT efficiency and increasing or decreasing the macroscopic velocity of DWM. The figure shows Δμ=v(+Hy)-v(-Hy)/J for different J and temperature T. The sign of Δμ directly reveals the internal DW magnetisation angle. Two sign changes occur, evidencing T_{MC} and T_{AC}. At T_{MC}, the dominant sublattice changes and the action of Hy reverses which by turn changes the angle. At T_{AC}, the tilt associated to the DWM reverses. Δμ reveals these changes very clearly. This approach relying on the application of a transverse field gives a T_{AC} value consistent with the mobility but based on intrinsic properties of the DW and not affected by the pinning.

[1] Haltz et al., PRB 99 (2019) [2] Hansen et al., JAP 66 (1989), Haltz et al., PRM 2 (2018) [3] Kim et al., Nat.Mat. 16 (2017), Caretta et al., Nat.Nano.13 (2018), Siddiqui et al.,PRB 121 (2018) [4] Thiaville et al., EPL 100 (2012), Parkin et al., Nat.Nano. 102 (2013)



Δμ *vs* J and *vs* T_{sp} rescaled on T. Inserts represent Kerr contrast and magnetization state for each ranges of T.

11:18

AI-13. Magnetic damping of non-collinear synthetic antiferromagnets probed by time-resolved magneto-optical Kerr effect. *A. Kamimaki*[1,2], S. Iihama[2,3], T. Taniguchi[4] and S. Mizukami[2,3] *1. Department of Applied Physics, Tohoku University, Japan, Sendai, Japan; 2. WPI-AIMR, Tohoku University, Japan, Sendai, Japan; 3. CSRN, Tohoku University, Japan, Sendai, Japan; 4. Spintronics Research Center, AIST, Tsukuba, Japan*

Antiferromagnet is the one of the important topics of current spintronics. In particular, synthetic antiferromagnet (SAF) is expected to be used for memory devices because of the tunability of its net magnetizations [1]. Considering magnetization dynamics in SAF, there are two magnetic resonances corresponding to an acoustic (AC) and optical (OP) mode. Besides them, a dynamic exchange coupling due to the spin-pumping should be discussed [2-5]. Previous study showed magnetization damping using microwave technique for SAFs in case of collinear magnetization configuration [5]. From an application point of view, it is also desired to examine magnetization damping in case of non-collinear magnetization configuration. In this work, we investigated two resonance modes for SAF in non-collinear magnetization configuration using all-optical means, and discussed the effect of dynamic exchange coupling on magnetic damping [6]. The stacking structure of SAF was Si/SiO_2 (subs.)/Ta(3)/CoFeB(3)/Ru(0.4)/CoFeB(3)/Ta (3) (thickness in nm). The samples were prepared by a magnetron sputtering. In the all-optical time-resolved magneto-optical Kerr effect (TRMOKE) measurements, a fluence of the pump was 1.5 mJ/cm^2 and an applied magnetic field angle was approximately 10° with respect to the film normal. Fig. 1 shows the typical TRMOKE results. The oscillations for

AC and OP modes were extracted by a fitting. Fig. 2 shows the effective damping for both modes obtained from the fitting. The solid and broken curves show the calculated results with and without the spin-pumping at the Ru/CoFeB interface, and the these results were well agreed with the experiments. It was clarified that the dynamic exchange coupling in SAF increases the effective damping only for the OP mode. A. Kamimaki thanks to the Graduate Programs of Spintronics at Tohoku University. This work was partially supported by KAKENHI (26103004, 19K15430) and JSPS Core-to-Core Program.

[1] R. A. Duine, K.-J. Lee, S. S. P. Parkin, and M. D. Stiles, Nat. Phys. 14, 217 (2018). [2] H. Tomita, A. R. Khorsand, T. Seki, A. Kirilyuk, A. Kimel, T. Rasing, and Y. Suzuki, J. Magn. Soc. Jpn. 36, 24 (2012) [3] K. Tanaka, T. Moriyama, M. Nagata, T. Seki, K. Takanashi, S. Takahashi, and T. Ono, Appl. Phys. Exp. 7, 063010 (2014). [4] T. Chiba, G. E. W. Bauer, and S. Takahashi, Phys. Rev. B 92, 054407 (2015). [5] H. Yang, Y. Li, and W. E. Bailey, Appl. Phys. Lett. 108, 242404 (2016). [6] A. Kamimaki, S. Iihama, T. Taniguchi, and S. Mizukami, submitted.

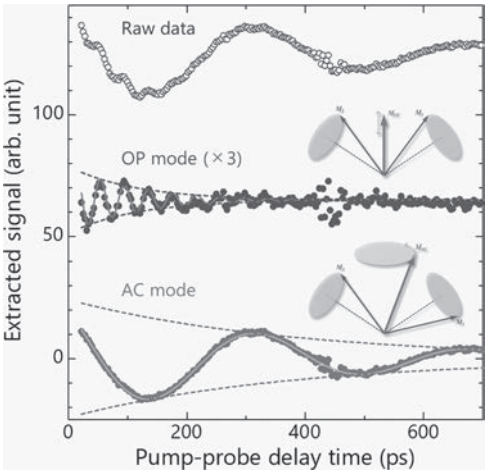


Fig. 1 TRMOKE signal obtained for CoFeB/Ru/ CoFeB SAF structures measured at $\mu_0 H$ = 0.27 T. Solid symbols are the extracted data of AC and OP mode by using fitting.

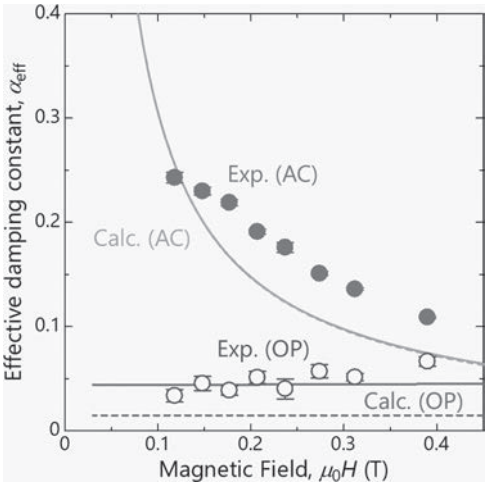


Fig. 2 Effective damping α_{eff} of the two modes as a function of $\mu_0 H$. Solid and open symbols represent the AC and OP modes, respectively.

Session AP
SPIN CALORITRONICS AND SPIN TRANSPORT PHENOMENA (Poster Session)

Peng Li, Chair
Auburn University, Auburn, AL, United States

AP-01. Thermoreflectance Measurement of the Spin Peltier Effect.
T. Yamazaki[1], R. Iguchi[2], T. Ohkubo[2], H. Nagano[1] and K. Uchida[2]
1. Nagoya University, Nagoya, Japan; 2. National Institute for Materials Science, Tsukuba, Japan

In recent years, "spin caloritronics", a fusion research field of correlation physics between heat and spin transport, has developed rapidly since the spin Seebeck effect was observed [1]. The spin Peltier effect (SPE) [2,3], the reciprocal phenomenon of the spin Seebeck effect, is referred to as the conversion of spin current into heat current in paramagnetic metal (PM)/ ferromagnetic insulator (FI) junction systems. In previous reports [3,4], the thermographic method is used and revealed that the SPE induces characteristic temperature modulation, where it is localized near the junction interfaces and approaches the steady state very rapidly (expected to be less than 1 ms [4]). While the experimental determination of temporal response is necessary for understanding the physical origin of the SPE and also for designing possible devices utilizing the SPE, no experimental results are obtained so far because of the low temporal resolution of the thermographic method (>1 ms), used in the previous studies. In this work, we demonstrate that the thermoreflectance method realizes the SPE measurement with high temporal resolution. Here, the thermoreflectance method determines the temperature through the reflectivity of the material. Following the previous thermographic studies, we employed this method in the frequency domain with the lock-in detection technique, i.e. the lock-in thermoreflectance (LITR) [5]. In our LITR measurement, the SPE is driven by the application of a charge current to the paramagnetic layer in the junction system, which induces a spin current via the charge-to-spin conversion (spin Hall effect [6]) in the paramagnetic layer (Fig. 1). The SPE-induced temperature change synced with the spin-current injection is extracted by monitoring the reflected intensity of the irradiated CW light (Fig. 2). As shown in Fig. 2, the lock-in detection enables exclusive detection of the SPE-induced temperature modulation, separated from that of Joule heating. We succeeded the SPE measurements by LITR under high lock-in frequency (up to 1 MHz) and determined its temporal response time.

[1] K. Uchida, S. Takahashi, K. Harii, *et al*., Nature, Vol. 455, p. 778 (2008) [2] J. Flipse, F. K. Dejene, D. Wagenaar, *et al*., Phys. Rev. Lett., Vol. 113, 027601 (2014) [3] S. Daimon, R. Iguchi, T. Hioki, *et al*., Nature Communications, Vol. 7, 13754 (2016) [4] R. Iguchi and K. Uchida, Jpn. J. Appl. Phys. Vol. 57, 0902B6 (2018) [5] C. A. Paddock and G. L. Eesley, J. Appl. Phys., Vol. 60, p. 285 (1986) [6] J. Sinova, Rev. Mod. Phys., Vol. 87, p. 1213 (2015)

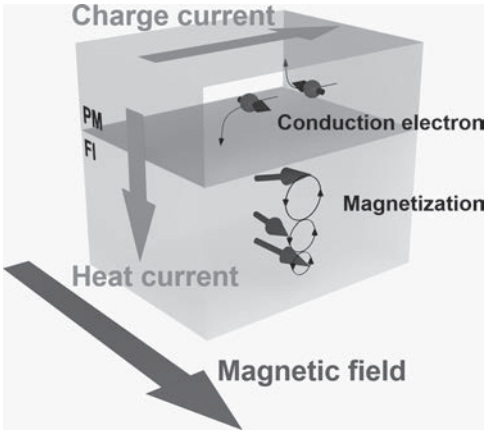


Fig. 1 Schematic illustration of the spin Peltier effect (SPE)

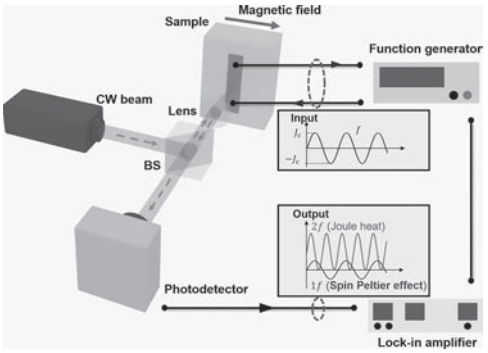


Fig. 2 Schematic image of the lock-in thermoreflectance (LITR)

AP-02. Electrical detection of spin Nernst effect using lateral spin valve structures. *R. Matsuda*[1], R. Suko[1], D. Ito[1] and T. Kimura[1,2] *1. Depertment of Physics, Kyushu University, Fukuoka, Japan; 2. Research Center for Quantum Nano-Spin Science, Fukuoka, Japan*

Recent developments of spintronics and spin-caloritronics indicate that a longitudinal heat current produces the transverse spin current owing to the spin-orbit interaction. This is known as spin Nernst effect[1,2,3] (SNE), which is a kind of spin-heat conversion. Several research groups reported the observation of SNE independently and found the similar tendency. In these experiments, they adapt multi-layered structures to perform the efficient spin injection and detection. However, in such layered structures, undesired signals originating from the ferromagnetic proximity effect[4] were superimposed on the SNE and make it difficult to analyze the actual SNE signal. To eliminate the influence of the magnetic proximity effect, we here develop the SNE devices based on lateral spin valve structures. Figure 1 shows the schematic illustration of the fabricated device for SNE. Here, Pt and CoFeAl wires are bridged by a Cu strip. As schematically shown in Fig. 1, the temperature gradient normal to the heavy metal/Cu junction was produced by the Joule heating in the heave metal. Owing to SNE, the transverse spin current is injected into the Cu strip through the side surface

of the Pt wire. The injected spin current can be electrically detected by a CoFeAl electrodes. By changing the magnetization direction of the CoFeAl, a rectangular-shape spin signal will be expected. Figure 2(a) shows the field dependence of the electric signal induced in the CoFeAl electrode. A rectangular shape signal was clearly observed, implying the electrical detection of the SNE of the Pt. To obtain more definite evidence, we also perform the similar experiment by using Ta wire. As seen in Fig.2(b), a clear rectangular shape signal is observed also in the Ta device. In the spin Hall effect, the sign of the spin Hall angle for Ta is opposite to that for Pt[5]. However, in the present experiment, we do not observe the sign reversal in the Ta. Although the reason is not clear at the moment, we may have to take into account the anomalous Nernst effect in the CoFeAl electrode.

[1] D. J. Kim, C. Y. Jeon, B. G. Park, Nature Communications 9, 1, 138 (2018). [2] S. Meyer et al., Nature Materials 16, 977 (2017). [3] P. Sheng, S. Mitani, and M. Hayashi, Science Advances 3, 7, e1701503 (2017). [4] M. Suzuki et al., Physical Review B 72, 8, 054430 (2005). [5] M. Morota, T. Kimura, and Y. Otani, Physical Review B 83, 5, 174405 (2011).

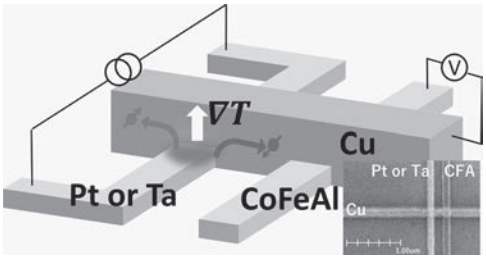


Fig. 1 Conceptual image of electrical detection of SNE together with the SEM image of the fabricated device.

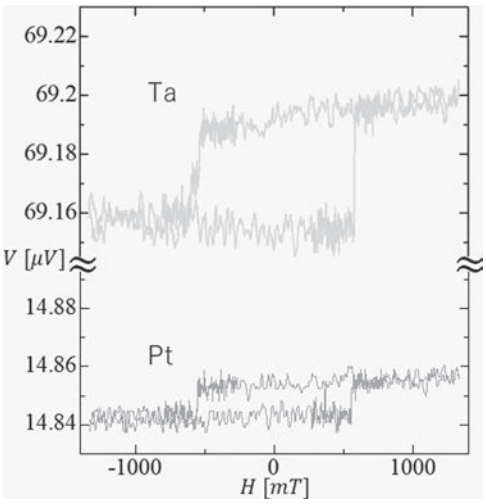


Fig. 2 SNEs signal for Pt and Ta wire measured at RT.

AP-03. Spin diffusion length and polarization of ferromagnetic metals measured by a spin-absorption technique in lateral spin valves.
G. Zahnd[1], *S. Ghosh*[1], L. Vila[1], V. Pham[1], M. Cosset-Cheneau[1], W. Lim[1], A. Brenac[1], P. Laczkowski[1], A. Marty[1] and J. Attané[1] *1. University of Grenoble Alpes, CEA, CNRS, INP-G, IRIG-Spintec, Grenoble, France*

Recent advances in spinorbitronics have evidenced the need for new characterization techniques. Parameters such as the damping, the polarization, the spin diffusion length, the Dzyaloshinskii-Moriya interaction (DMI) or the spin Hall angle are key factors in understanding and controlling various mechanisms: spin transfer torque [1], spin texture due to DMI [2], or charge-to-spin conversion based on spin-orbit coupling effects at Rashba interfaces [3], in the bulk of spin Hall effect (SHE) materials [4], or in surface states of topological insulators [5]. We present measurements of pure spin current absorption on lateral spin valves. By varying the width of the absorber we demonstrate that spin current absorption measurements enable one to characterize efficiently the spin transport properties of ferromagnetic elements. The analytical model used to describe the measurement takes into account the polarization of the absorber. The analysis of the measurements thus allows the determination of the polarization and the spin diffusion length of a studied material independently, contrary to most experiments based on lateral spin valves where those values are entangled. We report the spin transport parameters of some of the most important materials used in spin-orbitronics ($Co_{60}Fe_{40}$, $Ni_{81}Fe_{19}$, Co, Pt, and Ta), at room and low (10 K) temperatures. The obtained spin-dependent transport parameters are relatively close to values found in the literature for Pt [6], CoFe [7], NiFe [8], and Ta. We find a very low spin diffusion length for Ta (2 nm), quite low for NiFe, CoFe, and Pt (5.3, 6, and 3.8 nm, at room temperature, respectively). In contrast, the spin diffusion length of Co is found to be on the order of 10 nm at room temperature, smaller than in previous reports.

1. M. D. Stiles and A. Zangwill, Phys. Rev. B 66, 014407 (2002). 2. K. Zakeri, Y. Zhang, J. Prokop, T. H. Chuang, N. Sakr, W. X. Tang, and J. Kirschner, Phys. Rev. Lett. 104, 137203 (2010). 3. H. Min, J. E. Hill, N. A. Sinitsyn, B. R. Sahu, L. Kleinman, and A. H. MacDonald, Phys. Rev. B 74, 165310 (2006). 4. E. Saitoh, M. Ueda, H. Miyajima, and G. Tatara, Appl. Phys. Lett. 88, 182509 (2006). 5. C. Z. Chang, J. Zhang, X. Feng, J. Shen, Z. Zhang, M. Guo, K. Li, Y. Ou, P. Wei, L. L. Wang, and Z. Q. Ji, Science 340, 167 (2013). 6. J.-C. Rojas-Sánchez, N. Reyren, P. Laczkowski, W. Savero, J.-P. Attané, C. Deranlot, M. Jamet, J.-M. George, L. Vila, and H. Jaffrès, Phys. Rev. Lett. 112, 106602 (2014). 7. M. Johnson and R. H. Silsbee, Phys. Rev. Lett. 55, 1790 (1985). 8. S.D. Steenwyk, S. Y. Hsu, R. Loloee, J. Bass, and W. P. Pratt, J. Magn. Magn. Mater. 170, L1 (1997).

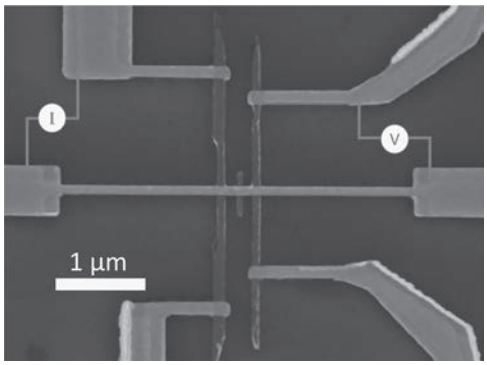


Fig. 1. Colored SEM Image of the spin-absorption device displaying the measurement configuration, and the ferromagnetic electrodes in red, the nonmagnetic channel in yellow, and the spin absorbing wire in blue.

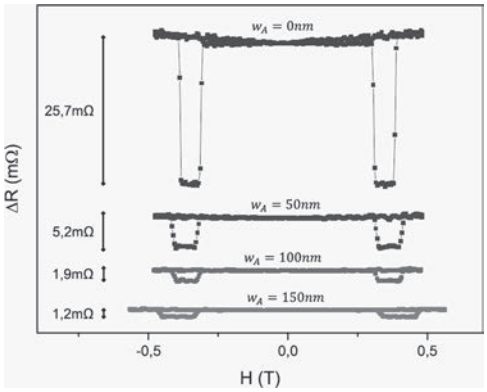
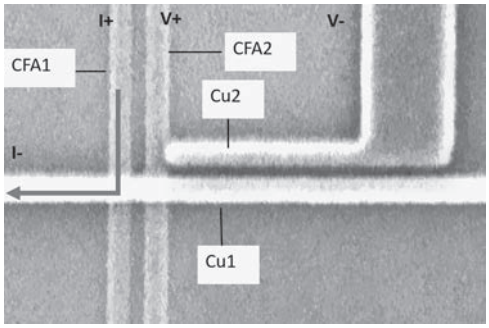


FIG. 2. Nonlocal measurements performed at room temperature on different devices. The spin signal amplitude is decreasing when the width of the absorbing wire increases. Different offsets have been set for each magnetoresistance curve, for graphical purposes.

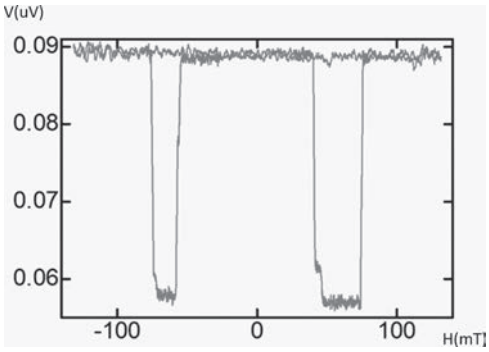
AP-04. Observation of the spin-dependent Peltier effect in lateral spin valve. *R. Suko*[1], R. Matsuda[1], D. Ito[1] and T. Kimura[1,2] *1. Dep. Physics, Kyushu University, Fukuoka, Japan; 2. Quantum Spin Research Center of Kyushu Univ., Fukuoka, Japan*

The discovery of the thermally excited spin current promoted the research on the conversion between the spin and heat, so called as spin caloritronics. As an opposite phenomena, the spin-current induced heating and cooling effect, namely the spin(-dependent) Peltier effect, has been reported by several groups very recently. In the reports, they used a complicated nanostructures lateral and vertical hybrid nanostructures or specially developed thermometer in order to detect the tiny signal. If the efficiency of the spin-heat conversion is sufficiently large, one can observe the spin-dependent Peltier effect (SDPE) more simply. Here, we demonstrated a relatively simple way for detecting the spin-dependent Peltier effect using a conventional lateral spin valve. Figure 1 shows the SEM image of the lateral spin valve used for the present study. Here, we adapt the CoFeAl (CFA), which has a large spin-dependent Seebek coefficient, indicating an efficient SDPE. The pure spin current generated from CFA1 flow through Cu1 and is effectively absorbed into the CoFeAl 2. The absorbed spin current produces the heat current which heat or cool the CFA2. The temperature change of the CFA2 due to the SDPE can detected as the Seebeck voltage between CFA2 and Cu2. Figure 2 shows a representative nonlocal signal measured at 20 K. A spin-valve like signal due to the SPE with the magnitude of 30nV was clearly obtained. From the change of the resistance, one can estimate the temperature change due to SDPE as 0.5mK. In the presentation, we will reports SDPE for other ferromagnetic metals and their temperature dependence.

J. Flipse, F. L. Bakker, A. Slachter, Direct observation of spin-dependent Peltier effect, nature nanotechnology, Vol.7, p.166-168 (2012) A. Slachter, F. L. Bakker, B. J. van Wees, Modeling of thermal spin transport and spin-orbit effects in ferromagnetic/nonmagnetic mesoscopic devices, Phys. Rev. B 84, 174408 (2011) S. Hu, J. Zhao, L. Wang, Substantial enhancement of thermal spin polarization in Py/Cu interface, PhysRevMaterials.2.104403(2018) S. Daimon, K. Uchida, R. Iguchi, Thermographic measurements of the spin Peltier effect in metal/yttrium-iron-garnet junction systems, Phys. Rev. B 96, 024424 (2017)



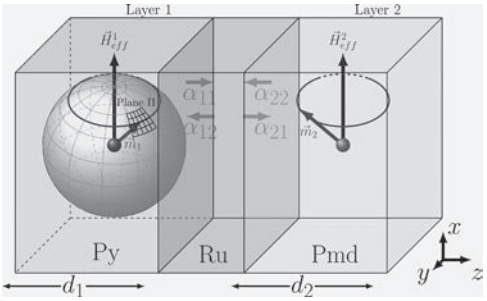
SEM image and schematic illustration of the fabricated device



Electrically detected spin-dependent Peltier signal

AP-05. Non-Reciprocal Spin Pumping in Asymmetric Magnetic Trilayers. *M. Pereiro*[1], Y. Pogoryelov[1], S. Jana[1], A. Kumar[2], S. Akansel[2], M. Ranjbar[3], D. Thonig[1], D. Primetzhofer[1], P. Svedlindh[2], J. Åkerman[3], O. Eriksson[1], O. Karis[1] and D.A. Arena[4] *1. Department of Physics and Astronomy, Uppsala University, Uppsala, Sweden; 2. Department of Engineering Sciences, Uppsala University, Uppsala, Sweden; 3. Department of Physics, University of Gothenburg, Gothenburg, Sweden; 4. Department of Physics, University of South Florida, Tampa, FL, United States*

In magnetic trilayer systems, spin pumping is generally addressed as a reciprocal mechanism characterized by one unique spin mixing conductance common to both interfaces. However, this assumption is questionable in cases where different types of interfaces are present in the material. Here, we present a general theory for analyzing spin pumping in cases with more than one unique interface. The theory is applied to analyze layer-resolved ferromagnetic resonance experiments on the trilayer system $Ni_{20}Fe_{80}$/Ru/$Fe_{49}Co_{49}V_2$ where the Ru spacer thickness is varied to tune the indirect exchange coupling. The results show that the spin pumping in trilayer systems with dissimilar magnetic layers is non-reciprocal. Our findings have importance on dynamics of spintronic devices based on magnetic multilayer materials.



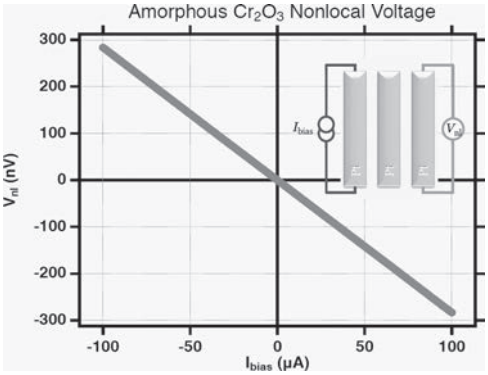
(Color online) Trilayer system composed of Permalloy (1) and Permendur (2) layers separated by a layer of Ruthenium. On the right-bottom of the figure the coordinate system used for the analytical derivations is shown. The blue arrow represents the precession of the spin in the y-z plane used in the model while the black arrow indicates the direction of the external magnetic field. The sphere represents the locus of constant magnetization length while II stands for the plane tangential to the surface of the sphere. The red-yellow arrows indicate the static (α_{ii}) and dynamic (α_{ij}) spin pumping dampings due to the currents flowing in and out of the layers. The thickness of the magnetic layers is represented by d_1 and d_2.

AP-06. Spin Transport in Disordered Magnetic Insulators. *L.A. Hernandez*[1], M. Roos[1], D.J. Wesenberg[1] and B.L. Zink[1] *1. Physics and Astronomy, The University of Denver, Denver, CO, United States*

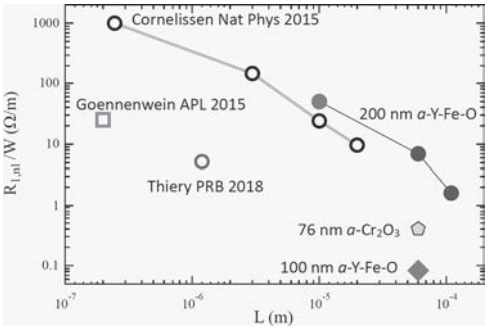
Much work has been done to explore spin transport through crystalline magnetic materials [1], yet recent work has shown that long range magnetic order is not a requirement for spin transport through insulators such as amorphous yttrium iron oxide (*a*-$Y_3Fe_5O_{12}$) [2]. Magnetic insulators are of special interest for applications in devices that use spin-based logic [3], and in this work we present the observation of spin transport in amorphous chromium oxide (*a*-Cr_2O_3), and the continued work on *a*-$Y_3Fe_5O_{12}$. Platinum leads inject spin current via the spin hall effect (SHE) and detect a non-local voltage (V_{nl}) via the inverse spin hall effect (ISHE) and the guard rail method is employed to mitigate electric charge leakage [4]. Results of 100 and 200 nm *a*-$Y_3Fe_5O_{12}$, and 76 nm *a*-Cr_2O_3 show a negative slope of the nonlocal voltage vs. injection current at 300 K, confirming the detection of a spin current via ISHE. Temperature dependence of *a*-$Y_3Fe_5O_{12}$ shows the onset of V_{nl} ~ 230 K corresponding with a feature in the magnetization. This gives more insight into the mechanisms of spin transport through

disordered magnetic insulators due to externally excited evanescent spin wave modes [5, 6]. Comparing the nonlocal spin transport of these disordered magnetic insulators with their crystalline counterparts shows that they are just as efficient at transporting spin angular momentum.

[1] V. Baltz *et al, Rev. Mod. Phys.* 90, 015005 (2018). [2] D. Wesenberg *et al, Nature* 13, 987–993 (2017). [3] J. Torrejon *et al, Nature* 547, 428 (2017). [4] D. Wesenberg *et al.,* (PRMats, submitted, 2019). [5] B. I. Halperin *et al, Phys. Rev. B* 16, 5 (1977). [6] R. Khymyn *et al, Phys. Rev. B* 93, 224421 (2016).



Nonlocal voltage measured as a function of injection current at 300 K and 0 field.



Comparison of spin transport through disordered magnetic insulators to crystalline magnetic insulators, with respect to lead separation.

Session AQ
MAGNETO-CALORIC AND MAGNETO-ELASTIC MATERIALS I (Poster Session)

Radhika Barua, Co-Chair
Virginia Commonwealth University, Richmond, VA, United States
Joao Sequeira Amaral, Co-Chair
Universidade de Aveiro, Aveiro, Portugal

AQ-01. Comparison on the ΔE effect in $Fe_{87}Ga_{13}$ alloy by doping Dy and Tb. *H.W. Chang*[1], S.U. Jen[2], D. Tseng[3], W. Cheng[4], W. Chang[1] and C. Ouyang[5] *1. National Chung Cheng University, Chia-Yi, Taiwan; 2. Academia Sinica, Taipei, Taiwan; 3. Tunghai University, Taichung, Taiwan; 4. NTUST, Taipei, Taiwan; 5. National Tsing Hua University, Hsinchu, Taiwan*

Fe-Ga alloys have attracted increasing attention due to good mechanical properties and large saturation magnetostriction (λ_s) at low magnetic field for the potential applications at acoustic sensors and magnetoelastic devices and sensors [1]. λ_s of Fe-Ga alloy is reported to be significantly increased by adding small amounts of Tb [2]. However, the worse ductility for $Fe_{100-z}Ga_z$ alloys with high Ga content e.g. z = 19-27 may limit the applications even though large magnetostriction is obtained [1-2]. Distinct from the previous literatures, more ductile Ga-lean $Fe_{87}Ga_{13}$ master alloy is adopted in this work. R-doping effects on the mechanical properties including Young's modulus (E) at magnetic field (H), that is ΔE effect, magnetic properties, magnetostriction, and magneto-mechanical coupling of quenched $Fe_{86.8}Ga_{13}R_{0.2}$ alloys prepared by induction melting (R=Tb and Dy) are studied. $\Delta E_s/E_0$ effect of $Fe_{87}Ga_{13}$ alloy is 6%, and it is significantly enhanced to 12% by doping 0.2% Dy, but reduced to 4.5% for Tb-doped alloy. The magnetostrictive sensitivity (dλ/dH) with R is similar to that of ΔE with R. For $Fe_{86.8}Ga_{13}R_{0.2}$ alloys, $\Delta E_s/E_0$ is proportional to the square of the magneto-mechanical coupling factor (K^2), theoretically calculated in term of permeability (μ), dλ/dH. Most importantly, strong ΔE effect or K due to high dλ/dH for $Fe_{86.8}Ga_{13}Dy_{0.2}$ alloy favors for applications. Large ΔE effect or magneto-mechanical coupling is considered to correlate to modified phase constitution by doping Dy. For Tb-doped alloy, increased λ_s might be related to the increase of Ga content in the matrix due to the appearance of minor Tb_2Fe_{17} phase. The decreased dλ/dH might result from increased coercivity and decreased μ because of the induction of Tb_2Fe_{17} phase and result in reduced ΔE effect and K. The findings of this work provide an effective pathway of enhancing the ΔE effect for Galfenol alloys.

[1] J. Atulasimha et al., Smart Mater. Struct. 20, 043001 (2011). [2] L.P. Jiang et al., Appl. Phys. Lett. 102, 222409 (2013).

AQ-02. Extended X-ray Absorption Fine Structure Spectroscopy for Flexible Spintronics. *S. Ota*[1,2], T. Hirai[1,2], T. Ina[3], T. Koyama[2,4] and D. Chiba[2,4] *1. Applied Physics, The University of Tokyo, Bunkyo, Japan; 2. The Institute of Scientific and Industrial Research, Osaka University, Ibaraki, Japan; 3. Japan Synchrotron Radiation Research Institute, Sayo, Japan; 4. Center for Spintronics Research Network at Osaka University, Toyonaka, Japan*

Adding flexibility to spintronic devices yields new functions [1]. Flexible electronic devices generally aim to be immune to an external strain, whereas flexible spintronic devices can make use of sensitivity to the external strain via the magnetoelastic effect [2-4]. Interestingly, reversible change in a magnetic anisotropy of ferromagnetic thin films formed on a flexible substrate has been realized even when stretch-induced tensile strain in the substrate exceeds 1%. However, under such a large strain, a strain transfer from the substrate is unobvious. To determine directly the change in an atomic distance under applying tensile strain, we conducted the extended X-ray absorption fine structure (EXAFS) spectroscopy of a Co film on a polyethylene naphthalate substrate. Figure 1 shows radial distribution functions of a 7-nm-thick Co obtained by EXAFS. In the EXAFS measurement, polarization of the X-ray is parallel to the tensile strain, where the spectrum mainly reflects an atomic structure in the tensile direction. Here, a peak for the nearest neighbor atoms clearly shifts. Atomic distance change of 0.3% at 1.6% substrate strain is determined by fitting analysis. The large difference between the atomic distance change and the substrate strain can be explained by a calculation assuming that the Co has an fcc(111)-oriented polycrystalline structure. The calculation expects 0.45% atomic distance change at 1.6% substrate strain if the substrate strain is perfectly transferred to the Co film. Thus, the EXAFS result is ~30% smaller than the perfect-transfer condition, most likely because of the reduced strain transfer. We also note that the effective magnetoelastic constant (*B*) similarly decreases when the Co thickness is 7 nm (Fig. 2) [3]. The authors thank K. Ochi, M. Suzuki, T. Nakamura, T. Namazu, R. Nishino and M. Kawasaki for useful discussion and technical help. This work was partly supported by the JSPS KAKENHI (Grant No. JP17J03125) and Spintronics Research Network of Japan.

[1] D. Makarov *et al., Appl. Phys. Rev.,* Vol. 3, p. 011101 (2016) [2] T. Uhrmann *et al.*, *J. Magn. Magn. Mat.,* Vol. 384, p. 209 (2006). [3] S. Ota *et al.*, *Nat. Electron.,* Vol. 1, p. 124 (2018). [4] H. Matsumoto *et al.*, *Appl. Phys. Lett.,* Vol. 114, p. 132401 (2019).

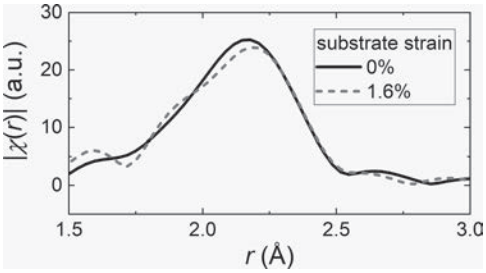


Fig. 1 Radial distribution functions of Co sample with and without strain.

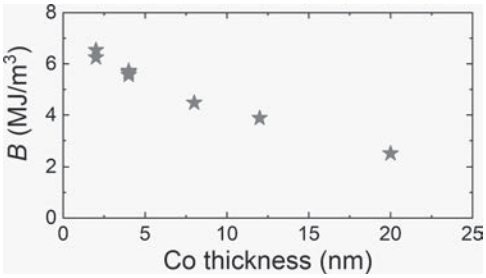
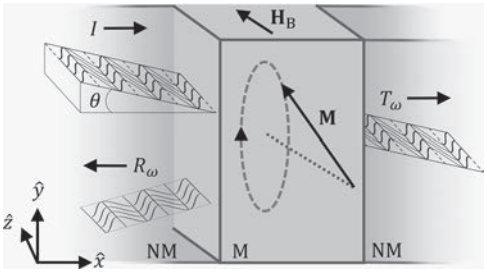


Fig. 2 Effective magnetoelastic constants (*B*) dependence on Co thickness. (Reproduced from [3].)

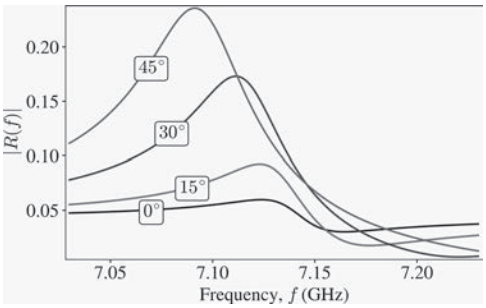
AQ-03. Controlling Acoustic Waves using Magnetoelastic Fano Resonances. *O. Latcham*[1], Y. Gusieva[2], A. Shytov[1], O. Gorobets[2] and V.V. Kruglyak[1] *1. University of Exeter, Exeter, United Kingdom; 2. Igor Sikorsky Kyiv Polytechnic Institute, Kyiv, Ukraine*

Magneto-elastic coupling between acoustic waves and magnetic procession may allow one to combine the low loss of acoustic waves and magnetic memory within the same devices. This may provide a route to devices that are more energy efficient than purely acoustic or magnetic devices. For instance, one can use acoustic waves as a signal carrier and then use their scattering from a magnetic inclusion as a means of control. Here, we explore theoretically how the strength of the magneto-elastic Fano resonance in the scattering of acoustic waves from an isolated magnetic slab (Fig.1) can be enhanced.[1] We find that the scattering strength is determined by the ratio of the linewidth due to the Gilbert damping and that due to the re-emission of acoustic waves. While the former is a material property, the latter depends on the magnetoelastic coupling strength, the slab width and the incidence angle. We calculate the ratio for different parameters of the slab and use it as a figure of merit by which to compare different magneto-elastic materials. We find that the oblique incidence angle may be used to enhance the resonant scattering (Fig.2) by enabling magneto-elastic coupling to the in-plane component of the elliptically polarized magnetic precession. In particular, an angle of incidence of about 15 degrees (Fig. 2) leads to a twofold increase in the figure of merit as compared to the normal incidence. The scattering strength may be further enhanced due to Bragg scattering in arrays of magneto-elastic slabs, which would thereby form a magnon-phonon crystal.

[1]O. S. Latcham, Y. Gusieva, A. V. Shytov, O. Y. Gorobets, V. V. Kruglyak, arXiv:1906.07297



Acoustic waves are incident at an angle on a thin magnetic slab (M) embedded within a non-magnetic matrix (NM) and are scattered with the transmission and reflection coefficients *T* and *R* respectively.



The frequency dependence of he reflection coefficient from a magnetic slab in the region of the Fano resonance is shown for differenet angles of incidence.

AQ-04. Simulation Design of Magnetic and Thermal Properties of Magnetorheological Elastomer Bushing. *W.M. Kiarie*[1], E.J. Barron III[1], M.D. Bartlett[1] and D.C. Jiles[2] *1. Materials Science and Engineering, Iowa State University, Ames, IA, United States; 2. Electrical and Computer Engineering, Iowa State University, Ames, IA, United States*

This paper presents a model of magnetic and thermal properties of magneto-rheological elastomer (MRE) in a novel design of a Semi-active Suspension Bushing (SSB). MREs are a class of composite materials consisting of soft magnetic particles embedded into a polymer matrix. Under the influence of a magnetic field the MRE is activated causing a change of stiffness in the bulk. Suspension bushings are designed to dampen frequencies that may cause discomfort to the driver. These bushings are considered passive, for they work effectively for a limited range of frequencies as designed. If operated outside these frequencies, they eventually lose their effectiveness. Therefore, SSB is designed such that it adjusts its frequencies accordingly depending on the road surface conditions. For this reason, the ability to controllably change the stiffness of MRE makes it highly desirable for use in SSB. The geometry and the electromagnetic circuit design have strong influences on the magnetic flux density and heat transfer properties. For effective performance of the SSB, high magnetic flux density is needed to effect large changes in stiffness this requires a large multi-turn coil leading to significant amount of heat output that can degrade the MRE. To balance these complexities, a Finite Element Analysis (FEA) is carried out to create a novel SSB, that optimizes the magnetic flux density and decreases the heat generated due to resistive losses. From the analysis, this novel design is observed to have a 24% increment in average magnetic flux density throughout the MRE with uniform radial distribution and a significant decrease in the heat generated.

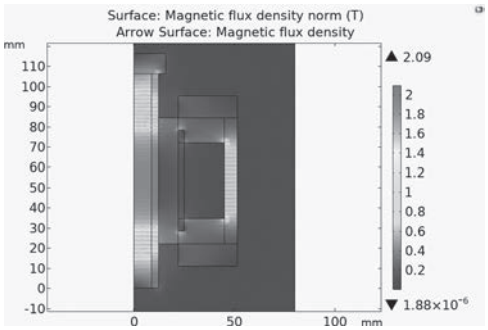


Fig 1: Magnetic flux density distribution of MRE bushing.

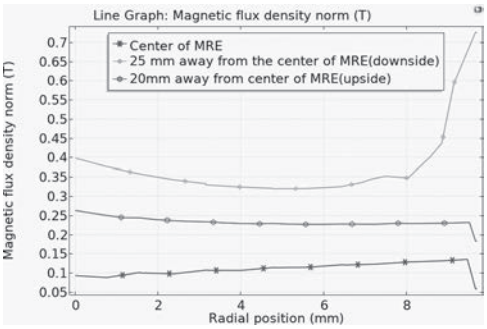


Fig 2: Magnetic flux density induced at different radial positions in the MRE.

AQ-05. Modeling and Fabrication of a Thin-Film Magnetorheological Elastomer Composite using Iron (III) Oxide Nanoparticles. *D.A. O'Mahoney*[1], A. El-Ghazaly[2] and J. Bokor[3] *1. Materials Science and Engineering, University of California, Berkeley, Berkeley, CA, United States; 2. Electrical and Computer Engineering, Cornell University, Ithaca, NY, United States; 3. Electrical Engineering and Computer Science, University of California, Berkeley, Berkeley, CA, United States*

Magnetorheological elastomers (MREs) are gaining interest for a number of applications[1-3]. However, little has been done to explore their applications in flexible electronics. This work looks at the possibility of using MREs to create flexible, programmable tactile surfaces with predictable deformation control. We took steps in realizing this goal through finite element modeling and fabrication of an MRE thin film device. The MRE was molded and fabricated on top of a nonmagnetic, flexible substrate, to create areas of compression and tension on opposite sides of the film when exposed to a magnetic field. Local control of the magnetic field was modeled using a surface

array of GdCo nanomagnetic dots (Fig. 1). Magnetic field simulations in COMSOL showed shallow field penetration from the nanodots. Because of this, a thin film elastomer was fabricated using nanoscale iron (III) oxide particles with diameter less than 50 nm. Previously MREs have only been created using micron sized magnetic particles in much thicker films[1-4]. Films with smaller particles have not been studied. The composite was fabricated by spin coating 4" silicon wafers with lift-off resist, followed by 6μm of SU-8 as the flexible substrate. The MRE was made by combining 30% iron (III) oxide nanoparticles and 70% Dowsil 734 by volume. This was spun onto the wafers at varying speeds giving final composite thicknesses between 55μm and 80μm after release from the silicon wafer. Displacement of the film was measured using a varying, external out-of-plane magnetic field. Results (Fig. 2) show vertical deformation of the films, with thinner films producing larger displacement maximizing at 58μm with an applied field of 800 Oe. These findings show that nanosized iron (III) oxide particles in an MRE produce measurable deformation and can be used in creating thin MRE films. The technique of spin coating an MRE on top of an SU-8 substrate proved to be successful and COMSOL simulations suggest that the addition of a nonmagnetic layer does not prevent field induced deformation.

[1] U. Ubaidillah, J. Sutrisno, A. Purwanto, Adv. Eng. Mater., Vol.17, p.563-597 (2015) [2] S. Lee, C. Yim, W. Kim, ACS Applied Materials & Interfaces., Vol. 7, p.19853-19856 (2015) [3] W. Li, X. Zhang, H. Du, Advances in Elastomers I: Blends and Interpenetrating Networks., Vol.11, p.357-374, (2013) [4] S. Marchi, A. Casu, F. Bertora, ACS Applied Materials & Interfaces., Vol. 7, p.19112-19118 (2015)

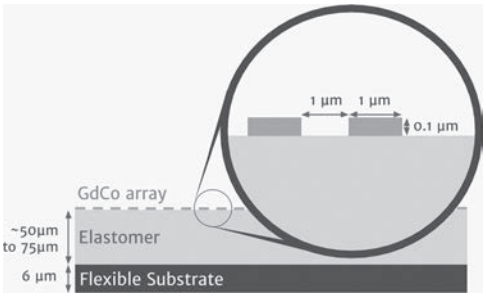


Fig. 1 - Device geometry for flexible programmable MRE film

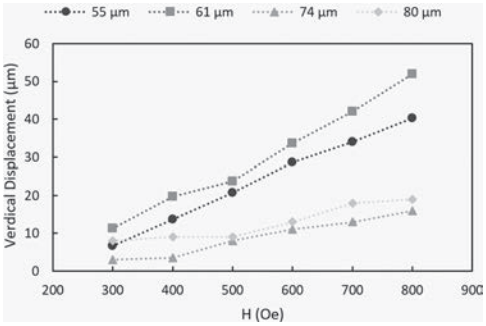
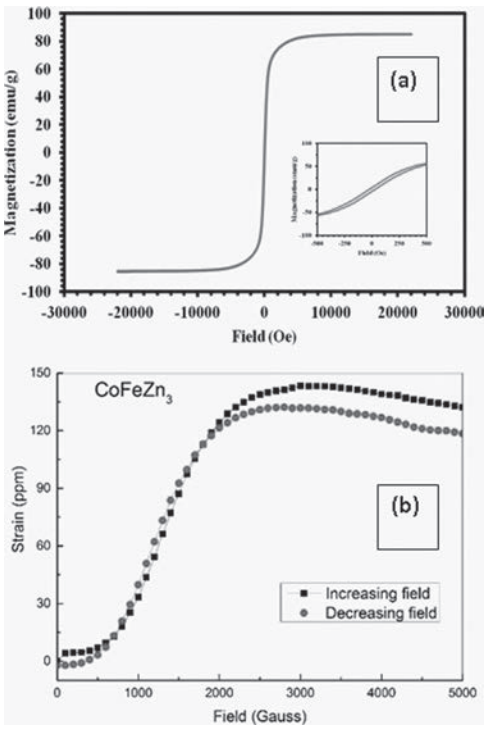


Fig. 2 - Vertical displacement of varying thicknesses of MREs in response to an external out-of-plane magnetic field

AQ-06. Hysteresis-free Highly Magnetostrictive Oxides. *S. Pokharel*[1], Z. Alyousef[1], M. Hassan[1], W. Morgan[1], M. Wuttig[2] and A. Lisfi[1] *1. Physics, Morgan State University, Baltimore, MD, United States; 2. Materials Science and Engineering, University of Maryland, College Park, MD, United States*

Hysteresis-free magnets displaying a large mechanical response under small magnetic fields are of a considerable interest to modern technology [1-2]. Cobalt ferrite can fulfill such requirement since it is distinguished by its large magnetostriction and good chemical stability. However, its moderate magnetization and large hysteresis can limit its technological performance. This research work aims to synthesize new ceramic material in the bulk phase that can exhibit a high magnetization and low anisotropy together with a sizable magnetostriction. The material of interest consists of Zn-doped cobalt ferrite, which is expected to offer the following enhanced properties over pure cobalt ferrite. (1) Doping with Zn can produce a significant increase in the magnetization. (2) The doped ceramic can display nearly hysteresis-free magnetic character while inheriting a large magnetostriction from cobalt ferrite. A series of Zn-doped cobalt ferrite samples was prepared with ball milling. The doped samples with different Zn concentrations were compacted and annealed at different temperatures up to 1500 °C. A good illustration of the enhanced properties is displayed in Fig. 1, which depicts the field dependence of the magnetization and the magnetostriction of Zn-doped cobalt ferrite prepared at 1400 °C. As shown by Fig. 1(a), the saturation magnetization of the Zn-doped sample (86 emu/g) exceeds that of pure single crystal cobalt ferrite (80 emu/g). Additionally, the material displays a reversible magnetic character with high magnetic susceptibility at low field and low saturation field. In term of striction, this doped ceramic exhibits a significantly large mechanical response (150 ppm) at low magnetic field. The detail of this investigation will be presented and discussed under a full study, which corroborates the results of this enhanced doped ceramic.

[1] H. P. Chopra, and M. Wuttig, Nature 340, 521 (2015) [2] A. Lisfi, T. Ren, A. Khachaturyan, and M. Wuttig, Appl. Phys. Lett. 104, 092401 (2014).



Field dependence of (a) the magnetization and (b) the magnetostriction of Zn-doped polycrystalline cobalt ferrite prepared at 1400 °C. Both the magnetization and the magnetostrictions are nearly hysteresis free and display high saturation values.

AQ-07. Magneto-optical Studies of Doped Magnetic Shape Memory Heusler alloys. *D. Kral*[1], V. Kopecky[2], L. Beran[1], J. Zemen[3], O. Heczko[2] and M. Veis[1] *1. Institute of Physics, Charles University, Prague, Czechia; 2. Institute of Physics, Academy of Sciences, Prague, Czechia; 3. Faculty of Electrical Engineering, Czech Technical University in Prague, Prague, Czechia*

Magnetic shape memory (MSM) alloys have been in the center of attention of many research groups for the past two decades. The MSM effect causes these extraordinary materials to strain to up to 12% of their original length if a moderate magnetic field (bellow 1 T) is applied[1]. This feature is rather appealing for contactless technology – its possible utilizations include sensorics and active/passive dumping, as well as a number of new paradigms,

such as contactless microfluidic pumps. The remarkable properties of MSM alloys are, however, rather limited by the temperature range in which the MSM effect occurs. Researchers have successfully used doping to widen this range[2], as it has been found that the effect is strongly influenced by changes in electronic structure. However, the exact relationship between the MSM effect and the electronic structure has not yet been found. We have investigated this relationship in a prototype MSM alloy, Ni-Mn-Ga. Electronic transitions manifest themselves in the spectral dependency of the dielectric tensor. Although one may obtain useful information by studying only its diagonal elements, the energies of the intraband transitions are more accurately determined from the off-diagonal parts[3]. In this work we studied bulk samples of Ni-Mn-Ga selectively doped with Fe. We have used spectroscopic ellipsometry along with magneto-optical spectroscopy to reconstruct the spectral dependency of both diagonal (Fig. 1) and off-diagonal (Fig. 2) parts of their dielectric tensor. The spectra have been parametrized using an original oscillator model to obtain energies of electronic transitions in the range from 0.7 to 6.5 eV. Our results are in excellent agreement with ab initio calculations, which proves that the mechanisms governing the operational range of MSM alloys can be easily studied by optical and magneto-optical methods.

1. Sozinov, A., Lanska, N., Soroka, A. & Zou, W. 12% magnetic field-induced strain in Ni-Mn-Ga-based non-modulated martensite. *Appl. Phys. Lett.* 102, (2013). 2. Khovailo, V. V. *et al.* Influence of Fe and Co on Phase Transitions in Ni-Mn-Ga Alloys. *Mater. Trans.* 44, 2509–2512 (2005). 3. Wittekoek, S., Popma, T. J. A., Robertson, J. M. & Bongers, P. F. Magneto-optic spectra and the dielectric tensor elements of bismuth-substituted iron garnets at photon energies between 2.2-5.2 eV. *Phys. Rev. B* 12, 2777–2788 (1975).

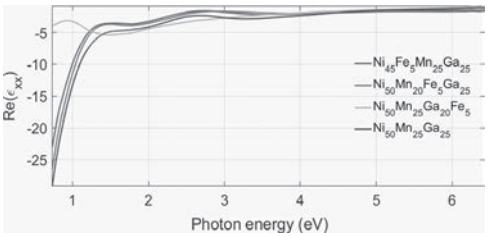


Fig. 1: Spectra of the real part of the diagonal dielectric function of Fe-doped Ni-Mn-Ga determined using spectroscopic ellipsometry.

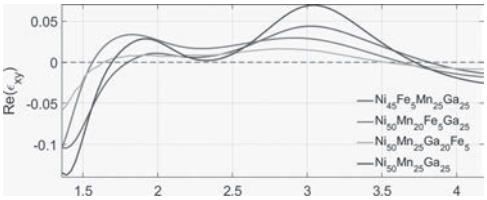


Fig. 2: Magneto-optical spectroscopy was used in tandem with spectroscopic ellipsometry to obtain the off-diagonal dielectric function of Fe-doped Ni-Mn-Ga (here only the real part is displayed).

AQ-08. Effect of film thickness on static and high frequency magnetic properties of $Fe_{100-x}Ga_x$ films with various Ga composition (x).

Y. Kawabe[1], T. Miyazaki[1,2] and Y. Endo[1,3] *1. Graduate School of Engineering, Tohoku University, Sendai, Japan; 2. Faculty of Engineering, Tohoku University, Sendai, Japan; 3. Center for Science and Innovation Spintronics, Tohoku University, Sendai, Japan*

Recently, much attention have been focused on magnetostrictive materials since their magnetostriction can be tuned easily by tensile stresses, electric fields and magnetic fields. Especially, Fe-Ga (Galfenol) alloys have been of much interest as one of the candidates for these materials because of their large magnetostriction, relative low saturation field, high Curie temperature, and good mechanical properties [1]. Therefore, Fe-Ga films are also studied intensively from both fundamental and application points of view. Previous reports on Fe-Ga films were focused on the effect of Ga composition on their static and high frequency (HF) magnetic properties [2-4]. While, details about the effect of film thickness on their properties are still open question. Herein, to clarify the effect of film thickness on static and HF magnetic properties of $Fe_{100-x}Ga_x$ films with several Ga compositions (x), we investigated their properties of these films in detail. Figure 1 shows change in the saturation magnetostriction (λ_s) and the in-plane effective damping constant ($\alpha_{//}$) in $Fe_{100-x}Ga_x$ films (x = 18.5, 24.9, and 33.4) with the film thickness (t). For every x, the tendency of λ_s for t is almost the same; λ_s increases for t < 30 nm, becomes maximum at t = 30 nm, and further decreases for t > 30 nm. Each value of λ_s becomes lower than those of a Fe-Ga alloy [1] and a polycrystalline Fe-Ga film [2]. In contrast, the relationship between $\alpha_{//}$ and t is the same for each x. In particular, $\alpha_{//}$ becomes maximum at t = 50 nm, and their $\alpha_{//}$ values are approximately 4 – 7 times as high as that of $Ni_{78}Fe_{22}$ films with the low magnetostriction. The reason for this might be due to the contribution of magnetic inhomogeneity such as large anisotropy dispersion, two-magnon scattering and so on. Therefore, it is suggested that both λ_s and $\alpha_{//}$ correlate each other for each x. This work was supported in part by JSPS KAKENHI Grant No. JP17H03226. This work was also supported in part by CIES collaborative research from CIES, Tohoku University, and ASRC in Japan.

[1] A. E. Clark *et al.*, IEEE Trans. Magn., 36, 3238 (2000) [2] N. A. Morley *et al.*, J. Appl. Phys., 105, 07A912 (2009) [3] Y. Endo *et al.*, J. Magn. Magn, Mater., 487, 165323 (2019) [4] Y. Kawabe *et al.*, T. Magn. Soc. Jpn., 3, 34 (2019)

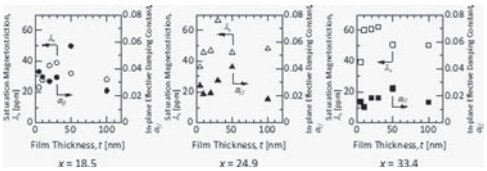


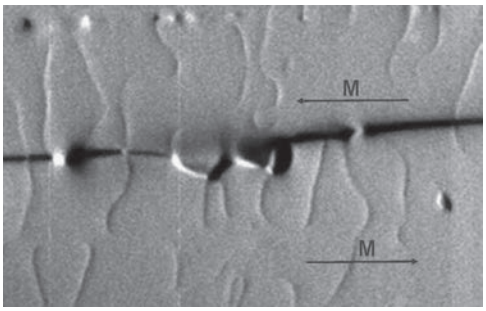
Fig. 1. Thickness dependence of λ_s and $\alpha_{//}$ for $Fe_{100-x}Ga_x$ films with x.

AQ-09. Interplay between magnetic domains and antiphase boundaries in Ni-Mn-Ga compound.

O. Heczko[1], L. Straka[1], L. Fekete[1], M. Vronka[1,2] and M. De Graef[2] *1. Magnetic Measurement and Materials, FZU - Institute of Physics CAS, Prague, Czechia; 2. Materials Science and Engineering, Carnegie Mellon University, Pittsburgh, PA, United States*

Heusler Ni-Mn-Ga compound is considered as an example of magnetoelastic multiferroics. The manifestation of the coupling between ferromagnetic and ferroelastic ordering is magnetically induced structural reorientation (MIR). The dramatic consequence of MIR is giant, up to 12% magnetic field induced strain and 90 deg switch of magnetization direction [1]. Moreover, it was shown recently that the increased coercivity provides further functionality [2, 3]. To understand this behavior, we studied the interactions between magnetic domain walls, twin boundaries and antiphase boundaries (APB) using magnetic force microscopy (MFM) and Lorenz TEM. To observe APB by MFM we used newly developed method [4]. Lorenz TEM was used to confirm the MFM observation and to determine the thickness of magnetic domain walls in the presence of APB. Both methods for observation of APB utilize the magnetic contrast arising from different magnetic properties of the boundary and bulk [5]. The magnetic contrast is only way how to observe APB since the conventional TEM methods failed in this material. The example of APB observation is in Fig 1. As the in-plane magnetization crosses randomly distributed APBs the weak magnetic contrast is generated, which is detected by magnetic force microscopy. The contrast from APB is bi-colored and weak compared to single color of magnetic domain wall (also in Fig1) and thus can be easily recognized. With easy magnetization axis perpendicular to surface the APB contrast is inundated by strong contrast arising from magnetic domains. From the detailed analysis follows that most of the magnetic domain walls are pinned on the APBs which agrees well with LTEM observation. Moreover, LTEM indicates that the magnetic domain walls pinned on the APB are much thinner compared to free domain walls [6]. It indicates that the pinning of magnetic domain walls on the APBs can be the main coercivity mechanism in 10M martensite and explain why increased density of APBs strongly enhances the magnetic coercivity [7].

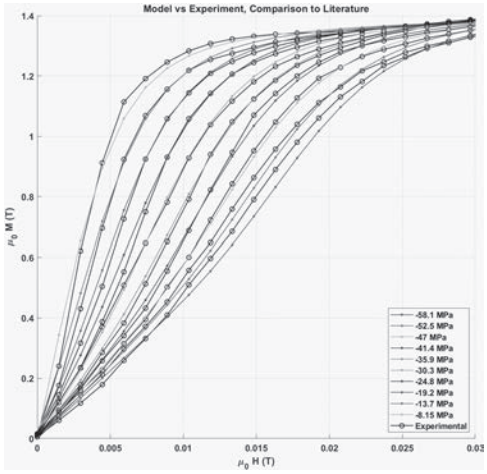
[1] O. Heczko, N. Scheerbaum, O. Gutfleisch, in: Magnetic shape memory phenomena, Springer US, New York 2009. [2] L. Straka et al., Scripta Mater. 87 (2014) 25–28 [3] Q. Peng et al., Scripta Mater. 127 (2017) 49-53. [4] L. Straka, L. Fekete, O. Heczko, Appl. Phys. Lett. 113 (17) (2018) 172901 [5] S.P. Venkateswaran, N.T. Nuhfer, M. De Graef, Acta Mater. 55 (8) (2007) 2621 [6] M. Vronka, O. Heczko and M. DeGraef, accepted to Applied Physics Letter, 2019 [7] L. Straka et al., Acta Mater. 169, 109 (2019).



Visualization of APBs and single magnetic domain wall by MFM. Magnetization directions are marked.

AQ-10. Modeling Low-Frequency Short-Range Mechanical Communication. *M.E. Goforth*[1] and J.P. Domann[1] *1. Biomedical Engineering and Mechanics, Virginia Tech, Blacksburg, WV, United States*

With respect to current methods, communicating at sub-VLF (<3kHz) frequencies is very difficult to achieve due to hardware constraints. Additionally, many applications such as communicating under water and in mines are practically impossible by propagating conventional electromagnetic waves. Conceptually, a device that only alters its surrounding magnetic field would be able to fill this current gap in technology. A model was developed to analyze a macroscale layered composite consisting of an aluminum beam coupled to a layer of magnetoelastic material which is driven at frequency by a piezoelectric layer. This device takes an electric signal to the piezoelectric layer which in turn vibrates the aluminum beam at a prescribed frequency (~1 kHz). The vibrating beam thus strains the magnetoelastic material altering its magnetization which affects the field surrounding the device. The model is on the continuum level which has been built up from the principles of micromagnetics. Since the operating frequencies being considered are "low," the LLG equations cannot be used. Hence, Boltzmann statistics have been used incorporating the magnetocrystalline, magnetoelastic, and Zeeman energies. The numerical FEA model takes prescribed initial conditions and material properties and inputs them into a segregated solver. The state of stress is first determined and this information is fed into the nonlinear constitutive solver. Here, Boltzmann statistics and a function for total energy are used to determine the most probable state of magnetization which determines the state of the surrounding magnetic field. The cycle continues with the state of stress being determined for the next step. The model has compared well to data presented in the literature, as well as inform experiments and prototypes attempting to prove the concept of "mechanical" communications.



AQ-11. EXAFS Analysis of SmFe2 Thin Films with Perpendicular Magnetic Anisotropy for Piezoelectric Magnetic Tunnel Junctions. *Y. Takamura*[1], H. Onozawa[1], S. Urashita[1], M. Tomita[1] and S. Nakagawa[1] *1. Department of Electrical and Electronic Engineering, Tokyo Institute of Technology, Tokyo, Japan*

Perpendicular magnetic tunnel junctions with a giant magnetostrictive free layer whose side wall is covered by piezo-electric materials, piezo-electric tunnel junctions (PE-MTJ) [1], is a promising spin device which overcome an intrinsic dilemma between high thermal stability and reducing critical current density for spin transfer torque magnetization switching. On a magnetization switching operation in PE-MTJs, the piezoelectric part applies pressure to the MTJ so that the magnetic anisotropy in the free layer, meaning energy barrier for magnetization switching, is lowered by inverse-magnetostrictive effect. Thus, the critical current density is dramatically reduced. As the free layer materials, we have been developed negative giant magnetostrictive $SmFe_2$ thin films, and successfully formed $SmFe_2$ thin films with perpendicularly magnetic anisotropy (PMA) by systematic investigation. However, the $SmFe_2$ thin films are amorphous, and thus the origin of the anisotropy is not understood. In this study, we carried out polarized extended X-ray absorption fine structure (EXAFS) measurements on $SmFe_2$ thin films with PMA to investigate the anisotropy in the coordination number. $SmFe_2$ thin films were sputter-deposited on W-buffered quartz substrates and capped with W. The standard condition of a substrate temperature during sputtering and post annealing temperature were 200°C and 500°C respectively. EXAFS measurements were done at a beamline BL-9C in High Energy Accretor Research Organization (KEK). EXAFS signals for Sm-L3 edges were clearly different between perpendicular and in-plane configurations, implying the existence of the difference in the coordination number neighboring a Sm atom in the depth direction and in-plane directions of the $SmFe_2$ films. This anisotropy can be the origin of the magnetic anisotropy and would be useful for further development of high quality giant magnetostrictive materials. This work was supported by JSPS KAKENHI Grant Number 18K18853. This work was performed under the approval of the Photon Factory Program Advisory Committee (Proposal No. 2018P004).

[1] Y. Takamura, et al., Solid State Electron., 128, 194 (2017).

AQ-12. Fabrication and magnetocaloric effect of Ni_2MnGa Heusler alloy nanowires. *Y. Zhang*[1], F. Qin[1], D. Estevez[1] and H. Peng[1] *1. Zhejiang University, Hangzhou, China*

As a type of functional material for multiple devices and sensors, Ni-Mn-Ga Heusler alloy has many attractive characteristics such as magnetic-field-induced strain (MFIS) and magnetocaloric effect (MCE). Much work has been done to prepare and study bulk, films, microwires and powders of Ni-Mn-Ga. It was found that the properties like mechanisms of phase

transition of Ni-Mn-Ga varied as its form changed. Among others, Ni-Mn-Ga nanowires remain to be investigated in terms of their structure and magnetic properties. Experimentally, Ni_2MnGa Heusler alloy nanowires were fabricated using electrospinning method. Optimized calcination and reduction annealing treatments warrant stable and uniform 2:1:1 phase structure which is expected to make vital contribution to magnetic property. The nanowires exhibit a magnetic phase transition between ferromagnetic and paramagnetic state near room temperature, as is in accordance with the mechanism existed in other forms of Ni-Mn-Ga alloys. However, positive slope in Arrott plot indicates that the scale of the magnetic phase transition is second order on contrary to most Ni-Mn-Ga bulk alloys. Moreover, due to the peculiarity of preparing method which results in small sum of residual antiferromagnetic oxides of transition metals, competition between ferromagnetic and antiferromagnetic phases is believed to lead to thermodynamic irreversibility at relatively low temperatures, as revealed by splitting feature observed from zero-field-cooled (ZFC) & field-cooled (FC) curves. For the interest of finding out the magnetocaloric effect of these Ni_2MnGa nanowires, the isothermal entropy change ($-\Delta S_m$) was calculated to be 0.35 J/(kgK), which is comparable to that of some Heusler alloy microwires, powders and films. It is worth noticing that the nanowires possess a fairly large working temperature range (T_{FWHW}) of 170 K which is much larger than that of many crystalline magnetocaloric materials; this could be attributed to the variety of subsystems caused by size distribution and composition fluctuation, which is outstanding at the nanoscale.

[1] V. Franco, J. S. Blazquez, J. J. Ipus, et al., Prog. Mater. Sci. 93, 112-232 (2017). [2] B. G. Shen, J. R. Sun, F. X. Hu, et at., Adv. Mater. 21, 4545-4564 (2009). [3] B. Tian, F. Chen, Y. X. Tong, et al., J. Alloy. Compd. 509, 4563-4568 (2011). [4] Y. V. B. de Santanna, M. A. C. de Melo, I. A. Santos, et al., Solid State Commun. 148, 289-292 (2008). [5] Y. D. Wang, Y. Ren, Z. H. Nie, et al., J. Appl. Phys. 101, 063530 (2007).

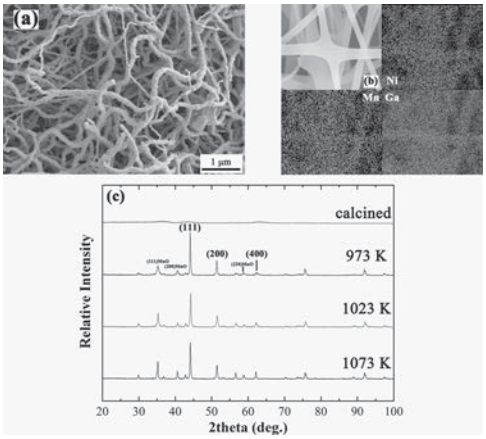


Fig. 1 (a) Morphology; (b) element distribution; (c) XRD patterns.

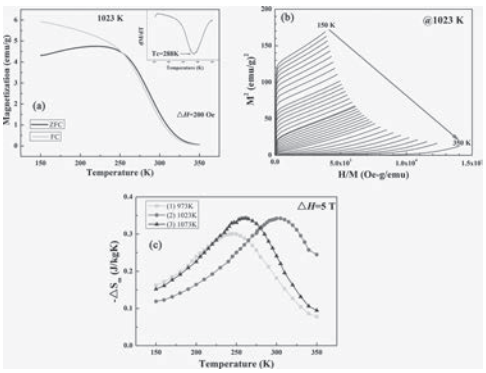
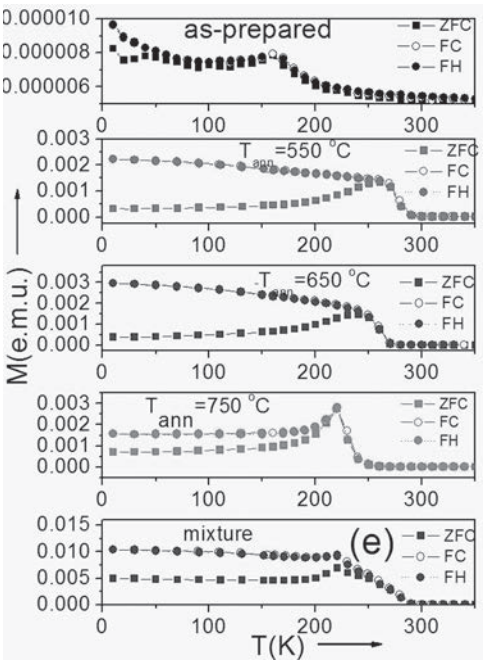


Fig. 2 (a) *M-T* curves with d*M*/d*T*-*T* curves in inset; (b) Arrott plot; (c) $-\Delta S_m$-*T* curves.

AQ-13. Tuning of second order phase transition of NiMnGa Heusler-type glass-coated microwires. C. Garcia[1], V. Zhukova[2,3], S. Shevyrtalov[4], M. Ipatov[2,3], P. Corte-Leon[2,3] and *A. Zhukov*[2,5] *1. Dpto de Física, Universidad Técnica Federico Santa María, Valparaiso, Chile; 2. Dept. Phys. Mater., Univ. Basque Country, UPV/EHU, San Sebastian, Spain; 3. Dpto. Física Aplicada, EIG, Univ. Basque Country, UPV/EHU, San Sebastian, Spain; 4. Immanuel Kant Baltic Federal University, Kaliningrad, Russian Federation; 5. Basque Foundation for Science, Ikerbasque, San Sebastian, Spain*

Heusler alloys can present magnetocaloric effect (MCE) [1,2], ferromagnetic shape-memory effect, half-metallic behaviour, and even superconductivity [1]. The conventional preparation method of Heusler alloys is arc-melting, followed by prolonged high temperature annealing [1,2]. However, recently rapidly quenching technique has been successfully employed for the Heusler-type ribbons and wires preparation [3,4]. This technological advance is of fundamental importance since most the proposed applications require miniaturized of Heusler-type materials [2-4]. The origin of high MCE effect of Heusler alloys is usually related to the first-order phase transition. However, the magnetic hysteresis that appears for first-order phase transitions may reduce the actual efficiency of the cooling process. Therefore, studies of the materials exhibiting the second-order phase transitions with a broader peak in the magnetic entropy change have attracted attention [5]. We present our last results on the tuning of the second-order phase transitions in Heusler-type NiMnGa glass—coated microwires prepared using Taylor-Ulitovsky method by annealing at temperatures ranging from 550 up to 750 ^oC. As-prepared Ni-Mn-Ga microwires exhibit a very weak magnetization at room temperature. However, annealed samples present ferromagnetic behaviour and second-order phase transition at nearly room temperatures. Additionally, both temperature dependence of magnetization, *M(T)*, as well as the corresponding Curie temperature, T_c, are considerably affected by the annealing conditions (annealing temperature and duration). Mixing of glass-coated microwires annealed at different conditions within the same bunch allows tuning of *M(T)* dependence and hence obtain broader second-order phase transition (see Fig). As discussed elsewhere [5] such expanding the temperature range over which a significant magnetic entropy change can be obtained is beneficial for the improvement of the refrigerant capacity. Observed *M(T)* and T_c dependence on annealing conditions has been discussed considering the relaxation of internal stresses distributed in complex way within the microwires.

[1]. Moya, et.al, Nature Materials, 13, 439-450 (2014) [2] D.C. Dunand, P. Müllner, Adv. Mater. 2011, 23, 216-232 [3] Novel Functional Magnetic Materials, Fundamentals and Applications (editor A. Zhukov), Springer Series in Materials Science, vol 231, Springer International Publishing, 2016, ISSN 0933-033X, DOI: 10.1007/978-3-319-26106-5 [4] A. Zhukov et al., Sci. Reports 8 (2018) 621 [5] V. Franco, et.al, Appl Phys. Lett. 88, (2006) 132509.



Temperature dependencies of magnetization of NiMnGa microwires.

AQ-14. Substitution effects on the magnetic phase transition and magnetocaloric effects in nanolaminated $AlFe_2B_2$ alloys. Y. Yan[1], T. Chen[2], *J. Chen*[3], Y. Yang[1], P. Jia[1], W. Cui[1,2] and Q. Wang[1] *1. Northeastern University, Shenyang, China; 2. Lanzhou University of Technology, Lanzhou, China; 3. Institute Of Electronics, CAS, Beijing, China*

Recently, a kind of novel transition-metal boride, called as MAB phase, possesses a general formulae of $(MB_2)_nMAl$ (n = 1, 2, 3) and layered crystal structure. M can be Cr, Mn, Co elements. But only for M = Fe, AlFe2B2 is ferromagnetic with phase transition temperature ranged between 280 ~ 320 K[1]. Due to the second-order nature, no hysteresis is desired and some attentions are paid to explore it as emerging magnetocaloric materials. In this work, the substitution effects of C for B and Ti, V for Fe have been studied. All alloys were prepared by arc-melting. The as-prepared ingots were annealed at 800ºC for 4 days followed by quenching into iced water. Structures and magnetic properties are studied by Bruker diffractometer and cryogenic VSM. The XRD patterns of AlFe2B2-xCx, AlFe2-yTiyB2 and AlFe2-zVzB2 show that the single-phase can be formed for x≤0.1, y<0.1 and z <0.1. More substitution leads into the impurities. The thermal magnetization curves of AlFe2B2-xCx alloys are shown in Fig. 1. The FM-PM phase transition occurs at 283K. With increased C substitution, the Tc is gradually increased. However, the almost flat M-T curve is observed for x=0.3 due to the decomposition of main $AlFe_2(B,C)_2$ phase. By minor Ti and V substitution for Fe, the T_c is decreased to 280 K due to magnetic dilution. Increased substitution does not further lead into decreased T_c due to the possible substitution limitation. All isothermal magnetization curves are reversible, indicating the second-order nature. The delta S is maximized at their respective T_c. Under the field of 7 T, delta Smax is 6.4 Jkg-1K-1. More C substitution leads into decreased delta Smax to 4 Jkg-1K-1 in $AlFe_2B_{1.9}C_{0.1}$, 4.8 Jkg-1K-1 in AlFe1.9Ti0.1B2 and 5 Jkg-1K-1 in AlFe1.9V0.1B2, due to the decreased magnetization.

1 Z. H. Zhang et al J. Magn. Magn. Mater., 484 154-158 (2019)

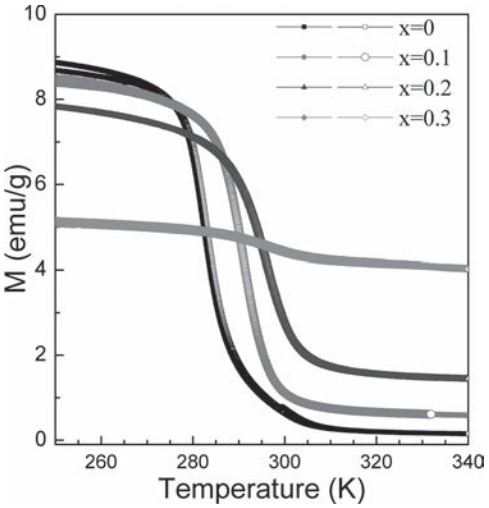


Fig. 1 The M-T curves of AlFe2B2-xCx (x=0, 0,1 and 0.2) alloys measured under 0.05 T. The solid and open symbols stands for the heating and cooling process respectively.

AQ-15. Lattice entropy change evaluated based on Debye approximation for $LaFe_{13-x}Si_x$ magnetocaloric materials. *Z. Yu*[1,2], J. Hao[1,3], F. Hu[1,2], J. Wang[1,2], J. He[3], J. Sun[1,2] and B. Shen[1,2] *1. Beijing National Laboratory for Condensed Matter Physics & State Key Laboratory of Magnetism, Institute of Physics, Chinese Academy of Sciences, Beijing, China; 2. School of Physical Sciences, University of Chinese Academy of Sciences, Beijing, China; 3. Division of Functional Material Research, Central Iron and Steel Research Institute, Beijing, China*

$La(Fe,Si)_{13}$-based materials have attracted many attentions since their discovery for giant magnetocaloric effect (MCE)[1,2]. The typical feature of $LaFe_{13-x}Si_x$ with first-order phase transition is the concurrent magnetic and lattice transitions. However, the lattice entropy change is usually difficult to measure. Gschneidner et al. found a relationship between the lattice entropy change and the lattice deformation (ΔV/V), which is given by $\delta[\Delta V/V(\%)]/\delta[\Delta S_{latt}]=0.08$(J/kgK)[3]. Yet, this empirical relationship is a rough approximation ignoring the specific Grüneisen parameter and Debye temperature, which affect the accurate evaluation of lattice entropy. Here, we report lattice entropy change evaluated based on Debye approximation for $LaFe_{13-x}Si_x$. Fig.1a displays the lattice parameter as a function of temperature for $LaFe_{13-x}Si_x$ with various Si concentrations. One can notice that the sharpness and the amount of lattice change around T_C become steeper and larger with the phase transition evolution from second-order to first-order. Fig.1b shows the calculated lattice entropy as a function of temperature after deducting the general contribution from lattice vibration. One can notice that the change of lattice entropy across phase transition can be as much as ΔS_{Latt} ~11.2 J/kg K for the $LaFe_{13-x}Si_x$ with x=1.2, and the ΔS_{Latt} increases linearly with decreasing Si content x (inset of Fig. 1b). We also measured the total entropy change ΔS_{Tot} across phase transition from heat flow curve using DSC instrument, and found the numerical value of ΔS_{Tot} increases from 2.4 to 28.3 J/kg K as Si content decreases from x=2.2 to 1.2 (Fig. 1c). For the materials with x=1.2, the ΔS_{Latt} accounts ~39% of ΔS_{Tot}. In addition, we also comparably measured the magnetic entropy change using the so-called normal and loop methods based on Maxwell relationship for the first-order compound with x=1.3[4]. The normal and loop methods can give consistent results in the process of descending magnetic field (Fig. 1d). The entropy change (~27.5 J/kg K) driven by 5 T almost reaches the total ΔS_{Tot} across phase transition.

1. K. A. Gschneidner, V. K. Pecharsky, et al, *Repotrs on progress in physics*, 68, 1479 (2005). 2. A. Fujita, *Acta Mater.* 169, 162(2019). 3. K. A. Gschneidner, Y. Mudryk and V. K. Pecharsky, *Scripta Materialia* 67 (6), 572-577 (2012). 4. J. S. Amaral, V. S. Amaral. *J. Magn. Magn. Mater.* 322, 1552–1557(2010).

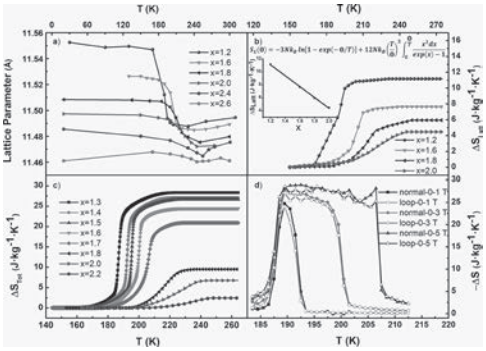


Fig.1. For $LaFe_{13-x}Si_x$, a) lattice parameters, b) ΔS_{Latt} based on Debye approximation, c) ΔS_{Tot} based on DSC, d) ΔS of $LaFe_{11.7}Si_{1.3}$

AQ-16. Withdrawn

AQ-17. Magnetostructural Phase Transitions and Magnetocaloric Effects in Sb Doped MnCoGe. *A. Aryal*[1], I. Dubenko[1], S. Talapatra[1], S. Stadler[2] and N. Ali[1] *1. Physics, Southern Illinois University, Carbondale, IL, United States; 2. Physics and Astronomy, Louisiana State University, Baton Rouge, LA, United States*

The effect of Sb doping on the structural, magnetic and magnetocaloric properties of the $Mn_{1-x}Sb_xCoGe$ system ($0 \le x \le 0.04$) have been investigated by room temperature X-ray diffraction, differential scanning calorimetry (DSC), and magnetization measurements. A change in crystal structure from orthorhombic to hexagonal was observed in the room temperature XRD data with increasing Sb concentration. Doping Sb for Mn in $Mn_{1-x}Sb_xCoGe$ results in a decrease in the martensitic transition temperature T_M. For the concentration range $0 \le x \le 0.015$, T_M was found to coincide with the ferromagnetic transition temperature (T_C), resulting in a first-order magnetostructural transition (MST) from paramagnetic hexagonal phase to ferromagnetic (FM) orthorhombic phase near room temperature. A drastic decrease in T_M by ~ 177 K relative to parent compound was found for x = 0.02. As T_M decreased below T_C (~ 268 K) of hexagonal phase a MST from FM hexagonal to FM orthorhombic phase was observed for compound with x = 0.02. Maximum values of magnetic entropy change in the vicinity of MST were found to be about 14.0 $Jkg^{-1}K^{-1}$, 10 $Jkg^{-1}K^{-1}$ and 8.5 $Jkg^{-1}K^{-1}$ for x = 0.01, 0.015 and 0.02, respectively, for ΔH = 5T. The large values of the ΔS_M at the first-order MST illustrates the potential of $Mn_{1-x}Sb_xCoGe$ compounds to be used in magnetic cooling technology. Acknowledgment: This work was supported by the U.S. Department of Energy (DOE), Office of Science, Basic Energy Sciences (BES) under Award No. DE-FG02-06ER46291 and DE-FG02-13ER46946.

AQ-18. Hysteresis Loss Reduction and Magnetocaloric Effect Improvement in the Ni-Co-Mn-In Alloys. *M. Ghahremani*[1], A. Aslani[2], M. Hosseinnia[3] and L.H. Bennett[2] *1. Computer Science, Mathematics, and Engineering, Shepherd University, Shepherdstown, WV, United States; 2. Electrical and Computer Engineering, George Washington University, Washington, DC, United States; 3. Clinical and Administrative Sciences, Notre Dame of Maryland University, Baltimore, MD, United States*

In this work $Ni_{45}Co_5Mn_{(37-x)}In_{(13+x)}$ alloys (x= 0, 0.4) were prepared using induction arc melting under argon atmosphere and their crystal structure, magnetostructural transitions, microstructures, magnetic, and magnetocaloric properties were systematically studied. The attributes of magnetostructural coupling have an important role in the magnetic behavior of these magnetofunctional alloys. This research exhibits that a strong magnetostructural coupling can be achieved over a wide temperature range in this alloy family. The M(H) and M(T) were measured under different fields and temperatures for the synthesized samples. The area between ascending and descending M(H) loops were calculated to study the hysteresis losses and to minimize their effect on the overestimation error of magnetic entropy change and relative cooling power. The effect of varying stoichiometry composition and applied magnetic field on the Curie temperature, magnetostructural transitions, magnetic and magnetocaloric properties and relative cooling power were studied. The impediment hysteresis losses of these alloys that have a first order phase transmission were considered to eliminate the overestimation of the magnetic entropy change using Maxwell's relations [1]. It's shown that by increasing the applied field the peak of entropy change curves shifts to lower temperatures. Additionally, a small variation in the stoichiometry composition broadens the magnetic entropy change curve and shifts the critical temperatures by about 36 K to around room temperature. Furthermore, the magnetization change accompanying the martensitic transformation is greatly improved, resulting in a large magnetic entropy change of 31 $Jkg^{-1}K^{-1}$ under 5 T across the magnetostructural transformation which is much higher than the values reported for other Ni-Mn rich alloys in literature. The broadened and higher peak of the entropy change curves produced a significantly high relative cooling power in $Ni_{45}Co_5Mn_{36.6}In_{13.4}$ (488 JKg^{-1}) and $Ni_{45}Co_5Mn_{37}In_{13}$ (317 JKg^{-1}) under 5 T applied field. These results are especially promising in finding high-performance magnetocaloric material for magnetic refrigeration systems [2-4].

[1] J. Liu, T. Gottschall, and K. Skokov, Nature Materials., Vol. 11, p.620 (2012) [2] L, Huang, D. Cong, and H. Suo, Applied Physics Letter., Vol. 104, p.132407 (2014) [3] J. Sharma, and K. Suresh, Journal of Alloys and Compounds., Vol. 620, p.329 (2015) [4] N. Bruno, C. Yegin, and I. Karaman, Acta Materialia., Vol. 74, p.66 (2014)

AQ-19. Magnetostructural transition and large magnetocaloric effect in transition metal-based multicomponent alloy with Ni_2In-type crystal structure. *A. Biswas*[1], A.K. Pathak[1], Y. Mudryk[1], V. Balema[1] and V.K. Pecharsky[1,2] *1. Ames Laboratory of US DOE, Ames, IA, United States; 2. Materials Science and Engineering, Iowa State University, Ames, IA, United States*

The coupling between structural and magnetic transitions in magnetic materials is paramount for a plethora of functional properties of materials including shape memory effect, barocaloric effect (BCE) and magnetocaloric effect (MCE). Recently, several Mn-containing compounds with the general formulae Mn*TX* (*T* = transition metal *X* = p-block element) have been reorted to exhibit magneto-structural transitions (MST)[1-3]. Generally, stoichiometric Mn*TX* alloys undergo martensitic structural transitions between the low-temperature TiNiSi-type orthorhombic and the high-temperature Ni_2In-type hexagonal phases in their paramagnetic states. Same materials also exhibit second-order magnetic transitions adopting different magnetic structures in various temperature regions depending on the composition. For example, MnNiSi has a structural transition around T_t ~ 1200 K, which is followed by a paramagnetic to ferromagnetic (FM) transition at T_C ~ 622 K[1]. By substituting Fe and Cr in Mn-site and Al in Si-site, we demonstrated that these two transitions can be coupled near room temperature, e.g., in $Mn_{0.4}Cr_{0.1}Fe_{0.5}NiSi_{0.94}Al_{0.06}$, resulting in an MST. Such coupling is rather uncommon among Mn*TX* alloys that do not contain expensive p-block elements, such as Ge or Ga. The Cr, Mn, and Al-substituted MnNiSi alloy exhibits large MCE with magnetic entropy change DS_M = -11 J/ Kg K at 2 T in the vicinity of its MST at ~270 K, which is comparable with other potential magnetocaloric materials[4]. Our results reveal a new potential magnetocaloric material, which is free from non-abundant elements, and is prepared by a simple, one-step arc-melting process. Acknowledgements: This work was performed at the Ames Laboratory under the auspices of CaloriCool®, funded by the Advanced Manufacturing Office and managed jointly by the Advanced Manufacturing Office and Building Technologies Office of the Office of Energy Efficiency and Renewable Energy of the United States Department of Energy (U.S. DOE). Ames Laboratory is operated for the U.S. DOE by Iowa State University under contract No. DE-AC02-07CH11358.

1. J. Liu et al., Sci. Rep. 6, 23386 (2016). 2. T. Samanta et al., Appl. Phys. Lett. 101, 242405 (2012). 3. Z. Wei et al., Adv. Elec. Mat. 1,1500076 (2015). 4. X. Moya et al., Nature Mat. 13, 439(2014).

Session AR
FERRITES AND RARE-EARTH MAGNETS
(Poster Session)

Durga Paudyal, Chair
Ames Laboratory, US DOE, Iowa State University, Ames, IA, United States

AR-01. Phase modification and coercivity improvement of melt spun $LaCo_5$ ribbons by Ti, Zr, or Hf substitution. *H.W. Chang*[1], Y. Guo[1], W. Chang[1], Y. Wong[1] and C. Shaw[2] *1. National Chung Cheng University, Chia-Yi, Taiwan; 2. Superrite Electronics Co. Ltd., Taipei, Taiwan*

Since the price surge of critical RE elements in 2011, it is significant to explore the RE-free or other abundant RE-containing permanent magnetic materials. La, one of the most abundant RE elements, is much cheaper than Nd, Pr, Sm, and Y due to its less usage. Unlike $SmCo_5$ alloy, $LaCo_5$ has not been attracted much attention due to the easy formation of impurity phases, such as $LaCo_{13}$ (1:13), La_5Co_{19} (5:19) and La_2Co_7 (2:7), despite its good magnetically intrinsic properties. The study related to the magnetic properties of $LaCo_5$ alloys so far is rare, and only ball-milling and mechanochemical synthesis to prepare $LaCo_5$ alloys are available. In this work, melt spinning is adopted to prepare $LaCo_5$-based ribbons, and the magnetic properties, crystal structure and microstructure of $LaCo_{5-x}M_x$ ribbons (M= Ti, Zr, and Hf; x=0.05-0.1) spun at 40 m/s are explored. Very low ${}_iH_c$ =0.8 kOe is obtained for $LaCo_5$ ribbon. Nevertheless, permanent magnetic properties of $LaCo_5$ ribbons are significantly enhanced by Ti, Zr, and Hf substitution for Co. The ${}_iH_c$ of the as spun ribbons is increased to 2.7-9.0 kOe for M=Ti, 5.2-8.1 kOe for M=Zr, and 4.8-9.0 kOe for M= Hf, respectively. The 2:7 and 1:13 phases diminished by M substitution with x=0.05, and almost suppressed for x=0.1 reveal that Ti, Zr, or Hf substitution is effective in suppressing the formation of impurity phases, stabilizing 1:5 phase, and accordingly enhancing the coercivity of the ribbons. XRD result analyzed by Rietveld refinement indicates that M tends to occupy 3g sites in 1:5 structure and the lattice constants are slightly changed. The occupancy of M at 3g sites may improve magnetocrystalline anisotropy field and thus contribute to coercivity enhancement and slight decrease in Curie temperature. M-doping is also helpful in refining the grain size from 100-150 nm to 30-50 nm and contributes to remarkable improvements of ${}_iH_c$ and the squareness of demagnetization curve. Besides, the coercivity of $LaCo_{5-x}M_x$ ribbons is mainly dominated by nucleation mechanism. Summarized with the above results, the suppressed impurity phase, the modified phase constitution, and the refined microstructure with M substitution significantly enhance coercivity of melt spun $LaCo_5$ ribbon.

None

AR-02. Structure factor and 3d - valence electron concentration considerations towards stabilization of the $SmFe_{5-y}Co_yNi_z$ phases using the high entropy alloy concept: special case $SmFe_3CoNi$. *D. Niarchos*[1,2], M. Gjoka[1], V. Psycharis[1] and E. Devlin[1] *1. Department of Materials Science, INN, NCSR "Demokritos", Athens, Greece; 2. AMEN-Technologies, Athens, Greece*

Although RCo5 (R=Rare-Earth) alloys with the CaCu5-type structure are stable and can be processed to make magnets withe nergy products in the range of 20-25MGOe, their Fe-rich counterparts with the same structure in bulk form are thermodynamically unstable [1].The energy of formation for the series $SmTM_5$ (TM=Fe, Co,Ni) is related to the number of 3d electrons in the system: the more 3d electrons, the more stable is the compound [2,3]. For example $SmNi_5$ is very stable, $SmCo_5$ less stable, and $SmFe_5$ unstable (positive energy of formation) as is seen in Fig. 1a. Given that the structure factors R_{Sm} and R_{TM} are almost the same across the $SmTM_5$ (TM=Fe, Co,Ni) series, the 3d electron concentration and the valence electron concentration are the important parameters for the stability of Fe-rich phases. In such structures the rare earth occupies the 1a site while the transition metal ions occupy two crystallographically different sites, 2c and 3g, in the space group P6/mmm, as shown in Fig. 1b. Previous efforts to substitute Co with Fe slightly improved the magnetization but the substitution is limited to less than 10 % [4]. In this work we will present data based on the high entropy alloy concept of the transition metals Fe_3Co-(Ni,Cu) [5]. In Fig. 2 we summarise our approach to creating $SmFe_3Co$-(Ni,Cu) by considering the heat of formation and the valence concentration of the stable compounds $SmNi_5$, $SmCo_5$ and $SmCu_5$, which, together with the structure factor, lead to the series $SmFe_3\{Co_{1-x}(Ni,Cu)_x\}$. A long anneal is needed to allow the diffusion of Co, Ni and Cu elements to occupy the remaining 2c sites, Fig. 1b. Crystallographic and magnetization data will be presented, which show a promising new magnetic material for permanent magnet applications. Acknowledgements: This project was partially supported by the H2020 – MSCA-RISE-*2015 INAPEM* and H2020-NMP23-2015

[1] J.M.D.Coey, Magnetism and Magnetic Materials, Cambridge University Press the Edinburgh Building, Cambridge CB2 8RU, UK, ISBN-13978-0-511-67743-4, eBook (NetLibrary), 2010. [2] P. Soderlind, A. Landa, I.L.M.Locht et al., Phys. Rev. B 96, 100404(R) (2017) [3] A. Landa, P. Soderlind, D. Parker et al, J Alloys Compd. v.765, p.659-663 (2018) [4] P. Kumar, A. Kashyap, B. Balamurugan et al., J of Physics: Condensed Matter v.26, 0642009 (2014) [5] Yeh, J. W et al, Adv. Eng. Mater. 6, p. 299-303 (2004)

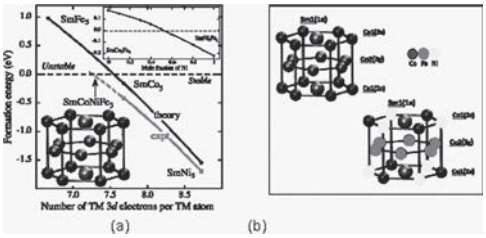


Fig. 1. a) Calculated (black circles) and experimental (red squares) formation energies (eV/cell). b) $SmCo_5$ structure-upper left and the proposed structure of $SmFe_3CoNi$ phase- lower right.

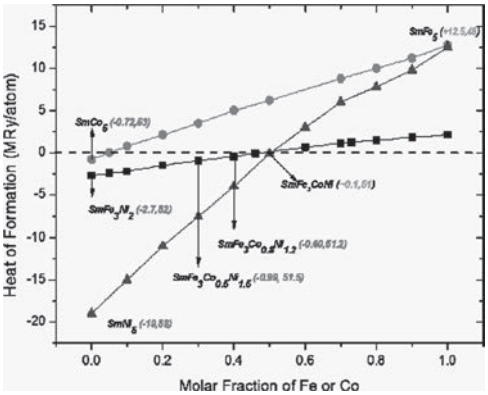


Fig. 2.Heat formation vs molar fraction of Fe or Co. Beside the alloy formulas, in parentheses, the energy of formation and the valence electron concentration/number are given.

AR-03. Effect of B on the Magnetic Properties for Sm-Fe-Co Thin Films. *Y. Tamazawa*[1], M. Kambayashi[2], G. Saito[1], M. Doi[1] and T. Shima[1] *1. Graduate School of Engineering, Tohoku Gakuin University, Tagajo, Japan; 2. Department of Electronic Engineering, Tohoku Gakuin University, Tagajo, Japan*

RFe$_{12}$ compounds with the tetragonal ThMn$_{12}$-type structure have been reported [1-4] and they are expected to show outstanding magnetic properties better than Nd-Fe-B sintered magnets, since RFe$_{12}$ compounds possess high saturation magnetization M_s and large magnetocrystalline anisotropy K_u. Recent study revealed that the addition of a light element nitrogen to the RFe$_{12}$ compounds can improve the magnetic properties by changing the average interatomic distances between Fe and Fe [5]. However, the influence of other light elements on the structure and magnetic properties of Sm(Fe, Co)$_{12}$ compounds has not been reported. In this study, Sm (Fe$_{0.8}$Co$_{0.2}$)$_{12}$B thin films with various B content and film thicknesses have been fabricated and their structure and magnetic properties have been investigated. The samples were prepared by using ultrahigh vacuum magnetron sputtering system with base pressure of less than 1.0×10^{-8} Pa. A V underlayer of 20 nm was deposited onto the MgO (100) single crystal substrate at T_s = 325 °C. Then, the Sm$_{11.3}$(Fe$_{0.8}$Co$_{0.2}$)$_{88.7}$B layer of 5 to 200 nm was deposited. The amount of B to the Sm$_{11.3}$(Fe$_{0.8}$Co$_{0.2}$)$_{88.7}$B layer was varied from 0 to 9 %. Finally, the V cap layer of 10 nm was deposited for the prevention of oxidation. The structural analysis was performed by the X-ray diffraction (XRD) and grazing incident X-ray diffraction (GIXD) with Cu-Kα radiation. The magnetization curves were measured by using a superconducting quantum interference device (SQUID) magnetometer in the magnetic fields up to ±70 kOe. The film composition was determined by an energy dispersive X-ray spectroscopy (EDX). All the measurements were performed at room temperature. From XRD patterns, the peak position of (002) and (004) from ThMn$_{12}$ phase was shifted to higher angle with increasing B content. From magnetization curves, H_c as high as 9.4 kOe was obtained in the Sm$_{11.3}$(Fe$_{0.8}$Co$_{0.2}$)$_{88.7}$B (100 nm) thin film when the amount of B addition is 5 at.%. Effect of the amount of B and film thickness on the crystal structure and magnetic properties for Sm(Fe, Co)$_{12}$ compounds will be discussed at the conference.

[1] Y. Hirayama, Y.K. Takahashi and K. Hono, Scr. Mater., 138, p.62-65 (2017) [2] T. Saito, F. Watanabe and D. Nishio-Hamane, J. Alloys Compd., 773, p.1018-1022 (2019) [3] P. Tozman, H. Sepehri-Amin and K. Hono, Acta. Mater., 153, p.354-363 (2018) [4] Y. Harashima, K. Terakura and T. Miyake, J. Appl. Phys., 120, 203904 (2016) [5] M. Akayama, H. Fujii and K. Tatami, J. Magn. Magn. Mater., 130, p.99-107 (1994)

AR-04. Magnetic properties of Sm(Fe,Zr)$_3$ melt-spun ribbons. T. Saito[1], T. Horita[1] and *Y. Ogawa*[1] *1. Chiba Institute of Technology, Narashino, Japan*

The SmFe$_3$ phase is a ferromagnetic phase with a rhombohedral structure [1-3]. It has been reported that the specimens with the SmFe$_3$-type phase exhibited coercivity and the coercivity of the SmFe$_3$-type phase can be improved by the small addition of zirconium (Zr) [4,5]. In order to examine the effects of Zr addition to the SmFe$_3$ phase, several Sm(Fe,Zr)$_3$ melt-spun ribbons were prepared in this study. The relationships between the structures and magnetic properties of the Sm(Fe,Zr)$_3$ melt-spun ribbons are examined. (Sm$_{1-x}$Zr$_x$)Fe$_3$ (x = 0–0.4) alloy ingots were prepared by induction melting under an argon atmosphere. The alloy ingots were induction melted and then ejected through an orifice with argon onto a copper wheel rotating at a surface velocity of 40 ms^{-1}. The melt-spun ribbons were annealed under an argon atmosphere at 773-1273 K for 1 h. The as-quenched melt-spun ribbons consisted of either fully or partly of the amorphous phase and showed low coercivity values. Heat treatment of the melt-spun ribbons resulted in the formation of the (Sm,Zr)Fe$_3$ phase. Figure 1 shows the dependence of the coercivity of the (Sm$_{1-x}$Zr$_x$)Fe$_3$ (x = 0–0.4) melt-spun ribbons on the annealing temperature. The coercivity of the melt-spun ribbons was drastically increased by heat treatment. The coercivity of the SmFe$_3$ melt-spun ribbon showed the maximum value when it was annealed at 973 K, while that of the (Sm$_{0.7}$Zr$_{0.3}$)Fe$_3$ melt-spun ribbon reached its maximum when annealed at 1173 K. The highest coercivity of 11.3 kOe was achieved in the (Sm$_{0.7}$Zr$_{0.3}$)Fe$_3$ melt-spun ribbon annealed at 1173 K.

[1] K. H. J. Buschow, J. Less-Common Metals 25,131 (1971). [2] J. F. Herbst and J. J. Croat, J. Appl. Phys. 53, 4304 (1982). [3] H. Samata, et al. Jpn. J. Appl. Phys. 36, 3492 (1997). [4] L. Schultz, et al. IEEE Trans. Magn. 26, 1373 (1990). [5] J. Wecker, et al. J. Appl. Phys. 69. 5847 (1991).

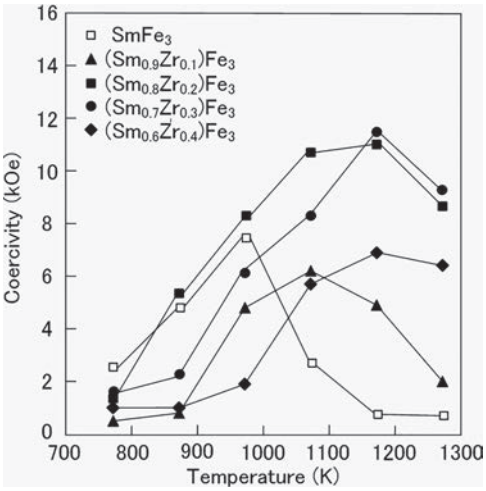


Figure 1 Dependence of the coercivity of the (Sm$_{1-x}$Zr$_x$)Fe$_3$ (x = 0–0.4) melt-spun ribbons on the annealing temperature.

AR-05. Production of anisotropic SmFe$_3$ magnets by hot deformation. *Y. Ogawa*[1], T. Saito[1] and D. Nishio-Hamane[2] *1. Chiba Institute of Technology, Narashino, Japan; 2. Institute for Solid State Physics, The University of Tokyo, Kashiwa, Japan*

It has been reported that the SmFe$_3$ phase is a ferromagnetic phase with a rhombohedral structure and that it is magnetically anisotropic [1–3]. Thus, the SmFe$_3$ phase can be considered as a possible candidate for permanent magnets if anisotropic magnets can be produced. In the case of Nd-Fe-B magnets, anisotropic Nd-Fe-B magnets have been produced by either the sintering of Nd-Fe-B powder or hot deformation of hot-pressed Nd-Fe-B magnets. The objective of the present study was to produce anisotropic SmFe$_3$ magnets by the hot deformation of hot-pressed SmFe$_3$ magnets.

The structures and magnetic properties of the hot-deformed $SmFe_3$ magnets are discussed. $SmFe_3$ alloy ingots were prepared by induction melting in an argon atmosphere. The alloy ingots were were induction melted and then ejected through an orifice with argon onto a copper wheel rotating at a surface velocity of 40 ms^{-1}. The melt-spun ribbons were comminuted into powders and then hot-pressed in a vacuum at 823 K under a pressure of 100 MPa by the spark plasma sintering (SPS) method. Hot deformation of the hot-pressed $SmFe_3$ magnets was performed in a vacuum at 973–1073 K under a pressure of ~200 MPa by the SPS method. X-ray diffraction and thermomagnetic studies revealed that the hot-deformed $SmFe_3$ magnet consisted of the $SmFe_3$ phase. Figure 1 shows the hysteresis loops of the $SmFe_3$ magnets hot-deformed at 1023 K, measured parallel and perpendicularly to the pressing direction. The magnetic anisotropy of the hot-deformed $SmFe_3$ magnets was confirmed by the existence of a higher remanence in the parallel direction than in the perpendicular direction. This indicates that anisotropic $SmFe_3$ magnets were successfully produced by the hot deformation of hot-pressed $SmFe_3$ magnets.

[1] K. H. J. Buschow, J. Less-Common Metals 25,131 (1971). [2] J. F. Herbst and J. J. Croat, J. Appl. Phys. 53, 4304 (1982). [3] H. Samata, et al. Jpn. J. Appl. Phys. 36, 3492 (1997).

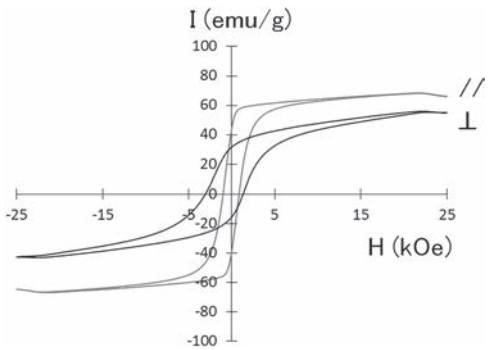


Figure 1 Hysteresis loops of the $SmFe_3$ magnets hot-deformed at 1023 K, measured parallel and perpendicularly to the pressing direction.

AR-06. Synthesis of $SmFe_5$ intermetallic compound. *T. Saito*[1] and D. Nishio-Hamane[2] *1. Chiba Institute of Technology, Narashino, Japan; 2. Institute for Solid State Physics, The University of Tokyo, Kashiwa, Japan*

Many efforts are being made to obtain new permanent magnet materials. One of the most promising candidates is the $SmFe_5$ phase, which has a hexagonal structure like that of the well-known $SmCo_5$ magnet. The $SmFe_5$ phase is a metastable phase and its formation has been reported only in sputtered films. It has been reported that the $SmFe_5$ phase can be stabilized by the addition of zirconium or titanium [1–3]. However, the addition of a nonmagnetic element results in a reduction of the saturation magnetization of the $SmFe_5$ phase. Since the formation of several metastable phases has been reported in binary Sm-Fe alloys [4], the $SmFe_5$ phase might be able to be produced by a rapid solidification process such as melt-spinning. The purpose of this study was to seek the possibility of producing binary Sm-Fe alloys with the $SmFe_5$ phase by optimizing the annealing conditions of rapidly quenched melt-spun ribbons. The relationship between the structures and magnetic properties of the Sm-Fe melt-spun ribbons is discussed. The $SmFe_5$ intermetallic compound was synthesized by the melt-spinning technique and subsequent annealing, as follows. $SmFe_5$ alloy ingots were prepared by induction melting under an argon atmosphere. The molten alloy ingots were then ejected through an orifice with argon onto a copper wheel rotating at a surface velocity of 40 ms^{-1}. The melt-spun ribbons obtained from this process were annealed under an argon atmosphere at 773–1273 K for 1 h. The specimens were examined by an X-ray diffraction (XRD) system, transmission electron microscope (TEM), and vibrating sample magnetometer (VSM). The TEM study revealed that the as-rapidly quenched $SmFe_5$ melt-spun ribbon consisted of nano-sized $SmFe_5$ grains. Subsequent annealing resulted in the crystal growth of the $SmFe_5$ grains. The optimally annealed $SmFe_5$ melt-spun ribbon exhibited a coercivity exceeding 1 kOe. Figure 1 shows a TEM micrograph of the $SmFe_5$ melt-spun ribbon annealed at 1073 K. The annealed specimen consisted of fine $SmFe_5$ grains of around 100 nm in diameter.

[1] F. Cadieu, et al. J. Appl. Phys. 55, 2611 (1984). [2] C. Lin, et al. J. Appl. Phys. 63, 3592 (1988). [3] Q. F. Xiao, et al. J. Appl. Phys. 82, 6170 (1997). [4] Y. Xingbo, et al. IEEE Trans. Magn. MAG-23, 3104 (1987).

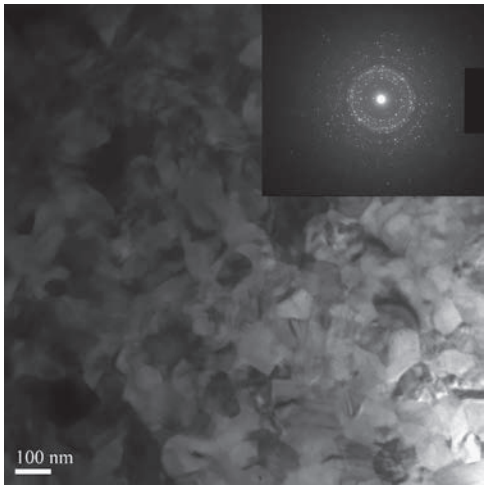
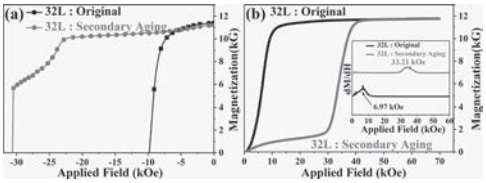


Figure 1 TEM micrograph of the $SmFe_5$ melt-spun ribbon annealed at 1073 K.

AR-07. Effect of Secondary Aging On Magnetic Properties of 2:17 SmCo Commercial Magnet. *Z. Xie*[1], D. Zhang[1], H. Zhang[1], W. Liu[1], Q. Wu[1], Q. Lu[1], Y. Li[1], Z. Ma[1] and M. Yue[1] *1. College of Materials Science and Engineering, Beijing University of Technology, Beijing, China*

Aging process has very important effect on coercivity of 2:17 SmComagnet. However, the effect of secondary aging on SmCo magnet need be further clarified. In this paper, the 2:17 SmCo commercial magnet (named 32L) was aged again, and the relationship between the coercivity and microstructure are studied. Fig. 1(a) shows the demagnetization curves of 32 L magnet before (black line) and after (red line) secondary aging. The coercivity of secondary aging magnet has been greatly improved from 9.83 kOe to 30.61 kOe after the secondary aging. The initial magnetization curves of the magnet were investigated, as shown in Fig. 1(b). Before the secondary aging, the magnet shows one step magnetization process, indicating that there is no pinning site against magnetic domain wall motion. However, after the secondary aging, the initial magnetization curve rise slowly below 3T magnetic field, which indicate stronger pinning force against magnetic domain wall motions [1]. From the first derivative curves shown in the inset of the figure, the corresponding pinning field are 6.97 kOe and 33.21 kOe, respectively. It shows that after the secondary aging, the pinning field is responsible for the enhancement of coercivity. The EPMA results of the magnet indicate that the Cu-lean grain boundary region is obvious in the secondary aging magnet. The secondary aging changes the distribution of Cu element in the magnet with low coercivity, and increases the strength of the pinning field, which is beneficial to the improvement of coercivity.

[1].H. Sepehri-Amin, J. Thielsch, J. Fischbacher, T. Ohkubo, T. Schrefl, O. Gutfleisch, K. Hono, Acta Materialia, 2017. 126: p. 1-10.



Demagnetization curves (a) and initial magnetization curves (b) of the 32 L magnet, and the inset shows the corresponding of first derivative curves before and after the secondary aging.

AR-08. Atomistic study on the pressure dependence of the melting point of $NdFe_{12}$. *C. Skelland*[1], T. Ostler[2], S.C. Westmoreland[3], R.F. Evans[3,6], R.W. Chantrell[3], M. Yano[4], T. Shoji[4], A. Kato[4], M. Ito[4], M. Winklhofer[5], G. Zimanyi[6], J. Fischbacher[7], T. Schrefl[7] and G. Hrkac[1]
1. University of Exeter, Exeter, United Kingdom; 2. Sheffield Hallam University, Sheffield, United Kingdom; 3. University of York, York, United Kingdom; 4. Toyota Motor Corporation, Toyota City, Japan; 5. The Carl von Ossietzky University of Oldenburg, Oldenburg, Germany; 6. UC Davis, Davis, CA, United States; 7. Danube University Krems, Krems an der Donau, Austria

Through atomistic simulation, we investigated how pressure affects the melting point of the $NdFe_{12}$ structure theorised by Miyake et al.[1], and recently grown epitaxially by Hirayama et al.[2]. Material constants from the literature, were used to fit Morse potentials using a genetic algorithm code and the General Utility Lattice Program (GULP), before running two-phase solid-liquid coexistence simulations in LAMMPS at various temperatures and pressures. Morse potentials for the interaction between identical atoms were fit to the material constants of the pure elemental forms of neodymium and iron (Table.1). In order to fit the final neodymium-iron potential two reference structures Nd_2Fe_{17}[3], and $NdFe_{12}$[2]were used, however as these structures have not been studied as thoroughly, only their lattice constants, comparative cohesive energies per atom, and a reasonable estimate of a similar young's modulus to $Nd_2Fe_{14}B$ are used for parameter fitting. An iterative process was used to fit the potentials, which varied the Morse potentials base parameters via random single percentage point scaling, and interchanging of similar parameters – known as *mutation*, and *cross-breeding* respectively. Each potential's absolute percentage difference from the expected values is calculated, and then scaled by a weighting function before being summed to give the *fitness* of the potential. The algorithm converges to a solution by discarding the potentials of poor *fitness* at the end of each iteration. We find the melting temperatures of neodymium and iron to be ~1700K, and ~3000K, overestimated by a factor 1.32, and 1.66 respectively (Fig.1). In expectation of the Fe-Fe interaction dominated $NdFe_{12}$ having a similar scaling to that of elemental iron, we predict a melting temperatures of ~1220K at ambient pressure, rising up to ~1270K at 500MPa. Further investigation will require the development of MEAM potentials for the current binary, and future ternary phases, using for example titanium and cobalt.

[1] T. Miyake, K. Terakura, Y. Harashima, et al., J. Phys. Soc. Jpn., 83(4), 043702 (2014). [2] Y. Hirayama, Y.K. Takahashi, S. Hirosawa, K. Hono., Scr. Mater, 95, 70-72 (2015). [3] Pablo Álvarez et al, J. Phys. Condens. Matter, 22 216005 (2010). [4] R. W. G. Wycoff, Interscience Publishers, 7-83 (1963). [5] Charles Kittel, 8th edition. Hoboken, NJ: John Wiley & Sons, Inc. (2005). [6] Tromans. D, IJRRAS, 6(4), pp.462-483 (2011). [7] G.V. Samsonov, IFI-Plenum, New York, USA (1968). [8] Adams, J.J., Agosta, D.S., Leisure, R.G. et al., J. Appl. Phys., 100(11), p.113530. (2006)

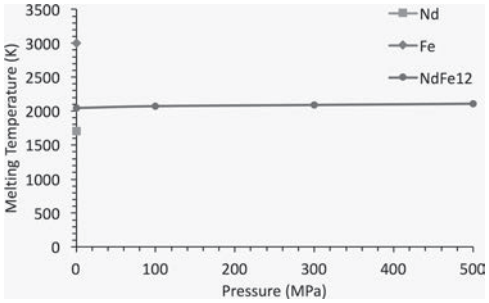


Fig1. Melting temperatures of $NdFe_{12}$with pressure, Nd and Fe at 0.1 MPa included for reference.

Table I
Fitting constant comparison

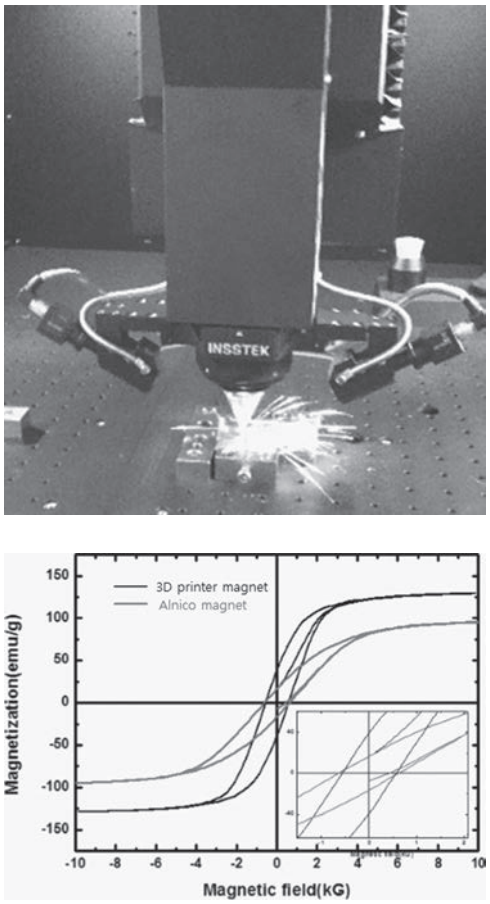
Constant	Nd-alpha (Calc.)	Nd-alpha (Exp.)	Fe-alpha (Calc.)	Fe-alpha (Exp.)
a (Å)	3.638	3.65[a]	2.875	2.867[a]
b (Å)	3.638	3.65[a]	2.875	2.867[a]
c (Å)	5.94	5.94[a]	2.875	2.867[a]
E (eV)	-6.823	-6.8[b]	-8.56	-8.56[b]
B (GPa)	33.349	32.7[b]	156.77	170.0[e]
c_{11} (GPa)	55.038	54.8[c]	167.22	239.26[e]
c_{12} (GPa)	31.41	24.6[c]	151.53	135.78[e]
c_{14} (GPa)	13.614	15.0[c]	151.53	120.72[e]
P (Km/s)	2.76	2.33[d]	5.447	4.91[d]

Calculated and experimental constants. With superscripts *a, b, c, d,* and *e* denoting values from references [4], [5], [6], [7], and [8] respectively.

AR-09. Fabrication of Permanent Magnet by 3D Printng Technique. *M. Lee*[1], Y. Choi[1], N. Tran[1], J. Ahn[1] and B. Lee[1] *1. Department of Physics and Oxide Research Center, Hankuk University of Foreign Studies, Yongin, The Republic of Korea*

Alnico magnets, which are made of alloy components of elements such as iron, nickel, cobalt and aluminum, do not exert strong magnetic force but are stable at high temperature of 650 degree celcius. It is alsoAlnico magnet is a permanent magnet with constant demand for applications such as in speakers, microphone and amplifier due to its superior hardness that are not damaged by strong impact. However, the molding cast used in the fabrication process must take into account the production period and cost., and the The shape of the permanent magnet is limited by the limitations of the shape of the molding cast. We This study present proposed a method for rapid production of high quality magnetic alloy by stacking metal pattern Less than a millimeter using 3D printer of laser cladding method. The laser is CW CO2 CO_2 laser and are maintained at an output of 400W. Purchased A purchased high purity alloy powder has an average size of 50-150um and can be molded into two or more types of powder. Metal powder is injected with inert gas at a rate of 4g/min to prevent oxidation during work, thus making high purity alloys and removing the need for vacuum system. The composition ratio of the injected powder and alloy powder was confirmed to be almost identical through XRF. The alloy produced was separated into two phases (magnetic phase and non-magnetic phase) through high temperature heat treatment, and the magnetic phase produced magnetic anisotropy by magnetic heat treatment. The microstructure was checked through SEM, and the magnetic properties were measured with VSM to compared the

permanent magnet properties with the actual alnico magnet. Permanent magnets made of laser cladding have properties similar to those of the actual alnico magnets, and the advantages of whichthat they can be easily molded can beand used in various industries.



AR-10. Unquenched Orbital Magnetic Moment in M-type Hexaferrites by Non-isovalent Substitution. *J. Kim*[1] and Y. Koh[2] *1. CALDES, Institute for Basic Science, Pohang, The Republic of Korea; 2. Max-Plank Korean Initiative, Pohang, The Republic of Korea*

The hard magnetic property of M-type hexaferrites are originated basically from the uniaxial crystal structure of magnetoplumbite and there have been a lot of works to enhance the property by modifying the magentic crystalline anisotropy energy or local spin magnetic moments through substituting varieties of cations for Sr and Fe sites. Smaller ionic size of La^{3+} induces a structural transition at low temperature and the excess charges from them can increase the ratio of Fe^{2+} ions with smaller spin magnetic moment in the antiparallel sites. The substituted Co ions for Fe sites have smaller local magnetic moments than Fe ions and their uneven distribution in differerent local sites is expected to change the magnetization too. In this work, we have measured X-ray absorption spectroscopy and X-ray magnetic circular dichroism on a series of M type Sr hexaferrites which have different substitution ratios of La and Co. They directly show that the Fe^{2+} are formed by the La and Co substitution and they are localized mostly at O_h sites. Also, we will show that the local symmetry distortion at O_h sites taken by Fe^{2+} induces a large unquenched orbital magnetic moment at the Fe^{2+} sites.

1. K. Uji, T.Waki. and H. Nakamura, J. Solid State Chem. 245, p.17 (2017) 2. Hiroaki Ueda, Yasuaki Tanioku, and Kazuyoshi Yoshimura, Phy. Rev. B 95, p.224421 (2017) 3. Chuanjian Wu, Zhoung Yu, and Zhongwen Lan, Sci. Rep. 6, p. 362300 (2016)

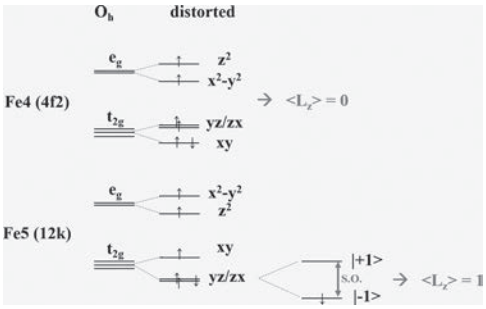


Fig. 1 Unquenced orbital moment of Fe^{2+} at 12k sites by spin-orbit coupling.

AR-11. Effect of Lanthanum Substitution on Magnetic Properties of $Ba_{4-x}La_xNi_2Fe_{36}O_{60}$ Hexaferrite. *X. Jiang*[1], X. Liu[1], T. Shen[1], Z. Yu[1], K. Sun[1], C. Wu[1] and R. Guo[1] *1. School of Materials and Energy, University of Electronic Science and Technology of China, Chengdu, China*

Hexagonal ferrites with c-axis texture have high magnetocrystalline anisotropy field (H_a). It it is benefit for achieving the ferrites with high remenence ratio (M_r/M_s) and coercivity (H_c), which are promising for implementing self-biased microwave ferrite devices [1,2]. U-type hexagonal ferrite has lower anisotropy field than that of M-type hexagonal ferrite [3]. It indicates that the U-type ferrite may have lower ferromagnetic linewidth (ΔH) which is benefit for reducing the insertion loss of the ferrite devices, but the lower anisotropy field of U-type hexagonal ferrite may give rise to the lower coercivity which is undesired. Lanthanum substitution was adopted to improve the remenence ratio and coercivity of U-type ferrites in the presented abstract. The La-substituted polycrystalline $Ba_{4-x}La_xNi_2Fe_{36}O_{60}$ (x=0.0-0.3) hexaferrites were prepared by a conventional ceramic method and wet magnetic field pressing with an external magnetic field of 2000 Oe. Effects of lanthanum substitution on magnetic properties of the sintered samples were investigated. Microstructures were examined using a scanning electron microscopy (SEM) shown in Fig. 1. The SEM picture shows that the grains align well along the external magnetic field. Saturation magnetization ($4\pi M_s$), remenence ratio, and coercivity were measured by a vibrating sample magnetometer (VSM) exhibited in Table 1. $4\pi M_s$ almost keeps changeless with the increase in x and it is appropriate for Ku-band ferrite devices, while M_r/M_s goes up obviously. La substitution increases the anisotropy constant (K_1) because of the change of the delocalized electrons [4]. The increasing in K_1 helps the grains align along the external field and improve the M_r/M_s. Coercivity also increases when x is 0.1. Anisotropy constant was also calculated by the intersection of magnetization curve (M-H) of easy axis (c-axis) and hard axis direction. K_1 increases obviously with the increase in x. Then anisotropy field goes up accordingly. It can be concluded that K_1 and H_a improves the c-axis orientation.

[1] V.G. Harris, Z. Chen and Y. Chen, J. Appl. Phys., 99, 08M911 (2006) [2] V.G. Harris, IEEE Trans. Magn., 48, 1075 (2012) [3] Z. Su, S. Bennett and B. Hu, J. Appl. Phys., 115, 17 (2014) [4] V. Chlan, K. Kouril and K. Ulicna, Phys. Rev. B, 92, 125125 (2015)

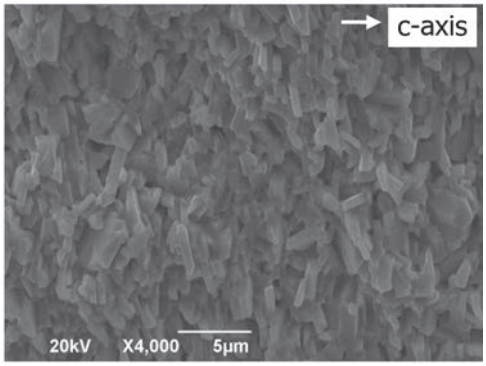


Fig. 1. SEM picture of the sintered $Ba_{3.8}La_{0.2}Ni_2Fe_{36}O_{60}$ hexaferrite

x	0	0.1	0.2	0.3
$4\pi M_s$ (Gs)	2956	2871	2862	2920
M_r/M_s	0.88	0.90	0.91	0.91
H_c (Oe)	1119	1220	1154	1123

Table 1 Magnetic properties of the sintered $Ba_{4-x}La_xNi_2Fe_{36}O_{60}$ hexaferrites

AR-12. Magnetic Properties of Mn substituted Strontium Ferrite Powders synthesized by the Molten Salt Method. *M. Kim*[1], H. Lee[1] and J. Kim[1] *1. Materials Science and Chemical Engineering, Hanyang University, Ansan-si, The Republic of Korea*

Hexagonal M-type ferrite magnets have been used in multiple applications such as motors, sensors, and etc. Because of their excellent high temperature stability and corrosion resistance, the M-type magnets have been widely used in severe operation conditions [1]. In particular, magnetic sensors in motors are strongly required to reduce their size and to enhance their accuracy. This indicates that M-type ferrite powders must be controlled to have a homogeneous structure with enhanced magnetic properties. In this study, the shape and size of ferrite powders were controlled by the molten salt method and changes in the coercivity were obtained by Mn substitution of strontium ferrite [2]. In order to obtain homogeneous mixtures, $SrCO_3$, Mn_2O_3, α-Fe_2O_3 and NaCl powders were mixed by ball milling at 300 rpm for 24 hr. These raw materials were calcined at various conditions using an alumina crucible in a box furnace under a heating rate of 10°C/min and a O_2 blowing rate of 3L/min. After the calcination, these synthesized powders were furnace cooled and washed with distilled water to remove residual NaCl powders and then dried in an oven at 60°C for 24 hr. The microstructures of fabricated ferrite powders were analyzed by a SEM and an XRD using CuKα radiation. The magnetic properties were measured by a VSM under 25 kOe. Figure 1 shows the morphology changes depending on the calcination condition. As shown in the figure 1, the two step calcination is an effective method to obtain homogenous morphology of the powders. Figure 2 shows the VSM results of fabricated strontium ferrite powders with different Mn concentrations. As shown in the figure 2, the coercivity of the strontium ferrites increases sharply with increasing the Mn concentration. These results show that the Mn substitution of strontium ferrite and the two step calcination process effectively improve the magnetic properties of strontium ferrite powders and are expected to be further improved by optimization of the calcination conditions [3].

[1] Kyumin Kim, Kwang-Won jeon, and Jongryoul Kim, IEEE Transactions on Magnetics., Vol. 52, Issue 7. (2016) [2] F.N.Tenorio-González, A.M. Bolarín-Miró, F.Sánchez-De Jesús, Journal of Alloys and Compounds, Vol. 695, p. 2083-2090 (2017) [3] Minyeol Kim, Kwiyoung Lee, and Jongryoul Kim, IEEE Transactions on Magnetics., Vol. 54, Issue 11. (2018)

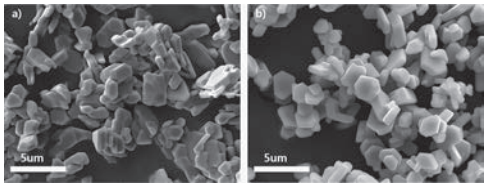


Fig. 1 SEM images of synthesized $SrFe_{12}O_{19}$ with calcination conditions a) at 1050°C for 1hr and b) at 850°C for 1hr and then at 1050°C for 1hr

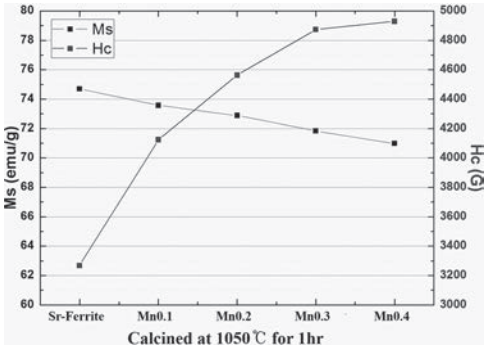


Fig. 2 Magnetic properties of Mn substituted strontium ferrite powders

AR-13. Effect of molten salt assisted calcination process in $SrFe_{12-x}Al_xO_{19}$ hexaferrite. *T.P. Poudel*[1], J. Mohapatra[2], D. Guragain[1], S. Yoon[3], D. Neupane[1], J. Liu[2] and S.R. Mishra[1] *1. University of Memphis, Memphis, TN, United States; 2. University of Texas at Arlington, Arlington, TX, United States; 3. Gunsan National Univeristy, Gunsan, The Republic of Korea*

Among ferrite families, M-type hexagonal ferrite, SrFe 12 O 19 (SrM) have great attraction due to their superior physical and chemical properties. SrM has applications from permanent magnet to electromagnetic wave absorber. Various strategies and synthesis technique have been used to prepare SrM viz. solid-state ball milling technique, hydrothermal technique, ceramics method, sol-gel, auto-combustion technique, co-precipitation method, and molten salt assisted method. Among these different techniques, the auto-combustion technique has been favored. However, agglomeration of particles has been often noticed with the auto-combustion technique, which affects the magnetic properties of SrM. We purpose a novel modified auto-combustion-molten salt technique for the synthesis of highly dispersed SrM nanoparticles. auto-combustion technique. As synthesized powder was mixed with NaCl thoroughly, and later heatedat 1100 o C for twelve hours. The calcined powder was thoroughly washed with methanol solution to obtain a highly dispersed SrM plate-like nanoparticles. We have prepared SrFe 12-x Al x O 19 with x= 0, 1, 2, 3, and 4. The structural and magnetic properties of molten-salt assisted SrM particles were compared with SrM synthesized via conventional auto-combustion technique, using XRD, FTIR, SEM, and VSM. The molten salt assisted powder showed plate-like morphology with an average size of 665 nm and thickness 86 nm (for x = 4). The surface area measured showed that molten salt assisted samples having a comparatively higher surface area of 25.15 m 2 /g for x = 4 samples vs. auto-combustion synthesized sample (14.67 m 2 /g). A reduction in magnetization (10.2 emu/g, for x = 4) and remanence (5.29 emu/g, x = 4), while enhancement in coercivity (20240 Oe, for x = 4) molten salt sample was observed when compared to that of samples prepared using auto-combustion technique only (Ms ~ 12 emu/g, Hc ~ 14888 Oe, and Mr~6.5 emu/g for x = 4). The EDX analysis shows that there is a presence of Na (0.1 atomic percentage) and Cl (0.4 atomic percentage) content in Molten salt assisted x = 4 samples. The molten salt assisted auto combustion technique could be a promising technique for applications requiring highly dispersed SrM nanoparticles.

AR-14. Effects of In^{3+} site occupancy on the magnetic properties of M-type strontium hexaferrite. C. Kim[2], B. Kim[1] and *S. Yoon*[1] *1. Department of Physics, Gunsan National University, Gunsan, The Republic of Korea; 2. Department of Physics, Kookmin University, Seoul, The Republic of Korea*

Effects of non-magnetic indium substitution on magnetic properties of M-type Strontium hexaferrites has been studied by first-principle calculation and crystallographic and magnetic measurements. The Indium doped samples $SrFe_{12-x}In_xO_{19}$ (x=0.25, 0.5, 0.75, 1.0) have been prepared by the auto-combustion method using metal nitrates and citric acid, followed by annealing at 1100 °C for 12 hours. Electron microscopy shows that the samples have hexagonal plate-like shape with the particle size ranging from 500~1000 nm and that the apparent size decrease with addition of indium. Lattice parameters show linear increase with increasing indium content, meaning the uniform solid solution is formed throughout the doping range (Fig 1). Figure 2 depicts the variations of saturation magnetization M_S and the coercivity H_C with indium content x obtained from room temperature VSM measurement. Whereas the H_C decreased monotonically with indium addition, the M_S first increase until x=0.5 reaching maximum but decrease thereafter. Effective magnetic anisotropy constants *K* are calculated as well from hysteresis curves using the law of approach to saturation method, and are 3.79×10^5, 3.70×10^5, 2.95×10^5, and 2.87×10^5 J/m^3 for x= 0.25, 0.5, 0.75 and 1.0, respectively. In view of the fact that 12k and 4f substitutions give rise to positive and negative contributions to M_S, this behavior strongly suggests that 12k site occupancy is more dominant when x>0.5. At the early stage of substitution, indium ions preferentially replace Fe^{3+} ions at $4f_2$ site [1]. However, if the occupation probability of the 12k site is almost equal, it can be anticipated that the two tendencies of site occupancy can compete at higher doping level. Density functional theory calculation has been performed to identify the possible substitution site of indium in accordance with experimental reports. The calculation found strong competition among different site occupations, which will be discussed in detail. Mossbauer spectra also show gradual decrease in $4f_2$ intensity, in support of the above conjecture.

[1] T. M. Clark, B. J. Evans, G. K. Thompson, and S. Freeman, J. Appl. Phys. vol.85, p. 5229 (1999).

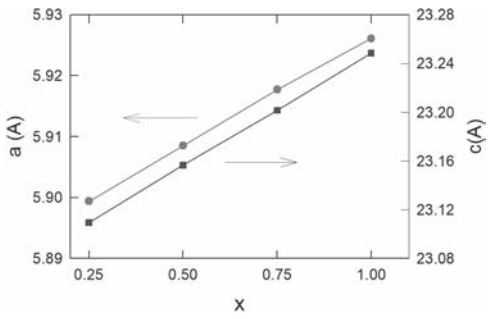


Fig. 1 Variation of lattice parameters with In^{3+} content x.

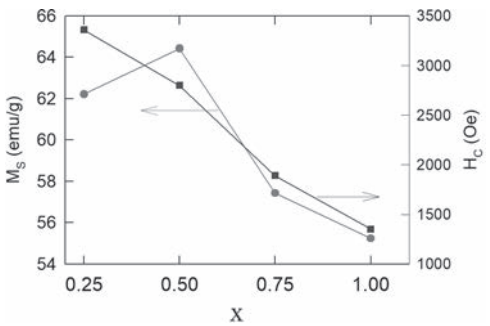


Fig. 2 Variations of saturation magnetization M_S and coercivity H_C with In^{3+} content x.

AR-15. Effect of perpendicular magnetic field assisted compaction on the magnetic and magnetostrictive properties of Cobalt Ferrite. *S. Indla*[1], G. Thotakura[2], A. Chelvane[3], T.V. Jayaraman[2] and D. Das[1] *1. School of Engineering Sciences and Technology, University of Hyderabad India, Hyderabad, India; 2. Mechanical Engineering, University of Michigan, Dearborn, MI, United States; 3. Advanced Magnetic Group, Defense Metallurgical Research Laboratory, Hyderabad, India*

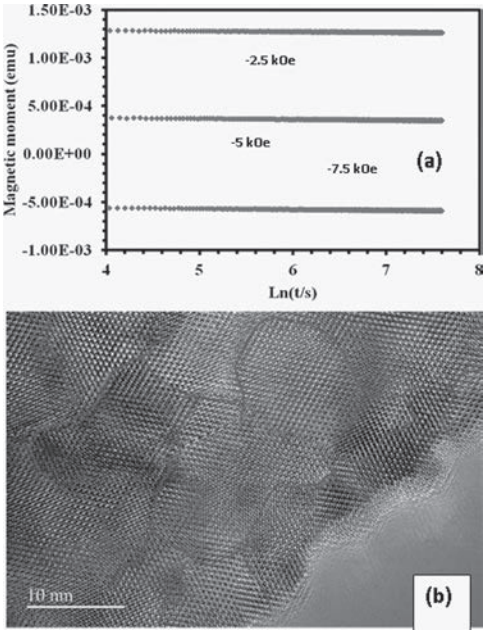
Polycrystalline $CoFe_2O_4$ powder was synthesized by combustion method followed by calcination [1]. Phase pure $CoFe_2O_4$ powder was pressed into pellets in a uniaxial hydraulic press under two different conditions: magnetic-field assisted pressing (MP) and normal pressing (NP) [2]. In the former, a magnetic field of 1 T is applied perpendicular to the applied pressure. Sintering of the green pellets at 1350°C for 12 h resulted in sintered pellets having ~80% of the theoretical density. X-ray diffraction revealed the presence of single phase cubic spinel structure in the sintered pellet while the scanning electron micrographs (SEM) of the as-sintered pellet showed the presence of micron-sized (~4 μm) ferrite grains. Magnetometry revealed that no significant change in magnetic properties, such as coercivity (43 kA/m for NP vs. 44 kA/m for MP), remanence (20 Am^2/kg and 19 Am^2/kg for NP and MP, respectively), and saturation magnetization (83 Am^2/kg for NP vs. 81 Am^2/kg for MP), between the two conditions. The magnetostriction was measured on a cubic pellet (~8 mm) with the strain gauge (350 Ohm) mounted on the flat surface of the pellet. Nearly 25% improvement in magnetostriction (168 ppm for MP vs. 134 ppm for NP sample) and 17% improvement in strain sensitivity (0.48×10^{-9} m/A to 0.56×10^{-9} m/A) were observed in the magnetic field assisted compacted sample compared to that compacted in the absence of a magnetic field.

[1] N. Somaiah, T. V. Jayaraman, P. A. Joy, and D. Das., J.Magn.Magn. Mater., 324, 2286 (2012) [2] S. Indla, A. Chelvane, A. Lodh, D. Das, J. Alloys. Compd. 779, 886-891 (2019)

AR-16. Magnetic Relaxation Process in Perpendicular Anisotropy Heterostructures. *Z. Alyousef*[1], M. Hassan[1], S. Pokharel[1], W. Morgan[1], M. Wuttig[2] and A. Lisfi[1] *1. Physics, Morgan State University, Baltimore, MD, United States; 2. Materials Science and Engineering, University of Maryland, College Park, MD, United States*

The increasing interest over magnetic media with perpendicular anisotropy is driven by fundamental science and technological demands such as data storage. Perpendicular magnetic media with small grains size and narrow switching field distribution have demonstrated their superior performance of high recording capacities. However, the media magnetic stability is compromised by the reduction of the grain size due to the thermal switching driven by the competition between thermal and magnetic anisotropy energies [1]. Cobalt ferrite is a promising ceramic for overcoming this problem due its large anisotropy that can be generated through its giant magnetostriction combined with epitaxial strain. In this paper, we elucidate the thermal stability of epitaxial $CoFe_2O_4$ hetero-structures with a large perpendicular anisotropy. The $CoFe_2O_4$ films were deposited by pulsed laser deposition from a polycrystalline target on (100) MgO substrate. The epitaxial nature of the films was confirmed through X-ray diffraction and transmission electron microscopy analyses. Magnetic relaxation measurements were performed with VSM under two different methods. (1) Direct measurement of the magnetization time dependence at constant applied magnetic field. (2) Measurement of hysteresis loops at different sweep rates of applied magnetic field in the range of 10-5000 Oe/s. As depicted by Fig. 1 (a) the time dependence measurements reveal a logarithmic decay of the magnetization over time and small magnetic viscosity weakly dependent on the external applied field. The investigation results will be presented and discussed based on the structural domains resulting from the epitaxy (Fig. 1(b)), the demagnetizing field imposed by the measurement geometry, the thermally activated irreversible process and the magnetization reversal mechanism in these epitaxial hetero-structures.

[1] Vassil Skumryev, Stoyan Stoyanov, Yong Zhang, George Hadjipanayis, Dominique Givord and Josep Nogués, *Nature* 423, 850-853 (2003)



(a) Magnetization time dependence of $CoFe_2O_4$ film measured along the easy axis (film plane normal) at 3 different applied fields (-7.5 kOe, -5 kOe and -2.5 kOe). (b) TEM picture showing nanometric structural domains delimited by blue lines boundaries.

AR-17. Strong dependence of exchange coupling on soft phase magnetization in hard/soft nanocomposites. *C. Pahwa*[1] and P. Sharma[1]
1. School of Physics & Materials Science, Thapar Institute of Engineering & Technology, Patiala, India

Existence of interfacial exchange coupling at nanoscale between high and low anisotropic ferrite can be exploited for tunable microwave devices. $BaFe_{12}O_{19}$ with high FMR (~35GHz) is extensively used in microwave devices upto W band. On contrary, spinel ferrites with low FMR frequency limit its application below 3 GHz [1]. To widen the operable frequency range; a composite ferrites could be an alternate for various microwave device applications. It is well reported, that nanoscale processing of composite ferrite show interfacial exchange coupling among the phases, and their effect on magnetic properties is vastly investigated [2]. However, role of different magnetization of soft ferrite and magnetic spin interaction across the interface in exchange-coupled system is one of the strong regime to investigate. In the present work, exchange-coupled nanocomposite with different magnetization of soft phase has been prepared. We observed strong dependence of exchange coupling on the magnetization of soft phase. The effect of exchange-coupling on magnetic and microwave properties was studied. Fig. 1 shows soft phase magnetization drastically affect the magnetization of exchange- coupled composite, which vastly deviates from theoretically calculated values. Interestingly, large difference between the magnetization of soft and hard phase provides better interfacial coupling. Fig. 2 depicts coupling dependent reflection losses in K_u-band, the multiple peaks in composite may paved the way for tunable microwave applications.

1. V.G. Harris, IEEE trans. Magn., 48 (3), 1075-1104, 2012. 2. D. Roy, C Shivakumara, P.S. Anil Kumar, J. Magn Magn. Mater., 321, L11-L14, 2009.

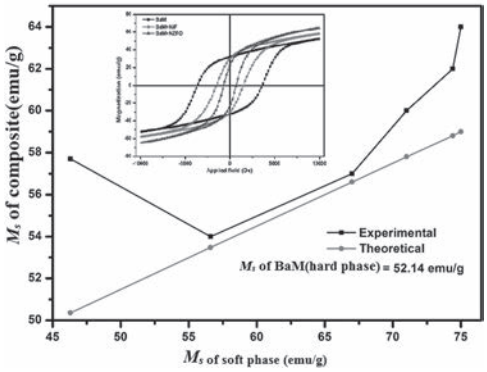


Fig.1 Variation in experimental and theoretical observed M_s of nanocomposite with M_s of soft phase and M-H loops (inset) of nanocomposites.

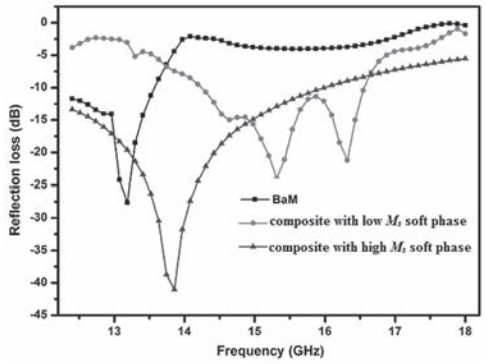


Fig. 2 Reflection losses with different M_s soft phase exchange-coupled nanocomposite.

Session AS
EDUCATION, OUTREACH, & PUBLIC ENGAGEMENT IN MAGNETISM
(Poster Session)

Barry L Zink, Co-Chair
University of Denver, Denver, CO, United States
Yukiko Takahashi, Co-Chair
NIMS, Tsukuba, Japan
Dafiné Ravelosona, Co-Chair
Center for Nanoscience and Nanotechnology, Palaiseau, France

AS-01. Exploring magnetic resonance with a compass. *D. Nelson*[1], E. Cookson[1], M. Anderson[1], D. McKinney[2] and I. Barsukov[1] *1. Physics and Astronomy, UC Riverside, Riverside, CA, United States; 2. Santa Rosa Academy, Menifee, CA, United States*

Magnetic resonance plays an important role in today's science, engineering, and medical diagnostics. Learning and teaching magnetic resonance is challenging since it requires advanced knowledge of condensed matter physics and quantum mechanics. Driven by the need to popularize this technologically impactful phenomenon, we develop an inexpensive table-top demonstration experiment. It unveils the magnetic resonance of a hand-held compass in the magnetic fields of a permanent magnet. The setup provides an immediate visualization of the underlying physical concepts and allows for their translation to broad student audiences. This work was supported by the National Science Foundation under Grant No. ECCS-1810541.

AS-02. Magnetic Fields Web Series: Engaging Middle School Students in STEM. *P. Pena Martin*[1], J. Isberg[1], E. Ertekin[1,3], V. Lorenz[1,2] and N. Mason[1,2] *1. Materials Research Laboratory, University of Illinois at Urbana-Champaign, Urbana, IL, United States; 2. Department of Physics, University of Illinois at Urbana-Champaign, Urbana, IL, United States; 3. Department of Mechanical Science and Engineering, University of Illinois at Urbana-Champaign, Urbana, IL, United States*

Web based media can make scientific content accessible to audiences far beyond the scientific community. We created a web series called "Magnetic Fields" that aims to introduce materials science, particularly concepts related to magnetism, and promote themes more general to STEM fields, such as persistence and the scientific process, through use of characters and a story geared towards a middle school audience. The goal is to build and maintain interest in science at an age where this tends to drop off. The four-episode arc follows a group of high school characters as they encounter a strange new material during a class field trip to a laboratory. The series is directed by John Isberg, with professional actors making up most of the cast. The series was initiated by scientists in the Illinois MRSEC, and the storyline was developed in collaboration with MRSEC students and faculty. The episodes were released in May 2019 through Youtube. We report on the process of creating this series, response to it upon release, and discussion of its use as an educational tool. The authors acknowledge primary support of the NSF through the University of Illinois at Urbana-Champaign Materials Research Science and Engineering Center DMR-1720633.



Fig.1 Scene from an episode of "Magnetic Fields." Photo by John Isberg.

AS-03. In-class experiments with smart phones for teaching upper-level electricity and magnetism. A. Davidson[1], A. Ranjan[2] and *X. Fan*[1] *1. Physics and Astronomy, University of Denver, Denver, CO, United States; 2. Cherry Creek High School, Greenwood Village, CO, United States*

Interactive-engagement method such as studio physics [1, 2], has demonstrated higher learning gains than traditional lecturing in intro-level physics classes. However, there have been limited applications in upper-level classes, such as Electricity and Magnetism (E&M), possibly because experiments on E&M topics can be too costly and sophisticated to be carried out in the classroom. Smart phone, which is equipped with magnetic field sensors, radio signal detectors and light sensors, provides a convenient platform for carrying out E&M-related experiments. In this poster, we will present three examples of the implementation of smart-phone-based studio physics in an E&M class for Physics majors: (1) Detection of earth magnetic field inclination; (2) quantifying skin depth of aluminum foil with cellphone tower signals; and (3) Measurement of Brewster's angle. Besides sensitive sensors, smart phone also has computational power, which can be explored to further expand the breadth and depth of the smart-phone-based studio physics. Due to the wide accessibility of smart phones and the simplicity of experimental setup, we expect this teaching technique can be easily transferred to other institutes in the world.

[1] Gok, T., *Assessment of the effectiveness of the hybrid studio format in introductory undergraduate physics.* Energy Education Science and Technology Part B-Social and Educational Studies, 2012. 4(1): p. 117-130. [2] Sorensen, C.M., A.D. Churukian, S. Maleki, and D.A. Zollman, *The New Studio format for instruction of introductory physics.* American Journal of Physics, 2006. 74(12): p. 1077-1082.

AS-04. The Use of Virtue Modules in Physics Lab Teaching. *W. Zhang*[1], R. Bidthanapally[1], T. Sebastian[2], Y. Xiong[1,3], H. Qu[3] and J. Sklenar[4]
1. Physics Department, Oakland University, Rochester, MI, United States; 2. THATec Innovation GmbH, Mannheim, Germany; 3. Electronic and Computer Engineering, Oakland University, Rochester, MI, United States; 4. Physics Department, Wayne State University, Detroit, MI, United States

Lab sessions in physics education connect the fundamental concepts to practical examples and are effective measures of the students' understanding and reasoning through ultimate real-world tests. Many topics in condensed matter physics are known to be challenging to convey in both lectures and labs. In addition, these topics are usually resource demanding, which has been one of the challenging issues. Here, we introduce and demonstrate the use of virtue lab modules for teaching physics labs and for effectively integrating research and education. Experiments that are relevant to magnetism and spintronics include, but not limited to, spin current detecting, microwave energy harvesting, and spin-based thermoelectric effects. An important highlight of these modules is the highly-interactive laboratory learning platform. In the class, each piece of experimental hardware (e.g. electrometers, oscilloscopes, etc) will be paired with a computer-based virtual module. The individual modules mimic the hardware, which the students can use to become familiar with the hardware, acquire real-time feedback, and visualize the data acquisition dynamics, on-demand and risk-free. The virtual component is also helpful for demonstrating delicate, shared hardware in class, without risk of damaging the actual instrumentation. These individual components are connected to a central operating system and the experiment can be re-programmed by simple coding and user-interfaced commands [1]. Work at Oakland University is supported by NSF DMR-1808892.

[1] THATec Innovation GmbH: https://www.thatec-innovation.com/

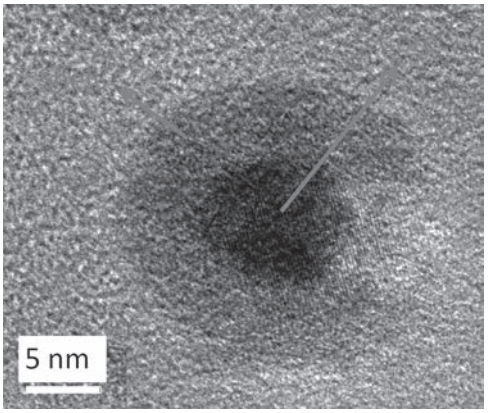
Session AT
NANO-ARRAYS, NOVEL STRUCTURES, AND SELF-ASSEMBLY I (Poster Session)

Karine Chesnel, Chair
Brigham Young University, Provo, UT, United States

AT-01. Comparative Study of Magnetic Properties of Fe_3O_4 Nanoparticles Produced by Pulsed Laser Deposition and Chemical Route.
W.S. Torres[1], N.R. Huaman[2], R. Bini[3], M.d. Santos[4], L.F. Cótica[3] and *D.L. Rocco[1,4] 1. Física, Universidade Federal Fluminese, Niterói, Brazil; 2. Centro Brasileiro de Pesquisas Físicas, Rio de Janeiro, Brazil; 3. Física, Universidade Estadual de Maringá, Maringá, Brazil; 4. Formação Geral, Centro Federal de Educação Tecnológica de Minas Gerais, Timóteo, Brazil*

Magnetite (Fe_3O_4) nanoparticles (NPs) have being intensely studied due to their semi-metallic nature, high Néel temperature (~850 K) and expected 100% spin polarization at room temperature. These properties make then a suitable candidate for spintronics sensors, as well biomedical applications[1]. It is well known that the NPs magnetic properties of this material are strongly dependent on the way they are synthesized and the substrate utilized[2]. Thus, our goal in this work was to prepare NPs of Fe_3O_4 using pulsed laser deposition (PLD) technique and to compare theirs structural and magnetic properties with the Fe_3O_4 NPs produced by a chemical route (CR) [3,4]. To PLD approach we starts from an iron target made by arc melting and using the wavelengths (λ) of 532 and 1064 nm with beam energy of 300 and 600 mJ, respectively, work pressure (argon) of 1.3 mbar. Transmission Electron Microscopy (TEM) revealed the formation of spherical NPs with core/shell morphology (Fig1) and with diameter of (8 ± 4) nm (1064 nm) and (16 ± 5) nm (= 532 nm). The as deposited NPs were exposed to air for 5 days, in order to oxidize them, and after that thermally treated at 600°C for 1 hour in order to accelerate the diffusion of oxygen through the material. X-ray diffraction technique with Rietveld's method was used to quantify the phases, and the percentages obtained were: 58% of Fe_3O_4 and 42% of α-Fe (532 nm) and 85% of Fe_3O_4 and 15% of α-Fe (1064 nm). Measurements of AC magnetization in different frequencies were carried out for the thermal treated NPs and these results were compared to the ones of Fe_3O_4 NPs synthesized by CR in which 100% of Fe_3O_4 was obtained. With the curves of the real part of magnetization versus temperature we got an estimation of the NPs blocking temperature (T_B) as being 257.6, 220.3 and 195.8 K for the ones obtained by CR, deposited with 532 and 1064 nm, respectively. As T_B is proportional to the medium diameter of the NP, we can see that the NPs deposited with 1064 nm have a diameter smaller than the ones deposited with 532 nm, which is in agreement with TEM image.

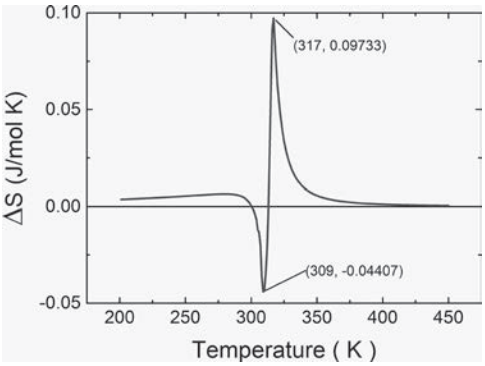
[1] A. Mitra et al., J. Phys. D: Appl. Phys.,51,085002 (2018). [2] S. Rajput et al., J. of Colloid and Interface Science, (2016). [3] C.G.S. Souza et al., J. Nanopart. Res, (2013). [4] Araújo-Neto et al., J. Magn. Magn. Mater., (2014).



TEM image of Fe_3O_4 nonparticle produced by pulsed laser deposition with λ = 532 nm. The core/shell strucuture is revealed in this image.

AT-02. Inverse magnetocaloric effect of densely packed ferromagnetic nanoparticles clusters.
C.M. Souza[1], L.L. Oliveira[2], *A.L. Dantas*[2] and A.S. Carriço[1] *1. Department of Physics, Federal University of Rio Grande do Norte, Natal, Brazil; 2. Department of Science and Technology, State University of Rio Grande do Norte, Natal, Brazil*

We present a theoretical discussion of the inverse magnetocaloric effect (IMCE) of clusters of ferromagnetic nanoparticles uniformly packed in ellipsoidal clusters. We apply the theoretical model to Gd nanoparticles with diameters in the 30 nm – 200 nm range, arranged in micrometer-sized clusters. The magnetocaloric effect (MCE) is strongly affected by the nanoparticles dipolar interaction, which leads to an up-shift of the Curie temperature and the values of temperature for the peaks in the isothermal entropy variations. We show that by switching off an external magnetic field of moderate strength the isothermal entropy variation of high-packing density nanoparticles clusters shows a double peak structure, with opposite signs, around the Curie temperature. The IMCE below the Curie temperature is due to the nucleation of the dipolar antiferromagnetic state (DAFS) and depends on the values of the packing density and the nanoparticles diameter, as well as the external field strength. We have found, for instance, that a 0.98 eccentricity cluster with a 2.37 μm major axis, holding 795 Gd nanoparticles with 30 nm diameter, packed with a density of 2.1 x 10^{15} nanoparticles/cm^3, shows a normal MCE, with no signature of dipolar effects, with ΔS=0.33 J/(mol K), at a temperature of T=294 K, in response to switching off a 0.5 T external magnetic field, as in bulk Gd. Using 60 nm diameter nanoparticles, the entropy variation displays a double-peak, as shown in Fig.1, with ΔS=-0.044 J/(mol K), at T_-=309 K and ΔS=0.097 J/(mol K), at T_+=317 K. At T_- the negative entropy change is due to the formation of a DAFS. For H_{ext}=0.5 T, the local field at most of the nanoparticles is smaller than the local field in the absence of the external magnetic field. Thus, when you switch off the external field, at most particles the local field increases, leading to a negative ΔS peak.



Isothermal entropy variation of a 0.98 eccentricity cluster with a 2.37 mm major axis, holding 795 Gd nanoparticles with 60 nm diameter, packed with a density of 2.1 x 10^{15} nanoparticles/cm^3, corresponding to switching off a 0.5 T external magnetic field.

AT-03. *In-situ* Alignment of Filament-based 3D Printed Magnetic Materials. *A. Sarkar*[1], S.M. A.[1], M. Paranthaman[2], M. Kramer[1], T. Lograsso[1], C. Haase[1] and I.C. Nlebedim[1] *1. AMES Laboratory, Ames, IA, United States; 2. Oak Ridge National Laboratory, Oak Ridge, TN, United States*

With the trend for rapid prototyping of parts and systems, additive manufacturing process like three-dimensional (3D) printing can advance the fabrication of shape-specific architectures for anisotropic permanent magnets involving expensive and critical rare-earth elements[1,2]. Although *in-situ* alignment will open new horizons for manufacturing of complex permanent magnets, integration of alignment systems into 3D printing processes is still a challenge. We will present a mechanism to address this challenge accomplished by integration of bonded magnet production, 3D printing, finite element modeling and system development. We have developed a mechanism to align magnetic materials using fused filament 3D printer with a novel magnetic field source architecture. The work addresses opportunities to integrate magnetic field into 3D printing process in order to enable printing, and alignment of anisotropic permanent magnets, without requiring further processing. The principle behind the analysis is rotation of magnetic particles in a molten matrix under low magnetic field. The alignment architecture was designed and optimized for weight and applied field. An in-depth finite element modeling and CAD was performed followed by prototyping of the magnetic field source. Magnetization vs. field measurements of extruded and printed Sm-Co in PLA polymer magnets, with and without alignment, confirmed alignment of magnetic particles. This process can be used for any permanent magnet composition or hybrid magnets. The work presents a benchmark for application of *in-situ* magnetic alignment of 3D printed bonded magnets in industrial and commercial applications. This work is supported by the Critical Materials Institute (CMI), an Energy Innovation Hub funded by the U.S. Department of Energy (DOE), Office of Energy Efficiency and Renewable Energy, Advanced Manufacturing Office. Ames Laboratory is operated for the U.S. Department of Energy by Iowa State University of Science and Technology under Contract No. DE-AC02-07CH11358. Authors are thankful to Electron Energy Corporation for providing the Sm-Co grinding swarfs used for this work.

[1] C. Huber, C. Abert, F. Bruckner, Appl. Phys. Lett., Vol. 109, p.162401, (2016). [2] L. Li, B. Post, V. Kunc, Scr. Mater., Vol. 135, p.100-104 (2017).

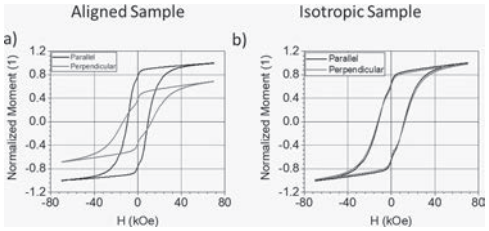
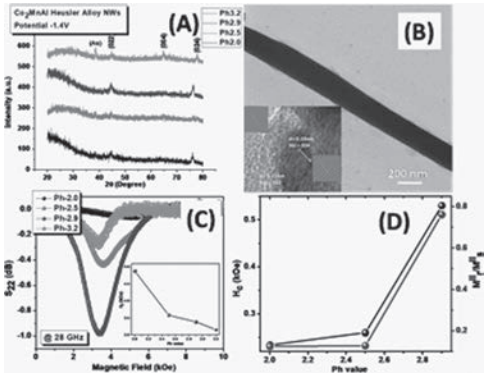


Fig.1. Normalized magnetic moment of, a) Aligned sample @ 1A current, and b) Isotropic sample.

AT-04. Modulation of static and dynamic properties of Co_2MnAl Nanowires through deposition parameters. M. Sharma[1], A. Das[1] and *B.K. Kuanr*[1] *1. Special Centre for Nanoscience, Jawaharlal Nehru University, New Delhi, India*

Full heusler alloys have emerged as a fascinating multifunctional material due to its excellent magnetic and electrical properties which can lead to potential applications in spintronics, thermoelectric, ferromagnetic shape memory and superconductors [1]. Recently a lot of research has been focused on bulk and thin film heusler alloys, however, very few reports studied the one-dimensional heusler alloy nanowires [2]. In the present work, Co_2MnAl heusler alloy nanowires have been successfully fabricated in anodic alumina templates using simple and low-cost electrodeposition technique at room temperature. We investigated the role of deposition parameters such as pH value of the electrolyte and deposition potential on the structural and magnetic properties of Co_2MnAl nanowires. It is observed that the crystallinity improves with the increase of pH value and optimized around pH=3.0. The XRD confirms the formation of B2 crystal type heusler alloys which is further verified by high-resolution transmission electron microscopy. The static magnetic properties revealed that the saturation magnetization, squareness, coercivity and uniaxial anisotropy of the nanowires increase with the increase in pH value. The highest remanent squareness of 76% is observed for pH=2.9. The dynamic measurements of heusler alloy nanowires have been studied by ferromagnetic resonance technique using the flip-chip method in the field-sweep mode at different applied frequencies ranging from 20-40 GHz. It is observed that the resonance field increases linearly with the increase in frequency for all samples. Further, the resonance field decreases to 35% with the increase of pH value of electrolyte, resulting in an increase in the effective field.

[1] T. Graf, C. Felser, and S. S. P. Parkin, Prog. Solid State Chem., 39, 1 (2011). [2] S. Khan, N. Ahmad, N. Ahmed, A. Safeer, J. Iqbal, and X. F. Han, J. Magn. Magn. Mater., 465, 462 (2018).



AT-05. Magnetic and catalytic properties of Co_xNi_{1-x} nanowires. J. Elkins[1], *J. Mohapatra*[1], M. Xing[1], J. Beatty[1] and J. Liu[1] *1. Department of Physics, University of Texas at Arlington, Arlington, TX, United States*

Many binary alloy systems have tunable properties and phase structures upon adjusting their compositions. CoNi is one of such systems that will change from hcp to fcc structure after the Ni content surpasses the threshold.

Therefore, it would be interesting to track the changes in the properties of CoNi nanoparticles as the amount of Ni reaches and surpasses the hcp/fcc threshold. CoNi bimetallic nanoparticles with varying Co:Ni concentrations were synthesized via a solvothermal approach. The changes in phase structure, morphology, magnetic properties, and catalytic hydrogenation were studied as the Ni content was increased. According to the XRD measurements, as the Ni content increased, the nanowires shifted from hcp to fcc structure, with nearly pure fcc at 50:50 Co:Ni ratio. Magnetic measurements show that as the Ni content is increased, the H_C and M_S decrease as shown in Figure 1. Contrary to the magnetic trend, the catalytic activity of the nanowires increases upon increasing Ni content. The addition of a thin Pt film sputtered on top of the CoNi films further increased the current density for hydrogen evolution reaction.

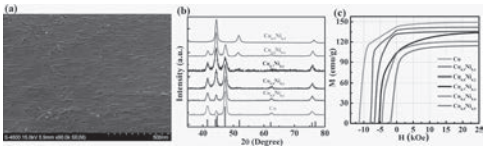


Figure 1. (a) Scanning electron microscope (SEM) micrographs of the aligned $Co_{0.9}Ni_{0.1}$ nanowire assemblies. (b) XRD patterns for Co_xNi_{1-x} (x = 0, 0.1, 0.2, 0.3, 0.4, and 0.5) alloys (c) Demagnetization measurements at room temperature of the aligned Co_xNi_{1-x} NWs assemblies.

AT-06. Effects of surface spin disorder on the magnetic properties of $CoFe_2O_4$ nanoparticles. *J. Mohapatra*[1], J. Beatty[1], J. Elkins[1], M. Xing[1] and J. Liu[1] *1. Department of Physics, University of Texas at Arlington, Arlington, TX, United States*

The effects of surface spin disorder are studied on the magnetic properties of two groups of $CoFe_2O_4$ nanoparticles with average size of 3.5 nm and 10 nm, respectively. Magnetization curves showed that the magnetic moment of the 3.5 nm $CoFe_2O_4$ nanoparticles (29 emu/g) is much smaller than the bulk materials (82 emu/g), whereas the 10 nm $CoFe_2O_4$ nanoparticle (75 emu/g) is comparable to the bulk value. The low magnetization in former case is attributed to the higher surface spin disorder. More importantly, the zero-field cooled and field-cooled magnetization loops of the 3.5 nm $CoFe_2O_4$ nanoparticles exhibited very high coercivity (27 kOe) and irreversible behavior even at a high field of 90 kOe (Figure 1a-b). Further, the measured training behavior indicates that the 3.5 nm $CoFe_2O_4$ nanoparticles have highly frustrated surface spins that rearrange much more slowly than the interior spins. On the other hand, the blocking behavior of 10 nm $CoFe_2O_4$ nanoparticles measured at various field strengths (50-5000 Oe) shows a strong dependence on the applied magnetic field (H_{app}). As the H_{app} is increased, the blocking temperature is found to be shifted to lower temperatures, a peculiar characteristic of super-spinglass systems (Figure 1c-d). Our experimental results demonstrate the origin of spinglass-like phenomenon at two different size scales.

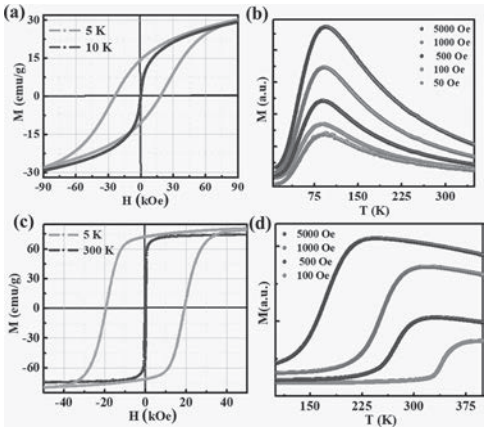


Figure 1. (a, c) Room temperature (300 K) and low temperature (5 K) hysteresis curves and (b, d) zero-filed-cooled magnetization curves of 3.5 nm and 10 nm $CoFe_2O_4$ nanoparticles, respectively.

AT-07. Designing Cobalt Nanowire Arrays. *J.G. Giuliani*[1], A. Galindo[1], J. Reyes[1] and K. Nash[1] *1. Physics, University of Texas at San Antonio, San Antonio, TX, United States*

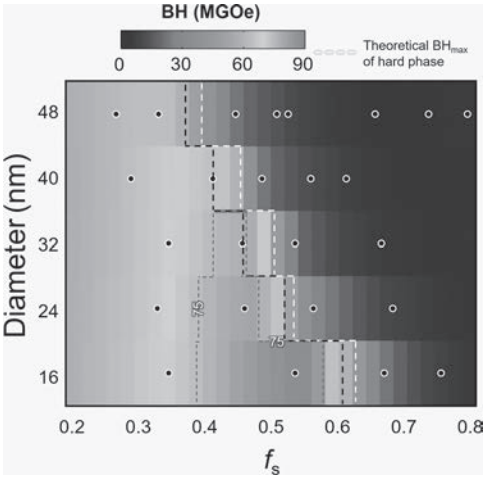
Cobalt (Co) is a popular element particularly for its magnetic properties, which makes it an ideal candidate for a variety of magnetic storage devices. More specifically, perpendicular magnetic storage devices (PMD) can benefit from cobalt's strong crystal anisotropy. However to achieve a viable device it is necessary to learn how to control the anisotropy orientation which has been the subject of much research. One such method of research is the use of self-supported anodic aluminum oxide-template-assisted electrochemical deposition (AAO-ED) to create ordered arrays of Co nanowires. This method allows for the tailoring of many aspects of the nanowires including the length, diameter, and the interwire distance by varying the AAO growth conditions. Also, by using various ED parameters it has been reported that the crystal structure can be altered from face-centered-cubic (FCC) to hexagonally-close-packed (HCP). Utilizing both the AAO and ED methods it should be possible to create nanowires with the correct crystal anisotropy for the use in PMD however; this remains a formidable challenge to achieve because of two main limitations. One limitation is that when the AAO self-supported templates are removed, the nanowires are left in a disordered state. The second heavily debated limitation is delineating the critical ED conditions in which to grow the nanowires to produce the desired crystal anisotropy. In this work, we introduce a variation of the AAO-ED technique, along with various ED growth conditions to synthesize Co nanowires. The ED growth condition parameters include pH, external magnetic fields, and substrate materials. Confirmation of the Co nanowire structures and their magnetic properties are confirmed with X-Ray Diffraction, scanning electron microscopy, focused ion beam milling, and with a vibrating-sample magnetometer. Overall this work demonstrates that these techniques allow for the synthesis of Co nanowires with specific crystal anisotropies to be directly synthesized onto almost any surface and subsequently retain the nanowire order even after the AAO has been removed which is ideal for the implementation into PMD devices.

Jason G Guiliani, John Cadena, and Carlos Monton, Nanotechnology 29 075301 (2018) M. Darques, L. Piraux, and U. Ebels, Appl. Phys. Lett. 86, 072508 (2005) M. P. Proenca, C. T. Sousa, and J. P. Araujo, J. Appl. Phys. 113, 093907 (2013) J. M. Garcia, A. Asenjo, J. Velazquez, and E. Ruiz-Hitzky, Journal of Applied Physics 85, 5480 (1999) A. Encinas, M. Demand, and L. Piraux, IEEE Transactions on Magnetics, VOL. 38, NO. 5, (2002) Michael Darques, Armando Encinas, Luc Piraux, J. Phys. D: Appl. Phys. 37 1411 (2004)

AT-08. The Practical Energy Product of Cylindrical Core/shell Consist of Soft- and Hard-magnetic Materials. *N. Kim*[1], H. Han[1], S. Lee[1] and K. Lee[1] *1. School of Materials Science and Engineering, Ulsan National Institute of Science and Technology (UNIST), Ulsan, The Republic of Korea*

The exchange-coupled soft-and hard-magnet has been considered as a good candidate for a future high-efficient permanent magnet since it can acquire high saturation magnetization and high coercivity from soft- and hard-magnets, respectively. However, to achieve such an ideal advantage from both magnets, very rigorous design of structures and mixing ratio are required. To do this, various types of exchange-coupled magnet has been investigated including multi-layer, mixture, core/shell structures. The cylindrical core/shell structure are particularly advantageous owing to large interface and versatility at controlling compositions and a demagnetization factor by dimensions. Since the energy product corresponds to the energy stored in the stray field produced by the magnet itself, it should be measured from demagnetizing field, H_d and the flux density, B at the remanent state. In this study, we investigate the energy product of the cylindrical core/shell structure, which do not mean the maximum energy product estimated from a hysteresis loop for a single aspect ratio, but the energy product considering H_d of the system at the remanent state by using micromagnetic simulations. As a model system, we adopted cylindrical core/shell structure composed of the soft-magnetic shell and the hard-magnetic core. To estimate the energy product, the hysteresis loops were calculated by applying external magnetic field along with easy axis and H_d and B. The results reveal that the energy product basically depends on the ratio but the dimension of the whole system contribute dominantly in the high energy product range. By optimizing the dimension and the ratio, the energy product can reach to very high value of 90 MGOe. We finally expanded this model to iterative array structure of the cylindrical core/shell.

[1] R. W. McCallum, L. Lewis, R. Skomski, M. J. Kramer, and I. E. Anderson, "Practical Aspects of Modern and Future Permanent Magnets," Annu. Rev. Mater. Res., vol. 44, no. 1, pp. 451–477, 2014. [2] E. F. Kneller and R. Hawig, "The exchange-spring magnet: A new material principle for permanent magnets," IEEE Trans. Magn., vol. 27, no. 4, pp. 3588–3600, 1991. [2] S. Mechanics, "Magnetic properties of core/shell nanoparticles with magnetic or nonmagnetic shells," vol. 4, pp. 0–20, 2012. [3] R. Skomski and J. M. D. Coey, "Giant energy product in nanostructured two-phase magnets," Phys. Rev. B, vol. 48, no. 21, pp. 15812–15816, 1993. [4] T. H. Rana et al., "Micromagnetism of MnBi:FeCo thin films," J. Phys. D. Appl. Phys., vol. 49, no. 7, pp. 3–8, 2016. [5] W. Zhanyong et al., "High coercivity Nd2Fe-14B/α-Fe nanocomposite magnets," Phys. B Condens. Matter, vol. 404, no. 8–11, pp. 1321–1325, 2009. [6] W. Liu, Z. Zhang, J. Fischbacher, and A. Kovacs, "Rational design of the exchange-spring permanent magnet," 2014. [7] E. Lottini et al., "Strongly Exchange Coupled Core|Shell Nanoparticles with High Magnetic Anisotropy: A Strategy toward Rare-Earth-Free Permanent Magnets," Chem. Mater., vol. 28, no. 12, pp. 4214–4222, 2016. [8] N. Kim, H.-S. Han, and K.-S. Lee, "A Limit to Predict Maximum Energy Product (BHmax) from the Magnetization Hysteresis Loop," J. Korean Magn. Soc., vol. 28, no. 5, pp. 205–211, 2018.



The phase diagram of the energy product according to the ratio of the soft-magnetic shell and the diameters of the hard-magnetic core. The energy product is plotted as black dots, and its color is linearly interpolated in each diameter. The black and white dashed line indicates that the calculated nucleation field is zero and the theoretical maximum energy product of the hard phase.

AT-09. Magnetic coupling of cementite nanoparticles within double-wall carbon nanotubes. W. Nieto[1], J. Chimborazo[2], A. Briones-Leon[2], O. Domanov[2], H. Shiozawa[2], T. Pichler[2], P. Ayala[2] and *D. Niebieskikwiat*[1] *1. Departamento de Física, Universidad San Francisco de Quito, Quito, Ecuador; 2. Faculty of Physics, University of Vienna, Vienna, Austria*

Studying the novelty of magnetism in carbon nanotubes is still intriguing and it has not been completely explored, despite a number of promising technological applications. In this study, we focus on the magnetic properties of bundles of double-walled, metallic carbon nanotubes with encapsulated cementite (Fe_3C) nanoparticles of ~3 nm in length inside their hollow core. These nanoparticles are not unintentional impurities, but have been deliberately introduced to fill the nanotubes with ferromagnetic material. Results of VSM magnetometry of the filled nanotubes give an anisotropy constant of ~$3x10^6$ erg/cm^3, much larger than the anisotropy of free cementite nanoparticles, indicating a strong magnetic coupling of the nanoparticles with the nanotubes. On the other hand, the calculated activation volume for magnetization reversal, of ~400 nm^3, shows that around 300 nanoparticles of cementite are mutually coupled through the conduction electrons of the nanotubes. Considering a spin diffusion length of 130 nm along the direction of the nanotubes, the activation volume suggests that magnetic coupling also occurs between neighboring nanotubes in the direction perpendicular to their axis, with a perpendicular magnetic correlation length of ~5-6 nm, i.e. involving four parallel nanotubes.

AT-10. Electrophoretic Deposition of Iron-Oxide Nanoparticles to Achieve Thick Nickel/Iron-Oxide Magnetic Nanocomposite Films. *S.C. Mills*[1], C.S. Smith[2], D.P. Arnold[2] and J. Andrew[1] *1. Materials Science and Engineering, University of Florida, Gainesville, FL, United States; 2. Electrical and Computer Engineering, University of Florida, Gainesville, FL, United States*

It is desirable to fabricate on-chip power components with both low loss and high magnetic saturation, which are typically not achievable with single-phase ferromagnetic materials. Magnetic nanocomposites fabricated from a low loss magnetic phase (e.g. ferrite) and a high magnetic saturation phase (e.g. nickel) can exhibit hybrid magnetic properties. To provide useful magnetic energy storage and power handling, thick (tens of microns) nanocomposites are needed [1,2]. Electro-infiltration—a process that electroplates a magnetic metal through a porous layer of nanoparticles—has

the potential to fabricate thick nanocomposites [3]. For the formation of a nanoparticle layer, solution-based methods, such as drop-casting, suffer a lack of control over film thickness and quality. Electrophoretic deposition (EPD), a method that deposits charged particles in colloidal suspensions via electrophoresis, can fabricate thicker magnetic nanoparticle films than other methods [4]. In this work, EPD is shown to be a viable option for assembling iron oxide nanoparticles into a mold, which can be subsequently electro-infiltrated with nickel to fabricate the final nanocomposite (~4.8 μm in thickness). The deposited films are imaged via scanning electron microscopy and energy dispersive x-ray spectroscopy to qualitatively observe the infiltration of the nickel between the iron oxide nanoparticles (Fig. 1). Further confirmation of successful composite formation is performed via vibrating sample magnetometry, showing the saturation magnetization value of the film (~473 kA/m) falls between that of the iron oxide nanoparticles (~280 kA/m) and the nickel (~515 kA/m) (Fig. 2). These results demonstrate the potential of EPD to fabricate electro-infiltrated magnetic nanocomposite films.

[1] Y. Nguyen, D. Bourrier, S. Charlot, J. Micromech. Microeng., Vol. 24, p. 1-10 (2014) [2] S.C. Mathuna, T. O'Donnell, N. Wang, IEEE Trans. Power Electron., Vol. 20, p. 585-592 (2005) [3] X. Wen, S. Kelly, J. Andrew, AIP Adv., Vol. 6, p. 1-6 (2015) [4] L. Besra, M. Liu, Progress in Mat. Sci., Vol. 52, p. 1-61 (2007)

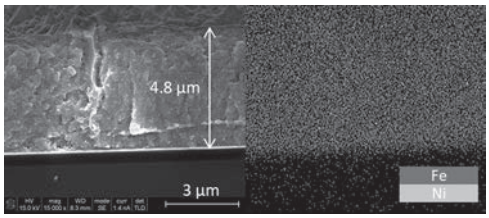


Fig. 1 – Scanning electron microscopy/electron dispersive x-ray spectroscopy images films fabricated via EPD of iron oxide nanoparticles followed by electro-infiltration of nickel, showing particles dispersed in the nickel matrix.

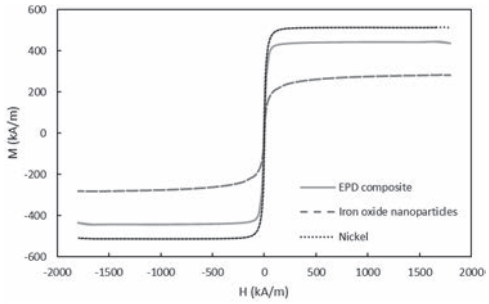


Fig. 2 – Hysteresis curves from vibrating sample magnetometry of the nanocomposite consisting of the electrophoretically deposited iron oxide nanoparticles, showing an averaging of the magnetic saturation of each constituent material.

AT-11. Withdrawn

AT-12. Withdrawn

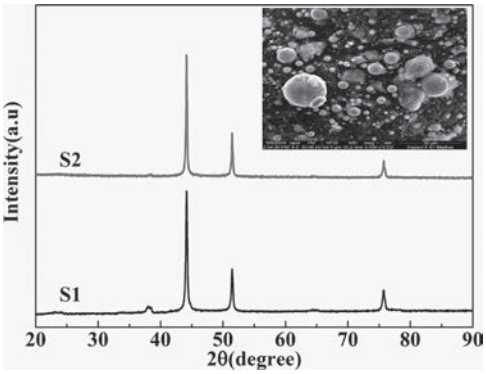
Session AU
NANOPARTICLES AND NANOWIRES
(Poster Session)

Ranko Heindl, Chair
San Jose State University, San Jose, CA, United States

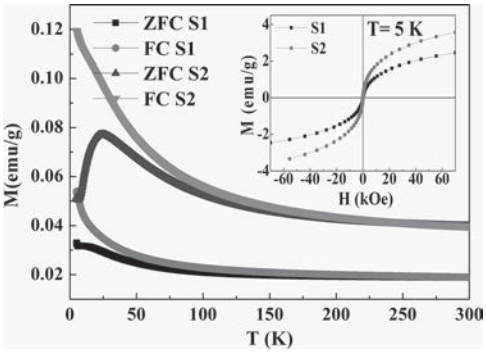
AU-01. Anomalous magnetic behavior in $Ni_{80}Cr_{20}$ nanoparticles prepared by electric explosion method of wire. *S. Vishvakarma*[2], S. Veeturi[2], P. Ranjan[1] and R. Sarathi[1] *1. Electrical Engineering, Indian Institute of Technology Madras, Chennai, India; 2. Physics, Indian Institute of Technology Madras, Chennai, India*

The remarkable magnetic properties observed in nanoparticles (NPs) that are different from their bulk counterparts. This is attributed to a complex interplay between finite size effect [1]. In the past considerable interest has been shown in the application of nickel–chromium (Ni–Cr) alloy NPs in for ferro-fluids and hyperthermia. The $Ni_{80}Cr_{20}$ NPs synthesized by physical and chemical methods, exhibited contrasting magnetic properties [2-4] i.e, NPs prepared by mechanical alloying exhibited ferromagnetism at room temperature compared to their non-magnetic bulk counterparts. It was suggested that the Cr-segregation in NiCr NPs results in ferromagnetic character and this is also supported by the Monte-Carlo simulations [4]. These observations suggest that the magnetic properties also depend on the synthesis process [2-4]. Therefore, in the present investigation we have synthesized $Ni_{80}Cr_{20}$ fine particles by electric explosion of wire. By varying the process conditions we have synthesized fine particles with different size distributions by wire explosion method (WEM) from commercially purchased Nichrome ($Ni_{80}Cr_{20}$) wire of 0.4 mm diameter. As prepared particles are of spherical shape and exhibit pure FCC phase (Fig.1). The samples prepared with different process conditions are termed as S1 and S2 respectively. Zero field cooled (ZFC) and field cooled (FC) magnetization curves suggest the presence of magnetic disorder and susceptibility does not follow Curie-Weiss behavior. The maximum observed in ZFC at T= 25K and sharp rise in FC curve is the signatures of presence of spin glass behavior (Fig.2). Although magnetic isotherm at T=5K showed coercivity for S1 and S2 samples 150 Oe and 80 Oe respectively, no spontaneous magnetization is observed. This rules out the possibility of AFM and weak ferromagnetic order. These observations are in contradiction to that of particles prepared by mechanical alloying. These anomalous magnetic properties will be discussed in details along with microstructure.

1-E. Winkler, R. D. Zysler, M. Vasquez Mansilla, D. Fiorani, D. Rinaldi, M. Vasilakaki and K. N. Trohidou, Nanotechnology, 2008, 19, 185702. 2-T. D. Xiao, S. Torban, P. R. Strutt, and B. H. Kear, Nanostructured Materials Vol. 7, No. 8, pp. 857-871, 1996. 3-I. Ban, J. Sterger, M. Drofenik, G. Ferk, and D. Makovec, ActaChim. Slov. 60, 750 (2013). 4-M. Bohra, P. Grammatikopoulous, R. E. Diaz, V.Singh, J. Zhao, J.-F. Bobo, A. Kuronen, F. Djurabekova, K. Nordlund, and M. Sowwan, Phys. Rev. Materials.1, 066001(2017).



XRD patterns of S1 and S2 samples. Inset: SEM image of S1 sample



ZFC-FC data as a function of T in a constant field of 100 Oe for S1 and S2 samples.Inset: Magnetic isotherm of S1 and S2 samples at T= 5 K.

AU-02. Magnetic spinel ferrite materials as high efficient and easily retrievable visible photocatalysts. Y. Jia[1] and *C. Liu*[1] *1. Physics, Hankuk University of Foreign Studies, Yongin, The Republic of Korea*

The development of efficient photocatalysts are now considered as one of the few approaches to solve the energy and environmental crisis around the world. Spinel ferrite materials, due to their suitable bandgap energy, have been increasingly investigated recently as promising photocatalysts under wide ranged solar light irradiation. The room temperature magnetization makes it possible to re-collect the spinel ferrite-based photocatalysts easily by using a normal magnet, which is a very important advantage as compared to non-magnetic photocatalyst. In this work, we plan to present our research research results on design and preparation of spinel ferrite-based photocatalyst with high efficiency in water system cleaning and CO2 reduction. A hydrothermal synthesis procedure was developed to prepare ferrite nanoparticles with good crystallinity and quite uniform size distribution. Non-metal element (N, S) doping was investigated to further adjust the bandgap energy for more efficient solar light absorption. The optical and photoelectrical characterizations will be present to evidence the desired properties for photocatalyst applications [1,2]. In addition, hetergeneous photocatalysts were also designed and prepared to enhance the light absorption and the separation of photo-generated electrons and holes. ferrite/TiO2, and ferrite/g-C3N4

composites were investigated in details for their photocatalystic applications in water system cleaning (CTC degradation, MO decomposition, etc), and showed relatively high efficiency due to the effective charge transfer across the interfaces of the composite materials [3,4]. Finally, we will also present our results in applying ferrite-composites for photocatalytic CO2 reduction. Their retrievability and stability in recycled usage will also be discussed. The results presented in this work are believed to provide important insights for developing novel photocatalysts based on spinel ferrite materials.

[1] Y.F. Jia, et al. RSC Advances 6, 76542 (2016). [2] Y.F. Jia, et al. J. Hazardous Materials 338, 447 (2017). [3] Y.F. Jia, et al. J. Industrial and Engineering Chemistry 47, 303(2017). [4] Y.F. Jia, et al. Materials Letters 45, 3509 (2016).

AU-03. Tailoring the energy product of cylindrical core-shell FePt@ $CoFe_2$ and FePt@Fe nanoparticles. Y.S. Santos[1], *L.L. Oliveira*[1], R.M. Souza[2], M.S. Nunes[3], A.L. Dantas[1] and A.S. Carriço[2] *1. Department of Science and Technology, State University of Rio Grande do Norte, Natal, Brazil; 2. Department of Physics, Federal University of Rio Grande do Norte, Natal, Brazil; 3. Department of Physics, State University of Rio Grande do Norte, Natal, Brazil*

We report a theoretical discussion of the impact core-shell composition on the maximum energy product (BH_{max}) of cylindrical core-shell FePt@$CoFe_2$ and FePt@Fe nanoparticles, with the magnetization along the cylindrical axis. For strong ferromagnetic core-shell interface exchange energy interaction, BH_{max} increases with the shell thickness. However, beyond a critical value of the shell thickness, BH_{max} turns a monotonically decreasing function of the shell thickness. The core-shell dipolar interaction favors the early alignment of the shell magnetization with the external field, in the demagnetization quadrant. Fe has a larger value of the exchange stiffness energy (25 x 10^{-12} J/m) than $CoFe_2$ (1.9 x 10^{-12} J/m). Thus, the exchange energy cost for a twist in the shell magnetization from aligned to the core magnetization to the direction opposite to the core magnetization at the shell surface, as required by the dipolar field, is larger in the FePt@Fe nanoparticles than in the FePt@ $CoFe_2$ nanoparticles. Thus, the critical shell thickness for Fe is larger than that of $CoFe_2$. We have found, for instance, that a 30 nm height and 7 nm FePt diameter core FePt@Fe nanoparticle, has the BH_{max} optimized for a 4 nm thick Fe shell. The FePt(7 nm)@Fe(4 nm) nanoparticle, for a magnetic field of H=-9 kOe, where the BH_{max} is reached, has the core and shell ferromagnetically coupled at the maximum value of the core-shell magnetization. For the same value of the magnetic field, a FePt(7 nm)@$CoFe_2$(4 nm) has the shell magnetization opposite to the core magnetization, with a large drop of the core-shell magnetization and the value of the BH_{max}. Thus, although having a smaller magnetization (M_s=1711 emu/cm^3) than $CoFe_2$(M_s=1887 emu/cm^3), Fe is the choice material for the shell, leading to a larger value of the BH_{max}. We have found, for instance, that a 30 nm height FePt(7 nm)@ Fe(4 nm) nanoparticle has a BH_{max} of 763.5 KJ/m^3, which is 88% larger than that of the FePt core (406.75 KJ/m^3). Also, with the same values of the FePt core diameter, and core-shell height, the best composition for a FePt@ $CoFe_2$ nanoparticle corresponds to a 2nm thick $CoFe_2$ shell, with a BH_{max} of 622.5 KJ/m^3.

AU-04. Compositional dependence of structural and magnetic properties of $Ga_{2-x}Fe_xO_3$ nanoparticles. *T. Han*[1] and T. Chen[1] *1. Department of Applied Physics, National University of Kaohsiung, Kaohsiung, Taiwan*

The $Ga_{2-x}Fe_xO_3$ (GF_xO) compound, is a quite interesting material due to simultaneous exhibit magnetic and electric orderings [1,2]. However, the physical properties of GF_xO at reduced grain sizes remain underexplored due to the challenges associated with their synthesis with a proper control over the crystalline phase. In addition, the effect of the Fe/Ga ratio on the magnetic properties of the nanosized GF_xO system has not yet been completely established. In this work, therefore, we prepare a series of GF_xO nanoparticles with $0.8 \leq x \leq 1.2$ using the sol-gel method to systematically study the effect of the Fe/Ga ratio on their structural and magnetic properties. All the samples of GF_xO with $0.8 \leq x \leq 1.2$ have been characterized by the powder XRD measurements and Rietveld refinements. All the observed peaks can be indexed by reflections of the $Pc2_1n$ orthorhombic structure of GF_xO, and no impurity phase was found. The determined lattice parameters are found to display a monotonic increase with the Fe content x. Composition of the GF_xO nanoparticles was confirmed by energy dispersive X-ray spectra. The evolution of the Néel temperature (T_N) of GF_xO samples versus their Fe-content (x) is given in Fig.1. It is found that with increasing Fe-content, up to 1.2, the T_N increases from 279 to 350 K. Moreover, the magnetic hysteresis curves measured below T_N exhibit two-phase-like magnetic behavior consisting of soft and hard magnetic phases. The results could be explained by the site-disorder of the cations in GF_xO nanoparticles.

[1]. T. Arima, D. Higashiyama, Y. Kaneko, J. P. He, T. Goto, S. Miyasaka, T. Kimura, K. Oikawa, T. Kamiyama, R. Kumai and Y. Tokura, Phys. Rev. B 70, 064426 (2004). [2]. B. Srimathy, Indranil Bhaumik, S. Ganesamoorthy, R. Bhatt, A. K. Karnal and J. Kumar, J. Alloys Compd. 590, 459 (2014).

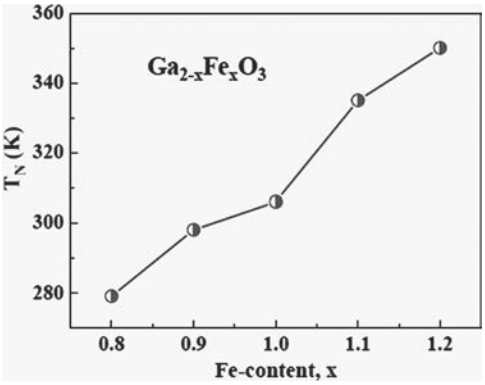
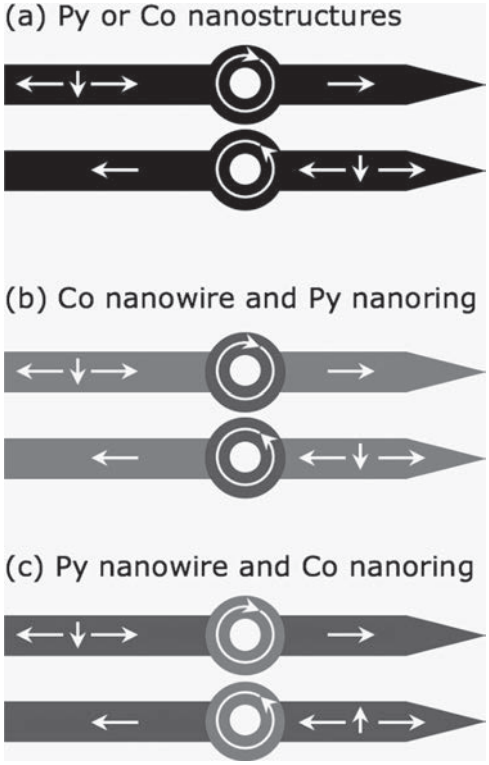


Fig.1 Néel temperature (T_N) versus Fe-content (x) for the $Ga_{2-x}Fe_xO_3$ samples.

AU-05. Controlling domain wall chirality by combining hard and soft magnetic materials in planar nanostructures with wire-ring morphology. *R. Corona*[1,3], S. Castillo[2,3], J. Escrig[1,3] and D. Altbir[1,3] *1. Física, Universidad de Santiago de Chile, Santiago, Chile; 2. Departamento de Ingenieria, Universidad Autonoma de Chile, Santiago, Chile; 3. CEDENNA, Santiago, Chile*

The study of the magnetization reversal process in ferromagnetic nanostructures continues attracting the attention of the scientific community due to several applications based on domain walls (DWs) and their dynamics [1-3]. Vortex domain walls exhibit a certain chirality that it is important to control for the use in potential technological applications. Gao *et al.* [4] studied a series of permalloy nanowires with an antisymmetric notch, concluding that the DW can keep or change its chirality, as it passes through a notch, depending on the geometric parameters of the system. Following these ideas, in this work we explore using micromagnetic simulations, a wire-ring structure, where we have alternated hard (cobalt) and soft (permalloy) magnetic materials. This wire-ring structure has been previously proposed by Corona *et al.* [5] for the nucleation of multiple DWs. The authors found that for thick rings, the magnetization reversal process began in the ring, while for thin rings, the process starts at the end of the wire with uniform width. However, the reversion process at the interface between the ring and the wire was not studied in detail and, in addition, only single material nanostructures were considered. In this work, we consider another variable and use materials with different coercivities for the ring and the wires. Our results evidence that, depending on the geometry, it is possible to control the DW chirality when it goes through the ring section. Therefore, this system can be used as a device that controls the chirality of the domain wall. Acknowledgments: The authors acknowledge financial support from Fondecyt 1160198 and 11170858, and Financiamiento Basal para Centros Científicos y Tecnológicos de Excelencia (CEDENNA), under project FB0807.

[1] G. Williams, M. Hunt, B. Boehm, A. May, M. Taverne, D. Ho, S. Giblin, D. Read, J. Rarity, R. Allenspach, and S. Ladak, *Nano Research* 11, 845 (2018). [2] M. Diegel, R. Mattheis, and E. Halder, *IEEE Trans. Magn.* 40, 2655 (2004). [3] J. Brandao and D. Atkinson, *Appl. Phys. Lett.* 109, 062405 (2016). [4] Y. Gao, B. You, X. Z. Ruan, M. Y. Liu, H. L. Yang, Q. F. Zhan, Z. Li, N. Lei, W. S. Zhao, D. F. Pan, J. G. Wan, J. Wu, H. Q. Tu, J. Wang, W. Zhang, Y. B. Xu, and J. Du, *Sci. Rep.* 6, 32617 (2016). [5] R. M. Corona, A. Aranda, J. L. Palma, C. E. Lopez, and J. Escrig, *Appl. Phys. Lett.* 105, 082406 (2014).



AU-06. Domain wall motion and coupled electron hopping relaxation in nanostructured magnetite. *R. Das*[1,2], V. Kalappattil[2], M. Phan[2] and H. Srikanth[2] *1. Faculty of Materials Science and Engineering, Phenikaa University, Hanoi, Vietnam; 2. Department of Physics, University of South Florida, Tampa, FL, United States*

Magnetite (Fe_3O_4) nanoparticles are not only promising for biomedical applications but also an excellent model for the study of nanomagnetism. Since most of the synthesis methods gave poorly crystalline, off stoichiometric Fe_3O_4 nanoparticles, the particle size dependence of Verwey transition has just recently been studied [1,2]. The low-temperature magnetic state of magnetite has remained a matter of debate till date, due to the presence of microtwinning in the monoclinic phase of Fe_3O_4 single crystals, which causes problem in neutron diffraction [3]. Most research on Fe_3O_4 was focused on the electric and magnetic properties near Verwey transition. There have been only a few reports on the low temperature (below 50 K) features, like Fe^{+2} ions electron relaxation. Kronmüller *et al*. observed two anomalies at ~25 and ~50 K in single crystals of Fe_3O_4 and attributed it to the relaxation of Fe^{+2} extra electrons [4]. However, no consensus has been reached on the origin of these anomalies. A clear understanding of the low temperature anomalies and the nature of Verwey transition in Fe_3O_4 nanoparticles is currently lacking, mainly due to the poor crystallinity of nanoparticles synthesized. In this study, we demonstrate that the low temperature anomalies observed in highly crystalline, stoichiometric Fe_3O_4 nanorods are associated with the coupled electron hopping relaxation process and domain wall motion. Both DC and AC susceptibility showed the presence of a hump around 35 K, which is associated with the relaxation of the Fe^{+2} extra electrons. Radio-frequency transverse susceptibility (TS) measurements indicated a noticeable increase in anisotropy field below ~ 25 K, which is attributed to the rearrangement of Fe^{+2} electrons in the octahedral site. TS measurements also revealed the domain wall freezing below ~ 35 K. A corroboration of DC, AC and TS susceptibility measurements has shed light on the complex nature of the low temperature anomalies in nanostructured magnetite.

[1] J. Lee, S. G. Kwon, J. G. Park and T. Hyeon, *Nano Lett.* 15, 4337 (2015). [2] R. Das, J. Alonso, Z. Porshokouh, V. Kalappattil, D. Torres, M. H. Phan, E. Garaio, J. A. Garcia, J. L. S. Liamazares and H. Srikanth, *J. Phys. Chem. C* 120, 10086 (2016). [3] M. Iizumi, T. F. Koetzel, G. Shirane, S. Chikazumi, M. Matsui and S. Todo, *Acta. Crystallogr.* 38, 2121 (1982). [4] H. Kronmüller, *J. Magn. Magn. Mater.* 4, 280 (1977).

AU-07. Effect of particle size variation on structural, magnetic and transport properties of Sol-gel derived nanocrystalline $La_{0.15}Pr_{0.45}Ca_{0.40}MnO_3$ perovskite manganites. *D. Raghav*[1], H.K. Singh[2] and G.D. Varma[3] *1. Physics, I.I.T. Roorkee, Roorkee, India; 2. CSIR NPL, New Delhi, India; 3. Physics, I.I.T. Roorkee, Roorkee, India*

In the present work we have investigated the effect of particle size on the structural, magnetic and transport properties of $La_{0.15}Pr_{0.45}Ca_{0.40}MnO_3$ system. $La_{0.15}Pr_{0.45}Ca_{0.40}MnO_3$ (LPC) materials have been synthesized using Sol-gel method and sintered at different temperature to get the samples of different particle sizes. Phase pureness of the synthesized samples has been confirmed by Retiveld refinement of the powder X- Ray diffraction (XRD) data, which authenticates orthorhombic structure with *Pnma* space group. All three lattice constants (a, b and c), bond lengths and bond angles increase with increasing particle size. The magnetization measurements (H@100 Oe) as a function of temperature exhibit paramagnetic (PM) to ferromagnetic (FM) transition and also bring out the hysteresis between the field cooled cooling (FCC) and field cooled warming (FCW) magnetization curves due to the coexistence of ferromagnetic (FM) and antiferromagnetic (AFM) phase [Fig. 1(a)]. Moreover, the divergence between the zero field cooled (ZFC) and FCW magnetization decreases with increasing particle size. The isothermal magnetization loops confirm the increase in the FM component at higher particle size at low temperature (5K) [fig.1(b)]. The temperature dependent resistivity measurements of all samples in zero magnetic field show no insulator to metal transition for the samples sintered at lower temperatures, but the sample sintered at higher temperature shows the metal to insulator transition. The data of resistivity have been fitted by using variable range hopping model (VRH). Characteristic temperature (T_0), localization length ($1/\alpha$) and average hopping distance (R) have been calculated by using this model. X-ray photoemission spectra of Mn2p and Mn2s core-level confirm dual valence state of Mn (Mn^{3+} and Mn^{4+}), which are responsible for the magnetic behaviour of LPCMO system. The detail correlation between the transport and observed magnetic properties of sintered LPCMO samples will be described and discussed in this paper.

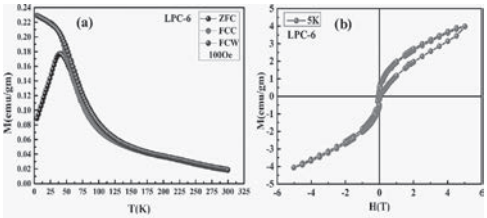


Fig. 1.- (a) Zero-field-cooled (ZFC), Field cooled cooling (FCC) and Field Cooled warming (FCW) Magnetization vs Temperature (M-T) measurements have been shown at 100 Oe magnetic field for LPC-6 nanocrystals. (b) Magnetic field versus magnetization (M-H) hysteresis curves for LPC- 6 sample at 5 K.

AU-08. Evaluation of magnetic properties in ferromagnetic martensite particle using type 304 stainless steel wire. *K. Kinoshita*[1] *1. Department of energy conversion science, Kyoto university, Kyoto, Japan*

Austenitic stainless steel, including type 304 stainless steel (SUS 304), is an interesting material as a magnetic composite because of the generation of ferromagnetic martensite particles upon plastic deformation. We developed a magnetic composite model for SUS 304, which is able to qualitatively express the permeability property [1]. However, the analysis results did not quantitatively agree with the experimental results. Miura et al. showed that a coercivity (H_c) of SUS 304 increased and then decreased with increasing martensite fraction [2]. This result suggests that the quantitative difference between the experimental and analysis result may be because we did not consider the possibility that the magnetization curve of the single martensite particle changed as its size and morphology varied. We need to confirm the hypothesis by measuring the magnetization curve for a single martensite particle; however, this is difficult because of the size and shape distributions of martensite particles. In this study, we attempted to weaken the effect of the distribution of martensite particles on the magnetization curve by decreasing the number of crystal grains per unit area using SUS 304 wires. The magnetization curve for the SUS 304 wires with an applied plastic tensile strain from 10 %–30% was measured using a squid magnet flux meter. Fig.1 shows the relationship between the plastic tensile strain and martensite fraction obtained by the saturation magnetization method. The martensite fraction for a wire diameter of 0.8 mm grew exponentially with increasing plastic tensile strain, and the behavior was the same as the results of the bulk material [3],[4]. However, for the wire diameter of 0.4 mm, the martensite fraction linearly increased, and this value was approximately 2/3 smaller than for the wire diameter of 0.8 mm. From the relationship between the H_c and the martensite fraction shown in Fig.2, the H_c increased and then converged. The variance of H_c per unit martensite fraction was larger for the wire diameter of 0.4 mm in which the number of grains was smaller.

[1] K. Kinoshita: Refinement of the magnetic composite model of type 304 stainless steel by considering misoriented ferromagnetic martensite particles, *AIP Adv*., 7, 056008 (2017). [2] K. Miura, S. Kobayashi, Y. Kamada, Y. Onuki and J. A. Szpunar: Relationship between morphology of strain-induced martensite phase and magnetic properties in austenitic stainless steels, *J. Jpn. Inst. Met. Mater.*, 78, 375 (2014). [3] G. B. Olson and M. Cohen: Kinetics of strain-induced martensitic nucleation, *Metall. Trans.*, 6A, 791 (1975). [4] S. K. Varma, J. Kalyanam, L. E. Murr, V. Srinivas: Effect of grain size on deformation-induced martensite formation in 304 and 316 stainless steels during room temperature tensile testing, *J. Mater. Sci. Lett.*, 13, 107 (1994).

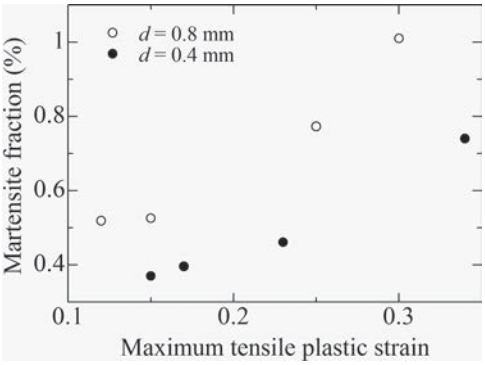


Fig.1 Relationship between maximum tensile plastic strain and martensite fraction.

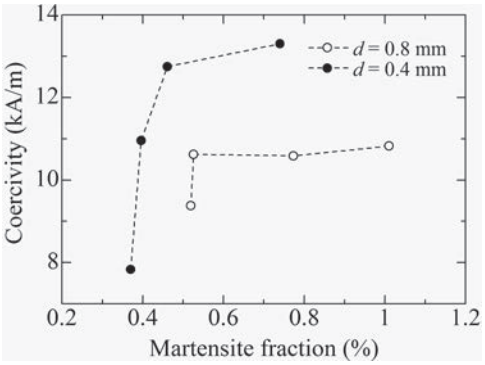


Fig.2 Relationship between martensite fraction and coercivity.

AU-09. Size-induced Enhancement of Room Temperature Magnetic Memory Effect in Fe-doped NiO Nanoparticles. *A.C. Gandhi*[1] and S.Y. Wu[1] *1. Department of Physics, National Dong Hwa University, Hualien, Taiwan*

In this study, we explore the role of size effect on the room temperature magnetic memory effect[1-3] from hydrothermally synthesized $Ni_{1-x}Fe_xO$ NPs (having a similar structure as NiO confirmed from synchrotron radiation X-ray diffraction)[4]. The effect of thermal treatment from 400°C to 800°C leads to increase of grain size from 8 to 35 nm (NiO) and 9 to 57 nm (1% Fe), suggesting Fe-doping has enhanced the crystal growth. A lattice expansion and microstrain are obtained from 8 nm NiO attributed to nickel vacancy defect and the effect of 1% Fe-doping (9 nm) resulted in further lattice expansion with reduced microstrain. On the further increase of grain size, lattice parameter approached to NiO bulk value of 4.177Å, whereas microstrain to zero. Above findings suggest that the dopant Fe^{3+} ions to move from ordered Ni^{2+} substitutional lattice sites to more disordered regions, such as surface regions. This dopant migration begins around ~500°C (27 nm) and is accompanied by suppression of disordered surface spins, and a corresponding enhancement in *n* with grain size suggests a relative increase of interparticle interaction possibly because of migration of dopant ions on the surface of NPs (Fig.1(a)). The value of *n* is obtained after analyzing time-dependent relaxation of magnetization M(t) at 300 K using $W(t)=t^{-n}$ ($W(t)=-(d/dt)\ln M(t)$).[5] The effect of interparticle interaction and broad size distribution in 1% sample leads to drastic enhancement in T_B from 140 K to far above 400 K with the increase of grain size from 9 nm to 57 nm (Fig.1(b)). An enhanced RT memory effect with grain size can be noted from Fig.2. Furthermore, both the spontaneous exchange bias (EB) field and coercivity drop with the increase of grain size. Our findings suggest that $Ni_{1-x}Fe_xO$ NPs system differs from a typical EB system. The thermal treatment at higher temperature might have resulted in the formation of interacting inverted core-shell type structure of $Ni_{1-x}Fe_xO$ NPs such that higher amount of Fe^{3+} ions are residing on the surface of NPs having a compensated AF-core.

[1] L. Xu, Y. Gao, A. Malik, etc., J. Mag. Mag. Mater., Vol. 469, p.504-509 (2019). [2] Z. Tian, L. Xu, Y. Gao, etc., Appl. Phys. Lett., Vol. 111(18), p.182406 (2017). [3] S. Dhara, R. R. Chowdhury, B. Bandyopadhyay, RSC Adv., Vol. 5(116), p.95695-95702 (2015). [4] A. C. Gandhi, R. Pradeep, Y.-C. Yeh etc., ACS Appl. Nano. Mater., Vol. 2, p.278-290 (2018). [5] M. Ulrich, J. García-Otero, J. Rivas, etc., Phys. Rev. B, 67(2), p.024416 (2003).

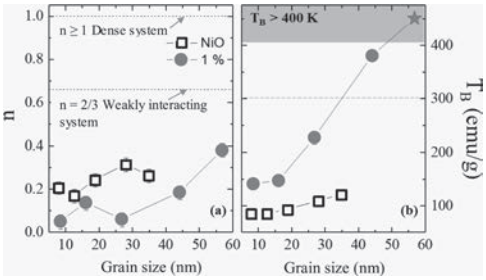


Fig.1 Size dependency of (a) *n* and (b) T_B of NiO and 1% $Ni_{1-x}Fe_xO$ samples.

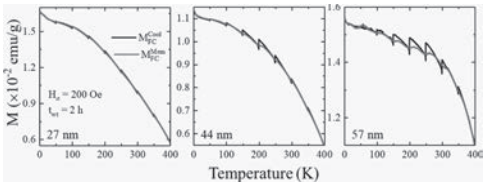
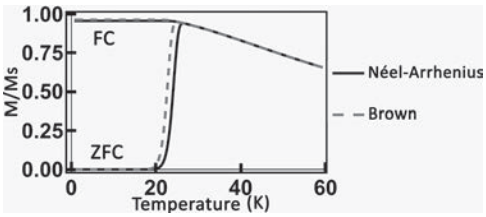


Fig.2 Magnetic memory effect measured from 27, 44, and 57 nm of 1% $Ni_{1-x}Fe_xO$ samples.

AU-10. Néel Relaxation Time and Blocking Temperature for Nanoparticle Magnetization as a Function of Static Applied Field.
C.R. Chalifour[1], N.R. Anderson[1], T.M. Crawford[2] and K. Livesey[1]
1. UCCS Biofrontiers Center and Department of Physics, University of Colorado Colorado Springs, Colorado Springs, CO, United States; 2. Department of Physics and Astronomy, SmartState Center for Experimental Nanoscale Physics, University of South Carolina, Columbia, SC, United States

The blocking temperature of a system of magnetic nanoparticles corresponds to the temperature separating ferromagnetic and superparamagnetic behavior. This quantity occurs at an inflection point in zero field cooled (ZFC) magnetization curves [1,2] and allows one to estimate the energy barrier for magnetization reversal. The blocking temperature is not a single temperature but rather a "blocking region" exists [1,2], arising from the stochastic behavior of magnetization reversal over a barrier [1,3]. The field-independent Néel-Arrhenius equation for the magnetization relaxation time $\tau_{NA}=\tau_0 e^{KV/kT}$, describes this stochastic behavior, where the characteristic attempt time τ_0 is taken as a constant on the order of nanoseconds [2], *KV* is the anisotropy energy barrier, and *kT* is the thermal energy. However, this form is inherently flawed because it does not consider that both the attempt time and barrier height can be altered by an applied field. We use a Néel relaxation time that depends on externally applied static fields, as found by Brown [4,5], and calculate its consequences on ZFC and field-cooled (FC) curves [1]. We examine the case of an assembly of noninteracting magnetic nanoparticles with easy axes aligned parallel to the applied field, show that the analytic model reduces to the expected result in the limiting case of zero applied field, and that the ZFC peak shifts to *lower* temperatures as a larger field is applied. This is shown in the figure where just a 50 Oe field shifts the ZFC peak down (red, dashed line) compared to the case where the field-dependence of is ignored (solid, black line). Our analytic results are in excellent agreement with results of numerical Landau-Lifshitz-Gilbert simulations. We have run the model with the addition of poly-disperse particle sizes and will discuss its implication on the interpretation of experimental results.

[1] K.L. Livesey *et al.* Sci. Rep. 8, 11166 (2018) [2] I.J. Bruvera *et al.* J. Appl. Phys. 118, 184384 (2015) [3] H. Maymiya *et al.* IEEE Trans. Magn. 41, 2294 (2005) [4] W.F. Brown, Jr. Phys. Rev. 130, 1677-1686 (1963) [5] W.T. Coffey *et al.* Phys. Rev. B 52, 15951 (1995) Funding is acknowledged from National Science Foundation awards DMR 1808412 and 1808426.



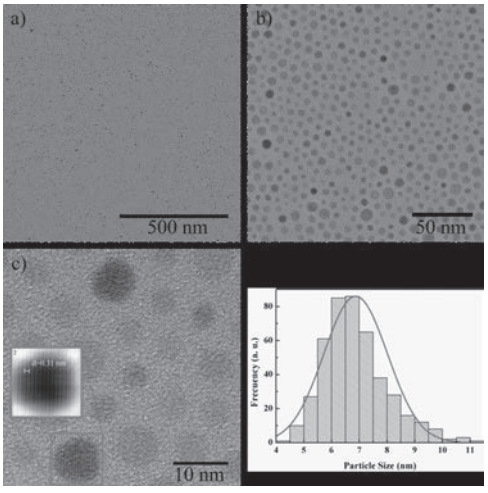
ZFC/FC magnetization curves for an assembly of 5 nm radius magnetite nanoparticles, aligned parallel to an externally applied field of 50 Oe.

AU-11. Withdrawn

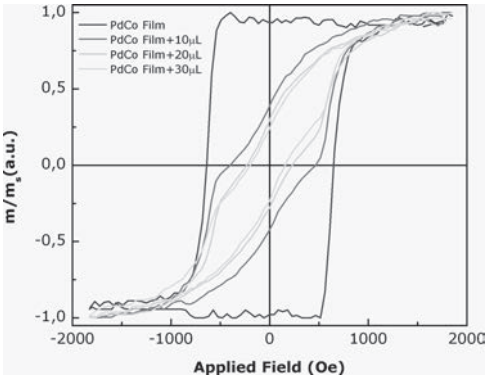
AU-12. Tailoring magnetic properties of PMA thin films due to the interaction with $CoFe_2O_4$ nanoparticles.
S. Michea[3,2], R. Freire[1,2], J. Palma[4,2], J. Denardin[1,2] and D. Altbir[1,2] *1. Physics, Universidad de Santiago de Chile, Santiago, Chile; 2. Center for the development of Nanoscience and Nanotechnology, Santiago, Chile; 3. Institute of Applied Chemical Sciences, Universidad Autónoma de Chile, Santiago, Chile; 4. Ciencias Básicas, Universidad Central de Chile, Santiago, Chile*

In this work, changes in hysteretic behavior for magnetic multilayer thin films with perpendicular magnetic anisotropy (PMA) under the influence of superparamagnetic nanoparticles are presented. Firstly, Si/[Pd(1.5nm)Co(0.3nm)] x10/Pd(2nm) magnetic thin films were fabricated by sputtering machine over a silicon substrate. Subsequently, $CoFe_2O_4$ nanoparticles (nps) were prepared using a stainless-steel reaction kettle with a Teflon-liner (20 ml) and were dispersed in hexane and stored at 4°C for further characterization and use. The magnetic characterization was carried out using an Alternate Gradient Force magnetometer. For the magnetic film, it is possible to observe the typical square behavior for thin film whit PMA. With 118 mg (each 10ml) of nps over the thin magnetic film, we observe a complete change in the magnetic behavior in both, remnant magnetization and coercivity. It is also possible to note a waist in the loop, which may be due to a chiral reversion process in film induced by the interaction with nps. The change in the main features of the hysteresis loop generates a great possibility of novel applications.

[1]S. Michea, S. Oyarzun, S. Vidal, J.C. Denardin. AIP Advances 7, 056310 (2017)



TEM images of $CoFe_2O_4$(a) at 20k, (b) 100k, (c) 600k times magnification, the inset image correspond to FFT-IFFT from the red square selection area



Magnetization curves for interaction between PdCo PMA thin film with $CoFe_2O_4$ nps in different quantities

AU-13. Room temperature ferromagnetic behaviour in Dy^{3+} doped dilute magnetic semiconductor nanoparticles. *S. Jindal*[1] and P. Sharma[2] *1. School of Physics and Material Science, Thapar Institute of Engineering and Technology, Patiala, India; 2. School of Physics and Material Science, Thapar Institute of Engineering and Technology, Patiala, India*

II-VI dilute magnetic semiconductors are promising material for application in electronics. Currently a great deal of attention is being focused on adding spin degree-of-freedom into semiconductor to create a new area of solid-state electronics, called spintronics [1]. Such materials need to be good semiconductors for easy integration in typical integrated circuits with high sensitivity to the spin orientation. The major material challenge is to magnetize and stabilize semiconductors with room temperature ferromagnetic ordering without significantly affecting the physical properties of semiconductors. Cadmium sulfide (CdS) is one of the promising II-VI semiconductor due to its inherent property of direct band gap of 2.42 eV and in green spectral range [2, 3]. Rare-earth (RE) elements play an important role in many functional materials and exhibit interesting magnetic and optoelectronic properties. Due to their highly localized 4f electrons, the direct f-f interactions between the neighbouring rare-earth atoms are very weak. This produces larger magnetic moments in 4f REs than 3d transition metals. Most of the earlier works on dilute magnetic semiconductor (DMS) were focused on TM doped ZnS, CdS. Since REs have higher magnetic moment than TMs, we expect to achieve higher magnetization with a few percentages of RE doping. In the present work, $Cd_{1-x}Dy_xS$ (x = 0.00, 0.05, 0.10 and 0.15) nanoparticles were synthesized by hydrothermal technique. The room temperature (*RT)* magnetic hysteresis loops of synthesized nanoparticles are shown in Fig.1. The magnetization increases upto x = 0.10, and then decreases. This increase in magnetization may due to the formation of various defects or vacancies with doping [4]. Fig.2 shows UV- visible absorption spectra with Tauc's plot of $Cd_{1-x}Dy_xS$ nanoparticles. The optical bandgap (E_g) enhances from 2.43 eV (x = 0.00) to 2.55 eV for x = 0.10. Further, for higher doping content E_g decreases. This blue shift in optical bandgap with doping can be attributed to the quantum confinement effect.

[1] C. Liu, F. Yun, H. Morkoc, J. Mater. Sci. Mater. Electron. 16, 555 (2005). [2] S. Shirakata, K. Ohkubo, Y. Ishii, T. Nakada, Sol. Energy Mat. Sol. Cells 93, 988 (2009). [3] C.B. Murray, D.J. Norris, M.G. Bawendi, J. Am. Chem. Soc. 115, 8706 (1993). [4] J. P. Tang, L. Wang, H. J. Luoc, W. Z. Xiao, Phys.Lett. A 377, 572 (2013).

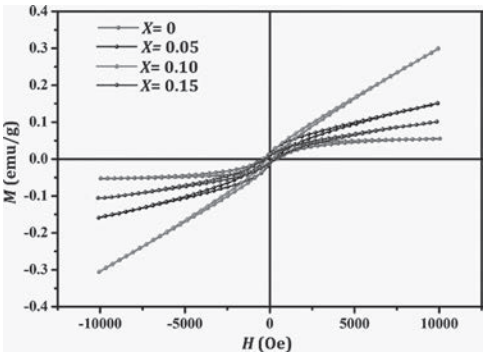


Fig. 1 *M-H* curves of $Cd_{1-x}Dy_xS$ nanoparticles.

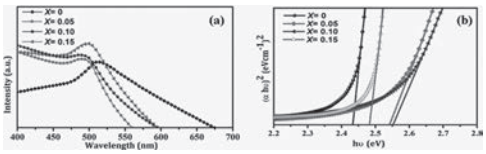


Fig 2 (a) *UV*–visible absorption spectra (b) Tauc's plot of $Cd_{1-x}Dy_xS$ nanoparticles.

AU-14. RE-doped Fe_3O_4 (RE = Eu, Gd, Er) nanoparticles for nanothermometry. *E. Correa*[1,2], B. Bosch-Santos[3,2], T. Sales[2], G. Cabrera-Pasca[4], B.S. Corrêa[2], O.F. Neto[2], A.W. Carbonari[2], V. Oleshko[1] and C. Dennis[1] *1. Material Measurement Laboratory, National Institute of Standards and Technology, Gaithersburg, MD, United States; 2. Nuclear and Energy Research Institute, Sao Paulo, Brazil; 3. NIST Center for Neutron Research, National Institute of Standards and Technology, Gaithersburg, MD, United States; 4. Federal University of Para, Abaetetuba, Brazil*

Temperature affects every physical system, chemical reaction, and biological process. A new method, magnetic nanothermometry, is being explored to measure temperature throughout a volume. This method uses large changes in magnetization as function of temperature, which cannot be obtained with current magnetic nano-objects (MNO). To get a large magnetization change we have examined the magnetic properties of RE-doped Fe_3O_4 (RE = Eu, Gd, Er) MNO. Samples were synthesized by co-precipitation. For the doped material, RE^{+3} were chosen in order to replace the Fe^{+3} in the $(Fe^{+2})(Fe^{+3})_2O_4$ structure. Structural characterization was performed by X-ray diffraction and transmission electron microscopy. Hyperfine interaction parameters as a function of temperature (300 K to 873 K) were obtained by perturbed angular g-g correlation (PAC) spectroscopy using $^{111}In(^{111}Cd)$ as probe nuclei. To fit the PAC spectra, the ^{111}Cd probes were considered to occupy three sites: tetrahedral, octahedral, and a third site where the probes are located at the nanoparticle surface [1]. The hyperfine magnetic field B_{hf} was calculated using the Larmor equation, and its behavior as a function of temperature follows a Brillouin-type transition. For example, the Curie temperature (T_C) obtained for 5% Er-doped was approx. 846 K (FIG. 1), which is higher than the expected T_C for pure Fe_3O_4 (approx. 722 K) [2]. Magnetization as a function of temperature shows a 70 % change in magnetization around 100 K for Er-doped Fe_3O_4 (FIG.2), which is an improvement in temperature on pure Fe_3O_4 (below 50 K) [3]. Current work is focused on correlating the temperature range in which the magnetization change occurs and determining if it depends on the dopant element.

1. E.L. Correa, B. Bosch-Santos, R.S. Freitas, M.P.A. Potiens, M. Saiki, A. W. Carbonari, *Nanotechnology*, 29 (2018) 205704. 2. I. T. Matos, B. Bosch-Santos, G. A. Cabrera-Pasca, A. W. Carbonari, *J. Appl. Phys.* 117 (2015) 17D511. 3. Y. Liu, Y. Wang, S. Zhou, S. Lou, L. Yuan, T. Gao, X. Wu, X. Shi, K. Wang, *ACS Appl. Mater. Interfaces*, 4 (2012) 4913.

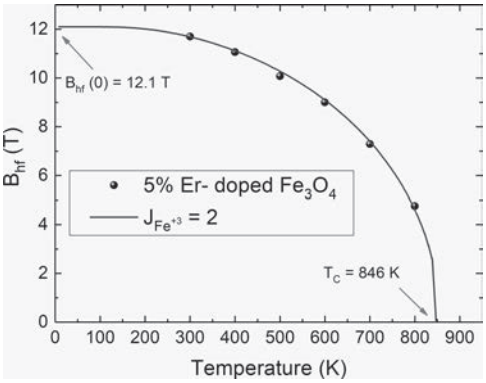


FIG. 1 – Hyperfine magnetic field as a function of temperature for 5% Er-doped Fe_3O_4 nanoparticles

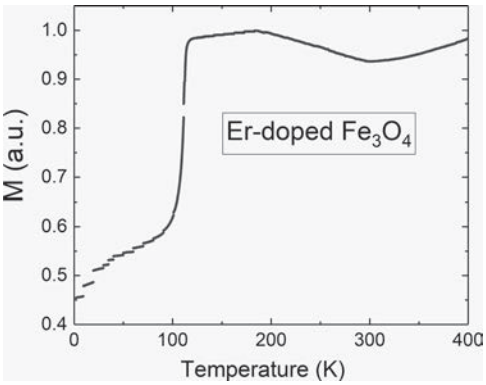


FIG. 2 – Normalized magnetization as function of temperature for Er-doped Fe_3O_4 nanoparticles

AU-15. Can natural oils improve the properties of magnetic nanoparticles? A systematic study of iron oxide nanoparticles coated with oils from Amazon fruits. B.S. Corrêa[1], M.S. Costa[2], G. Cabrera-Pasca[2], C. Sena[2], R.H. Pinto[2], R.N. Carvalho Jr[2], R.S. Freitas[3], M. Saiki[1], *E. Correa*[1] and A.W. Carbonari[1] *1. CERPQ, Instituto de Pesquisas Energéticas e Nucleares - IPEN, São Paulo, Brazil; 2. Faculdade de Ciências Exatas e Tecnologia, Universidade Federal do Pará - UFPA, Abaetetuba, Brazil; 3. Instituto de Física, Universidade de São Paulo, São Paulo, Brazil*

The use of nanoparticles coated with different materials have been studied by many researchers to improve the quality of nanomaterials for biomedical applications such as controlled drug delivery, image contrast and treatment of cancer by magnetic hyperthermia [1]. In this work, we used oils extracted from ucuúba (Virola surinamensis), bacaba (Oenocarpus bacaba Mart.) and açaí (Euterpe oleracea Mart.) to coat Fe_3O_4 nanoparticles. The ucuúba, bacaba and açaí are native trees of the Amazon forest, whose oils are rich in fatty acids, such as lauric, myristic, steatic, oleic, palmitic, and linoleic acid, with different proportions. These pure oils, free of solvents, were obtained by the extraction method with carbon dioxide in the supercritical state [2], and then added during the synthesis process of iron oxide nanoparticles by thermal decomposition method [3]. The results of X-ray diffraction confirmed the formation of Fe_3O_4 single phase. The average size around 3 nm and spherical morphology of the magnetite nanoparticles was determined by transmission electron microscopy. The study of magnetic properties revealed a saturation magnetization (Ms) enhancement and high values of the anisotropy constant for Fe_3O_4 samples when coated with açaí (91.4 emu.g^{-1}; 4.6 10^5 J.m^{-3}) and ucuúba (80.6 emu.g^{-1}; 9.3 10^5 J.m^{-3}) oils, which present a large percentage of saturated total fatty acid. The results indicate that nanoparticles with sizes smaller than around 5 nm present Ms values as high as those found in bulk Fe_3O_4 and higher than those usually obtained for nanoparticles coated with oleic acid [4]. The neutron activation analysis (NAA) nuclear technique was used to determine with high accuracy the mass of Fe in the Fe_3O_4 core of nanoparticles in order to normalize the magnetization values [5]. These results show that natural oils have a great potential to produce stable and quality nanoparticles as compared with conventional coated.

[1] F. B. Effenberger, A. W. Carbonari and L. M. Rossi, J. Magn. Magn. Mater., 417, 49–55 (2016). [2] C. C. R. Batista, M. S. Oliveira, M. E. Araújo et al., J. Supercritical Fluids 107, 364–369 (2016). [3] F. C. C. Oliveira, F. B. Effenberger, M. H. Sousa et al. Phys. Chem. Chem. Phys. 13, 13558–13564 (2011). [4] K. Parvin, J. Ma, J. Ly et al., J. Appl. Phys., 95, 7121-7123 (2004). [5] E.L. Corrêa, B. Bosch-Santos, R.S. Freitas et al., Nanotechnology 29, 205704 (2018).

Session AV
ORIGINS OF MAGNETIC ORDER I
(Poster Session)

Matthew Pufall, Chair
NIST, Boulder, CO, United States

AV-01. Ultrasound-Velocity Measurements in Spin-Frustrated Cobaltite $CoTi_2O_5$. *K. Takayanagi*[1], T. Watanabe[1], F. Kirschner[2], D. Prabhakaran[2], S. Blundell[2] and Y. Hara[3] *1. Nihon University, Tokyo, Japan; 2. Oxford University, Oxford, United Kingdom; 3. National Institute of Technology, Ibaraki College, Hitachinaka, Japan*

Orthorhombic cobaltite $CoTi_2O_5$ is considered to be a low-dimensional frustrated antiferromagnet with T_N = 26 K, which consists of magnetic Co^{2+} chains running along the crystal *a* axis [1]. For this compound, the experimentally-determined antiferromagnetic order below T_N is incompatible with the orthorhombic crystal structure above T_N [1]. Thus, in $CoTi_2O_5$, it is considered that, although the structural transition has not been experimentally observed so far, a spin-driven lattice distortion should coincide with the antiferromagnetic ordering at T_N, where the spin-lattice coupling lowers the crystal symmetry resulting in the release of frustration. Such a so-called spin-Jahn-Teller transition has experimentally been identified only in cubic chromite spinels ACr_2O_4 (A = Zn and Mg), where the magnetic Cr^{3+} ions form three-dimensional sublattice of corner sharing tetrahedra (pyrochlore lattice) [2]. For the verification of the spin Jahn-Teller effect in the low-dimensional antiferromagnet $CoTi_2O_5$, we perform ultrasound velocity measurements in the single-crystalline sample. The ultrasound velocity measurements have been proven to be a powerful tool for the study of spin-lattice-coupling-driven phenomena in the frustrated magnets [2,3,4]. Figures 1 and 2 respectively show temperature dependence of shear elastic moduli C_{55} and C_{66} in the orthorhombic $CoTi_2O_5$, which are respectively obtained by measuring the velocity of transverse ultrasound with propagation $k||a$ and polarization $u||c$, and that with $k||a$ and $u||b$. Both C_{55} and C_{66} exhibit monotonic hardening upon cooling, as is usually observed in solids [5]. Additionally, C_{66} exhibits a discontinuous change at $T_N \sim 26$ K as shown in the inset to Fig. 2. In the presentation in the conference, we report the experimental results in all the symmetrically-independent elastic moduli in the orthorhombic $CoTi_2O_5$.

[1] F. Kirschner *et al*., Phys. Rev. B, Vol. 99, p.064403 (2019) [2] T. Watanabe *et al*., Phys. Rev. B, Vol. 86, p.144413 (2012) [3] T. Watanabe *et al*., Phys. Rev. B, Vol. 92, p.174420 (2015) [4] T. Watanabe *et al*., Phys. Rev. B, Vol. 98, p.094427 (2018) [5] Y. P. Varshni, Phys. Rev. B, Vol. 2, p.3952 (1970)

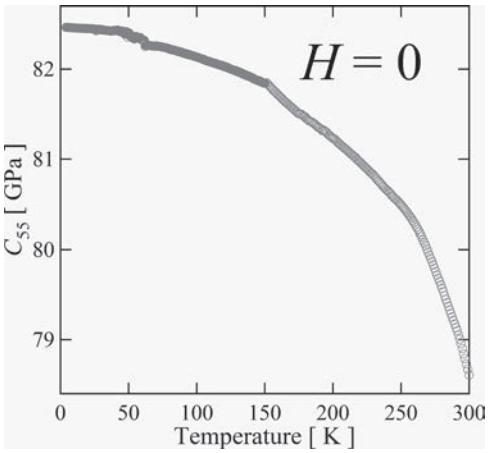


Fig. 1 Temperature dependence of shear elastic modulus C_{55}.

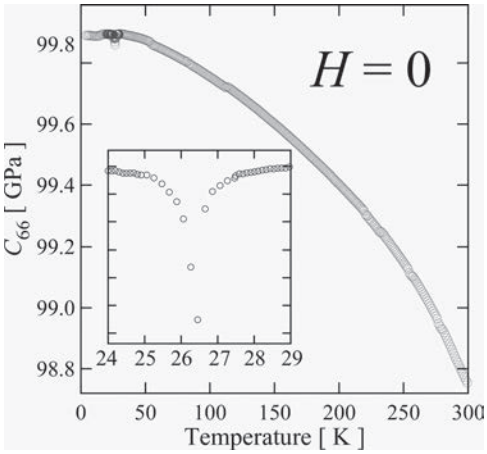


Fig. 2 Temperature dependence of shear elastic modulus C_{66}. The inset shows the expanded view of the data at around $T_N \sim 26$ K.

AV-02. Magnetic properties and the planer Hall effect of CoFeMnSi films. *K. Yamada*[1,2], T. Kimura[1], K. Elphick[2] and A. Hirohata[2] *1. Department of Physics, Kyushu University, Fukuoka, Japan; 2. Department of Electronic Engineering, University of York, York, United Kingdom*

Recently, a spin gapless semiconductor (SGS) attracts increasing attention because SGS has high resistivity, high spin polarization and a Dirac electron system. L. Bainsla *et al.* have reported the signature of SGS in a bulk CoFeMnSi(CFMS) crystal [1)]. H. R. Fu *et al.* have then reported an anomalous Hall effect in epitaxial CFMS thin films [2)]. On the other hand, a planer Hall effect (PHE) is useful for magnetic sensors as the PHE strongly depends on the direction of a magnetic field. In this presentation, we will report the PHE and magnetic properties of CFMS thin films. We prepared the films consisting of Ta (5)/Ru (5)/CFMS (20)/Ta (5) and Ru (5)/CFMS (10)/Ta (5) (thickness in nm) on Si substrates by high vacuum sputtering. At first, we measured the temperature T dependence of the conventional Hall effect introducing a magnetic field perpendicular to the film plane using an AC lock-in method. The Hall coefficient is found to increase with decreasing measurement temperature. This behavior shows that obtained films are semiconductor-like. Next, we measured the magnetic field H dependence of transverse magnetoresistance introducing a magnetic field horizontal to the film at T = 6 and 300K. The experimental configuration is shown in the inset of Fig 1(a). The magnetic field dependence of transverse resistance R_{XY} is shown in Fig 1(a), while the angle θ dependence of R_{XY} is shown in Fig 1(b). Here, the magnetic resistivity ρ_{XY} due to PHE is described as $\rho_{XY} = (\rho_{\perp}-\rho_{//}) \sin(2\theta)/2$ where $\rho_{\perp}$ and $\rho_{//}$ are the resistivity under magnetic fields applied transverse and parallel to the current, respectively. It is well known that two origins for PHE exist. One is an spin-orbit interaction due to the intrinsic magnetization and another is breaking of time reversal symmetry in Dirac electron systems [3)]. We found that PHE of CFMS films is not induced by the Dirac electrons but by their intrinsic magnetization as evidenced by the presence of hysteretic magnetic behavior. Such films can be useful from the viewpoints of fundamental physics and sensor applications.

1) L. Bainsla *et al.*, Phys. Rev. B Vol. 91, p.104408 (2015) 2) H. R. Fu *et al.*, Appl. Phys. Lett. Vol. 112, p.262406 (2018) 3) P. Li *et al.*, Phys. Rev B Vol. 98, p.121108(R) (2018)

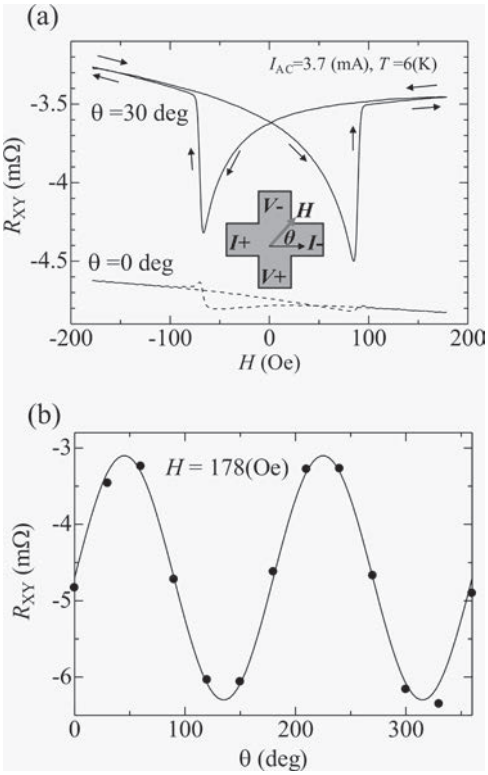


Fig.1 the *H* dependence (a) and the θ dependence (b) of the R_{XY}.

AV-03. Enhanced Room Temperature Ferromagnetism in MoS_2 by N Plasma Treatment. *B. Wang*[1], D. Zhang[1], H. Wang[1], H. Zhao[1], R. Liu[2], Q. Li[1], S. Zhou[3], L. Sun[2], J. Du[2] and Q. Xu[1] *1. School of Physics, Southeast University, Nanjing, China; 2. School of Physics, Nanjing University, Nanjing, China; 3. Institute of Ion Beam Physics and Materials Research, Helmholtz-Zentrum Dresden-Rossendorf, Dresden, Germany*

MoS_2 is a typical two-dimensional material of unique properties, which has important applications in semiconducting devices [1]. The introduction of ferromagnetism in MoS_2 may further extend its applications in spintronics. MoS_2 powders were prepared by hydrothermal method. N plasma was introuduced into a vacuum chamber with RF power of 100 W at N_2 pressure of 10 Pa for various durations at room temperature to treat MoS_2 powders. The morphologies of MoS_2 change little after the N plasma treatment. X-ray diffraction patterns and Raman spectra confirm the 2H structure, with little variation with increasing N plasma treatment time. The wavenumber difference of more than 24.5 cm^{-1} between E^1_{2g} and A_{1g} peaks indicates the thick layer structure [2]. X-ray photoelectron spectroscopy confirms the adsorption of N after the N plasma treatment, and higher valence state of Mo than +4 due to the bonding with N. The magnetic measurements show weak room temperature ferromagnetism of the as-prepared MoS_2 with saturated magnetization of only 1.13 memu/g after the subtraction of high field linear background, as shown in Fig. 1(a). With increasing the N plasma treatment time, the magnetization shows negligible variation. A sudden increase of saturated magnetization to 3.5 memu/g is achieved after the N plasma treatment for 30 min, shown in Fig. 1(b). However, the saturated magnetization drastically decreases with further increasing N plasma treatment time. To exclude the possible experimental errors, we repeated the experiment, and similar results were obtained. This indicates that the room temperature ferromagnetism can only be enhanced in a narrow period of N plasma treatment. First principle calculation has been performed to calculate the possible origin of ferromagnetism, and shows that only the chemical adsorbed N ions on S ions may form conjugated π bonds with adjacent Mo ions to have total magnetization of 0.75 m_B (inset of Fig. 1(b)), contributing to the observed room temperature ferromagnetism.

[1] P. Tang, J. J. Xiao, C. Zheng, S. Wang, and R. F. Chen, Acta Phys. -Chim. Sin. 29, 667 (2013) [2] C. Park, D. Chu, Y. Shon, J. Lee, and E. K. Kim, Appl. Phys. Lett. 110, 222104 (2017)

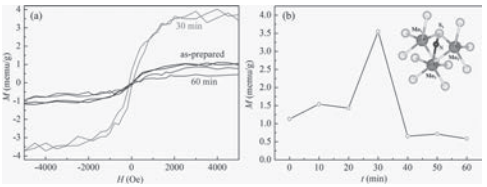


Fig.1 (a) The M-H curves of N plasma treated MoS_2 for 0, 30 and 60 min. (b) The saturated magnetization in dependence on the N plasma treating time. The inset shows the schematic structure of the location of adsorbed N ion.

AV-04. Substitution Effects on Magnetism of Laves-Phase Iron Compound $ZrFe_2$. *T. Suzuki*[1], Y. Fukushima[1], Y. Takei[1] and T. Watanabe[1] *1. Department of Physics. College of Science and Technology, Nihon University, Tokyo, Japan*

Transition-metal Laves-phase compounds AB_2 (B = transition-metal element) exhibit a variety of electron-correlation-driven novel phenomena such as the emergence of heavy-fermionic behavior in Sc-doped YMn_2 ($(Y_{1-x}Sc_x)Mn_2$) [1,2], and ferromagnetic quantum criticality in nonstoichiometric $NbFe_2$ ($Nb_{1-x}Fe_{2+x}$) [3,4]. Laves-phase iron compound $ZrFe_2$ is a metallic ferromagnet with $T_C \sim 620$ K [5], where Fe 3*d* electrons are expected to dominate the physical properties. This compound has C15-type cubic Laves-phase crystal structure, which contains Fe sublattice of corner-sharing tetrahedra (pyrochlore lattice). For the exploration of electron-correlation-driven phenomena, we study element substitution effects on the magnetism of $ZrFe_2$ by investigating structural, magnetic, and electrical properties of mixed crystals $Zr_{1-x}Fe_{2+x}$, $Zr(Fe_{1-x}B_x)_2$ (B = Mn and Co), and $(Zr_{1-x}A_x)Fe_2$ (A = Y, Nb, Ti, and Hf). Figures 1 and 2 respectively show temperature dependence of zero-field-cooled (ZFC) and field-cooled (FC) magnetic susceptibilities in polycrystalline $Zr(Fe_{1-x}Mn_x)_2$ and $Zr(Fe_{1-x}Co_x)_2$ ($x = 0.4 \sim 0.7$). We note here that, according to X-ray diffraction experiments at room temperature in these samples, $Zr(Fe_{1-x}Mn_x)_2$ with $x = 0.4 \sim 0.7$ crystallizes in C14-type hexagonal Laves-phase structure, while $Zr(Fe_{1-x}Co_x)_2$ with $x = 0.4 \sim 0.7$ crystallizes in C15-type cubic Laves-phase structure. From Figs. 1 and 2, it is evident that, for $ZrFe_2$, the ferromagnetic order is suppressed by substitution of Mn or Co for Fe. In the presentation in the conference, we report the experimental results in polycrystalline $Zr_{1-x}Fe_{2+x}$, $Zr(Fe_{1-x}B_x)_2$ (B = Mn and Co), and $(Zr_{1-x}A_x)Fe_2$ (A = Y, Nb, Ti, and Hf) in detail.

[1] H. Wada, M. Shiga, and Y. Nakamura, Physica. B, Vol. 161, p.197 (1987) [2] R. Ballou, E. Lelièvre-Berna, and B. Fåk, Phys. Rev. Lett., Vol. 76, p.2125 (1996) [3] M. Brando *et al.*, Phys. Rev. Lett., Vol. 101, p.026401 (2008) [4] S. Friedemann *et al.*, Nature Phys., Vol. 14, p.62 (2018) [5] E. Piegger and R. S. Craig, J. Chem. Phys., Vol. 39, p.137 (1963)

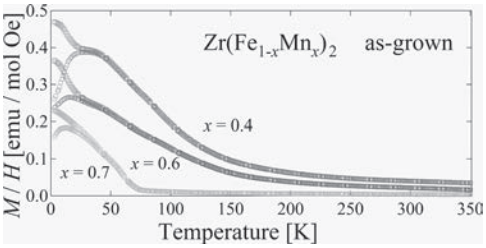


Fig. 1 Temperature dependence of ZFC and FC magnetic susceptibilities in $Zr(Fe_{1-x}Mn_x)_2$ polycrystals (x = 0.4, 0.6, 0.7).

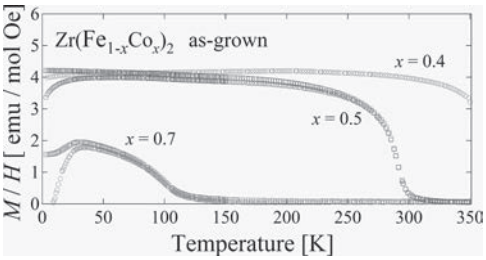


Fig. 2 Temperature dependence of ZFC and FC magnetic susceptibilities in $Zr(Fe_{1-x}Co_x)_2$ polycrystals (x = 0.4, 0.5, 0.7).

AV-05. Spin Wave Excitation in the Kitaev Honycomb Magnet α-$RuCl_3$.
S. Ji[1], S. Do[2], D. Voneshen[3] and K. Choi[4] *1. Neutron Science Center, Korea Atomic Energy Research Institute, Daejeon, The Republic of Korea; 2. Max Planck POSTECH, Pohang, The Republic of Korea; 3. ISIS Facility, Rutherford Appleton Laboratory, Didcot, United Kingdom; 4. Physics, Chung-Ang University, Seoul, The Republic of Korea*

Recently, α-$RuCl_3$ has been hailed as a promising candidate for the 2-dimensional Kitaev honeycomb model[1]. Due to its proximity to the Kitaev quantum spin liquid state[2,3], the compound simultaneously shows a broad continuum-like spin excitation and spin-wave modes from antiferromagnetically ordered spins. In this presentation, we provide a complete picture of magnetic excitation in α-$RuCl_3$. By using inelastic neutron scattering measurements with high resolution, we obtained clear spin wave excitations distinguishable from a broad continuum excitation. Our spin wave theory analysis with higher-order expansion not only identifies the spin wave modes by a minimal spin exchange model Hamiltonian but also suggests coexistence of fractional spin exictations and magnons in the compound. Furthermore, we present the magnetic field dependence of spin excitation and discuss about the possible field-induced quantum spin liquid state.

[1] K. W. Plumb *et al*., Phys. Rev. B, Vol. 90, p.041112 (2014) [2] S.-H. Do *et al*., Nature Physics, Vol. 13, p.1079 (2017) [3] L. J. Sandilands *et al*., Phys. Rev. Lett. Vol. 114, p.147201 (2015)

AV-06. Fabrication of noncentrosymmetric Nb/V/Ta superlattice and its superconductivity.
F. Ando[1], D. Kan[1], S. Nakamura[2], M. Naritsuka[2], Y. Kasahara[2], Y. Shiota[1], T. Moriyama[1], Y. Shimakawa[1], Y. Matsuda[2] and T. Ono[1] *1. Institute for Chemical Research, Kyoto University, Uji, Japan; 2. Department of Physics, Kyoto university, Kyoto, Japan*

Spin-orbit interaction (SOI) has recently been attracting intense attentions in the various fields of solid state physics, such as spintronics, topological matter, and unconventional superconductivity. In case of superconductors, the SOI with broken inversion symmetry significantly forbids the conventional classification of Cooper pairs and a mixed spin singlet-triplet state is expected to be realized [1]. There have been several reports of superconductors where the crystalline structure lacks a center of inversion, such as $CePt_3Si$ [2], $CeRhSi_3$ [3], and UIr [4]. Then, we can expect that an unconventional superconductivity can be explored in an artificial superlattice without inversion symmetry. In the present work, we show the crystal growth and conductivity of *ABC*-type superlattice [Nb/V/Ta] as a new platform to investigate an unconventional superconductivity. Nb, V, and Ta are all commonly-used superconducting elements and have body-centered cubic lattice structure. The $[Nb\ (t\ nm)/V\ (t\ nm)/Ta\ (t\ nm)]_n$ (n = 20/t and 40/t) superlattices were sputtered onto MgO(100) substrates at 750 degree. At first, we investigated the interfacial morphology and crystalline structure. Figure 1 shows the measured and calculated X-ray reflection curves for the superlattice (t = 1.0). Two noticeable Bragg peaks directly indicate that 2.8-nm-thick Nb/V/Ta multi-layers are periodically deposited with highly sharp interfaces. In addition, we confirmed the epitaxial growth of the superlattice by the combination of RHEED and X-ray diffraction. Finally, the electric resistivities were measured at low temperature as shown in figure 2. The inset of the figure is a photomicrograph of the processed film with the measurement configuration. It was found that the superlattices exhibited superconducting transitions [5]. In the presentation, we will discuss more details about the superconducting properties including critical magnetic fields.

[1] E. Bauer and M. Sigrist, Non-Centrosymmetric Superconductors: Introduction and Overview, (2012). [2] E. Bauer, G. Hilscher, and H. Michor, *et al.*, Phys. Rev. Lett., 92, 027003 (2004) [3] N. Kimura, K. Ito, and K. Saitoh, *et al.*, Phys. Rev. Lett., 95, 247004 (2005) [4] T. Akazawa, H. Hidaka, and T. Fujiwara, *et al.*, J. Phys. Condens. Matter, 16, L29 (2004) [5] F. Ando, D. Kan, and Y. Shiota, *et al.*, J. Magn. Soc. Jpn., 43, 2 (2019)

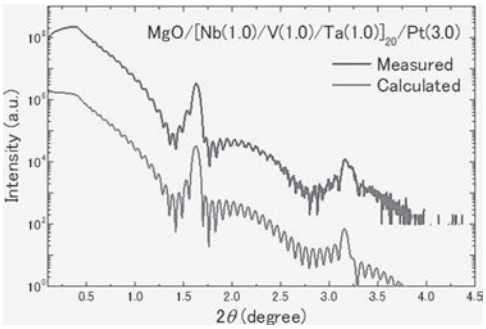


Fig.1 Measured (red) and calculated (blue) X-ray reflection curves for the superlattice $[Nb\ (1.0)/V\ (1.0)/Ta\ (1.0)]_{20}$/Pt (3.0).

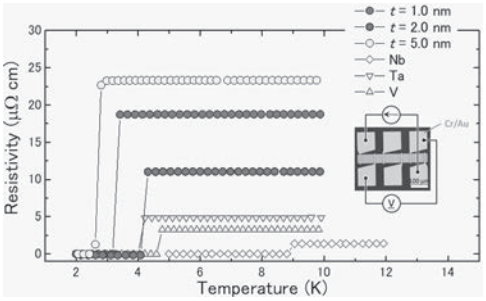


Fig.2 Temperature dependence of the electric resistivities for the superlattices (t = 1.0, 2.0, and 5.0) and 120-nm-thick Nb, V, Ta single layers.

AV-07. Substitution Effects on Magnetism of Spin-Frustrated Chromite and Ferrite Spinels.
K. Miura[1], Y. Koga[1], Y. Sugaya[1] and T. Watanabe[1] *1. Department of Physics, Nihon University, Tokyo, Japan*

Chromite spinel $CdCr_2O_4$ and ferrite spinel $CdFe_2O_4$ are considered to be typical spin-frustrated magnets, where orbital-inactive magnetic ions of Cr^{3+} ($3d^3$) with spin S = 3/2 and Fe^{3+} ($3d^5$) with S = 5/2 respectively form the sublattice of corner sharing tetrahedra (pyrochlore lattice). $CdCr_2O_4$ with the Weiss temperature Θ_W ~ -70 K exhibits an antiferromagnetic transition at T_N ~ 8 K in coincidence with the cubic-to-tetragonal lattice distortion [1,2]. On the other hand, for $CdFe_2O_4$ with Θ_W ~ -53 K, although the magnetic susceptibility exhibits an antiferromagnetic-transition-like anomaly at ~ 13 K, the

neutron scattering experiments revealed the absence of long-range magnetic order down to low temperature (1.5 K) [3]. We study substitution effects on the frustrated magnetism of $CdCr_2O_4$ and $CdFe_2O_4$ by investigating structural and magnetic properties of mixed crystals $Cd(Cr_{1-x}Fe_x)_2O_4$, $Cd(Cr_{1-x}B_x)_2O_4$ (B = V and Mn), and $Cd(Fe_{1-x}B_x)_2O_4$ (B = Mn and Co). Figure 1 shows temperature dependence of zero-field-cooled (ZFC) and field-cooled (FC) magnetic susceptibilities in polycrystalline $Cd(Cr_{1-x}Fe_x)_2O_4$. While $CdCr_2O_4$ (x = 0) exhibits an antiferromagnetic transition at T_N ~ 10 K, the mixed-crystal samples exhibit spin-glass-like behavior below ~ 10 K. Temperature dependence of ZFC and FC magnetic susceptibilities in $Cd(Cr_{1-x}Mn_x)_2O_4$ is shown in Fig. 2. The emergence of a ferromagnetic order in $Cd(Cr_{1-x}Mn_x)_2O_4$ with x = 0.4 ~ 0.7 is discovered, which should be driven by the substitution of e_g-orbital-active Mn^{3+} ($3d^4$) with S = 2 for orbital-inactive Cr^{3+} ($3d^3$) with S = 3/2. In the presentation in the conference, we report the experimental results in polycrystalline $Cd(Cr_{1-x}Fe_x)_2O_4$, $Cd(Cr_{1-x}B_x)_2O_4$ (B = V and Mn), and $Cd(Fe_{1-x}B_x)_2O_4$ (B = Mn and Co) in detail.

[1] H. Ueda *et al*., Prog. Theor. Phys. Suppl., Vol. 159, p.256 (2005)
[2] J. -H. Chang *et al*., Phys. Rev. Lett., Vol. 95, p.247304 (2005)
[3] K. Kamazawa *et al*., Phys. Rev. B, Vol. 70, p.024418 (2004)

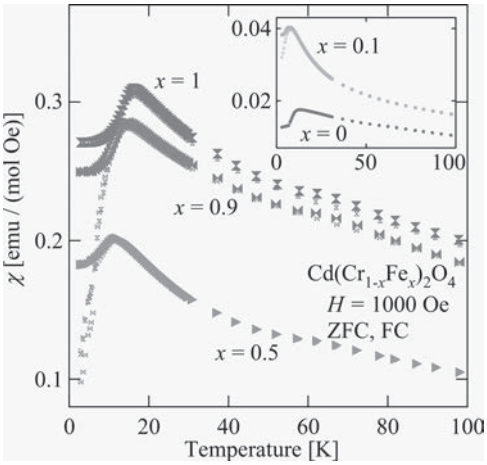


Fig. 1 Temperature dependence of ZFC and FC magnetic susceptibilities with H = 1000 Oe in $Cd(Cr_{1-x}Fe_x)_2O_4$ polycrystals (x = 0.5, 0.9, 1). Inset shows the data in the x = 0 and 0.1 samples.

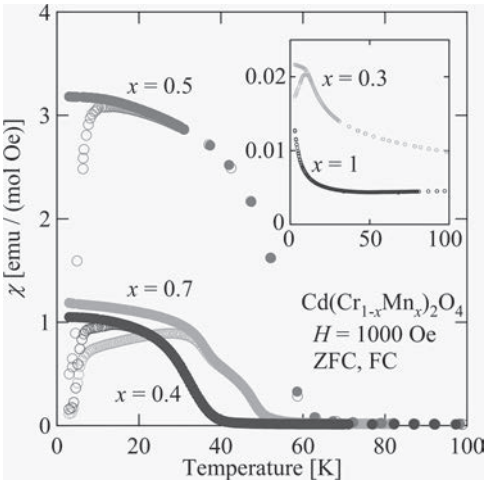


Fig. 2 Temperature dependence of ZFC and FC magnetic susceptibilities with H = 1000 Oe in $Cd(Cr_{1-x}Mn_x)_2O_4$ polycrystals (x = 0.4, 0.5, 0.7). Inset shows the data in the x = 0.3 and 1 samples.

AV-08. Superconductivity and magnetism of $Eu_{1-x}La_xFeAsF_{1-y}$. *S. Totsuka*[1], S. Demura[1] and Y. Takano[1] *1. Department of Physics, Nihon University, Tokyo, Japan*

After the discovery of superconductivity at 26 K in $LaFeAsO_{0.89}F_{0.11}$ [1], the isostructural superconducting compounds $Sr_{1-x}R_xFeAsF$ (R = rare earths) are found in 2009 [2]. This superconductivity is due to the electron doping. However, the superconductivity is not appeared by the F deficiency in $SrFeAsF_{1-y}$, irrespective of a same electron doping. We have previously investigated effects of the F deficiency in superconducting $Sr_{1-x}R_xFeAsF_{1-y}$ and found that T_C decreases with increasing y [3]. While Eu ion is divalent in EuFeAsF [4], it is trivalent in EuFeAsO [5]. The valence of Eu ion is sensitive to the chemical environment. In order to study the valence of Eu ion in $Eu_{1-x}R_xFeAsF_{1-y}$, we have prepared $Eu_{1-x}La_xFeAsF_{1-y}$, and investigated their electrical and magnetic properties. All samples were prepared by the solid state reaction. Stoichiometric amounts of raw materials FeF_2, EuAs, La, Fe and As were weighted, mixed and pressed into bars in Ar atmosphere. They were heated at 773 K for 5 h, and 1173 K for 60 h in an evacuated quartz tube. EuFeAsF is almost single phase and several impurity phases increase with increasing x and y. While the lattice constant a is unchanged for all samples, the lattice constant c decreases with the increase of x and y. Figure 1 shows the temperature dependence of the magnetic susceptibility (χ - T) of EuFeAsF. It obeys a Curie law. The absolute value is smaller than Eu^{2+} free ion value. There are two possibilities; one is a mixing of Eu^{2+} and Eu^{3+} ions, and the other is an antiferromagnetic interaction between Eu^{2+} ions. While the former can not reproduce the experimental result, the latter with the Weiss temperature of 5.5 K fits it. In χ - T curve of Eu_{1-x} La_xFeAsF, the hump considered to be due to a ferromagnetic impurity is observed in addition to the shifted Eu^{2+} ion value above x = 0.45. It increases with increasing x. Similar hump is observed in $Eu_{0.6}$ $La_{0.4}FeAsF_{1-y}$. Figure 2 shows $T_C - (x, y)$ phase diagram of $Eu_{1-x}La_xFeAsF_{1-y}$. Superconductivity is observed between x = 0.4 and 0.6. The highest T_C is about 37 K at x = 0.4, and T_C decreases with increasing y.

[1] Y. Kamihara, et al., J. Am. Chem. Soc., Vol. 130, p.3296 (2008)
[2] G. Wu, et al., J. Phys. Condensed Matter, Vol. 21, p.142203 (2009)
[3] Y. Murata, et al., 8th International Conference on f-elements, Udine, Italy (2012) [4] G. Wu, et al., Super. Chin. Sci. Bull., Vol. 54, p.1872 (2009)
[5] V. M. Dmitriev, et al., Fizika Nizkikh Temperatur, Vol. 35, p.659 (2009)

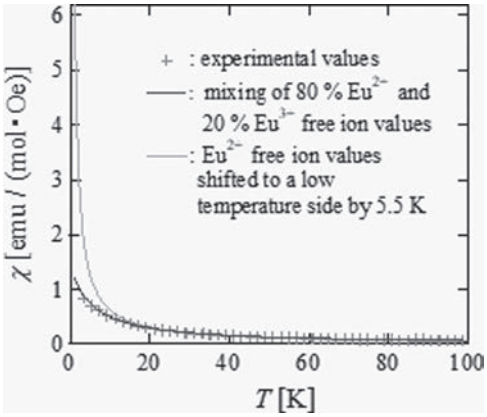


Fig. 1 Temperature dependence of the magnetic susceptibility of EuFeAsF

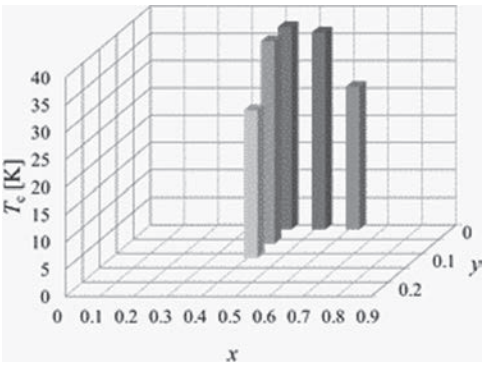


Fig. 2 T_C – (x, y) phase diagram of $Eu_{1-x}La_xFeAsF_{1-y}$

AV-09. Effects of Zn-Site Magnetic Substitution in Frustrated Chromite Spinel $ZnCr_2O_4$. *F. Tsujimura*[1] and T. Watanabe[1] *1. Department of Physics, College of Sience and Tecnology, Nihon University, Tokyo, Japan*

Chromite spinel $ZnCr_2O_4$ is a typical frustrated magnet, where the magnetic Cr^{3+} ions form the sublattice of corner sharing tetrahedra (pyrochlore lattice). This compound exhibits an antiferromagnetic transition in coincidence with the cubic-to-tetragonal structural contraction at T_N ~ 13 K, which is much lower than the Weiss temperature θ_W ~ -390 K [1]. For $ZnCr_2O_4$, it is considered that the spin-lattice coupling lowers the crystal symmetry resulting in the release of frustration, which is called spin Jahn-Teller effect [2,3]. We study effects of Zn-site magnetic substitution on the spin Jahn-Teller order of $ZnCr_2O_4$ by investigating structural and magnetic properties of mixed crystals $(Zn_{1-x}A_x)Cr_2O_4$ (A = Mn, Fe, Co, and Cu). For $ZnCr_2O_4$, it was previously reported that the small-amount nonmagnetic substitution of the Zn-site sensitively suppresses the spin Jahn-Teller order, resulting in the emergence of spin-glass-like behavior [4,5]. Figure 1 shows temperature dependence of zero-field-cooled (ZFC) and field-cooled (FC) magnetic susceptibilities in polycrystalline $(Zn_{1-x}A_x)Cr_2O_4$ (A = Mn, Fe, Co, and Cu) with x = 0.1. All the samples exhibit Curie-Weiss behavior at high temperatures above ~ 150 K (not shown). At low temperatures below ~10 K, the A = Mn, Co, and Cu samples exhibit the ZFC-FC hysteresis, indicating the emergence of spin-glass-like behavior. Additionally, the magnetic susceptibility of the A = Mn sample is rapidly enhanced upon cooling from ~ 30 K down to ~10 K. For the A = Fe sample, the magnetic susceptibility exhibits the ZFC-FC hysteresis below ~ 130 K. Figure 2 shows temperature dependence of ZFC and FC magnetic susceptibilities in polycrystalline $(Zn_{1-x}Mn_x)Cr_2O_4$ with x = 0 ~ 0.1. It is evident that the antiferromagnetic order (spin Jahn-Teller order) is sensitively suppressed by Mn substitution, resulting in the emergence of spin-glass-like behavior.

[1] H. Ueda *et al*., Prog. Theor. Phys. Suppl., Vol. 159, p.256 (2005) [2] Y. Yamashita and K. Ueda, Phys. Rev. Lett., Vol. 85, p.4960 (2000) [3] O. Tchernyshyov, R. Moessner, and S. L. Sondhi, Phys. Rev. Lett., Vol. 88, p.067203 (2002) [4] H. Martinho *et al*., Phys. Rev. B, Vol. 64, p.024408 (2001) [5] W. Ratcliff II *et al*., Phys. Rev. B, Vol. 65, p.220406(R) (2002)

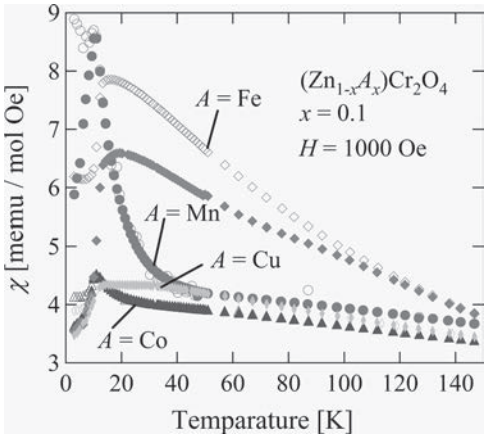


Fig. 1 Temperature dependence of ZFC and FC magnetic susceptibilities in $(Zn_{1-x}A_x)Cr_2O_4$ polycrystals with x = 0.1 (A = Mn, Fe, Co, and Cu).

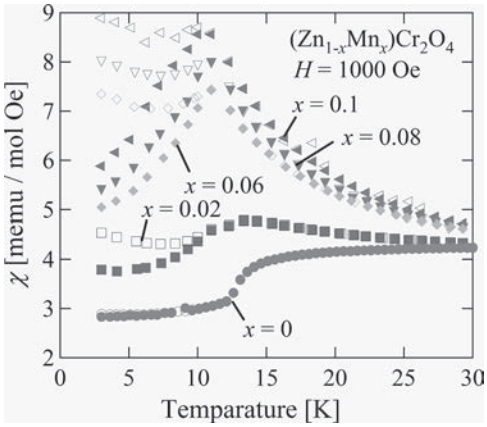


Fig. 2 Temperature dependence of ZFC and FC magnetic susceptibilities in $(Zn_{1-x}Mn_x)Cr_2O_4$ polycrystals (x = 0 ~ 0.1).

AV-10. Complex high field phase of the Kondo-lattice $CeRhIn_5$ unveiled by NMR. G. Lesseux[1], H. Sakai[2], Y. Tokunaga[2], S. Kambe[2], P. Kuhns[3], A. Reyes[3], J. Thompson[4], P. Pagliuso[1] and *R.R. Urbano*[1] *1. DEQ, State University of Campinas, Campinas, Brazil; 2. Advanced Science Research Center, Japan Atomic Energy Agency, Tokai, Japan; 3. National High Magnetic Field Laboratory, Tallahassee, FL, United States; 4. Los Alamos National Laboratory, Los Alamos, NM, United States*

Magnetic fields around B*~30T is proven to induce significant changes in the Fermi surface of the Kondo-lattice compound $CeRhIn_5$ as revealed by various macroscopic probes [1-4]. Although there is an increasing number of experimental signatures of a field-induced singularity emerging at B*, there is a lack of microscopic evidences for such a singularity due to inherent experimental challenges. Here, we report low temperature and high field ^{115}In Nuclear Magnetic Resonance (NMR) measurements of a high quality $CeRhIn_5$ single crystal through B*. Upon increasing the applied magnetic field along the c-axis at 0.5K, although a line broadening at high fields, no remarkable change of the planar In(1) signal was observed in the entire field range to 45T. Also, the formal Knight shift K′(1) was found to be virtally constant for all measured fields except at B* when it displays a dramatic discontinuity. Our results are the first microscopic evidences for the emergence of the singulatiry found at 30T. The interpretation is based on a scenario where a field-induced mixing of the crystal electric fields (CEF) energy levels is a key ingredient for the enhancement of hybridization between the Ce 4f and the conduction electrons c.e. resulting in a greater itinerant character of the f-electrons above B*. This ultimately may lead to a quantum critical point predominantly itinerant at B~50T in $CeRhIn_5$.

[1] Jiao, L. et al., Proceedings of the National Academy of Sciences 112, 673–678 (2015). [2] Moll, P. J. et al., Nature Communications 6 (2015). [3] Ronning, F. et al., Nature 548, 313–317 (2017). [4] Jiao, L. et al., arXiv:1711.06191 (2017).

AV-11. Realization of Various Weyl Semimetal Phases in Topoelectrical Circuit Models. *S. Rafi-Ul-Islam*[1], Z. Siu[1] and M.B. Jalil[1] *1. Electrical and Computer Engineering, National University of Singapore, Singapore*

We present an effective method to realize various Weyl semimetals (WSM) phases in three-dimensional topoelectrical (TE) circuit lattices composed of inductors and capacitors (Figs. 1a and 1b). The Laplacian of its admittance matrix at resonant frequency is given by L_{Weyl} (k)=i ω_r [(c_{Az}+c_{Bz}) cos k_z σ_o-(c_1+c_2 cos k_x + 2c_y cos k_y)σ_x - c_2 sin k_x σ_y -(c_{Az}-c_{Bz}) cos k_z σ_z] (1) where,ω_r, c_is and L_is are the resonant frequency, and coupling capacitances and inductances [1] respectively. Eq. 1 yields two pairs of Weyl points (WPs) located at (π, ± arccos((c_2-c_1)/2c_y), ±π/2) in *k* space. A capacitive (inductive) coupling between two B sublattice nodes along the z direction will cause the tilt strength (c_{Az}+c_{Bz}) to be greater (less) than the effective velocity term (c_{Az}-c_{Bz}) around the WP, giving rise to a pair of Type II (Type I) WPs shown in Fig. 1d (Fig. 1c). The Type-I and Type-II WSMs have closed elliptical and open hyperbolic iso-admittance contours (IAC) respectively (Fig. 2a and Fig. 2b). We calculated the impedance between two nodes by using the circuit Green's function [2], and classified the two Weyl phases by the impedance spectrum at resonance. Type-I WSMs show impedance peaks in the vicinity of WPs only (Fig. 2c), while Type-II WSMs exhibit many secondary peaks (Fig. 2d). This impedance behaviour is analogous to the vanishing and non-vanishing density of states at the WPs in the two WSM phases respectively. The experimental accessibility of TE circuit models makes it a ready platform for the study of novel transport phenomena in WSM-based nanodevices [3].

1. Imhof, Stefan, et al. *Nature Physics* 14.9 (2018): 925. 2. Lee, Ching Hua, et al." *Communications Physics* 1.1 (2018): 39. 3. Haenel, Rafael, et al." *arXiv preprint arXiv:1812.09862* (2018).

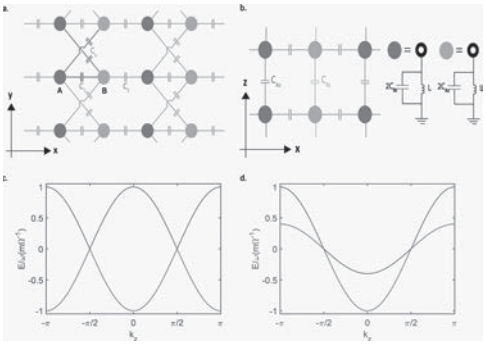


Fig. 1. Schematic of a TE circuit on the a. xy plane b. xz plane. The admittance band (E/ω) dispersion with c_1=c_2=0.716mF, c_y=0.167mF, L=1mH, c_{Az}=0.5mF, k_x=π, k_y=π/2 for c. Type-I WSM with c_{Bz}=-1/ω²L_B=-0.5mF and d. Type-II WSM with c_{Bz}=0.2 mF.

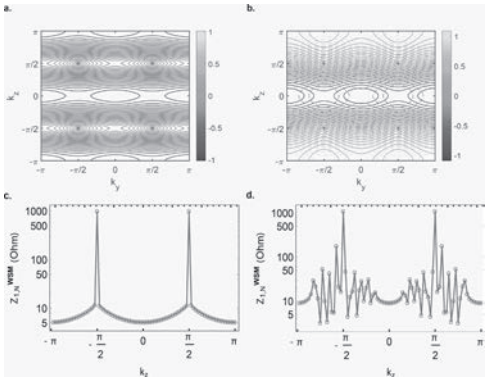


Fig. 2. Iso-energy contours for a. Type-I and b. Type-II WSM with same parameters in Fig. 1c and Fig. 1d respectively. Impedance spectrum of the c. Type-I d. Type-II WSM with 30-unit cells, c_2=0.95mF and N=60. Other parameters are the same as Fig. 1.

AV-12. Impurity effect of quantum spin trimer system $Na_2(Cu_{1-x}Ni_x)_3Ge_4O_{12}$. *R. Toma*[1] and Y. Yasui[1] *1. Physics, Meiji University, Kawasaki, Japan*

The quantum spin trimer system $Na_2Cu_3Ge_4O_{12}$ has the one-dimensional array of Cu_3O_8 trimers formed of edge-sharing three CuO_4 square planes which have Cu at center of square planes in Fig.1 [1]. The exchange interactions between Cu^{2+} spins, J_1, J_2 and J_3 were reported by analyzing magnetic susceptibility data and specific heat one [2]. The nearest-neighbor exchange coupling J_1 (J_1/k_B = 30 ± 20 K, antiferromagnetic) and the second-neighbor one J_2 (J_2/k_B = 340 ± 20 K) were reported by employing the isolated S = 1/2 Heisenberg trimer model above 70 K. In the low temperature region, two spins of the edge in the Cu_3O_8 trimer forms a nonmagnetic singlet by strong antiferromagnetic interaction J_2, and the spin left in the center of the Cu_3O_8 trimer forms one-dimensional chains by the exchange interaction J_3 (J_3/k_B = 18 ± 1 K) between the trimers, which was evaluated by S = 1/2 uniform Heisenberg chain model. $Na_2Cu_3Ge_4O_{12}$ exhibits antiferromagnetic transition at T_N = 2 K accompanied with ferroelectric transition (multiferroic phenomenon) [2]. In order to investigate the magnetic dynamics of the present system, we have studied impurity effect on magnetic susceptibility and specific heat of $Na_2(Cu_{1-x}Ni_x)_3Ge_4O_{12}$, where spin S = 1/2 of Cu^{2+} ions is replaced by S = 1 of Ni^{2+} ions. From the analyses of the specific heat and magnetic susceptibility, J_1 and J_2 are affected heavily by replacing Ni^{2+} ions with Cu^{2+} ions. On the other hand, J_3 and transition temperature T_N are had little effect by Ni-doping. We have observed the magnetic specific heat components newly appear at around 12 K by Ni-doping. In the presentation, we discuss the magnetic dynamics of $Na_2Cu_3Ge_4O_{12}$ by analyzing the magnetic susceptibility and specific heat data of the Ni-doping system.

[1]Mo *et al.*;Iong.Chem.45,3478-3480,(2006). [2] Yasui *et al.*;J.Appl. Phys.115, 17E125, (2014).

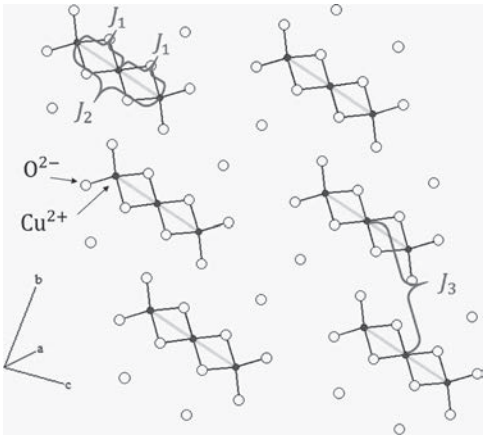


Fig.1 Schematics structure of $Na_2Cu_3Ge_4O_{12}$ cut into a plane of Cu_3O_8 trimers formed of edge-sharing three CuO_4 square planes [1]. The exchange coupling J_1, J_2 and J_3 are defined.

AV-13. Magnetic Properties of Frustrated Quantum Spin Chain System $Rb_2(Cu_{1-x}M_x)_2Mo_3O_{12}$ (M=Zn, Ni). *Y. Yasui*[1], Y. Okubo[1], S. Kittaka[2] and T. Sakakibara[2] *1. Physics, Meiji University, Kawasaki, Japan; 2. Institute for Solid State Physics, The University of Tokyo, Kashiwa, Japan*

We have investigated magnetic properties of the frustrated quasi-one-dimensional quantum spin system $Rb_2(Cu_{1-x}M_x)_2Mo_3O_{12}$ (M=Ni, Zn)., which are formed of edge-sharing CuO_4 square planes called as CuO_2 ribbon chains. The spin systems with the CuO_2 ribbon chains attract much attention, because the competition between the nearest-neighbor exchange interaction J_1 and the second neighbor interaction J_2 often induce the anomalous physical properties and exotic quantum states. Authors' group found that $Rb_2Cu_2Mo_3O_{12}$ exhibits the magnetic field induced ferroelectric transitions at $T_c \sim 8$ K [1]. The magnetic ground state of $Rb_2Cu_2Mo_3O_{12}$ is found to be non-magnetic state, which is the first example of non-magnetic ground state for CuO_2 ribbon chain systems [2]. Here, we have prepared several polycrystalline samples of partially substituted Zn^{2+} (S=0) or Ni^{2+} (S=1) to the Cu^{2+} (S=1/2) ions of $Rb_2Cu_2Mo_3O_{12}$. Measurements of the magnetic susceptibility (χ) and specific heat have been carried out for the spin systems, in order to understand the physics of non-magnetic state through the impurity effect on magnetic properties. For $Rb_2Cu_2Mo_3O_{12}$, the $\chi - T$ curve has a broad maximum at peak temperature $T_{max} \sim 13.5$K due to grow the antiferromagnetic short range ordering. With increasing Zn- or Ni- concentration, the values of T_{max} systematically decrease, and antiferromagnetic short range ordering is suppressed. The magnetic specific heat (C_{mag}) is evaluated by using specific heat data of a non-magnetic system $Rb_2Mg_2Mo_3O_{12}$. The $C_{mag}/T - T$ curve of x=0 has broad peak at ~ 8K. By the Zn- or Ni- doping, the broad peak of the $C_{mag}/T - T$ curve significantly is suppressed. Impurity effects of the Zn-doping on the magnetic properties have been found to be stronger than that of Ni-doping. For $Rb_2Cu_2Mo_3O_{12}$ below ~2 K, a dome-shape magnetic ordering phase exists in H-T phase diagram at the region of H_c (= 2.3 T) ≤ H < 13 T. By the Zn- or Ni- doping of x=0.01, temperature values of the phase boundary become higher than that of x=0, and the dome-shape magnetic ordering phase becomes stable. We present various magnetic properties of $Rb_2(Cu_{1-x}M_x)_2Mo_3O_{12}$ (M=Ni, Zn).

[1] Y. Yasui *et al*.: J. Appl. Phys. 113, 17D910 (2013). [2] Y. Yasui *et al*.: JPS Conf. Proc. 3, 014014 (2014).

AV-14. Magnetic properties of $Ba_3Co_{1-x}Ca_xRu_2O_9$. *A. Nagaya*[1], A. Horie[1], Y. Yasui[2], T.D. Yamamoto[3] and I. Terasaki[3] *1. Meiji University, Kawasaki, Japan; 2. Meiji University, Kawasaki, Japan; 3. Nagoya University, Nagoya, Japan*

We have measured magnetic susceptibility and specific heat on polycrystalline samples of $Ba_3Co_{1-x}Ca_xRu_2O_9$. The compounds with the general formula $Ba_3MRu_2O_9$ (M = Co, Ca, and Zn) have the Ru_2O_9 dimers, made from face-shared RuO_6 octahedra, connected with corner-shared MO_6 octahedra to form triangular lattice in the ab-plane. The magnetic ground states of the compounds are varied by the species of M. In $Ba_3CoRu_2O_9$, it is reported that Co^{2+} ($3d^7$) and Ru^{5+} ($4d^3$) ions have local spin and both spin systems exhibit an antiferromagnetic transition at $T_N \sim 100$ K [1]. On the other hand, the ground state of $Ba_3CaRu_2O_9$ is a non-magnetic state, because the Ru_2O_9 dimers are in the non-magnetic singlet state [2]. Recently, a novel type of spin liquid behavior has been reported in $Ba_3ZnRu_2O_9$ [3]. We have controlled the magnetic ground state from an antiferromagnetic order to non-magnetic state by making a solid solution system $Ba_3Co_{1-x}Ca_xRu_2O_9$. Measurements of the magnetic susceptibility and specific heat have been carried out on several polycrystalline samples of $Ba_3Co_{1-x}Ca_xRu_2O_9$. With increasing x, an antiferromagnetic transition temperature T_N decreases such as $T_N = 73$ K ($x = 0.3$), and 50 K ($x = 0.5$). The magnetic ground state of the spin systems is changed to a spin-glass state at around $x \sim 0.55$, where spin-glass transition temperature $T_{sp} = 26$ K ($x = 0.6$), and 6 K ($x = 0.8$). In the region of $x > 0.9$, the spin systems are found to have a non-magnetic ground state. We have also studied spin states of Co^{2+} ($3d^7$) and Ru^{5+} ($4d^3$) ions of $Ba_3Co_{1-x}Ca_xRu_2O_9$ by analyzing the magnetic specific heat and magnetic entropy. In the presentation, we discuss the magnetic properties and spin states of $Ba_3Co_{1-x}Ca_xRu_2O_9$.

[1] P. Lightfoot *et al*.: J. Solid State Chem. 89, 174 (1990). [2] M. S. Senn *et al*.: J. Phys.: Condens. Matter 25, 496008 (2013). [3] I.Terasaki *et al*.: J. Phys. Soc. Jpn. 86, 033702 (2017).

AV-15. Electron Quantum Interference in Epitaxial Antiferromagnetic NiO Thin Films. *J. Xu*[1], C. Zhou[1], M. Jia[1], G. Chen[4], Q. Li[2], A.K. Schmid[3] and Y. Wu[1] *1. Fudan University, Shanghai, China; 2. Lawrence Berkeley National Laboratory, Berkeley, CA, United States; 3. Lawrence Berkeley National Laboratory, Berkeley, CA, United States; 4. University of California, Davis, Davis, CA, United States*

Antiferromagnetic (AFM) spintronics has drawn significant attention recently due to its potential for low power consumption information storage and processing [1,2]. NiO is one of the most common AFM oxides, and becomes a fascinating candidate for investigating many novel spin-dependent phenomena in AFMs, such as spin Hall magnetoresistance, enhanced spin current transmission, THz magnons, and AFM switching by the spin-orbit-torque. All those spin-dependent transport properties should be closely correlated with the electronic structure of NiO, which has been paid little attention especially in ultrathin film range. In this contribution, we experimentally studied the electronic band structure of NiO films epitaxied on Ag(001). Utilizing the spin-polarized low energy electron microscopy in Lawrence-Berkeley National Laboratory, we measured the electron reflectivity as a function of NiO film thickness and electron energy. We found that the electron reflectivity oscillates systematically with electron energy and film thickness. Our experimental data can be well described by the phase accumulation model, which can be used to derive the band dispersion along the direction in the energy range of 3-8 eV and 12-20 eV above the Fermi surface. We also found that the electron reflectivity shows the weak quantum interference effect in CoO/Ag(001) system. Our work demonstrates the electron quantum interference effect inside the AFM thin films, which might provide further understandings of novel effects in the field of AFM spintronics.

[1] T. Jungwirth, X. Marti, P. Wadley, and J. Wunderlich, Nat. Nanotechnol. 11, 231 (2016). [2] V. Baltz, A. Manchon, M. Tsoi, T. Moriyama, T. Ono, and Y. Tserkovnyak, Rev. Mod. Phys. 90, 015005 (2018).

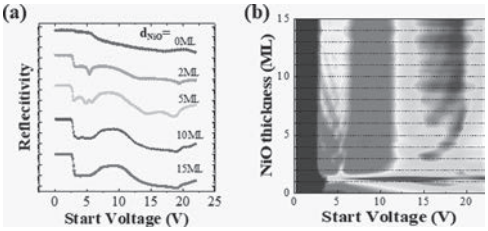
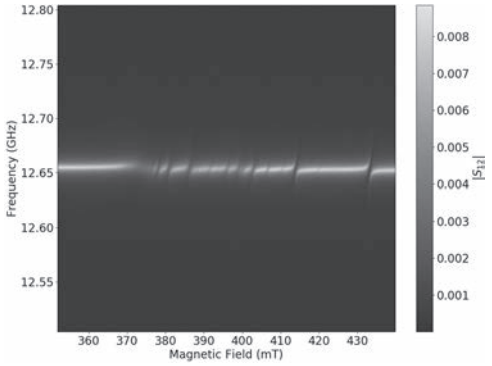


Fig 1. (a) The electron reflectivity from NiO(001) surface with different film thickness and electron energies. (b) Electron reflectivity as a function of start voltage and thickness plotted into a 2-dimentional color contour.

AV-16. Strong Coupling of a Ferromagnetic Sphere to a High-Tc Superconducting CPW Resonator. *I.W. Haygood*[1,2], E. Edwards[3,1], M. Pufall[1] and W.H. Rippard[1] *1. 687, NIST, Boulder, CO, United States; 2. Physics, University of Colorado - Boulder, Boulder, CO, United States; 3. IBM, Albany, NY, United States*

Hybrid quantum systems based on microwave cavity resonators and collective spin excitations in ferrimagnetic YIG structures have recently been explored at both room temperature and in the quantum limit [1]. These systems typically consist of a YIG element, often a mm-scale sphere, which couples to the RF magnetic field of a microwave cavity leading to level repulsion between the microwave cavity mode and the magnetostatic modes in the ferromagnet. These hybrid systems have been shown as possible candidates for use as quantum memories [2], microwave to optical transducers [3], single magnon detectors [4], and even parametric amplifiers[5]. Here we will present our work demonstrating coupling of a YIG sphere mounted to a ceramic rod coupled to a coplanar waveguide (CPW) resonator at 4 K. The system presented has the unique capability to tune the coupling to both the microwave and the coupling between the cavity and the YIG sphere. This allows us to access the strong-coupling, weak-coupling, magnetically-induced transparency, and Purcell regimes. We then discuss our plans to develop planar chip-based systems to scale the system by an order of magnitude. Finally, we will discuss how hybrid magnon-polariton systems coupled to a qubit can be used for fundamental magnetic measurements.

[1] R. G. E. Morris, A. F. Van Loo, S. Kosen, and A. D. Karenowska, "Strong coupling of magnons in a YIG sphere to photons in a planar superconducting resonator in the quantum limit," *Sci. Rep.*, vol. 7, no. 1, pp. 1–6, 2017. [2] X. Zhang, C. L. Zou, N. Zhu, F. Marquardt, L. Jiang, and H. X. Tang, "Magnon dark modes and gradient memory," *Nat. Commun.*, vol. 6, pp. 1–7, 2015. [3] R. Hisatomi *et al.*, "Bidirectional conversion between microwave and light via ferromagnetic magnons," *Phys. Rev. B*, vol. 93, no. 17, pp. 1–13, 2016. [4] D. Lachance-Quirion *et al.*, "Resolving quanta of collective spin excitations in a millimeter-sized ferromagnet," *Sci. Adv.*, vol. 3, no. July, p. e1603150, 2017. [5] X. Zhang, C. L. Zou, L. Jiang, and H. X. Tang, "Cavity magnomechanics," *Sci. Adv.*, vol. 2, no. 3, pp. 1–8, 2016.



Coupling between a CPW resonator and a YIG sphere. The many avoided crossings are evidence of coupling to many magnetostatic modes.

AV-17. Electron Correlation Effects and Magneto-Optical Property of Yttrium Iron Garnet. *H. Nakashima*[1], A.M. Pradipto[1], T. Akiyama[1], T. Ito[1] and K. Nakamura[1] *1. Physics engineering, Mie university, Tsu city, Japan*

Magneto-optical properties of YIG and other iron garnets have already been widely studied experimentally and envisaged in applications such as magneto-optical sensors. Theoretical first-principles approach has become an effective tool to investigate the electronic, magnetic and magneto-optical properties, however, only few theoretical reports are available due to the complexity of crystal structure and to the strong electron correlation for d-electrons. We have employed the constrained density functional theory (DFT) approach with linear response theory1) to calculate the Hubbard model parameter Ueff for the DFT+U treatment of the strong correlation. This method evaluates the Ueff values numerically by eliciting the difference in the second derivatives of the total energies of both the interacting and non-interacting electronic system. Calculations were performed by using the generalized gradient approximation2) to the DFT as implemented in the full-potential linearized augmented plane wave method3). A bcc unit cell of YIG (space group Ia-3d) contains a total of 160 atoms and, in our calculations, the lattice constant has been fixed to the experimental value (a=12.376 Å)4). There are two inequivalent Fe ion positions in YIG, i.e. those having octahedral and tetrahedral coordinations of oxygens, denoted here as FeO and FeT, respectively. In the present work, we have calculated the Ueff values to be 9.8 eV for FeO and 9.1 eV for FeT. We have applied the obtained Ueff values for the calculations of the electronic and magnetic properties and confirmed the validity of the Ueff value by comparing the band gap character with experimental observations. The spin magnetic moments of Fe atoms are 3.63 μB for FeO and -3.55 μB for FeT in the GGA calculation, while in the GGA+U calculation, they are 4.27 μB for FeO and -4.16 μB for FeT. We have calculated the complex dielectric function and magneto-optical Kerr effect (MOKE). Although the calculated dielectric function showed a difference compared to the experimental report, the overall MOKE spectra feature compares reasonably well with experiments. Further discussion on the discrepancy for our result of optical absorption as compared with experimental one will be presented.

1) K. Nakamura, Y. Kitaoka, T. Akiyama, T. Ito, M. Weinert, and A. J. Freeman, Phys. Rev. B Vol. 85, p.235129 (2012). 2) J. P. Perdew, K. Burke, and M. Ernzerhof, Phys. Rev. Lett. Vol. 77, p.3865 (1996). 3) M. Weinert, E. Wimmer, and A. J. Freeman, Phys. Rev. B Vol. 26, p.4571 (1982). 4) S. Geller and M. A. Gilleo, J. Phys. Chem. Solids Vol. 3, p.30 (1957).

AV-18. Delithiated $Fe_{1-x}Mg_xPO_4$ cathode materials: structural, magnetic, and Mössbauer studies. *H. Choi*[1], J. Kim[1] and C. Kim[1] *1. Department of Physics, Kookmin University, Seoul, The Republic of Korea*

Lithium-ion deficient $Fe_{1-x}Mg_xPO_4$ is a promising cathode material for batteries because of Mg ion is not electrochemically active. $Fe_{1-x}Mg_xPO_4$ (x = 0.01, 0.05, and 0.1) are synthesized by two-step method, which involves combining the solid-state reaction method and the chemical lithium deintercalation method. From the XRD analysis results, the crystal structure of $Fe_{1-x}Mg_xPO_4$ was an orthorhombic structure with *Pnma* space group. The magnetic properties of the sample were determined from vibrating sample magnetometer (VSM) and Mösssbauer spectroscopy, including their magnetic interactions, transition metal oxidation states, and structural ordering. The magnetic susceptibility (χ) of $Fe_{1-x}Mg_xPO_4$ was measured using VSM at temperatures from 4 to 290 K. Typical antiferromagnetic behavior can be found in the below Néel temperature (T_N). The magnetic parameters of $Fe_{1-x}Mg_xPO_4$ calculated from the fitted inverse susceptibility curves χ^{-1}(T). The T_N and curie constant decreases with increasing Mg content, which is consistent with the weakening of the antiferromagnetic exchange and a lower effective total magnetic moment after Mg substitution. Furthermore, for $Fe_{1-x}Mg_xPO_4$, the value of effective moment (μ_{eff}) decreases as expected with increasing Mg content. This can be explained the crystallographically strong deformation of $Fe(Mg)O_6$ octahedra. Mössbauer spectroscopy measurements at various temperatures were performed. The spectra at room temperature was fitted with one doublet, which having the isomer shift (δ) = 0.32–0.43 mm/s (Fe^{3+}). The large electric quadrupole splitting (1.46–1.92 mm/s) value is explained by the asymmetric local environment of the Fe atom. Below the T_N, the spectra of $Fe_{1-x}Mg_xPO_4$ were analyzed the eight resonance absorption lines (including two relatively small intensities). We can be obtained the mechanisms of the processes associated with lithium deintercalation in compounds based on LiMPO$_4$/MPO$_4$ from Mössbauer spectroscopy data.

[1] S. Yaroslavtsev, S. Novikova and A. Yaroslavtsev, Solid State Ion., Vol. 317, p.149 (2018)

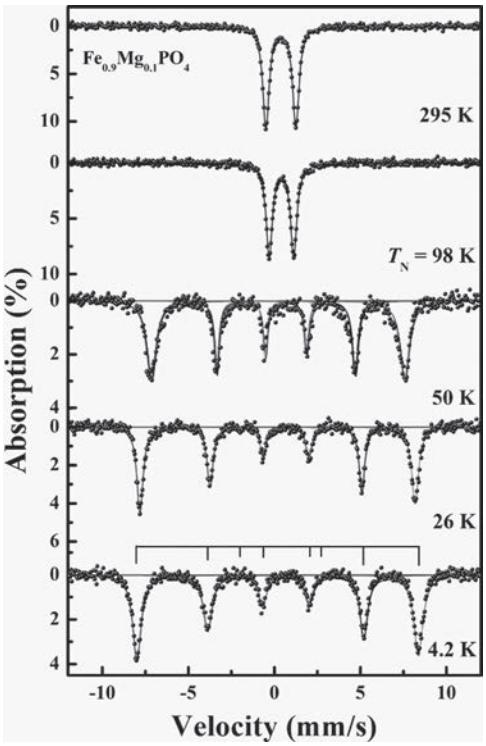


Fig. 1. Mössbauer spectra of $Fe_{0.9}Mg_{0.1}PO_4$ at various temperatures.

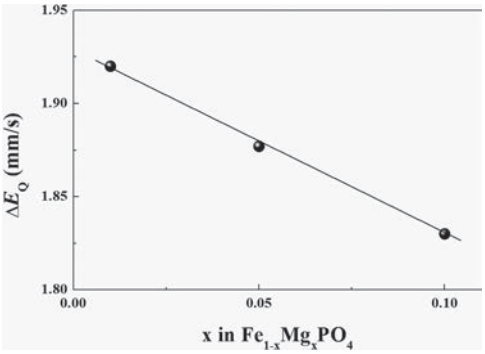


Fig. 2. Mg contents dependence of the electric quadrupole splitting of $Fe_{1-x}Mg_xPO_4$ at 4.2 K.

Session AW
SKYRMIONS
(Poster Session)

Dustin Allen Gilbert, Co-Chair
NIST Center for Neutron Research, Gaithersburg, MD, United States
Michalis Charilaou, Co-Chair
University of Louisiana at Lafayette, Lafayette, LA, United States

AW-01. Magnetoresistive Imaging of Magnetic Bubbles, Skyrmions, and Skyrmion Fabric. *I. Kao*[1], B. Parks[1] and S. Majetich[1] *1. Physics, Carnegie Mellon University, Pittsburgh, PA, United States*

Skyrmions have been proposed for use in racetrack memory,[1] where individual bits pass by a magnetoresistive electrode. There has been tremendous progress in imaging skyrmions,[2-4] and recent success using the Hall effect for sensing,[5] though the change in Hall resistance is a fraction of a mΩ. There is still a need for detection methods that could be incorporated into a memory device. Tunnel junctions have limitations to measure non-collinear spin textures, because the tunnel magnetoresistance (TMR) reflects the average over the area of the fixed layer electrode. Here we describe the use of tunnel magnetoresistance with a magnetic point contact that is small compared to the skyrmion diameter. To test this technique, the same regions of magnetic bubbles, skyrmions, or skyrmion fabric samples were imaged by magnetic force microscopy (MFM) in non-contact mode, and by conductive atomic force microscopy (CAFM) in contact mode. MFM detects a frequency shift due to the vertical magnetic force due to the fringe field of the sample, while CAFM measures tunnel magnetoresistance (TMR). The spin textures inferred from the images for the two methods are compared. The multilayer stack was Ta(3)Pt(10)$[Co(0.2)Ni(0.6)]_{20}$Pt(1)AlO_x(1) deposited by magnetron sputtering, where the numbers in parentheses are the film thicknesses in nanometers. From MFM, we saw magnetic bubbles enlarge and merge to form stripe domains at the nucleation field, while shrink and vanish in the single domain at the saturation field. In the MFM image (Fig.1), violet indicates a repulsive force where the moments of the tip and sample are antiparallel (AP), while blue indicates attraction due to parallel (P) moments. In the CAFM image (Fig.2) of tunnel current, red indicates low current (high resistance) expected for AP moments, while violet indicates high current (low resistance) expected for P moments. The images obtained at the same location show strong correlations. An MgO wedge sample was prepared to optimize the tunnel barrier thickness, and asymmetric skyrmion stacks are investigated, along with in-plane magnetized contacts for detection of skyrmion chirality.

1. A. Fert, V. Cros and J. Sampaio, Nat. Nanotech. Vol. 8, p. 152-156 (2013). 2. X. Z. Yu, Y. Onose and N. Kanazawa, Nature, Vol. 465, p. 901-904 (2010). 3. S. Woo, K. M. Song and H. S. Han, Nat. Commun., Vol. 8, 15573 (2017). 4. N. Romming, C. Hanneken and M. Menzel, Science, Vol. 341, p. 636-639 (2013). 5. D. Maccariello, W. Legrand and N. Reyren, Nat. Nanotech., Vol. 13, p. 233-237 (2018).

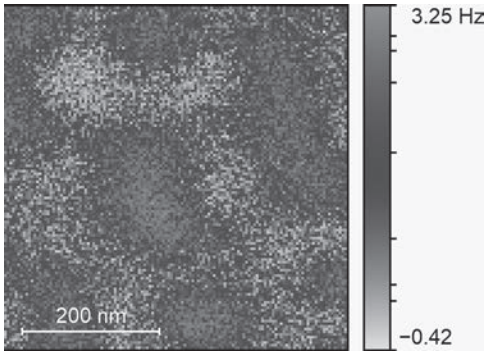


Fig. 1. MFM image at 52.7 kA/m.

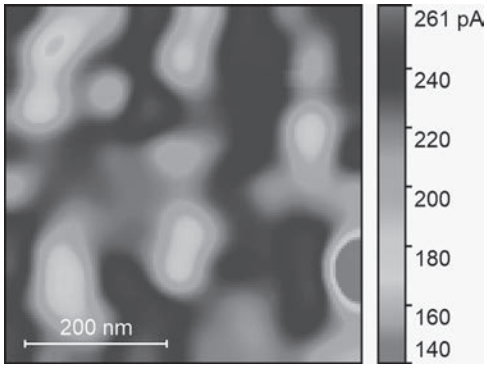


Fig. 2. TMR image at 52.7 kA/m at 300 mV.

AW-02. Realization of Ferro- and Ferri-magnetic skyrmions in Pt/Co/X based systems. *T. Lin*[1], S. Poellath[2], H. Liu[3], T. Xing[1], Z. Wang[1], Y. Sun[1], B. Ji[1], Y. Wu[3], J. Shen[3], C. Back[4] and N. Lei[1] *1. Beihang University, Beijing, China; 2. Universität Regensburg, Regensburg, Germany; 3. Fudan University, Shanghai, China; 4. Technische Universität München, Garching, Germany*

Magnetic skyrmions have attracted great attention and have been considered as potential candidates for next generation spintronics based memory and logics. To overcome some obstacles for future application of magnetic skyrmions, we designed various Pt/Co/X systems and experimentally realized skyrmions in them. To achieve skyrmion motion with high efficiency, we will introduce the study of Ferro-magnetic skyrmions in Pt/Co/W systems with large spin orbit coupling [1]. Besides skyrmion motion efficiency, skyrmion Hall effect is another obstacle for skyrmion-based applications. Facing this problem, we will show our experimental work on Ferri-magnetic Pt/Co/Tb multilayer skyrmion systems, which is promising to alleviate the skyrmion Hall effect. In addition, the temperature dependence of our Ferri-magnetic skyrmions is analyzed, in which the physical mechanism is preliminarily studied and discussed. Our realization of magnetic skyrmions

in different Pt/Co/X multilayer structures may provide alternative candidates to achieve highly efficient skyrmion motion and skyrmion-based applications.

[1] T.Lin, H.Liu and S. Poellath, PHYSICAL REVIEW B, Vol. 98, p.174425 (2018)

AW-03. Ultrafast nucleation and manipulation of antiferromagnetic skyrmion chains in nanotrack. *K. Khan*[1], N. Sisodia[1] and P.K. Muduli[1]
1. Physics, IIT Delhi, New Delhi, India

Chiral structures like skyrmions are promising candidates for future spintronic devices as they offer the advantage of ultra-dense storage and low power consumption [1,2]. To stabilize such chiral structures, Dzyaloshinskii-Moriya interaction (DMI) an antisymmetric magnetic exchange interaction is needed [3,4]. DMI can occur in some bulk magnetic materials with broken inversion symmetry or thin films of ferromagnetic/heavy metal (FM/HM) bilayer having strong spin-orbit coupling at the interface [5]. Both FM and antiferromagnetic (AFM) skyrmion can be translated by spin transfer torque via spin Hall effect. A disadvantage of FM skyrmion is skyrmion Hall effect (SkHE), which leads to an additional transverse motion (along the nanotrack width) of the skyrmion which can eventually lead to skyrmion destruction at the nanotrack edge. Recently, it has been reported, that AFM skyrmion can be translated along the nanotrack without SkHE due to zero topological charge [6]. In this work, by using micromagnetic simulation [9], we show an ultrafast nucleation and manipulation of AFM skyrmion by locally injecting a inplane spin polarized current. Recently it is reported that a single AFM skyrmion can be nucleated[8], by injecting 2 ns long out of plane spin polarized current pulse ($j = 5\times10^{13}$ Am^{-2}). Here, we use a 1 ns short dc inplane spin polarized current ($j = 5\times10^{13}$ Am^{-2}) in both AFM and FM layer, which nucleate a chain of seven AFM skyrmions in AFM layer, but there is no signature of FM skyrmion in FM layer as shown in Fig 1a. Interestingly, in Fig 1 (b) these chain of AFM skyrmions are also translated due to repulsion from newly created AFM skyrmion. In Fig 1 (c), we show the velocity of 1st nucleated AFM skyrmion which attains a steady state with a very high velocity of ~450 m/s after 0.2 ns. Our findings shows a potential way to create an AFM skyrmion chain and translate them with a constant velocity for racetrack based memory devices.

N. Nagaosa, & Y. Tokura, Nat. Nano. 8, 899–911 (2013). A. Fert, V. Cros, & J. Sampaio, Nat. Nano. 8, 152–156 (2013). T. Moriya, Phys. Rev. 120, 91 (1960). I. E. Dzialoshinskii, Sov. Phys. JETP 5, 1259 (1957). Cho, J. *et al*., Nat. Commun. 6, 7635 (2015) H. Xia et al., J. Phys. D: Appl. Phys. 50, 505005 (2017) X. Zhang, Y. Zhou & M. Ezawa, Sci. Rep, 6, 24795 (2016) A. Vansteenkiste, *et al.,* AIP Adv. 4, 107133 (2014).

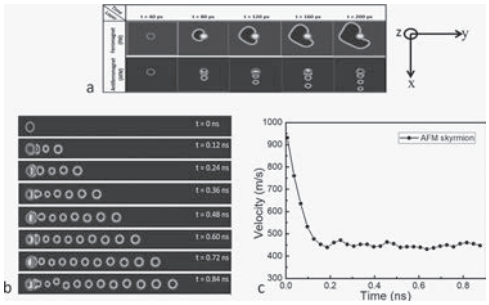


Fig1: (a) Behaviour of FM and AFM systems when an in-plane spin polarized current is injected in the area indicated by the red circle. (b) The snapshot AFM layer at different time showing creating of AFM skyrmions. (b) Velocity of 1st skyrmion as a function of time.

AW-04. Dipolar Stabilized Nano-Sized Spin Textures in Fe(Co)/Gd Multilayers. *M. Heigl*[1], M. Vanatka[2], P. Che[3], E. Catapano[3], Z.I. Maranloo[4], P. Böni[4], D. Grundler[3], M. Urbánek[2] and M. Albrecht[1] *1. Institute of Physics, University of Augsburg, Augsburg, Germany; 2. CEITEC BUT, Brno University of Technology, Brno, Czechia; 3. Institute of Materials (IMX) - Laboratory of Nanoscale Magnetic Materials and Magnonics, École Polytechnique Fédérale de Lausanne (EPFL), Lausanne, Switzerland; 4. Physic Department E21, Technical University of Munich, Garching, Germany*

Magnetic skyrmions are topologically protected chiral spin textures. Most skyrmion structures studied in today's research are stabilized by the Dzyaloshinskii-Moriya interaction [1]. Topologically similar spin structures have been observed in ferrimagnetic Fe/Gd multilayers stabilized by the competition between exchange, long-range dipolar, and domain wall energy [2,3]. In this work, Fe(Co)/Gd multilayers were deposited by magnetron sputtering at room temperature with up to 80 bilayers and varying individual layer thicknesses. The magnetic moment of the 3d-transition metals and the Gd layers are coupled antiparallel with the Gd moment being dominant over the whole temperature range. First, the structural properties of the films were investigated by X-ray reflectivity measurements and cross-section transmission electron microscopy. Both suggest a highly intermixed system still revealing a periodic modulation in composition along the growth direction. However, a co-sputtered homogeneous alloy with the same overall composition does not show the formation of non-trivial magnetic structures. The static magnetic properties were studied dependent on composition, magnetic field, and temperature by SQUID-VSM magnetometry, Lorentz transmission microscopy (LTEM), and magnetic force microscopy (MFM). The system shows a decrease in out-of-plane magnetic anisotropy and an increase in the magnetic moment for thicker Gd layers which leads to a shift of the stability range of the skyrmion phase to higher temperatures. The formation of skyrmions and bubbles was directly observed via field dependent MFM [Fig. 1] and LTEM [Fig.2]. The size of the observed spin objects is in the range of 100 nm. Additionally, the dynamic response of the spin textures was investigated by VNA ferromagnetic resonance measurements. With out-of-plane applied fields, we observed rich spectra containing spin wave excitations for skyrmions and stripe domains similar to [4].

[1] N. Nagaosa and Y. Tokura, Nat. Nanotech. 8, 899 (2013). [2] S. A. Montoya, et. al., Phys. Rev. B 95, 024415 (2017). [3] A. Singh, et. al., Nat. Commun. 10, 1988 (2019). [4] S. A. Montoya, et. al., Phys. Rev. B 95, 224405 (2017).

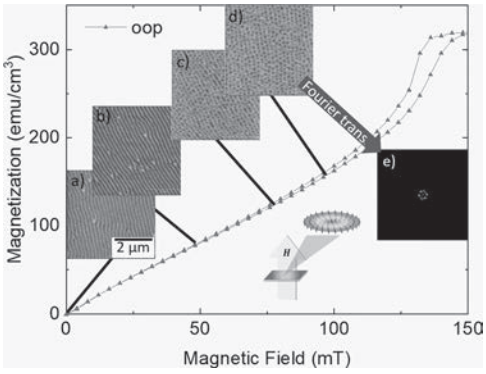


Fig. 1. Out-of-plane M-H hysteresis loop of $[Fe(0.35)/Gd(0.4)]_{80}$ with corresponding MFM images measured at room temperature.

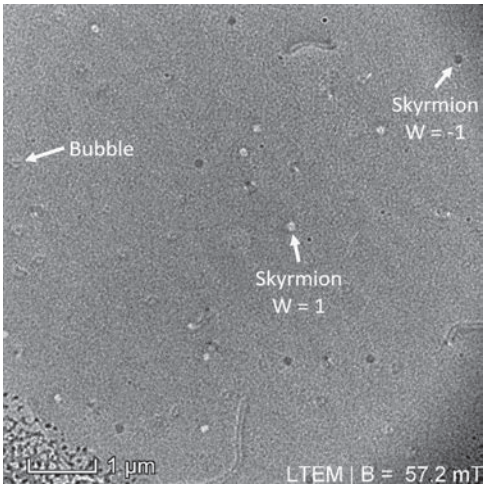
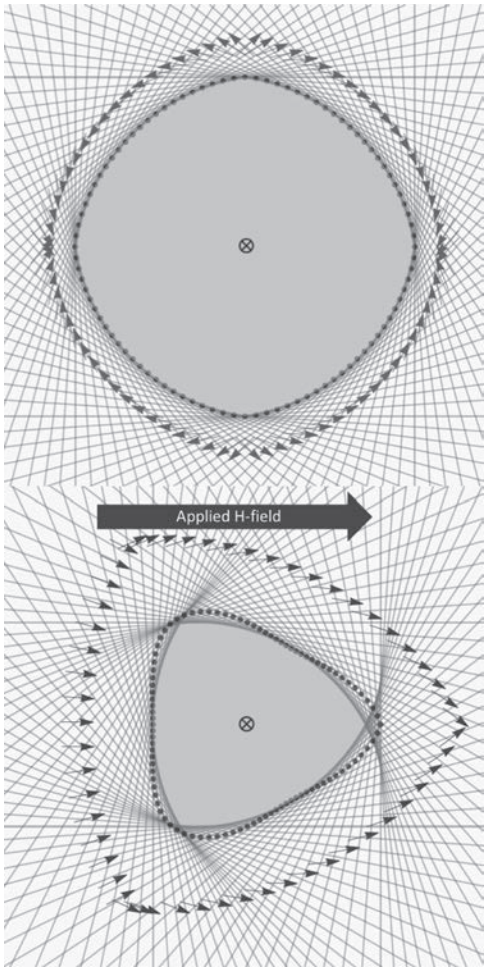


Fig. 2. LTEM image of bubbles and skyrmions with positive and negative chiralities W in $[Fe(0.35nm)/Gd(0.35nm)]_{80}$ measured at 150 K.

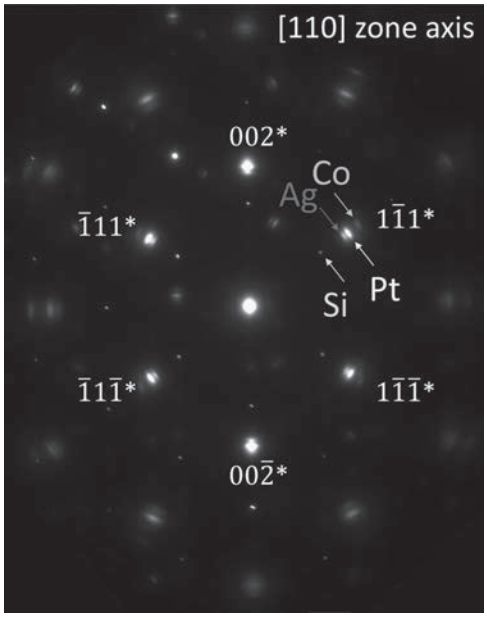
AW-05. Energetics, equilibrium shape and topology of skyrmions stabilized by the anisotropic Dzyaloshinskii-Moriya interaction in thin films with C_{2v} symmetry. *M.D. Kitcher*[1], T. Mewes[2], C.K. Mewes[3], M. De Graef[1] and V. Sokalski[1] *1. Materials Science and Engineering, Carnegie Mellon University, Pittsburgh, PA, United States; 2. Physics, University of Alabama, Tuscaloosa, AL, United States; 3. Physics and Astronomy/MINT, University of Alabama, Tuscaloosa, AL, United States*

2D C_{2V} magnetic systems exhibit both Rashba (D_R) and Dresselhaus (D_D) tensorial forms of the Dzyaloshinskii-Moriya interaction (DMI) according to the spin-orbit couplings present [1]. Equivalently, Moriya's rules, as applied to C_{2V} planes, do not uniquely choose the orientation of the DM vector, which is also modulated by the unit cell's asymmetry [2]. Overall, DMI is thus nominally anisotropic and hybridized, potentially stabilizing antiskyrmions as well as elliptical and Bloch-Néel (mixed) skyrmions as shown by [2] and [3]. Moreover, DMI character (i.e., $||D_R|| / ||D_D||$) and the unit cell's aspect ratio correlate to the DM vector's orientation. Ascertaining the existence and tunability of [anti]skyrmions in such systems is of technological interest and would elucidate the nature of DMI. This work models the equilibrium shape and internal wall magnetization of bubble domains (skyrmions being the limiting cases) in thin films with C_{2v} symmetry, using the Wulff construction and a domain wall (DW) energy dependent on the strength and character of DMI [3]. We show that for sufficiently strong DMI with no applied field, specific DM vector orientations stabilize antiskyrmions, while elliptical and/or mixed skyrmions are favored otherwise. An applied field was found to break the C_{2v} symmetry and stabilize domain shapes resembling ovals, teardrops and Reuleaux triangles. Relations between the domain shape, the unit cell's aspect ratio and the DM vector's orientation are discussed. Additionally, the effects of the DW's highly anisotropic energy on its elasticity and mobility will be reported. These findings are compared to micromagnetic simulations implemented within the M[3] package. Preliminary structural and magnetic measurements are introduced for a tunable C_{2v} thin film comprised of Si/Ag/Pt/Co (110) multilayers which we propose as an archetype for mirroring the optimal properties obtained from the above calculations.

1. U. Güngördü, R. Nepal, O. A. Tretiakov, K. Belashchenko, and A. A. Kovalev, Phys. Rev. B Vol. 93, p. 064428 (2016). 2. M. Hoffmann, B. Zimmermann, G. P. Müller, et al., Nat. Commun. Vol. 8, p. 308 (2017). 3. J. P. Pellegren, D. Lau, and V. Sokalski, Phys. Rev. Lett. Vol. 119, p. 027203 (2017).



Wulff construction showing equilibrium shape and internal wall magnetization for bubble domains with the DM vector normal to the domain wall with (bottom) and without (top) an applied in-plane field.



[110] zone axis electron diffraction pattern from Si/Ag/Pt/Co (110) thin film showing the C_{2v} symmetry.

AW-06. Magnetic skyrmion field-effect transistor. *I. Hong*[1] and K. Lee[1,2]
1. KU-KIST graduate school of converging science and technology, Korea University, Seoul, The Republic of Korea; 2. Department of Materials Science and Engineering, Korea University, Seoul, The Republic of Korea

In two-dimensional systems, the magnetic skyrmion has an integer topological charge Q, defined by $Q \equiv \int dA\ m.(\partial_x m \times \partial_y m)$. This nonzero Q makes magnetic skyrmions distinct from topologically trivial spin states with Q=0. Because of the topological effect, the magnetic skyrmion is expected to exhibit a high stability and to move fast at a low current [1], offering intriguing possibilities for the skyrmion to be used as information carrier in memory, logic, and oscillator devices. For device applications of magnetic skyrmions, it is important to understand the skyrmion Hall effect: a bending of skyrmion motion with respect to the direction of the driving force. Previous studies have focused on how to vanish the skyrmion Hall effect [2], because it can cause skyrmion annihilation and thus information loss. In this work, we take a different view from previous studies: we exploit the skyrmion Hall effect for device application, instead of vanishing it. We numerically study how spatially inhomogeneous Dzyaloshinskii-Moriya interaction (DMI) affects the transverse motion of a magnetic skyrmion. We find that when a magnetic skyrmion enters from a region with a DMI to another region with a different DMI δ_D, it exhibits very large transverse motion of which deflection angle and symmetry are distinct from the previously reported skyrmion Hall effect [3]. This unconventional skyrmion Hall effect is found to originate from an effective equilibrium spin-orbit-like torque due to the inhomogeneity of DMI [4]. By exploiting this large transverse motion of which direction and magnitude can be controlled by the DMI difference δ_D, we propose a skyrmion field-effect transistor based on the gate-controlled DMI, which was demonstrated in a recent experiment [5]. In the presentation, we show that the proposed skyrmion field-effect transistor can have the multibit states classified by the skyrmion position which is controllable by the magnitude and sign of the gate voltage.

[1] J. Sampaio *et al*., *Nat. Nanotechnol*. 8, 839-844 (2013). [2] Y. Hirata *et al*., *Nat. Nanotechnol*. 14, 232-236 (2019). [3] C. Reichhardt and C. J. O. Reichhardt, *New J. Phys*. 18, 095005 (2016). [4] S.-J. Lee *et al*., *Phys. Rev. B*, 96, 184433 (2017). [5] T. Srivastava *et al*., *Nano Lett*. 18, 4871-4877 (2018).



Fig. 1. Transverse motion of a magnetic skyrmion when it enters from the left region with a DMI (=D_1) to the right region with a different DMI (=D_2). Red and blue regions [(a) $\delta_D(=D_1-D_2)>0$ and (b) $\delta_D<0$] indicate the right regions.

AW-07. Skyrmions-Based Ultra-Low Power Electric-Field-Controlled Reconfigurable (SUPER) Logic Gate. Z. Zhang[1,2], Y. Zhu[1,2], *Y. Zhang*[1], K. Zhang[1], J. Nan[1], Z. Zheng[1], J. Wang[1], G. Wang[1], Y. Zhang[1,2] and W. Zhao[1] *1. Fert Beijing Research Institute, BDBC, School of Microelectronics, Beihang University, Beijing, China; 2. School of Electronics and Information Engineering, Beihang University, Beijing, China*

As a kind of topologically protected spin textures, skyrmions have been regarded as an excellent candidate for developing high-density, low-power memory and logic devices [1-4]. Unfortunately, owing to the presence of the skyrmion-Hall (Sky-Hall) effect and low motion velocity, the application of skyrmion-based device has been hindered. Compared with skyrmions in ferromagnetic (FM) materials, skyrmions in near-compensated ferrimagnetic (FIM) materials have higher motion velocity and negligible Sky-Hall angle [5-8]. This provides a brighter prospect of skyrmions for computing applications. In this paper, we propose a FIM skyrmion-based ultra-low power reconfigurable (SUPER) logic gate. By leveraging electric-field-controlled magnetic anisotropy (EFCMA) effect and skyrmion-skyrmion (Sky-Sky) interaction, various logic functions, such as AND, OR, XOR, NOT, etc., can be realized. Fig. 1 illustrates the schematic of the proposed SUPER logic gate. In order to propagate skyrmions via SOT effect, a driving current is injected into the heavy metal (HM) layer. Three voltage gates on the FIM film are used to control the trace of skyrmions to implement the logic operations. We also demonstrate the implementation of logic operations with simulation. As shown in Fig. 2(a)-(b), when "Vc1" is off and "Vc2" is on, AND logic operation can be achieved. If the input is (0,0), (0,1) or (1,0), there is no skyrmion arriving at the output MTJ, which gives the output '0'. If the input is (1,1), the cooperation of the driving current and the Sky-Sky interaction between the two skyrmions adds a new term of force on the skyrmions, which makes them bypass this gate and arrive at the output MTJ. The output is then '1'. Similarly, we also carry out other logical operations in this gate.

[1] A. Fert, V. Cros, and J. Sampaio, Nature Nanotechnology, Vol. 8, p. 152 (2013) [2] A. Fert, N. Reyren and V. Cros, Nature Reviews Materials, Vol. 2, p. 17031 (2017) [3] N. Nagaosa, and Y. Tokura, Nature Nanotechnology, Vol. 8, p. 899 (2013) [4] X. Zhang et al., Nature Communications, Vol. 8, p. 1717 (2012) [5] L. Shen et al., Physical Review B, Vol. 98, p. 134448 (2018) [6] S. Woo et al., Nature Communications, Vol. 9, p. 959 (2018) [7] A. Hrabec et al., Nature Communications, Vol. 8, p. 15765 (2017) [8] L. Caretta et al., Nature Nanotechnology, Vol. 13, p. 1154 (2018)

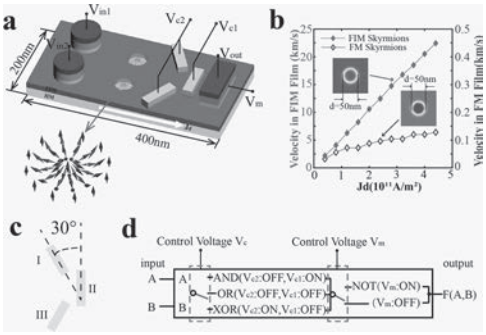


Fig.1 (a) Schematic of the proposed SUPER logic gate. (b) Velocity improvement of FIM skyrmion motions. (c) Special pattern of voltage gates. (d) Equivalent circuit of the SUPER logic gate with control voltages "Vc" and "Vm".

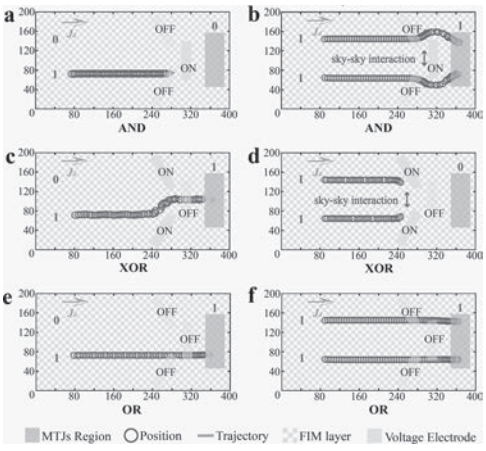


Fig. 2 (a)-(f) Three basic logic operations realizations and the traces of skyrmion motions.

AW-08. Manipulating Spin Chirality of Magnetic Skyrmion Bubbles by In-Plane Reversed Magnetic Fields in MnNiGa Magnet. *B. Ding*[1,2], J. Cui[1,2], H. Li[1,2], E. Liu[1,3], G. Wu[1], Y. Yao[1] and W. Wang[1,3] *1. Institute of Physics, Beijing, China; 2. University of Chinese Academy of Sciences, Beijing, China; 3. Songshan Lake Materials Laboratory, Dongguan, China*

Skyrmions, the particle-like topologically stable spin textures, are usually stabilized by the Dzyaloshinskii-Moriya interaction (DMI) in the noncentrosymmetric crystals but can also been identified in centrosymmetric magnets with uniaxial magnetic anisotropy. The dynamics of magnetic skyrmion and its response dynamics to external stimuli are important topics for the manipulation of skyrmions, indispensable for practical applications in spintronics. Contrary to DMI-stabilized skyrmions with a fixed chirality, skyrmion bubbles (SKBs) in centrosymmetric magnets possess two degrees of freedom, i.e., vorticity and helicity [1], making them suitable to manipulate spin chirality and topological texture through stimuli. In our previous work, the field free biskyrmion bubbles have been explored in centrosymmetric hexagonal MnNiGa alloys at room temperature via appropriate field cooling (FC) procedure [2-3]. In this work, motivated by the above-mentioned method, the generation of zero-filed skyrmion bubble lattice was obtained in $(Mn_{1-x}Ni_x)_{65}Ga_{35}$ (x=0.45). Furthermore, we report on the manipulated spin chirality of the field free SKBs at room temperature and observation of a collective effect of SKBs chirality reversal after applied with the in-plane magnetic field shown in Fig.1. Combining with quantitative analyses of micromagnetic simulation and data of LTEM, we have found that the controllable symmetry breaking of the SKB arising from thickness variation provide an ability to manipulate the collective behavior of the spin chirality with small external fields, leading to a promising application in nonvolatile spintronic devices for magnetic skyrmions.

1. Nagaosa and Y. Tokura, Nat. Nanotechnol. 8, 899 (2013). 2. W. H. Wang, Y. Zhang, G. Z. Xu, L. C. Peng, B. Ding, Y. Wang, Z. P. Hou, X. M. Zhang, X. Y. Li, E. K. Liu, S. H. Wang, J. W. Cai, F. W. Wang, J. Q. Li, F. X. Hu, G. H. Wu, B. G. Shen, and X.-X. Zhang, Adv. Mater. 28, 6887 (2016). 3. L. Peng, Y. Zhang, W. Wang, M. He, L. Li, B. Ding, J. Li, Y. Sun, X. G. Zhang, J. Cai, S. Wang, G. Wu, and B. Shen, Nano Lett. 17, 7075 (2017).

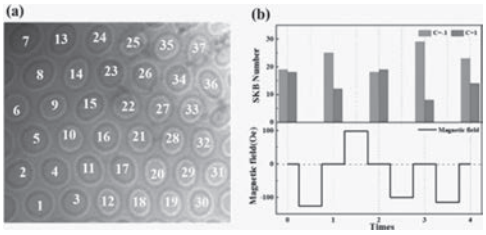


Fig.1 (a) L-TEM image was obtained at room temperature under zero magnetic field considered as the initial state. The numbered skyrmion bubbles are selected for further analyses. (b) The upper histogram shows the statistics number of C=1 and C=-1 chirality skyrmion bubbles. The orange and green bands indicate the numbers of the clockwise (C=-1) and counterclockwise (C=1) chirality of the skyrmion bubbles, respectively. Magnetic field dependence of times along with the experimental procedures is shown in the lower line chart.

AW-09. Topological spin structures at the spin reorientation transition in ferrimagnetic thin film alloys. *B. Seng*[2,1], N. Kerber[2,3], J. Bello[1], D. Schönke[2], F. Kammerbauer[2], M. Hehn[1], S. Mangin[1] and M. Kläui[2,3] *1. Institut Jean Lamour, Nancy, France; 2. Institute of Physics, Johannes Gutenberg Universität, Mainz, Germany; 3. Graduate School of Excellence MAINZ, Mainz, Germany*

Magnetic skyrmions are topologically stabilized spin textures particularly suitable for next generation spintronics devices, like the skyrmion-based racetrack memory. Recent studies confirmed the current-driven skyrmion dynamics in ultrathin ferromagnets [1]. However, the topological Magnus effect leads to a transverse motion of ferromagnetic skyrmions due to their non-zero topological charge [1]. Antiferromagnetically exchange-coupled skyrmions or compensated ferrimagnets could suppress this effect owing to an overall zero topological charge [2]. Especially at the angular momentum compensation temperature skyrmions dynamics is predicted to be collinear with the current [3]. We here explore ferrimagnets, such as GdFeCo multilayers where perpendicular anisotropy can be obtained for much thicker layers than for simple ferromagnets. Furthermore the compensation temperature can be tuned over a wide range by changing the deposition. Finally we show demonstrate at the spin reorientation transition worm domains as well as magnetic skyrmions can be observed.

[1] K. Litzius et al., Nature Phys. 13, 170 (2017) [2] Y. Hirata et al., Nature Nano. 14, 232 (2019) [3] J. Barker et al. Phys. Rev. Lett. 116, 147203 (2016)

AW-10. Use of magnetic skyrmions for the calculation of shortest path. *R. Tomasello*[1], G. Siracusano[2], F. Garesci[3], M. Raju[4], A. Giordano[5], Z. Zeng[6], C. Panagopoulos[4], M. Carpentieri[7] and G. Finocchio[5] *1. Institute of Applied and Computational Mathematics, Foundation for Research and Technology - Hellas, Heraklion, Italy; 2. Department of Electric, Electronic and Computer Engineering, University of Catania, Catania, Italy; 3. Department of Engineering, University of Messina, Messina, Italy; 4. Division of Physics and Applied Physics, School of Physics and Mathematical Sciences, Nanyang Technological University, Singapore; 5. Department of Mathematical and Computer Sciences Physical Sciences and Earth Sciences, University of Messina, Messina, Italy; 6. Key Laboratory of Nanodevices and Applications, Suzhou Institute of Nano-tech and Nano-bionics, Suzhou, China; 7. Department of Electric, Electronic and Computer Engineering, Polytechnic University of Bar, Bari, Italy*

Magnetic skyrmions are emerging as key elements of unconventional operations having unique properties such as small size and low current manipulation [1]. Very recently, it has been proposed to use skyrmions for unconventional applications, such as skyrmion based reshuffle for probabilistic computing [2,3] and reservoir computing [4–6]. In this work, we show how magnetic skyrmions can be useful in the solution of the shortest path optimization problem. In particular, the underlying physics is the same as memristive networks [7], where the inputs of the problem are the current and voltage distributions. On the contrary, the solution of the problem is achieved by using the final spatial distribution of the skyrmions, which behave similarly to real ant colonies when seeking the shortest path to food, but driven by a physical energy landscape. The capability of skyrmions to move on interconnected grids along complex trajectories [1] is the key feature which makes skyrmions the only candidate over other magnetic solitons, e.g. domain walls and vortex, to be used in this category of optimization problems. We analyze the skyrmion motion in a complex 2-dimensional synthetic antiferromagnetic system (Fig. 1). We compute the spatial distribution of the current by supposing to supply voltage between the terminals 1 and 2 (Fig. 1). We continuously nucleate a single skyrmion in correspondence of terminal 1, and then shift it by the spin-Hall effect. Each new skyrmion introduced into the system goes through the same path, as real ants follow the path with a larger amount of pheromone. After 130 ns, the best solution emerges (Fig. 1) and can be read by using state-of-the-art imaging techniques, such as MFM, STXM and MOKE.

[1] G. Finocchio et al. J. Phys. D. Appl. Phys. 49, 423001 (2016). [2] D. Pinna et al. Phys. Rev. Appl. 9, 064018 (2018). [3] J. Zázvorka et al. Nat. Nanotech. (2019). [4] D. Prychynenko et al. Phys. Rev. Appl. 9, 014034 (2018). [5] G. Bourianoff et al. AIP Adv. 8, 055602 (2018). [6] D. Pinna, G. Bourianoff, and K. Everschor-Sitte, arxiv:1811.12623 (2018). [7] Y. V. Pershin and M. Di Ventra, Phys. Rev. E 88, 013305 (2013).

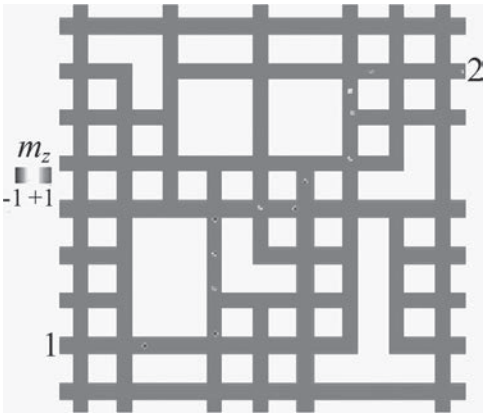


Figure 1: Example of final solution. Spatial distribution of the magnetization for the bottom layer of the SAF structure. The path identified by the skyrmion colony represents the final solution of the problem.

AW-11. Magnetic Phases of Skyrmion-Hosting $GaV_4S_{8-y}Se_y$ (y = 0, 2, 4, 8) Probed with Muon Spectroscopy. *K.J. Franke*[1,2], B. Huddart[1], T.J. Hicken[1], F. Xiao[3,4], S. Blundell[5], F.L. Pratt[6], M. Crisanti[7,8], J.A. Barker[9], S.J. Clark[1], A. Štefančič[7], M. Ciomaga Hatnean[7], G. Balakrishnan[7] and T. Lancaster[1]
1. Centre for Materials Physics, Durham University, Durham, United Kingdom; 2. School of Physics and Astronomy, University of Leeds, Leeds, United Kingdom; 3. Laboratory for Neutron Scattering, Paul Scherrer Institut, Viligen, Switzerland; 4. Department of Chemistry and Biochemistry, University of Bern, Bern, Switzerland; 5. Department of Physics, Oxford University, Oxford, United Kingdom; 6. ISIS Facility, STFC Rutherford Appleton Laboratory, Chilton, Didcot, United Kingdom; 7. Department of Physics, University of Warwick, Coventry, United Kingdom; 8. Institut Laue-Langevin, Grenoble, France; 9. Laboratory for Muon Spin Spectroscopy, Paul Scherrer Institut, Viligen, Switzerland

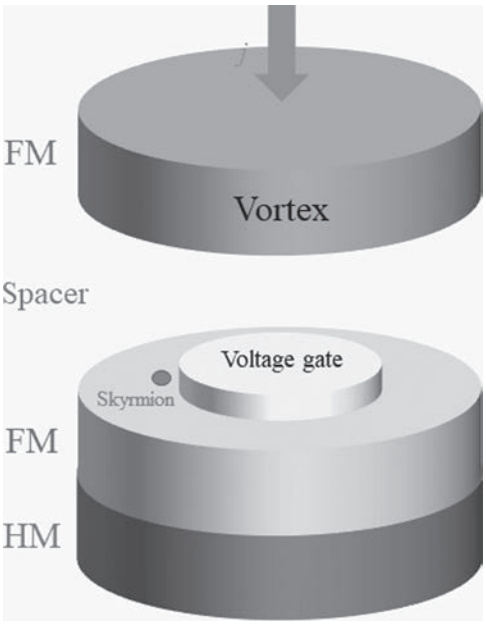
In recent years, a number of spectacular advances have demonstrated the existence, not only of magnetic skyrmions, but also their ordering into a skyrmion lattice (SL). The potential of skyrmions as high- density, low-power, data-storage and logic devices is driving their exploration. Skyrmions are topological spin textures stabilized by the competition between the antisymmetric Dzyaloshinskii-Moriya interaction (DMI) and the symmetric exchange interaction. The emergence of a Bloch-type SL phase has been observed in several magnetic materials with a chiral structure close to the paramagnetic to helical magnetically-ordered phase boundary. The formation of Néel-type skyrmions in bulk crystals with polar C_{nv} symmetry was only recently observed in $VOSe_2O_5$ [1], GaV_4S_8 [2,3], and GaV_4Se_8 [4]. Here, we present the results of a muon-spin rotation (μ^+SR) investigation of skyrmion-hosting materials GaV_4S_8 and GaV_4Se_8 and intermediate compounds from the $GaV_4S_{8-y}Se_y$ series, with y = 2 and 4 [5]. We present measurements in the longitudinal field (LF), transverse field (TF), and zero-field (ZF) geometries, allowing access to static and dynamic local magnetic properties. While GaV_4S_8 and GaV_4Se_8 are very similar in exhibiting a SL phase, we show that their magnetic behaviour is quite different. This is likely attributable to subtle (but significant) differences in the electronic ground states of the two systems. We find that the intermediate compounds with y = 2 and 4 do not undergo a transition to a state of long-range magnetic order, but instead show a glassy freezing of dynamics as the temperature is reduced. Our LF μ+SR measurements reveal that the skyrmion phases in GaV_4S_8 and GaV_4Se_8 give rise to emergent dynamics on the muon (microsecond) time scale, reflecting the slowing of magnetic fluctuations perpendicular to the applied field. In GaV_4S_8 these dynamics are observed over the temperature and field range where the SL was observed in single crystals. For GaV_4Se_8, the observed dynamics are more limited in their extent in the H–T phase diagram than the reported extent of the SL. It is thus plausible that the SL region of GaV_4Se_8 is less extensive than previously suggested.

[1] T. Kurumaji, et al. Phys. Rev. Lett. 119, 237201 (2017) [2] I. Kézsmárki, et al. Nat. Mater. 14, 1116 (2015) [3] J. S. White, et al. Phys. Rev. B 97, 020401 (2018) [4] S. Bordács, et al. Sci. Rep. 7, 7584 (2017) [5] K. J. A. Franke, et al. Phys. Rev. B 98, 054428 (2018)

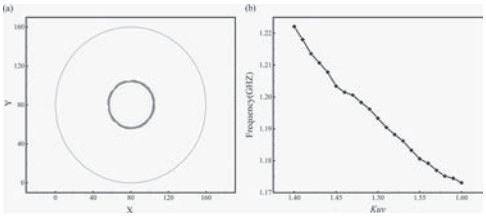
AW-12. Ferromagnetic Skyrmion nano-oscillators with voltage controlled magnetic anisotropy. *J. Guo*[1], X. Zhang[2], P. Pong[1], Y. Wu[3], H. Chen[4], W. Zhao[5] and Y. Zhou[2] *1. The University of Hong Kong, Hong Kong, Hong Kong; 2. The Chinese University of Hong Kong, Shenzhen, Shenzhen, China; 3. Fudan University, Shanghai, China; 4. Foshan University, Foshan, China; 5. Beihang University, Beijing, China*

Ferromagnetic (FM) skyrmion has been one of the most striking topological forms which are applied in spintronics devices such as spin transfer torque nano-oscillators (STNOs)[1]. Spin-transfer torque and Dzyaloshinskii-Moriya interaction (DMI) enable the movement of skyrmion on the nanodisk. However, Magnus force is far greater than boundary force, which will lead to the annihilation of skyrmion or staying at the central part on the nanodisk. This occurrence severely reduces the performance of STNOs. In recent research, voltage has shown the influence on the perpendicular magnetic anisotropy, known as voltage-controlled magnetic anisotropy (VCMA)[2, 3]. This effect can be explained as[4]: $K_{uv}=K_u+\theta V_b$, so the anisotropy coefficient can be modified by manipulating applied voltage. In order to effectively solve the problem above, we have designed a composited structure model shown in Fig.1, where the voltage gate is on the bottom FM layer. It proposes two anisotropy areas with different anisotropy coefficients in the inner area and outer area respectively. When K_{uv} of the inner area becomes larger than the K_u of the outer area to some extent, the inner area will show the repulsive force to the skyrmion. We hope to use this repulsive force to offset the magnus effect so that it can prevent skyrmion move to the central point of the nanodisk, making skyrmions move along the edge of the inner circular. The trajectory of skyrmion's motion of $K_{uv}=1.4\times10^6$ J/m^3 is illustrated in Fig. 2(a), We adopt Object Oriented Micromagnetic Framework (OOMMF)[5] for simulation and the typical parameters are as follows[6]: θ=0.02, DMI=4.0 mJ m^{-2}, A=15.0×10^{12} J/m, K=0.8×10^6 J/m^3, M_S=580×10^3 A/m, α=0.5, r=10 nm and R=80 nm. Assuming the voltage as a certain range from 0 to 100V. Fig. 2(b) shows that in a certain range of stable motion, with the increase of the K_{uv}, the frequency of oscillator will drop. Our results provide a promising method to modulate the frequency of STNOs by VCMA.

1. G. Finocchio, F. Büttner, R. Tomasello, M. Carpentieri and M. Kläui, J. Phys. D: Appl. Phys. 49 (42), 423001 (2016). 2. X. Chen, W. Kang, D. Zhu, X. Zhang, N. Lei, Y. Zhang, Y. Zhou and W. Zhao, IEEE Trans. Electr. Devices. (99), 1-7 (2018). 3. W. Kang, C. Zheng, Y. Huang, X. Zhang, Y. Zhou, W. Lv and W. Zhao, IEEE. Electr. Device. Lett. 37 (7), 924-927 (2016). 4. J. Wang, J. Xia, X. Zhang, G. Zhao, L. Ye, J. Wu, Y. Xu, W. Zhao, Z. Zou and Y. Zhou, J. Phys. D: Appl. Phys. 51 (20), 205002 (2018). 5. X. Zhang, Y. Zhou and M. Ezawa, Nat. Commun. 7, 10293 (2016). 6. J. Xia, Y. Huang, X. Zhang, W. Kang, C. Zheng, X. Liu, W. Zhao and Y. Zhou, J. Appl. Phys. 122 (15), 153901 (2017).



The simulated model of a skyrmion-based nano-oscillator. The skyrmion will move on the bottom FM layer.



(a) The trajectory of the stable motion, where the red line indicates skyrmion's motion. (b) The frequency of oscillator as a function of K_{uv} = (1.4-1.6)×10^6 J/m^3.

AW-13. Micromagnetic study of skyrmions in magnetic multilayers.
R. Tomasello[1], A. Giordano[2], M. Carpentieri[3], G. Yu[4] and G. Finocchio[2]
1. Institute of Applied and Computational Mathematics, Foundation for Research and Technology - Hellas, Heraklion, Greece; 2. Department of Mathematical and Computer Sciences Physical Sciences and Earth Sciences, University of Messina, Messina, Italy; 3. Department of Electrical and Information Engineering, Polytechnic University of Bar, Bari, Italy; 4. Institute of Physics, Chinese Academy of Sciences, Beijing, China

Magnetic skyrmions are topologically-protected magnetization textures characterized by a non-trivial topology [1]. Skyrmions are usually obtained in presence of the DMI, arising in systems lacking or breaking the inversion symmetry [1]. Recently, a growing interest have been devoted to magnetic multilayers [2–4], where tiny "hybrid skyrmions" can be stabilized at room temperature in absence of DMI. Such "hybrid skyrmions" are characterized by a thickness-dependent reorientation of their domain wall chirality and the equilibrium configuration depends on the interplay between dipolar interactions and DMI. In addition, theoretical studies have pointed out that SHE-driven skyrmion motion in these multilayers is characterized by a skyrmion Hall angle (SHA) dependent on the value of the DMI and/or on the number of repetitions of the ferromagnetic layer [3,5]. Therefore, by proper designing the IDMI and/or the number of repetitions, it is possible to achieve a zero SHA. Here, we micromagnetically investigate a squared 500x500nm^2 multilayer characterized by different 20 ferromagnetic repetitions, similarly to experimental studies [6]. At zero DMI, when the dipolar interactions are the dominant energy term, the hybrid skyrmion has a chirality going from an outward Néel skyrmion in the top layer to a Bloch skyrmion in the middle layer and to an inward Néel skyrmion in the bottom layer. On the other hand, when the DMI is increased, the Bloch skyrmion is shifted towards the upper layers, until, beyond a threshold DMI value, a pure Néel skyrmion is obtained along the whole thickness [3,4], as observed in Figure 1. We have also performed micromagnetic simulations as a function of the number of ferromagnetic repetitions, finding similar outcome. Our results are in agreement with recent experimental measurements [4]. Acknowledgements: This work has been supported by the project "ThunderSKY," funded by the Hellenic Foundation for Research and Innovation (HFRI) and the General Secretariat for Research and Technology (GSRT), under grant agreement No. 871.

[1] G. Finocchio *et al.*, J. Phys. D. Appl. Phys. 49, 423001 (2016). [2] S. A. Montoya *et al.*, Phys. Rev. B 95, 024415 (2017). [3] W. Legrand *et al.*, Sci. Adv. 4, (2018). [4] W. Li *et al.*, Adv. Mater. 31, 1807683 (2019). [5] I. Lemesh and G. S. D. Beach, Phys. Rev. B 98, 104402 (2018). [6] A. Soumyanarayanan *et al.*, Nat. Mater. 16, 898 (2017).

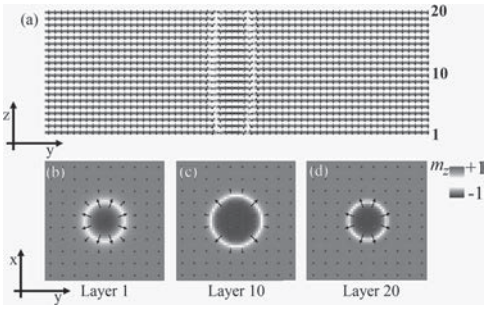


Figure 1: Pure Néel skyrmion. (a) Cross-sectional view of the 20-repeat multilayer. (b) – (d)Spatial distribution of the magnetization for different layers (top, middle, bottom).

AW-14. Suppressing the Skyrmion Hall Effect by Modulated Spin-Orbit Torques.
B. Göbel[1], A. Mook[2], J. Henk[2] and I. Mertig[2,1] *1. Max Planck Institute of Microstructure Physics, Halle (Saale), Germany; 2. Martin Luther University Halle Wittenberg, Halle (Saale), Germany*

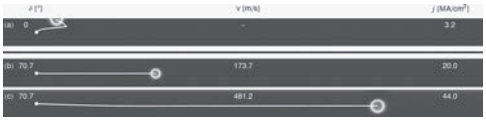
Magnetic skyrmions are envisioned as carriers of information in racetrack storage devices of the future [1]. Their non-trivial real-space topology brings about great stability but also the skyrmion Hall effect: When skyrmions are driven by currents, they are deflected towards the edge of the racetrack where they annihilate. Even in perfectly clean samples the skyrmions can only creep along the edge at limited velocities before they disappear [2]. Over the recent years, several alternative carriers of information have been proposed, which do not exhibit a skyrmion Hall effect, for example antiferromagnetic skyrmions [3,4], skyrmioniums [5], antiskyrmions [6], and skyrmions with a modulated in-plane magnetization [7]. However, the controlled generation of these particles still lacks experimental realization. Since the generation of Néel skyrmions is well understood, one is desired to find methods for suppressing the skyrmion Hall effect also for these particles. Here [2], we consider a ferromagnet on a heavy-metal layer, what leads to the stabilization of Néel skyrmions, which can be driven via spin-orbit torques. Instead of a conventional heavy metal like Pt we use a lower symmetric material, which allows for an injection of spins partially oriented along the racetrack direction [8]; cf. Fig. 1. We show by analytical considerations and micromagnetic simulations that the deflection angle decreases in this case and derive the condition for complete suppression of the skyrmion Hall effect [2]. Consequently, the skyrmion moves in the middle of the racetrack at velocities similar to those proposed for antiferromagnetic skyrmions [3]; cf. Fig. 2.

[1] J. Sampaio, V. Cros, S. Rohart et al., Nature Nanotechnol., 8, 839 (2013) [2] B. Göbel, A. Mook, J. Henk et al., Phys. Rev. B, 99, 020405(R) (2019) [3] J. Barker, O. Tretiakov, Phys. Rev. Lett., 116, 147203 (2016) [4] B. Göbel, A. Mook, J. Henk et al., Phys. Rev. B, 96, 060406(R) (2017) [5] B. Göbel, A. Schäffer, J. Berakdar et al., arXiv: 1902.06295 (2019) [6] S. Huang, C. Zhou, G. Chen et al., Phys. Rev. B, 96, 144412 (2017)

[7] K. Kim, K. Moon, N. Kerber et al., Phys. Rev. B, 97, 224427 (2018)
[8] M. Seemann, D. Ködderitzsch, S. Wimmer et al., Phys. Rev. B, 92, 155138 (2015)



Proposed mechanism to suppress the skyrmion Hall effect. Due to the spin Hall effect in the heavy metal, a charge current (white) leads to the injection of spins (orange) into the magnetic layer. Here, the skyrmion Hall angle arises for a skyrmion (circular object). Its magnitude depends on the orientation of the injected spins. Taken from [2].

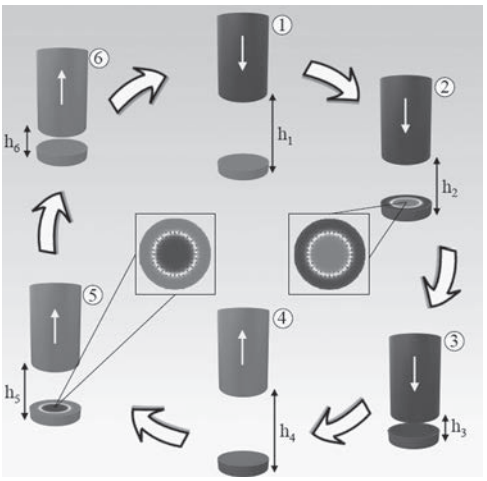


Micromagnetic simulations comparing the conventional and optimized setups. (a) Conventional Co/Pt racetrack, where the skyrmion annihilates at the edge. (b,c) Optimized racetrack with drastically increased velocities. Adapted from [2].

AW-15. Controlling the nucleation and annihilation of skyrmions with magnetostatic interactions. *N. Vidal-Silva*[1,2], A. Riveros[3], F. Tejo[3,2], J. Escrig[3,2] and D. Altbir[3,2] *1. University of Chile, Santiago, Chile; 2. Center for the Development of Nanoscience and Nanotechnology (CEDENNA), 917-0124 Santiago, Chile, Santiago, Chile; 3. Universidad de Santiago de Chile, Santiago, Chile*

In this work, and by means of analytical calculations and micromagnetic simulations, we explore the effect of the magnetostatic field generated by a magnetic cylindrical tip on the stability of skyrmions. Our results show that the interaction energy between the tip and the skyrmion plays a fundamental role in the stabilization of Néel skyrmions confined in nanodisks, allowing its nucleation and annihilation, and also providing precise control of its size and polarity. The magnetostatic field created by the tip can be used to control the polarity, chirality, and size of the core of the skyrmion, or create an almost homogeneous magnetic state, which is a particular case of a skyrmion with a core radius larger than the radius of the dot. The different states can be achieved by varying the distance between the tip and the dot, as shown in Fig. 1. Our analytical results show a good agreement with micromagnetic simulations and, as a highlighted result, we can show that from static energy calculations we can explain the dynamics associated with changes in the magnetostatic interaction. Based on our results, we propose a very simple and cyclic method to nucleate and annihilate skyrmions, as well as to control their polarity and chirality. This proposal could open new possibilities for logic devices taking advantage of all the degrees of freedom that skyrmionic textures have [1].

[1] N. Vidal-Silva, A. Riveros, F. Tejo, J. Escrig, and D. Altbir, https://arxiv.org/abs/1904.02775



Proposed cycle to nucleate and annihilate a skyrmion in a dot with a specific polarity and chirality by fixing the magnetization direction of the magnetic tip and its vertical separation with the dot.

AW-16. Skyrmions in Reduced Geometry. *K.L. Krycka*[1], J.J. Rhyne[1], J. Borchers[1], B. Balasubramanian[2,3] and D.J. Sellmyer[2,3] *1. NIST Center for Neutron Research, National Institute of Standards and Technology, Gaithersburg, MD, United States; 2. Physics and Astronomy, University of Nebraska, Lincoln, NE, United States; 3. Nebraska Center for Materials and Nanoscience, University of Nebraska, Lincoln, NE, United States*

This paper reports polarized beam small angle neutron scattering results on nanoparticle MnSi, illustrating the influence of restricted geometry on the formation of skyrmions. The nanoparticle films are produced by a cluster-deposition sputtering technique and show excellent uniformity of particle sizes with a deviation of around 20%. For this study 17.7 nm particle were chosen for which extensive magnetization and structural characterization has been performed. The magnetization data show anomalies in the magnetic susceptibility over limited temperature and applied field ranges that are characteristic of the formation of the skyrmion spin state [1]. The skyrmion effects are expected to be strongest near the Curie temperature where the Dzyaloshinshkii-Moriya interaction is dominant. For 17.7 nm nanoparticles sharp spikes appear in the magnetic susceptibility in fields of 70 Oe to 150 Oe in the temperature range 25 K to about 43 K (Tc = 39 K). At fields or temperatures significantly higher or lower than these ranges, no characteristic anomalies appear. For the neutron experiments, 75 K measurements (background) and 35 K measurements were compared over a Q-range of 0.03 nm^{-1} to 1.20 nm^{-1}. Measurements at 150 Oe showed no magnetic difference in temperature, while fields of 80 Oe and 100 Oe showed a temperature-dependent magnetic signal with shape similar to that of a 17 nm nanoparticle. Polarization analysis of the neutron spin further reveals signatures in both the non spin-flip and spin-flip channels, the latter of which is indicative of magnetic scattering from spins with components perpendicular to the applied field. These results will be analyzed in the context of the expected scatting associated with skyrmion formation.

[1] Bhaskar Das, Balamurugan Balasubramanian and David J. Sellmyer, Nanoscale 10, 9504 (2018)

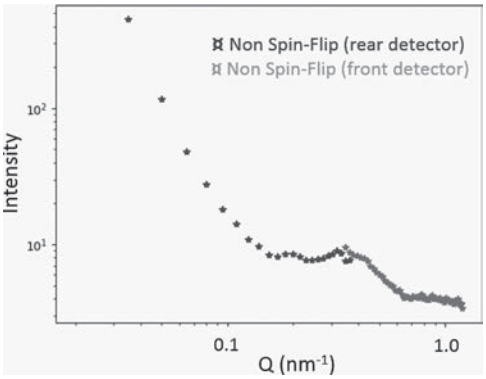


Figure 1. Non spin-flip neutron scattering of the MnSi nanoparticles at 100 Oe, 35 K probes structure and magnetism primarily parallel to B.

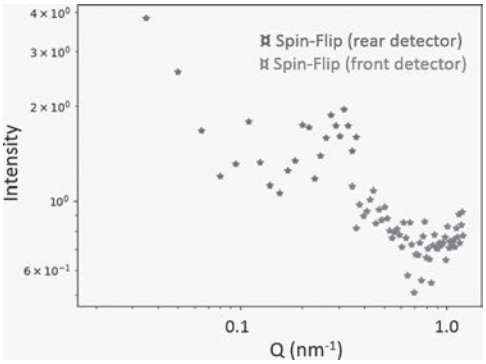
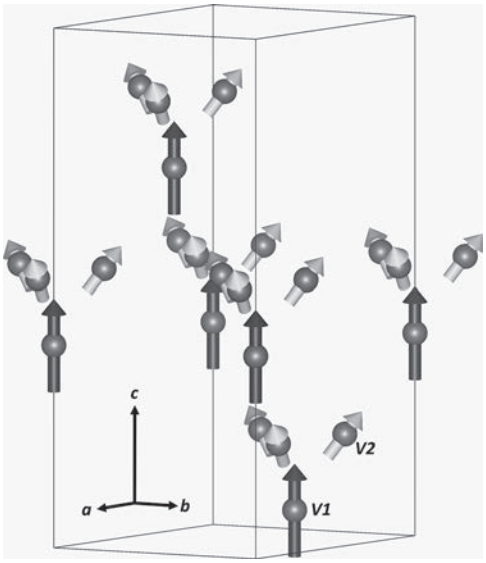


Figure 2. Spin-flip neutron scattering of the MnSi nanoparticles at 100 Oe, 35 K probes magnetism where the dominant component is perpendicular to B.

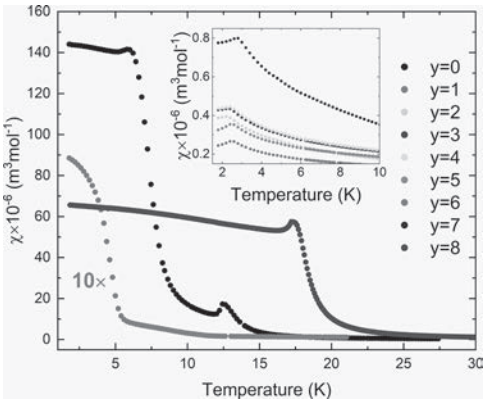
AW-17. Structural and magnetic studies of the skyrmionic materials $GaV_4S_{8-y}Se_y$. A. Štefančič[1], *S.J. Holt*[1], C. Ritter[2], M.J. Gutmann[3], M.R. Lees[1] and G. Balakrishnan[1] *1. Department of Physics, University of Warwick, Coventry, United Kingdom; 2. Institut Laue Langevin, Grenoble, France; 3. ISIS Facility, Oxfordshire, United Kingdom*

Recently, there has been considerable interest in the physics of magnetic skyrmions and the materials in which they are hosted due to their potential uses in spintronic devices [1]. Magnetic skyrmions are topological magnetic spin structures that were originally identified in materials belonging to the B20 class but have recently been found in other non-centrosymmetric materials [2]. Multiferroic GaV_4S_8 and GaV_4Se_8 have been shown to host Néel type skyrmions [3,4]. These two materials are isostructural forming in a low temperature *R*3*m* non-centrosymmetric space group but exhibit very different magnetic phase diagrams at low temperatures. In GaV_4S_8 and GaV_4Se_8 the magnetocrystalline anisotropies favour the formation of skyrmion magnetic spin textures constrained to particular crystallographic axis. We have undertaken investigations of several intermediate compositions of $GaV_4S_{8-y}Se_y$ to try to identify variations in magnetic behaviour across the series, in an attempt to investigate the possibility of observing skyrmions in the intermediate phases. Phase-pure polycrystalline solid-solutions have been successfully synthesized of the $GaV_4S_{8-y}Se_y$ ($0 \le y \le 8$) family and high-quality single crystals grown using the chemical vapour transport technique. We present the results of our detailed investigations of the crystal and magnetic structures of this series of materials as both powders and single crystals, using x-ray as well as neutron diffraction techniques (Figs. 1 & 2). These results are further supported by *dc* and *ac* magnetic susceptibility, and heat capacity measurements within the series.

[1] A. Fert, *et al.*, Nat. Nanotechnol. 8, 152 (2013). [2] S. Mühlbauer, *et al.*, Science 323, 915 (2009). [3] Y. Tokunaga, *et al.*, Nat. Commun. 6, 7638 (2015). [4] I. Kézsmárki *et al.*, Nat. Mater. 14, 1116 (2015).



Magnetic structure of GaV_4S_8 at 1.5 K determined by powder neutron diffraction. Magnetic moments are found to be localised on the vanadium sites in the R3m' magnetic space group.



***dc* magnetic susceptibility of the $GaV_4S_{8-y}Se_y$ series in an applied magnetic field of 10 mT. A large suppression in the susceptibility can be seen for the intermediate substitutions.**

AW-18. Unidirectional Manipulation of Magnetic Skyrmion Transmission via Asymmetric Modulation of Potential Energy Barrier. *D. Jung*[1], H. Han[1], N. Kim[1] and K. Lee[1] *1. School of Mechanical and Advanced Materials Engineering, Ulsan National Institute of Science and Technology (UNIST), Ulsan, The Republic of Korea*

Magnetic skyrmion is a self-localized chiral spin configuration with a topological protection, which holds promise as a digital information carrier in the future spintronics devices due to its advantages such as a nanoscale size, a topological stability, and a facile current-driven motion [1-3]. To realize competitive skyrmion-based devices, it is essential to understand interactions between the skyrmion and boundaries of devices. However, until now the potential energy of a skyrmion by general geometric boundaries has not been fully understood except for simple model in the limited situation such as one-dimensional ultrathin nanostrips or cylindrical dots [4-6]. In this work, we develop a methodology in determining the general potential energy of a skyrmion in a patterned thin films with arbitrary shape. We thus demonstrate that a current-driven skyrmion propagation can be unidirectionally manipulated (see FIG. 1) by forming asymmetrical potential energy profile through an asymmetric shape of device. Using a simple model based on the collective coordinates for skyrmion's motion, we reveal underlying physics of the dependence of the boundary force and spin-torque parameters on the manipulation of skyrmion dynamics. This work provides a fundamental

understanding of skyrmion's dynamics upon boundaries of devices as well as an efficient way to design skyrmion-based logic device such as a diode element by manipulating potential energies through the device shape.

[1] N. S. Kiselev, A. Bogdanov, R. Schäfer, and U. K. Rößler, J. Phys. D 44, 392001 (2011). [2] A. Fert, V. Cros, and J. Sampaio, Nat. Nanotechnol. 8, 152 (2013). [3] N. Nagaosa and Y. Tokura, Nat. Nanotechnol. 8, 899–911 (2013). [4] Z. V. Gareeva and K. Y. Guslienko, Phys. Solid State 60. 1146-1152 (2017). [5] A. R. Aranda et al., J. Magn. Magn. Mater. 465. 471-479 (2018). [6] K. Y. Guslienko, Appl. Phys. Express 11. 063007 (2018).

AW-19. Manipulation of magnetic skyrmions in a locally modified synthetic antiferromagnetic racetrack. R. Loreto[1], X. Zhang[2], Y. Zhou[2], M. Esawa[3] and *C.I. Levartoski de Araujo*[1] *1. Physics, Universidade Federal de Viçosa, Viçosa, Brazil; 2. The Chinese University of Hong Kong, Shenzhen, China; 3. University of Tokyo, Tokyo, Japan*

With the recent proposition of skyrmion utilization in racetrack memories at room temperature, skyrmionics has become a very attractive field. However, for the stability of skyrmions, it is essential to incorporate the Dzyaloshinskii–Moriya interaction (DMI) and the out-of-plane magnetic field into the system. In those skyrmion-based racetrack memories, the information encoded by skyrmions may be destroyed due to the skyrmion Hall effect in ferromagnetic racetracks, which can be surmounted by using alternative topological textures as skyrmionion [1] or resonant magnetic soliton [2]. Another approach would be the utilization of synthetic antiferromagnetic racetracks [3]. Hence, the manipulation of skyrmions in synthetic antiferromagnetic racetracks is important for practical applications. Here, we computationally study the interaction between a pair of skyrmions and a locally modified region in a synthetic antiferromagnetic racetrack, where the perpendicular magnetic anisotropy or thickness is locally adjusted to be different from that of the rest region of the racetrack. The skyrmion pair moves through the track with small pulse of current as demonstrated in Figure 1a. After currents switch of it is found that the skyrmions can be attracted, repelled, and even trapped by the locally modified region in a controllable manner (Figure 1b and 1c). Besides, we demonstrate that the skyrmion location can be precisely determined by the locally modified region. The possible manipulation of skyrmions by utilizing locally modified regions in a synthetic antiferromagnetic racetrack may be useful for future skyrmion-based applications.

1 - Göbel, Börge, et al., *arXiv preprint arXiv:1902.06295* (2019). 2 - R. P. Loreto et al., Journal of Magnetism and Magnetic Materials, v. 455, p. 25-31, (2018). 3 - X. Zhang, Y. Zhou and M. Ezawa, Nature communications, v. 7, p. 10293 (2016).

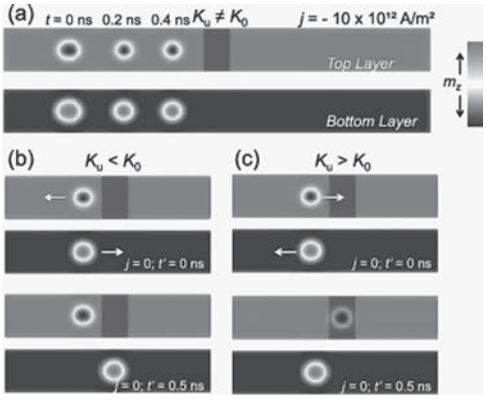


Fig. 1 - a) skyrmion pair moving after current pulse without skyrmion hall effect in a synthetic antiferromagnetic track, b) skyrmion repelled by a defect with lower anisotropy and c) skyrmion attracted by the deffect with higher anisotropy.

AW-20. Writing Skyrmions with a Magnetic Dipole. D. Garanin[1], *D. Capic*[1], S. Zhang[2], X. Zhang[2] and E. Chudnovsky[1] *1. CUNY Graduate Center at Lehman College, Bronx, NY, United States; 2. PSE, KAUST, Thuwal, Saudi Arabia*

In our already published paper, we demonstrate numerically on large spin lattices that one can write skyrmions in a thin magnetic film with a magnetic force microscope (MFM) modeled as a magnetic dipole of a few tens of nanometer in size. Nucleation of non-chiral skyrmions as well as chiral skyrmions formed by the Dzyaloshinskii-Moriya interaction has been investigated. Analytical model is developed that agrees with numerical results. It is shown that skyrmions can be written though a number of scenarios that depend on the experimental technique and parameters of the system. In one scenario, that branches into subscenarios of different topology, the magnetic dipole on approaching the film creates a skyrmion-antiskyrmion pair. As the dipole moves closer to the film it induces collapse of the antiskyrmion and creation of a non-zero topological charge due to the remaining skyrmion. In a different scenario the dipole moving parallel to the film nucleates a skyrmion at the boundary and then drags it inside the film. Possible implementations of these methods for writing topologically protected information in a magnetic film are discussed. This is an already published paper so I am not submitting it for publication at the conference; I would just like to present the findings.

D.A.Garanin, D.Capic, S.Zhang, X.X.Zhang, and E.M. Chudnovsky. Writing skyrmions with a magnetic dipole, Journal of Applied Physics 124, 113901-(8) (2018)

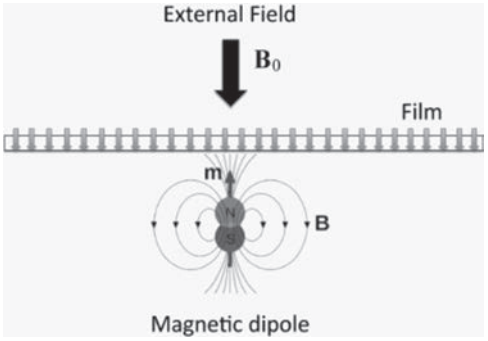


Fig 1. Nucleation of skyrmions via the competiting effects of an applied field and the dipole field from the MFM

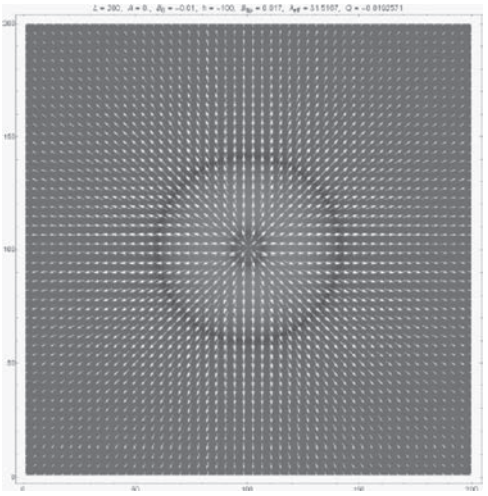


Fig 2. Creation of a skyrmion-antiskyrmion pair to conserve topological charge

Session BA
MAGNETO-IONICS: NEW PHENOMENA, MATERIALS, AND APPLICATIONS

Mingzhong Wu, Chair
Colorado State University, Fort Collins, CO, United States

INVITED PAPERS

1:30

BA-01. Electrolyte-Based Electrostatic and Electrochemical Control of Ferromagnetism in Perovskite Oxides. *C. Leighton*[1], J. Walter[1], H. Wang[1], B. Yu[1], G. Yu[1], A.J. Grutter[2], B.J. Kirby[2], J. Borchers[2], Z. Zhang[3], H. Zhou[3], T.R. Charlton[4], H. Ambaye[4], M. Fitzsimmons[4], P. Orth[1,5], B. Luo[1], T. Birol[1], B. Shklovskii[1], R. Fernandes[1], M. Greven[1] and D. Frisbie[1] *1. University of Minnesota, Minneapolis, MN, United States; 2. NIST Center for Neutron Research, Gaithersburg, MD, United States; 3. Advanced Photon Source, Argonne National Lab, Argonne, IL, United States; 4. Oak Ridge National Lab, Oak Ridge, TN, United States; 5. Iowa State University, Ames, IA, United States*

Ion-based manipulation of magnetic materials provides a promising route to electrically-controlled magnetism, of interest from both fundamental and device perspectives. Electrolytes such as ionic liquids and gels play a key role, through the foundational electric double layer transistor (EDLT) (Fig. 1). In EDLTs, massive capacitances (up to 100 μF/cm^2) enable induction of interfacial charge carrier densities up to 10^{15} cm^{-2} at just a few volts, *i.e.*, significant fractions of an electron/hole per unit cell in most materials. This is sufficient to induce and control electronic/magnetic order, properties, and phase transitions, generating great interest. Challenges remain, however, including understanding mechanisms, ultimate capabilities, and the universality of the approach [1]. In particular, it is now well established that both electrostatic and electrochemical gating mechanisms occur in EDLTs (Fig. 1), redox-based response in oxides providing a prominent example [1]. In this presentation I will review our recent work using epitaxial perovskite cobaltite thin films as model systems to understand mechanisms and capabilities of electrolyte gating for control of magnetism [2-5]. Through development of *operando* tools such as synchrotron X-ray diffraction (SXRD) [3] and polarized neutron reflectometry (PNR) [3,5], gate bias polarity asymmetry was first elucidated in these systems. In essence, positive gate voltages are found to induce oxygen vacancies (V_O), assisted by low enthalpy of formation and high diffusivity, while negative gate voltages favour electrostatic hole accumulation due to the thermodynamic stability of V_O [2,3]. Studies on other perovskite oxides have enabled separation of the influence of V_O formation enthalpy and diffusivity, highlighting the importance of the latter, and pointing to a potential route to understand and predict electrostatic *vs*. electerochemical response in electrolyte-gated oxides [1,6]. Electrical control of ferromagnetism in cobaltites was then achieved *via* both electrostatic [2,5] and electrochemical [2,3] mechanisms. Most recently, validating a theoretical prediction [4], optimization of *electrostatic* control of Curie temperature (T_C) has been achieved by gate-induced percolation from a nanoscopic magnetic cluster state (Fig. 2), confirmed by *operando* PNR [5]. Electrical control of T_C over a 150 K window was thus demonstrated, establishing new records for both *electrostatic* electrolyte gating, and complex oxide materials [5]. If time allows I will briefly show new results establishing that ferromagnetism can be electrically induced in EDLTs even from a *diamagnetic* starting point. Work supported by the NSF MRSEC and the DOE Center for Quantum Materials (specifically neutron scattering).

[1] Leighton, Nat. Mater. 18, 13 (2019). [2] Walter, Wang, Frisbie and Leighton, ACS Nano 10, 7799 (2016) [3] Walter, Yu, Yu, Grutter, Kirby, Borchers, Zhang, Zhou, Birol, Greven and Leighton, Phys. Rev. Materials 1, 071403(R) (2017) [4] Orth, Fernandes, Walter, Leighton and Shklovskii, Phys. Rev. Lett. 118, 106801 (2017). [5] Walter, Charlton, Ambaye, Fitzsimmons, Orth, Fernandes and Leighton, Phys. Rev. Materials 2, 111406(R) (2018). [6] Wang, Walter, Ganguly, Yu, Yu, Zhang, Zhou, Fu, Greven and Leighton, in press, Phys. Rev. Materials (2019).

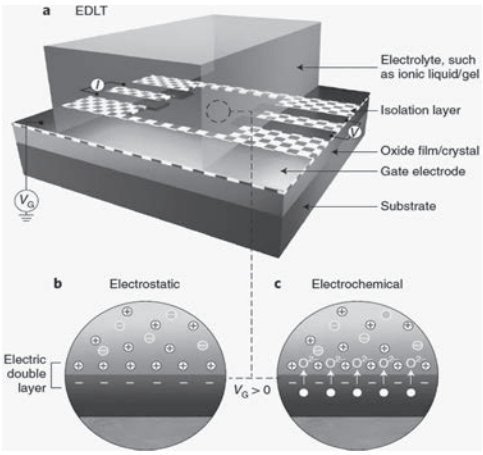


Fig. 1: (a) Oxide EDLT schematic showing (b) electrostatic and (c) electrochemical (via V_O formation) response. From [1].

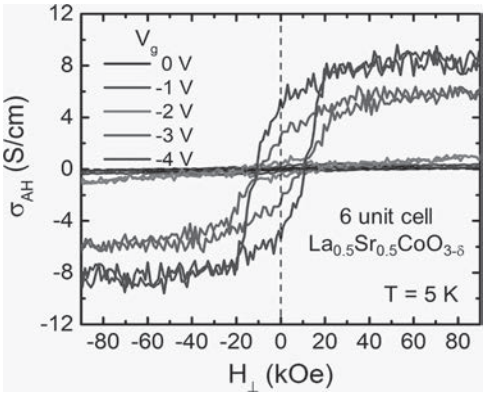


Fig. 2: 5 K magnetic field dependence of the anomalous Hall conductivity at multiple gate voltages in a 6-unit-cell-thick $La_{0.5}Sr_{0.5}CoO_{3-\delta}$ film. From [5].

2:06

BA-02. Voltage-controlled on-off ferromagnetism in dense and nanoporous transition-metal oxides. C. Navarro[1], A. Quintana Puebla[1], S. Robbennolt[1], A. Nicolenco[1], D. Baró[1], V. Sireus[1], E. Pellicer[1], J. Nogués[2,3], E. Menéndez[1] and *J. Sort*[1,3] *1. Physics, Universitat Autònoma de Barcelona, Cerdanyola del Vallès, Spain; 2. Catalan Institute of Nanoscience and Nanotechnology (ICN2), CSIC and The Barcelona Institute of Science and Technology, Cerdanyola del Vallès, Spain; 3. ICREA, Barcelona, Spain*

Manipulating magnetism with voltage has an enormous potential to boost energy efficiency in nanoscale device applications[1,2]. Recent works have indicated that voltage-driven ionic motion and related chemical reactions at or near magnetic interfaces (i.e., "magneto-ionic" effects) can enable considerable reversible, non-volatile changes of the magnetic properties, such as anisotropy direction, coercivity, domain wall pinning, exchange bias, spin reorientation, or magnetization. Thus, low-power voltage-reprogrammable magnetic materials are coming within reach and they may transform magnetics-based nanotechnologies. We have recently demonstrated the possibility to induce room temperature voltage-driven anionic and cationic motion of oxygen and cobalt, respectively, in a single 100 nm-thick polycrystalline paramagnetic Co_3O_4 dense film by electrolyte-gating. This effect results in controlled transitions from fully non-magnetic (paramagnetic) to ferromagnetic states[3]. Negative biasing (–10 V) reduces Co_3O_4 to Co, resulting in ferromagnetism, whereas, upon positive voltages, the process can be completely reversed, oxidizing Co back to Co_3O_4. The amount of Co and, thus, the induced ferromagnetism scales with time and the applied bias. Part of the induced ferromagnetism is permanent, but can be fully erased by applying positive voltages. The effect is self-sustained in the sense that no external oxygen acceptor/donor layers are required to obtain the desired effects. The presence of defects, such as oxygen and cobalt vacancies and grain boundaries (as evidenced by electron microscopy and positron annihilation spectroscopy), promote ion migration at room temperature, in absence of heat assistance, contrary to most previous works from the literature. Magneto-ionic effects have been also observed in electrolyte-gated nanoporous cobalt-ferrite[4] and Fe-oxide[5] films prepared by evaporation-induced self assembly combined with dip coating. By applying a negative voltage, cobalt ferrite becomes partially reduced, leading to an increase in magnetic moment at saturation of 15% and reduction in coercivity between 5-28%, depending on the voltage applied. These changes are mainly non-volatile but can be later reversed with a positive voltage to recover the initial properties. Similar studies, done on analogous films without the induced nanoporosity, reveal that the effects were much smaller, underscoring the importance of nanoporosity in our system. In the case of nanoporous Fe-oxide films, a maximum increase in magnetic moment at saturation by a factor of 13 and a noticeable (two-fold) increase of coercivity (after applying –50 V) were observed. Raman and X-ray photoelectron spectroscopy experiments again revealed the key role played by controlled oxygen ion migration in these effects[5]. All these results could have an imminent and strong economic impact in a wide range of technological fields, such as energy-efficient spintronic devices, magnetic sensors, magnetic actuators or magnetic memories.

[1] C. Navarro-Senent et al., *APL Materials* 7, 030701 (2019). [2] A. Molinari et al., *Adv. Mater.* 1806662 (2019). [3] A. Quintana et al., *ACS Nano* 12, 10291 (2018). [4] S. Robbennolt et al., submitted to *Sci. Rep.* (2019). [5] S. Robbennolt et al., submitted to *ACS Appl. Mater. Interfaces* (2019).

2:42

BA-03. Magneto-Ionic Control of Magnetism in Thin Ferromagnetic Films. *G. Beach*[1] *1. Department of Materials Science and Engineering, Massachusetts Institute of Technology, Cambridge, MA, United States*

Voltage control of magnetism has the potential to substantially reduce power consumption in spintronic devices, while offering new functionalities through field-effect operation. Magneto-electric coupling has usually been achieved using complex oxides such as ferroelectrics, piezoelectrics, or multiferroics. Here, I describe an alternative approach known as magneto-ionic switching [1,2], which relies on solid-state electrical gating of a mobile ionic species to modulate the properties of a thin ferromagnetic film. First, I will review our initial discoveries of voltage control of magnetism through solid-state electrochemical switching of the interfacial oxidation state [1-3] in thin metallic ferromagnets. In ultrathin ferromagnet/oxide bilayers, perpendicular magnetic anisotropy (PMA) arises from interfacial hybridization between the ferromagnetic 3d and oxygen 2p orbitals. By using GdOx as a gate oxide with high oxygen ion mobility, I show that O^{2-} can be reversibly displaced at a Co/GdOx interface with a small gate voltage, leading to unprecedented large, non-volatile changes to interfacial PMA by > 0.75 erg/cm^2 [3]. High-resolution cross-sectional transmission electron microscopy (TEM) and in-situ electron energy-loss spectroscopy (EELS) during bias application [2] directly reveals the reversible redox reaction taking place at the Co/GdO_x interface. By optimizing the device structure and geometry, I show that these effects can be achieved with switching times down to <100 microseconds [2], and can be integrated into devices [1,3] that can be gated locally to realize memory and logic functionalities. In the second part of the talk, I focus on our recent discovery [4] that magnetic anisotropy can be reversibly and nondestructively toggled at room temperature with a small gate voltage through H^+ pumping in all-solid-state heterostructures, eliminating the irreversibility and structural degradation that occurs in oxygen redox-based structures. I show that H_2O hydrolysis in ambient atmosphere catalyzed by a rare-earth oxide/noble metal interface can serve as a solid-state proton pump that enables nondestructive magnetic property gating with a modest voltage. We demonstrate reversible 90^o magnetization switching in a thin Co film at room temperature by either inserting H^+ at its interface with an oxide or loading hydrogen into an adjacent heavy metal layer. The mechanism permits both unipolar toggle switching and nonvolatile state retention, with no discernible irreversibility in magnetic properties of the ferromagnet after >2000 cycles. Moreover, since heavy metals like Pt and Pd that exhibit strong spin-orbit coupling are also well-known hydrogen storage materials that can be driven between a metal and metal-hydride phase, a host of spin-orbit induced phenomena at heavy-metal/ferromagnetic interfaces becomes accessible to voltage gating despite the fact that electric fields cannot be applied directly.

[1] U. Bauer, S. Emori, G. S. D. Beach, *Nature Nano.* 8, 411 (2013). [2] U. Bauer, L. Yao, A. J. Tan, P. Agrawal, S. Emori, H. L. Tuller, S. van Dijken, G. S. D. Beach, *Nature Mater.* 14, 174 (2015). [3] S. Emori, U. Bauer, S. Woo, G. S. D. Beach, *Appl. Phys. Lett.* 105, 222401 (2014). [4] A. J. Tan, M. Huang, C. O. Avci, F. Büttner, M. Mann, W. Hu, C. Mazzoli, S. Wilkins, H. L. Tuller, G. S. D. Beach, *Nature Mater.* 18, 35 (2019).

3:18

BA-04. Magneto-Ionic Control of Oxide Heterostructures beyond the Interfaces. P. Murray[2], D.A. Gilbert[3,4], A.J. Grutter[3], C.J. Jensen[1], A. Quintana[1], B.J. Kirby[3], D. Hernandez-Maldonado[5], M. Varela[5], Z.E. Brubaker[2,6], W. Liyanage[4], R.V. Chopdekar[2,7], V. Taufour[2], R.J. Zieve[2], J.R. Jeffries[6], E. Arenholz[7,8], Y. Takamura[2], J. Zhang[9], X. Zhang[9], J. Borchers[3] and *K. Liu*[1,2] *1. Georgetown University, Washington, DC, United States; 2. University of California, Davis, CA, United States; 3. National Institute of Standards and Technology, Gaithersburg, MD, United States; 4. University of Tennessee, Knoxville, TN, United States; 5. Universidad Complutense de Madrid, Madrid, Spain; 6. Lawrence Livermore National Laboratory, Livermore, CA, United States; 7. Lawrence Berkeley National Laboratory, Berkeley, CA, United States; 8. Cornell High Energy Synchrotron Source, Ithaca, NY, United States; 9. King Abdullah University of Science & Technology, Thuwal, Saudi Arabia*

Magneto-ionic approaches for modifying ion distributions in metal/oxide heterostructures offer exciting prospects to control material properties. Much of the progress so far has been limited to metal/oxide interfaces. Our recent studies show that such magneto-ionic effect, even though

initiated at metal/oxide interfaces, can extend deep into the rest of the oxide films and drastically tailor their physical properties, including antiferromagnetism [1-2], ferromagnetism [3,4] and superconductivity [5]. In studies of antiferromagnetic (AF) NiCoO, we have demonstrated a controllable positive exchange bias in GdFe/NiCoO due to redox-driven oxygen migration [1], and that the oxygen migration across the interface can be reversibly driven by an electric field [2]. More recently, we have observed an electrically enhanced exchange bias in Gd/NiCoO due to the magneto-ionic effect. A thin Gd capping layer deposited onto AF NiCoO initiates a solid-state redox reaction which reduces the oxide to ferromagnetic NiCo in a thin interfacial region. Upon field cooling, the hysteresis loop becomes exchange biased, demonstrating interfacial coupling between the NiCo and the remaining oxide. After electrically biasing the interface, driving O^{2-} ions towards the Gd layer, a ~15% enhancement of the exchange bias is observed, which can be reset by a subsequent field-cooling procedure (Fig.1). In studies of cuprates, we show a simple, scalable approach to tailor superconductivity in 100nm thick $YBa_2Cu_3O_{7-\delta}$ (YBCO) films via a chemically-driven ionic migration mechanism [5]. Using a thin Gd capping layer of up to 20 nm deposited onto 100 nm thick epitaxial YBCO films, oxygen is found to leach from deep within the YBCO. Progressive reduction of the superconducting transition is observed, with complete suppression possible for a sufficiently thick Gd layer (Fig. 2). These effects arise from the combined impact of redox-driven electron doping and modification of the YBCO microstructure due to oxygen migration and depletion. Our findings demonstrate an effective solid-state ionic approach to control a wide variety of magnetic functionalities, where the interface induced effect can go well into the quasi-bulk regime, opening up possibilities for electric gating. We are grateful to the support by the NSF (DMR-1610060, ECCS-1611424, DMR-1609855), nCORE SMART center (2018-NE-2861), DOE (DE-AC52-07NA27344 and DE-AC02-05CH11231), MINECO-FEDER (MAT2015-66888-C3-3-R and MAT2017-89599-R), and TALENTO program, Comunidad de Madrid.

[1]. D. A. Gilbert, et al, *Nat. Commun.,* 7, 11050 (2016). [2]. D. A. Gilbert, et al, *Nat. Commun.,* 7, 12264 (2016). [3]. A. J. Grutter, et al, *Appl. Phys. Lett.* 108, 082405 (2016). [4]. D. A. Gilbert, et al, *Phys. Rev. Mater.* 2, 104402 (2018). [5]. P. D. Murray, et al, submitted.

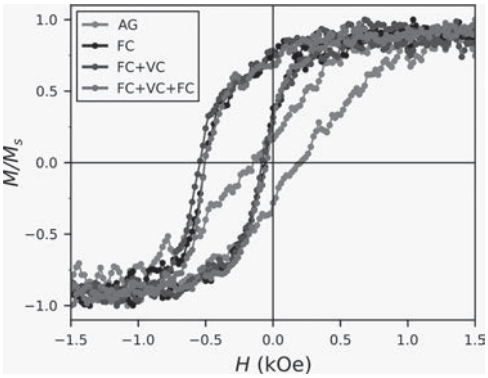


Fig. 1. Room temperature hysteresis loops of Gd/NiCoO in the as-grown (AG) state, after field cooling (FC), after voltage conditioning (FC+VC), and after a second field cooling procedure (FC+VC+FC).

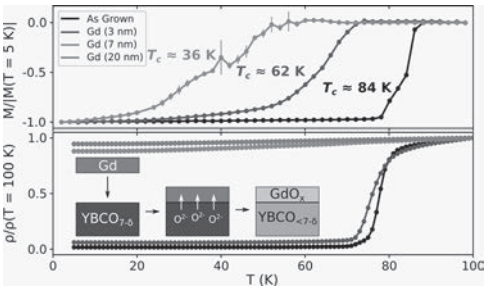


Fig. 2. Superconducting transition of YBCO films capped by Gd layers, measured by normalized magnetization (top) and resistivity (bottom), are suppressed by an interface-induced redox reaction.

3:54

BA-05. Ionically-controlled phase separation in cobaltite heterostructures. G. Rippy[1], L. Trinh[1], A.M. Kane[1], A. Ionin[1], M. Lee[1], R.V. Chopdekar[1], J. Christiansen-Salameh[1], D.A. Gilbert[2], A.J. Grutter[3], P. Murray[1], M. Holt[4], Z. Cai[4], K. Liu[5], Y. Takamura[1] and *R. Kukreja*[1]
1. University of California Davis, Davis, CA, United States; 2. University of Tennessee, Knoxville, TN, United States; 3. NIST, Gaithersburg, MD, United States; 4. Argonne National Laboratory, Lemont, IL, United States; 5. Georgetown University, Washington, DC, United States

Complex oxide heterostructures provide access to emergent functional and structural phases which are not present in the bulk constituent materials. Controlling ionic distribution and stoichiometry in complex oxide heterostructures has been utilized to significantly alter and tune the electronic, magnetic, and structural properties. Recently, deposition of a strong oxygen getter on top of an oxide thin film has emerged as a novel way to tailor oxygen stoichiometry and nanoscale functional properties [1-4]. However, the role played by nanoscale morphology, i.e. phase separation and defects in these oxide thin films and heterostructures remains largely unknown. In this talk, I will focus on Gd/$La_{0.67}Sr_{0.33}CoO_3$ (LSCO) heterostructures due to their high oxygen ion conductivity, as well as coupled magnetic and electronic properties of LSCO, which are strongly dependent on the oxygen stoichiometry. This combination of properties enable the ionic control of the functional properties of LSCO thin films through the presence of oxygen getter layers such as Gd. We utilize x-ray nanodiffraction to directly image the nanoscale morphology of LSCO thin films as they are progressively transformed from the equilibrium perovskite phase to the metastable brownmillerite (BM) phase with increasing Gd thickness. Our studies show the coexistence of perovskite and BM phases with a critical oxygen vacancy concentration threshold which leads to the formation of extended BM filaments. Strain maps reveal that the perovskite phase changes from compressive to tensile strain on opposite sides of a BM filament. Our studies provide an unprecedented nanoscale survey of the phase separation in the cobaltites and shed light on the formation of the metastable BM phase

1. Ferguson, J.D., et al., *Epitaxial oxygen getter for a brownmillerite phase transformation in manganite films.* Adv Mater, 2011. 23(10): p. 1226-30. 2. Gilbert, D.A., et al., *Ionic Tuning of Cobaltites at the Nanoscale.* Physical Review Materials, 2018. 2(10): p. 104402. 3. Grutter, A.J., et al., *Reversible control of magnetism in $La_{0.67}Sr_{0.33}MnO_3$ through chemically-induced oxygen migration.* Appl. Phys. Lett., 2016. 108: p. 082405. 4. Gilbert, D.A., et al., *Controllable positive exchange bias via redox-driven oxygen migration.* Nat Commun, 2016. 7: p. 11050.

Session BB
ANTIFERROMAGNETIC SWITCHING
Roman Khymyn, Chair
University of Gothenburg, Gothenburg, Sweden

CONTRIBUTED PAPERS

1:30

BB-01. Current-induced switching of the Néel vector in antiferromagnetic insulators/heavy metal bilayers. *L. Baldrati*[1], O. Gomonay[1], A. Ross[1,2], M. Filianina[1,2], R. Lebrun[1], R. Ramos[6], C. Leveille[1], T.R. Forrest[3], F. Maccherozzi[3], F. Kronast[4], S. Valencia[4], J. Sinova[1,2], E. Saitoh[5,6] and M. Kläui[1,7] *1. Institute of Physics, Johannes Gutenberg University Mainz, Mainz, Germany; 2. Graduate School of Excellence Materials Science in Mainz, Mainz, Germany; 3. Diamond Light Source, Didcot, United Kingdom; 4. Helmholtz-Zentrum Berlin fur Materialien und Energie, Berlin, Germany; 5. Department of Applied Physics, The University of Tokyo, Tokyo, Japan; 6. Advanced Institute for Materials Research, Tohoku University, Sendai, Japan; 7. Center for Quantum Spintronics, NTNU, Trondheim, Norway*

Antiferromagnets have potential to be the next building blocks of spintronic devices, thanks to the resonance frequencies in the THz regime, the absence of stray magnetic fields and the resulting resilience against external magnetic fields. These particular properties might enable ultrafast operation combined with high packing density, while spin transport in this class of materials is of interest for spin-logic based devices and was recently demonstrated to be possible over distances of 40 μm. [1] We have previously probed the spin transport properties of thermal magnons in crystalline epitaxial NiO(001) thin films [2], and found that the electrical reading of the magnetic moments is possible via spin Hall magnetoresistance (SMR) [3]. Here we show that one can electrically switch the orientation of the antiferromagnetic Néel vector via current pulses in the same system, without any ferromagnetic element. The switching of the antiferromagnetic moments is probed electrically (Fig. 1) and by direct imaging via x-ray magnetic linear dichroism – photo-emitted electron microscopy (Fig. 2). Both non-deterministic switching below the current threshold and deterministic switching above the current threshold are observed. We explain our results with a theoretical model involving spin torques acting directly on the domain walls and a ponder-omotive force that drives the antiferromagnetic domain walls. Resistance changes not related to the magnetic order are also induced by high density current pulses, as seen in a control sample with Pt only, which have to be considered to correlate the measured transverse resistance to the orienta-tion of the Néel vector. This writing method exploiting spin torques acting on antiferromagnetic materials can be used to realize antiferromagnetic memory elements with Hall cross shape, where combined electrical reading and writing operations are possible. [4,5] See also Ref. [6] (under revision).

[1] R. Lebrun, A. Ross, S. A. Bender et al., Nature Vol. 561, pp. 222 (2018). [2] L. Baldrati, C. Schneider, T. Niizeki et al., Phys. Rev. B Vol. 98, pp. 014409 (2018). [3] L. Baldrati, A. Ross, T. Niizeki et al., Phys. Rev. B Vol. 98, pp. 024422 (2018). [4] T. Moriyama, K. Oda, and T. Ono, Sci. Rep. Vol. 8, pp. 14167 (2018). [5] X. Z. Chen, R. Zarzuela, J. Zhang et al., Phys. Rev. Lett. Vol. 120, pp. 207204 (2018). [6] L. Baldrati, O. Gomonay, A. Ross et al., arXiv:1810.11326 (2018).

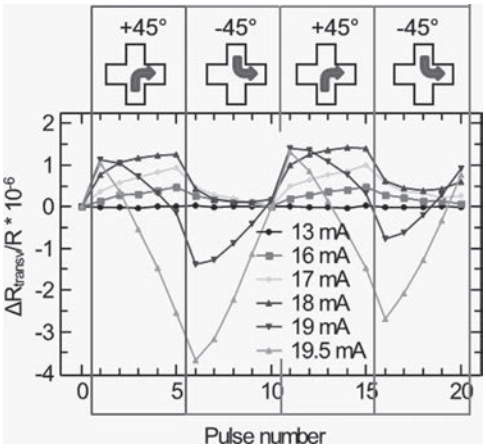


Fig.1: Variation of the transverse resistance after 1 ms long pulses of different current.

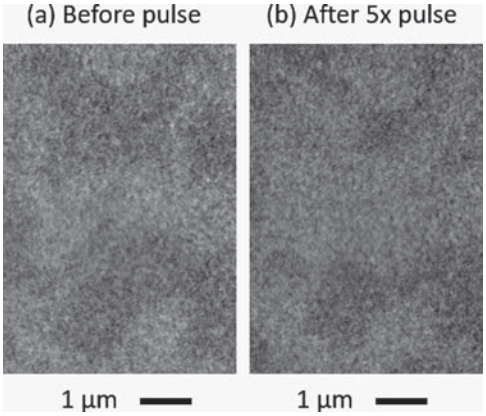


Fig.2: (a) Image of the antiferromagnetic domains before the application of a train of 5 pulses. (b) Image of the antiferromagnetic domains after the application of a train of 5 pulses above threshold.

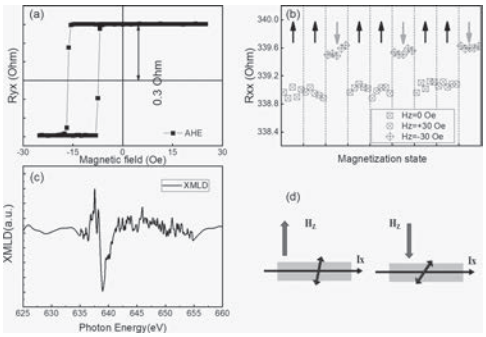
1:42

BB-02. Néel order variation in IrMn/CoFeB bilayer indicated by combined electrical and spectroscopic approach. *Y. Huang*[1], C. Yang[2], H. Wu[3], X. Che[3], K. Wang[3], C. Lai[2] and Y. Tseng[1] *1. National Chiao Tung University, Hsin-Chu, Taiwan; 2. National Tsing Hua University, Hsin-Chu, Taiwan; 3. University of California, Los Angles, Los Angles, CA, United States*

Perpendicular magnetization exchange-biased via the interfacial coupling with an adjacent antiferromagnet (AFM) serves as a key to realize the external field-free spin-orbit torque (SOT) switching. Currently, some AFM-based SOT devices have been reported that the AFM order would be modified through the spintronic effect [1][2][3]. This work investigates the

variation of AFM order in terms of anisotropic magneto-resistance effect (AMR) and x-ray linear magnetic dichroism (XMLD) in a Ta(2)/IrMn(5)/CoFeB(1.2)/MgO(2)/Ta(2) Hall bar device, where the thickness is in nanometer. The AHE measurement shows clear perpendicular Hex as Fig. 1(a). By varying the perpendicular magnetic field (Hz), we found a significant change on the longitudinal resistance (Rxx) of the Hall bar (Fig. 1(b)), where the low/high Rxx state was responsible for the Hz of +30 Oe/-30 Oe, respectively. This phenomenon is absent in the AFM-free device, suggesting the significant AMR effect arising from the tailorable AFM order upon varying Hz. To get a deeper insight into the AFM order, we perform the XMLD at Mn $L_{2,3}$ edge with a fixed linearly polarized X-ray and varied Hz (absorption difference, μ_{+Hz}-μ_{-Hz}). A clear XMLD feature is observed at Mn L_3 edge, suggesting the AFM order is capable of rotating with different Hz. The combined AMR and XMLD information reconstruct spin structure at the IrMn/CoFeB interface, which could be magnetically manipulated for the advanced AFM-based spintronic applications.

[1] P.-H. Lin, B.-Y. Yang, M.-H. Tsai, P.-C. Chen, K.-F. Huang, H.-H. Lin, and C.-H. Lai, Nature Materials 18, 335 (2019). [2] Y. Wang, C. Song, G. Wang, J. Miao, F. Zeng, and F. Pan, Advanced Functional Materials 24, 6806 (2014). [3] X. Marti, I. Fina, C. Frontera, J. Liu, P. Wadley, Q. He, R.J. Paull, J.D. Clarkson, J. Kudrnovský, I. Turek, J. Kuneš, D. Yi, J.-H. Chu, C.T. Nelson, L. You, E. Arenholz, S. Salahuddin, J. Fontcuberta, T. Jungwirth, and R. Ramesh, Nature Materials 13, 367 (2014).



(a) Hysteresis curve of IrMn/CoFeB with Hex of ~13 Oe acquired by anomalous Hall effect. (b) Longitudinal resistance (Rxx) of the device acquired by different magnetization states. Arrows in (b) stand for the magnetization state corresponding to the varied magnetic field. (c) XMLD spectrum at Mn L_3 edge obtained from the difference between the X-ray absorption spectra with Hz of 30 and -30 Oe. (d) Schemes to show the Néel order variation in IrMn/CoFeB bilayer upon applying a Hz upward and downward.

1:54

BB-03. Reliable Electrical Switching of Tri-State Antiferromagnetic Néel Order in *a*-Fe_2O_3 Epitaxial Films. *Y. Cheng*[1], S. Yu[1], M. Zhu[2], J. Hwang[2] and F. Yang[1] *1. Department of Physics, The Ohio State University, Columbus, OH, United States; 2. Department of Materials Science and Engineering, The Ohio State University, Columbus, OH, United States*

The ability to manipulate antiferromagnetic (AF) moments is a key requirement for the emerging field of antiferromagnetic spintronics. Electrical switching of bi-state AF moments has been demonstrated in metallic AFs, CuMnAs and Mn_2Au [1-4]. Recently, current-induced "saw-tooth" shaped Hall resistance was reported in Pt/NiO bilayers [5-8], while its mechanism is under debate. Here, we report the first demonstration of convincing, non-decaying, step-like electrical switching of tri-state Néel order in Pt/*a*-Fe_2O_3 bilayers (See Fig.1). Our experimental data shows the switching behavior of *a*-Fe_2O_3 Néel order among three stable states, which can be detected by the change of Hall resistance ΔR_{xy} through spin Hall anomalous Hall effect (SH-AHE). We also show that the observed "saw-tooth" Hall resistance is due to an artifact of Pt, not AF switching, while the signature of AF switching is step-like Hall signals (See Fig.2). Together with the Monte-Carlo simulations, we reveal the clear mechanism of AF Néel order switching and explain why only the first current pulse switches the Néel order. This demonstration of electrical control of magnetic moments in AF insulator (AFI) films will greatly expand the scope of AF spintronics by leveraging the large family of AFIs.

1. Wadley, P., et al., "Electrical switching of an antiferromagnet," *Science* 351, 587 (2016). 2. Meinert, M., Graulich, D. and Matalla-Wagner, T., "Electrical Switching of Antiferromagnetic Mn_2Au and the Role of Thermal Activation," *Phys. Rev. Appl.* 9, 064040 (2018). 3. Zhou, X. F., et al., "Strong Orientation-Dependent Spin-Orbit Torque in Thin Films of the Antiferromagnet Mn_2Au," *Phys. Rev. Appl.* 9, 054028 (2018). 4. Bodnar, S. Y., et al., "Writing and reading antiferromagnetic Mn_2Au by Néel spin-orbit torques and large anisotropic magnetoresistance," *Nat. Commun.* 9, 348 (2018). 5. Chen, X. Z., et al., "Antidamping-Torque-Induced Switching in Biaxial Antiferromagnetic Insulators," *Phys. Rev. Lett.* 120, 207204 (2018). 6. Gray, I., et al., "Spin Seebeck imaging of spin-torque switching in antiferromagnetic Pt/NiO heterostructures," *arXiv:1810.03997* (2018). 7. Moriyama, T., Oda, K., Ohkochi, T., Kimata, M. and Ono, T., "Spin torque control of antiferromagnetic moments in NiO," *Sci Rep* 8, 14167 (2018). 8. Baldrati, L., et al., "Mechanism of Néel order switching in antiferromagnetic thin films revealed by magnetotransport and direct imaging," *arXiv:1810.11326* (2018).

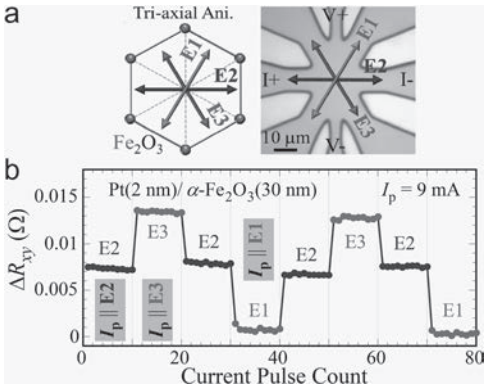


Figure 1 a, (Left). The *ab*-plane of α-Fe_2O_3 lattice with three in-plane easy axes labeled as E1, E2 and E3, where the double arrows represent the AF spins. (Right) Optical microscopy image of an eight-leg Hall cross of a Pt(2 nm)/α-Fe_2O_3(30nm) bilayer. b, A sequential pulse current of I_p = 9 mA is applied along one of the three easy axes (10 pulses for each segment) at 300 K and Hall resistance is detected by applying a 0.1 mA sensing current along E2.

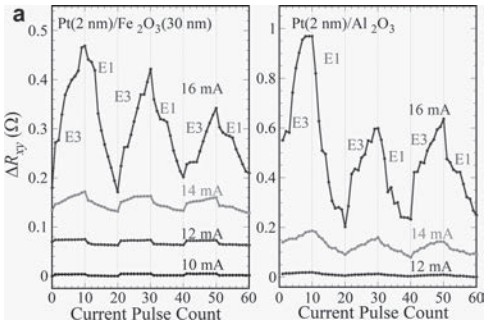


Figure 2. a, (Left). Evolution of ΔR_{xy} when the pulse current is switched between E3 and E1 (10 pulses each) for a Pt(2 nm)/α-Fe_2O_3(30 nm) bilayer. (Right) Same measurement for a 2 nm Pt control sample grown directly on Al_2O_3(001).

2:06

BB-04. Anisotropic Magnetoresistance and Nontrivial Spin Magnetoresistance in Pt/α-Fe_2O_3 Bilayers: Evidence for Magnetic Proximity Effect. *S. Yu*[1], Y. Cheng[1], A.S. Ahmed[1], M. Zhu[1], J. Hwang[1] and F. Yang[1] *1. The Ohio State University, Columbus, OH, United States*

Recently antiferromagnetic insulators(AFM) play an import role in spintronic research including the spin superfluid [1] and long distance spin transport [2]. However, magnetic proximity effect (MPE) has not been conclusively observed in antiferromagnet based systems. In this work, we observed anomalous Hall effect and anisotropic magnetoresistance in angular dependent magnetoresistance (ADMR) measurements in Pt on antiferromagnetic (AF) α-Fe2O3(0001) epitaxial thin films at 10 K, which provide evidence for the MPE[3]. The Néel order of α-Fe2O3 and the induced magnetization in Pt show a unique ADMR compared with all other FM and AF systems. In γ-scan of ADMR at 10 K, a sharp peak is observed when H is perpendicular to film (γ = 0° and 180°) at H = 1-14 T and the peak becomes narrower as H increases while the peak magnitude remains essentially the same. A macrospin response model is established and can explain the AF spin configuration and all main ADMR features in the Pt/α-Fe2O3 bilayers. This work was supported primarily the U.S. Department of Energy (DOE) under Grant No. DE-SC0001304 and partially supported by the Center for Emergent Materials, an NSF MRSEC, under Grant No. DMR-1420451

[1] Yuan, Wei, et al. "Experimental signatures of spin superfluid ground state in canted antiferromagnet Cr2O3 via nonlocal spin transport." *Science advances* 4.4 (2018): eaat1098. [2] Lebrun, R., et al. "Tunable long-distance spin transport in a crystalline antiferromagnetic iron oxide." *Nature* 561.7722 (2018): 222. [3] Cheng, Yang, et al. "Anisotropic Magnetoresistance and Nontrivial Spin Magnetoresistance in Pt/ α -Fe2O3 Bilayers: Evidence for Antiferromagnetic Proximity Effect." *arXiv preprint arXiv:1906.04395* (2019).

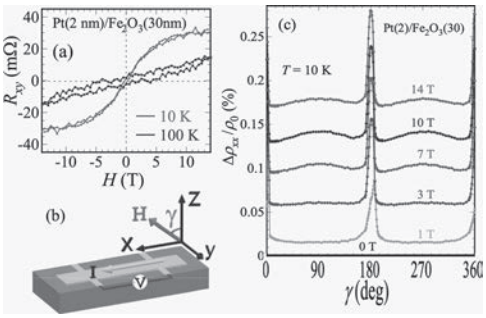


Fig.1 (a)Hall resistance for a Pt(2 nm)/α-Fe_2O_3(30 nm) bilayer at 10 and 100 K. (b)Schematics of γ (*zx*-plane) angular dependence measurements. (c)γ-scans of a Pt(2 nm)/α-Fe_2O_3(30 nm) sample at 10 K an various magnetic fields.

2:18

BB-05. Spin-Torque Induced Electrical Switching of Antiferromagnetic MnN. *M. Dunz*[1], T. Matalla-Wagner[1] and M. Meinert[1] *1. Center for Spinelectronic Materials and Devices, Department of Physics, Bielefeld University, Bielefeld, Germany*

Recently, it was shown that switching of magnetic moments via spin-orbit torque is possible in epitaxial films of antiferromagnetic NiO [1]. A spin-polarized current is generated in adjacent Pt layers and exerts a torque on the moments in the antiferromagnetic film. Here, we report on spin-torque induced switching of magnetic moments in polycrystalline films of antiferromagnetic MnN [2]. Ta (6 nm) / MnN (t_{MnN}) / Pt (4 nm) layer stacks are prepared via (reactive) sputter deposition at room temperature and patterned to star-shaped structures [3]. In Fig. 1, a typical measurement cycle is shown. First, current pulse bursts are sent through one of the pulse lines (red area) and the planar Hall resistance is measured after every burst. Afterwards, the antiferromagnet is left to relax for 10 minutes (grey area). Then, the same number of current bursts is sent through the orthogonal pulse line (blue area), leading to a reversion of the Hall resistance, again followed by relaxation. As can be seen in Fig. 1, the process is fully reversible. To investigate temperature and thickness dependence of the switching, samples with t_{MnN} = 6 nm and t_{MnN} = 9 nm are measured over a broad temperature range. Fig. 2 shows the switching efficiency of the first burst R_e [3] in dependence on the sample temperature T_S for both thicknesses. Higher T_S are needed to reach a certain efficiency in the thicker film as a result of increased anisotropy energy. Overall, R_e clearly increases with increasing T_S in both samples. The relaxation time constant decreases with increasing T_S and the switching efficiency is increased with increased current density. This is in line with the thermal activation model developed for Néel-order spin-orbit torque switching in CuMnAs [3] and Mn_2Au [4].

[1] T. Moriyama, K. Oda, T. Ohkochi, M. Kimata, and T. Ono, Sci. Rep., 8, 14167 (2018) [2] M. Meinert, B. Bueker, D. Graulich, and M. Dunz, Phys. Rev. B, 92, 144408 (2015) [3] T. Matalla-Wagner, M. Rath, D. Graulich, J. Schmalhorst, G. Reiss, and M. Meinert, arXiv: 1903.12387 [4] M. Meinert, D. Graulich, and T. Matalla-Wagner, Phys. Rev. Applied, 9, 064040 (2018)

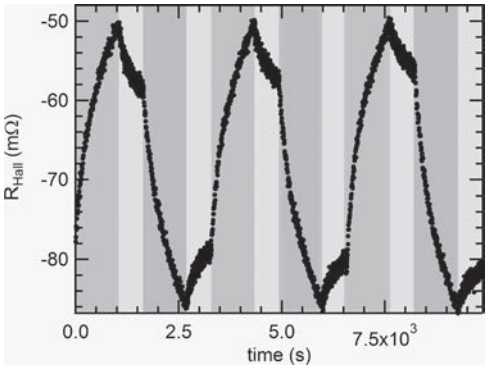


Fig. 1: Planar Hall resistance measurement during a typical pulse and relaxation cycle measured on a sample with t_{MnN} = 6 nm at 230 K with a current density of J = 5×10^{11} A/m^2.

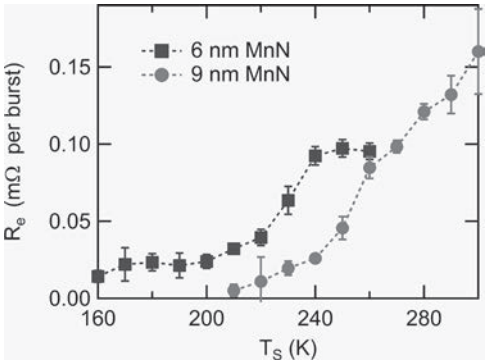


Fig. 2: Switching efficiency R_e in dependence on the sample temperature T_S measured for different t_{MnN} with a current density of J = 5×10^{11} A/m^2.

2:30

BB-06. Terahertz detector based on an antiferromagnetic spin-Hall oscillator. *V. Puliafito*[1], I. Medlej[2], I. Lisenkov[3], M. Carpentieri[4], B. Azzerboni[1], A.N. Slavin[5] and G. Finocchio[1] *1. University of Messina, Messina, Italy; 2. Lebanese University, Hadeth Beirut, Lebanon; 3. Winchester Technologies LLC, Boston, MA, United States; 4. Politecnico di Bari, Bari, Italy; 5. Oakland University, Rochester, MI, United States*

Spintronic devices based on antiferromagnetic materials work in the THz-frequency range, and are attracting a lot of attention from the scientific community [1-2]. In this field of research, a full micromagnetic framework for studying magnetization dynamics of antiferromagnets (AFMs), in particular under the influence of spin-orbit-torques, has been developed and compared successfully with analytical models [3]. The magnetization dynamics of current-driven AFMs is described as dynamics of two exchange-coupled sub-lattices by solving two Landau-Lifshitz-Gilbert equations including a torque term due to the spin-Hall effect. The exchange coupling of the sub-lattices includes the inhomogeneous intra-lattice, the homogeneous inter-lattice, and the inhomogeneous inter-lattice contributions. Within this micromagnetic framework, we perfomed modeling of an AFM spin-Hall oscillator [3,4]. In our numerical study, the oscillator consists of an AFM layer (40x40x5 nm^3) having a uniaxial anisotropy and coupled to a layer of a heavy metal. The AFM dynamics is described as precession of two coupled sub-lattice magnetizations m_1 and m_2 around the polarization p of the spin-Hall current, and may show a hysteretic behavior. The frequency of the generated signal shows a blue-shift with the increase of the applied current, from hundreds of GHz up to several THz, as expected [3]. In particular, the AFM oscillator demonstrates an interesting behavior in the sub-threshold regime. We studied the AFM resonance frequency (AFMR) of the oscillator, which defines the spectral "gap" of the device, as a function of different parameters. The most important result is that the AFMR frequency decreases with the increase of the direct electric current applied to the heavy metal, and converges to the self-oscillation frequency at and above the threshold current. This result, which agrees with a previous analytical model, demonstrates the possibility to use the sub-threshold oscillator as a current-tunable signal detector of a resonance type in the THz frequency range.

[1] Jungwirth et al. Nat. Phys. 14 200 2018. [2] Gomonay et al. Phys. Status Solidi RRL 11 1700022 2017. [3] Puliafito et al. Phys. Rev. B 99 024405 2019. [4] Khymyn et al. Sci. Rep. 7 43705 2017.

2:42

BB-07. Magnetoresitance Studies of the Tetragonal CuMnAs Single Crystal. J. Volny[1], K. Vyborny[2], D. Wagenknecht[1], E. Duverger-Nédellec[1], R. Colman[1] and *K. Uhlirova*[1] *1. Department of Condensed Matter Physics, Charles University, Prague, Czechia; 2. Department of Spintronics and Nanoelectronics, Institute of Physics AS CR, Prague, Czechia*

Emerging field of antiferromagnetic (AFM) spintronics is drawing a lot of attention due to promising applications in storage devices [1]. One of the promising materials is an AFM metal CuMnAs. Its transport properties have been mostly studied on thin films. So far the main focus has been on spin-orbit torque, allowing for a selective manipulation of magnetic moments in the AFM [2]. This amounts to an effective writing of information. As a method for readout, anisotropic magnetoresistance (AMR) is being used (although little explored), giving different readout signals for two orthogonal orientation of magnetic moments. In this work, we explore resistivity and AMR in a geometry which overcomes the limitations of thin films. To this end, we have prepared a transport device out of a bulk single crystal grain (small) of tetragonal CuMnAs [3] using Focused Ion Beam micromachining. This technique, allowing for precise control over sample geometry, lets us measure resisitivity along arbitrary crystallographic direction. For the first time, we report temperature dependence of both in-plane and out-of-plane resistivity, uncovering large structural transport anisotropy between both principal crystallographic axes. This is further discussed in context of *ab initio* calculations assuming various types of impurities in our samples. The AMR measurement in magnetic field B with rotation of the sample around c-axis (out-of-plane direction) shows only moderate response (~0.1 %) to B with saturation at around 6 T. In the first approximation, we could describe the dependence of the change of resistivity on the direction of B as $\Delta\rho(\theta) \sim \cos(2\theta)$ where θ is the angle between a-axis and B. However, we observe a tilt of the peaks towards higher θ for temperatures above 300 K and to the lower θ for temperatures under 300 K. This behaviour is discussed by means of the Stoner–Wohlfarth model for AFM suggesting an uniaxial magnetic anisotropy not pointing along any principal crystallographic axis. In addition, the calculated AMR values tend to be larger than experimental data, suggesting multidomain character of the sample.

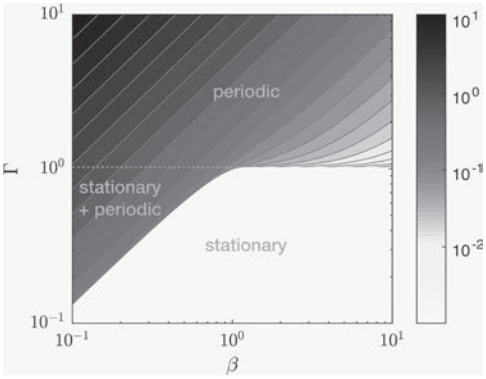
1. T. Jungwirth, X. Marti, P. Wadley, J. Wunderlich, Nat. Nanotechnol. 11, 231 (2016). 2. P. Wadley, B. Howells1, J. Zelezný, et al., Science 351, 587 (2016). 3. K. Uhlírová, E. Duverger-Nédellec, R. H. Colman, et al., J. Alloys Comp 771, 680 (2019)

2:54

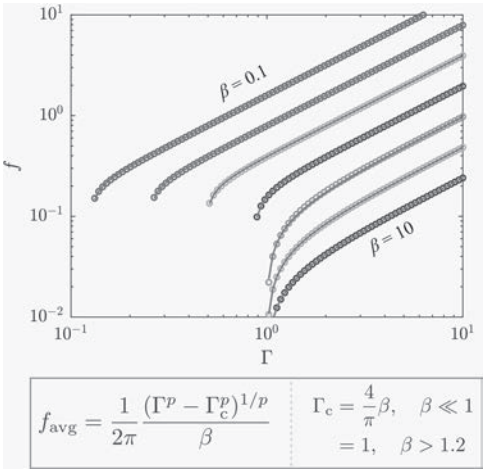
BB-08. Theory of Spin-Current-Induced Auto-Oscillations in a Biaxial Antiferromagnet. *A. Parthasarathy*[1], E. Cogulu[2], A.D. Kent[2] and S. Rakheja[1] *1. Department of Electrical and Computer Engineering, New York University, Brooklyn, NY, United States; 2. Center for Quantum Phenomena, Department of Physics, New York University, New York, NY, United States*

In antiferromagnetic materials with biaxial crystal symmetry, injection of a spin current polarized perpendicular to the Néel order can excite steady-state precession [1]. This phenomenon may be used to generate either a coherent signal [2] or a Dirac-delta-like impulses [3] at terahertz frequencies. Recent works have established that in the macrospin limit the spin-current dynamics of the Néel vector is equivalent to a classical damped pendulum in gravity forced with a constant torque, and have studied the problem numerically [1,3]. However, a general formulation of the problem and its analytic solutions are lacking. Based on the dynamics of a damped-driven pendulum [4] and its nonlinear dynamics, we explore the two-dimensional parameter space of spin-torque and Gilbert damping to determine the regimes of periodic and stationary solutions (see Fig. 1), and find the expression for the homoclinic bifurcation. Transient analytic solutions for the frequency of oscillation are determined in the limits of small and large damping; in the general case, we find a scaling function for the steady-state frequency (see Fig. 2). The results are analyzed in context of material properties of biaxial antiferromagnets such as NiO, CuMnAs, MnPt. We also propose experiments that can detect spin oscillations in antiferromagnets, such as by slowing down the dynamics by exploiting the hysteretic behavior: that sustaining the oscillations requires a lower current than initiating it. *This work was supported in part by the Semiconductor Research Corporation (SRC) and the National Science Foundation (NSF) through ECCS 1740136. S. Rakheja also acknowledges the funding support from the MRSEC Program of the NSF under Award Number DMR-1420073.*

[1] R. Cheng *et al*. "Ultrafast switching of antiferromagnets via spin-transfer torque," Phys. Rev. B 91, 064423 (2015). [2] R. Khymyn *et al*. "Antiferromagnetic THz-frequency josephson-like oscillator driven by spin current," Scientific reports 7, 43705 (2017). [3] R. Khymyn *et al*. "Ultra-fast artificial neuron: generation of picosecond-duration spikes in a current-driven antiferromagnetic auto-oscillator," Scientific Reports 8, 15727 (2018). [4] P. Coullet *et al*. "A damped pendulum forced with a constant torque," American Journal of Physics 73, 1122 (2005).



Heatmap of steady-state frequency (in units of resonance frequency) of the damped-driven pendulum equation in the parameter space of dimensionless torque Γ and damping β.



Scaling relationship for the average steady-state frequency.

3:06

BB-09. Electrical detection of Néel vector of a uniaxial antiferromagnetic insulator. *J. Li*[1], W. Yuan[1], M. Lohmann[1] and J. Shi[1] *1. Department of Physics and Astronomy, University of California, Riverside, Riverside, CA, United States*

Antiferromagnetic (AFM) materials may find novel spintronic applications thanks to their numerous interesting attributes: robustness against magnetic field perturbations, absence of stray fields, and ultrafast spin dynamics (1). However, one of the challenges in antiferromagnetic spintronics is that it is difficult to control and probe AFM spin order experimentally due to the lack of net magnetic moment. Here we report an electrical detection of the Néel order of antiferromagnetic insulator Cr_2O_3 (both crystal and epitaxial film) through magnetoresistance (MR) of normal metal (NM) layer deposited on top of Cr_2O_3. The Cr_2O_3 thin films are grown on Al_2O_3(11-20) substrate by pulsed laser deposition (PLD) and are characterized by reflection high-energy electron diffraction (RHEED), X-ray diffraction (XRD), and atomic force microscopy. We control the AFM Néel order of Cr_2O_3 by sweeping the external magnetic field at different orientations, and MR changes are observed during the spin-flop (SF) transition and continuous rotation of the Néel order. The MR variation as a function of magnetic field strength can be well understood by relative orientations between the AFM Néel order and current directions. We find that the MR is very sensitive to the interface properties. The MR of Pt changes sign after we etch the surface of Cr_2O_3 with argon-beam prior to the deposition of the Pt layer. And more interestingly, SF-induced MR jumps are not only observed in heavy metals such as Pt, Pd, and Ta, but also in light metal such as Cu on the etched Cr_2O_3. Our results suggest the interfacial spin-dependent scattering of conduction electrons from the AFM Néel order or the uncompensated interfacial magnetic moment plays an essential role in determining MR of AFM/NM. Furthermore, we demonstrate that the SF-induced MR jump can be used to track SF-field up to 300 K, which provides important information about exchange interaction and uniaxial anisotropy in Cr_2O_3. This work was supported as part of the SHINES, an Energy Frontier Research Center funded by the US Department of Energy, Office of Science, Basic Energy Sciences under Award No. SC0012670.

1. O. Gomonay *et al.*, Nature Physics 14, 213 (2018).

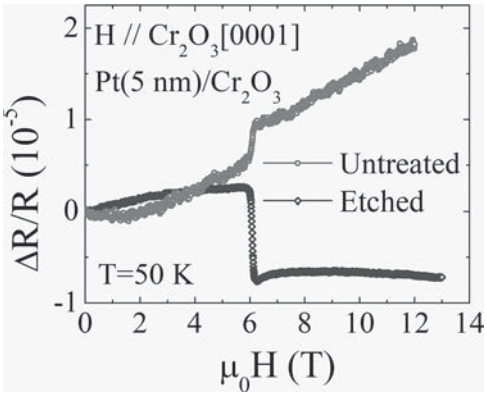


Fig. 1. Magnetoresistance of 5 nm Pt film on untreated and etched Cr_2O_3(10-10) crystal.

3:18

BB-10. Imaging Antiferromagnetic Domains in Nickel-oxide Thin Films by Magneto-optical Voigt Effect. *J. Xu*[1], C. Zhou[1], M. Jia[1], D. Shi[1], C. Liu[1], H. Chen[1], G. Chen[2], G. Zhang[3], Y. Liang[3], J. Li[4], W. Zhang[5] and Y. Wu[1] *1. Fudan University, Shanghai, China; 2. University of California, Davis, Davis, CA, United States; 3. Dalian Institute of Chemical Physics, Chinese Academy of Sciences, Dalian, China; 4. Shanghai Synchrotron Radiation Facility, Shanghai, China; 5. Oakland University, Rochester, MI, United States*

The emerging field of antiferromagnetic (AFM) spintronics is believed one of the most promising contenders for future energy-efficient, high-speed, robust information storage and processing [1-2]. However, the absence of a net magnetization in AFMs renders conventional magnetometry ineffective, which cast a great challenge in accessing their magnetic properties especially at the microscopic scale. To date, the photoemission electron microscopy (PEEM) based on X-ray magnetic linear dichroism effect (XMLD) [3] remains the most commonly adopted technique to study the AFM domains. Such a technique is not widely accessible and is difficult to be incorporated simultaneously with state-of-the-art magneto-transport measurements. In this contribution, we demonstrate the magneto-optical detection of antiferromagnetic domains in a collinear AFM thin film, i.e. NiO grown on MgO (001) substrate, utilizing the Voigt effect combined with a tabletop, magneto-optical microscopy technique. A large Voigt rotation up to 60 mdeg at room temperature can be observed for a 20-nm-thick NiO(001) film. By directly imaging the domain patterns, we are able to investigate the evolutions of domain configuration systematically under different thicknesses and temperatures. The XMLD-PEEM measurements confirm the AFM origin of the measured Voigt contrast. We elucidated on the surface spin-canting structure of NiO on MgO(001), and found that the AFM NiO spins are only partially tilted outward from the surface with a tilting angle of ~10°. As a tabletop technique, our approach to image the AFM domains utilizing the magneto-optic Voigt effect is considerably more accessible than user facility instruments such as XMLD-PEEM, and can also be made adaptable with

external magnetic fields or electric currents, which is extremely important in future experiments involving electric- and magnetic-field driven AFM dynamics and switching.

[1] T. Jungwirth, X. Marti, P. Wadley, and J. Wunderlich, *Nat. Nanotechnol.* 11, 231 (2016). [2] V. Baltz, A. Manchon, M. Tsoi, T. Moriyama, T. Ono, and Y. Tserkovnyak, *Rev. Mod. Phys.* 90, 015005 (2018). [3] J. Stöhr, A. Scholl, T. J. Regan, S. Anders, J. Lüning, M. R. Scheinfein, H. A. Padmore, and R. L. White, *Phys. Rev. Lett.* 83, 1862 (1999).

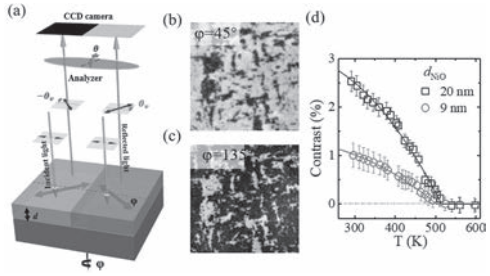


Fig. 1. (a) Schematics of magneto-optical microscopy measurement geometry. (b)-(c) The typical domain images of a 20 nm thick NiO film on MgO(100), obtained from the magneto-optical microscope at room temperature with φ=45° and 135°. (d) The Voigt contrasts as a function of temperature for 9 and 20 nm NiO films, respectively.

3:30

BB-11. Current-driven phase transition in a gradient-doped FeRh nanopillar: spin injection-triggered phase transformation and memristivity. R.C. Temple[1], J. Massey[1], T. Almeida[2], M. Rosamond[3], E. Linfield[3], K. Fallon[2], D. McGrouther[2], T. Moore[1], S. McVitie[2] and *C.H. Marrows[1] 1. School of Physics and Astronomy, University of Leeds, Leeds, United Kingdom; 2. School of Physics and Astronomy, University of Glasgow, Glasgow, United Kingdom; 3. School of Electronic and Electrical Engineering, University of Leeds, Leeds, United Kingdom*

FeRh has a first order antiferromagnetic (AF) to ferromagnetic (FM) transition at about 370 K in bulk. The transition temperature can be manipulated through magnetic field, strain, chemical doping and spin-polarised currents [1]. Due to this high versatility the material has been extensively investigated in recent years for its potential technological applications in heat-assisted magnetic recording [2], antiferromagnetic memory resistors [3] and electric field control of magnetic order [4]. We have recently shown that the transition is retained in islands patterned to few 100 nm dimensions [5] and that the use of a doping gradient can give a simple form of phase coexistence where the film separates into slabs with AF and FM order [6], separated by a planar phase boundary. We have fabricated few 100 nm diameter gradient doped devices through which electrical current can be driven vertically through the phase boundary (see Fig. 1). Since the AF phase has a substantially higher resistivity than the FM phase, the pillar resistance—comprising the series resistance of the two slabs—can be used as a proxy for the phase boundary position within the pillar. Driving current pulses (typically of 1 μs duration and ~10^{11} A/m^2 density) through the phase boundary results in a brief change in resistance due to Joule heating before the resistance relaxes to a new level that has shifted depending on the current flow direction (see Fig. 2). Trains of current pulses containing a few tens of mC of charge shift the resistance of the pillar by a few mΩ. The shift direction is consistent with the microscopic mechanism being spin injection from or into the FM phase slab that triggers the phase transition in a few nm wide region next to the phase boundary [7]. This represents memristive behavior, with potential application as artificial synapses in spintronic neuromorphic circuits.

[1] L. H. Lewis, C. H. Marrows, and S. Langridge, J. Phys. D: Appl. Phys. 49, 323002 (2016). [2] J.-U. Thiele, S. Maat, and E. E. Fullerton, Appl. Phys. Lett. 82, 2859 (2003). [3] X. Marti et al. Nat. Mater. 13, 367 (2014). [4] R. O. Cherifi et al. Nat. Mater. 13, 345 (2014). [5] R. C. Temple et al., Phys. Rev. Mater 2, 104406 (2018). [6] C. Le Graët et al. APL Mater. 3, 041802 (2015). [7] R. C. Temple et al., arXiv:1905.03573 [cond-mat.mtrl-sci].

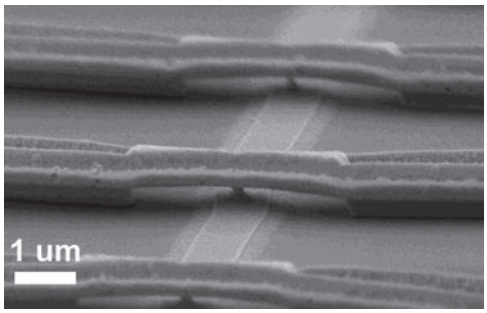


Figure 1: Scanning probe micrograph of 300 nm diameter gradient-doped FeRh nanopillar devices with flying bridge top contacts. The scale bar is 1 μm.

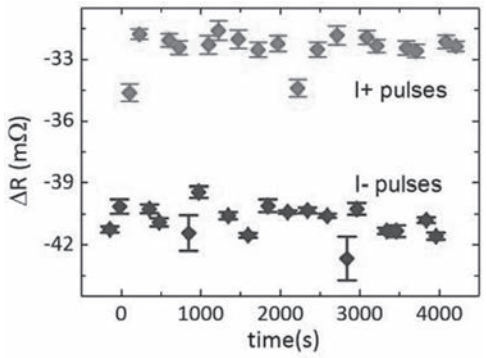


Figure 2: Change in nanopillar resistance after a train of 10^6 pulses of 1 μs duration and 30 mA amplitude. The sign of the shift is determined by the direction of current flow.

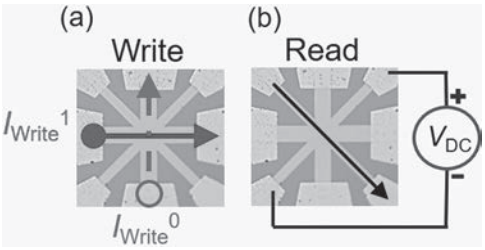
3:42

BB-12. Current-induced switching of antiferromagnet/non-magnet metallic structures. *S. DuttaGupta[1,2]*, A. Kurenkov[1,2], O. Tretiakov[3], G. Krishnaswamy[4], G. Sala[4], V. Krizakova[4], F. Maccherozzi[5], S.S. Dhesi[5], P. Gambardella[4], S. Fukami[2,1] and H. Ohno[2,1] *1. Center for Science and Innovation in Spintronics, Tohoku University, Sendai, Japan; 2. Research Institute of Electrical Communication, Tohoku University, Sendai, Japan; 3. School of Physics, University of New South Wales, Kensington, NSW, Australia; 4. Department of Materials, ETH Zurich, Zurich, Switzerland; 5. Diamond Light Source, Didcot, United Kingdom*

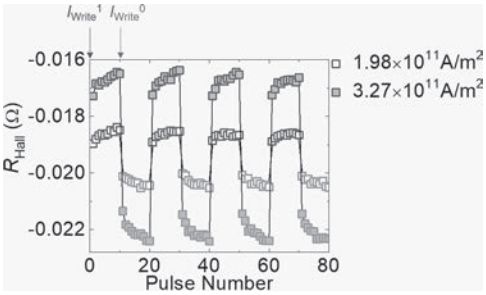
Utilization of antiferromagnets (AFMs) as functional components has opened new directions for next-generation low-power spintronic architectures [1-7]. A major roadblock concerns electrical recording of information in AFM devices without auxiliary ferromagnets. Previous investigations demonstrated the utilization of Néel spin-orbit torques (SOTs) [4,5] and/or interfacial SOTs in AFM-insulator/heavy metal (HM) [6,7] as a viable route for electrical manipulation. The realization of AFM devices using these materials is, however, limited by material choice and epitaxial structure constraints. Here, we demonstrate electrical writing in Mn-based polycrystalline metallic AFM/HM structures by spin-orbit torques (SOTs). The multilayer film with Si sub./buffer/PtMn(10)/Pt(5)/Ru(1) (AFM/HM, hereafter) (in nm) is grown by sputtering and patterned into star-shaped devices. Electrical writing is achieved by sourcing pulsed currents (I_{Write^1} and I_{Write^0}) along orthogonal directions while read-out was achieved by measuring transverse Hall resistance R_{Hall} (Fig. 1(a),(b)). Figure 2 shows the results of electrical writing for different current amplitudes. A combination of electrical measurements with X-ray magnetic imaging on identical structures shows

reorientation of antiferromagnetic Néel vector upon application of I_{Write}^{1} and/or I_{Write}^{0}. The present experimental results demonstrate the prospect of metallic AFMs for next generation antiferromagnetic spintronic architectures. A portion of this work was supported by JSPS KAKENHI 17H06511, 18KK0143, 19H00858, and Cooperative Research Projects of RIEC. O.A.T. acknowledges support by the Ministry of Science and Higher Education of the Russian Federation in the framework of Increase Competitiveness Program of NUST "MISiS" (No. K2-2019-006).

[1] T. Jungwirth, X. Marti, P. Wadley, Nature Nanotech. 11, 231 (2016). [2] S. Fukami, C. Zhang, S. DuttaGupta, Nature Mater. 15, 535 (2016). [3] V. Baltz, A. Manchon, M. Tsoi, Rev. Mod. Phys. 90, 015005 (2018). [4] P. Wadley, B. Howells, J. Zelezný, Science 351, 587 (2016). [5] S. Y. Bodnar, L. Šmejkal, I. Turek, Nature Commun. 9, 348 (2018). [6] T. Moriyama, K. Oda, T. Ohkochi, Sci. Rep. 8, 14167 (2018). [7] X. Z. Chen, R. Zarzuela, J. Zhang, Phys. Rev. Lett. 120, 207204 (2018).



Optical micrograph of device and schematic diagram of measurement. (a) writing scheme under application of I_{Write}^{1} and/or I_{Write}^{0}. (b) read-out achieved by measuring transverse voltage (V_{DC}) under application of read current.



Experimental results of electrical writing in AFM/HM for different J_{Pt}. J_{Pt} denotes the write current density in the HM.

3:54

BB-13. Tailorable Néel order via spin-orbit torque and the effect on field-free switching. *C. Yang*[1] and C. Lai[2] *1. Material Science and Engineering, National Tsing Hua University, Hsing Chu, Taiwan; 2. Material Science and Engineering, National Tsing Hua University, Hsing Chu, Taiwan*

As a modified structure of spin-orbit torque (SOT) device based on ferromagnet/heavy metal (FM/HM) bilayer, an antiferromagnet (AFM) adjacent to FM was currently regarded as a route toward to the application of field-free SOT switching due to the exchange bias (Hex) at FM/AFM interface (*1, 2*). In this study, we magnetically reconstruct the interface of Co/IrMn in a Pt/Co/IrMn Hall-cross device. In terms of Hex, anisotropic magneto-resistance, and X-ray linear dichroism (XMLD), a global Néel order modification driven by SOT effect has been found with a preferred orientation (anti)parallel to the electrical current we applied for SOT (Fig. 1(a)) and was tailorable while rotating the input current geometry (Fig. 1(b)). This modification on IrMn spin established an in-plane bias field of approximately 15 Oe at Co/IrMn interface, which enabled the partial Co switching being field-free. This nature was further investigated by means of engineering the interface of Co/IrMn with Ru dusting. The reduction of Hex in the Ru-dusted device showed great consistency with the reduction on the switchable component achieved by field-free manner. This work gives an insight into the manipulation of AFM state in HM/FM/AFM trilayer for field-free switching and advanced AFM-based spintronics.

1. Young-Wan Oh et al., Field-free switching of perpendicular magnetization through spin–orbit torque in antiferromagnet/ferromagnet/oxide structures. *Nature Nanotechnology* 11, 878 (2016). 2. A. van den Brink et al., Field-free magnetization reversal by spin-Hall effect and exchange bias. *Nature Communications* 7, 10854 (2016).

4:06

BB-14. Antiferromagnetic PtMn memory devices controlled by electric current. J. Shi[1], *V. Lopez*[2], F. Garesci[3], C. Wang[1], H. Almasi[1], M. Grayson[1], G. Finocchio[4] and P. Khalili Amiri[1] *1. Electrical Engineering and Computer Engineering, Northwestern University, Evanston, IL, United States; 2. Electrical Engineering and Computer Engineering, Northwestern University, Evanston, IL, United States; 3. Department of Engineering, University of Messina, Messina, Italy; 4. 3Department of Mathematical and Computer Sciences, Physical Science and Earth Sciences, University of Messina, Messina, Italy*

Antiferromagnet-based memories offer new potential capabilities such as picosecond time scale switching [1], immunity to magnetic fields, and the potential to realize high-density memory arrays due to the vanishing bit-to-bit dipole interactions. Electric control of the AFM order has been previously demonstrated in epitaxially grown AFMs with broken inversion symmetry such as CuMnAs [2, 3], and Mn_2Au, and in insulating NiO interfaced with a Pt layer [5,6]. In this work, we investigate current-induced switching in micrometer-scale circular memory bits based on the metallic antiferromagnet PtMn, which is already widely used as part of the pinned layer in in-plane magnetic tunnel junctions manufactured on CMOS. The device consists of a pillar of PtMn with thickness < 10 nm, grown by room-temperature sputter deposition on top of a heavy metal layer, i.e. Pt, which provides a spin current able to switch the AFM state. The device shows reversible switching in response to currents applied to the Pt layer, with opposite current polarities achieving opposite switching directions in the PtMn. The switching current density is ~2 MA/cm^2. We show that the switching process is essentially unaffected by external fields up to 16 T, and is robust over a wide temperature range. We also investigate the switching process by micromagnetic simulations, which shed light on the current-controlled domain structure of the device and the role of different torque terms in the switching process. Our results pave the way towards practical antiferromagnetic memories integrated on silicon.

[1] T. Jungwirth, J. Sinova, A. Manchon, X. Marti, J. Wunderlich, and C. Felser, "The multiple directions of antiferromagnetic spintronics," *Nature Physics,* vol. 14, pp. 200-203, 2018/03/01 2018. [2] K. Olejník, V. Schuler, X. Marti, V. Novák, Z. Kašpar, P. Wadley, R. P. Campion, K. W. Edmonds, B. L. Gallagher, J. Garces, M. Baumgartner, P. Gambardella, and T. Jungwirth, "Antiferromagnetic CuMnAs multi-level memory cell with microelectronic compatibility," *Nature Communications,* vol. 8, p. 15434, 05/19/ online 2017. [3] P. Wadley, B. Howells, J. Železný, C. Andrews, V. Hills, R. P. Campion, V. Novák, K. Olejník, F. Maccherozzi, S. S. Dhesi, S. Y. Martin, T. Wagner, J. Wunderlich, F. Freimuth, Y. Mokrousov, J. Kuneš, J. S. Chauhan, M. J. Grzybowski, A. W. Rushforth, K. W. Edmonds, B. L. Gallagher, and T. Jungwirth, "Electrical switching of an antiferromagnet," *Science,* vol. 351, p. 587, 2016. [4] S. Y. Bodnar, L. Šmejkal, I. Turek, T. Jungwirth, O. Gomonay, J. Sinova, A. A. Sapozhnik, H. J. Elmers, M. Kläui, and M. Jourdan, "Writing and reading antiferromagnetic Mn2Au by Néel spin-orbit torques and large anisotropic magnetoresistance," *Nature Communications,* vol. 9, p. 348, 2018/01/24 2018. [5] L. Baldrati, A. Ross, T. Niizeki, C. Schneider, R. Ramos, J. Cramer, O. Gomonay, M. Filianina, T. Savchenko, D. Heinze, A. Kleibert, E. Saitoh, J. Sinova, and M. Kläui, "Full angular dependence of the spin Hall and ordinary magnetoresistance in epitaxial antiferromagnetic NiO(001)/Pt thin films," *Physical Review B,*

vol. 98, p. 024422, 07/24/ 2018. [6] T. Moriyama, K. Oda, T. Ohkochi, M. Kimata, and T. Ono, "Spin torque control of antiferromagnetic moments in NiO," *Sci Rep,* vol. 8, p. 14167, Sep 21 2018.

4:18

BB-15. Non-Spin Torque Origin of Current-Induced Switching in an Antiferromagnet Insulator/Pt Bilayer Film. *P. Zhang*[1] and L. Liu[1]
1. Massachusetts Institute of Technology, Cambridge, MA, United States

Electrical control and detection of magnetic ordering inside antiferromagnets has attracted considerable interests, for the potential advantages in operating speed and device densities [1]. In contrast to ferromagnet, where the current induced torque on magnetic moments was first established and quantified via comparison with magnetic field's influence [2], the investigation on the spin torque mechanism in antiferromagnets represents a greater challenge, due to the lack of an independent method for controlling Néel vectors. Here by utilizing an antiferromagnetic insulator with Dzyaloshinskii-Moriya interaction [3], α-Fe_2O_3, we show that the Néel vector can be conveniently controlled with the application of a moderate external magnetic field, which is further used to examine the current induced magnetic dynamics. We find that the switching criteria employed in many of the previous studies -- the sawtooth feature in resistance or Hall resistance change is not necessarily related to the reorientation of Néel order. By further comparing the current and field-induced Néel vector tilting and through a systematic scaling study, we reveal the important role of magnetoelastic effect in current induced switching of this antiferromagnet. The spin torque effect induced switching, which is expected to be smaller and has the opposite sign as the magnetoelastic effect in our experiment, remains yet to be demonstrated.

[1] P. Wadley, B. Howells, and J. Zelezny, Science, Vol. 351, p.587 (2016) [2] L. Liu, O. J. Lee, and T. J. Gudmundsen, Phys. Rev. Lett., Vol. 109, p.096602 (2012) [3] S. J. Williamson and S. Foner, Phys. Rev., Vol. 136, p.A1102 (1964)

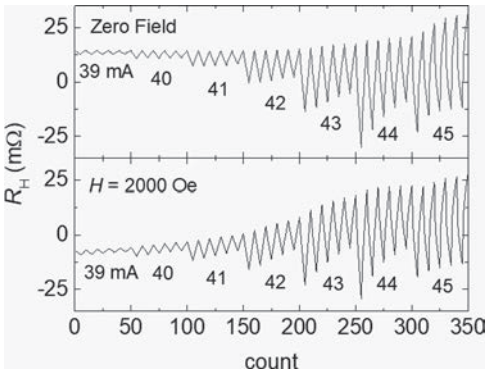


Fig. 1 The Fe2O3/Pt Hall cross device is being switched with current pulses along +45 and -45 deg directions, without and with in-plane magnetic field. Although 2000 Oe field should mostly saturate Fe2O3, the switching seems not affected at all.

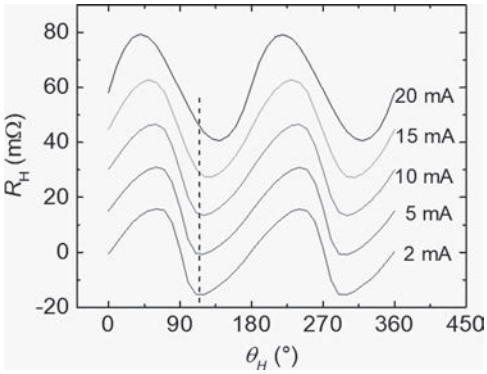


Fig. 2 The angle-dependent transverse spin hall magnetoresistance (SMR) of Fe2O3/Pt Hall cross device with 2000 Oe in-plane field. Curves are shifted vertically for comparison. With larger current applied, we see a significant peak shift and shape change, which indicates a change of the in-plane easy axis by current.

Session BC
SPIN-ORBIT TORQUE MRAM
Yu Zhang, Chair
University of Arizona, Tucson, AZ, United States

CONTRIBUTED PAPERS

1:30

BC-01. Spin-Orbit Torque Switching Scheme Based on Micromagnetic States. *C. Garg*[1], J. Zhang[2], T. Phung[1], C. Rettner[1], B. Hughes[1], S. Yang[1], Y. Jiang[2] and S.S.P. Parkin[1] *1. IBM Almaden Research Center, San Jose, CA, United States; 2. University of Science & Technology, Beijing, China*

Three-terminal spintronic devices based on the manipulation of a nanomagnet through spin-orbit torques[1] (SOT) are prospective candidates for high-speed cache memory. They are non-volatile, have essentially infinite endurance, and can operate at high speeds with low error rates[2]. However, their switching process is limited by an incubation time which is typical when the initial magnetization is collinear to the spin polarization. When the magnetization easy axis lies perpendicular to the spin polarization, switching is possible but requires an external field[3]. In this work, we demonstrate the use of non-uniform micromagnetic states to perform field-free deterministic switching. By employing this scheme, it becomes possible to control the magnetization switching direction for the same current polarity. We use this property to illustrate a potential nanomagnetic logic device. Lastly, we also explore the use of W(O) as an SOT generator and confirm its -50% spin Hall angle reported previously in a separate study[4].

1. Liu, L. et al. Science, 336 (6081), 555–558. (2012). 2. Aradhya, S. V. et al. Nano Lett, 16 (10), 5987–5992. (2016) 3. Fukami, S. et al. Nat. Nanotechnol, 11 (7), 621–625. (2016) 4. Demasius, K.-U et al. Nat. Commun, 7, 10644. (2016)

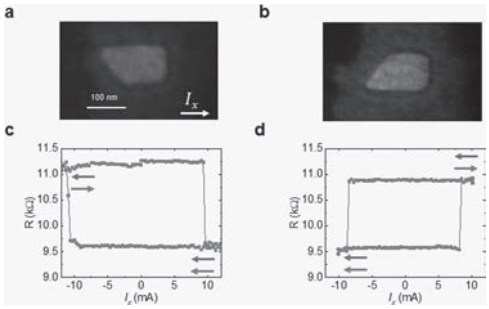


Figure 1. (a,b). SEM images of three-terminal devices patterned to demonstrate SOT switching. Application of current is collinear to magnetic easy axis of the device. (c,d). Loops showing switching behaviour as indicated by the change in resistance upon application of 1 ms current pulses.

1:42

BC-02. Iridium Enabled Field-free Spin-orbit Torque Switching of Perpendicular Magnetic Tunnel Junction Device. *Y. Liu*[1,3], B. Zhou[1,3], Z. Dai[2,3], E. Zhang[2,3] and J. Zhu[2,3] *1. Materials Science & Engineering, Carnegie Mellon University, Pittsburgh, PA, United States; 2. Electrical & Computer Engineering, Carnegie Mellon University, Pittsburgh, PA, United States; 3. Data Storage Systems Center, Carnegie Mellon University, Pittsburgh, PA, United States*

For spin-orbit torque (SOT) switching of a perpendicular magnet, an in-plane field is required for breaking the symmetry[1]. Although schemes have been demonstrated in external-field-free SOT switching of a perpendicular layer[2–4], practically integrating them with perpendicular MTJs (p-MTJs) still appears to be challenging. We have previously demonstrated field-free SOT switching of a perpendicular magnet via using an Ir layer for generating both SOTs and a steady exchange coupling in-plane field coupling with a synthetic antiferromagnetic structure (SAF)[5]. Here we report the experimental demonstration of its integration with p-MTJ devices, showing robust SOT writing of p-MTJs with size ranging from 500 nm to sub-50 nm, free of requirement for an external field. The film structure, as shown in Fig. 1(a), is substrate/ IrMn(5)/ Co(2)/ Ru(0.85)/ Co(2)/ Ir (1.35)/ FeCoB (1.2)/ MgO(1.2)/ FeCoB(1.3)/ Ta(0.5)/ [Co(0.4)/ $Pt(1)]_{x3.5}$/ Ru(0.85)/ [Co(0.4)/ $Pt(1)]_{x5.5}$/ Pt(7) (unit in nm). After deposition, the film is annealed at 300 ^{0}C for 10 min with a 5000 Oe magnetic field applied along -x direction. Fig. 1(b) shows the hysteresis loops of the film, exhibiting strong perpendicular anisotropy of the MTJ. The film is then patterned into three-terminal devices (Fig. 2(a)) for current-induced switching experiments. In Fig. 2 (b), we obtain well-defined switching of the p-MTJ at zero external field, as indicated by the sharp changes in MTJ resistance. With varying the pulse width (Fig. 2(c)), we observe that the switching current remains almost constant for pulse width from 5 μs down to 100 ns and starts to increase sharply with pulses shorter than 100 ns. Fig. 2(d) shows the effect of MTJ size on the threshold current. It can be seen that the threshold current is essentially constant for size greater than 150 nm and only slightly elevates at smaller MTJ size (down to 50 nm). Combined micromagnetic modeling providing physical insights will be presented in the talk.

[1] L. Liu, O.J. Lee, T.J. Gudmundsen, D.C. Ralph, and R.A. Buhrman, Phys. Rev. Lett. 109, 96602 (2012). [2] S. Fukami, C. Zhang, S. DuttaGupta, A. Kurenkov, and H. Ohno, Nat. Mater. 15, 535 (2016). [3] A. van den Brink, G. Vermijs, A. Solignac, et al. Nat. Commun. 7, 10854 (2016). [4] Y.-C. Lau, D. Betto, K. Rode, J.M.D. Coey, and P. Stamenov, Nat. Nanotechnol. 11, nnano (2016). [5] Y. Liu, B. Zhou, and J.J. Zhu, Sci. Rep. 1 (2019).

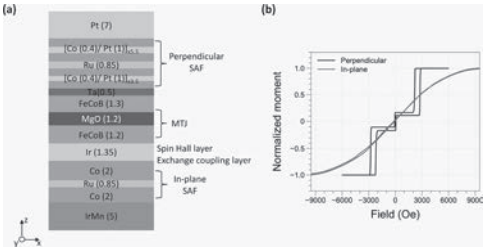


Fig.1(a) Film stack (in nanometer).(b) Hysteresis loops.

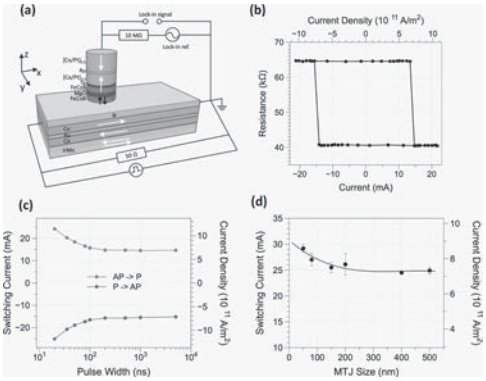


Fig.2(a) Schematic of the three-terminal device.(b) Current-induced switching at zero external field. Pulse width:200 ns. MTJ size:150 nm.(c) Switching current vs. pulse width.(d) Switching current vs. MTJ size.

1:54

BC-03. Ultrafast and energy-efficient spin–orbit torque switching in compensated ferrimagnets. *K. Cai*[1], Z. Zhu[1], J.M. Lee[1], R. Mishra[1], L. Ren[1], P. He[1], G. Liang[1], K.L. Teo[1] and H. Yang[1] *1. Department of Electrical and Computer Engineering, National University of Singapore, Singapore*

Spintronics aims to develop energy-efficient as well as high-speed magnetic logic and memory devices, and the spin-orbit torque is a promising approach for magnetization manipulation. However, conventional ferromagnetic spin-orbit torque systems have intrinsic limitations in operational speed due to their inherent magnetization dynamics. Alternatively, antiferromagnets and ferrimagnets with antiparallel exchange coupling exhibit faster spin dynamics, which shows the potential to overcome these limitations [1]. Here, we experimentally demonstrate an ultrafast spin–orbit torque induced magnetization switching in Pt/CoGd ferrimagnetic devices through time-domain measurements [2]. We find that the switching time can be easily reduced to the sub-nanosecond regime in ferrimagnets, corresponding to a ~10 times faster speed compared to ferromagnets (as shown in Figure 1a). Moreover, the switching energy efficiency is one to two orders of magnitude higher than that of ferromagnets [3]. In particular, a very high domain wall velocity of ~5.7 km s^{-1} is realized during switching (as shown in Figure 1b), which is in agreement with the analytical modeling and atomistic spin simulations. This work highlights the potential of the ultrafast and energy-efficient ferrimagnet based spin–orbit torque memory and computing applications.

[1] J. Yu, et al. Nat. Mater. 18, 29 (2019). [2] J. Yoon, et al. Sci. Adv. 3, e1603099 (2017) [3] R. Mishra, et al. Phys. Rev. Lett. 118, 167201 (2017)

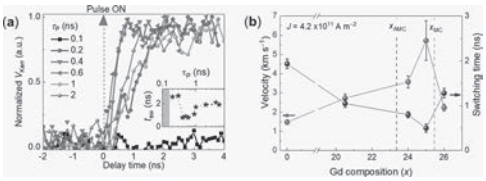


Fig. 1. (a) Temporal evolutions of MOKE signals for different pulse widths for $Co_{76}Gd_{24}$ with H_x = 1444 Oe and J = 4.2×10^{11} A m^{-2}. The switching time as a function of pulse duration is shown in the inset. (b) The extracted domain wall velocity and switching time as a function of Gd composition.

INVITED PAPER

2:06

BC-04. Gate-Tunable Inverse Spin Hall Effect in Ultrathin Pt. *S. Dushenko*[1,2] *1. The Institute for Research in Electronics and Applied Physics, University of Maryland, College Park/ National Institute of Standards and Technology, Gaithersburg, MD, United States; 2. Department of Electronic Science and Engineering, Kyoto University, Kyoto, Japan*

We report reversible modulation of up to two orders of magnitude of the inverse spin Hall effect (ISHE) in ultrathin platinum (Pt) using careful control of its thickness and an ionic gating technique.[1] The ISHE enables use of electric and spin currents in the same device, which is crucial for the future integration of spintronics and electronics. The ISHE[2,3] is governed by the spin-orbit interaction and is particularly strong in heavy metals. Due to the spin-orbit interaction, the scattering direction of the carriers depends on their spin direction. Thus, it couples the spin current with the charge current, allowing their interconversion. Following studies by Saitoh *et al*.[4] and Valenzuela *et al*.[5], Pt has become a dominant material choice for spin current detection due to the large ISHE[6] and easy fabrication. There have been many attempts to achieve control over the spin-charge conversion process. However, in contrast to semiconductors and two-dimensional systems, electric gating control over spin-charge conversion in heavy metals was considered out of reach because of high carrier density. In this study, we achieved the largest to date modulation of the metal resistivity in ultrathin Pt film. Such control over the carrier density allowed us to reversibly tune the amplitude of the ISHE in Pt over two orders of magnitude. *I-V* characteristics, ferromagnetic resonance (FMR) and the ISHE measurements were carried out at 250 K on 1.5 nm to 20 nm thick Pt films deposited on a 1.3 μm thick YIG ferrimagnetic layer. The voltage of an ionic gel (DEME-TFSI) top gate was set at room temperature and samples were cooled after the development of the electric double layer in the gel. Spin pumping was used to inject spin current in Pt by exciting FMR in the YIG at 9.12 GHz. Evidence for the ISHE modulation is derived from dramatic changes in the spin-charge conversion voltage, Pt resistance and FMR absorption spectra. Using the ionic gel top gate, the resistance of the Pt film was tuned up to 280% (Fig. 1). In contrast to the microwave absorption spectrum, electromotive force generated via the ISHE was strongly modulated with the application of the gate voltage. To isolate the ISHE from the large resistance changes, we report $I_{ISHE} = V_{ISHE}/R$. In the 2 nm thick Pt sample, the amplitude of the spin-charge conversion current was tuned from the I_{ISHE} = 3.0 nA at the gate voltage V_G = -2 V to I_{ISHE} = 0.1 nA at V_G = 2 V (Fig. 2). In our best sample, we achieve modulation of the V_{ISHE} and I_{ISHE} from 100% at V_G = -2 V down to 0.8% and 1.7%, respectively, at V_G = 2 V. The modulation of the spin-charge conversion current is reversible and reproducible between different measurements of the same sample, as well as between measurements of different samples with the same thickness. Our results can be used in the gate-tunable spin-charge converter devices. For example, it opens an exciting possibility of the gate-controlled spin-orbit torque magnetoresistive random-access memory (SOT-MRAM), where the spin current generated by the spin-charge conversion in heavy metal exerts a torque on the free magnetic layer.

[1] S. Dushenko, M. Hokazono, M. Shiraishi *et al*., *Nat. Commun.* 9, 3118 (2018). [2] N. S. Averkiev, and M. I. Dyakonov, *Sov. Phys. Semicond.* 17, 393 (1983). [3] A. A. Bakun, B. P. Zakharchenya, A. A. Rogachev *et al*., *Sov. Phys. JETP Lett.* 40, 1293 (1984). [4] E. Saitoh, M. Ueda, H. Miyajima *et al*., *Appl. Phys. Lett.* 88, 182509 (2006). [5] S. O. Valenzuela, M. Tinkham, *Nature* 442, 176 (2006). [6] T. Tanaka, H. Kontani, M. Naito *et al.*, *Phys. Rev. B* 77, 165117 (2008).

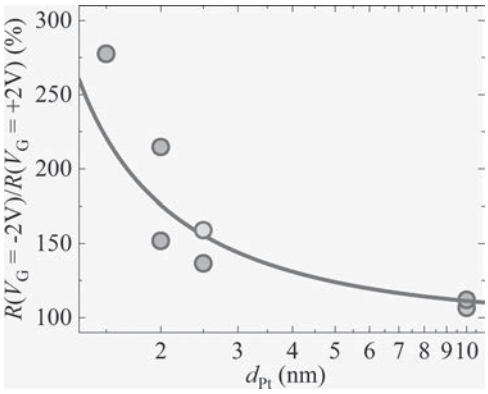


Fig. 1. Thickness dependence of the Pt resistance modulation $R(V_G = -2V)/R(V_G = +2V)$ with the gate voltage. Blue solid line shows theoretical calculation assuming the same number of carriers induced in all devices; purple filled circles are experimental data, each circle corresponds to a separate sample. The blue filled circle is the averaged resistance modulation obtained for 2.5 nm sample from 15 gate voltage sweeps. In agreement with the theoretical calculation, devices showed increased resistance modulation with the decreased thickness.

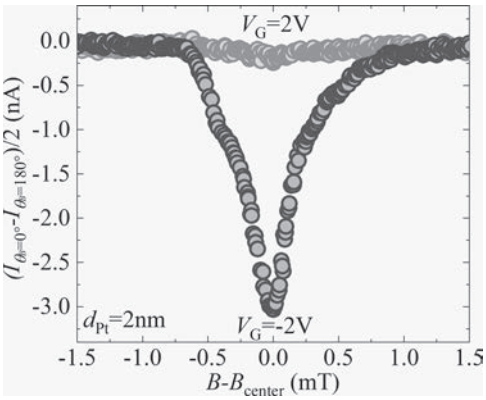


Fig. 2. The spin-charge conversion current in thin Pt films showing gate control. Spin-dependent component of the charge current (difference in the charge current between the opposite directions of the magnetic field $\theta_B = 0°$ and $\theta_B = 180°$) measured from $d_{Pt} = 2$ nm sample at gate voltage $V_G = -2.0$ V and $V_G = 2.0$ V.

CONTRIBUTED PAPERS

2:42

BC-05. Process control of tungsten β-phase window for spin-orbit torques MRAM applications. *K. Vudya Sethu*[1,2], S. Couet[1], J. Swerts[1], B. Soree[1,2], J. De Boeck[1,2], G.S. Kar[1] and K. Garello[1] *1. Imec, Leuven, Belgium; 2. ESAT, KU Leuven, Leuven, Belgium*

Spin-orbit torques (SOT) magnetic random-access memory (SOT-MRAM) is a new class of current based MRAM which is promising for embedded low-level cache applications [1, 2]. However, the critical current density required by SOT switching is presently too large and decreasing it remains a major challenge. A key parameter that influences threshold current for switching is the spin Hall angle (SHA) of the heavy metal used to generate SOT. Among heavy metals, W in beta phase has one of the highest SHA reported in the literature (~-30%) [3]. In imec, using our 300 mm platform, we successfully integrated W-based SOT-MTJ and demonstrated low power and sub-ns performances [4]. However, in our samples, beta-to-alpha transition of W occurs around 4 nm narrowing the process control and accessible thickness range. In addition, this phase transition dramatically reduces to 2 nm when inserting an adhesion layer to avoid stack delamination. Therefore, there is also a need to control and extend the beta phase window. In this presentation we will show that using oxygen and nitrogen (W(O,N)) doping during the sputter deposition of W allows for controlling and maintaining W beta-phase to more than 10 nm (Fig.1). We will next discuss that using this process it is possible to tune the perpendicular magnetic anisotropy (PMA) and we will also show that it remarkably enhances SHA up to -45% in optimized W(O,N) layers, which is one of the highest for W/CoFeB system with PMA free layer. We will conclude by presenting W(O,N)-based MTJ integrated devices properties (Fig.2) and the benefits that optimized W(O,N) layers bring to reduce threshold switching current.

[1] I.M. Miron et. al, Nature 476, 189–193 (2011), L. Liu et. al, Science 336, 555–558 (2012) [2] G. Prenat et. al, IEEE Trans. on Multi-Scale Computing Systems, 2, 49-60 (2016) [3] A. Manchon et. al, arXiv:1801.09636 [4] K. Garello et. al, *IEEE Symposium. on VLSI Circuit*, 81-82 (2018)

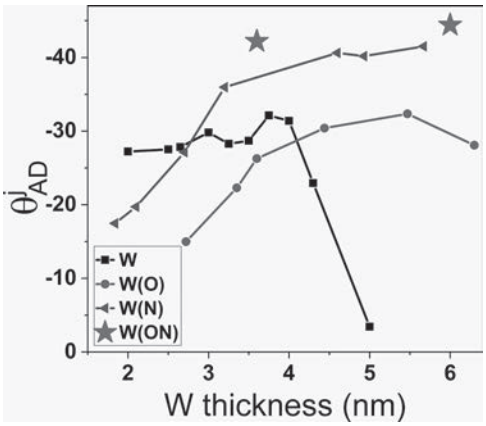


Fig.1: Anti-damping SOT as a function of thickness for different W samples prepared in the study

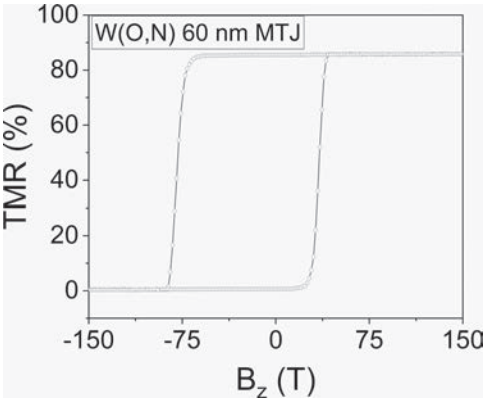


Fig.2: TMR of a 60 nm SOT-MTJ with 6nm W(O,N) used as SOT layer

2:54

BC-06. Design of an Erasable Spintronics Memory Based on Current-path-dependent Field-free Spin Orbit Torque. H. Zhou[1], Z. Wang[1], Z. Li[1], *C. Wang*[1], B. Wu[1] and W. Zhao[1] *1. Beihang University, Beijing, China*

Emerging spin orbit torque magnetic random access memory (SOT-MRAM) promises to overcome the speed and endurance issues of the spin transfer torque (STT) MRAM [1-2]. However, for the perpendicular-anisotropy SOT-MRAM, an undesirable magnetic field is required to achieve the deterministic switching [3-4]. Recently, we proposed a novel field-free SOT mechanism for the deterministic switching of the perpendicular magnetization [5], where an elliptical perpendicular-anisotropy magnetic tunnel junction (MTJ) is deposited above a heavy metal layer with a tilted long-axis. Two unidirectional currents flowing through different paths can deterministically switch the MTJ to P and AP states (low and high resistance states), respectively. In other words, the switched final state is only dependent on the current path instead of current direction. According to the final state, we call the two current paths P-path and AP-path, respectively (see Fig. 1). Here, based on this proposed SOT mechanism, we present an erasable spintronics memory. Take 4-bit memory as an example, four P-paths are connected to form the erasing channel, while four AP-paths are used as the programming channels (see Fig. 2). Non-volatile data can be written in two steps. In the first step, a reset current is injected into the erasing channel so that the states of four MTJs are all reset to '0' ('Step 1' in Fig. 2). In the second step, another one current is applied to the programming channel corresponding to 'MTJ1'. Then the 'MTJ1' is set to '1' ('Step 2' in Fig. 2). As a result, data '0010' is written into the memory. The switching could be achieved at sub-nanosecond latency and sub-hundred femto-joule energy. Thus our proposed memory is a good candidate for the embedded applications.

[1] S. W. Lee and K. J. Lee, Proc. IEEE, Vol. 104, p. 1831 (2016). [2] Z. Wang, Z. Li, Y, Liu, et al. in Proc. IEEE-ISCAS (2018). [3] I. M. Miron, K. Garello, G. Gaudin, et al. Nature, Vol. 476, p. 189 (2011). [4] L. Liu, C. F. Pai, Y. Li, et al. Science, Vol. 336, p. 555 (2012). [5] Z. Wang, Z. Li, M. Wang, et al. Nanotechnology. 2019. DOI: 10.1088/1361-6528/ab2831.

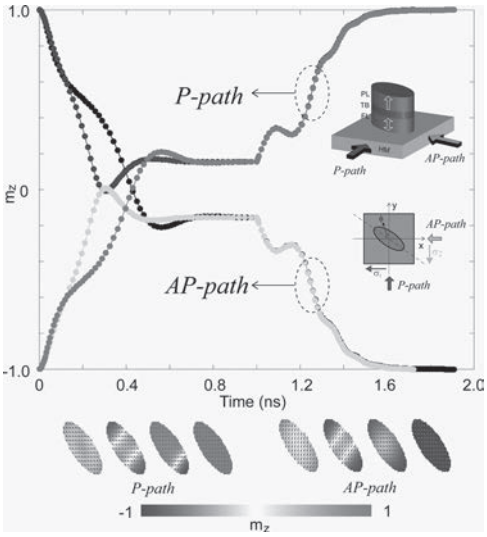


Fig. 1. The time evolution of z-component magnetization with the proposed SOT mechanism. Inset: the schematic of the proposed SOT device.

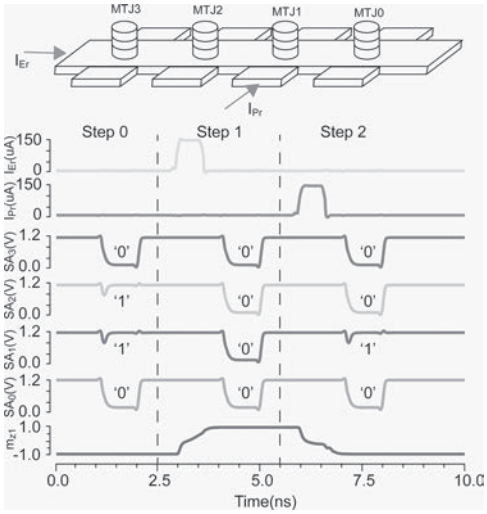


Fig. 2. Top: the schematic structure of the proposed erasable spintronics memory. Bottom: corresponding simulation reslults of the write operation. I_{Er}: erasing current. I_{Pr}: programming current. m_{z1}: z-component of the magnetization for MTJ1. SA_{0-3}, the output of the sensing amplifier for the MTJ_{0-3}.

3:06

BC-07. Ion Beam Etching Dependent of Spin-orbit Torque Memory Devices with Low Switching Current Density Enhanced by Hf Interlayers. *H. Ren*[1,2], S. Wu[3], E. Fullerton[1,2] and J. Sun[3] *1. Materials Science and Engineering, University of California San Diego, La Jolla, CA, United States; 2. Center for Memory and Recording Research, University of California San Diego, La Jolla, CA, United States; 3. IBM TJ Watson Research Center, Yorktown Heights, NY, United States*

Spin orbit torque (SOT) switching devices are promising for faster, more reliable and efficient switching compared to current magnetic memory technologies. However, large-scale fabrication of nano-scale SOT switching devices remains a challenge. Here we report some fabrication considerations of nano-sized, three terminal in-plane SOT switching devices with low switching current density by optimizing ion-beam etching conditions and by inserting Hf interlayers. As shown in figure 1(a), non-linear dependence of the critical switching field with bias current indicates the switching is caused by SOT current. We show that the angle and time of the ion beam etching is critical to avoid defects such as the shunting effect caused by redeposition at the junction pillar sidewall, trench effects around the base of junction pillar caused by reflected ions from the pillar side-wall during high angle etching, and a "big foot" effect caused by the shading of tall junction pillar. The switching behavior of the fabricated junctions is significantly affected by the junction pillar's in-plane aspect ratios due to demagnetization factor change, and by the insertion of Hf spacer interlayers which affects both interface spin-current transparency and interface anisotropy. We succeeded in bringing switching current densities down to 1.7×10^7 A/cm^2 through optimized etching, manipulation of the aspect ratio of the junctions and inserted Hf interlayers. The inserted Hf interlayers decreases 1/3 of the critical current required for switching as shown in figure 1(b). This study gives us a more comprehensive understanding of how to improve the fabrication process for application in mass production. Works at IBM supported by an IBM Summer Intern Program. Work at UCSD supported by Award # DE-SC0019273.

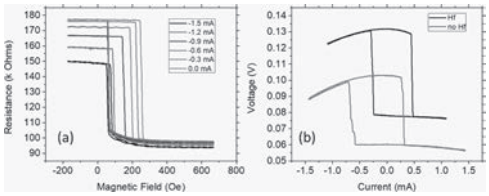


Figure 1. (a) Resistance vs magnetic field at various SOT currents. (b) SOT switching curves for the device with and without Hf interlayers.

3:18

BC-08. Highly Efficient Spin-Orbit Torque Magnetization Switching in a Perpendicularly Magnetized Ferromagnetic-Semiconductor Single Layer: Damping Like Torque and Field Like Torque. *M. Jiang*[1], H. Asahara[1], S. Sato[1], S. Ohya[1,2] and M. Tanaka[1,2] *1. Dept. of Electrical Engineering, The Univ. of Tokyo, Tokyo, Japan; 2. Center for Spintronics Research Network (CSRN), Graduate School of Engineering, The Univ. of Tokyo, Tokyo, Japan*

Spin-orbit torque (SOT) magnetization switching, which is induced by a spin current generated by a charge current, is a promising phenomenon that can be used to improve the performance of magnetoresistive random access memory. In our previous study, we achieved a highly efficient full SOT magnetization reversal in a GaMnAs single layer by applying a very low current density (J_c) of 3.4×10^5 A cm^{-2} [1], which is two orders of magnitude smaller than that required in the conventional SOT systems [2]. According to the Landau–Lifshitz–Gilbert (LLG) equation, the SOT is contributed by two parts; damping like torque (DLT) and field like torque (FLT). By fitting simulated results using the LLG equation to the experimental results, we clarified that the DLT is dominant during the magnetization switching in the 7-nm-thick GaMnAs single layer. Here, we explore the contributions of DLT and FLT by inducing the SOT switching in perpendicularly magnetized GaMnAs single layers with different thicknesses; d = 5 nm, 7 nm, 10 nm, and 15 nm as shown in Fig. 1. In the GaMnAs single layer with d = 5nm, SOT magnetization switching (dominated by DLT) is observed with $J_c = 1.6\times10^5$ A cm^{-2}, which is even smaller than that of our previous paper [1]. With the increase of d, the FLT starts to act on the magnetization switching and competes with the DLT. When d < 15 nm, J_c increases as d increases, which is caused by the enhancement of the contribution of FLT. At d = 15 nm, the switching polarity is totally reversed, indicating that the FLT becomes dominant. This result is understandable, considering that the acting direction of FLT is opposite to that of DLT. Our finding will advance the understanding on the contributions of DLT and FLT during the SOT switching in GaMnAs single layer. This work was partly supported by Grants-in-Aid for Scientific Research (No. 16H02095, No. 18H03860), CREST program of Japan Science and Technology Agency (JPMJCR1777), Spintronics Research Network of Japan (Spin-RNJ), and China Scholarship Council (No. 201706210086).

1. M. Jiang *et al., Nature Commun.* 10, 2590 (2019). 2. L. Liu *et al.*, *Phys. Rev. Lett.* 109, 096602 (2012).

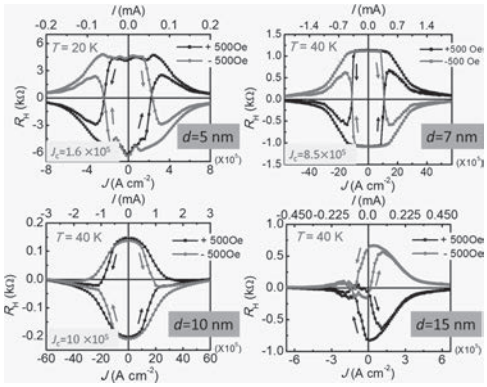


Fig. 1 Thickness dependent spin-orbit torque magnetization switching in a GaMnAs single layer. (The values in the yellow rectangles are *Jc* of the corresponding samples with a unit of A cm^{-2}.)

3:30

BC-09. Toggle Mode Spin-Orbit Torque Driven Perpendicular Magnetic Anisotropy MRAM. *N. Hassan*[1], S.P. Lainez-Garcia[1], F. Garcia-Sanchez[2,3] and J.S. Friedman[1] *1. Electrical & Computer Engineering, The University of Texas at Dallas, Richardson, TX, United States; 2. Istituto Nazionale di Ricerca Metrologica, Torino, Italy; 3. Departamento de Fisica Aplicada, Universidad de Salamanca, Salamanca, Spain*

Spin-orbit torque (SOT) is a high speed and energy efficient writing technology for magnetic random-access memory (MRAM) that prevents device degradation by separating the read-write path [1]. However, orthogonality between the in-plane polarized SOT current and thermally stable perpendicular magnetic anisotropy (PMA) inhibits deterministic MRAM switching. Several approaches have been proposed to break this symmetry, including an in-plane magnetic field [2], deformation of the device structure [3], tilted anisotropy [4], an antiferromagnet–ferromagnet bilayer system [5], and competing spin currents [6]. However, all of these approaches increase the fabrication complexity, are highly sensitive to the SOT current duration and magnitude, or increase the switching energy. We therefore propose toggle PMA SOT-MRAM [7], which exploits the precessional nature [8] of field-like SOT to achieve field-free and energy-efficient switching with a simple structure that is robust to the SOT current magnitude and duration. The structure is a three-terminal magnetic tunnel junction that consists of a heavy metal, free ferromagnet, insulating tunnel barrier, and compensating ferromagnet. A unidirectional SOT current applied through the heavy metal causes the free ferromagnet magnetization to stabilize at an excited steady state after crossing the hard axis plane. Switching off the excitation relaxes the magnetization to the nearest easy axis, thus completing a toggle cycle. Application of the next excitory pulse toggles the magnetization back to its initial state. Micromagnetic simulations demonstrate robust switching, with greater than 50% tolerance to applied SOT current magnitude. This deformation-free structure provides efficient data read-out, and the toggle switching can be leveraged for directional writing through a simple XOR between the current and incoming bits. The proposed device therefore provides a promising solution for compact, highly-efficient, and robust SOT-MRAM with PMA.

[1] S. P. Park, S. Gupta, N. Mojumder *et al.*, in *Proceedings of the 49th Annual Design Automation Conference on -DAC '12*, p. 492 (2012). [2] M. Cubukcu, O. Boulle, M. Drouard *et al.*, *Appl. Phys. Lett.*, vol. 104, no. 4, p. 042406 (2014). [3] G. Yu, P. Upadhyaya, Y. Fan *et al.*, *Nat. Nanotechnol.*, vol. 9, no. 7, pp. 548–554 (2014). [4] L. You, O. Lee, D. Bhowmik *et al*, *Proc. Natl. Acad. Sci.*, vol. 112, no. 33, pp. 10310–10315 (2015). [5] S. Fukami, C. Zhang, S. DuttaGupta *et al.*, vol. 15, no. 5, pp. 535–541 (2016). [6] Q. Ma, Y. Li, D. B. Gopman *et al.*, *Phys. Rev. Lett.*, vol. 120, no. 11, p. 117703 (2018). [7] W. Legrand, R. Ramaswamy, R. Mishra *et al.*, *Phys. Rev. Appl.*, vol. 3, no. 6, p. 064012 (2015). [8] N. Hassan, S. P. Lainez-Garcia, F. Garcia-Sanchez *et al.*, arXiv preprint arXiv: 1905.01125 (2019).

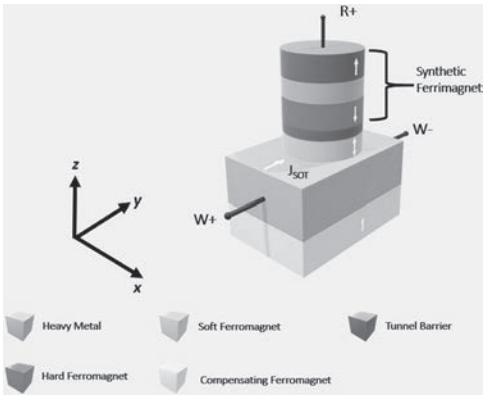


Fig. 1. Schematic of three-terminal toggle SOT-MRAM.

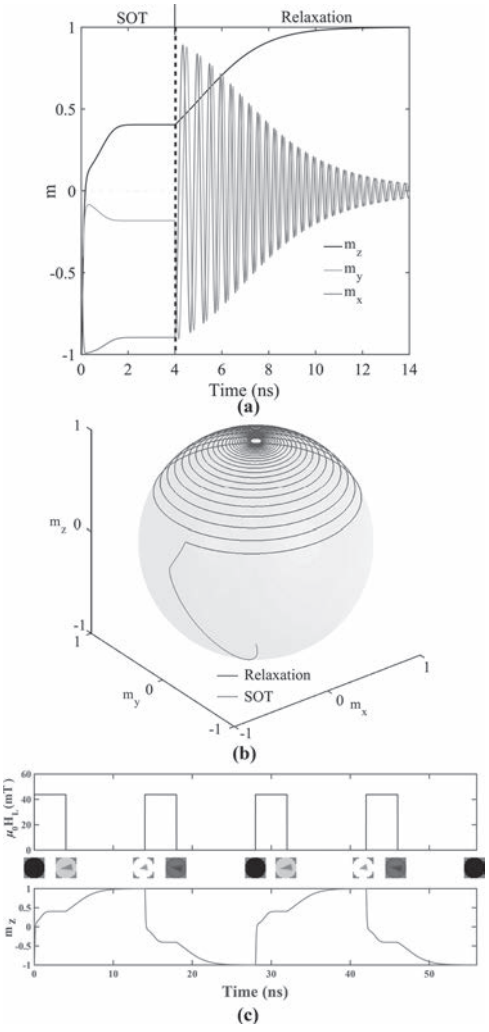


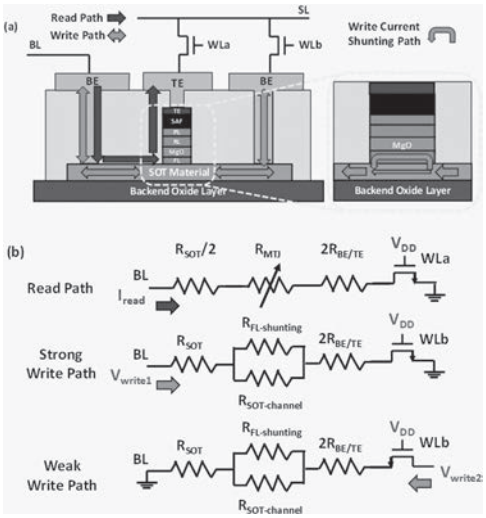
Fig. 2. (a) Time vs. free ferromagnet magnetization for single toggle operation. (b) Trajectory of the magnetization in 3D. (c) Consecutive toggle operations.

3:42

BC-10. Materials Requirements of High-Speed and Low-Power Spin-Orbit-Torque Magnetic Random-Access Memory. *X. Li*[1,2], C. Yao[2], M. DC[1], W. Tsai[3], S. Lin[3] and S. Wang[1,2] *1. Materials Science and Engineering, Stanford University, Stanford, CA, United States; 2. Electrical Engineering, Stanford University, Stanford, CA, United States; 3. TSMC, Hsinchu, Taiwan*

As spin-orbit-torque magnetic random-access memory (SOT-MRAM) is being intensively researched as the next-generation ultralow-power and high-speed on-chip cache memory solution [1], it is critical to identify the required materials properties to deliver the desired power and performance mandated by on-chip integration based on two transistor-one magnetic tunnel junction (2T-1MTJ) design. In this presentation, we will first discuss the circuit-level goals for replacing different levels of SRAM cache using SOT-MRAM. Then, array- and device-level materials requirement to achieve the above goals will be described, including the SOT material and the magnetic tunnel junction (MTJ). Last, we will briefly present an outlook of promising approaches to realize high-density 2-terminal SOT-MRAM crossbar architecture [2] and accompanying materials requirements. This work will provide important guidelines for SOT-MRAM materials and device research in the future. In particular, the typical 2 transistor-1 SOT-MTJ cell will be modeled in an effective circuit model as shown in Figure 1. Here, we include the parasitic resistance from the metal electrodes and the SOT layer, as well as the transistor itself. We will both analyze the read and write operation of the SOT-MTJ cell and their respective materials requirement. It is worth noting that a few works [3][4] have already discussed the write current shunting effect due to the ferromagnetic free layer (FL) sitting on top of the SOT layer during write operation as shown in Figure 1(a). However, to fully evaluate what are the best materials properties to be used in a SOT-MRAM cell, the transistors resistance and capacitance are also critical parameters to include. We find that to achieve the lowest power and latency, it is crucial to match the SOT layer material properties, such as resistivity, width, and length to that of the transistor if we consider the SOT efficiency of the material remains unchanged. The authors thanks NSF Center for Energy Efficient Electronics Science (E3S) and TSMC for financial support. This research was supported in part by ASCENT, one of six centers in JUMP, a Semiconductor Research Corporation (SRC) program sponsored by DARPA.

[1] F. Oboril, R. Bishnoi, M. Ebrahimi, and M. B. Tahoori, "Evaluation of Hybrid Memory Technologies Using SOT-MRAM for On-Chip Cache Hierarchy," *IEEE Transactions on Computer-Aided Design of Integrated Circuits and Systems,* vol. 34, pp. 367-380, 2015. [2] N. Sato, F. Xue, R. M. White, C. Bi, and S. X. Wang, "Two-terminal spin–orbit torque magnetoresistive random access memory," *Nature Electronics,* vol. 1, pp. 508-511, 2018/09/01 2018. [3] L. J. Zhu, D. C. Ralph, and R. A. Buhrman, "Highly Efficient Spin-Current Generation by the Spin Hall Effect in Au1-xPtx," *Physical Review Applied,* vol. 10, Sep 6 2018. [4] Q. Shao, H. Wu, Q. Pan, P. Zhang, L. Pan, K. Wong*, et al.*, "Room Temperature Highly Efficient Topological Insulator/Mo/CoFeB Spin-Orbit Torque Memory with Perpendicular Magnetic Anisotropy," in *2018 IEEE International Electron Devices Meeting (IEDM)*, 2018, pp. 36.3.1-36.3.4.



3:54

BC-11. Spin-Based Comparator Using Spin Hall Effect Driven Nanomagnets. *S. Wasef*[1], M. Alawein[1], S. Amara[1] and H. Fariborzi[1]
1. CEMSE, KAUST, Jeddah, Saudi Arabia

In this work, we propose a three-terminal magnetic tunnel junction (3T-MTJ) spin-based voltage comparator and a spin circuit model for the same. The proposed device utilizes a (α-β)-W channel (6.2 nm) of size 400 nm 400 nm, and it is represented by a spin Hall effect (SHE) circuit model [1]. One of the reasons of using (α-β)-W to produce transverse pure spin currents is its ability to provide similar spin current density to β-Ta and Pt but with lower resistivity [2]. The MTJ multilayer is comprised of CoFeB (2 nm) (free layer (FL))/MgO (0.6 nm)/CoFeB (5 nm) (reference layer (RL)) as in [3], and the size of the MTJ pillar is 40 nm 120 nm. The SHE, MTJ, and stochastic magnetization dynamics models are coupled in a self-consistent manner as in [4, 5] (Fig. 1(b)). The MTJ model is a representation of its varying conductance G = (GAP + GP)*(1 + P1.P2)*cos(Φ)/2 where P_1 (P_2) is the interface polarization factor of the FL (RL) of the 3T-MTJ calculated using Julliere's model for a TMR of 275% [3], and is the angle between the magnetizations of FL and RL. The operation of the comparator can be divided into two phases: (1) comparison phase, and (2) reset phase. First, the magnetic orientation of the FL is kept parallel to that of the RL. During the comparison phase, two voltage sources are connected to terminals T1 and T2 using clock controlled switches. Depending on the magnitude of the voltage across the SHE layer, a charge current flows and a transverse pure spin current is generated. The magnetic moment of the FL changes when the generated spin current exceeds the critical spin current required for switching [6]. During the reset phase T2 is connected to a 1 V supply and T1 is grounded to switch back the magnetic orientation of the FL to parallel state. A reading voltage of 1 V is used to read the output. Terminal T3 of the 3T-MTJ is connected to two inverters to produce a rail-to-rail output. We obtain a delay of 3.2 ns for a differential voltage of 400 mV (Fig. 2(a)).

[1]S. Hong, S. Sayed and S. Datta, "Spin Circuit Representation for the Spin Hall Effect," in *IEEE Transactions on Nanotechnology*, vol. 15, no. 2, pp. 225-236, March 2016. [2] Chi-Feng Pai, Luqiao Liu, Y. Li,H. "Spin transfer torque devices utilizing the giant spin Hall effect of tungsten" Appl. Phys. Lett. 101, 122404 (2012). [3] H. D. Gan, K. Mizunuma, S. Ikeda "CoFeB/MgO/CoFeB Magnetic Tunnel Junctions with Low Resistance-Area Product and High Magnetoresistance" 2009 International Conference on Solid State Devices and Materials, Sendai, 2009, pp1384-1385. [4] S. Manipatruni, D. E. Nikonov and I. A. Young, "Modeling and Design of Spintronic Integrated Circuits," in *IEEE Transactions on Circuits and Systems I: Regular Papers*, vol. 59, no. 12, pp. 2801-2814, Dec. 2012 [5] Alawein, Meshal, and Hossein Fariborzi. "Circuit Models for Spintronic Devices Subject to Electric and Magnetic Fields." *IEEE Journal on Exploratory Solid-State Computational Devices and Circuits* 4.2 (2018): 60-68. [6] Sun, J. Z. Spin-current interaction with a monodomain magnetic body: A model study. *Phys. Rev. B* 62, 570–578 (2000).

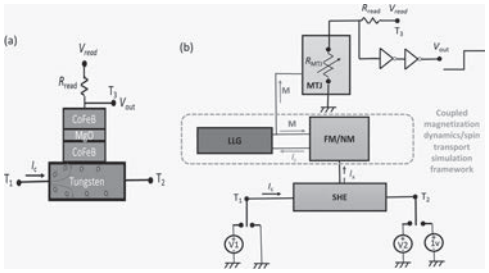
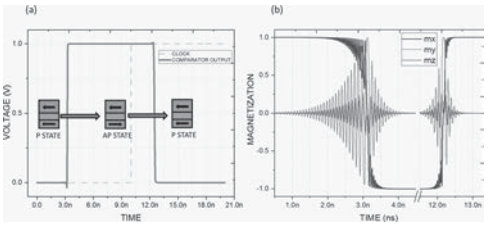


Fig. 1: (a) Three-terminal SHE comparator. (b) Circuit schematic of the comparator.



(a) Transient response of the comparator. (b) Magnetization dynamics of the FL in the comparison and reset phases.

4:06

BC-12. Spin orbit torque switching and thermal stability factor of W/CoFeB/MgO-based three terminal magnetic tunnel junctions. *S. Isogami*[1], Y. Shiokawa[2], A. Tsumita[2], T. Taniguchi[3], S. Mitani[1], T. Sasaki[2] and M. Hayashi[1,4] *1. Research Center for Magnetic and Sintronic Materials, National Institute for Materials Science, Tsukuba, Japan; 2. Technology & Intellectual Property HQ, TDK Corporation, Chiba, Japan; 3. Spintronics Research Center, National Institute of Advanced Industrial Science and Technology, Tsukuba, Japan; 4. The University of Tokyo, Tokyo, Japan*

Spin-orbit torque (SOT) induced magnetization switching in three-terminal magnetic tunnel junctions (MTJs)[1-4] is attracting great interest owing to its potential application for magnetic random access memories. Although there are similarities in the device structure between SOT-MRAM and the conventional spin transfer torque (STT)-MRAM, there remains many issues to be addressed in order for the SOT-based devices to compete with other technologies. We have studied the thermal stability factor (Δ) of three terminal MTJs using current and magnetic field induced magnetization switching. The Δ estimated from current (SOT) induced magnetization switching is studied as a function external bias field (H), duration and amplitude of the current pulse. The inset of Fig. 1(a) shows the device structure, the magnetic easy axis is orthogonal to the current flow direction (the SOT switching scheme is referred to as type-Y in ref. [3]). Figure 1(a) shows the magnetization switching hysteresis curve when current pulses with length of 50 ns and amplitude of V_{pulse} is applied to the W channel. An offset easy-axis field of $H_y \approx +50$ Oe was applied to compensate the dipolar magnetic field. We find symmetric switching for both positive and negative V_{pulse}. Figure 1(b) shows the switching probability with $H_y \approx$ —50 Oe, which favors antiparallel magnetic configuration. The switching probability is fitted using the thermally activated STT switching model with Δ and an intrinsic threshold current I_{c0} as the fitting parameters[5]. We find Δ for positive V_{pulse} is larger than that for negative V_{pulse}. The asymmetric Δ (against the current flow direction) is one of the characteristics we find for the SOT-induced magnetization switching. Details of the SOT-switching mechanism and its relation to the thermal stability factor will be discussed.

[1] I. M. Miron, et al., *Nature* 476, 189 (2011). [2] L. Liu, et al., *Science* 336, 555 (2012). [3] S. Fukami, et al., *Nature nanotech*. 11, 621 (2016). [4] H. Sato, et al., *IEEE Magn. Lett.* 3, 3000204 (2012). [5] M. Pakala, et al., *J. Appl. Phys*. 98, 056107 (2005).

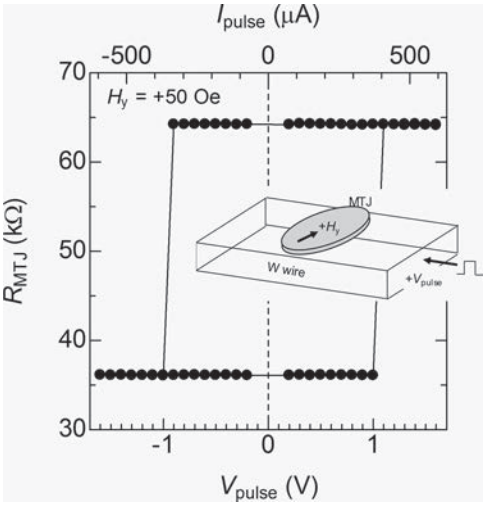


Fig. 1 Tunnel junction resistance (R_{MTJ}) plotted as a function of the current pulse amplitude (V_{pulse}) passed along the W channel. The pulse length is 50 ns, the external field (H_y) is +50 Oe. The inset represents schematic illustration of the three-terminal MTJ.

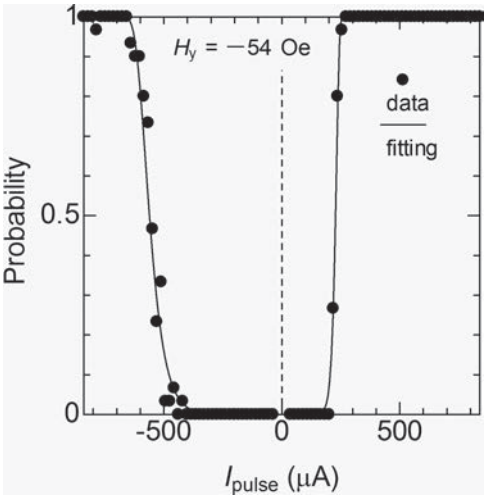


Fig. 2 Switching probability as a function of current pulse amplitude (I_{pulse}) with H_y = -54 Oe. Solid lines represent fitting results.

4:18

BC-13. Reduced thermal variation of perpendicular magnetic anisotropy in magnetically stiffened dual-W composite storage layer for STT-MRAM. *J. Chatterjee*[1], A. Chavant[1], F. Fettar[2], S. Aufftet[1], C. Ducruet[3], I. Joumard[1], L. Vila[1], R. Sousa[1], I. Prejbeanu[1] and B. Dieny[1]
1. Univ. Grenoble Alpes, CEA, CNRS, Grenoble INP, INAC-Spintec, Grenoble, France; 2. Univ. Grenoble Alpes, Inst. NEEL, Grenoble, France; 3. Crocus Technology, Grenoble, France

State-of-the-art spin-transfer-torque magnetic random access memory (STT-MRAM) is based on out-of-plane magnetized magnetic tunnel junctions (pMTJs) which comprise a composite storage layer (CSL) of the form (FeCoB/non-magnetic spacer (Ta, W, Mo etc.)/FeCoB). As STT-MRAM has to operate on a wide range of temperature (e.g. -40°C to 150°C for automotive applications), it is desirable to minimize the thermal variation of the magnetic and transport properties of pMTJs. In this context, we report a novel design of dual-W composite storage layer (dual W-CSL) of the form "FeCoB/W/ferromagnet/W/FeCoB", which brings additional degrees of freedom to further improve the performance of the storage layer and particularly reduce the thermal variation of its properties. A detailed investigation of the thermal variation of magnetic and electrical properties of such dual W-CSLs for various ferromagnet insertions($Fe_{72}Co_8B_{20}$, $Co_{60}Fe_{20}B_{20}$ and Co) characterized by different exchange stiffness is reported. In particular, cobalt insertion between two W laminations significantly enhances the effective perpendicular anisotropy at room temperature compared to that of the conventional CSL (FeCoB/W/FeCoB) and reduces the relative thermal variation of effective perpendicular anisotropy in the range 300 K-400 K, which is shown in Fig. 1. Moreover, as shown in Fig 2(a) and (b), STT-MRAM cells with 80 nm diameters comprising Co inserted dual-W-CSL exhibit in average 15% and 38% higher thermal stability factor (Δ) as well as 26 % and 15% higher tunneling magnetoresistance ratio (TMR) respectively at room temperature and 110 °C than those of conventional CSL. Despite the increase of Δ for the memory cells comprising the Co inserted dual-W-CSL compared to the conventional case, the STT-efficiency (Δ/I_{c0}) of the former cells still remain the same (Fig. 2(c)) which makes this storage layer promising for STT-MRAM applications.

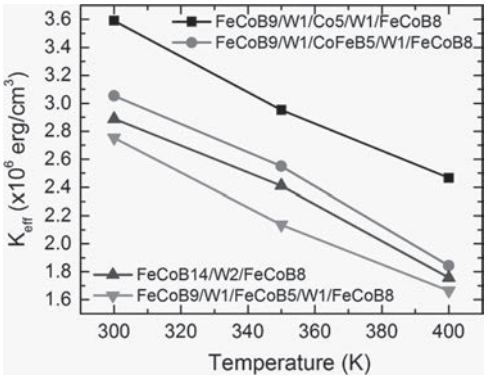


Fig.1 Effective perpendicular anisotropy of different composite storage layers as a function of temperature for 300, 350 and 400 K.

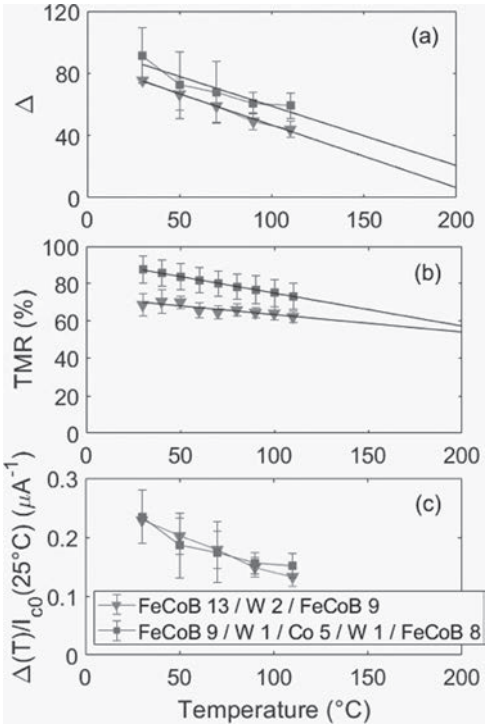


Fig.2 (a) Thermal stability factor (D) (b) TMR and (c) practical STT-efficiency as a function of temperature of the memory cells of 80 nm diameter for conventional CSL and Co laminated dual-W-CSL.

Session BD
MAGNETIZATION DYNAMICS: ULTRAFAST AND QUASIPARTICLE COUPLING I

Giovanni Finocchio, Chair
University of Messina, Messina, Italy

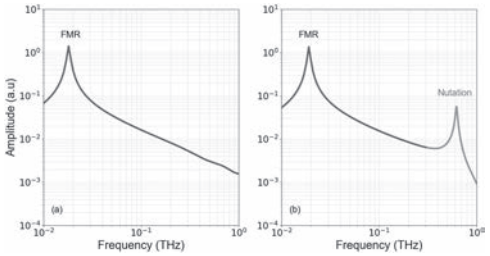
CONTRIBUTED PAPERS

1:30

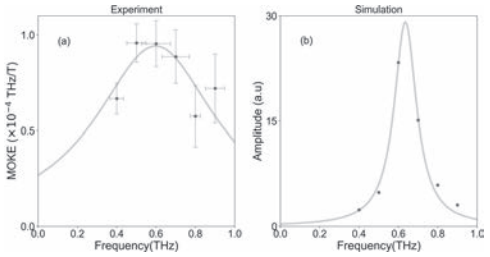
BD-01. Direct experimental evidence of inertial dynamics in ferromagnetic thin films. *K. Neeraj*[1], N. Awari[2], S. Kovalev[2], D. Polley[1], N. Zhou Hagström[1], A. Semisalova[9], B. Green[2], S. Arekapudi[3], V. Scalera[4], O. Hellwig[3,5], J. Wegrowe[6], M. Gensch[2,7] and S. Bonetti[1,8] *1. Department of Physics, Stockholm University, Stockholm, Sweden; 2. Helmholtz-Zentrum Dresden-Rossendorf, Dresden, Germany; 3. Institute of Physics, Chemnitz University of Technology, Chemnitz, Germany; 4. DIETI, University of Naples Federico II, Naples, Italy; 5. Institute of Ion Beam Physics and Materials Research, Helmholtz-Zentrum Dresden-Rossendorf, Dresden, Germany; 6. LSI, Ecole Polytechnique, CEA, CNRS, Palaiseau, France; 7. Institute of Optics and Atomic Physics, TU Berlin, Berlin, Germany; 8. Department of Molecular Sciences and Nanosystems, Ca' Foscari University of Venice, Venezia-Mestre, Italy; 9. Faculty of Physics, University of Duisburg-Essen, Duisburg, Germany*

It is known that the dynamics of magnetisation described by the Landau-Lifshits-Gilbert (LLG) equation [1] correctly models the reversal of a magnetic bit and hence the writing of digital information at nanosecond rates. Recently, the LLG equation was reformulated by including a physically correct inertial response [2] which predicts the appearance of spin nutations at a frequency much higher (in the terahertz range, i.e. at sub-picosecond timescales) than the spin precession described by the conventional LLG equation, typically at gigahertz frequencies. Here we show the first direct experimental evidence of inertial spin dynamics in ferromagnetic thin films in the sub terahertz frequency regime. We observed that when a ferromagnetically ordered spin system is driven by intense narrowband terahertz magnetic field pulses of tunable centre frequency, its behavior is similar to the one of a forced oscillator. By analyzing both amplitude and phase of the response, probed with femtosecond magneto-optical Kerr effect, we detect a broad resonance at approximately 0.6 THz, which we ascribe to nutation spin dynamics being driven by the terahertz magnetic field. From the experimental data, we were able to extract the angular momentum relaxation time, which we found to be on the order of 10 ps for three distinct samples with different Gilbert damping constant. Our experimental results are in good agreement with the numerical simulation of LLG equation with the inertial term. This work deepens our understanding of ultrafast magnetism and paves a new way towards controlling magnetism exploiting the nutation resonance.

1. Gilbert, T. L. IEEE transactions on magnetics, Vol.40, 3443–3449 (2004)
2. Ciornei, M. C., Rubí, J. M. & Wegrowe, J. E., Physical Review B, Vol.83, 1–4 (2011)



(a) LLG equation and (b) the inertial LLG equation showing the response (i.e. susceptibility) of a ferromagnetic system when an external ac magnetic field of varying frequency is applied. We see a ferromagnetic resonance (FMR) peak in both cases, and a nutation resonance peak for the inertial case.



(a) Maximum MOKE amplitude of amorphous CoFeB measured experimentally. (b) Maximum magnetization response amplitude of amorphous CoFeB calculated by solving the inertial LLG equation.

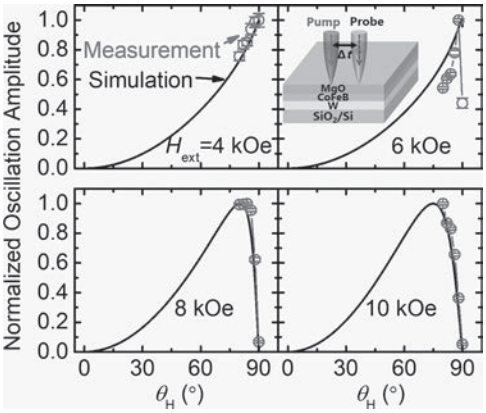
1:42

BD-02. Temperature Influence of Magnetization Dynamics in CoFeB Thin Films with TR-MOKE. *D.M. Lattery*[1], D. Zhang[2], D. Huang[1], P.A. Crowell[3], J. Wang[2] and X. Wang[1,2] *1. Mechanical Engineering, University of Minnesota Twin Cities, Minneapolis, MN, United States; 2. Electrical and Computer Engineering, University of Minnesota Twin Cities, Minneapolis, MN, United States; 3. Physics and Astronomy, University of Minnesota Twin Cities, Minneapolis, MN, United States*

Magnetic memory has recently shifted towards the use of magnetic thin films with large perpendicular magnetic anisotropy (PMA) to simultaneously satisfy the requirements in storage density and thermal stability. Understanding the magnetic switching process and its dependence on the Gilbert damping (α) of materials with large PMA is crucial for developing low-power consumption, ultrafast-switching, and high-thermal stability devices. The need to quantify α of materials with large PMA has resulted in the development of the all-optical ultrafast Time-Resolved Magneto-optical Kerr Effect (TR-MOKE) technique. While TR-MOKE has demonstrated its capability of capturing magnetization dynamics of materials with large PMA at high frequencies and fields, a quantitative analysis regarding the operational optimization of this emerging technique is still lacking. Through the application of a macrospin model based on the Landau-Lifshitz-Gilbert equation, the optimized operational conditions that produce the largest TR-MOKE signals are predicted.

As an experimental verification, we conducted TR-MOKE measurements on a representative sample of a CoFeB PMA thin film to show the excellent agreement of the model prediction with measurements. This analysis results in a better understanding on the external field influence on magnetization precession. With the results from this work and enhanced understanding of TR-MOKE measurements, we then determined the influence of annealing temperature in tungsten (W)-seeded CoFeB stacks. One of the most widely used PMA thin-film stacks is Ta/CoFeB/MgO; however, post-annealing at temperatures exceeding 350 °C leads to the failure of the CoFeB thin film to keep the PMA property. We replaced the Ta seed layer with W and discovered that this stack of W/CoFeB/MgO can sustain annealing temperatures up to 400 °C while still maintaining superb PMA properties and a relatively low Gilbert damping of ~0.02 at room temperature. Due to electronic heating, during the operation of these films in MRAM, it is necessary to understand the relaxation behavior at slightly elevated operational temperatures. For this reason, we also measure the increasing magnetic relaxation at environment temperatures up to 150 °C.

[1] D. Lattery, J. Zhu, D. Zhang, et al., Scientific Reports., Vol. 8, p.13395 (2018) [2] D. Lattery, D. Zhang, J. Zhu, et al., Applied Physics Letters., Vol. 113, p.162405 (2018)



1:54

BD-03. Light and THz induced magnetization dynamics in ultrathin PMA garnets. *L. Soumah*[1], S. Bonetti[1], A. Anane[2], V. Unikandanunni[1] and D. Polley[1] *1. Stockholm University, Stockholm, Sweden; 2. Universite Paris Sud CNRS Thales, Palaiseau, France*

Since the 60's, magnetic garnets have been the reference materials in terms of magnetization dynamics, due to their extremely low magnetic damping[1]. In those magnetic insulators, dynamics can be triggered differently: RF excitation, DC charge current (using spintronics phenomena[2]) or femtosecond-long light pulses[3–5]. Light-induced Ferromagnetic Resonance (FMR) precession can be observed on ferromagnetic garnets using λ=400 to 1300 nm pump. Femtosecond light pulses trigger magnetization dynamics through either impulsive (Inverse Cotton Mouton Effect[5] or Inverse Faraday Effect[4]) or displacive mechanisms (such as Photo-Induced Magnetic Anisotropy[3]). If light in the visible and near-infrared range is the most common way to induce magnetization dynamics, it is also possible to use the field from ultrafast terahertz (THz) light to obtain magnetization precession or demagnetization in metals[6,7]. However, THz induced magnetization dynamics in insulators remains an unexplored subject. Here, we investigate the magnetization dynamics induced by radiation of different wavelength, and hence possibly different light-matter interaction phenomena, in nanometer-thick $Bi_{0.3}Y_{2.7}Fe_5O_{12}$ films. Those films present high Faraday rotation coefficient, perpendicular magnetic anisotropy and low magnetic damping[8], and are thus ideal candidates for light-based pump-probe experiments. In those ultrathin films we induce magnetization dynamics using 400 nm light circularly and linearly polarized light (Figure 1 (a) and (b)) to establish the different processes involved into dynamics at those wavelengths. We also explore the potential of strong THz field pulses to generate magnetization dynamics in those films. Comparing the two excitation process mechanisms we draw conclusion on the most efficient approach.

1. Sparks, M. & Kittel, C. Ferromagnetic relaxation mechanism for Mz in yttrium iron garnet. *Phys. Rev. Lett.* 4, 232–234 (1960). 2. Kajiwara, Y. *et al.* Transmission of electrical signals by spin-wave interconversion in a magnetic insulator. *Nature* 464, 262–266 (2010). 3. Hansteen, F., Kimel, A., Kirilyuk, A. & Rasing, T. Femtosecond photomagnetic switching of spins in ferrimagnetic garnet films. *Phys. Rev. Lett.* 95, 1–4 (2005). 4. Koene, B. *et al.* Excitation of magnetic precession in bismuth iron garnet via a polarization-independent impulsive photomagnetic effect. *Phys. Rev. B - Condens. Matter Mater. Phys.* 91, 1–5 (2015). 5. Shen, L. Q. *et al.* Dominant role of inverse Cotton-Mouton effect in ultrafast stimulation of magnetization precession in undoped yttrium iron garnet films by 400-nm laser pulses. *Phys. Rev. B* 97, 1–15 (2018). 6. Hudl, M. *et al.* Nonlinear magnetization dynamics driven by strong terahertz fields. 1–6 (2019). 7. Polley, D. *et al.* THz-driven demagnetization with perpendicular magnetic anisotropy: Towards ultrafast ballistic switching. *J. Phys. D. Appl. Phys.* 51, (2018). 8. Soumah, L. *et al.* Ultra-low damping insulating magnetic thin films get perpendicular. *Nat. Commun.* 9, 1–6 (2018).

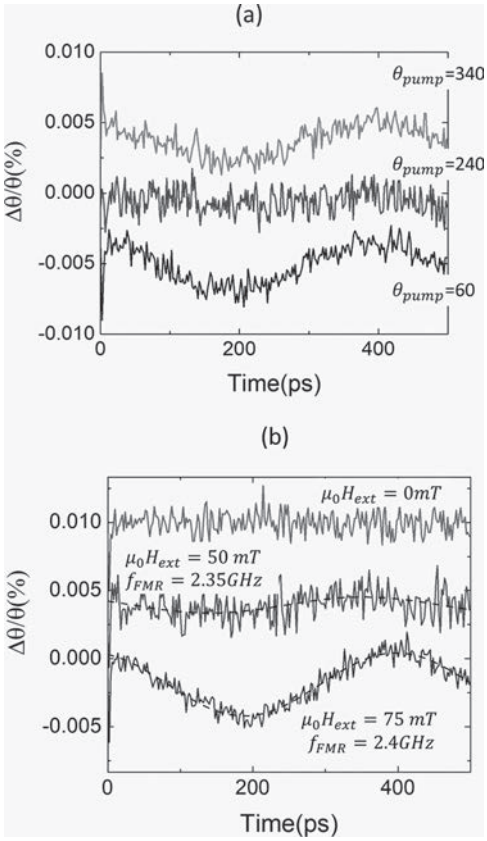


Figure 1 Evolution of Δθ/θ for 20 nm thick BiYIG//SGGG films after linearly polarized pump (λ=400nm) excitation. A tunable external field tilted 15° out of the plane is applied.(a) Polarization dependency of the oscillation suggests a non thermal origin of the magnetization dynamics' excitation and (b) the relaxation of the magnetization towards equilibrium in presence of the external field occurs at typical FMR frequency

2:06

BD-04. Magnetization dynamics of magnetotactic bacteria characterized by ferromagnetic resonance, micromagnetic simulations and scanning transmission x-ray microscopy ferromagnetic resonance.
T. Feggeler[1], B.W. Zingsem[1,2], R. Meckenstock[1], M. Winklhofer[3], D. Spoddig[1], H. Ohldag[4], A. Ney[5], M. Farle[1], H. Wende[1] and K. Ollefs[1]
1. Faculty of Physics, University of Duisburg-Essen, Duisburg, Germany; 2. Ernst Ruska-Centre for Microscopy and Spectroscopy with Electrons, Forschungszentrum Jülich GmbH, Jülich, Germany; 3. School of Mathematics and Science, University of Oldenburg, Oldenburg, Germany; 4. Advanced Light Source, Lawrence Berkeley National Laboratory, Berkeley, CA, United States; 5. Institute of Semiconductor and Solid State Physics, Johannes Kepler University, Linz, Austria

We present a comprehensive analysis of the magnetization dynamics of single magnetotactic bacteria of the types: a) Magnetospirillum Gryphiswaldense MSR-1 and b) Magnetospirillum Magnetotacticum MS-1 with individual chains of magnetite nanoparticles (particle diameter: a): 30 nm, b): 50 nm – 60 nm). The spectra of angular dependent ferromagnetic resonance (FMR) measurements at room temperature of single (multisegmented) nanoparticle chains show multiple angular dependent resonance lines originating from single particles and particle segments of the chain. A uniaxial shape anisotropy of the single chains with an easy axis along the chain axis is revealed. Formation of magnonic band gaps and band deformations are visible due to complex phase relationships in the dipolar coupled particle chain. These properties strongly depend on the arrangement of the nanoparticles in the chain and can be tailored by modifying the genetic code of the bacteria for use in applications e. g. magnonic logic devices. The complementary micromagnetic simulations are in good agreement to the experimental results, revealing the exact origin of the resonance lines. [1] A new approach to identify the origin of the resonances experimentally has been performed by using the element specific method of scanning transmission X-Ray microscopy ferromagnetic resonance (STXM-FMR) [2, 3], providing a lateral resolution down to 30 nm and a time resolution in the picosecond regime. First results at room temperature measured at the Fe L3-edge are shown, revealing a resonance response of a segment of a double segmented nanoparticle chain in a single wild type bacterium Magnetospirillum Magnetotacticum. Financial support: FWF Project No. I-3050, ORD-49 and DFG Project No. 321560838.

[1] B. Zingsem, et al., Nature Communications, in revision (2019). [2] S. Bonetti, et al., Rev. Sci. Instrum. 86, 093703 (2015). [3] T. Feggeler, et al., arXiv:1905.06772 [cond-mat.mes-hall] (2019).

2:18

BD-05. Anisotropic spin relaxation in epitaxial cobalt films following ultrafast demagnetization.
V. Unikandanunni[1], R. Medapalli[3], E. Fullerton[3] and S. Bonetti[1,2] *1. Department of Physics, Stockholm University, Stockholm, Sweden; 2. Department of Molecular Sciences and Nanosystems, Ca' Foscari University of Venice, Venice, Italy; 3. Center for Memory and Recording Research, University of California San Diego, San Diego, CA, United States*

The phenomenon of sub-picosecond demagnetization [1] has fascinated the magnetism community for the last two decades. Recently it was demonstrated that angular momentum from the spin system can be transferred to the lattice at ultrafast timescales via the microscopic version of the Einstein–de Haas effect [2]. The recovery of the spin order was suggested to happen via the Elliott-Yafet spin-flip scattering model [3]. Surprisingly though, there does not yet exist systematic studies on possible anisotropic demagnetization effects in epitaxial model systems, which would allow for probing the role of orientational spin-lattice coupling. We performed ultrafast demagnetization measurements on epitaxial hcp-cobalt thin film with the c-axis in the plane of the film by pumping the sample with 400-nm radiation and probing the magneto-optic effects in the longitudinal MOKE geometry using 800-nm radiation. The in-plane magnetic anisotropy of the sample enabled us to measure the demagnetization dynamics along two different directions, namely along the easy axis and at 45 degrees between the easy and hard axis (Fig. 1). Along these two directions, we observed a difference in the spin relaxation time. As shown in Fig. 2, the spin relaxation is systematically faster in the 45 degrees axis direction compared to the easy axis of magnetization, with only negligible (within the error bars) difference in the demagnetization magnitude and rate for the two different orientations. Repeated measurements with different relative polarization of both pump and probe show consistent evidence. The observed effect could be related to the anisotropic electron-phonon coupling in cobalt [4]. Our results emphasize the importance of the lattice symmetry in ultrafast demagnetization dynamics. Work at UCSD supported by the DOE award #DE-SC0018237.

1. E. Beaurepaire, J.C. Merle and J.Y. Bigot, Phys. Rev. Lett., Vol. 76, p.4250 (1996) 2. C. Dornes, Y. Acremann, M. Savoini et al., Nature, Vol.565, p.209 (2019) 3. E. Carpene, E. Mancini and S. De Silvestri, Physical Review B, Vol.78, p.174422 (2008) 4. Matthieu J Verstraete, J. Phys.: Condens. Matter., Vol.25, p.136001 (2013)

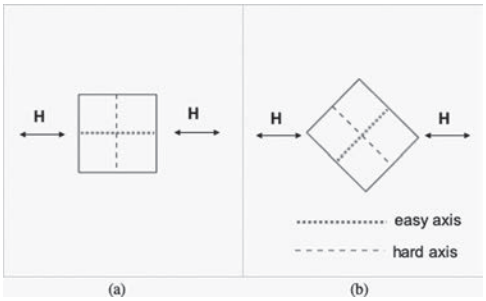


Figure 1 : Experimental schematic : The external magnetic field H is parallel to (a) the easy axis magnetization axis or (b) to the 45 degrees direction between easy and hard axis.

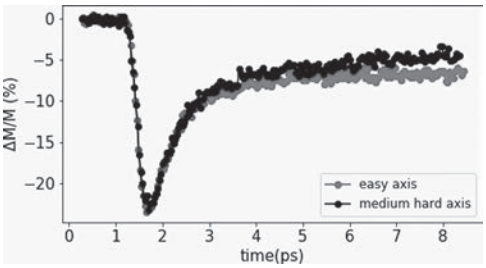


Figure 2: Magnetization dynamics measured with external field along easy and 45 degrees axis of magnetization in epitaxial cobalt. The pump is s-polarized, probe is p-polarized and the absorbed fluence is approximately 5 mJ/cm^2.

2:30

BD-06. Analysis of the linear relationship between asymmetry and magnetic moment at the M-edge of 3d transition metals. S. Jana[1,7], R. Malik[1], Y. Kvashnin[1], I.L. Locht[1], R. Knut[1], R. Stefanuik[1], I. Di Marco[1,6], A. Yaresko[4], M. Ahlberg[2], R. Chimata[1,8], M. Battiato[5], J. Soderstrom[1], O. Eriksson[1,3] and *O. Karis*[1] *1. Department of Physics and Astronomy, Uppsala University, Uppsala, Sweden; 2. Department of Physics, University of Gothenburg, Gothenburg, Sweden; 3. School of Science and Technology, Orebro University, Orebro, Sweden; 4. Max-Planck-Institut fur Festkorrperforschung, Stuttgart, Germany; 5. Nanyang Technological University, Singapore; 6. Department of Physics, POSTECH, Pohang, Pohang, The Republic of Korea; 7. Helmholtz-Zentrum Berlin, Berlin, Germany; 8. Argonne National Laboratory, Lemont, IL, United States*

The excitation of ferromagnetic material with an ultrashort laser pulse quench the magnetic moment rapidly on sub-picosecond timescales also called ultrafast magnetization, is one of the hot topics in modern magnetism[1]. For the last two decades, extensive efforts have been made to understand the origin of this ultrafast demagnetization[2,3,4]. The magneto-optical response of Fe and Ni is studied experimentally and theoretically during ultrafast demagnetization. We have performed pump-probe experiments in the transverse magneto-optical Kerr effect (T-MOKE) geometry using photon energies (40 to 72 eV) that cover the M-absorption edges of Fe and Ni. The asymmetry was calculated by measuring the reflection of light for two different magnetization directions of the sample. The observed variation of the magnetic asymmetry in the range of photon energies implies that the relation between magnetic asymmetry and sample magnetization is more complex than generally assumed[5]. Density functional theory (DFT) was used to calculate the magneto-optical response of different magnetic excitations: long-wavelength magnons, short wavelength magnons, and Stoner excitations. In case of Fe, the band structure is quite sensitive to the magnetic excitation, which results in the breakdown of the proportionality between the magnetization and magnetic asymmetry at and away from the resonance. Our modeling also reveals that during remagnetization Fe is to a reasonable approximation described by magnons, even though small non-linear contributions could indicate some degree of Stoner excitations as well. For Ni, the calculated asymmetry is not very sensitive to different magnetic excitations. However, due to the large magnetic asymmetry found for Ni experimentally, there is non-linearity in the relationship between asymmetry and the off-diagonal component of the dielectric tensor that underestimates the demagnetization by 12%. Our experimental and theoretical results emphasize the need for considering a coupling between asymmetry and magnetization that is more complex than a simple linear relationship and that is crucial for the microscopic interpretation of ultrafast magnetization experiments.

[1] Beaurepaire, E., Merle, J. C., Daunois, A., & Bigot, J. Y., Physical review letters, 76(22), 4250. (1996) [2] Zhang, G. P., & Hübner, W., Physical review letters, 85(14), 3025. (2000) [3] Koopmans, B., Malinowski, G., Dalla Longa, F., Nature Materials, 9(3), 259. (2009) [4] Stamm, C., Kachel, T., Pontius, N., Nature Materials, 6(10), 740. (2007) [5] Chan, L. O., Turgut, E., Teale, Physical Review X, 2(1), 011005. (2012)

2:42

BD-07. Ab-initio spin-lattice dynamics of low-dimensional clusters from tight-binding. *D. Thonig*[1], P. Bessarab[3,4], M. Pereiro[1] and O. Eriksson[1,2] *1. Department of Physics and Astronomy, Uppsala University, Uppsala, Sweden; 2. School of Science and Technology, Örebro University, Örebro, Sweden; 3. Science Institute of the University of Iceland, Reykjavik, Iceland; 4. Institute of Theoretical Physics and Astrophysics, University of Kiel, Kiel, Germany*

A profound concept in theoretical modelling is the separation of time scales in different reservoirs, for instance spin and lattice. However, in magnetocaloric [1] and multiferroic [2] materials such a reservoir separation is not feasible because of comparable exchange energies. Thus, a proper description combining the instantaneous dynamics of both, spin and lattice degrees of freedom, but also a deep understanding about the dynamical exchange mechanism between the reserviors are required. We will present our electronic structure approach of combined atomistic spin-lattice dynamics. Here, we apply our self-consistent, constrained, first-principles Tight Binding method, allowing us to calculate forces/torques without mapping to any particular effective Hamiltonian model. In particular for the spin degree-of-freedom it was shown [3] that this mapping is not feasible. Applying multiparameter perturbation theory to a disordered state in spin and lattice, we still are able to obtain 'parameters' in an effective bilinear spin-lattice Hamiltonian. This allows to compare ab-initio forces/torques with those obtained from an effective Hamiltonian, making a crucial statement about the validity of the classical spin-lattice model discussed in Ref. [4]. The current proposed self-consistent method will be applied to bulk Stoner magnets and low-dimensional systems. We reveal a significant discrepancies away from the bilinear model in both spin and lattice, especially under disorder. For instance, the hitherto assumed constant spin-spin exchange drastically varies strongly in time. Furthermore, indications for a dynamical anisotropic exchange interaction mediated by lattice vibration is exposed. Our approach will give, one hand, a new insight on exchange phenomena in a multi-reservoir system and, on the other hand, allows to study spin-lattice driven phenomena from a new first-principles perspective.

[1] G. E. W. Bauer, E. Saitoh and B. J. van Wees, Nature Materials., Vol. 11, p. 391–399 (2012) [2] R. Ramesh and N. A. Spaldin, Nature Materials., Vol. 6, p. 21 - 29 (2007) [3] A. Szilva, D. Thonig, P. F. Bessarab, et al., Phys. Rev. B., Vol. 96, p. 144413 (2017) [4] J. Hellsvik, D. Thonig, K. Modin, et al., Phys. Rev. B., Vol. 99, p. 104302 (2019)

2:54

BD-08. Terahertz induced Demagnetization in Magnetic Multilayers. *D. Polley*[1], K. Neeraj[1], V. Unikandanunni[1], S. Urazhdin[3] and S. Bonetti[1,2] *1. Department of Physics, Stockholm University, Stockholm, Sweden; 2. Department of Molecular Sciences and Nanosystems, Ca' Foscari University of Venice, Venice, Italy; 3. Department of Physics, Emory University, Atlanta, GA, United States*

In the last few years, strong table-top terahertz (THz) sources have been efficiently used to investigate spin-dynamics in different types of magnetic systems [1-3]. For metallic ferromagnets, defects-induced spin-lattice scattering appears to be more relevant than phonon scattering [1] and the THz-induced demagnetization amplitude is found to be more pronounced in multilayer films (ML) than for in-plane films [3]. Such observations paved the way to investigate the experimental realization of THz-induced 'ballistic switching' [4] in a table-top geometry. Here, we study the THz transport and the THz-induced ultrafast demagnetization dynamics in two ML films namely CoPt and CoNi. The complex conductivity is measured in the frequency range of 0.3-2.5 THz as shown in Fig. 1a, and has been analyzed with the Drude model. The d.c conductivity ($\sigma_{d.c.}$) and the Drude scattering timescale (σ_{Drude}) is smaller for CoPt (as shown in Table 1), due to the presence of the strong spin-orbit scattering element Pt and increased interface-scattering. THz-induced demagnetization spectra shown in Fig. 1b is measured in polar-magneto-optical Kerr effect geometry using strong THz radiation (~ 200 mT, fluence ~ 1 mJ/cm^2). The demagnetization amplitude is 52% larger in CoPt than CoNi and COMSOL simulation [5] confirms that absorbed energy difference alone cannot explain such a large change. The calculated Elliot-Yafet (EY) parameter (α_{EY}) [6] shows enhanced electron-phonon scattering rate in CoPt, which we suggest is due to enhanced spin-orbit coupling and interface scattering. This can explain the higher demagnetization amplitude in CoPt at the same THz field and fluence. The extracted electron-phonon relaxation timescale is slightly faster in CoNi than CoPt as shown in Table 1. The observation of large THz-induced demagnetization and its explanation in terms of enhanced EY scattering might open up efficient ways to induce THz-induced switching in ferromagnetic films.

1. S. Bonetti, M. C. Hoffmann, M.-J. Sher et. al., Phys. Rev. Lett. 117, 087205 (2016). 2. T. Kamfrath, A. Sell, G. Klatt et. al., Nat. Photon. 5, 31 (2011) 3. D. Polley, M. Pancaldi, M. Hudl et. al., J Phys. D Appl. Phys. 51, 084001 (2018) 4. I. Tudosa, C. Stamm, A. B. Kashuba et. al., Nature 428, 831(2004). 5. COMSOL Multiphysics v. 5.2. COMSOL AB, Stockholm, Sweden 6. D. Steiauf and M. Fähnle, Phys. Rev. B 79, 140401(R) (2009).

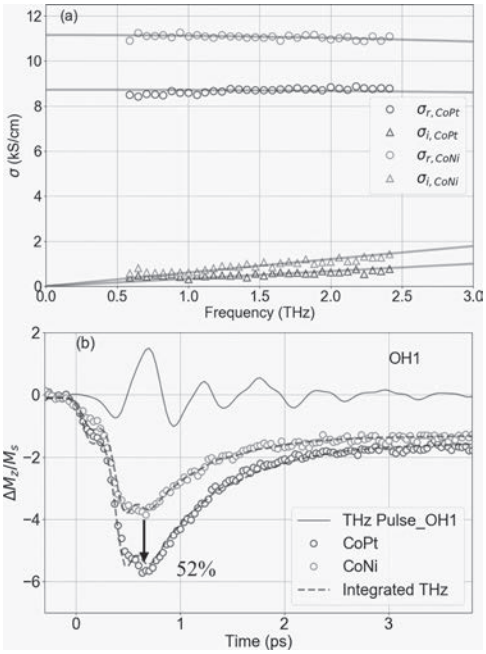


Fig. 1. (a) Complex THz conductivity for the two samples fitted with the Drude Model, (b) THz-induced demagnetization fitted with a phenomenological model, and temporal shape of the THz pulse used in the experiment generated with an OH1 crystal.

	CoPt	CoNi
$\sigma_{d.c.}$ (kS/cm)	8.70 ± 0.02	11.10 ± 0.04
τ_{Drude} (fs)	6.1 ± 0.3	8.7 ± 2.0
τ_M (fs)	33	100
α_{EY}	0.18	0.09
$\tau_{el-phonon}$ (fs)	640 ± 11	563 ± 12

Table 1. Fitted Parameters

3:06

BD-09. Spin Wave Relaxation by Eddy Currents in YIG/Pt Bilayers.
S.A. Bunyaev[1], A. Kreil[2], D.A. Bozhko[2], R.O. Serha[2], V.I. Vasyuchka[2], R.V. Verba[3], M.P. Kostylev[4], G.N. Kakazei[1], B. Hillebrands[2] and A.A. Serga[2] *1. Departamento de Fisica e Astronomia, IFIMUP-IN, Porto, Portugal; 2. Fachbereich Physik and Landesforschungszentrum OPTIMAS, Technische Universitat Kaiserslautern, Kaiserslautern, Germany; 3. Institute of Magnetism, Kyiv, Ukraine; 4. Faculty of Engineering and Mathematical Sciences, Physics, The University of Western Australia, Crawley, WA, Australia*

Single-crystal Yttrium Iron Garnet (YIG) is known as a material with the lowest Gilbert damping, which can be decreased or increased in electrically driven YIG/Pt bilayers by transfer of a spin torque from Pt to YIG films [1-3]. However, in the absence of an electric current in the Pt layer, the experimentally determined magnetic relaxation turns to be too high for practical applications [1]. Here, using the ferromagnetic resonance (FMR) technique, we show that the origin of this excessive damping is related to eddy currents induced in the Pt layer by magnetic oscillations excited in YIG film. Furthermore, we demonstrate a way to eliminate this relaxation mechanism. The experiment is performed using two 6.7-μm-thick YIG films grown by liquid phase epitaxy on a 500-μm-thick Gallium Gadolinium Garnet (GGG) substrate. One of the films serves as a reference, on another one YIG surface is covered by a 10 nm Pt layer, deposited by magnetron sputtering. The samples are fixed on the brass wall of a rectangular waveguide connected to an Anritsu vector network analyzer (VNA). The waveguide is placed inside electromagnet is such a way that orthogonal microwave, h_{rf} and magnetizing magnetic, H_0 fields are applied in the YIG film plane (Fig.1). For the reference YIG/GGG sample, the FMR linewidth Δf_{FMR} is independent of whether the sample is faced to the brass by YIG or by GGG side and is about 2.5 MHz. On the contrary, in the case of the Pt/YIG/GGG structure, Δf_{FMR} depends drastically on the fastening of the sample. If GGG is in contact with brass, the Δf_{FMR} increases up to 9.5 MHz. In the case, when Pt contacts the wall, Δf_{FMR} is almost the same as in the reference sample. This behavior can be understood if one attributes the observed Pt-related damping with Ohmic losses of eddy currents induced in a high resistive Pt layer. In such a case, the massive metallic wall electrically shunts the Pt layer and, thus, reduces the eddy current density in Pt. The shunting effect depends on a distance between Pt and the brass wall. The gradual increase of Δf_{FMR} with increase of this distance is clearly visible in Fig. 2. Developed analytical theory supports this explanation.

1. Z. Wang, Y. Sun, M. Wu, V. Tiberkevich et. al., Phys. Rev. Lett. 107, 146602 (2011). 2. R. O. Cunha, E. Padron-Hernandez, A. Azevedo et. al., Phys. Rev. B 87, 184401 (2013). 3. Z. Wang, Y. Sun, Y. Song et. al., Appl. Phys. Lett. 99, 162511 (2011).

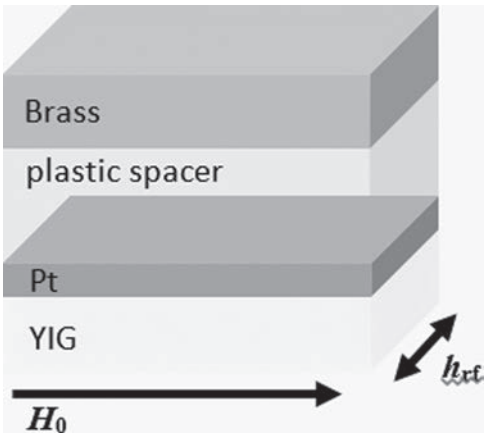


Fig. 1. Sample sketch.

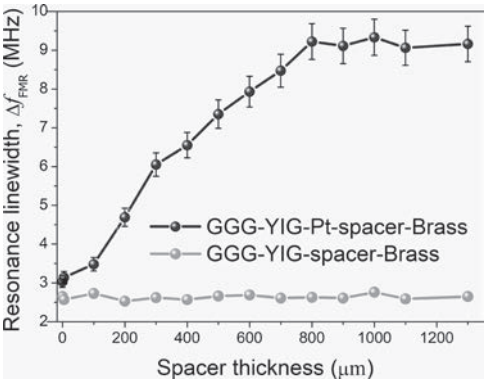


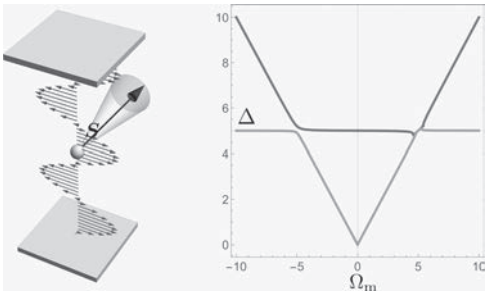
Fig. 2. Dependence of the linewidth.

3:18

BD-10. Microscopic Mechanisms of Level Attraction for a Coupled Magnon System in a Microwave Cavity. *I. Proskurin*[1,2], R. Macedo[3] and R.L. Stamps[1] *1. Department of Physics and Astronomy, University of Manitoba, Winnipeg, MB, Canada; 2. Institute of Natural Sciences and Mathematics, Ural Federal University, Ekaterinburg, Russian Federation; 3. School of Physics and Astronomy, University of Glasgow, Glasgow, United Kingdom*

Level attraction was proposed recently as a new universal type of interaction in dynamical nonequilibrium systems. In this regards it is analogous to synchronization of two harmonic oscillators, where one of the oscillators has a negative-mass instability [1,2]. This type of behavior is important in quantum information processing for realization of quantum amplifiers and mode entanglement [2]. Level attraction was recently demonstrated experimentally for cavity magnon-polaritons and interpreted in terms of macroscopic manifestation of the Lenz's effect in a dissipative system [3]. In this work, we consider the microscopic origins of level attraction for a coupled magnon system. By analyzing magnon response functions, we show that, in general, the attractive regime is related to an effective susceptibility of a diamagnetic type. There is a number of microscopic mechanisms that can contribute to this type of susceptibility depending on the type of interactions with another subsystem coupled to magnonic bath. For cavity magnon-polaritons, we analyze the contribution from the inverse Faraday effect and the Aharonov-Casher phase [4]. For the former scenario, we derive the effective susceptibility and the level attraction picture for the geometry shown in the Figure. We also demonstrate that in materials with flowing spin currents there is a relativistic mechanism of level attraction through the Aharonov-Casher effect of the cavity electric field. We estimate the magnitude of this effect and discuss its relevance to materials with Dzyaloshinskii-Moriya interactions. We extend our theory to the resonant absorption of magnons by the Bloch electrons in conducting materials and apply it to the Rashba materials with spin-orbit torques, where we demonstrate the origin of the attractive regime from the antidamping torque, which can be helpful for interpreting the available experimental data in these systems [5].

1. N. R. Bernier et al., Phys. Rev. A, Vol. 98, p. 023841 (2018). 2. J. Kohler et al., Phys. Rev. Lett., Vol. 120, p. 013601 (2018). 3. M. Harder et al., Phys. Rev. Lett., Vol, 121, p. 137203 (2018). 4. I. Proskurin, R. Macêdo, and R. L. Stamps, arXiv: 1904.11570 (2019). 5. A. J. Berger et al., Phys. Rev. B, Vol. 97, 094407 (2018).



Small ferromagnetic specimen interacting with the cavity mode via the inverse Faraday effect (left), and the level attraction picture between the magnon mode with frequency Ω and the cavity mode with the detunning parameter Δ (right).

3:30

BD-11. Abnormal anti-crossing dispersion in photon-magnon coupling. *B. Bhoi*[1], B. Kim[1] and S. Kim[1] *1. Department of Materials Science and Engineering, Seoul National University, Seoul, The Republic of Korea*

Understanding and exploiting the interactions of the excited modes in hybrid quantum systems are the keys to achieving the ambitious goal of quantum information processing [1-2]. Therefore, collectively excited modes (i.e., magnons) in ferromagnets, being coupled to elementary excitations of electromagnetic waves (photons), have increasingly been studied in a variety of hybrid systems [3-4]. The interaction (coupling) between the magnon and photon modes is usually demonstrated by showing the modes' splitting near their common resonant frequency within the so-called anti-crossing region or their level repulsion, as described well by a classical model for coupled oscillators and also by a two-level quantum model [4]. Herein, we report the experimental demonstration of an abnormal, opposite anti-crossing dispersion (or level attraction) in a photon-magnon (P-M) coupled system that consists of an Yttrium Iron Garnet film and an inverted pattern of split-ring resonator structure (noted as ISRR) in a planar geometry [5]. It was found that the normal shape of anti-crossing dispersion typically observed in P-M coupling is changed to its opposite anti-crossing shape just by changing the position/orientation of the ISRR's split gap with respect to the microstrip line axis along which ac currents are applied. The characteristic features of the opposite anti-crossing dispersion and its linewidth evolution were scrutinized with the help of analytical derivations based on electromagnetic interactions. We ascribed the observed opposite anti-crossing dispersion to the compensation of both intrinsic damping and coupling-induced damping in the magnon modes. This is achievable by controlling the relative strength and phase of the oscillating magnetic fields generated from the ISRR's split gap and the microstrip feeding line. We provided a phase diagram of the dispersion type in the P-M coupling region according to the strength and phase of the microwave magnetic fields acting on the hybrid system. The position/orientation of an ISRR's split gap provides a robust means of controlling the dispersion shape of anti-crossing and its damping in a P-M coupling, thereby offering more opportunity for advanced microwave-device designs.

[1] H. J. Kimble, Nature, Vol. 453, p.1023 (2008). [2] Z. Xiang, S. Ashhab, J. You, et al Rev. Mod. Phys., Vol. 85, p. 623 (2013). [3] B. Bhoi, B. Kim, S-K. Kim, et al Sci. Rep., Vol. 7, p.11930 (2017). [4] M. Harder and C.-M. Hu, in Solid State Physics, edited by R. E. Camley and R. L. Stamps (Academic Press, Cambridge, 2018), Vol. 69, p. 47 [5] B. Bhoi, B. Kim, S.-K. Kim, et al Phys. Rev. B Vol. 99, p.134426 (2019) [Editors' Suggestion].

3:42

BD-12. Lattice dynamics in magnetostrictive heterostructures excited by ps acoustic pulses. S. Zeuschner[2,3], *K. Dumesnil*[1], T. Parpiiev[4], T. Pezeril[4], A. Hillion[1], A. Anane[5], J. Pudell[2], L. Willig[2], M. Rossle[2], M. Herzog[2], A. von Reppert[2] and M. Bargheer[3,2] *1. Institut Jean Lamour, Nancy, France; 2. University of Potsdam, Potsdam, Germany; 3. Helmholtz Zentrum, Berlin, Germany; 4. Institut des Molécules et Matériaux, Le Mans, France; 5. UMphi, Saclay, France*

The control of the magnetization and/or the magnetization dynamics in a reliable, fast and energy-efficient way is of paramount interest for data storage, manipulation and signal processing. The possible control of magnetization via elastic strains (static and/or dynamic) is one of the promising paths that currently drives intense research activities, leading to the emergence of the so-called "straintronics". This work aims at exploring *both the magnetic and elastic dynamical responses* of magnetostrictive $TbFe_2$/Nb crystalline layered heterostructures, after excitation by femtosecond *laser-induced acoustic pulses*. The combination of ultrafast X ray diffraction (UXRD) with Magneto Optical Kerr Effect (MOKE) measurements permits to probe with time resolution the two degrees of freedom: the strain evolution in the different layers and the associated strain-induced magnetic changes in $TbFe_2$. When the excited $TbFe_2$ is the surface of the sample, a classical symmetric bipolar strain pulse is observed while a decomposition of the transient strain into an asymmetric bipolar and a unipolar pulses occurs when the excited $TbFe_2$ is capped with SiO_2. The inverse magnetostriction due to the unipolar strain pulses leads to a MOKE signal that linearly depends on the strain pulse amplitude measured through UXRD (Fig. 1). Linear chain model simulations accurately predict the timing and shape of UXRD and MOKE signals due to the strain reflections from multiple interfaces in the heterostructure [1]. MOKE thus appears to be a very sensitive probe for the

arrival of the multiple strain echoes at the top of the highly magnetostrictive $TbFe_2$ layer and complements bulk sensitive UXRD that provides quantitative information on strains with unit cell resolution and layer selectivity. The combination of MOKE and UXRD outlines a potential path towards an experimental calibration of the magnetoelastic coefficient for picosecond acoustic pulses, which constitutes an important step towards the manipulation of magnetization in giant magnetostriction materials.

[1] S. Zeuschner et al., Struct. Dyn. 6, 024302 (2019)

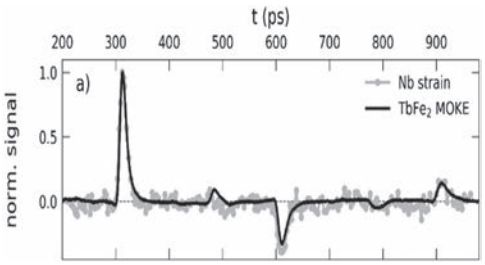


Fig. 1: Comparison of the coherent phonon strain contribution seen in the MOKE and UXRD signal, scaled to the maximum amplitude and shifted to overlap in time

3:54

BD-13. Gigahertz Frequency Antiferromagnetic Resonance and Strong Magnon-Magnon Coupling in the Layered Crystal $CrCl_3$. D. MacNeill[1], *J.T. Hou*[2], D. Klein[1], P. Zhang[2], J. Pablo[1] and L. Liu[2] *1. Physics, Massachusetts Institute of Technology, Cambridge, MA, United States; 2. Electrical Engineering and Computer Science, Massachusetts Institute of Technology, Cambridge, MA, United States*

Antiferromagnetic spintronics is an emerging field with the potential to realize high speed logic and memory devices. Compared to ferromagnetic materials, antiferromagnetic dynamics are less well-understood, partly due to their high instrinsic frequencies that require specialized terahertz techniques to probe. Here, we report broadband microwave absorption spectroscopy of the layered antiferromagnet insulator $CrCl_3$ [1]. We observe a rich structure of resonances arising from quasi-two-dimensional antiferromagnetic dynamics. Due to the weak interlayer magnetic coupling in this material, we are able to observe both optical and acoustic branches of antiferromagnetic resonance in the GHz frequency range and a symmetry-protected crossing between them. By breaking rotational symmetry, we further show that strong magnon-magnon coupling with large tunable gaps can be induced between the two resonant modes. All of these effects are captured with analytical solutions of the Landau-Lifshitz Gilbert equations, and the extracted values of exchange field and saturation magnetization are consistent with magnetometry measurements. Our results provide $CrCl_3$ as a versatile platform for studying antiferromagnetic dynamics with conventional microwave electronics. Furthermore, $CrCl_3$ can be cleaved to produce air-stable films down to the monolayer limit. Using van der Waals assembly, we can combine different magnetic materials to build antiferromagnetic devices and to induce magnon-magnon coupling by breaking sublattice exchange symmetry.

[1] D. MacNeill*, J. T. Hou*, D. R. Klein, P. Zhang, P. Jarillo-Herrero, and L. Liu, Gigahertz frequency antiferromagnetic resonance and strong magnon-magnon coupling in the layered crystal CrCl3, arXiv:1902.05669 (2019)

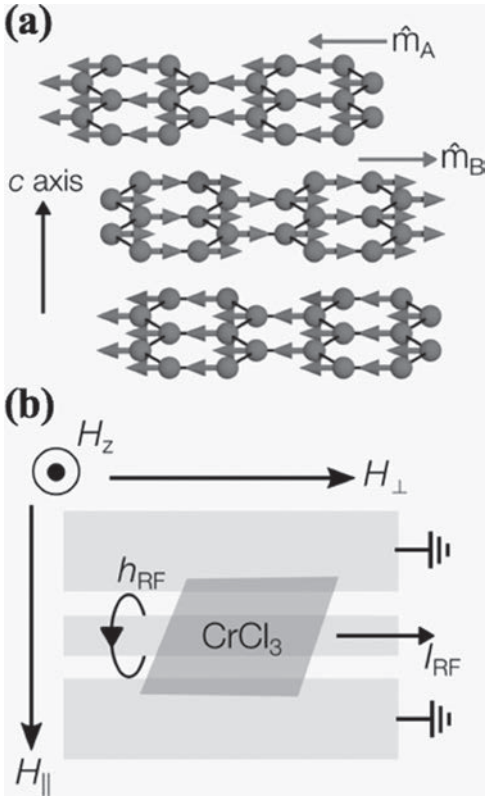


Fig. 1. (a) Magnetic structure of bulk $CrCl_3$ below the Neel temperature. The net magnetization direction alternates between layers. (b) Experimental schematic featuring a coplanar waveguide (CPW) with a $CrCl_3$ crystal placed over the signal line. The microwave transmission coefficient was measured as a function of applied magnetic field.

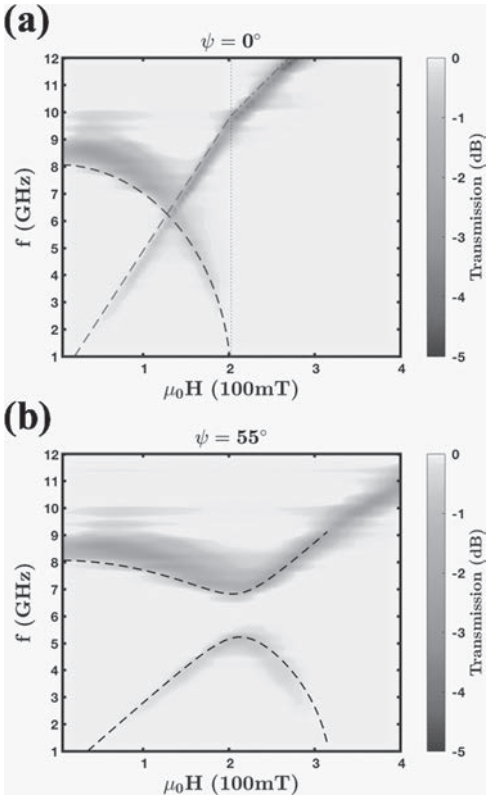


Fig. 2. Microwave transmission as a function of frequency and applied field at 1.56 K; the field is applied at an angle of a) Ψ = 0° and b) Ψ = 55° from the sample plane. The blue and red dashed lines in a) are fits of the optical and acoustic mode frequencies. A coupling gap is induced in b) due to rotational symmetry breaking.

4:06

BD-14. Greatly Enhanced Magnetoelastic Excitation of a Single Nanomagnet by Focusing Surface Acoustic Waves. *W. Yang*[1], M. Jaris[1] and H. Schmidt[1] *1. University of California Santa Cruz, Santa Cruz, CA, United States*

Elastic surface waves can significantly influence the magnetization dynamics of nanomagnets [1]. Surface acoustic waves (SAWs) can be optically generated by a nanowire array and used to excite narrow-band magnetization precessions in a single nanomagnet via magneto-elastic (MEL) coupling. This was used for time-resolved measurements of the SAW driven magnetization precession of a single nanomagnet and enabled direct determination of the intrinsic Gilbert damping of the nanomagnet [2]. Here, we demonstrated a dramatic enhancement of the MEL excitation of a single nanomagnet using focused SAWs (FSAWs) (Fig. 1a,b). We show the Kerr signal amplitude is almost 10 times larger than the optically excited (Fig. 1c). The Fourier amplitude of the MEL excitation shows a linear increase with increasing pump fluence (Fig. 1d). Thanks to the robust MEL excitation, we demonstrated for the first time the MEL controlled magnetization dynamics in sub-100nm single nanomagnets. Furthermore, we integrated four sets of nanowires with different pitch (Fig. 2a,b), which enables us to selectively excite magnetization dynamics of any one of four identical single nanomagnets at the corresponding four different resonant fields (Fig. 2c, d). The all-optical technique provides an alternative method of studying intrinsic spin dynamics of individual small nanomagnets, which have important implications for nanoscale spintronic devices and nanoscale magneto-mechanical devices.

[1]. Y. Yahagi et al. Phys. Rev. B 90 140405(R) (2014). [2] W.G. Yang et al. Phys. Rev. B 97 224410 (2018).

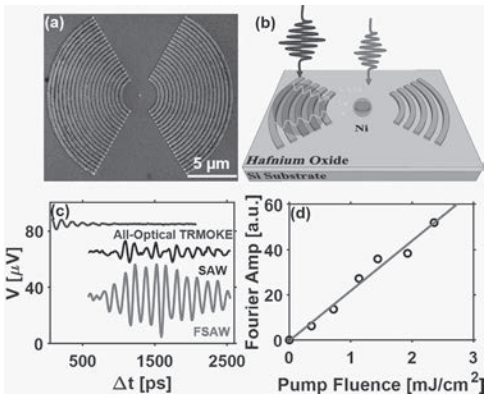


Fig. 1 (a) SEM image of a 200nm Ni nanomagnet surrounded by arc-shaped nanowires (p = 400nm) (b) Schematic plot of FSAW driven magnetization excitation in single nanomagnet (c) Time traces of the optically excited single Ni nanomagnet, the SAW and FSAW driven identical nanomagnet. (d) The Fourier amplitude of the FSAW driven magnetic precession versus the pump fluence.

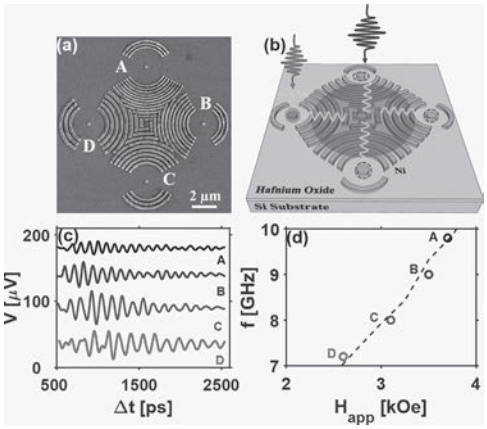


Fig. 2 (a) SEM image of four identical 200nm Ni nanomagnets surrounded by corresponding four pitches of nanowires with p = 250,300,350,400nm, respectively (b) Schematic plot of FSAW driven magnetization excitation (c) Time traces of the FSAW driven four nanomagnets (d) The precession frequency of the four nanomagnets at corresponding resonant fields. The dashed line is the intrinsic magnetic frequency.

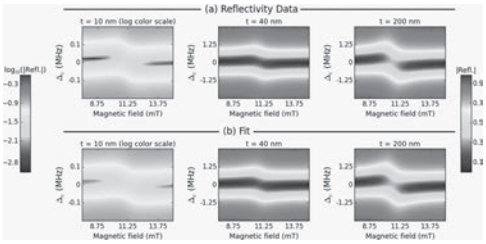
4:18

BD-15. Controlling the magnon-photon interface via a cavity Fano resonance. J. Gollwitzer[1], L. Bocklage[1,2], R. Röhlsberger[1,2] and *G. Meier*[3,2] *1. Deutsches Elektronen-Synchrotron DESY, Hamburg, Germany; 2. The Hamburg Centre for Ultrafast Imaging, Hamburg, Germany; 3. Max-Planck Institute for the Structure and Dynamics of Matter, Hamburg, Germany*

The interface between photons and magnons has introduced the opportunity to perform quantum information processing in macroscopic systems. So far, strong coupling and Rabi oscillations have been exploited to control the coupling between photons and magnons in microwave cavities (1–3). Here, we present a new scheme to achieve spectral control of magnon-photon coupling via Fano interference. The Fano resonance is controlled via cavity detuning, which acts as the background channel in the Fano picture at sufficiently low coupling. An incoherent term in the Fano picture, normally attributed to decoherence in open quantum systems (4,5), actually arises here due to the coupling of a discrete matter resonance with a resonant cavity mode. Magnon-photon hybridization at higher coupling strengths alters the

Fano phase relations and effects the breakdown of the Fano picture. These results establish spectral Fano control in cavity optomagnonics, which may lead to advances in room temperature quantum information processing.

1. X. Zhang, C.-L. Zou, J. Liang, and X. H. Tang, Phys. Rev. Lett.113, 156401 (2014). 2. X. Zhang, et al., Nat. Communications. 6, 8914 (2015). 3. L. Bai et al., Phys. Rev. Lett. 114, 227201 (2015). 4. A. Bärnthaler et al., Phys. Rev. Lett. 105, 056801 (2010). 5. A. A. Clerk, X. Waintal, and P. W. Brouwer, Phys. Rev. Lett. 86, 4636 (2001).



(a) Magnitude of the reflectivity showing the Purcell effect. The Kittel mode of the permalloy film couples to the cavity photon and shows up as a distortion in the cavity resonance. As the thickness of the permalloy film is increased the coupling factor g increases and the distortion becomes more pronounced. The diagrams on the left for the case t = 10 nm shows the reflectivity in the logarithmic color scale. (b) Fits to the data using a model based on a Jaynes Cummings Hamiltonian.

Session BE
SPIN CALORITRONICS

Felix Casanova, Chair
CIC nanoGUNE, Donostia-San Sebastian, Spain

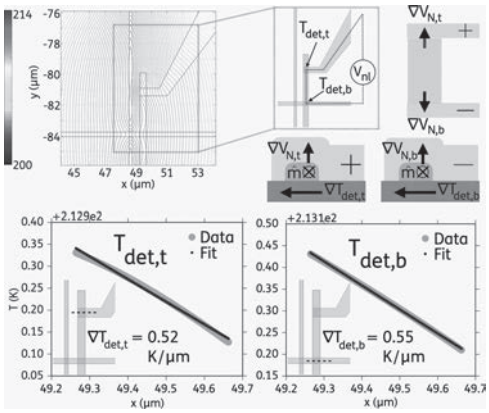
CONTRIBUTED PAPERS

1:30

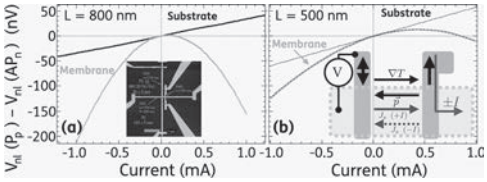
BE-01. Thermal Gradients and Anomalous Nernst Effects in Membrane-supported Non-Local Spin Valves. R.K. Bennet[1], A. Hojem[1,2] and *B.L. Zink*[1] *1. Physics & Astronomy, University of Denver, Denver, CO, United States; 2. Physics, UC San Diego, La Jolla, CA, United States*

Non-local spin valves (NLSVs) have the unique capability to separate charge and spin currents, and thus are an important tool for both applied and fundamental research in nanomagnetism.[1,2] Previous research shows that changes to the composition of the NLSV substrate can have a marked effect on the background non-local resistance by altering the substrate thermal conductance.[3] Our research demonstrates enhancement of non-local spin resistance by the anomalous Nernst effect (ANE) and dramatically lowered thermal conductance in NLSVs fabricated on Si-N membranes with a thickness of 500 nm.[4,5] In this membrane-supported construction, the thermal gradient is confined to nearly 2 dimensions. We therefore use 2D finite-element modeling of Py/Al NLSVs to present refined values as low as 0.17 for the Nernst coefficient of permalloy at 200 K. This is in good agreement with previously reported values.[6,7] We also discuss the rarely-measured temperature dependence of the Nernst coefficient of permalloy. This membrane-supported construction also leads to additional thermal spin injection effects, such as thermally-assisted electrical spin injection not seen in our bulk Si substrate-supported devices. We model this previously unknown effect as a contribution from phonon momentum interacting with the pure spin current in the Al channel.

[1] Jedema, et al. Nature 410, 345 (2001) [2] Ji, et al, APL 88, 052509 (2006) [3] Kasai, et al. APL 104, 162410 (2014) [4] Hojem, et al. (in preparation) [5] Bennet, et al. (resubmitted, PRB 2019) [6] Slachter, et al. PRB 84 020412(R) (2011) [7] Chuang, et al. PRB 96, 174406 (2017)



2D FEM of a Py/Al NLSV. Thermal gradients at the 2 detector junctions (Tdet,t and Tdet,b), determined by linear fits to the local temperature as a function of position across each contact, each generate a Nernst voltage. However, the overall detected Nernst voltage is the difference of these contributions due to the definition of the current path, shown schematically.



Direct comparison of spin-isolated (ANE removed) IV curves for substrate (blue) and membrane (orange) devices with FM separation distances of 800 (a) and 500 nm (b). The large in-plane thermal gradient in the membrane devices drives an additional nonlinear spin signal. Insets: SEM micrograph of a NLSV; and a schematic view of the charge current I, spin current Js (with direction in the channel dependent on polarity of I), thermal gradient, and average phonon momentum p.

1:42

BE-02. Sign reversal of anomalous and planar Nernst effects at low temperature for a $C1_b$-type NiMnSb half-Heusler alloy thin film. *H. Sharma*[1,2], *Z.* Wen[3], K. Takanashi[1,4] and M. Mizuguchi[1,2] *1. Institute for Materials Research, Tohoku University, Sendai, Japan; 2. CREST, Japan Science and Technology Agency, Kawaguchi, Japan; 3. National Institute for Materials Science, Tsukuba, Japan; 4. Center for Spintronics Research Network (CSRN), Tohoku University, Sendai, Japan*

The Nernst effect, thermally induced transversal voltage in the direction perpendicular to both the temperature gradient and the magnetization, is a valuable probe for the spin-orbit coupling phenomena in the field of spin caloritoronics [1-6]. The interplay between the anomalous Nernst effect (ANE), planar Nernst effect (PNE), pure spin-current and spin-polarized current generated by a thermal gradient is attracting many researchers. The ANE and PNE can be utilized to investigate the spin-orbit coupling phenomena through the interaction among spin, charge and heat. On the other hand, the $C1_b$-type half-metallic Heusler alloys are of intense research interest because of their exclusive properties due to the semiconducting behavior of the minority band with a gap at the Fermi level and thus leading to 100% spin polarization of conduction electrons [6-8]. This exceptional property may direct distinctive thermoelectric effects in half-metallic Heusler alloys, which augment the interest in the physical properties in the concerned materials. In this contribution, we present a systematic investigation of the ANE, PNE and Seebeck with in-plane applied thermal gradient (see in inset of Fig. 1a) at different temperatures for a $C1_b$-type NiMnSb half-Heusler alloy thin film. A clear reversal behavior of ANE and Seebeck (see in Fig. 1a) is observed at low temperatures ($T \leq 40$ K). In addition, the PNE switches (see Fig. 1b) from its fourfold $\sin\theta\cos\theta$ angular dependence behavior to twofold $\sin\theta$ angular dependence behavior at low temperatures ($T \leq 40$ K). This observed arbitrary behavior of ANE, Seebeck and PNE in $C1_b$-type NiMnSb half-Heusler alloy thin film will be discussed in details.

1. W. Nernst, Ann. Phys., 267, 760 (1887). 2. M. Mizuguchi, et al., Appl. Phys. Express 5, 093002 (2012). 3. Y. Sakuraba, K. Hasegawa, M. Mizuguchi, et al., Appl. Phys. Express 6, 033003 (2013). 4. K. Hasegawa, M. Mizuguchi, et al., Appl. Phys. Lett., 106, 252405 (2015). 5. H. Sharma, et al., Mate. Chem. Phys., 180, 390 (2016). 6. H. Sharma, M. Mizuguchi, et al.,

Jpn. J. Appl. Phys., 58, SBBI03 (2019). 7. Z. Wen, et al., Sci. Rep., 5, 18387 (2015). 8. Z. Wen, et al., arXiv:1902.07406 (2019).

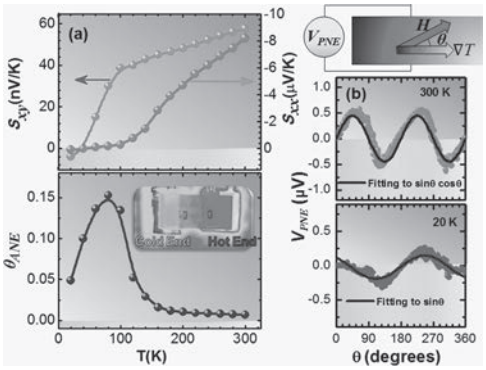


Fig. 1 (a) Temperature dependence of ANEs (left axis), Seebeck (right axis) effect, and temperature dependence of Nernst angle (θ_{ANE}). Inset shows the thermo-graphic image of the device used to measure ANE, (b) Angular dependence of the PNEs in applied magnetic field of 0.2 T at 300 K and 20 K with applied in-plane temperature gradient of 3 K.

1:54

BE-03. Large anomalous Nernst and Hall effects without magnetization scaling in $Fe_{1-x}Sn_x$ ordered alloy thin films.
M. Mizuguchi[1], H. Sharma[1], Y. Goto[2], A. Maeno[2], T. Nagahama[2], K. Watanabe[3], M. Tsujikawa[3] and M. Shirai[3] *1. Institute for Materials Research, Tohoku University, Sendai, Japan; 2. Graduate School of Engineering, Hokkaido University, Sapporo, Japan; 3. Research Institute of Electrical Communication, Tohoku University, Sendai, Japan*

The anomalous Nernst effect (ANE), one of the thermomagnetic effects studied for a long time, has recently attracted renewed attention. The ANE, which originates from fictitious fields in momentum space, is essential for clarifying the interplay among heat, spin, and charge in magnets[1]. It is indispensable to find the guiding principle to obtain materials with large ANE in order to realize a thermoelectric device based on the ANE. Thus, we have systematically investigated the ANE in ordered alloy thin films[2-4] and found the relation between the magnetic anisotropy and the ANE for the films. Recently, the metastable *B*2-type Fe-Sn alloys have been successfully fabricated by molecular beam epitaxy (MBE)[5]. This material attracts attention because large tunnel magnetoresistance is expected by combining with a MgO burrier layer. In this paper, we report the large ANE and anomalous Hall effect (AHE) in *B*2-type $Fe_{1-x}Sn_x$ ordered alloy films with various Sn composition (x). The films were grown on MgO(100) substrates by MBE. Transverse Seebeck coefficient (S_{xy}) loops and Hall resistivity (r_{xy}) as a function of the magnetic field were measured. For ANE measurements, one side of a sample was heated, and a temperature difference was induced along the long side of a rectangle sample. A magnetic field perpendicular to the sample plane was applied. Figure 1 shows Sn composition dependence of S_{xy} for $Fe_{1-x}Sn_x$ ordered alloy films measured at room temperature. Maximum S_{xy} is about 4 μV / K with x = 30 %. This value is exceedingly larger than ordinary ferromagnetic materials[2-4], and it is revealed that a Sn-doping into Fe site is very effective to enhance ANE of Fe. Surprisingly, the intensity of S_{xy} is not scaled to the saturation magnetization (M_s) of these films because M_s tends to decrease with increasing the Sn composition. This implies that the mechanism of the ANE in *B*2-type $Fe_{1-x}Sn_x$ is not simple and any interesting physics is involved in this phenomenon. Detailed comparison between ANE and AHE, and an insight on electronic structures of this material calculated by ab initio will be also discussed.

[1] M. Mizuguchi and S. Nakatsuji, Sci. Tec. Adv. Mater. 20, 262 (2019). [2] M. Mizuguchi, *et al*., Appl. Phys. Express 5, 093002 (2012). [3] K. Hasegawa, M. Mizuguchi, *et al*., Appl. Phys. Lett. 106, 252405 (2015). [4] H. Sharma, M. Mizuguchi, *et al*., Jpn. J. Appl. Phys. 58, SBBI03 (2019). [5] Y. Goto, T. Nagahama, *et al*., Jpn. J. Appl. Phys. 57, 120302 (2018).

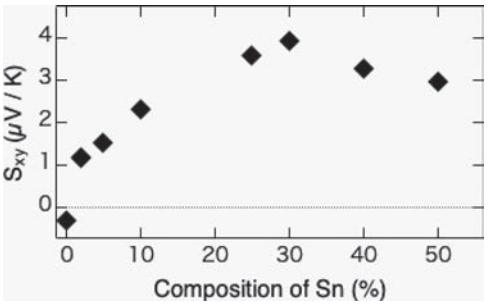


Figure 1. Sn composition dependence of S_{xy} for $Fe_{1-x}Sn_x$ ordered alloy films measured at room temperature.

2:06

BE-04. Light-induced thermal spin current. *Y. Chen*[1] and S. Huang[1] *1. Physics, National Taiwan University, Taipei, Taiwan*

In this work, we investigate the thermal spin current driven by light, including magnonic spin current of the spin Seebeck effect (SSE) and spin-polarized current of the anomalous Nernst effect (ANE) [1]. Unlike heating by electrical means, the light-induced thermal spin current by the SSE (see Fig. 1) and the ANE (see Fig. 2) can be enhanced, reduced, and its sign can even be reversed due to the intrinsic characteristic of the penetrating light. Most importantly, by reversing the direction of the incident light, we are able to qualitatively distinguish the contributions from the interfacial and bulk temperature gradients to the transverse spin accumulation. Most importantly, although the overall spin signals are strongly influenced by the frequency of light, the interfacial and bulk spin Seebeck coefficients are intrinsic and frequency independent. In addition, we observe a nearly instantaneous time response both from the SSE and the ANE during the light excitation, which highlight the importance of spin-to-charge conversion by the spin-orbit coupling for ultrafast spin caloritronics. We demonstrate light offers distinct heating mechanism to develop spintronic and spin caloritronic devices.

Ref. [1] Yi-Jia Chen and Ssu-Yen Huang, "Light-induced thermal spin current", Phys. Rev. B 99, 094426 (2019)

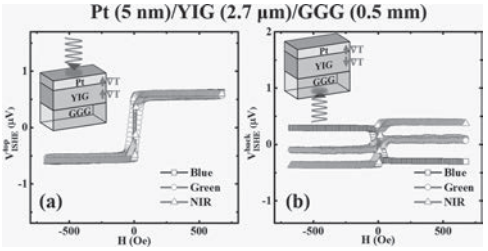


FIG. 1 Spin Seebeck signal induced by blue, green, and near-infrared (NIR) light, lighting on (a) top of Pt (5 nm)/YIG (2.7 μm)/GGG (0.5 mm), and (b) bottom of Pt (5 nm)/YIG (2.7 μm)/GGG (0.5 mm).

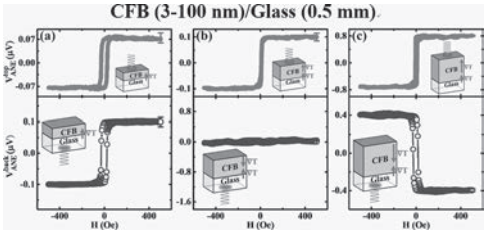


Fig. 2 V_{ANE} of (a) CFB (3 nm), (b) CFB (5 nm), and (c) CFB (100 nm) when illuminating the top and bottom by green light.

2:18

BE-05. Magnonic Spin Fluctuation in CuMn. *P. Wu*[1], Y. Tu[1], D. Qu[2], S. Lee[2] and S. Huang[1] *1. National Taiwan University, Taipei, Taiwan; 2. Institute of Physics, Academia Sinica, Taipei, Taiwan*

How to efficiently generate and manipulate spin current is one of the most important topics in the field of spintronics. Recently, strong interest has been focused on the enhancement of spin current by spin fluctuation. Most of the studies use long-range ordered magnetic materials such as ferromagnetic metals or antiferromagnetic insulators. In this work, we utilize $Cu_{1-X}Mn_X$ alloys over the entire composition range to study the influence of spin frustration and spin fluctuation, from antiferromagnetic to spin glass (SG) phase transition. We report the enhancement of the inverse spin Hall effect (ISHE) during spin fluctuation in conducting CuMn alloys by the spin Seebeck effect (SSE) measurement with YIG. By tuning composition in $Cu_{1-x}Mn_x$, the SG transition is systematically changed, as revealed by the blocking temperature (T_b). We demonstrate the ISHE signal can be significantly enhanced with a maximum at peak temperature T_p and subsequently suppressed by spin frozen at low temperature, as shown in Fig. 1. Most importantly, we found temperature dependent SSE signal is strongly influenced by the short-range spin fluctuation and always above its T_b. In addition, the value and the sign of the ISHE voltage vary with composition and correspond to the number of valence electrons. Thus, we provide a compelling and controllable method to significantly enhance the spin current through short-range SG system, which is beneficial for energy efficient spintronic devices.

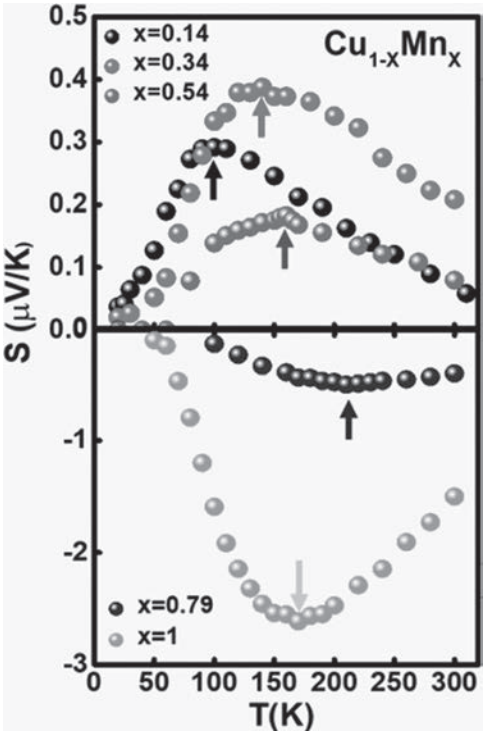


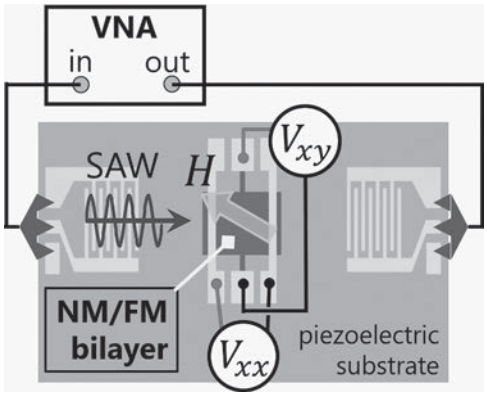
Fig. 1. The temperature dependent spin Seebeck coefficient of $Cu_{1-X}Mn_X$ with different at. % of Mn. The arrow indicates the corresponding peak of these curve (maximum value).

2:30

BE-06. Surface acoustic wave induced DC spin current in spin-orbit heterostructures. *T. Kawada*[1*], M. Kawaguchi[1], T. Funato[2], H. Kohno[2] and M. Hayashi[1,3] *1. Physics, The University of Tokyo, Tokyo, Japan; 2. Physics, Nagoya University, Nagoya, Japan; 3. National Institute for Materials Science, Tsukuba, Japan*

Spin current plays an important role in the field of spintronics. Spin rotation coupling, the interaction between spin angular momentum and mechanical rotation, is attracting significant interest as a source of spin current. The Rayleigh-type surface acoustic wave can produce lattice rotation in the radio-frequency range, allowing large spin-rotation coupling[1]. Recently, it has been shown that surface acoustic waves can generate spin current even in nonmagnetic metals with weak spin-orbit coupling[2]. Here, we show that a direct current (dc) electromotive force emerges in heavy metal/ferromagnetic metal bilayers when surface acoustic waves are excited. DC voltage across a Hall bar placed in between interdigital transducers (IDT) is measured while surface acoustic waves propagates between the IDTs[3]. The electromotive force is dependent on the magnetization direction of the ferromagnetic layer. Interestingly, the magnitude of the electromotive force that depends on the field angle increases with increasing thickness of the heavy metal layer until it saturates. The thickness dependence of the field-dependent electromotive force resembles that of the spin Hall magnetoresistance, which indicates that dc spin current is generated via excitation of lattice rotation.

[1] M. Matsuo, J. Ieda, K. Harii, E. Saitoh and S. Maekawa, Phys. Rev. B., Vol. 87, p.180402 (2013) [2] D. Kobayashi, T. Yoshikawa, M. Matsuo, R. Iguchi, S. Maekawa, E. Saitoh and Y. Nozaki, Phys. Rev. Lett., Vol. 119, p.077202 (2017) [3] T. Kawada, M. Kawaguchi and M. Hayashi, Phys. Rev. B., Vol. 99, p.184435 (2019)



Schematic illustration of the experimental setup.

INVITED PAPER

2:42

BE-07. Spin Transport at Heavy Metal/Ferromagnet Interfaces: Effective Spin-mixing Conductance and Spin Memory Loss. *L. Zhu*[1], D. Ralph[1] and R. Buhrman[1] *1. Cornell University, Ithaca, NY, United States*

Interfacial spin transport in heavy-metal /ferromagnet (HM/FM) systems is at the root of many spintronic phenomena. The spin current generated by the spin Hall effect of the HM [1-4] transports throught the HM/FM interface and exterts spin-orbit torques on the FM layer. In the reciprocal processes, the spin current due to spin pumping, spin seebeck effect and other effects transports through the HM/FM interface and can be detected by the inverse spin Hall effect of the HM. The effective spin-mixing conductance ($G_{eff}^{\uparrow\downarrow}$), the key

factor determining the spin transparency of a HM/FM interface, is typically ascertained from the inverse dependence of magnetic damping on the FM thickness under the assumption that spin pumping is the dominant mechanism affecting this dependence. This fails badly in many in-plane magnetized HM/FM systems in the nm-scale thickness regime [5], where instead the majority of the damping is from two-magnon scattering at the FM interface. If this is neglected, the result is an unphysical "giant" *apparent* $G_{eff}^{\uparrow\downarrow}$ and hence a considerable underestimation of both the spin Hall ratio and the spin Hall conductivity in inverse/direct spin Hall experiments. This talk will also report conclusive experiment evidence that interfacial spin orbit coupling linearly reduces the SOTs exerted on the FM layer by the spin currents generated in the HM [6] while interfacial intermixing at a Pt/Co interface can *increase* interfacial spin transparency [7], by approximately 30 %.

[1] Lijun Zhu et al., Variation of the giant intrinsic spin Hall conductivity of Pt with carrier lifetime, Sci. Adv. (in press). [2] Lijun Zhu et al., Phys. Rev. Appl. 11, 061004 (2019). [3] Lijun Zhu et al., Adv. Funct. Mater. 29,1805822 (2019). [4] Lijun Zhu, D.C. Ralph, R.A. Buhrman, Phys. Rev. Appl. 10, 031001 (2018). [5] Lijun Zhu, D. C. Ralph, and R. A. Buhrman, arXiv:1905.01577(2019). [6] Lijun Zhu, D. C. Ralph, and R. A. Buhrman, Phys. Rev. Lett. 122, 077201 (2019). [7] Lijun Zhu, D. C. Ralph, and R. A. Buhrman, Phys. Rev. B 99, 180404(R)(2019).

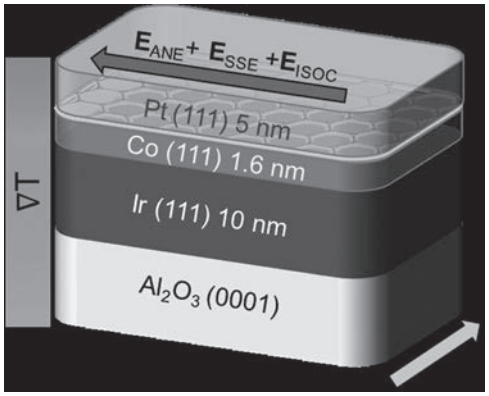
CONTRIBUTED PAPERS

3:18

BE-08. Disentangling the anomalous Nernst, spin Seebeck effect, and interfacial effects in epitaxial metal/Graphene/Cobalt heterostructures. *A. Anadón*[1], R. Guerrero[1], P. Jiménez-Cavero[2,3], A. Gudín[1], J. Díez-Toledano[1], P. Olleros[1], I. Lucas[2,3], L. Morellón[2,3], P. Antonio[3,4], M. Ibarra[2,3], R. Miranda[1,5], J. Camarero[1,5] and P. Perna[1] *1. IMDEA Nanociencia, Madrid, Spain; 2. Universidad de Zaragoza, Instituto de Nanociencia de Aragón, Zaragoza, Spain; 3. Física de la materia condensada, Universidad de Zaragoza, Zaragoza, Spain; 4. CSIC, 7Instituto de Ciencia de Materiales de Aragón, Zaragoza, Spain; 5. Física de la materia condensada, Instituto "Nicolás Cabrera" & IFIMAC, UAM, Madrid, Spain*

Conversion between spin and charge currents is essential in spintronics, since it enables a handful of potentially transformative phenomena such as modifying the magnetization of ultra-thin films by means of spin-orbit torque or generating energy by spin-current-driven rhermoelectric generation [1,2]. The inclusion of graphene in spintronics has allowed to unravel new arising spin-orbit effects unique of graphene/metal interfaces [3–5]. However, the thermal magnetotransport properties in Gr-based structures with perpendicular magnetic anisotropy have not been investigated at all. We have studied the thermal magnetotransport in Pt(Ta)/Gr/Co/Ir and Pt(Ta)/Co/Ir asymmetric epitaxial heterostructures on Al2O3(0001) single crystal substrates produced by means of a combination of DC sputtering, MBE and CVD techniques (see [3]). By applying a thermal gradient in the z direction (see figure 1) a transversal voltage can be observed in the y direction. This voltage is a combination of several effects arising from the magnetic (anomalous Nernst effect) and spin-orbit (Spin Seebeck effect) properties of the materials and interfaces involved. We have disentangled the origin of these components and observed that the inclusion of a graphene monolayer in the interface between cobalt and a metal can induce a significant interfacial contribution to the observed voltage.

[1] C. O. Avci et al., "Current-induced switching in a magnetic insulator," Nat. Mater., vol. 16, no. 3, pp. 309–314, 2017. [2] R. Ramos et al., "Unexpected enhancement of the spin Seebeck effect in Fe3O4 multilayer system," pp. 1–20, 2014. [3] F. Ajejas et al., "Unraveling Dzyaloshinskii–Moriya Interaction and Chiral Nature of Graphene/Cobalt Interface," Nano Lett., vol. 18, no. 9, pp. 5364–5372, Sep. 2018. [4] W. Yan, E. Sagasta, M. Ribeiro, Y. Niimi, L. E. Hueso, and F. Casanova, "Large room temperature spin-to-charge conversion signals in a few-layer graphene/Pt lateral heterostructure," Nat. Commun., vol. 8, no. 1, pp. 1–7, 2017. [5] B. Raes et al., "Determination of the spin-lifetime anisotropy in graphene using oblique spin precession," Nat. Commun., vol. 7, no. May, pp. 1–7, 2016.

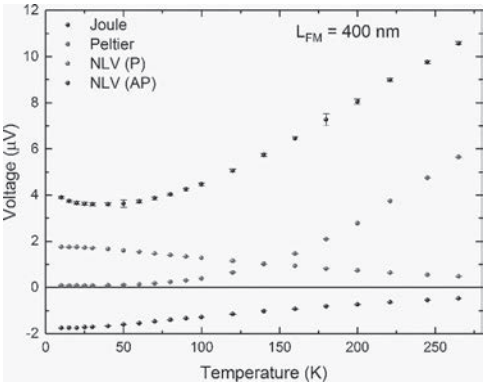


3:30

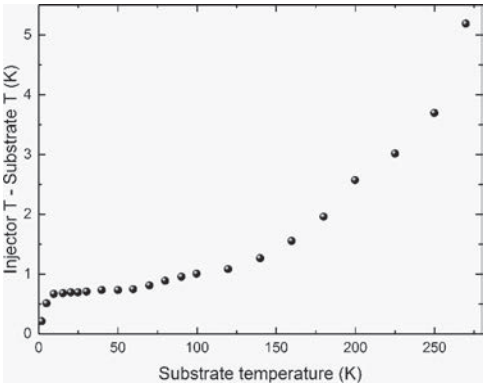
BE-09. Thermal effects in lateral spin valves. G. Stefanou[1], F. Menges[2], *K. Moran*[1], M. Ali[1], M. Rosamond[4], B. Gotsmann[3], R. Allenspach[3], G. Burnell[1] and B. Hickey[1] *1. Physics and Astronomy, University of Leeds, Leeds, United Kingdom; 2. University of Colorado, Boulder, CO, United States; 3. IBM, Zurich, Switzerland; 4. Electronic and Electrical Engineering, University of Leeds, Leeds, United Kingdom*

Our devices are fabricated in the clean-room using a combination of electron beam evaporation through a shadow mask defined by electron beam lithography in a PMMA/MMA resist and conventional optical lithography and lift-off techniques. The use of a 3-axes sample rotation stage coupled with a base pressure 10^{-10} mbar permits a flexible device design whilst retaining very clean interfaces between the Silver (Ag) and Permalloy (Py) electrodes. Using the non-local geometry, one can separate heat, charge and spin currents and thereby study the effect of these independently[1]. Thermally generated spin currents are known as spin caloritronics[2] and are intrinsically interesting. In lateral spin valves (LSVs) it is important to understand the origin of the thermal signals generated as their magnitude dominates the detected voltage, illustrated in figure 1. We study the heat diffusion in lateral spin valves using a DC current bias technique and taking advantage of the linear and quadratic field independent parts of the non-local IVs that are related to the thermal effects in the system. We separate the Joule heating and Peltier effect contribution from 270 K down to 2 K and calculate their decay lengths in the same temperature range. Using Scanning thermal microscopy[3] we map their heat spatial distribution at room temperature for the first time in a lateral spin valve system to aid the understanding of the aforementioned effects and develop an analytical model based on that. Coupling the experimental data with the analytical model, we predict a temperature rise at the injector junction of more than 5 ^{o}C at 270 K, depicted in figure 2. Finally, we investigate the correlation of the thermal signals to that of the spin transport, thermal conductivity and Seebeck coefficients in order to fully analyse the device's behaviour from 270 K to 2 K.

[1] F. L. Bakker, A. Slachter, J.-P. Adam, and B. J. van Wees, PRL 105, 136601, (2010) [2] G. E. W. Bauer, E. Saitoh and B. J. van Wees, Nature Materials 11, 391–399 (2012) [3] F. Menges, H. Riel, A. Stemmer, and B. Gotsmann, Review of Scientific Instruments 87, 74902 (2016)



Detected voltage as a function of temperature for heat and spin transport for a 400 nm separation device. No matter the temperature regime, the thermal signal dominates the detected signal.



The temperature increase of the injector junction from the substrate temperature as a function of the latter, as is was calculated using the theoretical model for an injected current of 500 μA.

3:42

BE-10. Magnetic Precession Induced by Surface Acoustic Waves in Magnetostrictive Nanostripes. *D. Castilla*[1], J.L. Prieto[1], M. Muñoz[1,2], G. Fuentes[1] and M. Sinusía[1] *1. Universidad Politécnica de Madrid, Madrid, Spain; 2. IMN-Instituto Micro y Nanotecnología, CSIC, Madrid, Spain*

We report a magnetic precession in a magnetostrictive nanostripe induced by a surface acoustic wave (SAW) resonator (see figure 1). This device was fabricated by EBL and sputtering deposition over a piezoelectric layer of ScAlN, 2 μm thick. The structure of the nanostripes is either Ni or FeCoB (35 nm) capped by a film of Pt (2 nm). By measuring Anisotropic Magnetoresistance loops for different amplitudes of the SAWs, we can measure a clear decrease of the coercivity in the samples. This is expected as the SAW is supplying an additional source of energy (stress) to the magnetization process. Interestingly, the SAW can also induce a non-resistive voltage (measured a zero current) in the nanostripe along the long axis. This is also a hysteretic voltage, dependent on the magnetization state. The comparison of the induced voltage V(H) with the AMR curve shows a clear relation. At high fields, the induced voltage is constant, which corresponds to a saturation state of the magnetization in the ferromagnet, when there is no precession of the magnetization (see figure 2). At low fields, ±100 Oe, a peak can be observed. This peak depends on the direction of the magnetization and occurs for the minimum in the AMR curve, i.e. when the magnetic moment of the sample has the largest component perpendicular to the long axis of the stripe. At this point, the torque induced by the SAW on the local magnetization is maximum and so it is the precession induced by the SAW. Within this work we present the results using different capping layers Pt, and Cr/Pt to determine if this SAW induced voltage has its origin in the Inverse Spin Hall Effect.

[1] M. Foerster, F. Macia, N. Statuto, et al. Nature Communications 8, 407 (2017). [2] S. Finizio, M. Foerster, M. Buzzi, et al., Physical Review Applied 1, 021001 (2014). [3] K. Roy, Spin 3, 1330003 (2013). [4] E. Chudnovsky, R. Jaafar, Physical Review Applied 2, 031002 (2016). [5] S. Parkin, M. Hayashi, L. Thomas, Science (New York, N.Y.) 320, 190 (2008). [6] K. Ando, S. Takahashi, J. Ieda, Journal of Applied Physics 109, 103913 (2011) [7] S.D. Ganichev, V Bel'kov, L.E. Goluv, Physical Review Letters, 92, 25 (2004)

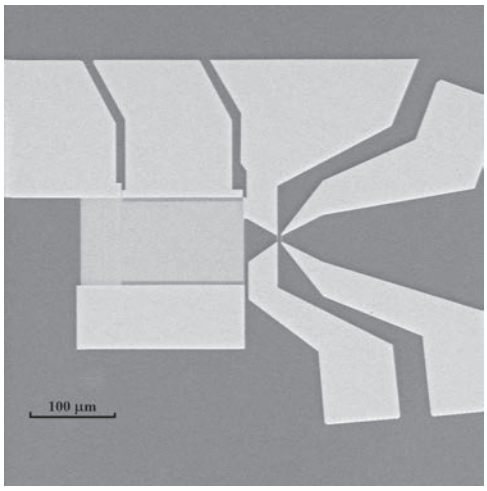


Fig 1. SEM image of the complete device. The device is divided in two halves. In the left half side is the SAW resonator and in the right half side the nanostripe and its contacts are placed. The nanostripe is placed 40 μm away from the resonator.

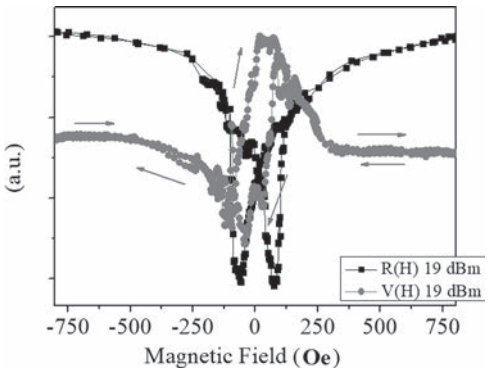


Fig 2. Comparison of the anisotropic magnetoresistance (R(H), black curve) and the induced non-resistive voltage as a function of the external magnetic field (V(H), red curve). Measurements are performed with the long axis of the nanostripe parallel to the external magnetic field.

3:54

BE-11. Enhancement of the spin pumping effect by magnon confluence process in YIG/Pt bilayers. T.B. Noack[1], V.I. Vasyuchka[1], D.A. Bozhko[1,2], B. Heinz[1], P. Frey[1], D.V. Slobodianiuk[3], O. Prokopenko[3], G.A. Melkov[3], P. Kopietz[4], B. Hillebrands[1] and *A.A. Serga*[1] *1. Fachbereich Physik and Landesforschungszentrum OPTIMAS, Technische Universität Kaiserslautern, Kaiserslautern, Germany; 2. James Watt School of Engineering, University of Glasgow, Glasgow, United Kingdom; 3. Faculty of Radiophysics, Electronics and Computer Systems, Taras Shevchenko National University of Kyiv, Kyiv, Ukraine; 4. Institut für Theoretische Physik, Universität Frankfurt, Frankfurt, Germany*

Spin pumping by dipolar-exchange magnons parametrically excited in in-plane magnetized Yttrium Iron Garnet / Platinum (YIG/Pt) bilayers was investigated in the presence of the longitudinal spin Seebeck effect (LSSE) [1].

When the microwave parametric pumping is applied to the sample, the electric voltage generated in the platinum layer via the inverse spin Hall effect (ISHE) results from contributions of two opposite spin currents formed by the LSSE and by the spin pumping from parametric magnons. In our field-dependent measurements of the spin pumping induced component of the ISHE-voltage, a clearly visible sharp peak is detected at high pumping powers. It is found that the peak position and the corresponding magnetic field are determined by the process of confluence of two parametrically exited magnons into one magnon possessing twice the frequency and the sum of the wavevectors of the initial magnons. The experimentally measured ISHE peak fields for different parametric pumping frequencies perfectly correspond to the calculated dependence without additional fitting parameters. The three-magnon confluence process constitutes an additional damping mechanism for the group of parametrically pumped magnons. Thus, for low pumping powers the confluence will decrease the total number of magnons in the system that results in the decreasing of the ISHE-voltage. Nevertheless, we demonstrate by numerical calculations that under the action of a rather strong parametric pumping field this confluence process results in the increase of the total number of magnons in the magnetic sample. This leads to the enhancement of the spin pumping effect in the YIG/Pt bilayer in the presence of the three-magnon confluence process.

T.B. Noack, V.I. Vasyuchka, D.A. Bozhko, B. Heinz, P. Frey, D.V. Slobodianiuk, O.V. Prokopenko, G.A. Melkov, P. Kopietz, B. Hillebrands, and A.A. Serga, *Enhancement of the spin pumping effect by magnon confluence process in YIG/Pt bilayers*, Phys. Stat. Solidi (b), 1900121 (2019)

4:06

BE-12. Enhanced magnon spin transport, magnon polarons and vector spin Seebeck effect detection in $NiFe_2O_4$ thin films on lattice-matched substrates. *T. Kuschel*[1] *1. Bielefeld University, Bielefeld, Germany*

We report on enhanced magnon spin transport properties in epitaxial $NiFe_2O_4$ (NFO) films grown on $MgGa_2O_4$ substrates compared to NFO films deposited on standard $MgAl_2O_4$ [1,2]. The reduction of the lattice mismatch from 3.2% to 0.8% decreases the number of antiphase boundary defects in the NFO films and, thus, improves structural and magnetic properties. Further, spin transport is strongly improved as we have studied by nonlocal magnon spin transport experiments with Pt injector and detector strips [2]. While the magnon spin diffusion length in the NFO films of around 3 μm is not changed drastically, the nonlocal spin transport signal is enhanced by two orders of magnitude. This increase is detectable for both electrically and thermally excited magnons. In addition, we observe spin transport signals in NFO that point to magnetoelastic coupling identified as magnon polarons [2]. These findings make lattice-matched NFO being an important alternative to $Y_3Fe_5O_{12}$ (YIG) in terms of spin transport properties. Finally, we use these lattice-matched NFO films to demonstrate a new vectorial magnetometry technique based on the longitudinal spin Seebeck effect (SSE) [3]. Placing four electrical contacts on top of Pd/NFO, we trace both in-plane magnetization components of the NFO. We identify different anisotropy contributions in NFO on lattice-matched substrates with (001) and (011) orientation and reconstruct the in-plane magnetization reversal process via the vector SSE technique [3].

[1] J. Shan et al., Appl. Phys. Lett. 110, 132406 (2017) [2] J. Shan et al., Appl. Phys. Lett. 113, 162403 (2018) [3] Z. Li et al., Appl. Phys. Lett. 114, 232404 (2019)

4:18

BE-13. Enhanced spin Seebeck effect in exchange-biased MgO/Fe_3O_4/Cu multilayers. *V. Kalappattil*[1], H. Nazari[1], S.G. Bhat[2], R. Das[1], A.P. Kumar[2], M. Phan[1] and H. Srikanth[1] *1. physics, University of South Florida, Tampa, FL, United States; 2. physics, Indian Institute of Science, Bangalore, India*

Spin Seebeck effect (SSE) along with spin pumping and spin Hall effect (SHE) is one of the most efficient ways to generate pure spin current [1]. Over the last decade, several approaches have been made to enhance the SSE voltage. One of the most effective methods established is through creating multilayers of Fe_3O_4 thin films [2]. In this study, we have fabricated high-quality multilayers of Fe_3O_4 (32 nm) thin films using pulsed laser deposition (PLD) on Magnesium Oxide (MgO) substrate separated by Cu (~10 nm) layers. As the number of layers increases, total magnetization drastically decreases due to the increased fraction of antiphase boundaries (APB), which leads to more antiferromagnetic interactions. Interestingly, we have achieved ~ 400% increase in the SSE voltage from one layer to three-layers, which can be attributed to the changes in interface magnetic anisotropy, spin mixing conductance (G) and characteristic length. Detailed magnetic characterization revealed a strong exchange bias of ~250 Oe present in the system mainly due to the presence of the AFM like antiphase boundaries. Building upon our previous studies on the SSE dependence on the magnetic anisotropy [3,4], we demonstrate, for the first time, the influence of exchange anisotropy on the SSE. Stronger exchange anisotropy in the sample subjected to a cooling field directly contributes to the generation and propagation of high-frequency magnons with short spin diffusion length. Although this leads to reduced thermal magnon numbers, spin wave pinning resulted in the coercivity enhancement and loop shift, similar to exchange bias in the field-cooled SSE. The ability to tune the spin current and propagation via exchanges anisotropy will give an extra degree of freedom in achieving new generation spintronics devices.

1. K. Uchida, et al., *Nat. Mater*. 9, 894(2010) 2. R. Ramos et al, *Phys. Rev. B* Vol. 92,p. 220407 (2015) 3. V. Kalappattil, et al., Sci. Rep. 7, 13316 (2017). 4. R. Das et al, *AIP Advances*, Vol.8, p. 055906, (2018)

Session BF
NANO-ARRAYS, NOVEL STRUCTURES, AND SELF-ASSEMBLY II

Ahmed A El-Gendy, Chair
University of Texas at El Paso, El Paso, TX, United States

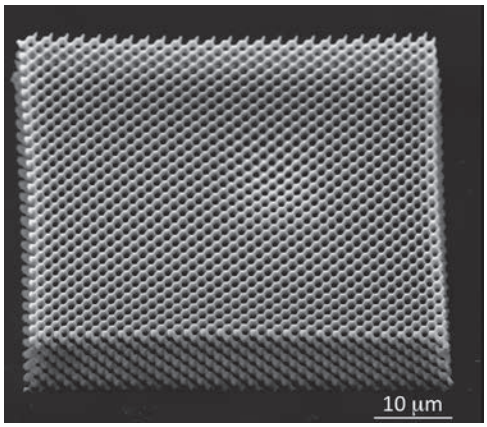
INVITED PAPER

1:30

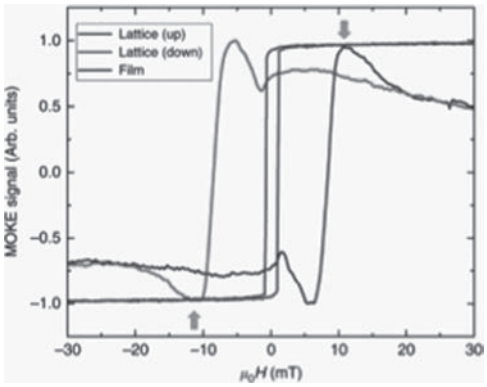
BF-01. Realisation of a 3D Frustrated Magnetic Nanowire Lattice.
S. Ladak[1], A. May[1], A. Van Den Berg[1], M. Hunt[1] and A. Hejazi[1] *1. School of Physics and Astronomy, Cardiff University, Cardiff, United Kingdom*

Patterning nanomagnets in three-dimensions [1] presents a new paradigm in condensed matter physics and allows access to a plethora of phenomena including spin textures that are topologically protected [2], ultrafast domain wall motion with an associated spin Cherenkov effect [3] and nanostructured frustrated systems with controlled degeneracy [4]. To date, the fabrication of single domain magnetic nanowires into complex 3D lattices has proven to be a formidable challenge. In this talk I will show that two-photon lithography (TPL), when combined with metallic deposition is a powerful methodology for realising 3D magnetic nanostructures. I will start by outlining why 3D nanostructuring is important, particularly within the context of frustrated magnetic materials, before detailing the physics of two-photon lithography and how this can be combined with other processes to transfer a polymer into a magnetic material. The challanges that one faces when trying to reach single domain wires with TPL will also be discussed. I will then show that using TPL and processing one can realise single domain $Ni_{81}Fe_{19}$ nanowires and arrange them into a 3D diamond-bond lattice geometry (Fig 1) [5]. The nanowires have a novel crescent-shaped cross-section with width of approximately 200nm, length of 1000nm and thickness 50nm. Finite element simulations suggest they switch via nucleation and propagation of vortex domain walls. The global switching of the lattice can be probed using optical magnetometry (Fig 2) and this shows a single sharp transition (H_c=8mT), suggesting that domain walls traverse the probed region with negligible pinning at upper vertices. Finite-element simulations upon building blocks of the diamond lattice (four-wire tetrapod structures) suggest a near degenerate set of ice-rules, indicating the system is a candidate 3D artificial spin-ice (3DASI). By carrying out magnetic force microscopy in a field and comparing obtained vertex contrast to simulations I will show that the spin texture upon the 3D lattice surface can be determined, paving the way to studies exploring ground state ordering within 3DASI systems that share lattice symmetry with their bulk counterparts.

[1] A. Fernandez-Pacheco, et al., Nature Communications, Vol. 8, p. 15756 (2017) [2] S. Da Col et al., Phys. Rev. B Vol. 89, 180405 (2014) [3] M. Yan et al., Appl. Phys. Lett. Vol. 99, 122505 (2011) [4] Y. Perrin, B. Canals and N. Rougemaille, Nature, Vol. 540, p. 410 (2016) [5] A. May et al., Communications Physics, Vol. 2, p. 13 (2019)



Scanning electron micrograph of 3D nanostructured magnetic lattice.



Magneto-optical Kerr effect loop of the 3D nanostructured magnetic lattice (red/black) and the sheet film (blue).

CONTRIBUTED PAPERS

2:06

BF-02. First Order Reversal Curves (FORCs) of Nano-engineered 3D Fe-Co Structures.
M. Al Mamoori[1,2], C. Schröder[3], J. Pieper[1], L. Keller[1], M. Huth[1] and J. Müller[1] *1. Institute of Physics, Goethe-University Frankfurt, Frankfurt am Main, Germany; 2. Institute of Materials Science, Technical University of Darmstadt, Darmstadt, Germany; 3. Institute for Applied Materials Research, Bielefeld University of Applied Science, Bielefeld, Germany*

A promising direction of developing complex new geometries of nanomagnets beyond planar arrays is the creation of three-dimensional structures, where unconventional spin textures emerge, paving the way towards novel nanomagnetic phenomena and applications. In a recent work [1,2], significant progress has become viable by an advanced platform of the direct-write process FEBID (focused electron beam induced deposition) combined with the possibility of high-resolution detection of small magnetic signals

using a home-built micro-Hall magnetometer. The latter device, based on a two-dimensional electron gas at the interface of a GaAs/AlGaAs heterostructure, allows to measure the local magnetic stray field of a single magnetic nanostructure. The major hysteresis loop measurements of a small (2 x 2) array of ferromagnetic Fe-Co nano-cubes and nano-tress, measured by the Hall sensor and supported by micromagnetic simulations, revealed complex vortex-like configurations developing through their magnetic elements [1,2]. In order to gain further insights into the hysteresis loops and mechanisms of magnetization reversal, (irreversible) magnetic interaction effects and coercivity distributions, we extend our studies by employing first-order reversal curves (FORCs) as a complementary tool for investigating the processes taking place during the complex magnetization reversal [3]. Here, we present FORC signatures of arrays of individual 3D CoFe nanomagnets as nano-cubes and nano-trees. Experimentally determined FORC diagrams seem to collectively reflect complex responses relevant to the vortex-like configurations through the magnetic elements. In comparison, a simple macro-spin model for both geometries appears to replicate the essential features observed in the experiment. Our objective is to develop a qualitative and, if possible, quantitative physical interpretation of these signatures.

[1] L. Keller et al., Scientific Reports 8, 6160, 2018 [2] M. K.I. Al Mamoori et al., Materials 11, 289 (2018). [3] M. Pohlit et al., Rev. Sci. Instr. 87, 113907 (2016).

2:18

BF-03. Determination of Demagnetizing Factors of Nanowire Arrays by Combining Experimental Data From First-Order Reversal Curves and Ferromagnetic Resonance. *K. Muster*[1] and R. Heindl[1] *1. Physics & Astronomy, San Jose State University, San Jose, CA, United States*

We developed a method for quantitative analysis of demagnetizing interactions between nanomagnets in an ordered 2D array by combining data from first-order reversal curves (FORC) with data obtained from ferromagnetic resonance (FMR). FORC measurement provides the Preisach distribution, a representation of magnetic reversal behavior in an external field. Preisach distributions of nanomagnet arrays have previously been quantitatively modeled with an additional uniform, internal field that is proportional to magnetization [1]. We developed a non-linear fit to the Preisach distribution to find: (1) the effective axial demagnetizing field strength, $H_{ds} = N_{ax}M_s$, where N_{ax} and N_{tr} are the demagnetizing factors in the axial and transverse directions with respect to the nanowires, and (2) a Gaussian Preisach distribution with respect to the internal field, $H_{int} = H - N_{ax}M$. Combining the FORC result, H_{ds}, with an FMR fit result, $(N_{ax} - N_{tr})M_s$, allowed us to algebraically solve for the array's effective demagnetizing factors. We tested this method on an ordered array of nickel nanowires with 4.6 ± 0.8 μm length and 80 nm diameter prepared by electrodeposition in a nanopore template. We determined the array's demagnetizing factor were $N_{ax} = 0.04 \pm 0.01$ and $N_{tr} = 0.476 \pm 0.006$. The axial demagnetizing factor was an order of magnitude larger than that of a theoretical isolated nanowire, and was comparable to the predicted value from the study of simulated nanowire arrays by Clime, et. al. [2]. Our experimental method provided quantitative evidence of the demagnetizing interaction between nanowires in an array.

[1] D. A. Gilbert, G. T. Zimanyi, R. K. Dumas, M. Winklhofer, A. Gomez, N. Eibagi, J. L. Vicent, and K. Liu, Sci. Rep., 4, p. 1 (2014) [2] L. Clime, F. Bron, P. Ciureanu, M. Ciureanu, R. W. Cochrane, and A. Yelon, J. Magn. Magn. Mater., 299, p. 487 (2006)

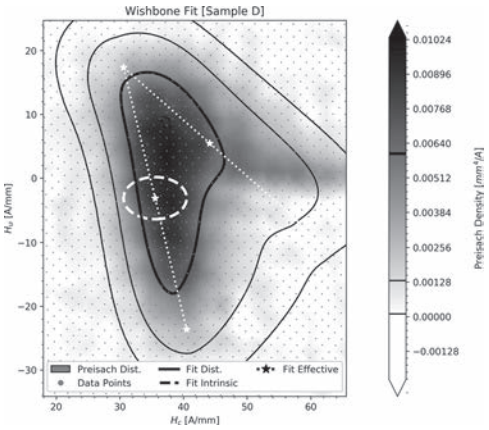


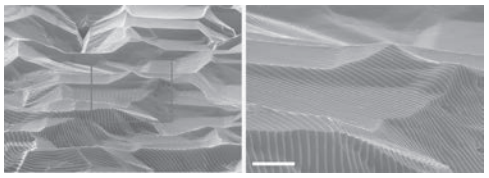
Fig. 1. The observed Preisach distribution was fit using a non-linear function that modeled a Gaussian intrinsic Preisach distribution transformed by a demagnetizing field.

2:30

BF-04. A New Approach of Constructing 3D Metallic Nanostructures on Arbitrarily-Shaped Substrate. *F. Chen*[1], R. Peng[1] and M. Wang[1] *1. Nanjing University, Nanjing, China*

Formation of three-dimensional (3D) nanostructures is an important step of advanced manufacture for new concept devices with novel functionality[1-4]. Despite of great achievements in fabricating nanostructures with state of the art lithography approaches, these nanostructures are normally made on flat substrates[5,6]. Up to now it remains challenging to build metallic nanostructures directly on a rough and bumpy surface. Here we demonstrate for the first time a unique way to fabricate metallic nanowire arrays on an arbitrarily-shaped surface by electrodeposition. Counter intuitively, here the growth direction of nanowire is perpendicular to its longitudinal axis, and the specific geometry of nanowires can be achieved by introducing specially designed shaped substrate. The spatial separation and the width of the nanowires can be tuned by voltage, electrolyte concentration and temperature in electrodeposition. By taking cobalt nanowire array as an example, we show that head-to-head and tail-to-tail magnetic domain walls can be easily introduced and modulated in the nanowire arrays, which is enlightening to construct new devices such as domain wall racetrack memory.

1.S. Parkin and S. Yang, Nature Nanotech., Vol.10, p.195 (2015) 2.A. Hirohata and K. Takanashi, J. Phys. D: Appl. Phys., Vol. 47, p.193001 (2014) 3.T. Ding, K. Song, K. Clays,et al., Adv. Mater. Vol.21, p.1936 (2009) 4.Y. Hayamizu, et al., Nature Nanotech. Vol.3, p.289 (2008) 5.C. Wagner and N. Harned, Nature Photon. Vol.4, p.24 (2010) 6.C. Vieu, et al., Appl. Surf. Sci. Vol.164, p.111 (2000)



INVITED PAPER

2:42

BF-05. Inter-particle magnetic correlations and fluctuations dynamics in assemblies of Fe3O4 nanoparticles. *K. Chesnel*[1], J. Rackham[1], B. Newbold[1], D. Griner[1], D. Smith[1], R. Harrison[2] and M. Transtrum[1]
1. Physics, BYU, Provo, UT, United States; 2. Chemistry, BYU, Provo, UT, United States

Magnetic nanoparticles (NPs) are increasingly used in biomedical applications such as drug and gene delivery, hyperthermia, or contrast agents for MRI. Magnetite (Fe3O4) NPs are good candidates for these applications due to their non-toxicity and long-life in the bloodstream. While the structural and magnetic properties of bulk Fe3O4 has been widely studied [1], knowledge is still lacking regarding the nanoscale magnetic behavior of collections of Fe3O4 NPs. In particular, when the NPs are small and superparamagnetic, it is useful to understand how the magnetic correlations evolve throughout cooling and heating. Here we use coherent x-ray resonant magnetic scattering (CXRMS) [2, 3] to probe nanoscale magnetic orderings in monolayers of Fe3O4 nanoparticles as illustrated in Figure 1. We show how magnetic orders depend on temperature throughout the blocking transition, as well as on particle size, varying from 5 to 11 nm [4] A model of the data using chains of NPs suggests the emergence of anti-ferromagnetic couplings for bigger particles when the field is reduced near zero. [5] Additionally, we exploit the coherence of the x-rays to investigate the dynamics of fluctuations via photo-correlation spectroscopy. We show a drastic change in the dynamics of fluctuation throughout the blocking transition between frozen state and superparamagnetic state.

[1] Verwey, *Nature* 144, 327 (1939); Fleet, *Acta Cryst. B* 37, 919-929 (1981) [2] Kortright *et al.*, *Phys. Rev. B* 71, 012402 (2005) [3] Chesnel et al., *Nature Communications,* 7, 11648 (2016) [4] Chesnel *et al.*, *Magnetochemistry* 4, 42-58 (2018) [5] Rackham *et al.*, *AIP Advances*, 9, 035033 (2019)

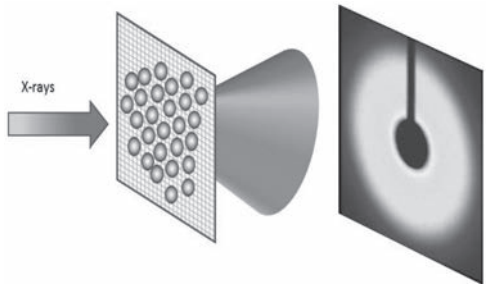


Figure 1: Layout for the x-ray resonant magnetic scattering (XRMS) measurement of a nanoparticle assembly.

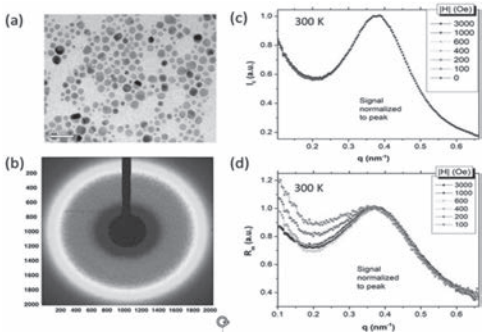
CONTRIBUTED PAPERS

3:18

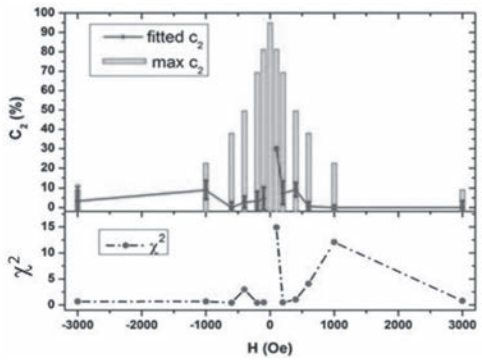
BF-06. Modeling Magnetic Correlations in Magnetite Nanoparticle Assemblies Using X-ray Magnetic Scattering Data. *J. Rackham*[1], K. Chesnel[1], M. Transtrum[1], A. Reid[2], R. Harrison[3], B. Newbold[1], S. Kotter[1], D. Smith[1] and D. Griner[1] *1. Physics, Brigham Young University, Provo, UT, United States; 2. SLAC National Accelerator Laboratory, Menlo Park, CA, United States; 3. Chemistry, Brigham Young University, Provo, UT, United States*

Magnetic nanoparticles are increasingly used in nanotechnologies and biomedical applications, such as drug targeting, MRI, and bio-separation [1-4]. Magnetite (Fe3O4) nanoparticles stand to be effective in these roles due to the non-toxic nature of magnetite and its ease of manufacture [5]. To be more effective in these applications, a greater understanding of the magnetic behavior of the individual magnetite nanoparticles is needed when a collection of them is used. This research seeks to discover the local magnetic ordering of ensembles of magnetite nanoparticles occurring at various stages of the magnetization process. To complete this study, we use resonant x-ray magnetic scattering, which provides information about the magnetic orders in the material, see Fig 1. Here we discuss the modeling of the magnetic scattering data using a one-dimensional chain of nanoparticles with a mix of ferromagnetic, anti-ferromagnetic, and random order. The model utilizes twelve variable parameters and we used a Levenberg-Marquardt algorithm to find the best fit parameters [6,7]. By fitting the model to the experimental data, we extracted information about the magnetic correlations in the nanoparticle assembly, shown in Fig 2.

[1] Frey N.A.; Peng S.; Cheng K.; Chem. Soc. Rev. 38, 2532-2542 (2009) [2] S. Mornet et al., J. Mater. Chem. 14, 2161 (2004) [3] E. Duguet et al., Nanomedicine 1(2), 157 (2006) [4] J. H. Gau et al., Acc. Chem. Res. 42(8),1097 (2009) [5] A. Ito et al., J. Biosci. Bioeng. 100, 1 (2005) [6] Levenberg, Kenneth (1944). Quarterly of Applied Mathematics. 2: 164–168 [7] Marquardt, Donald (1963). SIAM Journal on Applied Mathematics. 11 (2): 431–441.



(a) TEM image of sample. (b) Example XRMS image. (c) Charge scattering signal. (d) Magnetic scattering signal.



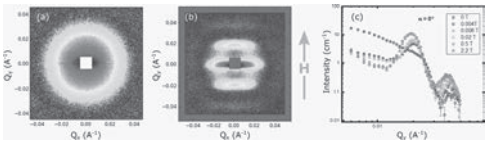
Fitted AF coverage (c2) including error bars at 95% confidence intervals for range of magnetic fields. The blue bars indicate the possible range for c2.

3:30

BF-07. Magnetic small-angle neutron scattering from self-assembled iron oxide nanoparticles influenced by field. N. Nandakumaran[1], T. Köhler[2], *L. Barnsley*[2], M. Feygenson[3], A. Feoktystov[2], O. Petracic[1] and T. Brückel[1] *1. Jülich Centre for Neutron Science (JCNS-2), Forschungszentrum Jülich GmbH, Jülich, Germany; 2. Jülich Centre for Neutron Science (JCNS) at Heinz Maier-Leibnitz Zentrum (MLZ), Forschungszentrum Jülich GmbH, Garching, Germany; 3. Jülich Centre for Neutron Science (JCNS-1), Forschungszentrum Jülich GmbH, Jülich, Germany*

Self-assembly of magnetic nanoparticles, in general, is of interest due to the broad range of applications in material science and biomedical engineering [1,2]. Parameters that affect self-assembly in nanoparticles include particle size, the applied magnetic field profile, concentration and synthesis routines [3]. A range of different sizes of iron oxide nanoparticles between 17 and 27 nm were investigated using polarized small-angle neutron scattering (SANS) at the KWS-1 instrument operated by the Jülich Centre for Neutron Science (JCNS) at Heinz Maier-Leibnitz Zentrum (MLZ) in Garching, Germany. Nanoparticles were dispersed in toluene and measured at room temperature in a range of applied fields between ±2.2 T. The observed self-assembly strongly depended on both nanoparticle size and applied field. For smaller particles (diameter ≤ 20 nm), there was no indication of self-assembly even at high concentration (1% v/v), while 27 nm nanoparticles assemble into linear chains even in low concentrations (0.42% v/v) and low field. The smallest nanoparticles (d = 17 nm) were studied by contrast variation; by altering the isotopic composition of the toluene solvent, the magnetization profile within the cores of the nanoparticles could be extracted with high-resolution when using a spin-polarized incident neutron beam [4]. For larger nanoparticle, the structural and form factors were obtained by sector analysis of the 2-D SANS patterns (Fig. 1(a) and (b)). The extracted structure factors suggest that the chains grow longer and straighter and align more closely with the field direction up until application of the maximum field (Fig. 1(c)). This is understood in terms of a minimization of the dipole energy of the nanoparticles in the presence of the applied field and neighbouring particles. The implications for the control of self-assembly of more complex nanoparticles will be discussed.

[1] G. Ozina, K. Hou, B. Lotsch, et. al., Materials Today, Vol. 12, p.12 (2009) [2] P. Tartaj, Current Nanoscience, Vol. 2, p.43 (2006) [3] Z. Fu, Y. Xiao, A. Feoktystov, et. al., Nanoscale, Vol. 8, p.18541 (2016) [4] A. Wiedenmann, Journal of Applied Crystallography, Vol. 33, p.428 (2000)



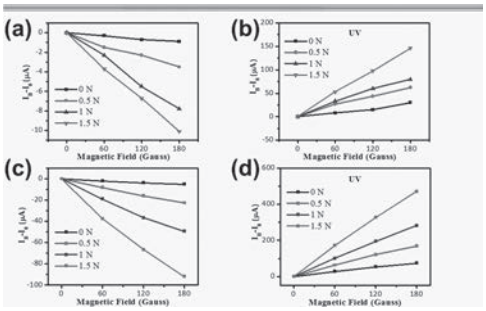
SANS pattern at room temperature in an applied field of 2.2 T of a) 20 nm and b) 27 nm nanoparticles (colour bar in logscale) c) Sector analysis of intensities from 27 nm nanoparticles along Q parallel to the applied field. A structural peak forms and becomes sharper with increasing field.

3:42

BF-08. Magnetic Field Study on Piezotronic and Piezo-Phototronic in ZnO and ZnO/Co_3O_4 Core/shell Nanowire Arrays. *W. Zhou*[1], S. Yan[1], Z. Zheng[1], S. Rai[1], M. Bhatt[1], L. Malkinski[1] and M. Retana[1] *1. Advanced Materials Research Institute, University of New Orleans, New Orleans, LA, United States*

Piezoelectric-related multi-property coupling effects have recently attracted much attention for developing next generation multi-functional devices. In this paper, the multi-property coupling effects among magnetic field, piezoelectricity and photoexcitation were investigated in ZnO nanowire arrays. The response of the current flowing through the array to the applied magnetic field was decreasing with increasing magnetic field strength. However, due to piezo-magnetotronic effect, the magnetically induced current was magnified by one order of magnitude by applying an external stress. In contrast, under UV light illumination, the magnetically induced current response increased with an increment of magnetic field strength, as the magnetic field is favorable to the separation of photo-induced electron-hole pairs. The magnetically-induced current response was enhanced by at least two orders of magnitude due to piezo-photo-magnetotronic effect. Furthermore, ZnO/Co_3O_4 core/shell heterojunction nanowire arrays was employed to improve the current responses up to 9 times and 3 times, under piezo-magnetotronic and piezo-photo-magnetotronic engagements, respectively, attributed to the improved charge carrier separation and transportation at the core/shell interface. This phenomenon projects a potential for multi-functional piezo-magnetotronic and piezo-photo-magnetotronic device development.

1. S. Rai, K. Wang, Y. Ding, et al., ACS NANo 9 (6), 6419-6427 (2015) 2. M. Peng, Y. Zhang, Y. Liu, M. Song, et al., *Adv. Mater. 26* (39), 6767–6772 (2014) 3. M.C. Wong, L. Chen, M.K. Tsang, et al. *Adv. Mater. 27* (30), 4488–4495 (2015)



The summary of the peak current difference of ZnO NWs (a) in dark and (b) under UV illumination the device, and of ZnO/Co3O4 NWs in (c) dark and (d) under UV illumination.

3:54

BF-09. The Limits of Frustration in Severely Deformed Fe-Cu Magnetic Alloys. M. Stückler[1], L. Weissitsch[1], S. Wurster[1], H. Krenn[2], P. Felfer[3], R. Pippan[1] and *A. Bachmaier*[1] *1. Erich Schmid Institute of Materials Science, Austrian Academy of Sciences, Leoben, Austria; 2. Institute of Physics, University of Graz, Graz, Austria; 3. Department of Materials Science and Engineering, Friedrich-Alexander Universität Erlangen-Nürnberg, Erlangen, Germany*

Severe plastic deformation is a relatively new technique for the preparation of nanocrystalline magnetic alloys. The advantage of high-pressure torsion, a method of severe plastic deformation, is that the as-deformed sample is already available in bulk form and the continuous application of an arbitrary amount of shear strain is possible, which can induce alloy formation (supersaturated solid solutions)[1]. In this study, the Fe-Cu system is investigated in the low Fe-containing region (≤25wt%Fe). Fe is immiscible with Cu as the phase diagram exhibits a negligible solubility[2]. Deformation-induced intermixing is obtained by high-pressure torsion, which leads to a partial dissolution of Fe in Cu possibly yielding supersaturated states. SQUID magnetometric measurements of the as-deformed state show contributions of thermal relaxation and frustration, which are disentangled with AC-mode measurements (Fig.1). The limit of the frustrated regime is well described with the de Almeida-Thouless Line[3] (Fig.2). The results obtained from magnetic measurements are correlated to microstructural analysis including atom probe tomography, where the different magnetic effects can be allocated to the distribution of Fe-atoms in the nanocrystalline Cu matrix.

Acknowledgements: This project has received funding from the European Research Council (ERC) under the European Union's Horizon 2020 research and innovation programme (grant agreement No 757333).

[1]K.S. Kormout, R. Pippan and A. Bachmaier, Advanced Engineering Materials, Vol.19.4, p.1600675 (2017) [2]J.Z. Jiang, C. Gente and R. Bormann, Materials Science and Engineering A, Vol. 242.1-2, pp. 268-277 (1998) [3]J. R. L. De Almeida and D.J. Thouless, Journal of Physics A: Mathematical and General, Vol.11.5, pp.983-990 (1978)

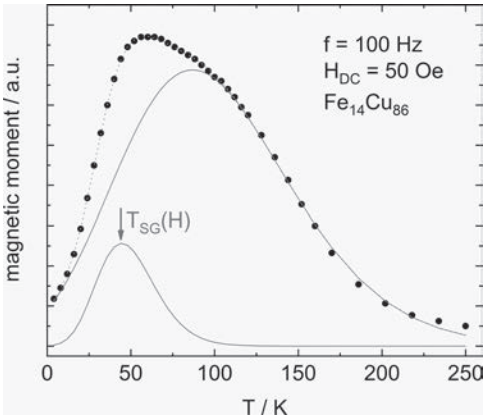


Fig.1: Results of an AC-SQUID measurement. The experimental values (black dots) are fitted by two lognormal peaks (solid curves).

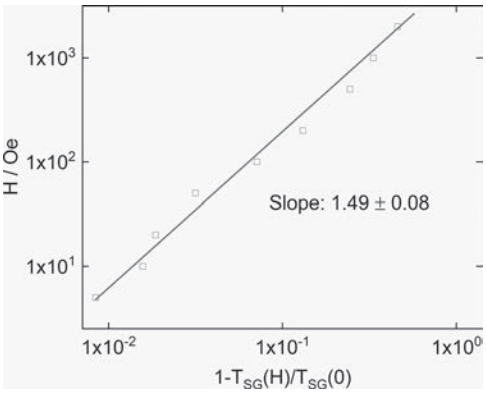


Fig.2: Almeida-Thouless Plot: the slope coincides with the theoretically proposed value of 1.5. Data recorded for 5Oe < H_{DC} < 2kOe.

4:06

BF-10. In-situ Growth Trajectory of Ni Nano Dendrites by Liquid Cell Electron Transmission Microscopy. *L. Zheng*[1,2], S. Zhao[2], J. Jiao[2], D. Zhou[1], M. Zhu[1], W. Li[1] and H. Zheng[3] *1. Central Iron & Steel Research Institute, Beijing, China; 2. Hebei University of Engineering, Handan, China; 3. Lawrence Berkeley National Laboratory, Berkeley, CA, United States*

Nickel has attracted an increasing attentions as one of the important transition metals due to its interesting properties and applications in catalysis [1], supercapacitor [2], hydrogen storage [3], magnetic storage devices [4], magnetic fluids [5], magnetic resonance imaging [6], magnetic carriers for drug targeting [7], and electrochemical sensor [8]. Morphology controlling is a critical technique for fabrication of nickel nanostructures since the properties depend on its morphology. Real-time observations with high temporal and spatial resolution is conducive to our understanding of nanostructure growth mechanism. Here we use in situ liquid cell transmission electron microscopy (LCTEM) to elucidate the growth trajectories of Ni nano dendrites. We have observed that nickel nanodendrites formed initially and fractal grew swiftly (Shown in Figure 1). We have calculated the fractal growth dimension and simulated the growth process of nano dendrites using diffusion-limited aggregation (DLA) model. The dendrite growth mechanism and kinetics have been explored, which give a way to grow metallic porous materials for novel applications.

[1] Önder Metin, et al, J. Am. Chem. Soc. 2010, 132, 1468-1469 [2] Qi Lu, et al, Angew. Chem. Int. Ed. 2011, 50, 6847-6850. [3] B. Liao, et al, J. Alloy & Compd. 2003, 356-357: 746-749. [4] H. Koo, et al, Appl. Phys. Lett. 2002, 81, 862. [5] Shuchun Zhao, et al, RSC Adv. 2015, 5, 41961. [6] A.B. Moradi, et al, European J Soil Sci., 2008, 59, 476-485. [7] Danny Bockenfeld, et al, Sep. Sci. Technol., 2010, 45(3), 355-363. [8] Eduardo G.C. Neiva, et al, J. Colloid Inter. Sci. 2016, 468, 34-41.

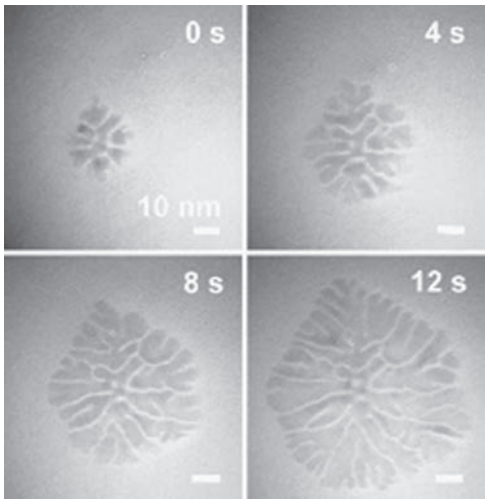


Fig. 1 Sequential TEM images from a movie show the growth of Ni dendrites

4:18

BF-11. Thermally activated dynamics in artificial Ising spin chains. N. Strandqvist[1], R. Rowan-Robinson[1], V. Kapaklis[1], B. Hjörvarsson[1], P. Steadman[4], R. Fan[4], O. Bikondoa[2,3] and *T.P. Hase*[2] *1. Materials Physics, Uppsala University, Uppsala, Sweden; 2. Physics, University of Warwick, Coventry, United Kingdom; 3. XMaS Beamline, European Synchrotron Radiation Facility, Grenoble, France; 4. Beamline I10, Diamond Light Source, Didcot, United Kingdom*

The length- and energy-scales within artificial arrays of nanostructures determines the magnetic order and emergent phenomena. The patterned element size and spacing defines the interaction energies, setting the global behavior and the dynamic window in which the mesospins of islands fluctuate. At low temperatures, there is insufficient energy to reverse islands resulting in a frozen mesospin manifold with only weak intra-island excitations. At higher temperatures, the flipping rate of individual islands rises, with a concomitant loss of long-range order. Thus, the dynamics are intrinsically related to the array configuration and evolve with temperature as island reversals act as grain boundaries between aligned regions. In this paper, we use resonant magnetic coherent x-ray scattering and correlation spectroscopies (via intensity-intensity temporal autocorrelation functions) to determine the dynamics of the mesospin manifold in simple Ising chains composed of FePd alloys [1 -4]. The use of a coherent beam introduces speckle into the diffraction pattern arising from the repeating in-plane structure (fig. 1). Each image reveals the magnetic disorder over the integration time (40-60 ms), with time correlations between images revealing the slow dynamics of the manifold (> seconds). We quantify the dynamics as a function of time, external field and temperature mapping out the dynamics across all relevant length scales in the array. By using samples with different element spacing, the effect of the coupling strength between the islands on the dynamics is elucidated. Our data is compared with photoemmision electron microscopy employing the x-ray magnetic circular dichroism (XPEEM) [5].

[1] E. Th. Papaioannou et al. J. Phys.: Condens. Matter 22, 236004 (2010). [2] V. Kapaklis et al Nat. Nanotechnology 9 514 (2014) [3] U. B. Arnalds et al New J. Phys. 18 023008 (2016) [4] U.B. Arnalds et al Appl. Phys, Lett.

105 042409 (2014) and V. Kapaklis et al. New. J. Physics 14 035009 (2012)
[5] E. Östman, et al J. Phys.: Condens. Matter 30 365301 (2018)

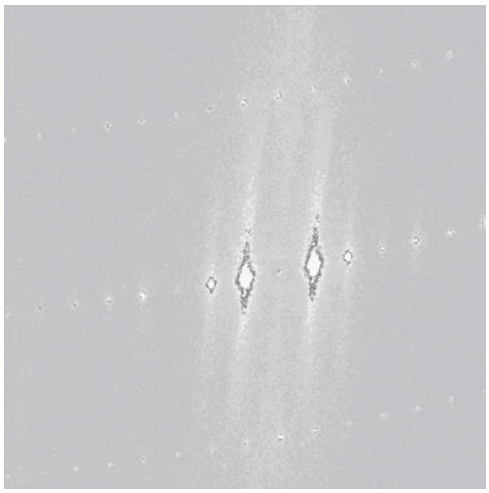


Fig. 1: Room temperature diffraction data recorded at the Fe L3 edge of a series of Ising chains. The coherent beam introduces speckle at each diffraction peak whose periodicity in the horizontal direction relates to the element spacing along a chain. The vertically offset rows come from the chain separation. The scattering angle is chosen to minimise the specular reflection from the surface (central point).

Session BG
MAGNETIC CHARACTERIZATION II: SCANNING PROBE, AND RESONANCE TECHNIQUES

Erick Omar Burgos Parra, Chair
CNRS, Paris, France

CONTRIBUTED PAPERS

1:30

BG-01. MRI of Magnetic Thin Film Structures and Devices.
S.E. Russek[1] *1. NIST, Boulder, CO, United States*

Magnetic nanostructures have been extensively used to modify magnetic resonance imaging (MRI) contrast, either increasing (paramagnetic ions such as Gd^{+3}) or decreasing signal (ferrite nanoparticles). Here, we present a study of imaging around microfabricated thin film structures using a 3T MRI. The images are derived from contrast in the water proton magnetization near the thin film structures. Fig.1 shows an optical image and MRI of a magnetic tunnel junction wafer immersed in water, where magnetic structures are clearly seen. While the best MRI resolution is ~ 125μm, features smaller than 10μm can be individually detected. Since the thin film structures can be precisely fabricated, it is possible to numerically calculate the magnetic fields and predict proton relaxation times (T1, T2, T2*), thereby providing a method to validate contrast models. The magnetic fields generated by thin film structures depend on materials, device size and shape, and direction of the applied field. Fig. 2a shows an MRI of 10nm thick Co thin film dot and line arrays. A large number of exotic materials can be rapidly evaluated for MRI contrast. Fig. 2b shows MRI contrast above antiferromagnetic CoO films near their Neel temperature. Contrast differences are seen due to CoO layer thickness as well as structures formed in the CoO. The contrast arises from both nonlocal interactions with the CoO-generated magnetic fields as well as local interactions from water molecules adsorbing to the surface.

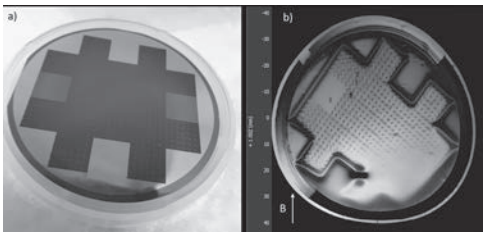


Fig. 1 a) Optical image of a 76mm-diameter magnetic tunnel junction (MTJ) wafer consisting of sensor arrays of elliptical junctions with size ~20μm. b) MRI of the wafer immersed in a water. The MTJ arrays can be seen as dark structures on a 2mm square grid. The black tri-lobed features seen in the upper left corner are small air bubbles.

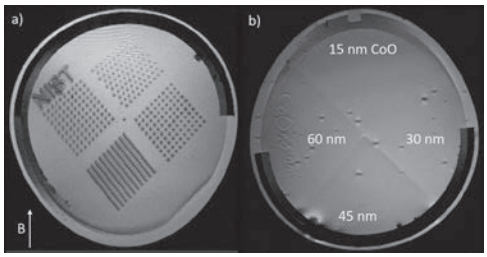


Fig.2 a) MRI of 10nm thick Co features including rectangular and hexagonal 1mm diameter dot arrays and 1mm wide lines. b) MRI of CoO films with wedges of different thickness. The water temperature was ~290K, which is close to the Neel temperature. The writing in the 60nm thick film is a region without CoO, clearly showing negative contrast provided by the CoO. The black tri-lobed features are small air bubbles.

1:42

BG-02. Electrodynamic theory of ferromagnetic resonance and its applications in precise measurements of ferromagnetic linewidth, permeability tensor and saturation magnetization. *J. Krupka*[1], A. Pacewicz[2], B. Salski[2] and P. Kopyt[2] *1. Institute of Microelectronics and Optoelectronics, Warsaw University of Technology, Warsaw, Poland; 2. Institute of Radioelectronics and Multimedia Technology, Warsaw University of Technology, Warsaw, Poland*

During the last few years the authors of this paper has developed rigorous electrodynamic theory of ferromagnetic resonance in spherical and rod shape, uniformly magnetized samples [1] – [3]. In this paper the state of the art in measurements of ferromagnetic linewidth, permeability tensor and saturation magnetization employing this theory is presented. It is shown that the electrodynamic theory allows significant improvements of measurement accuracy of these parameters with respect to the commonly used perturbation and magnetostatic theories. Contrary to the perturbation method the electrodynamic theory is not limited to small samples. It allows determination of the resonance frequencies and Q-factors for arbitrary size spherical and cylindrical gyromagnetic samples in suitably chosen metal enclosures. The influence of magnetic dielectric and conductor losses on the Q-factor is considered. Phenomena in lossy and dispersive gyromagnetic media related to the stored and dissipated electromagnetic energy in microwave resonators containing ferromagnetic samples are discussed in details. It is shown that the magnetic energy stored in dispersive gyromagnetic sample can be several orders of magnitude larger than for non-dispersive medium having identical but constant permeability. Results obtained with the electrodynamic theory for very small samples are identical to those obtained with perturbation and magnetostatic theories. Results of measurements of the ferromagnetic linewidth, permeability tensor and saturation magnetization on several single crystal and polycrystalline garnet samples are presented.

[1] J. Krupka, P. Aleshkevych, B. Salski, P. Kopyt, A. Pacewicz, Sci. Rep. 7 (1) 5750 (2017) [2] J. Krupka, P. Aleshkevych, B. Salski and P. Kopyt, IEEE Trans. Microwave Theory Tech, (2018) [3]J. Krupka, Meas. Sci. Technol. 29 (9) 092001 (2018)

1:54

BG-03. Withdrawn

INVITED PAPER

2:06

BG-04. Control and Local Measurement of the Spin Chemical Potential in a Magnetic Insulator. *C. Du*[1], T. Van der Sar[2], T. Zhou[3], P. Upadhyaya[4], F. Casola[3], H. Zhang[3], M. Onbasli[5], C. Ross[5], R. Walsworth[3], Y. Tserkovnyak[6] and A. Yacoby[3] *1. Physics, University of California, San Diego, La Jolla, CA, United States; 2. Delft University of Technology, Delft, Netherlands; 3. Harvard University, Cambridge, MA, United States; 4. Purdue University, West Lafayette, IN, United States; 5. Materials Science and Engineering, Massachusetts Institute of Technology, Cambridge, MA, United States; 6. Physics, University of California, Los Angeles, Los Angeles, CA, United States*

In recent decades, a large scientific effort has focused on harnessing spin transport for providing insights into novel materials and low-dissipation information processing. We introduce single spin magnetometry based on nitrogen-vacancy (NV) centers in diamond as a new and generic platform to locally probe spin chemical potentials which essentially determine the flow of spin currents. We use this platform to investigate magnons in a magnetic insulator yttrium iron garnet (YIG) on a 100 nanometer length scale. We demonstrate that the local magnon chemical potential can be systematically controlled through both ferromagnetic resonance and electrical spin excitation, which agrees well with the theoretical analysis of the underlying multi-magnon processes. Our results open up new possibilities for nanoscale imaging and manipulation of spin- related phenomena in condensed-matter systems.

C. H. Du et al., Science 357, 195 (2017)

CONTRIBUTED PAPERS

2:42

BG-05. Emerging widefield magnetic imaging applications using NV-diamond magnetic microscopy. *P. Kehayias*[1], E. Bussmann[1], T. Lu[1] and A. Mounce[1] *1. Sandia National Labs, Albuquerque, NM, United States*

Magnetically-sensitive nitrogen-vacancy (NV) color centers in diamond are gaining momentum as a standard tool for magnetic imaging in a diverse range of applications. Using a shallow layer of NV centers at the surface of a diamond chip, we image the NV fluorescence intensity with an optical microscope, which yields information about the magnetic field of nearby external magnetic sources. The benefits for using NVs for magnetic imaging include the following: 1. Being able to image many pixels in parallel (rather than raster-scanning a single-pixel detector) 2. Being able to reduce the sample-sensor standoff distance (as small as a few nanometers) to measure a larger magnetic field with better spatial resolution 3. Having micron-scale spatial resolution over a few-mm field-of-view 4. Allowing a wide range of working conditions (magnetic field strength, temperature, pressure, and frequency) NV magnetic microscopy is being used to investigate fundamental questions in paleomagnetism, biomagnetism, and superconductivity [1-3]. With the goal of extending the NV imaging capabilities to a wider array of scientific problems, we will report on our recent progress using NV imaging for applications relating to hardware security, electronics, fabricated micromagnets, and magnetic materials.

[1] D. R. Glenn et al., Geochemistry, Geophysics, Geosystems 18, 8 (2017). [2] D. Le Sage et al., Nature 496, 486-489 (2013). [3] Y. Schlussel et al., Phys. Rev. Applied 10, 034032 (2018).

2:54

BG-06. Interferometric Scanning Transmission Electron Microscopy of a Landau Domain. *A. Greenberg*[1], F. Yasin[1] and B.J. McMorran[1] *1. Physics, University of Oregon, Eugene, OR, United States*

Transmission electron microscopy is one of few methods capable of imaging magnetic features at the nanoscale. The sample's magnetic properties are inferred by measuring the phase shift imprinted on an electron's wavefront by a magnetic vector potential. Here we present the use of Interferometric Scanning Transmission Electron Microscopy (ISTEM) to measure magnetic phase.[1–4] In ISTEM, the electron beam is divided by a nanofabricated diffraction grating in an aperture above the sample (Fig. 1). The diffracted orders form spatially separated probes at the sample. We scan these probes across the specimen such that one of the probes interacts with the sample while others pass through vacuum. We image the interference pattern from which the phase shift induced by the sample on the interaction probe can be measured.[1–4] The best spatial resolution of a magnetic phase object attained, 1 nm, was achieved by Lorentz STEM with Differential Phase Contrast (DPC) analysis[5] although an atomic scale electron probe in a magnetic field free environment has been achieved.[6] There is an inherent tradeoff between DPC's spatial and phase resolution because the sensitivity of DPC depends on the ratio of the Lorentz deflection to the probe semi angle.[5] Because ISTEM measures the phase interferometrically, it does not suffer this trade off. As electron microscopes capable of forming a nanometer to subnanometer wide probe in a magnetic field-free environment become more common, ISTEM could be a powerful high-resolution magnetic phase measurement tool. We applied ISTEM to image a 1 um wide square composed of a layer of 25 nm thick permalloy and a layer of 100 nm thick silicon nitride. The square is supported by 200 nm wide tethers at each corner. A completely isolated thin film permalloy square has a vortex-like in-plane magnetic configuration known as a Landau domain. In the tethered square the Landau domain is altered because the domain walls fall to the side of each tether (Fig. 2). We confirm the measured magnetic induction by comparing it to standard Lorentz TEM measurements and micromagnetic simulation.

1. F. Yasin, T. Harvey, J Chess et al., Nano Lett., Vol. 18, p. 7118 (2018) 2. F. Yasin, K. Harada, D. Shindo et al., Appl. Phys. Lett., Vol. 113, p. 233102 (2018) 3. F. Yasin, T. Harvey, J. Chess et al., J. Phys. Appl. Phys., Vol. 51, p. 205104 (2018) 4. T. Harvey, F. Yasin, J. Chess et al., Phys. Rev. Appl., Vol. 10, p. 061001 (2018) 5. S. McVitie, D. McGrouther, S. McFadzean et al., Ultramicroscopy, Vol. 152, p. 57 (2015) 6. N. Shibata, Y. Kohno, A. Nakamura et al., Nat. Commun., Vol. 10 (2019)

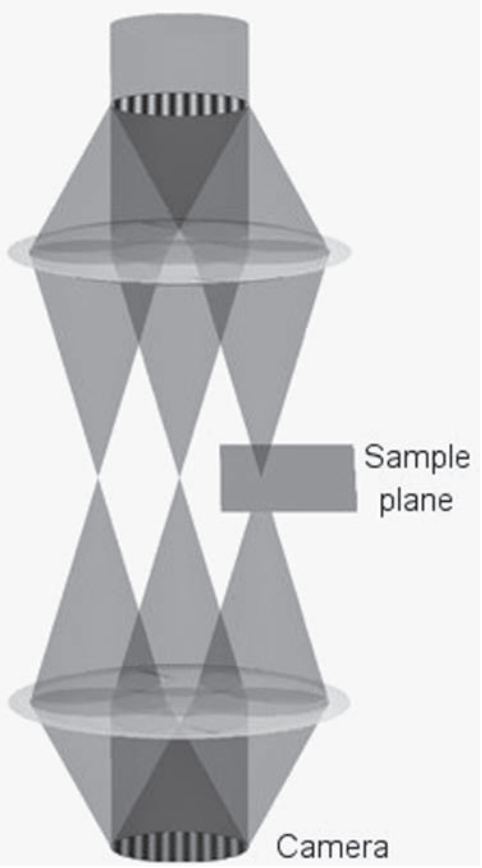


Figure 1. ISTEM experimental setup.

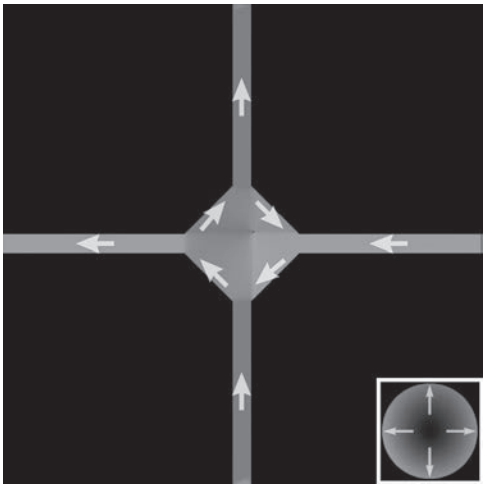


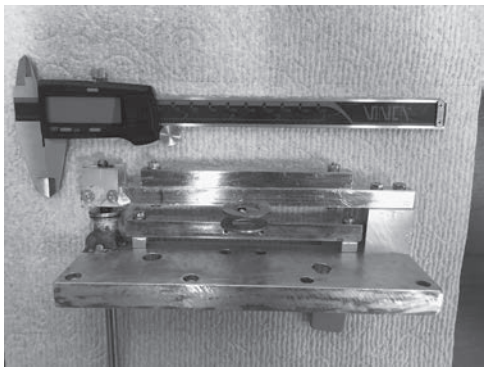
Figure 2. Micromagnetic simulation of tethered square magnetization (black indicates vacuum).

3:06

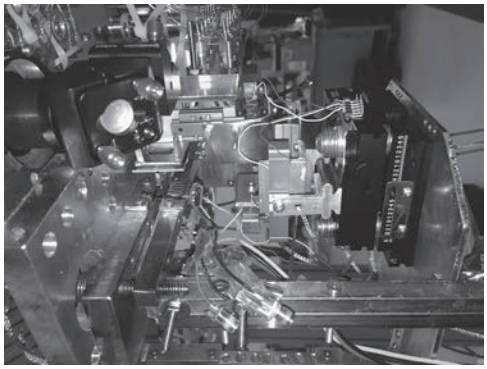
BG-07. Scanning Superconducting Quantum Interference Device (SQUID) setup for studies of magnetic materials under uniaxial stress or strain at millikelvin temperatures. *J. Franklin*[1], D. Davino[1] and I. Sochnikov[1] *1. Physics Department, University of Connecticut, Storrs, CT, United States*

Uniaxial strain is becoming an increasingly efficient tool for studying and controlling quantum materials. One of the challenges with the existing uniaxial stress or strain cells is combining the cells with microscopy techniques at ultra-low temperatures. Here, we demonstrate a unique copper bidirectional strain-stress cell. The cell is combined with an optical microscope and a scanning SQUID microscope. Benchmark measurements of magnetic signatures in strained quantum materials are demonstrated. This technique can lead to new discoveries such as enhanced superconductivity and new controlled magnetic states in various correlated material systems.

[1] C. Herrera, J. Cerbin, C. Dunnett et al. https://arxiv.org/abs/1808.03739



The copper strain-stress cell driven by a stainless steel lead-screw. The cell is preloaded and can apply tensile or compressive deformations at millikelvin temperatures.



The installed cell with the optics and the scanning SQUID setup.

3:18

BG-08. Validated Nano Scanning Hall Microscopy. *M. Gerken*[1], D. Momeni Pakdehi[1], T. Weimann[1], A. Solignac[2], K. Pierz[1], S. Sievers[1] and H. Schumacher[1] *1. Physikalisch-Technische Bundesanstalt, Braunschweig, Germany; 2. SPEC, CEA, CNRS, Université Paris-Saclay, Paris, France*

Scanning Hall Microscopy (SHM) is a versatile tool for the quantitative characterization of magnetic microstructures. However, application relevant structures are increasingly being scaled-down to the nanometer range and thus become smaller than the active area of commercially available sliding Hall sensors. Furthermore, the stray fields of nanoscale magnetic structures are rapidly decreasing with increasing distance to the sample. We here adopt SHM to these challenges by combining a reduced sensor size with unconventional materials and by positioning the sensors on a cantilever that can be used in standard scanning probe microscopes (SPM). We discuss the fabrication and characterization of Hall sensors with active areas down to 50 x 50 nm^2 fabricated out of gold and epitaxially grown graphene on SiC(0001) [1]. Figure 1 shows typical calibration curves for graphene and gold Hall sensors. A high sensitivity of 1615 V/AT and a resolution of 1.5 mT is achieved with the graphene nano sensor. Gold sensors show a lower sensitivity of about 3 mV/AT but better stability. Here, a resolution of 2 mT can be achieved. Gold nano Hall sensors are prepared on silicon cantilevers that can be directly integrated into commercial SPMs. Thus, allowing a measurement height of

down to 400 nm. By employing a metrological SPM developed at PTB [2] a 3D mapping of the sample stray field can be performed with a positioning accuracy of 0.5 nm. Figure 2 shows quantitative SHM data of a magnetic scale including a comparison to magneto-optical (MO) and simulation data. Furthermore, we will present an analysis of the uncertainty budget. This work was supported by the EMPIR JRP 15SIB06 NanoMag through EU and EMPIR participating countries within EURAMET.

[1] D. Momeni Pakdehi, J. Aprojanz, A. Sinterhauf, ACS Applied Materials & Interfaces, 10, 6039-6045 (2018) [2] G. Dai, X. Hu, S. Sievers, Rev. Scient. Instr., 89, 093703 (2018)

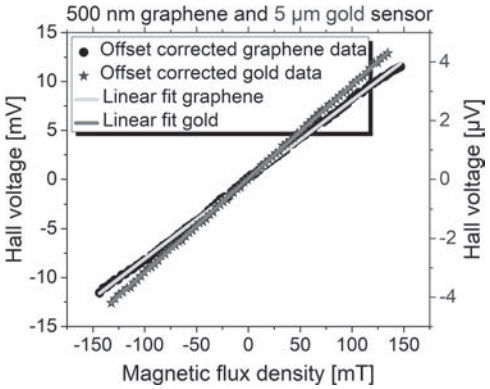


Fig. 1: Sensitivity from field dependent Hall voltage measurement for graphene and gold Hall sensors.

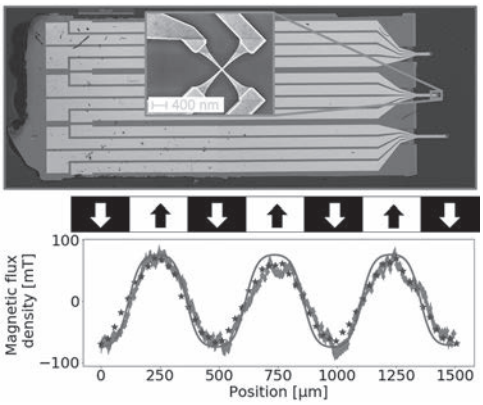


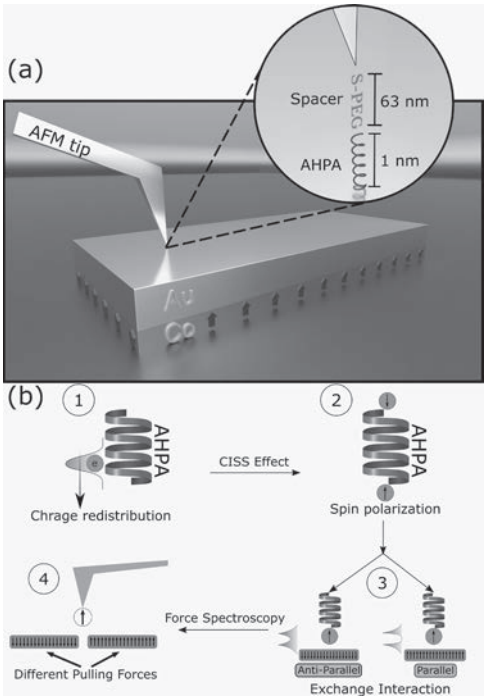
Fig. 2: Cantilever chip with scanning electron microscopy inset of a 50 nm Hall sensor out of gold symbolizes the scanning over a magnetic scale. Below is the data (red dots) measured with a 5 µm sensor at a height of 50 µm and its uncertainty (gray area) shown and compared to MO data (blue stars) and simulation (green line).

3:30

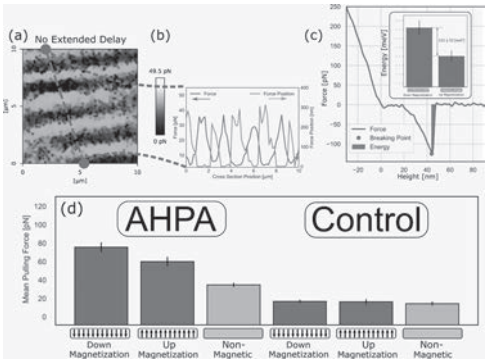
BG-09. Local Spin Exchange Microscopy by Chiral Molecules Adsorbed on an AFM Tip. *A. Ziv*[1], A. Saha[2], H. Alpern[1], N. Sukenik[1], L. Tomasz Baczewski[3], S. Yochelis[1], M. Reches[2] and Y. Paltiel[1]
1. Applied Physics, The Hebrew University, Jerusalem, Israel; 2. Institute of Chemistry, The Hebrew University, Jerusalem, Israel; 3. Institute of Physics, Polish Academy of Sciences, Warszawa, Poland

Local magnetic imaging at nanoscale resolution is highly desired for basic studies of magnetic materials, as well as for probing the reduction of magnetic memory size. However, such local imaging is hard to achieve by means of standard magnetic force microscopy (MFM) that exploits dipole-dipole interactions, where the resolution is fundamentally limited. While other magnetic imaging techniques such as spin polarized STM (SPSTM) and scanning squid microscopy (SSM) yielded highly resolved magnetic imaging, that lead to fundamental insights and research, they require low temperatures, high vacuum or strict limitations on the sample conditions. Other techniques such as MOKE and NV center are diffraction limited or able to probe weak magnetic stray fields only. In my talk, I will present a simple and robust method for locally resolved magnetic imaging based on the short-range spin exchange interactions that can be scaled down to atomic resolution. The presented method, realized at room temperature, requires a conventional AFM tip functionalized with a chiral molecule. In proximity to the measured magnetic sample, charge redistribution in the chiral molecule leads to a transient spin state, caused by the chiral induced spin selectivity (CISS) effect, followed by the exchange interaction with the imaged sample. This method acquires accurate results compared to methods based on measuring the magnetic stray field. Using the same tip with adsorbed chiral molecules, two oppositely magnetized samples were characterized, and magnetic imaging was performed. The method, we term CISS AFM, does not require high vacuum conditions, can be performed at room temperature and is simple to establish.

1. Dor, O. B. *et al. Nature Communications* 4, 2256 (2013). 2. Ben Dor, O. *et al. Nature Communications* 8, 14567 (2017). 3. Banerjee-Ghosh, K. *et al. Science* 360, 1331–1334 (2018). 4. Naaman, R., Paltiel, Y. & Waldeck. *Nature Reviews Chemistry* 3, 250 (2019).



(a) a chiral molecule is adsorbed on an Au AFM tip. (b)Imaging mechanism.



(a)Molecular spin exchange force mapping of magnetic stripes.(b) cross-section of the force mapping image, force is measured at close proximity to the surface.(c) Typical force dependence on the tip height. Inset: the mean pulling energy for the up and down direction of magnetization.(d)mean pulling force for two molecules, chiral (AHPA) and a control molecule. For AHPA, a difference in force exists between the up and down magnetization, which is absent in the control.

3:42

BG-10. Chirality probed in ferromagnetic and synthetic antiferromagnetic multilayers by quantitative MFM analysis at room temperature. *F. Ajejas*[1], W. Legrand[1], A. Haykal[2], Y. Sassi[1], A. Finco[2], S. Chouaieb[2], D. Maccariello[1], S. Collin[1], K. Bouzehouane[1], A. Vechiola[1], N. Reyren[1], V. Cros[1], V. Jacques[2] and A. Fert[1] *1. Unité Mixte de Physique, CNRS, Thales, Univ. Paris-Sud, Université Paris-Saclay, Palaiseau, France; 2. Laboratoire Charles Coulomb, Université de Montpellier and CNRS, Montpellier, France*

Dzyaloshinskii-Moriya interaction (DMI), a chiral exchange interaction, has attracted a great attention in the last years, because of its significant role in the stabilization of spin textures with a fixed chirality in thin films and magnetic multilayers (MML), such as chiral Néel domain walls (DW) [1] or skyrmions [2-3]. Depending on the direction of the DMI interaction vector, a counter clockwise (CCW) or clockwise (CW) chirality in the spin textures is stabilized. Extracting the sign of DMI and therefore the chirality sign has been experimentally assessed using different techniques e.g. Brillouin light scattering [4], asymmetric expansion of bubbles by Kerr microscopy [5], x-ray resonant magnetic scattering [6], or X- photoemission electron microscopy [7]. In this work, we present a novel method to determine the chirality of magnetization textures using magnetic force microscopy (MFM), an accessible tool in most laboratories. Two different systems have been characterized by AGFM and SQUID to extract magnetization and anisotropy values i.e. FM multilayers based on Pt(0.42)/Co(0.42)/Pd(0.42) and Pd(0.42)/Co(0.42)/Pt(0.42) and. SAF stacks which are composed of two (or more) FM thin layers (or blocks) separated by a thin spacer and coupled antiferromagnetically (AF) by RKKY interaction; with zero net magnetization. We acquire a series of MFM using variable scanning tip-surface distance to extract profiles of DWs. By comparing the MFM signal to micromagnetic simulations of the stray field emerging from the DW, the actual chirality can be assessed. Complementary characterizations of the DW stray field have been also performed using nitrogen vacancy (NV) microscopy relating quantitatively the stray fields in SAF. French ANR grant TOPSky TOPSKY (ANR-17-CE24-0025) and DARPA TEE program grant (MIPR#HR0011831554) and EU grant SKYTOP (H2020 FET Proactive 824123) are acknowledged for their financial support.

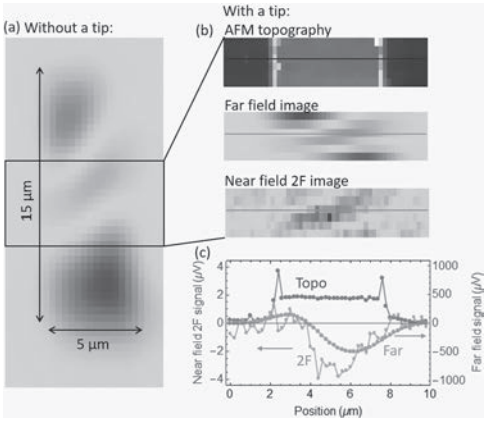
[1] A. Thiaville et al., EuroPhys. Lett, 100, 57002 (2012) [2] A. Fert, N. Reyren, V. Cros, Nat. Rev. Mat. 2, 17031 (2017). [3] C. Moreau-Luchaire et al., Nature Nanotechnology 11, 444 (2016) [4] M. Belmeguenai et al., Phys. Rev. B, 91 (2015) 180405(R) [5] F. Ajejas et al., Appl. Phys. Lett. 111, 202402 (2017); [6] J.Y. Chauleau et al., Phys. Rev. Lett. 120, 037202 (2018) [7] O. Boulle et al., Nature Nanotechnology 11, pages 449–454 (2016) [8] Marioni et al., Nano Letters. 18, 2263 –2267 (2018)

3:54

BG-11. Imaging Nanoscale Magnetization Using Scanning-Probe Magneto-Thermal Microscopy. *C. Zhang*[1], J. Bartell[1], J. Karsch[1], I. Gray[1] and G. Fuchs[1] *1. School of Applied and Engineering Physics, Cornell University, Ithaca, NY, United States*

Advanced magnetic microscopies are key to advancing our understanding and application of novel magnetic phenomenon such as skyrmions, spin-waves, and domain walls. However, due to the diffraction-limit of light, achieving the 10-100 nanometer spatial resolution and 10-100 picosecond temporal resolution required to image these phenomenon is beyond the reach of table-top techniques. To break free of the far-field diffraction limit, we have been developing a near-field magnetic microscope based on magne-to-thermo interactions: the time-resolved anomalous Nernst effect [1] and the time-resolved longitudinal spin Seebeck effect [2]. Our technique involves the excitation of plasmon-polaritons at the apex of a sharp gold tip. The resulting near-field tip-sample interaction creates a nanoscale thermal gradient for magneto-thermal microscopy [3]. Here, we study the near-field characteristics of our signal, demonstrate magnetic imaging of a multi-domain state, and present sub-optical diffraction spatial resolution. Our results suggest a new approach to nanoscale spatiotemporal magnetic microscopy in an accessible, table-top form to aid in the development of high-speed magnetic devices.

[1] J.M. Bartell, D.H. Ngai, Z. Leng, G.D. Fuchs, Nat. Commun. 6, 8460 [2] J. M. Bartell, C. L. Jermain, S. V. Aradhya, J. T. Brangham, F. Yang, D, C. Ralph, G. D. Fuchs, Phys. Rev. Appl. 7, 044004 [3] J. C. Karsch, J. M. Bartell, G. D. Fuchs, APL Photonics 2, 086103 (2017)



(a) Magnetic far field images of a multi-domain state in a 5 µm x 15 µm CoFeB/Hf/Pt sample without a tip. With a gold-coated tip, (b) images and (c) line cuts of tuning fork-AFM topography, the chopper-referenced far field signal, and the probe referenced at 2F (near field) signal. The spatial resolution in this sample is limited by the actual domain wall width in this sample.

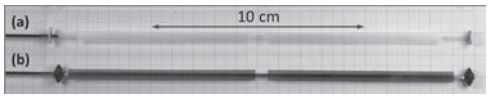
4:06

BG-12. *In situ* Compensation Method for High-Precision and High-Sensitivity Integral Magnetometry. *K. Gas*[1] and M. Sawicki[1] *1. Institute of Physics, Polish Academy of Sciences, Warsaw, Poland*

The most popular multipurpose commercial superconducting quantum interference device (SQUID) integral magnetometers are not object-selective probes, so the sought signal is very often buried in the magnetic response of the substrate or a carrier, which can be substantially contaminated by signals brought about by the chosen sample mount and magnetometer's instabilities. We report on a comprehensive method for mitigating these weak elements of integral magnetometry [1]. The method is based on the *in situ* magnetic compensation (on the sample holder level) of the vast majority

of the unwanted magnetic flux. This reduces the signal which is processed by the magnetometer up to two orders of magnitude, so the output is much less dependent on the inevitable fluctuations of some environmental variables which detrimentally reduce the real credibility of the outcome in the standard approach to precision magnetometry. Additionally, a two- to five-fold reduction in the absolute noise level has been observed. Practical solutions for the achievement of adequate compensation and proper expressions to evaluate the final results obtained in the compensational sample holder are given. Their universal form allows to practically employ one design of the compensational sample holder in investigations of a range of specimens characterized by different sizes, shapes and compositions. Importantly, the method does not require any modelling of the magnetometer output signal, nor any laborious fitting. All the necessary inputs to calculate the absolute magnitude of the net moment of the investigated object (e.g. magnetic layer) can be taken directly from the standard magnetometer output files. The method is tested to a very good result on some of the most demanding subjects as are single nm thin layers of dilute magnetic semiconductors. The solution given by us can be straightforwardly implemented in every field of activity where precise magnetic investigations are of a prime importance. This work has been supported by the National Science Centre, Poland through project DEC-2017/27/B/ST3/02470.

[1] K. Gas and M. Sawicki, Meas. Sci. Technol. (2019) accepted, https://doi.org/10.1088/1361-6501/ab1b03.



Compensational sample holders made by the authors. (a) Sapphire compensation on sapphire support, (b) GaP compensation on Si support.

Session BH
PATTERNED STRUCTURES AND ARTIFICIAL SPIN ICE
Yuan-Chieh Tseng, Chair
National Chiao-Tung University, Hsin-Chu, Taiwan

CONTRIBUTED PAPERS

1:30

BH-01. Creating 3D-Magnetic Textures in Synthetic Antiferromagnets by Focused Ion Beam Irradiation. *F. Samad*[1,2], L. Koch[2], G. Hlawacek[1], S. Arekapudi[2], M. Lenz[1] and O. Hellwig[1,2] *1. Institute of Ion Beam Physics and Materials Research, Helmholtz Zentrum Dresden Rossendorf, Dresden, Germany; 2. Chemnitz University of Technology, Chemnitz, Germany*

The Dzyaloshinskii–Moriya interaction (DMI) assisted emergence of 3D-magnetic textures in general and magnetic skyrmions, in particular, were hitherto typically observed in bulk B20-materials at low temperatures or in ferromagnetic multilayers at room temperature [1]. In contrast, we used a synthetic antiferromagnet (AF) [2] as a platform, consisting of perpendicular anisotropy Co/Pt-multilayers, AF coupled via Ru interlayers. Such a system provides the striking benefits of the absence of stray fields as well as high domain wall velocities [3], making it interesting for possible future data storage applications. The ground state energy balance was previously shown to depend on the ratio of dipolar energy and AF exchange energy [2], which increases with the Co layer thickness or Co/Pt-repetition number, thus yielding a phase transition to a ferromagnetic stripe domain state. Here, differently, we use focused He^+ ion beam irradiation with different fluences and energies, to modify the local interplay between dipolar and AF interlayer exchange energy. Thus, we were able to create a variety of laterally coexisting magnetic phases (see Fig. 1) and 3D-magnetic textures in different confinements. Detailed investigation of their interactions as well as their magnetic field reversal behavior were performed with in-field high-resolution magnetic force microscopy (MFM).

[1] Soumyanarayanan et al., Nat. Mater. 16, 898-904 (2017). [2] O. Hellwig et al., J. Magn. Magn. Mater. 319, 13-55 (2007). [3] Yang et al., Nat. Nanotechnol. 10, 221-226 (2015).

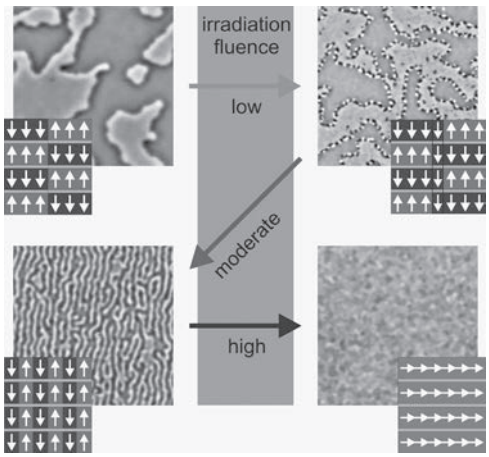


Fig. 1: MFM images (5 μm x 5 μm) showing the various types of domain structures observed in He^+-ion irradiated perpendicular AF-coupled $([Co/Pt]_6/Ru)_4$ multilayers, after in-plane demagnetization. In the insets the corresponding spin textures are indicated.

1:42

BH-02. Low temperature superspin glass behavior in a Co/Ag multilayer. E. Navarro[1], M. Alonso[1], A. Ruiz[1], C. Magen[2], U. Urdiroz[1], F. Cebollada[3], L. Balcells[4], B. Martínez[4], *J.M. González*[1] and F. Palomares[1] *1. Nanostructures and Surfaces, Instituto de Ciencia de Materiales de Madrid, Madrid, Spain; 2. Departamento de Materiales Magnéticos, Instituto de Ciencia de Materiales de Aragón, Zaragoza, Spain; 3. POEMMA-CEMDATIC, Universidad Politécnica de Madrid, Madrid, Spain; 4. Magnetic Materials and Functional Oxides, Institut de Ciència de Materials de Barcelona, Barcelona, Spain*

Superspin glass (SSG) magnetic order is commonly observed in granular metallic alloys, where a high degree of disorder on the magnetic particles positions constitutes a key ingredient for the collective freezing behavior. Here we present a study of the nanostructure and magnetic properties of a Co/Ag multilayer, a system that due to the stacking periodicity incorporates a reduced disorder in comparison with the granular solids. The multilayer was grown by molecular beam epitaxy on a clean MgO (001) surface, alternating Ag and Co deposition up to complete 32 periods. It was covered by a 3nm Ag cap layer, and the nominal thickness of the Co and Ag layers per period is 1 and 16 monolayers (ML), respectively. The sample was studied by X-ray reflectivity and diffraction, TEM, magnetometry (VSM and SQUID), and ac susceptibility. Our results indicated that: 1) a well-defined superlattice periodicity was built in the sample, see Fig.1; 2) Co layers were discontinuous, with a close-to-monodisperse distribution of Co particles (TEM mean diameter 1.6 nm) embedded in a Ag(001) matrix; 3) the sample exhibited hysteresis (not saturable at fields of up to 6 T) below ca. 14 K, and sharp zero-field cooling ac susceptibility peaks at a temperature range in correspondence with that associated to the hysteresis onset; 4) the ac field frequency dependence of real part of the susceptibility peak temperatures can be described by the Vogel-Fulcher law (Fig. 2) with a frequency shift parameter $\Gamma = 0.049$. We can thus conclude that, below the critical temperatures identified from the ac susceptibility curves, our sample behave as a SSG originated by the interparticle dipolar interactions, and that the degree of disorder built within the Co layers is sufficient to originate the observed magnetic collective behavior.

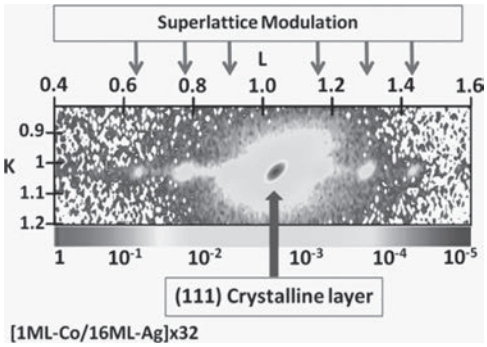


Fig. 1: Map of the reciprocal L-K space around the (111) reflection.

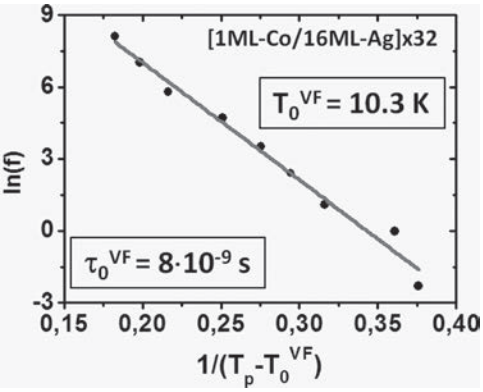


Fig. 2: Vogel-Fulcher fit of the experimental ac- data

1:54

BH-03. Thermally induced domain wall fluctuation in an antiferromagnetically ordered square artificial spin ice. *S. Roy*[1], X.M. Chen[1], B.W. Farmer[2], J.S. Woods[2], S. Dhuey[3], W. Hu[4], C. Mazzoli[4], S.B. Wilkins[4], I.K. Robinson[5], L.E. DeLong[2] and J.T. Hastings[6]
1. Advanced Light Source, Lawrence Berkeley National Laboratory, Berkeley, CA, United States; 2. Department of Physics, University of Kentucky, Lexington, KY, United States; 3. Molecular Foundry, Lawrence Berkeley National Laboratory, Berkeley, CA, United States; 4. NSLSII, Brookhaven National Laboratory, Upton, NY, United States; 5. Condensed Matter Physics and Materials Science Department, Brookhaven National Laboratory, Upton, NY, United States; 6. Department of Electrical and Computer Engineering, University of Kentucky, Lexington, KY, United States

Fluctuation and stochasticity are characteristics of material complexity that have been enduring themes in condensed matter and statistical physics research. Fluctuation provides basis for phase transitions and critical phenomena in statistical mechanics, order parameter field theories in quantum criticality etc. Systems that could be tailored so as to achieve phase transition is a candidate for studying effects of fluctuation. One such system is square Artificial Spin Ice (ASI), where magnetic nano-islands are arranged in a square lattice configuration. The shape anisotropy of the islands forces their magnetizations to align along their long axes, which gives them an Ising spin character. Geometrical constraints dictate the interactions between the Ising spins. In square ASI the arrangement of mutually perpendicular nanomagnets over a square lattice causes an asymmetry in the inter-island interactions that, in principle, favor an antiferromagnetic ground state. By choosing proper thickness of the nanomagnets it is possible to observe the paramagnet-to-antiferromagnet phase transition. In this work we have used resonant X-ray scattering to study the evolution of the antiferromagnetic Bragg peak in a square ASI that undergoes paramagnet-antiferromagnet phase transition around 380 K as a function of temperature. Further, we have used coherent soft X-ray Photon Correlation Spectroscopy (XPCS) to study thermally induced fluctuation of the domain wall as the phase transition temperature is approached. We observed an exponential slowing down of the fluctuation as the temperature is decreased. By analyzing the data within the framework of statistical mechanics we showed existence different type of fluctuations and relaxation. We observed two distinct regimes of domain wall motion; a low temperature ballistic and a high temperature diffusive type, as the sample goes through the antiferromagnetic phase transition. This work is supported by US DOE (Award# DE-SC0016519).

2:06

BH-04. Magnetic order and energy-scale hierarchy in artificial spin ice. *H. Stopfel*[1,2], E. Östman[2], I. Chioar[2], D. Greving[3], U.B. Arnalds[4], T.P. Hase[3], A. Stein[5], B. Hjörvarsson[2] and V. Kapaklis[2] *1. Engineering Sciences, Uppsala University, Uppsala, Sweden; 2. Physics and Astronomy, Uppsala University, Uppsala, Sweden; 3. Physics, University of Warwick, Coventry, United Kingdom; 4. Science Institute, University of Iceland, Reykjavik, Iceland; 5. Center for Functional Nanomaterials, Brookhaven National Laboratory, Upton, NY, United States*

The influence of different energy scales and their interplay is essential to explain and predict the properties of many physical systems. We present results on the magnetic order in thermalized artificial spin-ice structures[1,2], in particular the so-called Shakti and the modified Shakti lattices[3,4,5]. Due to the element sizes in these lattices, there are different activation energies at play for the interacting Ising-like elements[6]. While the Shakti lattice consists of short and long Ising-like elements, the modified Shakti lattice has only short elements. The different thermally active temperature regions for these elements are schematically shown in figure 1, emphasizing the two different energy scales present in these lattices. We image the thermally equilibrated magnetic states of the nanostructures using synchrotron-based photoemmision electron microscopy employing the x-ray magnetic circular dichroism to extract the magnetic orientation of each element. We demonstrate a clear impact on the magnetic ordering, by comparing results obtained from structures with one or two different activation energies. The differences are manifested in the analysis of the magnetic spin structure factors, in which the role of the activation energies is shows a distinct short-range order. These results highlight the potential of artificial spin-ice structures to serve as model systems for designing various energy-scale hierarchies and investigating their impact on collective dynamics and magnetic order.

[1] R. F. Wang et al., Nature 439, 303-306 (2006) [2] J. Cumings, Nature Physics 7, 7-8 (2011) [3] G. Chern et al., PRL 111, 1-5 (2013) [4] M. Morrison et al., NJP 15, 045009 (2013) [5] I. Gilbert et al., Nature Physics 9, 670-675 (2014) [6] H. Stopfel et al., PRB 98, 14435 (2018)

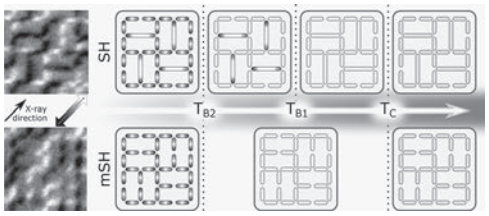


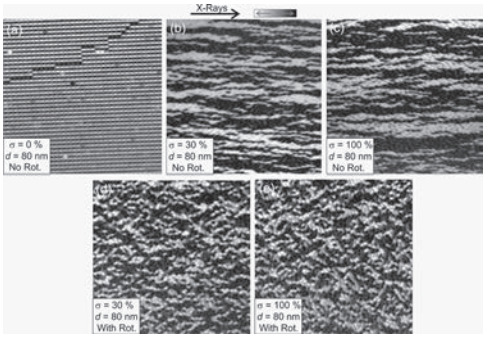
Figure 1: Representation of the different temperature regimes in which the Shakti (SH) and the modified Shakti (mSH) lattice are thermally active. Above the Curie-temperature, T_C, all islands are paramagnetic (light grey), below this temperature all islands are superparamagnetic (light blue). Below the blocking temperature of the long islands, T_{B1}, only the long islands are frozen-in and will not alter their magnetization direction during the measurement. Below T_{B2} all islands are frozen-in, with a blue magnetic north and a red magnetic south pole indicating their magnetization direction. At this temperature the PEEM measurements have been carried out, one examplary PEEM-image is shown on the left for SH and mSH lattice.

2:18

BH-05. Towards artificial Ising spin glasses. *M.D. Saccone*[1], A. Scholl[2], S. Velten[3,4], S. Dhuey[5], K. Hofhuis[6,7], C. Wuth[4], Y. Huang[8], Z. Chen[9], R.V. Chopdekar[2] and A. Farhan[2,7] *1. Physics, University of California Santa Cruz, Santa Cruz, CA, United States; 2. Advanced Light Source, Lawrence Berkeley National Laboratory, Berkeley, CA, United States; 3. Material Sciences Department, Lawrence Berkeley National Laboratory, Berkeley, CA, United States; 4. Institut für Nanostruktur- und Festkörperphysik, Universität Hamburg, Hamburg, Germany; 5. Molecular Foundry, Lawrence Berkeley National Laboratory, Berkeley, CA, United States; 6. Department of Materials, Laboratory for Mesoscopic systems, Zurich, Switzerland; 7. Laboratory for Multiscale Materials Experiments, Paul Scherrer Institut, Villigen, Switzerland; 8. Department of Materials Science and Engineering, University of California Berkeley, Berkeley, CA, United States; 9. School of Materials Science and Engineering, Harbin Institute of Technology, Guangdong, China*

From the study of sand piles [1] to descriptions of the human mind [2], spin glass research influences many disciplines. Patterned thin-film nanomagnets [3] are Ising type magnets that may be printed into nearly any two-dimensional pattern imaginable. Their ability to have their dynamics directly visualized makes them perfect candidates for spin glass model systems. However, it is uncertain whether or not spin glass phases at finite temperature exist in two dimensional systems like these [1,4]. Here we take the first step towards realizing spin glasses in artificial spin systems [5]. From an ordered grid of Ising type nanomagnet thin films we randomly alter the angular orientations and deviations. After thermal-annealing, we study the if the characteristic features of the spin glass phase are achieved. We record relaxation timescales together with magnetic susceptibility variations over temperature, revealing trends towards short-range order as randomness is increased, but falling short of pure spin-glass behavior. We then explore possibilities to directly construct spin glasses from existing glassy systems such as neural networks [6] and the Bethe lattice [7].

[1] Berthier, L., and G. Biroli. Rev. Mod. Phys. 83.2 (2011): 587. [2] Hudetz, A. G., C. J. Humphries, and Jeffrey R. Binder. Front. Syst.Neurosci. 8 (2014): 234. [3] Nisoli, C., R. Moessner, and P. Schiffer. Rev. Mod. Phys. 85.4 (2013): 1473. [4] Hartmann, A. K., and A. P. Young. PRB 64.18 (2001): 180404. [5] Saccone, M. et al. PRB 99.22 (2019): 224403. [6] Amit, D. J., Gutfreund, H., and H. Sompolinsky. PRA 32.2 (1985): 1007. [7] Mézard, M., and G. Parisi. Eur. Phys. J. B 20.2 (2001): 217-233.



XMCD images of a low-energy moment con guration achieved, following thermal annealing in (a) a fully ordered array of Ising-type nanomagnets, (b) a partially randomized array (σ = 30%) of parallel nanomagnets (no rotational disorder), (c) a fully randomized array (σ = 100%) of parallel nanomagnets (no rotational disorder), (d) a partially randomized array (σ = 30%) with rotational disorder, and (e) a fully randomized array (σ = 100%) with rotational disorder. The red scale bar indicates 1 m. We see a transition from a long-range ordered anti-ferromagnetic moment alignment for the ordered arrays, showing the characteristic dark- and bright lines (a), to a long-range ordered ferromagnetic state for the arrays with only positional disorder (b-c), ending in short-range ordered phases, when full randomness is introduced with rotational disorder (d-e).

2:30

BH-06. Thermal fluctuations in tetris vertex-frustrated artificial spin systems. *N.S. Bingham*[1], Y. Lao[2], X. Zhang[1], J.T. Batley[3], J. Sklenar[2], C. Leighton[3], C. Nisoli[4] and P. Schiffer[1,2] *1. Department of Applied Physics, Yale University, New Haven, CT, United States; 2. Department of Physics and Frederick Seitz Materials Research Laboratory, University of Illinois at Urbana-Champaign, Urbana-Champaign, IL, United States; 3. Department of Chemical Engineering and Materials Science, University of Minnesota, Minneapolis, MN, United States; 4. Theoretical Division and Center for Nonlinear Studies, MS B258, Los Alamos National Laboratory, Los Alamos, NM, United States*

Artificial spin ice systems [1] are arrays of interacting nanomagnetic islands originally designed to mimic the geometrical frustration of the complex pyrochlore spin ice materials. Each island has a single domain magnetization along its easy axis so the orientation can be treated as a single Ising spin. Recently, experimental realization of thermalized states [2] and slow thermal fluctuations, which drive lattices towards their ground state [3], have led to exciting new research in vertex-frustrated artificial spin ice. These are systems in which frustration is manifested in the allocation of ground state and excited state moment configurations at the lattice vertices. We have studied vertex-frustrated artificial spin ice using the tetris lattice (Fig. 1) [4] made with permalloy islands. We examined the temperature dependence of thermal fluctuations of moments along different island positions within the array using photoemission electron microscopy (PEEM) at various temperatures and lattice spacings using x-ray magnetic circular dichroism. We find that the moment fluctuations of the islands are highly dependent on nearest neighbor moment environments. Our results allow us to make a real space observation and characterization of the effects of neighboring moments on superparamagnetic behaviors of individual nanomagnet moments in this vertex-frustrated system and compare to results in square ice, where there is a well-defined and ordered ground state. NSB, YL, XZ, and PS are funded by the US Department of Energy, Office of Basic Energy Sciences, Materials Science and Engineering Division under grant number DE-SC0010778. JB and CL are sponsored by NSF through DMR. CN was supported by US Department of Energy under contract DE-AC52-06NA253962.

1. R. F. Wang et al. Nature 439, 303–306 (2006). 2. S. Zhang et al. Nature 500, 553–557(2013). 3. A. Farhan et al. Physical Review Letters 111, 57204 (2013). 4. I. Gilbert et al. Nature Physics 12, 162–165 (2016).

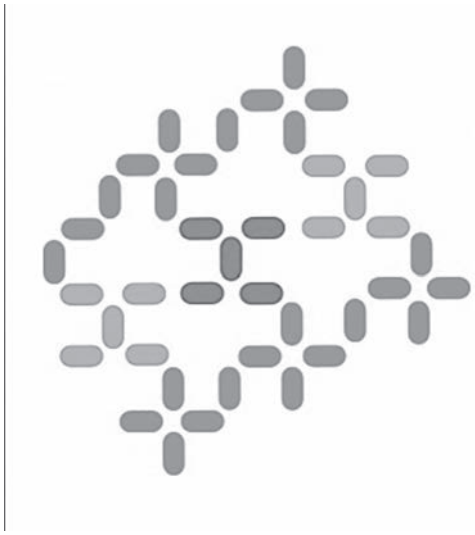


Figure 1: Schematic of the tetris lattice.

2:42

BH-07. Degenerate Ground States in Vertex-Frustrated Santa Fe Artificial Spin Ice. *X. Zhang*[1], Y. Lao[2], N.S. Bingham[1], J. Sklenar[2,3], J.T. Batley[4], R.V. Chopdekar[5], C. Leighton[4], C. Nisoli[6] and P. Schiffer[1,2] *1. Applied Physics, Yale University, New Haven, CT, United States; 2. Physics, University of Illinois Urbana and Champaign, Urbana, CT, United States; 3. Frederick Seitz Materials Research Laboratory, University of Illinois Urbana and Champaign, Urbana, IL, United States; 4. Chemical Engineering and Materials Science, University of Minnesota, Minneapolis, MN, United States; 5. Lawrence Berkeley National Laboratory, Berkeley, CA, United States; 6. Theoretical Division and Center for Nonlinear Studies, Los Alamos National Laboratory, Los Alamos, NM, United States*

Artificial spin ice systems (ASI) [1] are two-dimensional arrays of single-domain ferromagnetic nano-islands designed to study collective behavior of interacting magnetic systems. Vertex- frustrated ASI systems have highly degenerate ground states that are associated with the presence of excited vertices that are intrinsic to the lattice geometry, and these states can manifest a wealth of different emergent behavior [2]. One example of a vertex-frustrated ASI system is the Santa Fe lattice (Fig. 1a). Using a high temperature thermalization protocol [3], we have experimentally observed domains of the ground states of Santa Fe ASI (Fig. 1 b and C). We also performed Photoemission Electron Microscopy measurements as a function of lattice spacing and island moment to observe the kinetics behavior that driving Santa Fe ASI toward its ground state. Our results allow us to characterize ground state configurations and kinetics across different lattice parameters, demonstrating that Santa Fe lattice is an excellent candidate for studying novel order induced by vertex frustration. XZ, YZ, NB, JS, and PS are funded by the US Department of Energy, Office of Basic Energy Sciences, Materials Science and Engineering Division under grant number DE-SC0010778. JB and CL are sponsored by NSF DMR. CN was supported by US Department of Energy under contract DE-AC52-06NA253962. PEEM experiment was done in Lawrence Berkeley National Laboratory.

1.R. F. Wang, C. Nisoli, R. S. Freitas, *et. al.* Nature 439, 303–306 (2006). 2. M. J. Morrison, T. R. Nelson, and C. Nisoli, New J. Phys. 15, 045009 (2013). 3. S. Zhang, I. Gilbert, C. Nisoli, *et. al.* Nature 500, 553–557 (2013).

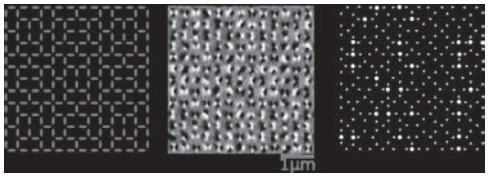


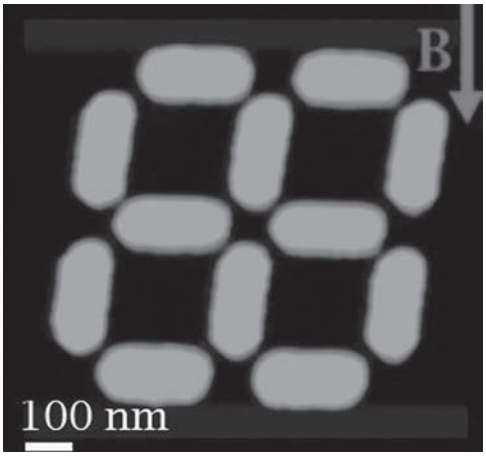
Figure 1: (a) Schematic for the Santa Fe lattice, (b) the MFM images after annealed at 545C, and (c) the spin map for (b). The open circles mark excited vertices.

2:54

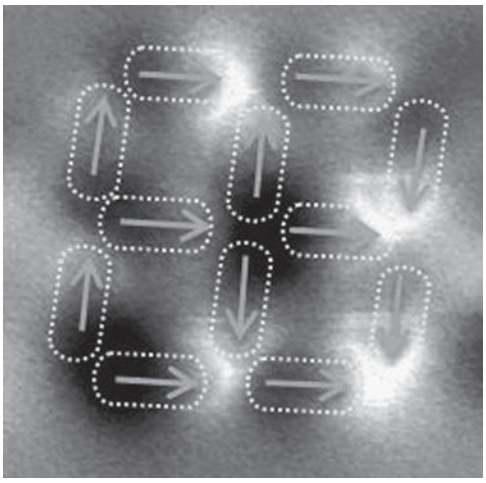
BH-08. Controlled generation of emergent magnetic monopole like states in square artificial spin ice systems. *N. Keswani*[1], Y. Nakajima[2], N. Chauhan[2], R. Singh[3], T. Som[3], S. Kumar[2] and P. Das[1] *1. Department of Physics, Indian Institute of Technology, Delhi, New Delhi, India; 2. Bio Nano Electronics Research Centre, Toyo University, Kawagoe, Saitama, Japan; 3. Institute of Physics, Bhubaneswar, India*

Artificial spin ice structures (ASI) have attracted great attention, serving as potential analogues for frustrated magnetic systems, such as bulk spin ice materials [1]. In 2008, Castelnovo *et al.* realized that excitations above the degenerated ground state, governed by the ice rule violation, could be interpreted as emergent quasiparticles that behave like magnetic monopoles. Such monopoles have been discussed in literature as magnetically charged particles in a dumbbell model where a dipole is considered as consisting of equal and opposite magnetic charges [2]. While most efforts have focused on study of array of artificial spin ice structures [3-6], little work has been done on understanding the switching behavior of individual nanoislands coupled by dipolar interactions in ASI systems [7]. In this work, we have investigated in details the magnetic switching behavior in individual vertices of square-ASI system composed of lithographically patterned nanoislands of dimensions 300×100×30 nm^3 of $Ni_{80}Fe_{20}$, as shown in Fig.1 (a). From magnetic force microscopy (MFM) investigations in presence of external field, we observe that an emergent monopole-like state can be predictably stabilized at about 425 G as shown in Fig.1 (b). The MFM image shows the 1-in/3-out magnetic state with magnetic charge $\sum Q = -2$ at vertex. Thus, we demonstrate the possibility of controlled generation of an emergent magnetic monopole in an isolated artificial square spin ice vertex. We also investigated the switching behavior of the individual nanoislands involved in the ASI structure and observe that the switchings can be controlled by the interplay of imperfections and dipolar interactions in these systems.

[1] R. Wang, *et al.*, Nature 439, 303 (2006). [2] C. Nisoli, *et al.,* Rev. Mod. Phys. 85, 1473 (2013). [3] C. Castelnovo, *et al.*, Nature 451, 42 (2008). [4] S. Ladak, *et al.*, New Journal of Physics 13, 063032 (2011). [5] A.L. Mól, *et al.,* Journal of Applied Phyics 106, 063913 (2009) [6] A. Farhan, *et al.*, Science Advances5, 6380 (2019). [7] N. Keswani and P. Das, AIP Advances 8, 101501 (2018).



AFM image of a lithographically patterned square-ASI structure of permalloy (single vertex with closed edges). Direction of applied field is shown by an arrow.



Corresponding MFM image showing 1-in and 3-out emergent monopole-like state at field of 425 G.

3:06

BH-09. Magnetic Configurations in Artificial Spin Ice subject to an External Bias Field during Demagnetization. *V. Parakkat*[1] and K. Krishnan[1] *1. Material Science and Engineering, University of Washington, Seattle, WA, United States*

The low energy states of artificial spin ice (ASI) arrays, fabricated of nano-magnets with large blocking temperatures, are traditionally probed by field demagnetization processes where a time varying external magnetic field in the form of a square wave with decreasing amplitude is applied in the plane of the rotating ASI [1,2]. These studies probe only zero field effects since the time average of the external field is zero in both laboratory and device frames. In contrast, we present here low energy states of an athermal square ASI of epitaxial Fe nanomagnets [thickness = 10 nm, width = 95 nm and length = 240 nm; Fig. 1(a)], subjected to a global magnetic field (H_G) applied in the rotating frame of reference of the ASI during demagnetization. In a square ASI, 16 different vertices are grouped into 4 different energy levels [3] as shown in Fig. 1b,c with their energies determined only by mutual magnetostatic interactions (at H_G = 0 Oe). We show that a field acting in the frame of reference of the ASI during demagnetization does not average to zero ($H_G \neq 0$ Oe) and hence adds Zeeman energy resulting in rearrangement of vertex energies. This breaks the spin reversal symmetry causing the energies of the vertices with moments parallel (antiparallel) to H_G to decrease (increase). This in turn modifies their population compared to that of a standard ASI (H_G =0). An H_G of fixed magnitude but applied at various angles w.r.t ASI axis also alters the energies of vertices and influences the shape and size of the T1 domains and the type of T2 domain walls (Fig. 1d). Striped features are observed in T1 domains when H_G is applied along the diagonal direction. The current study is in agreement with our recent work where each element of the ASI is subject to exchange-bias [4]. The ability to apply local and global fields can selectively control vertex energies, domains and domain wall configurations, opening a new pathway to compare and understand behavior of athermal and thermally active ASI arrays.

[1] R. F. Wang, C. Nisoli, R. S. Freitas, J. Li, W. Mcconville, B. J. Cooley, M. S. Lund, N. Samarth, C. Leighton, V. H. Crespi, and P. Schiffer, Nature 439, 303 (2006). [2] Y. Qi, T. Brintlinger, and J. Cumings, Phys. Rev. B 77, 094418 (2008). [3] C. Nisoli, R. Wang, J. Li, W. F. Mcconville, P. E. Lammert, P. Schiffer, and V. H. Crespi, Phys. Rev. Lett. 98, 217203 (2007). [4] V. M. Parakkat, K. Xie, and K. M. Krishnan, Phys. Rev. B 99, 054429 (2019).

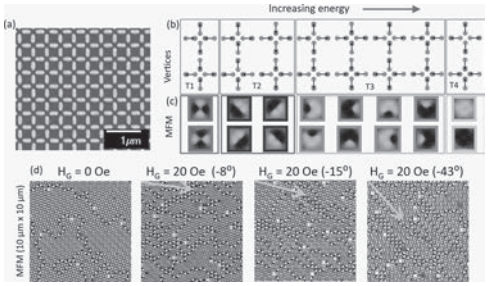


Fig. 1 a) SEM of square ASI with lattice constant ~ 380 nm. b) Schematic and c) MFM images of vertices with the color code highlight. d) MFM images of demagnetized ASI without and with H_G = 20 Oe at different angles (arrow).

3:18

BH-10. Interaction modifiers in artificial spin ices. E. Östman[1], *H. Stopfel*[2,1], I. Chioar[1], U.B. Arnalds[3], A. Stein[4], V. Kapaklis[1] and B. Hjörvarsson[1] *1. Physics and Astronomy, Uppsala University, Uppsala, Sweden; 2. Engineering Sciences, Uppsala University, Uppsala, Sweden; 3. Science Institute, University of Iceland, Reykjavik, Iceland; 4. Center for Functional Nanomaterials, Brookhaven National Laboratory, Upton, NY, United States*

We present here a generic solution to engineer the energy-landscape in fully planar magnetic nano-structures. This approach involves the mixing of nano-magnetic objects of distinctly different mesospin dimensionality[1]. In our example we use both elongated islands, spin dimensionality one, and discs, spin dimensionality two, to create a new type of square artificial spin ice (SASI) system dubbed modified SASI (mSASI) where a magnetic disc is placed in the center of each vertex. The disc mediate the interaction and therefore alters the effective coupling strengths between the elongated islands. In this way we can not only recover the degeneracy between Type-I and Type-II vertices, which is lost in SASI[2], but also promote an emergent magnetic order when the energy landscape is reversed, see Fig. 1. With the magnetic spin structure factor (SSF) we pinpoint the change of spatial correlations while altering the energy-landscape in mSASI. For a fixed lattice spacing, the decreasing of the gap size (G) and therefore an increase in the effective coupling leads to the magnetic SSF going from well defined bragg peaks (without interaction modifier), as expected when having large Type-I domains, to the characteristic intensity distribution which resamples the square-ice model for spin liquid (G=30), associated with an emergent Coulomb phase with slow decaying spin correlations[3,4,5]. Furthermore at the smallest gap size (G=15) the Type-I and Type-II population is reversed. Here the abundance of Type-II vertices give rise to an emergent flux lattice on the next length scale dictating the order of the spin system. The synergy

and cooperative behaviour between the two different mesospins provides a route for designing new types of magnetic metamaterials with rich magnetic phase diagrams and thermodynamics.

[1] E. Östman et al., Nature Physics 14, 375 (2018) [2] Wang, R. F. et al. Nature 439, 303–306 (2006). [3] Henley, C. L. Phys. Rev. B 71, 014424 (2005) [4] Henley, C. L. Annu. Rev. Condens. Matter Phys. 1, 179–210 (2010) [5] Perrin, Y. et al. Nature 540, 410–413 (2016)

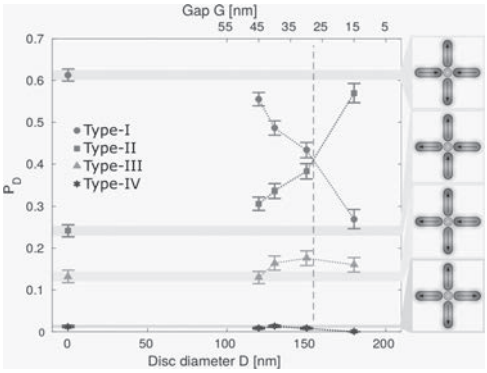


Fig. 1: Evolution of states depending on disc diameter/gap size in mSASI. A cross-over of the abundance of Type-I and Type-II vertices is seen in the measured population of states at a gap size of 30 nm, resulting in a reversed distribution for smaller gapes.

3:30

BH-11. Magnetization reversal mechanisms in Fe/NiO bilayers grown onto nanoporous alumina membranes and Si wafers. E. Navarro[1], M. Alonso[1], A. Ruiz[1], U. Urdiroz[1], M. Sánchez-Agudo[2], F. Cebollada[2], G. Domíguez-Cañizares[3], L. Soriano[3], A. Gutierrez[3], F. Palomares[1] and *J.M. González[1] 1. Nanostructures and Surfaces, Instituto de Ciencia de Materiales de Madrid, Madrid, Spain; 2. POEMMA-CEMDATIC, Universidad Politécnica de Madrid, Madrid, Spain; 3. Departamento de Física Aplicada, Universidad Autónoma de Madrid, Madrid, Spain*

We report on the Fe-thickness (5 nm – 20 nm) and temperature dependencies of the hysteretic parameters measured in two F/AF bilayer series: Fe/NiO/Al2O3 nanoporous membranes (series N) and Fe/NiO/Si wafers (series W). The Fe and NiO layers were deposited by pulsed laser ablation and magnetron sputtering, respectively. In both series different oxygen partial pressures (from 0% up to 70%) were implemented in the Ar plasma during NiO growth. The morphologies of both series (as imaged by atomic force microscopy) reflect those of their substrates and, particularly, the series N samples exhibit a six-fold columnar growth around each one of the nanopores (Fig. 1). The in-plane hysteresis loops measured (by means of a vibrating sample magnetometer) upon field cooling the samples down to different temperatures below 300 K evidenced (Fig. 2) the occurrence on the Fe 5 nm, series N samples of coercive forces larger than the Fe magneto-crystalline anisotropy field and decreasing with the increase of the NiO deposition oxygenpartial pressure. The series W samples including NiO layers deposited in the presence of oxygen, showed coercivities that were, for all the Fe thicknesses, below those measured on the corresponding series N samples. Our data are analysed, in close correlation to the deposits morphology, in terms of the occurrence of either propagation mediated reversal (collective mode linked to spatially averaged anisotropy) or localized switching (defect ruled mechanism taking place in a spatially confined environment). It is concluded that i) the magnetization reversal mechanism active in series N samples does not involve either propagation or domain wall pinning, and ii) the reversal events are spatially restricted to the Fe-covered, hexagonally closely packed dot-like tops of the NiO columns.

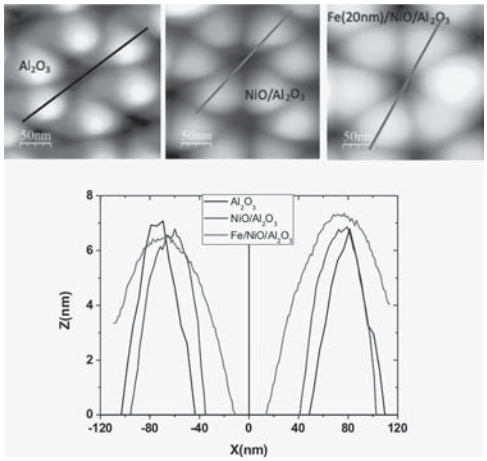


Fig. 1. Top: Atomic force microscope images of the region around a nanopore taken on, from left to right: the Al_2O_3 substrate, the NiO (30% oxygen) layer and Fe (20 nm) layer. Bottom: Profiles measured along the lines indicated in the images.

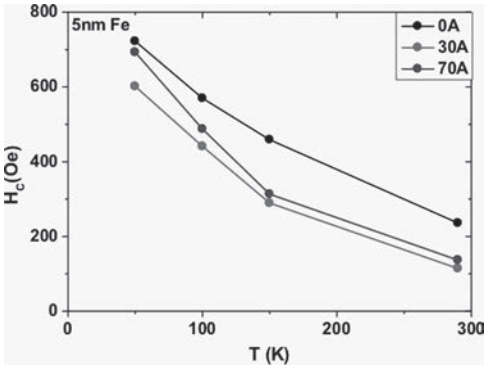


Fig. 2. Temperature dependencies of the coercivity in Fe (5 nm), series N samples deposited using 0% (0A), 30% (30A) and 70% (70A) oxygen-partial pressures.

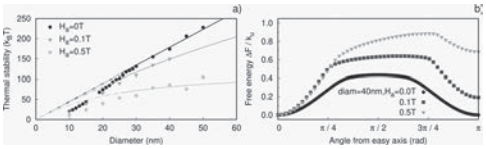
3:42

BH-12. Field and size dependence of the thermal stability in CoFeB/MgO systems. *A. Meo*[1], R.W. Chantrell[2] and R.F. Evans[2] *1. Department of physics, Mahasarakham university, Mahasarakham, Thailand; 2. Department of physics, University of York, York, United Kingdom*

The high anisotropy of CoFeB/MgO-based magnetic tunnel junctions (MTJs) provides the thermal stability (energy barrier/ thermal energy) required to store the information at a specific temperature. To further improve the reliability of these systems it is necessary to fully understand the dependence of the energy barrier on parameters such as system size, temperature and external field. The latter can be due to the stray field acting on the free layer arising from the fixed layer in a MTJ. Here we use an atomistic spin model performing constrained Monte Carlo simulations [1] to investigate the effect of an applied field on the energy barrier as function of diameter of CoFeB/MgO nanodisk at finite temperature. In zero field for small dimensions the spins behave as a macrospin and the thermal stability has the expected quadratic behaviour as function of diameter. Deviations from this behaviour occur as the system size approaches the single domain size and for larger diameters the thermal stability depends linearly on the diameter of the disk, as shown in Fig 1(a). The application of an external field along the easy axis direction, perpendicular to the system, makes the energy barrier between the two stable configurations nonequivalent, as shown in Fig 1(b). As a consequence the minimum barrier that the system magnetisation needs

to overcome decreases and tends towards a constant value for increasing applied fields. Above diameters of 30 nm this behaviour is well described by the droplet theory including the contribution of an external field and agrees with zero-temperature micromagnetic calculations presented in [2]. Further studies for larger diameters and including magnetostatic interactions are required to confirm the observed trends.

1) P. Asselin, R.F.L. Evans, J. Barker, R.W. Chantrell, *et al*, Phys. Rev. B 82, 054415 (2010). 2) G.D. Chaves-O'Flynn, G. Wolf, J.Z. Sun, and A.D. Kent, Phys. Rev. Appl. 4, 1 (2015).



a) Thermal stability as function of diameter for CoFeB/MgO dots at 300K for an external field Ha =0,0.1,0.5T applied along the positive z-direction. Points represent the data, while lines are the analytic model describing the droplet theory. Dotted lines are used for dimensions smaller than single domain size where the theory does not apply. b) Angular dependence of the energy barrier normalised by the maximum torque for CoFeB/MgO disks of diameter 40nm at 300K for Ha =0,0.1,0.5T.

3:54

BH-13. Tuning exchange bias and training effect in Co/CoO core/shell nanoparticle system by controlling surface defects. *M. Xing*[1], J. Mohapatra[1], J. Elkins[1], J. Beatty[1] and J. Liu[1] *1. Department of Physics, University of Texas at Arlington, Arlington, TX, United States*

A strategy is established to tune the exchange bias and training effect in Co/CoO nanoparticles of 14 nm size (Figure 1a) by controlling the surface defects. The surface defects in Co nanoparticles, and subsequently in the CoO shells, can be controlled by varying the Co-precursor to surfactant (hexadecylamine) mole ratio. The saturation magnetization of the freshly synthesized hcp-Co nanoparticles decreased from 144 emu/g to 126 emu/g with the increase of Co-precursor to surfactant mole content from 1:3 to 1:6, respectively. The low magnetization in the latter case is attributed to the higher surface spin disorder. Following surface oxidation, the sample with low surface spin disorder exhibited a giant exchange-bias field (H_{EB}) up to 2.7 kOe (Figure 1b), whereas the H_{EB} for the sample with high surface disorder is only 1.2 kOe. More importantly, the latter Co/CoO nanoparticles revealed prominent training effect (TE) of the H_{EB} with a large decrease of H_{EB} to 62 % from the first to the second cycles. The large training effects are attributed to spin-glass like behavior of the disorder spins at the interface of the Co/CoO core-shell. This conclusion is further supported by temperature dependent magnetization and thermal remanent magnetization measurements, which showed a spin-glass-like relaxation of CoO defect moments. These results provide a powerful approach towards manipulating and optimizing the exchange bias effects for applications.

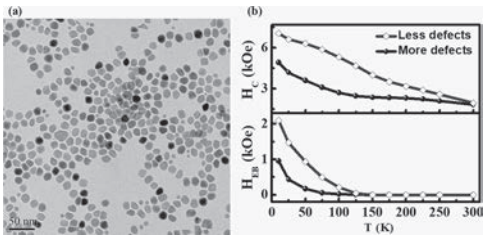


Figure 1. (a) TEM image of Co/CoO core-shell nanoparticles with average diameter 14 nm. (b) Temperature dependence of the coercivity and exchange bias fields of Co/CoO core-shell nanoparticles with different defect contents.

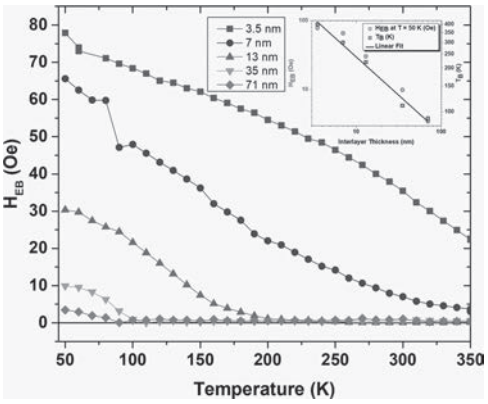
4:06

BH-14. Withdrawn

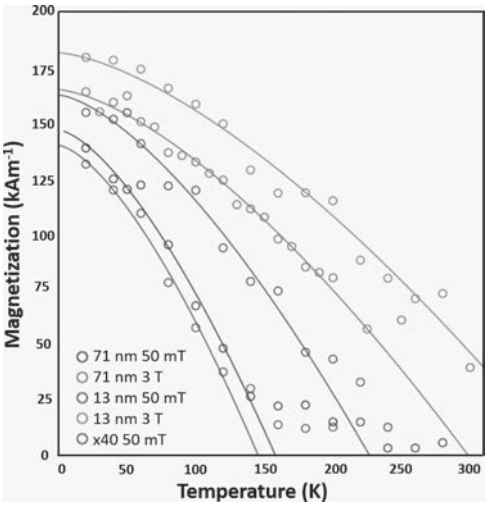
4:18

BH-15. Temperature and Thickness Dependent Coupling in PyCu Spin Valves Whose Interlayer Undergoes a Magnetic Phase Transition. *K. Repa*[1], B.J. Kirby[2] and C.W. Miller[1] *1. School of Chemistry and Materials Science, Rochester Institute of Technology, Rochester, NY, United States; 2. National Institute of Standards and Technology, Gaithersburg, MD, United States*

We studied spin valves (SV) of the form $Py_{0.8}Cu_{0.2}/Py_{0.4}Cu_{0.6}/Py_1Cu_0/IrMn$ (free/interlayer/pinned). The different Cu content gives each layer a distinct Curie temperature (T_C), which allowed us to study the SV as the interlayer undergoes a magnetic phase transition (T_C = 160 K). We also studied the magnetic properties of the system as a function of interlayer thickness (t = 3.5 nm - 71 nm). We examined each film via DC magnetometry to probe exchange bias (H_{EB}) of the free and pinned layers, and polarized neutron reflectometry (PNR) depth profiles to understand the contributions of each layer as a function of temperature. *M(H)* curves from 50 K to 350 K yielded H_{EB} for the free (*Fig 1*) and pinned ferromagnetic layers. The former shows a blocking temperature-like feature that is correlated with when the interlayer becomes magnetically ordered, which allows direct exchange throughout the stack. This feature has an inverse relationship with spacer layer thickness. In line with exchange bias theory, the magnitude of H_{EB} at constant temperature decreases as 1/t. Magnetic depth profiles from PNR (*Fig 2*) were used to obtain *M(T)* for t = 13 nm and 71 nm interlayers; a 37 nm control film of $Py_{0.4}Cu_{0.6}$ ("x40") was also measured. We found that proximity effects play an important role in the ordering of the interlayer. While the *M(T)* for t = 71 nm resembles that of the control at 50 mT, T_C is enhanced by 70 K for t = 13 nm. However, the magnetic depth profiles do not reveal evidence for a proximity induced enhancement of the interlayer order parameter- i.e. data at all conditions for all samples are consistent with uniform magnetization within the interlayer. Given that the exchange length in Py is ~5 nm, it is curious that we see such a significant and uniform enhancement across a 13 nm interlayer. This result could have wide reaching implications in the field of tunable thermomagnetic devices.



***$H_{EB}(T)$* for each spin valve with inset *$H_{EB}(t)$* and *$T_B(t)$* with linear fit.**



Interlayer *M(T)* curves from PNR at high and low field for indicated thicknesses; x40 is a single 37 nm thick film of the interlayer metal.

Session BI
NON-TRADITIONAL MAGNETIC MATERIALS

Bijoy K. Kuanr, Chair
University of Colorado at Colorado Springs, Colorado Springs, CO, United States

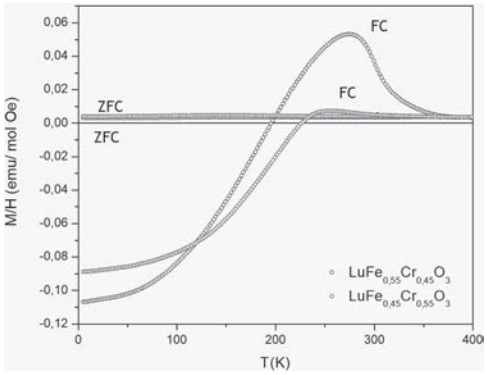
CONTRIBUTED PAPERS

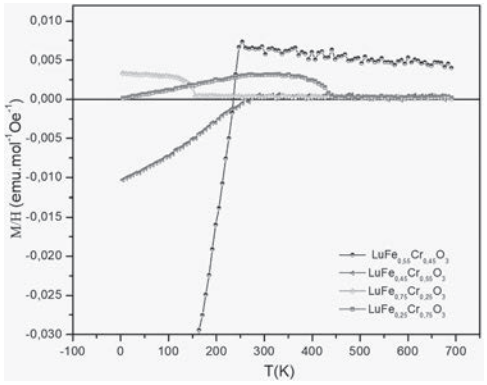
1:30

BI-01. Study of Magnetization Reversal in Orthorhombic Perovskites with Cation Lu^{3+}. *F.E. Lurgo*[1], O. Billoni[2], C. Martin[3] and R.E. Carbonio[1]
1. Departamento de Fisicoquimica, Facultad de Ciencias Quimicas, INFIQC-CONICET-Universidad Nacional de Córdoba, Córdoba, Argentina; 2. Facultad de Matemática, Astronomía, Física y Computación, Universidad Nacional de Córdoba, IFEG-UNC-CONICET, Córdoba, Argentina; 3. Laboratoire CRISMAT, Centre national de la recherche scientifique (CNRS)/ENSICAEN/UCBN, Caen, France

Rare earth orthoferrites and ortochromites of an ABO_3 composition, where A is a lanthanide and B is Fe or Cr, have been under study for several decades. The strong interaction between these two sublattices of the total magnetic moment could produce the phenomena vastly studied: Magnetization Reversal (MR). The MR make this material suitable to spintronic, sensors, thermally assisted random access memory devices, etc. The MR is phenomena in which the spontaneous magnetization changes its sign at a compensation temperatura (T_{comp}) under low magnetic field. Recent in our investigation group it was designed, synthetized and characterized the compound $LuFe_{0.5}Cr_{0.5}O_3$ determining a T_{comp} of 255K [1]. The MR of this compound it's because the two metal transition cations showed antisymmetric exchange interactions or Dzyaloshinskii-Moriya interactions [2] leading to weak antiferromagnetic behavior (WF). Four members of the perovskite family $LuFe_{1-x}Cr_xO_3$ (x= 0.25; 0.45;0.55;0.75) have been synthesized with different thermal treatment and characterized. A systematic study of the crystal and magnetic structure was performed by neutron powder diffraction combined with magnetization measurements. All the compounds crystallize in a *Pbnm* orthorhombic. The study of the magnetic structure vs temperature showed the transition Γ_2/Γ_4^{TM} to Γ_4^{TM} in the compound Cr-rich. The rest of the compositions showed Γ_4^{TM} in all the temperatures in good agreement with the magnetic measurements [3]. The compounds with near to x=0.5 show MR but if change the synthesis temperature, this phenomenon disappears. $LuFe_{0.25}Cr_{0.75}O_3$ don't show MR but with two different synthesis temperature the phenomenon appears. This results is because the different thermal treatment allows or not the cluster (inhomogeneous distribution of cations) formation. We have performed MonteCarlo simulations using the the following Hamiltonian of classical Heisenberg spins [4] lying in the nodes of a cubic lattice with N= (L x L x L) sites to reproduced the MR observed experimentally in a field cooling (FC) process and the cluster formation according the different thermal treatment.

[1] POMIRO, F. et. al., Phys.Rev. B 94,134402 (2016). [2] KANAMORI J., J. Phys. Chem. Solids 10; 87-98 (1959). [3] BERTAUT E. F., Acta Cryst. 24, 217 (1968). [4] BILLONI, O. et. al., J. Phys. Condens. Matter 28, 476003 (2016).





1:42

BI-02. The effect of phase separation on the structural and magnetic properties in $FeCoNi_{1+X}Cr_{1-X}Al$ high-entropy alloys. *S. Na*[1], P.K. Lambert[1], J. Park[2] and N.J. Jones[1] *1. Physical Metallurgy and Fire Performance Branch, Naval Surface Warfare Center, Carderock Division, West Bethesda, MD, United States; 2. Aerospace Engineering, University of Maryland, College Park, MD, United States*

High-entropy alloys (HEAs) generally contain five or more elements, often in equiatomic or near-equiatomic ratios. One of the most interesting HEAs from a magnetic perspective is the FeCoNiCrAl-based alloy system, which is highly attractive for investigating phase transformations and controlling small-scale microstructural features [1]. The phase transformation between BCC and FCC due to spinodal decomposition results in a significant change in magnetic properties, such as saturation magnetization [2]. In this work, we investigate the effects of annealing temperature on structural and magnetic properties in FeCoNiCrAl-based HEAs with varying Ni/Cr ratio. Ingots with nominal compositions of $FeCoNi_{1+X}Cr_{1-X}Al$ (X = 0 – 0.5) were prepared by arc melting and cut into discs for measurement. These discs were annealed at various temperatures from 300-1200 °C for 3 hours, then furnace cooled. The measured saturation magnetization (M_S) at room temperature strongly

depends on both the Ni/Cr ratio and annealing temperature, as shown in Fig. 1(a). These changing properties are associated with the change of FCC phase fraction, as determined by x-ray diffraction. Figure 1(b) shows hysteresis loops with different sample conditions in the equiatomic FeCoNiCrAl HEA. A wasp-waist hysteresis loop was found only after annealing at 600 °C, possibly due to negative (antiferromagnetic) exchange coupling between soft and hard magnetic phases in the BCC structure [3]. It was confirmed by MFM (see Fig. 1(c)-(d)) that the BCC phase is ferromagnetic, while the FCC phase is paramagnetic, as a ferromagnetic domain structure is clearly observed in the BCC structure.

[1] W.-R. Wang et al., *J. Alloys Compd.* 589, 143 (2014). [2] S. M. Na *et al.*, *AIP Advances* 9, 035010 (2019). [3] L. H. Bennett and E. D. Torre, *JAP* 97, 10E502 (2005).

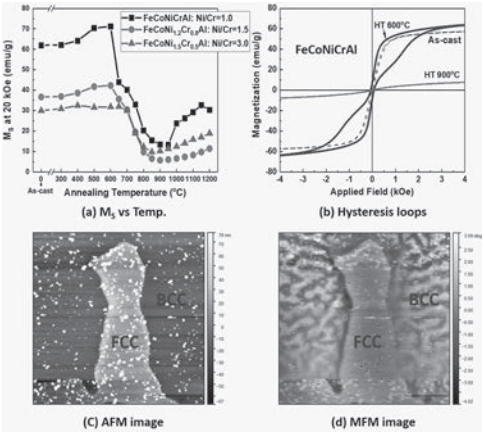


Figure 1. (a) Saturation magnetization at room temperature as a function of annealing temperature in $FeCoNi_{1+X}Cr_{1-X}Al$ HEAs, (b) magnetic field dependence of magnetization for the FeCoNiCrAl HEA samples with different conditions, and (c)-(d) AFM and MFM images taken from the same area of as-cast $FeCoNi_{1.5}Cr_{0.5}Al$ HEA, respectively.

1:54

BI-03. Inducing strong magnetism in non-magnetic $Cr_{20}Fe_{20}Mn_{20}Fe_{20}Co_{20}Ni_{20}$ by lattice-expansion. *M. Acet*[1] and A. Cakir[2] *1. Physics, Duisburg-Essen University, Duisburg, Germany; 2. Metallurgical and Materials Engineering, Mugla Sitki Kocman University, Mugla, Turkey*

Mixing numerous 3d-elements and subsequently melting them together or allowing them to undergo a solid-state reaction gives rise to random solid solutions with a high configurational entropy [1]. The classical example is the $Cr_{20}Fe_{20}Mn_{20}Fe_{20}Co_{20}Ni_{20}$ alloy with a 20% equiatomic composition forming a single FCC phase. It is paramagnetic at room temperature and has competing interactions at low temper- atures [2, 3]. This material has a valence electron concentration (*e/a*) = 8, which corresponds to that of elemental Fe, but instead of being BCC it is FCC. FCC-Fe has an enhanced enhanced anharmonicity known as anti-Invar. If FCC Fe could have been expanded, it would have been ferromagnetic with a high Curie temeprature T_C and a magnetic moment $\mu \approx 2.8\ \mu_B$. We show here first that $Cr_{20}Fe_{20}Mn_{20}Fe_{20}Co_{20}Ni_{20}$ can indeed be expanded by introducing carbon. We introduce carbon into the octahedral sites of this material and maintain (*e/a*) = 8 to obtain $Cr_{16}Fe_{16}Mn_{16}Fe_{16}Co_{16}Ni_{16}C_{20}$. This becomes FM with a Curie temperature $T_C = 400$ K with $\mu \approx 1.5\ \mu_B$ with room to increase.

[1] J. Yeh, et al., Adv. Eng. Mater. 6, 299-303 (2004). [2] Y. P. Wang, B. S. Li, H. Z. Fu, Adv. Eng. Mater. 11, 641 (2009) [3] O. Schneeweiss, et al., Phys. Rev. B 96, 014437 (2017).

2:06

BI-04. Mo4Ce4Al7C3 nanolaminates featuring ferromagnetism and mixed-valence states. *F. Wilhelm*[1], Q. Tao[2], D. Pinek[3], O. Chaix-Pluchery[3], A. Rogalev[1], C. Opagiste[4], L. Jouffret[5], A. Champagne[6], J. Charlier[6], J. Lu[2], L. Hultman[2], M.W. Barsoum[7], J. Rosen[2] and T. Ouisse[3] *1. ESRF, Grenoble, France; 2. Department of Physics, Chemistry, and Biology (IFM), Linköping University, Linköping, Sweden; 3. UGA, CNRS, Grenoble INP, LMGP, Grenoble, France; 4. UGA, CNRS, Institut Néel, Grenoble INP, Grenoble, France; 5. Institut de Chimie de Clermont Ferrand, Aubières, France; 6. Institute of Condensed Matter and Nanosciences, UCLouvain, Louvain-la-Neuve, Belgium; 7. Department of Materials Science and Engineering, Drexel University, Philadelphia, PA, United States*

Rare-earth (RE) compounds exhibit a variety of magnetic and electronic ground states through the hybridization between 4f and conduction electrons. In addition to the orbital and valence degrees of freedom generating a multitude of ground states, the discovery of new layered RE compounds that can act as precursors for the synthesis of two-dimensional (2D) magnetic materials is another fruitful avenue. The synthesis of three dimensional (3D) layered compounds such as RE in-plane ordered quaternary MAX phases (RE i-MAX) [1], which can be exfoliated to form magnetic 2D systems (e.g. MXene), in which the RE's magnetism is potentially transferred to the itinerant electrons and used for electron spin control and/or injection constitutes a real challenge. Here, we report on the electronic structure and magnetic properties of Mo4Ce4Al7C3, which belong to a recently discovered family of magnetically ordered nanolaminates with a Mo4RE4Al7C3 stoichiometry [2]. These phases, though of a different composition compared to the RE i-MAX phases, display the same characteristic in-plane chemical order of the Mo and RE elements. Powder sample was characterized with respect to structure and composition. Single crystals of Mo4Ce4Al7C3 were used for magnetization measurements. The crystal structure was investigated by means of x-ray diffraction and scanning transmission electron microscopy. Magnetization analysis reveals a ferromagnetic ground state with a Curie temperature of ~10.5 K. X-ray absorption near-edge structure at the Ce L3-edge provides experimental evidence that Ce is in a mixed-valence state. X-ray magnetic circular dichroism carried out at the Ce and Mo L3,2-edges shows that only the Ce atoms with 4*f*1 configuration occupying one of the two possible sites are ferromagnetically coupled, with a saturation moment of ~1.2μ*B* per atom.

[1] Q. Tao, J. Lu, M. Dahlqvist, A. Mockute, S. Calder, A. Petruhins, R. Meshkian, O. Rivin, D. Potashnikov, E. N. Caspi, H. Shaked, A. Hoser, C. Opagiste, R.-M. Galera, R. Salikhov, U. Wiedwald, C. Ritter, A. R. Wildes, B. Johansson, L. Hultman, M. Farle, M. W. Barsoum and J. Rosen, Chem. Mater. 31, 2476 (2019). [2] Q. Tao, T. Ouisse, D. Pinek, O. Chaix-Pluchery, F. Wilhelm, A. Rogalev, C. Opagiste, L. Jouffret, A. Champagne, J.-C. Charlier, J. Lu, L. Hultman, M. W. Barsoum, and J. Rosen, Phys. Rev. Mater. 2, 114401 (2018).

2:18

BI-05. Preliminary resistivity results on U_2Ni_2Sn single crystals. *I. Halevy*[1,2], A. Kolomiets[3], S. Mašková[1], A. Andreev[4], J. Prchal[1] and L. Havela[1] *1. Condensed Matter Physics, Charles University, Prague, Czechia; 2. Physics, IAEC-NRCN, Beer-Sheva, Israel; 3. Physics, Polytechnic National University, Lviv, Ukraine; 4. Physics, Academy of Sciences, Prague, Czechia*

U_2Ni_2Sn is a member of intermetallic compounds with the tetragonal Mo_2FeB_2 crystal structure, which has been studied intensively [1-3]. It orders antiferromagnetically at 25K with a propagation vector q=(0,0,1/2). Magnetization, magneto-acoustic, and neutron-diffraction experiments on a single crystal provide evidence that the uranium moments align parallel to the *c*-axis with the anisotropy energy of ≈170K, indicating that U_2Ni_2Sn can be classified as an Ising system. This behavior is rather exceptional, majority

of the isostructural uranium ternaries have U moments confined into the basal plane. Last results [1] are actually at variance with previous studies on polycrystals, which indicated different magnetic structure, and which were incompatible with the 5*f*-5*f* two-ion anisotropy model dominant in most of U band systems. Few single crystals of U_2Ni_2Sn were grown by the Czochralski method. The four-point technique was used to measure the resistivity as function of pressure and magnetic fields. We expect fast suppression of magnetic order with pressure, already the ambient pressure data yield an interesting insight. The first finding is that single crystal resistivity has better RRR value, reaching 10 for *i*//[110] and 3 for the [001] direction. None of the two directions exhibits the negative resistivity slope found for the polycrystal, and $r(T)$ shows merely a saturation. The magnetic propagation vector implies an influence of magnetic superzone gapping for [001], which can explain much higher residual resistivity in this direction. There is AF coupling between the U moments within the same basal-plane sheet, but it all happens within one-unit cell, accommodating 4 U atoms. Further differences are revealed by a numerical analysis. Fitting for *i*//[110] indicates the quadratic dependence, compatible with the high uniaxial anisotropy, not permitting a population of magnons with energy lower than the anisotropy gap. On the other hand, *i*//[001] exhibits an additional gap excitation term, with $\Delta \approx 50$K, i.e. much smaller than the anisotropy gap 170K. Such exchange gap has to be identified as a spin gap, suggesting an easy spin flipping along *c*.

[1] S. Mašková, A.V. Andreev, Y. Skourski, S. Yasin, D.I. Gorbunov, S. Zherlitsyn, H. Nakotte, K. Kothapalli, F. Nasreen, C. Cupp, H.B. Cao, A. Kolomiets, L. Havela, *Physical Review B.* (accepted 2019). [2] K. Kindo, T. Fukushima, T. Kumada, F.R. de Boer, H. Nakotte, K. Prokes, L. Havela, V. Sechovsky, A. Seret, J.M. Winand, J.C. Spirlet, J. Rebizant, *Journal of Magnetism and Magnetic Materials* 140-144 1369 (1995). [3] R.P. Pinto, M.M. Amado, M.E. Braga, M.A. Salgueiro, J.B. Sousa, B. Chevalier, D. Laffargue, J. Etourneau, *Journal of Magnetism and Magnetic Materials* 157/158 698 (1996).

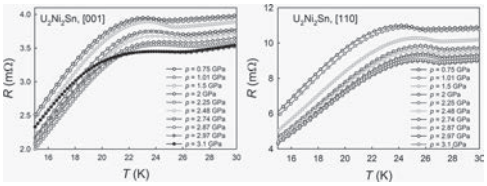


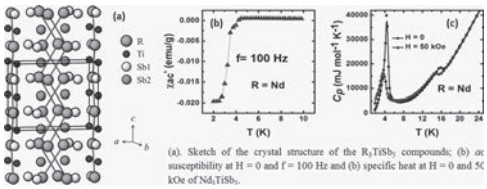
Fig 1. The temperature dependence of resistivity of U_2Ni_2Sn under pressure.

2:30

BI-06. Structure and physical properties of R_3TiSb_5 compounds (R = Ce, Pr, Nd). *A. Provino*[1,2], A.K. Pathak[3], C. Ritter[4], S.K. Dhar[5] and P. Manfrinetti[1] *1. Department of Chemistry, University of Genova, Genova, Italy; 2. Institute SPIN, Italian National Research Council, Genova, Italy; 3. Ames Laboratory, Ames, IA, United States; 4. Institut Laue-Langevin, Grenoble, France; 5. Condensed Matter Physics & Materials Science, Tata Institute of Fundamental Research, Mumbai, India*

Ternary rare-earth transition-metal antimonides R_3TiSb_5 (R = rare earth), anti-Hf_5CuSn_3-type (*h*P18, *P*6$_3$*/mcm*), are magnetically diverse. In the unit cell the R atoms occupy only the 6*g* site, Ti atoms the 2*b* site and Sb atoms the 4*d* and 6*g* sites. Depending upon R these compounds exhibit the most interesting physical properties, including antiferromagnetic Kondo lattices, heavy fermion, valence fluctuations, and possible superconductivity [1,2]. It was reported that the presence of a small amount of undetectable impurity phases makes it difficult to fully characterize without ambiguity the magnetic and transport properties of R_3TiSb_5 [1]; therefore, it is worth to further investigate the physical behaviors of these materials. Here, we present a study of the crystal structure from X-ray and neutron diffraction and magnetic, specific heat and transport properties of Ce_3TiSb_5, Pr_3TiSb_5 and Nd_3TiSb_5. The obtained results are unique among all the reported data so far. The ac-susceptibility and the specific heat of Nd_3TiSb_5 seem to indicate bulk superconductivity with $T_c = 4.5$ K, while neutron diffraction show the appearance of a commensurate magnetic order below $T_N = 5.5$ K. Ce_3TiSb_5, below about 7 K, sees two transitions corresponding to two different incommensurate magnetic structures, the appearance of which is strongly hysteretic. Pr_3TiSb_5, on the contrary, does not show any sign of long range magnetic order down to 1.5 K.

[1] S. H. D. Moore, L. Deakin, M. J. Ferguson, A. Mar, *Chem. Mater.* 14 (2002) 4867-4873. [2] M. Matin, R. Kulkarni, A. Thamizhavel, S. K. Dhar, A. Provino, P. Manfrinetti, *J. Phys.: Condens. Matter* 29 (2017) 145601 (7pp).



(a). Sketch of the crystal structure of the R_3TiSb_5 compounds; (b) ac susceptibility at H = 0 and f = 100 Hz and (b) specific heat at H = 0 and 5 kOe of Nd_3TiSb_5.

2:42

BI-07. Magnetic ordering of protons in NH_4I, NH_4Br and NH_4Cl. *F. Yen*[1], L. Meng[1], T. Gao[2] and S. Hu[3] *1. School of Science, Harbin Institute of Technology, Shenzhen, Shenzhen, China; 2. Shanghai University of Electric Power, Shanghai, China; 3. Southern University of Science and Technology, Shenzhen, China*

The methyl groups in hexamethylbenzene $C_6(CH_3)_6$ were recently found to become magnetically ordered below 118 K.[1-3] Naturally, we wondered whether similar behavior occurs in ammonium cations (NH_4^+) which are slightly more massive and possess a tetrahedron geometry. The ammonium halides were selected as there is ample literature concluding that their NH_4^+ exhibit hindered rotational motion even towards the lowest temperatures.[4-7] We present anomalies identified in the magnetic susceptibility of the ammonium halides NH_4I, NH_4Br and NH_4Cl at 232 K, 233 K and 243 K, respectively, which all coincide to the temperatures where geometric ordering of the NH_4^+ occur. To explain our results, we take into consideration that the orbital motion of the protons (H^+) also carries a magnetic moment and find that they are actually larger than that of the paired electrons. From such, the structural phase transitions are magnetically-driven as the system attempts to lift 8-fold energy degeneracies of the proton orbitals via Jahn-Teller distortions. Lastly, we discuss how magnetic ordering of NH_4^+ is rather ubiquitous in ammonia-based molecular solids.

1. F. Yen, Z. Z. Zhao, S. X. Hu, et al., *Angew. Chem., Int. Ed*., 56, 13675 (2017) 2. F. Yen, *J. Phys. Chem. C*, 122, 16304 (2018) 3. F. Yen, *J. Phys. Chem. C*, 122, 29628 (2018) 4. R. C. Plumb, D. F. Hornig, *J. Chem. Phys*., 21, 366 (1953) 5. H. S. Gutowsky, G. E. Pake, R. Bersohn, *J. Chem. Phys*., 22, 643 (1954) 6. T. Z. Lalowicz, *Acta Phys. Polon*., A56, 243 (1979) 7. A. R. Sharp, M. M. Pintar, *J. Chem. Phys*., 75, 2652 (1981)

2:54

BI-08. Ferromagnetism in 2D organic iron hemoglobin crystals based on nitrogenated conjugated micropore materials. *Y. Dahnovsky*[1], A. Pimachev[2], R.D. Nielsen[1] and A. Karonovich[3] *1. Physics and Astronomy, University of Wyoming, Laramie, WY, United States; 2. Aerospace Mechanics Research Center, University of Colorado Boulder, Boulder, CO, United States; 3. Physics, Virginia Polytechnic Institute and State University, Blacksburg, VA, United States*

In this work we study an environmentally stable, low-cost two-dimensional ferromagnetic semiconductor with possible applications in biomedicine, solar cells, spintronics, and energy and hydrogen storage. From first principle calculations we describe the unique electronic, transport, optical, and magnetic properties of a π-conjugated micropore polymer (CMP) with three iron atoms

placed in the middle of an isolated pore locally resembling heme complexes. We then study the stability of this material to an environment and how these properties change when bonded with CO, CO_2, and O_2. This material exhibits strong Fe-localized d_z^2 bands with a direct bandgap of 0.28 eV. The absorption coefficient and conductivity are roughly isotropic with conductivity in the energy range 0.3 - 8 eV. The material shows nonzero Faraday and Kerr rotation in the interval of 0.5-5.0 eV. This material is found to be a ferromagnet of an Ising type with long-range exchange interactions with a very high magnetic moment per unit cell, m = 6 μ_B. The estimated exchange integral is calculated to be about J_{nn} = 25 meV. The binding of CO, CO_2, and O_2 modifies the d_z^2 bands of the Fe ions with varying profiles and results in indirect bandgaps with values between 0.269 - 0.626 eV, 0.039 - 0.434 eV, and 0.291 - 0.347 eV for CO, CO_2, and O_2, respectively. The absorption coefficient becomes slightly anisotropic while conductivity remains isotropic with the same active energy regions. Both the absorption coefficient and conductivity have large modifications to the xy-components. The material remains ferromagnetic with the magnetic moment per unit cell decreasing to 4, 2, and 0 μ_B for gases attached to one, two, and three Fe ions per unit cell, respectively.

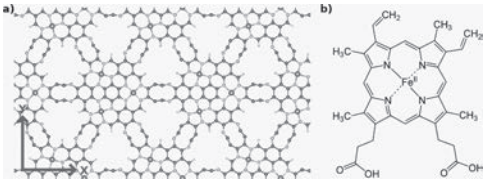


Fig. 1 Crystal structures of (a) the nitrogenated porous materials with three iron atoms inside the six-benzene-ring-CMP unit cell and (b) a heme group b molecule with an iron atom bound to the four nitrogen atoms.

3:06

BI-09. Ga- and Sc-substituted M-type ferrites for self-biasing circulators in LTCC microwave modules. M. Heidenreich[1], W. Gitzel[2], A. Jacob[2] and *J. Töpfer*[1] *1. Ernst-Abbe-Hochschule Jena, Jena, Germany; 2. Technical University Hamburg, Hamburg, Germany*

Future satellite communication technologies require microwave ferrites capable of being integrated in LTCC multilayer modules for applications in the K_a-band (26-40 GHz). Substituted hexagonal M-type Ba-ferrites $BaMe_xFe_{12-x}O_{19}$ exhibit significant potential as self-biasing microwave components such as for isolators and circulators and are well suited for the required frequency range. Ga- and Sc-substituted Ba ferrites with $0 \le x \le 2$ were prepared by the mixed oxide route. After calcination (1300 °C) and sintering (1400 °C) single-phase ferrites were obtained. For Ga-substitution, the lattice parameters a_0 decrease with x, while c_0 remains constant. In contrast, for Sc-substituted ferrites, both a_0 and c_0 increase with x, signaling a different substitution mechanism. Static magnetic measurements show that for both substitution series the saturation magnetization decreases with concentration of Ga or Sc. However, the coercivity slightly increases with Ga, whereas it decreases with Sc substitution, indicating respective changes of the anisotropy fields with substituent concentration. The ferromagnetic resonance frequency of the ferrites was determined by reflectance measurements in waveguides in U- and K-bands (30-60 GHz). The ferromagnetic resonance exhibits systematic shifts; for Ga FMR increases with y, whereas for Sc FMR is reduced. To implement ferrite layers into LTCC technology, the sintering behavior was modified by addition of BBSZ glass and sufficient densification at 900 °C was obtained. Ferrite tapes with x = 0.5 were co-fired with LTCC tapes. Alternatively, ferrite layers were screen-printed onto alumina substrates or LTCC tapes and fired at 850 – 900°C. Anisotropic ferrite layers were obtained by drying the films in a magnetic field. The texture of the films was characterized using XRD and EBSD. Ferrite layers were also applied by post-firing onto LTCC layers. Cofiring studies reveal the ferrite layers might be integrated into LTCC architectures. Circulators were fabricated and tested. The potential of such oriented hexagonal ferrite layers as integrated self-biased ferrite layers in microwave components is evaluated.

3:18

BI-10. Synthesis and Magnetic Characterization of Semi-Hard Magnetic Nanocrystalline Maraging Steel Powder. G. Thotakura[1], R. Goswami[2] and *T.V. Jayaraman*[1] *1. Mechanical Engineering, University of Michigan-Dearborn, DEARBORN, MI, United States; 2. Materials Science and Technology Division, Naval Research Laboratory, Washington, DC, United States*

Maraging steels are a particular class of high-strength steels that find themselves in a myriad aerospace and tooling applications [1]. A gap in the literature motivated to synthesize and investigate the magnetic properties of nanocrystalline maraging steel powders. Micron-sized nanocrystalline maraging steel powders were synthesized by mechanically milling the gas-atomized maraging steel powder. The structure of the as-milled steel powders was characterized by x-ray diffraction, scanning electron microscopy, and transmission electron microscopy; followed by the characterization of their magnetic properties from cryogenic temperatures to elevated temperatures (60 – 900 K). The phase constituents in mechanosynthesized alloy powder, at ambient temperature (300 K), was primarily martensite coupled with traces of retained austenite and intermetallics; atypical to traditional casting and forging techniques [2]. The magnetic saturation (σ_S) and coercivity (H_C) was estimated as ~165 Am^2/kg and ~5 kA/m, respectively. Both M_S and H_C decreased with the increase in temperature from cryogenic to elevated temperatures. Heat-treatment of the as-milled powder led to an increase in σ_S and a decrease in H_C, and the powders retained the nano-size grains. The change in magnetic properties from ambient temperature to cryogenic temperatures for the as-milled, as well as the heat-treated steel powders were less than 10%. The magnetic properties of the nanocrystalline steel were compared with their bulk counterparts as well as with similar nanocrystalline and commercially available semi-hard magnetic alloys [3]. The nanocrystalline maraging steel powder appears to have decent semi-hard magnetic properties.

[1] K. Rohrbach and M. Schmidt, ASM Handbook, Vol. 1 Properties and Selection: Irons, Steels, and High-Performance Alloys, p.793 (1990) [2] F. Zhu, Y.F. Yin, R.G. Faulkner, Materials Science and Technology, Vol. 27(1), p.395 (2011) [3] C. Moosbrugger, ASM Ready Reference: Electrical and Magnetic Properties of Metals, ASM International (2000)

3:30

BI-11. Theoretical and experimental study of influence of mixing the low-valent transition metal atoms (Y= V, and Cr) on the structural, magnetic, transport, and mechanical properties of the Heusler alloys $Fe_{3-x}Y_xGe$. *R. Mahat*[1,2], S. KC[1,2], S. Regmi[1,2], U. Karki[1,2], D. Wines[3], F. Ersan[3,4], R. White[1,5], C. Ataca[3], P. Padhan[6], A. Gupta[1,7] and P. LeClair[1,2] *1. Center for Materials for Information Technology (MINT), University of Alabama, Tuscaloosa AL 35487, Tuscaloosa, AL, United States; 2. Physics and Astronomy, Department of Physics and Astronomy, University of Alabama, Tuscaloosa AL 35487, Tuscaloosa, AL, United States; 3. Physics, Department of Physics, University of Maryland Baltimore County, Baltimore MD 21250, Baltimore, MD, United States; 4. Physics, Department of Physics, Aydin Adnan Menderes University, Aydin 09100, Turkey, Aydin, Turkey; 5. Metallurgical Materials Engineering, Department of Metallurgical Materials Engineering, University of Alabama, Tuscaloosa, AL 35487, Tuscaloosa, AL, United States; 6. Physics, Department of Physics, Nanoscale Physics Laboratory, Indian Institute of Technology Madras, Chennai-600036, India, Chennai, India; 7. Chemistry and Biochemistry, Department of Chemistry and Biochemistry, The University of Alabama, Tuscaloosa AL 35487, Tuscaloosa, AL, United States*

The detailed structural, magnetic, transport and mechanical properties of Heusler like $Fe_{3-x}Y_xGe$ (Y = V & Cr) alloys with ($0 \le x \le 1$) have been investigated experimentally and theoretically. With high temperature annealing (950°C), V-substituted alloys for $0.375 \le x \le 0.75$ are found to

crystallize in the cubic $L2_1$ structure, while alloys with $0 < x \leq 0.25$ crystallize in the hexagonal DO_{19}, the high temperature structure of the parent Fe_3Ge compound. Higher V concentrations for $x > 0.75$ are multi-phased at all annealing conditions. At a lower annealing temperature (650°C), V-substituted alloys for $0.25 \leq x \leq 0.75$ are found to crystallize in the $L2_1$ structure, while all single phase Cr-substituted alloys ($0 \leq x \leq 0.75$) found to crystallize in the DO_{19} structure. Vanadium substitution is observed to induce a diffusionless martensitic phase transformation from $L2_1$ to DO_{19} structure, as corroborated by Differential Scanning Calorimetry. The addition of Y significantly decreases the grain size, inhibiting the grain growth by pinning the grain boundary migration. All the alloys in the series are found to be soft ferromagnets at 5K with saturation magnetic moments and Curie temperatures decreasing as Y concentration increases. The extracted low temperature saturation moments are in close agreement with the expected Slater-Pauling values for the $L2_1$ phases, while the hexagonal samples have markedly higher values of saturation moments. First-principles calculations verified the experimental findings and revealed that Y substitution energetically favors one of the Fe sites in Fe_3Ge. The electrical resistivity measured from 5K to 400K shows a negative temperature coefficient of resistivity at high temperatures with increasing V concentration, attributed to impurities at the grain boundaries, while Cr-substituted samples show purely metallic behavior. Relatively high mechanical hardness values are also observed with hardness increasing with increasing Y content. Vanadium is found to play a central role in changing the mechanical properties, stabilizing the $L2_1$ structure, and shifting the martensitic transformation temperature to higher values from that of parent Fe_3Ge.

1. T. Graf, C. Felser, and S. S. Parkin, Progress in solid state chemistry 39, 1 (2011). 2. K. v. Buschow, P. Van Engen, and R. Jongebreur, Journal of magnetism and magnetic materials 38, 1 (1983). 3. F. Casper, C. Felser, R. Seshadri, C. P. Sebastian, and R. Pottgen, Journal of Physics D: Applied Physics 41, 035002 (2008). 4. H. Nakagawaand K. Kanematsu, Japanese Journal of Applied Physics 18, 1959 (1979). 5. A. Beitollahiand J. Booth, Journal of Physics: Condensed Matter 2, 2997 (1990). 6. R. M. Wentzcovitchand P. K. Lam, Phys. Rev. B 44, 9155 (1991)

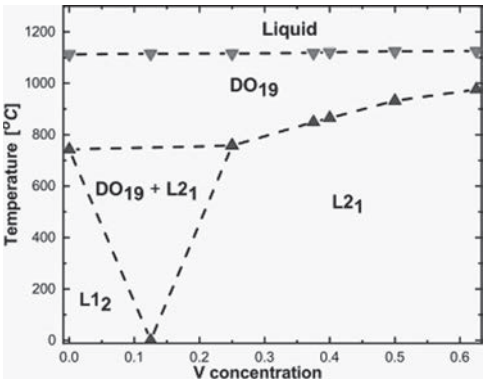


Fig1. Phase Diagram

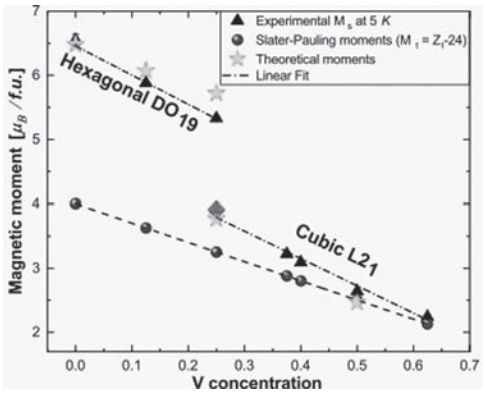


Fig2. Variation of magnetic moment.

3:42

BI-12. Self-Consistent Local Mean-Field Theory for Phase Transitions in FeRh. *B.R. McGrath*[1], K. Livesey[1] and R. Camley[1] *1. Physics, Center for Magnetism and Magnetic Nanostructures, University of Colorado, Colorado Springs, Colorado Springs, CO, United States*

FeRh has a phase transition from an antiferromagnetic state at low temperature to a ferromagnetic state near a temperature of 360 K. Various explanations for this behavior have been proposed over the past 20 years. However, many of the mechanisms are inconsistent with all the data. Early models were Ising like [1], but the large anisotropy fields necessary for this are not found in hysteresis curves. Using the four-spin Hamiltonian suggested by Barker and Chantrell [2], we obtain a complete theoretical description of the field/temperature phase diagram for this system. The theoretical results are in good agreement with experiments. For example, the transition temperature shifts downward as the external field is increased, with a reduction of about 25 K with the application of a 50 kOe field. Similarly, we find thermal hysteresis near the phase transition with a typical width of about 30-40 K. In-plane and out-of-plane magnetic field hysteresis loops also match well with experimental results. One of the advantages of the self-consistent local mean-field approach is that it can easily predict changes in behavior as a function of the thickness of the FeRh film. We find the four-spin Hamiltonian is particularly sensitive to the presence of a surface, with thinner films remaining ferromagnetic over a larger temperature range because the four-spin contribution to the energy (which favors the antiferromagnetic state) is smaller. This is clearly evident in Fig.1 which shows magnetization as a function of temperature for three different thicknesses of an FeRh film. We also note the presence of thermal hysteresis in each transition. We discuss our results in light of current experiments and device applications of FeRh, plus suggest future experiments to determine the interactions in FeRh.

[1] S. Maat, J.-U. Thiele, and E. E. Fullerton, Physical Review B, Vol 72, p 214432 (2005) [2] J. Barker and R. W. Chantrell, Physical Review B, Vol 92, p 094402 (2015)

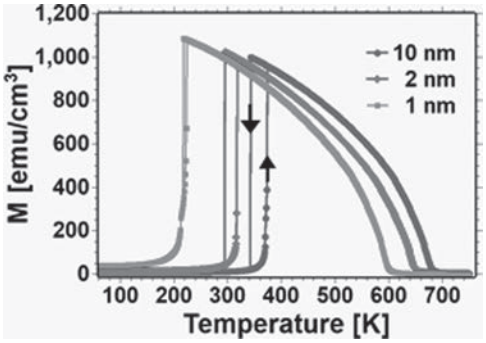


Fig. 1. Calculated magnetization as a function of temperature for FeRh films with different thicknesses. The low temperature phase is antiferromagnetic and has no net magnetic moment. The high temperature phase is ferromagnetic and has a typical decrease in magnetization as the temperature increases. As the film is made thinner, the transition temperature between the two phases is reduced.

3:54

BI-13. Magnetic and transport behavior in the non-centrosymmetric Nd_7Ni_2Pd compound. *A.K. Pathak*[2], Y. Mudryk[2], A. Provino[1], P. Manfrinetti[1] and V.K. Pecharsky[2,3] *1. Department of Chemistry, University of Genova, Genova, Italy; 2. Materials Science, Ames Laboratory, Ames, IA, United States; 3. Materials Science and Enginering, Iowa State University, Ames, IA, United States*

The studies of the R_7Pd_3 (R = rare-earth) compounds revealed interesting basic science and potential functional properties [1]. These compounds crystallize in the hexagonal Th_7Fe_3 structure type adopting non-centrosymmetric

space group symmetry $P6_3mc$, where the Pd atoms reside on a single 6*c* site, and R atoms occupy three different crystallographic sites (2×6*c* and 2*b*), resulting in three different magnetic sub-lattices formed by the lanthanide atoms. Crystallographic, magnetic, transport, and calorimetric investigations of Nd_7Ni_2Pd compound show that partial substitution of Pd with Ni changes the ground state from ferromagnetic in Nd_7Pd_3 to antiferromagnetic in Nd_7Ni_2Pd. The antiferromagnetic transition that occurs upon cooling at T_{N1} = 24.5 K is first order, and it is preceeded by a second order antiferromagnetic ordering at T_{N2} = 29 K. The electrical resistivity measurements show metallic behavior with magnetoresistance -12% at H = 30 kOe and T = 2 K. Temperature dependent x-ray powder diffraction clearly shows an anomaly in the lattice parameter *a* at ~30 K, however, there is no detectable structural distortion or volume discontinuity around 25 K, suggesting a significant weakening of the first-order transition compared to binary Nd_7Pd_3 [1]. Compared to the parent compound, Nd_7Ni_2Pd exhibits strong metamagnetic behavior with the application of an external magnetic field. Temperature dependence of lattice parameters as well as magnetic and electrical properties of Nd_7Ni_2Pd will be discussed. The Ames Laboratory is operated for the U. S. Department of Energy by Iowa State University of Science and Technology under contract No. DE-AC02-07CH11358. This work was supported by the Department of Energy, Office of Basic Energy Sciences, Materials Sciences Division.

[1] Mudryk et al., J. Phys.: Condens. Matter 31, 265801 (2019); Kadomatsu et al., J. Magn. Magn. Mater. 189, 335 (1998).

4:06

BI-14. Next-Generation Magneto-Optic Surface Plasmon Resonance-Based Sensors. *C. Rizal*[2,1] *1. Electrical Engineering and Computer Science, York University, Toronto, ON, Canada; 2. R&D, SeedNanoTech & Consulting, Brampton, ON, Canada*

Magneto-optic surface plasmon resonance (MOSPR) is relatively a new physics that has significant potential in the industry [1-3]. In this work, I will provide a brief background of the surface plasmon resonance (SPR) principle, followed by several aspects of magneto-optic SPR (MOSPR) and sensing schemes from the viewpoint of fundamental studies and potential applications [4-7]. I will discuss new sensitivity metrics developed by our group that would allow researchers to compare the performance of SPR and MOSPR-based sensors side by side. I will also discuss the merits of new MOSPR sensors over conventional SPR-based sensors and challenges faced by the MOSPR sensors in terms of their practical use and portability. I will end the presentation with potential new configurations and prospects of various MOSPR configurations. This work is considered significant to engineers, graduate and undergraduate students, and researchers of all levels involved in developing new classes of devices for sensing, imaging, environmental monitoring, toxic gas detection, and surveying applications to name a few.

1. C. Rizal. *IEEE Transactions on Magnetics,* Vol. 99, p. 1 (2018) 2. G. Armelles, A. Cebollada, A. Garcia-Martan, and M. U. Gonza¡lez, Advanced Optical Materials, Vol. 1, p. 2 (2013). 3. D. Regatos, B. Sepúlveda, D. Fariña, L. G. Carrascosa, and L. M. Lechuga, Optics Express, Vol. 19, p. 8336 (2011). 4. M. H. H. Hasib, J. N. Nur, C. Rizal, and K. N. Shushama, Condensed Matter, Vol. 4, p. 49 (2019) 5. C. Rizal, V. Belotelov, D. Ignatyeva.; A.K. Zvezdin, S. Pisana. *Condensed Matter*, Vol.4, p. 50 (2019) 6. B. Diaz-Valencia, J. Mejía-Salazar, O. N. Oliveira Jr, N. Porras-Montenegro, and P. Albella, ACS Omega, Vol. 2, p.7682 (2017) 7. D. Ignatyeva, P. Kapralov, G. Knyazev, S. Sekatskii, G. Dietler, M. Nur-E-Alam, M. Vasiliev, K. Alameh, and V. Belotelov, JETP letters, Vol. 104, p. 679 (2016)

4:18

BI-15. Tailoring the structural and electrical properties of Ba-Zn-Co M-type hexaferrites by lanthanum substitution for high frequency applications. N. Amin[1], *M. Ajaz-un-Nabi*[1], S. Nadeem[1], M.I. Arshad[1], K. Mahmood[1], A. Ali[1] and M. Sharif[1] *1. Physics, Government College University, Faisalabad, Faisalabad, Pakistan*

In the past couple of decades, hexaferrites have gained considerable attention due to their potential applications in industrial and technological fields. Their high resistivity and low losses made them a strong candidate for use in next generation high frequency microwave devices. In this study, $Ba_{0.5}Zn_{0.2}Co_{0.3}Fe_{12-y}La_yO_{19}$ (y=0, 0.1, 0.2, 0.3, 0.4, 0.5) nano hexaferrites were synthesized by co–precipitation method. The prepared powder was sintered at 1100 ^oC for 6 hours to assist to crystallization process. The formation of single phase hexagonal structure was confirmed using XRD. The crystallite size of prepared nano ferrites was found in the range of 12.5 – 28.1 nm. The characteristic band of hexagonal structure observed around 560 cm^{-1} in the FTIR spectra also confirmed the formation of M-type hexagonal phase. The current voltage measurements were performed to study the electrical character of prepared samples in the temperature range of 300 – 900 K. The highest values "2 x 10^{11} Ω cm" and "0.5 eV" of electrical resistivity and activation energy respectively, are observed for the sample with La content y = 0.2 at room temperature. The enhanced dc electrical resistivity due to La substitution indicates that the prepared hexaferrites are beneficial to reduce the eddy current losses for device fabrication in the high frequency range.

R. Topkaya, I. Auwal & A. Baykal, *Ceram. Int. 42* (2016)16296-16302. K. Rana, P. Thakur, A. Thakur, M. Tomar, V. Gupta, J. L. Mattei & P. Queffelec, *Ceram. Int. 42* (2016) 8413-8418. M. J. Iqbal & S. Farooq, Mater. Chem. Phys. 118 (2009) 308-313. L. Yuping, B. Daxin, W. Zhangzhong, Y. Zhang, C. Lizhao, Z. Guangcheng & W. Mengling, J. Alloys Compd. 734 (2018) 130-135. I. A. Auwal, A. Baykal, S. Güner, & H. Sözeri, Ceram. Int. 43 (2017) 1298-1303. A. Xia, T. Zhan, R. Sun, S. Su, J. Li, H. Zhang, H. Li & C. Jin, J. Alloys Compd. 784 (2019) 276-281. G. P. Nethala, R. Tadi, G. R. Gajula, K. N. C. Kumar & V. Veeraiah, Physica B 550 (2018) 136-144. D. E. Speliotis, IEEE Trans. Magn. 25 (1989) 4048. R. Gerber, R. Atkinson & Z. Simsa, J. Magn. Magn. Mater. 175 (1997) 79.

Session BP
2:14:1 PERMANENT MAGNET MATERIALS
(Poster Session)

Parashu Ram Kharel, Co-Chair
South Dakota State University, Brookings, SD, United States
Pelin Tozman, Co-Chair
National Institute for Materials Science, Tsukuba, Japan

BP-01. Withdrawn

BP-02. Crystallographic alignment and magnetic anisotropy in melt-spun Nd-Ce-Fe-B ribbons. *J. Zuo*[1], M. Zhu[1], W. He[2], M. Zhang[1], Y. Li[1] and X. Zhang[1] *1. School of Science, Inner Mongolia University of Science and Technology, Baotou, China; 2. Department of Materials Engineering, Baotou Vocational & Technical Collage, Baotou, China*

In this paper, crystallographic alignment and magnetic anisotropy were studied for $(Nd_{1-x}Ce_x)_{30}Fe_{69}B$ ribbons prepared via melt-spinning. Effect of Ce concentration and wheel speed on the crystal structure and magnetic properties of the ribbons were investigated. Alloy ingots with nominal composition of $(Nd_{1-x}Ce_x)_{30}Fe_{69}B$ (wt %,x=0~0.5) was prepared by induction melting. The as-cast ingots were crushed into blocks that were subjected to melt-spun treatment under different wheel speeds of 10, 20 and 30m/s. The resultant ribbons were examined by XRD with Cu *K*α radiation on the free side surface. The magnetic hysteresis loops of the ribbons were measured with a VSM with a maximum magnetic field of 3T along the ribbons length. The XRD patterns showed that under the wheel speed of 10 and 20m/s, the reflections such as (004), (006) become dominant in the XRD patterns, indicating remarkable *c*-axis crystal texture in the ribbons. As the wheel speed increased, however, the *c*-axis crystal texture weakened gradually. The relative intensity ratio of $I_{(004)}/I_{(410)}$ and $I_{(006)}/I_{(410)}$ under different Ce concentration and different wheel speeds were calculated. Under the wheel speed of 10m/s, the value of $I_{(004)}/I_{(410)}$ was two times higher than of $I_{(006)}/I_{(410)}$. Under the same Ce concentration, while increasing wheel speed, the $I_{(004)}/I_{(410)}$ firstly decreased then increases monotonously, bottomed at x=0.2; the value of $I_{(006)}/I_{(410)}$ presented decreasing-increasing-decreasing. Similar results were found under the wheel speed of 20 and 30m/s. These results indicated that the Ce concentration could affect the magnetic anisotropy of Nd-Ce-Fe-B ribbon. Fig.1 showed the magnetic measurement results under the wheel speed of 10m/s, while increasing the Ce concentration the remanence and intrinsic coercivity firstly dropped and bottomed at x=0.2, which was the same bottom point the relative intensity ratio of $I_{(004)}/I_{(410)}$, then abnormally raised with a further Ce concentration. The remanence ratio presented the same variation.

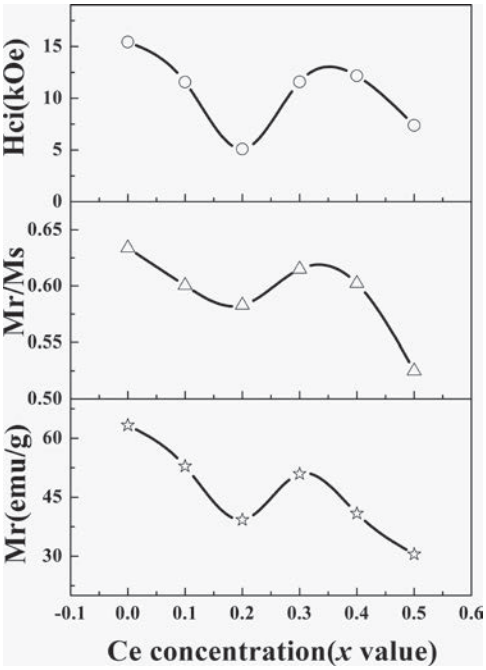


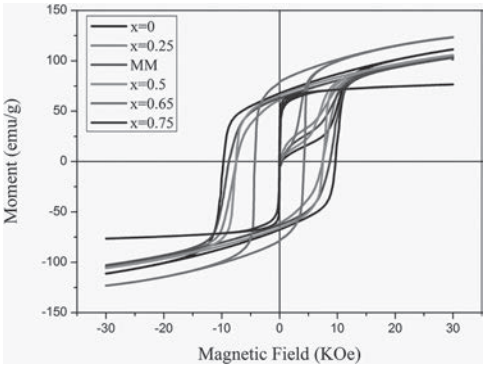
Fig.1 Magnetic properties of $(Nd_{1-x}Ce_x)_{30}Fe_{69}B$ melt-spun ribbons as a function of Ce concentration under 10m/s

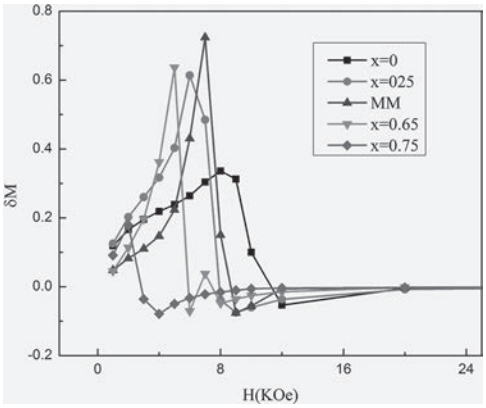
BP-03. Effect of Misch-Metal (MM) with the nature ratio on phase composition and magnetic properties in nanocrystalline $R_{30}Fe_{68.45}Al_{0.5}B_{1.05}$ ribbons. *F. Liu*[1,2], X. Wang[3,1], Y. Liu[1,2], X. Zhang[1,2] and Q. Ma[2,1] *1. School of Science, Inner Mongolia University of Science and Technology, Baotou, China; 2. Key Laboratory of Integrated Exploitation of Bayan Obo Multi-Metal Resources, Inner Mongolia University of Science and Technology, Baotou, China; 3. Division of Functional Materials, Central Iron & Steel Research Institute, Beijing, China*

The magnetic properties and microstructure of $R_2Fe_{14}B$ (R, rare earth) type magnets with nominal composition of $MM_{30}Fe_{68.45}Al_{0.5}B_{1.05}$ (MM, mischmetal) and $[Pr_{4.81}Nd_{16.38}(La_xCe_{1-x})_{78.76}]_{30}Fe_{68.45}Al_{0.5}B_{1.05}$ (x=0,0.25,0.5,0.65,0.75,1) prepared by melt spinning technique. Mischmetal (MM) is a typical mixed rare-earth in the mines with the nature ratio (28.63wt% La, 50.13wt% Ce, 4.81wt% Pr and 16.38wt% Nd), and the ratio of La to Ce is about 1:2. When the content of La is not 0, the intrinsic coercivity and the maximum energy product of $MM_{30}Fe_{68.45}Al_{0.5}B_{1.05}$ ribbon attains to the maximum of 9.8 kOe and 10 MGOe (Fig.1). With an increase of La content, both the saturation magnetization and remanence increase and then decrease with the maximum at x=0.65. When La content is more than 28.63wt%, the RFe_2 phase forms, which results in a decrease of the tetragonal phase content. The magnetization and Henkel plot (δM) measurements

indicate that the MM30Fe68.45Al0.5B1.05 ribbon has a relatively homogeneous microstructure and strong exchange-coupling interactions (Fig.2). The transmission electron microscope image verifies that the ribbons exhibit a homogeneous nanoscale microstructure. In addition, the Curie temperature Tc, the spin reorientation temperature TSR and thermal stability is investigated as a function of La content x, which demonstrates Tc, TSR and thermal stability of the ribbons are improved with proper amount of La. Furthermore, this work offers promise for developing MM-Fe-B based permanent magnets with high performance at low cost.

[1] R. X Shang, J. F. Xiong, D. Liu, et al, Chin. Phys. B, 26, 5 (2017). [2] W. L. Zuo, Sh. L. Zuo, R. Li, et al, J. Alloys Comp., 695, 1786(2016). [3] X. Q. Yu, M. Yue, W. Q. Liu, et al, JOURNAL OF RARE EARTHS,36(6),614, (2016).

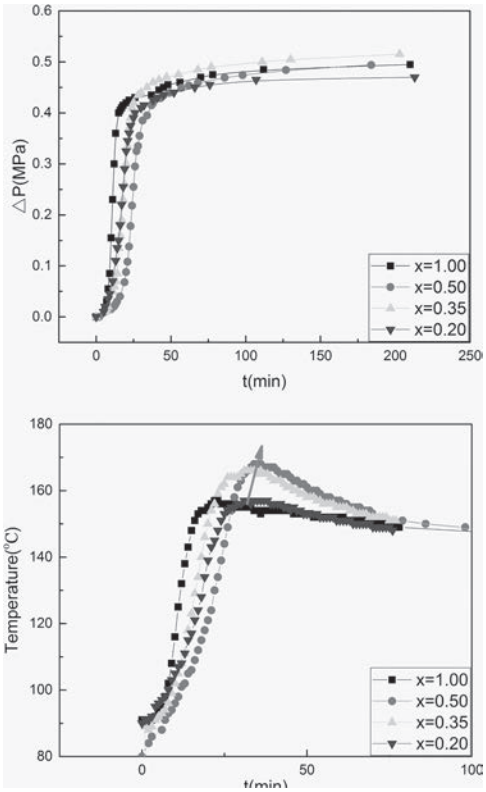




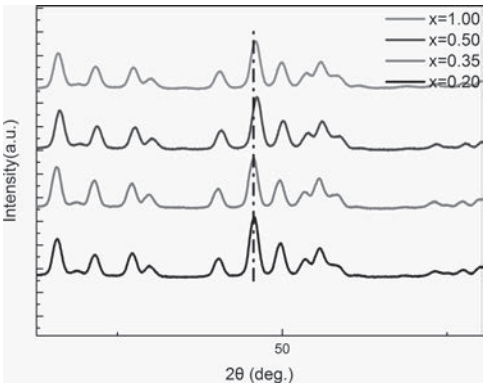
BP-04. Hydrogen Decrepitation Behaviors of Novel R-Fe-B Strip-Casting Alloys Based on Misch Metal. *Y. Liu*[1,2], X. Wang[1,2], F. Liu[1,2], Q. Ma[2,1], Y. Li[1,2] and X. Zhang[1,2] *1. School of Science, Inner Mongolia University of Science & Technology, Baotou, China; 2. Key Laboratory of Integrated Exploitation of Bayan Obo Multi-Metal Resources, Inner Mongolia University of Science& Technology, Baotou, China*

In order to reduce the Re-Fe-B material cost and balance the utilization of rare earth (Re) sources, misch metal(abbreviated as MM, is rich for La, Ce, Pr and Nd) substitution for Nd in the sintered magnet attract interest. Under the processing of fabricating Nd-Fe-B magnet, hydrogen decrepitation(HD) is widely use to obtain magnetic powder, however, the HD behaviors of Re-Fe-B strips base on MM may be complex. Therefore, HD behaviors of the $((PrNd)1\text{-}xMMx)_{30.8}Fe_{bal}Co_{1.4}B_{0.97}$ (x=0~1) (MM, Misch Metal)strips were study under 0.2 MPa pressure. We find that is similar to Nd-Fe-B, 2:14:1 tetragonal structure of Re-Fe-B strips base on MM is not broken during hydroden decrepitating. Whereas, when x<=0.50, the hydrogen absorption is more lagging as the ratio of MM/Re gets increasing. It should be ascribed to the grain cell volum changing. This finding suggests that La and Ce with stable 2:14:1 tetragonal structure upon HD process are promising alternatives for Nd However, to the $MM_{30.8}Fe_{bal}Co_{1.4}B_{0.97}$(x=1) strips, the hydrogen aborption behaviour is normal rapid, which may be attributed to the phase constitution of the strips(there exists $ReFe_2$ phase).

[1] R. X Shang, J. F. Xiong, D. Liu, et al, Chin. Phys. B, 26, 5 (2017). [2] W. L. Zuo, Sh. L. Zuo, R. Li, et al, J. Alloys Compd, 695, 1786(2016). [3] J. Y. Jin, G. H. Guo, Y. J. Zhang, B. X. Peng, Y. Sh. Liu, T. Y. Ma, M. Yan, AIP Adv. 8,056233(2018).



Variations of hydrogen pressure and temperature vs. time



XRD results of the hydrogen decrepitation powder of the ((PrNd)1-xM-Mx)30.8Fe66.83Co1.4B0.97

BP-05. Crystal structures and magnetic properties of synthesized Nd(Pr)FeCoB magnetic nanoparticles. A. Samardak[1], F. Nasirpouri[2], G. Ahmadpour[2], A. Portnyagin[1,3], E. Papynov[3,1], A.S. Samardak[1] and *A. Ognev[1] 1. School of Natural Sciences, Far Eastern Federal University, Vladivostok, Russian Federation; 2. Faculty of Materials Engineering, Sahand University of Technology, Tabriz, The Islamic Republic of Iran; 3. Institute of Chemistry Far Eastern Branch of Russian Academy of Sciences, Vladivostok, Russian Federation*

In this abstract, we report our experimental results for magnetic Nd-FeCo-B and Nd-Pr-Fe-Co-B nanoparticles synthesizing by a modified Pechini-type sol–gel method. Particle size, morphology, structures and elemental analysis of Nd(Pr)FeCoB oxide and reduced powders with cobalt additive varied from 0.05 up to 0.5 mole are investigated using XPS, SEM, TEM. The synthesized powders are composed from nearly spherical nanoparticles and irregular agglomerates with the presence of different phases in the microstructure of the Nd(Pr)FeCoB alloy. Magnetic hysteresis loop of NdFeB oxide and reduced powders with and without cobalt were measured. To better study of the magnetic behavior and its relationship to the microstructure and chemical composition, FORC results for NdFeCoB oxide powders are also obtained. Hysteresis loop of NdFeB oxide powders exhibits unusual magnetic behavior related with the presence and interaction between the paramagnetic and antiferromagnetic phases. But with the substitution of cobalt instead of iron in NdFeB oxide powders, hysteresis loop shows typical magnetic behavior. Also, the amount of M_r/M_s and H_c of NdFeB oxide powders are found to increase with cobalt content. Moreover, NdFeCoB oxide powders show lower and larger coercivity compared with reduced powders in H_2 atmosphere. The presence of soft CoFe magnetic phase in the microstructure of reduced powders in the H_2 atmosphere confirmed by the XRD pattern can be the main reason for this behavior. FeCo alloys have high saturation magnetization and low coercivity. The effects of the RE Pr on the magnetic behavior of the Nd(Pr)FeCoB powder will be show. This work has been supported by the Russian Science Foundation (project 19-72-20071).

BP-06. Chemical synthesis of $Nd_2Fe_{14}B$ particles with improved magnetic properties through wet ball milling process. *R. Kuchi*[1,2], S. Haider[1,2] and D. Kim[1,2] *1. Korea Institute of Geoscience and Mineral Resources, Korea Institute of Materials Science, Daejeon, The Republic of Korea; 2. Korea Institute of Materials Science, Changwon, The Republic of Korea*

$Nd_2Fe_{14}B$ based permanent magnets have attracted huge attention owing to its highest value of energy product (BH_{max}) and has been used enormously in electric motors for power generators, wind turbine generators, electric vehicles, energy conversion systems and many other novel applications. The simple chemical synthesis in this study including spray drying and reduction- diffusion process is very efficient startegy to obtain the $Nd_2Fe_{14}B$ particles. This technique offers a good plotform, and also inexpensive to produce permanent magnetic powders. The use of leached solution obtained from the monazite ore as a precursors could further decrease the production cost and is more economical way than utilisation of expensive inorganic salts (rare earths). In addition, the wet ball milling was introduced for particles after reduction-diffusion, on order to increase mangetic properties of $Nd_2Fe_{14}B$ particles. This can improve the dispersibilty of $Nd_2Fe_{14}B$ particles and separate out the by products which were formed during the reduction-diffusion process. The milled particles are subjected to washing process to get the final particles. However, milling is a key to enhance the magnetic properties of the final particles because the size, morphology and particle distribution strongly affect the coercivity, remenance and saturation magnetization. We investigated the magnetic properties of $Nd_2Fe_{14}B$ particles through wet ball milling in different solvents (Methanol, ethanol, and iso propanol) at different rotation speeds and time. At 200 rpm for 1 h, milling in ethanol resulted spherical particles with average size of 1.58 μm. This particles showed the corcivity of 2185 Oe, and remanence of 98 emu/g. This remanence is attributed to the pure $Nd_2Fe_{14}B$ phase and minimal defects and fractures of crystallites for the $Nd_2Fe_{14}B$ particles.

BP-07. Synthesis and characterzation of 1 dimensional NdFeB nano fiber using reduction-diffusion process. *N. Eom*[1], S. Noh[1] and B. Kim[1] *1. Korea Institute for Rare Metal, Korea Institute of Industrial Technology, Incheon, The Republic of Korea*

Neodymium-Iron-Boron (Nd-Fe-B) magnets are well known as the strongest magnets due to their high energy density than other magnetic materials such as ferrite and Sm-Co. These magnets have been widely used for motors, hard disc drive, and MRI. NdFeB based magnetic materials were generally synthesized using the classical powder metallurgy process and chemical synthesis methods for nanofibers. Among these processes, nanofibers fabricated by electrospinning are excellent for reproducibility and have a large aspect ratio. The electrospinning method is a simple and scalable nanostructure/microstructure fabricating process to produce 1-D-structured materials. By adjusting the amounts of each ingredient, typically the polymer, it is easy to control the dimensions and morphology of produced fiber. However, there has been little significant research reports on Nd-Fe-B fibers because the reduction of rare-earth elements oxide for Nd-Fe-B fibers is difficult without high temperatures with hydrogen. In this study, a novel method for the synthesis of neodymium-iron-boron (Nd-Fe-B) fibers was demonstrated by adopting three continuous processes: electrospinning, step heat treatment, and a facile reduction-diffusion which is new process. The structural and crystalline studies revealed that as-spun precursor fibers were transformed into $FeNdO_3$, Fe_2O_3, and $NdBO_3$ phases by non-isothermal heat treatment, and the oxide mixture fibers were reduced to the single Nd-Fe-B phase by the facile reduction-diffusion process. The morphology of the synthesized Nd-Fe-B material were analyzed by field emission scanning electron microscope (FE-SEM) and X-ray diffraction (XRD). The magnetic property as function of Nd-Fe-B wire diameter was conducted using vibrating sample magnetometer (VSM).

BP-08. Temperature dependent magnetization reversal process of a Ga-doped Nd-Fe-B sintered magnet based on first-order reversal curve analysis. *S. Okamoto*[1,2], K. Miyazawa[1], T. Yomogita[1], N. Kikuchi[1], O. Kitakami[1], K. Toyoki[3,2], D. Billington[3,2], Y. Kotani[3], T. Nakamura[3,2], T. Sasaki[2], T. Ohkubo[2], K. Hono[2], Y. Takada[4], T. Sato[4], Y. Kaneko[4] and A. Kato[5] *1. Tohoku University, Sendai, Japan; 2. ESICMM, NIMS, Tsukuba, Japan; 3. JASRI, Sayo, Japan; 4. Toyota Central R&D Labs., Nagakute, Japan; 5. Toyota Motor Corp, Susono, Japan*

Recently, a Ga-doped Nd-Fe-B sintered magnet has attracted much attention as a high-performance permanent magnet [1]. This magnet exhibits a unique behavior against annealing treatment. The coercivity of the as-sintered state is not large as about 1 T, however, it largely increases to be about 1.8 T after an optimum annealing treatment [2]. In this study, the magnetization reversal process of the Ga-doped Nd-Fe-B sintered magnet has been investigated using the first-order reversal curve (FORC) analysis. Fig. 1(a) shows the FORC diagram of the optimally annealed Ga-doped Nd-Fe-B sintered magnet measured at RT. The typical FORC diagram pattern of conventional Nd-Fe-B sintered magnets exhibit two spots at low and high field regions, respectively. According to our previous study, these two FORC spots correspond to multi- and single-domain magnetization reversals [3]. Contrary to these previous results, only one FORC spot is observed in Fig. 1 (a), indicating that the single-domain magnetization reversal is dominant in the Ga-doped Nd-Fe-B sintered magnet. To confirm the actual magnetization reversal process, we employed the soft X-ray magnetic circular dichroism (XMCD) microscopy observation performed at SPring-8. Fig. 2 shows the XMCD microscopy images taken along the reversal magnetization curve of the Ga-doped Nd-Fe-B sintered magnet. These XMCD microscopy images clearly evidence the single-domain magnetization reversal. At 200 °C, however, two FORC spots appear as shown in Fig. 1(b), that is similar to that of conventional Nd-Fe-B sintered magnets. This fact indicates that the magnetization reversal process of the Ga-doped Nd-Fe-B sintered magnet varies from the single-domain magnetization reversal at RT to the multi-domain magnetization reversal at high temperature, and this change in the magnetization reversal process crucially affects the temperature dependent coercivity of this magnet.

[1] K. Nakamura and T. Yamazaki, Japan Patent (2015) 5767788. [2] T. Sasaki et al. Scr. Mater. 113 (2016) 218. [3] K. Miyazawa et al., Acta Mater. 162 (2019) 1.

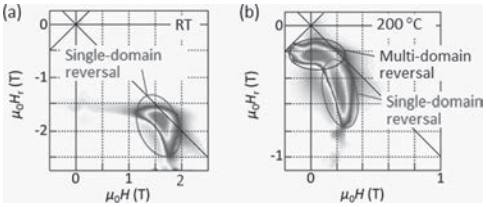


Fig. 1 FORC diagram patterns of a Ga-doped Nd-Fe-B sintered magnet measured at (a) RT and (b) 200 °C.

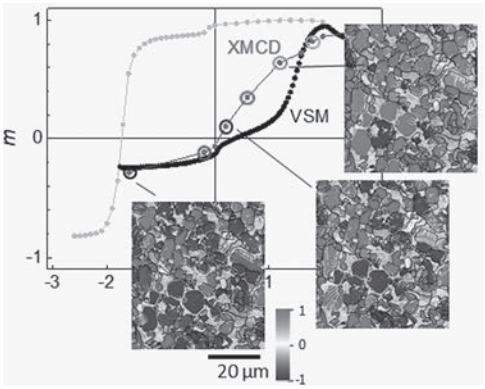


Fig. 2 XMCD microscopy imagens and magnetization curves of a Ga-doped Nd-Fe-B sintered magnet.

BP-09. Coercivity Mechanism of Ga-doped Nd-Fe-B Sintered Magnets. *Y. Matsuura*[1], T. Nakamura[2], K. Ishigami[2], K. Sumitani[2], K. Kajiwara[2], R. Tamura[3], M. Nagae[1] and K. Osamura[1] *1. Research Institute for Applied Sciences, Kyoto, Japan; 2. Japan Synchrotron Radiation Research Institute (JASRI), Sayo, Japan; 3. Tokyo University of Science, Tokyo, Japan*

The alignment dependence and angular dependence of coercivity (ALDC and ANDC, respectively) of aligned and isotropically aligned Ga-doped $Nd_{14.79}Ga_{0.57}B_{5.24}Co_{1.11}Fe_{bal.}$ were investigated and compared with those of the Nd–(Dy)–Fe–B sintered magnets and ferrite magnets [1], [2], [3]. The ALDC was similar to those of Nd–(Dy)–Fe–B magnet and the ferrite magnet. The coercivity of Ga-doped Nd–Fe–B magnets decreased as the alignment improved. It is postulated that every grain reversed independently by the magnetic domain walls. The angle of magnetization reverse area (θ_1) (AMRA) for the coercivity [2] as a reversed magnetization area at coercivity was calculated and compared with the θ_1 that was obtained from the experimental ALDC. The AMRA that was calculated from the ALDC increased, and was similar to the Nd–(Dy)–Fe–B sintered magnets and ferrite magnets [2], [3]. The AMRA of the aligned Ga-doped magnets was 41.4° at coercivity, which is wider than the 40.7° of the ferrite magnets [3]. Figure 1 shows the ANDC of the Ga-doped Nd–Fe–B sintered magnets and ferrite magnets. The ANDC of the Ga-doped Nd–Fe–B sintered magnets is expected to be similar to the ferrite magnet but slightly lower than the ferrite magnets as established from the AMRA. The ANDC of these magnets decreases from 0° to 40° and increases after 40°. The ANDC behavior might be explained by the coherent rotation model. However, the relationship between the ALDC and ANDC suggests that these phenomena originate from the magnetic domain wall motion. Figure 2 shows the ANDC of isotropically aligned Ga-doped Nd–Fe–B sintered magnets and ferrite magnets. These results support our proposed coercivity mechanism; for aligned magnets, the magnetic domain walls are pinned at grains that are tilted in easy magnetization directions or the c-axis is tilted from the easy magnetization of the magnet. When the magnetic domain walls are de-pinned from the pinning sites, they jump through several grains, which determines the coercivity.

(1) Y. Matsuura, R. Ishii, J. Hoshijima, J. Magn. Magn. Mater. 336 (2013) 88-92 (2) Y. Matsuura, T. Nakamura, K. Sumitani, AIP Advances, 8, 015226 (2018) (3) Y. Matsuura, IEEE Transaction on Magnetics, 54(11), 2101405 (2018)

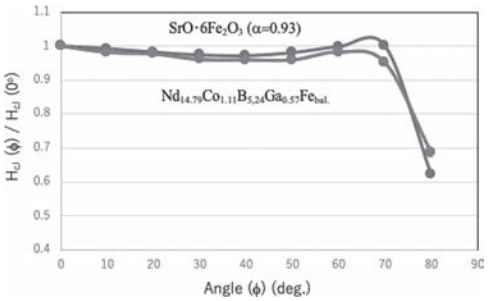


Fig.1 ANDC of Ga-doped Nd–Fe–B sintered magnets with α = 0.947and ferrite magnets α = 0.93 [2], where α is the alignment

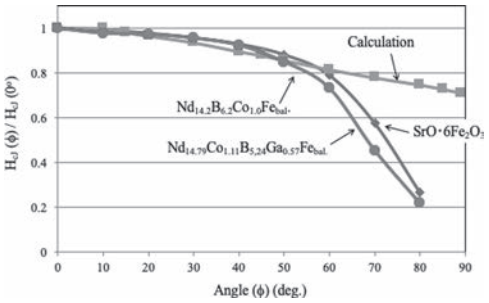


Fig.2 ANDC of isotropically aligned (α=0.5) Ga-doped Nd–Fe–B sintered magnets and ferrite magnets [2]

BP-10. Liquid phase diffusion source of heavy rare-earth for enhancing coercivity of grain-boundary-diffusion-processed Nd-Fe-B-type magnet. J. Choi[1], *H. Kwon*[1], B. Kim[1] and J. Lee[2] *1. Pukyong National University, Busan, The Republic of Korea; 2. Korea Institute of Materials Science, Changwon, The Republic of Korea*

Nd-Fe-B-type magnet has been exclusively used for rotor magnet in traction motor of HEV and EV, but it still has one big drawback: poor thermal stability (high temperature coefficient of coercivity (b)) due to low Curie temperature (T_c). Standard approach for solving this problem is sufficiently enhancing room temperature coercivity by means of grain boundary diffusion (GBD) of heavy rare-earth (HRE), such as Tb or Dy. Commonly used diffusion sources of the HRE for GBD are HRE fluoride or oxide salts. As these salts exist as solid during GBD process, diffusion of HRE towards interior is inherently sluggish. It is expected that using HRE diffusion sources in liquid form would lead to speedier diffusion of HRE, thus leading to more rapid and efficient coercivity enhancement. By a lucky chance, we could find a good candidate of diffusion source of Dy in DyF_3 – LiF binary system, which becomes liquid during GBD annealing. Promising liquid diffusion source containing Dy is available in two-phase region (solid DyF_3 + liquid (DyF_3 – LiF)) above peritectic line (~ 815 °C) in DyF_3 – LiF binary system, and the peritectic temperature is desirably lower than typical GBD annealing temperature for Nd-Fe-B-type magnet. In this study, efficacy of using liquid phase Dy diffusion source for enhancing coercivity in GBD-processed Nd-Fe-B-type magnet was investigated. Commercial (Nd,Pr)-Fe-Co-Cu-B-type sintered magnet was coated with (DyF_3 – LiF) mixture having desired composition. The coated Nd-Fe-B magnet was annealed at 820 °C and then quenched, and followed by ageing at 550 °C. It was found that the (DyF_3 – LiF) mixture having 10 vol% liquid (DyF_3 – LiF) + 90 vol% solid DyF_3 at annealing temperature was the best for enhancing coercivity of the Nd-Fe-B-type magnet (Fig. 1(a)). More importantly, it was also revealed that more rapid and consistently higher coercivity enhancement was achieved by using liquid phase diffusion source containing Dy with respect to solid

DyF_3 diffusion source (Fig. 1(b)). Overall, the magnet GBD-processed with Dy-containing liquid phase diffusion source outperformed the one processed with solid DyF_3.

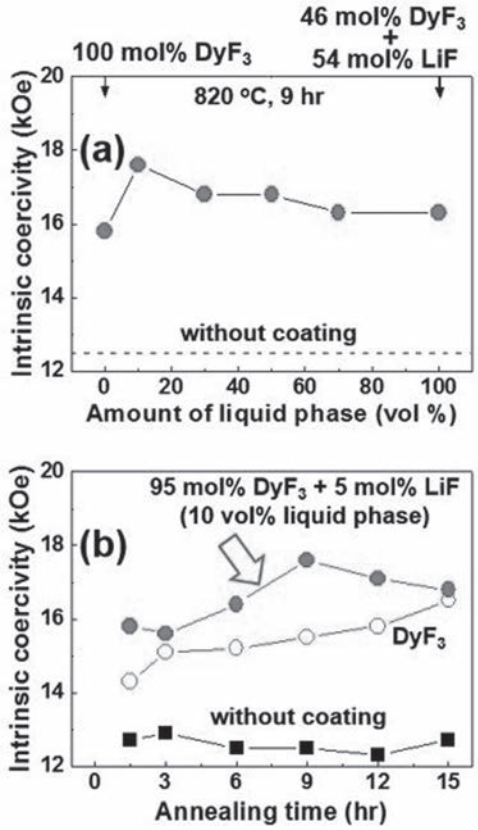
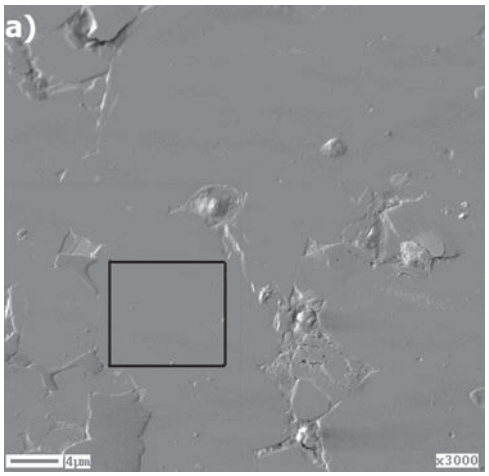


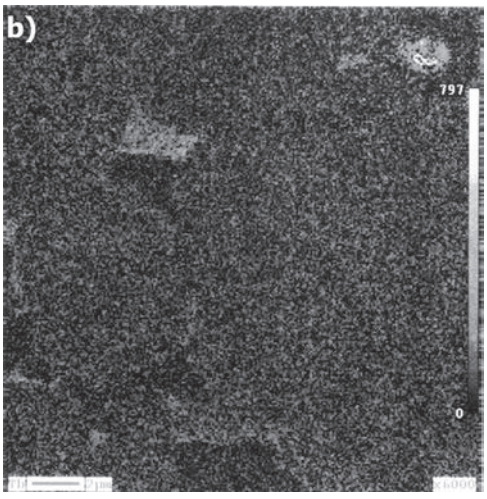
Fig. 1. Coercivity variation in Nd-Fe-B-type magnet GBD-processed using liquid phase Dy diffusion source.

BP-11. Application of Hydrogen-Containing REM-Based Additions in Designing Nd-Fe-B Magnetic Materials. *K. Skotnicova*[1], N.B. Kolchugina[2], G.S. Burkhanov[2], M. Kursa[1], T. Cegan[1], A. Lukin[3], O. Zivotsky[1], P. Prokofev[2], N. Dormidontov[2], J. Jurica[1] and B. Smetana[1] *1. Regional materials science and technology centre, VSB-Technical University of Ostrava, Ostrava, Czechia; 2. Baikov Institute of Metallurgy and Materials Science, Russian Academy of Sciences, Moscow, Russian Federation; 3. JSC SPETSMAGNIT, Moscow, Russian Federation*

The focusing of new technologies on the formation of inhomogeneous distribution of heavy rare-earth metals (REMs) in the hard magnetic Nd-Fe-B materials is the scientific importance of the problem of increase in their functional properties [1-3]. Our novel manufacturing process of these materials includes strip casting, hydrogen decrepitation and treatments in a hydrogen atmosphere, high-energy milling plus mechanical alloying of multicomponent mixtures [4]. We studied the role of alloying REMs and their alloys with transition metals, which were added in the form of hydride or hydrided compounds (TbH_x, DyH_x, ScH_x, Tb_3CoCu, Dy_3CoCu) to initial Nd-Fe-B-based powder mixtures in the course of their mechanical activation, in the formation of phase composition, microstructure, fine structure of grains and given hysteretic properties of hard magnetic materials based on $(RR')_2Fe_{14}B$ compositions. New knowledge on the formation of structured state of $(RR')_2Fe_{14}B$-phase grains, namely, the formation in them of compositional inhomogeneities of heavy REMs, and on the creation of optimum grain surface, Nd-rich grain boundary phase, was acquired. The found Tb distribution inhomogeneities (see Fig.1) are typical of different compositions containing Tb, in the total case, for compositions with a heavy REM. The magnets prepared with 2 and 4 wt.% TbH_2 demonstrates 52 and 90% increase in $_jH_c$ and only 4 and 10% decrease in B_r as compared to those of magnets prepared without the hydride additions, respectively. This effect manifests itself more substantially in using some manufacturing processes, such as strip casting, hydrogen decrepitation, mechanical alloying of binary powder mixtures, etc. Along with the formed core-shell grain structure, the nonuniformity of principal hard-magnetic phase leads to the increase in structure-sensitive magnetic parameters. Magnets prepared with DyH_2 addition demonstrate the higher thermal stability of hysteretic properties at the expense of higher lattice rigidity in the presence of heavy REM. The modified manufacturing process allows us to prepare magnets with the wide range of hysteretic characteristics in using unified initial Nd-Fe-B strip-casting alloy. (Projects LTARF18031 and 14.616.21.0093).

1. O. Gutfleisch, M.A. Willard, E. Bruck, et al., Magnetic Materials and Devices for the 21st Century: Stronger, Lighter, and More Energy Efficient, Advanced Material, Vol. 23, pp. 821-842 (2011). 2. Y. Zhang, T. Ma, X. Liu, et al., Coercivity enhancement of Nd-Fe-B sintered magnets with intergranular adding (Pr, Dy, Cu)-Hx powders, Journal of Magnetism and Magnetic Materials, Vol. 399, pp. 159-163 (2016). 3. H. Sepehri-Amin, Y. Une, T. Ohkubo, et al., Microstructure of fine-grained Nd-Fe-B sintered magnets with high coercivity, Scripta Materialia vol. 65, pp. 396-399 (2011). 4. G. S. Burkhanov, N. B. Kolchugina, A. A. Lukin, et al., Structure and Magnetic Properties of Nd-Fe-B Magnets Prepared from DyH_2-Containing Powder Mixtures, Inorganic Materials: Applied Research, Vol. 9, pp. 509-516 (2018).





BP-12. Comparison on the coercivity enhancement of sintered NdFeB magnets by grain boundary diffusion with low-melting (Tb, R)$_{75}$Cu$_{25}$ alloys (R = Y, La, and Ce). *Y. Wong*[1], H.W. Chang[1], Y. Lee[1], W. Chang[1], C. Chiu[2] and C. Mo[3] *1. Department of Physics, National Chung Cheng University, Chia-yi, Taiwan; 2. New Materials Research & Development Dept., China Steel Corp., Kaohsiung, Taiwan; 3. R&D Department, Himag Magnetic Corporation, Pingtung, Taiwan*

NdFeB sintered magnets exhibit the highest energy product ($(BH)_{max}$) among all developed permanent magnets due to the outstanding magnetically intrinsic properties of $Nd_2Fe_{14}B$. Traditionally, Dy or Tb is generally added to the Nd-Fe-B magnets to enhance the coercivity ($_iH_c$) for the applications at higher temperature. Since the price surge of critical RE elements in 2011 and also the trade war arises this year, how to reduce the usage of Dy or Tb in the magnets while keeping high coercivity for practical applications becomes the crude issue again. Nevertheless, the grain boundary diffusion (GBD) technique has been developed to conquer this challenge. In this work, significant coercivity enhancement of the commercial NdFeB magnets, 5 mm in thickness, with the magnetic properties of $(BH)_{max}$ = 48.4 MGOe and $_iH_c$ = 17.5 kOe is demonstrated through GBD with low-melting $Tb_{55}R_{25}Cu_{25}$ alloys (R = None, Y, La, Ce). The experimental results show that the adoption of $Tb_{55}R_{25}Cu_{25}$ alloys as GBD sources is effective in increasing coercivity to 29.0 kOe for R = None, 23.8 kOe for R = Y, 25.6 kOe for R = La, 28.0 kOe for R = Ce, respectively. $(BH)_{max}$ is slightly reduced to 46.2-48.2 MGOe. The preferential appearance of Cu at grain boundary and triple junction of the grains and the core-shell structure occurred due to Tb at grain surface remarkably enhances the coercivty. Interestingly, higher coercivity enhancement per wt% Tb usage (Δ_iH_c/wt%Tb) of 7.2 kOe/wt% for the magnet with $Tb_{55}Ce_{25}Cu_{25}$ than 5.9 kOe/wt% for that with $Tb_{75}Cu_{25}$ has been found due to the magnetic isolation effect caused by the preferential appearance of Ce at GB, though slightly lower coercivity enhancement for the samples with R = Y, La, and Ce. Lower melting point of 637 ^oC for $Tb_{55}Ce_{25}Cu_{25}$ than $Tb_{75}Cu_{25}$ (743 ^oC) leads to larger diffusion depth of Tb into the magnet and therefore contributes to higher Δ_iH_c/wt%Tb for the magnet with R=Ce. The coercivity mechanism through micromagnetic model and thermal stability with temperature coefficients of the above samples will be discussed in this presentation. The results of this study suggest the low-melting $Tb_{55}R_{25}Cu_{25}$ alloys for GBD process is cost effective in enhancing the coercivity of sintered NdFeB magnets.

None

BP-13. PLD-fabricated Pr-Fe-B thick film magnets applied to small motors. *S. Takeichi*[1], K. Inoue[1], K. Takashima[1], A. Yamashita[1], T. Yanai[1], M. Nakano[1] and H. Fukunaga[1] *1. Nagasaki University, Nagasaki, Japan*

Although a cylinder-type small motor comprising a rare earth bonded magnet on a stainless shaft has been conventionally used, it is difficult to achieve the high values of residual magnetization and $(BH)_{max}$ of the magnets because each motor contains a nonmagnetic phase such as a thermosetting resin. In the study, preparation of miniaturized magnets without non-magnetic materials was carried out using PLD (Pulsed Laser Deposition) method [1]. In order to deposit a Pr-Fe-B thick film magnet on a stainless shaft, we optimized Pr contents of Pr-Fe-B films on stainless substrates through the evaluation of magnetic together with mechanical properties. Then, an approximately 250 μm-thick Pr-Fe-B film magnet which has superior magnetic properties compared with those of a conventional bonded magnet could be obtained on a stainless shaft applicable to a small motor. A rotated $Pr_XFe_{14}B$ (X=1.8~2.4) target was ablated using a Nd-YAG pulse laser in the vacuum atmosphere to deposit Pr-Fe-B film magnets on stainless substrates and shafts, respectively. In order to crystallize an as-deposited Pr-Fe-B film with amorphous structure, a pulse annealing (PA) method was utilized. Figure 1 shows the relationship between the peeling phenomenon and Pr contents in as-deposited Pr-Fe-B films on stainless substrates. In the thickness range from 10 to 100 μm, Pr-Fe-B films with the Pr content above 15 at. % tended to peel from the substrates. This result is considered to be attributed to the different linear expansion coefficient between a stainless (10.3×10^{-6} K^{-1}) and Pr element (6.7×10^{-6} K^{-1}). On the other hand, an increase in Pr contents of the samples enabled us to enhance the magnetic properties compared with those of a conventional bonded magnet. We, therefore, deposited a Pr-Fe-B film with the Pr contents of slightly less than 15 at. % on a stainless shaft. Resultantly, a PLD-made 250 μm-thick film on a stainless shaft with the diameter of around 0.5 mm could be prepared. We also found that the coercivity of the film was about 1250 kA/m which was applicable to a small motor.

[1] M. Nakano, Y. Chikuba, M. Oryoshi *et al.*, *IEEE Trans. Magn.* vol. 51, #2102604-1~4(2015).

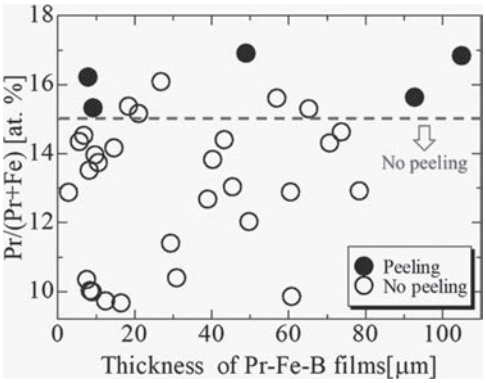
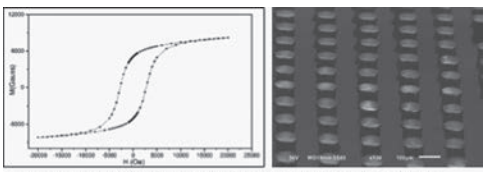


Fig. 1 Observation of peeling phenomenon as a function of Pr amounts (Pr/(Pr+Fe)) in as-deposited Pr-Fe-B films with various thicknesses on stainless substrates

BP-14. Synthesis of Nd-Fe-B/Fe hybrid micro-magnets. *N. Gunduz Akdogan*[1], O. Akdogan[2] and B. Misisrlioglu[3] *1. Piri Reis University, Istanbul, Turkey; 2. Bahcesehir University, Istanbul, Turkey; 3. Sabanci University, Istanbul, Turkey*

There is an overgrowing interest in the synthesis of high-performance micro magnets due to their wide application areas in MEMS, microfluidics, and micro-robotics. In addition, they possess great potential to become a model system for the development of next-generation hard magnets. In this study, NdFeB/Fe hybrid micro-magnets have been synthesized by a photolithography technique. NdFeB and Fe micro powders in the form of nano-thin flakes have been synthesized by one step surfactant assisted planetary ball milling. The fabricated nano-thin flakes with different lateral sizes have been obtained by varying the milling time. Room temperature coercivities of up to 3.1 kOe for NdFeB has been achieved after milling for 8 hr (Fig. 1a). Photoresist and powders of NdFeB and Fe have been mixed at various powder-to-resist ratios. SU-8 has been chosen as the photoresist due to its resistance to chemicals and its suitability to be utilized in MEMS technology. Micro islands of SU-8/NdFeB/Fe have been prepared according to the manufacturer's recommendations for pure SU-8. The hybrid micromagnets in disk form (height: 50 μm and diameter: 100 μm) have been successfully produced. (Fig. 1b.) The evolution of magnetic, structural and microstructural properties of these micro magnets will be reported. Successful fabrication of hybrid micro-magnets using the methodology prescribed in this work can pave the way for the development of next-generation MEMS. This work was supported by TUBITAK project: 116C080. Photolithography has been conducted in Sabanci University Nanotechnology Application Center.

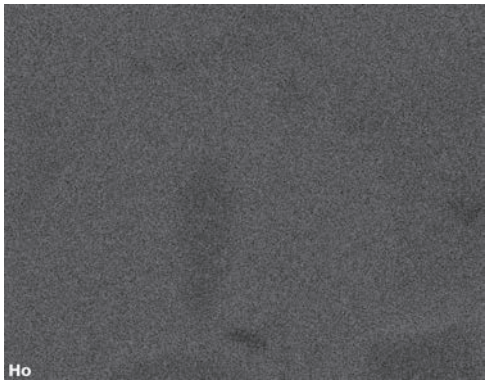

Fig. 1. a) Hysteresis loop of NdFeB nanoflakes, b) SEM image of micro islands

a) Hysteresis loop of NdFeB nanoflakes, b) SEM image of micro islands

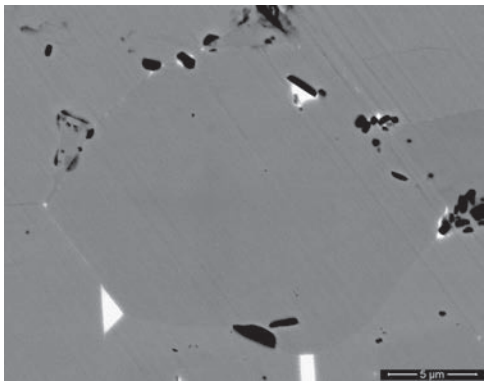
BP-15. (Pr, Ho)-Fe-B Magnets for Low-Temperature Applications.

N. Kolchugina[1], A. Lukin[2], G.S. Burkhanov[1], K. Skotnicova[3], *O. Zivotsky*[4], M. Kursa[3], N. Dormidontov[1], P. Prokofev[2], Y. Koshkid'ko[1,5], T. Cegan[3], T.P. Kaminskaya[6] and B. Ginzburg[6] *1. Baikov Institute of Metallurgy and Materials Science, Russian Academy of Sciences, Moscow, Russian Federation; 2. JSC SPETSMAGNIT, Moscow, Russian Federation; 3. Regional Materials Science and Technology Centre, VSB-Technical University of Ostrava, Ostrava, Czechia; 4. Department of Physics, VSB-Technical University of Ostrava, Ostrava, Czechia; 5. Institute of Low Temperature and Structure Research, Polish Academy of Sciences, Wroclaw, Poland; 6. Physical Department, Moscow State University, Moscow, Russian Federation*

Currently, processes named as grain boundary diffusion and grain boundary restructuring are widely used as approaches, which allow one to improve hysteretic properties of Nd-Fe-B-based magnets, namely, to enhance the coercivity and reduce the heavy rare-earth consumption of Nd–Fe–B sintered magnets simultaneously. Some progresses have been made in efforts to introduce heavy rare-earth metals (REMs) in the form of hydrides. In recent years, permanent magnets based on $(Nd,Pr)_2Fe_{14}B$ compound are of interest for investigators owing to the possibility to use these magnets at low and cryogenic temperatures. In contrast to $Nd_2Fe_{14}B$ compound (at 135 K, its easy-magnetization axis anisotropy changes to easy-axis cone anisotropy), the $Pr_2Fe_{14}B$ compound does not undergo the spin-reorientation transition, and the natural increase in the hysteretic parameters with decreasing temperature can be adequately used. In the present study, we investigate the effect of HoH_2 hydride addition on the hysteresis loop parameters of sintered Pr-Fe-Ti-Al-Cu-B magnets. The magnets were prepared by traditional powder metallurgy technology, and 3 wt. % HoH_2 was added to the powder at the fine-milling stage. The magnets demonstrate the monotonic increase in all hysteretic parameters with decreasing temperature up to 4.2 K. The structure of the magnets was studied in detail by scanning electron microscopy (SEM/EDX - Fig. 1), and the formation of so-called "core-shell" structure was demonstrated (Fig. 2), which is assumed to favor the marked improvement of hysteretic properties of Pr-Fe-B-based magnets. The coercive force and maximum energy product at 4.2 K are H_c = 5420 kA/m and $(BH)_{max}$ = 352 kJ/m^3, respectively. Domain structure of the magnets was studied perpendicular and parallel to the magnet texture using magnetic force microscopy. The data obtained indicate the well-formed magnetic texture. The average domain width is 1.2-1.8 μm.



The distribution of Ho in the matrix grains of Pr-Fe-B sintered magnet prepared from the powder mixture with 3 wt.% HoH_2.



SEM image of $Pr(Ho)_2Fe_{14}B$ phase grain showing so-called "core-shell" structure, i.e. cores of grains are Ho-depleted, whereas the edges of grains are Ho-enriched.

Session BQ
VOLTAGE-CONTROLLED MAGNETIC ANISOTROPY AND SWITCHING I (Poster Session)

Tatsuya Yamamoto, Co-Chair
National Institute of Advanced Industrial Science and Technology, Tsukuba, Japan
Aliona Nicolenco, Co-Chair
Autonomous University of Barcelona, Bellaterra, Spain

BQ-01. Influence of HfO_2 Interlayers on Magnetocrystalline Anisotropy in Fe|MgO|Fe Magnetic Tunnel Junction: First-Principles Investigation.
W. Chen[1], J. Zhang[2], B. Yang[1], T. Yu[3] and *X. Han*[1] *1. Institute of Physics, Beijing, China; 2. Huazhong University of Science and Technology, Wuhan, China; 3. Sichuan University, Sichuan, China*

Perpendicular magnetic anisotropy (PMA) is important for MgO based magnetic tunnel junction and magnetic random access memory (MRAM) to be large-scale integrated due to high thermal stability and low critical switching current. Here, we applied density function theory to study the effect of HfO_2 inserting layers on PMA of Fe|MgO|Fe tunnel junction. It was found that the magnetocrystalline anisotropy (MCA) of the junction for 5 layers Fe electrode was up to 1.95 mJ/m^2 with one unit cell HfO_2 interlayer, while 1.72 mJ/m^2 without the interlayer. More importantly, analyzed by the layer and orbital-resolved MCA based on second-order perturbation theory, MCA characters and the underlying mechanism of PMA become very different after inserting HfO2. The remarkable difference is the MCA contribution of the second interfacial Fe layers, which is about 0.4 mJ/m^2 for Fe|MgO|Fe junctions, while larger than 0.7 mJ/m^2 for Fe|HfO_2|MgO|HfO_2|Fe junctions. Furthermore, Fe-dz^2 and O-pz hybridization plays a crucial role on MCA contribution from the first interfacial Fe layers since the interfacial Fe-O bond length reduces from 2.20 Å to 1.77 Å with inserting the HfO_2 layers. Besides, the reduction in Fe-O bond length can redistribute the orbital-resolved electrons of the second and third closest Fe layer to the interface to enhance their absolute values of MCA contributions, which results in the strong dependence of MCA on Fe thickness.

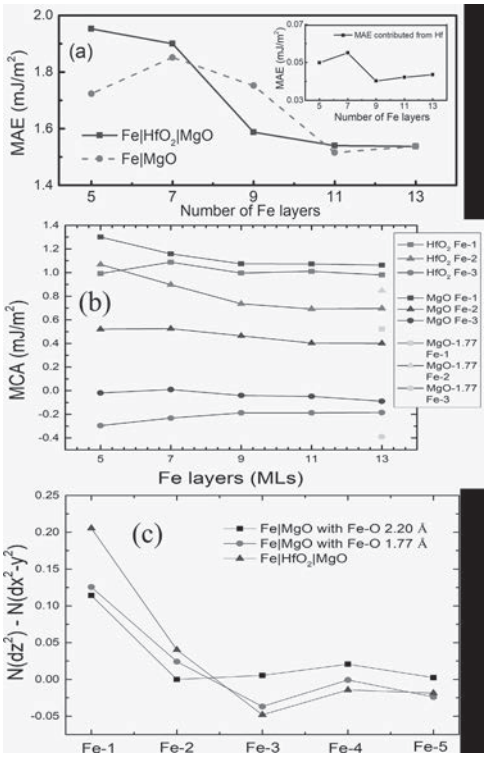


FIG. 1. (a) MCA for different number of Fe layers in supercell, where dashed lines and solid lines represent Fe|MgO|Fe and Fe|HfO_2|MgO|HfO_2|Fe junctions, respectively. (insert) Interface MCA contributed by Hf atoms in Fe|HfO_2|MgO|HfO_2|Fe junction. (b) MCA contribution of the closest (Fe-1), the second closest (Fe-2) and the third closest (Fe-3) Fe layer to the interface for three supercells with different Fe layers, where red, blue and green represent Fe|HfO_2|MgO, Fe|MgO and artificial Fe|MgO with Fe-O bond length of 1.77 Å, respectively. (c) Difference of orbital-resolved electrons N(dz^2) and N(dx^2-y^2) for three supercells with 13 ML Fe layers.

BQ-02. Strong bias effect on voltage-driven torque at epitaxial Fe-MgO interface.
S. Miwa[1,2], Y. Jibiki[1], J. Fujimoto[3], M. Goto[1] and Y. Suzuki[1] *1. Graduate School of Engineering Science, Osaka University, Toyonaka, Japan; 2. The Institute for Solid State Physics, The University of Tokyo, Kashiwa, Japan; 3. Institute for Chemical Research, Kyoto University, Uji, Japan*

Torque can be provided to induce magnetization in nanomagnets directly by electric current and/or voltage. This technique enables electric current (voltage)-to-spin conversion without electromagnetic induction, and has been intensively studied for memory device applications. Among the various kinds of torque, torque induced by spin-orbit splitting has recently been found [1,2]. However, quantitative understanding of bulk-related torque and

interface-related torque is still lacking [3] due to their identical symmetry for current-in-plane devices. In this presentation, we propose that a pure interface-related torque can be characterized by spin-torque ferromagnetic resonance with a current-perpendicular-to-plane tunnel junction utilizing tunnel anisotropic magnetoresistance [4]. We prepared epitaxial Fe-MgO-V tunnel junctions with various MgO thicknesses giving a wide range of current density. As a result, we found that the interface-related current-driven torque was negligible but the voltage-driven torque increased as the MgO thickness decreased. The maximum voltage-driven torque was as large as 2.8×10^{-5} J/(Vm^2). This is comparable to the VCMA at an Fe-MgO interface of 180 fJ/Vm, which is larger than any reported VCMA-induced voltage-driven torque. The voltage-driven torque shows nonlinear DC bias voltage dependence, with a maximum around zero DC bias as shown in Fig. 1(a); thus, an electronic state in the vicinity of the Fermi level at Fe-MgO interface is likely to be of importance to generate the large voltage-driven torque. An interface resonant state at Fe-MgO was also found in the vicinity of the Fermi level from the conventional tunnel spectroscopy (Fig. 1(b)) as well as tunnel anisotropic magnetoresistance spectroscopy. This surface-state-sensitive electric modulation of magnetic properties provides new insight in the field of interface magnetism. A part of this work was supported by JSPS KAKENHI (Nos. JP26103002), TEPCO Memorial Foundation, and The Asahi Glass Foundation.

[1] L. Liu *et al.*, Phys. Rev. Lett. 106, 036601 (2012). [2] L. Liu *et al.*, Science 336, 555 (2012). [3] J. Kim *et al.*, Nat. Mater. 12, 240 (2013). [4] S. Miwa *et al.*, Phys. Rev. X 7, 031018 (2017).

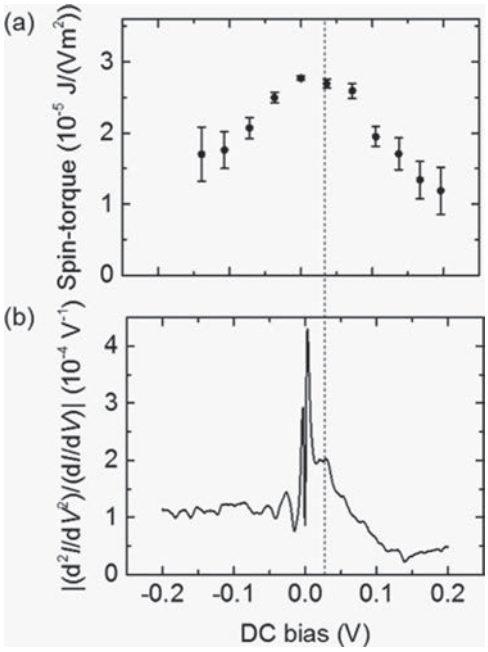


Fig. 1 (a) Spin-torque and (b) Tunnel spectra in Fe-MgO-V tunnel junction.

BQ-03. Strain Mediated Current-induced Magnetization Switching in PMN-PT/Ta/Pt/Co/Pt Heterostructures. M. Wang[1], *X. Xu*[1], J. Miao[1] and Y. Jiang[1] *1. school of materials science and engineering, University science and technology of Beijing, Beijing, China*

Current-induced spin-orbit torques (SOT) induced magnetization switching and electric filed controlled magnetism in ferroelectric materials are two interesting topics with potential application in spintronic devices [1-7]. However, the research of the strain mediated SOT switching on ferroelectric substrates is still limited. Therefore, it is important to clarify the mechanism of the strain mediated electric field induced SOT switching. In this work, we study strain mediated SOT induced magnetization switching in $PbMg_{1/3}Nb_{2/3}O_3$-$PbTiO_3$ (PMN-PT)/Ta (1)/Pt (3)/Co (1.3)/Pt (1) (thickness in nanometer) multilayers. The film was patterned into a Hall bar using EBL and an Ar ion milling technique. The multilayer takes on a perpendicular magnetic anisotropic state on the basis of the figure of the Hall resistance (R_H) as a function of the out-of-plane magnetic field. R_H-I curves under external in-plane magnetic field H_x=100 Oe is shown in Figure 1, the magnetic field is applied along the positive current direction. The changes of resistance ΔR of the clockwise switching loops can respond to the extent of the magnetization switching. Along the magnetic field direction, applying an electric field of E=10 kV/cm, the magnetization switching becomes close to full switching compared with E=0 kV/cm under H_x=100 Oe. Therefore, the effective magnetic anisotropy field can promote the magnetization switching under the external magnetic field. We can also observe the easy axis rotated in hysteresis loops before and after applying E=10 kV/cm in Figure. 2. According to our experiments, strain modulation of interface magnetic anisotropy plays an essential role in manipulating the SOT induced magnetization switching. By applying the electric-filed E=10 kV/cm, the magnetization switching can be increased about 40%, which suggests that magnetization witching can be realized with lower external in-plane magnetic field or even zero field.

[1] Shunsuke Fukami. et al, Nature Mater., 4566, 535-542 (2016). [2] Young-Wan Oh. et al, Nature Nano., 109, 1-8 (2016). [3] W. J. Kong. et al, Appl. Phys. Lett., 109, 132402 (2016) [4] G. Q. Yu. et al, Nature Nano., 94, 548-554 (2014). [5] K. M. Cai. et al, Nature Mater., 4886, 1-6(2017). [6] B. Peng. et al, Acs Nano., 11, 7b01547 (2017). [7] Y. Qu. et al, Phys. Rev. Appl. Nano., 8, 044006 (2017).

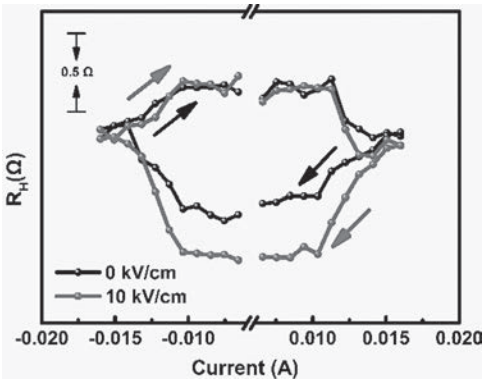


Figure 1. The current-induced magnetization switching probed by anomalous hall effect under in-plane magnetic field with H_x=100 Oe.

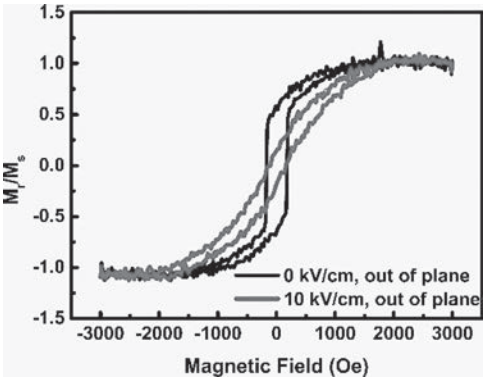


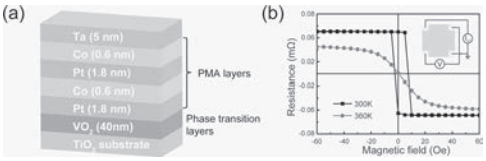
Figure 2. Out of-plane magnetic hysteresis loops for the multiferroic heterostructure with PMA measured at E=0 kV/cm and E=10 kV/cm.

BQ-04. Phase-transition-induced magnetic anisotropy change in VO_2/(Co/Pt)$_2$ heterostructure. *W. Guodong*[1], X. Lin[1], Z. Si[1] and W. Zhao[1] *1. Beihang University, Beijing, China*

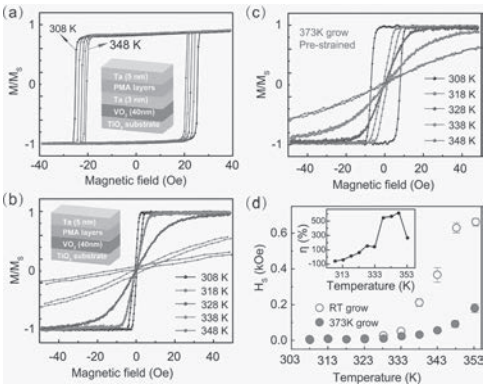
Perpendicular magnetic anisotropy (PMA) is one of the most significant technologies to be used in next generation spintronics devices as its potential in promoting thermal stability and device miniaturization. It is an important

issue to find an efficient way to modulate its property in the process of PMA application. In this work, we report the phase-transition controlled magnetic anisotropy modulation in the VO_2/(Co/Pt)$_2$ heterostructure, where VO_2 is introduced into the system to applied an interfacial strain by its metal-insulator transition. Fig.1 (a) shows the schematic drawing of the phase-transition controlled modulation of magnetic anisotropy (PCMA) heterostructure used in this work. The Hall resistance (R_{Hall}) was measured to investigate the magneto-transport properties of the PCMA film. Fig.1(b) shows the R_{Hall}-H curves of the sample at 300 K and 360 K. The difference of the curves between 300 K and 360 K shows that the phase change of VO_2 can indeed regulate PMA properties of the sample. To further investigate the magnetic modulation effect in this heterostructure, magnetization measurements were performed by MOKE. As shown in Fig. 4, only faint shrinking of coercive field can be detected in a sample with 3 nm Ta inserted between VO_2 and PMA layers. However, for the ordinary sample a significant variation of H_S is observed (Fig.4 (b)). This sharp contrast confirms that the modulation effect relies on the interface coupling between VO_2 and PMA layers. The modulation effect is further studied by a comparison between the ordinary sample and a pre-strained one which is prepared with the PMA layers deposited at 373 K. The variation of *Hs* for these two samples has been summarized in Fig.5 (d). The inset gives the difference ratio which value reaches 620%. It reflects that if the interfacial strain effect is pre-released, the modulation effect would be highly weakened. The present result is expected to provide guidelines for the improvement of the efficiency of PMA modulation and benefits the development of spintronic research.

Guodong Wei, Xiaoyang Lin, Zhizhong Si, Na Lei, Yanxue Chen, Sylvain Eimer, and Weisheng Zhao, Appl. Phys. Lett. 114, 012407 (2019)



Film preparation and characterization



PMA modulation results

BQ-05. Mechanism of Voltage-Induced Change in Magnetism of Pt/Co with HfO_2 Dielectric Layer. *T. Hirai*[1,2], T. Koyama[2,3] and D. Chiba[2,3]
1. Department of Applied Physics, The University of Tokyo, Bunkyo-ku, Japan; 2. The Institute of Scientific and Industrial Research, Osaka University, Ibaraki-shi, Japan; 3. Center for Spintronics Research Network, Ibaraki-shi, Japan

Voltage control of magnetism (VCM) in transition metal (TM) has a potential to realize ultra-low-power spin manipulation in future spintronic devices. Two mechanisms have been proposed as the origin of VCM; the modification of the electronic state by electrostatic charge doping at the TM/dielectric oxide (DO) interface[*1] and thermally-activated chemical effect in the TM layer.[*2] In this talk, we show that the quality of the DO layer determines which mechanism dominates the VCM.[*3] The DO layer quality strongly depends on its deposition temperature. This result is expected to be the key for both pursuing the underlying physics of VCM effect and expanding the possibility of the application of the field-effect spin devices. We fabricated two Pt/Co capacitor structures with the HfO_2 DO layer deposited at 150°C (sample A) and 60°C (sample B) using atomic layer deposition. The frequency-dependent phase angle (θ-*f*) measured using LCR meter for both samples are shown in Fig. 1. In sample A, θ shows -90° for a wide range of *f* as a conventional capacitor whereas the peculiar θ-*f* relation is observed in sample B, indicating that the high quality DO layer is formed in sample A. As for the VCM effect, the anomalous Hall (AH) measurement is performed under gate voltage V_G. In sample A, the change in coercivity H_c and the 2-wire resistance R (~0.02%) following to V_G change without delay can be seen (Fig. 2 (a)). This means the effect of electrostatic charge accumulation is dominant in VCM using high quality DO. On the other hand, in sample B, the modulation of R is much larger (~10%) and H_c greatly changes in the range of ~20 to 0 mT (Fig. 2 (b)). The gradual changes in R and H_c are observed even though V_G is fixed. Moreover, the values do not go back to the initial state when setting V_G = 0 V. These results indicate that the voltage-driven redox reaction is dominant in the sample with the low-quality DO. This work was partly supported by JSPS KAKENHI and Spintronics Research Network of Japan.

[*1] K. Nakamura, R. Shimabukuro, and Y. Fujiwara *et al*., *Phys. Rev. Lett.* Vol. 102, p.187201 (2009). [*2] U. Bauer, L. Yao, and A. Tan *et al*., *Nat. Mater.* Vol. 14, p. 174 (2015). [*3] T. Hirai, T. Koyama, and D. Chiba, *Appl. Phys. Lett.* Vol. 112, p. 122408 (2018).

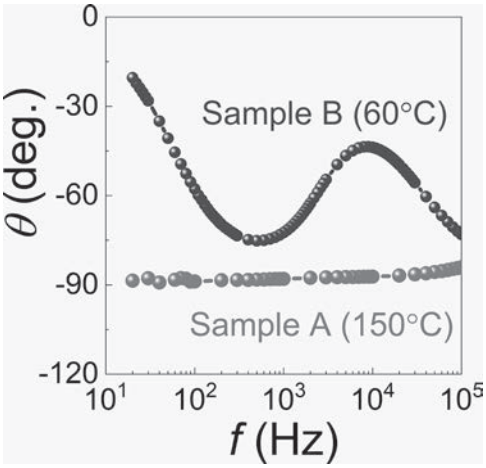


Fig.1 θ-*f* characteristic for sample A and B.

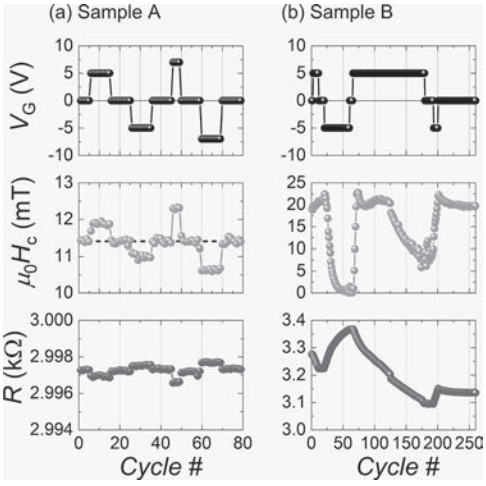
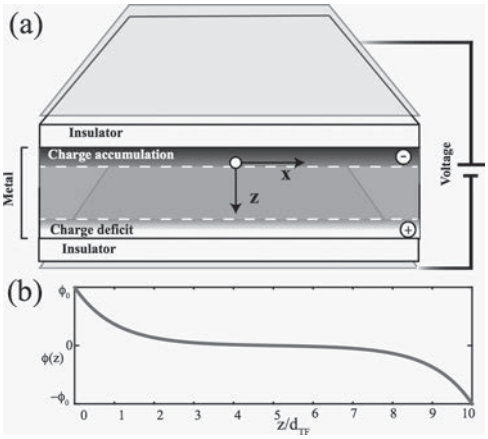


Fig.2 V_G, H_c, and R as a function of cycle for each AH measurement of (a) sample A and (b) B.

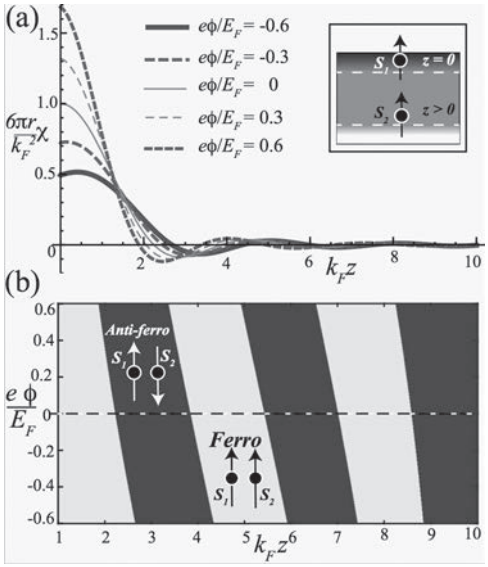
BQ-06. Voltage-Control of the RKKY Exchange. *A.O. Leon*[1], J. d'Albuquerque e Castro[2], J. Retamal[3], A. Cahaya[4] and D. Altbir[3]
1. Instituto de Fisica, Pontificia Universidad Catolica de Valparaiso, Valparaiso, Chile; 2. Instituto de Fisica, Universidade Federal do Rio de Janeiro, Rio de Janeiro, Brazil; 3. Departamento de Fisica, CEDENNA, Universidad de Santiago de Chile, USACH, Santiago, Chile; 4. Department of Physics, Universitas Indonesia, Depok, Indonesia

The electric-field-induced manipulation of magnetic systems has gained much attention in recent years. Typical examples include voltage-controlled magnetic anisotropy [1,2] and the voltage induced manipulation of exchange. In the second case, the effect of voltages applied to magnetic multilayers in insulator stacks has been studied [3-5]. However, the consequences of applying electric fields on the exchange interaction of single particles are not fully explored. The indirect exchange interaction between magnetic moments in metals is named Ruderman-Kittel-Kasuya-Yosida (RKKY). The coupling constant, known as the RKKY function, depends on the separation distance. In this work [6], we study a non-magnetic metal sandwiched by two insulators and subject to a voltage bias (see Fig. 1). One impurity is at the top interface, and we study the interaction with another impurity at a different position. We show the voltage-induced modification of both the strength and the wavenumber of the RKKY function. Figure 2(a) shows the RKKY function for two magnetic particles at opposing interfaces and Fig. 2(b) illustrates the type of coupling (Ferro- and Antiferromagnetic) for several applied fields and separation distances. As this figure illustrates, the type of coupling can be switched from Ferro- to Antiferromagnetic orders, and vice-versa, by voltages. The interaction can also be switched off. Finally, possible applications to switching dynamics are also discussed. We thank financial support from Postdoctorado FONDECYT 2019 No. 3190030, Financiamiento Basal para Centros Cientificos y Tecnologicos de Excelencia FB 0807, and Air Force Office of Scientific Research No. FA9550-18-1-0438.

[1] Y. Shiota, T. Maruyama, T. Nozaki, et al., Appl. Phys. Express 2, 063001 (2009). [2] T. Nozaki, Y. Shiota, S. Miwa, et al., Nat. Phys. 8, 491 (2012). [3] C.-Y. You, S.D. Bader, J. Magn. Magn. Mater. 195, 488 (1999). [4] M. Y. Zhuravlev, A. V. Vedyayev, and E. Y. Tsymbal, J. Phys.: Condens. Matter 22, 352203 (2010). [5] T. Newhouse-Illige, Y. Liu, M. Xu, Nat. Comm. 8, 15232 (2017). [6] A. O. Leon, J. d'Albuquerque e Castro, J. C. Retamal, et al., Accepted by Physical Review B.



Setup. (a) Two insulators sandwich a metal, and the stack is subject to a potential Φ_0 along the z-axis. (b) Potential profile $\Phi(z)$. A voltage shifts the Fermi level at the interfaces and modifies the RKKY interaction.



Electric-potential-induced change in the RKKY function along the z-axis. (a) The RKKY oscillations modify their wavelength as well as their magnitude. (b) Type of coupling (ferro- or antiferromagnetic) as a function of the voltage and the distance between impurities.

BQ-07. Electric control of exchange bias in Co/FeO$_x$ bilayer by resistive switching. L. Wei[1], R. Liu[1], Y. Yuan[1], J. Wang[1], L. Sun[1], B. You[1], W. Zhang[1], Q. Xu[2] and *J. Du*[1] *1. Department of Physics, Nanjing University, Nanjing, China; 2. School of Physics, Southeast University, Nanjing, China*

Electric control of exchange bias (EB) in ferromagnet/antiferromagnet (FM/AFM) bilayer provides a pathway for full electric control of magenetism, which is of great importance in developing energy-efficient spintronic devices. Among various mothods people used before, very recently we proposed a new way to realize non-volatile, repeatable electric control of EB at room temperature by resistive switching (RS) with an antiferromagnetic resistive layer [1]. However, this can only be operated when high-density magnetic filaments are formed/ruptured at the FM-AFM interface during the RS process. In this work, the electrol of EB has been accomplished by interface-barrier-type RS, which is much easier to be realized in comparison with the filament mechanism described in Ref. [1]. The Ti(2 nm)/Pt(50 nm)/FeO$_x$(65 nm)/Co(2.6 nm)/ITO(50 nm) multilayer device was made by magnetron sputtering on Si(100) substrate with the diameter of the top electrode of about 160 μm, as sketched in the inset of Fig. 1(a). The FeO$_x$ ($x \approx 3$) layer was made by reactive rf sputtering with $P_{Ar} : P_{O2} = 2:1$. The *I-V* curve shown in Fig. 1(a) indicate typical bipolar RS effect in the device and the on/off ratio is larger than 10^3. The in-plane magnetic hysteresis (*M-H*) loops were measured by a commercial focused MOKE with the spot size of about 100 μm. Figure 1(b) shows that the EB field (H_E) is 116 Oe and 122.5 Oe and the coercivity (H_C) is 66 Oe and 112.5 Oe at the low- and high resistance states (LRS and HRS), respectively. Therefore, compared with LRS, H_E increases a little but H_C increases significantly at HRS. All the measurements were performed at room temperature and the results repeat well. The migration of the oxygen vacancies under different voltages is considered to mediate the interfacial barrier height, leading to the bipolar RS effect and distinctly different exchange coupling as well at LRS and HRS for the FeO$_x$/Co bilayer.

[1] L. J. Wei, Z. Z. Hu, G. X. Du, Y. Yuan, J. Wang, H. Q. Tu, B. Xiao, S. M. Zhou, J. T. Qu, H. W. Liu, R. K. Zheng, Y. Hu, J. Du, Adv. Mater. 30, 1801885 (2018).

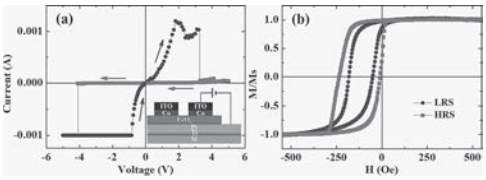


Fig.1 *I-V* curve (a) and *M-H* loops at LRS and HRS (b) for the Ti/Pt/ FeO_x/Co/ITO multilayer device.

BQ-08. Voltage-Induced High-Speed Domain Wall Motion in a Synthetic Antiferromagnet. L. Chen[1], M. Shen[1], Y. Peng[1], X. Liu[1], W. Luo[1], J. Ou-Yang[1], B. Zhu[1], S. Chen[1], L. You[1], X. Yang[1] and *Y. Zhang*[1]
1. Huazhong University of Science and Technology, Wuhan, China

Voltage-induced motion of a magnetic domain wall (DW) has potential in developing novel devices with ultralow dissipation [1, 2]. However, the speed for the voltage-induced DW motion (VIDWM) in a single ferromagnetic layer is usually very low. In this work, we proposed VIDWM with high speed in a synthetic antiferromaget (SAF) [3]. The velocity for the coupled DWs in the SAF is significantly higher than its counterpart in a single ferromagnetic layer. Strong interlayer antiferromagnetic exchange coupling plays a critical role for the high DW velocity since it inhibits the tilting of DW plane with strong Dzyaloshinskii-Moriya interaction [4]. On the other hand, the Walker breakdown of DW motion is also inhibited due to the stabilization of moment orientation under a strong interlayer antiferromagnetic coupling. In theory, the voltage-induced gradient of magnetic anisotropy is proved to be equal to an effective magnetic field that drives DW [1, 5].

1. K. Yamada, S. Murayama, and Y. Nakatani, Appl. Phys. Lett. 108, 202405 (2016). 2. W. Lin, N. Vernier, G. Agnus, K. Garcia, B. Ocker, W. Zhao, E. E. Fullerton, and D. Ravelosona, Nat. Commun. 7, 13532 (2016). 3. S.-H. Yang, K.-S. Ryu, and S. Parkin, Nat. Nanotech. 10, 221 (2015). 4. M. Shen, Y. Zhang, L. You, and X. Yang, Appl. Phys. Lett. 113, 152401 (2018). 5. Y. Zhang, S. Luo, X.Yang, and C, Yang, Sci. Rep. 7, 2047 (2017).

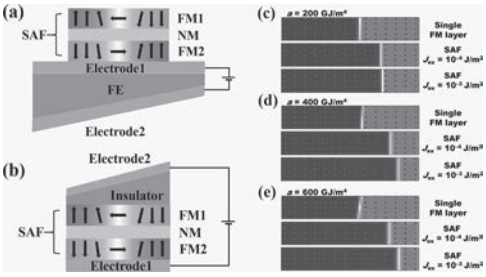


Fig. 1. Schematic of voltage-induced DW motion based on multiferroic behavior (a) and manipulation of charge state at metal/insulator interface (b); (c) - (e). DW motion under different voltage-induced gradient of magnetic anisotropy energy in a single FM layer and in the SAFs with different interlayer exchange coupling.

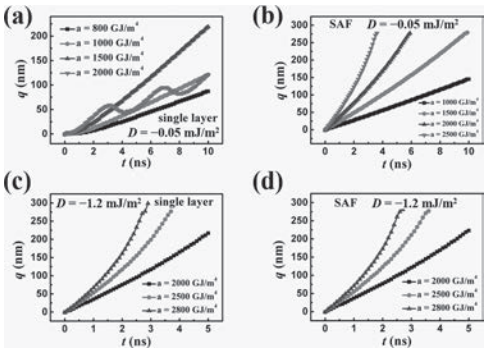
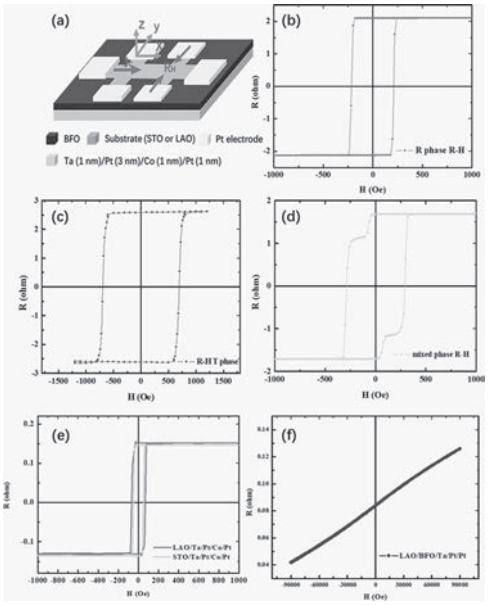


Fig. 2. Time dependence of central position of DW in a single layer for (a) D = –0.05 mJ/m² and (c) D = –1.2 mJ/m² and an SAF for (b) D = –0.05 mJ/m² and (d) D = –1.2 mJ/m² (J_{ex} = –10⁻³ J/m²).

BQ-09. Steplike anomalous Hall effect switching in mixed BFO-based heterostructure. P. Liu[1], *Y. Jiang*[1], J. Miao[1], K. Meng[1], J. Chen[1] and Z. Li[1]
1. School of Materials Science and Engineering, University of Science and Technology Beijing, Beijin, China

$BiFeO_3$ (BFO)-based heterostructure has a big potential in magnetoelectric coupling and spintronic applications. And different phases in BFO films also brings on various functionalities. [1] Therefore, the research on the combination with BFO-based heterostructure and different phases of BFO has received much attention. [2,3] In this study, the perpendicular magnetic anisotropy (PMA) is realized in BFO-based heterostructures with different phases. Figure (a) shows the schematic diagram of the Hall bar structure. The anomalous Hall effect (AHE) of R-, T- and mixed phase BFO hetero were measured in Figure (b-d). The anomalous Hall resistance of every samples exhibit good perpendicular magnetic anisotropy (PMA) in room temperature (RT). Interestingly, a steplike switching is found in the AHE of mixed-phase hetero. Referring to fig. (b) and (c), the H_c' s results of steplike signals do not correspond with the results in pure R phase and T phase. As the mixed-phase BFO is not the single superposition about pure T phase regions and R phase regions, the steplike signals in mixed-phase hetero are also not the sum of pure R phase signals and T phase signals. Some contrastive measurements are also shown in fig. (e) and (f). Considering the mixed-phase BFO can be reversibly controlled via polarization field, our results have a prospect on spintronic and memory devices.

[1] A. Spaldin and M. Fiebig, Science 2005, 309, 391-392. [2] W. Eerenstein, N. D. Mathur and J. F. Scott, Nature 2006, 442, 759-765. [3] J. Wang, J. B. Neaton, H. Zheng, V. Nagarajan, S. B. Ogale, B. Liu, D. Viehland, V. Vaithyanathan, D. G. Schlom, and U. V. Waghmare, Science 2003, 299, 1719-1722.



(a) Schematic diagram of the Hall bar structure. (b-d) AHE curve of R-phase hetero, T-phase hetero and mixed-phase hetero measured at RT. (e) AHE curves of LAO/Ta (1 nm)/Pt (3 nm)/Co (1 nm)/Pt (1 nm) and STO/Ta (1 nm)/Pt (3 nm)/Co (1 nm)/Pt (1 nm). (f) the AHE curve of LAO/BFO (mixed phase)/Ta (1 nm)/Pt (3 nm)/Pt (1 nm).

BQ-10. Theoretical Study on Voltage-Controlled Exchange Coupling via Nonmagnetic Metal Layers. *K. Ohgane*[1], Y. Yahagi[1], D. Miura[1] and A. Sakuma[1] *1. Applied Physics, Tohoku University, Sendai, Japan*

Control of the spin Seebeck diode effect (SSDE) [1] has been desired to realize magnonic logic circuits. The SSDE is the phenomenon that the amplitude of a magnon current induced by the spin Seebeck effect depends on the direction of the tempareture gradient applied on magnonic spin tunneling junctions (MSTJs), which have the structure of FI/NM/FI (FI: ferromagnetic insulator, NM: nonmagnetic layer). Recently, we showed that the SSDE strongly depends on the magnetization direction in FIs [2]. As a next step, we consider a possibility to control the SSDE electrically. In the SSDE, the presence of an exchange coupling, Jeff, between the FIs is essential because it is just the tunneling amplitude of magnons between the FIs. In this study, we aim to electrically control Jeff and to reveal its dominant factors from microscopic viewpoints. The inset in Fig. 1 is a schematic view of the MSTJ that a bias voltage, V, is applied, and the main figure shows our result for Jeff vs. V calculated on the basis of a tight-binding model for conductive electrons in NM (now we consider 2 mono-layers case, for simplicity), and we found features as follows: (1) at zero bias, the sign of Jeff depends on model parameters, (2) however, in a strong voltage range, Jeff has the positive sign in the 2 mono-layers case, that is, the magnetic coupling between FIs is ferromagnetic, (3) therefore, as shown in the case 1 of Jeff<0 at zero bias, the Jeff monotonically decreases with increasing V, (4) on the other hand, as shown in the case 2 of Jeff<0 at zero bias, the sign of the Jeff changes at a threshold voltage V0. From the above, the case 2 is very important in applications of the SSDE in the sense that the effect may be efficiently controllable by the voltage; for example, in integrated magnon circuits with many MSTJs, one can locally break a circuit by applying V0 on the MSTJ. In the conference, we will further discuss the voltage-controlled SSDE, focusing on its dependences on NM thickness and electron density.

[1] J. Ren and J. X. Zhu, Phys. Rev. B, Vol. 88, p. 094427 (2013) [2] D. Miura and A. Sakuma, J. Phys. Soc. Jpn. Vol. 87, p. 125001 (2018)

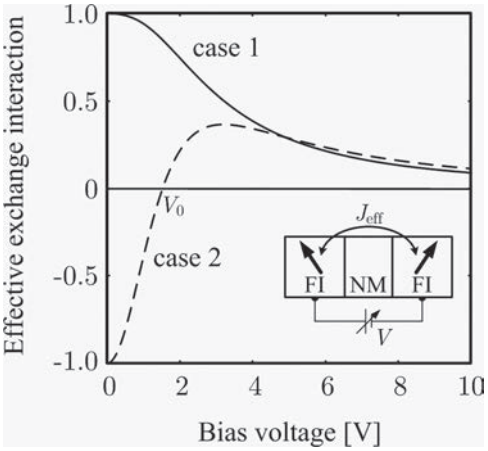
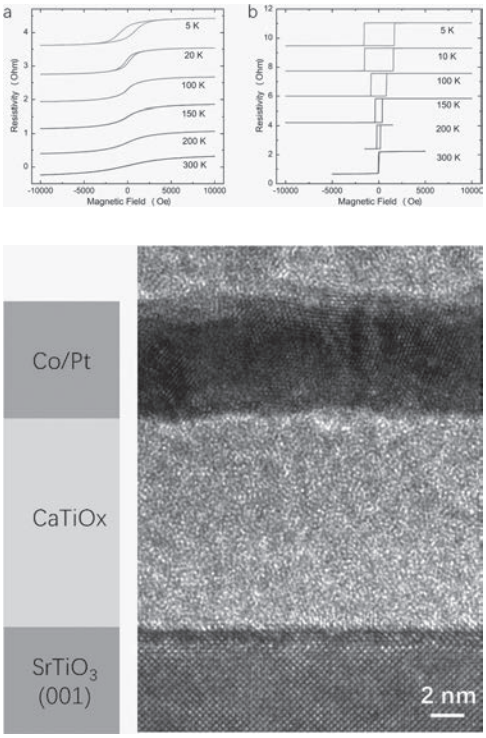


Fig. 1 The bias voltage V dependence of the effective exchange coupling Jeff, where the amplitude of Jeff is normalized at zero bias, and V0 is the threshold value giving Jeff=0. The inset shows a schmatic of voltage-biased MSTJs.

BQ-11. Improving Perpendicular Magnetic Anisotropy in $SrTiO_3$/Co/Pt Films by Inserting $CaTiO_x$ Layer. *Z. Zhang*[1], Z. Li[1], Y. Jiang[1], X. Xu[1], K. Meng[1], Y. Wu[1], J. Chen[1] and J. Miao[1] *1. university of science and technology beijing, Beijing, China*

The integration of metallic spintronic devices and multifunctional oxides with perovskite structure can induce coupling between functionalities such as ferroelectricity and the spin transport properties. However, the perpendicular magnetic anisotropy (PMA) of the magnetic films is difficult to be achieved when they are directly deposited on perovskite oxide substrates according to literature research,[1] therefore, related devices for example spin orbital torques (SOT) induced magnetization switching device cannot be realized.[2] The control of interfacial structure and oxidation state of magnetic elements by oxygen migration is effective in tailoring the magnetic properties.[3] Here, we study the effect of $CaTiO_x$ spacer on $SrTiO_3$(STO)/$CaTiO_x$/Co/Pt films and Both magnetization vs. magnetic field (M-H) and Hall resistivity vs. magnetic field (R-H), as shown in Figure 1, at different temperature are measured. It can be found that the spacer can improve the PMA of magnetic films. By varying the spacer thickness, the PMA to planar magnetic anisotropy transition temperature can also be tailored. The high resolution transmission electron microscopy (HR-TEM) image of the film suggests the $CaTiO_x$ layer is amorphous while Co/Pt layer is polycrystalline, as shown in Figure 2. The energy dispersive X-ray spectroscopy (EDS) and electron energy loss spectroscopy (EELS) in TEM are also used to study the chemical stoichiometry of the films. The X-ray photoelectron spectroscopy (XPS) indicates the Co valence state is reduced by insertion of $CaTiO_x$ between Co and $SrTiO_3$. Our results suggest the $CaTiO_x$ spacer can stabilize the metallic state of ultrathin Co and strengthen the PMA. More importantly, the $CaTiO_x$ compound is more compatible with functional perovskite oxides than other oxides such as MgO which is normally used to achieve PMA of magnetic layer, therefore, amorphous or epitaxial $CaTiO_x$ layer could serve as a good spacer layer to achieve the integration of the single crystalline perovskite functional films and metallic magnetic devices, and further tuning of spin transport properties by functionalities from perovskites, such as nonvolatile electric field modulation of SOT.

[1] Li, Y. *et al.* Manipulation of magnetization by spin-orbit torque, *Adv. Quantum Technol.* 2, 1800052 (2019). [2] Yu, G. *et al.* Switching of perpendicular magnetization by spin–orbit torques in the absence of external magnetic fields. *Nature Nanotechnol.* 9, 548-554 (2014). [3] Bauer, U. *et al.* Magneto-ionic control of interfacial magnetism. *Nature Materials* 14, 174(2015)



BQ-12. Magnetic bipolar transistor based on ZnO/NiO/Si Heterostructure using Pulsed Laser Deposition. H. Kaur[1], M. Sharma[2], R.K. Ghosh[2], S. Mohapatra[1] and *B.K. Kuanr*[2] *1. Indrapratha University, New Delhi, India; 2. Special Centre for Nanoscience, Jawaharlal Nehru University, Delhi, India*

With the advent of technology, a magnetic transistor could be the potential candidate for non-volatile data storage and improved device performance as compared to traditional transistors [1]. Transition metal oxides (TMOs) have attracted much attention due to their unique properties for new generation electronics [2]. In this work, a magnetic bipolar transistor was fabricated by growing p-NiO and n-ZnO thin films on n-type silicon wafer by pulsed laser deposition technique with in-situ annealing at 670° C in the presence of oxygen. The structural characterization of these films was done by X-ray diffraction (XRD), and Raman spectroscopy, optical properties of the deposited films were done by UV-visible spectroscopy, and magnetic properties were studied by vibrating sample magnetometer (VSM). The I-V characteristics of the fabricated transistor were tested in common emitter (CE[L1]) configuration with DC biasing. Junction parameters such as ideality factor, barrier height, series resistance, q-point, and amplification gain were determined by using conventional output characteristics. The ideality factor and barrier height for NiO/Si is calculated to be 0.056 and 0.09 eV and for ZnO/NiO is 0.202 and 0.32 eV respectively. Interestingly, the anti-ferromagnetic semiconducting nature of NiO in the presence of oxygen vacancies basically helped in spin-polarized bipolar transport in these devices [3, 4]. The diode and transistor showed a linear increase in current with the applied magnetic field and therefore the current amplification in these devices can be controlled by spin; making attractive for spintronic applications.

[1] S. Jiang, L. Li, Z.Wang, J. Shan, and K. F. Mak, 2019. Nature Electronics, 2(4), 159. [2] R. Karsthof, H. von Wenckstern, and M.Grundmann, 2015. IEEE Transactions on Electron Devices, 62(12), 3999-4003. [3] V. Verma, and M.Katiyar. 2015. J. Phys. D: Appl. Phys. 48, 235003. [4] J. Fabian, I. Zutić, and S. D. Sarma, 2004. Appl. Phys. Lett. 84, 85.

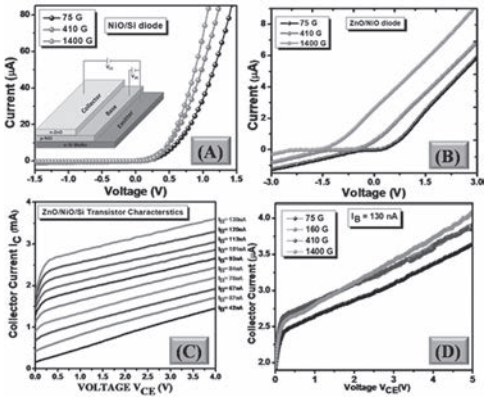


Fig.1: Diode characteristics for various applied magnetic field (A) NiO/Si (inset: schematic of a fabricated device) (B) ZnO/NiO (C) transistor characteristics of ZnO/NiO/Si at various base current (D) transistor characteristics for various magnetic field.

BQ-13. Ferroelectric polarization control of the Hall resistance in $BiFeO_3/SrRuO_3$. *Z. Ren*[1], J. Miao[1], P. Liu[1], K. Meng[1], J. Chen[1], X. Xu[1] and Y. Jiang[1] *1. School of Materials Science and Engineering, University of Science & Technology Beijing, Beijing, China*

$SrRuO_3$ (SRO) is a complex oxide perovskite with itinerant ferromagnetism, which has fascinating properties originating from the strong spin-orbit coupling.[1] Most interestingly, the temperature dependence of Hall resistance (R_{xy}) is not only nonmonotonic, but also the sign will change at a critical temperature. It can be attributed to the change of electron distributions around Fermi energy.[2] The electron distributions around Fermi energy or the Fermi level position can also be affected by ferroelectric polarization, this raises the possibility of electrically modulating the R_{xy} in SRO. The sample of $(La_{0.3}Sr_{0.7})MnO_3$ (LSMO) (10 nm)/$BiFeO_3$ (BFO) (100 nm)/SRO (20 nm) was epitaxially grown on atomically-flat $SrTiO_3$(001) substrate by pulsed laser deposition (PLD), the bottom layer of LSMO (10 nm) is as the bottom electrode. We measured the R_{xy} by sweeping the magnetic field Hex perpendicular to the sample surface from 50 K to 120 K. Fig. 1 shows temperature dependence of R_{xy}-H in SRO/BFO, it is obvious that R_{xy} is nonmonotonic. To investigate the polarization-field-induced effects on the Rxy of heterostructure BFO/SRO, the gate voltage with +/- 9V (upward/downward polarization of BFO) in the Hall bar was applied. Fig.2 shows the Rxy of initial state, oppositely switched state and reversibly switched state for heterostructures, when ferroelectric polarization is from upward to downward, decrease of R_{xy} are clearly observed. When ferroelectric polarization is switched back to the original state, R_{xy} are indeed switched back to the initial state. These results confirm that the R_{xy} are mainly modulated by the ferroelectric polarization along the out-of-plane direction. In summary, the polarization-field-induced effects on the Rxy of heterostructure BFO/SRO were investigated. We found that both the magnitude and sign of R_{xy} can be modulated by manipulating the polarization of BFO.

[1] Koster, G., Klein, L., Siemons, W., Rijnders, G., Dodge, J. S., Eom, C. B., ... and Beasley, M. R., Rev of Mod Phys,84(1), 253 (2012). [2]Fang, Z., Nagaosa, N., Takahashi, K. S., Asamitsu, A., Mathieu, R., Ogasawara, T., ... & Terakura, K, Science, 302(5642), 92-95 (2003).

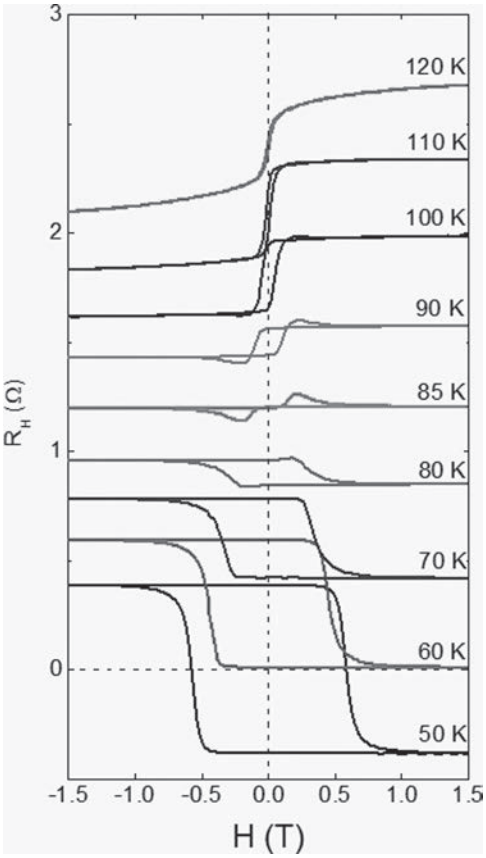


Figure 1. Temperature dependence of R_{xy}-H in BFO/SRO

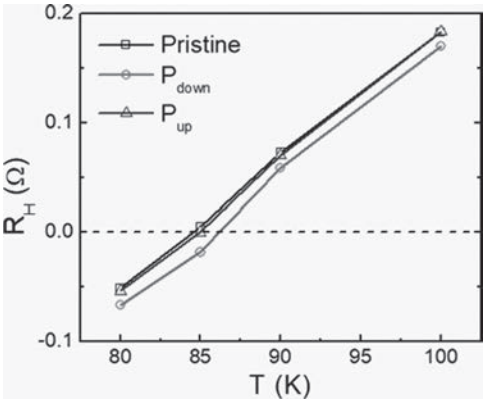


Figure 2. Temperature dependence of R_{xy} in as-grown state, oppositely switched state and reversibly switched state in BFO/SRO

BQ-14. Electric Field Manipulation of Propagating Spin Wave Properties in Ultrathin CoFeB Films. S. Choudhury[1], B. Rana[2], K. Miura[3], H. Takahashi[3], *A. De*[1], A. Barman[1] and Y. Otani[2,4] *1. S. N. Bose National Centre for Basic Sciences, Kolkata, India; 2. Center for Emergent Matter Science, RIKEN, Wako, Japan; 3. Research and Development Group, Hitachi, Ltd., Kokubunji, Japan; 4. Institute for Solid State Physics, University of Tokyo, Kashiwa, Japan*

Magneto-electric coupling enables us to control the magnetic properties of magnetic materials by voltage *i.e.* electric field which is one of the key requirements for realizing ultralow power spintronics devices. One of the most promising phenomena is the recently discovered electric field controlled magnetic anisotropy (ECMA), generally observed at the interface between 3*d*-ferromagnet (FM) and oxide [1]. Among them, the CoFeB/MgO interface has gained great attention. Generally, SW properties are modulated by charge current induced method which produces unavoidable Joule heating. However, ECMA can be used to modulate SW properties at ultralow power consumption. Here, we report an experimental study on the modulation of propagating SW frequency in ultrathin $Co_{20}Fe_{60}B_{20}$ (CoFeB) films by tuning interfacial perpendicular magnetic anisotropy (iPMA) by an electric field applied through a top metal gate electrode. The devices were fabricated by a combination of UV-maskless photolithography and electron beam lithography from heterostructures: Ta(10nm)|CoFeB(t = 1.6, 1.8, 2.0 nm)|MgO(2nm)|Al_2O_3(10nm), deposited on Si/SiO_2 substrate by rf magnetron sputtering [2]. The SW signals are detected by measuring inverse spin Hall effect voltage (V_{ISHE}) across the Ta layer underneath CoFeB films (Fig. 1(a)). Figure 1(b) shows a typical SW signal measured as a function of frequency for 2 nm-thick CoFeB film at $\mu_0 H_{ext}$ = 160 mT. To modulate SW frequency, a dc gate voltage is applied from a voltage source. Figure 1(b) shows that the resonance frequency either decreases or increases under the application of negative or positive gate voltages due to the increment or decrement of iPMA with negative or positive gate voltages. We have also measured SW signals from other lower thicknesses of CoFeB films and observed significant modulation of SW frequency with gate voltage (V_{DC}) due to the higher magneto-electric coefficient.

[1] T. Maruyama, Y. Shiota, T. Nozaki, K. Ohta, N. Toda, M. Mizuguchi, A. A. Tulapurkar, T. Shinjo, M. Shiraishi, S. Mizukami, K. Ando, Y. Suzuki, Nat. Nanotechnol., 4, 158 (2009). [2] B. Rana, Y. Fukuma, K. Miura, H. Takahashi, Y. Otani, Appl. Phys. Lett., 111, 052404 (2017).

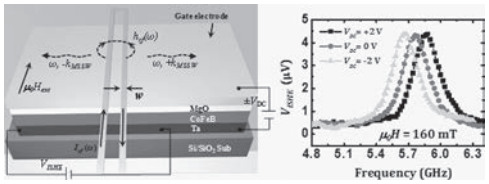


Figure 1. (a) Schematic of the electric field-controlled SW device. (b) Inverse spin Hall signal (V_{ISHE}) obtained from the device with CoFeB thickness of 2.0 nm using the nanoscale antenna of width w = 600 nm under the application of different dc voltage (V_{DC}) at bias magnetic field $\mu_0 H_{ext}$ = 160 mT.

BQ-15. High-speed write error rate evaluation of a voltage-torque magnetic random access memory cell. *S. Tamaru*[1], T. Yamamoto[1], T. Nozaki[1] and S. Yuasa[1] *1. Spintronics Research Center, National Institute of Advanced Industrial Science and Technology (AIST), Tsukuba, Japan*

Voltage-torque magnetic random access memory (VT-MRAM) based on a magnetic tunnel junction (MTJ) is a promising candidate for the next generation solid state memory. In VT-MRAM, the free layer magnetization is toggled by applying a short voltage pulse to the MTJ cell to excite coherent precession over half cycle[1]. The resistance of a VT-MRAM cell is very high, typically of the order of 100 kΩ. These properties result in very fast and low power write operations. However, they adversely affect the read speed. Therefore, the maximum write error rate (WER) evaluation speed in the conventional system is about 4 kbps, which is too slow because the WER has to be lower than 10^{-10} for practical applications[2]. To overcome this problem, we developed a high-speed WER evaluation system, whose block diagram is shown in Figure 1[3]. In the new system, a high-speed semiconductor analog switch (SW) switches the connection to the MTJ cell between the read and write channels, and a custom amplifier/comparator circuit is directly connected to the SW to detect the magnetization state of the MTJ cell with a minimum time constant. Figure 2 shows the waveform of the amplifier output observed when the WER is evaluated at 500 kbps. During the write cycle, the waveform stays 0 V. When the system transitions from the write to the read cycle, the waveform first discontinuously jumps due to charge injection of the SW, then converges to either high or low level depending on the magnetization state of the MTJ cell. The figure shows that the waveform has a large enough read window at the end of the read cycle.

This result confirms that it can actually evaluate the WER at 500 kbps, which is 2 orders of magnitude faster than the conventional system. In the presentation, the detail of the WER evaluation system, including the design guideline, the factors limiting the WER evaluation speed and some strategies for further enhancing the speed.

1) Y. Shiota, et al., Nat. Mater. Vol 11, p39 (2012). 2) T. Yamamoto, et al., J. Phys. D Vol 52, p164001 (2019). 3) S. Tamaru, et al., Jpn. J. Appl. Phys. Vol 58, p060905 (2019).

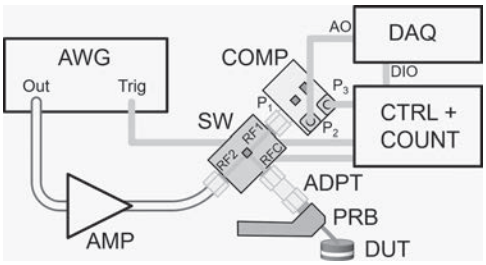


Fig. 1, Block diagram of a high-speed WER evaluation system developed in this work.

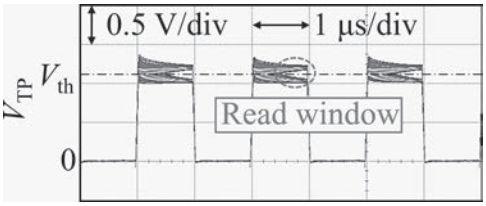


Fig. 2, Waveform at the amplifer output when the system is evaluating the WER at 500 kbps.

BQ-16. Voltage-induced switching with long tolerance of voltage-pulse duration in a perpendicular MRAM. *R. Matsumoto*[1], T. Sato[1,2] and H. Imamura[1] *1. Spintronics Research Center, National Institute of Advanced Industrial Science and Technology (AIST), Tsukuba, Japan; 2. Department of Electrical and Electronic Engineering, Faculty of Engineering, Chiba Institute of Technology, Narashino, Japan*

Voltage-induced magnetization switching [1-5] has been attracting a great deal of attention because it enables low-power-consumption writing in magnetoresistive random access memory (MRAM), but this writing method requires the adjustment of the voltage-pulse duration (t_p) to obtain low write error rate (WER). The range of t_p where WER is below 1×10^{-3} has been only several hundred picoseconds [4, 5]. We call this range of t_p as the tolerance of t_p just for convenience. The long tolerance of t_p is desirable because of the distribution of t_p from pulsed power supply in MRAMs and the distribution of precession periods among the MRAM cells. In this study [6], we theoretically investigate the voltage-induced magnetization switching with the long tolerance of t_p [1] in a perpendicular MRAM cell shown in Fig. 1(a). Before and after the voltage pulse, the free layer is relaxed at $K_{eff}^{(pre)}$ = 70 kJ/m^3 and $K_{eff}^{(post)}$ = 40 kJ/m^3. Here K_{eff} is the effective perpendicular anisotropy constant including the demagnetization energy and $K_{eff}^{(+V)}$ in Fig. 1 represents K_{eff} during t_p. In Fig. 1(b), types of the magnetization dynamics at 0 K are classified in $K_{eff}^{(+V)}$ – the Gilbert damping (α) space. Between the two solid curves, the switching with the long tolerance of t_p is available by utilizing the damping torque. Even under thermal agitation at 300 K, WER lower than 10^{-3} is obtained in 0.5 ns ≤ t_p ≤ 10 ns (see Fig. 1(c)). The tolerance of t_p is much longer than 1 ns. We will also show that WER can be reduced by increasing the external magnetic field (H_{ext}) and/or decreasing θ (see Fig. 1(a)) with increasing $K_{eff}^{(pre)}$. This work was partly supported by the ImPACT Program of the Council for Science, Technology and Innovation, and JSPS KAKENHI Grant No. JP16K17509.

[1] Y. Shiota *et al*., Nat. Mater., Vol. 11, p. 39 (2012). [2] S. Kanai *et al*., Appl. Phys. Lett., Vol. 101, p. 122403 (2012). [3] C. Grezes *et al*., Appl. Phys. Lett., Vol. 108, p. 012403 (2016). [4] Y. Shiota *et al*., Appl. Phys. Express, Vol. 9, p. 013001 (2016). [5] T. Yamamoto *et al*., J. Phys. D: Appl. Phys., Vol. 52, p. 164001 (2019). [6] R. Matsumoto *et al*., Appl. Phys. Express, Vol. 12, p. 053003 (2019).

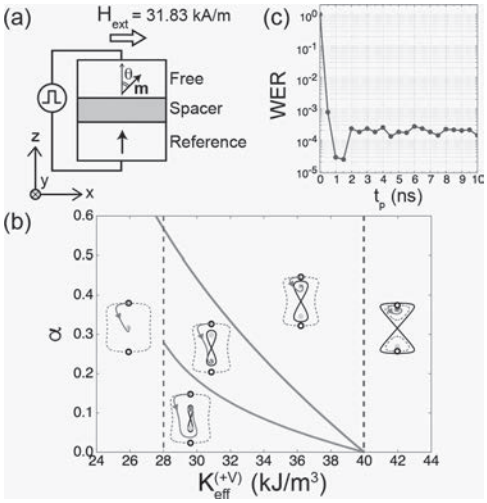


Fig. 1 (a) MRAM and definitions of (*x, y, z*) and θ. (b) Types of magnetization dynamics. In each schematic illustration, curve with triangle represents trajectory of magnetization (*m*) during t_p viewed from +*x* direction, and open and solid circles represent equilibrium directions of *m* at $K_{eff}^{(pre)}$ and $K_{eff}^{(+V)}$. (c) t_p dependence of WER at 300 K. In Langevin simulation, $K_{eff}^{(+V)}$ = 33 kJ/m^3, α = 0.17 and the volume of the free layer is 140^{2}π×2 nm^3.

BQ-17. Voltage assisted magnetization switching in ferromagnetic (Ga,Mn)N. *D. Sztenkiel*[1], K. Gas[1,2], M. Foltyn[1], N. Gonzalez Szwacki[3], D. Hommel[2,4], T. Dietl[5,6] and M. Sawicki[1] *1. Institute of Physics, Polish Academy of Sciences, Warszawa, Poland; 2. Institute of Experimental Physics, University of Wroclaw, Wroclaw, Poland; 3. Institute of Theoretical Physics, University of Warsaw, Warszawa, Poland; 4. PORT Polish Centre for Technology Development, Wroclaw, Poland; 5. International Research Centre MagTop, Polish Academy of Sciences, Warszawa, Poland; 6. WPI-Advanced Institute for Materials Research, Tohoku University, Sendai, Japan*

Switching of magnetization direction between two stable states separated by an energy barrier is one of the most important processes for magnetic recording and information storage [1]. This is conventionally done by applying an external magnetic field or spin polarized currents. One way to reduce the energy required for magnetization switching while maintaining sufficiently high magnetic anisotropy energy is to control the magnetization direction by other means than the external magnetic field or charge current. An electric field-control of magnetic anisotropy is a promising candidate. We anticipate that this can be accomplished in (Ga,Mn)N-based structures, in which the magnitude and the sign of magnetic anisotropy can be changed by appropriate material engineering and by an electric field. Recently, we have shown that a strong coupling between piezoelectricity and magnetism exists in paramagnetic $Ga_{1-x}Mn_xN$ with x = 0.025 [2]. In these piezoelectric systems a voltage V applied across the crystal strains it linearly. This in turn deforms the crystal field which surrounds the magnetic ions and so modifies their magnetic anisotropy. Now, by using molecular beam epitaxy grown structures we investigate the magnetoelectric effect at $T \geq 2$ K in the ferromagnetic state. We observe an electric field-induced decrease of coercivity, shown in the Fig. 1, and a non-reversible magnetization switching for magnetic fields close to the coercive field (not shown). The work is supported by the National Science Centre, Poland, through projects DEC-2018/31/B/ST3/03438, DEC-2011/02/A/ST3/00125, DEC-2016/23/B/ST3/03575

and DEC-2014/12/S/ST3/00549. We also acknowledge the access to the computing facilities of the Interdisciplinary Centre for Mathematical and Computational Modelling at the University of Warsaw.

[1] D. Chiba, *et al.*, Appl. Phys. Lett., Vol. 103, p. 142418 (2013)
[2] D. Sztenkiel *et al.*, Nature Comm., Vol. 7, p. 13232 (2016)

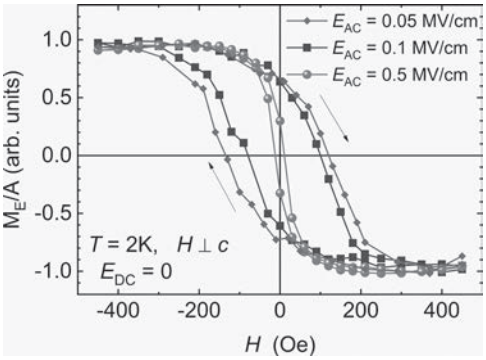


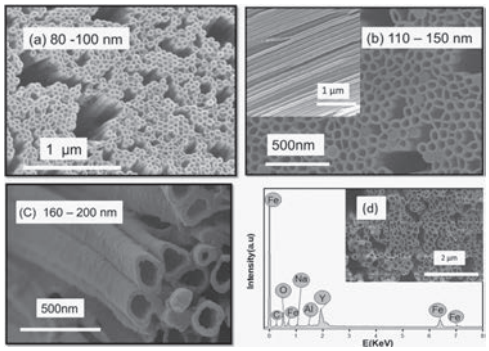
Fig. 1. Magnetic field H dependence of the normalized amplitude of the sample's magnetic moment induced by an acoustic-frequency sinusoidal electric field E_{AC} at T = 2 K measured along the magnetic easy axis.

Session BR
FERRITES
(Poster Session)

Pilar Marin, Chair
Universidad Complutense de Madrid, Madrid, Spain

BR-01. Fabrication and characterization of YIG nanotubes. X. Zhang[1], S. Parajuli[1], J. Feng[1], G. Yu[1] and *X. Han[1] 1. Chinese Academy of Science, Instite of Physics, Beijing, China*

We have successfully synthesized Y3Fe5O12 (yttrium iron garnet, YIG) nanotubes (NTs) of different diameters using a conventional sol-gel method in anodized aluminum oxide (AAO) templates. An annealing process at 800 °C is performed to get a pure phase of YIG. The room-temperature magnetization measurements show that the coercivity decreases significantly as the diameter of nanotubes increases. The temperature dependence of magnetic moments in field-cooled (FC) and zero-field-cooled (ZFC) modes indicates that YIG NTs transform from ferromagnetic-like (FM-like) state to superparamagnetic (SPM) state when temperature decreases (in the region of 310 K–400 K). The Blocking temperature dramatically decreases as the size of YIG NTs reduces. In the FM-like state, the temperature-dependent coercivity in three different samples yields a 1/2 power law of the temperature. The temperature dependence of saturation magnetization in three different samples can be well fitted to Bloch's T3/2 law. Characterization of ferromagnetic resonance (FMR) is conducted, which indicates the Gilbert damping parameter of YIG NTs is around $7\sim9 \times 10^{-3}$.



BR-02. The effect of gadolinium substitution in inverse spinel Nickel Ferrite: structural, magnetic, and mossbauer study. *T.P. Poudel*[1], B.K. Rai[2], S. Yoon[3], D. Neupane[1], D. Guragain[1] and S.R. Mishra[1]
1. Department of Physics and Material Science, University of Memphis, Memphis, TN, United States; 2. Oak Ridge National Laboratory, Oak Ridge, TN, United States; 3. Gunsan National University, Gunsan, The Republic of Korea

Nickel ferrite is an inverse spinel ferrite with nickel ions located at the B site the iron ions at both A and B sites. $NiFe_2O_4$ is regarded as a superior candidate for microwave devices and sensor application because of high resistivity and intermediate magnetization. Any change in cationic distribution can alter their cationic distribution, and hence, one can achieve the required change in magnetic and dielectric properties. Doping the parent spinel ferrite with rare-earth ions leads to structural disorder and lattice strain, thereby enhancing the electrical and magnetic parameters. The rare-earth element, Gadolinium, doped $NiGd_xFe_{2-x}O_4$ ($0<x<0.1$) materials were synthesized using the sol-gel route. X-ray diffraction analysis (XRD) showed that the specimens exhibited a single-phase spinel structure up to $x = 0.1$. The lattice parameter and induced strain increased with an increase in the Gd^{3+} content. The magnetic parameters derived from hysteresis loops show a decrease in saturation magnetization (Ms) and coercivity (Hc) value with Gd^{3+} substitution and reaching a minimum value of Ms ~ 39 emu/g and Hc ~ 110 kOe at $x = 0.1$. The magnetocrystalline anisotropy, as determined from the Law of Approach to saturation magnetization, is observed to be highest for $x = 0.1$ at 5K with the value $K1 \sim 1.53 \times 10^6$ J/m^3. The Curie temperature decreased to 898 K at $x = 0.1$ from 918 for $x = 0.0$. Hyperfine parameters were derived from fitting Mössbauer spectra. The Mossbauer spectral analysis indicated that iron was in the Fe^{3+} state, the magnetic hyperfine field at both the sites tended to decrease, and isomer shift of B site increased while that of A site remained invariant with an increase in the Gd^{3+} content. Furthermore, migration of Ni^{2+} from B site to A site was observed with the increase in the Gd^{3+} occupancy at the B site in the sample. The structural, magnetic, and Mossbauer results are elucidated by the occupancy of Gd^{3+} at the octahedral (B) site in the inverse spinel $NiFe_2O_4$ ferrite. Our study suggests that with the judicious Gd^{3+} doping in Ni-ferrite, soft ferrite properties can be enhanced for potential application in radio and microwave range application.

BR-03. Enhanced magnetic and magnetodielectric properties of Al-doped gallium ferrite nanoparticles. *T. Han*[1], Z. Tu[1] and Y. Huang[1]
1. Department of Applied Physics, National University of Kaohsiung, Kaohsiung, Taiwan

Gallium ferrite, $GaFeO_3$ (GFO), has ferrimagnetic (FM) and piezoelectric orderings and has been intensively studied recently for its potential application as a magnetoelectric ferrimagnet [1]. Site-disorder in bulk GFO is reported to be induced by adopting different preparation methods, which are shown to affect the magnetic properties significantly [1-3]. Moreover, the physical properties of GFO at reduced grain sizes remain underexplored due to the challenges associated with their synthesis with a proper control over the crystalline phase. In addition, the origin of the doping effects on the correlation between the site-disorder and magnetism in the nanosized GFO system has not yet been completely established. Therefore, it is worthy to explore the possibility of tuning the magnetic properties of doped GFO nanoparticles. In this work, we prepare a series of $Ga_{1-x}Al_xFeO_3$ (GAFx) ($0 \le x \le 0.5$) nanoparticles by the sol-gel method to systematically study the effect of Al-doping on their structural, magnetic, and magnetodielectric (MD) properties. The X-ray diffraction pattern analysis indicated that all samples have an orthorhombic structure with $Pc2_1n$ space group. Al substitutions slightly modify lattice parameters and induce lattice distortion within the same crystalline structure. The average grain sizes of the GAFx nanoparticles are around 28 nm. Interestingly, the magnetic characterization indicates that with increasing Al-content, up to 0.5, the FM transition temperature (T_C) increases from 310 to 350 K. The magnetization has been enhanced due to doping of Al^{3+} in GFO compared to that of the pristine sample. The cause of magnetic enhancement could be explained from the modification exchange interaction due to the substitution of smaller size cations of Al^{3+} in place of relatively larger size cations of Ga^{3+}. The dielectric constant of each GAFx sample is strongly perturbed by the external magnetic field. It is to be noted that the value of MD increases in the Al-doped samples for different applied magnetic fields. Furthermore, the simultaneous improvement of magnetic behavior and MD coupling effect in Al-doped GFO are prominent candidates for the applications of room temperature multiferroic devices.

[1]. T. Arima, D. Higashiyama, Y. Kaneko, J. P. He, T. Goto, S. Miyasaka, T. Kimura, K. Oikawa, T. Kamiyama, R. Kumai, and Y. Tokura, Phys. Rev.

B 70, 064426 (2004). [2]. M. B. Mohamed, A. Senyshyn, H. Ehrenberg, and H. Fuess, J. Alloys Compd. 492, L20 (2010). [3]. K. Sharma, V. R. Reddy, D. Kothari, A. Gupta, A. Banerjee, and V. G. Sathe, J. Phys.: Condens. Matter 22, 146005 (2010).

BR-04. Tailoring of Magnetic Spectra of Magneto-Dielectric Composites by Grain and Particle-Size Distributions of Ferrite Inclusions. *Q. Li*[1], Y. Chen[2] and V. Harris[1] *1. Department of Electrical and Computer Engineering, Northeastern University, Boston, MA, United States; 2. Innovation Center, Rogers Corporation, Burlington, MA, United States*

Magneto-dielectric composites, in the form of magnetic particles dispersed in an electrically insulating matrix, are promising candidate materials for high frequency applications, such as VHF up to 5G wireless communications.[1] Such magneto-dielectric materials require particularly high permeability and low magnetic loss, which are closely related to both the grain size and the particle size of the magnetic fillers.[2,3] This work reports an extended effective medium theory (EMT) including the grain-size distribution and the particle-size distribution to predict the magnetic spectra of magneto-dielectric composites. Starting with solving the frequency response of domain wall motion, the grain-size dependent dynamic susceptibility of a ferrite grain is derived.[4,5] Figure 1 shows the theoretical permeability spectra of Co-Ti substituted M-type barium ferrites with grain sizes of 5, 10 and 15 μm, respectively. Then, the permeability spectrum of the polycrystalline ferrite is calculated from a model of crystalline ferrite grains with a certain size distribution surrounded by thin, non-magnetic grain boundaries. The effective permeability of the magneto-dielectric composite is finally obtained from the extended EMT formula considering the particle-size distribution of ferrite inclusions. The proposed EMT formula is experimentally verified by the measured permeability spectra of Co-Ti substituted M-type barium ferrite ($BaCo_{1.15}Ti_{1.15}Fe_{9.7}O_{19}$)/paraffin composites prepared by the conventional ceramic process with specifically designed grain-size and particle-size distributions. Taking the grain-size dependent intrinsic permeability into consideration, the modified EMT formula describes a more accurate model to predict the effective permeability of magneto-dielectric composites filled with polycrystalline ferrite particles over a wide frequency range. It also provides an effective tool to optimize the magnetic properties of magneto-dielectric composites by tailoring both the grain-size and the particle-size distributions of the ferrite inclusions in various polymer matrices.

[1] V. G. Harris, A. Geiler, Y. Chen *et al*., J. Magn. Magn. Mater., Vol. 321, p. 2035 (2009). [2] Q. Li, Y. Chen, and V.G. Harris, J. Magn. Magn. Mater., Vol. 453, p. 44 (2018). [3] Q. Li, Y. Chen, and V.G. Harris, J. Appl. Phys., Vol. 125, p. 185107 (2019). [4] A. Globus, P. Duplex, and M. Guyot, IEEE Trans. Magn., Vol. 7, p. 617 (1971). [5] B. K. Das and P. Chaudhari, J. Mater. Sci., Vol. 13, p. 84 (1978).

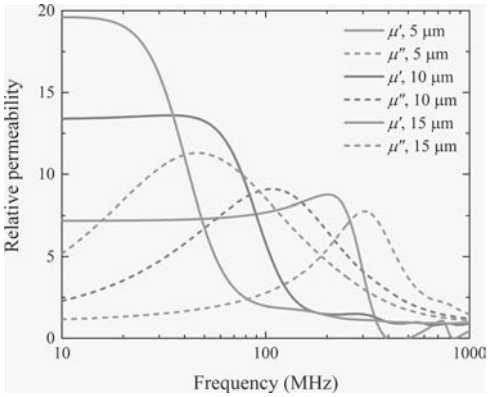


Fig. 1. Permeability spectra of Co-Ti substitueted M-type barium ferrites with different grain sizes.

BR-05. Impedance Engineered Ultra-High Frequeny Low-Loss Co_2Z Ferrite Composites for Broadband RF Applications. *P. Kulik*[1], G. Winter[1], K. Murphy[1], J. Adams[1], O. Obi[2] and V. Harris[1] *1. ECE, Northeastern University, Boston, MA, United States; 2. Kostas Research Institute at Northeastern University, Burlington, MA, United States*

The demand for miniaturized and high performing broadband communication systems in the GHz frequency range is steadily growing due to severely crowded and rapidly changing modern commercial and military spectral environments. Hexaferrite composites have proven to be one of the few key enablers in providing miniaturized form factors due to their high permeability and permittivity as well as their capability to reach high resonance frequencies up to 100 GHz [1]. In this work, we demonstrate a broadband and low loss ferrite composite engineered for equivalent permittivity and permeability at 0.2-1.2 GHz. For the first time in $\mu = \varepsilon$ engineered Co_2Z hexaferrites, single domain grains are controlled to less than 1 μm allowing reduction in losses. Additionally, co-polymers of isobutylene and maleic anhydride (ISOBAM) were employed to achieve theoretical densities (~5.37 g/cm^3, Co_2Z ferrite [2]). Polycrystalline Co_2Z ferrites, having a nominal composition of $Ba_3Co_{2+X}Ir_XFe_{24-2X}O_{41}$, where x=0 to x=.1, were prepared by a solid-state process. $BaCo_3$, IrO_2, Co_3O_4, and Fe_2O_3 of high purity were mixed and calcined in oxygen for 5-8 hours at 900-1000 °C, which then were ball milled for 18-24 hours to reduce the grain size to under 1 μm. The grain size was measured by scanning electron microscope as shown in Fig. 1. After ball-milling, ISOBAM was added as a binder and mixed for several minutes. Samples were then pressed to form toroids with an inner diameter of 3 mm and an outer diameter of 7 mm. The toroids were pressed by a cold isostatic press in order to maximize compaction before sintering in oxygen for 4-6 hours at 1000-1250 °C. Finally, samples were measured using the Agilent E864A PNA and a 7 mm precision airline. Samples showed a density of 5.36 g cm^{-3} which is 99% of the theoretical density. Low magnetic loss tangents were achieved as shown in Fig. 2. These results show that a nine-time reduction in size can be achieved while maintaining an impedance of 360 Ω close to that of free space over a broadband.

[1] S.B.S Magham, et al., J. Magn. Magn. Mater., vol. 441, pp. 303–309 (2017). [2] Pullar., Progress in Materials Science., vol. 57, pp.1191-1334(2012).

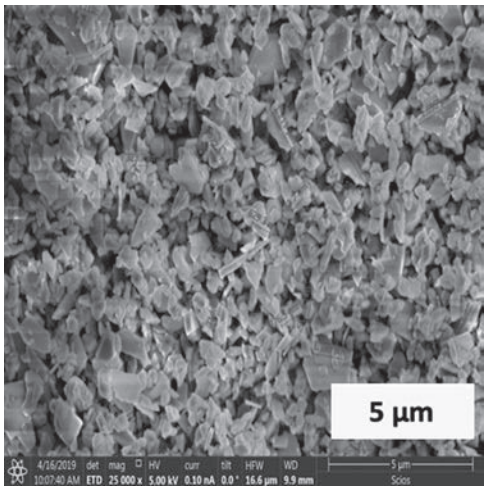


Fig.1

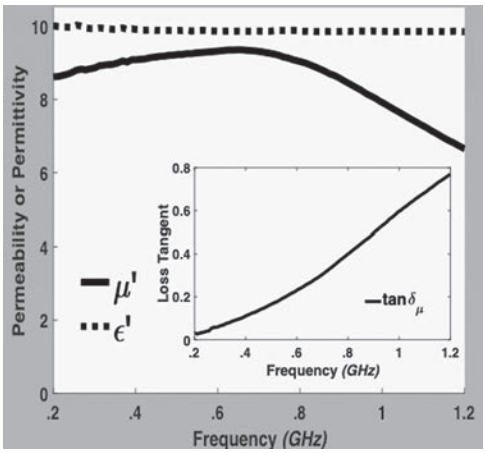


Fig.2

BR-06. Epitaxial magnesium aluminum ferrite films grown by magnetron sputtering. *M. Mishner*[1], A. Jara[1] and I. Krivorotov[1] *1. Physics and Astronomy, University of California, Irvine, Irvine, CA, United States*

Thin films of magnetic insulators are extensively used in nano-magnonics and spin caloritronics. Up to date, most research efforts in these fields employ films of yttrium iron garnet (YIG). While much progress has been made using YIG-based devices, YIG is not ideally suited for patterned magnonic crystals due to its low saturation magnetization, which results in weak dipolar interactions among individual nanomagnets of the crystal. Therefore, epitaxial films of magnetic insulators with high saturation magnetization and low damping are highly desirable. Recently, growth of thin films of magnesium aluminum spinel ferrite $MgAl_{0.5}Fe_{1.5}O_4$ (MAF) with high saturation magnetization and low damping by pulsed laser deposition was reported [1]. Here we have developed a method for growth of epitaxial thin films of MAF by radio-frequency magnetron sputtering. MAF films were deposited onto lattice-matched (001)-oriented $MgAl_2O_4$ substrates from a stoichiometric target in a mixture of Ar and O_2 gases. We varied the partial pressures of O_2 and the substrate temperature to optimize epitaxial growth of the MAF films. At the substrate temperature of 550°C, high quality epitaxial growth is achieved as evidenced by the appearance of strong Laue oscillations in θ-2θ X-ray diffraction scans and rocking curve full-width-at-half-maximums of 0.04° for an 18 nm thick MAF film as shown in Fig. 1. Ferromagnetic resonance measurements made as a function of magnetic field angle in the film plane reveal high effective saturation magnetization $4\pi M_{eff}$ = 15.2 kOe, g = 2.01 ± 0.04 and an in-plane cubic anisotropy field of H_a = 933 Oe. A g-factor near 2.0 verifies that the films show minimal spin-orbit coupling needed to achieve low magnetic damping. We will discuss the dependence of Gilbert damping parameter on the film growth conditions and post-annealing treatment.

[1] S. Emori *et. al.*, Nano Lett., 18(7), p. 4273-4278 (2018)

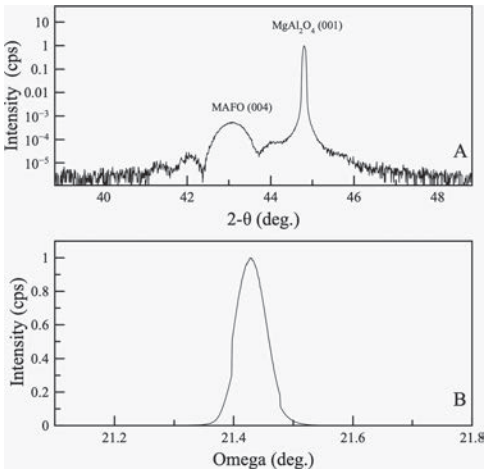


Fig. 1. (a) X-ray diffraction θ-2θ scan and (b) rocking curve of 18 nm thick MAF film grown on $MgAl_2O_4$ (001) via RF sputtering.

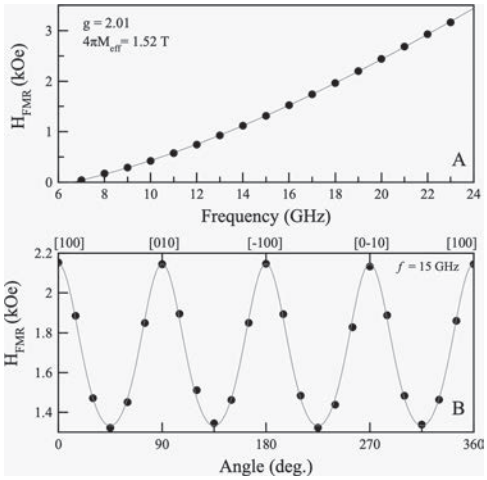


Fig. 2. In-plane ferromagnetic resonance field as a function of (a) frequency and (b) in-plane magnetic field direction for an 18 nm thick epitaxial MAF film.

BR-07. Di-valent doping effect on structural and magnetic properties of nanocrystalline $Pr_{0.7}Ba_{0.2}Sr_{0.1}MnO_3$. *M. .*[1], A. Gaur[1] and R.N. Mahato[1] *1. School of Physical Sciences, Jawaharlal Nehru University, New Delhi, India*

Nowadays, magnetic refrigeration (MR) technology is considered as an alternative to the conventional vapor pressure cycle, due to its environmental-friendly nature and higher cooling efficiency [1]. The basic principle of the magnetic refrigeration technology is the magnetocaloric effect which can be defined as the change in entropy of a magnetic material on applying the magnetic field. The magnetocaloric effect (MCE) is characterized mainly by the isothermal magnetic entropy change (ΔS_M) and the relative cooling power (RCP). Thus, it is of great importance to search the magnetic materials which can possibly exhibit large values of magnetic entropy changes close to the room temperature at lower applied fields. In the present work, we have synthesized the nanocrystalline $Pr_{0.7}Ba_{0.2}Ca_{0.1}MnO_3$ sample using the sol-gel method. The Rietveld refinement of the X-ray diffraction (XRD) pattern (recorded at room temperature) confirmed the formation of the rhombohedral crystal structure with space group. The temperature dependent magnetization M(T) measurements suggested that the sample undergo paramagnetic to ferromagnetic phase transition and the Curie temperature was found to be ~ 128 K and M(T) plot is shown in Fig. 1. The field dependence of magnetization M(H) data at 2 K showed the formation of hysteresis loop which

indicates the presence of ferromagnetism in the sample at lower temperatures and the linear behavior of M(H) at 300 K confirms the paramagnetic nature of the sample at room temperature. The slopes of the Arrott plots for the present sample are positive indicating the second order of magnetic phase transition, as per the Banerjee criterion [2]. The maximum value of magnetic entropy change and relative cooling power (RCP) were found to be ~2.3 J $kg^{-1}K^{-1}$ and 230 Jkg^{-1} for a field change of 5 T. The relatively large values of $|\Delta S_M|$ and RCP make the present compound promising for magnetic refrigeration technology.

[1] I. Hussain, S. N. Khan, E. J. Kim, S. E. Jeon, and B. H. Koo, Ceram. Int. 44, 2892 (2018). [2] S.K. Banerjee, Phys. Rev. Lett. 12, 1 (1964).

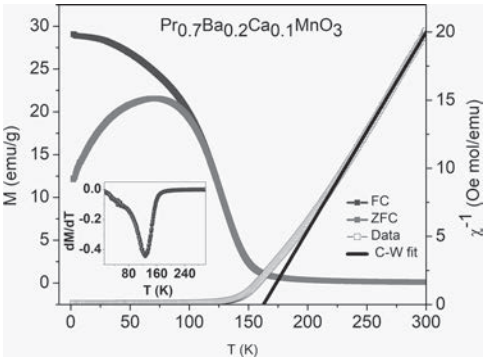


Fig. 1 Temperature dependence magnetization for nanocrystalline $Pr_{0.7}Ba_{0.2}Ca_{0.1}MnO_3$ sample at an applied magnetic field of 500 Oe and the corresponding Curie-Weiss fit. The insets show the derivative plot (dM/dT vs. T).

BR-08. Tunable high-frequency magnetic and dielectric properties of NiZnCo ferrite/resin magneto-dielectric composites. *Z. Zheng*[1], Z. Xiong[1], X. Wu[1] and Q. Feng[1] *1. School of Information Science and Technology, Southwest Jiaotong University, Chengdu, China*

Nowadays, as the rapid development of electronic and communication technology, the various devices are developing towards miniaturization and lightweight, especially the devices with small size and high performance are ever increasingly demanded. A challenge in this process is that the reduced size of device often produces performance degradation due to the fact that the performance of many devices is dependent on their size. In recent years, magneto-dielectric ferrite materials have received considerable attention and show unique advantage for miniaturized and high-performance radio frequency (RF) and microwave devices, such as in the applications of antennas, EBG structures, LC filters, oscillators, magnetic sensors, etc. In this work, a series of magneto-dielectric composite materials that consist of NiZnCo ($Ni_{0.5}Zn_{0.3}Co_{0.2}Fe_2O_4$) spinel ferrites and low-loss resin (weight ratio x = 0, 2, 4 and 6 wt% respectively) are synthesized for their potential applications as novel high-frequency magneto-dielectric materials. The magnetic and dielectric properties of the samples are investigated over a wide frequency range of 0.1–5 GHz. It is revealed that the permeability and permittivity are significantly tunable through the variation of composite ratio. With increasing x from 0 to 6 wt%, μ′ and permittivity ε′ are varied in the range of about 2.0~6.5 and 5.0~8.5 respectively. These variations are carefully analyzed based on the magnetic circuit model and effective medium theory. Correspondingly, the magnetic losses and impedance performances are effectively modulated. The microstructure and densification of the composite samples are also analyzed in detail to correlate with the variations of the magnetic and dielectric properties.

[1]Z. Zheng, et al, J. Appl. Phys. 121 063901 (2017). [2]Z. Zheng, et al, IEEE Trans. Magn. 54 18191621 (2018). [3]V. G. Harris, IEEE Trans. Magn., 48, 1075–1104, (2012). [4]Z. Su, et al, Appl. Phys. Lett., 105, 062402 (2014). [5]J. L. Mattei, et al, J. Magn. Magn. Mater. 447 9-14 (2018). [6]R. C. Pullar, Progr. Mater. Sci., 57, 1191-1334, (2012). [7]Z. Zheng, et al, J. Amer. Ceram. Soc., 97, 2016-2019, (2014).

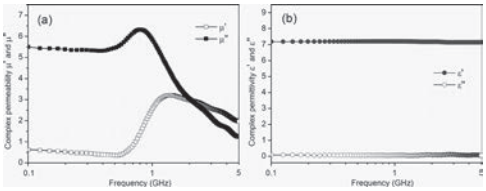


Fig. 1. The typical (a) complex permeability and (b) complex permittivity for the NiZnCo ferrite/resin composite materials over the frequency range of 0.1–5 GHz.

BR-09. Structural Characterization, Magnetic Properties, and Spin Transport in $NiFe_2O_4$ Thin Film Grown on Lattice Matched Substrates. *S. Regmi*[1,2], Z. Li[1,2], A. Srivastava[1,2], R. Mahat[1,2], S. KC[1,2], A. Rastogi[3], Z. Galazka[4], T. Mewes[1,2] and A. Gupta[1] *1. Center for Materials for Information Technology, The University of Alabama, Tuscaloosa, AL, United States; 2. The Department of Physics and Astronomy, The University of Alabama, Tuscaloosa, AL, United States; 3. Materials Science and Technology Division, Oak Ridge National Laboratory, Oak Ridge, TN, United States; 4. Leibniz-Institut fur Kristallzuchtung, Max-Born-Str. 2, Germany*

Spinel ferrite thin films have been widely studied from the past few decades because of their potential applications in the microwave and high-frequency device fabrications. These materials possess low coercivity, high saturation magnetization, and high remnant magnetization. Here, we report the epitaxial growth of $NiFe_2O_4$ thin films on two different isostructural substrates i.e. $MgGa_2O_4$ (MGO) and $ZnGa_2O_4$ (ZGO) using pulsed laser deposition technique. These substrates have lattice mismatch of 0.62% and 0.04%, respectively with bulk $NiFe_2O_4$. Our result shows that the films on $MgGa_2O_4$ substrate have considerable strain because of the tetragonal distortion in the crystal structure, whereas the films on lattice matched $ZnGa_2O_4$ substrate are free of strain and cubic in structure. The magnetometry data suggests that the film strain is the principal factor for magnetic anisotropy contribution in $NiFe_2O_4$ film. Moreover, we show that the reduction in magnetic strain anisotropy greatly impacts the effective Gilbert damping constant obtained from ferromagnetic resonance (FMR) measurement. We further show that there is an enhancement in spin voltage generation in spin Seebeck effect (SSE) experiment as a combined effect of lower damping and lower film strain.

1. Z. Galazka, S. Ganschow, R. Schewski, APL Materials 7, 022512 (2019) 2. A. V. Singh, B. Khodadadi, J. B. Mohammadi, Advanced Materials 29, 1701222 (2017) 3. B. Heinrich, "Spin relaxation in magnetic metallic layers and multilayers," in Ultrathin Magnetic Structures III: Fundamentals of Nanomagnetism, edited by J. A. C. Bland and B. Heinrich (Springer Berlin Heidelberg, Berlin, Heidelberg, 2005) pp. 143–2103

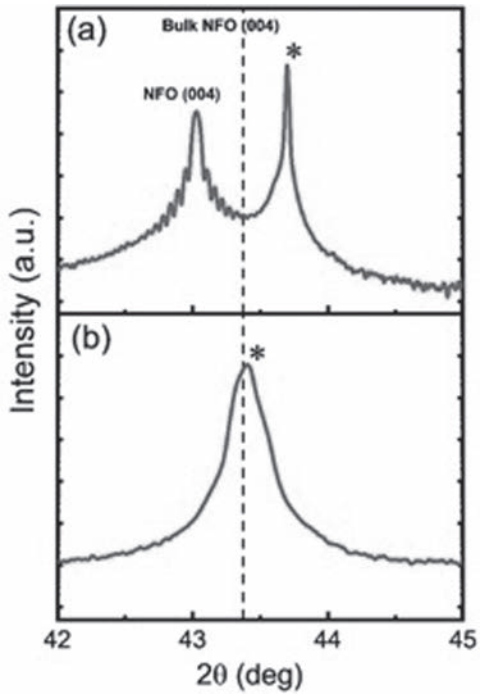


Figure 1. Partial 2θ-ω scans around 004 peak of the substrate and ≈ 200 nm NFO films deposited on (a) $MgGa_2O_4$ and (b) $ZnGa_2O_4$ substrates. (*) represents the substrate peaks.

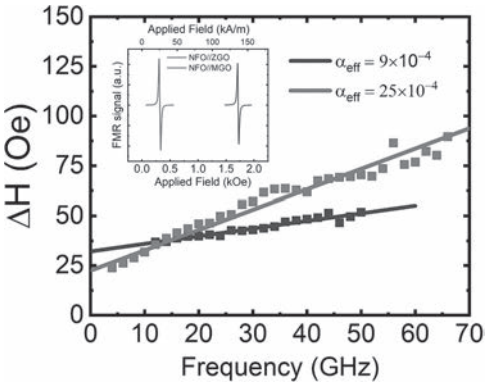


Figure 2. The variation of microwave frequency with FMR linewidth for NFO//MGO and NFO//ZGO films. The inset shows the typical FMR spectra for NFO//MGO and NFO//ZGO films at 10 GHz.

BR-10. Magnetic Properties of Polycrystalline Y-type Hexaferrite $Ba_{2-x}Sr_xNi_2(Fe_{1-y}Al_y)_{12}O_{22}$ using Mössbauer Spectroscopy. *J. Kim*[1], H. Choi[1] and C. Kim[1] *1. Kookmin University, Seoul, The Republic of Korea*

Synthesis of the polycrystalline $Ba_{2-x}Sr_xNi_2(Fe_{1-y}Al_y)_{12}O_{22}$ (x = 0.0, 1.5, y = 0.00, 0.01, 0.03) was accomplished by the polymerizable complex method. The samples were investigated for the crystallographic and the magnetic properties by x-ray diffraction (XRD), vibrating sample magnetometer (VSM), and Mössbauer spectrometer. The Mössbauer spectra were obtained by a conventional spectrometer with a ^{57}Co source in a Rh matrix in the temperature range from 4.2 to 295 K. From refined XRD patterns, all samples were confirmed of the rhombohedral structure with space group *R*-3*m*. Also, we were able to identify six distinguish sublattices, which are four octahedral sites ($18h_{VI}$, $3b_{VI}$, $6c_{VI}$, and $3a_{VI}$) and two tetrahedral sites ($6c_{IV}$*, $6c_{IV}$). The lattice constant of a_0 and c_0 decrease by Sr, Al substitution because the ionic radius of Sr^{2+} (1.12 Å) is smaller than that of Ba^{2+} (1.34 Å) and the ionic radius of Al^{3+} (0.535 Å) is smaller than that of Fe^{3+} (0.645 Å). The zero-field-cooled (ZFC) measurement between 4.2 and 295 K applied 100 Oe shows that spin transition temperature (T_S). Substitution of Sr ions increased T_S. Al ions were further substituted after Sr ions were substituted, and T_S increased to around room temperature. The Mössbauer spectra were fitting six distinguish sublattices: $18h_{VI}$, $3b_{VI}$, $6c_{VI}$, $6c_{IV}$*, $6c_{IV}$, and $3a_{VI}$. The measured isomer shift of all samples indicated that the charge state of Fe ions is Fe^{3+}. The Mössbauer spectra according to temperature change confirmed the changes in the magnetic hyperfine field curves at T_S.

[1] Y. Chang, K. Zhai, and Y. Sun, J. Phys. D-Appl. Phys., Vol.51, p.264002 (2018)

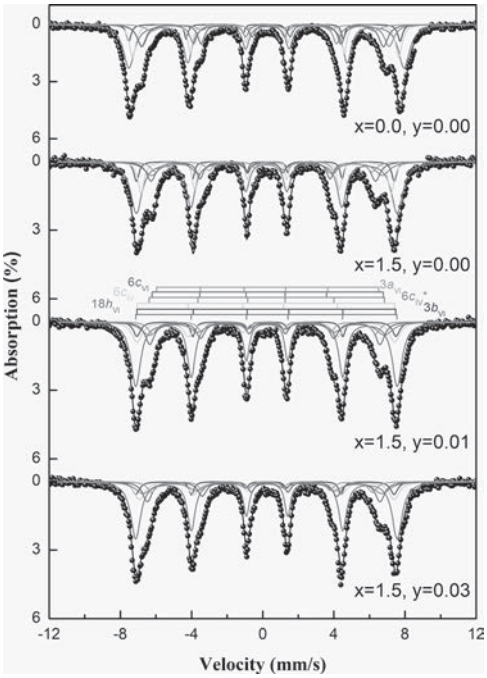


Fig.1. Mössbauer spectra of the $Ba_{2-x}Sr_xNi_2(Fe_{1-y}Al_y)_{12}O_{22}$ at 295 K.

BR-11. Static and dynamics magneto-viscoelasticity in $Co_{1-x}Zn_xFe_2O_4$ ($0 \le x \le 1$) based magnetic nanofluid. *A. Singh*[1], A. Rathi[1], P. Kumar[1], R. Pant[1], G. Basheed[1] and K.K. Maurya[1] *1. Indian reference Material (BND), AcSIR-National Physical laboratory, New Delhi, India*

The study of rheological characteristics of magnetic nano-fluid plays an important role in device development, as magnetic control on fluid behavior is a promising field in numerous applications. The present work investigates the magneto viscoelastic behavior of Zn substituted cobalt ferrite based magnetic fluid synthesized by surface modified chemical Co-precipitation route. The crystalline spinel phase and purity of all the samples have been confirmed by X-ray diffraction (XRD) and High-resolution transmission electron microscopy (HRTEM). The crystallite size calculated by W-H methods which are corroborated with HRTEM. The room temperature magnetic measurements confirm systematic decrease in saturation magnetization. Although for x = 0.4 the decrease is slightly low as compared to other composition. This has been confirmed from viscoelastic measurements performed in dynamics and oscillatory mode using magentorheometer. The steady-state rheograms (viscosity vs shear rate curve) shows a decrease in dynamics viscosity behavior with the increase of Zn substitution. The rheograms for all compositions are well fitted with power-law confirming the shear thinning behavior with n ≤1. Also from magneto-sweep rheograms (viscosity vs magnetic field), we have found that the steady increase in viscosity with increase in magnetic field is due to the formation of a chain like structure which causes an interruption in smooth streamline flow of the MNFs. With a small addition of Zn, we have observed a drastic decrease in the viscosity of fluid behavior. Field-induced viscoelastic behavior of Co-Zn MFs in static and dynamic mode provides significant information for optimization of MNFs for various applications

[1] Noorjahan, S. Pathak, K. Jain, R.P. Pant, Improved magneto-viscoelasticity of cross-linked PVA hydrogels using magnetic nanoparticles, 2017. [2] R.K. Sharma, V. Sebastian, N. Lakshmi, K. Venugopalan, V.R. Reddy, A. Gupta, Variation of structural and hyperfine parameters in nanoparticles of Cr-substituted Co-Zn ferrites, Physical Review B, 75 (2007) 144419.

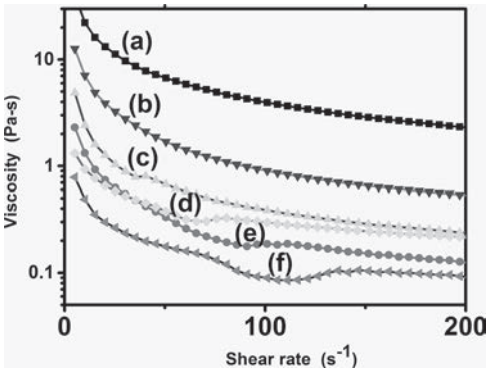


Fig.1: shows rheogram of $Co_{1-x}Zn_xFe_2O_4$ (a) x = 0.0, (b) x = 0.2, (c) x = 0.4, (d) x = 0.6, (e) x = 0.8, (f) x = 1.0

BR-12. Study of complex permeability spectra of Co-substituted Ni-Zn ferrite composites and processing of ferrite thin sheets for RF applications. *P. Lathiya*[1] and J. Wang[1] *1. Electrical Engineering, University of South Florida, Tampa, FL, United States*

Introduction: With the recent advancements related to imminent rollout of 5G and IoT technologies, there is a growing demand for soft magnetic materials for different applications such as radio frequency circuits, antennas, isolators, circulators, and interference suppressors etc. Ni-Zn ferrites exhibit excellent soft magnetic properties such as high resistivity, high permeability and low magnetic loss for both low and high frequency applications. To meet the performance specifications for aforementioned applications, thin Ni-Zn sheets with a high permeability and low magnetic loss is desired. In this work, we present a new method to prepare thin Ni-Zn ferrite sheets with high permeability and low magnetic loss. More specifically, Co-substitution was used to achieve desired properties of Ni-Zn powders and thin sheets were prepared subsequently using a doctor blade coater. Experimental Section: Co-substituted (Co: x-0.2, 0.18, 0.15) $Ni_{0.65-x}Co_xZn_{0.35}Fe_2O_4$ ferrite was synthesized by a conventional solid-state method. The calcined granular powders were mixed with 5 wt% PVA binder to make cylindrical test samples and sintered in air at 1100 °C. For the preparation of thin Ni-Zn ferrite sheet, PVA was used as the binder and the thin sheets were obtained using a doctor blade coater. Results: Substitution of Cobalt in Ni-Zn ferrite increases the real part of permeability from 6.5 (x=0.20) to 8.5 (x=0.15) at 250 MHz. Similarly, the imaginary part of permeability increases from 0.12 to 0.24. An increase in magnetic loss from 0.18 to 0. 28 is observed as the amount of cobalt is decreased from 0.2 to 0.15. Further increase of Cobalt to substitute Nickel decreases the real part of permeability. Conclusion: The variation in composition for Ni-Zn and doping strongly influence the dynamic magnetic properties of the soft magnetic ferrites. The cobalt substitution has exhibited a direct effect on combined high permeability and low magnetic loss of ferrites at RF and microwave frequencies. Future work: Further experiments will be conducted on thin sheets to measure FMR frequency and loss measurements using strip-line cavity method. Also, we are exploring the process methodology of 3D printing Ni-Zn ferrites using PVA binder.

H. Su, H.W. Zhang, and Y. K. An, *Physica Status Solidi a- Appl. Mater. Sci.* 204, 576-580 (2007). E. Peng, X. Wei and J. Ding, *RSC Adv.*7, 27128 (2017). D. Kokkinis, M. Schaffner and A. R. Studart, *Nature Commun.* 10,1038 (2015).

BR-13. Precursor effects and field-induced short-range order above the Verwey transition in single Fe_3O_4 crystals. C. Boekema[1] and *C. Morante*[1] *1. Physics & Astronomy, San Jose State University, San Jose, CA, United States*

The internal fields in single crystals of magnetite (Fe_3O_4) have been previously studied through muon-spin rotation (μSR). [1] By Maximum-Entropy (MaxEnt, ME) μSR [2] we analyze Fe_3O_4 μSR data with external fields parallel to the <111>, <110> or <100> axis. We optimize the ME peak-to-noise ratio by varying the filter time and time interval. [2] Several μSR time series indicate a beat pattern. Using MEμSR, a second frequency signal is seen at *non-zero* fields in the temperature range above the Verwey transition (T_V= ~123 K). At zero field, MEμSR confirms with much improved precision the existence of one frequency signal found earlier [1] by curve fitting (CF) and Fourier transformation (FT). We compare our room temperature (RT) field-dependent MEμSR results for <110> Fe_3O_4 with those found at 205 K to study a second order phase transition at the Wigner temperature (T_W= ~247 K). At RT and 205 K for fields below the demagnetization field and parallel to <110> Fe_3O_4, a second MEμSR frequency is observed, *missed* by CF and FT. These secondary magnetic fields fall on the extended magnetization curves below and above T_W. At RT a small field induces a short-range order similar to the precursor effects in the T_V– T_W interval. At 205 K within that precursor T-interval, we observe a comparable RT-disordered state. The existence of these additional internal fields are likely related to phonon-assisted 3d-electron(-spin) hopping and short-range order behaviors. [3] Our MEμSR studies lead to a better understanding of the local magnetism in this Mott-Wigner glass. [1, 3] Research is supported by DOE-LANL, AFC & SJSU.

[1] C Boekema *et al*, Hpf Interactions 31 487 (1986); Phys Rev B31 1233 (1985). [2] C Boekema and MC Browne, MaxEnt 2008, AIP Conf Proc #1073 p260 (2008) [3] C Boekema *et al*, Proc 11th Int M2S Conf (2015).

BR-14. Wideband Square Spiral Metamatereial Absorbers Based on Flaky Carbony Iron/Epoxy Composites. *R. Yang*[1], J. Yang[1] and S. Lo[1] *1. Aerospace and Systems Engineering, Feng Chia University, Taichung, Taiwan*

Radar absorbing materials (RAMs) also known as microwave absorbers, which can absorb and dissipate incident electromagnetic waves by converting them to thermal energy, are widely used in the fields of radar-cross section reduction (stealth technology), electromagnetic interference reduction (EMI) and human health protection. Metamaterials (MMs) are artificial subwavelength periodic structures engineered to have properties that may not be found in nature. In this paper, a broadband and thin microwave absorber composed of metal-base planar metamaterials sandwiched between two layers of flaked-shaped carbonyl iron (FCI) composites is presented. FCI powder was prepared by ball milling spherical carbonyl iron powder and then added to epoxy resin to prepare FCI composite (FCIC) samples with different weight fractions. A coaxial transmission/reflection method is used to obtain the complex permittivity (ε′-jε″) and permeability (μ′-jμ″) of FCIC samples at 2-18 GHz. Figure 1 shows the complex permittivity and permeability of the FCIC with weight ratios of 30, 40, 50, 60 and 70 wt.% of magnetic fillers, respectively. With these electromagnetic characteristics, a broadband, polarization-insensitive and thin metamaterial absorber comprising of arrays of square spirals imbedded between two different layers of FCIC is optimally designed through a genetic algorithm. Figure 2 shows a schematic of bandwidth-enhanced metamaterial absorbers and the reflection loss of the optimally designed metamaterial absorbers with or without the embedded MM layer. The planar metamaterial is etched on a 0.1 mm-thick FR4 with each unit consisting of four identical spiral structures with different rotational angles to enhance the polarization insensitivity. The thickness of the upper layer (50 wt.% of FCI) is 1.93 mm and the bottom layer (70 wt.% of FCI) is 0.76 mm. The absorbing bandwidth below -10 dB is extended to from 4.8 GHz to 9.1 GHz with the embedded MM layer.

Reference [1] R. B. Yang, and W. F. Liang, J. Appl. Phys. 109, 07A311 (2011). [2] M. A. Ei-AAsser, J. Nanophotonics, 8, 083085 (2014). [3] Q. Ye, Y. Liu and H. Lin, Appl. Phys. A, 107, p.155 (2012). [4] X. Huang, H. Yang and S. Yu, J. Appl. Phys., 113, 213516 (2013).

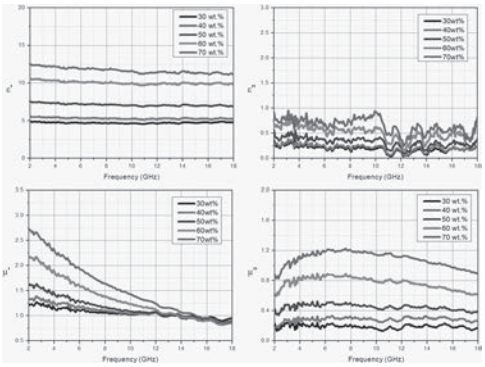


Fig. 1. Real and imaginary parts of complex permittivity and permeability of FCIC for different weight ratios of FCI.

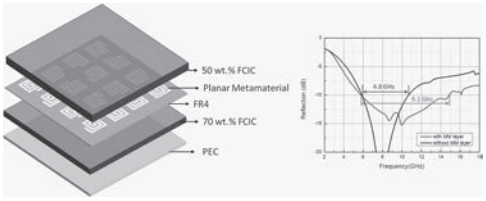


Fig. 2. A schematic of bandwidth-enhanced metamaterial absorbers and the reflection loss of the metamaterial absorbers with or without the embedded MM layer.

BR-15. Study of structural, electrical, and magnetic properties of rare-earth Tb^{3+} doped $NiFe_2O_4$ ferrite. *D. Guragain*[1], T.P. Poudel[1], B.K. Rai[2], S. Yoon[3] and S.R. Mishra[1] *1. University of Memphis, Memphis, TN, United States; 2. Oak Ridge National Lab, Oak Ridge, TN, United States; 3. Gunsan National University, Gunsan, The Republic of Korea*

$NiFe_2O_4$, a ferrimagnetic inverse spinel, has a high specific resistance, low losses in high-frequency applications, low coercivity, a moderate saturation magnetization with positive magneto-crystalline anisotropy. Doping the parent spinel ferrite with rare-earth ions leads to structural disorder and lattice strain, thereby enhancing the electrical and magnetic parameters. The present work delineates study on terbium doped $NiTb_xFe_{2-x}O_4$ ($0<x<0.1$) ferrite to understand the influence of a rare-earth ion (Tb^{3+}) on structural, electrical and magnetic properties of Ni-ferrites. We have successfully synthesized spinel type ferrites $NiTb_xFe_{2-x}O_4$ (x=0.0 to 0.1) by sol-gel auto combustion followed by heat treatment, and characterization is done by XRD, FTIR, SEM, SQUID, LCR meter and Mossbauer spectroscopy. The Rietveld analysis shows that the lattice parameter and induced strain increased with an increase in the Tb^{3+} content in the ferrite. The crystallite size decreased with increasing Tb^{3+} content due to grain refinement. The octahedral band in FTIR show a progressive variation with Tb^{3+} doping in Ni-ferrite. The magnetic parameters derived from the room temperature RT hysteresis loops show a decrease in saturation magnetization, from 54.9 emu/g (x=0) to 26.06 emu/g (x=0.1) and coercivity value from 164 Oe to 94 Oe at x = 0.1. A significance reduction in magnetization results from lattice distortion and magnetic dilution upon replacing Fe^{3+} with Tb^{3+}. The Curie temperature decreased from 921 at x=0 to 904 K at x = 0.1 due to weakening of Fe^{3+}-O^{2-}—Fe^{3+} super-exchange interaction, while the electrical resistivity peaked at $3x10^8$ for x=0.1. Hyperfine parameters were derived from fitting Mossbauer spectra at RT. The Mossbauer spectral analysis indicated that iron was in the Fe^{3+} state, the magnetic hyperfine field at both the sites tended to decrease, and isomer shift at B site increased while that of A site remained invariant with an increase in the Tb^{3+} content. Furthermore, migration of Ni^{2+} from B site to A site was observed with the increase in the Tb^{3+} occupancy at the B site in the sample. The structural, magnetic, and Mossbauer results are elucidated by the occupancy of Tb^{3+} at the octahedral (B) site in $NiFe_2O_4$.

BR-16. Withdrawn

BR-17. Temperature Dependence of Antiferromagnetic Coupling at the YIG-GGG Interface. *M. Roos*[1], B.J. Kirby[2], P. Quarterman[2], J. Ding[3], M. Wu[3] and B.L. Zink[1] *1. Physics and Astronomy, University of Denver, Denver, CO, United States; 2. Center for Neutron Research, NIST, Gaithersburg, MD, United States; 3. Department of Physics, Colorado State University, Fort Collins, CO, United States*

Yttrium iron garnet (YIG) is a ferrimagnetic insulator that has been extensively studied for spintronic applications due to its low Gilbert damping.[1] High quality ultra thin YIG with remarkably low damping is often grown and annealed on gadolinium gallium garnet (GGG) due to exceptional lattice matching. During the high temperature anneal gadolinium atoms embed into the YIG crystal, creating a thin Gd-infused layer ($(Gd_{1-x}Y_x)Fe_5O_{12}$). Recent evidence shows antiferromagnetic coupling between this interfacial layer and the crystalline YIG film.[2,3] In this work we use SQUID magnetometry and spin-polarized neutron reflectometry (PNR) to confirm antiparallel alignment of the interface layer and reveal complex temperature-dependent interactions between the GGG substrate, $(Gd_{1-x}Y_x)Fe_5O_{12}$ layer and YIG thin film. Neutron nuclear scattering of 20 nm crystalline YIG film grown on GGG[1] shows a roughly 3nm $(Gd_{1-x}Y_x)Fe_5O_{12}$ layer. PNR magnetization profiling describes antiparallel alignment of the $(Gd_{1-x}Y_x)Fe_5O_{12}$ up to room temperature for low fields, and enhancement of the interfacial antiferromagnetism with decreasing temperature. While magnetometry shows the magnetization closely agrees with literature for room temperature[2], we find a different temperature dependent evolution down to 2 K. Magnetometry reveals the GGG has field-dependent negative thermoremanent magnetization, and overall shows more complicated magnetism than a simple paramagnet at all temperatures studied. This is possibly related to defects in the substrate. The role of the $(Gd_{1-x}Y_x)Fe_5O_{12}$ interface layer's magnetic properties in ultra thin film spintronic devices is still an open question, as the impact of the GGG substrate to the interface dynamics is non-negligible. A more thorough characterization process of GGG might be important when selecting device substrates.

[1]. H. Chang, P. Li, W. Zhang, T. Liu, A. Hoffmann, L. Deng, and M. Wu, IEEE Magnetics Letters 5, 1 (2014) [2]. A. Mitra, O. Cespedes, Q. Ramasse, M. Ali, S. Marmion, M. Ward, R. M. D. Brydson, C. J. Kinane, J. F. K. Cooper, S. Langridge, and B. J. Hickey, Sci. Rep. 7, 11774 (2017). [3] J. Gomez-Perez, S. Vélez, L. McKenzie-Sell, M. Amado, J. Herrero-Martín, J. López-López, S. Blanco-Canosa, L. E. Hueso, A. Chuvilin, J. W. A. Robinson, and F. Casanova, Phys. Rev. Applied, 10, 044046 (2018)

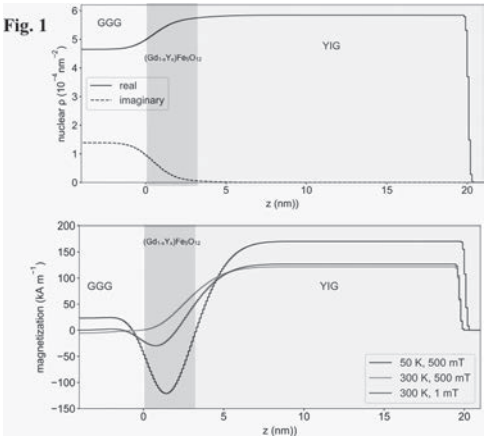


Fig. 1. PNR nuclear density (top) and magnetization (bottom) profiles at various temperatures and fields. Interface is paramagnetic at room temperature only with sufficient field applied.

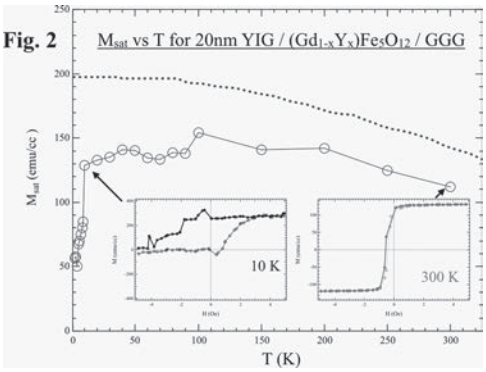


Fig. 2. Magnetization vs temperature. The magnetization at low temperatures is much lower than reported for 40nm films[2]. Depression from bulk expectation (red dots) occurs at all temperatures.

Session BS
EDUCATION, OUTREACH, & PUBLIC ENGAGEMENT IN MAGNETISM
(Poster Session)

Barry L Zink, Co-Chair
University of Denver, Denver, CO, United States
Dafiné Ravelosona, Co-Chair
Center for Nanoscience and Nanotechnology, Palaiseau, France
Yukiko Takahashi, Co-Chair
NIMS, Tsukuba, Japan

BS-01. Exploring magnetic resonance with a compass. *D. Nelson*[1], E. Cookson[1], M. Anderson[1], D. McKinney[2] and I. Barsukov[1] *1. Physics and Astronomy, UC Riverside, Riverside, CA, United States; 2. Santa Rosa Academy, Menifee, CA, United States*

Magnetic resonance plays an important role in today's science, engineering, and medical diagnostics. Learning and teaching magnetic resonance is challenging since it requires advanced knowledge of condensed matter physics and quantum mechanics. Driven by the need to popularize this technologically impactful phenomenon, we develop an inexpensive table-top demonstration experiment. It unveils the magnetic resonance of a hand-held compass in the magnetic fields of a permanent magnet. The setup provides an immediate visualization of the underlying physical concepts and allows for their translation to broad student audiences. This work was supported by the National Science Foundation under Grant No. ECCS-1810541.

BS-02. Magnetic Fields Web Series: Engaging Middle School Students in STEM. *P. Pena Martin*[1], J. Isberg[1], E. Ertekin[1,3], V. Lorenz[1,2] and N. Mason[1,2] *1. Materials Research Laboratory, University of Illinois at Urbana-Champaign, Urbana, IL, United States; 2. Department of Physics, University of Illinois at Urbana-Champaign, Urbana, IL, United States; 3. Department of Mechanical Science and Engineering, University of Illinois at Urbana-Champaign, Urbana, IL, United States*

Web based media can make scientific content accessible to audiences far beyond the scientific community. We created a web series called "Magnetic Fields" that aims to introduce materials science, particularly concepts related to magnetism, and promote themes more general to STEM fields, such as persistence and the scientific process, through use of characters and a story geared towards a middle school audience. The goal is to build and maintain interest in science at an age where this tends to drop off. The four-episode arc follows a group of high school characters as they encounter a strange new material during a class field trip to a laboratory. The series is directed by John Isberg, with professional actors making up most of the cast. The series was initiated by scientists in the Illinois MRSEC, and the storyline was developed in collaboration with MRSEC students and faculty. The episodes were released in May 2019 through Youtube. We report on the process of creating this series, response to it upon release, and discussion of its use as an educational tool. The authors acknowledge primary support of the NSF through the University of Illinois at Urbana-Champaign Materials Research Science and Engineering Center DMR-1720633.



Fig.1 Scene from an episode of "Magnetic Fields." Photo by John Isberg.

BS-03. In-class experiments with smart phones for teaching upper-level electricity and magnetism. A. Davidson[1], A. Ranjan[2] and *X. Fan*[1] *1. Physics and Astronomy, University of Denver, Denver, CO, United States; 2. Cherry Creek High School, Greenwood Village, CO, United States*

Interactive-engagement method such as studio physics [1, 2], has demonstrated higher learning gains than traditional lecturing in intro-level physics classes. However, there have been limited applications in upper-level classes, such as Electricity and Magnetism (E&M), possibly because experiments on E&M topics can be too costly and sophisticated to be carried out in the classroom. Smart phone, which is equipped with magnetic field sensors, radio signal detectors and light sensors, provides a convenient platform for carrying out E&M-related experiments. In this poster, we will present three examples of the implementation of smart-phone-based studio physics in an E&M class for Physics majors: (1) Detection of earth magnetic field inclination; (2) quantifying skin depth of aluminum foil with cellphone tower signals; and (3) Measurement of Brewster's angle. Besides sensitive sensors, smart phone also has computational power, which can be explored to further expand the breadth and depth of the smart-phone-based studio physics. Due to the wide accessibility of smart phones and the simplicity of experimental setup, we expect this teaching technique can be easily transferred to other institutes in the world.

[1] Gok, T., *Assessment of the effectiveness of the hybrid studio format in introductory undergraduate physics.* Energy Education Science and Technology Part B-Social and Educational Studies, 2012. 4(1): p. 117-130. [2] Sorensen, C.M., A.D. Churukian, S. Maleki, and D.A. Zollman, *The New Studio format for instruction of introductory physics.* American Journal of Physics, 2006. 74(12): p. 1077-1082.

BS-04. The Use of Virtue Modules in Physics Lab Teaching. *W. Zhang*[1], R. Bidthanapally[1], T. Sebastian[2], Y. Xiong[1,3], H. Qu[3] and J. Sklenar[4] *1. Physics Department, Oakland University, Rochester, MI, United States; 2. THATec Innovation GmbH, Mannheim, Germany; 3. Electronic and Computer Engineering, Oakland University, Rochester, MI, United States; 4. Physics Department, Wayne State University, Detroit, MI, United States*

Lab sessions in physics education connect the fundamental concepts to practical examples and are effective measures of the students' understanding and reasoning through ultimate real-world tests. Many topics in condensed

matter physics are known to be challenging to convey in both lectures and labs. In addition, these topics are usually resource demanding, which has been one of the challenging issues. Here, we introduce and demonstrate the use of virtue lab modules for teaching physics labs and for effectively integrating research and education. Experiments that are relevant to magnetism and spintronics include, but not limited to, spin current detecting, microwave energy harvesting, and spin-based thermoelectric effects. An important highlight of these modules is the highly-interactive laboratory learning platform. In the class, each piece of experimental hardware (e.g. electrometers, oscilloscopes, etc) will be paired with a computer-based virtual module. The individual modules mimic the hardware, which the students can use to become familiar with the hardware, acquire real-time feedback, and visualize the data acquisition dynamics, on-demand and risk-free. The virtual component is also helpful for demonstrating delicate, shared hardware in class, without risk of damaging the actual instrumentation. These individual components are connected to a central operating system and the experiment can be re-programmed by simple coding and user-interfaced commands [1]. Work at Oakland University is supported by NSF DMR-1808892.

[1] THATec Innovation GmbH: https://www.thatec-innovation.com/

Session BT
MAGNETOELECTRIC BEHAVIOR
(Poster Session)

Ramanathan Mahendiran, Chair
National University of Singapore, Singapore

BT-01. Magnetotransport of $SrIrO_3$ Films on (110) $DyScO_3$. A. Jaiswal[1,2], A. Zaitsev[1], R. Singh[2], R. Schneider[1] and *D. Fuchs*[1] *1. Institute for Solid-State Physics, Karlsruhe Institute of Technology, Karlsruhe, Germany; 2. Department of Physics, Indian Institute of Technology Delhi, Delhi, India*

Epitaxial perovskite (110) oriented $SrIrO_3$ (SIO) thin films were grown by pulsed laser deposition on (110) oriented $DyScO_3$ (DSO) substrates with various film thickness t (2nm < t < 60 nm). All the films could be produced with stoichiometric composition, in single orthorhombic phase and with high crystallinity. The films display untwinned and nearly strain free growth over the complete thickness range. The nearly perfect in-plane lattice matching of DSO with respect to SIO and similar orthorhombic symmetry of DSO and SIO result in a full epitaxial in-plane alignment, i.e., the *c*-axis of DSO and SIO are parallel to each other with only slightly enlarged d_{110} out-of plane lattice spacing (+0.38%) due to the rather small in-plane compressive strain by the DSO substrate. Measurements of the magnetoresistance (MR) were carried out for current flow along the [001] and [1-10] direction of DSO and magnetic field perpendicular to the film plane. MR appears to be distinct different for both directions. The anisotropy $MR_{001}/MR_{1\text{-}10} > 1$ increases with decreasing T and is especially pronounced for the thinnest films where, in addition, hysteretic field dependence appears. The results strongly indicate magnetic ordering in the SIO films. The ordering temperature T^* is between 2K and 5 K, and the coercive field H_c amounts to 2-5 T. Both, T^* and H_c are very similar to the field-induced magnetic order of Dy moments in DSO which strongly suggests substrate induced magnetism in the SIO films.

BT-02. Spintronic Terahertz Emission by Ultrafast Spin-Charge Current Conversion in Organic-Inorganic Hybrid Perovskites. *W. Zhang*[1,2], K. Cong[3], E. Vetter[4], Y. Liang[5], Y. Li[1,2], Q. Zhang[3], Y. Xiong[1,6], R. Schaller[3], A. Hoffmann[2], W. You[5], H. Qu[6], H. Wen[3] and D. Sun[4] *1. Physics Department, Oakland University, Rochester, MI, United States; 2. Materials Science Division, Argonne National Laboratory, Lemont, IL, United States; 3. Advanced Photon Source, Argonne National Laboratory, Lemont, IL, United States; 4. Physics Department, North Carolina State University, Raleigh, NC, United States; 5. Chemistry Department, University of North Carolina, Chapel Hill, NC, United States; 6. Electronic and Computer Engineering, Oakland University, Rochester, MI, United States*

Hybrid Metal Halides (HMHs) is a new class of synthetic semiconductors prepared by low-temperature solution processing with a large chemical and structure 'universe' given the synthetic versatility of their molecular cations. While the family of HMHs has shown remarkable performance in photovoltaic and optoelectronic applications, their rich spintronic functionalities have yet to be fully utilized. We report the successful observation of the inverse Rashba-Edelstein Effect (IREE) in a prototypical 3D-HMH material, $CH_3NH_3PbBr_3$ polycrystalline thin films and single crystals, driven by spin-pumping from a $Ni_{80}Fe_{20}$ (NiFe) ferromagnetic metal. We found a large surface-dominated IREE spin-to-charge conversion efficiency, which is comparable to that observed in more traditional Rashba-type systems (e.g., Bi/Ag, etc.). The THz emission can be controlled by the magnetic field, and furthermore, exhibits a unidirectional behavior and peculiar laser linear polarization dependence. Considering that HMH materials are grown from solution, our findings demonstrate a substantial advance towards low-cost, low-temperature processable HMH-based spintronics applications. This work was supported by AFOSR FA9550-19-1-0254. E.V. and D.S. were thankful for NCSU start-up and NCSU-Nagoya Collaboration Grants. Work at Argonne was supported by DOE, BES, Materials Science and Engineering Division. The use of Center for Nanoscale Materials at Argonne was supported by DOE, BES, under contract no. DE-AC02-06CH11357.

BT-03. Hysteretic temperature dependent spin-wave response associated with phase transitions in V_2O_3/Ni/NiFe thin films. *Y. Chen*[2], N. Vargas[1], P. Salev[1], P.N. Lapa[1], I. Schuller[1] and A.D. Kent[2] *1. Department of Physics and Center for Advanced Nanoscience, University of California San Diego, La Jolla, CA, United States; 2. Center for Quantum Phenomena, Department of Physics, New York University, New York City, NY, United States*

Spin-torque nano-oscillators (STNOs) are a new class of microwave oscillators with operating frequencies that can be precisely tuned by external magnetic fields, injected spin currents, or prior states. We report a study of the hysteretic magnetization dynamics of a V_2O_3/Ni/NiFe heterostructure associated with the structural phase transition (SPT) and metal-insulator transition (MIT) of V_2O_3 near 150 K [1]. Ferromagnetic resonance (FMR) was measured with a dc magnetic field applied perpendicular to the sample plane for different thicknesses of Ni/NiFe bilayers between 50 and 300 K. The phase transitions in V_2O_3 induces a clear increase of the FMR resonant fields, indicating the strong coupling between V_2O_3 structural/electronic state and the spin-wave modes in the adjacent ferromagnetic bilayers. In addition, the resonance fields are hysteretic, showing clear shifts between sample cooling and heating (Figure 1). The FMR linewidths are also enhanced at temperatures lower than 150 K. The FMR results show that the spin-wave modes of the V_2O_3/Ni/NiFe thin films can be tuned by external parameters (such as applied magnetic fields) as well as state of V_2O_3. This makes the heterostructure studied a good candidate for realizing non-volatile STNOs and potential devices for neuromorphic computing [2]. Vibrating sample magnetometer (VSM) and magneto-optic Kerr effect (MOKE) characterization of the V_2O_3/Ni/NiFe samples will be presented along with the temperature-dependent FMR results. This work is supported by the Quantum Materials for Energy Efficient Neuromorphic Computing Energy Frontier Research Center funded by the U.S. Department of Energy (DOE), Office of Science, Basic Energy Sciences (BES), under Award DE-SC0019273.

[1] J. G. Ramírez *et al.* "Collective mode splitting in hybrid heterostructures," Phys. Rev. B 93, 214113 (2016). [2] M. Romera *et al.* "Vowel recognition with four coupled spin-torque nano-oscillators," Nature 563, 230-234 (2018).

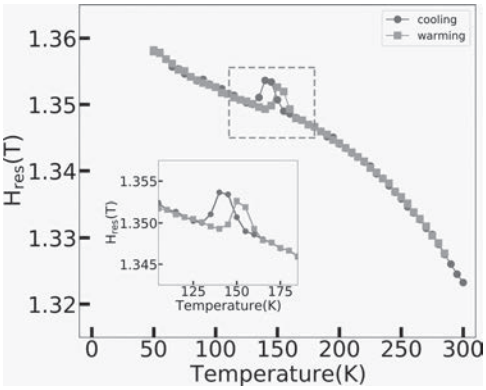


FIG. 1: FMR resonant fields of V_2O_3(100 nm)/Ni(10 nm)/NiFe(10 nm)/Pt(3 nm) as a function of temperature during the cooling and heating processes from 50 to 300 K.

BT-04. Investigating the Magnetic Ground state of the Skyrmion Host Material Cu_2OSeO_3 using Long-Wavelength Neutron Diffraction.
K.J. Franke[1,2], P.R. Dean[1], M. Ciomaga Hatnean[3], M.T. Birch[1], D. Khalyavin[4], P. Manuel[4], G. Balakrishnan[3] and P.D. Hatton[1] *1. Centre for Materials Physics, Durham University, Durham, United Kingdom; 2. School of Physics and Astronomy, University of Leeds, Leeds, United Kingdom; 3. Department of Physics, University of Warwick, Coventry, United Kingdom; 4. ISIS Facility, STFC Rutherford Appleton Laboratory, Chilton, Didcot, United Kingdom*

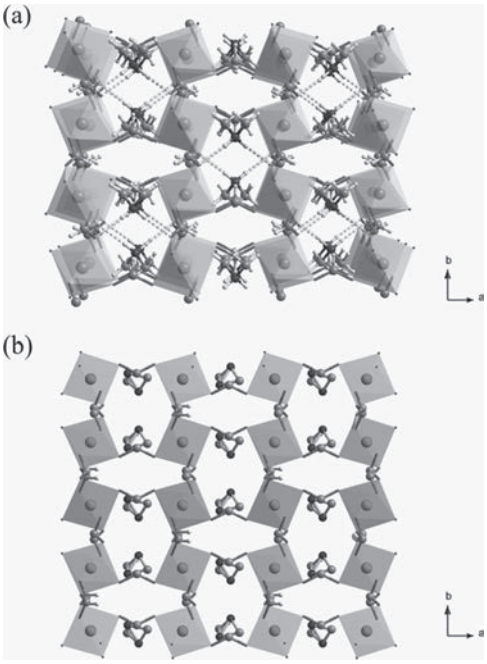
Skyrmions are topologically protected, nano-sized swirls of spins found in a range of magnetic materials. In recent years a number of advances have demonstrated the existence, not only of magnetic skyrmions, but also their ordering into a skyrmion lattice (SL) in several magnetic materials with a chiral structure. This symmetry can lead to the formation of an antisymmetric Dzyaloshinskii-Moriya interaction (DMI). Competition between the symmetric exchange interaction and the DMI leads to a magnetic ground state that generally consists of helices, long period magnetic structures where the magnetisation rotates in a plane perpendicular to the propagation direction. The magnetic phase diagram of multiferroic Cu_2OSeO_3 resembles that of other skyrmion hosting systems, consisting of a helical (H) ground state, a conical (C) phase in applied fields, a field polarised (FP) phase in large applied fields, and a SL phase in a pocket in applied field and temperature just below T_c [1]. Previous investigations have either shown that Cu_2OSeO_3 is a ferrimagnet [2] without addressing the chiral nature of the magnetic ground state, or investigated the chirality without taking into account ferrimagnetism [1,3-5]. Here we investigate the microstructure of the magnetic phases of Cu_2OSeO_3 and address the question of whether the ground state H structure is also ferrimagnetic. Using time-of-flight long-wavelength neutron diffraction on a single crystal sample, we observe magnetic satellites around the (0-11) diffraction peak not accessible to other techniques. Furthermore, our measurements uniquely allow us to distinguish helical from conical spin textures in reciprocal space. We show successive transitions from H to C to FP as the external magnetic field is increased in the magnetically ordered phases, and the formation of a skyrmion lattice with propagation vectors perpendicular to the field direction in a region of the field-temperature phase diagram that is consistent with previous reports [1,3]. We use powder diffraction measurements to determine the magnetic microstructure of the FP and H phases, and show that not only the FP phase but also the H ground state are made up of ferrimagnetic clusters instead of individual spins [6].

[1] S. Seki, et al. Science 336, 198 (2012) [2] J.-W. G. Bos, C. V. Colin, and T. T. M. Palasta, Phys. Rev. B 78, 094416 (2008) [3] T. Adams, et al. Phys. Rev. Lett. 108, 237204 (2012) [4] S. Seki, et al. Phys. Rev. B 85, 220406 (2012) [5] J. H. Yang, et al. Phys. Rev. Lett. 109, 107203 (2012) [6] K. J. A. Franke, et al. in preparation (2019)

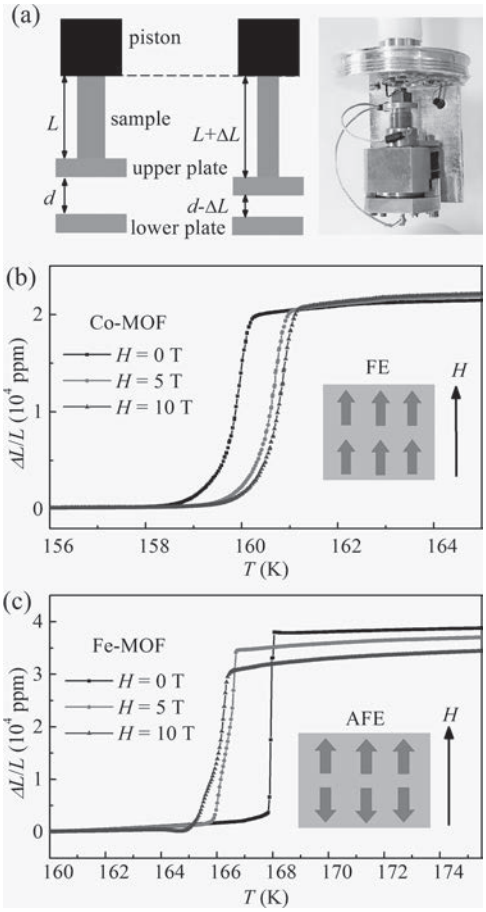
BT-05. Magnetic-Field Tuning of Hydrogen Bond Order-Disorder Transition in Metal-Organic Frameworks.
Y. Sun[1], Y. Ma[1], J. Cong[1] and Y. Wang[2] *1. Institute of Physics, Chinese Academy of Sciences, Beijing, China; 2. Department of Chemistry, Nankai University, Tianjing, China*

The ordering of polar hydrogen bonds can induce ferroelectricity or antiferroelectricity. This process is usually immune to external magnetic fields so that magnetic control of hydrogen bonds is very challenging. We find that the ordering of hydrogen bonds in the perovskite metal-organic frameworks $[(CH_3)_2NH_2]M(HCOO)_3$ (M=Fe, Co) can be manipulated by applying magnetic fields [1]. After cooling in a high magnetic field, the order-disorder transition of hydrogen bonds shifts to a lower or higher temperature, depending on antiferroelectricity or ferroelectricity induced by hydrogen bond ordering. Besides, the order-disorder transition leads to a giant thermal expansion, exceeding ~35000 and ~20000 ppm for M = Fe and Co, respectively, which is much higher than that of inorganic ferroelectrics. The influence of magnetic field on hydrogen bond ordering is discussed in terms of the magnetoelastic coupling.

[1] Y. Ma, Y. Wang, J. Cong, and Y. Sun, Phys. Rev. Lett. (in press).



The structure of the metal-organic framework $[(CH_3)_2NH_2]M(HCOO)_3$ with M=Fe and Co, respectively.



(a) Schematic of a capacitance dilatometer. The linear expansion/ striction of the sample is transformed into the change in the capacitance which is precisely measured by a capacitance bridge. Temperature dependence of the linear thermal expansion along the [012] direction in several magnetic fields for (b) the ferroelectric Co-MOF and (c) the antiferroelectric Fe-MOF. The order-disorder transition of hydrogen bonds induces a large change in length. After cooling in a high magnetic field, the transition temperature shifts to a higher temperatur for the Co-MOF but to a lower temperature for the Fe-MOF.

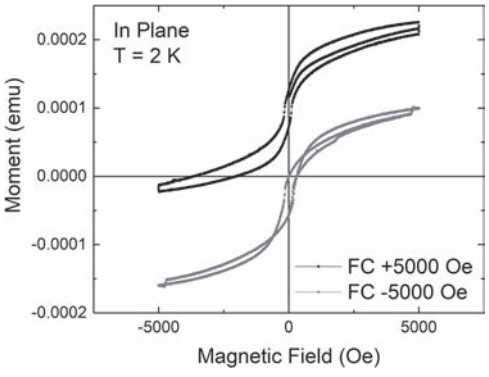
BT-06. Solution-Processed Yttrium Iron Garnet Thin Films as Novel Magnetostrictive Materials. *S.K. Patel*[1], C.T. Karaba[1] and S. Tolbert[1]
1. Chemistry and Biochemistry, University of California - Los Angeles, Los Angeles, CA, United States

Multiferroic antennas have the potential to revolutionize modern technology since they can be made orders of magnitude smaller than conventional antennas.[1] Successful multiferroic antennas have previously employed metallic magnetostrictive materials due to their optimal magnetic properties, including having low coercivity, high saturation magnetization, and high magnetostriction.[2] However, the radiation efficiency of such antenna devices is limited by the high conductivity of metallic magnetostrictive materials, causing significant electrical losses in RF systems.[3] Yttrium iron garnet ($Y_3Fe_5O_{12}$, or YIG) is a promising alternative to metallic magnetostrictive materials due to its extremely low Gilbert damping.[4] Additionally, YIG exhibits acceptable magnetic properties for a RF applications including a relatively low anisotropy field and low coercivity.[5] Despite these advantages, YIG intrinsically exhibits near-zero magnetostriction. Theoretical and experimental data has shown that doping YIG with ruthenium (substituting for iron) and with cerium (substituting for yttrium) can significantly increase magnetostriction due to increased spin-orbit coupling in bulk, single crystal materials.[6,7] In this work, we synthesize doped YIG thin films to use as new magnetostrictive materials, which would improve radiation efficiency upon integration into multiferroic antennas. We utilize solution-processing for facile stoichiometry control as well as integratability into future devices. The synthesis and characterization of these magnetostrictive YIG materials will be presented.

1. T. Nan, H. Lin, and Y. Gao, Nature Communications, Vol. 8, p.296-303 (2017). 2. Z. Yao, E. Wang, S. Keller, G. Carman, IEEE transactions on antennas and propagations, Vol. 63, p. 3335-3344 (2015). 3. H. Chang, P. Li, and W. Zhang, IEEE Magnetics Letters, Vol. 5, 6700104 (2014). 4. R. Pêna-Garcia, A. Delgado, Y. Guerra, E. Padrón-Hernández, Materials Letters, Vol.161, p. 384-386 (2015). 5. M. Musa, R. Azis, N. Osman, Results in Physics, Vol. 7, p. 1135-1142 (2017). 6. R. Comstock, R. and J. Raymond, Journal of Applied Physics, Vol. 38, pp. 3737-3739 (1967). 7. R. Krishnan, V. Cagan, and M. Rivoire, AIP Conference Proceedings, Vol. 5, pp. 704 (1972).

BT-07. Exchange Bias in $La_{0.7}Sr_{0.3}CrO_3/La_{0.7}Sr_{0.3}MnO_3/ La_{0.7}Sr_{0.3}CrO_3$ Heterostructures. *R. Olmos*[1], H. Iturriaga[1], D.S. Blazer[1], K. Gandha[2], C.I. Nlebedim[2], D.P. Kumah[3] and S. Singamaneni[1] *1. Physics, University of Texas at El Paso, El Paso, TX, United States; 2. Critical Materials Institute, Ames Laboratory, Ames, IA, United States; 3. Physics, North Carolina State University, Raleigh, NC, United States*

In the recent past, heterostructures of magnetic oxide thin films have attracted a great deal of research excitement due to very interesting physical properties such as antiferromagnetic interlayer coupling, tunable exchange-bias, interfacial driven magnetic properties and high mobility electron gas across the interfaces. In this work, we report on the comprehensive magnetic properties observed from the heterostructures of (2 unit cells)$La_{0.7}Sr_{0.3}CrO_3$/ (8 unit cells)$La_{0.7}Sr_{0.3}MnO_3$/ (2 unit cells)$La_{0.7}Sr_{0.3}CrO_3$, which are epitaxially deposited on $SrTiO_3$ substrate by plasma-assisted oxide molecular beam epitaxy at a growth temperature of 800° C. The thickness of each layer and valence states of elements were inferred from the aberration-corrected high-angle annular dark field-scanning transmission electron microscopy, electron energy loss spectroscopy, and energy dispersive x-ray spectroscopy chemical maps. Using Quantum Design SQUID magnetometer, the magnetic properties were studied when the magnetic field was applied both in-plane and out of plane of this sample. The Curie temperature of this structure is found to be at 290 K. Most significantly, at 2 K, we observed a complete up/down shift (along the magnetization axis) of hysteresis loop when the sample was cooled under the magnetic field of ±5000 Oe in the in-plane configuration. We believe that the strong antiferromagnetic (super) exchange coupling of Mn-Cr across the two interfaces is responsible for the observed exchange bias. We will present and discuss our in-detailed experimental findings collected on this heterostructure as a function of temperature and magnetic field.



BT-08. Strain-affected Modulation of Oxygen Ions Transfer in Topotactic Phase Transition. *J. Li*[1,2], J. Wang[1,2], C. Zhang[1,2], K. Qiao[1,2], F. Hu[1,2], J. Sun[1,2] and B. Shen[1,2] *1. Institute of Physics, Chinese Academy of Sciences, Beijing, China; 2. School of Physical Sciences, University of Chinese Academy of Sciences, Beijing, China*

Recent studies have shown that the topotactic phase transition is of great significance to the application of complex oxides in the fields of energy technology, ferroelectrics and catalyst.[1-3] Therefore, not only the degrees of freedom such as lattice, charge, orbit, and spin, but also the transfer of ions need to be considered in the design and regulation of functional materials. We grew 40 nm perovskite $La_{0.7}Sr_{0.3}CoO_{3-\delta}$ (LSCO) films on $(LaAlO_3)_{0.3}$-$(SrAl_{0.5}Ta_{0.5}O_3)_{0.7}$ (LSAT) and $LaAlO_3$ (LAO) substrates by pulsed laser deposition. The pristine perovskite films with different strains were vacuum annealed under different temperature (300-500 degrees Celsius). The X-ray diffraction (XRD) results identify a series of samples with structures from perovskite to brownmillerite (Fig. 1a and 1b). The lattice volume calculated from the (008) peak position shows a continuous expansion with the annealing temperature (Fig.1c), indicating an enhancement of the strain with the escape of oxygen ions in both films. Meanwhile, for both films, the normalized integral intensity of the brownmillerite characteristic (00$\underline{1}$0) peak shows a gradual saturation with the increase of the annealing temperature (Fig. 1d). However, an unexpected decrease appears in the film on LAO when the temperature further increases up to 500 degrees Celsius, indicating a reduction in the order degree of oxygen vacancies. Our results manifest that the strain in the film prefers suppressing the formation of long-range order of oxygen vacancies although the escape of oxygen ions is insusceptible to the strain type. In addition, large changes in magnetic and electrical properties were found in both films during the topotactic phase transition. Our work reveals the influence of strain on the evolution of oxygen ions transfer in topotactic phase transition, which provides new possibilities for the development of functional materials and devices in the future.

(1) Lu, N., Zhang, P., Zhang, Q., Qiao, R., He, Q., Li, H. B., Wang, Y., Guo, J., Zhang, D., Duan, Z., Li, Z., Wang, M., Yang, S., Yan, M., Arenholz, E., Zhou, S., Yang, W., Gu, L., Nan, C. W., Wu, J., Tokura, Y. & Yu, P. *Nature* 2017, 546, 124-128. (2) Kim, Y.-M., Morozovska, A., Eliseev, E., Oxley, M. P., Mishra, R., Selbach, S. M., Grande, T., Pantelides, S. T., Kalinin, S. V. & Borisevich, A. Y. *Nat. Mater.* 2014, 13, 1019. (3) Zhang, Z., Schwanz, D., Narayanan, B., Kotiuga, M., Dura, J. A., Cherukara, M., Zhou, H., Freeland, J. W., Li, J., Sutarto, R., He, F., Wu, C., Zhu, J., Sun, Y., Ramadoss, K., Nonnenmann, S. S., Yu, N., Comin, R., Rabe, K. M., Sankaranarayanan, S. K. R. S. & Ramanathan, S. *Nature* 2017, 553, 68.

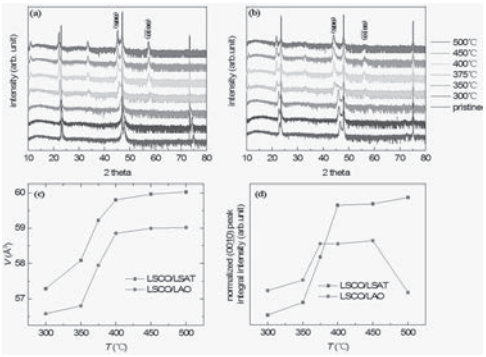


Fig. 1. a, b, Evolution of the XRD pattern of LSCO/LSAT (a) and LSCO/LAO (b) films vs annealing temperature. c, Annealing temperature-dependent unit cell volume for LSCO/LSAT and LSCO/LAO films. d, Normalized annealing temperature-dependent (00$\underline{1}$0) peak integral intensity for LSCO/LSAT and LSCO/LAO films.

BT-09. Analysis of thermal effects in current driven magnetic wires. *T. Sawa*[1], S. Sumi[1], P. Van Thach[1], K. Tanabe[1] and H. Awano[1] *1. Toyota Technological Institute, Nagoya, Japan*

Current-driven domain walls in magnetic nanowires will be one of the attractive candidates for the next generation of low energy consumption memory devices. When domain walls on magnetic nanowires are driven by injected electric current, it is necessary to consider also Joule heating effect for the DW motion. So far, have been few reports on it. Therefore, heat generation and absorption are evaluated in detail. For the measurement, we use a nanoMDS which can observe the magnetic domain image and heat distribution on the magnetic wire with TMR head and Ni sensor [1]. Samples of TbFe alloy magnetic wire with a platinum cover was prepared by sputtering on a thermally oxidized silicon substrate. The wire is 6 um width, 20 um length, and 10 nm thickness. A DC current of 17 mA (current density of 5.7 $\times$ 10^{10} A/m^2) is applied into the nanowire. The measured image of the heat distribution is shown in Fig.1. A temperature gradient from the center of the sample to the electrode was observed. Next, To see the asymmetry component, temperature distribution was measured when the direct current direction was reversed, and a difference image with the above result was taken. The results are shown in Figure 2. In the figure, the red area indicates heat generation, and the blue area indicates heat absorption. It can be confirmed that the left end of the sample generates heat and the right end absorbs heat. From this, we succeeded in seeing the asymmetric heat generation and heat absorption generated by the thin wire. This work was partly supported by JSPS Grant-in-Aids for Scientific Research (17H03240), the MEXT-Supported Program Research Foundation at Private University (2014-2019)

[1] T. Chikamatsu, A. Ogawa, and T. Mizuno; Magnetics Japan 6(6), 357(2011)

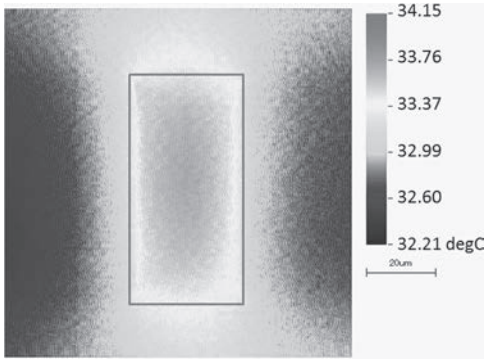


Figure 1 Measurement results of the heat distribution with DC current density of 5.7 ×10^{10} A/m^2. The sample part is represented by a black square.

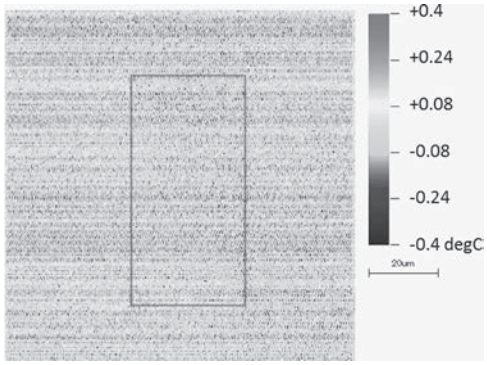


Figure 2 Difference image of temperature distribution in different current directions. The red area indicates heat generation (left edge of the sample), and the blue area indicates heat absorption (right edge of the sample).

BT-10. Tuning Magnetic Anisotropy and Exchange Bias by Interfacial Engineering in Pervoskite Oxide Suplerlattice. *H. Huang*[1], J. Zhang[1], B. Shen[1] and J. Sun[1] *1. Beijing National Laboratory for Condensed Matter & Institute of Physics, Chinese Academy of Sciences, Beijing, China*

The interfacial in oxide heterostructures providing a rich playground to explore emergent interfacial phenomena that arise due to electronic, spin, or orbital reconstruction. One good example is tunning the magnetic anisotropy (MA) of materials by interfacial engineer. Herein we report huge perpendicular magnetic anisotropy of $La_{2/3}Sr_{1/3}MnO_3$ (LSMO) when it sandwiches between $La_{0.8}Sr_{0.2}CoO_{3-\delta}$ (LSCO) on $SrTiO_3$ (STO) substrate, different from the bare LSMO with in-plane magnetic anisotropy. The sketch of LSCO/LSMO/LSCO is shown in Fig 1(a), and the high-angle annular dark-field (HAADF) image of the cross-section is shown in Fig 1(b). Noting that MnO_6 octahedron is connected to CoO_4 tetrahedron at interface of trilayer, enhanced lattice distortion of MnO_6 octahedron near interface, inducing orbital reconstruction and PMA properties[1,2]. The thermomagnetic (MT) curves of the trilayer with in-plane (IP) and out-of-plane (OP) mode are shown in Fig 1(c), and the red triangles mark stands for spin reorientation. The anisotropy constant of the trilayer is calculated as shown in Fig 1(d), the maximal anisotropy constant is as large as ~1.88×10^6 erg/cm^3 at 10K. More interesting, the coercivity enhancement and exchange bias (EB) phenomenons by interfacial effect are also discovered in LSCO/LSMO/LSCO trilayer[3]. The hysteresis loops of trilayer are shown in Fig 2(a). The maximal coercivity field of trilayer is ~6000 Oe at 10K, more than two order than bare LSMO, as shown in Fig 2(b). The minor hysteresis loops after 5T and -5T bias fields at 10K are shown in Fig 2(c). EB of the trilayer is clearly seen and the EB shift as a function of temperature is shown in Fig 2(d).

[1]J Zhang, Z Zhong, X Guan *et al*, Symmetry mismatch-driven perpendicular magnetic anisotropy for perovskite/brownmillerite heterostructures, *Nat. Commun.* 9, 1923 (2018) [2] J Zhang, X Chen, Q Zhang *et al*, Magnetic anisotropy controlled by distinct interfacial lattice distortions at the $La_{1-x}Sr_xCoO_3/La_{2/3}Sr_{1/3}MnO_3$ interfaces, *ACS Appl. Mater. Interfaces,* 10, 40951 (2018). [3] B Li, R. V. Chopdekar, *et al,* Tuning interfacial exchange interactions via electronic reconstruction in transition-metal oxide heterostructures, Tuning interfacial exchange interactions via electronic reconstruction in transition-metal oxide heterostructures, *Appl. Phys. Lett,* 109, 152401 (2016)

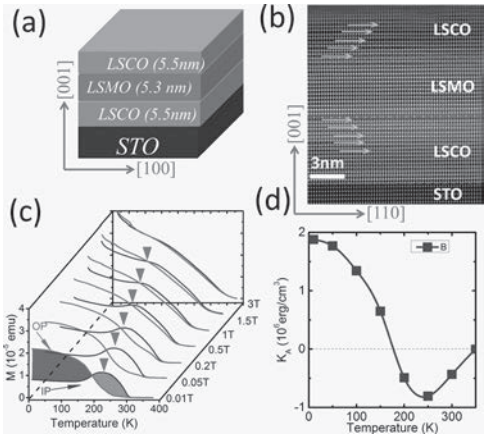


Fig 1(a) The sketch of LSCO/LSMO/LSCO trilayer. (b) HAADF image of trilayer and yellow arrows represent dark stripes. (c) MT curves of the trilayer with IP or OP mode, and red triangles stands for spin reorientation. (d) The anisotropy constant oftrilayer asfunction of temperature.

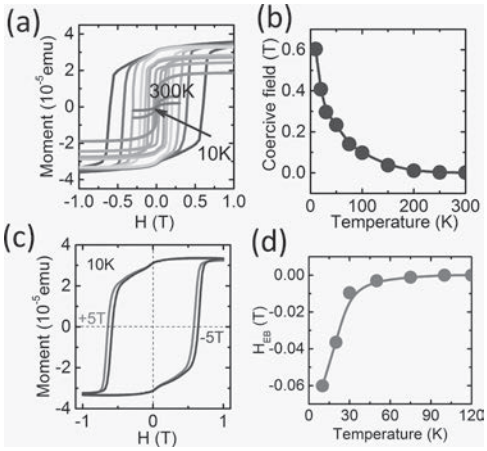
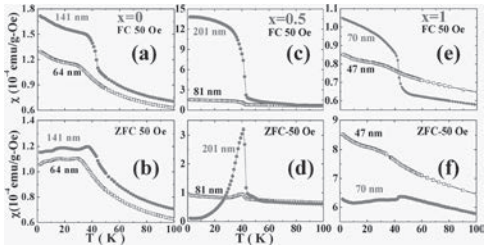


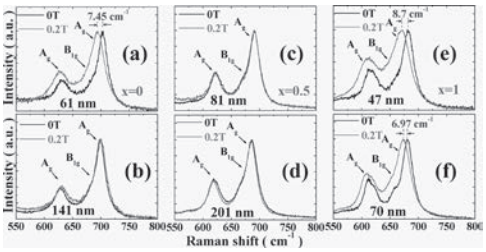
Fig 2(a) The hysteresis loops of LSCO/LSMO/LSCO trilayer at different temperature. (b) The coercivity field as a function of temperature. (c) The minor hysteresis loops of trilayer after 5T and -5T bias fields at 10K. (d) The exchange bias shift as a function of temperature.

BT-11. Inteplay Between Doping and Size Effects of Multiferroic $Y_{1-x}Eu_xMn_2O_5$ Nanorods. T. Hsu[1], *C. Yang*[1], Y. Tung[1], C. Kao[1], W. Wu[1] and K. Lin[2] *1. Chung Yuan Christian University, Taoyuan, Taiwan; 2. Yuan Ze University, Taoyuan, Taiwan*

$Y_{1-x}Eu_xMn_2O_5$ nanorod samples (x = 0, 0.5, and 1) were prepared by hydrothermal method. Each x composition contains two sizes. X-ray diffraction analysis shows that the lattice constants increased with increasing Eu doping and the nanorod size. Magnetic susceptibility experiments revealed that all six samples exhibited antiferromagnetic peaks at around 43 K under zero magnetic field cooling, and all converted to ferromagnetic ones as cooling with a magnetic field. The x = 0.5 sample displayed a relative larger magnetic susceptibility before and after phase transition in both zero field cooling (ZFC) and field cooling (FC), which implied that the doping effect increased the magnetic response near the magnetic phase transition. In the all three difference x of samples, the small-sized nanorods exhibited a weaker change in magnetic susceptibility experiments near the magnetic phase transition temperature. This observation shows that the size effect weakens the strength of the magnetic order. Room temperature Raman spectra of x = 0.5 samples show no shift of all peaks in both <*Lc*> = 81 nm and 201 nm sizes under the zero and 0.2 T magnetic fields. Only the small size of 65 nm YMn_2O_5 sample exhibited peak shift at 0.2 T. In the contrast, all sizes of $EuMn_2O_5$ samples show the peaks shift by the magnetic field. These observations imply that the size effect weakens the force constant between th e magnetic ions in the crystal, so that resulted in the external magnetic field can shift the Raman peaks. However, the doping effect enhanced the force constant and overcome the size effect, thus reducing the influence of the Raman peak on the external field.

Nicola A. Spaldin, S.-W. Cheong, and Ramamoorthy Ramesh, *Physics Today*, October 38-43 (2010). W. Eerenstein, N. D. Mathur, J. F. Scott., *Nature* 442, 759 (2006). Nicola A. Spaldin and Manfred Fiebig, *Science* 309, 391 (2005). E. Asher, H. Rieder, H. Schmid, and H. Stossel, *J. Appl. Phys*. 37, 1404 (1966).





BT-12. Inverse Magnetocaloric Effect in the Cycloidally-modulated Skyrmion Material GaV_4S_8: New Insights into the Metamagnetic Phase Evolution of Noncollinear Spin Textures. *E. Clements*[1], R. Das[7,8], G. Pokharel[2,3], D. Mandrus[4,5], M. Osofsky[6], H. Srikanth[1] and M. Phan[1] *1. Physics, University of South Florida, Tampa, FL, United States; 2. Physics & Astronomy, University of Tennessee Knoxville, Knoxville, TN, United States; 3. Quantum Condensed Matter Division, Oak Ridge National Lab, Oak Ridge, TN, United States; 4. Materials Science and Engineering, University of Tennessee Knoxville, Knoxville, TN, United States; 5. Materials Science and Technology Division, Oak Ridge National Lab, Oak Ridge, TN, United States; 6. Naval Research Lab, Washington, DC, United States; 7. Faculty of Materials Science and Engineering, Phenikaa University, Hanoi, Vietnam; 8. Phenikaa Research and Technology Institute, A&A Green Phoenix Group, Hanoi, Vietnam*

The inverse magnetocaloric effect in materials with noncollinear spin textures reveals essential details about their complex ordering and magnetization processes, including spin fluctuations and thermally-activated metamagnetism. [1,2] Near the paramagnetic (PM) to helicoid and skyrmion lattice (SkL) transitions in B20 FeGe, positive isothermal entropy change to an applied magnetic field (ΔS_M) was associated with the first-order nature of the chiral fluctuation-enhanced transition. [3] Multiferroic GaV_4S_8 (GVS) displays a cycloidally-modulated Néel skyrmion lattice under the influence of easy axis anisotropy. Among several unique phase transitions, the strong anisotropy drives an expansion of the cycloid pitch as temperature is lowered and leads to a ferromagnetic (FM) ground state. [4] GVS also displays magnetoelectric coupling, evident from the excess spin-driven polarization of the magnetic textures. [5] Thus, GVS is an ideal system to examine the effects of anisotropy, coexisting order parameters, and modulated spin ordering on magnetic field-induced caloric effects. We exploit the magnetocaloric effect to analyze ΔS_M as a function of temperature (T) and field (H) across the magnetic phase diagram of GVS (T_C = 13 K). Detailed magnetization versus T data was collected with H applied along each of the three principle cubic axes: [111], [110], [100]. Below 11 K, ΔS_M decreases in a step-like fashion across sequential Cyc to SkL and SkL to FM metamagnetic transitions due to field-induced spin ordering. However, for a narrow temperature regime below T_C, a ridge of positive ΔS_M separates the modulated states from the PM phase. The nature of phase evolution from high T in GVS has not been investigated, and the results open important questions about the mechanisms driving the formation of a noncollinear texture from a disordered phase. By analyzing incremental changes in entropy, dS/dH, we verify the extent of the increasing entropy regime at lower temperatures. Below ~ 5 K, a broad dome of $\Delta S_M > 0$ exists within the expected FM phase. Our results reveal an extended incommensurate-commensurate transition that agrees with the scenario of an anisotropy-driven conversion of the spin cycloid into the FM ground state.

[1] N. Biniskos, K. Schmalzl, S. Raymond et al., Phys. Rev. Lett. 120, 257205 (2018) [2] E. M. Clements, R. Das, L. Li et al., Sci. Rep. 7, 6545 (2017) [3] J.D. Bocarsly, R.F. Need, R. Seshadri et al., Phys. Rev. B 97, 100404(R) (2018) [4] E. Ruff, S. Widmann, P. Lunkenheimer et al., Sci. Adv. 1, 1500916 (2015) [5] J. White, A. Butykai, R. Cubitt et al., Phys. Rev. B 97, 020401(R) (2018)

BT-13. Magnetization studies of Magnetoelectric Coupling in $0.8BaTiO_3$-$0.20Mn_{0.1}Zn_{0.9}Fe_2O_4$ Ceramic Composite. *A. Farheen*[1] and R. Singh[1] *1. School of Physics, University of Hyderabad, Hyderabad, India*

Multiferroics are the materials that contain at least two ferroic orders in them such as electric, magnetic and elastic behaviour simultaneously [1]. The coupling interaction present in the multiferroic materials between various order parameters can develop new effects, such as magnetoelectric effect. [2]. The multiferroic properties of ferromagnetic- ferroelectric composites are due to induced electric polarization in the magnetic order and vice versa. Therefore, the composite multiferroics offer a way to attain magnetic and ferroelectric ordering simultaneously. Composite of $0.8BaTiO_3$+$0.20Zn_{0.9}Mn_{0.1}Fe_2O_4$ was synthesized via solid-state route. X-ray diffraction pattern and microstructure of the sample confirm the coexistence of $BaTiO_3$ (BTO) and $Zn_{0.9}Mn_{0.1}Fe_2O_4$ phases without any detectable third phase. Clear hump in magnetization vs. temperature ($M(T)$) plots (Fig.1(i)) around BTO structural phase transition temperature is an evidence of the origin of strain mediated magnetoelectric coupling. Derivative of zero field-cooled curve (dM/dT vs. temperature plot, Fig.1(ii)) shows clear hump around 190 and 280K which coincide with BTO transition temperatures and not observed in pure ferrite sample. It is well known that BTO has different crystal structure depending upon temperature due to different lattice strains, which represent different ferroelectric phases respectively. The lattice strain generated in BTO phase could be a possible reason for the occurrence of peaks in M (T) plot around transition temperatures. Due to well interface matching this strain will be transferred to the ferrite phase which alters the magnetization of ferrite phase in the composite. Further, sample exhibit magnetic hysteresis (Fig.1(iii)) behaviour which indicates the soft ferromagnetic behaviour of composites with much lower value than pure ferrite. This indicates the existence of non-magnetic ferroelectric phase with ferrite phase [3]. The presence of magnetic and electric hysteresis loop confirms ferromagnetic ordering as well as ferroelectric ordering in the composite sample.

[1] N. A. Spaldin and M. Fiebig, *Science,* vol. 309 (5733), 391-392, 2005. [2] S. W. Cheong and M. Mostovoy, *Nature Materials*, Vol. 6, 12-20, 2007. [3] T. Kimura, T. Goto, H. Shintani, et al *Nature*, Vol. 426, 55-58, 2003.

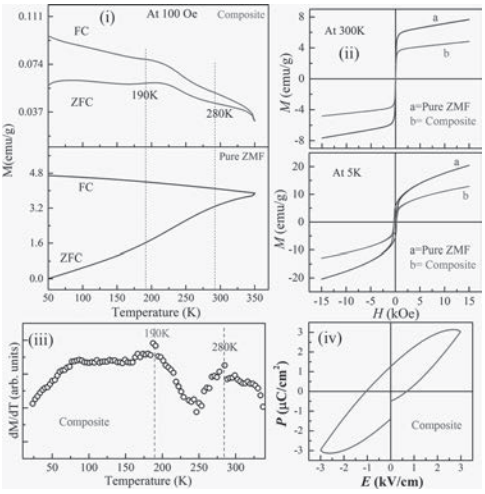
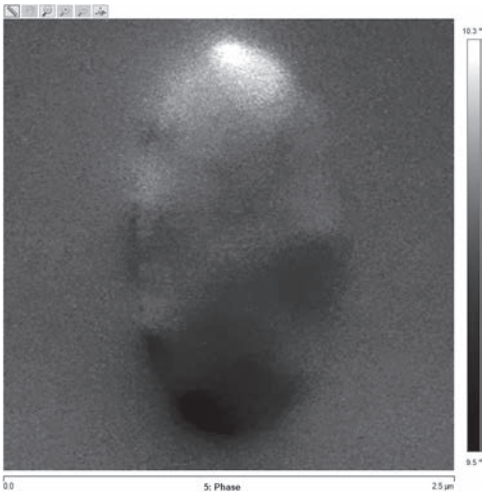


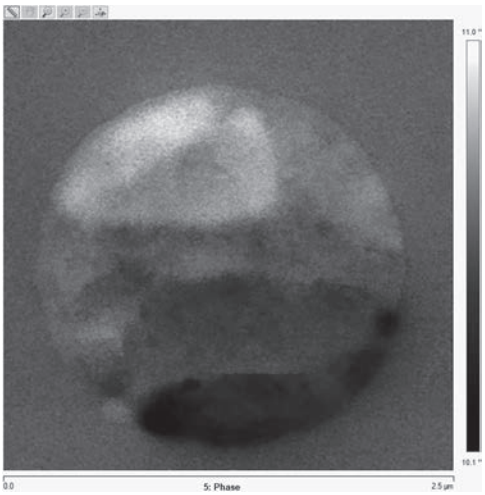
Figure1. M(T), M(H), dM/dT vs. T and P(E) plots of composite

BT-14. Metastable Multi-Domain Effects in FeGa Magnetoelectric Heterostructures for Cell Sorting. *M. Guevara*[1], R. Khojah[2], K. Fitzell[3], G. Carman[1] and C.S. Lynch[1] *1. Mechanical and Aerospace Engineering, University of California, Los Angeles, Los Angeles, CA, United States; 2. Bioengineering, University of California, Los Angeles, Los Angeles, CA, United States; 3. Chemical and Biomolecular Engineering, University of California, Los Angeles, Los Angeles, CA, United States*

Cell Sorting (CS) has been implemented in the field of biomedical devices with potential applications in cell therapy. Current methods of CS lack the ability to control individual cells and optimum imaging feedback. A new method of CS has been proposed that has the potential to overcome these challenges. It consists of using magnetoelectric heterostructure in a microfluidic channel to capture cells containing magnetic particles. An array of FeGa elliptical microstructures on top of PMN-PT is used to capture and release super paramagnetic (SPM) beads. Using the shape anisotropy of the microstructure, a metastable multi-domain (MD) state can be achieve and used to capture SPM beads. Due to the instability of these MD state, the magnetic state can be switching from MD to vortex state through a strain mediated method. Preliminary modeling work has shown the dependency of the MD state on the shape and size (aspect ratio and major axis diameter, respectively). The MD state can be optimized to enhance magnetic flux (e.g. bead capture) and the energy barrier required to switch it into vortex. The MD state observed in the modeling work matches observations using magnetic force microscopy (MFM) imaging, showing that the MD state has an effective magnetization along the easy axis, therefore allowing magnetic flux to leave the structure generating a magnetic field gradient that produces a force on SP particles. The effects of this force are observed in the microfluidic imaging, where the SPM beads are attracted to the poles of the nanoscale magnets.

[1] H. Sohn, M. E. Nowakowski, C. Liang, J. L. Hockel, K. Wetzlar, S. Keller, B. M. McLellan, M. A. Marcus, A. Doran, A. Young, M. Kläui, G. P. Carman, J. Bokor, and R. N. Candler, ACS Nano, 2015, 9 (5), 4814-4826. [2] V. Sampath, N. D'Souza, D. Bhattacharya, G. M. Atkinson, S. Bandyopadhyay and J. Atulasimha, Nano Lett., 2016, 16, 5681-5687. [3] R P Cowburn 2000 J. Phys. D: Appl. Phys. 33 R1. [4] D. Bhattacharya, M. M. Al-Rashid, N. D'Souza, S. Bandyopadhyay, and J. Atulasimha, Nanotechnology, 2017, 28, 015202. [5] R. Lo Conte, Z. Xiao, C. Chen, C. V. Stan, J. Gorchon, A. El-Ghazaly, M. E. Nowakowski, H. Sohn, A. Pattabi, A. Scholl, N. Tamura, A. Sepulveda, G. P. Carman, R. N. Candler, and J. Bokor, Nano Lett., 2018, 18, 1952-1961. [6] C-Y. Liang, S. M. Keller, A. E. Sepulveda, A. Bur, W-Y. Sun, K. Wetzlar, and G. P. Carman, Nanotechnology, 25, 2014, 435701.

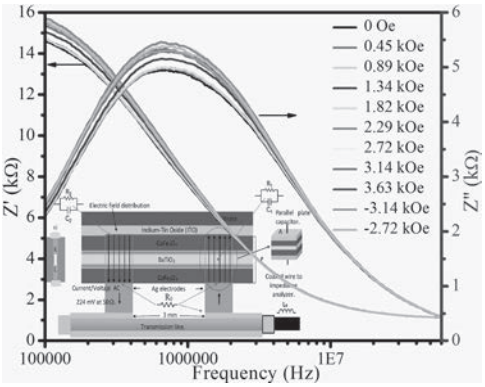


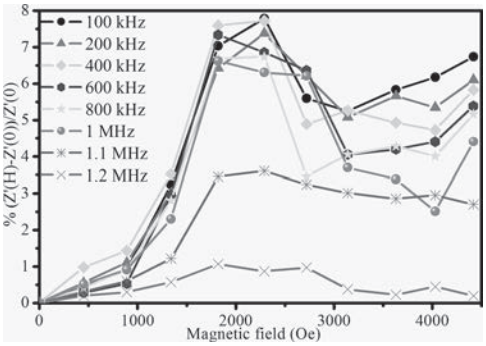


BT-15. Magnetodielectric and electric transport properties of ITO/$CoFe_2O_4$/$BaTiO_3$/$CoFe_2O_4$ multilayer composite. *E. Lopez Moreno*[1], H. Montiel[1] and G. Alvarez Lucio[2] *1. Micro and Nanotecnology, National Autonomous University of Mexico, Mexico City, Mexico; 2. Science and Tecnology, Autonomous University of Mexico City, Mexico City, Mexico*

The magnetodielectric characterization of ITO/$CoFe_2O_4$/$BaTiO_3$/$CoFe_2O_4$ multilayer by Impedance Spectroscopy (IS) is presented for the FM/insulator/FM system deposited by Pulsed Laser Deposition (PLD) on the semiconductor Indium-Tin Oxide (ITO) coated substrate with Ag top electrodes. GIXRD studies confirm spinel-type and hexagonal crystal structure of cobalt ferrite ($CoFe_2O_4$) and barium titanate ($BaTiO_3$) layers, respectively. Raman spectroscopy studies confirm spinel-type structure of $CoFe_2O_4$, while $BaTiO_3$ has a mixture of phases (hexagonal, tetragonal, and amorphous phases). Vibrating Sample Magnetometry (VSM) at room temperature reveals ferromagnetic behavior with high coercivity of 2.9 KOe of multilayer composite, while for individual layers of $CoFe_2O_4$ and $BaTiO_3$ have diamagnetic and ferromagnetic properties, respectively. The chemical characterization was carried out X-ray Photoelectron Spectroscopy (XPS) confirming the correct elemental composition. Real and Imaginary part of impedance data have remarkable changes at different DC magnetic field intensities with an analogous behavior to the magnetoimpedance phenomenon. Furthermore, impedance Z*, electric permittivity ε* and AC conductivity show frequency dependence with changes under magnetic field providing magnetodielectric properties at room temperature. The electric transport of the composite is discussed in terms of the electric response of individual layers where hopping conduction mechanism is attributed to $CoFe_2O_4$, while in $BaTiO_3$ structural disorder or defects can modify the electronic band structure. The obtained multilayer composite we obtained can be proposed as a magnetocapacitive system as it is supported by impedance measurements.

Acknowledgements. The authors acknowledge the LUCE laboratory for the Raman measurements, also we like to thank C. Sánchez-Aké (ICAT-UNAM) for providing the PLD system, and A. Conde Gallardo (CINVESTAV-IPN) for magnetic measurements. We tank to Adriana Tejeda Cruz (IIM-UNAM) and L. Huerta Arcos (IIM-UNAM) for GIXRD and XPS measurements, respectively. Funding information: The authors also acknowledge the financial support provided by the DGAPA-UNAM through the research project PAPIIT AG100517.

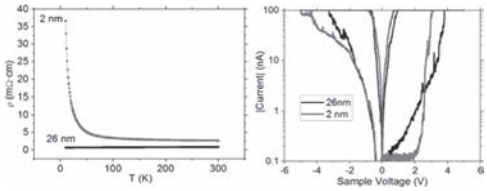




BT-16. Resistive Switching behavior on semimetallic $SrIrO_3$ thin films. V. Fuentes[1], B. Vasic[2], Z. Konstantinovic[2], L. Balcells[1], A. Pomar[1] and *B. Martinez[1] 1. Magnetic Materials and Complex Oxides, ICMAB-CSIC, Bellaterra, Spain; 2. Institute of Physics Belgrade, University of Belgrade, Belgrade, Serbia*

The relation between Metal Insulator Transitions (MIT) and Resistive Switching (RS) is important from the fundamental point of view, but also highly relevant because of the possible applications of RS based devices in non-volatile memories [1]. We studied RS of 5d $SrIrO_3$thin films in the vicinity of a MIT triggered by the reduction of thickness [2]. RS was studied for two characteristic cases: 1. in a thick film which behaves like a semimetal, and 2. in a very thin film which has undergone the MIT and is in an insulating state (see Figure 1). Local electrical properties were measured by means of Conductive Atomic Force Microscopy (C-AFM). In the case of very thin and initially insulating films, I/V curves presented an abrupt increase of the current intensity only for high enough sample voltage indicating a sharp transition into low resistance state (LRS). On the other hand, in the case of initially semimetallic films, this transition was less pronounced without clear threshold voltage for the switching into LRS (see Figure 2). As a result, such different behavior indicates that the MIT has indeed a high impact on the RS. Possible mechanisms of RS in both samples involving oxygen vacancies will be discussed.

1. E. Janod et al., Advanced Functional Materials 25.40 (2015): 6287-6305.
2. A. Biswas et al., Journal of applied physics 116.21 (2014): 213704



Right: MIT triggered by the reduction of thickness. Inset: C-AFM current map with a region in the High Resistance State (dark) and a region in the Low Resistance State (inner bright square). Left: I/V characteristic curves of $SrIrO_3$ thin films showing RS behavior in samples with thickness of 2 nm and 26 nm.

BT-17. Design of efficient p-type spin caloritronic devices using flexible macroscopic interconnected nanowire networks. *T. da Câmara Santa Clara Gomes*[1], F. Abreu Araujo[1], N. Marchal[1] and L. Piraux[1] *1. Institute of Condensed Matter and Nanosciences, Université catholique de Louvain, Louvain-La-Neuve, Belgium*

Spin-dependent thermoelectric mechanisms are at the heart of the rapidly emerging field of spin caloritronics and are crucial steps in designing next generation heat management devices [1,2,3]. Highly efficient flexible spin caloritronic devices using macroscopic network films made of interconnected FM/Cu multilayered nanowires (FM = Co, NiCo, NiFe) were recently fabricated by direct electrodeposition into 3D nanoporous polymer host with no sample size limitation (see Fig. 1) [4,5]. Large magneto-thermoelectric effects have been observed and the spin-dependent Seebeck coefficients were directly obtained, being both negative (n-type) in all those systems. However, significant boost in magneto-thermoelectric performance can be expected in FM/Cu systems where the Seebeck coefficients for the spin-up and spin-down electrons have opposite signs. Such sign asymmetry is possible because the sign and magnitude of the diffusion thermopower depend strongly on the energy derivative of the density of states at the Fermi level, and has already been demonstrated in some FM dilute alloys [6,7]. Moreover, practical thermometric device required both p- and n-type elements. Here, interconnected nanowire networks made of diluted CoCr and NiCr alloys (<5% of Cr) are studied, revealing large modifications in the magneto-transport and thermoelectric properties, as shown in Fig. 2. Negative anisotropic magnetoresistance have been observed, highlighting the large effect of Cr on the density of state (reversal of the resistivity spin asymmetry coefficient) [8]. Moreover, large positive Seebeck coefficients have been obtained in interconnected nanowire networks made of diluted NiCr alloys, opening the door to magnetically tunable p-type thermoelectric devices and, thus, p-n spin caloritronic junctions.

[1] J. He and T.M. Tritt, Science, 357, 6358 (2017). [2] G.E.W. Bauer, E. Saitoh and B.J. van Wees, Nature Materials, 11, 391 (2012). [3] S.R. Boona, R.C. Myers and J.P. Heremans, Energy Environ. Sci., 7, 885 (2014). [4] T. da Câmara Santa Clara Gomes, F. Abreu Araujo and L. Piraux, Science Advances, 5(3), eaav2782 (2019). [5] F. Abreu Araujo, T. da Câmara Santa Clara Gomes and L. Piraux, Advanced Electronic Materials (in press). [6] T. Farrell and D. Greig, Journal of Physics C: Solid State Physics, 3(1), 138 (1970). [7] M.C. Cadeville and J. Roussel, Journal of Physics F: Metal Physics, 1(5), 686 (1971). [8] I. A. Campbell, A. Fert and O. Jaoul. Journal of Physics C: Solid State Physics, 3(1S), S95 (1970).

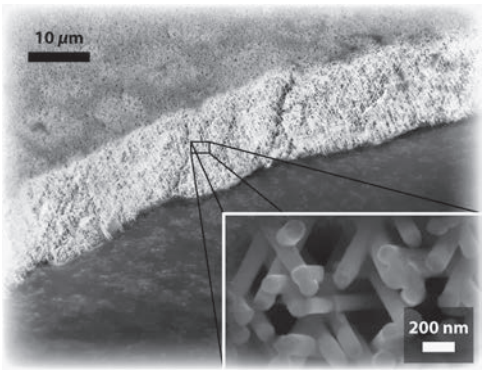


Fig.1: SEM image of a self-supported interconnected NW network film. The inset highlights the NW branched structure.

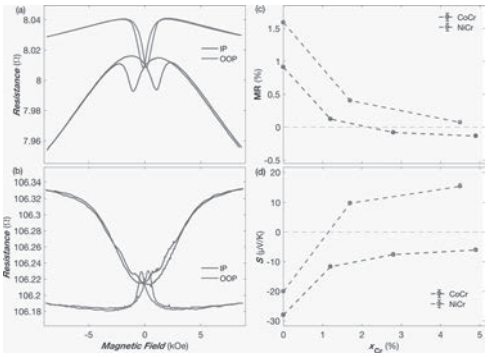


Fig. 2: (a-b) Anisotropic magnetoresistance curves for interconnected nanowire networks made of (a) Co and (b) diluted CoCr alloy (5% of Cr). (c) Magnetoresistance ratio MR and (d) Seebeck coefficient *S* with respect to the Cr contain in interconnected nanowire networks made of CoCr and NiCr diluted alloys.

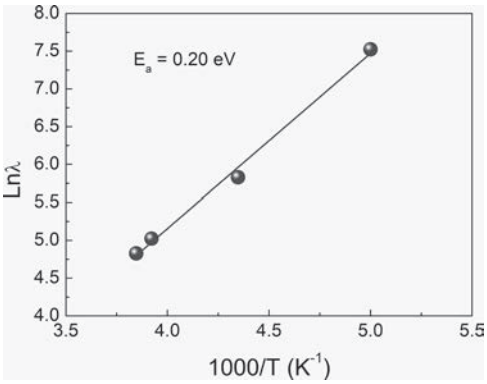
BT-18. Interplay between magneto-elasticity and magneto-electricity in FePt/$BaTiO_3$. *Q. Ain*[1], D. Odkhuu[2], S.H. Rhim[1] and S.C. Hong[1] *1. University of Ulsan, Ulsan, The Republic of Korea; 2. Incheon National University, Incheon, The Republic of Korea*

Using first-principles calculations, the interplay between magneto-electricity (ME) and magneto-elasticity (MEL) is investigated. As a prototype, magnetization of epitaxial FePt heterostructure on $BaTiO_3$ is explored, where TiO_2-terminated interface is taken into account. In particular, the interfacial ME coefficient,a_l= $3.56x10^{-9}$ $G.cm^2/V$, one order larger than Fe/$BaTiO_3$ interface [1], as a consequence of considerable difference in magnetization under the polarization (P) reversal at the interface. Furthermore, strain (η) significantly modifies the interfacial electronic structure when P>0 as compared to P<0. At zero-strain, out-of-plane magnetization is preferred regardless of polarization directions. However, at η =1.75%, magnetization switches from out-of-plane (P<0) to in-plane (P>0). The interplay is analyzed by the different responses of out-of-plane (*xz*and *yz*) and in-plane (*xy* andx^2-y^2) orbitals with respect to strain and polarization, where the magnetization direction is governed by and matrices.

C.-G. Duan, S.S. Jaswal, and E. Y. Tsymbal, *Phys. Rev. Lett*. 97, 047201 (2006).

BT-19. Effect of the magnetic impurity on the charge diffusion in highly dilute Ce doped $LaMnO_3$. G. Cabrera-Pasca[1], B. Bosch-Santos[2], A. Burimova[2], E. Correa[3] and *A.W. Carbonari*[2] *1. Faculdade de Ciências Exatas e Tecnologia, Universidade Federal do Pará - UFPA, Abaetetuba, Brazil; 2. CERPQ, Instituto de Pesquisas Energéticas e Nucleares - IPEN, São Paulo, Brazil; 3. Materials Science Laboratory, National Laboratory of Standards and Technology - NIST, Gaithersburg, MD, United States*

$LaMnO_{3+\delta}$ is a complex oxide, which, depending on the oxygen excess concentration δ, presents different crystalline structure and interesting magnetic and electric properties such as colossal magnetoresistance, polaron dynamics, multiferroic behavior, and charge-orbital ordering. This complexity requires different characterization techniques to draw a picture as complete as possible allowing a good understanding of these phenomena. Here, we have used the perturbed angular correlation (PAC) technique to measure hyperfine interactions at La and Mn sites of $LaMnO_{3+\delta}$ (δ ~0.15) using ^{140}Ce (at La sites) and ^{111}Cd (at both La and Mn sites) as probe nuclei in order to investigate within an atomic scale the magnetic and electric interactions in this compound. Results show that ^{111}Cd nuclei occupy quite high symmetric local sites in agreement with a rhombohedral structure. The magnetic hyperfine field (B_{hf}) measured with ^{111}Cd at La sites is very small (B_{hf} = 0.40 T) due to the supertransferred magnetic field from Mn neighbors through oxygen orbitals. On the other hand, ^{140}Ce nuclei at La sites present a saturation field of around 3.7 T much higher than that expected for La sites (due to the weak transfer field by superexchange mechanism). In addition, for temperature range above the magnetic ordering (200-300 K) a dynamic hyperfine interaction was observed characterized by the attenuation parameter λ(T) whose temperature dependence allowed to determine the activation energy (E_a) associated to the polaron diffusion, as displayed in Fig. 1.



BT-20. Magnetization dynamics of epitaxially grown manganite thin films on (001) oriented ferroelectric PMN-PT substrates. *S. Pati*[1], T. Usami[1] and T. Taniyama[1] *1. Department of Physics, Nagoya University, Nagoya, Japan*

Interfacial multiferroic materials comprising of a ferromagnetic (FM) and a ferroelectric (FE) layer have attracted great attention due to their interesting voltage controlled magnetic phenomena and its applicability in energy efficient spintronic devices [1,2]. Among FM oxides, perovskite manganites particularly $La_{1-x}Sr_xMnO_3$ (LSMO) have potential for a vast range of applications due to the unique properties such as half metallicity, i.e., high spin polarization, and high Curie temperature. In this work, we report on the static and dynamic magnetic properties of LSMO thin films epitaxially grown on (001) oriented ferroelectric (1-x)$Pb(Mg_{1/3}Nb_{2/3})O_3$-x$PbTiO_3$ (PMN-PT, with x=0.3). 100-nm-thick LSMO films were grown using a pulsed laser deposition technique equipped with a Nd:YAG laser of wavelength 266 nm at 650°C. XRD measurement confirms epitaxial growth of samples having out-of-plane lattice parameter c=3.843 Å. Temperature dependent magnetization shows that the Curie temperature, T_C, is around 355 K. In-plane magnetic anisotropy is confirmed from the M-H curve measurements, while the in-plane angular dependence of the remanence ratio reveals isotropic nature of the sample in the plane at room temperature. Room temperature

ferromagnetic resonance (FMR) was measured in in-plane magnetic fields using a vector network analyzer with a coplaner waveguide. A clear single dispersion of the FMR is seen, in contrast to the double dispersion structure on a $SrTiO_3$ substrate. Fitting of the Kittel's equation estimates the effective saturation magnetization of 280 G, the inhomogeneous broadening ($\Delta H(0)$) of 72.6 Oe, and the effective Gilbert damping (α_{eff}) of 0.036. This ensures the high quality of the LSMO based interfacial multiferroic structure, given the immediate relaxation of the lattice mismatch at the LSMO/PMN-PT interface, in agreement with the x-ray diffraction data. From the combined results, the lattice mismatch induced strain in LSMO plays an important role for controlling the static and dynamic magnetic properties. This work was supported in part by JST CREST Grant Number JPMJCR18J1, JSPS KAKENHI Grant Numbers JP17H03377, JP18F18353, the Asahi Glass Foundation, and the Kato foundation for Promotion of Science.

[1] Y. Shirahata et al., *NPG Asia Mater.* 7, e198 (2015). [2] J. Okabayashi et al., *npj Quantum Mater.* 4, 21 (2019).

Session BU
MAGNETIC TUNNEL JUNCTIONS
(Poster Session)

Takahide Kubota, Co-Chair
Tohoku University, Sendai, Japan
Sumito Tsunegi, Co-Chair
AIST, Tsukuba, Japan

BU-01. The Formation Mechanism of the Insulating Amorphous BN Barrier in Magnetic Tunnel Junctions Prepared by Sputtering. *T. Ichinose*[1], K. Elphick[2], A. Hirohata[2] and S. Mizukami[1,3] *1. WPI-Advanced Institute for Materials Research, Tohoku University, Sendai, Japan; 2. Department of Electronic Engineering, University of York, York, United Kingdom; 3. Center for Science and Innovation in Spintronics (Core Research Cluster) and Center for Spintronics Research Network, Tohoku University, Sendai, Japan*

The development of barrier materials for magnetic tunnel junctions (MTJs) have attracted immense attention recently. The one of the candidates is BN. The hexagonal BN barrier has been prepared by using chemical vapor deposition (CVD) or exfoliation. [1, 2] However, in these techniques, the crystal size is limited in micrometer scales, and the transfer of small flakes requires the exposure to atmosphere. Thus, the large-scale deposition and conventional microfabrication techniques should be developed to grow a BN barrier layer. Although the amorphous BN (a-BN) could be formed on various substrates with large-scale, [3] the MTJs with a-BN have not been reported. The one of the issues is preparation of insulating BN due to the difficulty of nitridation. In this work, a-BN thin films were prepared by using sputtering which is suitable for large-scale deposition, and the formation mechanism of insulating BN was investigated, resulting in the observation of the tunnel magnetoresistance (TMR) ratio comparable to that in MTJs with h-BN prepared via CVD or exfoliation. [4] MTJ stacking structures composed of Ta(5)/ Ru(10)/ $Ir_{22}Mn_{78}$(10)/ Co(4)/ BN(t_{BN})/ Co(3)/ Ta(3)/ Ru(7) (thickness in nanometers) were deposited on Si/ SiO_2 substrates via sputtering. All the films were deposited at room temperature (~290 K), and the post-annealing at 523–673 K under a magnetic field of 2 kOe was performed. The magnetization of the bottom Co in the as-deposited sample was ~ 850 emu/cm^3 which was smaller than that of bulk Co, indicating nitridation due to the deposition of a BN overlayer. After post-annealing, the magnetization of the bottom Co layer increased to ~ 1400 emu/cm^3. In addition to the recovery of magnetization of bottom Co, the resistance of MTJs increased 2–3 orders of magnitude. These indicated that the N diffused from a bottom Co into a BN barrier layer via annealing because the Co-N is thermodynamically unstable, which reduced the N deficiency in the BN. The insulating a-BN formed via N diffusion could be used as the tunneling barrier of the MTJs, which showed the TMR ratios of -0.2% (-0.7%) at 300 K (10 K). This work was supported in part by JST CREST (No. JPMJCR17J5), JSPS Core-to-Core Program, and EPSRC (EP/M02458X/1).

[1] M. P.-Banci *et al.*, ACS Nano, vol. 12, p. 4712 (2018). [2] Z. Wang *et al.*, Nano Lett., vol. 18, p. 4303 (2018). [3] N. R. Glavin *et al.*, Adv. Funct. Mater., vol. 26, p. 2640 (2016). [4] T. Ichinose *et al.*, submitted.

BU-02. Effect of Fe and FeCo insertion on MgO-interface of TbFe-Co-based perpendicular magnetic tunnel junction. R.C. Bhatt[1,2], L. Ye[1,2], M. Guo[1,2] and *T. Wu*[1,2] *1. Graduate School of Materials Science, National Yunlin University of Science and Technology, Taiwan, Yunlin, Taiwan; 2. Taiwan SPIN Research Center, National Yunlin University of Science and Technology, Taiwan, Yunlin, Taiwan*

The MgO barrier layer interface is crucial not only for perpendicular magnetic anisotropy of the magnetic layer but also for the preservation of spin alignment for the large tunnel magneto-resistance[1,2]. Here, we study the effect of inserting Fe and FeCo thin layers between the MgO and the magnetic layer in the TbFeCo-based perpendicular magnetic tunnel junction. First, we deposited TbFeCo-MgO half structures as a reference and free layers separately and then the magnetic tunnel junction full structure. Further, in these half and full structures, we inserted Fe and FeCo thin layers to change the MgO interface. The minor and major hysteresis loops of different full structures are compared with the hysteresis curves of free and reference layer half structures, respectively. It is observed that in both the reference and free layer half structures the coercivity decreases on inserting Fe or FeCo thin layer, however, the magnetization remains nearly the same except FeCo for which it is increased. In MTJ full structure, the magnetization decreases to the nearly same value for Fe and FeCo insertion whereas the free layer coercivity increases with Fe and FeCo insertion. The transmission electron microscope images of without and with FeCo insertion MTJ show the MgO interface smoothness for the latter case. We found that the MgO interface roughness could be improved by the insertion of Fe and FeCo thin layer (1-2 nm), however, the effect of MgO interface reconstruction has a different impact on magnetic properties of the TbFeCo-based MTJ.

[1] I-J. Shin, B-C. Min and J-P. Hong, IEEE Trans. Magn. 45, 2393 (2009). [2] S.C. Li, T.J. Chen and C.H. Chang, J. Appl. Phys. 99, 2 (2006).

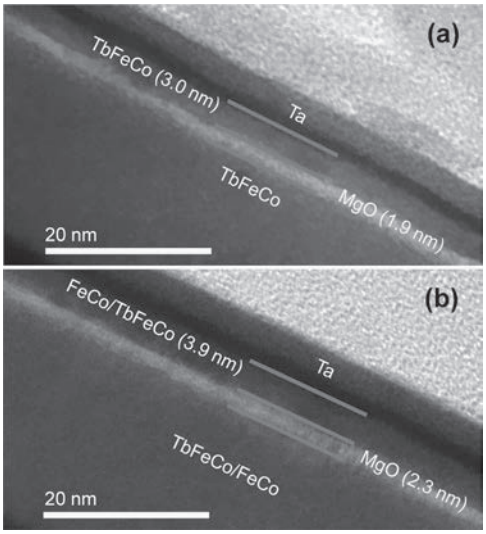


Fig. 1 Transmission electron microscope images of (a) SiO_x/Ta/TbFeCo/MgO/TbFeCo/Ta and (b) SiO_x/Ta/TbFeCo/FeCo/MgO/FeCo/TbFeCo/Ta structures showing the change in roughness of the MgO interface.

BU-03. Role of Boron in Sustaining Magnetic Thermal Tolerance in MgO/CoFeB/Mo Magnetic Tunnel Junction. *C. Yang*[1], C. Yang[1] and C. Lai[1] *1. Materials Science and Engineering, National Tsing Hua University, Hsinchu, Taiwan*

CoFeB/MgO-based magnetic tunnel junction (MTJ) has been considered an outstanding candidate to be applied to the embedded spin-transfer-torque magnetic random access memory (STT-MRAM). This work systematically studies the issues arising from the interdiffusion in an MgO/CoFeB/Mo MTJ system in terms of varying CoFeB's stoichiometries and the temperature of thermal annealing. Employing an Mo cap on CoFeB [1,2] enables the thermal endurance above 400 °C with a sustainable perpendicular anisotropy, which features less diffusion than Ta on the presence of reduced deadlayer (DL). By varying the stoichiometry of CoFeB, $Co_XFe_YB_{20}$ & $Co_XFe_YB_{30}$ [3,4], the magnetic properties of CoFeB were found in a wide tailorable window as a result of the competing diffusion mechanism between CoFeB and adjacent Mo. A clear suppression on DL was achieved upon increasing B composition to 30 at% (Fig. 1) at all the investigated annealing temperatures, which further boosted the H_k in nature. In addition, B also played a significant role of preventing the perpendicular anisotropy from thermal issue above 400 °C. A monotonic increasing on K_{eff} can be observed on the samples with high B composition (Fig. 2), which was absent in the previous reports and suggested the significant improvement of the thermal tolerance in this CoFeB/Mo combination. An optimized MTJ based on this MgO/CoFeB/Mo heterostructure has been proposed to be applied to the high temperature of BEOL process.

[1] T. Liu, Y. Zhang, J. W. Cai, and H. Y. Pan, Sci. Rep. 4, 5895 (2014) [2] K. Watanabe et al., Jpn. J. Appl. Phys., 56, 0802B2 (2017) [3] H. Honjo et al., IEEE. Trans. Mag. 52, 3401104 (2016) [4] J. P. Pellegren et al. AIP Advances 7, 055901 (2017)

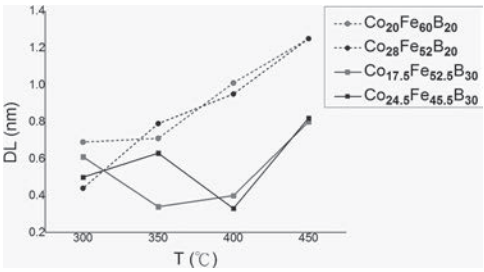


Fig. 1 Magnetic dead layer (DL) thickness as a function of annealing temperature. DL is obtained by the intersection of Ms-thickness$_{CoFeB}$ curve.

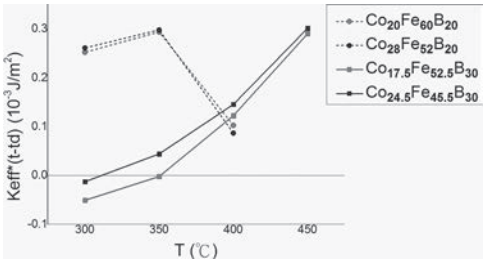
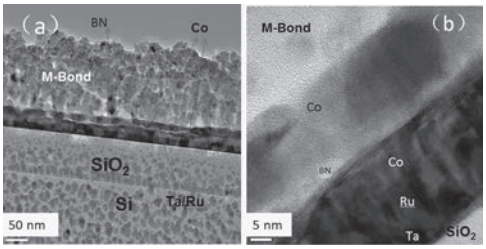


Fig. 2 K_{eff} x ($t-t_d$) versus annealing temperature for all the investigated CoFeB samples. Here K_{eff} is defined by M_s x H_k/2, t=1.5 nm and t_d is the DL thickness corresponding to which obtained at the specific annealing temperature.

BU-04. Investigation on the structural property of the sputtered hcp-phase Boron Nitride tunnel barrier for spintronic applications. *C. Peng*[1] and D. Zhang[1] *1. Electrical and Computer Engineering, University of Minnesota, twin cities, Minneapolis, MN, United States*

As a key building block of the next-generation high density non-volatile memory devices, magnetic tunnel junctions (MTJs) based on MgO tunnel barrier have attracted a significant attention in past decades due to the good performances (1). However, when the MgO tunnel barrier keeps thinning down to realize ultra-low RA with optimal spin transfer torque switching, there are challenges including the non-uniformity, defects and pinholes of MgO tunnel barrier. In addition, to apply the hcp phase perpendicular magnetic anisotropy materials for MTJ stacks, there is a limit for the cubic MgO tunnel barrier. Recently, it was found that the hexagonal boron nitride (hcp-BN) is a promising candidate as a tunnel barrier (2,3). The inert nature of hcp-BN provides a potential good control on the morphology and interface at the atomic scale and could minimize the defects. In this study, MTJ stacks with the hcp-BN tunnel barrier were prepared with a structure of Ta(4 nm)/Ru(20 nm)/Co(7 nm)/BN(8.4 nm)/Co(7 nm)/Ta(5 nm). All the samples were developed on Si/SiO_2 substrates by a magnetron sputtering system with the base pressure better than 5.0×10^{-8} Torr. The Ta (4 nm)/Ru (20 nm) seed layer was deposited at room temperature, and all other layers were deposited at 340°C. Nitrogen/Argon gas was used to deposit the hcp-BN tunnel barrier. The structural property of the MTJ stack is characterized through the cross-sectional TEM. As shown in Fig.1, the Ta/Ru/Co forms a high quality hcp texture, then induces the hcp texture BN layer as well as the top Co layer. This clearly shows that we successfully developed the hcp-BN tunnel barrier for fabricating the hcp textured perpendicular MTJ devices. Magnetic and transport measurements for the prepared MTJ stacks will be reported in the full paper

1. S. Yuasa, et al., Giant room-temperature magnetoresistance in single-crystal Fe/MgO/Fe magnetic tunnel junctions. Nature Materials 3, 868 (2004). 2. S. Parkin, et al., Giant tunnelling magentoresistance at room temperature with MgO (100) tunnel barriers. Nature Materials 3,862(2004) 3. L. Britnell, et. al., Electron Tunneling through Ultrathin Boron Nitride Crystalline Barriers. Nano Letters 12, 1707 (2012). 4. M. Piquemal-Banci, et al., Magnetic tunnel junctions with monolayer hexagonal boron nitride tunnel barriers. Appl. Phys. Lett. 108, 102404 (2016).



BU-05. Tunnel magnetoresistance effect in CoFeB/MgO/metastable bcc Co_3Mn tunnel junctions. K. Kunimatsu[1,2], *T. Tsuchiya*[3], K. Elphick[4], T. Ichinose[2], K. Suzuki[2,5], A. Hirohata[4] and S. Mizukami[2,3] *1. Department of Applied Physics, Tohoku University, Sendai, Japan; 2. WPI Advanced Institute for Materials Research, Tohoku University, Sendai, Japan; 3. Center for Science and Innovation in Spintronics (Core Research Center) and Center for Spintronics Research Network, Tohoku University, Sendai, Japan; 4. Department of Electronic Engineering, University of York, York, United Kingdom; 5. Center for Spintronics Research Network, Tohoku University, Sendai, Japan*

A bulk Co-rich CoMn binary disordered alloy has an antiferromagnetic fcc phase as thermodynamically stable phase [1]. On the other hand, metastable ferromagnetic bcc Co-Mn films have been prepared by molecular beam epitaxy (MBE) technique on optimum substrates such as GaAs [2] and MgO [3]. Here, we report, for the first time, relatively large tunnel magnetoresisitance (TMR) effect in magnetic tunnel junctions (MTJs) comprising of bcc Co-Mn electrode. The stacking structures of the Co-Mn films and the MTJs were MgO(001) sub./ Cr (40)/ Co-Mn(10)/MgO(2)/ Ta(3) and MgO(001) sub./ Cr (40)/ Co-Mn (10)/ Mg (0.4)/ MgO (2)/ CoFeB (4.5)/ Ta (3)/ Ru (5) (thickness is in nm), respectively. The samples were prepared by a magnetron sputtering system. The film composition was $Co_{74}Mn_{26}$ (at.%). The crystalline structures were characterized by x-ray diffraction (XRD) and transmission electron microscopy (TEM). The magnetic properties were measured by a vibrating sample magnetometer (VSM). The microfabrication of the MTJs were performed using a standard photolithography technique. The TMR effect was measured by a four-probe method at room temperature. The out-of-plane XRD measurements showed the 002 peaks from bcc Co_3Mn, however, those from fcc Co-Mn were not detected. The saturation magnetization M_s was approximately 1640 emu/cm^3. This value is similar to the magnetic moment value evaluated by x-ray magnetic circular dichroism for bcc $Co_{76}Mn_{24}$ alloy films [3], rather than that of fcc CoMn alloys with the similar Mn concentration. The MR curves measured at RT for the 40×2 μm^2 MTJ annealed at 350°C is shown in Figure 1. The resistance changes depending on the magnetization configuration are observed, however, the antiparallel state would not be well defined because the MTJ is a pseudo-spin valve type. The maximum TMR ratio was observed as 158% at the annealing temperature of 350°C for 1 hour. The TEM images showed the coherent epitaxial growth of the MgO barrier on the (001) Co_3Mn electrode, indicating possible coherent tunneling [4]. This work was partially supported by CREST (No. JPMJCR17J5), and JSPS Core-to-Core Program.

[1] A. Z. Menshikov, G. A. Takzei, Yu. A. Dorofeev, V. A. Kazan- stev, A. K. Kostyshin, and I. I. Sych, Zh. Eksp. Teor. Fiz. 89, 1269 (1985) [Sov. Phys. JETP 62, 734 (1985)]. [2] D. Wu, G.L. Liu, C. Jing, Y.Z. Wu, D. Loison, G.S. Dong, X.F. Jin, and D.-S. Wang, Phys. Rev. B 63, 214403 (2001). [3] R.J. Snow, H. Bhatkar, A.T. N'Diaye, E. Arenholz, and Y.U. Idzerda, J. Magn. Magn. Mater. 419, 490 (2016). [4] K. Kunimatsu, T. Tsuchiya, K. Elphick, Tomohiro Ichinose, Kazuya Z. Suzuki, A. Hirohata, and Shigemi Mizukami, submitted.

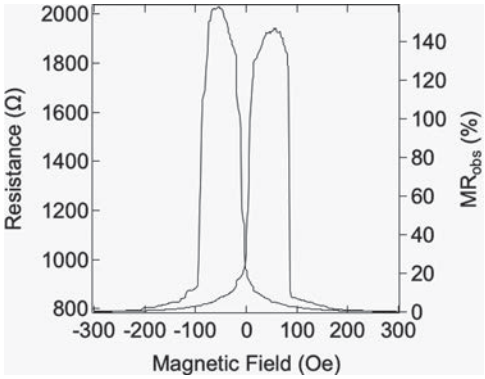


Figure 1: TMR curves of the MTJ with the Co_3Mn electrode.

BU-06. Interface Characterisation Using Non-Destructive Method in MTJ. *K. Elphick*[1], T. Ichinose[2], S. Mizukami[2] and A. Hirohata[1] *1. University of York, York, United Kingdom; 2. Tohoku University, Sendai, Japan*

In the past decade Magnetic random access memory (MRAM) has overcome serval obstacles which increased the performance. [1] Magnetic tunnel junction (MTJ) is the predominant storage unit in MRAM. The performance of MTJ is highly dependent on the barrier interface in MTJ. The most common methods to characterise atomic interfacial structure is high-resolution transmission electron microscopy (HRTEM). [2, 3] However, this is known as a destructive imaging method where the device will be destroyed permanently. We are here to introduce a non-destructive method relying on back-scattered electrons which carries abundant information from the barrier interface. [4] MTJs consisting of Si(substrate)/Ta(5)/Ru(10)/Ta(5)/ CoFeB(10)/ MgO(2)/ CoFeB(2)/ Ta(3)/ Ru(5) (thickness in nm) were prepared by using magnetron sputtering at room temperature. Non-destructive characterisation method was undertaken on two distinctive MTJs, where the corresponding TMR ratios were almost 30 times different. The used acceleration voltages were estimated by the CASINO simulation. [5] SEM images were acquired using 16.4keV and 16.2keV to characterise the top MgO/CoFeB interface, whilst 16.6keV and 16.4keV were used to characterise the bottom CoFeB/ MgO interface. Figure 1a shows the images after image subtraction between the two images collected at two voltages above. Black and white dots in the middle of MTJ were observed representing pinholes in high TMR MTJ. On the other hand, the low TMR MTJ shown in Figure 1b contains fewer black dots. These results may suggest that the high TMR junction may create some pinholes due to the CoFeB/MgO crystallization process. Our results confirm that the capability of the non-destructive method in charaterising MTJ samples. It delivers supportive information for understanding the selective sample interface quality, which can be fed back to the fabrication process. This work is partially supported by JSPS-EPSRC Core-to-core programme (EP/M02458X/1) and JST CREST (JPMJCR17J5). The authors thank financial and technical support by JEOL UK to develop the non-destructive imaging.

[1] S. Bhatti et al., Materials Today 20, 530 (2017). [2] S. W. Ryu et al., J. Alloy. Comp. 747 505 (2018). [3] M. Li et al., Appl. Sur. Sci. 488 30 (2019). [4] A. Hirohata., Nat. Commun. 7 12701 (2016). [5] P. Hovington et al., Scanning 19 1 (1997).

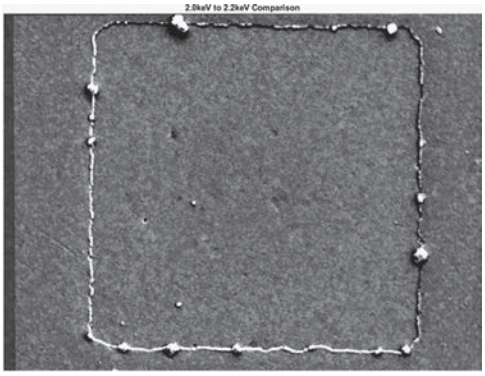
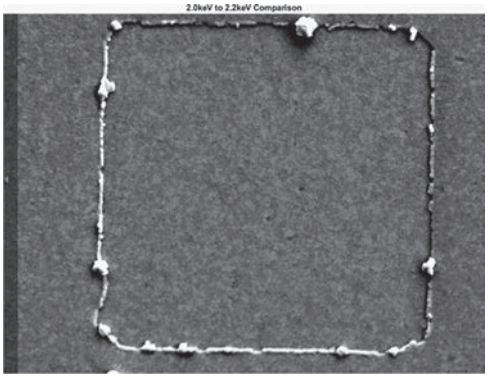


Figure 1. SEM images focusing on the top CoFeB/MgO interface of (a) High TMR; and (b) Low TMR MTJs.



(b) Low TMR MTJs.

BU-07. Effect of capping material on the reduction of write current in perpendicular magnetic-tunnel-junctions for STT-MRAM application.
H. Tomita[1,2], K. Nakamura[1], S. Bosu[1,2], K. Nagasaka[1,2], A. Gomi[1], A. Fukushima[2], H. Kubota[2], K. Yakushiji[2], S. Yuasa[2], H. Maehara[3,2] and N. Watanabe[1] *1. Tokyo Electron Technology Solutions, Nirasaki, Japan; 2. Spintronics Research Center, National Institute of Advanced Industrial Science and Technology (AIST), Tsukuba, Japan; 3. Tokyo Electron Limited, Tokyo, Japan*

Perpendicular magnetic-tunnel-junctions (p-MTJs) with large MR ratio and lower resistance-area (*RA*) products [1] are required for spin-transfer-torque (STT) magnetic random access memory (STT-MRAM) applications. Recently, STT-MRAM has attracted much attention for its potential to replace SRAM, in particular for Last Level Cache (LLC) applications by taking advantage of its non-volatility and scalability. However, LLC applications require high-speed operation, low write current, and as well as low power consumption. One of the major challenges is to develop efficient pMTJ devices with low current operation in order to overcome the bottleneck for substitution of SRAM. In this study, we systematically investigated the effect of capping layer material on magnetic, and electric transport properties to reduce write current in pMTJ devices. In comparison with conventional MgO capping layer [2-4], we used Mg, Ru, and Ta as cap materials to control damping factor, and effective magnetic moment, M_s of the free layer, thereby to reduce the write current. The pMTJ films were prepared by DC magnetron sputtering using Tokyo Electron EXIM™ sputtering system. And the MgO tunnel barrier layer formed by natural oxidation process after metallic Mg layer deposition. Fig. 1(a) shows a schematic image of MTJ films. After deposition, MTJ films were followed by 400 degC post annealing for 1 hour. MR and *RA* properties (Fig. 1(b) and (c)) are almost independent of capping layer material. However, Ms considerably reduces for all other capping layers than conventional MgO cap. From the STT-switching properties of cylindrical nano-pillar pMTJ devices in Fig2, write current (I_{c0}) reduces about 30% than MgO capping layer for using Mg, Ru, or Ta capping layers with maintaining a high thermal stability factor, Δ over 70. In the presentation, we will also discuss the detailed STT-switching properties such as pulse width dependence with different cap materials.

[1] K. Nakamura et al., Intermag, CF-02 (2017) [2] S. Ikeda, et. al., Appl. Phys. Lett. 93 082508 (2008) [3] S. Ikeda, et. al., Nature. Mat. 9 721 (2010) [4] H. Sato, et. al., Appl. Phys. Lett. 101 022414 (2012)

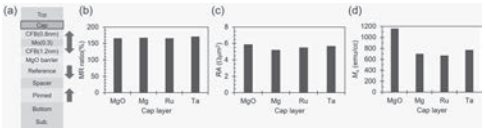


Fig 1 (a) Schematic MTJ film structure. Film properties (b)MR ratio, (c) RA, and (d) Ms of MTJs with MgO, Mg, Mo and Ta capping layer.

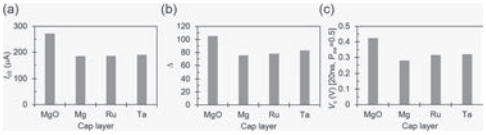


Fig 2 STT-switching properties of patterned pMTJs, (a) I_{c0}, (b) Δ and (c) write voltage (V_c).

BU-08. Development of thermally robust perpendicular MTJ for embedded MRAM application.
S. Bosu[1,2], H. Tomita[1,2], K. Nakamura[1], Y. Tanaka[1], K. Nagasaka[1,2], A. Gomi[1], A. Fukushima[2], H. Kubota[2], K. Yakushiji[2], S. Yuasa[2], H. Maehara[3,2] and N. Watanabe[1] *1. Tokyo Electron Technology Solutions Limited, Nirasakai, Japan; 2. Spintronics Research Center, National Institute of Advanced Industrial Science and Technology (AIST), Tsukuba, Japan; 3. Tokyo Electron Limited, Tokyo, Japan*

Despite recent advances in STT-MRAM technology [1,2], improvement of thermal stability and energy efficiency still remains challenges because of the practical requirement of wide operating temperature range. Furthermore, a perpendicular magnetic tunnel junction (pMTJ) must possess a high thermal budget to withstand semiconductor back-end-of-line (BEOL) [3] process for embedded MRAM application. We report, development of the thermally robust (up to 250 °C) pMTJ by optimizing magnetization, M_s and anisotropy field H_k of CoFeB(CFB) free layer(FL). Low RA(~ 5 Ωμm^2) pMTJ films with high TMR ratio (~165%) were prepared by DC magnetron sputtering with the MgO barrier fabricated by natural oxidation process after metallic Mg layer deposition using Tokyo Electron EXIM™ sputtering system. Fig.1 shows a schematic structure of MTJ film based on two FLs separated by a Mo spacer. In this study we have investigated the effect of CFB FL2 thickness(t_{FL2}) on magnetic and transport properties to improve the thermal stability factor Δ. M_s increases linearly with increasing t_{FL2}(Fig.2(a), whereas, H_k is constant at t_{FL2}= 0.6, 0.8 nm and suddenly drops over 30% at t_{FL2}=1nm(Fig.2(b). Temperature (T) dependence of delta of pMTJ devices with electrical critical diameter, eCD = 80 nm in Fig.2(c) reveals that the Δ increases with increasing t_{FL2}, and decreases monotonically with increasing T. A considerably high Δ = 60 maintained even at T= 200 °C for t_{FL2} = 1 nm. Detail characterization and evaluation results will be reported in the presentation.

[1] S. Ikeda, *et al*., Nat. Mater. 9, 721-724 (2010) [2] M.-C Shih, *et al*., Tech. Dig. Pap.symp. VLSI Technol 2016, 14.1(2016) [3] L. Thomas *et al*., J. Appl. Phys. 115, 172615 (2014)

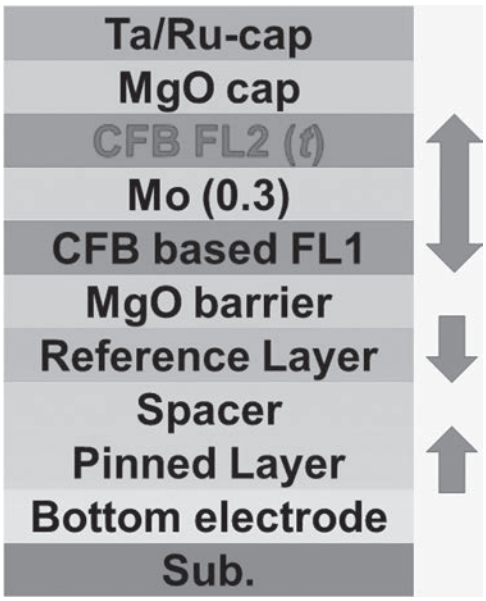


Fig.1: Schematic diagram of MTJ film structure.

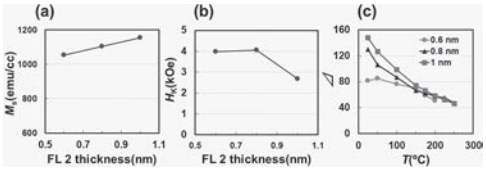


Fig. 2: (a) Magnetization, M_s (b) anisotropy field, H_K as a function of FL2 thickness. (c) temperature dependence of thermal stability factor, Δ for different FL2 thicknesses.

BU-09. Second order interfacial magnetic anisotropy for MgO/CoFeB/Ta films. *T. Ogasawara*[1], M. Oogane[1,2], M. Tsunoda[3] and Y. Ando[1,2]
1. Applied physics, Tohoku University, Sendai, Japan; 2. CSIS, Tohoku University, Sendai, Japan; 3. Electronic engineering, Tohoku University, Sendai, Japan

Magnetic tunnel junctions (MTJs) with MgO can exhibit a high tunnel magnetoresistance (TMR) ratio [1], which leads to the development of highly sensitive magnetic sensor devices [2]. For their electric vehicle applications, a linear output, i.e. low nonlinearity should be achieved for the safe operations, where nonlinearity has been recently reported to depend on the second order magnetic anisotropy, K_2 [3]. Hence, controlling K_2 is significantly important for the reduction of nonlinearity in MTJ sensor devices. Therefore, we have systematically investigated the CoFeB thickness dependence of K_2 and discuss its interfacial contribution in MgO/CoFeB/Ta films. The samples with the stacking of Ta(3)/MgO(2)/$(Co_{1-x}Fe_x)_{80}B_{20}$ (1.2-2.0)/Ta(5) (thickness in nm) were deposited on SiO_2 substrates using dc/rf sputtering at room temperature. All samples were post annealed at 300ºC for the CoFeB crystallization. The magnetic properties were characterized using a SQUID and an angular dependent FMR with microwave frequency of 9.4 GHz. Figure 1 shows an angular dependent resonance field, H_{res} for 1.4-nm-thick CoFeB with x=75. The small dip shown at around θ_H = 33 deg. is due to the easy cone state, which is realized under the condition of K_2/K_1^{eff}<-0.5, where K_1^{eff} is effective perpendicular magnetic anisotropy. Hence, we confirmed the presence of K_2 in CoFeB film. For the investigation of an interfacial effect, as shown in Figure 2, we plotted the areal K_2 against effective thickness, extracting dead layer, t_d of 0.2-0.5 nm for each x. The apparent linear relationships indicate the existence of interfacial K_2, $K_i^{(2)}$ similarly to well defined interfacial K_1^{eff}, $K_i^{(1)}$ [4]. Also, all compositions show negative $K_i^{(2)}$, implying that thinner film prefers smaller K_2 in contrast of well know positive $K_i^{(1)}$. We also found that the $K_i^{(2)}$ increases as increasing x, and shows the maxima of -0.024 erg/cm^2 at x = 100. The control of $K_i^{(2)}$ by CoFeB composition is significantly important to realize a reduction of K_2 leading to small nonlinearity in MTJ sensor devices.

[1] S. Yuasa, T. Nagahama, A. Fukushima, Y. Suzuki, and K. Ando, Nat. Mater. 3, 868 (2004). [2] K. Fujiwara, M. Oogane, Y. Ando et al., Appl. Phys. Express 11 023001 (2018). [3] T. Ogasawara, M. Oogane, M. Tsunoda, and Y. Ando, JSAP spring meeting, 9p-PB1-65 (2019) [4] S. Ikeda, et al, Nature Mater. 9, 721 (2010).

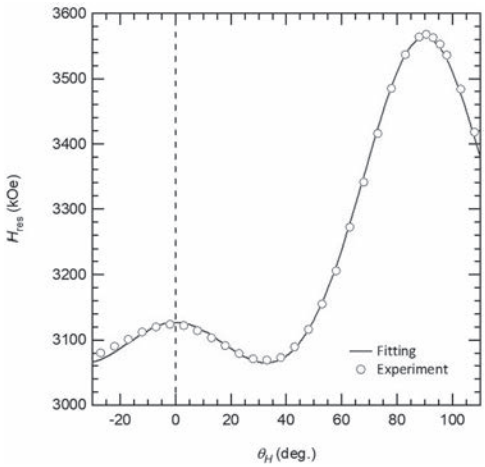


Fig.1 Angular dependent H_{res} of CoFeB (1.4) at x=75

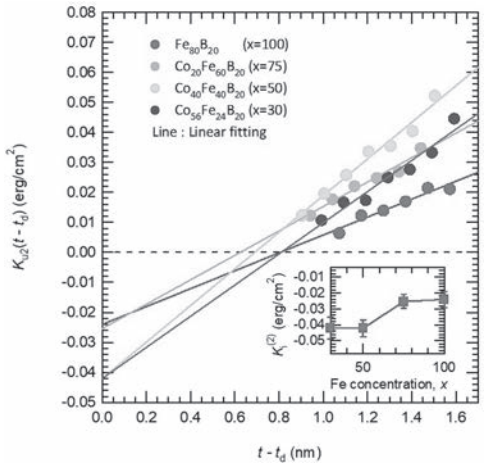


Fig.2 Areal K_2 dependence on effective thickness. The inset shows $K_i^{(2)}$ for each compositions.

BU-10. Detecting interfacial quadrupoles at Fe/MgO interfaces by X-ray magnetic linear dichroism. *J. Okabayashi*[1], Y. Iida[2], Q. Xiang[2], H. Sukegawa[2] and S. Mitani[2] *1. The University of Tokyo, Tokyo, Japan; 2. NIMS, Tsukuba, Japan*

Magnetic tunnel junctions using MgO barrier have been developed by exploiting the strong perpendicular magnetic anisotropy (PMA) of 1.4 MJ/m^3 at the interfaces between MgO and Fe [1]. As a fundamental understanding of PMA induced at the interface between ferromagnetic layer and MgO barrier layer, the interfacial electronic and magnetic states have to be clarified explicitly. There are numerous studies for the interfacial PMA between MgO and Fe including x-ray magnetic circular dichroism (XMCD) and the first-principles calculations [2,3]. For investigating the PMA energy, it is necessary to evaluate the anisotropy of not only orbital magnetic moments but also quadrupole moments through the interfacial strain [2]. In order to investigate the detailed site- and element-specific magnetic properties, we focus on the novel technique using x-ray magnetic linear dichroism

(XMLD) for PMA interfaces which enables to detect the quadrupole and magnetic anisotropy. In this presentation, we report the XMLD technique adopting for PMA at Fe/MgO interfaces and discuss the origin of PMA beyond the anisotropic orbital moments. Samples grown by electron-beam evaporation methods on MgO substrates are stacked as Cr buffer layer and the 0.7-nm-thick Fe layer with MgO capping layer. Post annealing was performed to enhance PMA. XMLD measurements were performed at room temperature using linear polarized beams. Fe $L_{2,3}$-edge X-ray absorption spectra exhibit clear metallic line shapes. XMLD intensities of 2.7 % are detected by the linearly polarized beam. XMLD sum rule suggests that the integrals of XMLD line shapes are proportional to quadrupole moment Q_{zz} and PMA energy [4]. We confirmed that the sign of Q_{zz} is positive; that is, $3dz^2$ orbitals are slightly elongated to out-of-plane direction. Therefore, the results of XMLD are consistent with those analyzed by XMCD line shapes. As for the origin of PMA in Fe/MgO interfaces, we found that orbital moment anisotropy can be a main factor for PMA with the small contribution of Q_{zz}. These results are comparable with the theoretical calculations [2]. In the presentation, we discuss the site-specific magnetic and quadratic properties of Fe/MgO interfaces using XMLD technique.

[1] J.W. Koo *et al.*, Appl. Phys. Lett. 103, 192401 (2013). [2] K. Masuda and Y. Miura, Phys. Rev. B 98, 224421 (2018). [3] J. Okabayashi *et al.*, Appl. Phys. Lett. 105, 122408 (2014). [4] P. Carra *et al.*, Physica B 192, 182 (1993).

BU-11. Polycrystalline $Co_2Fe_{0.4}Mn_{0.6}Si$ Heusler alloy thin films with high *B*2 ordering and small magnetic anisotropy for magnetic tunnel junction based sensors. *N. Kudo*[1], M. Oogane[1], M. Tsunoda[2] and Y. Ando[1] *1. Applied Physics, Tohoku University, Sendai, Japan; 2. Department of Electronic Engineering, Tohoku University, Sendai, Japan*

The measurement of the magnetic field from the heart was successfully demonstrated at room temperature using magnetic tunnel junctions (MTJs) based sensor [1]. However, the sensitivity of MTJs-based sensor is still short for detection of the brain field. Since the sensitivity is defined as TMR ratio / $2H_k$ (H_k: magnetic anisotropy field of the free layer), high TMR ratio and small H_k are required. The $Co_2Fe_{0.4}Mn_{0.6}Si$ (CFMS) Heusler alloy is a candidate to realize the high sensitivity because of the high spin polarization and small H_k [2]. In particular, the polycrystalline CFMS films are useful for reduction of H_k by averaging of the crystalline magnetic anisotropy in the film plane. However, fabrication of the polycrystalline films with high *B*2-phase ordering parameter (S_{B2}), which is required for high spin polarization, is quite difficult. In this study, polycrystalline CFMS thin films were prepared on SiO_2 substrates to realize both high *B*2 ordering and small H_k. To optimize S_{B2} and soft magnetic property of CFMS films, Si/ SiO_2 sub./ Ta(5)/ CoFeB(5)/ Mg(0.4)/ MgO(10)/ CFMS(d_{CFMS})/ Ta(5) (thickness in nm) structure was fabricated by sputtering method and were annealed at various temperature (T_a) in a magnetic field of 1 T. MTJ devices with structure of Si/ SiO_2 sub./ Ta(5)/ CoFeB(5)/ Mg(0.4)/ MgO(10)/ CFMS(75)/ Mg(0.3)/ MgO(2)/ CoFeB(3)/ CoFe(2)/ IrMn(10)/ Ta(5) were also fabricated and characterized by DC 4-probe method. Fig. 1 shows the T_a dependence of S_{B2} for 25-100 nm thick CFMS films. We observed the highest S_{B2} of 83% for 75-nm-thick CFMS films with T_a = 500°C. The obtained S_{B2} was extremely high for polycrystalline Heusler thin films. Fig. 2 shows the T_a dependence of H_k for CFMS films with various d_{CFMS}. The lowest H_k of 4.0 Oe was achieved under the condition of d_{CFMS} = 75 nm and T_a = 500°C. We have also confirmed a small H_k in TMR curves for MTJ devices. The optimized polycrystalline CFMS thin films with high *B*2 ordering and small H_k can realize a very high sensitivity in MTJs-based sensors.

[1] Kosuke Fujiwara *et al.,* : Appl. Phys. Express 11 023001(2018) [2] H-x Liu *et al*., J. Phys. D : Appl. Phys., 48, 164001(2015)

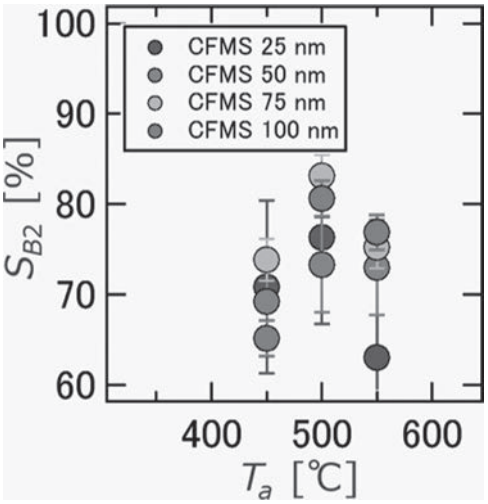


Fig.1 : Annealing temperature dependence of S_{B2} in CFMS films

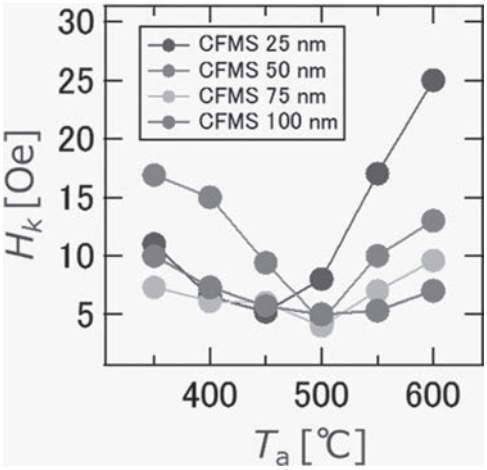


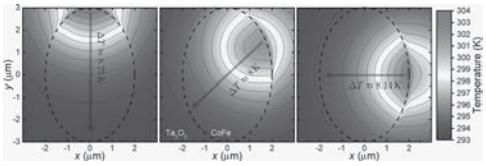
Fig.2 : Annealing temperature dependence of H_k in CFMS films

BU-12. Generating temperature gradients in three-dimensions, the Anomalous Nernst effect in magnetic tunnel junctions. U. Martens[1], T. Huebner[2], H. Ulrichs[3], O. Raimer[2], T. Kuschel[2], R. Tamming[4], C. Chang[4], R. Tobey[4], A. Thomas[5], M. Münzenberg[1] and *J. Walowski*[1] *1. Greifswald University, Greifswald, Germany; 2. Bielefeld University, Bielefeld, Germany; 3. Göttingen University, Göttingen, Germany; 4. Zernike Institute for Advanced Materials, Groningen, Netherlands; 5. IFW, Dresden, Germany*

Thermomagnetic effects are the key elements for energy efficient spintronic and sensing applications. Their application field is the usage of the otherwise wasted heat generated in ever-smaller electronic circuits. In a systematic investigation of three-dimensional temperature gradients created by localized laser heating in magnetic devices, we study the generated thermomagnetic voltages in magnetic devices [1]. We measure the tunnel magneto-Seebeck effect (TMS) and extract the anomalous Nernst effect (ANE) generated on a nanometer length scale by micrometer sized temperature gradients in magnetic tunnel junctions (MTJs). The best conditions to generate the TMS in MTJs is to create the highest possible, homogeneous temperature difference through the layer stack i.e. having the same temperature at each layer thickness. Therefore, the ANE can be extracted by analyzing the influence of in-plane temperature gradients on the TMS in in-plane magnetized pseudo spin valve MTJs based on CoFeB electrodes with uniaxial magnetic anisotropy (UMA) and an MgO tunnel barrier. The direction-controlled

temperature gradients are created by a focused cw diode laser spot. The spatial extent of the measured effects is defined by the elliptically shaped MTJ sized 6 μm×4 μm, while the spatial resolution is given by the laser spot size and the step size of its lateral translation. We investigate the influence of the CoFeB electrodes UMA on the generated ANE voltage in by systematically rotating the temperature gradient in the MTJs plane. Our measurement method is highly sensitive to low voltages and yields an ANE coefficient of $K_N \approx 1.6\times10^{-8}$V/TK for the used CoFeB composition. This is slightly lower than was found for other CoFeB compositions. At such a high sensitivity, the generated ANE effect allows to expand the MTJs' functionality from simple memory storage to nonvolatile logic devices and in combination with the UMA opens new application fields, for example, direction-dependent temperature sensing.

[1] U. Martens et al., Communications Physics, Volume 1, Article number: 65 (2018)



Rotating the in-plane temperature gradients in an elliptically shaped MTJ generated by placing the laser heating spots at the edges.

BU-13. Applying Oblique-Incidence Deposition to Tailor Magnetic Properties of CoFeB in Single Thin Films and TMR Stacks. *K. Schlage*[1], S. Willing[1,2], T. Gurieva[1], M. Ramin Moayed[1] and R. Röhlsberger[1,3] *1. DESY, Hamburg, Germany; 2. PIER Helmholtz Graduate School, Hamburg, Germany; 3. The Hamburg Centre for Ultrafast Imaging, Hamburg, Germany*

CoFeB has developed into one of the most used magnetic materials for tunneling magnetoresistance (TMR) applications. To exploit the TMR effect in a CoFeB-MgO-CoFeB stack, an annealing step is required for templated crystallization and the relative orientation of magnetization in the two CoFeB electrodes needs to change in external magnetic fields. In practice, the latter is often achieved by pinning one of the magnetic layers in an exchange bias structure. Recently, we showed that oblique-incidence deposition (OID) is an easy and flexible technique to tailor the magnetic properties of ultrathin films by inducing additional shape anisotropy [1]. The two angular degrees of freedom during sputter deposition freely tune the orientation of magnetization as well as the coercive field in every single magnetic layer of a multilayer stack. In this contribution, we present the interdependencies of film thickness, deposition angles, thermal annealing and resulting magnetic properties in single CoFeB layers and TMR stacks. From a scientific point of view, OID-CoFeB is very interesting due to a sensitive balance of different anisotropy terms that leads to an anomalous in-plane rotation of magnetization that relaxes upon annealing. From the application point of view, it is possible to tailor switching fields and functionalities of TMR-stacks for the first time in a simple and convenient fashion by choosing appropriate deposition angles and layer thicknesses. A thorough understanding of the OID parameters' influence on magnetic and magneto-resistive properties of CoFeB itself and embedded in a TMR stack could pave the way to custom-designed TMR sensors in the future.

[1] K. Schlage, L. Bocklage and R. Röhlsberger, Adv. Funct. Mater. 26, 7423 (2016)

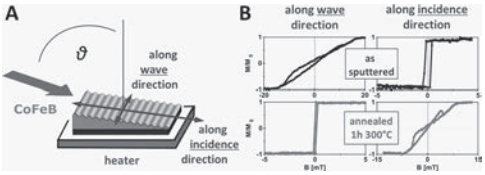


Fig. 1) (A) The wavy surface profile obtained through OID adds a shape anisotropy that supports a magnetic easy axis perpendicular to the particle incidence. (B) However, in thin CoFeB layers, the magnetization is oriented along the incidence direction (sharp switching) in the as-sputtered state and only rotates into the OID-induced direction upon annealing.

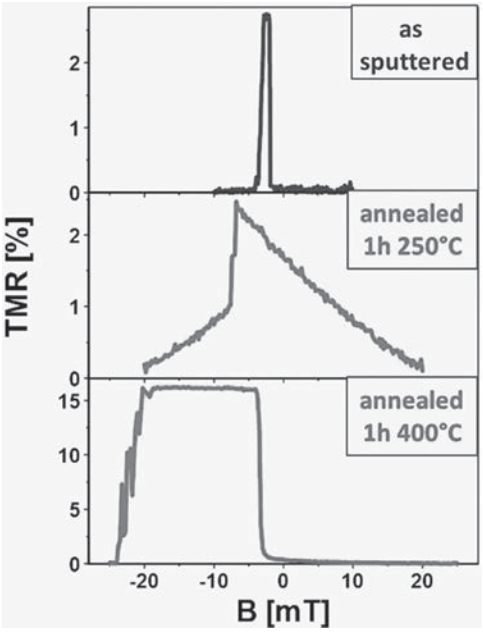


Fig. 2) A TMR stack with OID-induced parallel easy axes shows the 90°-rotation in one of its layers upon partial annealing at low temperature, but assumes the expected plateau shape after about 350°C.

BU-14. Large tunnel magnetoresistance effects in Fe_3O_4(001)/MgO(001)/Fe(001) epitaxial magnetic tunnel junctions. S. Yasui[1], J. Okabayashi[2], T. Yanase[3], T. Shimada[3] and *T. Nagahama*[3] *1. CSE, Hokkaido University, Sapporo, Japan; 2. Research Center for Spectrochemistry, University of Tokyo, Tokyo, Japan; 3. Graduate School of Engineering, Hokkaido University, Sapporo, Japan*

The Fe_3O_4, which is a typical iron oxide with spinel structure, has attracted much attention because of the potential as a spintronic material. It is predicted to be a half-metal with -100% spin polarization theoretically[1], so that large tunnel magnetoresistance (TMR) ratio is expected in the magnetic tunnel junctions (MTJ) with Fe_3O_4 electrodes. However, the TMR ratio remains small value, though many research groups have been worked on the Fe_3O_4-MTJs[2]. Moreover, the sign of the TMR effect varies according to the papers. This is a crucial issue to develop the spintronics with magnetic oxides matters. In this study, we fabricated fully epitaxial Fe_3O_4(001)/MgO(001)/Fe(001) junctions and observed the TMR ratio of -55%. Samples were fabricated by an MBE system with the base pressure of 5×10^{-8}Pa. The sample structures were MgO(001) substrate / MgO(20 nm) / NiO(5nm) / Fe_3O_4(60 nm)/MgO(2.5nm)/Fe(10nm)/Au(30nm). Fe_3O_4 thin film was formed by reactive deposition at a substrate temperature (Tsub) of 573K in an O_2 gas atmosphere of 4×10^{-4} Pa. Then the films were annealed at T_{sub} of 873K for 30 minutes in an O_2 gas atmosphere. MgO tunnel barrier and Fe/Au top electrodes were deposited at room temperature. The junctions of 10x10 μm^2 were fabricated by photolithography, Ar ion milling, and sputtering.

To examine the magnetic states at Fe_3O_4/MgO interface, The XMCD measurements were performed at BL-7A in the Photon Factory (KEK). Figure 1 showed the TMR curve of the Fe_3O_4-MTJ at 80K. We observed TMR of -55% which is the largest TMR ratio in Fe_3O_4-MTJ as far as we know. The negative TMR corresponded with negative spin polarization predicted theoretically. The shape of the TMR curve had small squareness indicating incomplete antiparallel magnetic configuration. The TMR ratio increased with decreasing temperature monotonically, which is similar behavior to previous reports[3]. The bias dependence of TMR and XMCD spectra will be also discussed.

[1] A. Yanase and K. Siratori, J. Phys. Soc. Jpn. 53, 312–317 (1984). [2] M. Opel et al., Phys. Status Solidi A 208 232 (2011). [3] G. Hu and Y. Suzuki, Phys. Rev. Lett. 89, 276601 (2002).

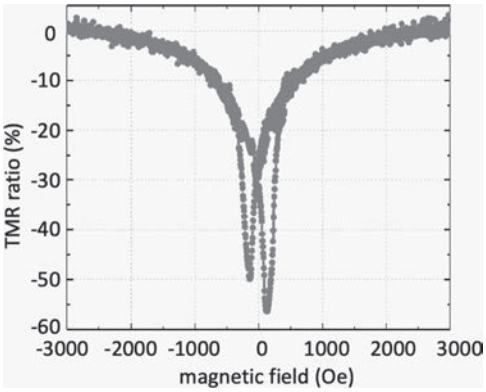


Fig. 1 TMR curve of Fe_3O_4(60 nm)/MgO(2.5nm)/Fe(10nm)/Au(30nm) at 80K.

BU-15. Effects of Resistance States on the Magnetoresistance in Ni/Al_2O_3/Ni by Resistive Switching. *G. Wang*[1], L. Sun[2], S. Zhou[3], Q. Li[1], J. Du[2] and Q. Xu[1] *1. School of Physics, Southeast University, Nanjing, China; 2. School of Physics, Nanjing University, Nanjing, China; 3. Institute of Ion Beam Physics and Materials Research, Helmholtz-Zentrum Dresden-Rossendorf, Dresden, Germany*

The resistive switching (RS) in various materials has attracted much attention due to its interesting physics and potential applications.[1] Conductive filaments have been widely reported as an important mechanism of unipolar resistive switching (URS), which can be manifested by the observation of magnetoresistance (MR) effect if ferromagnetic metallic filaments are formed.[2] In this work, Pt film as bottom electrode, then Ni and Al_2O_3 layers were deposited in turn on SiO_2/Si substrates at room temperature. An array of Ni top electrodes were deposited to obtain the Ni/Al_2O_3/Ni/Pt capacitors. Typical URS can be clearly observed in Figure 1. The device initially is in high resistance state (HRS). After the forming process with current compliance of 1 mA, the device changes to low resistance state (LRS). The LRS changes to HRS at voltage of 0.68 V with increasing voltage from 0 V, which is called the set process. And HRS changes to LRS again at the voltage of 3.84 V during the subsequent voltage sweeping from 0 V. It is understood that Ni^+ ions migrate into Al_2O_3 layer to form the metallic Ni conductive filaments under the external electric field.[2] To further confirm this, we perform the MR measurements. Clear MR effect can be observed when the device is in LRS. We further change the field direction from in-plane to perpendicular, similar positive MR curve can be observed, in contrast the conventional anisotropic MR in Ni film, suggesting the possible giant MR (GMR) effect.[3] No MR is detected in HRS due to the broken of filaments. We further add resistors of various resistance values in serial connect to the device to modify the resistance of the device in LRS (63 Ω, 97 Ω, 114 Ω, 126 Ω). Similar GMR effect is observed, however, the MR value continuously decreases with increasing the resistance in LRS. With increasing the resistance in LRS, the diameter of Ni conductive filaments becomes smaller. Thus, the nonmagnetic scattering at the surfaces of filaments increases, leading to the decrease of MR value.

1. K.M. Kim, D.S. Jeong, C.S. Hwang, Nanotechnology 22, 254002 (2011). 2. D. Zhao, S. Qiao, Y. Luo, et al., ACS Appl. Mater. Interfaces. 9, 10835 (2017). 3. M. Viret, D. Vignoles, D. Cole, et al., Phys. Rev. B. 53, 8464 (1996).

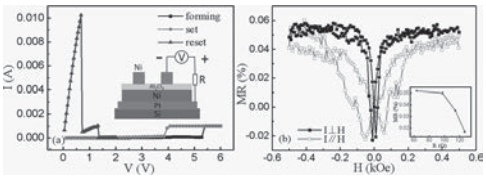


Figure 1. (a) the RS curves, (b) GMR behavior of the device in LRS of 63 Ω. The inset in (a) is the schematic diagram for I–V measurements, and in (b) is the MR in dependence on resistance of LRS.

Session BV
SPIN-ORBIT TORQUES II
(Poster Session)

Aleksandr Kurenkov, Chair
Tohoku University, Sendai, Japan

BV-01. Effect of dc sense current on switching behavior of TbFeCo for SOT applications. *R.C. Bhatt*[1,2], L. Ye[1,2], Y. Zou[1,2], S. Ciou[3], J. Wu[3] and T. Wu[1,2] *1. Graduate School of Materials Science, National Yunlin University of Science and Technology, Taiwan, Yunlin, Taiwan; 2. Taiwan SPIN Research Center, National Yunlin University of Science and Technology, Taiwan, Yunlin, Taiwan; 3. Department of Physics, National Changhua University of Education, Changhua, Taiwan*

The tuning of magnetization, coercivity, and spin-orbit torque (SOT) through composition, film thickness and temperature in the rare earth-transition metal ferrimagnets have revealed enormous possibilities for spintronics applications[1-5]. The control of electrical current in nanoscale devices is important for advanced applications of spintronics. In this work, the influence of a wide range of dc sense currents on the anomalous Hall voltage and switching field in Tb-rich TbFeCo thin film structure have been studied. we deposited Tb-rich TbFeCo thin film structure with a Ta/MgO capping layer. The blanket film showed perpendicular magnetic anisotropy (PMA). The anomalous Hall measurements on two Hall bar widths of 5 and 10 μm were carried out with a series of dc sense currents. The coercivity (H_C) and the switched state anomalous Hall resistivity (ρ_{AHE}) are found to be decreasing with increasing the dc sense current. A sharp drop in ρ_{AHE} and H_C is observed after 1 mA sense current. The investigation on V_{AHE} variation with sense current revealed linear behavior except at large current, where V_{AHE} either drops or saturates. The V_{AHE} behavior is explained by considering the current induced SOT and the Joule heating knowing that the V_{AHE} is proportional to the perpendicular component of magnetization M_Z. At large currents, the SOT field pushes the magnetization away from the Z-direction which drops the M_Z. Further, Joule heating at large currents also drops down the M_Z. The switching speed is estimated by reciprocal of the difference in the saturation and the nucleation field. It is argued that at large dc currents, the switching speed is higher for 10 μm in comparison to the 5 μm Hall bar width. The Joule heating is larger for 10 μm width in comparison to the 5 μm width, which supports the fast switching behavior. This study initiates the sense current effect on device performance in various spintronic applications.

[1] J. Finley and L. Liu, Phys. Rev. Appl. 6, 1 (2016). [2] R.C. Bhatt, L.-X. Ye and Y.-C. Luo, J. Appl. Phys. 125, 113902 (2019). [3] W. Li, J. Yan, and M. Tang, Phys. Rev. B 97, 184432 (2018). [4] R. Ando, T. Komine, and S. Sato, AIP Adv. 8, 056316 (2018). [5] K. Ueda, M. Mann and P.W.P. deBrouwer, Phys. Rev. B 96, 064410 (2017).

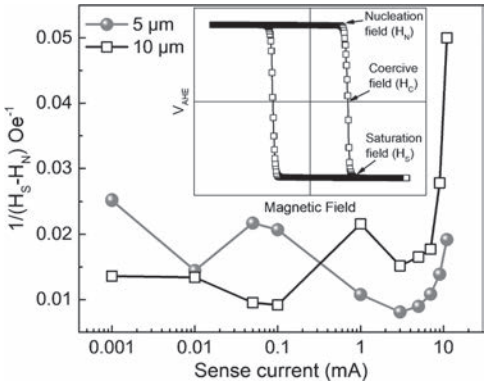


Fig. 1. The plot of reciprocal of difference in saturation field and nucleation field (H_S-H_N) with the applied dc sense current for the two Hall bar widths 5 and 10 μm. The inset defines the various fields in a typical anomalous Hall loop.

BV-02. Spin-Orbit Torques in In-plane Magnetized Systems Driven by Breaking of Inversion Symmetry. *D. Gupta*[1], A. Kumar[1], P. Gupta[1], N. Chowdhury[1] and P.K. Muduli[1] *1. Physics, Indian Institute of Technology Delhi, New Delhi, India*

The injection of charge current into a system comprising of a heavy metal (HM) and a ferromagnet (FM) can produce a spin-orbit torque (SOT)[1], which can be used to manipulate the magnetization of the FM layer. SOT can have two origins, namely, spin Hall effect[2] (in bulk HM layer), and Rashba effect[3] (at FM/HM interfaces). Harmonic Hall measurements have been widely used to study SOT in systems with perpendicular magnetization anisotropy[4,5]. In this work, we have studied two different sputter deposited in-plane magnetized anisotropic systems; NiFe(10 nm)/Ta(2 nm) (S1) and Ta(5 nm)/CoFeB(10 nm)/MgO(4 nm) (S2) to investigate the role of breaking of the inversion symmetry in SOT generation. We have fabricated Hall bar structures (500×50 μm^2) using lift-off technique. We used a recently proposed harmonic Hall measurement[6] method to simultaneously measure the damping like (H_{DL}) and field-like (H_{FL}) effective fields. In this measurement, we use a vector magnet assembly, which consists of two electromagnets. The field along the x-axis was used to saturate the sample while the field along the y-axis was varied and the first (R_w) and second (R_{2w}) harmonic resistances were measured. Figure 1 (a, b) shows the variation of R_{2w} with the applied field in the perpendicular direction of current (H_y) in the presence of the fixed field H_x = ±100 Oe and ±200 Oe for S1 and S2 respectively. According to Ref. 5, the sign of R_{2w} should change on reversing the direction of magnetization or the magnetic field. In the case of S1, R_{2w} does not show any sign change on reversing the sign of H_x, while, R_{2w} does changes its sign with the H_x for S2. This result shows the absence of SOT in S1. The presence of oxide layer, which breaks the inversion symmetry along the growth direction, is found essential to observe SOT. We have quantified the H_{DL} and H_{FL}. A linear variation is obtained for their current dependence and is shown in Fig. 1 (c, d).

[1] A. Manchon and S. Zhang, Phys. Rev. B 79, 094422 (2009). [2] J. Hirsch, Phys. Rev. Lett. 83(9), 1834 (1999) [3] A. Manchon *et al.* Nat.

Mater. 14(9), 871 (2015) [4] U.H. Pi *et al.* Appl. Phys. Lett. 97(16), 162507 (2010). [5] K. Garello *et al.* Nat. Nanotechnol. 8(8), 587 (2013). [6] F. Luo *et al.* Phys. Rev. B 95, 174415 (2017)

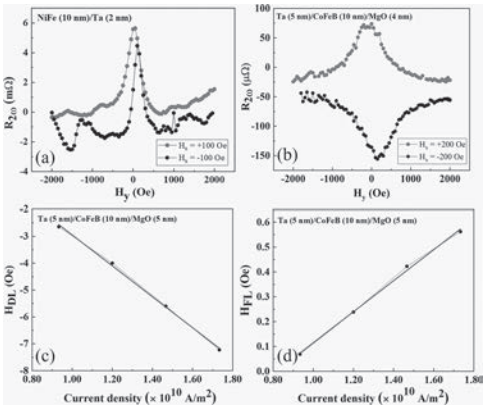


Fig1:Variation of R_{2w} with the applied field (H_y) in presence of constant field H_x in two opposite directions for (a) NiFe(10nm)/Ta(2nm) and (b) Ta(5nm)/CoFeB(10nm)/MgO(4nm) at current density of 0.8×10^{10}A/m^2 and 1.73×10^{10}A/m^2 respectively, and the current dependence of (c) H_{DL} and (d) H_{FL} for S2.

BV-03. Spin-Orbit Torque Driven Perpendicular Magnetization Reversal in Pt/(Co/Ni) Patterned Multilayers. *N. Figueiredo-Prestes*[1,2], S. Collin[1], J. Zarpellon[2], L. Vila[3], N. Reyren[1], D.H. Mosca[2] and J. George[1] *1. Unité Mixte de Physique, CNRS, Thales, Univ. Paris-Sud, Université Paris-Saclay, Palaiseau, France; 2. Universidade Federal do Paraná, Curitiba, Brazil; 3. Université Grenoble Alpes, CEA, CNRS, Grenoble INP, INAC, SPINTEC, Grenoble, France*

An important goal of current spintronics research is the development of efficient and reliable ways to produce spin-polarized electrical currents. In classical spintronics, such spin-polarized currents are obtained when a charge current passes through a magnetic material. A new approach for the generation of spin-polarized electrical currents takes advantage of the spin-dependent scattering notably observed in heavy metals. This phenomenon is related to the spin Hall effect (SHE) and could be extended to Edelstein effect in 2D materials [1]. Spin-orbit torques (SOT) produced by such spin currents have the advantage to eliminate the need for a magnetic layer and to dissociate the spin current from the charge current. It is established that using small in-plane fields, it is possible to reverse thin magnetic layers with perpendicular anisotropy [2]. Nevertheless, the origin and the microscopic understanding of the spin current absorption mechanisms at the interface are still debated. Here, we present a recent work on the perpendicular magnetization reversal induced by SOT of micronic and submicronic patterns of [Co(0.2nm)/Ni(0.6nm)]x5 multilayer films on top of 6-nm-thick Pt electrodes. The electrically induced switching process details is probed by anomalous Hall effect measurements and Kerr microscopy. It leads, as recently reported [3], to a deterministic nucleation of magnetic domain involving the field- and damping-like torques and the Dzyaloshinskii-Moriya interaction (DMI). We measured switching diagrams for disks (Figure 1) for in-plane field directions and current. In light of these experiments and micromagnetic simulations, we will discuss the key parameters needed to understand the magnetization reversal.

[1] J. Sinova, S. O. Valenzuela, J. Wunderlich *et al*, *Reviews of Modern Phys*ics 87, 1213 (2015) [2] I. M. Miron, K. Garello, G. Gaudin *et al*, *Nature* 476, 189 (2011); L. Liu, C. Pai, Y. Li *et al*, *Science* 336, 555 (2012); J.-C. Rojas-Sánchez, P. Laczkowski, J. Sampaio *et al*, *Applied Physics Letters* 108, 082406 (2016) [3] M. Baumgartner, K. Garello, Johannes Mendil *et al*, *Nature Nanotechnol*ogy 12, 980 (2017)

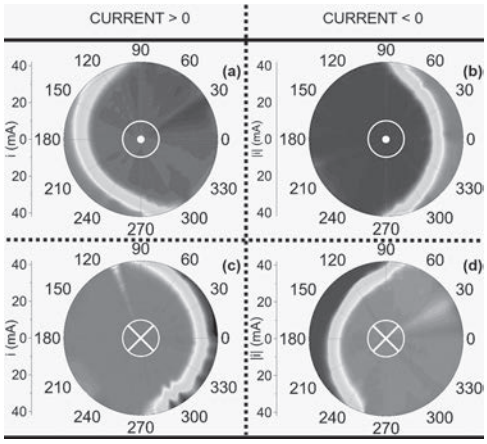


Figure 1: Color-coded AHE resistances as a function of the current amplitude (radial axis) and the direction of the external field (polar axis). Blue corresponds the low-resistance state, where the disks' magnetizations point towards the Pt layer, *i.e.* $m_z < 0$; red corresponds $m_z > 0$.

BV-04. Spin-orbit torque acting on a perpendicularly-magnetized Py. *T. Chen*[1], Y. Ou[2], R. Buhrman[2] and C. Pai[1] *1. National Taiwan University, Taipei, Taiwan; 2. Cornell University, Ithaca, NY, United States*

Current-induced spin-orbit torque is an efficient mechanism to drive magnetization switching [1]. When a charge current flowsin heavy metal (HM) layer with large spin-orbit interaction, the spin Hall effect (SHE) therein generates a transverse spin current that will flow into the ferromagnetic layer (FM). However, the transmission of this spin current or spin transparency at the HM/FM interface will also strongly affect the resulting SOT efficiency acting on the FM layer. The effective dampinglike SOT (DL-SOT) efficiency of a particular heterostructure therefore should be expressed as, where and represent the internal spin Hall ratio of HM and the HM/FM interfacial spin transparency factor, respectively. In this work, we show that Py, a commonly used soft ferromagnetic material with weak anisotropy, which iswidely used as in-plane magnetized FM layer in the ST-FMR measurement [2], can become perpendicularly magnetized while depositing Ta buffer layer with Hf or Zr insertion layers (ILs) and an MgO capping layer. By using harmonic voltage measurement [3] and hysteresis loop shift measurement [4], the damping like spin-orbit torque efficiency are systematically characterized and the current-induced switching are also demonstrated in both heterostructures. We find that though Ta has a significant spin Hall effect, the DL-SOT efficiencies are small in systems with the Ta/Py interface compared to that obtained from the control sample with the traditional Ta/CoFeB interface. Our results indicate that the spin transparency for the Ta/Py interface is much less than that for the Ta/CoFeB interface, which might be related to the variation of spin mixing conductance for different interfaces.

[1] L. Q. Liu, C.-F. Pai, Y. Li, H. W. Tseng, D. C. Ralph, and R. A. Buhrman, Science 336, 555 (2012). [2] L. Q. Liu, T. Moriyama, D. C. Ralph, and R. A. Buhrman, Phys. Rev. Lett. 106, 036601 (2011). [3] J. Kim, J. Sinha, M. Hayashi, M. Yamanouchi, S. Fukami, T. Suzuki, S. Mitani, and H. Ohno, Nature Materials 12, 240 (2012). [4] C. F. Pai, M. Mann, A. J. Tan, and G. S. D. Beach, Physical Review B 93, 144409 (2016).

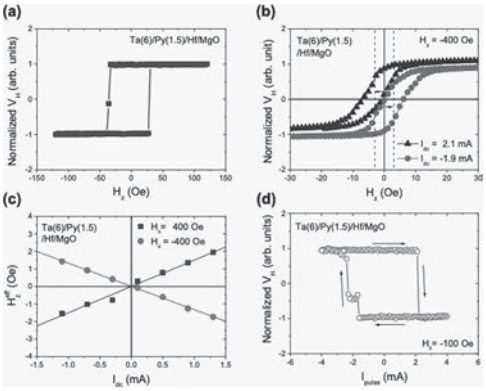


Fig 1. (a) Out-of-plane hysteresis loop from a Ta(6)/Py(1.5)/Hf(0.2)/MgO(2) Hall-bar device obtained from anomalous Hall effect (AHE). (b) Current-induced hysteresis loop shift measurement results obtained from a Ta(6)/Py(1.5)/Hf(0.2)/MgO(2) Hall-bar device with H_x= -400 Oe and different applied currents I_{dc}. (c) Current-induced effective field of a Ta(6)/Py(1.5)/Hf(0.2)/MgO(2) as functions of Idcfor H_x= ±400 Oe. (d) Current-induced switching loop of a Ta(6)/Py(1.5)/Hf(0.2)/MgO(2) Hall-bar device measured with H_x= -100 Oe.

BV-05. Material and Thickness investigation in Ferromagnet/Ta/CoFeB Trilayers for Enhancement of Spin-orbit torque and Field-free Switching. Y. Oh[1], *J. Ryu*[1] and B. Park[1] *1. Materials Science and Engineering, Korea Advanced Institute of Science and Technology, Daejeon, The Republic of Korea*

The generation of spin current in a magnetic nanostructure has drawn a great deal of attention because it can be used to efficiently manipulate the magnetization via in-plane current induced spin-orbit torque (SOT)[1, 2]. In a conventional SOT structure of a heavy metal (HM)/ferromagnet (FM) bilayer, the direction of spin polarization is aligned in the film plane, thus an external magnetic field is required for the SOT-induced switching of perpendicular magnetization. On the other hand, our previous study demonstrated that a spin current generated at FM/Ti interface in FM/Ti/CoFeB magnetic trilayers[3,4] has spin polarization along out of plane direction, enabling field-free switching. Here, we report SOTs in FM (CoFeB, NiFe)/Ta/CoFeB trilayers, in which the spin current generated by spin Hall effect (SHE) in Ta can be combined with the interface-generated spin current at the FM/Ta interface. Figure 1 shows the first (V_{1w}) and second (V_{2w}) harmonic Hall voltages as a function of in-plane magnetic fields (B_x or B_y) for the samples with various Ta thicknesses t_{Ta}. This shows that the sign of the SOTs depends on the FM when t_{Ta} is thinner than 1.5 nm, demonstrating that the SOTs are dominated by the spin current in bottom FM/Ta interface. However, as t_{Ta} increases, the sign of the SOTs follows spin Hall angle of Ta, indicating the SOTs mainly rely on the SHE in Ta. Furthermore, we observe field-free magnetization switching in the Ta thickness ranges, where a sizable amount of the interface-generated spin current in the CoFeB/Ta bilayers is present (Fig. 2). Our study demonstrates that SOTs in trilayers are determined by the contributions of interface-generated spin current in bottom FM/Ta and SHE in Ta, suggesting that a proper material combination in the trilayer provides a way for optimistic material engineering of SOT-based applications.

[1] I. M. Miron *et al*., Nature (London) 476, 189 (2011). [2] L. Liu *et al*., Science, 336, 555 (2012). [3] S-h. C. Baek *et al.*, Nat. Mater. 17, 509 (2018). [4] V. P. Amin, J. Zemen, M. D. Stiles, 121, 125805 (2018).

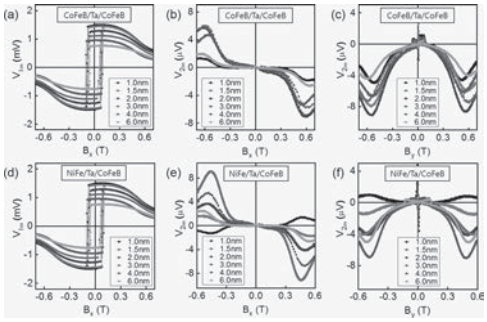


Fig. 1. Harmonic Hall measurement. (a) V_{1w} and (b, c) V_{2w} vs B_x and B_y in CoFeB/Ta/CoFeB. (d) V_{1w} and (e, f) V_{2w} vs B_x and B_y in NiFe/Ta/CoFeB.

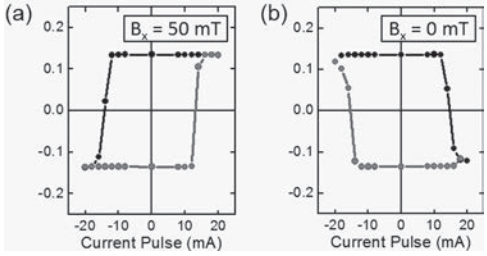


Fig. 2. SOT-induced switching in CoFeB/Ta/CoFeB with (a) B_x=50 mT and (b) B_x=0 mT. Note that magnetization of bottom CoFeB in (b) is aligned to –x direction.

BV-06. Yttrium Iron Garnet Thin Films with Perpendicular Anisotropy and Low Damping — Sputtering Growth and Spin-Orbit Torque-Induced Switching. *J. Ding*[1], C. Liu[1], Y. Zhang[1,2], U. Erugu[3], Z. Quan[4], R. Yu[5], S. Mo[1], S. Yang[1], O. Lockwood[1], H. Ding[5], X. Xu[4], J. Tang[3], X. Yang[2] and M. Wu[1] *1. Colorado State University, Fort Collins, CO, United States; 2. Huazhong University of Science and Technology, Wuhan, China; 3. University of Wyoming, Laramie, WY, United States; 4. Shanxi Normal University, Linfen, China; 5. Nanjing University, Nanjing, China*

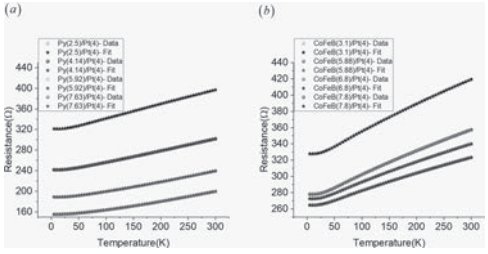
One can use spin-polarized currents or spin currents to drive domain wall motion in magnetic thin film strips or wires. This phenomenon has potential applications in energy-efficient memory and logic devices, such as race-track memory. To realize high-dense memory, thin films with perpendicular magnetic anisotropy (PMA) are needed; to achieve fast domain wall motion, films with low damping are desired since in general the speed of domain walls is inversely proportional to the damping constant. To date, the research on this subject has been based mainly on metallic PMA thin films that usually show relatively large damping due to magnon-electron scattering. It is well known that damping in magnetic insulator $Y_3Fe_5O_{12}$ (YIG) is lower than in any other magnetic materials, but the anisotropy in YIG films is usually very weak and the magnetization is usually confined in-plane due to the demagnetization field. Here we report the realization of low-damping YIG thin films with PMA. The films are epitaxially grown on single-crystal, (111)-oriented, substituted gadolinium gallium garnet (SGGG) substrates by sputtering. Due to the lattice mismatch between the films and the substrates, in-plane tensile strain presents in the YIG films and induces strong PMA in the films. The films show smooth surfaces, (111) orientation, square magnetic hysteresis loops, and low damping. For example, a 6-nm-thick YIG film showed a rms surface roughness of 0.3 nm, an effective PMA field of 2200 Oe, a coercive field of 60 Oe, a hysteresis loop squareness of almost 100%, and a Gilbert damping constant of about 4.8×10^{-4}. Note that the damping constant was determined using perpendicular fields; it is about one or two orders of magnitude lower than the values reported previously for PMA thin films. Anomalous Hall effect (AHE) was detected in YIG(6 nm)/Pt(5 nm) bi-layers. Via AHE measurements, current-induced magnetization switching was demonstrated on the YIG/Pt

bi-layers at room temperature. The switching current density is 0.8 MA/cm^2, which is significantly lower than in most of the previous spin-orbit torque-induced magnetization switching experiments.

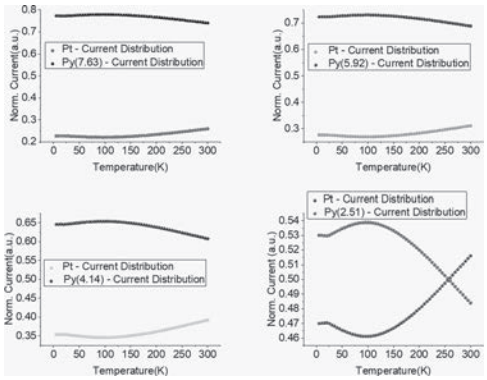
BV-07. Spin-Orbit Torque in Heavy Metal/ Ferromagnetic Bilayers.
H. Kannan[1], Y. Ou[2], R. Barri[3], H. Chen[3], K. Haughey[3], M. Doty[2] and J. Xiao[3] *1. BE Metals, Intel Corporation, Hillsboro, OR, United States; 2. Materials Science and Engineering, University of Delaware, Newark, DE, United States; 3. Physics and Astronomy, University of Delaware, Newark, DE, United States*

In the past, the current-driven spin-orbit torques (SOT) in metallic ferromagnetic/heavy metal (FM/HM) bilayers were analyzed by neglecting the current in FM layer. However, it has been revealed recently that an electric current through a FM layer can introduce SOT not only in a neighboring FM layers [1,2], but also in itself [3]. Therefore, the contribution to SOT from the current in FM layer in FM/HM bilayers cannot be ignored. While developing analytical expressions for interface contribution to current-induced SOT, Kim, et al [4] have concluded, that the currents in both FM and non-magnetic (NM) layers contribute to the SOTs with additive field-like torque and canceling damping-like torque. In this work, we aim to verify the contribution to SOT from the FM layer in FM/HM bilayers. We design the bilayers with the same HM (Pt) but FMs of markedly distinct resistivities, such as NiFe and CoFeB. Therefore the current distribution is very different in HM and FM layers in two systems. In addition, the temperature coefficients of resistivity (α) for the chosen materials are also very different with $\alpha_{CoFeB} << \alpha_{NiFe} \sim \alpha_{Pt}$. Consequently, the current distribution in HM and FM remains similar in Pt/NiFe but changes in Pt/CoFeB as a function of temperature. The temperature dependent resistance of the bilayer structures are shown in Fig. 1, and derived temperature dependent current distributions in FM and HM layers are depicted in Fig 2. The temperature dependence of field-like and damping-like torques have been measured using magneto-optical Kerr (MOKE)-based spin-orbit torque magnetometer [5]. Experimental results will be compare to theoretical predictions.

[1] A. M. Humphries, T. Wang, E. R. J. Edwards, S. R. Allen, J. M. Shaw, H. T. Nembach, J. Q. Xiao, T. J. Silva, and X. Fan, Nature Communications 8, 911 (2017). [2] S. C. Baek, V. P. Amin, Y.-W. Oh, G. Go, S.-J. Lee, G.-H. Lee, K.-J. Kim, M. D. Stiles, B.-G. Park, and K.-J. Lee, Nature Materials 17, 509 (2018). [3] Y. Du, S. Karube, H. Gamou, J. Ryu, S. Takahashi, M. Kohda, and J. Nitta, ArXiv:1807.10867 [Cond-Mat] (2018). [4] K. W. Kim, K. J. Lee, J. Sinova, H. W. Lee, and M. D. Stiles, Phys. Rev. B 96, 104438 (2017). [5] X. Fan, A. R. Mellnik, W. Wang, N. Reynolds, T. Wang, H. Celik, V. O. Lorenz, D. C. Ralph, and J. Q. Xiao, Appl. Phys. Lett. 109, 122406 (2016).



(a) Temperature dependent resistance data and fitting for Py(t)/ Pt(4) sample with various Py thicknesses. (b) Temperature dependent data and fitting for CoFeB(t)/ Pt(4) sample with various CoFeB thicknesses.

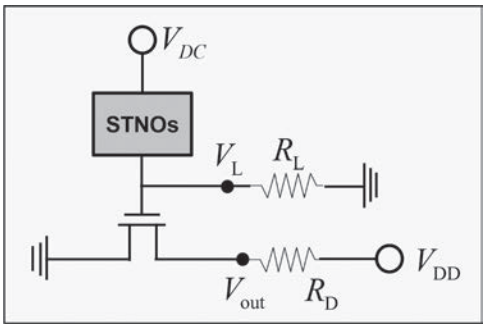


Temperature dependent normalized current distributions in Py and Pt layers in the Py(t) / Pt(4) sample.

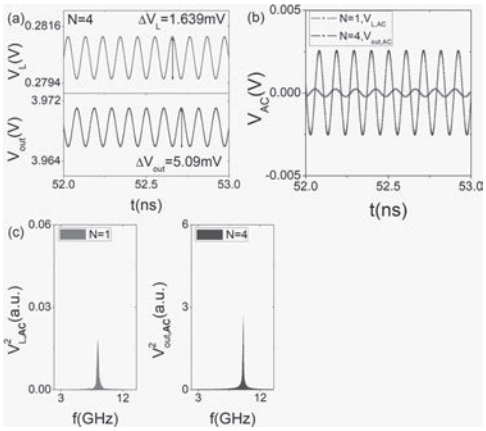
BV-08. High Power Spin Torque Nano-Oscillators Integrated Directly on a MOSFET. *D. Kang*[1], W. Jeong[1], J. Lee[1] and M. Shin[1] *1. KAIST, Daejeon, The Republic of Korea*

Spin torque nano-oscillators (STNOs) have been significantly studied over the past few decades due to their potentials for practical application as devices in the gigahertz band [1-4]. It is necessary to increase the output power and reduce the linewidth for practical application of STNOs [5]. Here, employing a macrospin simulation and the Technology-Computer-Aided-Design (TCAD) device simulator, we investigated the output power of synchronized STNOs integrated directly on a metal-oxide-semiconductor field-effect-transistor (MOSFET), where both electrical and magneto-dipolar coupling between the STNOs induce the synchronization of STNOs [Fig. 1]. Our proposed model not only overcomes the issue of the noise generated from a metal wire between STNOs and an amplifier but also maintains the degree of integration by minimizing the area of devices. The operating principle of this model is simple. The DC voltage induces the magnetization precession of the free layer, and the combination of the GMR (TMR) effect and magnetization precession induces the voltage oscillation across the load resistance acting as the gate voltage of the MOSFET. The voltage across the load resistance can be amplified in a normally-on MOSFET in this model. We found that the output power is greatly enhanced by amplifying the AC voltage generated by synchronized STNOs. For example, in case of the serially connected STNOs, the output power obtained upon the amplication of four synchronized STNOs is approximately 118.8 times larger than the output power of the single STNO [Fig. 2]. Futhermore, we reveal that the number of serially connected STNOs is theoretically unlimited within the cutoff frequency of the MOSFET.

J. Smith, J. Doe and M. Howard, Journal Name., Vol. X, p.XX (2016) [1] J. C. Slonczewski, J. Magn. Magn. Mater., 159, L1 (1996) [2] L. Berger, Phys. Rev. B, 54, 9353 (1996) [3] S. I. Kiselev et al., Nature, 425, 380 (2003) [4] I. N. Krivorotov, N. C. Emley and R. A. Buhrman, Science 307, 228 (2005) [5] Y. Zhou, S. Bonetti, and J. Akerman, IEEE Trans. Magn., 45, 2421 (2009)



Schematic illustration of STNOs directly integrated on a MOSFET that is connected to drain resistance, R_D. In this model, the voltage across the load resistance (V_L) acts as the gate voltage of the MOSFET.



(a) Comparison of V_L and V_{out} for N=4, where N is number of STNOs and V_{out} is the output voltage of the MOSFET. (b) Time evolutions of $V_{L,AC}$ for N=1 and $V_{out,AC}$ for N=4. (c) Comparison of $V^2_{L,ac}$ for N=1 and $V^2_{out,ac}$ for N=4 in the frequency domain.

BV-09. Angular Characterization of the Spin-Orbit Effective Fields.

H. Yang[1] and X. Qiu[1] *1. School of Physics Science and Engineering, Tongji University, Shanghai, China*

Spin-orbit torque (SOT) in heavy metal (HM)/ferromagnet (FM) heterostructures opens a new avenue to switch magnetization and move magnetic textures in an efficient and fast manner [1-4]. In studies of SOT, the existing techniques to evaluate SOT effective fields, such as the DC, AC and FMR measurement, have been still restricted by many factors such as the anisotropy, the artifacts from the thermal gradient and planar effect *etc*. [5]. Therefore, it is necessary to develop a versatile and general technique to accurately characterize SOT effective fields to advance the development of spin-orbitronic. In this work, we showed the characterization of the sign and amplitude of SOTs by angular measurements. Compared to most of the previous measurements, this angular characterization does not require perquisites of the strong perpendicular anisotropy thus it is capable for more general schemes. The large second harmonic Hall signal contribution of the thermal gradient caused by Joule heating can be readily removed by the external field (H_{ext}) dependence. Fig. 1 shows the finite element analysis of the current induced thermal gradient and the characterization of anti-damping effective field (H_L). As shown Figs. 2(a) and (b), the SOTs cause the oscillation of magnetization in two geometries and the oscillation amplitude decreases with the H_{ext} increases while the thermal gradient contribution did not affect. By analyzing the H_{ext} dependence of the second harmonic voltage, the SOTs effective field and thermal effect can be determined as shown in Figs.2c. Our work provides a comprehensive and versatile method to characterize SOTs and paves the necessary foundation for the spin-orbitronic studies.

[1] I.M. Miron, K. Garello, G. Gaudin, et al., Nature, Vol. 476, p. 189 (2011) [2] L. Liu, C.-F. Pai, Y. Li, et al., Science, Vol. 336, p. 555 (2012) [3] L. Liu, O.J. Lee, T.J. Gudmundsen, et al., Phys. Rev. Lett., Vol. 109, p. 096602 (2012) [4] A. Brataas, A.D. Kent and H. Ohno, Nat. Mater., Vol. 11, p. 372 (2012) [5] X. Qiu, Z. Shi, W. Fan, et al., Adv. Mater., Vol. 30, p. 1705699 (2018)

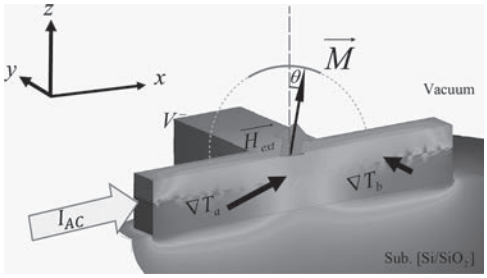


Fig. 1 Experimental setup in longitudinal geometry, the finite element analysis of thermal gradient caused by the current.

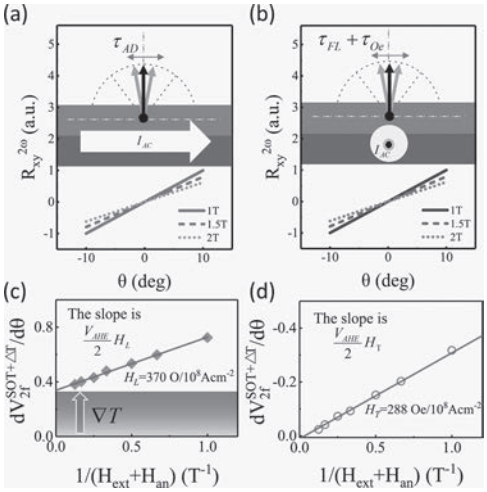


Fig. 2 Ta (2)/Cu (3)/CoNi (1.8)/Pt (4) (in nm). (a)(b), The second harmonic Hall voltage. The insets show the periodic oscillation of magnetization caused by current induced effective fields in two geometries. (c)(d), The slope of the red fitted line reflect the SOT effective fields. The red bar shows the vertical thermal gradient contribution in longitudinal geometry and it does not exist in transverse geometry.

BV-10. Spin-orbit torques in low-resistive mixed phase Ta Thin Films.

A. Kumar[1], R. Sharma[1], S. Chaudhary[1] and P.K. Muduli[1] *1. Department of Physics, Indian Institute of Tachnology Delhi, New Delhi, India*

Current-induced spin-orbit torques (SOTs) in ferromagnet/heavy metal (FM/HM) heterostructures provide the opportunity for magnetization switching[1] and auto-oscillations[2]. SOTs can enhance or compensate the Gilbert damping (α_{eff}) depending upon the direction of current flow. Initially, spin Hall effect is considered as essential for SOTs, however, recent studies have suggested breaking of inversion symmetry at the FM/HM interface due to Rashba effect also contributes to a large extent[3]. In this work, we have studied the current induced modulation of α_{eff} using spin-torque ferromagnetic resonance (ST-FMR) technique in NiFe (10 nm)/Ta (10 nm) bilayers. Here, we have optimized the growth of Ta thin films for low resistive mixed phase (α+β)-Ta having a high spin Hall angle (θ_{SH} = -0.17)[4]. The electrical resistivity for Py and Ta thin films are ρ_{Py} = 33 μΩ-cm and ρ_{Ta} = 68 μΩ-cm, which results in 32% total current passing through Ta. The rectangular mesa of size 16×40 μm^2 of NiFe/Ta bilayer deposited using DC magnetron sputtering and fabricated using optical lithography for STFMR measurements. Figure 1(a) shows observed STFMR spectra for 5 GHz RF frequency (*f*), observed spectra can be fitted with Lorentzian equation (Red line)[5] to determine symmetric (V_S), asymmetric (V_A) voltage signal, linewidth (ΔH) and resonance field (H_R). Inset of Fig. 2 shows *f* vs. ΔH, where the red line shows

a linear fit to the observed data to calculate α_{eff}. Current-induced modulation of α_{eff} for +6 mA to -6 mA is shown in Fig. 2. We have found 34.6% current modulation in α_{eff} for current density ($J_{C,Ta}$) = 2.8×10^{10} A/m^2. The high current modulation and θ_{SH} in mixed phase Ta compared to their β-phase counterpart can be understood by the interplay of bulk spin Hall effect and interfacial Rashba type effects. These results are very promising for the rapid developments in the fabrication of efficient spin Hall effect based devices.

1.L. Liu, *et al.*, Science 336, 555 (2012). 2.V. E. Demidov, *et al.*, Nat. Mat.11, 1028 (2012). 3.D. Tiwari, *et al.*, Appl. Phys. Lett. 111, 232407 (2017). 4.A. Kumar, *et al.*, Phy. Rev. B 98, 104403 (2018). 5.L. Liu, *et al.*, Phy. Rev. Lett. 106, 036601 (2011).

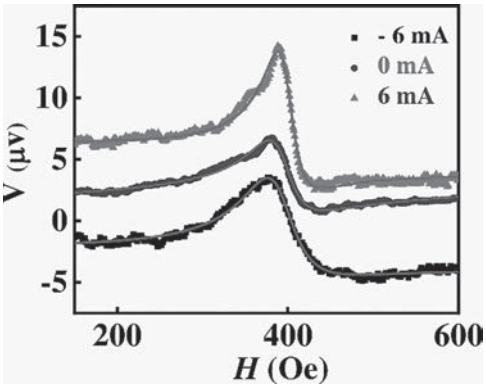


Figure 1 ST-FMR measurements of NiFe(10 nm)/Ta(10 nm) for 5 GHz of RF frequency (Red line shows fitting of observed data using Lorentzian equation).

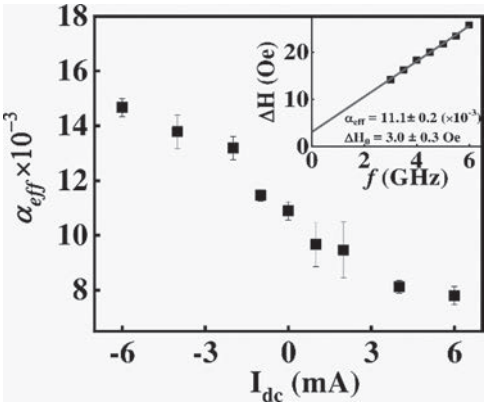
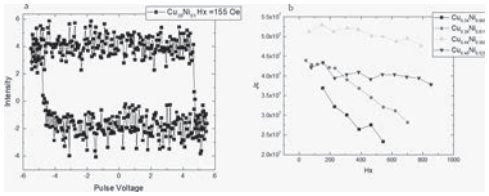


Figure 2 Current modulation of Gilbert damping for +6 mA to -6 mA bias current, inset shows ΔH vs. f, red line shows fitting using linear fit to calculate α_{eff}.

BV-11. Switching Perpendicular Ferromagnetic Layer by Spin Orbital Torque from Cu_xNi_{1-x} Non-heavy Metal. *Y. Yen*[1], P. Lin[1] and C. Lai[1]
1. Material Science and Engineering, National Tsing Hua University, Hsinchu, Taiwan

Spin orbital torque (SOT) has become a promising candidate for MRAM switching method due to it's fast switching speed and low switching power consumption. Contribution of spin current by SOT is believe to correlate with Z number of element due to spin orbital interaction such as Pt, Pd, Ta elements. Recent research also shows spin hall effect from non-heavy metal such as Cr, Ni, CuO. A research published recently shows nearly unity spin hall angle in $Cu_{40}Ni_{60}$ system measured by ferromagnetic resonance technique[1]. In this work we use Cu_xNi_{1-x} (x=0.34, 0.39, 0.44, 0.48) as spin current source to switch perpendicular magnetized Co/Ni multilayer. The critical switching current density is at the level of 3 – 6 x 10^7 A/cm^2, comparable to Pt case. The high switching efficiency of perpendicular ferromagnetic layer by non-heavy metal provides a much cost-effective spin current source compare to noble metals. The film stack is Si/SiO2/Ti (5)/Cu_xNi_{1-x} (6)/[Co (0.3)/Ni (0.6)]x2/Ti (2) fabricated by magnetron sputtering. Composition of the sample is determined by ICP-MS result. Numbers in parentheses are thickness in nm. Films were pattern into devices with lithography system with lift-off technique with a linewidth of 10 um. The switching test is conduct under various Hx and magnetization is measured by micro magneto-optic Kerr effect (MOKE) system. The shunting current into CuNi layers is calculated by resistivity measured from 4-point probe experiment on sheet film. Figure 1a shows typical switching behavior from $Cu_{0.39}Ni_{0.61}$ sample. Figure 1b shows critical switching current density versus applied Hx. We successfully demonstrate perpendicular ferromagnetic layer switching by non-heavy metal with low critiical swtching current densty, which can be used as both cost effectve and energy effcient spin current source.

1. Mark W. Keller and others, 'Near-Unity Spin Hall Ratio in N i x C u 1 – x Alloys', *Physical Review B*, 99.21 (2019), 214411 <https://doi.org/10.1103/PhysRevB.99.214411>.



BV-12. Spin torques on the surface of magnetic topological insulators with hexagonal warping. *Y. Imai*[2], T. Yamaguchi[1], A. Yamakage[2] and H. Kohno[2] *1. National Institute of Advanced Industrial Science and Technology, Tsukuba, Japan; 2. Department of Physics, Nagoya University, Nagoya, Japan*

Recently, two-dimensional Dirac electrons on the surface of magnetic topological insulator (MTI) have been attracting attention in spintronics. Usually, the Dirac electrons are modeled by a linear-dispersion model, but it was found experimentally [1] and pointed out theoretically [2] that the dispersion of Dirac electrons on some topological insulators, such as Bi_2Te_3 [3], is deformed hexagonally, and such "hexagonal warping" can be important in certain phenomena. For example, it was shown that the quantum anomalous Hall effect is induced by in-plane magnetization [4,5]. On the other hand, spin torques on the surface of MTI were studied without hexagonal warping and it was demonstrated that the ordinary spin-transfer torque and the dissipative correction (beta torque) do not exist on the surface of MTI [6]. In this work, we investigate spin torques due to Dirac electrons with hexagonal warping, including the spin-transfer torque and the beta torque. First, we list all possible form of spin torques allowed by symmetry. We introduce three viewpoints to classify the torques, which are viewpoints of spin-transfer torque, spin-orbit torque, and the one which does not allow a simple interpretation. Then, we show the result of microscopic calculation for each spin torque. We found that the spin-transfer torque and the beta torque arise due to the hexagonal warping. We also found that a nonequilibrium Dzyaloshinskii-Moriya interaction is induced by in-plane electric field owing to the hexagonal warping.

[1] Y. L. Chen *et. al*., Science 325, 178 (2009). [2] L. Fu, Phys. Rev. Lett. 103, 266801 (2009). [3] M. Nomura *et. al.*, Phys. Rev. B 89, 045134 (2014). [4] R. S. Akzyanov and A. L. Rakhmanov, Phys. Rev. B 99, 045436 (2019). [5] R. S. Akzyanov and A. L. Rakhmanov, Phys. Rev. B 97, 075421 (2018). [6] A. Sakai and H. Kohno, Phys. Rev. B 89, 165307 (2014).

BV-13. Enhanced Spin-Orbit Torques and Multi-Level Current-Induced Switching in W/CoTb/Pt Heterostructure. *Z. Zheng*[1,2], Y. Zhang[1], X. Feng[1], K. Zhang[1], J. Nan[1], Z. Zhang[1,2], G. Wang[1], J. Wang[1], N. Lei[1], Y. Zhang[2] and W. Zhao[1] *1. School of Microelectronics, Beihang University, Beijing, China; 2. School of Electronics and Information Engineering, Beihang University, Beijing, China*

Spin-orbit torque (SOT) driven magnetization switching in Ferrimagnets (FIMs) can inspire variety of low-power, high-speed and multifunctional spintronic devices [1-4]. Recently, SOT efficiency in FIM/heavy metal systems has been found to be increased when FIM is approaching its magnetic compensation point [3-5]. However, the effective spin Hall angle cannot be obviously augmented owing to the net magnetization reduction [1,2,6], which degrades FIM's future application potential. Here, we investigate enhanced SOT effect in a heterostructure composed of a near-compensated CoTb layer sandwiched by W and Pt layers (see Fig. 1a), where CoTb is a typical rare-earth-transition-metal (RE-TM) ferrimagnetic alloy with bulk perpendicular magnetic anisotropy (PMA) and W has the opposite spin Hall angle against Pt [7-8]. As shown in Fig. 1b, beyond a large SOT efficiency (58.6×10^{-10} Oe m^2/A), 1.84 times damping-like effective spin Hall angle and 20% switching power consumption can also be achieved simultaneously by optimizing the thickness of Pt layer, compared with SOT performance in conventional W/CoTb structure. We further carry out current-induced multi-level magnetization switching in Pt(3nm)/CoTb(2nm)/W(5nm)/CoTb(4nm)/Pt(3nm) stack (see Fig. 2a). Anomalous Hall effect (AHE) curve in Fig. 2b confirms that zero coupling effect exists between two CoTb layers. By sweeping current pulse under a certain in-plane magnetic field along the current direction, four magnetization states ($CoTb_{thin,\uparrow}$, $CoTb_{thick,\downarrow}$), ($CoTb_{thin,\downarrow}$, $CoTb_{thick,\downarrow}$), ($CoTb_{thin,\downarrow}$, $CoTb_{thick,\uparrow}$) and ($CoTb_{thin,\uparrow}$, $CoTb_{thick,\uparrow}$) can be achieved in sequence (see Fig. 2c), which doubles the capacity of normal SOT devices. Our work combining efficient and multi-bit magnetization switching provides an alternative route to leverage ferrimagnetic material in future spintronic devices.

[1] J. Finley, and L. Liu, Phys. Rev. Appl., Vol. 6, p. 054001 (2016). [2] S. Je, et al, Appl. Phys. Lett., Vol. 112, p. 062401 (2018). [3] K. Kim, et al, Nat. Mater., Vol. 16, p. 1187 (2017). [4] S. Siddiqui, et al, Phys. Rev. Lett., Vol. 121, p. 057701 (2018). [5] V. López-Flores, et al, Phys. Rev. B, Vol. 87, p. 214412 (2013). [6] W. Ham, et al, Appl. Phys. Lett., Vol. 110, p. 242405 (2017). [7] L. Liu, et al, Phys. Rev. Lett., Vol. 106, p. 036601 (2011). [8] C. F. Pai, et al, Appl. Phys. Lett., Vol. 101, p. 122404 (2012).

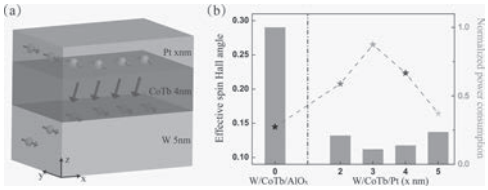


Fig. 1 (a) Schematic of the W/CoTb/Pt heterostructure. (b) Effective spin Hall angle and power consumption tendencies versus Pt thickness.

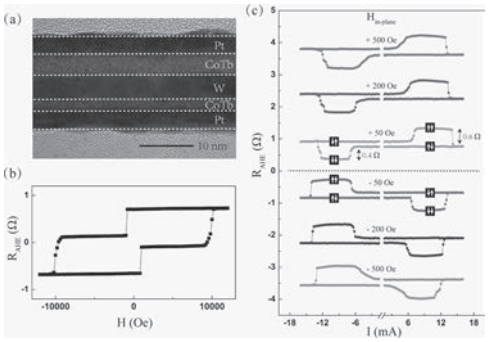
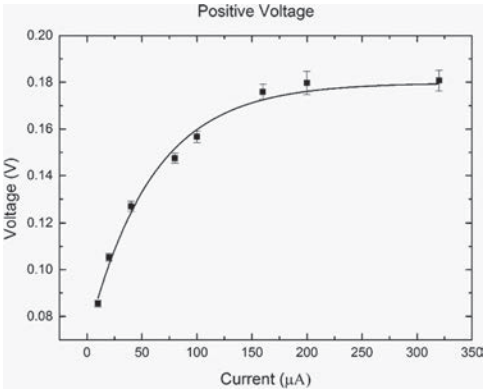


Fig. 2 (a) Cross-section image of the stack. (b) AHE measurement of the fabricated Hall bar. (c) Four-state current-induced magnetization switching.

BV-14. Detecting spin hall signals of permalloy and heavy metal using inverse spin Hall effect. *K. Lai*[1], D. Shiu[1], C. Chang[1] and L. Horng[1] *1. National Changhua University of Education, Changhua, Taiwan*

In the spin Hall effect, a current passed through sample. The spin–orbit coupling induced spin polarized electrons accumulation of inverse signal on either side of the sample. Conversions between charge current into spin current which are called the inverse spin Hall effect. We made a multi-terminal device with a Ta Hall bar and a permalloy nanowire spin injector to detect inverse spin Hall effect. In this device, we read out different signal from magnetic state of permalloy. We using magneton sputtering and e-beam lithography to made devices and measured by four point probes at room temperature. We find asymmetry shift of inverse shin Hall voltage at different magnetic states and find difference signal in opposite current.

L. Thomas, R. Moriya, C. Rettner, S.S.P. Parkin, Science 330 1810 (2010). Axel Hoffmann, IEEE TRANSACTIONS ON MAGNETICS, VOL. 49, NO. 10, OCTOBER (2013). Hiroyuki Awano, Journal of Magnetism and Magnetic Materials 383 50–55 (2015).



BV-15. Spin-orbit torque switching in a T-type magnetic configuration. W. Kong[1], *C. Wan*[1], C. Fang[1] and X. Han[1] *1. Chinese Academy of Sciences, Institute of Physics, Beijing, China*

Different symmetry breaking ways determine various magnetization switching modes driven by spin-orbit torque (SOT) and breed diverse spin dynamics. For instance, an applied or effective symmetry breaking field parallel to applied current is indispensable to switch magnetization with perpendicular anisotropy by SOT [1-3]. Besides of this switching mode, here we demonstrate a distinct field-free switching mode in a T-type magnetic system with the structure of MgO/CoFeB/Ta/CoFeB/MgO where a perpendicular layer was coupled to an in-plane layer with a uniaxial easy axis. Switching current was applied orthogonal to the easy axis and thus also normal to an in-plane effective field experienced by the perpendicular layer. By symmetry analysis, we found that the perpendicular layer could become switchable if the in-plane layer was first switched by the current. These switching modes realized in the T-type magnetic system might expedite the birth of novel multi-state spin memory or spin logic devices which are fully operational by pure electric manners [4].

[1] L. Q. Liu, O. J. Lee, T. J. Gudmundsen, et al. Phys. Rev. Lett. 109, 096602 (2012). [2] X. Zhang, C. H. Wan, Z. H. Yuan, et al. Phys. Rev. B, 94, 174434 (2016). [3] X. Wang, C. H. Wan, W. J. Kong, et al. Adv. Mater. 30, 1801318 (2018) [4] W. J. Kong, C. H. Wan, X. Wang, et al. Nat. Commun, 10:233 (2019).

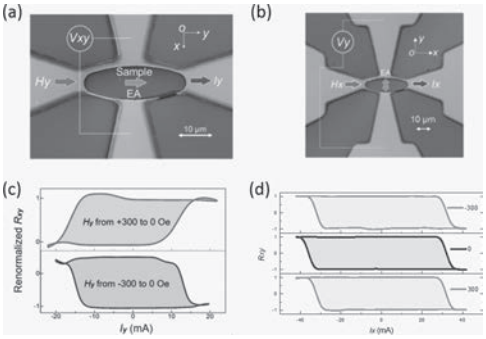


Fig.1 (a) Structure of a patterned film of Type-z switching. (b) Structure of a patterned film of Type-T switching. (c) Field-free switching of the Hall bar of Type-Z mode. (d) Field-free switching of the Hall bar of Type-T mode

Session BW
BIOMAGNETISM, BIOMEDICAL, AND MAGNETIC FLUIDS I (Poster Session)

Paola Tiberto, Chair
INRIM, Torino, Italy

BW-01. Thermal Performance Evaluation of a Ferrofluid Filled Power Transformer by 3-D Magnetic-Thermal-Fluidic Coupled Analysis.
Y. Zhang[1], S. Ho[1], W. Fu[1], X. Yang[2] and H. Wu[1] *1. The Hong Kong Polytechnic University, Hong Kong, Hong Kong; 2. Hebei University of Technology, Tianjin, China*

I. Introduction Power Transformer is one of the key equipment in power grid, and its thermal performance is critical for the safe operation. In order to improve the inherently low thermal conductivity of transformer oil, oil-based nanofluids, which are manufactured by dispersing nanoparticles of large thermal conductivity into transformer oil, are widely studied [1]. Compared with the ordinary nanofluids, the ferrofluids (magnetic nanofluids) prepared with colloidal magnetic nanoparticles have another advantage, which is to utilize external magnetic field to force the circulation [2]. In order to evaluate the cooling capacity of ferrofluid in power transformers, a magnetic-thermal-fluidic coupled analysis [3], in which two separated solvers are indirectly coupled, is conducted in this paper. II. Numerical model The thermal analysis of ferrofluid filled power transformers is a typical multi-physics problem, which couples the magnetic, fluid and thermal field. A coupled numerical model is built for the analysis, and the interaction between fields is taken into consideration by modifying the governing equations. The temperature dependent material properties, such as saturation magnetization, viscosity, and thermal conductivity, are considered to model the practical two-way coupling. The magnetic field is discretized and solved with finite element method, while the finite volume method is used to solve the fluidic-thermal field. To save the computational resources, two sets of meshes are employed, and data transfer between fields are realized by the mapping between meshes. Based on the estimate of the flow pattern, adjustment of the governing equations of the fluid field may be required. As shown in Fig. 1, a three-phase oil natural cooling transformer (10-0.4kV, 50Hz and 50kVA), in which the regular transformer oil is replaced by the Fe_3O_4/oil ferrofluid (0.1% volume fraction of nanoparticles), is modelled to evaluate the performance of ferrofluid. The derived results will be compared with the oil cooled transformer to showcase the improvement in cooling ability.

[1] D. Liu, Y. Zhou, Y. Yang, L. Zhang, F. Jin, IEEE Transactions on Electrical Insulation, vol. 23, p. 2757-2767 (2016) [2] L. Pislaru-Danescu et al., IEEE Transactions on Industry Applications, vol. 49, p. 1289-1298 (2013) [3] J. Smolka, O. Biro, and A. J. Nowak, Archives of Computational Methods in Engineering, vol. 16, p. 319-355 (2009)

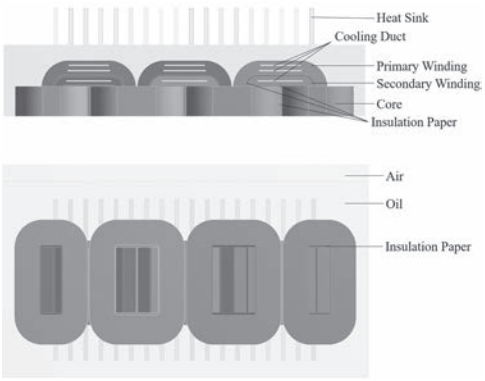
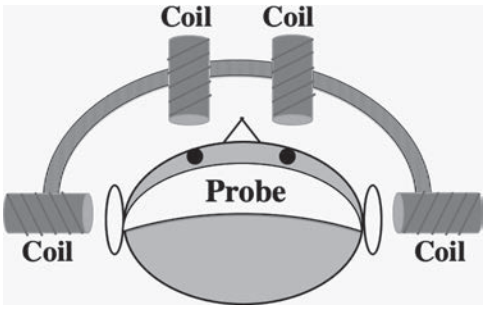


Fig. 1. The numerical model of the ON transformer.

BW-02. Practical Application of ELF Stimulation to Early Diagnosis System for Detecting Mild Cognitive Impairment.
H. Nakagawa[1], M. Sugai[1] and S. Ueno[2] *1. Department of Electrical and Electronic Engineering, Tokyo Denki University, Tokyo, Japan; 2. Department of Applied Quantum Physics, Kyushu University, Fukuoka, Japan*

Up to the present, numerous techniques have been developed to investigate human brain functions for application in both therapeutic and preventive medicine. Our previous trial using ELF stimulations provided a new finding concerning the fail in the phosphene sensitivity caused by aging of more certain age [1]. As our new attempt, for the rapid progress to the development of early diagnosis system for detecting a mild cognitive impairment (MCI), we examined the prefrontal hemodynamics corresponding to retinal responsibilities with ELF-inducing phosphene, employing functional near-infrared spectroscopy (fNIRS) analysis. In this research, four iron-core coil systems were used for ELF magnetic stimulations. Their capabilities of performing the task are very high and controllable, as shown in Fig. 1. The ELF stimulations to subjects' eyes were carried out in the same way as in a previous report [2]. Hemodynamic changes at the prefrontal regions were measured using an fNIRS instrument (Hitach HOT121B). The relative concentration of total hemoglobin, and the pulse as well as the heart beat fluctuation index (LF/HF: LF, low frequency; HF, high frequency) were measured with a prefrontal probe every 0.1 s during each measurement session (rest–task–rest). Additionally, subjects' localizations in their retinal regions for the phosphenes were recorded by filling in an original form. For detecting the connection between retinal activities and prefrontal hemodynamics during the measurement session, we attempted to evaluate the changes of our subjects' autonomic nervous system. The LF/HF index is considered to reflect the activity condition of the autonomic nervous system of the human body. As it turned out, the connection between retinal activities and prefrontal hemodynamics during ELF stimulations may be able to provide preventive solutions for some conditions of an MCI. Besides, judging from the essential low energies of ELF fields, the stimulations may also provide clinical safety for the development of early diagnosis system for detecting an MCI.

1) H. Nakagawa *et al.*, J. Appl. Phys. 115, 17E311 (2014). 2) H. Nakagawa and S. Ueno, IEEE Trans. Magn. 51, 5000604 (2015).



BW-03. Control of Magnetic Particle Size in Magnetic Fluid and Its Effect on Rheological Properties. *S. Chen*[1] and D. Li[1] *1. Country State Key Laboratory of Tribology, Tsinghua University, Beijing, China*

Magnetic fluid exhibits liquid behavior coupled with the ability to response to external magnetic field, thus has been widely used in many devices, such as seals, sensors and dampers[1-3]. Rheological properties are theoretical base and key to common problems in applications. And size of magnetic particles has a significant influence on rheological properties[4]. In this work, we prepared 4 samples with different magnetic particle size by controlling precursor solution concentration during chemical coprecipitation process (concentration decreased with sample number) and investigated rheology properties of these samples. The flow curves were fitted according to Herschel-Bulkley model. With the increase of magnetic field, consistency increased, demonstrating magnetoviscous effect, flow index decreased, gradually deviating from 1, showing stronger non-Newtonian behaviors, and yield stress increased, indicating formation of more complex microstructures. As we can see from Fig. 1, magnetoviscous effect got weaker from No.1 to No.3 sample, but increased at No. 4 sample. Fig. 2 showed the viscoelastic properties. Storage modulus experienced a plateau and then decayed by power law, while loss modulus increased to a peak after a plateau and then decayed by power law with a different decay index. The intersection of the two moduli could be treated as a transition from solid-like to liquid-like behavior. With the increase of applied field, the moduli increased, and the transition shear stain decreased. According to experimental results, magnetic fluid exhibited field-controlled rheology properties, which could be explained by formation and destruction of microstructures. There were two opposing mechanisms. With the reduction of precursor solution concentration, the size of particle produced by chemical reaction got smaller. Meanwhile, surfactants became insufficient to completely coat magnetic particles due to an increased specific surface area, causing the particles to aggregate and form clusters which strongly enhanced magnetoviscous effect and viscoelastic effect.

[1] Y. Chen and D. Li, Acta Armamentarii, Vol. 32, p.1428-1432 (2011) [2] T. Medvegy, Á. Molnár, G. Molnár and Z. Gugolya, Journal of Magnetism and Magnetic Materials, Vol. 428, p.189-193 (2017) [3] Marinică, O., D. Susan-Resiga, F. Bălănean, et al, Journal of Magnetism and Magnetic Materials, Vol. 406, p.134-143 (2016) [4] Chen, S. and D. Li, Journal of Magnetics, Vol.22 p.605-609 (2017)

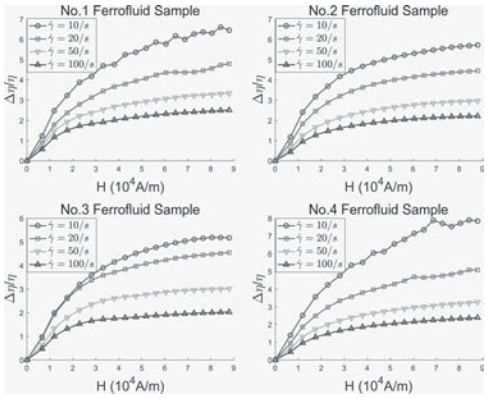


Fig.1 Dependence of viscosity on magnetic field under different shear rates

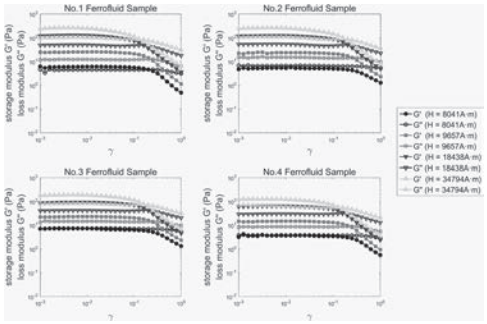


Fig.2 Viscoelasitic properties of the samples under different magnetic field

BW-04. Structure and Magneto-viscosity of Ba-Sr Ferrite Ferrofluid. *N. Gautam*[1] and R. Singh[1] *1. School of Physics, University of Hyderabad, Hyderabad, India*

M type-ferrite family is well known because of their unique magnetic properties. The optimized Ba-Sr ferrite (BSF) nanoparticles of $Ba_{0.8}Sr_{0.2}Fe_2O_4$ composition were synthesized using hydrothermal process at 200 ^{0}C in autoclave for 24 hours. The nanoparticles were coated with DBSA and Oleic acid to prevent cluster formation and dispersed in water and silicone oil for preparing the water based and silicon oil based ferrofluids (FF). The transmission electron micrographs (TEM) show the hexagonal structure of nanoparticles. The magnetization (M(H)) plots at 300 K, 5 K and M (T) plots in ZFC and FC modes in100 Oe applied field of the nanoparticles show ferromagnetic behaviour. The magneto-viscosity results recorded using rheometer are shown in Fig. 2. Different hysteresis behavior in the magneto-viscosity plots (fig 2) at 1 s^{-1} shear rate for the DBSA based and silicone oil based ferrofluids respectively. This is due to the different relaxation rates of formed chains in the ferrofluids when the magnetic field is removed [1]. The silicone oil based FF showed slower relaxation with higher viscosity compared to DBSA based FFdue to the stronger formed magnetic chains [1]. The magnetic hysteresis of DBSA based FF found to be more compared to the silicone oil based FF due to its response in different colloids and applied magnetic field. The silicone oil based FF is found to be more stable FF compared to DBSA water based FF. The flow curves at different magnetic fields show power law behavior. The viscosity showed higher variation at low shear rates due to strong chain formation which is controlled by the magnetic field over flow field [1]. These magneto-viscosity properties are useful in heat absorber application.

[1] Nisha Gautam, G.Thirupathy and R.Singh AIP Advances 7, 056727 (2017)

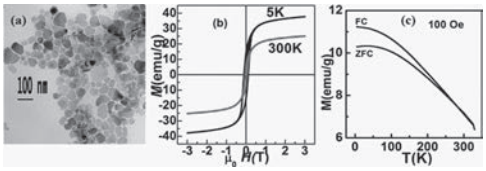


Fig.1 TEM micrograph (a), and *M*(*H*) plots (b) and FC/ZFC (c) of the nanoparticles of $Ba_{0.8}Sr_{0.2}Fe_{12}O_{19}$ respectively

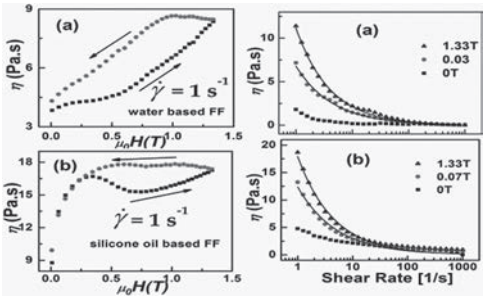


Fig. 2 Magneto viscosity plots at the shear rate of 1 s^{-1} (left) and the flow curves at different magnetic fields (right) of the ferrofluids of $Ba_{0.8}Sr_{0.2}Fe_{12}O_{19}$ DBSA based (a) and $Ba_{0.8}Sr_{0.2}Fe_{12}O_{19}$ silica oil based (b) respectively

BW-05. Reaction field-dependent spin-correlated radical pair model: A new insight into liposomal DDS. *H. Nakagawa*[1] *1. Department of Electrical and Electronic Engineering, Tokyo Denki University, Tokyo, Japan*

The therapeutic use of magnetic field effects on spin-correlated radical pair mechanisms is a new approach for applications to liposomal drug-delivery systems (DDSs). The pair mechanisms are known as the one and only phenomenon by which magnetic fields can switch over chemical reaction paths. It goes without saying that the use of magnetic fields has a certainly long-range potential when aided with high substance permeability. As a matter of course, their essential forces must be of low energies. As previously reported [1], the liposomal DDS methodology is regulated mainly via *S-T* intersystem crossing and magnetic relaxation (Fig. 1). A further detailed evaluation of the drug-release potential and invasivity was carried out for the rapid progress of the methodology. The instrument mainly consists of: a computer-controlled monochromator (Nikon, G250), two of regulated DC power supplies (Kikusui, PAK6 and PMC18) and an original detector enabled to monitor the degree of the photoreactivity of anti-cancer flutamide (FM) in liposomal membranes. Small unilamellar vesicles containing FM were prepared by the membrane filtration method [2], [3]. Under exposure to static/pulsating magnetic fields, FM in the liposomal membrane was excited by an emission wavelength of 325 nm. To compare magnetic field effects on the behaviour of the model membranes, the delayed fluorescence was measured as well as the spectral changes with absorbance at 380 and 260 nm after the emission. According to the measurement results, it was obvious that a pulsating field influences the pair mechanism in the process of membrane peroxidations induced by reactive oxygen species—mainly, excited singlet oxygen ($^1O_2$). This finding might be expected to reveal new knowledge for resolving important clinical problems. And the liposomal drug-release technology with magnetic controls must be one of the most adaptable DDS.

1) H. Nakagawa and M. Ohuchi, IEEE Trans. Magn., 55, 5000104 (2018). 2) H. Nakagawa *et al.*, Ann. Oncol. 26, P8.06 (2015). 3) H. Nakagawa *et al.*, Ann. Oncol. 26, P2.06 (2015).

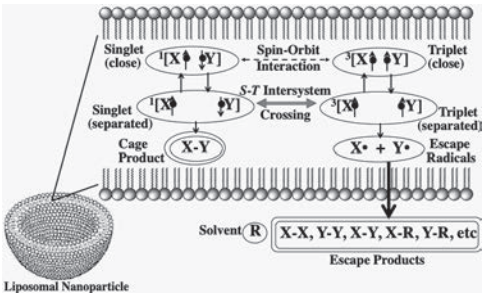


Fig. 1. Scheme for liposomal DDS *via* intramembranous radical pair mechanism.

BW-06. Magnetic Field Effects on Reaction Field-Dependent Radical Pair System. *H. Nakagawa*[1] *1. Department of Electrical and Electronic Engineering, Tokyo Denki University, Tokyo, Japan*

It goes without saying that magnetic field effects on radical pair mechanisms are known as the one and only phenomenon by which magnetic fields can switch over chemical reaction paths despite of their low energies. We previously demonstrated the design of liposomal nanoparticles modified with 2,2'-azobis(2,4-dimethylvaleronitrile) to show the broad potential opportunities in drug delivery systems [1]. In our present research, we considered examining magnetic field effects of combined AC/DC fields to measure the physicochemical changes of liposomal membranes peroxidized by reactive oxygen species. Each dry film composed of various molar ratios of phospholipids, photosensitizers and antenna pigments was hydrated by vortexing them with some appropriate buffer solutions. Each of the dispersions was transferred to a Mini-Extrudor (Avanti Polar Lipids, Inc.) to produce small unilamellar liposomal nanoparticles. Irradiation of the nanoparticles and exposure to magnetic fields were carried out in the same way as in our previous report [2]. ^{1}H- and ^{13}C-NMR spectra of reaction products in methanol-d_4 were obtained with a JEOL JNM A-600 (600.05 MHz) spectrometer at 27°C. Chemical shifts (δ) were referred to internal CD_2HOD at 3.35 ppm for ^{1}H-NMR and $^{13}CD_3OD$ at 49.0 ppm for ^{13}C-NMR. FAB mass spectrum was recorded by a JEOL JMS SX-102 mass spectrometer. HPLC was performed using a Shimadzu SCL-10A system controller equipped with a LC-10AS pump and a SPD-10AV detector. As it turned out, we found the possibility that a pulsating field influences the pair mechanism in the process of membrane peroxidations induced by excited singlet oxygen ($^1O_2$). Comparison of our experimental results showed no relationship between lipophilic and hydrophilic radical scavenging activity, suggesting the possibility of the existence of some types of magnetic field effects on radical pair mechanisms. Accordingly, further studies on the reaction field-dependent radical pair system are now under investigation.

1) H. Nakagawa *et al.*, J. Appl. Phys. 105, 07B323 (2009). 2) H. Nakagawa and M. Ohuchi, IEEE Trans. Magn. 55, 5000104 (2019).

BW-07. Methyl Orange Adsorption onto magnetic removable Fe_3O_4 / Carbon (AC, GO, PGO) nanocomposites. *G.C. Hermosa*[1], C. Liao[1], S. Wang[2] and A. Sun[1] *1. Chemical Engineering and Materials Science, Yuan Ze University, Zhongli District, Taiwan; 2. Department of Materials and Mineral Resources Engineering, National Taipei University of Technology, Taipei, Taiwan*

Dyes are widely used to color products in textile, leather tanning, cosmetics, pigment and many other industries. Effluents discharged from these industries cause potential hazards to environment and human health. Hence, the removal of dyes from water/wastewater has gained a huge attention in recent years. Adsorption as one of the most effective methods for wastewater treatment has been successfully applied to reduce hazardous inorganic/organic pollutants present in the effluents. Adsorbents such Activated Carbon (AC), Graphene Oxide (GO) and Porous Graphene Oxide (PGO) exhibit good adsorption capacity owing to their high specific area, adequate pore size distribution and relatively high mechanical strength. In spite of the

advantages of these adsorbents, the separation and recovery from water is still hard as it causes secondary pollution. Combined magnetic nanoparticles with sorbents as to recover particles from the water that provides a simple and economically friendly for various applications. In this study, carbonaceous nanomaterials (AC, GO and PGO) were synthesized and attached to Fe_3O_4 magnetic powder for the effective removal of synthetic Methyl Orange (MO). AC and GO were successfully conjugated with Fe_3O_4 whilst PGO was not due to its surface functional groups. Batch adsorption experiments were performed and showed significant removal efficiency of 90% at the first ten minutes for Fe_3O_4/AC nanocomposite. Analysis of adsorption equilibrium revealed that AC/Fe_3O_4 is well fitted with Langmuir model, a homogeneous adsorption having an adsorption capacity of 270 mg/g. The GO/Fe_3O_4 can fit with both Langmuir and Freundlich models indicating multilayer adsorption on the surface of the adsorbent with an adsorption capacity of 81.9 mg/g. Both adsorbents follow the pseudo second order kinetics model showing high R^2 values. The adsorbents demonstrated advantageous superparamagnetic properties for their easy recovery from aqueous solutions and prospective applications to toxic removal in water and wastewater.

L. Ai, Y. Zhou, and J. Jiang, Desalination., Vol. 266, pp. 72-77 (2011). J. Sokolowska-Gajda and H.S. Freeman, Dyes and Pigment., Vol.30, pp.1-20 (1996). P.J.M. Carrott and R.A. Roberts, Colloids and Surfaces.,Vol. 58, pp. 385-500 (1991). M. Yu, J. Li, and L. Wang, Chem. Eng. J., Vol. 310, pp.300-306 (2017). W. Konicki, M. Aleksandrzak, and E. Mijowska, Chem. Eng. Res. Des., Vol. 123, pp.35-49 (2017).

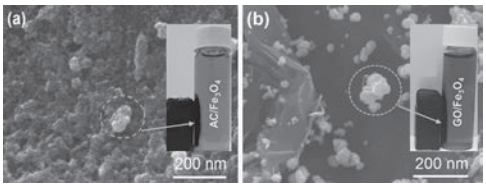


Fig.1. Difference in the adsorption performance for (a) AC/Fe_3O_4 and (b) GO/Fe_3O_4 in relation to their morphologies

BW-08. ELF Magnetic Effects on Forced Metamorphosis of Mexican Axolotls (*Ambystoma mexicanum*). *H. Nakagawa*[1] and T. Tadokoro[1]
1. Department of Electrical and Electronic Engineering, Tokyo Denki University, Tokyo, Japan

Objective: Up to the present, a wide variety of intestinal microflorae (e.g., Proteobacteria, Firmicutes, Bacteroidetes, Actinobacteria, and Verrucomicrobia) have been isolated from the gut microbial community of salamander larvae [1]. Nevertheless, judging from the best of our knowledge, there are almost no reported studies of the observation of their behaviors under exposure to magnetic fields. Our previous report already provided a novel finding about the influences of a gradient or an extremely low frequency (ELF) magnetic field on amphibian metamorphosis induced forcibly with a thyroid hormone [2]. In this study, as our new attempt, we investigated the gradient/ELF magnetic effects on serious anorexia with respect to the forced metamorphosis of Mexican axolotls (*Ambystoma mexicanum*). Methodology: Before performing this experiment, axolotls were individually kept in 0.85-L square boxes containing a de-chlorinated water (0.7 L) without aeration at a temperature of 24°C under illumination of 250 $\mu Em^{-2}s^{-1}$ on a 12 : 12 h L : D photocycle. They had become accustomed to being given food rotating of a solid / a tubifex worm; and additionally, they were acclimatized to our experimental environment at least a week. Exposures of thyroxine (T_4)-administrated axolotls to magnetic fields were performed using a strong permanent magnet (17 T/m), as well as an air-cored coil system (5.0 mT at 10–100 Hz). The survival rates of the axolotls influenced by the presence of T_4 were monitored every day, and the digestive capacities were evaluated minutely. Discussion: From our experimental results, we found that the initiation timings of the field exposures affect the survival rates of the following salamanded axolotls. Particularly, there were a few distinct patterns that revealed a serious anorexia in each of the salamanded bodies. We postulated that some changes in the behaviors of their intestinal microflorae might be induced, because of a kind of stress under the exposures. Therefore, further detailed evaluations of the methodology are now under investigation. Our data could prove to be helpful for future reference with respect to a magnetic control study of gut microbial community.

1) M. C. Bletz*et al.*, Nature Comm. 7, 133699 (2016). 2) H. Nakagawa and M. Ohuchi, IEEE Trans. Magn. 54, 5000405 (2018).

BW-09. Magnetic field control of moiré fringes on guanine crystal plate surface utilizing its optical interference pattern. *H. Asada*[1], E. Muneyama[1], R. Nagai[1], T. Kimura[1] and M. Iwasaka[2] *1. Yamaguchi University, Ube, Japan; 2. Hiroshima University, Higashi-Hiroshima, Japan*

Periodically aligned guanine crystals (GCs) exhibit a structural color caused by the light interference effect. So far, we have reported that the optical interference stripe pattern is observed at a smooth broadest surface of biogenic GC (102) plane combining with mirror surface substrates [1]. Moiré fringes are created by superimposing periodic or quasi-periodic network of lines. This technique is now established as an important metrological tool such as super-resolution microscope. In this study, we observed the GC plate of goldfish floating in water over the herringbone patterns (HBPs) and found that the moiré fringes were appears on GC surface utilizing its optical interference pattern. This measurement technique has the advantage of being magnetically controllable, which was demonstrated experimentally, because the orientation of GC can be controlled magnetically due to the diamagnetic anisotropy [2]. HBPs of Cr film were fabricated by using microfabrication techniques. Figure 1 shows microscope images of GC floating in water over 1/1 μm line and space (L/S) HBP on (a) Si and (b) glass substrates. As clearly seen in both the images, different moiré fringes appear on the GC surface. Figure 1(c) shows a schematic view of overlapping HBP and interference strips. The moiré fringes in Figs. 1(a) and (b) are reproduced. These results indicate that the various moiré fringes can be obtained by rotating the GC according to the rotation of the in-plane magnetic field. Applying the vertical magnetic field of several hundred mT, the GC is oriented so that the short-axis of the (102) plane is parallel to the field [2]. This property enables to continuously change the inclination angle between the substrate and the (102) plane according to the rotation of GC caused by the magnetic field change. As shown in Figs.2 (a)-(c), the interference pattern period becomes wider due to the decrease of the inclination angle of GC. This means that the magnification ratio of moiré fringes can be changed magnetically (see Figs. 2(d)-(e)). We also successfully observed the moiré fringes in the case of 0.5/0.5 μm L/S HBP. This work was supported by JST-CREST Grant number JPMJCR16N1, Japan.

[1] T. Sogame et al., IEEE Trans. Magn., 54, 2501504/1-4(2018). [2] M. Iwasaka et al., Appl. Phys. Express, 6, 037002/1-4(2013).

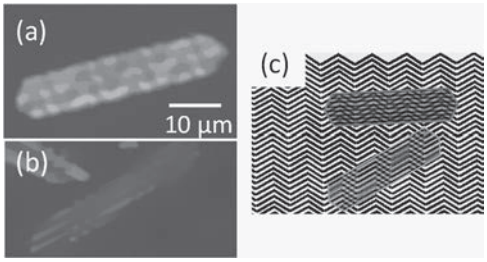


Fig. 1

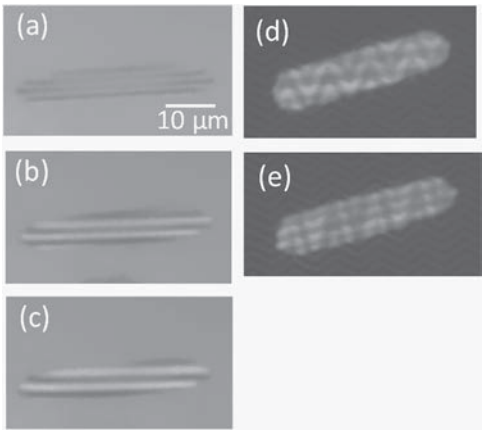


Fig. 2

BW-10. High-efficient catalytic reduction of 4-nitrophenol with magnetically recoverable Cu-Fe_3O_4 nanocrystals. *Y. Yang*[1], J. Guo[1], P. Si[1] and H. Ge[1] *1. Zhejiang Province Key Laboratory of Magnetism, China Jiliang University, Hangzhou, China*

Nowadays, the serious water pollution and water resources crisis cause damaging consequences and a threat to human life [1,2]. Among the harmful toxins and compounds, 4-nitrophenol (4-NP) is widely present in waste water from printing, textile, petrochemical and pharmaceutical industries. It becomes one of the most difficult water pollutants to tackle since it has high solubility and stability in water. 4-NP not only cause serious ecological problems, but also cause carcinogenic or devastating effects on humans and wildlife [3-5]. Meanwhile, magnetically recoverable noble metal nanoparticles are promising catalysts for chemical reactions[6]. In this paper, a highly efficient Cu-Fe_3O_4 nanocatalyst was fabricated through hydrothermal method. When loaded with Cu nanoparticles, the Cu-Fe_3O_4 nanocatalyst exhibits high efficiency in catalytically reduce 4-NP to 4-aminophenol (4-AP), the 4-NP is able to be fully degraded in a period shorted than a minute [Figure 1]. With the increase of Cu dosage, the time for complete degradation of the 4-NP is gradually decreases. For the $Cu_{1.0}$-Fe_3O_4 nanocatalyst, the complete degradation of the 4-NP sharply reduced to 5s and the conversion rate reaches at least 98%. As shown in Figure 2, the Cu-Fe_3O_4 nanocatalyst demonstrated good magnetic recoverability and high conversion in 1 min (>98%) after 8 successive cycles. The results here provide a simple and environmentally friendly choice for preparing magnetic noble nano-catalyst and stimulate the study of highly efficient catalysts for 4-NP reduction.

[1] L. Qin, et al, Sci. Total Environ. 652,93 (2019). [2] X. Y. Wang, et al, ChemCatChem 10, 4143 (2018). [3] X. Y. Yang, et al, ACS Appl. Mater. Inter. 10, 23154 (2018). [4] K. Gu, et al, Small 14, 1801812 (2018). [5] R. S. Cai, et al, Small 14, 1703734(2018). [6] L. Shang, et al, Adv. Funct. Mater. 27,1606215(2017).

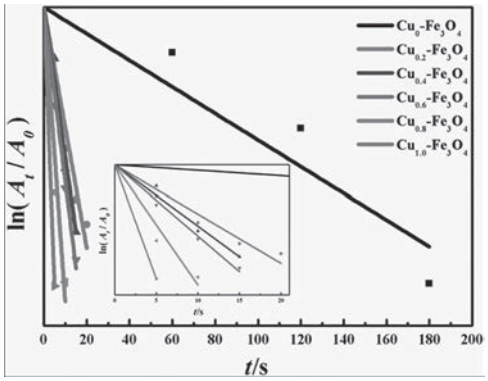


Fig. 1. The corresponding ln C_t/C_0 versus reaction time for the reduction of 4-NP over various contrast catalysts.

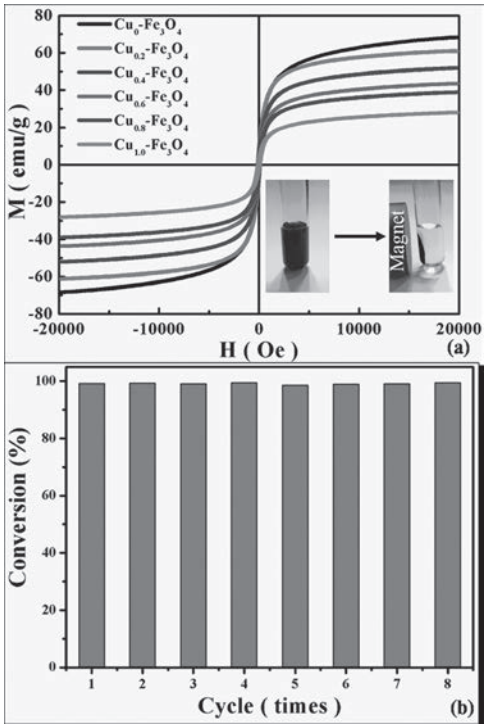
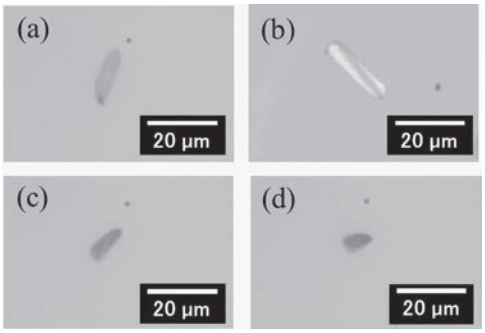


Fig.2. The M-H loops of Fe_3O_4, $Cu_{0.2}$-Fe_3O_4, $Cu_{0.4}$-Fe_3O_4, $Cu_{0.6}$-Fe_3O_4, $Cu_{0.8}$-Fe_3O_4 and $Cu_{1.0}$-Fe_3O_4. The inset shows the partly enlarged M-H loops and the photographs of the magnetic separation. (b) Recycle use of $Cu_{1.0}$-Fe_3O_4 nanoparticles for the reduction of 4-NP.

BW-11. Magnetic orientation of biogenic guanine crystal plate combined with magnetic nanoparticles. *R. Nagai*[1], M. Kurahashi[1], K. Kishimoto[1], T. Koyanagi[1], M. Iwasaka[2] and H. Asada[1] *1. Yamaguchi University, Ube, Japan; 2. Hiroshima University, Higashi-Hiroshima, Japan*

A biogenic guanine crystal (GC) is receiving much attention due to its unique optical properties such as high reflectivity. Diamagnetic anisotropy of GC enables to magnetically align the orientation of GC in water, though the field of hundred mT is needed[1]. So far, we reported that the orientation of GC with the ferromagnetic film can be controlled by a low magnetic field[2,3]. In this study, we examined the combination of magnetic nanoparticles (NPs) and GCs for magnetic orientation in order to maintain the optical transparency of GC and successfully confirmed that GC can be oriented by a low magnetic field. Goldfish GCs were dropped in water dispersed with Fe_2O_3 NPs having the size ≥50 nm. After shaking, the liquid was sealed in a micro-chamber. The magnetic fields were applied by a three-axis Helmholtz coil. The magnetization curve of NP in the low field range was almost saturated at 1 Oe with the value of 13 emu/cc. Microscope images of GC without magnetic field are shown is Figs.(a) and (b). A few NPs (probable three) are attached to the side of GC. It is found that Fe_2O_3 NP is attached preferentially to the side of GC. Moreover, the clear undisturbed light interference pattern is observed, meaning that NPs do not cause crystal distortion and do not affect the optical properties. Next, the magnetic orientation experiments were done. As shown in Figs.(c) and (d), increasing vertical field ((c) 0.1 and (d) 1.0 mT), GC stands on so that the long-axis of (102) plane is parallel to the vertical field like GC with the ferromagnetic film as reported before[2,3]. This motion seems to occur so that the magnetization of NP becomes parallel to the GC (102) plane to decrease the magnetic field component orthogonal to the (102) plane generated by NP, that is, to decrease the diamagnetic energy of GC. The magnetization of NP is oriented parallel to the external field direction, resulting in the orientation of GC. The magnetic orientation field is comparable to that of ferromagnetic film/GC hybrid plate, meaning that NP is quite effective to reduce the orientation field. The NP number and size dependence of magnetic orientation are also presented. This work was supported by JST-CREST Grant number JPMJCR16N1, Japan.

[1] M. Iwasaka et al., Appl. Phys. Express, 6, 037002(2013). [2] T. Sogame et al., IEEE Trans. Magn., 54, 2501604(2018). [3] T. Sogame et al., IEEE Trans. Magn., 55, 5000604(2019).



BW-12. Design and Development of a Highly Focused Coil for Transcranial Magnetic Stimulation on Small Animals. *I.C. Carmona*[1], D. Kumbhare[2], M.S. Baron[3,4] and R.L. Hadimani[1,5] *1. Dept. of Mechanical and Nuclear Engineering, Virginia Commonwealth University, Richmond, VA, United States; 2. Dept. of Neurosurgery, Virginia Commonwealth University, Richmond, VA, United States; 3. McGuire Research Institute, Hunter Holmes McGuire Veterans Affairs Medical Center, Richmond, VA, United States; 4. Southeast Parkinson's Disease Research, Education and Clinical Center (PADRECC), Hunter Holmes McGuire Veterans Affairs Medical Center, Richmond, VA, United States; 5. Dept. of Biomedical Engineering, Virginia Commonwealth University, Richmond, VA, United States*

TMS is a non-invasive technique used to regulate the synaptic activity of neurons in the human brain improving the functionality of several regions and bringing effective treatment to different neurological and psychiatric disorders. Many of these conditions can be treated by applying external magnetic fields to superficial regions of the brain, but most of them originate in deeper areas difficult to stimulate without overstimulation of the cortex. The study of the complete mechanism that intervenes in the progression of these diseases and their relation with the networks between brain regions in animals is needed to stimulate the deeper regions by employing the cortical areas of these networks. However, the stimulation of small areas in animals like rodents is not easy, since most of the studies in TMS use commercial equipment for human, with power and coil geometries not designed for small animals. In mice and rats, e.g., the use of standard human TMS coils does stimuli the whole body of the animal, instead of a targeted area. This work presents the design and evaluation of a focused conical coil with a MnZn ferrite core to increase the magnetic flux in areas as small as 1mm^2 using finite element analysis software, ANSYS Maxwell. The coil has an angle of opening of 5.71 degrees that shifts the point of maximum flux density towards the tip - closer to the objective - rising the flux while reducing the area. The results show B-flux magnitudes at the air-core interface without and with tip-sharpening (Fig.1) of up to 0.57T and 0.56T, respectively, while flux densities of up to 0.30T and 0.15T (Fig.2) at 4.25mm from the tip to the brain surface (average lambda-bregma distance in adult mice) were observed. The values demonstrate the usefulness of the coil to perform *in vivo* experimentation on rodents for the identification of fiber tracts and brain networks. Further work on the coil and rat stimulator construction are in progress, expected to complete before the MMM 2019 conference. This study was funded in part by the Dpt. of VA Biomedical Lab Research and Development 2I01BX001147-05A2 merit review award (M. Baron, PI).

1. S.D. March, S.J. Stark, R. L Hadimani, et al., "Thermal and Mechanical Analysis of Novel Transcranial Magnetic Stimulation Coil for Mice", IEEE Transactions On Magnetics, Vol. 50, No. 9 (Sep. 2014). 2. L. J. Crowther, R. L. Hadimani, A. G. Kanthasamy, and D. C. Jiles, "Transcranial Magnetic Stimulation of Mouse Brain Using High-Resolution Anatomical Models", J. Appl. Phys. Vol. 115, No.17, p. 17B303 (Jan. 2014). 3. S. D. March, S. McAtee, M. Senter, et al, "Focused and Deep Brain Magnetic Stimulation Using New Coil Design in Mice", 6th Annual International IEEE EMBS Conference on Neural Engineering, San Diego, CA (6-8 Nov. 2013). 4. M TWilson1, A D Tang2, 3, K Iyer2, et el., "The challenges of producing effective small coils for transcranial magnetic stimulation of mice", Biomedical Physics & Engineering Express, Vol 4 (Apr. 2018).

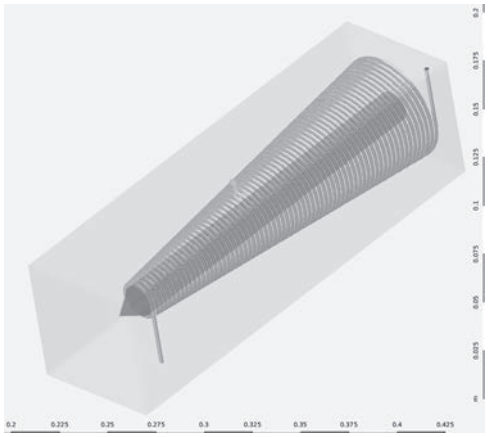


Fig. 1) Conical coil with sharpened MnZn ferrite core.

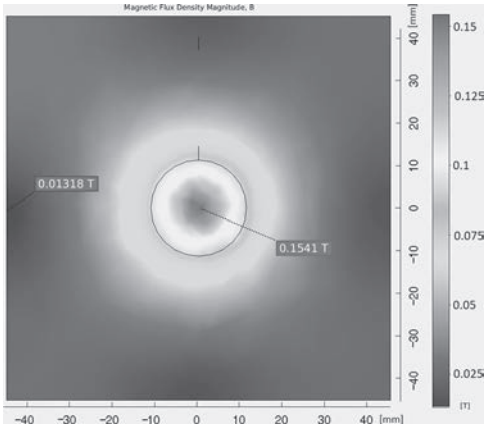


Fig. 2) B-flux magnitude at y= -4.25mm.

BW-13. Study of magnetic micelles as a drug carrier for anti-inflammation treatment. *C. Tsou*[1], F. Dong[1], W. Wang[2], Y. Huang[1], C. Su[3], T. Chen[1] and T. Ger[1] *1. Biomedical Engineering, Chung Yuan Christian University, Taoyuan City, Taiwan; 2. Nephrology, Tao-Yuan General Hospital, Ministry of Health and Welfare, Taoyuan City, Taiwan; 3. Institute of Biomedical Engineering and Nanomedicine, National Health Research Institutes, Miaoli County, Taiwan*

The chemical synthesis, biocompatibility and drug delivery study of pH-dependent temperature response magnetic micelles were investigated. The micelles of grafted modified magnetic nanoparticles which called magnetic micelles, were used as they have magnetic manipulation characteristics for accumulating the micelles in the lesion area through external magnetic field. Drug carrier micelle was characterized by Fourier transform infrared spectroscopy (FT-IR), Transmission electron microscope (FEG-TEM), critical micelles concentration (CMC), low critical solution temperature (LCST) superconducting quantum interference device (SQUID) and the thermogravimetric analysis (TGA). Micelles were divided into cell viability testing and inflammation assessment. We used lipopolysaccharide (LPS) to induce the inflammatory response in RAW264.7 mouse macrophages/monocyte and co-culture with multi-functional drug carrier micelles for inflammatory evaluation. This study provided multi-functional micelles as the anti-inflammation drug carrier with good biocompatibility, while maintaining the

characteristics of pH-dependent temperature response and magnetic properties. It is suggesting that these magnetic micelles can be a good candidate for anti-inflammatory therapy in the further clinical trial.

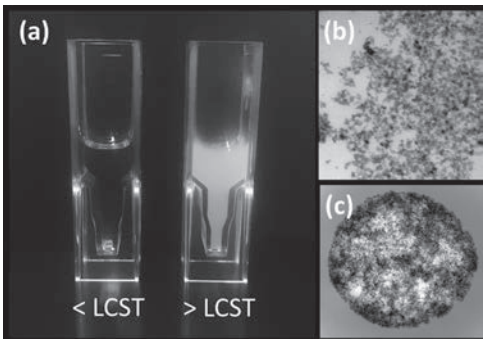


Figure. (a) With increasing temperature exceed LCST, the transmittance rapid decline in rapid, and the color change of magnetic micelles from initial transparent to milky. (b) TEM image of magnetic nanoparticles. (c) TEM image of single magnetic micelle.

BW-14. Noncontact Manipulation of Magnetic Particles Using Arrays of Permanent Magnets. *N. Riahi*[1] and A. Komaee[1] *1. ECE, Southern Illinois University, Carbondale, IL, United States*

Magnetic manipulators provide a unique ability for noncontact control of magnetic or magnetically tagged objects, which is of particular interest for medical and biochemical applications, including drug targeting, cell sorting, and magnetic tweezers. The current technology focuses on electromagnets to produce magnetic fields, while permanent magnets are well known to make stronger force compared to the electromagnets of the same size. This feature can lead to more compact, more efficient, and yet less expensive magnetic manipulators. The main drawback of the permanent magnet manipulators is the need to control the magnetic field by mechanically changing the position of magnets, and the highly nonlinear nature of this class of manipulators. We investigated the effectiveness of feedback control to overcome this nonlinearity. Our study is focused on the magnetic manipulator of Fig.1, which is comprised of six identical radially magnetized cylindrical magnets, spaced equally around a circular petri dish in which a magnetic object can move freely inside a viscous fluid. Each magnet in this setup is equipped with a servomotor, so that they can rotate individually to adjust the total magnetic field in the petri dish. By computer simulations, we implemented state feedback control to steer the magnetic particle along a desired reference trajectory. We then improved the results by adding integral action to the controller. The controllers were designed for a state-space model describing the dynamics of system with the position and velocity of the particle as the state vector and the angular positions of the magnets as its control vector. This nonlinear dynamics was first approximated by a linear model to facilitate the control design procedure. Since integral action constantly compensates for linear approximation error of the state space model, it can enlarge the region of attraction, i.e., the set of points over which the closed-loop system remains stable. As Fig.2 shows, this improvement results in the enlargement of tracking area by more than twice.

[1] A. Ito, M Shinkai and H Honda, Journal of bioscience and bioengineering.,Vol 100, p. 1-11, (2005) [2] J.L. Corchero, and A. Villaverde, Trends in biotechnology, Vol 27, p. 468-476, (2009)

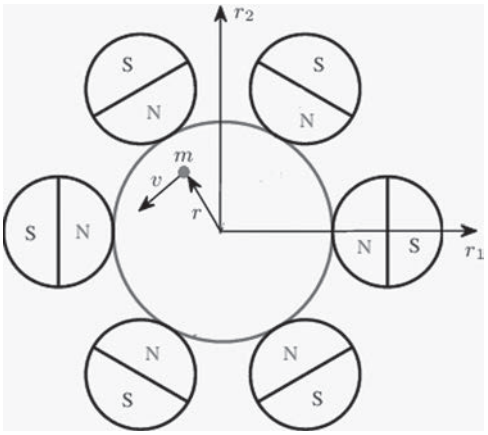


Fig.1 Schematic diagram of the magnetic manipulator

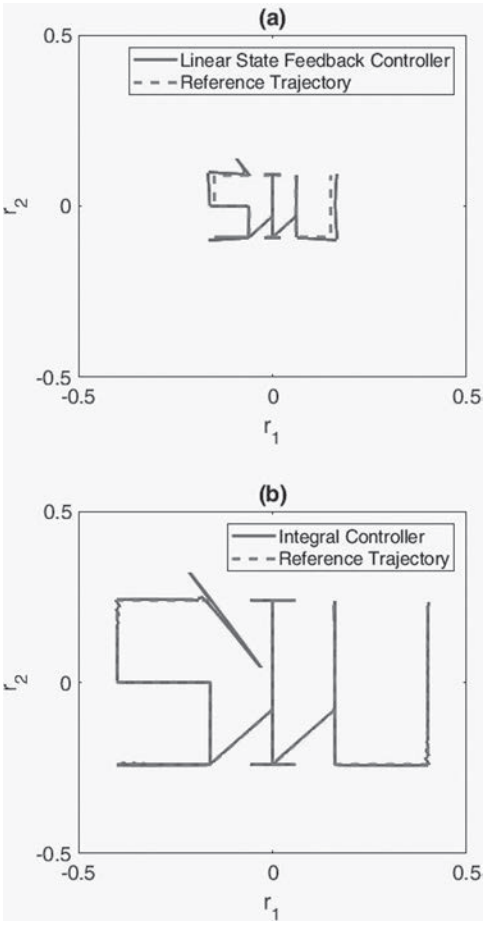


Fig.2 trajectory of the magnetic object and reference path under state feedback (a), and integral control (b)

BW-15. Safety issues of electric field induced in human body by a high field Magnetic Resonance Imaging system. *M. Trapanese*[1], G. Ala[1], P. Romano[1], F. Viola[1], G. Rizzo[1], M. Midiri[2], S. Salerno[2] and M. Galia[2] *1. Dipartimento Ingegneria, Palermo University, Palermo, Italy; 2. Biomedicina, Neuroscienze e Diagnostica avanzata, Palermo University, Palermo, Italy*

Safety issues and discussions associated with magnetic resonance imaging (MRI) systems and procedures have been intense over last years: the main topic has been the disputed assertions about the role of electromagnetic fields

in carcinogenesis or the promotion of abnormalities in growth and development On the contrary, since the introduction of MRI in the early 1980s, more than 100,000,000 diagnostic procedures (estimated) have been completed worldwide, with relatively few major incidents. However, recently the level of magnetic field used in commercial MR has been increased (up to 3T) and the safety issues have increased accordingly. As a result, in order to enhance the level of safety for the workers, European and Italian standards have recently fixed several value limit of the induced electric field that must not be exceeded. This limit is 1.1V/m. In this work, we evaluate analytically, numerically and experimentally the level of the induced electric field in proximity of MRI machine in a moving human body. The calculation has been performed by assuming several movement schemes. The analytical approach allows us to adapt the results to several cases and several level of magnetic field. The numerical approach has been based of a finite element method software where suitable models of moving human body and MR device have been implemented. The MR has been modelled as a coil of radius equal to the main commercial models and human body has been modelled as a water volume with some dielectric inserts. Finally, an experimental approach has been performed. All the approaches indicate that the limit imposed by the regulation is always respected for MRI device which a magnetic field up to 1.5T, for higher level of field the level of induced electric field can be exceeded in case of rapid movement of the arms.

BW-16. Withdrawn

Session CA
MACHINE LEARNING IN MAGNETISM

Thomas Schrefl, Chair
Danube University Krems, Wiener Neustadt, Austria

INVITED PAPERS

8:30

CA-01. Machine learning and high-throughput methods for the accelerated discovery of new magnets. *S. Sanvito[1] 1. School of Physics and CRANN, Trinity College Dublin, Dublin, Ireland*

The development of novel materials is a strong enabler for any technology, and often technology and materials innovation cannot be separated. Unfortunately the process of finding new materials, optimal for a given application, is lengthy, often unpredictable and has a low throughput. Here I will describe a systematic pathway to the discovery of novel materials, which demonstrates an unprecedented throughput and discovery speed. The method can be applied to any materials class and any potential application. I will use the example of magnetism to introduce the main features of the method, and I will demonstrate the discovery of several new high-performance magnets. Furthermore, I will highlight how such high-throughout schemes can be combined with machine-learning methods for data-mining to extract novel materials designing rules and for identifying new prototypes for further investigation. Based on an extensive electronic structures library of Heusler alloys containing 236,115 prototypical compounds, we have filtered those alloys displaying magnetic order and established whether they can be fabricated at thermodynamical equilibrium [1]. Specifically, we have carried out a full stability analysis for intermetallic Heuslers made only of transition metals. Among the possible 36,540 prototypes, 248 are found thermodynamically stable but only 20 are magnetic. The magnetic ordering temperature, T_C, has then been estimated by a regression calibrated on the experimental T_C of about 60 known compounds. As a final validation we have attempted the synthesis of a few of the predicted compounds and produced two new magnets. One, Co_2MnTi, displays a remarkably high T_C in perfect agreement with the predictions, while the other, Mn_2PtPd, is a complex antiferromagnet. In the second part of my talk I will discuss the use of machine-learning methods for predicting the Curie temperature of ferromagnets, based solely on their chemical composition, and for sorting magnets into hard and soft [2]. In particular I will discuss how to develop meaningful feature attributes for magnetism and how these can be informed by experimental and theoretical results. I will also show a potential promising scheme for extracting information from published literature. All these together can pave the way for the large-scale design of novel magnetic materials at unprecedented speed.

[1] Stefano Sanvito, Corey Oses, Junkai Xue, Anurag, Tiwari, Mario Zic, Thomas Archer, Pelin Tozman, Munuswamy Venkatesan, J. Michael D. Coey and Stefano Curtarolo, Accelerated discovery of new magnets in the Heusler alloy family, Science Advances 3, e1602241 (2017). [2] James Nelson and Stefano Sanvito, Predicting the Curie temperature of ferromagnets using machine learning, arXiv:1906.08534 (2019)

9:06

CA-02. Machine learning enhanced characterization of magnetic materials. *K. Ono[1] 1. High Energy Accelerator Research Organization (KEK), Tsukuba, Japan*

The recent development of materials informatics (MI) accelerates the efficiency of material fabrication and enables the automated and high precision characterization and analysis of materials. In the characterization and analysis of magnetic materials, machine learning techniques make it possible to measure a desired physical quantity optimally and shortly, and high-throughput experiment has been developed along with the automation of measurements. However, while measurement throughput has been increased, analysis of measurement data, that is, extraction of desired physical quantities and material characteristics from measurement data, is almost always performed by skilled experts. It is often to be a bottleneck for research and development of materials. We have studied optimization, automation, and acceleration of measurement and data analysis for magnetic materials. These studies not only significantly reduce human intervention in measurement and analysis but also commoditize characterization of material that only experts could ever perform. Furthermore, the measurement and analysis results become reproducible. It is considered to be an essential technology for future materials developments.

[1]T. Ueno, H. Hino, A. Hashimoto, Y. Takeichi, M. Sawada and K. Ono, npj Computational Materials 4, 4 (2018). [2] Kotaro Saito, Masao Yano, Hideitsu Hino, Tetsuya Shoji, Akinori Asahara, Hidekazu Morita, Chiharu Mitsumata, Joachim Kohlbrecher and Kanta Ono, Sci. Rep. 9, 1526 (2019) [3] Yuta Suzuki, Hideitsu Hino, Masato Kotsugi and Kanta Ono, npj Computational Materials 5, 39 (2019).

9:42

CA-03. Classification and optimization of a magnet's microstructure. *A. Kovacs[1], T. Schrefl[1], J. Fischbacher[1], L. Exl[2], N. Sakuma[3], M. Ito[3], A. Kinoshita[3], T. Shoji[3] and A. Kato[3] 1. Department for Integrated Sensor Systems, Danube University Krems, Wiener Neustadt, Austria; 2. WPI c/o Faculty of Mathematics, University of Vienna, Vienna, Austria; 3. Advanced Material Engineering Div., Toyota Motor Corporation, Higashifuji, Japan*

Growing demands for permanent magnets are predicted for green technology applications such as sustainable energy production and eco-friendly transport. With the quest for rare-earth reduced or rare-earth free permanent magnets, an optimal control of the magnet's microstructure becomes increasingly important. For example, grain boundary engineering and the use of core-shell grain structures have high potential to improve coercivity while reducing the material costs. In other fields of materials research, data driven machine learning approaches have been applied recently, in order to obtain a deeper understanding of the material's microstructure on its properties [1]. In the talk we present an automated search and optimization tool for the granular microstructure of permanent magnets. Machine learning is a method to relate microstructure and hysteresis properties of

a permanent magnet. Once built, the model can be used to replace time consuming micromagnetic simulations as design tool that predicts coercivity or energy density quickly. The machine learning tool chain needs (i) key features that characterizes a magnet's microstructure, (ii) fast methods for data generation, (iii) a machine learning predictor that is trained to predict hysteresis properties for a given microstructure, and (iv) model validation and interpretation. Similar to conventional materials modeling machine learning can be applied at different length scales. Key features of a grain are the crystallographic orientation, the position within the magnet, the sphericity, the maximum dihedral angle, and the number of neighbors. On a sub-grain scale, important features are the intrinsic magnetic properties of core, shell and grain boundary phase together with its spatial dimensions. For feature selection we apply cross-correlation and drop redundant features (see Figure 1). To generate hysteresis data quickly, we use a reduced order micromagnetic model for multigrain systems or fast parallel micromagnetic solvers for single grains. We train a random forest classifier with switching field maps computed with reduced order micromagnetics. This classifier is used to predict the weak grains where nucleation of a reversed domain will occur first. By identifying the features that cause low coercive grains, we have a handle to improve coercivity efficiently [2]. We developed an automated tool for the optimization and design of the core-shell structure in a permanent magnet. A universal deep Bayesian optimizer [3] is used to randomly sample a high dimensional feature space for the grain. A finite element model reflecting a specific feature set is generated and coercive field and energy density product are computed. Evaluating different machine learning models for predicting coercivity, we achieved the best regression scores with a gradient boost model. An uncertainty measure tells us whether the predicted coercive field for a given input can be trusted or should be recalculated with the micromagnetic solver. The machine learning models help to enhance the understanding and can be used for optimization: (i) The computed feature importance tells us which parameters have to be improved first before others become more relevant. For example, a feature identified as highly important is the magnetization of the grain boundary phase. The partial dependence plot (see Fig. 2) shows how the coercive field changes with the grain boundary magnetization while averaging over all other features of the model. (ii) Using classification, we can identify the grains that cause a low or a high coercive field. (iii) The use of local linear surrogate models tells us how feature changes near a specific design point affect coercivity or energy density product.

[1] A. Mangal and E. A. Holm, Int. J. Plast., Vol. 111, p.122-34 (2018) [2] L. Exl et al, J. Phys. Mater. 2, 014001 (2019) [3] F. Häse, L. M. Roch, C. Kreisbeck, A. Aspuru-Guzik, ACS Cent. Sci., Vol. 4, p.1134-1145 (2018)

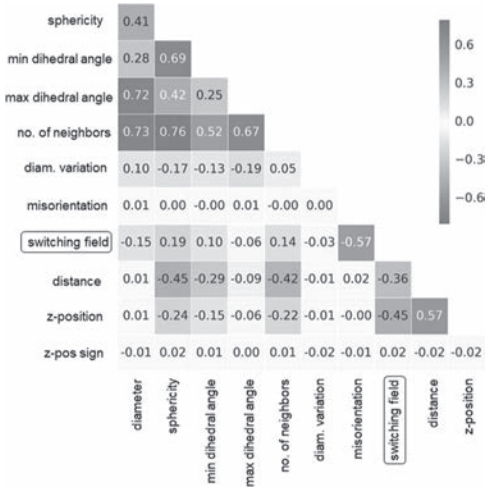


Fig. 1 Correlation between features that characterize a grain of a magnet.

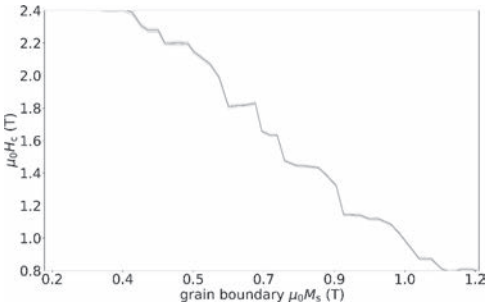


Fig. 2 Predicted change of coercivity with the grain boundary magnetization.

10:18

CA-04. Neural network based magnetic hysteresis modeling.
C. Serpico[1] *1. University of Napoli "Federico II", Napoli, Italy*

Magnetic Hysteresis in a moderately large ferromagnet arises as a consequence of the presence of a multiplicity of metastable equilibrium states. The magnetization of the ferromagnet, for a given external magnetic field, can assume many different values depending on the past history of the magnetic system [1]. This behavior depends both on intrinsic properties of the media (anisotropy, exchange interactions) and on extrinsic characteristics such the shape, the density of impurities and defects. This leads to a considerably complex phenomenon which is very difficult to be described using first principles physical modeling. The complexity of hysteresis, on the other hand, can be effectively handled by using machine learning techniques based on neural network [2]. The fact that hysteresis is a memory effect seems to require the use of dynamic neural networks [3]. However, by using a suitable framework to describe the mechanism of memory update in hysteretic systems, based on Preisach Model [4], this problem can be circumvented and it is possible to use only memoryless neural networks such feed-forward neural networks [3]. These aspects will be illustrated in the talk in detail. The last part of the talk will be devoted to an overview of the developments made in the last decades in the application of machine learning technique to hysteresis modeling [5].

[1] I.D. Mayergoyz, Mathematical Models of Hysteresis, Springer, New York (1991) [2] G. James, D. Witten, T.Hastie and R. Tibshirani, An Introduction to Statistical Learning, Springer, New York (2013) [3] J.A. Hertz, A.S. Krogh, and R.G. Palmer, Introduction to the Theory of Neural Computation, Addison-Wesley, Redwood City, CA (1991) [4] C. Serpico, C. Visone, IEEE Transactions on Magnetics, Vol. 34, p. 623 – 628 (1998) [5] A.A. Adly, S.K. Abd-El-Hafiz, Journal of Advanced Research, Vol. 5, p. 615-627 (2014)

10:54

CA-05. Estimation of the Magnetic Field Distribution through Deep Learning.
D. Lowther[1] and A. Khan[1] *1. Elec and Comp Eng, McGill University, Montreal, QC, Canada*

In the analysis and design of electromagnetic devices, the distribution of the magnetic field is crucial to determining the performance of the device. The air gap field is needed for the force generated in a motor or actuator; the eddy currents and hysteresis losses in the components of the device give rise to local losses and thus lead to local heating and potential failure of a device; etc. Computing the field through the solution of the partial differential equations that result, in non-radiating systems, from Ampere's and Faraday's laws can be slow and thus limit the interactivity of any design space exploration. Solving the field equation is equivalent to replacing the construction of physical prototypes a with virtual prototyping process which can reduce overall costs and time but is rarely capable of providing a designer with

performance feedback which would allow an interactive exploration of a design space. The physics equations which are solved are, themselves, a set of rules which have been developed based on logical deductions drawn from the outputs of a series of experiments. In a sense, they are surrogates which represent real world performance. The question can be asked as to whether other surrogates can be created. For example, is it possible to estimate the field distribution with suitable fidelity from just the input data, i.e. the geometry, material properties, the excitations and a series of examples connecting these inputs to the observed field distributions, without using the physics equations directly. If so, there are two potential benefits that could be derived from this approach. The first is that the field estimates could be used to accelerate existing numerical solution systems. Many solvers are, in fact, optimizers and work on minimizing the error in the solution. If a good estimate of the solution can be provided, the solver can reach a solution very much faster. The second benefit comes with the speed at which an estimate can be obtained, potentially allowing the effect of design modifications to be evaluated interactively. Additionally, the estimation system should be able to provide a level of certainty with its estimate, i.e. to suggest where its prediction might be in error. The goal here is to try to simulate the performance of a design engineer who is capable of estimating the impact of changes on device performance largely through experience. Over the last few decades the idea of estimating the field distribution has been explored using machine learning based on neural networks. There has been some success in achieving the first benefit using relatively simple systems [1]-[3] when the estimates are used along with an adaptive solver. However, obtaining an estimate of sufficient accuracy to be useful for design exploration has proven more difficult [3]. Basically, the computational power and network architectures that were considered were insufficient to achieve a result which met the goal. More recently, the development of deep learning systems based around convolutional neural networks and treating the field solution as an "image" or "pattern" related to the input data has shown some promise. The paper will discuss some of the history behind the use of machine learning and artificial intelligence in the area of magnetic field estimation and describe a recent system based on a convolutional neural network which has had reasonable success both in estimating a field solution and in determining the errors and their locations in the prediction [5].

1. D. Dyck, M.Eng. thesis, McGill University, (1990). 2. D.A.Lowther, D.N.Dyck, IEEE Transactions on Magnetics, Vol. 29, pp. 1927-1930 (1993). 3. F. Dandurand and D. A. Lowther, IEEE Transactions on Magnetics, vol. 35, pp. 1817-1820 (1999). 4. A. Auclair, M.Eng. thesis, McGill University, (2004) 5. A. Khan, V. Ghorbanian and D. Lowther, IEEE Transactions on Magnetics, (early access), pp. 1-4 (2019).

Session CB
SPIN TRANSPORT IN ANTIFERROMAGNETS

Samik DuttaGupta, Chair
Tohoku University, Sendai, Japan

INVITED PAPER

8:30

CB-01. Magnetization Switching Utilizing Topological Surface States.

M. Wu[1], P. Li[1], J. Kally[2], S. Zhang[3], T. Pillsbury[2], J. Ding[1], G. Csaba[4], J. Ding[3], J. Jiang[3], Y. Liu[5], R. Sinclair[5], C. Bi[6], A. DeMann[1], G. Rimal[7], W. Zhang[8], S. Field[1], J. Tang[7], W. Wang[6], O. Heinonen[3], V. Novosad[3], A. Hoffmann[3] and N. Samarth[2] *1. Colorado State University, Fort Collins, CO, United States; 2. Pennsylvania State University, University Park, PA, United States; 3. Argonne National Laboratory, Lemont, IL, United States; 4. Pazmany Peter Catholic University, Budapest, Hungary; 5. Stanford University, Stanford, CA, United States; 6. University of Arizona, Tucson, AZ, United States; 7. University of Wyoming, Laramie, WY, United States; 8. Oakland University, Rochester, MI, United States*

Materials with strong spin-orbit coupling can convert a charge current to a spin current, and vice versa. Heavy metals are one class of such materials in which the spin-orbit coupling is associated with the spin Hall effect in the bulk or the interfacial Rashba effect. When a heavy metal film is interfaced with a ferromagnetic (FM) film, the spin-orbit coupling-produced spin current in the heavy metal can exert a torque on the magnetization in the FM film, which is the so-called spin-orbit torque (SOT). This SOT can be used to switch magnetization, drive domain-wall motion, or excite magnetization precession. Due to the spin-momentum locking of the topological surface states (TSS), topological insulators (TIs) are expected to host spin-orbit coupling that is considerably stronger than in heavy metals and can thereby produce substantially larger SOT. In fact, very recently there have been several experimental demonstrations of SOT-induced magnetization switching in TI/FM bi-layers.[1-7] The demonstrated switching efficiencies were all higher than in the heavy metal/FM counterparts. The FM films in those studies, however, were all conductive, with conductivities either about one order of magnitude higher than or comparable to the conductivities of the TI films. A straightforward consequence of this is the severe shunting current in the FM film, which not only limits the switching efficiency but may also cause certain thermal issues. In addition, the conductive nature of the FM components has a much more serious consequence – the TSS may have been largely spoiled by the FM films and may not account for the observed strong SOT effects. Previous works have shown that interfacing a TI with a conductive FM film can result in a significant modification or even complete suppression of the TSS in the TI.[8-12] One can eliminate the above issues simply by replacing the conductive FM components with insulating FM materials. A recent theoretical work compared the effects of conductive and insulating FM films on the TSS in TI/FM heterostructures. It showed that, in stark contrast with the conductive FM case, the TSS in a TI/magnetic insulator (MI) structure can be largely preserved, except for opening of a small gap at the Dirac point when strong coupling exists at the interface.[10] This presentation reports the demonstration of TSS-induced switching in a TI/MI bi-layered structure where the TI layer is a Bi_2Se_3 film consisting of 6 quintuple layers, and the MI layer is a 5-nm-thick $BaFe_{12}O_{19}$ film that has large magneto-crystalline anisotropy and shows an effective perpendicular anisotropy field of about 22 kOe. The switching response in the $BaFe_{12}O_{19}$ film strongly depends on the charge current applied to the Bi_2Se_3 film. When a constant magnetic field is applied in the film plane, the charge current in the Bi_2Se_3 film can switch the magnetization in the $BaFe_{12}O_{19}$ film between the up and down states. When the magnetization is switched by sweeping an obliquely applied magnetic field with a constant charge current in the Bi_2Se_3 film, the current can cause the switching field to decrease or increase, depending on the current polarity, by as much as 4000 Oe. A decrease in temperature (T) results in a monotonic reduction in the switching current in the field-fixed measurements and a monotonic increase in the change of switching field in the current-fixed measurements. This result evidently indicates the presence of strong SOT responses at low T, while the latter can be attributed to the presence of strong TSS due to enhanced surface state conductivity and decreased bulk state conductivity. When compared with $Pt/BaFe_{12}O_{19}$, the SOT efficiency is comparable at room temperature but is about 30 times higher at T=3 K. These results demonstrate the merits of TSS in manipulating magnetization and thereby shed light on the applications of topological insulators in spintronic devices.

[1] Y. Fan, P. Upadhyaya, X. Kou, M. Lang, S. Takei, Z. Wang, J. Tang, L. He, L. -T. Chang, M. Montazeri, G. Yu, W. Jiang, T. Nie, R. N. Schwartz, Y. Tserkovnyak, K. L. Wang, Magnetization switching through giant spin–orbit torque in a magnetically doped topological insulator heterostructure. *Nat. Mater*. 13, 699–704 (2014). [2] J. Han, A. Richardella, S. A. Siddiqui, J. Finley, N. Samarth, L. Liu, Room-temperature spin-orbit torque switching induced by a topological insulator. *Phys. Rev. Lett*. 119, 077702 (2017). [3] Y. Wang, D. Zhu, Y. Wu, Y. Yang, J. Yu, R. Ramaswamy, R. Mishra, S. Shi, M. Elyasi, K.-L. Teo, Y. Wu, H. Yang, Room temperature magnetization switching in topological insulator-ferromagnet heterostructures by spin-orbit torques. *Nat. Commun*. 8, 1364 (2017). [4] K. Yasuda, A. Tsukazaki, R. Yoshimi, K. Kondou, K. S. Takahashi, Y. Otani, M. Kawasaki, and Y. Tokura, Current-nonlinear Hall effect and spin-orbit torque magnetization switching in a magnetic topological insulator. *Phys. Rev. Lett.* 119, 137204 (2017). [5] Y. Li, Q. Ma, S. X. Huang, C. L. Chien, Thin films of topological Kondo insulator candidate SmB_6: Strong spin-orbit torque without exclusive surface conduction. *Sci. Adv*. 4, eaap8294 (2018). [6] M. DC, R. Grassi, J.-Y. Chen, M. Jamali, D. R. Hickey, D. Zhang, Z. Zhao, H. Li, P. Quarterman, Y. Lv, M. Li, A. Manchon, K. A. Mkhoyan, T. Low & J.-P. Wang, Room-temperature high spin–orbit torque due to quantum confinement in sputtered $Bi_xSe_{(1-x)}$ films. *Nat. Mater*. 17, 800 (2018). [7] N. Khang, Y. Ueda, P. H. Hai, A conductive topological insulator with large spin Hall effect for ultralow power spin–orbit torque switching. *Nat. Mater.* 17, 808 (2018). [8] L. A. Wray, S.-Y. Xu, Y. Xia, D. Hsieh, A. V. Fedorov, Y. S. Hor, R. J. Cava, A. Bansil, H. Lin, M. Z. Hasan, A topological insulator surface under strong Coulomb, magnetic and disorder perturbations. *Nat. Phys*. 7,32–37 (2011). [9] J.-C. Rojas-Sánchez, S. Oyarzún, Y. Fu, A. Marty, C. Vergnaud, S. Gambarelli, L. Vila, M. Jamet, Y. Ohtsubo, A. Taleb-Ibrahimi, P. Le Fèvre, F. Bertran, N. Reyren, J.-M. George, and A. Fert, Spin to charge conversion at room temperature by spin pumping into a new type of topological insulator: α-Sn films. *Phys. Rev. Lett*. 116, 096602 (2016). [10] J. Zhang, J. P. Velev, X. Dang, E. Y. Tsymbal, Band structure and spin texture of Bi_2Se_3 3*d* ferromagnetic metal interface. *Phys. Rev. B* 94, 014435(2016). [11] J. M. Marmolejo-Tejada, K. Dolui, P. Lazic, P.-H. Chang, S. Smidstrup, D. Stradi, K. Stokbro, B. K. Nikolic, Proximity band structure and spin textures on both sides of topological-insulator/ferromagnetic-metal interface and their charge transport probes. *Nano Lett*. 17, 5626 (2017). [12] Y. T. Hsu, K. Park, E. A. Kim, Hybridization-induced interface states in a topological insulator-magnetic metal heterostructure. *Phys. Rev. B* 96, 235433 (2017).

CONTRIBUTED PAPERS

9:06

CB-02. Large Enhancement in Spin Transport Efficiency in $Y_3Fe_5O_{12}$/NiO/Pt Heterostructures. *E. Cogulu*[1], D. Roy[2], J. Ding[3], H. Ohldag[4], M. Wu[3] and A.D. Kent[1] *1. Center for Quantum Phenomena, Department of Physics, New York University, New York, NY, United States; 2. Department of Physics, Indian Institute of Technology Ropar, Rupnagar, India; 3. Department of Physics, Colorado State University, Fort Collins, CO, United States; 4. Advanced Light Source, Lawrence Berkeley National Lab, Berkeley, CA, United States*

The spin Seebeck effect (SSE), where a thermal gradient in a ferromagnet generates spin current, is a widely used method to generate and study spin waves. Further, there has been increasing interest in characterizing spin transport, specifically, in thin insulating antiferromagnets (AFM). This is not only because they can transmit spin waves efficiently while providing electrical isolation, but also because they can provide insight about the nature of the transport and how it relates to the magnetic order in the AFM. We have studied heterostructures of the form ferromagnet-antiferromagnet-heavy metal ($Y_3Fe_5O_{12}$(YIG)-NiO-Pt) to detect spin transport flow through NiO. A temperature gradient is created by applying high current densities to the heavy metal (Pt) while the spin current is detected by the inverse spin Hall effect in the heavy metal. A lock-in technique is used to measure the 2nd harmonic response as a function of temperature and in-plane magnetic field, which sets the magnetization of YIG layer (inset Fig. 1). We have found a sharp increase in the SSE amplitude around 110 K (Fig. 1). The fact that the peak is not present in our control samples (YIG/Pt) suggests that the origin is either the NiO layer or the YIG/NiO interface. In addition, we have conducted X-ray Magnetic Circular Dichroism Absorption Spectroscopy (XMCD) to gain insight into the magnetic order (Fig. 2). For 5 nm thickness of NiO, we observe a change in the circular dichroism of nickel and iron near 100 K which is associated with a change in the coupling of Fe and Ni moments. Results on samples with varied NiO thickness and external magnetic field are used to identify the origin of this large enhancement and sharp peak in the spin-transport efficiency.

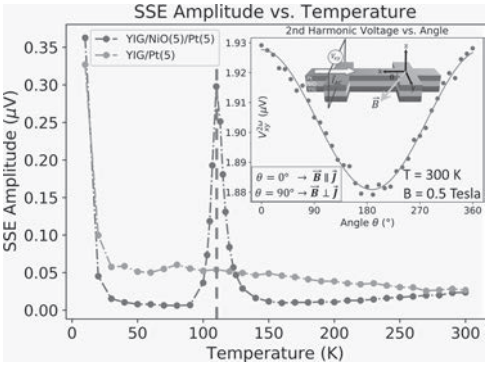


Fig. 1: Temperature dependence of the Spin Seebeck Effect in YIG/NiO/Pt and YIG/Pt samples. The sharp increase of the SSE amplitude around 110 K is only present in samples with NiO layers. The inset shows the measurement geometry and a sine fit to the field angular dependence.

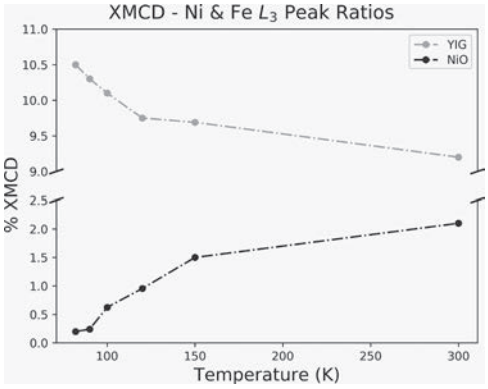


Fig. 2: XMCD of nickel and iron inside the heterostructure. The change around 100 K suggest the coupling between iron and nickel magnetic moments change near the SSE peak temperature.

9:18

CB-03. Roles of Magnon Angular Momentum in Non-collinear Magnetic System. *Y. Cheng*[1] and S. Zhang[1] *1. University of Arizona, Tucson, AZ, United States*

Magnons and electrons are essential angular momentum carriers in spintronics. For the collinear ferromagnets and antiferromagnets, the angular momentum of each magnon is quantized in the direction of the order parameter with the magnitude \hbar. The interaction between magnons and electrons yield a number of spin transport phenomena such as spin transport torques, spin-magnon current conversion at interfaces, and magnon drag effects. We study the magnon spectrum and its associated spin transport in non-collinear antiferromagnets. We consider a standard antiferromagnetic Heisenberg Hamiltonian with a Dzyaloshinskii-Moriya interaction and an easy-axis anisotropy in a two-dimensional triangular and Kagome lattice. We first determine the energy-momentum dispersion of the magnons and the corresponding average angular momentum of each magnon. Note that the angular momentum is no longer an eigenvalue of the magnon. The directions of the angular momentum and the linear momentum, known as spin-momentum locking, become nontrivial. We then investigate the magnon spin accumulation in the presence of an external spin current injection, spin-magnon drag, and the electron conductivity due to the scattering of these magnons. The results will be compared with those of magnon transport for collinear magnetic systems.

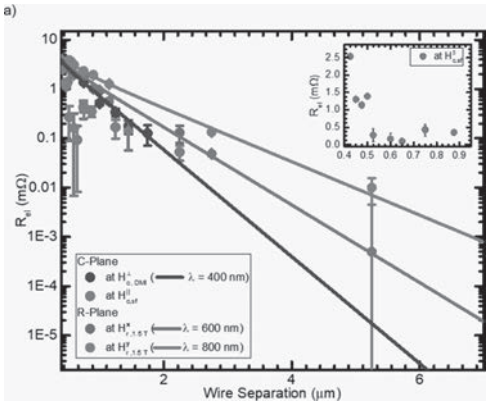
9:30

CB-04. Tunable long-distance spin-transport in antiferromagnetic insulators. R. Lebrun[4], A. Ross[4], O. Gomonay[4], D. Grave[1], A. Kay[1], A. Qaiumzadeh[2], S. Bender[3], C. Ulloa[3], *L. Baldrati*[4], S. Becker[4], D. Ellis[1], F. Kronast[5], R. Duine[3,2], A. Brataas[2], A. Rothschild[1] and M. Kläui[4,2] *1. Department of Materials Science and Engineering, Technion-Israel Institute of Technology, Haifa, Israel; 2. Center for Quantum Spintronics, Norwegian University of Science and Technology, Trondheim, Norway; 3. Utrecht University, Utrecht, Netherlands; 4. Johannes Gutenberg University, Mainz, Germany; 5. Helmholtz-Zentrum Berlin für Materialen und Energie, Berlin, Germany*

In contrast to ferromagnets, antiferromagnets benefit from enhanced stability with respect to applied external fields, magnetization dynamics at THz frequencies and a lack of stray fields [1,2]. Many theoretical studies have been undertaken describing the mechanisms through which antiferromagnets could allow for the propagation of spin current across the long distances in antiferromagnets, which would be required for integration into information transfer and logic devices [3,4]. Here we demonstrate that in the most common insulating antiferromagnet, hematite (α-Fe2O3) [5], a

diffusive magnonic spin current is able to propagate over micrometers in both single crystals [5] and thin films [6]. With a low damping and characteristic frequencies of hundreds of GHz, this compound allows antiferromagnetic spin-waves to propagate as far as in YIG, a ferromagnetic material with the lowest known damping, which is the material of choice for magnonic devices. We detect a first harmonic signal, related to the spin conductance, that exhibits a maximum at the spin-flop reorientation, while the second harmonic signal, related to the Spin Seebeck conductance, is linear in the amplitude of the applied magnetic field. The first signal is dependent on the direction of the Neel vector of the antiferromagnet and the second one depends on the induced magnetic moment due to the field. From the power and distance dependence, we unambiguously distinguish long-distance transport based on diffusion [5] from predicted spin superfluidity [4]. To understand the mechanisms behind magnon propagation, we extract the critical fields using the spin-Hall magneto-resistance technique [7], allowing for a precise determination of the magnetic anisotropies without the need for synchrotron-based facilities. We finally discuss establish the interactions between antiferromagnetic spin-waves and domain walls, and demonstrate that one can even achieve zero-field, room temperature magnon transport in insulating antiferromagnets[6].

[1] T. Jungwirth, X. Marti, P. Wadley, and J. Wunderlich, Nat Nano 11, 231 (2016). [2] V. Baltz, A. Manchon, M. Tsoi, T. Moriyama, T. Ono, and Y. Tserkovnyak, Rev. Mod. Phys. 90, 015005 (2018). [3] S. A. Bender, H. Skarsvåg, A. Brataas, and R. A. Duine, Phys. Rev. Lett. 119, 056804 (2017). [4] S. Takei, B. I. Halperin, A. Yacoby, and Y. Tserkovnyak, Physical Review B 90, 094408 (2014). [5] R. Lebrun, A. Ross, S. A. Bender, A. Qaiumzadeh, L. Baldrati, J. Cramer, A. Brataas, R. A. Duine, and M. Kläui, Nature 561, 222 (2018). [6] A. Ross, R. Lebrun, O. Gomonay, D. Grave, A. Kay, L. Baldrati, S. Becker, A. Qaiumzadeh, S. Bender, C. Ulloa, D. Ellis, F. Kronast, G. Jakob, R-A. Duine, A. Brataas, A. Rothschild, M. Kläui (2019) [7] R. Lebrun, A. Ross, O. Gomonay, S. Bender, L. Baldrati, F. Kronast, A. Qaiumzadeh, J. Sinova, A. Brataas, R. Duine, and M. Kläui, *Communications Physics* 2, 50 (2019)



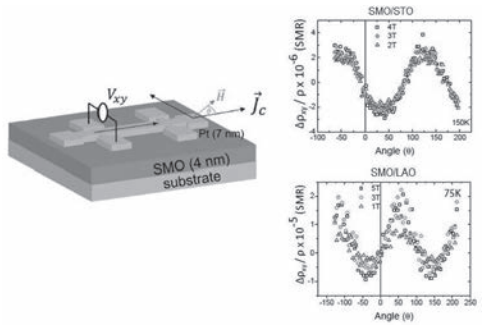
Distance dependence of the spin-transport signal for antiferromagnetic thin films of hematite with different growth orientations.

9:42

CB-05. Realization of spin current across the interface of Pt and thin films of antiferromagnetic manganites. *A. Das*[1], A. Watson[1], A. Burema[1], P. Zhang[1] and T. Banerjee[1] *1. Zernike Institute for Advanced Materials, University of Groningen, Groningen, Netherlands*

Antiferromagnets are incipient material choice to study long distance magnon transport across an insulating channel, given their fast magnetization dynamics and robustness against stray fields[1,2]. The detection of spin currents and spin wave excitations in antiferromagnets, exploiting the (inverse-)spin hall effect on heavy metal electrodes, have attracted lot of attention in recent years. However, complex oxides, with their rich magnetic phase diagram, are relatively unexplored. In particular, manganite thin films, due to the strong coupling between the orbital degrees of freedom and magnetic exchange interactions are worth exploring. In this work, we demonstrate a scalable spin current in antiferromagnetic thin films of (SMO), detected using a Hall bar made of Pt. By growing SMO films epitaxially on two different substrates ($SrTiO_3$ and $LaAlO_3$), we tailor the strain, from compressive in the former to tensile in the latter. This gives rise to different orbital occupancies, thus different magnetic orderings. We further investigate the influence of partial pressure of oxygen, during the growth of thin SMO films, on the spin current at different temperatures. We find that the resultant mixed structural phases of perovskite and brownmillerite exhibit an exchange bias in SMO on both substrates. Spin Hall magnetoresistance (SMR) studies on differently strained SMO thin films [3], show a phase shift in the angular dependence of the SMR signal, allowing a differentiation between ferromagnetic and antiferromagnetic moments. This work highlights the strong correlation of magnetic ordering with structural properties, such as epitaxial strain and oxygen vacancy-induced orbital occupancies, inherent in transition metal oxides, and demonstrate the suitability of SMO for magnon transport. Fig. 1: (right panel) Hall bar geometry of Pt patterned on SMO with charge current making an angle θ with the applied magnetic field in-plane to the charge transport. (Left panel) Transverse SMR response at Pt/SMO interface grown on $SrTiO_3$ (top) and $LaAlO_3$ (bottom). The phase shift of 90 degrees indicate an anti-ferromagnetic (top) to ferromagnetic (bottom) ordering in SMO.

1. R. Lebrun et al., Nature 561, 222 (2018) 2. J. Fischer et al., Phys. Rev. B, 97, 014417 (2018) 3. A. Das et al., submitted (2019)



9:54

CB-06. Spin currents in antiferromagnetic insulators: optical excitation, zitterbewegung, and magnon conductivity. *I. Proskurin*[1,2] and R.L. Stamps[1] *1. Department of Physics and Astronomy, University of Manitoba, Winnipeg, MB, Canada; 2. Institute of Natural Sciences and Mathematics, Ural Federal University, Ekaterinburg, Russian Federation*

Antiferromagnetic insulators are of interest for creating and transmitting spin currents, which is a key issue in spintronics. Spin currents in antiferromagnets can be excited by various methods [1] including spin-Seebeck and spin-Nernst effects, spin pumping from a ferromagnet, spin injection, and photo-excitation [2]. It has been suggested that a magnon spin current in antiferromagnetic materials is affected by interband tunneling [2]. Based on the special features of magnon dynamics in antiferromagnets [3], we demonstrate that the interband terms in the magnonic spin current correspond to the zitterbewegung (trembling motion) effect expected for magnon wave packet dynamics [4]. We show how these terms contribute to the mechanism of optical excitation of spin currents proposed in Ref. [2]. This mechanism involves polarized light and is motivated by the photogalvanic effect in metals, where circularly polarized light can produce a direct electron photocurrent, which direction depends on the polarization. In electron Dirac materials, interband effects are significant near the band crossing.

In particular, they are responsible for the minimal conductivity of graphene [5]. By analogy, we discuss similar effects in the spin conductivity of magnons, which is determined as a linear response coefficient to the eclectic field via the Aharonov-Casher phase. The effect can be interpreted as a magnon contribution to the electric dipole moment created by the magnon spin current.

[1] V. Baltz et al., Rev. Mod. Phys., Vol. 90, p. 015005 (2018) [2] I. Proskurin, et al., Phys. Rev. B, Vol. 98, p. 134422 (2018). [3] I. Proskurin, et al., Phys. Rev. Lett., Vol. 119, p. 177202 (2017) [4] W. Wang, et al., Phys. Rev. B, Vol. 96, p. 024430 (2017). [5] M. I. Katsnelson, Eur. Phys. J. B, Vol. 51, p. 157 (2006).

10:06

CB-07. Effect of Dzyaloshinskii–Moriya and Dipolar Interactions in the Propagation Length of Thermally Excited Magnons in Low Anisotropy Antiferromagnets. R. Yanes[1] and *L. Lopez-Diaz*[1] *1. Applied Physics, University of Salamanca, Salamanca, Spain*

Long-range spin transport in low anisotropy antiferromagnets has been recently proved [1,2]. The increase of the spin conductance around the spin-flop transition (B_{sf}) is interpreted in terms of the field dependent gap between the two magnon modes carrying opposite angular momentum [1,3]. However, the mechanisms that couple spin accumulation to antiferromagnetic order enabling transport over long distances are not well understood yet. In particular, the role played by Dzyaloshinskii–Moriya interaction (DMI), essential to explain the equilibrium states under field in some cases [1], and dipolar interactions, usually neglected in antiferromagnets, is to be elucidated. We use an atomistic spin localized model to investigate the propagation of thermally excited spin currents (SCs) in a bi-partite antiferromagnet under the effect of an external field along the easy axis, analyzing the role of DMI and dipolar interaction. The parameters are chosen so that the spin-flop transition occurs around B_{sf} =6 T, close to the value obtained for α-Fe2O3 in [1]. As observed in Fig.1, the influence of dipolar interaction is negligible in equilibrium, whereas DMI smooths out the spin-flop transition favouring the gradual orientation of the Neel vector, n. Starting from equilibrium, thermal fluctuations are introduced in a region on the left side corresponding to T=50K, whereas the rest of the system is at T=0. Thermal magnons are excited and they propagate along the x-axis. The propagation length of this SC, L_{SC}, is computed and the results are presented in Fig.2. A sharp increase of the propagation length around B_{sf} is obtained, in good agreement with experimental results [1]. Interestingly, this increase is more pronounced when dipolar interactions are included, yielding propagation lengths in the order of 400 nm. This result suggests that dipolar interactions might be partially responsible for the long distance propagation of SC in low anisotropy antiferromagnets close to B_{sf}. The detailed mechanism behind this result is a consequence of the appearance of significant net angular momentum and the spatial rotation of n around B_{sf}.

[1] R. Lebrun et al, Nature Vol. 561, p. 222 (2018) [2] S. Seki et al, Phys. Rev. Lett. Vol 115, p. 266601 (2015) [3] S. A Bender et al, Phys. Rev. Lett. Vol 119, p. 056804 (2017)

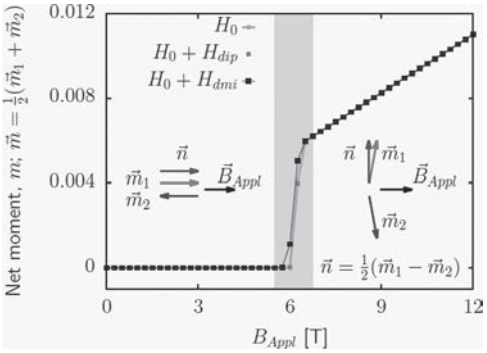


Fig. 1 Field dependence of the net magnetic moment

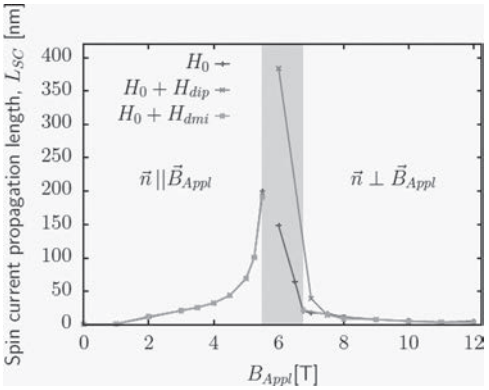


Fig. 2 Field dependence of spin current propagation length.

10:18

CB-08. Spin Seebeck effect from antiferromagnetic magnons in epitxial Cr_2O_3 films. *W. Yuan*[1], J. Li[1], V.H. Ortiz[1] and J. Shi[1] *1. UC Riverside, Riverside, CA, United States*

A temperature gradident can generate pure spin currents in ferro- and ferri-magnetic materials that can be detected by the inverse spin Hall effeect (ISHE), which is called spin Seebeck effect (SSE). Recently, SSE has been reported in antiferromagnetic (AFM) insulators, such as Cr_2O_3 single crystal [1] and MnF_2 thin films [2]. As the easy-axis field increases, the SSE signal shows a step-like jump at the spin-flop (SF) transition. However, it is still unclear whether AFM SSE requires a field-induced static magnetic moment. Here we report a study of the SSE in Cr_2O_3 thin films, which are epitaxially grown on pre-annealed Al_2O_3(11-20) substrates using a high vacuum pulsed laser deposition system. The lattice structure of Cr_2O_3 films is characterized by reflection high energy electron diffraction and X-ray diffraction. After deposition of a 5 nm Pt (or Ta) layer on Cr_2O_3, we fabricate the SSE devices by covering with a 80 nm Al_2O_3 insulating layer and then Cr(45 nm)/Au(5 nm) layers as a heater. Systematic measurements of SSE in Cr_2O_3/Pt and Cr_2O_3/Ta heterostructures are performed as a function of magnetic field and temperature. The SSE signal clearly shows a sign reversal across the SF transition while sweeping the magnetic field along the c-axis of Cr_2O_3, which is consistent with the SSE result observed in our Cr_2O_3 single crystal samples. The sign revcersal at the SF transition suggests that AFM magnons carry opposite angular momenta below and above SF transition. The magnitude of the SSE signal increases with decreasing temperature, reaches a maximum at T = 8 K, and then starts to decrease towards zero. Our observations can be explained by a model based on AFM magnons and is consistent with our presious report on SSE in FeF_2 epitaxial thin films [3]. This work is partly supported by SHINES, an Energy Frontier Research Center funded by the US Department of Energy, Office of Science, Basic Energy Sciences under Award No. SC0012670.

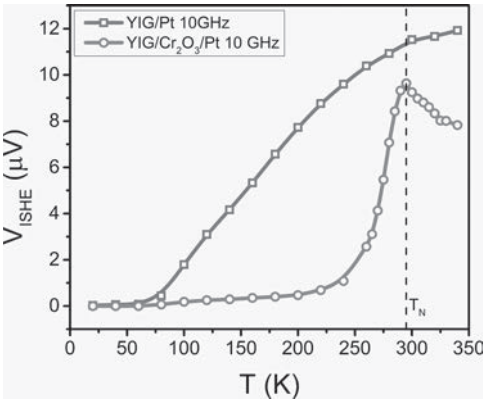
[1] S. Seki et al, Phys. Rev. Lett. 115, 266601 (2015). [2] Stephen M Wu et al, Phys. Rev. Lett. 116, 097204 (2016). [3] J. Li et al, Phys. Rev. Lett. 122, 217204 (2019).

10:30

CB-09. Spin Current Suppression by Antiferromagnetic Ordering in Spin Pumping in $Y_3Fe_5O_{12}/Cr_2O_3$/Pt Heterostructure. *V.H. Ortiz*[1], J. Li[1], B. Arkook[1], W. Yuan[1], I. Barsukov[1] and J. Shi[1] *1. Physics and Astronomy, University of California Riverside, Riverside, CA, United States*

Antiferromagnetic insulators (AFMI) have recently attracted a great deal of attention due to many unique interesting properties [1]. For example, thin AFMI layers are found to enhance spin current transmission around the antiferromagnetic phase transition temperature when they are inserted between a ferrimagnetic insulator (FMI) and a heavy metal (HM), such as the NiO and CoO layers in $Y_3Fe_5O_{12}$(YIG)/NiO/Pt [2] and YIG/CoO/Pt [3]. In a recent work [4], a sharp decrease of spin Seebeck effect (SSE) signal below Néel temperature of Cr_2O_3 was reported in a YIG/Cr_2O_3/Pt heterostructure. It was suggested that the blockage of spin current was caused by the spin-orbit torque absorption exerted by the relative spin orientation of the FMI/AFMI layers. However, this proposed picture has not been validated. In this work, we report a greatly suppressed spin current transmission due to the presence of AFM ordering in spin pumping (SP) experiments in YIG/Cr_2O_3/Pt heterostructures. We grew a 10 nm Cr_2O_3 film on epitaxial YIG (111) film using a high-vacuum pulsed laser deposition (PLD) system and then post-annealed it in oxygen prior to the deposition of Pt layer. Coplanar waveguide SP devices were fabricated on top of the film, and systematic measurements of SP and SSE signals were carried out as a function of microwave frequency, magnetic field, and temperature. We observed a significant suppression of both SP and SSE signals below the AFM phase transition of Cr_2O_3 films (T_N~295 K), which is very similar to what was reported by Z. Qiu *et al* [4]. However, our high-resolution transmission electron microscopy study revealed that the Cr_2O_3 is a randomly oriented polycrystalline thin film, contradicting the previously proposed model [4]. Our experimental results suggest that the spin current blockage may be caused by the large magnon gap of AFM material that prevents the magnon diffusion from the ferrimagnet. This work was supported as part of the SHINES, an Energy Frontier Research Center funded by the US Department of Energy, Office of Science, Basic Energy Sciences under Award No. SC0012670.

[1] V. Baltz, A. Manchon, M. Tsoi, T. Moriyama, T. Ono, and Y. Tserkovnyak, Rev. Mod. Phys. 90, 015005 (2018). [2] A. Prakash, J. Brangham, F. Yang, and J. P. Heremans, Phys. Rev. B 94, 014427 (2016). [3] W. W. Lin, K. Chen, S. F. Zhang, and C.-L. Chien, Phys. Rev. Lett. 116, 186601 (2016). [4] Z. Qiu, D. Hou, J. Barker, K. Yamamoto, O. Gomonay, and E. Saitoh, Nature Mater. 17, 577 (2018).



Comparison of spin pumping signal magnitude for YIG/Pt and YIG/Cr_2O_3/Pt heterostructures.



TEM image of YIG/Cr_2O_3/Pt heterostructure

10:42

CB-10. Observation of AC spin current propagation through epitaxial NiO layers. *M. Dabrowski*[1], T. Nakano[1,2], D. Newman[1], D. Burn[3], A. Frisk[3], Q. Li[4], M. Yang[4], C. Klewe[5], P. Shafer[5], E. Arenholz[5], Z.Q. Qiu[4], G. van der Laan[3] and R. Hicken[1] *1. Physics and Astronomy, University of Exeter, Exeter, United Kingdom; 2. Spintronics Research Center, National Institute of Advanced Industrial Science and Technology (AIST), Tsukuba, Japan; 3. Magnetic Spectroscopy Group, Diamond Light Source, Didcot, United Kingdom; 4. Department of Physics, University of California at Berkeley, Berkeley, CA, United States; 5. Advanced Light Source, Lawrence Berkeley National Laboratory, Berkeley, CA, United States*

The use of insulating antiferromagnets (AFM) as a medium to transport spin angular momentum has generated great excitement. Thin NiO films not only transmit but can also enhance a spin current [1, 2]. So far experiments have been limited to the detection of dc spin current and mainly performed on polycrystalline NiO layers. By employing element specific x-ray ferromagnetic resonance (XFMR) [3] we demonstrate transport of ac spin current, generated via spin pumping within a NiFe layer, through adjacent epitaxial NiO(001) layers. For a FeCo/NiO/NiFe multilayer, magnetization precession at the resonant frequency of the NiFe is also observed in the FeCo, with the phase of precession being very similar in both layers. The amplitude of precession of the sink FeCo layer (a measure of the amplitude of the spin current propagating through NiO) depends on the NiO thickness. The amplitude reaches a maximum at 6 nm of NiO and decays exponentially above this thickness (see Fig.1), in a similar manner to that in both previous experimental reports concerning the dc spin current [1, 2] and theoretical studies [4, 5]. For comparison, we present results for FeCo/NM(5nm)/NiO/NiFe, where the NiO is decoupled from the sink layer by insertion of a 5 nm thick non-magnetic (NM) layer of Ag or Pd. The magnetization precession of the FeCo sink layer at the NiFe resonance has amplitude nearly one order of magnitude smaller than for the case of directly coupled layers. Furthermore, the precession of the sink layer exhibits a bipolar variation of phase that is a signature of spin transfer torque associated with ac spin current transmitted through the NiO layer [3]. Our results suggest that the observed propagation of ac spin current within NiO layers is mediated by coherent magnons, rather than by diffusion of thermal magnons.

[1] H. Wang, C. Du, P. C. Hammel, and F. Yang, PRL 113, 097202 (2014). [2] C. Hahn, G. de Loubens, V. V. Naletov, J. B. Youssef, O. Klein, and M. Viret, EPL (Europhysics Letters) 108, 57005 (2014). [3] J. Li, L. R. Shelford, P. Shafer, A. Tan, J. X. Deng, P. S. Keatley, C. Hwang, E. Arenholz, G. van der Laan, R. J. Hicken, and Z. Q. Qiu, Phys. Rev. Lett. 117, 076602 (2016). [4] R. Khymyn, I. Lisenkov, V. S. Tiberkevich, A. N. Slavin, and B. A. Ivanov, PRB 93, 224421 (2016). [5] S. M. Rezende, R. L. Rodríguez-Suárez, and A. Azevedo, PRB 93, 054412 (2016).

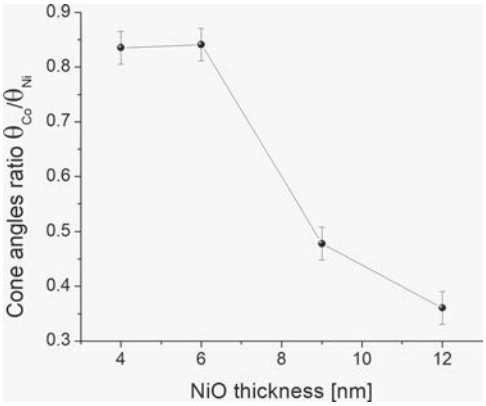


Figure 1. Ratio of Co (sink) and Ni (pump) cone angle for different thickness of NiO layer. Values were extracted from XFMR measurements on MgO(001)/MgO(5nm)/$Fe_{75}Co_{25}$(5nm)/NiO(x)/Fe(1nm)/$Ni_{80}Fe_{20}$(25nm)/MgO(3nm) structures at 4 GHz excitation frequency.

10:54

CB-11. Excitation of Ultrashort Spin Waves in Anisotropic Antiferromagnets by a Domain Wall Driven by Spin Current.
R. Khymyn[1], R. Ovcharov[3], J. Åkerman[1,4] and B.A. Ivanov[2,3] *1. Department of Physics, University of Gothenburg, Gothenburg, Sweden; 2. Institute of Magnetism, Kyiv, Ukraine; 3. Faculty of Radiophysics, Electronics and Computer Systems, Taras Shevchenko National University of Kyiv, Kyiv, Ukraine; 4. Materials and Nanophysics, KTH Royal Institute of Technology, Kista, Sweden*

Antiferromagnets (AFMs) have great benefits for the future spintronic applications [1] involving high frequencies (up to THz) and high speeds (up to dozens of km/s) of magnetic excitations. Also, the AFM spin-torque nano-oscillators (STNOs), in which the applied spin current rotates the Neel vector [2-4], do not require an external magnetic field for their operation. Advanced devices will require high-speed propagating spin waves (SWs) as signal carriers, i.e. SWs with the high k-vectors, the excitations of which remains challenging. We demonstrate theoretically and by micro-magnetic simulations that the simple spin texture, such as an AFM domain wall (DW), driven by spin current, can be a source of the propagating SWs with substantially high frequencies and short wavelengths, comparable to the exchange length of the AFM. We consider AFM with the anisotropy and/or Dzyaloshinskii-Moriya interaction (DMI) with n-fold rotational symmetry in the hard plane. In the proposed generator the spin current, which polarization is directed along the principal axis, excites the precession of the Neel vector within the DW. The threshold current is defined by the value of the in-plane anisotropy, and frequency of the DW precession ω_{DW} is tuneable by the strength of the spin current. We show that the above precession of the DW leads to the excitation of two modes of magnons with the frequencies with $(n\pm1)\omega_{DW}$, where n is the order of the anisotropy and/or DMI symmetry [5]. A robust emission of the propagating SWs into the AFM strip takes place in the case, when $(n\pm1)\omega_{DW} > \omega_{AFMR,}$ where ω_{AFMR} defines the frequency of antiferromagnetic resonance. Consequently, the maximum achievable frequency of SWs is $(n+1)\omega_{AFMR}$, which corresponds to a very short wavelengths of the SW, comparable with the exchange length, especially for the hexagonal AFMs. The excitation of the high wavevectors is possible due to the substantially small width of the DW in AFM and is hard to achieve by any other method.

[1] O. Gomonay, V. Baltz, A. Brataas & Y. Tserkovnyak Nature Physics Vol. 14, 213–216 (2018) [2] R. Khymyn et al., Sci. Rep. Vol. 7, 43705 (2017) [3] O. Sulymenko et al., Phys. Rev. Applied, Vol. 8, 064007 (2017) [4] V. Puliafito et al., Physical Review B Vol. 99, 024405 (2019) [5] E. V. Gomonai et al., Zh. Eksp.Teor. Fiz. Vol. 97, 307 (1990)

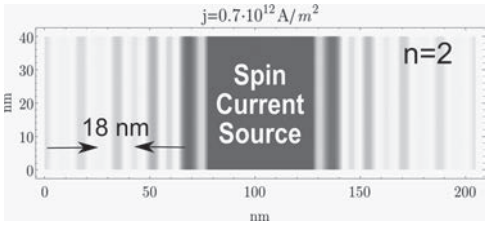
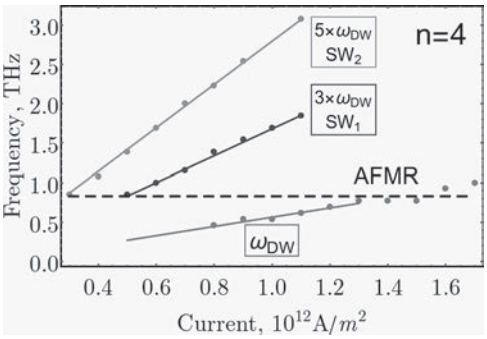


Image of the generated SW for n=2 extracted from the simulations

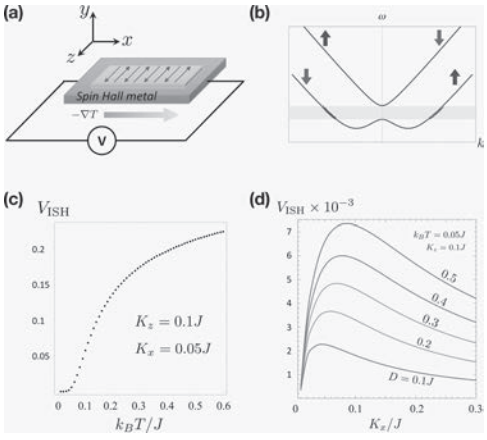


Frequencies of the DW precession and generated SWs vs applied direct current for n=4 (cubic anisotropy). The AFM resonance is shown by the dashed line.

11:06

CB-12. Magnon spin-Edelstein effect in an antiferromagnetic insulator. *R. Cheng*[1,2] *1. Electrical and Computer Engineering, University of California, Riverside, CA, United States; 2. Physics, University of California, Riverside, CA, United States*

In an antiferromagnetic insulator with biaxial anisotropy and the Dzyaloshinskii-Moriya interaction (DMI), symmetry ensures a spin-momentum locking similar to the gapped Rashba electrons. A temperature gradient can generate an interfacial magnon accumulation with a preferred spin polarization, realizing the magnonic counterpart of the spin Edelstein effect. This thermally-driven magnonic spin accumulation can be injected into an adjacent heavy metal and converted into a measurable voltage. It is found that the magnon spin-Edelstein coefficient increases monotonically with an increasing temperature and an increasing DMI, but, it depends non-monotonically on the magnetic anisotropy.



(a) Schematic device geometry. (b) Magnon band structure with the spin-momentum locking occurring in the shaded region. (c) Temperature dependence of the spin Edelstein coefficient. (d) In-plane anisotropy dependence of the spin Edelstein coefficient at different values of DMI.

11:18

CB-13. Investigation of the spin Seebeck effect in an antiferromagnetic insulator. *C. Liu*[1], D. Hong[1], J. Pearson[1] and A. Bhattacharya[1] *1. Material Science Division, Argonne National Laborotory, Lemont, IL, United States*

Recent years have seen rapid development in the area of spin caloritronics. In particular, the spin Seebeck effect (SSE) has been observed in a diverse class of magnetic systems. One interpretation of the SSE is based on thermal excitation of magnons in the bulk. Spin angular momentum is then transferred from those magnons to the normal metal through the local spin pumping process. While other theories for the SSE place more emphasis on the role of spin dependent scatterings at the magnetic material/normal metal interface. To elucidate the mechanism of the SSE, we performed the SSE measurements using an antiferromagnetic insulator. The epitaxial thin films were grown using RF sputtering. The unique response of the magnetic sublattice in this AFM to the applied magnetic field enables us to identify the role of surface magnetic moments in the SSE in an atomic length scale. By taking angular dependence measurement, we observe clear spin-flop transitions and the response of the thermal excitations of magnons owing to the difference in spinwave dispersion induced by the applied magnetic field. We performed the SSE measurements on samples with different thicknesses, which provide further insights on the exact mechanism of the SSE. Acknowledgments: all work at Argonne was supported by the US Department of Energy, Office of Science, Basic Energy Sciences, Materials Sciences and Engineering Division. The use of facilities at the Center for Nanoscale Materials, an Office of Science user facility, was supported by the US Department of Energy, Basic Energy Sciences under Contract No. DE-AC02-06CH11357.

Session CC
MAGNETIC TEXTURES AND MAGNETIZATION DYNAMICS I

Yayoi Takamura, Chair
University of California, Davis, Davis, CA, United States

CONTRIBUTED PAPERS

8:30

CC-01. Chaotic Pattern and Bit Generation in a Nanocontact Vortex Oscillator. *M. Yoo*[1], D. Rontani[2], J. Létang[1], S. Petit-Watelot[3], T. Devolder[1], M. Sciamanna[2], K. Bouzehouane[4], V. Cros[4] and J. Kim[1]
1. Centre de Nanosciences et de Nanotechnologies, CNRS, Univ. Paris-Sud, Université Paris-Saclay, Palaiseau, France; 2. Laboratoire Matériaux Optiques, Photonique et Systèmes, CentraleSupélec, Université de Lorraine, Metz, France; 3. Institut Jean Lamour, CNRS, Université de Lorraine, Nancy, France; 4. Unité Mixte de Physique, CNRS, Thales, Univ. Paris-Sud, Université Paris-Saclay, Palaiseau, France

Nanocontact vortex oscillators (NCVOs) are spin-torque devices, where large current densities drive vortex gyration around a nanocontact on a magnetoresistive multilayer. In contrast to other types of spin torque oscillators, NCVOs exhibit unique dynamical states caused by the self-phase locking between the core gyration and the periodic switching of the core. When the ratio between these two frequencies is irrational, chaotic dynamics appears [1]. Because of the random-like feature of chaotic signals, much effort has been devoted to understanding how to exploit these waveforms for information technologies, such as random number generation, encryption, and encoding information via symbolic dynamics [2-4]. In this work, we investigate experimentally the chaotic time series of an NCVO at 77 K. From the signals, we are able to identify a well-defined series of patterns (Fig. (a)). The patterns are the building blocks of the time series and denoted by their *pn* number, where *p* is the vortex-core polarization, and *n* is an integer number of required core gyration for the switching. We analyze the pattern sequence by reconstructing the attractor (Fig. (b)), and then extract symbolic dynamics (Fig. (c)) from a suitable Poincaré surface (Inset of Fig. (b)). Bit sequences generated from the symbolic dynamics (Fig. (c)) are found to be maximal complexity in the chaotic regime, which is suggestive of a chaotic state subject to thermal noise. This is confirmed by the computation of the Shannon block entropy and the Lempel-Ziv complexity [5, 6]. Finally, we show that the characteristics of the chaotic sequences can be controlled electrically. These results support the feasibility of chaos-based information processing using spintronic nanodevices.

[1] S. Petit-Watelot, J.-V. Kim, A. Ruotolo *et al*., Nat. Phys. Vol. 8, p.682 (2012) [2] M. Virte, E. Mercier, H. Thienpont *et al*., Opt. Express Vol. 22, p.17271 (2014) [3] A. Argyris, D. Syvridis, L. Larger *et al*., Nature Vol. 438, p.343 (2005) [4] W. L. Ditto and S. Sinha, Chaos Vol. 25, p.097615 (2015) [5] A. Lesne, J.-L. Blanc, and L. Pezard, Phys. Rev. E Vol. 79, p.046208 (2009) [6] A. Lempel and J. Ziv, IEEE Trans. Inf. Theory Vol. IT-22, p.75 (1976)

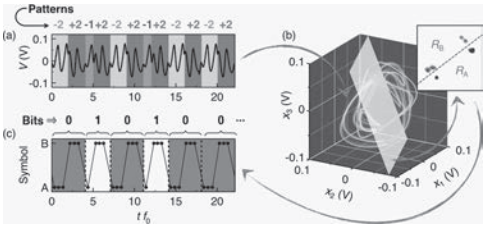


Fig. (a) Time series from a NCVO at the chaotic regime. f_0 is the gyration frequency. The patterns are distinguished by colors. (b) The attractor reconstructed from the measured signal in (a). The white plane represents a Poincaré surface. The inset shows the Poincaré map and the dashed line is a partition for the symbolic dynamics. (c) Symbolic dynamics calculated from the Poincaré map. The generated bits are represented in grayscale.

8:42

CC-02. Bloch Type Rotation Chirality in Spin Helix in Monolayer Fe on Ir(110) by Spin Polarized STM. *J.A. Fischer*[1], T. Knispel[1], M. Bagchi[1], J. Brede[1], V. Tseplyaev[2], M. Hoffmann[2], S. Bluegel[2] and T. Michely[1] *1. II. Physikalishes Institut, Universität zu Köln, Cologne, Germany; 2. Peter Grünberg Institut and Institute for Advanced Simulation, Forschungszentrum Jülich, Jülich, Germany*

Magnetic films that come into contact with heavy metals have a wealth of interesting interfacial phenomena that include interfacial Dzyaloshinskii-Moriya interaction (DMI), which may lead to chiral magnetic structures. Most work on interfacial DMI is based on films that exhibit C_{3v} symmetry. Such a high-symmetry interface is known to only support Néel type spin helices and skyrmions. [1] Here, the DMI is isotropic and can be described by exactly one micromagnetic parameter. This is different for systems exhibiting C_{2v} symmetry like the (110) surface of an fcc crystal, for which is predict to show anisotropic DMI leading to various scenarios of topological pattern formation. [2] Here, we report a spin-polarized scanning tunneling microscopy and spectroscopy study that reveals a magnetic stripe phase, due to a spin helix with a period of 1.2 nm along the [-1 1 0] direction in a monolayer of Fe on unreconstructed Ir(110). On the basis of our detailed magnetic field dependent measurements we conclude that the chirality of the spin helix is surprisingly of Bloch type, where the rotation is perpendicular with the propagation direction. This contradicts the spin helix induced by an interface in-plane DMI vector. Combined with theoretical insights, we discuss our findings in terms of the formation energy in systems with C_{2v} symmetry. The work is supported by the CRC 1238 of the Deutsche Forschungsgemeinschaft (DFG).

[1] S. Heinze et al. Nat. Phys. Vol.7, p.713 (2011). [2] M. Hoffmann et al. Nat. Commun. Vol.8, p.308 (2017).

8:54

CC-03. X-ray Imaging of the Bloch Points in an Asymmetric Nanodisk. *H. Han*[1], M. Jung[2], Y. Yu[3], S. Lee[1], S. Yoon[2], W. Chao[4], P. Fischer[5,6], J. Hong[2], M. Im[4] and K. Lee[1] *1. School of Materials Science and Engineering, Ulsan National Institute of Science and Technology (UNIST), Ulsan, The Republic of Korea; 2. Department of Emerging Materials Science, Daegu Gyeongbuk Institute of Science and Technology (DGIST), Daegu, The Republic of Korea; 3. Advanced Light Source, Lawrence Berkeley National Laboratory, Berkeley, CA, United States; 4. Center for X-ray Optics, Lawrence Berkeley National Laboratory, Berkeley, CA, United States; 5. Materials Sciences Division, Lawrence Berkeley National Laboratory, Berkeley, CA, United States; 6. Department of Physics, University of California, Santa Cruz, Santa Cruz, CA, United States*

A Bloch point (BP) is a singularity in a ferromagnetic material at which the local magnetization vanishes. BP has a novel physical character such as pining in between atomic lattices, and the spin-Cherenkov effect [1, 2]. Furthermore, it has been known that the switching of vortex and skyrmion cores is mediated by the injection and propagation of the BP with changing the local topological number of the spin structures [3, 4]. However, the experimental study on the basic physics of BP such as atomic-scaled pinning and dynamics has not yet been elucidated due to difficulties of generating a stable BP in magnetic nanostructures which is easy to measure. In this presentation, we report experimental observations of the BPs stabilized in a magnetic vortex structure in an asymmetrically shaped permalloy ($Ni_{80}Fe_{20}$) nanodisks [5] by using the magnetic transmission soft X-ray microscopy (MTXM) at the Advanced Light Source [6]. We figured out clearly the types of BPs according to its surrounding structures. Furthermore, we observed the stable movement of the BPs under the static magnetic field. Our findings provide a way to stabilize a BP in a patterned nanostructure and it is expected to stimulate the experimental study on fundamental static and dynamic behaviors of BP.

[1] S.-K. Kim, and O. Tchernyshyov. Phys. Rev. B. 88, 174402 (2013) [2] R. Hertel and C, Andreas. in Magnetic Nano- and Microwires (ed. Vazquez, M.) 653–677 (2015). [3] A, Thiaville. and J, Miltat. Europhys. Lett. 26, 57 (1994). [4] T. Senthil. *et al*. Science 303, 1490-1494 (2004). [5] M.-Y Im, H.-S. Han, *et al.* Nature Commun. 10, 593 (2019) [6] Fischer, P. *et al.* Mater. Today 9, 26–33 (2006).

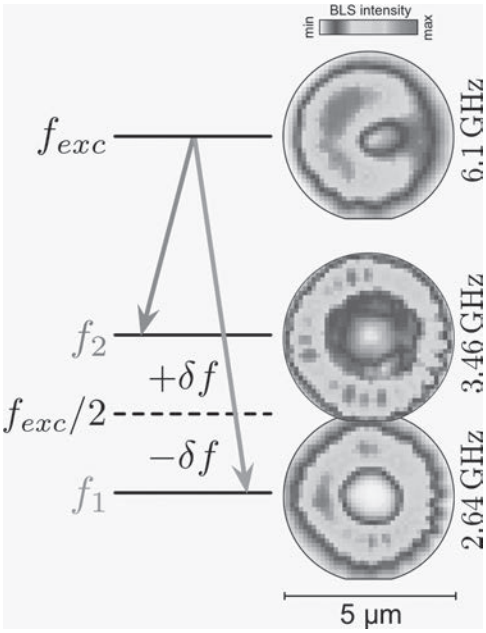
INVITED PAPER

9:06

CC-04. How to Generate Whispering Gallery Magnons. *K. Schultheiss*[1], R.V. Verba[2], F. Wehrmann[1], K. Wagner[1], L. Korber[1], T. Hula[1], T. Hache[1], A. Kakay[1], A.A. Awad[3], V. Tiberkevich[4], A.N. Slavin[4], J. Fassbender[1] and H. Schultheiss[1] *1. Institute of Ion Beam Physics and Materials Research, Helmholtz-Zentrum Dresden-Rossendorf, Dresden, Germany; 2. Institute of Magnetism, National Academy of Sciences of Ukraine, Kyiv, Ukraine; 3. Department of Physics, University of Gothenburg, Gothenburg, Sweden; 4. Department of Physics, Oakland University, Rochester, MI, United States*

One of the most fascinating topics in current quantum physics are hybridized systems, in which resonators of different quantum systems are strongly coupled. Prominent examples are circular resonators with high quality factors that allow the coupling of optical whispering gallery modes to microwave cavities or magnon resonances. However, the coupling to magnons with finite azimuthal wave vectors has not yet been achieved due to the lack of efficient excitation schemes. I will present the generation of whispering gallery magnons with unprecedented high azimuthal wave vectors via nonlinear 3-magnon scattering in a µm-sized magnetic vortex state disc [1]. These modes exhibit a strong localization at the disk's perimeter and practically zero amplitude in an extended area around the vortex core. They originate from the splitting of the fundamental radial magnon modes (see Figure), which can be resonantly excited in a vortex texture by an out-of-plane microwave field. I will shed light on the basics of this non-linear scattering mechanism from experimental and theoretical point of view. Using Brillouin light scattering (BLS) microscopy, the frequency and power dependence of this nonlinear mechanism is investigated. The spatially resolved mode profiles give evidence for the localization at the disk's boundaries and allow for a direct determination of the modes' wavenumber. Furthermore, time resolved BLS in combination with pulsed microwave excitation revealed the temporal evolution of the 3-magnon splitting and its dependence on the applied microwave power.

[1] K. Schultheiss et al. Physical Review Letters 122, 097202 (2019).



Left side: Schematic illustration of the 3-magnon scattering process. The magnon mode excited at f_{exc} splits in two secondary modes with frequencies f_1 and f_2, equally spaced around half the excitation frequency. Right side: Two-dimensional profiles of the whispering gallery magnons measured by BLS microscopy.

CONTRIBUTED PAPERS

9:42

CC-05. Three-Magnon Splitting in Vortex-State Magnetic Nanodots. *R.V. Verba*[1], L. Korber[2,3], V. Tiberkevich[4], K. Schultheiss[2], H. Schultheiss[2,3] and A.N. Slavin[4] *1. Institute of Magnetism, Kyiv, Ukraine; 2. Helmholtz-Zentrum Dresden–Rossendorf, Dresden, Germany; 3. TU Dresden, Dresden, Germany; 4. Oakland University, Rochester, MI, United States*

Spin waves in ferromagnetic micro- and nanostructures demonstrate a great variety of nonlinear phenomena at moderate excitation power. In particular, using the nonlinear effect of 3-magnon splitting it is possible to built frequency-selective power limiters [1], and excite highly non-uniform magnon modes, which are not accessible to direct linear excitation [2]. Also, properties of 3-magnon interaction drastically depend on the geometry of the ferromagnetic structure, and on its static magnetic configuration. In this work, we present a theory of 3-magnon splitting in a *vortex-state* magnetic nanodot. Using vector Hamiltonian formalism [3], we demonstrate, that 3-magnon spitting of a magnon mode with radial and azimuthal numbers (n_3, m_3) into modes (n_1, m_2) and (n_2, m_2) obeys the following selection

rules: conservation of the azimuthal number $m_3=m_1+m_2$, and, for a radially symmetric initial mode ($m_3=0$), inequality of the radial number of resultant modes, $n_1 \neq n_2$. The last rule, however, is relaxed in small dots due to the increasing role of the vortex core. The coefficient $V_{12,3}$ describing the efficiency of the 3-magnon interaction significantly depends on the resultant modes, as it is shown in Fig, 1b for the example of splitting of the second radial (2,0) mode of a vortex-state Permalloy disk (50 nm thickness, 5 μm diameter). Although the resonance condition for the 3-magnon splitting (zero detuning, Fig. 1a) is satisfied for several pairs of the resultant modes, the larger efficiency $V_{12,3}$ requires splitting into (0,5)+(2,-5) modes, in full accordance with the experiment [2]. Varying the driving frequency, one can control the splitting process, and the resultant modes can be changed e.g. to (1,*m*)+(2,-*m*) at 8.9-9 GHz. Thus, the developed theory allows one to predict both the splitting channels and the splitting thresholds. Also, this theory is useful for the investigation of the stimulated sub-threshold 3-magnon processes in magnetic vortices.

[1] A. D. Boardman, S. A. Nikitov, Phys. Rev. B 38, 11444 (1988). [2] K. Schultheiss, et al., Phys. Rev. Lett. 122, 097202 (2019). [3] O. Dzyapko, et al., Phys. Rev. B 96, 064438 (2017).

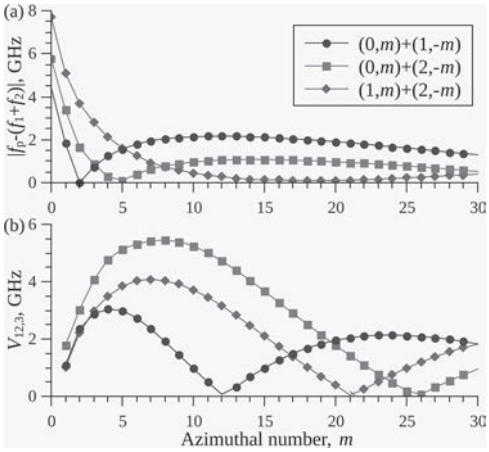


Fig.1. Detuning from resonance condition (a), and 3-magnon interaction efficiency (b) for splitting process (2,0)→(n_1,*m*)+(n_2,-*m*) and driving frequency of 8.3 GHz.

9:54

CC-06. Withdrawn

10:06

CC-07. In-situ GHz Dynamics of Hybrid Skyrmions Probed with SANS. *N. Tang*[1], S. Montoya[3,2], L. W.L.N.C.[1], S.K. Patel[2,4], L. J. Quigley[1], A.J. Grutter[5], M. Fitzsimmons[6], E. Fullerton[2], J. Borchers[5], L. DeBeer-Schmitt[6] and D.A. Gilbert[1] *1. Materials Science Department, University of Tennessee, Knoxville, Knoxville, TN, United States; 2. CMRR, University of California, San Diego, San Diego, CA, United States; 3. Naval Information Warfare Systems Command, San Diego, CA, United States; 4. Physics Department, University of California, San Diego, San Diego, CA, United States; 5. NIST Center for Neutron Research, National Institute of Standards and Technology, Gaithersburg, MD, United States; 6. High Flux Isotope Reactor, Oak Ridge National Laboratory, Oak Ridge, TN, United States*

Magnetic skyrmions are nano-scale chiral spin configurations which present fascinating physical behaviors due to their topological qualities, and are attractive for next-generation data storage and logic devices. These chiral structures can support long-range dynamic modes, including breathing modes and gyration modes which can be excited using ferromagnetic resonance (FMR) [1]. The frequency of these dynamics – typically in the gigahertz range – presents additional opportunities for microwave frequency electronics. In this work, we us small angle neutron scattering (SANS) as a real-space, in-situ probe to capture the dynamics in hybrid skyrmion structures under RF applied fields. Specifically, our team has recently demonstrated magnetic skyrmions with a hybrid configuration – with a flux-closure defined Néel caps on the top and bottom, and Bloch configuration at the equatorial band – in Gd/Fe multilayer films, which are stable at ambient conditions [2, 3]. Using an in-plane RF field with an out-of-plane static field, dynamic gyration modes are excited in the skyrmions. These gyration modes were probed using Doppler-shift contrasted SANS. In this technique, we recognize that neutrons scattering from a moving object pick-up an additional energy. In the case of the gyration mode, the dynamics occur in a plane that is orthogonal to the neutron beam. As a result, the neutrons pick-up a transverse velocity, proportional to the speed and direction of the skyrmion motion at the time of scattering. For the case of gyrating skyrmions, this manifests as a broad ring on the detector, with a radius proportional to the velocity. By analyzing the distribution of the scattering pattern the speed and path of the gyration is extracted. Work at UCSD supported by DOE award No. DE-SC0003678.

[1]. S. A. Montoya et al., Phys. Rev. B 95, 224405 (2017) [2]. S. A. Montoya et al., Phys. Rev. B 95, 024415 (2017) [3]. R. D. Desautels et al., arXiv:1904.13274

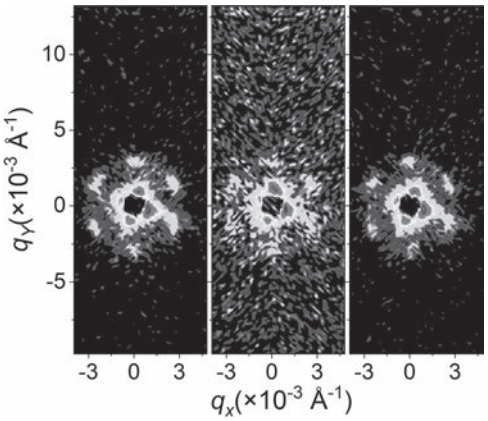


Figure 1 Small angle neutron scattering (SANS) measurements of the skyrmion thin-films in an RF field, at the applied external fields: (a) 140 mT (below resonance), (b) 150 mT (at resonance), and 160 mT (above resonance).

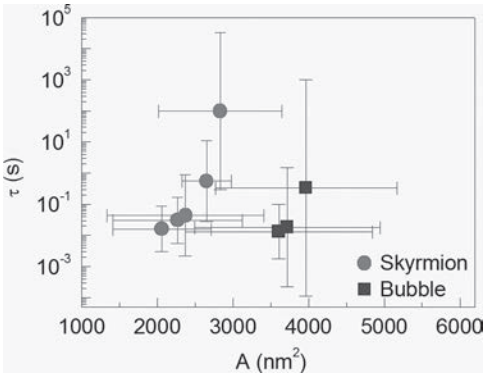
10:18

CC-08. Direct demonstration of topological stability of magnetic skyrmions. *S. Je*[1], H. Han[2], S. Kim[3], S. Montoya[4], W. Chao[1], I. Hong[5], E. Fullerton[6], K. Lee[2], K. Lee[5], M. Im[1] and J. Hong[7] *1. Lawrence Berkeley National Laboratory, Berkeley, CA, United States; 2. Ulsan National Institute of Science and Technology, Ulsan, The Republic of Korea; 3. University of Missouri, Columbia, MO, United States; 4. Space and Naval Warfare Systems Center Pacific, San Diego, CA, United States; 5. Korea University, Seoul, The Republic of Korea; 6. University of California–San Diego, La Jolla, CA, United States; 7. Daegu Gyeongbuk Institute of Science and Technology, Daegu, The Republic of Korea*

The concept of topological protection in a continuum model precludes a continuous deformation between topologically inequivalent configurations[1]. Motivated by this concept, there has been a great expectation that nontrivial magnetic structures at a nanoscale, i.e. magnetic skyrmions, can stay robust against thermal agitations, providing a breakthrough in ultrahigh density magnetic memory applications[2]. Despite the substantial importance of the concept of topological protection, however, the experimental assessment

has remained elusive due to difficulties in evaluating the stability of topologically inequivalent magnetic textures in the same material at the same conditions[3]. Here either the skyrmion state or the topologically trivial bubble state is selectively prepared, and we experimentally show that the magnetic skyrmions, of which decay involves surpassing a topological barrier, exhibit far longer lifetime τ than topologically trivial bubbles (Fig. 1), directly evidencing the topological stability in a real discrete system. Our work has far-reaching implications for taming and exploiting the topology of magnetic materials towards the ever-dense and more-stable magnetic devices.

1. H.-B. Braun, Adv. Phys. 61, 1-116 (2012). 2. J. Sampaio, et al., Nat. Nanotech. 8, 839–844 (2013). 3. J. Wild, et al., Sci. Adv. 3, e1701704 (2017).



10:30

CC-09. Large terahertz magnetization response in ferromagnetic nanoparticles embedded in a semiconductor. *S. Ohya*[1], T. Ishii[1], H. Yamakawa[2], T. Kanaki[1], T. Miyamoto[2], N. Kida[2], H. Okamoto[2] and M. Tanaka[1,3] *1. Department of Electrical Engineering and Information Systems, The University of Tokyo, Tokyo, Japan; 2. Department of Advanced Materials Science, Graduate School of Frontier Science, The University of Tokyo, Kashiwa, Japan; 3. Center for Spintronics Research Network (CSRN), Graduate School of Engineering, The University of Tokyo, Tokyo, Japan*

Ultra-fast coherent magnetization reversal within a picosecond, which will be an essential technique for ultra high-speed spintronics in the future, is expected to be realized by irradiation with a nearly monocyclic terahertz pulse. Till now, coherent magnetization modulation by terahertz pulses has been reported for several ferromagnetic thin films; however, the modulation ratio reported so far has been typically less than 1% of the saturation magnetization even with extraordinarily strong terahertz electric fields. Here, we demonstrate a large modulation up to 20% of the magnetization with terahertz pump-pulse irradiation to MnAs ferromagnetic nanoparticles embedded in a semiconductor GaAs (GaAs:MnAs) (Figs. 1,2) [1]. We show that, when using semiconductor-based ferromagnetic materials, the influence of the "electric field" component of the terahertz pulse has much more dominant than that of the magnetic-field component [2], unlike in metallic materials. In GaAs:MnAs, a strong electric field can be applied to each nanoparticle, leading to the large modulation. This work was partly supported by Grants-in-Aid for Scientific Research (No. 26249039, 18H03860, ISHO1011, 16H02095), Spintronics Research Network of Japan, and CREST, Japan Science and Technology Agency (Grant No. JPMJCR1661, JPMJCR177).

[1] T. Ishii, H. Yamakawa, T. Kanaki, T. Miyamoto, N. Kida, H. Okamoto, M. Tanaka, and S. Ohya, Appl. Phys. Lett. 114, 062402 (2019). [2] T. Ishii, H. Yamakawa, T. Kanaki, T. Miyamoto, N. Kida, H. Okamoto, M. Tanaka, and S. Ohya, Sci. Rep. 8, 6901 (2018).

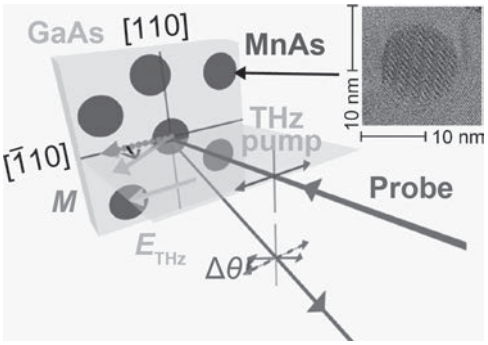


Fig. 1: Schematic illustration of the experimental setup. The terahertz pump pulse, whose polarization plane is expressed by the yellow plane, is focused on the GaAs:MnAs sample surface, and the following probe pulse detects the excited dynamics. The yellow arrow represents the terahertz electric field E_{THz} (yellow arrow). The in-plane magnetization (pale red dotted arrow) is modulated toward the sample normal by the terahertz pump pulse. The inset is the transmission-electron-microscopy lattice image of a MnAs nanoparticle in GaAs.

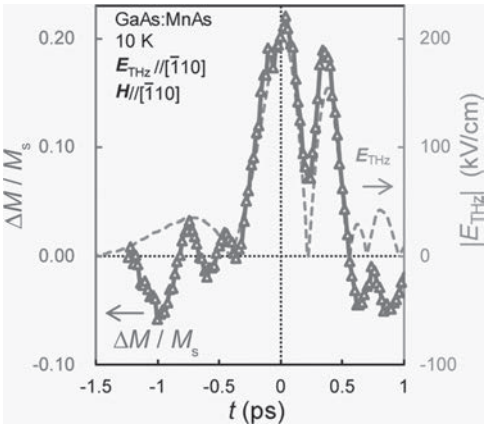


Fig. 2: Time evolution of the ratio of the modulated magnetization ΔM to the saturated magnetization M_s (red triangles, left axis), which was measured using the magnetooptical Kerr effect, and the time evolution of the terahertz electric field $|E_{THz}|$ (green dotted curve, right axis).

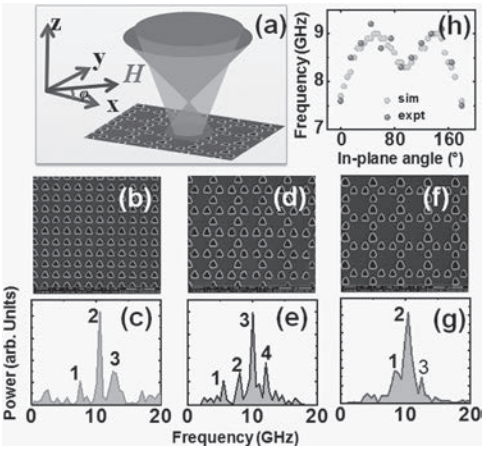
10:42

CC-10. Active Control of Ultrafast Magnetization Dynamics and Configurational Anisotropy in Triangular Shaped Ferromagnetic Antidot Lattice with Varying Symmetry. *A. De*[1], S. Mondal[1], S. Sahoo[1], K. Dutta[1], A. Adhikari[1], Y. Otani[2] and A. Barman[1] *1. Bose National Centre for Basic Sciences, Kolkata, India; 2. University of Tokyo, Tokyo, Japan*

Spin-wave (SW) dynamics in lithographically patterned nanomagnet arrays have attracted huge interest to the scientific community due to their rich physics and potential applications in magnetic memory, sensors, logic and on-chip communication devices. Here, we present the efficient modulation of SW spectra in 200-nm wide triangular shaped $Ni_{80}Fe_{20}$ antidot lattices (ADL) arranged in different symmetry, namely square, rectangular, hexagonal, honeycomb and octagonal symmetry with different lattice constants of 400, 500, 600 and 700 nm. Further, the anisotropy properties of the square and octagonal lattices have been studied by varying the orientation of the in-plane bias magnetic field. The triangular holes create inhomogeneous internal magnetic fields resulting in effective pinning centres for SWs created by the asymmetric demagnetized regions. This is mainly responsible for the observed tunability of the SW dynamics and the configurational anisotropy. Experimental studies with Time-Resolved Magneto-Optical Kerr Effect (TR-MOKE) microscopy show a rich variation of the SW spectra

with the variation of the lattice symmetry as well as the lattice constant. The SW modes in both square and octagonal lattices possess strong anisotropic behaviour as a function of the in-plane bias field orientation, which originates from the variation of the asymmetric demagnetized regions around the triangular shaped holes. The square lattice shows a four-fold anisotropy with superposition of a weak six fold anisotropy. On the other hand, for the octagonal lattice a mixture of eight-fold and six-fold anisotropy is observed. Micromagnetic simulations qualitatively reproduce the experimentally observed modes and the simulated mode profiles reveal the presence of different types of extended and quantized standing SW modes in these samples. The simulated magnetostatic field distributions underpinned the observed variation in the SW spectra leading towards an extensive understanding of SW dynamics in this new type of magnonic crystal.

1. A. Khitun, M. Bao, K.L. Wang, J. Phys. D: Appl. Phys. 43, 264005 (2010). 2. O. Hellwig, A. Berger, T. Thomson, E. Dobisz, Z.Z. Bandic, H. Yang, D.S. Kercher, E.E. Fullerton, Appl. Phys. Lett. 90, 162516 (2007). 3. A. Barman, A. Haldar, Solid State Phys. 65, 1 (2014). 4. A. Barman, S. Barman, Phys. Rev. B 79, 144415 (2009).



10:54

CC-11. Stimulated, continuous, and wave vector selective magnon excitation using rapid demagnetization from high repetition rate femtosecond laser pulse trains. *S. Muralidhar*[1*], A. Aleman[1], A.A. Awad[1], R. Khymyn[1], D. Hanstorp[1] and J. Åkerman[1,2] *1. Department of Physics, University of Gothenburg, Gothenburg, Sweden; 2. KTH Royal Institute of Technology, Stockholm, Sweden*

Magnonics provides interesting prospects in miniaturization and optimization of high frequency devices where magnons/spin waves (SWs) are the information carriers. Optical excitation of SWs in thin magnetic films was first observed in 2002 using rapid demagnetization from femtosecond (fs) laser pulses [1]. However, due to the high damping coefficients of magnetic materials, continuous emission of SWs using this approach has not yet been possible. With fs-laser repetition rates being typically 80 MHz and lower, the time duration between pulses is much longer than the time constant of SW damping. However, this has recently changed with 1 GHz repetition rate fs-lasers now being available, which allows magnetic excitation every 1ns, i.e. on the same time scale as the SW decay [2]. We here use μ-focused Brillouin Light Scattering (μ-BLS) as probe, which affords us excellent spatial resolution and high sensitivity to both thermal and optically excited SWs. The results using a 20 nm NiFe thin film are shown in Fig.1(a) where the BLS counts are plotted on a logarithmic scale as a function of SW frequency for four different laser powers and together with the laser off (thermal SWs only). As the laser power is increased, we find a pronounced exponential enhancement of the BLS counts when the SW frequency matches harmonics of the 1 GHz rep-rate. While the enhancement is the strongest around the ferromagnetic resonance (~8 GHz), substantial additional SW intensity is observed also at 7 and 9 GHz. To study the spatial extent of the generated SWs, we acquired line scans of the BLS counts. At 7 GHz the SWs appear localized to the pump region. The SWs at 8 and 9 GHz instead show propagation along the direction perpendicular to the in-plane component of the applied magnetic field (H_{in}). By changing the in-plane component angle and the strength of the magnetic field, we can control the direction and spatial pattern of the SW emission.

[1] M. van Kampen et. al., Phys. Rev. Let. 88, 227201/1 (2002). [2] Jackl, M. et. al. Phys. Rev. X. 7, 021009 (2017).

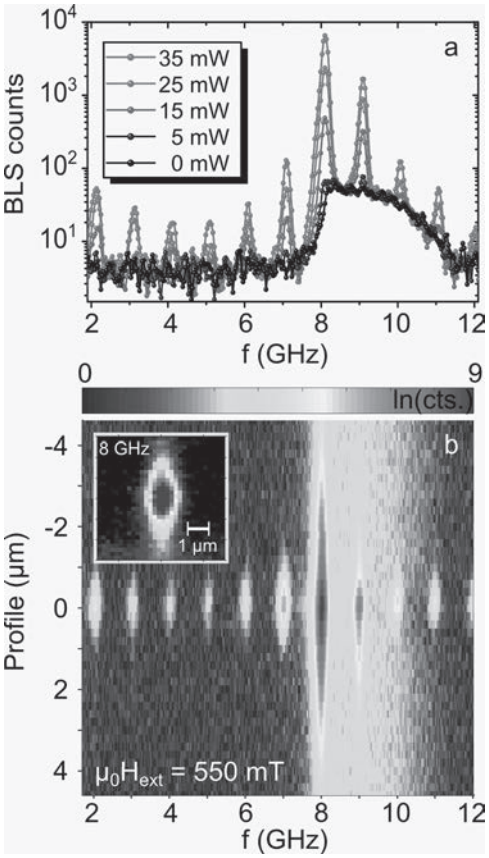


Figure 1: (a) BLS spectra at 5 different laser powers for an applied field strength of 550 mT. (b) Linear profile of the spinwave propagation at different frequencies. The inset shows a 2D profile of the propagation for the mode at 8GHz.

11:06

CC-12. Investigating optically excited THz spanding spin waves in noncollinear magnetic heterostructures. *T. Lichtenberg*[1], M.H. Janssen[1], R. Lavrijsen[1] and B. Koopmans[1] *1. Applied Physics, Eindhoven University of Technology, Eindhoven, Netherlands*

In recent years, spin waves have received significant interest due to their potential use as information carriers in Joule-heat-free data transfer and processing. Recently, it was discovered that fs laser pulses can be used to excite THz standing spin waves in noncollinear magnetic heterostructures [1, 2]. The basic principle of this phenomenon is sketched in the inset of fig. 1. A fs laser pulse generates a spin current between the two neighboring ferromagnetic layers, allowing for interlayer angular momentum transfer. The injected spin current is absorbed on a relatively short length scale (~1 nm). This causes a depth dependence of the spin-transfer torque and thus the magnetization canting, which creates the ideal environment for higher order spin wave excitation. In this work, we study the excited first order THz spin waves in a $[Co(0.2)/Ni(0.6)]_{4x}$/Co(0.2)/Cu(0-30)/Co(5)/Pt(2) stack

using optical pump-probe experiments. More specifically, we investigate the influence of the Cu spacer layer on their damping and phase. The first order modes are presented for several spacer thicknesses in fig. 2. Micromagnetic simulations have been performed in support of these experiments. These simulations accurately predict the spin wave dispersion, and extensions to extract phase information are on the way. We report that the typical length scale for interlayer angular momentum transfer in this stack is ≈13 nm, which is much smaller than the spin diffusion length of Cu. This indicates a simple picture of a demagnetization induced diffusive spin current is insufficient to fully describe the observed spin transfer. By measuring the phase of the first order rather than the homogeneous mode, a higher resolution is obtained for studying the injected spin current in the time domain. Preliminary results indicate that the current absorption time increases from 50 to 300 fs within the studied range (fig.2). This experiment thus allows us to further elucidate the spin transfer mechanism in our experiments.

[1] I. Razdolski, D. Bovensiepen, A. Melkinov *et al*., Nature communications 8, (2016) [2] M.L.M. Lalieu, R. Lavrijsen, B. Koopmans *et al*., Physical Review B 99, 184439 (2019)

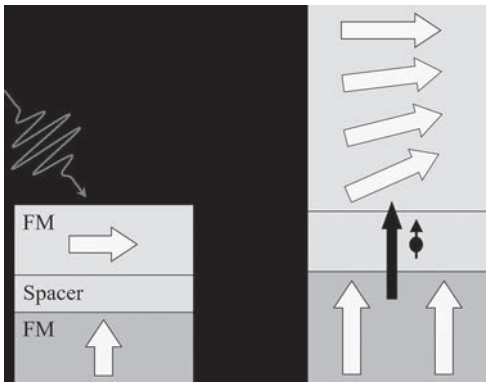


Fig. 1: Schematic representation of the sample after laser excitation and spin current absorption.

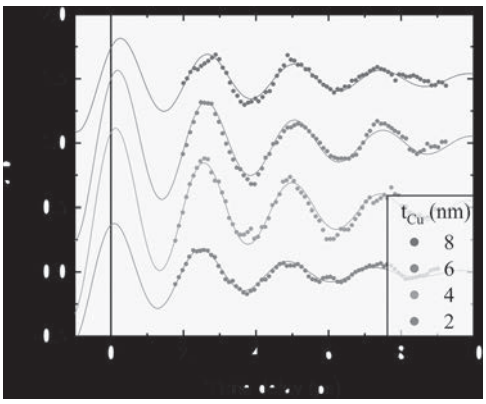


Fig. 2: Optically excited first order modes, for various spacer thicknesses. The lines represent fits with a damped cosine.

11:18

CC-13. Terahertz Magnonics on Garnet Ferrite Thin Films and their Neuromorphic Application. *H. Tabata*[1] *1. School of Engineering, University of Tokyo, Tokyo, Japan*

Spin-waves in magnetic insulators maintain several centimeters [1]. Because there are no conductive electrons in magnetic insulators, spin-wave of magnons, which are the collective motion of spins angular momentum, can be propagated over a long distance. In addition, spin pumping technique enables to convert the spin-wave spin-currents into conduction electron spin-currents [2]. High-energy magnons which are called as electromagnons (EMs) is expected to be excited by the electric field component of THz wave [3]. In this study, samarium ferrite garnet (SmIG) was selected as the target material. The epitaxial strain rate of SmIG is largest in all of rare-earth iron garnets (RIGs) because the lattice constant of SmIG is largest in all of RIGs. RIGs are ferrimagnetic and dielectrics at RT, and transparent in a wide range of THz region. Moreover, spin fluctuation because the spin fluctuation can be observed in THz region and it is expected to mimetic neuromorphic signal processing [4]. Figure shows the THz spectroscopy of the SmIG films. The complex permittivity of the film in THz regime was extracted using the way described in [5]. Because the phonons do not change their excitation energy in accordance with magnetization strength, these absorption peaks are considered to be EMs. The higher energy peak is due to the Brillouin Zone-edge magnon mode (EMBZ), and the lower energy peak is due to the harmonic magnon mode (EMH) [6]. The EMs were observed only in the strained SmIG film, whereas they were not observed in the relaxed SmIG film, as we designed. The increment of excitation energies of EMs is saturated above 0.35 T, being coherent with a MCD result. We estimated the spin-wave spin-current properties of Ems using D'yakonov-Perel (DP) model; $\Gamma \propto \omega^2\tau$, where Γ is the scattering probability of spin precession, ω is the resonant angular frequency and τ is the relaxation time of the electrons. Electromagnons are detected in the strained Sm3Fe5O12 ultrathin film, using a transmittance THz time-domain spectroscopy.

[1] Schneider, T. *et al*., Appl. Phys. Lett. 92, (2008) 022505. [2] Saitoh, E. *et al*., Appl. Phys. Lett. 88, (2006) 182509. [3] A. Pimenov, *et al.*, Nat. Phys. 2, 97-100 (2006) [4] H. Kuroe, et al., Phys. Rev. B 55, 409 (1997) [5] N. Kida, M. Hangyo, M. Tonouchi, Phys. Rev. B, 62, (2000) 18 [6] M. Mochizuki, *et al*., Phys. Rev. B 80, (2009) 1344416 [7] M.Adachi *et al.*, Appl.Phys. Express 8, (2015) 043002

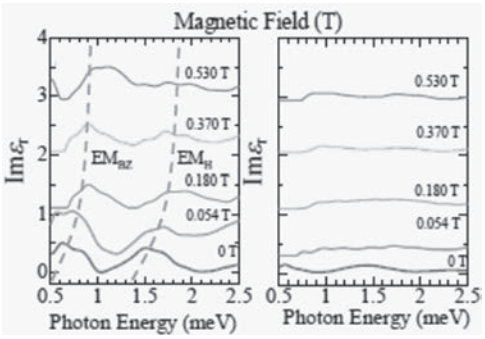


Fig.1 THz spectra of strained SmIG and non-strained SmIG thin films

Session CD
SPIN-ORBIT TORQUES III

Joseph Sklenar, Chair
Northwestern University, Evanston, IL, United States

CONTRIBUTED PAPERS

8:30

CD-01. Spin-orbit torque estimation in perpendicularly magnetized trilayers. *R. Guerrero*[1], A. Anadón[1], A. Gudín[1], J. Díez-Toledano[1], P. Olleros[1], F. Ajejas[1], M. Muñoz[2], J. Camarero[1,3], R. Miranda[1,3] and P. Perna[1] *1. nanomagnetism, IMDEA nanoscience, Madrid, Spain; 2. Instituto de Micro y Nanoelectronica, Madrid, Spain; 3. DFMC, Universidad Autonoma de Madrid, Madrid, Spain*

Spin polarized currents are employed to efficiently manipulate the magnetization of ferromagnetic ultrathin films (below 2 nm) by exerting a torque on them. When these spin currents are generated by means of the spin-orbit interaction it is known as spin-orbit torque (SOT)[1,2]. In this work, we present a new technique to quantify the SOT efficiency based on the measurement of the non-linearities of dc current-voltage characteristics in Hall bar devices. We have experimentally studied the SOT TaOx/Co/Pt asymmetric stack with perpendicular magnetic anisotropy and compared the results with the second harmonic technique. The presented technique requires a lesser current than the used in the second harmonic technique, see reference [3] and yields directly the effective field per unit of current density in a single experiment. The results obtained show large torques due to the different Spin Hall angles of platinum and tantalum that induce a large spin current density in the cobalt layer [4].

[1] Amin, V. P. & Stiles, M. D. Spin transport at interfaces with spin-orbit coupling: Formalism. *Phys. Rev. B* 94, 104419 (2016). [2] Amin, V. P. & Stiles, M. D. Spin transport at interfaces with spin-orbit coupling: Phenomenology. *Phys. Rev. B* 94, 104420 (2016). [3]Kim, J. *et al.* Layer thickness dependence of the current-induced effective field vector in Ta|CoFeB|MgO. *Nat. Mater.* 12, 240–245 (2012). [4] Woo, S., Mann, M., Tan, A. J., Caretta, L. & Beach, G. S. D. Enhanced spin-orbit torques in Pt/Co/Ta heterostructures. *Appl. Phys. Lett.* 105, 212404 (2014).

8:42

CD-02. Spin orbit torque arising from the interfacial scattering in an Fe/Ru Interface. *Q. Liu*[1], K. Meng[1], Y. Wu[1], J. Chen[1], Z. Li[1], J. Miao[1], X. Xu[1] and Y. Jiang[1] *1. University of science and technology Beijing, Beijing, China*

Controlling magnetization of nanodevices through the spin-orbit torque(SOT) offers a wide spectrum of opportunities to integrate magnetic functions[1]. However, up to now, the study of SOT is limited to systems consisting of heavy metal (HM), where the HM has a strong spin-orbit coupling (SOC) (such as Pt, W, etc.)[2-4]. In this work, samples of Ru/Fe/HfO_2 structures were deposited at room temperature on oxidized silicon wafers. According to the magnetic field H dependence of the out-of-plane magnetization M and anomalous hall resistance R with temperature as shown in Fig. 1 (c) and (d), We found that the Ru/Fe/HfO_2 films has better perpendicular magnetic anisotropy and thermal stability. Then, the current-induced magnetization switching behaviors in Ru/Fe/HfO_2 films were measured with applying a non-zero in-plane field H. Although the spin Hall angle (SHA) of Ru is small as compared with those from Ta- or W-based heterostructures, reversible current-induced SOT switching of a thermally stable Ru/Fe/HfO_2 heterostrutures can still be achieved as shown in Fig. 2 (a) and (b). To quantitatively determine the strength of the spin-orbit effective fields, the non-adiabatic harmonic Hall voltage measurements were carried out at room temperature. The harmonic measurements by applying a sinusoidal AC current with the amplitude of 5×10^6 A/cm^2 at 300 K are taken as an example as shown in Fig. 2 (c). According to the calculated H values plotted with respect to the applied current in Fig. 2 (d), the SHA in Ru/Co/HfO_2 is calculated to be 0.045. The effective field induced in Ru/Fe/HfO heterostruture is comparable with that generated by SHE of Pt. In conclusion, our results suggest a new opportunities for fundamental study of spin dynamics and transport in ferromagnetic systems.

[1] L. Liu, D. C. Ralph, and R. A. Buhrman, Phys. Rev. Lett. 109, 096602 (2012). [2] C.-F. Pai, D. C. Ralph, and R. A. Buhrman, Appl. Phys. Lett. 101, 122404 (2012). [3] J. Kim, S. Mitani and H. Ohno, Nat. Mater. 12, 2340 (2013). [4] K. Garello, G. Gaudin, and P. Gambardella, Appl. Phys. Lett. 105, 212402 (2014).

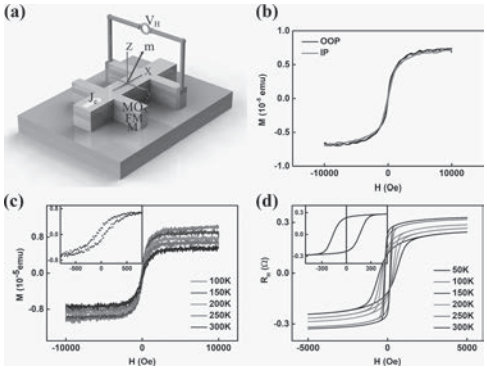


Fig. 1 (a) The Hall bar sturcture. (b) M-H curves of the out-of-plane magnetization (OOP) and the in-plane magnetization(IP). M-H curves of the OOP magnetization (c) and R_H-H curves (d) with temperature.

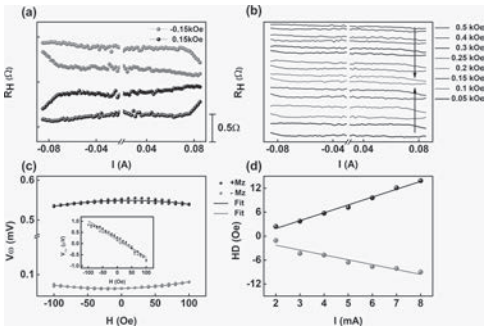


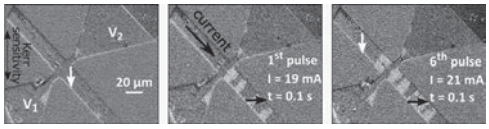
Figure 2 (a) and (b) R_H-I curves with different in-plane external fields. (c) The first V_ω and second $V_{2\omega}$ harmonic (inset) Hall voltages plotted against the small in-plane external fields. (d) Current-induced effective field H_D versus applied current.

8:54

CD-03. Characterization of field- and current-induced magnetization switching in epitaxial Au/Fe/MgO(001). P. Gospodaric[1], E. Mlynczak[1], A. Kakay[2], *L. Plucinski*[1], I. Soldatov[3], R. Schäfer[3], D. Buergler[1], J. Fassbender[2] and C.M. Schneider[1] *1. PGI-6, FZ Juelich, Juelich, Germany; 2. HZDR, Dresden, Germany; 3. IFW, Dresden, Germany*

We have studied an epitaxial Fe(001) ultra-thin film sandwiched between the MgO substrate and an epitaxial Au thin film. We performed a thorough characterization of the field- and current induced magnetization reversal in the Au/Fe bilayers using magneto-transport measurements and Kerr microscopy. The magnetic properties of the Fe film were studied in the Hall bar geometry via the planar Hall effect. The analysis shows the characteristic four-fold in-plane magneto-crystalline anisotropy of Fe(001) layers, present due to the high crystalline quality of the films. We observe changes in the hysteretic response of the magnetization to the external magnetic field when a high current density is applied to the Au/Fe Hall bar wire. Kerr microscopy of the Hall bars reveals further details on the switching mechanism in presence and absence of a high current density. By comparing field- and current-induced magnetic hystereses the information on the current-induced effective fields can be obtained. Previously we have investigated the magnetization dependent spin-orbit gaps in Fe thin films on Au(001) using angle-resolved photoemission [1], and the growth of Fe on Au using LEEM/PEEM [2]. The spin-orbit torque (SOT) is considered as one of the most promising ways of current-induced switching of ferromagnets and antiferromagnets. In heavy metal/ferromagnet bilayers for example, the spins in the ferromagnetic layer can be manipulated via SOT with an in-plane electric current. Our study points out the considerable effect of the Oersted field for the switching mechanism in Au/Fe heterostructures. Figure shows the evolution of in-plane domains in the Au/Fe Hall bar after applying current pulses monitored by Kerr microscope. Our results demonstrate that only the area close to the Hall cross contributes significantly to the transverse magnetoresitance signal.

[1] E. Mlynczak et al., Fermi surface manipulation by external magnetic field demonstrated for a prototypical ferromagnet, Phys. Rev. X 6, 041048 (2016) [2] P. Gospodaric et al., Localized segregation of gold in ultra-thin Fe films on Au(001), Phys. Rev. B 97, 085409 (2018)



Kerr microscope snapshots of the evolution of in-plane domains in the Au/Fe Hall bar after applying indicated current pulses.

INVITED PAPER

9:06

CD-04. Manipulating exchange bias by spin–orbit torque. P. Lin[1], H. Lin[2] and *C. Lai*[1] *1. Department of Materials Science and Engineering, National Tsing Hua University, HsinChu, Taiwan; 2. Department of Physics, National Tsing Hua University, HsinChu, Taiwan*

Inspired by the success in switching FM magnetization by various electrical means, AFM spintronics has received a great deal of attention in recent years. While most efforts have focused on electrical manipulations of a bulk AFM, interfacial effects between FM and AFM layers are also vitally important for spintronic devices. Here we demonstrate that applying current pulses to heavy metal/FM/AFM trilayers causes concurrent switching of FM magnetization and exchange bias (EB), shown in Fig. 1, but with different underlying mechanisms[1]. This implies that the FM magnetization and EB can be manipulated independently. When comparing with the conventional field-annealing approach to generate EB, SOT determines the FM magnetization direction and further provides effective disturbance to align the interfacial spins between the FM/AFM layers to the FM magnetization. We further develop a time-resolved resistance measurement technique to eliminate the possibility of EB reversal due to joule heating effects. Not only the direction of the exchange bias can be reversed, but its strength can also be controlled by electric current pulses, which can be correlated to the alignment of interfacial spins and current-induced reorientation of N'eel ordering. With further investigation and optimization along this direction, the current-pulse-induced EB shall have significant impacts on the SOT-MRAM and other spintronic devices.

[1]P. H. Lin, B. Y. Yang, M. H. Tsai, H. H. Lin, C.H. Lai, Nat. Mater. 18, 335, (2019)

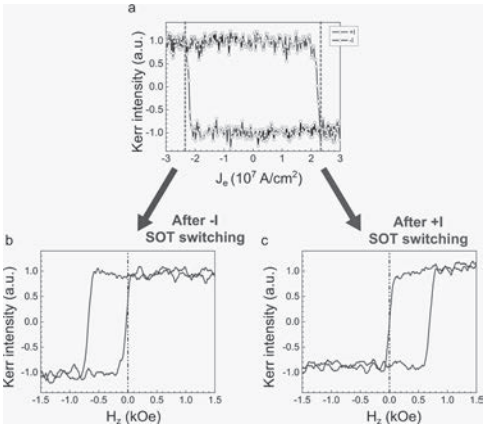


Fig. 1: Concurrent SOT switching for FM magnetization and exchange bias. a. SOT switching curves of FM magnetization in the presence of a longitudinal field Hx=300 Oe for sample Pt 2 nm/Co 1.2 nm/ IrMn 8nm. Dotted lines denote the current density thresholds in the Pt layer for the concurrent SOT switching. b,c. After the concurrent SOT switching, not only is the FM magnetization flipped, but the exchange bias is also reversed. The negative pulse (red line) flips the magnetization (from negative to positive) and the exchange bias (shifted easy-axis loop to the left) at the same time. The opposite SOT switching is observed when the positive pulse (blue line) is applied.

CONTRIBUTED PAPERS

9:42

CD-05. A magneto-optical study of spin-orbit torque acting on a nano-ellipse with in-plane magnetization. P.S. Keatley[1], *P. Androvitsaneas*[1], K.O. Chatzimpaloglou[1], T. Manago[2,1], G. Mihajlovic[3], L. Wan[3], J. Katine[3] and R. Hicken[1] *1. University of Exeter, Exeter, United Kingdom; 2. Fukuoka University, Fukuoka, Japan; 3. HGST, San Jose, CA, United States*

In-plane magnetized elements activated by spin-orbit torque (SOT) show great promise for future magnetic memory applications. SOT switching of in-plane magnetized ellipses at the centre of a Pt Hall cross has been studied via the differential planar Hall effect [1]. Time-resolved (TR) scanning Kerr microscopy (SKM) revealed the action of SOT on GHz frequency magnetization precession [2]. The SOT generated by a sub-nanosecond current pulse can yield relaxation that depends on field history, and a transient out-of-plane deflection. However the presence of an associated Oersted (Oe) field prevents full characterisation of the SOT [3]. Here, SKM was used in quasi-static (QS) and spin torque ferromagnetic resonance (ST-FMR) modes to explore the SOT and the Oe-field effects in different sized ellipses. The polar Kerr effect was used to detect the change in the magnetization in response to (i) a modulated DC current (QS mode), and (ii) a combination

of microwave (RF) and DC current (ST-FMR mode). The current passes through a Pt (6 nm) Hall cross parallel to the ellipse minor (hard) axis. The associated Oe-field and the polarization of spins traversing the Pt/CoFeB interface due to the spin Hall effect are parallel to the major (easy) axis. Ellipses with size 0.4×1 to 2×5 μm² were studied. In QS mode, the out-of-plane deflection was found to be maximum, when the magnitude of the applied field was close to the anisotropy field, and perpendicular to the spin polarization and Oe-field. This is in agreement with analytical calculations. ST-FMR mode spectra reveal a shift to the resonance field as a function of magnetic field angle, but little change in the spectral shape when the DC current is zero. A DC current of 10 mA yields marked differences in the amplitude and linewidth that are ascribed to SOT enhancement or compensation of the magnetic damping. A shift in resonance field, of opposite sign to either side of the hard axis, is ascribed to a combination of the DC Oe-field torque and the field-like SOT. Detailed analysis is in progress to disentangle the Oe-field and SOT contributions.

[1] G. Mihajlović et al., Appl. Phys. Lett., 109, 192404 (2016). [2] P. S. Keatley et al., 'Picosecond reorientation of in-plane magnetization within a nano element by spin orbit torque' FB-14, 2019 Joint MMM-Intermag, Washington DC. [3] X. Fan et al., Nat. Comms. 5, 3042 (2014).

9:54

CD-06. Effect of Interface Engineering in Pt/CoFeB/MgO Heterostructures on Spin-Orbit Torque. *S. Kim*[1,4], H. Lee[2], J. Park[2], Y. Oh[2], S. Park[3], W. Ham[4], Y. Kotani[5], T. Nakamura[5], M. Suzuki[5], T. Ono[4,6], K. Lee[7,8] and B. Park[2] *1. Department of Physics, University of Ulsan, Ulsan, The Republic of Korea; 2. Department of Materials Science and Engineering, Korea Advanced Institute of Science & Technology (KAIST), Daejeon, The Republic of Korea; 3. Division of Scientific Instrument, Korea Basic Science Institute (KBSI), Daejeon, The Republic of Korea; 4. Institute for Chemical research, Kyoto University, Kyoto, Japan; 5. Japan Synchrotron Radiation Research Institute (JASRI), Sayo, Japan; 6. Center for Spintronics Research Network (CSRN), Osaka University, Osaka, Japan; 7. Department of Materials Science and Engineering, Korea University, Seoul, The Republic of Korea; 8. KU-KIST Graduate School of Converging Science and Technology, Korea University, Seoul, The Republic of Korea*

Spin-orbit toque (SOT) has been widely investigated because it allows efficient manipulation of the perpendicular magnetisation in HM/FM heterostructures using an in-plane current [1,2]. Since then, much effort has been devoted to finding materials with a large SOT-induced switching efficiency, which however has to be further enhanced for the realisation of energy-efficient SOT-based spintronic devices. In this study, we have successfully achieved two folds enhancement in SOT and resultant switching efficiency in Pt/CoFeB systems by an interfacial modification involving Ti insertion (Fig. 1). Our spin pumping and X-ray magnetic circular dichroism experiments reveal that such significant enhancements originate from improved spin transparency by suppressing Pt proximity effect at the interface and/or an additional spin current generated of non-magnetic interface. Two significances of our results can be summarized. 1) The perpendicularly magnetised Pt/CoFeB system is a promising candidate for SOT-based spintronic device application because Pt is a highly conductive material with a sizable spin Hall angle and CoFeB has a large spin polarization in conjunction with crystalline MgO, thereby resulting in a large tunnel magnetoresistance. However, SOT in the Pt/CoFeB layer has been reported to be smaller than other Pt/FM bilayers systems so far. Therefore, our result of the enhancement in effective spin Hall angle of Pt/CoFeB promises potential applications in high-performance SOT devices. 2) And more, our result is the first observation that SOT can be enhanced by 100% by an interfacial engineering involving 3*d* metal insertion whereas other studies have shown that SOT decreases by the insertion of a 3*d* metal interfacial layer [4, 5]. In this work, we clearly demonstrate that interface engineering affords an effective approach to improve SOT and thereby magnetisation switching efficiency.

Reference 1. I.M. Miron, et al. Nature 476, 189 (2011). 2. L. Liu, et al. Phys. Rev. Lett. 109, 096602 (2012). 3. H.-Y. Lee, et al. APL Mater. 7, 0631110 (2019). 4. W. Zhang, et al. Nat. Phys. 11, 496 (2015). 5. X. Fan, et al. Nat. commun. 5, 3042 (2014).

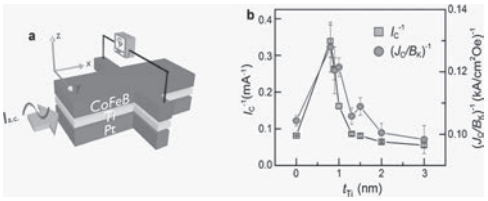


Figure 1. a. Schematic image of the Pt/Ti/CoFeB device. b. Switching efficiency of the device in terms of the Ti-thickness [3].

10:06

CD-07. High Thermal Stability of Perpendicular Magnetic Anisotropy and Current Induced Spin-orbit Torque in Zr/CoFeB/MgO Stacks. *T. Zhu*[2] and X. Zhan[1] *1. Dongguan Neutron Science Center, Dongguan, China; 2. Institute of Physics, Chinese Academy of Sciences, Beijing, China*

The manipulation of the magnetization in an energy efficient and fast way can be achieved in a magnetic multilayer with perpendicular magnetic anisotropy (PMA) [1-3]. Among the PMA material systems, the heavy metal buffered or capped CoFeB/MgO multilayer, such as Ta/CoFeB/MgO, is of frequently employed owing to its advantage in excellent PMA property [1]. The manipulation of magnetization in CoFeB can be realized through both spin transfer torque or spin orbit torque generated in heave metal underlayer. However, the commercialization of such structures requires PMA to be compatible with COMS integrated circuits, which generally can endure the annealing above 400°C. Here, we reported that the PMA in Zr/CoFeB/MgO, which was used 4d metal as the underlayer, is found to be robust up to 450°C. The origin of PMA is investigated by using polarized neutron reflectometry (PNR) [4], which is a technique sensitive to the compositional and magnetic depth profiles of thin film samples which enables us to discuss the role of boron in the formation of PMA. Meanwhile, we have investigated the spin-orbit torques in the perpendicularly magnetized Zr/CoFeB/MgO stacks.

[1] S. Ikeda, et al. Nat. Mater. 9, 721 (2010) [2] D. C. Worledge, et al. Appl. Phys. Lett. 98, 022501 (2011) [3] C. F. Pai, et al. Appl. Phys. Lett. 104 082407 (2014) [4] T. Zhu, et al. Appl. Phys. Lett. 100, 202406 (2012)

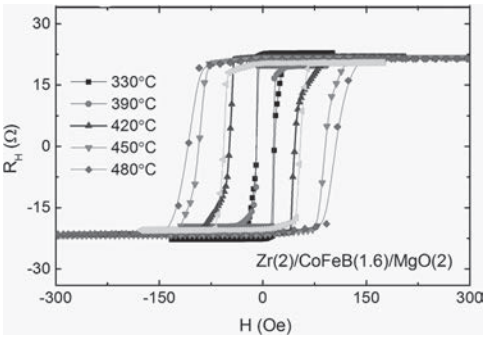


Fig. 1. Anomalous Hall resistance loops of samples annealed at elevated temperatures.

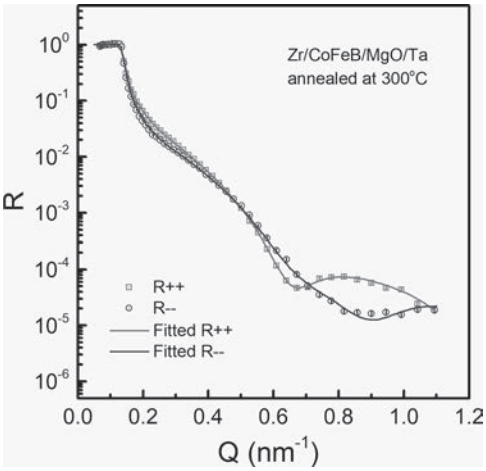


Fig. 2. PNR curves as a function of wavevector transfer Q for Zr/CoFeB/MgO

10:18

CD-08. Current-Driven Magnetization Switching and Large Spin Orbit Torque in Ferrimagnet $GdMn_{2.5}Ge_{1.5}$ Thin Film. *L. Ren*[1], L. Liu[1], K. Cai[1], Y. Liu[1], J. Chen[1], H. Yang[1] and K. Teo[1] *1. National University of Singapore, Singapore*

Antiferromagnets have attracted lots of attentions because of no stray fields and faster spin dynamics than ferromagnets. [1, 2] Unfortunately, the challenges of operating the antiferromagnets impede their applications. However, compensated ferrimagnets combine the advantages of the low magnetic moment of antiferromagnets and the ease of realizing magnetic reading and controlling of ferromagnets. [3, 4]. Especially some investigations on spin-orbit torque of have been reported, which provide a promising platform for high-speed spintronic applications [5-7]. Here we report that compensated $GdMn_{2.5}Ge_{1.5}$ films were deposited on MgO substrates. The structure of the film was characterized by XRD and HRTEM. The results indicate that the films are tetragonal with (001) preferred orientation. Magnetic properties indicate that the T_{comp} is about 115 K and the coercivity decreases with increasing or decreasing temperature for either above or below T_{comp}, and that the maximum H_C reaches larger than 7 T near T_{comp}, while the magnetization reaches zero moment. Besides, the transport properties and Harmonic Hall voltages of the film were also measured using Hall bridge method. Some of the results are shown in Figures (a) and (b), from which we can find that the sign of anomalous Hall resistance above compensation temperature is opposite to that bellow the T_{comp}, and that the spin orbit torque effective field are evaluated as 9.54mT/10^{10}Am^{-2} at 300K, which is much higher than reported values in heavy metal/ferromagnet systems and is attributed to the bulk spin orbit torque effect in our film here. Moreover, at 300K we also found the Hall resistance switching at a current density of 4×10^{10}Am^{-2} under an external magnetic field, as shown in Figure (c). With temperature decreasing, the switching threshold of current density and the Hall resistance switching ratio both increase. Our experiment results provide alternative candidate for the compensated ferrimagnet spintronic applications.

[1] P. Wadley *et al*., Science, 351, 6273 (2016). [2] S. Yu. *et al*., Nat. Commun. 9, 348 (2018). [3] A. H. MacDonald and M. Tsoi, Phil. Trans. R. Soc. A 369, 3098 (2011). [4] J. Kubler and C. Felser, Europhys. Lett. 108, 67001 (2014). [5] J. Finley *et al*., Phys. Rev. Appl. 6, 054001 (2016). [6] R. Mishra, *et al*., Phys. Rev. Lett. 118, 167201 (2017). [7] J. Finley *et al*., Adv. Mat. 31, 1805361 (2019).

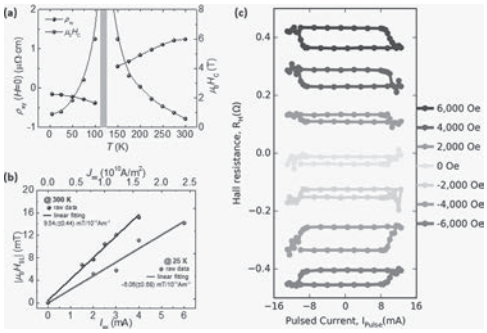


Figure (a) Temperature dependence of coercivity and spontaneous Hall resistivity of the $GdMn_{2.5}Ge_{1.5}$ film. (b) Evaluation of spin orbit torque effective field at 300 K and 25 K. (c) Current-driven Hall resistance switching at different external field

10:30

CD-09. Large Spin Orbit Torque Generated by Mn_3Sn Weyl Semimetal Thin Films. *S. Hu*[1] and X. Qiu[1] *1. School of physics science and engineering, Tongji University, Shanghai, China*

Non-collinear antiferromagnet Mn_3Sn has attracted great attention for its novel properties, such as large anomalous Hall effect [1], unique spin Hall physics [2], and negative magnetoresistance in association with Weyl nodes [3]. As Weyl semimetals are predicted to possess efficient charger-spin conversion due to their intriguing band structure and spin-momentum locking in both the surface and bulk states [4-6], the Weyl semimetallic character of Mn_3Sn shows great prospects for spin-orbitronic memory and logic applications Here, we report the large spin orbit torque (SOT) and its driven efficient perpendicular magnetization switching in Mn_3Sn/Cu/$[Ni/Co]_n$ heterostructures at room temperature. Mn_3Sn (0001) thin film was deposited on single crystalline MgO (111) substrates by dc magnetron sputtering. Figure 1(a) shows the X-ray diffraction spectrum of 40 nm-thick Mn_3Sn films, which exhibits strong (0001) preferred orientation. The positive magnetoconductance, an important feature of Weyl semimetal, is shown in Fig. 1(b) [3]. Figure 2(a), (b) are the first and second harmonic measurements of Mn_3Sn/Cu/$[Ni/Co]_n$ and β-Ta/Cu/$[Ni/Co]_n$ heterostructures to quantify the SOT effective fields. We observe that the spin orbit torque generated by Mn_3Sn is nearly one order larger than β-Tantalum [7]. Figure 2(c) shows the corresponding SOT-induced magnetism switching curves. A much lower critical J_C of 4.17×10^6A cm^{-2} is needed to switch the magnetization in Mn_3Sn heterostructure when comparing to the β-Ta heterostructure. Our results demonstrate the Mn_3Sn Weyl semimetal for highly efficiency spin-orbitronic applications.

[1] S. Nakatsuji, N. Kiyohara and T. Higo, Nature, Vol. 527, p. 212 (2015) [2] M. Kimata, H. Chen, K. Kondou, et al., Nature, Vol. 565, p. 627 (2019) [3] K. Kuroda, T. Tomita, M.T. Suzuki, et al., Nat. Mater., Vol. 16, p. 1090 (2017) [4] J. Jiang, F. Tang, X.C. Pan, et al., Phys. Rev. Lett., Vol. 115, p. 166601 (2015) [5] Y. Sun, Y. Zhang, C. Felser, et al., Phys. Rev. Lett., Vol. 117, p. 146403 (2016) [6] I. Belopolski, S.-Y. Xu, Y. Ishida, et al., Phys. Rev. B, Vol. 94, p. 085127 (2016) [7] L. Liu, C.-F. Pai, Y. Li, et al., Science, Vol. 336, p. 555 (2012)

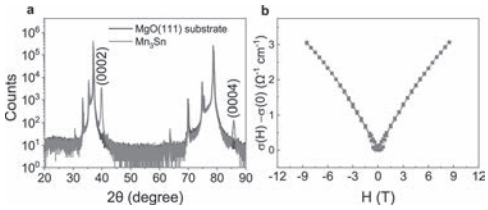


Fig. 1 (a), XRD patterns of the 40 nm Mn_3Sn films on MgO (111) substrate. (b), Magnetic field dependences of the magnetoconductivity at room temperature.

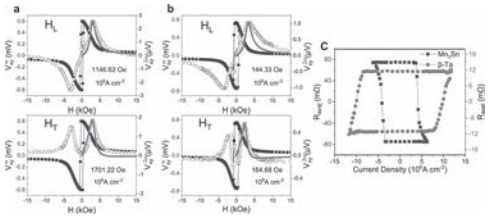


Fig. 2 First and second harmonic loops of Mn_3Sn/Cu/$[Ni/Co]_n$ and Ta/Cu/$[Ni/Co]_n$ heterostructures are shown in (a), (b). (c), R_{AHE} as a function of current density for Mn_3Sn and β-Tantalum based heterostructures at 300 K.

Session CE
SPIN WAVES: EXCITATION & MANIPULATION

Hendrik Ohldag, Chair
Lawrence Berkeley National Laboratory, Berkeley, CA, United States

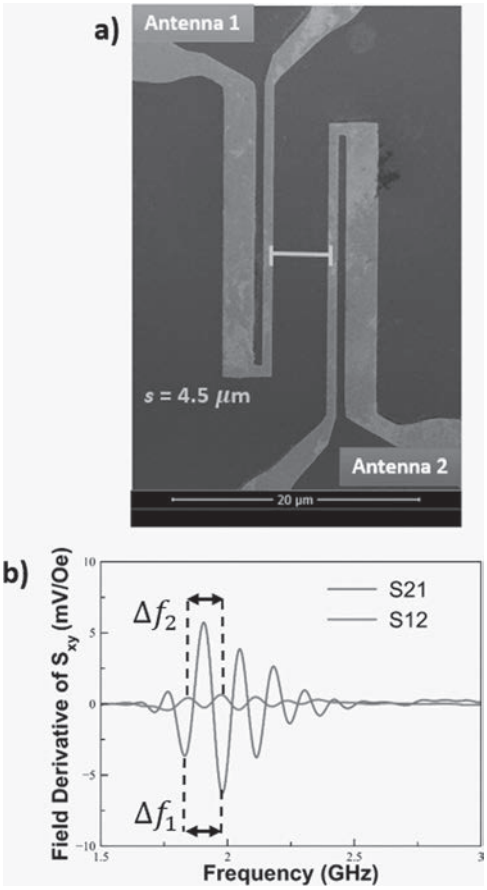
CONTRIBUTED PAPERS

8:30

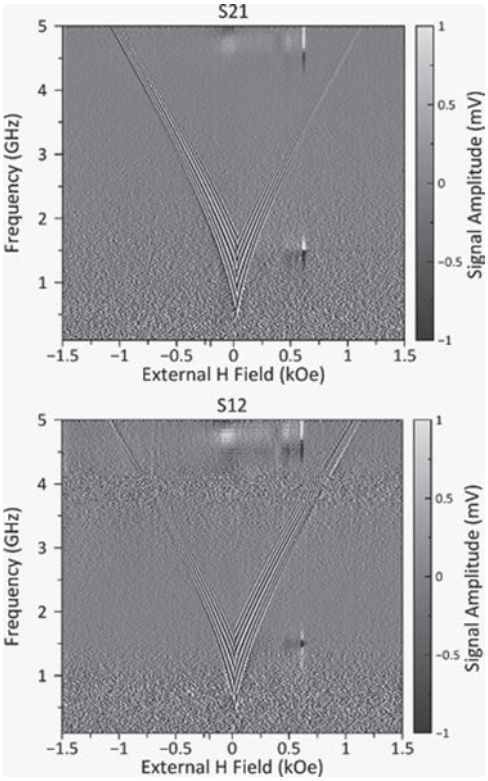
CE-01. Non-Reciprocal Short-Wavelength Spin Waves in Thin YIG Films. *A. Khan*[1], T. Liu[2], M. Wu[2] and I. Krivorotov[1] *1. Physics, University of California, Irvine, Irvine, CA, United States; 2. Physics, Colorado State University, Fort Collins, CO, United States*

Non-reciprocal microwave devices such as circulators, isolators and phase shifters based on field-biased bulk ferrites have been extensively used for microwave signal processing over many decades. However, these magnetic device designs cannot be scaled down to chip-integrable, nanoscale dimensions. An alternative route towards non-reciprocal nanoscale magnetic devices is based on non-reciprocal short-wavelength spin waves in thin magnetic films [1]. Here we report observation of strongly non-reciprocal propagation of short-wavelength spin waves in 40 nm thick films of yttrium iron garnet (YIG). For these measurements, we employed e-beam lithography to pattern two coplanar strip Ti/Au microwave antennas on top of the YIG film as shown in Fig. 1a, which can excite spin waves with wavelengths as short as 420 nm. Spin wave propagation between the antennas is measured using a microwave network analyzer as a function of magnetic field applied in the sample plane perpendicular to the spin wave propagation direction. Fig. 1b shows magnetic field derivative of the measured S_{21} and S_{12} parameters as a function of frequency [2]. The data reveals significant non-reciprocity of the spin wave dispersion relation. Using this data, we calculate group velocities of 668 m/s and 583 m/s for the left and right propagating spin waves, respectively. Fig. 2 shows the dependence of field derivatives of S_{21} and S_{12} parameters as a function of magnetic field and frequency. These data reveal that spin wave non-reciprocity is observed over a wide range of magnetic fields and frequencies. We will discuss possible origins of the observed non-reciprocity of short-wavelength spin waves in these thin YIG films [3].

[1] M. Jamali et al., Scientific Reports 3, 3160 (2013) [2] H. Maier-Flaig et al., Rev. of Sci. Instr. 89, 076101 (2018) [3] M. Kostylev, Jour. of Appl. Phys. 115, 233902 (2014)



a) SEM image of Ti/Au coplanar strip antennas on top of YIG film separated by 4.5 μm. b) Comparison of field derivatives of S_{21} and S_{12} at 200 Oe applied parallel to the antennas. Group velocities for right- and left-propagating spin waves calculated from Δf_1 and Δf_2 are 668 m/s and 583 m/s, respectively, revealing strong non-reciprocity of spin wave dispersion relation.



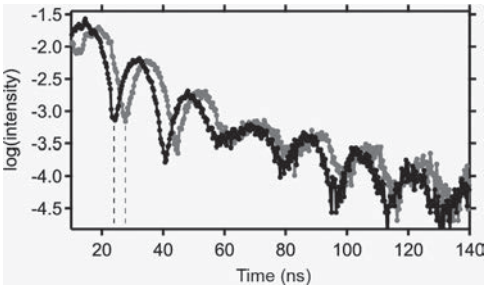
Field derivative of S_{21} and S_{12} as a function of frequency and field.

8:42

CE-02. Nuclear Quantum Phase Control by Transient Magnons. *L. Bocklage*[1,2], J. Gollwitzer[1], C. Strohm[1], C.F. Adolff[1,2], K. Schlage[1], I. Sergeev[1], O. Leupold[1], H. Wille[1], G. Meier[3,2] and R. Röhlsberger[1,2] *1. DESY, Hamburg, Germany; 2. The Hamburg Centre for Ultrafast Imaging, Hamburg, Germany; 3. Max-Planck Institute for the Structure and Dynamics of Matter, Hamburg, Germany*

Quantum optics requires coherent light-matter interactions. Recently, quantum optical concepts have been established in the hard X-ray regime utilizing nuclear resonances of Mössbauer isotopes [1,2]. However, direct coherent control is still a great challenge at hard X-ray energies and its corresponding sub-attosecond time scales. Here, we show that the quantum phase of 57-Fe Mössbauer nuclei embedded in a thin ferromagnetic film can be coherently controlled with zeptosecond temporal accuracy via a transient magnon. We use this collective spin excitation to modulate the magnetic hyperfine interactions of the nuclei in the sample [3]. In this way, the phase of a collectively excited nuclear state, the nuclear exciton, can be controlled on the zeptosecond time scale, as monitored via quantum beats between different hyperfine-split levels. The nuclei are excited with a resonant synchrotron pulse at an energy of 14.4 keV. The quantum beat in the X-ray emission of the nuclei is shown in Fig. 1. The temporal beat on a nanosecond scale results from the interference of the nuclear dipole transition moments of two interacting nuclear levels. When a transient magnon is excited during the lifetime of the nuclear excition (blue bar in Fig.1) a phase shift is induced in the quantum beat. This phase shift directly relates to the phases of the involed dipole transition moments, where we determine phase shift down to one zeptosecond. Our quantum control method opens new perspectives for precision phase control of X-rays in extreme metrology applications. Furthermore, magnonic applications, such as spin wave logic or spin-caloritronics, can be extended to the field of quantum state control.

[1] R. Röhlsberger et al., Science 328, 1248 (2010). [2] J. Haber et al., Nat. Photonics 11, 720 (2017). [3] L. Bocklage et al., Phys. Rev. Lett. 114, 147601 (2015).



Nuclear quantum beat of 57-Fe Mössbauer nuclei. Black shows the nuclear X-ray emission without magnon excitation. When the transient magnon is excited during the time indicated by the blue bar the quantum beat (red) experiences a phase shift (dashed lines).

8:54

CE-03. Introducing Coherent Time Control to Cavity-Magnon-Polariton Modes. *T. Wolz*[1], A. Stehli[1], A. Schneider[1], I. Boventer[1,2], R. Macedo[3], A.V. Ustinov[1,4], M. Kläui[2] and M. Weides[1,3] *1. Institute of Physics, Karlsruhe Institute of Technology, Karlsruhe, Germany; 2. Institute of Physics, Johannes Gutenberg University, Mainz, Germany; 3. James Watt School of Engineering, University of Glasgow, Glasgow, United Kingdom; 4. Russian Quantum Center, National University of Sicence and Technology MISIS, Moscow, Russian Federation*

By connecting light to magnetism, cavity-magnon-polaritons (CMPs) [1-3] can build links from quantum computation to spintronics. As a consequence, CMP-based information processing devices have thrived over the last five years, but almost exclusively been investigated with single-tone spectroscopy. However, universal computing applications will require a dynamic control of the CMP on demand and within nanoseconds. In this work, we perform fast manipulations of the different CMP modes with independent but coherent pulses to the cavity and magnon system. We change the state of the CMP from the energy exchanging beat mode to its normal modes (Fig. 1) and further demonstrate two fundamental examples of coherent manipulation: First, a dynamic control over the appearance of magnon-Rabi oscillations, i.e., energy exchange, and second, a complete energy extraction (Fig. 2) by applying an anti-phase drive to the magnon. Our results show a promising approach to control different building blocks for a quantum internet and pave the way for further magnon-based quantum computing research.

[1] H. Huebl, C. Zollitsch, J. Lotze, Physical Review Letters, 111, 127003 (2013) [2] X. Zhang, C.-L. Zou, L. Jiang, Physical Review Letters, 113, 156401 (2014) [3] Y. Tabuchi, S. Ishino, T. Ishikawa, Physical Review Letters, 113, 083603, (2014)

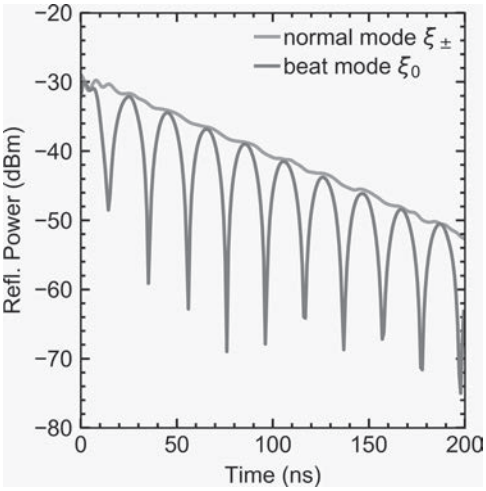


Fig.1 Time-resolved cavity response of the CMP's normal mode compared to the beat mode.

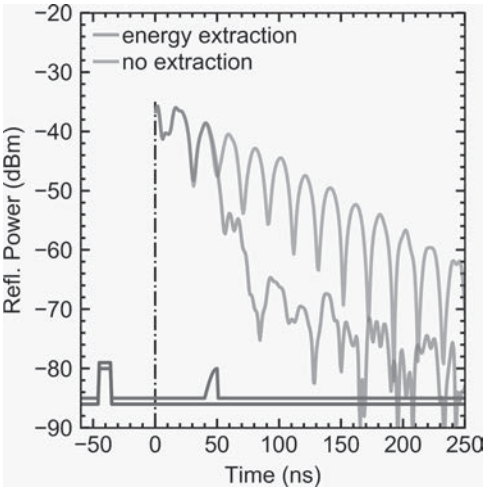


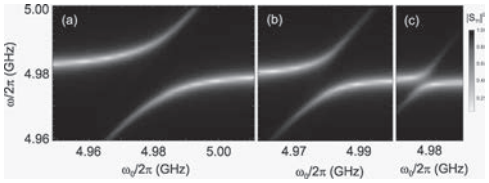
Fig.2 Cavity time trace showing a complete energy extraction in the system. An anti-phase pulse applied to the magnon system counters the energy coming from the cavity. Blue and brown lines display the applied pulse sequences to the magnon system and cavity, respectively.

9:06

CE-04. Excitation Vector Field and Polarization Effect on Cavity-Magnon-Polaritons. *R. Macedo*[1], D.A. Bozhko[1], R. Holland[1], J. Barbosa[1] and M. Weides[1] *1. James Watt School of Engineering, University of Glasgow, Glasgow, United Kingdom*

In recent years we have witnessed a growing interest in cavity-magnon-polaritons. These are hybrid light–matter quasiparticles originating from the strong coupling between magnons and cavity photons [1,2]. Thereby, combining light and magnetism in such way, it is possible to combine quantum information with spintronics. By using this emergent phenomenon, it is possible to engineer devices including, gradient memory and radiofrequency-to-optical transducers. In order to enable more functionality, it is particularly interesting to engineer and understand the coupling strength between elements of a hybrid system – a property which works as a measure for coherent information exchange. This coupling is strongly dependent on the field configuration within the cavity, and hence, the position at which the magnetic sample is placed. In this work, the importance of the field configuration within the cavity is demonstrated but also shown, how different polarisation states can affect the behaviour of cavity magnon polaritons. In Figure 1 we show the measured reflection (S_{11}-parameter) of a YIG sphere placed inside a square microwave cavity, which exemplifies how the coupling can change as a function of the field profile at the sample position. We also show how the polarisation states within different cavity geometries can affect said coupling strength and behaviour of the overall hybrid system. We use the perturbation method to verify our experimental findings. This is done by finding analytical expressions for the field profiles inside the cavity which couple with specific permeability tensor components – these can be calculated through classic LLG equations. Finally, we expect that by being able to control and understand the behaviour of cavity-magnon-polaritons will open up new avenues for, and better manipulate, exchange of information as well as bridging the gap between quantum information and spintronics applications.

[1] D. Zhang, X.-Q. Luo, Y.-P. Wang, T.-F. Li, and J. Q. You, *Nat. Commun.* 8 1368 (2017). [2] Boventer, I., Pfirrmann, M., Krause, J., Schön, Y., Kläui, M. and Weides, M., Phys. Rev. B, 97, 184420 (2018)



The measured ω-H reflection (S_{11}) mapping of the cavity magnon polariton of a YIG sphere placed in a square microwave cavity at positions (a) 2.5 mm, (b) 10 mm, and (c) 15 mm away from the caity wall.

9:18

CE-05. Parametric Pumping of Forward Volume Spin Waves by Surface Acoustic Waves. *N. Nujhat*[1], A. Jander[1] and P. Dhagat[1] *1. Electrical Engineering and Computer Science, Oregon State University, Corvallis, OR, United States*

We demonstrate the parametric pumping of forward volume magnetostatic spin waves (FVMSW) by surface acoustic waves (SAW) in a yttrium iron garnet (YIG) thin film. Parametric pumping of spin waves has application in magnonic signal processing devices, where forward volume modes of spin waves are preferred due to their single-valued dispersion characteristics. Although parametric pumping of spin waves can also be achieved using microwave magnetic fields [1, 2], such pumping of the FVMSW modes is precluded by their circular precession. We have predicted theoretically [3], and now show experimentally, that SAW can pump FVMSW in a magnetostrictive film such as YIG. The experimental device, illustrated in Fig. 1, consists of aluminum interdigitated transducers with an overlying piezoelectric ZnO film for generating SAW, and coplanar waveguide antennas for exciting and detecting spin waves, both fabricated lithographically on a 1μm thick YIG film on a gadolinium gallium garnet (GGG) substrate. A magnetic bias field directed perpendicular to the film plane supports FVMSW propagation between the antennas. The SAW generated by the interdigitated transducers propagate in the YIG film, transverse to the spin waves. The acoustic transducers are driven at a pump frequency of f_p=*2366* MHz while the spin wave antenna is driven near half of this frequency to generate a spin wave signal at f_s=*1183* MHz+Δf. By the energy and momentum conservation rules for parametric interactions, an idler spin wave is generated at $f_i=f_p-f_s$. This idler wave travels counter to the direction of the signal spin wave and is picked up by the same antenna. As shown in Fig. 2a, the observed idler frequency varies with Δf, an evidence of the nonlinear parametric interactions between the spin and acoustic waves. The intensity of the generated idler is plotted as a function of signal wave power and acoustic pump power in Fig. 2b showing that the idler power is a product of the signal and pump powers.

[1] P. A. Kolodin *et al*., "Amplification of Microwave Magnetic Envelope Solitons in Thin Yttrium Iron Garnet Films by Parallel Pumping," *Phys.*

Rev. Lett., vol. 80, no. 9, pp. 1976, (1998). [2] T. Brächer, P. Pirro, and B. Hillebrands, "Parallel Pumping for Magnon Spintronics: Amplification and Manipulation of Magnon Spin Currents on the Micron-scale," *Physics Reports*, vol. 699, pp. 1-34, (2017). [3] I. Lisenkov, A. Jander, and P. Dhagat, "Magnetoelastic Parametric Instabilities of Localized Spin Waves Induced by Traveling Elastic Waves," *Phys. Rev. B*, vol. 99, no. 18, pp. 18433, (2019).

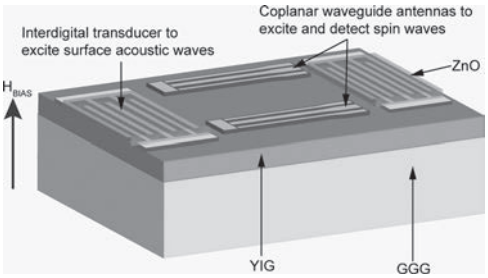


Fig. 1. Illustration of the device to study parametric pumping of FVMSW by SAWs.

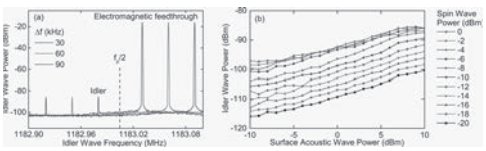


Fig. 2. Experimental results showing the parametrically generated idler wave power for (a) different signal frequency offsets, and (b) as a function of signal and SAW pump power.

9:30

CE-06. Code Correlation of Binary-Phase-Shift-Keying Microwave Signals Using Parametric Pumping of Spin Waves. M. Hansen[1], I. Lisenkov[2], H. Liu[1], P. Dhagat[1] and *A. Jander*[1] *1. Electrical Engineering and Computer Science, Oregon State University, Corvallis, OR, United States; 2. Winchester Technologies LLC, Burlington, MA, United States*

We demonstrate the cross-correlation of binary code words, up to 16 bits in length, using a simple microwave device based on parametric pumping of spin waves. With two binary-phase-shift-keying (BPSK) microwave signals applied at the inputs, the correlator generates an output that is a BPSK microwave signal encoded with the cross-correlation of the input codes. Microwave correlators [1-3] are useful for radar and communications systems employing code division multiple access (CDMA) schemes. The correlator device, illustrated in Fig. 1a, consists of a narrow microstrip antenna and wider pumping strap for respectively generating and parametrically pumping spin waves in an adjacent yttrium iron garnet (YIG) film. A BPSK microwave signal with carrier frequency 1.2 GHz applied to the microstrip antenna generates a backward volume magnetostatic spin wave which travels beneath the pumping strap. A second BPSK microwave signal, with twice the carrier frequency, applied to the pumping strap produces a microwave magnetic field which parametrically pumps the spin wave, generating a counter-propagating idler spin wave. The modulation of the input waveforms depends on the binary code signal and reference codes, where the pump code is time-reversed and compressed by a factor of two for proper operation. As shown in Fig. 1b, the resulting idler wave is modulated with the cross-correlation of the two inputs. With an estimated time-bandwidth product of 22, the correlator should be able to process binary code words of up to 22 bits in length. As shown in Fig 2, we have tested all possible combinations of 7 bit codes with the results closely matching the theoretically expected correlation. We have further demonstrated the correlation of 16 bit code words using a subset of possible codes, specifically the Walsh-Hadamard codes often used in CDMA systems. Agreement between the correlator output and the expected results is excellent.

[1] R. Brocato *et al.*, "UWB communication using SAW correlators," *Proceedings. 2004 IEEE Radio Wirel. Conf. (IEEE Cat. No.04TH8746)*, pp. 267–270, 2004. [2] Y. V Kobljanskyj, G. A. Melkov, A. A. Serga, V. S. Tiberkevich, and A. N. Slavin, "Effective microwave ferrite convolver using a dielectric resonator," vol. 1645, no. August 2002, pp. 1–4, 2008. [3] V. I. Vasyuchka, G. A. Melkov, V. A. Moiseienko, A. V Prokopenko, and A. N. Slavin, "Correlation receiver of below-noise pulsed signals based on parametric interactions of spin waves in magnetic films," *J. Magn. Magn. Mater.*, vol. 321, pp. 3498–3501, 2009.

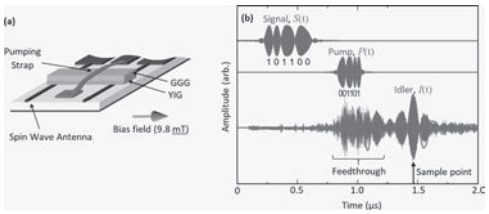


Fig. 1. (a) Illustration of the spin wave correlator. (b) Typical input and output signals for the autocorrelation of binary code 101100.

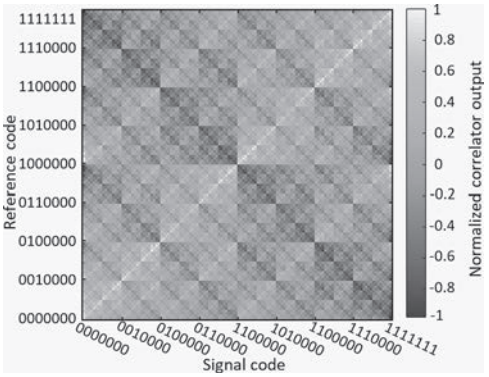


Fig. 2. Measured cross-correlation of all possible 7-bit codes. The data represent the amplitude of the idler wave sampled at the point indicated in Fig. 1b.

INVITED PAPER

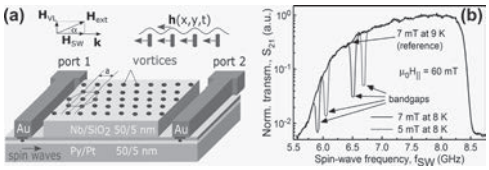
9:42

CE-07. Magnon-Fluxon Interaction in Ferromagnet/Superconductor Heterostructures. *O.V. Dobrovolskiy*[1,2], R. Sachser[2], T. Brächer[3], T. Böttcher[3], V.V. Kruglyak[4], R. Vovk[5], V. Shklovskij[5], M. Huth[2], B. Hillebrands[3] and A. Chumak[1,3] *1. Nanomagnetism and Magnonics, University of Vienna, Vienna, Austria; 2. Physikalisches Institut, Goethe University, Frankfurt am Main, Germany; 3. Technical University of Kaiserslautern, Kaiserslautern, Germany; 4. University of Exeter, Exeter, United Kingdom; 5. V. Karazin Kharkiv National University, Kharkiv, Ukraine*

The field of magnonics considers the operations with data carried by spin waves and their quanta, magnons [1]. Nowadays, the new direction of cryogenic magnonics attracts increasing attention. The decrease in temperature, in particular, results in the reduction of thermal population *n* of magnons below 1 opening access to single-magnon quantum physics [2, 3]. Moreover, this allows for combining magnonics with superconductivity [3-6]. Ferromagnetism and superconductivity are fundamental cooperative phenomena in condensed matter physics. Entailing opposite spin orders, they share an essential conceptual similarity: Disturbances in magnetic ordering in magnetic materials can propagate in the form of spin waves (magnons) while magnetic fields penetrate type II superconductors as a lattice of magnetic flux quanta (fluxons). Despite a rich choice of wave and quantum

phenomena predicted, magnon-fluxon coupling has lacked experimental scrutiny so far. In this talk, a selection of our recent results [6] on the interaction of spin waves with the flux lattice in ferromagnet/superconductor Py/Nb bilayers will be presented - see Fig. 1. In this system we found the magnon frequency spectrum to exhibit a Bloch-like band structure (as shown in Fig. 1(b)) which can be tuned by the biasing magnetic field. Furthermore, the frequency spectra of spin waves scattered on the flux lattice moving under the action of a transport current in the superconductor exhibit Doppler shifts. The resonance absorption of spin waves is explained by their inelastic scattering on the vortex lattice constituting a reconfigurable magnonic crystal [7]. The observed Doppler shifts arise due to the modified dispersion relation for spin waves scattered on the moving vortex lattice constituting a moving Bragg grating. In addition, manipulation of spin waves and tailoring of their transmission spectra in Py will be exemplified by using adjacent Nb layers with nanofabricated pinning potential landscapes.

[1] A. V. Chumak, V. I. Vasyuchka, A. A. Serga, et al., Nat. Phys. 11, 453 (2015). [2] Y. Tabuchi, S. Ishino, A. Noguchi, et al., Science 349, 405 (2015). [3] I. A. Golovchanskiy, N. N. Abramov, M. Pfirrmann, et al., Phys. Rev. Appl. 11, 044076 (2019). [4] A. A. Bespalov, A. S. Mel'nikov, and A. I. Buzdin, Phys. Rev. B 89, 054516 (2014). [5] I. A. Golovchanskiy, N. N. Abramov, V. S. Stolyarov, et al., Adv. Func. Mater. 28, 1802375 (2018). [6] O. V. Dobrovolskiy, R. Sachser, T. Brächer, et al., Nat. Phys. 15, 477 (2019). [7] A. V. Chumak, A. A. Serga, and B. Hillebrands, J. Phys. D: Appl. Phys. 50, 244001 (2017).



(a) Sketch of the experimental system. (b) Fluxon-induced reconfigurable magnonic crystal: Bandgaps in the spin-wave transmission spectra in Py are observed when the Nb layer contains an array of Abrikosov vortices.

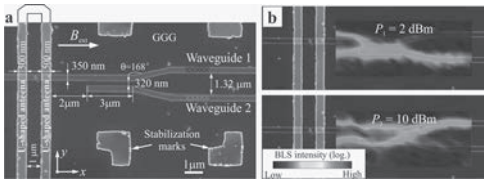
CONTRIBUTED PAPERS

10:18

CE-08. Realization of a Nanoscale Magnonic Directional Coupler for All-Magnon Circuits. Q. Wang[1], M. Kewenig[1], M. Schneider[1], R.V. Verba[2], B. Heinz[1], M. Geilen[1], M. Mohseni[1], B. Lägel[1], F. Ciubotaru[3], C. Adelmann[3], S. Cotofana[6], C. Dubs[4], T. Brächer[1], P. Pirro[1] and *A. Chumak*[5,1] *1. University of Kaiserslautern, Kaiserslautern, Germany; 2. Institute of Magnetism, Kyiv, Ukraine; 3. Imec, Leuven, Belgium; 4. INNOVENT e.V. Technologieentwicklung, Jena, Germany; 5. Nanomagnetism and Magnonics, University of Vienna, Vienna, Austria; 6. Delft University of Technology, Delft, Netherlands*

Spin waves, and their quanta magnons, are of great interest as potential data carriers in future low-energy computing devices [1]. The phase of a spin wave provides an additional degree of freedom, while the scalability of structures and wavelengths down to the nanometer regime [2, 3] are further advantages. Recently, a set of magnonic data processing units was demonstrated. Nowadays, the challenge is the realization of an integrated magnonic circuit [4]. Such a circuit requires the development of a universal reconfigurable unit for performing different logic operations with a nonlinear functionality to cascade multiple units. Here, we present the experimental realization of a nanoscale magnonic directional coupler which fulfills all these criteria [4]. A SEM image of the structure fabricated from an 85 nm thick Yttrium Iron Garnet (YIG) is shown in Fig. 1a. The two spin wave waveguides, each of 350 nm width, are separated by a gap of 320 nm. A U-shaped antenna is used to excite spin waves and space-resolved Brillouin Light Scattering (BLS) spectroscopy is exploited for detection. It is shown experimentally [4] and numerically [5] that the data is coded into the spin wave amplitude is guided towards one of its two outputs depending on the signal frequency, magnitude, and on the magnetic field. By controlling these degrees of freedom, the multi-functionality and reconfigurability of the device is achieved. The nonlinear switching of the output by changing the spin wave amplitude is demonstrated in Fig. 1b. Particularly, this ability opens a path for the realization of all-magnon integrated circuits. The operation of the directional coupler as a multiplexer, fan-out, AND, and XOR logic gates, as well as a half-adder, is demonstrated. This research has been supported by ERC Starting Grant 678309 MagnonCircuits, FET-OPEN project CHIRON (801055), by the DFG through the SFB/TRR-173 "Spin+X" (B01) and DU 1427/2-1 and by the Ministry of Education and Science of Ukraine (0118U004007).

[1] A.V. Chumak, V.I. Vasyuchka, A.A. Serga, *et al.,* Nat. Phys. 11, 453 (2015). [2] Q. Wang, B. Heinz, R. Verba, *et al.*, Phys. Rev. Lett. 122, 247202 (2019). [3] C. Liu, J. Chen, T. Liu, *et al.*, Nat. Commun. 9, 738 (2018). [4] Q. Wang, R. Verba, T. Brächer, *et al.*, arXiv:1905.12353 (2019). [5] Q. Wang, P. Pirro, R. Verba, *et al.*, Sci. Adv. 4, e1701517 (2018).



(a) *SEM image of the directional coupler (shaded in blue) with the U-shaped antenna. (b) Nonlinear functionality of the directional coupler. Two-dimensional BLS maps of the spin wave intensity for different input powers.*

10:30

CE-09. Creating Rogue Waves in Magnetic Thin Films. *M. Copus*[1] and R. Camley[1] *1. Physics, Center for Magnetism and Magnetic Nanostructures, University of Colorado at Colorado Springs, Colorado Springs, CO, United States*

Rogue waves in oceans are a well-known phenomenon where a large wave that can overturn a ship spontaneously arises. We study whether it is possible to create a rogue wave in a magnetic system. We do this in micromagnetics by starting the system initially with a rogue wave configuration, for example where the spins in the center of the film are raised out of plane by a few degrees (see Fig. 1), and then letting the system evolve in time. Instead of collecting data over the entire sample and using time reversal to produce the rogue wave[1], we collect time-dependent magnetic data at a small number of receiver sites in the sample. Playing back the time reversed signal at the receiver sites from a system beginning in equilibrium we can create rogue waves which are several times larger than the average amplitude of the noise. By playing back just the fields above the film, but with larger amplitudes, one can get large angular deviations at the initial site, over 10 degrees. Fig. 1 shows the initial rogue wave and the regenerated wave produced by four sites. In our example the intial rogue wave has a diameter of 50 nm and the calculation is for a Permalloy film 5 nm thick in a field of 1 kOe. In addition, we find that it is possible to create multiple rogue waves and we can create more rogue waves than the number of recording sites. Unlike the ocean, magnetic systems are anisotropic and tunable. The reconstruction can be influenced by several variables including saturation magnetization, damping, exchange stiffness, external field strength, dynamic field strength, sensor placement, and material size and shape. Because of the large angular deviations possible at the rogue wave, we discuss the effect of nonlinearities in the reconstruction. To finish, we discuss potential applications.

[1] A. Przadka, S. Feat, P. Petitjeans et al, Physical Review Letters, Vol 109, p. 064501 (2012)

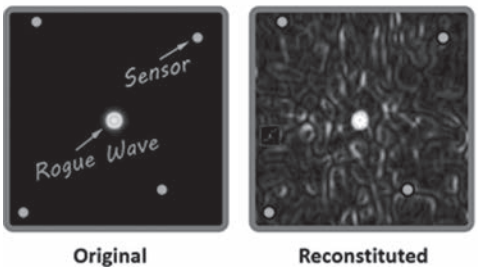


Fig. 1. An example of an initial rogue wave and its reconstruction. The system is initially in an equilibrium state with all the spins in the plane of the film except those near the center which are raised by a few degrees in angle. The system is released, evolves in time and the motions and fields are recorded (for about 2 ns) at the receivers. When the signals at the receivers are time reversed and played, a reconstructed wave appears.

10:42

CE-10. Chiral Spin Waves in Obliquely Magnetized Magnetic Films. *C.A. Trevillian*[1] and V. Tiberkevich[1] *1. Physics, Oakland University, Rochester Hills, MI, United States*

Recently, the chiral properties of spin waves (SWs) became a subject of intensive research [1-4]. SW chirality may lead to a frequency splitting of counter-propagating SW excitations [1] and might be important for effective SW excitation [3, 4] and propagation [2] in nano-scale magnetic systems. Here, we studied chiral SW properties in a simple, yet not fully understood magnetic system lacking mirror symmetry—obliquely magnetized (OM) magnetic film with SWs propagating along the direction of projection of the bias field (see Fig. 1 (a)). Using numerical simulations, we investigated spectra and profiles of dipole-exchange SWs propagating in OM films under varying bias field orientations. We found that for all magnetization angles $0° < \theta < 90°$, the propagating SWs possess a definite chirality that reverses upon the mirror reflection of the bias field direction. Fig. 1 (c) and (d) show the instantaneous profiles of dynamic SW magnetization across the film thickness for "original" (H) and "mirror-reflected" (H′) systems, respectively. The two SW profiles have a clearly visible spiral character with opposite chiralities. The chiral nature of SWs is most pronounced for $\theta \approx 80°$ and gradually diminishes when the bias field approaches in-plane or normal-to-plane directions. It is interesting to note, that, in the considered geometry, other usual manifestations of SW chirality are absent. In particular, frequencies and time-averaged amplitude profiles of SWs remain unchanged upon mirror reflection (see Fig. 1 (b)). One of the direct consequences of the chiral nature of SWs is the presence of transversal exchange spin currents carried by SWs. Such transversal spin currents in OM films have been reported previously [5, 6] and might be important for spintronic applications. The natural SW chirality in OM geometry may also be used for more efficient SW excitation and detection [3, 4].

[1] M. Mohseni et al., "Chiral excitations of magnetic solitons driven by their own inertia", *arXiv:1905.01085* (2019). [2] M. Mohseni et al., "Backscattering Immunity of Dipole-Exchange Magnetostatic Surface Spin Waves", *Phys. Rev. Lett.* 122, 197201 (2019). [3] J. Chen et al., "Excitation of unidirectional exchange spin waves by a nanoscale magnetic grating", *arXiv:1903.00638* (2019). [4] T. Yu et al., "Chiral excitation of spin waves in ferromagnetic films by magnetic nanowire gratings", *Phys. Rev. B* 99, 134424 (2019). [5] D. Bozhko et al., "Wavelength-dependent transformation of dipole-exchange magnon modes in obliquely magnetized YIG films", CD-10, MMM-2017 (Pittsburgh, USA, Nov. 2017). [6] H. Musiienko-Shmarova et al., "Dipolar-exchange magnon and phonon spectra in arbitrarily magnetized yttrium-iron-garnet films", Magnonics-2017 (Oxford, England, Aug. 2017).

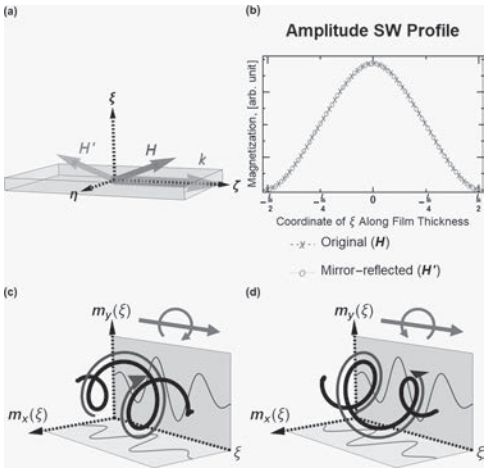


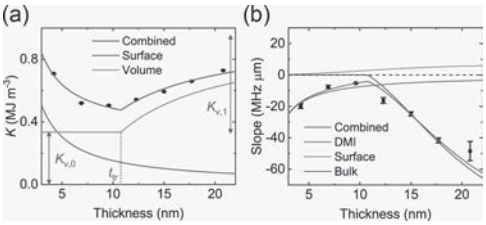
Fig.1: (a) Sketch of the studied OM film. *k* is the SW wavevector, *H* and *H′* show the directions of the bias field in the "original" and "mirror-reflected" systems. (b) Time-averaged amplitude profiles of SWs. (c) and (d) Instantaneous profiles of SWs in the "original" (c) and "mirror-reflected" (d) systems.

10:54

CE-11. Extracting the Dzyaloshinskii–Moriya interaction from propagating spin waves. *J. Lucassen*[1], C. Schippers[1], M. Verheijen[1], R. Duine[1,2], H. Swagten[1], B. Koopmans[1] and R. Lavrijsen[1] *1. Applied Physics, Eindhoven University of Technology, Eindhoven, Netherlands; 2. Institute for Theoretical Physics, Utrecht University, Utrecht, Netherlands*

Thin film magnetism has seen a large increase in the investigations of the interfacial Dzyaloshinskii–Moriya interaction (iDMI) because of its ability to stabilize complex chiral spin textures. This interaction can be quantified by investigating the frequency difference between oppositely propagating spin waves. [1] However, as the films become thicker this frequency difference reduces and quantification becomes more difficult. Moreover, other effects such as a differences in the interfacial anisotropies between the top and bottom of the ferromagnetic layer start playing a role. [2] Here, we disentangle different contributions to spin wave frequency non-reciprocity utilizing all-electrical Propagating Spin Wave Spectroscopy (PSWS) to extract the iDMI. [3] Non-reciprocities as a function of Co thickness in Pt/Co/Ir, Pt/Co/Pt and Ir/Co/Pt are investigated to separate the different contributions to this non-reciprocity. In fig. 1 we show our measured data including fits based on a model we have developed. The striking correspondence allows the extraction of the individual components to the spin-wave frequency non-reciprocity. From the fits we find a DMI that demonstrates the expected sign change when going from Pt/Co/Ir to Ir/Co/Pt. The model also provides us with the difference in interfacial anisotropies, and a large new contribution from a thickness dependent change in the crystalline phase of Co, the presence of which is confirmed using transmission electron microscopy data. These insights will open up new avenues to investigate, quantify and disentangle the fundamental mechanisms governing the iDMI, and pave a way towards engineered large spin-wave non-reciprocities for magnonic applications.

[1] J. Cho, N.-H. Kim, S. Lee et al., Nature Communications 6, 7635 (2015). [2] O. Gladii, M. Haidar, Y. Henry, M. Kostylev et al., Phys. Rev. B 93, 054430 (2016). [3] J. Lucassen, C. F. Schippers, L. Rutten et al., arXiv:1901.11108 (2019).



11:06

CE-12. Electrical Study of Spin-Wave Propagation in Nanoscale CoFeB Waveguides. *F. Ciubotaru*[1], D. Narducci[1,2], G. Talmelli[1,2], I. Radu[1] and C. Adelmann[1] *1. Imec, Leuven, Belgium; 2. Department of Materials Engineering, KU Leuven, Leuven, Belgium*

Spintronic devices are promising candidates to complement CMOS technology to improve both throughput and energy consumption. Especially spin-wave-based majority gates show potential for functional scaling, circuit simplification, and ultralow power consumption. For competitive applications, spin-wave devices need to be miniaturized down to the nanoscale. Hence, the characteristics of spin waves in sub-μm structures are of crucial importance. Moreover, scaling the magnetic volume leads to low spin-wave intensities which are a challenge for the electrical characterization of such devices. Here, we report on electrical characterization of spin waves in nanoscale waveguides. The width of the investigated CoFeB waveguides range from single μm-wide structures to multiple waveguides with widths down to 160 nm. Spin waves are excited and detected by inductive antennas (*cf.* Fig. 1a). By all-electrical spin-wave spectroscopy, we investigate the spin-wave propagation characteristics in different types of waveguides in the Damon-Eschbach geometry. We demonstrate that the spin waves can be efficiently detected in 160-nm-wide waveguides even after 1.5 μm propagation (*cf.* Fig. 1b). The shift of the FMR frequency, the changes in the spin-wave band, and the decay characteristics are studied in devices with different waveguide width, gap between waveguides, and propagation distance. The results are explained by modifications of the internal effective field, the dipolar coupling between adjacent waveguides, and the dispersion relation. The obtained results are crucial for the understanding of propagating spin wave modes in ultra-scaled waveguides and open paths to use spin waves in applications, where dimensions in the order of 100 nm and parallel processing are required. The funding from the European Union's Horizon 2020 research and innovation program within the FET-OPEN project CHIRON under grant agreement No. 801055 is acknowledged.

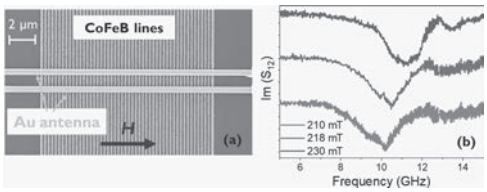


Fig. 1. (a) Scanning electron micrograph of a device with fifty 160-nm-wide lines separated by 130-nm-wide gaps. (b) Electrical spin-wave transmission data for different external bias fields. The spin-wave bandwidth shifts to higher frequencies with increasing field as expected for surface waves.

11:18

CE-13. Reflection-less width-modulated magnonic crystal. P. Frey[1], A.A. Nikitin[2], D.A. Bozhko[3,1], S.A. Bunyaev[4], G.N. Kakazei[4], A.V. Ustinov[2], B.A. Kalinikos[2], F. Ciubotaru[5], A. Chumak[6,1], Q. Wang[1], V. Tiberkevich[7], B. Hillebrands[1] and *A.A. Serga*[1] *1. Fachbereich Physik and Landesforschungszentrum OPTIMAS, Technische Universität Kaiserslautern, Kaiserslautern, Germany; 2. Department of Physical Electronics and Technology, St. Petersburg Electrotechnical University, St. Petersburg, Russian Federation; 3. James Watt School of Engineering, University of Glasgow, Glasgow, United Kingdom; 4. IFIMUP and IN-Institute of Nanoscience and Nanotechnology, Departamento de Fisica, Universidade do Porto, Porto, Portugal; 5. imec, Leuven, Belgium; 6. Nanomagnetism and Magnonics, University of Vienna, Vienna, Austria; 7. Department of Physics, Oakland University, Rochester, MI, United States*

Magnonic crystals receive a lot of attention in spintronics, due to their great potential for information processing technologies [1]. The main features of these crystals are the presence of bandgaps in the spin-wave spectra. The bandgaps are formed due to the Bragg reflections on the artificially created periodic structures. It is possible to influence the properties of the crystals using different designs of these structures within a magnetic material. Recently, potential of edge- and width-modulated waveguiding structures for creation of macro- and micro-sized magnonic crystals was demonstrated [2-5]. In this work, we studied spin-wave propagation in longitudinally magnetized width-modulated yttrium-iron-garnet (YIG) waveguides by means of both Brillouin light scattering and microwave spectroscopies. The waveguides were produced by chemical etching of a YIG film of 8.5 μm-thickness. Short pulses (30 ns) of backward volume magnetostatic spin waves (BVMSW) were excited, close to the ferromagnetic resonance frequency and their propagation was visualized and measured, both in pass and rejection frequency bands (see Fig. 1). We found, that the width-modulated magnonic crystal shows a new underlying mechanism for the formation of a band gap structure, where no back reflection of the spin-wave pulse is observed. Such a reflection-less magnonic crystal is a promising candidate for the realization of frequency selective or multi-component devices.

[1] A.V. Chumak, A.A. Serga and B. Hillebrands, *Magnonic crystals for data processing*, J. Phys. D: Appl. Phys. 50, 244001 (2017) [2] A.A. Nikitin *et al.*, *A spin-wave logic gate based on a width-modulated dynamic magnonic crystals*, Appl. Phys. Lett. 106, 102405 (2015) [3] F. Ciubotaru *et al.*, *Magnonic band gap design by the edge modulation of micro-sized waveguides,* J. Phys. D: Appl. Phys. 45, 255002 (2012) [4] A.V. Chumak *et al.*, *Spin-wave propagation in a microstructured magnonic crystal*, Appl. Phys. Lett. 95, 262508 (2009) [5] G.N Kakazei et al., *Ni80Fe20 film with periodically modulated thickness as a reconfigurable dimensional magnonic crystal,* Appl. Phys. Lett. 104, 042403 (2014)

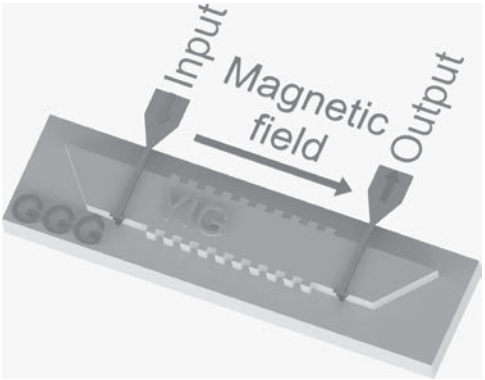


Fig 1: Sketch of the experimental setup for the width-modulated YIG structure. The sketch shows the orientation of the external magnetic field as well as the excitation and receiving antennas.

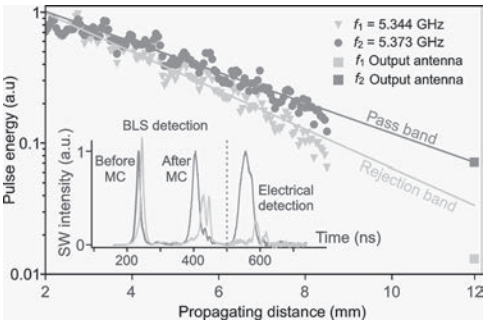


Fig 2: Main panel: Energy of SW pulses at different positions along the MC. Solid circles and triangles -- experimental data as measured by the BLS technique; lines -- exponential fits. Solid squares at 12 mm correspond to the results of microwave measurements. Inset: Temporal profiles of the SW pulses at the input and output of the MC as measured by BLS, in comparison with signals measured by the output microwave antenna.

Session CF
TUNNEL MAGNETORESISTANCE AND GIANT MAGNETORESISTANCE

Aurelie Marion Spiesser, Chair
National Institute of Advanced Industrial Science and Technology (AIST), Tsukuba, Japan

CONTRIBUTED PAPERS

8:30

CF-01. Epitaxial magnetic tunnel junction with Co_2MnGa Heusler alloy electrode on a large-sized Si wafer. *T. Nakano*[1], S. Miwa[2], T. Higo[2], A. Fukushima[1], S. Yuasa[1], S. Nakatsuji[2,3] and K. Yakushiji[1] *1. Spintronics Research Center, National Institute of Advanced Industrial Science and Technology, Tsukuba, Japan; 2. The Institute for Solid State Physics, The University of Tokyo, Kashiwa, Japan; 3. Department of Physics, The University of Tokyo, Tokyo, Japan*

Magnetic tunnel junctions (MTJs) have been intensively explored for various device applications. We recently realized a fully epitaxial MTJ on a large-sized Si wafer, thanks to the development of a NiAl seed layer and a Mg-Al-O barrier [1]. This technology is compatible with CMOS process, and simultaneously enables us to employ novel single-crystalline materials such as ordered alloys. Here, we focus on Co_2MnGa Heusler alloy which is classified as a Weyl magnet exhibiting topological functions such as giant anomalous Nernst effect [2,3]. Films were deposited on an 8" bare Si(001) wafer using a mass-production sputtering apparatus (Canon-Anelva C-7100). Prior to the film deposition, a native oxide layer on the wafer was removed with hydrofluoric acid. Microstructural analysis was carried out by high-resolution transmission electron microscopy (TEM). MTJ films were microfabricated by electron beam lithography process and then its tunnel magnetoresistance (TMR) properties were measured by dc four-probe method. Figure 1 shows a cross-sectional TEM image of an MTJ consisting of substrate/NiAl (25)/Cr (20)/Fe (3)/Co (0.4)/Mg-Al-O/Co_2MnGa (7.5)/capping layers (unit in nm). All the layers, up to the Co_2MnGa electrode, epitaxially grew on the Si wafer. The Co_2MnGa layer was found to contain $B2$- and $L2_1$-ordered structures by electron beam diffraction. Figure 2 shows an TMR curve of an MTJ with a 10-nm-thick Ir-Mn layer inserted on the Co_2MnGa electrode under the magnetic field parallel to the Fe[100] (Co_2MnGa[100]) direction. Parallel and antiparallel magnetization alignments are realized, where the Fe/Co bilayer has a smaller coercivity than that of the Co_2MnGa layer. The TMR ratio was higher than 130% and the resistance-area (RA) product was 123 Ωμm^2. Such a performance of the MTJ supports a high degree of order in the Co_2MnGa electrode. These results demonstrate that this epitaxial growth technology is applicable to an Heusler alloy and can open up utilization of other novel spintronic materials. This work was in part supported by CREST (No. JPMJCR18T3), Japan Science and Technology Agency.

[1] K. Yakushiji, *et al*., submitted. [2] A. Sakai, *et al*., Nature Physics 14, 1119 (2018). [3] H. Reichlova, *et al*., Applied Physics Letters 113, 212405 (2018).

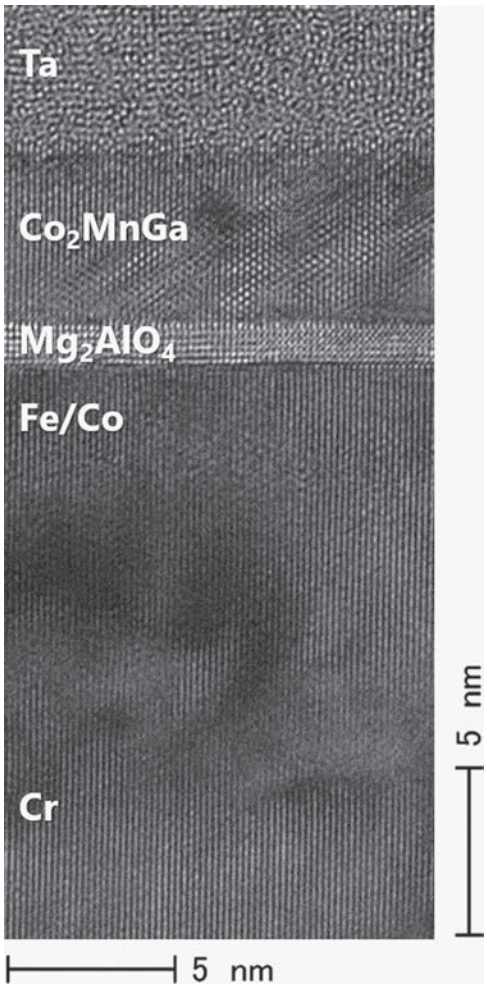


Fig. 1. Cross-sectional TEM image of an epitaxial MTJ.

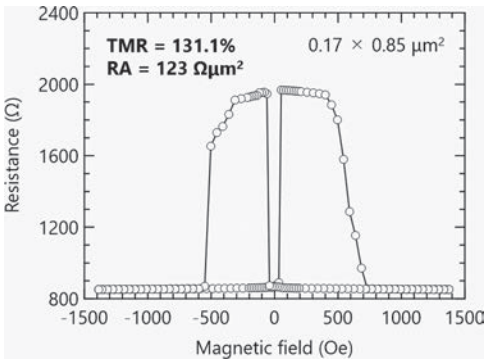


Fig. 2. Representative TMR curve of a microfabricated MTJ.

8:42

CF-02. CMOS-compatible $L1_0$ FePd perpendicular magnetic anisotropy thin film via a fcc Ru seed-layer for spintronic applications. *D. Zhang*[1], D.M. Lattery[2], R. Wu[3], J. Liu[1], D.B. Gopman[4], A. Mkhoyan[3], X. Wang[2] and J. Wang[1] *1. Department of Electrical and Computer Engineering, University of Minnesota, Minneapolis, MN, United States; 2. Department of Mechanical Engineering, University of Minnesota, Minneapolis, MN, United States; 3. Dept. of Chemical Engineering & Materials Science, University of Minnesota, Minneapolis, MN, United States; 4. Materials Science and Engineering Division, National Institute of Standards and Technology, Gaithersburg, MD, United States*

$L1_0$ FePd is a promising candidate for applications in ultralow energy and ultrahigh density spin memory devices, such as spin-transfer-torque magnetic random-access memory (STT-MRAM) due to its high PMA (K_u~ 2×10^7 erg/cm^3), low damping constant (α~0.002), and low processing temperature which are the key features for satisfying the demand of high thermal stability and low critical current spintronic devices (1-4). In order to obtain high-textured FePd thin films with better performance, the seed layer plays a significant role. In this work, $L1_0$ perpendicular FePd thin films on MgO (001) single crystalline substrates were developed with the fcc phase Cr/Ru seed layer by a magnetron sputtering system with the base pressure less than 5.0×10^{-8} Torr. After the sample deposition, the FePd samples were post-annealed at 400 ^{o}C and 500 ^{o}C, respectively, using a high-vacuum furnace. Then their crystal structures were investigated as a function of the post-annealing temperatures, as shown in Fig. 1 It is clearly found that the (001) and (002) diffraction peaks are observed for all of the FePd samples, which indicates that the Cr/Ru seed layer can induce the high-textured crystalline structure of the FePd thin films. We also found that the intensity of these two peaks slightly increases with the increase of the post-annealing temperature, suggesting the crystallinity of the FePd thin films improves. In addition, the damping constant of these Cr/Ru-seeded FePd thin films are investigated by the TR-MOKE and FMR technologies. The ultralow damping constant~0.009 is obtained for the Cr/Ru-seeded FePd thin film. These results demonstrate that the Cr/Ru-seeded FePd thin films can be used to develop the spin memory devices, which can integrate with the current CMOS technology.

1 S. Iihama, A. Sakuma, H. Naganuma, et. al., Appl. Phys. Lett. 105, 142403 (2014) 2. S. Iihama, A. Sakuma, H. Naganuma, et al., Phys. Rev. B 94, 174425 (2016) 3. D.L. Zhang, K.B. Schliep, R. J. Wu, et al., Appl. Phys. Lett. 112, 152401 (2018) 4. D.L. Zhang, C. Sun, Y. Lv, et al., Phys. Rev. Applied 9, 044028 (2018)

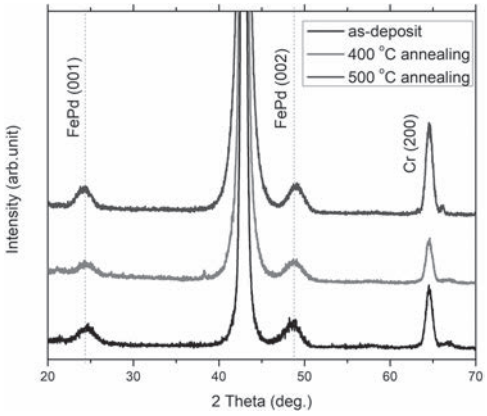


Fig.1 Out-of-plane XRD patterns of the Cr/Ru-seeded L10-phase FePd at the different annealing temperatures

8:54

CF-03. Low-Frequency Electronic Noise and Charge Transport Dynamics in Electrically Tunable AlO_x-based Magnetic Tunnel Junctions. *J. Hong*[1], C. Hung[2], I. Martinez[3], C. Gonzalez-Ruano[3], F.G. Aliev[3], D. Ling[1] and M. Lin[2,4] *1. Department of Physics, Tamkang University, New Taipei City, Taiwan; 2. Department of Physics, National Taiwan University, Taipei City, Taiwan; 3. Depto Fisica de la Materia Condensada, Universidad Autonoma de Madrid, Madrid, Spain; 4. Institute of Atomic and Molecular Sciences, Academia Sinica, Taipei City, Taiwan*

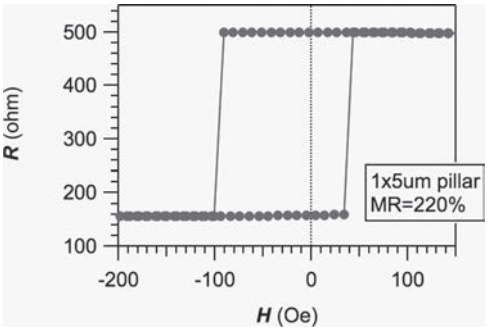
Voltage-controlled charge transport properties of AlO_x-based magnetic tunnel junctions (MTJs) have been revolutionized to generate emergent functionality capable of reversibly manipulating resistive switching and tunneling magnetoresistance in a single device, which is promising for multibit nonvolatile memory applications. We demonstrate that the AlO_x-based MTJs can be reversibly tuned by the voltage switching, which causes the change in device resistance and magnetoresistance. The I-V curve, resistance-temperature (R-T) characteristics and low-frequency noise spectroscopy have been experimentally investigated to understand the charge transport dynamics. The Hooge's parameter extracted from the measured 1/f noise varies significantly as the MTJs are tuned from the high resistance state to the low resistance state. This distinct feature can be qualitatively explained by an empirical formulation of mobility fluctuations, indicating that the (re)distribution/(re)migration of oxygen ions and inevitable oxygen vacancies in the AlO_x barrier play an important role in manipulation of the resistance states of the device. Our work develops a phenomenological model of the microscopic charge transport dynamics associative with the resistive switching in the AlO_x-based MTJs.

9:06

CF-04. Fully epitaxial magnetic tunnel junction with a spinel-type Mg-Al-O barrier on an 8″ silicon wafer. *K. Yakushiji*[1], T. Nakano[1], A. Fukushima[1], A. Sugihara[1] and S. Yuasa[1] *1. AIST, Tsukuba, Japan*

So far, standard MTJs consist of a CoFeB/MgO-based textured stack for its high MR ratio and low resistance-area (RA) product. Despite such favorable results, the performance has nearly reached a ceiling due to restrictions imposed by the characteristics of the materials and the poly-crystallinity. The use of single-crystalline stacks can likely overcome these difficulties. However, the fully epitaxial MTJs to date have not been deemed practical, because they must be fabricated on a small piece of single-crystalline substrate. That is, none as yet have been fabricated on commercial silicon wafers. In this study, we fabricated a fully epitaxial MTJs on a large Si wafer for the first time [1]. An MTJ stack was fabricated on an 8″ bare Si wafer with (001)-oriented single crystal. A wafer was wet-etched in 1% DHF acid for 10 sec. Films were deposited using a PVD apparatus (C-7100, Canon-Anelva). First, we developed a B2-type Ni-Al seed layer [2] as a (001) oriented template on a Si wafer. The best smoothed surface with Ra ~ 0.15 nm was obtained at Ni = 44 at%. Although similar B2-type alloys such as Co-Al, Fe-Al and Ru-Al were also developed, their surfaces were not so smooth as that for Ni-Al. Then, in-plane magnetized MTJ stacks were fabricated as follows: Si-wafer/ Ni-Al (25) / Cr (20) / Fe (3.0) / Co (0.4) / Al (0.4-0.6) / RF-sputtered MgO (0.6-1.5) / Co (0.4) / Fe (2.5) / Ir-Mn (10) / capping (nm). The benefit of the Al insertion before RF-MgO is that it maintains epitaxy while avoiding plasma damage to the underlying ferromagnetic layer. The bilayer Al/MgO was annealed (in-situ at 480°C for 7 min.), which formed the Mg-Al-O barrier layer. Figure shows a typical R-H minor loop for an MTJ with 1x5 um rectangle shape. It exhibited high MR ratio of 220% with sharp magneto-flips. HR-TEM image revealed a nearly perfect epitaxial stack with a (001) orientation. The lattice constant of the spinel-type Mg-Al-O barrier was 0.410 nm. A wafer-level fully epitaxial MTJ is now a reality. It will affect the performance of every spintronics device to come. This work was supported by the ImPACT Program of the Council for Science, Technology, and Innovation.

[1] K. Yakushiji et al., submitted. [2] J. M. Chen et al., APL Materials 4, 056104 (2016).



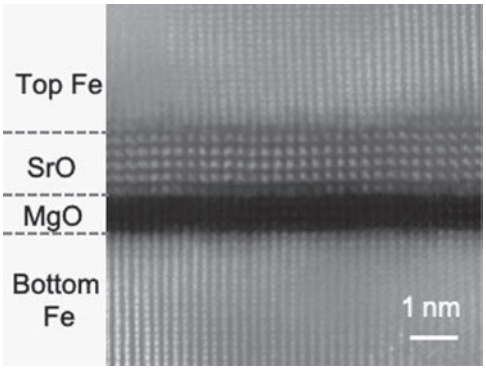
R-H minor loop for a fully-epitaxial MTJ with a 1x5um pillar.

9:18

CF-05. Spin-Polarized Coherent Tunneling in Fully Epitaxial Magnetic Tunnel Junctions with SrO Tunnel Barrier. *A.M. Spiesser*[1], S. Kon[1,2], Y. Yasukawa[2], S. Yuasa[1] and H. Saito[1] *1. Spintronics Research Center, AIST, Tsukuba, Japan; 2. Department of Electrical and Electronic Engineering, Chiba Institute of Technology, Narashino, Japan*

An efficient way to induce a large spin polarization in Si is to take advantage of the spin filtering effect in epitaxial ferromagnet/crystalline oxide tunnel barriers. With this method, we recently demonstrated the creation of a giant spin accumulation in Si using epitaxial Fe/MgO tunnel contacts[1,2] and found that the tunnel spin polarization (*P*) of Fe/MgO on Si can reach up to ~ 90% at 10 K[2]. However, for MgO thicknesses below 1 nm, we observed a rapid drop of the *P* to values below 25 %[2], which might be attributed to the lower crystalline quality of thin MgO layers due to the large lattice mismatch between MgO and Si (22%). This can suppress spin-dependent coherent tunneling transport near the interface and limit the *P* of the Fe/MgO tunnel contact. A low *P* for thin tunnel barrier thicknesses would be a major obstacle for achieving large magnetoresistance (MR) in a two-terminal Si-based lateral device. From a crystal growth viewpoint, rock-salt type SrO is better lattice-matched to Si than MgO (the lattice mismatch between SrO and Si is 4.9%). Thus, if spin-polarized coherent tunneling through SrO can be achieved, SrO might be a more suitable tunnel barrier for achieving high MR ratio in Si devices. Here, we fabricate magnetic tunnel junctions (MTJs) with an epitaxial SrO tunnel barrier and examine its ability for spin-dependent tunneling by measuring MR effect. The structure of the MTJ consists of Au (10 nm) / Co (20 nm) / SrO (1.5 nm) / MgO (1.0 nm) / Fe (30 nm) on a MgO(001) substrate. From the scanning transmission electron microscopy (STEM) image of the MTJ (Fig. 1), we observe a fully epitaxial Fe(001)/SrO(001)/MgO(001)/Fe(001) structure without significant diffusion or intermixing. Magneto-transport measurements reveal high MR ratios up to 90% at room temperature, indicating that spin-polarized coherent tunneling occurs through SrO. In addition, for equivalent barrier thicknesses, the resistance-area products of the MTJs with SrO are comparable to that of epitaxial Fe/MgO/Fe MTJs. Therefore, SrO presents valuable properties as a novel tunnel barrier for high MR ratio in Si-based lateral devices. This work was supported by JSPS KAKENHI (Grant No. 18K13807, A.S.).

1. A. Spiesser H. Saito,Y. Fujita *et al.*, Phys. Rev. Appl. 8, 064023 (2017) 2. A. Spiesser H. Saito, S. Yuasa, *et al.*, to be published in Phys. Rev. B, 2019



STEM image of Fe/SrO/MgO/Fe MTJ.

9:30

CF-06. Towards highly customized GMR and TMR sensors via oblique-incidence deposition. *M. Ramin Moayed*[1], S. Willing[1,2], T. Gurieva[1], L. Bocklage[1,3], K. Schlage[1] and R. Röhlsberger[1,3] *1. Deutsches Elektronen-Synchrotron DESY, Hamburg, Germany; 2. PIER Helmholtz Graduate School, Hamburg, Germany; 3. The Hamburg Centre for Ultrafast Imaging, Hamburg, Germany*

Giant magnetoresistance (GMR) and tunnel magnetoresistance (TMR) as the heart of spintronics have attracted much interest. Magnetic sensors based on these effects have shown to be of great importance since they are small, robust, energy-efficient, and capable of providing accurate data without physical contact. Such sensors have been employed for many applications including information technology, automotive control, and industrial process management. One major issue of these sensors is the control of the easy axis and the coercive field of one or both magnetic layers without the limitations of interlayer exchange or exchange-biased pinning. Here we present an easy and highly flexible method to address this problem: oblique-incidence deposition (OID) [1]. By adjusting the polar and azimuthal deposition angle, an additional and definable shape anisotropy is induced into the system that tailors the magnetic properties of each layer (Figure 1). Based on this technique we are able to realize custom-designed GMR and TMR sensors which exhibit high performance and novel functionalities. For these sensors, the signal strength, temperature stability, and system reliability have been optimized by comprehensively investigating the stack configurations and preparation steps (Figure 2) in order to exploit the method on industrial scales [2]. Our insight opens new pathways to further expand the use of magnetoresistive systems, especially GMR and TMR sensors.

[1] K. Schlage, et al.," Spin-Structured Multilayers: A New Class of Materials for Precision Spintronics", Adv. Funct. Mater.26, 7423 (2016). [2] K. Schlage et al., "An apparatus for depositing material on the surface of a substrate", European patent application EP18179694.7 (2018/pending).

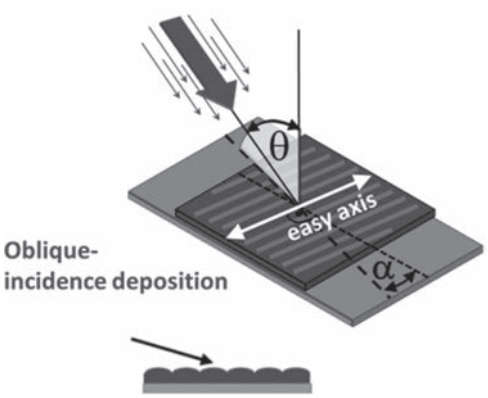


Fig. 1. Oblique-incidence sputter deposition forms a wavy surface which defines the magnetic properties of ultra-thin films via additional shape anisotropy. An easy axis is established perpendicular to the deposition direction. By varying the polar deposition angle (θ), the coercive field can be tuned over a wide range.

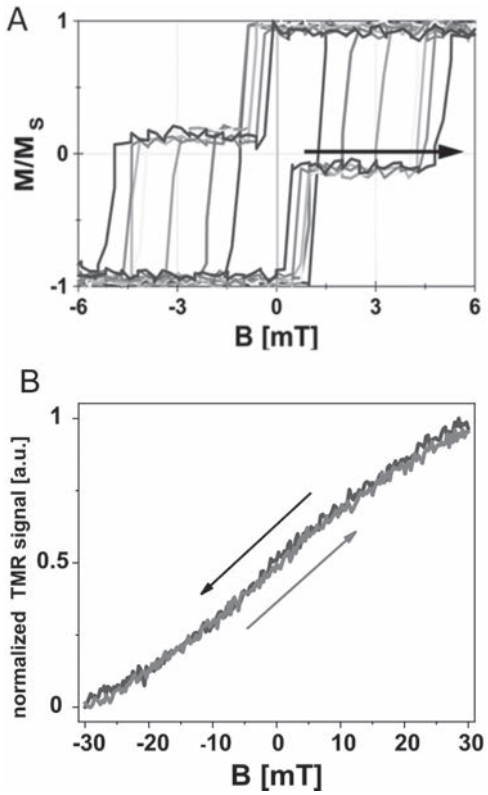


Fig. 2. Functionality of OID based CoFeB/MgO/CoFeB TMR sensors. (A) Magneto-optical Kerr effect (MOKE) measurements of a system with parallel easy axes. The switching field can be tuned by changing the OID configurations (OID angle or thickness). (B) TMR measurements of a system with a 90° crossing of the easy axes. The signal shows a diagonal response to external magnetic fields. The slope and working field range can be adjusted via the OID parameters.

9:42

CF-07. Analysis of the spin-dependent transport in CPP-GMR devices with self-organized Ag-In:Mn-Zn-O nanocomposite spacer.
T. Nakatani[1], T. Sasaki[1], Y. Sakuraba[1] and K. Hono[1] *1. Research Center for Magnetic and Spintronic Materials, National Institute for Materials Science, Tsukuba, Japan*

We studied the mechanism of the improved MR ratio ($\Delta R/R$) of the current current-perpendicular-to-plane giant magnetoresistance (CPP-GMR) devices with a Ag-In:Mn-Zn-O nanocomposite spacer. Polycrystalline pseudo spin-valve structures with Cu-lead / Ta(2) / Ru(2) / CoFe(0.5) / CoFeBTa(1.5) / $Co_2(Mn_{0.6}Fe_{0.4})Ge$ (CMFG)(5) / CoFe(0.4) / spacer / CoFe(0.4) / CMFG(5) / CoFeBTa(1.5) / Ru(8) (thickness in nm) were fabricated with Ag(0.4 nm)/IZO(1.30-1.75 nm) and AIZO (Ag 20-36 at. %)(1.2 nm) films as the spacer layers. As shown in Fig. 1, the devices with AIZO showed much larger $\Delta R/R$ (*e.g.* ~50% at RA ~0.08 Ω μm^2) than those with Ag/IZO bi-layer (*e.g.* $\Delta R/R$ ~30% at RA ~0.1 Ω μm^2). Scanning transmission electron microscopy revealed that for both AIZO and Ag/IZO cases the actual spacer layers were a heterogeneous Ag-In:Mn-Zn-O nanocomposite, where Ag-In alloy paths are distributed in a Mn-Zn-O matrix. This structure is considered to form by an oxidation-reduction reaction between Mn in CMFG and In_2O_3 in IZO as reported recently [2]. In this nanostructure structure, electric current is thought to flow through the Ag-In paths, which gives rise to enhancements of RA and $\Delta R/R$ known as current-confined-path (CCP) CPP-GMR [2]. However, the lateral size of the Ag-In CCP formed from the AIZO precursor layer was found to be larger (~7 nm in diameter) than that from the Ag/IZO precursor (~3 nm). We analyzed the spin-dependent transport in these devices from the point of view of effective spin resistance [3]. The ratio of the effective spin resistance of the CMFG ferromagnetic layer (r_F) to that of the Ag-In CCP (r_{CCP}) are plotted as a function of the resistivity of Ag-In (ρ_N) which cannot be deduced from these experiments. As shown in Fig. 2, r_F/r_{CCP} for AIZO is closer to 1 for a wide range of ρ_N than that for Ag/IZO, indicating a better matching of effective spin-resistance between ferromagnetic layer and spacer for the case of AIZO precursor. This explains the larger $\Delta R/R$ for the devices with the AIZO precursor.

[1] Nakatani *et al*. J. Appl. Phys. 124, 223904 (2018). [2] Fukuzawa *et al*. IEEE Trans. Magn. 40, 2236 (2004). [3] Sato *et al*. IEEE. Trans. Magn. 44, 2608 (2008).

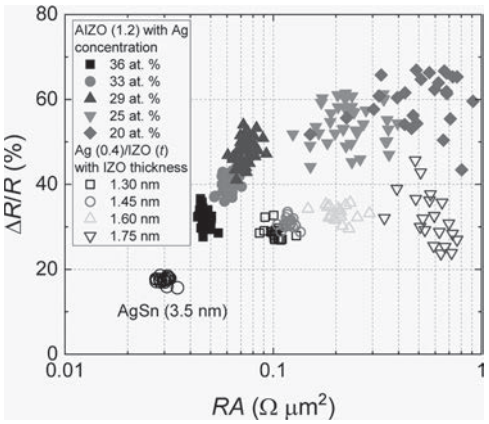


Fig.1 *RA* vs. $\Delta R/R$ of CPP-GMR devices with Ag/IZO and AIZO precursors for spacer.

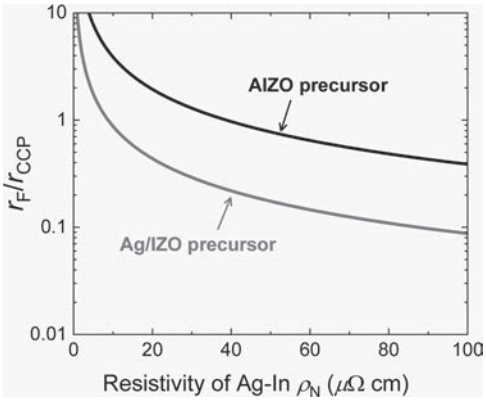


Fig. 2 The ratio of the effective spin resistance of ferromagnetic layer (r_F) to that of CCP (r_{CCP}) as a function of Ag-In resistivity (ρ_N).

9:54

CF-08. Thermally Assisted Magnetisation Reversal in Giant Magneto-Resistive Junctions. *A. Hirohata*[1], W.J. Frost[1], T. Kubota[2], R. Ramos[2], E. Saitoh[2,3] and K. Takanashi[2] *1. Department of Electronic Engineering, University of York, York, United Kingdom; 2. Institute for Materials Research, Tohoku University, Sendai, Japan; 3. The University of Tokyo, Tokyo, Japan*

The wide range of spin-caloric effects, such as the spin-Seebeck [1], Peltier [2] and Nernst [3] effects, have great potential to improve device efficiency by utilising waste heat. Ferromagnetic insulators (FMI) can generate spin-waves via the spin-Seebeck effect when exposed to a thermal gradient. These gradients are ubiquitous in current operated devices, such as giant magneto-restive (GMR) devices and tunnelling magnetoresistance junctions (MTJs). In this study, an unconventional current-perpendicular-to-plane (CPP)-GMR device has been fabricated where the insulating AlO has been replaced with the FMI Fe_2O_3. A Heusler-alloy GMR multilayer of $Co_2Fe_{0.4}Mn_{0.6}Si$ (CFMS) (5)/$Ag_{0.78}Mg_{0.22}$ (5)/ CFMS (5) (thickness in nm) was grown via ultra-high-vacuum sputtering on a MgO(001) substrate with a Cr (20)/Ag (40) seed layer and was capped by Ag(2)/Au (5) layers. The seed and Heusler alloy layers were annealed at 650ºC and 500ºC respectively. Photo- and electron-beam lithography followed by Ar-ion milling were used to fabricate a series of elongated pillars with major axes between 100 - 800 nm. As shown in Fig. 1, the milling was stopped ~1 nm into the bottom CFMS layer. For adhesion a Cr (1)/AlO (2) insulating layer was deposited underneath a 5 nm Fe_2O_3 channel around the GMR pillar. Figure 2 shows a typical MR sweep for one of these devices. When the field is swept from negative-to-positive a wide anti-parallel switch is seen with a small rotational component and a GMR of (10.2 ± 0.1) %. However, when the field is swept from positive-to negative a sharp, narrow reversal is observed with a much larger GMR of (32.8 ± 0.1) %. The difference is due to the spin-wave generated in the FMI enhancing the reversal in one direction. Furthermore the magnetisation of the Fe_2O_3 does not reverse due to its higher coercivity, and therefore couples with some moments in the free-layer, preventing a complete reversal. The asymmetry can also be observed in current-driven reversal, with switching currents as low as (3 ± 0.5) x10^7 A/cm^2. More details will be presented at the meeting.

[1] K. Uchida *et al*., *Nature*, Vol. 455, 778 (2008). [2] J. Flipse *et al*., *Phys. Rev. Lett.,* Vol. 113, 027601 (2014). [3] S. Meyer *et al*., *Nature Mater*., Vol. 16, 977 (2017).

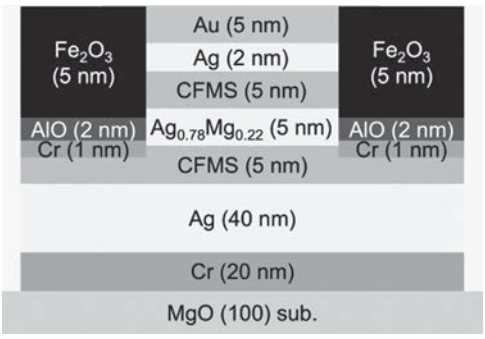


Figure 1. Schematic of thermally-assisted GMR device

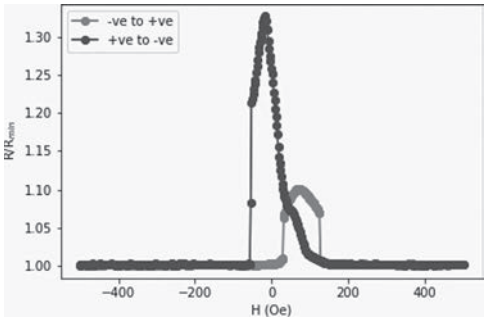


Figure 2. Typical asymmetry observed with spin-Seebeck enhancement via Fe_2O_3.

10:06

CF-09. Tunable Long-Term and Short-Term Memories in a Single Magnetic Tunnel Junction Based Synapse. *N. Prasad*[1*], S. Banerjee[1] and L. Register[1] *1. Electrical and Computer Engineering, University of Texas at Austin, Austin, TX, United States*

In this paper, we present an artificial synapse design based on a magnetic tunnel junction (MTJ)-based spin transfer torque random access memory (STTRAM), as depicted in Fig 1. This device is intended to function as a single stochastic electronic synapse for long-short term memory (LSTM) networks (Fig. 1(a)). LSTM networks have been shown to have a distinct edge over other neural networks when processing sequences of data, such as time-ordered video frames, speech, or connected hand-writing recognition [1]. Changes in the synaptic strength are mapped to the MTJ conductance, which is stochastically varied via spin-transfer torque resulting from input current stimuli [2]. This snowman-shaped free ferromagnetic (FM) layer (Fig. 1(b)) provides a meta-stable intermediate magnetic state (Fig. 2, center) to provide short term plasticity (STP) and associated forgetting behavior, as in a biological synapse. Repeated spin-current stimulations, while the MTJ remains in the STP state, then can cause a permanent change in the magnetic state and associated MTJ conductance to provide long-term potentiation (LTP). For the device with magnetic domains shown in Fig. 2, the room temperature lifetime of the STP state is estimated to be ~10 microseconds, while the lifetime of the LTP state is estimated to be ~100 years, based on the minimum-energy paths for switching obtained through micromagnetic simulation. The snowman shaped FM offers the advantage of tailoring the barriers to switching, along with their associated lifetimes, through variation of the device dimensions (Fig. 1(b)). We also analyze the stochastic switching characteristics of the synapse and demonstrate image recognition behavior on a cross-bar array of these synapses.

1. K. Greff, R. K. Srivastava, J. Koutník, et al., *IEEE Transactions on Neural Networks and Learning Systems*, vol. 28, no. 10, pp. 2222–2232 (2017). 2. A. Sengupta and K. Roy, *Phys. Rev. Applied*, vol. 5, no. 2, p. 024012 (2016).

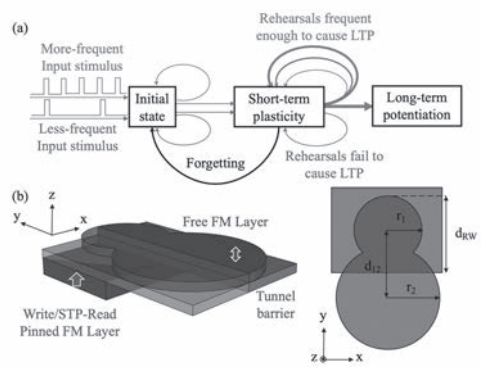


Fig 1. (a) Long-short term memory (LSTM). (b) Snow-man-shaped STTRAM electronic synapse for LSTM.

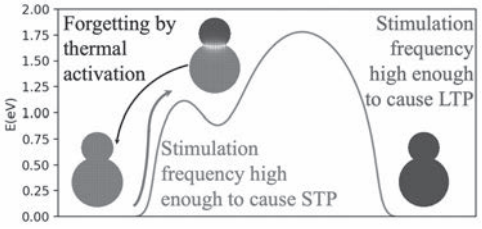


Fig 2. Minimum energy path for switching for the device of Fig. 1(b) as obtained by micromagnetic simulation, for free FM layer of 1 nm thickness with r_1 = 25 nm, r_2 = 40 nm, d_{12} = 55 nm, d_{RW} = 60 nm, and d_R = 40 nm. Material parameters considered are saturation magnetic moment M_s = 1100 kA/m, uniaxial anisotropy constant K_u = 0.8 MJ/m^3, damping constant α = 0.01 and exchange energy constant A_{ex} = 10 pJ/m.

10:18

CF-10. Electrical Control of Magnetoresistance in 2D van der Waals Spin Valve. *W. Yang*[1], X. Wang[1], X. Lin[1] and W. Zhao[1]
1. Microelectronics School, Beihang University, Beijing, China

Spintronics in two-dimensional (2D) van der Waals (vdW) heterostructure is one of the research hotspots recently. With the advent of two-dimensional ferromagnetism and two-dimensional tunneling magnetoresistance (TMR), further explorations of magnetoresistance in 2D van der Waals spin valve and investigations of the modulation effect have been key issues in this field. In this work, we report a large magnetoresistance effect in 2D vdW spin valve of $VSe_2/WSe_2/VSe_2$, where VSe_2 and WSe_2 are adopted as 2D ferromagnetic layer and 2D spacer layer, respectively. A TMR ratio up to 10^{6}% can be achieved in such a device at room temperature, which originates from the interfacial enhanced spin filtering effect. Electrical gating effect further implements voltage control of magnetoresistances in this spin valve (ranging from -15% to about 10^{6}%), which highlights the gate tunability feature of 2D spintronics and enables innovative device applications such as spin logics.

10:30

CF-11. TMR Detection of Skyrmions: Simulations of Current Spreading and Spin Polarization. *H. Chen*[1] and S. Majetich[1] *1. Physics, Carnegie Mellon University, Pittsburgh, PA, United States*

Skyrmions have potential interest for sensing, memory, and logic devices [1-2]. Here we have used simulations to investigate electrical detection of skyrmions through vertical tunneling. When current passes through regions with different spin orientations, it can obscure the contrast in the local tunnel magnetoresistance (TMR). A spin polarized current needs to be strongly localized around the contact. The model system used a cylindrical contact 30 nm in diameter, separated by a thin oxide tunnel barrier from a multilayer stack that can support skyrmions or magnetic bubbles. We divided a 180 nm diameter skyrmion with a 20 nm core into 9 cylindrical layers, with uniform spin orientation inside each shell (Fig. 1a). For clarity only two of the twenty horizontal repeat units in the stack are shown and 3 of the shells. Fig. 1b shows the vertical component of the current density through a cross-section of the stack corresponding to the dashed red box of Fig. 1a. Current is injected vertically, but some travels out laterally (orange arrows), so the footprint of the skyrmion bubble will be larger than the contact diameter. The conductivity at the edge of skyrmion is set at the bulk value σ_0 for it has the same spin direction as the contact. At the center, spins antiparallel to the contact spins are characterized by a conductivity σ_c. The shells were fit by an empirical cosine relation based on the relative spin orientations. Fig. 2 shows the resistance measured when the contact is at different locations relative to the skyrmion. Anisotropic conductivities of σ_c=0.6σ_0, 0.8σ_0 yielded TMR contrast of 66.2%, and 25.7%, respectively. This same approach is used to simulate with asymmetric skyrmion stacks and chirality detection in Bloch skyrmions.

1. R. Tomasello, E. Martinez, R. Zivieri, L. Torres, M. Carpentieri, G. Finocchio, *Scientific Reports* 4, 6784 (2014). 2. X. Zhang, G. P. Zhao, H. Fangohr, J. P. Liu, W. X. Xia, J. Xia, F. J. Morvan, *Scientific Reports* 5, 7643 (2015).

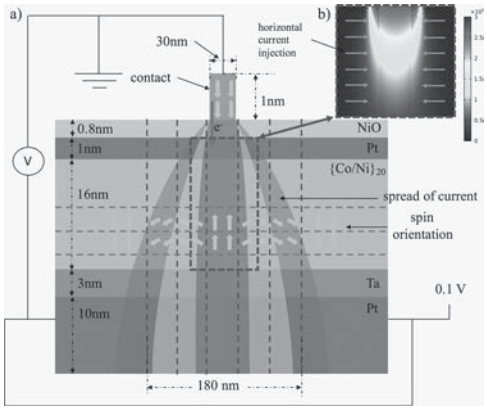


Fig 1. a) Schematic of experimental setup with skyrmionic stack Pt(10 nm)/Ta(3 nm)/{Co(0.2 nm)/Ni(0.6 nm)}$_{20}$/Pt(1 nm)/NiO(0.8 nm) for TMR detection. b) Relative distribution of current density (vertical component only) around the contact.

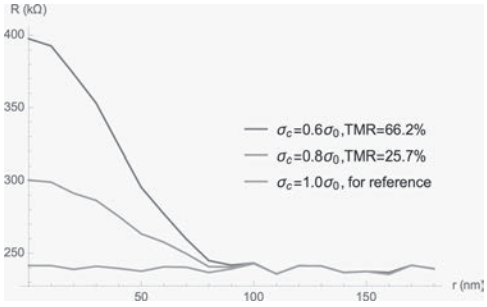


Fig 2. TMR simulation with different center conductivity. r is the contact position relative to the center of the skyrmion. The TMR anisotropy depends on σ_c /σ_0.

10:42

CF-12. Phenalenyl-based Organic Barriers for Tunnel Junctions.
N. Jha[1], *C. Denker*[1], A. Pariyar[2], P.K. Vardhanapu[2], H.S. Mohamad[1], A. Azinfar[1], A. Ahrens[3], T. Meyer[3], J. Walowski[1], C.A. Helm[1], M. Seibt[3], S. Mandal[2] and M. Münzenberg[1] *1. Institut für Physik, Universitaet Greifswald, Greifswald, Germany; 2. Department of Chemical Sciences, IISER, Kolkata, India; 3. IV. Physikalisches Institut, Georg-August Universtitaet Goettingen, Goettingen, Germany*

Phenalenyl (PLY) based molecules are appealing for spintronic applications as demonstrated by the formation of a spinterface, showing tunnel magneto-resistance close to room temperature (RT). The spinterface formation leads to the unique property, that a magnetic tunnel junction (MTJ) with a PLY barrier requires only one ferromagnetic metal layer (FM), while the other magnetic layer is formed in the organic barrier directly at the FM/organic barrier interface [1]. In the present study, we compare three different kinds of PLY molecules (PLY, zinc methyl phenalenyl (ZMP), PLY-Cu[2]) as a barrier material for tunnel junctions. In addition, we introduce a new 3-D shadow mask technology allowing for reducing the junction size of in-situ structured devices down to 3 x 6 μm^2 (Fig. 1). Further investigations reveal an AFM rms-roughness of less than 0.7 nm and TEM imaging indicates sharp and well-defined interfaces. Consequently, the current depends non-linearly on the voltage for average barrier thicknesses exceeding 4.8 nm measured by a calibrated quartz microbalance (QCM), the resistance depends exponentially on the barrier thickness and the resistance shows no significant temperature dependence. This evidences tunneling as a conduction mechanism. Magneto-resistive characteristics appear applying a few mV, while memristive properties require voltages in the Volt range. The memristive resistance change is found for all three types of PLY and can be up to a factor of 2. Furthermore, it is stable and reproducible for at least about 100 cycles. Extremely high MR signals are observed at room temperature up to 1000% for FM/PLY-Cu/FM and FM/PLY-Cu/non-magnetic metal layer (NM), but only for some junctions and with improvable stability (Fig. 2).

[1] K. V. Raman, A. M. Kamerbeek, A. Mukherjee et al., Nature, Vol. 493, p. 509 (2013) [2] A. Mukherjee, T. K. Sen, S. K. Mandal et al., J. Chem. Sci., Vol. 123, p. 139 (2011)

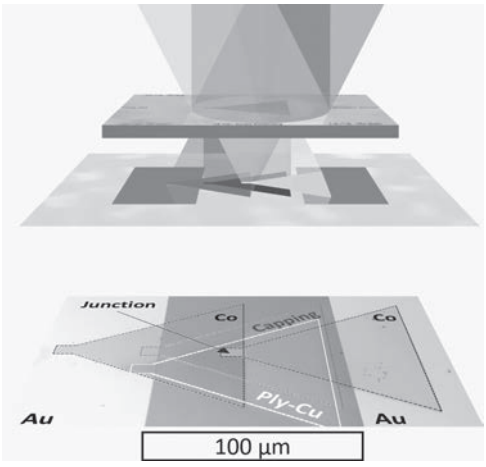


Fig. 1: Sketch of 3D shadow mask device fabrication and resulting device

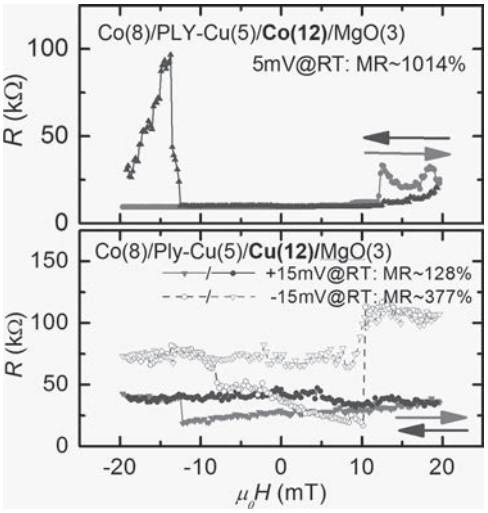


Fig.2: Magneto-resistance (MR) measurements for FM/PLY-Cu/FM and FM/PLY-Cu/NM

10:54

CF-13. Very Fast Current-Induced Domain Wall Motion with Speed of over 2.5 km s^{-1} Driven by Spin Orbit Torques in Ferrimagnetic GdFeCo Wires. *P. Van Thach*[1,2], S. Sumi[1] and H. Awano[1] *1. Toyota Technological Institute, Nagoya, Japan; 2. Institute of Materials Science, Vietnam Academy of Science and Technology, Hanoi, Vietnam*

Current-induced domain wall motion (CIDWM) in magnetic nanowires has been of great attention in spintronic field during a past decade due to its potential applications such as magnetic memory and logic devices [1]. Previous studies showed that CIDWM-driven by spin-orbit torques (SOTs) is more effective than that driven by conventional spin-transfer torques (STTs). In addition, SOTs can move the DWs along and against the current-flow direction, while STTs only move the DWs against the current-flow direction [2, 3]. Recently, the CIDWM with very high DW velocities of around 1 km/s at current densities of 2 - $3.5x10^{12}$ A/m^2 has been observed in magnetic wires based on antiferromagetically-coupled structures [4, 5], which made these antiferromagetic structures more promising for realizing CIDWM-based magnetic memory devices with low-power consumption and high-speed operation. In this work, we investigated the CIDWM in ferrimagnetic GdFeCo wires having Gd antiferromagnetically coupled with FeCo. Thin films with a structure of Pt(5 nm)/$Gd_{1-(x+y)}Fe_xCo_y$(8 nm)/SiN(10 nm) were deposited on thermally-oxidized Si substrates using a magnetron sputtering system. Magnetic properties of the films were examined by polar Kerr effect. As shown in Fig. 1, the films exhibit the perpendicular magnetic anisotropy. The CIDWM in the GdFeCo wires is investigated by a polar Kerr microscopy. Fig. 2 (a, b and c) show the polar Kerr images taken before, after applying a current to the wire, and in a differential mode, respectively. The DWs were moved in the current-flow direction, which indicates that SOTs are responsible for the CIDWM. We found that the CIDWM with a very fast DW speed of over 2.5 km/s at a current density < $2x10^{12}$ A/m^2 was observed in these GdFeCo wires, and it is strongly dependent on Gd and FeCo compositions. This research was partially supported by the Ministry of Education, Culture, Sport, Science and Technology, Japan - Supported Program for Strategic Research Foundation at Private University (2014-2020) and JSPS KAKENHI (Nos. 17H03240 and 18K14128).

[1]. Parkin, S. S. P et al., Science 320, 190–194 (2008). [2]. Satoru Emori et al., Nat. Mater. 12, 611–616 (2013). [3]. Do Bang et al., Phys. Rev. B 93, 174424 (2016). [4]. S.-H. Yang et al., Nat. Nanotechnol. 10, 221 (2015). [5]. Caretta, L. et al. Nat. Nanotechnol. 13, 1154–1160 (2018).

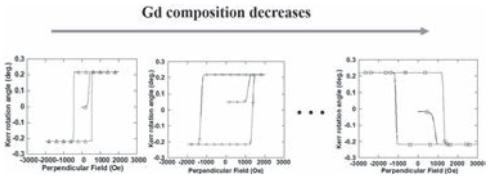


Fig. 1. representative results of polar Kerr loops measured for Pt(5nm)/ GdFeCo(8 nm)/SiN(10 nm) films with various compositions

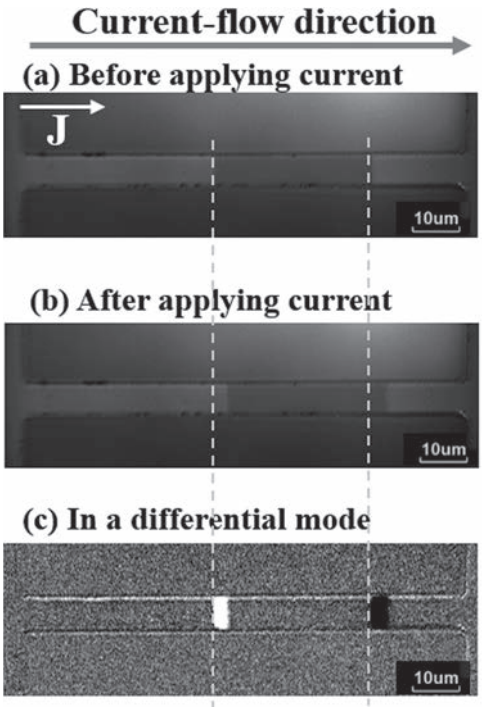


Fig. 2. Polar Kerr images of the GdFeCo wire

Session CG
INTERFACES: PERPENDICULAR ANISOTROPY AND DMI

Patrick Quarterman, Chair
NIST Center for Neutron Research, Gaithersburg, MD, United States

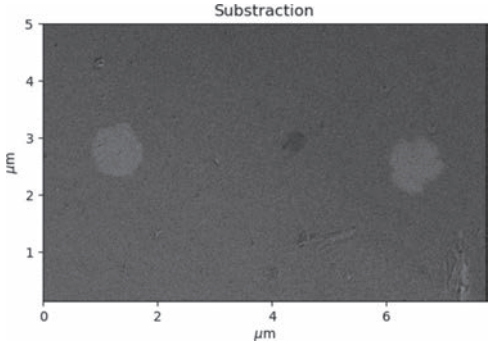
CONTRIBUTED PAPERS

8:30

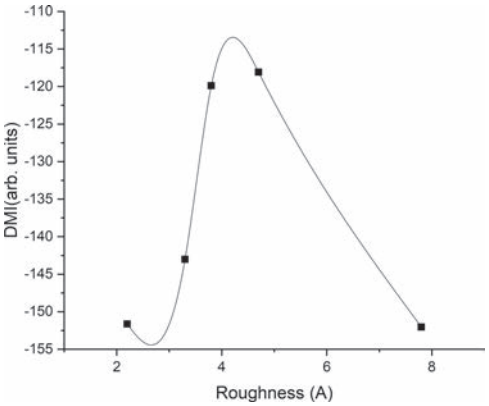
CG-01. Dzyaloshinskii-Moriya interaction in Pt/Co/Ta multilayers with engineered interfacial roughness. *A. Mora Hernandez*[1], A. Hindmarch[1], M. Belmeguenai[2], Y. Roussigné[2] and A. Stashkevich[2] *1. Physics Department, Durham University, Durham, United Kingdom; 2. Physics Department, Université 13 Paris, Villetaneuse, France*

The Dzyaloshinskii-Moriya Interaction (DMI) determines the type and symmetry of non-uniform magnetic structures. The DMI comes from the spin-orbit-interaction, and arises as a result of broken inversion symmetry in bulk magnetic crystals with low symmetry or at interfaces between a ferromagnet and a nonmagnetic material with strong spin-orbit coupling. DMI is important for spintronics as it stabilizes Néel domain walls with high velocities under current excitation, and stabilizes magnetic skyrmions which are potential candidates for new data storage and processing technologies. As that DMI depends of the symmetry of the system, interfacial roughness further breaks the symmetry at the interface in a heterostructure. Here, we describe how controlled induced interfacial roughness can be used to tailor the DMI in model Pt/Co/Ta thin-film multilayer structures. In thin-films, the effect of the DMI is to act as in-plane magnetic field. This influences both the slow, field-driven, dynamics of magnetic domain walls, and the faster, thermally driven, motion of spin-wave excitations. Magneto-optic Kerr effect (MOKE) microscopy is used to quantify the strength of the DMI indirectly (figure, left) via the asymmetric growth of bubble-like domains. Brillouin Light Scattering (BLS) is also used to directly quantify the DMI from the asymmetry induced in the spin-wave dispersion. The influence of engineered interface roughness on DMI as measured by BLS is shown in the figure (right).

[1] M. Belmeguenai et. al, Phys Rev Appl 9, 044044 (2018) [2] R. M. Rowan-Robinson et. al, Sci Reports: 7: 16835 (2017) [3] M. Belmeguenai et.al, Phys Rev B 93, 174407 (2016) [4] M. Tokac et. al, AIP Advances 7, 115022 (2017) [5] M. Belmeguenai et. al, IEEE Trans Mag: 51, 11, (2015)



Magnetic Domain Bubbles in Pt/Co/Pt multilayer using MOKE microscopy.



DMI strength versus induced interface roughness in Pt/Co/Ta measured by BLS.

8:42

CG-02. Reversible control of Dzyaloshinskii-Moriya interaction at graphene/Co interface via hydrogen absorption. *B. Yang*[1], Q. Cui[1], J. Liang[1], A. Hallal[2], M. Chshiev[2] and H. Yang[1] *1. Ningbo Institute of Materials Technology and Engineering, Chinese Academy of Sciences, Ningbo, China; 2. Univ. Grenoble Alpes, CEA, CNRS, Grenoble INP, IRIG-SPINTEC, Grenoble, France*

Chiral order magnetic structure such as domain wall and skyrmion are attractive for the development of future information storage. The Dzyaloshinskii-Moriya interaction (DMI), which originates from spin orbit coupling (SOC) in inversion symmetry broken system, plays a crucial role in the formation of these spin helix magnetic textures. Therefore, tuning the magnitude and chirality of DMI is beneficial for creation and manipulation the magnetic textures for spintronic applications. Recently, it was found that graphene could induce DMI in Co/Gr heterostructure due to the Rashba effect [1]. Hydrogenated graphene can enlarge the spin-orbit coupling of carbon atoms. Therefore, we suppose that a larger DMI may appear in the hydrogenated graphene system. Moreover, hydrogen has smaller size, lower atomic weight and weaker binding energy, indicating the possibility for devices with faster speed by hydrogen migration. Recently, A. J. Tan *et al*. found that a 90° magnetization switching with H^+ insertion at Co/GdO_x interface by external electric field [2]. Whether the hydrogen can influence the DMI has not been reported. In this paper, using first principles calculations, we find that the DMI oscillates with a period of 2 monolayer (ML) as the function of Co thickness ranging from 1ML to 5ML. This oscillation may come from the quantum well states of Co-d_{xz} and d_z^2 orbitals between graphene and vacuum. Moreover, the DMI gradually decreases as a function of H concentration. In most of the cases, anti-clockwise chirality of Co/Gr could be tuned to clockwise one. For Co(2ML)@Gr-4/8H, the strength of DMI can reach -1.0 meV/cell. Our analysis using density of states combined with first order perturbation theory reveals that the spin-splitting and the occupation of Co-*d*

orbitals, especially the d_{xz} and d_{z^2} states, play a crucial role in changing the magnitude and the chirality of DMI in hydrogenated graphene/Co system. Our understanding of the DMI will provide guideline for experimental and theoretical investigations on the chiral related magnetic systems.

[1] H. Yang, G. Chen and M. Chshiev, Nat. Mater. 17, 605 (2018). [2] A. J. Tan, M. Huang and G. S. D. Beach, Nat. Mater. 18, 35 (2019).

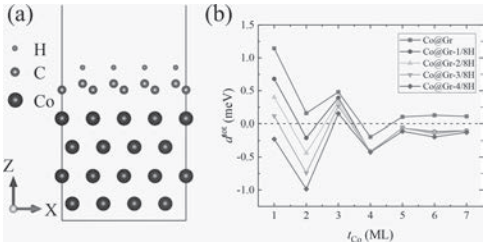


Fig. (a) Schematic diagram of Co(4ML)@Gr-4/8H. (b) DMI strength as a function of Co thickness ranging from 1ML to 7ML for different hydrogen concentration.

8:54

CG-03. Withdrawn

INVITED PAPER

9:06

CG-04. Chirally Coupled Nanomagnets. *Z. Luo*[1,2], T. Dao[1], A. Hrabec[1,2], J. Vijayakumar[2], A. Kleibert[2], M. Baumgartner[1], E. Kirk[1,2], J. Cui[1,2], T. Savchenko[2], G. Krishnaswamy[1], L. Heyderman[1,2] and P. Gambardella[1]
1. ETH Zurich, Zurich, Switzerland; 2. PSI, Villigen, Switzerland

Magnetically coupled nanomagnets have many potential applications including nonvolatile memories, logic gates, and sensors. For these applications, the most effective magnetic couplings have been found to occur between the magnetic layers in a vertical stack. However, in order to realize functional two-dimensional networks of coupled nanoscale magnetic elements such as those used for magnetic logic devices [1] and artificial spin ices [2], it is desirable to engineer the lateral magnetic couplings in a controllable way. Up to now, this has been achieved by exploiting the long-range dipolar interaction. This interaction is nonlocal and scales inversely with the magnetic volume, which limits its use in applications involving nanometer sized structures and thin films. In this work, we demonstrate an alternative method to control the lateral coupling between adjacent magnetic nanostructures [3] based on the interfacial Dzyaloshinskii-Moriya interaction (DMI), which emerges from the combination of spin-orbit coupling and broken inversion symmetry at the interface of ferromagnets and heavy metals. This coupling is mediated by chiral domain walls between out-of-plane and in-plane magnetic regions and dominates the behavior of nanomagnets below a critical size (Fig. 1a). We have exploited this concept for various applications, making use of the fact that the chiral coupling is much stronger than the dipolar coupling. For example, we have created stable synthetic lateral antiferromagnets (Fig. 2a), skyrmionic structures with different numbers of concentric rings (Fig. 2b), and artificial spin ices based on either a square lattice (Fig. 2c) or a kagome lattice (Fig. 2d). In addition, we have demonstrated field-free current-induced switching between multistate magnetic configurations in the chirally coupled nanomagnets via spin-orbit torques. Our work therefore provides a platform to design tailor-made arrays of correlated nanomagnets with a future perspective to achieve all-electric control of planar logic gates and memory devices.

[1] H. Arava, P. M. Derlet, J. Vijayakumar, et al., Nanotechnology, Vol. 29, p.265205 (2018) [2] L.J. Heyderman and R.L. Stamps, J. Phys.: Condens. Matter., Vol. 25, p.363201 (2013) [3] Z. Luo, T. P. Dao, A. Hrabec, et al., Science, Vol. 363, p.1435 (2019)

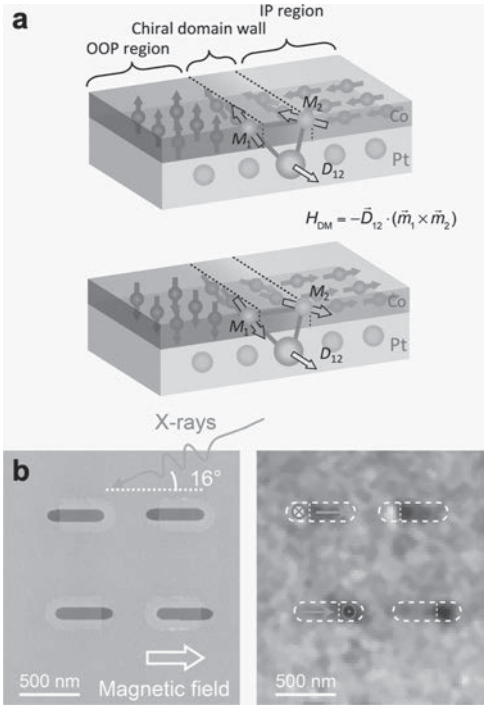


Fig. 1. Chiral coupling between OOP and IP magnets. (a) Schematics of the coupled magnetization states favored by the DMI in adjacent OOP (red) and IP (blue) regions of a Pt/Co/AlOx trilayer. (b) Scanning electron micrograph of coupled OOP-IP elements (left) and their x-ray photoemission electron microscopy (X-PEEM) image (right).

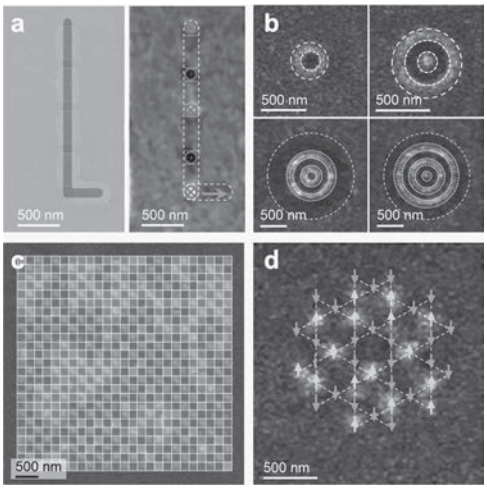


Fig. 2. Lateral synthetic antiferromagnets based on chiral coupling. (a) Scanning electron micrograph and X-PEEM image of a chain structure including five OOP regions. (b) MFM images of synthetic skyrmions with 1, 2, 4, and 5 IP rings. (c) Coloured MFM image of an artificial spin system consisting of OOP elements arranged on a square lattice and acting like Ising-like moments coupled via IP spacers. Antiferromagnetic domains are shaded in green and purple. (d) MFM image of an artificial kagome spin system. The green and purple arrows indicate the orientation of the magnetization of the OOP region.

CONTRIBUTED PAPERS

9:42

CG-05. Interfacial magnetic properties in 3*d*-transition metal alloy thin films with Pt underlayer. *N. Kim*[1], J. Kim[1], E. Baek[1], J. Kim[1] and C. You[1] *1. Daegu Gyeongbuk Institute Science & Technology, Daegu, The Republic of Korea*

The Slater-Pauling curve explained successfully the magnetic moment variation as a function of the number of electrons for wide range of *3d*-transition metal alloys system[1]. The interfacial magnetic properties of ultra-thin *3d*-transition layers such as Co, Fe, CoFe, and CoNi with Pt underlayer are investigated as a function of the number of electrons, they are important in the spin-transfer-torque and spin-orbit-torque device applications[2-4]. In this work, we investigated the interface perpendicular magnetic anisotropy (PMA) and interfacial Dzyaloshinskii-Moriya interaction (iDMI) of ultra-thin Fe_xCr_{1-x}, Co, Fe, Ni, and Co_xNi_{1-x} alloys on the Pt under layer whose strong spin-orbit coupling is important. By employing Brillouin light scattering (BLS) measurements, we obtained the interface PMA and iDMI energy density as shown in the Fig. 1 (a) and (b). Surprisingly, they show very similar tendency to the Slater-Pauling curve, it increases with the number of electron, and shows maximum between Fe and Co. After the maximum, it decreases linearly. We already reported that the interface PMA and iDMI showed strong correlations in our previous studies[5] because of their common physical origin, the strong spin-orbit coupling. Furthermore, it has been already reported that the iDMI is proportional to the exchange stiffness, which is also related with the saturation magnetization[6]. Therefore, it is not surprising that the interface PMA and iDMI showed the similar dependence with the Slater-Pauling curve. Based on our finding, we can claim that the interface PMA and iDMI can be finely tuned by adjusting the Fermi level of the ferromagnetic layers.

1. R. C. O' Handley, "Modern Magnetic Materials -Principles and Applications", John Wiley & Son, p.150~152 (2000). 2. J. Cho *et al.*, Nat. Comm. 6, 7635 (2015). 3. N.-H. Kim *et al.*, Appl. Phys. Lett. 107, 142408 (2015). 4. J. Cho *et al.*, IEEE Trans. MAG 54, 6, 1-4 (2018). 5. N.-H. Kim *et al.*, Appl. Phys. Express 10, 103003 (2017). 6. Hans T. Nembach *et al.,* Nat. Phys. 11, 825–829 (2015).

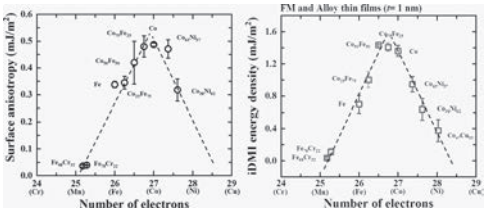


Figure 1. The result of BLS measurement (a) surface anisotropy (K_S), (b) iDMI energy density as a function of number of electrons.

9:54

CG-06. Perpendicular magnetic anisotropy of Cu_2Sb-type (Mn-Cr)AlGe films onto thermally oxidized silicon substrates. *T. Kubota*[1,2], Y. Kota[3], K. Ito[1,2], R.Y. Umetsu[1,2], M. Sun[1], M. Mizuguchi[1,2] and K. Takanashi[1,2] *1. Institute for Materials Research, Tohoku University, Sendai, Japan; 2. Center for Spintronics Research Network, Tohoku University, Sendai, Japan; 3. National Institute of Technology, Fukushima College, Iwaki, Japan*

Perpendicularly magnetized films with high uniaxial magnetocrystalline anisotropy energy, K_u, and small saturation magnetization, M_s, are of the interest for developing magnetoresistive random access memories with giga-bit class memory capacity for future. Cu_2Sb-type MnAlGe is a material showing relatively large K_u of 5×10^6 erg/cm^3 and small M_s of about 300 emu/cm^3[1][2]. MnAlGe possesses a merit that the films exhibit (001)-orientation also onto amorphous substrates, e.g. glass substrates[3], which is suitable for applying to magnetic tunnel junctions using MgO barrier with (001) orientation. On the other hand, the moderate K_u is a drawback which is necessary to be improved. Substitution of Cr for the Mn site is a way to manipulate the magnetic properties of MnAlGe. The enhancement of ferromagnetic Curie temperature was reported for poly-crystalline bulk (Mn-Cr)AlGe [4,5], however, there has been no report on K_u so far. In this study, Cr concentration dependence of magnetic properties was investigated for (Mn-Cr)AlGe films onto thermally oxidized Si substrates. The films were fabricated using ultra-high vacuum magnetron sputtering machine, and the stacking structure was as follows: Si, SiO_2 sub.|(Mn-Cr)AlGe 100 nm|MgO 2 nm|Ta 3 nm. All layers were deposited at room temperature, and after the deposition of the capping layers, annealing was carried out using a vacuum furnace at 500 °C. The Cr concentration was changed from 0 to 0.45 in the stoichiometry. The (001)-textured Cu_2Sb-type structures were confirmed by x-ray diffraction profiles for all samples, successfully. Magnetization curves were measured by using vibrating sample magnetometer for the out-of-plane and in-plane directions at room temperature, and all samples exhibited perpendicular magnetization. Values of M_s and K_u are summarized in Table I. The K_u is successfully enhanced by the Cr-substitution. First principles calculations were also carried out for evaluating K_u, and the possible mechanism of the enhancement will be discussed in the presentation. This work was partially supported by the Murata Science Foundation.

[1] K. Shibata, H. Watanabe, H. Yamauchi, and T. Shinohara, *J. Phys. Soc. Jpn.* 35, 448 (1973). [2] S. Mizukami, A. Sakuma, A. Sugihara, T. Kubota, Y. Kondo, H. Tsuchiura, and T. Miyazaki, *Appl. Phys. Express* 6, 123002 (2013). [3] R. C. Sherwood, E. A. Nesbitt, J. H. Wernick, D. D. Bacon, A. J. Kurtzig, and R. Wolfe, J. Appl. Phys. 50, 1704 (1971). [4] H. Ido, T. Kamimura, and K. Shirakawa, *J. Appl. Phys.* 55, 2365 (1984). [5] H. Masumitsu, S. Yoshinaga, Y. Mitsui, R. Y. Umetsu, M. Hiroi, Y. Uwatoko, and K. Koyama, *J. Magn. Magn. Mater.* 456, 104 (2018).

	M_S (emu/cm^3)	K_U (10^6 erg/cm^3)
$Mn_{1.07}Al_{0.88}Ge_{1.05}$	223	2.5
$(Mn_{0.76}Cr_{0.28})Al_{0.94}Ge_{1.06}$	308	7.3

Table I: Saturation magnetization, M_s, and perpendicular magnetic anisotropy energy, K_u, of (Mn-Cr)AlGe films.

10:06

CG-07. The Surface Spin Flop in Fully Tunable Synthetic Antiferromagnets with Perpendicular Magnetic Anisotropy. *B. Böhm*[1], N.S. Kiselev[2], D. Pohl[3,5], L. Fallarino[4], L. Koch[1], B. Rellinghaus[3,5], K. Nielsch[5] and O. Hellwig[1,4] *1. Institute of Physics, Chemnitz University of Technology, Chemnitz, Germany; 2. Forschungszentrum Jülich and JARA, Jülich, Germany; 3. Dresden Center for Nanoanalysis, TU Dresden, Dresden, Germany; 4. Institute of Ion Beam Physics and Materials Research, Helmholtz-Zentrum Dresden-Rossendorf, Dresden, Germany; 5. IFW Dresden, Dresden, Germany*

Antiferromagnets (AFs) are of emerging interest due to their wide variety of useful properties at the micro and nanoscale. Despite the macroscopically vanishing magnetic remanent moment and therefore high stability with respect to external magnetic field, AFs may provide other unique magnetic static states as well as promising characteristics for dynamic applications like high domain wall velocities and excitation frequencies up to the THz regime [1, 5]. Synthetic antiferromagnets (SAFs), consisting of AF-coupled ferromagnetic layers via thin non-magnetic spacer layers [2], maintain the main characteristics of intrinsic AFs. Additionally, SAFs offer a high degree of tunability and easy integration, thus making them interesting for a wide range of applications [3-5]. One unique AF phenomenon, whose observation became possible through the emergence of SAFs, is the Surface Spin Flop (SSF) [6, 7]. Here, for an even number of AF-coupled layers at sufficiently high field, a vertical AF domain wall is nucleated at one of the surfaces of the SAF and then, as the external field is further increased, propagates

towards the center of the SAF. For even higher fields, the vertical AF domain wall expands into the Bulk Spin Flop state with a canting between adjacent magnetic layer moments [8]. So far, the observation of the SSF in SAFs was limited to epitaxial systems with in-plane uniaxial magneto crystalline anisotropy. We will present the SSF for the first time in SAFs with perpendicular magnetic anisotropy caused by the interfaces of Co/Pt multilayers (Fig. 1). The fact that single crystalline substrates are no longer needed, paves the way for further investigations of the SSF state as well as for applications. Furthermore, we demonstrate the possibility to stabilize the vertical AF domain wall even at remanence, thereby making it readily available also for low field investigations and applications.

[1] S.-H. Yang, K.-S. Ryu and S. Parkin, Nat. Nanotechnol. 10, 221 (2015) [2] P. Grünberg, R. Schreiber, Y. Pang, M. B. Brodsky and H. Sowers, Phys. Rev. Lett. 57, 2442 (1986) [3] O. Hellwig, A. Berger and E. E. Fullerton, Phys. Rev. Lett. 91, 197203-1 (2003) [4] O. Hellwig, A. Berger, J. B. Kortright and E. E. Fullerton, J. Magn. Magn. Mater. 319, 13 (2007) [5] R. A. Duine, Kyung-Jin Lee, Stuart S. P. Parkin and M. D. Stiles, Nat. Phys. 14, 217 (2018) [6] D. L. Mills, Phys. Rev. Lett. 20, 18 (1968) [7] R. W. Wang, D. L. Mills, E. E. Fullerton, J. E. Mattson and S. D. Bader, Phys. Rev. Lett. 72, 920 (1994) [8] F. Keffer and H. Chow, Phys. Rev. Lett. 31, 1061 (1973)

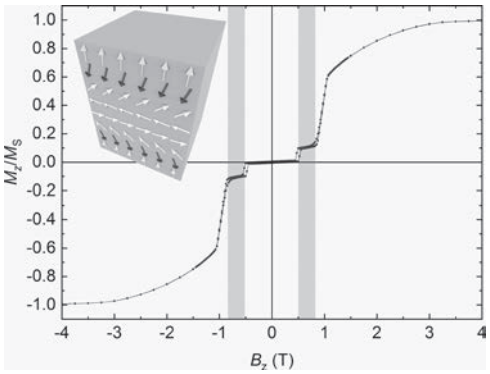
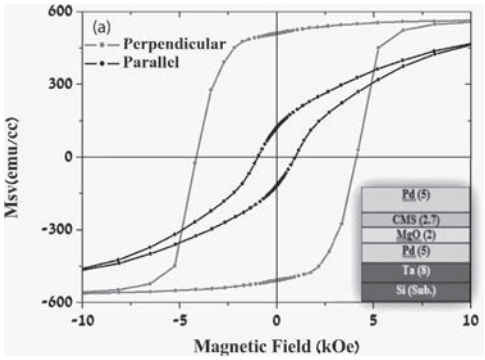


Fig. 1: Magnetization curve with the Surface Spin Flop (SSF) states occuring in the green regions. The laterally homogeneous vertical AF domain wall originating from the SSF is indicated in the inset.

10:18

CG-08. Interface alloying of ultra-thin films as a source of perpendicular magnetic anisotropy. A. Basha[2,3], H. Fu[5], G. Levi[2,4], *G. Leitus*[1], A. Kovacs[6], C. You[5] and A. Kohn[2,3] *1. Chemical Research Support, Weizmann Institute of Science, Rehovot, Israel; 2. Department of Materials Science and Engineering, Tel Aviv University, Tel Aviv, Israel; 3. Tel Aviv University Center for Nanoscience and Nanotechnology, Tel Aviv University, Tel Aviv, Israel; 4. Wolfson Applied Materials Research Center, Tel Aviv University, Tel Aviv, Israel; 5. School of Materials Science and Technology, Xi'an University of Technology, Xi'an, China; 6. Ernst-Ruska Centre for Microscopy and Spectroscopy with Electrons, Forschungszentrum Jülich, Jülich, Germany*

Novel spin-electronic devices require electrodes that inject electrons with both high in-polarization and perpendicular magnetic anisotropy (PMA). We investigate structural origins of PMA using a test case of ultra-thin Co2MnSi films prepared by magnetron sputter-deposition, adjacent to a MgO layer to represent a tunneling barrier, and to a Pd buffer layer. We measure PMA, with an energy density of 7.8 ± 1.8 Merg/cc at 5 K, when a Pd layer is adjacent to Co2MnSi, following annealing in a narrow temperature range, around 350 °C. This ferromagnetism originates from nanometer scale regions, below 5 nm in size, having a relatively low saturation magnetization, 550 ± 50 emu/cc at low temperatures. Following thermal annealing, significant compositional interdiffusion between Co2MnSi films and adjacent layers, Co with Pd and Mn with MgO, was observed by electron energy-loss and angle resolved X-ray photoelectron spectroscopies. Aberration-corrected transmission electron microscopy shows that Co2MnSi does not crystallize while at the interface with Pd, nanometer-scale crystallites of FCC solid solution CoPd with {1 1 1} texture are identified. We conclude that these Pd rich CoPd crystallites, characterized by large magnetostriction, are a source for PMA.



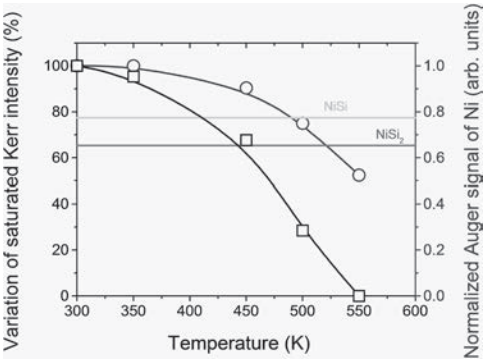
M-H loops measured at 5 K for Pd/CMS/MgO/Pd multilayer annealed at 350 °C. The notations "perpendicular" and "parallel" refer to directions of the applied external magnetic field with respect to the plane of the film.

10:30

CG-09. Evolutions of magnetic phases driven by compositional changes for ultrathin Ni/Si(111). C. Chang[1], Y. Chow[1], C. Hsieh[1], P. Jiang[1] and *J. Tsay*[1] *1. Department of Physics, National Taiwan Normal University, Taipei, Taiwan*

Metal-semiconductor interfaces have attracted considerable interest because of their promising applications as semiconductor devices and possible use as new functionalities in semiconductor technology [1,2]. As a magnetic material, nickel has an advantage of a relatively low Curie temperature, which permits it to be used in studies of critical phenomenon near room temperature. There are relatively few reports dealing with the magnetic properties of ultrathin Ni layers on silicon surfaces and chemical compositions of these materials at the interface. We report herein on the correlation between the morphology, composition, and magnetic properties of ultrathin Ni/Si(111) films. At room temperature, the dominant species produced at the interface is NiSi, which is produced by the spontaneous formation of strong bonds between Ni and Si atoms. We established a chemical shift-related concentration model for determining the amount of ultrathin Ni silicides by assuming that a Ni layer is formed over a NiSi layer with the total coverage as a constraint. At elevated temperatures, the compositional changes as monitored using Auger electron spectroscopy shows a strong correlation with the magnetic responses (Figure 1). From systematical explorations, a magnetic phase diagram for Ni/Si(111) was established showing three regimes. The interdiffusion of Ni and Si atoms at the interface as well as the morphological characteristics play important roles on the boundaries of phase transitions.

[1] Yu-Ting Chow, Bin-Han Jiang, Cheng-Hsun-Tony Chang and Jyh-Shen Tsay, Phys. Chem. Chem. Phys. 20, 1504-1512 (2018). [2] Cheng-Hsun-Tony Chang, Pei-Cheng Jiang, Yu-Ting Chow, Hsi-Lien Hsiao, Wei-Bin Su, and Jyh-Shen Tsay, Enhancing silicide formation in Ni/Si(111) by Ag-Si particles at the interface, Scientific Reports, 2019, in press.



10:42

CG-10. Alternate monoatomic layer deposition of Fe and Ni on Al_2O_3 (0001) using PLD. *T. Miyashita*[1], H. Ito[1], T. Kumagai[1], T. Koganezawa[2], T. Miyamachi[3], F. Komori[3] and M. Kotsugi[1] *1. Tokyo University of Science, Tokyo, Japan; 2. JASRI, Hyogo, Japan; 3. ISSP of The University of Tokyo, Chiba, Japan*

Development of novel magnetic materials is an important issue in the realization of spintronics devices or electric vehicles. Recently, huge attention has been focused on rare-earth-free high-performance magnetic materials from the viewpoint of elemental strategy. Our proposed FeNi ordered alloy shows strong magnetization and large magnetic anisotropy without rare earth elements, and it is a potential candidate satisfying these requirements [1]. A number of studies have been carried out on FeNi ordered alloys such as material fabrication, functional analysis and theoretical calculation so far [2, 3]. Here, we focused on the $L1_1$-FeNi ordered alloy, which is expected to show a higher uniaxial magnetic anisotropy K_u by the first principle calculation. In this study, we attempt to construct $L1_1$-FeNi by alternate monoatomic layer deposition of Fe and Ni by using pulsed laser deposition (PLD). We analyzed the crystal structure and magnetic properties, and discussed their correlation [4]. Experimentally, Al_2O_3(0001) substrate was heat-treated to obtain a clean surface. Thereafter, Cu was vapor-deposited using a PLD apparatus using an Nd: YAG laser (266 nm) as a light source as an underlayer. The preparation of $L1_1$-FeNi was performed using monoatomic alternate deposition on the optimized underlayer. Evaluation of surface crystallinity was RHEED, evaluation of surface flatness was AFM, evaluation of crystal structure was Synchrotron radiation-based X-ray diffraction, evaluation of magnetic characteristics was SQUID magnetometer was used. Fig. 1 shows the magnetic hysteresis by SQUID. Fig. 1 (a) shows the magnetic hysteresis of FeNi/ Cu/ Al_2O_3, and Fig. 1 (b) shows the magnetic hysteresis of $L1_0$-FeNi. The figure shows that the spontaneous magnetization is oriented in the in-plane direction in both samples. At this time, calculate the magnetic anisotropy energy K_u. The evaluated K_u was 9.8×10^6 erg/cc for FeNi/ Cu/ Al_2O_3 in (a) and 8.4×10^6 erg/cc for $L1_0$ FeNi in (b). From the above, it was confirmed that the FeNi alloy on the Al_2O_3 substrate fabricated this time had high magnetic anisotropy.

[1] M. Kotsugi, C. Mitsumata, and M. Oshima, Appl. Phy. Express 3, 013001, (2010) [2] M. Saito, H. Ito, and M. Kotsugi, Applied Physics Letters 114, 072404, (2019) [3] M. Kotsugi, M. Mizuguchi, and Y. Watanabe, Journal of Magnetism and Magnetic Materials 326, 235-239 (2013) [4] H. Ito, M. Saito, and M. Kotsugi, AIP Advances 9, 045307, (2019)

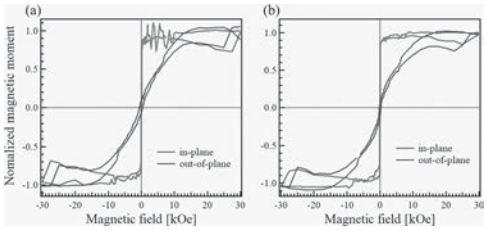


Fig 1. Magnetic hysteresis of (a) FeNi/Cu/Sap. Sub and (b) $L1_0$-FeNi. Both ware measured at 100 K

10:54

CG-11. Significant perpendicular magnetic anisotropy induced by chemisorbed small organic molecules on ferromagnetic films. *A. Fernandes Cauduro*[1], G. Chen[2], M. Robertson[2], R. Lo Conte[3], M. Madsen[4], A.K. Schmid[1] and K. Liu[2,5] *1. Molecular Foundry, Lawrence Berkeley National Laboratory, Berkeley, CA, United States; 2. Physics, UC Davis, Davis, CA, United States; 3. Materials Science and Engineering, UC Berkeley, Berkeley, CA, United States; 4. NanoSYD, University of Southern Denmark, Soenderborg, Denmark; 5. Physics, Georgetown University, Washington, DC, United States*

Molecular spintronics has become a very promising field for the next generation of spin-valve based devices due to their chemical tunability,[1] low spin relaxation mechanisms[2] and novel interfacial interactions between ferromagnets and organic molecules.[3] When small organic molecules are in contact with more reactive metals such as ferromagnet films, the interactions at the interface may lead to the formation of chemical bonds between the molecular adsorbates and the film, creating new hybrid metal-organic interface states that directly affect the electronic and magnetic properties of the adsorbed molecule.[3] In this work, we study small organic molecules/ferromagnets interface effects by imaging the magnetization vector at the surface using spin-polarized low-energy electron microscopy (SPLEEM). We found that the out-of-plane to in-plane spin reorientation transition occurs at thicker Ni films in the presence of bathocuproine (BCP) overlayer compared to bare Ni films, indicating that a significant perpendicular magnetic anisotropy (PMA) is induced at the BCP/Ni interface at room temperature. Systematic Ni thickness dependent measurements allow the quantification of PMA induced by the BCP overlayer. This is somewhat similar to what has been reported in the graphene/ferromagnet system.[4] Our experimental observations suggest that the metal-organic interface plays a fundamental role in inducing the PMA. In addition, this work opens up possibilities for studying the adsorbed molecule's composition and morphology that may lead to new insights in designing novel organic spin-valve devices with tunable anisotropy. Supports by the NSF (DMR-1610060 and DMR- 1905468), UCOP (MRP-17-454963), and DOE (DE-AC02-05CH11231)are gratefully acknowledged.

[1]C. Barraud, et al, Nat. Phys. 6, 615 (2010). [2]M. Cinchetti, et al Nat. Mater. 16, 507 (2017). [3]K. V. Raman, et al, Nature 493, 509 (2013). [4]H. Yang, et al, Nano Lett. 16, 145 (2016).

11:06

CG-12. Evolution of Bulk Perpendicular Magnetic Anisotropy and AHE in CoFeBGd Alloy Films: Composition and Temperature Dependence. O.A. Inyang[1], B. Nicholson[1] and *D. Atkinson*[1] *1. Physics, Durham University, Durham, United Kingdom*

Thin-film ferrimagnetic rare earth-transition metals (RE –TM) alloys have been studied and used in technology over decades. Research interest has re-emerged due to the bulk perpendicular magnetic anisotropy (PMA) and magnetisation response to field and spin-orbit torques around the ferrimagnetic compensation point [1-4] The bulk PMA is hosted by an amorphous microstructure resulting from the addition of sufficient RE into a TM lattice,

and while studies have given insight into the origin of the PMA [5-8], details of the origin and control of bulk PMA are poorly understood. Here the aim is to further understand bulk PMA and AHE with RE content and the temperature dependence around the ferrimagnetic compensation. Previous studies have focused on adding a RE, typically Gd or Tb, into crystalline Fe, Co or CoFe alloy that leads to the amorphous structure. The emerging bulk PMA has been linked to texturing of the amorphous phase. To investigate the link between structure, composition and bulk PMA and AHE, we report, for the first time, on the of addition of Gd to the already amorphous alloy CoFeB, as a function of Gd concentration. We also demonstrate the critical role of the underlayer in developing bulk PMA and show that the anisotropy depends on temperature around the compensation point. Multilayers of NM(5nm)/Gdx(Co20Fe60B20)1-x(t)/Ta were studied as a function of Gd content, thickness and the Non-Magnetic underlayer. Magnetisation was investigated with longitudinal and polar MOKE and Hall magnetometry. Fig. 1 shows the development of the anisotropy in CoFeBGd with Gd content. No magnetic response was observed at the compensation at 21.9 % Gd. Significantly, the role of the underlayer is important, with some cases creating a bulk PMA, while in others the magnetisation is in-plane for the same amorphous ferrimagnetic alloy. Furthermore, temperature measurements show that the anisotropy is also very sensitive to the ferrimagnetic state around the compensation, switching between PMA and in-plane magnetisation.

[1] R. Mishra et al, Phys. Rev. Lett. 118, 167201 (2017) [2] K-J Kim et al, Nature Mater. 16, 1187 (2017) [3] J. Finley and L. Liu, Phys. Rev. Appl. 6, 054001 (2016) [4] N. Roschewsky et al, Phys. Rev. B 96, 064406 (2017) [5] R.C. Taylor and A. Gangulee J. Appl. Phys. 47, 10, 4666 (1976) [6] A.G. Dirks and H.J. Leamy IEEE Trans. Magn. 14, 5, 835 (1978) [7] F. Hellman and E.M. Gyorgy Phys. Rev. Letts. 68, 1391 (1992) [8] N. Bergeard et al, Phys. Rev B 96, 064418 (2017)

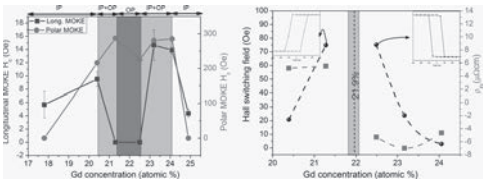


Figure 1: (a) In-plane and out-of-plane switching fields as a function of Gd concentration and (b) Anomalous Hall effect magnitude and switching field as a function of Gd concentration in GdCoFeB alloy.

11:18

CG-13. Mapping of Magnetic Metastable States in Synthetic Antiferro- and Ferrimagnets with Perpendicular Magnetic Anisotropy.
R. Salikhov[1], F. Samad[1,2], L. Koch[2], B. Böhm[2] and O. Hellwig[1,2] *1. Institute of Ion Beam Physics and Materials Research, Helmholtz-Zentrum Dresden-Rossendorf, Dresden, Germany; 2. Physical faculty, Chemnitz University of Technology, Chemnitz, Germany*

Magnetic multilayers (MLs) with perpendicular magnetic anisotropy (PMA), such as Co/Pt or Co/Pd, are the host materials for a variety of metastable magnetic configurations, e.g. aligned or labyrinth stripe domains, bubble domains and their mixtures. The magnetic morphology at remanence mostly depends on the specific demagnetization routine using an external magnetic field [1], whereas the characteristic size of the magnetic objects (domain period or bubble radius) is mostly determined by the design parameters of the magnetic MLs (e.g. the thickness of Co layer, periodicity and the number of repeats X) [1,2]. Interleaving the Co/Pt blocks by Ru or Ir layers, which promote antiferromagnetic (AF) interlayer coupling between PMA ML blocks, results in a class of artificial magnetic structures, known as synthetic antiferromagnets (SAFs) with PMA. The AF interlayer exchange energy alters the typical energy balance, thus modifying the morphology and characteristic size of magnetic domain states in PMA SAFs [1]. Stabilisation of magnetic bubble domain states in SAFs is of particular practical interest [3], whereas other new magnetic configurations are of interest for fundamental research. Here we present the mapping of magnetic states in SAFs for different demagnetization protocols and ML parameters by means of monitoring the remanent magnetization M_R during the AC or DC demagnetization process itself and performing magnetic force microscopy (MFM) imaging at the intermediate states of interest (Fig. 1). The aligned stripe domain state is characterised by almost zero M_R, whereas bubble domains [4] and mixed states (Fig. 1) manifest themselves by an enhanced M_R. The magnetic states for SAFs with tuneable parameters such as Co thickness and repetition number X will be presented. We will also discuss the magnetic behaviour in synthetic ferrimagnets, where the two ML block sub-lattices have different magnetic moments.

[1] O. Hellwig, A. Berger, J. B. Kortright, JMMM, Vol. 319, p.13-55 (2007) [2] I. Lemesh, F. Büttner, G. S. D. Beach, Phys. Rev. B, Vol. 95, p.174423 (2017) [3] K. Chesnel, A. S. Westover, C. Richards, Phys. Rev. B, Vol. 98, p.224404 (2018) [4] A. Hubert, R. Schäfer, Magnetic Domains, Springer Berlin (2009)

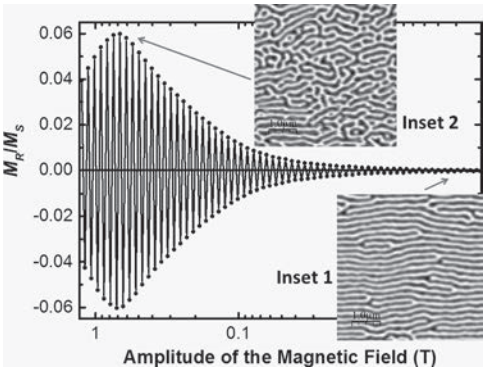


Fig. 1 M_R normalised to saturation magnetization M_S for different field amplitudes applied during the AC demagnetization process for the $\{[Co/Pt]_8/Co]/Ru\}_{18}$ PMA SAFs. The inset 1 shows an MFM image of aligned stripe domains. The inset 2 presents the mixed labyrinth and bubble domain states with largest M_R.

Session CH
INTEGRATED INDUCTORS, TRANSFORMERS AND POWER ELECTRONICS

Pilar Marin, Chair
Universidad Complutense de Madrid, Madrid, Spain

INVITED PAPER

8:30

CH-01. Electro-infiltrated Nickel/Iron-oxide and Permalloy/Iron-oxide Nanocomposite Films for On-chip Power Converters. *C.S. Smith*[1], S. Savliwala[2], S.C. Mills[3], J. Andrew[3], C. Rinaldi[2,4] and D.P. Arnold[1]
1. Electrical and Computer Engineering, University of Florida, Gainesville, FL, United States; 2. Chemical Engineering, University of Florida, Gainesville, FL, United States; 3. Materials Science and Engineering, University of Florida, Gainesville, FL, United States; 4. J. Crayton Pruitt Family Department of Biomedical Engineering, University of Florida, Gainesville, FL, United States

On-chip power inductors and transformers require ferromagnetic core materials that offer large frequency bandwidth, low loss, and relatively high permeability. Where traditional core materials typically lack one or more of these parameters, magnetic nanocomposites have garnered interest for their hybrid magnetic properties and potential to concurrently meet all device specifications [1]. In this work, the fabrication and characterization of two soft magnetic nanocomposite films are described: ~4-μm-thick nickel/iron-oxide, and ~2-μm-thick permalloy/iron-oxide. These composites are made using electro-infiltration, where a magnetic nanoparticle phase is deposited into a mold, and then a magnetic metal matrix phase is electroplated through the voids between these particles [2]. Testing shows that both composites provide a high permeability attributed to the metal matrix phase, but also an increased bandwidth and modestly low losses attributed to the iron-oxide nanoparticle inclusion phase. At 10 MHz, the nickel/iron-oxide nanocomposite exhibits a relative permeability of ~23, with a loss tangent of ~0.1, and the permalloy/iron-oxide nanocomposite exhibits a relative permeability of ~136, with a loss tangent of ~0.15 (Fig. 1). These materials are also explored structurally through scanning/transmission electron microscopy and energy dispersive x-ray spectroscopy, and results show that the ~31 nm diameter iron-oxide nanoparticles are dispersed throughout both composites. A dense, void-free interface between the nanoparticle phase and metal matrix phase is also observed, suggesting complete infiltration of the voids between particles (Fig. 2).

[1] C. Sullivan, D Harburg, J Qiu, IEEE Trans. Power Electron., Vol. 28, p. 4342–4353 (2016) [2] X Wen, J Starr, J Andrew, J. Micromechanics Microengineering, Vol. 24, p. 1-5 (2014)

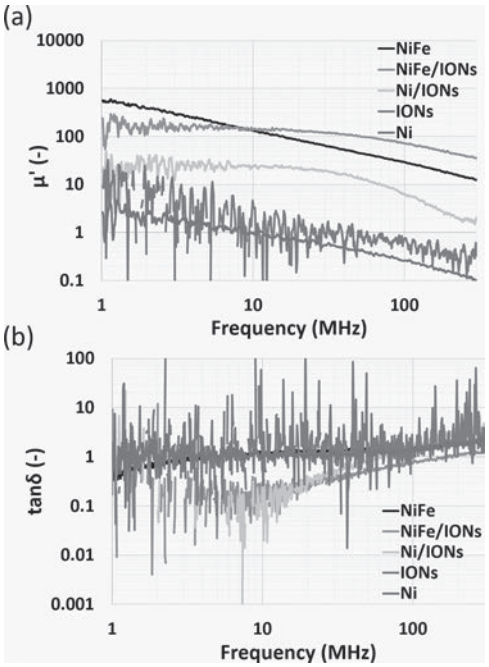


Fig 1. (a) Real part of the permeability and (b) loss tangent (μ"/μ') of composites and their constituent materials. Note that the composites maintain relatively high permeabilities and low loss tangents up to 10 MHz, providing a larger frequency bandwidth than their constituent materials.

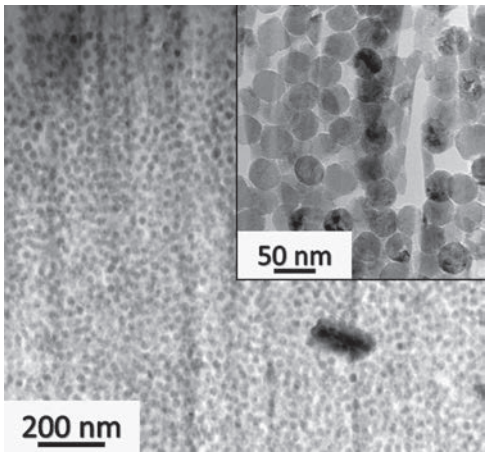


Fig 2. S/TEM image of Ni/IONs composite layer (inset: zoom-in of composite layer).

CONTRIBUTED PAPERS

9:06

CH-02. Spray-coated magnetic planar inductor for compact IoT sensor node. T. Hara[1] and *M. Yamaguchi*[2,3] *1. Design center, RICOH Electronic Devices Co., Ltd., Ikeda, Japan; 2. Department of Electrical Engineering, Tohoku University, Sendai, Japan; 3. New Industry Creation Hatchery Center, Tohoku University, Sendai, Japan*

A 'sensor node' typically consists of sensor(s), microprocessor, transceiver and battery power supply [1]. Since a compact IoT wireless sensor node needs a small and high efficiency power supply, this paper reports a magnetic powder composite thin film inductor. The composite is spray-coated at room temperature that offers quick, low temperature and high step coverage microfabrication technology for better mass productivity for integrated DC/DC converter [2], [3]. Ni-Cu-Zn spinel ferrite particles (mean diameter = 0.61 μm, initial permeability = 544 @ 1MHz) and epoxy precursor were mixed and spray-coated on a Si-substrate to the thickness of 62.6 μm. The fraction of ferrite particles was 19.5 wt%. SEM image revealed that the ferrite particles were uniformly distributed and did not sedimented in epoxy precursor. RF measurement by the shielded-loop type permeameter [4] clarified that the real part of relative permeability was 1.32 at low frequency, and the FMR frequency was 3.0 GHz. A 3 x 3 mm^2 planer air-core inductor was firstly made on a Si substrate. The coil was made of 1 μm-thick Al, line/space was 56/9 μm, and had 10 turns. Then, using a spray coater, the diluted magnetic powder composite with solvent was sprayed on to the air-core to the thickness of 62.8 μm without insulator in between. The composite covered entire coil surface well, including the coil height steps, as shown in Fig. 1. The thickness of spray-coat is controllable in a wide range from 0.1 μm to several tens μm. Fig. 2 shows the impedance $R_s + j\omega L_s$ of the inductor measured by an impedance analyzer. The inductance L_s was increased whereas the R_s was constant as frequency increased up to 20 MHz. Magnetic powder composite enhanced the Ls from 157 nH to 205 nH (30%) up to 5 MHz. This enhancement is achieved by low permeability but thick magnetic powder composite film processed by the proposed spray-coating process. The permeability and corresponding inductance can be increased by further process development to increase the volume fraction of ferrite. Collaboration with Junichi Konishi (RICOH Co., Ltd.) is highly appreciated.

[1] D. Galer, U. Kumar, 'eMaintenance,' Chapter 1, Elsevier Inc. (2017). [2] A. W. Lotfi, et al, "Integrated, High-Frequency DC-DC Converter Technologies Leading to Monolithic Power Conversion," CIPS 2012, Paper 07.5 (2012). [3] Y. Kondo et al., "Embedded planar power inductor technology for package-level DC power grid," ICEP-IAAC., pp. 814-817 (2015) [4] M. Yamaguchi, Y. Miyazawa, et al., "A New 1MHz-9GHz Thin-Film Permeameter Using a Side-Open TEM Cell and a Planar Shielded-Loop Coil,", Trans. Magnetic Society of Japan, 3, pp. 137-140 (2003).

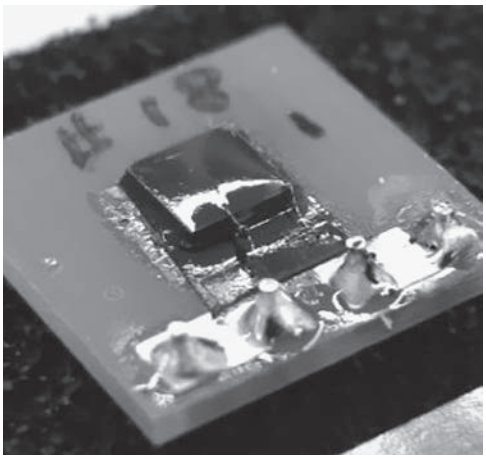


Fig. 1 Fabricated spray-coated magnetic planar inductor

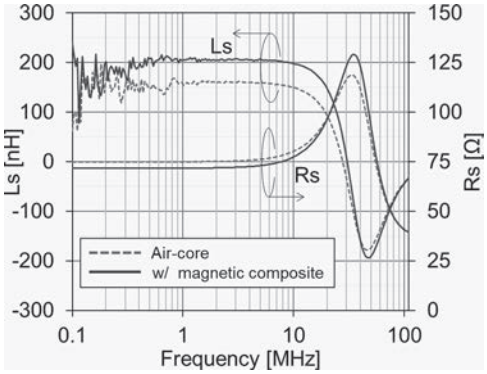


Fig. 2 Measuerd impedance of spray-coated magnetic planar inductor

9:18

CH-03. Microtransformer on Silicon with CoFeB Magnetic Core for High-Frequency Signal Applications. *D. Dinulovic*[1], M. Shousha[1,2] and M. Haug[1] *1. R&D, Würth Elektronik eiSos GmbH & Co. KG, Garching, Germany; 2. Electrical Power & Machines, Cairo University, Giza, Egypt*

One of the important development challenges for monolithic solutions for Internet of Things (IoT), wireless communication, and many portable devices is the integration of on-chip inductors and transformers with magnetic materials on silicon [1-3]. The most recent works in this technical field show not only big improvement in integration technology and magnetic material research but also the development of new micro inductors and microtransformers and their implementation in many electrical applications [4-8]. This paper presents the development of a microtransformer with a bar magnetic core fabricated on silicon substrate using thin-film technology. The microtransformer device can be applied for higher frequencies up to 20 MHz. The microtransformer features a bar magnetic core and primary and secondary windings with a minimum distance between primary and secondary side of 30 μm. Both windings are identical with 12 turns each. The dimension of a single turn is 620 μm x 40 μm x 1 μm (L x W x T) with a 10 μm distance between turns. The winding material is copper fabricated using physical vapor deposition (PVD) process. As magnetic material for microtransformer core, a CoFeB alloy is used, which is also fabricated using PVD process. The magnetic core consists of two layers with dimensions of 1400 μm x 500 μm with a thickness of 0.4 μm and oxide gap in-between of 0.8 μm. The insulation material is a combination of SiO_2 and Si_3N_4. The microtransformer device is remarkably small and the chip size is only 1.6 mm x 0.8 mm. The inductance of the device is about 40 nH. The breakdown voltage is about 1500 V. The thickness of deposited copper material is only 1 μm, therefore, the microtransformer device shows an electrical resistance of about 7 Ω, hence this device is suitable for using in signal applications. Figure 1 shows a fabricated microtransformer. In the full paper, the design, fabrication and evaluation will be presented.

[1] D. S. Gardner, G. Schrom, F. Paillet, B. Jamieson, T. Karnik and S. Borkar, IEEE Transactions on Magnetics, vol. 45, no. 10, pp. 4760-4766, Oct. 2009. [2] P. R. Morrow, C. Park, H. W. Koertzen and J. T. DiBene, IEEE Transactions on Magnetics, vol. 47, no. 6, pp. 1678-1686, June 2011. [3] D. V. Harburg, X. Yu, F. Herrault, C. G. Levey, M. G. Allen and C. R. Sullivan, 7th International Conference on Integrated Power Electronics Systems (CIPS), Nuremberg, 2012, pp. 1-6. [4] H. Wu, M. Lekas, R. Davies, K. L. Shepard and N. Sturcken, IEEE Transactions on Magnetics, vol. 52, no. 7, pp. 1-4, June 2016, Art. No. 8401204. [5] D. Dinulovic, M. Shousha, M. Haug, S. Beringer and M. C. Wurz, IEEE Transactions on Magnetics, vol. 53, no. 11, pp. 1-7, Nov. 2017, Art no. 4700107. [6] H. T. Le et al, IEEE Transactions on Power Electronics, vol. 34, no. 1, pp. 74-85, Jan. 2019. [7] D. V. Harburg et al., IEEE Journal of Emerging and Selected Topics in Power Electronics, vol. 6, no. 3, pp. 1280-1294, Sept. 2018 [8] Z. Yue et al., 2019 IEEE International Solid- State Circuits Conference - (ISSCC), San Francisco, CA, USA, 2019, pp. 244-246.

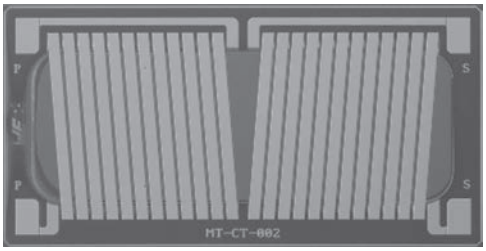


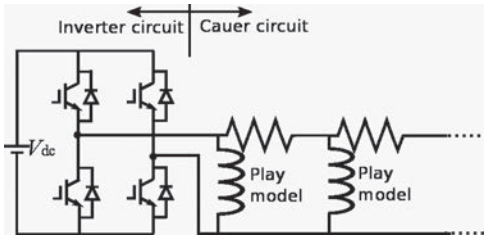
Fig.1: Completed microtransformer

9:30

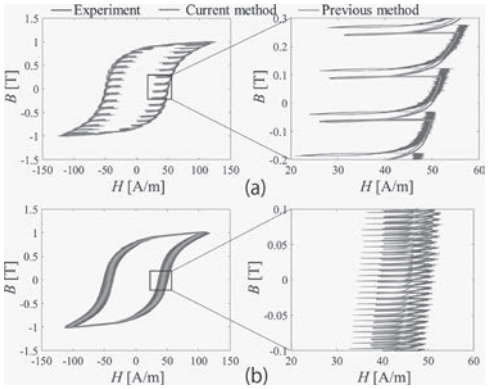
CH-04. Magnetic Hysteresis Phenomena under PWM Inverter Excitation by using Coupled Analysis between Electricity and Magnetism in Circuit Simulator. *A. Yao*[1] and T. Hatakeyama[1]
1. Department of Electrical and Computer Engineering, Toyama Prefectural University, Imizu, Japan

Pulse width modulation (PWM) excitation is often used for control in motor drive system. Many studies have shown that the high frequency components caused by PWM waveforms induce complex dynamic hysteretic magnetic loops in soft magnetic materials (used as a motor core)[1-5]. To realize the high-efficiency motor system, it is necessary to numerically represent the dynamic hysteretic loops of soft magnetic materials. Previous studies have shown that the play model[6] with the Cauer circuit[7-11] (PMCC) can express hysteretic loops. Recently, some researchers have realized a weak coupling analysis of magnetic field and electric circuit by using PMCC[8,11]. However, there has been no report on a strong coupling analysis to express magnetic hysteretic loops by using PMCC. In this study, we develop the strong coupling analysis in a circuit simulator. Figure 1 shows schematic of the strong coupling analysis with the inverter circuit and the hysteresis model. In our study, we apply PMCC to the circuit simulator (PSIM, Powersim) to realize the numerical calculation of magnetic hysteresis properties under PWM inverter excitation by using the strong coupling analysis. See Refs. 10, 11 for details of numerical methods based on PMCC. Figure 2 plots the magnetic hysteresis loops of magnetic materials under PWM inverter excitation with a carrier frequency of 1 and 20 kHz. The experimental results are consistent with the numerical loops calculated by the strong coupling analysis (current method). We realize accurate representations for hysteresis loops especially in high carrier frequency region compared with results of the previous method[11] (weak coupling analysis). The evaluation errors of iron losses calculated by strong and weak coupling analysis are about 3.5 % and 10 % at 20 kHz, respectively. These results open the way to further research in low loss motor system based on coupled studies of magnetic and semiconductor properties.

[1] M. Kawabe, T. Nomiyama, A. Shiozaki, H. Kaihara, N. Takahashi, and M. Nakano, Behavior of minor loop and iron loss under constant voltage type PWM inverter excitation, IEEE Transactions on Magnetics, 48 (11), 3458–3461 (2012). [2] A. Yao, K. Tsukada, S. Odawara, K. Fujisaki, Y. Shindo, N. Yoshikawa, and T. Yoshitake, PWM inverter-excited iron loss characteristics of a reactor core, AIP Advances, 7 (5), 056618 (2017). [3] A. Yao and K. Fujisaki, Iron loss characteristics under pwm inverter excitation at high ambient temperatures, The 11th International Symposium on Linear Drives for Industry Applications (LDIA2017), 1–3 (2017). [4] A. Yao, T. Sugimoto, S. Odawara, and K. Fujisaki, Core losses of a permanent magnet synchronous motor with an amorphous stator core under inverter and sinusoidal excitations, AIP Advances, 8 (5), 056804 (2018). [5] A. Yao, T. Sugimoto, S. Odawara, and K. Fujisaki, Core loss properties of a motor with nanocrystalline rotor and stator cores under inverter excitation, IEEE Transactions on Magnetics, 54 (11), 1–5 (2018). [6] T. Matsuo and M. Shimasaki, An identification method of play model with input-dependent shape function, IEEE Transactions on Magnetics, 41 (10), 3112–3114 (2005). [7] Y. Shindo and O. Noro, Simple circuit simulation models for eddy current in magnetic sheets and wires, IEEJ Transactions on Fundamentals and Materials, 134 (4), 173–181 (2014). [8] S. Odawara, K. Fujisaki, T. Matsuo, and Y. Shindo, Evaluation of magnetic properties considering semiconductor properties by using numerical technique coupling inverter circuit analysis to magnetic analysis (in japanese), IEEJ Transactions on Industry Applications, 135 (12), 1191–1198 (2014). [9] T. Miyazaki, T. Mifune, T. Matsuo, Y. Shindo, Y. Takahashi, and K. Fujiwara, Equivalent circuit modeling of dynamic hysteretic property of silicon steel under pulse width modulation excitation, Journal of Applied Physics, 117 (17), 17D110 (2015). [10] A. Yao, S. Odawara, and K. Fujisaki, Iron loss and hysteretic properties under pwm inverter excitation at high ambient temperatures, IEEJ Journal of Industry Applications, 7 (4), 298–304 (2018). [11] S. Odawara and K. Fujisaki, Influence rate of semiconductor on-voltage in inverter circuit on iron loss inside a non-oriented electrical steel sheet, IEEE Transactions on Magnetics, 54 (5), 1–8 (2018).



Schematic of strong coupling analysis with inverter circuit and PMCC in circuit simulator.



Hysteresis loops under PWM inverter excitation. (a) Carrier frequency of 1 kHz, (b) 20 kHz.

9:42

CH-05. Core loss calculation for power electronics converter excitation from a sinusoidal excited core loss data. *H. Matsumori*[2], T. Shimizu[1], T. Kosaka[2] and N. Matsui[2] *1. Tokyo Metropolitan University, Tokyo, Japan; 2. Nagoya Institute of Technology, Aichi, Japan*

Advances in power semiconductor devices such as SiC, GaN, etc. have significantly enhanced the power-density of power electronic converters. By increasing the switching frequency, the volume of magnetic components, i.e. inductors and transformers can be reduced [1], [2]. However, the reduced surface area of the magnetic component leads to increased thermal resistance and temperature stresses. Therefore, the core loss analysis of magnetic cores is important for high-power-density converter design. The core loss data provided by core manufacturers is usually based on sinusoidal excitations, whereas in most cases the magnetic cores in power converters are under square voltage excitations and the DC bias condition. One solution is to approximate the sinusoidal wave to a square wave [3-7], yet its accuracy is affected by the DC bias characteristic of the core loss. Another solution is

using square voltage and the DC bias excited core loss data [8-12]. However, the square waveforms are described by the amplitude, the frequency, and the duty ratio, which leads to a wide range of test conditions [13]. The authors thus propose a core loss calculation method for power electronics converter excitation from a sinusoidal excited core loss data. This method is based on Brockmeyer's theory shown in [5] and adapts to calculate core loss under DC bias excitation conditions. Furthermore, the core loss test conditions are reduced since the required core loss data used in this method is only to add DC bias characteristics to the sinusoidal excitation core loss data provided by the core manufacturers. In order to validate the proposed method, first, the core losses under sinusoidal and square voltage excitation are measured by BH analyzer with DC bias excitation unit, as shown in Fig.1. And then, the measured values under square voltage excitation and the calculated values from sinusoidal excited core loss data are compared. The evaluation result of the Sendust core (Toho Zinc.corp: HK-08SS) is shown in Fig. 2. The core losses on DC bias Ho= 4000 A/m is calculated within 2.2% error. The detail of the proposed method and the others result are explained in the final paper.

[1] J. Itoh, T. Araki, and K. Orikawa, "Experimental Verification of EMC Filter Used for PWM Inverter with Wide Band-Gap Devices", IEEJ Journal of Industry Applications, Vol.4, No.3, pp.212-219, 2015. [2] D. Reusch, J. Glaser, "Improving DC-DC Converter Performance with GaN Transistors", in Proc. of IEEE Energy Conversion Congress and Exposition (ECCE) 2015. [3] K. Venkatachalam, C. R. Sullivan, T. Abdallah, and H. Tacca, "Accurate prediction of ferrite core loss with nonsinusoidal waveforms using only Steinmetz parameters," Proc. IEEE Workshop Comput. Power Electron., pp. 36–41, 2002. [4] M, Mingkai, and Fred C. Lee, "A new core loss model for rectangular AC voltages," in proc. of IEEE Energy Conversion Congress and Exposition (ECCE). pp. 5214-5220, 2014. [5] M. Albach, T. Durbaum, and A. Brockmeyer, "Calculating core losses in transformers for arbitrary magnetizing currents a comparison of different approaches." in 27th Annual IEEE Power Electronics Specialists Conference, vol. 2, pp. 1463–8, 1996. [6] J. Reinert, A. Brockmeyer, and R. De Doncker, "Calculation of losses in ferro- and ferrimagnetic materials based on the modified Steinmetz equation," in Proc. of 34th Annual Meeting of the IEEE Industry Applications Society, vol.3, pp. 2087–92, 1999. [7] J. Li, T. Abdallah, and C. R. Sullivan, "Improved calculation of core loss with nonsinusoidal waveforms," in Proc. of IEEE Industry Applications Society Annual Meeting, pp. 2203-2210, 2001. [8] H. Matsumori, T. Shimizu, K. Takano, H. Ishii, "Evaluation of Iron Loss of AC Filter Inductor used in Three-Phase PWM Inverters Based on an Iron Loss Analyzer (ILA)," IEEE Trans. on Power Electronics, vol.31, pp.3080-3095, 2016. [9] Yoshihiro Miwa, Toshihisa Shimizu, Koushi Takano, Hitoshi Ishii, "Calculating the Iron Losses in Gapped Inductors Using the Loss-Map Method," IEEJ Journal of Industry Applications, vol.8, No.1, pp. 57-65, 2019. [10] H. Matsumori, T. Shimizu, X. Wang and F. Blaabjerg, "A practical iron loss model for filter inductors of switched power converters," IEEE Journal of Emerging and Selected Topics in Power Electronics, vol.6, pp.29-39, 2018. [11] J. Mühlethaler, J. Biela, J. W. Kolar, and A. Ecklebe, "Core losses under the DC bias condition based on steinmetz parameters," IEEE Trans. Power Electron., vol. 27, pp. 953–963, 2012. [12] C. R. Sullivan, J. H. Harris, E. Herbert, "Core Loss Predictions for General PWM Waveforms from a Simplified Set of Measured Data," in Proc. of Applied Power Electronics Conference and Exposition, pp.1048-1055, 2010.

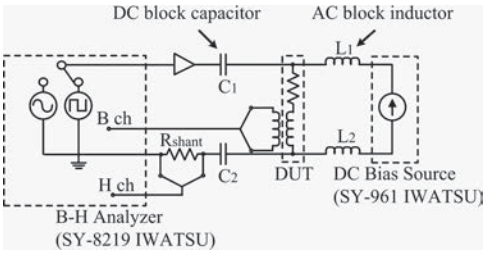


Fig.1 core loss measurement system.

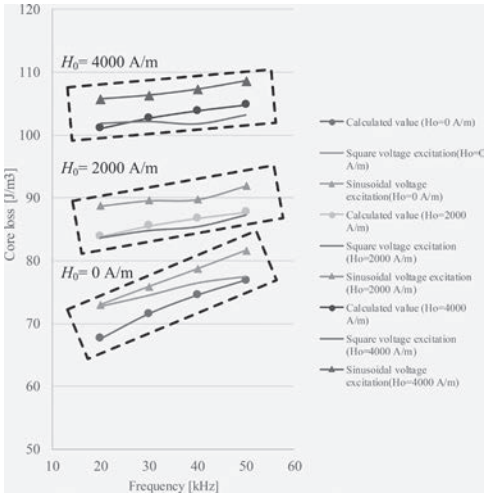


Fig.2 loss evaluation result

9:54

CH-06. Transient Potential Distribution on Transformer Winding Considering the Effect of Core Lamination Stack. *S. He*[1], D. Huang[1], X. Feng[1], Y. Wang[1], J. Deng[2] and J. Li[1] *1. Electrical Engineering, Xi'an Jiaotong University, Xi'an, China; 2. Maintenance and Test Center of EHV Power Transmission Company, China Southern Power Grid, Guangzhou, China*

The potential distribution of windings under impulse voltage is very important for the design of transformer inter-turn insulation especially for large capacity transformers such as UHVDC converter transformer. Quite a lot of equivalent circuit models for transformer winding have been proposed for the potential distribution calculation assuming that the influence of magnetic core is negligible at frequencies higher than 10kHz. However, lightning Impulse or VFTO waveforms usually contain abundant frequency components higher than 10kHz. At above situations the magnetic core plays an important role during the transient procedure. To obtain a more comprehensive model and also to provide a more accurate potential distribution of transformer winding, in this paper, the equivalent circuit representation of UHVDC converter transformer winding is given taking into consideration of comprehensive frequency characteristic of core lamination stack. Considering skin effect and saturation effect, the equivalent relative permeability of lamination stack is studied and implemented in the calculation of frequency-dependent parameters such as resistance, self- and mutual- inductances. The equivalent circuit model is realized in MATLAB and the surge propagation process in the winding, the winding potential distribution under transient overvoltage is studied carefully. The initial potential distribution and Interturn potential gradient distribution are shown in Fig.1 and Fig.2, respectively. The calculation results may provide more accurate winding potential distribution prediction for transformer inter-turn insulation design. Detailed calculation results and analysis will be shown in the full paper.

[1] Shuang H, Yuhao L, Zheng Z. The Journal of Engineering. 2019(16):2921-5 [2] Leon, F., Semlyen, A. IEEE Trans. Power Deliv.1994,9,pp.231–23 [3] Deswal D, De Leon F.IEEE Transactions on Power Delivery, 2019:1-1. [4]Preis K, Renhart W, Rabel A. IEEE Transactions on Magnetics, 2017,PP(99):1-4

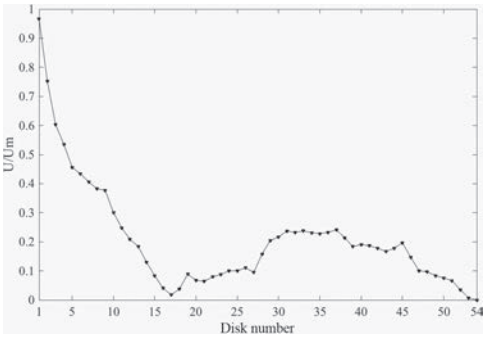


Fig.1 initial potential distribution

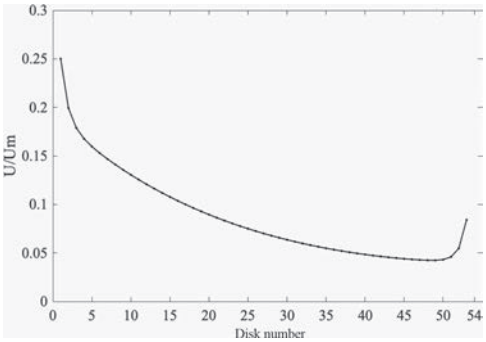


Fig.2 interturn potential gradient distribution

10:06

CH-07. Reduced Basis Finite Element Modelling of Transformers with Stranded Conductors. *I. Gürbüz*[1], A. Lehikoinen[2], U. Aydin[1], P. Rasilo[3], E. Takala[4] and A. Belahcen[1] *1. Department of Electrical Engineering and Automation, Aalto University, Espoo, Finland; 2. Smeklab Oy, Espoo, Finland; 3. Faculty of Information Technology and Communication Sciences, Tampere University, Tampere, Finland; 4. Trafotek Oy, Turku, Finland*

The windings of transformers and electrical machines sometimes consist of several stranded parallel conductors to reduce AC-losses. Although using stranded parallel conductors instead of large conductors reduces the skin effect losses, circulating currents are inevitable because of the uneven distribution of the current among the strands [1]. Several authors with variety of different methods have addressed the issue of modelling individual strands, that is computationally heavy due to large number of unknowns. However, very few of the presented methods are able to model parallel strands [2]. In this paper, a reduced basis approach is proposed to analyze the proximity effect and circulating currents in transformers with stranded parallel conductors while reducing the needed computation time. This method is heavily inspired by the reduced basis approach earlier proposed for rotating electrical machines with multi conductor windings [2]. In the reduced basis approach, the model geometry is divided into non-winding and winding domains. Instead of solving the AVI formulation directly, the vector potential of the winding domains (a_w) and voltages of the windings (u_i) are expressed with a matrix system in terms of the vector potential of the non-winding domain (a_n), its boundary (a_b) and the currents flowing through individual conductors (i_i). Next, this matrix system is inserted into the other rows of the AVI formulation to eliminate a_w and u_i in order to obtain the reduced matrix system, from which a_n, a_b, and u_i are solved first. Finally, a_w and u_i are solved from the initially found matrix system by using the solutions of previous computations. The proposed approach is applicable for both time-harmonic and time-stepping analysis. In case of a non-conforming mesh between the non-winding and winding domains, the method is achieved by using an interpolation (or projection) matrix. Also, having identical winding domains makes the computation efficiency of the approach better as the same matrix system expressions can be used for all identical domains. The method enables to observe eddy-current and circulating current losses in the windings as well as core losses.

[1] C.R. Sullivan, IEEE Transactions on Power Electronics, vol. 14, no. 2, pp. 283–291, 1999 [2] A. Lehikoinen, A. Arkkio, and A. Belahcen, 2016 XXII International Conference on Electrical Machines (ICEM), pp. 1-7, 2016

10:18

CH-08. Modelling and Measurement of Magnetic Properties of Anode Saturable Reactor Under Impulse Excitation. *C. Zhang*[1,2], J. Wang[2], Y. Li[2] and Q. Yang[2] *1. Ohio State University, Columbus, OH, United States; 2. Hebei University of Technology, Tianjin, China*

In high-voltage DC transmission system, the anode saturable reactor is crucial to protect the switching device from over-current fault in the converter valve. Since the core loss of saturable reactor under impulse excitation produce significant heat, which may cause large temperature rise and reduce the lifespan of insulation. The classical Steinmetz model based on the empirical and loss separation technique is only applicable to the perfect waveform at 50/60 frequency[1]. S. Barg developed a new empirical method to estimate magnetic core loss under non-sinusoidal magnetic induction[2]. When using the T-Ω method, the effects of lamination core loss are considered by introducing an additional field component in lamination [3]. It would cost too much computation burden to refine mesh of laminated steel layer by layer considering impulse eddy current effects. In order to reduce the complexity of numerical algorithm, the multi-scale numerical method is introduced into the electromagnetic eddy current[4]. The saturable reactor made of ultra-thin silicon steel is used in the 12-pulse rectifier converter valve, which can limit the changing rate of current in the circuit. Firstly, the magnetic properties of the ultra-thin silicon steel is measured. Based on magnetic properties data, an improved magnetic property simulation model is proposed to estimate core loss under the switch-on and switch-off working condition. The stray capacitor and reactor form a high frequency oscillation as shown in Fig. 1, thus the switching process would cause significant current harmonic and extra core loss. One single core with air-gap is simulated by transient electromagnetic simulation shown in Fig. 2, when the current of the reactor is the same as in the real operating conditions. Eddy current and hysteresis loss are much higher than excess losses. The additional eddy losses in the lamination are calculated by 3D transient magnetic field considering the fringing magnetic flux flowing into the silicon steel lamination plane. Finally, the temperature-rise test is carried out by infrared thermometer in order to verify the proposed core loss model.

[1] E. Agheb and H. K. Hoidalen, “Modification of empirical core loss calculation methods including flux distribution,” *IET Electric Power Applications*, vol. 7, no. 5, pp. 381-390, May. 2013. [2] S. Barg, K. Ammous, H. Mejbri and A. Ammous, “An improved empirical formulation for magnetic core losses estimation under nonsinusoidal induction,” *IEEE Transactions on Power Electronics*, vol. 32, no. 3, pp. 2146-2154, Mar. 2017 [3] D. Lin, P. Zhou, Q. M. Chen, N. Lambert and Z. J. Cendes, “The effects of steel lamination core losses on 3D transient magnetic fields,” *IEEE Transactions on Magnetics*, vol. 46, no. 8, pp. 3539-3542, Aug. 2010. [4] I. Niyonzima, R. V. Sabariego, P. Dular, F. Henrotte and C. Geuzaine, “Computational homogenization for laminated ferromagnetic cores in magnetodynamics,” *IEEE Transactions on Magnetics*, vol. 49, no. 5, pp. 2049-2052, May. 2013.

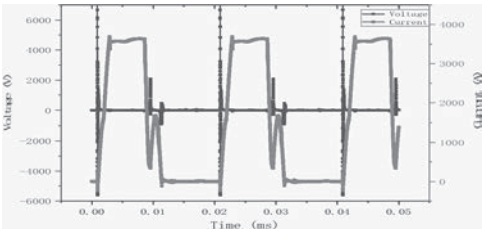


Fig 1. Voltage and current waveform of the saturated reactor.

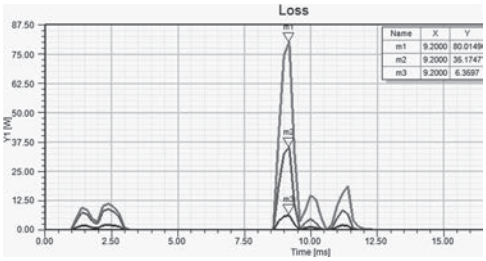


Fig 2. Core loss of reactor

10:30

CH-09. Influence of magnetization fixture winding on magnet flux profile and performance of isotropic bonded NdFeB motor.

R.C. Angara[1], N.E. Onal[1], K.W. Hsu[1], P. Villar[1] and *N.K. Sheth*[1]
1. Research and Development, Neo Performance Materials (S) Pte Ltd, Singapore

Isotropic bonded NdFeB magnets are used in automotive and home appliance motors due to their superior magnetic properties which helps in achieving increased motor efficiency and power density. The magnetizing fixture winding configuration is critical in achieving the desired performance[1,2] . In this paper the effect of fixture winding configurations on resultant magnet flux profile and motor performance is presented for a 4-pole automotive accessory motor. Magnetizing fixtures are designed using to achieve 3T magnetizing field on the magnet. It is observed that when the number of turns is kept the same, but the conductor diameter reduced by 29%, the magnetization profile becomes more radial and resulting in 20% higher peak to peak cogging torque in motor. Using two-dimensional (2D) finite element analysis (FEA), the magnetization fixtures are designed for six different conductor configurations for the winding. Figure 1 shows four of the conductor configurations evaluated. For each configuration a 2D FEA is performed to arrive at magnetized magnet profile and motor performance. Table I summarizes the flux integral of magnetized magnet profile and corresponding motor perfromence. From this table it is observed that for a 4-pole magnet, the '1-column' conductor arrangement where-in the conductors are arranged along the radial direction resulted in radial flux profile and highest flux integral per pole. On the other side the flux integral per pole is minimum and the flux profile becomes more sinusoidal when '1 row' arrangement in which the conductors are arranged along a concentric arc from fixture core surface is used. The higher flux per pole with radial magnet flux profile, results in higher back-emf and peak to peak cogging torque for '1-column' configuration. The lowest flux integral per pole and the Halbach magnet flux results in lowest back-emf and cogging torque. The designed magnetization fixtures were built, magnets are magnetized, and the motor performance is evaluated. The experimental results are in good agreement with the simulation results.

1. Y. N. Zhilichev, "Precise Multipole Magnetization of Disc Magnet for Sensor Application", IEEE Trans on Magnetics, Vol. 39, Issue 5, pp 3301-3303, Sep 2003. 2. Seok-Myeong Jang, Han-Wook Cho, Sung-Ho Lee, Hyun-Sup Yang, and Yeon-Ho Jeong, "The Influence of Magnetization Pattern on the Rotor Losses of Permanent Magnet High-Speed Machines", IEEE Trans on Magnetics, Vol. 40, Issue 4, pp 2062-2064, Jul 2004.

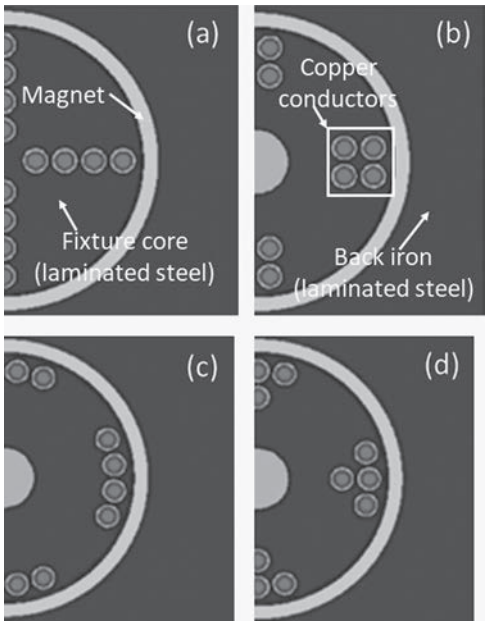


Fig.1. Various conductor arrangements (a) 1 column (b) 2 column (c) 1 row (d) Delta

Conductor configuration in the fixture slot	Flux Integral per pole (T-°mech)	Motor back-emf integral (V-*mech)	Peak-to-peak cogging torque (mN-m)
1 column	27.32	330	48
2 column	25.12	323	11
1 row	21.91	293	10
Delta	24.28	311	10

Table I Effect of conductor configuration on magnet flux and motor performance

10:42

CH-10. Design of Directing Permanent Magnet of U-Shape Interior Ferrite Permanent Magnet Synchronous Motor for Electric Vehicles.

H. Won[1], Y. Hong[1], M. Choi[1] and W. Lee[1,2] *1. Department of Electrical and Computer Engineering and Center for Advanced Vehicle Technologies, The University of Alabama, Tuscaloosa, AL, United States; 2. RF Product Development Group, Samsung Electro-Mechanics, Suwon-si, The Republic of Korea*

Recently, U-shaped interior permanent magnet synchronous motor (UIPMSM) received much attention due to the possibility of employing rare-earth less ferrite permanent magnet (PM) [1-2]. To further improve the motor performance, the design of UIPMSM with barrier shaping and rotor overhanging method was proposed [1-2]. However, these methods either require high precision tools or reduce torque density. In this paper, we propose a new hybrid directing PM (D-PM) method that enhances the ferrite motor performance without requiring expensive tools and increasing volume. Two types of UIPMSM are rectangular- (R-) and trapezoidal (T-) UIPMSM, having the same dimensions and specification of IPMSM used in Toyota Prius 2010 in Fig. 1 [3]. These UIPMSMs were used to validate our D-PM method and simulated for motor performance using ANSYS Maxwell 2D. While NMF-12F ferrite having B_r of 0.46 T and H_{ci} of 4.13 kOe are used for pillar PM [4], three types of PM having 1) B_r of 0.4 T and H_{ci} of 5.02 kOe, 2) B_r of 0.4 T and H_{ci} of 10 kOe, and 3) B_r of 1.2 T and H_{ci} of 10 kOe were used for D-PM. Fig. 2 shows the resulting efficiency map of R- and T- UIPMSM. As the H_{ci} of D-PM increases from 4.13 to 10 kOe, the maximum torque (T_{max}) of both motors increased from 152.3 to 161 Nm for R-UIPMSM and 159.4 to 167.6 Nm for T-UIPMSM. The size of each efficiency region increased by 1-3% for both motors, while maintaining maximum speed (ω_{max}) of 14,000 revolutions per minute (rpm). By increasing the B_r of D-PM from 0.4 to 1.2

T, the T_{max} and ω_{max} increased from 161 to 166.5 Nm and 14,000 to 16,000 rpm, respectively, for R-UIPMSM, and 167.6 to 171.5 Nm and 14,000 to 16,000 rpm, respectively, for T-UIPMSM. Further, as shown in Fig. 2 (b) and (d), the efficiency region shifted its region to higher torque and lower speed region. As a result, we found that as increasing B_r and H_{ci} of D-PM, T_{max} and ω_{max} of UIPMSM increase without modifying the main motor design. Also, adjustable efficiency regions can be achieved without requiring high precision dies and large motor volume. This work was supported in part by NSF-I/UCRC for EV-STS under Grant number 1650564.

[1] W. Wu, X. Zhu, and L. Quan, 2016 IEEE Vehicle Power and Propulsion Conference, pp. 1-6 (2016) [2] W. Kim, I Jang, and C Jin, IEEE Transactions on Magnetics, vol. 51, iss. 3, pp. 8202004 (2015) [3] M. Olszewski, *FY2011 Oak Ridge National Laboratory,* pp. 1 (2011) [4] H. Won, Y. K. Hong, and W. Lee, AIP Advances, vol. 8, pp. 056811 (2018)

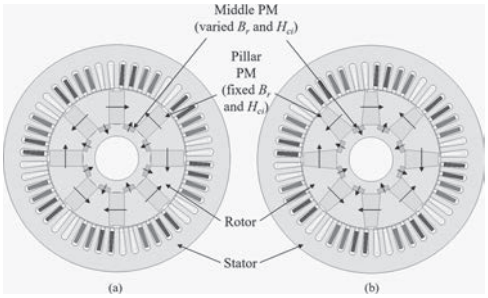


Fig. 1. Design of (a) R- and (b) T-UIPMSM

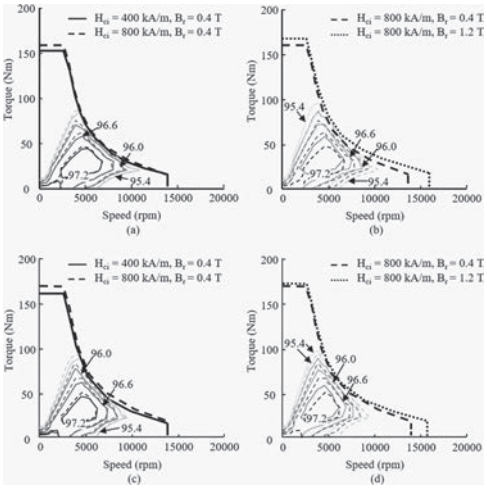


Fig. 2. Efficiency map of (a-b) R- and (c-d) T-UIPMSM

10:54

CH-11. An ironless linear permanent magnet generator for the conversion of sea waves energy. *M. Trapanese*[1] and V. Frazitta[1]
1. Dipartimento di Ingegneria, Palermo University, Palermo, Italy

Linear permanent magnet generators are widely considered for the direct conversion of energy contained in sea waves [1-3]. Both planar and tubular structures have been proposed and all these structures present several advantages: relative high efficiency, simplicity of the structures, high sturdiness. However, as all the other linear machines they present some drawbacks: oscillations in the movement, distortion in the generated electromotive force (emf), high level of vibration in the translator. In this paper we focus our attention on the parasitic oscillations of the translator. The oscillation in the movement of the translator are caused by the presence of a high cogging force that is strongly related to the use of iron. Cogging force is generated by the fact that magnetic energy presents a deep minimum when the length of the magnetic flux lines reaches a minimumin the presence of iron. This effect negatively influences the dinamic equations of the generator and strongly reduced the conversion effciency. Thanks to a 3D FEM simulator and in order to reduce the parasitic effects, we have studied the features of a ironless PM generator in a multiphysics approach and we have studied several possible designs of a PM linear generator for the conversion of sea waves energy developing an optimization procedure. Numerical simulations showed that an optimized design can reach efficiency comparable to that of an iron based PM linear generator with a great reduction of parasitic effects. A structure of the stator has been chosen and built. Finally, in order to verify, our optimization approach several structures of rotor have been built and tested. This has led us to validate our approach to the optimization of cogging torque.

[1] Leijon, M.; Bernhoff, H.; Agren, O.; Isberg, J.; Sundberg, J.; Berg, M.; Karlsson, K.E.; Wolfbrandt, A. “Multiphysics simulation of wave energy to electric energy conversion by permanent magnet linear generator”, IEEE Transactions on energy conversion vol. 20, N.1, pp. 219- 224, 2005. [2] Polinder H., Gardner F. and Vrisema V., “Linear PM generator for wave energy conversion in the AWS”, in Proc. ICEM 2000, Espoo, Finland, 2000. [3]Saha C.R., O’Donnell T., Loder H., Beeby S. and Tudor J., “Optimization of an Electromagnetic Energy Harvesting Device”, IEEE Trans. On Magn, vol. 42, No. 10, October 2006, pp.3509-3511.

11:06

CH-12. Optimal Design of a 314kW-class IPMSM for Railway Vehicles Using Hydrogen Fuel Cells. *J. Lim*[1], H. Lee[1], T. Kim[2], J. Lee[1], K. Seo[1], G. Jeong[3] and C. Park[1] *1. Korea National University of Transportation, Uiwang-si, The Republic of Korea; 2. Electrical and Computer Engineering Department, University of Michigan-Dearborn, Dearborn, MI, United States; 3. Electrical Engineering, Hanyang University, Seoul, The Republic of Korea*

Conventional diesel railway vehicles have produced many air pollutants. As a result, studies on the commercialization and development of a diesel/battery hybrid railway vehicles have been conducted in Japan and other countries [1]. However, as disadvantages of the continuous use of diesel such as air pollution, carrying on fuel and low efficiency of internal combustion engine, New type hybrid battery vehicle is needed [2]. One of next-generation railway vehicle technologies is a hydrogen fuel cells vehicle that uses hydrogen as a power source and combines a rechargeable battery that can be charged using regenerative power [3]. Since the hydrogen fuel cell vehicle is equipped with a hydrogen tank and a battery, interior permanent magnet synchronous motor(IPMSM) with a higher output density than an induction motor should be used for heavy-weight components such as traction motors [4]. However, IPMSM have high no-load back electromotive force (back EMF) in high-speed of coasting running sections and are difficult to control. In particular, since it is to the limit value of the phase voltage of the hydrogen fuel cell vehicle much lower than that of the electric railway using the existing catenary, the back EMF is required to be very low (Phase back EMF voltage 866V or less, Conventional phase back EMF voltage 1617V). In order to meet the rated output with low back EMF, high current must be used, but the size of the motor is increased. However, due to the mounting the traction motor on the existing bogie, the constraint of the bogie space must be satisfied. The following table shows the back EMF, electrical and mechanical constraints of this hydrogen fuel cell vehicle. In order to design a IPMSM with high output density under such harsh electrical and mechanical constraints, this paper perform basic design such as characteristic analysis according to various motor parameters. Then, optimal design is performed. It will be also presented to the results of performance analysis of demagnetization, thermal and stiffness of an optimum designed motor in this paper.

[1] J.J. Mwambeleko, T. Kulworawanichpong, “Battery and accelerating-catenary hybrid system for light rail vehicles and trams”, *Proceedings of 2017 International Electrical Engineering Congress*, pp.1-4, 2018 [2] S. M. Lim, S. W. Sung, Y. K. Lee, “Technical Trends of Hydrogen fuel cell railway rolling stock”, *2018 Annual Meeting & Annual Conference of*

the Korean Society for Railway, pp314-317, 2018 [3] J. S. Lee, "Hydrogen Fuel-Cell/Battery Hybrid Train", *Journal of the Korean Society for Railway*, 22(1), pp.19-26, 2019 [4] G. C. Jeong, C. B. Park, S. Y. Oh, "A study on rotor shape design according to structure characteristics of IPMSM for urban railway vehicle traction", *2014 Autumn Conference & Annual Meeting of the Korean Society for Railway*, pp597-602, 2014

Design condition	Unit	Value
Rated Output	kW	314
Rated Speed	rpm	1,810.8
Maximum Speed	rpm	5,031.5
Stator Outer Diameter	mm	≤513
Stack Length	mm	≤273
Phase back EMF (at Maximum speed)	V	< 866
Torque (at Rated speed)	Nm	> 1657.5

Table 1. Constraints of a 314kw-class IPMSM

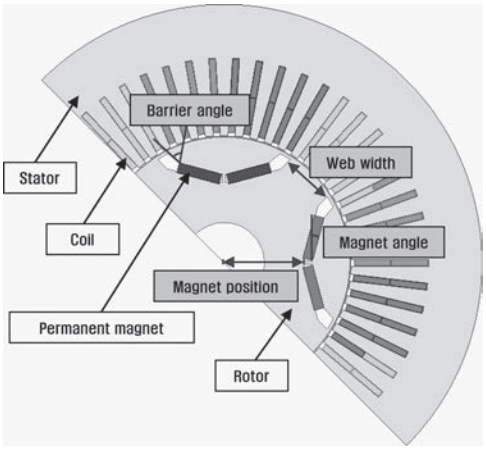


Fig. 1. Cutaway view of a 314-class IPMSM periodic model

Session CI
2:14:1 PERMANENT MAGNETS: PROCESSING AND PROPERTIES/HIGH FREQUENCY DEVICES

Arjun K Pathak, Co-Chair
Ames National Laboratory, Ames, IA, United States
Karen Livesey, Co-Chair
University of Colorado at Colorado Springs, Colorado Springs, CO, United States

CONTRIBUTED PAPERS

8:30

CI-01. Enhancing the coercivity and thermal stability of Nd-Fe-B sintered magnets by grain boundary diffusion process. *S. Kim*[1], H. Lee[1], D. Kim[2], J. Kim[1], J. Roh[3] and W. Lee[1] *1. Yonsei University, Seoul, The Republic of Korea; 2. Star Group, Daegu, The Republic of Korea; 3. Kyungpook National University, Sangju, The Republic of Korea*

High-coercivity Nd-Fe-B sintered magnets have been widely used in a variety of practical and industrial applications since their discovery in1984 [1,2], but there is still a need to be able to operate magnets for a long period of time without reducing coercivity in high-temperature environments. In a general way, the coercivity of Nd-Fe-B magnets can be improved by partially replacing Nd with Dy, Tb, or both. However, due to the high cost and scarcity of these heavy rare-earth elements, it is necessary to develop alternatives more economically [3,4]. One of such alternatives is to reduce the use of heavy rare-earth elements and minimize the loss of remanence and energy product through the utilization of the grain boundary diffusion process. [5,6] In this study, we employed consecutive heat treatment-driven Tb-H diffusion to fabricate large-size Nd-Fe-B magnets exhibiting enhanced coercivity without any decrease of B_r and $(BH)_{max}$. In detail, the coercivity of the base magnet increased by 62.7% after grain boundary diffusion process, whereas B_r and $(BH)_{max}$ concomitantly decreased by 1.66% and 1.43%, respectively. To investigate the relationship between Tb-diffused area and coercivity enhancement, we performed a microstructure analysis based on electron probe microanalysis compositional maps. We have found that core-shell structures generated in a stepwise annealing process successfully suppressed the nucleation of reverse domains at Nd-rich phase/main phase interfaces and therefore enhanced magnet coercivity without decreasing remanence and energy product (Fig.1). Furthermore, for practical applications in high-temperature environments, we should consider not only coercivity of Nd-Fe-B magnets but also thermal stability, such as flux loss, temperature coefficients (β), and squareness. For this reason, we have improved thermal stability parameters as well as coercivity through the changes in heat treatment conditions and diffusion materials. As a result, we obtained the Nd-Fe-B sintered magnet with a coercivity lower than the maximum coercivity but with much better thermal stability.

[1] M. Sagawa, S. Fujimura, N. Togawa, H. Yamamoto, Y. Matsuura, J. Appl. Phys., Vol. 55, p.2083 (1984) [2] J.J. Croat, J.F. Herbst, R.W. Lee, F.E. Pinkerton, J. Appl. Phys., Vol. 55, p.2078 (1984) [3] O. Gutfleisch, M.A. Willard, E. Bruck, C.H. Chen, S.G. Sankar, J.P. Liu, Adv. Mater., Vol. 23, p.821 (2011) [4] S. Hirosawa, Y. Matsuura, H. Yamamoto, S. Fujimura, M. Sagawa, H. Yamauchi, J. Appl. Phys., Vol. 59, p.873 (1986) [5] K.T. Park, K. Hiraga, M. Sagawa, Proc. 16th Int. Workshop Rare-earth Magnets and Their Applications, p. 257 (2000) [6] H. Nakamura, K. Hirota, M. shimao, T. Minowa, M. Honshima, IEEE Trans. Magn., Vol. 41, p.3844 (2005)

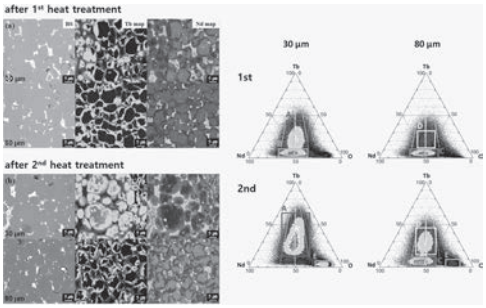


Figure 1. EPMA profiles and ternary diagrams of (a) 1st heat treatment and (b) 2nd heat treatment by depth (30, 80 μm)

8:42

CI-02. Detection of elemental magnetization reversal events in a micropatterned hot-deformed Nd-Fe-B magnet. *T. Yomogita*[1], N. Kikuchi[1], S. Okamoto[1,2], O. Kitakami[1], S. Hossein[2], T. Ohkubo[2], K. Hono[2], K. Hioki[3] and A. Hattori[4] *1. IMRAM, Tohoku University, Sendai, Japan; 2. ESICMM, NIMS, Tsukuba, Japan; 3. Daido Steel Co. Ltd., Nagoya, Japan; 4. Daido Electronics Co. Ltd., Nakatsugawa, Japan*

Although Nd-Fe-B magnets exhibit the highest maximum energy product $(BH)_{max}$ among all of the permanent magnetic materials [1], the coercivity remains as small as about 1/3 of the anisotropy field. Since the coercivity process in permanent magnet includes enormous number of magnetization reversal events, it is essentially important to measure the elemental magnetization reversal events to solve the coercivity problem. For this purpose, ultra-high sensitivity of the magnetization detection for a microsized magnet sample is required. In this study, a hot-deformed (HD) Nd-Fe-B magnet is patterned into a microsized cross-shape using focused ion beam (FIB), and anomalous Hall effect (AHE) is adopted to detect the elemental step of magnetization reversal. The HD magnet consists of well aligned platelet small grains with 300 nm in diameter and 70 nm in thickness [2]. Owing to this unique microstructure, HD magnet has enough high tolerance for process damage. AHE measurement detects electric signal proportional to the perpendicular magnetization component of the cross patterned area with ultra-high sensitivity. Fig. 1 shows the SEM image of the cross-patterned HD magnet with the AHE cross area of 0.9 μm in width and 1 μm in thickness. Fig. 2 shows the AHE curves of the HD magnet repeatedly measured three times. The stepwise AHE signal is clearly confirmed. Taking into account the AHE cross area size and the included grain size, each step height corresponds to the magnetization reversal of a single grain. Moreover, these three AHE curves overlaps, indicating that each step is repetitive. The inset of Fig. 2 shows an expanded part of the AHE curves. The step position slightly fluctuates due to the thermal agitation [3-4]. The thermal activation analysis for these elemental magnetization events will make us to understand the background physics of the magnetization reversal of the HD magnet.

[1] M. Sagawa et al., J. Appl. Phys. 55 (1984) 2083 [2] J. Liu et al., Acta Mater. 61 (2013) 5387 [3] L. Néel, Adv. Phys. 4 (1955) 191 [4] R. Street et al., Proc. Phys. Soc. A62 (1949) 562

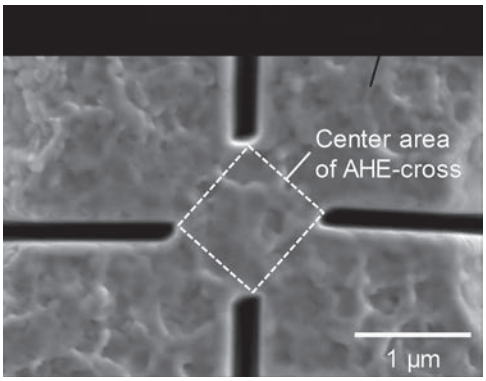


Fig. 1 SEM image of a cross-shaped HD Nd-Fe-B magnet for AHE measurement.

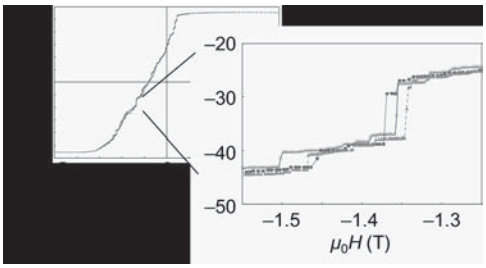


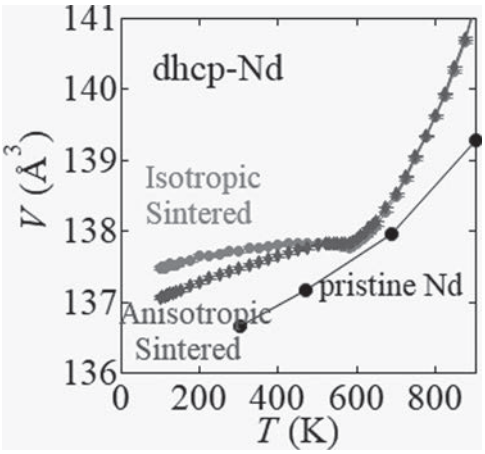
Fig. 2 Three times repeatedly measured AHE curves of micropatterned HD Nd-Fe-B magnet.

8:54

CI-03. Influence of magnetostriction on the lattice constants of the secondary phases in Nd-Fe-B sintered magnets studied by synchrotron X-ray diffraction. *S. Kobayashi*[2,1], A. Martín-Cid[2,1], K. Toyoki[2,1], H. Okazaki[2,1], S. Hirosawa[1] and T. Nakamura[2,1] *1. Elements Strategy Initiative Center for Magnetic Materials (ESICMM), National Institute for Materials Science, Tsukuba, Japan; 2. Japan Synchrotron Radiation Research Institute (JASRI), Sayo-cho, Japan*

Nd-Fe-B permanent magnets have been intensively studied in order to improve the magnetic properties, especially, coercivity. It has been reported that the lattice strain in the $Nd_2Fe_{14}B$ crystalline grain in the Nd-Fe-B magnet affects the magnetic anisotropy, and hence the coercivity [1-3]. However, there are few experimental reports on the lattice strain in the $Nd_2Fe_{14}B$ phase so far [4]. In our previous synchrotron X-ray diffraction (XRD) study [5], the lattice constants of each constituent phase in an anisotropic Nd-Fe-B-Cu sintered magnet are slightly different from those of the pristine metal or compounds. This result implies the presence of internal strain in sintered magnets. In this study, we have measured temperature dependent synchrotron XRD and determined precise lattice constants of the $Nd_2Fe_{14}B$ phase and secondary phases in the several types of samples: isotropic and anisotropic Nd-Fe-B-Cu as-sintered magnets, their powdered samples, and powder samples obtained from a coarse single crystal which we used as a reference sample without lattice strain. While temperature variations of lattice constants of the $Nd_2Fe_{14}B$ phase are quite similar for all the samples above Curie temperature (T_C), the temperature variations below T_C are different between sintered magnets and their powdered samples. The comparison of the lattice constants of the $Nd_2Fe_{14}B$ phase clarifies the presence and absence of internal strain in sintered magnets and powdered samples, respectively. The internal strain in the isotropic as-sintered magnet is larger than that in the anisotropic magnet. In addition, unit cell volume of each secondary phase in sintered magnets is larger than those of pristine metal or compounds and each secondary phase in powdered sintered magnets below T_C. These results indicate that internal stain in sintered magnets varies lattice constants of all the constituent phases. We thank T. Nishiuchi of Hitachi Metals, Ltd. for supplying the samples. A part of this work is supported by ESICMM under the outsourcing project of MEXT.

[1] M. Yi *et al*., Phys. Rev. Appl. 8, 014011 (2017). [2] G. Hrkac *et al*., Appl. Phys. Lett. 97, 232511 (2010). [3] C. H. de Groot and K. de Kort, J. Appl. Phys. 85, 8312 (1999). [4] Y. Murakami *et al*., Acta Materialia 101, 101 (2016). [5] N. Tsuji *et al*., Acta Mater. 154, 25 (2018).



Temperature variation of unit cell volumes of dhcp-Nd in isotropic and anisotropic Nd-Fe-B-Cu as-sintered magnets, and pristine Nd [5].

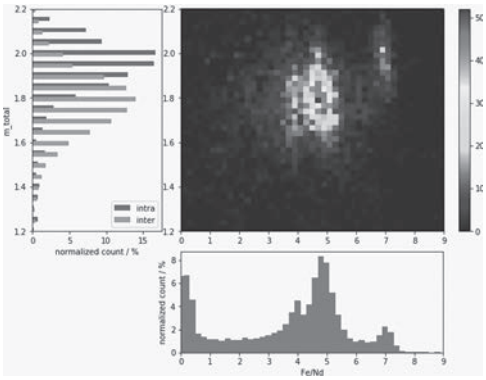
9:06

CI-04. Determination of Local Magnetic Moments in the Fractured Surface of a Nd-Fe-B Sintered Magnet by a Soft X-ray Microscope. *A. Martín-Cid*[1,2], D. Billington[1,2], K. Toyoki[1,2], Y. Kotani[1,2], S. Kobayashi[1,2], H. Okazaki[1], S. Hirosawa[2] and T. Nakamura[1,2] *1. Japan Synchrotron Radiation Research Institute (JASRI), Sayo, Japan; 2. Elements Strategy Initiative Center for Magnetic Materials (ESICMM), Tsukuba, Japan*

Permanent magnets (PM) used in energy-related applications occasionally operate under strong demagnetizing fields and at elevated temperatures of about 150 °C or more. One of the most desirable properties of PM that operate under such conditions is the coercivity. Nowadays, the main type of PM used in these high demanding applications are the Nd-Fe-B sintered magnets, which usually use the scarce heavy rare earth (HRE) elements such as Tb or Dy to improve their coercivity and thermal stability. In order to avoid the use of the scarce HRE, it is important to have a good knowledge of the effect of the microstructure and the grain boundary (GB) phases on the magnetic properties of a magnet. It has been known that the magnetic properties of the GB phase is associated with the coercivity through nucleation of magnetic domains and the pinning effect of the magnetic domain wall displacement. The evaluation of the magnetic properties of the GB phase is, therefore, crucial for the study of permanent magnets. Soft X-ray magnetic circular dichroism (XMCD) with the total electron yield (TEY) regime is a surface sensitive probe for element specific magnetic moments. XMCD measurements previously showed the magnetic properties of the GB phase exposed in the fractured surface [1]. The estimated values were, however, those averaged over a wide area with significant inhomogeneity. In this work, we present the distribution of the local Fe magnetic moments estimated by the sum rule analysis for XMCD spectra. The local XMCD spectra were recorded using the scanning soft XMCD microspectroscopy technique with the spatial resolution of about 100 nm [2,3] and it was possible to discern the magnetic moment of Fe from the intragranular fracture (related

to the $Nd_2Fe_{14}B$ phase) and the intergranular fracture (related at some extent with the GB phase). The value obtained for the intragranular fracture was ~2 μ_B, similar to that obtained by Mössbauer spectroscopy [4]. We thank T. Nishiuchi of Hitachi Metals, Ltd. for supplying the samples. Part of this work is supported by ESICMM under the outsourcing project of MEXT.

[1] T. Nakamura et al. Appl. Phys. Lett., Vol. 105, p. 202404 (2014) [2] Y. Kotani et al., J. Synchrotron Rad., Vol. 25, p. 1444-1449 (2018) [3] D. Billington et al., Phys. Rev. Mater., Vol. 2, p. 104413 (2018) [4] H. Onodera et al., J. Magn. Magn. Mater., Vol. 68, p. 6 & 15 (1987)



Distribution of Fe magnetic moments related to the Fe/Nd composition ratio. The $Nd_2Fe_{14}B$ phase corresponds with Fe/Nd = 7.

9:18

CI-05. Magnetic States of Rare-Earth Atoms in $(Nd,Ce,La)_2Fe_{14}B$ Investigated by Powder Neutron Diffraction. *T. Hawai*[1], M. Yano[2], T. Shoji[2], J.R. Hester[3] and K. Ono[1] *1. High Energy Accelerator Research Organization (KEK), Tsukuba, Japan; 2. Toyota Motor Corporation, Toyota, Japan; 3. Australia's Nuclear Science and Technology Organisation (ANSTO), Lucas Heights, NSW, Australia*

The most popular rare-earth magnet $Nd_2Fe_{14}B$ is necessary for industrial applications because of its strong coercivity originated from anisotropy of Nd. On the other hand, Nd is much costly than Fe and B, so that if a low Nd content magnet as strong as $Nd_2Fe_{14}B$ is realized, its commercial effect should be significant. The most abundant rare-earth elements Ce and La have a much lower cost than Nd, thus they are strong candidates for a low Nd content magnet. In general, Ce is in non-magnetic Ce^{4+} state. However, when Ce^{3+} state is stable, Ce has a magnetic moment and could work as a substitution for Nd. Previous research reported that a rare-earth atom with larger ionic radius prefers a position with a larger volume [1]. The magnetic Ce^{3+} has larger ionic radius (1.15 Å) than that of non-magnetic Ce^{4+} (1.01 Å) [2]. Therefore, to expand a cell for stabilization of Ce^{3+}, La (1.17 Å) is doped as a spacer. Previous study reported that Ce in $(Ce,La)_2Fe_{14}B$ has no moment [3]. Following the previous results, we focused on $(Nd,Ce,La)_2Fe_{14}B$. In this work, powder neutron diffraction experiments were performed to evaluate magnetic moment on rare-earth site and Ce state. The powder samples of $Nd_2Fe_{14}B$, $(Nd_{0.75}Ce_{0.225}La_{0.075})_2Fe_{14}B$, $(Nd_{0.5}Ce_{0.375}La_{0.125})_2Fe_{14}B$, and $Ce_2Fe_{14}B$ were measured on ECHIDNA at ANSTO [4]. Natural B was substituted with ^{11}B due to strong neutron absorption. Figure 1 shows an observed diffraction pattern of $(Nd_{0.5}Ce_{0.375}La_{0.125})_2Fe_{14}B$ together with a result of Rietveld analysis. The experimental data was well explained by the calculated pattern. The magnetic moment on 4*f* site changes almost proportionally to Nd content (Fig. 2). In contrast, the magnetic moment on 4*g* site shows only a little decrease against the decrease of Nd content. The reported magnetic moment on rare-earth sites in $(Nd,Ce)_2Fe_{14}B$ quickly decrease with decreasing Nd content [3]. This result suggests that magnetic Ce^{3+} state is stable thanks to La dope. The details will be discussed.

[1] K. Saito, S. Doi, T. and K. Ono, J. Alloy. Compd., 721, 476 (2017) [2] R. D. Shannon, Acta Crystallographica, A32, 751 (1976) [3] C. V. Colin, M. Ito, M. Yano, N. M. Dempsey, E. Suard and D. Givord, APL, 108, 242415 (2016) [4] M. Avdeev and J. R. Hester, J. Appl. Cryst., 51, 1597 (2018)

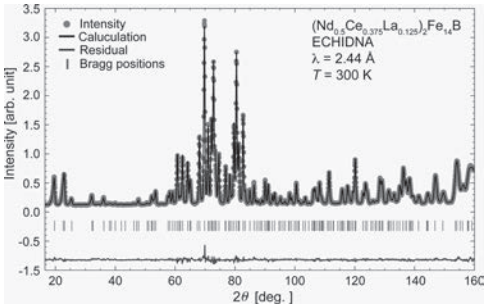


Fig. 1: The diffraction pattern of Nd 50% sample together with a Rietveld refinement result.

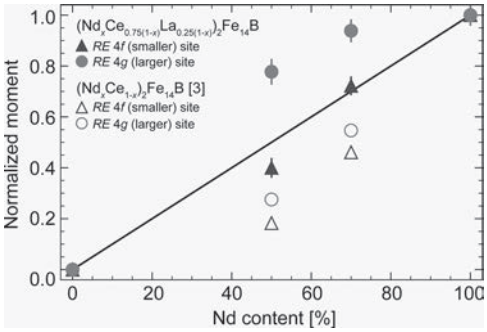


Fig. 2: The Nd content dependence of rare-earth moments. The moments shown here are normalized by the Nd moments of $Nd_2Fe_{14}B$.

9:30

CI-06. A mixed-valence model for $Ce_2Fe_{14}B$ compounds. *H. Tabata*[1], T. Yoshioka[1,2] and H. Tsuchiura[1,2] *1. Department of Applied Physics, Tohoku University, Sendai, Japan; 2. National Institute for Materials Science (NIMS), ESICMM, Tsukuba, Japan*

Because of the recent intensive use of Nd and Dy for high performance Nd-Fe-B permanent magnets, there is an urgent need to develop novel, economically attractive magnetic materials. Ce-based, or at least Ce-substituted permanent magnets, will be of particular interest because Ce is the most abundant rare-earth element. It is well known, however, that Ce-based magnetic materials such as $Ce_2Fe_{14}B$ usually do not have high magnetocrystalline anisotropy as a consequence of the less tightly-bound 4f electronic clouds in those systems. Theoretically, much less is known about the 4f electronic states of Ce ions in the $Ce_2Fe_{14}B$ because the modern first-principles calculations techniques still have problems to treat them. Thus in this study, we propose an alternative theoretical model to understand how the 4f electrons behave, and how these materials loses magnetocrystalline anisotropy. This model is essentially a cluster-type model which consists of Ce 4f orbital degrees of freedom and several surrounding ligand orbitals. The hybridization amplitude between the 4f and ligand orbitals is given as a parameter V in this model. This model reduces to the localized spin model in a limit with V=0, which has been widely used for rare-earth based permanent magnets [1]. Figure 1 shows the temperature dependences of the magnetic anisotropy constant K_1 obtained by using the present model. We find that the experimental data [2] can be well described at any temperature, when we take V=1100K. The localized spin model extremely overestimates K_1, as also shown in Fig. 1. The V dependences of K_1 and the 4f electronic density N_{4f} are shown in Fig. 2. We can see that N_{4f} first rapidly decreases

but becomes almost independent with increasing V. However, K_1 decreases monotonically even when N_{4f} is nearly constant around 0.5. This results may correspond to the weak magnetic anisotropy of $Ce_2Fe_{14}B$.

[1] M. Yamada, H. Kato, H. Yamamoto, and Y. Nakagawa, Phys. Rev. B 38 (1987) 620. [2] Satoshi Hirosawa, Yutaka Matsuura, Hitoshi Yamamoto, Setsuo Fujimura, Masato Sagawa, and Hiroshi Yamauchi, J. Appl. Phys. 59 (1986) 873.

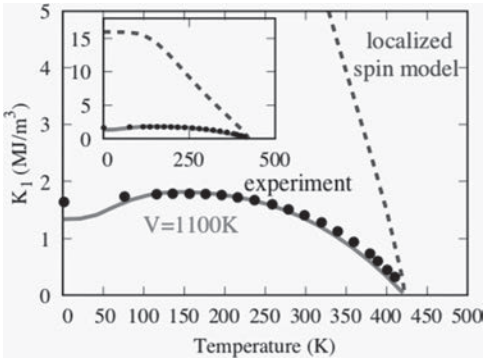


Fig. 1. The temperature dependence of magnetic anisotropy constants K_1, in the cluster model for V=1100K (solid lines), localized spin model (broken lines), and an experimental result (circles) [2].

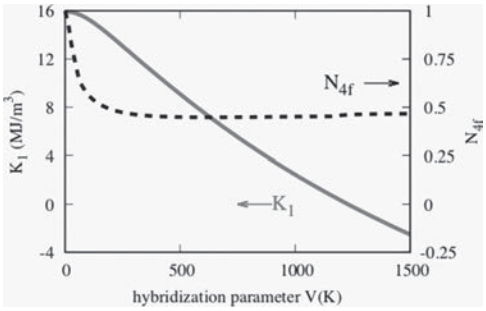


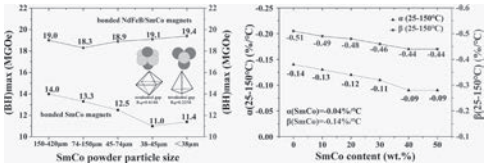
Fig. 2. The K_1 and 4f electronic density N_{4f} in the cluster model as functions of the hybridization parameter V.

9:42

CI-07. Magnetic properties of anisotropic bonded NdFeB/SmCo permanent magnets. *S. An*[1,3], Z. Ma[2], W. Li[1], H. Zhang[1] and T. Yin[1]
1. School of Materials Science and Engineering, Henan University of Science and Technology, Luoyang, China; 2. College of Materials Science and Engineering, Beijing University of Technology, Beijing, China; 3. Collabororative Innovation Center of Nonferrous Metals, Henan University of Science and Technology, Luoyang, China

Anisotropic bonded NdFeB permanent magnets have wide potential applications in the areas such as brushless DC motors, spindle motors, and stepping motors due to their excellent processing property and high magnetic properties. Anisotropic NdFeB bonded magnets prepared by hydrogen-disproportionation–desorption-recombination (HDDR) process have large energy product at room temperature, however, they are not stable at ~100°C, which is the working temperature of many electric motors. In order to improve their temperature stability, we developed bonded NdFeB/SmCo magnets and investigated the effects of powder particle size and SmCo content on their magnetic properties. We proposed a model to clarify the filling effect of the powder, which played a key role in the enhanced energy product when reducing the SmCo particle size. As for the SmCo content, the bonded magnets showed improved thermal stability with the increase of SmCo mass percent. And through adjusting the SmCo content, the remanence temperature coefficient and coercivity temperature coefficient from 25-150°C were able to be regulated in the range of -0.14%/°C to -0.04%/°C and -0.51%/°C to -0.14%/°C, respectively. This work provides a design strategy and a facile route to improve the magnetic properties and thermal stability of the bonded magnets.

[1] O. Gutfleisch, K. Güth, T. G. Woodcock, et al., Adv. Energy Mater. 3, 151-155 (2013). [2] N. Poudyal, V. V. Nguyen, C. B. Rong, et al., J. Phys. D Appl. Phys. 44, 335002 (2011). [3] D.-w. Shin, D.-s. Kim, B. Madavali, et al., J. Magn. Magn. Mater. 482, 280-286 (2019). [4] P. Saravanan, A. N. Sharma, V. Chandrasekaran, J. Magn. Magn. Mater. 321, 138-3143 (2009). [5] H. Sepehri-Amin, T. Ohkubo, K. Hono, et al., Acta Mater. 85, 42-52 (2015). [6] S. An, W. Li, K. Song, et al., J. Magn. Magn. Mater. 469, 113-118 (2019). [7] M. S. Walmer, C. H. Chen, M. H. Walmer, IEEE Trans. Magn. 36, 3376-3381 (2000). [8] G. C. Hadjipanayis, W. Tang, Y. Zhang, et al., IEEE Trans. Magn. 36, 3382-3387 (2000).



10:06

CI-09. Measuring THz Magnons in Metamaterials made of Ultrathin Magnetic Layers. P.M. Yarbrough[1], K. Livesey[1], R. Camley[1] and *R. Macedo*[2] *1. Department of Physics, University of Colorado at Colorado Springs, Colorado Springs, CO, United States; 2. James Watt School of Engineering, University of Glasgow, Glasgow, United Kingdom*

In recent years there has been growing interest in THz magnons as spin waves in this frequency range can be used for applications, such as spin-wave logic devices [1]. Due to their short lifetimes, however, high-frequency magnons can be difficult to measure. THz magnons are common in antiferromagnets, but more difficult to create and measure in metallic ferromagnets. Here we present a calculation showing that infrared magnons can be detected in metallic ferromagnets using standard reflection and attenuated total reflection (ATR) measurements [2]. We consider a layered structure of alternating thin magnetic and nonmagnetic materials. Thin ferromagnetic films have standing spin waves with resonance frequencies in the 100 – 500 GHz range, much higher than those typically found in bulk ferromagnets. We use an entire-cell effective-medium calculation to find the magnetic permeability of our metamaterial. We then calculate reflectivity as a function of frequency. We employ the geometry shown in Fig. 1 where the incident THz radiation is Transverse Electric (TE)-polarised. As can be observed from Fig. 2(a), there are appreciable dips (10%) in the reflectivity at infrared magnon resonance frequencies, for realistic material parameters. Here we have used Fe as the magnetic material composing our layered structure with 343 nm total thickness. The ATR geometry is similar to that pictured in Fig. 1 but we now add a dielectric prism a distance d_{gap} above the magnetic composite material, creating an air gap in which allows for evanescent waves to travel into the composite. The dips at resonance frequencies are now substantial, with reductions of 30% in the reflectivity seen in Fig. 2(c). We note that ferromagnetic and ferrimagnetic elements are widely used for applications in the 1-50 GHz range, and this work opens the way for those applications to be extended to much higher frequencies between 50 GHz and 1 THz.

[1] Chumak, A. V., et al. *Nat. Phys.* 11 453-461 (2015). [2] P. M. Yarbrough, K. L. Livesey, R. E. Camley and R. Macedo, *Phys. Rev. Applied* (In Press).

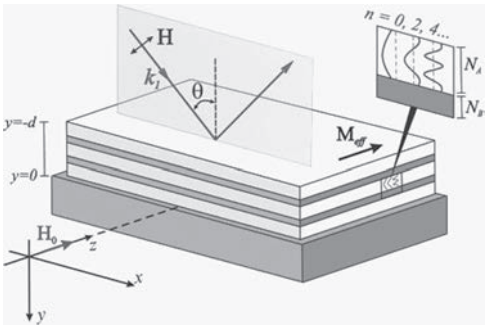


Fig 1. Geometry of reflection for TE-polarised incident radiation onto the metamaterial.

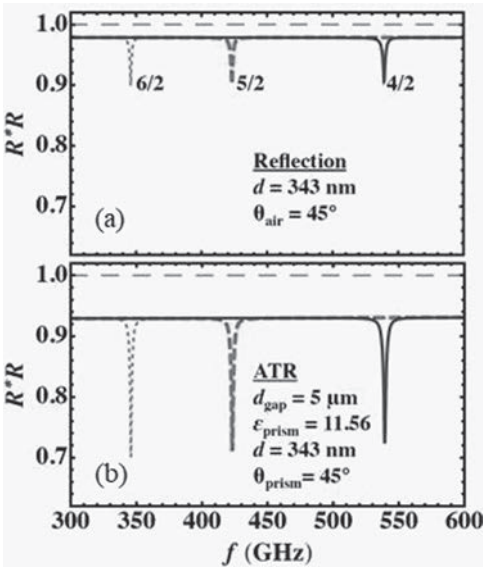


Fig 2. (a) Reflectivity and (b) ATR spectra for a magnetic metamaterial made from alternating 4, 5 and 6 atomic layers of Fe and 2 atomic layers of a nonmagnetic material - 4/2 (blue solid line), 5/2 (red dashed line), and 6/2 (green dashed line).

10:18

CI-10. Strongly Absorbing Optic Mode in Ferromagnetic Multilayers: Application to Signal Processing Devices. R. Macedo[1,2], P. Couture[2], R. Camley[2], K. Livesey[2] and *Z. Celinski[2] 1. SUPA School of Physics and Astronomy, University of Glasgow, Glasgow, United Kingdom; 2. Physics, Center for Magnetism and Magnetic Nanostructures, University of Colorado at Colorado Springs, Colorado Springs, CO, United States*

Metallic ferromagnetic layers have been used in signal processing devices to produce microscopic filters and phase shifters [1]. Most of these studies employed a single ferromagnetic film. Here, in contrast, we explore the behavior of a magnetic multilayer system with antiferromagnetic coupling between the ferromagnetic films. This work is motivated by a recent theoretical prediction [2] that such a structure could show significant absorption at higher frequencies in the optic mode, even with no external biasing field. This is very different from the single film results where there is no optic mode, and the operational frequency is generally low for small external biasing fields. While it is possible to use shape anisotropy or internal anisotropy to raise the operational frequency [3, 4] each of these methods has drawbacks. To test the theory, we grew both Fe/Cu and Fe/Cr multilayers embedded into a coplanar waveguide (CPW) structure. The polycrystalline samples had Cu or Cr layers which were 1 nm thick, ensuring an antiferromagnetic coupling between the 1.4 nm thick Fe films with ten repetition of the Fe/ spacer structure. The multilayer stack was covered by a 60 nm thick Cu film. The CPW geometry was defined by photolithography and lift-off. The MOKE measurements, seen in Fig. 1, indicate a weak antiferromagnetic coupling. Network analyzer measurements, shown in Fig. 2, for the Fe/Cu structure show a significant dip in transmission for low biasing fields. As the biasing field is increased, the transmission dip becomes smaller and moves to lower frequencies, in agreement with theoretical calculations. With further increases in biasing, the transmission dip moves to higher frequencies, and in fact is now the, weakly absorbing acoustic mode of a nearly ferromagnetically aligned structure. While the frequencies measured here are relatively small, stronger antiferromagnetic coupling could lead to significantly higher operational frequencies.

[1] R Camley, Z Celinski, T Fal et. al. J. Magn. and Magn. Mater. Vol 321, p 2048 (2009) [2] R Macêdo, K Livesey, and R Camley, Appl. Phys. Lett, Vol 113, p. 121104 (2018) [3] Z Wang, Y-Y Song, Y Sun, Appl. Phys. Lett, Vol. 97, p 072509 (2010) [4] I. Harward, R. Camley, and Z. Celinski, Appl. Phys. Lett. Vol 105, p. 173503 (2014)

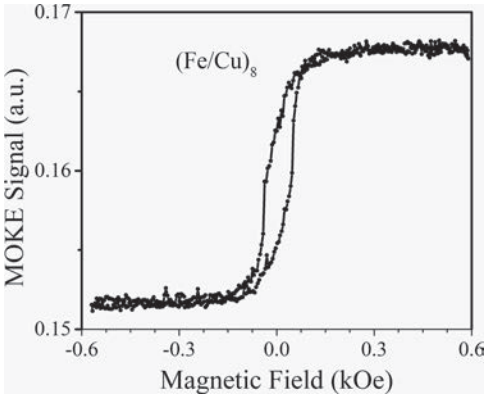


Fig. 1 MOKE hysteresis curve for the Fe/Cu sample. Note the saturation slightly above 100 Oe indicates that above this value the magnetic structure is all aligned with the field.

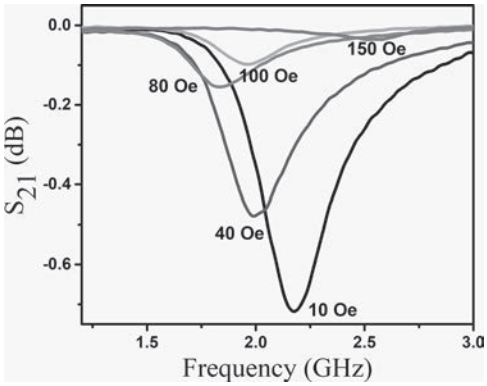


Fig. 2 Examples of transmission as a function of frequency for different static applied fields.

10:30

CI-11. Injection Locking of Spin-Torque Oscillator with Perpendicularly Magnetized Free Layer. *T. Yamaguchi*[3], N. Akashi[1], K. Nakajima[1,2], S. Tsunegi[3], H. Kubota[3] and T. Taniguchi[3] *1. Graduate School of Information Science and Technology, The University of Tokyo, Tokyo, Japan; 2. JST, PRESTO, Saitama, Japan; 3. Spintronics Research Center, National Institute of Advanced Industrial Science and Technology (AIST), Tsukuba, Japan*

Injection locking of a spin torque oscillator (STO) by alternative current (AC) or microwave field has been studied extensively [1-4]. The main purpose of the injection locking is the reduction of noise in STO, which is preferable for practical devices such as magnetic sensor. Injection locking is also important for new applications, such as phased array radar and reservoir computing [5,6]. For example, the performance of the reservoir computing was shown to be significantly improved recently by a phase control in microwave field [6]. So far, injection locking has been studied for an in-plane magnetized or vortex STO [1-3]. On the other hand, the injection locking of a perpendicularly magnetized STO is not fully understood yet, although STO as such is attractive due to its high emission power [4]. In this work, a theoretical study is developed on the injection locking by AC of an STO consisting of a perpendicularly magnetized free layer and an in-plane magnetized reference layer [7]. Figure 1 shows the frequency detuning between STO and AC. The frequency locking was observed over a wide range, almost 2 mA, of direct current (DC). An explanation for such behavior, contrary to the in-plane magnetized system [1-3] where the locking rage is less than 1 mA, is the orthogonal alignment in the magnetizations of the free and reference layers, since the AC spin torque should have a projection to the precession direction for locking, and thus, the locking range is proportional to the tangent of the relative angle between the magnetizations [8]. Figure 2 shows the temporal magnetization oscillation for several DC values. As phase difference between the STO and AC depends on the free running frequency, the STO phase varies by changing the DC. The wide locking range and phase tunability found in this work indicate that an array of the present STOs can shift the equal phase surface of an injected signal, which guarantees the applicability of STOs to phased array radar. This work was based on the results obtained from a project commissioned by NEDO.

1. W. H. Rippard *et al*., Phys. Rev. Lett. 95, 067203 (2005). 2. B. Georges *et al*., Phys. Rev. Lett. 101, 017201 (2008). 3. E. Iacocca and J. Akerman, Phys. Rev. B 87, 214428 (2013). 4. S. Urazhdin *et al*., Phys. Rev. Lett. 105, 237204 (2010). 5. J. Torrejon *et al*., Nature 547, 428 (2017). 6. S. Tsunegi et al., Appl. Phys. Lett. 114, 164101 (2019). 7. H. Kubota *et al*., Appl. Phys. Express 6, 103003 (2013). 8. A. Slavin and V. S. Tiberkevich, Phys. Rev. B 72, 092407 (2005).

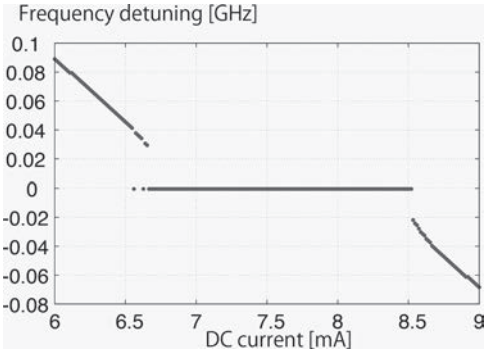


Fig.1:Frequency detuning between STO and AC. The detuning becomes zero in the locked state.

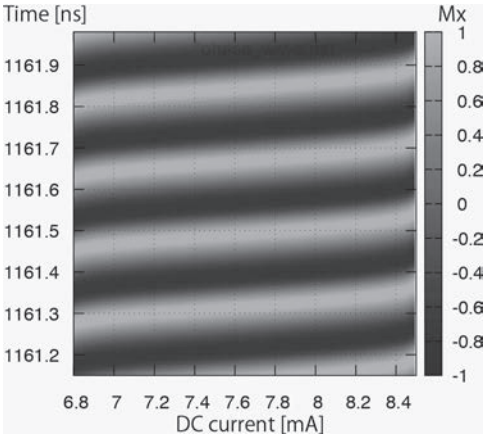


Fig.2:Time evolutions of the in-plane component of the magnetizations for several DC values.

10:42

CI-12. Maser operation of two magnetic tunnel junctions with positive gain. *Y. Yamada*[1], M. Goto[1,4], T. Yamane[2], N. Degawa[2], T. Suzuki[2], A. Shimura[2], S. Aoki[2], J. Urabe[2], S. Hara[2], S. Miwa[3,4] and Y. Suzuki[1,4] *1. Graduate School of Engineering Sciences, Osaka University, Osaka, Japan; 2. TDK Corporation, Tokyo, Japan; 3. Institute for Solid State Physics, University of Tokyo, Tokyo, Japan; 4. Center for Spintronics Research Network, Osaka University, Osaka, Japan*

Magnetic tunnel junction (MTJ) is attracting attention for next generation microwave signal sources. Recently, it was reported that the microwave reflection signal from MTJ is amplified by spin-torque from heat-induced magnetic anisotropy change [1]. In addition, we reported that the transmission signal is amplified with a similar mechanism [2]. These results suggest that, using multiple MTJs which amplify the signal at same frequency region, the maser could be excited. In this study, we first investigate the microwave emission from an MTJ with heat induced torque. Then, we put it in a feedback loop circuit and observed auto oscillation of the MTJ. Furthermore, we put two MTJs in the loop and observed strong non-linear increase in the emission power suggesting MASER operation of the MTJs. The film structure is buffer layer / IrMn (7 nm) / CoFe / Ru / CoFeB / MgO barrier (1 nm) / FeB (2 nm) / MgO cap (t_{MgO} =0.3 nm, 0.4 nm) / metal cap. Figure 1 shows the set up for RF power measurement with feedback loop circuit. The DC voltages were applied to the MTJs through bias-tee. The loop signal is measured through the directional coupler. Total gain without sample in loop circuit is adjusted to the negative gain of -0.44 dB by using external amplifier and attenuator. The total cable length of the loop circuit is about 11.5 m. Figure 2 shows the power spectrum density of the loop circuit with two MTJs at the resolution bandwidth of 0.1 MHz. The curve shows sharp peak at 4.809 GHz with side band peaks. The frequency difference between the side peaks is about 19 MHz. The side peaks are observed due to the standing wave in the cavity which is the same mechanism as a multi-mode laser system. In our experiment, the feedback loop acts as microwave cavity and provides the delay. The observed frequency difference of 19 MHz would correspond to a delay line 11.5 m. In addition to this result, the peak intensity amplified by two MTJs is 15 times higher than that amplified by one MTJ. This result suggests MASER operation of the MTJs.

[1] M. Goto *et al*., Nature Nanotechnology. 14, 40-43 (2019) [2] Y. Yamada, M. Goto *et al*., Japan Society of Applied Physics Autumn meeting (2018)

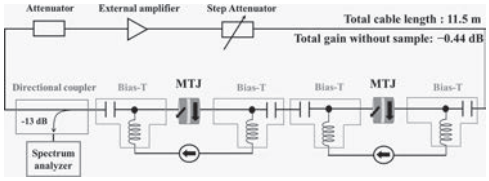


Fig. 1. Set up for RF power measurement with feedback loop circuit.

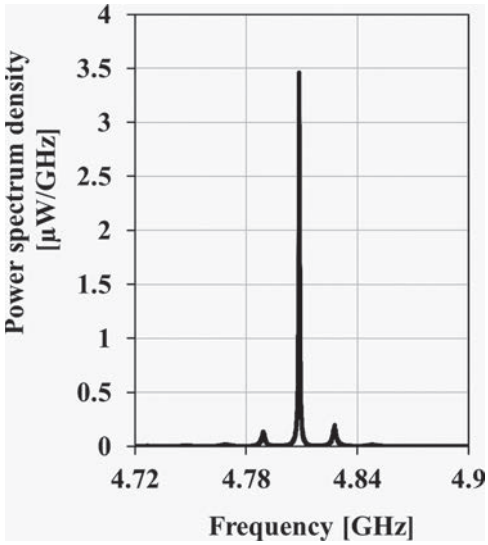


Fig. 2. RF emission spectrum when the two MTJs are in the loop circuit.

10:54

CI-13. Enhanced broadband RF detection in nanoscale magnetic tunnel junction by interface engineering. *L. Zhang*[1,2], B. Fang[1], J. Cai[1], G. Finocchio[3] and Z. Zeng[1,2] *1. Nano Fabrication Facility, Suzhou Institute of Nano-Tech and Nano-Bionics, CAS, Suzhou, China; 2. School of Nano Technology and Nano Bionics, University of Science and Technology of China, Hefei, China; 3. Department of Mathematical and Computer Sciences, Physical Sciences and Earth Sciences, University of Messina, Messina, Italy*

Energy harvesting technologies offer a promising approach to capture energy from ambient sources, such as vibration, heat, and electromagnetic waves. Among them, the ambient radio-frequency (RF) electromagnetic signals provide an attractive energy source for applications in self-powered portable electronics [1, 2]. However, currently available microwave detectors based on semiconductors do not meet the practical requirements for energy harvesting applications. The theoretical work proposed a spin-torque microwave detector with out-of-plane precession for RF energy harvesting [3]. Later on, the experimental work reported a broadband rectifier using magnetic tunnel junction (MTJ) [4]. Our recent work [5] demonstrated that spin-torque microwave detectors based on MTJ with a canted free layer are capable to convert RF power to DC voltage in a broadband frequency. The resulted DC voltage by spin-torque microwave detector can power a nanodevice, suggesting that the spin-torque microwave detectors could be served as building blocks for self-powered nanosystems. In the ambient conditions, there are several high-frequency RF energy sources – e.g. Wi-Fi and 3G/4G mobile signals. Hence a broadband signal detection is essential for energy harvesting applications. Here we show that the bandwidth of RF detection can be tunned by adjusting the perpendicular anisotropy (PMA) in the nanoscale magnetic tunnel junction. We designed an MTJ with a wedge CoFeB free layer to study the effect of PMA on the RF detection performances since the PMA in the free layer is related to the free-layer thickness [6]. An ultra-wide RF detection bandwidth of more than 3 GHz is achieved with the assistance of an external bias magnetic field when the CoFeB thickness is 1.61 nm. Even without external bias fields, a bandwidth of 1.8 GHz is realized under the thickness of 1.65 nm, which covers the most commonly used 3G/4G communication bands. Therefore, our results suggest that the spintronic diode offers a prospective approach for energy harvesting applications.

[1] S. Priya, & D. J. Inman, Energy harvesting technologies (Springer, 2009). [2] S. Hemour, & K. Wu, *Proc. IEEE* 102, 1667-1691(2014). [3] O. V. Prokopenko, *et al*. *J. Appl. Phys.* 111, 123904 (2012). [4] M. Tarequzzaman *et al*. *Appl. Phys. Lett.* 112, 252401 (2018). [5] B. Fang *et al*. *Phys. Rev. Applied* 11, 014022 (2019) [6] S. Ikeda, *et al*. *Nat. Mater*. 9, 721 (2010).

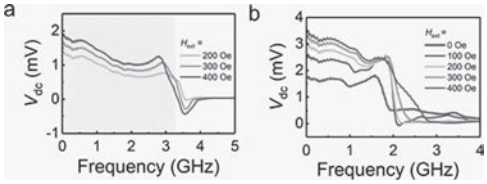


Fig. 1. (a) and (b) Broadband detection as a function of RF frequency at different magnetic field for the device with a free layer of 1.61 nm and 1.65 nm, respectively.

11:06

CI-14. Strong Coupling of Magnons to Microwave Photons in Three-Dimensional Printed Resonators. J. Bourhill[1,2], S. Ben Ammar[1], G. Cochet[3], A. Manchec[3] and *V.M. Castel*[1,2] *1. IMT Atlantique, Technopole Brest-Iroise, CS 83818, Brest, France; 2. Lab-STICC (UMR 6285), CNRS, Technopole Brest-Iroise, Brest, France; 3. Elliptika (GTID), Brest, France*

In recent years, a new light–matter interaction platform has been developed [1-2] by combining microwave (MW) photons residing in a resonant cavity with magnons in magnetic materials with a high spin density, such as yttrium iron garnet (YIG) [3]. The use of a standard three-dimensional (3-D) cavity for MW applications seems difficult to combine with concepts of integration, compactness, cost, and miniaturization. Here, we propose to take advantage of the geometric configuration of a re-entrant MW cavity to counterbalance this problem, which is becoming more and more critical by reducing the working frequency. MW re-entrant cavities offer many advantages in terms of frequency tunability, volume reduction, and control of the MW magnetic field distribution while keeping a high Q factor. Such cavities have been used for decades for a variety of applications, such as high Q resonator or sensors, and in different research area from the observation of spin wave propagation [3] to studies of cavity magnon–polaritons [4]. A range of experimental and simulations results are presented for two YIG/cavity systems, demonstrating the strong coupling signature (see Fig.1) between a YIG thin film resonator and photons generated by a 3-D re-entrant cavity elaborated by additive manufacturing (see Fig.2). A frequency dependence of the coupling strength was observed for both cavities, which differ only with the inner post height. Additive manufacturing opens an innovative path for the development of a new class of 3-D tunable filters based on re-entrant cavities, adjustable inner posts (including exotic shape), iris aperture, and magnon-photon coupling control. Such elaboration procedure combined to re-entrant cavities features improve the integration of YIG/Pt systems without increasing the intrinsic loss rate of the cavity, adding another degree of freedom in terms of tunability [5].

[1] Y. Tabuchi, S. Ishino, Y. Nakamura, Phys. Rev. Lett., Vol. 113, p.083603 (2014) [2] L. Bai, M. Harder, Y.P. Chen, X. Fan X, J.Q. Xiao, C-M. Hu, Phys. Rev. Lett., Vol. 114, p.227201 (2015) [3] J.R. Eshbach, Phys. Rev. Lett., Vol. 8, p.357 (1962) [4] M. Goryachev, J. Bourhill, M. Kostylev, M.E. Tobar, *Phys. Rev. B*, Vol. 97, p.155129 (2018) [5] V. Castel, A. Manchec, G.E.W. Bauer, Phys. Rev. B, Vol. 96, p.064407 (2017)

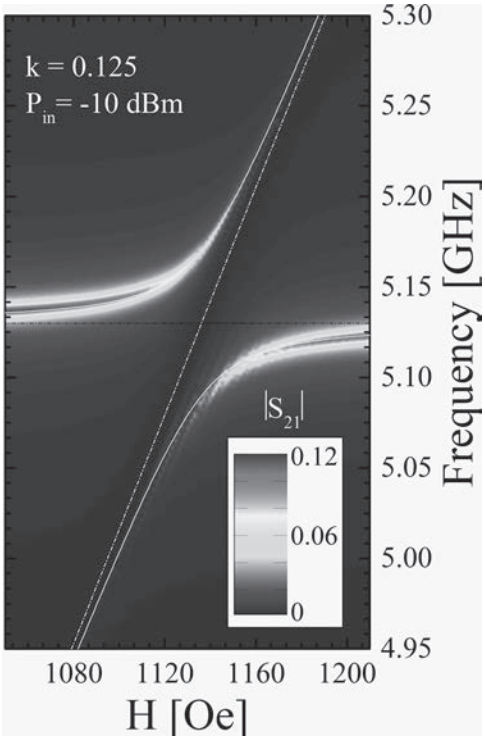


Fig.1 Experimental observation of the anticrossing region at room temperature with the dark mode. Measurement of the transmission amplitude |S21| of the resonator system as function of the frequency and the applied static magnetic field.

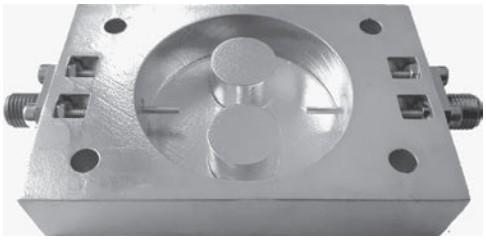


Fig.2 Photograph of the 3-D printed cavity (without lid).

11:18

CI-15. 3D Double Post Re-entrant Microwave Cavities as a Powerful Tool for Strong Photon-Magnon Coupling. *J. Bourhill*[1], V.M. Castel[1], M. Goryachev[2] and M. Tobar[2] *1. IMT-Atlantique, Brest, France; 2. University of Western Australia, Perth, WA, Australia*

3D re-entrant cavities offer a unique platform for microwave photon-magnon coupling in magnetic materials. A double post architecture (see Fig. 1) allows RF magnetic field focusing over a magnetic sample placed between the posts, generating orders of magnitude improvements in coupling strength compared to standard TM microwave cavities. These systems have successfully demonstrated achieving the strong coupling regime with coupling strengths equal to a sizeable percentage of the system's total energy [1,2] (see Fig. 2). Futhermore, the spatial separation of E and B fields within the cavity permit the presence of conductive layers, allowing utilisation of Spin-Hall devices [3]. Finally, the possibility of broad in-situ tuneability of the resonant frequency of these cavities results in an extremely versatile device, which will have important ramifications for microwave filtering applications and cavity quantum electrodynamics experiments. A range of experimental and simulation results are presented demonstrating the adaptability of these cavities towards the goals of achieving large coupling parameters, low microwave losses or high field uniformity, the latter being important for the suppression of coupling to higher order magnetic modes [4] for the purposes of clean filtering protocols. Successful manufacturing of these cavities has been demonstrated via 3D printing [5], further adding to their list of benefits through reduced cost and weight, and improved reproducibility, allowing mass production of such systems from a commercial standpoint, but also scalability of experimental tests of fundamental physics such as dark matter detection [6].

[1] M. Goryachev, W.G. Farr and D.L. Creedon, Phys. Rev. Applied, Vol. 2(5), pp. 054002, (2014) [2] M. Goryachev, S. Watt and J. Bourhill, Phys. Rev. B, Vol. 97(15), pp. 155129, (2018) [3] V. Castel, R. Jeunehomme and J.B. Youssef, Phys. Rev. B, Vol. 96, pp. 064407, (2017) [4] J. Bourhill, N. Kostylev and M. Goryachev, Phys. Rev. B, Vol. 93(14), pp. 144420, (2016) [5] V. Castel, S.B. Ammar and A. Manchec, IEEE Mag. Lett., Vol. 10, pp. 1-5, (2019) [6] G. Flower, J. Bourhill and M. Goryachev, Physics of the Dark Universe, Vol. 25, pp. 100306, (2019)

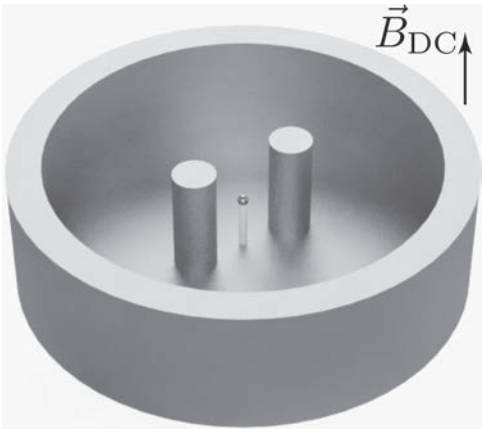


Fig. 1. 3D double post re-entrant cavity architecture with magnetic sphere positioned between the posts.

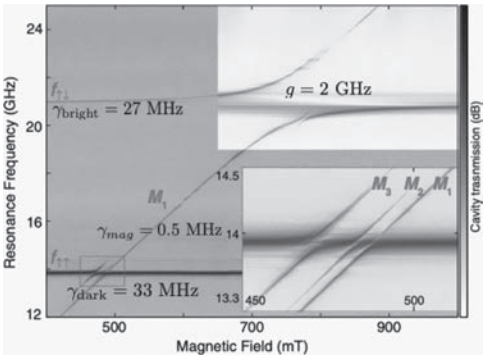


Fig. 2. Magnetic spectroscopy of cavity system with YIG sphere, demonstrating photon-magnon coupling strength of 2 GHz (~ 10% of system energy).

Session CP
ANTIFERROMAGNETIC SPINTRONICS II
(Poster Session)

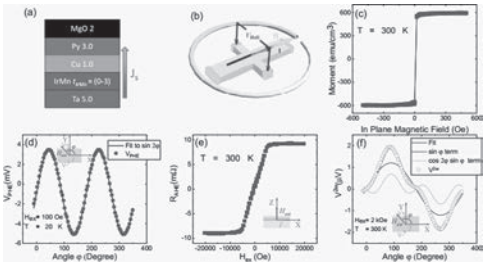
Yoichi Shiota, Chair
Kyoto Uniersity, Uji, Japan

CP-01. Chiral-driven switching of antiferromagnets in a confined thin film. *T. Kim*[1], S. Han[2] and B. Cho[1] *1. School of Material Science and Engineering, Gwangju Institute of Science and Technology, Gwangju, The Republic of Korea; 2. Division of Navigation Science, Mokpo National Maritime University, Mokpo, The Republic of Korea*

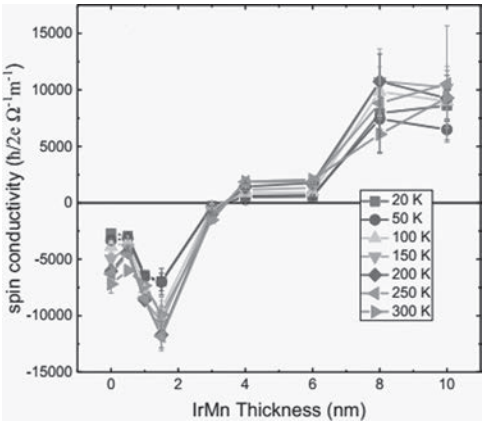
In the development of spin-based electronic devices, a particular challenge is the manipulation of the magnetic state with high speed and low power consumption. While many studies have focused on the spin-orbit torque (SOT), based on strong spin-orbit coupling, the torque-driven devices (as well as the charge-based ones) have fundamental limitations: Joule heating, phase mismatching and overshooting. To overcome these limitations, we report alternative switching scenario of antiferromagnetic insulator through theoretical and numerical demonstration. In two-dimensional geometry, as the electric field is applied to the magnetic system, the inversion symmetry of magnetic system is broken, and thereby two magnetic interactions are triggered: Dzyaloshinskii-Moriya (DM) interaction and pseudo-dipole anisotropy. The competition between the DM interaction, the exchange and crystalline anisotropy in thin film results in spiral structure with symmetric and antisymmetric configurations. By tuning DM strength, each symmetric state is energetically determined, which is enable to reverse magnetization. As a result, the switching power is estimated as ~1 pW, which is extremely lower than ~ μW of SOT-driven devices with various magnetic tunnel junction structures. Our finding provides promising opportunities to realize the rapid and energy-efficient electrical manipulation of magnetization for future spin-based electronic devices.

CP-02. Competition between Electronic and Magnonic Spin Currents in Metallic Antiferromagnet. *Y. Wen*[1], F. Zhuo[1], A. Manchon[1] and X. Zhang[1] *1. King Abdullah University of Science and Technology, Thuwal, Saudi Arabia*

We investigate the spin-orbit torque in a Ta/IrMn/Cu/NiFe multilayer heterostructure and relate it to spin current transmission through the IrMn layer. We identify several spin current transport regimes as a function of temperature and thickness of the IrMn layer. To interpret this experiment, we developed a drift-diffusion model accounting for both electron and magnon transport in the heterostructures. This model allows us to discriminate between the contributions of electrons and magnons to the total spin current in IrMn. We find that the electron-magnon spin convertance is one order of magnitude larger than the interfacial electronic spin conductance, while the magnon diffusion length is about ten times longer than the electronic spin relaxation length. This study demonstrates that magnonic spin transport dominates over electronic spin transport even in disorder metallic antiferromagnets.



(a) Illustration of the deposited film stack. (b) Schematic of second harmonic measurements. Cyan array denotes the in-plane rotated magnetic field. (c) Magnetic moment measured with the in-plane magnetic field at 300 K. (d) Anomalous Hall resistance measured at 300 K. (e) Planar Hall voltage measured by the locked-in amplifier at 20 K with in-plane constant magnetic field 100 Oe. (f) A typical second harmonic voltage measured at 300 K with in-plane magnetic field 2 kOe. The red line shows the fit of data. The blue and yellow line shows sinφ and sinφcos2φ term, respectively. Data is captured in IrMn 3 nm samples.



Spin conductivity as a function of IrMn thickness at various temperatures.

CP-03. Dirac nodal line metal for topological antiferromagnetic spintronics. *D. Shao*[1], G. Gurung[1], S. Zhang[2] and E.Y. Tsymbal[1] *1. Department of Physics and Astronomy, University of Nebraska-Lincoln, Lincoln, NE, United States; 2. College of Science, Beijing University of Chemical Technology, Beijing, China*

Topological antiferromagnetic (AFM) spintronics is an emerging field of research, which exploits the Néel vector to control the topological electronic states and the associated spin-dependent transport properties. A recently discovered Néel spin-orbit torque has been proposed to electrically manipulate Dirac band crossings in antiferromagnets; however, a reliable AFM material to realize these properties in practice is missing. Here, we predict that room temperature AFM metal $MnPd_2$ allows the electrical control of the Dirac nodal line by the Néel spin-orbit torque. Based on first-principles density functional theory calculations, we show that reorientation of the

Néel vector leads to switching between the symmetry-protected degenerate state and the gapped state associated with the dispersive Dirac nodal line at the Fermi energy. The calculated spin Hall conductivity strongly depends on the Néel vector orientation and can be used to experimentally detect the predicted effect using a proposed spin-orbit torque device. Our results indicate that AFM Dirac nodal line metal MnPd2 represents a promising material for topological AFM spintronics.

[1] Ding-Fu Shao, Gautam Gurung, Shu-Hui Zhang, and Evgeny Y. Tsymbal, "Dirac nodal line metal for topological antiferromagnetic spintronics," Phys. Rev. Lett. 122, 077203 (2019).

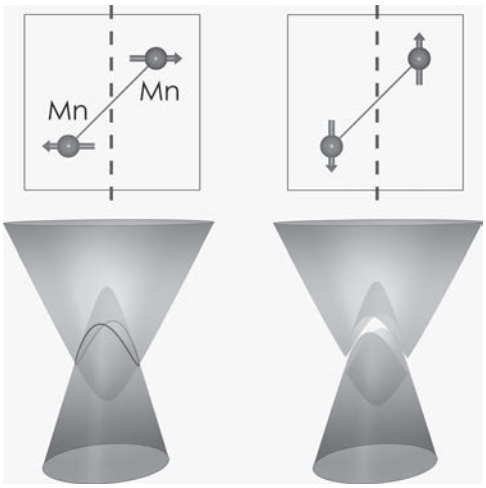


Fig. 1. Switching of the Dirac nodal line state from degenerate to gapped (bottom panels) of by reorientation of the antiferromagnetic order parameter (indicated by arrows on the top panels).

CP-04. Structural and Magnetic Property of Co Doped Mn_3Ga Antiferromagnetic Heusler Alloys. Y. Yoshihara[1,2], K. Elphick[2], M. Samiepour[2], H. Uchida[1], M. Inoue[1] and *A. Hirohata*[2] *1. Department of Electrical and Electronic Information Engineering, Toyohashi University of Technology, Toyohashi, Japan; 2. Department of Electronic Engineering, University of York, York, United Kingdom*

Antiferromagnetic (AF) Heusler alloys, especially Mn_2YZ (Y: transition metals and Z: other metals), has been intensively investigated due to their device applicability. Because of their large exchange bias induced at their interface against a ferromagnetic (FM) layer, they can be a potential candidate to replace rare metals, particularly IrMn which commonly used for MR head in HDD or MRAM applications. Fe-doped Mn_3Ga, *i.e.*, $D0_{19}$ Mn_2FeGa, has been predicted to form a collinear spin orientation [1]. Previously we observed both in and out-plane exchange bias experimentally [2]. In this study we study the influence of a FM element doped in an AF Heusler alloy, namely Co doped Mn_3Ga, via the observation of exchange bias and Hall effects. Layer stacks consisting of Ta (5)/Ru (35)/Mn_3Ga (30)/CoFe(3.3) or [Co (1.0)/Pt (1.6)]$_3$/Ta (5) (thickness in nm) were deposited for in- and out-of-plane anisotropy studies, respectively. They were grown by magnetron sputtering at room temperature and doping was achieved by adding Co pegs on the Mn_3Ga target. Blocking temperature (T_B) measurement was performed at activation temperatures T_{act} by the York Protocol [3]. Hall bar devices was fabricated by the lift off method using the stacks consisting of Ta (5)/Ru (35)/Mn_3Ga (30)/Ta (10). Figures 1 and 2 show in- and out-of-plane magnetization curves of $Mn_{2.18}Co_{1.09}Ga$ activated at T_{act} = 100~300 K, respectively. Loops are found to shift to a positive field with increasing T_{act}. Out-of-plane magnetization curves show better squareness than in-plane ones. T_B is estimated to be 197 and 186K for in- and out-of-plane, respectively. These results suggest the Co doped Mn_3Ga transforms the triangular spin configuration into the collinear one as expected. Hall measurements reveal the resistivity is 132 nΩ·m, which is almost the same to bulk Ta. This indicates a current predominantly flows through the Ta capping layer, which is an ideal situation for the spin Hall effect measurements. The details of these results will be presented in our presentation.

[1] A. Kundu and S. Ghosh, *Intermetallics,* Vol. 93, p.209 (2018). [2] T. Ogasawara *et al*., *J. Magn. Magn. Mater.,* Vol. 484, p.307 (2019) [3] K. O'Grady *et al*., *J. Magn. Magn. Mater.,* Vol. 322, p.883 (2010)

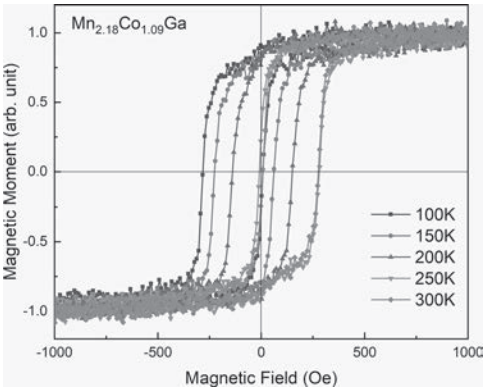


Fig. 1. In-plane magnetization curves of $Mn_{2.18}Co_{1.09}Ga$ (30)/CoFe (3.3) bilayers.

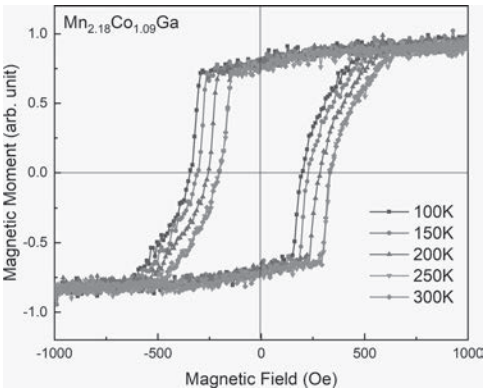


Fig. 2. Out-of-plane magnetization curves of $Mn_{2.18}Co_{1.09}Ga$ (30)/ [Co (1.0)/Pt (1.6)]$_3$ bilayers.

CP-05. Degenerated Orthogonal Spin States in Antiferromagnetic NiO(111) on Fe(110). *M. Slezak*[1], P. Drozdz[1], W. Janus[1], J. Korecki[1,2], A. Koziol-Rachwal[1], K. Matlak[1], M. Szpytma[1], M. Zajac[3] and T. Slezak[1] *1. AGH University of Science and Technology, Krakow, Poland; 2. Jerzy Haber Institute of Catalysis and Surface Chemistry PAS, Krakow, Poland; 3. National Synchrotron Radiation Centre SOLARIS, Jagiellonian University, Krakow, Poland*

The aim of antiferromagnetic (AFM) spintronics is to complement or replace ferromagnets (FM) in the active components of spintronic devices [1,2]. For magnetic control of AFMs spin orientation, two main possible routes are application of very strong external magnetic field or to employ the magnetic proximity effects at the AFM-FM interface. Depending on particular AFM-FM interfacial coupling, relatively small magnetic field is required in order to rotate the AFM spins [3]. In this report, we combine interfacial AFM-FM exchange interaction and temperature induced spin reorientation transition (SRT) in FM layer, in order to implement zero-field switching of AFM spins. In epitaxial NiO(111)/Fe(110) bilayers, we take the advantage of intrinsic hysteretic nature of the temperature induced SRT in Fe(110) layer and at given temperature we directly document the existence of degenerated orthogonal magnetic states in AFM NiO(111) sublayer. We used XMLD and XMCD techniques in order to follow the magnetic properties of epitaxial NiO(111)/Fe(110) bilayers. We find that the NiO spins are fully rotatable and always perpendicularly oriented with respect to Fe magnetization that direction can be controlled by external magnetic field or via the thickness or

temperature driven, 90-degree, in-plane SRT of Fe(110) [4,5]. The thickness and preparation recipe of Fe(110) buffer layer can be fine tuned in such a way that temperature driven SRT in Fe takes place at the desired temperature. For example, in Fig. 1 we present temperature dependence of XMCD (rescaled) and XMLD (R_{L2} ratio as defined for example in [6]) in NiO(40 Å)/ Fe(90 Å) bilayer. Fe sublayer undergoes a temperature driven in-plane SRT from [1-10] at high temperature to [001] at low temperature. We observe large thermal hysteresis of the SRT and consequently, in both Fe and NiO layers, at (230, 270 K) temperature range, two degenerated magnetic states can be stabilized at given temperature. Specifically, on the cooling branch within temperature hysteresis the ($FM_{[1-10]}$, $AFM_{[001]}$) magnetic state is stable while on the heating branch the system persists in the orthogonal ($FM_{[001]}$, $AFM_{[1-10]}$) state.

[1] D. Kriegner et al., Nature Communications 7 11623 (2016) [2] B. G. Park et al, Nature Materials 10 347 (2011) [3] J. Wu et al., Phys. Rev. Lett. 104 217204 (2010) [4] M. Slezak et al., Scientific Reports 9 889 (2019) [5] M. Slezak et al., JMMM 475 195 (2019) [6] Y. Z. Wu et al., Phys. Rev. B 74 212402 (2006)

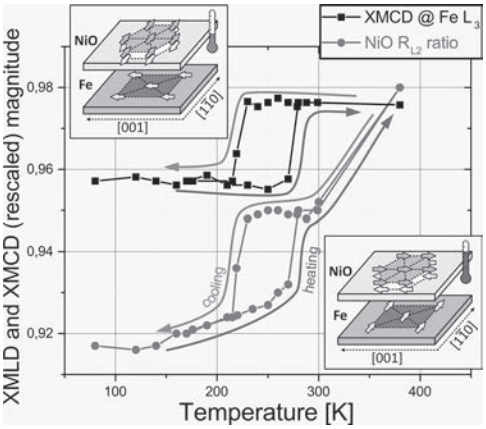


Fig.1 Temperature dependence of XMLD and XMCD in NiO(111)/ Fe(110) bilayer.

CP-06. Spintronics of magnetoelectric antiferromagnetic thin films. T. Kosub[1] and *D. Makarov*[1] *1. Helmholtz-Zentrum Dresden-Rossendorf, Dresden, Germany*

Thin film magnetoelectric antiferromagnets (AF) have potential to revolutionize spintronics due to their inherently magnetic-field stable magnetic order and high-frequency operation. To explore their application potential, it is necessary to understand modifications of the magnetic properties and magnetoelectric responses of AF thin films with respect to their bulk counterparts. Our approach is based on the electron transport characterization of magnetic responses of thin film antiferromagnets [1-4]. This task is difficult as minute uncompensated surface magnetization of antiferromagnets needs to be detected, which imposes strict requirements to the sensitivity of the method. We will outline our developments of zero-offset anomalous Hall magnetometry [3] applied to study the physics of insulating magnetoelectric Cr2O3 antiferromagnets. To build a reliable description of the material properties, the analysis of the transport data is backed up by structural characterization and real space imaging of AF domain patterns using NV microscopy [1,2]. Considering grainy morphology of thin films, we address questions regarding the change of the intergranular exchange [2], criticality behavior and switching of the order parameter [3]. The fundamental understanding of the magnetic microstructure of magnetoelectric α-Cr2O3 thin films and the possibility to read-out its antiferromagnetic order parameter all-electrically enabled the entirely new recording concept where a magnetoelectric memory cell can be addressed without using a ferromagnet, the purely antiferromagnetic magnetoelectric random access memory (AF-MERAM) [1]. In addition to the outline of the memory concept, we discuss on the physics of the readout signal in α-Cr2O3 interfaced with Pt [4].

[1] T. Kosub et al., Nat. Commun. 8, 13985 (2017). [2] P. Appel et al., Nano Letters 19, 1682 (2019) [3] T. Kosub et al., Phys. Rev. Lett. 115, 097201 (2015). [4] R. Schlitz et al., Appl. Phys. Lett. 112, 132401 (2018).

CP-07. Tunnel Magnetoresistance Properties in the Magnetic Tunnel Junctions with the Plasma Oxidized Cr_2O_3 Barrier. *T. Ichinose*[1], K. Elphick[2], A. Hirohata[2] and S. Mizukami[1,3] *1. Advanced Institute for Materials Research, Tohoku University, Sendai, Japan; 2. Department of Electronic Engineering, University of York, York, United Kingdom; 3. Center for Science and Innovation in Spintronics (Core Research Cluster) and Center for Spintronics Research Network, Tohoku University, Sendai, Japan*

There has been growing interest in the antiferromagnetic spintronics due to the high-speed operation, no stray fields etc. [1] Cr_2O_3 known to be the magnetoelectric material with the antiferromagnetic ordering under the Néel temperature of 310 K would show the intriguing spin dependent transport phenomena such as magnetoresistance effects mediated by antiferromagnetic and/or magnetoelectric nature. [2] In this work, the spin-dependent transport properties in the magnetic tunnel junctions (MTJs) with a Cr_2O_3 barrier were investigated. The stacking structures of Cr_2O_3(20)/ Ta(5) and Cr_2O_3(2)/ Co(3)/ $Ir_{22}Mn_{78}$(10)/ Ta(3)/ Ru(7) were prepared on the Si/ SiO_2/ Ta(5)/ Ru(20)/ Co(4) underlayers. (thickness in nm) The structural and transport properties were measured by using the x-ray diffraction (XRD), the 4-terminal prober, and the physical property measurement system. The Cr_2O_3 thin films were prepared by using the 90° off-axis cathode followed by the plasma oxidation to reduce the oxygen vacancies. The MTJs were post-annealed at 523 K under a magnetic field of 2 kOe. The Cr_2O_3 (006) peak could be observed in the XRD profiles of 2θ/ω scans for the 20-nm-thick Cr_2O_3 films. In the corundum oxides, the (006) diffractions were weak in contrast to the (104) peaks: For instance, the intensity ratio $I_{(006)}/I_{(104)}$ in the Cr_2O_3 powder sample was 0.15. On the contrary, sputtered Cr_2O_3 showed the $I_{(006)}/I_{(104)} \sim 8.8$, indicating high orientation of Cr_2O_3 to the (001) direction. The dielectric breakdown strength could be improved from 0.3 V to 1 V via the plasma oxidation, which could originate from the reduction of the oxygen vacancies. The MTJs with the Cr_2O_3 barrier showed the tunnel magnetoresistance (TMR) ratio of 1% (4%) at 300 K (10 K). In the TMR curves at < 100 K, the increase of coercive fields and anisotropy in the Co layers could be observed, indicating antiferromagnetic order of Cr_2O_3. This is the first observation of TMR in MTJs with the antiferromagnetic Cr_2O_3 barrier. The work was partially supported by KAKENHI (JP18H05947) and JST CREST (No. JPMJCR17J5).

[1] V. Baltz *et al.*, Rev. Mod. Phys., vol. 90, p. 015005 (2018). [2] K. Wang *et al.*, Sci. Rep., vol. 5, p. 15498 (2015).

CP-08. Crystallographic Structure Dependent Current-induced Switching in NiO/Pt Bilayer. *S. Hu*[1] and X. Qiu[1] *1. School of Physics Science and Engineering, Tongji University, Shanghai, China*

Spintronics mainly focus on manipulating magnetic moments of ferromagnetic materials. Recently, antiferromagnet has drawn a lot of attentions for its self-canceled stray fields, ability to against the external field and ultra-fast spin dynamics [1]. Several works have demonstrated electrical switching of metallic antiferromagnet CuMnAs and insulating antiferromagnet NiO [2-4]. However, more detailed discussions about whether the structure dominates the switching behavior is lacking. Here, we report the current-induced switching of antiferromagnetic insulator and its strong crystallographic structure dependent behavior in NiO/Pt bilayer by probing transvers resistance. Figure 1 (a) and (b) show the cross-sectional HR-TEM of the $SrTiO_3$/ NiO/Pt and the X-ray diffraction spectrum of 30nm-thick NiO films grown on different substrates, indicating epitaxially growth of NiO on $SrTiO_3$ and different crystallographic structures of NiO are successfully obtained. Figure 2 shows the strong crystallographic structure dependent switching behavior for NiO/Pt deposited on four different substrates, which reflected in the aspects of critical and degenerative J_C as well as ΔR_H. Both the crystallographic structure of NiO and the thermal conductivity of substrates can be responsible to the observations. The inset shows the writing and probing

geometry, two orthogonal writing pulses will switch the transvers resistance to different state. Furthermore, electron energy loss spectrum mapping reveals that the redistribution of oxygen in NiO after electrical switching which could be in strong correlation with the current-induced switching of antiferromagnetic insulator. Our works provide a vital way to tune critical switching current density and enhance switching amplitude in insulating antiferromagnet/Platinum bilayer.

[1] T. Jungwirth, X. Marti, P. Wadley, et al., Nat. Nanotechnol., Vol. 11, p. 231 (2016) [2] P. Wadley, B. Howells, J. Zelezný, et al., Science, Vol. 351, p. 587 (2016) [3] X. Chen, R. Zarzuela, J. Zhang, et al., Phys. Rev. Lett., Vol. 120, p. 207204 (2018) [4] T. Moriyama, K. Oda, T. Ohkochi, et al., Sci. Rep., Vol. 8, p. 14167 (2018)

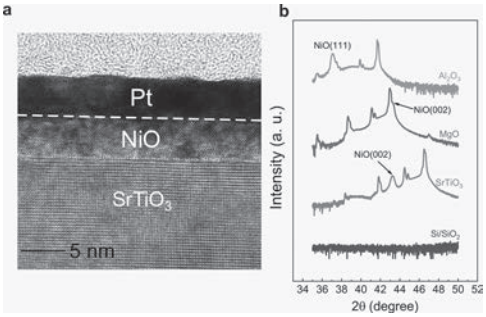


Fig. 1 (a), High-resolution TEM images of $SrTiO_3$(100)/NiO/Pt. (b), XRD spectrum of the 30nm-thick NiO grown on Al_2O_3(0001), MgO (100), $SrTiO_3$ (100) and Si/SiO_2 substrates, respectively.

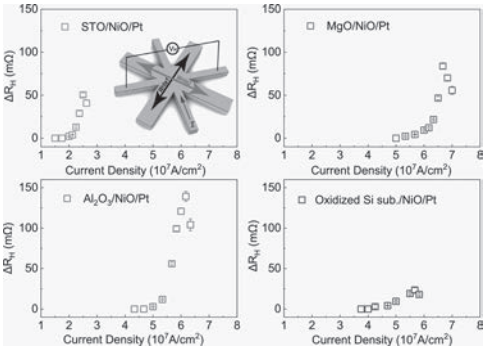
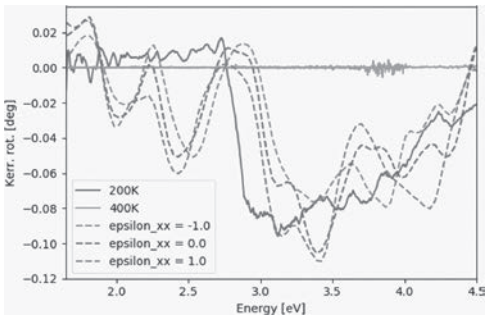


Fig. 2 Current-induced switching of NiO/Pt grown on different substrates. Inset is the writing and probing geometry, the writing current will turn to orthogonal directions after 10 pulses. The transverse resistance is defined as R_H.

CP-09. Magneto-optical Kerr Spectroscopy of Mn_3AN Non-collinear Antiferromagnetic Thin Films. *K. Krizanova*[3], L. Beran[3], J. Zázvorka[3], F. Johnson[2], D. Boldrin[2], A. Mihai[2], B. Zou[2], L. Cohen[2], M. Veis[3] and J. Zemen[1] *1. Czech Technical University, Prague, Czechia; 2. Imperial College London, London, United Kingdom; 3. Charles University, Prague, Czechia*

Mn_3NiN and Mn_3GaN belong to a family of Mn-based antiperovsktie nitrides with general formula Mn_3AN. In the bulk form, this class of materials has attracted much interest due to phenomena such as temperature independent resistivity, abnormal thermal expansion, or barocaloric effects [1, 2] in the last decade. Here we focus on thin films which have shown potential for spintronic applications very recently, e.g., Piezomagnetic effect [3] and Anomalous Hall Effect [4] have been demonstrated on various perovskite oxide substrates. So far there has been one observation of MOKE in the Mn_3AN family [5]. However, the agreement with the available simulated MOKE spectra [6] is relatively poor, possibly due to an intentional N-deficiency in the Mn_3GaN1-x film [5]. We present magneto-optical spectra of Mn_3AN (A= Ni, Ga) thin films on substrates with different lattice parameters (BTO, STO, LSAT) which induce various strain. The samples were grown by pulsed laser deposition. The magneto-optical spectra were measured by rotating analyzer method in the spectral range from 1.5 to 4.5 eV. The samples were cooled down in in-plane field of 0.9 T from the paramagnetic state across the Neel temperature for each polarity of the magnetic field. The Kerr rotation spectra were obtained by the subtraction of the spectra at each polarity. Figure 1 shows a comparison of measured (solid lines) and simulated (dashed lines) spectra in stoichiometric Mn_3NiN thin films on BTO with strain, e_{xx}~ 0.1%, due to lattice mismatch with substrate. Our simulations rely on the Projector-Augmented Wave method (PAW) and linear response theory as implemented in the VASP code [7]. They assume the triangular G^{4g} and canted triangular states are assumed in the simulations for cubic and strained lattices ($|e_{xx}|> 0$), respectively. We observe semi-quantitative agreement of our measured and simulated spectra. Moreover, the amplitude of the measured spectrum is an order of magnitude larger than MOKE measured in hexagonal Mn_3Sn [8]. It is also in agreement with predictions of ref. [6].

[1] D. Boldrin, L. F. Cohen et al.: *Phys. Rev. X*, 8, 041035 (2018). [2] D. Matsunami et al.: *Nature Materials*,14, 73–78 (2015). [3] D. Boldin, L. F. Cohen et al.: *ACS Appl. Mater. Interfaces*, 10, 18863 (2018). [4] D. Boldrin, L. F. Cohen et al.: *arXiv*:1902.04357 (2019). [5] S. Ishino et al.: *AIP Advances*8.5, 056312 (2018). [6] Y. Mokousov et al.: *Phys. Rev. B*, 99, 104428 (2019). [7] G. Kresse and J. Hafner, *Phys. Rev. B*47, 558 (1993); ibid. 49, 14251 (1994). [8] T. Higo et al.: *Nature photonics*, 12.2, 73 (2018).



CP-10. Modification of Antiferromagnetic State by Spin-Orbit Torque. J. Wu[1], *C. Yang*[1] and C. Lai[1] *1. National Tsing Hua University, Hsing Chu, Taiwan*

The spin-orbit torque (SOT) device with an orthorhombic current/in-plane magnetization geometry has demonstrated its potential on the deterministic switching dynamics and low-power consumption [1]. In this work, we exhibit the field-free SOT switching in a PtMn/CoFeB bilayer studied by using a magnetic force microscope (MFM) and magneto-optical Kerr magnetometer (MOKE). PtMn is an antiferromagnet with considerable spin Hall effect as typical heavy metals, which is capable of triggering the magnetization switching of adjacent CoFeB with a critical current density of 3.9×10^7 A/cm^2. Fig. 1(a) and 1(b) show the MFM images of the two magnetic states driven by pulse current upward and downward, leading to magnetization leftward and rightward, respectively. Furthermore, in Fig. 1(c) the hysteresis loops acquired from the two magnetic states show a clear variation on exchange bias (±160 Oe), suggesting the spin configuration at the PtMn/CoFeB interface can be modified by the spin Hall effect from PtMn itself. The SOT-driven field-free switching captured by exchange bias offers a novel approach for exploring the AFM state modification in FM/AFM bilayer.

[1] S. Fukami, T. Anekawa, C. Zhang, and H. Ohno, Nat. Nanotechnol. 11, 621 (2016)

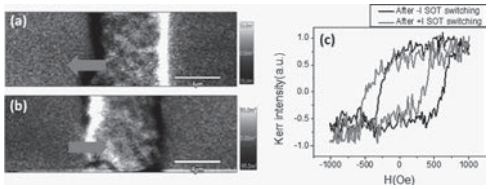


Figure 1. Monitoring the SOT switching using magnetic force microscope and magneto-optical Kerr magnetometer (a)(b) MFM images of the device with magnetization leftward (a) and rightward (b) acquired after applying a pulse current of 3.9×10^7 A/cm^2 downward (-I) and upward (+I), respectively. The opposite contrast at the edges of the device reveals the magnetization switching after applying current. The red arrows in (a) and (b) represent the magnetization direction. (c) Hysteresis curves of the PtMn/CoFeB acquired from the two magnetic states in (a) and (b). A clear change of the exchange bias from +160 Oe to -160 Oe was captured by L-MOKE.

CP-11. Tunable Magnetic-Phase Order and Magnetic Anisotropy in FeRh Multilayers: First-Principles Prediction. *D. Odkhuu*[1,2] *1. Department of Physics, Incheon National University, Incheon, The Republic of Korea; 2. Institute of Physics and Technology, Mongolian Academy of Sciences, Ulaanbaatar, Mongolia*

Phenomena originating from spin-orbit interaction such as magnetic anisotropy, Rashba-type interactions, or topological insulators have drawn huge attention for its intriguing physics as well as possibilities for applications. In particular, modern spintronics relies on perpendicular magnetic anisotropy (PMA) and its switchable feature in an antiferromagnetic material. In this presentation, we will report results of our recent first-principles calculations on viable routes by applying electric-field and strain effects that can lead to tunable magnetic-phase order and magnetization direction in recently proposed antiferromagnet-based magnetic tunnel junctions, including FeRh films on MgO(001) and $BaTiO_3$(001) substrates. We will also discuss on the tremendous effects of heavy transition-metal (HTM) contact layers on the magnetic-phase transition from an antiferromagnetic to a ferromagnetic order and large PMA found in HTM/FeRh/MgO and HTM/FeRh/$BaTiO_3$ multilayers.

CP-12. Anomalous Hall effect in antiferromagnetic antiperovskite $Mn_3Ni_{1-x}Cu_xN$ films. *T. Hajiri*[1], K. Zhao[2], R. Miki[1], H. Chen[3], P. Gegenwart[2] and H. Asano[1] *1. Nagoya University, Nagoya, Japan; 2. Augsburg University, Augsburg, Germany; 3. Colorado State University, Fort Collins, CO, United States*

Antiferromagnet (AFM) spintronics is an emergent field of research because AFMs have a great potential to take the place of ferromagnets [1]. However, since the AFM spins align alternating directions of magnetic moments on individual atoms, the resulting zero net magnetization makes hard to detect AFM ordering electrically. Although it is well known that the anomalous Hall effect (AHE) in conventional ferromagnet is proportional to the net magnetization, the large AHE is realized in noncollinear antiferromagnet Mn_3X (X = Sn, Ge, Pt) [2, 3, 4]. The symmetry analysis expects that antiperovskite nitride Mn_3AN can exhibit large AHE [5], and recently, we realize AHE in polycrystalline sintered pieces and epitaxial thin films of $Mn_3Ni_{1-x}Cu_xN$ [6]. In this presentation, we report the thin film growth and AHE of antiferromagnetic $Mn_3Ni_{1-x}Cu_xN$ films. Figure 1 shows the out-of-plane magnetic hysteresis loops of $Mn_3Ni_{0.35}Cu_{0.65}N$ films on MgO(111) substrate. A weak remnant magnetization is clearly observed with the saturation magnetization of ~0.003 μB/Mn above 50 K and 0.01 μB/Mn at 2 K. Figure 2 shows AHE measurements results of $Mn_3Ni_{0.35}Cu_{0.65}N$ films on MgO (111) substrate. The clear AHE signal is obtained below 180 K. Both magnetization and AHE exhibit similar coercive field, indicate that the obtained AHE is directly related to the noncollinear AFM order. The normalized anomalous Hall conductivity by the magnetization exceeds 6000 (Ω●cm●μB/Mn)$^{-1}$ at 50K, which is much larger than that of typical ferromagnet Fe of 135 (Ω●cm●μB/Fe)$^{-1}$. From the symmetry analysis based on noncollinear Γ_{4g} magnetic order, the obtained AHE can be explained by the non-vanishing Berry curvature in momentum space.

[1] H. V. Gomonay and V. M. Loktev, Low Temp. 40, 17 (2014). [2] S. Nakatsuji *et al*., Nature 527, 212 (2015). [3] N. Kiyohara *et al*., Phys. Rev. Appl. 5, 064009 (2016). [4] Z. Liu et al., Nat. Electron.1, 172 (2018). [5] G. Gurung *et al*., Phys. Rev. Mater. 3, 044409 (2019). [6] K. Zhao *et al*., arXiv:1904.05678 (2019).

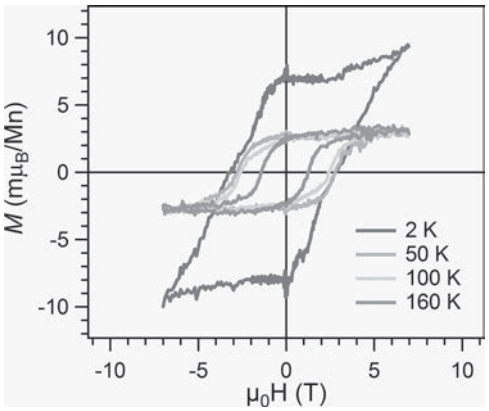


Fig. 1. Out-of-plane magnetic hysteresis loops of $Mn_3Ni_{0.35}Cu_{0.65}N$ films on MgO (111) substrate.

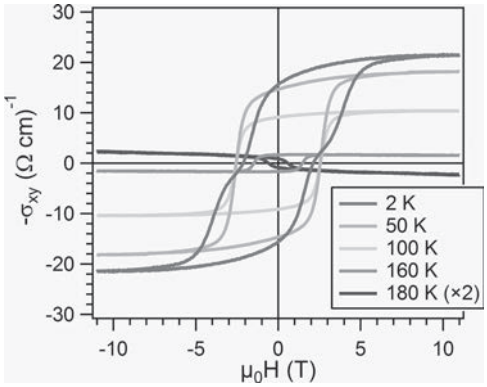


Fig. 2. Anomalous Hall conductivity versus external field of Mn3Ni0.35Cu0.65N films on MgO (111) substrate.

CP-13. Spin Transport Properties in Antiferromagnetic $L1_2$-ordered Mn_3Ir Thin Films. *H. Iwaki*[1], T. Moriyama[1], T. Ikebuchi[1], K. Oda[1], Y. Shiota[1] and T. Ono[1] *1. Institute for Chemical Research, Kyoto University, Uji, Japan*

There is a growing interest in spin dependent transport due to the Berry-phase and topological effect often manifested by the anomalous Hall effect (AHE). The magnitude of the AHE has been phenomenologically believed to be proportional to the magnitude of the spontaneous magnetization. However, since the intrinsic AHE emerges due to the interplay between the Berry curvature and the spin-orbit coupling, the spontaneous magnetization is not always necessary to show AHE. One example is the antiferromagnetic Mn_3Sn with a chiral Kagome lattice [1]. While it has negligibly small net magnetization, a sizable AHE has been observed due to the Berry curvature associated with the chiral magnetic structure. Similar giant AHE has been predicted for the Mn_3X family (X = Sn, Ge, Ir, Pt, etc.) [2,3]. In this work, we investigated AHE in $L1_2$-ordered Mn_3Ir. We prepared thin films with the structure: MgO(100) substrate / Mn_3Ir (20nm) / SiO_2(5nm). The Mn_3Ir layer was grown at various substrate temperatures (T_s = 300°C ~ 600°C) to promote the epitaxy as well as the intermetallic ordering. X-ray diffraction (XRD) shows a superlattice (100) peak for the sample grown at T_s > 400°C indicating that the $L1_2$ ordering is established (Fig. 1.). Hall

resistances (R_{Hall}) of each sample were measured with a Hall cross structure using a physical-property measurement system (PPMS) with the magnetic field applied perpendicular to the sample plane. R_{Hall} of the ordered samples varies nonlinearly with respect to the field B and draws a hysteresis curve (Fig. 2.) which is akin to the AHE behavior. In the presentation, we will discuss in more detail the correlation between the $L1_2$-ordering and the AHE-like behavior.

1) S. Nakatsuji, N. Kiyohara, and T. Higo, Nature., Vol.527, p.212 (2015). 2) H. Chen, Q. Niu, and A. H. MacDonald, Phys. Rev. Lett., Vol.112, p.017205 (2014). 3) N. Kiyohara, T. Tomita, and S. Nakatsuji, Phys. Rev. Applied., Vol.5, p.064009 (2016).

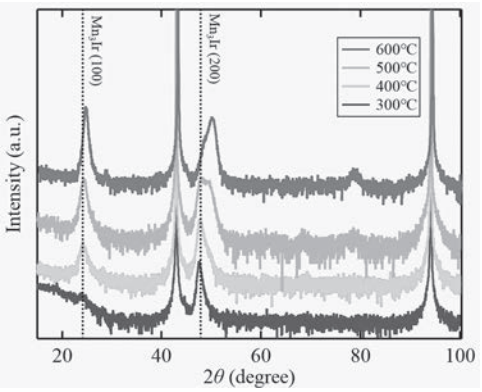


Fig. 1. θ-2θ XRD spectra of the epitaxial Mn_3Ir (100) films deposited at various T_s.

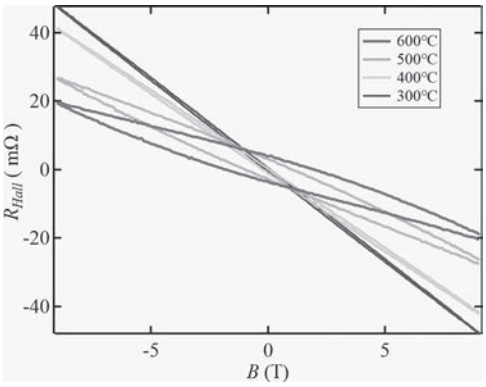


Fig. 2. R_{Hall} as a function of the magnetic field.

CP-14. Crystal orientation dependence of the spin current transmission in single crystalline NiO thin films. *T. Ikebuchi*[1], T. Moriyama[1], K. Oda[1], H. Iwaki[1] and T. Ono[1] *1. ICR, Kyoto University, Uji, Japan*

Spin current transmission in antiferromagnetic materials is one of the intriguing phenomena in the emerging antiferromagnetic spintronics [1]. We previously investigated the spin current transmission in a polycrystalline NiO by means of the spin pumping effect and estimated the spin propagation length λ_{NiO} to be 22±3 nm [2]. In this work, we prepared single crystalline NiO thin films with various crystal orientations and investigated the crystal orientation dependence of the spin current transmission. NiO (t_{NiO}) / $Fe_{20}Ni_{80}$ (5) / SiO_2 (5) (unit: nm) multilayers were deposited on an Al_2O_3 (0001) and a MgO (001) substrate by magnetron sputtering. From the XRD and RHEED images, the NiO films were found to be epitaxially grown with (111) and (001) orientation on the Al_2O_3 (0001) and the MgO (001) substrates, respectively. Ferromagnetic resonance (FMR) measurements were performed by the homodyne detection technique [3]. FMR spectra were taken at room temperature by sweeping an external field with a fixed frequency. The Glibert damping constant α is estimated from the FMR spectra. We focus on the enhancement of α due to the spin pumping effect with respect to the NiO thickness, which reflects the spin transmission in NiO [2]. α is plotted as a function of NiO thickness (Fig. 1) for (111) and (001) epitaxially grown NiO films. The asymptotic fitting based on the spin pumping model [4] results in λ_{NiO}=68±10 nm for the NiO (111). On the other hand, for NiO (001), α does not change much in the measured thickness range, which may suggest λ_{NiO} could be gigantic. Furthermore, in order to assure that spin current passed through the NiO layer, the enhancement of α in Pt/NiO/Py trilayer thin films was also investigated. The details will be discussed in the talk.

[1] T. Jungwirth, X. Marti, and J. Wunderlich, Nat. Nanotechnol. 11, 231-241 (2016) [2] T. Ikebuchi, T. Moriyama, and T. Ono Appl. Phys. Express 11, 073003 (2018) [3] T. Ikebuchi, T. Moriyama, and T. Ono Appl. Phys. Express 11, 053008 (2018) [4] Y. Tserkovnyak, A. Brataas, and B. I. Halperin, Rev. Mod. Phys. 77, 1375 (2005)

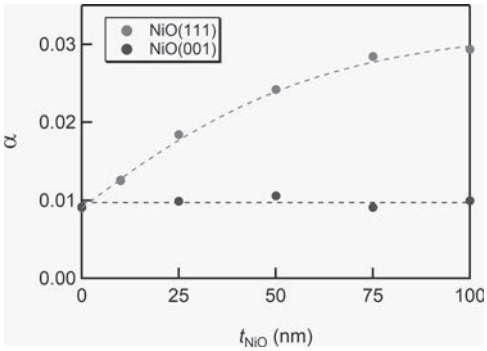


Fig. 1 α as a function of t_{NiO} in single crystalline NiO films.

CP-15. Spin transport across antiferromagnent in an ferromagnent/ antiferromagnet/heavy metal trilayer device. *P. Lin*[1], B. Yang[1], P. Lee[1] and C. Lai[1] *1. Materials Science and Engineering, National Tsing Hua University, Hsinchu, Taiwan*

Antiferromagnent (AFM) now become a promising candiate in spintronics research. Here, we study the interaction between spin current and antiferromagnent. The spin diffusion length of metallic antiferromagnent is around 2 nm[1]. However, there is a recent report demonstrating that the spin current can penerate the 12 nm metallic FeMn[2]. The magnon transportation for this thicker region is proposed. In this study, we use ferromagnent (FM) with perpendicular magnetic anisotropy (PMA) for it can achieve higher density, switching speed and thermal stability in futue application[3]. Also, the spin-orbit torque (SOT) switching is performed to probe the spin current transportation. The [Co/Ni] multilayers/FeMn t_{FeMn}/Pt 5 (unit:nm) trylayer structure is fabricated by magnetron sputtering. The FeMn thickness (t) is varied from 0 to 14 nm. Surprisingly, the FM switching is observed through all the FeMn thickness. Fig. 1a exhibits the swiching for t_{FeMn} = 14nm under in-plane magnetic field (Hx) = 300 Oe. Besides the FM swiching, the exchange bias switching is also observed as shown in fig. 1b, c.[4] This shows an unexpected result that the SOT switching could still take place with inserting an thick AFM between [Co/Ni] multilayers and Pt. The magnon transpotation across thick FeMn is a possible explanantion. In summary, by demonstrated the spin-orbit switching in FM/AFM/Pt structure, we provide another mean to study the spin transpotation in AFM.

1. Zhang, W. *et al.* Spin Hall effects in metallic antiferromagnets. *Phys. Rev. Lett.* 113, 196602 (2014). 2. Saglam, H. *et al.* Spin transport through the metallic antiferromagnet FeMn. *Phys. Rev. B* 94, 140412(R) (2016). 3. Ikeda, S. *et al.* A perpendicular-anisotropy CoFeB--MgO magnetic tunnel junction. *Nat. Mater.* 9, 721-724 (2010). 4. Lin, P.-H. *et al.* Manipulating exchange bias by spin-orbit torque. *Nat. Mater.* 18, 335–341 (2019)

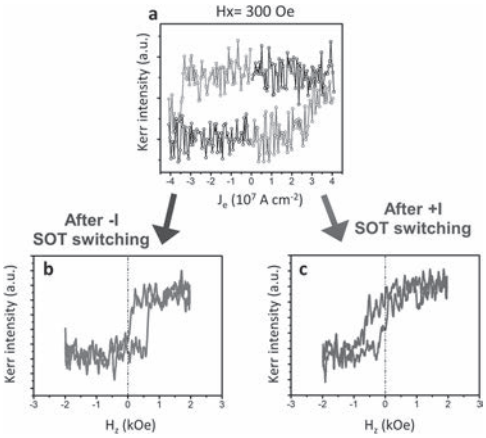


Fig. 1. Concurrent SOT switching for FM magnetization and exchange bias. a, SOT switching curves of FM magnetization in the presence of an in-plane magnetic field Hx = 300 Oe. The blue curve denotes SOT switching starting from -M (magnetization) with positive pulses. The red curve denotes SOT switching starting from +M with negative pulses. The black curve denotes SOT switching starting from +M (-M) with positive (negative) pulses. b,c, After the concurrent SOT switching, not only is the FM magnetization flipped, but the exchange bias is also reversed.

CP-16. Fabrication of Antiferromagnetic Mn_3Sn Epitaxial Thin Films and Anomalous Hall Effect in Them. *T. Ikeda*[1], M. Tsunoda[2], M. Oogane[1], S. Oh[3], T. Morita[3] and Y. Ando[1] *1. Department of Applied Physics, Tohoku University, Sendai, Japan; 2. Department of Electronic Engineering, Tohoku University, Sendai, Japan; 3. Institute for Super Materials, ULVAC Inc., Tsukuba, Japan*

In bulk single crystals of antiferromagnetic Mn_3Sn, an anomalous Hall effect (AHE) with significant amplitude as large as ferromagnetic materials was observed [1]. For applications of this large AHE to practical devices such as MRAMs, researches for growth techniques and characterizations in thin film form are necessary. Previously, we succeeded in fabricating polycrystalline Mn_3Sn thin films on SiO_2 sub. and observed the large AHE in them [2], [3]. However, its magnitude was smaller than bulk's one because of the existence of grains whose orientations do not contribute to the AHE. Therefore, controlling crystal orientation is essential to obtain larger AHE. The purpose of this research is to fabricate Mn_3Sn epitaxial thin films and to evaluate their properties. 50-nm-thick films were deposited on MgO (111) sub. by sputtering at room temperature (R.T.). After the deposition, thermal annealing was performed to promote crystallization. Diffraction peaks originated from Mn_3Sn phase were observed in the XRD profile for the samples annealed at 400°C or higher as shown in Fig. 1. Detailed structural analyses clarified that the Mn_3Sn phase has epitaxial relationship as Mn_3Sn [110](001) // MgO [110](111), meaning successful fabrication of c-plane oriented epitaxial Mn_3Sn thin films. The *MH*-curve exhibited weak ferromagnetic behavior in the c-plane. Saturation magnetization at R.T. was almost same to the bulk's one. On the other hand, it showed linear behavior against applied magnetic field along c-axis, similar to the bulk's response. The Hall curves measured with a field normal to the film plane are shown in Fig. 2. Negligibly small negative AHE was observed in the present epitaxial sample, differently from the previous polycrystalline sample. This behavior is well corresponding to the *MH*-curve response along c-axis as same as the bulk's one. It thus implies that large AHE comparable to the bulk's one will be obtained when the current flows along the thickness direction. Results for the other oriented films will be presented.

[1] S. Nakatsuji *et al*., Nature 527, 212–215 (2015). [2] T. Ikeda *et al*., Appl. Phys. Lett. 113, 222405 (2018). [3] T. Ikeda *et al*., IEEE Trans. Magn. 10.1109, 2899223 (2019).

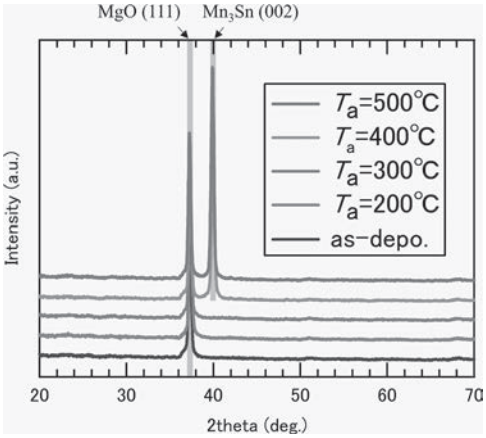


Fig.1 XRD patterns of the samples on MgO (111) sub., as-deposited and annealed at various temperatures.

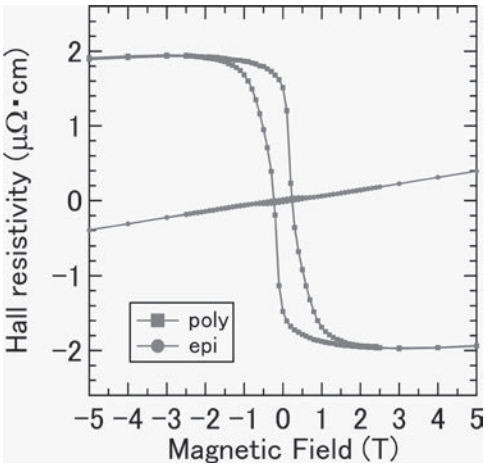


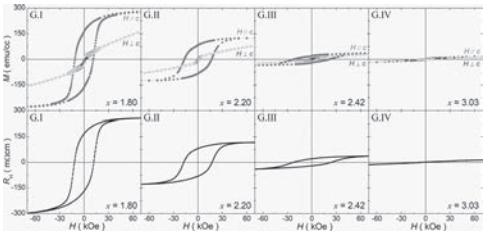
Fig.2 Hall curves measured for the present epitaxial thin film and polycrystalline thin film.

CP-17. Gradual phase transition from ferromagnetic tetragonal to antiferromagnetic cubic states in Mn_xGa ($1.8 \leq x \leq 3.0$) thin films. Y. Jang[1], W. Yoo[1], H. Bang[1], C. Kim[1], Y. Lee[2], K. Lee[3] and *M. Jung*[1] *1. Department of Physics, Sogang University, Seoul, The Republic of Korea; 2. Korea Institute of Science and Technology, Seoul, The Republic of Korea; 3. Mainz University, Mainz, Germany*

The $D0_{22}$ tetragonal structure of Mn_3Ga has a ferrimagnetic state with the net magnetization of about 150 emu/cc [1]. The deficiency of manganese introduces vacancies in the Mn I sites, while maintaining the tetragonal crystal structure. The $D0_{22}$ tetragonal phase in Mn_xGa is formed in a wide range of Mn concentration x from 1.8 to 2.9 [2]. In the case of Mn_2Ga, only Mn II atoms are left and aligned ferromagnetically, so that the magnetization increases up to 400 emu/cc [3]. The cubic phase of Mn_3Ga is anticipated to possess collinear antiferromagnetic order and complete spin polarization as one of the key materials to lower energy loss in spintronic device applications. Our preliminary experiments have demonstrated the cubic phase in Mn_3Ga films displays an antiferromagnetic transition at T_N = 400 K [4]. Thus, one can naturally expect the change of magnetic and electronic properties dependent on the crystal structure from tetragonal Mn_2Ga to cubic Mn_3Ga. In this study, we report the systematic results on the phase change from a ferromagnetic tetragonal structure to an antiferromagnetic cubic structure in a wide range of Mn composition ($1.80 \leq x \leq 3.03$) in Mn_xGa thin films. The structural, magnetic, and electronic properties of Mn_xGa thin films are investigated as varying the Mn composition. The variation of x in Mn_xGa films dramatically changes the crystal structure as well as the magnetic properties. With increasing x, we observe the gradual phase

transition from a ferromagnetic tetragonal state to an antiferromagnetic cubic state. The structural characterization reveals that the $D0_{22}$ tetragonal structure of Mn_2Ga is slowly transformed to the $L1_2$ cubic structure of Mn_3Ga. Two phases coexist around $x = 2.4$. The magnetization is systematically reduced as x increases, ending to an antiferromagnetic state of cubic Mn_3Ga, and the electrical resistivity increases with x. Such highly tunable magnetic and electronic properties in Mn_xGa phase simply by the variation of the Mn/Ga ratio provide advantages to be used for spintronic device applications.

[1] E. Krén and G. Kádár, Solid State Commun., 1970, 8, 1653-1655. [2] H. Niida, T. Hori, H. Onodera, Y. Yamaguchi and Y. Nakagawa, J. Appl. Phys., 1996, 79, 5946-5948. [3] S. Mizukami, T. Kubota, F. Wu, X. Zhang, T. Miyazaki, H. Naganuma, M. Oogane, A. Sakuma and Y. Ando, Phys. Rev. B, 2012, 85, 014416. [4] H. W. Bang, W. Yoo, C. Kim, S. Lee, J. Gu, Y. Park, K. Lee and M. H. Jung, 2019, arXiv:1901.09524.



Magnetization $M(H)$ and Hall resistivity R_H curves for G.I ($x = 1.80$), G.II ($x = 2.20$), G.III ($x = 2.42$), and G.IV ($x = 3.03$).

CP-18. Withdrawn

Session CQ
BIOMEDICAL APPLICATIONS I
(Poster Session)

Bethanie Stadler, Chair
University of Minnesota, Minneapolis, MN, United States

CQ-01. Using repetitive paired-pulse transcranial magnetic stimulation for evaluation of motor cortex excitability. T. Torii[1], A. Sato[1], *M. Iwahashi*[2] and K. Iramina[3] *1. Medical Care and Welfare Engineering, Tokai University, Kumamoto, Japan; 2. Clinical Engineering, Komatsu University, Komatsu, Japan; 3. Graduate School of Sytems Life Sciences, Kyushu University, Fukuoka, Japan*

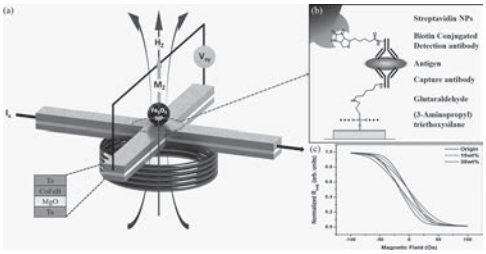
Transcranial magnetic stimulation (TMS) is a noninvasive human brain stimulation method, in which a magnetic field is used to induce eddy currents in the cortex. TMS has mostly been applied to the treatment of brain or neurological diseases, and studies of brain function. However, there has been relatively little research investigating cortical excitability induced by TMS. Previous studies have used a long duration of magnetic stimulation to evaluate cortical excitability (e.g., 0.1 Hz magnetic stimulation for 15 minutes). The present study examined whether cortical excitability could be evaluated using repetitive paired-pulse TMS for a short duration. The inter-stimulus intervals (ISIs) between the conditioning (first) stimulus and the test (second) stimulus were 1000 ms, 200 ms and 100 ms, and magnetic stimulation intensity was 110% of the resting motor threshold. A total of 20 stimuli were delivered to primary motor cortex using paired-pulse TMS at 10 s intervals. The results revealed no significant correlations between the number of stimulations and average motor-evoked potential (MEP) amplitudes at each ISI. However, weak negative correlations were observed for 200 and 100 ms ISIs. This decreasing tendency indicates a cumulative cortical impact of repetitive paired-pulse TMS with ISIs of 200 and 100 ms. Therefore, repetitive paired-pulse TMS with 200 and 100 ms ISIs may require an interval of 10 s or more to avoid exerting a cumulative impact. In addition, MEP amplitude with an ISI of 200 ms increased in the second stimulation ($p < 0.05$), and MEP amplitude with an ISI of 100 ms decreased dramatically ($p < 0.01$). However, MEP amplitude with a 1000 ms ISI did not change significantly. Previous research suggested that successive stimulation at a frequency of 1 Hz or less inhibited cortical excitability. The current findings suggested that cortical excitability after the first stimulation was facilitated at 200 ms, and inhibited at 100 ms. In contrast, repetitive paired-pulse TMS may appear to not affect the cortex after 1000 ms from first stimulation. Thus, the current findings indicate that repetitive paired-pulse TMS with an ISI of 1000 ms could be used to evaluate cortical excitability.

1. *R. Chen et al., Depression of motor cortex excitability by low-frequency transcranial magnetic stimulation, Neurology, 48(5), 1398–1403, 1997.* 2. *T. Kujirai et al., Corticocortical inhibition in human motor cortex, J Physiol., 471, 501–519, 1993.* 3. *E. M. Wassermann, Risk and safety of repetitive transcranial magnetic stimulation: report and suggested guidelines from the International Workshop on the Safety of Repetitive Transcranial Magnetic Stimulation, Electroencephalogr Clin Neurophysiol. 108(1), 1–16, 1998.* 4. *F. Maeda et al., Interindividual variability of the modulatory effects of repetitive transcranial magnetic stimulation on cortical excitability, Exp Brain Res., 133, 425–430, 2000.*

CQ-02. Immunoassay Using a CoFeB/MgO Perpendicular Magnetic Sensor. *C. Cheng*[1], K. Chang[1], S. Kao[1] and Y. Tseng[1] *1. National Chiao Tung University, Hsinchu, Taiwan*

This work reports on a Hall sensor using CoFeB/MgO perpendicular magnetic structure for immunoassays. Fe_3O_4 nanoparticles (NPs) were used to bind to a biotin-avidin system and conjugated antibody on the sensor surface for antigen capture. The amount of bound NP can quantitatively reflect the antigen concentration by monitoring the R_{AHE}-H (anomalous Hall effect (AHE) resistance vs magnetic field) change of the sensor. This is because the R_{AHE}-H is determined by the stray-field yielded by the attached NPs. The sensor presented reproducible R_{AHE} change with antigen-concentration dependence for H < 100 Oe. This demonstrates the potential of the sensor as an electronic-based immunoassay detector. The sensor's detecting sensitivity was tunable with the interfacial magnetic anisotropy of the state-of-the-art CoFeB/MgO heterostructure [1]. The combination of the CoFeB/MgO stack and a perpendicular magnetic coil is the core of the design, at which the coil is to trigger the NPs' stray field as well as to enable the AHE measurement. COMSOL Multiphysics simulation was combined with experiments to explore the sensor's detection limit. Arduino prototyping platform was employed to test the modularization of the proposed sensor, through which the read-out signal could be magnified by a factor of ten. The proposed sensor may facilitate the idea of digital medicine with spintronic technology.

[1]: S. Ikeda et al., *Nature Mater*. 9, 721 (2010)



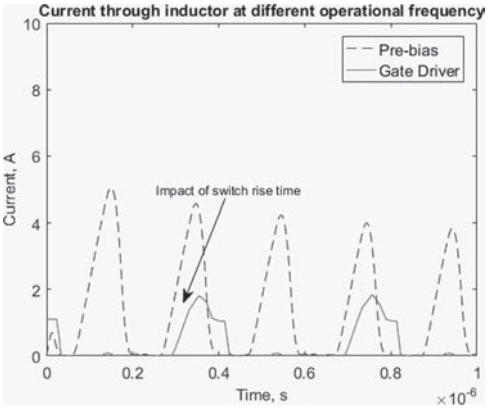
(a) Illustration for the design and measurement of the proposed Hall bio-sensor. The Hall device is composed of a Ta/CoFeB/MgO/Ta stack. Functionalization is placed at the intersection part of the Hall device, which allows a local binding of Fe_3O_4 NPs. (b) Detail of the functionalization on the sensor surface for biological sensing. 3-Aminopropyl triethoxysilane (APTES) conjugated glutaraldehyde is to bind the antibody, which functionalizes the sensor surface and enables the capture of the antigen. The biotin-conjugated detection antibody binds the antigen to the NPs that are streptavidin-functionalized. (c) R_{AHE} change with various antigen/NP concentrations. Origin refers to the antigen/NP-free condition.

CQ-03. Monophasic pulsed field generation with an optimized switching mechanism. *N. Prabhu Gaunkar*[1], W. Theh[1] and M. Mina[1] *1. Electrical and Computer Engineering, Iowa State University, Ames, IA, United States*

Pulsed magnetic fields play a significant role in the application space of magnetic resonance, medical therapy, and brain stimulation since magnetic moments/neurons produce predictable responses to pulsed fields [1,2]. Specific parameters such as pulsed-field magnitude, frequency and repetition rate, are controlled to observe the different biological phenomena. In essence, all these parameters depend on the pulsed field switching mechanism. Thus, the focus of this work is to evaluate and improve the pulsed field switching process for a monophasic pulsed field generator. The designed pulsed field generator is relevant for low-field magnetic resonance applications. It must be noted that several conventional pulsed field switching

methods exist [3,4] but most of these are designed for high-field systems and aren't directly applicable to low-field applications. In the low-field magnetic resonance application space, localized pulsed fields in the frequency range of 5-10 MHz with fields <0.1 T are used [5]. Switching devices (such as FETs or transistors) are connected to inductive loads to obtain pulsed currents correspondingly leading to the generation of pulsed fields. However, it is observed that the rise time of the switching device affects the pulsed currents and thus lower pulsed fields or delayed responses are obtained [5]. To overcome the impact of the switching rise time on the pulsed fields, simulations were performed to verify rise time minimization techniques such as pre-biasing, charging gate capacitance, and use of gate drivers. Design considerations and improvements presented by these different techniques will be discussed as a part of this work. The design of an improved monophasic pulsed field generator will be presented and compared to prior designs [5,6].

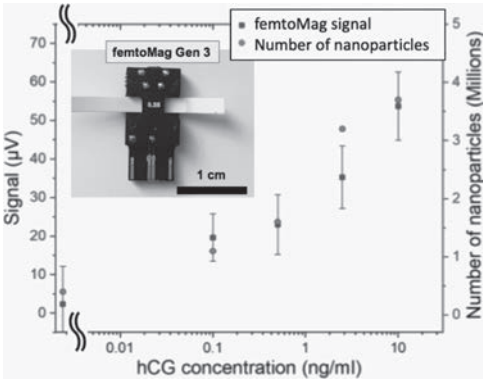
[1]. A. Oliviero, L. Mordillo Mateos, P. Arias, I. Panyavin, G. Foffani, and J. Aguilar, The Journal of physiology 589, no. 20 (2011): 4949-4958. [2]. J. Lerch, A. Van der Kouwe, A. Raznahan, T. Paus, H. Johansen-Berg, K. L. Miller, S. M. Smith, B. Fischl, and S. N. Sotiropoulos, Nature Neuroscience 20, no. 3 (2017): 314. [3]. J. Liu, Y. Wang, Y. Chen, H. Xiong, and W. Sun, Review of Scientific Instruments 90, no. 1 (2019): 016101. [4]. J. Selvaraj, P. Rastogi, N. Prabhu Gaunkar, R. L. Hadimani, and M. Mina, 54(11), 5200405, 2018 [5]. N. Prabhu Gaunkar, R. Weber, M. Mina, and D. Jiles. 53(11), 6501004, 2017. [6]. N. Prabhu Gaunkar, J. Selvaraj, W. Theh, R. Weber, and M. Mina, AIP Advances 8, no. 5 (2018): 056814.



Comparison of simulated pulsed currents for switching circuits using a pre-bias circuit (blue) and a gate driver (red)

CQ-04. Point-of-care ultrahigh sensitivity magnetic lateral flow assay.
M. Khodadadi[1], J. Trabuco[1], L.V. Chang[1], K. Kourentzi[1], R. Willson[1] and *D. Litvinov*[1] *1. University of Houston, Houston, TX, United States*

Today, many highly quantitative biomarker detection tools for medical diagnostics are readily available in state-of-the-art centralized clinical laboratories. However, there remains a critical need for inexpensive, versatile, and high-sensitivity diagnostic platforms which can bring the performance to the point of care (POC) or doctor's office. Our team has developed an ultrasensitive point of care biosensor based on the miniaturized inductive detector of magnetic reporter nanoparticles (10^{-10} emu detection limit) in a test line of a lateral flow assay (like a pregnancy test). This technology represents a new general biosensor platform that can be broadly useful in various areas of molecular diagnostics, therapy monitoring, biomarker detection, and biomedical research. The biosensor prototype performance was evaluated using a standard hCG model system with well-established LFA immunochemistry based on readily available, well-characterized and inexpensive antibodies. The LFA half-strip was prepared on a nitrocellulose membrane with an absorbent pad. Polyclonal anti-α hCG antibody and anti-mouse antibody (1μg/cm each) were used to functionalize the test and control lines, respectively. hCG model protein was diluted in LFA Buffer and 10 μL of each sample was mixed with 1 μL (~10^8) of conjugated 200nm Adembeads functionalized with mouse monoclonal anti-β hCG and the 3 mm half-strip was dipped in the mixture. The test line and control line on each strip was measured by passing the strip through the femtoMag chip and recording the signal in real-time. For system calibration, each line was cut from the LFA strip to be measured in the AGFM. The Figure compares the test line measurements for an LFA with various concentration of hCG using the biosensor and an AGFM. The number of magnetic nanoparticles reported is estimated from the AGFM measurements using a calibration sample with known amounts of 200 nm Adembeads.



The biosensor (left) and AGFM (right) is used to quantify the number of magnetic nanoparticles immobilized in the test line of an LFA test strip using various concentration of hCG pregnancy hormone. The blank sample (left-most data point) has no hCG and represents the amount of non-specifically bound particles.

CQ-05. Magnetically Activated Cell Capture and Release using Spin Orbit Torque.
V.M. Estrada[1], R. Zheng[1], G. Carman[1] and A. Sepulveda[1] *1. Mechanical and Aerospace Engineering, University of California, Los Angeles, Los Angeles, CA, United States*

Cell sorting has become an indispensable technique for a variety of biological and biomedical applications. With the development of fields such as personalized medicine and new breakthroughs in cancer treatments, more modern cell sorting techniques aimed at addressing the problems at hand are needed now more than ever. Magnetically activated cell sorting (MACS) has quickly become one of the most widely used techniques due to its high performance in throughput, selectivity, and ease of use. Recently, there has been much research and development aimed at creating MACS devices in the microfluidic regime[1]. This is due to the many benefits of using such devices. These benefits include: low cost, the ability to run fast low volume experiments, and the ability to capture and release cells while simultaneously culturing them within a device. In this paper we present a novel method of capturing and releasing magnetically activated cells using spin orbit torque (SOT) to change the magnetization of magnetic films with perpendicular magnetic anisotropy (PMA) placed within a microfluidic device. SOT has been shown to be a reliable method of manipulating the magnetization of magnetic memory devices with PMA[2] and for this reason it was chosen as the method of operation. This device is an improvement on current microfluidic cell sorting approaches due to its simple mechanism and high selectivity. The paper includes both modeling and experimental data to verify the theoretical mechanism proposed.

[1]Iv, C. W., Reyes, C. D., & López, G. P. (2015). Microfluidic cell sorting: A review of the advances in the separation of cells from debulking to rare cell isolation. *Lab on a Chip, 15*(5), 1230-1249. doi:10.1039/c4lc01246a [2]Kwak, W., Kwon, J., Grünberg, P., Han, S. H., & Cho, B. K. (2018). Current-induced magnetic switching with spin-orbit torque in an interlayer-coupled junction with a Ta spacer layer. *Scientific Reports, 8*(1). doi:10.1038/s41598-018-22122-1

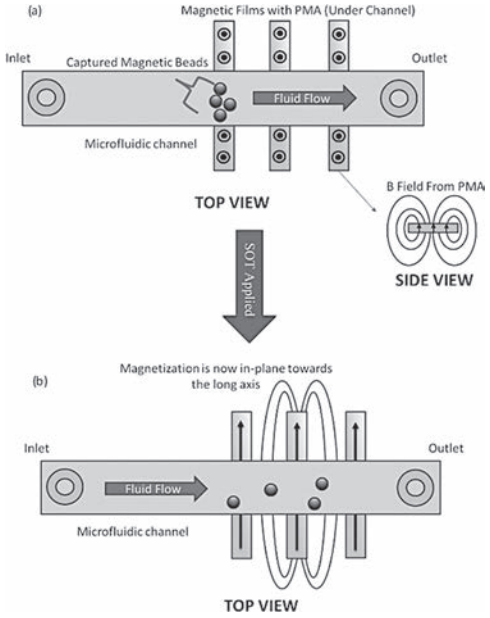


Fig. 1 Schematic of the proposed Device and Operation Principle. (a) The magnetic beads are captured due to a strong magnetic field gradient at the surface of the films due to their PMA. (b) The beads are released due to the drag force of the fluid overcoming the magnetic attraction of the beads to the film. This occurs because the magnetization has changed from out of plane to in-plane. The change in magnetization is performed by running a current that exerts a SOT on the films.

CQ-06. Magnetic Properties and Hyperthermia Behavior of Iron Oxide Nanoparticle Clusters. *S. Pourmiri*[1], V. Tzitzios[2,3], G.C. Hadjipanayis[1], B. Meneses Brassea[4] and A.A. El-Gendy[4] *1. Physics, University of Delaware, Newark, DE, United States; 2. Department of Chemical Engineering, Khalifa University of Science and Technology, Abu Dhabi, United Arab Emirates; 3. NCSR Demokritos, Athens, Greece; 4. Physics, University of Texas at El Paso, El Paso, TX, United States*

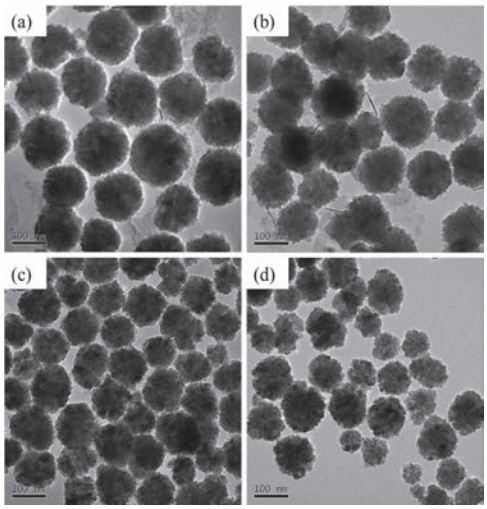
Magnetic iron oxide nanoparticles have a great potential for magnetic hyperthermia, due to their low cost, tunable properties, and biocompatibility. In particular, Iron oxide nanoparticle clusters have been found to have higher magnetization and better colloidal stability than individual nanoparticles, making them better suited for magnetic hyperthermia [1]. In this study, Fe_3O_4 nanoparticle clusters have been made from two different sizes of individual nanoparticles. The synthesis was done by adding a CTAB aqua solution to individual Fe_3O_4 nanoparticles, which were mixed in chloroform. It has been observed that the time, temperature and CTAB concentration were the three important factors for controlling the size, shape and collective behavior of the clusters. The impact of each of these three factors on the aggregation behavior of clusters has been studied. Powder XRD studies shows that the clusters have the Fe_3O_4 phase. Dynamic Light Scattering (DLS) shows that the clusters can have a hydrodynamic diameter in the range of 100 to 200 nm. The growth of nanoparticle clusters has been studied by TEM measurements and is in a good agreement with the DLS values. Magnetic measurements show that saturation magnetization of clusters can be changed from 52 emu/g to 68 emu/g by just changing the size of individual particles from 7 nm to 11 nm. Also, the blocking temperature for Fe_3O_4 clusters was increased from 250 K to 300 K which confirms the stronger collective behavior in the case of bigger nanoparticles. The magnetic hyperthermia behavior of the clusters is studied, and it is seen that by increasing the size of nanoparticles, the SAR value for clusters was increased from 14 W/g to 67 W/g.

[1] P. Qiu, C. Jensen, N. Charity, R. Towner and C. Mao, Journal of the American Chemical Society., 132(50) (2010).

CQ-07. Investigations of the effective parameters on the synthesis of monodispersed magnetic Fe_3O_4 by solvothermal method for biomedical applications. G.C. Hermosa[1], W. Chen[1], H. Wu[1], C. Liao[1], S. Wang[2], Y. Chen[1,3], C. Koh[3] and *A. Sun*[1] *1. Department of Chemical Engineering and Materials Science, Yuan Ze University, Taoyuan, Taiwan; 2. Department of Materials and Mineral Resources Engineering, National Taipei University of Technology, Taipei, Taiwan; 3. Department of Surgery, Far Eastern Memorial Hospital, New Taipei, Taiwan*

Iron oxide nanoparticles, such as magnetite (Fe_3O_4) is by far the most commonly employed in different fields in particular in biomedical applications. These nanoparticles are especially interesting, because of their excellent chemical stability, low toxicity, readily accessibility, high coercivity and inexpensiveness, which makes it a promising material. All these technological and medical applications require that the nanoparticles are superparamagnetic with smaller sizes and the overall particle size distribution is narrow so that the particles have uniform physical and chemical properties. To apply superparamagnetic nanoparticles for biomedical applications, the nanoparticles should be monodispersed for controlled biodistribution and contrast effects. Therefore, much effort has focused on the development of Fe_3O_4. The solvothermal process is one of the successful methods to obtain Fe_3O_4 fine particles with highly uniform sizes, hydrophilic surface and aqueous dispersibility. These characteristics can be altered by changing certain experimental parameters, including water and stabilizing agent amount and pH. In this study, monodispersed magnetite nanoparticles were obtained by investigating the different synthesis parameters of the solvothermal method. The morphology and chemical structure of the Fe_3O_4 nanoparticles were characterized by FT-IR, XRD, SEM, TEM, DLS and VSM. Results indicated that the without the addition of water as it forms the minor phase of iron instead of magnetite. Furthermore, the size of nanoparticles is tunable in the range of 50 to 150 nm by changing the amounts of water, PSSMA and NaOH. The amount of PSSMA restricts the growth of the nanoparticles and narrow the size distribution and a hydrophilic surface was obtained. Synthesized magnetite nanoparticles were successfully conjugated with carbon dots for bio-imaging application. The resulting nanoparticles exhibited good fluorescence characteristics. Cytotoxicity tests confirmed that nanoparticles are non-toxic. The synthesized monodispersed magnetite nanoparticles are good potential candidates for biomedical applications in the future.

J. Liu, Z.K. Sun and Y. Deng, Angew. Chem. Int. Ed., 48, 5875 –5879 (2009). L. Feng, M. Caoa and X.Y. Maa, J. Hazard. Mater., 217–218, 439–446 (2012). P. Tartaj, M.P. Morales and G.C. Sabino, Adv. Mater., 23, 5243–5249 (2011). D. Zhang, S.Y. Wei and C.D. Kaila, Nanoscale, 2, 917–919 (2010). G. Salazar-Alvarez, M. Muhammed and A.A. Zagorodni, Chem. Eng. Sci., 61,4625-4633 (2006).



Microstructures of synthesized nanoparticle with (a) 0 (b) 0.5 (c) 1 and (d) 1.5 of PSSMA.

CQ-08. A Simple and Rapid Detection System of Oral Bacteria in Liquid Phase for Point-of-Care Diagnostics using Magnetic Beads.
L. Ton That[1,2], S. Takahashi[1], H. Onodera[2], K. Okita[2], S. Yabukami[1,2], K. Yokota[1,2], M. Furuya[1], H. Kanetaka[1], Y. Miura[3] and H. Takahashi[3]
1. Tohoku University, Sendai, Japan; 2. Tohoku Gakuin University, Tagajo, Japan; 3. JNS Co., Ltd., Natori, Japan

Magnetic beads have gained great interest in recent years for use in biomedical applications such as microorganism detection, hyperthermia therapy, and drug delivery. Currently, ac susceptibility, magnetic relaxation, and remanence-based methods have been developed for microorganism detection by measuring the magnetic field from magnetic nanoparticles bound to microorganisms via detecting antibodies [1]. In this study, we evaluated a simple and rapid detection system of oral bacteria in liquid phase for point-of-care diagnostics using magnetic nanoparticles. We focused on the response of nanoparticles to applied switching magnetic field, i.e. the magnetic moments of the nanoparticles without the bacteria can be easily reversed by switching magnetic field compared to the nanoparticles with the bacteria [2]. Figure 1 shows schematic diagram of laboratory-made system. The system consists of a giant magneto-impedance (GMI) sensor, driving coil (3000 turns), NdFeB magnet (5 mm x 4 mm x 3 mm) and rotor. Firstly, the cultured bacteria sample using magnetic nanoparticles of 500 nm in diameter was magnetized by the NdFeB magnet for 600 sec. Next, a switching magnetic field was applied to the sample for 30 sec by driving coil, then the sample rotated slowly close to the GMI sensor and the magnetic field from magnetic nanoparticles was measured by the sensor. The strength and direction of switching magnetic field were changed to evaluate the response of nanoparticles. Figure 2 shows the relationship of the output signal from the sensor and the number of bacteria with *Porphyromonas gingivalis* and *Pseudomonas aeruginosa* cultured. The results show that the output signal to the switching magnetic field became larger as the number of bacteria increased. Furthermore, it was possible to detect the bacteria in liquid phase with the concentration below 10^5 CFU/ml, which was the same sensitivity as other microbial sensors currently used in point-of-care diagnostics.

[1] K. Enpuku et al., Supercond. Sci. Technol., Vol. 30, pp. 053002 (2017)
[2] W.F. Brown, J. Appl. Phys., Vol. 34, pp. 1319 (1963)

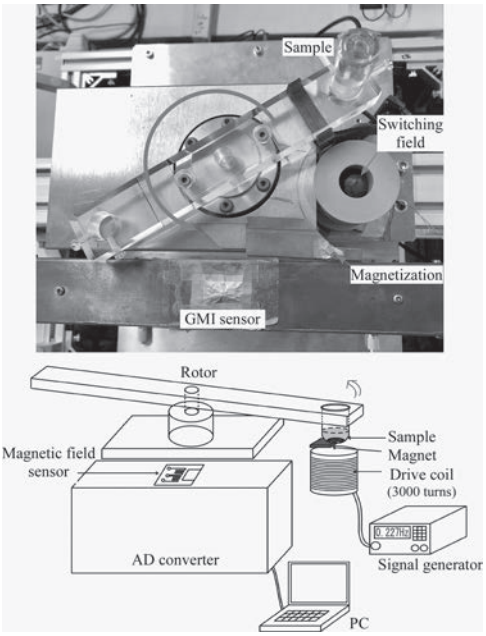


Fig. 1 Schematic diagram of laboratory-made system for detecting bacteria in liquid phase using magnetic nanoparticles.

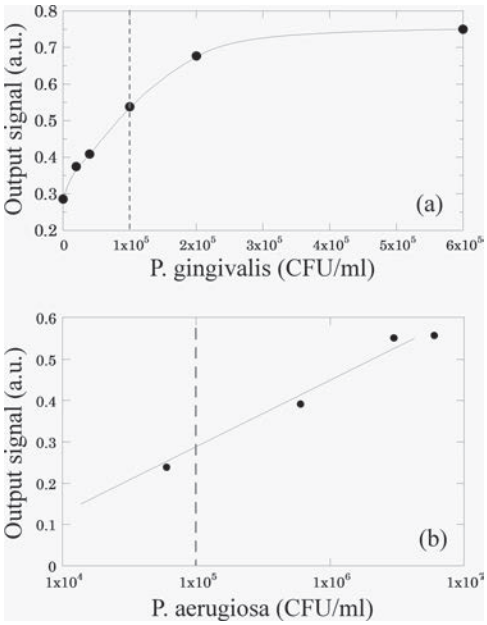


Fig. 2 Relationship between the output signal from GMI sensor and number of bacteria with (a) Porphyromonas gingivalis and (b) Pseudomonas aeruginosa.

CQ-09. Magnetic Characterization Change by Solvents of Magnetic Nanoparticles in Liquid-phase Magnetic Immunoassay.
K. Jinno[1], B. Hiramatsu[1], K. Tsunashima[1], K. Fujimoto[1], K. Sakai[1], T. Kiwa[1] and K. Tsukada[1] *1. Graduate School of Interdisciplinary Science and Engineering in Health Systems, Okayama University, Okayama, Japan*

Magnetic nano-particles (MNPs) have been studied for medical diagnostic purposes—as the imaging agents of MRI, hyperthermia, and drag delivery. Among them, a highly sensitive magnetic immunoassay (MIA) has been developed. The MIA generally uses polymer-coated MNP beads, on the surface of which antibodies are immobilized to detect conjugation with antigens. Conventional immunoassays need to be washed to remove unbounded antibodies from solutions; however, the MIA can estimate the number of conjugated antibodies without being washed because the AC magnetic properties of MNP beads vary when the antibodies are bounded with antigens. Thus, we studied the AC magnetic properties of MNPs under various conditions and substances using a developed MNP measurement system. Variations in the AC magnetic properties are observed owing to variations in the volume, which results in the moment of rotation of beads by conjugation; therefore, the viscosity of the sample solution is considered to affect the AC magnetic properties. Our study revealed that the MNP beads in the serum solution exhibited AC magnetic properties different from those of MNP beads in the buffer solution though the viscosity of the solution was similar. To investigate the influence of serum on the AC magnetic properties, the concentration dependence of sodium chloride in the solution was first measured, because the sodium (Na^+) and chloride (Cl^-) ions in the serum dominate the ion balance of the serum. Resovist was used as MNPs, and susceptibility as a function of the concentration of Na^+ was measure. The results show that the magnetic properties depend on the concentration of Na^+ in the solution as well as the difference in viscosities. We conclude that this dependence was caused by the aggregation of MNPs by shielding the surface charge of the MNPs by ions, which was supported by our AC susceptibility and light scattering measurements for the same MNPs solutions. In this study, we have also evaluated the difference in magnetic properties for different substances as well as different coating and sizes of MNPs. Evidently, the optimization of substances is required for applying the MIA to practical medical diagnosis.

CQ-10. Superparamagnetic gold coated iron nanoparticles for hyperthermia treatment of cancer. M. Sanad[1], B. Meneses Brassea[1], S. Pourmiri[2], G.C. Hadjipanayis[2] and *A.A. El-Gendy*[1] *1. Physics, University of Texas at El Paso, El Paso, TX, United States; 2. Physics and Astronomy, University of Delaware, Newark, DE, United States*

Core/shell iron/gold nanoparticles have been synthesized using wet chemical method. The synthesis conditions have been tailored to obtain monodispersed, biocompatible and high magnetic properties that needed for efficient hyperthermia. The morphology and crystal structure of the prepared core/shell samples have been characterized using SEM, TEM and XRD. The data yielded spherical like shape and identical core/shell morphology with average sizes of 10, 20, 40 nm with FCC structure for iron core and cubic structure for gold shells. The magnetization dependence on external magnetic field exhibited superparamagnetic behavior with saturation magnetization (MS) of 168, 150, and 135 emu/g for sizes of 10, 20, 40 nm respectively. Feasibility of hyperthermia has been measured for particles solution of 5mg/ml under different applied magnetic field and frequencies in the range of 100-500 Oe and 144-304 kHz respectively. The particles showed good dispersion in water and observable increase in the heating rate and the heating power or specific absorption rate (SAR) ranging from 1.5-3.5 C/min and of 20-150 W/g respectively. The data reveal the potential of Fe@Au superparamagnetic nanoparticles for hyperthermia treatment of cancer.

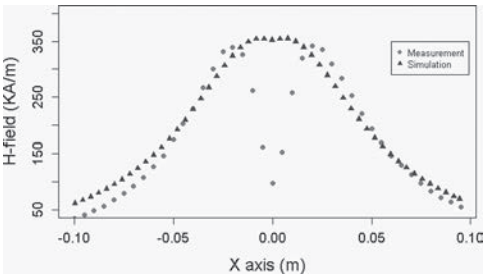
CQ-11. Self-regulating magnetic hyperthermia (SrMH) of Ni_xCu_{1-x} nanoparticles. B. Meneses Brassea[1], S. Pourmiri[2], M. Sanad[1], M. Ortega[1], G.C. Hadjipanayis[2] and *A.A. El-Gendy*[1] *1. Physics, University of Texas at El Paso, El Paso, TX, United States; 2. Physics and Astronomy, University of Delaware, Newark, DE, United States*

NixCu1-x (x=0.2-0.5) nanoparticles have been synthesized with a proper size distribution by reducing a Ni and Cu from metal precursor's using sol-gel route followed by annealing at different temperatures. These particles have been synthesized to be used for controlled self-regulating magnetic hyperthermia applications (SrMH). We have investigated the morphology and crystal structure of the particles revealing spherical shape with average size ranging from 20-50 nm and FCC cubic structure for different compositions of NixCu1-x alloy. The magnetic properties exhibited ferromagnetic behavior with saturation magnetization (MS) ranging from 8-20 emu/g at 300 K and Curie temperature ranging from 42-45°C within the limit of the therapeutic temperature range of 42-46°C. The feasibility of hyperthermia has been performed under the therapeutic limits of alternating magnetic field and frequency. The samples exhibited heating rate and a significant dissipated heating power or measured as specific absorption rate (SAR) ranging from 0.1-1.6 C/min and 20-100 W/g, respectively. The dissipated heating power of the samples saturated after reaching their Curie temperature at 42-45°C revealing their feasibility for self-regulation hyperthermia.

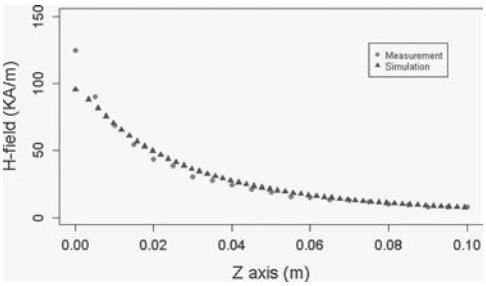
CQ-12. Testing of the prototype of a novel TMS coil with improved focality: Quadruple Butterfly Coil. *X. Zhong*[1], P. Rastogi[1], Y. Tang[1] and D.C. Jiles[1] *1. Electrical and Computer Engineering, Iowa State University, Ames, IA, United States*

Transcranial magnetic stimulation (TMS) is a non-invasive neuromodulation technique that is used or investigated for various neurological disorders such as major depressive disorder, Parkinson's disease, and obsessive compulsive disorder. The design of TMS coil has always been a popular topic in TMS studies as the coil geometry can affect the distribution of induced electric field significantly. A novel coil called Quadruple Butterfly Coil (QBC) has been introduced to improve the focality of stimulation [1]. Recently the prototype of QBC has been fabricated by Jali Medicals which gives us the opportunity to test the validation of this prototype as well as the computational simulation results. A Hall probe and a gaussmeter were used to measure the actual magnetic field strength provided by the prototype of QBC. Measurements were taken along two directions, one is along x axis going through from the center to the end of the two windings of QBC, the other is along z axis moving away from the surface of QBC perpendicularly. The results for the two directions are shown in Figure 2 and 3 from which we can see a good match between the measurements and the simulation results. Therefore, the QBC prototype has shown its success and in turn validate the computational simulations.

[1] P. Rastogi, E. G. Lee, R. L. Hadimani, and D. C. Jiles, "Transcranial Magnetic Stimulation-coil design with improved focality," *AIP Adv.*, vol. 7, no. 5, 2017.



Comparison of measurement data and simulation data along the X axis



Comparison of measurement data and simulation data along the Z axis

CQ-13. A Highly Tunable Skyrmion-based Neurostimulator (SkyNS) for Low-Power Cellular-Level Implantable Magnetic Stimulation. *R. Saha*[1], K. Wu[1], D. Su[2] and J. Wang[1] *1. Electrical & Computer Engineering, University of Minnesota, Minneapolis, MN, United States; 2. Chemical Engineering and Material Science, University of Minnesota, Minneapolis, MN, United States*

Bonmassar *et. al* [1] had explored the possibility of implantable micromagnetic stimulation (μMS) by using commercially available sub-mm sized microcoils to stimulate deep target neuronal tissues. Magnetic field can permeate deep through the biological tissues and the induced electric field from the magnetic neurostimulators are spatially asymmetric, thereby supporting selective activation of neurons [2]. This gives implantable μMS an added edge over deep brain stimulation (DBS) or transcranial magnetic stimulation (TMS). Nevertheless, μMS has been reported to consume 10^3 times greater energy than conventional DBS electrodes which causes detrimental thermal effects on tissues [3]. Here, we propose SkyNS [4], a skyrmion-based neurostimulator of dimension 500 nm × 200 nm × 1 nm with a barrier of higher perpendicular magnetic anisotropy (PMA) situated at the center that operates on a current of 2.71 μA and consumes a power of 1.434 nW. On solving the Landau–Lifshitz–Gilbert (LLG) equation, it was studied that the displacement of magnetic skyrmions in a heavy metal/ferromagnetic metal (HM/FM) bilayer generates a time varying magnetic field (see Fig. 1) which according to Faraday's Law of Electromagnetic Induction, induces an electric field (see Fig. 2) large enough to trigger neuron stimulation. Magnetic material properties including Dzyaloshinskii-Moriya interaction (DMI), PMA of barrier and surrounding thin film and device dimensions on stable skyrmion nucleation and smooth skyrmion dynamics have been extensively tuned to meet the therapeutic specifications for cellular-level neurostimulation. This work provides another proof-of-concept to exploit our proposed spintronic neurostimulators [5,6,7,8] as ultra-low power, implantable magnetic nanostimulators.

[1] G. Bonmassar, S.W. Lee and D.K. Freeman et.al, *Nature communications,* vol. 3, p. 921, 2012. [2] S. W. Lee, F. Falleger and B.D.F. Casse et. al,

Science advances, vol. 2, no. 12, p. e1600889, 2016. [3] Z. B. Kagan, J. T. Mize and P. Kosta et. al, *IEEE Transactions on Neural Systems and Rehabilitation Engineering,* vol. 27, no. 5, pp. 937-946, 2019. [4] R. Saha, K. Wu and D. Su et. al, *arXiv preprint arXiv:1901.01349,* 2019. [5] J.P. Wang, W.C. Low and D.C. Mahendra et. al, US Patent App. 15/130,371, 2016. [6] K. Wu, D. Su and R. Saha et. al, *arXiv preprint arXiv:1903.02726,* 2019. [7] D. Su, K. Wu, R. Saha et. al, *arXiv preprint arXiv:*1906.08701, 2019. [8] R. Saha, K. Wu and D. Su et. al, "Applying Spintronic Nanodevices in Cellular-Level Magnetic Neurostimulation", Neuromodulation Symposium, Minneapolis, MN, USA, 17-18 April, 2019.

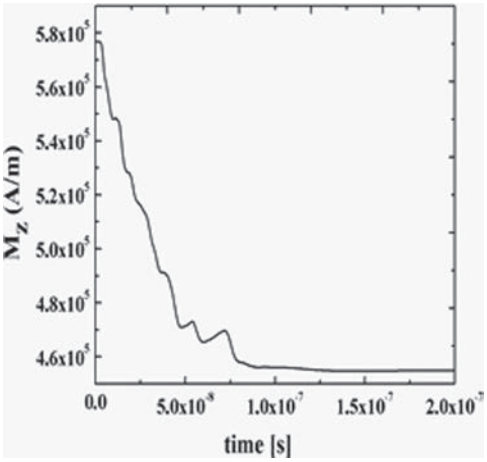


Fig.1. Rate of change of magnetization due to displacement of magnetic skyrmions in the HM/FM bilayer for a single pulse current of 10^{10} A/m^2 of duration 200 ns.

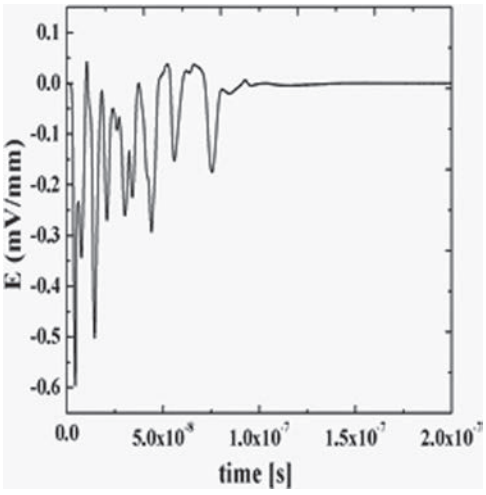


Fig.2. Induced electric field from displacement of magnetic skyrmions in the HM/FM bilayer sufficient for neurostimulation.

CQ-14. Magnetic Nanoparticle Relaxation Dynamics-Based Magnetic Particle Spectroscopy for Rapid and Wash-Free Molecular Sensing.

K. Wu[1], J. Liu[1], D. Su[2], R. Saha[1] and J. Wang[1] *1. Department of Electrical and Computer Engineering, University of Minnesota, Minneapolis, MN, United States; 2. Department of Chemical Engineering and Material Science, University of Minnesota, Minneapolis, MN, United States*

Magnetic nanoparticles (MNPs) have been extensively used as contrasts and tracers for bioimaging, heating sources for tumor therapy, carriers for controlled drug delivery, and labels for magnetic immunoassays. Here, we describe a MNP Brownian relaxation dynamics-based magnetic particle spectroscopy (MPS) method for the quantitative detection of molecular biomarkers. In MPS measurements, the harmonics of oscillating MNPs are recorded and used as a metric for the freedom of rotational motion, which indicates the bound states of the MNPs. These harmonics can be collected from microgram quantities of iron oxide nanoparticles within 10 seconds. Since the harmonics are largely dependent on the quantity of the MNPs in the sample, the MPS bioassay results could be biased by the deviations of MNP quantities in each sample, especially for the very low concentration biomarker detection scenarios. On the other hand, the ratios of the 3rd to the 5th harmonics (R35) at different drive field frequencies have also been used as a MNP quantity-independent metric for characterizing the biomarker concentrations/quantities from samples. Fig. 1 summarizes the harmonic ratios, R35, from six samples as we vary the drive field frequency from 500 Hz to 20 kHz. The harmonic ratios R35 increases as the concentrations/quantities of streptavidin increases. Herein, we report three MNP concentration/quantity-independent metrics for characterizing the bound states of MNPs in MPS. Using a streptavidin-biotin binding system as a model, we demonstrate the feasibility of using MPS and MNP concentration/quantity-independent metrics to sense these molecular interactions, showing this method can achieve rapid, wash-free bioassays, and is suitable for future point-of-care (POC), sensitive, and versatile diagnosis [1].

[1] Wu, K., et al. Magnetic Nanoparticle Relaxation Dynamics-Based Magnetic Particle Spectroscopy for Rapid and Wash-Free Molecular Sensing. ACS Applied Materials & Interfaces. DOI: 10.1021/acsami.9b05233

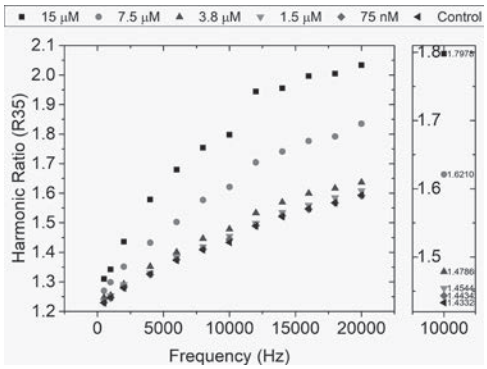


Figure 1. MPS measurements of the ratio of the 3rd to the 5th harmonics (R35) of six MNP samples in different bound states. (a) The harmonic ratios, R35, from six samples as we vary the from 500 Hz to 20 kHz. The inset figure summarizes the R35 under a drive field frequency of for vials I – VI, the R35 values are: 1.7978 (15 mM), 1.6210 (7.5 mM), 1.4786 (3.8 mM), 1.4544 (1.5 mM), 1.4434 (75 nM), and 1.4332 (control, 0 nM), respectively.

Session CR
DAMPING, INTERFACES, AND ANISOTROPY II
(Poster Session)

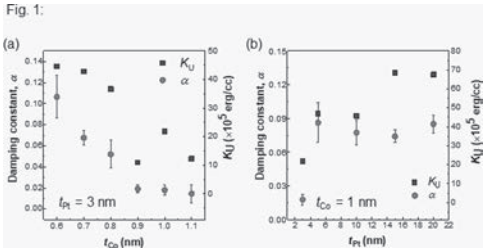
Grant A. Riley, Chair
NIST, Boulder, CO, United States

CR-01. Dynamic magnetic property in Pt/Co/Cr_2O_3/Pt stack films with perpendicular magnetic anisotropy. *T. Nguyen*[1,2], Y. Shiratsuchi[3], H. Sato[4,1], S. Ikeda[4,1], T. Endoh[4,1] and Y. Endo[5,1] *1. Center for Science and Innovation in Spintronics, Tohoku University, Sendai, Japan; 2. Center for Spintronics Research Network, Tohoku University, Sendai, Japan; 3. Graduate School of Engineering, Osaka University, Suita, Japan; 4. Center for Innovative Integrated Electronic Systems, Tohoku University, Sendai, Japan; 5. Graduate School of Engineering, Tohoku University, Sendai, Japan*

Ferromagnetic (FM)/non-magnetic (NM) stack films with perpendicular magnetic anisotropy (PMA) are of increasing interest in spintronics devices with various enriched functionalities [1]. To realize these devices, understanding their dynamic magnetic properties such as the Gilbert damping constant (α) is one of the most important requests. Until now, the relationship between PMA and α for these films was reported, and the results were, however, dispersed among the variation of layered structure [2,3]. Herein, we choose the perpendicularly magnetized Pt/Co/Cr_2O_3/Pt stack films, where Cr_2O_3 is insulating at room temperature with a weak spin-orbit coupling, which enabled us to focus on the dynamic magnetic properties at the Pt/Co interface. Then, we investigate the change in PMA and α with the thickness of Co (t_{Co}) and Pt (t_{Pt}) layers, and discuss their correlation in these stack films. The changes in the perpendicular magnetic anisotropy energy density (K_U) and α of Pt(t_{Pt})/Co(t_{Co})/Cr_2O_3(200 nm)/Pt stacks with t_{Co} and t_{Pt} are shown in Fig. 1 (a) and (b), respectively. In case of the fixed t_{Pt} = 3 nm, K_U decreases as t_{Co} increases except for 0.9 nm. α linearly decreases with the increase of t_{Co} up to 0.9 nm, and saturates for t_{Co} above 0.9 nm. On the other hand, in case of the fixed t_{Co} = 1 nm, as t_{Pt} increases, K_U increases for t_{Pt} below 5 nm, keeps constant for 5 nm ≤ t_{Pt} ≤ 10 nm, again increases for t_{Pt} up to 15 nm, and then saturates for t_{Pt} above 15 nm. α increases as t_{Pt} increases and saturates as t_{Pt} excesses 5 nm. Thus, each behavior of α in the range of thinner t_{Co} (≤0.8nm) and t_{Pt} (≤10nm) is very similar to those of K_U, implying that α is correlated with K_u in these stack films. Therefore, these results reveal that the origin of α is mainly derived from the spin-orbital coupling (SOC) and α value depends on the strength of SOC [4]. In addition, these results could suggest the non-negligible role of the spin-diffusion in the Pt capping layer [5]. Acknowledgment: The authors acknowledge the Core Research Cluster program of Tohoku Univ., Japan. This work was also supported by JSPS KAKENHI Grant Nos. 17K18991, 16H03832, 16H02389, 19H00825. Figure captions: Fig. 1: The changes in α and K_U with (a) t_{Co}; and (b) t_{Pt}.

[1] S. Ikeda *et al.*, Nat. Mater. 9, 721 (2010). [2] S. Mizukami *et al.*, Appl. Phys. Lett. 96, 152502 (2010). [3] S. Pal *et al*., Appl. Phys. Lett. 98, 082501 (2011). [4] H-S. Song *et al*., Appl. Phys. Lett. 103, 022406 (2013). [5] E. Barati *et al*., Phys. Rev. B 93, 054402 (2014).

Fig. 1:



CR-02. Optically Detected Spectroscopy of Magnons Generated in Nonlinear Ferromagnetic Resonance using NV Centers in Diamond. *B. McCullian*[1], A. Thabt[1], B.A. Gray[2], M.S. Wolf[2], A.S. Ahmed[1], V.P. Bhallamudi[3], D.V. Pelekhov[1], M.R. Page[2] and P.C. Hammel[1] *1. Physics, Ohio State University, Columbus, OH, United States; 2. Materials and Manufacturing Directorate, Air Force Research Laboratory, Dayton, OH, United States; 3. Department of Physics, Indian Institute of Technology Madras, Madras, India*

We have used nitrogen-vacancy (NV) centers in diamond to optically detect and spectroscopically map magnons generated in the nonlinear regime of ferromagnetic resonance (FMR) in thin films of low damping NiZnAl ferrite, a material which shows promise for voltage control of magnetization [1]. The spin-state dependence of fluorescence intensity in NV centers enables sensitive optical detection of fluctuating magnetic fields at NV spin transition frequencies which are in the few-GHz range. Applied to ferromagnetic dynamics, this has enabled local, off-resonant spectroscopy of driven uniform-mode FMR [1-3] by monitoring the field-noise associated with NV-resonant magnons generated by the FMR damping process. The low damping of NiZnAl allows us to increase microwave power and drive into the nonlinear FMR regime. NV measurements at high microwave power show very small NV-resonant magnon population at the uniform mode FMR condition, and instead a large occupation of NV-resonant magnons at the field and frequency of the broadened FMR shoulder. To rule out possible heating and very large cone angle effects, we perform stripline FMR at various temperatures, microwave powers, microwave duty cycles, and static magnetic field sweep rates [4-6]. We attribute both the broadened FMR line and the strong generation of magnons at the FMR shoulder to a spinwave instability process. This direct probe of magnons enables study of nonlinear FMR behavior that may have important implications for magnetic switching in memory applications.

[1] S. Emori, et al., Advanced Materials., 29, 1701130 (2017) [2] C. S. Wolfe, et al., Physical Review B, 89, 180406 (2014) [3] C. S. Wolfe, et al., Applied Physics Letters, 108, 232409 (2016) [4] D. Labanowski, et al., Science Advances, eaat6574 (2018) [5] J. Lustikova, et al., Journal of Applied Physics, 177, 073901 (2015) [6] Y. T. Zhang, et al., Journal of Applied Physics, 63, 5433 (1988) [7] Y. T. Zhang, et al., IEEE Transactions on Magnetics., Vol. 22 Issue 5 p.993-995 (1986)

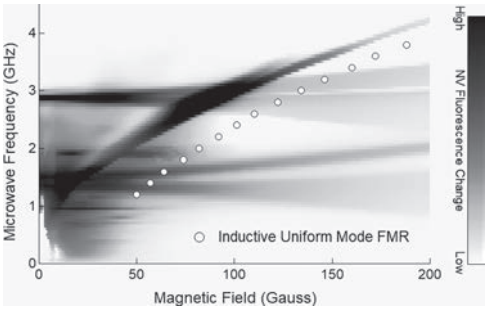


Figure 1: NV detected magnon spectroscopy Change in NV photoluminescence from NiZnAl ferrite at high microwave drive power. Nanodiamonds are drop cast on ferrite surface. Static magnetic field swept along the ferrite <100> crystalline axis. Inductively detected uniform mode FMR (white circles) shows clear spectroscopic separation from the NV fluorescence response.

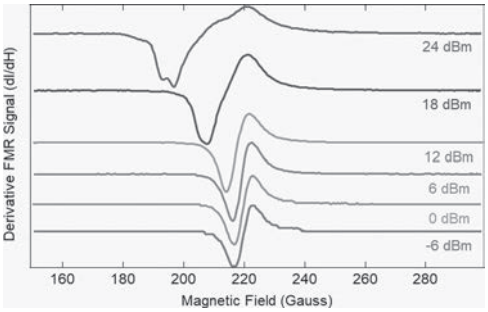


Figure 2: FMR Line Broadening Field-modulated stripline detected FMR at 4 GHz with a swept static magnetic field oriented along <100> for different microwave input powers. The FMR line shows significant broadening with increasing microwave intensity, characteristic of spinwave instability.

CR-03. Fourth-order Magnetic Anisotropy and Interfacial Damping of Co/Ni Multilayers. *A. Rai*[1,2], A. Sapkota[1,2], A. Pokhrel[1,2], M.P. Li[3], M. De Graef[3], C.K. Mewes[1,2], V. Sokalski[3] and T. Mewes[1,2] *1. Department of Physics and Astronomy, The University of Alabama, Tuscaloosa, AL, United States; 2. Center for Materials for Information Technology, The University of Alabama, Tuscaloosa, AL, United States; 3. Department of Materials Sciences and Engineering, Carnegie Mellon University, Pittsburgh, PA, United States*

Co/Ni multilayers have been known to exhibit large and tunable perpendicular magnetic anisotropy (PMA) [1] and relatively low intrinsic damping [2]. In this study we investigated a series of Pt/(Co/Ni)xN/Ir multilayers grown on Si/SiO2 with a Ta adhesion layer and Pt/Ta capping layer. Using broadband ferromagnetic resonance (FMR) and elevation angle dependent measurements, we find the presence of a strong fourth-order contribution to the perpendicular anisotropy. We are able to fit the elevation angle resonance field data and extract both the second and fourth-order anisotropy constants (shown in Fig 1) by using the Smit-Beljers relation [3]. Using the frequency dependence data of the linewidth, we are able to determine the effective Gilbert damping parameter. The effective Gilbert damping increases linearly with the inverse thicknesses of the multilayer, indicating an interfacial contribution to the damping process as shown in Fig 2. We find the spin-mixing conductance to be $g_{\uparrow\downarrow,eff} = (3.1 \pm 0.1) \times 10^{19}$ m^{-2}. Acknowledgements: DARPA TEE: D18AP00011 & NSF-CAREER #1452670

1. G. Daalderop, P. Kelly and F. D. Broeder, Physical Review Letters., vol 68, p:682-685 (1992) 2. J. M. Shaw, H. T. Nembach and T. J. Silva, Journal of Applied Physics., vol 108, p: 093922 (2010) 3. J. Smith and H. Beljers, Philips Research Reports., vol 10, p:113 (1955)

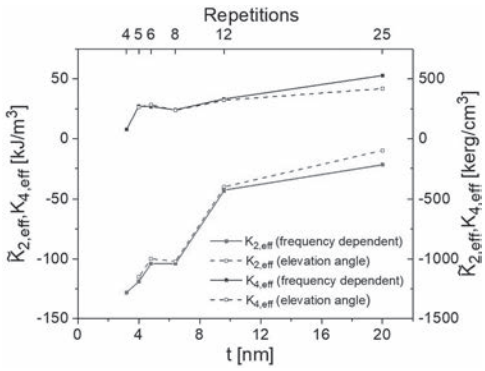


Fig 1: Comparison of second and fourth-order anisotropies using frequency dependent and elevation angle dependent measurements.

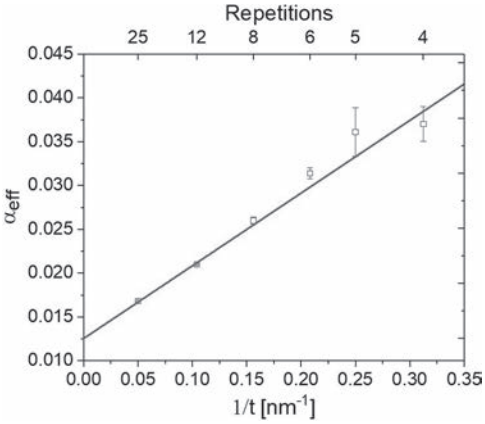
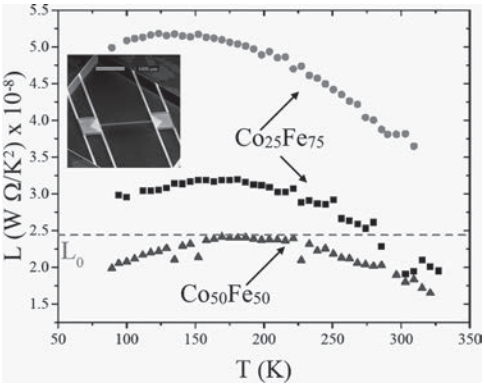


Fig 2: Variation of effective Gilbert damping with the inverse Co/Ni thicknesses.

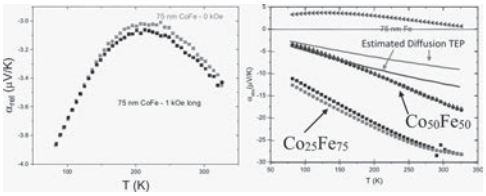
CR-04. Non-electronic Contributions to Thermal Conductivity in a Low-Damping Ferromagnetic Metal. *M.R. Natale*[1], D.J. Wesenberg[1], E. Edwards[2], J.M. Shaw[2] and B.L. Zink[1] *1. Physics & Astronomy, University of Denver, Denver, CO, United States; 2. NIST, Boulder, CO, United States*

Low Gilbert damping materials have many potential applications in the field of spintronics and spincaloritronics. While low-damping magnetic insulators have been studied for decades, recent work has shown that carefully engineered metals can achieve similarly low damping parameter [1]. Low damping suggests that spin waves could contribute to heat transport in such metals[2], though this has yet to be conclusively shown[3]. Here we use suspended Si-N thermal isolation platforms to address this issue by careful examination of the Wiedemann-Franz law in two compositions of Co-Fe alloys, $Co_{25}Fe_{75}$(CoFe-A) and $Co_{50}Fe_{50}$ (CoFe-B). This allows us to better understand how damping affects heat transport via charge, magnons, and phonons. CoFe-A, where the lowest Gilbert damping is seen, has large positive "violations" of the Wiedemann-Franz law, showing non-electronic contributions to thermal conductivity. Comparison to temperature- and field-dependenent Seebeck measurements on the sample samples, which show large contributions beyond simple diffusive thermopower, provides further insights on the non-electronic contributions to thermal conductivity.

[1] M. A. W. Schoen, *et al.*, Nature Physics 12 839 (2016) [2] M. Beens, *et al*., J.Phys. D: Applied Physics 51 394002 (2018) [3] S. Srichandan, *et al*., PRB 98 020406 (2018)



Measured Lorenz number, L=k/σT, for two Co-Fe alloys. Compositions with low Gilbert damping give L far above the free-electron value, indicating large non-electronic contributions to thermal conductivity.



Left: **Relative Seebeck coefficient for Co-Fe shows magnetic field dependence consistent with magnon contributions to thermopower.** ***Right:*** **Absolute thermpower for Co-Fe dramatically exceeds estimated diffusion thermopower, especially in compositions with low damping.**

CR-05. First Principle Calculations for Gilbert Damping Constants of Heusler Alloys in the Consideration of Spin Fluctuation. *R. Hiramatsu*[1], S. Shirakihara[1], D. Miura[1] and A. Sakuma[1] *1. Applied Physics, Tohoku University, Sendai, Japan*

The magnetization damping is of critical importance for development of magnetic devices. In particular, low Gilbert damping are required to achieve high speed and low power consumption devices. Therefore, it has attracted much interest to study magnetic materials with the small damping constants. Especially, because of theoretical prediction about the low damping [1], Heusler alloys have been studied for long time. On the basis of the theory, the low damping comes from the half metallicity of the systems. Thus, it is considered that breaking the half metallicity, such as spin fluctuations, affects on the damping constants. The purpose of our research is to evaluate the effect of spin fluctuations on the damping constants in half metals, on the basis of first principle calculations. To achieve this aim, we assume that the spin direction is restricted to one axis, and the spin fluctuations are expressed by varying the ratio between up and down spins, which was proposed in our previous study [2]. For the calculations of the electronic structures, we employ the first principle tight-binding linear muffin-tin orbital method and apply the coherent-potential-approximation for the spin configurations. The Gilbert damping constants are evaluated on the basis of the torque-correlation model [3]. In addition, to convert spin fluctuations ratio to temperature, we use an experimental results of temperature dependence of magnetization in $L2_1$ structure [4]. Figure 1 and 2 show temperature (T) dependence of the damping constants and the spin polarization at the Fermi level in Co_2MnAl, with $L2_1$, B2 structure, respectively. T_C denotes the Curie temperature of $L2_1$ structure. In the both systems, we can observe that the damping constant is temperature independent in the region of nearly half metal. Whereas, at high temperature range, the damping constants increase with increasing temperature. In the conference, we will also show the property of A2 structure and other Heusler alloys such a Co_2MnSi, and argue its trend in detail.

[1] C. Liu, C. K. A. Mewes, M. Chshiev, T. Mewes and W. H. Butler, Appl. Phys. Lett., Vol. 95, p.022509 (2009). [2] D. Ozaki, D. Miura and A. Sakuma, IEEE Trans. Magn., Vol. 53, p.1300604 (2017). [3] V. Kamberský, Phys. Rev. B, Vol. 76, p.134416 (2007). [4] P. J. Webster, J. Phys. Chem. Solids, Vol. 32, pp.1221-1231 (1971).

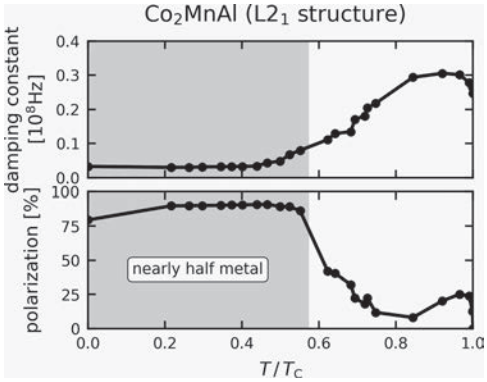


Fig. 1. Calculated results of T dependence of damping constant and polarization in Co_2MnAl $L2_1$ structure.

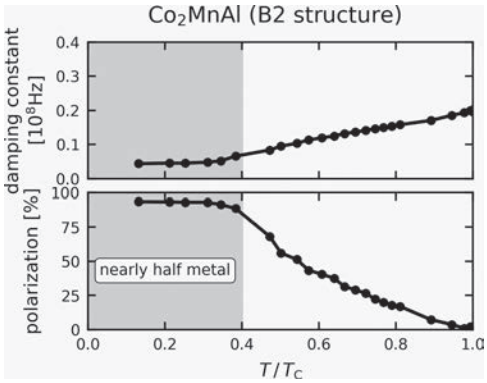


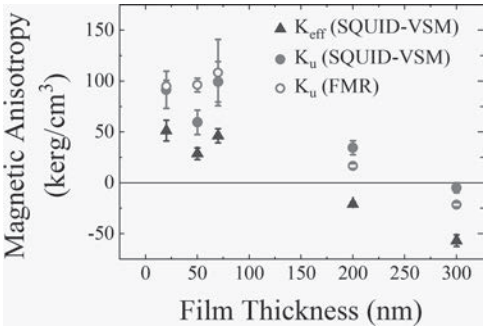
Fig. 2. Calculated results of T dependence of damping constant and polarization in Co_2MnAl B2 structure.

CR-06. Strain-Induced Perpendicular Magnetic Anisotropy and Gilbert Damping of $Tm_3Fe_5O_{12}$ Thin Films. *O. Ciubotariu*[1], A. Semisalova[2], K. Lenz[2] and M. Albrecht[1] *1. Institute of Physics, University of Augsburg, Augsburg, Germany; 2. Institute of Ion Beam Physics and Materials Research, Helmholtz-Zentrum Dresden-Rossendorf, Dresden, Germany*

Over the past years, iron garnets thin films have attracted a lot of attention in the field of spintronics and magnonics due to the superior magnetic properties of $Y_3Fe_5O_{12}$ (YIG). The insulating nature and low Gilbert damping (10^{-4}) make YIG the prototype material for the investigation of fundamental phenomena with potential applications in spin-wave-based technologies. In this regard, the control of the magnetic easy axis direction would open new potential applications. Tensile strained films grown on largely mismatched substrates or implemented in engineered heterostructures show perpendicular magnetic anisotropy (PMA) [1,2]. Other rare-earth iron garnets can also possess PMA when grown under tensile or compressive strain depending on the sign of the magnetostriction constant. Such an example is $Tm_3Fe_5O_{12}$ (TmIG) [3]. However, despite contradicting reports, no systematic study was performed to investigate the effect of TmIG film thickness grown on sGGG(111) substrates on the structural and magnetic properties. In this study, TmIG films with thicknesses between 20 and 300 nm are epitaxially grown by pulsed laser deposition on sGGG(111) substrates. Structural characterization shows that films thinner than 200 nm show in-plane tensile strain, thus exhibiting PMA due to strain-induced magnetoelastic anisotropy. However, with increasing film thickness a relaxation of the unit cell is observed resulting in the rotation of the magnetic easy axis towards the sample plane due to the dominant shape anisotropy. Furthermore, the Gilbert

damping parameter is found to be in the range of 0.02 for the entire film series. Our results show promising properties needed for the integration of TmIG films in heterostructures designed for spin-wave propagation.

[1] G. Li et al., APL Materials 7, 041104 (2019). [2] J. Fu et al., Applied Physics Letters 110, 202403 (2017). [3] C.O. Avci et al., Nature Materials 16, 309 (2017).



Dependence of magnetic anisotropy on TmIG film thickness.

CR-07. Ferrimagnetic Domain Wall Dynamics through the Compensation Points. *E. Haltz*[1], J. Sampaio[1] and A. Mougin[1] *1. Laboratoire de Physique des Solides, Orsay, France*

The manipulation of magnetisation via spin current offers new perspective for processing and storage of non-volatile information. To increase the efficiency of spin torques on magnetic texture (by Spin-Transfer-Torque (STT) or Spin-Orbit-Torque (SOT)), it is proposed to use materials mixing different magnetic sub-lattices antiferromagnetically coupled (AFC) [1]. The conventional mechanisms involved in this new dynamics have to be revisited. Here, new simulations or analytical approaches are developed in rare earth-transition metal amorphous ferrimagnetic alloys whose properties are tuneable changing the temperature or the chemical composition [2]. At so-called compensation points, the net magnetisation or the net angular momentum vanishes. Recent experimental studies, including our work, show very interesting properties as the fast Domain Wall motion (DW,) driven by field or SOT [3] crossing compensation points. The magnetic properties of GdCo ferrimagnetic alloy are simulated using mean field theory. Quantitative values are used in micro-magnetic simulations to investigate DW dynamics under field, STT or SOT. To mimic the magnetic alloy structure, micro-magnetic simulations consider two magnetic momentums of Gd and Co interacting each other by AFC. Field acts on both sub-lattices whereas, as expected, the spin injection interact only with the Co population. DWM driven by field and spin current simulated for a large range of chemical composition reveals translational or precessional modes separated by Walker-like threshold (including DMI [4]). As a further support, two analytical approaches are used. First, in a strong AFC approximation, it is possible to consider the alloy as a ferromagnet with effective parameters. Calculations using standard q-φ model (q, the DW position, and φ its internal magnetisation angle) explain most of results. However, few of the effective parameters exhibit non-physical divergences at compensation points. The laters are solved considering an eventual tilt between magnetic moments of both sub-lattices. In a new model, 2 couples of coordinates (q1- φ1 and q2- φ2, one for each sub-lattice) describe two AFC DWs and a tilt can arise from any a difference (q1-q2) or (φ1-φ2).

[1] Haltz et al., PRB 99 (2019) [2] Hansen et al., J.Appl. Phys 66(2) (1989), Haltz et al., Phys.Rev.Mat. 2 (2018) [3] Kim et al., Nat.Mat. 16 (2017), Caretta et al., Nat.Nano.13 (2018), Siddiqui et al.,PRB 121 (2018) [4] Thiaville et al., EPL 100 (2012)

CR-08. Temperature Dependence of Magnetic Resonance in Ferrimagnetic GdFeCo Alloys. *T. Okuno*[1], S. Kim[2,4], T. Moriyama[1], D. Kim[1], H. Mizuno[1,3], T. Ikebuchi[1], Y. Hirata[1], H. Yoshikawa[5], A. Tsukamoto[5], K. Kim[6], Y. Shiota[1], K. Lee[7,8] and T. Ono[1,9] *1. Institute for Chemical Research, Kyoto University, Uji-City, Japan; 2. Department of Physics and Astronomy, University of Missouri, Columbia, MO, United States; 3. Institute for Solid State Physics, University of Tokyo, Kashiwa, Japan; 4. Department of Physics and Astronomy, University of California Los Angeles, Los Angeles, CA, United States; 5. College of Science and Technology, Nihon University, Funabashi, Japan; 6. Department of Physics, Korea Advanced Institute of Science and Technology, Daejeon, The Republic of Korea; 7. Department of Materials Science & Engineering, Korea University, Seoul, The Republic of Korea; 8. KU-KIST Graduate School of Converging Science and Technology, Korea University, Seoul, The Republic of Korea; 9. Center for Spintronics Research Network (CSRN), Graduate School of Engineering Science, Osaka University, Osaka, Japan*

Antiferromagnetic spintronics has been gaining much attention in both fundamental and practical points of view [1,2]. Antiferromagnetically-coupled ferrimagnets have recently been emerging as useful material platforms for studying antiferromagnetic dynamics since we can use conventional techniques for ferromagnets to investigate them. Both field-driven [3] and current-driven [4,5] domain-wall dynamics in ferrimagnets are found to be fastest at the angular momentum compensation temperature T_A, indicating that the magnetic dynamics becomes antiferromagnetic-like. In the context of the antiferromagnetic-like dynamics, however, the ferrimagnetic resonance (FiMR) has not been fully clarified. In this presentation, we revisit the FiMR in ferrimangetic GdFeCo compounds theoretically and experimentally, and show the rigorous analysis for the FiMR. For this study, we used a 5-nm SiN/10-nm $Gd_{25.0}Fe_{65.6}Co_{9.4}$/5-nm Pt/100-nm SiN/Si substrate. We measured spin-torque induced FiMR spectra at several temperatures T between 220 K and 295 K by using the homodyne technique. It is found that the spectral linewidth of the resonance peak strongly depends on T. From those FiMR spectra, we calculate the two versions of the effective Gilbert damping parameter: α_{FM} based on the conventional expressions of ferromagnetic resonance [6] and α_{FiM} based on our theory for FiMR that accounts for the difference between the net spin density and the saturated total spin density in ferrimagnets. As shown in Fig. 1, α_{FM} increases significantly as T approaches T_A, in good agreement with Ref. [6], while α_{FiM}(≈0.01) is insensitive T to in sharp contrast to α_{FM}. This indicates that the T dependence of the spectral linewidth in FiMR is attributed to the T dependence of the net spin density instead of that of α_{FM}. Our results provide a clear evidence that properly defined Gilbert damping parameter α_{FiM} of ferrimagnets is insensitive to T, which is consistent with some recent reports [7,8].

[1] T. Jungwirth, X. Marti and P. Wadley, Nat. Nanotechnol., Vol. 11, p.231 (2016) [2] V. Baltz, A. Manchon and M. Tsoi, Rev. Mod. Phys., Vol. 90, p.015005 (2018) [3] K.-J. Kim, S. K. Kim and Y. Hirata, Nat. Mater., Vol. 16, p.1187 (2017) [4] S. A. Siddiqui, J. Han and J. T. Finley, Phys. Rev. Lett., Vol. 121, p.057701 (2018) [5] L. Caretta, M. Mann and F. Büttner, Nat. Nanotechnol., Vol. 13, p.1154 (2018) [6] C. D. Stanciu, A. V. Kimel and F. Hansteen, Phys. Rev. B, Vol. 73, p.220402(R) (2006) [7] A. Kamra, R. E. Troncoso and W. Belzig, Phys. Rev. B, Vol. 98, p.184402 (2018) [8] D.-H. Kim, T. Okuno and S. K. Kim, Phys. Rev. Lett., Vol. 112, p.127203 (2019)

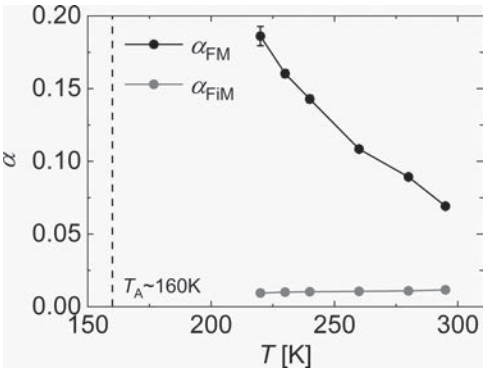
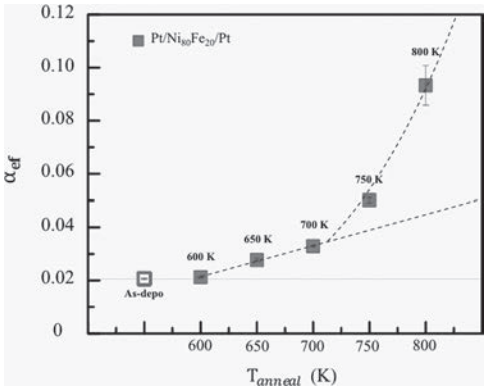


Fig. 1 The effective Gilbert damping parameter α_{FM} and the properly defined Gilbert damping parameter α_{FiM} as functions of temperature.

CR-09. Thermal intermixing effect on Gilbert damping of sputter-grown Pt/$Ni_{80}Fe_{20}$/Pt sandwich trilayers. *Y. Kim*[1], B. Kim[1], B. Bhoi[1], Y. Kim[1] and S. Kim[1] *1. Material science, Seoul National University, Seoul, The Republic of Korea*

In this work, we investigated the intermixing effect on the Gilbert damping constant of sputter-grown Pt/Py/Pt trilayer films. In order to enable intermixing at both Pt/Py interfaces, we post annealed them in the same vacuum environment for 30 min by varying the annealing temperature up to 800 K. We examined the structural changes among all of the samples by X-ray diffractometry (XRD), at the interfaces using TEM, and the magnetic properties using VSM measurement; then, we obtained the Gilbert damping constant by the VNA-FMR technique. According to the VNA-FMR results, = 0.0206 for the as-deposited sample and = 0.0932 for the sample annealed at 800 K. In the annealing temperature range up to 600 K, the Gilbert damping constant was nearly unchanged, ranging from 0.0206 to 0.0212. This can be explained by the competition between the spin pumping effect and the sharp interface effect on the Gilbert damping constant. Above the 600 K annealing temperature, the Gilbert damping constant began to increase, and in the annealing temperature range of 700 – 800 K, it showed a drastic increase, from 0.0329 to 0.0932. Such an increase in the Gilbert damping constant could be accounted for by intermixing, the stoichiometric compound, and the formation of the non-magnetic dead layer at the interface. The XRD data revealed that the crystallinity of the interface increased up to the 600 K annealing temperature, but that above it, there was increased interface roughness as well as degradation of the crystallinity and texture of the Pt phase. Additionally, above the 700 K annealing temperature, formation of the stoichiometric compound between Py and Pt and the structural transformation from ordered L12-FCC to disordered A1-FCC[2] were observed. Furthermore, the average diffusion length[3,4] of the atoms imparted a consistency of structural change, as observed by XRD. This research establishes that the intermixing effect on Gilbert damping, allows for understanding of the interfacial effect and provides insight into the optimization of complex low-damping-constant multi-layer spintronic devices with various interfaces.

[1] I.V. Vernyhora and S. M. Bokoch, ISRN Thermodynamics, 2012, 917836 (2012) [2] V.D. Divya and A. Paul, J. Mater. Res., 26, 18, 2384-2393 (2011) [3] T. Kaiser and W. Jäger, J. Appl. Phys., 103, 063913 (2008)



The effective Gilbert damping constant for all samples annealed at different temperature for 30 minute.

CR-10. Enhanced damping effect of FeNiN film due to two magnon scattering. *Z. Zhu*[1], H. Feng[1], J. Wang[1] and Q. Liu[1] *1. Key Laboratory for Magnetic and Magnetic Materials of the Ministry of Education, Lanzhou University, Lanzhou, China*

The magnetic damping behavior of soft magnetic films have been widely investigated due to their application in high frequency microwave devices, spintronic devices or magnetic random access memory. Generally, effective damping is divided into intrinsic Gilbert damping and extrinsic relaxation mechanisms. The doping is considered as an effective method to adjust the magnetic damping. Meanwhile, the static magnetic properties of thin films will also change. In order to suppress the impact of dopant on static magnetic properties. The light element Nitrogen was used as dopant to adjust magnetic damping. we prepared FeNiN films by magnetron sputtering technology. Five different samples were prepared by varying the Nitrogen partial pressure with 0, 5%, 10%, 15%, 20%, and we will represent the samples with symbols S1~S5, respectively. Ferromagnetic resonance (FMR) was used to study the enhanced magnetic damping. The experimental results show that nitrogen doping significantly affects the magnetic damping of the samples, while its effect on the coercivity is negligible. The analysis of angular dependence of FMR indicates the enhanced damping is mainly from two magnon scattering (TMS). Fig. 1 presents angular dependences of FMR linewidth and theoretical fitting curves. θ is the angle between applied magnetic field and film plane. With the rise of Nitrogen partial, TMS (the green diamond) gradually become a very important part of FMR linewidth. Gilbert damping of samples increases, and TMS increases more sharply. The shape of angular dependent FMR linewidth curves even transforms from "field dragging type" to "TMS type". Our experiments and analysis point out that one can strictly distinguish the types of damping stemmed from doping process. The prepared FeNiN films maintain the excellent soft magnetic properties with large effective damping, which meet the requirements of many devices, such as spin-torque nano-oscillator, etc.

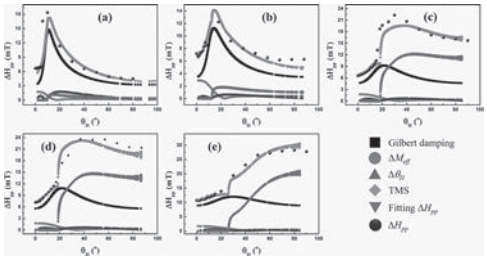


FIG. 1. The measured angular dependences of FMR linewidth (dark blue dots) and the fitting data of different samples. (a) ~ (e) represents the results of S1 ~ S5, respectively

CR-11. Manipulation of Magnetic Anisotropy by Pt Under-Layer Thickness in Pt/Co/Pt Films. *J. Yu*[1], D. Kim[1], J. Chang[1], J. Park[1], Y. Park[1,2], D. Kim[3], B. Min[2] and S. Choe[1] *1. Physics and Astronomy, Seoul National University, Seoul, The Republic of Korea; 2. Spin Convergence Research Center, Korea Institute of Science and Technology, Seoul, The Republic of Korea; 3. Institute for Chemical Research, Kyoto University, Kyoto, Japan*

Magnetic domain-wall (DW) dynamics has received a substantial attention owing to its academic interest as well as its possibility to state-of-the-art application of magnetic memory and logic devices [1]. In the creep regime, it has been known that the DW dynamics strongly depends on the creep-scaling constant that is directly correlated to the magnetic anisotropy [2]. Here, we show that the magnetic anisotropy can be systematically manipulated by adjusting the thickness of non-magnetic Pt under-layer in Pt/Co/Pt films and consequently, the DW dynamics can be finally controlled. In this study, 5.0-nm Ta/t_{Pt}^{u}-nm Pt/0.3-nm Co/1.5-nm Pt films were fabricated on a Si/100-nm SiO_2 substrate by using dc and ac magnetron sputtering, where t_{Pt}^{u} varied from 1.5 to 8 nm. Then, the magnetic anisotropy field H_K was characterized by the extraordinary-Hall-voltage measurement scheme [3] and the creep-scaling constant was measured by observing the DW motion through a magneto-optical Kerr effect (MOKE) microscope equipped with an out-of-plane electromagnet [2]. Figure 1 shows the plot of H_K and with respect to t_{Pt}^{u}, respectively. The figure unambiguously shows that H_K and are closed correlated: both increases as t_{Pt}^{u} increases and then, saturates at a critical value of t_{Pt}^{u}. Examination based on the x-ray diffraction suggests that the close correlation between H_K and is possibly attributed to their common relation to the crystallinity of the Pt under-layers.

[1] S. S. P. Parkin, M. Hayashi, and L. Thomas. Science 320, 190 (2008) [2] D.-H. Kim, B.-C. Min, and S.-B. Choe. Appl. Phys. Lett. 104, 142410 (2014) [3] K.-W. Moon, S.-B. Choe and K.-H. Shin. Rev. Sci. Instrum. 80 113904 (2009)

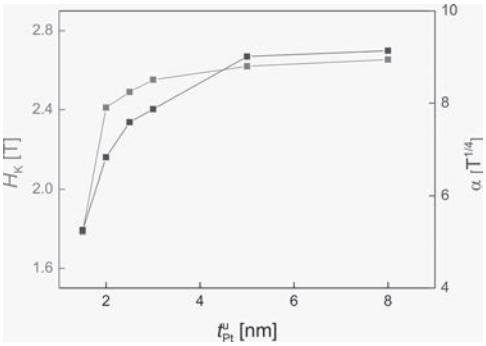


Fig.1 Plots of H_K and with respect to t_{Pt}^{u}.

CR-12. Gilbert Damping Variation via Disorder in B2 Ordered Co_2MnAl Full Heusler Alloy System. *V. Barwal*[1], N. Behera[2], S. Husain[2], A. Kumar[2], P. Svedlindh[2] and S. Chaudhary[1] *1. Physics, Indian Institute of Technology Delhi, New Delhi, India; 2. Department of Engineering Sciences, Uppsala University, Uppsala, Sweden*

Co-based Heusler alloys are in demand due to their half-metallicity, high spin polarization, high Curie temperature T_c and low damping constant, etc. Co_2MnAl (CMA) is one of the Co-based full Heusler alloys which exhibits high T_c~697 K and large spin polarization (~78%). CMA has considerable research interest due to its compatibility with the most semiconducting substrates and topological properties. In the present work, the Mn concentration dependent magnetization dynamic properties of *B2* ordered CMA full Heusler alloy are investigated.$Co_{2+x}Mn_{1-x}Al$ (CMA) Heusler alloy thin films grown on Si (100) by varying Co/Mn concentration at fixed growth temperatures (T_s) of 400 deg.C using DC-magnetron sputtering are investigated. XRD patterns revealed the formation of *B2* ordered phase in the film with exact stoichiometry. Ferromagnetic resonance (FMR) technique is employed to determine the Gilbert damping constant, which is found to be 0.0045±0.0002 for the perfect stoichiometric film which is a record low value in the CMA Heusler alloy thin films. The Co/Mn concentration based tunable Gilbert damping constant in CMA Heusler alloy is investigated and the lowest value of damping constant is found to be 0.0045. The tunability of Gilbert damping provides the opportunity to apply Heusler alloy materials in different fields of the spintronic devices. The low damping constant is inevitably important for spintronic applications.

The effect of Mn content on magnetism and half-metallicity of off-stoichiometric Co_2MnAl Journal of Magnetism and Magnetic Materials 387 (2015) 118–126 Disorder and weak localization effects in $Co_2Mn_x Ti_{1-x}$ Al Heusler alloy thin films: M Aftab *et al* 2012 *J. Phys. D: Appl. Phys.* 45 475001 Magnetic properties of full-Heusler alloy $Co_2Fe_{1-x}Mn_xAl$ films grown by molecular beam epitaxy Appl. Phys. Lett. 97, 232506 (2010); doi: 10.1063/1.3525376 Doping and disorder in the Co_2MnAl and Co_2MnGa half-metallic Heusler alloys PHYSICAL REVIEW B 74, 172412 2006

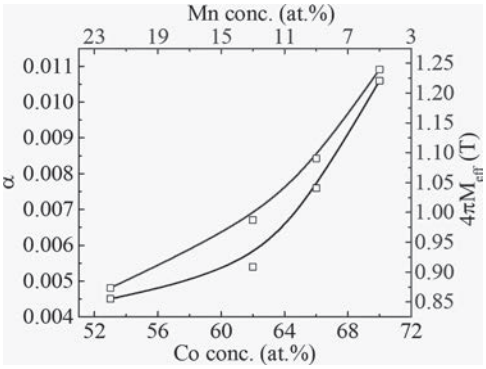


Fig. 1 Changing damping coefficient and Effective Magnetization as a function of Co/Mn concentration

CR-13. Paramagnetic resonance in $La_{0.6}Ca_{0.4}MnO_3$ detected by magnetoimpedance method using a copper 'stripcoil'. U. Chaudhuri[1], A. Chanda[1] and *R. Mahendiran*[1] *1. Physics, National University of Singapore, Singapore*

Electron paramagnetic resonance (EPR) and ferromagnetic resonance (FMR) in colossal magnetoresistive Mn-oxides have been extensively studied using the microwave cavity perturbation technique at a fixed resonance frequency of the cavity, typically 9.8 GHz. [1] Conventional EPR/FMR spectrometers record the field derivative of the microwave power absorbed by the sample while *dc* magnetic field (H_{dc}) is swept through resonance. Here, we show detection of EPR signal $La_{0.60}Ca_{0.40}MnO_3$ by measuring the effective changes in magnetoimpedance of a copper stripcoil surrounding the sample. In our method, *rf* current from an impedance analyzer flows through a stripcoil surrounding the sample which creates an *rf* magnetic field inside it, along its axial direction, [2] which excites t_{2g} core electrons of Mn^{3+}/Mn^{4+} ions to make Zeeman transitions between spin split levels upon sweeping *dc* magnetic field. Fig. 1 (a) shows a plot of magnetization (M) versus applied magnetic field (H) and M vs T in the inset for the sample. These curves indicate that the sample is paramagnetic at 300 K and it undergoes a transition to ferromagnetic state below 260 K. Fig. 1 (b) illustrates the percentage changes in magnetoresistance ($\Delta R/R_0$) and magnetoreatance ($\Delta X/X_0$) at 2.5 GHz which are the apparent resistance and reactance changes of the sample as picked up by the stripcoil. $\Delta R/R_0$ decreases gradually and shows an abrupt increase at a critical field H_{cr} which corresponds to a pronounced dip in $\Delta X/X_0$. In Fig. 1 (c) and (d) display the evolution of $\Delta R/R_0$ and $\Delta X/X_0$ respectively, from 0.5 GHz to 2.5 GHz. We can see that the H_{cr} increases linearly with frequency (f) of the current in the stripcoil which follows the relation $f = (g/2\pi)H$, where g is the gyromagnetic ratio as expected for EPR. The electrical detection of spin dynamics in the paramagnetic sample shown here urgently needs theoretical explanation.

[1] A. Shengelaya *et al. Phys. Rev. B* 61, 5888 (2000); M. T. Casua *et al*. 58, 3233 (1998); V. A. Ivanshin et al. J. Superconductivity, 15, 523 (2002); S. S. Rao et al, J. Phys. Condens. Mat. 21, 196005 (2009). [2] U. Chaudhuri, M. Kumari, and R. Mahendiran. *IEEE Trans. Magn.* 54, 2801104 (2018).

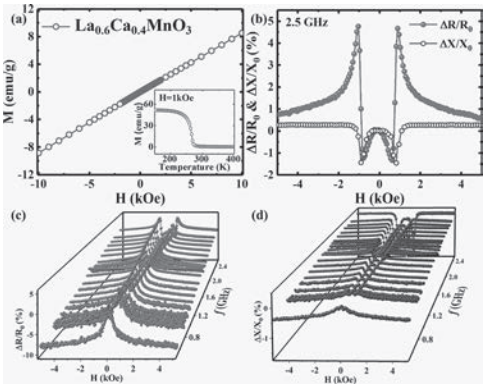


Fig. 1 (a) *M* versus *H* for $La_{0.6}Ca_{0.4}MnO_3$ at 300 K. Inset: *M* vs *T* with *H* = 1 kOe. (b) Magnetoresistace ($\Delta R/R_0$) and magnetoreactance ($\Delta X/X_0$) at 2.5 GHz as measured by the Cu-stripcoil. Evolution of (c) $\Delta R/R_0$ and (d) $\Delta X/X_0$ with varying *dc* magnetic field while increasing the frequency of *rf* current in the stripcoil.

CR-14. Dynamic Magnetic Properties of Amorphous $Fe_{80}B_{20}$ Thin Films and its Relation to their Interfaces. *U. Urdiroz*[1], B.M. Teixeira[2], F. Palomares[1], J.M. Gonzalez[1], N. Sobolev[2,3], A. Mayoral[4] and F. Cebollada[5]
1. Instituto de Ciencia de Materiales de Madrid (CSIC), Madrid, Spain; 2. Departamento de Física and I3N, Universidade de Aveiro, Aveiro, Portugal; 3. National University of Science and Technology "MISiS", Moscow, Russian Federation; 4. Advanced Microscopy Laboratory, Nanoscience Institute of Aragon (LMA-INA)., Zaragoza, Spain; 5. POEMMA-CEMDATIC - ETSI de Telecomunicación, Universidad Politécnica de Madrid, Madrid, Spain

We analyze the ferromagnetic resonance field H_r and linewidth of pulsed laser ablation deposited, amorphous Fe-B films based on the characteristics of their film-substrate and film-capping interfaces. Two pairs of films (20 nm thick) were deposited onto MgO (001) (M films) and Corning® glass (C films) substrates, respectively. A film out of each pair was capped with a 5 nm Au layer whereas the other was kept uncapped. All films exhibit a uniaxial dc MOKE hysteresis with the easy axis (e.a) parallel to one substrate side (C) or to one diagonal (M). The in-plane (IP) angle dependence of H_r in the C films (Fig. 1a) showed a uniaxial anisotropy component typical of amorphous alloys, with no traces of higher order components. The magnetoelastic coupling with the stresses at the substrate-film interface is proposed as the source of this anisotropy and of the extrinsic contribution to the linewidth, showing the same angle dependence as H_r (Fig. 1b). The origin of a peak splitting observed in the angular region associated to the linewidth maxima is discussed in terms of different mechanisms, based on magnon scattering [1, 2] or local resonance [3]. The larger linewidth of the uncapped C film, in comparison to the capped C one, can be attributed to the oxide layer formed at its free surface. The M films present, in addition to a uniaxial anisotropy, a weaker cubic (biaxial IP) component (Fig. 2a), due to the presence, observed by transmission electron microscopy, of a 1 nm thick Fe epitaxial layer at the Fe-B/MgO interface. The extrinsic linewidth contribution exhibited by the capped M film (Fig. 2b) has a four-fold angle dependence, which, consequently, must be associated to the occurrence of exchange coupling between the Fe epitaxial layer and the amorphous Fe-B layer. In contrast with this result, the linewidth of the uncapped M film (Fig. 2b) shows an angle evolution correlated neither to the cubic nor to the uniaxial components of the anisotropy, and which is likely ruled by the oxide layer present at the deposit free surface.

[1] R.D. McMichael, D.J. Twisselmann, J.E. Bonevich, A.P. Chen, W.F. Egelhoff, and S.E. Russek, J. Appl. Phys. 91, 8647 (2002). [2] M. Körner, K. Lenz, R.A. Gallardo, M. Fritzsche, A. Mücklich, S. Facsko, J. Lindner, P. Landeros, and J. Fassbender, Phys. Rev. B 88, 054405 (2013). [3] R.D. McMichael, D.J. Twisselmann, A. Kunz, Phys. Rev. Lett. 90, 227601 (2003).

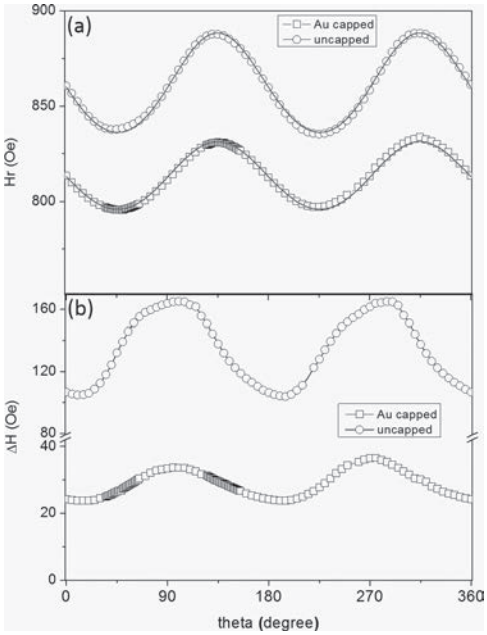


Fig. 1. Angular dependence of the resonance field (a) and linewidth (b) of the C films.

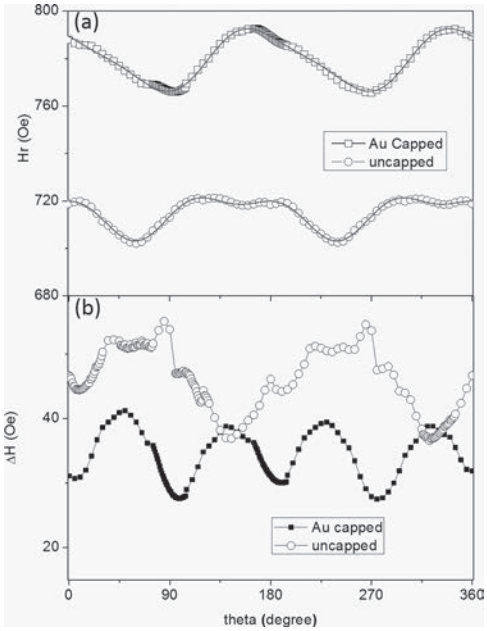


Fig. 2. Angular dependence of the resonance field (a) and linewidth (b) of the M films.

CR-15. Time dynamics and magnetic viscosity measurements in inhomogeneous $La_{0.7}Sr_{0.3}MnO_3$ films. *N. Mottaghi*[1], S. Kumari[2], M.S. Seehra[1] and M. Holcomb[1] *1. Physics and astronomy, West Virginia University, Morgantown, WV, United States; 2. Department of Physics, The Pennsylvania State University, University Park, PA, United States*

Recently we have reported on the role of so-called magnetic dead layers/regions in the bulk magnetic properties of a 7.6 nm thin of $La_{0.7}Sr_{0.3}MnO_3$ (LSMO) grown on $SrTiO_3$ (STO) substrate[1, 2] showing that this sample was magnetically inhomogeneous containing spin clusters embedded in a ferromagnetic phase.[2] It was suggested that these spin clusters are responsible for the observed hysteresis loop inversion and negative magnetization in the temperature dependent magnetization (*M*-*T*) measurements and these spin clusters act like a superparamagnetic phase.[1, 2] Here we report a systematic study of the magnetic relaxation ($M(t)$) in similar magnetically inhomogeneous LSMO/STO (001) thin films but with thickness = 12, 21.2, 32 and 37 nm. As before[1, 2], these films were fabricated by pulsed laser deposition (PLD). Measurements of magnetization were done as follows: Samples are cooled in magnetic field $H = +50$ Oe to the measuring temperature. After the temperature becomes stable, H is set to zero and time dependence of $M(t)$ is recorded for t up to 2 hours yielding the long-time logarithmic relaxation rate shown in Fig. 1. Similar measurements were repeated for other temperatures after warming the sample each time to $T > T_C$ and then cooling back to the measuring temperature in $H = +50$ Oe. The data of M vs. t follows the Eq. $M(t) \approx M_0 - S(H, T) \ln(t)^3$, with S being the magnetic viscosity and M_0 the magnetization at $t = 0$. In addition to the temperature dependence of S, we also report the temperature of M_{stable}, the final value of the magnetization the system reaches after 2 hours. Temperature variations of M_{stable} and S for the four films (Fig. 2) show that S has the maximum values for all the samples at the temperature where M_{stable} switches sign from positive to negative values. These results of peaks in S and sign change in M_{stable} are interpreted in terms of co-existence of multiple magnetic phases in these inhomogeneous films.

[1] N. Mottaghi, R.B. Trappen, S. Kumari, C.Y. Huang, S. Yousefi, G.B. Cabrera, M. Aziziha, A. Haertter, M.B. Johnson, M.S. Seehra, and M.B. Holcomb, J. Phys. Condens. Matter 30, 405804 (2018). [2] N. Mottaghi, M.S. Seehra, R. Trappen, S. Kumari, C.-Y. Huang, S. Yousefi, G.B. Cabrera, A.H. Romero, and M.B. Holcomb, AIP Adv. 8, 056319 (2018). [3] E.P. Wohlfarth, J. Phys. F Met. Phys. 14, L155 (1984).

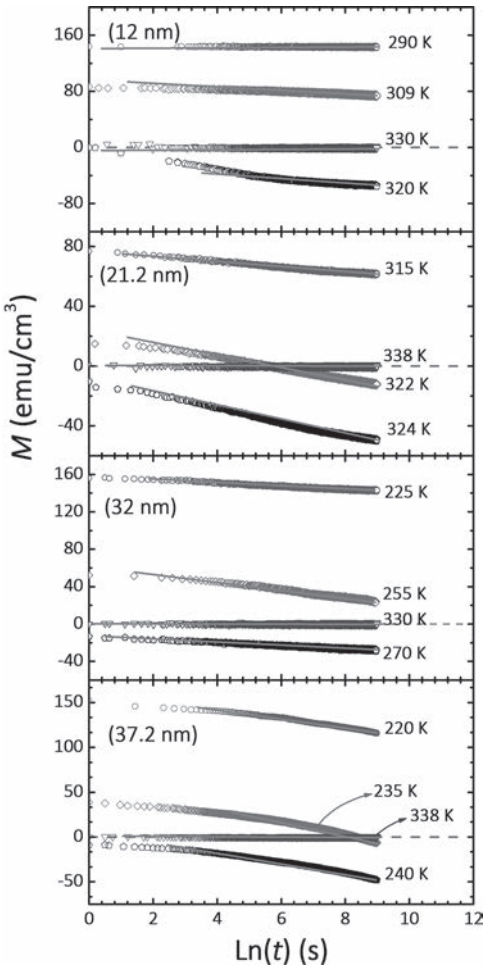


Fig. 1. Selected $M(t)$ of LSMO/STO films. The solid red line is the fit to the Eq.: $M(t) \approx M_0 - S(H, T) \ln(t)$.

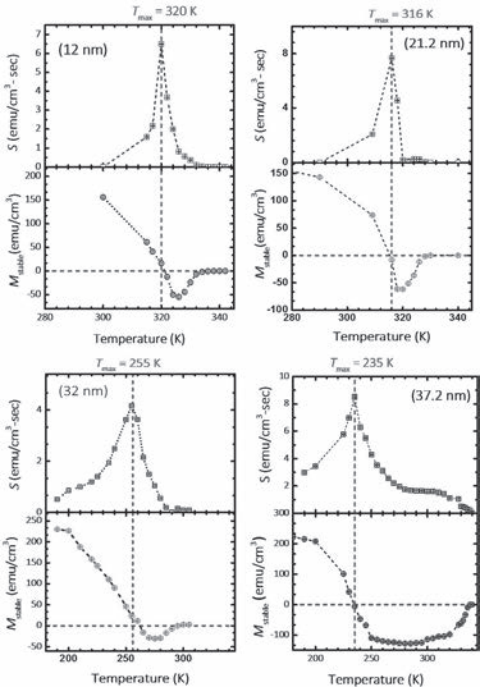


Fig. 2. Results of the fitting to Eq.: $M(t) \approx M_0 - S(H, T) \ln(t)$ of samples. S and M_{stable} the magnetic viscosity and the final value of M at the end of each measurement.

CR-16. Damping Enhancement of Permalloy/Ho Bilayers Induced by Spin Pumping Effect at Room Temperature. M. Tian[1], Q. Chen[1], L. Cao[1], Z. Kou[1], M. Jalali[1], *Y. Zhai*[1], J. Wang[2], B. You[2] and J. Du[2]
1. School of Physics, Southeast University, Nanjing, China; 2. School of Physics, Nanjing University, Nanjing, China

Spin pumping effect in FM/NM bilayers attracts more interests because it can tailor magnetization dynamic damping. Interface and NM layer play crucial roles in spin current generation based on the effect. For Permalloy (Py), the magnetization dynamic damping (α) is quite small due to the quenched orbital magnetic moments, which restricts the applications in spintronic devices. Spin pumping occurred on the interface between Py and the NM films with larger L-S coupling could improve the α of Py indirectly. Rare earth materials as NM layers have showed a stronger spin pumping effect, such as Tb(Terbium)[1]. Ho is also a heavy rare earth material with paramagnetism at room temperature and larger orbital moment L. In this paper, we investigate the α by spin pumping in Py/Ho bilayers by frequency dependence of Ferromagnetic Resonance (FMR). Various thicknesses of Ta(5)/Py(10)/Ho(d)/Ta(2) films are fabricated by magnetron sputtering. Results show that the α increases with the increasing thickness of Ho layer and then tends to a stable value at about 0.03828 as shown in Fig.1, which agrees with the trend of the spin pumping behavior. By fitting the experimental data based on spin pumping principle, the spin diffusion length of Ho and spin mixing conductance are obtained, which indicate that a stronger L-S coupling in the Ho layer than that in heavy metal Pt gives main contributions of α enhancement. From the saturation magnetization, it decreases with the function of the thickness of Ho layer d, which may tell us that an antiferromagnetic interface in Py/Ho exists. The magnetic moments Py may induce the non-zero magnetic moment of Ho during atomic layers near adjacent Py layer. This non-zero magnetic moment is possibly anti-parallel to the one of Py layer. It is reported that an antiferromagnetic interface can increase the damping coefficient [2]. Therefore, in our research, antiferromagnetic interface also plays an important role in the damping enhancement in Py/Ho bilayer. The detailed discussion and analysis will be described in the full text. This work was supported by NSFC (Grant No 61427812, 51571062).

[1]J. Yue et al., "The influence of interface on spin pumping effect in Ni80Fe20 /Tb bilayer," AIP Adv., vol. 6, no. 5, (2016) [2]W. Lin, K. Chen, S. Zhang, and C. L. Chien, "Enhancement of Thermally Injected Spin Current through an Antiferromagnetic Insulator," Phys. Rev. Lett., vol. 116, no. 18, pp. 1–6, (2016)

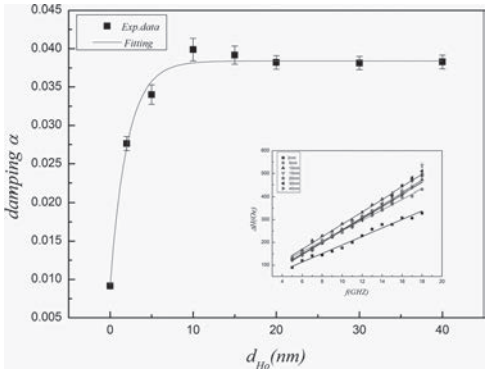


Fig.1 damping as a function of Ho thickness. Inset is the linewidth variation of ΔH vs Ho thickness.

Session CS
EDUCATION, OUTREACH, & PUBLIC ENGAGEMENT IN MAGNETISM
(Poster Session)

Barry L Zink, Co-Chair
University of Denver, Denver, CO, United States
Dafiné Ravelosona, Co-Chair
Center for Nanoscience and Nanotechnology, Palaiseau, France
Yukiko Takahashi, Co-Chair
NIMS, Tsukuba, Japan

CS-01. Exploring magnetic resonance with a compass. *D. Nelson*[1], E. Cookson[1], M. Anderson[1], D. McKinney[2] and I. Barsukov[1] *1. Physics and Astronomy, UC Riverside, Riverside, CA, United States; 2. Santa Rosa Academy, Menifee, CA, United States*

Magnetic resonance plays an important role in today's science, engineering, and medical diagnostics. Learning and teaching magnetic resonance is challenging since it requires advanced knowledge of condensed matter physics and quantum mechanics. Driven by the need to popularize this technologically impactful phenomenon, we develop an inexpensive table-top demonstration experiment. It unveils the magnetic resonance of a hand-held compass in the magnetic fields of a permanent magnet. The setup provides an immediate visualization of the underlying physical concepts and allows for their translation to broad student audiences. This work was supported by the National Science Foundation under Grant No. ECCS-1810541.

CS-02. Magnetic Fields Web Series: Engaging Middle School Students in STEM. *P. Pena Martin*[1], J. Isberg[1], E. Ertekin[1,3], V. Lorenz[1,2] and N. Mason[1,2] *1. Materials Research Laboratory, University of Illinois at Urbana-Champaign, Urbana, IL, United States; 2. Department of Physics, University of Illinois at Urbana-Champaign, Urbana, IL, United States; 3. Department of Mechanical Science and Engineering, University of Illinois at Urbana-Champaign, Urbana, IL, United States*

Web based media can make scientific content accessible to audiences far beyond the scientific community. We created a web series called "Magnetic Fields" that aims to introduce materials science, particularly concepts related to magnetism, and promote themes more general to STEM fields, such as persistence and the scientific process, through use of characters and a story geared towards a middle school audience. The goal is to build and maintain interest in science at an age where this tends to drop off. The four-episode arc follows a group of high school characters as they encounter a strange new material during a class field trip to a laboratory. The series is directed by John Isberg, with professional actors making up most of the cast. The series was initiated by scientists in the Illinois MRSEC, and the storyline was developed in collaboration with MRSEC students and faculty. The episodes were released in May 2019 through Youtube. We report on the process of creating this series, response to it upon release, and discussion of its use as an educational tool. The authors acknowledge primary support of the NSF through the University of Illinois at Urbana-Champaign Materials Research Science and Engineering Center DMR-1720633.



Fig.1 Scene from an episode of "Magnetic Fields." Photo by John Isberg.

CS-03. In-class experiments with smart phones for teaching upper-level electricity and magnetism. A. Davidson[1], A. Ranjan[2] and *X. Fan*[1] *1. Physics and Astronomy, University of Denver, Denver, CO, United States; 2. Cherry Creek High School, Greenwood Village, CO, United States*

Interactive-engagement method such as studio physics [1, 2], has demonstrated higher learning gains than traditional lecturing in intro-level physics classes. However, there have been limited applications in upper-level classes, such as Electricity and Magnetism (E&M), possibly because experiments on E&M topics can be too costly and sophisticated to be carried out in the classroom. Smart phone, which is equipped with magnetic field sensors, radio signal detectors and light sensors, provides a convenient platform for carrying out E&M-related experiments. In this poster, we will present three examples of the implementation of smart-phone-based studio physics in an E&M class for Physics majors: (1) Detection of earth magnetic field inclination; (2) quantifying skin depth of aluminum foil with cellphone tower signals; and (3) Measurement of Brewster's angle. Besides sensitive sensors, smart phone also has computational power, which can be explored to further expand the breadth and depth of the smart-phone-based studio physics. Due to the wide accessibility of smart phones and the simplicity of experimental setup, we expect this teaching technique can be easily transferred to other institutes in the world.

[1] Gok, T., *Assessment of the effectiveness of the hybrid studio format in introductory undergraduate physics.* Energy Education Science and Technology Part B-Social and Educational Studies, 2012. 4(1): p. 117-130. [2] Sorensen, C.M., A.D. Churukian, S. Maleki, and D.A. Zollman, *The New Studio format for instruction of introductory physics.* American Journal of Physics, 2006. 74(12): p. 1077-1082.

CS-04. The Use of Virtue Modules in Physics Lab Teaching. *W. Zhang*[1], R. Bidthanapally[1], T. Sebastian[2], Y. Xiong[1,3], H. Qu[3] and J. Sklenar[4] *1. Physics Department, Oakland University, Rochester, MI, United States; 2. THATec Innovation GmbH, Mannheim, Germany; 3. Electronic and Computer Engineering, Oakland University, Rochester, MI, United States; 4. Physics Department, Wayne State University, Detroit, MI, United States*

Lab sessions in physics education connect the fundamental concepts to practical examples and are effective measures of the students' understanding and reasoning through ultimate real-world tests. Many topics in condensed

matter physics are known to be challenging to convey in both lectures and labs. In addition, these topics are usually resource demanding, which has been one of the challenging issues. Here, we introduce and demonstrate the use of virtue lab modules for teaching physics labs and for effectively integrating research and education. Experiments that are relevant to magnetism and spintronics include, but not limited to, spin current detecting, microwave energy harvesting, and spin-based thermoelectric effects. An important highlight of these modules is the highly-interactive laboratory learning platform. In the class, each piece of experimental hardware (e.g. electrometers, oscilloscopes, etc) will be paired with a computer-based virtual module. The individual modules mimic the hardware, which the students can use to become familiar with the hardware, acquire real-time feedback, and visualize the data acquisition dynamics, on-demand and risk-free. The virtual component is also helpful for demonstrating delicate, shared hardware in class, without risk of damaging the actual instrumentation. These individual components are connected to a central operating system and the experiment can be re-programmed by simple coding and user-interfaced commands [1]. Work at Oakland University is supported by NSF DMR-1808892.

[1] THATec Innovation GmbH: https://www.thatec-innovation.com/

Session CT
MAGNETIC ALLOYS AND COMPOUNDS
(Poster Session)

Nicholas John Jones, Co-Chair
Naval Surface Warfare Center, Bethesda, MD, United States
Mehmet Acet, Co-Chair
Duisburg-Essen University, Duisburg, Germany

CT-01. Microwave absorption properties of Y-Co_2Z/PANI composites. *N. Tran*[1], H. Nguyen[1], Y. Choi[1], M. Lee[1], T. Phan[1] and B. Lee[1] *1. Department of Physics, Hankuk University of Foreign Studies, Yongin, The Republic of Korea*

In recent years, the growing development of wireless devices has caused microwave polluted environment. Therefore, the demand for microwave absorbers in the GHz range is much increasing. Ferrites are concerned to be the best choice for industrial purpose because of their high resistivity, high saturation as well as excellent electromagnetic properties [1-3]. Z-type hexaferites have high resonance frequency f_r and large permittivity μ in the GHz range. Furthermore, the composites of Z-type hexaferrites/conductive polymers can be used to enhance the microwave absorption in the minimum reflection loss (RL) as well as effective bandwidth absorption. To understand the role of doping and composite on the microwave absorption properties of Z-type hexaferites, composites of Y-doped $Ba_3Co_2Fe_{24}O_{41}$ and polyaniline (PANI) were prepared. $Ba_{3-x}Y_xCo_2Fe_{24}O_{41}$ (x = 0, 0.2 and 0.4) samples were synthesized by solid state reaction method. Their composites with PANI were then prepared with hexaferrites (H) and PANI (P) ratio H/P = 9/1. The composites together with 7%wt. epoxy were ground and pressed into the toroidal shape (with D = 7 mm and d = 3 mm) then dried at 170 °C/0.5 h. Electromagnetic wave absorption properties of these composites were studied by a PNA-X Network Analyzer in the frequency range of 0.1 – 18 GHz. The absorption properties versus the toroidal thickness (t) were also carried out. RL of the composites was strongly dependent on x and t. With t decreasing, the absorption frequency moved toward the high frequency range. All the samples had minimum RL < –10 dB, which represented capacity of incident wave absorbing of materials up to 90%. The largest bandwidth of microwave RL < –10 dB was obtained in the range of 13.8 – 17.8 GHz for x = 0.4. Considering microwave RL < –8 dB (~84% of incident wave being absorbed), the sample x = 0 can be covered for a huge frequency range of 3.95 – 16.54 GHz at t = 2 mm. Meanwhile, the minimum RL = –29.5 dB (~99.9% of incident wave being absorbed) was archived at frequency of 11.4 GHz for x = 0.2 with t = 2.5 mm. These results suggest that Y-Co_2Z/PANI composites are potential candidates for microwave absorption.

[1] M. Mehdipour and H. Shokrollahi, "Comparison of microwave absorption properties of $SrFe_{12}O_{19}$, $SrFe_{12}O_{19}/NiFe_2O_4$, and $NiFe_2O_4$ particles," *J. Appl. Phys.,* vol. 114, no. 4, p. 043906, 2013. [2] X. T. Tang *et al.*, "Microwave absorption performance enhanced by high-crystalline graphene and $BaFe_{12}O_{19}$ nanocomposites," *J. Appl. Phys,* vol. 119, no. 20, p. 204301, 2016. [3] S. Ozah and N. S. Bhattacharyya, "Nanosized barium hexaferrite in novolac phenolic resin as microwave absorber for X-band application," *J. Magn. Magn. Mater.,* vol. 342, pp. 92-99, 2013.

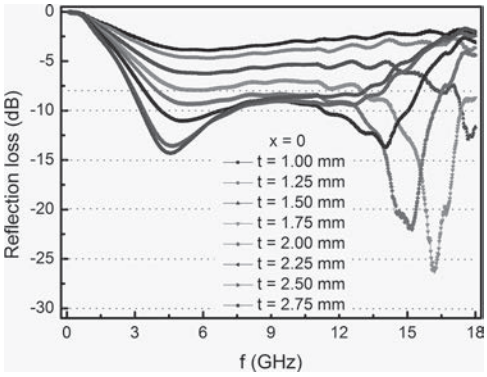


Fig. 1. RL vs t of the sample x = 0.

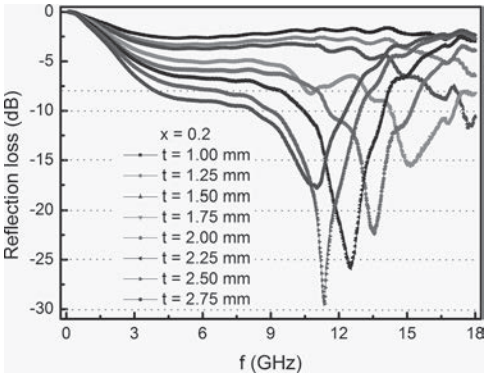


Fig. 2. RL vs t of the sample x = 0.2.

CT-02. Microwave absorption properties of core-shell structured FeCoNi/PMMA filled in composites. *K. Kim*[1], W. Jang[1], S. Mallesh[1] and S. Lee[2] *1. Physics, Yeungnam University, Gyeongsan, The Republic of Korea; 2. Composites Research Division, Korea Institute of Materials and Science, Changwon, The Republic of Korea*

The electromagnetic (EM) absorbers have been required the essential factors such as high absorption ability, broad bandwidth, and lightweight [1, 2]. To enhance the ability of EM absorption, the permittivity and permeability of absorber should be controlled for impedance matching. In general, the carbonyl Iron particles (CIP), ferrites and carbon based materials have been widely employed in EM absorber for tuning the permittivity and permeability. Especially, the specific gravity of the metallic and ceramic fillers is relatively high. In order to reduce the weight of EM absorbers, the core-shell structured fillers synthesized by electroless plating that the 100 nm thick-FeCoNi shell was coated on the surface of PMMA beads (approximately 3 μm) as shown in Fig. 1. To verify the enhancement of EM properties of FeCoNi@PMMA, which were compared with those of the spherical CIP (BASF, EW) with similar size of PMMA. The magnetization values of FeCoNi@PMMA and CIP were 170 emu/g and 191 emu/g, respectively.

The FeCoNi@PMMA and the CIP were dispersed in paraffin matrix, respectively, which composites were pressed into the toroidal shape to measure EM properties by using 7 mm coaxial line with vector network analyzer up to 18 GHz. The real part of permittivity of FeCoNi@PMMA of 55 wt.% in composite exhibited from 15 to 12 although the CIP with same weight ratio was 4. The real part of permeability of FeCoNi@PMMA and CIP composites were slightly decreased from 1.5 to 1 with the increment of frequency. The minimum reflection losses (RL) of FeCoNi@PMMA composites exhibited from -21.4 dB@13.3 GHz for 1.5 mm to -19.3 dB@6.1 GHz for 3 mm, which values were much larger than those of CIP with the same weight ratio as shown in Fig. 2. As results, the core-shell structured lightweight FeCoNi@PMMA is one of good candidate filler material for EM absorber. We'll present the analytical results in detail and discuss in presentation.

[1] Bin Zhang, Jun Wang, Junpeng Wang, SiqiHuo, Bin Zhang, Yushan Tang, Microwave absorption properties of lightweight absorber based on $Fe_{50}Ni_{50}$-coatedpoly(acrylonitrile) microspheres and reduced graphene oxide composites, J. Magn. Mag. Mater. 413 (2016) 81-88. [2]Seung-geun Jeon, Jinu Kim, Ki Hyeon Kim, Microwave absorption properties of graphene oxide capsulated carbonyl iron particles, Appl. Surf. Sci. 475 (2019) 1065-1069.

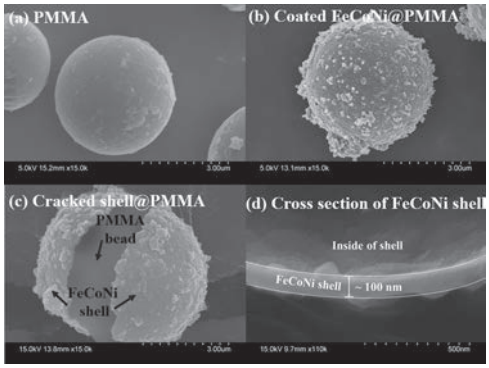


Fig. 1 SEM images of (a) PMMA bead, (b) FeCoNi@PMMA, (c) the cracked surface of FeCoNi layer and (d) the cross sectional view of FeCoNi shell.

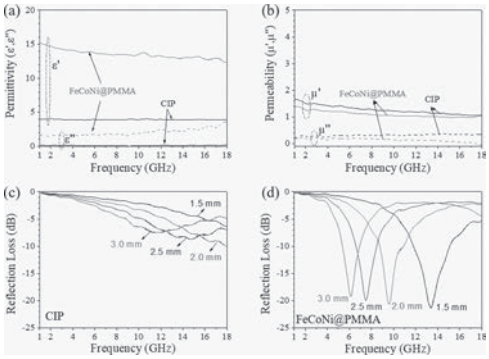


Fig. 2 (a) the permittivity, (b) permeability of FeCoNi@PMMA and CIP and the reflection loss of (c) CIP, (d) FeCoNi@PMMA composites with the variation of thickness.

CT-03. In-detailed Study of Magnetic, Dielectric and Microwave Properties on $MnFe_2O_4$ Nano-Hollow Spheres. *D. Mandal*[1] and K. Mandal[1] *1. Condensed Matter Physics & Material Sciences, S.N.Bose National Centre for Basic Sciences, Kolkata, India*

From the detail studies of structural, magnetic, dielectric and microwave properties, $MnFe_2O_4$ (MFO) nano-hollow spheres (NHS) are found interesting towards its application in high-frequency devices as well as in bio-medical fields. Single crystal MFO NHS of size ~ 250 nm is synthesized in one step template free solvothermal method and the morphology is analyzed through FESEM and TEM micrographs. The crystallographic phase is determined using profile analysis of XRD pattern. Room temperature magnetization (M) study on MFO NHS displays its soft ferrimagnetic nature with H_C, M_R and M_S values of 127.7 Oe, 15.3 emu/g and 57.8 emu/g respectively. Domain structures of NHS and temperature dependence of M are predicted from the Day plot and Bloch's power law. Variation of dielectric properties such as permittivity (ε), and ac conductivity (σ) of these NHS with frequency (1 Hz – 1MHz) is explained on the basis of Maxwell-Wagner two-layer model for space charge and cationic interactions in between tetra- and octahedral sites. Permeability (μ), ε, and Reflection loss (RL) are studied in widely used X-Band (8-12 GHz) frequency range on composites filled (20 wt% and thickness of 2 mm) with sample. Hollow cavity of NHS leads to a lower density as well as multiple internal reflections enhances Electro-Magnetic wave absorption (optimal RL ~ - 32 dB at 11.7 GHz) and a broad band-width (W) of ~ (9.4 – 12) GHz having RL < -10 dB (absorption > 90%) [1]. These properties ensure its potentiality as light-weight, size efficient microwave absorbing material.

1. D. Mandal, A. Gorai and K. Mandal, Journal of Magnetism and Magnetic Materials, Vol. 485, p. 43-48 (2019)

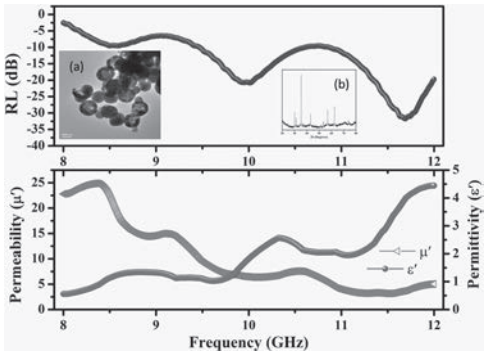


Fig. 1: Variation of RL, μ′ and ε′ with Frequency; inset (a) TEM micrograph and (b) XRD Plot of MFO NHS

CT-04. Magnetic and microwave absorption properties of Co-doped $SrFe_{12}O_{19}$ M-type hexaferrites. *H. Nguyen*[1], N. Tran[1], Y. Choi[1], J. Ahn[1], T. Phan[1] and B. Lee[1] *1. Department of Physics, Hankuk University of Foreign Studies, Yongin, The Republic of Korea*

Many studies have demonstrated that strontium hexaferrite (SrM) is a potential candidate for radar-absorbing materials (RAMs) [1-3]. By substituting either Sr^{2+} or Fe^{3+} with other elements, changing the permittivity (ε_r) and permeability (μ_r) [1, 2], one can improve the magnetic and microwave absorption (MWA) properties of SrM, prticularly for the Co doping because it is a fast relaxer with high magnetocrystalline anisotropy. Basing on this suggestion, we have prepared $SrCo_xFe_{12-x}O_{19}$ (x = 0 - 1) samples and studied their magnetic and MWA properties. The results obtained from magnetization measurements indicated an increase of the saturation magnetization (M_s) with increasing x in $SrCo_xFe_{12-x}O_{19}$, namely from ~36 emu/g for x = 0 to 46 emu/g for x = 1, see Fig. 1. Meanwhile, excepting for x = 0, the coercivity (H_c) reduces from ~3.7 kOe for x = 0.1 to 1.7 kOe for x = 1. These changes are related to the replacement of Co^{2+} for Fe^{3+} in different polyhedral sites of the M-type structure that changes the local geometrical structures and exchange interactions between Fe ions. Such changes influence directly the MWA properties. To investigate the MWA properties, we selected typical samples (x = 0, 0.4, and 0.8), pressed into toroid-shaped devices, and performed frequency (f)-dependent measurements of ε_r and μ_r in the range f = 0.1-18 GHz. After recording the ε_r and μ_r data with different toroidal thicknesses (t, 1.75-2.75 mm), we calculated f- and t-dependent reflection loss (RL). We have found that while x = 0 does not show the MWA possibility (RL ≈ 0), the others with x = 0.4 and 0.8 show good MWA possibility at frequencies f = 9-17 GHz. The best MWA performance has been found for x = 0.4 with t = 2 mm. For this sample, two absorption ranges at 9.8~12 and 13~17 GHz with RL < -10 dB are observed. Particularly, the minimum RL obtained at 10.9 GHz is about -49 dB,

corresponding to >99.99% microwave absorption (see Fig. 2), which is much larger than absorption values reported previously. These features demonstrate that the Co doping improved remarkably the magnetic and MWA properties of $SrCo_xFe_{12-x}O_{19}$ at high fequencies, above 9 GHz.

[1] X.S. M. Liu, F. Song, J. Xiang, X. Meng, J. Solid State Chem., 184 (2011) 871-876. [2] S. Choopani, N. Keyhan, A. Ghasemi, A. Sharbati, R.S. Alam, Mater. Chem. Phys., 113 (2009) 717-720. [3] M.M. R.S. Alam, H. Nikmanesh, J. Ventura, M. Rostami Magn, J. Magn. Mater., 402 (2016) 20-27.

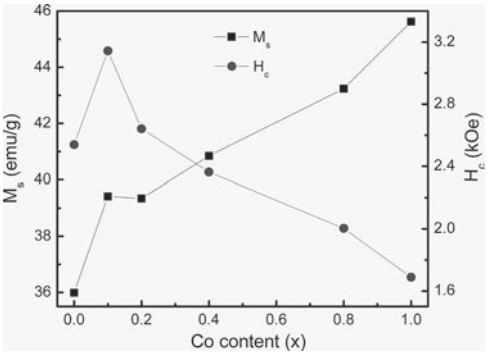


Fig. 1. M_s and H_c as a function of (x)

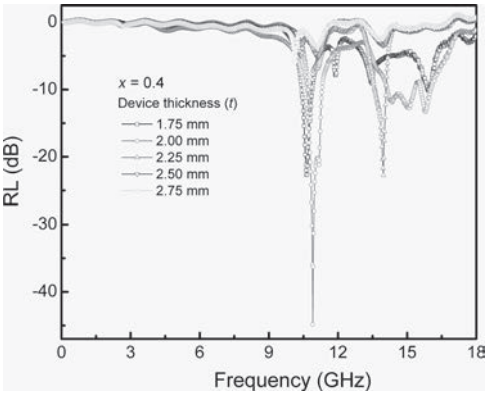


Fig. 2. RL vs t values for x = 0.4 at f = 0.1-18 GHz.

CT-05. Improved microwave properties of C-axis oriented La-Co substituted barium hexaferrite thick films for high frequency device applications. *S. Mahadevan*[1] and P. Sharma[1] *1. School of Physics and Materials Science, Thapar Institute of Engineering & Technology, Patiala, India*

M-type barium hexaferrite (BaM) has gained considerable attention in high frequency device applications due to its intriguing magnetic and microwave properties. The large uniaxial magnetocrystalline anisotropy (H_a ~17 kOe) associated with self-bias nature overcome the requirement of an external biasing field, which miniaturize the size of devices[1]. The operational frequency of microwave devices was strongly depended on intrinsic magnetic properties[2], i.e., saturation magnetization and H_a. Over the decades, large efforts have been made to tailor the magnetic properties by partial cationic substitution for Fe or Ba. However, magnetic and microwave studies related to simultaneous substitution for Fe and Ba is scarcely investigated. In the present work, $Ba_{0.85}La_{0.15}Fe_{12-x}Co_xO_{19}$ (x = 0 - 1) samples were prepared by solid-state ceramic method. Their structural, magnetic and microwave properties were investigated with micro Raman, VSM and VNA. We observe that cobalt substitution (x = 0.20) shows drastic increase in reflection loss (RL < -20 dB; absorption >99%) at K_u-band, which is 50% improved as compare to unsubstituted BaM shown in fig. 1. Our results suggest that the improvement is ascribed to dilution of H_a associated with cobalt substitution. Further, the material was utilized to fabricate oriented screen printed thick films of ~74 μm, which is a 26% reduction in thickness with respect to the previous reports[3,4]. Its morphological and magnetic properties were investigated by SEM and VSM respectively. Fig.2 shows the VSM plot of oriented thick film sintered at 1275 °C.

[1] V.G. Harris, IEEE Trans. Magn. 48, 1075 (2012). [2] Y. Chen, A.L. Geiler, T. Sakai, S.D. Yoon, C. Vittoria, and V.G. Harris, J. Appl. Phys. 99, 1 (2006). [3] Y. Chen, A.L. Geiler, T. Sakai, S.D. Yoon, C. Vittoria, and V.G. Harris, J. Appl. Phys. 99, 08M904 (2006). [4] Z. Chen, A. Yang, K. Mahalingam, K.L. Averett, J. Gao, G.J. Brown, C. Vittoria, and V.G. Harris, Appl. Phys. Lett. 96, 242502(1 (2006).

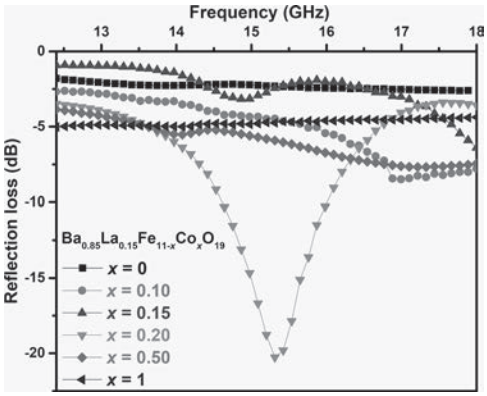


Fig 1. Reflection loss spectra of $Ba_{0.85}La_{0.15}Fe_{12-x}Co_xO_{19}$.

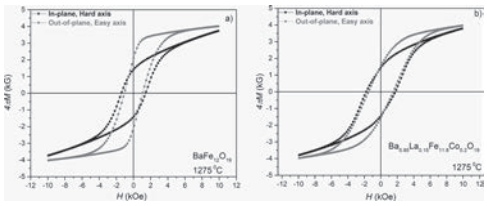


Fig 2. Hysteresis loops of a) $BaFe_{12}O_{19}$ & b) $Ba_{0.85}La_{0.15}Fe_{11.8}Co_{0.2}O_{19}$ screen printed thick film sintered at 1275 °C

CT-06. Magnetic properties and microstructures of Fe-doped $(Ti_{1-x}Fe_x)_3AlC_2$ MAX phase and their delaminated MXene. N. Zhao[1], T. Chen[2], *J. Chen*[3], P. Jia[1], W. Cui[1] and Q. Wang[1] *1. Northeastern University, Shenyang, China; 2. Lanzhou University of Technology, Shenyang, China; 3. Institute Of Electronics, CAS, Beijing, China*

MAX phases, with with a chemical formula of $M_{n+1}AX_n$ (n= 1~3), are a family consisting of inherently nanolaminated compounds. Here M is the early transition metal, A is an A group elements and usually Al, and X is C and/or N. Al can be easily etched by acid, leading into the delaminated emerging 2D MXene by sonication. Some studies have been focused on the magnetic substitution on M site of MAX phase. But there are seldom reports on the further delamination to MXene of magnetic doped MAX phase. The $(Ti_{1-x}Fe_x)_3AlC_2$ (x = 0, 0.025, 0.05, 0.075, 0.1) powders were prepared by the conventional solid state reaction. The MXene samples were prepare by the typical etching process. The structural evolution was characterized by X-ray diffraction, TEM and SEM. Magnetic properties were characterized by Cryogenic VSM. XRD patterns of (Ti1-xFex)3AlC2 (x = 0.025, 0.05, 0.075 and 0.1) are compared in Fig. 1. For small doping amount x ≤ 0.05, all peaks corresponds to 3:1:2 MAX phase. More doping leads into the (Ti,Fe)C cubic phase for x = 0.075 and 0.1. By etching and delamination, a broadened (002) peak at 2θ ≈ 6o and a weak (004) peak at 2θ ≈ 18o are observed due to the expanded c lattice parameter. The SEM images after acid etching show the typical accordian-like morphology. While, after sonication and delamination, the 2D nanosheets are formed and show the six-fold symmetry of diffraction patterns. The Curie temperature of (Ti1-xFex)3AlC2 (x = 0.025, 0.05, 0.075) is measured by M-T curves and gradually increased from 210 K to 260 K, indicating the weak ferromagnetism. The MXene "paper" can be

prepared from all three MXene. The excellent electromagnetic shielding properties were obtained for the frequency between 2-18GHz and the The best electromagnetic interference of ~ 35 dB is achieved, which means that more than 99.9% of the incident energy is reflected by the prepared "paper".

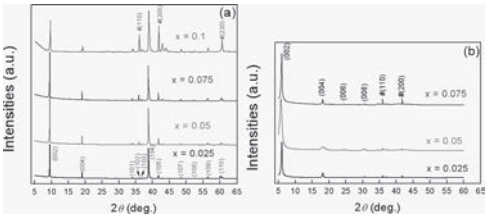
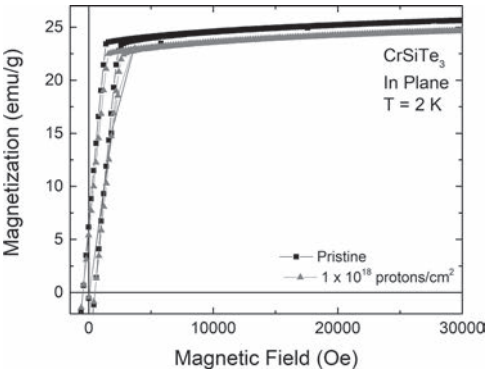


Fig.1 The XRD patterns of (Ti1-xFex)3AlC2 (x = 0.025, 0.05, 0.075 and 0.1) MAX phase and the corresponding MXene.

CT-07. Fluence Dependent Magnetic Properties of Proton Irradiated van der Waals CrSiTe. *H. Iturriaga*[1], R. Olmos[1], D.S. Blazer[1], L.M. Martinez[1], K. Gandha[2], C.I. Nlebedim[2], Y. Liu[3], C. Petrovic[3], L. Shao[4], Q. Wang[5] and S. Singamaneni[1] *1. Physics, University of Texas at El Paso, El Paso, TX, United States; 2. Critical Materials Institute, Ames Laboratory, Ames, IA, United States; 3. Condensed Matter Physics and Materials Science Department, Brookhaven National Laboratory, Upton, NY, United States; 4. Department of Nuclear Engineering, Texas A&M University, College Station, TX, United States; 5. Department of Physics and Astronomy, West Virginia University, Morgantown, WV, United States*

The research on van der Waals magnetic materials is rapidly progressing after the discovery of monolayer ferromagnetism in CrI_3 two years ago. Proton irradiation is an effective tool in manipulating the magnetic properties of these materials. The main goal of this work is to study the magnetic properties of $CrSiTe_3$ (CST), which is a layered ferromagnetic material associated with the Curie temperature of 32 K. We find the Curie temperature for the 10^{18} protons/cm^2 irradiated sample to be 37 K. A comparison between a 10^{18} protons/cm^2 irradiated sample and a pristine sample showed a 4% change in magnetization at 2 K in the in-plane direction. Furthermore, comparing isothermal magnetization in different crystal orientations confirms the presence of magnetocrystalline anisotropy and reveals that the easy axis is along the in-plane direction. We will present and discuss our comprehensive experimental findings on the magnetic properties of CST such as saturation magnetization, coercive field, and Curie temperature by varying the proton fluence from 10^{15} to 10^{18} protons/cm^2.



CT-08. Preparation and characterization of flexible FeRh thin films. *Y. Xie*[1], B. Wang[1], H. Yang[1] and R. Li[1] *1. Ningbo Institute of Industrial Technology, Chinese Academy of Sciences., Ningbo, China*

Flexible magnetic devices are one of the indispensable flexible devices.[1] Meanwhile, CsCl-type FeRh alloy have been used widely as one of the magnetic layers in magnetic devices.[2-4]. Therefore, it is essential to develop a method to fabricate flexible FeRh films. In this work, we present a convenient method to fabricate flexible wrinkled FeRh films via coating and transfer process. From the curvature radii dependent magnetic measurement, it can be obtained that the magnetic properties of FeRh is stable under different bending strain. As schematically illustrated in Fig. 1(a), the substrates used in this work were cleaved NaCl single crystals that can be dissolved in water. FeRh films were deposited on the top of soluble NaCl crystal by dc magnetron sputtering, as shown in Fig. 1(b). During deposition, there are great disparities in the thermal expansion coefficient of FeRh and NaCl crystal substrates. Consequently, the grown films display random wrinkles. Subsequently, polydimethylsiloxane (PDMS) were coated on the top side of the wrinkled film surface using spin coating technique, as schematically shown in Fig. 1(c). After the spin coating process, the NaCl crystal is peeled from the FeRh films, by means of dissolution, leading to a PDMS elastomeric template covered with the FeRh film (Fig. 1(d)). Fig. 2(a) shows the temperature dependent magnetization of FeRh/PDMS. With decreasing of curvature radii from ∞ to 1.5 mm, the temperature dependence of magnetic behaviors of FeRh/PDMS keeps almost unchanged, indicating that the magnetic properties are stable when the sample is under different strains generated via bending of the simple. Fig. 3(b)-3(c) show the hysteresis loops of FeRh/PDMS with different curvatures radii, which were measured at 250 and 400 K, respectively. Similarly, the magnetic hysteresis loop is almost unchanged as the curvature decreased from ∞ to 1.5 mm.

[1] D. Makarov, et al., Appl. Phys. Rev. 3, 011101 (2016). [2] M. Fallot, Ann. Phys. 10, 291 (1938). [3] J. S. Kouvel, *et al.* J. Appl. Phys. 33, 1343 (1962). [4] A. I. Zakharov, *et al.* Sov. Phys. JETP 19, 1348 (1964).

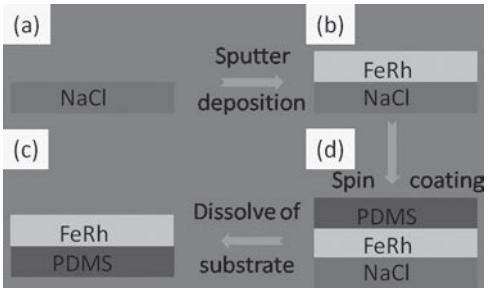


FIG.1. Step-by-step process for fabricating flexible FeRh/PDMS with random wrinkles.

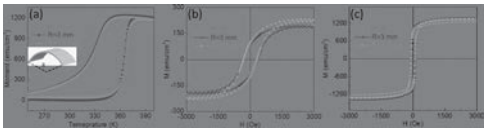


FIG.2. (a) Temperature dependent magnetization for FeRh/PDMS under various curvature radii in an applied magnetic field of 0.2 T. Typical hysteresis loops under various curvature radii measured at 250 K (b) and 400 K (c) for FeRh/PDMS.

CT-09. Spectral reflectivity crossover and direct-write of ferromagnetic patterns in FeRh thin films. *O. Van't Erve*[1], M. Currie[1], I. Mazin[1], C.D. Cress[1], J. Prestigiacomo[1] and S.P. Bennett[1] *1. Naval Research Lab, Washington, DC, United States*

Metamagnetic transition in FeRh, the transition from antiferromagnetic (AF) to ferromagnetic (FM) above room temperature, has been subject to many investigations. Several methods have been employed to investigate the various structural, magnetic, and electronic characteristics as the material undergoes this transition. In this work, we investigate the frequency dependent reflectance, which is a fast and easy probe and is found to display a clear and distinct signature coincident with this transition. Complimenting these experimental finds, our first principle calculations reveal that the dramatic difference in electronic structure between the ferro- and antiferromagnetic phases of FeRh leads to a characteristic crossover in the energy dependence

reflectivity, whereby the reflectivity difference between the two phases changes sign at E=~0.79 eV (1400 nm). Developing means to control the metamagnetic transition is also of high interest. To this end, we will demonstrate the successful direct write of ferromagnetic patterns in FeRh. For this we utilized a He-ion microscope to implant He ions with a specific dose, as determined by the microscope settings, into arbitrarily shaped regions. This sample was then transferred to a Magneto Optical Kerr Effect Microscope to characterize the local magnetic properties and study the effects of He implantation (energy and dose) on the metamagnetic properties of FeRh.

[1] S. P. Bennett, M. Currie, O. M. J van't Erve and I. I. Mazin, "Spectral Reflectivity Crossover at the Metamagnetic Transition in FeRh Thin Films," *Optical Materials Express* Vol 9, No. 7 / 1 July 2019 / 2870

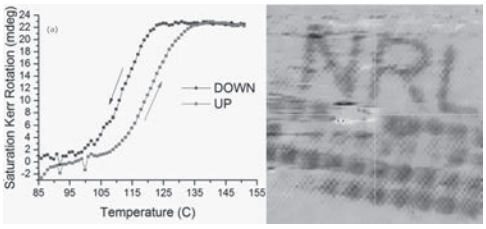
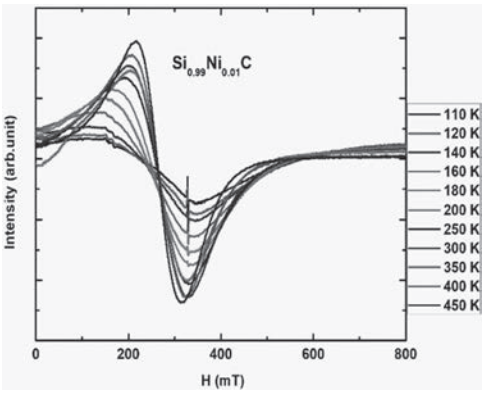


Figure 1: (a) Saturation Kerr rotation (taken at H=1250 Oe) as a function of temperature heating and cooling through the metamagnetic transition to display the temperature hysteresis of magnetic to antimagnetic phase of FeRh as deposited. (b) Kerr image of FeRh at RT after He implantation by He ion beam, contrast shows ferromagnetic versus antiferromagnetic regions (squares are 25 x 25 um2).

CT-10. On the magnetic interactions and spin dynamics in 3d transition metal doped 3C-SiC. *G. Moharana*[1], S. Singh[2] and H. Narayanan[1] *1. Physics, Indian Institute of Technology Madras, Chennai, India; 2. IMMT BBSR, BBSR, India*

We have synthesized Cr, Mn, Co and Ni (1, 3, 5) % doped 3C-SiC polycrystalline samples by Thermal Plasma technique. X-Ray Diffraction (XRD) revealed that the structure is Cubic (space group F4-3m) for all the three samples. XRD and Raman spectra indicates that the samples have crystallized in single phase and confirms the incorporation of the dopants into the host matrix. The temperature variation of Raman spectra reveals the roles of the defects in the structural stability and its effect on magnetic properties of the materials. The variation of Longitudinal Optical Mode (LO) and transverse Optical mode (TO) with temperature and different concentration has been analysed. The Site occupancy and valence state of dopant ions were investigated by variable Temperature Electron Spin Resonance spectroscopy (VT-ESR) and XPS study. The spectrum of pure SiC sample has shown the feature of resonance at resonance field Hr= 338.05mT, corresponding to g value of 2.00 which could be due to defects present in the sample (Vsi,Vc).

1.T. Dietl, H. Ohno, F. Matsukura, J. Cibert, and D. Ferrand, Science 287, 1019 (2000). 2. Zhao Huang, Qianwang Chen, Journal of Magnetism and Magnetic Materials., 313 111–114, 2007. 3. C G Jin et al, J. Phys. D: Appl. Phys. 41 035005, 2008.



Temperature variation of EPR spectra showing asymmetry and spectral broadening due to strong dipolar interaction. A small EPR signal from defect is shown in figure.

CT-11. Spin Reorientation in $R_XSm_{1-X}FeO_3$ Perovskites (R= Pr or Nd). *F.E. Lurgo*[1], C. Martin[2] and R.E. Carbonio[1] *1. Departamento de Fisicoquimica, Facultad de Ciencias Quimicas, Universidad Nacional de Córdoba, INFIQC-UNC-CONICET, Córdoba, Argentina; 2. Laboratoire CRISMAT, Centre National de la Recherche Scientifique (CNRS)/ENSICAEN/UCBN, Caen, France*

Design, development and understanding of novel functional magnetic materials are essentially important for numerous applications such as magnetic data storage devices, sensors and in the field of biomedicine [1,2]. Lanthanide orthoferrites and orthocromites have been under exhaustive study for several decades. These materials show a variety of striking effects resulting from the coupling between the two magnetic sublattices. This strong interations between these two sublattices could produce a phenomenon vastly studied: spin reorientation (SR). The orthoferrites $SmFeO_3$, $NdFeO_3$ and $PrFeO_3$ present reorientation of spin at temperatures already reported (470-490K for Sm, 66-158K for Nd and 50-85K for Pr) [3-6]. If one of these lanthanides, Pr or Nd are mixed with Sm in a composition such that the T_{SR} decreases to 300 K would be fantastic, because it could be potentially observing magneto-electric properties at room temperature. In the present work, three different compositions of two different perovskites of the $R_xSm_{1-x}FeO_3$ family (R=Pr, Nd) have been synthesized to obtain magneto-electric materials at room temperature. All these compounds crystallize in a *Pbnm* orthorhombic unit cell. ZFC and FC dc magnetic susceptibility curves as a function of temperature were measured in warming for all the members. The magnetic behavior depends on the rare earth. The study of the magnetic structure vs temperature showed the occurrence of a progressive spin orientation in all the compositions and is possible switch the T_{SR} with different compositions of rare earth cations on A site.

[1] R.F. Service Science, 314,1898 (2006) [2] Moser A. et. al. J. Phys. D 35,157 (2002) [3] Gorodetsky G. and Levinson L. Solid State Comunications 7,67-70 (1969) [4] White R. L. J. App. Physics 40, 1061-1069 (1969) [5] Zhou Z. et. al. J. of Alloys and Compounds 583,21-31(2014) [6] Ramesh J. et. al. J. of Alloys and Compounds 711,300-304(2017)

CT-12. A comparison between Al and Si substitution effects on structural and magnetic properties of Mn_3Ge with tetragonal $D0_{22}$ structure. *H. Okada*[1,2] and Y. Syoji[2] *1. Faculty of Engineering, Tohoku Gakuin University, Tagajo, Japan; 2. Graduate School of Engineering, Tohoku Gakuin University, Tagajo, Japan*

Mn-based alloys with tetragonal structure have attracted much attention in the field of spintronics and permanent magnet [1,2]. Mn_3Ge with $D0_{22}$ structure exhibits a ferrimagnetic ordering and strong uniaxial magnetocrystalline anisotropy without 4*f* elements. It has been known that magnetic properties of the Mn-based alloys are strongly influenced by number of the valence electron. On the other hand, theoretical investigations have predicted that

the magnetic state is sensitive to structural properties [3,4]. In this work, we have investigated structural and magnetic properties of Al- and Si-substituted Mn_3Ge to clarify the relationship between structural and magnetic properties of the alloys. It is known that Mn-rich composition is required for obtaining a single phase of the $D0_{22}$ structure in Mn-Ge alloys. In this work, the single phase is obtained at x = 0.0-0.2 for $Mn_{3.03}Ge_{0.97-x}Al_x$ and y = 0.0-0.4 for $Mn_{3.09}Ge_{0.91-y}Si_y$. The lattice constants a and c estimated from the X-ray diffraction data linearly decreases with increasing Si content. This is due to the substitution with Si atom having smaller ionic radius than Ge atom. As the result, the unit cell volume shrinks with the increasing Si content. The axial ratio c/a is mostly constant, indicating that the unit cell volume is isotropically contracted by the Si substitution. On the other hand, the replacement of Ge with Al leads to an increase in the parameter a and a decrease in the parameter c. Consequently, the unit cell volume is slightly expanded. The Al substitution effects are consistent with the results of the Ga-substituted Mn_3Ge [5]. Therefore, it is considered that the structural properties are influenced by number of the valence electron in addition to ionic radius. As shown in Fig.1, Spontaneous magnetization estimated using the law of approach to saturation increases with increasing Al content, whereas the magnetization decreases with increasing Si content. These results imply that the structural properties such as the unit cell volume and the atomic distance between Mn atoms play an important role for the magnetic properties of the alloy.

[1] B. Balke et. al., Appl. Phys. Lett. 90, 152504 (20107) [2] J. M. D. Coey, J. Phys., Condens. Matter 26, 064211 (2014) [3] D. Kim et al., Phys. Rev. B 90, 144413 (2014). [4] S. Khmelevskyi et al., Phys. Rev. B 93, 184404 (2016). [5] H. Okada et al., IEEE Trans. Magn. 53, 1000506 (2017)

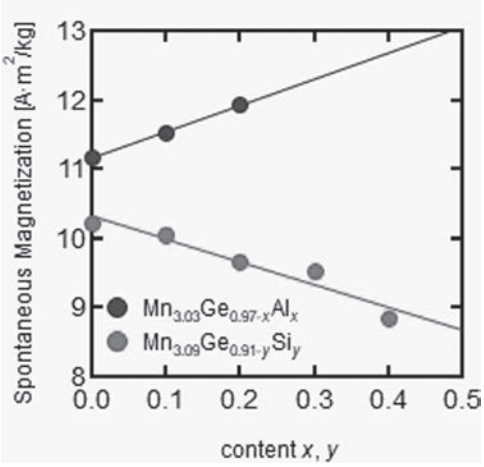


Fig.1 Spontaneous magnetization of $Mn_{3.03}Ge_{0.97-x}Al_x$ and $Mn_{3.09}Ge_{0.91-y}Si_y$.

CT-13. Investigation of the structural and magnetic phase transition of Ga-doped $Eu_3Ir_4Sn_{13}$. *R.M. Grossi*[1], A. Fahl[1], K.R. Pakuszewski[1], J.C. Souza[1], A. Ribeiro[1], C. Adriano[1] and P. Pagliuso[1] *1. Unicamp, Campinas, Brazil*

$Eu_3Ir_4Sn_{13}$ is an intermetalic compound, the so-called Remeika cubic phase $R_3M_4Sn_{13}$ (R = rare earth, M = transition metal). $Eu_3Ir_4Sn_{13}$ presents a structural distortion at T* ~ 57K with a propagation vector (0 1/2 1/2). In addition it presents an antiferromagnetic (AFM) order below T_N ~ 10K where we observe a commensurate magnetic propagation vector (0 1/2 1/2) identical to the one observed for the structural distortion [3]. In this work we present the evolution of the magnetic and structural properties of $Eu_3Ir_4Sn_{13-x}Ga_x$ studied by electrical resistivity, specific heat and magnetic susceptibility. The results have shown that the Ga doping suppresses the structural transitions and barely changes de magnetic one. We will also present results of X Ray powder diffraction under applied pressure of the undoped compound were we found a change of the powder pattern of the super lattice peaks for pressure higher that 3.2 Gpa.

[1] J.P. Remeika et al., Solid State Commun. 34, 923 (1980) [2] H. Sato, et al., Physica 630, 186 (1993) [3] J. R. L. Madergan, et al., IEEE transactions on magnetics, 49, 4652 (2013). [4] L. Medonça Ferreira et al, PhysicaB, 384 (2006)

CT-14. Preparation of Highly Magnetic and Dispersible FeCoNi-Graphene Hybrid Materials using a Low Temperature Process for Electromagnetic Absorbing Film. K. Lee[1], *S. Lee*[1], K. Kim[2], B. Jung[1] and T. Kim[1] *1. Korea Institute of Materials Science, Changwon, The Republic of Korea; 2. Yeungnam University, Gyeongsan, The Republic of Korea*

Magnetic metal and graphene hybrid is a suitable material for electromagnetic wave absorbing film due to high electric and magnetic properties [1, 2]. However, hydrothermal process and heat treatment at high temperature decreases the productivity of the hybrid material. In this work, a strategy for preparation of FeCoNi and graphene hybrid materials without heat treatment and hydrothermal method is described. Electroless plating is used to grow the magnetic metal particles on the surface of graphene without reduction by heat treatment at high temperature. We find that the conventional electroless plating method is inappropriate for the synthesis of FeCoNi@graphene hybrid materials with high saturation magnetization. Therefore, we propose a new electroless plating method and observe the morphological, structural and magnetic properties of the synthesized FeCoNi@graphene hybrid materials. The FeCoNi@graphene prepared by the new synthesis method has a different morphology (see Figure 1) and crystal structure from that prepared by the conventional one. Saturation magnetization value of the hybrid material is 63.1 emu/g when the ratio of FeCoNi to graphene is 1:1, and the maximum is 171.6 emu/g when the FeCoNi ratio is increased. When the ratio of FeCoNi to graphene is 4:1, both magnetic property (120.4 emu/g) (see Figure 2) and dispersion stability of the hybrid material can be achieved. The FeCoNi@graphene hybrid is well dispersed in tetrahydrofuran, and thus it is fabricated into a free-standing and flexible composite film by mixing with thermoplastic polyurethane. High permeability of the FeCoNi@graphene film results in high EM wave absorbing performance due to impedance matching. These results provide important progress not only towards the commercialization of EM wave absorbing film for healthcare, electronic reliability, and tactical security applications, but also towards the development of magnetic metal and graphene hybrid materials based on a scalable process.

[1] F. Meng, H. Wang, F. Huang, Y. Guo, Z. Wang, D. Hui, Z. Zhou, Graphene-based microwave absorbing composites: A review and prospective, Compos. Part B 137 (2018) 260-277. [2] X. Ding, Y. Huang, J. Wang, H. Wu, P. Liu, Excellent electromagnetic wave absorption property of quaternary composites consisting of reduced graphene oxide, polyaniline and FeNi3@SiO2 nanoparticles, Appl. Surf. Sci. 357 (2015) 908-914.

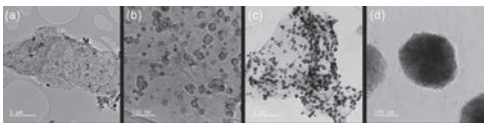


Fig 1. TEM micrographs of (a, b) FeCoNi@graphene(C) hybrids and (c, d) FeCoNi@graphene(D) hybrids.

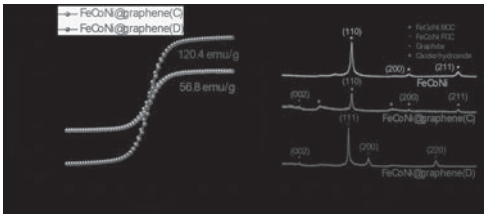


Fig 2. (a) MS values of FeCoNi@graphene and (b) XRD profiles of FeCoNi@graphene hybrids and FeCoNi nanoparticles.

CT-15. First-principles study of magnetic properties of NO_2 absorbed on $SnSe_2$ monolayer. W. Cheng[1], H. Fuh[2] and *C. Chang*[3] *1. Graduate Institute of Applied Physics, National Taiwan University, Taipei, Taiwan; 2. Department of Chemical Engineering & Materials Science, Yuan Ze University, Taoyuan, Taiwan; 3. Department of Physics, National Taiwan University, Taipei, Taiwan*

Recently, two-dimensional transition metal dichalcogenides (2D-TMDs) materials has gained great attention due to its weak van der Waals type layer structure. Moreover, the flake and few-layers $SnSe_2$ have also been used as high performance photodetector[1] and high-mobility field-effect transistor[2] applications. Moreover, $SnSe_2$ is also a good candidate for gas sensing. This study simulates the interactions of NO_2 and NH_3 gas molecules absorbed on $SnSe_2$ monolayer respectively via a first-principles approach based on density-functional theory (DFT). The calculation includes both the van der Waals force interaction and spin polarization. Fig. 1 (a) and (b) show the crystal structures of monolayer $SnSe_2$ adsorbed with NO_2 and NH_3 molecules, respectively. The distances between gas molecules and $SnSe_2$ are about 3Å means the interaction between gas molecules and $SnSe_2$ monolayer is in the range of physisorption. Fig. 2 (a)~(d) represent the band structures of NO_2 and NH_3 adsorption on $SnSe_2$ monolayer. The magnetic moment of NO_2-$SnSe_2$ system is about $1.0\mu_B$. In Fig. 2(a) and (b) are the spin decomposed band structure of SnSe2 adsorbed with NO_2. Firstly, there are two flat bands between the E_F which located in about -0.2eV and 0.8eV. The spin-up electrons are occupied below the E_F and the spin-down electrons are occupied up the E_F. This kind of band structure distribution also induces the magnetic moment after NO_2 adsorbs on the $SnSe_2$ monolayer. However, the magnetic moment of NH_3-$SnSe_2$ system is about $0.0\mu_B$. Due to the band occupation of the spin-up and spin-down electrons of NH_3 are the same location which shown in Fig.2 (c) and (d). The difference of magnetic moment induced by different gases sensing is similar with graphene-based gas sensor[3][4]. In conclusion, the magnetic moment would be induced when NO_2 adsorbs $SnSe_2$ monolayer which provides experimental researcher to further investigation.

[1] P. Yu, X. C. Yu, W. L. Lu, H. Lin, L. F. Sun, K. Z. Du, F. C. Liu, W. Fu, Q. S. Zeng, Z. X. Shen, C. H. Jin, Q. J. Wang, and Z. Liu, Adv Funct Mater 26 (1), 137 (2016). [2] Chenglei Guo*,* Zhen Tian*,* Yanjun Xiao*,* Qixi Mi*, and Jiamin Xue*, Appl. Phys. Lett. 109, 203104 (2016) [3] Miao Zhou, Yun-Hao Lu, Yong-Qing Cai, Chun Zhang and Yuan-Ping Feng, Nanotechnology, 22, 385502 (2011) [4] Youngbin Lee, Sangho Lee, Yubin Hwang, Yong-Chae Chung, Applied Surface Science, 289, 445– 449(2014)

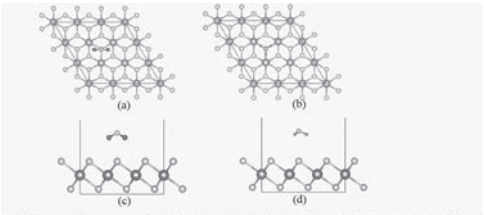


Fig. 1 The crystal structures of monolayer $SnSe_2$ adsorbed with NO_2 molecules in top view (a) and side view (c), as well as the structure adsorbed with NH_3 molecules in (b) and (d).

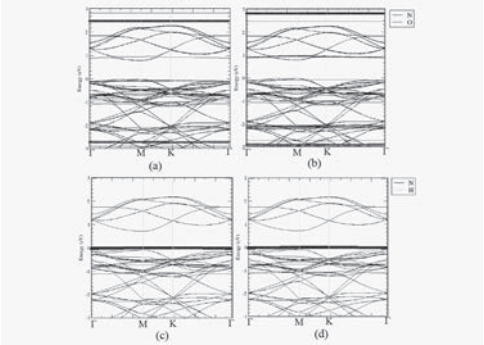


Fig. 2 The band structures of NO_2 molecules adsorption on monolayer $SnSe_2$ with (a)spin-up and (b)spin-down electrons, as well as the band structure of NH_3 molecules adsorption with (c)spin-up and (d) spin-down electrons. The blue and red lines denote the bands occupied by N atom and O atom of NO2 in (a)~(b), respectively. The blue and grey lines denote the bands occupied by N atom and H atom of NH3 in (c)~(d), respectively.

CT-16. A Study on the Improvement of Torque Density and THD Performance through the Injection of Ferrofluid into the Magnet Tolerance of IPMSM. *I. Yang*[1], D. Kim[1], S. Song[1], S. Lee[1], K. Kim[2] and W. Kim[1] *1. Gachon University, Gyeonggi-do, The Republic of Korea; 2. Halla University, Gangwon-do, The Republic of Korea*

When inserting a permanent magnet into a rotor core of IPMSM (Interior Permanent Magnet Synchronous Motor), it is ideal that the size of the permanent magnet and the insertion space correspond to each other. However, it is difficult to insert the permanent magnet when the sizes of insertion space and the permanent magnet are the same. Magnet tolerance between the rotor core and the permanent magnet is necessarily required. Increased magnet tolerance can reduce the performance and there is a problem with driving motor at high speed that can cause vibration between the permanent magnet and the magnet tolerance. And vibration causes noise. In order to prevent vibration in the magnet tolerance, an adhesive is inserted into the magnet tolerance to fix the permanent magnet. In this case, the magnet tolerance doesn't contribute to performance improvement. In this paper, a method to improve performance by injecting ferrofluid into the magnet tolerance of IPMSM for 4WD hydraulic control system and changing the rotor shape. The ferrofluid is a magnetic liquid which consists of water or oil mixed with ultrafine powder. The ferrofluid has a higher permeability than vacuum. Therefore, it is possible to improve the performance by reducing magnetic resistance when the ferrofluid is injected into the magnet tolerance. To verify the proposed rotor configuration, two rotor parameters and four target functions were set for the proposed model which the shape of the barrier and the position of the magnet were changed while the ferrofluid was injected in and the conventional model. And the rotor design was proceeded respectively through FEM (Finite Element Method). It was confirmed whether the conventional model and the proposed model satisfied the target specification of IPMSM for 4WD hydraulic control system or not. The design process was verified through prototype manufacture and testing. The proposed model had higher performance than the conventional model in terms of torque, THD and efficiency except cogging torque. This study is expected to be applied to robot, aviation, medical, and other fields requiring high performance and high efficiency motors.

[1] Alexy O.Ivanov, "Magnetic Properties Of Dense ferrofluids", Journal of Magnetism and Magnetic Materials, 252, 135-137, 2002. [2] Dr. Duane Hanselman, "Brushless Motors Magnetic Design, Performance and Control", E-Man Press LLC, 2012, 113. [3] Babak Assadsangabi, "Ferrofluid-Assisted Micro Rotary Motor for Minimally Invasive Endoscopy Applications", IEEE on MEMS, 200-203, 2014

Session CU
MAGNETIC CHARACTERIZATION III: INSTRUMENTATION
(Poster Session)

Thomas Thomson, Co-Chair
University of Manchester, Manchester, United Kingdom
Neil Dilley, Co-Chair
Purdue University, W Lafayette, IN, United States

CU-01. Influence of the random interaction among magnetic moments on the magnetization in cobalt ferrite nanoparticles. *C.R. Stein*[2,4], M.J. Stoffes Júnior[1], J. André-Filho[4], T.R. Covas[2] and P.C. Morais[3,4]
1. Physics, Federal Institute of Rondônia – IFRO, Porto Velho, Brazil; 2. Federal Univerity of Goiás, Goiânia, Brazil; 3. Catholic University of Brasília, Brasilia, Brazil; 4. University of Brasília – UnB, Brasilia, Brazil

Systems comprising magnetic nanoparticles (MNPs) are unique in both structure and properties, thus allowing different applications. However, interactions among MNPs are difficult to address in real systems. Regarding MNPs interactions, several experimental results have been reported in the literature, but few theoretical approaches have been proposed to explain the behavior of such a complex system. In this study, we report on the morphological, structural and magnetic investigation of cobalt ferrite nanoparticles (CFN) synthesized by co-precipitating Co^{2+} and Fe^{3+} in alkaline medium at increasing temperatures, from 25 to 95 °C [1,2]. X-ray diffraction data of the as-synthesized CFN revealed samples with high degree of crystallinity and average crystallite size in the range of 5 nm to 11 nm as the synthesis temperature increases [3]. Hysteresis cycles (*M* versus *H*) were recorded at 5 K, 100 K and 300 K whereas field-cooled (FC) and zero-field-cooled (ZFC) magnetization curves (*M* versus *T*) were obtained in the range of 5 K to 300 K while varying the applied field in the range of 50 Oe to 100 Oe. The room-temperature *M* versus *H* data were well described by averaging out the first order Langevin function with a lognormal distribution function of magnetic moments [4]. However, at low temperatures, deviations from the classical superparamagnetic regime are observed and generally attributed to single-particle blocking effects and/or random interactions among MNPs [5,6]. The dependence of the magnetization in different temperatures is herein reported and explained using a new phenomenological approach. Three samples are tested, and the results are discussed in terms of such a new empirical model. The proposed interpretation is thought to be applicable to other MNPs systems.

[1] N. Boda; G. Boda; K. C. B. Naidu; M. Srivivas; K. M. Batoo; D. Ravinder; A. P. Reddy, Journal of Magnetism and Magnetic Materials Vol 473, p. 228 – 235 https://doi.org/10.1016/j.jmmm.2018.10.023 (2019) [2] A. Sathya, P. Guardia, R. Brescia, N. Silvestri, G. Pugliese, S. Nitti, L. Manna, T. Pellegrino, Chem. Mater. Vol. 28, 1769 – 1780 DOI: 10.1021/acs.chemmater.5b04780 (2016). [3] C. R. Stein; M. T. S Bezerra, G. H. A Holanda, J. André-Filho, P. C. Morais, AIP Advances, Vol. 8, 056303 – 1 – 6. DOI: 10.1063/1.5006321, (2018). [4] Z. Huang, F. Tang, Journal of Colloid and Interface Science Vol. 281 p. 432 – 436. DOI: doi.org/10.1016/j.jcis.2004.08.121 (2005). [5] E. Ferrari, F. Da Silva, M. Knobel, Physical Review B Vol. 56 6086 – 6093. DOI: doi.org/10.1103/PhysRevB.56.6086 (1997). [6] S. Rout, M.Senthil Kumar, D.K. Aswal, S.K. Gupta, Physica B Vol. 405 345 – 351 (2010). DOI:10.1016/j.physb.2009.08.076.

CU-02. gFORC: A GPU Accelerated First-Order Reversal-Curve Calculator. F. Gross[1], J.C. Martínez García[2], S.E. Ilse[1], G. Schütz[1], E. Goering[1], M. Rivas[2] and *J. Gräfe*[1] *1. Max Planck Institute for Intelligent Systems, Stuttgart, Germany; 2. University of Oviedo, Gijón, Spain*

First-order reversal-curves (FORCs) [1] are a powerful tool, increasingly used in material science as well as nano-magnetism [2-4]. Ideally, it can access microscopic interactions and coervities without the need for lateral resolution [5]. Unfortunately, the conventional fitting algorithm requires lots of computational effort to overcome noise, inherently present in the measurement data. Here we present a fast Fourier transform (FFT) evaluation approach exploiting the manifold of Fourier space to decrease the computing time by a factor of 200. Comparing baseline resolutions of the conventional and the FFT algorithm, we are able to deduce an analytical equation to transform the smoothing factor *SF* of a FORC diagram into real field resolution *R*. To validate the proposed algorithm we compare three representative FORC measurements evaluated with both approaches (Fig. 1). All of the FORC densities show exceptionally good agreement. Not only does the FFT algorithm show the typical *reversal ridge* [6] for fully reversible processes (*cf.* Fig 1c) & d)), it also perfectly recovers the behavior of a multi-phase system with complex interactions between soft and hard magnetic phases [7] (*cf.* Fig 1e) & f)) over a wide range of smoothing factors. The achieved speed up allows us to utilize an autocorrelation approach [8] which was previously computationally prohibitive. This autocorrelation allows us to judge objectively whether a FORC diagram is under- or oversmoothed at a given smoothing factor (Fig. 2). In the first part (gray box, left), the noise of the FORC diagram is reduced which increases the correlation (undersmoothing). The last part (gray box, right) is highly oversmoothed which causes destruction of information. The part between noise and signal reduction (green box) illustrates the region of optimum smoothing in which noise is suppressed sufficiently but no information destroyed. In summary, the proposed algorithm speed up FORC calculations and allows to replace the *SF* concept with real field resolutions. It automatically determines the optimum smoothing and enables unprecedented advanced FORC evauation.

[1] Mayergoyz, I.D., Physical Review Letters, 56(15): p. 1518-1521 (1986) [2] Gräfe, J., *et al*., Physical Review B, 93(1): p. 014406 (2016) [3] Dobrotă, C.-I. and A. Stancu, Journal of Applied Physics, 113(4): p. 043928 (2013) [4] Pike, C.R., *et al*., Physical Review B, 71(13): p. 134407 (2005) [5] Gräfe, J., *et al*., Review of Scientific Instruments, 85(2): p. 023901 (2014) [6] Pike, C. R., Physical Review B, 68: p. 104424 (2003) [7] Groß, F., *et al*., Physical Review B, 99(6): p. 064401 (2019) [8] Heslop, D., *et al*., Journal of Magnetism and Magnetic Materials, 288: p. 155-167 (2005)

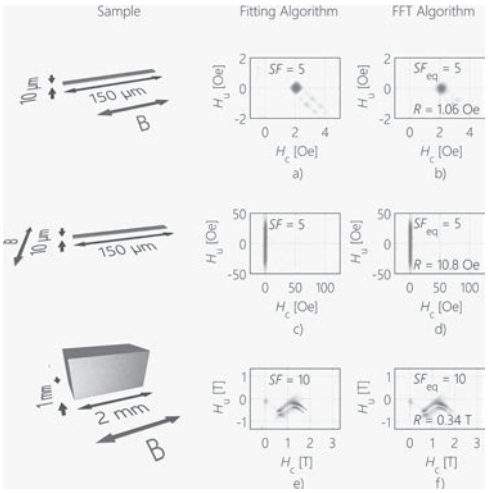


Fig. 1: Comparison of FORC diagrams (Fitting & FFT).

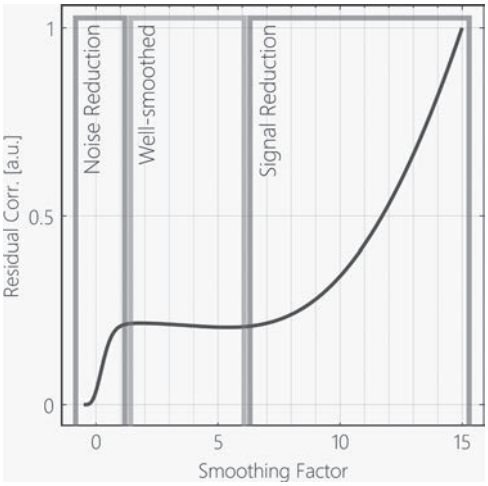


Fig. 2: Objective criterion for the optimum smoothing factor.

CU-03. Study of Mechanical Resonance Induced by Magnetostriction in Cyclic Structures Based on FeSi. *J. Li*[1], B. Qu[2] and K. Yu[3] *1. State Key Laboratory of Control and Simulation of Power System and Generation Equipments, Tsinghua University, Beijing, China; 2. State Key Laboratory of Reliability and Intelligence of Electrical Equipment, Hebei University of Technology, Tianjin, China; 3. Global Information and Telecommunication Institute, Waseda University, Tokyo, Japan*

The noise produced by motors and power transformers is harmful and its reduction is the hot subject in continuous research. Such systems are likely to be in resonance and become more vociferous, and the resonance may be mechanical or magnetic forces. The interaction between the deformation due to magnetostriction and mechanical resonance of a structure made up of laminated steel sheets is investigated in this paper. The resonance phenomena are generally studied and analyzed by considering that the frequency and the spatial distribution of the electromagnetic forces coincide with the natural frequency and the modal shape of the corresponding structure. It is observed that the magnetostriction may induce a resonance without the need to combine these two conditions. Two cyclic sheets structures of square and circular consisting of cold-rolled grain-oriented (GO) and non-grain oriented (NO) electrical steels are used to confirm this assumption. Finite element (FE) calculations and measurements are made and compared with vibration displacements. The results of the mechanical resonance induced by ferromagnetic magnetostrictive strain are shown, as well as the corresponding vibration spectrums. 1. The mechanical resonance induced by magnetostrictive deformation has been studied. The resonance occurs when the natural frequency of the laminated steel sheets structure corresponds to the multiple of the excitation frequency. The vibration behavior of the laminated structure shows a ferromagnetic behavior which similar to the modelling. 2. The study confirms that the magnetostriction is likely to cause the resonance of a ferromagnetic materials even at very low amplitudes of excitation, and may be even more important for high power devices. Due to the presence of harmonics in the magnetizing field, so, the consideration of their influence on the deformation is necessary. 3. This paper has shown that the magnetostriction can be involved in the mechanical resonance of a laminated structure, and should be considered in the design stage.

[1] S. S. Mbengue, N. Buiron and V. Lanfranchi, Sensors, Vol. 16, No. 4, pp. 553-556 (2016) [2] M. Liu, O. Hubert, X. Mininger, et al, IEEE Transactions on Magnetics, Vol. 53, No. 8, pp. 1-11 (2017) [3] P. Pellerey and V. Lanfranchi, IEEE Transactions on Magnetics, Vol. 48, No. 2, pp. 983-986 (2012) [4] M. Liu, O. Hubert, X. Mininger, et al, IEEE Transactions on Magnetics, Vol. 52, No. 2, pp. 1-12 (2016)

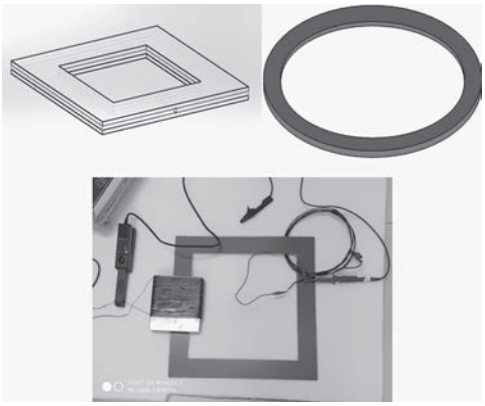


Fig. 1. Test verification models for magnetostriction based on two cyclic sheets structures of square and circular.

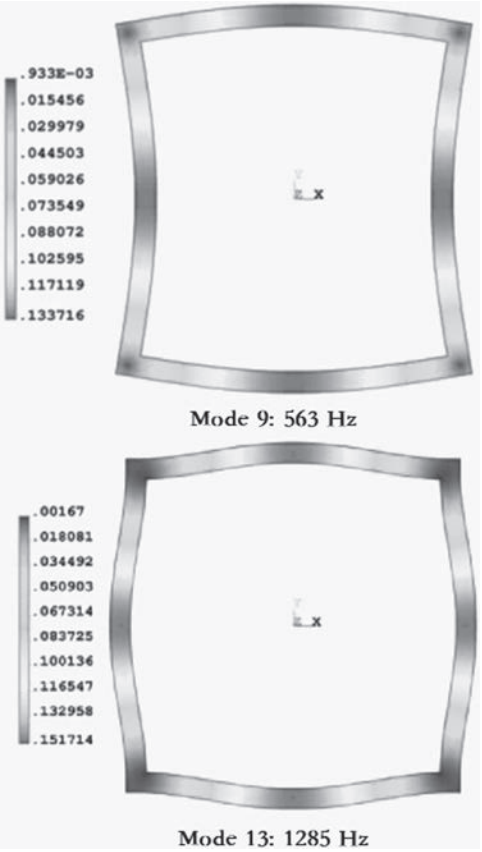


Fig. 2. Simulation of deformation modes in the square cyclic structure.

CU-04. Ultra-broadband and ultra-high sensitivity permeability measurements by transformer coupled permeameter. *S. Tamaru*[1], H. Kubota[1], N. Kikuchi[2] and S. Okamoto[2] *1. Spintronics Research Center, National Institute of Advanced Industrial Science and Technology (AIST), Tsukuba, Japan; 2. IMRAM, Tohoku University, Sendai, Japan*

Many high frequency magnetic components are made of magnetic particles, which are first prepared by crashing an ingot, next undergo various processes such as micro-forging and annealing, then are either sintered or dispersed into polymer resin and solidified into the final form. Its permeability is measured on the final form due to limited sensitivities of permeameters currently available[1-3]. Therefore, one can only infer the effect of each of the processes on the permeability from the measurement result on the final form, which is very inefficient and often misleading for the development of high frequency magnetic components. For this reason, a technique to measure the permeability of magnetic particles with a sufficiently high sensitivity has been strongly sought. To accomplish this goal, we have developed a permeability measurement technique, which we named as "transformer coupled permeameter (TC-permeameter). Figure 1 shows the block diagram. A magnetic particle is sandwiched by two short terminated coplanar waveguides (CPWs). These two CPWs are electrically insulated by Kapton tape, thus this structure forms a loosely coupled transformer. Each CPW is connected to the port 1 and 2 of a vector network analyzer that measures S_{21} twice, first under the magnetic field of interest, and second under a sufficiently strong magnetic field to saturate the magnetic particle. The difference of S_{21} under these two magnetic fields reflects the permeability. Figure 2 shows the permeability of a single Permalloy particle with a lateral size of approximately 100 μm and thickness of 0.5 μm, which is similar to the size of magnetic particles contained in commercial noise suppression sheets, measured by the TC-permeameter. The figure shows that the permeability can be measured from 10 MHz up to 20 GHz with a high signal-to-noise ratio. In the presentation, the measurement principle of the TC-permeameter, including the jig structure, the reason why this technique can enhance the sensitivity and how to calibrate the system to give the absolute value will be explained.

1) A. M. Nicolson and G. F. Ross, IEEE Trans. Instrum. Meas. 19.4, 377 (1970). 2) M. Yamaguchi et al. T. Mag. Soc. Jpn. Vol. 3, p137 (2003). 3) S. Takeda and H. Suzuki, J. Magn. Soc. Jpn., Vol. 33, P171 (2009).

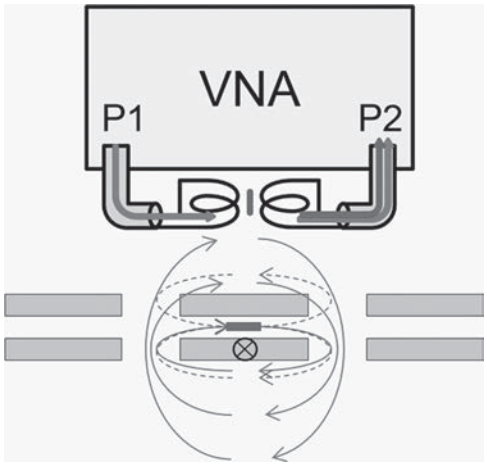


Fig. 1, Block diagram of the TC-Permeameter.

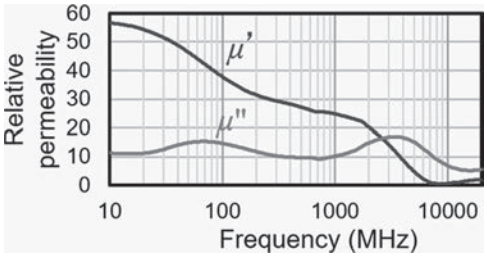


Fig. 2, Complex relative permeability of a single Permalloy particle over 10 MHz – 20 GHz.

CU-05. Inexpensive Setup for Accurate Characterization of the Ferromagnetic Linewidth of Garnet Spheres. *A. Pacewicz*[2], J. Krupka[2], P. Aleshkevych[1], B. Salski[2] and P. Kopyt[2] *1. Institute of Physics, Polish Academy of Sciences, Warsaw, Poland; 2. Warsaw University of Technology, Warsaw, Poland*

The theory, design and operation of an inexpensive but accurate setup for ferromagnetic linewidth (ΔH) measurement of garnet spheres is presented. The fixture consists of a microwave Q-meter, rectangular cavity, hand-adjustable magnet, quartz sample tube and personal computer. From a single Q-factor measurement, as well as the diameter and saturation magnetization of the sample, the linewidth is obtained based on the recently proposed characteristic equation for a spherical gyromagnetic resonator placed in a metal enclosure [1]. The setup can handle any coupling regime between the sample and cavity. For strong coupling, which occurs for sufficiently narrow ΔH, the magnet is positioned in such a way that the Q-factors of the sample and cavity modes are similar [2]. For weak coupling, i.e. when the cavity mode is perturbed, the minimum value of the Q-factor is sought. In either case ΔH is quickly obtained with the aid of a precomputed database. The influence of factors such magnetic anisotropy or dielectric losses on ΔH is shown to be negligible in most practical scenarios. A variety of mono- and polycrystalline yttrium iron garnet samples have been measured in two TE_{102} cavities operating at ca. 5 GHz and 10 GHz. Where possible, the obtained results are compared to a perturbation theory approach.

[1] J. Krupka, B. Salski, P. Kopyt, Scientific Reports, Vol. 6, pp. 34739 (2016) [2] J. Krupka, P. Aleshkevych, B. Salski, Measurement Science and Technology, Vol. 29, pp. 025501 (2018)

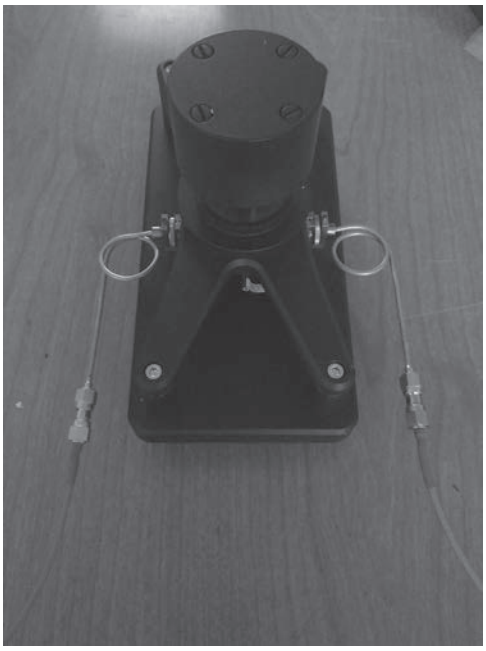


Fig. 1. Photograph of a version of the linewidth measurement fixture operating at ca. 10 GHz.

CU-06. Measurement uncertainties of complex permeability effects in ferrite material under compressive stress. *J. Le Gallou*[1] *1. DMAT, CEA, Monts, France*

To achieve non-destructive control of materials properties, a general broad band measurement technique of complex permeability under stress has been demonstrated some years ago, based on a short-circuited line (one-port measurement/reflection only) [1]. Despite the fact that the application of an external stress can change drastically the values of the permeability, most of the studies have evidenced the influence of a stress on static magnetic properties only, but few works have led into the field of the dynamic magnetic properties. As shown figure 1, the sample is inserted between an alumina layer of already characterized EM spectral permittivity and the short circuit. Broad band measurement of the complex reflection coefficient S_{11} is performed using a vector network analyzer, in a coaxial line geometry. The complex permeability of the MUT sample is retrieved using the one-to-one well described Nicholson and Weir correspondence procedure, from this two-phase material configuration formed by the alumina cylinder placed side-by-side of the sample. To apply a compressive, uniaxial controllable state of stress, the mechanical setup, as shown in figure 1, allows the alumina layer to apply the designed force on the whole surface of the parallel sides of the sample, to create an uniform stress. Such applied pressure is monitored by a force sensor connected to the computer. The developed programs allow to define the VNA and extensometer measuring conditions and to calculate the complex permeability as a function of stress (see figure 2). The dynamic permeability measurements versus stresses are carried out in a standard APC7 sample, in a coaxial wave guide, between 1 MHz and 6 GHz at room temperature. The configuration presented allows to determine accurately the microwave properties of the material under compressive and uniaxial stress. This technique is used to investigate the properties of a soft NiZn ferrite. Many new results on the permeability under mechanical stress of this material will be presented at the conference (example: sensitivity of the permeability as a function of stress speed).

[1] M. Ledieu, A.L. Adenot and O. Acher, “Permeability Measurement of Ferrite Under Stress Up to 6 GHz”, IEEE Transactions on Magnetics, 36 n° 5 (2000)3254-3256.

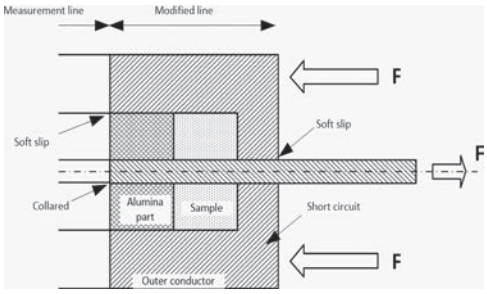


fig. 1: coaxial setup

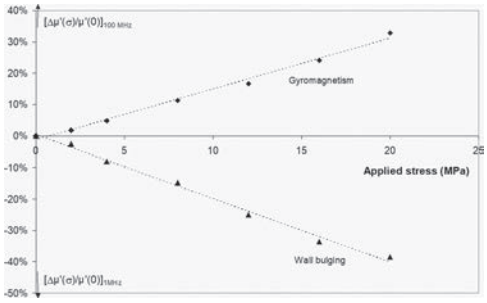


fig. 2: evolution of the relative variations of permeabilityversus stress (0 up to 15 MPa)

CU-07. Determination of Anisotropy Constants of a Magnetic Thin Film Sample Using Ferromagnetic Resonance (FMR) Spectra. *K.I. Masood*[1], P. Dhagat[1] and A. Jander[1] *1. EECS, Oregon State University, Corvallis, OR, United States*

An experimental procedure, using angle- and strain-dependent ferromagnetic resonance (FMR) spectra to[J1] determine anisotropy constants (K_u, K_1, K_2) and magnetoelastic constants (B_1, B_2) of crystalline thin films, is illustrated in this work. Application of FMR spectra for determining anisotropic constants of magnetic thin films is a well-researched topic [1-5]. Experimental field vs. resonant frequency data are fitted with the theoretical model to extract the anisotropy constants. However, determination of all five constants requires measurements as a function of magnetization angle and strain. Our experimental setup is designed to do this by providing full vector control of the applied magnetic field as well as the ability to apply a bending moment to the sample under test. The arbitrary magnetic field vector is applied by an orthogonal pair (y and z direction) of superconducting electromagnets coupled with automated sample rotation about the z axis as illustrated in Fig. 1(a). Simultaneously, a custom sample-holder is used to bend the sample as shown in Fig. 1(b). A four point bending mechanism is used to generate uniform strain, which can be calculated from the sample geometry, the applied force, the distance (shown as ‘c’ in Fig. 1(b)) between the fulcra, and the elastic modulus of the substrate. The push rod is connected to a voice-coil actuator to modulate the strain in the sample. An example measurement in our instrument is shown in Fig. 2(a), where the angle dependence of the FMR frequency for a Mn doped YIG film is shown. This figure also demonstrates the effect of out-of-plane magnetic field (labeled as ‘Bz’). The effect of applied strain is shown in Fig. 2(b). A gradient descent method is used to fit the FMR data with the Smit-Beljers model and thereby extracting the unknown constants.

[1] A. Smith, Review of Scientific Instruments, vol. 39, no. 3, pp. 378–385, (1968). [2] S. Bushnell, W. Nowak, S. Oliver, and C. Vittoria, Review of scientific instruments, vol. 63, no. 3, pp. 2021–2025, (1992). [3] S. Goel, S. Ohya, M. Tanaka et al., Physical Review B, vol. 99, no. 1, pp. 014431-014436, (2019). [4] J. Duquesne, C. Hepburn, P. Rovillain, and M. Marangolo,

Journal of Physics: Condensed Matter, vol. 30, no. 39, p. 394002, (2018). [5] S. Lee, S. Grudichak, J. Sklenar, C. Tsai, M. Jang, Q. Yang, H. Zhang, andJ. B. Ketterson, Journal of Applied Physics, vol. 120, no. 3, p. 033905, (2016).

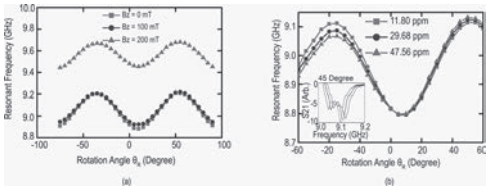


Fig 1. Resonance frequency for a Mn-doped YIG thin film as the sample is rotated in the x-y plane while (a) the Bz is varied and (b) the strain is varied. The asymmetry in the strain induced curves is due to wave-guide tilt. The inset in (b) shows the FMR spectra at 45 degree.

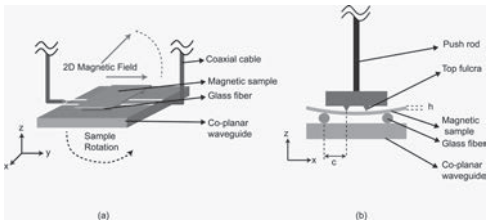


Fig 2. Illustration of our (a) experimental procedure with 3D vector magnetic field capability and (b) custom sample holder for modulating the film strain.

CU-08. Displaying FORC Distributions without Information Loss.
P.B. Visscher[1] *1. MINT Center, University of Alabama, Tuscaloosa, AL, United States*

The First Order Reversal Curve (FORC) method[1] is designed to extract more information about a magnetic system than a simple M(H) loop. Specifically, in a system of irreversible Preisach hysterons (each characterized by a down-switching field H_R and an up-switching field H) FORC gives the distribution $\rho(H,H_R) = -\frac{1}{2}\partial^2 M(H,H_R) / \partial H\, \partial H_R$. However, existing programs for displaying this FORC distribution lose much of the information in the FORC measurement. Specifically, (1) By construction, the FORC distribution ρ contains no information on reversible components. (2) There may be nonzero density ρ beyond the maximum H of the FORC curves. (3) The most common (Princeton Measurements) protocol for FORC measurement does a calibration measurement at saturation before each FORC curve which cannot be recovered from the display. We have written a public-domain display program ("FORC+")[2,3] which is designed to preserve all of the information in the FORC measurement, in the sense that the FORC curves $M(H_R, H)$ (where H_R is the reversal field), as well as the calibration measurements $M(H_R, H_{cal})$ can be exactly recovered from the displayed data. Fig. 1 shows a schematic view of the display. The density is displayed as a color plot. However, to recover the original M, we also need some first derivatives as boundary conditions – physically these are the reversible switching field distribution[4] and a Lost Hysteron distribution $\partial M(H,H_R)/\partial H_R$ at the end of the FORC and at the calibration field H_{cal} that indicates how much density was lost by not measuring to high enough field H.

[1] A. P. Roberts, D. Heslop, X. Zhao, and C. R. Pike, Rev. Geophys., Vol. 52, p. 557–602(2014). [2] P. B. Visscher, FORC+ (stand-alone FORC analysis program for Windows), http://MagVis.org [3] P. B. Visscher, http://arxiv.org/abs/1610.09199 (2016). [4] Joseph B. Abugri, P. B. Visscher, Subhadra Gupta, P. J. Chen and R. D. Shull, J. App. Phys. (2018). [5] Joseph B. Abugri *et al,* J. Appl. Physics, accepted June 2019, http://arxiv.org/abs/1903.03568.

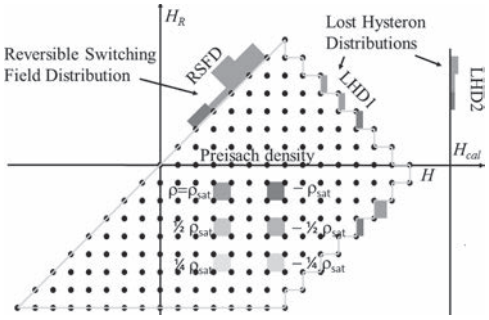


Fig. 1. Schematic of FORC+ display, retaining all the information of the FORC measurement. Each black dot is a measurement point (each horizontal row of black dots is a FORC curve). Discrete second derivative (Preisach density) is calculated for each square plaquette (6 nonzero values are shown). Each pixel of orange or blue color represents exactly the same amount of magnetization, whether it is in the Preisach density, the reversible SFD, or the two Lost Hysteron Distributions.

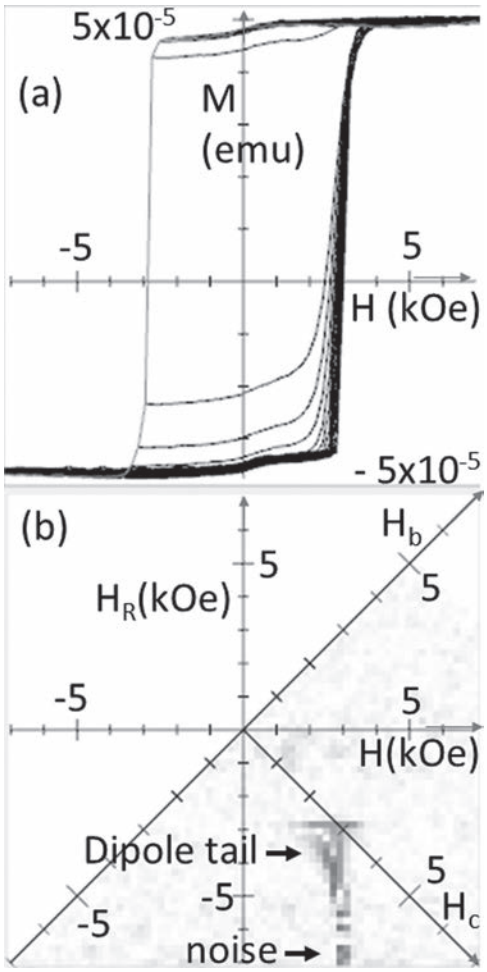


Fig. 2. FORC curves from a system with rapid domain-wall motion (CoPd alloy film, courtesy of J. B. Abugri), showing sharp features that are lost if smoothing is used.

CU-09. Suspension Force Modeling and Electromagnetic Performance Analysis on the Integrated Five Degrees of Freedom DC Four-Pole Hybrid Magnetic Bearing. *X. Ye*[1], Q. Gu[1] and T. Zhang[1] *1. Huaiyin Institute of Technology, Huai'an, China*

Modern ultra-high speed power transmission system puts forward new performance requirements for magnetic suspension motor [1], such as high power density, high suspension force density and high critical speed. The existing magnetic suspension motors usually use 1-DOF axial magnetic bearings, 2-DOF radial magnetic bearings and 3-DOF radial-axial magnetic bearings to form a 5-DOF magnetic suspension support system to support the rotor [2], which results in the longer axial length, lower critical speed, lower power density and suspension force density. Moreover, compared with AC HMB, DC HMB are uncoupled in every direction and easy to control. Therefore, to solve the above problems, an integrated DC HMB which can achieve 5-DOF stable suspension is proposed in this paper. The proposed 5-DOF DC HMB integrates the functions of two radial magnetic bearings and one axial magnetic bearing. It can realize 5-DOF stable suspension in one unit, which is of great importance to improve the critical speed, power density and suspension force density of magnetic suspension motor. Firstly, the structure and suspension mechanism of the integrated 5-DOF four-pole DC HMB are analyzed. Then, the mathematical models of suspension force are deduced by the equivalent magnetic circuit method. Thirdly, the three-dimensional finite element model is established according to the prototype parameters, and the three-dimensional magnetic circuit is analyzed. The relationships between the suspension forces and the control currents are calculated, and the experimental prototype has been manufactured. The simulation and experimental results verify the correctness of the suspension mechanism and the mathematical models. The structure of integrated 5-DOF DC HMB is shown in Fig. 1(a). Fig. 1(b) shows the magnetic circuits. Fig. 2(a), Fig. 2(b) and Fig. 2(c) show the distribution of bias flux density. Fig.2(e), Fig.2(f) and Fig.2(g) show the distribution of resultant magnetic flux density. The force-current relationships are shown in Fig. 2(h). It can be seen that the calculated values of the finite element method agree with those of the mathematical models.

[1] W. Zhang and H. Zhu, "Control System Design for a Five-Degree-of-Freedom Electro-spindle Supported With AC Hybrid Magnetic Bearings," *IEEE/ASME Transactions on Mechatronics*, vol. 20, no. 5, pp. 2525-2537, Oct. 2015. [2] X. Sun *et al*., "Performance Analysis of Suspension Force and Torque in an IBPMSM With V-Shaped PMs for Flywheel Batteries," *IEEE Transactions on Magnetics*, vol. 54, no. 11, pp. 1-4, Nov. 2018, Art no. 8105504.

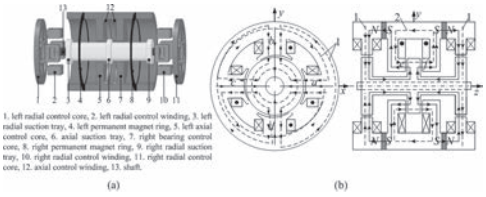


Fig.1 Structure and magnetic circuits

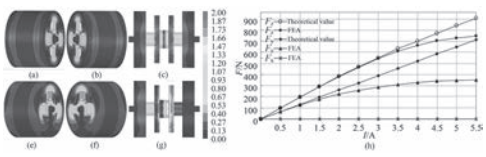


Fig.2 Simulation results

CU-10. Effects of an external magnetic field on the hyperfine parameters in RE_2O_3 (RE = Gd, Er) nanoparticles measured by perturbed angular correlation spectroscopy. *E. Correa*[1,2], B. Bosch-Santos[3], R.N. Saxena[2], G. Cabrera-Pasca[4] and A.W. Carbonari[2] *1. Material Measurement Laboratory, National Institute of Standards and Technology, Gaithersburg, MD, United States; 2. Nuclear and Energy Research Institute, Sao Paulo, Brazil; 3. NIST Center for Neutron Research, National Institute of Standards and Technology, Gaithersburg, MD, United States; 4. Federal University of Para, Abaetetuba, Brazil*

The RE_2O_3 (RE = rare-earth) oxides present three different structures depending on the RE ionic radii: hexagonal (A-type), monoclinic (B-type) or cubic (C-type). In the latter, RE ions occupy two non-equivalent cation sites: asymmetric 24d sites and symmetric 8b sites. Gd_2O_3 and Er_2O_3 crystallize in this structure and have a paramagnetic behavior, although Er_2O_3 also orders antiferromagnetically below 4 K. Due to the high magnetic moment of Gadolinium ions, Gd^{3+} chelates have been used as a contrast agent for magnetic resonance imaging[1]. An investigation of the localized magnetic moment behavior on Gd and Er sites in Gd_2O_3 and Er_2O_3 nanoparticles (NPs), within an atomic resolution, under the influence of an external magnetic field (EMF), is very necessary mainly because the high neutron absorption cross-section of Gd prevents the use of neutron diffraction[2]. In this paper, hyperfine interactions, measured by Perturbed Angular Correlation (PAC) spectroscopy using $^{111}In \rightarrow ^{111}Cd$ as probe nuclei, were used to investigate the behavior of each RE site in Gd_2O_3 and Er_2O_3 NPs with and without the application of an EMF of 0.5 T. NPs were synthesized by thermal decomposition and characterized by transmission electron microscopy and X-ray diffraction. Results show that the contribution of RE atoms at 24d sites is invariant with temperature whereas the contribution from RE atoms at 8b sites is so that the hyperfine magnetic field (B_{hf}) increases in Er_2O_3 and decreases in Gd_2O_3 when temperature decreases indicating an opposite alignment of Gd magnetic moments at the 8b symmetric sites.

[1] M. Absinta et.al., Neurology, 85, 18-28 (2015). [2] B. J. Kennedy, M. Avdeev, Aust. J. Chem. 64, 119–121 (2011).

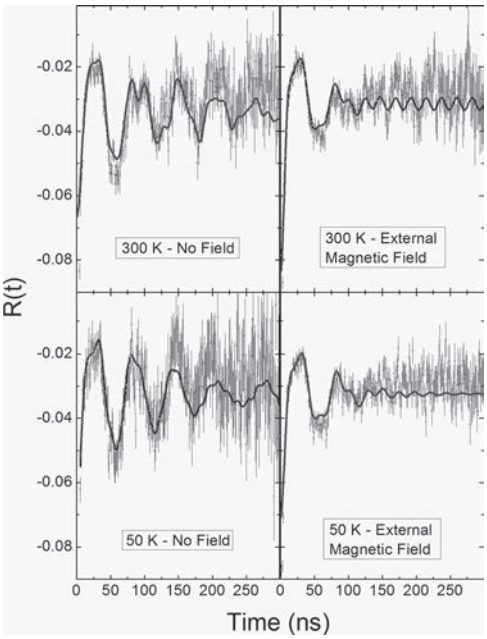


Fig.1 - Perturbation functions of Gd_2O_3 sample with and without the application of an external magnetic field

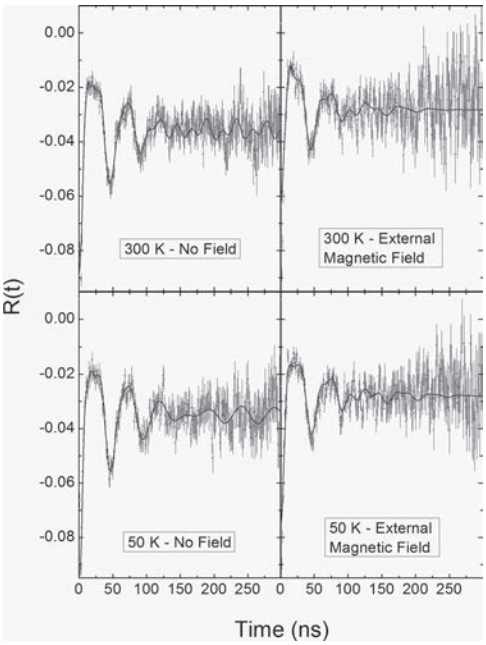


Fig.2 – Perturbation functions of Er_2O_3 sample with and without the application of an external magnetic field

CU-11. Macroscopic magnetization tunneling in the Josephson φ_0 junction. *G. Kim*[1] *1. Physics and Astronomy, Sejong University, Seoul, The Republic of Korea*

A quest to understand the quantum tunneling of magnetization(M) in nanomagnets has been a topical issue of intensive theoretical and experimental studies. At extremely low temperature the magnitude of M is frozen out and its orientation becomes an interesting dynamical variable. Since the direction of M is intrinsically determined by the anisotropy energy, there are two or more equilibrium orientation of M. Many studies have focused on the switching rate of individual nanoparticles for observing magnetic tunneling in the magnetic field. In recent years special interest has emerged in the tunneling rate manipulated by a Josephson current. As is well known, an influence of ferromagnetism on superconductivity is much stronger than the opposite one of the superconductivity on the ferromagnetism because the exchange interaction for ferromagnet (~100 K) is much larger than the order parameter for conventional superconductor (~ 1K). However, relativistic interactions responsible for the direction of M in nanomagnets (~ 1 K or less) are expected to be of the same order as the superconducting order parameter. Such a possibility was recently studied by Chudnovsky[1] who investigated the tunneling rate of M in the Josephson φ_0 junction. In fact, such a junction was proposed by Buzdin[2] who studied the Josephson junction between superconductors with a weak link formed by a noncentrosymmetric magnetic metal, and present the current-phase relation, $j=j_c\sin(\varphi-\varphi_0)$ where the phase φ_0 is proportional to M perpendicular to the gradient of the asymmetric spin-orbit potential. However, in the previous works they considered the spin dynamics controlled only by the bias current. In this work we consider quantum tunneling of M in the Josephson φ_0 junction with an external magnetic field as well as the bias current, and present diverse features of the tunneling rate which depends on two external controlling parameters. Spin-coherent-state path integrals are used to obtain analytic expressions for the tunneling rate for various crystal symmetries, with special attention to the field effect of currents. We will discuss optimal conditions giving the possibility of observing quantum tunneling of M coupled with Josephson current.

[1] E. M. Chudnovsky, Phys. Rev. B 93, 144422 (2016). [2] A. Buzdin, Phys. Rev. Lett. 101, 107005 (2008); F. Konschelle and A. Buzdin, *ibid.* 102, 017001 (2009).

CU-12. Research on High Frequency Magnetic Properties for Nanocrystalline Alloys Under Alternating and Rotational Magnetizations. M. Yang[1,2], *Y. Li*[1,2], Q. Yang[1,2], S. Yue[1,2], C. Zhang[1,2] and H. Sun[1,2] *1. School of Electrical Engineering, Hebei University of Technology, State Key Laboratory of Reliability and Intelligence of Electrical Equipment, Tianjin, China; 2. School of Electrical Engineering, Hebei University of Technology, Key Laboratory of Electromagnetic Field and Electrical Apparatus Reliability of Hebei Province, Tianjin, China*

Compared with silicon steel sheets, nanocrystalline alloys have higher permeability and lower conductivity, and it can be made into thinner strips, which makes it more easily magnetized and have lower eddy current loss. Therefore, nanocrystalline alloys have great high frequency performance. Compared with ferrite, nanocrystalline alloys have higher saturation magnetic density, which can further reduce the volume of electrical equipment and effectively improve power density. The rotating magnetic field will exist at the corner joint of laminated and blocky cores, and the rotating loss will be quite different from the alternating loss. In order to improve the accuracy of loss prediction, it is necessary to measure the rotational magnetic properties of related core materials [1]. At present, electrical equipment is gradually developing towards high frequency and miniaturization, and the application of novel materials such as nanocrystalline alloys is more extensive. In order to widen the application of nanocrystalline alloys in engineering practice, it is necessary to measure and analyze the magnetic properties of these materials and to make their physical properties clearer so as to give full play to their application value [2]. In this paper, a novel high-frequency 2-D magnetic tester for nanocrystalline alloy is proposed. The alternating and rotating magnetic properties of this material are studied from 1 kHz to 20 kHz. And the differences of magnetic properties between easy and difficult magnetization directions of nanocrystalline alloy in alternating magnetic fields are systematically investigated, and combined the experimental data of 2-D rotating magnetic properties, the macroscopic phenomenon of the magnetic anisotropy is analyzed from the view of the microstructure of the material. The relationship between rotation loss and alternating loss of nanocrystalline alloys under different axial ratios of elliptical magnetic field excitation is analyzed.

[1] S. Yue, Y. Li and Q. Yang, IEEE Transactions on Magnetics., Vol. 55, p.1-5(2019) [2] L. Chen, Y. Wang and Z. Zhao, IEEE Magnetics Letters., Vol. 8, p.1-5 (2017)

CU-13. Independent Control of Anti-parallel and Parallel State Thermal Stability Factors in Magnetic Tunnel Junctions for Telegraphic Signals with Two Degrees of Tunability. *B.R. Zink*[1], Y. Lv[1] and J. Wang[1] *1. Electrical and Computer Engineering, University of Minnesota, Minneapolis, MN, United States*

Magnetic tunnel junctions (MTJs) with low thermal stability at room temperature have been proposed as read units in probabilistic-bits, or p-bits [1]. However, networks of multiple interconnected MTJs may be particularly sensitive to device-to-device variations of thermal stability from design targets [2]. Recently, we generated tunable telegraphic signals using a thermally stable MTJ through proper control over an external bias field and a DC voltage bias [3], which is illustrated in Fig. 1. Not only does this provide a solution to issues associated with device to device variations, but it also introduces the possibility of p-bit designs that are compatible with state of the art MRAM technology. Furthermore, our results demonstrated that the average anti-parallel (AP) and parallel (P) state dwell times could be tuned independently, giving a second degree of tunability to the signals generated. In this work, we expand on this method in two important ways. First, we demonstrate the applicability of our method to p-bit designs by modelling the transfer function using existing p-bit models. Fig. 2 shows that the device's transfer function can be adjusted with slight modifications to the bias field, where the bias voltage is treated as the input and the percentage of time that the MTJ spends in the AP-state (referred to as the AP-rate) is treated as the output. This allows for the possibility of p-bit circuits capable of on-chip

corrections against device-to-device variations of their thermal stabilities. Second, we identify the physical mechanisms that allow for two degrees of tunability in the output signal, which is explained via the Néel-Brown model. This study provides both applicability and predictability to the dual-biasing method.

[1]. R. Faria, K. Y. Camsari, and S. Datta, *IEEE Magn. Lett.*, vol. 8, pp. 1-5, (2017). [2]. V. Ostwal, P. Debashis, R. Faria, Z. Chen, and J. Appenzeller,*Sci. Rep.*, vol. 8, no. 1, (2018). [3]. B. R. Zink, Y. Lv, and J.-P. Wang, *J. Appl. Phys.*, vol. 124, no. 15, (2018).

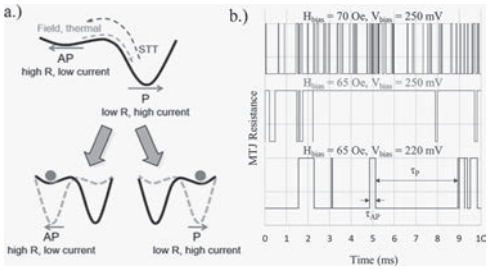


Fig. 1. **a.) Evolution of the energy band diagrams as the MTJ fluctuates between the AP and P states. b.) Time-domain plots acquired by the oscilloscope, shown in a 10 ms window to illustrate the stochastic nature of the signals produced.**

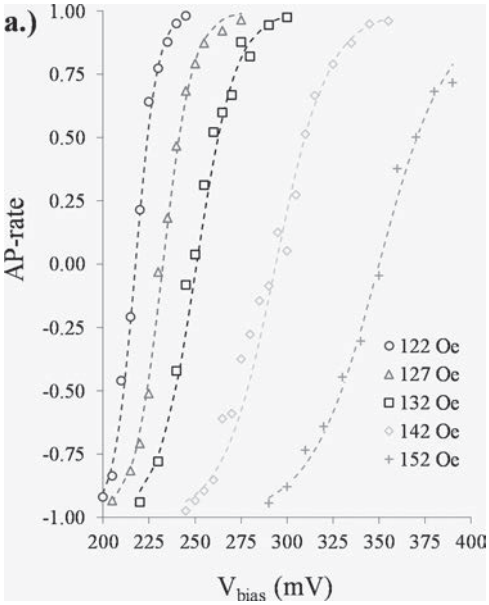
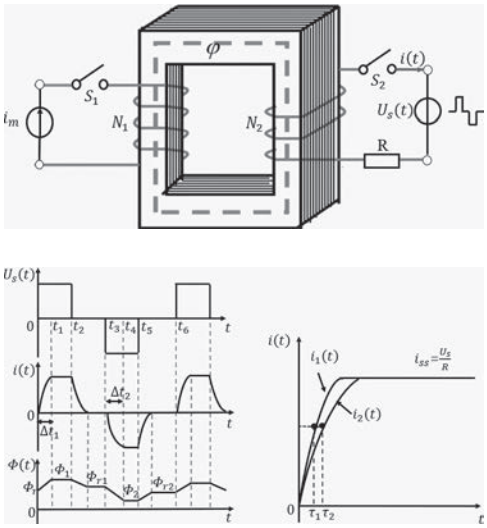


Fig. 2. AP-rate versus V_{bias} at several fixed bias fields.

CU-14. Based on Transient Current Analysis a Measurement Method of Residual Flux Density Used in Single-phase Power Transformer.
H. Cailing[1] *1. Hebei University of Technology, Tianjin, China*

With the rapid development of AC/DC ultra-high voltage (UHV) transmission technology, large capacity transformer has been more and more widely used [1]. As the transformer closes without load, if there is residual flux in the core, the magnetic saturation of the core will be accelerated, resulting in larger inrush current (the peak value can reach 6-8 times of the rated current) [1]. To avoid large inrushing current the study of residual flux in the power transformer is particularly necessary. Gauss meter and fluxgate sensor are used to measure the residual flux of iron core [2-3], but there is a lot of interference and some error in the instrument itself. Some scholars have proposed that residual flux by integral of the measured voltage at switching-off time of transformer can be calculated [4]. Other scholars judge the residual flux by establishing the relationship between residual flux and measurable current [5]. However, none of the methods mentioned in the above references can accurately measure the residual flux. Therefore, this paper proposes a new residual flux density measurement method used in the single-phase power transformer through establishing the basic relationship between residual flux density Br and time constant T of winding transient current i(t) under different Br when loading positive and negative constant voltage signals Us to measuring winding. Basic model of the single-phase power transformer core is shown in Fig.1. N_1 and N_2 are the turn number of preset residual flux winding (winding1) and measuring winding (winding2). The residual flux is preset by loading current excitation im in winding 1, and Us is loaded in winding 2 to detect $i_1(t)$ and $i_2(t)$. The basic principle of the proposed method is shown in Fig. 2. It can be seen that T is different when the flux increases or decreases. Through theoretical analysis and 3-D finite element simulation analysis. The direction of Br is judged by comparing T, and the magnitude of Br can be calculated by the establishing empirical formulas of Br and T. Finally, the validity and accuracy of the proposed residual flux density measurement method are verified by experiments.

[1]D S, R N. Service Restoration of Distribution Networks Considering Switching Operation Costs and Actual Status of the Switching Equipment[J]. IEEE Transactions on Smart Grid, 2015, 6(3):1227-1232.[2] F C, Ma X. Introduction to Engineering Electromagnetic Field [M]. Beijing: Higher Education Press, 2000.[3]C D, O V. A New Method to Evaluate Residual Flux Thanks to Leakage Flux, Application to a Transformer[J]. IEEE Transactions on Magnetics, 2014, 50(2):1005-1008.[4]T D, L J D, J B. Single-Phase Transformer Inrush Current Reduction Using Prefluxing[J]. IEEE Transactions on Power Delivery, 2012.[5]Ge W, W Y. Residual Flux in the Closed Magnetic Core of a Power Transformer[J]. IEEE Transactions on Applied Superconductivity, 2014, 24(3):1-4.



CU-15. Effect of Uniaxial and Biaxial Stress on Alternating Magnetic Properties of Silicon Steel Sheet.
Y. Dou[1,3], *Y. Li*[1,3], C. Zhang[1,3] and J. Zhu[2] *1. State Key Laboratory of Reliability and Intelligence of Electrical Equipment, Hebei University of Technology, Tianjin, China; 2. School of Electrical and Information Engineering, University of Sydney, Sydney, NSW, Australia; 3. Key Laboratory of Electromagnetic Field and Electrical Apparatus Reliability of Hebei Province, Hebei University of Technology, Tianjin, China*

Laminated silicon steel sheet, which is widely applied in electrical engineering, such as cores of power transformers and electrical machines, usually subject to mechanical stress. Magnetostriction will occur once mechanical stress exists, and therefore additional power loss is produced [1, 2]. In general, stress is caused by a number of factors such as material processing, machine manufacturing and operating conditions. To optimize the utilization of silicon steel, the measurement of magnetic properties is required, especially under stress. Although the effect of stress on magnetic properties has been extensively studied, the experiments were always conduct at power

frequency which was not enough to separate the iron losses and study the stress effects on different loss components. This paper focuses on the effect of uniaxial and biaxial stress on hysteresis loop shape, maximum permeability of the material and power loss characteristics. In addition, based on the measurements under different stress situation under various frequency, the total loss can be separate into three loss component, hysteresis loss, classical eddy loss and excess loss using conventional loss separation te chnique. Detailed loss separation process will be presented in the full manuscript.

[1] Lobue M, Sasso C, Basso V, et al. Journal of Magnetism & Magnetic Materials, Vol. 215(3), p.124-126 (2000). [2] Moses A J, IEEE Transactions on Magnetics, Vol.15(6), p.1575-1579 (1979).

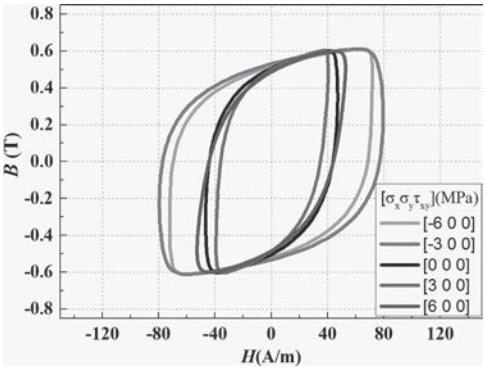


Fig.1 B-H hysteresis loops under tensile and compressive stress along RD at Bmax=0.6T.

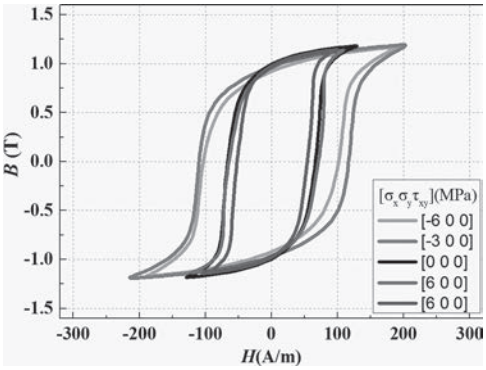


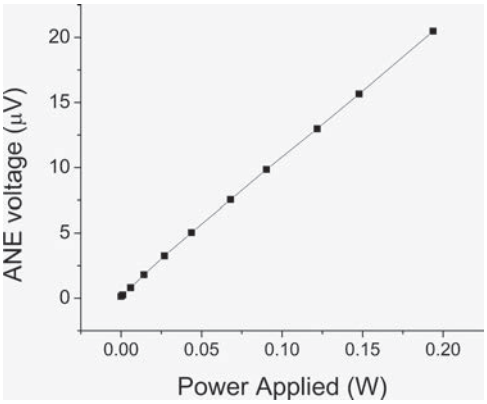
Fig.2 B-H hysteresis loops under tensile and compressive stress along RD at Bmax=1.2T.

CU-16. Hysteresis loop tracer based on the anomalous Nernst effect induced by the asymmetric dissipation of Joule heating.

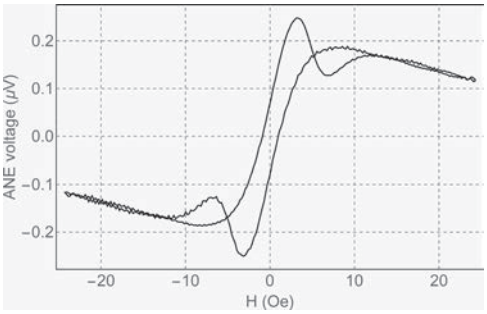
C.A. Gonzalez-Fuentes[1], C. Romanque[1], C. Orellana[1] and C. Garcia[1]
1. Physics, UTFSM, Valparaiso, Chile

Magneto-transport measurements techniques, often imply the application of an electrical current on ferromagnetic thin film stripe. As collateral effect, there is always a generation of some amount of Joule heating on the stripe. Given the typically orders of magnitude differences between the thermal conductivities of the ambient and the substrate, this results in an out-of-plane thermal gradient originated by the asymmetric dissipation of Joule heating [1]. This, in turn, may give origin to Anomalous Nernst Effect (ANE) voltages. This effect is normally an unwanted artifact that must be removed from the data analysis, being specially relevant in Second Harmonic Detection of Spin-Orbit Torques [2]. In this work we demonstrate that the above mentioned effect can be conveniently exploited for the study of ANE on thin ferromagnetic films. We test this idea on a NiFe thin film (20nm) shaped into 4-terminal Hall bar, in which the heating current is injected through 2 extremes of the Hall bar and the ANE generated voltages are measured at the two other extremes. As expected, the results showed an excellent linearity between the power applied and the ANE voltage. However, the H-loop curve presents some distortion that we attribute to the non-uniform thermal gradient across the thickness of the film. Our method is very attractive from the experimental point of view given that only electrical connections to the sample are required to study the ANE, without the needing of an external heating or cooling hardware.

[1] C. O. Avci et al., Phys. Rev. B 89, 214419 (2014). [2] M. Hayashi, J. Kim, M. Yamanouchi, and H. Ohno, Phys. Rev. B 89, 144425 (2014).



Experimental check of the linearity between the power applied to the sample and the ANE voltage detected



Hysteresis loop measured on a 20nm thickness NiFe sample employing the our proposed method

Session CV
MAGNETORESISTANCE, MAGNETOIMPEDANCE, AND HALL EFFECT (Poster Session)

Tao Qu, Co-Chair
University of Minnesota, Minneapolis, MN, United States
Paul A Crowell, Co-Chair
University of Minnesota, Minneapolis, MN, United States

CV-01. Strain effects on the magnetotransport properties of transition metals. *R.J. Gonzalez Hernandez*[1], B. Dupe[2] and J. Sinova[2] *1. Department of Physics, Universidad del Norte, Barranquilla, Colombia; 2. Institute of Physics, Johannes Gutenberg University Mainz, Mainz, Germany*

The Anomalous Hall Effect (AHE) is a phenomenon which consists of an extra anomalous transverse voltage developing when current is passed through ferromagnetic material in a magnetic field [1]. In this work, we studied the dependence of strain and magnetization effect on the intrinsic anomalous Hall conductivity (AHC) in 3d metal Fe-bcc, Co-fcc, Co-hcp, and FeCo structure. For Fe-bcc case, the AHC shows a slightly decreasing with the increase of pressure, being this associate to the magnetization dependence with the lattice constant. However, the AHC for lattices constants above of 2.95A shows a downturn around 70%, even when the magnetization has increased. This decreasing seems to be related to a transition of d-states occupations above this lattice constant. The computation of the anomalous Hall conductivity was carried out using ab-initio calculations (included the effect of spin-orbit interaction for the ferromagnetic state) and the Wannier interpolation technique for the application of the Kubo-Greenwood formula [2].

1] N. Nagaosa, J. Sinova, S. Onoda, A. H. MacDonald, and N. P. Ong, "Anomalous Hall effect," *Rev. Mod. Phys.*, vol. 82, no. 2, pp. 1539–1592, (2010). [2] X. Wang, J. R. Yates, I. Souza, and D. Vanderbilt, "Ab initio calculation of the anomalous Hall conductivity by Wannier interpolation," *Phys. Rev. B - Condens. Matter Mater. Phys.*, vol. 74, no. 19, pp. 1–15 (2006).

CV-02. Perfection of theoretical model for high frequency MI effect of ferromagnetic amorphous microwires. Y. Wang[1], *F. Qin*[1], Y. Zhao[1], D. Estevez[1], D. Makhnovskiy[1] and H. Peng[1] *1. Zhejiang University, Hangzhou, China*

The Co-based amorphous microwires have a significant magnetoimpedance effect (MI) effect for the excellent soft magnetic properties, nearly zero negative magnetostriction coefficient and the unique magnetic domain structure. Based on the MI effect, the material has excellent sensing properties and can be widely used in the field of sensors, especially high frequency sensors for its high magnetic permeability. However, there is currently a lack of research on high frequency MI effect. And in high frequency, the interaction between the amorphous wire and the electromagnetic field is complex, and the existing theoretical models cannot match the high frequency MI experiment results very well. We developed an accurate method, broadband impedance measurements, for measuring the magnetoimpedance effect (MI) of ferromagnetic microwires from 100 kHz up to 15 GHz. Through the measurements, we obtained the MI curves at different frequencies and the impedance spectrums under different magnetic fields of the amorphous microwires with a nominal composition of Co68.7Fe4Si11B13Ni1Mo2.3, fabricated by Taylor–Ulitovsky method. The MI profiles (Fig.1(a)) shows that a new maximum of impedance appears with the frequency increasing from a few hundred MHz to GHz; its value and the corresponding magnetic field also increase with increasing frequency. In contrast, the magnetic field corresponding to the original maximum in relatively lower frequency remains almost unchanged. The phenomenon cannot be expressed by the existing theoretical model. The impedance spectrum (Fig.1(b)) indicates that the microwires undergo the transition from natural resonance to ferromagnetic resonance with the magnetic field increasing. A multilayer planar domain model is therefore proposed herein to describe these experiment results, which introduces the effect of axial domains (inner layer) on impedance at relatively higher frequency. The new maximum of impedance results from the ferromagnetic resonance of the inner layer based on the analyses of the model on the experimental results.

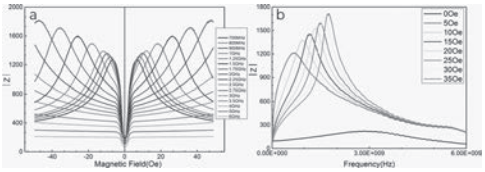


Fig. 1 (a) The MI curves at different frequency. (b) The impedance spectrum of the sample at different magnetic field.

CV-03. The Effects of Annealing Rate and Temperature on Ta/TbFeCo bilayers. *L. Ye*[1,2], C. Lee[1,2], R.C. Bhatt[1,2], S. Chang[1,2], J. Wu[3] and T. Wu[1,2] *1. Graduate School of Materials Science, National Yunlin University of Science and Technology, Douliou, Taiwan; 2. Taiwan SPIN Research Center, National Yunlin University of Science and Technology, Douliou, Taiwan; 3. Department of Physics, National Changhua University of Education, Changhua, Taiwan*

Among various perpendicularly anisotropic magnetic materials, amorphous rare-earth-transition metal RE-TM alloys have attracted much interest due to the advantages of tunable magnetic properties and suitable perpendicular magnetic anisotropy (PMA) strength. Furthermore, RE-TM alloys are anti-parallel coupled systems that can be switched by spin-orbit torques (SOT). In this study, the magnetic properties of the structure Ta/TbFeCo/MgO with various Tb contents, annealing rise rate and temperatures are explored. The film stack consists of structures SiNx/Ta(4 or 10nm)/TbFeCo(10nm)/ MgO(4nm). The samples were then annealed at different annealing rate from 10 ^{o}C/min to 50 ^{o}C/min and holding time from 10 min to 30 min with temperatures ranging from 100 to 150 °C. We found that fast rise rate and low temperature annealing could help to improve PMA and significantly increase the saturation magnetization and squareness. The best Tb composition ratio for the required PMA depends on the annealing conditions. Figure 1 and Figure 2 show the magnetic hysteresis loops for the TM-rich and RE-rich samples under various annealing conditions, respectively. One can see that the both the squareness and coercivity increase with temperature rise rate, but decrease with temperature and holding time. In additions, the anomalous Hall Effect (AHE) measurements on Hall bar were carried out with a series of dc sensing currents. PMA, The AHE measurement results and TEM microstructure properties will be presented and meticulously discussed. This work was supported by the National Science Council of Taiwan, Republic of China, under Contract No. NSC 107-2112-M-224 -001 -MY2.

[1] Witold Skowronski et al., Applied Physics Letters 109, 062407 (2016) [2] J. Kim et al., Nat. Mater. 12, 240–245 (2012). [3] Ramesh Bhatt et al., Journal of Applied Physics, 125, 113902 (2019)

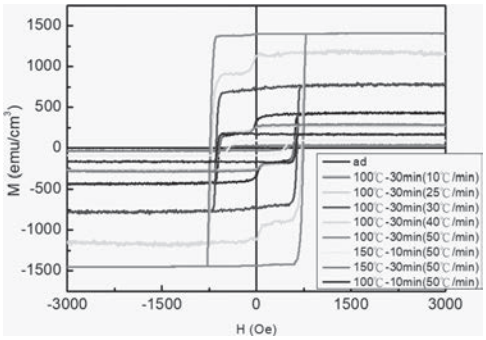


Figure 1 The magnetic hysteresis loops with various annealing conditions for the TM-rich sample.

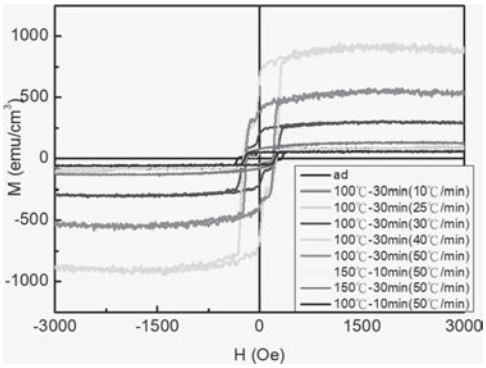


Figure 2 The magnetic hysteresis loops with various annealing conditions for the RE-rich sample.

CV-04. Magnetotransport Properties of Epitaxial Terbium Nanowires. *G.A. Newman*[1], C.S. Taylor[1], L.J. Calvano[1], P.D. Sparks[1], J.C. Eckert[1], S.K. Patel[2] and E. Fullerton[2] *1. Physics, Harvey Mudd College, Claremont, CA, United States; 2. Center for Memory and Recording Research, University of California, San Diego, La Jolla, CA, United States*

Rare earth materials are of great interest because of their rich magnetic properties that play a critical role in current technology and are of potential use in future technologies such as antiferromagnetic spintronics [1]. The high orbital moment and strong spin-orbit interactions make rare-earths appealing for spin-Hall and inverse spin-Hall effects. Further, as materials are scaled down in size for technological application, finite-size effects emerge which alter the properties in confined structures and illuminate the nature of the magnetic transitions [2, 3]. We are interested in studying thin epitaxial films grown on ultrathin seed layers, making the films appropriate for magnetotransport and spintronic measurements. Bulk terbium exhibits ferromagnetic (FM) and weak helical antiferromagnetic (AF) phases [4]. Here, we study these phases in Tb that has been confined in one or more dimensions to magnetic length scales. Thin films of Tb (0001) were deposited by DC magnetron sputtering on MgO (100) and MgO (111) substrates with W seed and capping layers and patterned by electron beam lithography into wires with widths ranging from 100 nm to 4 μm and voltage lead gaps ranging from 100 nm to 16 mm. The FM, AF, and paramagnetic (PM) phases were measured in moment vs. applied field measurements (see Fig. 1) by vibrating sample magnetometry. In magnetoresistance measurements, anomalies in resistance vs. temperature and resistance vs. field (see Fig. 2) determined the phase diagrams for different wire widths and applied field directions. As the wire widths are decreased to magnetic length scales, we are able to measure the transition in individual domains. Work at HMC was funded in part by the Jean Perkins Foundation, Florida State University, and Los Alamos National Laboratory. Work at UCSD supported by DOE award No. DE-SC0003678.

[1] V. Baltz et al., Rev. Mod. Phys. 90, 015005 (2018) [2] E. Weschke, et al. Phys. Rev. Lett. 93, 15 (2004) [3] V. Uhlír, et al. Nature Communications. 7, 13113 (2016) [4] V. Zverev, et al. J. Phys.: Condens. Matter. 26, 066001 (2014)

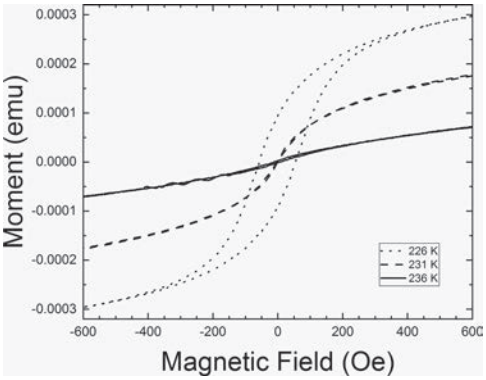


Fig. 1 Moment vs. field applied along the wire axis in the FM (226 K, dotted line), AF (231 K, dashed line), and PM (236, solid line) phases

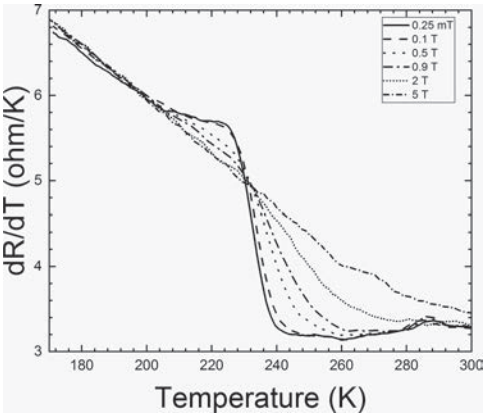


Fig. 2: Derivative of the resistance vs. temperature at different fields applied along the wire axis for a 4 μm terbium wire. At low fields, the wire exhibits FM, AF, and PM phases. The AF state vanishes at high fields

CV-05. Electron transport and magnetoresistance in highly oriented epitaxial magnetite nanorods. *R. Das*[1,2], V. Kalappattil[2], M. Phan[2] and H. Srikanth[2] *1. Faculty of Materials Science and Engineering, Phenikaa University, Hanoi, Vietnam; 2. Department of Physics, University of South Florida, Tampa, FL, United States*

Recent advancements in miniaturization of devices are motivating research at nanoscale. Fe_3O_4 is a promising material for room temperature spintronic device application due to its 100% spin polarization, half metallic behavior and high Curie temperature (T_C = 850 K). Numerous fascinating properties arise from the spin-polarized transport, particularly the magnetoresistance (MR) [1]. At room temperature, MR of 10% has been observed in bulk and polycrystalline Fe_3O_4, which is well below the theoretical value [2]. This could be due to defects, off-stoichiometry, strain effects and interfaces. Moreover, in nanoscale random distribution of tunneling barriers, complex transport channels and crystallite orientations further affect the spin transport properties. One-dimensional nanostructures with unique electron transport properties have shown potential for nanoelectronic devices [1]. However, there has been no report on magnetotransport of an oriented array of magnetite nanorods. In this study, we report the electron transport and MR

in chemically grown highly oriented epitaxial Fe_3O_4 nanorods on a (001) $SrTiO_3$ substrate. Resistance vs. temperature (R-T) data exhibited a sharp increase in the resistance at 120 K, which can be attributed to the Verwey transition whose presence affirmed the high crystallinity of the Fe_3O_4 nanorods. Negative MR values of 0.8% and 2.2% at 0.4 T were observed at 300 and 100 K, respectively. This can be ascribed to the spin-polarized electron transport across the antiphase boundaries. The sharp MR peaks of 200, 410 Oe at 300 and 100 K, respectively, are close to the coercive field as observed from the M-H loop. Recently, we have shown that the epitaxial nanorods exhibit biaxial magnetic anisotropy at room temperature [3]. The results obtained identify epitaxial nanorods as useful materials for room temperature data storage and spintronic devices that necessitate tunable anisotropic magnetotransport property.

[1] D. Zhang, Z. Liu, S. Han, C. Li, B. Lei, M. P. Stewart, J. M. Tour and C. Zhou, *Nano Lett.* 4, 2151 (2004). [2] G. Hu and Y. Suzuki, *Phys. Rev. Lett.* 89, 276601 (2002). [3] S. Chandra, R. Das, V. Kalappattil, C. Harnegea, R. Nechache, M.H. Phan, F. Rosei, and H. Srikanth, *Nanoscale* 9, 7858 (2017)

CV-06. Anomalous Hall Effect in FePt/Fe3O4 Core/Shell Nanoparticle Thin Films. F. Sun[1], Y. Li[2,1], *M. Bian*[3,1], S. Yang[2], Y. Hou[3] and H. Zeng[1]
1. Department of Physics, University at Buffalo, SUNY, Buffalo, NY, United States; 2. Department of Material Physics, Xi'an Jiaotong University, Xi'an, China; 3. Department of Materials Science and Engineering, Peking University, Beijing, China

The anomalous Hall effect (AHE), as a consequence of spin-orbit coupling, occurs in ferromagnetic material and plays an important role in the experimental research. The AHE in molecular-beam epitaxy L10 FePt thin films has been measured and the side jump mechanism was proven to be dominating. [1] On the other hand, magnetic properties of core/shell FePt/Fe3O4 Nanoparticles has been studied and the hysteresis loops showed that the magnetic hard core and the magnetic soft shell were exchange-coupled. [2] We synthesized FePt/Fe3O4 Core/Shell Nanoparticles with shell thickness 0-5 nm using two steps high temperature organic phase method. The synthesized Nanoparticles were spin coated onto Si/SiO2 substrates and annealed under UHV to obtain a nanoparticle film. The as-made thin films were characterized by SEM, AFM, EDS and XRD. The AHE as a function of film thickness and annealing temperature were systematically investigated. The mechanisms of the AHE in such nanoparticle systems were also investigated.

[1] J. Yu, U. Ruediger and A. D. Kent, Journal of Applied Physics 87.9 (2000): 6854-6856. [2] Hao Zeng, Jing Li, Z. L. Wang, J. P. Liu and Shouheng Sun, Nano letters 4.1 (2004): 187-190.

CV-07. Perpendicular magnetic anisotropy in TbFeCo/MgO structure with underlayer Ta/Hf. *L. Ye*[1,2], R.C. Bhatt[1,2], C. Lee[1,2] and T. Wu[1,2]
1. Graduate School of Materials Science, National Yunlin University of Science and Technology, Douliou, Taiwan; 2. Taiwan SPIN Research Center, National Yunlin University of Science and Technology, Douliou, Taiwan

To attain perpendicular magnetic anisotropy (PMA) for MRAM structure, a number of material systems like RE-TM alloys, Co/Pt and FePt multilayers etc. have been explored as a magnetic recording layer in pMTJs. The RE-TM alloys, in particular the amorphous TbFeCo alloys have advantage of low saturation magnetization, large PMA and significant thermal stability, therefore, are expected to have low critical current density for spin-torque-induced magnetization switching. The heavy-metal underlayer has strong spin-orbit coupling (SOC) which can provide a lower critical current and fast magnetization switching. In this study, the interfacial PMA in (Ta or Hf)/TbFeCo/MgO/Ta structures are investigated and the effectiveness of two kinds of heavy-metal Hf and Ta underlayers are explored. The PMA of TbFeCo are found to be critically relied on several aspects like Tb-concentration (Tb sputtering power), underlayer material (Hf/Ta), annealing temperature and heating rate of annealing. The crystalline phase of the underlayer was optimized by changing the film thickness and observed by XRD and resistivity measurements. It is observed that for the Hf underlayer the PMA can be obtained in as-deposited samples irrespective of the Tb-concentration with squareness close to 1. To see the heat treatment effect, samples were annealed at different (i) heating rate, (ii) annealing temperature and (iii) holding time. We found that fast heating rate and low temperature annealing improves PMA in FeCo-dominant films; however, the PMA reduces when Tb-concentration is increased. Figure 1 and Fig. 2 show the magnetic hysteresis loops for as-deposited and annealed Hf (4nm)/TbFeCo/MgO/Ta structure, respectively. To further investigate the effect of Tb composition and annealing conditions on PMA, the anomalous Hall effect, XRD, and TEM characterizations will be presented and meticulously discussed. This work was supported by the National Science Council of Taiwan, Republic of China, under Contract No. NSC 107-2112-M-224 -001 -MY2.

[1]S. Ikeda et al., Nature Mater. 9, 721 (2010). [2]Zhengyang Zhao et al., Appl. Phys. Lett. 106, 132404 (2015)

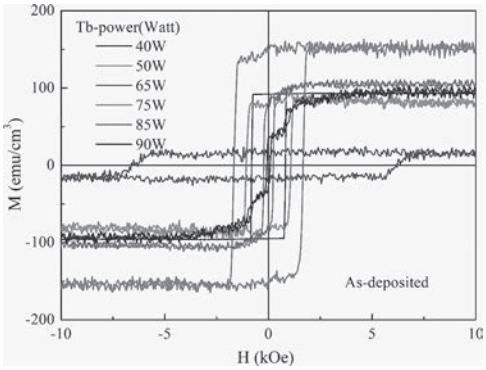


Figure 1 The magnetic hysteresis loops for differently Tb-powered as-deposited samples.

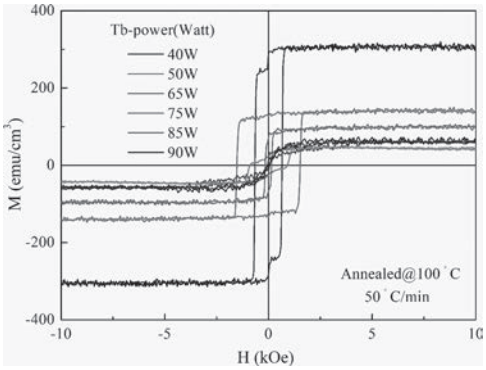


Figure 2 The magnetic hysteresis loops for differently Tb-powered samples after annealing.

CV-08. First-principles study of anomalous Nernst effect in 2D ferromagnet and materials with nontrivial spin textures. *F. Ishii*[1], R. Syariati[2], S. Minami[2] and H. Sawahata[2] *1. Nanomaterials Research Institute, Kanazawa University, Kanazawa, Japan; 2. Graduate School of Natural Science and Technology, Kanazawa University, Kanazawa, Japan*

We are interested in getting higher thermoelectric conversion efficiency by magnetic materials. We have been studying Berry-phase-mediated thermoelectric effects, namely anomalous Nernst effect (ANE), which is a heat-to-electricity conversion observed in magnetic materials and directly related to he contribution of the anomalous Hall conductivity (AHC) [1-4]. We discussed AHC mainly driven by an effective magnetic field, Berry curvature, induced by spin-orbit interaction and spin chirality. We performed first-principles density functional calculations[5] for hypothetical

2D materials[1-2], half-metallic 2D ferromagnet[3] and and 3D half-metallic half-Heusler alloys[4]. We found that the spin-orbit interaction and spin chirality driven Berry curvature indeed generates large ANE. We predicted that the carrier tuning enhances thermoelectric efficiency. We will discuss how to find new materials with large Berry-phase-mediated thermoelectric effects in mainly 2D materials.

[1] Y.P. Mizuta and F. Ishii, Sci. Rep. Vol. 6, p.28076 (2016). [2] Y.P. Mizuta, H. Sawahata, and F. Ishii, Phys. Rev B, Vol. 98, p.205125 (2018). [3] R. Syariati, S. Minami, H. Sawahata, F. Ishii, submitted. [4] S. Minami, F. Ishii, Y.P. Mizuta, and M. Saito, Appl. Phys. Lett. Vol. 113, p.032403 (2018). [5] T. Ozaki et al., OpenMX, http://www.openmx-square.org.

CV-09. Magnetic and Transport Properties of MnRh Thin Films.

L.J. Calvano[1,2], S.K. Patel[1], C.S. Taylor[2], G.A. Newman[2], P.D. Sparks[2], J.C. Eckert[2] and E. Fullerton[1] *1. Center for Memory and Recording Research, University of California, San Diego, La Jolla, CA, United States; 2. Harvey Mudd College, Claremont, CA, United States*

There is increasing interest in studying materials that exhibit complex magnetic order and phase transitions that couple electronic, magnetic and electronic degrees of freedom. MnRh and FeRh are such materials that show an antiferromagnetic (AF) low-temperature phase to a ferromagnetic (FM) high-temperature phase transition for potential applications such as in magnetic recording, magneto-calorics or antiferromagnetic spintronics.[1-3] In bulk, the binary alloy MnRh undergoes a transition to the AF state during cooling at approximately 150 K and to the FM state during warming near room temperature.[4] In this work, we fabricate epitaxial MnRh thin films on MgO substrates (see Fig. 1) using DC magnetron sputtering. These films exhibit an AF-FM transition with a broad thermal hysteresis that can be seen in magnetometry measurements, as shown in Fig. 2. We conduct a systematic study in these films, showing a shift in the transition to higher temperature with larger Mn:Rh ratios. We also make transport measurements, which demonstrate a dramatic change in resistivity between the AF and FM states. By fabricating nanowires using electron-beam lithography, we confine the system in multiple dimensions to domain size length scales and are able to probe the transition more carefully in individual domains.[3] Work at UCSD funded by Award # DE-SC0019273. Work at HMC funded by the Jean Perkins Foundation, Florida State University, and Los Alamos National Laboratory.

[1]M. Sharma, et al. *J. Appl. Phys*. 109, 083913 (2011). [2]T. Moriyama, et al. *Appl. Phys. Lett*. 107, 122403 (2015). [3]V. Uhlír, et al. *Nature Communications*. 7, 13113 (2016). [4]J.S. Kouvel, et al. *J. Appl. Phys*. 34, 1095 (1963).

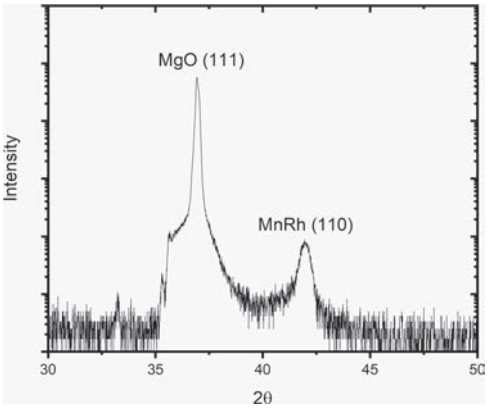


Fig. 1: Room temperature X-ray diffraction for a MnRh thin film grown on MgO (111).

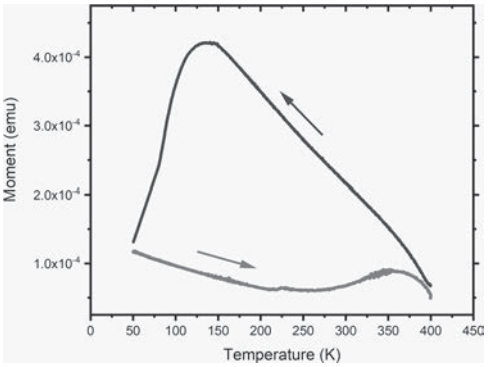


Fig. 2: Moment vs. temperature for a MnRh film exhibiting a FM-AF transition around 100 K and the AF-FM transition near 400 K.

CV-10. Anomalous Hall effect in Hexagonal Magnetic Alloy Fe_5Sn_3.

H. Li[1,2], J. Chen[1,2], B. Ding[1,2], E. Liu[1,3], H. Zhang[1], X. Xi[1], G. Wu[1] and W. Wang[1,3] *1. Institute of Physics, Chinese Academy of Sciences, BeiJing, China; 2. University of Chinese Academy of Sciences, BeiJing, China; 3. Songshan Lake Materials Laboratory, Dongguan, China*

Anomalous Hall effect (AHE) has been explored for a long time in ferromagnetic materials and there are some different origins which relate to AHE in different materials [1]. In general, there are three origins of AHE which can be classified into intrinsic and extrinsic mechanisms, respectively. The former is originated from influence of Berry phase generated from momentum-space[2] and the latter is from scattering which also can be divided into side jump[3] and skew scattering[4,5] because of the different scattering reasons. In hexagonal magnet Fe_5Sn_3, the AHE is investigated during the current flows along c-axis and magnetic field parallels to ac-plane. As shown in Fig.1, with temperature reduced, the slopes of the Hall resistivity ρ_{xy} carves in saturation region changes from positive to negative, which means the species of charge carriers change at low temperatures. This special phenomena could be originated from the influence of magnetic structure on Fermi surface.

[1] Naoto Nagaosa, Jairo Sinova, Shigeki Onoda, A. H. MacDonald, and N. P. Ong, Reviews of Modern Physics 82 (2), 1539 (2010). [2] T. Jungwirth, Q. Niu, and A. H. MacDonald, Phys Rev Lett 88 (20), 207208 (2002). [3] L. Berger, Physica 30 (6), 1141 (1964). [4] J. Smit, Physica 21 (6), 877 (1955); [5] J. Smit, Physica 24 (1), 39 (1958).

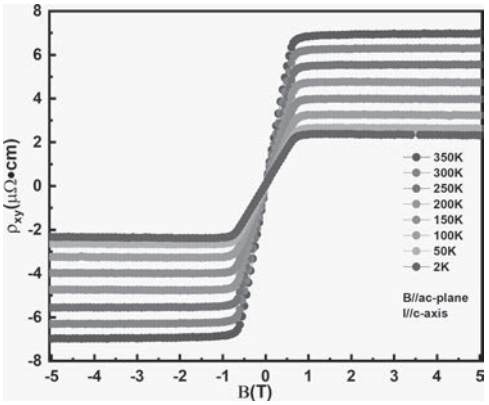


Fig. 1 Hall resistivity ρ_{xy} as a function of magnetic field B which parallels to ac-plane at various temperatures.

CV-11. Withdrawn

CV-12. Fabrication of $D0_{19}$- and B2-type Fe_3Sn epitaxial films and comparison of magneto-transport properties. A. Maeno[1], Y. Goto[1], M. Tsujikawa[2,3], M. Shirai[2,3], T. Yanase[4], T. Shimada[4] and *T. Nagahama*[4]
1. CSE, Hokkaido University, Sapporo, Japan; 2. RIEC, Tohoku University, Sendai, Japan; 3. CSRN, Tohoku University, Sendai, Japan; 4. Graduate School of Engineering, Hokkaido University, Sapporo, Japan

The alloys consisted of 3d-transition metals and Sn has attracted much attention because of novel characteristics. For example, Mn_3Sn was reported to show large anomalous Hall effect (AHE) or anomalous Nernst effect (ANE) [1]. Fe_3Sn_2 also expected to exhibit large AHE because of the crystal structure involving Kagome lattice[2,3]. So far, most of the experiments were performed using single crystal samples. To use them in the devices, thin film fabrication technique is indispensable. Recently, we succeeded in the fabrication of B2 type Fe_3Sn epitaxial films[4] which exhibited large ANE. On the other hand, $D0_{19}$ type Fe_3Sn phase was also reported in the literature. In this study, we fabricated the epitaxial growth of $D0_{19}$ Fe_3Sn and compare the magneto-transport characteristics to B2-type Fe_3Sn. The samples were prepared by Molecular Beam Epitaxy (MBE) method. Stacking structures were as follows: Al_2O_3 (0001) substrate / Pt (111) 6nm (buffer layer) / $D0_{19}$-Fe_3Sn (0001) 30 nm/ Al_2O_3 5nm (cap layer). The temperature of substrates during the depositions were 673 K for $D0_{19}$-Fe_3Sn. B2 Fe_3Sn layer was deposited at a temperature of 373 K on MgO(001) substrate, then the films were annealed at 573 K for 30 min. The epitaxial growth was confirmed by RHEED and XRD θ-2θ measurements. Figure 1 shows the anomalous Hall effect of B2 and $D0_{19}$ Fe_3Sn thin films. Both Fe_3Sn films exhibited clear Hall effect because they were ferromagnetic materials. The Hall resistivity of B2 was 7 times larger than that of $D0_{19}$ Fe_3Sn. Such small Hall effect for $D0_{19}$ alloy could be attributed to the anisotropic crystal structure[1]. The saturation fields of AHE were very different between B2 and $D0_{19}$ because $D0_{19}$ Fe_3Sn has in-plane magnetic anisotropy. The longitudinal MR will be also discussed.

1. S Nakatsuji et al., Nature 527 212 (2015) 2. Linda Ye et al., Nature 555 638 (2018) 3. Y. Satake et al., Scientific reports, 9, 3282, (2019) 4. Y. Goto et al., Jpn. J. Appl. Phys., 57, 120302, (2018)

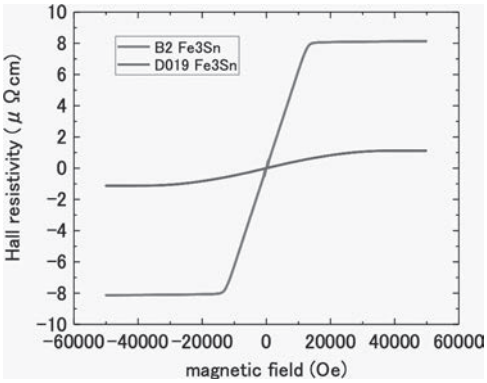


Fig.1 Hall resistivity of B2- and $D0_{19}$- Fe_3Sn at room temperature.

CV-13. Withdrawn

CV-14. Enhanced MR Raio and Low Coercivity in Dual-Spin-Valve GMR Stack with Synthetic Antiferromagnetic Couplings. *N. Fukatani*[1], M. Ichimura[1] and J. Hayakawa[1] *1. Hitachi Ltd., Hikigun, Japan*

In recent years, giant magnetoresistance (GMR) effect has been used in many application such as low magnetic field sensor, current sensor, and read heads in hard disc drives due to their small size, high sensitivity, low power consumption, and low cost[1, 2]. Except for a reading heads in hard disc drives, GMR sensors are required to show high MR ratio and low coercivity (H_c) with low stray field regardless of their thickness because the thickness of GMR stacks is not critical for the performance of GMR sonsors. Important design parameters are number of spin-dependent electron scattering layers, crystallinity, and the interface sharpness. In this study, we fabricated dual-spin-valve GMR stacks with synthetic antiferromagnetic couplings in order to enhance GMR ratio with low H_c in a current-in-plane configuration toward the sensitive magnetic sensor applications. The dual-spin-valve GMR stack is composed of Si/SiO sub.//seed layer/IrMn(6)/ CoFe(2.6)/ Ru(0.85)/CoFe(2.6)/Cu(2.5)/CoFe(1)/NiFe(3.5)/CoFe(1)/ Cu(2.5)/CoFe(2.6)/Ru(0.85)/CoFe(2.6)/IrMn(6)/capping layer (all thickness in nm), which were deposited by magnetron sputtering technique. The micro structure was investigated using scanning transmission electron microscope (STEM) with a energy dispersive X-ray spectroscopy (EDX). The MR curves were measured by a four-probe method by applying magnetic field. Figure 1 shows a vertical STEM-EDX element mapping image of the GMR stack. The layered film structures which consist of a few nm films are clearly observed. The crystal structure of the GMR stack is identified to be highly oriented (111) structure from the fast Fourier transformed diffraction patterns. Figure 2 shows MR curves for the dual-spin-valve and the conventional single-spin-valve GMR stack. The MR ratio in the dual-type is increased up to 13.1 %, which is about 1.3 times higher than that of the single-type of 9.8 %. The H_c estimated from Fig.2 is below 10 Oe, which is comparable to that of the practical GMR sensors. Therefore, present dual-spin-valve GMR stack is promising for realizing high sensitive magnetic sensors.

[1] A. Bernieri, G. Betta, L. Ferrigno, and M. Laracca, IEEE Sens. J. 13, 4513 (2013). [2] L. Jogschies, D. Klaas, R. Kruppe, J. Rittinger, P. Taptimthong, A. Wienecke, L. Rissing, and M. C. Wurz, IEEE Sens. J. 15, 28665 (2015).

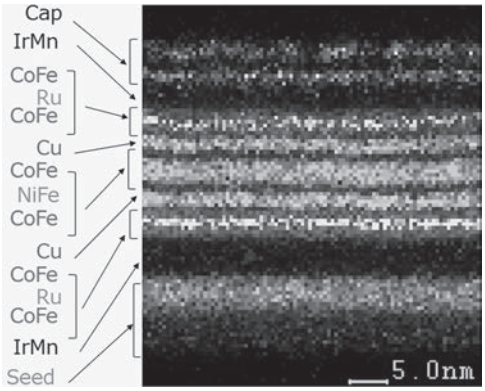


Fig. 1 The vertical STE-EDX element mapping image of GMR stacks.

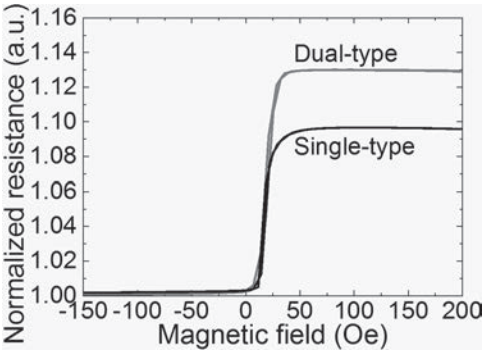


Fig. 2 The MR curves for dual- and single-spin-valve GMR stacks.

CV-15. Magnetotransport Properties Probed by Terahertz Time-Domain Spectroscopy on Ferromagnetic Thin Films.
L. Huang[1], S. Lee[1], D. Kim[1], Y. Zhao[1], S. Kim[2], H. Shin[2], J. Park[2], H. Kim[3], J. Hong[3] and D. Kim[1] *1. Chungbuk National University, Cheongju, The Republic of Korea; 2. Pohang Accelerator Laboratory, Pohang, The Republic of Korea; 3. Daegu Gyeongbuk Institute of Science & Technology, Daegu, The Republic of Korea*

Terahertz (THz) properties of various materials have drawn a great attention recently. Since THz time-domain-spectroscopy (TDS) is used to investigate optical conductivity, under external magnetic fields, THz TDS could reveal useful information regarding magnetotransport behavior of ferromagnetic samples. For TDS, a beamsplitter is used to split one ultrafast pulse from Ti:sapphire regenerative amplified laser system into two pulses and different portions of the THz pulse can be measured at the detector and thus, mapping out the THz pulse in the time-domain[1]. Here, we report our experimental investigation on spin-dependent conduction behavior in ferromagnetic Fe metallic films with different thickness by means of TDS developed at Pohang Accelerator Laboratory. It is considered that, in case of ferromagnetic transition metals, carriers are mostly taken by sp-band Fermi-level electrons, while localized electrons scatter with spin-dependent momentum at spin-split d-band, where the spin-dependent transport behavior occurs. The spin-dependent optical conductivity is analyzed based on the Drude model[2]: $\sigma(\omega) = \sigma_0(1\text{-}i\omega\varsigma)^{-1}$ with consideration of the spin-dependent density and momentum scattering/relaxation time of conducting electrons at Fermi levels[3]. THz-TDS under various external magnetic fields in the range 0 – 150 Oe for different thickness have been analyzed, where the amplitude of transmitted signal showed an obviously increasing trend with respect to the external magnetic field, as seen in Fig. 1, which can be understood based on the sample conductivity and number of spin/charge carriers[4]. This research has been supported by [Grant No. 2018R1A2B3009569] and by Max Planck POSTECH/KOREA Research Initiative Program [Grant No 2016K1A4A4A01922028] through the National Research Foundation of Korea (NRF).

[1] H. Kang, Y.-H. Ahn, D.-Y. Koh, S.-H. Kim, J.-H. Park, and H. Lee, J. Phys. Chem. C 119, 21353 (2015). [2] M. Scheffler, M. Dressel, M. Jourdan, and H. Adrian, Nature 438, 1135 (2005). [3] Z.-M. Jin, A. Tkach, F. Casper, V. Spetter, H. Grimm, A. Thomas, T. Kampfrath, M. Bonn, M. Kläui, and D. Turchinovich, Nature Phys. 11, 761 (2015). [4] Z. Mics, A. D'Angio, S.-A. Jensen, M. Bonn, and D. Turchinovich, Appl. Phys. Lett. 102, 231120 (2013).

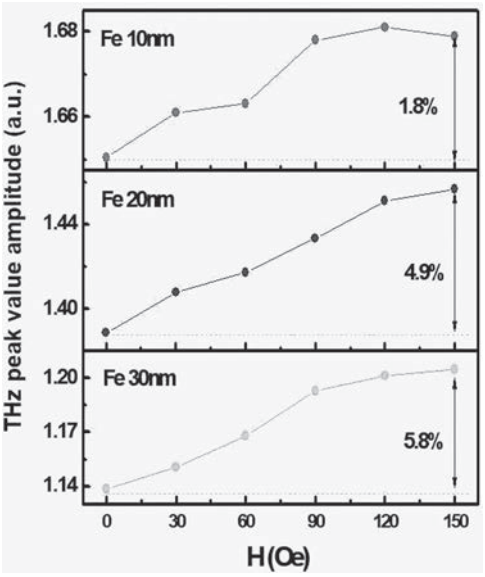


Fig. 1. THz-TDS peak amplitude under different magnetic fields for 10-, 20-, and 30-nm Fe films.

CV-16. Large Magnetoresistance at Small Magnetic Field and Reconfigurable Boolean Logic Functions Based on Diode-enhanced Giant Magnetoresistance Effect.
J. Nan[1], K. Zhang[1], S. Yan[1], Z. Zhang[1,2], Z. Zheng[1,2], G. Wang[1], Y. Zhang[1], Y. Zhang[1,2] and W. Zhao[1] *1. Fert Beijing Research Institute, BDBC, School of Microelectronics, Beihang University, Beijing, China; 2. School of Electronic and Information Engineering, Beihang University, Beijing, China*

Magnetoresistance (MR) plays a key role for spintronic devices [1-3]. Recently, diode-enhanced MR has been reported to achieve large MR ratio [4-6]. In this paper, we proposed an alternative to realize large MR at small magnetic field by combining giant MR (GMR) effect with the nonlinear transport property of the diode. The GMR film stack (Fig. 1(a)) [7] is patterned into a strip and then connected to a Zener diode and two resistors R_1, R_2 (Fig. 1(b)). The apparent resistance R is defined as R=V/I, where V is the voltage measured by the voltmeter and I is the applied current. The MR ratio is defined as MR=(R(H)-R(0))/R(H), where R(H) is the apparent resistance under magnetic field H. The MR of the GMR strip (Fig. 1(c)) is amplified by the switching behavior of the diode, resulting in a dramatic change in the apparent resistance of the system (Fig. 1(d)). MR ratio up to 5389% is realized with a magnetic field as small as 50 Oe. This proposal has the potential for realizing reconfigurable Boolean logic functions. As shown in Fig. 2(a), two GMR strips are connected in series. The aligned low-resistance state and anti-aligned high-resistance state of the GMR strip are regarded as logic input "1" and "0", respectively. The pinning direction of the two strips should be opposite to each other, thus the two logic inputs can be set to (0,1), (1,1), (1,0) and (0,0) by applying different magnetic fields (see Fig. 2(b)). Fig. 2(c) shows the I-V curves of the proposed circuit with these four sets of logic inputs. The critical voltage separating logic output "0" and "1" is 0.13 V. For example, setting the working current to 6.1 mA can achieve logic function AND. The working current for logic function OR is 6.4 mA. The details are summarized in Fig. 2(d). This work can help to build future high-performance computing systems.

[1] G. A. Prinz, Science, Vol. 282, no. 5394, pp. 1660–1663 (1998) [2] A. Ney, et al., Nature, Vol. 425, pp. 485–487 (2003) [3] A. D. Kent and D. C. Worledge, Nature Nanotechnology, Vol. 10, pp. 187–191 (2015) [4] J. Chen, et al., Applied Physics Letters, Vol. 105, 193508 (2014) [5] Z. Luo, et al., Advanced Materials, Vol. 28, no. 14, pp. 2760–2764 (2016) [6] K. Zhang, et al., Advanced Electronic Materials, Vol. 5, no. 3, 1800812 (2019) [7] S. Yan, et al., Sensors, Vol. 18, no. 6, 1832 (2018)

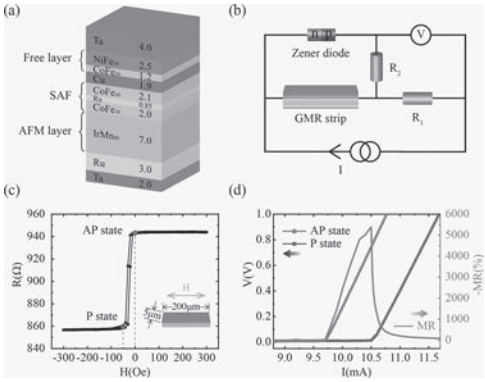
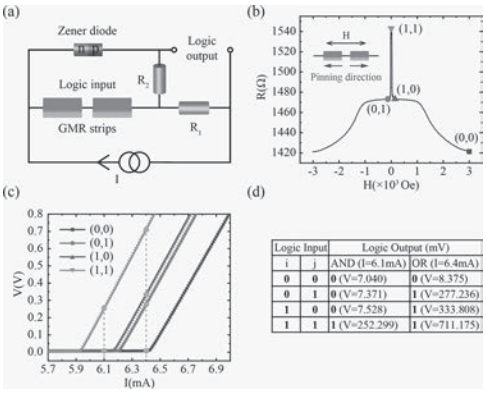


Fig.1 (a) Film stack of the GMR strip. (b) Schematic of the proposed scheme to achieve large MR ratio. (c) R-H loop of the GMR strip. (d) I-V curves and MR ratio of the proposed system.



Logic Input		Logic Output (mV)	
i	j	AND (I=6.1mA)	OR (I=6.4mA)
0	0	0 (V=7.040)	0 (V=8.375)
0	1	0 (V=7.371)	1 (V=277.236)
1	0	0 (V=7.528)	1 (V=333.808)
1	1	1 (V=252.299)	1 (V=711.175)

Fig.2 (a) Circuit schematic for realizing Boolean logic functions. (b) R-H loop of the two connected GMR strips. (c) I-V curves of the circuit with four sets of logic inputs. (d) Detailed configurations for logic functions.

CV-17. Withdrawn

CV-18. Magnetic and Transport Properties of Multilayered EuO/Pt Thin Films. *N. Shrestha*[1], J.R. Murphy[1], W.D. Rice[1] and J. Tang[1] *1. Physics and Astronomy, University of Wyoming, Laramie, WY, United States*

Research on europium monoxide (EuO) has been done extensively in the last decade because of the physics of this interesting magnetic semiconductor and its potential applications in spintronics. In order to examine the spin-orbit proximity effect, we have prepared multilayered EuO/Pt thin films on Si (001) substrates by pulsed laser deposition (PLD) using europium (Eu) metal as target. The magnetic and transport properties of the EuO/Pt films have been studied as a function of temperature and magnetic field with a Physical Property Measurement System (PPMS). The magnetic data show increased Curie temperature from 70 K to 140 K which is characteristic of oxygen deficient samples (Fig. 1) and is described by a magnetic polaron model [1]. The transport measurements (Fig. 2) reveal contributions from various conducting channels including the interface between EuO and Pt [2]. At the lowest temperatures, the resistivity ρ exhibits an exp ($1/T^{1/2}$) temperature dependence for some samples. The transport measurements reveal both positive magnetoresistance (PMR) and negative magnetoresistance (NMR) originating from spin-orbit scattering and weak localization effect. There is a strong enhancement in the magnetic anisotropy from its bulk value, which results from strong spin-orbit coupling across the EuO/Pt interface.

[1] P. Liu and J. Tang, Physical Review B 85, 224417 (2012). [2] G. Rimal and J. Tang, Physical Review B 98, 144442 (2018). This work was supported by National Science Foundation (Grant No. DMR-1710512).

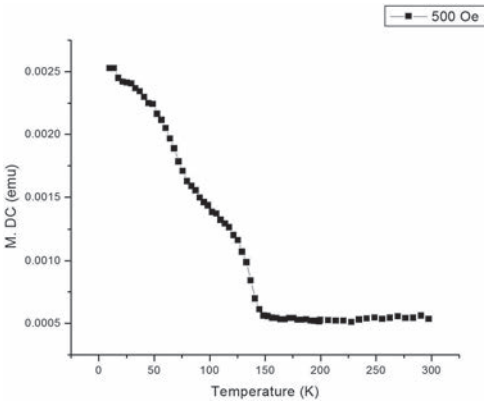


Fig. 1The temperature dependent magentic moment for the EuO/Pt thin film.

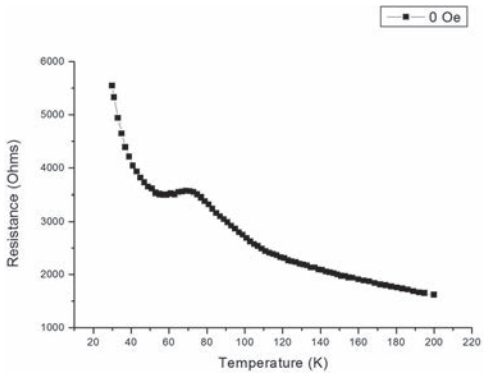


Fig. 2 The temperature dependence of the resistance.

Session CW
RARE-EARTH-FREE MAGNETS
(Poster Session)

Feng Yan, Co-Chair
The University of Alabama, Tuscaloosa, AL, United States
Tetsuji Saito, Co-Chair
Chiba Institute of Technology, Chiba, Japan

CW-01. Uniaxial magnetic anisotropy and bcc-bct-fcc transformation of FeCo caused by the addition of V and N elements. *T. Hasegawa*[1], C. Shirai[1] and Y. Takemasa[1] *1. Department of Materials Science, Akita University, Akita, Japan*

The energy utilized by the magnets depends on the magnitudes of the saturation magnetization (Ms) and uniaxial magnetic anisotropy (Ku). FeCo with the body-centered cubic (bcc) structure is a well-known magnetic material characterized by the highest Ms and very high Tc values among various transition metal alloys. Although FeCo-based materials exhibit the strong magnetic properties, their low Ku magnitudes make them unsuitable for the fabrication of permanent magnets. However, if the Ku of FeCo could be increased to a sufficiently high value, one of the strongest permanent magnets would be obtained. Recent our studies[1] revealed that the epitaxial FeCo thin films with the body-centered tetragonal (bct) structure and thicknesses of several nanometers exhibited Ku values of 10^6 J/m^3 due to epitaxial stress, which required further stabilization. Two methods can be used to stabilize the bct structure: (I) applying a uniaxial stress to the FeCo lattice via epitaxial effects and (II) adding a third element to the FeCo structure. The addition of certain third elements (II) is expected to generate a tetragonal distortion in the FeCo lattice leading to the relaxation of the local stress in their vicinity. In our previous study,[2] we focused on the use of the combination of V and C, N elements as the third additive element because of its ability to form a bcc, which was subsequently transformed into the fcc with an increase in the third element content. We expected that a stabilization of the bct structure occurs at the boundary between the bcc phase and the fcc phase. In this study, the effect of the N addition into FeCoV films on their tetragonal deformation was investigated. Figures 1(a) and 1(b) shows the in-plane XRD and the out-of-plane XRD patterns of the FeCoVN films deposited directly on the MgO substrate, respectively. The bcc-bct-fcc transformation depending on the N content (x) is observed. At x = 2.0 at% in the bct region, a high Ku of 10^6 J/m^3 are obtained. This work was supported by NEDO.

[1] T. Hasegawa et al., Scientific Reports 7, 13215 (2017). [2] T. Hasegawa et al., Scientific Reports 9, 5248 (2019).

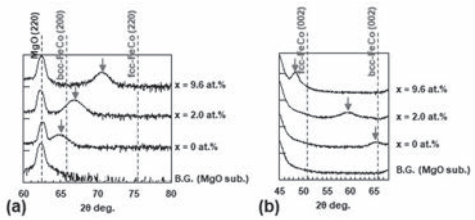


Fig. 1. (a) In-plane and (b) out-of-plane XRD patterns recorded for the MgO(100) substrate/$(Fe_{0.5}Co_{0.5})_{90-0.9x}V_{10-0.1x}N_x$ (0≤x≤9.6 at.%, t=20 nm)/ SiO2 (t=5 nm) continuous films.

CW-02. Large perpendicular anisotropy of highly (001) oriented MnAl film fabricated on CoGa buffer layer. *D. Oshima*[1], T. Kato[2] and S. Iwata[1] *1. Institute of Materials and Systems for Sustainability, Nagoya University, Nagoya, Japan; 2. Department of Electronics, Nagoya University, Nagoya, Japan*

$L1_0$-phase MnAl is one of promising candidates for the memory layer in spin transfer torque magnetic random access memory since it exhibits a large perpendicular magnetic anisotropy and a small Gilbert damping [1]. In previous reports, (001) oriented MnAl films were grown on Cr or Cr alloy buffer layer [1]. Recently, highly (001) oriented MnGa films were grown on CoGa buffer layers which exhibit an excellent magnetic property even for the thickness < 5 nm [2]. In this study, we prepared MnAl films on CoGa(001) buffer layers by magnetron sputtering. The film stack was Cr (2 nm) / MnAl (5 or 15 nm) / CoGa (0 or 30 nm) / Cr (20 nm) / MgO(001) sub. Cr and CoGa buffer layers were deposited at 400 °C and annealed at 600 °C after the deposition. The MnAl layer was grown at T_s and annealed at T_a after the deposition. Figure 1 shows *M-H* loops, atomic force microscope (AFM) images, and x-ray diffraction (XRD) profiles of the 5-nm-thick MnAl films grown on the Cr or CoGa buffer layer. In this case, T_s was set to be 200 °C and post-annealing was not carried out. By using the CoGa buffer layer, MnAl film exhibited a saturation magnetization of 400 emu/cc and almost unity squareness ratio. The value of the perpendicular anisotropy was roughly estimated to be 7 Merg/cc from the in-plane curve. The surface flatness was also improved by using the CoGa buffer layer. In XRD profiles, 001 and 002 MnAl peaks were clearly observed and intensities of these peaks were larger for the sample with the CoGa buffer than that without the CoGa buffer. Further improvements of the magnetic property and the surface flatness by post-annealing at T_a = 500 °C were confirmed, it is concluded that the insertion of the CoGa buffer layer was effective to improve the (001) orientation and magnetic property of MnAl.

[1] M. Hosoda et. al., J. Appl. Phys., vol. 111, 07A324 (2012). [2] K. Z. Suzuki, Jpn. J. Appl. Phys., vol. 55, 010305 (2016).

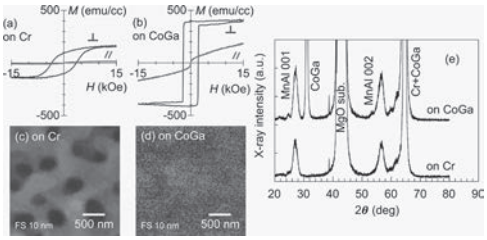


Fig. 1 (a), (b) *M-H* curves, (c), (d) AFM images, and (e) XRD profiles of MnAl films grown on (a), (c), (e) Cr or (b), (d), (e) CoGa buffer layer.

CW-03. Structural and magnetic properties of $Mn_{53.3-x}Al_{45}C_{1.7}Ti_x$ (x = 0, 0.5, 1.0, 1.5) melt spun ribbons. *J.S. Trujillo Hernandez*[2,1], J.A. Tabares[1] and G.A. Pérez Alcázar[1] *1. Physics Department, Universidad del Valle, Cali, Colombia; 2. Facultad de Ciencias Naturales y Matematicas, Universidad de Ibagué, Ibagué, Colombia*

The binary Mn-Al alloy is a promising rare-earth free hard magnetic materials due to its intrinsic magnetic properties and low cost of the raw materials. The effect of Ti addition on the magnetic properties and the phase stability of the Mn-Al system is investigated. For this purpose, $Mn_{53.3-x}Al_{45}C_{1.7}Ti_x$ (x = 0; 0.5; 1.0; 1.5) alloys were subject to melt spinning at 20 m/s wheel speeds and annealing under different temperatures. The X-ray diffraction patterns and scanning electron microscope images indicates that was possible to obtain pure ε-phase after melt spinning at 20 m/s for all compositions. For all the other solidification conditions, the melt spun ribbons show undesired secondary phases (T, β and γ_2). Annealing the single phase ribbons above 550°C has shown a clear transformation from the high temperature e-phase to the desired τ-phase. Magnetic measurements indicate a slight increase in the coercivity values with increasing Ti concentration and an increase in Curie temperature by 20 K with addition of Ti. The highest values of magnetic properties were obtained for $Mn_{51.8}Al_{45}C_{1.7}Ti_{1.5}$ alloy: M_s(3T) = 93.6 Am²/kg, μ_oH_c = 0.198 T, M_r = 43.3 Am²/kg, and T_c = 650 K.

[1] J. M. D. Coey, Journal of Physics: Condens. Matter., 26, 064211, (2014). [2] Q. Zeng, I. Baker, J. B. Cui, Z. C. Yan, Journal of Magnetism and Magnetic Materials, 308, 214-226, (2007). [3] Hong Jian, Konstantin P. SkoKov, Oliver Gutfleisch, Journal of Alloys and Compounds, 622, 524-528, (2015).

CW-04. Effect of Al doping on magnetic properties of LTP-MnBi alloys. *H. Lee*[1], M. Kang[1], G. Lee[1] and J. Kim[1] *1. Materials Science and Chemical engineering, Hanyang University, Ansan, The Republic of Korea*

Recently, there has been much interest in the development of rare-earth free permanent magnets. Among several candidates, a low temperature phase (LTP) MnBi intermetallic compound has been attracted much attention due to its high magneto-crystalline anisotropy coefficient (K = 10^7 erg/cm³), curie temperature (T_c = 775 K) and positive coercivity temperature coefficient.[1-2] Up to now, most studies have focused on increasing the ratio of the LTP phase in MnBi powders due to its low processing temperature but few studies have been conducted to improve its magnetic properties. The first principle calculation showed that addition of Al could increase the saturation magnetization (M_s).[3-4] Therefore, in this study, LTP-MnBi alloys doped with Al were fabricated in order to investigate the effects of Al on the magnetic properties. In this experiment, Mn, Bi and Al raw materials were arc-melted under an argon atmosphere to prepare $(Mn_{54}Bi_{46})Al_x$ (x = 0, 1, 3, 5) alloys. Then, MnBi-Al ingots were inductively re-melted to obtain homogeneously mixed ribbons through the melt-spining process. These melt-spun ribbons were annealed at 573 K for 24 hours under an argon atmosphere to finally produce high quality LTP-MnBi alloys. Figure.1 shows the XRD patterns of annealed MnBi-Al alloys. It can be clearly seen that only LTP-MnBi single phase is developed in specimens containing less than 1 at.% Al. The further increase of the Al concentration results in the formation of the Al_8Mn_5 phase, which remains excess Bi. Figure.2 shows the M-H curves of the alloys measured by VSM at 2.5 T. This demonstrates that the addition of 1 at.% Al increase the M_s of the MnBi alloy from 60.9 to 62.2 emu/g. As expected, the further increase of Al concentration decreases the M_s due to the formation of the non-magnetic phases. The above results suggest that the addition of Al can increase the saturation magnetization of the LTP MnBi phase as the single phase of LTP-MnBi is maintained. This increase may be due to that Al atoms occupy the interstitial sites of the hexagonal MnBi phase. In order to clarify the effects of the Al addition, the microstructural analysis is under investigation.

1. W. E. Stutius and Tu ChenT. R. Sandin, AIP Conference Proceedings 18, 1222 (1974) 2. X. Guo, X. Chen and Z. Altounian, PHYSICAL REVIEW B, Vol. 46, p.22(1992) 3. R. F. Sabiryanov and S. S. Jaswal, PHYSICAL REVIEW B, Vol. 53, p.1(1996) 4. V.V. Ramakrishna, S. Kavita, Ravi Gautam, Journal of Magnetism and Magnetic Materials, Vol. 458, p.25(2018)

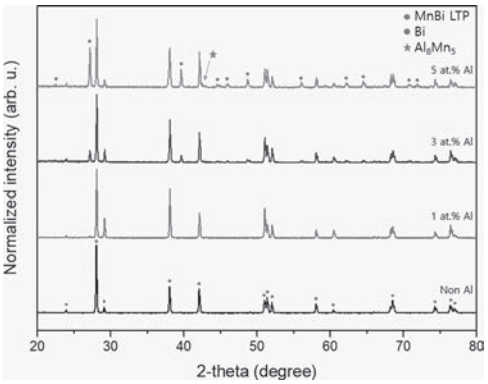


Fig.1 XRD pattern of MnBi-Al.

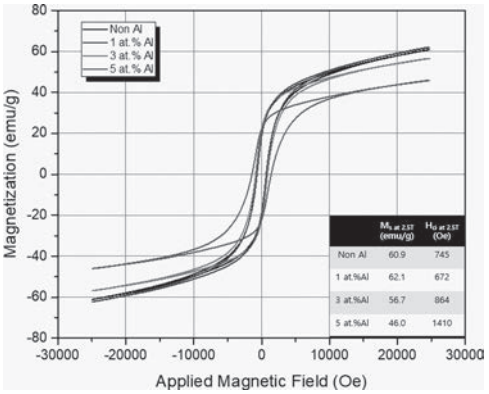


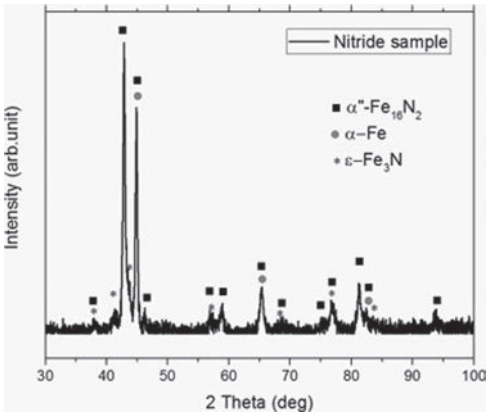
Fig.2 M-H curve measured by VSM at RT.

CW-05. Withdrawn

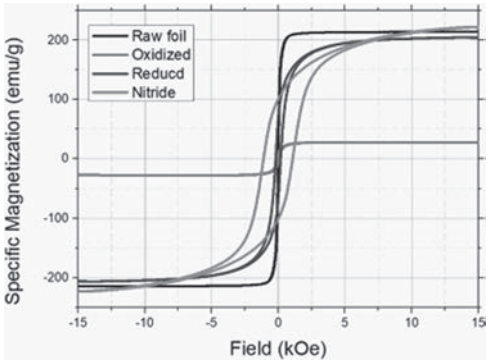
CW-06. α″-$Fe_{16}N_2$ Foils with a Positive Temperature Coefficient of Coercivity. *J. Liu*[1], G. Guo[1], F. Zhang[1], B. Ma[1] and J. Wang[1] *1. University of Minnesota, Minneapolis, MN, United States*

α″-$Fe_{16}N_2$ has been getting more attention as a candidate of rare-earth-free magnets due to its unique magnetic properties, such as high saturation magnetization (M_s ~ 2.9 T),[1], [2] relatively large magnetocrystalline anisotropy (~1.0×10^7 erg/cm³) [3]–[5], and low coercivity temperature dependence. [6] Nanoparticles (NPs) are widely used to prepare α″-$Fe_{16}N_2$ by a low-temperature method (<200 °C) because of the higher nitrogen diffusivity for NPs.[7] However, several challenges remain for NPs approach such as easy to be oxidized, difficult to handle, and relatively low packing density. Bulk form α″-$Fe_{16}N_2$ like foils or ribbons could potentially address those challenges. However, the nitrogen diffusivity in the bulk forms needs to be enhanced to obtain high phase volume ratio of α″-$Fe_{16}N_2$. Here, we proposed to use Fe foils and tune the microstructure of these Fe based foils to make them suitable for fabricating α″-$Fe_{16}N_2$ foils by a low-temperature nitridation process. The Fe foils (~25 μm) were oxidized in air and then reduced by H_2. A porous structure was formed in these foils, in which the nitrogen diffusivity was enhanced significantly. After the reduction, a nitridation was proceeded using ammonia gas at the temperature lower than 200 °C, and nitride foil with a high phase volume ratio of α″-$Fe_{16}N_2$ were obtained. Magnetic properties of these nitride foils were characterized with coercivity around 1.1 kOe and M_s around 222 emu/g higher than the reduced Fe foil (~ 205 emu/g). The achieved magnetic anisotropy of these nitride foils is up to 7×10^6 erg/cm³. Temperature-dependent hysteresis loops indicated that the nitride foils have a small coercivity temperature coefficiency (positive) from 300 K to 425 K. It is about an order of magnitude smaller than that of commercial NdFeB magnets (negative). This could allow new applications for α″-$Fe_{16}N_2$ magnets. The good magnetic performances of α″-$Fe_{16}N_2$ foils make it a promising candidate for rare-earth-free magnets.

[1] N. Ji, X. Liu, and J.-P. Wang, "Theory of giant saturation magnetization in α″-$Fe_{16}N_2$: role of partial localization in ferromagnetism of 3d transition metals," *New J. Phys.*, vol. 12, no. 6, p. 063032, Jun. 2010. [2] J.-P. Wang *et al.*, "Fabrication of $Fe_{16}N_2$ Films by Sputtering Process and Experimental Investigation of Origin of Giant Saturation Magnetization in $Fe_{16}N_2$," *IEEE Trans. Magn.*, vol. 48, no. 5, pp. 1710–1717, May 2012. [3] H. Takahashi, M. Igarashi, A. Kaneko, H. Miyajima, and Y. Sugita, "Perpendicular uniaxial magnetic anisotropy of $Fe_{16}N_2$ [001] single crystal films grown by molecular beam epitaxy," *IEEE Trans. Magn.*, vol. 35, no. 5, pp. 2982–2984, 1999. [4] N. Ji *et al.*, "Perpendicular magnetic anisotropy and high spin-polarization ratio in epitaxial Fe-N thin films," *Phys. Rev. B*, vol. 84, no. 24, p. 245310, Dec. 2011. [5] X. Li *et al.*, "Heavy-Metal-Free, Low-Damping, and Non-Interface Perpendicular $Fe_{16}N_2$ Thin Film and Magnetoresistance Device," *Phys. status solidi – Rapid Res. Lett.*, vol. 13, p. 1900089, Apr. 2019. [6] J. Liu *et al.*, "α″ -$Fe_{16}N_2$ Foils Prepared by a Low-Temperature Nitridation Method: a Candidate for Rare-Earth-Free Magnets." (to be submitted) [7] T. Ogawa *et al.*, "Challenge to the Synthesis of α″-$Fe_{16}N_2$ Compound Nanoparticle with High Saturation Magnetization for Rare Earth Free New Permanent Magnetic Material," *Appl. Phys. Express*, vol. 6, no. 7, p. 073007, Jul. 2013.



x-ray diffraction pattern of a nitride foil



Hysteresis loops of foil samples at each step at 300 K

CW-07. Synthesis and magnetic properties of α″-$Fe_{16}N_2$ nanowires using an electrospinning method. *M. Kang*[1], G. Lee[1], J. Lee[1], Y. Choa[1] and J. Kim[1] *1. Hanyang University, Ansan, Ansan, The Republic of Korea*

In recent decades, there have been many attempts to develop new hard magnetic materials with high energy product ($BH_{(max)}$) and rare-earth free elements. An iron nitride phase, α″-$Fe_{16}N_2$, has received much attention due to the giant magnetic moment. Using this high magnetic moment, the α″-$Fe_{16}N_2$ phase was estimated to have a theoretical energy product of the 135 MGOe [1]. However due to the low crystalline anisotropy constant, the coercivity of α″-$Fe_{16}N_2$ magnetic materials was reported to be less than about 2.2 kOe. This means that the coercivity must be increased to use α″-$Fe_{16}N_2$ as a permanent magnet. In this study, one-dimensional α″-$Fe_{16}N_2$ nanowires with high aspect ratios were fabricated to induce the shape anisotropy for high coercivity using an electrospinning method. [2] In this experiment, electro-spun Fe/PVP precursor nanowires were prepared by electrospinning and then annealed at 700°c for 1 hr to obtain iron oxide nanowires in air. These annealed iron oxide nanowires were reduced in a hydrogen atmosphere at 300~400°c for 2 hr. The reduced iron nanowires were then nitrided at 140~170°c for 6~24 hr using ammonia gas. Figure 1 shows the morphology of fabricated nitrided nanowires. As shown in the figure, the wires with a diameter of 150 ~ 350 nm are successfully fabricated and their aspect ratio is also higher than 50. The XRD analysis of the wires indicated that the fraction of the α″-$Fe_{16}N_2$ phase reached 93.7 wt.%. Figure 2 shows the magnetic properties of the nitrided nanowires. The magnetization and coercivity of the nanowires measured 176.2 emu/g and 1215.5 Oe, respectively. It is considered that this low coercivity is caused by the fine grains of the nitrided nanowires. Thus, in order to improve the magnetic properties, various pre-heat treatment conditions before the nitridation of the iron wires have been examined. As a result, the pre-heat treatment is found to be an effective way to increases their initial grain size.

[1] Wang, J. P. et al., Magnetics, IEEE Transactions on 48, 1710–1717 (2012) [2] M. Tobise et. al., J. Magn. Soc. Jpn., 41, 58-62 (2017)

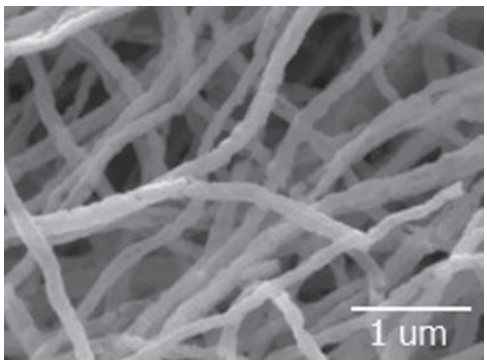


Fig 1. FE-SEM image of iron nitride nanowires

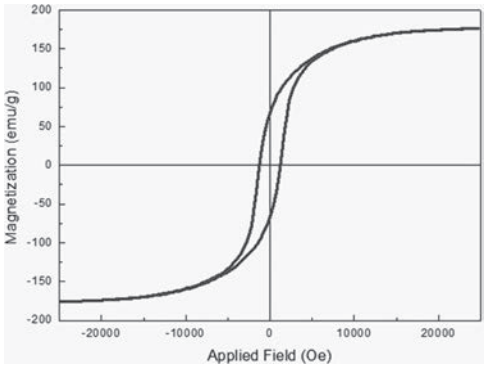


Fig 2. Hysteresis loop for the nitride nanowire

CW-08. Design of $Fe_{16}N_2$ magnets assisted with antiferromagnetic matrix. *X. Hang*[1] and J. Wang[2,1] *1. Chemical Engineering and Materials Science, University of Minnesota, Minneapolis, MN, United States; 2. Electrical and Computer Engineering, University of Minnesota, Minneapolis, MN, United States*

Permanent magnets have traditionally been made with rare-earth (RE) elements. However, the environmental cost of RE mining and processing, as well as RE supply risks make it urgent to develop RE-free permanent magnets. $Fe_{16}N_2$, with its high saturation magnetization (M_s), is a promising candidate material for such purpose. However, even though $Fe_{16}N_2$ has decently large uniaxial anisotropy (K = 1.0 – 1.8 x 10^7 erg/cm^3), bulk $Fe_{16}N_2$ magnets made so far are limited with low coercivity (1200 – 2000 Oe), so are $Fe_{16}N_2$ nanoparticles (1000 – 3000 Oe). Thus, it is desirable to search

for new approaches to enhance its coercivity to make practical iron nitride magnets for a broad range of applications. Here, we propose the use of exchange coupling to an antiferromagnet (AFM) as a means to increase coercivity of $Fe_{16}N_2$ magnets. We studied nanometer-sized single-domain AFM-FM bilayers, using material constants of $Fe_{16}N_2$ as input. The dependence of coercivity on the two key parameters, AFM anisotropy and interface coupling strength, is reported within a simplified two-spin model, assuming uncompensated interface. We showed that, by proper choice of AFM materials, coercivity and $(BH)_{max}$ can be effectively enhanced. Our results guide the design of AFM-FM composite magnets and apply well to semi-hard materials like $Fe_{16}N_2$.

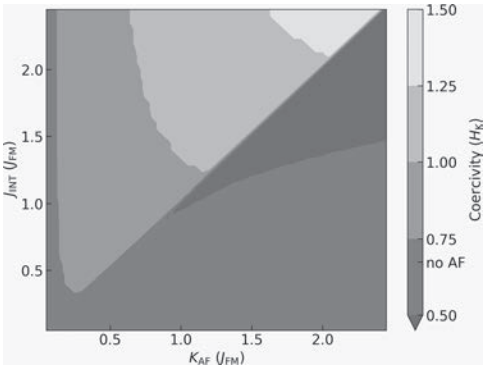


Fig. 1. Coercivity of the AFM-FM composite magnets as a function of AFM anisotropy and interface coupling strength. The coercivity of a single FM is marked on the scale bar.

CW-09. Characteristics of a rare earth free $L1_0$-FeNi hard magnet developed through annealing of FeNiPC amorphous alloys. J. Kim[1] and *H. Yim[1] 1. Sookmyung Women's University, Seoul, The Republic of Korea*

The rare-earth-free hard magnetic $L1_0$-FeNi phase found in cosmic meteorites demonstrates potential as a nextgeneration permanent magnet. However, it is very difficult to artificially produce the $L1_0$-FeNi phase due to the low atomic diffusion coefficients of Fe and Ni near the order-disorder transition emperature (~320 °C). Therefore, FeNiPC amorphous alloy systems exhibiting crystallization temperature (T_x) near the transition temperature were investigated. The amorphous alloys were annealed at T_x, resulting in high atomic diffusion. The structural and microstructural characterizations of annealed ribbons revealed the formation of $L1_0$-FeNi phase through observation of the superlattice peak. The magnetic property, such as coercivity (H_c), also indicated the formation of $L1_0$-FeNi phase, because the maximum H_c value is 641 Oe after the annealing process.

[1] R. Skomski, J.M.D. Coey, Permanent Magnetism, Institute of Physics, Bristol, 1999. [2] S. Chikazumi, Physics of Magnetism, Wiley, New York, 1964. [3] R. Skomski, J.M.D. Coey, Scripta Mater. 112 (2016) 3–8. [4] O. Gutfleisch, M.A. Willard, E. Bruck, C.H. Chen, S.G. Sankar, J.P. Liu, Adv. Mater. 23 (2010) 821–842.

CW-10. Magnetic domain wall pinning and rapid thermal annealing in $L1_0$ -FePt/SiO_2 thin films. *J. Chiou*[1], H. Chang[2], C. Chi[1], C. Hsiao[1] and A. Ranjan[1] *1. National Tsing Hua University, Hsinchu, Taiwan; 2. National Chung Cheng University, Chia-Yi, Taiwan*

Highly ordered $L1_0$ FePt thin films with a strong (001) texture were successfully fabricated on amorphous silicon substrate by co-sputtering and rapid thermal annealing. The main focus of this work is to obtain the preferred orientation structure on amorphous SiO_2. The growth of thin films with controlled texture on the amorphous substrate would be beneficial for economic consideration as compared to with the MgO underlayer, which is pretty expensive. The perpendicular coercivity was enhanced by increasing the heating rate by increasing dislocation densities induced from strain. Dominant pinning sites to restrict the domain wall motion are the strain field of dislocation in FePt $L1_0$ films, because the domain wall width are similar to the range of strain field associated with dislocations. Higher in plane tensile stress was induced in the film by increasing the heating rate during the RTA. Structures were identified by X-ray diffractometer (Simadzu-6000) with the Cu Kα radiation, the strain mapping was performed using the GPA-Phase software (HREM Research Inc.). A spherical aberration corrected (scanning) TEM (JEOL JEM-ARM 200F) operated at 200 kV equipped with an energy-dispersive X-ray spectroscopy (EDS) was used for chemical composition and microstructural analyses. Magnetic hysteresis loops of samples were measured by SQUID, (Quantum Design MPMS-XL). Keyword: GPA-graphical phase analysis, SQUID-superconducting quantum interference device, RTA-rapid thermal annealing.

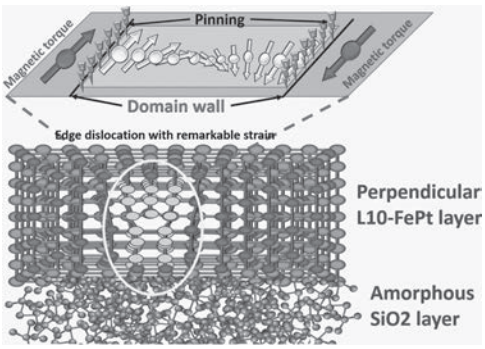


Fig 1. Table of content

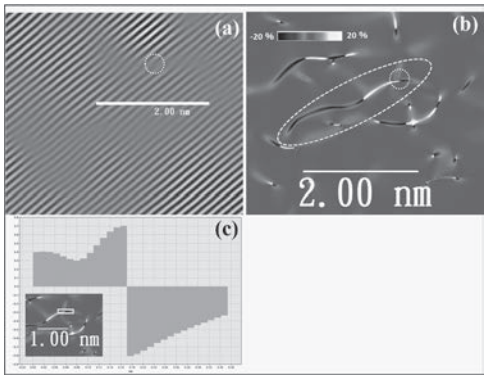


Fig 2. comparison of TEM and GPA images that confirm the dislocation and its strain field range. (a). TEM image can be obtained by choosing and doing FFT of diffraction points, dislocations can be seen in white dot line circles. (b). Results of GPA image that shows the strain field of dislocation (yellow dot line ellipse) about 3-4 nm. (c). Figure shows the strain of edge dislocation (-0.82 to 0.70) that marked in region.

CW-11. High-temperature properties of Fe-Pt film-magnets prepared by electroplating method. T. Yanai[1], *Y. Omagari*[1], S. Furutani[1], A. Yamashita[1], M. Nakano[1] and H. Fukunaga[1] *1. Electricity and Electronics, Nagasaki University, Nagasaki city, Japan*

An $L1_0$ ordered Fe-Pt alloy is one of the well-known hard-magnetic materials, and active studies on Fe-Pt films with high coercivity have been carried out in the field of recording media. Although the saturation magnetic polarization of the Fe-Pt films is smaller than that of Nd-Fe-B films, the Fe-Pt films show relatively high remanence due to a remanence enhancement effect [1], suggesting that the Fe-Pt films are hopeful materials as isotropic permanent magnets. Taking advantage of high remanence and high coercivity of the TM-Pt alloy, some researchers have reported TM-Pt thick-films as small magnets [2-3], and we also reported the Fe-Pt thick-films prepared by an electroplating method [4]. For applying the films as magnets to small electric devices, we need to consider the thermal stability of the magnetic properties. In the present study, we, therefore, evaluated the high-temperature properties of the electroplated Fe-Pt thick-films. We carried out electroplating to obtain

the Fe-Pt thick films by using a direct current. Almost the same bath composition and the plating condition were used as our previous study [4]. The compositions of the as-plated Fe-Pt films were determined by SEM-EDX, and the hysteresis loops were measured with a VSM in the temperature range from 25 to 200°C. Figure 1 shows the coercivity of the annealed Fe-Pt thick-films as a function of the measurement temperature. As shown in Fig.1, the coercivity of all films decreased with increasing the measurement temperature. The thermal coefficient of H_c was approx. -0.21 %/K and this value is superior to that for typical Nd-Fe-B [5]. Figure 2 shows the demagnetization curves of annealed $Fe_{50}Pt_{50}$ and $Fe_{55}Pt_{45}$ films at 25°C and 200°C. Although high coercivity could be obtained for the $Fe_{55}Pt_{45}$ film compared with that for the $Fe_{45}Pt_{55}$ one, the squareness was inferior. Thus, we consider that the $Fe_{50}Pt_{50}$ thick-films are preferable to operate the films under high-temperature. The coercivity at 150°C was 700 kA/m, and this value is higher than that of some reports for Nd-Fe-B-system magnets [6]. From these results, we confirmed that the electroplated Fe-Pt film-magnets can be applied to small magnets required high thermal stability.

[1] E. F. Knellerand and R. Hawig, *IEEE Trans. Magn.*, 27, 3588 (1991) [2] W. F. Liu, S. Suzuki, D.S Li, and K. Machida, *J. Magn. Magn. Mater,* 302, 201 (2006) [3] S. Thongmee, J. Ding, J. Y. Lin, D. J. Blackwood, J. B. Yi, and J. H. Yin, *J. Appl. Phys.*, 101, 09K519 (2007) [4] T. Yanai, K. Furutani, T. Ohgai, M. Nakano, K. Suzuki, and H. Fukunaga, *J. Appl. Phys.*, 117, #17A744, (2015) [5] G. Bai, R. W. Gao, Y. Sun, et al., *J. Magn. Magn. Mater*, 308, 20-23 (2007) [6] Jhon J. Croat, Jan F. Herbst, Robert W. Lee, et al., *J. Appl. Phys.*, 55, 2078-2081, (2015)

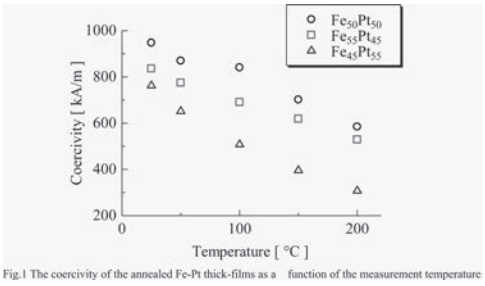


Fig.1 The coercivity of the annealed Fe-Pt thick-films as a function of the measurement temperature.

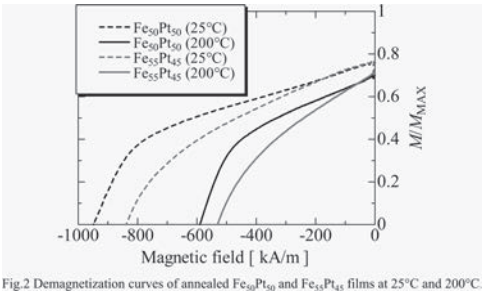


Fig.2 Demagnetization curves of annealed $Fe_{50}Pt_{50}$ and $Fe_{55}Pt_{45}$ films at 25°C and 200°C.

CW-12. Effect of chloride ion on crystal structures and magnetic properties of electroplated Fe-Pt film-magnets. *S. Furutani*[1], Y. Omagari[1], R. Hasama[1], A. Yamashita[1], T. Yanai[1], M. Nakano[1] and H. Fukunaga[1] *1. Nagasaki University, Nagasaki-shi, Japan*

$L1_0$ Fe-Pt films are attractive film-magnets for medical devices since they have good hard magnetic properties and high biological safety [1], and we reported some Fe-Pt thick-films (>10 μm) with a high coercivity (> 700 kA/m) prepared by an electroplating method [2]. In the recent study, we investigated the effect of NaCl concentration in plating baths on the coercivity of the films and pointed out that a possibility of enhancement in the coercivity by the Na ion [3]. When varying the NaCl concentration, not only the Na ion concentration but also the Cl ion one varies, suggesting that the Cl ion also has a possibility of coercivity enhancement. In the present study, we electroplated the Fe-Pt films from plating bath with various concentration of the Cl ion and evaluated structural and magnetic properties. We electroplated $Fe_{50}Pt_{50}$ film-magnets using a direct current on Cu plates. The plating bath consisted of $FeSO_4$(1-12 g/L), $Pt(NO_2)_2(NH_3)_2$(10 g/L), $H_6N_2O_3S$(25 g/L), and citric acid(30 g/L). To vary the Cl ion concentration without the change in the Na ion concentration, we used $FeCl_2$ and NH_4Cl. The films were annealed at 700°C for 5-60 min in a vacuum to order the Fe-Pt crystalline phase. Figure 1 shows the coercivity and Δ2θ of the annealed $Fe_{50}Pt_{50}$ films as a function of the Cl ion concentration. Since the diffraction peak of fcc (200) for the as-plated film is split into two peaks of fct (002) and (200) due to the development of the $L1_0$ ordering by the annealing, we can estimate the degree of the $L1_0$ ordering from the peak splitting Δ2θ. The Cl ion concentration was calculated from the amount of $FeCl_2$ or NH_4Cl in the bath. As shown in Fig. 1, the coercivity and the Δ2θ decreased with increasing the Cl ion concentration. This result implies that the Cl ion concentration affects the degree of the ordering and high Cl ion concentration of is not preferable to obtain high coercivity. Figure 2 shows the coercivity of the Fe-Pt films prepared from the Cl-ion-contained baths as a function of the amount of $NaSO_4$. The coercivity was increased by the addition of $NaSO_4$. From these results, we found that the $L1_0$ ordering is prevented by the Cl ion and enhanced by the Na one.

[1] H. Aoyama, Y. Honkura, *J. Magn. Soc. Jpn*, 20 (1996) 237. [2] T. Yanai, K. Furutani, T. Ohgai, M. Nakano, K. Suzuki, and H. Fukunaga, *J. Appl. Phys.*, 117 (2015) #17A744. [3] T. Yanai, J. Honda, R. Hamamura, H. Yamada, N. Fujita, K. Takashima, M. Nakano, and H. Fukunaga, J*, Alloys Compd.* 752, 133 (2018).

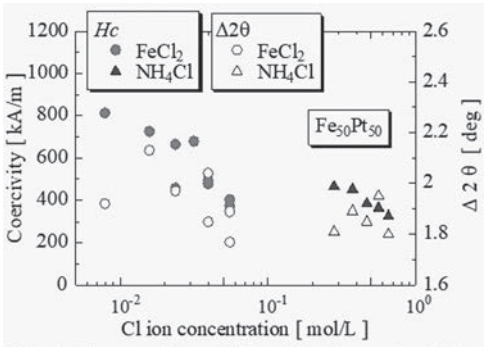


Fig. 1. The coercivity and the diffraction peak splitting between (002) and (200), $\Delta 2\theta$, for the annealed $Fe_{50}Pt_{50}$ films as a function of the Cl ion concentration.

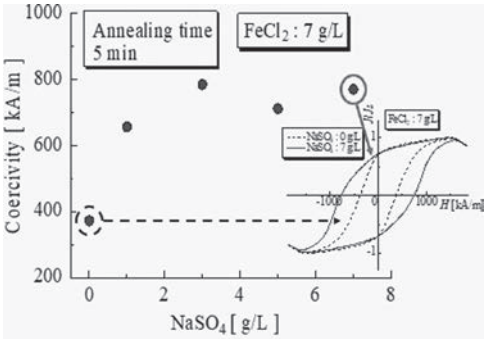


Fig. 2. The coercivity of the Fe-Pt films prepared from the Cl-ion-contained baths as a function of the amount of $NaSO_4$. The J-H loops for the baths with and without $NaSO_4$ are shown as an inset.

CW-13. Periodic Magnetic Domains in Singlecrystalline Cobalt Dendrites Fabricated by Electrodeposition. *F. Chen*[1], C. Li[1], R. Peng[1] and M. Wang[1] *1. Physics, Nanjing University, Nanjing, China*

The magnetic structure of a singlecrystalline nanostructures can be fundamentally influenced by the magnetocrystalline anisotropy, which is determined by the crystallographic orientation of the material. The competition of the magnetocrystalline anisotropy and the shape anisotropy enriches

the magnetic patterns of micro/nanostructures.[1] The traditional fabrication method to deposit singlecrystalline films such as molecular beam epitaxy is time-consuming and expensive. In this report, we demostrate an easy and cheap electrochemical method to deposit singlecrystalline dendrites in an ultrathin layer of electrolyte. Singlecrystalline cobalt dendrites are fabricated by electrodeposition on surface of any insulating or semi-conducting substrates. The size of the dendrites can be tuned by adjusting the magtitude of the applied voltage. Periodic magnetic domains and stripe domains are imaged by magnetic force microscopy in the dendrites. The periodicity of the magnetic domain is related to the size, the shape and the crystallographic orientation of the cobalt dendrites. We expect that this fabrication approach can be applied to construct singlecrystalline nanostructures with perpendicular magnetocrystalline anisotropy.

1. F. Chen, et al. Phys. Rev. B, Vol. 93, p.054405 (2016)

CW-14. Buffer layer dependence of magnetic properties and crystal structures for C38-type MnGaGe films. *M. Sun*[1,2], T. Kubota[1,3], K. Ito[1,3], S. Takahashi[4], Y. Sonobe[4] and K. Takanashi[1,3] *1. Institute for Materials Research, Tohoku University, Sendai, Japan; 2. Graduate School of Engineering, Tohoku University, Sendai, Japan; 3. Center for Spintronics Research Network, Tohoku University, Sendai, Japan; 4. Samsung R&D Institute Japan, Yokohama, Japan*

In the society of Internet of Things, the competition of memory development is becoming more and more serious. Among various memories, magnetoresistive random access memory (MRAM) attracts great attention for its non-volatile attribute and high-working-speed, recently. From the viewpoint of data retention for longer than 10 years, thermal stability factor Δ defined as $K_u V/k_B T$ must be larger than 60, where K_u, V, k_B, and T are uniaxial magnetic anisotropy energy, cell volume, Boltzmann constant and temperature, respectively. With the further integration of memory devices, K_u must be high enough to ensure the large Δ for the ferromagnetic layers in tunnel junctions of MRAM cells. According to the above reasons, our group has been working on C38-type MnGaGe films. In our previous study, the saturation magnetization of 260 emu/cm^3 and the K_u of 8.1 × 10^6 erg/cm^3 were found in a MnGaGe film deposited on MgO (100) substrate [1]. The M_s is comparatively small and the K_u is larger than that of CoFeB [2]. However, a problem is relatively large crystalline orientation dispersion which resulted in the poor squareness of magnetization curves. To improve the crystalline orientation of MnGaGe films, we have investigated the buffer layer dependence of magnetic properties and crystal structures for C38-type MnGaGe films. The stacking structure was as follows: MgO (100) substrate/buffer layer(s)/ MnGaGe (*t*)/MgO (2 nm)/Ta (5 nm). The layer thickness, *t* was varied from 5 nm to 100 nm. Different types of buffer layers such as Cr (60 nm), Cr (60 nm)/Pt (5 nm), Cr (20 nm)/Ru (40 nm) and Cr (60 nm)/ MgO (2 nm) were used. A 100-nm-thick MnGaGe sample using the Cr/MgO hybrid buffer layer exhibited the best squareness of 81% for the magnetization curve, and the full-width at half maximum of 002 peak for the rocking curve was reduced to 1.1°. In addition, perpendicular magnetization was observed down to the thickness of 5 nm for the MnGaGe sample using the Cr/MgO hybrid buffer layer. Samples using other buffer layers will also be discussed in this presentation. This work was partially supported by the Murata Science Foundation and Cooperative Research Project of CRDAM-IMR, Tohoku Univ. MS and TK thank Issei Narita for technical supports.

[1] M.-l. Sun, *et al., The 2019 Joint MMM-Intermag Conference,* DH-09 (2019). [2] S. Ikeda *et al., Nat. Mater.* Vol. 9, p. 721 (2010).

CW-15. Structure and Magnetic Properties for Fe-Mn-Ga-Sn Thin Films Prepared by Alternate Monoatomic Layer Deposition Method. *F. Nakagawa*[1], M. Doi[1] and T. Shima[1] *1. Graduate School of Engineering, Tohoku Gakuin University, Tagajo, Japan*

Since Nd-Fe-B sintered magnets possess high $(BH)_{max}$ of all permanent magnets, they have been used for variety of applications such as motors, sensors and actuators. However, hard magnetic properties are deteriorated with increasing temperature. Accordingly, substitution of heavy rare-earth (HRE) elements such as Dy and Tb for Nd is essential for increasing thermal stability. Recently, due to the scarce and localized natural resources of the HRE elements, HRE-free or less permanent magnet is strongly required. One of the candidate is Mn-based magnet. It is reported that the XA-type Fe_2MnGa alloy, which is formed when Fe is added to the MnGa alloy, has a high saturation magnetization (M_s) as high as 1300 emu/ cc, a high magnetocrystalline anisotropy, and a Curie temperature. Furthermore, it has been studied theoretically that XA-type crystal structure of Fe_2MnGa in which the ferromagnetic phase is stabilized by the partially substitution of Ga with Sn partially. In this study, in order to confirm the enhancement of the magnetic properties for FeMnGa thin films, alternate layer deposition method have used to prepare FeMnGa and FeMnGaSn thin films, and their structure and magnetic properties have been also investigated. The samples were deposited on a MgO (100) single crystal substrate using an ultrahigh vacuum sputtering (UHV) system. The total film thickness was fixed at 20 nm, and the number of stacking period n was fixed at 60 times. The Fe-Mn-Ga-Sn layer was deposited at 100 °C and them annealed at 400 °C. Cr layer of 10 nm was deposited to a thickness of 10 nm for the purpose of preventing oxidation. A X-ray diffractometer (XRD) and a superconducting quantum interference device (SQUID) were used to evaluate the crystal structure and the magnetic properties, respectively. The M_s was slightly increased with increasing Sn content (x), and the largest M_s of 830 emu/ cc was successfully obtained for $[FeMn/ FeGa_{1-x}Sn_x]_{60}$ (x = 0.8) thin films. It was confirmed that the addition of Sn into FeMnGa thin films led to increase M_s by 20 % as compared to the FeMnGa thin films. Effect of N_2 addition (0 to 5 %) on the crystal structures and magnetic properties for the FeMnGaSnN thin films will be discussed at the conference.

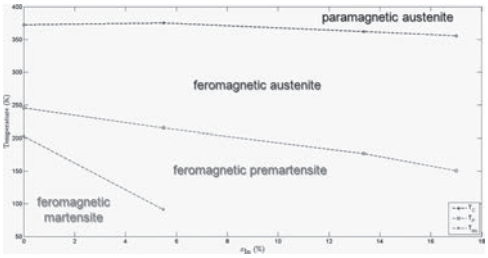
[1] H. Niida, T. Hori and Y. Nakagawa, J. Appl. Phys., 79, 5964 (1996) [2] Y. Takahashi, H. Makuta and M. Doi, T. Magn. Soc. Japan, 1, 30-33 (2017) [3] T. Gasi, A.K. Nayak and C. Felser, J. Appl. Phys., 113, 17E301 (2013)

CW-16. Compositional dependence of critical temperatures in $Ni_2MnGa_{1-x}In_x$ single crystals. *P. Cejpek*[1], P. Opletal[1], P. Dolezal[1], K. Vlaskova[1] and M. Dopita[1] *1. Department of Condensed Matter Physics, Charles University, Praha, Czechia*

Ni_2MnGa is a good model system of the shape memory alloy family. These materials are frequently studied because of their possible application as micropumps [1], sensors or actuators [2]. Shape memory effect is connected to the martensitic transformation and to the magnetically induced reorientation (MIR). Therefore, the study of these materials under various external conditions is the key to understand the martensitic transformation, which is still not fully described. Previous studies showed that critical temperatures of the Ni_2MnGa related compounds are strongly dependend on their composition. For example, Ni_2MnGa has the martensitic transformation around 200 K [3], but the alloy with the slightly different composition $Ni_{50}Mn_{28}Ga_{22}$ [4] has the martensitic transformation at 338 K. According to abovementioned facts we decided to study properties of Ni_2MnGa single crystals with respect to indium doping (galium is replaced). As the MIR occurs by twin boundary motion, a single crystal is the basic prerequisite for any significant effect as the presence of grain boundaries can block the motion of twin boundaries. The single crystals were prepared by Bridgman method in the induction furnace (growing speed 0.5 mm/h). The material $Ni_2MnGa_{1-x}In_x$ was previously studied in the form of polycrystals [5] but the results obtained on single crystals apparently differ as it is shown in this work. Electrical resistivity, magnetisation and specific heat measurements were performed to obtain the critical temperatures. All obtained critical temperatures (Curie temperatures, temperatures of martensitic and premartensitic transformation) decrease with the increasing indium content (shown in Figure 1). Contrary to the results previously published on polycrystals [5], the decreasing tendency is much faster – the polycrystalline samples exhibited martensitic transformation even in the sample with 15% of indium, but we did not observed any martensitic transformation on single crystals with the indium content above 10%.

[1] A.R. Smith et al., Microfluidics and Nanofluidics 18 (2015) 1255-1263, https://doi.org/10.1007/s10404-014-1524-6 [2] A. Hobza et al., Sensors and Actuators A 269 (2018) 137-144, https://doi.org/10.1016/j.sna.2017.11.002

[3] P. Cejpek et al., Journal of Alloys and Compounds 775 (2019) 533-541, https://doi.org/10.1016/j.jallcom.2018.10.113 [4] O. Heczko et al., Acta Materialia 115 (2016) 250-258, https://doi.org/10.1016/j.actamat.2016.05.047 [5] M. Khan et al., Journal of Physics: Condensed Matter 16 (2004) 5259–5266, https://doi.org/10.1088/0953-8984/16/29/017



The phase diagram obtained from the magnetisation data. T_C – Curie temperature, T_P – temperature of premartensitic transformation, T_{Ms} – temperature of martensitic transformation

CW-17. Electronic, magnetic, and structural properties of Fe_2MnSn Heusler alloy. B.R. Dahal[1], A. Maruf[1], S. Prophet[2], Y. Huh[1], *P.R. Kharel*[1] and P. Lukashev[2] *1. Department of Physics, South Dakota State University, Brookings, SD, United States; 2. Department of Physics, University of Northern Iowa, Cedar Falls, IA, United States*

Recently, Heusler alloys and compounds have attracted much attention because of their interesting properties with prospects for spintronics, energy technology and magnetocaloric applications. Most of the Heusler alloys are cubic in crystal structure but some non-cubic (tetragonal or hexagonal) alloys have shown high magnetic anisotropy with potential for various magnetic applications. We have performed a combined computational and experimental study of one such compound, Fe_2MnSn. Our density functional theory calculation indicates that this compound has two energetically close crystal phases: cubic $L2_1$ and hexagonal $D0_{19}$, with the latter having slightly lower energy (few meV per 16-atom cell). Electronic structure calculation indicates that both the cubic and hexagonal phases are ferromagnetic, with magnetization values of 6.50 μ_B/f.u. in the hexagonal phase, and 6.04 μ_B/f.u. in the cubic phase. The magnitude of spin polarization is relatively small in both cubic and hexagonal phases (~22% in hexagonal, and ~26% in cubic phases). These theoretically predicted structural and magnetic properties are consistent with our experimental investigation carried out on Fe_2MnSn alloy prepared by arc-melting and annealing. The room temperature x-ray diffraction pattern shows that the dominant phase in the alloy is hexagonal $D0_{19}$ (space group: $P6_3/mmc$) with a small amount of cubic impurity phase. The temperature dependence of magnetization *M(T)* measurement displays ferromagnetic behavior with Curie temperature of 338 K, Figure 1. As shown in the inset of Fig. 1, the field dependent magnetization *M(H)* at 100 K shows a high value of saturation magnetization of 122 emu/g. Strong ferromagnetic nature with potentially high magnetic anisotropy in the hexagonal phase, high Curie temperature and saturation magnetization indicates that the Fe_2MnSn has potential for magnetic applications. We will also present the effect of Mn concentration in the structural and magnetic properties of this material.

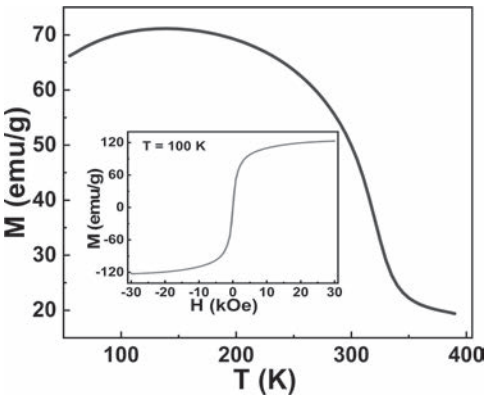


Figure 1: The temperature dependence of magnetization of Fe_2MnSn Heusler alloy. Inset: Field dependence of magnetization

Session DA
GIANT SPIN ORBIT TORQUES BEYOND SPIN HALL

Emilie Jué, Chair
National Institute of Standards and Technology, Boulder, CO, United States

INVITED PAPERS

1:30

DA-01. Interface-Generated Spin-Orbit Torques and Currents.
V. Amin[3,2], P. Haney[2] and *M.D. Stiles*[1] *1. Alternative Computing Group, National Institute of Standards and Technology, Gaithersburg, MD, United States; 2. Nanoscale Processes and Measurements Group, National Institute of Standards and Technology, Gaithersburg, MD, United States; 3. Maryland NanoCenter, University of Maryland, College Park, MD, United States*

Spin-orbit torques couple angular momentum from the lattice to the magnetization. The electrons' spin and orbital moments are intermediaries of this angular momentum flow, which is mediated by the crystal field potential, spin-orbit coupling and the exchange interaction. This variety of angular momentum sources and flows complicates the analysis of the resulting torques. The coupling between the magnetization and the spins always occurs through the local exchange interaction in the ferromagnet. However the coupling of the spins to the orbital moments (spin-orbit coupling) can not only occur there but also in the adjacent non-magnetic layer, at the interface between them, or in an additional ferromagnetic layer or its interface. In these latter cases, transport of spins determines the resulting torques in the ferromagnet. The reduced symmetry of the thin films means that torques that result from all of these sources of angular momentum have the same symmetry, making different mechanisms quite difficult to distinguish experimentally. Never-the-less, it is useful to isolate and identify the specific mechanisms of underlying spin-orbit torques because the resulting models can suggest ways to try to optimize the torque. Interfaces are crucially important in spin-orbit torque systems: they provide inversion symmetry breaking; they convert spin currents into torques; and their reduced symmetry gives rise to Rashba-like spin-orbit coupling localized there. Semiclassical models that describe bulk-like transport in the interior of layers coupled with spin-dependent transmission and reflection at interfaces provide a way to discuss various mechanisms that can give rise to torques. Such models also describe how spin currents are converted into torques at the interface, as well as how interfaces generate spin currents which that are converted into torques in an adjacent or remote ferromagnetic layer. One goal of spin-orbit torque research is to identify mechanisms to generate torques that can deterministically switch a ferromagnetic layer with a perpendicular easy axis. A bilayer of materials that can be each treated as isotropic forbids such torques by symmetry. However, if a second ferromagnetic layer is added, its (fixed) magnetization can break the symmetry of the system and allow such torques. These symmetry breaking torques can be driven by spin currents from the bulk of this second ferromagnetic layer or can be generated by its interface with the nonmagnetic spacer layer.

V. P. Amin, Junwen Li, M. D. Stiles, and P. M. Haney (accepted for publication in Phys. Rev. B). V. P. Amin, J. Zemen, and M. D. Stiles, Phys. Rev. Lett. 121, 136805 (2018). V. P. Amin and M. D. Stiles, Phys. Rev. B 94, 104420 (2016). V. P. Amin and M. D. Stiles, Phys. Rev. B 94, 104419 (2016).

2:06

DA-02. Spin-Orbit Torque Driven by Planar Hall Current.
E.A. Montoya[1], C. Safranski[1] and I. Krivorotov[1] *1. Department of Physics and Astronomy, University of California, Irvine, Irvine, CA, United States*

Spin-orbit torques in bilayers of ferromagnetic (FM) and nonmagnetic (NM) materials create potential for energy efficient spintronic devices. Previously studied spin Hall [1] and Rashba [2] torques originate from spin-orbit interactions within the NM layer and at the FM/NM bilayer interface, respectively. In this talk, we report on the discovery of a spin orbit toque arising from planar Hall current in the FM material of the bilayer [3]. This spin orbit torque driven by planar Hall current, or planar Hall torque (PHT) for brevity, exhibits biaxial symmetry in the plane defined by the bilayer normal and the applied electric field (xz plane in Fig. 1) and can act as positive or negative damping. The unusual symmetry of PHT can be deduced from the angular dependence of the planar Hall current [4] in the FM layer and is distinctly different from the uniaxial symmetry of the spin Hall torque (SHT) as illustrated in Fig. 1. We fabricate 40-50 nm wide nanowires from Al_20_3(0001)/Ta(3.0 nm)/NM/FM/Ta(4.0 nm), where FM = [Co(0.85 nm)/Ni(1.28 Nm)]$_2$/Co(0.85 nm) and NM=Au, Pd, or Pt. We characterize spin orbit torques by means of field-modulated spin torque ferromagnetic resonance (ST-FMR) measurements. The antidamping component of the SOTs is deduced from the dependence of the ferromagnetic resonance linewidth ΔH on direct current density J_{dc} applied to the nanowire. The slope of the line $\Delta H(J_{dc})$ quantifies the strength and sign of the anti-damping SOT. Fig. 2 shows angular dependence of the slope of $\Delta H(J_{dc})$ for three different NM materials. This figure shows that the magnitude of SHT depends on the NM material while the magnitude of the PHT is nearly the same for all three NM materials, lending further support to the planar Hall effect in the FM layer being the origin of the novel SOT. Fig. 2 demonstrates that the magnitude of PHT is similar to that of the giant SHT of Pt and that strong PHT can be present in a system with negligibly small SHT (e.g. FM/Au). Finally, we demonstrate that the planar Hall torque is large enough to excite auto-oscillations of the FM layer magnetization, allowing one to create a planar Hall nano-oscillator [4,5]. Furthermore, the magnetization angle that maximizes PHT also maximizes the dynamic change in resistance due to anisotropic magnetoresistance (AMR). This is in contrast to the spin Hall nano-oscillator where the anti-damping action of SHT is maximized at magnetization angles where dynamic response of AMR is minimized. Therefore, we show the efficiency of the PHT nano-oscillator exceeds that of the SHT nano-oscillator. The discovery of the planar Hall torque [3] expands the class of materials for energy efficient manipulation of magnetization by giant SOTs.

[1] L. Liu, C.-F. Pai, Y. Li, et. al., Science, Vol. 336, p.555 (2012) [2] I. M. Miron, K. Garello, G. Gaudin, et. al., Nature, Vol. 476, p.189 (2011) [3] C. Safranski, E. A. Montoya, and I. N. Krivorotov, Nature Nanotechnology, Vol. 14, p.27 (2019) [4] T. Taniguchi, J. Grollier, and M. D. Stiles, Physical Review Applied, Vol. 3, p.044001 (2015) [5] A. Slavin and V. Tiberkevich, IEEE Transactions on Magnetics, Vol. 45, p.1875 (2009) [6] S. I. Kiselev, J. C. Sankey, I. N. Krivorotov, et. al., Nature, Vol. 425, p.380 (2003)

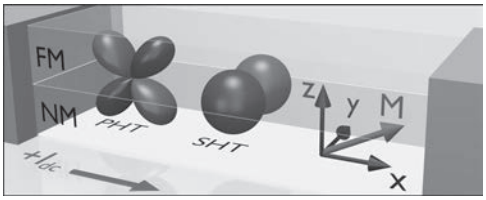


Figure 1 - Schematic illustrating the angular dependence of damping-like SOT in NM/FM bilayers (red corresponds to negative damping while blue corresponds to positive damping for $I_{dc} > 0$).

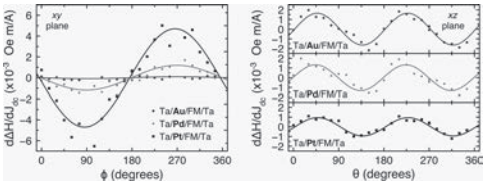


Figure 2 - Angular dependence of SOTs in FM/NM bilayers for NM = Au, Pd, and Pt: (a) SHT in the xy plane; (b) PHT in the xz plane.

2:42

DA-03. Iron Garnet Films for Spintronics. *C. Ross*[1], G. Beach[1], E.R. Rosenberg[1], J. Bauer[1], T. Fakhrul[1], C. Avci[1], L.M. Caretta[1] and B. Khurana[1] *1. Massachusetts Institute of Technology, Cambridge, MA, United States*

Ferromagnetic insulator thin films have emerged as an important component of magnonic, spintronic and magnetooptical devices. Yttrium iron garnet in particular is an excellent insulator with low damping, and has been incorporated into heterostructures that exhibit a plethora of spintronic and magnonic phenomena including spin pumping, spin Seebeck, proximity effects and spin wave propagation. Rare earth (RE) garnet films are both magnetic and magnetoelastic, and their properties can be manipulated by choice of composition and substrate. We demonstrate robust perpendicular anisotropy (PMA) in epitaxial films of bismuth, thulium, europium, dysprosium and terbium iron garnets with high structural quality down to a thickness of 2.5 nm, about 2 unit cells, resulting from lattice mismatch strain. PMA was also induced by thermal mismatch stress in polycrystalline films of EuIG grown on quartz or DyIG on silicon, with grain size exceeding 10 μm diameter. Substitution on the Fe sites is also effective in tuning properties, with Sc raising the magnetization and lattice parameter and lowering Curie temperature in Tb(Fe,Sc) garnet. RE garnet/Pt bilayers exhibit efficient spin transmission across the garnet/Pt interface, with a spin mixing conductance that is similar for different RE garnets and for polycrystalline and single crystal films. RE garnet films exhibit a Dzyaloshinskii-Moriya interaction originating at the garnet/substrate interface which stabilizes skyrmions and chiral magnetic textures. Spin orbit torque from a Pt overlayer drives domain wall motion at room temperature at velocities exceeding 2 km/s in TmIG and 4 km/s in Bi-substituted YIG. Iron garnets also exhibit magnetooptical activity and high transparency in the infrared, and we demonstrated integrated optical isolators with isolation ratios of up to 40 dB comprising Bi and Ce garnets. These results illustrate the potential of garnets to provide a path towards devices with combined spintronic and optical functionality. Support of the nCORE SMART Center, NSF and DARPA is gratefully acknowledged.

Nature Nanotech. 14 561 (2019), Optica 6 473 (2019), ACS Photonics 5, 5010 (2018), Phys. Rev. Mater. 2, 094405 (2018), Nature Materials 16, 309–314 (2017), Adv. Electron. Mater. 3 1600376 (2017), Phys. Rev. B 95 115428 (2017)

3:18

DA-04. Spin-Orbit Torques in Metal-Based Heterostructures. *K. Ando*[1] *1. Keio University, Yokohama, Japan*

The fundamental building block of spin-orbitronics is the generation of spin-orbit torques, which enable electric manipulation of magnetization. The source of the spin-orbit torques is spin-orbit interaction in solids. When a charge current passes through a heavy metal with strong spin-orbit coupling, electrons with opposite spins are deflected in opposite directions, resulting in the generation of a transverse spin current, which is known as the spin Hall effect. Another source of the charge-to-spin conversion is the Rashba-Edelstein effect, where a charge flow in a Rashba two-dimensional electron gas results in the creation of a non-zero spin accumulation. The generated spin current and spin accumulation give rise to the spin-orbit torques. Here, we discuss recent experimental results on the generation of the spin-orbit torques in metal-based heterostructures [1-3]. We show that oxidation of the most widely used spintronic material, Pt, turns the heavy metal into an electrically insulating generator of the spin-orbit torques, which enables the electrical switching of perpendicular magnetization in a ferrimagnet sandwiched by insulating oxides [2]. The spin-orbit torques generated by the Pt oxide can be controlled electrically through voltage-driven oxygen migration. We also show that the intrinsic mechanism originating from the Berry curvature is responsible for the generation of the spin-orbit torque through the spin-orbit coupling at ferromagnetic-metal/metal-oxide interface [3].

[1] H. An, Y. Kageyama, Y. Kanno, N. Enishi, and K. Ando, Nature Communications 7, 13069 (2016). [2] H. An, T. Ohno, Y. Kanno, Y. Kageyama, Y. Monnai, H. Maki, J. Shi, and K. Ando, Science Advances 4, eaar2250 (2018). [3] T. Gao, A. Qaiumzadeh, H. An, A. Musha, Y. Kageyama, J. Shi, and K. Ando, Physical Review Letters 121, 017202 (2018).

3:54

DA-05. Spin-orbit-torques from low-symmetry materials. *D. Ralph*[1], G. Stiehl[1], D. MacNeill[1], V. Gupta[1], J. Mittelstaedt[1], S. Karimeddiny[1], M. Guimaraes[1], N. Reynolds[1], N. Sivadas[1], I. El Baggari[1], L. Kourkoutis[1], C. Fennie[1] and R. Buhrman[1] *1. Cornell University, Ithaca, NY, United States*

In most experiments performed to date, spin-orbit torques have an important limitation -- the component of torque that can compensate magnetic damping is required by symmetry to lie within the device plane and perpendicular to the applied current, i.e. the spin current has a Rashba-type symmetry. This means that spin-orbit torques can drive the most current-efficient type of magnetic reversal (antidamping switching) only for magnetic devices with in-plane anisotropy, not the devices with perpendicular magnetic anisotropy that are needed for high-density applications. In principle, the types of symmetry-breaking within a spin-source material that are necessary for generating other components of spin-orbit torque can be produced in at least two ways: by using materials that have low crystalline symmetry or an appropriate type of magnetic order. Here I will focus on experimental results from the Cornell group using materials with low crystalline symmetries. We have investigated torques generated within bilayers in which a ferromagnetic layer is integrated with different low-symmetry transition-metal dichalcogenide (TMD) semi-metals and metals: WTe_2, $TaTe_2$, $MoTe_2$, and strained $NbSe_2$. The low crystalline symmetries of the TMDs can indeed allow an out-of-plane antidamping torque of the type desired to drive the most efficient switching mode for magnets with perpendicular anisotropy. In WTe_2 and $MoTe_2$, this component has a surprising dependence on the number of TMD layers, being much weaker for 2-layer samples than for either single-layer or thicker samples. This dependence is not yet understood. We have also observed current-induced torques with an unusual Dresselhaus symmetry. This contribution appears to arise primarily from resistance anisotropy rather than a direct spin-orbit torque. The different TMD materials can generate current-induced torques with a surprising range of contrasting properties even though the underlying crystal symmetries are

similar, indicating that the torques depend not only on global broken symmetries but also on microscopic factors. The same fabrication techniques that allow us to incorporate air-sensitive TMD materials into spin-orbit devices also allow devices made using recently-discovered 2-dimensional magnetic materials. We have combined mechanically-exfoliated thin flakes of the insulating 2D ferromagnet $Cr_2Ge_2Te_6$ into bilayers with the spin-orbit metal Ta. These samples exhibit spin-orbit induced switching of the out-of-plane magnetic moment of $Cr_2Ge_2Te_6$ at record-low levels of current density. I will present initial results to understand the magnetoresistance of these samples and to characterize the strength of the spin-orbit torque. Support from DOE, SRC/DARPA, and NSF.

D. MacNeill et al., *Nature Physics* 13, 300 (2017). D. MacNeill et al., *Phys. Rev. B* 96, 054450 (2017). M. H. D. Guimarães et al., *Nano Lett.*18, 1311 (2018). G. M. Stiehl et al., *ACS Nano* 13, 2599 (2019). G. M. Stiehl et al., arXiv:1906.01068.

Session DB
SPIN TRANSPORT AND MAGNETISM IN 2D MATERIALS

Nadya Mason, Chair
University of Illinois at Urbana-Champaign, Urbana, IL, United States

INVITED PAPER

1:30

DB-01. Tunable spin-to-charge conversion in van der Waals heterostructures at room temperature. *W.F. Savero Torres*[1], L.A. Benítez[1,2], J.F. Sierra[1], M. Timmermans[1], J.H. Garcia[1], S. Roche[1,3], M. Costache[1] and S.O. Valenzuela[1,3] *1. Catalan Institute of Nanoscience and Nanotechnology (ICN2), CSIC and the Barcelona Institute of Science and Technology (BIST), Barcelona, Spain; 2. Universitat Autonòma de Barcelona, Barcelona, Spain; 3. Institució Catalana de Recerca i Estudis Avancats (ICREA), Barcelona, Spain*

Spin Hall and spin galvanic effects provide a versatile tool for spin-current generation without ferromagnets [1,2]. They have been widely studied during the last years, giving rise to the emergent field of spin-orbitronics and providing new routes for developing spintronic devices [1,3]. However, despite the diversity of existing bulk materials and the recent advent of interfacial and low-dimensional effects, room temperature electric-field control of the interconversion between charge and spin currents remains elusive [1,2]. In this talk, we will show that strong and controllable spin-to-charge (StC) conversion can be obtained in engineered graphene-based heterostructures at room temperature. By using spin precession experiments, we will first demonstrate that large spin Hall signals in graphene/Pt heterostructures enable full characterisation of both spin transport in graphene and StC conversion in Pt [4]. We will then show that StC conversion driven by the spin galvanic and the spin Hall effects can be unambiguously detected in Hall bar devices made of graphene interfaced with a semiconducting transition metal dichalcogenide [5]. Our findings clearly indicate that StC conversion arises from proximity-induced spin-orbit coupling in graphene. Remarkably, the corresponding conversion efficiencies in this heterostructure can be tailored by electrostatic gating in magnitude and sign, with a magnitude that is comparable to the largest efficiencies reported to date. Such unprecedented electric-field tunability provides a novel route for spin generation free from magnetic materials and a new building block for the development of ultra-compact magnetic memory technologies. We acknowlegde the support from the European Union's Horizon 2020 research and innovation programme Graphene Flagship CORE 2, under grant agreement No. 785219, by the European Research Council under Grant Agreement No. 306652 SPINBOUND, by the Spanish Ministry of Economy and Competitiveness, MINECO (under Contracts FIS2015- 62641-ERC, MAT2016-75952-R, and SEV-2017-0706 Severo Ochoa), and by the CERCA Programme and the Secretariat for Universities and Research, Knowledge Department of the Generalitat de Catalunya 2017 SGR 827.

[1] J. Sinova, S.O. Valenzuela, J. Wunderlinch, C. H. Back, Rev. Mod. Phys. 87, 1213 (2015) [2] A. Manchon, H.C. Koo, J. Nitta, S.M. Frolov & R.A. Duine. Nature Mater. 14, 871-882 (2015) [3] S. Manipatruni *et al*. Nature. 565, 35-42 (2019) [3] W. Savero Torres *et al.* 2D. Mater. 4 041008 (2017) [4] L. A. Benítez, W. Savero Torres *et al*. Unpublished.

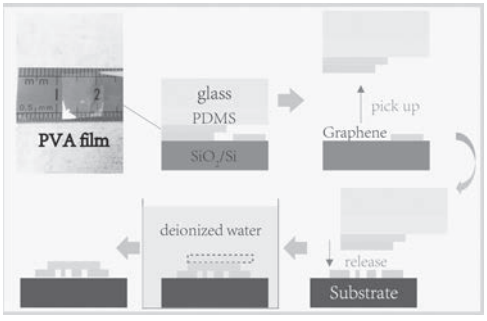
CONTRIBUTED PAPERS

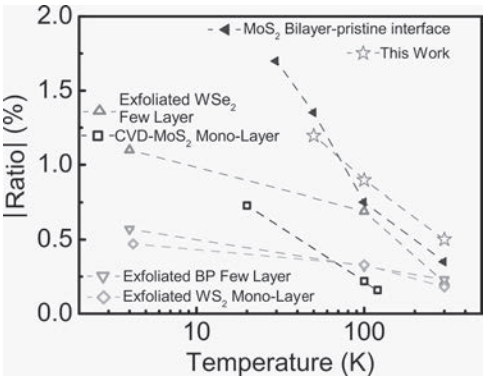
2:06

DB-02. Universal Transfer and Stacking Technique of van der Waals Heterojunctions for Spintronics. *Y. Cao*[1], X. Wang[1], X. Lin[1] and W. Zhao[1] *1. Beihang University, Beijing, China*

Integrating layered two-dimensional (2D) materials into 3D heterostructures offers opportunities for novel material functionalities and applications in electronics[1] and spintronics[2]. The resulting 2D material transfer and high-quality heterostructures construction techniques are crucial to preserve cleanliness and morphology of 2D material surfaces[3] which come in contact with transfer mediator and flexible stacking control of various 2D materials. In this work, we introduce a free standing poly vinyl alcohol (PVA) film to meet the above requirements. The pre-fabricated PVA film enables ultraclean, accurate and selective 2D materials' interface and contact engineering, including a partial transfer with one micron resolution, flexible stacking of both angle and position, and even transfer of 2D materials with pre-deposited metal films. Such a universal and convenient technique is suitable for 2D materials no matter mechanically exfoliated or chemical vapor deposited (CVD) growth. We further illustrate the practical superiority of this method by a WSe2 vertical spin valve device, whose performance verifies the applicability and advantage of such a method for spintronics. Our PVA-assisted transfer process would certainly promote the development of fundamental research and wafer-scale device application of 2D nanostructures.

[1] Cao. Y, Fatemi. V and Fang. S; Nature, Vol. 556, p.43–50.(2018) [2] Wang. Z,Gutiérrez-Lezama. I and Ubrig. N, Nat. Commun., Vol. 9, p.2516,(2018) [3] Wood. J.D, Doidge. G.P and Carrion. E.A, Nanotechnology, Vol. 26, p.055302, (2015)



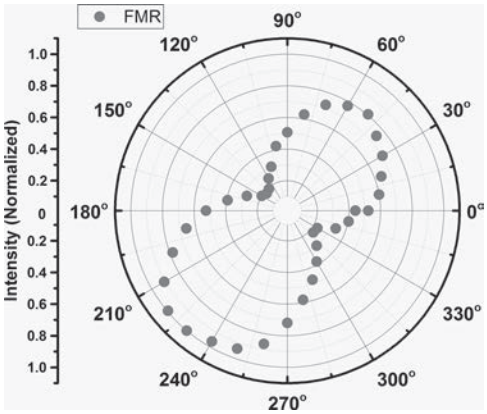


2:18

DB-03. Observation of Ferromagnetic Resonance in Quasi-2D Ferromagnet CrI_3 using Magneto-Raman Spectroscopy. *R. Valdes Aguilar*[1], A. McCreary[2], T. Mai[1,2], J.R. Simpson[3,2], F.G. Utermohlen[1], N. Trivedi[1] and A.R. Hight Walker[2] *1. Physics, The Ohio State University, Columbus, OH, United States; 2. NIST, Gaithersburg, MD, United States; 3. Towson University, Baltimore, MD, United States*

There is a growing interest in the discovery and understanding of the fundamental physics of magnetic materials in two dimensions (2D) [1-3]. In particular, efforts continue on one of the original 2D ferromagnets, CrI_3, in order to understand whether the interlayer interactions are ferro- or antiferromagnetic [4-10]. The interplay of these magnetic interactions and excitations, structural distortions [4], and their response in a magnetic field is important for a fundamental understanding that can drive potential applications [1,2,11]. To this end, we study in detail the structural and magnetic excitations of CrI_3 in single crystalline thin flakes using inelastic light scattering in a magnetic field, i.e. magneto-Raman spectroscopy. We find that for fields above 6 T we observe the scattering from the zone center magnon, the ferromagnetic resonance, with a linear dependence on the magnetic field in this range. This behavior is well explained by the classical Kittel formula [12] that predicts a value of the zero-field resonance at approximately 45 GHz with an effective g-factor of 2. We also find that as a function of the scattered polarization angle with respect to the incoming polarization, the intensity has a two-fold symmetric pattern without nodes (i.e. the signal does not vanish) as shown in the figure. This indicates that some of the components of the Raman response tensor are complex, which is typically only expected for resonant scattering [13]. We will discuss the possible reasons for this behavior and compare it to that expected for the lattice excitations.

[1] M. Gibertini, et al. "Magnetic 2D materials and heterostructures". Nat. Nanotechnology, 14 408 (2019). [2] K.S. Burch, et al. "Magnetism in two-dimensional van der Waals materials". Nature 563 47 (2018). [3] M.A. McGuire. "Crystal and Magnetic Structures in Layered, Transition Metal Dihalides and Trihalides". Crystals 7 121 (2017). [4] M.A. McGuire, et al. "Coupling of Crystal Structure and Magnetism in the Layered, Ferromagnetic Insulator CrI3". Chem. Mater. 27 612 (2015). [5] B. Huang, et al. "Layer-dependent ferromagnetism in a van der Waals crystal down to the monolayer limit". Nature, 546 270 (2017). [6] J.L. Lado and J. Fernandez-Rossier. "On the origin of magnetic anisotropy in two dimensional CrI3". 2D Materials, 4 035002 (2017). [7] D.R. Klein, et al. "Probing magnetism in 2D van der Waals crystalline insulators via electron tunneling". Science 360 1218 (2018). [8] N. Sivadas, et al. "Stacking-dependent magnetism in bilayer CrI3". Nano Lett. 18 7658 (2018). [9] P. Jiang, et al. "Stacking tunable interlayer magnetism in bilayer CrI3". Phys. Rev. B 99 144401 (2019). [10] S.W. Jang, et al. "Microscopic understanding of magnetic interactions in bilayer CrI3". Phys. Rev. Materials 3 031001 (2019). [11] T. Song, et al. "Giant tunneling magnetoresistance in spin-filter van der Waals heterostructures". Science 360 1214 (2018). [12] C. Kittel. "On the Theory of Ferromagnetic Resonance Absorption". Phys. Rev. 73 155 (1948). [13] H.B. Ribeiro, et al. "Unusual Angular Dependence of the Raman Response in Black Phosphorous". ACS Nano 9 4270 (2015).



2:30

DB-04. Efficient magnetization switching and Dzyaloshinskii-Moriya interaction in WTe_2/ferromagnet heterostructures. *S. Shi*[1,2*], Z. Zhu[1], K. Cai[1], S.D. Pollard[1], J. Wang[3,2], P. He[1], G. Eda[3,2], G. Liang[1] and H. Yang[1,2] *1. Electrical and computer engineering, National University of Singapore, Singapore; 2. Centre for advanced 2D materials, National University of Singapore, Singapore; 3. Department of physics, National University of Singapore, Singapore*

Weyl semimetal WTe_2 has been discovered to have strong spin-orbit coupling and a large spin polarization protected by time-reversal symmetry in both the surface and bulk states [1,2]. However, magnetization switching using the above interesting properties has not been demonstrated so far. Utilizing WTe_2 as a spin current source, here we report current-induced magnetization switching without assistive magnetic fields in WTe_2/Py heterostructures at room temperature. An extremely small charge current density of ~1.58×10^5 A cm^{-2} as shown in Fig. 1 and the thickness-dependent charge-to-spin conversion efficiency in Fig. 2 with the current along the b-axis in the WTe_2 layer are found. Furthermore, a strong Dzyaloshinskii-Moriya interaction (DMI) with a DMI constant up to –1.8 mJ m^{-2} is identified at the WTe_2/Py interface from the chiral domain wall tilting. The demonstration of efficient current-driven magnetization switching and sizable interfacial DMI in WTe_2/ferromagnet heterostructures open a new avenue for the Weyl semimetal based spintronic device applications.

[1] J. Jiang, F. Tang, X. Pan, *et al.*, Phys. Rev. Lett., 115, 166601 (2015). [2] B. Feng, Y. Chan, Y. Feng, *et al.*, Phys. Rev. B, 94, 195134 (2016).

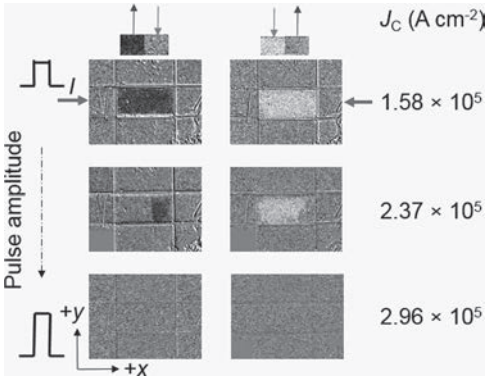


Fig 1. Switching process captured by MOKE images. The left-hand side of the MOKE images show the magnetization is switched from the +*y* to –*y* direction by current pulses in the +*x* direction.

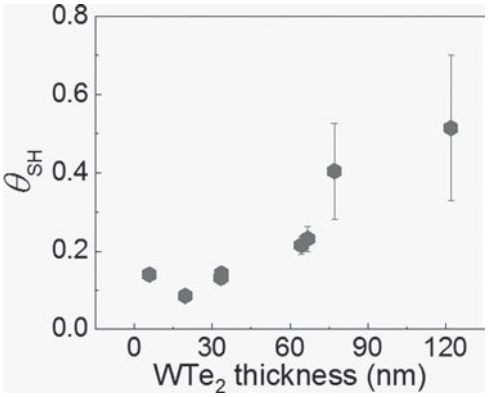


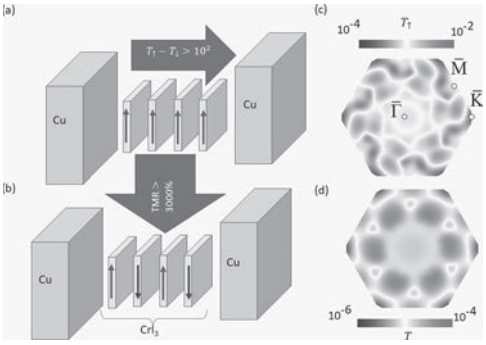
Fig 2. Thickness dependent charge-to-spin conversion efficiency of WTe_2 from ST-FMR averaged between 6 and 7 GHz.

2:42

DB-05. Spin Filtering in CrI_3 Tunnel Junctions. *T.R. Paudel*[1] and E.Y. Tsymbal[1] *1. Department of Physics and Astronomy & Nebraska Center for Materials and Nanoscience, University of Nebraska-Lincoln, Lincoln, NE, United States*

The recently discovered magnetism of two-dimensional (2D) van der Waals crystals has attracted a lot of attention. Among these materials is CrI_3 – a magnetic semiconductor exhibiting transitions between antiferromagnetic and ferromagnetic orderings under the influence of an applied magnetic field. Here, using first-principles methods based on density functional theory, we explore spin-dependent transport in tunnel junctions formed of fcc Cu (111) electrodes and a CrI_3 tunnel barrier. We find about 100% spin polarization of the tunneling current for a ferromagnetically-ordered four-monolayer CrI_3 and tunneling magnetoresistance of about 3,000% associated with a change of magnetic ordering[1]. This behavior is understood in terms of the spin and wave-vector dependent evanescent states in CrI_3 which control the tunneling conductance. We find a sizable charge transfer from Cu to CrI_3 which adds new features to the mechanism of spin-filtering in CrI_3-based tunnel junctions. Our results elucidate the mechanisms of spin filtering in CrI_3 tunnel junctions and provide important insights for the design of magnetoresistive devices based on 2D magnetic crystals and possibly of using conventional metallic electrode for enhanced performance, thereby broadening design space of such devices beyond 2D Van der Walls heterostructures.

1. Paudel, T. R. & Tsymbal, E. Y. *ACS Appl. Mater. Interfaces* 11, 15781–15787 (2019).



Tunneling transmission in Cu/CrI_3/Cu tunnel junctions. Schematics of the tunnel structure with FM (a) and AFM (b) CrI_3 barrier layers sandwiched between Cu electrodes and corresponding k||-resolved transmission across the 2D Brillouin zone (c) and (d)

2:54

DB-06. Band gaps and 3d-band splittings on the electronic structures in 2D magnetic materials: Application of Quasiparticle Self-Consistent GW method. *Y. Lee*[1], T. Kotani[2] and L. Ke[1] *1. Ames Laboratory, Ames, IA, United States; 2. Department of Applied Mathematics and Physics, Tottori University, Tottori, Japan*

Using (Quasiparticle Self-Consistent GW) QSGW method, we investigate the electronic structures in magnetic 2D van der Waals (m2dvdW) materials, including $CrGeTe_3$, VI_3, CrI_3, and Fe_3GeTe_2 ---four of the most studied m2dvdW systems to date. QSGW yields non-local potential missing in density functional theory (DFT). The non-local potential contains both off-site and inter-site parts. The off-site non-locality is crucial to better describe the band gap for semiconductors while the DFT+*U* like on-site non-locality enhances the band separation within an atom. In comparison with DFT, QSGW enhances the band gaps in $CrGeTe_3$ and VI_3 due to the off-site and on-site non-local potentials, respectively. Mainly because of the occupied 3d is pushed down relative to anion bands, QSGW predicts an entirely different picture for the transport properties in CrI_3 and VI_3. Furthermore, we found that defects such as vacancy and impurity introduce localized states in the bandgap, which may explain the discrepancy between QSGW bandgap and experiments. The effects of spin-orbit coupling on band structures are also discussed. Finally, we discuss the limitation of usual DFT+*U* method from the view of its ability to mimic QSGW.

3:06

DB-07. Effect of Random Anisotropy on Magnetic Long Range Order of Two-Dimensional Magnets. *P. Tang*[1,2], X. Han[2] and S. Zhang[1] *1. Physics, The University of Arizona, Tucson, AZ, United States; 2. Institute of Physics, Chinese Academy of Sciences, Beijing, China*

Recent experimental discovery of new classes of two-dimensional magnets demands a revisit of mechanisms of ferromagnetism of 2D materials. Two essential factors limit the long range order of ferromagnetism with short-range exchange interactions. The number of Goldstone magnons excited at any nonvanishing temperature would diverge for isotropic exchange Hamiltonian in two-dimension systems [1] and thus an anisotropy gap is needed to suppress the thermal fluctuation. The random field, which exists for any film with imperfection, is another source of destabilizing the long range order via formation of the domain structure [2]. Furthermore, the random field also reduces the effective anisotropy and thus it always suppresses the Curie temperature. We consider the influence of the random anisotropy rather than the random field on the magnetic ordering. We argue that the model of the random anisotropy is more appealing than the random field since the magnetic anisotropy is due to spin-orbit coupling at the 2D surface and the symmetric breaking occurs in the direction perpendicular to the film. By using the Green's function approach, we find a quantitative relation between the Curie temperature and the random anisotropy, and we show there are distinct differences when compared with the results of the random field.

[1] N. D. Mermin and H. Wagner, Phys. Rev. Lett. 17, 1307 (1966)
[2] Yoseph Imry and Shang-keng Ma, Phys. Rev. Lett. 35, 1399 (1975)

3:18

DB-08. Giant enhancements of perpendicular magnetic anisotropy and spin-orbit torque by a MoS_2 layer. *Q. Xie*[1], W. Lin[1], B. Yang[2], X. Shu[1], S. Chen[1], L. Liu[1], X. Yu[1], M. Breese[1], T. Zhou[5], M. Yang[3], Z. Zhang[3], S. Wang[3], H. Yang[4], J. Chai[3], X. Han[2] and J. Chen[1] *1. National University of Singapore, Singapore; 2. Chinese Academy of Sciences, Beijing, China; 3. Agency for Science, Technology and Research, Singapore; 4. Chinese Academy of Sciences, Ningbo, China; 5. Hangzhou Dianzi University, Hanzhou, China*

The unique properties of two-dimensional transition metal dichalcogenides (2D TMCDs) including a well-defined single atomic layer thickness, inversion symmetry breaking and strong spin-orbit coupling have motivated 2D TMCDs-based research to seek their potential applications in spintronic devices.[1-3] At the same time, magnetic tunnel junction (MTJ) with ferromagnets possessing a perpendicular magnetic anisotropy (PMA) is attracting increasing attention because it is a promising candidate for achieving next-generation high-density non-volatile memory devices with low-energy-consumption.[4,5] To improve the area density of spintronic devices, a large PMA of the storage layer is required to overcome the thermal fluctuation of the magnetic moment in spintronic application.[6] Many efforts have been made to enhance PMA of the ferromagnetic layer. For example, Chshiev. M et al. reported that the PMA at the Fe/MgO interface can be effectively tuned by electric field.[7] Recently, spin-orbit torque (SOT) has been proposed to switch the magnetization of the free layer in MTJs at lower power consumption and faster speed.[8-10] The SOT is generated from the heavy metal, like Pt[8] and Ta[10] or Rashba effect due to the broken structure symmetry. In order to maintain the thermal stability of the cell at the reduced size and reduce the switching current density, it is desirable to enhance the PMA and SOT efficiency simultaneously in the structure of MTJs. In this work, we investigated the effects of 2D MoS_2 as the underlayer on the magnetic properties and SOT efficiency of Pt/$[Co/Ni]_2$. We found that the PMA and SOT efficiency are significantly enhanced after inserting the MoS_2 underlayer, which reaches a maximum at the structure with a 2 nm Pt. The maximum enhancements of PMA and SOT efficiency are around 3 and 17 times higher than those without MoS_2 underlayer, respectively. First principles calculation and XAS reveal that the MoS_2 underlayer results in the modification of the orbital hybridization at Pt/Co interface, which is responsible for the enhancement of both PMA and SOT efficiency.

[1] W. Feng, Y. Yao, D. Xiao, *Phys. Rev. B* 86, 165108(2012). [2] X. Xu, D. Xiao, T. F. Heinz, *Nat. Phys*.10, 343(2014). [3] A. Manchon, S. M. Frolov, R. A. Duine, *Nat. Mater.*14, 871(2015). [4] D. Sander, S. O. Valenzuela, A. Berger, *J. Phys. D.* 50, 363001(2017). [5] S. Ikeda, K. Miura, H. Ohno, *Nat. Mater.* 9, 721(2010). [6] S. Ikeda, J. Hayakawa, H. Ohno, *IEEE Trans. Electron Devices* 54, 991(2007). [7] F. Ibrahim, H. X. Yang, M. Chshiev, *Phys. Rev. B* 93, 014429(2016). [8] L. Liu, O. J. Lee, R. A. Buhrman, *Phys. Rev. Lett.*109, 096602(2012). [9] I. M. Miron, K. Garello, P. Gambardella, *Nature* 476, 189(2011). [10] L. Liu, C.-F. Pai, R. A. Buhrman, *Science* 336, 555(2012).

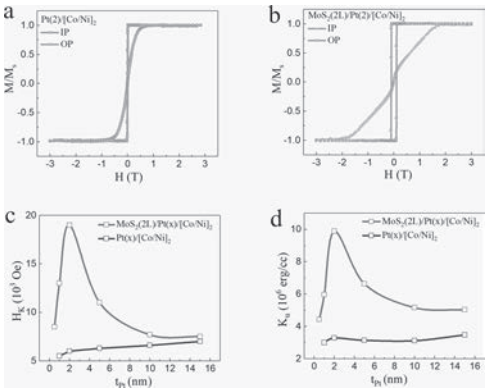


Fig. 1 Enhancement of perpendicular magnetic anisotropy of [Co/Ni] by MoS_2

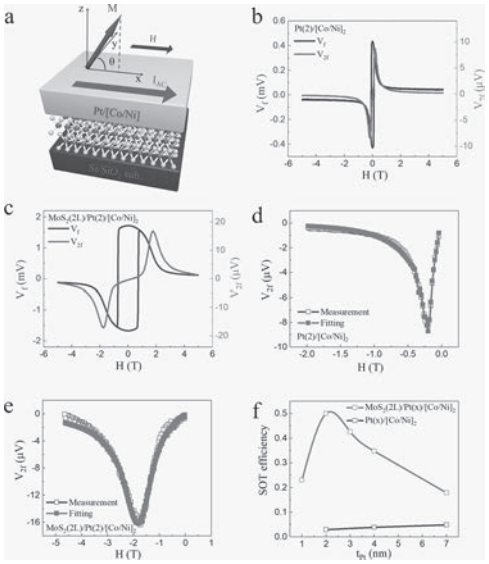


Fig. 2 Estimation of SOT efficiency enhanced by MoS_2

3:30

DB-09. Surface spin-flop transition in CrI_3 probed by Pt. *T. Su*[1,2], M. Lohmann[2], J. Li[2], M. Al ghamdi[2], K. Watanabe[3], T. Taniguchi[3] and J. Shi[2] *1. International Center for Quantum Materials, Peking University, Beijing, China; 2. Physics and Astronomy, University of California, Riverside, Riverside, CA, United States; 3. National Institute for Materials Science, Tsukuba, Japan*

Two-dimensional (2D) magnetic materials have attracted enormous research attention in recent years. As an important member of this family, CrI_3 has been observed to exhibit a soft ferromagnetic behavior in bulk crystals and antiferromagnetic interlayer coupling in ultra-thin flakes. However, how magnetic properties of the surface layers differ from those of the bulk layers is not clear. Because CrI_3 is insulating, in this work, we perform transport measurements in a conducting material such as Pt that is in proximity with CrI3. Due to the short-range nature of the proximity coupling, the acquired magneto-transport properties in the conducting materials reflect the magnetic properties of the surface layer of CrI3. We fabricate the devices by putting exfoliated CrI_3 flake on top of a pre-patterned thin channel of Pt on a bottom flake of BN, followed by covering the heterostructure with a top BN layer to avoid degradation. We observe an unambiguous jump at ~ 2 T in the magnetoresistance of Pt which is confirmed to come from the presence of the CrI_3. We have fabricated similar devices by replacing Pt with few-layer graphene but did not observe the magnetoresistance jump. We have further

explored the current density dependence of the magnetoresistance jump and found that it only appears at large current densities. Since simple spin-flips would not cause any magnetoresistance jump, our results suggest a surface spin-flop transition in CrI3. We will discuss the role of the spin-orbit torque and spin-orbit coupling in the surface spin flop transition.

3:42

DB-10. Structural, electrical and magnetotransport properties of layered $FeGe_2$ thin films. *J. Herfort*[1], S. Gaucher[1], D. Czubak[1], B. Jenichen[1] and M. Ramsteiner[1] *1. Paul-Drude-Institute for Solid State Electronics, Berlin, Germany*

The solid-phase epitaxy of Ge thin films over Heusler alloy surfaces was investigated recently as a solution to create lattice-matched ferromagnet-semiconductor heterostructures for vertical spin valves.[1] A persistent challenge in this field is the growth of epitaxial semiconductors over metals by MBE, a limiting factor for a number of envisaged applications in the field of spintronics. In order to solve this issue, amorphous Ge was deposited on ferromagnetic quasi-Heusler compound Fe_3Si and crystallized slowly by annealing. Instead of pure Ge, the resulting single-crystalline films were shown to consist of a new 2D polymorph of $FeGe_2$ with space group P4mm. TEM studies reveal a layered structure with monolayer Fe planes sandwiched between tetragonal Ge bilayers.[2] The material does not exist in a bulk form, its creation being interpreted as an ordering phenomenon induced by minimization of the elastic energy of the epitaxial film.[2] It is possible to isolate the material on an insulating GaAs substrate by first growing a few monolayers of crystalline Fe_3Si, and then an amorphous Ge fim with a thickness ratio such as to obtain the right stoichiometry for $FeGe_2$. Electrical measurements conducted on $FeGe_2$ films indicate a thickness dependence of their resistivity. Magnetotransport at low temperature reveal a strong anomalous Hall effect. In addition, we investigated vertical spin valve structures based on this novel 2D material as an intermediate layer between the two Heusler alloy films Fe_3Si (bottom) and Co_2FeSi (top). At room temperature, these spin valves exhibit a magnetoresistance effect of around 0.3%. A decrease of the operating temperature leads to a reduced magnetoresistance effect due to a phase change in the $FeGe_2$ layer from a non-magnetic into the ferromagnetic state. At cryogenic temperatures, the magnetoresistance value depends in a complex manner on the sample orientation relative to the external in-plane magnetic field. Two spin valve-like signals appear with opposite signs for orthogonal orientations. The analysis of the observed anisotropic behavior allows for the extraction of information on the spin transport behavior of the $FeGe_2$ film sandwiched between two ferromagnetic Heusler alloy films.

[1] S. Gaucher *et al*., Appl. Phys. Lett. 110, 102103 (2017). [2] B. Jenichen *et al*., Phys. Rev. Mat. 2, 051402 (2018).

3:54

DB-11. Current-driven magnetization switching in a van der Waals ferromagnet Fe_3GeTe_2. X. Wang[1], J. Tang[1], X. Xia[2], Y. Liu[1], Z. Han[2], G. Zhang[1], *G. Yu*[1] and X. Han[1] *1. Beijing National Laboratory for Condensed Matter Physics, Institute of Physics, Chinese Academy of Sciences, Beijing 100190, China, Beijing, China; 2. Shenyang National Laboratory for Materials Science, Institute of Metal Research, Chinese Academy of Sciences, Shenyang, China, Shenyang, China*

The recent discovery of ferromagnetism in two-dimensional (2D) van der Waals (vdW) materials holds promises for novel spintronic devices with exceptional performances. However, in order to utilize 2D vdW magnets for building spintronic nanodevices such as magnetic memories, key challenges remain in terms of effectively switching the magnetization from one state to the other electrically. Here, we devise a bilayer structure of Fe_3GeTe_2/Pt, in which the magnetization of few-layered Fe_3GeTe_2 can be effectively switched by the spin-orbit torques (SOTs) originated from the current flowing in the Pt layer. The effective magnetic fields corresponding to the SOTs are further quantitatively characterized using harmonic measurements. Our demonstration of the SOT-driven magnetization switching in a 2D vdW magnet could pave the way for implementing low-dimensional materials in the next-generation spintronic applications.

[1] X. Wang, J. Tang, X. Xia, C. He, J. Zhang, Y. Liu, C. Wan, C. Fang, C. Guo, W. Yang, Y. Guang, X. Zhang, H. Xu, J. Wei, M. Liao, X. Lu, J. Feng, X. Li, Y. Peng, H. Wei, R.Yang, D. Shi, X. Zhang, Z. Han, Z. Zhang, G. Zhang, G. Q. Yu* and X. Han "Current-driven magnetization switching in a van der Waals ferromagnet Fe_3GeTe_2"(In press)

4:06

DB-12. Pressure-Dependent Reduction of Magnetic Ordering in $Fe_{3-x}GeTe_2$. *D.J. O'Hara*[1,2], Z.E. Brubaker[1], R. Stillwell[1], E. O'Bannon[3], A. Baker[1], D. Weber[4], C. Park[5], J.E. Goldberger[4], R. Kawakami[6], J.R. Jeffries[3] and S.K. McCall[1] *1. Materials Science Division, Lawrence Livermore National Laboratory, Livermore, CA, United States; 2. Materials science and engineering, University of California, Riverside, Riverside, CA, United States; 3. Physics Division, Lawrence Livermore National Laboratory, Livermore, CA, United States; 4. Chemistry and Biochemistry, The Ohio State University, Columbus, OH, United States; 5. X-ray science division, Argonne National Laboratory, Argonne, IL, United States; 6. Physics Department, The Ohio State University, Columbus, OH, United States*

Among the recently discovered two-dimensional (2D) van der Waals magnets, Fe_3GeTe_2 is of particular interest due to its high Curie temperature, T_c, strong perpendicular magnetic anisotropy, and tunable magnetic properties depending on the concentration of Fe and its thickness. In this work, the magnetic, electronic, and structural properties of van der Waals-layered, Fe-deficient $Fe_{3-x}GeTe_2$ were systematically investigated by application of high pressure. Electrical and magneto-transport measurements show a ~70 K decrease in the T_c with an increasing pressure up to ~14 GPa. The resistivity of $Fe_{3-x}GeTe_2$ shows a change from a metallic ($d\rho/dT > 0$) to a less metallic ($d\rho/dT < 0$) phase at ~8 GPa, while the magnetoresistance (MR) is negative with an increase in magnitude (below T_c) with pressure. High-pressure x-ray diffraction (HP-XRD) shows no phase change in the hexagonal crystal structure for pressures up to ~29 GPa but a clear shift in the lattice spacing. The decrease in the T_c is due to the lattice shrinkage from pressurization which leads to a weakening of the exchange interaction, while the increase in MR may be related to shrinkage of the van der Waals gap leading to a stronger interlayer coupling. These results indicate that the application of pressure can complement other external stimuli such as chemical doping and strain when manipulating the material properties of van der Waals magnets which are of high interest for next-generation spintronic technologies. Prepared by LLNL under contract DE-AC52-07NA27344.

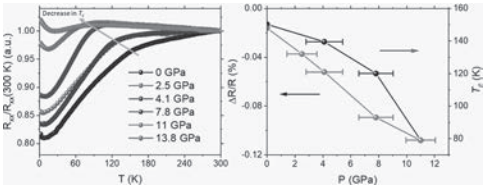


Figure 1. Temperature-dependent resistance (left), MR and Curie temperature (right) $Fe_{3-x}GeTe_2$ as a function of pressure showing decrease in T_c and increase in MR at higher pressures.

4:18

DB-13. Quasi-2D Magnon Identification by Magneto-Raman Spectroscopy in Antiferromagnetic $FePS_3$. *J.R. Simpson*[2,1], A. McCreary[1], T. Mai[1], R. Valdes Aguilar[3] and A.R. Hight Walker[1]
1. National Institute of Standards & Technology, Gaithersburg, MD, United States; 2. Physics, Towson University, Towson, MD, United States; 3. Physics, The Ohio State University, Columbus, OH, United States

The recent discovery that van der Waals-bonded magnets retain long range magnetic ordering down to a single layer opens avenues in fundamental physics and potential applications of these novel materials.[1,2] One such material is $FePS_3$, a high spin (S=2), Mott insulator where the Fe atoms form a honeycomb lattice.[3] In bulk, $FePS_3$ has been shown to be a quasi-two-dimensional, Ising antiferromagnet,[4] with emergent features in the Raman spectra below the Néel temperature, $T_N \approx 120$ K. Using magne-to-Raman spectroscopy as an optical probe of magnetic structure, we report the temperature and magnetic field dependence of a Raman-active magnon in the magnetically ordered state with a low-temperature frequency of 3.6 THz (121 cm^{-1}). Contrary to previous work that interpreted this feature as a phonon[5], our Raman data shows the expected frequency shifting and splitting of the magnon as a function of temperature and magnetic field, respectively. In addition, we measure the symmetry behavior of the magnon using polarization-dependent Raman spectroscopy and explain the result using the magnetic point group of $FePS_3$.

[1] C. Gong *et al.*, *Nature* 546, 265 (2017). [2] B. Huang *et al.*, *Nature* 546, 270 (2017). [3] P. A. Joy and S. Vasudevan, *Phys Rev. B* 46, 5425 (1992). [4] K. C. Rule, G. J McIntyre, S. J. Kennedy, and T. J. Hicks, *Phys. Rev. B* 76 (2007). [5] J. U. Lee *et al.*, *Nano Letters* 16, 7433 (2016).

Session DC
SKYRMIONS IN NEW MATERIALS
Myoung-Woo Yoo, Chair
Paris-Sud University, Palaiseau, France

INVITED PAPER

1:30

DC-01. New materials and devices in skyrmionics: Skyrmion-based artificial synapse and skyrmion lattice in van der Waals magnets.
S. Woo[1] *1. IBM TJ Watson Research Center, Yorktown Heights, NY, United States*

The field of skyrmionics has been actively investigated across a wide range of topics during the last decade, mainly inspired by the fascinating physical properties of magnetic skyrmions. [1] In this talk, we present our recent experimental achievements on the new material platform and device scheme where magnetic skyrmions can be stabilized and harnessed to realize non-conventional energy efficient future spintronics applications. In the first part of the talk, using ferrimagnetic multilayers, we demonstrate a fully functional skyrmion-based electronic device, where skyrmions are written, driven, read and erased electrically on a single device at room temperature. [2] In particular, we demonstrate a skyrmion-based artificial synaptic device designed for neuromorphic computing and thus artificial neural network (ANN), which could be used in broader technology fields in the future. Figure 1 summarizes the experimental demonstration of such skyrmion-based synaptic devices. Figure 1a illustrates the schematic of a skyrmion-based artificial synapse and its working principle, where skyrmions play the role of neurotransmitters in biological systems. In a skyrmion synapse, the synaptic weights are proportional to the number of skyrmions in synapse. Therefore, the electric current-controlled accumulation and dissipation of skyrmions within an active synaptic device area can imitate the linear variations of synaptic weights during potentiation and depression, respectively. Figure 1b demonstrates the experimentally measured electrical operation of a skyrmion synapse, where the corresponding magnetic configuration of each resistance state is also imaged by scanning transmission X-ray microscopy (STXM) as shown in Fig. 1c. In this talk, we further present an skyrmion synapse-based ANN and the pattern recognition simulation. [2] In the second part of the talk, we present a new novel material platform, van der Waals (vdW) ferromagnetic crystals, where magnetic skyrmions and their lattice structure can be stabilized. Very recently, it has been reported that 2D vdW crystals can also have long-range intrinsic ferromagnetism in few materials with strong magnetic anisotropy [3, 4]. This discovery of 2D magnets opened a whole new door toward 2D heterostructure-based spintronics, as a result, there appeared significant following interests and efforts revealing the possibility of such devices by demonstrating the magnetoresistance effect in 2D magnets [5], gate-tunable 2D magnets [6] and so on. Due to the broken inversion symmetry and expected large spin-orbit coupling of vdW magnets, vdW magnets might permit the presence of Dzyaloshinskii-Moriya (DM) interaction that could stabilize magnetic skyrmions. In this talk, we present such demonstration of magnetic skyrmions and their crystal formation in ferromagnetic vdW crystals, Fe_3GeTe_2 [7]. Figure 2 summarizes the experimental observations. Figure 2a first illustrates the schematic of crystalline structure of Fe_3GeTe_2 vdW crystal. Figure 2b then shows an observed exemplary STXM image taken at T=100 K and B_z=0 mT, showing the ordered skyrmion lattice (SkX) structure. In this talk, we describe the current-induced generation of skyrmion lattice in detail, as shown in Fig. 2b., as well as the underlying physical mechanism behind the formation of skyrmion lattice in vdW crystals. [7]

[1] A. Fert *et al. Nat. Rev. Mater.* 2, 17031 (2017). [2] K.M. Song *et al. submitted* (2019) [3] Gong, C. *et al. Nature* 546, 265–269 (2017). [4] Huang, B. *et al. Nature* 546, 270–273 (2017). [5] Song, T. *et al. Science* 360, 1214–1218 (2018). [6] Deng, Y. *et al. Nature* 563, 94 (2018). [7] T.-E. Park *et al. submitted* (2019)

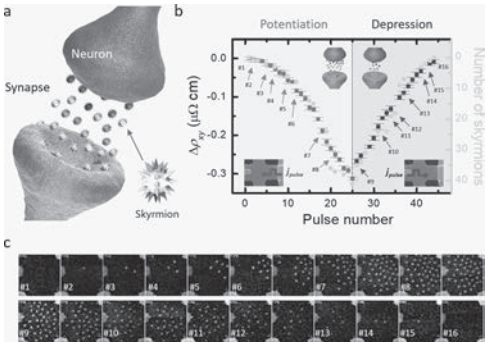


Figure 1. (a) Schematic drawing of skyrmion-based artificial synapse and its working principle. (b) The measured Hall resistivity change and calculated skyrmion number as a function of injected pulse number. (c) Sequential STXM images showing skyrmion populations after injecting unipolar current pulses along the track, with polarities as indicated in (b).

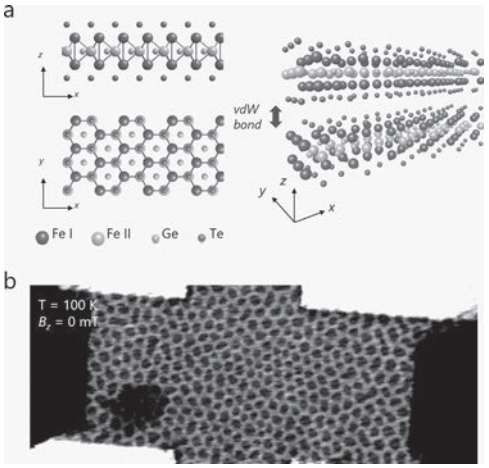


Figure 2. (a) Schematic drawing of the crystalline structure of Fe_3GeTe_2. (b) Observation of magnetic skyrmion crystal in Fe_3GeTe_2 using STXM at 100 K in the absence of magnetic field.

CONTRIBUTED PAPERS

2:06

DC-02. Topological Hall Effects and Topological Spin Hall Effects Caused by a Skyrmion and a Skyrmionium. *Y. Ishida*[1] and K. Kondo[1]
1. Research Institute for Electronic Science, Hokkaido Univ., Sapporo, Japan

Magnetic skyrmions are topological solitons which behave like particles and have been paid much attention in the field of spintronics. Since their structures are topologically protected, it is difficult to destroy their structures and deform them to other magnetic structures. Therefore, it is considered that skyrmions can carry one bit of information and are expected to become candidates for high-density memories in the spintronics fields. In order to apply skyrmions to the spintronics devices, it is mandatory to read information by detecting the existence of skyrmions. This can be resolved using the topological Hall effect (THE). THE originates from the fact that skyrmions create an emergent magnetic field affecting itinerant electrons in ferromagnets. Moreover, this field also causes the topological spin Hall effect (TSHE). This is because the emergent fields are opposite to each other for itinerant electrons with different spins. In our study, we investigate THE and TSHE for Néel-type and Bloch-type skyrmions using the tight binding model, respectively. The Hamiltonian consists of the nearest neighbor hopping and the exchange coupling between spins of itinerant electrons and magnetization of a ferromagnet. For simplicity, we set the hopping parameter t and the strength of exchange coupling J_H equal to one. Figure 1 and Figure 2 show joint density of states (DOS) and topological (spin) Hall angles θ_{TH} (θ_{TSH}) for different fermi energy ε_f in the case of a Néel-type skyrmion, respectively. In the case of a Bloch-type skyrmion, we have obtained almost identical results. As shown in Fig. 2, manifestation of THE and TSHE strongly depends on the fermi energy of itinerant electrons. This result implies that the fermi energy is an important factor to apply skyrmions to spintronics devices. Moreover, we have obtained joint DOS and (spin) Hall angles in the case of a skyrmionium and found that they are totally different from those of skyrmions. At the conference, we are going to discuss both the results of the skyrmions and the skyrmioniums in detail.

[1] Y. Ishida and K. Kondo, 2018 International Conference on Solid State Devices and Materials, (Tokyo, Japan), 2018 [2] N. Nagaosa and Y. Tokura, Nat. Nanotechnol., Vol. 8, p.899 (2013) [3] A. Fert, V. Cros, and J. Sampaio, Nat. Nanotechnol., Vol. 8, p.152 (2013) [4] P. B. Ndiaye, C. A. Akosa, and A. Manchon, Phys. Rev. B, Vol. 95, p.064426 (2017) [5] G. Yin, Y. Liu, Y. Barlas, *et al*., Phys. Rev. B, Vol. 92, p.024411 (2015)

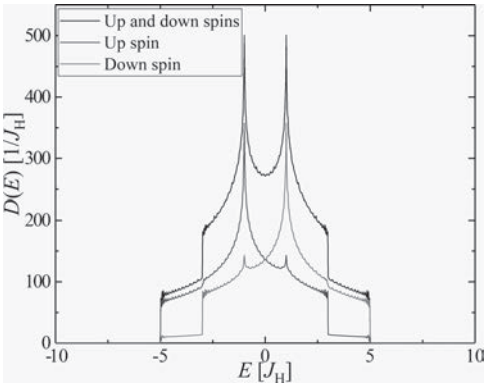


Fig. 1. Joint DOS of a system in the case of a Néel-type skyrmion.

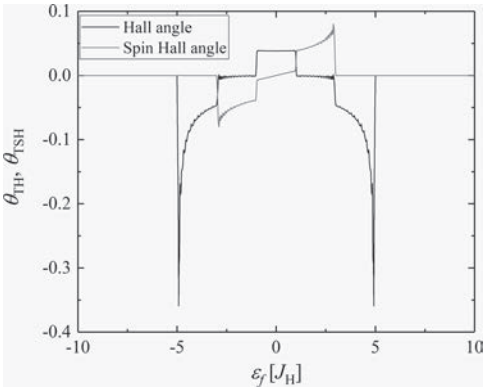


Fig. 2. Topological (spin) Hall angles θ_{TH} (θ_{TSH}) of a system in the case of a Néel-type skyrmion.

2:18

DC-03. Spin-Hall Topological Hall Effect in Highly Tunable Pt/Ferrimagnetic-Insulator Bilayers. A.S. Ahmed[1], *A.J. Lee*[1], N. Bagués[2], B. McCullian[1], A. Thabt[1], A. Perrine[2], P. Wu[1], J.R. Rowland[1], M. Randeria[1], P.C. Hammel[1], D.W. McComb[2,3] and F. Yang[1] *1. Physics, The Ohio State University, Columbus, OH, United States; 2. Center for Electron Microscopy and Analysis, The Ohio State University, Columbus, OH, United States; 3. Materials Science and Engineering, The Ohio State University, Columbus, OH, United States*

Electrical detection of topological magnetic textures, such as skyrmions, is currently limited to conducting materials. While magnetic insulators offer key advantages for skyrmion technologies with high speed and low loss, they have not yet been explored electrically. Here, we report a prominent topological Hall effect in $Pt/Tm_3Fe_5O_{12}$ (TmIG) bilayers below, at, and above room temperature. Fig. 1 shows Hall resistivity and topological Hall resistivity versus out-of-plane magnetic field (H) where a prominent peak in the data indicates a strong topological Hall signal for a 1.85 nm thick TmIG film. Secondly, our pristine TmIG epitaxial films down to 1.25 unit cell thickness allow for tuning of topological Hall stability over a broad range of temperatures (T) from 200 to 465 K through atomic-scale thickness control. Fig. 2 shows *H-T* phase diagrams for several TmIG thicknesses with the color scale representing the magnitude of topological Hall resistivity. These regions of skyrmion stability scale with TmIG thickness, and consequently, the thickness dependent Curie temperature of the films. The electrical detection of topological magnetic textures in Pt is made possible by a novel phenomenon: "spin-Hall topological Hall effect" (SH-THE), where the interfacial spin-orbit torques allow spin-Hall-effect generated spins in Pt to experience the unique topology of the underlying skyrmions in TmIG. This novel electrical detection phenomenon paves a new path for utilizing a large family of magnetic insulators in future skyrmion technologies.

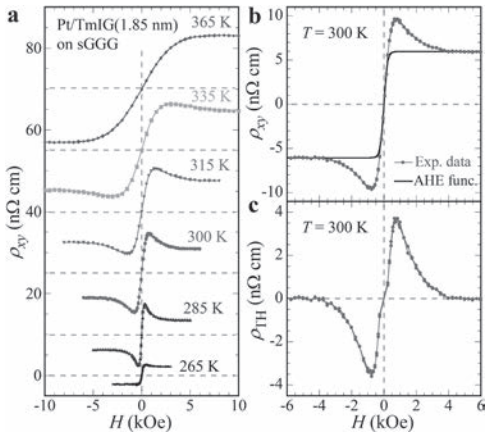


Fig. 1. a) Hall resistivity vs. applied magnetic field at various temperatures for a Pt(2 nm)/TmIG(1.85 nm)/sGGG(111) film. b) Room temperature Hall resistivity where the magnetization is approximated as a tanh(H/H_0) function to represent the AHE contribution, where H_0 is a fitting parameter. c) Room temperature topological Hall resistivity.

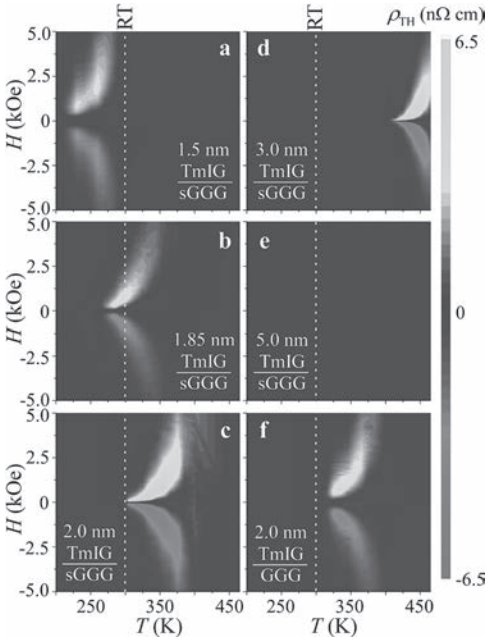


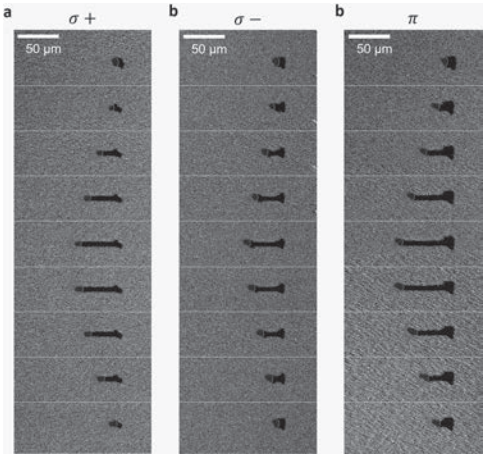
Fig. 2. Hall resistivity phase diagrams for Pt(3 nm)/TmIG(t)/sGGG(111) with a) t = 1.5 nm, b) t = 1.85 nm, c) t = 2 nm, d) t = 3 nm, and e) t = 5 nm. As the TmIG thicknesses increases, the temperature window of shifts towards higher temperatures. F) H-T phase diagram for Pt(3 nm)/TmIG(2 nm)/GGG(111) where the TmIG film has in-plane anisotropy.

2:30

DC-04. All Optical Motion of Chiral Domain Walls and Skyrmion Bubbles. *L.M. Caretta*[1], F. Buettner[1], F. Steinbach[2], D. Suzuki[1], B. Pfau[2], C. von Korff Schmising[2], S. Eisebitt[2] and G. Beach[1] *1. MIT, Cambridge, MA, United States; 2. Max-Born-Institut, Berlin, Germany*

Manipulation of magnetism with femtosecond laser excitations began with the observation of ultrafast demagnetization in ferromagnets[1,2] and was soon followed by the discovery of all optical switching (AOS) in GdFeCo[3]. Today, the mechanism of AOS is well understood, enabling low-power, sub-picosecond manipulation of magnetism for spintronics[4]. Deterministic, single shot AOS is limited to rare-earth transition metal ferrimagnets, whereas in transitional metal (TM) ferromagnets, helicity dependent, multi-shot switching occurs through a thermal demagnetization and re-magnetisation process resulting from helicity-dependent propagation of domain walls (DWs)[5]. This gave rise to the study of helicity-dependent optical DW motion in TM ferromagnets and ferromagnetic semiconductors. Simultaneously, it was discovered that the Dzyaloshinskii-Moriya Interaction (DMI) can be present in non-centrosymmetric materials systems, giving rise to new chiral forms of spin textures, such as skyrmions and homochiral Neel DWs[6,7]. Moreover, the same DMI that gives rise to AOS in ferrimagnetic systems also gives rise to ultra-small and ultrafast current-driven spin textures[8], making ferrimagnets the one of the most promising technologies for beyond-CMOS data storage and computing. However, the role of the chirality in all optical domain wall motion (AO-DWM) has been nearly neglected. Here, we systematically study the role of DMI in AO-DWM of ferrimagnetic GdCo. We achieve deterministic, single shot thermally-driven motion of chiral Neel DWs in Co-rich Pt/GdCo/Ta trilayers exhibiting significant DMI. We find that that the DW motion does not depend on light helicity, but rather on the orientation of the DW (Neel versus Bloch), revealing the role of the DMI in AO-DWM for the first time. Micromagnetic simulations, in combination with atomistic simulations, support this observation, indicating that coherent AO-DWM in GdCo necessitates Neel DWs. Moreover, we demonstrate that this same principle can be applied to drive to skyrmion bubbles all-optically for the first time.

1 Beaurepaire, E. *et al. Phys. Rev. Lett.* 76, 4250–4253 (1996) 2 Koopmans, B. *et al. Nat. Mater.* 9, 259–265 (2010) 3 Radu, I. *et al. Nature* 472, 205–208 (2011) 4 Vahaplar, K. *et al. Phys. Rev. Lett.* 103, 117201 (2009) 5 El Hadri, M. S. *et al. Phys. Rev. B* 94, 064412 (2016) 6 Emori, S. *et al. Nat. Mater.* 12, 611–616 (2013) 7 Woo, S. *et al. Nat. Mater.* 15, 501–506 (2016) 8 Caretta, L. *et al. Nat. Nanotechnol.* 13, 1154–1160 (2018)



Sequential MOKE images AO-DWM in Pt(6 nm)/GdCo(6 nm)/Ta(4 nm) for a) right b) left and c) linearly polarized light. Red circle indicates laser position.

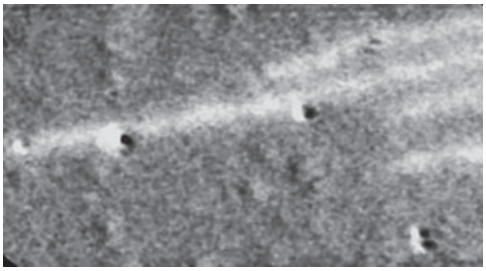
2:42

DC-05. Temperature dependent skyrmion Hall angle in ferrimagnets. *M. Vogel*[1], X. Wang[2], P.N. Lapa[3], J. Pearson[1], R. Divan[4], X. Cheng[2], A. Hoffmann[1] and S.G. te Velthuis[1] *1. Materials Science Division, Argonne National Laboratory, Lemont, IL, United States; 2. Department of Physics, Bryn Mawr College, Bryn Mawr, PA, United States; 3. Physics Department, University of California, San Diego, CA, United States; 4. Center for Nanoscale Materials, Argonne National Laboratory, Lemont, IL, United States*

Analogous to the Hall effect where electronic charges moving in the presence of a magnetic field acquire a transverse velocity, magnetic solitons with non-zero topological charges (i.e. skyrmions and chiral domains walls) exhibit the skyrmion Hall effect [1], which opens up new possibilities for manipulating the trajectories of these quasiparticles. The skyrmion Hall

effect has been theoretically predicted to vanish for antiferromagnetic skyrmions because of the cancelation of opposite topological charges [2] and experimentally demonstrated to vanish in ferrimagnets at the compensation temperature [3]. We present a study of current driven domain wall dynamics in artificially ferrimagnetic multilayers: Ta(4 nm)/Pt (5 nm)/[Co (0.5 nm)/Gd (1 nm)/Pt(1 nm)]$_{10}$/Al (2 nm). The magnetic texture in different layers of the multilayer films are coherent and antiferromagnetically aligned. Here we experimentally investigate the temperature dependence of the current driven magnetization dynamics from room temperature down to temperatures below the compensation point at around 100 K and show a dependency of the skyrmion Hall angle and domain wall speeds on the applied temperature. *Work at Argonne was supported by the US-DOE, Office of Science, MSED. Use of the Center for Nanoscale Materials, an Office of Science user facilities, was supported by the US-DOE, Office of Science, BES, under contract no. DE-AC02-06CH11357.* Work at Bryn Mawr College is supported by NSF (DMR #1708790).

[1] W. Jiang, X. Zhang, G. Yu et. al., *Nature Physics*,13(2), 162–169 (2017) [2] J. Barker & O. Tretiakov, *Phys. Rev. Lett.* 116, 147203 (2016). [3] Y. Hirata, D.-H Kim, S. Kim et al., *Nature Nanotechnology*, *14*(3), 232–236 (2019).



Current driven elongation of magnetic bubble domains in Co/Gd/Pt multilayers at 280 K

2:54

DC-06. Persistence of chiral domain walls in synthetic ferrimagnetic skyrmions through spin reorientation transition in [Co/Gd/Pt]$_{10}$ multilayers. *X. Wang*[1], A.T. Clark[1], P.N. Lapa[2], R.V. Chopdekar[3], Z. Xiao[3,4], C.M. Quispe Flores[5], A. Fiagbenu[1], M. Vogel[2], J. Pearson[2], K. Buchanan[5], S.G. te Velthuis[2], A. Hoffmann[2] and X. Cheng[1] *1. Department of Physics, Bryn Mawr College, Bryn Mawr, PA, United States; 2. Materials Science Division, Argonne National Laboratory, Lemont, IL, United States; 3. Advanced Light Source, Lawrence Berkeley National Laboratory, Berkeley, CA, United States; 4. Electrical and Computer Enginnering, Univeristy of California, Los Angeles, Los Angeles, CA, United States; 5. Department of Physics, Colorado State University, Fort Collins, CO, United States*

Antiferromagnetic skyrmions, compared to their counterpart ferromagnetic skyrmions, have richer physics and offer technological advantages for spintronic device applications, because of their insensitivity to stray fields, compensation of skyrmion Hall effects and expected high mobility [1-3]. Here we report the realization of zero-field synthetic ferrimagnetic skyrmions at room temperature in [Co/Gd/Pt]$_{10}$ multilayers and the investigation on the stability of the chiral domain walls of such synthetic ferrimagnetic skyrmions between 33 K and 300 K. Synthetic ferrimagnetic skyrmions, in which Co and Gd layers are antiferromagnetically coupled across the interfaces of the multilayer, were created in a sputtered Ta(4 nm)/Pt (5 nm)/[Co (0.5 nm)/Gd (1 nm)/Pt(1 nm)]$_{10}$/Al (2 nm) multilayer by a well-defined magnetic field treatment. These skyrmions, once formed, are stable at room temperature and zero field. The spin configuration of the Co and Gd layers were imaged by element-specific synchrotron x-ray photoemission electron microscopy (PEEM) at zero field, while the temperature decreased from 300 K to 33 K and then increased back to 55 K. PEEM imaging reveals that the antiferromagnetically coupled Co and Gd skyrmion pairs are stable over a large temperature range from about 300 K to 55 K. At 50 K the magnetization of the core area of the skyrmion pairs starts to rotate from the original out-of-plane direction to in-plane. This spin reorientation transition (SRT) becomes more pronounced when the temperature is decreased further to 33 K. However, the domain wall regions are preserved during this SRT, and after the temperature is increased back to above 50 K, the same skyrmions are recovered to the their identical state before the SRT. Micromagnetic simulations were performed to understand the SRT in context of the presence of chiral domain walls. The observed temperature dependent spin configuration changes in the [Co/Gd/Pt]$_{10}$ multilayers can be attributed to the competition among the ferromagnetic exchange coupling within the Gd spins and Co spins, antiferromagnetic exchange coupling between the interfacial Gd and Co spin, and the interfacial Dzyaloshinskii–Moriya interaction.

[1] X Zhang *et al.,* Nature Communications 7, 10293 (2016) [2] M Stier *et al.,* Physics Review Letter 118, 267203 (2017) [3] S Woo *et al.,* Nature Communications 9, 959 (2018)

INVITED PAPER

3:06

DC-07. Magnetic skyrmions, bimerons and antiskyrmions in new materials. *Y. Zhou*[1] *1. School of Science and Engineering, The Chinese Univerisity of Hong Kong (Shenzhen), Shenzhen, China*

In this talk, I will discuss our recent work of magnetic skyrmions, bimerons and antiskyrmion in new material systems, i.e., antiferromagnets, ferrimagnet and frustrated magnets [Nature Electronics, 1, 288-296, (2018); Nature Communications, 9, 959, (2018); Nature Physics, 13, 162–1169 (2017); Nature Communications, 8, 1717, (2017); Nature Communications, 7, 10293 (2016)]. It is shown that the skyrmion Hall effect can be partially or completely suppressed in ferri-, antiferro- or frustrated materials in comparison to ferromagentic materials, making magnetic skyrmions in the new systems suitable for memory applications. In addition, I will discuss the novel physics of these intriguing topological spin textures in the new materials systems and highlight their potential device applications.

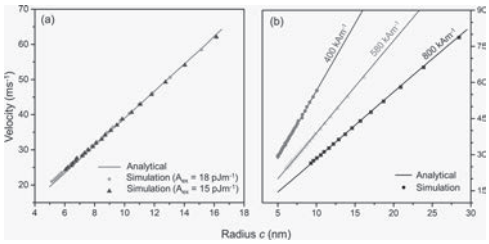
CONTRIBUTED PAPERS

3:42

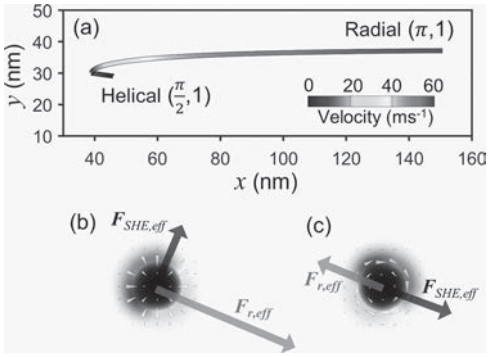
DC-08. An accurate model for skyrmion dynamics under spin-orbit torques. *W. Gan*[1], I. Purnama[1], J.C. Martinez[2] and W. Lew[1] *1. Nanyang Technological University, Singapore; 2. Singapore University of Technology and Design, Singapore*

While many experimental works have demonstrated that the spin-orbit torques play a critical role in propelling skyrmions, the phenomenon has not been modelled completely. In this work, we develop an analytical model to accurately describe skyrmion dynamics under the influence of spin-orbit torques by incorporating the contribution from the spin Hall effect and the Rashba effect. We show that the spin Hall effect leads to the emergence of a force with an amplitude that depends solely on the skyrmion size and a direction that depends only on the skyrmion configuration. The result suggests that small skyrmion used for hi-density devices will suffer from deteriorated performance due to their slow speed. Comparison with micromagnetics confirm the accuracy of our model over a wide range of material parameters and skyrmion configurations. Using our model prediction for the helical-type skyrmions, we find that, despite their very low skyrmion Hall angle, they were found to move much slower in nanowires as compared to the high skyrmion Hall angle radial-type skyrmions. The counter-intuitive results were explained by a force amplification effect that arises due to the edge repulsion from the nanowire. We further provide examples on how this

amplification effect can be exploited for higher skyrmion speeds. In conclusion, our work provides a fundamental understanding of skyrmionics and insights for possible exploitation or elimination of the skyrmion Hall effect, while predicting a scalability challenge for skyrmion devices.



Verification of model with micromagnetic simulations. (a) The skyrmion radius and shape from micromagnetics was tuned by an applied magnetic field or a modification of exchange stiffness, respectively. (b) Plot of velocity versus radius with the saturation magnetization varied.



Displacement of two different skyrmions types under the same spin Hall current of 1 MA/cm² after 3 ns. (b-c) Illustration of the force amplification of the effective forces acting on (b) a radial skyrmion and on (c) a helical skyrmion at equilibrium.

3:54

DC-09. Vanishing skyrmion Hall effect at the angular momentum compensation temperature of a ferrimagnet. *Y. Hirata*[1], D. Kim[1], S. Kim[2,3], D. Lee[4], S. Oh[5], D. Kim[6], T. Nishimura[1], T. Okuno[1], Y. Futakawa[7], H. Yoshikawa[7], A. Tsukamoto[7], Y. Tserkovnyak[2], Y. Shiota[1], T. Moriyama[1], S. Choe[6], K. Lee[4,5] and T. Ono[1,8] *1. Chemistry, Institute for Chemical Research, Uji, Japan; 2. Physics and Astronomy, University of California Los Angeles, Los Angeles, CA, United States; 3. Physics and Astronomy, University of Missouri, Columbia, MO, United States; 4. Materials Science and Engineering, Korea University, Seoul, The Republic of Korea; 5. Nano-Semiconductor and Engineering, Korea University, Seoul, The Republic of Korea; 6. Physics and Institute of Applied Physics, Seoul National University, Seoul, The Republic of Korea; 7. College of Science and Technology, Nihon University, Funabashi, Japan; 8. Ceneter for Spintronics Research Network, Osaka University, Osaka, Japan*

Moving skyrmions with non-zero topological charges and finite fictitious magnetic fields exhibit the skyrmion Hall effect, which is detrimental for applications such as skyrmion racetrack memory[1]. Recently, it was predicted that the skyrmion Hall effect vanishes for antiferromagnetic skyrmions because their fictitious magnetic field, proportional to net spin density, is zero[2]. In this work, we experimentally demonstrate the vanishing skyrmion Hall effect in the vicinity of the angular momentum compensation temperature T_A[3] by using ferrimagnetic compound GdFeCo. We measured current-driven transverse elongation of pinned ferrimagnetic bubbles in perpendicularly magnetized ferrimagnetic GdFeCo/Pt film by using MOKE (Fig. 1). And we confirmed that the angle between the current and bubble elongation directions, vanishes at the angular momentum compensation temperature T_A (=287±5 K) where the net spin density vanishes (Fig. 2). To interpret these results, we developed a simple theory for the elongation of a pinned magnetic bubble driven by SOT. Specifically, we modelled an elongated bubble with one pinned end at the origin as a composite object that consisted of a half skyrmion ($Q = \pm 1/2$) at the free end and a straight rod that connected the two ends, and the elongation angle $\theta = \theta_{SkH}$ with $\theta_{SkH} \approx \tan^{-1}(2s_{net}Q\lambda/\alpha s_{total}r)$ where s_{net} is the net spin density, s_{total} is the sum of the sublattice spin density magnitudes, α is the Gilbert damping constant, λ is the domain wall width that forms the bubble boundary and r is the radius of the half skyrmion. As the temperature approaches T_A, s_{net} goes to zero and, consequently, the elongation angle θ_{SkH} goes to zero. This implies the skyrmion Hall effect vanishes at T_A, as was experimentally observed. Combined with theoretical and numerical support, our observation demonstrates that the fictitious magnetic field for magnetic skyrmions is proportional to s_{net} and skyrmion Hall effect vanishes at T_A[4].

[1] W. Jiang, X. Zhang and G. Yu, Nat. Phys., Vol. 13, p.162–169 (2016) [2] S. K. Kim, K.-J. Lee and Y. Tserkovnyak, Phys. Rev. B, Vol. 95, 140404(R) (2017) [3] K.-J. Kim, S. K. Kim and Y. Hirata, Nat. Mater., Vol. 16, p.1187-1192 (2017) [4] Y. Hirata, D.-H. Kim and S. K. Kim, Nat. Nanotechnol., Vol. 14, p.232-236 (2019)

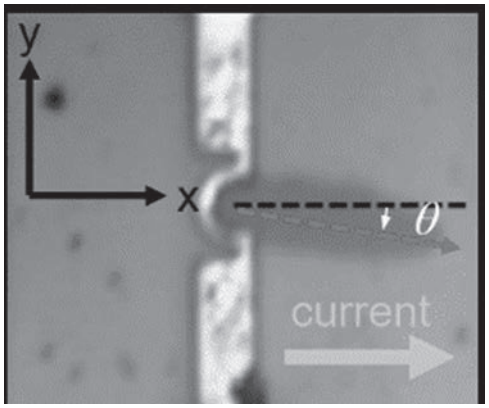


Fig. 1 MOKE image of the current driven elongation of the bubble domain.

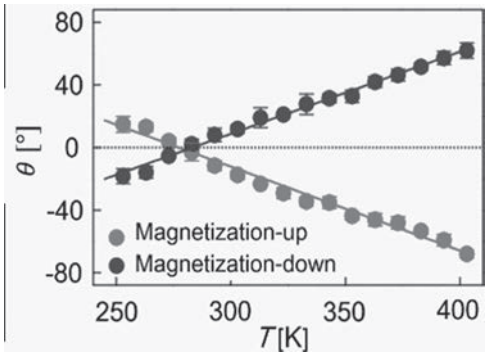


Fig. 2 Elongation angle θ as a function of temperature (*T*) for each magnetization state.

Session DD
ULTRAFAST CONTROL OF MAGNETISM
Stefano Bonetti, Chair
Stockholm University, Stockholm, Sweden

INVITED PAPER

1:30

DD-01. All-optical single shot magnetization switching mediated by angular momentum transfer in spin-valve. *S. Iihama*[1,2], J. Igarashi[2,3], Y. Xu[2], M. Deb[2], G. Malinowski[2], M. Hehn[2], J. Gorchon[2], E. Fullerton[2,4], S. Fukami[3,5], S. Mizukami[1,5] and S. Mangin[2] *1. Advanced Institute for Materials Research, Tohoku university, Sendai, Japan; 2. Institut Jean Lamour, Universite de Lorraine, Nancy, France; 3. Laboratory for Nanoelectronics and Spintronics, Tohoku University, Sendai, Japan; 4. Center for Memory and Recording Research, University of California San Diego, La Jolla, CA, United States; 5. Center for Science and Innovation in Spintronics (CSIS), Tohoku University, Sendai, Japan*

In recent years, the manipulation of magnetization solely by the ultrashort laser pulse has attracted attention for future ultrafast and low-energy spintronics devices [1-10]. GdFeCo has been predominant materials system showing all-optical single-shot magnetization switching. The magnetization switching of GdFeCo is driven by a transient ferromagnetic-like states and transfer of angular momentum between Gd and FeCo sublattices [1,2]. However, restriction to Gd-based ferrimagnetic material limits potential spintronics device applications. Moreover, all-optical magnetization switching in magnetic multilayer, in which magnetic layers are decoupled, is unexplored. In this study, we demonstrated that all-optical single shot magnetization switching can be realized even in ferromagnetic film, which is mediated by transfer of angular momentum in spin-valve structure [11]. This demonstration provides new way to deterministically switch ferromagnetic films with a single optical pulse. The spin-valve structure used in this study consists of a ferromagnetic [Co/Pt] layer and a ferrimagnetic GdFeCo layer where the two magnetic layers were magnetically decoupled by a thick Cu spacer layer. The ultrashort laser pulses irradiate sample from the film side (GdFeCo layer) and the magneto-optical Kerr effect images are obtained from the substrate side. It is observed that the ferromagnetic layer is switched by the irradiation of single femtosecond laser pulse to the GdFeCo layer even when we insert a 30-nm-thick Cu layer. When we insert Pt spin scattering layer in the Cu spacer layer, single shot switching of ferromagnetic layer decayed with increasing Pt layer thickness. Thus, we conclude that the all-optical switching of ferromagnetic layer is attributed to the transfer of angular momentum from GdFeCo layer to the Co/Pt layer. In the presentation, we will show the details of the experimental results as well as recent experiments using different ferromagnetic materials. In addition, time-resolved experiments using pump-probe technique as well as electrical detection of all-optical switching in spin-valve will be presented. This work was partially supported by the SAKURA program. S. I. acknowledges Sasakawa Foundation, JSPS KAKENHI (No. 19K15430). J.I. acknowledges GP-Spin, JST-OPERA, DIARE, Tohoku University and JSPS KAKENHI (No. 19J12926). Work at UCSD supported by the BES Award DE-SC0018237.

[1] I. Radu *et al*. Nature 472, 207 (2011) [2] T. A. Ostler *et al*. Nat. Commun. 3, 666 (2012) [3] C. D. Stanciu *et al*. Phys. Rev. Lett. 99, 047601 (2007) [4] S. Mangin *et al*. Nat. Mater. 13, 286 (2014) [5] C. -H. Lambert *et al*. Science 345, 1337 (2014) [6] A. Stupakiewicz *et al*. Nature 542, 71 (2017) [7] Y. Yang *et al*. Sci. Adv. 3, e1603117 (2017) [8] Y. Xu *et al*. Adv. Mater. 29, 1703474 (2017) [9] J. Gorchon *et al*. Appl. Phys. Lett. 111, 042401 (2017) [10] M. L. M. Lalieu *et al*. Phys. Rev. B 96, 220411 (2017) [11] S. Iihama *et al*. Adv. Mater. 30, 1804004 (2018)

CONTRIBUTED PAPERS

2:06

DD-02. Ultrafast Holographic Imaging at the European XFEL. *N. Zhou Hagström*[1], N. Kerber[2], M. Schneider[3], C. Günther[3,4], M. Beg[5], R. Rosca[5], M. Pancaldi[1], K. Neeraj[1], D. Polley[1], R. Jangid[6], N. Agarwal[5], L. Le Guyader[5], R. Carley[5], A. Yaroslavtsev[5], L. Mercadier[5], G. Mercurio[5], R. Gort[5], J. Zhu[5], T. Kluyver[5], M. Bergemann[5], E. Kamil[5], A. Philippi-Kobs[7], M. Riepp[7], W. Roseker[7], L. Müller[7,8], G. Grübel[7,8], E. Jal[9], T.J. Silva[10], J.M. Shaw[10], C. Sanchez Hanke[11], R. Kukreja[6], N. Jaouen[12], H. Fangohr[5], S. Eisebitt[3,4], M. Kläui[2], A. Scherz[5] and S. Bonetti[1,13] *1. Department of Physics, Stockholm University, Stockholm, Sweden; 2. Institute of Physics, Johannes Gutenberg-University Mainz, Mainz, Germany; 3. Max Born Institute for Nonlinear Optics and Short Pulse Spectroscopy, Berlin, Germany; 4. Institut für Optik und Atomare Physik, Technische Universität Berlin, Berlin, Germany; 5. European XFEL GmbH, Schenefeld, Germany; 6. Department of Materials Science and Engineering, University of California Davis, Davis, CA, United States; 7. Deutsches Elektronen-Synchrotron DESY, Hamburg, Germany; 8. Universität Hamburg, Hamburg, Germany; 9. LCPMR, Sorbonne Université, Paris, France; 10. Quantum Electromagnetics Division, National Institute of Standards and Technology, Boulder, CO, United States; 11. Diamond Light Source, Oxford, United Kingdom; 12. Synchrotron SOLEIL, Saint Aubin, France; 13. Department of Molecular Sciences and Nanosystems, Ca' Foscari University of Venice, Venezia-Mestre, Italy*

In the past two decades, researchers have been able to observe ultrafast magnetic dynamics driven by femtosecond laser pulses, revolutionizing our view on magnetism [1,2]. Despite the progress of the last decade in the description of ultrafast magnetism, the understanding of the fundamental physics that allows for the ultrafast transfer of angular momentum is still only partial, historically hampered by the lack of experimental techniques suited to fully explore these phenomena. However, the recent appearance of coherent X-rays generated at free electron lasers (FELs), has given researchers access to a whole new set of capabilities to unveil this elusive phenomenon. With its superconducting linear accelerator, the European XFEL is the only existing high-repetition FEL. The increased number of photons hugely improves the statistics and allows to effectively perform time-resolved imaging experiments with femtosecond resolution. The SCS beamline for soft X-rays has a new state-of-the-art detector (DSSC) that matches the high repetition rate offered by the FEL. We will show the first images taken with the DSSC detector at a record repetition rate of 1.1MHz. Using holographic reconstruction techniques, we were able to image spin structures in a CoFeB nanodot using femtosecond X-ray pulses. Our experiment shows that the European XFEL and hence future superconducting FELs are facilities where it is possible to perform imaging with combined high temporal and spatial resolution. While our first images on ultrathin CoFeB are limited to ~20 nm spatial and ~500 fs temporal resolution due to temporary limitations at the European XFEL, we anticipate that these new machine will open up for achieving combined 10 nm and 10 fs resolution in a single measurement. Such combined resolution will allow for a deeper

understanding of the fundamental processes in the puzzling phenomenon of ultrafast magnetism, directly probing the spatial and temporal length scale of the spin-orbit and exchange interactions.

[1] E. Beaurepaire *et al.*, Physical Review Letter, Vol. 76, p.4250 (1996)
[2] C. D. Stanciu *et al.*, Physical Review Letter, Vol. 99, p.047601 (2007)

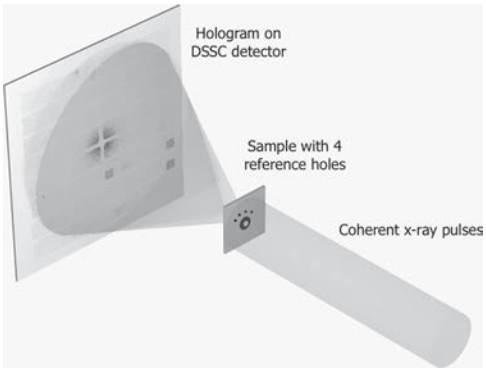


Fig.1 Schematic of the experiment. The image on the DSSC detector is the measured X-ray Magnetic Circular Dichroism intensity. The reference structure is four circular apertures. The object is a CoFeB nanodot.

2:18

DD-03. Ultimate Speed Limits for Deterministic All-Optical Toggle Switching. *Y. van Hees*[1], B. Koopmans[1] and R. Lavrijsen[1] *1. Department of Applied Physics, Eindhoven University of Technology, Eindhoven, Netherlands*

In order to use single pulse all-optical switching (AOS) for future ultrafast data storage or logic applications, a better understanding is needed of the ultimate switching rates that can be achieved to assure deterministic AOS. In this contribution, we experimentally investigate double pulse AOS behaviour in a Co/Gd bilayer [1] as a function of picosecond time delay between two fs laser pulses which can individually induce AOS (fig. 1). As seen in fig. 2, we demonstrate that there is a clear delay threshold for deterministic switching of 50-100 ps (leading to data rates of 10-20 GHz). We introduce and discuss simulations describing this process using the microscopic three-temperature model (M3TM) [2], which can already qualitatively reproduce single and double switching as well as thermal demagnetization behaviour seen in the experiments (fig. 2). This model allows us to unravel the determining factors for the time-delay threshold. For instance, we find that this threshold is strongly dependent on the relative laser fluence of the incident pulses, which we will also demonstrate experimentally. Interestingly, matching with previous modeling work [3], these simulations show that it is possible to switch the magnetization a second time even when the system has not fully relaxed to saturation yet. Optical double-pump-probe measurements are underway to experimentally investigate the ps-timescale dynamics of this non-equilibrium switching mechanism. This work demonstrates the exciting potential of single pulse AOS for future ultrafast magnetic storage and logic applications. Moreover, the bilayer nature of the system under investigation grants (interface) engineering opportunities which can push this so-called rapid-fire performance of future devices even further.

[1] M.L.M. Lalieu et al. *Physical Review B* Vol. 96, p. 220411 (2017) [2] A.J. Schellekens and B. Koopmans, *Physical Review B* Vol. 87, p. 020407 (2013) [3] U. Atxitia and T.A. Ostler, *Applied Physics Letters* Vol. 113, p. 062402 (2018)

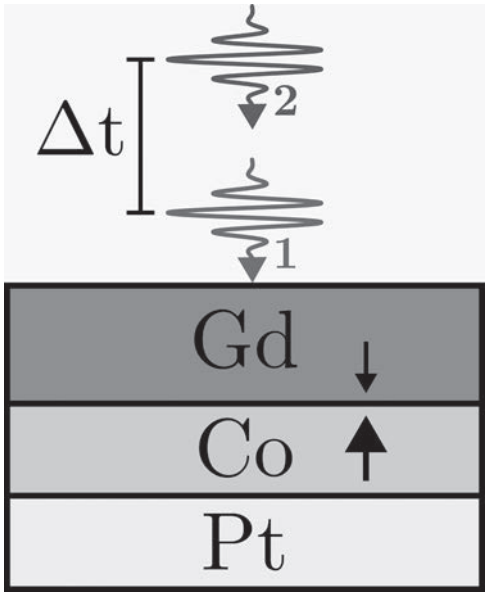


Fig. 1: Sketch of the experiment.

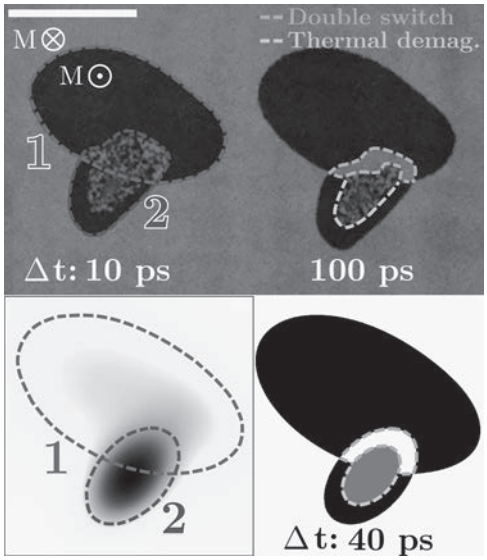


Fig. 2: Top: Kerr microscopy image (scale bar 50 µm) of domains written using spatially overlapping ps-delayed laser pulses in a Co/Gd bilayer. Bottom: Spatial mapping of laser power intensity profiles and domains obtained with this mapping via M3TM double pulse simulations.

2:30

DD-04. Pathways for deterministic all-optical switching of magnetization. C. Davies[1], T. Janssen[1], J. Mentink[2], A. Tsukamoto[4], A. Kimel[2], L. van der Meer[1], A. Stupakiewicz[3] and *A. Kirilyuk*[1] *1. FELIX Laboratory, Radboud University, Nijmegen, Netherlands; 2. Institute for Molecules and Materials, Radboud University, Nijmegen, Netherlands; 3. Faculty of Physics, University of Bialystok, Bialystok, Poland; 4. College of Science and Technology, Nihon University, Chiba, Japan*

We demonstrate how femto- or picosecond-long heat pulses enable single-shot all-optical switching (AOS) of magnetization in ferrimagnets[1]. By realistically modelling a generic ferrimagnet as two coupled macrospins[2], we show that the net magnetization can be reversed via distinctly different pathways, using a heat pulse with duration spanning all relevant timescales within the non-adiabatic limit (Fig. 1). This understanding is validated by

experiments studying the material and optical limits at which the switching process in GdFeCo alloys loses its reliability. Specifically, we numerically and experimentally reveal the existence of a critical pulse-duration threshold for $Gd_x(FeCo)_{100-x}$ alloys, whereby thermal pulses with durations below and above t_c are capable and incapable respectively of achieving deterministic AOS. The size of t_c scales monotonically and dramatically with x (Fig. 2) – increasing x from 22 to 27 leads to t_c increasing by a factor of more than 40. Our interpretation and results resolve a significant controversy[3] about how relatively "slow" pulses can achieve magnetization reversal, and also provide new guidelines for how deterministic AOS can be achieved in suitable ferrimagnets using tailored thermal pulses[4].

[1] T. A. Ostler *et al.*, Nature Comms. 3, 666 (2012). [2] J. H. Mentink *et al.*, Phys. Rev. Lett. 108, 057202 (2012). [3] J. Gorchon *et al.*, Phys. Rev. B 94, 184406 (2016). [4] C. S. Davies *et al.*, Preprint at arXiv:1904.11977 (2019).

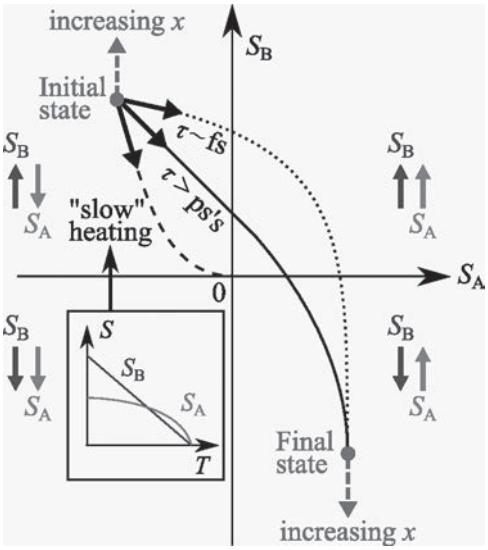


Fig. 1 Conceptual phase map showing the different pathways for thermally-induced relaxation and recovery of the constituent-resolved angular momentum *S*. The thick green dots indicate positions of equilibrium. Excitation of the ferrimagnet by thermal pulses of varying duration lead to different trajectories. Shown in the inset is the adiabatic thermal dependence of the angular momentum.

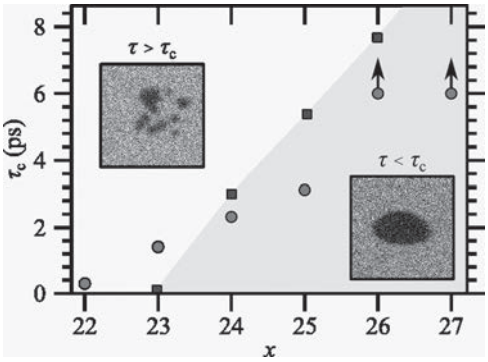


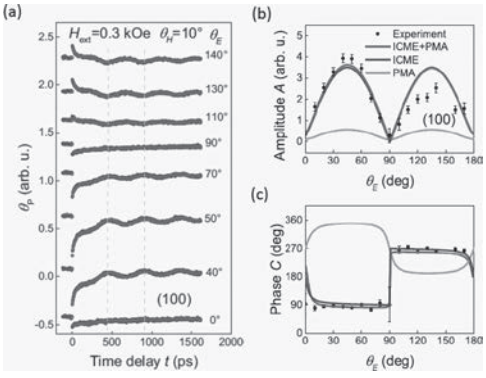
Fig. 2 The critical pulse-duration threshold t_c is plotted (red circles) as a function of alloy composition, measured using pulses of photon energy 1.55 eV. Deterministic AOS is achieved if $t < t_c$ but disabled if $t > t_c$. Also shown are the calculated values of t_c (blue squares). Insets: Typical background-corrected magneto-optical images, of side length 100 μm, obtained for $Gd_{23}(FeCo)_{77}$ showing deterministic AOS (bottom-right panel, t = 1.4 ps) and demagnetization (top-left inset, t = 1.5 ps). The contrast in the images is proportional to the out-of-plane component of magnetization.

2:42

DD-05. Control of Magnetization Precession Excitation via Tuning Ultrafast Laser Polarization Direction. J. Shi[1], L. Shen[1], L. Zhou[3], Y. Dai[4], H. Zhao[1], H. Xia[1], D. Wu[3,5], S. Zhou[4] and *H. Zhao*[2,1]
1. Department of Optical Science and Engineering, Fudan University, Shanghai, China; 2. Key Laboratory of Micro and Nano Photonics Structure, Fudan University, Shanghai, China; 3. Department of Physics, Nanjing University, Nanjing, China; 4. Physics Department, Tongji University, Shanghai, China; 5. National Laboratory of Solid State Microstructures, Nanjing University, Shanghai, China

The interaction of an ultrashort laser pulse with magnetic materials may be used to manipulate spins at the time scale of picoseconds [1, 2]. This provides a feasible way to significantly improve the speed of information storage and operation based on the spins of magnetic materials. However, this manipulation normally originates from the light induced heat effect. Because of the slow heat diffusion, the repetition frequency of this spin manipulation is greatly limited. Therefore, it is important to search nonthermal ways to control the spins at the ultrafast time scale. Although the circularly polarized light was used to nonthermally stimulate the coherent spin rotation in a variety of magnetic materials via the inverse Faraday effect, using linearly polarized light to nonthermally drive the magnetization motion at the ultrafast time scale is much less demonstrated. Here, we present two methods using linearly polarized light to manipulate the magnetization of magnetic materials via the ultrafast nonthermal effect. One way is the excitation of magnetization precession via the inverse Cotton-Mouton effect in undoped yttrium iron garnet (YIG) films [3], as shown in Fig. 1, and the other way is the excitation of magnetization precession via the optical rectification in combination of the inverse piezoelectric effect in a ferromagnetic/ferroelectric heterostructure ($Co/BiFeO_3$). For both effects, the precession amplitude and/or precession phase depend on the polarization direction of the linearly polarized laser pulse.

[1] Z. Zheng, H. B. Zhao, *et al*., "Ultrafast modulation of exchange coupling induced anisotropy in Fe/CoO by laser induced charge transfer", Applied Physics Letters 110, 172401 (2017) [2] J. Y. Shi, H. B. Zhao, *et al*., "Impact of ultrafast demagnetization process on magnetization reversal in $L1_0$ FePt revealed using double laser pulse excitation", Applied Physics Letters 112, 082403 (2018) [3] L. Q. Shen, H. B. Zhao, *et al.*, "Dominant role of inverse Cotton-Mouton effect in ultrafast stimulation of magnetization precession in undoped yttrium iron garnet films by 400-nm laser pulses", Physical Review B 97, 224430 (2018).



(a) Time evolution of the modulated magneto-optical Kerr angle (θ_p) due to the magnetization precession in YIG (001) excited by ultrafast laser pulses with different polarization direction (θ_E). (b) and (c) The amplitude and phase of the magnetization precession as a function of θ_E. The solid lines are fitting curves using inverse Cotton-Mouton effect (ICME) and photo-induced magnetic anisotropy (PMA).

2:54

DD-06. Selective All-Optical Toggle Switching Defined by Spin Currents in FM/Cu/Co/Gd Systems. *Y. van Hees*[1], P. van de Meugheuvel[1], B. Koopmans[1] and R. Lavrijsen[1] *1. Department of Applied Physics, Eindhoven University of Technology, Eindhoven, Netherlands*

Single pulse all-optical switching (AOS) of magnetization by fs laser pulses has been proposed as a candidate for future data storage applications. However, in this regard it is limited by being a toggle mechanism, which is independent of the inital magnetization direction. In this contribution, we show that spin currents generated in a magnetic reference layer can significantly impact single pulse AOS in a Co/Gd bilayer. Using this mechanism, we demonstrate selective toggle switching which only depends on the magnetization direction of the reference layer. The system under investigation (fig. 1) consists of a Co/Ni multilayer separated by a Cu spacer from a Co/Gd bilayer, the latter of which shows single pulse AOS [1]. Upon fs laser illumination the Co/Ni multilayer demagnetizes, generating spin currents which flow through the Cu spacer to the top Co/Gd. We conjecture that the additional spin angular momentum deposited into the top Co layer may add as an additional bias to provoke or prevent switching into the reversed state. We find (fig. 2) that the threshold laser fluence for single pulse AOS is lower when the moments of the Co/Ni multilayers and the top Co layer are initially antiparallel. Here the effect is found to be >10%, with more systematic studies underway for further tuning and understanding. Furthermore, we prove that this phenomenon is driven by spin currents by demonstrating that the effect vanishes when inserting a Pt spin sink layer. We show that our mechanism allows for laser fluence dependent deterministic setting of the magnetization state of the top Co/Gd layer based on the reference layer magnetization direction, which could lead to new applications in data storage and logic.

[1] M.L.M. Lalieu et al. *Physical Review B* Vol. 96, p. 220411 (2017)

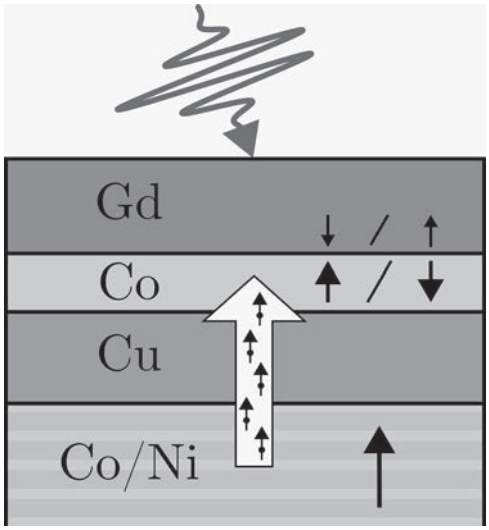


Fig. 1: Sketch of the experiment.

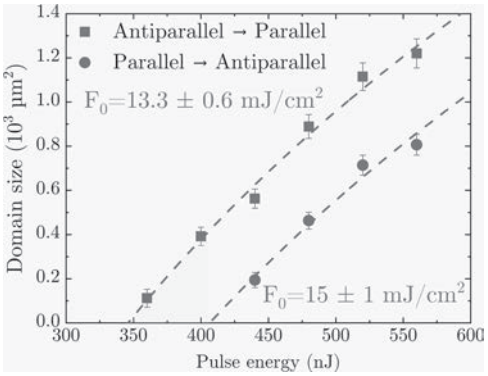


Fig. 2: Measurements of domain sizes switched with single pulse AOS in a [Co(0.2)/Ni(0.6]x4/Cu/Co(1)/Gd(3) system when the initial top Co layer magnetization is aligned parallel (blue circles) or antiparallel to the Co/Ni moment. Dashed lines are fits used to extract the threshold fluence F_0 assuming a Gaussian laser spot profile. For pulse energies within the shaded region, the final magnetization state of the illuminated area will always align with the Co/Ni magnetization.

3:06

DD-07. Comparing all-optical switching in (synthetic-)ferrimagnetic multilayers and alloys. *M. Beens*[1], M. Lalieu[1], A. Deenen[1], R. Duine[2,1] and B. Koopmans[1] *1. Applied Physics, Eindhoven University of Technology, Eindhoven, Netherlands; 2. Utrecht University, Utrecht, Netherlands*

All-optical switching (AOS) refers to the switching of the magnetization by femtosecond laser pulses and has a high potential to be used in future magnetic memory devices. After the discovery of AOS in ferrimagnetic GdFeCo alloys [1], AOS was also demonstrated in Pt/Co/Gd multilayers [2]. The latter allows for easy interface-engineering to optimize its magnetic properties. An important question that arises is to what extent the switching of ferrimagnetic alloys and synthetic ferrimagnets relies on the same physics. Our research shows that the conditions for switching the ferrimagnetic alloys and synthetic ferrimagnets are strikingly different [3]. We experimentally show that Pt/FM/Gd multilayers can be switched for a relatively thick ferromagnetic (FM) layer, which indicates that the switching mechanism in synthetic ferrimagnets is independent of a possible compensation temperature. In contrast, for the alloys it is believed that it is crucial to have a significant magnetization compensation. These different conditions are verified by our microscopic model, which describes the laser-induced dynamics in ferrimagnetic alloys and synthetic ferrimagnets on an equal footing. The model includes Elliott-Yafet spin-flip scattering and exchange scattering between multiple spin sublattices, which correspond to the sublattices of a ferrimagnetic alloy or the atomic monolayers of a synthetic ferrimagnet. In agreement with our experiments, Fig. 1 shows that Co/Gd bilayers can be switched for an arbitrary thickness of the Co layer, i.e., both with and without the presence of a magnetization compensation temperature. In contrast, Fig. 2 shows that GdCo alloys can only be switched near the compensation point. The role of spin transport on the robustness of the switching mechanism in the synthetic ferrimagnets will be discussed.

[1] C.D. Stanciu, F. Hansteen, A.V. Kimel, A. Kirilyuk, A. Tsukamoto, A. Itoh and Th. Rasing, Phys. Rev. Lett. 99, 047601, (2007) [2] M.L.M. Lalieu, M.J.G. Peeters, S.R.R. Haenen, R. Lavrijsen and B. Koopmans, Phys. Rev. B, 96, 220411, (2017) [3] M. Beens, M.L.M. Lalieu, A.J.M. Deenen, R.A. Duine and B. Koopmans, in preparation, (2019)

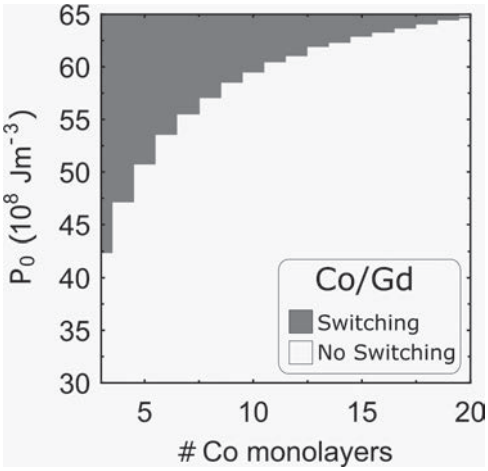


Fig. 1. Phase diagram of AOS in Co/Gd bilayers, for the number of Co monolayers versus laser power P_0. Switching is found even for relatively thick Co layers.

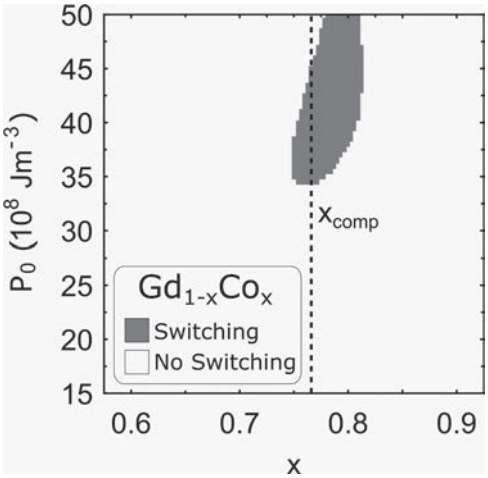


Fig. 2. Phase diagram of AOS in $Gd_{1-x}Co_x$ alloys, for the Co concentration x versus laser power P_0. x_{comp} is the compensation point, for which the compensation temperature equals room temperature. Switching is only found near x_{comp}.

3:18

DD-08. Enhanced Ultrafast Switching Dynamics at the Nanoscale.

A. El-Ghazaly[4], B. Tran[1], A. Ceballos[2], C. Lambert[3], A. Pattabi[5], S. Salahuddin[5], F. Hellman[1,2] and J. Bokor[5] *1. Physics, University of California Berkeley, Berkeley, CA, United States; 2. Materials Science and Engineering, University of California Berkeley, Berkeley, CA, United States; 3. Materials, ETH Zurich, Zurich, Switzerland; 4. Electrical and Computer Engineering, Cornell University, Ithaca, NY, United States; 5. Electrical Engineering and Computer Science, University of California Berkeley, Berkeley, CA, United States*

Reduction of switching time and energy are the keys to the success of future MRAM devices [1,2]. In recent years, much attention has been given to the material GdFeCo as a result of its unique ability to reverse its magnetization in picosecond timescales in response to only a single femtosecond laser pulse excitation [3-5]. Early attempts to observe this behavior at the nanoscale, however, were impeded by either the weak anisotropy and loss of perpendicular magnetization in nanoscale patterns of GdFeCo alloys [6] or the inhomogeneity of the local, but higher anisotropy in continuous films of TbFeCo alloys [7,8]. In this work, after first demonstrating helicity-independent all-optical switching in GdCo nanoscale patterned dots, we characterize their time-resolved magnetization switching behavior as a function of diameter [9]. GdCo dots of diameter d and spacing 2d were made to fill uniform arrays of size 25 μm x 25 μm, such that the laser probe beam (diameter 15 μm) would measure a summation of the magnetization from many dots of the same size. The time resolved magneto-optic Kerr effect (TR-MOKE) behavior in Fig. 1 indicates clear evidence of faster magnetization reversal for smaller dot sizes, despite increased noise in those arrays resulting from laser interference, edge effects, and other non-idealities. Figure 2 summarizes the switching time as a function of dot diameter, where a 75% reversal threshold was chosen. Increased switching speed at smaller dimensions is believed to be a result of enhanced electron-phonon and spin-lattice coupling, which cause a reduction in the time necessary to transfer heat from the electrons and spins to the lattice, allowing the magnetization to settle faster to its reversed state [9]. These results can be further extrapolated to demonstrate the potential impact in nanoscale integrated systems, where in Fig. 2, a 20 nm dot is expected to switch its magnetization in less than 2 ps, two orders of magnitude less than precessional switching processes [10].

[1] S. Tehrani, et al., *IEEE Transactions on Magnetics,* 35, 2814 (1999). [2] X. Dong, et al., *Design Automation Conference* (2008). [3] B. Koopmans, et al., *Nature Materials, 9,* 3 (2010). [4] I. Radu, et al., *Nature*, *472,* 7342 (2011). [5] T. A. Ostler, et al., *Nature Communications*, *3*, 666 (2012). [6] L. Le Guyader, et al., *Applied Physics Letters,* 101, 2 (2012). [7] M. Finazzi, et al., *Physical Review Letters,* 110, 17 (2013). [8] T. M. Liu, et al., *Nano Letters*, 15, 6862 (2015). [9] A. El-Ghazaly, et al., *Applied Physics Letters*, *114*, 23 (2019). [10] H. Zhao, et al., *Journal of Physics D: Applied Physics*, *45*, 2 (2012).

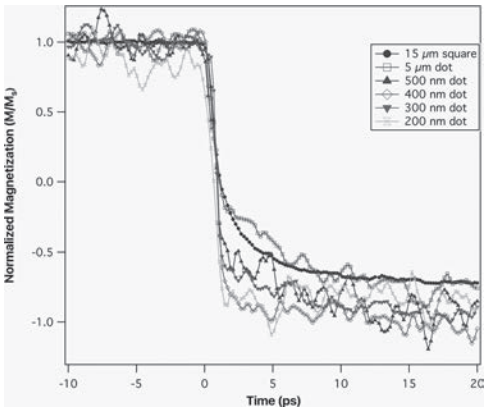


Fig 1. TR-MOKE measurements of magnetization reversal in patterns from 15 μm down to 200 nm.

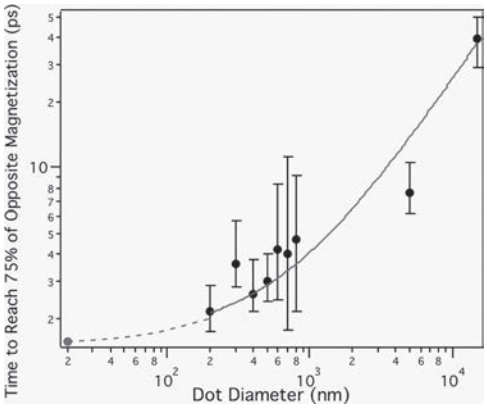


Fig 2. Summary of reversal times, based on a 75% reversal threshold, for different pattern diameters. Dotted line shows extrapolation to a 20 nm dot.

3:30

DD-09. Ultrafast helicity-independent all-optical magnetization reversal of Co/Pt multilayers coupled with CoGd. *J. Chatterjee*[1], A. Pattabi[1], M. Ruiz[2], S. Salahuddin[1,3], F. Hellman[2,3] and J. Bokor[1,3]
1. Department of Electrical Engineering and Computer Sciences, University of California, Berkeley, Berkeley, CA, United States; 2. Department of Physics, University of California, Berkeley, Berkeley, CA, United States; 3. Lawrence Berkeley National Laboratory, 1 Cyclotron Road, Berkeley, CA, United States

Ultrafast helicity-independent all-optical switching (HI-AOS)[1] as well as ps current-pulse driven magnetization reversal[2] of a ferrimagnetic GdFeCo illuminated the pathway of realizing ultrafast magnetization reversal of a ferromagnet[3]. Recently, HI-AOS of Co/Pt multilayers (MLs), coupled with GdFeCo has been demonstrated[3,4]. However, as the perpendicular magnetic anisotropy of GdFeCo decreases with device scaling[5], the stacks where a ferromagnet is coupled with GdFeCo are not ideal for applications. Therefore, we have investigated the magnetic properties as well as magnetization dynamics of Co/Pt MLs coupled with CoGd, in which HI-AOS is recently been reported in nano-devices. The stacks studied are configured as "Pt seed /$[Co/Pt]_2$ /Co /Pt (t nm) /CoGd /Pt cap", where the intermediate Pt spacer thickness is varied (t= 0.25, 0.5, 1 and 5 nm). The hysteresis loops of the samples shown in Fig. 1(a) were measured by polar magneto optical Kerr effect (MOKE). The MLs are ferromagnetically coupled with CoGd for t<5 nm. They exhibit single shot HI-AOS with laser pulse widths from 60 fs to 3.5 ps as presented in Fig 1 (b) and (c), which opens up the possibility to reverse the magnetization of Co/Pt MLs using charge current pulses of similar pulsewidth (~ 3.5 ps). The MLs and CoGd are decoupled, for t=5 nm and only the magnetization of CoGd is toggled under successive optical pulses. Hence, we believe that the HI-AOS of Co/Pt MLs is mediated by exchange coupling through the Pt spacer. Finally, the magnetization dynamics of the ferromagnetically coupled stacks are characterized by time-resolved MOKE measurements, which is presented in Fig. 2. The magnetization of the stacks reverse within a ps time-scale irrespective of the spacer layer thickness. Such a fast magnetization reversal of a ferromagnet exploiting the exchange bias with CoGd will be promising for ultrafast memory and storage applications.

[1]I. Radu, K. Vahaplar, C. Stamm, et al. Nature 472, 205 (2011). [2]Y. Yang, R.B. Wilson, J. Gorchon et al. Sci. Adv. 3, e1603117 (2017). [3]J. Gorchon, C.H. Lambert, Y. Yang, et al. Appl. Phys. Lett. 111, (2017). [4]S. Iihama, Y. Xu, M. Deb et al., Adv. Mater. 30, 1 (2018). [5]A. El-Ghazaly, B. Tran, A. Ceballos, et al. Appl. Phys. Lett. 114, 232407 (2019).

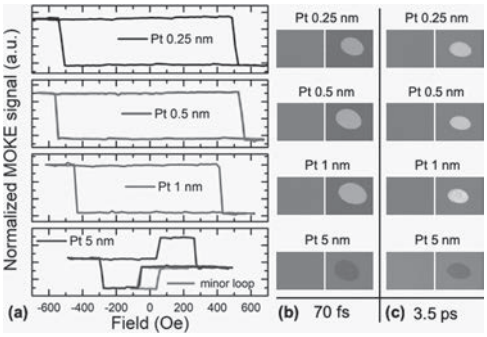


Fig.1 (a) M(H) loops measured by polar MOKE and (b), (c) single shot HI-AOS by 70fs and 3.5 ps laser pulse respectively of the samples with variable Pt spacer thickness.

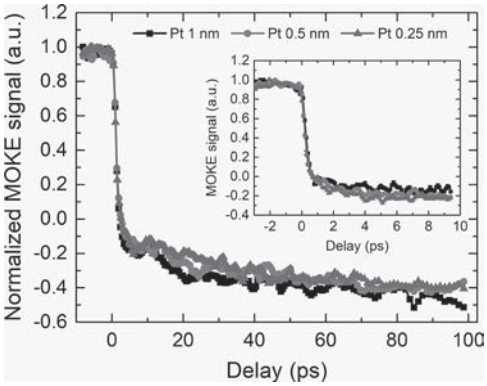


Fig.2 Time resolved MOKE signal of the stacks with 0.25, 0.5 and 1nm Pt spacers at incident fluence of 117 J/m^2. Inset: Similar graph for smaller time scale.

3:42

DD-10. Field Dependence of Time-Resolved All-Optical Toggle Switching in Co/Gd Bilayers. *M. Peeters*[1], Y. van Ballegooie[1], M. Beens[1], R. Lavrijsen[1] and B. Koopmans[1] *1. Applied Physics, Eindhoven University of Technology, Eindhoven, Netherlands*

Originally discovered in ferrimagnetic GdFeCo alloys [1], AOS gives rise to a toggle switch of the magnetization on the picosecond timescale after excitation with an ultrashort laser pulse. Recently, it was shown that single-pulse AOS can also be found in ferrimagnetic Co/Gd bilayers [2], opening up new possibilities for (interface) engineering of the stack, which makes it highly suitable for future spintronic applications [3]. However, up until now only static measurements of AOS in Co/Gd have been reported. We report on the first time-resolved measurements of all-optical switching in Co/Gd for applied fields between 0 and 500 mT, performed with a time-resolved MOKE setup. In order to measure the time-dependence of the toggle switching process, we detect at half the repetition rate of the laser (100 kHz), selecting only every other pulse. Thus, we do not need to rely on a reverse magnetic field to bring the magnetic state back to the original orientation after the switch. We show that in Co/Gd bilayers the switching happens on the same picosecond timescale as in GdFeCo alloys. As visible in Fig. 1, the magnetization recovery on very short timescales displays a strong dependence on the external field, even for fields that are orders of magnitude smaller than the exchange fields that drive the magnetization recovery. We will present numerical simulations using the M3TM applied to alloys and bilayers on equal footing. From comparing our magnetic-field dependent experimental results with those simulations, we conjecture that the magnetization reversal is a strongly non-homogeneous across the exciting laser spot. Also, the recovery process is suggested to be a complex process of local magnetization dynamics and domain wall propagation on longer time scales. Our current efforts are aimed at shedding more light on this non-homogeneous and multiple time scale dynamics. We expect that this research will provide an important next step in the understanding of AOS in ferrimagnets.

[1] C.D. Stanciu, F. Hansteen and Th. Rasing, Phys. Rev. Lett. Vol. 99, p.047601 (2007) [2] M.L.M. Lalieu, M.J.G. Peeters and B. Koopmans, Phys. Rev. B, Vol. 96, p.220411 (2017) [3] M.L.M. Lalieu, R. Lavrijsen and B. Koopmans, Nature Communications, Vol. 10, p.110 (2019)

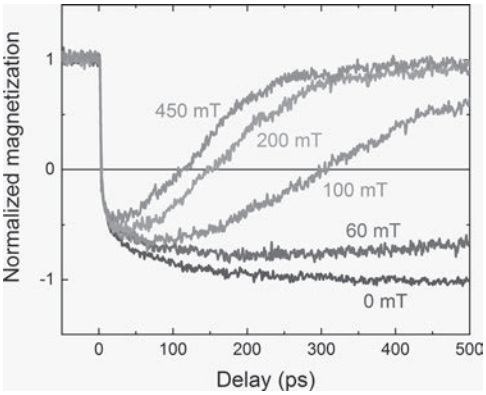
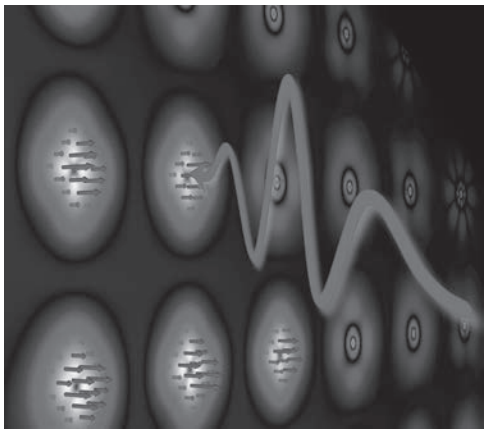


Fig 1: Time-dependent magnetization traces of Co/Gd for different applied fields. In these experiments the applied field is oriented in the positive direction.



Coherent in the step of light - spin current at the Ni/Pt interface.

INVITED PAPER

3:54

DD-11. Light-wave dynamic control of magnetism. *M. Münzenberg*[1]
1. Institute of Physics, Greifswald University, Greifswald, Germany

Ultrafast magnetism, attosecond lasers and methods using x-ray pulses to explore structural dynamics is reaching new limits - attosecond magnetism. Recent major milestones, from hard x-ray bunches to attosecond pulses, are breaking frontiers and time records. This allows the observation and study of coherent spin processes. The phenomena is originating from coherent charge transfer, driven by a few cycle laser pulse. Today, the fully controlled electric field evolution of ultrashort laser pulses permits the direct and ultrafast control of electronic properties of matter and is the cornerstone of light-wave electronics. In sharp contrast, because there is no first order interaction between light and spins, the magnetic properties of matter can only be affected indirectly on the much slower tens-of-femtosecond timescale in a sequence of optical excitation followed by the rearrangement of the spin structure. Here we record an orders of magnitude faster magnetic switching with sub-femtosecond response time by initiating optical excitations with near-single-cycle laser pulses in a ferromagnetic layer stack. The unfolding dynamics are tracked in real-time by a novel attosecond time-resolved magnetic circular dichroism (atto-MCD) detection scheme revealing optically induced spin and orbital momentum transfer (OISTR) in synchrony with light field driven charge relocation. We present the first incarnation of attomagnetism observes light field coherent control of spin-dynamics in the initial non-dissipative temporal regime and paves the way towards coherent spintronic applications with Petahertz clock rates.

[1] F. Siegrist, J. A. Gessner, M. Ossiander, C. Denker, Y.-P. Chang, M. C. Schroeder, A. Guggenmos, Y. Cui, J. Walowski, U. Martens, J. K. Dewhurst, U. Kleineberg, M. Münzenberg, S. Sharma, M. Schultze, "Light-wave dynamic control of magnetism", Nature (2019) http://dx.doi.org/10.1038/s41586-019-1333-x

Session DE
SKYRMIONS IN MULTILAYERS I

Ivan Lisenkov, Chair
Winchester Technlogies, LLC, Burlington, MA, United States

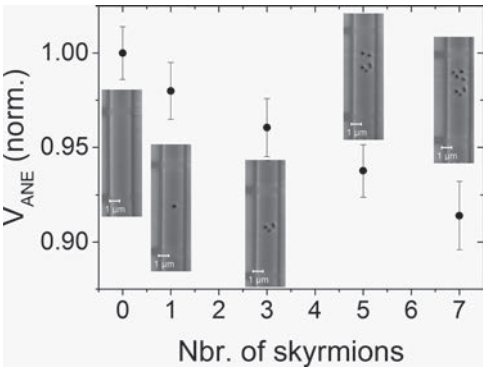
INVITED PAPER

1:30

DE-01. Thermoelectric signature of individual skyrmions. *A. Fernández Scarioni*[1], C. Barton[2], H. Corte-León[2], S. Sievers[1], F. Ajejas[3], W. Legrand[3], N. Reyren[3], V. Cros[3], O. Kazakova[2] and H. Schumacher[1] *1. Physikalisch-Technische Bundesanstalt, Braunschweig, Germany; 2. National Physical Laboratory, Teddington, United Kingdom; 3. Unité Mixte de Physique, CNRS, Thales, Univ. Paris-Sud, Université Paris-Saclay, Palaiseau, France*

The electrical detection and characterization of individual skyrmions at room temperature is a key requirement both for future devices and fundamental studies. So far, skyrmions in multilayers have been electrically detected by their signature in the anomalous Hall effect (AHE) [1]. While AHE detection is limited to Hall crosses, here we show that the anomalous Nernst effect (ANE) [2], the thermoelectric analogue of the AHE, allows non-invasive detection, counting and characterization of individual skyrmions in complete nanowires at room temperature. We use a combined ANE – in situ magnetic force microscopy (MFM) setup to identify the ANE signature of individual skyrmions in Co|Ru|Pt multilayer nanowires. First, a set of skyrmions is nucleated by a current pulse through the wire. Then, MFM is used to characterize the number, size, and spatial distribution of the skyrmions. A transverse thermal gradient from a microheater induces an ANE signal proportional to the out-of-plane magnetization of the wire, which is electrically detected. To derive the ANE signature of individual skyrmions, the stray field of the MFM tip is used to delete individual skyrmions one by one and the respective ANE signals are compared. We demonstrate the ANE based detection and counting of individual skyrmions and study the field dependence of the ANE signature of individual skyrmions. This new non-invasive tool could prove useful for applications and fundamental studies of the topological Nernst effect.

[1] D. Maccariello, et al, Nat. Nanotech. 13, 233 (2018) [2] P. Krzysteczko, et al, Phys, Rev, B 95, 220410 (2017)



ANE voltage as a function of the number of skyrmions present in the nanowire. For every measurement of the ANE voltage an MFM measurement was performed, yielding the number of skyrmions in the nanowire.

CONTRIBUTED PAPERS

2:06

DE-02. The 3-dimensional depth profile of magnetic skyrmion tubes. *W. Liyanage*[1], L.J. Quigley[1], S. Montoya[2,3], N. Tang[1], T. Liu[4], M. Fitzsimmons[5,6], S.q. Sinha[7], R. Kawakami[4], J. Borchers[8], E. Fullerton[2], B.B. Maranville[8], L. DeBeer-Schmitt[6], A.J. Grutter[8] and D.A. Gilbert[1] *1. Materials Science and Engineering, University of Tennessee, Knoxville, TN, United States; 2. CMRR, University of California, San Diego, La Jolla, CA, United States; 3. Naval Information Warfare Systems Command, San Diego, CA, United States; 4. Department of Physics, The Ohio State University, Columbus, OH, United States; 5. Department of Physics, University of Tennessee, Knoxville, TN, United States; 6. Oak Ridge National Laboratory, Oak Ridge, TN, United States; 7. Department of Physics, University of California, San Diego, La Jolla, CA, United States; 8. NCNR, National Institute of Standards and Technology, Gaithersburg, MD, United States*

Magnetic skyrmions are the focus of intense research due to their fundamental qualities as a topologically stabilized pseudo-particle and their potential applications to next-generation magnetic information technologies. These chiral spin structures are frequently presented as 2D projection of a complex 3D topological structure, however, this picture ignores the three-dimensional tube-like structure of the skyrmion. Previous works have suggested interesting physics, including magnetic monopoles, may exist within the depth of the skyrmion. Recently, we have demonstrated the realization of hybrid skyrmions stable at room temperature and zero magnetic field in Gd/Fe multilayers [1]. These skyrmions are stabilized by magnetic dipolar interactions, rather than the traditional Dzyaloshinskii–Moriya interaction.[1,2] As part of the dipolar stability, flux-closure domains form at the top and bottom surfaces of the film; TEM results reveal a Bloch-type azimuthal winding at the equator. In this work, we use grazing incidence small-angle neutron scattering (GISANS), shown in Figure 1, and polarized neutron reflectometry (PNR), to determine the depth profile of the skyrmion. Specifically, in the GISANS and PNR patterns, the specular data capture the depth-dependent magnetic structure of the skyrmions, averaged across the sample plane. Since the structure is highly symmetric in-plane, the depth-resolved average cannot determine the structure alone. The off-specular GISANS data captures the in-plane structure. Measuring both data, we resolve the full depth profile of the skyrmion. To interpret the data, a micromagnetic simulation of the skyrmions was developed; the specular and off-specular patterns were calculated from the model and compared to the experimental results. By iteratively improving the model the simulated pattern was made to accurately reproduce the experiment. For comparison, a prototypical skyrmion thin-film of FeGe is also measured. Work at UCSD supported by DOE (DE-SC0003678); neutron work was performed on VSANS and PBR at NCNR, and supported by CHRNS (NSF:DMR-1508249).

[1]. R. D. Desautels et al., arXiv:1904.13274 [2]. S. A. Montoya et al., Phys. Rev. B 95, 024415 (2017)

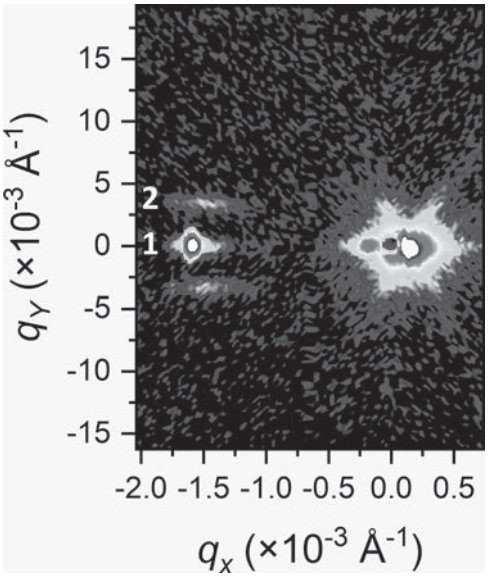


Figure 1 GISANS data with the specular and off-specular features labeled "1" and "2", respectively.

2:18

DE-03. Anatomy of skyrmionic textures in magnetic multilayers. W. Li[1], I. Bykova[2], S. Zhang[3], *G. Yu*[1], R. Tomasello[4], M. Carpentieri[5], Y. Liu[1], Y. Guang[1], J. Gräfe[2], M. Weigand[2], T. Hesjedal[3], G. Finocchio[6], X. Han[1] and G. Schütz[2] *1. Beijing National Laboratory for Condensed Matter Physics, Institute of Physics, Chinese Academy of Sciences, Beijing, China; 2. Max Planck Institute for Intelligent Systems, Stuttgart, Germany; 3. Department of Physics, Clarendon Laboratory, University of Oxford, Oxford, United Kingdom; 4. Institute of Applied and Computational Mathematics, Heraklion-Crete, Greece; 5. Department of Electrical and Information Engineering, Polytechnic of Bari, Bari, Italy; 6. Department of Mathematical and Computer Sciences, Physical Sciences and Earth Sciences, University of Messina, Messina, Italy*

Room-temperature magnetic skyrmions in magnetic multilayers are considered as information carriers for future spintronic applications. Currently, a detailed understanding of the skyrmion stabilization mechanisms is still lacking in these systems. To gain more insight, it is first and foremost essential to determine the full real-space spin configuration. Here, we apply two advanced X-ray techniques, based on magnetic circular dichroism, to investigate the spin textures of skyrmions in $[Ta/CoFeB/MgO]_n$ multilayers[1]. First, by using ptychography, a high-resolution diffraction imaging technique, we determined the two-dimensional out-of-plane spin profile of skyrmions with a spatial resolution of 10 nm. Second, by performing circular dichroism in resonant elastic X-ray scattering, we demonstrate that the chirality of the magnetic structure undergoes a depth-dependent evolution. This suggests that the skyrmion structure is a complex three-dimensional structure rather than an identical planar texture throughout the layer stack. The analyses of the spin textures confirm the theoretical predictions that the dipole-dipole interactions together with the external magnetic field play an important role in stabilizing sub-100-nm-diameter skyrmions and the hybrid structure of the skyrmion domain wall. Our combined X-ray-based approach opens the door for in-depth studies of magnetic skyrmion systems, which allows for precise engineering of optimized skyrmion heterostructures.

[1] W. Li#, I. Bykova#, S. Zhang#, G. Q. Yu*, R. Tomasello, M. Carpentieri, Y. Liu, Y. Guang, J. Gräfe, M. Weigand, D. M. Burn, G. van der Laan, T. Hesjedal, Z. Yan, J. Feng, C. Wan, J. Wei, X. Wang, X. Zhang, H. Xu, C. Guo, H. Wei, G. Finocchio*, X. Han, G. Schütz "Anatomy of Skyrmionic Textures in Magnetic Multilayers"*Advanced Materials* 31, 1807683 (2019)

2:30

DE-04. Controlling skyrmion bubble confinement by dipolar interactions. *T. Lichtenberg*[1], F.C. Ummelen[1], H. Swagten[1] and B. Koopmans[1] *1. Applied Physics, Eindhoven University of Technology, Eindhoven, Netherlands*

Magnetic skyrmions are whirls in the magnetization in which neighboring spins are rotated with respect to each other with a specific chirality. They are robust against annihilation, are less hindered by pinning sites or defects than magnetic domain walls (DWs), and their size can be in the order of nanometers. These properties make them suitable for data storage. For the envisioned skyrmion racetrack memory device [1, 2], skyrmions must be stable in small geometrically confined structures. Therefore, understanding and being able to control the interaction between skyrmions and the edge of the magnetic structure is crucial to the development such devices. In this work addressing dipolar interactions in confined structures, we show that it is possible to use focused ion beam irradiation (FIB) to control the stability and confinement of skyrmion bubbles in an entirely novel way [3]. FIB is used to locally decrease the magnetic anisotropy of a Pt/Co/Ir stack, such that skyrmion bubbles are stable within the irradiated region (fig. 1). We observe that skyrmion bubbles are located throughout the entire geometry if the background magnetization within the structure points in the same direction as the surrounding. Conversely, when the magnetization direction is opposite, a clear repelling bubble-edge interaction is observed, indicated by the red dashed line. Thus, we demonstrate it is possible to tune the skyrmion bubble confinement with a magnetic field. Finally, we calculate theoretically how skyrmion bubble stability changes in the vicinity of an edge due to a change in dipolar interactions. The observed behavior matches well with these calculations, indicating that dipolar interactions are dominant in determining the positions of skyrmion bubbles with respect to edges and to each other.

[1] J. Sampaio, A. Thiaville, and A. Fert *et al*., "Nucleation, stability and current-induced motion of isolated magnetic skyrmions in nanostructures," Nature Nanotechnology 8, 839–844 (2013). [2] A. Fert, V. Cros, and J. Sampaio, "Skyrmions on the track," Nature Nanotechnology 8, 152–156 (2013). [3] F.C. Ummelen, T. Lichtenberg, B. Koopmans *et al.* Manuscript submitted for publication.

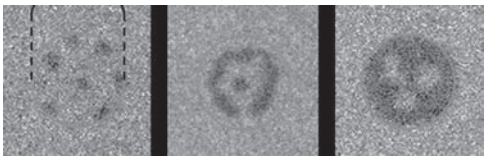


Fig. 1: skrymion stabilization in a small circular area irradiated with a focused ion beam, for various applied magnetic fields. Dark and light areas are opposing out-of-plane magnetization directions. The blue rectangles denote the edges of the regions and the red dashed line indicates the bubble confinement region.

INVITED PAPER

2:42

DE-05. Detection, Motion and Nucleation of Skyrmions. K. Zeissler[1,2], S. Finizio[3], *C. Barton*[1], A. Huxtable[2], J. Massey[2], M. Rosamond[2], E. Linfield[2], A.V. Sadovnikov[4], S. Nikitov[4], J. Raabe[3], T. Moore[2], G. Burnell[2], O. Kazakova[1] and C.H. Marrows[2] *1. National Physical Laboratory, Teddington, United Kingdom; 2. University of Leeds, Leeds, United Kingdom; 3. Paul Scherrer Institut, Villigen, Switzerland; 4. Saratov State University, Saratov, Russian Federation*

The study of topological objects has emerged as a fascinating phenomenon in solid state research from both the fundamental and the applied perspectives. An exciting candidate in this field of research is the magnetic skyrmion

which is unaltered by certain elastic transformations such as a stretching, bending or twisting [1]. The skyrmion's topology introduces unique characteristics in the way in which it interacts with electrons, other skyrmions and defects and on how it responds to a driving force [2]. This talk will address aspects of skyrmion creation, motion and detection at room temperature in cobalt based multilayer devices. Individual skyrmions are detected using Hall resistivity. A skyrmion size independent contribution to the Hall resistivity was observed which was found to be dependent on the number of skyrmions in the disc [3] (Fig. 1a). Scanning transmission x ray microscopy (STXM) was used to image the devices' out of plane magnetization while the Hall resistance was measured *in situ*. Current driven motion is observed in amorphous cobalt based devices. Recent publications have shown experimental deviations from the rigid skyrmion motion theory in form of a velocity dependence of the skyrmion Hall angle [4,5]. Here, we will discuss the diameter dependence of the skyrmion Hall angle with a constant average skyrmion velocity at 6 ± 1 m/s evaluated from STXM images. Here, we show a skyrmion diameter independent skyrmion Hall angle in systems where moving skyrmions and pinned skyrmions coexist (Fig. 1b). Furthermore, the potential for laboratory based local field assisted skyrmion creation is outlined (Fig. 1c). This work was funded by Horizon 2020 MagicSky, TOPS EMPIR and received funding from the EU H2020 research and innovation programme (grant agreement N 654360), benefitting from the access provided by the Paul Scherrer Institut (Villigen) within the NFFA Europe Transnational Access Activity framework.

[1] Braun H. et al Adv Phys. 61, 1 (2012) [2] Nagaosa N. et al. Nat Nanotech. 8, 899 (2013) [3] Zeissler K et al. Nat. Nanotech. 13, 1161 (2018) [4] Litzius K. et al. Nature Phys. 13 170 (2017) [5] Jiang W. et al. Nature Phys. 13, 162 (2017)

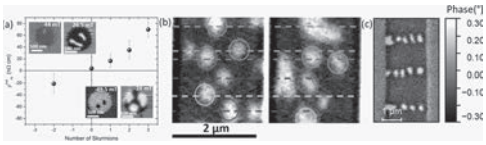


Fig 1:(a) Magnetization independent contribution to the Hall resistivity versus number of skyrmions in disc. STXM images of one, two, and three skyrmions are inset. (b) STXM images of initial skyrmion state (color coded lines) and state after current pulse induced motion. (c) Local magnetic field controlled skyrmion creation in a wire imaged by magnetic force microscopy.

CONTRIBUTED PAPERS

3:18

DE-06. Magnetic Skyrmion Nanolithography. *A.S. Samardak*[1], A. Ognev[1], A. Kolesnikov[1], A.V. Sadovnikov[2,3], S. Nikitov[2,3], I. Soldatov[4], A. Talapatra[5], J. Mohanty[5], Y. Kim[6], I. Cha[6] and Y. Kim[6] *1. School of Natural Sciences, Far Eastern Federal University, Vladivostok, Russian Federation; 2. Laboratory "Metamaterials", Saratov State University, Saratov, Russian Federation; 3. Kotel'nikov Institute of Radioengineering and Electronics RAS, Moscow, Russian Federation; 4. Leibniz Institute for Solid State and Material Research (IFW-Dresden), Dresden, Germany; 5. Indian Institute of Technology Hyderabad, Hyderabad, India; 6. Department of Materials Science and Engineering, Korea University, Seoul, The Republic of Korea*

We present the nucleation of skyrmions and the formation of skyrmion lattices by magnetic force microscopy (MFM) in "heavy metal/ferromagnet"-based multilayers with PMA and the interfacial Dzyaloshinsky-Moriya interaction. Stray fields induced by a standard magnetic moment tip during a multi-pass scanning result in the spontaneous nucleation of zero-field lattices of skyrmions with size of 100-150 nm, which were observed by MFM using a low magnetic moment tip. Ordered skyrmion lattices have the periodicity of about 150 nm, Fig.1. The physical process of a high dense skyrmion lattice fabrication is supported by the micromagnetic simulations. The appropriate conditions under which a confined skyrmion lattice with the hexagonal arrangement and the desired spatial geometry is formed have been defined. These results open a pathway for a maskless skyrmion nanolithography (SkNL) with sub-100 nm resolution, where each skyrmion plays role of a pixel in a final topological image. SkNL can be used to create regions of complex shape covered with skyrmions, Fig.2. The flexibility and further development of this approach related to the topological modification of the environment will make it possible to obtain regions with a minimum size corresponding to the skyrmion lattice period. The alignment of skyrmions into ordered geometric regions will allow one to fabricate skyrmion-based magnonic crystals and assign trajectories of a complex shape for the propagation of spin waves in a skyrmion lattice. Another promising aspect of tSkNL is the possibility of studying the interaction of skyrmions with a labyrinth domain structure and the features of the dynamic properties of skyrmions and chiral domain walls. The work is supported by RFBR (18-52-53038 and 19-02-00530) and Minobrnauki (state task 3.5178.2017).

1. A.G. Kolesnikov, M.E. Stebliy, A.S. Samardak, A.V. Ognev. *Sci. Rep.* 8, p.16966 (2018). 2. A.G. Kolesnikov, V.S. Plotnikov, E.V. Pustovalov, A.S. Samardak, L.A. Chebotkevich, A.V. Ognev. *Sci. Rep.* 8, p.15794 (2018). 3. G.W. Kim, A.S Samardak, Y.J. Kim, I.H. Cha, A.V. Ognev, A.V. Sadovnikov, S.A. Nikitov, Y.K. Kim. *Phys. Rev. Applied* 9, p.064005 (2018). 4. P. Neilinger, T. Ščepka, M. Mruczkiewicz, J. Dérer, D. Manca, E. Dobročka, A.S. Samardak, M. Grajcar, V. Cambel. *Appl. Surf. Sci.* 462, p.202 (2018). 5. A.S. Samardak, A.G. Kolesnikov, M.E. Stebliy, L.A. Chebotkevich, A.V. Sadovnikov, S.A. Nikitov, Abhishek Talapatra, Jyoti Mohanty, A.V. Ognev. *Appl. Phys. Lett.* 112, p.192406 (2018). 6. M.E. Stebliy, A.G. Kolesnikov, A.V. Ognev, E.V. Stebliy, X. Wang, H.F. Han, A.S. Samardak. *Phys. Rev. Applied* 11, p.054047 (2019).

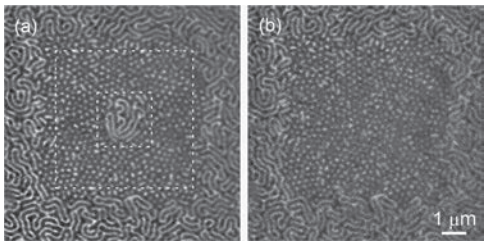


Fig.1. MFM images for the Ta/(Pt/CoFeSiB/W)$_{10}$ multilayer with the square area filled up by skyrmions and with the residual labyrinth structure in the center (a) and the same area with the high dense skyrmion lattice (b) after the multi-pass MFM scanning in the tapping mode.

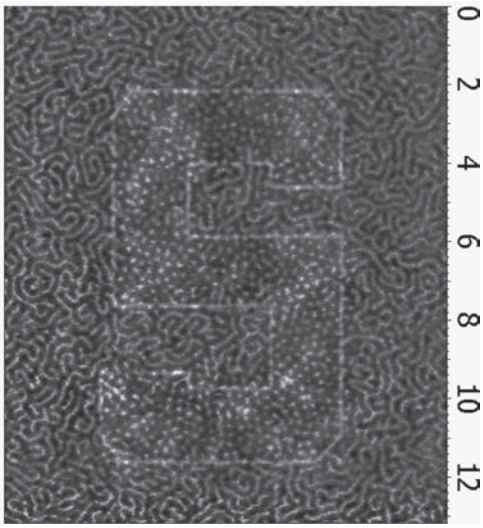


Fig.2. Realization of "S" symbol by the skyrmion nanolithography on the surface of the Ta/(Pt/CoFeSiB/W)$_{10}$ film. The MFM image size is 11×13 mm^2.

3:30

DE-07. Nonvolatile creation and annihilation of fixed magnetic skyrmions using VCMA. *D. Bhattacharya*[1], S. Razavi[2], H. Wu[2], B. Dai[2], K. Wang[2] and J. Atulasimha[1] *1. Virginia Commonwealth University, Richmond, VA, United States; 2. University of California, Los Angeles, Los Angeles, CA, United States*

Current control of magnetic skyrmion motion has been investigated widely for its potential to realize racetrack like memory devices [1, 2]. Although Voltage Control of Magnetic Anisotropy (VCMA) has shown great promise to implement low power consuming memory devices by minimizing I^2R loss, control of magnetic skyrmions using VCMA has not been extensively studied yet. Some recent theoretical proposals have shown utilizing VCMA to manipulate skyrmions can be the basis of small footprint energy efficient nanomagnetic memory devices [3-5]. In this work, we demonstrate VCMA induced nonvolatile creation and annihilation of skyrmions in an antiferromagnet/ferromagnet/oxide heterostructure film (Ta/IrMn/CoFeB/MgO/Al_2O_3) [6]. Due to competing interactions (i.e. PMA, DMI and exchange bias), skyrmions and worm domains formed in CoFeB layer of 1.13 nm thickness without requiring any external bias magnetic field (Fig. 1, left column). Thereafter, we applied a negative voltage of -7 V (electric field of -0.16 V/nm) across the stack which resulted in an increase of PMA. We observed that after withdrawing the voltage, the skyrmions (and the worm domains) were annihilated and the magnetization reoriented in the perpendicular direction (Fig. 1, middle column). On the other hand, application of a positive voltage pulse reduced PMA of the system which proved to be a favorable condition for skyrmion formation from a saturated out of plane oriented state (Fig. 1, right column). Furthermore, we observed creation of skyrmions from chiral domains while increasing PMA. Finally, we performed detailed micromagnetic modeling to understand the underlying physics (Fig. 2). This study could provide a future pathway to control single skyrmion in an MTJ like device using VCMA. Acknowledgment: D.B and J.A are supported in part by the NSF CAREER grant CCF-1253370, NSF ECCS 1609303, VCU Quest Commercialization Grant and Virginia Microelectronics Seed Grant. S. A. R., H. W., B. D. and K. W. are supported in part by the NSF ECCS 1611570 and NSF NERC for Translational Applications of Nanoscale Multiferroic Systems (TANMS).

1. A. Fert et al, *Nat. Nanotechnol., vol. 8, no. 3, pp. 152–156, 2013* 2. X. Zhang et al, *Sci. Rep., 5, p. 9400, 2015.* 3. D. Bhattacharya et al, *Sci. Rep., 6, 31272, 2016.* 4. Y. Nakatani et al, *Appl. Phys. Lett., vol. 108, no. 15, 2016.* 5. D. Bhattacharya et al, *ACS Appl Mat. Inter. 10 (20), pp 17455–17462, 2018.* 6. D. Bhattacharya et al, *arXiv:1904.00701, 2019.*

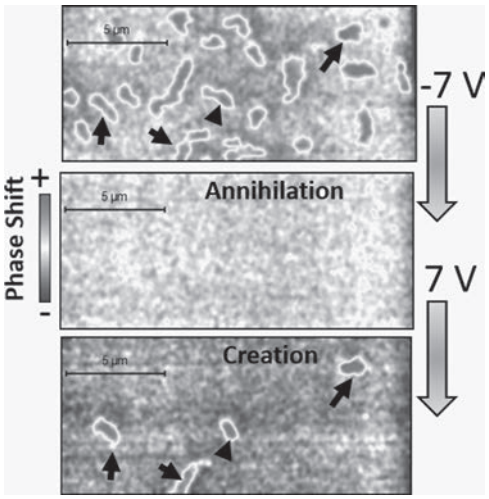


Fig 1. Annihilation and creation of skyrmions due to increase and decrease in perpendicular magnetic anisotropy

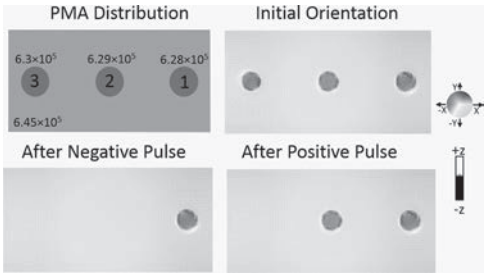


Fig 2. Micromagnetic simulation

3:42

DE-08. Skyrmion nucleation in Pt/Co/Ni-based thin film heterostructures. *J.A. Brock*[1], S. Montoya[2], M. Im[3,4] and E. Fullerton[1] *1. Center for Memory and Recording Research, University of California, San Diego, La Jolla, CA, United States; 2. Naval Information Warfare Systems - Pacific, San Diego, CA, United States; 3. Center for X-Ray Optics, Lawrence Berkeley National Laboratory, Berkeley, CA, United States; 4. Department of Emerging Materials Science, Daegu Gyeongbuk Institute of Science and Technology, Daegu, The Republic of Korea*

Magnetic skyrmions have attracted significant attention given their efficient motion in response to electrical currents and their topological stability due to their integer winding number [1]. For applications, the reliable nucleation of skyrmions that are stable in zero field at room temperature is of continued interest. Previously, it has been shown that the Joule heating from electrical current pulses may assist in nucleating skyrmions from stripes in systems with an interfacial Dzyaloshinskii-Moriya interaction (iDMI) [2,3]. In this presentation, experimental studies of Co/Ni/Pt thin-film heterostructures with moderate iDMI will be discussed. Using full-field transmission soft X-ray microscopy, we have observed a current-induced skyrmion phase can be generated at room temperature. We find a complete stripe-to-skyrmion transformation (within the field of view) by applying a 300 μs-long current pulses of density 5 x 10^{11} A/m^2 in an out-of-plane magnetic field of H = 3 kOe in 10 μm-wide wires of the composition $[Co/Ni/Pt]_{30}$. By reducing the moment and effective perpendicular anisotropy in samples of the form $[Co/Tb(0.4\ nm)/Ni/Pt]_{20}$, the current and field necessary to accomplish the same transition reduces to 1 x 10^9 A/m^2 and Hz = 350 Oe, respectively. Furthermore, the Joule heating needed to nucleate skyrmions is also reduced by

orders-of-magnitude. In both systems, the skyrmions remain stable over a range of magnetic fields, including at zero field. By investigating the effect of different current pulse amplitude, pulse duration, and applied magnetic fields, we find a sub-mJ difference in the Joule heating needed to completely transform stripe domains into skyrmions and that which has no action is found – suggesting Joule heating may not completely explain the energetic impetus of the stripe-to-skyrmion transition in these materials (Fig. 1). This work is supported by the US Department of Energy under grant DE-FOA-0001810.

[1] I.M. Miron, *et al.*, Nature Mat. 9, 230 (2010) [2] I. Lemesh, K. Litzius, M. Bottcher, *et al.*, Adv. Mat. 30, 2805461 (2018) [3] W. Legrand, D. Maccariello, N. Reyren, *et al.*, Nano Lett. 17, 2703 (2017)

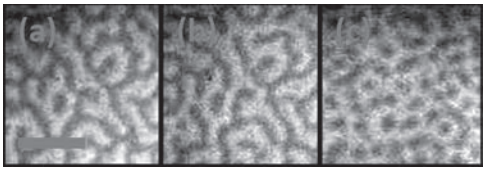


Fig. 1 In an out-of-plane field of 500 Oe, MTXM images (collected at the Co L-edge) of magnetic features in the $[Co/Ni/Pt]_{20}$ sample (a) before current pulses are applied, after a current density 2.5 x 10^{11} A/m^2 was applied for (b) 50 µs and (c) 60 µs. (bar = 500 nm)

3:54

DE-09. Temperature dependence of skyrmion size in a Ir/Fef/Co/Pt multilayer film. A. Yagil[1], M. Raju[2], R. Tomasello[3], G. Finocchio[4], S. Chiappini[5], O.M. Auslaender[1], C. Panagopoulos[2] and *M. Reznikov*[1]
1. Physics, Technion, Israel Institute of Thechnology, Haifa, Israel; 2. Physics and Applied Physics, Nanyang Technological University, Singapore; 3. Institute of Applied and Computational Mathematics, Foundation for Research and Technology-Hellas, Heraklion, Greece; 4. Department of Mathematical and Computer Sciences Physical Sciences and Earth Sciences, University of Messina, Messina, Italy; 5. Istituto Nazionale di Geofifica e Vulcanologia - INGV, Rome, Italy

Skyrmions are nanometer-scale magnetic domains which can be attributed a non-trivial topological charge. Their size and stability make them candidates for high-density magnetic memory. Skyrmions have been observed at low temperatures in certain bulk crystals and thin films lacking inversion symmetry. Recently, Ir/Fe/Co/Pt multi-stack films have been shown to host magnetic skyrmions at ambient conditions [1,2]. Here we present magnetic force microscopy (MFM) imaging of skyrmions in the temperature range 5-200K. We studied a sample with 20 repeats of [Ir(1)/Fe(0.5)/Co(0.5)/Pt(1)], where numbers in the parentheses represent layer thickness in nm. Isolated skyrmions in the film appear at an external magnetic field B≈0.3T. The skyrmions shrink and proliferate with temperature. Special care was taken to maintain a constant height of the MFM tip of ≈30nm above the surface, which allowed assessment of the temperature dependence of the skyrmion size. The examples of the MFM scans are shown in Fig. 1. Contrary to expectations [3], we found that skyrmions shrink and proliferate with temperature; the observed skyrmion radius r_m at half maximum decreases from ≈32nm at 5K to ≈24nm at 200K. Due to the blurring effect of the tip, the actual skyrmion radius r_s is much smaller, r_s≈22nm at 5K. For smaller r_m blurring contributes even more, so we expect that r_m=24nm corresponds to r_s<14nm. The reduction of r_s is accompanied by a decrease of the amplitude of the MFM signal, although the decrease, by a factor 3 from 5K to 200K, is significantly smaller than expected due to the decrease of r_s and of the saturation magnetization M_s with temperature. We analyzed skyrmions by minimizing the micromagnetic energy functional [3], which depends on material parameters, from which M_s and the effective anisotropy K_{eff} are known experimentaly [1], and B is set externally. Although K_{eff}, which favors large skyrmions, reduces strongly with temperature, we find its influence on size to be small. In contrast, the reduction of M_s and Dzyaloshinckii-Moria interactions with temperature can explain the observed size change.

1. A. Soumyanarayanan, M. Raju, A. L. Gonzalez Oyarce, et al., Nature. materials, Vol.16, p. 898, (2017) 2. M. Raju, A, Yagil, A. Soumyanarayanan, et al., Nature Communications, Vol.10, p. 696 (2019) 3. R. Tomasello, K. Guslienko, M. Ricci, et al., Phys. Rev. B 97, p. 060402 (2018)

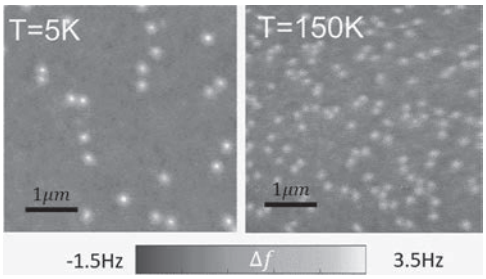


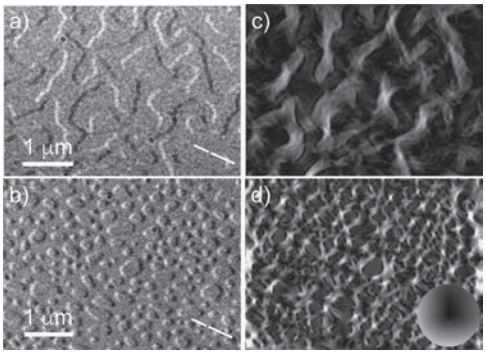
Fig. 1. MFM scan

4:06

DE-10. Observation of zero-field skyrmion arrays in Pt/Co/Ni/Ir-based multi-layers. *M.P. Li*[1], M. De Graef[1] and V. Sokalski[1] *1. Materials Science & Engineering, Carnegie Mellon University, Pittsburgh, PA, United States*

Magnetic skyrmions have drawn a great deal of attention due to the efficiency by which they can be manipulated with electric current for use in spintronic devices. The spin structure of skyrmions results from the Dzyaloshinskii-Moriya interaction (DMI), but skyrmion arrays also often require a perpendicular field to become the ground state. Here we observe skyrmion arrays that are stable in the absence of a perpendicular field in Pt/Co/Ni/Ir-based thin films with a range of DMI strengths using Lorentz transmission electron microscopy (LTEM). Multi-layers of $[Pt/(Co/Ni)_M/Ir]_N$ were deposited onto Si_3N_4 TEM membranes via magnetron sputtering. The ferromagnetic thickness, M, can be varied to effectively tune interfacial DMI without loss of perpendicular magnetic anisotropy. We have previously shown interfacial DMI is sufficient to support chiral Néel domain walls and isolated Néel skyrmions in this system.[1] Fresnel-mode LTEM was performed on an aberration-corrected FEI Titan G2 80-300 in Lorentz-mode. In the demagnetized state, the magnetic domain pattern is irregular (Fig 1) where contrast is only visible with the application of sample tilt confirming Néel DWs. *Ex situ* application of a sufficiently large in-plane magnetic field produces a skyrmion array in the remnant state (Fig 1). Although the precise mechanism for this observation remains under investigation, the in-plane field will significantly reduce the DW energy, thereby, enabling a much finer initial domain size as the in-plane field is reduced below the saturation field, H_k. In these relatively thin samples dipolar interactions do not immediately drive the system to a labyrinth or stripe pattern as in conventional bubble materials. Rather, the combination of pinning and topological stability of 360° Néel transitions between skyrmions preserves a refined size distribution. This method, coupled with our tunable materials system, provides a means to investigate skyrmions out of equilibrium for the development of future spintronic devices.[2]

[1] M. Li, D. Lau, M. De Graef, and V. Sokalski, *Phys. Rev. Mater.,* Vol. 3, p. 064409 (2019). [2] This research is supported by the Defense Advanced Research Project Agency (DARPA) program on Topological Excitations in Electronics (TEE) under grant number D18AP00011. The authors also acknowledge use of the Materials Characterization Facility at Carnegie Mellon University supported by grant MCF-677785.



a,c) LTEM images and b,c) in-plane induction maps of $[Pt/(Co/Ni)_5/Ir]_2$ in its a,b) demagnetized state and c,d) remnant state after application of in-plane magnetic field. Samples were imaged with a sample tilt of 20°.

4:18

DE-11. High-Frequency Domain Wall Oscillations in Ferromagnetic Nanowire with a Nanoscale Dzyaloshinskii–Moriya Interaction (DMI) Region. *D. Kumar*[1], R. Sbiaa[2], P. Sengupta[1] and S. Piramanayagam[1]
1. School of Physical and Mathematical Sciences, Nanyang Technological University, Singapore; 2. Department of Physics, Sultan Qaboos University, Muscat, Oman

It has been almost fifty years since Dzyaloshinskii and Moriya have observed and explained the non-collinear interaction between spins. However, only recently, the Dzyaloshinskii–Moriya Interaction (DMI) has picked up the interest of researchers [1]. Domain wall (DW) devices with interfacial DMI, exhibiting Chiral DW motion with high speed and Skyrmions are some examples [2, 3]. On the fundamental front, DMI has attracted interest because of its role in stabilizing several magnetic phases with non-collinear and non-coplanar spin orderings. Many of these phases exhibit exotic low energy excitations obeying fractional statistics and drive unconventional electronic transport phenomena such as linear magneto-resistance and topological Hall effect. In most of the studies involving DMI so far, the investigations were focussed on a ferromagnetic layer which is entirely under DMI. In this study, we have investigated a distinctive scenario, where DMI acts only in a narrow region of a ferromagnetic nanowire. Through micromagnetic simulations, we have observed that the DW oscillates with the microwave frequency for a limited range of geometrical and magnetic parameters (as shown in Fig. 1). Fig. 1 (c) shows the discrete phase diagram for DW pinning (smaller DMI) and oscillation (higher DMI). When an electrical current flows along the nanowire, STT pushes the DW. However, the DW also experiences an additional restoring force in this DMI modified region. As a result, DW was found to oscillate. The oscillation frequency (*f*) linearly increases with the current density while it does not depend on d. A good tunability of "*f*" was observed with the magnetic parameters as shown in Fig. 2. We have developed an analytical model, which explains our findings of the simulations. The details will be presented during the conference.

A. Thiaville, S. Rohart, É. Jué, V. Cros and A. Fert, EPL (Europhysics Letters) 100, 57002 (2012). I.M. Miron, K. Garello, G. Gaudin, P.J. Zermatten, M.V. Costache, S. Auffret, S. Bandiera, B. Rodmacq, A. Schuhl, and P. Gambardella, Nature 476, 189 (2011). S.H. Yang, K.S. Ryu, and S. Parkin, Nature nanotechnology 10, 221 (2015).

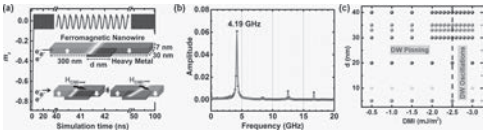


Fig. 1. (a) Variation of *z*-component of magnetization (m_z) as a function of simulation time for d= 30 nm, DMI= -3 mJ/m² and J= 5 x 10^{11} A/m². Inset: the schematic of the proposed nanotrack, (b) the fast Fourier transform of Fig. 1 (a), and (c) discrete phase diagram for DW oscillations.

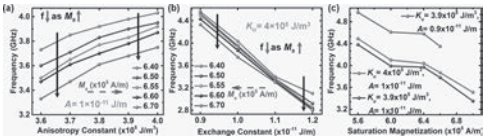


Fig. 2. Dependence of "*f*" on (a) anisotropy constant, (b) exchange constant and (c) saturation magnetization.

Session DF
NEUROMORPHIC COMPUTING

Jean Anne C. Incorvia, Chair
University of Texas at Austin, Austin, TX, United States

INVITED PAPER

1:30

DF-01. Physical Reservoir Computing based on Spin Torque Oscillator with Synchronization. *S. Tsunegi*[1], T. Taniguchi[1], K. Nakajima[2,3], S. Miwa[4], K. Yakushiji[1], A. Fukushima[1] and H. Kubota[1] *1. Spintronics Research Center, National Institute of Advanced Industrial Science And Technology (AIST), Tsukuba, Japan; 2. Graduate School of Information Science and Technology, The University of Tokyo, Bunkyo-ku, Japan; 3. PRESTO, JST, Kawaguchi, Japan; 4. The Institute for Solid State Physics, The University of Tokyo, Kashiwa, Japan*

Recently, spintronics devices have been applied to artificial neural networks. In particular, reservoir computing (RC) based on spin torque oscillators (STOs) is an interesting research target, which enables us to classify and calculate a time sequence of input data such as spoken languages and movies [1]. Several functionalities of STOs, such as small size and nonlinearity, are preferable to the RC. The smallness of the device size, however, causes serious problems such as a large noise in the STO. Thermal fluctuation disturbs the magnetization oscillation, and gives randomness in its amplitude and phase [2]. The reduction of the noise from STO is highly required to improve the performance of RC. Synchronization phenomena such as forced synchronization have been known to be useful to reduce the noise from STO [3]. However, the performance of RC with synchronized STO has not been studied yet. In this work, we investigated the oscillation properties of a vortex-type STO synchronized to microwave field from the viewpoint of physical RC. As a figure of merit, we measured the short-term memory and parity-check capacities [4,5] by using the phase modulation of the microwave as a binary input. Figure 1 shows schematics of experimental. The modulated microwave field was applied to the STO, and causes transient dynamics of the vortex core. Since the transition dynamics depends on the sequence of the input data, the dynamics has the functionality of short-term memory. Optimizing the microwave amplitude, the short-time memory capacity was maximized to be 3.6 as shown in Fig. 2. Note that this value is two times larger than that without synchronization [6,7]. The parity-check capacity was also evaluated for the first time, which was 3.1 at maximum. The results demonstrated that the synchronized STO has a great potential to be applied in RC. This work was based on the results obtained from a project commissioned by NEDO.

[1] J. Tirrejon *et al*., Nature 547, 428 (2017) [2] M. Keller *et al*., Appl. Phys. Lett. 94, 193105 (2009) [3] R. Lebrun *et al*., Phys. Rev. Lett. 115, 017201 (2015) [4] K. Nakajima *et al*., J. R. Soc. Interface 11, 20140437 (2014) [5] T. Furuta *et al*., Phys. Rev. Appl. 10,034063 (2018) [6] S. Tsunegi *et al*., Jpn. J. Appl. Phys. 57,120307 (2018) [7] S. Tsunegi *et al*., Appl. Phys. Lett. 114,164101 (2019)

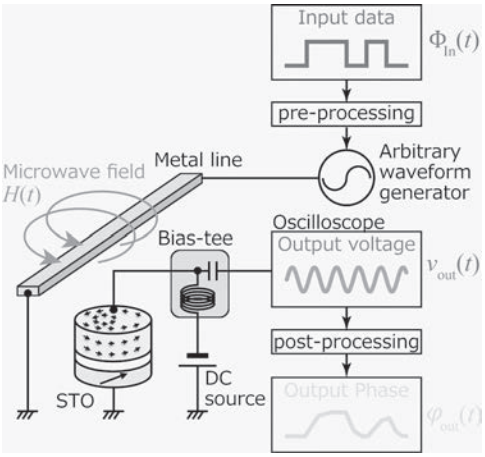


FIG. 1. Schematics of the measurement circuit. The microwave field is applied to the STO, where the phase of the microwave field is changed according to the binary data sequence input to an arbitrary waveform generator.

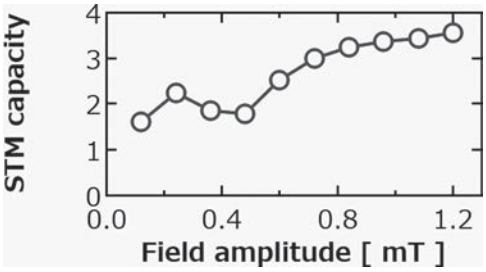


FIG. 2. Relation between amplitude of microwave field and short-term memory (STM) capacity.

CONTRIBUTED PAPERS

2:06

DF-02. Oxygen-Migration-Based Magnetic Device Emulating a Biological Synapse. *R. Mishra*[1], D. Kumar[1] and H. Yang[1] *1. Electical and Computers Engineering, National University of Singapore, Singapore*

Electronic emulation of the biological synapse, which is the memory and learning element of the brain, is an important step towards the realization of brain-inspired computing systems. However, a complementary metal-oxide-semiconductor–based implementation of a synapse is not scalable due to the power and area inefficiency[1]. It is therefore essential to develop alternative material and device concepts that can mimic the synaptic functionalities in an energy-efficient way[2-3]. We demonstrate a nanosized energy-efficient three-terminal artificial synapse, with a separate read and write path, based on a magnetic material (Co) that could generate both positive and negative synaptic outputs. Devices from the structure MgO/Pt/Co were covered with gate oxide, GdO_x. The Co layer acts as the main functional layer of the

synapse. The weight of the magnetic synapse is defined using the measure of net Co magnetization and it is quantified with the anomalous Hall resistance (R_{AHE}). The synaptic weight is modulated by applying an electric field on the GdO_x gate which results in the movement of oxygen ions[4] in and out of the Co layer as shown in Fig. 1. Synaptic potentiation and depression is shown in Fig. 2(a). When V_g pulses of +10 V and 50 ms duration are applied on the magnetic synapse, an increase in R_{AHE} is observed. Spike time dependent plasticity (STDP) of the magnetic synapse as shown in Fig. 2(b) results in weight modulation whose magnitude depends on the relative arrival of pre and postsynaptic spikes similar to that observed in the biological brain. The magnetic synapse can emulated other synaptic functions as well such as spike magnitude and rate-dependent plasticity, and the transition from short-term to long-term plasticity. Our results[5] suggest the viability of a spintronic synapse in neuromorphic computing.

1. E. Farquhar and P. Hasler, IEEE Transactions on Circuits and Systems I: Regular Papers 52, 477 (2005). 2. S. H. Jo, T. Chang, I. Ebong et al., Nano Letters 10, 1297 (2010) 3. J. Torrejon, M. Riou, F. A. Araujo et al., Nature 547, 428 (2017). 4. U. Bauer, L. Yao, A. J. Tan et al., Nature Materials 14, 174(2014). 5. R. Mishra, D. Kumar and H. Yang, Physical Review Applied 11, 054065 (2019).

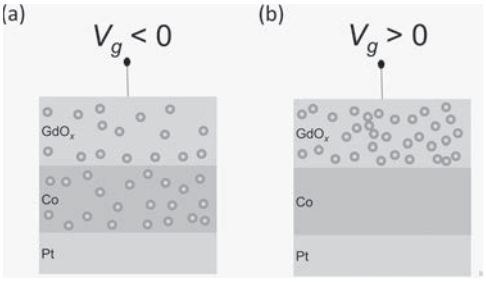


Fig. 1. State of the magnetic synapse under the application of (a) negative and (b) positive V_g. Blue spheres represent oxygen ions.

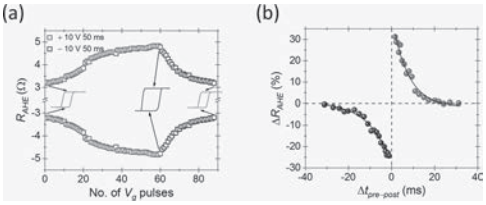


Fig. 2. (a) Potentiation and depression of the magnetic synapse. The Co magnetization state is switched between positive and negative state to emulate positive and negative synaptic weight. (b) Dependence of synaptic weight on relative timing of the pre and postsynaptic pulses.

2:18

DF-03. Hardwired MTJ Circuits for Stochastic Computing. *B. Parks*[1] and S. Majetich[1] *1. Physics, Carnegie Mellon University, Pittsburgh, PA, United States*

Magnetic tunnel junctions (MTJs) have been proposed as components of logic gates for stochastic computing [1]. The two resistance states of an MTJ, parallel and antiparallel, are used as logical 1 and 0. When the energy barrier to magnetization reversal is low compared to the thermal energy, the MTJ switches between 1 and 0 stochastically. The average dwell time before another switch can be tuned, using spin transfer torque (STT), such that the resistance is instantaneously digital yet analog in time average. When these STT-controlled stochastic MTJs are electronically coupled, the same circuit may be used to multiply and factor numbers. In-plane magnetized films were deposited consisting of SiO_2/Ta(5)/CoFeB(2.5)/MgO(1)/CoFeB(2.5)/Ru(0.85)/CoFe(2.5)/IrMn(8)/Ru(10), where the numbers in parentheses are the thicknesses in nanometers. The IrMn layer pins the CoFe layer, which in turn pins the CoFeB reference layer. We patterned these films into MTJ pillars with platinum leads and wire bond pads (Figure 1a). As shown in Figure 1b, the feedback between devices is regulated using resistance in series with transimpedance amplifiers to modulate the input current. We set the probability of the 1 state for each device using independent input currents and then allow the feedback mechanism to fluctuate about that set probability. Figure 2 shows binarized experimental measurements of the resistance of an MTJ for two different STT currents. The mean of the product of the two measurements agrees with the product of the two means to within 3% with an averaging time of 300 μs. This approach is extended to demonstrate invertible logic operations.

Camsari, Kerem Yunus, et al. “Stochastic p-bits for invertible logic.” *Physical Review X* 7.3 (2017): 031014.

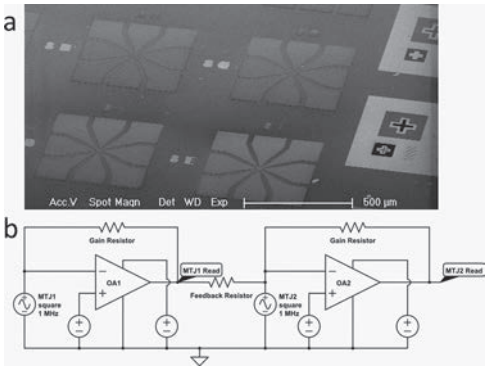


Figure 1: a) MTJ pillars lay at the center of each of the star-shaped bond pad structures. b) Transimpedance amplifiers are used to read the state of each MTJ and to provide feedback between devices such that the state of one device can influence the state of another.

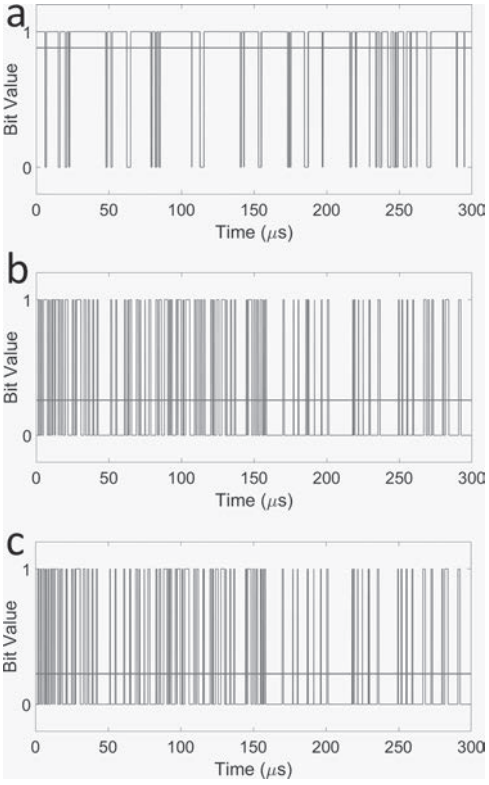


Figure 2: Measured bit values are shown in blue with mean values in red. A current of 52.5 μA results in a mean of 0.89 (a) while a current of 142 μA gives a mean of 0.26 (b). The product of the two measurements (c) gives a mean of 0.23, the same as the product of the means.

2:30

DF-04. Advantage of domain wall synapse over RRAM synapse for "on-chip" learning in hardware Fully Connected Neural Network. *D. Kaushik*[1], U. Singh[2], U. Sahu[1] and D. Bhowmik[1] *1. Electrical Engineering, Indian Institute of Technology Delhi, New Delhi, India; 2. Electronics and Communication Engineering, Delhi Technological University, New Delhi, India*

Resistive RAM (RRAM) has been widely used as synapse in hardware Neural Network (NN) [1,2,3]. Here we demonstrate advantage of recently proposed spin orbit torque driven Domain Wall (DW) device (Fig1a) [4,5] as synapse compared to RRAM for "on-chip" learning (training in hardware) in NN. RRAM synapse is simulated using VerilogA module in SPICE circuit simulator, benchmarked on HfOx device (Fig1c) [1]. Though conductance and hence weight increases gradually with increasing gate voltage pulses of short duration (200 ns), a RESET pulse (6 μs) that consumes large amount of time and energy is needed to decrease conductance [1,2,3]. Still conductance drops abruptly (Fig1d). This affects accuracy in "on-chip" learning because weights need to change gradually. Similar issue occurs in Phase Change Memory (PCM) synapse [3]. Using 2-RRAM or PCM devices per synapse overcomes accuracy issue to a degree [2,3,6] but occasional RESET pulses increase time and energy for "on-chip" learning, e.g, when we train a Fully Connected NN (FCNN) made of RRAM synapses on popular Fisher's Iris dataset [7] 6 RESET pulses were needed within 50 epochs for a particular synapse (Fig2c). However in DW synapse conductance varies symmetrically and linearly with current pulse of opposite polarities because of the nature of DW motion as observed in our micromagnetic simulations, benchmarked against experimental data on Pt/CoFe/MgO structure [4,5,8] (Fig1a,b). Hence when we design FCNN on SPICE simulator with micromagnetic model of DW synapse present in it as VerilogA module (Fig2a), the same 3 ns long current pulse of Fig1b increases and decreases the weight of the synapses (Fig2b) as needed during training on same dataset. No RESET pulse is needed. Hence total energy in synaptic weight update during "on-chip" learning on DW synapse NN is 9 orders lower than that in RRAM NN and time for learning is also much less (Fig2d).

[1] P. Chen and S. Yu, IEEE Trans. Electron Devices. vol. 62, no. 12, 2015. [2] C. Li, D. Belkin, Y. Li et al. Nature Comm. vol. 9, no. 2385, 2018. [3] H. Tsai, S. Ambrogio, P. Narayanan et al. J. Phys. D: Appl. Phys. vol. 51, no. 283001, 2018. [4] A. Sengupta and K. Roy, IEEE Trans. on Circuits and Systems-I, vol. 63, no. 12, 2016. [5] D. Bhowmik, U. Saxena, A. Dankar et al. J. Magn. Magn. Mater. Vol. 489, no. 165434, 2019. [6] G. W. Burr, R. M. Shelby, S. Sidler et al. IEEE Trans. on Electron Devices, vol. 62, no. 11, 2015. [7] R. A. Fisher, Annual Eugenics, vol. 7, no. 2, pp. 179-188, 1936. [8] S. Emori, U. Bauer, S. M. Ahn et al. Nature Materials vol. 12, p. 611-618, 2013.

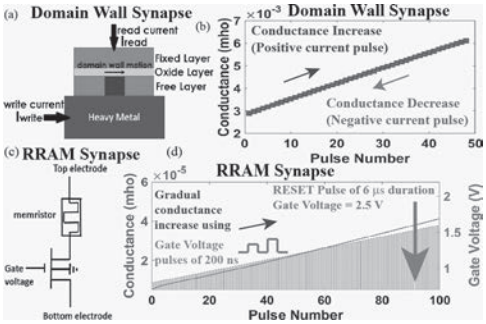


Fig 1. Schematic and conductance response of Domain Wall synapse ((a),(b)) and RRAM synapse ((c),(d))

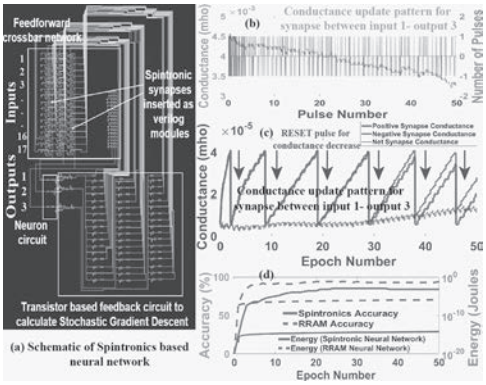


Fig 2. (a) Schematic of DW synapse based FCNN designed on SPICE (b) Conductance update scheme for a particular DW synapse in circuit of (a) (c) Update scheme in same synapse if made of RRAM (d) Accuracy and energy consumption comparison

INVITED PAPER

2:42

DF-05. Artificial Synapse and Neuron Based on the Dynamics of Spintronic Devices. *A. Kurenkov*[1,2], S. DuttaGupta[1,2], C. Zhang[1], S. Fukami[1,2], Y. Horio[1] and H. Ohno[1,2] *1. RIEC, Tohoku University, Sendai, Japan; 2. CSIS, Tohoku University, Sendai, Japan*

The human brain can perform complex cognitive tasks with amazing efficiency which is far superior to von Neumann machines. While there has been considerable progress in software-based artificial intelligence dedicated to specific tasks, building neural networks of the efficiency and complexity of the brain will require reproducing its architecture in hardware. A major obstacle here is that functionalities of the unit elements—synapses and

neurons—are complex and very different. This either forces their implementation in different material systems or requires a large number of CMOS elements to build a single neuron/synapse. Here we will show how spintronics can help to reconcile the contradictory requirements of synapses and neurons and realize them in a lean and biologically plausible way by considering an antiferromagnet/ferromagnet heterostructure with field-free spin-orbit torque switching[1,2]. First, control of its switching mode from binary to analog-like[3] will be discussed. This is an essential requirement to realize binary firing/nonfiring states of the neuron and analogue weight memorization of the synapse in the same material stack. Next, we will show that a uniform mechanism of "local time" can drive the functionalities of synapses and neurons despite their differences. To realize such mechanism in the considered spintronic devices, their dynamical properties under current pulses down to 1 ns will be analyzed. After identifying a suitable dynamical process, it will be used as a timer and thereby as a basis for artificial synapses and neurons. Finally, all the discussed physical properties will be combined to demonstrate units with inherent synapse- and neuron-like properties, made from the same material and driven by a uniform principle[4]. We will show that the devices respond like their biological counterparts, which makes them promising candidates for future artificial spiking neural networks, and discuss their operation. A portion of this work was supported by JSPS KAKENHI 17H06093, 18KK0143 and 19K15428, JST-OPERA, JSPS Core-to-Core Program and Cooperative Research Projects of RIEC.

[1] I. Miron et al., Nature 476, 189 (2011). [2] S. Fukami, A.K. et al., Nature Mater. 15, 535 (2016). [3] A. Kurenkov et al., Appl. Phys. Lett. 110, 092410 (2017). [4] A. Kurenkov et al., Adv. Mater. 31, 1900636 (2019).

CONTRIBUTED PAPERS

3:18

DF-06. The recognition accuracy and power consumption of weightless neural network adopting spin-torque MRAM with a high write error rate. *H. Arai*[1] and H. Imamura[1] *1. AIST, Tsukuba, Japan*

The weightless neural network (NN) is a memory-based NN that has the benefit of simple and quick learning [1]. The weightless-NN is basically a pattern recognition system, but can recognize subjects having noise. Though it is an old technology, its performance is as good as that of conventional machine learning methods for classification tasks. Spin-torque magnetic random access memory (ST-MRAM) has attracted much attention as a fast and low-power non-volatile memory. The use of ST-MRAM instead of conventional volatile memories can reduce the power consumption of a weightless-NN because it consumes much less leakage power. In addition, the write error rate (WER) of ST-MRAM increases with decrease of the current density [2]. Therefore the power consumption for writing bits can be reduced if one accepts a high WER. However, little attention has been paid to the effects of the use of memories with a high WER on the accuracy as well as the power consumption of the weightless-NN. We investigated the recognition accuracy and power consumption of the weightless-NN consisting of ST-MRAM with a high WER. We numerically performed multi-class classification for binary images of hand-written digits in MNIST database [3]. We found that the weightless-NN works well even if the write error appears in the RAMs. As shown in Fig.1, the curve for the case with WER=10^{-3} corresponds to that for the case without the write error. In addition, the maximum accuracy is comparable for that for the case without the write error, and retained up to 10^{-3} of WER for 10 trials, shown in Fig.2(a). We also evaluated the power consumption until reaching the maximum accuracy and found that it can be reduced owing to the trade-off relation of ST-MRAM between WER and power consumption, shown in Fig.2(b).

[1] W. Thomas, I. Aleksander, and P. Bowden, Sensor Review 4, 120 (1984). [2] H. Lie, et al., J. Mag. Mag. Mat. 358-359, 233 (2014). [3] Y. Lecun, C. Cortes, and C. J. C. Burges, http://yann.lecun.com/exdb/mnist/.

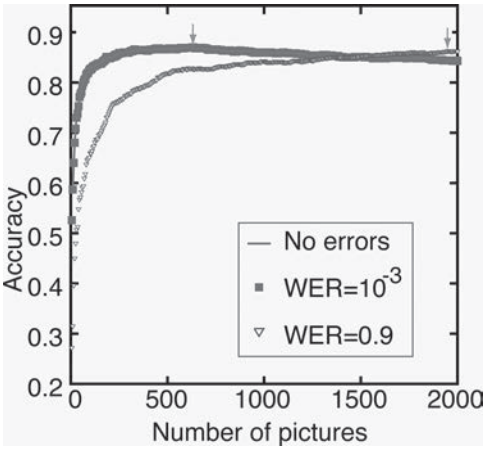


Fig.1 Typical learning history of the weightless-NN. Arrows indicate the maximum accuracy.

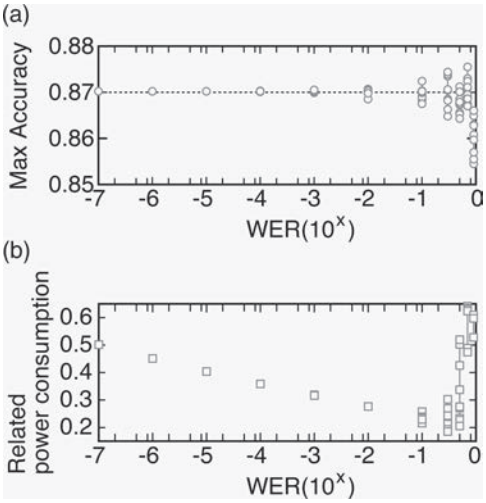


Fig.2(a) Distribution of maximum accuracy for 10 trials with different WER. The dotted line shows the result for the case without write error. (b) Distribution of the power consumption until reaching the maximum accuracy shown in Fig.2(a), where the power consumption for WER=10^{-15} is normalized to 1.0.

3:30

DF-07. Implementation of Spike Time Dependent Plasticity (STDP) enabled supervised learning in a Spiking Neural Network (SNN) using Domain Wall (DW) motion based neurons and synapses. *U. Sahu*[1], A. Pandey[2], K. Goyal[3] and D. Bhowmik[1] *1. Electrical Engineering, Indian Institute of Technology Delhi, New Delhi, India; 2. Electrical and Computer Engineering, Georgia Institute of Technology, Atlanta, GA, United States; 3. Mechanical Engineering, Indian Institute of Technology Delhi, New Delhi, India*

Spin orbit torque driven Domain Wall (DW) and skyrmionic devices have been proposed as Leaky Integrate Fire (LIF) neurons [1,2] and Spike Time Dependent Plasticity (STDP) exhibiting synapses [3,4,5] in Spiking Neural Network (SNN). Only testing has been shown in [1], using spintronic devices only for neurons. Training has been shown in [3,4]. But only the synapses are spintronic in [3,4] and not neurons. Here we have shown training, for the first time to the best of our knowledge, on SNN designed with both spintronic (DW based) synapses and neurons (Fig. 1(a)). Also in [3,4] STDP enabled unsupervised learning scheme is followed for training [6], But here we follow a STDP enabled supervised scheme [7,8]. DW synapse,

proposed in [4,9], is simulated using micromagnetics on "mumax3", benchmarked against experimental data on Neel DW motion in Pt (heavy metal) /CoFe(ferromagnet)/MgO heterostructures due to in-plane current (write current or I_{write}) reported in [10] and used in the designed SNN (Fig. 1(b)). To incorporate STDP property we design transistor based circuit operating in sub-threshold regime [4] on SPICE circuit simulator that applies 3ns long I_{write} pulse on the synapse. Magnitude of I_{write}, and hence DW position and hence conductance and weight of DW synapse, show exponential dependence on time difference between spikes of pre and post-neuron with time constant (τ_{STDP} = 1.5 μs)- characteristic of STDP (Fig. 1(c),1(d)). DW neuron (Fig. 2(a)) is designed next with LIF characteristic such that time difference between two consecutive spikes is in the order of τ_{STDP} and hence three orders higher than time duration of I_{write} pulse for DW synapse (Fig. 2(b)). High classification accuracy is obtained for designed SNN on the popular Fisher's Iris dataset of flowers [11] and MNIST database of handwritten digits [12] (Fig. 2(c),(d)). Such high accuracy (85%) for MNIST is obtained for first time in the case of this STDP enabled supervised learning algorithm [7,8]. Synaptic weights form impression of the digits just like in [6] showing successful training (Fig.2(e)).

[1] N. Hassan *et al.* J. Appl. Phys., vol. 124, no. 152127, 2018. [2] S. Li, W. Kang, Y. Huang et al. Nanotechnology, vol. 28, p. 31LT01, 2017. [3] T. Bhattacharya, S. Li, H. Yangki et al. IEEE Access, vol. 7, p. 5034, 2019. [4] A. Sengupta, A. Banerjee, and K. Roy, Devices, Circuits, and Systems, Phys. Rev. Appl. vol. 6, no. 064003, 2016. [5] Y. Huang, W. Kang, X. Zhang et al. Nanotechnology, vol. 28, p. 08LT02, 2017 [6] P. U. Diehl and M. Cook, Front. Comput. Neurosci. vol. 9, no. 99, 2015. [7] A. Biswas, S. Prasad, S. Lashkare, and U. Ganguly. arxiv. 1612.02233, 2016 [8] S. Prasad, A. Biswas, A. Shukla and U Ganguly. International Conference on Artificial Neural Networks (ICANN) 2017 [9] A. Sengupta and K. Roy, IEEE Transactions on Circuits and Systems- I, vol. 63, no. 12, 2016. [10] S. Emori, U. Bauer, S. M. Ahn et al., Nature Materials, vol. 12, p. 611-616, 2013. [11] R. A. Fisher, Annual Eugenics, vol. 7, no. 2, pp. 179-188, 1936. [12] Y.LeCun, L. Bottou, Y. Bengio et al. Proceedings of the IEEE 86, p. 2278-2324, 1998

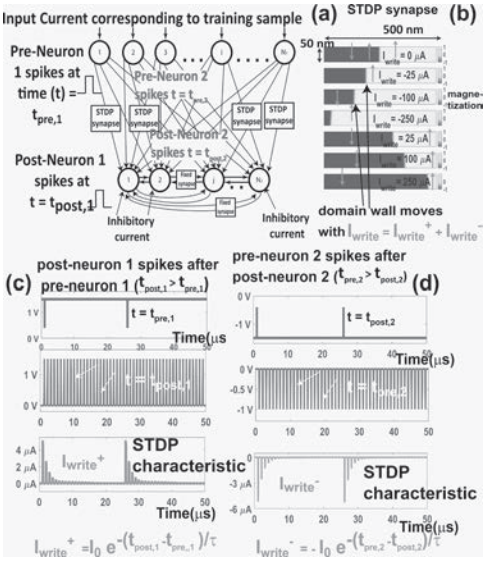


Fig 1. (a) Designed SNN (b) DW synapse with STDP characteristic in I_{write}

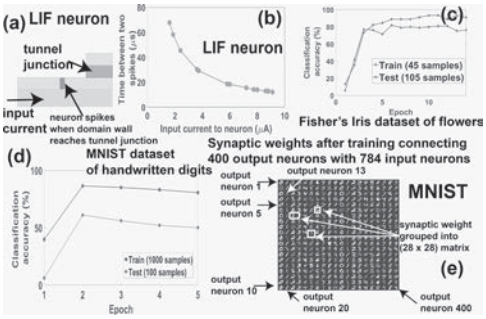


Fig 2. (a), (b) Designed DW neuron showing LIF property (c),(d)(e) Training on datasets

INVITED PAPER

3:42

DF-08. Neuromorphic computing using two-dimensional arrays of spin Hall nano-oscillators. *J. Åkerman*[1] *1. Department of Physics, University of Gothenburg, Gothenburg, Sweden*

Mutually synchronized spin torque nano-oscillators (STNOs) are one of the promising platforms for bioinspired computing and microwave signal generation [1,2]. Using STNOs one can achieve 90% recognition rate in spoken vowels [3]. However, in order to do more complex tasks, larger scale synchronized oscillators are needed, something that is not easily done with the STNOs demonstrated so far. In my talk, I will describe a different type of spin current driven device called spin Hall nano-oscillators (SHNOs), which can generate microwave frequencies over a very wide frequency range [4]. The SHNOs are based on 50 – 120 nm wide nano-constrictions in Pt(5)/Hf(0.5)/NiFe(3) trilayers (all numbers in nm). When multiple nano-constrictions are fabricated close to each other (300 – 1200 nm separation) they can mutually synchronize and chains of up to nine nano-constrictions have been demonstrated to exhibit complete synchronization [5]. For the first time, we can now also synchronize two-dimensional SHNO arrays with as many as 8 x 8 = 64 SHNOs [6]. The mutual synchronization is observed both electrically and using scanning micro-BLS microscopy. Both the output power and linewidth of the microwave signal improves substantially with increasing number of mutually synchronized SHNOs, such that quality factors of about 170,000 can be reached. Following the approach of Romera et al [3], we also demonstrate neuromorphic computing using a 4 x 4 SHNO array with two injected microwave signals as inputs. Given their high operating frequency (~10 GHz), ease of fabrication, and highly robust synchronization properties, nano-constriction SHNO arrays are the most promising candidates for neuromorphic computing based on large oscillator networks.

[1] J. Grollier, D. Querlioz, and M. D. Stiles, Proc. IEEE 104, 2024 (2016) [2] J. Torrejon et al, Nature 547, 428 (2017) [3] M. Romera et al, Nature 563, 230–234 (2018) [4] T. Chen, R. K. Dumas, A. Eklund, P. K. Muduli, A. Houshang, A. A. Awad, P. Durrenfeld, B. G. Malm, A. Rusu, and J. Åkerman, Proc. IEEE 104, 1919 (2016) [5] A. A. Awad, P. Durrenfeld, A. Houshang, M. Dvornik, E. Iacocca, R. K. Dumas, and J. Åkerman, Nature Physics 13, 292–299 (2017) [6] M. Zahedinejad, et al. arXiv:1812.09630 (2018)

Session DG
BIOMEDICAL APPLICATIONS II
Maciej Zborowski, Chair
Cleveland Clinic, Cleveland, OH, United States

INVITED PAPER

1:30

DG-01. Towards Organ Cryopreservation: Nanowarming Using Magnetic Nanowires. *B. Stadler*[1,2], D. Shore[2], A. Ghemes[3], O. Dragos[3], Z. Gao[4], Q. Shao[4], A. Sharma[4], J. Um[1], I. Tabakovic[1,3] and J.C. Bischof[4]
1. Electrical and Computer Engineering, University of Minnesota, Minneapolis, MN, United States; 2. Chemical Engineering and Materials Science, University of Minnesota, Minneapolis, MN, United States; 3. National Institute of R&D for Technical Physics, Iasi, Romania; 4. Mechanical Engineering, University of Minnesota, Minneapolis, MN, United States

Magnetic nanoparticles have proven useful for contactless heating in biological applications, such as hyperthermia in cancer therapy. A relatively new application, nanowarming cryopreserved organs [1-3], requires uniform heating that is much faster than 50°C/min to avoid crystallization of vitrified cryoprotective agents (CPA), which act as antifreeze buffers. Unlike iron oxide nanoparticles, magnetic nanowires (MNWs) have high saturation magnetizations (M_s) and high magnetic anisotropies, which are ideal for magnetic heating in an alternating magnetic field (AMF).[4] Here, Au-tipped MNWs were coated with polyethylene glycol (PEG) and specific absorption rates (SAR) were measured in glycerol to mimic the viscosity of a typical CPA. SAR increased when using metals with increasing M_s ($Co_{35}Fe_{65}$ > Fe > Co > Ni), reaching 1610 ± 20 W/g metal at 1 mg metal/ml glycerol for $Co_{35}Fe_{65}$ nanowires using 190 kHz and 20 kA/m. Aligning these nanowires parallel to the AMF increased SAR up to 2010 W/g $Co_{35}Fe_{65}$. Next, $Co_{35}Fe_{65}$ nanowires were used to nanowarm vitrified VS55, a common CPA. Nanowarming rates up to 1000 °C/min (5 mg $Co_{35}Fe_{65}$/ml VS55) were achieved, Fig. 1a, which is 20x faster than the critical warming rate for VS55 and other common CPAs. In this talk, magnetic measurments such as the area of minor loops, Fig. 1b, and design rules for optimized MNWs will be presented. To check for cytotoxicity, human dermal fibroblast cells exposed to VS55, and $Co_{35}Fe_{65}$ nanowire concentrations of 0, 1 and 2.5 mg Fe/ml, and all cases showed similar (high) cell viability. With the ability to provide rapid and uniform heating, MNWs have excellent potential for nanowarming cryopreserved tissues, in addition to enrichment [5] and MRI contrast [6] as shown previously.

[1] Giwa, S, JK Lewis, L Alvarez, R Langer, AE Roth, GM Church, JF Markmann, DH Sachs… JC Bischof, et al. "The promise of organ and tissue preservation to transform medicine." *Nature biotechnology* 35, no. 6 (2017): 530. [2] Manuchehrabadi N... M Garwood, CL Haynes, JC Biscof, Science translational medicine. 2017 Mar 1;9 (379): eaah4586. [3] Bischof, JC, 11. Nanowarming: a new concept in tissue and organ preservation. *Cryobiology* 71, no. 1 (2015): 167. [4] Authors of this abstract, Nanoscale, accepted May 2019. DOI:10.1039/C9NR01182J [5] DE Shore, T Dileepan, JF Modiano, M. Jenkins, BJH Stadler, Nature Sci Reports 8 (2018). [6] DE Shore, SL Pailloux, JJ Zhang, T Gage, DJ Flannigan, M Garwood, VC Pierre, BJH Stadler, Chem Comm 52 12634 (2016).

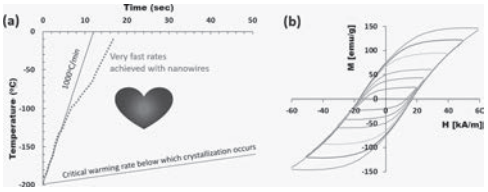


Fig. 1- a) Showing great promise for cryopreservation of organs, magnetic nanowiress were shown to nanowarm vitrified cryoprotective agent VS55 20x faster than the necessary critical warming rate. b) The area of minor loops can be tailored to optimize nanowarming.

CONTRIBUTED PAPERS

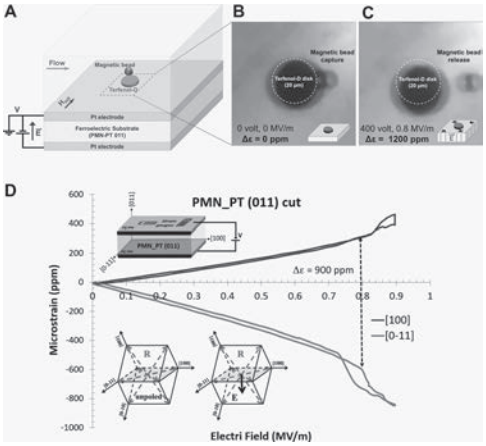
2:06

DG-02. Programmable Multiferroic Micromagnets for Single-Cell Manipulation. *R. Khojah*[1], Z. Xiao[2], M.K. Panduranga[3], M. Goiriena-Goikoetxea[5], R.V. Chopdekar[4], J. Bokor[5], G. Carman[3], R. Candler[2] and D. Di Carlo[1] *1. Bioengineering, University of California Los Angeles, Los Angeles, CA, United States; 2. Electrical Engineering, University of California Los Angeles, Los Angeles, CA, United States; 3. Mechanical and Aerospace Engineering, University of California Los Angeles, Los Angeles, CA, United States; 4. Advanced Light Source, Lawrence Berkeley National Laboratory, Berkeley, CA, United States; 5. Electrical Engineering and Computer Sciences, University of California Berkeley, Berkeley, CA, United States*

Precise and programmable magnetic fields at the microscale can improve the resolution of magnetic cell sorting to a single-cell level for personalized cell therapy applications. Current technologies comprising soft and hard magnetic materials enable bulk cell separation but are currently unable to be actuated for programmable magnetic capture/release of target single-cells from a larger cell population [1]. These previous materials lack programmability to release cells while electromagnets are programmable but lack localization of a sufficient force to capture single-cells. This work demonstrates a new generation of programmable multiferroic devices that promises precise and tunable capture/release of cells across massive arrays [2]. Magnetoelastic Terfenold-D microstructures ($Tb_{0.3}$ $Dy_{0.7}$ $Fe_{1.92}$) microstructures (diameter 5-100 μm) were fabricated using photolithography and dry etching methods on a (011)-cut PMN-PT piezoelectric substrate (Fig.1A). Single-domain structures are established in Terfenol-D microdisks (20 μm) after the application and removal of a 0.5 T saturating magnetic field. Magnetic beads and magnetically-labeled cells were introduced in the device via microfluidic channels with a steady flow rate of 5 μL/min, where single-cells were captured and arrayed on Terfenol-D microdisks (Fig.1B), then subsequently released with an applied electric field (Fig.1C). An electric field of 0.8 MV m^{-1} induces compressive strain of 900 ppm along [100] direction and tensile strain of 300 ppm along [0-11] direction (Fig.1D). The resulting total strain of 1200 ppm, perturbs the single domain state due to magnetic anisotropy variation following which magnetic beads were released from the Terfenol-D micromagnets to the outlet of the microchannel. This programmable

strain-coupled multiferroic device provides an array-addressable element that can serve as the basis for massively parallel single-cell sorting via electronic actuation of magnetoelastic Terfenol-D microstructures.

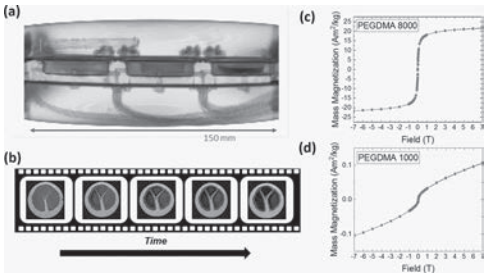
[1] S. Rampini, et al., Lab on a Chip 16, 3645 (2016) [2] Xiao, Zhuyun, et al., Multifunctional Materials 1.1 (2018): 014004.



2:18

DG-03. *In-Situ* Visualization of Iron Oxide Nanoparticle Growth Within a Hydrogel Network Using Magnetic Resonance Imaging (MRI). *S. Oberdick*[1,2], G. Zabow[2], K.E. Kennan[2], M.E. Poorman[1,2] and S.E. Russek[2] *1. Physics, University of Colorado Boulder, Boulder, CO, United States; 2. Applied Physics Division, NIST, Boulder, CO, United States*

It is challenging to monitor the growth of nanoparticles over the course of synthesis without perturbing the system or arresting the synthesis at successive times for analysis. Magnetic resonance imaging (MRI) is a powerful tool for non-invasive characterization of magnetic nanoparticles due to its inherent sensitivity to magnetic materials. Here, we describe a series of *in-situ* characterization experiments, measuring iron oxide nanoparticles as they grow within size-constraining hydrogels. Polyethylene glycol-based hydrogels were loaded into a custom, temperature-controlled MRI-compatible reaction chamber. Within the reactor, magnetic nanoparticles were grown within the crosslinked hydrogel via coprecipitation of iron chloride salt solutions. The diffusion of reactants through the hydrogel was monitored and visualized using T_2^* maps throughout the course of the reaction, which is particularly sensitive to the presence of magnetic nanoparticles. Quantitative T_1, T_2, and susceptibility maps of the hydrogel were also acquired at multiple time points during the reaction. The dynamic measurements in the MRI can be compared against SQUID magnetometry to correlate the DC magnetic properties, such as saturation magnetization and susceptibility, to relaxation times. Moreover, we have developed a SQUID compatible reaction vessel to directly connect datasets from magnetometry to MRI as a function of time. We describe how to engineer the magnetic properties of the hydrogel/nanoparticle composite by changing size, density and composition of particles, and explore how they impact MRI. Finally, we discuss applications of the hydrogel/nanoparticle system for developing bio-iron mimics and "living reference objects" for MR characterization of the transition from healthy iron types to pathological types within a tissue mimicking environment.



(a) MRI scan of reactor for *in-situ* observation of nanoparticle synthesis in hydrogel (b) Time series of gradient echo MRI images, contrast change indicates growth of particles in hydrogel (c) Room temperature M-H curve for 15 nm particles in PEGDMA 8000 with high magnetization (d) Room temperature M-H curve for 1.5 nm particles in PEGDMA 1000 with low magnetization

2:30

DG-04. Cell Tracking using Iron Nanowires as MRI T2 Contrast Agent. *A.I. Martínez Banderas*[1], A. Aires[2], S. Plaza-García[2], L. Colás[2], J.A. Moreno[3], T. Ravasi[1], J.S. Merzaban[1], P. Ramos-Cabrer[2,4], A.L. Cortajarena[2,4] and J. Kosel[3] *1. Division of Biological and Environmental Sciences and Engineering, King Abdullah University of Science and Technology, Thuwal Jeddah, Saudi Arabia; 2. CIC BiomaGUNE, Donostia-San Sebastián, Spain; 3. Division of Computer, Electrical and Mathematical Sciences and Engineering, King Abdullah University of Science and Technology, Thuwal Jeddah, Saudi Arabia; 4. Ikerbasque, Basque Foundation for Science, Bilbao, Spain*

Cell tracking by magnetic resonance imaging (MRI) is a key tool in cell therapy that enables achieving the therapeutic potential of cells after implantation into a host.[1] MRI is a non-invasive imaging technique for cell monitoring, and requires labelling the cells with contrast agents.[2] Iron nanowires with their strong magnetic properties and biocompatibility are excellent materials for MRI applications.[3, 4] In this work, the capability of iron nanowires to perform as contrast agents for cell detection through MRI was investigated. Using a 1.5 T system, iron nanowires were first evaluated as longitudinal (T1) and transversal (T2) contrast agents, revealing a great potential to enhance the T2 contrast with transversal relaxivity (r_2) values of ~40 $s^{-1}mM^{-1}$. The effects of the different variables such as oxidation level and surface coating of the nanowires on the T2 contrast were further studied by measuring their r_2 values at 7 T with values higher than 200 $s^{-1}mM^{-1}$, from which two of the tested formulations were selected. The suitability of iron nanowires to label cells for detection through MRI was first demonstrated in T2-weighted images of the labeled cells implanted in vitro in a tissue-like environment. Cellular internalization of the nanowires was assessed by iron quantification and confocal microcopy. We found a high sensitivity with the possibility to detect a minimum of 25 cells/μL with a concentration of nanowires as low as 0.8 μg of Fe/mL, thus preventing toxic effects. Finally, a selected formulation of nanowires was used to label cells prior to their implantation in the parenchyma of mice brain at two different concentrations. A high sensitivity was achieved allowing almost single cell detection after in vivo implantation persisting for at least 40 days. The nanowires-based cellular detection opens a window for studies in cancer treatment, regenerative medicine and cellular migration where nanowires could be also magnetically guided to the target area.

1. M. Hoehn, D. Wiedermann, C. Justicia, The Journal of Physiology, 584, 25-30 (2007). 2. A. J. L. Villaraza, A. Bumb, M. W. Brechbiel, Chemical Reviews, 110 (5), 2921-2959 (2010). 3. D. Shore, S. L. Pailloux, J. Zhang, Chemical Communications, 52 (85), 12634-12637 (2016). 4. S. Meng-Meng, S. Wen-Jing, B. Hong, Biomaterials, 31 (7), 1509-1517 (2010).

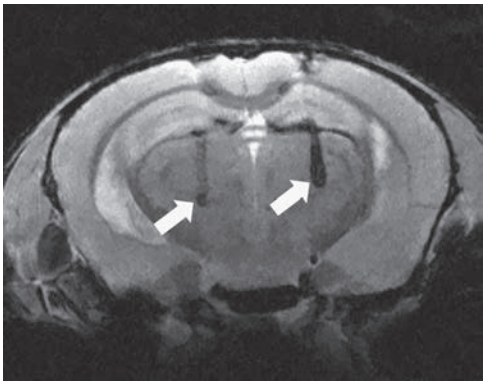


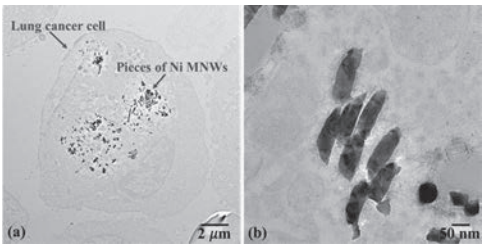
Figure. Axial MRI image of a mouse brain 40 days after implantation of cells labeled with iron nanowires. Approx. 10 cells were injected in the left hemisphere (left arrow), while approx. 100 cells were injected in the right hemisphere (right arrow).

2:42

DG-05. Magnetic isolation and identification of exosomes using magnetic nanowires and magnetosomes. *Z. Nemati Porshokouh*[1,2], J. Alonso Masa[3], M. Zamani Kouhpanji[1], J. Um[1], L. Gandarias[4], D. Gandia[5], A. Muela[4,5], M. Fdez-Gubieda[5,6], R. Franklin[1], J. Modiano[7,2] and B. Stadler[1,2] *1. Electrical and Computer Engineering, University of Minnesota, Minneapolis, MN, United States; 2. Masonic Cancer Center, University of Minnesota, Minneapolis, MN, United States; 3. CITIMAC, Universidad de Cantabria, Santander, Spain; 4. Dpto. Inmunología, Universidad del País Vasco (UPV/EHU), Leioa, Spain; 5. BCMaterials, Leioa, Spain; 6. Depto. de Electricidad y Electrónica, Universidad del País Vasco (UPV/EHU), Leioa, Spain; 7. Veterinary Clinical Sciences, University of Minnesota, St Paul, MN, United States*

There is a new drive for personalized cancer prevention and treatment, but there are still unmet medical needs, such as more effective biomarkers. In order to survive and metastasize, cancer cells use exosomes, microvesicles that contain materials unique to each cell. Therefore, these exosomes present as potential biomarkers.[1] We found that cancer cells can internalize magnetic nanowires (MNWs)[2] and package them into exosomes, enabling their magnetic isolation. Here, we employed Fe/Au and Ni MNWs, and also used more conventional iron oxide-based nanoparticles: magnetosomes synthesized by magnetotactic bacteria.[3] Osteosarcoma (OSCA-8) cells were incubated with Fe/Au and Ni MNWs for 48 hours before imaging with fluorescence and transmission electron microscope (TEM). The OSCA-8 cells internalized PEG-coated MNWs better than bare MNWs, and these MNWs were fragmented into small pieces in lysosomes inside the cells. Magnetosomes were also located inside the lysosomes, but they remained nearly intact. In addition, we repeated the experiments with human cancer cells, e.g. bone (U2OS), lung (a549), and breast (mcf7), and obtained similar results, Fig. 1. Next, exosomes were isolated using both magnetic and non-magnetic methods. TEM images show that exosomes indeed packaged small pieces of MNWs or individual magnetosomes. We analyzed the exosome size distribution using a nanoparticle tracking analyzer (NanoSight) and found that exosomes isolated magnetically had similar size distributions to those isolated non-magnetically. Importantly, the magnetic isolation takes about 10 minutes compared to two days for non-magnetic isolation. Our data show that MNWs are potential candidates for fast, inexpensive magnetic exosome isolation, and our goal is to use these MNWs for RF identification of exosomes. The methodology developed in this study should be transferable to identify exosomes from virtually any type of cancer cells.

1 M. Scott, in *AACR Annual Meeting*, 2017, pp. 817–817. 2 A. Sharma, *Nanotechnology*, 2015, 26, 135102. 3 M. L. Fdez-Gubieda, *ACS Nano*, 2013, 7, 3297–3305.



(a) Human lung cancer cell (a549), and (b) magnified image of fragmented Ni MNWs in lysosome inside the cell.

2:54

DG-06. Can Magnetic Nanoparticles Operate as Temperature Sensitive MRI Contrast Agents in the Motional-Narrowing Regime? *J.H. Hankiewicz*[1,2], J. Stroud[1], J. Stoll[1], Y. Garbovskiy[1], S.E. Russek[2], S. Jurga[3], M. Kempka[3], T. Zalewski[3] and Z. Celinski[1] *1. Biofrontiers, University Colorado Colorado Springs, Colorado Springs, CO, United States; 2. National Institute of Standards and Technology, Boulder, CO, United States; 3. NanoBioMedical Center, Adam Mickiewicz University, Poznan, Poland*

Our earlier study [1] confirmed usefulness of micrometer size magnetic particles as novel exogenous temperature sensitive contrast agents for MRI thermometry. These particles, suspended in hydrogels, produce temperature dependent dipolar magnetic fields and provide images with temperature dependent intensities using T2* weighted gradient echo sequences. Although such large particles can be delivered to the tissue of interest by injection, they cannot diffuse beyond the area of injection. Additionally, safety concerns prevent such large particles from being used for *in vivo* studies. Here, we investigate using smaller $Co_{0.3}Zn_{0.7}Fe_2O_4$ ferrite particles, which solves the problem of retention in tissue. Their magnetic properties, specifically transition temperature and magnetization vs temperature, were determined with a SQUID magnetometer while crystallographic structure was studied with XRD [2]. Batches of different sized nanoparticles were obtained using sonication and sedimentation. Particles were tested in aqueous solution by DLS. Two groups of nanoparticles were selected with hydrodynamic sizes of 150 and 50 nm. Particles were suspended in 1 % agar water gels with a concentration of 0.3 mM and tested using a 9.4 T preclinical MRI scanner in temperature from 5 to 50 ^{o}C. The apparent diffusion coefficient (ADC) of water was measured at 3 T. Relative image intensities (the ratio of image intensities of pure agar to agar doped with particles), presented in Fig. 1, showed strong temperature dependence for larger particles (150 nm) and longer echo time (TE). We attribute weak temperature dependence of image intensities observed in samples doped with 50 nm particles to the averaging effect of local dipolar field due to fast diffusion of water molecules (Fig. 2). With such small particles present protons are no longer in the static dephasing regime but rather in the motional-narrowing regime, where motion of water molecules cannot be neglected [3, 4, 5]. In the future, we will study smaller particles in higher concentrations to obtain a stronger temperature dependence images and optimize TE.

[1] J. H. Hankiewicz *et al* Nature Comm. 7, p.12415 (2016) [2] J.H. Hankiewicz *et al* J. Magn. and Magn. Mater. 469, p.550 (2019) [3] D.A. Yablonskiy and E.M. Haacke, Magn. Reson. Med. 32, p.749 (1994) [4] P. Gillis, F. Moiny, and R.A. Brooks Magn. Reson. Med. 47 p.257 (2002) [5] A. Roch et al. J. Magn. Magn. Mater.293, p.532 (2005)

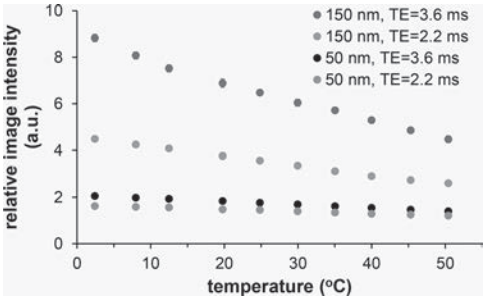


Fig.1. Relative MR image intensity as the function of temperature.

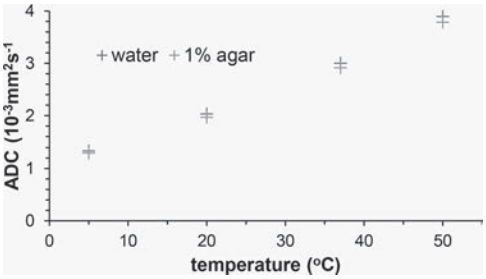


Fig.2. Apparent diffusion coefficient in water and in 1% agar gel.

3:06

DG-07. Oleic acid functionalized Fe_3O_4 magnetic nanoparticles and its adsorption capability of oil for potential biomedical applications. *G.C. Hermosa*[1], K. Chen[1], C. Liao[1], S. Wang[2], Y. Chen[3,4], C. Koh[4] and A. Sun[1] *1. Department of Chemical Engineering and Materials Science, Yuan Ze University, Taoyuan, Taiwan; 2. Department of Materials and Mineral Resources Engineering, National Taipei University of Technology, Taipei, Taiwan; 3. Chemical Engineering and Materials Science, Yuan Ze University, Taoyuan, Taiwan; 4. Surgery, Far Eastern Memorial Hospital, New Taipei, Taiwan*

Hypertension is caused by excessive oils present in the blood vessels and is a global epidemic at present. Though the conventional method such as different drug blockers are available, they still face challenges regarding adverse effects which can greatly limit their efficacies. Oleic acid (OA) is a good lipophilic material, which already widely used in nanoparticle synthesis since it can form a protective layer and can strongly be bonded to the nanoparticles. In recent years, Fe_3O_4 (commonly known as magnetite) is the choice of researchers because of their, high moment at low magnetic field, superparamagnetic property, stability at physiological conditions, biocompatibility and excellent adsorption capacity. In order for the OA suitable to be controlled *in vivo* applications and for an easy recovery from aqueous solutions, they are coated with magnetite nanoparticles. Henceforth, in this work, magnetite was synthesized via co-precipitation method and modified with different amounts for oleic acid (x=0.5, 1, 2 mL) with the evaluation of the synthesis process parameters (temperature, H_2O amount and pH), in seeking to understand the adsorption capability of oil for potential biomedical usage. The morphology and chemical structure of the OA coated Fe_3O_4 nanoadsorbents were characterized by FT-IR, XRD, SEM, VSM and MTT assay for the cytotoxicity test. Successful coating was confirmed by FTIR and showed COO- groups within the spectra. The results indicated that the adsorption capacity was 588, 833 and 1000 mg/g for x= 0.5, 1 and 2 mL respectively. An increase in the amount of OA leads to the decrease in magnetization but still demonstrated a superparamagnetic property for an easy recovery. Grain size was evaluated, and was found out to be in the range of 8nm-10nm. The adsorbent is well fitted on the Langmuir model suggesting a monolayer adsorption. Regarding the adsorption kinetics, the adsorbent follows the pseudo second order with high $R^2 = 0.98$. The nanoadsorbent exhibited a high cell viability rate signifying low toxicity. Therefore, the synthesized nanoparticle is a good candidate for biomedical applications as such for hypertension treatment, as shown in this study.

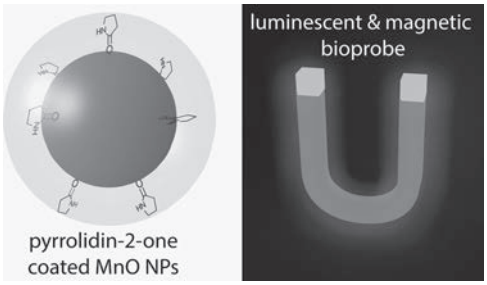
N. Jović Orsini, B. Babić-Stojić, and G. F. Goya, *Journal of Magnetism and Magnetic Materials,* vol. 449, pp. 286-296, (2018). X. Wang, Y. Shi, R. W. Graff, D. Lee, and H. Gao, *Polymer,* vol. 72, no. Supplement C, pp. 361-367, (2015). H.-C. Roth, S. P. Schwaminger, M. Schindler, F. E. Wagner, and S. Berensmeier, *Journal of Magnetism and Magnetic Materials,* vol. 377, pp. 81-89, (2015). M.-J. Chen, H. Shen, X. Li, J. Ruan, and W.-Q. Yuan, *Chemical Papers,* vol. 70, no. 12, pp. 1642-1648, (2016). L. Zhang, R. He, and H.-C. Gu, *Applied Surface Science,* vol. 253, no. 5, pp. 2611-2617, (2006).

3:18

DG-08. New MnO-based Nanoparticle Contrast Agents for Magentic Resonance Imaging. *S. Trudel*[1], A. Banerjee[1] and B. Tomanek[2] *1. Chemistry, University of Calgary, Calgary, AB, Canada; 2. Clinical Neurosciences, University of Calgary, Calgary, AB, Canada*

Multimodal probes are an asset for simplified, improved medical imaging. In particular, fluorescence and magnetic resonance imaging (MRI) are sought-after combined capabilities. Here, we show that pyrrolidin-2-one capped manganese oxide nanoparticles (MnO^{pyrr} NPs) combine MRI with fluorescence microscopy to function as efficient bifunctional bionanoprobes. We employ a one-pot synthesis for ca. 10 nm MnO NPs, wherein manganese(II) 2,4-pentadionate is thermally decomposed using pyrrolidin-2-one as a solvent and capping ligand. The MnO^{pyrr} NPs are soluble in water without any further post-synthetic modifications. The r_1 relaxivity and r_2/r_1 ratio indicate these NPs are potential T_1 MRI contrast agents at clinical (3 T) and ultra-high (9.4 T) magnetic fields. Serendipitously, the as-prepared NPs are photoluminescent. The unexpected luminescence is ascribed to the modification of the pyrrolidin-2-one during the thermal treatment. MnO^{pyrr} NPs are successfully used to enable fluorescence microscopy of HeLa cells, demonstrating bifunctional imaging capabilities. A low cytotoxic response in two distinct cell types (HeLa, HepG2) supports the suitability of MnO^{pyrr} NPs for biological imaging applications. Additionaly, we have investigate the shape-dependent MRI capabilities of MnO-based contrast agents. A variety of shapes (spheres, cubes, octapods, agglomerated particles) are obtained by modifying the synthetic protocol, and their MRI capabilities evaluated through relxivity and relaxation dispersion measurements.

A. Banerjee, G.E. Bertolesi, C.-C. Ling, B. Blasiak, A. Purchase, O. Calderon, B. Tomanek, S. Trudel, ACS Appl. Mater. Interfaces, vol. 11, p. 13069 (2019)



3:30

DG-09. 2D and 3D magnetic nanoparticles for biomedical applications.
P. Tiberto[1], F. Celegato[1], G. Barrera[1], M. Coisson[1] and M. Cialone[2]
1. Advanced Materials and life sciences, INRIM, Torino, Italy;
2. Chemistry, Università di Torino, Torino, Italy

Magnetic nanoparticles of controlled size have raised a broad technological interest in different areas such as catalysis, photonics, and biomagnetism. Fe-Pd alloys possess outstanding magnetic and mechanical properties making them suitable for different applications and due to their high magnetic saturation and metallic nature they are here studied for biomedical applications depending on nanostructures shape. In this work, 2D and 3D nanostructures have been obtained by exploiting two bottom-up processes starting from a continuous layer and their magnetic properties have been compared and discussed. $Fe_{70}Pd_{30}$ films have been deposited on Si substrates (previously coated with a MgO sacrificial layer) by rf-sputtering (film thickness 30 nm). Fabrication of 2D FePd nanodisks (NDs) is performed by nanolithography exploiting self-assembling of polystyrene nanospheres (starting diameter 500 nm) [1]. NDs with controlled diameter (≈300 nm, see Fig. 1a) have been obtained. The room-temperature magnetization process of detached NDs is characterized by a vortex core, (see hysteresis curve in Fig. 1c). This feature is very promising for magnetic hyperthermia being marked by high saturation magnetisation and zero remanence to prevent aggregation. As an alternative route to synthesize 3D nanoparticles (NPs), solid-state dewetting has been performed [2]. Here, to promote dewetting, the as-deposited thin films are subsequently submitted to a furnace annealing in vacuum atmosphere at 834 °C for 1000 s and spherical nanoparticles are obtained (≈300 nm diameter and height, see Fig. 1b). The NPs room-temperature hysteresis loop (see Fig.1 d) indicates a magnetisation process typical of a soft magnetic alloy, but still with a considerable hysteresis loop area. The specific loss power (SLP) at 100 kHz (field amplitude 30 – 60 mT) of both NDs and NPs dispersed in water have been measured through a calibrated non-adiabatic setup [3]. SLP values much larger than those achieved with conventional magnetite or ferrite nanoparticles are achieved in both nanostructures.

[1] P. Tiberto at al, JAP (2015) [2] G. Barrera et al, J. Alloys and Comp. 742 (2018) 751 [3] M. Coisson et al. *Biochem. Biophys. Acta* 1861 (2017) 1545.

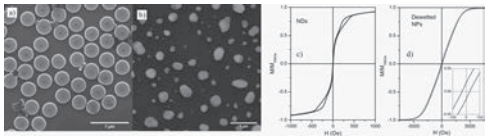


Fig. 1. SEM image of FePd nanodisks (a) and nanoparticles (b) attached on MgO substrate; room-temperature hysteresis curve for nanodisks (c) and nanoparticles (d).

3:42

DG-10. Laser Monitoring of Dynamic Behavior of Magnetic Nanoparticles in Magnetic Field Gradient.
K. Tsunashima[1], K. Jinno[1], B. Hiramatsu[1], K. Fujimoto[1], K. Sakai[1], T. Kiwa[1], M. Saari[2] and K. Tsukada[1] *1. Graduate School of Interdisciplinary Science and Engineering in Health Systems, Okayama University, Okayama, Japan; 2. Faculty of Electrical and electronic Engineering, Universiti Malaysia Pahang, Pekan, Malaysia*

Magnetic nanoparticles (MNPs) have been extensively studied in the field of biotechnology and medicine. The MNPs for bio- or medical purpose are generally used for magnetic correction of antibodies in a conventional immunoassay and drug delivery. Additionally, we have studied magnetic immunoassays to detect bio-based materials in solutions with high sensitivity. Manipulation of MNPs by a magnetic gradient in solutions is an excellent option to promote reactions of MNPs with bio-materials. However, the dynamic behavior of MNPs generally depends on various properties of MNPs and solutions. In this study, a laser transmission system (LTS) has been developed to evaluate dynamic movement of MNPs in a solution with changing gradient fields. Figure 1 shows the schematic of the LTS. A laser (with a wavelength of λ~635 nm) was focused in the glass cell, which was filled with the MNPs solution. The transmitted laser beam was pass through a pin-hole and a polarizer to cut off the scattered laser beam, and subsequently focused on a Si photodiode. The detector's output increased by decreasing the concentration of MNPs (in the region where the laser was focused), and the localized concentration of MNPs was measured. Here, a permanent magnet was mounted on a linear stage to change the distance from the cell, and the gradient field change was monotonically. Figure 2 shows the output signal of the Si photodiode while the distance between the cell and the magnet changed from 4 mm to 49 mm. The speed was at ~10 mm/s. We used Resovist of 50 mg/mL as the MNPs, and the serum was mixed in the solution. The result indicates that the MNPs were first localized near the magnet and diffused over the cell, and the diffusion speed decreased with increasing serum concentration. Our series of measurements on the same solutions using dynamic light scattering (DLS) method, zeta-potential measurement, and magnetic susceptibility measurement suggest that the difference in the diffusion speed can not only be attributed to viscosity of the solution but also to the aggregation of the MNPs.

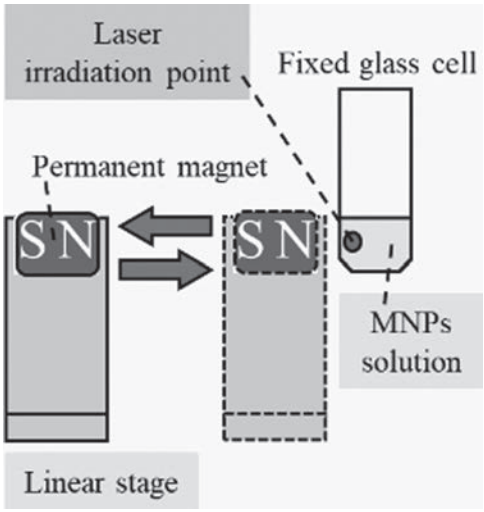


Fig 1. System configuration.

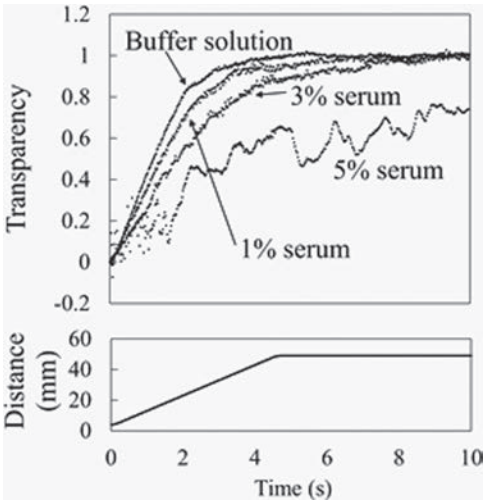


Fig 2. Difference of lag by serum concentration.

3:54

DG-11. Towards Development of a Temperature Contrast Agent for MRI Guided Laser Ablations. J.H. Hankiewicz[1], N. Alghamdi[1], K. Gorny[2], D. Woodrum[2], A. Anderson[3,2], A. Cruz Hernandez[4], J. Brown[4] and *Z. Celinski*[1] *1. Biofrontiers, University Colorado Colorado Springs, Colorado Springs, CO, United States; 2. Radiology, Mayo Clinic College of Medicine, Rochester, MN, United States; 3. Philips Healthcare, Best, Netherlands; 4. Colorado Center for Nanomedicine and Nanosafety, University of Colorado Anschutz Medical Campus, Aurora, CO, United States*

Current MRI-guided laser ablations use proton resonance frequency (PRF) shift for real-time monitoring of tissue heating [1]. PRF thermometry, however, is easily inhibited by the presence of adipose tissue, tissue movement and/or phase drift caused by magnetic field instablility or inhomogeneity [2]. Recently, we developed a new method of MRI thermometry (tMRI), using magnetic particles, which circumvents these problems [3]. These particles embedded in tissue create a temperature dependent local dipolar magnetic field that modulate the field homogeneity of the MRI scanner. Resulting intensities in T2* weighted gradient echo MR images allow us to obtain spatial temperature maps. $MgFe_2O_4$ ferrite is nontoxic at low concentrations [4]. $Mg_{1-x}Zn_xFe_2O_4$ 2 μm particles, in $0.5 \leq x \leq 0.75$ range, were tested. Magnetic properties, using SQUID, were studied between 5 to 350 K. Cell viability and reactive oxygen species production was studied following exposure to ferrite particles at concentrations of 30-240 mg/mL. Adding Zn to $MgFe_2O_4$ reduces the Curie temperature and provides biocompatible compounds. Water proton NMR linewidth, in agar gel with embedded particles, was measured between 278 to 323 K. Preliminary MRI results were obtained with a laser ablation system shown in Fig. 1. Fig. 2 shows mass magnetization vs. temperature for all compositions. Magnetization of ferrites decreases with increasing Zn content and temperature. Between 278 and 323 K, a 30% reduction of proton NMR linewidth, correlated with decreasing magnetization, was found. In laser heating experiments, 1.5 T MRI images taken at 313 and 338 K, show a 20% change of intensity, indicating that our tMRI method can provide real-time temperature maps during MRI-guided laser ablation procedure [5].

[1] D.A. Woodrum, *et al.* J. Vasc. Interv. Radiol. 22, p.929 (2011) [2] V. Rieke and K. Butts Pauly K. J. Magn Reson Imaging 27, p.673 (2008) [3] J.H. Hankiewicz, *et al.* Nature Comm. p.12415 (2016) [4] S. Kanagesan, *et al.* J. Nanomat. 2013, p.865024 (2013) [5] T. Lee *et al.* Rev. Urol.16, p.55 (2014)

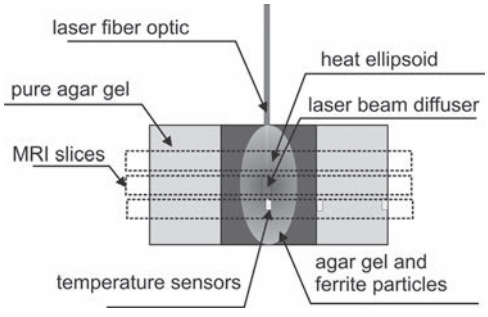


Fig.1. Diagram of phantom heating setup. Inner core of the phantom with ferrite particles consists of 240 mg/mL concentration of x=0.64 composition. Heating was accomplished using 980 nm, 20 W laser.

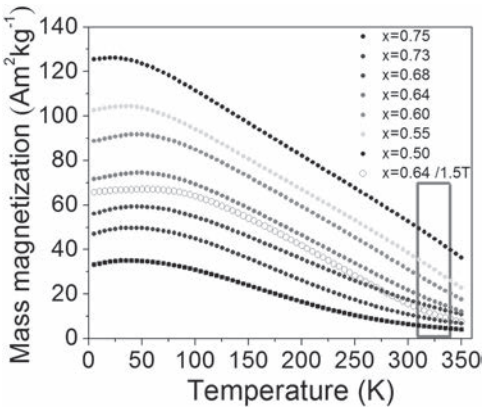


Figure 2. Mass magnetization data of $Mg_{1-x}ZnxFe_2O_4$ ferrite at 3.0 T and at 1.5 T (only for x=0.64; open red circles). The red rectangle window shows the targeted temperature range for particle application in MRI guided laser ablations (308-338 K).

4:06

DG-12. Evaluation of Local and Global Induced Temperature Therapeutic Profile in Magnetic and Photo-thermal Nanoparticle-based Therapies. *A. Espinosa*[1], G. Castro[2,3], J. Reguera[4,5], A. Curcio[6], C. Castellano[7], C. Wilhelm[6], M. García[8] and A. Muñoz-Noval[9] *1. IMDEA Nanociencia, Madrid, Spain; 2. Instituto de Ciencia de Materiales de Madrid (ICMM-CSIC), Madrid, Spain; 3. Spanish CRG - ESRF-European Synchrotron Radiation Facility, Grenoble, France; 4. BCMaterials - Basque Center for Materials, Applications and Nanostructures - UPV/EHU, Leioa, Spain; 5. Ikerbasque - Basque Foundation for Science, Bilbao, Spain; 6. Laboratoire Matière et Systèmes Complexes, University Paris Diderot, Paris, France; 7. Dipartimento di Chimica, Università degli Studi di Milano, Milano, Italy; 8. Instituto de Cerámica y Vidrio, Consejo Superior de Investigaciones Científicas (ICV-CSIC), Madrid, Spain; 9. Dpto. Física Materiales - Facultad CC. Fisicas, Universidad Complutense de Madrid, Madrid, Spain*

Achieving to determine the local temperature of nano-objects would suppose a major breakthrough in many technological and scientific fields. In biomedicine, magnetic and photo-induced hyperthermia therapies [1-3] employ nanoparticles as heating sources for therapeutic purposes, whose protocols are based on global temperature measurements. However, local heating effects produced at the nanoparticle surface are a key issue to evaluate the onset of thermal doses and quantify possible side effects derived from achieving high local temperatures (i.e. destroying healthy cells in the tissue, degradation of proteins and enzymes in the extracellular medium, etc). In this work, we explore the use of the extended X-ray absorption fine structure (EXAFS) analysis as an universal and accurate *in situ* probe to determine the local temperature at the nanoscale.[4] We will compare the temperatures measured in magneto-photothermal nanoparticles subjected to hyperthermia conditions by means of EXAFS spectroscopy and by infrared thermographic imaging as macroscopic temperature methods in different biological environments.

[1] A. Espinosa, J. KolosnjajTabi, A. AbouHassan *et al.*, Adv. Funct. Mater. 28, 1803660 (2018). [2] A. Espinosa, A. Curcio, S. Cabana *et al.*, ACS Nano (2018). [3] A. Curcio, A. K. Silva, S. Cabana *et al.*, Theranostics 9, 1288 (2019). [4] B. Van de Broek, D. Grandjean, J. Trekker *et al.*, Small 7, 2498 (2011).

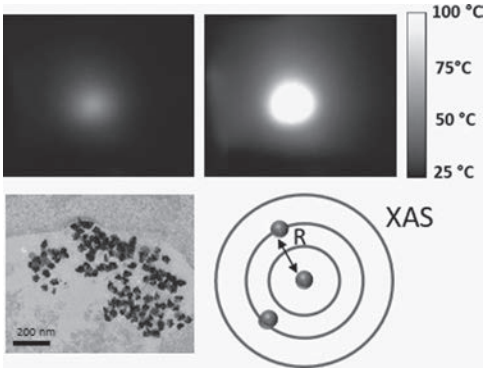


Fig. 1. A) Macroscopic thermographic images of magnetic and photothermal NPs subjected to hyperthermic conditions. B) Magneto-photothermal NPs incubated in cancer cells. C) Nanomaterial absorbing atoms in X-ray absorption spectroscopy (XAS) measurements.

4:18

DG-13. Effect of direct-current magnetic field on the specific absorption rate of metamagnetic CoMnSi: A potential approach to switchable hyperthermia therapy. *K.C. Ugochukwu*[1], M.M. Sadiq[2,3], L. Meagher[1], M.R. Hill[2,3], K.G. Sandeman[4,5], A. Haydon[6], J. Lickliter[7] and K. Suzuki[1] *1. Department of Materials Science and Engineering, Monash University, Clayton, VIC, Australia; 2. Department of Chemical Engineering, Monash University, Clayton, VIC, Australia; 3. CSIRO, Private Bag 33, Clayton South MDC, VIC, Australia; 4. Department of Physics, Brooklyn College of The City University of New York, 2900 Bedford Avenue, Brooklyn, NY, United States; 5. Physics Program, The Graduate Center, CUNY, New York, NY, United States; 6. Department of Medical Oncology, Alfred Hospital, Melbourne, VIC, Australia; 7. Nucleus Network, Melbourne, VIC, Australia*

Magnetic particle hyperthermia has been proposed as a promising, minimally invasive and targeted cancer therapy [1]. So far, the majority of published works have focused on superparamagnetic (SPM) and ferromagnetic (FM) materials [1,2]. SPM materials have an intrinsic low response to alternating-current (a.c.) magnetic field and yield a low specific absorption rate (SAR). FM materials, on the other hand, even though they have high SAR values, they have the tendency to agglomerate and form large particle aggregates, even in zero applied field, which could potentially lead to occlusion of blood vessels. A possible approach utilizing the high magnetization of the FM state for SAR while preventing the agglomeration effect is to use a metamagnetic transition where the FM state is induced by a bias field. In this proof of concept study, we employed MnCoSi (MnCoSi) [3], where a first-order magnetic transition is known to take place. A CoMnSi ingot was prepared by arc melting under a purified Ar atmosphere. The ingot was annealed at 1123 K for 216 ks and ground to particles which were < 30 mm. The SAR was measured at 212.0 kHz and 31.0 kA/m. The room-temperature magnetization curve was found to show little remanent magnetization and no tendency of agglomeration for the CoMnSi powders was observed via optical microscopy. The magnetization curve showed an abrupt increase in magnetization to 67.7 Am^2/kg at $m_0H = 1$ T, reflecting the metamagnetism of this compound. The SAR measured under a direct-current (d.c.) bias field of 1.0 T was 10.7 W/g, indicating a moderate heating effect in the ferromagnetic state. Moreover, MnCoSi showed an anisotropic SAR that depended on the direction of the applied d.c. bias field. These results indicate that the heating power of metamagnetic materials can be controlled by the applied d.c. bias field, opening a new direction in the search for controlled hyperthermia cancer therapy.

[1] E. A. Périgo *et al*., Fundamentals and advances in magnetic hyperthermia, Appl. Phys. Rev. 2, 041302 (2015). [2] E. C. Abenojar *et al*., Structural effects on the magnetic hyperthermia properties of iron oxide nanoparticles, Prog. Nat. Sci: Mater. Inter. 26, 440 (2016). [3] K. G. Sandeman *et al*., Negative magnetocaloric effect from highly sensitive metamagnetism in $CoMnSi_{1-x}Ge_x$, Phys. Rev. B 74, 224436 (2006).

Session DH
EMERGENT PHENOMENA IN COMPLEX OXIDES

Michel Viret, Co-Chair
CEA, Gif sur Yvette Cedex, France
Dan Read, Co-Chair
Cardiff University, Cardiff, United Kingdom

INVITED PAPER

1:30

DH-01. $LaTiO_3$/ $SrTiO_3$ Interfaces: From Giant Rashba Spin Splitting to Edge State Conduction. M. Veit[1,2], R. Arras[3], B. Ramshaw[4,5], M. Chan[4], D. Yi[2], R. Pentcheva[6] and *Y. Suzuki*[1,2] *1. Applied Physics, Stanford University, Stanford, CA, United States; 2. Geballe Laboratory for Advanced Materials, Stanford University, Stanford, CA, United States; 3. CEMES, University of Toulouse, Toulouse, France; 4. Los Alamos National Laboratory, Los Alamos, NM, United States; 5. Laboratory for Atomic and Solid Statre Physics, Cornell University, Ithaca, NY, United States; 6. Department of Physics and Center for Nanointegration, University of Duisburg-Essen, Duisburg, Germany*

The Mott insulator/ band insulator interface of $LaTiO_3$/ $SrTiO_3$ was first shown to exhibit metallicity due to electronic reconstruction by Ohtomo and Hwang many years ago. Since then there has been little subsequent study of this system in comparison to the $LaAlO_3$/$SrTiO_3$ interface. We have recently found that the low dimensional metallic behavior at the $LaTiO_3$/ $SrTiO_3$ interface is accompanied by giant Rashba spin-orbit coupling. Evidence for giant Rashba spin splitting is manifest in two sets of Shubnikov-de Haas oscillations associated with an inner and outer Fermi surface, Berry phase of π, substantial anisotropic magnetoresistance and a weak anti-localization correction to the magnetoconductivity. Together these results indicate a giant Rashba coupling which is an order of magnitude larger than other complex oxide interfaces. By gating the samples with an electric field, we observe (i) quantized resistance peaks which are independent of sample dimensions in a conventional 6-terminal Hall bar geometry, (ii) a strong negative magneto-conductance near the quantized peaks in resistance, and (iii) nonlocal transport in a 4-terminal geometry. All of these observations are consistent with edge state conduction and the quantum spin Hall effect. †This work was funded by the Vannevar Bush Faculty Fellowship of the Department of Defense under Contract No. N00014-15-1-0045.

CONTRIBUTED PAPERS

2:06

DH-02. Current-induced effective magnetic field in $La_{0.67}Sr_{0.33}MnO_3$/ $LaAlO_3$/$SrTiO_3$. *M. Yamanouchi*[1,2], T. Oyamada[2] and H. Ohta[1,2] *1. Research Institute for Electronic Science, Hokkaido University, Sapporo, Japan; 2. Graduate School of Information Science and Technology, Hokkaido University, Sapporo, Japan*

Recently, we have reported that the sign of the planar Hall effect (PHE), which originates from the spin-orbit interaction (SOI), for $La_{0.67}Sr_{0.33}MnO_3$/ $LaAlO_3$/$SrTiO_3$ (LSMO/LAO/STO) is opposite to that for LSMO/STO at low temperature [1]. This observation suggests that the SOI in LSMO is modified by LAO/STO and generation of current-induced effective magnetic field H_{eff} originating from the SOI is expected in LSMO/LAO/STO. In this work, we investigated H_{eff} in LSMO/LAO/STO structures. LSMO(18)/LAO(0,2,6)/STO structures were grown on STO (001) substrates by pulsed laser deposition, where numbers in parentheses are nominal film thicknesses in unit cells (u.c.). The LAO(6)/STO is conductive, whereas the LAO(2)/STO is insulating, which is consistent with the formation of a two-dimensional electron system (2DES) at the LAO/STO interface with a thicker LAO (>= 4 u.c) layer [2,3]. The structures were processed into a Hall bar structure having a 10-mm wide channel along [100] and two pairs of Hall probes. The magnetic field angle dependence of transverse resistance R_{yx}, which is dominated by the PHE, shows that all the structures have an in-plane biaxial magnetic anisotropy with the easy axes almost along <110> and the sign of the PHE coefficient for LSMO(18)/LAO(6)/STO is opposite to that for LSMO(18)/LAO(0,2)/STO at low temperature. After aligning magnetization direction along [-110], we measured variation of R_{yx} reflecting the switching of magnetization direction from [-110] to [-1-10] by sweeping H in [0-10] under various currents. The switching magnetic field is larger for negative current than that for positive current in LSMO(18)/LAO(6)/STO, which shows that H_{eff} is exerted on magnetization. Similar H_{eff} is observed in LSMO(18)/LAO(0,2)/STO, however the direction is opposite. The sign of the PHE coefficient and H_{eff} depend on the presence of a 2DES, suggesting that H_{eff} observed in LSMO/LAO/STO is related to the SOI modulation caused by formation of a 2DES at LAO/STO.

[1] M. Yamanouchi *et al*., AIP Advances 9, 035129 (2019). [2] A. Ohtomo and H. Y. Hwang, Nature 427, 423 (2004). [3] S. Thiel *et al*., Science 313, 1942 (2006).

2:18

DH-03. Spin susceptibility of topological Kondo insulator. *P. Goswami*[1] *1. Physics, University of Delhi, D.B. College, New Delhi, India*

A topological insulator is a material with topologically protected metallic boundaries and an insulating bulk. The strongly-correlated Kondo variety [1-4], such as SmB_6, has recently been widely investigated owing to its promise of being the first realized topological Kondo insulator (TKI). We study here a generic TKI system by performing a mean-field theoretic (MFT) calculation within the frame-work of slave-boson protocol. We assume infinite Hubbard-type interaction among the quasi-localized electrons (QLE). We also investigate the consequences of break-down of the time-reversal symmetry (TRS) due to bulk substitutional magnetic impurities (MIs), such as Co atoms. These impurities couple with itinerant electrons of the system. One of the note-worthy outcome is the impurities change the single-particle excitation spectrum in a fundamental way. We obtain the grand canonical potential of the system and self-consistent equations for MFT parameters minimizing the potential with relative to these parameters. The parameters enforce constraints on the pseudo-particles due to the infinite Coulomb repulsion and the need of the formation of singlet states between an itinerant electron and a localized fermion at each lattice site in order to have a Kondo insulator. A fundamental quantity describing the magnetic response of a system is the spin susceptibility. The Kondo screening mechanisms are mostly characterized by this quantity. We have calculated the bulk spin susceptibility of the generic TKI system in the metallic and insulating phases of the system at a fixed chemical potential and found them behaving

differently with relative to change in the field corresponding to the localized moments. The difference between the metallic and insulating phase is in the sign of nearest neighbor hopping of QLE : It is positive for the metallic and negative for the insulating phase.

[1]M. Dzero, Kai Sun, V. Galitski, and P. Coleman, Phys. Rev. Lett. 104, 106408 (2010). [2] *M. Dzero*, K. Sun, P. Coleman, and V. Galitski, *Phys. Rev.* B 85, 045130 (2012). [3] J. Werner and F. F. Assaad, Phys. Rev. B 88, 035113 (2013). [4] J. Werner and F. F. Assaad, Phys. Rev. B 89, 245119 (2014).

2:30

DH-04. Epitaxial growth of RVO_3 by ozone assisted MBE towards multiferroism in $(LaVO_3)_n/(PrVO_3)_m$ superlattices. *G. Masset*[1], O. Copie[1], K. Dumesnil[1], J. Ghanbaja[1] and S. Andrieu[1] *1. Institut Jean Lamour, Nancy, France*

Transition metal oxides with perovskite structure (ABO_3) attract an increasing interest driven by their wide range of physical properties and the opportunity to functionalize them in nanometric heterostructures for new electronic devices. The current study focuses on rare-earth (RE) vanadates ($REVO_3$). In decreasing temperature, these materials undergo first a V *3d-t_{2g}* orbitals ordering accompanied by a structural transition (symmetry lowering), followed by a spin ordering at lower temperature [1]. *Ab initio* calculations predict that (i) a shift of RE atoms (X_5^- displacements) could induce hybrid improper ferroelectricity in layered structures combining different cations, and that (ii) the coupling of polarization to Jahn-Teller distortions could let envision a direct and strong coupling between polarization and magnetism [2]. Our objective is thus to synthetize a multiferroic material in combining strains and interfaces engineering in $AVO_3/A'VO_3$ superlattices. The systems are grown in a Molecular Beam Epitaxy chamber with controlled ozone pressure. Single films of $LaVO_3$ and $PrVO_3$ have been first synthesized on $SrTiO_3$ (001) substrates. RHEED and X-ray diffraction analysis permit the optimization of the growth window (deposition temperature and ozone pressure) to obtain highly controlled 2D growth and stoichiometry. Electronic microscopy (TEM and STEM) experiments highlight the orthorhombic structure and the three growth domains on the square symmetry surface of $SrTiO_3$. The accurate determination of the atomic positions [3] enabled us to observe the X_5^- displacements of rare-earth atoms required for the appearance of ferroelectricity. Magnetic measurements confirm ordering temperatures ($T_{Néel}$) in agreement with stoichiometric bulk compounds. $(LaVO_3)_n/(PrVO_3)_m$ superlattices of high quality have then been grown, even for thinnest individual layers (one unit cell). Electrical transport measurements are planned very soon to explore the ferroelectricity in $(LaVO_3)_n/(PrVO_3)_m$ superlattices. These results will constitute a significant advance in the understanding of the electronic properties of oxide-based heterostructures, in particular for the emergence of their ferroelectric and multiferroic characters.

[1] S. Miyasaka, Y. Okimoto and M. Iwama, Phys. Rev. B 68, 100406 (2003) [2] J. Varignon, NC. Bristowe and E. Bousquet, Scientific Reports 5, 15364 (2015) [3] H. Meley, Karandeep and L. Oberson, APL Materials 6, 046102 (2018)

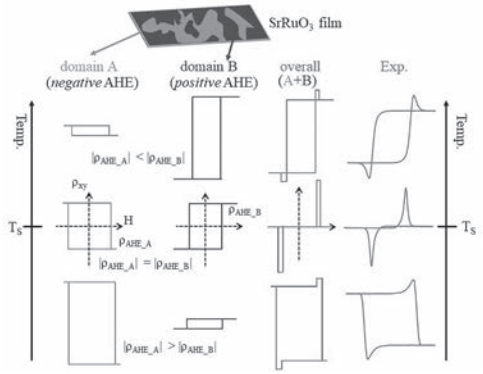
INVITED PAPER

2:42

DH-05. Transverse resistivity anomalies in the ferromagnetic oxide $SrRuO_3$ and their interpretation: Topological or Traditional? *D. Kan*[1] *1. Kyoto University, Uji, Japan*

Transport phenomena yielding voltages transverse to electric currents, such as anomalous and topological Hall effects have been a subject of intensive investigations in recent years. Here, we show that epitaxial thin films of the ferromagnetic oxide $SrRuO_3$ exhibit transverse resistivity anomalies associated with magnetization reversal [1], which is quite similar to what have been claimed to be the emergence of the topological Hall effect (THE) due to formations of topologically non-trivial magnetic textures, such as skyrmions. Our thorough investigations revealed that the anomalies are enhanced at a certain temperature at which the sign of the anomalous Hall effect reverses. Based on our experimental observations, we proposed a model considering inhomogeneous magnetoelectric properties (such as the anomalous Hall coefficient and coercive field) in the material [2]. Our analyses fully explain every feature of the transverse resistivity anomalies without resorting to the THE. In this presentation, I will also present time and field sweep rate dependence of the transverse resistivity anomalies in $SrRuO_3$ and discuss their origin.

[1] D. Kan and Y. Shimakawa, Physica Status Solidi B 255, 1800175 (2018). [2] D. Kan, T. Moriyama, K. Kobayashi, and Y. Shimakawa, Phys. Rev. B 98, 180408R (2018). "*Editor's Suggestions*"



Schematics of the proposed model for the transverse resistivity anomalies in $SrRuO_3$

CONTRIBUTED PAPERS

3:18

DH-06. Unusual Magnetic and Electric Properties of $SrRuO_3$(111) Thin Films. *J. Flores*[1], K. Meng[1], A.S. Ahmed[1] and F. Yang[1] *1. Physics, The Ohio State University, Columbus, OH, United States*

Oxide thin films offer a wide platform for investigating the effects of lattice strain due to the variety of substrates with similar lattice parameters. Lattice distortions have been known to cause significant changes to the magnetic and electrical properties. $SrRuO_3$ has been shown to have enhanced magnetization when grown on $SrTiO_3$(111) as opposed to the conventional (001)-orientation. Here we explore the structural, magnetic, and electric properties of epitaxial $SrRuO_3$ films grown on $SrTiO_3$(111). $SrRuO_3$ films were grown by off-axis dc magnetron sputtering on treated $SrTiO_3$(111) substrates. Crystalline quality of the films was verified by X-ray diffractometry and atomic force microscopy showing epitaxial growth and sub-nanometer roughness. In Fig. 1, SQUID magnetometry measurements show a magnetization of 2 μ_B/Ru and ~1μ_B/Ru for 5nm and 35nm films respectively. The difference in magnetic moment suggest a different spin configuration in the 5nm films in comparison to the 35nm films. In the ultra-thin regime we expect the $SrRuO_3$ to be completely strained to the substrate whereas in 35nm the film has partially relaxed resulting in a lower net moment due to contributions from the unstrained system. Resistivity measurements indicate metallic behavior in films down to 5nm, smaller than previously reported. Hall measurements showed a nonlinear response not seen in $SrRuO_3$ grown on STO(001). Fig. 2 shows a nonlinearity that exists in thicknesses ranging from 5-15nm showing up near the coercive field. The effect is not seen in 35nm $SrRuO_3$ where the film has relaxed. We will explore the possible origin of the unusual behavior by a thickness dependence study of the structural, magnetic, and electric properties.

Grutter, A. J. *et al.* Appl. Phys. Lett.4–6 (2009) Grutter, A. J., Wong, F. J., Arenholz, E., Vailionis, A. & Suzuki, Y. Phys. Rev. B - Condens. Matter Mater. Phys.85, 1–8 (2012) Chang, J., Park, Y. S., Lee, J. W. & Kim, S. K. J. Cryst. Growth 311, 3771–3774 (2009) Koster, G. *et al.* Rev. Mod. Phys.84, 253–298 (2012) Ziese, M., Vrejoiu, I. & Hesse, D. Phys. Rev. B - Condens. Matter Mater. Phys .81, (2010). Ziese, M., Jin, L. & Lindfors-Vrejoiu, I. J. Phys. Mater. (2019).

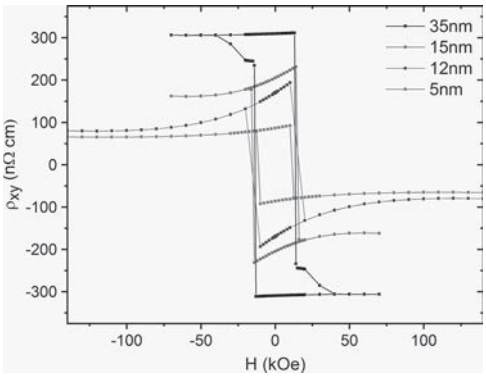


Fig. 2 Hall resistivity measurement at 20K of 5, 12, 15, and 35nm $SrRuO_3$ films deposited on $SrTiO_3$(111). A linear background was determined by fitting in high field and subtracted from data. Significant curvature is seen in the 5, 12, and 15nm films and vanishes in the 35nm sample.

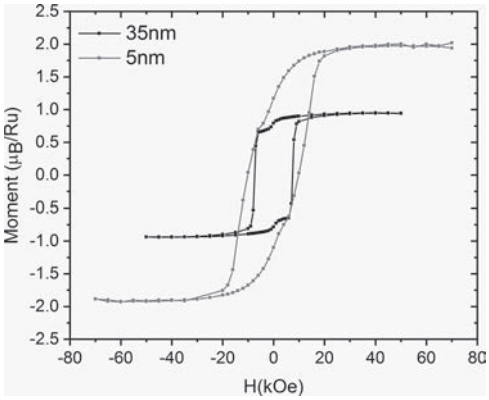


Fig. 1 Magnetic hysteresis of 5nm and 35nm $SrRuO_3$ grown $SrTiO_3$(111) taken at 20K. The moment of the 35nm film is approximately half of that of the 5nm film and closer to moments typically reported in (001)-oriented films.

3:30

DH-07. Strain-induced Majority Carrier Inversion in Ferromagnetic Epitaxial $LaCoO_{3-\delta}$ Thin Films. *V. Chaturvedi*[1], J. Walter[1], A. Paul[1], J. Jeong[1], B. Yu[2], Z. Zhang[3], H. Zhou[3], A.J. Grutter[4], B.J. Kirby[4], J. Borchers[4], A. Mkhoyan[1], M. Greven[2], T. Birol[1] and C. Leighton[1]
1. Chemical Engineering and Materials Science, University of Minnesota, Minneapolis, MN, United States; 2. School of Physics and Astronomy, University of Minnesota, Minneapolis, MN, United States; 3. Advanced Photon Source, Argonne National Laboratory, Argonne, IL, United States; 4. NIST Center for Neutron Research, National Institute of Standards and Technology, Gaithersburg, MD, United States

$LaCoO_3$ (LCO) has been extensively studied due to its thermally-assisted spin-state crossover, deriving from the small difference between crystal field and Hund's exchange energies. Bulk LCO is thus a diamagnetic insulator below ~30 K, above which the spin-state crossover is initiated. Relatively recently, ferromagnetic (FM) order in epitaxial LCO thin films [1], in stark contrast to the bulk, has gathered attention. While stabilization of a finite spin-state and FM interactions under tensile strain are known to play a role, no consensus has emerged as to the origin of the FM. Additionally, due to the insulating nature, little attention has been paid to transport. Here, we present a study of epitaxial LCO (8-22 nm thick) grown under both tensile (on $SrTiO_3$, LSAT) and compressive strain (on $LaAlO_3$, $SrLaAlO_4$), emphasizing magnetism and transport. Based on X-ray diffraction, atomic force microscopy, and scanning transmission electron microscopy (STEM), the films are phase-pure, smooth, epitaxial, and fully strained, from -1.5 to 2.5% mismatch. STEM reveals oxygen vacancy ordering, with orientation controlled by strain-state, similar to Sr-doped LCO [2,3]. Tensile films exhibit ferromagnetism with saturation magnetization 1-1.5 μ_B/Co and Curie temperature ~80 K, consistent with prior work (Fig. 1a). Polarized neutron reflectometry reveals relatively uniform magnetization depth profiles. Most notably, transport, which is semiconducting, reveals an unanticipated correlation between strain-state and majority carrier type (Fig. 1b & c). FM is found to be associated with inversion to *n*-type, supported by density functional theory calculations indicating significant changes in conduction band effective mass under strain. We have thus revealed an important additional clue to the origin of the controversial FM in this system. Work supported by DOE Center for Quantum Materials under DOE-SC0016371.

[1] Fuchs, Pinta, Schwarz, Schweiss, Nagel, Schuppler, Schneider, Merz, Roth, and v. Löhneysen, Phys. Rev. B 75, 144402 (2007). [2] Gazquez, Bose, Sharma, Torija, Pennycook, Leighton, and Varela, APL Mater. 1, 12105 (2013). [3] Walter, Bose, Cabero, Yu, Greven, Varela, and Leighton, Phys. Rev. Materials 2, 111404(R) (2018).

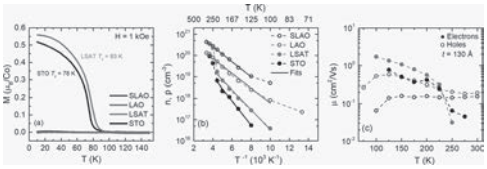


Fig. 1 (a) Temperature (*T*) dependence of magnetization (*M*, field-cooled) at 1 kOe in-plane measuring field (b) Hall electron or hole density (log scale, solid symbols for electrons, open symbols for holes) vs. inverse temperature (*T*) (c) Corresponding mobility (log scale) vs. *T* for 130-Å-thick $LaCoO_{3-\delta}$ films on various substrates.

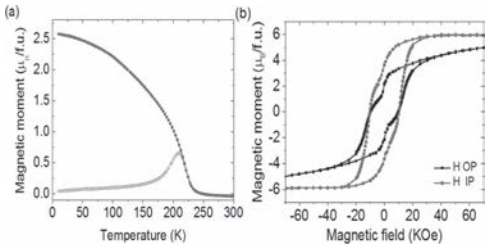
3:42

DH-08. La_2CoMnO_6 Ordered Double Perovskite Epitaxial Thin Films Grown by Polymer Assisted Deposition. H. Wang[1], J. Gazquez[1], C. Frontera[1], M. Chisholm[2], A. Pomar[1], N. Mestres[1] and *B. Martinez*[1]
1. Magnetic Materials and Complex Oxides, ICMAB-CSIC, Bellaterra, Spain; 2. Materials Science and Technology Division, Oak Ridge National Laboratory, Oak Ridge, Oak Ridge, TN, United States

Double perovskite La_2CoMnO_6 (LCMO) thin films are highly attractive due to their insulating ferromagnetic behavior and magnetodielectric effect near room temperature, making it a promising material for applications into new devices and spintronics.[1] However these properties are strongly dependent on the ordered arrangement of cations in the double perovskite $A_2BB'O_6$structure.[2] Therefore, many efforts have been made to improve the level of cationic ordering to obtain optimal properties while suppressing antisite defect formation. In this work, high quality epitaxial LCMO films were grown on (001) $SrTiO_3$ substrates by polymer assisted deposition (PAD).[3] This technique allows an easy control of stoichiometry by mixing different metal-polymer precursor solutions with the corresponding metal molar ratios. The precursor solutions were spin coated on (001)-STO substrates and the resultant coatings were thermally treated at 900 °C in flowing oxygen. We show that the particular crystallization and growth process conditions of PAD (very slow rate, close to thermodynamic equilibrium conditions) promote high crystallinity and quality of the films, as well as B-site cationic ordering. The LCMO films show saturation magnetization values of about 6 μ_B/f.u. and a Tc≈230K, thus indicating full cationic ordering of Co^{2+}/Mn^{4+} in a double perovskite structure Confirmation of the achievement of full Co/Mn

cationic ordering was found by scanning transmission electron microscopy (STEM) measurements; EELS maps indicated the ordered occupancy of B-B' sites by Co/Mn cations.

References [1] L. Lopez-Mir, C. Frontera, H. Aramberri, et al., *Sci. Rep.* 2018, *8*, 861 [2] R. Galceran, C. Frontera, L. Balcells, et al., *Appl. Phys. Lett.* 2014, *105*, 242401 [3] Q. X. Jia, T. M. McCleskey, A. K. Burrell, et al., *Nat. Mater.* 2004, *3*, 529



Temperature dpendence of the magnetization (a) and M-H loops recorded (b) at 10K for a LCMO/STO film, displaying saturation magnetization value close to 6 μB/f.u. in good agreement with the theoretical value for fully ordered samples

3:54

DH-09. Interfacial control of chiral magnetic interactions and Hall effect in iridate-manganite superlattices. *E. Skoropata*[1], J. Nichols[1,2], J. Ok[1], R.V. Chopdekar[3], C. Eun Sang[4], A. Rastogi[1], C. Sohn[1], X. Gao[1], T. Farmer[1], R.D. Desautels[1], Y. Choi[5], D. Haskel[5], S. Okamoto[1], M. Brahlek[1] and H. Lee[1] *1. Oak Ridge National Laboratory, Oak Ridge, TN, United States; 2. University of Arkansas at Little Rock, Little Rock, AR, United States; 3. Lawrence Berkeley National Laboratory, Berkeley, CA, United States; 4. National High Field Magnet Laboratory, Tallahassee, FL, United States; 5. Argonne National Laboratory, Argonne, IL, United States*

One of the most intriguing outcomes of symmetry breaking and spin-obit interactions in magnetic systems is the possibility to create non-collinear and chiral spin textures. The Dzyaloshinskii-Moriya interaction (DMI) results from strong spin-orbit coupling and broken inversion symmetry to generate magnetization rotations with fixed chirality. The discovery of magnetic skyrmions originating from strong DMI in metal thin films has led to an explosion of efforts to manipulate magnetic phases originating from interfaces. I will describe our progress to understand interface-induced magnetism in epitaxial 3*d*/5*d* iridate/manganite superlattices. Our previous work on high-quality epitaxially stabilized $SrMnO_3/SrIrO_3$ superlattices revealed charge-transfer induced interfacial collinear ferromagnetism and an anomalous Hall effect [1,2]. In $LaMnO_3/SrIrO_3$ superlattices, we find a large additional topological Hall effect arising from the interaction of charge carriers with a noncoplanar chiral spin texture induced by interfacial DMI [3]. I will describe how the interfacial atomic layer stacking and symmetry enabled by the nonmagnetic A-sites determine the competition between collinear and chiral magnetic interactions originating from the oxide interface. These results will be compared with magnetometry measurements, soft and hard x-ray experiments, which provide a comparison of the bulk and interface electronic and magnetic properties. Our findings provide insight to the manipulation of chiral magnetism from atomic-scale control of DMI at oxide interfaces.

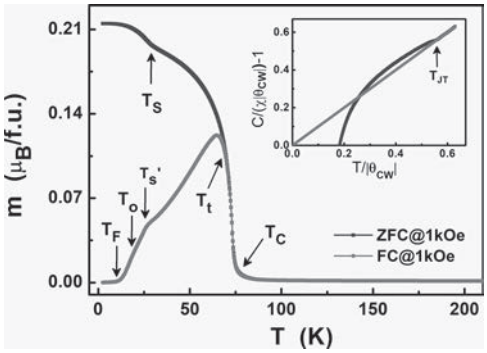
This work was supported by the U.S. Department of Energy, Office of Science, Basic Energy Sciences, Materials Sciences and Engineering Division. [1] J. Nichols *et al.*, *Nat. Commun.* 7, 12721 (2016). [2] S. Okamoto *et al.*, *Nano Lett.* 17, 2126 (2017). [3] P. Bruno *et al.*, *Phys. Rev. Lett.* 93, 096806 (2004).

4:06

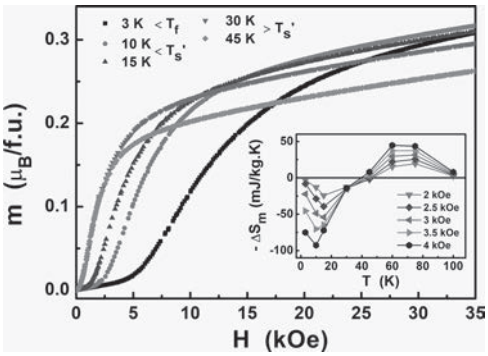
DH-10. Size evolution of magnetostructural transitions in spin and orbital-frustrated $NiCr_2O_4$: A possible magnetic multiferroic. *A. Rathi*[1], P. Babu[2], A. Awasthi[3], P. Rout[4], R. Pant[1] and G. Basheed[1] *1. AcSIR, CSIR-National Physical Laboratory (NPL) Campus, New Delhi, India; 2. UGC-DAE Consortium for Scientific Research, R-5 Shed, B. A. R. C., Mumbai, India; 3. UGC-DAE Consortium for Scientific Research, D. A. University Campus, Indore, India; 4. CSIR-National Physical Laboratory (NPL), New Delhi, India*

Frustrated magnetism has been at the forefront of modern condensed matter physics [1]; alongside its fundamental importance, spin frustration stabilize complex spin textures like in type-II multiferroics, generally antiferromagnets (AFM) [2] etc. Meanwhile, spinel ferrimagnet (FiM) chromite, ACr_2O_4 with Cr^{3+} ions on frustrated pyrochlore lattice have provided a great platform to study "spiral" multiferroicity with low-filed electric polarization reversal, as in cubic $CoCr_2O_4$ [3]. Here, we dare to undertake another spinel FiM chromite $NiCr_2O_4$ with Jahn-Teller (JT) active Ni^{2+} ions, which are expected to suppress the geometrical frustration via structural distortions. We study in detail the magneto-structural transitions in spin and orbital-frustrated $NiCr_2O_4$ from bulk to nanoscale by neutron diffraction (ND), magnetization, specific heat and magneto-dielectric measurements. The Jahn-Teller (JT) distortion temperature is reduced down to $T_{JT} \approx 268$ K on nanoscale (from its bulk value of 310 K) [4]; the nanoscale confinement further induces a significant enhancement in the magnetic collinearity, leading to (longitudinal) FiM ordering at higher Tc ≈ 100 K than in bulk $NiCr_2O_4$ at 70 K. Moreover, the ordering of frustrated (transverse) AFM interactions (at $T_S \approx 30$ K with frustration index, $f = |\theta_{CW}|/T_N \approx 18$ in bulk) is not observed on nanoscale down to 3 K; this suggests the possible co-existence of magnetic ordering and a spin-liquid state in nanochromite $NiCr_2O_4$. More importantly, another low-temperature transition is observed for bulk $NiCr_2O_4$ at $T_f \approx 8$ K in high magnetic fields in both magnetization and magneto-dielectric measurements, suggesting a field-induced type-II multiferroicity in $NiCr_2O_4$. The study concludes that structural transitions/distortions in $NiCr_2O_4$ are stabilized by magneto-elastic effects, spin and orbital frustration.

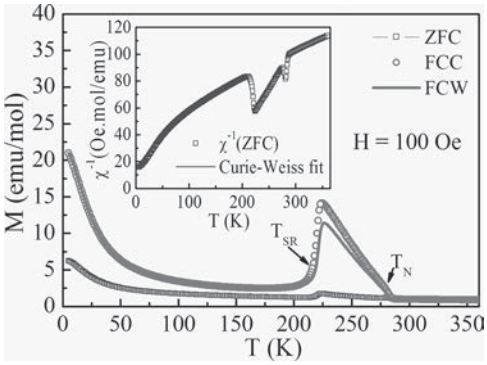
1. C. Lacroix, P. Mendels, and F. Mila, Introduction to Frustrated Magnetism: Materials, Experiments, Theory (Springer, New York, 2011). 2. Y. Tokura, S. Seki and N. Nagaosa, Rep. Prog. Phys. 77 076501 (2014). 3. Y. Yamasaki, S. Miyasaka, Y. Kaneko, Phys. Rev. Lett. 96, 207204 (2006). 4. A. Rathi, P.D. Babu, P.K. Rout, J. Magn. Magn. Mater. 474, 585 (2019).



The temperature dependence of 'field-cooled' (m^{FC}) and 'zero-field-cooled' (m^{ZFC}) dc magnetization of bulk $NiCr_2O_4$ in an applid magnetic field of 1kOe. The inset shows the rearranged Curie-Weiss plot, constructed out of the m^{FC} data.



The m-H Isotherms for bulk $NiCr_2O_4$ at selected low temperatures. The inset shows the temperature dependence of magnetic entropy at low fields.



The magnetization vs. temperature curves taken for an applied field of 100 Oe in ZFC, FCC and FCW protocals (inset) Curie-Weiss fit of inverse susceptibility data

4:18

DH-11. Spin Reorientation, Metamagnetism and Spin-Phonon Coupling in Polycrystalline $EuFe_{0.5}Mn_{0.5}O_3$. *K. Chandran*[1], P. Lekshmi[1] and s. P N[1] *1. Physics, Indian Institute of technology Madras, Chennai, India*

Rare earth orthoferrites ($RFeO_3$) are receiving attention these days owing to their interesting applications in sensors, magneto-optic properties, multi-ferroics, spin switching, optical control of spins and domain wall physics, etc. $EuFeO_3$ exhibits similar properties like all other orthoferrites and have high octahedral rotations due to the smaller size of the Eu^{3+} ion. In many $RFeO_3$ the substitution of different magnetic at the Fe site is found to tune the magnetic transitions and change the nature of spin reorientation due to modified crystallographic and magnetic features. In the present work, 50% of Mn ion is substituted at the Fe site in order to create an equal distribution of Mn ions in the Fe matrix. Polycrystalline samples of $EuFe_{0.5}Mn_{0.5}O_3$ were synthesized by a sol-gel route. Rietveld refinement of Synchrotron XRD patterns taken at different temperatures down to 15 K were fitted with orthorhombic unit cell having *Pbnm* space group without any structural change in the measured temperature range. Thermomagnetic measurements indicate the presence of a magnetic transition around 280 K, due to the AFM ordering of Fe^{3+}/Mn^{3+} sublattice, followed by a sharp drop in the magnetization at 220 K, due to the spin reorientation (SR) of Fe/Mn spins. The presence of weak ferromagnetism is reflected by the increase in bulk magnetization below the transition and a minor hysteresis loop observed in M(H) isotherms. The modified magnetic interactions coupled with the co-existence of multiple magnetic ions (Er/Fe/Mn) further establish metamagnetic transition and Griffith like features in $EuFe_{0.5}Mn_{0.5}O_3$. Additionally, in order to investigate the phonon behavior across the magnetic transitions, Raman spectrum was taken at several temperatures ranging from 170 K to 300 K. Spin phonon coupling is observed at both antiferromagnetic transition and SR transition. The presence of high T_N, sharp spin reorientation transition, Griffith like behavior, metamagnetic transitions and spin-phonon coupling makes this material suitable candidate for practical applications.

Session DI
SPIN, MAGNETISM, AND SUPERCONDUCTIVITY

Elena Y Vedmedenko, Chair
University of Hamburg, Hamburg, Germany

INVITED PAPER

1:30

DI-01. Emergent Phenomena in the Shastry-Sutherland Model System as Function of Magnetic Field, Pressure and Chemical Doping.
S. Haravifard[1] *1. Physics, Duke University, Durham, NC, United States*

The physics of Mott insulators holds the key that might unlock some of the most pressing problems in condensed matter physics, such as the long-sought Resonating Valence Bond (RVB) superconductivity [1]. A particularly important proposal involves the doping-induced superconductivity in spin-1/2 orthogonal dimers on a square lattice, the so-called Shastry-Sutherland (SS) model as realized physically in the Mott insulator SrCu2(BO3)2 (SCBO) [2,3]. Furthermore, SCBO has been studied vigorously for its extremely rich phase diagram and exotic properties at high magnetic fields [4], while recently it has been attracting additional attention as a bosonic topological insulator candidate which is suggested to host chiral edge modes of triplon bound states at low magnetic field regime, and for the proposals of novel states emerging as function of pressure. [5] Therefore, it is of great interest to shed light on the roles magnetic field, pressure, and chemical doping play in tuning the underlying interactions in SCBO. Additionally, understanding the interplay between pressure, chemical doping, and magnetic field in SCBO (at both high and low fields regimes) provides critical information and reveals a fresh prospective, illuminating the path to advancing our knowledge of topological phenomena and emergent quantum states in SCBO and similar systems of interest. In this talk, I present a comprehensive study of the field- [6], pressure- [7] and chemical doping-induced [8] novel emergent states in SCBO. We use multiple complementary measurement techniques to probe static and dynamic magnetic structure, magnetization, and magnetic susceptibility at fields up to 65 T, pressures up to 5 GPa, and cryogenic temperatures, conducted for several doping concentrations. Our numerical simulations performed using DMRG and iPEPS techniques complement these results, providing firsthand description of the intriguing experimental observations.

[1] Xu, Guangyong, G. Aeppli, M. E. Bisher et al., Science 289, 419 (2000). [2] B. S. Shastry & B. Sutherland, Phys. B+C. 108, 1069 (1981). [3] H. Kageyama, K. Yoshimura, R. Stern et al., Physical Review Letters 82, 3168 (1999). [4] K. Kodama, M. Takigawa, M. Horvatić et al., Science 298, 395 (2002). [5] A. P. McClarty, F. Krüger, T. Guidi et al., Nature Physics 13, 736 (2017). [6] S. Haravifard, D. Graf, A. E. Feiguin et al., Nature Communications 7, 11956 (2016). [7] S. Haravifard, A. Banerjee, J. van Wezel et al., Proceedings of the National Academy of Sciences 111, 14372 (2014). [8] Z. Shi, W. Steinhardt, D. Graf et al., Nature communications 10, 2439 (2019).

CONTRIBUTED PAPERS

2:06

DI-02. Ferromagnetic order in a cuprate superconductor.
R.l. Greene[1], T. Sarkar[1], N.R. Poniatowski[1] and P. Mandal[1] *1. Physics, University of Maryland, College Park, MD, United States*

Conventional wisdom dictates that the mysterious and extraordinary properties of the cuprates arise from doping an antiferromagnetic (AFM) Mott Insulator. Such a picture can account for the increase of the superconducting (SC) transition temperature (Tc) with increasing doping as a consequence of the competition between the AFM and SC orders, but not for the decrease of Tc beyond optimal doping. In fact, there is no satisfactory theoretical explanation for this decline of Tc. In this work, we report the emergence of a ferromagnetic (FM) phase beyond the superconducting dome in the electron-doped cuprate $La_{2-x}Ce_xCuO_4$ (LCCO) as evidenced by resistivity, magneto- thermopower and magnetization experiments. This unexpected discovery suggests that a quantum phase transition occurs at the end of the SC dome and that a competition between superconductivity and FM could provide an explanation for the decrease in Tc in the overdoped cuprates. Our findings show that the physics of the overdoped cuprates is much richer than previously thought, and pose a challenge to most proposed models of the cuprates.

T. Sarkar, P.R. Mandal, N.R. Poniatowski, and R. L. Greene, arXiv:1902.11235

2:18

DI-03. Vortex state study of superconducting Fe(Te, Se) thin films deposited on $SrTiO_3$ substrate by pulsed laser deposition technique.
R. Kumar[1], D. Mitra[1] and G.D. Varma[1] *1. Physics, I.I.T. Roorkee, Roorkee, India*

Superconducting thin films of two thicknesses have been fabricated on (*100*) oriented $SrTiO_3$ (STO) substrates using the target of composition $Fe_{1.05}Te_{0.50}Se_{0.50}$ by pulsed laser deposition technique. The structural and transport properties of the fabricated thin films have been investigated and the results indicate the enhancement in the superconducting properties with increasing thickness of the thin films. The onset of the superconducting transition temperature of the grown thin films of thicknesses ~82 nm and ~179 nm are ~12.10 and 12.62 K at 0 T magnetic field, respectively. To estimate the upper critical fields $H_{C2}(0)$, thermally activated energy (TAE) and vortex phase diagram, the magnetoresistance measurements have been performed in the magnetic field range of 0 - 8 T. $H_{C2}(0)$ has been calculated by Ginzburg Landau (GL) theory as well as by Werthamer-Helfand-Hohenberg (WHH) model by taking the criterion of 90%, 50% and 10% of normal state resistivity and the corresponding GL coherence lengths have also been calculated. In the present work, the TAE has been estimated by conventional Arrhenius relation and modified thermally activated flux flow (TAFF) theory [Fig. 1]. The power law dependence of TAE, shows prominently the possible planer defects in the system. From the modified TAFF model, the values of fitting parameter 'q' suggests the 3 dimensional behaviour of the vortices for both the grown thin films. The detail correlations among the structural and superconducting properties of both the thin films have been discussed in this paper.

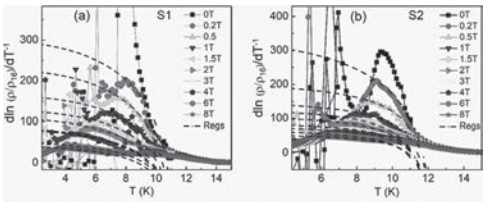


Figure 1: $d\ln(\rho/\rho_{16})/dT^{-1}$ versus T (K) plots at different magnetic fields for the calculation of TAE using modified TAFF model for both the thin films.

2:30

DI-04. Magnetic Screening Effects in Superconductor/Ferromagnet Heterostructures. *P. Quarterman*[1], N. Satchell[2], B.J. Kirby[1], R. Loloee[2], N. Birge[2] and J. Borchers[1] *1. NIST, Gaithersburg, MD, United States; 2. Michigan State University, East Lansing, MI, United States*

Ferromagnetic Josephson junctions are a viable candidate for low power cryogenic memory alternative compared to traditional CMOS technologies. Magnetic screening properties of superconductors in proximity to ferromagnetic materials are of interest due to recent predictions of a long-range magnetic field in the superconductor induced by proximity effect [1]. These additional screening currents may account for several experimental observations, most notably in Co/Nb/Cu stacks where an anomalous Meissner effect has been reported [2]. Prior to this work, we characterized analogous Nb films with polarized neutron reflectivity (PNR), modelled the Meissner effect, and extracted the London penetration depth which matches the known value. In this work, we report on our progress characterizing samples which are expected to exhibit the predicted 'electromagnetic proximity effect.' Specifically, we have carried out PNR measurements on Ni(2.8)/Nb(200) bilayers and Ni(2.8)/AlO_x(3)/Nb(200) samples to probe screening-effect distortions in Nb when in proximity of a ferromagnet. Figure 1 shows the spin asymmetry, as determined from the polarized neutron reflectometry for both samples at 3 K, and the sample with an oxide interlayer at 12 K. In the Ni/AlO_x/Nb sample, the spin asymmetry is understood by modeling the Meissner effect in conjunction with the ferromagnetic Ni layer at 3 K, and just the ferromagnetic component at 12 K. When the Ni and Nb are in direct contact, PNR shows that the Meissner effect is suppressed, and the data cannot be described by the same Meissner and ferromagnetic model. The data analysis we discuss in this work highlights the sensitivity of the spin asymmetry to anomalous suppression of field screening in Ni/Nb heterostructures.

[1] S. Mironov et al., Appl. Phys. Lett. 113, 022601 (2018) [2] M. G. Flokstra et al., Phys. Rev. Lett. 120, 247001 (2018)

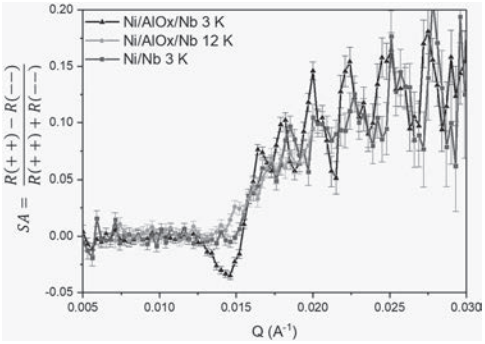


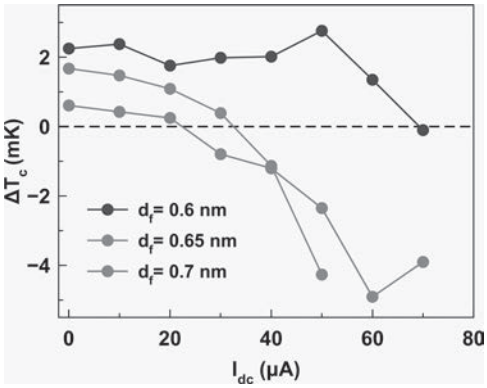
Figure 1: Spin asymmetry data for Ni/Nb bilayers (purple), and Ni/AlO_x/Nb layers measured at 3 (black) and 12 K (orange). The dip near Q = 0.015 $Å^{-1}$ in the black curve is characteristic of traditional Meissner screening.

2:42

DI-05. Spin Hall Current Dependence of Superconducting Transition Temperature in Superconductor/Spin-Valve Nanowires. *A. Jara*[1], I. Krivorotov[1], E. Moen[2] and O. Valls[2] *1. Physics and Astronomy, University of California - Irvine, Irvine, CA, United States; 2. School of Physics and Astronomy, University of Minnesota, Minneapolis, MN, United States*

Superconductor/ferromagnetic (S/F) heterostructures have been a focus of intensive research over the past two decades. Apart from their importance for the understanding of fundamental physics of the superconducting proximity effect, S/F nanostructures may find applications in low-power cryogenic computing [1]. Competition between superconducting and ferromagnetic ordering in S/F heterostructures can lead to unusual types of magneto-transport effects emerging from the proximity effect at the S/F interfaces such as odd-triplet superconductivity and spin-polarized supercurrents. A prominent example of an S/F proximity effect is the spin switch effect (SSE) observed in S/F/F superconducting spin valve multilayers, in which the superconducting transition temperature T_c is controlled by the angle Φ between the magnetic moments of the F layers [2]. Here we present an experimental study of SSE in Nb/Co/Cu/Co/CoO nanowires measured as a function of bias current flowing in the plane of the layers. In this structure, the magnetization of the top Co layer is pinned by a strong exchange bias from the antiferromagnetic CoO layer, while the magnetization of the bottom (free) Co layer can be easily rotated in the plane of the sample by a relatively small magnetic field. These measurements reveal an unexpected dependence of $T_c(\Phi)$ on the bias current: $T_c(\pi) - T_c(0)$ changes sign with increasing current bias (Fig. 1). We attribute the origin of this bias dependence of the SSE to a spin Hall current, induced by the bias current and perpendicular to the plane of the multilayer, which suppresses the critical temperature of the multilayer. We rule out other possible explanations on either qualitative or quantitative grounds. The bias dependence of SSE can be important for hybrid F/S devices such as those used in cryogenic memory for superconducting computers as device dimensions are scaled down to the nanometer length scale. We will present detailed measurements of the magnitude of this effect as a function of bias current and the thickness of the free magnetic layer.

[1] D. S. Holmes, A. L. Ripple, M. A. Manheimer, IEEE Trans. Appl. Supercond. 23, 1701610 (2013). [2] A. A. Jara, C. Safranski, I. N. Krivorotov, C. T. Wu, A. N. Malmi-Kakkada, O. T. Valls, and K. Halterman, Phys. Rev. B 89, 184502 (2014).



Dependence of $\Delta T_c = T_c(\pi) - T_c(0)$ on current bias I_{dc} for three Nb(20 nm)/Co(d_f)/Cu(6 nm)/Co(2 nm)/CoO_x(2 nm) devices with different values of the free layer thickness d_f.

2:54

DI-06. Unprecedented Electronic Structure, Magnetic Anisotropy and Orbital Moment in Rare Earth (RE) - Cobalt Systems. *D. Paudyal*[1], R. Choudhary[1] and R. Skomski[2] *1. Ames Laboratory, Ames, IA, United States; 2. University of Nebraska, Lincoln, NE, United States*

We have used theory and computation to investigate the magnetic properties of Fe substituted RE-Co systems. Many features of these systems are consistent with past research. Figure 1 examplifies the theoretically calculated magnetocrystalline anisotropies and formation energies of SmCo5-xFex as a function of Fe content. Some of the electronic structure findings are seemingly contradictory to past research. The disagreement is not caused by numerical errors or accidental mistakes but reflects how the many-electron nature of the rare-earth 4f electrons is interpreted by crystal-field and local spin density approximation with Hubbard model and spin orbit coupling (LSDA+U+SOC) theories. The two-sublattice crystal-field theory is known to describe a broad variety of RE-Co properties, such as the temperature dependence of magnetization and anisotropy, but it is not a first-principle approach. By contrast, our first-principle approach, LSDA+U, yields a substantial orbital-moment quenching, which violates Hund's rules and is contradictory to conventional knowledge accumulated over several decades of rare-earth research. Rationalizing the orbital-moment quenching in terms of the dependence of the charge distribution (Fig. 2) on the magnetization angle, we argue that medium- and long-run future research will be necessary to reconcile experiment, sublattice models, and first-principle calculations for RE-Co materials. This work is supported by the Critical Materials Institute, an Energy Innovation Hub funded by the U.S. Department of Energy, Office of Energy Efficiency and Renewable Energy, Advanced Manufacturing Office. The work in Nebraska was supported by the US Department of Energy (Grant No. DE-FG02-04ER46152) and performed in part in the Nebraska Nanoscale Facility and the Nebraska Center for Materials and Nanoscience which are supported by NSF NNCI #1542182, and the Nebraska Research Initiative.

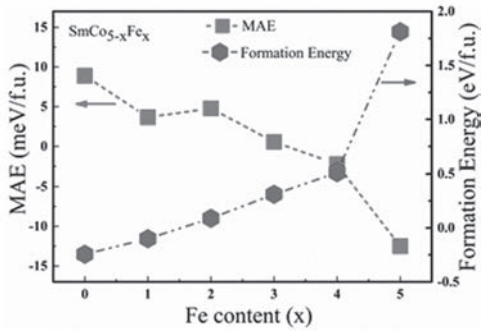


Fig 1. Theoretically calculated magnetocrystalline anisotropies and formation energies of $SmCo_{5-x}Fe_x$ as a function of Fe content.

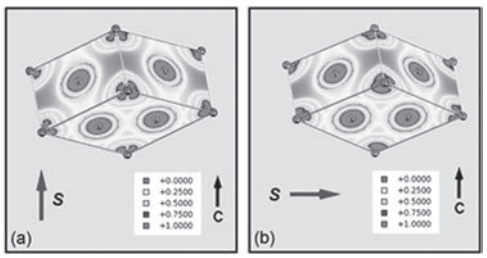


Fig 2. The charge density as calculated by DFT: (a) easy direction and (b) hard direction. The charge density has ranged from 0 to 1 e/Å^3.

3:06

DI-07. Exchange interaction and Curie temperature in R_2Co_2Al. *X. Liu*[1], Z. Altounian[2] and C.I. Nlebedim[1] *1. Ames Lab, Ames, IA, United States; 2. Physics, McGill University, Montreal, QC, Canada*

We present the magnetization, exchange interaction and Curie temperature of R_2Co_2Al (R=Nd, Sm, Gd, Tb, Dy, Ho, Er, Tm) and also the effects of Fe-substitution for Co. R_2Co_2Al with R = Nd, Sm, Gd, Tb, Dy, Ho, Er, and Tm crystallizes in the W_2CoB_2-type orthorhombic structure[1]. These compounds display complex magnetoresistance and magneto-caloric effects around the magnetic transition temperature,[2–4] which is intimately related to their magnetic exchange interaction. Our study is based on a first principles DFT calculation and a linear response method with the Heisenberg model. The crystallographic parameters are fully relaxed with the PAW (projector augmented wave) method, implemented in the QuantumEspresso package. The optimized crystal parameters are in good agreement with the experimental values[1]. The calculated magnetic moments are mainly contributed by the R-atom's 4*f* electrons. The Co atoms display a small induced magnetic moment of about 0.2-0.3 μ_B, and are antiferromagnetically coupled with the spin magnetic moment of the R-atoms, in agreement with neutron diffraction results[4]. The exchange interaction parameters were derived from the calculated band structures using a linear response method. We found that the values of the nearest R-R inter-site exchange coupling constants are comparable to those of R-Co and Co-Co pairs. These results imply that the small magnetic moments, induced at the Co sites, are important for stabilizing the magnetic structure in R_2Co_2Al compounds. Based on the Heisenberg model, the estimated trends in the mean field Curie temperatures are in good agreement with the experimental results (Fig. 1). Further, the calculations for $Gd_2(Co,Fe)_2Al$ with the W_2CoB_2-type structure indicate that Fe has a magnetic moment of 1.2 μ_B, which enhances the R-Co(Fe) inter-site exchange interaction, confirming the important role of the magnetic moment of Co(Fe) in this system. The calculated mean field Curie temperatures are 113 K and 366 K for Gd_2Co_2Al and virtual Gd_2Fe_2Al compounds, respectively.

[1] M. Pani, F. Merlo, and M.L. Fornasini, Z. Kristallogr., 217, 415 (2002). [2] K. Sengupta, K.K. Iyer, and E. V Sampathkumaran, Phy.Rev. B, 72, 054422 (2005). [3] H. Fu, M. Zou, M.S. Guo, Q. Zheng, and X.T. Zu, J. Alloys. Compd. 62, 4 (2011). [4] A. V Morozkin, V.K. Genchel, A. V Garshev, V.O. Yapaskurt, O. Isnard, J. Yao, R. Nirmala, S. Quezado, and S.K. Malik, J. Magn. Magn. Mater. 442, 36 (2017).

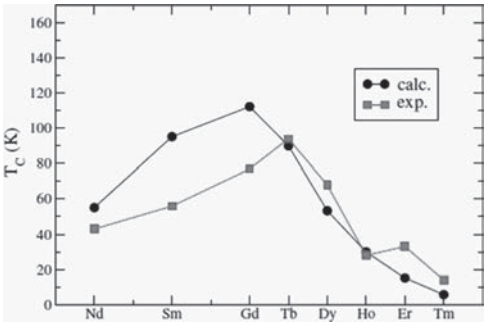


Fig.1 Calculated (circle) and experimental (square) Curie temperature in R_2Co_2Al with R=Nd, Sm, Gd, Tb, Dy, Ho, Er, and Tm.

INVITED PAPER

3:18

DI-08. Spin Current: a Probe for Quantum Materials. *W. Han*[1]
1. Peking University, Beijing, China

Spin current generally means the electron-mediated current with spin polarization after the discovery of giant and tunneling magnetoresistances in 1980s. Recently, new types of spin current in quantum materials have been found, which are mediated by magnons, superconducting (SC) quasiparticles, spinons etc. These quantum materials have exhibited fascinating spin-dependent properties, which are attractive for future spintronics applications [1]. In this talk, I will discuss some primary experimental results to illustrate how spin current could be a powerful probe for new quantum materials. I will discuss the SC quasiparticle-mediated spin current as a probe for spin dynamics of an s-wave superconducting film [2], which might be useful to probe the spin dynamics for unconventional superconducting thin films. I will also discuss the spin superfluid-mediated spin current for the probe of novel quantum phase of spin superfluidity/superconductor ground states. The spin current in canted antiferromagnet Cr_2O_3 is investigated, which provides important experimental signatures of the spin superfluid ground states [3]. At the end, I will present the current status and the outlook of this exciting direction of using spin current as a probe for quantum materials [4].

[1] W. Han*, Y. Otani, and S. Maekawa, npj Quantum Materials, 3, 27 (2018). [2] Y. Yao, Q. Song, Y. Takamura, J. Cascales, W. Yuan, Y. Ma, Y. Yun, X. C. Xie, J. S. Moodera, and W. Han*, Physical Review B 97, 224414 (2018). [3] W. Yuan, Q. Zhu, T. Su, Y. Yao, W. Xing, Y. Chen, Y. Ma, X. Lin, J. Shi*, R. Shindou, X. C. Xie*, and W. Han*, Science Advances, 4, eeat1098 (2018). [4] W. Han*, S. Maekawa and Xin-Cheng Xie, Nature Materials (Under review).

CONTRIBUTED PAPERS

3:54

DI-09. Lattice and magnetic excitations in CrAs: A Raman spectroscopy study. *K. Sen*[1], Y. Yao[1], R. Heid[1], A. Omoumi[1], F. Hardy[1], K. Willa[1], M. Merz[1], A. Haghighirad[1] and M. Le Tacon[1] *1. Institute for Solid State Physics, Karlsruhe Institute of Technology, Eggenstein-Leopoldshafen, Germany*

Following the discovery of high-temperature superconductivity in Fe-based compounds, several transition-metal pnictides have been investigated [1–4]. CrAs is a representative of this family of compounds, which undergoes a first-order transition from a high-temperature paramagnetic state to a low-temperature non-collinear double-helical magnetic state below T_N= 265 K [5]. Concomitantly, it exhibits a giant structural anomaly which involves the abrupt expansions of the crystallographic b-axis by 4 % and the unit cell volume by 2.2 % below T_N [6]. This helical magnetic ground state gets suppressed upon chemical doping or hydrostatic pressure. In the latter case, bulk superconductivity with a maximum T_c of 2 K has been reported [7], making this system the first Cr-based superconductor to date. Moreover, recently observed quantum critical behavior in CrAs suggests that this is an unconventional superconductor [8]. Despite the evident interplay between the lattice and magnetic degrees of freedom in CrAs, only a few studies of the spin and lattice dynamics of this system have been reported to date. We have addressed this issue using polarized Raman scattering. Large renormalizations of the phonon energies and linewidths are observed across T_N, which along with the results of first-principle calculations suggest the presence of a sizeable spin-phonon coupling in this compound. Furthermore, we observe two broad modes around 350 and 1700 cm^{-1} in the magnetic phase, which we associate with two-magnon Raman scattering, providing one of the few examples of magnetic Raman scattering from a non-collinear magnet.

[1] Y. Kamihara *et al.*, J. Am. Chem. Soc. 130, 3296 (2008). [2] M. Rotter *et al.*, Phys. Rev. Lett. 101, 107006 (2008). [3] F.-C. Hsu *et al.*, Proc. Natl. Acad. Sci. 105, 14262 (2008). [4] X. C. Wang *et al.*, Solid State Commun. 148, 538 (2008). [5] K. Selte *et al.*, Acta Chem. Scand. 25, 1703 (1971). [6] T. Suzuki and H. Ido, J. Appl. Phys. 73, 5686 (1993). [7] W. Wu *et al.*, Nat. Commun. 5, 5508 (2014). [8] M. Matsuda *et al.*, Phys. Rev. X 8, 031017 (2018).

4:06

DI-10. Origin of Itinerant Carriers in an Antiferromagnetic $LaFe_{1-x}Mo_xO_3$ Studied by X-ray Spectroscopies. *D. Phuyal*[1], S. Mukherjee[1], S. Jana[1,2], C.U. Segre[3], L. Simonelli[4], S.M. Butorin[1], H. Rensmo[1] and O. Karis[1] *1. Department of Physics and Astronomy, Uppsala University, Uppsala, Sweden; 2. Methods and Instrumentation for Synchrotron Radiation, Helmholtz-Zentrum Berlin, Berlin, Germany; 3. CSRRI & Department of Physics, Illinois Institute of Technology, Chicago, IL, United States; 4. BL22 CLÆSS, CELLS-ALBA Synchrotron, Barcelona, Spain*

We report on the electronic structure of a Mo-doped $LaFeO_3$ at the crossover from insulating to metallic phase transition. Comprehensive x-ray spectroscopic methodologies are used to understand core and valence electronic structure as well as crystal structure distortions associated with the electronic transition. Despite the antiferromagnetic (AFM) ordering at room temperature[1], we show direct evidence of itinerant carriers at the Fermi level revealed by resonant photoemission spectroscopy (RPES) at the Mo L_3 edge. RPES data taken at the Fe L_3 edge show spectral weight near the valence band edge and significant hybridization with O 2*p* states necessary to account for AFM ordering. Resonant inelastic x-ray scattering (RIXS) spectra taken across Fe $L_{2,3}$ edges show electron correlation effects (U) driven by Coulomb interactions of *d* electrons as well as broad charge-transfer excitations for $x \geq 0.2$ where the compound crossovers to a metallic state. Site substitution of Fe by Mo ions in the Fe-O_6 octahedra enhances the separation of the two Fe-O bonds and Fe-O-Fe bonding angles relative to the orthorhombic $LaFeO_3$, but no considerable distortions are present to the overall structure. Mo ions appear to be homogeneously doped, with average valency of both metal sites monotonically decreasing with increasing Mo concentration. This insulator-to-metal phase transition with AFM stability is primarily understood through interaction strengths between correlation (U) and bandwidth (W). These results highlight the important role of extrinsic carriers in stabilizing a unique phase transition that can guide future efforts in antiferromagnetic-metal spintronics.

1. S. Jana, S. K. Panda, D. Phuyal, Physical Review B 99 075106 (2019).

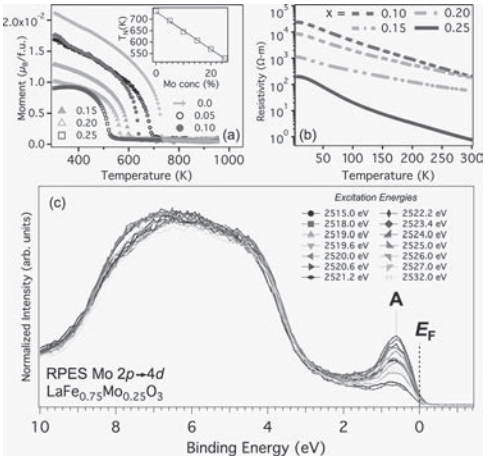


Fig. 1 - (a) Temperature dependence on magnetization for all compositions. (b) The resistivity vs. temperature plots, and (c) Mo resonant photoemission showing spectral intensity at E_F.

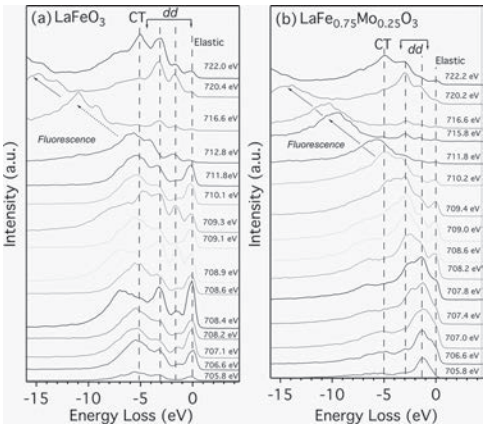


Fig. 2 Fe $L_{2,3}$ edge RIXS spectra for (a) the undoped parent $LaFeO_3$, (b) x = 0.25 Mo doped sample where crossover to metallicity occurs. The metallic sample maintain a strong *d* correlation.

4:18

DI-11. Fine Tuning of Canted Magnetization in Stepped Fe Films Through Thickness Variation, Au Capping and Quantum Confinement. M. Dabrowski[1], M. Cinal[2] and *M. Przybylski*[3] *1. Department of Physics and Astronomy, University of Exeter, Exeter, United Kingdom; 2. Institute of Physical Chemistry of the Polish Academy of Sciences, Warszawa, Poland; 3. Academic Centre for Materials and Nanotechnology, AGH University of Science and Technology, Kraków, Poland*

Our results demonstrate that well defined canted magnetization can be achieved without application of an external field. By taking advantage of broken symmetry of a vicinal substrate, we show that magnetic anisotropy of Fe films grown on the Ag-stepped surface results in the canted magnetization with its azimuthal orientation locked within the plane perpendicular to the step edges. The value of the tilting angle can be precisely tuned by changing the thickness of Fe film and Au overlayer. This is possible thanks to continuous rotation of magnetization from out-of-plane to in-plane direction with increasing thickness of Fe and the fact that the direction of magnetization rotation can be reversed by covering Fe films with Au layers. At low temperatures, QWS formed within Fe films come into play and contribute to the magnetocrystalline anisotropy, resulting in periodic modulations of the tilting angle, which substantially affects the magnetization rotation associated with the SRT. The analysis of the proposed theoretical model reveals that the ferromagnetic system grown on vicinal surface can only be fully described if two additional, step-induced, anisotropy constants are included in the magnetic anisotropy energy of the film. The model reproduces the experimental findings and predicts that the tilting of magnetization results from the superposition of the three uniaxial magnetic anisotropies acting within the vertical plane perpendicular to the step edges. The step-induced anisotropy term with the easy axis oriented at 45^o or –45^o to the terrace plane affects the tilting angle significantly. The presence of this term is crucial for explaining the reversed rotation of magnetization upon covering the stepped Fe films by Au. The presented methods allow for fine engineering of canted magnetization state and can be beneficial for control of the magnetization direction via voltage or optical pulses since tilted magnetization provides an additional torque and reduces the external energy required to switch the magnetization.

M. Dabrowski, M. Cinal, A. K. Schmid, J. Kirschner, and M. Przybylski, Phys. Rev. B, Vol.99, p.184420 (2019)

Session DP
2D AND TOPOLOGICAL MATERIALS
(Poster Session)

Fatima Ibrahim, Chair
Université Grenoble Alpes, CEA, CNRS, Grenoble, France

DP-01. Controlling the Magnetic Properties of $MoSe_2$ Monolayer by Mn and Cr Substitutional Doping and Vacancy Clustering: A First-Principles Study. *M.B. Kanoun*[1] and S. Goumri-Said[1] *1. Physics, Alfaisal University, Riyadh, Saudi Arabia*

The search for spintronic materials remains a continuous priority [1,2] due to promising new functionalities for future information technologies. The recent discovery of two-dimensional (2D) materials [4] provides a way to overcome these difficulties and new research area for materials science and technology. These 2D materials have revealed large potential for the new generation low-dimensional transistors, photo-emitting devices and spintronics devices due to their distinct crystal structures and electronic properties [3,4]. Here, we report the effect of Mn and Cr doping on electronic and magnetic properties of $MoSe_2$ monolayer using first principles calculations based on density functional theory within generalized gradient approximation [5], as implemented in the Vienna Ab initio Simulation (VASP) code [6]. The interactions between electrons and ions were described by the projector-augmented wave (PAW) method [7]. The layered structures of $MoSe_2$ have a sandwich structure which is composed of three atomic layers with one Mo layer between two Se, as shown in Fig. 1. A 4 × 4 × 1 $MoSe_2$ monolayer supercell structures containing 32 Se and 16 Mo atoms is built. To explain the role of the Mn -doping on the electronic structure, we calculated the density of states (DOSs) as shown in Figures 2 (a and b). The DOSs showed that the substitution of Mn at Mo site can induce spin polarized state and introduces highly localized orbitals within the energy band gap region of the un-doped compounds. Indeed, the polarized charges mainly rise from the localized Mn 3d states with weak contribution of the delocalized 4d states of the Mo atom and p states of Se atom (Fig. 2b). For Cr doping, it is known that the Cr atom is isoelectronic to Mo which shows an identical behavior of valence band and conduction band maximum between doped system and pristine monolayer. Then, we aim to study and control the magnetic properties of $MoSe_2$ monolayer by including single or double Se vacancies cluster near Cr/Mn atoms to enhance magnetism in doped system.

[1] T. Dietl, 9, 965–974 (2010). [2] S. Wolf, D. Awschalom, R. Buhrman, et al, Science 294, 1488–1495 (2001). [3] H. Li, J. Wu, Z. Yin and H. Zhang, Acc. Chem. Res., 47, 1067 (2014). [4] M. B. Kanoun, J. Alloys Compounds, 748, 938-942 (2018) [5] J. P. Perdew, K. Burke, M. Ernzerhof, Phys. Rev. Lett. 77, 3865 (1996). [6] G. Kresse, J. Furthmuller, Comput. Mater. Sci. 6, 15-50 (1996). [7] P. E. Blochl, Phys. Rev. B 50, 17953 (1994).

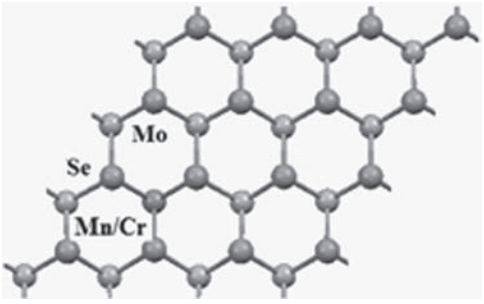


Fig 1. Top views of monolayers $MoSe_2$ doped Mn/Cr atoms

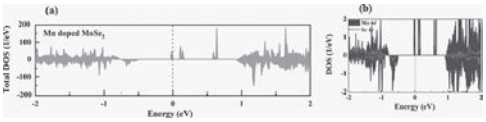


Fig 2. Total and partial density of states of the Mn/Cr doped $MoSe_2$. Spin up and spin down correspond to positive and negative values, respectively.

DP-02. Magnetotransport properties of Ni-nanoparticle-decorated graphene. E. Argüello[1], P. Ducos[1], Z. Gao[2], A.T. Johnson[2] and *D. Niebieskikwiat[1] 1. Departamento de Física, Universidad San Francisco de Quito, Quito, Ecuador; 2. Department of Physics and Astronomy, University of Pennsylvania, Philadelphia, PA, United States*

In this work, we characterize the effect of Ni magnetic nanoparticles on the magnetotransport properties of chemical vapor deposition (CVD) graphene. The magnetoresistance of a Ni-nanoparticle-decorated Graphene Resistor (Ni-GR, nanoparticles diameter ~ 7 nm) is measured while sweeping the magnetic field at different temperatures and compared with measurements done on the unmodified Graphene Resistor (GR), with no nanoparticles, as a control sample. Our results show that, in the presence of Ni nanoparticles, the commonly observed zero-field peak of the resistivity is widely suppressed, while the high field magnetoresistance shows a fourfold enhancement as compared to the GR sample. These results are discussed in terms of electron-electron-interaction corrections to the Drude conductivity, as well as weak localization effects arising from quantum interference phenomena at low magnetic fields. On one hand, the magnetic interaction of graphene with the Ni nanoparticles frustrates quantum interference, suppressing weak localization. On the other hand, a possible charge transfer between Ni and graphene may reduce the carrier density, increasing the carrier's mean free time and affecting both, weak localization and electron-electron interaction contributions to the conductivity of graphene.

DP-03. Topological spin-Hall effect in 2D Cr-halogenated materials. *Y. Dahnovsky*[1] and A. Zadorozhniy[1] *1. Physics and Astronomy, University of Wyoming, Laramie, WY, United States*

We study the THE in various systems on 2D magnetic materials. The focus will be on the spin textures in the atomic thin 2D materials (CrI<s_3, $CrCl_3$, and $CrBr_3$). The system consists of two layers: one is a CrI_3 layer while the other is $CrCl_3$. We have selected such a system such a system because it provides an interesting spin texture: a CrI_3 layer is a ferromagnet with an out-of-plane magnetic moment while a $CrCl_3$ layer is also a ferromagnet with an in-plane magnetization. The calculations of a topological Hall current will help us to understand how a spin texture affects the transport and magnetic properties of the system. From the estimations a skyrmion size is about 30-40 nm. The computations of a spin Hall effect and magnetoresistance require the calculations of the nonequilibrium distribution function, which we will determine from the kinetic Boltzmann equation. The distribution function describes by a 4 × 4 matrix because of different spin projections and the spin-dependent momenta of conducting electrons. However, if we consider two layers, there are two types of electrons: (1) the electrons are from CrI_3 layer and (2) the electrons are from $CrCl_3$ layer. Thus, the matrix

becomes 8 × 8. The matrix elements contain various parameters such as effective masses, exchange constants, etc., that will be found from the first principle calculations. The reason why such system exhibit topological Hall effect is because the scattering transition probability matrix has an antisymmetric part with respect to the scattering angle. The scattering asymmetry acts as an effective magnetic field, which sign can be either the same for both spin projections of an incident electron, hence leading to a *topological charge Hall effect*, or opposite for different electron spin projections, *leading to the topological spin Hall effect*.

DP-04. Demonstration of low Schottky barrier height in monolayer MoS_2 field effect transistor with ferromagnetic metal contacts. *S. Gupta*[1], F. Rortais[1], R. Ohshima[1], Y. Ando[1], T. Endo[2], Y. Miyata[2] and M. Shiraishi[1] *1. Kyoto University, Japan, Kyoto, Japan; 2. Tokyo Metropolitan University, Tokyo, Japan*

Molybdenum disulfide (MoS_2) is a semiconductor with a sizable band gap, which makes it promising for semiconducting electronics.1 A high on/off ratio (~10^8) and high carrier mobility at room temperature have been demonstrated in MoS_2-based field effect transistor (FET).[2] However, the large electrical potential drop due to high Schottky barrier at the metal/ semiconductor-MoS_2 junction may strongly limit the performance of MoS_2-based devices, which remains an open challenge for the integration of MoS_2 in future technology. We report electronic properties of monolayer MoS_2 based FET devices using permalloy (Py) as ferromagnetic (FM) metal contact. Monolayer MoS_2 channels were directly grown on SiO_2/Si substrate via chemical vapor deposition technique. To determine the Schottky barrier height (SBH), two-probe source-drain current-voltage (I_{DS}-V_{DS}) curve measurements (Fig. 1) were carried out as a function of temperature and gate voltage (V_g). Figure 2(a) shows that I_{DS}-V_{DS} curves are almost linear at 300 K. As temperature decreases to 10 K, I_{DS}-V_{DS} curves show strong deviation from linearity and significant reduction in I_{DS} (Fig. 2b). This suggests that the device goes in the off state at low temperatures. The increase in I_{DS} with V_g shows the tunability of FET characteristics (Fig. 2). SBH was estimated using an activation energy method by employing the 2D thermionic emission equation.3 SBH for Py/MoS_2 contacts was found to be +28.4 meV for V_g = 0 V, which is the smallest value reported so-far for any direct metal / monolayer MoS_2 contact. With the application of gate voltage (+10 V), SBH reduces to a negative value of -6.8 meV, revealing ohmic behavior of Py/MoS_2 contacts. Low SBH with the control of the ohmic nature of FM contacts is a primary requirement for MoS_2 based spintronics and therefore using directly grown MoS_2 channels in the present study can pave a path towards high performance devices for large scale applications.

1. Q. H. Wang *et al*., Nat. Nanotechnol. 7, 699 (2012). 2. B. Radisavljevic *et al*., Nat. Nanotechnol. 6, 147 (2011). 3. A. Anwar *et al*., J. Appl. Phys. 85, 2663 (1999).

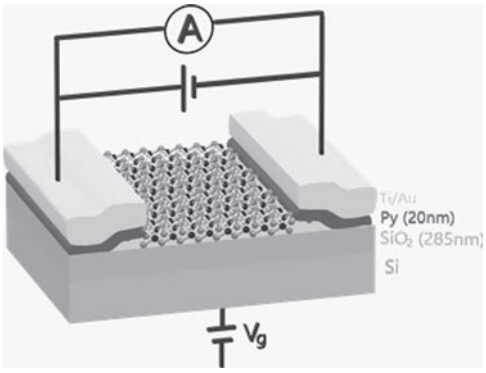
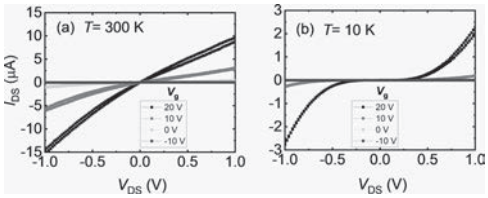


Fig 1. The schematic of a monolayer MoS_2 FET device and measurement configuration for two-probe I_{DS}-V_{DS} curves.

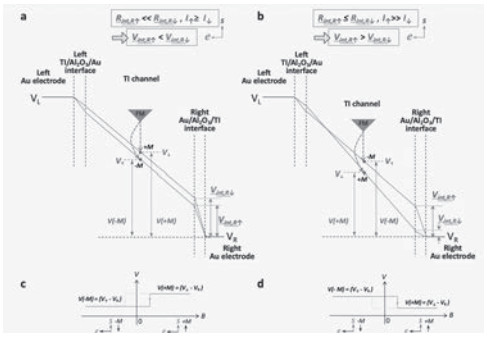


Figu2. I_{DS}-V_{DS} characteristics of a monolayer MoS_2 FET (a) at T= 300 K and (b) at T= 10 K as a function of back gate voltage (V_g).

DP-05. Electrical detection of current generated spin in topological insulator surface states: Role of interface resistance. *C.H. Li*[1], O. Van't Erve[1], C. Yan[2], L. Li[2] and B. Jonker[1] *1. Naval Research Lab, Washington, DC, United States; 2. Physics and Astronomy, West Virginia University, Morgantown, WV, United States*

Current generated spin polarization in topological insulator (TI, e.g., Bi2Se3) surface states due to spin-momentum locking has been detected recently using FM/tunnel barrier contacts, where the projection of the TI spin onto the magnetization of the FM is measured as a voltage [1]. However, opposing signs of the spin voltage have been reported [e.g., 1-4], which had been tentatively attributed to the coexistence of trivial 2DEG states on the TI surface which may exhibit opposite current-induced polarization [4,5]. Models based on electrochemical potential have been developed to derive the sign of the spin voltage expected for the TI surface states [3]. However, these models only consider the spin-dependent electrochemical potential for the spin-up and spin-down electrons in the TI channel, and do not take into account key experimental parameters such as the interface resistance. Specifically, in most studies, a blanket layer of tunnel barrier material such as Al_2O_3that is often deposited on the TI as the first step (for capping and/ or to simplify fabrication). It is therefore also present at the interfaces of the current injecting contacts, which can be nonlinear and/or asymmetric [6,7]. Here we present a Mott two-spin current resistor model which takes into account these parameters, and show that such inclusions can lead to a crossing of the voltage potential profiles for the spin-up and spin-down electrons within the channel (Fig. 1), which can lead to measured spin voltages of either sign [6,7]. These findings offer a resolution of the ongoing controversy regarding opposite signs of spin signal reported in the literature, and further highlight the intricate nature of the seemingly straightforward electrical measurement of current generated spin in TI surface states, where experimental parameters such as spin dependent resistances in both the channel and at current injecting interfaces must be considered to accurately account for the sign of spin voltage measured.

[1] C. H. Li et al., *Nature Nanotech*. 9, 218 (2014). [2] J. Tian et al., *Sci. Rep.*5, 14293 (2015). [3] F. Yang, et al., *Phys. Rev. B*94, 075304 (2016). [4] C. H. Li et al., *Nature Communications*, 7, 13518 (2016). [5] S. Hong, *Phys. Rev. B*. 86, 085131 (2012). [6] C. H. Li et al., *Nature Communications*, 10, 2523 (2019). [7] C. H. Li et al., *Sci. Rep.,*9, 6906 (2019).



Voltage profiles for the spin-up (blue) and spin-down (red) electrons for a left flowing current, for the case (a) $V_{int,R\uparrow}$<$V_{int,R\downarrow}$and (b) $V_{int,R\uparrow}$>$V_{int,R\downarrow}$, and their corresponding predicted lineshapes (c) and (d), respectively.

DP-06. Giant Spin-Orbit Torque in Sputtered Perpendicular Bi_2Te_3/FM Films. *H. Yang*[1] and X. Qiu[1] *1. School of Physics Science and Engineering, Tongji University, Shanghai, China*

The large charge-to-spin conversion efficiency of topological insulator (TI) has attracted great attention for ultra-low power consumption magnetic storage and logic applications [1, 2]. It has been demonstrated that the TI such as Bi_2Se_3 can be used to switch the magnetization of ferromagnetic Co-Tb alloy with perpendicular anisotropy at low current densities [3]. Recently, extremely efficient spin-orbit torque in sputtered Bi_xSe_{1-x} has been reported. However, the presence of intercalated Ta may decrease the device efficiency and complicates the transmission of spin current [4]. Direct exertion of spin-orbit torque from TI to a directly contacted ferromagnet with perpendicular anisotropy is still much awaited to explore. In this work, we study the spin-orbit torque in a perpendicular magnetized Ta/Cu/[CoNi]/Bi_2Te_3/TaO_x by magnetron sputtering shown in Fig. 1. By characterizing spin-orbit torque by second harmonic measurements, a giant spin-orbit toque is found at low temperature and the spin Hall angle increases with decreasing the temperature shown in Fig. 2a and b. More remarkably, we found the current density required for the magnetization switching is extremely low,~1.3×10^6 Acm^{-2} at 5 K, which is one order of magnitude smaller than Ta. In addition, comparing to Ta sputtered Bi_2Te_3 show much lower power consumption as shown in Fig. 2d. The giant spin-orbit torque found in Ta/Cu/[CoNi]/Bi_2Te_3/TaO_x at low temperature can be ascribed to the strengthened topological surface state. The giant spin-orbit torque, efficient perpendicular magnetization switching and the ultra-low power consumption with sputtered Bi_2Te_3 show great prospects for topological spintronics applications.

[1] H. Zhang, C.-X. Liu, X.-L. Qi, et al., Nat. Phys., Vol. 5, p. 438 (2009) [2] A.R. Mellnik, J.S. Lee, A. Richardella, et al., Nature, Vol. 511, p. 449 (2014) [3] J. Han, A. Richardella, S.A. Siddiqui, et al., Phys. Rev. Lett., Vol. 119, p. 077702 (2017) [4] M. Dc, R. Grassi, J.Y. Chen, et al., Nat. Mater., Vol. 17, p. 800 (2018)

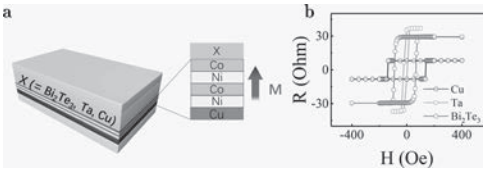


Fig. 1 a, Sub/Ta (3)/Cu (2)/Co-Ni (1)/X (4)/TaO_x (2) (in nm), X= (Bi_2Te_3, Ta, Cu). b, Hall resistance R_H as a function of *H* applied in the out-of-plane direction.

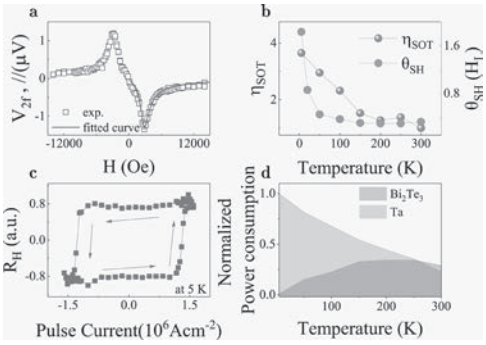


Fig. 2 Results of Sub/UL/[Co-Ni] (1) /Bi_2Te_3 (4)/TaO_x (2) (in nm) structure. a, Second harmonic voltage at full H range. b, The temperature dependence of η_{SOT} and $\theta_{SH}(H_L)$ in sputtered Bi_2Te_3/Co-Ni films. c, Current-induced switching with extremely low current density at 5 K. d, For current-induced magnetization switching, Bi_2Te_3 consumes less power than Ta.

DP-07. Helicity-dependent photo-induced magnetoresistance in topological insulator/semiconductor heterostructures. *T. Guillet*[1], C. Zucchetti[2], A. Marchionni[2], F. Bottegoni[2], A. Marty[1] and M. Jamet[1] *1. Univ. Grenoble Alpes, CEA, CNRS, Grenoble INP, IRIG-Spintec, Grenoble, France; 2. LNESS-Dipartimento di Fisica, Politecnico di Milano, Milan, Italy*

We report the observation of a new kind of magnetoresistance effect, which is the result of the interplay between two spin accumulations at the topological insulator/semiconductor interface. For this purpose, we grow single crystalline Bi_2Se_3 thin films on Ge (111) by molecular beam epitaxy and make microdevices shown in Fig. 1a and 1b where pure spin currents with in-plane spin polarization are generated by optical spin orientation in Ge. The scattering of circularly polarized light on the right (left) edge of a Pt stripe creates a pure spin current in germanium with in-plane orientation pointing to the right (left) respectively [1,2]. The spin accumulation generated in Ge by the laser spot diffuses to the spin detector (Bi_2Se_3 here). The distance between the Pt bars and the spin detector can be as large as 10 μm thanks to the long spin diffusion length of low-doped Ge. When passing a DC current in the Bi_2Se_3 spin detector, a second spin accumulation is induced by the Edelstein effect at the Bi_2Se_3/Ge interface. Experimentally the light circular polarization is modulated ω=50 kHz and we apply DC current in the detector. We observe an helicity-dependent photovoltage (HDP) at ω, which changes sign when the current direction or the spin orientation in Ge are reversed. The HDP scales linearly with the DC current, laser power and degree of circular polarisation [3]. We interpret these results by analogy with the uniaxial spin Hall magnetoresistance (USMR) in heavy metal/ferromagnet bilayer, where the ferromagnet is replaced by an out-of-equilibrium spin accumulation. This type of experiments enables to explore new physics and test our best understanding of spin-dependent phenomena.

[1] C. Zucchetti *et al.,* Phys. Rev. B 96, 014403 (2017) [2] F. Bottegoni *et al.,* Nature Materials 13, 790–795 (2014) [3] T. Guillet *et al.,* to be submitted

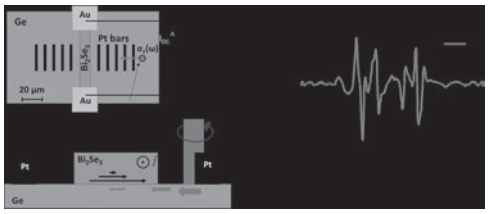


Fig. 1 a) Illustration of the microdevice used for optical spin orientation. b) A first spin accumulation is generated below the detector using the scattering of circularly polarized light, a second is induced in the detector by the Rashba Edelstein effect when applying a DC current. c) Integrated profiles of the sample reflectivity (bottom) and the helicity-dependent photovoltage signal (top), HDP with opposite signs are observed when the laser impinges opposite edges or when the DC current direction is reversed.

DP-08. Mapping Giant Spin-Charge Conversion to the Band Structure in a Topological Oxide Two-Dimensional Electron Gas. D.C. Vaz[1], *M. Cosset-Chéneau*[2], A. Johansson[3,4], B. Göbel[3], F. Bruno[5], G. Singh[6], S. McKeown[5], F. Trier[1], A. Sanders[1], P. Bruneel[7], M. Vivek[7], N. Bergeal[6], F. Baumberger[5], H. Okuno[8], A. Barthelemy[1], A. Fert[1], L. Vila[2], I. Mertig[3,4], J. Attané[2] and M. Bibes[1] *1. Unité Mixte de Physique CNRS, Thales, Univ. Paris-Sud, Université Paris-Saclay, Palaiseau, France; 2. Spintec, Institut Nanosciences et Cryogénie, Univ. Grenoble Alpes, CEA, CNRS, Grenoble, France; 3. Max Planck Institute of Microstructure Physics, Halle, Germany; 4. Institute of Physics, Martin Luther University Halle-Wittenberg, Halle, Germany; 5. Department of Quantum Matter Physics, University of Geneva, Geneva, Switzerland; 6. Laboratoire de Physique et d'Etude des Matériaux, ESPCI Paris, PSL Research University, CNRS, Paris, France; 7. Laboratoire de Physique des Solides, CNRS, Univ. Paris-Sud, Université Paris-Saclay, 91405, Orsay, France; 8. Univ. Grenoble Alpes, CEA, Grenoble INP, INAC-MEM, Grenoble, France*

While classical spintronics has traditionally relied on ferromagnetic metals as spin generators and spin detectors, spin-orbitronics exploits the interplay between charge and spin currents enabled by the spin-orbit coupling (SOC) in non-magnetic systems. An efficient spin-charge interconversion can be obtained through Spin Hall Effect and Inverse Spin Hall Effect in heavy metals such as Pt or Ta. Yet a more efficient conversion can be obtained by exploiting the direct and inverse Edelstein effects at interfaces where broken inversion symmetry induces a Rashba SOC. Although the simple Rashba picture of split parabolic bands is usually used to interpret such experiments, it fails to explain the largest conversion effects and their relation to the actual band-structure. Here, we demonstrate a giant spin-to-charge conversion effect by means of Spin Pumping FMR in an interface-engineered high-carrier-density SrTiO3 two-dimensional electron gas. We use angle-resolved photoemission and Boltzmann calculations to map its peculiar gate dependence. We show that the conversion process is amplified by enhanced Rashba-like splitting due to orbital mixing, and in the vicinity of avoided band crossings with topologically non-trivial order. Our results indicate that oxide 2DEGs are strong candidates for spin-based information readout in novel memory and transistor designs. In parallel, they confirm the promise of topology as a new ingredient to expand the scope of complex oxides for spintronics.

DP-09. Higher-Order Topological Insulator Taking into Consideration Uniaxially Anisotropic Hopping. *S. Komori*[1] and K. Kondo[1] *1. Research Institute for Electronic Science, Hokkaido University, Sapporo, Japan*

Topological materials have attracted enormous attention in the field of condensed matter physics from about a decade ago. Recently, it is found that there exist new types of topological insulators (TIs) having topologically protected gapless hinge states. They are called "higher-order topological insulators (HOTIs)". Then, HOTIs have been investigated intensively by theoretical and experimental researchers. Generally, the systems with gapless boundaries of codimension n are called "nth-order TIs". Conventional TIs are classified as 1st-order TIs in this sense. Schindler *et al*. constructed the model of 2nd-order chiral TIs based on Wilson-Dirac type 1st-order TIs. It is known that the model is distinguished by Z_2 topological invariant termed mirror Chern number (C_m). However, in the case of anisotropic systems, both the electron structure and the topological phase have not yet been investigated to our knowledge. In this study, we are going to investigate the model with uniaxially anisotropic hopping strength in the z-direction. Fig. 1 shows the electron density of the anisotropic model. We can confirm most electrons exist at the hinges. The Wilson loop method is utilized for calculating the mirror Chern number C_m of our model. Fig. 2 shows the trajectory of the Wilson loop. The trajectory wraps once around the cylinder, which corresponds to $C_m = 1$ and means that the gapless hinge states exist. Using the above C_m, we have obtained the topological phase diagram of the model with changing the hopping strengths. It is found that the phase diagram suggests that the Z_2 invariant of 2nd-order TIs reflects the Z_2 index of 1st-order strong TIs. This result is expected to serve as a criterion to realize a new kind of HOTI. At the conference, we are going to talk about the differences from the isotropic model. Moreover, we are going to compare the topological phase diagram of 1st-order TIs with that of 2nd-order TIs and discuss the features of their phases in detail.

[1] Frank Shindler *et al*., *Sci. Adv*., Vol. 4, No. 6 (2018) [2] S. Komori and K. Kondo, 74th Annual Meeting The Physical Society of Japan, (Hakata, Japan) 2019

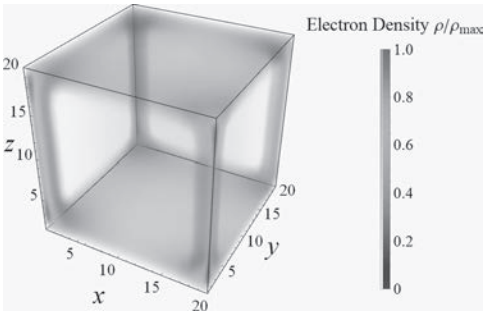


Fig. 1. Electron density of our model in the topological phase. Most electrons exist at the hinges.

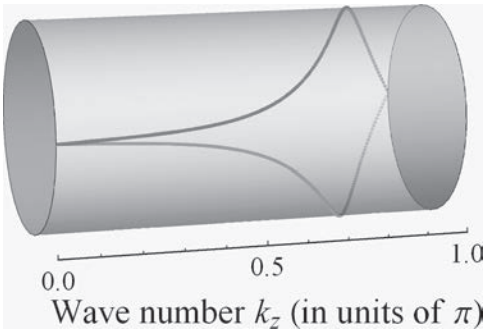


Fig. 2. Wilson loop in the topological phase. Nontrivial winding is related to the existence of gapless hinge states.

DP-10. Strong Spin-textures Anisotropy of Ultra-Thin 3*d* Transition Metals Induced by Topological Surface States. *S. Laref*[1] and A. Manchon[1] *1. Physical Science and Engineering Division, King Abdullah University of Science and Technology (KAUST), Thuwal, Saudi Arabia*

Topological insulators (TIs) such as Bi_2Se_3, Bi_2Te_3, and Sb_2Te_3 have attracted remarkable consideration because of their strong surface states, which are introduced by strong spin-orbit coupling (SOC) and protected by time-reversal symmetry (TRS). In particular, there is tremendous interest in heterostructures composed of transition metal magnetic layers deposited on TI surfaces as such system can display quantized anomalous Hall effect, as well as extremely large spin-charge conversion efficiency. Based on density functional theory calculations, we rigorously study the spin-momentum locking performance of a wide range of transition metals (3*d*-TM) adsorbed on Bi_2Se_3. Our results show that monolayer anisotropy is initiated by the hybridization of spin-polarized states on 3*d*-TM with spin-momentum locked surface states conducting electrons on the TI. Additionally, we demonstrate that the spin texture on the 3*d*-TM monolayer becomes momentum dependent, enabling the emergence of large spin-charge conversion processes. The bottom surface of the slab, interfaced with vacuum, shows delocalized Bi and Se *p*-orbitals forming an unperturbed Dirac cone, while the top surface of the slab, interfaced with the 3*d*-TM overlayer, displays localized *p*-states with strong spin texture. Indeed, the excess of 3*d*-TM electronic charge pushes down the top layer Dirac cone towards lower energy, and the distortion on the point of Dirac comes from the hybridization of 3*d*-TM and TI. Finally, the 3*d*-TM absorbed on the hollow adsorption site at the top surface display localized *d*-states that acquire a spin texture through proximity effect with the TI. The strength of the spin texture on the TI and 3*d*-TM orbitals are reported for the whole range of 3*d* transition metal series.

DP-11. Characterization of Traps in Sputtered Topological Insulator FET (TI-FET). *P. Sahu*[1], J. Chen[2] and J. Wang[2,1] *1. School of Physics and Astronomy, University of Minnesota, Minneapolis, MN, United States; 2. Department of Electrical and Computer Engineering, University of Minnesota, Minneapolis, MN, United States*

Topological insulators have captured the attention of condensed matter physicists for their highly spin-polarized conducting surface states. Such materials allow us to make dissipation less spin channels for spintronic applications. Recently, high charge-to-spin conversion and vice-versa was reported in sputtered topological insulators [1-3]. Non-stoichiometric 2D materials often have open bonds at the surface, which can be a source of ionic traps [4]. Topological insulators are especially susceptible to this, since a small change in surface conduction can produce a substantial change in the overall transport property. In order to understand this mechanism, we start by chemically characterizing the depth profile of the film using X-ray photoelectron spectroscopy at different sputter etch times. Going deeper into the film, a change in the shape and position of Bi4f peaks can be seen. This change is attributed to the oxidation of Bismuth near the top interface. We also observe Mg^{2+} impurities through the film, which is a strong candidate for mobile ion traps. The atomic force microscopy shows a relatively rough surface, which is due to the formation of crystal twins [5]. These films are then fabricated into FET structures with SiO_2 dielectric (t ~ 70 nm) deposited by CVD. We measure the resistivity of the film as a function of gate voltage. The transport measurements depict a very clear and strong hysteretic behavior. Negative to positive gate sweep shows a maximum and vice versa. Such strong long-delay hysteresis can be attributed to the movement and trapping of ions across the interface. We further develop a detailed semi-empirical model to explain the effects of ionic traps on transport properties (carrier density, mobility and conductivity). This allows us to calculate the effective trap density due to gate voltage. We fit the model into our experiment to get the important parameters relating the trap density with gate voltage.

[1] Mahendra DC, et al. Nature Materials, Vol 17, Issue-9, 2018 [2] P. Sahu et al. Applied Physics Letters, 112(12), p.122402, 2018 [3] M. DC et al. Applied Physics Letters, 114(10), p.102401, 2019 [4] J.R. Weber et al. PRB 87, 035203, 2013 [5] Kriegner et al. J Appl Crystallogr. 2017, 369-377

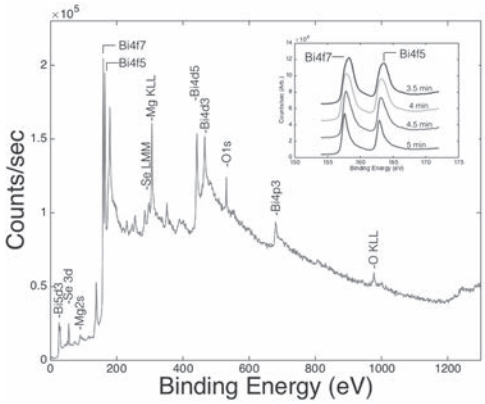


Fig.1. XPS spectra of the sample after 3 min Ar sputter to remove the MgO capping layer. Inset: Bismuth depth-profile spectra at different Ar sputter etch times.

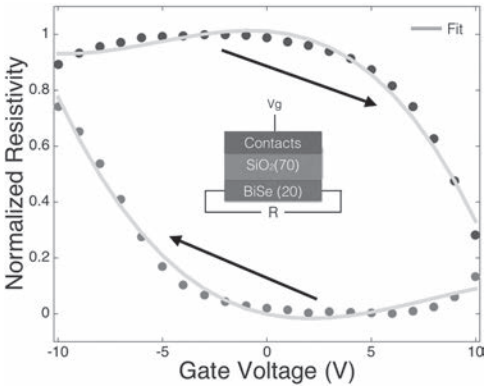


Fig.2. Normalized resistivity as a function of gate voltage for forward and reverse sweep.

DP-12. Highly Efficient Spin-to-Charge Current Conversion at Room Temperature in Strained HgTe Surface States. P. Noel[1], *M. Cosset-Chéneau*[1], C. Thomas[2], P. Ballet[3], L. Vila[1], T. Meunier[2] and J. Attané[1] *1. Univ. Grenoble Alpes, CEA, CNRS, Grenoble INP, INAC, SPINTEC, Grenoble, France; 2. Institut Néel, C.N.R.S. and Université Joseph Fourier, Grenoble, France; 3. Univ. Grenoble Alpes, CEA, LETI, MINATEC Campus, Grenoble, France*

Spin current manipulation in spintronic requires finding an efficient way to transform charge currents into spin currents, and vice-versa. If classical spintronics generally relies on magnetic materials, the spin manipulation can also be achieved by harnessing the Spin Orbit Coupling (SOC) in non-magnetic materials such as topological insulators. The main interest of topological insulators lies in their surface states, which possess a linear Dirac-like dispersion, and a spin momentum locking. A flow of electric current in the 2DEG leads to a spin accumulation. The direction of the accumulated spins is parallel to the surface, and perpendicular to the electron motion direction. This effect is known as the Edelstein Effect, while the reverse spin-to charge-conversion effect is known as the Inverse Edelstein Effect (IEE). Recent results suggest that surfaces of topological insulators have a strong potential for spintronics, both for the generation or detection of spin currents through direct or inverse Edelstein effects. Among these newly discovered class of materials, strained HgTe is a promising one, as it is an archetypal topological insulator, compatible with electronic and optoelectronic applications. Gap opening and Topological insulator properties can be induced in HgTe by applying a tensile strain that can be achieved by epitaxy of HgTe on a substrate with a larger lattice constant, such as CdTe. We present the study of spin to charge interconversion in strained HgTe thin films by ferromagnetic resonance spin pumping in cavity. The spin to charge current conversion rate, the inverse Edelstein length, was measured to be up to 2 nm, one to two orders of magnitude larger than in Bi-based topological insulators. Moreover, the non-conventional thickness dependence of the conversion rate allows to ascribe this conversion to the topological surface states [1].

[1] P. Noël et al., Phys. Rev. Lett. 120, 167201 (2018)

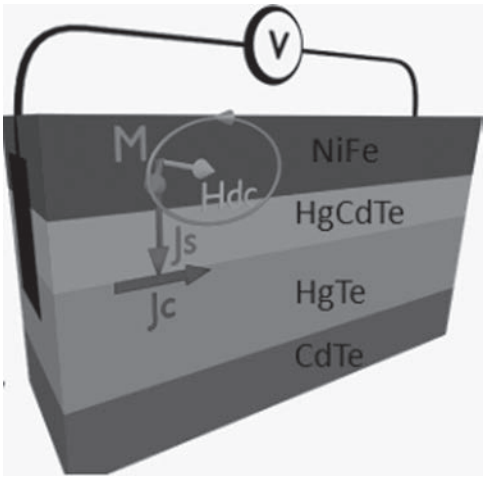
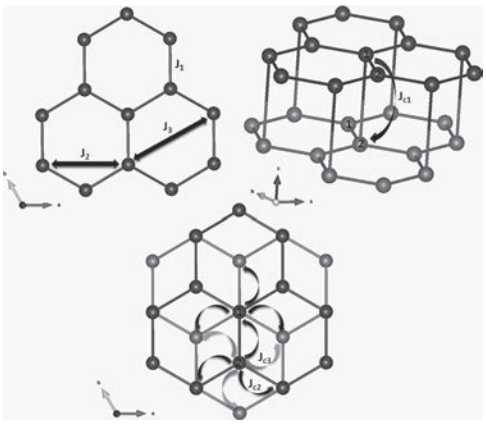


fig. 1: Geometry of the spin pumping by ferromagnetic resonance (FMR) measurement setup, and stack used for the measurement.

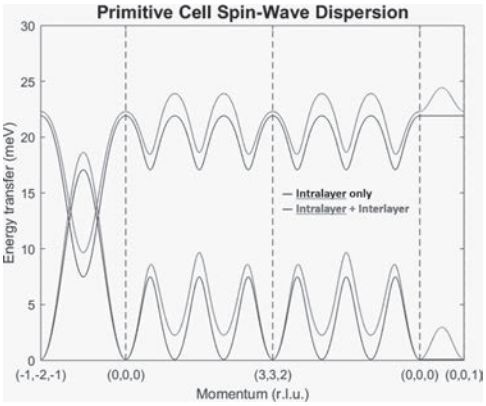
DP-13. Bulk and Layered Magnetic Properties of Two-Dimensional van der Waals ferromagnetic VI_3. *E.E. Gordon*[1] and L. Ke[1] *1. Division of Materials Science & Engineering, Ames Laboratory, Ames, IA, United States*

Two-dimensional (2-D) magnetic materials have recently gained significant focus due to potential film and device applications. VI_3, a new ferromagnetic material, has gained recent interest due to experimental evidence suggesting VI_3 is easily cleavable down to a few layers, and being the first know hard 2-D van der Waals magnetic material. We investigate VI_3's bulk, bilayer, and monolayer intrinsic magnetic properties via density functional theory (DFT) within VASP. Our DFT + *U* calculations agree well with the experimentally determined ferromagnetic insulating ground state, experimental bulk band gap, experimental bulk Curie temperature (T_c), predicts a small change in the T_c as a function of the number of layers (similar to what is found in CrI_3), and predicts a similar spin-wave spectra to CrI_3 along high-symmetry hexagonal paths. A change in the spin-wave spectra along high-symmetry hexagonal paths is seen as interlayer exchange interactions are included as xy-components are present within some extracted interlayer exchanges. Layer-dependent magnetization experiments are suggested to explore T_c as a function of the number of layers and inelastic neutron scattering experiments are suggested to explore the possibility of a spin-wave gap, as present in CrI_3, due to Dzyaloshinkii-Moriya (DM) interactions along the second nearest neighbor intralayer interaction.

[1] B. Huang, G. Clark, and E. Navarro-Moratalla, Nature 546, 270 (2017). [2] S. Tian, J.-F. Zhang, and C. Li, J. Am. Chem. Soc. 141, 5326 (2019). [3] T. Kong, K. Stolze, and E. I. Timmons, Adv. Mater. 31, 1808074 (2019). [4] S. Son, M. J. Coak, and N. Lee, Phys. Rev. B 99, 041402(R) (2019). [5] J. He, S. Ma, and P. Lyu, J. Mater. Chem. C, 4, 2518 (2016). [6] S. Toth, and B. Lake, J. Phys. Condens. Matter 27, 166002 (2015). [7] L. Chen, J.-H. Chung, and B. Gao, Phys. Rev. X 8, 041028 (2018).



Blue spheres represent V within 1 plane and red spheres represent V in the plane below. J_1, J_2, and J_3 spin exchanges represents the nearest-neighbor, 2nd nearest-neighbor, and 3rd nearest-neighbor interactions within the V hexagonal ab-plane. J_{c1}, J_{c2}, and J_{c3} spin exchanges represents the nearest-neighbor, 2nd nearest-neighbor, and 3rd nearest-neighbor interactions between V planes. Curved arrows represent interactions of the blue plane V with the red plane V. V(1) spin exchanges along the +c (-c) direction is the same as V(2) spin exchanges along the -c (+c) direction.



Spin-wave spectra plots of VI_3 using extracted spin exchange interactions along hexagonal high symmetry paths, i.e., Γ -> K, Γ -> M, Γ -> A. Black (red) lines represent the spin-wave spectra excluding (including) interlayer spin exchanges. Plots were created using the SpinW program.

DP-14. Experimental evidence of the valley Nernst effect in WSe_2. M. Dau[1], C. Vergnaud[1], *T. Guillet*[1], A. Marty[1], C. Beigné[1], S. Gambarelli[2], V. Maurel[2], H. Okuno[3] and M. Jamet[1] *1. Univ. Grenoble Alpes, CEA, CNRS, Grenoble INP, IRIG-Spintec, Grenoble, France; 2. Univ. Grenoble Alpes, CEA, CNRS, IRIG-SYMMES, Grenoble, France; 3. Univ. Grenoble Alpes, CEA, IRIG-MEM, 38000 Grenoble, France, Grenoble, France*

We study the interplay between thermoelectricity and the valley degree of freedom in monolayers of WSe_2. By using van der Waals epitaxy, high quality WSe_2 mono and multilayers are grown on epitaxial graphene on SiC over large areas (Fig. 1a and 1b). Using such millimeter-sized sample, we are able to apply well-defined temperature gradients and demonstrate the very strong Seebeck response of this material. In a second step, we use the ferromagnetic resonance-spin pumping technique to (i) apply the temperature gradient by off centering the sample in the RF cavity and (ii) address a single valley using the spin pumping through spin-valley coupling (Fig. 1c). The combination of a temperature gradient and the valley polarization leads to the valley Nernst effect in WSe_2 that we detect electrically in the RF cavity (Fig. 1d). The Nernst coefficient we measure is in very good agreement with the predicted value. This effect can be exploited to generate large transverse valley currents for valleytronics applications.

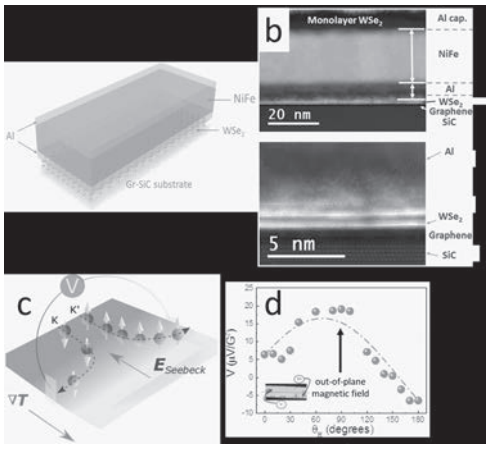


Fig.1 : (a) Sketch of the WSe2/metallic stack to study the Valley Nernst effect. (b) Cross sectional transmission electron microscopy images of the full stack. (c) Illustration of the valley Nernst effect when a temperature gradient is applied and a single valley is addressed. (d) Valley Nernts effect voltage measured by the FMR-spin pumping technique.

DP-15. Spin and Valley Transport in Strained Silicene Heterojunctions: Zigzag versus Armchair Interface. *Z. Siu*[1] and M.B. Jalil[1] *1. Electrical and Computer Engineering, National University of Singapore, Singapore*

In this work, we study the spin and valley transport across silicene[1] heterojunctions consisting of a strained[2] central segment sandwiched between two semi-infinite unstrained leads. We employ a tight-binding Hamiltonian obtained by generalizing the procedure in Ref. 3 to account for arbitrarily distorted lattices. The strain displaces the Dirac points and introduces angular anisotropies into the Fermi surfaces (FS). Fig. 1a shows a schematic diagram of a heterojunction with zigzag interfaces. Fig 1b shows that due to the anisotropy of the strained central segment FS for a given value of incidence angle φ_j, the corresponding conserved value of k_x cuts across different portions of the central segment FS. This results in differing transmission between the two valleys, and hence spin and valley polarizations (Fig 1c) of the resultant transmitted current. Fig 2 shows a schematic diagram of a heterojunction with armchair interfaces. In contrast to the zigzag interface in Fig 1b where the halves of the central FS propagating from the source to drain in the two valleys are symmetrical to each other, in the armchair interface the halves of the central FS propagating in the correct direction are asymmetrical in the two valleys (Fig 2b). This induces an asymmetrical spin and valley polarization of the transmitted current with respect to the incidence angle, in contrast to the zigzag interface where the polarizations are symmetrical (Fig 2c).

1. C.-C Liu, W. Feng and Y. Yao, Phys. Rev. Lett., Vol. 107, p. 076802 (2011); B. Aufray et. al., Appl. Phys. Lett., Vol. 96, 183102 (2010); P. De Padova et. al., Appl Phys. Lett., Vol. 96, pp. 261905 (2010). 2. V. M. Pereira and A. H. C. Neto, Phys. Rev. Lett., Vol. 103, pp. 046801 (2009); F. Guinea, M. I. Katsnelson and A. K. Geim, Nat. Phys., Vol. 6, pp. 30 (2010). 3. C. C. Liu, H. Jiang and Y. Yao, Phys. Rev. B., Vol 84, pp. 195430 (2011).

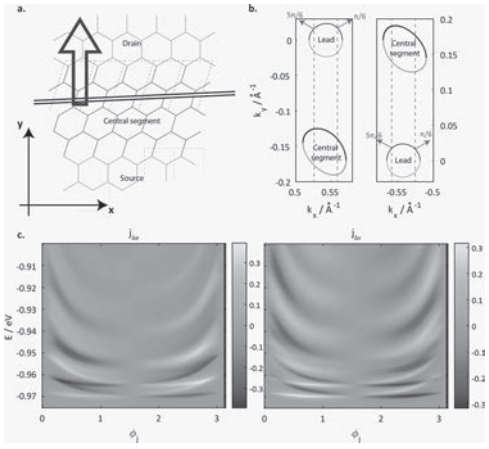


Fig. 1 a. Schematic diagram of a silicene heterojunction consisting of a strained central segment sandwiched between semi-infinite unstrained leads with interfaces along the zigzag direction. b. The lead and source FS in the two valleys. The black portions denote states propagating in the +y direction, and the points marked 5π/6 and π/6 the states with these incidence angles. c. The spin (left) and valley (right) current polarizations as functions of φ_j and Fermi energy E_f.

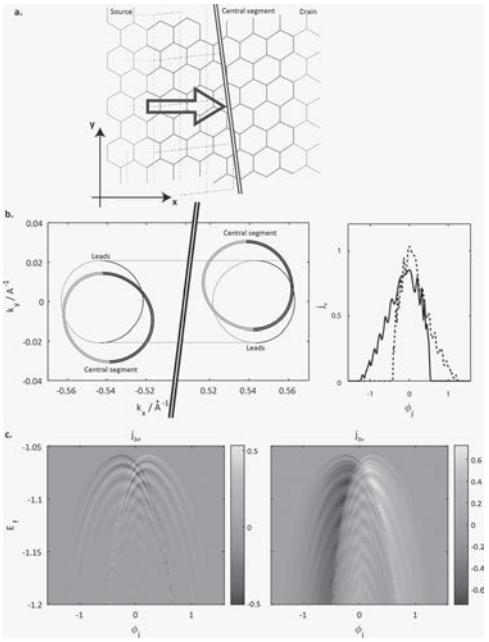


Fig. 2 a. Schematic diagram of a silicene heterojunction with interfaces along the armchair direction. b. (left) The lead and source Fermi surfaces in the two valleys and (right) the valley resolved transmission at one particular E_f. c. The spin (left) and valley (right) current polarization

DP-16. Spin reorientation in quasi-2D ferromagnet Cr_5Te_8. *Y. Chen*[1], J.G. Lin[1,2], C. Kuo[3] and C. Lue[3] *1. Center for Condensed Matter Science, National Taiwan University, Taipei, Taiwan; 2. Center for Atomic Initials for New Materials, National Taiwan University, Taipei, Taiwan; 3. Department of Physics, National Cheng Kung University, Tainan, Taiwan*

$Cr_{1-\delta}Te$ is a family of metal-deficient hexagonal half-metal with strong spin-orbit coupling and crystalline anisotropy, which could be a good candidate for the spintronics applications. Recently, a critical analysis on magnetization revealed a unique 2D to quasi-2D type of ferromagnetic transition near 230 K in trigonal Cr_5Te_8,[1] leading to a prominent question of how this dimensional transition affects magnetic properties. In this work, the

temperature-dependent magnetic anisotropy in a Cr_5Te_8 single-crystal slab was studied by means of ferromagnetic resonance (FMR) across the dimensional transition. The temperature dependence of in-plane and out-of-plane magnetization shows a switch of easy-axis near the transition. The results of angular-dependent FMR field (Fig. 1) confirms a spin reorientation transiting the easy axis from *a*-*b* plane to the direction title by ~π/4 as cooling from 260 to 200 K. A numerical simulation indicates this spin reorientation involving with the sign reversal of 2nd-order magnetic anisotropy from negative to positive and a substantial enhancement of 4th-order crystal magnetic anisotropy for T < 240 K. In summary, our results suggest a strong enhancement of crystal anisotropy below the temperature of 2D to quasi-2D transition, corresponding to a structure anomaly through the strong spin-orbital coupling in Cr_5Te_8.

[1] Yu Liu and C. Petrovic, PHYSICAL REVIEW B, Vol. 96, pp.134410 (2017)

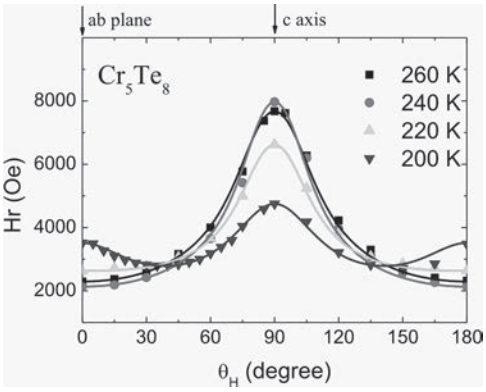
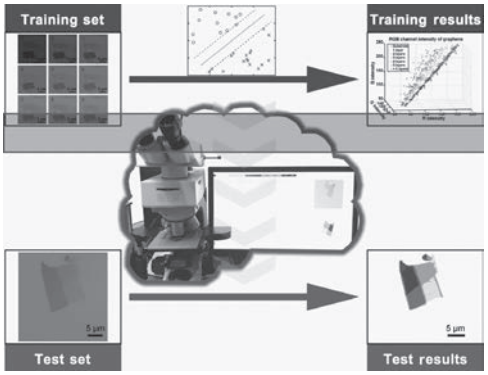


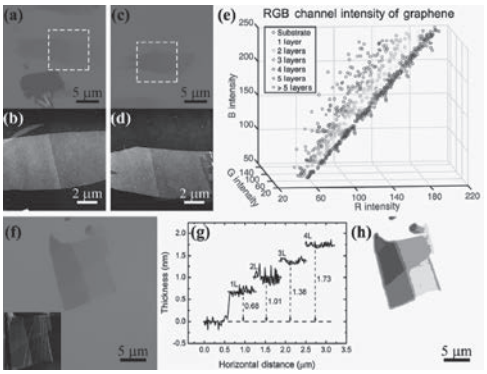
Fig. 1 Angular dependences of resonance field at various temperatures. Solid lines are the fitting curves using Kittel equation.

DP-17. The application of machine learning on the optical identification of two-dimensional nanostructures. X. Lin[1], Z. Si[1], W. Fu[1], *X. Wang*[1], G. Wei[1] and W. Zhao[1] *1. Microelectronics, Beihang University, Beijing, China*

Two-dimensional (2D) materials and their heterostructures, with wafer-scale synthesis methods and fascinating properties, have attracted significant interest and triggered revolutions in corresponding device applications. However, facile methods to realize accurate, intelligent, and large-area characterizations of these 2D nanostructures are still highly desired. Herein, we report the successful application of machine-learning strategy in the optical identification of 2D nanostructures. The machine-learning optical identification (MOI) method endows optical microscopy with intelligent insight into the characteristic color information of 2D nanostructures in the optical photograph. The experimental results indicate that the MOI method enables accurate, intelligent, and large-area characterizations of graphene, molybdenum disulfide, and their heterostructures, including identifications of the thickness, existence of impurities, and even stacking order. With the convergence of artificial intelligence and nanoscience, this intelligent identification method can certainly promote fundamental research and wafer-scale device applications of 2D nanostructures.

[1] Lin, X., Si, Z., Fu, W., Yang, J., Guo, S., Cao, Y., Zhang, J., Wang, X., Liu, P., Jiang, K. & Zhao, W., Nano Res. 11, 6316-6324 (2018). [2] Lin, X., Su, L., Si, Z., Zhang, Y., Bournel, A., Zhang, Y., Klein, J., Fert, A. & Zhao, W., Physical Review Applied 8, 034006 (2017).





DP-18. Controllable growth of 2D magnetic and non-magnetic van der Waals crystals via temperature-oscillating chemical vapor transport. *Z. Li*[1,2], X. Xi[1] and W. Wang[1] *1. State Key Laboratory for Magnetism, Beijing National Laboratory for Condensed Matter Physics, Institute of Physics, Chinese Academy of Sciences, Beijing, China; 2. University of Chinese Academy of Sciences, Beijing, China*

Dimensionality effect exhibited by two-dimensional (2D) van der Waals (vdW) materials has recently attracted considerable interest due to their convenience for mechanically exfoliating, transferring and stacking to fabricate novel heterojunction devices [1]. Thus growing highly crystalline single crystals is of vital importance for studying intrinsic physical property. However, comparing bottom-up with top-down synthetic strategies for obtaining low dimensional layers, it is found that physical and chemical vapor deposition methods are lacking in defect control. As for $NbSe_2$, disorder-induced localization of Cooper pairs appears to strongly suppress the superconductivity [2]. As a result, the superconducting transition temperature of these bottom-up grown samples [3-5] are 2 kelvin degrees lower than samples exfoliated from bulk form [6, 7]. Therefore, chemical vapor transport (CVT) and mechanical exfoliation should be the most reliable and low-priced method for obtaining high-quality 2D vdW single crystals. Herein, we developed an innovative design for growing 2H-NbSe2 single crystals with controlled morphology and quality via temperature-oscillating CVT process. In combination of a thermodynamics calculation, we grew crystals under different degrees of supersaturation, and obtained various shapes of crystals from screw-dislocated types to homogeneously hexagon types. The formation mechanisms of morphology was quantitative explained with the Burton-Cabrera-Frank (BCF) model. And the quality of obtained single crystals was characterized by XRD, HRTEM and electrical resistance measurements. It should be noted that the growth at higher temperature tended to decompose and generate more selenium vacancy [8]. Our designed temperature-oscillating method could reduce the growth temperature to the lowest value ever reported in the same reaction, and the best grown samples had the exceptional RRR≈61 and Tc≈7.4K. Furthermore,

this temperature-oscillating technique could be universally applicable among other CVT reactions. We also succeeded in growing 2D magnetic crystals Fe_3GeTe_2, CrI_3, and so on.

1. Bhimanapati, G.R., et al., ACS Nano, 2015. 9(12): p. 11509-11539. 2. Khestanova, E., et al., Nano Letters, 2018. 18(4): p. 2623-2629. 3. Ugeda, M.M., et al., Nature Physics, 2015. 12: p. 92. 4. Wang, H., et al., Nature Communications, 2017. 8(1): p. 394. 5. Lin, H., et al., Nature Materials, 2019. 6. Xi, X., et al., Nature Physics, 2015. 12: p. 139. 7. Xi, X., et al., Nature Nanotechnology, 2015. 10: p. 765. 8. Igaki, K. and S. Nishine, Transactions of the Japan Institute of Metals, 1979. 20(5): p. 219-226.

DP-19. A New Method for Probing the Light-controlled Ferromagnetism in a Two-dimensional van der Waals Heterostructure System.
V. Ortiz-Jimenez[1], V. Kalappattil[1] and M. Phan[1] *1. Physics, University of South Florida, Tampa, FL, United States*

Van der Waals heterostructures of transition metal dichalcogenides (TMDs) have been a subject of great interest in recent years due to their outstanding electrical, magnetic, and optical properties [1,2]. A plethora of potential applications have emerged as a result, such as spintronics, valleytronics, and quantum computing technology among many others. It has been shown that as a consequence of the magnetic proximity effect, magneto-optical properties of non-magnetic TMDs may be induced or enhanced by stacking them with other magnetic TMDs [3]. In this work, we show a van der Waals heterostructure composed of VSe_2 monolayer/MoS_2 bilayer grown on SiO_2, in which the presence of the VSe_2 layer enhances the magnetization of the MoS_2 layer. Interestingly, the presence of VSe_2 enables us to use light to control the magnetization of the heterostructure. This phenomenon has been probed using the magnetic LC-resonance principle. This technique employs a soft ferromagnetic Co-based microwire coil driven near resonance with an RF signal. The microwire shows an excellent giant magneto-impedance (GMI) effect, so it is very sensitive to small magnetic fields. When driven near resonance, the coil becomes highly sensitive to changes in magnetic flux through its core. By placing the van der Waals structure at the core of the coil and exciting the material with a laser, we were able to measure the changes in magnetization of the heterostructure. We observed how the magnetization is dependent on the laser power, which would allow us to tune it within a certain range. The tunability of the magnetization is associated with the excellent photon absorption of the MoS_2 bilayer which creates electron-hole pairs that mediate the magnetization. These findings may inspire novel two-dimensional spintronic devices that exploit light-controlled ferromagnetism.

[1] C. Zhao, et al., Nature Nanotechnology 12, 757 (2017) [2] T.C. Song, et al., Science 360, 1214 (2018) [3] I. Zutic, et al., Proximitized Materials. Materials Today 22, 85 (2019)

DP-20. Lateral non-local black phosphorus spin valve.
C. Li[1], X. Xu[1], Y. Wu[1], K. Meng[1], J. Miao[1] and Y. Jiang[1] *1. University of Science and Technology Beijing, Beijing, China*

Two dimensional materials(2D materials), such as graphene,MoS_2,-MoS_2,BN, due to long spin diffusion length etc., have been widely applied in spintronics. Nowadays, black phosphorus(BP) is a promising material in this field [1]. The black phosphorus(BP), which is a new kind 2D material, has a direct bandgap and the electron mobility and the spin relaxation length of bP are comparable with graphene [2]. With increasing the thickness of BP, the size of bandgap changes from 2 eV to 0.35 eV. In this work, we discuss the influence of BP, as a spin channel, on spin injection and spin transport. The schematic of the lateral non-local spin valve is showed in Fig.1(a). Firstly, we purchased bP layers with the Scotch tap by the means of mechanical exfoliation. Then, BP was transferred onto Si/SiO2 substrate. Fig.1(b) shows the Raman spectra of BP with different thicknesses which can detect the layer of BP. To form a non-local spin valve, we deposited 4 electrodes with different widths on a certain bP stripe with 1.5 nm Al_2O_3 followed by 40nm Co [3]. The Al_2O_3 layer is a tunnel layer to filter current and get pure spin current. Fig.1(c) and Fig.1(d) shows non-local spin valve signals of a same sample in 300K and 50K. Both in 300 K and 50 K, signals are obvious which means efficient spin injection and spin transport. Of course, the curve in 50 K seems more smooth without thermal effect. We also estimated the spin diffusion length λ is 594 nm by an equation[4,5]. Although the spin diffusion length of BP is not comparable with graphene, there still many works to do to achieve more excellent feature.

[1] Avsar A, Tan J Y, Kurpas M, et al, Nature Physics. 13, 888–893 (2017). [2] Khandelwal A, Mani K, Karigerasi M H, et al, Mater. Sci. Eng. B, 221, 17-34(2017). [3] Zhao B, et al, J. Magn. Magn. Mater, *432*, 291-295(2017). [4] S. Takahashi, S. Maekawa, Phys. Rev. B, 67, 052409(2003). [5] M. Popinciuc, C. Józsa, P.J. Zomer, N. Tombros, A. Veligura, H.T. Jonkman, B.J. van Wees, Phys. Rev. B, 80, 214427(2009).

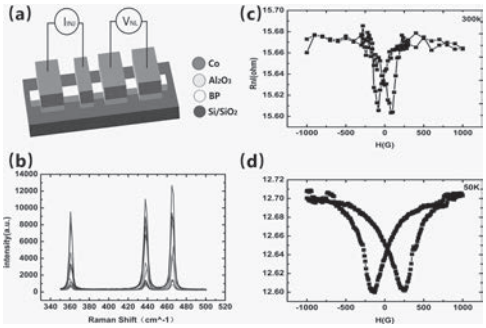


Fig.1(a) The schematic of non-local spin valve with BP. (b) The Raman spectra of different BP samples. (c) and (d) The non-local signals of the same BP sample in 300 K and 50 k.

Session DQ
MAGNETOCALORIC MATERIALS I
(Poster Session)

Karl G. Sandeman, Co-Chair
Brooklyn College of The City University of New York, Brooklyn, NY, United States
Mohamed Balli, Co-Chair
International University of Rabat, Rabat, Morocco

DQ-01. Structural, magnetic, and magnetocaloric characterization of Mn_2FeGe Heusler alloy. *A. Aryal*[1], J. Sánchez Llamazares[2], J. Zamora[2], C. Sanchez-Valdes[3], I. Dubenko[1], D. Mazumdar[1], S. Talapatra[1], S. Stadler[4] and N. Ali[1] *1. Physics, Southern Illinois University, Carbondale, IL, United States; 2. Instituto Potosino de Investigación Científica y Tecnológica A.C., San Luis Potosí, Mexico; 3. División Multidisciplinaria, Ciudad Universitaria, Universidad Autónoma de Ciudad Juárez, Chihuahua, Mexico; 4. Physics and astronomy, Louisiana State University, Baton Rouge, LA, United States*

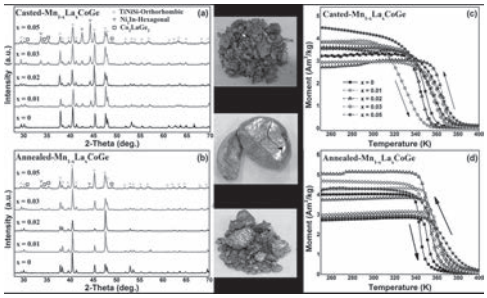
Theoretical studies on manganese-rich Mn_2FeGe Heusler alloy through first principle calculations have found that this material is nearly half-metallic, a ferrimagnetic and stabilizes in the inverse Heusler-type crystal structure [1, 2]. In this work we present structural, magnetic, and magnetocaloric properties of Mn_2FeGe of nominal composition synthesized in bulk form by arc melting and as rapidly solidified melt-spun ribbons. X-ray diffraction results show that the alloy crystallizes into the hexagonal DO_{19} crystal structure at room temperature with a small trace of a secondary phase. Mn_2FeGe was found to be ferro/ferrimagnetic at low temperatures undergoing a well-defined magnetic transition of second order at a Curie temperature (T_C) of ~ 202 K for bulk and 192 K for melt-spun ribbons. A ground state magnetization values of ~ 1.6 μ_B/f.u. (in bulk) and 1.7 μ_B/f.u. (ribbons) were found. These magnetization values obtained for the polycrystalline Mn_2FeGe are in good agreement with the value 2.0 μ_B/f.u. predicted by the Slater-Pauling rule. Further theoretical investigations are necessary to understand the properties of the hexagonal structure. Maximum absolute values of magnetic entropy change at T_C were found to be 1.6 $Jkg^{-1}K^{-1}$ ($\mu_0\Delta H$ = 5 T) and 0.9 $Jkg^{-1}K^{-1}$ ($\mu_0\Delta H$ = 2 T) for bulk and ribbons, respectively. Corresponding values of refrigerant capacity for bulk and melt-spun ribbons were found to be 128 Jkg^{-1} ($\mu_0\Delta H$ = 5 T) JKg^{-1} and 40 Jkg^{-1} ($\mu_0\Delta H$ = 2 T). Acknowledgments. This work was supported by the U.S. Department of Energy (DOE), Office of Science, Basic Energy Sciences (BES) under Award No. DE-FG02-06ER46291 (SIUC), DE-FG02-13ER46946 (LSU) and the NSF CAREER grant (ECCS 1846829). The authors acknowledge financial support received from Laboratorio Nacional de Investigaciones en Nanociencias y Nanotecnología (LINAN, IPICyT). J. Zamora is grateful to CONACyT-Mexico for supporting his postdoctoral position at IPICyT. C.F.S is grateful to DMCU-UACJ for supporting his research stays at IPICyT; also, for the financial support received from SEP-CONACyT, Mexico (Grant No. A1-S-37066). Authors are thankful for the technical support of M.Sc. B.A. Rivera Escoto and A.I. Peña Maldonado.

[1] H. Z. Luo, H. W. Zhang, and H. B. Xu, J. Appl. Phys., 103, 083908 (2008) [2] J. Ma, J. He, and William H. Butler, Phys. Rev. B 98, 094410 (2018)

DQ-02. Phase transitions and magnetic properties in $Mn_{1-x}La_xCoGe$ system. *P. Zhang*[1], H. Zhang[2], H. Imam[2] and B. Song[2] *1. Shaanxi University of Science & Technology, Xi'an, China; 2. Beijing University of Technology, Beijing, China*

MnCoGe is the most intensively studied compound among the newly discovered MM′X system with so-called Curie temperature window (CTW) behavior [1]. Many efforts have been made to build and enlarge the CTW. The most successive way so far is substitutions on the transition metal sites (Mn or Co) with elements such as Fe, V, Ti, Cu, Ni and Zn, or substitutions on the main group element site (Ge) with Ga or Al. In this work, we use rare-earth element La to replace Mn and address the phase stability as well as the martensitic transformation of the system. The $Mn_{1-x}La_xCoGe$ compounds with x = 0, 0.01, 0.02, 0.03, and 0.05 were prepared by arc melting under a high purity argon atmosphere. From Fig. (a), we can see that the increase in La content will increase the percent of hexagonal phase, and there is also the sign of secondary phase. This indicates that the martensitic transition temperature (T_M) gradually decreases and eventually below room temperature. However, the subsequent annealing process causes the increase of T_M because the hexagonal phase almost disappears in Fig. (b). Temperature dependence of the magnetization of the $Mn_{1-x}La_xCoGe$ compounds before and after annealing process are shown in Fig. (c, d). The as-casted samples show abrupt transitions with obvious thermal hysteresis along the increase of La content, which is a sign of magnetostructural transition. On the other hand, the annealed samples only show simple transition from ferromagnetism to paramagnetism, confirming the increase of T_M. Further investigations reveal that the substitution on transition metal site with La can help to establish the magnetostructural coupling and thus CTW by causing Ge deficiency beside Mn defficiency in the MnCoGe system.

[1] Liu E.K., W. Zhu, L. Feng, J.L. Chen, W.H. Wang, G.H. Wu, H.Y. Liu, F.B. Meng, H.Z. Luo, Y.X. Li, EPL, 2010, 91 (1): 17003.



XRD patterns of the (a) as-casted and (b) annealed $Mn_{1-x}La_xCoGe$ series. M-T curves measured under a magnetic field of 0.01T in both heating and cooling modes for the (a) as-casted and (b) annealed $Mn_{1-x}La_xCoGe$ series. The three photos shows the appearance of the as-casted $Mn_{0.99}La_{0.01}CoGe$, $Mn_{0.95}La_{0.05}CoGe$ and the annealed $Mn_{0.95}La_{0.05}CoGe$.

DQ-03. Influence of A-site Cation Size-Disorder on the Magnetocaloric Response of $La_{0.6}Ca_xSr_{0.4-x}MnO_3$ Nanoparticles. *C.S. Hunt*[1], R. Barua[2] and E. Carpenter[2] *1. Chemistry, Virginia Commonwealth University, Richmond, VA, United States; 2. Nuclear and Mechanical Engineering, Virginia Commonwealth University, Richmond, VA, United States*

Magnetic refrigeration is an energy-efficient and environmentally-friendly alternative to the conventional vapor-compression refrigeration systems. The key component of a magnetic cooling device is a working magnetocaloric material that demonstrates significant magnetocaloric effect (MCE) - large magnetic entropy and temperature change (ΔS and ΔT, respectively)

upon application and removal of a magnetic field - in the proximity of a room temperature magnetic phase transition [1]. To this end, manganites having the general formula $La_{1-x}M_xMnO_3$ (M=Ca, Sr, Ba etc.) have attracted considerable attention in the last decade. In particular, $La_{0.6}Ca_{0.4}MnO_3$ compounds exhibit the largest MCEs among the existing manganites (ΔS= 5 J/kgK at μH=3T) [2]. We have recently observed an enhanced MCE in $La_{0.6}Ca_{0.4}MnO_3$ nanoparticles (NPs) – a feature attributed to alteration of free energy terms dependent upon the surface area and volume of finite systems [3]. Building on this work, $La_{0.60}Ca_x\ Sr_{0.40-x}MnO_3$ ($0<x<0.4$) nanoparticles were synthesized via a modified Pechini sol-gel method, as verified by powder x-ray diffraction and laser ablation-inductively coupled plasma-mass spectrometry. The temperature-dependence of the magnetic entropy change between 200K and 300K in a magnetic field of μH=3T was evaluated by means of Maxwell's relations and isothermal MH curves. The reported values of ΔS_{max} increase from 1.5 J $kg^{-1}K^{-1}$ to 4.7 J $kg^{-1}K^{-1}$ as x increases from 0 to 0.4, Figure 1. The results show a clear positive correlation between calcium concentrations and the value of -ΔS, suggesting that a larger atom at the calcium site negatively impacts the magnetocaloric effect, thereby decreasing magnetic refrigeration viability.

1. V. Franco, J.S. Blazquez, and B. Ingale, Annual Review of Materials and Research. Vol. 42, pp. 305-342 (2012) 2. V.M. Andrade, R.J. Carabello Vivas, and S.S. Pedro, Acta Materialia. Vol. 102, pp. 49-55 (2016) 3. M.H.M. Tsui, D.T. Dryer and A. A. Elgendy, RSC Advances, Vol. 7, pp 46589-46593 (2017)

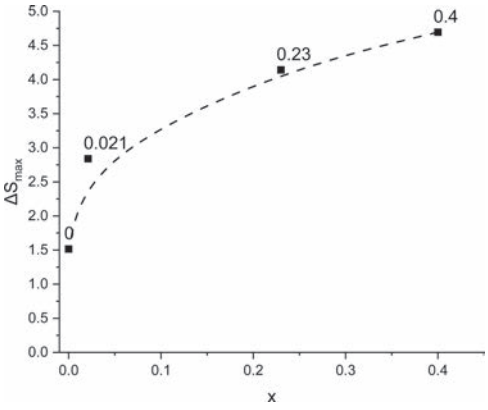


Figure 1. Dependence of ΔS_{max} values on chemical doping (x) in $La_{0.60}Ca_xSr_{0.4-x}MnO_3$ nanoparticles. The dotted line serves as a guide to the eye to indicate increase in ΔS_{max} with an increase in x. The values of x are reported with an error of approximately ±5%.

DQ-04. Geometrically designed Gd-alloy microwire arrays with enhanced magnetocaloric properties for energy-efficient magnetic refrigeration. *C. Hung*[1], H. Srikanth[1] and M. Phan[1] *1. Physics, University of South Florida, Tampa, FL, United States*

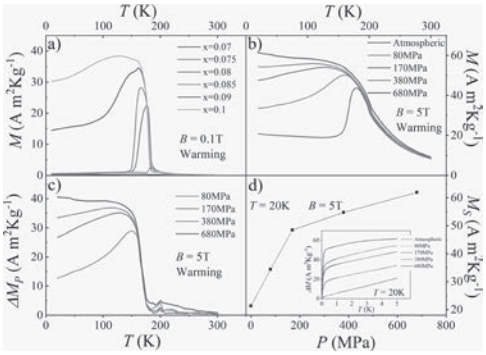
Magnetic refrigeration (MR) based on the magnetocaloric effect (MCE) with its high efficiency, tunable device, and environmental friendliness is a promising alternative to the vapor compression based cooling technology. In an actual cooling device, however, the geometry of a magnetic refrigerant is crucial as it strongly affects the operating frequency, the heat exchange rate and consequently the cooling power of the device. Magnetocaloric wire-shaped materials have been theoretically and experimentally shown to have improved mechanical strength, lower viscosity, and greater MCE performance as compared to their bulk counterparts or the particle and ribbon forms [1,2]. Our recent findings of the large MCEs in melt-extracted Gd-alloy microwires have opened the door for realizing this technology [2,3]. In the present study, we propose a new geometrical design method for enhancing the cooling power of a magnetic refrigerant by arranging magnetocaloric wires (e.g. soft ferromagnetic $Gd_{55}Al_{20}Co_{25}$ microwires) into laminate-like structures. In multilayer systems, layers are orthogonally arranged to each other, forming a grid-like structure. Magnetocaloric experiments showed larger values of magnetic entropy change (ΔS_M) over wider temperature ranges in the laminated microwires relative to a single microwire or a bundle of microwires, as a result of the enhanced wire-wire and layer-layer interactions. Both the magnetic interactions between wire-layers and geometric effect arising from the wires' arrangement play important roles in determining the MCE performance. The even-layer systems show significantly enhanced ΔS_M values (~9.8 J/kg.K) compared to the odd-layer ones (~8.5 J/kg.K). Among the systems investigated, the highest relative cooling power (RCP ~ 918 J/kg at 5T), which is the product of the maximum ΔS_M and the temperature span, is achieved for the four-layer system. The newly designed Gd alloy wire-based structures are promising for energy-efficient MR technology.

[1] M. D. Kuz'min, Appl. Phys. Lett. 90, 251916 (2007). [2] N. S. Bingham, H. Wang, F. Qin, H. X. Peng, J. F. Sun, V. Franco, H. Srikanth, and M. H. Phan, Appl. Phys. Lett. 101, 102407 (2012). [3] H.X. Shen, D.W. Xing, J.L. Sánchez Llamazares, C.F. Sánchez-Valdés, H. Belliveau, H. Wang, F.X. Qin, Y.F. Liu, J.F. Sun, H. Srikanth, and M.H. Phan, Appl. Phys. Lett. 108, 092403 (2016).

DQ-05. Giant baromagnetic effect in Sn-doped MnNiGe. *F. Shen*[1], F. Liang[1], J. Hao[1], F. Hu[1], J. Wang[1], J. Chen[2], L. He[1], T. Liang[2], J. Sun[1] and B. Shen[1] *1. Institute of Physics, Chinese Academy of Sciences, Beijing, China; 2. Spallation Neutron Source Science Center, Dongguan, China*

Pressure sensor (PS) has important application in artificial intelligence and modern industries. Baromagnetic effect (BME), i.e. pressure-induced magnetic moment change, is regarded as the candidate technology for new PS. The reported large BME in $Mn_3Ga_{0.95}N_{0.94}$ [1] has gained great attention. The origin comes from the pressure-induced spin re-orientation from Γ^{5g} antiferromagnetic (AFM) to M-1 ferrimagnetic phase. Recently, the ternary metallic compounds MM'X (M, M' = transition metals, X = main elements) have attracted renewed attention due to their barocaloric effect [2], and giant negative thermal expansion [3]. In the MM'X family, the MnNiGe alloy possesses a martensitic structural transiton from austenite (with ferromagnetic (FM) ground state) to martensite (with AFM ground state) [4]. By doping the Sn into the Ge site, the martensite become unstable and can be easily converted to austenite by pressure. A giant BME is therefore achieved. $MnNiGe_{1-x}Sn_x$ ($0.07\leq x\leq 0.1$) compounds were prepared by arc-melting technique (Fig. 1a). Here, the critical composition (x = 0.085) is chosen to study the BME. The results show that an application of hydrostatic pressure is able to increase the magnetization significantly (Fig. 1b). Neutron powder diffraction reveal that the origin is closely relative to collapse of AFM structure enforced by pressure and establishment of FM structure. We quantify the BME by ΔM_P ($\Delta M_P = M(T, P) - M(T, P_0)$), where M(T, P) is the magnetization under different temperature and pressure, and P_0 stands for the atmospheric pressure (Fig. 1c). The maximal ΔM_P reaches 40.5 A m^2Kg^{-1} at 20K under 680MPa, which is three times larger than the maximum ΔM_P (13.0 A m^2Kg^{-1} under 1000MPa) of the well-known material $Mn_3Ga_{0.95}N_{0.94}$ [1], and the ΔM_P can maintain above 30 A m^2Kg^{-1} below 160K. The pressure dependent spontaneous magnetization (M_S) is also measured (Fig. 1d), and intrinsic mechanism of the giant BME relative to the evolution of magnetic structure is discussed. Fig.1. a) M-T under 0.1 T for $MnNiGe_{1-x}Sn_x$ ($0.07\leq x\leq 0.1$). b) M-T and c) ΔM_P–T under 5 T and different pressures, and d) M_S–P at 20K for $MnNiGe_{1-x}Sn_x$ (x=0.085). The inset shows the corresponding M–H curves for the M_S–P.

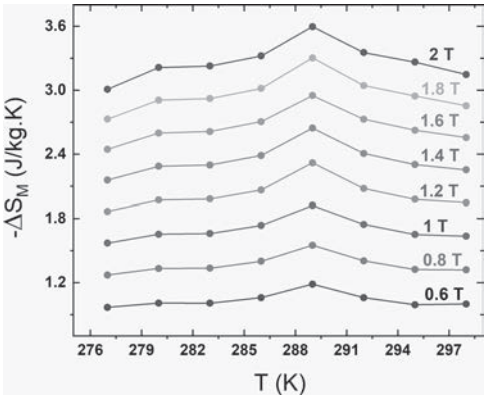
1. K. W. Shi, Y. Sun, J. Yan, et al., Adv. Mater., Vol. 28, p.3761-3767 (2016) 2. R. R. Wu, L. F. Bao, F. X. Hu, et al., Sci. Rep., Vol. 5, p.18027 (2015) 3. Y. Y. Zhao, F. X. Fu, L. F. Bao, et al., J. Am. Chem. Soc., Vol. 137, p.1746-1749 (2015) 4. W. Bazela, A. Szytula, J. todorovic, et al., Phys. Stat. Sol. (a)., Vol. 38, p.721-729 (1976)



DQ-06. Fe-Ni-Al-Zr Amorphous Thin Films for Magnetic Refrigerants near Room Temperature. *R. P*[1], P. Svedlindh[1] and G. Andersson[1] *1. Uppsala University, Sweden, Uppsala, Sweden*

Amorphous Fe-Zr-based thin films are suitable candidates for magnetic refrigeration due to the relationship between their magnetic and microstructural properties. These systems have the advantage of low cost, due to that they are free of rare-earth elements, and they can exhibit large changes in magnetic entropy close to room temperature at relatively low applied fields (< 2 tesla), while being free from magneto-structural phase transitions. Furthermore, they exhibit higher electrical resistivity, relatively larger values of refrigerant capacity (RC) and tunable Curie temperature in the amorphous phase compared to that of rare-earth based films at room temperature. Fe-Zr based amorphous films $(Fe_{1-x}Ni_x)_{90}Zr_{10}$ and $(Fe_{0.95}M_{0.05})_{90}Zr_{10}$, with M being one of Al, Si, Ga, Ge and Sn, have been studied as candidate materials for room temperature magnetic refrigeration with larger values in RC [1, 2]. In the present studies, Fe-Ni-Al-Zr (FNAZ) amorphous thin films were prepared at room temperature, using DC magnetron sputtering by co-deposition of individual elemental targets. The presence of Ni and Al improves the magnetic moment and minimizes the eddy currents respectively in these films. An order-disorder transition temperature of 289 K for a specific FNAZ amorphous film was determined using SQUID magnetometry at an applied field of 100 Oe. A magnetic entropy change (ΔS_M) of 3.58 J/kgK at an applied of 2 T was observed close to the order-disorder temperature. The magnitude of this value makes the material a possible candidate for future room temperature magnetic refrigeration applications.

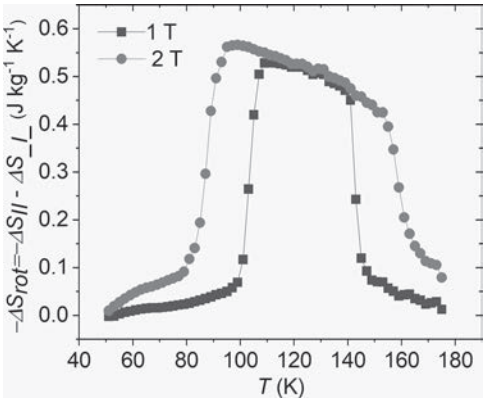
1. Y. K. Fang et al., Magnetocaloric effect in Fe-Zr-B-M (M = Mn, Cr, and Co) amorphous systems, J. Appl. Phys. 105, 07A910 (2009). 2. Hiroshi Maeda et al., Fe-Zr amorphous alloys for Magnetic Refrigerants near Room Temperature, J. Japan Inst. Metals. Vol. 47, No.8(1983), pp. 688-691



Magnetic entropy change (ΔS_M) in one of the FNAZ amorphous film at an applied field of 2 T

DQ-07. Rotating Magnetocaloric Effect in the Region of Spin-Reorientation Transition in the Fe_7Se_8 Single Crystal. *I. Radelytskyi*[1,2] and Y. Konopelnyk[2] *1. Jülich Centre for Neutron Science at MLZ, Garching, Germany; 2. Institute of Physics PAS, Warsaw, Poland*

Trigonal Fe_7Se_8 (3c type) shows in constant magnetic fields a spin-reorientation transition from the easy *c*-axis to the easy *c*-plane near the temperature $T_R \approx 125$ K, as a first-order phase transition. This transition is induced by temperature and/or by an applied magnetic field. We investigated a Fe_7Se_8 single crystal by magnetization measurements above and below T_R and observed first order metamagnetic field induced transitions. The maximum rotating entropy change was evaluated from magnetization data using the Maxwell equation to be about $\Delta S_{rot} \approx 0.566$ J /(kg K) for H = 2T. The calculated refrigeration capacity is equal $RC_{rot} \approx 35.71$ J/kg for H=2 T, which is twice time bigger that conventional magnetocaloric effect at the same magnetic field magnitude. A one-ion model of the rotating magnetocaloric effect has been developed and its predictions have been compared with experimental data.



DQ-08. Near Room Temperature Magnetocaloric Effect in CrTe1-xSbx Alloys. M.K. Hamad[1], E. Martinez-Teran[2], Y. Maswadeh[3], R. Hamad[1], E.G. Alnahari[1], *A.A. El-Gendy*[2] and K.A. Ziq[1] *1. Physics, King Fahd University of Petroleum & Minerals, El Damam, Saudi Arabia; 2. Physics, University of Texas at El Paso, El Paso, TX, United States; 3. Department of Physics and Science of Advanced Materials Program, Central Michigan University, Mt. Pleasant, MI, United States*

We investigated the structural, magnetic properties and magnetocaloric effect in CrTe1-xSbx with different Sb concentration ($0 \le x \le 0.2$). Rietveld refinement of the XRD patterns revealed that the Sb substituted samples are pure phase hexagonal structure with P63/mmc (194) space group. However, the Sb-free sample (CrTe) contains a non-reacted minority phase. Moreover, a small concentration of Sb (~5%) was enough to produce samples with pure hexagonal structure. The magnetic properties of CrTe1-xSbx have also been investigated. The magnetic susceptibility revealed that ferromagnetic transition temperature decreases gradually in the range (330-285K) with Sb substitutions. Moreover, the molecular field coefficient γm obtained from the susceptibility also showed a gradual reduction with increasing Sb concentration, indicative of a weakening of the ferromagnetic interaction. Magnetization isotherms have been used to investigate the magnetocaloric effect in CrTe1-xSbx polycrystalline with $0 \le x \le 0.2$. We observed a significant enhancement in the maximum entropy change (deltaS max) and the rate of cooling power (RCP) upon Sb substitutions in a maximum cycling field at 3 Tesla. These results indicated that CrTe1-xSbx is a potential candidate as a room temperature magnetocaloric material.

DQ-09. Tuning of structural transition and phase stability in MnCo(Ge, V) system. H. Imam[1], *H. Zhang*[1], B. Song[1], Q. Lu[1], W. Liu[1], Y. Li[1], Z. Altounian[2] and M. Yue[1] *1. College of Materials Science and Engineering, Beijing University of Technology, Beijing, China; 2. Center for the Physics of Materials, Department of Physics, McGill University, Montreal, QC, Canada*

MnCoGe compound possesses a highly tunable martensitic transformation from low temperature TiNiSi-type structure to high temperature Ni_2In-type structure, which makes it a prototype for the investigation of magnetostructural coupling of the well-known MM'X systems [1]. Recently, all-d-metal Heusler system Ni-Mn-Ti-Co has been reported, in which low-valence-electron-element Ti can play the role as main-group element in traditional Heusler compounds by means of d-d hybridization. Base on this idea, a substitution of V for Ge in MnCoGe compound has been investigated in this work to understand the structure transition, phase stability and magnetic behavior of the system. Fig.(a) shows the patterns of the $MnCoGe_{1-x}V_x$ (x=0.005, 0.01, 0.015, 0.02, 0.03 and 0.04) compounds. They can be indexed as TiNiSi-type orthorhombic phase, mixed with a growing amount of Ni_2In-type hexagonal phase. This indicates that the martensitic transformation temperatures are decreased by V doping. Fig.(c) shows the BSEM and EDS results of the x = 0.04 samples. One can see that there are two different contrasts, dark one and grey one, corresponding to the $Mn_{0.91}CoGe_{0.96}V_{0.04}$ and $Mn_{0.91}CoGe_{0.70}V_{0.03}$ phases, respectively. The temperature dependence of the magnetization of the $MnCoGe_{1-x}V_x$ samples were studied in both the cooling and heating processes, as seen in Fig.(b). The increase of thermal hysteresis between the cooling and heating processes along V doping indicates that the phase transition temperature is decreased and eventually the magnetostructural coupling is established. The isothermal entropy change -ΔS was derived using the Maxwell relation and shown in Fig.(d), in which the largest $-\Delta S_{Max}$ is 10 J/kgK for x = 0.015. The values of the refrigerant capacity were also calculated and the largest one is 129.5 J/kg for x = 0.015. These results prove that d-d hybridization in MM'X systems can also help to achieve the magnetostructural coupling and thus realize magnetocaloric effect.

[1] Liu E.K., W. Zhu, L. Feng, J.L. Chen, W.H. Wang, G.H. Wu, H.Y. Liu, F.B. Meng, H.Z. Luo, and Y.X. Li, EPL, Vol. 91 (1), p.17003 (2010)

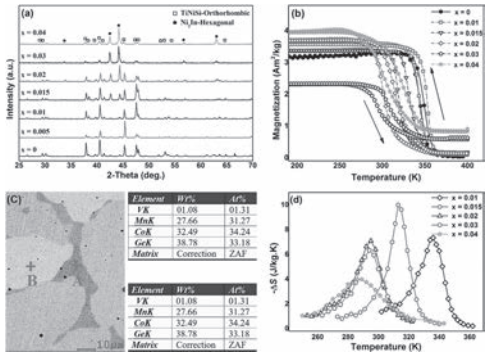


Fig. (a) XRD patterns and (b) M-T curves under a magnetic field of 0.01T of the $MnCoGe_{1-x}V_x$ series; (c) BSEM and EDS of $MnCoGe_{0.9}6V_{0.04}$; (d) isothermal magnetic entropy changes of the $MnCoGe_{1-x}V_x$ series

DQ-10. Quadrupolar ordering effect on magnetocaloric effect in rare-earth tetraborides. *M. Song*[1], K. Cho[1], J. Lee[1] and B. Cho[1] *1. Gwangju institute science and technology, Gwangju, The Republic of Korea*

The interplay of charge, spin, orbital and lattice degrees of freedom has recently received much attention due to its potential to improve the magnetocaloriceffect (MCE) for the purpose of magnetic cooling applications. The exotic inverse MCE is observed in rare-earth tetraborides, $Ho_{1-x}Dy_xB_4$ (x = 0.0, 0.5, and 1.0), and the strong coupling of magnetic dipole moments with quadrupole moments is found to induce the MCE in the presence of geometric frustration of 4*f* moments. It is remarkable that the maximum entropy change is realized in the critical fields below H = 5 T, which depends on the x values. So, it enables to induce a field-tuned entropy change and to bring about a significant advantage for several applications. On the other hand, ErB_4 and TmB_4 show the maximum entropy changes of 11.4 J/kgK, and 12.6 J/kgK with the critical field of » 40 kOe, respectively, which are significantly smaller than those of $Ho_{1-x}Dy_xB_4$. Although ErB_4 and TmB_4 have a similar structural and magnetic properties to those of $Ho_{1-x}Dy_xB_4$, i.e, the consecutive magnetic transitions, magnetization plateau, and strong anisotropy, those compounds are found to have strong competition between Zeeman effects and magnetic frustration, instead of the quadrupolar interaction. Thus, it supports the fact that the strong coupling between quadrupolar and magnetic dipolar moments plays important role in the exotic giant MCE in rare-earth tetraborides system.

DQ-11. Magnetostructural Transition and Giant Magnetocaloric Effect near Room Temperature in Al doped $(Mn_{0.6}Fe_{0.4})NiSi$ Alloys. *S. Ghosh*[1], P. Sen[2] and K. Mandal[1] *1. Condensed Matter Physics & Material, S. N. Bose National Centre for Basic Sciences, Kolkata, India; 2. Physics group, Variable Energy Cyclotron Centre, Kolkata, India*

MnNiSi [1] compound exhibits a first order structural transition, beyond a magnetic transition at T_C = 622 K, from orthorhombic TiNiSi-type structure to a hexagonal Ni_2In-type structure at a high temperature about ~1210 K in the paramagnetic region which is not suitable for room temperature magnetic refrigeration and it is desired to lower the structural transition to room temperature in the magnetically ordered ferromagnetic (FM) state. Magnetoresponsive properties of the above system are related to change in magnetization across its phase transitions. Therefore it is crucial to couple both magnetic and structural transition to achieve giant magnetocaloric effects in this alloy [2]. Here, first order magnetostructural transition (MST) between ferromagnetic orthorhombic and paramagnetic hexagonal structure and giant magnetocaloric effect near room temperature are observed in transition metal based low cost Al doped $(Mn_{0.6}Fe_{0.4})NiSi_{1-x}Al_x$ (x = 0.06, 0.07 and 0.08) alloys. Isothermal magnetic entropy change (ΔS_M) as large as ~ 35.1 and 6.52 $Jkg^{-1}K^{-1}$ is found for the alloy with x = 0.07 due to a change of 50 and 10 kOe magnetic field respectively. Interestingly, no noticeable field induced metamagnetic behavior is observed during heating cycle for these alloys which is very advantageous in respect of efficiency of these materials as refrigerant [3]. Moreover field dependence of ΔS_M data during heating cycle show universal behavior and are fitted well with a Lorentz function. Giant value of ΔS_M associated with large relative cooling power (RCP = 182.5 J/kg, for ΔH = 50 kOe) observed for the alloy of x = 0.07 enable the alloy as a potential candidate for magnetic refrigerant.

[1] V. Johnson and C. G. Frederick, Phys. Status Solidi 20, 331 (1973) [2] T. Samanta, D. L. Lepkowski, A. U. Saleheen, A. Shankar, J. Prestigiacomo, I. Dubenko, A. Quetz, I. W. H. Oswald, G. T. McCandless, J. Y. Chan, P. W. Adams, D. P. Young, N. Ali, and S. Stadler, Phys. Rev. B 91, 020401 (2015) [3] S. Ghosh, P. Sen, and K. Mandal, IEEE Trans. Magn. 54, 1 (2018)

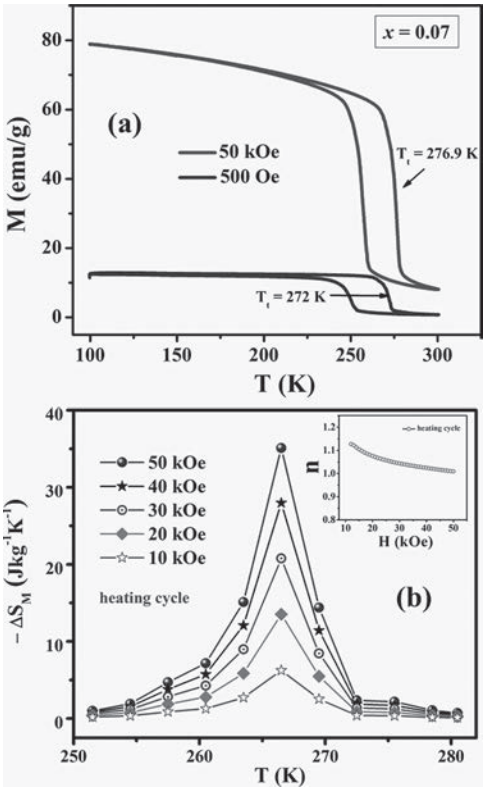
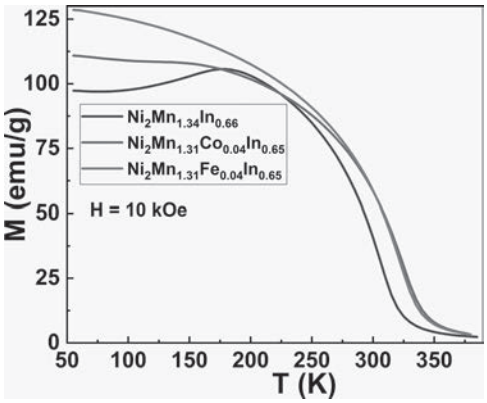


Fig.1: (a) M-T curves for the alloy x = 0.07 in presence of 500 Oe and 50 kOe magnetic field (b) Magnetic entropy change estimated from isothermal M-H curve as a function of temperature for the different field variation of x = 0.07 alloy in heating cycle [Inset: the exponent n as a function of magnetic field in heating cycle]

DQ-12. Magnetocaloric effect in Ni_2MnIn-based Heusler alloys with second-order phase transition. *B.R. Dahal*[1], Z. Lehmann[1], Y. Huh[1] and P.R. Kharel[1] *1. Department of Physics, South Dakota State University, Brookings, SD, United States*

Magnetic materials with second-order phase transition near room temperature exhibiting strong magnetocaloric effect (MCE) are preferred for room temperature magnetic refrigeration technology because these materials are free from magnetic and thermal hysteresis.[1] The MCE in Ni-Mn-In-based Heusler alloys have been widely investigated for their application in magnetic refrigeration but the main focus is in the MCE near their magnetostructural (first-order) phase transitions due to the observed large value of entropy change. We are interested to investigate the MCE of Ni-Mn-In-based alloys with elemental composition close to the critical composition between the first and second order phase transitions. We have investigated the structural, magnetic, and magnetocaloric properties of $Ni_2Mn_{1+x}In_{1-x}$ alloys prepared using arc-melting and vacuum annealing. We have found that the $Ni_2Mn_{1.34}In_{0.66}$ alloy shows a clear second-order phase transition near room temperature (Tc = 305K) with substantial MCE, but it also shows a first order phase transition(FOPT) when cooled below room temperature, Fig. 1. However, the first-order phase transition in $Ni_2Mn_{1.34}In_{0.66}$ can be completely suppressed with partial substitution of Mn with Fe or Co. We have found that the FOPT is highly suppressed in $Ni_2Mn_{1.31}Co_{0.04}In_{0.65}$ and completely suppressed in $Ni_2Mn_{1.31}Fe_{0.04}In_{0.65}$ alloys with a slight increase in saturation magnetization and Curie temperature, Fig. 1. The magnetic entropy change calculated from the isothermal magnetization *M(H)* curves measured at 30 kOe fields indicate that the maximum entropy change in $Ni_2MN_{1.31}Co_{0.04}In_{0.65}$ and $NI_2Mn_{1.31}Fe_{0.04}In_{0.65}$ alloys are 3.95 $Jkg^{-1}K^{-1}$ and 4.30 $Jkg^{-1}K^{-1}$, respectively. The corresponding relative cooling power near their Curie temperatures are 205 Jkg^{-1} and 211 Jkg^{-1}, respectively. These values are relatively high for rare-earth-free magnetocaloric materials showing second-order phase transitions near room temperature. We will also discuss the effect of annealing on the crystal structure and MCE of these alloys.

[1]M.-H. Phan, S.-C Yu, J Magn Magn Mater 308, 2, 325-340 (2007).



Temperature dependence magnetizations *M(T)* measurements of $Ni_2Mn_{1.34}In_{0.66}$, $Ni_2Mn_{1.31}Co_{0.04}In_{0.65}$, and $Ni_2Mn_{1.31}Fe_{0.04}In_{0.65}$ Heusler alloys.

DQ-13. Magneto-elastic coupling in $AlFe_2B_2$-based compounds. *R. Barua*[1,2], B. Lejeune[2], Y. Mudryk[3], B.A. Jensen[3], M. Kramer[3], V.K. Pecharsky[3] and L. Lewis[2,4] *1. Department of Mechanical & Nuclear Engineering, Virginia Commonwealth University, Richmond, VA, VA, United States; 2. Department of Chemical Engineering, Northeastern University, Boston, MA, United States; 3. Division of Materials Sciences and Engineering, Ames Laboratory, Ames, IA, United States; 4. Department of Mechanical and Industrial Engineering, Northeastern University, Boston, MA, United States*

Understanding structure-magnetic property correlations provides insight into the fundamental drivers underlying the magnetocaloric effect (MCE) in $AlFe_2B_2$-based compounds, thus enabling fine-tuning of their functional response for potential magnetic cooling applications. To this end, samples of nominal composition $Al_{1.2}Fe_2B_2$ and $Al_{1.1}Ga_{0.1}Fe_2B_2$ were synthesized via casting, followed by annealing at 1040 °C for 3 days. Both single-phase samples adopt the expected orthorhombic (space group *Cmmm*) crystal structure wherein the Fe and B atoms form Fe_2B_2 layers that are separated by Al monolayers along the *b*-axis, Fig 1. Energy dispersive spectroscopy indicates that the solid solubility of Ga in the $AlFe_2B_2$ lattice is limited; hence the addition of Ga appears to favor non-stoichiometric enrichment by Fe.[1] Intriguingly, a 16 K increase in Curie temperature and 60% improvement in the magnetic entropy change was observed in the $Al_{1.1}Ga_{0.1}Fe_2B_2$ specimen (T_C=290 K; ΔS=4.4 J/kgK at μ_0H=2T), relative to $Al_{1.2}Fe_2B_2$ (T_C=274 K; ΔS=2.6 J/kgK at μ_0H=2T).[1] The noted changes in the magnetic character of the samples motivated examination of the temperature dependence of the lattice parameters and three significant interatomic distances within the coordination polyhedron of B (shaded in Fig. 1) - $d_{Al\text{-}Fe}$, $d_{(Fe\text{-}Fe)c}$ and $d_{(Fe\text{-}Fe)ab}$ - by X-ray Diffraction. In both samples, the *a*- and *b*-parameters increase upon heating while the *c*-parameter decreases, confirming a small volumetric thermal expansion of ~0.2 % in the temperature range 100 K - 325 K. In $Al_{1.1}Ga_{0.1}Fe_2B_2$, a broad discontinuity in $d_{Al\text{-}Fe}$ and an abrupt change in $d_{(Fe\text{-}Fe)ab}$ is noted through the magnetic transition, Fig. 2. These two structural features are largely absent in $Al_{1.2}Fe_2B_2$. It is surmised that magnetostructural coupling is stronger in $Al_{1.1}Ga_{0.1}Fe_2B_2$ than in $Al_{1.2}Fe_2B_2$ and is likely the underlying basis of the enhanced MCE in this sample. Acknowledgements: ARPA-E (DEAR00000754); U.S Department of Energy (DE-AC02-07CH11358).

[1] R. Barua et. al., J. Alloys Compd. 777, pp. 1030 (2019). [2] B. T. Lejeune et. al., J. Magn Magn. Mater. 482, pp. 262 (2019)

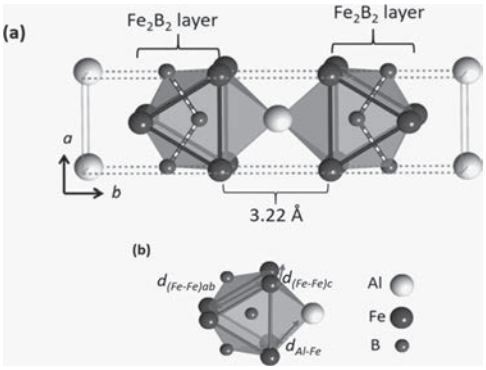


Fig 1. Crystal structure of $AlFe_2B_2$. Within the coordination polyhedron of boron, three key interatomic distances are identified.

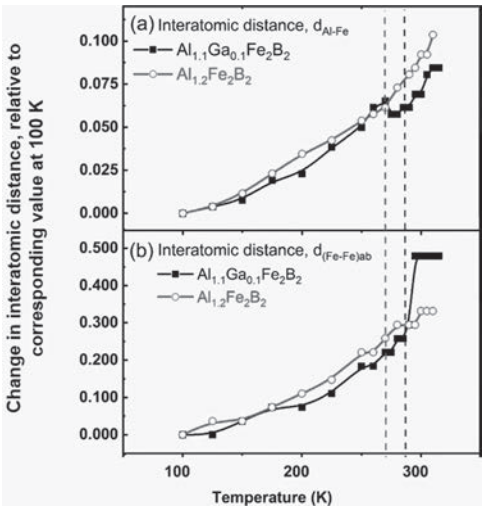


Fig 2. Temperature-dependencies of the interatomic distances. The dotted lines mark the corresponding Curie temperatures.

DQ-14. Magnetocaloric effect and magnetic properties of $Gd_{(1-x)}Nd_{(x)}$ alloys. *R.d. Rodrigues*[1], É. Usuda[2,3], L. Soares de Oliveira Paixão[2], C. Salazar Mejia[4], K. Roberto Pirota[1] and A. Magnus Gomes Carvalho[2]
1. DFMC, UNICAMP, Campinas, Brazil; 2. Laboratório Nacional de Luz Síncrotron, Campinas, Brazil; 3. Departamento de Ciências Exatas e da Terra, UNIFESP, Diadema, Brazil; 4. Hochfeld-Magnetlabor Dresden, Helmholtz-Zentrum Dresden - Rossendorf e.V. (HZDR), Dresden, Germany

Magnetic materials undergo temperature variation when exposed to an external magnetic field, this is said to be the magnetocaloric effect [1]. In the past two decades, the interest in magnetocaloric effect has grown by the scientific community mainly due to the application for eco-friendly magnetic refrigeration. Moreover, it is interesting that magnetocaloric materials can also be used for magnetic hyperthermia treatments [2]. Among the magnetocaloric materials, gadolinium was one of the first and most important elements investigated so far due to its remarkable magnetic properties at close to room temperature [1]. In this work, we studied the intermetallic alloys of gadolinium and neodymium with different compositions to understand the magnetocaloric effect and magnetic properties using experimental and computational methods. A set of five samples were prepared by arc-melting method with the following compositions: $Gd_{90}Nd_{10}$, $Gd_{80}Nd_{20}$, $Gd_{70}Nd_{30}$, $Gd_{60}Nd_{40}$, $Gd_{50}Nd_{50}$. The samples were characterized using two commercial magnetometers and X-ray diffraction (XRD) analyses. The results indicate that both magnetic transition temperature and saturation magnetization can be modified by changing the composition of Gd and Nd as shown in Fig. 1 and Fig. 2. It is reasonable to infer that the addition of Nd atoms changed the magnetic interaction between the magnetic atoms of alloys and thereby the magnetic properties [3]. Our perspectives are to investigate the magnetic ordering of our samples using X-ray magnetic circular dichroism (XMCD) measurements, specifically, we expect to obtain information about the local magnetism of the chemical elements in our samples, distinguishing the contributions of the magnetic orbital and spin moments of each element and compare the experimental and theoretical results.

[1] Franco, V., Blázquez, J. S., Ipus, J. J., Law, J. Y., Moreno-Ramírez, L. M., & Conde, A. (2018). Magnetocaloric effect: From materials research to refrigeration devices. Progress in Materials Science. https://doi.org/10.1016/j.pmatsci.2017.10.005 [2] Tishin, A. M., Spichkin, Y. I., Zverev, V. I., & Egolf, P. W. (2016). A review and new perspectives for the magnetocaloric effect : New materials and local heating and cooling inside the human body Une synthèse et de nouvelles perspectives pour l′ effet magnétocalorique : Nouveaux matériaux et chauffage et refroidissement. International Journal of Refrigeration, 68, 177–186. https://doi.org/10.1016/j.ijrefrig.2016.04.020 [3] Xiao, S., & Chen, Y. (2016). Magnetic properties and magnetic exchange interactions in Gd1-xREx-(RE=Pr, Nd) alloys. Journal of Rare Earths, 34(5), 489–494. https://doi.org/10.1016/S1002-0721(16)60054-6

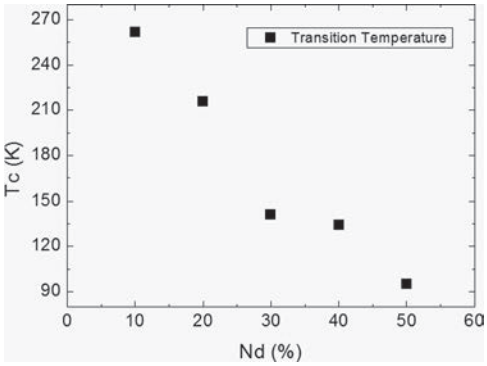


Fig 1: Transition temperature as a function of neodymium content.

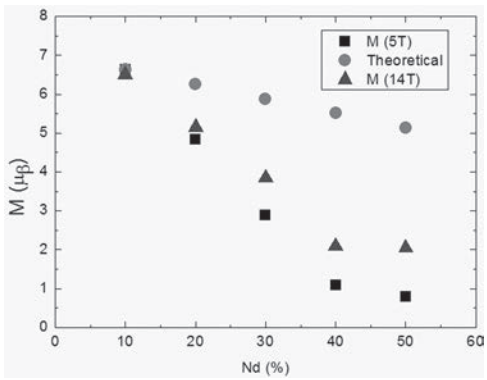


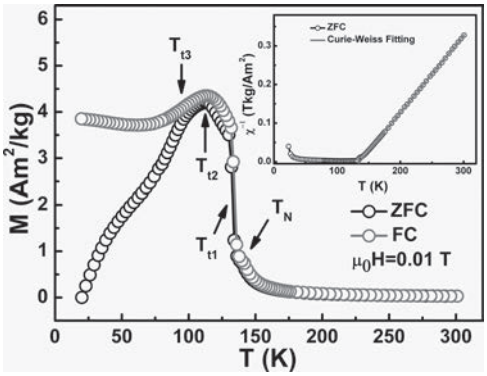
Fig 2: Theoretical saturation magnetization and experimental magnetization at 5 T and 14 T as a function of neodymium content.

DQ-15. Magnetic properties and large magnetocaloric effect in R_3NiSi_2 (R=Tb, Dy) compounds. *J. Liu*[4,3], W. Liang[4,3], L. Wang[2], J. Xu[1], X. Zheng[1], T. Zhao[4], F. Hu[4,3], J. Sun[4,3] and B. Shen[4,3] *1. University of Science & Technology Beijing, Beijing, China; 2. Capital Normal University, Beijing, China; 3. University of Chinese Academy of Sciences, Beijing, China; 4. Institute of Physics, Chinese Academy of Sciences, Beijing, China*

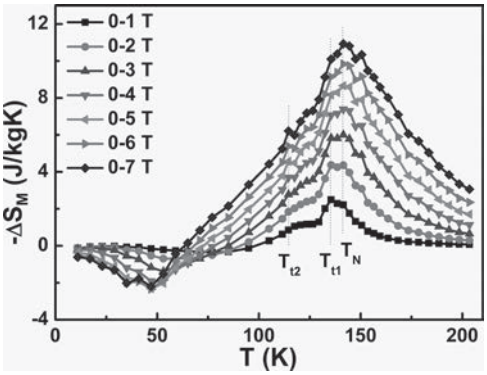
Gd_3NiSi_2 compound present a reasonable magnetocaloric effect (MCE) than other recently reported R-Ni-Si systems [1] and the crystal structure had extensively been investigated [1-4]. In this work, orthorhombic polycrystalline R_3NiSi_2 (Tb, Dy) compounds were prepared using arc-melting method and the magnetic properties and magnetocaloric effect were investigated in detail. Magnetic measurements on R_3NiSi_2 indicated that there were several

magnetic phase transitions in both compounds. As temperature decreases, Tb_3NiSi_2 compound experienced a paramagnetic (PM) to antiferromagnetic (AFM) transition at T_N and an AFM to ferromagnetic (FM) transition at T_{t1}. When the temperature continue to reduce, Tb_3NiSi_2 compound underwent a FM to FM transition T_{t2} and an FM to AFM transition at T_{t3}. Not only normal MCE, but also inverse MCE can be found in Tb_3NiSi_2 compound. Under a field change of 0–7 T, the maximal value of inverse and normal MCE were about 2.3 J/kgK and 11.1 J/kgK for Tb_3NiSi_2 compound, respectively. As for Dy_3NiSi_2 compound, transition temperature T_{t3} cannot been observed compared with Tb_3NiSi_2 compound. And only normal MCE was verified with the maximal value at about 10.8 J/kgK for a field change of 0-7 T. Considering of normal and inverse MCE, Tb_3NiSi_2 shows considerable refrigerant capacity among the R_3NiSi_2 (Tb, Dy) compounds, indicating its potential applications in middle temperature magnetic refrigeration.

[1] S. Tencé, S. Gorsse and E. Gaudin, Intermetallics, Vol. 17, p. 115-119 (2009). [2] K. Klepp and E. Parthé, Acta Cryst., Vol. 37, p. 1500-1504 (1981). [3] K. Klepp and E. Parthé, J. Less-Common. Met., Vol. 83, p. 33-35 (1982). [4] A. V. Morozkin, V. Svitlyk and Y. Mozharivskyj, J. Magn. Magn. Mater., Vol. 349, p. 201-207 (2014).



The ZFC-FC curves measured at a field of 0.01 T for the Tb_3NiSi_2 compound. The inset displays the temperature dependence of reciprocal magnetic susceptibility χ^{-1} and the Curie-Weiss fitting.



Magnetic entropy changes each as a function of temperature for Tb_3NiSi_2 under the magnetic field changes of 0–1 T, 0–2 T, 0–3 T, 0–4 T, 0–5 T, 0–6 T, 0–7 T.

DQ-16. Magnetic properties and magnetocaloric effect in $Ho_{1-x}Tm_xGa$ (x=0.2, 0.3, 0.4) compounds. *S. Yang*[1,2], X. Zheng[1], J. Xu[1], S. Shao[1], J. Zhang[1], S. Wang[1], J. Liu[2], Y. Zhang[2], Y. Liu[2], Z. Xu[3], L. Wang[4] and B. Shen[2,1] *1. School of Materials Science and Engineering, University of Science and Technology Beijing, Beijing, China; 2. State Key Laboratory for Magnetism, Institute of Physics, Chinese Academy of Sciences & University of Chinese Academy of Sciences, Beijing, China; 3. National Institute of Metrology, Beijing, China; 4. Department of Physics, Capital Normal University, Beijing, China*

Magnetic refrigeration has drawn much attention during the last decades because of the advantages on energy efficiency and environment friendliness compared with conventional refrigeration. [1-3] Magnetic refrigeration is based on magnetocaloric effect (MCE) and the MCE materials with low transition temperatures can be used for low temperature refrigeration such as gas liquefaction. A lot of low temperature MCE materials have been reported, including TmGa and HoGa compounds. [4-5] In this work, the influence of Tm-substitution for Ho atoms on the magnetic property and MCE of HoGa compound was studied in detail. According to powder X-ray diffraction (XRD) measurements, $Ho_{1-x}Tm_xGa$ (x=0.2, 0.3, 0.4) compounds are all pure phases. Magnetic measurements (Fig.1a) show that $Ho_{1-x}Tm_xGa$ (x=0.2, 0.3, 0.4) compounds exhibit three successive magnetic transitions: ferromagnetic (FM)-I to FM-II, FM-II to antiferromagnetic (AFM), and AFM to paramagnetic (PM) transition. The FM-I to FM-II transition comes from spin reorientation (SR) which has been studied already.[4] The other two transitions have been reported in TmGa compound.[5] As the content of Tm increases, the T_{FA} and T_N decreases monotonically from 54.5 K to 42.0 K and 55.5 K to 44.0 K, respectively. T_{SR} changes little and almost keeps at about 20.0 K, in good accordance with the results of $Gd_xEr_{1-x}Ga$ compounds. [6] It is found that two peaks can be observed on the ΔS_M curves for all $Ho_{1-x}Tm_xGa$ (x=0.2, 0.3, 0.4) compounds (Fig.1b). The two peaks get closer in temperature with the content of Tm increasing. More specially, the maximal magnetic entropy change $(-\Delta S_M)_{max}$ at T_{SR} increases from 5.9 J/kg K with x=0.2 to 15.6 J/kg K with x=0.4, indicating a larger magnetic order change around T_{SR}. As for refrigerant capacity (RC), it increases monotonously from 393.9 J/kg to 553.8 J/kg with increasing Tm. Therefore, Tm-substitution for Ho atoms has a positive influence on the performance of HoGa compound.

1. V. K. Pecharsky and K. A. Gschneidner, Phys. Rev. Lett. 78, 4494 (1997) 2. F. X. Hu, B. G. Shen, J. R. Sun, Z. H. Cheng, G. H. Rao, and X. X. Zhang, Appl. Phys. Lett. 78, 3675 (2001) 3. O. Tegus, E. Brück, K. H. J. Buschow, and F. R. de Boer, Nature 415, 150 (2002) 4. J. Chen, B. G. Shen, Q. Y. Dong, and J. R. Sun, Solid State Commun. 150, 157 (2010) 5. Z. J. Mo, J. Shen, L. Q. Yan, C. C. Tang, J. Lin, J. F. Wu, J. R. Sun, L. C. Wang, X. Q. Zheng, and B. G. Shen, Appl. Phys. Lett. 103, 052409 (2013) 6. X. Q. Zheng, J. Chen, L. C. Wang, R. R. Wu, F. X. Hu, J. R. Sun, and B. G. Shen, J. Appl. Phys. 115, 17A905 (2014)

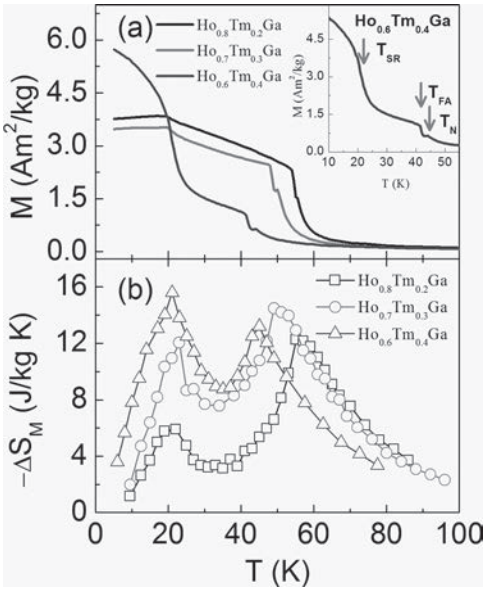


Fig. 1 (a) Temperature dependences of magnetization under the magnetic field of 0.01 T for $Ho_{1-x}Tm_xGa$ (x=0.2, 0.3, 0.4) compounds. (b) Temperature dependences of $-\Delta S_M$ for a field change of 0-5 T for $Ho_{1-x}Tm_xGa$ (x=0.2, 0.3, 0.4) compounds.

DQ-17. Comparison of Magnetic Entropy Change Measured in Standard and Loop Modes for $Ni_{50}Mn_{35}In_{15}$. *F. Liang*[1,2], Z. Yu[1,2], F. Hu[1,2], J. Hao[1,2], F. Shen[1,2], K. Qiao[1,2], J. Li[1,2], J. Wang[1,2], J. Sun[1,2] and B. Shen[1,2]
1. Beijing National Laboratory for Condensed Matter Physics and State Key Laboratory of Magnetism, Insititute of Physics, Beijing, China; 2. School of Physical Sciences, University of Chinese Academy of Sciences, Beijing, China

The validity of entropy change (ΔS) calculated by Maxwell relation from magnetization isotherms has been widely discussed in the first-order magnetostructural transition during the last decades[1-5]. Here, by both standard and loop modes, we investigate the entropy change ΔS of $Ni_{50}Mn_{35}In_{15}$ alloy, which exhibits first-order magnetostructural transition from high temperature cubic phase to low temperature tetragonal phase. Considering the thermodynamics of the first-order phase transition process, the rationality of the entropy change calculated by Maxwell relation is discussed in $Ni_{50}Mn_{35}In_{15}$. The *M-T* curves under 0.01 T, 5 T, and *M-H* curves in the phase transition region on cooling is shown in Fig. 1 (a) and (b), respectively. In the two-phase region, the initial increase of magnetization indicates the magnetization process of ferromagnetic (FM) martensite phase. At higher field, the structural transition from non-magnetic tetragonal phase to ferromagnetic cubic phase is responsible for the further increase of magnetization. As shown in Fig. 1 (c), during cooling process, there exists obvious difference between the standard and loop mode in the branch of ascending magnetic field. The isothermal entropy change calculated from both standard and loop process under magnetic field of 1 T, 2 T and 5 T is shown in Fig. 1 (e) (ascending process) and Fig. 1 (f) (descending process). Compared with the standard process, the peak value of is lowered from 30 J $kg^{-1}K^{-1}$ to 25 J $kg^{-1}K^{-1}$ under field change of 0-5 T in loop process. However, the magnetization of standard and loop modes keep consistent in the branch of descending magnetic field, as shown in Fig. 1 (d). This can be explained that the driven direction of the phase transition by temperature and magnetic field is converse in cooling and ascending process but consistent in cooling and descending process. Mechanism related to coexistence of multiphase is discussed.

[1] A. Giguère and M. Foldeaki, Phys. Rev. Lett., Vol. 83, p.2262 (1999). [2] L. Caron, Z. Q. Ou and T. T. Nguyen, J. Magn. Magn. Mater., Vol. 321, p.3559–3566 (2009). [3] J. S. Amaral and V. S. Amaral, J. Magn. Magn. Mater., Vol. 322, p.1552–1557 (2010). [4] A. Magnus G. Carvalho, A. A. Coelho and P. J. von Ranke, J. Alloys. Comp., Vol. 509, p.3452–3456 (2011). [5] Weibin Cui, Wei Liu, and Zhidong Zhang, Appl. Phys. Lett., Vol. 96, p.222509 2010.

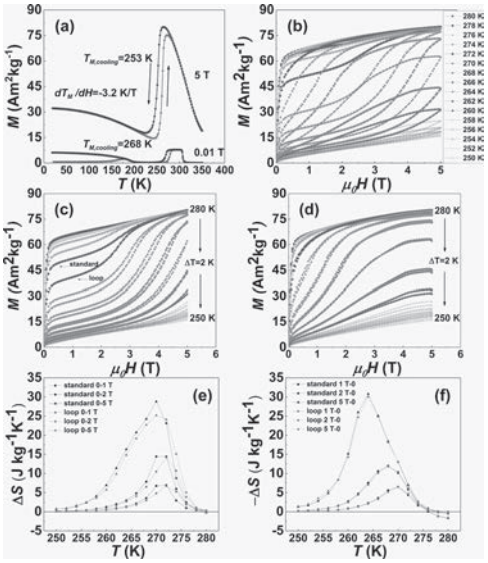


Fig.1. *M-T* curves of $Ni_{50}Mn_{35}In_{15}$ under 0.01 T and 5 T (a); *M-H* curves measured using standard mode (b); comparison of *M-H* curves using standard and loop modes on cooling during ascending (c) and descending process (d); comparison of *DS* of in two modes for ascending process (e) and descending process (f).

DQ-18. Multiferroic Polymer Composites with Combined Magnetoelectric and Multicaloric Effects. *I. Baraban*[1], V. Rodionov[1], A. Amirov[1,2] and A. Kamantsev[1,3] *1. Laboratory of Novel Magnetic Materials, Immanuel Kant Baltic Federal University, Kaliningrad, Russian Federation; 2. Amirkhanov Institute of Physics, Daghestan, Russian Federation; 3. Kotelnikov Institute of Radio Engineering and Electronics, Moscow, Russian Federation*

Recently, the great scientific interest has focused on the design of smart materials, which exhibit large caloric effects (CE) combined with strong magnetoelectric (ME) coupling, for biomedicine and energy efficient technologies. As known, caloric materials are observed adiabatic temperature (isothermal entropy) changes, when the applied external field (magnetic, electric, mechanic) changes. Depending on type of external field stimulus, these caloric effects deals to magnetocaloric, electrocaloric and mechanocaloric effects. The phenomena relates with observation of two or more caloric effect, called as multicaloric effects and the materials, which demonstrate these effects-multicalorics. Multiferroics are advanced materials for multicaloric studies and the ME composites were proposed for it, due to their strong ME coupling. In this connection, recent studies conducted a search for multicalorics with high caloric effects and ME coupling around room temperature. The new multiferroic polymer composites with large magnetocaloric and ME effects around room temperature were fabricated, their structure, magnetic and ME properties were studied. Polymeric 0-3 type composites FeRh / PVDF and GdGeSi / PVDF, consisting of magnetocaloric microparticles $Fe_{50}Rh_{50}$ and $Gd_5Ge_{1.6}Si_{2.4}$ embedded into a piezopolymer matrix of polyfilidendenedluoride (PVDF) in mass ratios from 2 to 40%. The methodics for fabrication of flexible polymer ME composites based on magnetocaloric microparticles (Fe-Rh and Gd-Ge-Si) were developed, their structure and basic physical characteristics were studied in detail. Preliminary experiments on samples with mass fractions of the magnetic phase of 2 and 12% observed the presence of a ME interaction in the vicinity of the magnetic phase transition temperature of the magnetocaloric component of the composite, which can be used for applications in smart composites. In was experimentally demonstrated that the introduction of Gd-Ge-Si

microparticles into an electroactive PVDF with a volume fraction of 2 and 12%, gives rise to a ME coupling and, consequently, a multicaloric effect. *The work was supported by Russian Science Foundation (project #18-79-10176).*

Planes, T. Castan, A. Saxena, Philos. Mag. 94,1893-1908 (2014) S. Fahler, U.K. Robler, O. Kastner, J. Eckert, G. Eggeler, H. Emmerich, P. Entel, S. Muller, E. Quandt, K. Albe, Adv. Eng. Mater. 14 10-19 (2012) I.Flerov, E. Mikhaleva, M. Gorev, A. Kartashev, Phys. Solid State. 57, 429–441 (2015) A. Starkov, I. Starkov, J. Exp. Theor. Phys. 119, 258-263 (2014) M.M. Vopson, Solid State Commun. 152, 2067-2070 (2012) Ce-Wen Nan, M. I. Bichurin, Shuxiang Dong, D. Viehland, and G. Srinivasan, J. Appl. Phys. 103, 031101-1-031101-35 (2008)

DQ-19. Ising Model Simulations of the Magnetocaloric Material $Gd_5(Si_xGe_{1-x})_4$. *A. Evans*[1], M. Gao[2] and D. Read[1] *1. Physics & Astronomy, Cardiff University, Cardiff, United Kingdom; 2. Engineering, Cardiff University, Cardiff, United Kingdom*

The magnetocaloric effect (MCE) is characterized by an adiabatic change of temperature resulting from a varying external magnetic field. Recently, the giant MCE (GMCE) has become of greater interest due to its enhancement of the temperature response[1,2] achieved by coupling the effect with a crystallographic phase transition. New materials discoveries have allowed for MCE use at or close to room temperature[2]. An MCE based refrigeration system would allow for less environmentally harmful materials to be used with a higher efficiency and lower energy consumption[3]. The Ising model has previously been used to study MCE materials[4], based on modeling a set of localized sites in a 3D system each with an associated spin value. Here we employ the RKKY interaction, commonly used to describe the coupling in rare earth materials, in order to model the coupling strength as a function of bond length. We have investigated the effects of a changing inter-site distance, corresponding coupling and the associated energy for the crystal phases of GdSiGe. Our simulations show that a transition from an orthorhombic to monoclinic GdSiGe phase is energetically favourable over a temperature range of 96K to 300K, dependent upon a term introduced into the Hamiltonian to represent the bond energy (E) between interstitial slabs. Calculations show that a ferromagnetic orthorhombic phase exists as a lower energy state of the system than a ferromagnetic monoclinic phase (see figure 1). Increasing the bond energy (E) shows an increasing transition temperature up to 300K where the monoclinic phase is no longer favoured. Figure 2 shows that the peak value of the entropy change decreases as higher temperature transitions are achieved with increasing bond energy (E), calculations are shown for zero field and for magnetic fields of 5T.

[1] R. Hadimani, J. Silva, A.Pereira, Appl. Phys. Lett., Vol.106, p.032402 (2015) [2] V. Pecharsky, K. Gschneider, Jr., Phys. Rev. Lett., Vol. 78, p.4494 (1997) [3] V.Franco, J.Blazquez, B. Ingale, Annu. Rev. Mater. Res., Vol. 42, p.305 (2012) [4] A. Ikeda, H. Kawamura., J. Phys. Soc. Jpn., Vol. 145, p.073707 (2008)

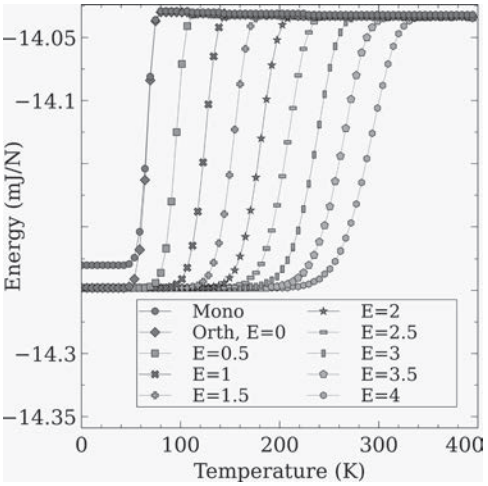


Figure 1 - Energy per site plotted as a function temperature for monoclinic and orthorhombic phases with varying bond energy (E)

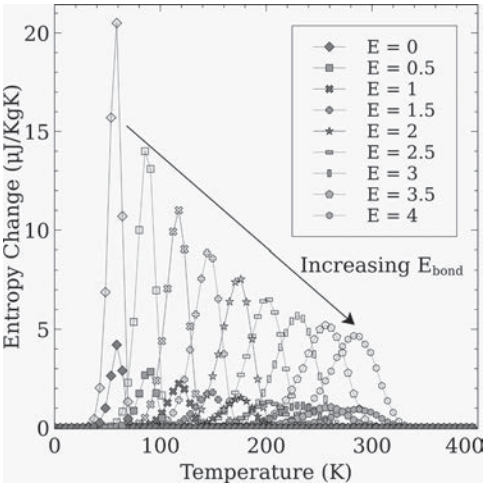


Figure 2 - Entropy change as a function of temperature associated with varying bond energy (E). Open symbols are 5T calculations closed symbols represent those in zero field

Session DR
HEUSLER ALLOYS AND MAGNETIC SEMICONDUCTORS I
(Poster Session)

Wei Zhang, Co-Chair
Oakland University, Rochester, MI, United States
Maciej Sawicki, Co-Chair
Institute of Physics, Polish Academy of Sciences, Warszawa, Poland

DR-01. NMR Studies of the Ground State of $Ni_{50-x}Co_xMn_{35}In_{15}$ (x=1, 2.5) and $Ni_{45}Co_5Mn_{37}In_{13}$ Heusler Alloys. *A. Aryal*[1], I. Dubenko[1], S. Pandey[1], S. Talapatra[1], V. Chlan[2], H. Stepankova[2], V. Matveev[3], M. Blinov[4], V. Prudnikov[4], A. Granovsky[4], E. Lähderanta[5], S. Stadler[6] and N. Ali[1]
1. Physics, Southern Illinois University, Carbondale, IL, United States; 2. Department of Low Temperature Physics, Charles University in Prague, Prague, Czechia; 3. Faculty of Physics, Saint-Petersburg State University, Saint-Petersburg, Russian Federation; 4. Faculty of Physics, Lomonosov Moscow State University, Moscow, Russian Federation; 5. Lappeenranta University of Technology, Lappeenranta, Finland; 6. Physics and Astronomy, Louisiana State University, Baton Rouge, LA, United States

At least three temperature induced phase transitions at $T=T_1$, T_M/T_A and, T_C related to ferromagnetic order of martensitic phase (FMMP), martensitic transitions (MT) and, ferromagnetic order of austenitic phase (FMAP), respectively, have been detected in the result of magnetic studies of off-stoichiometric Heusler alloys of $Ni_{50-x}Co_xMn_{35}In_{15}$ (x=1, 2.5) and $Ni_{45}Co_5Mn_{37}In_{13}$. The phase transition temperatures are found to be depended on alloy composition. The ground state (T=4.2 K and external field H=0) of the alloys was found to be characterized by three main lines; two, partially overlapping, in the higher frequency, (300-450) MHz, (most likely corresponding of manganese resonance lines) and one at lower frequency of about 200 MHz. Significant shift the spectrum of $Ni_{45}Co_5Mn_{37}In_{13}$ of about 100 MHz to higher frequencies was observed. This effect indicates approximately one third of the increased magnetic moment in the $Ni_{45}Co_5Mn_{37}In_{13}$. The correlation of magnetizations obtained from magnetic moment and NMR studies is discussed. Acknowledgment: This work was supported by the U.S. Department of Energy (DOE), Office of Science, Basic Energy Sciences Award No. DE-FG02-06ER46291 (SIUC) and DE-FG02-13ER46946 (LSU).

DR-02. Ferromagnetism in C-doped ZnO powder: the role of oxygen vacancies and carbon defects. *S. Akbar*[1,2], S. Hasanain[3,4], M. Jamil[8], G. Jaffri[5,6], S. Shah[7] and P. Rudolf[9]
1. Physics Department, Zernike Institute of Advanced Materials, Groningen University, The Netherlands, Groningen, Netherlands; 2. Department of Physics, Quaid-i-Azam University, Islamabad, Pakistan; 3. Department of Physics, Quaid-i-Azam University, Islamabad, Pakistan; 4. COMSTECH Secretariat, 33-Constitution Avenue, Islamabad, Pakistan; 5. Physics Department, Quaid-i-Azam University, Islamabad, Pakistan; 6. Department of Physics and Astronomy, University of Delaware, Delaware, DE, United States; 7. Department of Physics and Astronomy, University of Delaware, Delaware, DE, United States; 8. Department of Physics, Quaid-i-Azam University, Islamabad, Pakistan; 9. Department of Physics, Zernike Institute of Advanced Materials, Groningen University, The Netherlands, Groningen, Netherlands

We report on defects in C-doped ZnO powders and their role as a source of ferromagnetism in these compounds. The samples were prepared by standard solid-state reaction and sintering in either reducing (95 % Ar + 5 % H) or nitrogen atmosphere. For the samples sintered in a reducing atmosphere X-ray diffraction and X-ray photoelectron spectroscopy data gave evidence for C substitution at Zn sites (C_{Zn}) and for carbon in interstitial sites (C_i). X-ray photoelectron and Auger spectroscopy studies also demonstrated the presence of oxygen vacancies, zinc interstitials (Zn_i) and defect complexes involving C-C bonds. Magnetization studies showed room temperature ferromagnetism in these powders, with the saturation magnetization being largest for compositions with high concentration of carbon defect complexes with (C-C) bonds and with high Zn_i concentration. We relate the Zn_i and the defect complexes with C-C bonds to the formation and stabilization of Zn vacancies and thus support the prediction that ferromagnetism in ZnO type oxides is associated with cation (zinc) vacancies. Samples sintered in nitrogen, an atmosphere which favours hole doping, showed instead diamagnetic behaviour.

1. H. Pan, J. B. Yi, L. Shen, Physical Review Letters 99 (12), 127201 (2007). 2. S. Zhou, Q. Xu, K. Potzger, Applied Physics Letters 93 (23), 232507 (2008). 3. S. Akbar, S. K. Hasanain, M. Abbas, Solid State Communications 151 (1), 17-20 (2011). 4. H. S. Hsu, Y. Tung, Y. J. Chen, physica status solidi (RRL) – Rapid Research Letters 5 (12), 447-449 (2011). 5. D. K. Mishra, J. Mohapatra, M. K. Sharma, Journal of Magnetism and Magnetic Materials 329, 146-152 (2013). 6. J. W. Park, D. H. Kim, S.-H. Choi, Journal of the Korean Physical Society Vol. 57 (No. 6), 1482-1485 (2010). 7. K. Parmod, K. M. Hitendra and K. Asokan, EPL (Europhysics Letters) 110 (6), 67006 (2015). 8. X. Zhang, Y. H. Cheng, L. Y. Li, Physical Review B 80 (17), 174427 (2009).

DR-03. Vacancy and doping modulated magnetic properties of InN monolayer. *R. Chaurasiya*[1], N. Kumar[1] and A. Dixit[1] *1. Physics, Indian Institute of Technology Jodhpur, Jodhpur, India*

The monolayers are widely explored because of their nteresting electronic properties with potential in next generation the optoelectronic devices [1-3]. InN monolayer is one of the most interesting materials in semiconductor. Bulk InN is a narrow band gap material with very high electronic mobility [4-6]. Thermoelectric devices, solar cells and high speed electronic devices are realized with InN and nanostructuring may lead to further enhancement in these properties. InN monolayer may be a promising material with desired physical properties for such applications [7-8]. In nitride semiconductors, the experimental and theoretical work is focused on understanding the properties of bulk materials and their potential in electronic devices such as light emitting diodes (LEDs), field effect transistors (FET) [9]. There are efforts to understand nanostructured systems and researchers have explored III-Nitride monolayers for their optoelectronic properties. However, there are limited studies available on magnetic properties of InN monolayer. We investigated the onset of magnetization in thermodynamically stable InN monolayer, Fig 1. by modulating the vacancy defects such as In, N, both In/N and the antisite defects such as In↔N sites. The light elemental dopants such as B, Be, C, F, Li, and O at N site are investigated to understand the change in magnetic properties of InN monolayer. In, N and In/N vacancy defects showed 3.00 μ_B, 0.00 μ_B and 2.00 μ_B magnetic moment, respectively, whereas antisite vacancies do not exhibit any mangetization in InN monolayer. Further, we observed 0.04 μ_B, 0.91 μ_B and 1.09 μ_B magnetic moment with the extrinsic B, Be, and C dopants, respectively while other dopants do not exhibit any magnetization. Thus, we showed the onset of magnetic ordering by manipulating the vacancy and dopant defects. The microscopic origin of magnetic behaviour will be discussed in terms of computed charge density, electronic band structure and density of states.

1. F. Schedin, A. K. Geim, S. V. Morozov, E. W. Hill, P. Blake, M. I. Katsnelson, K. S. Novoselov, Nature Materials, 6, 652, (2007) 2. J. W. Orton, C. T. Foxon, *Reports on progress in physics* 61, 1 (1998) 3. S. C. Jain, M. Willander, J. Narayan, R. V. Overstraeten, *Journal of Applied Physics*, *87*(3), 965-1006 (2000). 4. M. Farzan, S. M. Elahi, H. Salehi, M. R. Abolhassani, *Optics Communications*, *395*, 293-300 (2017). 5. R. Goldhahn, P. Schley, A. T. Winzer, G. Gobsch, V. Cimalla, O. Ambacher, O., ... & W. J. Schaff, *physica status solidi (a)*, *203*(1), 42-49 (2006). 6. Y. S. Lu, C. C. Huang, J. A. Yeh, C. F. Chen, S. Gwo, *Applied Physics Letters*, *91*(20), 202109 (2007). 7. N. Sofikiti, N. Chaniotakis, J. Grandal, M. Utrera, M., M. A. Sanchez-Garcia, E. Calleja, ... & A. Georgakilas, *Applied Physics Letters*, *95*(11), 113701 (2009). 8. W. Lim, J. S. Wright, B. P. Gila, S. J. Pearton, F. Ren, W. T. Lai, K. H. Chen, *Applied Physics Letters*, *93*(20), 202109 (2008). 9. Y. V. Davydov, A. A. Klochikhin, V. V. Emtsev, S. V. Ivanov, V. V. Vekshin, F. Bechstedt, A. Yamamoto, *physica status solidi (b)*, *230*(2), R4-R6 (2002).

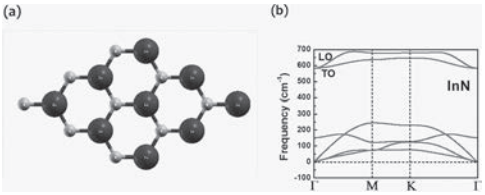


Figure 1: (a) Optimized structure and (b) phonon dispersion curve for InN monolayer

DR-04. Spin wave resonance study in a series of etched ferromagnetic semiconductor films. *X. Liu*[1], Y. Zhou[1], S. Bac[2,1], S. Lee[2], M. Dobrowolska[1] and J.K. Furdyna[1] *1. Physics, University of Notre Dame, Notre Dame, IN, United States; 2. Physics, Korea University, Seoul, The Republic of Korea*

Although ferromagnetic semiconductor films have already been investigated for the last two decades, some fundamental issues still puzzle the researchers in this field. One of these issues is how the magnetic anisotropy field is distributed along the growth direction. Two models, the volume inhomogeneity model and surface inhomogeneity model, are proposed to address the inconsistent features observed in spin wave resonance (SWR) studies.[1] To solve such inconsistencies, a series of etched samples formed by wet-etching a 158-nm GaMnAs film for 2min, 4min, 7min and 10min were studied by XRD, SQUID and FMR. The thicknesses of the etched GaMnAs films were determined by XRD measurements, using the oscillations observed in ω-2θ scans around the GaAs (004) plane, as shown in Fig. 1. It should be mentioned that the XRD peaks from GaMnAs films are constant for all etched samples, indicating the Mn content to be the same along the growth direction. Magnetizations of the films are measured by SQUID as a function of field and temperature, and are the same for all etched samples. However, SWR measurements obtained with dc field perpendicular to the sample plane at 4K (Fig. 2) reveal a series of modes which vary linearly as a function of field, indicating a parabolic magnetic anisotropy field along the growth direction. However, such a magnetic anisotropy profile is inconsistent with the position of the main FMR peak as a function of film thickness in etched samples. In order to reconcile such inconsistencies, we conducted angular dependent SWR measurements in all etched samples to map the surface anisotropy using the newly reported spherical surface pinning model.[2] These results suggest the approach to reconcile the inconsistencies between the two inhomogeneity models. For completeness, we also plan to carry out similar measurements on GaMnAsP films to further expand our understanding to magnetic systems with perpendicular anisotropy.

1. H. Puszkarski, and P. Tomczak, Scientific Reports 4, 6135 (2014). 2. H. Puszkarski, and P. Tomczak, Surface Science Reports 72, 351–367 (2017).

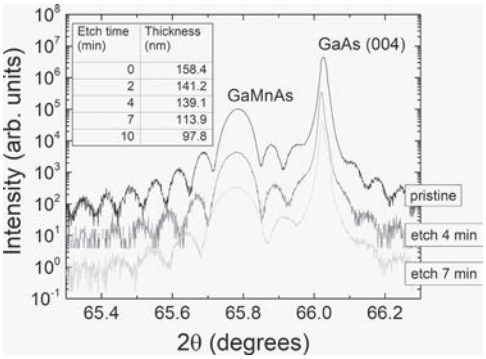


Fig. 1 XRD spectra measured at (004) plane of a series of etched GaMnAs samples at 4K. The Inside table shows the thickness obtained from Pendellosung oscillations.

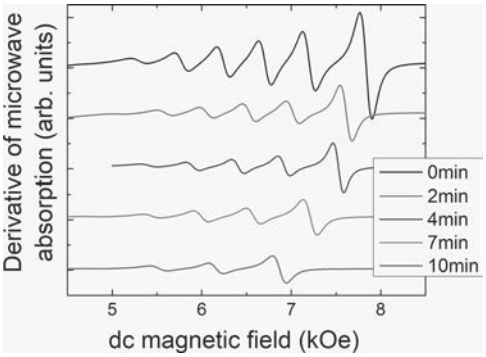
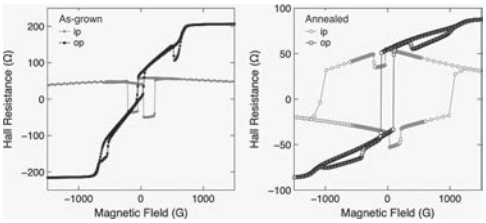


Fig. 2 SWR spectra when dc field H is perpendicular to the sample plane of etched GaMnAs samples at 4K.

DR-05. Effect of annealing on magnetic properties of graded GaMnAsP film. *S. Bac*[1,2], K. Lee[1], S. Lee[1], X. Liu[2], M. Dobrowolska[2] and J.K. Furdyna[2] *1. Department of Physics, Korea University, Seoul, The Republic of Korea; 2. Department of Physics, University of Notre Dame, Notre Dame, IN, United States*

Ferromagnetic films with out-of-plane (OP) magnetic anisotropy have been extensively studied because of the wide applications in magnetic devices with perpendicular magnetization[1,2]. Magnetic easy axes of ferromagnetic semiconductor GaMnAs, which is normally in the film plane when it is grown on GaAs substrate[3], can be changed to OP by alloying GaMnAs with phosphorus. Here we investigate magnetic properties of GaMnAsP thin film with graded phosphorus composition. The phosphorus content was varied from 0 % to 30 % along the vertical direction in the film. Hall measurement of as-grown graded GaMnAsP film showed the presence of both in-plane (IP) and OP magnetization in the film. Transitions involving these magnetization are distinguished in the figure: the sharp transitions at very low fields represent the reversal of the OP magnetization characteristic of the phosphorus-rich part of the graded sample; and the transitions at higher fields correspond to rotation of IP magnetization between IP easy axes. Both types of transitions are accompanied by their own hystereses. From the analysis of anomalous and planar Hall effects, the portion of magnetic components with OP and IP easy axes was obtained to about 20 % and 80 %, respectively, in the graded film. After low temperature annealing of the sample, the Curie temperature increases in both components, and the coercive field is enhanced in the film, especially for the component with vertical magnetic easy axis. The most prominent feature of the annealing effect for our graded GaMnAsP film is the significant change in the ratio of magnetic components with OP and IP easy axes. Specifically, the ratio of the OP magnetization in the annealed GaMnAsP film increased to nearly 60 % of the entire film, while the IP component reduced to 40 %, thus showing that the relative portions of the graded GaMnAsP film with magnetization having OP and IP easy axes can be selectively controlled by the annealing process.

[1] H. J. Richter, Journal of Physics D: Applied Physics, Vol. 40, p.R149 (2007) [2] B. Dieny and M. Chshiev, Review of Mordern Physics Vol. 89, p.025008 (2017) [3] D. Shin, S. Chung, S. Lee, *et al.*, Physical Review B, Vol. 76, p.035327 (2007)



Magnetic field dependence of the anomalous (black) and the planar (red) Hall resistances measured on the as-grown (left) and the annealed (right) graded GaMnAsP film at 10 K.

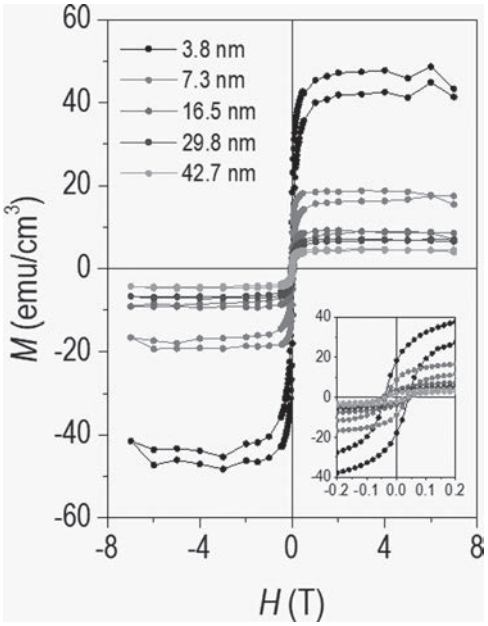
DR-06. Muon-Spin-Relaxation Study of Ferromagnetic Insulator (Ga,Mn)N. *K. Gas*[1], T. Prokscha[2] and M. Sawicki[1] *1. Institute of Physics, Polish Academy of Sciences, Warsaw, Poland; 2. Laboratory for Muon Spin Spectroscopy, Paul Scherrer Institute, Villigen PSI, Switzerland*

$Ga_{1-x}Mn_xN$ belongs to the well-known family of dilute ferromagnetic semiconductors which exhibits low-temperature ferromagnetism driven by ferromagnetic superexchange among the Mn^{3+} ions. However, in this material systematic information about the uniformity and of the volume fraction of the ferromagnetic phase and on the distribution of internal fields is generally lacking. We report here on the results of the very first studies of spatial homogeneity of ferromagnetic phase in the $Ga_{1-x}Mn_xN$ using muon-spin-relaxation (μSR) spectroscopy applied to a single phase and high quality molecular beam epitaxy grown $Ga_{1-x}Mn_xN$ layer with x = 10% and Curie temperature T_C = 10 K [1]. Our μSR measurements revealed that the magnitude of the asymmetry parameter A started to saturate (or the magnetic volume fraction rolled off to zero) at temperatures being about 5 and 10 K above the value of the T_C established beforehand for this sample by SQUID magnetometry [1]. These temperature scans were obtained for 50 and 1500 Oe in transverse field (TF) configuration, respectively, and are indicative that the magnetic configurations of Mn species are strongly affected by the external field, at least on a time scale relevant to μSR. Another rather unexpected finding of our μSR measurements is the observation that the temperature dependence of the TF μSR depolarization rate λ has truly a λ-like shape, when plotted in a log-log scale, peaking strongly at T = 20 K, that is where A starts to saturate. Above this temperature λ obeys a clear power law dependence on T, $\lambda \sim T^{-\alpha}$, where $\alpha > 0.2$ μs^{-1}, corresponding to a previously observed similar dependence of magnetic susceptibility in $Ga_{1-x}Mn_xN$ [2]. We assign this nonstandard dependence to a gradual formation of coupled neighbor spin clusters (spin pairs, triplets, etc.) on lowering temperature. Importantly, these clearly non-zero values of λ are seen well above T_C in a very well characterized single phase material [1]. This work has been supported by the National Science Centre, Poland through grants DEC-2014/12/S/ST3/00549 and DEC-2018/31/B/ST3/03438.

[1] K. Gas *et al*, J. Alloys Compd. Vol. 747, p. 946 (2018). [2] S. Stefanowicz *et al*, Phys. Rev. B Vol. 88, p. 081201(R) (2013).

DR-07. Investigating Surface-Induced Ferromagnetism in Pristine SnO_2 Film. *J. Kim*[1], S. Song[1], Y. Choi[1], D. Lee[1], H. Kim[2], H. Lee[2], J. Bae[3] and S. Park[1,3] *1. Physics, Pusan National University, Busan, The Republic of Korea; 2. Core Research Facilities, Pusan National University, Busan, The Republic of Korea; 3. Busan Center, Korea Basic Science Institute, Busan, The Republic of Korea*

The understanding ferromagnetic origin in semiconducting oxides, known as d^0-ferromagnetism, is an important subject not only for the fundamental interests but also for the potential applications in modern spin-based semiconductor devices. For example, SnO_2 film exhibits reproducible ferromagnetism well above room temperature even without magnetic cation doping. Since conventional super-exchange or double-exchange interactions cannot explain a long-range ordering in this system, defects have been considered as the source of the room temperature ferromagnetism. However, the main reason for the ferromagnetic order in SnO_2 is still unclear due to the lack of experimental evidence. We investigated the film thickness-dependent magnetic property of pristine SnO_2 films to understand the role of defects (either tin or oxygen vacancies) on the ferromagnetism. We found that the magnetization in the unit of surface area was consistent with respect to the film thickness, deducing a magnetic moment resides at the film surface or interface. Based on X-ray photoelectron spectroscopy, the amount of oxygen vacancy at the surface was consistent as well as the magnetization, supporting a magnetic ground state is induced at the surface of SnO_2 film by the oxygen vacancy. These works are supported in part by NRF-Korea (NRF-2017K1A3A7A09016305 and NRF-2018R1D1A1B07045663) and Korea Basic Science Institute (KBSI) grant (C38529) to Sungkyun Park.



DR-08. Large Tunable Magnetoresistance in Half-Heusler Compound RPtBi (R=rear earth). *J. Chen*[1,2], H. Li[1,2], B. Ding[1,2], Z. Li[1,2], Z. Hou[3], E. Liu[1,4], H. Zhang[1], X. Xi[1], G. Wu[1] and W. Wang[1,4] *1. Institute of Physics, Chinese Academy of Sciences, BeiJing, China; 2. University of Chinese Academy of Sciences, BeiJing, China; 3. South China Normal University, Guangzhou, China; 4. Songshan Lake Materials Laboratory, Dongguan, China*

Heusler is multifunctional platform to study the physical properties for their large amounts of compounds and the high tunableness. Recently, large amounts of half-Heusler compounds were predicted to be topological semimetals, which host diversity novel physical properties. The one of physical properties is large magnetoresistance, which has potential applications in future high-performance magnetoelectric devices. As the previous literature report, the large nonsaturating positive MR were observed in YPtBi[1] and LuPtBi[2]. But the haf-Heusler RPtBi (R=heavy rear earth) has not been systematic study. Here, we will present the results of (Tb, Ho, Er, Tm)PtBi. The carrier type of compounds change from single carrier to two type of carriers with the atomic number Z increasing. And the electron-hole-compensated play an important role in getting large MR. The compounds ErPtBi and TmPtBi with two kinds of carriers host a large MR, which is up to 1400% and 1800%, respectively. And comparing the values of MR, we can find the fact that the MR can be tune effectively by rear earth R.

[1] Shekhar C, Kampert E, Förster T, et al. arXiv preprint arXiv:1502.00604(2015). [2] Hou Z, Wang W, Xu G, et al. Physical Review B, 92(23): 235134(2015).

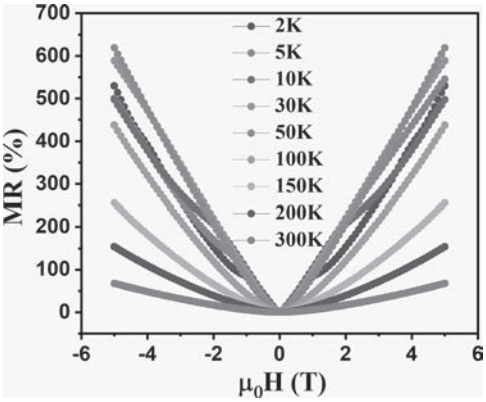


Fig. 1 The magnetic field dependence of MR at different temperatures for ErPtBi.

DR-09. Resonant inelastic soft x-ray scattering under magnetic field for Mn_2VAl Heusler alloy. *R.Y. Umetsu*[2,3], H. Fujiwara[1], F. Kuroda[4,5], H. Fujii[4,5], T. Oguchi[4,5], A. Sekiyama[1], J. Miyawaki[6,7], Y. Harada[6,7] and S. Suga[4] *1. Graduate School of Engineering Science, Osaka University, Toyonaka, Japan; 2. Institute for Materials Research, Tohoku University, Sendai, Japan; 3. Center for Spintronics Research Network, Tohoku University, Sendai, Japan; 4. Institution of Scientific and Industrial Research, Osaka University, Ibaraki, Japan; 5. CMI2-MaDIS, National Institute for Materials Science, Tsukuba, Japan; 6. Institute for Solid State Physics, The University of Tokyo, Kashiwanoha, Japan; 7. Synchrotron Radiation Research Organization, The University of Tokyo, Sayo-cho, Japan*

Since half-metallic ferro- or ferrimagnets have been theoretically predicted in many kinds of Heusler alloys [1,2], a large number of investigations have been carried out from the interest in the field of spintronics. When electrons around the Fermi energy (E_F) are completely spin-polarized, a system must be very useful as a ferromagnetic electrode for the tunnel magnetoresistance and spin injection as well as various spin utilizable devices. In the present study, bulk sensitive resonant inelastic soft x-ray scattering (RIXS) was performed under an external magnetic field in order to verify the half-metallic electronic states of V and Mn 3*d* electrons in the ferrimagnet Mn_2VAl Heusler alloy. RIXS for V and Mn 2*p* core excitation was measured at room temperature using the ultrahigh resolution soft X-ray emission spectroscopy in BL07LSU of SPring-8, Japan, with using a single crystal of Mn_2VAl. For the measurement, external magnetic field of 0.25 T was applied by a permanent magnet [3,4]. The *d*-*d* excitation due to the t_{2g}-e_g splitting is clearly observed for V in Mn_2VAl under the L_3-edge excitation, and the loss energy is comparable to the splitting energy between the theoretically predicted e_g and t_{2g} states. The delayed branching off in the V 3*d*-2*p* fluorescence peak from the elastic peak demonstrates the nearly absent V 3*d* partial density of states (PDOS) around E_F. Figures show RIXS spectra measured at incoming photon energy, $h\nu_{in}$ of 512.5 eV (a) and 638.6 eV (b) at the V and Mn L_3-edges for Mn_2VAl alloy, respectively, together with the difference between them (MCD). The RIXS-MCD of the fluorescence peaks of Mn 3*d*-2*p* transition under the L_3-edge indicates negative two peak's behavior with clear hn_{in} dependence. Such an MCD behavior is reproduced in consistence with the calculated spectra, suggesting the half-metallicity of Mn_2VAl Heusler alloy [5].

[1] J. J. Kübler, A. R. Williams, C. B. Sommers, *Physical Review B*, 1983, 28, 1745. [2] S. Ishida, S. Akazawa, Y. Kubo, J. Ishida, *Journal of Physics F: Metal Physics*, 1982, 12, 1111 [3] J. Miyawaki, S. Suga, H. Fujiwara, H. Niwa, H. Kiuchi, Y. Harada, *Journal of Synchrotron Radiation*, 2017, 24, 449. [4] J. Miyawaki, S. Suga, H. Fujiwara, M. Urasaki, H. Ikeno, H. Niwa, H. Kiuchi, Y. Harada, *Physical Review B*, 2017, 96, 214420. [5] R.Y. Umetsu, H. Fujiwara, K. Nagai, et al., *Physical Review B*, 2017, 99, 134414.

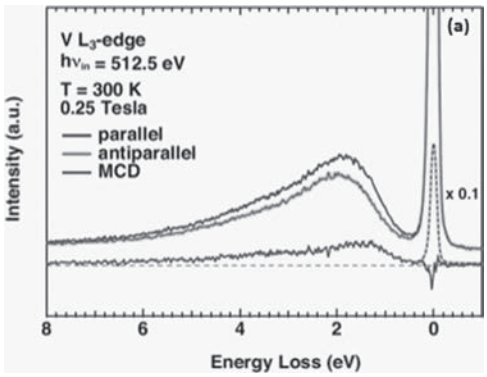


Figure (a) shows resonant inelastic x-ray scattering (RIXS) spectra measured at incoming photon energy, $h\nu_{in}$ of 512.5 eV at the V L_3-edge for Mn_2VAl alloy, together with the difference between them (MCD).

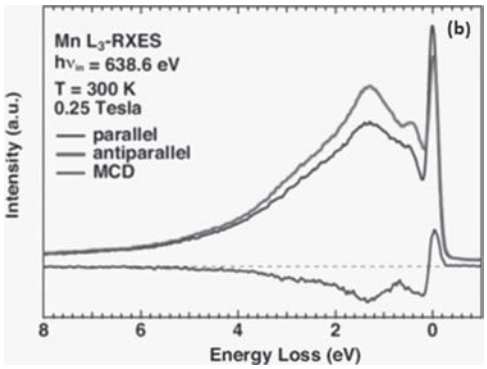


Figure (b) shows RIXS spectra measured at $h\nu_{in}$ of 638.6 eV at the Mn L_3-edge for Mn_2VAl, together with the MCD.

DR-10. Disorder and the Spin Gapless Semiconductor, Mn_2CoAl. R.G. Buckley[1,2], T. Butler[1], C. Pot[1], N.M. Strickland[1] and *S. Granville*[1,2] *1. Robinson Research Institute, Victoria University of Wellington, Lower Hutt, New Zealand; 2. MacDiarmid Institute for Advanced Materials and Nanotechnology, Wellington, New Zealand*

Band structure calculations of Heusler alloy Mn_2CoAl have identified it as a potential spin-gapless semiconductor [1]. However, more recent calculations indicate significant sensitivity of the band structure to deviations from the ideal stoichiometry and inter-site disorder [2,3]. Experimental reports to date [4-7] have generally not invoked disorder to understand the physical properties of Mn_2CoAl. We present a study of DC sputtered Mn_2CoAl films on MgO using temperature and field-dependent resistance, magnetisation, and anomalous Hall measurements. We also report reflection spectroscopy from the far infrared to the UV. Interestingly, in general the temperature-dependent resistivities reported in the literature, including ours, show the same behaviour, notably the same magnitude and a small, negative temperature coefficient of resistivity (100-700 μΩcm and -2 x 10-4 ppm/K respectively). This behaviour is often seen in highly disordered metals rather than semiconductors. We have successfully employed a weak localisation model to describe this behaviour emphasising the role of disorder (Fig. 1). This conclusion is supported by the infrared reflection study where the response at energies below the inter-band absorption can be understood largely by a single Drude term with a relatively large scattering-rate similar to that calculated from the DC resistivity data (Fig. 2). Moreover, we observe that the magnetic behaviour is also consistent with significant compositional and anti-site disorder. We conclude that the characteristics of our Mn_2CoAl thin films result from disorder rather than intrinsic properties. These characteristics are common to most published reports on this material to date, indicating that significantly more care needs to be taken to isolate the role of disorder and correctly identify the behaviour of potential spin-gapless semiconductor materials.

[1] X.L. Wang, Phys. Rev. Lett. 100, 156404 (2008). [2] J. Kudrnovský, V. Drchal and I. Turek, Phys. Rev. B 88, 014422 (2013). [3] I. Galanakis, K. Özdoğan, E. Sasioğlu et al., J. Appl. Phys. 115, 093908 (2014). [4] S. Ouardi, G.H. Fecher, C. Felser et al., Phys. Rev. Lett. 110, 100401 (2013). [5] M.E. Jamer, B.A. Assaf, T. Devakul et al., Appl. Phys. Lett. 103, 142403 (2013). [6] G.Z. Xu, Y. Du, X.M. Zhang et al., Appl. Phys. Lett. 104, 242408 (2014). [7] K. Arima, F. Kuroda, S. Yamada, T. Fukushima, T. Oguchi, and K. Hamaya, Phys. Rev. B 97, 054427 (2018).

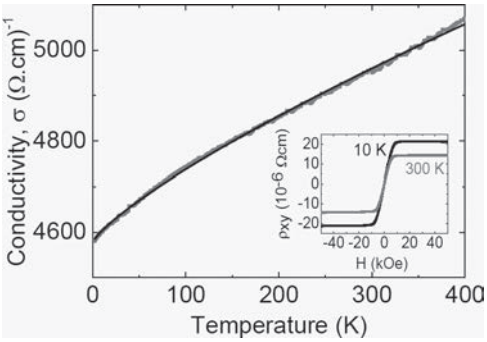


Fig. 1: DC conductivity vs temperature (red points) and weak localisation model (black line). Inset: anomalous Hall resistivity.

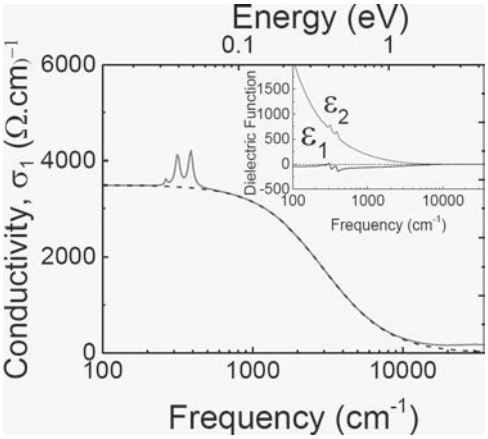


Fig. 2: Real part of the frequency dependent conductivity (red line) derived from the reflectivity. The black dashed line is the Drude component of the model. Inset: real and imaginary parts of the complex dielectric function.

DR-11. Magnetic properties and tunnel magnetoresistance effect of fully compensated ferrimagnetic Mn-Co-V-Al Heusler alloy. *T. Tsuchiya*[1] and S. Mizukami[2,1] *1. Center for Science and Innovation in Spintronics (Core Research Center) and Center for Spintronics Research Network, Tohoku University, Sendai, Japan; 2. WPI Advanced Institute for Materials Research, Tohoku University, Sendai, Japan*

Mn-Co-V-Al Heusler alloy is one of candidate for a fully compensated ferrimagnet(FCF). $(Mn\text{-}Co)_2VAl$ was predicted to be a FCF, however, the Curie temperature was lower than room temperature (RT) [1]. Recently, the magnetization compensation was experimentally observed in a Mn_2(Co-V)Al alloy [2-3]. Furthermore, the Curie temperature was estimated to be 695 K, which was higher than RT. The half-metallicity of Mn_2(Co-V)Al was demonstrated by first principles calculation [3]. However, there are no reports to fabricate the Mn_2(Co-V)Al film. In this study, we investigated the magnetic properties of the Mn_2(Co-V)Al films and the tunnel magnetoresistance (TMR) effect for the magnetic tunnel junctions with its electrode to gain insight into its half-metallicity. Samples were prepared by the magnetron sputtering. The stacking structures of the single layer samples and MTJs were MgO(001) sub./ Mn-Co-V-Al (30)/ MgO (2)/ Ru (2) and MgO(001) sub./ Mn-Co-V-Al (30)/ Mg (0.4)/ MgO (2)/ CoFe (5)/ IrMn (10)/ Ru (8) (thickness is in nm), respectively. The Mn-Co-V-Al layer was deposited at 700°C and the other layers were deposited at the room temperature (RT). The crystalline structures were characterized by x-ray diffraction (XRD). The magnetic properties were measured by a vibrating sample magnetometer (VSM). The microfabrication of the MTJs were performed using a standard photo-lithography technique. The TMR effect was measured by a four-probe method. The XRD measurements indicated that Mn_2VAl and $Mn_2Co_{0.5}V_{0.5}Al$ samples have the $L2_1$ or XA ordering. The magnetization for Mn-Co-V-Al films were smaller than the bulk value. However, its composition dependence was similar to that for bulk experiments, and the magnetization compensation was confirmed for $Mn_2Co_{0.5}V_{0.5}Al$. The TMR effects were observed for Mn-Co-V-Al films and the TMR ratios were -0.5%, 0.12% and 0.05% for Mn_2VAl, Mn_2CoAl and $Mn_2Co_{0.5}V_{0.5}Al$, respectively. These signs of TMR effects for Mn-Co-V-Al were consistent with the spin polarization for those alloys predicted from the first principles calculation. The origin of the small TMR ratio will be discussed. This work was partially supported by KAKENHI(No. 18H05948) and CREST(No. JPMJCR17J5).

[1] B. Deka et al., Journal of Alloys and Compounds 662 510e515 (2016) [2] P. V. Midhunlal et al., J. Phys. D: Appl. Phys. 51 075002 (2018) [3] D. Benea et al., Journal of Magnetism and Magnetic Materials 475 229 (2019)

DR-12. Experimental and theoretical investigations of half-metallic $Co_{2-x}Fe_xCrAl$ (x = 0.25, 0.50 and 0.75) Heusler alloys. *A.K. Patel*[1], L. Bainsla[2], V. Yenugonda[1], K. Suresh[1] and A. Alam[1] *1. Physics, IIT Bombay, Mumbai, India; 2. WPI Advanced Institute for Materials Research, Tohoku University, Sendai, Japan*

Heusler alloys gained renewed interest for the last three decades due to the discovery of half-metallic property in some of the alloys [1]. Recent studies have shown that equiatomic Heusler alloy CoFeCrAl is interesting due to the halt metallic nature [2]. In this work, we have explored the structural and the magnetic properties of $Co_{2-x}Fe_xCrAl$ (x = 0.25, 0.50 and 0.75) using experimental and theoretical tools. All the arc melted alloys crystalize in $L2_1$ structure. Rietveld refined room temperature XRD for $Co_{1.50}Fe_{0.50}CrAl$ is shown in fig. 1(a). The absence of (111) reflection indicates the B2 type of disorder, possibly resulting from the nearly equal electronegativities of Al and Cr. Fig. 1(b)-(d) show the field dependent magnetization of $Co_{2-x}Fe_{x}$-CrAl. The moments for x = 0.50 and 0.75 are close to the estimated moments using the Slater-Pauling rule and hints at the half-metallic nature. T_C of $Co_{2-x}Fe_xCrAl$ (x = 0.25, 0.50 and 0.75) are found to be 540, 696 and 530 K respectively. Hence, these compositions are suitable for room temperature spintronic applications. Electronic structure calculations show that half-metallic nature is present for x = 0.50 and 0.75. Fig 2(a) shows the spin-resolved DOS for x = 0.50 and fig. 2(b) shows the unit cell used for it. Other possible disorders for x= 0.50 were also considered and calculations carried out. Half-metallic nature is found to be robust irrespective of the disorder. All the three compositions of $Co_{2-x}Fe_xCrAl$ are found to crystallize in $L2_1$ structure. The compositions for x= 0.50 and 0.75 follow the Slater-Pauling rule, which hints the possibility of half-metallic nature. Maximum anomalous Hall effect is found to be 1.81 μΩ-cm and decreases with increasing temperature, which is following the magnetization. Theoretical simulation confirms the half-metallic nature irrespective of antisite disorder for x=0.50 and 0.75 compositions. Hence it can be concluded that these two compositions are potential candidates for spintronic applications.

[1] R. A. de Groot. et al. Phy. Rev. Lett. 50, 2024 (1993). [2] Lakhan Bainsla et al. JMMM 394, 82 (2015) [3] Rodriguez-Carvajal, J. Physica B 192, 55 (1993) [4] P. Giannozzi et al. JPCM 21, 395502 (2009).

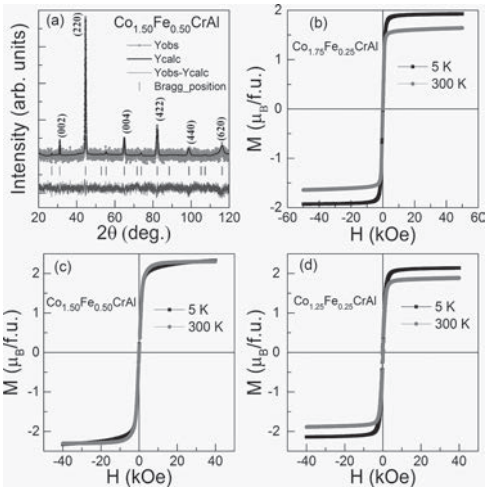


FIG. 1. (a) Room temperature XRD of $Co_{1.5}0Fe_{0.50}CrAl$. (b-d) Field dependent magnetization at 3 and 300 K for $Co_{2-x}Fe_xCrAl$ (x = 0.25, 0.50 and 0.75) respectively.

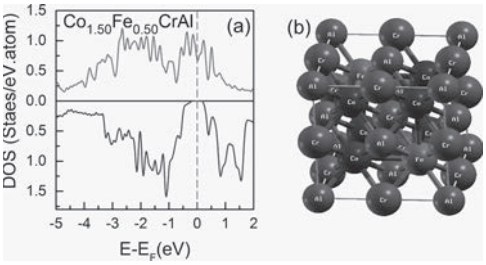


FIG.2 (a) Spin resolved DOS. (b) Unit cell for $Co_{1.50}Fe_{0.50}CrAl$.

DR-13. Resistivity Anomaly in Weyl Semimetal Candidate – $MoTe_2$.
D. Suri[1,6], C. Linderalv[2], B. Karpiak[3], S.K. Singh[3], A. Dankert[3], R. Sankar[4,5], F. Chou[4,5], P. Erhart[2], S.P. Dash[3] and R. Patel[1] *1. Department of Physics, Birla Institute of Technology and Science Pilani, K K Birla Goa Campus, Zuarinagar, India; 2. Department of Physics, Chalmers University of Technology, Göteborg, Sweden; 3. Department of Microtechnology and Nanoscience, Chalmers University of Technology, Göteborg, Sweden; 4. Institute of Physics, Academia Sinica, Taipei, Taiwan; 5. Center for Condensed Matter Science, National Taiwan University, Taipei, Taiwan; 6. Francis Bitter Magnet Laboratory and Plasma Science and Fusion Center, Massachusetts Institute of Technology, Cambridge, MA, United States*

Transition metal dichalcogenides (TMDCs) have received a lot of attention due to a plethora of exciting physical phenomena and their excellent electronic, optical, thermal and mechanical properties [1-3]. TMDCs can exist in several different phases displaying a variety of electronic properties including semiconducting, metallic, superconducting, topological insulators and Weyl Fermionic states. TMDCs also possess high spin-orbit coupling (SOC), which gives rise to spin polarized surface states in topological insulators and Weyl semimetals. Here, we present our investigations on Weyl semi-metal candidate $MoTe_2$ by both electronic transport experiments and density functional theory (DFT) calculations. The basic material properties were investigated by electron, thermal and magneto-transport measurements. We observed the structural phase transition from 1T' to T_d in both resistivity and Seebeck coefficient measurements, and significant spin-orbit coupling as evident from weak anti-localization signatures (Figure 1). The samples exhibit a very large and strongly anisotropic resistivity anomaly in the T_d phase of $MoTe_2$ that occurs between 25 and 50 K. This is up to 13% in the temperature window between 25 and 50 K, which is found to be strongly anisotropic. Based on the experimental data in conjunction with density functional theory calculations, we conjecture that the anomaly can be related to the presence of defects in the system. These findings open opportunities for further investigations and understanding of the transport behavior in these newly discovered semi-metallic layered systems.

[1] Keum et al, Nature Physics 11, 482 (2015). [2] Qi et al, Nature communications 7, 11038 (2016). [3] D. Suri and R S Patel, Applied Physics Letters 110, 233108 (2017).

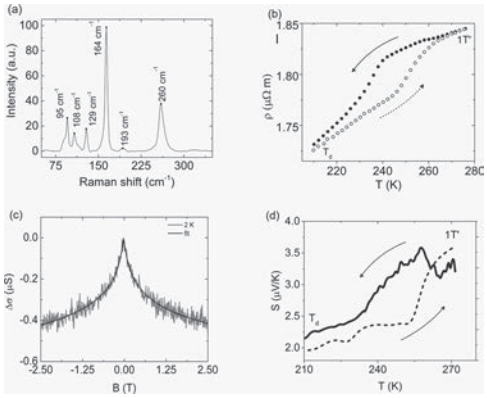
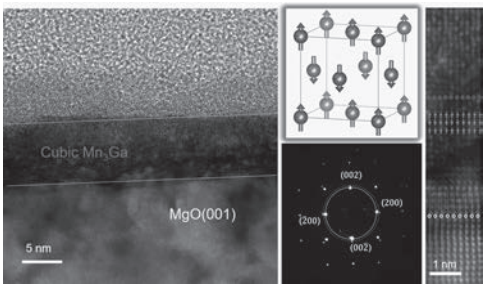


Figure 1: (a) Raman spectra of $MoTe_2$ bulk showing characteristic features of 1T' phase. (b) Resistivity as a function of temperature showing thermal hysteresis at 240 K (c) Differential conductivity versus out-of-plane field showing localization effect (d) Seebeck coefficient as a function of temperature showing thermal hysteresis at 240 K, the onset being the same as that for hysteresis in electronic resistivity.

DR-14. Structural, magnetic, and electrical properties of collinear antiferromagnetic heteroepitaxy cubic Mn_3Ga thin films.
H. Bang[1], W. Yoo[1], C. Kim[1], S. Lee[2], J. Gu[3], Y. Park[4], K. Lee[5] and *M. Jung*[1] *1. Department of Physics, Sogang University, Seoul, The Republic of Korea; 2. Department of Physics and Astronomy, Sejong University, Seoul, The Republic of Korea; 3. Department of Physics and Astronomy, California State University LongBeach, Long Beach, CA, United States; 4. National Nanofab Center, Daejeon, The Republic of Korea; 5. Mainz University, Mainz, Germany*

Mn-based Heusler compounds have been received of great interest due to the tetragonally distorted structure showing half-metallic ferrimagnetism, which has an advantage of low saturation magnetization requisite for spin-transfer-torque based spin devices. The magnetization of tetragonal Mn_3Ga vanishes over a wide range of temperature because the magnetic moments of two Mn sublattices are antiferromagnetically aligned with different magnitude [1,2]. However, the tetragonal distortion tends to destroy the compensated ferrimagnetism as well as the half-metallic behavior [1,3]. In theory, Mn_3Ga can crystallize in an ordered $D0_3$ cubic phase, which is predicted to display half-metallicity with collinear antiferromagnetic order, anticipating both complete spin polarization and zero net magnetic moment [4,5]. However, the ordered phase of cubic Mn_3Ga has not been experimentally verified yet in a bulk or film form. In the present work, we have successfully fabricated hetero-epitaxial Mn_3Ga films with stable cubic phase by using RF magnetron sputtering method. We report the structural, magnetic, and electrical properties of the cubic Mn_3Ga (C-Mn_3Ga), in comparison with the tetragonal phase (T-Mn_3Ga). The structural analyses reveal that C-Mn_3Ga deposited with low RF power crystallizes in the disordered Cu_3Au-type fcc structure, and it transforms to T-Mn_3Ga as the power increases. Compared to theoretical calculations for ordered cubic phase, Ga atoms exchange their positions with MnI and MnII atoms to have an equal number of MnI and MnII atoms, and the spin moments are aligned ferromagnetically in layers which are stacked antiferromagnetically. We find the antiferromagnetic transition at T_N = 400 K for C-Mn_3Ga, while the ferrimagnetic transition at T_C = 800 K for T-Mn_3Ga. Furthermore, the electrical resistivity is higher in the antiferromagnetic phase of C-Mn_3Ga than that in the ferrimagnetic phase of T-Mn_3Ga.

1) B. Balke, G. H. Fecher, J. Winterlik, and C. Felser, Appl. Phys. Lett. 90, 152504 (2007). 2) H. Kurt, K. Rode, M. Venkatesan, P. Stamenov, and J. M. D. Coey, Phys. Rev. B 83, 020405(R) (2011). 3) L. Wollmann, S. Chadov, J. Kübler, and C. Felser, Phys. Rev. B 92, 064417 (2015). 4) L, Wollmann, S. Chadov, J. Kübler, and C. Felser, Phys. Rev. B 90, 214420 (2014). 5) G. Y. Gao, and K. -L. Yao, Appl. Phys. Lett. 103, 232409 (2013).



Transmission electron microscope image and transmission electron diffraction pattern of cubic Mn_3Ga film and MgO substrate.

DR-15. Drastic Violation of the Basic Correlation Between the Hall Effect and Resistivity in the Heusler Alloy $Ni_{45}Cr_5Mn_{37}In_{13}$.
S. Pandey[1,3], M. Blinov[2], A. Aryal[3], I. Dubenko[3], V. Prudnikov[2], E. Lähderanta[4], A. Granovsky[2], N. Kazachkova[2], S. Stadler[5] and N. Ali[3]
1. Department of Physics, University of California San Diego, La Jolla, CA, United States; 2. Faculty of Physics, Lomonosov Moscow State University, Moscow, Russian Federation; 3. Department of Physics, Southern Illinois University Carbondale, Carbondale, IL, United States; 4. Lappeenranta University of Technology, Lappeenranta, Finland; 5. Department of Physics & Astronomy, Louisiana State University, Baton Rouge, LA, United States

Two metamagnetic Heusler alloys based on $Ni_{45}Cr_5Mn_{37}In_{13}$ with differing Mn concentrations (by 0.2 at. %) were studied using magnetization, resistivity, and Hall resistivity measurements. It is shown that this small variation in composition leads to fundamental changes in magnetic properties. Near the martensitic phase transitions, the anomalous Hall coefficient (R_S) was found to increase with temperature while the resistivity (ρ) decreases. Thus, in the case of $Ni_{45}Cr_5Mn_{37}In_{13}$, the general correlation between R_S and ρ, considered as applicable for all crystalline and amorphous ferromagnetic alloys, breaks down completely. We explain this behavior in the framework of an s-d model where it is assumed that the resistivity and anomalous Hall effect (AHE) are determined by different groups of current carriers. The obtained results on the AHE can shed light on the long-standing discussion regarding the mechanism of the martensitic transition in Heusler alloys. Acknowledgements:This work was supported by the Office of Basic Energy Sciences, Material Science Division of the U.S. Department of Energy, DOE Grant No. DE-FG02-06ER46291 (SIU) and DE-FG02-13ER46946 (LSU).

DR-16. Effect of stoichiometry on crystal structure and magnetism in $Mn_{3-x}Cr_xGa$ ($0 \le x \le 2$) Heusler alloy.
S. Perween[1,2], A. Rathi[1,2], B. Gahtori[1,2] and *G. Basheed*[1,2] *1. National Physical Laboratory, Delhi, India; 2. NPL -Campus, Academy of Scientific and Innovative Research (AcSIR), Delhi, India*

The Cr doped tetragonal $D0_{22}$ Mn_3Ga Heusler alloy has been emerged as an potential candidate for spintronics applications after observation of Mn_2CrGa [1] as a half metallic ferrimagnet with high Curie temperature (T_c ~ 800 K) but interestingly in cubic structure (B2-type). In order to obtain high magneto crystalline anisotropy, many groups [2, 3] have done theoretical and experimental studies to search for the possibility of phase transformation from a cubic to tetragonal phase. Here, we have synthesized the full series of Cr-doping, $Mn_{3-x}Cr_xGa$ (x = 0, 0.5, 1, 1.5, 2) alloys synthesized by arc melting method. The $D0_{22}$ symmetry holds upto x = 0.5, after which the disordering of tetragonal symmetry is observed, which leads to an observation of a mixed phase (~ 85% $D0_{22}$ & ~15% B2-type) and (~ 40% $D0_{22}$ & 60 % B2-type) for x = 1 (Mn_2CrGa) & 1.5, respectively, and finally, single phase B2-type cubic phase for x = 2 ($MnCr_2Ga$). In initial magnetization study with Vibrating sample magnetometer (VSM, 2T), the magnetization for x = 0.5 increases with spontaneous magnetization, M_s ~ 24 emu/g, remanent M_r ~ 18 emu/g (only at 2T field) and minimal decrease of H_c from parent Mn_3Ga. In end members from Mn_3Ga (x = 0) to $MnCr_2Ga$ (x = 1), the magnetic nature changes from hard magnet (Hc = 3.71 kOe for x =0) to soft magnet (Hc = 1.53 kOe for x = 2), as seen in Fig.1. The coercivity mechanism of $Mn_{3-x}Cr_xGa$ (x = 0.5, 1) is evaluated from field dependence Ms and Hc through hysteresis loops up to 2T [see Fig. 2] where the alloys confirm the movement of domain wall with low impedance through nucleation mechanism. The more detailed structural and magnetic measurements are going on to understand the effect of Cr-doping on destabilization of tetragonal $D0_{22}$ phase and adoption of B2-type cubic symmetry and its role on magnetization in these alloys. *Key words: Heusler alloy, spintronics, magneto crystalline anisotropy*

References: W. Zhang et. al., AIP Advances 6, 056218 (2016). X.-Z. Li et. al., Acta Materialia 140, 188 (2017) H. G. Zhang, J. Chen, E. K. Liu, M. Yue, Q. M. Lu, W. Wang, and G. H. Wu (2016).

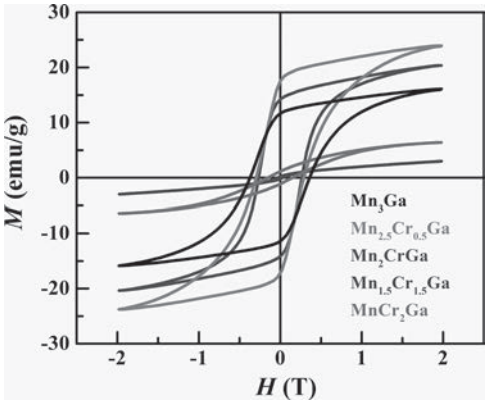


Fig.1: Room temperature field dependant magnetization curves of $Mn_{3-x}Cr_xGa$ (x = 0, 0.5, 1, 1.5, 2) alloys.

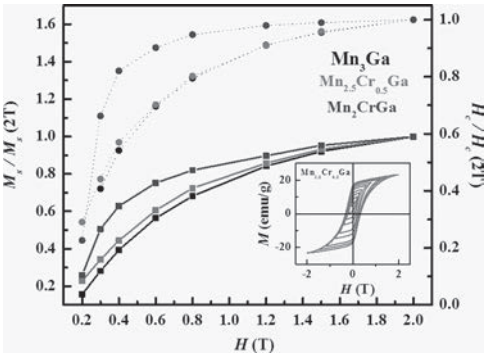


Fig.2: The variation of magnetization, M_s (squares) and coercivity, H_c (circles) from minor M(H) loops of $Mn_{3-x}Cr_xGa$ (x = 0, 0.5, 1) alloys. The inset shows the minor loop for x= 0.5.

Session DS
EDUCATION, OUTREACH, & PUBLIC ENGAGEMENT IN MAGNETISM
(Poster Session)

Barry L Zink, Co-Chair
University of Denver, Denver, CO, United States
Dafiné Ravelosona, Co-Chair
Center for Nanoscience and Nanotechnology, Palaiseau, France
Yukiko Takahashi, Co-Chair
NIMS, Tsukuba, Japan

DS-01. Exploring magnetic resonance with a compass. *D. Nelson*[1], E. Cookson[1], M. Anderson[1], D. McKinney[2] and I. Barsukov[1] *1. Physics and Astronomy, UC Riverside, Riverside, CA, United States; 2. Santa Rosa Academy, Menifee, CA, United States*

Magnetic resonance plays an important role in today's science, engineering, and medical diagnostics. Learning and teaching magnetic resonance is challenging since it requires advanced knowledge of condensed matter physics and quantum mechanics. Driven by the need to popularize this technologically impactful phenomenon, we develop an inexpensive table-top demonstration experiment. It unveils the magnetic resonance of a hand-held compass in the magnetic fields of a permanent magnet. The setup provides an immediate visualization of the underlying physical concepts and allows for their translation to broad student audiences. This work was supported by the National Science Foundation under Grant No. ECCS-1810541.

DS-02. Magnetic Fields Web Series: Engaging Middle School Students in STEM. *P. Pena Martin*[1], J. Isberg[1], E. Ertekin[1,3], V. Lorenz[1,2] and N. Mason[1,2] *1. Materials Research Laboratory, University of Illinois at Urbana-Champaign, Urbana, IL, United States; 2. Department of Physics, University of Illinois at Urbana-Champaign, Urbana, IL, United States; 3. Department of Mechanical Science and Engineering, University of Illinois at Urbana-Champaign, Urbana, IL, United States*

Web based media can make scientific content accessible to audiences far beyond the scientific community. We created a web series called "Magnetic Fields" that aims to introduce materials science, particularly concepts related to magnetism, and promote themes more general to STEM fields, such as persistence and the scientific process, through use of characters and a story geared towards a middle school audience. The goal is to build and maintain interest in science at an age where this tends to drop off. The four-episode arc follows a group of high school characters as they encounter a strange new material during a class field trip to a laboratory. The series is directed by John Isberg, with professional actors making up most of the cast. The series was initiated by scientists in the Illinois MRSEC, and the storyline was developed in collaboration with MRSEC students and faculty. The episodes were released in May 2019 through Youtube. We report on the process of creating this series, response to it upon release, and discussion of its use as an educational tool. The authors acknowledge primary support of the NSF through the University of Illinois at Urbana-Champaign Materials Research Science and Engineering Center DMR-1720633.



Fig.1 Scene from an episode of "Magnetic Fields." Photo by John Isberg.

DS-03. In-class experiments with smart phones for teaching upper-level electricity and magnetism. A. Davidson[1], A. Ranjan[2] and *X. Fan*[1] *1. Physics and Astronomy, University of Denver, Denver, CO, United States; 2. Cherry Creek High School, Greenwood Village, CO, United States*

Interactive-engagement method such as studio physics [1, 2], has demonstrated higher learning gains than traditional lecturing in intro-level physics classes. However, there have been limited applications in upper-level classes, such as Electricity and Magnetism (E&M), possibly because experiments on E&M topics can be too costly and sophisticated to be carried out in the classroom. Smart phone, which is equipped with magnetic field sensors, radio signal detectors and light sensors, provides a convenient platform for carrying out E&M-related experiments. In this poster, we will present three examples of the implementation of smart-phone-based studio physics in an E&M class for Physics majors: (1) Detection of earth magnetic field inclination; (2) quantifying skin depth of aluminum foil with cellphone tower signals; and (3) Measurement of Brewster's angle. Besides sensitive sensors, smart phone also has computational power, which can be explored to further expand the breadth and depth of the smart-phone-based studio physics. Due to the wide accessibility of smart phones and the simplicity of experimental setup, we expect this teaching technique can be easily transferred to other institutes in the world.

[1] Gok, T., *Assessment of the effectiveness of the hybrid studio format in introductory undergraduate physics.* Energy Education Science and Technology Part B-Social and Educational Studies, 2012. 4(1): p. 117-130. [2] Sorensen, C.M., A.D. Churukian, S. Maleki, and D.A. Zollman, *The New Studio format for instruction of introductory physics.* American Journal of Physics, 2006. 74(12): p. 1077-1082.

DS-04. The Use of Virtue Modules in Physics Lab Teaching. *W. Zhang*[1], R. Bidthanapally[1], T. Sebastian[2], Y. Xiong[1,3], H. Qu[3] and J. Sklenar[4] *1. Physics Department, Oakland University, Rochester, MI, United States; 2. THATec Innovation GmbH, Mannheim, Germany; 3. Electronic and Computer Engineering, Oakland University, Rochester, MI, United States; 4. Physics Department, Wayne State University, Detroit, MI, United States*

Lab sessions in physics education connect the fundamental concepts to practical examples and are effective measures of the students' understanding and reasoning through ultimate real-world tests. Many topics in condensed

matter physics are known to be challenging to convey in both lectures and labs. In addition, these topics are usually resource demanding, which has been one of the challenging issues. Here, we introduce and demonstrate the use of virtue lab modules for teaching physics labs and for effectively integrating research and education. Experiments that are relevant to magnetism and spintronics include, but not limited to, spin current detecting, microwave energy harvesting, and spin-based thermoelectric effects. An important highlight of these modules is the highly-interactive laboratory learning platform. In the class, each piece of experimental hardware (e.g. electrometers, oscilloscopes, etc) will be paired with a computer-based virtual module. The individual modules mimic the hardware, which the students can use to become familiar with the hardware, acquire real-time feedback, and visualize the data acquisition dynamics, on-demand and risk-free. The virtual component is also helpful for demonstrating delicate, shared hardware in class, without risk of damaging the actual instrumentation. These individual components are connected to a central operating system and the experiment can be re-programmed by simple coding and user-interfaced commands [1]. Work at Oakland University is supported by NSF DMR-1808892.

[1] THATec Innovation GmbH: https://www.thatec-innovation.com/

Session DT
MAGNETIC CHARACTERIZATION IV: PHOTON, ELECTRON AND NEUTRON BASED TECHNIQUES (Poster Session)

Hendrik Ohldag, Chair
Lawrence Berkeley National Laboratory, Berkeley, CA, United States

DT-01. Super-Resolution Magnetic Microscopy using Nitrogen-Vacancy Centers in Diamond. *N. Mosavian*[1], B.A. Richards[1], P. Kehayias[2] and V.M. Acosta[1] *1. Center for High Technology Materials and Department of Physics and Astronomy, University of New Mexico, Albuquerque, NM, United States; 2. Sandia National Labs, Albuquerque, NM, United States*

Nitrogen-vacancy (NV) centers are point defects in diamond whose fluorescence is sensitive to magnetic fields. They are among the most sensitive magnetic field sensors and are now routinely used for quantitative magnetic imaging [1]. Typically the imaging resolution is limited by optical diffraction to a few hundred nanometers. We are developing a new tool that uses 2-D optical lattices (Fig. 1) and the nonlinear optical properties of NV centers to realize parallel magnetic microscopy with a resolution that may approach 10 nanometers. We intend to use the microscope to study the nanoscale magnetic properties of superparamagnetic nanoparticles and correlated electron materials, such as superconductors.

[1] I. Fescenko, A. Laraoui, J. Smits, N. Mosavian, P. Kehayias, J. Seto, L. Bougas, A. Jarmola, V. M. Acosta, "Diamond magnetic microscopy of malarial hemozoin nanocrystals." Physical Review Applied 11, 034029 (2019).

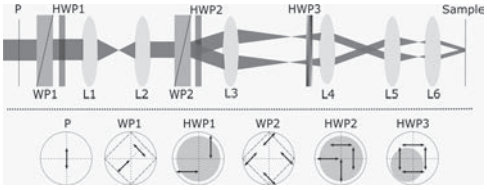


Figure 1: 2D optical lattices. Top: Optical setup to obtain a 2-D optical lattice. An unpolarized 637 nm laser beam passes through the polarizer P before entering the first Wollaston prism WP1. The relay lenses L1 and L2 project the two beams onto a second Wollaston prism WP2, resulting in four symmetric beams with equal power. Lenses L3, L4, and L5 project the beams onto the back aperture of the objective (L6). The end result is a 2D square optical lattice with a pitch of ~0.5-1 micrometers (depending on the choice of objective). Bottom: Polarization of beams after each optical element. Three half wave plates (HWP) are placed in different locations to generate the desired polarization for interference. The gray area indicates the region covered by each HWP.

DT-02. Ultrafast Magnetic Spectroscopy, Scattering and Full-Field Imaging Using Tabletop High Harmonic Sources. *P.C. Johnsen*[1], R. Karl[1], J. Thurston[1], J. Knobloch[1], C. Gentry[1], H. Kapteyn[1] and M. Murnane[1] *1. JILA / CU Boulder, Boulder, CO, United States*

We present scattering and full field imaging of magnetic nanostructures and dynamics using EUV high harmonic sources. By harnessing the high spatial and temporal coherence, as well as the ability to shape the polarization and orbital and spin angular momentum, we can uniquely spectroscopically probe and image very fast spin dynamics, on few-femtosecond timescales on up.

DT-03. Polarization analysis on the small-angle neutron scattering diffractometer KWS-1: A faster, more versatile instrument. *L. Barnsley*[1], A. Feoktystov[1], E. Babcock[1], Z. Salhi[1] and H. Frielinghaus[1] *1. Jülich Centre for Neutron Science (JCNS) at Heinz Maier-Leibnitz Zentrum (MLZ), Forschungszentrum Jülich GmbH, Garching, Germany*

A number of upgrades have been made to the KWS-1 small-angle neutron scattering (SANS) instrument, operated by the Jülich Centre for Neutron Science (JCNS) and located at the research reactor FRM II of the Heinz Maier-Leibnitz Zentrum (MLZ) in Garching, Germany. A neutron flux on the sample of 1×10^8 cm^{-2} s^{-1} makes it one of the most intense SANS instruments in the world, while an optional double-disc chopper can reduce wavelength spread down to $\Delta\lambda/\lambda = 1\%$ [1], allowing for high resolution measurements. In this presentation, we will describe two recent upgrades, aimed towards optimization of studies of nanoscale magnetic correlations. The first is the installation of an upgraded detector. In September 2018, we were able to achieve commissioning of a new detector consisting of an array of ^{3}He tubes interfaced with fast electronics (supplied by GE Reuter Stokes, OH, USA) to minimize dead-time for high-intensity measurements. An increase in the total detected area resulted in a new maximum Q-range of 0.7 Å^{-1}, a 60% improvement over the previous geometry. ^{3}He provides improved discrimination from background events, increasing signal-to-noise, while a faster detector response allows us to increase the source aperture for even shorter measurement times. In-line with our development of KWS-1, particularly for the magnetic SANS community, we report on recent developments for the option of measuring with polarization analysis. An analyser cell with polarized ^{3}He allows detection of all four scattering cross-sections with a Q_{max} exceeding 0.06 Å^{-1}. The ^{3}He cell is contained inside a μ-metal chamber, designed in-house by our JCNS ^{3}He group, to ensure a high degree of uniformity of the magnetic field at the cell position. In recent experiments, a cell lifetime of more than 90 hours was achieved. A new option for in-situ polarization of a ^{3}He cell, allowing for time-independent analyzing efficiency of post-scattered neutrons, will be discussed.

[1] A. Feoktystov, H. Frielinghaus, Z. Di, et. al., Journal of Applied Crystallography, Vol. 48, p.61 (2015)

DT-04. Second harmonic response of magnetic nanoparticles enhanced by a static bias magnetic field perpendicular to an alternating excitation field for magnetic particle imaging. S. Ota[1], K. Nishimoto[2], T. Yamada[2] and *Y. Takemura*[2] *1. Department of Electrical and Electronic Engineering, Shizuoka University, Hamamatsu, Japan; 2. Department of Electrical and Computer Engineering, Yokohama National University, Yokohama, Japan*

Magnetic particle imaging (MPI) has attracted attention as a medical imaging technique using magnetic nanoparticles (MNPs) as tracers [1]. The harmonic signals of MNPs generated on applying an alternating-current (AC) magnetic field are detected for MPI. In a previous research, we studied the effects of a particle structure on the harmonics [2]. In this study, we reveal a large second harmonic on the application of an AC field with a direct-current (DC) bias magnetic field instead of the third harmonic shown in conventional research works. We prepared the Fe_3O_4 nanoparticles commercially distributed as M-300 by Sigma Hi-Chemical Inc., which were bonded with epoxy to form the measured sample. Two types of directions were set for the

AC field, H_{AC}, DC bias field, H_{DC}, and signal detection. In set A and B, H_{AC} was respectively perpendicular and parallel to H_{DC}, which in turn was parallel to the signal detection (Fig. 1(a)). The intensity and frequency of H_{AC} were 4 kA/m and 10 kHz, respectively. The gradient of H_{DC} was 1 T/m. The second harmonic, M_2, measured in set A and B is denoted as $M_{2,A}$ and $M_{2,B}$, respectively. The third harmonic, M_3, was measured in set B without H_{DC}. Figure 1(b) shows the AC magnetization curve measured in set A with an H_{DC} of 2.4 kA/m. Figure 2 shows the dependence of $M_{2,A}$, $M_{2,B}$, and M_3 on the distance from the point of zero H_{DC} as the field-free point (FFP). M_2 increases with the increase in the intensity of H_{DC} up to 8 kA/m. Tanaka *et al.* also showed that $M_{2,B}$ was larger than M_3 [3]. In this study, it was shown that $M_{2,A}$ was larger than $M_{2,B}$, and both of which were larger than M_3 depending on the directions of H_{AC}, H_{DC}, and the signal detection. M_2 was not associated with a non-linear response of the magnetization to H_{AC}. In conclusion, H_{DC} perpendicular to H_{AC} increased M_2, which was larger than M_3. M_2 was significantly affected by the relationship between the directions of H_{AC}, H_{DC}, and the signal detection. The dependence of M_2 on the frequency and intensity of H_{AC} was also presented.

[1] B. Gleich and J. Weizenecker, Tomographic imaging using the nonlinear response of magnetic particles, Nature 435, 1214 (2005). [2] S. Ota, Y. Matsugi, T. Nakamura, R. Takeda, Y. Takemura, I. Kato, S. Nohara, T. Sasayama, T. Yoshida, and K. Enpuku, Effects of size and anisotropy of magnetic nanoparticles associated with dynamics of easy axis for magnetic particle imaging, J. Magn. Magn. Mater., 474, 311–318 (2019). [3] S. Tanaka, T. Suzuki, K. Kobayashi, S.-H. Liao, H.-E. Horng, H.-C. Yang, Analysis of magnetic nanoparticles using second harmonic responses, J. Magn. Magn. Mater., 440, 189–191 (2007).

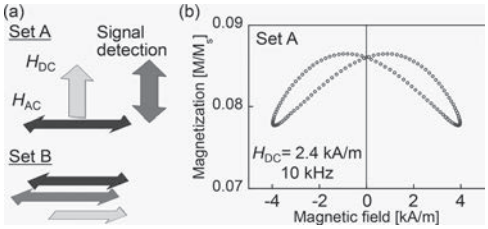


Fig. 1 (a) Experimental set of the directions of H_{AC}, H_{DC}, and the signal detection. (b) AC magnetization curve measured in set A.

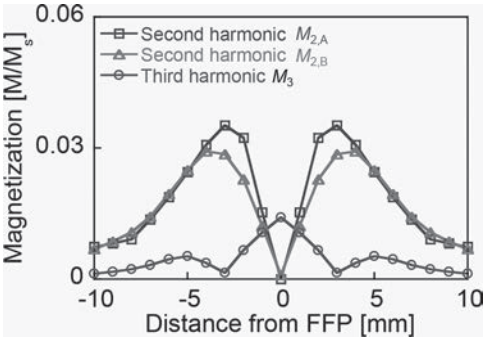
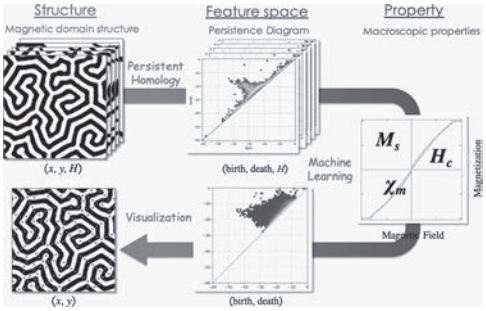


Fig. 2 Dependence of $M_{2,A}$, $M_{2,B}$, and M_3 on the distance from the FFP.

DT-05. Automated visualization of the origin of the coercivity by using persistent homology. *M. Kotsugi*[1,2], T. Yamada[1,2], C. Mitsumata[2], T. Ueno[3], I. Obayashi[4,5], K. Akagi[5,2] and Y. Hiraoka[6,2] *1. Tokyo University of Science, Katsushika, Japan; 2. NIMS-MI2I, Tsukuba, Japan; 3. QST, Sayo, Japan; 4. RIKEN-AIP, Tokyo, Japan; 5. Tohoku Univ., Sendai, Japan; 6. Kyoto Univ., Kyoto, Japan*

Coercivity is one of the most important magnetic property in ferromagnetic materials for use in widespread applications, i.e. the core loss of soft magnets or the maximum energy product of hard magnets. It is the intensity of the external magnetic field to reduce the magnetization from saturation to zero. However, the detailed mechanism, how the macroscopic coercivity correlates to the microscopic magnetic domain structure, has not been perfectly understood yet. Here, we used "persistent homology", and developed an automated visualization technique of the origin of coercivity in the magnetic domain structure (Fig. 1)[1]. Persistent homology is an algebraic tool for measuring the topological features of shape, and it can offer the feature extraction of the spatial fluctuation in the magnetic domain. Moreover, the combination with machine learning offers us to establish a correlation between microscopic structure and macroscopic property [2]. In the experiment, we applied persistent homology to the magnetic domain of Bi-substituted rare-earth iron garnet. (1) We examine the availability of persistent homology for the feature extraction of the magnetic domain. (2) We investigate the systematic change of the feature respect to the external magnetic field. (3) We visualized pinning center on the original magnetic domain in combination with principal component analysis. As a result, we confirmed that persistent homology can accurately extract the feature of labyrinth magnetic domain, especially striped structure, blanched structure and terminated structure. The extracted feature synchronizes to the magnetic domain reversal process, and sensitive to the change of the external magnetic field. We automatically visualized the pinning center in the original magnetic domain structure that contributes to coercivity. Moreover, the projected points are corresponding to the topological defects, and it offers us to describe the non-equilibrium state in the microstructure. We could demonstrate that persistent homology is a useful approach to data-driven magnetic domain analysis for the first time.

[1] T. Yamada and M. Kotsugi et al. Vac. Surf. Sci. 62, (2019), 153-160 [2] I. Obayashi et al. J. Appl. Comp. Topo. 1 (2018) 421-449



Visualization of the origin of the coercivity in the magnetic domain structure by using persistent homology and machine learning.

DT-06. Precision Magneto-optical Measurements of Magnetically Doped Mn-PbSnSe. *L. Riney*[1], B. Assaf[1], G. Krizman[2], X. Liu[1], J. Wang[1] and L. de Vaulchier[2] *1. University of Notre Dame, South Bend, IN, United States; 2. Ecole Normale Supérieure, Paris, France*

Recently, the topological crystalline insulator $Pb_{1-x}Sn_xSe$ has been of interest due to its ability to exhibit tunable trival and non-trivial topological phase transitions with varying Sn content. In this work, we explore magnetically doped Mn-$Pb_{1-x}Sn_xSe$ using magneto-optical techniques with a magnetic field that varies from 0 to 17T to perform Landau-level spectroscopy. We measure the exchange parameters of Mn-$Pb_{1-x}Sn_xSe$ in various fields and temperatures ranging from 1.6K to 200K. With a high enough mobility (>3000cm^2/Vs), we are able to probe the Landau-levels of our samples at 3T and above. We find that our measurements agree well with our k.p theory model that includes magnetization terms to account for the Mn doping. Magnetic topological insulators are of particular interest because they exhibit naturally gapped surface states which have the potential to exhibit a topologically protected quantum anomalous Hall conductive state.

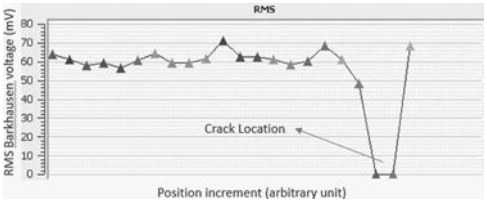
DT-07. Use of AC Faraday Rotation as a Complementary Technique in Material Characterization. *M. Syed*[1], J. Monarch[1], W.J. Li[1] and N. Fried[1] *1. Physics & Optical Engineering, Rose-Hulman Institute of Technology, Terre Haute, IN, United States*

Magnetic measurements like Hall Effect, etc. have a long history of providing useful information related to material characterization. Here, we study glasses using a very sensitive AC Faraday rotation (FR) setup to show that magneto-optic techniques can also be utilized to study types of samples that are not necessarily known for their magnetic response. Samples included in this study are widely used in technological and research applications ranging from microscopy to solar cell applications. The experimental setup employs a stabilized He-Ne lase (633 nm) along with AC magnetic field that enables lock-in detection. We investigate a series of glass samples that include borosilicate glass and quartz subjected to UV treatment and glass with transparent conducting oxide films (TCO). The TCO samples include the more widely used Indium Tin Oxide (ITO) and the relatively newer Fluorine doped ITO. Various other measurements like absorbance, four-point probe, and ellipsometry have been conducted on these samples as well. We plan to discuss the results of these measurements in conjunction with FR measurements to show how a standard magneto-optic measurement can work in concert with these other measurements to provide characterization outcomes that are more consistent than the ones obtained from a single measurement. We will discuss the role played by sample thickness (substrate and TCO films), carrier concentration, and resistivity and how they relate to the framework of a FR measurement.

DT-08. C-scan imaging with magnetic Barkhausen emission measurements for the detection of shallow surface micro-cracks. N. Prabhu Gaunkar[2], *G. Prabhu Gaunkar*[1] and D.C. Jiles[2] *1. Mechanical Engg, IIT Goa, Farmagudi, India; 2. Electrical and Computer Engineering, Iowa State University, Ames, IA, United States*

Surface cracks can develop in components due to residual stresses, fatigue, stress corrosion cracking, corrosion fatigue, etc., Different NDT methods are employed to detect and monitor such cracks. Magnetic Barkhausen Noise (MBN) analysis is one such technique that is used for in-situ examination of microstructural anomalies or stress patterns. In the present work, we study the applicability of MBN for the detection of surface cracks. A part through surface crack was created by controlled fatigue loading of a martensitic stainless steel plate. The surface of the sample was scanned for BN emissions in incremental steps parallel and perpendicular to the crack. Measurements of MBN signal strength were recorded and assessed. Typical values for scans across the crack at its mid-length and in the vicinity of the crack tip are shown in Fig.1. It is observed that the number of MBN events drop significantly as the test spot location approaches the crack. Minimum MBN is thus observed whilst traversing the crack. Two distinct minima in the MBN peak amplitude are seen for scans just ahead of the crack tip. The estimated magnetic permeability also shows a similar pattern. The drop in the MBN signal is attributed to the localized deformation that accompanies the crack growth forming a plastic zone of much wider thickness than the crack itself. During the scan, the plastic zone gets detected along with the crack. The pinning sites in the form of dislocations along with the void within the crack are responsible for the drop in the recorded MBN. The detection sensitivity thus gets enhanced since material adjacent to the crack that is plastically deformed contributes to the signal detected thus revealing the presence of a crack. The double minima seen ahead of the crack tip are attributed to the characteristic residual stress pattern inherited from the typical butterfly shaped stress field ahead of a growing crack. C-scan mapping of component surfaces with miniature Barhausen Emission probes can thus provide a cost-effective and sensitive non-destructive examination tool for ferromagnetic materials.

[1].Stewart, D. M., K. J. Stevens, and A. B. Kaiser. "Magnetic Barkhausen noise analysis of stress in steel." *Current Applied Physics* 4, no. 2-4 (2004): 308-311. [2]. Yelbay, H. Ilker, Ibrahim Cam, and C. Hakan Gür. "Non-destructive determination of residual stress state in steel weldments by Magnetic Barkhausen Noise technique." *NDT & E International* 43, no. 1 (2010): 29-33. [3]. Mierczak, L., D. C. Jiles, and G. Fantoni. "A new method for evaluation of mechanical stress using the reciprocal amplitude of magnetic Barkhausen noise." *IEEE Transactions on Magnetics* 47, no. 2 (2010): 459-465. [4]. Sorsa, Aki, Kauko Leiviskä, Suvi Santa aho, and Toivo Lepistö. "Quantitative prediction of residual stress and hardness in case-hardened steel based on the Barkhausen noise measurement." *Ndt & E International* 46 (2012): 100-106.



RMS Barkhausen voltage measured along sample with crack

DT-09. Crystal & Magnetic Structure Studies of Li-ion Battery Materials with Neutron Powder Diffraction. *S. Lee*[1] *1. Kaeri, Daejeon, The Republic of Korea*

Neutron powder diffraction experiment is the most powerful experimental tool to give unique information for study of an electrochemical reaction mechanism. For examples, the microscopic structural deformation of a light element such as Lithium-ion and oxygen-ion in unit cell could be distinguished by only neutron diffraction. The information about the distribution of Li-ion is strongly correlated in the conduction mechanism. Also, the stability of structure in Li-ion battery materials depends on the change of site occupancy of Li-ion. Another merit of neutron diffraction for Li-ion battery is the strong penetration property of neutron. This property of neutron can be studied the conduction process using Li-ion battery full system. We have been developing protocols that allow for analysis of electrochemical cell reactions "in-situ," that is, methods for monitoring a battery while it is undergoing charging and discharging. But there are still many problems to be overcome such as a large neutron diffraction background of battery system and the inappropriate analysis of overlapped diffraction pattern based on very complicated multi-phase. In this talk, we will introduce the crystal and magnetic structure studies of battery materials using high resolution neuron powder diffraction (HRPD) in HANARO. For examples, we have investigated the magnetic and crystal structure of $Na_xFe_3(PO_4)_2(P_2O_7)$ ($1 \le x \le 4$) with a mixed polyanion framework using neutron powder diffraction. The new compounds contained three-dimensional (3D)-sodium paths supported by P2O7 pillars in the crystal. The de/sodiation of the $Na_xFe_3(PO_4)_2(P_2O_7)$ electrode occurs via a one-phase reaction with a reversible Fe2+/Fe3+ redox reaction and accompanies an exceptionally small volumetric change of less than 4%. Very interestingly, we have observed a very strong spin-lattice coupling behavior in this compound. Even though, the spin ordering of this material is happened at a low temperature, the trials to understand a strong correlation between spin and lattice within electrode materials are valuable to open an opportunity which realizes the new concept's second battery to be controlled the conduction property of electrode by the spin ordering.

DT-10. Kerr Effect Microscope with Rotating Analyzer for Exact Spatial Determination of Kerr Angle of Magnetic Domains. *J. Zázvorka*[1], A. Papackova[1], L. Beran[1], L. Nowak[1], V. Kletečka[1], T. Maleček[1] and M. Veis[1] *1. Charles University, Prague, Czechia*

Magneto-optical (MO) methods are used as highly sensitive non-destructive techniques to probe physical properties of various magnetic materials down to the nanometre scale. Spatially resolved MO experiments are suited for visualization of magnetic domains larger than 150 nanometres [1]. There are many advantages of magneto-optical microscopy, such as non-destructiveness, possible high time resolution, low requirements on samples and easy manipulation with them. MO microscopy posses a way to analyse large variety of nanostructured magnetic materials [2]. As disadvantage of the MO microscopy, the obtained results represent only optical contrast and for advanced

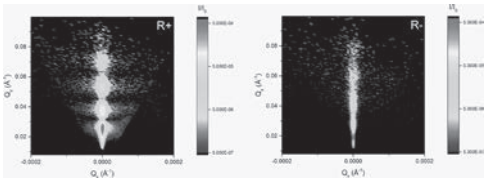
investigation a comparison with additional methods, e.g. magnetometry or anisotropy measurements, needs be used. We report on the development of a magneto-optical Kerr effect (MOKE) microscope that employs the rotating analyser method. This technique is usually used in spectroscopic measurements and allows for obtaining the exact value of the Kerr rotation of the studied system directly form the captured pictures with the accuracy of several millidegrees resolution. Spatial imaging of the Kerr rotation, combined with sub-pixel domain wall detection and image post-processing techniques, is useful for detailed characterization of magnetic properties. e.g. nucleation and stability of magnetic domains, pinning, magnetic transport, etc. Combined in a setup with a high-speed camera, capable of capturing 100 fps, dynamics of magnetic domains can be captured as well. To demonstrate the setup capabilities, we present exemplary measurements and characterization of several samples, such as NiFe permalloy gratings, domain structures of Bi:YIG garnets and investigation of domains in magnetic shape memory material Ni_2MnGa.

[1] I. V. Soldatov, R. Schäfer, Phys. Rev. B. 95 (2017) 1–6. doi:10.1103/PhysRevB.95.014426. [2] I. V. Soldatov, R. Schäfer, Rev. Sci. Instrum. 88 (2017) 073701. doi:10.1063/1.4991820.

DT-11. POLREF: Time of flight Polarised Reflectometer for Magnetism. *C. Kinane*[1] and A. Caruana[1] *1. STFC, Rutherford Appleton Laboratory, Oxford, United Kingdom*

Polarised Neutron Reflectometry (PNR) measures surfaces, buried interfaces and layers, yielding information about layer thicknesses, densities, surface/interface roughness and interdiffusion. Uniquely it can provide the magnetic equivalents of these quantities, including the total in-plane magnetisation [1,2]. A large variety of thin film phenomena can be investigated using the POLREF beamline, including topological insulators, proximity-induced and fundamental magnetism, superconductivity and spintronic devices. Furthermore, POLREF has the capability to perform off-specular PNR and specular Polarisation Analysis (PA) measurements. If the problem can be made flat and is in the right length scales (~1 nm – 200 nm) then it can be probed by PNR. The POLREF time of flight PNR beamline is located in the second target station at the ISIS neutron and Muon source [3,4]. With a polarised wavelength band of 2-15Å (PEff~96%), low instrument backgrounds of I/I0 < 10-7 and a resolution of dQ/Q better than 1%, QMAX = 0.25-0.3 Å-1 is routinely accessible for small (10x10 mm) samples within reasonable count times. The POLREF beamline has gone through a number of recent upgrades. Upgrades of the spin flippers and analyser system have improved the capability of the beamline to measure samples with larger moments or weaker spin flip signals when using the PNR and PA modes. The 1D linear detector efficiency has also been upgraded and now is fully commissioned into the user program providing full off-specular capability in the NR and PNR (see Figure 1) modes and some off-specular PA capability (the maximum Qx being restricted by the analysing mirror). Here, we will present the current capabilities of the POLREF beamline, including science highlights and how to get access to the ISIS neutron facility and POLREF beamline.

[1] J.F. Ankner, G.P. Felcher, J. Magn. Magn. Mater, 200, 741-754 (1999) [2] S. J. Blundell and J. A. C. Bland, PRB, 46, 3391 (1992) [3] J.R.P. Webster et al, Eur. Phys. J. Plus, 126: 112 (2011) [4] https://www.isis.stfc.ac.uk/



DT-12. Control and observation of ferromagnetic domains in resistive random access memory conducting filament nanostructures formed in epitaxial NiO thin films. *E. Lee*[1] and J. Son[1] *1. Kyung Hee University, Yong-in, The Republic of Korea*

We investigated resistive random access memory (RRAM) characteristics of epitaxial NiO thin films and using microcapacitor in micrometer scale and conducting atomic force microscope (CAFM) in nanometer scale. CAFM and magnetic force microscope were used to form and observe RRAM filament nanostructures of nanodots, nanorads, and nanorings. Depending on the size of the CAFM tip, the size of the nanodots was determined and nanodots with diameters of about 5 nm could be formed. Since the CF nanostructures have ferromagnetic properties, It was possible to control the magnetization directions of the nano-rad and nano-rings by the magnetic field formed by applying voltage to the CAFM tip.

DT-13. Magnetic Bubble States and Their Current-Driven Motion in C-Added MnNiGa. *S. Zuo*[1,2], J. Liu[1,2], K. Qiao[1,2], T. Zhao[1], F. Hu[1,2], J. Sun[1,2] and B. Shen[1,2] *1. Institute of Physics, Chinese Academy of Sciences, Beijing, China; 2. University of Chinese Academy of Sciences, Beijing, China*

Topological magnetic domains have received intensive attention due to their potential applications in the magnetic recording and memory devices [1]. Previous research reveals that biskyrmions can be observed in MnNiGa alloy with a wide temperature range [2], which would change into magnetic bubbles after the substitution of Y, but the bubble density is low similar to biskyrmions in MnNiGa [3]. Magnetic domains in C-added MnNiGa have been directly observed in the present work by means of Lorentz TEM. Magnetic bubbles with high density were obtained after the addition of C without changing the crystal structure. Furthermore, the bubble density and diversified spin configurations are systematically manipulated via combining the electric current with perpendicular magnetic fields. The magnetic bubble lattice at zero field were achieved and magnetic bubble states with uniform type-I or –II bubbles were observed after the optimized manipulation. Physics related to the magnetic domain evolution is discussed for present alloy, which probably stimulate further exploration of the universal phenomenon and mechanism.

[1] S. Parkin, M. Hayashi and L. Thomas, Science, 320,190–194 (2008). [2] W. Wang, Y. Zhang, G. Xu, et at., Adv. Mater., 28, 6887–6893 (2016). [3] S. L. Zuo, Y. Zhang, L. C. Peng, et at., Nanoscale, 10, 2260–2266 (2018).

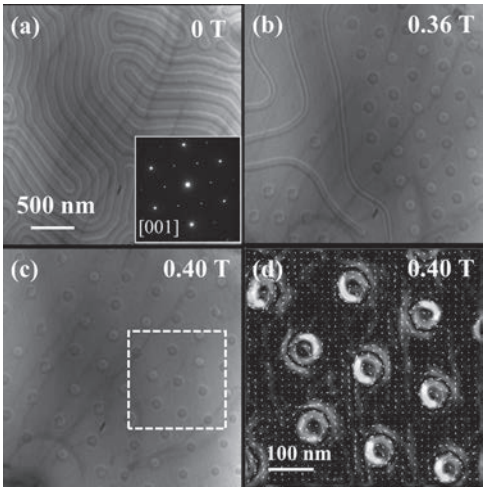


Fig. 1 Magnetic domain evolution in MnNiGaC alloy under perpendicular magnetic fields the inset showing the selected area electron diffraction, and (d) corresponding spin textures of magnetic bubbles obtained by transport-of-intensity equation analysis in the selected area by white square.

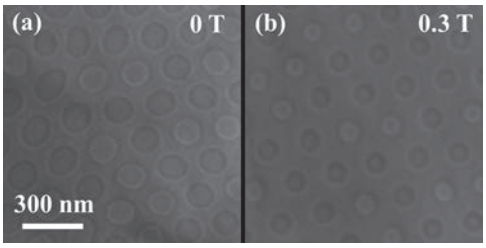


Fig. 2 Lorentz TEM images of uniform type-I bubble in (a) residual sate after the electric current manipulation and (b) at a perpendicular magnetic field of 0.3 T based on the residual state in MnNiGaC.

DT-14. Scanning laser magneto-optical microscopy for the study of magnetization dynamics of magnetic nanoparticles. R. Soucaille[1], M.E. Sharifabad[2], N. Telling[2] and *R. Hicken*[1] *1. University of Exeter, Exeter, United Kingdom; 2. Keele University, Stoke-on-Trent, United Kingdom*

Detailed characterization of magnetic nanoparticle (MNP) dynamics is needed to improve the efficiency of magnetic hyperthermia as a cancer therapy. It is necessary to investigate the MNPs within the cellular environment since the specific absorption rate of energy depends upon the spacing between the MNP and their agglomeration state. We have developed a scanning laser magneto-optical microscope to probe the magneto-optical response of the MNPs. The polarization rotation induced by the Faraday effect is small (typically less than 100 mdeg) and other sources of polarization or intensity change can cloud the characterization of the MNPs so that it is important to optimize all elements of the microscope design. Since the magneto-optical response depends upon the wavelength of the light, we have studied both the low-field AC susceptibility (ACS) and high field AC response of MNPs in solvent at different wavelengths. We report the wavelength dependence of the magneto-optical response in the 400 to 900nm range. For magnetite nanoparticles the magneto-optical response changes sign around 560 nm, while we also find that the optical ACS shows a response different to that expected from linear response theory. We have related this response to a change in the MNP configuration in the magnetic fluid. Another important aspect of the measurement system is the electromagnet that has been designed to optimize high frequency magnetic field generation with minimum loss. The magnet delivers a polar magnetic field while also providing an optical path for Faraday measurements. We finally developed a beam scanning Faraday microscope, that employs galvo mirrors and exploits the same electromagnet, to explore the dynamics of MNPs. The beam scanning microscope provides a fast and versatile means of mapping the magnetization dynamics and other processes that can affect the light polarization. Different schemes for the detection of the polarization change have been compared, including modulation of polarization and use of a balanced bridge detector. Measurements of the domain structure within a Co/Pt multilayer deposited on a glass substrate confirm that the microscope is well suited to the study of thin transparent magnetic structures.

DT-15. Element Specific Magnetometry of Buried Layers by HAXPES. *A. Gloskovskii*[1], G. Fecher[2], K. Ederer[1], C. Schlueter[1], G. Schönhense[3] and W. Drube[1] *1. Photon Science / Deutsches Elektronen-Synchrotron DESY, Hamburg, Germany; 2. Max Planck Institute for Chemical Physics of Solids, Dresden, Germany; 3. Institut für Physik, Johannes Gutenberg-Universität, Mainz, Germany*

The intensity and shape of photoelectron lines of magnetic materials depend on the relative orientation of the sample magnetization, the photon helicity vector and the electron emission direction. In the hard X-ray regime, the photon polarization can be conveniently modified utilizing the phase shift produced by a diamond phase plate in the vicinity of a Laue or Bragg reflection. A single-stage in-vacuum diamond phase retarder has been built for the HAXPES beamline P22 at PETRA III (Hamburg, Germany) [1]. The electronic and magnetic properties of buried CoFe and Co_2MnSi nano-layers were studied using the linear and circular magnetic dichroism in the angular distribution of photoelectrons [2, 3]. The layers were remanently magnetized *in-situ* and probed using HAXPES at PETRA III (beamline P09). It is demonstrated that magnetic dichroism in HAXPES is an effective and powerful technique to perform element specific magnetometry of deeply buried (~10 nm) ferromagnetic and antiferromagnetic materials, which are inaccessible with conventional soft X-ray photoelectron spectroscopy. The data analysis allows the determination of the relative orientation of magnetization in the different layers of these complex nano-structured samples. We are operating a time-of-flight HAXPES setup with spinfilter option at P22 [4]. The instrument is providing momentum and spin-resolved HAXPES with unmatched efficiency for the user community. It takes advantage of the unique time structure of the reduced bunch filling modes of PETRA III, offering rather large bunch separation of up to 192 ns (with 40 bunches) owing to the large circumference of the storage ring (2.3 km).

1. C. Schlueter, A. Gloskovskii, K. Ederer et al., AIP conference proceedings 2054(1), 040010 (2019). 2. A. Gloskovskii, G. Stryganyuk, G.H. Fecher et al., J. El. Spec. Rel. Phenom. 185, 47 (2012). 3. G.H. Fecher, D. Ebke, S. Ouardi et al., SPIN 04, 1440017 (2014). 4. S. Babenkov, K. Medjanik, D. Vasilyev et al., Comms. Phys. in print (2019).

Session DU
BIOMEDICAL APPLICATIONS III
(Poster Session)

Shin Yabukami, Chair
Tohoku University, Sendai, Japan

DU-01. Immuno-magnetic sorting of circulating tumor cells using microstructured NdFeB-PDMS composites. *D. Le Roy*[4], L. Descamps[1], S. Mekkaoui[1], E. Laurenceau[2], M. Audry[1], A. Deman[1], J. Garcia[3] and L. Payen[3] *1. Univ. Lyon 1, INL, Villeurbanne, France; 2. Ecole Centrale Lyon, INL, Lyon, France; 3. Hospices Civils Lyon, Lyon, France; 4. Univ. Lyon 1, ILM, Villeurbanne, France*

Circulating tumor cells (CTCs) are found to be valuable indicators of cancer stage [1]. Monitoring CTCs can serve to analyze treatment response and carry out personalized therapy [2]. However, recovering CTCs is challenging due to their scarcity in blood: few ppm at most. Microfluidic devices are interesting tools for cellular handling as they offer precise spatial and temporal control. Moreover, these devices can be easily made in low cost polymers such as polydimethylsiloxane (PDMS). In view to isolate CTCs, immuno-magnetic based micro-devices offer high selectivity and the possibility to recover living cells for subsequent analysis [3]. An external magnet is often used to create a magnetic flux pattern, but larger gradients, so reachable forces, are obtained when integrating micrometer-sized magnetic flux sources in the close region of the fluidic channel. Microstructured composites, made of magnetic particles and a polymer, is an efficient way to integrate micro-flux sources, and breakswith standard approaches [4]. Here we investigate mixtures of NdFeB particles with PDMS. During the PDMS reticulation, a magnetic field pattern serves to create arrays of NdFeB particle agglomerates, used as magnetic traps. Depending on the NdFeB concentration, one can vary the traps size and density. Figure 1(a-b) shows reconstructed 3D views from X-ray tomography, and a schematic of the microfluidic device. We first used model magnetic beads (12 µm) to assess trapping performances of the composites under varying fluidic conditions. We then performed preliminary experiments to specifically immuno-capture WBCs. To do so, WBCs were magnetically labelled with nanoparticles. We observed efficient WBC trapping using NdFeB-PDMS composites in microfluidic devices (Figure 1 (c-d)). These results demonstrate the potential of this approach for the immuno-magnetic sorting ofCTCs, either by positive selection, or by any negative selection through the capture of WBCs in pre-filtered blood sample.

[1] M. Pore et al, Clinical lung cancer (2016) 17:535-42 [2] J. M. Jackson et al, Chem. Soc. Rev. (2017) 46, 4245 [3] C. Hyungseok et al, Lab Chip (2017) 17, 4113 [4] S. Mekkaoui et al, Microfluid. Nanofluid. (2018) 22: 119

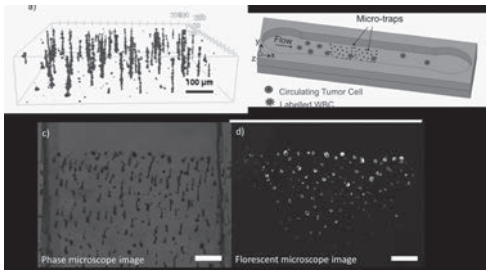


Fig. 1 : (a) X-ray tomography view of a NdFeB-PDMS membrane. (b) Device schematic. (c-d) Phase and fluorescent microscope images of WBCs captured on micro-traps. The scale bar in (c-d) is 100 µm.

DU-02. Flexibility of Undulating Magnetic Microbead Swimmers. *Y. Li*[1] and S. Chen[1] *1. Department of Mechanical and Aerospace Engineering, Chung Cheng Institute of Technology, National Defense University, Taoyuan, Taiwan*

The effect of curvature on the propulsive efficiency of the magnetic microswimmer subjected to an external field is investigated experimentally. The overall field is composed of a homogeneous static field H_d and a dynamical sinusoidal field H_y with a maximum amplitude H_p and an adjustable frequency f, that is, $H_y = H_p \sin(2\pi ft)$. The swimmer is obtained by combining the self-assembling ability of microsized superparamagnetic particles composed the iron oxide magnetite embedded in polystyrene microspheres suspended in distilled water. The flexibility of the swimmer can be determined by the value of C_{max}, a dimensionless ratio of the diameter of the magnetic particle to the swimmer's radius of curvature. Fig. 1(a) shows the sequential images of L2S2 swimmer (comprising two large and two small particles) and L1S3 swimmer (comprising one large and three small particles) swimming in an identical external field. It is noted that the undulating pattern of L2S2 is quite different from that of L1S3. Additionally, L2S2 has higher propulsive efficiency than that of L1S3. Fig. 2 shows the comparison of the swimming velocity for the L2S2 and L1S3 swimmers steered in different field conditions with various C_{max}. The velocities of both swimmers nearly linearly increase with the flexibility and reach the highest values at their corresponding C_{max}. The velocity of L2S2 is more sensitive to the flexibility than the counterpart of L1S3. In addition, L2S2 longer than the L1S3 obtains the maximum velocity of 3.16 µm/s when C_{max} =0.35, while the L1S3 possesses a maximum velocity of 1.5 µm/s at the flexibility of C_{max} =0.48. Our experimental results indicate that not only the flexibility is an essential controlling parameter for the propulsive efficiency, the length (or wetted area) of the swimmer which determines the friction for pulling the swimmer perpendicular to its long axis is a dominated factor for the propulsion generation as well.

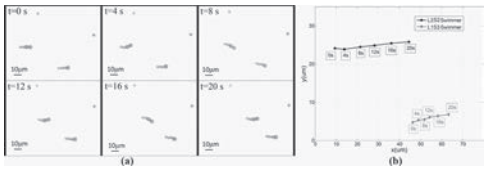


Fig.1 (a) Sequential images of L2S2 and L1S3 swimmers waggling in field strength of H_p=2000 A/m, H_d=1930 A/m, and frequency of f=10Hz. (b)Moving trajectories of the swimmers shown in Fig. 1(a).

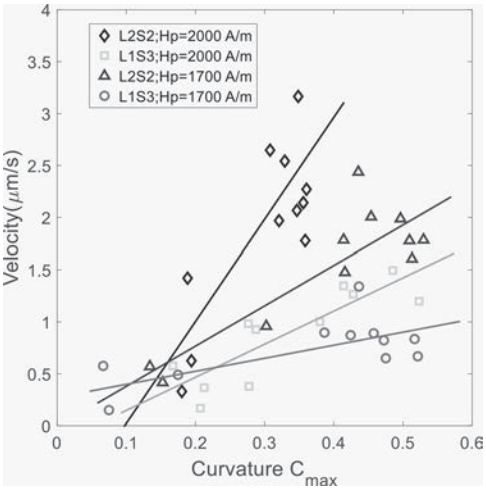
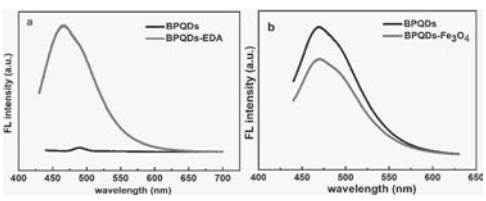


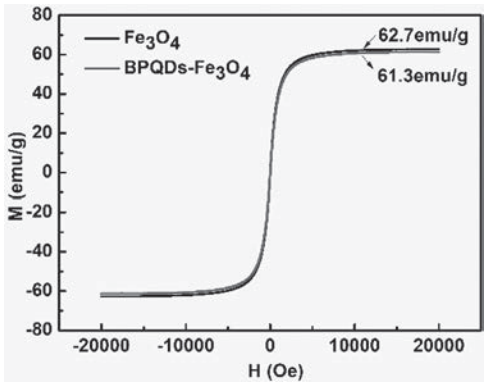
Fig.2 Comparison of the maximum velocities for different types of microswimmers with various flexibility.

DU-03. Fe_3O_4-BPQDs Nanoplatforms as Dual Mode Detection Probe. *Y. Ma*[1], X. Xu[1] and Y. Jiang[1] *1. School of Materials Science and Engineering, University of Science and Technology Beijing, Beijing, China*

The magnetic nanoplatforms involving black phosphorus quantum dots (BPQDs) and Fe_3O_4 nanoparticles will become a novel dual mode detection probe to improve accuracy of medical diagnosis and detection. Black phosphorus quantum dots (BPQDs) has unique optical properties and biocompatibility [1,2], while they have groups on surface and therefore can be decorated to avoid oxidation and weak emission [3-4]. The passivated BPQDs can bonded to superparamagnetic Fe_3O_4 nanoparticles, which are widely used as T_2 magnetic resonance imaging (MRI) contrast agent. Here, high fluorescent BPQDs are synthesized by thermal-pyrolysis and then effectively surface passivated by reaction with ethylenediamine (EDA). As shown in Figure. 1a, the fluorescent intensity of passivated BPQDs-EDA is much higher than pure BPQDs. The enhanced PL is contributed to high yield of BPQDs and P-N bond on the surface introduced by passivation. As shown in Figure. 1b, Fe_3O_4 nanoparticles are coated with chitosan, which can prevent the fluorescence quenching of BPQDs due to Fe_3O_4 NPs effectively. The magnetic nanoplatforms have a saturation magnetization (Ms) of 61.3 emu/g, while the Ms of Fe_3O_4 NPs is 62.7 emu/g in Figure. 2. It means that the magnetic nanoplatform can used as novel MRI contrast agent. According to our experiments, by successfully assembling the passivated BPQDs and Fe_3O_4 NPs, the dual-mode detection of MRI and fluoresce imaging can be effectively achieved in vivo.

[1] M. Z. Rahman, C. W. Kwong, K. Davey, S. Z. Qiao, Energy Environ. Sci., 2016, 9, 709. [2] S. Zhang, J. Yang, R. J. Xu, F. Wang, W. F. Li, M. Ghufran, Y. W. Zhang, Z. F. Yu, G. Zhang, Q. H. Qin, Y. R. Lu, ACS Nano., 2014, 8, 9590. [3] G. Eda, Y.-Y. Lin, C. Mattevi, H. Yamaguchi, H.-A. Chen, I. S. Chen, C.-W. Chen, M. Chhowalla, Adv. Mater., 2010, 22, 505. [4] M. A. Sk, A. Ananthanarayanan, L. Huang, K. H. Lim, P. Chen, J. Mater. Chem. C., 2014, 2, 6954.





DU-04. Investigating the Role of Pulsed Magnetic Field Intensity on the Growth and Proliferation of N27 Dopaminergic Neuronal Cells. *J. Boldrey*[1], L. Que[1], I. Schneider[2], R.L. Hadimani[3] and D.C. Jiles[1] *1. Electrical and Computer Engineering, Iowa State University, Ames, IA, United States; 2. Chemical and Biological Engineering, Iowa State University, Ames, IA, United States; 3. Mechanical and Nuclear Engineering, Virginia Commonwealth University, Richmond, VA, United States*

Much of the biomedical research to find the causes of and treatments for Parkinson's Disease (PD) and Alzheimer's Disease (AD) is performed using cell lines from animals that model the behavior of cells in the human brain that are linked to PD and AD. The N27 dopaminergic cell line is well-established in neurodegenerative disease research. [1] [2]. Transcranial Magnetic Stimulation (TMS) has been approved by the US Food and Drug Administration (FDA) as a method for treating major depressive disorder (MDD), obsessive-compulsive disorder (OCD) and certain types of migraine headaches [3]. However, the effect of TMS type fields at the cellular level are not fully understood. Recent studies have shown that monophasic pulsed magnetic fields generated by a TMS stimulator increases growth and proliferation of N27 cells in vitro [4] [5] [6]. In TMS therapy, each session is tailored to the specific patient by establishing a base threshold level of magnetic field strength (H). This is performed by aiming the stimulation coil at the patient's motor cortex and finding the minimum intensity level to make the patients thumb visibly twitch. This H field intensity baseline, called the motor threshold (MT), is then multiplied by a specified percentage set by the therapy protocol established by the FDA. Different patients have different MTs. Therefore, the intensity of the H field delivered to the brain cells of different patients should also vary. Recent studies have shown that monophasic pulsed magnetic fields generated by a TMS stimulator increases growth and proliferation of N27 cells in vitro [4] [5] [6]. The goal of our research is to investigate the effects of different H field intensities on N27 cells. By modulating the H field, an exploration was made into the role of variable H field intensity experienced during TMS therapy due to different MT between patients. The results of our research will increase our understanding of the effects of magnetic fields at the cellular level, increase the knowledge of the underlying mechanisms behind TMS, and contribute the ongoing research into treatments for PD and AD.

[1] "Time, Sex, Gender, History, and Dementia." Rocca, Walter A., 31.1 (2017): 76–79. *PMC*. Web. 1 Aug. 2018 [3] "FDA permits marketing of transcranial magnetic stimulation for treatment of obsessive compulsive disorder," Case Medical Research, 2018. [Online]. Available: https://www.fda.gov/newsevents/newsroom/pressannouncements/ucm617244.htm. [Accessed: 18-Mar-2019]. [4] "Cellular level studies and coil system design for transcranial magnetic stimulation", Meng, Yiwen, (2015), https://lib.dr.iastate.edu [5] "On-Chip Studies of Magnetic Stimulation Effect on Single Neural Cell Viability and Proliferation on Glass and Nanoporous Surfaces", Xiangchen Che, Shalini Unnikandam-Veettil and Ian Schneider, ACS Applied Materials & Interfaces 2018 10 (34) [6] "Effects of Magnetic Stimulation on the Proliferation of Dopaminergic Neuronal Cells Grown in Extracellular Matrix", Xiaojing Zhong, Long Que and Ian Schneider, INTERMAG Conference, Singapore, April 23-27, 2018

DU-05. Selective Separating and Retrieving Mechanism of Untethered Magnetic Robot for the Application of Human Vascular Disease.
J. Park[1], W. Lee[1], J. Kim[1], E. Jung[1], N. Kim[1] and G. Jang[1] *1. Hanyang University, Seoul, The Republic of Korea*

Because untethered magnetic robot (UMR) can be controlled remotely and precisely utilizing external magnetic field (EMF) generated by magnetic navigation system, UMR has been actively investigated to be applied to various biomedical fields such as vascular disease treatment [1]. However, propulsive force of UMR is not enough to move forward to target lesion against the high blood flow velocity up to 70 cm/s. Also, it is difficult to effectively deliver and retrieve UMR in blood vessels. In this paper, we proposed an integrated magnetic robot (IMR) and selective separating and retrieving (SSR) mechanism to overcome these limitations of UMR. The proposed IMR is consisted of a flexible-legged UMR(FLUMR) [2] and a tethered delivery catheter as shown in Fig. 1(a). Assembled magnet (AM) which is composed of two axially magnetized half-ring type magnets, is equipped at distal tip of the catheter and at \rear part of the FLUMR. SSR mechanism separates the FLUMR from the catheter by generating a repulsive force in coupling part and attaches the FLUMR with the catheter by generating an attractive force in coupling part as shown in Fig. 1(b). The magnetic moment of AMs is designed to be zero in such a way that the FLUMR does not move even though magnetic field is applied during the navigation of IMR. To verify the SSR mechanism, we prototyped IMR and conducted an experiment as shown in Fig. 2(a) and (b). FLUMR was selectively separated by applying more than 10 mT at 7.4 Hz which generates sufficient external magnetic torque when the spacer thickness between the magnets of AMs is 0.5 mm. Finally, we verified the navigation and SSR mechanism of IMR by *in vitro* experiment with the pseudo blood vessel (Y-shaped glass tube filled with water) as shown in Fig. 2(c). This study can contribute to expanding the application field of UMR by proposing safe and effective navigation and retrieval methods of UMR.

B. J. Nelson, I. K. Kaliakatsos, and J. J. Abbott, Annual Review of Biomedical Engineering., Vol. 12, p. 55–85 (2010) W. Lee, J. Nam, and G. Jang, IEEE Transactions on Industrial Electronics., Vol. 65, p. 1388–1397 (2018)

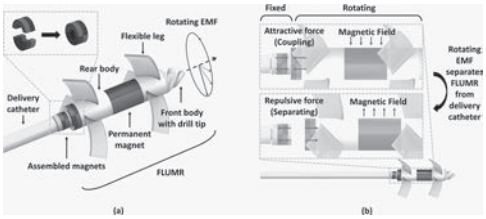


Fig. 1 (a) Structure of the IMR. (b) Attractive and repulsive magnetic force between AMs with the application of rotating EMF.

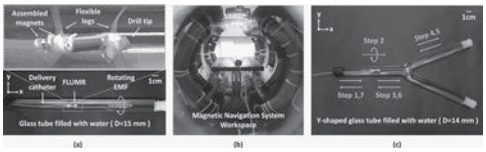


Fig. 2 (a) Prototyped IMR. (b) Experimental setup (c) *in vitro* experiment to verify the mechanism.

DU-06. Effect of Microstructure on r_2 Relaxivity for T_2 Weighted Magnetic Resonance Imaging in Magnetite Nanoparticles.
B. Park[2,1], M. Ko[2] and Y. Kim[2] *1. Research Institute of Engineering and Technology, Korea University, Seoul, The Republic of Korea; 2. Department of Materials Science and Engineering, Korea University, Seoul, The Republic of Korea*

Magnetite (Fe_3O_4) nanoparticles (NPs) have been considered as reagents for T_2 weighted magnetic resonance imaging (MRI) because they can accelerate spin-spin relaxation of adjacent protons by appearing a magnetic field [1]. In particular, since r_2 relaxivity, an indicator of T_2 contrast, is directly related to the magnetic moment and size of the NPs, control of diameter and surface are key factors to achieve high relaxivity [2]. Recently, it was reported that clustered Fe_3O_4 NPs (c-Fe_3O_4 NPs) composed of assemblies of several crystallites can exhibit high r_2 values [1]. However, it was difficult to precisely control the crystallite size of NPs smaller than 100 nm in a chemical route. In this study, we present a synthetic method by which we can control the diameter (D) and crystallite size (C) separately. The relevant c-Fe_3O_4 NPs were prepared by hydrothermal polyol process in the presence of iron(Fe^{3+}) chloride, sodium acetate, water, and ethylene glycol. We were able to control the crystallite size by changing the ratio of sodium acetate and water, which act as sources of OH^- ion during forming Fe_3O_4 phase. Figure 1 shows TEM images of two groups with different crystallite sizes. S1 (D: 30 nm) and S2 (D: 42 nm) consist of crystallites with a size of 15 nm and L1 (D: 25 nm), L2 (D: 34 nm), and L3 (42 nm) consist of crystallites with a size of 26 nm. As shown in Fig. 2, the c-Fe_3O_4 NPs with larger granule size has high saturation magnetization (M_s) and coercivity (H_c) resulting in high r_2 relaxivity. The r_2 values increased as the number of crystallites constituting the NP decreased in both groups. It should be noted that the microstructural changes play critical roles in magnetic NP design for T_2 weighted MRI.

[1] W. Zhang et al., Theranostics, Vol. 8, p. 2521 (2018) [2] J. Huang et al., ACS Nano, Vol. 4, p. 7151 (2010)

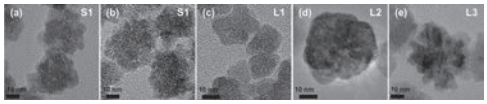


Fig. 1. TEM images of two groups of c-Fe_3O_4 NP with different crystallite sizes of (a, b) 15 nm and 26 nm (c-e).

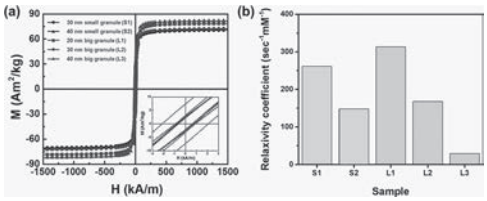


Fig. 2. Magnetic hysteresis curves and T_2 relaxivity coefficient of c-Fe_3O_4 NPs.

DU-07. Experimental Validation of an Analytical Model for Diametrically Magnetized Permanent Magnets.
N. Riahi[1] and A. Komaee[1] *1. ECE, Southern Illinois University, Carbondale, IL, United States*

Our team is devoted to development of noncontact permanent magnet manipulators for a variety of biomedical applications. The ultimate goal is to replace the existing electromagnet manipulators with more compact, more effective, and less expensive devices by employing permanent magnets that offer superior strength-to-size-ratio and energy efficiency. A key component toward this goal is the availability of reliable models for the magnetic fields generated by the permanent magnets of various geometries. Finite-Element Method is usually the most accurate approach to use. However, the undeniable need for analytical methods in design and dimension optimization for several applications including micro-actuators, have led to some analytical models for various types of permanent magnets. In particular, we are interested in an analytical 2-D model proposed in [1] for diametrically magnetized cylindrical magnets, a simplified and modified version of 3-D model presented in [2]. Before using this model in our design, the accuracy of model is verified experimentally, as reported below. Employing a SENIS MMS-1-RS 3-axis magnetic field mapper with accuracy of 0.5%, we measured the magnetic field around a diametrically magnetized magnet RX04X0DIA from KJ-Magnets. The magnetization factor was estimated from empirical data by LS method to be incorporated into the analytical model. The magnet dimensions appearing in the model were directly measured. Fig.1. compares the calculated and measured fields along the north pole direction of the magnet. The graphs indicate reasonably close match in particular as moving further from the magnet. For the entire area

around the magnet, the relative error between the analytic and empirical magnetic fields is illustrated in Fig.2. Since the magnet is not necessarily perfectly manufactured, it is not fully symmetric and asymmetry in the relative error is observed. Overall, the relative error over the area around the magnet does not exceed 11%. This relatively small error confirms that the analytical model in [1] can be safely used in our future work.

[1] M. Fontana, F. Salsedo and M. Bergamasco, Sensors, Vol.13.6, p. 7618-7632 (2013) [2] R. Ravaud, G. Lemarquand and V. Lemarquand, IEEE Trans. Mag, Vol. 44, p. 1982–1989 (2008)

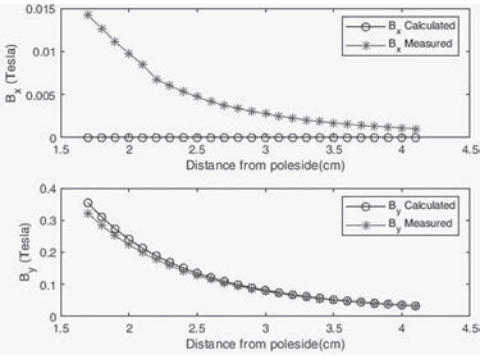


Fig.1 Comparing the calculated and measured fields along the north pole of the magnet

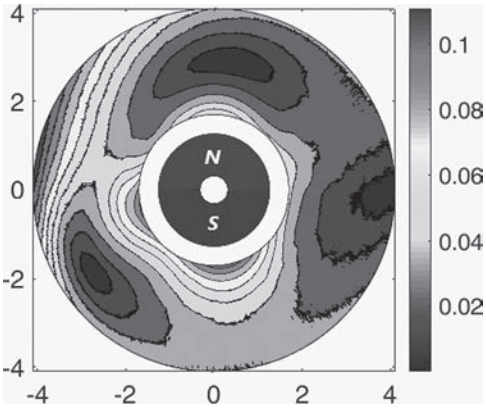


Fig.2 Relative error between analytical model and empirical data

DU-08. Development of a procedure for experimental mapping of electric field induced by TMS in an anatomically accurate brain phantom. *H. Magsood*[1] and R.L. Hadimani[1] *1. Virginia Commonwealth University, Richmond, VA, United States*

Transcranial magnetic stimulation (TMS) is therapeutic and diagnostic technique for various neurological and psychiatric disorders [1], [2]. There are extensive modeling and simulation studies to understand the effect of TMS coils on the brain [3], [4]. However, there is a lack of experimental and physical models for examining the brain stimulation. Previous experiments attempted to measure e-field on a conducting material that mimic the electrical conductivity of the brain but lacked the geometric/anatomical accuracy. We previously reported a newly developed brain phantom that is geometrically/anatomically accurate and has an averaged conductivity closely matching the human brain [5]. This work is an attempt to establish a methodology to map the e-field from the magnetic field applied on material like the brain. Previous work was based on the measurement of the electric field and characterization of the TMS coils but on highly conductive probes in air [6][7]. Our analogy of mapping the e-field on the brain phantom is divided in three part. The first is the mapping of the e-field induced on an oscilloscope probe to help characterizing TMS coils and establish a reference for measurements. The second part is the mapping of e-field from the voltage measurement on electrically conductive sheet (a composite of polydimethylsiloxane, PDMS and multi-walled carbon nanotubes, MWCNT) made with the same material composition of the brain phantom in order to simplify the geometry. The third part is to map the e-field from the brain phantom which is in progress. The upper half of Fig. 1 shows the e-field constructed from the voltage reading on the reference oscilloscope probe. The result trend is consistent with the previous modeling and computational studies[8]. The lower half of Fig. 1 shows the results of constructing the e-field from the electrically conductive sheet. The high electric field can be attributed to the polarization effect of the conductive polymer.

[1] S. H. Lisanby, B. Luber, T. Perera, and H. a. Sackeim, "Transcranial magnetic stimulation: applications in basic neuroscience and neuropsychopharmacology.," *Int. J. Neuropsychopharmacol.*, vol. 3, no. 3, pp. 259–273, 2000. [2] E. M. Wassermann and S. H. Lisanby, "Therapeutic application of repetitive transcranial magnetic stimulation: a review," *Clin. Neurophysiol.*, vol. 112, pp. 1367–1377, 2001. [3] F. Syeda, K. Holloway, and R. L. Hadimani, "Computational analysis of transcranial magnetic stimulation in the presence of deep brain stimulation probes," no. May, 2017. [4] M. Windhoff, A. Opitz, and A. Thielscher, "Electric field calculations in brain stimulation based on finite elements: An optimized processing pipeline for the generation and usage of accurate individual head models," *Hum. Brain Mapp.*, vol. 34, no. 4, pp. 923–935, 2013. [5] H. Magsood, C. H. A. Serrate, A. A. El-Gendy, and M. R. L. Hadimani, "Anatomically accurate brain phantoms and methods for making and using the same," *US Pat. US2019005762 3A1*, vol. 1, 2019. [6] J. O. Nieminen, L. M. Koponen, and R. J. Ilmoniemi, "Experimental characterization of the electric field distribution induced by TMS devices," *Brain Stimul.*, vol. 8, no. 3, pp. 582–589, 2015. [7] P. M. Glover and R. Bowtell, "Measurement of electric fields due to time-varying magnetic field gradients using dipole probes," *Phys. Med. Biol.*, vol. 52, no. 17, pp. 5119–5130, 2007. [8] F. Hoeft, D. A. Wu, A. Hernandez, G. H. Glover, and S. Shimojo, "Electroncally switchable sham transcranial magnetic stimulation (TMS) system," *PLoS One*, vol. 3, no. 4, 2008.

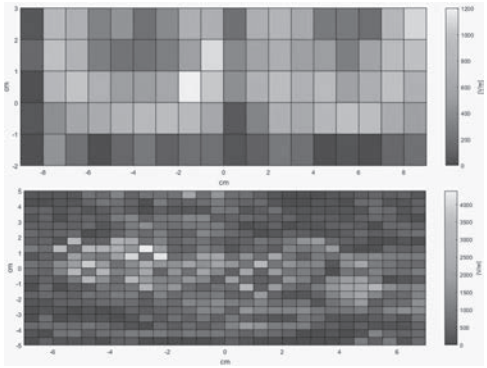


Fig.1. (upper) the e-field constructed on the reference oscilloscope probe. (Lower) the electric field form the electrically conductive sheet PDMS+MWCNT

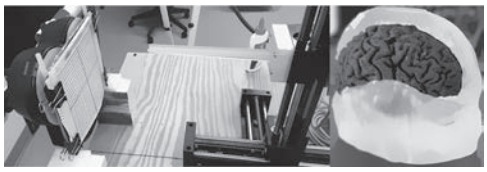


Fig.2. Experimental set up of the TMS coils and the electrically conductive sheet and the brain phantom.

DU-09. Detailed Analysis of Specific Absorption Rate of Magnetic Nanowires for Biomedical Applications. *M. Zamani Kouhpanji*[1,2], A. Ghoreyshi[1], D. Bilardello[4], P.B. Visscher[3] and B. Stadler[1] *1. Electrical and Computer Engineering, University of Minnesota Twin Cities, Minneapolis, MN, United States; 2. Biomedical Engineering, University of Minnesota Twin Cities, Minneapolis, MN, United States; 3. Physics and Astronomy, University of Alabama, Tuscaloosa, AL, United States; 4. Institute for Rock Magnetism, University of Minnesota Twin Cities, Minneapolis, MN, United States*

Magnetic nanowires have found applications in electronic and spintronic devices, in green technologies, such as water purification agents, and in biomedical applications, such as thermal therapies and RNA/DNA extraction agents [1-3]. To truly design properties optimized for each application, quantification of the intrinsic reversible and irreversible magnetization mechanisms is important, but so far elusive [4]. Here, a novel mathematical approach is proposed to quantitatively distinguish the intrinsic irreversible versus reversible magnetization mechanisms of the nickel nanowire arrays using first order reversal curves (FORC). The energy barrier, domain wall length, effective anisotropy constant, switching field, and coercivity were calculated to identify the reversal mechanism and calculate the specific absorption rate (SAR) of the nanowires, Figure 1. Furthermore, the angular-dependent coercivity (ADC) was measured to validate the FORC results. The FORC data show that the energy barrier of the nickel nanowires (Figure 1a) increased as their diameter increased which could lead to larger energy generation, suitable for thermal therapeutic applications. However, since the larger nanowires have larger volumes, their SAR values decreased resulting in lower efficiency per volume (and per mass) for thermal therapeutic applications, Figure 1b. A good agreement was found between the results of the ADC and FORC techniques, Figure 1d. However, ADC predicted the effective anisotropy slightly larger than FORC, Figure 1c, which is closer to what reported in previous literature [5].

[1]: Maqableh, M.M., Huang, X., Sung, S.Y., Reddy, K.S.M., Norby, G., Victora, R.H. and Stadler, B.J., 2012. Low-resistivity 10 nm diameter magnetic sensors. *Nano letters*, *12*(8), pp.4102-4109. [2]: Daniel Shore, Adrian Ghemes, Oana Dragos, Zhe Gao, Qi Shao, Joseph Um, Anirudh Sharma, Ibro Tabakovic, John Bischof, and Bethanie JH Stadler, "Nanowarming using Au-Tipped $Co_{35}Fe_{65}$ Ferromagnetic Nanowires." Accepted in *Nanoscale*. [3]: Fernandez-Roldan, J.A., Serantes, D., del Real, R.P., Vazquez, M. and Chubykalo-Fesenko, O., 2018. Micromagnetic evaluation of the dissipated heat in cylindrical magnetic nanowires. *Applied Physics Letters*, *112*(21), p.212402. [4]: Visscher, P.B., 2016. FORC+: A method for separating reversible from irreversible behavior using first *order reversal curves. arXiv preprint arXiv:1610.09199. [5]: Vivas, L.G., Vazquez, M., Escrig, J., Allende, S., Altbir, D., Leitao, D.C. and Araujo, J.P., 2012. Magnetic anisotropy in CoNi nanowire arrays: analytical calculations and experiments. Physical Review B, 85(3), p.035439.*

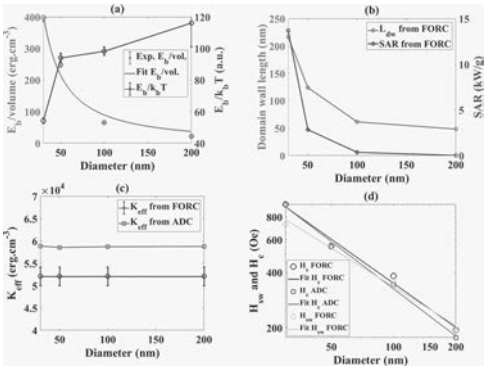
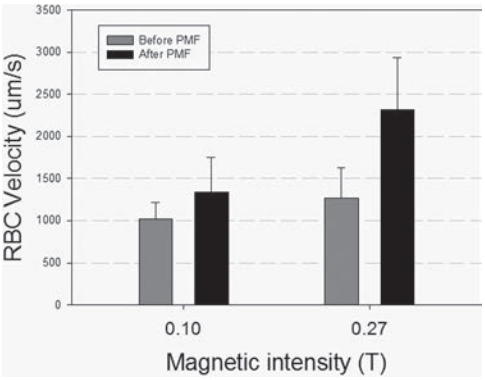


Figure 1: (a) the energy barrier for irreversible switching of the magnetic nanowires, (b) domain wall length and SAR, where the time is the round trip of domain wall along the nanowire length, (c) effective anisotropy constant, and (d) coercivity and switching field.

DU-10. Study on the Blood Flow in Stenosed Microvascular Model under Pulsed Magnetic Field. S. Han[1], J. Mok[1] and *H. Lee*[1] *1. Sangji University, Wonju, The Republic of Korea*

The use of pulsed magnetic field (PMF) was proposed as an alternative non-invasive medical treatment for influencing human physiology, via inducing electric current in deep tissue with the rapidly changing field of the magnetic impulses and has been reported to be effective in improvement of blood circulation.[1] It is widely known that abnormal peripheral blood circulation due to intravascular stenosis causes ischemic diseases and blood circulatory disorders. Since the stenosis occur due to hemodynamic and geometric characteristics of blood vessels, as well as pathological and physiological factors, therefore, present study has tried to investigate the influence of PMF on hemodynamic characteristics in blood vessel with stenosis. Stenosed microvascular channels were fabricated using polydimethysiloxane (PDMS). Red Blood Cell (RBC) suspension with hematocrit (Ht) of 5~20% was prepared using phosphate buffer saline (PBS) and it was injected into micro-channel with the blood flow rate of 1 μl/h using syringe pump. The changes in blood flow and deformation of RBCs were examined before and after PMF stimulus. These hemodynamic information on RBC passing through the stenotic region might provide the treatment of blood circulatory disorders.[2] Our PMF stimulator has the maximum intensity of 0.27T at a transition time of 102 μs with pulse intervals of 1Hz. The blood flow velocities of RBC in the micro-channel having a diameter of 15μm and stenosis rate of 30% increased by 32% and 89% after PMF stimulus with intensities of 0.1T and 0.27 T, respectively.(Fig.1) And the RBC deformability near the stenosis increased by an average of 30% after PMF stimulus. Our study shows that PMF plays an important role in hemorheologic and hemodynamic properties. In order to extend our results to clinical applications, we need develop more indicators for hemorheologic characteristics such as viscosity and resistance, and need further experiment with diverse PMF condition such as pulse shape, pulse duration, or repetition rate.

[1] Yonghyeok Jo, Hyoje Ahn, Kyunghun Shin, et al., *IEEE Transactions on Magnetics, vol.* 54(11), p.5000503 (2018) [2] O.K. Baskurt, and H.J. Meiselman, Semin Thromb Hemost, vol 29(5), p. 435-450 (2003)



The comparison of RBC flow velocities in the stenosed micro-channel before and after PMF stimulus vs. PMF strength of 0.1T and 0.27 T.

DU-11. Cavity-shaped magnet for highly sensitive magnetic detection of magnetic nanoparticles in breast cancer patients. *A. Kuwahata*[1], M. Kusakabe[2,1], S. Chikaki[1], I. Saito[3] and M. Sekino[1] *1. The University of Tokyo, Tokyo, Japan; 2. Matrix Cell Research Institute Inc., Ibaraki, Japan; 3. iMed Japan Inc., Tokyo, Japan*

Recent clinical studies demonstrated the feasibility of a magnetic sentinel lymph node biopsy using magnetic nanoparticles (MNPs) and a dedicated magnetic probe [1-3] to diagnosis cancer metastasis in breast cancer patients. Our handheld magnetic probe with a conventional column-shaped permanent magnet and a Hall sensor [3] can effectively generate larger magnetic fields (B) to magnetize MNPs compared with the magnetic probe with a coil. However, a large gradient of magnetic fields (∇Bz ~ 160 mT/mm) around

the magnet has been an obstacle to employ high-sensitive magnetic sensors (e.g., a magneto-impedance sensor) for detecting the MNPs at a further distance. This study presents a novel configuration of a permanent magnet to overcome the above issue. We proposed the cavity-shaped magnet with zero gradient of the magnetic field at the magnetic null area where $B \sim 0$. Figure 1 shows the two-dimensional distribution of magnetic fields calculated by the finite element method. The narrow magnetic null area of the conventional magnet is shown in Fig. 1(a). By contrast, the proposed cavity-shaped magnet produces the wider magnetic null (Fig. 1(b)). Although the cavity area of the magnet produces the zero gradient, the strength magnetic fields are still large. The small ring magnet located at the tip of the magnet plays an important role to eliminate the large magnetic field under keeping the zero gradient, resulting in the novel configuration magnet with $\nabla Bz \sim Bz \sim 0$. In addition, at the further distance ($Z > 11$ mm), the magnetic sensitivity of the cavity-shaped magnet shows the larger value compared with that of the conventional magnet, as shown in Fig. 2. These results indicate the proposed magnet is useful for the enhancement of the detection performance of the magnetic probe. We will present the detailed characteristics of the cavity-shaped magnet and the application of highly sensitive magnetic sensors.

[1] M. Shiozawa, A. T. Lefor, Y. Hozumi *et al.*, *Breast Cancer* 20, 223 (2013). [2] M. Douek, J. Klaase, I. Monypenny *et al.*, *Surg. Oncol.* 21, 1237 (2014). [3] M. Sekino, A. Kuwahata, T. Ookubo *et al.*, *Scientific Reports* 8, 1195 (2018).

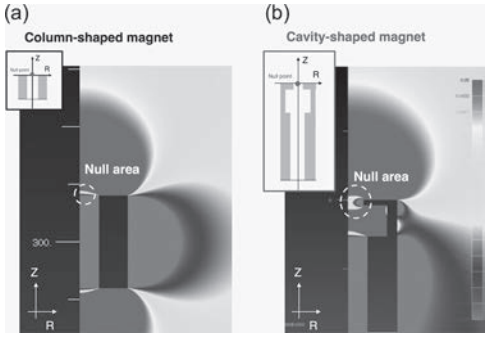


Fig 1. Two-dimensional distribution of magnetic field generated by (a) the conventional column-shaped magnet and (b) novel cavity-shaped magnet. Wider magnetic null area exists in the cavity-shaped magnet.

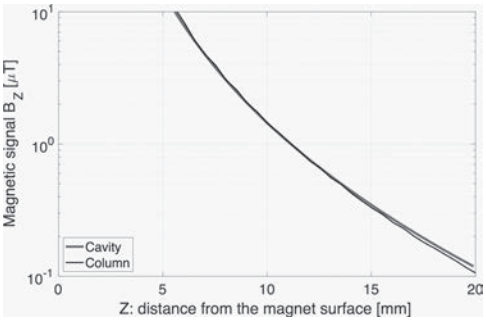


Fig 2. Magnetic sensitivity of the conventional column-shaped magnet and cavity-shaped magnet with respect to the MNPs of 5 µL.

DU-12. Exploring exchange-coupled cobalt ferrite/iron oxide and iron oxide/cobalt ferrite core/shell nanoparticles for advanced magnetic hyperthermia. *J. Robles-Garcia*[1], E. Fuller[2], R. Das[3], M. Phan[1] and H. Srikanth[1] *1. Physics, University of South Florida, Tampa, FL, United States; 2. Physics, Ohio State University, Columbus, OH, United States; 3. Phenikaa Unversity, Hanoi, Vietnam*

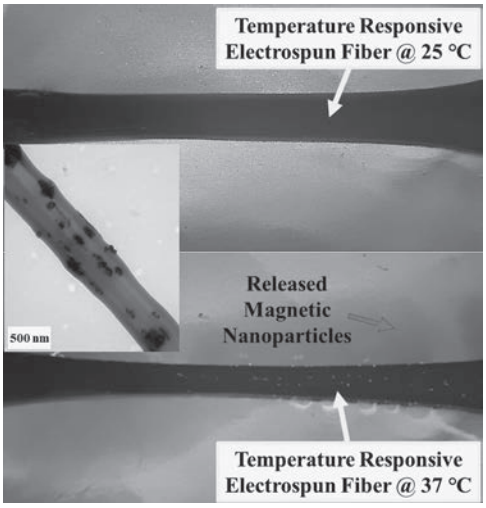
Iron/iron oxide core/shell nanoparticles have recently been exploited as a promising candidate for magnetic hyperthermia, owing to their biocompatible and expectedly enhanced magnetic properties. However, atomic diffusion between the core (Fe) and shell (Fe_3O_4 or γ-Fe_2O_3) hindered the heating capacity of these nanoparticles, making them impractical for application in magnetic hyperthermia [1]. To overcome this, we propose the design and synthesis of exchange-coupled cores/hell nanoparticles with exchange coupling between soft (Fe_3O_4) and hard ($CoFe_2O_4$) magnetic phases. We have systematically studied the effects of the core and shell composition/thickness on the heating efficiency in both $Fe_3O_4/CoFe_2O_4$ and $CoFe_2O_4/Fe_3O_4$ core/shell nanoparticles. The nanoparticles were synthesized using thermal decomposition of organometallic precursors. Transmission electron microscopy (TEM) showed formation of spherically shaped $CoFe_2O_4/Fe_3O_4$ and $Fe_3O_4/CoFe_2O_4$ nanoparticles. Magnetic measurements showed high saturation magnetization (MS~70 emu/g) and a superparamagnetic behavior for the nanoparticles at room temperature. Magnetic hyperthermia measurements indicated a large increase in specific absorption rate (SAR) for $Fe_3O_4/CoFe_2O_4$ compared to $CoFe_2O_4/Fe_3O_4$ nanoparticles of same size (~10 nm). The heating efficiency of $CoFe_2O_4/Fe_3O_4$ increased to ~200 W/g as compared to $Fe_3O_4/CoFe_2O_4$ (~159 W/g). The increase in SAR is attributed to the increases in both the saturation magnetization and the effective magnetic anisotropy field.

1. Z. Nemati, J. Alonso, H. Khurshid, M.H. Phan, and H. Srikanth, *RSC Advances* 6, 38697 (2016)

DU-13. Development of Temperature Responsive Electrospun Fiber for Magnetic Nanoparticles Releasing. *T. Chen*[1], C. Huang[1], C. Tsou[1] and T. Ger[1] *1. Biomedical Engineering, Chung Yuan Christian University, Taoyuan City, Taiwan*

In this study, we present a temperature responsive magnetic nanoparticle embedded fiber which was fabricated through the electrospun process. The electrospun fibers could be temperature increasing by the alternating magnetic field (AMF) because of the magnetic nanoparticles in fibers. Temperature responsive material of PNIPAAm changed the compound structure at the low critical solution temperature which was 32 °C and expressed the morphology variation between shrunken and swollen state. With this behavior, we observed that the magnetic nanoparticles with the fiber release out during the temperature variation, made it got the potential to be applied in the magnetic particles releasing platform and could be further used in the field of hyperthermia treatment. The surface morphology of the electrospun fibers were characterized by the transmission electron microscope and the magnetic property was measured by superconducting quantum interference device. High frequency alternative magnetic field machine was use to triggered the temperature response behavior and recorded by the thermal infrared image system. The fibers morphology variation under the AMF was recorded by the CCD camera system. The results showed that the temperature responsive fibers were successfully fabricated by the electrospun process with the magnetic nanoparticles and the captured image showed the releasing of magnetic nanoparticles behavior under the AMF trigged.

T. R. Ger, H.T. Huang and M.F Lai, Journal of Applied Physics., vol.115, p.17B908 (2014) T. Y. Chen, C. K. Huang, and T.R. Ger, AIP Advances., vol. 9, p.035339 (2019)



Images of the temperature responsive electrospun fiber and the magnetic nanoparticles releasing

DU-14. Image-based feedback control of a distal part of magnetic catheter to enhance a path-following capability of its position and orientation. *N. Kim*[1], W. Lee[1], J. Kim[1], E. Jung[1], J. Park[1] and G. Jang[1] *1. Convergence Mechanical Engineering, Hanyang University, Seoul, The Republic of Korea*

Various methods to control a magnetic catheter (MC) have been widely investigated to follow the path precisely. Some of the prior researchers have controlled a distal tip position of MC by utilizing various beam models [1], [2], [3]. They did not include the effect of external forces, such as pulsatile flow and heartbeat, which continuously change in real time. These methods have a potential problem to move the distal part of MC with large tilting angle which may damage blood vessel during navigation. We propose an image-based feedback control method to reduce the position error and tilting angle of the distal part of MC with respect to the pre-defined path. This method does not utilize a beam model but determines the required magnetic field from the positions of 2 markers. Fig. 1(a) shows 2 markers on MC and normal distances (d_1, d_2) of each marker from the pre-defined path. We classified the states of MC into 17 cases as shown in Fig.1(b) and decided the required magnetic field by comparing d_1 with d_2 as shown in Fig.1(c). The proposed method controls the magnetic field to minimize, and the middle point between 2 markers indicates how precisely the MC follows the path. To verify the proposed control method, we conducted *in vitro* experiment following a pre-defined path with commercial MC and traced the trajectories of 2 markers as shown in Fig.2. The trajectories are the area in which the distal part between d_1 and d_2 sweeps during navigation. As shown in Fig.2, the proposed method contains the pre-defined path around the central part of the trajectory. The results show that the proposed method reduces position error and tilting angle of the distal part in comparison with the method to control only a distal tip position. This research can contribute to improving a safe control of MC and can be utilized to automatic control of MC using deep learning by big data classification of various states of the catheter.

[1] Vi N. T. Le, N. H. Nguyen, and P. Pratten, Medical Physics, Vol. 43, no. 650 (2016) [2] N. Kim, S. Lee, and G. Jang, AIP Advances, Vol. 8, no.5 (2018) [3] J. Edelmann, A. J. Petruska and B.J. Nelson, The International Journal of Robotics Research, Vol.36, no. 1 (2017).

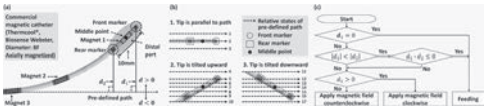


Fig.1 (1)2 markers on MC and normal distances (d_1, d_2). (b)17 cases of MC states. (c)Flowchart to determine the required magnetic field.

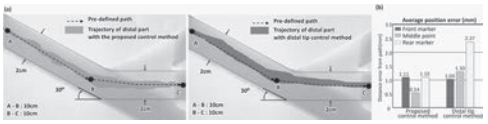


Fig.2 (1) Trajectories in which the distal part sweeps during navigation. (b)Average normal distances of 2 markers and middle point.

DU-15. Enhanced Steering Capability of the Distal End of a Magnetic Catheter by Utilizing Magnets with Optimized Magnetization Direction. *E. Jung*[1], W. Lee[1], J. Kim[1], N. Kim[1], J. Park[1] and G. Jang[1] *1. Mechanical Engineering, Hanyang University, Seoul, The Republic of Korea*

Conventional catheters can only be controlled from outside of a patient's body by a medical doctor which makes it difficult to precisely control the distal end of catheter. Magnetic navigation system (MNS) and magnetic catheter (MC) have been developed to overcome this limitation of conventional catheters [1,2]. Magnets in a MC make it possible to control the MC's distal end by applying an external magnetic field (EMF) generated by MNS to the magnets [3]. Conventional MCs are made of multi-magnets with same magnetization direction which tend to align along the direction of EMF. However, these MCs cannot deform only the distal end of the MC but whole MC. It does not provide precise navigating ability and it also damages blood vessel when navigating through a steeply bifurcated branch of complex blood vessel. In this paper, we propose a MC that can generate large curvature to precisely navigate through complex blood vessel. The proposed MC is composed of a flexible tube, three magnets as shown in Fig. 1(a). To design the magnetization direction of magnet1 (Φ_1) and magnet2 (Φ_2), we defined two parameters *k* (the curvature of the MC's distal end) and *D* (the vertical displacement of MC's proximal end) as shown in Fig. 1(b). We optimized *k* and *D* by utilizing Euler-Bernoulli beam theory with the application of EMF for 6 cases that satisfies $0°\leq\Phi_2\leq\Phi_1\leq180°$ (Φ_1, Φ_2=0°, 90°, 180°). We prototyped the optimized MC with enhanced steering capability in case of Φ_1=180° and Φ_2=90°. We verified its performance by comparing the curvature of the conventional MC (30.1 m^{-1}) with that of the proposed MC (77.5 m^{-1}) under same EMF (100 mT) as shown in Fig.2(a), (b). Finally, we confirmed that the proposed MC can precisely and successfully navigate through a bifurcated glass tube with -140° *in vitro* experiment as shown in Fig. 2(c).

B. J. Nelson, I. K. Kaliakatsos, and J. J. Abbott, Annual Review of Biomedical Engineering., Vol. 12, p. 55 (2010) N. Kim, S. Lee, W. Lee, and G. Jang, AIP Advances, Vol. 8, p. 056708 (2018) J. Nam, W. Lee, and G. Jang, IEEE Transactions on Industrial Electronics, Vol. 65, p. 5673 (2018)

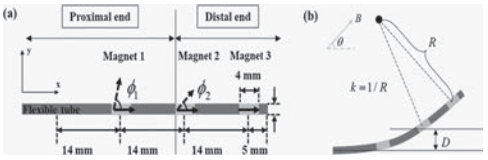


Fig. 1 (a) Structure of MC and design variables of magnet 1 and 2 (Φ_1 and Φ_2). (b) Curvature (*k*) and maximum vertical displacement (*D*) to optimize Φ_1 and Φ_2 to enhance the steering ability of MC's distal end.

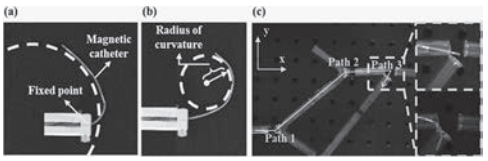


Fig. 2 (a) Curvature of conventional MC. (b) Curvature of proposed MC. (c) *In vitro* experiment to verify the steering capability of proposed MC (Right-top: conventional MC, right-bottom: proposed MC).

Session DV
SENSORS I
(Poster Session)

Simon Greaves, Chair
Tohoku University, Sendai, Japan

DV-01. Structue and Output Voltage Model Optimization of Magnetostrictive Force Sensor. *B. Wang*[1,2], X. Cui[1,2], W. Huang[1,2] and L. Weng[1,2] *1. State Key Laboratory of Reliability and Intelligence of Electrical Equipment, Tianjin, China; 2. Key Laboratory of Electromagnetic Field and Electrical Apparatus Reliability of Hebei Province, Tianjin, China*

A force sensor plays an increasingly important role. It is complementary to visual perception and can be widely used in robotic grasping of objects and daily life. Since most of the existing magnetostrictive force sensor output voltage models do not consider the influence of magnetostriction on the output voltage, the model calculations are deviated from the experimental results. It is essential to establish a output voltage model that can accurately reflect the material mechanism for the magnetostrictive force sensor. A novel output voltage model is proposed considering the external forces, the bias magnetic field, and the magnetostriction. In order to prove the accuracy of the sensor output voltage model,a magnetostriction sensor for precise sensing of small external forces is designed. It consists of a sheet cantilever beam, a coil, a hard contact, a Hall element, a skeleton, and a silicone casing (Fig.1). The cantilever beam is magnetostrictive material Fe-Ga or Fe-Co sheet, which has a favorable magnetostriction combined with mechanical strength, and fast response speed. The sensor output voltage designed in this paper is studied through experiments,The output voltage of the design force sensor are measured and analyzed. It is found that the results of the theoretical calculation are consistent with the experimental ones (Fig.2). We can see that the output voltage of the sensor gradually increases as the external force increases when the magnetostriction and bias magnetic fields are constant. The results show that the proposed output voltage model of the force sensor has high accuracy and the designed force sensor has good practicability.

[1] Zhao Y, Li J and Liu Y, et al. Journal of Magnetism & Magnetic Materials, Vol. 451, p.587 (2018) [2] Atulasimha J, Flatau A B, Chopra I, et al. Proceedings of SPIE - The International Society for Optical Engineering, Vol. 5387, p.487 (2004) [3] Wun-Fogle M, Restorff J B, Clark A E, et al. Journal of Applied Physics, Vol.97, p.881 (2005)

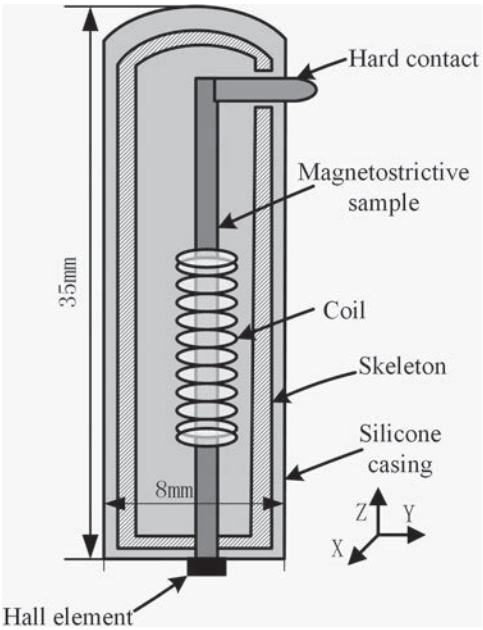


Fig. 1. Structural of the force sensor.

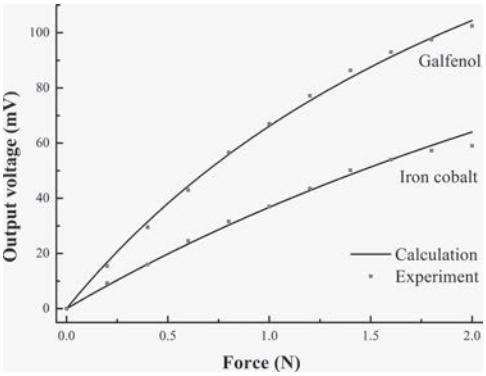


Fig. 2. The Output voltage of the force sensor.

DV-02. A Highly Sensitive Coplanar Line Thin Film Sensor for Magnetocardiographic Measurement. H. Kudo[1], H. Uetake[3], H. Onodera[2], *L. Ton That*[1,2], S. Yabukami[1,2], J. Hayasaka[3] and K. Arai[3] *1. Tohoku University, Sendai, Japan; 2. Tohoku Gakuin University, Tagajo, Japan; 3. Research Institute for Electromagnetic Materials, Tomiya, Japan*

Highly sensitivity thin film sensors operating at room temperature are gaining more attention for use in biomagnetic measurement because they are much cheaper and easier to operate than SQUID, and can be easily integrated into sensor arrays compared to large-scale induction coils and fluxgate sensors. In previous studies, we successfully detected magnetocardiogram signals without magnetic shielding [1]. To enhance the sensitivity, this study developed a new coplanar line thin film sensor composed of CoNbZr,

SrTiO and Cu/Cr films mounted by flip chip bonding, then examined the phase change to the film thickness and the signal and noise level under a low-frequency magnetic field. As shown in Fig. 1, the sensor element was fabricated by depositing an amorphous CoNbZr film on a glass substrate by RF sputtering and processing coplanar lines of Cu film by liftoff through SrTiO film. CoNbZr film was annealed in a rotating magnetic field, then in a static magnetic field to induce transverse magnetic anisotropy. Cr film used to improve the contact between SrTiO film and Cu film. To evaluate the sensor, dc magnetic field of 0–10 Oe was changed slowly in the longitudinal direction of the coplanar by a Helmholtz coil, and the phase change of the carrier was detected by a network analyzer. The carrier frequency was 0.3 MHz–4 GHz. Fig. 2(a) shows the relationship between the thickness of CoNbZr film and the slope of phase change with respect to external magnetic field. The sensor had good characteristics with a maximum phase change of 295.8 deg/Oe and a gain of over –40 dB for CoNbZr film thickness of 1 μm under the carrier frequency of 1670 MHz and external magnetic field of 4.5 Oe. We considered that the magnetization is easily aligned in the plane, thereby magnetization rotation with less dispersion can be obtained. Next, we measured the output spectrum of the carrier under a weak magnetic field of 20 Hz and 2.7×10^{-9} T using a laboratory-made setup [2]. As shown in Fig. 2(b), the noise level achieved was approximately 100 pT/√Hz around 20 Hz.

[1] S. Yabukami et al., J. Magn. Soc. Jpn., Vol. 38, pp. 25-28 (2014)
[2] H. Uetake et al., IEEE Trans. Magn., Vol. 50 (11), pp. 4007604 (2014)

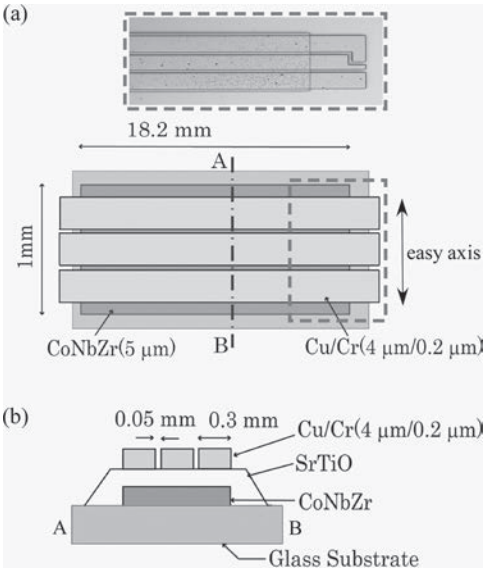


Fig. 1 Thin film sensor with (a) top and (b) cross-sectional views.

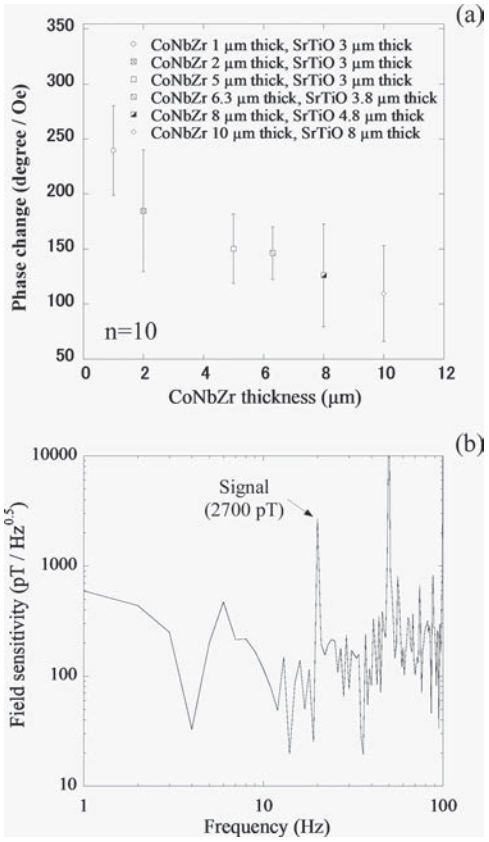


Fig. 2 (a) Phase change as a function of CoNbZr film thickness, and (b) Signal and noise level using the sensor.

DV-03. Design and Output Characteristics of Magnetostrictive Flexible Tactile Sensor Array. *L. Weng*[1], S. Gao[1], B. Zhang[1], S. Liu[1], B. Wang[1] and W. Huang[1] *1. Hebei University of Technology, Tianjin, China*

Tactile information is essential in determining physical properties of objects[1]. Various types of tactile sensors have been proposed, which can be categorized as piezoresistive[2], piezoelectric, capacitive, and optical sensors[3]In practical applications, the tactile sensor is required to detect multi-contact information and achieve flexible[4]. A magnetostrictive tactile sensing unit based on the Villari effect of iron-gallium alloys (Galfenol) line was designed and integrated into an flexibly array. The output characteristics of the flexible magnetostrictive tactile sensor array were tested. The magnetostrictive tactile sensing unit is composed of Galfenol wires, Hall sensor, contact, permanent magnets, and shell, as shown in Fig.1 (a). When the contact of tactile sensing unit touches an object, the Galfenol wires are deformed and the magnetic induction changes, which further cause the change of output voltage in Hall sensor. The sensing unit is consisted of three Galfenol wires with length of 10 mm and a diameter of 0.5 mm as the transducing component. Two permanent magnets are installed in the side wall of the shell to provide bias magnetic field. The Hall sensor is placed on the back side of shell. The contact is used to transfer force to bend the wires. The size of the sensing unit is 7.5 mm × 4.4 mm × 4.5 mm, and the weight is 0.56 g. The flexible array integrated with a 2 × 3 matrix magnetostrictive tactile sensing unit is fabricated on a flexible printed circuit (FPC), as shown in Fig.1 (b). Two adjacent sensing units share permanent magnets. Fig. 2 shows the relationship between the output voltage of magnetostrictive tactile sensing unit and the applied force F in the bias magnetic field of 2.5 kA / m. The results show that the output voltage increases with the increase of force applied to the unit. When the force increases to 3 N, the output voltage reaches 183.9mV. The sensitivity is 61.3 mV/ N in the range of 0 - 3 N.

[1] Zou L, Ge C, Wang Z., Sensors, Vancouver, vol.17, p. 2653(1-24),Nov.2017. [2] Zhang T, Jiang L and Liu H, IEEE Transactions on Neural Systems & Rehabilitation Engineering. Shenzhen, vol.26, p.1391-1399, Jul.2018 [3] Jung M, Kim K and Kim B, Nanoscale. vol.9, p.17212-17219,Nov. 2017 [4] B. Zhang, B. Wang and Y. Li, IEEE Transactions on Magnetics. Tianjin, vol. 54, p. 4002205, Nov.2018.

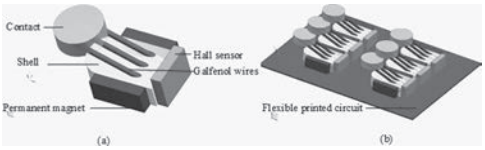


Fig. 1 Structure of magnetostrictive tactile sensing unit (a) and integrated flexible array (b)

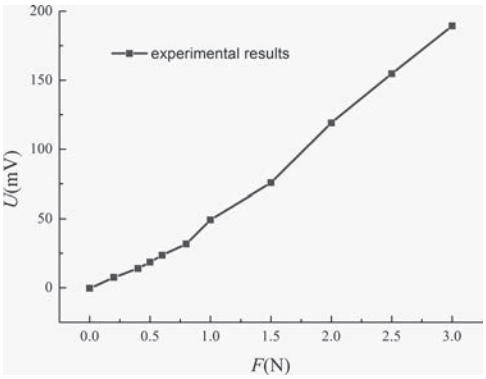


Fig.2 Relationship between output voltage and applied force.

DV-04. Controlling domain configuration for the sensing layer of magnetic tunneling junction by using exchange bias. *S. Ranjbar*[1], M. Al-Mahdawi[2], M. Oogane[1,2] and Y. Ando[1,2] *1. Applied Physics, Tohoku University, Sendai, Japan; 2. Center for Science and Innovation in Spintronics (Core Research Cluster), Organization for Advanced Studies, Tohoku University, Sendai, Japan*

Magnetic tunnel junctions (MTJs) are becoming important for magnetic field sensing applications, like the bio-magnetic sensing. However, the low-frequency noise is still a major challenge for low-field sensing. We expect that the main origin of magnetic noise of MTJs is the fluctuating domain walls at the center of MTJ device. The purpose of this study is controlling the multidomain structure in the sensing layer by using an exchange bias from an antiferromagnetic (AFM) layer. In this study, we used PtMn as an AFM layer because it shows higher blocking temperature (410 C) than other AFMs such as IrMn [1]. Additionally, PtMn has a large unidirectional anisotropy constant (J_k = 0.24 erg/cm^2) which is comparable with IrMn [2, 3]. We studied the effect of exchange bias on the micro-patterned Permalloy (Py: $Ni_{80}Fe_{20}$) sensing layer. We deposited (A) single Py (70 nm) layer, and (B) $Pt_{48}Mn_{52}$ (15nm)/Py (60 nm) exchange-biased films on thermally-oxidized silicon substrates. After annealing at 370 C, sample B showed a small coercivity and exchange bias (7 Oe). After micro-fabrication into 50 μm × 50 μm square pillars, we measured the domain structure by Magneto Optical Kerr Effect (MOKE) microscopy. Figures 1 (a,b) show the domain configurations of samples A and B at zero field, respectively. Sample A has a simple closure domain at the center, whereas sample B exhibits a more complicated structure but with a single domain at the center region due to exchange bias overcoming the magnetostatic energy. The dashed rectangle shown in the MOKE images is the area of pinned layer for MTJ devices. Therefore, sample B is promising for decreasing the magnetic noise due to single domain at the center of PtMn/Py sensing layer. This work was supported by the S-Innovation program, Japan Science and Technology Agency (JST) and by JSPS KAKENHI Grant Number JP19K15429.

[1] S. RANJBAR, M. TSUNODA, Muftah Al-Mahdaw, M. OOGANE, Y. ANDO, Composition Dependence of the Exchange Anisotropy in Pt_xMn_{100-x}/Co_yFe_{100-y} Films (2019). (submitted) [2] S. RANJBAR, M. TSUNODA, M. OOGANE, Y. ANDO, Composition Dependence of Exchange Anisotropy in PtxMn1-x/Co70Fe30 Films, Jpn. J. Appl. Phys. (2019). [3] Du, Yuqing, et al. *Applied Physics Letters* 96.22 (2010).

DV-05. Improving Filmed Planar Inductor by Grooved Gratings for Sensor Applications. *X. Zhou*[1], Y. Wen[1], Y. Mu[1] and P. Li[1] *1. Shanghai Jiao Tong University, Shanghai, China*

Soft magnetic materials have relative permeabilities that are extremely sensitive to an applied magnetic field and they are always made into a specific structure such as a film structure for miniaturization and circuit integration. A filmed inductor, which consists of a planar coil sandwiched by two soft magnetic films, can show different inductances under various external magnetic fields[1]~[2]. When sensing an applied field, the films are magnetized so that the film permeability changes. Ideally, the inductance will change dramatically as much as the permeability's variation, which suggests a great potential for magnetic sensor applications[3]. However, as no closed-up magnetic circuit is formed in the film, demagnetization and flux leakage are inevitable. Hence, the inductance variation cannot perform so high as the ideal condition and the performances of the device is constrained accordingly. In this paper, we propose an approach of improving the filmed inductor's performances by producing grooved gratings on the film surfaces. First, the relationship between demagnetization and film structure is studied. The results reveal that grooved gratings not only reduce demagnetization by thinning the film, but also generate stray field whose component has the same direction as the applied field. Thus, as shown in Fig.1, the internal field (effective field) is enhanced and the variation of effective permeability is improved. On the other hand, as the filmed coil is a device that converts electrical energy into magnetic energy and stores it, the more field induced by the coil current concentrated in the film, the larger inductance the device obtains. We precisely calculate the flux in the film and the coil inductance through Maxwell's equations. In Fig.2, compared with the coil sandwiched by smooth films, the current-induced field is enhanced in the film, and both the inductance and its variation rate with different permeabilities are improved significantly. Finite-element simulations also indicate a good agreement with our analysis which suggests a more sensitive inductor in magnetic sensor applications.

Y.Wang, Y.Wen and F.Song, *Applied Physics Letters,* Vol.112, p.182403(2018) F.Song, Y.Wen and P.Li, *IEEE Transactions on Magnetics*, Vol.55, p.4001505(2019) Y.Wen, F.Song and P.Li, *IEEE Transactions on Magnetics*, Vol.54, p.4001906(2018)

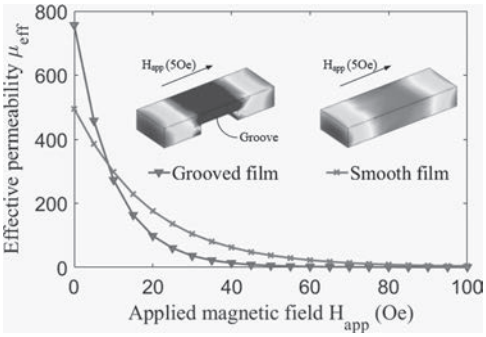


Fig.1 Improvement of film permeability by a groove

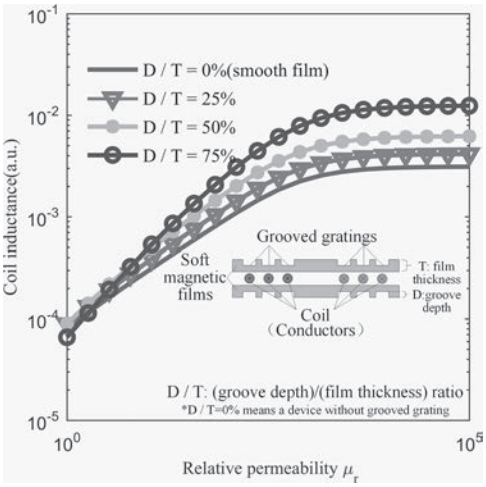


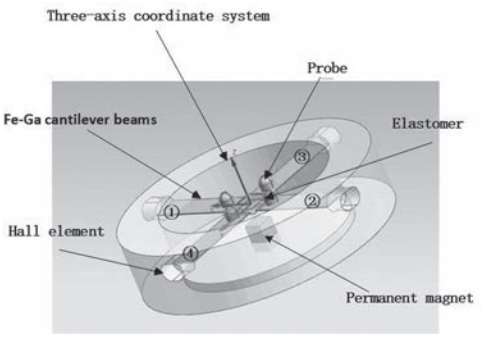
Fig.2 Enhancement of coil inductance by grooved gratings

DV-06. Withdrawn

DV-07. Analysis of Output Characteristic Model of 3D Tactile Sensor Based on Cantilever Beams. *L. Wan*[1] and B. Wang[1] *1. Hebei University of Technology, Tianjin, China*

Tactile sensing and recognition are indispensable for new generation intelligent robot. Along with the development of the intelligent robotic hand, tactile sensing and recognition technologies have increasingly attracted a wide attention. In this paper, a novel tactile sensor of three-axis detection is developed, which based on the material of Fe-Ga alloy. The relationship between the output voltage of the tactile sensor and the force signal of texture surface has been analyzed and the structure of tactile sensor has been designed. The 3D tactile sensor mainly composed of four Fe-Ga cantilever beams, the permanent magnet, four Hall elements, four probes and an elastomer shaped as fingertips, as shown in Fig.1. In order to increase the flexibility of the tactile sensor, the four probes at the free end are wrapped together in elastomer, while the other end is installed at a cylindrical base, 90 degrees apart from each other. The maximum magnetostrictive coefficient of the cantilever beam exceeds 280ppm along the rolling direction. The cylindrical base has the radius of 11mm and the fingertip-like the elastomer has the height of 5mm. The 3D tactile sensor is mounted on the support bracket and can touch the surface texture of the object from different angles. The contact between the elastomer and the surface of the object moving at a certain speed forms a contact surface, whose normal stress and shear stress can be analyzed according to the three-dimensional stress state. After the elastomer of 3D tactile sensor is deformed by external object, the positions of the four probes fixed at the free end of the cantilever beam are changed, and drive the Fe-Ga sheet to move up and down. According to Fig.1, the results of the analysis and simulation show that the normal stress on the four probes is the same in the same direction; one shear stress acts on the cantilever beams in the x-axis direction is equal in the magnitude but opposite in direction; the same is true for the cantilever beams in the y-axis direction. Therefore, the four output voltages of the 3D tactile sensor, related with the stress can reflect the texture information of the object surface from three dimensions.

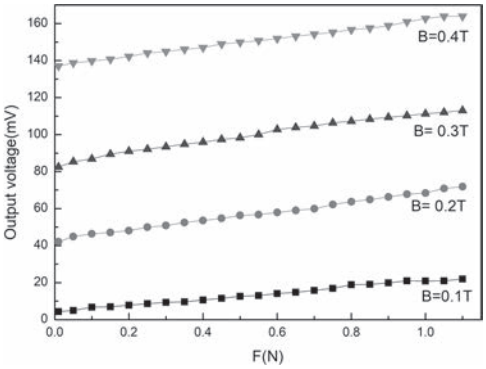
[1] Zhang T, Liu H, Jiang L, et al. “Development of a flexible 3-D tactile sensor system for anthropomorphic artificial hand,” IEEE sensors journal, vol.13, no.2, pp.510-518, 2013. [2] Luyu Zhang, Bowen Wang, Ying Sun, Ling Weng, and Peng Wang. ”Analysis of output characteristic model of magnetostrictive displacement sensor under a helical magnetic field and stress,” IEEE transactions on applied superconductivity, vol.26, no.4, June 2016. [3] Liu S, Wang L, Feng X, et al. “Ultrasensitive 2D ZnO piezotronics transistor array for high resolution tactile imaging,” Advanced Materials, vol.29, no.16, 2017.



DV-08. The output characteristic of texture tactile sensor based on the inverse-magnetostrictive effect and the surface texture detection. *L. Wan*[1] and B. Wang[1] *1. Hebei University of Technology, Tianjin, China*

Humans rely on sense of touch for perception and control of the body, grasping, manipulating, and identifying objects via their physical properties, such as texture, shape, and stiffness. The perception of the textural properties of object is one the most challenging task in robotics. In order to extract robust features from the generated raw tactile signals during tactile object exploration, the key is to design a set of novel tactile sensor. However, research work on the tactile sensor, based on the inverse-magnetostrictive effect, is rare. Therefore, it is necessary to investigate the output characteristic of the texture tactile sensor based on the inverse -magnetostrictive effect. The output voltage model for the texture tactile sensor has been developed, according to the inverse-magnetostrictive effect, the Jiles-Atherton model, the hall effect and the strain theory of the beam. The output voltage detected by the Hall element is mainly related to the bias magnetic field, the contact depth, the contact pressure angle, the width of the ridge and the groove of the object surface. The contact depth is determined by the normal force applied to the texture tactile sensor. The prototype of the texture tactile sensor is manufactured, based on $Fe_{83}Ga_{17}$ alloy sheet, which has the length of 10mm, the width of 3mm, and the thickness of 0.1mm. Fig.1 shows the relationship between output voltage of texture tactile sensor and normal force under different magnetic induction. The experimental result shows that output voltage increases with increasing normal force (in the range 0-1.15N). From the data in Fig.1, the ratio of output voltage to normal force is 16mv/N, 27mv/N, 28mv/N,24.5mv/N, while the magnetic induction changes from 0.1T to 0.4T. Therefore, the normal force and the magnetic induction from the permanent magnet provide the basis for the design of the tactile sensor. In addition, the texture tactile sensor mounted on an artificial fingertip has been designed to detect surface textures of different dimensions. The output signal generated during the exploratory movement of the finger reliably correlates to all the widths of grooves and ridges of the surface textures under investigation.

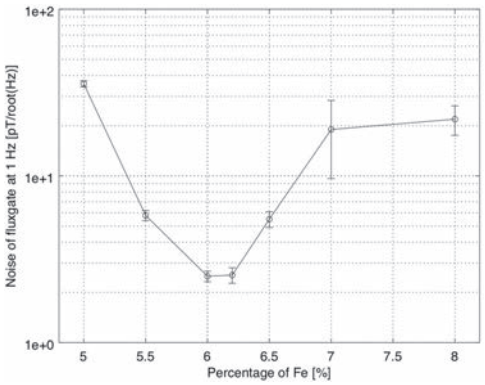
[1] R. S. Johansson and J. R. Flanagan, “Coding and use of tactile signals from the fingertips in object manipulation tasks,” Nature Rev. Neurosci., vol. 10, pp. 345–359, 2009. [2] Kaboli, Mohsen, and Gordon Cheng. “Robust tactile descriptors for discriminating objects from textural properties via artificial robotic skin.” IEEE Transactions on Robotics34.4 (2018): 985-1003. [3] Jamali, Nawid, and Claude Sammut. “Material classification by tactile sensing using surface textures.” *2010 IEEE International Conference on Robotics and Automation*. IEEE, 2010.



DV-09. Dependence of the noise of an orthogonal fluxgate on the composition of its amorphous wire-core. *M. Butta*[1,2], M. Vázquez[2], R. Pérez del Real[2] and E. Calle[2] *1. Faculty of Electrical Engineering, Czech Technical University in Prague, Prague, Czechia; 2. Consejo Superior de Investigaciones Científicas - CSIC, Instituto de Ciencia de Materiales de Madrid, Madrid, Spain*

Amorphous magnetic wires have been used for long time as cores of orthogonal fluxgate sensors as well as for other sensors such as GMI. Despite the good results in terms of the noise [1] of the fluxgates based on such wires we still have limited information about the origin of this noise. In this paper we study the dependance of the noise on the composition of the wires. We casted amorphous wires changing the composition $(Co_{100-x}Fe_x)_{72.5}Si_{12.5}B_{15}$ for different values of x: 5, 5.5, 6, 6.2, 6.5, 7 and 8. We changed the relative amount of iron and cobalt keeping the total amount of these two elements unchanged to the respect of silicon and boron. By doing so we changed the magnetostriction of the alloy, because of the different compensation between positive and negative contribution to magnetostriction brought by iron and cobalt [2]. The wires were produced by water quenching and they all had diameter between 120 and 130 μm. We manufactured three sensors for each composition using wires produced with three different master alloys and three casting processes to avoid the effect of the random defects due to the manufacturing process. There wires were cut in 8 cm long pieces and used as cores for orthogonal fluxgate. Each core had 2 wires connected in series and soldered on a fiberglass substrate at 3 mm distance. Finally a 2500 turns pick up coil was wound around the cores. All sensors showed resonance at a value of frequency around 40 kHz. We then measured the noise using 50 mA DC current in the wires added to an AC component at 40 kHz with different values of amplitude. The lowest noise was obtained for all sensors around 40 mA. Fig. 1 shows the dependence of the noise at 1 Hz vs. the percentage of iron in the wire. We clearly see that the minimum noise (about 2.5 pT/√Hz) is achieved between 6 and 6.2 % of iron, which should give the minimum magnetostriction [2]. This indicates that a component of the noise in orthogonal fluxgates is caused by the magnetostriction connected to the stress introduced to the wires during casting and during the assembling of the sensor.

[1] Butta M, Schutte B.P., Low-Noise Orthogonal Fluxgate Using Flipped Current Joule Annealing, IEEE Transactions on Magnetics, Vol. 55, Iss. 7 (2019 [2] Magnetostriction of amorphous $(Co_{1-x}Fe_x)_{75}Si_{15}B_{10}$ ribbons ($0 \leqq x \leqq 0.12$) and its temperature dependence, November 1984 Solid State Communications 52(7):701–703



Dependence of the noise at 1 Hz of an orthogonal fluxgate on the percentage x of iron in the wires used as its core for composition $(Co_{100-x}Fe_x)_{72.5}Si_{12.5}B_{15}$

DV-10. Elastomer Based Force Sensor Fabricated by 3D Additive Manufacturing. *M.G. Kisic*[1], N.V. Blaz[1], L.D. Zivanov[1] and M.S. Damnjanovic[1] *1. Department of Power, Electronic and Telecommunication Engineering, University of Novi Sad, Faculty of Technical Sciences, Novi Sad, Serbia*

Numerous sensors with ferrite materials are fabricated for specific sensing applications [1, 2]. A large number of innovative sensors demonstrated very good performances of silicone rubber Ecoflex for realization of various sensors [3]. In this paper a new simple soft inductive magnetic sensor for force measurement is presented. The working principle of the sensor is based on the variation of the inductance caused by distance changes of ferrite in close proximity to the inductor. The sensor consists of a casing, an inductor, a piece of ferrite and a layer of elastomer (Fig. 1.). For the fabrication of inductor are used 3D printer and silver. The rectangular spiral inductor has outer dimensions of 21x25mm^2, 8 windings, and lines of width and spacing of 600 μm. At comparison of various fabrication technologies additive technology is one of the more reliable which enables the realization of cost-effective sensors with enhanced features. The dimensions of the used ferrite are 21x25x3.7mm^3. Two liquid parts of Ecoflex (vol. 1+1 ml) are mixed, poured into the 3D printed mold (in the shape of a matrix with outer dimensions of 21x25x1.5mm^3), cured under room temperature for 4 hours after which it is demolded from the mold. Sensor's elastic layer is in the form of a matrix in order to achieve a better elasticity of Ecoflex and sensitivity of the sensor. Ecoflex rubbers open new opportunities for designs of the sensor simultaneously with good performances due to their good properties. The casing of the sensor is 3D printed, with 4 pins in the corners in order to hold all the components together. All fabricated parts of the sensor are placed in the casing and the characterization of developed sensor is done by employing Impedance Analyser4194A and in house developed forcer. The Ecoflex deforms under the applied force which decreases distance between the inductor and the ferrite and causes the increase in the inductance of the sensor (Fig. 2.). The measurements are done for the forces up to 2N and the obtained sensitivity is 2nH/N.

1. Lj. Zivanov, M. Damnjanović, N. Blaz et al., 19th Chapter Soft ferrite applications in book Magnetic, Ferroelectric, and Multiferroic Metal Oxides, Elsevier, pp. 1-658 (2018) 2. M.G. Kisic, N. V. Blaz, K. B. Babkovic et al., IEEE Transactions on Magnetics, Vol. 51, No. 1, art. no. 4002004, pp. 1-4 (2015) 3. H. Wang, D. Jones, G.de Boer et al., IEEE Sensors Journal, Vol. 18, No. 19, pp. 7793-7801 (2018)

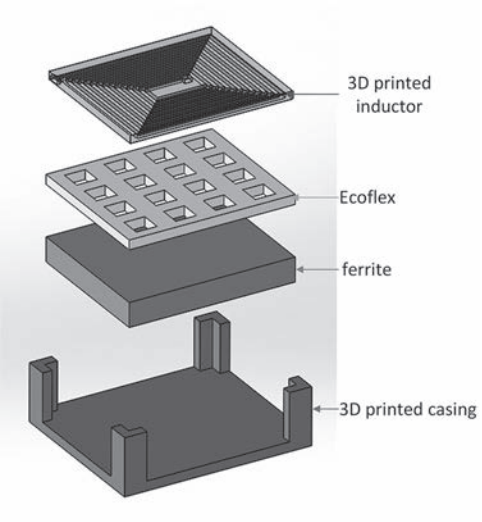


Fig. 1. Exploded 3D model of the sensor.

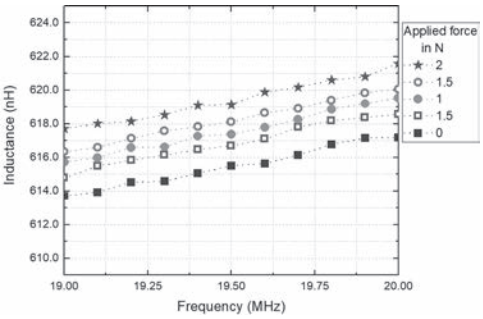
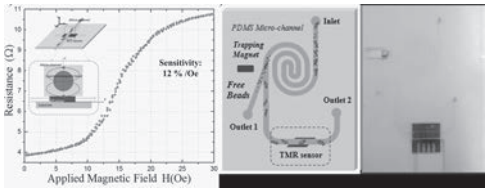


Fig. 2. The frequency dependence of the inductance for different applied forces.

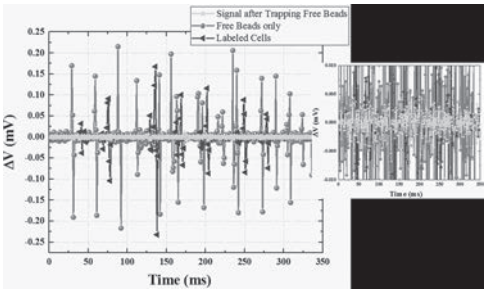
DV-11. High-Performance Magneto-Resistive Cytometer of Filtered Magnetically Labeled Cells. *S. Amara*[1], M. Alawein[1] and H. Fariborzi[1] *1. CEMSE, King Abdullah University of Science and Technology, Thuwal, Saudi Arabia*

Flow cytometers provide rapid and reliable analytical capabilities, making them an important tool for biological and biomedical analyses. We propose a compact magnetic biosensor cytometer with Tunneling Magneto-Resistive (TMR) sensors suitable for the detection of cells labeled with superparamagnetic beads. This concept has a number of distinct advantages. Firstly, biological samples hardly contain any magnetic material; therefore the detection background is intrinsically low. Secondly, TMR sensors for label detection can be integrated on-chip [1-6]. A spiral microfluidic device with a trapping magnet is implemented to filter free beads and separate them from labeled cells. The curvilinear micro-channels under continuous flow presents an inherent Dean Vortex which focus larger labeled cells against the inner wall, with inertial lift forces. The trapping magnet is added to further improve the separation of free beads from labeled cells. The labeled cells are directed to pass by the TMR sensor, where their passage is detected. The cytometer consists of TMR sensor with a high sensitivity of 12%/Oe (Fig.1.a) and a curvilinear polydimethylsiloxane micro-channel (Fig.1.b). The beads, magnetized by 15 Oe external field, are used to label the human embryonic kidney cells 293. The stray fields of the bead can be sensed by the MTJ, if the magnetic bead is within the sensing region. The sensor is first tested using free beads in a simple linear PDMS micro-channel. When magnetic beads pass over the TMR sensor, the resistance of the sensor changes, causing a variation of the sensor output voltage (Fig. 2). When free beads are filtered by the micro-fluidic channel, no significant peak is detected. When injecting cell-bead compounds (after 24h of incubation), signals are observed even after filtering, indicative of labeled cells passing by the sensor. The results prove the efficiency of the implemented filter and sensor system for detection of magnetically labeled cells.

[1] F. Li and J. Kosel: "An efficient biosensor made of an electromagnetic trap and a magneto-resistive sensor". Biosensors and Bioelectronics, 59, pp. 145-150 (2014). [2] Kotitz, R., Matz, H., Trahms, L., Koch, H., Weitschies, W., Rheinlander, T., Semmler, W., Bunte, T., 1997. IEEE Trans. Appl. Superconduct. 7 (2), 3678–3681. [3] Graham, D., Ferreira, H., Feliciano, N., Freitas, P., Clarke, L., Amaral, M., 2005. Sens. Actuators B 107 (2), 936–944. [4] Megens, M., Prins, M., 2005. J. Magn. Magn. Mater. 293 (1), 702–708. [5] Millen, R., Kawaguchi, T., Granger, M., Porter, M., 2005. Anal. Chem. 77 (20), 6581–6587. [6] Wirix-Speetjens, R., Fyen, W., Xu, K., De Boeck, J., Borghs, G., 2005. IEEE Trans. Magn. 41 (10), 4128–4133.



TMR sensor based Cytometer : a) R(H) plot with used sensing concept inset. b) Schematic of the spiral microfluidic device with a trapping magnet.



Real-time ΔV indicating free beads and labeled cells passage over the TMR sensor

DV-12. Magneto-mechano-electric devices operating in torque mode without magnetic bias field. *J. Wu*[1], Z. Hu[1], Z. Wang[1], Z. Zhou[1] and M. Liu[1] *1. Xi'an Jiaotong University, Xi'an, China*

Giant magnetoelectric coefficient is discovered in laminated composites consisting of piezoelectric and magnetostrictive layers, where the magneto-mechano-electric coupling effect is mediated by strain.[1-3] To obtain the highest ME coefficients under a small AC magnetic field, magnetostrictive layer in ME composites must be DC biased to the point of maximum slope in the strain-magnetic field curve, inducing an ME voltage via piezoelectric effect.[4-6] Here, we propose a stress-mediated magneto-mechano-electric structure operating in torque mode without DC bias, which can be designed as a magnetic field sensor, a magnetic energy harvester, or a magnetic compass. NdFeB permanent magnets combined with elastic layers are employed to induce compressive stress on piezoelectric layer via torque effect under an external magnetic field, thus the structure is suitable for magnetic field sensing and energy harvesting. The proposed ME sensor detects both DC and AC magnetic fields, of which the sensitivities are ~0.01 Oe and ~0.001 Oe, respectively. A barbell-shaped magneto-mechano-electric device that mediated by stress reveals excellent performance for harvesting low-frequency magnetic field energy, presenting a low resonate frequency (<50 Hz), a ME coefficient higher than 1 V/cm Oe, a high output voltage (>10 V @ 10 Oe), and a maximum output power of ~10.5 μW. A magnetoelectric compass is designed for detecting the direction of an in-plane AC magnetic field. The intensity sensitivity and angle sensitivity of the proposed ME compass are 0.01 Oe and 0.2°, respectively. The multiple

functionalities realized in the magneto-mechano-electric devices without DC bias field show great potential for low power applications.

[1] Junyi Zhai, Shuxiang Dong, Zengping Xing, Jiefang Li, and D. Viehland. Appl. Phys. Lett. 89, 083507 (2006). [2] Henry Greve, Eric Woltermann, Hans-Joachim Quenzer, Bernhard Wagner, and Eckhard Quandt. Appl. Phys. Lett. 96, 182501 (2010). [3] Meng-Chien Lu, Lei Mei, Dae-Yong Jeong, Jing Xiang, Huaqing Xie, and Q. M. Zhang. Appl. Phys. Lett. 106, 112905 (2015). [4] M. I. Bichurin, R. V. Petrov, and V. M. Petrov. Appl. Phys. Lett. 103, 092902 (2013). [5] Jungho Ryu, Shashank Priya, Kenji Uchino, and Hyoun-Ee Kim. Journal of Electroceramics, 8, 107–119, 2002. [6] Zhaoqiang Chu, Huaduo Shi, Weiliang Shi, Guoxi Liu, Jingen Wu, Jikun Yang, and Shuxiang Dong. Adv. Mater. 2017, 1606022.

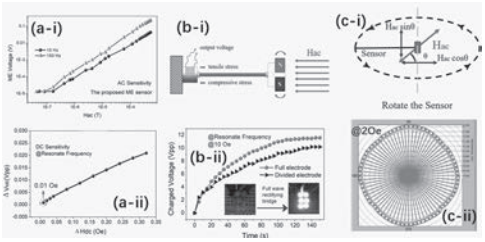


Fig 1. (a-i) AC Sensitivity of the ME sensor; (a-ii) DC Sensitivity of the ME sensor; (b-i) structure diagram of the barbell-shaped magneto-mechano-electric device; (b-ii) the variation of the voltage across capacitor with respect to charging time under 10 Oe AC magnetic field, the capacitor is charged by the barbell-shaped MME device; (c-i) diagram of test principle for the proposed ME compass; (c-ii) experimental results of ME compass for detecting arbitrary in-plane AC magnetic field of 2 Oe intensity;

DV-13. Investigation of low-frequency noise dependent on serial MTJs with various junction areas. *Z. Jin*[1], Y. Wang[1], M. Oogane[1,2] and Y. Ando[1,2] *1. Applied of Physics, Tohoku University, Sendai, Japan; 2. Center for Science and Innovation in Spintronics, Tohoku university, Sendai, Japan*

Magnetic tunnel junctions (MTJ) have received much attention due to their ultra-high tunnel magnetoresistance (TMR) [1], which can be used as high-sensitivity magnetic sensors to detect small variations in magnetic fields. To date, many studies focus on enhancement in TMR to improve sensitivity. However, the reduction of low-frequency noise is a noticeable issue for improvement of MTJ performance. Previous studies indicated that an integrated MTJ sensor could suppress low-frequency noise [2], and the electrical 1/*f* noise is related to junction area [3]. Since the choice of MTJ area has an important effect on low-frequency noise, this study investigated the low-frequency noise properties in serial MTJs with various junction areas. The stacking structure of films was SiO2 sub./Ta(5)/Ru(10)/Ta(5)/$Ni_{80}Fe_{20}$(70)/Ru(0.9)/$Co_{40}Fe_{40}B_{20}$(3)/MgO(1.6)/$Co_{40}Fe_{40}B_{20}$(3)/Ru(0.9)/$Co_{75}Fe_{25}$(5)/$Ir_{22}Mn_{78}$(10)/Ta(8)(in nm). Three types of 20 serial-MTJs sensor were fabricated with junction areas of 598 μm^2, 1520 μm^2, and 4488 μm^2, respectively. In addition, their transfer curves, noise power spectral densities, and Signal/Noise (S/N) ratio were measured. Figure 1(a) shows noise power spectral densities of serial MTJs with junction areas at a bias voltage of 100 mV and zero magnetic field. The dominant 1/*f* can be determined at the low-frequency region. The result indicated that the low-frequency noise can be decreased by increasing junction area. Figure 2(a) shows the output signals from the sensors when a 23 Hz AC magnetic field was applied from Helmholtz coils which shows clear voltage peaks. Fig. 2(b) shows the dependence of S/N ratio ($V_{peak}/V_{background}$) on the junction area at a bias voltage of 100 mV. Owing to small low-frequency noise, the high S/N ratio was obtained in the serial MTJs with a large junction area (4488 μm^2). This study indicated the choice of junction area is very important to reduce noise power and enhance the detectivity of the MTJ sensor.

[1] S.Yuasa, T. Nagahama, A. Fukushima, et al., Nat. Mater. 3, 868, (2004) [2] K. Fujiwara, M. Oogane, T. Nishikawa, et al., J. Phys. Soc. Jpn. 52, 04CM07, (2013) [3] Z. Lei, G. Li, W. Egelhoff, et al., IEEE Trans. Magn. 47, 602, (2011).

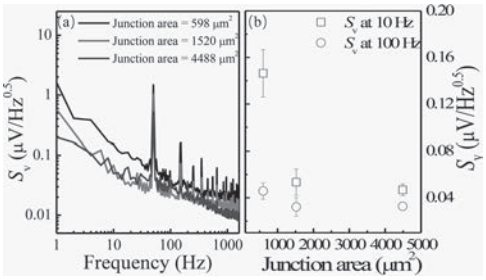


Fig.1(a) Noise power spectral density as a function of the frequency of the different sensors. (b) Dependence of noise power (10 Hz and 100 Hz) on the junction area.

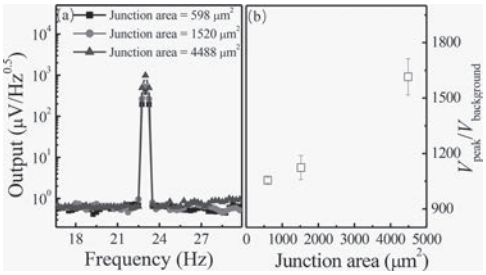


Fig. 2(a) The output signals from the different sensors. (b) Dependence of S/N ratio on the junction area.

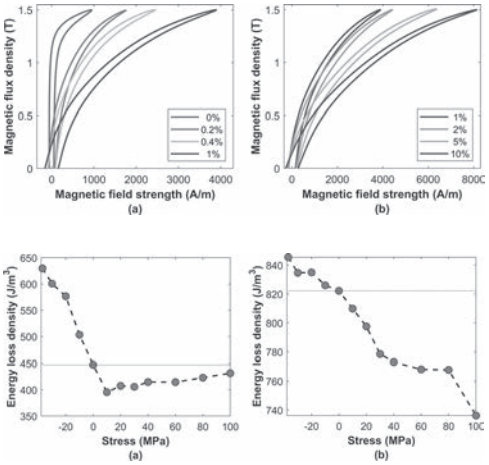
Session DW
SOFT MAGNETIC MATERIALS
(Poster Session)

Masaki Nakano, Chair
Nagasaki University, Nagasaki, Japan

DW-01. Effect of Plastic and Elastic Deformations on Magnetic Properties of Electrical Steel Sheets. *U. Aydin*[1,3], P. Rasilo[2], F. Martin[1], A. Belahcen[1], R. Kouhia[3], S. Laakso[4], L. Daniel[5] and A. Arkkio[1] *1. Department of Electrical Engineering and Automation, Aalto University, Espoo, Finland; 2. Electrical Energy Engineering, Tampere University, Tampere, Finland; 3. Civil Engineering, Tampere University, Tampere, Finland; 4. Department of Mechanical Engineering, Aalto University, Espoo, Finland; 5. CentraleSupélec, Univ. Paris-Sud, Université Paris-Saclay, Sorbonne Université, GeePs UMR CNRS 8507, Paris, France*

Electrical steel sheets are widely used in electromagnetic devices as core material. During the manufacturing of these devices the core undergoes plastic and elastic deformations. These deformations affect the magnetic properties of the material which in return affects the performance of the electromagnetic devices [1-3]. In addition, it is important to understand the effect of elastic stresses imposed in plastically deformed materials in order to develop magnetic methods for nondestructive evaluation. This paper studies for the first time the effect of simultaneous plastic and elastic deformations on the magnetic properties and iron losses of M400-50A electrical steel. The dog-bone shaped steel specimens were prepared by pre-straining the samples to various plastic strain levels ranging from 0.2% to 10% using a universal testing machine. A custom made uniaxial single sheet tester from [4] was then used to measure the magnetic characteristics of the samples under alternating field and various additional tensile and compressive elastic stresses. The magnetic flux density (*B*) and magnetic field strength (*H*) were measured by *B*-coil and tunneling magneto resistive sensor at the middle of the specimen, respectively. The supply voltage waveform of the magnetizing device was controlled to obtain sinusoidal flux density at the measurement area. *B-H* loops were measured at various flux density amplitudes and magnetizing frequencies. In Fig. 1 (a) and (b) the measured *B-H* loops for various pre-strained samples are shown. The plastic deformation increases the coercive field and decreases the permeability significantly compared to undeformed sample. These effects are attributed to change in dislocation density and pinning sites as a result of the plastic deformation. In Fig. 2 (a) and (b) the variation of the energy loss density of undeformed and 1% deformed sample at 10 Hz and 1.5 T peak flux density with respect to the applied elastic stress is shown. The detailed analysis of the effect of plastic deformation together with elastic stress on the magnetic properties and on different iron loss components in electrical steel sheets will be studied in the full paper.

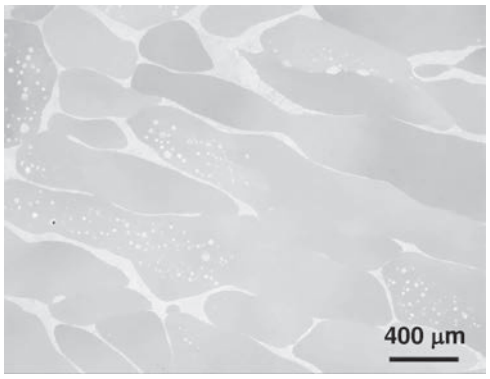
[1] M. Hofmann, H. Naumoski, U. Herr, H. H. Herzog, "Magnetic properties of electrical steel sheets in respect of cutting: micromagnetic analysis and macromagnetic modeling," *IEEE Trans. Magn.,* vol 52, iss. 2, pp. 2000114, Feb. 2016. [2] V. E. Iodache, E. Hug, N. Buiron, "Magnetic behaviour versus tensile deformation mechanisms in a non-oriented Fe-(3 wt.%)Si steel," *Mat. Sci. Eng. A,* vol. 359, iss. 1-2, pp. 62-75, Oct. 2003. [3] L. Vandenbossche, S. Jacobs, D. V. Hoecke, E. Attrazic, "Impact of mechanical stresses on the magnetic performance of non-oriented electrical steels and its relation to electric machine efficiency," *IEEE Transportation Electrification Conference and Expo (ITEC),* Jun. 2015. [4] Singh, D., Rasilo, P., Martin, F., Belahcen, A., Arkkio, A., "Effect of Mechanical Stress on Excess Loss of Electrical Steel Sheets," *IEEE Trans. Magn*., vol. 51, no. 11, pp. 1001204, Nov. 2015.

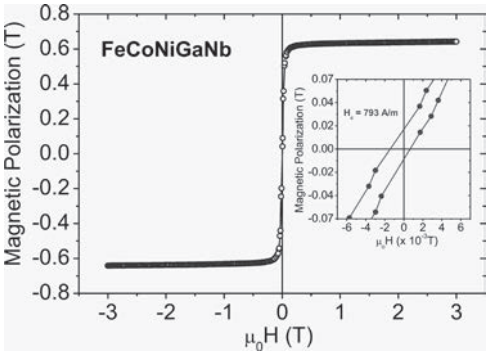


DW-02. Soft Magnetic Properties of a FeCoNiGaNb High Entropy Alloy. *C. Bormio-Nunes*[1], F. Martins Cardoso[1] and P. Pereira[1] *1. Engenharia de Materiais, Universidade de São Paulo - Escola de Engenharia de Lorena, Lorena, Brazil*

Soft magnetic material (SMM) applications comprise diverse requirements that are frequently tough and challenging for their design and fabrication. The SMMs must have a maximum permeability, small coercive force, hysteresis loss and remanent magnetization, as well as high saturation magnetization. AC applications involve equipments as power supply transformers, DC-DC Converters, electric motors and the most important issue is the material energy loss. Here we report a class of SMM material based on high-entropy alloys (HEAs) [1]. The alloy is composed of Fe, Co, Ni, Ga and Nb. The alloy has two phases, where the majority phase has a fcc structure. The second phase occupies only 9% of the volume and is richer in Nb compared to the main phase. The FeCoNiGaNb microstructure is shown in Fig. 1. Although the material is not single phase, the soft magnetic properties of the material are favorable. Magnetization measurements as a function of applied magnetic field made on a PPMS/VSM system from QD at 300K are depicted in Fig. 2. The attained coercive field is H_c = 793 A/m, the remanent magnetization is14 mT and the saturation polarization 0.68 T. Extrapolation of the magnetization vs temperature data, measured in the interval between 4 and 310 K, by using second order polynomial and exponential decay curves resulted in Curie temperatures of 721K (448 C) and 851K (578 C) respectively. The elimination of the second phase should have a positive effect on magnetic properties causing a decrease of H_c value, because it can be acting as domain wall pinning centers. In addition, if the second phase is not ferromagnetic, which is expected since it is Nb rich, the increase of the saturation magnetization is probable. Complementary data of resistivity, plus new data on the single phase alloy will be presented.

[1] Y. Zhang, T. Zuo, Y. Cheng, P.K. Liaw. Scientific Reports, v. 3, p. 1455; 2013.





DW-03. Effects of neutron irradiation on magnetic first-order reversal curves in reactor pressure vessel steels. *S. Kobayashi*[1], H. Murakami[1], A. Horvath[2], L. Almasy[2], F. Gillemot[2] and A. Feoktystov[3] *1. Iwate University, Morioka, Japan; 2. Hungarian Academy of Science, Budapest, Hungary; 3. Forschungszentrum Julich GmbH, Garching, Germany*

Magnetic method is one of useful non-destructive evaluation techniques for irradiation hardening in reactor pressure vessel (RPV) steels. Recent magnetic measurements revealed the competing mechanism due to recovery and formation of nanoscale features, which contribute to magnetic softening and hardening, respectively [1]. While neutron-irradiated materials have been investigated by measuring a major loop, first-order reversal curves (FORCs), which are one type of minor loops, have been rarely measured, primarily due to a difficulty of installing large FORC measurement system in hot cell laboratory. Here, we report results of the first attempt of measuring FORCs for neutron-irradiated RPV steels. Russian-type VVER440 and high-Ni VVER1000 steels [2], were neutron-irradiated at 290^{O}C up to a fluence of 4.3 x 10^{19} n/cm^2. FORC distribution as a function of switching field Hc and interaction field Hu, was obtained by analyzing FORCs [2]. Figs. 1(a) and 1(b) show a FORC diagram for VVER440 before and after neutron irradiation. The FORC diagram has a single FORC distribution peak on the Hc axis, which slightly shifts towards a lower Hc after irradiation. Figs. 1(c) and 1(d) show a change in the peak position $H_{c,p}$ and width parameter s of the FORC distribution peak along the Hc axis, obtained by least-squares fits assuming lognormal distribution function. For VVER440, both $H_{c,p}$ and s decrease with neutron fluence, while those for VVER1000 are almost constant. A decrease of $H_{c,p}$ reflects a magnetic softening due to recovery. On the other hand, a decrease of s indicates that magnetic inhomogeneity originating from a mixture of magnetically hard (bainite) and soft (ferrite) phases, is reduced for VVER440, while matrix microstructure is rather stable for VVER1000. The present investigations demonstrate that FORCs provide useful microstructural information for irradiated materials, which was not revealed by conventional hysteresis measurements.

[1] S. Kobayashi, T. Yamamoto, D. Klingensmith, G.R. Odette, H. Kikuchi, Y. Kamada, J. Nucl. Mater. 422, 158 (2012). [2] S. Kobayashi, F. Gillemot, A. Horvath, M. Horvath, L. Almasy, Q. Tian, A. Feoktystov, AIP Advances, 7, 056002 (2017).

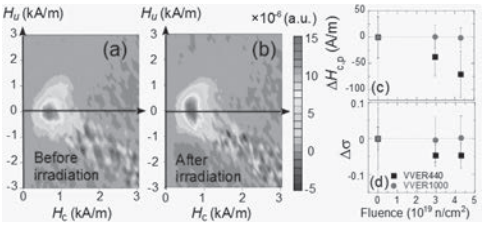
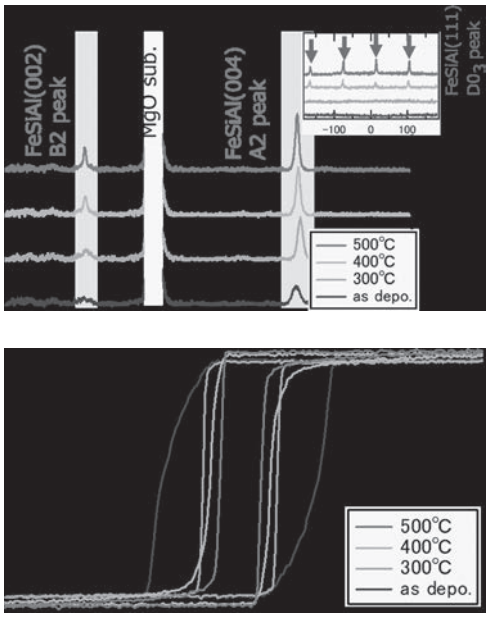


Fig.1. FORC diagram for VVER440, (a) before and (b) after neutron irradiation up to a fluence of 4.3x10^{19} n/cm^2. Neutron fluence dependence of a change of (c) peak position and (d) width parameter of a FORC distribution peak along the Hc direction.

DW-04. FeSiAl Thin Films with Low Magnetic Anisotropy for the Free Layer of Magnetic Tunnel Junction Based Sensors. *S. Akamatsu*[1], M. Oogane[1,3], M. Tsunoda[2,3] and Y. Ando[1,3] *1. Applied Physics, Graduate School of Engineering, Tohoku University, Sendai, Japan; 2. Electronic Engineering, Graduate School of Engineering, Tohoku University, Sendai, Japan; 3. Center for Spintronics Research Network, Tohoku University, Sendai, Japan*

Soft magnetic materials such as NiFe, CoFeSiB have been used for a free layer in magnetic tunnel junctions (MTJs) for bio-magnetic field sensor because of their soft magnetic properties [1, 2]. However, these materials need to form a complicated stacking structure with CoFeB, facing to MgO barrier, to obtain high tunnel magnetoresistance (TMR) ratio. In this work, we focus on $Fe_{85}Al_{9.6}Si_{5.4}$ (Sendust) alloy which has $D0_3$-ordered structure and shows very low anisotropy associated with the $D0_3$ structure in bulk. By using Sendust film as a free layer of MTJs, both low magnetic anisotropy and high TMR ratio might be realized because of the coherent tunneling due to its good epitaxial relationship with MgO barrier and structural similarity to bcc-Fe[3]. However, FeSiAl thin films with nm-order thickness have never been fabricated, so we didn't know whether FeSiAl thin film could be fabricated, have $D0_3$-ordered structure and show soft magnetic property. We optimized post-annealing temperature to obtain FeSiAl thin film with such structural and magnetic property. All films with the stacking structure of MgO(20)/FeAlSi(30)/Ta(5) (in nm) were deposited on MgO (001) substrates using magnetron sputtering. After the deposition, the films were annealed at = 300-500 degrees for 1 hour. Their crystal structure, surface roughness, and magnetic properties were measured by X-ray diffraction (XRD), atomic force microscope (AFM) and vibrating sample magnetometer, respectively. Fig. 1 shows the XRD patterns for prepared FeAlSi films. For f-scan measurements, four-fold symmetric (111) peaks from $D0_3$-ordered structure were observed at = 400 and 500 degrees. We firstly succeeded in the fabrication of $D0_3$-ordered FeAlSi epitaxial thin films grown on MgO substrates. Fig. 2 shows magnetization curves for FeAlSi films with various T_a. The film annealed at =500 degrees showed the lowest = 1.8 Oe because of the $D0_3$ ordering. The obtained small H_c is comparable to NiFe [1] and CoFeSiB [2] films. We also confirmed by AFM measurement that $D0_3$-ordered FeAlSi films possess a low surface roughness of R_a~0.3 nm. The fabricated $D0_3$-ordered FeAlSi thin film with soft magnetic property is a promising candidate for a free layer of MTJ based sensors.

[1] K. Fujiwara et al., Jpn. J. Appl. Phys., Vol. 52, p.04CM07 (2013). [2] D. Kato et al., Appl. Phys. Express., Vol. 6, p.103004 (2013). [3] W. H. Butler et al., Phys. Rev. B, Vol. 63, p.054416 (2001).



DW-05. Magnetization Process and Loss Decomposition in Fiber-Laser-Irradiated Grain-Oriented Steel Sheets. *S. Dobak*[1], J. Fuzer[1], P. Kollar[1], I. Petryshynets[2] and F. Kovac[2] *1. Institute of Physics, Faculty of Science, P. J. Safarik University, Kosice, Slovakia; 2. Division of Metal Systems, Institute of Materials Research, Slovak Academy of Sciences, Kosice, Slovakia*

Progress in loss reduction of grain-oriented (GO) steels, the key material for large-scale power transformers, has been achieved by generating thermomechanical stress to induce the artificial domain refinement [1,2]. Its influence on the bulk DC behavior has recently been understood by advanced domain imaging [2]. Little, however, is concluded on the quantitative correlation between dynamic excess loss and domain formation, affected by post-processing, playing a chief role in loss prediction at working frequencies. In this study we discuss how selective laser-irradiation, particularly designed to improve the dynamic loss response (Fig. 1), stimulate homogenization of discrete magnetization process with the attention to its theoretical assessment encompassing hysteresis and excess loss counterparts. Electric-spark-cut 3.2% Si GO sheets were stress-relief annealed and exposed to fiber laser scribing of either solid (continuous) or dotted (pulse) lines. A matrix of line spacing L (4–10 mm) and beam irradiated power P (12–240 W) was imposed to instigate domain walls (d.w.s) rearrangement, due to the interaction with residual stress pattern, in a controlled fashion. The loss in continuously treated sheet at low L decreased by 40% at $f \geq 50$ Hz while in pulse one by 16% even at 10 times higher P. By resorting to the statistical considerations on activated d.w.s [3], the dynamic d.w.-generated loss $W_{exc,calc}$ can be calculated (Fig. 2). Excellent predictive capability allows for mapping the effect of L and P on the number n of d.w.s, involved in magnetization reversal at the same time, defining the f-evolving domain structure to quantifiable extent. Such analysis, supported by domain imaging, revealed that $n(f \rightarrow 0) \sim 10–50$ increases with lower L and higher P resulting in moving width of a distribution of local d.w. pinning fields $\Delta H_c \sim 5–23$ A/m. Higher f brings about the extra domain refinement and ensuing smoothing of underlying process with further increase of n up to ~ 100 at $f = 200$ Hz and $J_p = 1.5$ T. *Support by the Slovak Research and Development Agency [APVV-18-0207] is acknowledged.*

[1] J.M. Silveyra, et al., Science, Vol. 362, p. 418 (2018). [2] P. Rauscher, et al., Sci. Rep., Vol. 6, p. 38307 (2016). [3] G. Bertotti, IEEE Trans. Magn., Vol. 24, p. 621 (1988).

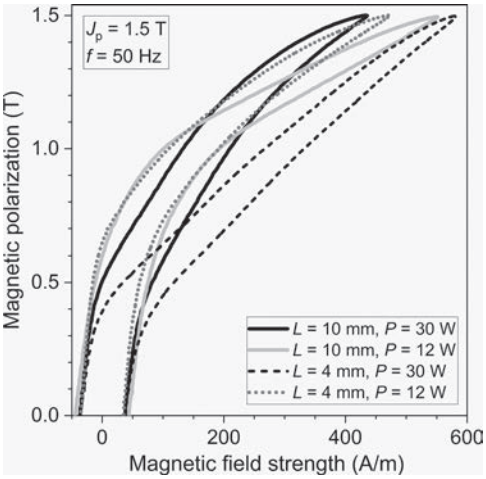


Fig. 1 Part of hysteresis loops for selected *L* and *P*.

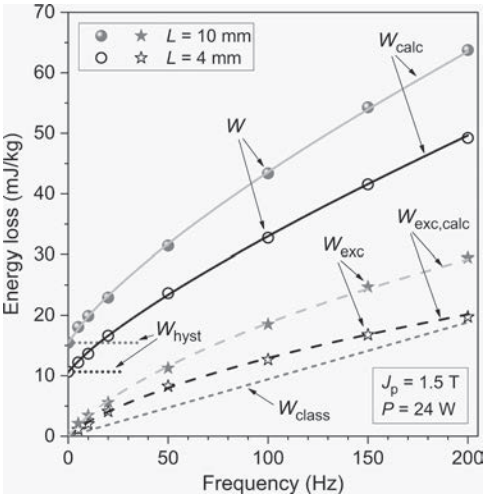


Fig. 2 Loss decomposition after continuous scribing for selected *L* at defined *P*.

DW-06. Magnetoimpedance studies on electrodeposited NiFe composite wires. *S. Vasam*[1] and S. Veeturi[1] *1. Physics, Indian Institute of Technology Madras, Chennai, India*

The giant magnetoimpedance effect has been observed in composite wires that consist of a highly conductive non-magnetic inner core and soft magnetic shell [1]. Experimental and theoretical studies have demonstrated that the presence of highly conductive inner core in composite wires results in significant increase of GMI effect [2]. The GMI is proportional to the skin depth, which varies with permeability (μ), conductivity (σ) and frequency (ω). In this work, we present the effect of core-wire diameter and its conductivity on GMI effect is studied experimentally. The electrodeposition of NiFe on 0.1(*C1)*, 0.2(*C2)*, 0.4(*C3)*, 0.6(*C4)* and 1.17(*C5) mm* diameter wires was done. Further magnetoimpedance measurements were also carried out on NiFe deposited on Ag ($0.63*10^8(\Omega m)^{-1}$), Cu ($0.58*10^8(\Omega m)^{-1}$) and $Ni_{80}Cr_{20}$ ($0.66*10^6(\Omega m)^{-1}$) wires. The electrodeposition was carried by using, $NiSO_4.6H_2O$ (0.2M), $FeSO_4.7H_2O$ (0.025M), H_3BO_3 (0.4M), NH_4Cl (0.28M), and Sodium saccharin (1g/L) bath. Magneto-impedance (MI) was measured using a IM 3536 impedance analyser. As shown in Fig.1, a maximum GMI value (705%) was observed at 50 kHz for NiFe/Ag while for sample deposited on Cu-wire (611%) was observed at 80 kHz. This could be due to higher conductivity of Ag core-wire. on the other-hand a maximum GMI value of 96% was observed at 500 kHz for the sample deposition on $Ni_{80}Cr_{20}$ wire. These observations suggest that if the conductivity of the substrate is increased maximum GMI values are shifted to low frequency

region (500kHz to 20kHz). From Fig.2. we observe high magnetoimpedance (611%) in case of C1 while for C5 the maximum MI drops to 31%. From the present observations we conclude that the frequency at which maximum magnetoimpedance is observed can be controlled by varying the substrate conductivity. On the other-hand the GMI values and sensitivity can be enhanced by choosing highly conducting substrates. As the thickness of the Cu-wire is increased maximum GMI value is observed to decreaseThe detailed experimental data supported by theoretical simulations.

M.A. Correa, et al, (2019), J.Magn.Magn.Mater, 485, 75-81. N.A Buznikov, et al, (2006), J.Magn.Magn.Mater, 296, 77-88. Panina LV, Mohri K. (1994), Appl Phys Lett, 65, 1189-91.

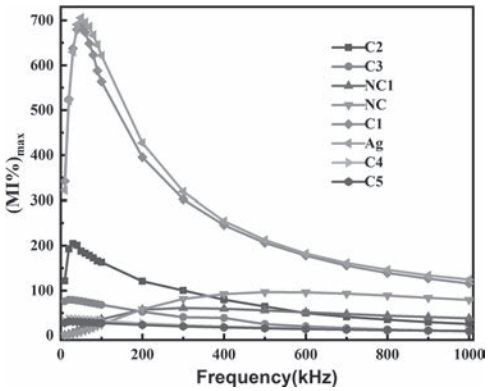


Fig.1. ($MI\%)_{max}$ as a function of frequency.

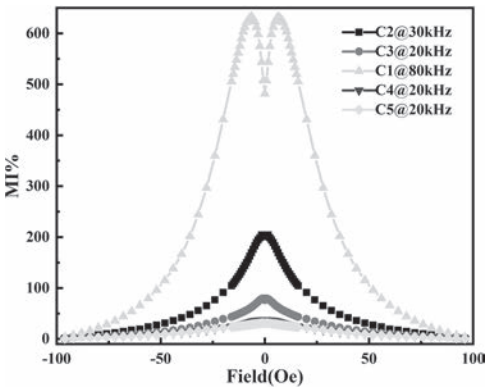
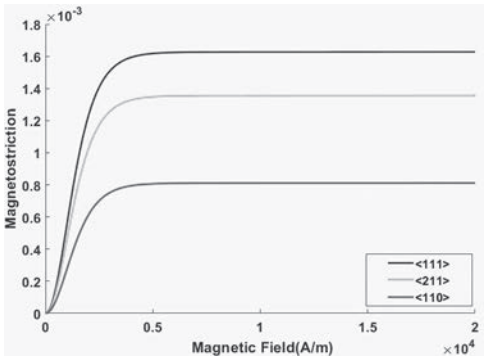


Fig.2. Magnetoimpedance as a function of external magnetic field.

DW-07. A Statistical Method for Modeling the Magneto-elastic Coupling Behavior of Magnetic Materials. *X. Yuan*[1] and L. Li[1] *1. North China Electric Power University, Beijing, China*

In order to accurately model the magnetization and loss properties of magnetic materials, a physic based model is needed to describe the phenomenon of magneto-mechanical coupling [1]. Since these phenomena usually have relatively complex nonlinear relationships, few macroscopic constitutive equations can accurately describe the effects of stress on the magnetic susceptibility and magnetostriction of the magnetic materials [2]. At the microscopic scale, the magnetic susceptibility and the magnetostriction of the magnetic materials is related to the structure of magnetic domains [3], which affects the technical properties of magnetic materials. As the intensity of the external magnetic field increases, the domain walls move and results in an increase in the number of domains whose directions are closer to the direction of the external magnetic field and a decrease in the number of domains whose directions are far from the direction of the external magnetic field. In the case of the application of stress, the stress state will also have an influence of this process which leads to the macroscopical magnetic susceptibility and magnetostriction of the magnetic materials [4] [5]. The potential energy of a magnetic domain in the magnetic materials is divided into exchange energy, magneto-static energy, magneto-crystalline energy and elastic energy. For each possible magnetization direction, the higher potential energy leads to the lower existence probability. In this paper, the existence probability of each possible magnetization direction is calculated, and the statistical method is used to model the magnetization process of the magnetic material. The magnetostriction and magnetization of two magnetic materials, giant magnetostrictive material Terfenol-D and iron-cobalt alloy are modelled by using the statistical method. Fig.1 shows the calculated macroscopic magnetostrictions of the single crystal of Terfenol-D in different directions under the applied external magnetic field. Fig.2 shows the calculated magnetization of iron-cobalt alloy under the external magnetic field and different applied uniaxial mechanical stresses.

[1] Daniel, Laurent, et al. “Reversible magneto-elastic behavior: A multiscale approach.” Journal of the Mechanics and Physics of Solids 56.3(2008):1018-1042. [2] Buiron N, Hirsinger L, Billardon R. “A multi-scale model for magneto-elastic couplings[J]”. Le Journal de Physique IV, 1999, 09(PR9):Pr9-187-Pr9-196. [3] Hubert, A., Schäfer, R., 1998. Magnetic Domains. Springer, Berlin. [4] L. Daniel, “An Analytical Model for the Effect of Multiaxial Stress on the Magnetic Susceptibility of Ferromagnetic Materials,” *IEEE Transactions on Magnetics*, vol. 49, no. 5, pp. 2037-2040, May 2013. [5] Graham, C. D. Physics of Ferromagnetism :[M]// Physics of ferromagnetism. Clarendon Press ;1997.



DW-08. Magnetic properties of Fe-Ni-system films prepared by electroless deposition. *R. Tanaka*[1], R. Ueno[1], K. Mieda[1], J. Kaji[1], A. Yamashita[1], T. Yanai[1], M. Nakano[1] and H. Fukunaga[1] *1. Nagasaki University, Nagasaki-Shi, Japan*

Fe-Ni alloys are well-known as soft magnetic materials with excellent soft-magnetic properties, and we have reported the good soft magnetic properties of Fe-Ni films prepared by an electrodeposition method [1-3]. An electroless deposition method is also chemical technic to obtain films, and the process has some advantages such as thickness uniformity, economic viability, and high selectivity of substrates. Although some researchers have reported Fe-Ni films with good magnetic properties prepared by an electroless deposition [4-6], deposition rates were not enough high (< 10 μm/h). In the present study, we developed an electroless deposition process with high deposition rate for Fe-Ni-system films. The plating bath was consisted

of $NiSO_4$-$6H_2O$:50 g/L, $FeSO_4$-$7H_2O$:70 g/L, $C_6H_5Na_7$-$2H_2O$ (Trisodium Citrate Dihydrate): 110 g/L, $(NH_4)_2SO_4$ (Ammonium Sulfate): 60 g/L, $NH_4OSO_2NH_2$ (Ammonium Amidosulfate):25 g/L, H_3BO_3: 25 g/L, $(CH_3)_2NH$-BH_3 (Dimethylamine-Borane): 5 g/L. A Cu plate was used as a substrate, and the pH of the bath was adjusted to 7.5 using KOH. The bath temperature was changed from 70 to 80°C. Figure 1 shows the thickness of the Fe-Ni films as a function of the plating time. As shown in Fig.1, the thickness tends to increase with increasing the bath temperature. The deposition rate estimated from liner fitting curves was approx. 15 μm/h, and this rate is higher than that for Ref. 4. Although we can obtain high deposition rate, the surface condition was inferior as shown in the inset. To improve the surface conditions, we investigated a replacement of Ni with Co in the Fe-Ni film. Figure 2 shows the coercivity as a function of the Co content. The coercivity shows almost the same value up to 25 at.%-Co followed by a dramatic increase. The surface conditions were improved by the Co substitution. From these results, we found that a small amount of Co is effective to improve the surface condition of the electroless-deposited-Fe-Ni films without deterioration of good soft magnetic properties.

[1] X. Hou, S.Liu, S.Yang, J.Li, B.Guo, *Science China,* 56, (2013),84. [2] M. Theis, S. Ediger, M.T Schmitt, J.E. Hoffmann, M. Saumer, *Physica Atatus Solidi A,* 210, (2013),853 [3] T. Shimokawa, T.Yanai, K. Takahashi, M. Nakano, K. Suzuki, and H. Fukunaga, *IEEE Trans. Magn*., 48, (2012),2907 [4] A. F. Schmeckenbecher, *J. Electrochem. Soc*.,113, (1966),778 [5] M. Matsuoka, T. Hayashi, *Plat. Surf. Finish*. 69, (1982), 53 [6] R. Anthony, B. J. Shanahan, F. Waldron, C. Ó.Mathúna, J. F. Rohan, *Appl. Surf. Sci*., 357, (2015), 385

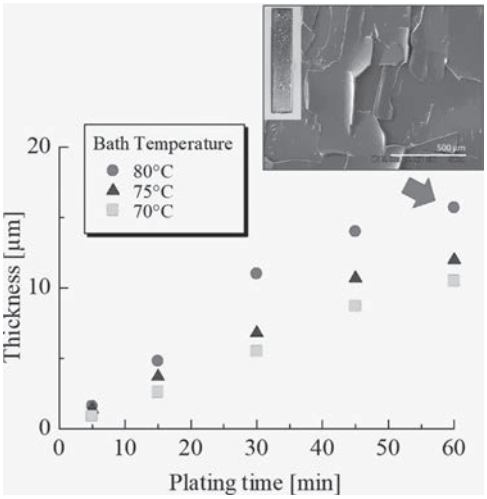


Fig.1 Thicknesses of the Fe-Ni films as a function of the plating time

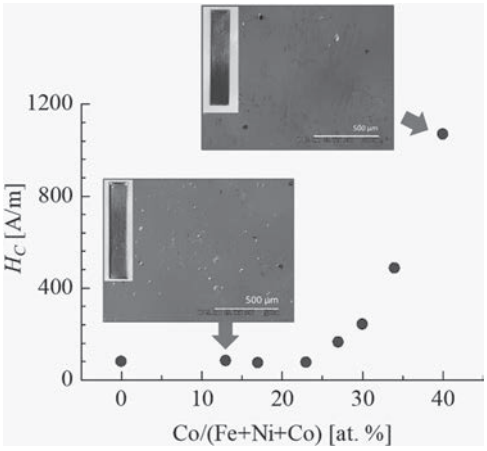


Fig.2 The coercivity the Fe-Ni films as a function of the Co content. The insets indicate an SEM images of the Co-added Fe-Ni films.

DW-09. Magnetic Loss Reduction in FeGa/NiFe Laminates for Strain-Mediated Multiferroic Micro-Antenna Applications. *K. Fitzell*[1], A. Acosta[1], C. Rementer[1,2], J.D. Schneider[3], J. Hu[3], A. Sepulveda[3], G. Carman[3] and J.P. Chang[1] *1. Chemical & Biomolecular Engineering, University of California, Los Angeles, Los Angeles, CA, United States; 2. Lam Research, Fremont, CA, United States; 3. Mechanical & Aerospace Engineering, University of California, Los Angeles, Los Angeles, CA, United States*

The ability to reduce the size of antennae would enable a revolution in wearable and implantable electronic devices. Multiferroic antennae, composed of individual ferromagnetic and piezoelectric phases, could reduce antenna size by up to five orders of magnitude through the efficient coupling of magnetization and electric polarization via strain. This strategy requires a material with strong magnetoelastic coupling and acceptable magnetic losses at high frequency. In this work, nanoscale laminates containing alternating layers of FeGa (possessing large magnetostriction but poor loss properties) and NiFe (possessing excellent loss properties but virtually no magnetostriction) were fabricated via DC magnetron sputtering to combine the complementary properties of the two magnetic phases, resulting in a composite material with a small coercive field, narrow ferromagnetic resonance linewidth, and high permeability (Rementer et al., 2017). Optical magnetostriction measurements confirmed that these laminates retain the large saturation magnetostriction of FeGa (200 με) while enhancing the piezomagnetic coefficient (7 ppm/Oe), allowing for optimal piezomagnetic actuation at substantially reduced magnetic bias fields. To further enhance the magnetic loss properties at high frequency, ultrathin layers of Al_2O_3 were incorporated into the multilayer materials to reduce the conductivity and mitigate the generation of eddy currents. The effect of Al_2O_3 thickness, FeGa:NiFe volume ratio, and multilayer architecture on the soft magnetic properties was studied, resulting in a 50% reduction in the ferromagnetic resonance linewidth. Optimized magnetic laminates were shown to exhibit a small coercive field (<20 Oe), narrow ferromagnetic resonance linewidth (<50 Oe), and high relative permeability (>500) while maintaining excellent magnetoelastic coupling, showing great promise for the use of FeGa/NiFe/Al_2O_3 laminates in strain-mediated micro-scale communications systems.

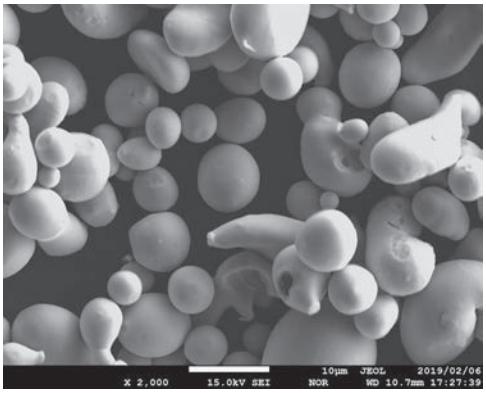
1. C. R. Rementer, K. Fitzell, Q. Xu, et al., Applied Physics Letters, Vol. 110 (24), 242403 (2017)

DW-10. Development of Rapid Cooling Atomizing Method and Production of High-B_s Nanocrystalline Powder with Large Particle Sizes. *K. Uji*[1], T. Tomita[1], K. Yoshida[1], T. Takahashi[1] and h. kuwata[1] *1. Tohoku magnet institute Co., LTD., Sendai, Japan*

An expectation for a nanocrystalline soft magnetic powder is increasing for a purpose of miniaturization and enhancing an efficiency of electronic devices. It seems to be important to achieve both a high saturation magnetic density, B_s, and a low coercivity, H_c, of a soft magnetic powder. In order to produce a high-B_s nanocrystalline powder, it is strongly required to produce an amorphous precursor with a quite rapid quenching rate. Yoshida[1] reported a new atomizing machine named as "HPWA/YK" which is based on a water atomization, and production of a $Fe_{83.3}Si_4B_8P_4Cu_{0.7}$ nanocrystalline powder with 5μm in an average diameter. A frequency dependent of a permeability of a soft magnetic core depends on particle size distribution. Therefore, it is important to produce powder of various particle sizes. However, it was difficult to obtain an amorphous precursor with a relatively large particle size (>10μm) avoiding precipitation of undesirable crystal grain. In this work, nanocrystalline powder with various particle sizes were produced using "HPWA/YK" machine. A molten metal with a composition of $Fe_{83.3}Si_4B_8P_4Cu_{0.7}$ was atomized in two steps. The fluid of the primary atomization and the secondary atomization were high pressure nitrogen gas and high pressure water, respectively. As a result, it was found that the cooling rate increased as the ratio of the gas pressure and water pressure increased, and amorphous precursor powder with particle size in the range of 5μm to 10μm were obtained. Finally, the amorphous powder having an average particle size of 18μm was obtained by removing the fine particles using an air flow classifier. After nanocrystallization, the B_s was revealed

as 1.68 T. It was exceedingly higher than that of conventional atomized amorphous powder (B_s < 1.4 T). In addition, it showed the low coercivity (128 A/m). These results indicate the evolution of cooling capability of the "HPWA/YK" machine.

[1] K. Yoshida, T. Takahashi, and K. Kuwata, AIP Advances 9, 035218 (2019)



A SEM image of the powder produced by the "HPWA/YK" (P_{gas}/P_{water} = 0.067)

DW-11. Soft Magnetic Co-rich Nanocrystalline Alloys for GMI Applications at Elevated Temperatures. F. Andrejka[1], *J. Marcin*[1], P. Svec[2] and I. Skorvanek[1] *1. Institute of Experimental Physics SAS, Kosice, Slovakia; 2. Institute of Physics SAS, Bratislava, Slovakia*

Technological demand for soft magnetic materials, which offer a reasonably large magnetic induction and at the same time are capable of operation at elevated temperatures has led to an increased interest in HITPERM-type FeCo-based nanocrystalline alloys prepared by devitrification of melt-spun amorphous precursors [1]. These alloys usually show a strong response to the magnetic field annealing, which can be used for tailoring the shape of their hysteresis loops for desired applications [2,3]. Heat treatment in magnetic field was also found to be a powerful tool for tuning of giant magnetoimpedance (GMI) characteristics in HITPERM alloys [4]. In this work, a controllable field annealing induced magnetic anisotropy was produced in series of Co-rich $(Co_{1-x}Fe_x)_{81}Nb_7B_{12}$ (x=0, 0.14 and 0.25) nanocrystalline alloys. The amorphous precursors were nanocrystallized at 773 K for 1 hour in longitudinal (LF) or transversal (TF) magnetic field. Reference samples were annealed in zero (ZF) magnetic field. Special attention is focused on testing the high temperature stability of soft magnetic properties and GMI characteristics in temperature range from 293 K to 573 K. The magnetoimpedance measurements are performed over a frequency range 0.1 – 100 MHz. The GMI response of LF annealed samples exhibits a single-peak behavior in whole frequency range investigated. On the other hand, ZF and TF annealed samples are characterized by a double-peak behavior. Our results show that the samples with higher amount of Co exhibit a stronger GMI response. The highest values of ΔZ/Z ratio ≈ 310% and sensitivity η ≈ 23%/Oe were observed at frequency 90 MHz for $Co_{81}Nb_7B_{12}$ sample annealed in transverse magnetic field. Application potential of such materials for construction of GMI magnetic sensors capable of operation at high temperatures is briefly highlighted. *This work was supported by the projects APVV-15-0621, VEGA 2/0171/19 and JRP SAS-TUBITAK MAGSAT.*

[1] M.A. Willard, D.E. Laughlin, M.E. McHenry et al., J. Appl. Phys., 84, 6773-6778 (1998) [2] I. Skorvanek, J. Marcin, T. Krenicky et al. J. Magn. Magn. Mater. 304, 203-207 (2006) [3] J.S. Blazquez, J. Marcin, F. Andrejka et al. J. Alloys. Compd. 658, 367-371 (2016) [4] A. Chaturvedi, N. Laurita, A. Leary et al. J. Appl. Phys. 109, 07B508 (2011)

DW-12. Oxygen dependence of transparent amorphous magnetic thin films Co-Fe-Ta-B-O magnetization: experiments and simulations. *C. Xiong*[1] and X. Zhang[1] *1. Material Science and Engineering, Tsinghua University, Beijing, China*

Quaternary alloy Co-Fe-Ta-B with very high Young's modulus and fracture strength has extraordinary soft magnetic properties and unusual magnetic behaviors like spin reorientation transition. Recently, researchers made the magnetic thin film transparent by oxygen doping. So that a lot of interesting electric, magnetic and optic properties are generated, which brings it a potential to fabricate magnetic semiconductor. These properties are very sensitive to the oxygen content in Co-Fe-Ta-B-O system. We fabricated the films $(Co_{20}Fe_{47}Ta_{20}B_{13})_{1-x}O_x$ of ~100 nm in thickness by using magneto sputtering method. The oxygen content x can be divided into 3 regions. First is the metallic region when x is less than 0.37, the magnetization behavior is like soft bulk metal material with a multi-domain structure and a coecivity less than 120 Oe. Second, when x increases to 0.37~0.48, the coecivity at low temperature will be largely increased (maximum ~1000 Oe at x=0.41) and the magnetization behavior is like magnetic granular films composed of single domain granules. This region is called hybrid region with magnetic granules in insulating matrix. When x is larger than 0.48, the magnetization gets weak. This region is called insulator region. The magnetic phase diagram (Fig. 2) shows three magnetic states ferromagnetic(FM), superparamagnetic(SPM) and paramagnetic (PM) at different temperature and composition. A magnetic granular model was also built to simulate the magnetization properties by using Monte Carlo method. The Hamiltonian of the system is composed of Zeeman energy, anisotropy energy, exchange interaction energy and magneto static interaction energy. The simulation result shows that the percolation effect in magnetic granule system causes the transition of metal and hybrid region and the missing of exchange interaction between adjacent granules in hybrid and insulator region causes the difference in temperature dependent magnetic properties.

[1] A. Inoue, B. Shen, H.Koshiba et.al. Nat.Mater., Vol. 2, p.661 (2003) [2] B.Shen, A. Inoue and C Chang. App. Phys. Lett., Vol. 85, p.4911 (2004) [3] P. Sharma, H. Kimura and A. Inoue. J. App. Phys., Vol.100, p.083092 (2006) [4] N. Chen, Li H, A. Hirata et.al. Mater. Des., Vol. 132, p.208 (2017) [5] W. Liu, H. Zhang, J. Shi et.al. Nat. Comm. Vol.7, p. 13497 (2016) [6] W. Sun, A. Saleemi, Z. Luo et.al. J. App. Phys. Vol. 122, p. 165101 (2017) [7] C. Xiong, C. Chen, W. Sun et.al. Chin. Phys. Lett. Vol. 36, p. 077502 (2019)

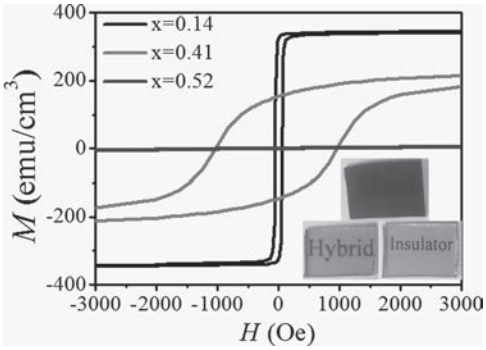


Fig.1 Typical magnetization curve of $(Co_{20}Fe_{47}Ta_{20}B_{13})_{1-x}O_x$ thin films (measured at 2K) and optical images when x belongs to metal (x=0.14), hybrid (x=0.41) and insulator region (x=0.52)

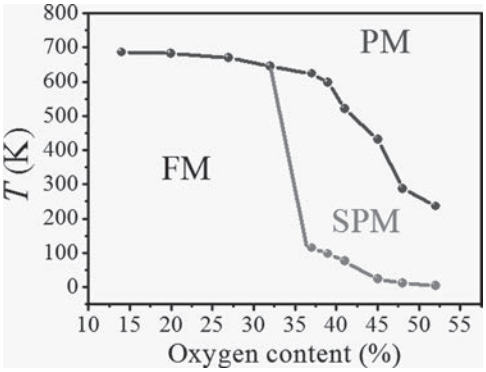


Fig.2 Magnetic phase diagram of $(Co_{20}Fe_{47}Ta_{20}B_{13})_{1-x}O_x$ thin films

DW-13. Strain Induced Anisotropy in Nanocomposite $Co_{74.6}Fe_{2.7}Mn_{2.7}Nb_4Si_2B_{14}$. *A. Srivastava*[1,2], K. Cole-Piepke[1,2], A. Koenig[3], T. Burton[3], C.K. Mewes[1,2], T. Mewes[1,2], G. Thompson[3], R. Noebe[4] and A. Leary[4] *1. Center for Materials for Information Technology, University of Alabama, Tuscaloosa, AL, United States; 2. Physics and Astronomy, University of Alabama, Tuscaloosa, AL, United States; 3. Department of Materials and Metallurgical Engineering, University of Alabama, Tuscaloosa, AL, United States; 4. Materials and Structures Division, NASA Glenn Research Center, Cleveland, OH, United States*

We report on broadband ferromagnetic resonance (FMR) characterization of strain induced magnetic anisotropy in nanocomposite $Co_{74.6}Fe_{2.7}Mn_{2.7}Nb_4Si_2B_{14}$ ribbons, about 22 mm wide and 22 microns thick, produced by a single roller melt spinning process[1]. The in-plane angular variation of resonance field shows a uniaxial anisotropy with the spin cast direction (also the direction of applied stress during annealing) as the hard axis (figure 1(a)), which is commonly observed in these type of ribbons[2]. A higher value of stress during the annealing process gives rise to an increased anisotropy value (H_u) as determined by both broadband FMR and in-plane angle dependent FMR measurements (figure 1(b)). The relative permeability (μ_r) calculated by using effective magnetization (M_{eff}) and uniaxial anisotropy (H_u) (obtained from FMR) is compared with relative permeability values obtained from measurements on bulk toroid samples and both are found to be in good agreement (figure 2). This indicates that FMR measurements on small samples could be used for determining the permeability of bulk cores wound from these ribbons. The effective magnetization and gyromagnetic ratio calculated from broadband FMR[3] show no significant dependence on degree of stress on the ribbon during annealing.

[1] A. Leary, V. Keylin and A. Devaraj, Journal of Materials Research, vol. 31, pp. 3089-3107 (2016) [2] O. V. Nielsen and H. J. V. Nielsen, Solid State Communications, vol. 35, pp. 281-284 (1980) [3] B. Heinrich and J. A. C. Bland, Ultrathin magnetic structures II vol. 2: Springer Science & Business Media (2006)

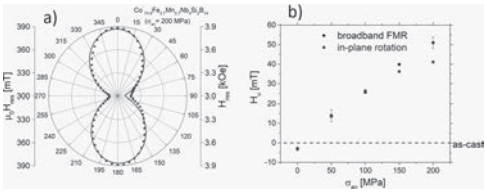


Fig.1: a) In-plane angular variation of resonance field of ribbon annealed at 200 MPa. b) Dependence of uniaxial anisotropy field H_u on the stress during annealing.

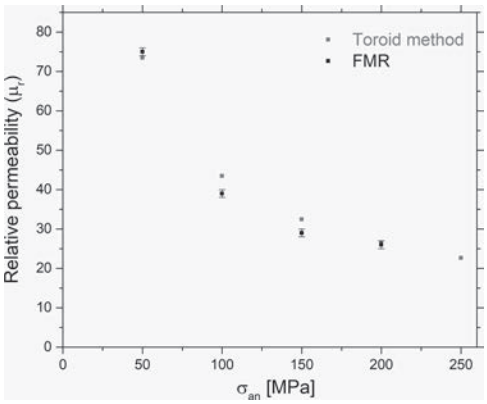


Fig. 2: Comparison of the relative permeability as function of the stress during annealing.

DW-14. Role of Jahn-Teller Distortions and Ferrimagnetic Transitions in $(Co_{1-x}Cu_x)Cr_2O_4$ (x = 0.5, 0.25) Nanoparticles. *P. Mohanty*[1], C. Sheppard[1], B. Doyle[1], E. Carleschi[1] and A. Prinsloo[1] *1. Department of Physics, University of Johannesburg, Johannesburg, South Africa*

The normal spinel ferrimagnet $CoCr_2O_4$ with T_C 93–97 K [1–3] demonstrates multiferroic properties due to a spiral ordering at 26 K [2–4]. In addition, a lock-in transition appears at 15 K [3]. Structurally, $CoCr_2O_4$ retains the cubic phase down to 11 K [4]. In contrary, the normal spinel $CuCr_2O_4$ only crystallizes into the cubic phase above 853 K [1]. The tetrahedral crystal field around Cu^{2+} in the cubic phase causes fully occupied low energy *e* levels and triply degenerate t_2 levels that leads to a cooperative lattice distortion from cubic to tetragonal symmetry below 853 K with a disputed ambient temperature structure [1]. Jahn-Teller (JT) activity of the Cu elevates the frustration in the Cr^{3+} sublattice [1]. Neutron diffraction studies confirm the magnetic structure of $CuCr_2O_4$ consisting of two canted Cr^{3+} sublattices with a net magnetic moment and a Cu^{2+} sublattice that couples antiferromagnetically to the net moment of the Cr^{3+} sublattices below 135 K [1]. Compression of CuO_4 tetrahedra towards a square planar configuration accounts for the tetragonal to orthorhombic phase transition at ~ 130 K [1]. Looking at such strong links between the distinct degrees of freedom motivates exploring new classes of multifunctional systems specifically at the nanoscale [5]. In this direction, current work focuses on the modification of structural and magnetic properties upon substituting Cu at the Co site in $CoCr_2O_4$. In order to do so, $(Co_{1-x}Cu_x)Cr_2O_4$ (x = 0.5, 0.25) nanoparticles were synthesized through sol-gel techniques. XRD reveals the cubic structure at ambient temperature for x = 0.25 and 0.5, with average crystallite sizes of ~21 nm and ~13 nm, respectively. JT distortion becomes prominent for x = 0.75. The temperature dependent magnetization studies reveal the T_C remains similar for both the samples: 101.6(4) K for x = 0.5 and 100.2(3) K for x= 0.25. However, the feature related to T_S has been enhanced for x = 0.25, where as it becomes suppressed for x = 0.5. Hysteresis loops measured at low temperature show enhanced constriction for x = 0.25 quite distinct from both chromites. Changes in the valence band and core level electronic structure from XPS support these observations.

[1] M. R. Suchomel, D. P. Shoemaker, and L. Ribaud, *Phys. Rev. B* 86 (2012) 054406. [2] Y. Yamasaki, S. Miyasaka, Y. Kaneko,J.-P. He,T. Arima, and Y. Tokura, *Phys. Rev. Lett.* 96 (2006) 207204. [3] K. Tomiyasu, J. Fukunaga, and H. Suzuki, *Phys. Rev. B* 70 (2004) 214434. [4] G. Lawes, B. Melot, K. Page, C. Ederer, M. A. Hayward, Th. Proffen, and R. Seshadri, *Phys. Rev. B* 74 (2006) 024413. [5] P. Mohanty, C.J. Sheppard, A.R.E. Prinsloo, W.D. Roos, L. Olivi, and G. Aquilanti *J. Mag. Mag. Mat.* 451 (2018) 20.

DW-15. *In-vitro* evaluation of $Zn_xFe_{3-x}C$ ($0 \le x \le 1$) nanoparticles for magnetic hyperthermia treatment. *A. Gangwar*[1], K.V. Matte[2], K. Neogi[2], M.S. Muthu[2], S. Kumar[3], A. Sharma[4], S. Singh Meena[5] and N.K. Prasad[1] *1. Metallurgical Engineering, IIT(BHU) Varanasi, Varanasi, India; 2. Pharmaceutical Engineering, IIT(BHU) Varanasi, Varanasi, India; 3. Metallurgical Engineering, NIT, Rourkela, Rourkela, India; 4. Metallurgical and Materials Engineering, IIT, Bombay, Mumbai, India; 5. Solid State Physics Division, BARC, Mumbai, Mumbai, India*

In this present study, $Zn_xFe_{3-x}C$ ($0 \le x \le 1$) MNP_S were synthesized using the simple and cost-effective sol-gel technique. The carbide phase for these samples (size range = 12-45 nm) was obtained after calcination at 700 C in N_2 atmosphere which was confirmed by X-ray diffraction, electron diffraction, and Mössbauer spectroscopy. The samples contain Fe, Zn, and C which was indicated by X-ray photoelectron spectroscopy. The saturation magnetization (M_S) value for $x = 0.1$ sample was 58 Am^2/kg which has decreased minutely with increased Zn substitutions. In contrast, the M_S values were 68 Am^2/kg for pure Fe_3C and the value decreased continuously with Co substitution due to antiferromagnetic coupling [1-2]. The heating abilities of their ferrofluids prepared using F127 polymer exhibited comparable specific absorption rate (SAR) values as that of iron oxides [3]. The maximum, SAR as well as intrinsic loss power (ILP) values were 85 W/g and 1.9 nHm^2/kg for $x = 0.7$, at 25 mT external magnetic field. The cytotoxicity of these MNP_S was examined with human lung adenocarcinoma A549 cells using SRB assay and found to be compatible up to 1 mg/mL.

A. Gangwar, G. Singh, S. K. Shaw, *New J. of Chem*, 43, 3536, (2019) A. Gangwar, S.S Varghese, Sher Singh Meena, *Journal of magnetism and magnetic materials*, 481, 251-256, (2019) A. Gangwar, S. K. Alla, M. Srivastava, *Journal of magnetism and magnetic materials*, 401, 559-566, (2016)

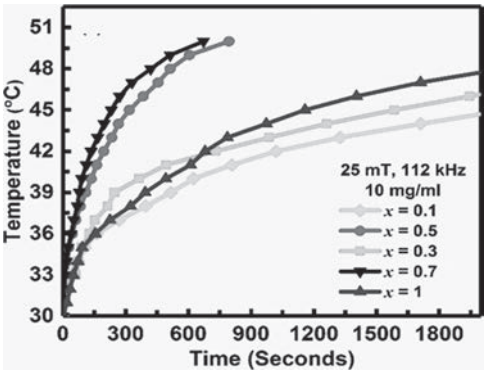


Fig. 1 Temperature *vs.* Time curves for $Zn_xFe_{3-x}C$ nanoparticles

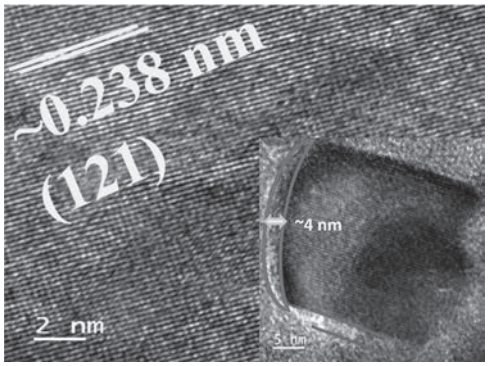


Fig. 2 High-resolution TEM micrograph for $ZnFe_2C$ nanoparticles

DW-16. Electroplated Fe-Co films prepared in citric-acid-based plating baths. *K. Mieda*[1], R. Tanaka[1], J. Kaji[1], A. Yamashita[1], T. Morimura[1], T. Yanai[1], M. Nakano[1] and H. Fukunaga[1] *1. Nagasaki University, Nagasaki-shi, Japan*

To reduce the coercivity of soft magnetic materials, a reduction in the grain size is one of the effective methods [1]. We found out that Fe-Ni films electroplated by citric-acid-based baths have nano-structure and show low coercivity due to the grain the refinement effect [2]. Although Fe-Co alloys have high saturation magnetization, coercivity of typical Fe-Co alloys is higher than that of Fe-Ni ones. In the present study, for reduction in coercivity of Fe-Co alloys, we employed a citric-acid-based plating bath for preparation of Fe-Co films and evaluated magnetic and strucural properties of the films. We plated Fe-Co films on Cu substrates using a direct current. The bath contains $225 - x$ [g/L] of $CoSO_4$, x [g/L] of $FeSO_4$, 10 g/L of $C_6H_8O_7$-H_2O, 10 g/L of NaCl, 5 g/L of $C_7H_4NNaO_3S$-$2H_2O$, 1 g/L of $C_{12}H_{25}OSO_3Na$. The current density, the plating time, and the bath temperature for the electroplating were set at 200 mA/cm^2, 2.5 min, and 50°C, respectively. Figure 1 shows the coercivity H_c and the saturation magnetization M_s as a function of the Fe content in the Fe-Co films. The change in M_s over the Fe content almost agreed with the expected change from the Slater-Pauling curve. The maximum M_s was 221 emu/g around $Fe_{70}Co_{30}$. In contrast, we obtained the minimum value of coercivity around $Fe_{70}Co_{30}$. These results indicate that we can obtain the Fe-Co films with high M_s and low H_c by adjusting Fe content around 70 at.%. To confirm reasons of low coercivity, we carried out structural analyses. Figure 2 shows XRD patterns of the films. As shown in Figure 2, the diffraction peaks of the $Fe_{70}Co_{30}$ film were very weak compared with those of other films. The result for the X-ray analysis implies that the grain size decreases with increasing Fe content, and the $Fe_{70}Co_{30}$ film has a very fine structure. To obtain direct evidence of the structure, a TEM observation was carried out and the result is shown in Fig.2 as an inset. Large grains were not observed, and we confirmed that the fine structure effectively works to reduce the coercivity. From these results, we concluded that the citric-acid-based bath is attractive for obtaining Fe-Co films with high M_s and low H_c.

[1] G. Herzer, IEEE Trans. Magn., Vol. 26, pp. 1397-1402 (1990). [2] T. Shimokawa, T. Yanai, K. Takahashi, M. Nakano, K. Suzuki, and H. Fukunaga, IEEE Trans. Magn., Vol. 48, pp. 2907-2909 (2012).

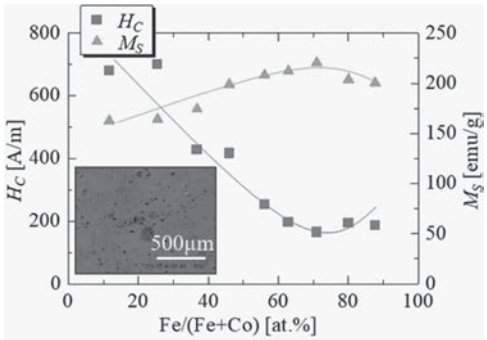


Figure 1. Coercivity and saturation magnetization as a function of the Fe content of the Fe-Co films. An SEM image of $Fe_{70}Co_{30}$ film was shown as an inset.

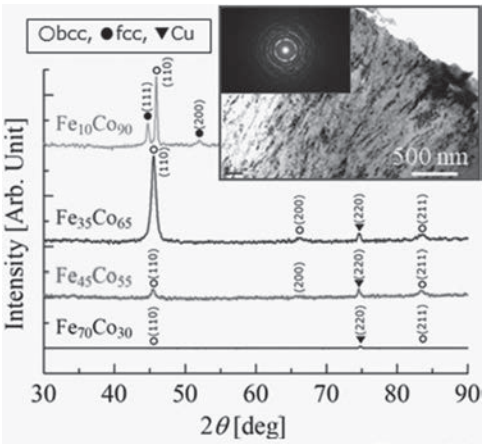
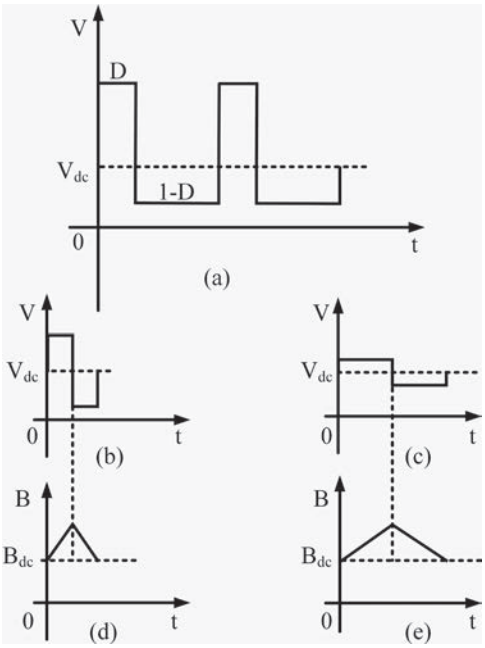


Figure 2. XRD patterns of Fe-Co films with different Fe contents. A TEM image of $Fe_{70}Co_{30}$ film was shown as an inset.

DW-17. Iron Loss Separation Model Under DC Bias for Filter Inductors of Power Electronic Converters. H. Sun[1,2], *Y. Li*[1,2], S. Yue[1,2] and M. Yang[1,2] *1. State Key Lab of Reliability and Intelligence of Electrical Equipment, Hebei University of Technology, Tianjin, China; 2. Key Lab of EFEAR of Hebei Province, Hebei University of Technology, Tianjin, China*

The calculation of iron losses in inductive components is difficult because of complex excitations and has not yet been entirely solved. In particular, it is impossible to predict the influence of dc bias and duty cycle on the iron losses simultaneously without extensive measurements [1]. In this paper, nanocrystalline ring FT-3KS is used as sample. A separation model for predicting iron losses under rectangular waveform considering dc bias, such as shown in Fig. 1(a) in filter inductors is introduced. The iron losses of filter inductors under rectangular waveform considering dc bias is evaluated, which shows that the proposed model not only accurately predicts the iron losses but also identifies the hysteresis loss part. For a given duty cycle D, the total hysteresis loss or total eddy current loss under a fundamental waveform [see Fig.1 (a)] is the sum of two loss quantities. The first one is calculated with a frequency f1=f/2D and the second one is calculated with a frequency f2=f/2(1-D) [2] [3]. Since the parameters of the separation model are frequency dependent and they are only valid for a limited frequency range, different parameters is used in order to fit with measurements under different duty cycles and increase the accuracy of the iron loss model in this paper. A more detailed description of the model will be presented in full paper. This result indicates that the proposed model can model the iron loss under rectangular waveform considering dc bias condition. The iron loss value calculated by using the proposed model is compared with the measurement results. The calculation error is within 3%. A well-known empirical characteristics of the hysteresis loss is explained. The hysteresis loss will be independent with exciting voltage waveforms. These results are useful not only for iron loss calculation, but also for the optimal design of electronics applications.

[1]Muhlethaler J, Biela J, Kolar J W. IEEE Transactions on Power Electronics, 2012, 27(2):953-963. [2]Matsumori H, Shimizu T, Wang X. IEEE Journal of Emerging & Selected Topics in Power Electronics, 2018, PP (99):1-1. [3]Barg S, Ammous K, Hanen M, et al. IEEE Transactions on Power Electronics, 2016:1-1.



DW-18. Improvement in soft magnetic properties exchange-coupled Fe-Ni/$Fe_{22}Ni_{78}$ bilayer films. *J. Kaji*[1], R. Tanaka[1], K. Mieda[1], A. Yamashita[1], T. Yanai[1], M. Nakano[1] and F. Hirotoshi[1] *1. Nagasaki University, Nagasaki, Japan*

For typical soft magnetic materials, both high saturation magnetization and low coercivity are required. Although $Fe_{22}Ni_{78}$ alloys are one of hopeful soft magnetic materials due to their extremely low coercivity, the saturation magnetization is relatively low. To increase in the saturation magnetization of $Fe_{22}Ni_{78}$-based alloys, we recently proposed exchange-coupled Fe-Ni/$Fe_{22}Ni_{78}$ bilayer films and confirmed that the bilayer films enable us to increase the saturation magnetization keeping low coercivity [1]. It is well-known that annealing often improves soft magnetic properties due to relaxing residual stresses. In the present study, we employed annealing to improve the soft magnetic properties of our previously-proposed bilayer films. We carried out the electroplating to obtain the Fe-Ni films using a direct current. The plating bath and conditions were described elsewhere [1]. Ni and Cu plates were used as electrodes, and 75 mm^2 Fe-Ni/$Fe_{22}Ni_{78}$ films were electroplated on the Cu plate. The films were annealed at 250 - 410°C for 60 min in a vacuum. The strength of the exchange coupling strongly depends on grain sizes, and we need to keep the fine structure to obtain good soft magnetic properties [2]. Figure 1 shows the grain size of the $Fe_{22}Ni_{78}$ and $Fe_{58}Ni_{42}$ single layer films as a function of the annealing temperature. As shown in Fig.1, dramatic grain growth was observed at 360°C for the $Fe_{22}Ni_{78}$ films. As the exchange coupling becomes weak with the increase in the grain size, the result for Fig.1 suggests that we need to set the annealing temperature below 360°C to obtain strong coupling between $Fe_{22}Ni_{78}$ and $Fe_{58}Ni_{42}$ layers of the double-layer films. Figure 2 shows the coercivity of the $Fe_{58}Ni_{42}$/$Fe_{22}Ni_{78}$ bilayer film as a function of the annealing temperature. The coercivity decreased with increasing the annealing temperature up to 350°C which was expected value from Fig.1. The saturation magnetization of the bilayer film was 120 emu/g, and this value was much higher than that for Ref.1. From these results, we found that the annealing without the grain growth improves the soft magnetic properties of the exchange coupled Fe-Ni/$Fe_{22}Ni_{78}$ bilayer film.

[1] T. Yani, J. Kaji, K. Kouda, K. Takashima, M. Nakano, H. Fukunaga, *IEEE Transactions on Magnetics*, 54 (2018) #2002503. [2] G. Herzer, *IEEE Transaction on Magnetics,* 26, (1990) 1397.

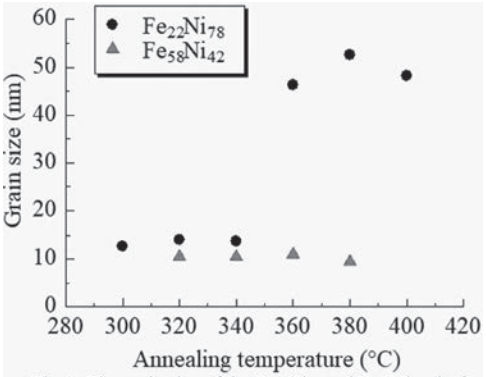


Fig. 1. The grain size of the $Fe_{22}Ni_{78}$ and $Fe_{58}Ni_{42}$ single layer films as a function of the annealing temperature.

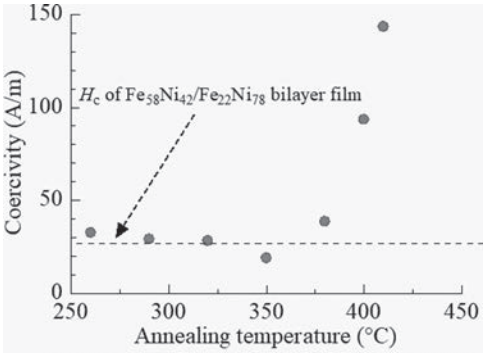


Fig.2 The coercivity of the $Fe_{58}Ni_{42}/Fe_{22}Ni_{78}$ bilayer film as a function of the annealing temperature.

Session XA
MEMORIAL SESSION FOR JOHN SLONCZEWSKI

Alina Maria Deac, Chair
Helmholtz-Zentrum Dresden-Rossendorf, Dresden, Germany

INVITED PAPERS

6:15

XA-01. Spin-transport physics – a gift from John, a new field of science. *J. Sun*[1] *1. IBM T. J. Watson Research Center, Yorktown Heights, NY, United States*

John Slonczewski passed away in May this year. It is a great loss to the condensed matter physics community. With sadness and a fond memory, I will reflect on our journey with John over the last two decades or so together at IBM Research and beyond. As an example of the inspiration derived from working with John, I will give a brief review of my studies on the development of the scientific basis for spin-transfer torque and related device and materials physics, and share some fond memories of those good times we had together. I got to know John in the mid-1990s at IBM Research, when my studies transitioned from superconductivity to magnetics. John patiently mentored me through my early adventures in magnetism. He was even then, and indeed much earlier, already well-aware of the new physics spin-dependent transport could bring. He urged us to take a closer look at high current-density spin transport and angular momentum conservation. The rest is history in the making, to this day. We now have spin-transfer torque physics and devices, magnetic tunnel junctions, and spin-orbit and thermal magnonic sources for even more efficient generation and propagation of spin-current. These new concepts are deeply rooted in John's creative thinking and encyclopedic understanding of magnetism. Take the example of spin-transfer torque. Twenty-three years ago, John published his seminal work on spin-transfer torque and its resulting magnetic switching. This concept has now been widely accepted. New terms have been added to the Landau-Lifshitz-Gilbert equation, and development is well under way to utilize this effect for a new type of all-solid-state, CMOS-integrated magnetic random-access memory. John's impact to our field cannot be overstated. Thanks to John's vision and deep insight, today we have many new topics blossoming in spin-transport physics. John's solid, stoic approach to the search for a sound, lasting scientific understanding will continue to guide me in my future work. Thank you, John.

7:00

XA-02. J. C. Slonczewski: From Bubble to MRAM. *S. Maekawa*[1,2] *1. Center for Emergent Matter Science, Riken, Wako, Japan; 2. Kavli Institute for Theoretical Sciences, Beijing, China*

Dr. John C. Slonczewski passed away in May, 2019, at the age of 90. He was constantly a front runner in magnetism research for more than 60 years. His interest in magnetism was from basic physics to its applications. In 1975, I had an opportunity to join his group at IBM Watson Research Center in Yorktown Heights, New York, where the main subject of research was to develop magnetic bubble memory. At the time, to increase the memory density, magnetic bubbles with sub-micron size were expected. One of the problems, however, was how to detect such a small bubble. John, as the leader of the bubble project at IBM, proposed that we develop a magnetic tunnel junction as a sensor of the weak magnetic field of the bubbles. We worked on various aspects of magnetic bubbles and magnetic tunnel junctions. John's formalism was always expressed in beautiful mathematics. We can see examples of this beauty in his book entitled "Magnetic Domain Walls in Bubble Materials", published together with A. P. Malozemoff. He also extended his study on the spin dynamics in magnetic metals. He then discovered the spin transfer torque and thereby opened the door to STT-MRAM. John was a great teacher for me. He visited Japan several times and we enjoyed our collaboration. When phone-calls interrupted our discussion in my office, he warned me saying "you are not concentrating on physics!". My wife and I are proud that John and Esther called us "our Daughter and Son". He kept his interest in physics until the end of his life. He always encouraged me saying that you are still young. We miss John, but we are happy to have his physics with us.

Session EA
PHYSICS AND APPLICATIONS OF SYNTHETIC ANTIFERROMAGNETS (SAFS)

Olav Hellwig, Chair
Chemnitz University of Technology, Chemnitz, Germany

INVITED PAPERS

8:30

EA-01. The fundamental properties and applications of synthetic antiferromagnetc systems. *E. Fullerton[1] 1. Center for Memory and Recording Research, University of California San Diego, La Jolla, CA, United States*

The discovery of indirect exchange coupling of ferromagnetic layers (FM) across thin transition-metal layers [1] allowed the ability to form thin-film heterostructures where the adjacent FM layers are antiferromagnetically (AF) coupled. These materials are referred to as synthetic antiferromagnets (SAFs) as they are magnetically isomorphic to many natural forming AF materials. Advantages of SAFs is that is possible to tune the moment of the FM layers, the anisotropy (both strength and orientation) and the interlayer coupling allowing the design of model systems to probe complex behavior in AF systems. SAFs are particularly attractive for studying field-induced phase transitions in AF films because the exchange interaction that couples adjacent ferromagnetic layers is comparable to the Zeeman energy in modest applied fields. In addition, finite size and surface effects are more pronounced in SAFs and can be well controlled by the individual thicknesses of their composing layers [2,3]. One example is the observation of the surface spin-flop transition that was theoretically predicted to occur in AF materials [4]. SAFs have also become important components in modern magnetic and spintronic devices. First used as reference magnetic layer in giant magnetoresistance read heads [5] they are also used as longitudinal recording media [5], soft underlayers in perpendicular recording media and both reference and free layers in MRAM cells [6]. SAFs also have unusual dynamic properties [1] making them suitable for novel nano spin-torque oscillators, materials for all-optical switching [7], and fast current induced domain wall motion [8]. I will review the fundamental properties of SAFs in both the in-plane and perpendicular orientations [3] and then describe how these properties make them well-suited for applications.

[1]. P. A. Grünberg, Rev. Mod. Phys. 80, 1531 (2008). [2]. B. Dieny, P. Gavigan, & J. P. Rebouillat, J. Phys. Condens. Matter 2, 159–185 (1990). [3]. O. Hellwig, J. B. Kortright, A. Berger and E. E. Fullerton, J. Magn. Magn. Mater. 319, 13 (2007). [4]. R. Wang, et al., Phys. Rev. Lett. 72, 920–923 (1994). [5]. R. McFadyen, E. E. Fullerton, and M. J. Carey, MRS Bulletin 31, 379-383 (2006). [6]. D. Apalkov, B. Dieny, and J. M. Slaughter, Proc. IEEE 104, 1796-1830 (2016). [7]. S. Mangin et al., Nature Materials 13, 286–292 (2014). [8]. S.-H. Yang, K. S. Ryu, and S. S. P. Parkin, Nature NanoTech 10, 221–226 (2015)

9:06

EA-02. Tuning magnetic phases in synthetic antiferromagnets with perpendicular anisotropy via control of micromagnetic energy balance. *N.S. Kiselev[1] 1. Peter Grünberg Institute and Institute for Advanced Simulation, Forschungszentrum Jülich, Jülich, Germany*

The term synthetic antiferromagnets (SAFs) is typically used for magnetic multilayer systems with antiferromagnetic interlayer exchange coupling. SAFs with strong perpendicular magnetic anisotropy (PMA) represent an exceptional class of systems characterized by a large variety of magnetic phase transitions [1]. Similar to natural magnetic crystals the phase transitions in SAF can be induced both by external stimuli (e.g. applied magnetic field) and by a change in the internal energy balance (e.g. due to competition between magnetocrystalline PMA and easy-plane shape anisotropy induced by demagnetizing fields) [2]. The uniqueness of SAFs lies in the possibility to control the balance between different energy terms in a very wide range independently [2], while in the most of natural magnetic crystals i) this range typically is quite limited, ii) it is hard to change of a particular energy term without impact on the others. In this presentation, I will discuss how the competition between different energy terms as anisotropy, interlayer exchange coupling between nearest layers, and the long-range magnetostatic coupling between all layers lead to the formation of complex three dimensional (3D) magnetic states, which may correspond to the ground state of the system or metastable phases. Besides that, I will discuss the role of surface-induced Dzyaloshinskii-Moriya interaction, responsible for the stabilization of chiral magnetic textures, in the formation of complex states in SAF. The accent in my talk will be made on the metamagnetic transitions and the stabilization of localized states such as magnetic bubble domains [3] and skyrmions [4] in multilayers with strong interlayer exchange coupling and PMA. I will also briefly discuss possible practical applications of metamagnetic bubble domains (or skyrmions) in SAF (Fig.1) for data encoding in new nonvolatile memory devices.

[1] O. Hellwig, T.L. Kirk, J.B. Kortright, A. Berger, and E.E. Fullerton, “A new phase diagram for layered antiferromagnetic films” Nat. Mater. 2, 112 (2003). [2] O. Hellwig, A. Berger, J.B. Kortright, and E.E. Fullerton, “Domain structure and magnetization reversal of antiferromagnetically coupled perpendicular anisotropy films” J. Mag. Mag. Mat. 319, 13 (2007). [3] N.S. Kiselev, C. Bran, U. Wolff, L. Schultz, A.N. Bogdanov, O. Hellwig, V. Neu, and U.K. Rößler, “Metamagnetic domains in antiferromagnetically coupled multilayers with perpendicular anisotropy” Phys. Rev. B 81, 54409 (2010). [4] A.K. Nandy, N.S. Kiselev, S. Blügel, “Interlayer Exchange Coupling: A General Scheme Turning Chiral Magnets into Magnetic Multilayers Carrying Atomic-Scale Skyrmions” Phys. Rev. Lett. 116, 117202 (2015).

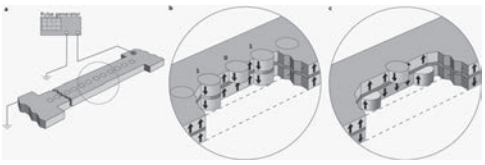


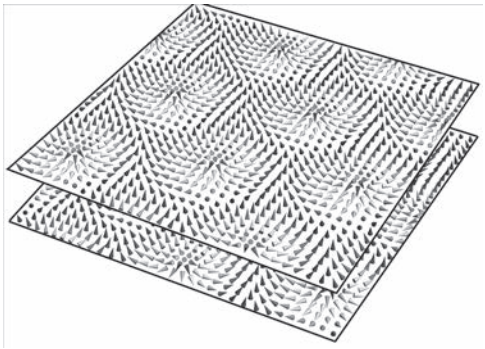
Fig. 1 (a) Schematic representation of a racetrack nano-stripe. (b) Chain of metamagnetic and ordinary bubble-skyrmions representing a stream of zeros and ones respectively. (c) Chain of alternate metamagnetic bubbles situated in the top and in the bottom ferromagnetic stack - the case of strong IEC.

9:42

EA-03. Perspectives of Synthetic Antiferromagnetic Spintronics.
R. Duine[1,2] *1. Physics, Institute for Theoretical Physics, Utrecht, Netherlands; 2. Physics, Eindhoven University of Technology, Eindhoven, Netherlands*

Spintronic and nanomagnetic devices often derive their functionality from layers of different materials and the interfaces between them. This is especially true for synthetic antiferromagnets — two or more ferromagnetic layers that are separated by metallic spacers or tunnel barriers and which have antiparallel magnetizations. Here, we discuss the new opportunities that arise from synthetic antiferromagnets, as compared to crystal antiferromagnets or ferromagnets. In particular, I will discuss applications for magnonics, magnon spintronics, and skyrmionics [2] (see figure).

[1] R. A. Duine, Kyung-Jin Lee, Stuart S. P. Parkin & M. D. Stiles, Nature Physics 14, 217 (2018). [2] E. van Walsem, *et al*., arXiv:1812.08082.



10:18

EA-04. Using Synthetic AntiFerromagnetic (SAF) Structures for Biomedical Applications. T. Vemulkar[1], J. Verheyen[1], S. Leulmi Pichot[1], E. Welbourne[1], M. Stanton[1], D. Petit[1] and *R. Cowburn*[1] *1. Cavendish Physics Laboratory, University of Cambridge, Cambridge, United Kingdom*

Magnetic materials are currently used in a number of biomedical applications such as therapy, diagnostics, separation and sorting, with hyperthermia therapy being the most well-known. To date, most biomedical magnetism uses very simple magnetic materials – typically superparamagnetic iron oxide nanoparticles (SPION). This talk will describe a new approach in which physical vapour deposition (sputtering) combined with lithography is used to form large numbers of nano- and micro-structures across a silicon wafer, which are then released into solution to form a highly functional magnetic liquid [1]. The advantage of this approach over SPION is that phenomena such as RKKY coupling, spin textures and interfacial anisotropy can all be used to make the magnetic properties of the liquid more advanced and therefore better suited to particular biomedical applications. Of particular importance is the creation of synthetic antiferromagnetic (SAF) layer structures with perpendicular magnetic anisotropy (PMA). These combine the key requirements of having low or zero remanence, moderate coercivity and high anisotropy. The low or zero remanence prevents agglomeration in liquid [2]; the moderate coercivity allows a high moment to be recreated once the particles are absorbed into the relevant biological species; the high anisotropy allows strong mechanical torques to be generated for mechano-biological therapies and detection. In this talk we show latest experimental results in using magnetic nanostructures to treat glioblastoma brain tumours in mice [3], including combining with radiotherapy for enhanced cell damage, and to detect early stage kidney cancer by performing ELISA-like assays on the surface of the magnetic nanostructures.

[1] T.Vemulkar, R.Mansell, R.P.Cowburn et al. Applied Physics Letters 107,012403 (2015) [2] T.Vemulkar, E.N.Welbourne, R.P.Cowburn et al. Applied Physics Letters 110, 042402 (2017) [3] Yu Cheng, M. E. Muroski, R.P.Cowburn et al. Journal of Controlled Release 223, 75 (2016)

10:54

EA-05. Giant Tunneling Magnetoresistance in van der Waals Layered Antiferromagnet. *T. Song*[1], X. Cai[1], Z. Fei[1], M. Tu[4], X. Zhang[3], C. Carnahan[3], M. McGuire[2], D. Cobden[1], D. Xiao[3], W. Yao[4] and X. Xu[1] *1. University of Washington, Seattle, WA, United States; 2. Oak Ridge National Laboratory, Oak Ridge, TN, United States; 3. Carnegie Mellon University, Pittsburgh, PA, United States; 4. University of Hong Kong, Hong Kong, Hong Kong*

Synthetic antiferromagnets and magnetic multilayer devices that exploit magnetoresistance are the backbone of magnetic sensing and data storage technologies. Similar to synthetic antiferromagnets, few-layer chromium triiodide (CrI_3) is a recently discovered layered antiferromagnetic insulator in its natural crystal form even down to the atomically thin limit. In this talk, we will report giant tunneling magnetoresistance in the layered antiferromagnet based on van der Waals (vdW) heterostructures in which atomically thin CrI_3 acts as a spin-filter tunnel barrier sandwiched between graphene contacts. We demonstrate tunneling magnetoresistance which is drastically enhanced with increasing CrI_3 layer thickness, reaching a record 57,000% for magnetic multilayer structures using four-layer CrI_3 at low temperatures. In a dual-gated structure, a pair of bistable magnetic states in four-layer CrI_3 can be switched reversibly by electrostatic gating, demonstrating a new kind of voltage-controlled vdW spintronic devices. Moreover, we demonstrate the control of 2D magnetism by hydrostatic pressure. The antiferromagnetic interlayer coupling in CrI_3 can be more than doubled and even change the sign. In bilayer CrI_3, pressure can change the stacking arrangement which induces a transition from layered antiferromagnetic to ferromagnetic phases. In trilayer CrI_3, pressure can create coexisting domains of three phases, one ferromagnetic and two distinct antiferromagnetic. Our work provides ample opportunities to engineer novel spintronic devices using layered antiferromagnets based on vdW heterostructures with voltage and pressure tunabilities.

1. T. Song, X. Cai, M. Tu *et al*., Giant tunneling magnetoresistance in spin-filter van der Waals heterostructures, Science 360, 1214–1218 (2018). 2. T. Song, M. Tu, C. Carnahan *et al*., Voltage control of a van der Waals spin-filter magnetic tunnel junction, Nano Lett. 2019, 19, 915–920 (2019). 3. T. Song, Z. Fei, M. Yankowitz *et al*., Switching 2D magnetic states via pressure tuning of layer stacking, arXiv:1905.10860 (2019).

Session EB
SPINS AND MAGNETISM IN TOPOLOGICAL MATERIALS

Hongxin Yang, Chair
Chinese Academy of Sciences, Ningbo, China

CONTRIBUTED PAPERS

8:30

EB-01. Spin-to-charge conversion in topological insulator/ semiconductor heterostructures probed by optical spin orientation. *T. Guillet*[1], C. Zucchetti[2], A. Marchionni[2], F. Bottegoni[2], A. Marty[1] and M. Jamet[1] *1. Univ. Grenoble Alpes, CEA, CNRS, Grenoble INP, IRIG-Spintec, Grenoble, France; 2. LNESS-Dipartimento di Fisica, Politecnico di Milano, Milan, Italy*

Topological insulators (TIs) are predicted to host exotic properties like topologically protected surface states (TSS) showing Dirac-like band dispersion and strong spin-momentum locking. Such characteristics make this class of materials ideal for the generation and the detection of spin currents. In this work, we grow single crystalline Bi_2Se_3 thin films on low n-doped (10^{16} cm^{-3}) Ge (111) by molecular beam epitaxy. Germanium is an optically active material with a long spin diffusion length ($l_{sf} \approx 10$ µm at room temperature) and it is compatible with the current silicon technology platform. We propose an original method to probe the spin-to-charge conversion in TIs by taking advantage of the Ge optical properties. We design microdevices (Fig. 1a) where pure spin currents with in-plane spin polarization are generated by optical spin orientation in Ge when the laser beam hits the edge of Pt bars [1,2]. Spin currents are then detected in a non-local geometry by the inverse Rashba-Edelstein effect in a Bi_2Se_3 bar at room temperature. We modeled the spin-to-charge conversion to estimate the efficiency of the process and we find λ_{IREE} =30 pm. When multiplied by the Bi_2Se_3 spin diffusion length, this value is comparable to the one obtained in a Pt bar in place of the Bi_2Se_3 using the same experimental conditions. However, Pt and Bi_2Se_3 show opposite spin-charge conversion and the possible reason for this sign change will be discussed in this presentation [3]. Our results highlight the efficiency of Bi_2Se_3 as a spin detector and pave the way toward spintronic devices without using ferromagnetic compounds.

[1] C. Zucchetti and al, Phys. Rev. B 96, 014403 (2017) [2] F. Bottegoni and al, Nature Materials 13, 790–795 (2014)



Fig. 1 a) Illustration of the microdevice used for optical spin orientation. b) Integrated profiles of the sample reflectivity (bottom) and the inverse Rashba-Edelstein effect signal (top). The scattering of circularly polarized light on the right (left) edge of a Pt stripe will create a pure spin current in germanium with in-plane orientation pointing to the right (left) respectively. The spin current is then absorbed and converted into a charge current in the Bi_2Se_3 bar by inverse Rashba-Edelstein effect.

8:42

EB-02. Butterfly-shaped magnetoresistance and topological Hall effect induced by spin fluctuations on triangular lattice. *H. Taniguchi*[1], M. Watanabe[1], M. Tokuda[1], S. Suzuki[1], T. Ibe[1], T. Arakawa[1,2], H. Yoshida[3], H. Ishizuka[4], K. Kobayashi[1,5] and Y. Niimi[1,2] *1. Graduate School of Science, Osaka University, Toyonaka, Japan; 2. Center for Spintronics Research Network, Osaka University, Toyonaka, Japan; 3. Graduate School of Science, Hokkaido University, Sapporo, Japan; 4. Department of Applied Physics, University of Tokyo, Bunkyo, Japan; 5. Graduate School of Science, University of Tokyo, Bunkyo, Japan*

Since the discovery of graphene, there have been many reports on two-dimensional (2D) materials. Especially, 2D materials showing phase transitions have attracted much attention not only from the viewpoint of fundamental physics but also for potential applications to atomic-layers [1,2]. The motivation of the present study is to fabricate conductive 2D antiferromagnets (AFMs) and to investigate unique magnetic states through electrical transport. The triangular AFMs induce *magnetic frustration* because of the geometrical spin configurations and bring about rich magnetic properties unique to the geometrical frustrations. Ag_2CrO_2 is one of the layered triangular AFMs with electrical conductivity (see the inset of Fig. 1). This material exhibits a unique thermodynamic property, so-called *partially disordered (PD) state*, below the AFM transition temperature T_N [3-6]. However, the magnetic structure of the PD state is not still elucidated because the single crystal has not been synthesized yet. In this work, we have fabricated a micrometer-size Ag_2CrO_2 which is presumably a single crystal [7], and mesured magnetotransport in order to investigate the effect of PD spin fluctuations on the electrical transport property. A clear butterfly-shaped magnetoresistance was observed only when the magnetic field direction is out-of-plane. The amplitude of the MR takes a maximum at $T \sim T_N$ (Fig. 1). These results indicate that spin fluctuations near T_N strongly affects the butterfly-shaped MR. Next, we have measured the Hall resistivity as shown in the inset of Fig. 2. Apparently, the Hall slope changes with increasing temperatures. The derivative of ρ_{yx} is plotted as a function of T in Fig. 2. It has a cusp structure near T_N where the butterfly-shaped MR is strongly enhanced. The observed Hall effect can be explained by a recent theoretical model based on the extrinsic topological Hall effect where the fluctuation of spins produces a finite scalar chirality due to the interfacial Dzyaloshinskii-Moriya interaction [8].

[1] C. Gong *et al*., Nature, Vol. 546, p265 (2017) [2] B. Huang *et al*., Nature, Vol. 546, p270 (2017) [3] H. Yoshida *et al*., J. Phys. Soc. Jpn. Vol. 80, p123703 (2011) [4] T. Takagi and M. Mekata, J. Phys. Soc. Jpn. Vol. 64, p4609 (1995) [5] M. Matsuda *et al.,* Phys. Rev. B Vol. 85, p144407 (2012) [6] J. Sugiyama *et al.,* Phys. Rev. B Vol. 88, p184417 (2013) [7] H. Taniguchi *et al*., AIP Adv. Vol. 8, p025010 (2018) [8] H. Ishizuka and N. Nagaosa, New J. Phys. Vol. 20, p123027 (2018)

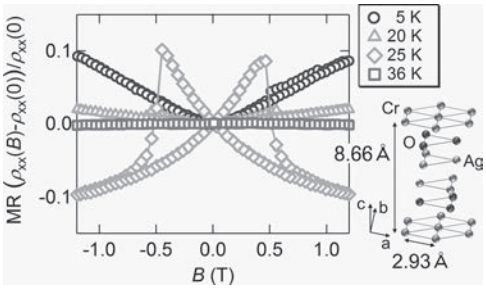


Fig.1 : MR of a Ag_2CrO_2 thin film at different temperature. The inset shows the Ag_2CrO_2 crystal structure.

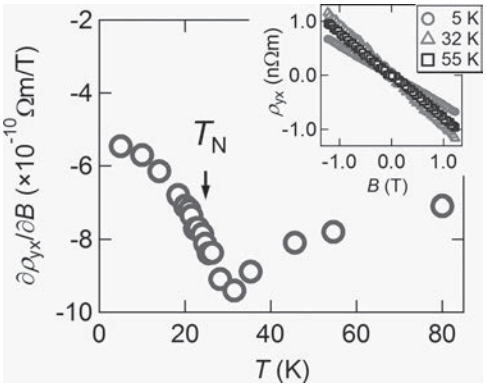


Fig.2 : The derivative of ρ_{yx} is plotted as a function of *T*. The inset shows ρ_{yx} at typical temperatures.

8:54

EB-03. Study of surface-spin accumulation in topological insulators using scanning tunneling microscopy. *S. Tyagi*[1], M. Dreyer[2], D. Bowen[2], D. Hinkel[2], A.L. Friedman[2], P. Taylor[3], R.E. Butera[2], C. Krafft[2] and I. Mayergoyz[1] *1. University of Maryland, College Park, MD, United States; 2. Laboratory for Physical Sciences, College Park, MD, United States; 3. US Army Research Laboratory, Adelphi, MD, United States*

Topological insulators are currently a very active area of research in spintronics due to their unique physical properties as well as their promising applications. Among these properties is the ninety-degrees locking between the spin and momentum of electrons in the topologically protected surface mode. This property results in surface accumulations of spin-polarized electrons caused by bias current flow through the topological insulators. In our work, we report the experimental study of this surface spin-polarized electron accumulation for Bi_2Se_3 by using Scanning Tunneling Microscopy with tungsten as well as iron-coated tungsten tips. The central idea of this study is to explore the asymmetries in electron tunneling caused by such surface spin-accumulation due to bias currents through the samples. We have experimentally observed two types of the above asymmetries in the tunneling currents: (a) for different polarities of tunneling voltages, and (b) for different directions of bias currents through the Bi_2Se_3 sample. The first type of asymmetry was detected by using tungsten tips, and it manifests in appreciable difference between the tunneling currents when spin polarized electrons tunnel from the sample to the tip as compared to the other way around. In the case of tungsten tips, no asymmetry was observed in tunneling currents by changing the direction of bias current through the Bi_2Se_3 sample. However, in the case of Fe-coated tungsten tips, this asymmetry was clearly pronounced. This can be related to the phenomenon of spin-dependent tunneling between Fe-coated tungsten tip and the sample. Many experimental results revealing these asymmetries are obtained. Here, we present two sample results. Fig. 1 illustrates the asymmetry in the tunneling currents for opposite polarities of tunneling voltage and various bias current pulses through the sample observed by using tungsten tip. Fig. 2 reveals the asymmetry in the tunneling current from the sample to the Fe-coated tungsten tip caused by changing the direction of the bias current through the sample.

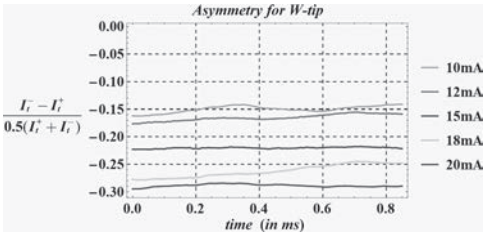


Fig.1 I_t^+ and I_t^- are tunneling currents for opposite polarities of tunneling voltage

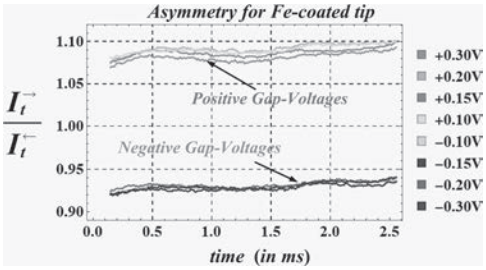


Fig.2 $I_t^{\rightarrow}$ and $I_t^{\leftarrow}$ are tunneling currents for opposite directions of bias current pulses

INVITED PAPER

9:06

EB-04. Surface State Magnetoresistance in Proximity Magnetized Topological Insulators. *N. Mason*[1], J. Sklenar[1], J. Oh[1], Y. Zhang[2] and M. Gilbert[3] *1. Physics, University of Illinios at Urbana-Champaign, Urbana, IL, United States; 2. Materials Science, University of Illinois at Urbana-Champaign, Urbana, IL, United States; 3. Electrical and Computer Engineering, University of Illinois at Urbana-Champaign, Urbana, IL, United States*

Topological insulators (TIs) have a variety of unique transport properties, including strong spin-orbit coupling and symmetry-protected spin-momentum locked surface states. These properties have driven significant interest in understanding the science and device potential of systems that combine TIs with magnetism. In particular, proximity magnetization—i.e., placing a layer of magnetic material in direct contact with the TI—can be used to control the surface state symmetry, and thus the transport properties. In this talk, I will discuss transport measurements of TIs proximity magnetized by magnetic insulators and metals, where in both cases out-of-plane magnetic anisotropy leads to gapping of the TI surface state. For the TI Bi2Se3 on the magnetic insulator YIG, we experimentally observe a new MR effect, that is identified as anisotropic magnetoresistance consistent with a magnetized surface state. For Bi2Se3 coupled to a Co/Pt multilayer, which has a perpendicular magnetic anisotropy, resistance switching is observed for every magnetic field direction. These results are consistent with magnetic anisotropy out of the sample plane opening an energy gap between the surface states, and provide insights into the fundamental mechanisms of magnetic proximity and interface interactions in topological systems. This work is supported by DARPA under ONR 14-17-1-3012 and NSF DMR 17-20633 through the MRSEC program.

CONTRIBUTED PAPERS

9:42

EB-05. Magnetoelectric Induced Topological Phases in Graphene on Chromia Interface. *H. Takenaka*[1], S. Sandhoefner[1], A. Kovalev[1] and E.Y. Tsymbal[1] *1. University of Nebraska-Lincoln, Lincoln, NE, United States*

Topological antiferromagnetic (AFM) spintronics is an emerging field of research, which involves the topological electronic states coupled to the AFM order parameter known as the Néel vector. Recently, the control of these states is successfully envisioned through manipulation of the Néel vector by spin-orbit torques driven by passing electric currents. Here, using interface of graphene on Cr_2O_3 (0001) surface, we propose a different approach favorable for low-power AFM spintronics, where the control of the topological states in a two-dimensional material, such as graphene, is performed via the proximity effect by the voltage induced switching of the Néel vector in an adjacent magnetoelectric AFM insulator, such as chromia. Using density functional theory and tight-binding Hamiltonian approaches, we model the graphene/Cr_2O_3 (0001) interface and demonstrate non-trivial band gaps, differently open in the graphene Dirac bands near the *K* and *K′* valleys. This gives rise to an unconventional quantum anomalous Hall effect with the onset of an additional quantized value or the emergence of the valley Hall effect. The electrically switchable AFM order parameter in Cr_2O_3 determines the sign of the quantum anomalous Hall conductance. Furthermore, the Chern numbers which depend on the Néel vector orientation across the 180° AFM domain wall in Cr_2O_3 indicate the appearance and transformation of the five different topological phases in graphene as shown in Figure and the emergence of the chiral edge states due to the discontinuous changes. These topological properties are controlled by voltage through magnetoelectric switching of the AFM insulator with no need for spin-orbit torques.

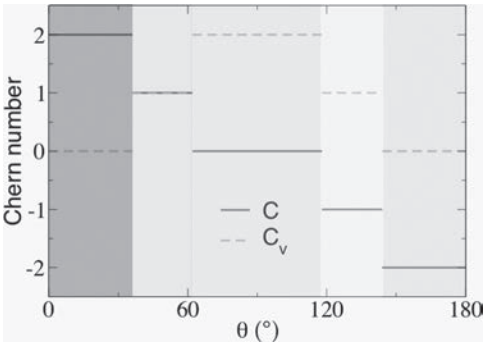


Fig.1 The phase diagram of Chern numbers for the graphene bands as a function of magnetization angle across 180° domain wall in chromia.

9:54

EB-06. Adiabatic and Resonant Spin Pumping in Two-dimensional Quantum Spin Hall Insulator. *Y. Araki*[1], T. Misawa[2] and K. Nomura[3] *1. Advanced Science Research Center, Japan Atomic Energy Agency, Tokai, Japan; 2. Institute for Solid State Physics, The University of Tokyo, Kashiwa, Japan; 3. Institute for Materials Research, Tohoku University, Sendai, Japan*

We present our theoretical work on spin pumping into a two-dimensional (2D) quantum spin Hall inslator (QSHI). QSHI is a topological insulator in 2D exhibiting gapless helical edge stats, which are responsible for the quantized spin Hall conductivity. Recent theories [1] and experiments [2] have demonstrated the QSHI phase in a monolayer of transition metal dichalcogenide 1T'-WTe_2, which can be easily engineered in contrast to traditionally-known HgTe/CdTe and InAs/GaSb quantum wells. While the theory of spin pumping is well established in normal metals by focusing on the spin-dependent electron scattering at the interface [3], it is unreliable for topologically nontrivial interfaces in such systems. In the present work, we consider a junction of a ferromagnet and a 2D QSHI at its 1D edge (Fig. 1), and demonstrate the pumping of angular momentum from the spin-precessing ferromagnet into the QSHI [4]. Using the Floquet theory for the electrons on the helical edge states, we analytically show that the time-periodic precession of the magnetization drives a charge current on the edge, for the whole range of precession frequency. This edge current can be regarded as a consequence of the inverse spin Hall effect intrinsic to the QSHI, which converts the injected spin current into a transverse charge current [5,6]. By varying the precession frequency of the magnetization and the coupling strength at the junction, we find a clear crossover between two regimes: the adiabatic regime, where the slow magnetization precession drives a quantized pumping, and the resonant regime, where the fast precession leads to a suppressed pumping. We also incorporate the effect of orbital dependence in the exchange coupling at the edge, and show numerically that it shifts the crossover point between the adiabatic and resonant regimes.

[1] X. Qian, J. Liu, L. Fu, and J. Li, Science 346, 1344 (2014). [2] S. Tang *et al.*, Nat. Phys. 13, 683 (2017). [3] Y. Tserkovnyak, A. Brataas, G. E. W. Bauer, and B. I. Halperin, Rev. Mod. Phys. 77, 1375 (2005). [4] Y. Araki, T. Misawa and K. Nomura, *paper in preparation*. [5] X.-L. Qi, T. L. Hughes and S.-C. Zhang, Nat. Phys. 4, 273 (2008). [6] S.-H. Chen, B. K. Nikolić and C.-R. Chang, Phys. Rev. B 81, 035428 (2010).

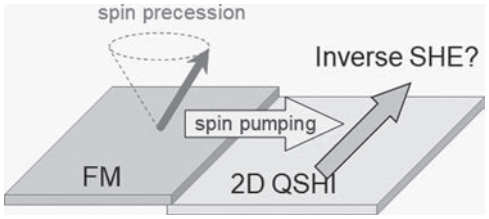


Fig.1 Schematic picture of the spin pumping from the precessing ferromagnet (FM) into the quantum spin Hall insulator (QSHI).

10:06

EB-07. Antiferromagnetic topological insulator $MnBi_2Te_4$ and its applications. *M.M. Otrokov*[1,2], I.P. Rusinov[3,4], M. Blanco-Rey[5,6], M. Hoffmann[7], A.Y. Vyazovskaya[3,4], S.V. Eremeev[8,3], Y.M. Koroteev[8,3], A. Ernst[7], P.M. Echenique[5,6], A. Arnau[1,5] and E.V. Chulkov[5,6] *1. Centro de Física de Materiales (CFM-MPC), Centro Mixto CSIC-UPV/EHU, San Sebastian, Spain; 2. IKERBASQUE, Basque Foundation for Science, Bilbao, Spain; 3. Tomsk State University, Tomsk, Russian Federation; 4. Saint Petersburg State University, Saint Petersburg, Russian Federation; 5. Departamento de Física de Materiales, Universidad del País Vasco (UPV/EHU), San Sebastian, Spain; 6. Donostia International Physics Center (DIPC), San Sebastian, Spain; 7. Institut für Theoretische Physik, Johannes Kepler Universität, Linz, Austria; 8. Institute of Strength Physics and Materials Science, Tomsk, Russian Federation*

Using state-of-the-art first-principles methods as well as Monte Carlo simulations, we have predicted the van der Waals block-layered compound $MnBi_2Te_4$ to be AFMTI [1,2]. An interlayer AFM ordering makes $MnBi_2Te_4$ invariant with respect to the combination of the time-reversal (Θ) and primitive-lattice translation ($T_{1/2}$) symmetries, $S = \Theta T_{1/2}$, which gives rise to the Z_2 classification of AFM insulators, $Z_2 = 1$ for this material. The *S*-breaking (0001) surface of $MnBi_2Te_4$ exhibits a giant band gap in the topological surface state thus representing an ideal platform for the observation of the quantized magnetoelectric coupling and intrinsic axion insulator state. Our prediction is confirmed experimentally by means of structural, transport, magnetic, angle- and spin-resolved photoemission spectroscopy measurements, with the first observation reported in Ref. [1]. In the 2D limit, we predict $MnBi_2Te_4$ to show a unique set of thickness-dependent magnetic and topological transitions, which drive it through FM and (un)compensated

AFM phases, as well as quantum anomalous Hall (QAH) and zero plateau QAH states [3]. Thus, $MnBi_2Te_4$ is the first stoichiometric material predicted to realize the zero plateau QAH state intrinsically. This state has been theoretically shown to host the exotic axion insulator phase. The discovery of the first AFMTI $MnBi_2Te_4$ opens new direction in the field of magnetic TIs that focuses on intrinsically magnetic stoichiometric compounds [4]. Apart from $MnBi_2Te_4$ itself, its FM building blocks can be utilized for the creation of topologically-nontrivial heterostructures [5,6]. Using the growth mechanism reported in [6], we theoretically propose a conceptually new type of interface between a trivial magnetic insulator and a nonmagnetic TI [7].

[1] M.M. Otrokov, I. I. Klimovskikh, et al., arXiv:1809.07389. [2] S.V. Eremeev, M.M. Otrokov, E.V. Chulkov, J. Alloys Compd. 709, 172 (2017). [3] M.M. Otrokov, I.P. Rusinov, M. Blanco-Rey, et al., Phys. Rev. Lett. 122, 107202 (2019). [4] Z.S. Aliev, et al., J. Alloys Compd. 789, 443 (2019). [5] M.M. Otrokov, T.V. Menshchikova, et al., 2D Mater. 4, 025082 (2017). [6] T. Hirahara, S.V. Eremeev et al., Nano Lett. 17, 3493 (2017). [7] S.V. Eremeev, M.M. Otrokov, E.V. Chulkov, Nano Lett. 18, 6521 (2018).

10:18

EB-08. Giant Spin Hall Angle in $Bi_{1-x}Sb_x$ Semimetals Driven by Thermally Excited Dirac-like Electrons. *Z. Chi*[1,2], Y. Lau[1,2] and M. Hayashi[1,2] *1. Department of Physics, The University of Tokyo, Tokyo, Japan; 2. National Institute for Materials Science, Tsukuba, Japan*

Charge-to-spin conversion induced spin-orbit torques in heavy metals (HM)/ ferromagnet (FM) heterostructures have attracted significant attention for its potential application in magnetic memory technologies. In order to obtain a high spin conversion efficiency, a variety of materials have been studied[1,2]. Due to its large spin orbit coupling, Bi has been predicted to possess a large spin Hall conductivity (SHC)[3,4]. However, up to date, the spin conversion efficiency of Bi has been reported to be extremely small compared to 5*d* transition metals[5,6]. In this presentation, we report experimental findings of large spin-orbit torque in $Bi_{1-x}Sb_x$/CoFeB bilayers prepared by magnetron sputtering. The Sb concentration dependence of the SHC is in good agreement with that calculated using a tight binding approach[4], indicating that the spin current has an intrinsic origin. Surprisingly, we find the strength of SHC in BiSb increases with increasing temperature, by nearly a factor of 3 when the measurement temperature is varied from 10 K to 300 K. We infer this temperature driven enhancement of the SHC is due to the increased number of thermally excited Dirac-like electrons located at the Bi *L*-valleys with large Berry curvature.

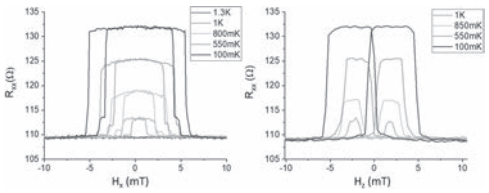
[1] L. Liu *et al.*, Science 336, 555-558 (2012). [2] A. R. Mellnik *et al.*, Nature 511, 449-451 (2014). [3] Y. Fuseya *et al.*, Journal of the Physical Society of Japan 81, 093704 (2012). [4] C. Sahin *et al.*, Physical Review Letters 114, 107201 (2015). [5] D. Z. Hou *et al.*, Applied Physics Letters 101, 042403 (2012). [6] H. Emoto *et al.*, Physical Review B 93, 174428 (2016).

10:30

EB-09. Spin valve-like magnetoresistance of a topological insulator in proximity to a perpendicular magnet. *J. Oh*[1], V. Humbert[1], J. Sklenar[1] and N. Mason[1] *1. Physics, University of Illinois at Urbana-Champaign, Urbana, IL, United States*

Topological insulators (TIs) have a variety of unique transport properties, one of which is symmetry-protected surface states with spin-momentum locking. Efforts have been made to control the surface states by breaking time reversal symmetry via proximity magnetization, which is achieved by placing a magnetic layer in direct contact with the TI.[1,2] In parallel, other works demonstrated in similar TI/ferromagnetic systems that the magnetic layer's magnetization can be switched with electric current through TI due to the TIs' exceptional spin-to-charge conversion ratio.[3,4] We report an exotic spin valve-like magnetoresistance switching response observed at low temperatures in heterostructures of the TI, Bi_2Se_3, adjacent to a Co/Pt multilayer with perpendicular magnetic anisotropy. The magnetoresistance is hysteretic in magnetic field and nearly isotropic, as evidenced by the resistance state switching when either in-plane or out-of-plane magnetic fields are applied. In-plane angle dependence and temperature dependence of the field sweep imply that the effect does not arise from Co/Pt magnetization, but rather from the TI. The results indicate that ferromagnetism induced in a TI via proximity coupling can be probed through magnetoresistance measurements. *This work is supported by NSF under DMR 17-10437 and DMR 17-20633 through the MRSEC program, and DARPA under ONR 14-17-1-3012.

[1] M. Lang, M. Montazeri, M. C. Onbasli, X. Kou, Y. Fan, P. Upadhyaya, K. Yao, F. Liu, Y. Jiang, W. Jiang, K. L. Wong, G. Yu, J. Tang, T. Nie, L. He, R. N. Schwartz, Y. Wang, C. A. Ross, K. L. Wang, *Nano letters* 14.6 (2014): 3459-3465. [2] P. Wei, F. Katmis, B. A. Assaf, H. Steinberg, P. Jarillo-Herrero, D. Heiman, and J. S. Moodera, *Physical review letters*110.18 (2013): 186807. [3] J. Han, A. Richardella, S. A. Siddiqui, J. Finley, N. Samarth, and L. Liu *Physical review letters* 119.7 (2017): 077702. [4] Y. Wang, D. Zhu, Y. Wu, Y. Yang, J. Yu, R. Ramaswamy, R. Mishra, S. Shi, M. Elyasi, KL. Teo, Y. Wu and H. Yang, *Nature communications* 8.1 (2017): 1364.



Abrupt magnetoresistance (MR) change observed for magnetic field swept along the current, H_x (left), and out-of-plane direction, H_z (right), in Bi_2Se_3/[Co/Pt] device at different temperatures. Sudden MR rise/drop occur at much lower fields (<7mT) than the switching field of Co/Pt multilayer (50mT). The square MR behavior becomes more suppressed as the temperature is raised before disappearing after 1K. Such result indicate that abrupt MR change arises from ferromagnetism induced in Bi_2Se_3.

10:42

EB-10. Spin-orbit torque switching of ferromagnets and ferrimagnets by topological surface states. *H. Wu*[1], P. Zhang[1], P. Deng[1], Y. Xu[2], S. Razavi[1], S. Mangin[2] and K. Wang[1] *1. Department of Electrical and Computer Engineering, University of California, Los Angeles, Los Angeles, CA, United States; 2. Institut Jean Lamour, CNRS UMR 7198, Université de Lorraine, Nancy, France*

Utilizing spin-orbit torque (SOT) to manipulate the magnetic order provides a promising route for low power-dissipation spintronic devices [1-4]. To date, the improvement of SOT efficiency is still a major challenge to further reduce the power dissipation of SOT-based devices, where topological insulators (TIs) with spin-momentum locked surface states promise a giant SOT compared to conventional heavy metals (HMs) with bulk spin-orbit coupling (SOC). Here, in the first part, we systematically study the SOT from topological insulators and heavy metals in a series of ferromagnet-based structures [TI(HM)/Ti/CoFeB/MgO] at room temperature. The effective spin Hall angle θ_{SH} of TIs is one order of magnitude larger than HMs, at the same time the resulted switching current density J_c is one order of magnitude smaller, indicating the high charge-spin conversion efficiency from topological surface states, as shown in Table 1. By tuning the Fermi level, we find the SOT is significantly enhanced near the Dirac point with the most insulating bulk contribution. In the second part, we change the ferromagnetic CoFeB to the ferrimagnetic GdFeCo. With tuning the magnetic moment of GdFeCo by its composition, we find that the SOT efficiency is enhanced

near the compensation point with the zero magnetic moment, as shown in Fig. 1. The switching current density J_c reaches as low as 1.2×10^5 A cm^{-2}, where the switching speed could be as fast as several picoseconds. This work demonstrates the ultrahigh SOT efficiency from topological surface states.

[1] Y. Fan, P. Upadhyaya, X. Kou, M. Lang, S. Takei, Z. Wang, J. Tang, L. He, L.-T. Chang, M. Montazeri, G. Yu, W. Jiang, T. Nie, R. N. Schwartz, Y. Tserkovnyak and K. L. Wang, Nature Materials 13, 699 (2014). [2] J. Han, A. Richardella, S. A. Siddiqui, J. Finley, N. Samarth and L. Liu, Physical Review Letters 119 (7), 077702 (2017). [3] M. Dc, R. Grassi, J.-Y. Chen, M. Jamali, D. Reifsnyder Hickey, D. Zhang, Z. Zhao, H. Li, P. Quarterman, Y. Lv, M. Li, A. Manchon, K. A. Mkhoyan, T. Low and J.-P. Wang, Nature Materials 17 (9), 800-807 (2018). [4] N. H. D. Khang, Y. Ueda and P. N. Hai, Nature Materials 17 (9), 808-813 (2018).

	$\lvert J_c \rvert$ (10^6 A cm^{-2})	$\lvert \chi_{SOT} \rvert$ (10^{-6} Oe A^{-1} cm^2)	$\lvert \theta_{SH} \rvert$	σ (10^4 Ω^{-1}m^{-1})	$\lvert \sigma_{SH} \rvert$ (10^4 $\frac{\hbar}{2e}$ Ω^{-1}m^{-1})	t_s (nm)	$\lvert q_{ICS} \rvert$ (nm^{-1})	P_D (10^{16} W m^{-3})
$(BiSb)_2Te_3$	0.52	62.7	2.32	1.83	4.25	1.5	1.55	0.15
Bi_2Te_3	2.43	1.94	0.07	15.0	1.05	1.5	0.05	0.39
SnTe	1.46	34.1	1.26	5.45	6.87	1.5	0.84	0.39
Ta	3.44	4.50	0.17	34.3	5.83	1.9	0.09	0.35
W	4.57	3.35	0.12	38.8	4.66	2.1	0.06	0.54
Pt	33.5	0.29	0.01	87.2	0.87	7.3	0.001	12.8

Table 1. Switching current density $|J_c|$, SOT efficiency $|\chi_{SOT}|$, effective spin Hall angle $|\theta_{SH}|$, conductivity σ, spin Hall conductivity $|\sigma_{SH}|$, spin source thickness t_s, interfacial charge-spin conversion efficiency $|q_{ICS}|$ and power dissipation P_D in TI(HM)/Ti/CoFeB/MgO structures.

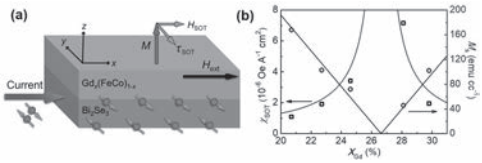


Figure 1. (a) Schematic of spin-orbit torque (SOT) induced magnetization switching in the Bi_2Se_3/GdFeCo structure. (b) Saturation magnetization M_s and SOT efficiency as a function of Gd concentrations.

10:54

EB-11. Non-local electrical detection of helical surface states in three-dimensional topological insulators. *S. Jafarpisheh*[1,2], F. Volmer[1], Z. Wang[3], Y. Ando[3], C. Stampfer[1,2] and B. Beschoten[1] *1. 2nd Institute of Physics and JARA-FIT, RWTH Aachen University, Aachen, Germany; 2. Peter Grünberg Institute (PGI-9), Forschungszentrum Jülich, Jülich, Germany; 3. Physics Institute II, University Cologne, Cologne, Germany*

Spin-momentum locking on the surface of three-dimensional (3D) topological insulators (TIs) is a unique property that can be utilized in the future spintronic devices. A crucial step toward this goal is the direct detection of the surface states in transport measurements. A major problem, however, is the conductive bulk which acts as a parallel channel in transport and makes it extremely difficult to distinguish the contribution of the surface-states in conventional magneto-transport measurements. A solution is to perform non-local measurements where transport characteristics are investigated outside the region between the two current leads [1]. Due to the large spin-orbit coupling, the spin-diffusion length inside the bulk channel of TIs is very small and therefore, no bulk contribution is expected in the non-local signal. In contrast, the surface-states are expected to fully enclose the bulk of a strong 3D TI and therefore giving rise to a non-local spin-polarized current. Spin-sensitive studies of the non-local current thus allow to unambiguously probe the spin-momentum locking of the surface states. Here, we report on non-local spin transport measurements on exfoliated $BiSbTeSe_2$ flakes. We utilize potentiometric measurements by using ferromagnetic sensing electrodes to confirm the spin-momentum locking of the conducting surface states throughout the whole surface layer of the crystal. The spin signals in both local and non-local geometries are strongly temperature dependent and disappear at 50 K that excludes the dominance of magnetic fringe-fields from the ferromagnetic electrodes as origin of the spin signals. Furthermore, we identify thermally activated transport through bulk states at higher temperatures, which explains the disappearance of the surface states contribution by the loss of the non-local spin signal.

[1] S. Wolgast *et al*., Phys. Rev. B, Vol. 88, p.180405 (2013)

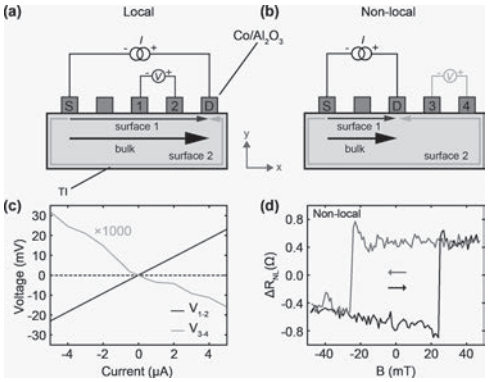


Figure 1: Measurement configurations in (a) local (b) non-local geometries. (c) I-V characteristics of the two geometries. (d) Spin-sensitive measurements in the non-local configuration.

11:06

EB-12. Observation of opposite current-induced spin polarization in bulk-metallic Bi_2Se_3 and bulk-insulating Bi_2Te_2Se topological insulator thin flakes. *J. Tian*[1,2], C. Sahin[3], I. Miotkowski[1], M.E. Flatté[3] and Y.P. Chen[1] *1. Physics and Astronomy, Purdue University, West Lafayette, IN, United States; 2. Physics & Astronomy, University of Wyoming, Laramie, WY, United States; 3. Physics and Astronomy, University of Iowa, Iowa City, IA, United States*

One of the most fundamental and exotic properties of 3D topological insulators (TIs) is spin-momentum-locking (SML) of their topological surface states (TSSs), making 3D TI a promising candidate for future spintronics. [1-3] However, real 3D TI materials may also host other conductive channels, [4] such as a trivial two-dimensional electron gas (2DEG) with strong Rashba type spin-orbit interaction (SOI) and bulk spin Hall (SH) states. All the three states can possibly contribute to the current induced spin polarization (CISP), making the determination of the origin of the observed CISP in 3DTIs difficult. Here, we directly compare the CISPs in both bulk-insulating Bi_2Te_2Se (BTS221) and bulk-metallic Bi_2Se_3 thin flakes by spin potentiometry.[5] In bulk insulating BTS221 samples, the measured CISP can be unambiguously ascribed to the SML of TSS, whereas an opposite CISP is observed in bulk metallic Bi_2Se_3 samples, consistent with the expectations of Rashba SOI of the 2DEG due to band bending. We further calculated the intrinsic SH conductivity of the bulk Bi_2Se_3 and discussed its possible contribution to the measured CISP. Our results give the direct transport evidence of the opposite signs of the spin helicity in TSS and the outer Fermi surface of Rashba 2DEG in 3D TIs, opening ways for potential applications in 3D TI-based spintronics.

[1] J. Tian, I. Childres, H. Cao, et al., *Solid State Commun.,* Vol. 191, p.1 (2014). [2] J. Tian, I. Miotkowski, S. Hong, et al., *Sci. Rep.,* Vol. 5, p.14293 (2015). [3] J. Tian, S. Hong, I. Miotkowski, et al., *Sci. Adv.* Vol. 3, p.e1602531 (2017). [4] J. Tian, H. Seokmin, S. Shehrin, et al., *Nat. Commun.,* Vol. 10, p.1461 (2019). [5] J. Tian, C. Sahin, I. Miotkowski, et al., (2019).

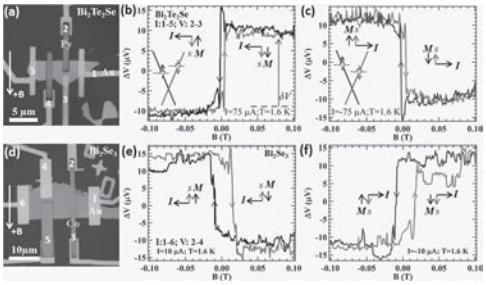


Fig. 1 Current-induced opposite spin polarizations in bulk-insulating Bi_2Te_2Se (BTS221) and bulk-metallic Bi_2Se_3 thin flakes. (a) Optical image of a typical BTS221 device. (b,c) The voltage (ΔV) measured by an FM (Py, electrode "2") spin detector as a function of the in-plane magnetic field (*B*) at *I*= 75 μA (b), and -75 μA (c). The purple arrow represents the extracted spin signal $\delta V = \Delta V_{+M} - \Delta V_{-M}$. (d) Optical image of a representative Bi_2Se_3 device. (e,f) Voltage (ΔV) measured by a Co (electrode "2") spin detector as a function of the in-plane *B* field at *I*= 10 μA (e), and -10 μA (f).

11:18

EB-13. Point Contact Spectroscopy of Zero-energy Modes in Topological Materials. G.P. Mazur[1], K. Dybko[1,2], A. Szczerbakow[2], J.Z. Domagala[2], A. Kazakov[1], M. Zgirski[2], E. Lusakowska[2], S. Kret[2], J. Korczak[1,2], T. Story[1,2], *M. Sawicki*[2] and T. Dietl[1,2] *1. International Research Centre MagTop, Institute of Physics, Polish Academy of Sciences, Warszawa, Poland; 2. Institute of Physics, Polish Academy of Sciences, Warszawa, Poland*

Point-contact spectroscopy of several topological materials reveals a phase transition to a low temperature phase that is characterized by low-energy modes superimposed on an energy gap showing a Bardeen-Cooper-Schrieffer (BCS) type of criticality. This behavior is not accompanied by a bulk superconductivity, which points to either local superconductivity or to the emergence of an unfamiliar ground state specific to topological matter. As indicated experimentally [1] and suggested theoretically [2], one of these can be a correlated many body state at surface atomic steps in topological crystalline insulators, exhibiting low-energy excitations. Here we show [3], employing a soft point-contact method that a conductance gap with a broad zero bias conductance peak or Andreev-type characteristics develop at junctions of Ag with topological surfaces of diamagnetic, paramagnetic, and, most notably, ferromagnetic quaternary PbSnMnTe. However, our state of the art structural characterization and magnetometry has not revealed presence of any superconducting nanoclustering. Nevertheless, the temperature dependence of the gap shows a BCS-like critical behavior with the critical temperature up to 4.5 K and the magnitudes of the critical fields independent of the orientation of the magnetic field in respect to the surface plane. This implies the emergence of a collective low-temperature phase, whose appearance is insensitive not only to the magnetic state of the metallic part of the junction, but also to the magnetic character of the topological material. The body of the accumulated evidences indicates that this new phase can be linked to carriers occupying 1D topological states adjacent to surface atomic steps, which undergo a transition to a collective state at sufficiently low temperatures and magnetic fields. The work has been supported by the Foundation for Polish Science through the IRA Programme co-financed by EU within SG OP, the National Science Centre, Poland through UMO-2015/19/N/ST3/02626 and UMO-2017/27/B/ST3/02470 projects.

[1] P. Sessi, D. Di Sante, A. Szczerbakow, F. Glott, S. Wilfert, H. Schmidt, T. Bathon, P. Dziawa, M. Greiter, T. Neupert, G. Sangiovanni, T. Story, R. Thomale, and M. Bode, Science Vol 354, 1269 (2016). [2] W. Brzezicki, M. M. Wysokinski, and T. Hyart, arXiv:1812.02168 (2018). [3] G. P. Mazur, K. Dybko, A. Szczerbakow, A. Kazakov, M. Zgirski, E. Lusakowska, S. Kret, J. Korczak, T. Story, M. Sawicki, and T. Dietl, arXiv: 1709.04000 (2017).

Session EC
SPIN CURRENTS AND RESULTING SPIN TORQUES I

Markus Münzenberg, Chair
Universität Greifswald, Greifswald, Germany

CONTRIBUTED PAPERS

8:30

EC-01. High Spin Hall Conductivity and Current-Induced Magnetization Switching by α-W. *W. Liao*[1], T. Chen[1], Y. Ferrante[3], S.S.P. Parkin[2] and C. Pai[1] *1. Materials Science and Engineering, National Taiwan University, Taichung, Taiwan; 2. Max Plank Institute of Microstructure Physics, Halle, Germany; 3. IBM Research-Almaden, San jose, CA, United States*

The spin Hall effect from 5d transition metal can convert charge current into spin current that can further exert spin-orbit torques to switch the magnetization of adjacent magnetic layers. Among all 5d transition metals, amorphous-W (or β-W) has the largest damping-like spin-orbit torque efficiency ~ 0.20-0.50. However, compared to other materials systems which also possess large spin-orbit torque efficiency such as Pt [1], amorphous W is less favorable due to its relatively high resistivity ($\rho^{\text{amorphous-W}}$~ 200-300 μΩ-cm), and therefore requires higher power consumption to achieve current-induced magnetization switching. In this work, we find that W in its conductive and crystalline phase (α-W) has the possibility to possess larger spin-orbit torque efficiency with lower resistivity ($\rho^{\alpha\text{-W}}$~ 20-40 μΩ-cm). Through comprehensive study on W/CoFeB/MgO and the reversed MgO/CoFeB/W, we find that although α-W shows lower spin-orbit torque efficiency ~ 0.04 [2-3], the spin Hall conductivity of α-W ($|\sigma_{SH}^{\alpha\text{-W}}|=3.71\times10^5\ \Omega^{-1}m^{-1}$) is roughly three times higher than that of amorphous-W ($|\sigma_{SH}^{\text{amorphous-W}}|=1.05\times10^5\ \Omega^{-1}m^{-1}$), which suggests that we can possibly achieve higher spin-orbit torque efficiency in α-W by further tuning its resistivity [4-6]. Moreover, we perform current-induced magnetization switching using α-W as the spin Hall source, which has not been reported previously. Our findings suggest that conductive and high spin Hall conductivity α-W is promising for future low power consumption spin-orbit torque memory application.

[1] N. H. D. Khang, Y. Ueda, P. N. Hai, Nat. Mater. 2018, 17, 808. [2] T. C. Wang, T. Y. Chen, C. F. Pai, Phy Rev Mater 2018, 2, 014403. [3] C. F. Pai, M. Mann, G. S. D. Beach, Phys. Rev. B 2016, 93, 144409. [4] M. Morota, Y. Niimi, Y. Otani, Phys. Rev. B 2011, 83, 174405. [5] E. Sagasta, Y. Omori, F. Casanova, Phys. Rev. B 2016, 94, 060412. [6] E. Sagasta, Y. Omori, F. Casanova, Phys. Rev. B 2018, 98, 060410.

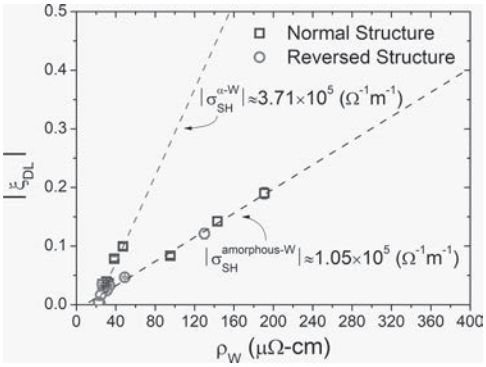


Fig.1 The magnitude of damping-like spin-orbit torque efficiency $|\xi_{DL}|$ vs resistivity of the normal (blue squares) and reversed (red circles). The dashed lines represent linear fits to the data, and the slopes correspond to the spin Hall conductivity of two different phases.

8:42

EC-02. Ultra-Low Switching Current Density in All-Amorphous W-Hf/CoFeB/TaO_x Films. *K. Fritz*[1], L. Neumann[2] and M. Meinert[1] *1. Center for Spinelectronic Materials and Devices, Department of Physics, Bielefeld University, Bielefeld, Germany; 2. Argelander Institute for Astronomy, Bonn University, Bonn, Germany*

In our previous work [1], we investigated the spin Hall effect of W-Hf thin films, which exhibit a phase transition from a segregated phase mixture to an amorphous alloy below 70% W. Accompanied by a jump in resistivity, the spin Hall angle shows a pronounced maximum at the composition of the phase transition. A maximum spin Hall angle of θ_{SH} = -0.20 was obtained for amorphous $W_{0.7}Hf_{0.3}$. Due to their amorphous character, the films are expected to contain few pinning centers and, therefore, to show fast domain wall motion, making them interesting in the context of current induced SOT switching. Using polar Kerr microscopy, we study current induced domain wall motion and magnetization switching of all-amorphous $W_{0.66}Hf_{0.34}$/CoFeB/TaO_x stacks with perpendicular magnetic anisotropy and large spin Hall angle. We observe current induced domain wall motion without an in-plane assist field, indicating Néel-type domain walls. Investigations of magnetization switching as a function of H_x and current pulse-widths τ reveal switching current densities as low as 3×10^9 A/m² in the dc limit. We accredit the low switching current densities to a weak pinning [2], caused by the amorphous character of the sample and the associated small grain size with respect to the domain wall width [3]. Our assumption is supported by observations of the switching process, which takes place via nucleation and subsequent expansion of a single, smooth domain. Measurements of the domain displacement upon current injection for $\mu_0 H_x = 0$ reveal a low depinning current density of 3.9×10^{10} A/m² at a pulse width of 500 ns. We verify the correlation between switching and depinning current density by investigations of a Ta/CoFeB/MgO/Ta reference sample, which shows critical current densities of at least one order of magnitude larger, respectively.

[1] K. Fritz, S. Wimmer, H. Ebert, and M. Meinert, Phys. Rev. B, 98, 094433 (2018) [2] O. J. Lee, L. Q. Liu, C. F. Pai, Y. Li, H. W. Tseng, P. G. Gowtham, J. P. Park, D. C. Ralph, and R. A. Buhrmann, Phys. Rev. B, 89, 024418 (2014) [3] W. Legrand, D. Maccariello, N. Reyren, K. Garcia, C. Moutafis, C. Moreau-Luchaire, S. Collin, K. Bouzehouane, V. Cros, and A. Fert, Nano Lett., 17, 2703-2712 (2017)

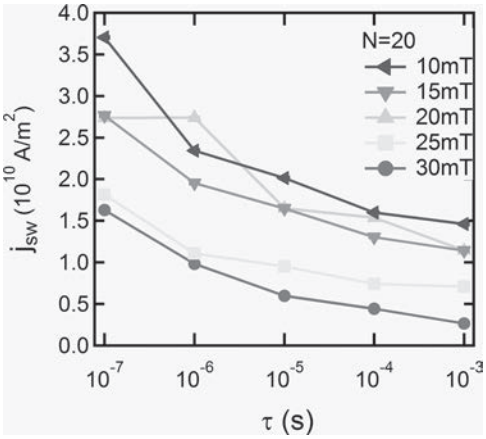


Fig.1 Switching current density of W-Hf as a function of τ for different $\mu_0 H_x$.

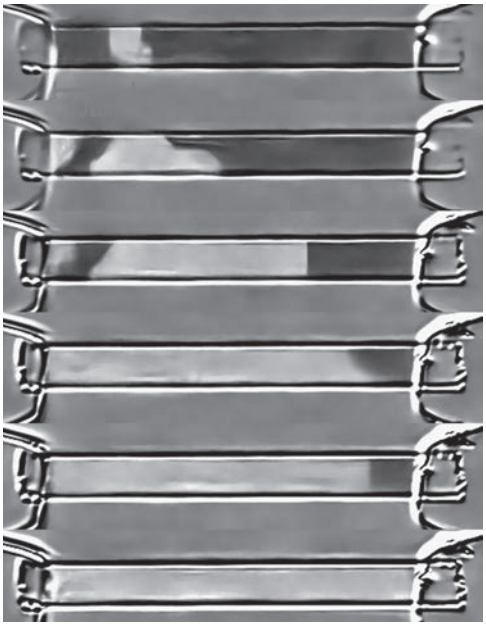


Fig. 2 CIMS in W-Hf with $\mu_0 H_x$ = 20 mT and single pulses ($j = 2\times10^{10}$ A/m^2, $\tau = 1\times10^{-4}$ s).

8:54

EC-03. Spin Planar Hall Effect. *V. Amin*[1,2], P. Haney[2] and M.D. Stiles[2] *1. University of Maryland, College Park, MD, United States; 2. National Institute of Standards and Technology, Gaithersburg, MD, United States*

Ferromagnets generate spin currents under an applied electric field. For example, the charge current driven by an electric field in ferromagnets is spin-polarized because majority and minority carriers have different conductivities. However, in the presence of spin-orbit coupling, the spins of individual electrons in ferromagnets are tilted from the axis of the exchange field. One consequence of this misalignment is that, under an applied electric field, electrons can carry a substantial spin current flowing perpendicularly to the electric field with spin directions both longitudinal and transverse to the magnetization. These spin currents are associated with several mechanisms including the spin Hall effect and the spin anomalous Hall effect. In this talk, we explore another mechanism that it is closely related to the Hall current arising from the anisotropic magnetoresistance. We refer to this phenomenon as the spin planar Hall effect, and present first principles transport calculations giving its strength and magnetization dependence in transition metal ferromagnets. The strength of the generated spin currents is proportional to the charge current conductivity of the ferromagnetic layer. We compute the full spin current tensor to probe all spin directions and compare the spin currents associated with the spin planar Hall effect to all spin currents allowed by symmetry. We find that in Co, the spin current with spin direction transverse to the magnetization has an associated conductivity of approximately 3000 [cm Ohm]$^{-1}$, which exceeds most estimates of the spin Hall conductivity in Pt. To help guide the interpretation of experiments, we also present calculations of the spin planar Hall effect in magnetic heterostructures to quantify their transmission through interfaces and the spin torques they exert. This work was supported by the Cooperative Research Agreement between the University of Maryland and the National Institute of Standards and Technology Center for Nanoscale Science and Technology, Award No. 70NANB14H209, through the University of Maryland.

INVITED PAPER

9:06

EC-04. Manipulating spin currents with graphene-based heterostructures. *F. Casanova*[1,2] *1. CIC nanoGUNE, San Sebastian, Spain; 2. IKERBASQUE, Bilbao, Spain*

The integration of the spin in charge-based electronic devices has revolutionized both sensing and memory capability in microelectronics. Further development in spintronic devices requires electrical manipulation of spin current as well as spin-charge interconversion for logic operations. Graphene has raised as an outstanding spin transporter due to its weak spin-orbit coupling (SOC) [1]. However, a strong SOC is required for an electrical control of the spin state, as in the seminal proposal of Datta and Das [2], or to achieve spin-charge interconversion, via the spin Hall effect [3]. In this talk, I will show how SOC can be induced in graphene by proximity with another material, allowing us to manipulate spin currents. A very simple approach by combining Pt with a graphene channel already shows a very large spin-to-charge voltage output at room temperature [4], opening up exciting opportunities for spin-orbit logic circuits. A radically different approach is by engineering a van der Waals heterostructure which combines graphene with MoS_2, a transition metal dichalcogenide with strong SOC and semiconducting properties. The spin transport in the graphene channel is modulated between ON and OFF states by tuning the spin absorption into the MoS_2 layer with a gate electrode [5]. Our demonstration of a spin field-effect switch using 2D materials identifies a new route towards spin logic operations for beyond CMOS technology. Furthermore, the van der Waals heterostructure at the core of our experiment allows us to unambiguously demonstrate experimentally [6] a predicted spin Hall effect in graphene due to spin-orbit proximity with the MoS_2 [3]. The combination of long-distance spin transport and spin Hall effect in different parts of the same material gives rise to an unprecedented spin-to-charge conversion efficiency, opening up exciting opportunities in a variety of future spintronic applications [6].

[1] J. Ingla-Aynes et al., Nano Lett. 16, 4825 (2016). [2] S. Datta and B. Das, Appl. Phys. Lett. 56, 665 (1990). [3] J. H. Garcia et al., Nano Lett. 17, 5078 (2017). [4] W. Yan et al., Nat. Commun. 8, 661 (2017). [5] W. Yan et al., Nat. Commun. 7, 13372 (2016). [6] C. K. Safeer at al., Nano Lett. 19, 1074 (2019).

CONTRIBUTED PAPERS

9:42

EC-05. Determination of Spin Freezing Temperature in Nanoscale Spin Glasses. *H. Taniguchi*[1], M. Tokuda[1], T. Taniguchi[1], T. Arakawa[1,2], B. Gu[3], T. Ziman[4], S. Maekawa[5], K. Kobayashi[1,6] and Y. Niimi[1,2]
1. Graduate School of Science, Osaka University, Toyonaka, Japan; 2. Center for Spintronics Research Network, Osaka University, Toyonaka, Japan; 3. Kavli Institute for Theoretical Sciences, University of Chinese Academy of Sciences, Beijing, China; 4. Institut Laue Langevin, LPMMC, Université Grenoble-Alpes, Grenoble, France; 5. Center for Emergent Matter Science, RIKEN, Wako, Japan; 6. Graduate School of Science, University of Tokyo, Bunkyo, Japan

Spin current is the central concept in spintronics. The effective generation and detection of spin current have been intensively studied so far in this field. Recently, it has been demonstrated spin currents can detect magnetic fluctuations in magnetic metals in a very sensitive manner [1,2]. Spin glass, a magnetic ordering state with complex spin structures, is a typical example to demonstrate it. According to recent spin Hall effects (SHEs) in a spin glass CuMn [2], the SH signal starts to decrease at a temperature labeled as T^*, which is 4 times higher than the spin frozen temperature T_{fM} determined from the magnetization measurement. Due to the randomness of the Mn impurities in Cu, most of the Mn spins are randomly frozen below T_{fM}, but the SH signal continuously decreases even below T_{fM}. This experimental fact indicates the real spin frozen temperature T_f of the nanowire might be lower than T_{fM}. In this work, we have performed SHE measurements in $Cu_{99.5-x}Mn_xBi_{0.5}$ alloys with much higher Mn concentrations (x = 4.2, 8.2 and 10.6) than the previous work [2], in order to investigate the SH signals at much lower temperatures than T_{fM}. We have measured the SHEs with the spin absorption method [3] in the lateral spin valve structure (see the inset of Fig. 1). Figure 1 shows η, the SH angles of $Cu_{99.5-x}Mn_xBi_{0.5}$ normalized by that of $Cu_{99.5}Bi_{0.5}$, as a function of temperature. η starts to decrease at T^*, and becomes completely zero at a temperature indicated by the arrow in Fig. 1. From comparison with the theoretical calculation, the real spin frozen temperature T_f of nanowire is the temperature where η becomes zero. To support our conclusion, we plot T_f, T_{fM} and T^* as a function of the Mn concentration x in Fig. 2. For all the investigated x region, T_f is always lower than $T_{fM,}$ and increases almost linearly with increasing x. The present result demonstrates that the SHE measurement is a powerful method to detect the magnetic property in a tiny sample, which cannot be realized by the superconducting quantum interference device.

[1] D. H. Wei *et al*., Nat. Commun. Vol. 3, p.1058 (2012) [2] Y. Niimi *et al*., Phys. Rev. Lett. Vol. 115, p.196602 (2015) [3] Y. Niimi and Y. Otani, Rep. Prog. Phys. Vol. 78, p.124501 (2015)

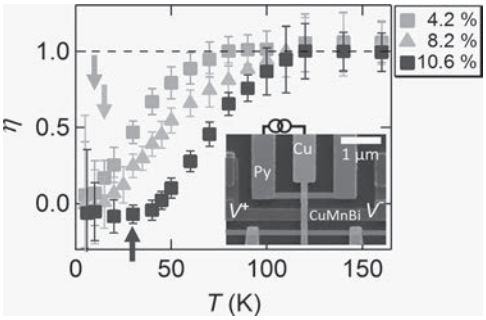


Fig.1 : Temperature dependence of η. The arrows indicate T_f. The inset shows an SEM image of typical device.

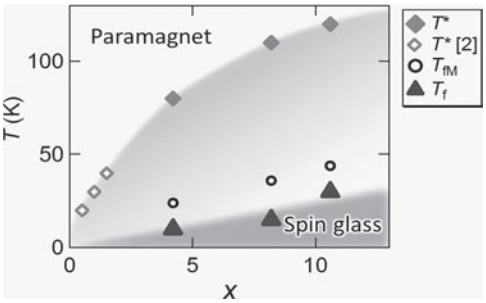


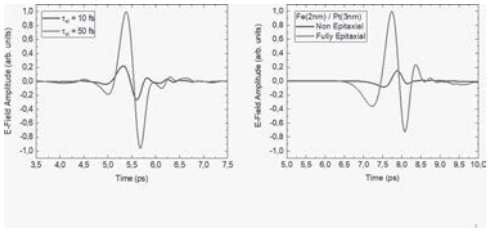
Fig.2: Relations of T^*, T_{fM} and T_f with the Mn concentration x for $Cu_{99.5-x}Mn_xBi_{0.5}$.

9:54

EC-06. Enhanced Performance of Spintronic Terahertz Emitters Based on Defect Engineering. *L. Scheuer*[1], D. Nenno[1], G. Torosyan[2], A. Brodyanski[3], R.H. Binder[4], H.C. Schneider[1], R. Beigang[1] and E.T. Papaioannou[1] *1. Physics, TU Kaiserslautern, Kaiserslautern, Germany; 2. Photonic Center Kaiserslautern, Kaiserslautern, Germany; 3. Institut für Oberflächen- und Schichtanalytik (IFOS) and Landesforschungszentrum Optimas, Kaiserslautern, Germany; 4. College of Optical Sciences, Tucson, AZ, United States*

Metallic magnetic heterostructures consisting of ferromagnetic (FM) and non-magnetic (NM) thin films are revealed as novel sources of THz radiation combining the field of THz physics with the field of spintronics. Recent studies have nicely shown the effect in different FM/NM systems considering the influence of the layer thicknesses, substrates, geometrical arrangement and excitation energy [1-4]. However, in these former studies the significance of the crystal structure of the metallic layers was not yet investigated. Here, we reveal the defect density of the crystal structure as a major factor to engineer the THz generation regarding electric field amplitude and bandwidth of the spectrum. To support the experimental findings, we employ a theoretical model based on the Boltzmann transport equation that accounts for the differences in elastic electron scattering lifetime in the layers and for the transmission of spin-polarized hot carriers at the FM/NM interface. We experimentally show the role of the defect density by studying relaxed epitaxial, deformed epitaxial and fully non-epitaxial Fe/Pt bilayers. We control the emitted THz spectra by modifying the defect density that results in (a) changing the elastic electron-defect scattering lifetime in Fe and Pt and in (b) the interface transmission for spin-polarized, non-equilibrium electrons. A decreased defect density increases the electron-defect scattering lifetime which results in a significant enhancement of the THz-signal amplitude and shifts the spectrum towards lower THz frequencies. Furthermore, we introduce the parameter of the interface transmission that is correlated to the ability of the interface to transfer spin currents into the NM layer. The transmission influences the spectral amplitude of the emitted THz field but conserves the composition of the spectrum.

[1] T. Seifert et al., Nat. Photon. 10, 483–488 (2016) [2] Y. Wu et al., Adv. Mater. 29, 1603031 (2017) [3] G. Torosyan et al., Scientific Reports 8, 1311 (2018) [4] E. Papaioannou et al., IEEE Transactions on Magnetics 99, 1-5 (2018)



Numerical simulation for the THz E-field amplitude of the spintronic Fe (2 nm) / Pt (3 nm) emitter for different elastic scattering lifetimes τ_{Pt} of the electrons (left) and measured THz-E-field amplitude of this emitter grown fully epitaxial resp. non-epitaxial (right).

10:06

EC-07. Making Magnonic Spin Currents Useful – Controlling Spin Transport. J. Cramer[1], F. Fuhrmann[1], R. Lebrun[1], L. Baldrati[1], A. Ross[1], T. Niizeki[2], R. Ramos[2], D. Hou[2], Z. Qiu[2], E. Saitoh[2,3] and *M. Kläui*[1]
1. Physics, Johannes Gutenberg University Mainz, Mainz, Germany; 2. IMR, Tohoku University, Sendai, Japan; 3. Applied Physics, University of Tokyo, Tokyo, Japan

Magnon-based spintronic applications enable a promising alternative to charge-driven devices for information transport and processing [1]. We explore key aspects of magnon spintronics necessary to functionalize such spin currents: we develop the efficient interconversion of spin and charge information by the (inverse) spin Hall effect in the binary alloy $Cu_{1-x}Ir_x$ [2]. In this material, the spin Hall effect exhibits a complex composition dependence, with a maximum spin Hall angle near 40% Ir content. Beyond that, DC and THz signals are compared, showing similar behavior showing functionality of the spin-to-charge conversion up to THz speeds. To functionalize the spin transport for instance for magnon logic as a key requirement of magnon spintronics, the spin-dependent (inverse) spin Hall effect in metallic ferromagnets like Co or $Co_{60}Fe_{20}B_{20}$ is demonstrated [3]. We then use this to build a magnon spin-valve type element: in ferromagnetic resonance spin pumping and non-local spin transport measurements it is shown that the spin detection efficiency strongly depends on the angle between that ferromagnet's magnetization and the spin current polarization vector [4]. We explain this by the distinct properties of spin-up and spin-down electrons in the ferromagnet and allows to implement a spin valve like effect with an amplitude of up to 120% [4]. Finally to purely control the transport also in a lateral geometry, we use gates that allow us to control the spin propagation [5].

[1] Chumak *et al.*, Nat. Phys. 11, 453 (2015) [2] Cramer *et al.*, Nano Lett. 18, 1064-1069 (2018) [3] Cramer et al., Phys. Rev. B 99, 104414 (2019) [4] Cramer *et al.*, Nat. Commun. 9, 1089 (2018) [5] J. Cramer et al., arxiv:1906.05631 (2019)

10:18

EC-08. Influence of alloying Ta and V on spin-orbit torque efficiency in W/CoFeB/MgO junctions. *G. Kim*[1], Y. Kim[1], I. Cha[1], T. Kim[1], M. Lee[1] and Y. Kim[1] *1. Materials science and engineering, Korea University, Seoul, The Republic of Korea*

Spin-orbit torque (SOT) can efficiently manipulate the magnetization using in-plane current injection in normal metal/ferromagnet/oxide (e.g., W/CoFeB/MgO) structures. The SOT can be utilized for low energy writing operation in MRAM devices as well as fast domain wall motion in patterned strips. However, one of the main impediments to realize SOT devices is a low charge-to-spin conversion efficiency as quantified by a physical property called spin Hall angle (SHA). To increase the value of SHA, previous studies focused on modifying the fabrication method of the W layers either by reactive sputtering [1] or by multistep deposition [2] to preserve metastable beta-W phase which offers the highest SHA among various 3d-5d transition metals. Recently, theoretical calculation predicts that Ta incorporation in the beta-W lattice can enhance the spin Hall conductivity of the W itself [3]. In this study, we considered adding vanadium (V) in the W layer to investigate its influence on the SOT behaviors while maintaining the perpendicular magnetic anisotropy (PMA) in the W/CoFeB/MgO junctions. We chose V because it has the same number of outermost electrons as Ta. Thus, we expected the electrical property of V is similar to that of Ta. Different compositions of Ta and V in W/W-Ta (or V)/CoFeB/MgO/Ta films were sputter-deposited and underwent 300°C annealing. Subsequently, Hall bar devices with widths of 5 μm were patterned by photolithography. To estimate the effective field of SOT in our sample, we employed the low-frequency harmonics method and domain wall depinning and propagation model [4]. We only considered the damping-like torque (DLT) component because the field-like torque (FLT) contribution is known to be at least an order of magnitude smaller. Unlike Ta, V-alloyed devices showed PMA up to about 70 at% of V alloying. In the case of V, the SHA value reached about 0.5 compared to that of pure W which is 0.36. However, a nonlinear SOT behavior upon V compositional change remains unknown at the moment.

[1] K-U. Demasius et al., Nat. Commun. 7, 10644 (2016) [2] W. Chen et al., Phys. Rev. B 98, 134411 (2018) [3] X. Sui et al., Phys. Rev. B 96, 241105(R) (2017) [4] O.J. Lee et al., Phys. Rev. B 89, 024418 (2014)

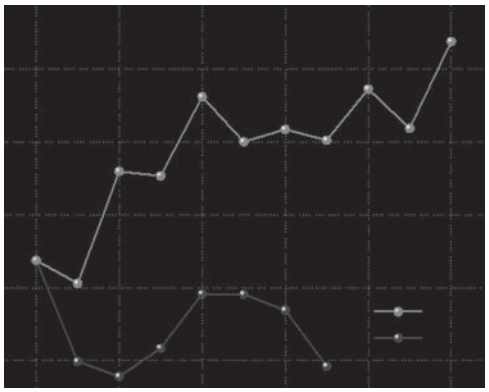


Fig.1. Damping-like SOT efficiency in Ta and V-alloyed structures.

10:30

EC-09. Self-Induced Inverse Spin Hall Effect in Ferromagnets: Demonstration through Non-Monotonous Temperature-Dependence. O. Gladii[1], L. Frangou[1], A. Hallal[1], R.L. Seeger[1], P. Noel[1], G. Forestier[1], S. Aufftet[1], M. Rubio-Roy[1], P. Warin[1], L. Vila[1], S. Gambarelli[2], M. Chshiev[1] and *V. Baltz*[1] *1. Univ. Grenoble Alpes / CNRS / CEA, SPINTEC, Grenoble, France; 2. Univ. Grenoble Alpes / CEA, Symmes, Grenoble, France*

The generation of a spin current and its further conversion to a charge current have attracted considerable attention, facilitating advances in fundamental physics and closely related applications in the field of spintronics. In this work, we investigated the overlooked and incompletely understood self-induced inverse spin Hall effect in spin pumping ferromagnetic resonance experiments [1,2]. When magnetic moments are precessing, the angular momentum of 3d-electrons is transferred to 4s-conduction electrons leading to a spin-polarized current in the ferromagnet. A diffusive flow of spins is further caused by non-uniform magnetization ascribed to asymmetric spin relaxation at the different interfaces. Spin-orbit interactions in the ferromagnet further ensures spin-charge conversion via the inverse spin Hall effect. We performed systematic temperature-, thickness- and angular- dependent measurements of transverse voltage in spin pumping ferromagnetic resonance experiments with permalloy films (NiFe). Our experimental data revealed non-monotonous temperature-dependence of the self-induced transverse voltage. The experiments were found in qualitative agreement with our results of first-principle calculations unravelling the skew scattering and the side-jump plus intrinsic

contributions to the temperature-dependent spin Hall conductivity. More specifically, similar amplitudes but opposite signs were calculated for the two contributions. We obtained similar sets of experimental data whatever the material in contact with NiFe: SiO2, MgO, AlOx oxides, Cu and Pt metals, supporting the bulk origin of the effect. Insights on the direction of the self-induced current were obtained by addition of a buffer or capping reference layer of Pt to the stack. This study contributes to our understanding of self-induced inverse spin Hall effect in ferromagnets. It further underlines that the self-induced conversion in the ferromagnet can be as efficient as that of noble metals like Pt, as a caveat for the need to carefully consider them when investigating spin-orbit-related effects in materials for spintronics [3].

[1] A. Tsukahara, Y. Ando, Y. Kitamura *et al*, Phys. Rev. B 89, 235317 (2014). [2] K. Kanagawa, Y. Teki, E. Shikoh, AIP advances 8, 055910 (2018). [3] O. Gladii, L. Frangou, A. Hallal *et al*, to be published.

10:42

EC-10. Giant spin Hall effect in ultrathin Au/Si multilayers. *M. El Hadri*[1], J. Gibbons[2], Y. Xiao[1], H. Ren[1], H. Wang[1], A. Hoffmann[2] and E. Fullerton[1] *1. Center for Memory and Recording Research, University of California, San Diego, La Jolla, CA, United States; 2. Materials Science Division, Argonne National Laboratory, Lemont, IL, United States*

The investigation of the spin-orbit coupling effect in Au has gained increased interest in the past decade, since such a heavy metal combines the properties of a relatively long spin diffusion length [1] and strong spin-orbit coupling. While initial studies by Seki *et al*. reported a giant spin Hall angle (SHA) of 0.11 in Au (10 nm) [2], follow up thickness dependence studies showed an absence of such a giant SHA in thicker Au films [3-6], thus questioning the microscopic origin of the giant spin Hall effect in Au. To further elucidate the microscopic origin of the spin Hall effect in Au, we investigated the non-local transport in single Au films and ultrathin Au/Si multilayers patterned into mesoscopic Hall bar structures (Fig. 1a). We showed that the effective spin Hall angle of Au is inversely proportional to the thickness and is significantly enhanced in ultrathin Au/Si multilayers, where the thickness of the individual Au layers is scaled down to 2 nm (Fig. 1b). This variation behavior was further corroborated by independent spin-torque ferromagnetic resonance measurements. Finally, we investigated the spin-orbit torque efficiency in Au/Tb_xCo_{1-x} and $[Si/Au]_N/Tb_xCo_{1-x}$, where the top ferrimagnetic TbCo layer shows robust perpendicular magnetic anisotropy. Our observations provide insights into the microscopic origin of the giant spin Hall effect in Au, highlighting the significant role of ultrathin Au in emerging spintronic devices. Acknowledgments: This work was supported as part of Quantum Materials for Energy Efficient Neuromorphic Computing, an Energy Frontier Research Center funded by the U.S. DOE, Office of Science.

[1] J.-H. Ku, J. Chang, H. Kim *et al*. *Appl. Phys. Lett*. 88, 172510 (2006). [2] T. Seki, Y. Hasegawa, S. Mitani *et al*. *Nat. Mater.* 7, 125-129 (2008). [3] G. Mihajlovic, J. E. Pearson, M. A. Garcia *et al*. *Phys. Rev. Lett.* 103, 166601 (2009). [4] T. Seki, I. Sugai, Y. Hasegawa *et al*. *Solid State Commun.* 150, 496-499 (2010). [5] J.T. Brangham, K.-Y. Meng, A. S. Yang *et al*. *Phys. Rev. B* 94, 054418 (2016). [6] C. Chen, D. Tian, H. Zhou *et al*. *Phys. Rev. Lett.* 122, 016804 (2019).

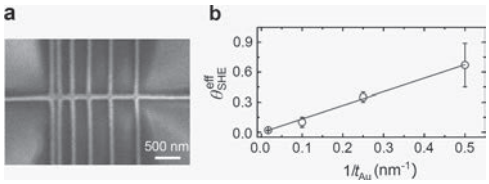


Fig. 1: (a) Top-view SEM image of Au (2 nm)/Si (2 nm) multilayers patterned into a Hall bar device with six vertical 90 nm-wide wires separated by various distances and bridged by a horizontal one. (b) Measured effective SHA as a function of the inverse thickness of Au measured for Au (t_{Au} = 10, 60 nm) films, as well as Au (t_{Au} = 2 nm)/Si (2 nm) and Au (t_{Au} = 5 nm)/Si (4 nm) multilayers. The blue line is a linear fit to the data.

10:54

EC-11. Spin Hall effect investigated by spin Hall magnetoresistance in $Pt_{100-x}Au_x$/CoFeB/MgO systems. *Y. Saito*[1], N. Tezuka[2,3], S. Ikeda[1,3], H. Sato[1,4] and T. Endoh[1,5] *1. Center for Innovative Integrated Electronic Systems, Tohoku University, Sendai, Japan; 2. Department of Materials Science, Graduate School of Engineering, Tohoku University, Sendai, Japan; 3. Center for Spintronics Research Network, Tohoku University, Sendai, Japan; 4. Center for Science and Innovation in Spintronics, Tohoku University, Sendai, Japan; 5. Department of Electrical Engineering, Graduate School of Engineering, Tohoku University, Sendai, Japan*

Current-induced spin-orbit torque (SOT) originating from the spin-Hall effect (SHE) in heavy metal/ferromagnet (HM/FM) systems has attracted attention due to their potential application in the efficient manipulation of magnetization of nano magnets in SOT-MRAM, skyrmion and domain wall devices. For the application to a large scale integration, the efficient SOT operation (high spin Hall angle $|\theta_{SH}|$) in low resistivity (ρ_{xx}) HM is necessary [1]. One of the ideas for realizing this is increase in an intrinsic SHE. Taking into account the recent ab initio electronic structure calculation [2] and rigid band model, studying SHE in $Pt_{1-x}Au_x$ is one of the good candidates. Actually, a maximum magnitude of $|\theta_{SH}|$ was observed in $Pt_{0.75}Au_{0.25}$/Co system by measuring harmonic response, and a maximum magnitude of ρ_{xx} was also observed at same alloy composition (x=0.25) [3]. However, it is not clear whether mechanism of a high $|\theta_{SH}|$ is related to the increase in an intrinsic SHE. In this paper, we prepared $Pt_{1-x}Au_x$/CoFeB/MgO systems with various $Pt_{1-x}Au_x$ thicknesses and x under sputtering conditions using Kr gas by which Pt with high ρ_{xx} was observed. These systems are patterned into the microscale Hall bar by photolithography and Ar ion milling, and annealed at 300°C. SHE in $Pt_{1-x}Au_x$/CoFeB/MgO system with various x by means of spin Hall magnetoresistance (SMR) was studied. As a result, we found that the amplitude in SMR signals increases with increasing x, even though the ρ_{xx} values of $Pt_{1-x}Au_x$ monotonically decrease with increasing x as shown in inset of Fig.1. The analysis based on the drift diffusion model reveals that the increase in SMR originates from an enhancement of $|\theta_{SH}|$ (Fig. 1). These results indicate that the increase in $|\theta_{SH}|$ for $Pt_{1-x}Au_x$ systems is clearly related to increase in an intrinsic SHE. In this presentation, we will report the details of SMR, θ_{SH} and spin diffusion length. This work was supported by the JST OPERA (JPMJOP1611) and JSPS KAKENHI (15H05699, 19H00844).

[1] Y. Saito et al., Appl. Phys. Exp. 12, 053008 (2019). [2] G. Y. Guo et al., Phys. Rev. Lett. 100, 096401 (2008). [3] L. Ahu et al., Phys. Rev. Appl. 10, 031001 (2018).

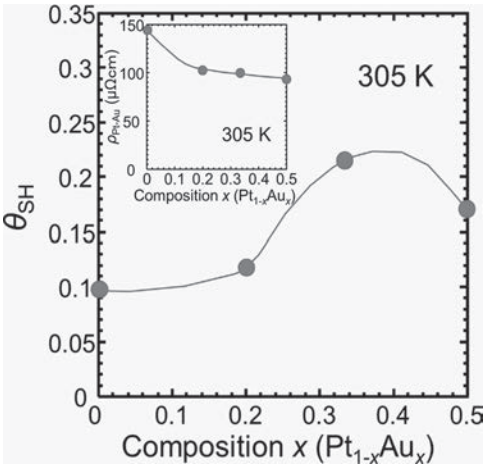


Figure 1 Estimated magnitude of the $|\theta_{SH}|$ as a function of Au concentration x in $Pt_{1-x}Au_x$ alloy HMs. Inset shows the resistivity of $Pt_{1-x}Au_x$ vs x.

11:06

EC-12. Spin Hall Magnetoresistance and Proximity Induced Magnetism in CoFeTaB-Pt Bilayers. *O.A. Inyang*[1,5], K. Moran[2], C. Kinane[3], L. Bouchenoire[4], B. Hickey[2], D. Atkinson[1] and A. Hindmarch[1]
1. Department of Physics, Durham University, Durham, United Kingdom; 2. Department of Physics and Astronomy, University of Leeds, Leeds, United Kingdom; 3. ISIS neutron facility, Rutherford Appleton Laboratory, Didcot, United Kingdom; 4. XMaS beamline, ESRF, Grenoble, France; 5. Department of Physics, Akwa Ibom State University, Mkpat Enin, Nigeria

Recently, pure spin current has been proposed for next-generation energy efficient spintronic devices. At the interface of ferromagnetic (FM) – nonmagnetic (NM) bilayer, there is spin-mixing due to electron scattering, influenced by magnetic defects. In this work, the impact of the imaginary component of spin mixing conductance is decoupled by longitudinal and transverse magnetoresistance measurements in CoFeTaB(CFTB)-Pt interfaces, in conjunction with polarized neutron reflectometry (PNR) which provides information on magnetic dead-layers and x-ray resonant magnetic reflectivity (XRMR) which provides element specific information on proximity induced magnetization in Pt. Structures consisting of Pt/CFTB/Pt, Pt/CFTB and CFTB/Pt thin-films were sputter deposited onto Si/SiO2 substrates. Magnetoresistance measurement was undertaken in three angular sweep geometries (xy (α), yz (β) and xz (γ) planes). Room-temperature PNR, XRMR and x-ray diffraction (XRD), were used to isolate the various contributions to the magnetoresistance. Proximity-induced magnetization in Pt is observed to be larger at the CFTB/Pt interface in comparison to Pt/CFTB interface (Fig 1). PNR reveals a reduced magnetic moment at the upper CFTB region within the sample. XRD measurement suggests that interfacial moment formation in Pt due to proximity effect has a dependence on the microstructure. Interpretation of the complicated interplay of magnetoresistance phenomena reveals that the majority of the in-plane magnetoresistance originates from the spin-Hall effect in Pt (spin Hall magnetoresistance (SMR) ratio of ~0.2) [1,2]. Hall-geometry measurement showed the transverse SMR effect, which indicates a significant contribution from the imaginary component of the spin-mixing conductance [3]. This is attributed to magnetic polarization of Pt, as confirmed from XRMR, which causes the precession of the spin current about the local Pt moment at the interface resulting in tilting of the interfacial spin polarization relative to that generated by the spin-Hall effect [4].

[1] H. Nakayama et al, Phys. Rev. Lett. 110, 206601 (2013). [2] M. Isasa et al, Appl. Phys. Lett. 105, 142402 (2014). [3] S. Meyer et al., Appl. Phys. Lett. 106, 132402 (2015). [4] X. Xia et al., Phys. Rev. B. 65, 220401 (2002).

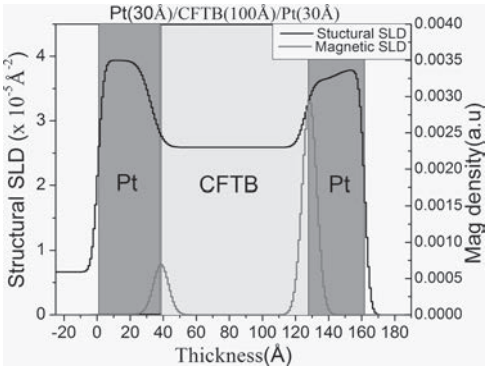


Fig 1: XRMR SLD profile of Pt(30 Å)/CoFeTaB(60Å)/Pt(30Å)

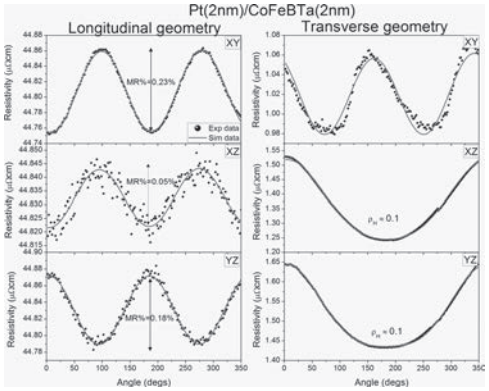


Fig 2: Magnetoresistance measurements of Pt(20 Å)/CoFeTaB(20Å).

11:18

EC-13. Temperature dependent spin Hall angles of Pt thin films with different crystalline structures. *H. Wang*[1], Y. Xiao[1] and E. Fullerton[1]
1. University of California, San Diego, La Jolla, CA, United States

Spin-orbit coupling plays a central role in modern spintronic research [1] and to the formation of many exotic quantum phases in strongly correlated material systems [2]. To date, the spin Hall angle, the figure of merit for spintronic applications, has been intensively studied in a variety of material systems spanning from transition metals, semiconductors, to complex oxides. A comprehensive understanding of its underlying mechanism promises to bring new functionalities to the next-generation energy efficient spin Hall devices. Here, we deposit CoNi multilayers with perpendicular magnetic anisotropy on a series of 5*d* heavy metal Pt thin films with different crystalline structures [Fig. 1(a)]. The spin Hall angles obtained by harmonic Hall measurements follow a monotonic increase in the order of single crystalline Pt, polycrystalline Pt, and doped Pt thin films [Fig. 1(b)]. Remarkably, they exhibit distinct temperature dependent variation behavior, underlining the multiple contributing mechanisms of spin-orbit coupling in Pt thin films with different crystalline structures [3]. Our results also point to the possibility of tuning the spin-to-charge conversion efficiency by engineering the crystalline textures in a variety of transition metals. Acknowledgement: This work was supported as part of Quantum Materials for Energy Efficient Neuromorphic Computing, an Energy Frontier Research Center funded by the U.S. DOE, Office of Science.

Reference: 1. J. Sinova et al., *Rev. Mod. Phys*. 87, 1213 (2015). 2. X.-L. Qi and S.-C. Zhang, *Rev. Mod. Phys*. 83, 1057 (2011). 3. M. Isasa et al., *Phys. Rev. B* 91, 024402 (2015).

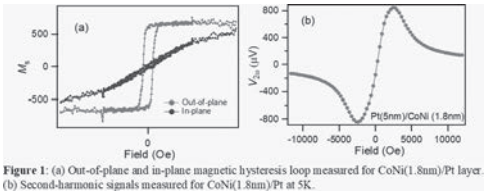


Figure 1: (a) Out-of-plane and in-plane magnetic hysteresis loop measured for CoNi(1.8nm)/Pt layer. (b) Second-harmonic signals measured for CoNi(1.8nm)/Pt at 5K.

Session ED
SKYRMIONS IN MULTILAYERS II

Katharina Zeissler, Co-Chair
University of Leeds, Leeds, United Kingdom
Craig Barton, Co-Chair
University of Manchester, Manchester, United Kingdom

INVITED PAPER

8:30

ED-01. Interactions of Chiral Magnetic Textures with Electrical Currents Studied with X-ray Microscopy. *S. Finizio*[1], K. Zeissler[2], A. Huxtable[3], S. Wintz[1,4], S. Mayr[1,5], J. Bailey[1,6], M. Langer[1], G. Burnell[3], C.H. Marrows[3] and J. Raabe[1] *1. Paul Scherrer Institut, Villigen PSI, Switzerland; 2. National Physical Laboratory, Teddington, United Kingdom; 3. University of Leeds, Leeds, United Kingdom; 4. Max Planck Institut für Intelligiente Systeme, Stuttgart, Germany; 5. ETH Zürich, Zürich, Switzerland; 6. EPFL, Lausanne, Switzerland*

After recent developments in the design and manufacturing processes of perpendicularly magnetized (PMA) materials exhibiting anti-symmetric exchange (or Dzyalonshinsky-Moriya – DM) interaction, the study of the chiral magnetic textures stabilized in these materials has attracted much attention in the magnetism research community. Chiral magnetic configurations include e.g. chiral domain walls, helical states, and magnetic skyrmions. In particular, magnetic skyrmions, chiral magnetic configurations exhibiting a non-trivial topology, have been extensively investigated. This is due to their interesting properties, which include an energy barrier against annihilation at defect sites [1], and the possibility of manipulating them with low current densities [2], leading to the proposal to employ these magnetic configurations as an information carrier [3]. The possibility to manipulate these magnetic textures with electrical currents is not limited to magnetic skyrmions. Various effects, including e.g. spin-orbit torques (SOT), have been discovered and employed to electrically manipulate these spin configurations, and the study of these effects and their consequences has also enjoyed an heightened attention in the recent years. The experimental investigation of these chiral spin configurations and of their electrical manipulation requires a non-invasive technique capable of visualizing the magnetic configuration at sub-um spatial resolution, and of resolving the dynamical processes at sub-ns temporal resolution under *in-operando* conditions. A suitable set of techniques encompassing all of these requirements is given by time-resolved X-ray microscopy. In particular, time-resolved scanning transmission X-ray microscopy has been successfully employed for the investigation of numerous dynamical processes in chiral magnetic systems. In this contribution, after an overview of time-resolved X-ray microscopy techniques, we will present the experimental investigation of the manipulation of various chiral magnetic configurations with electrical currents using time-resolved X-ray microscopy at high spatial and temporal resolution. In particular, we will focus on the study of the current-induced domain wall motion (CIDWM) of Neel-type magnetic domain walls [4], and on the nucleation and manipulation of Neel-type magnetic skyrmions [5]. The SOT-induced CIDWM of Neel-type domain walls was investigated on Pt/CoB/Ir microwires of different geometries. Here, we could directly visualize the effect of the wire's geometry on the motion and inertia of the domain wall. These investigations will be employed to provide a direct experimental verification of the theoretical models currently used to describe the CIDWM. As mentioned above, it has been proposed to employ magnetic skyrmions to encode digital information. Proposed designs of skyrmionic data processing devices include variations of the magnetic racetrack memory [3]. Such designs usually rely on three components: nucleation/deletion [5,6], current-driven motion [7], and electrical detection [8] of the magnetic skyrmions. Here, we present a time-resolved X-ray microscopy investigation of the skyrmion nucleation dynamics in absence of external magnetic fields achieved by the injection of an electrical current pulse across a nano-engineered nucleator structure fabricated on top of a Pt/CoB/Ir microwire. With these measurements, we could demonstrate the reliable current-induced nucleation of magnetic skyrmions in absence of external magnetic fields with pulse widths down to 100 ps, and observe that the nucleation process is driven by a synergy between SOT-induced switching of the magnetization and thermal effects due to the Joule heating of the current pulse. Part of this work has received funding from the EU-H2020 programme (Grant No. 654360) having benefitted from the access provided by PSI in Villigen within the framework of the NFFA-Europe Transnational Access Activity.

[1] F. Büttner et al., Scientific Reports 8, 4464 (2018) [2] N. Nagaosa et al., Nature Nanotechnology 8, 899 (2013) [3] A. Fert et al., Nature Nanotechnology 8, 152 (2013) [4] S. Finizio et al., Nano Letters 19, 184 (2019) [5] S. Finizio et al., arXiv :1902.10435 [6] S. Woo et al., Nature Electronics 1, 288 (2018) [7] K. Litzius et al., Nature Physics 13, 170 (2017) [8] K. Zeissler et al., Nature Nanotechnology 13, 1161 (2018)

CONTRIBUTED PAPERS

9:06

ED-02. Evolution of Skyrmion Character with Interfacial Chiral Interactions in Co/Pt-Based Multilayers. X. Chen[1,2], M. Lin[1], H. Tan[1], A. Tan Kok Cheng[1], J. Kong[3], K. Khoo[3], H. Tan[1,2] and *A. Soumyanarayanan*[4,5] *1. A*STAR Institute of Materials Research and Engineering, Singapore; 2. A*STAR Data Storage Institute, Singapore; 3. A*STAR Institute of High Performance Computing, Singapore; 4. A*STAR Institute of Materials Research and Engineering and Data Storage Institute, Singapore; 5. Physics, National University of Singapore, Singapore*

Magnetic skyrmions can be stabilized at room temperature with sub-100 nm sizes in multilayer films and are promising candidates for next-generation in-memory computing applications. The structure and stability of these small skyrmions is derived from the chiral interaction generated at the ferromagnet/heavy metal interfaces [1]. Although nominally symmetric structures like Pt/Co/Pt multilayers have negligible DMI, asymmetric structures such as Ir/Co/Pt, Pt/Co/MgO, and Ir/Fe/Co/Pt can acquire large values of DMI needed to stabilize small skyrmions. These stack structures also offer a large latitude of tunability – one can access a wide phase-space of magnetic textures, manipulating their size, density and configurations (isolated or lattice array) by varying the thickness of individual layers [2]. To understand the role of the various interactions in generating magnetic textures, we investigated this tunable stack structure using a series of complementary magnetic microscopy techniques – magnetic force microscopy (MFM), magnetic transmission soft x-ray microscopy (MTXM) and Lorentz transmission electron microscopy (L-TEM). Combined with previous theoretical work, we differentiate between domain walls of Bloch and Néel character, and further

between achiral bubbles, chiral bubbles and skyrmions (see e.g. Fig. 1) [3]. Next, using a combination of microscopic imaging and magnetometry techniques, we elucidate that skyrmions and chiral bubbles have contrasting thermodynamic signatures – which point to a dichotomy in their creation and annihilation mechanisms, which are then verified using field-dependent Lorentz microscopy measurements. Direct comparisons with micromagnetic simulations elucidate the microscopic mechanisms underlying the nucleation, propagation and destruction of these magnetic textures. This work establishes a platform for quantifying the helicity, topology, and stability of functional room temperature skyrmions, paving the way for the development of skyrmion-based devices.

[1] A. Soumyanarayanan et al., Nature 539, 509 (2016). [2] A. Soumyanarayanan et al., Nature Materials 16, 898 (2017). [3] X. Chen et al., Unpublished.

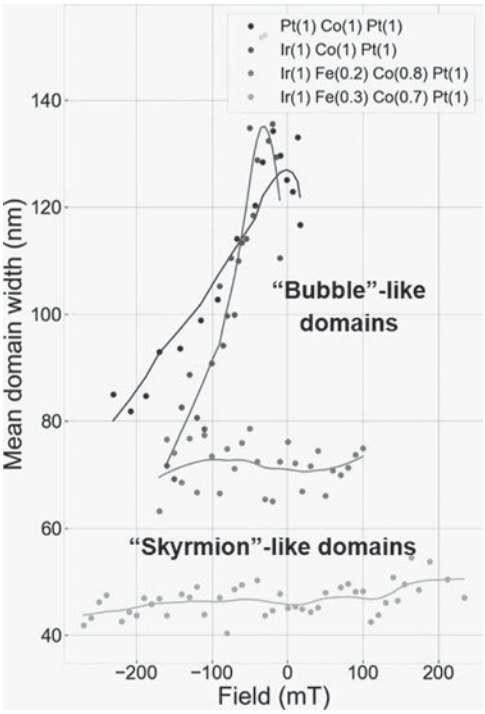


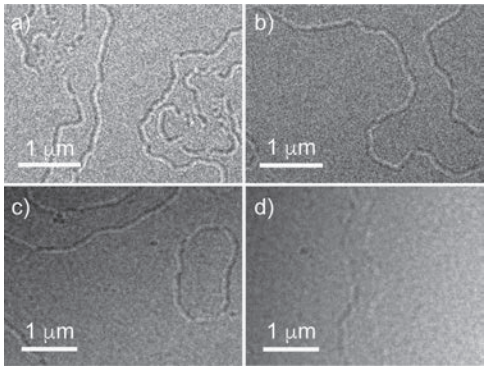
Fig. 1 Field evolution of mean domain width for varying interfacial chiral interactions, as measured by full-field microscopy, suggesting a dichotomy in domain character.

9:18

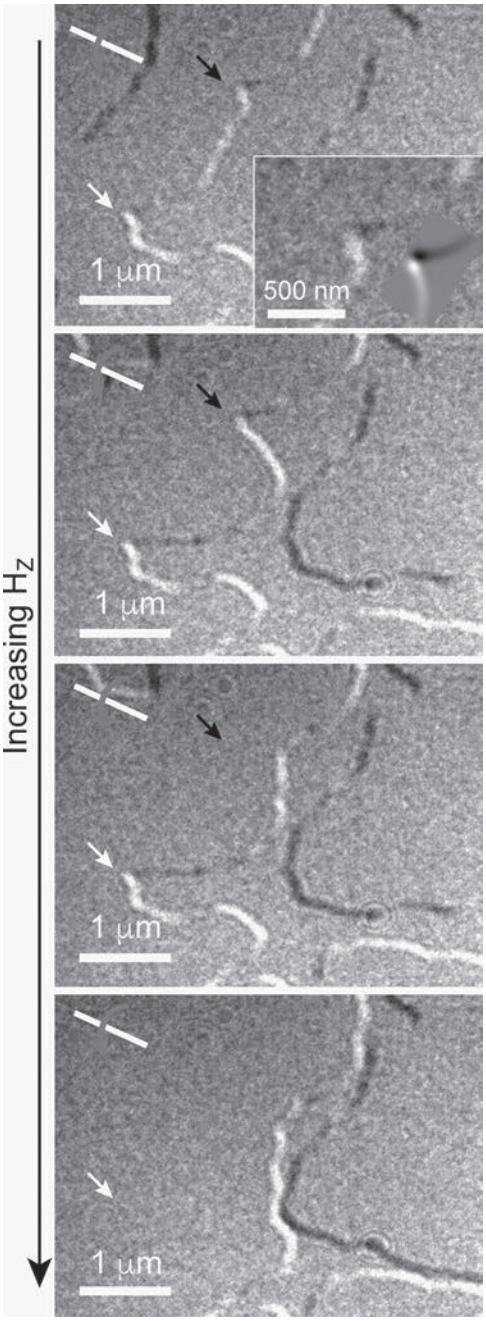
ED-03. Imaging magnetic domain wall skyrmions in Pt/Co/Ni/Ir-based multi-layers using Lorentz transmission electron microscopy. *M.P. Li*[1], A. Sapkota[3], A. Rai[3], A. Pokhrel[3], R. Cheng[4], D. Xiao[1,2], T. Mewes[3], C.K. Mewes[3], M. De Graef[1] and V. Sokalski[1] *1. Department of Materials Science & Engineering, Carnegie Mellon University, Pittsburgh, PA, United States; 2. Department of Physics, Carnegie Mellon University, Pittsburgh, PA, United States; 3. Department of Physics and Astronomy/ MINT Center, The University of Alabama, Tuscaloosa, AL, United States; 4. Department of Electrical and Computer Engineering, University of California, Riverside, CA, United States*

Magnetic domain wall (DW) skyrmions are 360° transitions of magnetization along a chiral Néel DW with a topological charge of C=±1. Much like 2D skyrmions originate from magnetic bubbles and the Dzyaloshinskii-Moriya interaction (DMI), DW skyrmions are the successor to vertical Bloch lines (VBLs). The structure of these objects has been calculated analytically and through micromagnetic energy minimization with excellent agreement and has been predicted to display a unique signature in Fresnel mode Lorentz transmission electron microscopy (LTEM).[1] DW skyrmions are predicted to be stable in ultrathin magnetic films where the magnetization is uniform through its thickness and DMI is appreciable. Here we experimentally image DW skyrmions by LTEM using the tunable Pt/Co/Ni/Ir system.[2] $[Pt/(Co/Ni)_M/Ir]_N$ multi-layers were deposited by magnetron sputtering onto Si_3N_4 membranes. Fresnel mode LTEM was performed on an aberration-corrected FEI Titan G2 80-300 operated in Lorentz mode. Micromagnetic simulations were performed using M[3] and used to calculate theoretical Fresnel mode images.[3] LTEM images of M=4-10, N=1 samples display a significant Bloch component of the DW which fades with decreasing M. However, clusters of VBLs are found including 2π VBLs which are topological equivalent to, but much larger than, DW skyrmions. This suggests DW skyrmions could be supported if DMI is further increased via a reduction in M. Further decreasing M to 3 (with N=2 to preserve TEM contrast) supports the formation of chiral Néel DWs. Dipole-like contrast is observed along DWs from the formation of DW skyrmions as predicted from simulated LTEM images. A perpendicular magnetic field is applied *in situ* to drive DW motion where pinning is observed at the location of DW skyrmions. As the field is increased, DW skyrmions annihilate concurrent with an abrupt movement of the DW. Factors governing DW skyrmion stability and *in situ* behavior will be discussed along with their prospects for future spintronic applications.[4]

[1] R. Cheng, M. Li, A. Sapkota, *et al*. *Phys. Rev. B.*, Vol. 99, p. 184412 (2019). [2] M. Li, D. Lau, M. De Graef, and V. Sokalski, *Phys. Rev. Mater.,* Vol. 3, p. 064409, (2019). [3] "Micromagnetics code M[3]," http://magneticslab.ua.edu/micromagnetics-code.html. [4] This research is supported by the Defense Advanced Research Project Agency (DARPA) program on Topological Excitations in Electronics (TEE) under grant number D18AP00011. The authors also acknowledge use of the Materials Characterization Facility at Carnegie Mellon University supported by grant MCF-677785.



LTEM images of $[Pt/(Co/Ni)_M/Ir]_1$ where M= a) 10, b) 8, c) 6, and d) 4.



LTEM images of DW skyrmions in $[Pt/(Co/Ni)_3/Ir]_2$ with perpendicular magnetic field applied in-situ and calculated Fresnel mode image of a DW skyrmion.

9:30

ED-04. Current-Inudced Skyrmion Nucleation/Annihilation in Synthetic Antiferromagnetic Multilayers. *R. Juge*[1], Q. Zhang[1], K. Rana[1], M. Foerster[2], L. Aballe[2], B. Sarpi[3], S. Stanescu[3], R. Belkhou[3], J. Gräfe[4], M. Weigand[4], J. Vogel[5], S. Aufftet[1], G. Gaudin[1] and O. Boulle[1] *1. SPINTEC, Univ. Grenoble Alpes, CNRS, CEA-IRIG, Grenoble INP, Grenoble, France; 2. CIRCE beamline, ALBA Synchrotron Light Facility, Cerdanyola del Vallès, Barcelona, Spain; 3. Hermès beamline, SOLEIL Synchrotron, Saint-Aubin, France; 4. Max Planck Institute for Intelligent Systems, Stuttgart, Germany; 5. Néel Institute, Grenoble, France*

Magnetic skyrmions are nanoscale whirling spin configurations. Their small size, topological protection and the fact than they can be manipulated by small in-plane current densities have opened a new paradigm to manipulate the magnetisation at the nanoscale. This has led to proposal for novel memory and logic devices in which the magnetic skyrmions are the information carriers. The recent observation of room-temperature magnetic skyrmions [1,2,3,4] and their current-induced manipulation [4,5,6,7] in sputtered ferromagnetic nanotracks have lifted an important bottleneck toward the practical realisation of such devices. Notably, due to their quantised topological charge, moving magnetic skyrmions are subject to a gyrotropic force which leads to their deviation from the trajectory imposed by the current [5,6,7]. This "skyrmion Hall effect" is an important issue for reliable current-induced manipulation in track geometries as it tends to drive the skyrmions towards the edge of the track, leading to their annihilation. Recently, it was proposed that the use of Synthetic AntiFerromagnetic (SAF) multilayers would allow to suppress the skyrmion Hall effect due to opposite gyrotropic forces on the skyrmions in each AF-coupled ferromagnetic layers, allowing in turn a faster and more reliable current-induced skyrmion motion [8,9]. Here we report on the observation and current-induced nucleation of skyrmions in SAF multilayers at room temperature and zero external magnetic field. SAF composed of (Pt/Co/Ru) multilayers with vanishing magnetisation and perpendicular magnetic anisotropy were grown using magnetron sputtering. Using X-ray microscopy XMCD-PEEM, we observed the chiral Néel texture of SAF skyrmions and DWs at zero external field. Using STXM, we demonstrated the reproducible current-induced nucleation/annihilation of SAF skyrmions with diameters in the 100 nm range induced by the local injection of ns-long pulses at zero field. Time-resolved pump-probe STXM experiments reveal that the nucleation occurs within the first ns of the current pulse injection. Our results pave the way for the current-induced manipulation of SAF skyrmions in technology-relevant sputtered magnetic tracks.

[1] Jiang *et al.*, Science 349, 283 (2016) [2] Moreau-Luchaire *et al.*, Nature Nanotechnology, 11, 444 (2016) [3] Boulle *et al.*, Nature Nanotechnology 11, 449 (2016) [4] Woo *et al.*, Nature Materials 15, 501 (2016) [5] Jiang *et al.*, Nature Physics 13, 162 (2017) [6] Litzius *et al.*, Nature Physics 13, 170 (2017) [7] Juge *et al.*, arXiv:1904.08275 (2019) [8] Zhang *et al.*, Nature Communications 7, 0293 (2016) [9] Tomasello *et al.*, Journal of Physics D: Applied 50, 325302 (2017)

9:42

ED-05. Antiferromagnetic skyrmions in synthetic antiferromagnetic multilayers at room-temperature. W. Legrand[1], *F. Ajejas*[1], A. Haykal[2], Y. Sassi[1], A. Finco[2], S. Chouaieb[2], D. Maccariello[1], S. Collin[1], K. Bouzehouane[1], A. Vechiola[1], N. Reyren[1], V. Cros[1], V. Jacques[2] and A. Fert[1] *1. Unité Mixte de Physique CNRS/Thales, Palaiseau, France; 2. Laboratoire Charles Coulomb, Université de Montpellier and CNRS, Montpellier, France*

Magnetic skyrmions are non-collinear chiral spin textures stabilized in magnetic materials by interfacial Dzyaloshinskii-Moriya interaction (DMI). Recently room-temperature skyrmions in ferromagnetic films and multilayers has been demonstrated and they show promise for encoding information bits in new computing technologies [1]. Despite many recent progresses, ferromagnetic order in thick layers or multilayers [2-3] generates dipolar fields

that prevent from reaching expected ultra-small skyrmion sizes. Moreover, in ferromagnetic systems, a transverse deflection of moving skyrmions is present that hinder their efficient manipulation. Antiferromagnetic skyrmions could lift these limitations [4-5]. Here we demonstrate that room-temperature antiferromagnetic skyrmions can be stabilized in synthetic antiferromagnetic (SAF) systems. We elaborate a material system in which perpendicular magnetic anisotropy, antiferromagnetic coupling and chiral order can be adjusted concurrently. Utilizing interlayer electronic coupling to an adjacent bias layer, we demonstrate by Magnetic Force Microscopy that the spin-spiral state obtained in a SAF system with vanishing perpendicular anisotropy can be turned into isolated antiferromagnetic skyrmions (see Fig. 1). These observation of small AF skyrmions in SAF has been also achieved using NV microscopy in which the potential perturbation from the tip are not existing. In addition, we provide model-based estimations of their size and stability, showing that room-temperature stable antiferromagnetic skyrmions below 10 nm in radius can be anticipated in further optimized SAF systems [6]. Antiferromagnetic skyrmions in SAF systems may thus solve major issues associated to ferromagnetic skyrmions for low-power spintronic devices. French ANR grant TOPSky TOPSKY (ANR-17-CE24-0025), and DARPA TEE program grant (MIPR#HR0011831554) and EU grant SKYTOP (H2020 FET Proactive 824123) are acknowledged for their financial support.

[1] A. Fert, N. Reyren, V. Cros, Nat. Rev. Mat. 2, 17031 (2017) [2] C. Moreau-Luchaire et al., Nat. Nanotechnol. 11, 444 (2016) [3] W. Legrand et al., Nano Letters 17, 2703 (2017) [4] X. Zhang et al., Nat. Commun. 7, 10293 (2016) [5] R. Tomasello et al, Scien. Rep. 4, 6784 (2014) [6] W. Legrand et al, unpublished (2018)

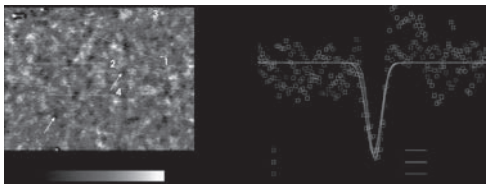


Figure 1: (Left) MFM image (phase) of SAF skyrmions. (Right) Corresponding cross sections of the phase signal.

9:54

ED-06. Withdrawn

INVITED PAPER

10:06

ED-07. Skyrmion diffusion in thin film multilayers. *U. Nowak*[1]
1. Physics Department, University of Konstanz, Konstanz, Germany

Skyrmions are topologically protected quasi-particles that can appear in ferromagnetic thin-films multilayers and are increasingly discussed as possible building blocks for spintronic applications. Skyrmion diffusion [1] has been demonstrated in a recent combined experimental and theoretical study [2]. While being of fundamental interest as the type of diffusion yields information on transport and dissipation processes, thermally activated diffusion processes can also serve as a sensitive tool to analyze system properties. We use the stochastic Landau-Lifshitz-Gilbert equation to simulate diffusive motion of Skyrmions in a PtIr/Fe-bilayer on a Pd surface. Here, the frustration of the isotropic exchange interactions in connection with the Dzyaloshinskii-Moriya interaction is responsible for the creation of skyrmionic structures with various topological charges [3]. We demonstrate the dependence of the diffusive motion on the topological properties and on the Gilbert damping parameter by calculating the diffusion coefficient for skyrmionic structures with different topological charges. Our simulations reveal that in this system skyrmionic structures are deformed by the Dzyaloshinskii-Moriya interaction rendering them elongated. This deformation leads to anisotropic diffusive behavior and rotational Brownian motion in a periodic potential, which in combination lead to a transition from anisotropic Brownian motion at short time scales to isotropic on longer time scales.

[1] Schütte et al., Phys. Rev. B 90, 174434 (2014). [2] Zázvorka et al., Nat. Nanotech., (2019) [3] Rózsa et al., Phys. Rev. B 95, 094423 (2017).

CONTRIBUTED PAPERS

10:42

ED-08. Controlling long-range skyrmion lattices using field and temperature in Fe/Gd multilayers. *L. DeBeer-Schmitt*[1], R. Desautels[2,1], N. Tang[3], S. Montoya[4,5], L. W.L.N.C.[6], S.K. Patel[4,8], M. Fitzsimmons[1,6], E. Fullerton[4], J. Borchers[7] and D.A. Gilbert[3] *1. Neutron Scattering Division, Oak Ridge National Laboratory, Oak Ridge, TN, United States; 2. Seagate Inc, Londonderry, United Kingdom; 3. Material Science Depeartment, University of Tennessee, Knoxville, TN, United States; 4. CMRR, University of California San Diego, La Jolla, CA, United States; 5. Naval Information Warfare Systems Command, San Diego, CA, United States; 6. Physics, University of Tennessee, Knoxville, TN, United States; 7. NIST Center for Neutron Research, National Institute of Standards and Technology, Gaithersburg, MD, United States; 8. Physics, University of California San Diego, La Jolla, CA, United States*

Ordered magnetic skyrmion lattices presents a lush playground of new and interesting physics to explore. This opportunity is provided, in part, due to the non-trivial topological nature of the skyrmion. Currently, a significant effort is being made to realize skyrmion-driven devices. These efforts are focused on designing and developing materials that can support skyrmions under ambient conditions. We have recently fabricated thin-films of amorphous Fe and Gd multilayers that support skyrmions and skyrmion lattices at room temperature and zero applied magnetic field. These skyrmions are stabilized by dipolar interactions, rather than the Dzyaloshinskii–Moriya interaction (DMI). By varying the film thickness and alloy composition we can alter the balance of the dipole interactions relative to the exchange and anisotropy, thus facilitating control of the skyrmion size, pitch, and field stability. Using small angle neutron scattering (SANS), we demonstrated that once formed these dipole skyrmions are stable over a large field and temperature range (including positive/negative/zero magnetic field and temperatures between 10K and 325 K, in a single film). Interestingly, we observe temperature and field dependent changes in the scattering vector (Q) for peak scattering related to the skyrmion lattice spacing. We observed two effects while changing the magnetic field; i). ramping the field results in a decrease in Q suggesting an increased skyrmion lattice, and ii). when applying an field in the opposite direction to (i), to that used to establish the skyrmion lattice we observe an increase Q before leaving the lattices stability window. The origin of this change in scattering vector has led us to identify a key requirement necessary for the range of stability that we have observed in these amorphous thin films. Work at UCSD supported by DOE award No. DE-SC0003678. GP-SANS work is supported by the U.S. DOE, Office of Science (OS), Basic Energy Sciences (BES), Scientific User Facilities Division at ORNL and is managed by UT-Battelle, LLC for the U.S. DOE. VSANS access was provided by the Center for High Resolution Neutron Scattering, a partnership between NIST and the NSF under Agreement No. DMR-1508249.

[1]. R. D. Desautels et al., arXiv:1904.13274 (2019) [2] S. A. Montoya, et al. Phys. Rev. B 95, 024415 (2017)

10:54

ED-09. Thermal Brownian Motion of Skyrmion for Ture Random Number Generation. *Y. Yao*[1], X. Chen[1], W. Kang[1] and W. Zhao[1]
1. Beihang University, Beijing, China

The current driven skyrmion motion and its application for racetrack memory have been extensively studied in theories and in experiments [1,2]. However, the thermal induced dynamics of skyrmion at room temperature leads to various problems for racetrack memory. Meanwhile, a wide variety of concepts or prototypes have been proposed by utilizing the dynamics of skyrmion. In this work, we exploit and take the advantages of thermal Brownian motion of skyrmion [3-6] for random number generation. In our design, a skyrmion is generated at the center of an elliptical disk consisting of a rectangular region and two semicircular regions. With no external excitation, the skyrmion is only affected by regional boundaries and thermal disturbance, and its dynamics are consistent with Brownian motion, as shown in Fig. 1(a). In this case, a random data bit sequence can be obtained by periodically detecting the position of the skyrmion relative to the center. Specifically, if the skyrmion locates in the left region, indicating a bit of "0", otherwise, indicating a bit of "1" or vice versa. In order to obtain a reliable random data bit sequence, the detection interval is suggested to be over 10 ns depending on the temperature. The corresponding distribution map of the skyrmion location is shown in Fig. 1(b). We can find that probability of bit "0" or "1" equals to ~50% given a long enough data bit sequence (e.g., over 1000 bits). The National Institute of Standards and Technology (NIST) test results, as shown in Table I, show that our proposed design can achieve true random number generator (TRNG) at ultra-low power. Furthermore, we can easily configure the probability between bit "0" and bit"1" by modulating the equilibrium position of the skyrmion with anisotropy gradient. This work provides a ultra-low-power TRNG for stochastic or probabilistic computing [3-7] by exploiting the naturally thermal induced Brownian motion of skyrmion. More details will be presented in the conference.

[1] A. Fert, et al., Nature Nanotechnology, vol. 8, (2013). [2] W. Kang, et al., Proc. IEEE, vol. 12, (2016). [3] D. Pinna, F. A. Araujo, J.-V. Kim, et al., Physical Review Applied, vol. 9, (2018). [4] J. Miltat, S. Rohart, and A. Thiaville, Physical Review B, vol. 97, (2018). [5] T. Nozaki, Y. Jibiki, M. Goto, et al., Applied Physics Letters, vol. 114, (2019). [6] Y. Liu, Z. Wang, Z. Li, et al., IEEE-NANO, (2018). [7] J. Zázvorka, et al., Nature Nanotechnology, vol. 4, (2019).

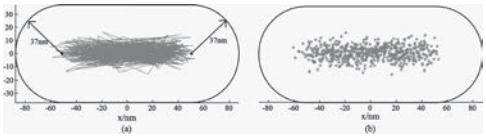


Fig. 1. (a) Thermal Brownian motion of skyrmion in an elliptical simulation disk at room temperature. (b) Spatial distribution of the location of skyrmion.

	Test	P-value		Success/Fail
1	Frequency	0.716998		Success
2	Block Frequency	0.119433		Success
3	Runs	0.337499		Success
4	Longest Run of Ones	0.808069		Success
5	FFT	0.305078		Success
6	Approximate	1.000000		Success
7	Cumulative Sums	0.604709	0.329312	Success
8	Serial	0.824844	0.907266	Success
9	Non-Overlapping Template Matching	All sub-test success		

Table I. NIST test results of the generated random numbers.

11:06

ED-10. Skyrmiogenesis: Skyrmion–antiskyrmion asymmetry from pair generation. U. Ritzmann[1,2], B. Dupe[3], R. Camley[4] and *J. Kim*[5]
1. Department for Physics and Astronomy, Uppsala University, Uppsala, Sweden; 2. Department of Physics, Freie Universität Berlin, Berlin, Germany; 3. Institut für Physik, Johannes Gutenberg-Universität Mainz, Mainz, Germany; 4. Department of Physics and Energy Science, University of Colorado, Colorado Springs, CO, United States; 5. Centre de Nanosciences et de Nanotechnologies, CNRS, Univ. Paris-Sud, Université Paris-Saclay, Palaiseau, France

Topological non-collinear magnetic textures called skyrmions are the subject of intense research due to their stability and nontrivial dynamics. They represent key components for future technologies such as racetrack memories [1,2] or bio-inspired computing devices [3]. In such systems, an important requirement is the controlled generation of skyrmions. Here we discuss in detail how a skyrmion gas can be generated through the trochoidal motion of an initial antiskyrmion seed [4]. The dynamics is driven by current-induced spin-orbit torques, which deform the antiskyrmion core and leads to the emergence of the helicity as a dynamical variable. During trochoidal motion, a skyrmion–antiskyrmion pair is nucleated from the deformed core, much in the same way as a vortex–antivortex pair being nucleated prior to vortex core reversal. In contrast to the vortex core case, the skyrmion–antiskyrmion pair separates because skyrmions and antiskyrmions execute different motion under these torques [4]. Skyrmions readily propagate away from the region of generation through linear motion, while the trochoidal motion of antiskyrmions mean they remain more localized to the generation region. Remarkably, each antiskyrmion created becomes a subsequent source of pair generation. Increased scattering between antiskyrmions leads to annihilation, which results in an overall excess of skyrmions in the system. An example of the generation from a single antiskyrmion is shown in Fig. 1. We investigated how the generation rate and skyrmion excess depend on the spin-orbit torque parameters. Due to the attractive interaction between skyrmions (through the frustrated exchange interaction), a crystallite of the excess skyrmions gradually forms. These results provide insight into how skyrmion ensembles may be created in realistic materials. This work was supported by the Horizon2020 Framework Programme of the European Commission (H2020-FETOPEN-2014-2015-RIA) under Contract No. 665095 (MAGicSky) and the Agence Nationale de la Recherche under Contract No. ANR-17-CE24-0025 (TOPSKY).

[1] S. Parkin *et al.*, Science 320, 190-194 (2008). [2] A. Fert *et al.*, Nat. Nanotechnol. 8, 152-156 (2013). [3] D. Pinna *et al.*, Phys. Rev. Appl. 9, 064018 (2018). [4] U. Ritzmann *et al*., Nat. Electron. 1, 451 (2018).

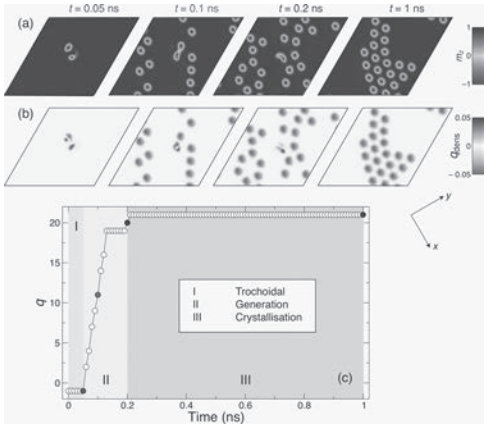


Fig.1 Skyrmion-antiskyrmion pair generation. Snapshots of the (a) mz component and (b) topological charge density. (c) Total topological charge as a function of time.

11:18

ED-11. Skyrmions in Ta/CoFeB-wedge/MgO. *C. Denker*[1], S. Nielsen[2], H. Heyen[1], E. Lage[2], Y.L. Junk[1], J. Walowski[1], M. Münzenberg[1] and J. McCord[2] *1. Institut fuer Physik, Universitaet Greifswald, Greifswald, Germany; 2. Institute for Materials Science, Christian-Albrechts-Universitaet zu Kiel, Kiel, Germany*

Magnetic skyrmion racetrack memories are interesting candidates for future data storage applications. We investigate different generation approaches as well as pinning center distribution and strength for magnetic skyrmions in Ta/CoFeB/MgO trilayers. This layer stack forms a bottom electrode with a tunnel barrier of a magnetic tunnel junction (MTJ) which are promising for the electrical reading and writing of skyrmions. Continuous CoFeB thickness wedges provide precise control for the relative average thickness of 3-6 pm defining the magnetic anisotropy. Skyrmions appear as a part of the out-of-plane hysteresis in a 13(6) pm wide window of CoFeB thickness directly followed by a transition to in-plane magnetic anisotropy at 1383(40) pm. This parameter range is extended by 10(6) pm using pulsed in-plane fields for skyrmion generation. Zero-field stable skyrmion bubbles nucleate from a slightly out-of-plane tilted in-plane remanent magnetic field application. The diffraction limit for diameter measurements in magnetooptical Kerr microscopy is circumvented by intensity evaluation leading to a noise-limited size limit below 100 nm. External magnetic field and effective anisotropy allow tuning the skyrmion size and density. In addition, we investigate energy landscapes for skyrmions by current induced hopping motion in a stripe with regions of different defect types and densities, since skyrmion motion tracking allows us to access the pinning center distribution and strength. We access the hopping regime by applying 50 μs long current pulses of about 5 x 10^{12} A/m^2 with a repetition rate of 20 Hz in a 10 μm wide stripe (Fig. 1). We observe forward and backward motion at an overall average speed of about 1 μm/s, corresponding to 1 mm/s during the current pulses, taking the duty cycle into account. While the Hall angle is masked in the individual traces by the influence of an inhomogeneous energy landscape, it is distinguishable in the average of the traces.

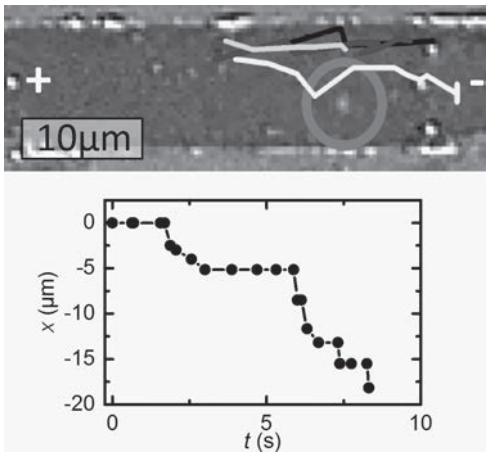


Fig. 1: 4 Representative tracked skyrmions. The red highlighted skyrmion is heavily pinned and immobile. The typical displacement vs. time dependence in the direction of the electrons in the graph of the yellow trace clearly indicates hopping motion

Session EE
ANTIFERROMAGNETIC ORDER AND DOMAINS

Elizabeth Skoropata, Chair
Oak Ridge National Laboratory, Oak Ridge, TN, United States

CONTRIBUTED PAPERS

8:30

EE-01. Magneto-electric driven antiferromagnetic domain reversal and domain wall dynamics. *K. Toyoki*[1], Y. Shiratsuchi[1], H. Yoshida[1], S. Watanabe[1], Y. Kotani[2], T. Nakamura[2] and R. Nakatani[1] *1. Department of Materials Science and Engineering, Graduate School of Engineering, Osaka University, Suita, Japan; 2. Japan Synchrotron Radiation Research Institute, Sayo, Japan*

Antiferromagnetic (AFM) spintronics offers the variety of new physics such as the ultrafast spin/domain wall (DW) dynamics as well as the promising application such as the ultrahigh density magnetic storage. Controlling AFM spins is a main difficulty in this field and we have been demonstrated that the magneto-electric (ME) effect is one of the solutions to resolve the problem [1-3]. Cr_2O_3 is a proto-typical ME-AFM material and the AFM order parameter (the Néel vector) was switchable by the ME field, i.e., the simultaneous application of magnetic (*H*) and electric (*E*) fields. One of the remaining questions is the switching process including the dominant dynamics, which we investigated in this work based on magnetic domain observations using the scanning soft X-ray magnetic circular dichroism microscope [4]. Pt/Co/Au/Cr_2O_3/Pt stacked film was used as the sample. First, the sample was cooled to 285 K, below the Néel temperature of Cr_2O_3 under H = -4 kOe to induce the exchange bias. At 285 K, H (+40 kOe) and variable E (DC or pulse) were simultaneously applied to control the ME-AFM domain state. The magnetic domain pattern was observed after removing the ME fields, i.e. H = 0 kOe and E = 0 V/m. In these processes, the negative H was not applied and the positive exchange bias is only the driving force to switch the magnetic domain state in removing H (+40 kOe to 0 kOe). The element-specific domain imaging revealed that ferromagnetic and AFM domains were spatially coupled [5] meaning that the FM domain is a replica of the ME-AFM domain and resultantly, the exchange bias polarity. Namely, the change in the observed FM domain pattern corresponds to that of the ME-AFM domain inducing the positive exchange bias. The results indicate that the switching process of the ME-AFM magnetization is proceeded by the nucleation of the reversed ME-AFM domain and the propagation of DW, in similar fusion of the ordinal FM materials [6]. The change in the propagation length with the pulse duration gives the ME-AFM DW velocity v. With increasing E, v exponentially increases followed by linear increase indicating the change from the creep motion to the DW flow. The highest v in the studied ME condition is ~22 m/s at $E = 1.3\times10^3$ kV/cm [7].

[1] T.V.A. Nguyen, Y. Shiratsuchi *et al*., Appl. Phys. Express 10, 083002 (2017). [2] T.V.A. Nguyen, Y. Shiratsuchi *et al*., J. Appl. Phys. 122, 073905 (2017). [3] T.V. A. Nguyen, Y. Shiratsuchi *et al*., J. Appl. Phys. 123, 233902 (2018). [4] Y. Kotani, K. Toyoki *et al*., J. Synchrotron Rad. 25, 1444 (2017). [5] Y. Shiatsuchi, *et al*., AIMS Mater. Sci. 2, 484 (2015). [6] Y. Shiratsuchi K. Toyoki *et al*., Appl. Phys. Lett. 113, 242404 (2018). [7] Y. Shiratsuchi K. Toyoki *et al*., APL Mater. 6, 121104 (2018).

8:42

EE-02. A Journey into the Antiferromagnetic Spin Textures of $BiFeO_3$. *A. Haykal*[1], J. Fischer[2], W. Akhtar[1], A. Finco[1], J. Chauleau[3], C. Carrétéro[2], N. Jaouen[4], M. Bibes[2], M. Viret[3], S. Fusil[2,5], V. Garcia[2] and V. Jacques[1] *1. Laboratoire Charles Coulomb CNRS-UM2, Montpellier, France; 2. Unité Mixte de Physique, CNRS, Thales, Palaiseau, France; 3. SPEC, CEA, CNRS, Gif-sur-Yvette, France; 4. Synchrotron SOLEIL, Gif-sur-Yvette, France; 5. Université d'Evry, Université Paris-Saclay, Evry, France*

Antiferromagnetic (AF) thin films are currently attracting considerable excitement for low dissipative spintronic devices [1,2]. However, most of conventional real-space magnetic microscopy techniques cannot probe the AF order at the nanoscale because magnetic moments are mostly compensated, resulting in very low magnetic signals. This is a major obstacle to the fundamental understanding of nanoscale AF order and its response to external stimuli, such as spin polarized currents or electric fields. To release the full potential of AFs for next-generation spintronics, the nanoscale control and imaging capabilities that are now routine for ferromagnets must be extended to AF materials. Here we show that scanning magnetometry based on a single nitrogen–vacancy (NV) defect in diamond is ideally suited for imaging complex AF orders at the nanoscale, even under ambient conditions. As a proof of principle, we report on the first real-space visualization of a non-collinear AF order in a thin film of bismuth ferrite $BiFeO_3$(BFO), a room-temperature multiferroic material in which the AF order is intimately linked to the ferroelectric one via magnetoelectric coupling. We first image the cycloidal AF order in a BFO thin film and demonstrate that magneto-electric coupling can be exploited to manipulate the cycloid propagation direction by an electric field [3]. We then investigate the effect of epitaxial constraint on the behaviour of the AF order in strained BFO thin-films [4]. Different substrates were used for the growth in order to tune the strain. Using scanning NV-magnetometry, we proved that tuning strain can stabilize different propagation directions of the cycloid, can change the plane in which the cycloid rotates or can collapse the cycloid into G-type antiferromagnetic domains in highly strained films. These results demonstrate how BFO can be used to design reconfigurable AF spin textures on demand.

[1] V. Baltz et al., Antiferromagnetic spintronics, Reviews of Modern Physics 90, 015005 (2018). [2] T. Jungwirth et al., Antiferromagnetic spintronics, Nature Nanotechnology 11, 231-241 (2016). [3] I. Gross, W. Akhtar et al, Nature, 549, 252–256 (2017).

8:54

EE-03. Mapping Spin Textures in Epitaxial Oxide Ferromagnet-Antiferromagnet Heterostructures with X-ray Photoemission Electron Microscopy. *R.V. Chopdekar*[1], Y. Jia[2], M. Lee[2] and Y. Takamura[2] *1. Advanced Light Source, Lawrence Berkeley National Laboratory, Berkeley, CA, United States; 2. Materials Science and Engineering, University of California, Davis, Davis, CA, United States*

Interest in antiferromagnetic (AFM) spintronic devices has surged due to the possibility of obtaining ultrafast magnetization dynamics with no stray field,[1] and complex oxide heterostructures offer a route to tailor AFM

spin textures via their many degrees of freedom and sensitivity to epitaxial strain. However, an absence of stray field makes visualizing AFM domain structures difficult though conventional techniques. We show that X-ray photoemission electron microscopy (X-PEEM) combined with both x-ray linear and circular dichroism can spatially resolve the ferroic domain structure and quantify spin axis orientation in AFM and ferromagnetic (FM) layers of a model system of alternating FM $La_{0.7}Sr_{0.3}MnO_3$ and G-type AFM $La_{1-x}Sr_xFeO_3$ (x=0 or 0.3). In contrast to thicker layers where the spin axis cants out of plane,[2] in the limit of few unit-cell thick layers for (001)-oriented samples the AFM spin axis lies in the plane of the film. For (111)-oriented superlattices, a subset of spins cant along low-index <110> directions and exhibit spin flop coupling to the FM layer, and a subset of spins have spin axes that lie within the (111) plane.[3] The coupling at AFM/FM interfaces for both orientations allows for control of the AFM domain structure through magnetization rotation of the FM layer, and we have recently shown that shape anisotropy offers an additional degree of freedom to control complex oxide AFM domain orientation.[4] X-PEEM with variable x-ray polarization offers a powerful local probe to determine the AFM spin axis on the scale of single AFM domains, and enables a fuller understanding of how the similar energy scales of shape anisotropy and interfacial exchange can be engineered in order to design spin textures in oxide heterostructures.

1. Baltz et al, Rev. Mod. Phys 90, 015005 (2018). 2. Takamura et al, Phys. Rev. B 80, 180417 (2009). 3. Jia, Chopdekar et al, Phys. Rev. B. 92, 094407 (2015); Jia, Chopdekar et al, Phys. Rev. B. 96, 214411 (2017). 4. Lee et al, Phys. Rev. Mater. 1 014402 (2017).

INVITED PAPERS

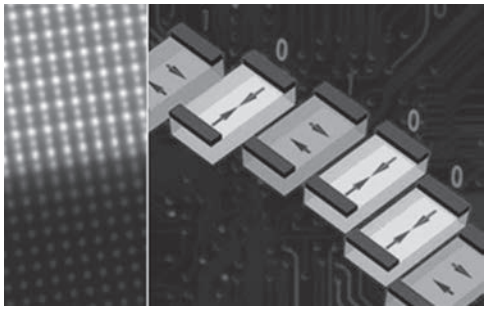
9:06

EE-04. Electric control of antiferromagnetic/ferromagnetic order.

I. Fina[1,2] 1. Institut de Ciència de Materials de Barcelona (ICMAB-CSIC), Bellaterra, Spain; 2. IGSresearch, La Poble de Mafumet, Spain

Devices mainly based on antiferromagnetic materials will not easily substitute those based on ferromagnetic materials. However, the research during the last years on antiferromagnetic materials for applications has raised exponentially [1,2]. Antiferromagnetic materials concentrate numerous features that encourage the research on its integration in devices for both information processing and storage: i) antiferromagnetically-coupled moments are not altered by moderate magnetic fields, ii) the absence of dipolar interactions allow the stability of multiple magnetic configurations, iii) the nearly null stray fields reduces the cross-talk among neighboring elements within the same device and makes them invisible for the commercial magnetic read-devices, iv) they are more abundant in nature than ferromagnets and generally display higher magnetic ordering temperatures. These exclusive characteristics make antiferromagnetic materials very interesting for some niche applications, for instance, security. The same fundamental characteristic that makes antiferromagnetic materials interesting, the absence of net magnetic moment, hampers their characterization because null magnetic moment makes their manipulation (write) and measurement (read) challenging. In my talk, I will cover my contributions on the process of "writing in antiferromagnets". I will focus on its writing by using external magnetic fields, by the help of either the exchange spring effect [3,4] or heat [5,6], as reviewed in ref. [1]. However, as one might anticipate, these methodologies are very costly from the energetic point of view, and simplify the read process remains as a challenge [2]. Electric control of antiferromagnetic order at low temperature is possible in a variety of antiferromagnetic materials [7,8]. However, I will mainly focus on the thermal and electric control of the combined antiferromagnetic/ferromagnetic orders present at room temperature in FeRh films [9-11]. The electric control of antiferromagnetic/ferromagnetic orders produce large effects in an energy efficient manner. The coexistence between both magnetic orders can help to simplify the reading process, while preserving some of the main characteristics that make antiferromagnetic materials interesting. Potential routes towards applications will be discussed.

[1] X. Martí, I. Fina, and T. Jungwirth. IEEE Transactions on Magnetics 51, 2900104 (2015). [2] I. Fina, X. Marti. IEEE Transactions on Magnetics 53, 2500107 (2017). [3] I. Fina, X. Marti, D. Yi, J. Liu, J. H. Chu, C. Rayan-Serrao, S. Suresha, A. B. Shick, J. Zelezný, T. Jungwirth, J. Fontcuberta, R. Ramesh. Anisotropic magnetoresistance in an antiferromagnetic semiconductor. Nature Communication 5, 4671 (2014). [4] R. Galceran, I. Fina, J. Cisneros-Fernández, B. Bozzo, C. Frontera, L. López-Mir, H. Deniz, K.-W. Park, B.-G. Park, Ll. Balcells, X. Martí, T. Jungwirth & B. Martínez. Scientific Reports 6, 35471 (2016). [5] D. Petti, E. Albisetti, H. Reichlová, J. Gazquez, M. Varela, M. Molina-Ruiz, A. F. Lopeandía, K. Olejník, V. Novák, I. Fina, B. Dkhil, J. Hayakawa, X. Marti, J. Wunderlich, T. Jungwirth, and R. Bertacco. Applied Physics Letters 102, 192404 (2013). [6] X. Marti, I. Fina, C. Frontera, R.J. Paull, J.D. Clarkson, J. Kudrnovský, I. Turek, D. Yi, Jian Liu, J.-H. Chu, C. Nelson, E. Arenholz, Q. He, L. You, S. Salahuddin, J. Fontcuberta, T. Jungwirth, R. Ramesh. Nature Materials 13, 367 (2014). [7] I. Fina, L. Fàbrega, X. Martí, F. Sánchez, and J. Fontcuberta. Physical Review Letters 107, 257601 (2011). [8] I. Fina, L. Fàbrega, X. Martí, F. Sánchez, and J. Fontcuberta. Applied Physics Letters 97, 232905(2010). [9] J. D. Clarkson, I. Fina, Z. Q. Liu, Y. Lee, J. Kim, C. Frontera, K. Cordero, S. Wisotzki, F. Sanchez, J. Sort, S. L. Hsu, C. Ko, L. Aballe, M. Foerster, J. Wu, H. M. Christen, J. T. Heron, D. G. Schlom, S. Salahuddin, N. Kioussis, J. Fontcuberta, X. Marti and R. Ramesh, Scientific Reports 7, 15460 (2017). [10] I. Fina, A. Quintana, J. Padilla-Pantoja, X. Marti, F. Macià, F. Sanchez, M. Foerster, L. Aballe, J. Fontcuberta, and J. Sort, ACS Applied Materials and Interfaces 9, 15577 (2017). [11] I. Fina, A. Quintana, X. Martí, F. Sánchez, M. Foerster, L. Aballe, J. Sort, and J. Fontcuberta, Applied Physics Letters 113, 152901 (2018).



9:42

EE-05. Multi-stimuli manipulation of domains in multiferroics.

J. Chauleau[1] 1. SPEC, CEA Saclay, Gif-sur-Yvette, France

Antiferromagnets (AF) are currently in the limelight thanks to recent breakthroughs demonstrating the efficient effect of spin currents in interacting with the AF order parameter [1,2]. So far, due to the lack of net magnetization, controlling AF distributions has been rather challenging. Current-induced AF control also opens new perspectives in Terahertz magnetization dynamics. On the materials side, antiferromagnets represent the large majority of magnetic materials. Some of them show several simultaneous ordered phases and are commonly called 'multiferroics'. As a result, when the AF order is coupled to a net polarization, it may be controlled by applying a voltage. Generally speaking, multiferroic materials [3] are the focus of an intense research effort due to the significant technological interest of multifunctional materials as well as the rich fundamental physics lying in the coupling of various order parameters. Among all multiferroics, $BiFeO_3$ (BFO) is a material of choice because its two ordering temperatures (ferroelectric FE and AF) are well above room temperature. In addition a large magnetoelectric coupling has been demonstrated in single crystals as well as in thin films. Second harmonic generation has proven to be a powerful and elegant way to assess complex multiferroïc textures and to unentangle the different contributions at play [4]. In this presentation, we will present a study demonstrating the possibility to use second harmonic generation (SHG) to access the micron sized distribution of AF domain

(Figure 1) in a multiferroic thin film [5]. Subsequently, we will study their ultrafast dynamics by assessing the time evolution of the multiferroic texture when subjected to an intense femtosecond light pulse. Eventually we will discuss how they could be efficiently manipulated by the internally optically rectified sub-picosecond electric fields. This opens the door to an all-optical terahertz control the AF order, independently of the electric polarization, but still using the magnetoelectric effect.

[1] T. Jungwirth, X. Marti, P. Wadley and J. Wunderlich *Nature Nanotech*. 11, 231 (2016) [2] P. Wadley and al. *Science* 351, 587 (2016) [3] N. Spalding and M. Fiebig, *Science*, 309, 391 (2005) [4] M. Fiebig & al., *Nature*, 419, 818, (2002) [5] J.-Y. Chauleau & al., *Nature Materials*, 16, 803, (2017)

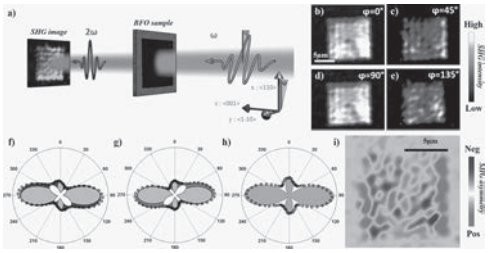


Fig.1 SHG study of antiferromagnetic domains in BiFeO3 thin epitaxial layer. (a) SHG experiemental configuration. (b-e) SHG intensity images for different incident light polarization direction, \phi. (f-h) 3 kind of Polarization angular dependence of the SHG intensity observed in the ferroelectric monodomain. (i) Reconstructed AF domains image. From [5]

CONTRIBUTED PAPERS

10:18

EE-06. Chiral antiferromagnetic and electric orders at multiferroic domain walls in $BiFeO_3$ striped films. J. Chauleau[1], S. Fusil[3], T. Chirac[1], V. Garcia[3], p. Thibaudeau[4], J. Tranchida[5], I. Gross[6], W. Akhtar[6], A. Finco[6], M. Bibes[3], V. Jacques[6], N. Jaouen[2] and *M. Viret*[1] *1. IRAMIS/ SPEC, CEA Saclay, Gif sur Yvette cedex, France; 2. Synchrotron Soleil, Saint Aubin, France; 3. Unité mixte de physique CNRS/Thales, Palaiseau, France; 4. CEA – DAM le Ripault, Monts, France; 5. Sandia National Laboratories, Albuquerque, NM, United States; 6. Université de Montpellier and CNRS, Montpellier, France*

Chirality, a foundational concept throughout science, may arise at ferromagnetic domain walls[1] and in related objects such as skyrmions[2]. A vast literature has emerged in recent years concerning these topological objects and their potential use in memories or magnetic-based logic. Chiral textures should also exist in other types of ferroics such as antiferromagnets for which theory predicts that they should move faster for lower power[3], and ferroelectrics where they should be extremely small and possess unusual topologies[4,5]. A significant effort is now being devoted to generating such structures in ferroelectrics and antiferromagnets but so far with limited success. We will present here the concomitant observation of antiferromagnetic and electric chiral textures at domain walls in the room-temperature ferroelectric antiferromagnet $BiFeO_3$[6]. This observation is achieved by combining several reciprocal and real-space characterization techniques. Both electric and antiferromagnetic chiralities are evidenced at room-temperature in this multiferroic compound where domain walls represent very particular regions in space where the different orders have to adapt. We reveal here the presence of both electric chirality and periodic chiral antiferromagnetic objects along the domain walls. These are backed by dynamical atomistic spin simulations able to reproduce the observed textures. The mechanisms underlying their formation and their relevance for electrically controlled topological oxide electronics and spintronics will be discussed.

1. Emori, S., Bauer, U., Ahn, S.-M., Martinez, E. & Beach, G. S. D. Current-driven dynamics of chiral ferromagnetic domain walls. *Nat. Mater.* 12, 611–616 (2013). 2. Fert, A., Reyren, N. & Cros, V. Magnetic skyrmions: advances in physics and potential applications. *Nat. Rev. Mater.* 2, 17031 (2017). 3. Barker, J. & Tretiakov, O. A. Static and Dynamical Properties of Antiferromagnetic Skyrmions in the Presence of Applied Current and Temperature. *Phys. Rev. Lett.* 116, 147203 (2016). 4. Nahas, Y. *et al.* Discovery of stable skyrmionic state in ferroelectric nanocomposites. *Nat. Commun.* 6, 8542 (2015). 5. Gonçalves, M. A. P., Escorihuela-Sayalero, C., García-Fernández, P., Junquera, J. & Íñiguez, J. Theoretical guidelines to create and tune electric skyrmions. *ArXiv180601617 Cond-Mat* (2018). 6. J.-Y. Chauleau, T. Chirac, S. Fusil, V. Garcia, W. Akhtar, J. Tranchida, P. Thibaudeau, I. Gross, C. Blouzon, A. Finco, M. Bibes, B. Dkhil, D.D. Khalyavin, P. Manuel, V. Jacques, N. Jaouen, M. Viret, Electric and antiferromagnetic chiral textures at multiferroic domain walls, under revision in Nature Materials.

10:30

EE-07. Control of Highly Anisotropic Ferroelastic Domains in $LaCoO_3$ Films and Ferromagnetism Using Strain and Pressure. *T.R. Charlton*[1], E. Guo[1,7], R. Desautels[1], D. Lee[1], M. Roldan[2], Z. Liao[1], H. Ambaye[1], J.J. Molaison[1], R. Boehler[1,3], D. Keavney[4], A. Herklotz[1,5], T.Z. Ward[1], H. Lee[1] and M. Fitzsimmons[1,6] *1. Oak Ridge National Laboratory, Oak Ridge, TN, United States; 2. Eyring Materials Center, Arizona State University, Tempe, AZ, United States; 3. Geophysical Laboratory, Carnegie Institution for Sciences, Washington, DC, United States; 4. Advanced Photon Source, Argonne National Laboratory, Lemont, IL, United States; 5. Institute for Physics, Martin-Luther-University Halle-Wittenberg, Halle (Saale), Germany; 6. Department of Physics and Astronomy, University of Tennessee, Knoxville, TN, United States; 7. Beijing National Laboratory for Condensed Matter Physics and Institute of Physics, Chinese Academy of Sciences, Beijing, China*

The coupling of ferroelastic and ferromagnetic order parameters in materials offers a means to achieve novel multiferroic applications. We observe that one dimensional ferroelastic domains in $LaCoO_3$ thin films are intimately linked to its magnetization. Unidirectional structural modulation is achieved by the selection of substrate or growth plane, which produces broken in-plane rotational symmetry. Structural modification either through film growth or application of pressure is shown to affect the magnetism. These modifications perturb the crystal field energy, which leads to an unexpected in-plane anisotropy of the orbital configuration and the magnetization. Here, we will present the structural and magnetic depth profile of a $LaCoO_3$ film under hydrostatic pressure (0 to 1.6 GPa). We observe the that the structural density increases more in the center of the $LaCoO_3$ than at the interfaces. Additionally, we find that the magnetization decreases considerably (20% per GPa) with increasing pressure. Work funded by the U.S. Department of Energy, Basic Energy Sciences

10:42

EE-08. Possible Emergence of a Skyrmion Phase in Ferroelectric $GaMo_4S_8$. *H. Zhang*[1], J. Chen[1], P. Barone[2], K. Yamauchi[3], S. Dong[1] and S. Picozzi[2] *1. School of Physics, Southeast University, Nanjing, China; 2. Institute for Superconducing and Innovative Materials and devices (CNR-SPIN), Consiglio Nazionale delle Ricerche, Chieti, Italy; 3. Institute of Scientific and Industrial Research, Osaka University, Ibaraki, Osaka, Japan*

$GaMo_4S_8$ is a member of the lacunar spinel AM_4X_8 family (A = Ga and Ge; M = V, Mo, Nb, and Ta; X = S and Se), which have shown an incredibly rich physical phenomenology. Moreover, an extended Néel-type Skyrmion lattice phase was observed in GaV_4S_8 and GaV_4Se_8.[1-3] This was consistent with symmetry considerations, predicting a Néel-type Skyrmion lattice phase to be observed in polar magnets with C_{nv} crystal symmetry. As for $GaMo_4S_8$, a structural transition was observed from point group T_d to C_{3v} at $T_s \approx$ 45.5K. At high temperatures, the structure shows ideal Mo_4

tetrahedron, with equivalent Mo ions and Mo-Mo bond-lengths. However, in the low-temperature polar structure, the Mo_4 cluster is compressed along the [111] direction, leading to a difference between apical (Mo_1) and planar (Mo_2) ions. Furthermore, $GaMo_4S_8$ was found to be ferromagnetic below $T_c \approx 19.5$K, with one unpaired electron for each Mo_4 cluster. Stimulated by large potential interests in $GaMo_4S_8$, we performed both Density Functional Theory calculations and Monte Carlo (MC) simulations. By means of PBEsol+*U* approach and using the Berry phase method, we first focus on ferroelectric properties. We estimate a polarization along the [111] direction of about 1.4μC/cm^2, consistent with Mo_1-Mo_2 bonds to be shorter than Mo_2-Mo_2 bonds. From the magnetic properties point of view, the magnetization is found to be quite homogeneous within the Mo_4-tetrahedron, the magnetic moments being $0.24\mu_B$ for Mo_1 and $0.22\mu_B$ for Mo_2. We find a sizeable Dzyaloshinskii-Moriya (DM) interaction, with a ratio of DM with respect to Heisenberg exchange interactions (*J*) up to 0.74. In addition, due to the magnetocrystalline anisotropy in $GaMo_4S_8$, anisotropic spin exchange interactions (*J*) and single ion anisotropy are considered. Finally, a classical spin model was used as basis for MC simulations, considering DM, anisotropic spin exchange interactions (*J*) and single ion anisotropy, as evaluated from first-principles. While the magnetic ground state is found to be a spin cycloid at low temperatures, we predict the emergence of a Néel-type Skyrmion lattice phase in the phase diagram upon applying a magnetic field. [4]

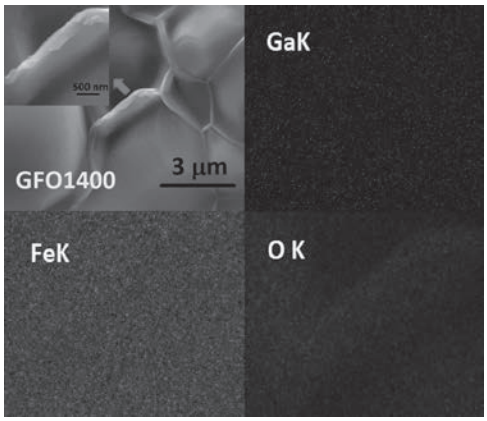
[1] I. Kézsmárki, S. Bordács, P. Milde, E. Neuber et al., Nat. Mater. 14, 1116 (2015) [2] E. Ruff, S. Widmann, P. Lunkenheimer, et al., Sci. Adv. 1, e1500916 (2015) [3] Y. Fujima, N. Abe, Y. Tokunaga, et al., Phys. Rev. B 95, 180410(R) (2017) [4] H. M. Zhang, S. Dong and S. Picozzi et al., Phys. Rev. B accepted (2019)

10:54

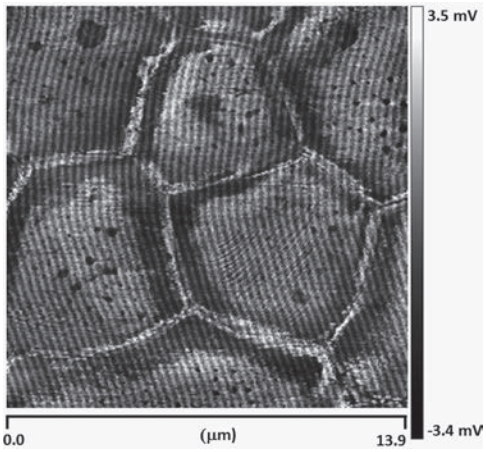
EE-09. Presence of Conductive Path at the Grain Boundaries of Multiferroic $GaFeO_3$. *S. Ghose*[1] and K. Mandal[1] *1. CMPMS, SNBNCBS, Kolkata, India*

Multiferroic Gallium Ferrite ($GaFeO_3$) is a promising material for the application in advanced device fabrication due to its substantial magnetoelectric coupling [1,2]. But the presence of high leakage in $GaFeO_3$ shadows the possibility of its application [3,4]. The conduction mechanism behind this exceptionally high leakage current in $GaFeO_3$ is still not identified properly. Here we have investigated the variation of leakage conduction with the changes in morphologies especially at the grain boundaries due to the heat treatment temperature during sample preparation. A partial decomposition is identified at the grain boundaries above 1325 ^{0}C though the melting temperature of $GaFeO_3$ is 1520 ^{0}C [5]. Ridge like structures form at the grain boundaries due to this partial decomposition. These ridges have introduced conducting paths which act as conducting channels for the leakage electrons to propagate through the material. Interestingly, C-AFM image shows that oxygen vacancies at the near grain boundaries produce poor conductive regions. Small polaron hopping could be the effective transport mechanism present at the grain boundaries of $GaFeO_3$.

[1] J. H. Jung, M. Matsubara, T. Arima, J. P. He, Y. Kaneko and Y. Tokura, Phys. Rev. Lett., 93, 037403 (2004). [2] Y. Ogawa, Y. Kaneko, J. P. He, X. Z. Yu, T. Arima, Y. Tokura, Phys. Rev. Lett., 92, 047401 (2004). [3] V. Singh, A. Daryapurkar, S. S. Rajput, S. Mukherjee, A. Garg and R. Gupta, J. Am. Ceram. Soc., 100, 5226 (2017). [4] N. Sharma, A. K. Mall, R. Gupta, A. Garg and S. Kumar, Appl. Phys. A, 123, 536 (2017). [5] H. J. Vanhook, J. Am. Ceram. Soc., 48, 470 (1965).



The SEM image and EDAX mappings of $GaFeO_3$ sample.



The C-AFM image of $GaFeO_3$ sample.

11:06

EE-10. Ion irradiation effect in complex oxides: Another degree of freedom or complexity? *S. Zhou*[1], C. Wang[1], P. Pandey[1], M. Helm[1], S. Gemming[1,6], C. Chang[2], R. Ganesh[3], D. Chen[4] and Y. Chu[5] *1. Institute of Ion Beam Physics and Materials Research, Helmholtz-Zentrum Dresden-Rossendorf, Dresden, Germany; 2. Department of Physics, National Cheng Kung University, Tainan, Taiwan; 3. The Institute of Mathematical Sciences, Chennai, India; 4. Institute for Advanced Materials and Guangdong Provincial Key Laboratory of Optical Information Materials and Technology, South China Normal University, Guangzhou, China; 5. Department of Materials Science and Engineering, National Chiao Tung University, Hsinchu, Taiwan; 6. Institute of Physics, Technische Universität Chemnitz, Chemnitz, Germany*

Inter-relations among charge, spin, orbital and lattice parameters are largely demonstrated in multi-functional oxide materials, which exhibit a variety of exotic properties, ranging from superconductivity, insulator-metal transition, colossal magnetoresistance, charge ordering, and orbital ordering, etc. In particular, tilting a delicate energy balance in lattice interactions and kinetics, achieved by temperature, pressure or chemical control, may result in exotic phenomena in these systems. However, fine-tailoring such interactions has proven difficult. In this context, defect engineering by ion irradiation, which can introduce strain and electronic disorder, has emerged as a powerful technique to fine tune complex phases of oxide thin films. In this contribution, we show that ion irradiation can modify the magnetic and electrical transport properties in a broad variety of materials, including spinel $NiCo_2O_4$, perovskite $BiFeO_3$, $SrRuO_3$ and $LaNiO_3$ [1-4]. Diverse magnetic, structure and magneto-transport modifications, which are inaccessible by

conventional film growth methods, have been obtained. For instance, the transport in $LaNiO_3$ can be driven from metallic phase into an Anderson insulator by directly tuning the electronic mean free path via irradiation-induced disorder [4]. In $BiFeO_3$, we have obtained a super-tetragonal phase with the largest c/a ratio ~ 1.3 that has ever been experimentally achieved in $BiFeO_3$ [2]. This may lead to strong polarization enhancement. By comparing the effect in different materials, we will also point out the complexity in understanding the tailoring of oxides by ion beams.

[1] P. Pandey, Y. Bitla, M. Zschornak, M. Wang, C. Xu, J. Grenzer, D. C. Meyer, Y. Y. Chin, H. J. Lin, C. T. Chen, S. Gemming, M. Helm, Y. H. Chu, S. Zhou, Enhancing the Magnetic Moment of Ferrimagnetic $NiCo_2O_4$ via Ion Irradiation driven Oxygen Vacancies, APL Materials 6, 066109 (2018) [2] C. Chen, C. Wang, X. Cai, C. Xu, C. Li, J. Zhou, Z. Luo, Z. Fan, M. Qin, M. Zeng, X. Lu, X. Gao, U. Kentsch, P. Yang, G. Zhou, N. Wang, Y. Zhu, S. Zhou, D. Chen, J-M. Liu, Controllable defect driven symmetry change and domain structure evolution in $BiFeO_3$ with enhanced tetragonality, Nanoscale 11, 8110 (2019) [3] C. Wang, C. Chen, C.-H. Chang, H.-S. Tsai, P. Pandey, C. Xu, R. Böttger, D. Chen, Y.-J. Zeng, X. Gao, M. Helm, S. Zhou, Defect-induced exchange bias in a single $SrRuO_3$ layer, ACS Appl. Mater. Interfaces, 27472 (2018).

11:18

EE-11. Concept of artificial magnetoelectric materials via geometrically controlling curvilinear helimagnets. *O. Volkov*[1], U. Roessler[2], J. Fassbender[1] and D. Makarov[1] *1. Helmholtz-Zentrum Dresden-Rossendorf, Dresden, Germany; 2. Leibniz Institute for Solid State and Materials Research Dresden, Dresden, Germany*

Magnetoelectric materials are of the great interest due to their unique coupling of the magnetic and electrical order parameters, offering exciting prospectives for energy efficient memory, logic and sensor devices. However, a sizeable magnetoelectric coupling for technologically relevant applications is obtained for a limited set of single-phase bulk materials. Typically, this restriction can be removed by using two-phase materials, containing strain-coupled magnetoelectric heterostructures based on piezoelectric-magnetostrictive bilayers. Although the concept is promising, there is a clear limitation regarding the fact that strain-induced changes result in the modification of all intrinsic magnetic parameters, in particular anisotropic couplings. Ideally, it would be advantageous that electric field control of magnetic state is achieved without change of global intrinsic magnetic parameters. We propose a novel type of artificial magnetoelectric material [1], which allows an electric field-induced deterministic switching between magnetic states without influencing intrinsic magnetic parameters. The proposal refers to geometrically curved helimagnets [2,3] embedded in a piezoelectric matrix or sandwiched between two piezoelectric layers. In contrast to typical strain-coupled magnetoelectric heterostructures, we exploit the geometric coupling between the piezoelectric matrix and curvilinear helimagents. Namely, a small geometrical deformation causes a drastic modification of magnetic state of the helimagnet through a magnetic phase transition between a homogeneous magnetic state and a periodical one. Resulting transformations of the average magnetization from non-zero to zero value can be uniquely assigned to logical “1” and “0”. This paves the way towards the realization of novel magnetoelectric devices with geometrically tunable and deterministically switchable magnetic states. We provide not only the general concept but also show analytical validation for a prototypical example of torsional nanospring helimagnets. Furthermore, we put forth a discussion on the feasibility of the experimental realization of the concept including the choice of materials and fabrication approaches.

[1] O. M. Volkov et al., J. Phys. D: Appl. Phys. (2019). doi:10.1088/1361-6463/ab2368. [2] O. M. Volkov et al., Scientific Reports 8, 866 (2018). [3] R. Streubel et al., J. Phys. D: Appl. Phys. (Topical Review) 49, 363001 (2016).

Session EF
APPLICATIONS OF SPIN-TORQUES INCLUDING NEUROMORPHIC COMPUTING

Witold Skowronski, Chair
AGH University of Science and Technology, Krakow, Poland

CONTRIBUTED PAPERS

8:30

EF-01. Spintronic Nano-Neurons: Using Spin-Torque Nano Oscillators for Solving Machine Learning Tasks. *F. Abreu Araujo*[1], M. Riou[2], J. Torrejon[2], S. Tsunegi[3], D. Querlioz[4], K. Yakushiji[3], A. Fukushima[3], H. Kubota[3], S. Yuasa[3], M.D. Stiles[5] and J. Grollier[2] *1. IMCN, Université catholique de Louvain, Louvain-la-Neuve, Belgium; 2. Unité Mixte de Physique CNRS/Thales, Palaiseau, France; 3. Spintronics Research Center, National Institute of Advanced Industrial Science and Technology (AIST), Tsukuba, Japan; 4. Centre de Nanosciences et de Nanotechnologies, Palaiseau, France; 5. Center for Nanoscale Science and Technology, National Institute of Standards and Technology, Gaithersburg, MD, United States*

The brain displays many signatures of non-linear dynamical behavior, including synchronization and complex transient behavior. These observations have inspired a whole class of neuromorphic concepts based on complex networks of interconnected non-linear nodes. Hardware systems for neuromorphic computing are usually tested using the so-called reservoir computing neural network architecture [1], a machine learning approach. One of the preferred tasks for benchmarking such devices is automatic speech recognition [2-7]. However, this task requires acoustic transformations from sound waveforms with varying amplitudes to frequency domain maps that can be seen as feature extraction techniques (see Fig. 1). Depending on the conversion method, these may obscure the contribution of the neuromorphic hardware to the overall speech recognition performance. Here, we quantify and separate the contributions of the acoustic transformations and the neuromorphic hardware to the speech recognition success rate [8]. We show that the non-linearity in the acoustic transformation plays a critical role in feature extraction. We compute the gain in word success rate provided by a reservoir computing device compared to the acoustic transformation only (see Fig. 2) and show that it is an appropriate benchmark for comparing different hardware. Finally, we experimentally and numerically quantify the impact of the different acoustic transformations for neuromorphic hardware based on magnetic nano-oscillators.

[1] H. Jaeger, and H. Haas, *Science* 304, 78–80 (2004) [2] L. Appeltant *et al.*, *Nat. Commun.* 2, 468 (2011) [3] Y. Paquot *et al.*, *Sci. Rep.* 2, 287 (2012) [4] D. Brunner *et al.*, *Nat. Comm.* 4, 1364 (2013) [5] K Vandoorne *et al.*, *Nat. Comm.* 5, 3541 (2014) [6] J. Torrejon, M. Riou, F. Abreu Araujo, J. Grollier *et al.*, *Nature* 547, 428-431 (2017) [7] M. Riou, F. Abreu Araujo, J. Torrejon, J. Grollier, *IEDM 2017* (2017) [8] F. Abreu Araujo, M. Riou, J. Grollier *et al.*, *arXiv:1906.02812* (2019)

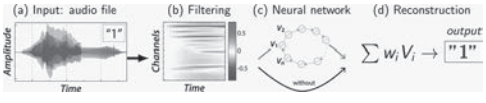


Fig. 1. Principle of spoken digit recognition. (a) Audio waveform. (b) Filtering to frequency channels for acoustic feature extraction. (c) The filtered input is injected into the neural network or directly used to construct the output (no neural network). The neural network is composed of *N* interconnected filtered inputs. (d) For each digit, the response of the neural network (or directly the filtered output) is constructed from a linear combination of neuron states.

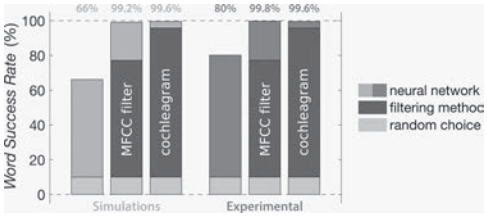


Fig. 2. Contributions to the spoken digit recognition rate. The random choice level is shown in grey, the filtering methods in blue, and the neural network under the reservoir computing approach in green and orange for the simulations and experiments, respectively.

8:42

EF-02. Meander Domain Wall Device as a Synaptic Element for Neuromorphic Computing. *N. Sernicola*[1], T. Jin[1], D. Kumar[1], W. Lew[1], R. Sbiaa[2] and S. Piramanayagam[1] *1. Division of Physics and Applied Physics, School of Physical and Mathematical Sciences, Nanyang Technological University, Singapore; 2. Department of Physics, Sultan Qaboos University, Muscat, Oman*

Artificial intelligence (AI) has recently become an integral part of our daily lives and its applications are plentiful and growing. The vast majority of these applications rely on algorithms running on a traditional von Neumann architecture, where the physical separation of the processing unit from memory causes a bottleneck that greatly increases power consumption, especially for AI applications. In contrast, the human brain is capable of performing highly complex tasks, consuming just 20 W. Neuromorphic computing (NC) is a new computational paradigm that tries to emulate the functioning of the brain[1]. Recently, a synaptic application of domain wall devices has been proposed based on the multiple states of anomalous Hall resistance[2]. In our study, we have investigated a magnetic tunnel junction (MTJ) synaptic device with a meander structure, which has the potential to exhibit much higher changes in resistance and controllable pinning, which is suitable for commercial applications. CoFeB based MTJs were prepared in the form of meander domain wall devices, where the position of the DW, which is controlled by spin orbit torque (SOT), dictates multiple resistance states. Figure 1 shows the scanning electron microscope images of the meander devices. In this meander structure, the corners act as pinning sites. Figure 2 shows the simulation results of the pinning of a domain wall along a corner of a nanowire. The simulation results confirm that the edges of the meander structure pin the domain walls. The experimental results of the electrical measurements will be presented.

[1] Burr, Geoffrey W., et al., *Advances in Physics: X* 2.1 (2017) [2] Borders W A, Akima H, Fukami S, *Appl. Phys. Express* 10 013007 (2017)

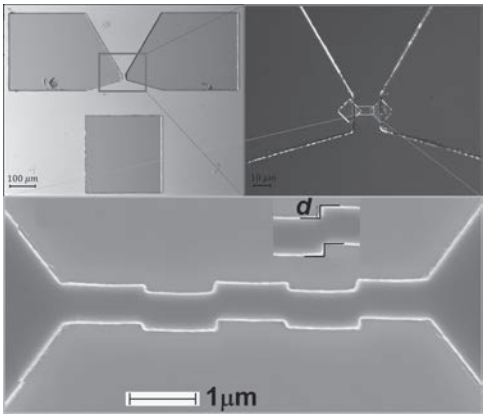


Fig 1: Optical (top) and scanning electron microscope (bottom) images of the meander domain wall device at various levels of zoom with 400 nm width and d = 100 nm.

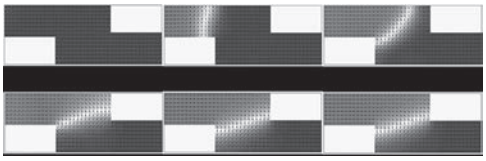


Fig 2: Micromagnetic simulations of the domain wall pinning along a single step of a meander domain wall device.

8:54

EF-03. Neuromorphic computing with magnetic Josephson junctions. *M.L. Schneider*[1], C.A. Donnelly[2], A. Wynn[3], I.W. Haygood[1], S.E. Russek[1], M. Pufall[1], P. Hopkins[1] and W.H. Rippard[1] *1. NIST, Boulder, CO, United States; 2. Electrical Engineering, Stanford, Palo Alto, CA, United States; 3. MIT Lincoln Laboratory, Lexington, MA, United States*

Neuromorphic computing can improve both the speed and efficiency of many computational tasks such as image recognition and internet search. Our recent work on Josephson junctions with magnetic nano-particles in the barrier demonstrated devices with quasi-analog control of the Josephson critical current. These devices can tune the Josephson critical current by more than 1,000 % by adjusting the amount of spin order between the nano-particles. [1] These devices can be combined with naturally spiking Josephson junctions to implement artificial neural networks directly in hardware. The single flux quantum pulses produced by Josephson junctions in the voltage state are analogous to the action potentials in biological neurons and superconducting transmission lines act as axons distributing the signals with near lossless transmission. The magnetic nano-clustered Josephson junctions form a high-speed energy efficient synaptic element that can control the weighting to form a spiking neural network. We combine these elements to make a new neuromorphic architecture with the potential to be applied to problems that are currently addressed by artificial neural networks.[2] We will also present our recent experimental results which confirm agreement between our simulated synaptic design and circuits fabricated with the MIT-Lincoln Laboratory Josephson junction process. Figure 1 shows the simulated synaptic transfer covering the critical current tuning range demonstrated in a clustered magnetic Josephson junction (squares), which are in good agreement with the 4 test circuits shown in circles. The agreement between these test circuits enables more rapid development of neuromorphic architectures that include these novel magnetic Josephson junctions.

[1] M. L. Schneider, et al., Sci. Adv., Vol. 4, p.e1701329 (2018) [2] M. L. Schneider, C. A. Donnelly and S. E. Russek, J. of App. Phy. Vol. 124, p. 161102 (2018)

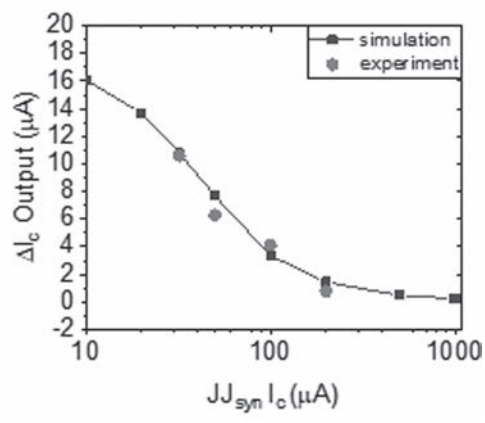


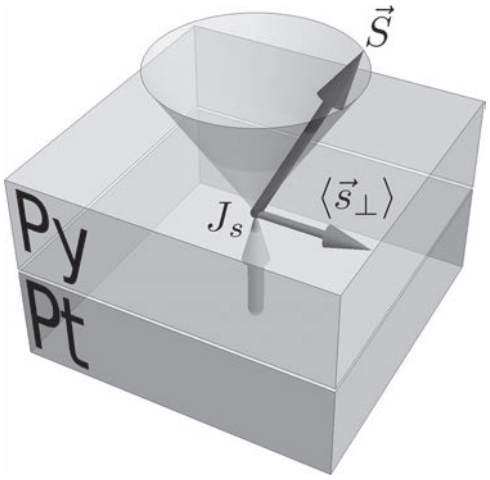
Fig 1. Change in output neuron current as a function of synapse critical current value

9:06

EF-04. Mode Attraction and Antiresonance in a Dynamic Rashba System with Spin-Orbit Torques. *I. Proskurin*[1,2] and R.L. Stamps[1] *1. Department of Physics and Astronomy, University of Manitoba, Winnipeg, MB, Canada; 2. Institute of Natural Sciences and Mathematics, Ural Federal University, Ekaterinburg, Russian Federation*

Mode attraction has recently attracted attention in optomechanical, opto-magnonic, and optodynamical systems inside microwave cavity resonators. Together with negative-mass instability, this effect has been experimentally realized in an number of systems including cavity magnon-polaritons and cold atom ensembles [1,2]. On grounds that this type of behavior should be ubiquitous and is expected in a wide variety of nonequilibrium driven systems [3]. An interesting class of meta-materials where this type of instabilities can be probed is the spin-orbit torque oscillators where a spin current in the Rashba layer is able to produce an antidamping effect on the magnetic oscillator. Experimentally, a transition from the resonance to the antiresonance has been reported in Py/Pt bilayers [4]. We propose that this effect is related to the level attraction between the ferromagnetic resonance in Py layer and the interband electron transitions in the Pt layer. We theoretically identify a level attraction regime in a coupled electron-magnon system. We show how this effect is related to the relative dynamic population of the Bloch band and interband transitions. This theory is applied to the Rashba Hamiltonian interacting with a magnetic oscillator in the antidamping torque geometry. In this case, the transition from the usual hybridization between the magnons and the resonant interband electron transitions to the mode attraction regime depends on dynamic spin accumulations that can be produced by a spin current flowing in the Rashba material. We estimate the relevant physical parameters, such as the threshold current strength, necessary for experimental detection. The resonant instability in spin-orbit torque systems, which is described by the mode attraction scenario, can be interesting for future designing of fully quantum spintronic devices such as transducers and quantum amplifiers.

1. M. Harder et al., Phys. Rev. Lett., Vol, 121, p. 137203 (2018). 2. J. Kohler et al., Phys. Rev. Lett., Vol. 120, p. 013601 (2018). 3. I. Proskurin, R. Macêdo, and R. L. Stamps, arXiv: 1904.11570 (2019). 4. A. J. Berger et al., Phys. Rev. B, Vol. 97, 094407 (2018).



Schematic picture of the spin torque oscillator where spin current in the Pt layer creates a spin accumulation on the surface with the Py slab.

9:18

EF-05. Synchronization and Chaos in Spin Torque Oscillator with Two Free Layers. *T. Taniguchi*[1] *1. Spintronics Research Center, National Institute of Advanced Industrial Science and Technology (AIST), Tsukuba, Japan*

Spin torque oscillator (STO) as a microwave source for microwave assisted magnetization reversal (MAMR) has been an exciting research subject for a decade [1-4]. Microwave emitted from an STO is applied to magnetic recording bits in a hard-disk drive, and reduces the reversal field. The latest design of STO for MAMR consists of two ferromagnetic layers called spin-injection and field-generation layers, where the former injects spin current into the latter and excites the magnetization oscillation [5]. Importantly, both layers can be regarded as free layers because the STO has no pinned layer. The magnetization dynamics of this STO is still not fully understood, yet an effort to experimentally observe the dynamics was reported recently [6]. In this work, a theoretical study on the magnetization dynamics in an STO consisting of two free layers, namely CoFe and NiFe used in the experiment [6], is presented [7]. Two layers are coupled via dipole interaction and spin-transfer effect. Solving the Landau-Lifshitz-Gilbert equation, we find three dynamical phases, as shown in Fig. 1. The first one is a synchronization in low current region, where the oscillation frequencies of two layers are identical. Note that synchronized magnetization oscillations cannot be detected by the conventional method employing tunnel or giant magnetoresistance (MR) effect. This is because the relative angle between the magnetizations is constant in the synchronized state; see also Fig. 1, where the oscillation frequency of MR is zero. In fact, no MR signal was observed experimentally in low current region [3]. However, it does not necessarily indicate that there is no magnetization oscillation. We believe its existence in the low current region, and is applicable to MAMR. The second phase is the magnetization oscillations with different frequencies. The third phase is chaos, which serves no contribution MAMR but might be interesting for other applications such as random number generator. This work was supported by NEDO.

1. J.-G. Zhu *et al*., IEEE Trans. Magn. 44, 125 (2008). 2. H. Suto *et al*., J. Appl. Phys. 112, 083907 (2012). 3. K. Kudo *et al*., Appl. Phys. Express 8, 103001 (2015). 4. S. Bosu *et al*., Appl. Phys. Lett. 108, 072403 (2016). 5. J.-G. Zhu, Dual side spin transfer spin torque oscillator for microwave assisted magnetic recording in Joint MMM-Intermag Conference, San Diego, CA, USA, Jan. 2016, AB-11. 6. W. Zhou *et al*., Appl. Phys. Lett. 114, 172403 (2019). 7. T. Taniguchi, J. Magn. Magn. Mater. 438, 281 (2019).

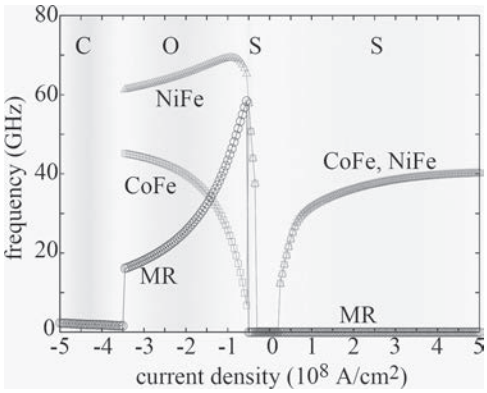


Fig. 1: Dependences of oscillation frequencies of CoFe, NiFe, and magnetoresistance (MR) on current density. The labels "S", "O", and C" indicate the synchronization, oscillations with different frequencies, and chaotic.

9:30

EF-06. Nonlinear dynamics of spin-torque nano-oscillators with delayed feedback. J. Williame[1], A. Difini Accioly[1], D. Rontani[2], M. Sciamanna[2] and *J. Kim*[1] *1. Centre de Nanosciences et de Nanotechnologies, CNRS, Univ. Paris-Sud, Université Paris-Saclay, Palaiseau, France; 2. Laboratoire Matériaux Optiques, Photonique et Systèmes, CentraleSupelec, Université de Lorraine, Metz, France*

Delayed feedback, whereby the output signal of a system is sent back into its input with amplification and delay, can result in a variety of nonlinear behaviors [1]. For spin-torque nano-oscillators (STNOs) in which magnetization is driven into self-oscillation by spin-transfer torques, delayed feedback can improve spectral properties such as the emission linewidth [2,3]. Here, we present theoretical results on the complex transient response and chaotic behavior in STNOs subject to delayed feedback. We considered model oscillator systems in which the output is generated by changes in the tunneling magnetoresistance, which is subsequently fed back as variations in the input drive current [4]. Fig. 1 shows possible phases for a macrospin oscillator operating near the transition between the in-plane (IPP) and out-of-plane (OPP) precession regimes. By tuning the delay and amplification of the self-injected signal, we have identified new dynamical regimes in this system such as chaos, IPP/OPP switching with complex transients, and oscillator death. Fig. 2 shows the power spectral density as a function of delay in the nonlinear oscillator [5], where the frequency is strongly dependent on the amplitude. For this system, well-defined modulated states evolve to chaotic behavior as the delay is increased. These delayed feedback schemes open up a new field of exploration for STNOs, where complex transient states might be useful for applications such as reservoir computing [6]. This work was supported by the Agence Nationale de la Recherche under Contract No. ANR-17-CE24-0008 (CHIPMuNCS).

[1] E. Schöll and H. G. Schuster, *Handbook of Chaos Control* (Wiley, 2008). [2] V. S. Tiberkevich *et al*., Sci. Rep. 4, 3873 (2014). [3] G. Khalsa *et al*., Appl. Phys. Lett. 106, 242402 (2015). [4] J. Williame *et al*., Appl. Phys. Lett. 114, 232405 (2019). [5] J.-V. Kim *et al*., Phys. Rev. Lett. 100, 017207 (2008). [6] L. Appeltant *et al*., Nat. Commun. 2, 468 (2011); J. Torrejon *et al*., Nature 547, 428 (2017).

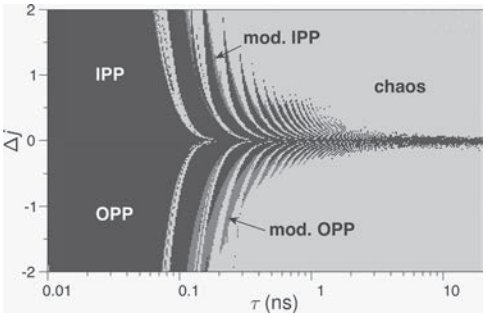


Fig. 1: Phase diagram of macrospin oscillator with delayed feedback, showing in-plane precession (IPP), out-of-plane precession (OPP), and chaos.

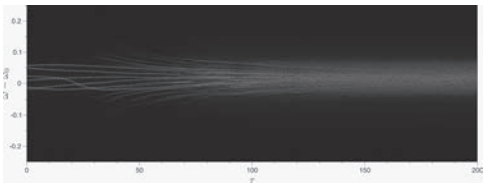


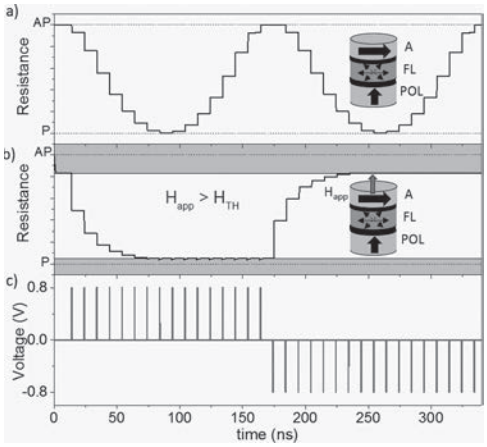
Fig. 2. Power spectral density map showing frequency as a function of feedback delay in the nonlinear oscillator model.

9:42

EF-07. Macrospin simulation with dry friction of a spintronic memristor based on angular variation of TMR. *M. Mansueto*[1], A. Chavent[1], U. Ebels[1], R. Sousa[1], L. Buda-Prejbeanu[1], I. Prejbeanu[1] and B. Dieny[1] *1. CEA - IRIG, Spintec, Grenoble, France*

Nowadays, brain-like networks are the best example of efficient and low power consumption computational tool for big data analysis tasks. In this context, the development of a proper hardware is essential and memristive devices, with their synapse-like behavior, represent a key element for this purpose. Our objective is to conceive a spintronic memristor based on the angular variation of TMR in an in-plane junction with the magnetic state controlled by spin transfer torque. One of the main challenge is represented by the realization of a special magnetic media (FL) able to stabilize the magnetization along several directions in the plane of the layer. Here we are developing such a media by exploiting the ferromagnet/antiferromagnet (F/AF) coupling in a trilayer F/AF/F [1]. For critical thicknesses of the AF layer, the strength of the coupling at the frustrated interface ensures the stability of the magnetization independently on its direction. Here we demonstrate that such system can be well described by inserting a dry friction term in the LLG equation for which the total damping is $a = \alpha + b/(dM/dt)$, with α the Gilbert damping and b the dry friction parameter [2] (model used in [3],[4],[5],[6]). For a thin film system with zero anisotropy, macrospin simulations show that the magnetization can be stabilized in any in-plane direction (isotropic coercivity). The possibility to control the magnetization position has been investigated considering a static and a rotating in-plane magnetic field. The STT effect from an out-of-plane polarizer (POL) has also been simulated with and without a static in-plane field. For all the four cases, an analytical solution has been found and compared to the macrospin simulations with good agreement. Finally, simulations of the full device (as in the inset) show the expected memristive behavior through the application of short pulses (100ps) and of a transverse in-plane magnetic field that insures the monotonicity of the resistance variation with the voltage polarity between the parallel P and antiparallel AP state. Fig a) shows the resistance variation under the effect of voltage pulses as in c). The memristive behavior is shown in b) where a transverse in-plane field is applied.

[1] M. Mansueto et al., under review [2] W. Baltenperger, J.S. Helman, *Dry friction in micromagnetics,* IEEE Trans. Magn. 27 (1991) 4772–4774 [3] J. A. Holyst and W. Baltensperger, *Influence of dry magnetic friction on the ferromagnetic resonance,* Solid State Communications, Vol. 82, No. 10, pp. 763-765, (1992) [4] A. Visintin, *Modified Landau-Lifshitz equation for ferromagnetism,* Physica B 233 (1997) 365-369 [5] M. P. Magiera et al., *Magnetic friction: From Stokes to Coulomb behavior,* Physical Review B 84, 212301 (2011) [6] G. Consolo et al., *Mathematical modeling and numerical simulation of domain wall motion in magnetic nanostrips with crystallographic defects,* Applied Mathematical Modelling 36(2012) 4876–4886



9:54

EF-08. Pronounced Scaling of the Tunnel Spin Polarization of Fe/MgO/silicon Contacts with MgO Thickness. *A.M. Spiesser*[1], H. Saito[1], S. Yuasa[1] and R. Jansen[1] *1. Spintronics Research Center, AIST, Tsukuba, Japan*

The discovery of giant tunnel magnetoresistance in crystalline Fe/MgO/Fe magnetic tunnel junctions[1,2] greatly accelerated the development of practical spintronic applications. Inspired by this success, crystalline MgO has also widely been used in semiconductor spintronic devices. Indeed, it has been shown that a charge current across a FM/MgO/semiconductor tunnel junction results in spin injection into the semiconductor[3-6]. With this approach, we recently demonstrated the creation of a giant spin accumulation in Si using Fe/MgO tunnel contacts[6]. However, some important questions remain, such as how the tunnel spin polarization (TSP) varies as a function of the MgO thickness and what is the role of symmetry-based spin filtering due to coherent tunneling in Fe/MgO tunnel contacts on Si. Here we report on these two aspects[7]. The Fe/MgO contacts were deposited on a Si substrate having a 70 nm-thick heavily-doped Si(001) channel and a MgO thickness (t_{MgO}) varying from 0.75 nm to 2.3 nm. The spin current produced by a charge current across the Fe/MgO/Si tunnel junction was measured using the standard 4-terminal nonlocal geometry. The TSP was extracted from the magnitude of the nonlocal spin-valve and Hanle signals. As shown in Fig. 1, the TSP depends sensitively on t_{MgO}, increasing from values below 1 % at small thickness, to values in the 90 to 95 % range for t_{MgO} above 2 nm. Such a near-perfect spin polarization of the tunnel current indicates that symmetry-based spin filtering due to coherent tunneling occurs in Fe/MgO tunnel contacts on Si, despite the significant lattice mismatch. The unexpected drop of the TSP below 1 nm of MgO is attributed to the lower crystalline quality of thin MgO layers, as supported by TEM. The scaling of the TSP can be well described (Fig. 1) by assuming coherent spin-dependent tunneling, but excluding the first 0.7 nm of MgO, which has lower quality. The pronounced scaling of the TSP with MgO thickness, as revealed here, has important implications for achieving large magnetoresistance in Si-based devices.

1. S. S. P. Parkin, C. Kaiser, A. Panchula, *et al.*, Nature Mater. 3, 862 (2004) 2. S. Yuasa, T. Nagahama, A. Fukushima, *et al.*, Nature Mater. 3, 868 (2004) 3. X. Jiang, R. Wang, R. M. Shelby, *et al.*, Phys. Rev. Lett. 94, 056601 (2005) 4. T. Suzuki, T. Sasaki, T. Oikawa, *et al.*, Appl. Phys.

Express 4, 23003 (2011) 5. M. Ishikawa, T. Oka, Y. Fujita, *et al.*, Phys. Rev. B 95, 115302 (2017) 6. A. Spiesser H. Saito, Y. Fujita, *et al.*, Phys. Rev. Appl. 8, 064023 (2017) 7. A. Spiesser H. Saito, S. Yuasa *et al.*, to be published in Phys. Rev. B, (2019)

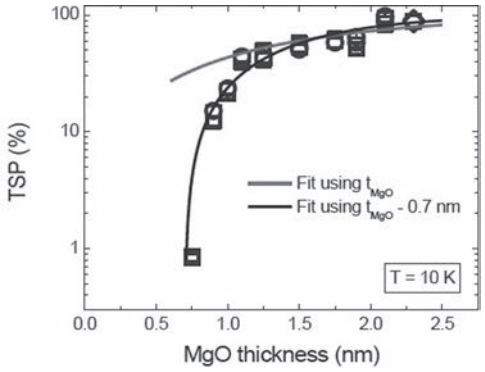


Fig.1 Scaling of the TSP of Fe/MgO tunnel contacts on Si with MgO thickness. The black solid line is a fit assuming coherent tunneling, but excluding 0.7 nm of MgO.

10:06

EF-09. Spin Signals in Two-terminal Devices with a Nonmagnetic Channel and Ferromagnetic Tunnel Contacts. *R. Jansen*[1], A.M. Spiesser[1], H. Saito[1], Y. Fujita[1], S. Yamada[2], K. Hamaya[2] and S. Yuasa[1] *1. 1National Institute of Advanced Industrial Science and Technology (AIST), Tsukuba, Japan; 2. Osaka University, Toyonaka, Japan*

Spintronic devices typically consist of a combination of ferromagnetic (FM) and non-magnetic (NM) materials in various device geometries. Nonlocal 4-terminal devices have been instrumental in fundamental studies of spin accumulation and pure spin currents. But since 4-terminal devices are not easily integrated in practical spintronic systems, attention is shifting to two-terminal (2T) lateral devices. Unlike nonlocal devices, spin signals in 2T devices are not very well understood. Here we report on spin transport in 2T devices with a Si channel and Fe/MgO tunnel contacts. We reveal two aspects that are crucial for the understanding of the 2T spin signals: (i) The conversion of the spin accumulation in the channel into a detectable voltage across a biased tunnel contact is shown to be strongly nonlinear [1], causing the spin-detection efficiency P_{det} of the FM tunnel contact to be different from the tunnel spin polarization, and strongly bias dependent. Consequently, contrary to expectation, the two FM contacts do not contribute equally to the detected spin signals. In fact, most of the 2T spin signal is generated at one of the FM contacts, while for the other contact, the bias polarity is such that $P_{det} \sim 0$ so that it contributes little or nothing. (ii) Spin voltages in 2T devices are shown to contain not only the expected contributions due to spin transport from one electrode to the other, but also local contributions from the spin accumulation in the Si created and detected at each of the two contacts separately [2]. The salient features of the 2T spin signals therefore differ from those in nonlocal devices. For instance, the 2T Hanle signals for parallel (P) and antiparallel magnetization (AP) have unequal amplitude (figure 1). The local and transport contributions to the 2T spin signal can be disentangled and described by the same set of device parameters as the nonlocal spin signals measured in the same devices [3]. Our conclusions apply also to 2T devices with a channel made from other semiconductors (GaAs, Ge), normal metals, or two-dimensional materials such as graphene and van der Waals crystals.

[1] R. Jansen, A. Spiesser, H. Saito, Y. Fujita, S. Yamada, K. Hamaya and S. Yuasa, Nonlinear electrical spin conversion in a biased ferromagnetic tunnel contact, Phys. Rev. Appl. 10, 064050 (2018). [2] A. Spiesser, Y. Fujita, H. Saito, S. Yamada, K. Hamaya, S. Yuasa and R. Jansen, Hanle spin precession in a two-terminal lateral spin valve, Appl. Phys. Lett. 114, 242401 (2019). [3] A. Spiesser, H. Saito, Y. Fujita, S. Yamada, K. Hamaya, S. Yuasa and R. Jansen, Giant spin accumulation in silicon nonlocal spin-transport devices, Phys. Rev. Appl. 8, 064023 (2017).

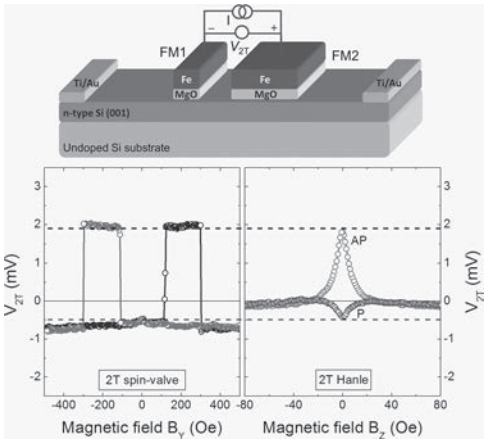


Fig.1 Two-terminal spin-valve and Hanle spin signals for a Si device with Fe/MgO tunnel contacts.

10:18

EF-10. Understanding of mechanism for gate-controlled spin accumulation in Si-based lateral spin valve. *S. Lee*[1], F. Rortais[1], R. Ohshima[1], Y. Ando[1], Y. Suzuki[2], H. Koike[3] and M. Shiraishi[1] *1. Department of Electronic Science and Engineering, Kyoto University, Kyoto, Japan; 2. Graduate School of Engineering Science, Osaka University, Toyonaka, Japan; 3. Advanced Products Development Center, TDK, Ichikawa, Japan*

One of the main advantages of semiconductor as spin transport channel is that both charge- and spin- transport properties can be modified by a gate voltage. Even if much effort has been dedicated for Si-based spin transistor, because of its long spin lifetime, the origin of the variation of the spin accumulation with applied gate voltage is still unclear [1, 2]. In this research, we aimed to understand the physical origin and the dominant mechanisms of the gate-controlled spin accumulation voltage in Si-based lateral spin valve device. For our research, we used Silicon-on-insulator based lateral spin valve (LSV) device, which consists of two ferromagnetic contacts and two nonmagnetic contacts on the top of the non-degenerate silicon channel with a carrier density of 5×10^{17} cm^{-3}. In addition, a gate voltage (V_G) was applied between the back side of the sample and a nonmagnetic contact of the device. V_G dependences of the electrical channel conductivity (σ_{Si}) and the spin diffusion length (λ_{Si}) of the LSV device, shown in figure 1, demonstrate the importance of σ_{Si} which was modified by several orders of magnitudes with applied V_G. Finally, local 3-terminal spin accumulation voltage (ΔV_{L3T}) was measured at various injection currents (I_{inj}) and applied V_G as summarized in figure 2. The control by a gate of the spin accumulation voltage is well described by a competition between spin drift effect and the conductivity mismatch. At positive V_G, the spin drift effect is decreased because the drift velocity is reduced by the accumulated carriers. However, at negative V_G the spin resistance of the channel is enhanced, which is increasing the conductivity mismatch and so reducing the spin injection/detection efficiency. At high I_{inj} and negative V_G, because drift velocity is reaching the saturation, the conductivity mismatch is the dominant mechanism. Both effects were included in our 1-dimensional model to explain the experimental results of the spin signal dependence with V_G. Our experimental demonstration of the competition between the conductivity mismatch and the drift effect, paves the way toward an efficient gate voltage control of spin signals.

[1] T. Sasaki, M. Shiraishi *et al*., Phys. Rev. Appl. 2, 34005 (2014). [2] T. Tahara, M. Shiraishi *et al.*, Appl. Phys. Express 8, 113004 (2015).

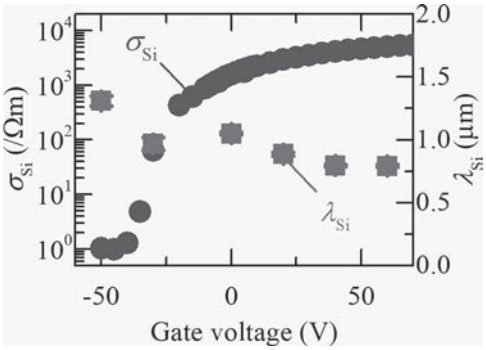


Fig 1. V_G dependence of σ_{Si} and λ_{Si}

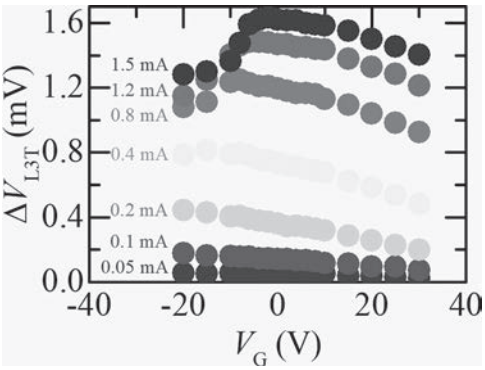


Fig 2. V_G dependence of ΔV_{L3T}

10:30

EF-11. Withdrawn

10:42

EF-12. Crystalline-orientation Dependent Charge-spin Conversion and SOT Switching of Epitaxial Pt Films. *Y. Xiao*[1], H. Wang[1] and E. Fullerton[1] *1. Center for Memory and Recording Research, La Jolla, CA, United States*

The discovery of spin Hall effect (SHE) in heavy metals leads to effective charge current to spin current conversion [1,2]. The spin current can be employed to manipulate magnetic moment reorientation by spin-orbit torque (SOT). Similar to the anomalous Hall effect (AHE) in ferromagnets, the SHE in nonmagnetic conductors is contributed by spin skew scattering [3], side jump scattering [4] and intrinsic scattering [5]. In this context, engineering the crystallinity and defects in heavy metals provides an approach to delve in the underlying mechanism. Here, we fabricate Co/Ni multilayers with perpendicular magnetic anisotropy (PMA) on a series of epitaxial Pt layers with different crystalline orientations and doped impurities. The epitaxy nature of Pt and magnetic anisotropy of Co/Ni structures are confirmed by X-ray diffraction (XRD) (Fig. 1a) and vibrating sample magnetometry (VSM) (Fig. 1b) measurements, respectively. The charge-to-spin conversion efficiencies of different Pt layers are studied by SOT switching and harmonic Hall measurements (Fig. 1c, Fig. 1d). The measured spin Hall angles (SHA) of Pt layers with different textures and purities exhibit pronounced variations which can be correlated to the electrical resistivity and defects providing insights into the dominant scattering mechanism behind the spin Hall effect in heavy metals. This work was supported as part of Quantum Materials for Energy Efficient Neuromorphic Computing, an Energy Frontier Research Center funded by the U.S. DOE, Office of Science.

1) A. A. Bakun, A. A. Zakharchenya, B. P.and Rogachev et al. *Sov. Phys. JETP* 40, 1293 (1984). 2) J. Hirsch, *Phys. Rev. Lett.* 83, 1834 (1999). 3) J. Smit, *Physica* 24, 39 (1958). 4) L. Berger, *Phys. Rev. B* 2, 4559 (1970). 5) J. Luttinger, Phys. Rev. 112, 739 (1958).

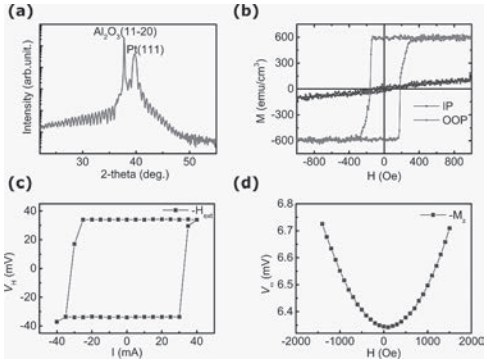


Figure 1: (a) XRD spectra on epitaxial Pt (111) film. (b) Perpendicular magnetic anisotropy obtained on Pt/Co/Ni stacks by VSM measurements. (c) Current-induced switching by probing anomalous Hall resistance. (d) First harmonic Hall signal on Pt/Co/Ni stacks.

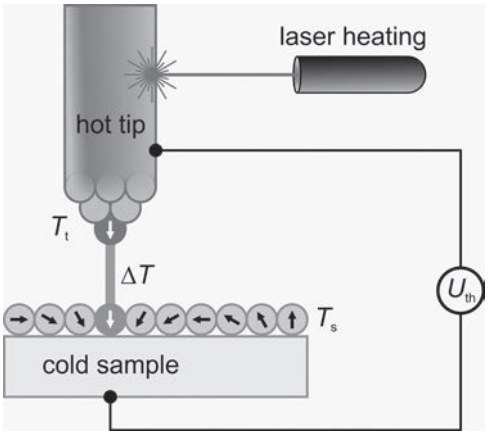
INVITED PAPER

10:54

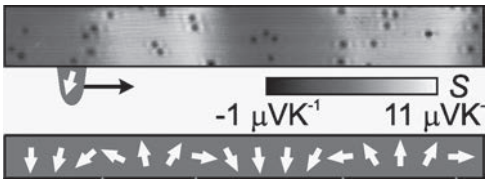
EF-13. Magneto-Seebeck Tunneling on the Atomic Scale. *C. Friesen*[1], H. Osterhage[1], J. Friedlein[1], A. Schlenhoff[1], R. Wiesendanger[1] and S. Krause[1] *1. Institute of Applied Physics and Interdisciplinary Nanoscience Center Hamburg, University of Hamburg, Hamburg, Germany*

The ongoing effort to fabricate electronic and spintronic devices at ever smaller size scales inevitably leads to a dramatic increase in heat generation. This ultimately sets a limit on the devices that can be constructed. Thus a detailed understanding of the coupling between charge, spin, and heat transport at the nanometer scale is a critical prerequisite for the design of such devices [1]. The tunneling of spin-polarized electrons across a magnetic tunnel junction, driven by a temperature gradient, is a fundamental process for the thermal control of electron spin transport, and previous studies have confirmed that large switching ratios are possible [2]. The possible applications of this effect, e.g. the efficient conversion of waste heat into spin currents, or the magnetic control of heat transfer on the atomic scale, have implications both for basic research and future technological applications. We experimentally investigated the atomic-scale details of this magneto-Seebeck tunneling by approaching a magnetic probe tip to a magnetic sample at cryogenic temperatures, with vacuum serving as the tunneling barrier [3,4]. By using a laser to heat the tip and measuring the resulting thermopower across the junction, while scanning across the spin texture of the sample, spin-resolved Seebeck coefficients are determined with atomic-scale lateral resolution. These direct tip-heating results were confirmed using predictions from rectification compensation and bias spectroscopy [3]. The experiments were performed at low temperatures and in UHV conditions, on the Fe/W(110) multilayer system (T = 50 K) [5], as well as on the Fe monolayer on Ir(111) (T = 25.3 K) [6], using a bulk Cr tip and active bias compensation [7]. The non-collinear spin structures present in these sample systems, and the atomic-scale lateral resolution of spin-polarized scanning tunneling microscopy, allowed for the imaging of a continuous range of relative tip-sample magnetization orientations. The results will be presented in terms of spin-averaged effects (including spin-orbit coupling) and magneto-Seebeck tunneling. Finally, a possible realization of a purely heat-driven magnetic sensor will be envisaged, potentially being an atomic-scale building block for integrated circuits in future spintronics devices.

[1] G. Bauer, E. Saitoh, B. van Wees, Nature Materials, Vol. 11, pp. 391-399 (2012). [2] M. Walter, et al., Nature Materials, Vol. 10, pp. 742-746 (2011). [3] C. Friesen, et al., Journal of Physics D: Applied Physics, Vol. 51, p. 324001 (2018) [4] C. Friesen, et al., Science, Vol. 363, pp. 1065-1067 (2019). [5] S. Meckler, et al., Physical Review Letters, Vol. 103, p. 157201 (2009). [6] S. Heinze, et al., Nature Physics, Vol. 7, pp. 713-718 (2011). [7] P. Muralt, D. Pohl, Applied Physics Letters, Vol. 48, pp. 514-516 (1986).



Schematic of the experimental method. The tip-sample potential, U_{th}, generated by the heating of the STM tip with an external laser, is modulated by the magnetic state of the tunnel junction.



Map of atomic-scale magneto-Seebeck coefficients on the Fe double-layer on W(110), showing the characteristic alternating out-of-plane domain pattern. Image taken using a bulk Cr tip at T_{STM} = 50 K.

Session EG
VOLTAGE-CONTROLLED MAGNETIC ANISOTROPY AND SWITCHING II

Ilya Krivorotov, Chair
University of California, Irvine, Irvine, CA, United States

CONTRIBUTED PAPERS

8:30

EG-01. Higher Order Magnetic Anisotropy in a Perpendicularly Magnetized Epitaxial Ultrathin Fe Layer under Various Applied Voltage. *A. Sugihara*[1], T. Nozaki[1], H. Kubota[1], H. Imamura[1], A. Fukushima[1], K. Yakushiji[1] and S. Yuasa[1] *1. National Institute of Advanced Industrial Science and Technology, Tsukuba, Japan*

Recently, voltage-controlled magnetic anisotropy (VCMA) effect at a ferromagnetic metal/dielectric material interface attracts much attention as the key technology for voltage-torque magnetic random access memory (MRAM). For the stable operation, VCMA coefficient ξ is required to be 600-1500 fJ/Vm.[1)] However, demonstrated ξ value (≲290 fJ/Vm) in magnetic tunnel junctions (MTJs) is much lower than the required value and its improvement is the current main issue. To make a strategy to improve ξ value, we need more systematic studies on the relationship between magnetic anisotropy and VCMA effect which give clues to clarify the mechanism of VCMA effect. In this study, we investigated the thickness and applied voltage dependences of first and second order magnetic anisotropy, K_1 and K_2 respectively, in an ultrathin Fe film. A fully epitaxial MTJ consisting of Cr buffer/ultrathin Fe free layer (t_{Fe})/MgO barrier (2.3 nm)/Fe pinned layer (10 nm) was grown on an MgO(001) single crystal substrate. In this film, easy axis of the free layer is perpendicular and that of the pinned layer is in-plane. The film was fabricated into micrometer-sized devices to measure tunnel magnetoresistance (TMR) curves under the application of in-plane magnetic fields and various electrical voltages (V) at room temperature. K_1 and K_2 were evaluated with Sucksmith-Thompson method[2)] from magnetization curves given from the TMR curves. Figure shows V dependence of K_1, K_2, K_1+K_2, intrinsic K_1 (K_{1int}), and effective uniaxial magnetic anisotropy $K_{u,\,eff}$ evaluated by the area method for t_{Fe} of (a) 0.40 nm and (b) 0.64 nm. They show clearly different trend that all the magnetic anisotropy constants have strong dependence on V at t_{Fe} = 0.40 nm while have virtually no dependence on V at t_{Fe} = 0.64 nm. We can also find that change in K_1 term is partly compensated by that in K_2 term at t_{Fe} = 0.40 nm. ξ value in the K_1 term reaches -600 fJ/Vm, being two times higher than that of effective one observed in the Cr/Fe/MgO systems.[3)] These results imply that individual control of K_1 and K_2 is the key factor for enhancement of the VCMA coefficient.

1) T. Nozaki, T. Yamamoto, S. Miwa, M. Tsujikawa, M. Shirai, S. Yuasa, and Y. Suzuki, Micromachines 10, 327 (2019). 2) W. Sucksmith, and J. E. Thompson, Proc. R. London A 225, 362 (1954). 3) T. Nozaki, A. Kozioł-Rachwał, W. Skowronski, V. Zayets, Y. Shiota, S. Tamaru, H. Kubota, A. Fukushima, S. Yuasa, and Y. Suzuki, Phys. Rev. Appl. 5, 044006 (2016).

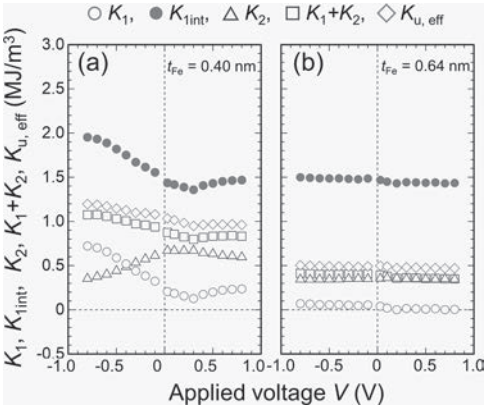


Fig. V dependence of K_1, K_2, K_1+K_2, K_1 (K_{1int}), and $K_{u,\,eff}$ for t_{Fe} of (a) 0.40 nm and (b) 0.64 nm.

8:42

EG-02. Voltage-controlled tunability of threshold current and frequency in spin Hall nano-oscillators. *H. Fulara*[1,2], M. Zahedinejad[1], R. Khymyn[1,2], M. Dvornik[1], S. Fukami[3], S. Kanai[3], H. Ohno[3] and J. Åkerman[1,2] *1. Department of Physics, University of Gothenburg, Gothenburg, Sweden; 2. NanOsc AB, Kista, Sweden; 3. Laboratory for Nanoelectronics and Spintronics, Research Institute of Electrical Communication, Tohoku University, Sendai, Japan*

Spin Hall nano-oscillators (SHNOs) have recently emerged as one of the most promising spintronics devices as they are CMOS compatible tunable microwave nanoscale sources and exhibit robust mutual synchronization phenomena both in long chains and two-dimensional arrays desired for neuromorphic computing applications [1,2]. However, more complex cognitive tasks in neuromorphic vowel recognition have been limited so far due to the lack of fine control over an individual SHNO of these synchronized networks [3]. It would be highly advantageous if an energy efficient route such as electrostatic gating can potentially manipulate the device functionalities in order to perform more complex tasks using synchronized SHNO networks for novel applications. Here we demonstrate how electrostatic gating can substantially modulate the operational characteristics, such as threshold current and auto-oscillation frequency, in nano-constriction based W(5nm)/CoFeB(1.7nm)/MgO(2nm) electrically gated SHNOs. High frequency microwave measurements carried out in SHNO devices clearly exhibit a large overall modulation of about 22% in threshold current with ΔV_G = 4V and frequency tunability with a rate of 12 MHz/V (see Fig. 1). Our detailed analysis employing spin-torque ferromagnetic resonance (ST-FMR) measurements suggest that the observed noticeable tunabilities are caused by the voltage-controlled Gilbert damping constant [4], interfacial magnetic anisotropy [5], and spin Hall efficiency in our SHNOs. The unusual observation of simultaneous achievement of large spin Hall efficiency and low damping constant contrary to spin-transparency models is indicative of voltage controlled reversible changes in the electronic structure at the

CoFeB/MgO interface. Our findings pave a way for an energy efficient fine control of individual oscillators in chains or arrays of SHNOs manipulating the synchronization behavior for neuromorphic computing applications [3].

[1] A. A. Awad, P. Dürrenfeld, A. Houshang, M. Dvornik, E. Iacocca, R. K. Dumas, and J. Åkerman, Nat. Phys. 13, 292-299 (2017). [2] M. Zahedinejad, A. A. Awad, S. Muralidhar, R. Khymyn, H. Fulara, H. Mazraati, M. Dvornik, and J. Åkerman, arXiv preprint arXiv:1812.09630 (2018). [3] M. Romera, P. Talatchian, S. Tsunegi, F. A. Araujo, V. Cros, P. Bortolotti, J. Trastoy, K. Yakushiji, A. Fukushima, H. Kubota, S. Yuasa, M. Ernoult, D. Vodenicarevic, T. Hirtzlin, N. Locatelli, D. Querlioz, and J. Grollier, Nature 563, 230 (2018). [4] A. Okada, S. Kanai, M. Yamanouchi, S. Ikeda, F. Matsukura, and H. Ohno, Appl. Phys. Lett. 105, 052415 (2014). [5] M. Endo, S. Kanai, S. Ikeda, F. Matsukura, and H. Ohno, Appl. Phys. Lett. 96, 212503 (2010).

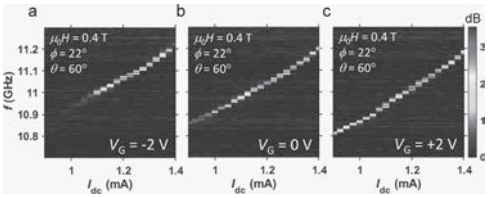


Fig. 1: Spin-wave auto-oscillations vs. current on an electrically gated w = 150 nm SHNO device, showing a tunability of both threshold current and frequency with different gate voltages (a) V_G= -2 V, (b) V_G= 0 V and (c) V_G= +2 V.

8:54

EG-03. Pseudo-magnetization as a New Order Parameter for Voltage Controlled Magnetism. *O. Hassan*[1], K.Y. Camsari[1] and S. Datta[1]
1. Electrical and Computer Engineering, Purdue University, West Lafayette, IN, United States

Traditional spintronic devices process information by encoding it in the orientation of magnetization. This requires a write operation that ensures a deterministic 180° switching of magnetization direction to flip "0" to "1". On the other hand, voltage controlled magnetism (VCM) by voltage control of magnetic anisotropy or by synthetic multiferroics naturally lead to ±90° switching of magnetization, that necessitates assisting mechanisms such as spin-transfer-torque or magnetic fields in addition to VCM. Here, we show how a new order parameter which we call *pseudo-magnetization*, that encodes magnetic anisotropy information rather than magnetization, combined with the unique characteristics of low barrier nanomagnets (LBM) [1] can be used for applications in memory and unconventional computing paradigms. Using an experimentally established circuit model [2] that describes the physics of synthetic multiferroics such as coupled magnetostrictive and piezoelectric materials (for example PMN-PT/CoFeB) we show how pseudo-magnetization can be imprinted and read-out directly by electrical voltage [3,4] without the use of magnetic tunnel junctions.

[1] O. Hassan, R. Faria, K.Y. Camsari, J.Z. Sun, and S. Datta, IEEE Magnetics Letters, Vol. 10, pp.1-5 (2019) [2] K.Y. Camsari, R. Faria, O. Hassan, B.M. Sutton, and S. Datta, Physical Review Applied, Vol. 9(4), p.044020 (2018) [3] A. Klimov, N. Tiercelin, Y. Dusch, S. Giordano, T. Mathurin, P. Pernod, V. Preobrazhensky, A. Churbanov, and S. Nikitov, Applied Physics Letters, Vol. 110(22), p.222401 (2017) [4] T. Shen, V. Ostwal, K.Y. Camsari, and J. Appenzeller, arXiv preprint (arXiv:1901.01368) (2019)

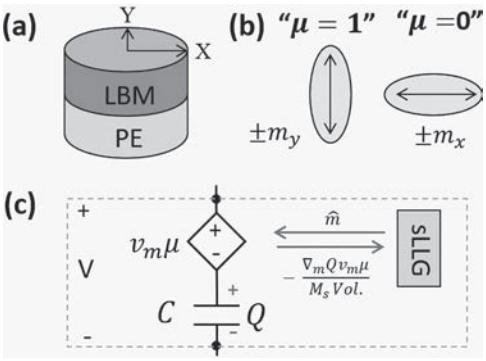


Fig.1 Schematic representation of (a) coupled low barrier nanomagnet (LBM) and piezoelectric (PE) synthetic multiferroic structure with (b) *pseudo-magnetization* states (μ). (c) Equivalent circuit model of the structure where v_m is the back-voltage due magnetoelectric effect and Q is the resulting μ dependent variable charge on the piezoelectric capacitor C.

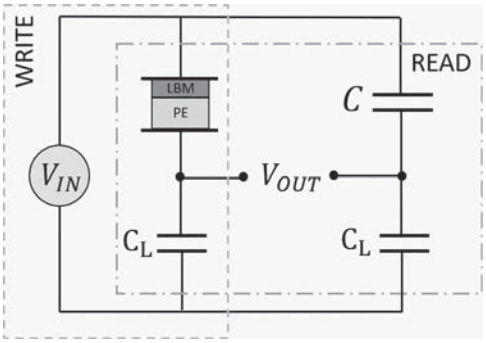


Fig. 2 Electric circuit for read and write operation. Write operation is achieved through input voltage V_{IN}, and the information is read through the V_{OUT} of the bridge circuit.

INVITED PAPER

9:06

EG-04. Voltage-induced dynamic magnetization switching with low write error rate. *T. Nozaki*[1], T. Yamamoto[1], H. Imamura[1], M. Endo[2], T. Nozaki[1], M. Konoto[1], H. Ohmori[2], Y. Higo[2], H. Kubota[1], A. Fukushima[1], M. Hosomi[2] and Y. Suzuki[1,3] *1. Spintronics Research Center, AIST, Tsukuba, Japan; 2. Sony Semiconductor Solutions Corp., Atsugi, Japan; 3. Graduate School of Engineering Science, Osaka Univ., Toyonaka, Japan*

Dynamic magnetization switching using a voltage-controlled magnetic anisotropy (VCMA) effect is an ultimate writing technology for future spintronic devices, such as voltage-torque MRAM. We have performed fundamental demonstrations of the VCMA effect in fully solid state devices[1]*, repeatable voltage-induced dynamic switching*[2] *and large enhancement of VCMA effect by an introduction of heavy metal materials*[3]*. An important remaining technical issue for developing a voltage-torque MRAM is the demonstration of low write error rate (WER).* In this work, we performed systematic investigations to realize the reliable switching from the viewpoints of materials design and the electrical control of spin dynamics. Macro-spin model simulation revealed that high thermal stability, *i.e.* high perpendicular magnetic anisotropy (PMA), and low damping constant are key parameters to suppress the write error[4]. Firstly, in conventional CoFeB/MgO based magnetic tunnel junctions, we maximized the PMA and VCMA coefficient by optimizing the CoFe composition and post-annealing process[5].

Figure 1 shows an evaluation example of pulse duration dependence of WER for the MTJ with the free layer of 1.1 nm-thick $(Co_{50}Fe_{50})_{80}B_{20}$ post-annealed at 250°C. WER of lower than 10^{-6} has been achieved by a single pulse voltage application. We also found that WER can be reduced by intentional control of pulse shape[6]. For example, Figure 2 shows the rise- and fall- time dependence of WER. Introduction of fall-time of 0.15 ns resulted in the reduction of WER. Optimal fall-time, which causes the uncompensated PMA, can suppress the relaxation dynamics after the switching process, leading to the reduction in the WER. For further reduction in the WER, enhancement in the VCMA coefficient is also demanded. Recent activities on the materials design using a heavy metal doping technique will also be introduced. Large VCMA coefficient surpassing -350 fJ/Vm has been observed in the Ir-doped Fe layer with an introduction of optimized CoFe termination layer.

[1] T. Maruyama *et al. Nat. Nanotechnol. 4, 158 (2009).* [2] Y. Shiota *et al. Nat. Mater.* 11, 39 (2012). [3] T. Nozaki *et al. NPG Asia Mater.* 9, e451 (2017). [4] Y. Shiota *et al. Appl. Phys. Exp.* 9, 013001 (2016). [5] T. Yamamoto *et al. J. Phys. D: Appl. Phys.* 52, 164001 (2019). [6] T. Yamamoto *et al. Phys. Rev. Appl.* 11, 014013 (2019).

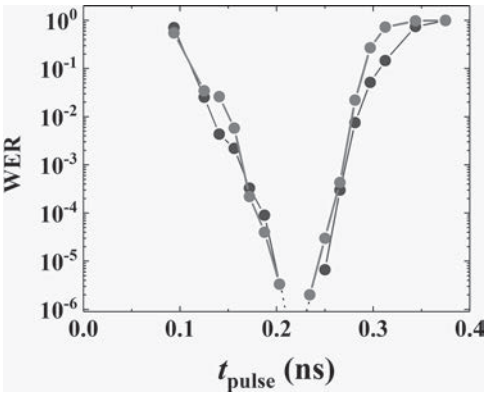


Figure 1 Pulse duration time dependence of WER for the voltage-induced dynamic switching

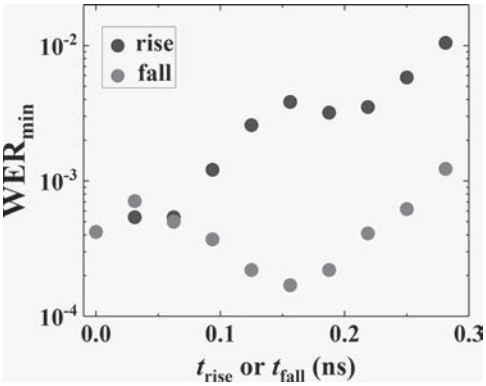


Figure 2 Influence of rise- and fall-time for the writing pulse on the minimum WER

CONTRIBUTED PAPERS

9:42

EG-05. Voltage-torque-driven magnetization switching using microwave-superimposed voltage pulse. *T. Yamamoto*[1], T. Nozaki[1], H. Imamura[1], S. Tamaru[1], K. Yakushiji[1], H. Kubota[1], A. Fukushima[1], Y. Suzuki[1,2] and S. Yuasa[1] *1. Spintronics Research Center, National Institute of Advanced Industrial Science and Technology, Tsukuba, Japan; 2. Graduate School of Engineering Science, Osaka University, Toyonaka, Japan*

Voltage-torque (VT) provides unique ways of manipulating the magnetization in ferromagnetic thin-films, as exemplified by the induction of ferromagnetic resonance (FMR) [1] and magnetization switching [2]. Since the VT-driven magnetization switching is mediated by magnetization precession around an effective field, the switching probability (P_{sw}) exhibits a periodic oscillation as a function of write pulse width. However, the magnetization damping gradually reduces the precession angle and thus it is generally difficult to achieve a well-controlled magnetization switching using a long write pulse. In this work, we tackle this technological issue by attempting to *swing* the magnetization using the VT. We show that the VT generated from a microwave voltage effectively counteracts against the magnetization damping and that substantially improves P_{sw} over a wide range of pulse width. The VT-driven magnetization switching is investigated for a CoFeB/MgO/CoFeB magnetic tunnel junction (MTJ). Microwave voltages as well as square voltage pulses are simultaneously generated by using an arbitrary waveform generator. We employed waveform correction procedure as described in Ref. [3] to ensure that the waveform applied to the MTJ becomes just as we designed. Figure 1 displays the result of VT-driven magnetization switching using microwave-superimposed voltage pulses. As expected from the VT-driven FMR experiment [1], a substantial improvement of P_{sw} is obtained when f is set to the FMR frequency ($f = f_0$). However, the most remarkable improvement of P_{sw} is observed for $f = 2f_0$. We employ a simple model to explain the experimental observations, and also show that the VT can actually swing the magnetization with the utmost efficiency when $f = 2f_0$. This work was partly supported by ImPACT Program of Council for Science, Technology.

[1] Y. Shiota et al., *Nat. Mater.*, Vol.11, p.39 (2012). [2] T. Nozaki et al., *Nat. Phys.*, Vol.8, p.491 (2012). [3] S. Tamaru et al., *Jpn. J. Appl. Phys.*, Vol.57, p.073002 (2018).

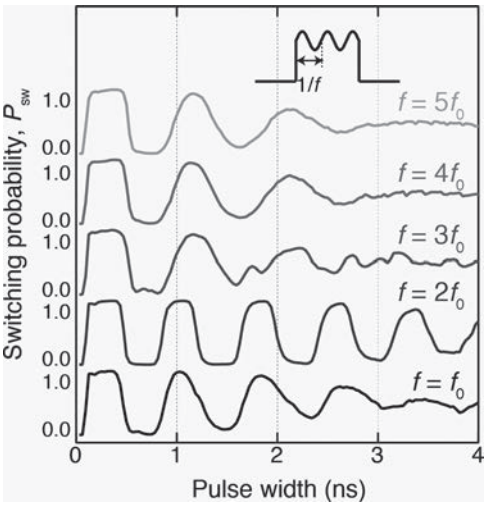


Figure 1

9:54

EG-06. Voltage Induced 180 Degree Switching of the Néel Vector in a Ferrimagnet by Solid-State Ionic Gating. *M. Huang*[1], L.M. Caretta[1], J. Bartell[1] and G. Beach[1] *1. Department of Materials Science and Engineering, Massachusetts Institute of Technology, Cambridge, MA, United States*

The rapid increase of data being generated nowadays requires denser and more energy efficient data storage than is currently available. Controlling magnetism by an electric field is a promising way to manipulate magnetism that could enable ultralow-power, high-density magnetic memory and logic devices [1], [2]. However, 180 degree switching of magnetization is not straightforward because the electric field does not break time-reversal symmetry. Motivated by the recent discovery that hydrogen pumping in an solid state structure can be used to control magnetic anisotropy in metallic heterostructures [3], here we examine the effects of proton gating on ferrimagnetic order in rare earth-transition metal alloys. Prior work has shown that hydrogen loading into ferrimagnets can control their compensation temperature [4]. Here we show that the dominant lattice of GdCo ferrimagnetic thin films at room temperature can be reversibly toggled by hydrogen loading/unloading into the material controlled through a gate voltage in an all-solid-state structure. We examine Pd(6nm)/CoGd(6nm)/Pd(10nm)/GdOx(30nm)/Au(3nm) structures with perpendicular magnetic anisotropy. In these structures, a positive gate bias applied to the top electrode generates protons through hydrolysis of ambient moisture in the air, as shown previously [3]. We find that proton injection into the CoGd leads to a significant decrease in the compensation temperature, which we attribute to a decrease in the Gd moment due to hydrogen localization near the rare earth. With a fixed perpendicular bias field, we show that a gate voltage can induce 180° magnetic switching of the sublattices by shifting the magnetic compensation temperature above and below room temperature. We show that this switching can occur on relatively fast timescales and is reversible over at least 100 cycles. The study provides a new direction in magneto-ionic control of magnetism and a new route towards low power nonvolatile magnetic memory.

[1] F. Matsukura, Y. Tokura, and H. Ohno, *Nat. Nanotechnol.*, vol. 10, no. 3, pp. 209–220 (2015). [2] E. Y. Tsymbal, *Nat. Mater.*, vol. 11, no. 1, pp. 12–13 (2011). [3] A. J. Tan *et al.*, *Nat. Mater.*, vol. 18, no. 1, pp. 35–41 (2019). [4] J. H. Schelleng, D. W. Forester, P. Lubitz, and C. Vittoria, *J. Appl. Phys.*, vol. 55, no. 6, pp. 1805–1807 (1984).

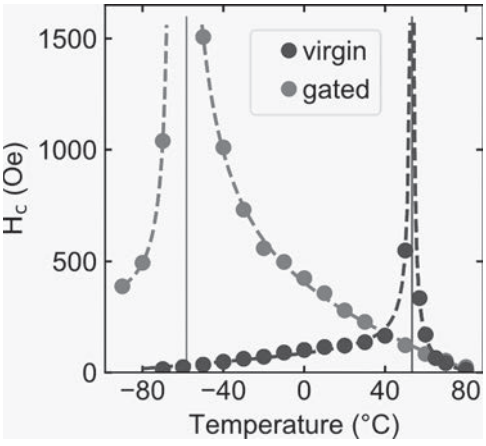


Fig.1 H_c versus temperature showing compensation temperature change of CoGd by solid-state ionic gating.

10:06

EG-07. Highly efficient magneto-ionic control of interfacial magnetism using YSZ gate oxide. *K. Lee*[1], S. Jo[1], J. Park[2], A. Tan[3], J. Son[2], J. Chang[1], G. Beach[3] and S. Woo[4] *1. Center for Spintronics, Korea Institute of Science and Technology, Seoul, The Republic of Korea; 2. High Temperature Energy Materials Research Center, Korea Institute of Science and Technology, Seoul, The Republic of Korea; 3. Department of Materials Science and Engineering, Massachusetts Institute of Technology, Cambridge, MA, United States; 4. TJ Watson Research Center, IBM, Yorktown Heights, NY, United States*

Voltage control of magnetism has been a forefront subject of spintronics research for many years[1,2]. Among the few suggested methods, magneto-ionic control of magnetism has demonstrated significant modulation of magnetic anisotropy on the order of ~ 1 erg cm^{-2} [3,4]. However, prior work[3-5] utilized voltage-induced oxygen migration, which suffered from irreversible oxidation damage[5] and high operation temperature[4]. Recently, it has been demonstrated that, hydrogen-based magneto-ionic devices could offer enhanced device capabilities such as high reliability (>2000 cycles) and fast switching (~100 ms) at room temperature (RT).[6] In these devices, solid-state electrochemical water splitting using atmospheric humidity was shown[6] to provide a source of mobile protons that could be driven through a gate oxide to reversibly switch the magnetic properties. Here we demonstrate that the performance, in particular "switching speed", of hydrogen-based magneto-ionic devices can be significantly enhanced using yttria-stabilized zirconia (YSZ) gate oxide. We first compared the device switching efficiencies using various oxide materials, including gadolinium-doped ceria (GDC), barium cerium yttrium zirconate (BZCY) and YSZ, which are all well-known proton conducting oxides. Hydrogen-induced anisotropy modulation was observed in all devices (Fig. 1), revealing the generality of this mechanism. However, switching speed was oxide-dependent and the fastest for YSZ. We then systematically study the YSZ thickness-dependent switching speed, and as shown in Fig. 2, we demonstrate sub-5 ms magnetic anisotropy switching, exceeding the temporal resolution of current measurement set-up and exhibiting ~ two orders of magnitude faster than the state-of-the-art device reported to date at RT.[6] In this talk, we will also discuss further engineering that could push the switching speed down to the 10~100 times of nanoseconds.

1. Matsukura, F. *et al. Nat. Nanotechnol.* 10, 209–220 (2015). 2. Song, C. *et al. Prog. Mater. Sci.* 87, 33–82 (2017). 3. Bauer, U. *et al. Nat. Mater.* 14, 174–181 (2015). 4. Bi, C. *et al. Phys. Rev. Lett.* 113, 267202 (2014). 5. Gilbert, D. A. *et al. Nat. Commun.* 7, 12264 (2016). 6. Tan, A. J. *et al. Nat. Mater.* 18, 35-41 (2019).

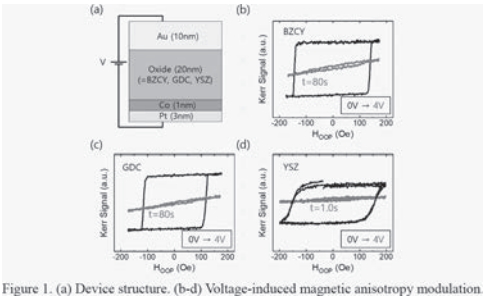


Figure 1. (a) Device structure. (b-d) Voltage-induced magnetic anisotropy modulation.

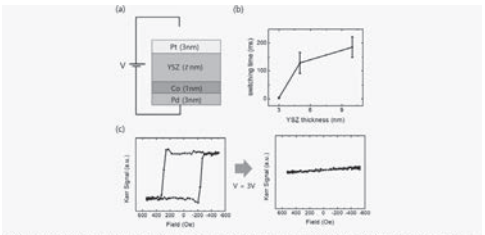


Figure 2. (a) Device structure. (b) Magnetization switching speed as a function of YSZ gate oxide thickness. Note that magnetization switching refers 90-degree rotation of spins from out-of-plane to in-plane. (c) Out-of-plane hysteresis loops upon the application of V=6V.

10:18

EG-08. Impact of spin transfer torque on the write error rate of a voltage-torque MRAM. *H. Imamura*[1] and R. Matsumoto[1] *1. Spintronics RC, AIST, Tsukuba, Japan*

Voltage-torque (VT) switching is an attractive method for low-power writing of a magnetoresistive random access memory (MRAM), which is based on voltage control of magnetic anisotropy [1-7]. The basic structure of a magnetic tunnel junction for VT MRAM is the same as that for spint-ransfer-turque (STT) based MRAM except for the value of resistance-area product. VT MRAM has much larger resistance-area product than STT MRAM to suppress the current density, or energy loss by Joule heating at the operating voltage. Although Joule heating reduces as the resistance increases, the read time increases with increase of the resistance because it is determined by the *RC* time constant, where *R* and *C* are the resistance and capacitance of the MRAM cell, respectively. The resistance of the MRAM cell should be designed to balance the energy consumption and read time. The write error rate (WER) is another key metric to characterize the performance of the MRAM cell. The WER of STT-MRAM can be lowered below 10^{-11} by increasing the applied current density [9]. The WER of VT MRAM is still higher than that of STT MRAM, which ranges form 10^{-3} to 10^{-5} [6-8]. Attempts are being made to reduce the WER by improving materials [7] as well as by shaping voltage pulse [8]. Until now the WER of VT MRAM has been studied in the high-resistance condition to eliminate the effects of STT. However, for practical application, the resistance should be lowered to decrease the read time. It is important to know the minimum current density (J) below which the impact of STT on the WER is negligible. Here we theoretically analyze the WER of a perpendicularly magnetized VT MRAM with special attention to the impact of STT [10]. We show that the STT assists or suppresses the precessional motion of the magnetization depending on the direction of the initial state, i.e. up-polarized or down-polarized. There is a characteristic value of the current density above which the precessional motion, and therefore magnetization switching, is forbidden by the STT for one direction of the switching. We found that for typical material parameters the WER is insensitive to STT below a current density of 10^{10} A/m^2 as shownin Fig. 1.

[1] M. Weisheit, et al., Science 315, 349 (2007). [2] T. Maruyama, et al., Nature Nanotechnology 4, 158 (2009). [3] T. Nozaki, et al., Applied Physics Express 7, 093005 (2014). [4] C. Grezes, et al., Applied Physics Letters 108, 3 (2016). [5] S. Kanai, et al., Applied Physics Letters 108, 2014 (2016). [6] Y. Shiota, et al., Applied Physics Express 9, 013001 (2016). [7] Y. Shiota, et al., Applied Physics Letters 111, 2 (2017). [8] T. Yamamoto, et al., Physical Review Applied 11, 014013 (2019). [9] J. J. Nowak, et al., IEEE Magnetics Let- ters 2, 2 (2011). [10] H. Imamura and R. Matsumoto, Physical Review Applied 11, 064019 (2019)

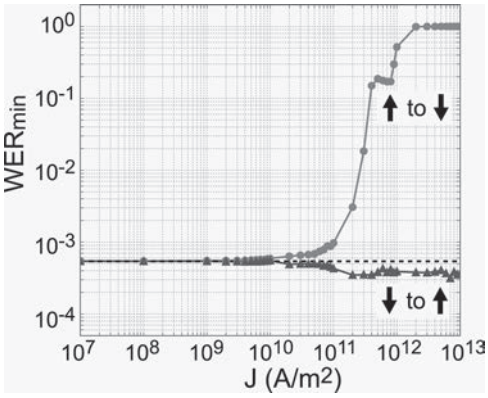


Fig.1 Current density dependence of WER.

10:30

EG-09. Temperature dependence of VCMA in $SrTiO_3$\Co\Pt trilayers: insights into the mechanism. *B.F. Vermeulen*[1,2], J. Swerts[2], S. Couet[2], M.I. Popovici[2], Y. Wu[5,2], W. Kim[2], G.S. Kar[2], P.J. Roussel[2], J. Vande Vondel[3], K. Temst[4], G. Groeseneken[5,2] and K.M. Martens[1,2] *1. Laboratorium voor Halfgeleiderfysica, KULeuven, Leuven, Belgium; 2. imec, Leuven, Belgium; 3. Laboratory for Solid State Physics and Magnetism, KULeuven, Leuven, Belgium; 4. Instituut voor Kern- en Stralingsfysica, KULeuven, Leuven, Belgium; 5. Department of Electrical Engineering, KULeuven, Leuven, Belgium*

The Voltage Control of Magnetic Anisotropy (VCMA) effect has been widely demonstrated using MgO as the functional oxide [1, 2]. Recently, we showed an increase of the VCMA effect up to above 200 fJ/Vm using a $SrTiO_3$\Co\Pt trilayer. The ultrathin (10 nm) layer of $SrTiO_3$ is grown using Atomic Layer Deposition and has a relative permittivity k around 40. However, the mechanism driving the anisotropy change in $SrTiO_3$\Co\Pt remains unclear. One hypothesis may be that the larger permittivity of $SrTiO_3$ enhances the accumulated charge, and hence the VCMA [3]. To understand the mechanism, we measure the VCMA effect in $SrTiO_3$\Co\Pt trilayers as a function of decreasing temperature, between 300K and 5K. At first, the effect decreases from the room temperature value of 186 fJ/Vm down to 165 fJ/Vm at 100K (see Fig. 1). Below 100K, the VCMA effect drops more sharply, down to 30 fJ/Vm at 50K and becomes indistinguishable below. The decrease of the VCMA effect strength is unexpected according to previous reports [4]. Capacitance-Voltage (CV) measurements were performed to measure the permittivity k of the STO as a function of decreasing temperature (Fig. 1). They show that the k-value also decreases by 5% down to 77K. The decrease of the permittivity is ascribed to de-activation of defects in the ALD- grown STO layer, which leads to a decrease in the apparent dielectric constant [5]. The decrease of the VCMA amplitude is not proportional to the change in the permittivity, which shows that an additional effect is at play; in particular, the sudden drop at the lowest temperatures suggests that another mechanism arises and suppresses VCMA altogether. The impact of the temperature onto the band structure at the STO\Co interface may play a crucial role in the effect reported here.

[1] Maruyama, T. et al. Nature Nanotechnology 4, 158 (2009) [2] Kita, K. et al., JAP 112, 033919 (2012) [3] Duan et al., PRL 101, 033919 (2008) [4] Nakazawa, S. et al., APL 110, 062406 (2017) [5] Padovani, IEEE TED 66, 1892 (2019)

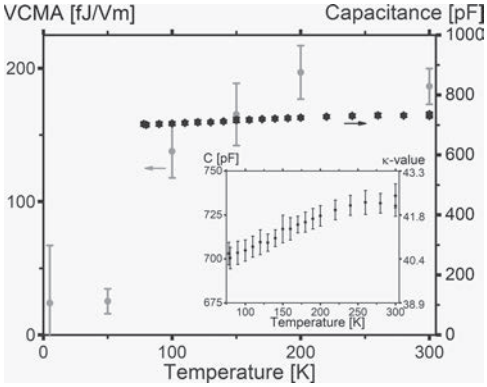


Fig.1 The VCMA effect decreases sharply with decreasing temperature, below 100K. The capacitance and hence the permittivity k decrease as well, albeit to a lesser extent.

10:42

EG-10. Electric-field induced spin pumping in an in-plane magnetized CoFeB/MgO junction. *A. Deka*[1], B. Rana[2], R. Anami[1], K. Miura[3], H. Takahashi[3], Y. Otani[4,2] and Y. Fukuma[1,2] *1. Computer Science and Systems Engineering, Kyushu Institute of Technology, Iizuka, Japan; 2. Center for Emergent Matter Science, RIKEN, Wako, Japan; 3. Research and Development Group, Hitachi Ltd., Kokubunji, Japan; 4. Institute for Solid State Physics, University of Tokyo, Chiba, Japan*

Recently the possibility of controlling magnetization of a ferromagnetic metal by applying an electric-field at its interface was demonstrated by Weisheit *et al* [1]. It has the potential to eliminate the need for high charge current densities of the order ~1×10^{11} Am^{-2} that is typically required to control magnetization in spin transfer torque or spin orbit torque experiments. However, voltage torque on magnetization is zero for an in-plane or out-of-plane magnetized films. So an external bias field is always needed to tilt the magnetization away from the film plane or normal [2]. Here we will present our observation that by inducing an interfacial in-plane magnetic anisotropy, we can have a non-zero voltage torque in an in-plane magnetized CoFeB film. This enables us to demonstrate electric-field induced spin pumping from an in-plane magnetized CoFeB thin film into an adjacent heavy metal (Ta) layer. As shown in Fig. 1, the resulting DC inverse spin Hall voltage obtained from the electric-field induced spin pumping is observed to be over 10 times higher compared with the spin pumping induced by magnetic fields [3]. Such a control of the interfacial magnetic anisotropy proposes a new design for future ultralow power spintronic devices, wherein the excitation and switching of magnetization can be controlled purely by electric-fields.

1. M. Weisheit, *et al.,* Science, vol 315, p. 349–351 (2007). 2. T. Nozaki, *et al.,* Nat. Phys., vol 8, p. 491–496 (2012). 3. Y. Tserkovnyak, A. Brataas and G. E. W. Bauer, Phys. Rev. Lett., vol 88, p. 117601 (2002).

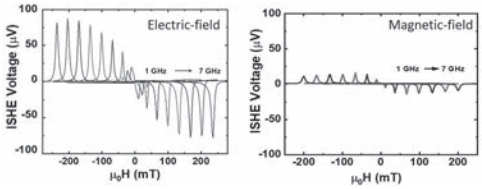


Figure 1

10:54

EG-11. Study of GHz VCMA Precessional Switching Speed in BEOL-Compatible Perpendicular MTJ. *Y. Wu*[1,2], W. Kim[1], S. Couet[1], K. Garello[1], S. Rao[1], B.F. Vermeulen[1,2], S. Van Beek[1], S. Kundu[1], S. Houshmand Sharifi[1], F. Yasin[1], J. Swerts[1], D. Crotti[1], J. Van Houdt[1,2], G. Groeseneken[1,2] and G.S. Kar[1] *1. IMEC, Leuven, Belgium; 2. KULeuven, Leuven, Belgium*

Magnetization switching by voltage control of magnetic anisotropy (VCMA) effect allows for lower power and ultra-fast writing (sub-ns) of perpendicular magnetic tunnel junction (pMTJ) devices [1,2]. VCMA functions in applying electric-field (*EF*) that removes the energy barrier (E_b) to induce precessional switching [1]. The precession frequency f_P, in other words, the switching speed ($V_S = 2f_P$), varies with both *EF* and in-plane magnetic field (B_{IP}) [2,3]. In this work, we use BEOL-compatible MgO/CoFeB/Ta based pMTJ devices to study their characteristics of VCMA-induced precessional switching. We first measure the switching probability (P_S) distribution as a function of pulse width (*PW*). f_P is estimated by fitting the first period of P_S *vs. PW (see* Fig.1(a) inset). V_S is clearly characterized by two representative regimes. First, below the critical *EF* (EF_C), there is a non-precessional phase where switching occurs by thermal activation, hence no switching speed can be deduced. Second, above EF_C is the acceleration regime, in which higher *EF* increases progressively V_S (Fig. 1(a)). Such EF_C varies with B_{IP}, since B_{IP} contributes in lowering the energy barrier along its direction. This variation is also studied and examined by micromagnetic simulation (Fig. 1(b)). In the acceleration regime, a positive energy difference (ΔE) induces precessional switching, in which f_P is expressed as γB_{eff}. Additionally, there is a characteristic *EF* (EF_{C0}) that can remove E_b without assistance of B_{IP}. At such EF_{C0}, B_{IP} will contribute completely in executing precessional switching, where f_P can be approximated as γB_{IP}, and V_S is a characteristic speed of $2\gamma B_{IP}$. Both experimental and simulation results agree well with the prediction (Fig. 2). This work was supported by IMEC's Industrial Affiliation Program on MRAM devices.

[1] P. Khalili Amiri et al., IEEE Trans. Magn. 51(11), 3401507 (2015). [2] C. Grezes et al., Appl. Phys. Lett. 108, 012403 (2016) [3] C. Grezes et al., AIP Advances 6, 075014 (2016)

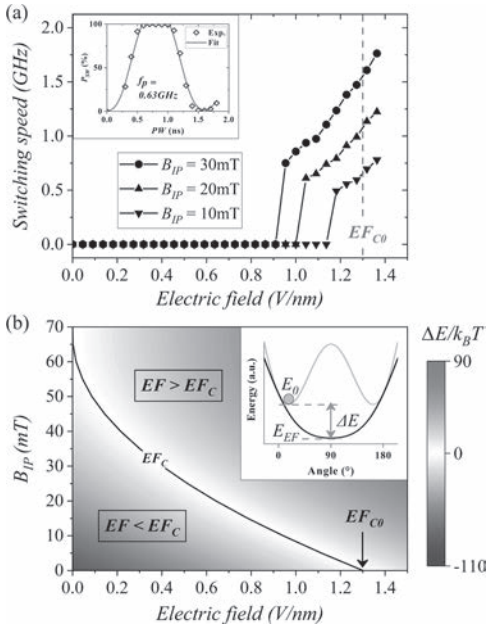


Fig. 1. (a) Experimental switching speeds as a function of *EF* at various B_{IP}. Inset: example of fitting f_P in experimental P_S vs. *PW*. (b) Simulation of ΔE ($=E_0-E_{EF}$). Inset: example of ΔE calculation, with gray and black curves being the energy diagram at *EF=0* and at *EF=1V/nm*, respectively.

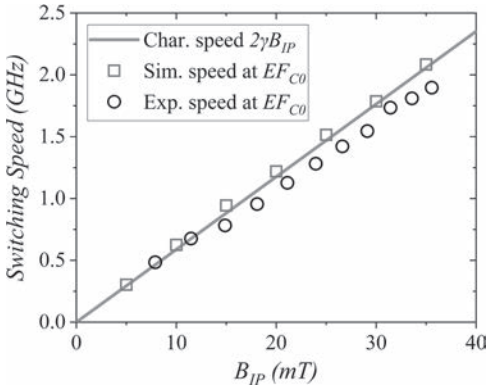


Fig. 2. Comparison of experimental and simulation switching speeds at EF_{C0} to the predicted characteristic speed.

11:06

EG-12. Voltage Tuning of Switching Probability in Voltage-controlled Switching. *A. Fukushima*[1], T. Yamamoto[1], T. Nozaki[1], K. Yakushiji[1], H. Kubota[1] and S. Yuasa[1] *1. Spintronics Research Center, National Institute of Advanced Industrial Science and Technology (AIST), Tsukuba, Japan*

We have developed a new type of random number generator (RNG), named spin dice, which employs stochastic switching events in MTJs [1]. In the case of voltage-controlled switching [2], switching of both directions, parallel (P) to antiparallel (AP), and AP to P, are caused by the same unipolar voltage pulse, and random numbers are generated by mixing the both switching results. In addition, when the switching probabilities of P to AP and AP to P have the same voltage dependence [3], average of the generated random numbers becomes nearly identical, as shown in Fig. 1(a), which shows that the change in switching probability is not directly related to the average of generated random numbers. In order to precisely measure the switching probability, classification of the switching events depending on the initial state (P or AP) is necessary, which however, becomes costly and complicated. By tuning the switching probability to 0.5, we divide the generated random numbers in every 2-bits and count the occurrence of 4-pattern (00, 01, 10, 11). For the ideal random numbers, the occurrence frequency of the 4-patterns should be the same. Figure 1(b) shows the voltage dependence of the occurrence of the 4-patterns. Contrary to voltage dependence of the average of generated random numbers, frequencies of the 4-patterns change linearly against the voltage and the voltage dependence of the frequency of (00, 11) has opposite sign to that of (10, 01). Consequently, it is possible to generate well balanced random numbers by tuning the occurrence frequency of the 4-patterns to be the same value 0.25. It is important for a well-balanced randomness source to tune the switching probability under the unipolar bias (voltage or magnetic field) where P to AP and AP to P switchings are mixed. Further, intentional control (manipulation) of the switching probability could be useful to realize a probabilistic computing element such as p-bit [4]. This work was funded by ImPACT Program of Council for Science, Technology and Innovation (Cabinet Office, Government of Japan).

[1] A. Fukushima *et al.*, Appl. Phys. Express 7, 083001 (2014). [2] Y. Shiota *et al.*, Nat. Mater. 11, 39 (2012). [3] A. Fukushima *et al.*, Intermag 2018, FC-08 (2018). [4] K. Y. Camsari *et al.*, Phys. Rev. X 7, 031014 (2017).

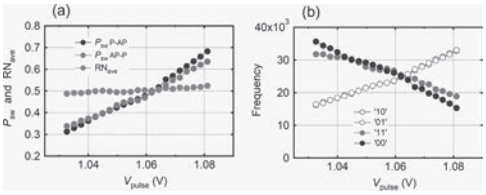


Fig. 1 (a) Voltage dependence of switching probability and average of the generated random numbers, (b) Voltage dependence of occurrence of the 4-patterns (00, 01, 10, 11).

11:18

EG-13. Giant Electric Field Modulation of Magnetism in Ferrimagnetic Heusler Heterostructures. Q. Sun[1], S. Kwon[1] and *N. Kioussis*[1] *1. California State University, Northridge, Northridge, CA, United States*

The demand for higher density, higher speed, and more energy-efficient magnetoelectric random access memory (MeRAM) requires the search of novel materials and magnetic tunnel junction stacks with voltage-controlled magnetic anisotropy (VCMA) efficiency greater than the 1000 fJ/(Vm) challenge.[1] To date, the realization of MeRAM relies primarily on ferromagnetic (FM) based heterostructures, which exhibit low perpendicular magnetic anisotropy (PMA) and low VCMA efficiency. On the other hand, the E-field manipulation of magnetism in *ferrimagnetic* Heusler nanojunctions, which are considered to be potential candidates in spintronic devices, remains unexplored thus far both theoretically and experimentally. In this talk, we will present predictions of ab initio electronic structure calculations of the VCMA of Ir/Mn_3Ga/MgO heterostructures, in which the ultrathin ferrimagnetic Mn_3Ga has the tetragonal DO_{22} structure.[2] We find that the Mn_{II}-Mn_{II}- (Mn_I-Ga-) terminated interfaces exhibit large out-of-plane (in-plane) magnetic anisotropy (MA). More importantly, the calculations reveal colossal PMA and VCMA efficiency of about one order of magnitude higher than the values reported today. We demonstrate that both the MA and VCMA depend critically on the heavy metal thickness. We also predict a sign reversal of the VCMA efficiency from the Mn_{II}-Mn_{II} to the Mn_I-Ga-terminated interface. We demonstrate that the dominant contribution to both the PMA and VCMA arises from the strong spin-orbit-coupling of Ir and the E-field induced shift of the Ir *d*-derived orbitals. These findings provide useful guiding rules in the design of more energy-efficient ferrimagnetic-based MeRAM devices. Supported by NSF Grant No. ERC TANMS-1160504

[1] Y. Shiota, T. Nozaki, F. Bonell, S. Murakami, T. Shinjo, and Y. Suzuki, Induction of coherent magnetization switching in a few atomic layers of FeCo using voltage pulses, Nat. Mater. 11, 39 (2012). [2] Rode, K. *et al.* Site-specific order and magnetism in tetragonal Mn_3Ga thin films. Phys. Rev. B 87, 184429 (2013).

Session EH
RARE-EARTH-FREE PERMANENT MAGNETS

Hideto Yanagihara, Chair
University of Tsukuba, Tsukuba, Japan

INVITED PAPER

8:30

EH-01. A New Generation of MnBi Permanent Magnets.
G.C. Hadjipanayis[1], A. Gabay[1] and J. Cui[2,3] *1. University of Delaware, Newark, DE, United States; 2. Iowa State University, Ames, IA, United States; 3. Ames Laboratory, Ames, IA, United States*

MnBi magnets, notable for the positive temperature coefficient of their coercivity, are recognized as promising rare-earth-free alternatives to the lower-grade rare-earth magnets, such as the bonded Nd-Fe-B magnets. The intrinsic magnetic properties of the key MnBi "low-temperature phase" (LTP) allow for a maximum energy product $(BH)_{max}$ up to 20 MGOe. The powder metallurgy approach using ball-milled fine powders has been nearly universally explored in numerous earlier studies – ultimately yielding MnBi powders with a nominal $(BH)_{max}$ up to 15 MGOe [1]. However, sintering of the fine MnBi powders into anisotropic magnets is accompanied by a partial loss of both the LTP and coercivity, so the $(BH)_{max}$ reported for the magnets sintered from single-crystal powders does not exceed 8.4 MGOe [2]. Here, we present a new approach to manufacturing of bulk MnBi magnets which involves neither the fine milling nor the lengthy homogenization process which is usually required to initially obtain the LTP. Instead, melt-spinning of the appropriately alloyed MnBi is used to generate nanograins of the "high-temperature phase" which later transform into larger, but still submicron LTP grains [3]. The melt-spun ribbons are compacted to a full density at the low temperature of 150 °C and then subjected to a short (less than an hour) annealing at 260-300 °C in a moderately strong magnetic field of 30 kOe to increase the LTP fraction to 97-98% and to partially align the easy magnetization directions of the LTP crystallites. The best magnets are characterized by LTP grains approximately 0.5 um in size and they exhibit at room temperature a remanence of 7 kG, a coercivity of 5 kOe and a $(BH)_{max}$ up to 11.5 MGOe; more importantly, the $(BH)_{max}$ remains greater or equal to 10 MGOe for the temperatures between 5 °C and 125 °C. We will discuss the development of the material based on the structural and thermal data and identify the research areas in need of further exploration. In particular, the observed negative correlation between the texture and the coercivity, which is hindering further improvement of the new MnBi magnets, remains poorly understood. The work was supported by the US DOE through grants EE0007794 and DE-FG02-90ER45413.

[1] Y.C. Chen, S. Sawatzki, S. Ener, H. Sepehri-Amin, A. Leineweber, G. Gregori, F. Qu, S. Muralidhar, T. Ohkubo, K. Hono, O. Gutfleisch, H. Kronmüller, G. Schütz, E. Goering, AIP Adv. 6 (2016) 125301. [2] N. Poudyal, X. Liu, W. Wang, V.V. Nguyen, Y. Ma, K. Gandha, K. Elkins, J.P. Liu, K. Sun, M.J. Kramer, J. Cui, AIP Adv. 6 (2016) 056004. [3] A.M. Gabay, G.C. Hadjipanayis, J. Cui, J. Alloys Compd. 792 (2019) 77.

CONTRIBUTED PAPERS

9:06

EH-02. The Effect of Sn Addition on the Magnetic and Physical Properties of Mn-Bi Magnetic Materials.
J. Park[1], Y. Yang[1], J. Kim[1] and C. Choi[1] *1. Functional Powder Material Department, Korea Institute of Materials Science, Changwon, The Republic of Korea*

Ferromagnetic low temperature phase (LTP) MnBi alloy possesses maximum energy product, $(BH)_{max}$, of about 17 MGOe at 290 K [1], therefore, LTP MnBi is a promising candidate to fill the gap between rare-earth and rare-earth free permanent magnets. However, the low phase transformation (PT) temperature and segregation of Mn from MnBi liquid at 446 °C [2] are the major obstacles to producing a high density bulk magnet for high efficiency sustainable energy applications. Therefore, in this work, we have fabricated Sn diffused MnBi powders and bulks at lower temperature than the PT temperature to prevent phase decomposition and increase the density. LTP MnBi powder was prepared by ingot casting using induction melting, followed by crushing, sieving, and magnetic separation. The obtained powder was then mixed with Sn submicron powder using low energy ball milling in ethanol. The mixed powder was dried in a glove box and annealed/hot pressed at 245 °C for 30 min to produce a high density Sn diffused LTP MnBi bulk magnetic materials. Figure 1 shows the Sn wt.% dependence of the density for the Sn diffused LTP MnBi bulk magnetic materials. The density increases with increasing Sn wt.% up to 2 %, then begin to decrease with increasing Sn content. It was found that the small amount of Sn preferentially reacts with remaining Bi, and excessive Sn reacts with MnBi. The variation of the Bi/MnBi phase ratio in Fig. 2 indicates that the increasing Sn content promotes the formation of LTP MnBi, therefore, results in the enhanced M_r/M_s ratio and $(BH)_{max}$. In this presentation, detailed experimental procedures and analyses of physical and magnetic properties of the Sn addition to MnBi alloy will be discussed.

[1] R. G. Pirich and D. J. Larson, Jr., Patent 4,784,703. 15 Nov. 1988. [2] J. Cui, J. P. Choi, and G. Li, J. Phys. Condens. Matter, vol. 26, p.064212 (2014).

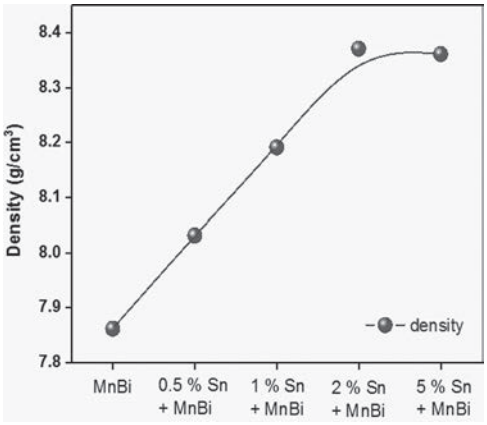


Fig. 1. Sn wt.% dependence of the density for MnBi/Sn bulk magnetic materials.

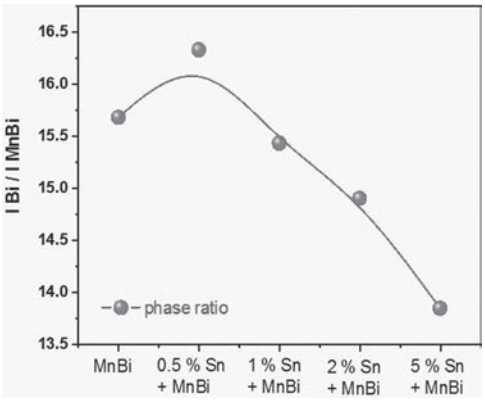


Fig. 2. Sn wt.% dependence of the Bi/MnBi ratio for MnBi/Sn bulk magnetic materials.

9:18

EH-03. Effect of Quench Rate on the Magnetic Properties of Cr Doped MnBi Melt Spun Ribbons. *K. Anand*[1], N. Christopher[1] and N. Singh[1]
1. Physico Mechanical Metrology Division, CSIR-National Physical Laboratory, Delhi, India

The ferromagnetic intermetallic compound MnBi in its low-temperature phase (LTP) has long been a material of interest, particularly in the field of rare-earth-free permanent magnet materials. However, because of the decomposition of LTP MnBi into $Mn_{1.08}Bi$ and liquid Bi upon heating to 628 K, its synthesis is a matter of concern. In view of the potential of melt spinning and the scope of optimizing various process parameters, the present study is focussed on the effect of quenching rate on $Mn_{47}Bi_{50}Cr_3$ ribbons. Addition of Cr to MnBi led to decoupling of structural and magnetic transition temperature, resulting in the formation of a stable compound. The ribbons produced via melt spinning at different wheel speeds of 20, 25, 30 and 35 Hz, were analyzed for its phase, microstructure and magnetic properties. Due to a higher rate of cooling induced on the melt, the crystallite size as determined from Scherer's formula decreased from 80 nm to 32 nm for the ribbons melt spun at 20Hz and 35Hz respectively. This was confirmed from the microscopic studies as well, where grain size as observed from scanning electron microscopy (Fig. 1) is found to be inversely proportional to wheel speed and cooling rate. This could be attributed to the high cooling rate causing an increased number of nucleation sites and reduced grain size, which in turn leads to a high value of coercivity. The maximum coercivity of 11.1 kOe and saturation magnetization of 55 emu/g is obtained for the ribbons melt spun at 25Hz (Fig. 2). This suggests that the initial grain size and the magnetic property of the ribbon depend on the crystal growth rate, heterogeneous nucleation frequency, and the time required for solidification on the surface. By optimizing the process parameters associated with melt spinning technique, high performance nanocrystalline $Mn_{47}Bi_{50}Cr_3$ alloy has been synthesized by carefully adjusting the wheel speed and thereby controlling the quench rate.

1 B.W. Roberts, Phys. Rev. 104, 607 (1956) 2 N.V. Rama Rao, G.C. Hadjipanayis, Journal of Alloys and Compounds, 629, 80–83 (2015) 3 Prabhakar R. Bandaru, Timothy D. Sands, Yukiko Kubota, Ernesto E. Marinero, Applied Physics Letters, 72, 18 (1998) 4 A. M. Gabay, G. C. Hadjipanayis, J. Cui, AIP Advances 8, 056702 (2018)

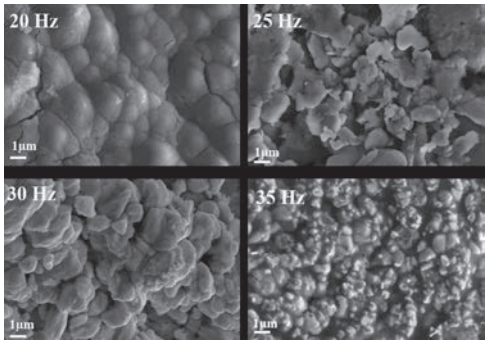


Fig. 1: SEM images of $Mn_{47}Bi_{50}Cr_3$ ribbons melt spun at various wheel speeds of 20, 25, 30, and 35 Hz, showing the effect of varying wheel speed on particle size and morphology

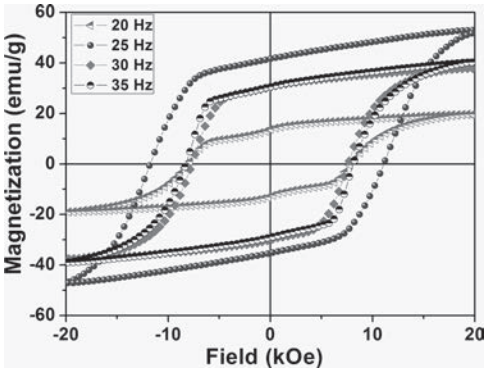


Fig. 2: Room temperature MH curve of $Mn_{47}Bi_{50}Cr_3$ ribbons melt spun at various wheel speeds of 20, 25, 30, and 35 Hz

9:30

EH-04. Phase Transformation and Large Coercivity in Severely Deformed MnAl Alloys Doped with B+N Elements. P. Si[1], H. Ge[1], *C. Choi*[2] and J. Du[3] *1. College of Materials Science & Engineering, China Jiliang University, Hangzhou, China; 2. Powder & Ceramic Division, Korea Institute of Materials Science, Changwon, The Republic of Korea; 3. School of Material Science & Engineering, Shanghai University, Shanghai, China*

The B-N-doped MnAl alloys were prepared by using induction melting and post annealing process. Elemental doping is usually employed to stabilize the metastable binary MnAl alloys [1, 2]. It has been well-known that C can stabilize the ferromagnetic τ-phase MnAl effectively. The boron-doped τ-MnAl has also been studied previously [3, 4]. Herein we show that the co-doping of B+N elements can also stabilize the τ-phase MnAl, which were obtained by controlling the cooling process of ε-phase from high temperatures and by annealing the water-quenched ε-phase at elevated temperatures, respectively. The massive phase transformation of ε→τ in the B-N-doped MnAl is activated at 680 K and accomplished at 760 K, as shown in Fig. 1. Coercivity development is crucial for applications of MnAl-based alloys as magnets [2-7]. Ball milling is most frequently employed to develop coercivity in magnetic powders of MnAl-based alloys [2-8]. However, the coercivity decreases significantly when the milled magnetic powders were consolidated into bulk [8]. In this work, the coercivity of the τ-phase MnAl doped with B+N was developed by using a high-pressure severe deformation process, during which bulk samples with large coercivity were obtained directly from the original τ-phase bulk alloys. The microstructure and the magnetic properties of the samples were studied.

[1] T. Mix, F. Bittner, K.-H. Müller, L. Schultz, T.G. Woodcock, Acta Mater., 128,160(2017) [2] J. Cui, M. Kramer, L. Zhou, et al., Acta Mater. 158,118(2018) [3] S. Kontos, H. Fang, J. Li, et al., J. Magn. Magn.

Mater. 474,591(2019) [4] Z. Xiang, C. Xu, T. Wang, et al., Intermetallics 101,13(2018) [5] S. Zhao, Y. Wu, J. Wang, et al., J. Magn. Magn. Mater. 483,164(2019) [6] J. Z. Wei, Z. G. Song, J. B. Yang, et al., AIP Adv. 4,127113(2014) [7] J. Rial, M. Villanueva, E. Céspedes, et al., J. Phys. D: Appl. Phys. 50,105004(2017) [8] R. Madugundo, O. Koylu-Alkan, and G. C. Hadjipanayis, AIP Adv. 6,056009(2016)

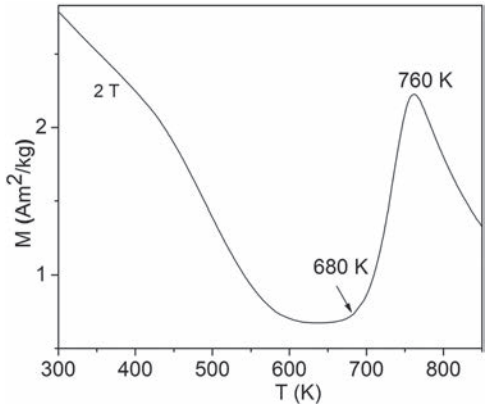


Fig. 1. The M-T plot of the ε-phase B-N-doped MnAl measured with increasing temperature.

9:42

EH-05. Enhancement of Maximum Energy Product in Exchange-Coupled Fe_3O_4 Coated $BaFe_{12}O_{19}$ Nanocomposites. F. Mohseni[1,2], R.C. Pullar[2], J.M. Vieira[2] and *J.S. Amaral*[1] *1. Department of Physics and CICECO, University of Aveiro, Aveiro, Portugal; 2. Department of Materials and Ceramic Engineering and CICECO, University of Aveiro, Aveiro, Portugal*

Recent economic and environmental concerns have prompted intensive research on the development and optimisation of rare-earth free permanent magnets, in particular of ferrites. M-type barium hexaferrites ($BaFe_{12}O_{19}$, BaM) are a type of technologically important, low-cost permanent magnet, with high Tc and high resistance to oxidation and corrosion. Their magnetic performance can be improved upon by exploring exchange-coupling mechanisms, to increase their competitiveness with existing rare-earth magnets [1, 2]. The present investigation explores the exchange-coupling mechanism and shows the correlation between the structural, microstructural, compositional and magnetic properties of BaM hexaferrite and Fe_3O_4 nanocomposites. Via a sol-gel auto combustion method, flake-like BaM particles were prepared and afterwards coated with magnetite nanoparticles using a hydrothermal method. The exchange-spring mechanism was then optimized via the control of nanocomposite phase fractions and heat treatment conditions. Electron microscopy results show that 10 nm sized magnetite nanoparticles were developed as the shell of ultra-thin BaM nanoparticles. We observed the exchange coupling between the hard and the soft magnetic phases requiring no post-heat treatment. The obtained flake-like BaM/Fe_3O_4 nanocomposite exhibits a saturation magnetization of 90 emu/g and a coercivity of ~ 3.5 kOe at room temperature for the sample with a BaM to magnetite weight ratio of 9:1. The magnetic measurements indicate an >50% increase in the saturation magnetization (Ms) in each of the nanocomposite samples compared to the annealed BaM. The results also show a 75% increase in the energy product (BH)max at room temperature in the BaM/Fe_3O_4 9:1 hard/soft nanocomposite, compared to the parent hard phase, which is significantly larger than previous studies [3, 4]. The results are significant in the sense that a simultaneous >30% enhancement in the Ms and the (BH)max of the prepared nanocomposite compared to a commercial BaM powder.

[1] N. Poudyal and J.Ping Liu, Journal of Physics D: Applied Physics 46 (4), p.043001 (2013). [2] R. C. Pullar, Progress in Materials Science 57 (7), p.1191–1334 (2012). [3] Y. Lin et al, Journal of Alloys and Compounds 739, p.202-210 (2018). [4] K. P. Remya et al, Journal of Magnetism and Magnetic Materials 406, p.233–238 (2016).

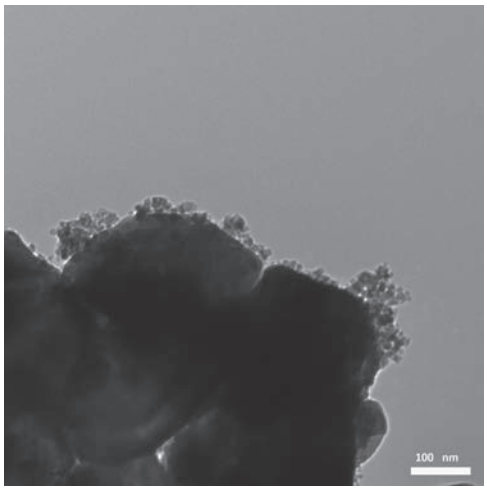


Fig. 1 TEM image of the as-coated BaM/Fe_3O_4 nanocomposite powder

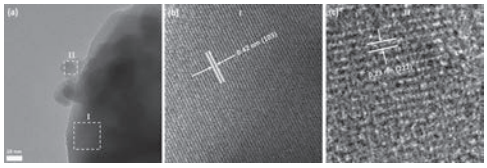


Fig. 2 HRTEM of the interface between Fe_3O_4 and BaM nanoparticles

9:54

EH-06. High Coercivity of Rare-earth Free Alnico Thin Film. X. Han[1], H. Won[3], M. Choi[3], L. Guo[1], Z. Liu[1], R. Wang[1,2], L. Li[1], Y. Hong[3,2] and *F. Yan*[1,2] *1. Department of Metallurgical and Materials Engineering, The University of Alabama, Tuscaloosa, AL, United States; 2. Alabama Transportation Institute, The University of Alabama, Tuscaloosa, AL, United States; 3. Department of Electrical and Computer Engineering and Center for Advanced Vehicle Technologies, The University of Alabama, Tuscaloosa, AL, United States*

The microstructure of Alnico IX permanent magnet (PM) is composed of spinodally decomposed ferromagnetic $L1_0$ Fe-Co rich (α_1) rods embedded in paramagnetic $L1_2$ Al-Ni rich (α_2) matrix. The coercivity (H_{ci}) of Alnico is originated from a shape anisotropy of α_1 rod, instead of magneto-crystalline anisotropy (K_1), resulting in low H_{ci} of 1.4 kOe compared to that of K_1 based PM. To enhance H_{ci} and understand its mechanism, Alnico V was sputter deposited on Si/SiO_2 (100) substrate wafer, showing increase in H_{ci} from 0.74 to 1.8-6.5 kOe [1-3]. The papers postulated that this increase may be attributed to inter-diffusion between Si/SiO_2 substrate and sputtered Alnico V films, yet without providing solid evidence. Especially, α_1 composition was investigated for magnetic properties in neither thin film nor bulk form, but mostly, direct deposition of Alnico V on Si/SiO_2. In this paper, we have sputter deposited α_1 phase alloy ($Fe_{52}Co_{35.8}Al_{5.6}Ni_{5.3}Ti_{0.9}Cu_{0.4}$) on (111) oriented Pt(100 nm)/TiO_2/SiO_2/Si substrate to study the effects of inter-diffusion and annealing on the H_{ci} for various α_1 film thickness (t = 100-140 nm). Fig. 1 shows the magnetic hysteresis loop of as-deposited and annealed films with different t. As-deposited 100 nm thick film is magnetically very soft with H_{ci} = 0.05 kOe. In contrast, after annealing at 800 °C, H_{ci} remarkably increases to 5.4 kOe for 140 nm film, exhibiting pronounced enhancement with increasing t. To understand the mechanism, X-ray diffraction pattern and the elemental line-scan profiles of energy x-ray dispersive spectroscopy across the thin film layers and interfaces were performed. The results shown in Fig. 2 reveal that the increase in H_{ci} is attributed to inter-diffusion among Co, Fe, and Pt in the annealed film, resulting

in the formation of large K_1, 50 nm spherical tetragonal $L1_0$ (Co, Fe)Pt phase, thereby large H_{ci}. This work was supported in part by NSF-I/UCRC for EV-STS under Grant No. 1650564 and NSF-CMMI under Grant No. 1463301.

[1] O. Akdogan and G. Hadjipanayis, *Journal of Physics: International Conference on Magnetism*, vol. 200, pp. 1 (2010) [2] O. Akdogan, W. Li, and G. Hadjipanayis, *Journal of Nanoparticle Research*, vol. 14, no. 891, pp. 1 (2012) [3] D. Patroi, M. Codescu, and E. Patroi, *Optoelectronics and Advanced Materials – Rapid Communication*, vol. 5, no. 10, pp. 1130 (2011)

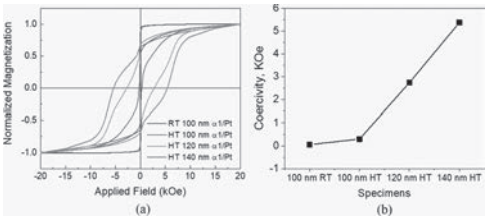


Fig. 1. (a) Magnetic hysteresis loops and (b) H_{ci} of as-deposited and annealed films with different *t*.

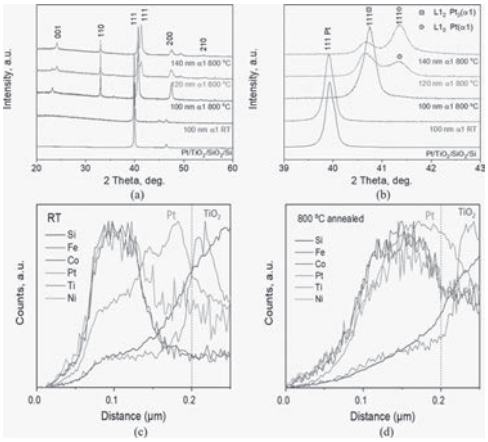


Fig. 2. (a) Overall and (b) enlarged x-ray diffraction patterns of and energy x-ray dispersive spectroscopy for (c) as-deposited and (d) annealed films.

10:06

EH-07. Nanoporous FePt alloys with ultrahigh coercivity. *W. Zhang*[1], D. Ma[1], Y. Wang[1], K. Yubuta[2], Y. Li[1], P. Sharma[2] and R.Y. Umetsu[2]
1. Dalian University of Technology, Dalian, China; 2. Institute for Materials Research, Tohoku University, Sendai, Japan

Nanoporous magnets have attracted the growing interest of researchers for possible applications in the field of nano-biotechnology. In addition, a variety of novel functionalities may be found by impregnation of other functional materials into the pores to form new nanocomposites. It is known that Fe-Pt alloys composed of an ordered face-centered-tetragonal FePt ($L1_0$-FePt) phase have gained considerable attention for the fabrications of high performance permanent magnets and ultrahigh density magnetic data storage media due to the extremely high magnetocrystalline anisotropy. Template-based techniques via annealing with FePt nanoparticles were used to fabricate an ordered nanoporous structure with an $L1_0$-FePt phase [1], but this method is technically difficult and time-consuming to implement. In this work, for fabricating nanoporous magnets by simple and effective approach, the Fe-Pt-B nanocomposite alloys [2] consisting of hard $L1_0$-FePt and soft Fe_2B magnetic phases have been electrochemical etched in H_2SO_4 aqueous solution. The structure and properties of the etched alloys were investigated. A novel nanoporous alloy with a single $L1_0$-FePt phase has been fabricated by etching an $Fe_{60}Pt_{10}B_{30}$ nanocomposite alloy. The Fe_2B phase is selectively removed from by electrochemical etching, while the preserved $L1_0$-FePt phase forms a uniform open bicontinuous interpenetrating ligament–channel structure with a ligament size of ~15 nm. The nanoporous $L1_0$-FePt alloy possesses a very high coercivity of 18.5 kOe. For understanding the magnetic behavior of the nanoporous alloy, the micromagnetic simulation has been carried out.

[1] F. Iskandar, T. Iwaki, T. Toda, K. Okuyama, Nano Lett., 5, 1525 (2005). [2] W. Zhang, D. V. Louzguine, A. Inoue, Appl. Phys. Lett., 80, 4998 (2004).

10:18

EH-08. Co nano-cluster inclusions in $L1_0$-FePt matrix as a model system of nanocomposite magnets. C. Paléo[1], F. Wilhelm[2], T. Epicier[3], V. Dupuis[1] and *D. Le Roy*[1] *1. Univ. Lyon 1, ILM, Villeurbanne, France; 2. E.S.R.F., Grenoble, France; 3. INSA Lyon, Villeurbanne, France*

Nanocomposite materials is a promising route to develop new permanent magnets with unprecedented performances. Theoretical calculations predicted a potential energy product of 1 MJ/m^3, which is twice as large as the one of best $Nd_2Fe_{14}B$ magnets produced today [1]. But these calculations also pointed out the absolute necessity to confine the softer phase in nano-sized grains, typically smaller than 10 nm, which cannot be obtained with conventional process for mass scale material fabrication. So far only very few experimental works with encouraging results have been reported on such exchange-spring magnet [2]. Further experimental investigations are needed to assess the full potential of nancomposite for designing high energy product magnetic materials. We recently prepared Co@FePt transition metal (TM)-based nanocomposite films from low energy cluster beam deposition technique (LECBD) of Co clusters, *in situ* embedded in FePt matrix independently produced by alternative electron gun [3,4]. This nanofabrication route gives a fine control over the microstructure. Co cluster inclusions can be selected in size prior their deposition, between 1 and 10 nm. The cluster to matrix volume ratio is adjusted controlling the thickness of each Co, Fe, Pt individual layers. Annealing is a crucial step to drive the initial Fe and Pt multilayers to the high-magnetic anisotropy $L1_0$ phase with a limited cluster-matrix interdiffusion. X-rays Diffraction revealed a thermal transition to a chemically ordered $L1_0$-FePt alloyed matrix with a partial texture on Si substrate while environmental-TEM and EDX analyses allowed us to observe the partial diffusion of the Co clusters in the hard matrix. Recently, X-ray absorption spectroscopy measurements (EXAFS, XLD and XMCD) were performed on annealed Co@FePt nanocomposite at Fe and Co K-edges at the ESRF. The structural analysis proved that the Co clusters don't entirely mix with the matrix during annealing. The study of such model system could give insights about the role of the nanostructure on magnetic hardness and could thus guide the development of mass scale synthesis processes. This work is supported by the ANR collaborative project "SHAMAN": Soft in HArd MAgnetic Nanocomposites (2017-20).

1. Skomski R. and Coey J. M. D. Phys. Rev. B 48, 15812 (1993) 2. Balasubramanian B., et al, Scientific reports 4, 6265 (2014) 3. Tournus F. et al, Journal of Magnetism and Magnetic Materials, vol. 323, p. 1868 (2011) 4. Liu Y. et al, Appl. Phys. Lett. 99, 172504 (2011)

10:30

EH-09. A Two-dimensional Magnet Based on the Shell-Ferromagnetic Effect. *A. Cakir*[1] and M. Acet[2] *1. Metallurgical and Materials Engineering, Mugla Sitki Kocman University, Mugla, Turkey; 2. Physics, Duisburg-Essen University, Duisburg, Germany*

Shell-ferromagnetism is a macroscopic monopolar effect which occurs when off-stoichiomentric Hesulers in the form $Ni_{50}Mn_{45}X_5$ (*X*: Al, Ga, In Sn, Sb) are temper-annealed at 650 K in a magnetic-field. In this top-down process, the material decpomposes and results in the formation of 2-5 nm full-Heusler cubic ferromagnetic $Ni_{50}Mn_{25}X_{25}$ laminar precipitates embedded coherently

in an antiferromagnetic tetragonal $Ni_{50}Mn_{50}$ matrix [1]. The spins at the interface shell layer become strongly pinned in the direction of the annealing field. The precipitates have a coercivity exceeding 15 T, but comprise at most 10 % of the material so that the magnetization remains low; at most at 8 Am^2kg^{-1}. It would be desirable to have this coercivity with the full magnetization of the full-Heusler, namely 80 Am^2kg^{-1}, which would give a large energy product. To overcome this issue, we prepare this time with a bottom-up process two-dimensional $Ni_{50}Mn_{50}/Ni_{50}Mn_{25}X_{25}/Ni_{50}Mn_{50}$ multilayers with 100/5/100 nm thicknesses. The layers are initiallly incoherent, but after temper-annealing at 650 K in a magnetic field, the coherency increases, and the spins at the interface become strongly pinned in the direction of the annealing field as in the case of the shell-ferromagnet leading to a two dimensional magnet.

[1] A. CAkir, M. Acet, and M. Farle, Sci. Rep. 6, 28931, 2016

10:42

EH-10. Rehabilitation of "Failed" Ferromagnetic Materials.
A. Palasyuk[1], T.N. Lamichhane[1,2], V. Taufour[3], O. Palasyuk[1,4], S. Bud'ko[1,2] and P. Canfield[1,2] *1. Ames Laboratory, Ames, IA, United States; 2. Department of Physics and Astronomy, Iowa State University, Ames, IA, United States; 3. Department of Physics, University of California, Davis, Davis, CA, United States; 4. Department of Material Science and Engineering, Iowa State University, Ames, IA, United States*

To find new, practical, magnetic materials is a highly challenging task since great efforts have been already invested world-wide in exactly this activity. A vast variety of approaches, materials systems, and techniques have been tried, most unsuccessfully. A new approach – *rehabilitation* – is proposed as a state-of-the-art strategy for finding new magnetic materials. The idea is based on converting materials that lack the desired ferromagnetic ground state, uniaxial anisotropy and/or required crystal structure into strong ferromagnets. This is achieved by tuning of the "failed" materials with dopants that leads to the appearance of the required permanent magnet characteristics and makes these compounds suitable for use as potential magnets. For example, in $(Fe_{1-x}Co_x)_2B$ at $x = 0.3$, the undesirable easy-plane magneto-crystalline anisotropy changes to the desired easy-axis anisotropy. Similarly, the theoretical work found that Sb substitution into the planar ferromagnet Fe_3Sn rendered this material uniaxial with significant anisotropy [1], and ongoing experimental work shows ways towards practical realization and "rehabilitation" of this rare-earth-free ferromagnet. In another case, the Pauli paramagnet $CeCo_3$, upon being doped with nonmagnetic Mg, exhibits sufficiently strong magnetic characteristics (a Curie point of 450 K and substantial uniaxial anisotropy) to warrant consideration as a permanent magnet [2], see Figure. Finally, there is the $Ce_2(Co,Fe)_{17}$ system. Having excellent intrinsic characteristics, i.e., magnetization above 1.3 T and Curie temperatures above 500 °C, this system possesses rather weak uniaxial magnetocrystalline anisotropy (with anisotropy fields of ~ 1 – 1.5 T). However, our recent experiments show that introduction of refractory metals into this system "rehabilitates" its anisotropy characteristics close to practical values of ~ 2.5 – 3 T, keeping other important parameters (magnetization and Curie temperature) on the same high level. Our method of rehabilitation greatly increase the number of potential compounds for development as accessible permanent magnets.

[1] B. C. Sales, B. Saparov, M. A. McGuire et al., Scientific Reports., 4, 7024 (2014) [2] T. N. Lamichhane, V. Taufour, A. Palasyuk et al., PR Applied., 4, 024023 (2018)

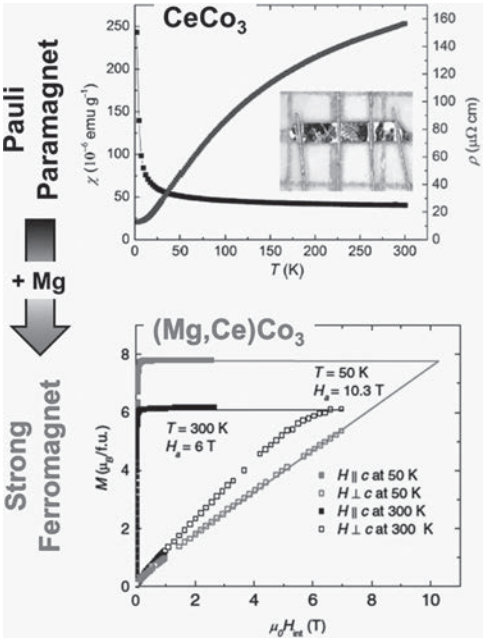


Figure. Transformation of Pauli paramagnet $CeCo_3$ into strong ferromagnet through Mg-doping.

10:54

EH-11. First Principles Study of Doped RE-TM_5 Systems for the Development of Hard Magnetic Properties.
H. Ucar[1], R. Choudhary[2] and D. Paudyal[2] *1. Chemical and Materials Engineering, California Polytechnic University, Pomona, Pomona, CA, United States; 2. Ames Laboratory, Ames, IA, United States*

In this study, we explore the influence of substitutional and interstitial impurities in RE-TM_5 (RE: rare earth, TM: transition metal) compounds on their hard magnetic properties such as magnetic anisotropic energy, (MAE), and saturation magnetization, M_s using density functional theory (DFT). The structure of RE-TM_5 is that of a $CaCu_5$ as the prototype (P6/mmm, No.191), and it can be described as alternating layers of hexagonal nets formed by the TM atoms (2c) with the RE sitting at the center of the net, and planes of TM atoms (3g) arranged in a Kagome network. The favorable arrangement of this TM_5 network is possibly driving the formation of a large orbital magnetic moment of TM atoms that couples with the spin moment via SO coupling which leads to large MAE and M_s values [1-3]. This was predicted by a first principles study that found comparable MAE values for the YCo_5 as well as the hypothetical Co_5 having the same $CaCu_5$ structure with yttrium replaced by a vacancy [4]. Inspired by the earlier research, we investigate here the role of interstitial dopings - nitrogen, boron, hydrogen - at the tetrahedral interstices of RE-TM_5 as well as the substitutional dopings, most notably cerium, at the RE site in determining the MAE and M_s. In addition, we elucidate the role of exchange correlation approximations such as local spin density approximations (LSDA) and generalized gradient approximation (GGA) formulation in determining the MAE and M_s by analyzing their corresponding density of states (DOS) as shown in table 1 and fig. 1. As indicated with arrows, the change in DOS between the [100] axis (shaded curve) and the [001] axis (dashed lines) within the GGA is more significant than the LSDA method especially for the Co($3g_2$) site. This difference might be one of the reasons for MAE value within the GGA being higher and closer to the experimental findings. This research is supported by the Critical Materials Institute, an Energy Innovation Hub funded by the U.S. Department of Energy, Office of Energy Efficiency and Renewable Energy, Advanced Manufacturing Office.

[1] A. Asali, J. Fidler, D. Suess, J. Magn. Magn. Mater., Vol. 485, p. 61, (2019). [2] Alameda J M, Givord D, Lemaire R and Lu Q 1981 J. Appl. Phys. Vol. 52 p. 2079, (1981). [3] Schweizer J and Tasset F 1980 J. Phys. F: Met. Phys. Vol. 10, p. 2799, (1988). [4] P. Larson, I. I. Mazin, and D. A. Papaconstantopoulos, Phys. Rev. B Vol. 67, p. 214405 (2003). [5] Manh Cuong Nguyen, Yongxin Yao, Cai-Zhuang Wang, Kai-Ming Ho and Vladimir P Antropov J. Phys. Condens. Matter Vol. 30, p. 195801, (2018).

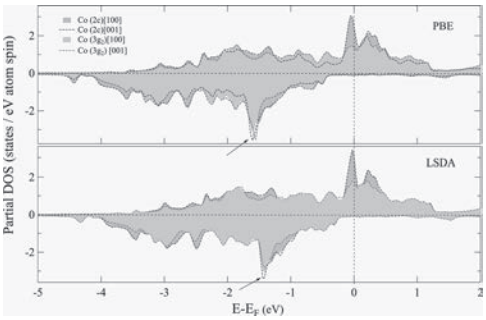


Fig. 1: The PDOS of crystallographically inequivalent Co sites along the [100] and [001] direction.

Table I: Local spin and orbital magnetic moments of $LaCo_5$ in units of (u_B/fu) with GGA and LSDA as two different exchange correlation parameters.

	$LaCo_5$		
Atomic Sites	GGA (S/L)	LSDA (S/L)	GGA + U at Co sites (S/L) [a]
Interstitial	0.60	0.43	
La	-0.186 / 0.0823	-0.153 / 0.007	-0.283 / 0.027
Co(2c)	1.574 / 0.103	1.492 / 0.108	1.628 / 0.152
Co($3g_1$)	1.556 / 0.085	1.465 / 0.0857	1.663 / 0.139
Co($3g_2$)	1.557 / 0.119	1.467 / 0.124	1.663 / 0.139
Total moment	7.431	7.362	8.71
MAE (meV/fu)	1.41	0.552	4.402

[a]Ref. [5]

11:06

EH-12. Data integration approach for multiple-sublattice ferromagnetism in rare-earth permanent magnets based on *ab initio* electronic structure and neutron diffraction measurements.
M. Matsumoto[1], T. Hawai[1] and K. Ono[1] *1. High Energy Accelerator Research Organization, Tsukuba, Japan*

Rare-earth permanent magnet (REPM) requires both of strong magnetization and accordingly strong coercivity all through the given operation temperature range for practical utilities like traction motors of electric vehicles. Main-phase ferromagnets in REPM are made of at least two sublattices, namely, transition-metal (TM) sublattice for high-temperature ferromagnetism and rare-earth (RE) sublattice for uni-axial magnetic anisotropy as the intrinsic source of coercivity. Often each of the TM and RE sublattice is further split into multiple sublattices: the champion magnet compound $Nd_2Fe_{14}B$ is made of two Nd sublattices, Nd(4f) and Nd(4g), and six Fe sublattices, Fe($16k_1$), Fe($16k_2$), Fe($8j_1$), Fe($8j_2$), Fe(4e), and Fe(4c) and the particular roles of those sublattices have been discussed: Nd(4g) sublattice contributes more to the intrinsic magnetic anisotropy [1], also helps with Ce to enhance the intrinsic magnetism [2], and Fe($8j_1$) sublattice seems to be preferred by Co [3,4]. Given that the site preference of dopant elements can critically influence the possible merit of a ferromagnet in question, we implement a data integration approach between theory and experiment to quantitatively analyse the site occupation of dopants, magnetic moments and the lattice structure in order to assess the intrinsic properties of REPM compounds as realistically as possible. Rietveld analysis of neutron diffraction data is combined with *ab initio* electronic structure calculations to determine the relevant observables self-consistently between the experimental data derived from the diffraction pattern and the *ab initio* data for the ferromagnetic state. Results for (Sm,Zr)$(Fe,Co,Ti)_{12}$ [5] are presented to reveal the background mechanism behind the apparent site preference of the dopants Zr, Co, and Ti distribution all over RE and TM sublattices in the host ferromagnet, $SmFe_{12}$. Such integrated data elucidates the missed points behind the apparent observation and helps to build the right strategy for the improvement of intrinsic magnetism in REPM.

[1] D. Haskel, J. C. Lang, Z. Islam, A. Cady, G. Srajer, M. van Veenendaal, P. C. Canfield, Phys. Rev. Lett. 95, 217207 (2005). [2] X. Tang, H. Sepehri-Amin, MM, T. Ohkubo, K. Hono, Acta Materialia 175, 1 (2019). [3] J. F. Herbst and W. B. Yelon, J. Appl. Phys. 60, 4224 (1986). [4] MM, preprint [arXiv:1812.10945]. [5] P. Tozman, H. Sepehri-Amin, Y. K. Takahashi, S. Hirosawa, K. Hono, Acta Mater. 153, 354 (2018).

11:18

EH-13. Correlation Corrections in Rare-Earth Transition-Metal Permanent Magnets.
R. Skomski[1], B. Balasubramanian[1] and D.J. Sellmyer[1] *1. Physics and Astronomy & NCMN, University of Nebraska, Lincoln, NE, United States*

Electron-electron interactions going beyond the local spin density approximation (LSDA) yield corrections to the description of metallic permanent magnets. We use model calculations to estimate these correlation corrections, which involve two or more Slater determinants. The LSDA works well for iron-series elements, including atomic-scale imperfections and disordered alloys. The approximation is based on an independent-electron density functional that allows a description in terms of individually rotating spins [1], and the same is true for extensions such as the LSDA+*U*. Quasi-local extensions involving gradients improve quantitative predictions, but the example of Hartree-Fock calculations, which are highly nonlocal without going beyond the independent-electron picture, show that locality is not the primary consideration. In fact, many features of the transition-metal sublattices of permanent magnets are Heisenberg-like [2], and the quantum-mechanical treatment of these strongly correlated model yield quantum spin liquid (QSL) corrections [3] to quantities such as the Curie temperature. These corrections scale as $1/z$, where z is the number of nearest neighbors. The rare-earth sublattice is much more severely affected by correlations. In principle, density-functional theory provides an exact description of the rare-earth ground state, but there is no general expression for the density functional [4] and known density-functional approximates for high correlated systems look very different from LSDA. As an example, we discuss Sm^{3+}, where the spin $S = 5/2$, or 5 μ_B, and the orbital moment $L = 5$, or 5 μ_B, are antiparallel and may naively be expected to yield a zero net moment. In fact, from Hund's rules it is well-known that $g = 2/7$ for Sm^{3+}. This indicates that spin and orbital moment form an obtuse angle in the vector model and explains the observed Sm contribution to the magnetization. The example of Sm^{3+} shows that the corresponding moment error is comparable to the moment itself, and this can also be shown to be true for the magnetocrystalline anisotropy, affecting both sign and magnitude. — This research is supported by DOE BES (DE-FG02-04ER46152).

[1] A. I. Liechtenstein *et al.*, "Local spin density functional approach to the theory of exchange interactions in ferromagnetic metals and alloys", J. Magn. Magn. Mater., Vol. 67, p. 65 (1987). [2] P. Fulde, Electron Correlations in Molecules and Solids, Springer, Berlin 1991. [3] R. Skomski, "Exchange Interaction", in: Handbook of Magnetism, Eds. J. M. D. Coey and S. S. Parkin, Springer, Berlin 2020. [4] E. H. Lieb, "Density functionals for coulomb systems", Int. J. Quantum Chem., Vol. 24, p. 243 (1983).

Session EI
EFFECTS OF DIMENSIONALITY

Anna Isaeva, Chair
TU Dresden, Dresden, Germany

INVITED PAPER

8:30

EI-01. 2D Magnetism and Novel Spintronic Devices. *C. Gong*[1]
1. University of Maryland, College Park, MD, United States

Magnetism, one of the most fundamental physical properties, has revolutionized significant technologies such as data storage and biomedical imaging, and continues to bring forth new phenomena in emergent materials and device architectures. The recently discovered magnetic 2D van der Waals materials (hereafter abbreviated as "2D magnets") [1,2] provide ideal platforms to enable the atomic-thin, flexible, lightweight magneto-optic and magnetoelectric devices. The seamless integration of 2D magnets with dissimilar electronic and photonic materials further opens up exciting possibilities for unprecedented properties and functionalities. In this talk, I will speak on our experimental observation of the 2D magnetism in 2D magnets, and show the possibility of using such atomically thin magnetic flatlands to develop novel spintronic devices [3,4] such as low-power magnetoresistive memories, high-efficiency spin field-effect transistors, and phase-change bio- or chemical sensors.

1. C. Gong et al., Nature 546, 265-269 (2017). 2. C. Gong et al., Science 363, eaav4450 (2019). 3. S. Gong et al., PNAS 115, 8511-8516 (2018). 4. C. Gong et al., Nature Communications 10, 2657 (2019).

CONTRIBUTED PAPERS

9:06

EI-02. Magnetic interactions and excitations in 2D van der Waals materials. *L. Ke*[1] *1. Ames Laboratory, Ames, IA, United States*

The magnetic 2D van der Waals (m2DvdW) materials [1,2] have received significant attention recently due to their potential applications in spintronics. It is of great interest to unravel the underlying magnetic mechanisms that could guide the bandstructure engineering to improve the magnetic properties in these systems. We investigate the origins of magnetic properties such as exchange interactions, magnetocrystalline anisotropy (MA), and magnetic excitations in magnetic 2D van der Waals materials. To unravel the origin of MA in these systems, we use a recently-developed realistic tight-binding Green's function framework [3] to compute and resolve MA energy (MAE) efficiently into sublattices. We found that the inter-sublattice contribution (between the magnetic-atom sublattice and the heavy-atom sublattice) to MAE is significant. Magnetic interactions and spin-wave dispersions in various m2DvdW systems are calculated using a linear response method. Results are compared with available inelastic neutron scattering measurements. Finally, methods beyond density functional theory are used to investigate the effects of non-local potentials on the magnetic properties in m2DvdW systems. This work is supported by the U.S. Department of Energy, Office of Science, Office of Basic Energy Sciences, Materials Sciences and Engineering Division, and Early Career Research Program. Ames Laboratory is operated for the U. S. Department of Energy by Iowa State University under Contract No. DE-AC02-07CH11358.

[1] B. Huang, G. Clark, E. Navarro-Moratalla, D. R. Klein, R. Cheng, K. L. Seyler, D. Zhong, E. Schmidgall, M. A. McGuire, D. H. Cobden, W. Yao, D. Xiao, P. Jarillo- Herrero, and X. Xu, Nature 546, 270 (2017). [2] C. Gong, L. Li, Z. Li, H. Ji, A. Stern, Y. Xia, T. Cao, W. Bao, C. Wang, Y. Wang, Z. Q. Qiu, R. J. Cava, S. G. Louie, J. Xia, and X. Zhang, Nature 546, 265 (2017). [3] L.Ke, Phys. Rev. B, 99:054418 (2019).

9:18

EI-03. The Effect of High Pressure on Ferromagnetic Properties of the van-der-Waals Materials VI_3 and CrI_3. M. Kratochvilova[1], *K. Uhlirova*[1], J. Valenta[1], S. Son[2,3], P. Proschek[1], J. Prchal[1], V. Sechovsky[1] and J. Park[2,3]
1. Department of Condensed Matter Physics, Charles University, Prague, Czechia; 2. Center for Correlated Electron Systems, Institute for Basic Science, Seoul, The Republic of Korea; 3. Department of Physics and Astronomy, Seoul National University, Seoul, The Republic of Korea

Despite belonging to well-studied layered transition metal trihalides, the VI_3 and CrI_3 compounds received significant attention only recently [1-6]. They are reported ferromagnetic (FM) at temperatures below T_C = 50 K [1] and 61 K [5], respectively. Calculations predict that the FM order may persist into monolayer form [7, 8], suggesting that VI_3 and CrI_3 could be promising materials for spintronics. In bulk materials the interlayer exchange interactions play an important role. The hierarchy of exchange interactions and dimensionality of magnetism can be effectively tuned by hydrostatic pressure particularly due to the weak van der Waals bonding between the FM layers. Recently published magnetization data in lower hydrostatic pressures (p £ 1 GPa) suggest pressure-induced increase of T_C, both, in VI_3 [1] and CrI_3 [6]. We measured the magnetic properties of the VI_3 and CrI_3 single crystals at ambient and high hydrostatic pressures up to 3.5 GPa. The peak in the $\chi'(T)$ dependence of VI_3 confirms T_C = 50 K at ambient pressure. Besides, 3 additional side peaks in $\chi'(T)$ data are observed between 52 and 60 K. These $\chi'(T)$ anomalies are almost intact by increasing p up to 0.8 GPa. Above 0.8 GPa, all peaks merge into one and T_C increases abruptly to 60 K at 1.6 GPa. This result is in line with the p evolution of magnetization around T_C [1]. From 1.6 and 3.5 GPa, T_C increases linearly at a rate of 4.1 K/GPa. A significantly different behavior was observed in CrI_3. A single peak in $\chi'(T)$ is observed at T_C = 60 K in ambient pressure and stays at the same temperature in pressures up to 1.5 GPa in contrast to data from Ref. [6]. Between 1.5 and 3 GPa, T_C decreases linearly at a rate of - 2.3 K/GPa. Besides the dominant peak in χ' corresponding to T_C, another peak at T_1 = 50 K emerges in 0.7 GPa, showing analogous T vs. p evolution. The observed contrasting pressure dependence in the VI_3 and CrI_3 compounds indicates considerably different hierarchy of interlayer exchange interactions in the two compounds. Results will be discussed considering also data from the uniaxial-stress and higher hydrostatic-pressure (> 3.5 GPa) experiments which are in progress.

S. Son, M. J. Coak, N. Lee, J. Kim, T. Y. *Phys. Rev. B* 99, 041402(R) (2019) S. Tian, J.-F. Zhang, Ch. Li, T. Ying, S. Li*J. Am. Chem. Soc.* 141 5326-5333 (2019) T. Kong, K. Stolze, E. I. Timmons, *Adv.Mater.* 31 (2019) 1808074. G. T. Lin, X. Luo, F. C. Chen, *Appl. Phys. Lett.* 112 (2018) 072405. M. A. Guire, H. Dixit, V. R. Cooper, Chem. Mater. 27 (2015) 612–620. S. Mondal, M. Kannan, M. DasPhys. Rev. B 99 (2019) 180407(R). J. He, S. Ma, P. Lyu, J. Mater. Chem. C 4 (2016) 2518. H. Wang, F. Fan, S. Zhu EPL, 114 (2016) 47001.

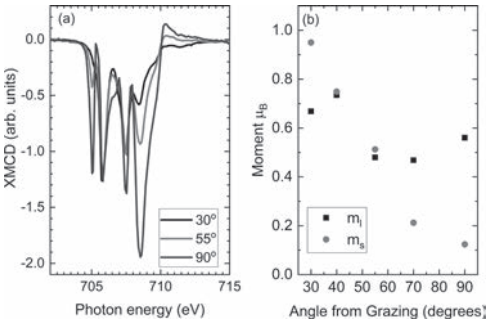
9:30

EI-04. Magnetic Spectroscopy of One-Dimensional Iron Chains.

A. Baker[1], N. Vargas[4], F. Torres[2], M. Kiwi[2], T. Willey[1], I. Schuller[4] and C. Monton[3] *1. Materials Science Division, Lawrence Livermore National Laboratory, Livermore, CA, United States; 2. Universidad de Chile, Santiago, Chile; 3. University of Texas, San Antonio, TX, United States; 4. University of California, San Diego, CA, United States*

We report on unusual magnetic properties that arise in one-dimensional (1d) iron (Fe) chains with lengths of 10 – 200 nm, in thin film and superlattices. The Fe chains are grown using iron phthalocyanine (FePc) molecules, and in superlattices with metal-free-phthalocyanines (H2Pc). The Pc molecules act as templates for their metal centres, leading to arrays of independent, highly-oriented 1D chains [1]. The coercivity of the films is constant, but in superlattices increases with chain length, due to a combination of direct exchange and Dzyaloshinskii-Moriya interactions, where the magnetization reversal is governed by chiral symmetry breaking at the FePc/H2Pc interfaces. XAS measurements reveal the presence of hybridization and disorder at the interfaces, a potential mechanism for such interactions. XMCD sheds further light on the highly anisotropic magnetic character of the samples, with strong quenching or enhancement of spin angular momentum as magnetization is rotated from parallel to perpendicular to the chain. The orbital angular momentum, in contrast, is significantly more isotropic than previous reports [2], although still largely unquenched. The versatility and control offered in these samples provides a versatile testbed of 1D magnetism and the crucial role of interfaces in the magnetic states that arise.

[1] Willey et al, J. Chem. Phys, 139, 034701 (2013) [2] Gargiani et al, Phys. Rev. B, 87, 165407, (2013) Work supported by the Department of Energy's Office of Basic Energy Science under grant DE FG02 87ER-45332, the National Science Foundation under grant No. 1804414 and 1805585, and AFOSR Grant FA9550-16-1-0122. Prepared by LLNL under Contract DE-AC52-07NA27344.



(a) Example XMCD spectra for [FePc(10nm)/H2Pc(5nm)]$_4$ superlattices, showing strong anisotropy characteristic of well-oriented Pc films. (b) extracted spin and orbital angular momentum as a function of angle, using magneto-optical sum rules and assuming nh = 2.669. The anisotropy of the orbital angular momentum does not match the expected sin(θ) behavior, which is observed for the spin.

9:42

EI-05. Chiral magnetic ordering in ultra-short 1D iron chains.

M. Kiwi[1], N. Vargas[2], F. Torres[1], A. Baker[3], J. Lee[3], T. Willey[3], I. Schuller[2] and C. Monton[4] *1. Physics, Universidad de Chile, Santiago, Chile; 2. Physics, University of California, San Diego, San Diego, CA, United States; 3. Material Science Div., Lawrence Livermors National Lab, Berkely, CA, United States; 4. Physics, Univ. of Texas, San Antonio, San Antonio, TX, United States*

The discovery of unconventional atomic-scale chiral ferromagnetic ordering in one-dimensional (1D) ferromagnetic chains is reported. The iron chain superlattices (SLs) were fabricated by a novel method that allows for precise control of composition and length, only a few atoms long (7 to 200 atoms), as shown in Fig. 1. The magnetic response is strongly dependent on the boundary conditions imposed on the end atoms of the Fe chains by electronic hybridization with H. The coercive field increases with the Fe chain length with hybridized boundaries (SLs), whereas in chains not subject to hybridization the coercive field remains constant (films). This implies that the electronic environment of the end atoms determines the magnetic response of these 1D chains [1,2]. The evolution of the coercive field with the length of the 1D chains is systematic and monotonic. Surprisingly, the films have a coercive field independent of chain length (Fig. 2) whereas the SLs show a definite increase as a function of length well beyond any possible experimental error. This linear dependence extends to the shortest lengths (t_{FePc}= 3 nm and 5 nm), which could only be measured in SLs. Remarkably, there is a significant difference between the coercive field evolution with FePc thickness between films and the SLs for the same total length of the chains compared to the single layer in the SLs. The relevance of this discovery is that it seems to contradict the Mermin-Wagner theorem [3], which asserts that in for one or two-dimensional Heisenberg systems with isotropic short ranged interactions, there can be no spontaneous ferro- or antiferromagnetic long-range order at T>0. However, a semi-classical model that includes short-range exchange and Dzyaloshinskii-Moriya interactions quantitatively explains the results [4].

1 C. Monton, I. Valmianski, and I. K. Schuller, Appl. Phys. Lett. 101, 133304 (2012). 2 F. Bartolomé *et al.*, J. of Appl. Phys. 117, 17A735 (2015). 3 N. D. Mermin and H. Wagner, Phys. Rev. Lett. 17, 1133 (1966). 4 F. Torres, D. Altbir, and M. Kiwi, Europhys. Lett. 106, 47004 (2014).

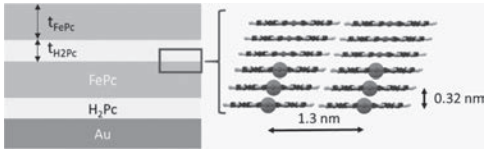


Fig.1 Schematic diagram of a FePc/H_2Pc superlattice and molecular orientation of the samples grown on Au-coated sapphire. The thickness of the H_2Pc and FePc is t_{H2Pc} and t_{FePc}, respectively. The period of the superlattice is Λ= t_{H2Pc} + t_{FePc}.

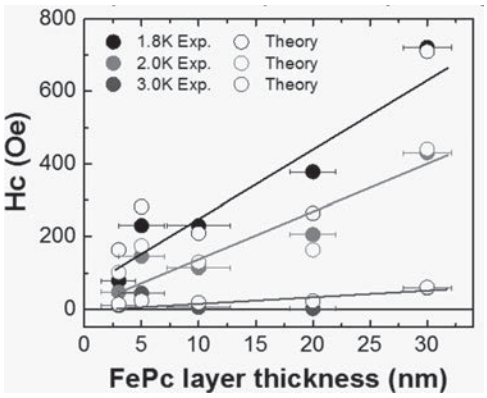


Fig.2 Coercive field dependence on FePc thickness for three different temperatures. Experimental results (full circles) and theoretical model prediction (open circles) are in excellent agreement.

9:54

EI-06. Magnetic Correlations at Different Length Scales in the Solid Solution Alloy Ni-V Close to the Ferromagnetic Critical Point Revealed with Small Angle Neutron Scattering. *A. Schroeder*[1], S. Bhattarai[1], J.L. Lussier[1], A. Gebretsadik[1] and K.L. Krycka[2] *1. Physics, Kent State University, Kent, OH, United States; 2. NIST, Gaithersburg, MD, United States*

We present small angle neutron scattering (SANS) data (non polarized, half polarized and full polarized using a He3 cell as spin filter) collected at NG7SANS at NIST on well characterized polycrystalline Ni(1-x)V(x) samples with x=0.10 and x=0.11 with confirmed random atomic distribution [1]. These ferromagnetic (FM) samples are close to the quantum critical point x_c=0.116 where the FM order of Ni is suppressed with critical temperatures T_c approaching zero. Magnetization and muSR data recognized a quantum Griffiths phase with coexisting static order and magnetic fluctuations [1]. SANS is an ideal tool to reveal the different magnetic correlations length scales in this disordered FM but resolving the small magnetic scattering remains a challenge since it is dominated by the nuclear contribution of Ni. We will show the advantages of a polarization analysis [2] in identifying the main magnetic contributions at different length scales in Ni-V. Through angular dependent spin flip scattering we can recognize magnetic short-range fluctuations in both compounds that are strongest at T_c but remain still present at the lowest temperature (see Figure 1). Neutron depolarization at very low magnetic fields and increased Porod-terms below T_c indicate the onset of long-range order within domains. The angular dependence of non spin flip interference terms reveals the anisotropic magnetic scattering of aligned domains and frozen short range clusters in enhanced magnetic fields. These data confirm magnetic correlations at various length scales (from micrometer to 5nm) in Ni-V close to the quantum critical point.

[1] R. Wang, A. Gebretsadik, S. Ubaid-Kassis, A. Schroeder et al, Phys. Rev. Lett. 118, 267202 (2017) [2] K. Krycka et al, J. Appl. Cryst. 45, 554-565 (2012)

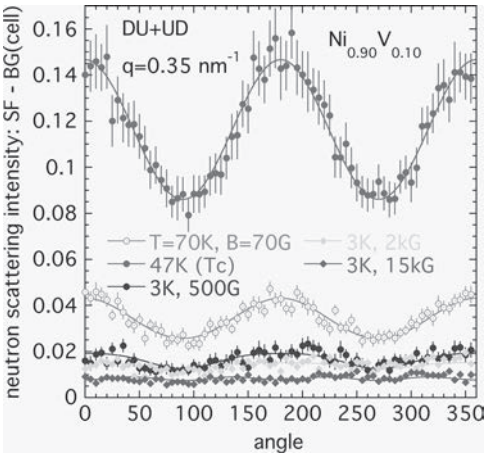


Figure 1: Spin flip scattering (magnetic in origin) vs. angle θ (within 2D detector) for Ni(1-x)V(x) with x=0.10 for different temperatures and magnetic fields (at θ=0° along the polarization direction of the neutron perpendicular to the beam). Data are shown at the wave vector with radius q=0.35±0.15nm^{-1}, cell background is subtracted. Solid line is fit [2] that reveals magnetic intensities with isotropic (M_{iso}^2) and anisotropic (m_x^2) electronic contributions: Int(SF) = 1/3 M_{iso}^2 [1+cos^{2}θ] + m_x^2 cos^{2}θ sin^{2}θ + 2/3 I_V^2.

10:06

EI-07. Secnond Spin Phase Transition in Spin Spiral $ZnCr_2Se_4$ at Low Temperatures. *S. Park*[1], S. Kwon[2], S. Lee[1], S. Khim[3], D. Bhoi[3], C. Park[3] and K. Kim[3] *1. Department of Physics, KAIST, Daejeon, The Republic of Korea; 2. University of Waterloo, Waterloo, ON, Canada; 3. Department of Physics and Astronomy, Seoul National University, Seoul, The Republic of Korea*

In the past decades, bond frustrated Heisenberg antiferromagnet $ZnCr_2Se_4$ has attracted attention in various aspects. $ZnCr_2Se_4$ undergoes a transition to a Spiral spin order occurs at T_N=21 K in zero magnetic field. As the applied magnetic field increases, the spin state changes to conical structure and then to the fully saturated ferromagnet [1]. Magnetoelectricity[2] and pseudo Goldstone mode[3] were explained based on this understanding. At low temperatures, the magnetic susceptibility shows unusual field dependence[1,4] applied during cooling, which has been simply regarded as an effect due to the multidomain state. In this work, we report magnetic susceptibility and Cr and Se NMR results obtained at various temperatures and fields. As the temperature decrease below 6 K, the magnetic susceptibilities of the zero field cool and field cool split like a spin glass. The NMR relaxation rates in Fig. 1 shows a lambda-shape anomaly near the temperature of the susceptibility split. Both experimental results suggest the existence of additional spin phase transition. The transition temperature depends on the applied magnetic field. The intensity of the low frequency peak of the Cr and Se NMR spectra (inset of Fig.2.) rapidly decays approaching the transition and then revives at lower temperatures as in Fig.2. This is understood as the transition from the incommensurate spiral spin order to the random spin distribution.

[1] J. Hemberger, et. al., Phys. Rev. Lett., Vol. 98, 147203 (2007) [2] H. Murakawa, et. al., J. Phys. Soc. Jpn., Vol. 77, 043709 (2008) [3] Y. V. Tymoshenko, et. al., Phys. Rev. X, Vol. 7, 041049 (2017) [4] C. C. Gu, et. al., Phys. Rev. Lett., Vol. 120, 147204 (2018)

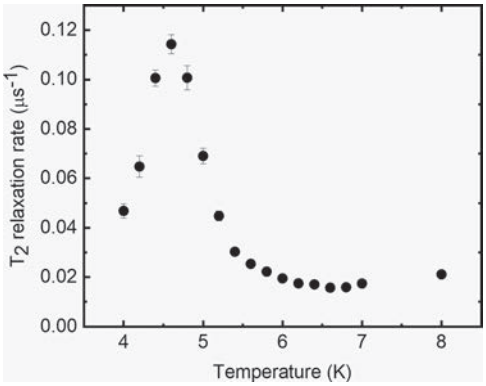


Fig.1 Temperature dependence of T_2 relaxation rate

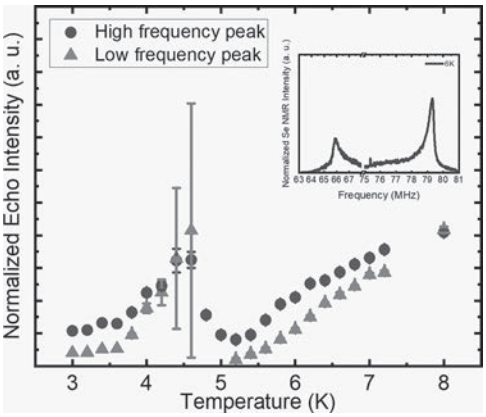


Fig.2 Normalized echo intensity measured at various temperature. (Inset) Zero field Se NMR spectrum measured at 6 K.

INVITED PAPER

10:18

EI-08. Giant Antiferromagnetic Response in a Two-dimensional Spin-orbit Mott Insulator. *L. Hao*[1], D. Meyers[2], H. Suwa[1], J. Yang[1], H. Xu[3], C. Batista[1], M.P. Dean[2] and J. Liu[3] *1. Department of Physics and Astronomy, University of Tennessee, Knoxville, TN, United States; 2. Department of Condensed Matter Physics and Materials Science, Brookhaven National Laboratory, Upton, NY, United States; 3. Department of Materials Science and Engineering, University of Tennessee, Knoxville, TN, United States*

Antiferromagnetic (AFM) materials started to gain traction owing the advantages of reliability, ultrafast dynamics, etc. in spintronic applications. In this regard, Mott insulators can be an appealing candidate because of the robust AFM ground state due to the strong electron-electron correlation. Moreover, exploring AFM order is fundamentally important for understanding emergent phenomena, like high-*T*c superconductivity and quantum criticality. In our recent work, we investigated AFM order in layered iridates, which is a newly established Mott system similar to cuprates but features a strong spin-orbit coupling. By building the spin-orbit Mott insulators as superlattices composed of perovskite $SrIrO_3$ and $SrTiO_3$, we gained controllability in the strength and sign of interlayer exchange interaction [1]. This enables one to reach the two-dimensional limit of the antiferromagnet, where the ordering temperature is only governed by magnetic anisotropy. The two-dimensional antiferromagnet preserves a hidden SU(2) symmetry, which was first proposed in cuprates but never experimentally realized. More specifically, model analysis reveals that Dzyaloshinskii–Moriya interaction in the square-lattice magnet does not contribute to the spin anisotropy. The extremely strong two-dimensional critical fluctuations enable us to achieve giant AFM responses to sub-tesla uniform external fields. The observed field-induced logarithmic increase of the AFM ordering (Fig. 1) demonstrates a new pathway for designing efficient AFM spintronics [2].

[1] L. Hao, D. Meyers, C. Frederick, G. Fabbris, J. Yang, N. Traynor, L. Horak, D. Kriegner, Y. Choi, J.-W. Kim, D. Haskel, P.J. Ryan, M.P.M. Dean, and J. Liu, *Two-Dimensional J_{eff}=1/2 Antiferromagnetic Insulator Unraveled from Interlayer Exchange Coupling in Artificial Perovskite Iridate Superlattices*, Phys. Rev. Lett. 119, 027204 (2017). [2] L. Hao, D. Meyers, H. Suwa, J. Yang, C. Frederick, T.R. Dasa, G. Fabbris, L. Horak, D. Kriegner, Y. Choi, J.-W. Kim, D. Haskel, P.J. Ryan, H. Xu, C.D. Batista, M.P.M. Dean, and J. Liu, *Giant magnetic response of a two-dimensional antiferromagnet*, Nat. Phys. 14, 806–810 (2018).

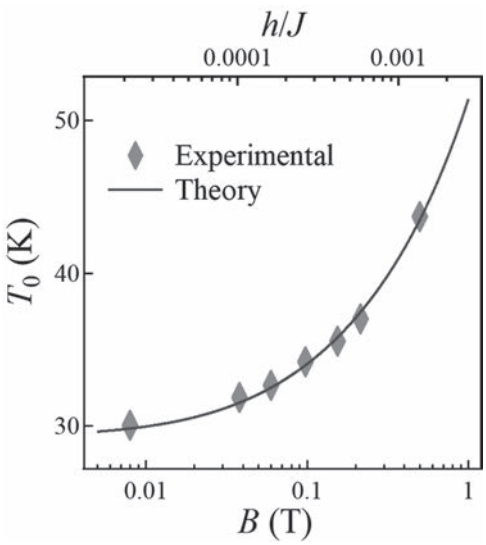


Fig. 1. Comparison between the measured field-dependence of the ordering temperature T_0 (Markers) and the logarithmic increase (line) expected for a quasi-2D antiferromagnet with a hidden SU(2) symmetry [2].

CONTRIBUTED PAPERS

10:54

EI-09. Spin disorder near nonmagnetic impurities in $YMnO_3$. *S. Lim*[1], H. Sim[2,3], K. Park[2,3], J. Park[2,3] and S. Lee[1] *1. Department of Physics, KAIST, Daejeon, The Republic of Korea; 2. Center for Correlated Electron Systems, Institute for Basic Science (IBS), Seoul, The Republic of Korea; 3. Department of Physics and Astronomy, Seoul National University, Seoul, The Republic of Korea*

Magnetic moment is induced around nonmagnetic impurities in geometrically frustrated magnets due to readjustment of neighboring spins. This vacancy-induce magnetism is in contrast to the magnetic impurities in nonmagnetic bath. We studied effects of nonmagnetic Al/Ga impurities in magnetic bath $YMnO_3$ by the magnetization, heat capacity, and NMR measurements. Suppression of Neel order with increasing doping rate was evidenced by the heat capacity and M-T curve which also shows the Curie tail. We found that the vacancies in frustrated magnets release the local frustration partially by readjustment of the spin directions around the impurity. A Monte-Carlo simulation [1] predicts that a nonmagnetic impurity in 120° spin structure carries magnetic moment of $\langle m \rangle \sim 0.04S$. Impurity moment estimated from our susceptibility data is $\langle m \rangle \sim 0.1S$. Interestingly, our NMR results show that the amplitude of the impurity moment $|m|$ is an order of magnitude bigger than that of the bulk average value $|\langle m \rangle|$. Triangular spin structure predicts the angle-dependent spectrum with 60° symmetry, while the observed spectrum (Fig. 1) was not. This means that the direction of the neighboring spins generating the hyperfine field at a nonmagnetic impurity site is quite random. The magnitude of the impurity moment estimated from the distribution of the hyperfine field is $|m| \sim S$. The spins compensating the missing magnetic moment near a nonmagnetic impurity in $YMnO_3$ are disordered.

[1] A. Wollny *et al.*, Phys. Rev. Lett. Vol. 107, p.137204 (2011).

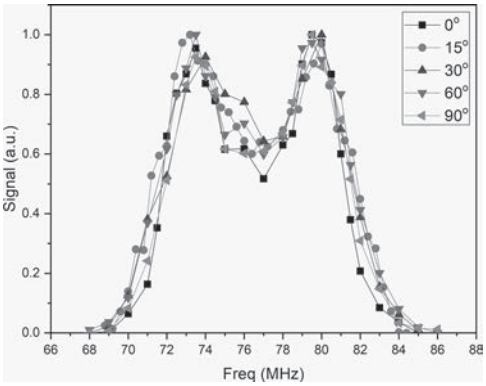


Fig. 1: Angle independence of ^{27}Al NMR spectra of $YMn_{0.9}$ $Al_{0.1}O_3$ obtained at 4 K and 7 T. The external field is rotated from the crystal axis [110] to [1-10].

11:06

EI-10. Understanding Magnetic Exchange Interactions through the Pressure Dependence of the Susceptibility in FeCoNiCuMn High Entropy Alloys. *A.E. Perrin*[1], S.K. McCall[2], M. McElfresh[2], D.E. Laughlin[1] and M. McHenry[1] *1. Materials Science and Engineering, Carnegie Mellon University, Pittsburgh, PA, United States; 2. Lawrence Livermore National Lab, Livermore, CA, United States*

Curie temperature engineering in metals with direct exchange interactions is based on understanding the dependence of Tc on interatomic distances and magnetic d-orbital overlap that determine J_{ex} as described by the Bethe-Slater curve. The Bethe-Slater curve predicts the dependence J_{ex} on D/d, with D the transition metal interatomic spacing and d the spatial extent of magnetic d-orbitals. We analyze the pressure (P) dependence of the Curie temperature, T_c, in a FeCoNiCuMn high entropy alloy (HEA), considering d-orbital contraction to explain changes in magnetic exchange interactions (J_{ex}) with reference to the Bethe-Slater curve. We combine considerations of d-radius contraction based on the composition dependence of T_c in g-Fe-Ni with experimental magnetic measurements of T_c (Fig. 1a) and data for the P-dependence of lattice constants (Fig. 1b) to calculate the contribution of changes in atomic spacing and d-orbital radii to J_{ex}. Unlike many textbook discussions of the dependence of J_{ex} on D, we show that the contraction of the d-orbitals with P accounts for the majority of the T_c change in this HEA system, which is very clear when the term accounting for the change in atomic spacing is plotted against the term accounting for change in d-orbital extent (Fig. 1c).

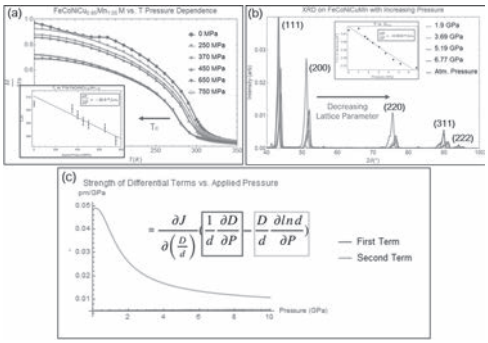


Fig.1 (a) Magnetization versus temperature for an FeCoNiCuMn HEA with linearly decreasing T_c versus pressure. (b) XRD data showing linearly decreasing atomic spacing with applied pressure. (c) The strength of the contributions from atomic spacing deriative term versus d-orbital extent derivative term to the change in T_c vs pressure.

11:18

EI-11. Influence of sample quality on the physical properties of the S=1 antiferromagnetic spin-ladder CaV_2O_4. S. Hiller[1], S. Guitarra[1], A. Caneiro[2], M. Salamon[3] and *D. Niebieskikwiat*[1] *1. Departamento de Física, Universidad San Francisco de Quito, Quito, Ecuador; 2. Instituto Balseiro - Centro Atómico Bariloche, Bariloche, Argentina; 3. The University of Texas at Dallas, Richardson, TX, United States*

In this work we study the magnetic and transport properties of different CaV_2O_4 samples. This compound presents quasi one-dimensional (1D) V chains, with an antiferromagnetic (AFM) S=1 spin-ladder ground state. Due to this 1D characteristic, it is expected that the physical properties of CaV_2O_4 are very sensitive to impurities, defects, and disorder in general. Indeed, different previous works show dissimilar results about the magnetic response of this vanadium oxide. Here, we study several CaV_2O_4 samples prepared by different methods and conditions (solid-state and wet-chemical routes), showing the influence of the sample quality on the physical properties of this material. We find that defects in CaV_2O_4 induce local ferromagnetic correlations that generate exchange bias. Also, electrical transport can be satisfactorily described by a Variable-Range Hopping (VRH) model with a characteristic exponent for each sample determined by the density of defects in the V chain. Notably, the nitrate decomposition route produces a better quality sample with a higher order temperature.

Session EP
MRAM, MAGNETIC LOGIC, NEUROMORPHIC COMPUTING, AND RELATED DEVICES (Poster Session)

Satoru Emori, Co-Chair
Virginia Tech, Blacksburg, VA, United States
Ye Du, Co-Chair
Tohoku University, Sendai, Japan

EP-01. Non-volatile NDR-assisted Magnetic Half-adder. *Z. Lu*[1] and X. Zhang[1] *1. School of Material Science & Engineering, Tsinghua University, Beijing, China*

Conventional logic gates in computers based on CMOS are volatile and require frequent communication with external storage units, which causes the von-Neumann bottleneck that limits computers' speed [1]. Magnetic logic device, however, benefiting from magnetic material's non-volatile feature, has become a promising candidate to achieve logic-in-memory architecture to solve this problem[2]. In order to build the counterpart of CMOS-based arithmetic logic units (ALU) using spin-based logic devices, both logic functions and arithmetic functions should be achieved. In recent years, widespread research has been conducted and people have found several ways to realize simple logic gates such as AND, OR, NAND, NOR and NOT[3][4], but only few based on STT-MTJ could perform arithmetic functions in experiments because of risk of tunnel barrier breakdown and complex peripheral CMOS circuit[5]. Here, we proposed a noval non-volatile magnetic logic device working at room temperature based on coupling of anomalous Hall effect of Ta/CoFeB/MgO multilayers with perpendicular magnetic anisotropy (PMA) and negative differential resistance (NDR) phenomenon in semiconductor. With simple peripheral circuit consist of semiconductor elements with NDR, our device not only could perform Boolean logic operations AND, NOR, XOR and XNOR, but could also work as a half-adder without cascading. Since the logic function of our device was not resulted from spin transfer torque, there was little risk of device breakdown caused by tunneling barrier damage. By randomly changing the logic input of our device continually, the reliability of our device was also confirmed. Since our device is current-driven, it has the potential to bridge the von-Neumann bottleneck by integrating computing with memory writing via spin orbit torque-induced magnetization switching.

[1] Z. Luo, Z. Lu, C. Xiong, et al. Advanced Materials. Vol. 29, p.1605027 (2017) [2] G. A. Prinz, Science., Vol. 282, p.1660 (1998) [3] S.-h. C. Baek, K.-W. Park, D.-S. Kil, et al. Nature Electronics., Vol. 1, p.398-403 (2018) [4] W. J. Kong, C. H. Wan, X. Wang, et al. Nature communications. Vol. 10, p.233 (2019) [5] S. Matsunaga, J. Hayakawa, S. Ikeda, et al. Applied Physics Express. Vol. 1, p.091301 (2008)

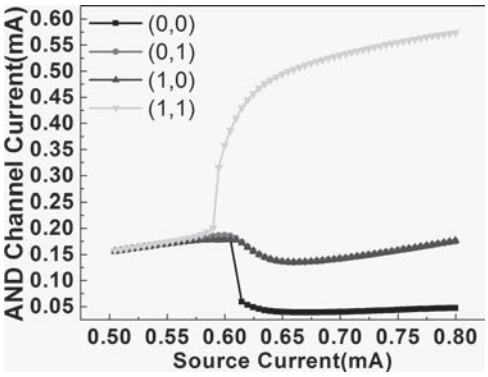


Fig.1 Output current in AND output channel corresponding to different logic inputs.

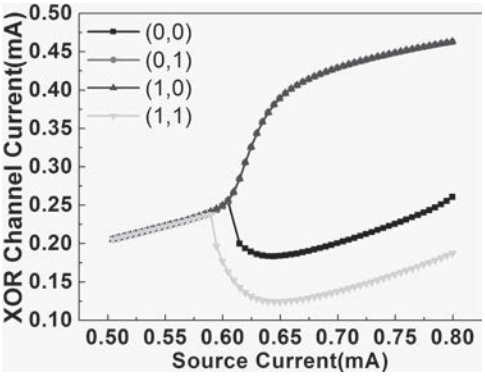


Fig.2 Output current in XOR output channel corresponding to different logic inputs, Fig.1 and 2 proved that our device was capable of working as a half-adder.

EP-02. Closely packed magnetic tunnel junction arrays for reservoir computing. *H. Kubota*[1], K. Yakushiji[1], A. Fukushima[1], S. Tamaru[1], S. Tsunegi[1], T. Taniguchi[1], A. Sugihara[1], T. Nozaki[1], T. Yamamoto[1], T. Nozaki[1], S. Yuasa[1], M. Goto[2,3], K. Takahashi[2], H. Nomura[2,3] and Y. Suzuki[2,3] *1. National Institute of Industrial Science and Technology (AIST), Tsukuba, Japan; 2. Osaka University, Toyonaka, Japan; 3. CSRN-Osaka, Toyonaka, Japan*

Magnetically coupled nanomagnets have been investigated for many years as an energy-efficient resource of computation[1]. The magnetic coupling causes magnetic frustration, which can drive information processing with low energy cost. High integration of the nanomagnets, which is established in modern MRAM technology[2], would enhance the computational capability. Recently reservoir computing, which is one of the frameworks in recurrent neural network, is intensively investigated because of simple learning process and high compatibility with electronic hardware[3-6]. H. Nomura et al. simulated that a dipole-coupled 2x10 magnetic dot array can perform binary logic functions using reservoir computing scheme[7]. In this study, we develop a physical reservoir using an MTJ array. In the array, the gap between MTJ dots (*g*) should be very small (~20 nm) so that the magnetic coupling is strong enough. Individual electric access to the dots is necessary to detect magnetizations in the dots influenced by the coupling. The MTJ films prepared by a UHV magnetron sputtering had a stack of buffer layer/Co-Pt based fixed layer/MgO/CoFeB free layer/MgO cap layer/metal cap layer, where CoFeB free layer was basically perpendicularly magnetized. The film had an MR ratio of about 100% and resistance-area product of about 3 $\Omega\mu m^2$. After deposition, the films were patterned into 8×8 MTJ arrays with various *g* and diameter of dot (*d*) using EB lithography combined with etching and lift-off technique. Fig. 1 shows a SEM image of the fabricated reservoir, in which fine patterns of top leads (Cu) were connected to central 2×6 dots. Cross-sectional TEM observation indicated that the MTJ dots had tapered shape and that the free layers in neighboring dots were isolated. The smallest *d* and *g* were 60 nm and 20 nm, respectively. Such a small gap can realize strong magnetic coupling required in the reservoir computing operation. This research and development is partly supported by the Ministry of Internal Affairs and Communications.

1) R.P. Cowburn and M.E. Welland, Science. 287, 1466 (2000). 2) S.-W. Chung, et al., IEEE IEDM, p. 27.1.1 (2016). 3) L. Appeltant, et al., Nat Commun. 2, 468 (2011). 4) K. Nakajima, et al., Sci Rep. 5, 10487 (2015). 5) J. Torrejon, et al., Nat. 547, 428 (2017). 6) R. Nakane, et l., IEEE Access. 6, 4462 (2018). 7) H. Nomura, et al., Jpn. J. Appl. Phys. 58, 070901 (2019).

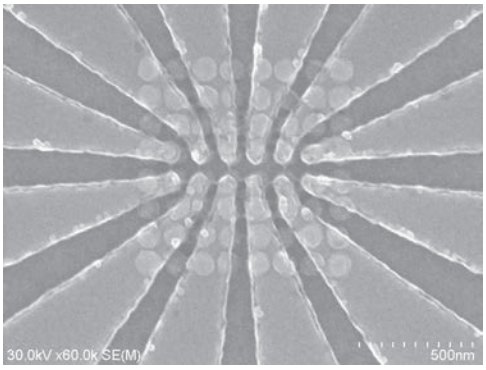


Fig. 1 A SEM image of the reservoir of an 8×8 MTJ array with *d*=80 nm and *g*=40 nm. Top leads were connected to central 2×6 dots. MTJ dots under the top leads are visible because of high voltage observation (30 kV).

EP-03. Investigation of Radiation Effect on Magnetic Tunnel Junction against Proton and Ion Beam. *J. Park*[1], J. Kim[1], J. Ryu[1], J. Jeong[1] and B. Park[1] *1. Materials Science and Engineering, Korea Advanced Institute of Science and Technology (KAIST), Daejeon, The Republic of Korea*

Conventional semiconductor-based electronic devices can cause errors when they are exposed to cosmic rays. Magnetic memory has been proposed as an alternative because it consists of a metal structure free from radiation-induced errors in principle. Although there are several reports on the radiation hardness of magnetic random access memory (MRAM) [1,2] and magnetic tunnel junction (MTJ) [3,4], their radiation conditions were limited to a dose level of up to $1x10^{12}cm^{-2}$ and an energy of MeV ranges. In this study, we investigate the radiation hardness of MTJ for proton and Cr ion beams of dose levels up to $1x10^{14}cm^{-2}$ using an in-plane MTJ of Ta(5)/Pt(10)/IrMn(30)/CoFeB(5)/MgO(2)/CoFeB(10) /Ru(5) and a perpendicular MTJ of W(4)/CoFeB(1.2)/MgO(3.5)/CoFeB(2.0)/W(4)/Ru(5) structures, where the numbers in parentheses are in nm. We observed that the magnetic hysteresis and tunnel magnetoresistance (TMR) of MTJs were not affected by proton irradiation of an energy of 20 MeV and dose levels up to $1x10^{14}cm^{-2}$, thus demonstrating good radiation hardness in response to the proton beam (Fig. 1). On the other hand, when a MTJ was irradiated by a Cr ion beam of an energy of 20 keV and dose levels up to $1x10^{14}cm^{-2}$, its magnetic properties or TMR deteriorated (Fig. 2). Simulation study shows that the protons penetrate through the entire MTJ structure, leaving negligible displacement damages, whereas Cr ions deposit within the MTJ structure, inducing significant damage. Our study suggests that the degradation of the MTJ may stem from radiation-energy dependent displacement damage in the magnetic layers, which can be avoided by the introduction of a proper protective layer.

[1] D. N. Nguyen and F. Irom, 2007 9th European Conference on Radiation and Its Effects on Components and Systems (2007) 628-631. [2] R. R. Katti *et al.*, 2009 IEEE Radiation Effects Data Workshop (2009) 103-105 [3] Harold Hughes *et al.*, IEEE Trans. Nucl. Sci. 59(6) (2012) 3027-3033. [4] Daisuke Kobayashi *et al.*, IEEE Trans. Nucl. Sci. 61(4) (2014) 1710-1716.

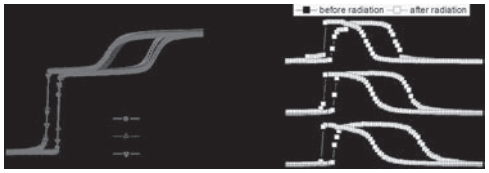


Fig.1 (a)Magnetic hysteresis curves and (b) TMR curves after 20MeV proton beam irradiation with $1x10^{12}cm^{-2}$, $1x10^{13}cm^{-2}$, $1x10^{14}cm^{-2}$.

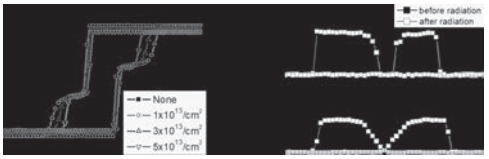


Fig.2 (a)Magnetic hysteresis curves and (b) TMR curves after 20keV Cr ion beam irradiation with $1x10^{13}cm^{-2}$, $3x10^{13}cm^{-2}$, $5x10^{13}cm^{-2}$.

EP-04. Six-State Magnetic Tunnel Junction Memory Driven by Spin Hall Effect. *M. Alawein*[1], S. Amara[1], S. Wasef[1], U. Myrzakhan[1] and H. Fariborzi[1] *1. Electrical Engineering, King Abdullah University of Science and Technology, Thuwal, Saudi Arabia*

This work reports the fabrication and characterization of a memory based on spin Hall effect driven nanomagnet with six-fold configurational anisotropy [1]. The proposed memory (Fig. 1(a)) is comprised of a $Pt/Ni_{81}Fe_{19}$ (Py) multilayer, and its states are written and read electrically. The six-state nanomagnet is made by patterning a 3-nm-thick Py in the shape of an equilateral triangle [2] to introduce a six-fold configurational anisotropy (Fig. 1(b)), the presence of which is verified by OOMMF (Fig. 1(c)). For writing, a charge current is passed between a pair of pads. The charge current in Pt generates a transverse spin current that switches the Py magnetization. The magnetic information is read via a magnetic tunnel junction (MTJ), which can be either symmetric or asymmetric, where the latter type consists of a tilted elliptical layer and is used to remove resistance degeneracy. The reading is done by measuring the MTJ resistance which varies according to [3–5] $R_\beta = (1/2)(R_P + R_{AP}) - (1/2)(R_{AP} - R_P)\cos(\beta)$ where R_P and R_{AP} are the resistances in the parallel and antiparallel states, respectively. After every read operation, a writing process follows by passing a current of magnitude I_{write} = 10 mA. Figs. 2(a) and 2(b) shows tunnel magnetoresistance (TMR) plots for the symmetric and asymmetric MTJs, respectively. For the symmetric (asymmetric) MTJ, a minimum resistance separation of 6.3% (3.5%) was observed. In addition, in Fig. 2(c) we show TMR plots of five different asymmetric MTJ samples, and in Fig. 2(d) we show resistance-time curve of an asymmetric MTJ. We have also investigated the memory's read endurance by performing pulsed measurements until the MgO breakdown (Fig. 2(e)).

[1] R. Cowburn, A. Adeyeye and M. Welland, *Physical Review Letters*, vol. 81, no. 24, pp. 5414-5417 (1998). [2] M. Alawein, S. Amara and H. Fariborzi, *IEEE Magnetics Letters*, vol. 10, pp. 1-5 (2019). [3] S. Wasef et al., *Proc. 2nd IEEE Electron Devices Technology and Manufacturing Conf.*, pp. 298-300 (2018). [4] Y. Telepinsky et al., *Applied Physics Letters*, vol. 108, p. 182401 (2016). [5] Y. Zheng et al., *IEEE Transactions on Magnetics*, vol. 38, pp. 2850-2852 (2002).

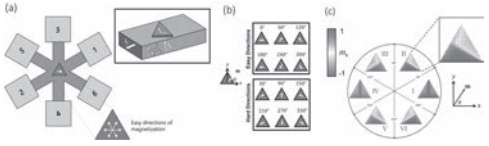


Fig.1 (a) Six-state memory structure. The inset illustrates the transverse spin current injected into Py due to the passage of a charge current in Pt. (b) Easy and hard directions of magnetization. (c) OOMMF simulation of a 3-nm-thick Py of side length a = 3 μm illustrating the stable "buckle" states.

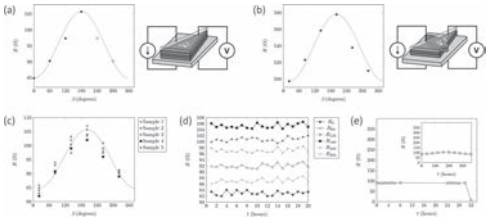


Fig.2 TMR curves of the (a) symmetric (a = 3 μm) and (b) asymmetric (a=5 μm) MTJs. (c) TMR curves of five different samples (a = 5 μm). (d) 20 hours retention measurements of a sample (a = 5 μm). (e) Endurance measurements of a sample (a = 5 μm).

EP-05. $L1_0$-(MnCo)Al thin film with high perpendicular magnetic anisotropy grown on Pt seed layer. *L. Yu*[1], M. Oogane[1], M. Tsunoda[2] and Y. Ando[1] *1. Department of Applied Physics, Tohoku University, Sendai, Japan; 2. Department of Electrical Engineering, Tohoku University, Sendai, Japan*

Spin-orbit torque (SOT) induced magnetization switching in heavy metal (HM) / ferromagnetic metal (FM) heterostructures has been devoted lots of research attention as it shows promise for future ultrafast and power conservation magnetic memories [1]. For FM layers, magnetic thin films with high perpendicular magnetic anisotropy (PMA) are needed, which promote research of Mn-based alloys, such as $L1_0$-MnAl with high PMA [2]. These Mn-based alloys have always been deposited on buffer layers such as Cr, CoGa, etc. [3-4], instead of heavy metals or heavy metal-based alloys which were well studied to possess a high spin Hall angle, such as Pt and PtMn [5-6], and the properties such as magnetic features and crystal structures of these Mn-based alloys deposited on Pt or PtMn are still unrevealed. In this work, we report the crystal and magnetic properties of $L1_0$-(MnCo)Al thin films (light-doped Co into MnAl) deposited on Pt seed layer. All the samples were prepared by magnetron sputtering system. The stacking structures were MgO(001) sub. / Pt (5) / $Mn_{0.97}Co_{0.03}Al$ (20) / Ta (3) in nm. The substrate temperature (T_s) has been tuned from 150°C to 400°C during the deposition of MnCoAl layer. The crystal structure and magnetic properties were respectively measured by X-ray diffraction (XRD) and superconducting quantum interference device (SQUID). Fig. 1 shows the XRD patterns of the prepared films with various T_s. The $L1_0$ MnCoAl (001, 002) peaks are the signature of crystallization in tetragonal $L1_0$ phase. 001 and 002 peaks disappeared when T_s above 300°C, which indicate the transition to other phases. On the other hand, the intensity of Pt (002) peak decreased with increasing T_s, which was considered that Pt diffused into (MnCo)Al layers at a high temperature. Fig. 2 shows the magnetic properties of prepared samples shown in Fig. 1. Although PMA magnitude K_u^{eff} decreased rapidly with temperature above 300°C corresponding to the phase transition which has been observed in Fig. 1, we have achieved a high K_u^{eff} of 4 Merg/cc at T_s = 300°C in the (MnCo)Al films grown on Pt seed layer.

[1] Ramaswamy, *et al*. Appl. Phys. Rev. 5.3, p.031107 (2018). [2] Mizukami, S., *et al*. Scr. Mat. 118, p.70-74 (2016). [3] Li, Mingyang, *et al*. Applied Physics Letters 103.3, p.032410 (2013). [4] Suzuki, K. Z., *et al*. Applied Physics Letters 112.6, p. 062402 (2018). [5] Sinova, Jairo, *et al*. Reviews of Modern Physics 87.4, p. 1213 (2015). [6] Baltz, V., *et al*. Reviews of Modern Physics 90.1, p. 015005 (2018).

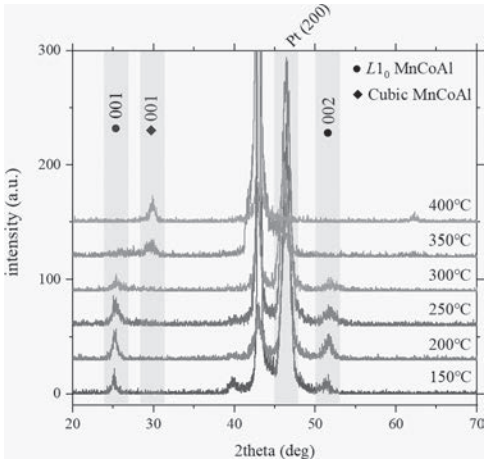


Fig. 1 XRD pattern of (MnCo)Al films grown with various T_s.

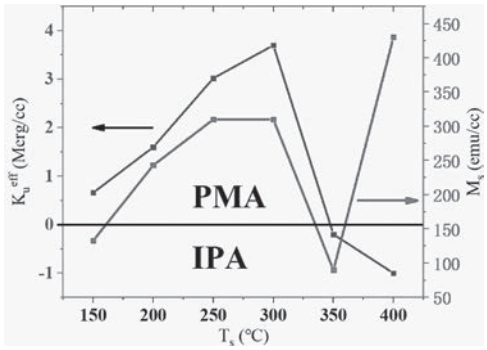


Fig. 2 magnetic properties of (MnCo)Al films grown with various T_s

EP-06. STT-MRAM Error Correction Technology Based on LDPC Coding. *X. Zhang*[1] and Y. Jiang[1] *1. Internet of Things Engineering, Jiangnan University, Wuxi, China*

Spin-transfer torque magnetic random access memory (STT-MRAM) is a new generation non-volatile memory. It is regarded as the most popular memory because of its fast reading/writing speed and "unlimited" endurance [1]. As a single device, STT-MRAM is consistent of a magnetic tunnel junction (MTJ) and a metal oxide semiconductor (MOS). STT-MRAM implements information writing by controlling the direction and magnitude of current flowing through the MTJ. The information reading is performed by detecting the voltage across the MTJ. The writing error of MTJ is usually occurs when the pulse width is less than the switch time or the applied current is less than the switch current I_{CO}. The reading error occurs when the read current is larger than I_{CO}, resulting in an error flip from 1 to 0 or 0 to 1. In STT-MRAM arrays, a single cell's read and write failures will cause the row or the column to fail. It is necessary to design error correction circuits in the array of STT-MRAM to improve overall performance. Well known, static random access memory (SRAM), dynamic random access memory (DRAM), and Flash use error-correcting codes (ECC) to reduce the error rate [2-4]. Recently, some researchers have paid more attention to studying ECC in STT-MRAM. C. Yang et al studied the Bose-Chaudhuir-Hocquenghem (BCH) error correction mechanism for STT-MRAM [5]. As the storage capacity of MRAM increases, the error rate gradually increases. BCH will not be able to meet the requirements. As we all known, the performance of the Low Density Parity Check (LDPC) code not only approaches the Shannon limit, but also has strong error correction capability. In this work, we used LDPC code with higher error correction capability in STT-MRAM for the first time, as far as the authors know. Firstly, we introduced the basics of the STT-MRAM model and LDPC codes. Secondly, we designed and simulated LDPC codes for STT-MRAM read and write failures. Finally, the results are discussed and analyzed. Our research shows that LPDC codes

have the advantages of high coding rate and fast decoding speed compared to other ECCs. This work is supported by the National Natural Science Foundation of China (No.61774078).

[1] J. J. Kan, C. Park, C. Ching et al., 2016 IEEE International Electron Devices Meeting, p.27.4.1 (2016) [2] S.-S. Pyo, C.-H. Lee, G.-H. Kim et al., IEEE International Symposium on Circuits and Systems, p.2517 (2009) [3] P. Reviriego, A. Sánchez-Macian, and J. A. Maestro, 18th IEEE International On-line Testing Symposium IEEE Computer Society, p.79 (2012) [4] K.-C. Ho, P.-C. Fang, H.-P. Li et al., IEEE International Solid-State Circuits Conference Digest of Technical Papers. IEEE, p.222 (2013) [5] C. Yang, Y. Emre, Y. Cao et al., EURASIP Journal on Advances in Signal Processing, Vol.211, p.1 (2012).

EP-07. Industrial Level Thermal Model of STT-MTJ Device with Parameter Extraction. *Y. Jiang*[1] and L. Jiang[2] *1. Jiangnan University, Wuxi, China; 2. UC Berkeley, Berkeley, CA, United States*

Spin-Transfer Torque RAM (STT-RAM) has emerged as a potential candidate for Universal memory. The development of industrial level spice model of STT-MTJ device is a key aspect of exploring the potential of STT-RAM. Several SPICE compatible MTJ models have been reported in the past for the simulation of the spintronic circuit. For a SPICE model to be useful in industrial level in MRAM simulation work, the model should be applicable at different temperature and at the same time be fully-compatible with SPICE. To satisfy these requirements, the industrial level thermal model with parameter extraction is proposed in the paper. To set up a compact model to describe the thermal properties of the MTJ device, three key parameters, conductance at 0 K (G_0), polarization at 0 K (P_0) and a material-dependent constant (α), are extracted from experimental measurements. The influence of the temperature on the conductance of the MTJ device can be described accurately by using the extracted parameters. Simulation based on the compact temperature model is conducted to demonstrate the feasibility of the designed thermal model, showing wide range of linearity. Beyond the static thermal property, the dynamic thermal reaction is also included in the thermal model. To verify the above analysis, the thermal reaction is observed by the model's simulation. The simulation results are shown in Fig.1, corresponding to different states, varied from 1.03 ns to 3.31 ns. It can be seen that the thermal transition can be done in nano-seconds at suitable pulse amplitude. Above all, the thermal model for spin-transfer-torque operated magnetic tunnel junction (STT-MTJ) is proposed and described in Verilog-A language, which led to more accurate electrical simulations while maintaining better efficiency without obvious additional run time and memory resource.

[1] Yanfeng Jiang, Jian-Ping Wang, "Magnetic Tunnel Junction-Based Spin Register for Nonvolatile Integrated Circuits," *IEEE Transactions on Electron Devices,* vol. 59, pp. 2917-2923, 2012. [2] Y. Jiang, Y. Lv, M. Jamali, and J.-P. Wang, "Spin analog-to-digital convertor using magnetic tunnel junction and spin Hall effect," *IEEE Electron Device Letters,* vol. 36, pp. 511-513, 2015. [3]J.A.Katine, R.A.Buhrman, E.B.Myers, and D.C.Ralph, "Current-driven magnetization reversal and spin-wave excitations in co/cu/co pillars," *Physical Review Letters,* vol. 84, pp. 3149-3152, 2000.

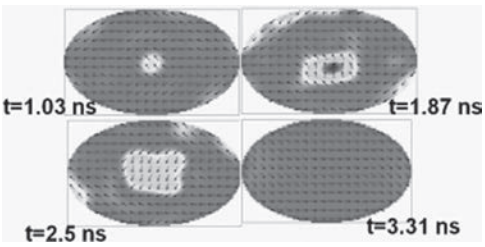


Fig.1 Simulation results of the dynamic thermal reaction by using the thermal model

EP-08. Passive and active microwave signal detection using magnetic tunnel junctions with perpendicular magnetic anisotropy. *A. Sidi El Valli*[1], V. Iurchuk[1], N. Lamard[1], A. Chavent[1], J. Langer[2], J. Wrona[2], B. Dieny[1], I. Prejbeanu[1], L. Vila[1], R. Sousa[1] and U. Ebels[1] *1. Univ. Grenoble Alpes, CEA, CNRS, G-INP, IRIG-SPINTEC, Institute of Engineering Univ. Grenoble Alpes, SPINTEC, Grenoble, France; 2. Singulus Technologies AG, Kahl, Germany, Kahl, Germany*

Perpendicular magnetic tunnel junctions (pMTJs) are key elements for the development of spin transfer torque magnetic memories (STT-MRAM). pMTJs exploit the interfacial perpendicular magnetic anisotropy (iPMA) to define the out-of-plane orientation of the free (FL) and reference layers (RL) [1]. Meanwhile pMTJs are also expected to provide microwave spintronic functions such as rf signal generation and detection giving added value for multifunctional operation. Here we report on the microwave signal detection of such pMTJs with similar stacks as presented in [2] and evaluate the obtained performances for applications such as rf power harvesters [3] and frequency selective demodulators. The detection method is based on the rectification effect that generates a DC voltage signal when the frequency of the rf input signal to be detected is close to the FL or RL ferromagnetic resonance frequency. Measurements were performed (i) without dc current (passive detection) and with dc current (active detection), (ii) under in-plane and out of plane static magnetic fields as well as (iii) for devices of different FL magnetization orientation by varying the FL thicknesses: t_{FL}=1.4 out-of-plane and t_{FL}=1.8 nm in-plane. It is found that the DC output voltage V_{dc} lies in the 1-10mV range for the different measurement conditions and devices. For devices with t_{FL}=1.8 nm, we demonstrate a strong dependence of V_{dc} on the device diameter, with an increase by a factor of three (five) reaching values of 5mV (V_{dc}=28mV) when reducing the diameter from 150 nm to 40 nm for passive (active) detection at input power levels of -5 dBm. These findings give prospect to utilize pMTJs as nanoscale microwave detectors for power harvesting and/or for short range communication applications. The authors acknowledge funding support from the Fondation Nanosciences, Grenoble; from ERC MagiCAL (N° 669204) and the EU Horizon 2020 project GREAT (No. 687973).

[1] S. Ikeda, et al., Nature Materials 9, 721 (2010) [2] W. Skowronski, et al., Appl. Phys. Express 5, 063005 (2012) [3] B. Fang, et al., AIP Adv. 6, 125305 (2016)

EP-09. The Design of 1Gb Parallel STT-MRAM with Pipeline Architecture. *G. Zhang*[1] and Y. Jiang[1] *1. School of Internet of Things Engineering, Jiangnan University, Wuxi, China*

Spin transfer torque (STT) magnetic RAM (MRAM) is the only emerging memory technology that combines endurance, speed and energy efficiency of SRAM and DRAM with non-volatility of flash. In write operation, the STT-MRAM memory array receive the addresses and control commands through control register. And the input data and clock signals are submitted into the memory array by a register. Compare with conventional STT-MRAM, the pipeline architecture of STT-MRAM has an additional register between memory array and sense amplifier as shown in Fig.1. The first decode output A0 from the previous clock can be latched by the additional register in the rising edge of the next clock. So the decode output A1 can be fetched in the second clock, and the A0 can be amplified by SA at the same time. In the third clock, the address A2 can be decoded and the A1 can be latched. As a result, the total data read time will be greatly shortened as shown in Fig.2. Therefore the pipeline STT-MRAM has the better real-time response and lower-latency memory access. It is necessary for STT-MRAM to improve the read efficiency. Until now, there have been a great number of studies in pipeline architecture of various memories, such as DRAM, SRAM, and Flash [1-3]. Recently, K. Swaminathan *et al* have utilized the characteristics of STT-MRAM for providing protection of all storage structures in the pipeline, which can reduce soft error vulnerability and enhance system reliability [4]. In this paper, 1Gb parallel STT-MRAM with pipeline architecture has been demonstrated. Firstly, 1Gb STT-MRAM memory array is divided into suitable several blocks to enhance operation efficiency. Secondly, based on the design of blocks and SA, an additional register is

arranged between each decoder and SA. Finally, the overall circuit structure is simulated and discussed. The results show that the pipeline architecture of 1Gb parallel STT-MRAM can greatly shorten the total read time and enhance the read performance.

[1] O. Takahashi, S. H. Dhong, M. Ohkubo, IEEE International Solid-state Circuits Conference Digest of Technical Papers, p.396-397 (2000) [2] Z. Lin, X. Wu, Z. Li, Lin Z, IEEE Journal of Solid-State Circuits, vol.52, p. 669-677 (2017) [3] S. Kajiyama, M. Fujito, and H. Kasai, IEEE Asian Solid-state Circuits Conference, p.257-260 (2009) [4] K. Swaminathan, R. Mukundrajan, N. Soundararajan, Proceedings of the 2011 IEEE Computer Society Annual Symposium on VLSI, p.236-241 (2011)

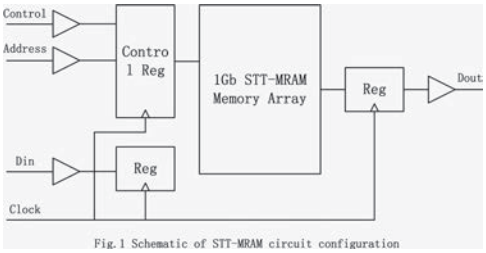


Fig. 1 Schematic of STT-MRAM circuit configuration

Fig.1

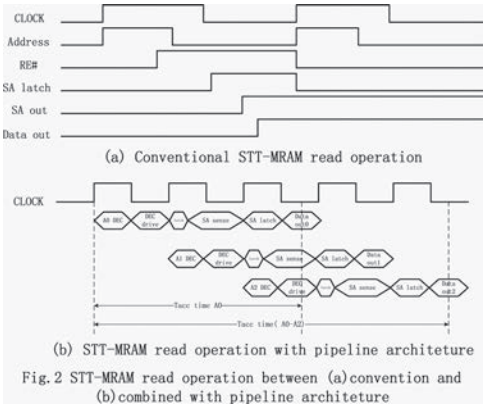


Fig. 2 STT-MRAM read operation between (a)convention and (b)combined with pipeline architeture

Fig.2

EP-10. Synchronization of Stochastic Magnetic Oscillators Based on Thermally Stable Magnetic Tunnel Junctions by Supply Voltage Modulation. *Y. Lv*[1], R. Bloom[1], B.R. Zink[1] and J. Wang[1] *1. Department of Electrical and Computer Engineering, University of Minnesota, Minneapolis, MN, United States*

Synchronization of stochastic oscillators is one of the key tasks for developing oscillator based probabilistic computing schemes. Spintronic stochastic oscillators made of thermally unstable magnetic tunnel junctions (MTJs) can be synchronized by alternating current applied on the MTJ generating alternating spin-transfer torque (STT)[1]. On the other, a thermally stable MTJ can also be driven by a static voltage source to act as a stochastic oscillator[2]. In this work, we experimentally demonstrate synchronization of stochastic magnetic oscillators based on such thermally stable MTJs As shown in Fig. 1, when the MTJ is in antiparallel (AP) state, it switches to parallel (P) state due to reduced energy barrier by magnetic field (H_{ext}) and thermal fluctuation. When in P state, the MTJ draws more current from the supply voltage source, and more STT switches it back to AP state. In this way, thermally stable MTJ is driven to stochastically oscillate between two states. Then we add a square wave modulation to the supply voltage (Fig. 1, left). When the supply voltage is slightly higher, stronger STT favors P to AP transition, while when the supply voltage is lower, external field makes AP to P transition more likely. Therefore, although the oscillation of MTJ is still stochastic to some extent, it is clearly synchronized to the supply voltage modulation. Fig. 2 shows experiment results. The V_{supply} is modulated as a square wave on an offset; the V_{MTJ} is the MTJ's current sensed by a resistor that represents its oscillation (high voltage is P state). The MTJ's oscillation is synchronized to supply voltage modulation while exhibiting some randomness. Furthermore, correlation between the V_{MTJ} and V_{supply} is shown as C_M XNOR C_S (and its time average). The XNOR of the two is greater than 0.5 so that the synchronization is confirmed.

[1] N. Locatelli *et al.*, "Noise-Enhanced Synchronization of Stochastic Magnetic Oscillators," *Phys. Rev. Appl.*, vol. 2, no. 3, p. 034009, Sep. 2014. [2] B. R. Zink, Y. Lv, and J. P. Wang, "Telegraphic switching signals by magnet tunnel junctions for neural spiking signals with high information capacity," *J. Appl. Phys.*, vol. 124, no. 15, p. 152121, Oct. 2018.

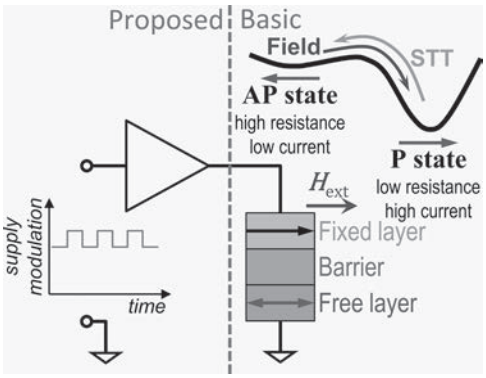


Fig. 1. Basic operation of thermally-stable-MTJ-based stochastic oscillator (right) and proposed synchronization by supply voltage modulation (left).

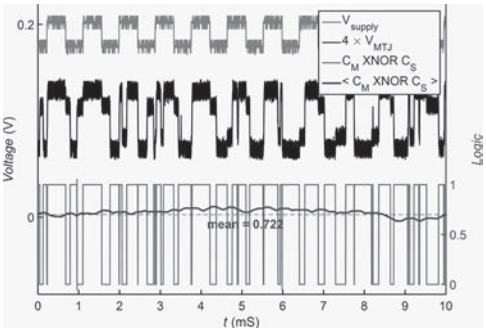


Fig. 2. Measured waveform of modulated V_{supply} (grey) and V_{MTJ} (black), and C_M XNOR C_S (sky blue) and time average of C_M XNOR C_S (blue), where C_M and C_S are logic values of V_{supply} and V_{MTJ} respectively. Note that V_{MTJ} is enlarged by 4 for clarity.

EP-11. Micromagnetic study of fast switching mechanism in perpendicular double MTJ with a switchable reference layer. *C. Yoshida*[1], T. Tanaka[1], T. Ataka[1] and A. Furuya[1] *1. Fujitsu Limited, Kawasaki, Japan*

It has been reported that a dynamic double magnetic tunnel junction (DD-MTJ) with a fixed reference (FR) and a switchable reference (SR) layers showed a high thermal stability, a low switching current, and good manufacturability [1, 2]. In this study, we investigate the effect of SR layer on spin transfer torque (STT) switching in a perpendicular 30 nm DD-MTJ (Fig. 1(a)) using micromagnetic simulation [3] including thermal fluctuations at 300K. Time evolutions of normalized z-component of the magnetization ($<M_z>$) of SR, F1, F2, and FR layers are shown in Figs. 1(b) and (c). Under a negative voltage, initial P/P (SR↓/F1-F2↓) state first switched to AP/P state (SR↑/F2-F1↓). Once two reference layers (SR and FR) becomes antiparallel, the spin torques coming from both side add up to accelerate the speed of switching. After switching to AP/AP state (SR↑/F2-F1↑), the spin torque acting on SR layer and eventually became P/AP state (SR↓/F2-F1↑) [1]. Similarly, under a positive voltage, initial P/AP states switches to final P/P state in the reverse order. Since STT-switching is a probabilistic event, 100 switching trials were simulated under the voltage of -2 and 2.5 V for the

DD-MTJ at 300K. Then switching time of first SR reversal (t_{SR}) and subsequent free layer reversal (t_{SR+F}) were obtained at 80% switching probability (Fig. 2). The fast STT switching was achieved in the MTJ with small $M_{s\text{-}SR}$ of 0.25 T; the switching time was reduced by 41% at V = -2.0 V and by 22% at V = 2.5 V compared to the single reference MTJ. Note that switching time of DD-MTJ (t_{SR+F}) includes the switching time of SR (t_{SR}) which increases with increasing $M_{s\text{-}SR}$. We found that the DD-MTJ with smaller $M_{s\text{-}SR}$ is a promising as a high-performance cache for embedded applications.

[1] A. V. Khvalkovskiy et al., J. Appl. Phys. Vol.124, p.133902 (2018) [2] K. Tsunoda et al., IEDM Tech. Dig. p.665 (2012). [3] Fujitsu Ltd. [Online] Available: http://www.fujitsu.com/global/about/resources/news/pressreleases/2015/0324-01.html

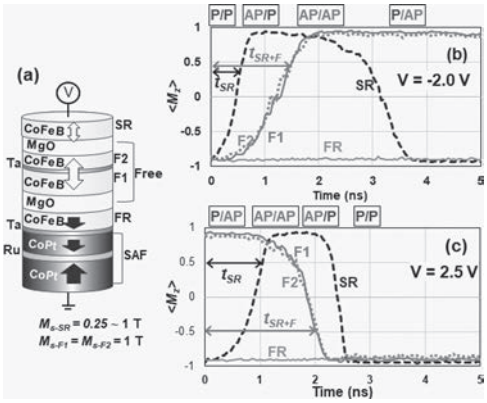


Fig. 1 (a) Schematic structure of 30 nm-DD-MTJ. Time evolution of <M_z> for SR, F1, F2, and FR layers under the voltage of (b) -2.0 V and (c) 2.5 V.

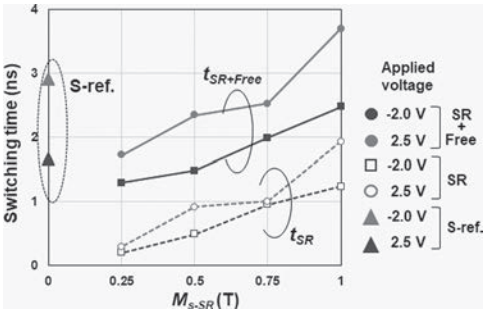
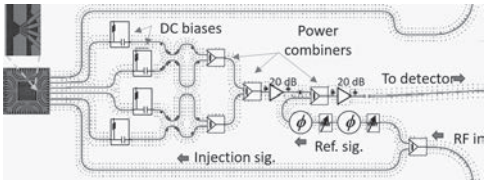


Fig. 2 Switching time as a function of $M_{s\text{-}SR}$.

EP-12. Coupled Spin-Torque-Oscillator based Distance Computation: *M. Pufall*[1], W.H. Rippard[1], E. Jué[1], M. Koo[2], Y. Shim[2], k. Roy[2], G. Csaba[3] and W. Porod[4] *1. National Institute of Standards and Technology, Boulder, CO, United States; 2. Purdue University, Lafayette, IN, United States; 3. Pazmany University, Budapest, Hungary; 4. Notre Dame University, South Bend, IN, United States*

Recent research on spin torque oscillators (STOs) has shown the possibility of using coupled oscillator network as a core computing primitive for non-Boolean computation, because they are CMOS compatible, highly integrable, scalable, and frequency/phase tunable. A basic computation that is amenable to non-Boolean hardware is the degree-of-match between two vectors, which can be parametrized by a distance metric such as the Euclidean distance norm L2. In this poster, we describe the design and experimental demonstration of a new architecture for a hybrid spintronic/CMOS hardware prototype that computes a multi-dimensional norm.[1] The hybrid system is composed of an array of four injection-locked STOs (see Figure) and a CMOS detector, we experimentally demonstrate a system composed of giant magnetoresistance (GMR)-based STO devices. We theoretically show that phase dynamics of the system inherently introduce non-linearity that makes the system appropriate to measure the distance between two multi-dimensional vectors, that when loaded into the hybrid system, produce an output voltage that is proportional to the L2^{2} norm. The experimental results are then used to parametrize larger-scale simulations of coupled oscillator computing using realistic device parameters, and demonstrate that oscillator-based distance computation scales favorably with increasing input dimension and are tolerant to device variations. In the poster, we estimate the energy efficiency of such an architecture. In addition, we also quantitatively analyze noise propagation in the detection circuit, which uses several stages of amplification to detect the phase response from the GMR devices used, and discuss the impact of improving STO device performance (e.g., MR, phase noise) on the distance computation.

[1] Koo, M, Shim, Y., Rippard, W.H., Pufall. M.R., Roy, K., submitted.



SEM of 4 oscillator array, and schematic of microwave signal conditioning board

EP-13. Time-Resolved Study of the Switching of Spin Transfer Torque Random Access Memories. *P. Bouquin*[1,2], S. Rao[2], S. Couet[2], S. Kundu[2], D. Crotti[2], J. Swerts[2], G.S. Kar[2] and T. Devolder[1] *1. Centre de Nanosciences et Nanotechnologies, Palaiseau, France; 2. IMEC, Leuven, Belgium*

We use time-resolved measurements to study the switching mechanism in STTMRAM [1]. Our samples are disk-shaped pillars of diameter ranging from 25 nm to 150 nm [2]. We study the devices time-resolved conductance response to fast rising voltage steps. Following [3] we describe the switching in two steps: an incubation delay during which the conductance is quiet followed by a fast change of the conductance called the transition time. We study the impact of the diameter of the disk and of the voltage step amplitude on both delays. The statistics of the incubation delay span from the μs to the ns range when increasing the applied voltage. The transition time also decreases with increasing voltage but at a slower rate. We observe an event-to-event variability in the switching path for the larger diameters (Fig. 1), but much less for the smaller one. This variability also depends on voltage: for the largest voltages applied it is not observed and all switching events present a sharp transition. Thus, two regimes can be identified: for low voltages the total switching time is given by the incubation delay (not shown), while for larger voltages one should solely consider the transition time (Fig. 2). Varying the diameter has an impact on both delays. The incubation delay cannot be decreased as fast for the smaller devices compared to the larger ones for the same voltage range. The transition time is also linked to the diameter since the switching path that undergoes the magnetization in such a disk is expected to depend on disk size [4]. The variability in the switching path observed at larger diameter can be explained by domain wall related phenomena such as oscillations of the wall position or pinning. We can extract a characteristic diameter for those phenomena, which gives information on the size dependence of the switching path on real devices.

[1] A. V. Khvalkovskiy et al, J. Phys. D: Appl. Phys, 46, 139601 (2013) [2] S.Couet et al, Appl. Phys. Lett., 111, 152406 (2017) [3] C.Hahn et al, Phys. Rev. B, 94, 214432 (2017) [4] P.Bouquin et al, Appl. Phys. Lett, 113, 22408 (2018)

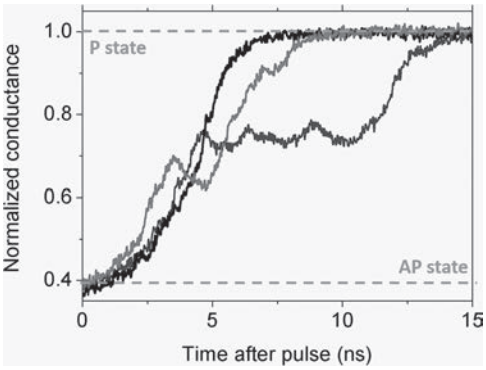


Fig. 1: Single shots of the switching from anti-parallel to parallel state for a 114 nm diameter device under a voltage step of 530 mV. The conductance is normalized to a P-state reference.

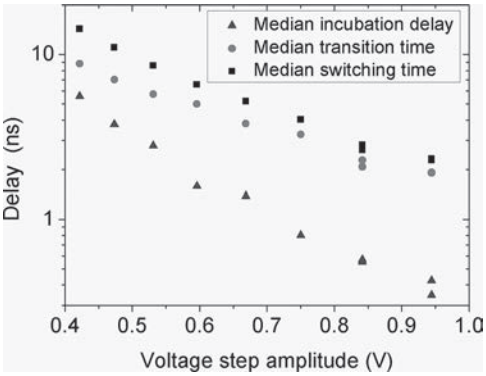


Fig. 2: Voltage dependence of both delays and of the total switching time for a 114 nm device, in the transition time regime. Each voltage point is extracted from 100 single shots.

EP-14. Thermally assisted STT switching MRAM cell using hybrid memory layer consisting of CoPd/Pd and Co/Pd multilayers. *W. Zhao*[1], T. Kato[1], D. Oshima[2], Y. Sonobe[3], S. Takahashi[3] and S. Iwata[2] *1. Department of Electronics, Nagoya University, Nagoya, Japan; 2. Institute of Materials and Systems for Sustainability, Nagoya University, Nagoya, Japan; 3. Sumsung R&D Institute Japan, Yokohama, Japan*

Spin transfer torque (STT) switching is considered as a promising writing scheme to realize a Gbit-class magnetic random-access memory (MRAM). Memory cells with high thermal stability Δ and low switching current density J_c are required for the high-density MRAM. We have designed bi-multilayers (MLs) stack with a high Curie temperature (T_C) Co/Pd and a low T_C CoPd/Pd MLs for the memory layer to realize the efficient STT-switching [1, 2]. In this work, we fabricated GMR junctions using the hybrid memory layer with a stack of $[Co/Pd]_{3\text{-}N}$ / $[CoPd/Pd]_N$ and investigated structural dependence of J_c and Δ at various of temperatures to study the switching efficiency of the hybrid memory layer. The layer stack of Si substrate with a surface oxide layer / Ta (10) / $Cu_{70}Ta_{30}$ (150) / Pt (5) / $[Pt (1.0) / Co (0.6)]_6$ ML / Cu (2.5) / $[Co (0.6) / Pd (1.0)]_{3\text{-}N}$ ML / $[Co_{48}Pd_{52} (0.4) / Pd (1.2)]_N$ ML / Cu (5) / Ta (5) (thickness is in nm) was sputter deposited and fabricated into a current perpendicular to the plane giant magneto-resistance (CPP-GMR) junctions with pillar diameters of 120-300 nm. STT switching of the hybrid memory layer was confirmed by measuring the resistance of the CPP-GMR pillar after injecting the current with a pulse width τ of 10 μs - 100 ms. The intrinsic critical current density J_{c0} was estimated by extrapolating the STT switching current density J_c to τ = 1 ns, and the thermal stability factor Δ was estimated from the slope of the pulse width dependence of J_c. Fig. 1 shows the temperature dependence of Δ and J_{c0} of the hybrid memory layer with $N = 0$ and 2. J_{c0} and Δ for $N = 0$ was almost constant up to ~170°C. On the other hand, significant reduction of J_{c0} and Δ was confirmed for $N = 2$ at high temperature of ~170°C. Interestingly, Δ for $N = 2$ was almost constant up to 100°C then reduced significantly. This tendency is quite attractive for thermally assisted MRAM suggesting the hybrid memory layer is suitable to realize the efficient MRAM cells.

[1] Machida et al., IEEE Trans. Magn., 53, 2002205 (2017). [2] W. Zhao et al., IEEE Trans. Magn., 54, 3450405(2018).

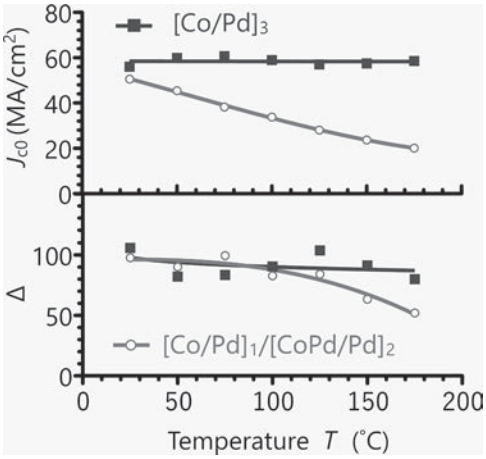


Fig. 1 Temperature dependence of intrinsic critical current density J_{c0} and thermal stability factor Δ of the hybrid memory layer of $[Co/Pd]_{3\text{-}N}$ / $[CoPd/Pd]_N$.

EP-15. Spintronic Processing in Memory for Convolutional Neural Network Based on STT-MRAM. *H. Zhang*[1], W. Kang[1], Y. Zhang[1] and W. Zhao[1] *1. Beihang University, Beijing, China*

The traditional von-Neumann computer architecture is facing increasingly serious problems due to the limitation of the band width between the CPU and memory. In this situation, processing-in-memory is considered as a promising method to solve this bottleneck issue[1]. Recently, emerging nonvolatile memories (NVMs) has shown a fascinating prospect to realize PIM because of their inherent characteristic [2-6]. In this paper, we leverage STT-MRAM with an improved sequential logic method as the logic paradigm to realize convolutional neural network computing. Here, the STT-MRAM is selected from the NVMs because it has more mature technology and better application prospects. As shown in Figure.1, different logic functions can be realized within one write and read cycle. [7]. Besides, a one-bit full adder can be achieved within 5 write and read cycles based on this logic paradigm [8]. For the convolutional neural network, the basic is the convolutional computing. Figure.2 (a) shows the realization of a multiplication operation between two 4-bit operands. First, the operand X is stored 4 times with shift. Then, the 4 rows perform "and" logic operations with each bits of Y, respectively. In the end, add these 4 rows together to obtain the product. As shown in figure.2 (b), the convolutional kernel computing is consists of 9 multiplication operations and 8 add operations. Besides, as shown in figure.2 (c), a block contains 8 sub-arrays, which can perform logic operations simultaneously, and a memory is consists of many blocks. Therefore, it can support high parallelism calculations. By disassembling the computing process, when the convolutional kernel is 3X3 and the precision is 4-bit, one single convolution computing can be achieved within ~90 write and read cycles in one block.

[1] Y. Xie, *IEEE DATE*, pp: 964-969(2013) [2] S. Li, C. Xu, Q. Zou, J. Zhao, et al., *ACM/EDAC/IEEE DAC*, pp. 1-6(2017) [3] M. Soeken, P. E. Gaillardon, S. Shirinzadeh, R. et al., *Computer*, vol. 50, pp. 35-40(2017) [4] J. Lee, D. I. Suh, and W. Park, *J. Appl. Phys*., vol. 117, pp. 17D717(2015) [5] Z. R. Wang, Y. T. Su, Y. Li, et al., *IEEE Electron Device Lett.*, vol. 38, pp. 179-182(2017) [6] A, Sengupta, G. Srinivasan, D. Roy, et al., *IEEE IEDM*, pp. 15-6(2018) [7] H. Zhang, W. Kang, K. Cao, et al., *IEEE Trans. Electron Devices*, Vol. 66, pp. 2017-2022(2019) [8] H. Zhang, W. Kang, B. Wu, et al., *IEEE Trans. Nanotechnol*., Vol. 18, pp. 473-483(2019)

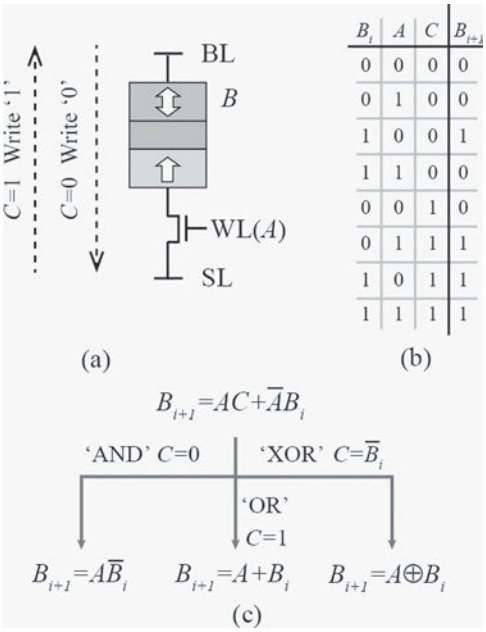


Figure.1. (a) Bit-cell structure of the 1T1MTJ-based STT-MRAM. (b) Truth table depending on the three input logic operands. (c) Principle of implementing reconfigurable logic functions.

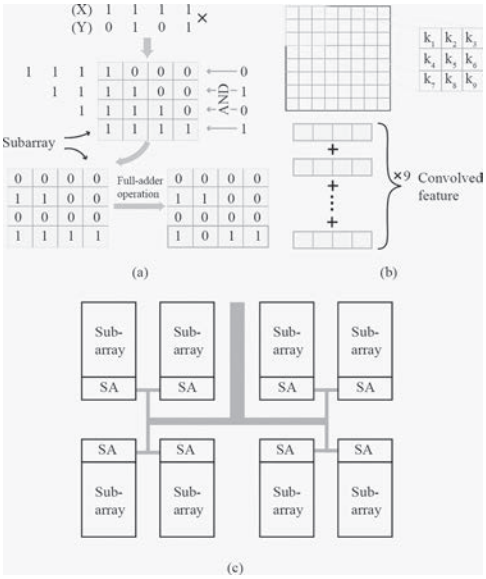


Figure.2 (a) Principle of the realization of multiplication operation. (b) Leveraging the proposed PIM paradigm to obtain convolved feature. (c) Structure of single block, which consists of 8 sub-arrays.

EP-16. Domain Wall Mediated Reversal Dynamics in Perpendicular Magnetic Tunnel Junctions with SAF Free Layer. *O. Bultynck*[1,2], V. Nguyen[2], S. Couet[2], D. Wan[2], E. Raymenants[1,2], B. Soree[1,2], M. Heyns[1,2], I. Radu[2] and T. Devolder[3] *1. KU Leuven, Leuven, Belgium; 2. imec, Leuven, Belgium; 3. Novel magnetic devices, C2N, Palaiseau, France*

In this work, we study the spin transfer torque induced magnetic reversal dynamics of a conventional dual-MgO CoFeB reference [1] versus a synthetic antiferromagnetic (SAF) free layer (FL) in a magnetic tunnel junction (MTJ) device. SAF thin-films exhibit increased magnetic domain wall (DW) velocities [2], and reduced pinning [3] compared to their ferromagnetically coupled counterparts. These properties are attributed to the presence of DMI and antiferromagnetic exchange coupling, leading to a stabilized Néel DW configuration. These properties are expected to be key for DW motion based devices, such as the racetrack memory [4] or the spin-torque majority gate [5]. We apply a time-resolved conductance measurement technique [6] which allow us to study the evolution of the perpendicular magnetic component down to the ns timescale (Fig.1). The measured responses contain a stochastic incubation delay before switching onset, and subsequent dynamics during the reversal time. Multiple dynamics with diverse physical origins are identified during the MTJ reversal process, such as: DW pinning, DW oscillation, backhopping, and self-heating. Exponentially distributed pinning times dominate the dynamics in the thermal regime of the dual-MgO reference devices. This is strongly suppressed in the SAF based devices (Fig.2). In the intrinsic regime, the DW velocity become the limiting property, with the SAF devices having shorter reversal times (Fig.2 inset). We conclude that the domain wall physics at play in a SAF stack can help enhance the reversal in the confined dimensions of a patterned device.

[1] S. Couet, J. Swerts, S. Mertens, et al., IEEE Magn. Lett. vol. 7, 3103004 (2016) [2] S.-H. Yang, K.-S. Ryu, and S. Parkin, Nat. Nanotechnol vol. 10, p.221–226 (2015) [3] H. Saarikoski, H. Kohno, C. H. Marrows, and Gen Tatara, Phys. Rev. B vol. 90, 094411 (2014) [4] M. Hayashi, L. Thomas, R. Moriya, C. Rettner, and S. S. Parkin, Sci. vol. 320, p.209-211 (2008) [5] D. E. Nikonov, G. I. Bourianoff, T. Ghani, IEEE Electron Device Lett. vol. 32, p.1128 – 1130 (2011) [6] T. Devolder, Joo-Von Kim, F. Garcia-Sanchez, *et al.*, Phys. Rev. B vol. 93, 024420 (2016)

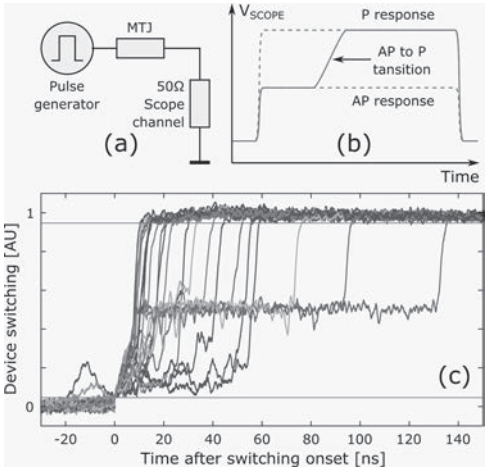


Fig.1: (a) Measurement setup, where fixed amplitude pulses are transmitted through the devices and (b) the conductance is recorded in a time-resolved fashion. (c) Single shot measurements, with incubation delay omitted, demonstrating pinning in dual-MgO.

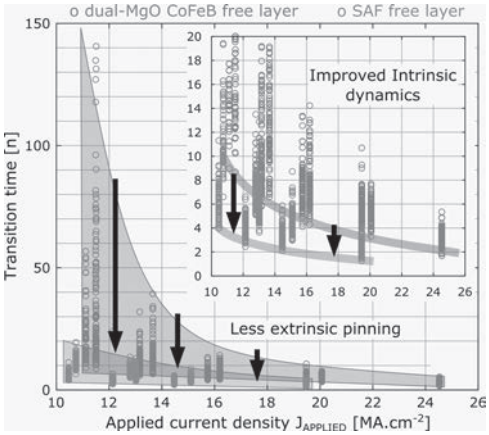


Fig.2: Distribution of transition times extracted form single shot measurements, comparing dual-MgO (red) and SAF based free layer (blue). Most notable, is the suppression of exponentially distributed pinning times. A speed increase is also achieved in the intrinsic dynamics (zoom inset). Both effects are attributed to the antiferromagnetic configuration.

EP-17. A Study of Domain Wall Switching and Structural Properties of Perpendicular $Co_{25}Pd_{75}$ Alloys for STT-RAM Applications. *S. Gupta*[1], P.B. Visscher[8], B.D. Clark[2,3], J.B. Abugri[2], K.E. Tippey[4,7], I.M. Oikonomou[5], P. Komninou[5] and J. Gong[6] *1. Metallurgical and Materials Engineering, University of Alabama, Tuscaloosa, AL, United States; 2. Electrical and Computer Engineering, University of Alabama, Tuscaloosa, AL, United States; 3. Intel Corporation, Tuscaloosa, OR, United States; 4. Metallurgical and Materials Engineering, Colorado School of Mines, Golden, CO, United States; 5. Physics, Aristotle University of Thessaloniki, Thessaloniki, Greece; 6. Seagate Technology, Bloomington, MN, United States; 7. EVRAZ, Portland, OR, United States; 8. Physics and MINT Center, University of Alabama, Tuscaloosa, AL, United States*

We have found that perpendicular magnetic anisotropy (PMA) Co_xPd_{100-x} alloys are a simple means of pinning the reference layer in CoFeB-MgO based magnetic tunnel junctions [1]. Composition, thickness and seed layers were varied. After optimization of the CoPd alloy composition with respect to coercivity, perpendicular anisotropy and magnetoresistance at a nominal Co concentration of 25 atomic percent, various seed layers were investigated [2]. The coercivity was found to be significantly higher for Ta/Pd and Ta/Ru/Ta seed layers. Structural characterization of these stacks by X-ray diffraction and high resolution cross-sectional transmission electron microscopy revealed that the CoPd alloy grown on the Ta/Pd seed layer had much better crystallinity than that grown on MgO or Ta [3]. Magnetic force microscopy was performed on these stacks to observe the switching properties and matched with first order reversal curves (FORC) as shown in Figure 1. The switching process begins with nucleation and dendritic growth of a spongy region which expands to fill the film [4]. The sharp drop in M produced by this switching gives very fine structure in the FORC distribution, which is clearly seen in a new visualization program, FORC+ [5-6].

1. B. D. Clark et al., J. Magn. Magn. Matls. Vol. 436, 113 (2017). 2. J. Abugri et al., Proc. 2019 IEEE Workshop on Microelectronics and Electron Devices (WMED), Boise, Idaho, April 26, (2019). 3. J. B. Abugri et al. (in preparation, 2019). 4. J. B. Abugri et al. J. Appl. Phys. (accepted) 2019. 5. FORC+: open-source program for FORC analysis, http://MagVis.org. 6. J. B. Abugri at al., J. Appl. Phys. Vol. 124, p. 043901 (2018).

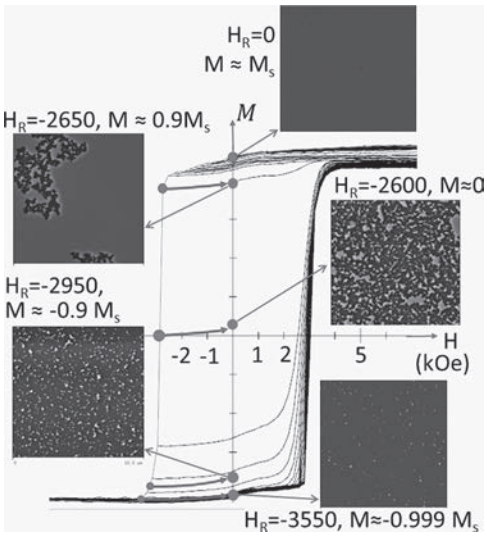


Fig. 1. FORC curves of CoPd alloy film with TaPd seed. The system was brought to each of the 5 red dots along the switching path (at a field H_R), then brought to H=0 (blue dot) along the FORC (black curve). The blue arrow from the blue dot points to an inset 10 µm x 10 µm MFM image at the blue dot (H=0).

Session EQ
MAGNETIC TEXTURES AND MAGNETIZATION DYNAMICS II (Poster Session)

Christoph Klewe, Chair
Lawrence Berkeley National Laboratory, Berkeley, CA, United States

EQ-01. Stoichiometry Controlled Ultrafast Demagnetization in $Co_2Fe_XMn_{1-X}Si$ Heusler Alloy. S. Pan[1], T. Seki[2,3], *A. De*[1], K. Takanashi[2] and A. Barman[1] *1. Condensed Matter Physics and Material Sciences, Satyendranath Bose National Centre for Basic Sciences, Kolkata, India; 2. Institute for Materials Research, Tohoku University, Sendai, Japan; 3. Center for Spintronics Research Network, Tohoku University, Sendai, Japan*

Ultrafast demagnetization is a vital research field in magnetism since its discovery in 1996. $Co_2Fe_XMn_{1-X}Si$ Heusler alloy (HA) with perfect stoichiometric ratio (X) has band gap in minority spin band leading to very low magnetic damping and longer demagnetization time. Very few articles [1-2] demonstrate the ultrafast demagnetization in $Co_2Fe_XMn_{1-X}Si$ HA with only X=0 (CMS) and X=1 (CFS). As the earlier reports lack the variation of ultrafast demagnetization time with intermediate X values, the exact mechanism behind ultrafast demagnetization in this HA remains an open question. Here, we experimentally investigate the ultrafast demagnetization in $Co_2Fe_XMn_{1-X}Si$ with different values of X, i.e. the ratio between Fe and Mn. The time-resolved traces of Kerr rotation have been analyzed using three temperature model [3] to extract the ultrafast demagnetization time (τ_M). Interestingly, we obtain maximum τ_M of ~350 fs for X = 0.4 as shown in Fig. 1. On both side of X=0.4, τ_M decreases. This trend follows the variation of density of states (DOS) at Fermi level (E_F) with X. In HA because of low DOS at E_F, the spin-orbit coupling mediated spin-flip scattering channels become narrower and therefore, τ_M enhances. Fig. 1 also represents the variation of magnetic Gilbert damping constant (α) with stoichiometry. α shows the lowest value for X=0.4 in contrast to τ_M. Fig. 2 represents the variation of τ_M with $1/\alpha$ which fits with a linear equation. This indicates that both damping and ultrafast demagnetization are controlled by the same spin-orbit coupling strength owing to the DOS at E_F. As the DOS increases, spin-orbit coupling mediated spin-flip scattering increases and τ_M decreases with increasing α and vice-versa. In addition, the inverse relation in between α and τ_M proves the presence of dominant inter-band scattering in HA [4].

1. G. M. Muller, J. Walowski, M. Djordjevic, et al., Nat. Mater. 8, 56 (2009). 2. D. Steil, S. Alebrand, T. Roth, et al., Phys. Rev. Lett. 105, 217202 (2010). 3. B. Koopmans, G. Malinowski, F. Dalla Longa, et al., Phys. Nat. Mater. 9, 259 (2013). 4. M. Fahnle, J. Seib, C. Illg, Phys. Rev. B 82, 144405 (2010).

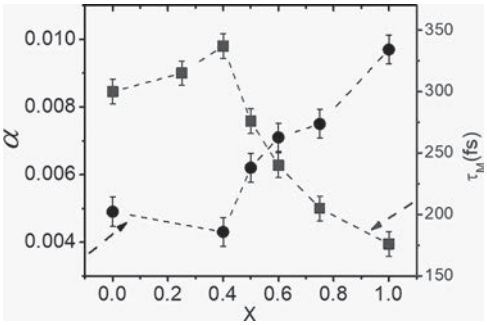


***Figure*. 1 Variation of damping parameter (α) and demagnetization time (τ_M) with stoichiometry (X).**

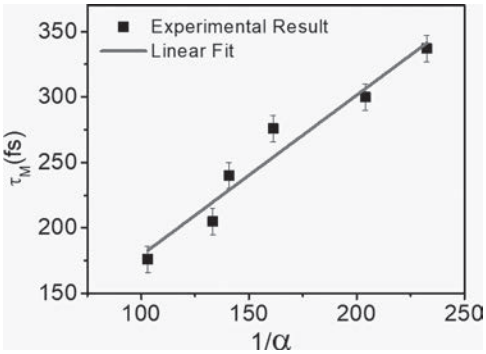


***Figure*. 2 Variation of demagnetization time (τ_M) with inverse of damping parameter (α).**

EQ-02. Reconfigurable Magnonic Band Structure with Field-Bifurcation Dynamics in Coupled Ferromagnetic Nanodot Array. A.K. Mondal[1], C. Banerjee[1], A. Adhikari[1], A.K. Chaurasiya[1], S. Choudhury[1], *A. De*[1], J. Sinha[1,2] and A. Barman[1] *1. S. N. Bose National Centre for Basic Sciences, Kolkata, India; 2. SRM Institute of Science and Technology, Kattankulathur, India*

The quest for advanced spin-based computational technology began a few decades ago with the understanding that the charge-based technology would cease to fulfill the ever-increasing demands of miniaturization, speed, and energy consumption. The field of magnonics, a sub-field of modern magnetism, aims to meet some of these demands using spin waves (SWs), a coherent propagation of magnetic excitation arising from precession of magnetic moments. Periodically modulated ferromagnetic nanostructures, i.e. magnonic crystal (MC), give rise to allowed and forbidden magnonic bands[1]. They have already shown great potential in building various on-chip microwave communication devices. In this work, we have studied the static and dynamic magnetic properties of a MC in the form of a two-dimensional array of rounded rectangular nanodots made of $Ni_{80}Fe_{20}$. The competition between the demagnetizing and the shape anisotropy fields gives rise to a tunable spin configuration, resulting in a transition from magnetic leaf state to S-state upon decreasing the magnetic field from saturation. Finally, a magnetic vortex state is formed at AC demagnetization state, as observed by magnetic force microscopy. We have further studied the magnonic band structure (MBS) by Brillouin light scattering technique and plane-wave method (PWM) by numerically solving the linearized Landau-Lifshitz equation[2]. Our results reveal a fully reconfigurable MBS and band gap (BG) at different bias field (H), namely H = 850 Oe (leaf-state) and H = 330 Oe (S-state). Interestingly, a remarkable shift in the position of the BG at H = 330 Oe in vortex-state give rise to a new phenomenon, namely the bifurcation dynamic[3]. In the vortex-state, the competition between the asymmetric distribution of magnetic field components probably gives rise to an asymmetric periodic magnetic potential energy leading towards the shift in the MBS and BG in this system. We gratefully acknowledge the financial support from S. N. Bose National Centre for Basic Sciences (grant no.: SNB/AB/18-19/211).

1. C. Banerjee *et.al*, Phys. Rev. Appl. 8, 014036 (2017). 2. M. Krawczyk *et. al*, Phys. Rev. B 77, 054437 (2008). 3. S.H. Strogatz Nonlinear Dynamics and Chaos, 1st edn., Addison-Wesley (1994).

EQ-03. Microwave Power Controlled Nonlinear Ferromagnetic Resonance in $Ni_{80}Fe_{20}$ Nano-Cross Array. K. Adhikari[1], S. Sahoo[1], A.K. Mondal[1], *A. De*[1], Y. Otani[2,3] and A. Barman[1] *1. S. N. Bose National Centre for Basic Sciences, Kolkata, India; 2. Institute for Solid State Physics, Kashiwa, Japan; 3. CEMS-RIKEN, Wako, Japan*

Ferromagnetic nano-cross structures manifest a variety of anisotropic spin-wave (SW) properties[1-2], which are crucial for their applications in spintronic and magnonic devices. Here, we demonstrate a rigorous experimental and micromagnetic simulations study about the effect of microwave excitation power (P) on ferromagnetic resonance (FMR) in $Ni_{80}Fe_{20}$ (permalloy; Py) nano-cross array. The experimental results show a remarkable microwave power-dependent shift of the FMR frequency where the sign of the frequency shift depends on the strength of the applied bias magnetic field (H). For lower H values, the power-dependent shift is positive in frequency, whereas for higher H values the power-dependent shift is negative in frequency, above a certain threshold power (P_{th}). Further interesting properties including SW mode softening and mode splitting have also been efficiently controlled by varying P value. To explain the origin of the power-dependent frequency shift, we start with the macrospin model in linear regime, which is possible in nano-cross array system only at higher H values when all spins are parallel to bias field direction. In such a case, the FMR frequency decreases with the increment of P. However, at lower H values, spins of vertical arms in nano-cross align nearly perpendicular to H due to strong configurational anisotropy, which is likely the reason for increment of FMR frequency with the increase of P at lower H values. The rf field which is perpendicular to the bias field does not allow sharp change of static spin configuration with the increment of bias field at higher P values which is the reason for nearly vanishing of SW mode softening. Remarkably, numerically simulated spatial distribution of power and phase profiles reveal that at P = -15 dBm, the lowest frequency SW mode shows a mixed backward volume (BV; n) and Damon Eshbach (DE; m) like character with mode quantization numbers n=6, m=3. Whereas at P = +4 dBm, both the newly generated SW modes due to SW mode splitting show incoherent character. The rich magnetization dynamics of nano-cross array are promising for applications in microwave assisted fast magnetic storage, logic and communication devices.

[1] K. Adhikari, et al, J. Appl. Phys. 121, 043909 (2017). [2] K. Adhikari, et al, Phys. Rev. Appl. 10, 044010 (2018).

EQ-04. Extending the Intrinsic Memory of the Spintronic Nano-Neuron Through Time-Delayed Feedback. M. Riou[2], *F. Abreu Araujo*[1], J. Torrejon[2], B. Garitaine[2], P. Bortolotti[2], V. Cros[2], S. Tsunegi[3], K. Yakushiji[3], A. Fukushima[3], H. Kubota[3], S. Yuasa[3], D. Querlioz[4], M.D. Stiles[5] and J. Grollier[2] *1. IMCN, Université catholique de Louvain, Louvain-la-Neuve, Belgium; 2. Unité Mixte de Physique CNRS/Thales, Palaiseau, France; 3. Spintronic Research Center, National Institute of Advanced Industrial Science and Technology (AIST), Tsukuba, Japan; 4. Center for Nanoscience and Nanotechnology, Palaiseau, France; 5. Center for Nanoscale Science and Technology, National Institute of Standards and Technology, Gaithersburg, MD, United States*

The recent demonstration of neuromorphic computing with spin-torque vortex oscillators [1-3] has opened a path to energy efficient data processing. The success of this demonstration hinged on the intrinsic short-term memory of the oscillators. In this study [4], we extend the memory of the spin-torque nano-oscillators through time-delayed feedback. We leverage this extrinsic memory to increase the efficiency of solving pattern recognition tasks that require memory to discriminate different inputs. The large tunability of these non-linear oscillators allows us to control and optimize the delayed feedback memory using different operating conditions of applied current and magnetic field. A single oscillator with time multiplexing projects the initial problem in a higher dimensional state, turning it into a linearly separable problem. We tested this computation scheme on a temporal pattern recognition task, sine and square waveform classification, which requires memory and non-linearity. The error rate drops from 10.8 % without feedback to 0.16% with feedback (see Fig. 2).

[1] J. Torrejon, M. Riou, F. Abreu Araujo, J. Grollier *et al.*, *Nature* 547, 428-431 (2017) [2] M. Riou, F. Abreu Araujo, J. Torrejon, J. Grollier, *IEDM 2017* (2017) [3] M. Romera, F. Abreu Araujo, J. Grollier *et al., Nature* 563, 230–234 (2018) [4] M. Riou, F. Abreu Araujo, J. Grollier *et al.*, *arXiv:1905.02695* (2019)

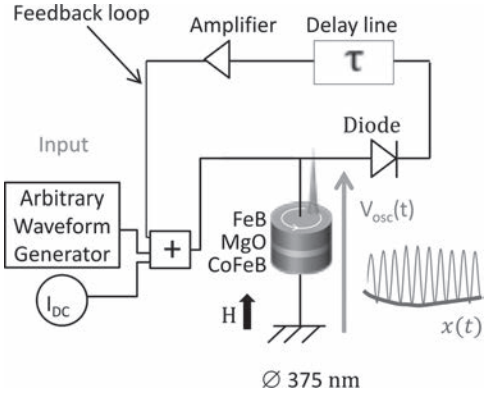


Fig. 1: Experimental setup. The spin-torque vortex oscillator is subjected to a DC current and a perpendicular magnetic field giving rise to an oscillating voltage V_{osc}. The time-varying input is generated by an arbitrary waveform generator. A diode allows measuring the amplitude of the oscillations x(t), which is used for computation. Finally, the feedback loop consists of an electronic delay line and an amplifier.

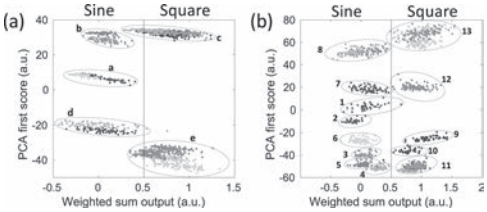


Fig 2: 2D visualization of the higher dimension mapping obtained from the experiments for all the different inputs: (a) without feedback. Five clusters are observed. The separation between sine and square cases is the vertical black solid x = 0.5. For perfect recognition, points corresponding to sine input should be left to this line and points corresponding to square input should be to the right. Without feedback, several points are mixed up between sine and square cases. The error rate is 10.8 %, (b) with feedback. Thirteen clusters are observed confirming that feedback enables the oscillator to separate inputs by remembering sequences of two consecutive inputs. The final classification is almost perfect with only 0.16 % error rate.

EQ-05. Influence of Vortex Configuration on the Spin-torque Diode Effect for Unbiased RF Energy Harvesting. *M. Jotta Garcia*[1], S. Wittrock[1], J. Moulin[2], S. Menshawy[1], R. Ferreira[3], A. Solignac[2], U. Ebels[4], P. Bortolotti[1] and V. Cros[1] *1. Unité Mixte de Physique CNRS, Thales, Univ. Paris-Sud, Université Paris-Saclay, 91767 Palaiseau, France; 2. SPEC, CEA-Saclay, CNRS, Université Paris-Saclay, 91191 Gif-sur-Yvette, France; 3. International Iberian Nanotechnology Laboratory, Braga, Portugal; 4. SPINTEC, CEA-Grenoble, CNRS and Université Grenoble Alpes, 38054 Grenoble, France*

Spin-torque nano-oscillators (STNOs) are spintronic devices based on the excitation of precession modes in frequencies ranging from 100 MHz up to tens of GHz [1]. A particular layout for these devices is one in which the free layer exhibits a vortex magnetization in its equilibrium state, presenting four possible polarity/chirality magnetic configurations. The spin-transfer induced precession of the vortex core in STNOs is especially relevant because, in addition to being a model system for the study of magnetic dynamics, they provide excellent signal characteristics and are promising candidates for next-generation devices and applications, such as rf

generation [2], detection [3] or bio-inspired computing [4]. Here, we focus on the detection and harvesting of low-power rf signals, in the case where the STNO is operating in the sub-critical regime. Two different rf-to-dc modes appear in vortex-based STNOs, the spin-torque diode effect [5] and the vortex core expulsion [6]. While the vortex core expulsion mode allows for larger detection sensitivities, it occurs only above a certain rf power threshold and it relies on the application of a dc current [3]. The spin-torque diode effect, on the other hand, is a rectification effect which does not require any biasing or external magnetic field, and is expected to increase in sensitivity with decreasing rf power [7], down to the device's detection threshold, making it highly suitable for energy harvesting applications. This effect can be seen, even without any external stimulus, in all the vortex configurations i.e. chirality and core polarity. However, their influence on the rectified signal's amplitude and shape has yet to be fully described. Here, we investigate through noise measurements how the different configurations affect the spin-torque diode response. Furthermore, in order to achieve high sensitivities and low rf power thresholds, we explore the connection in series of multiple STNOs with very close resonance frequencies, both experimentally and through simulations. The work is supported by the French ANR project "SPINNET" ANR-18-CE24-0012.

[1] S. Kiselev et al., Nature Vol. 425, 380 (2003); A. Dussaux et al., Nat. Comm. Vol. 1, 8 (2010) [2] S. Wittrock et al., Phys. Rev. B Vol. 99, 235135 (2019) [3] A. S. Jenkins et al., Nat. Nanotech. Vol. 11, 360 (2016) [4] M. Romera et al., Nature Vol. 563, 230–234 (2018); J. Torrejon et al., Nature Vol. 547, 428-431 (2017) [5] A. A. Tulapurkar et al., Nature 438, 339-342 (2005) [6] S. Menshawy et al., AIP Advances Vol. 7, 056608 (2017) [7] P. Skirdkov et al., Appl. Phys. Lett. Vol. 113, 242403 (2018); B. Fang et al. Phys. Rev. Applied Vol. 11, 014022 (2018)

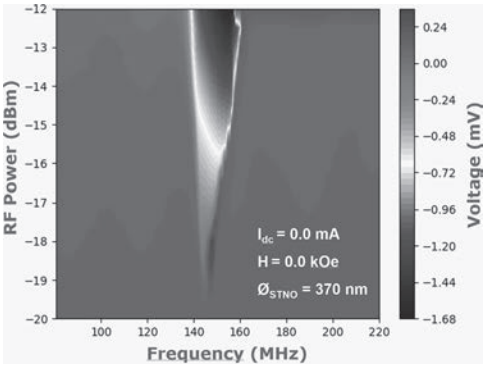


Fig.1 Map of the spin-torque diode voltage with rf injection power, for one chirality/polarity vortex configuration.

EQ-06. Coupling of spin waves propagating along domain walls with magnetic vortex in thin-film nanostrip cross-structure. *H. Park*[1], J. Lee[1], J. Yang[1] and S. Kim[1] *1. Department of Material Science and Engineering, Seoul National University, Seoul, The Republic of Korea*

A spin wave is the collective excitation occurring in the lattice of spins. It was recently demonstrated that the energy density required to switch or transfer single-digit information in spin-wave-based devices is less than that in conventional electronic transistors[1]. With the aid of nanotechnology[2], the quite large feature size of current magnonic devices fabricated by optical lithography can be down-scaled to several nanometers. Thus, spin waves provide a new pathway for future information processing devices in terms of energy-cost efficiency. Furthermore, spin-wave modes confined in narrow potential wells of magnetic domain walls have been intensively studied owing to their aspects of fundamental interest as well as their possible applications to logic gates[3]. Confinements of spin waves inside narrow, sub-100nm channels such as domain walls[4] promise to further reduce power consumption in magnonic devices and to increase the relatively low group velocities of spin waves[5]. Here, we report on a micromagnetic simulation study of interactions between spin waves propagating along narrow domain-wall channels and a magnetic vortex in a thin-film nanostrip cross-structure. The specific modes of the spin waves propagated well in the narrow potential wells of the domain walls, and then interacted with a magnetic vortex when they went through the vortex soliton. Via this interaction, characteristic eigenmodes of the vortex motions appeared, resulting in elliptical gyration motions of several specific frequencies[6]. The gyration motions could be interpreted by the sum of clockwise and counter-clockwise circular eigenmodes excited by spin waves of corresponding resonance frequencies[7]. According to the action-reaction effect, the phases and amplitudes of the spin waves after their interaction with the vortex were modified differently in the three different arms.

[1] A. V. Chumak, A. A. Serga, and B. Hillebrands, Nature Commun. 5, 4700 (2014). [2] J. A. Briggs, G. V. Naik, T. A. Petach, B. K. Baum, D. Goldhaber-Gordon, and J. A. Dionne, Appl. Phys. Lett. 108, 051110 (2016). [3] F. Garcia-Sanchez, et al. Phys. Rev. Lett. 114, 247206 (2015). [4] E. Albisetti, et al. Commun. Phys. 1, 56 (2018). [5] G. Duerr, K. Thurner, J. Topp, R. Huber, and D. Grundler, Phys. Rev. Lett. 108, 227202 (2012). [6] B. Krüger, A. Drews, M. Bolte, U. Merkt, D. Pfannkuche, and G. Meier, Phys. Rev. B 76, 224426 (2007). [7] K.-S. Lee and S.-K. Kim, Phys. Rev. B 78, 014405 (2008).

EQ-07. Determination of magnetization alignment speed by observing nucleation process of magnetic vortices. *T. Ohkochi*[1,2], M. Oura[2], H. Osawa[1], A. Yamaguchi[3,2], H. Fujiwara[4,2], A. Sekiyama[4,2] and T. Kinoshita[1] *1. Japan Synchrotron Radiation Research Institute, Sayo, Japan; 2. RIKEN/SPring-8, Sayo, Japan; 3. University of Hyogo, Kamigori, Japan; 4. Osaka University, Toyonaka, Japan*

Magnetic vortices are formed in micron-sized magnetic thin film discs as a consequence of competition between magnetstatic- and exchange-energies. [1] These two magnetic energies have been known for a long time as important parameters to describe microscopic and macroscopic magnetic structures in materials in the equilibrium state. Although investigations of the dynamics of magnetic vortex cores which are already formed have been carried out intensively [2,3], time-constant of the emergence of these energies has not been discussed so far. This study is attempted to solve the question "How fast can the magnetizations align?", by observing the nucleation process of the magnetic vortices just after the transient demagnetization by laser heat pulses, using photoemission electron microscopy combined with magnetic circular dichroism effect (XMCD-PEEM, Fe $L_{2,3}$-edge). The experiments have been performed at BL17SU in SPring-8. "As-grown" $Ni_{81}Fe_{19}$ (permalloy) thin-film discs with their diameter up to 6 μm formed clear magnetic vortex structure, reflecting very soft property of the permalloy's magnetizations (Fig. 1). However, as shown in Fig. 2, most of the discs whose diameter exceed 3 μm showed random multi-domains after the ultrafast laser pulse irradiation (Ti: Sapphire (λ=800 nm), 100 fs-width, 20 mJ/cm^2), while all the discs smaller than 2 μm-diameter formed vortex structure as expected in the equilibrium state. Considering that the typical magnetization recovery time of metallic alloy systems after the demagnetization by femtosecond pulses is approximately 100 ps, [4] the experimental result shows that the magnetic exchange energy works very quickly within the recovery time (otherwise, neither vortex nor multi-domain (microscopically aligned magnetizations) structures would not be formed) and that the spreading velocity of the magnetostatic energy is tentatively determined to 2 (μm) / 100 (ps) = 20 (m/s).

[1] T. Shinjo, T. Okuno, R. Hassdorf *et al*., Science, Vol. 289, p.930 (2000). [2]A. A. Tulapurkar, Y. Suzuki, A. Fukushima *et al*., Nature, Vol. 438, p.339 (2005). [3]S. Kasai, P. Fischer, M. -Y. Im, K. Yamada *et al*., Phys. Rev. Lett., Vol. 101, p.237203 (2008). [4] K. Takubo, K. Yamamoto, Y. Hirata *et al*., Appl. Phys. Lett., Vol. 110, p.162401 (2017).

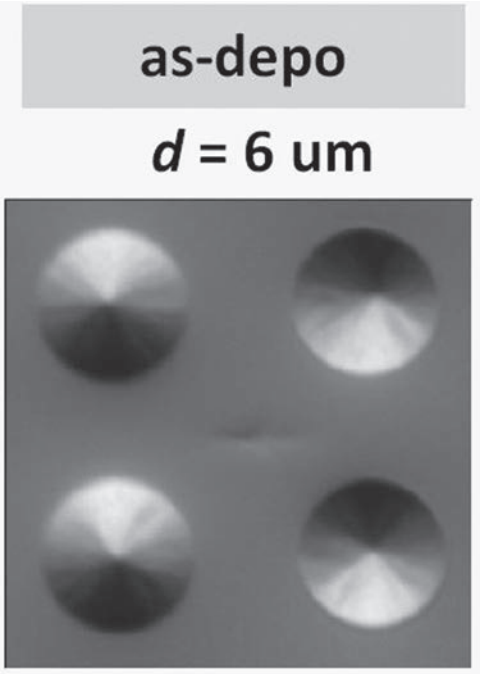


Fig.1 Magnetic domain (XMCD-PEEM) image of $Ni_{81}Fe_{19}$ discs with 6 µm diameter (as-grown state).

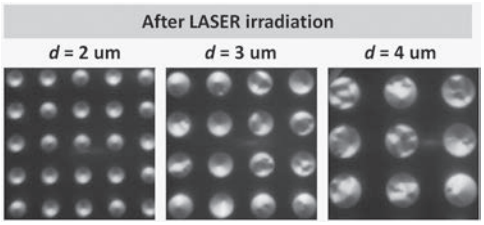


Fig.2 XMCD-PEEM images of $Ni_{81}Fe_{19}$ discs with various diameters after irradiation of laser pulses whose fluence is 20 mJ/cm². A spot size of the laser is approximately 300 x 500 µm² which is sufficiently larger than the disc size.

EQ-08. Core Orbit of a Rigid Vortex Magnetic Texture. D. Carvajal[1], *A. Riveros*[2] and J. Escrig[2,3] *1. Departamento de Matemática y Ciencia de la Computación, Universidad de Santiago de Chile, Santiago, Chile; 2. Departamento de Física, Universidad de Santiago de Chile, Santiago, Chile; 3. Center for the Development of Nanoscience and Nanotechnology (CEDENNA), Santiago, Chile*

In physics, conserved quantities are key to understand and describe physical phenomena. These conserved quantities are formally related by the Noether theorem and the lagrangian description both in classical mechanics and field theory. Here we found the orbit equation of the trajectory of the core center for a rigid vortex texture in terms of two conserved physical quantities, namely the energy E and a vector with direction perpendicular to the orbit-plane, $A = -L + G\,|r_c\,|2 / 2$ where G, L and r_c are the topological gyrovector, standard angular momentum and core position of the vortex texture, respectively. Also, the condition for bounded orbits are explicitly obtained. We show analytically, through a similar strategy for the orbit description of the reduced mass in the well know Kepler problem [1], that in absence of a dissipation term, for small deviation of the core [2], the orbit trajectory is bounded between two concentric circles, with the dot center outside the core motion region (Fig1a). Instead, under a dissipation dyadic term proportional to the damping coefficient, A is no longer conservative, and by solving numerically the generalized Thiele equation [3] we show that the core moves into the dot center (a similar behavior was observed in Ref.[4], by micromagnetic simulations using OOMMF[5].) or moves away, depending of the chirality of the vortex texture and the intensity of the applied in plane magnetic field (Fig1b,c respectively). We acknowledge support from Fondecyt under grants 3180470, 1150952 and Financiamiento Basal para Centros Científicos de Excelencia, CEDENNA, grant FB0807.

[1] H. Goldstein, C. Pool, and J. Safko, Classical Mechanics, third Edition 2001 Addison-Wesley.(1951). [2] K. Yu. Guslienko, V. Novosad, Y. Otani, H. Shima, K. Fukamichi, Appl. Phys. Lett. 78, 3848 (2001). [3] A.A. Thiele, Phys. Rev. Lett. 30, 230 (1973); J. Appl.Phys. 45,377 (1974); A. R. Volkel, G. M. Wysin, and F. G. Mertens, Phys. Rev. B, 50, 12711 (1994). [4] K. Yu. Guslienko, B. A. Ivanov, and V. Novosad, Journal of Applied Physics 91, 8037 (2002). [5] M. J. Donahue and D. G. Porter, OOMMF Users Guide, Version 1.0, Interagency Report NIST IR 6376, Gaithersburg, MD (1999).

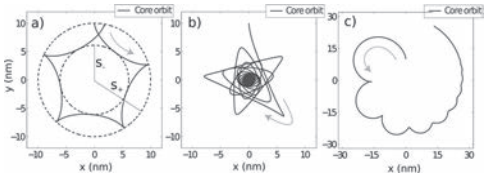


Fig.1: Orbit trajectory of the core center of a magnetic vortex texture in a cobalt dot of radius 100 nm in presence of magnetic field of 30 mT in the x-direction, the dot plane corresponds to the xy-plane and the origin is located at the dot center. (a) In absence of a dissipation dyadic. Instead, (b,c) under a dissipation term for a vortex with chirality in clockwise and counter-clockwise direction, respectively.

EQ-09. Coupling between gyrating motion and breathing mode of a magnetic skyrmion. *K. Wang*[1], S. Ying[1] and G. Xiao[1] *1. Department of Physics, Brown University, Providence, RI, United States*

Magnetic skyrmions, together with their dynamics including trajectories of the centre of skyrmion mass and breathing modes (oscillatory variation of the skyrmion radius) have been generating considerable interest for both fundamental and technology reasons.[1-5] The trajectories illustrate the nature of skyrmion motion. They allow us to determine the value of inertial mass.[3] Breathing modes have been observed for both stable and dynamically stabilized skyrmions.[5] These Gigahertz eigenmode dynamics have been proposed to be information carriers, as analogous to propagating spin waves. Coupled gyrating motion and breathing modes between neighbouring skyrmions have been explored.[1,2] However, coupling between the two modes of a skyrmion, and theoretical descriptions, remain elusive. In this work, we identify both gyrating motion and breathing modes when manipulating skyrmions in a racetrack.[4] The gyrating motion of a skyrmion is suggested, via a Thiele equation derived from the micromagnetic model, to be coupled to the breathing mode dynamics. We study spin-orbit torque and boundary effects on collective motions of both modes. We note that the mass density is a more meaningful parameter compared with the inertial mass when studying the skyrmion dynamics.

[1] J. Kim, J. Yang, Y.-J. Cho, B. Kim, and S.-K. Kim, Sci. Rep. 7, 45185 (2017). [2] J. Kim, J. Yang, Y.-J. Cho, B. Kim, and S.-K. Kim, J. Appl. Phys. 123, 053903 (2018). [3] I. Makhfudz, B. Krüger, and O. Tchernyshyov, Phys. Rev. Lett. 109, 217201 (2012). [4] K. Wang, L. Qian, S.-c. Ying, X. Gang, and X. Wu, Nanoscale 11, 6952 (2019). [5] Y. Zhou, E. Iacocca, A. A. Awad, R. K. Dumas, F. Zhang, H. B. Braun, and J. Åkerman, Nat. Commun. 6, 8193 (2015).

EQ-10. Dissipative magnetic solitons: nucleation and annihilation timescales and multiple soliton modes. *N. Statuto*[1], C. Hahn[3], J. Hernàndez Ferras[1], A.D. Kent[2] and F. Macià[1] *1. University of Barcelona, Barcelona, Spain; 2. New York University, New York, NY, United States; 3. Physikalisch-Technische Bundesanstalt, Braunschweig, Germany*

Collective magnetic excitations, such as spin waves are attracting a growing interest for their potential in technological applications. In particular, dissipative droplet solitons (DD) and their topological homologous, known as dynamical skyrmions (DS) [1], were proposed as the building blocks for new applications beyond binary computing and memory devices [2]. Those magnetic excitations can be created in magnetic thin films with uniaxial anisotropy by a spin-polarized current flowing through an electrical nanocontact. Applications require high control of the nucleation and annihilation of magnetic solitons as well as an understanding of their intrinsic stability and their behavior against external perturbations. Here, we combine experimental data and micromagnetic simulations to understand the creation and the annihilation process for both DD and DS as well as their stability [1,3]. Simulations and room-temperature data indicate that creation and annihilation processes present different timescales since the creation process has associated an incubation time that depends sensitively on the initial magnetic state of the nanocontact [3]. Low-temperature data shows the existence of different and quantized DD modes that are accessed by varying applied fields and currents [4] and those different accessible modes in addition to their nonlinearity and stochasticity, which could be exploited in neuromorphic [2] or reservoir computing [5].

[1] N. Statuto, J. M. Hernàndez, A. D. Kent and F. Macià, Nanotechnology, Vol. 29, num. 32 (2018) [2] N. Locatelli, V. Cros & J. Grollier Nature Materials volume 13, pages 11–20 (2014) [3] J. Hang, C. Hahn, N. Statuto, F. Macià, and A. D. Kent, Sci. Rep. 8, 6847 (2018). [1] N. Statuto, C. Hahn, J. M. Hernàndez, A. D. Kent, and F. Macià Phys. Rev. B 99, 174436 (2019) [5] D. Pinna, F. Abreu Araujo, J.-V. Kim, V. Cros, D. Querlioz, P. Bessiere, J. Droulez, and J. Grollier, Phys. Rev. Appl. 9, 064018 (2018).

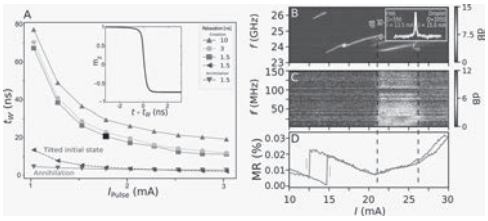


Fig.1: A, Incubation time for annihilation and creation process as a function of the applied current pulse amplitude. Tilted magnetization at the initial state reduce the incubation time. High (B) and low (C) and dc (D) resistance as a function of the applied current at fixed perpendicular field of 850 mT and in-plane field applied of 50 mT. Droplet nucleates at 12.5 mA with a quality factor up to 2000 (inset). Then at 21mA the main high-frequency peak splits into three weaker peaks with lower frequencies, the low-frequency noise increase and the MR shows a change in trend.

EQ-11. The effects of Dzyaloshinskii Moriya interactions on the dynamics of magnetic vortices. *C.M. Quispe Flores*[1], K. Livesey[2] and K. Buchanan[1] *1. Physics, Colorado State University, Fort Collins, CO, United States; 2. Physics, University of Colorado, Colorado Springs, CO, United States*

We have studied the effects of the DMI on the resonance frequencies of magnetic vortices confined in magnetically soft cylindrical nanodots using two approaches: micromagnetic simulations and semi-analytical solutions of the linearized Landau-Lifshitz (LL) equation. Simulations show that without DMI only the odd radial-type modes are excited, whereas when we increase the DMI strength, higher order modes are excited including even modes as shown in Fig.1. Semi-analytical solutions were obtained based on the approach outlined in \cite{guslienko2005vortex} where the linearized LL equation is reduced to a single integro-differential equation that is solved numerically as an eigenvalue problem. The effective torque exerted by the DMI produces two uncoupled integro-differential equations, and the problem is consequently more complicated than the dipolar-only solution. The solution to the LL equation can be expressed as an eigenvalue problem of the form $ i \lambda_n \mathbf{m}_n(\rho) = \int_V \hat{\Gamma } (\rho,\rho′) \mathbf{m}_n(\rho') d^3 \mathbf{r} $ where radially-symmetric solutions are assumed, and the imaginary λ_n values are related to the eigenfrequencies by $ \omega_n =-i \gamma M_0 \lambda_n $. Using this approach, the kernel $\hat{\Gamma } (\rho,\rho') $ may contain the magnetostatic \cite{guslienko2011magnetostatic,kostylev2007dipole}, exchange and DMI contributions. When the DMI is non-zero, the static effective fields must be included in the dynamic calculations since the static magnetization $\mathbf{M}_0$ is tilted by an angle $\psi(\rho)$ with respect to the azimuthal direction, where $\psi(\rho)$ is well described by a Cauchy function. Thus, it is necessary to locally rotate the orthogonal system (ρ,ϕ,z) to a new orthogonal system (ρ',ϕ',z) tilted by the angle $\psi(\rho)$ to ultimately obtain the system eigen-frequencies under the assumptions $|\mathbf{m}|<<|\mathbf{M}_0|= M_s$ and $\mathbf{M_0} \times \mathbf{H_{eff,0}}=0 $. The results for zero DMI agree quite well with experimental results and theoretical calculations reported in \cite{guslienko2005vortex}, and our calculations agree well with micromagnetic simulations performed with DMI.

K. Y. Guslienko, W. Scholz, R. Chantrell, and V. Novosad, Physical Review B 71, 144407 (2005). K. Y. Guslienko and A. N. Slavin, Journal of Magnetism and Magnetic Materials 323, 2418 (2011). M. Kostylev, G. Gubbiotti, J.-G. Hu, G. Carlotti, T. Ono, and R. Stamps, Physical Review B 76, 054422 (2007).

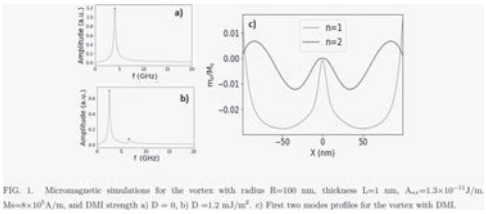


FIG. 1. Micromagnetic simulations for the vortex with radius R=100 nm, thickness L=1 nm, A_{ex}=1.3×10^{-11}J/m, Ms=8×10^{5}A/m, and DMI strength a) D = 0, b) D =1.2 mJ/m^2. c) First two modes profiles for the vortex with DMI.

Figure 1

EQ-12. Time-dependent ab initio insight to the ultrafast demagnetization mechanism. *Z. Chen*[1] and L. Wang[1] *1. Lawrence Berkeley National Laboratory, Berkeley, CA, United States*

Laser induced ultrafast demagnetization process has a great potential in future spintronic devices. Ever since its discovery, this subject has been studied intensively. However, the fundamental physics is still not well understood. There are several long-standing problems regarding the demagnetization mechanism. One major issue is the remarkable underestimation in ab initio simulation. At the same intensity of laser, the theoretical demagnetization rate can be ten times smaller than the experimental observation. Here, we present an ultrafast real-time time-dependent density functional theory method, together with atomic Landau-Lifshitz-Gilbert model, to investigate this problem. Our results show that one important reason for the underestimation is the missing of initial spin disorder, which can significantly enhance the demagnetization to the experimentally observed rate. This spin disorder connects the electronic structure theory with the phenomenological three-temperature model. We have also systematically studied the roles of various interactions which are heavily debated. In particular, we found that electron-electron interaction and spin-orbit interaction play extremely important roles, while electron-phonon and light-spin interactions are not essential.

EQ-13. Analytical calculation of fringe field and magnetization in $V[TCNE]_{x\sim2}$ cylindrical disks. *D.R. Candido*[1,2] and M.E. Flatté[1,2]
1. Department of Physics and Astronomy and Optical Science and Technology Center, University of Iowa, Iowa City, IA, United States; 2. Pritzker School of Molecular Engineering, University of Chicago, Chicago, IL, United States

The collective magnetic excitations in magnetic materials – also known as magnetostatic spin waves [1,2] – have been investigated and studied due to their long spin lifetimes and absence of ohmic losses. These spins waves are created through the application of an alternating magnetic field in ferrimagnetic materials. Here, we solve the Maxwell's equations in the magnetostatic limit for a ferrimagnetic $V[TCNE]_{x\sim2}$ disk [3] on top of a diamond substrate. More specifically, we calculated analytically the spectrum, the magnetization and the fringe fields using the pinning condition at both bottom and top surfaces. We also perform the relaxation of the used pinning condition and investigate its consequence in both fringe fields, spectrum and magnetization. We calculate those quantities for in plane and out of plane magnetic fields. The material is based on work supported by the U.S. Department of Energy, Office of Basic Energy Sciences, under Award Number DE-SC0019250.

[1] R. W. Damon and J. R. Eshbach, J. Phys. Chem. Solids 19, 308 (1961). [2] R. W. Damon and H. van de Vaart, Journal of Applied Physics 36, 11 (1965) [3] Na Zhu, Xufeng Zhang, I. H. Froning, Michael E. Flatté, E. Johnston-Halperin and Hong X. Tang., Applied Physics Letters 109, 082402 (2016)

EQ-14. Parallel-pump FMR based Non-linear Magnon Dynamics in Magnetic Insulators. *A. Venugopal*[1], T. Qu[1] and R. Victora[1] *1. Electrical and Computer Engineering, University of Minnesota, Minneapolis, MN, United States*

Non-linear magnetic response of magnetic insulator materials is often used in the realization of radio-frequency (RF) devices such as Frequency Selective Limiters (FSLs) [1]. These devices are used at the front end of communication receivers to limit power levels of RF signals that exceed a certain preset threshold. In order to design FSLs with better performance, much remains to be understood in terms of generation as well as subsequent interactions of magnons created by RF pumping. We have used high-performance parallel computation based CUDA simulations and a theoretical model for magnon scattering to explore the direct and parametric generation of magnons, excited by microwaves in parallel pumped configurations [3]. The sample is 1-100 um thick and we use periodic boundary conditions. The DC magnetic field is applied in-plane and the RF field is linearly polarized and parallel to the DC field. We first determine the dispersion relation which plays a vital role in the understanding of nonlinearly generated magnons. We then study the effect of ferrimagnet thickness, RF frequency, power, and DC magnetic field, on properties like frequency response, operational bandwidth, and power absorption of the material (Figure 1). It is found that the degree of non-linearity can be controlled using parameters like RF power and damping of the magnetic system. Analytically, Holstein and Primakoff based analysis is used to arrive at the threshold RF amplitude. We also study non-linear damping in the magnetic system which arises at RF powers higher than the corresponding threshold. Excellent agreement over a wide range of fields (Figure 2) between high power experimental and simulation results has been obtained using only low power parameters.

[1] J. D. Adam and F. Winter, *IEEE Trans. Magn.,* vol. 49, no.3, pp. 956-962, March. 2013. [2] E. Schlomann, *J. Appl. Phys*., vol. 33, no.2, Feb.1962. [3] H. Kurebayashi, O. Dzyapko, V. E. Demidov D. Fang, A. J. Ferguson, and S. O. Demokritov, Appl. Phys. Lett., vol. 99, no. 162502, 2011.

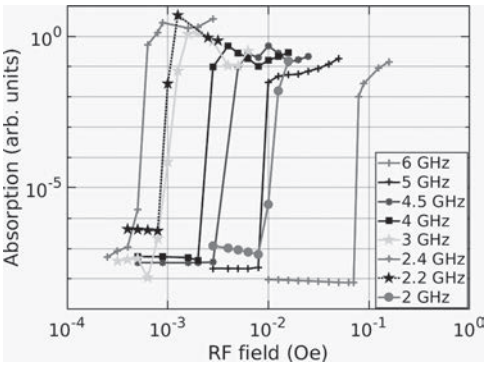


Fig. 1 Absorption (imaginary part of susceptibility) vs RF power for various RF frequencies, all calculated at 100 Oe.

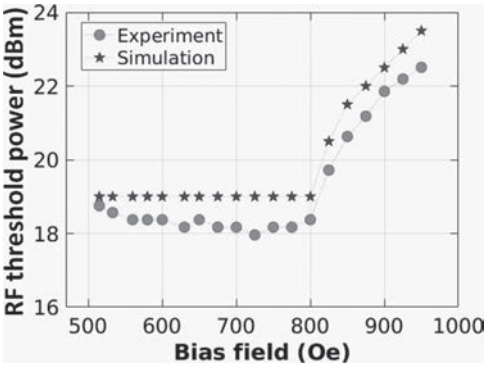


Fig 2. Comparison of simulation results with experimental data [3] for the butterfly curve for 5.1 um thick YIG sample in parallel configuration.

Session ER
MAGNETIZATION DYNAMICS: ULTRAFAST AND QUASI-PARTICLE COUPLING II (Poster Session)

Stefano Bonetti, Chair
Stockholm University, Stockholm, Sweden

ER-01. Influence of Magnetic Anisotropy on the Ultrafast Magnetization Dynamics of Gd-Fe Thin Films with Different Thicknesses. S. Mondal[1], A. Talapatra[2], J. Chelvane[3], *A. De*[1], S. Sahoo[1], J. Mohanty[2] and A. Barman[1]
1. Condensed Matter Physics and Material Sciences, S. N. Bose National Centre for Basic Sciences, Bidhan Nagar, India; 2. Department of Physics, Indian Institute of Technology Hyderabad, Hyderabad, India; 3. Defence Metallurgical Research Laboratory Hyderabad, Kanchan Bagh, India

Rare earth-transition metal (RE-TM) alloys are multisublattice ferrimagnets, which gained huge scientific attention due to the fast and highly damped spin dynamics useful for ultrafast ringing-free precessional switching in magneto-optical recording. Femtosecond laser-induced magnetization reversal was initially observed in Gd-based ferrimagnetic alloys [1]. We have demonstrated magnetic anisotropy controlled ultrafast magnetization dynamics as a function of film thickness in e-beam evaporated amorphous Gd-Fe films [2]. Employing a two-color time-resolved magneto-optical Kerr effect (TRMOKE) magnetometer [3] the ultrafast demagnetization, remagnetization, precession and damping have been investigated (Fig. 1(a)). A weak out-of-plane magnetic anisotropy (~10^5 erg/cc) developed in the films with increasing thickness is quantified from the field dispersion of precessional frequency and static magnetic characterizations. This feature is contradictory to conventional ferromagnetic thin films. The direction of the bias magnetic field is varied from in-plane to out-of-plane configuration. Tunability of the orientations of magnetization is achieved due to the growth of the anisotropy. The frequency and decay time for Kittel mode and perpendicular standing spin-wave (PSSW) modes were modulated from 0.3 ns to 0.9 ns with the variation of frequency (Fig. 1 (a)-(c)). The role of several extrinsic effects, *i.e.* two-magnon scattering, magnetic inhomogeneity, and multimodal dephasing, in opening up additional energy dissipation channels has been elucidated. Effective damping of the films is found to vary over a broader range of 0.02 to 0.15 which may find applications in various magnonic and spintronic devices. We acknowledge the financial support from S. N. B. N. C. B. S. (Grants No. SNB/AB/18-19/211). S.M. acknowledges DST for the INSPIRE fellowship. J.M. acknowledges the financial support from SERB, Govt. of India, (Grants No. EMR/2016/006794).

[1] C. D. Stanciu, F. Hansteen, A. Kimel, A. Kirilyuk, A. Tsukamoto, A. Itoh and Th. Rasing, Phys. Rev. Lett. 99, 047601 (2007). [2] A. Talapatra, J. Arout Chelvane, and J. Mohanty, J. Magn. Magn. Mater. 448, 360-366 (2018). [3] A. Barman and J. Sinha, Spin dynamics and damping in ferromagnetic thin films and nanostructures (Springer, Switzerland, 2018).

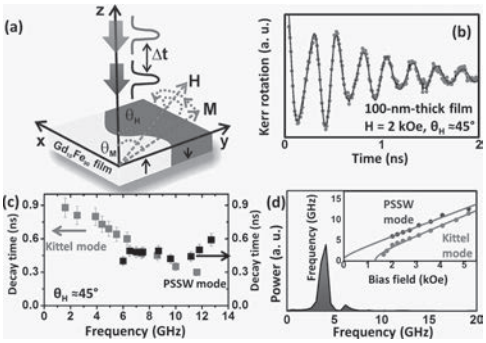


Fig.1 (a) Schematic of experimental geometry, (b) Time-resolved Kerr rotation data for 100-nm-thick Gd-Fe film with the damped sinusoidal fit. (c) Variation of decay time with frequency. (d) Spin-wave spectra showing multiple modes. Field dispersion of frequency is shown at the inset.

ER-02. Phonon Transport Properties Obtained from Phonon Driven Ferromagnetic Resonance. *C. Zhao*[1,2], M. Vogel[1], Y. Li[1], J. Holanda[1], Z. Zhang[1], J. Pearson[1], W. Zhang[3], Q. Liu[2], V. Novosad[1], J. Wang[2] and A. Hoffmann[1] *1. Materials Science Division, Argonne National Laboratory, Lemont, IL, United States; 2. Key Laboratory of Magnetism and Magnetic Materials of the Ministry of Education, Lanzhou University, People's Republic of China, Lanzhou, China; 3. Department of Physics, Oakland University, Rochester, MI, United States*

We have investigated the phonon transport modulated by magnetization dynamics in Ni/$LiNbO_3$ hybrid heterostructures. In these devices, we excite at microwave frequencies surface acoustic waves (SAW) using interdigitated transducer. The SAW then drives subsequently ferromagnetic resonance FMR in the Ni film, which we analyze by considered both phonon attenuation and generation. At the microscopic level, angular momentum conversation requires the simultaneous transformation of angular momentum from magnons to phonons. Therefore, the line shape of the phonon transport transmission power is significant to study magnon-phonon interaction and the concomitant transformation of angular momentum in this process. Fig. 1(a) shows a schematic illustration of the magnon-phonon interaction during SAW driven FMR. Due to the magnon-phonon interaction, phonons will redistribute angular momentum and energy between magnons and phonons, which can enhance SAW transmission. Fig. 1 (b) shows the magnetic field H dependence of the transmission power at $\theta = 60°$ for an annealed device. The attenuation of the phonon results in dips in the transmission power via FMR absorption at FMR filed. At the same time, the magnon and phonon interaction enhances the phonon transmission at the higher field ($\eta>1/2$), which results in peaks for the transmission power, as shown in Fig. 1 (b). The parameter η is related to the magnon-phonon interaction, at a different frequency (f = 3.56 GHz, 2.24 GHz, 1.61 GHz, and 0.97 GHz), and can be obtained as 3.1, 3.0, 3.6 and 7.1 from the theoretical fits for the annealed device. When $\eta \leq 1/2$, only the peaks near field are observed in the transmission power, which agrees with the line shape for the as-grown device. Thus, the magnon-phonon coupling becomes more pronounced for annealed devices.

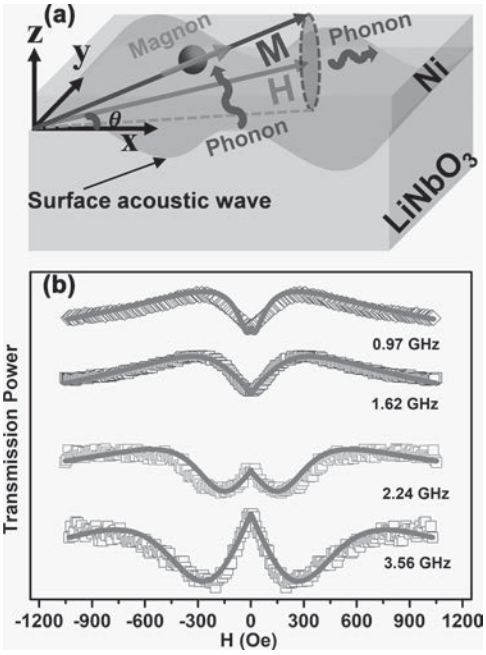


Figure 1 (a) shows schematic illustration of magnon-phonon interaction during SAW driven FMR; (b) shows magnetic field *H* dependence of the transmission power for an annealed device at θ = 60°. The symbols are experiment data, and solid lines are theoretical fits.

ER-03. Direct light-induced spin transfer between different elements in a spintronic Heusler material via femtosecond laser excitation. *C. Gentry*[1], P. Tengdin[1], A. Blonsky[1], D. Zusin[1], M. Gerrity[1], L. Hellbruck[2], M. Hofherr[2], J.M. Shaw[3], Y. Kvashnin[4], E.K. Delczeg-Czirjak[4], M. Arora[3], H. Nembach[3], T.J. Silva[3], B. Stadtmuller[2], S. Mathias[5], M. Aeschlimann[2], H. Kapteyn[1], D. Thonig[4], K. Koumpouras[6], O. Eriksson[4,7] and M. Murnane[1] *1. Department of Physics and JILA, CU Boulder, Boulder, CO, United States; 2. University of Kaiserslautern, Kaiserslautern, Germany; 3. Quantum Electromagnetics Division, National Institute of Standards and Technology, Boulder, CO, United States; 4. Department of Physics and Astronomy, University Uppsala, Uppsala, Sweden; 5. Georg-August-Universitat Gottingen, Physikalishes Institut, Gottingen, Germany; 6. Department of Engineering Sciences and Mathematics, Lulea University, Lulea, Sweden; 7. School of Science and Technology, Orebro University, Orebro, Sweden*

Heusler compounds are exciting materials for future spintronics applications because they display a wide range of tunable electronic and magnetic interactions such as metallicity, superconductivity, and giant magneto-resistance. However, the ultimate speed at which spins can be manipulated in materials is still an open question. We use a femtosecond light pulse to directly transfer spin polarization from one element to another in a half-metallic Heusler material, Co_2MnGe. This spin transfer initiates as soon as light is incident on the material, showing that we can spatially transfer angular momentum between neighboring atomic sites on timescales less than 10 fs. The observation is made possible by the ability of ultrafast high harmonic pulses to simultaneously and independently probe the magnetic state at two atomic sites, Co and Mn, during laser excitation. We find that the magnetization of Co is enhanced by the laser pulse, while that of Mn rapidly quenches. By comparing our measurements to density functional theory, we show that the optical excitation *directly* transfers spin from one magnetic sub-lattice to another, via preferred spin-polarized excitation pathways. The enhancement of ferromagnetic order demonstrates direct manipulation of spins via light, thus providing a path towards spintronic logic devices such as switches that can operate on few femtosecond or even faster timescales.

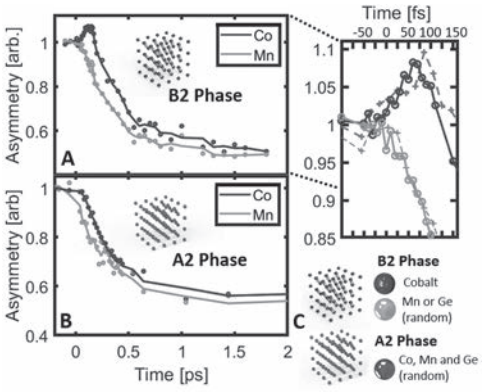


Fig. 1 Element resolved ultrafast magnetization dynamics following excitation by femtosecond laser in the (A) half-metallic B2 phase. Co magnetization increases as Mn decreases. (B) Element resolved ultrafast magnetization dynamics in the non half-metallic A2 phase. There is no enhancement of the Co magnetization.

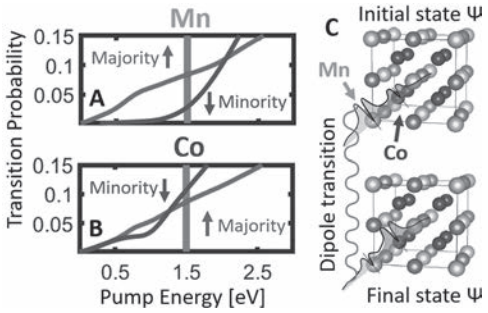


Fig. 2 The probability for exciting a spin up (majority) vs. spin down (minority) electron from the valence band in the B2 phase for different pump energies in (A) Mn sites. For a 1.55 eV pump, the probability is higher for spin up electrons to be excited from Mn. (B) Probability for excitations in Co sites. In contrast to the Mn result, the probability is higher for minority electrons to be excited in Co.

ER-04. Ultrafast Demagnetization Processes in Low-Damping Ni-Ferrite Films. R. Knut[1], *R. Malik*[1], R. Stefanuik[1], Y. Kvashnin[1], D. Thonig[1], A. Gupta[2], O. Eriksson[1], O. Karis[1] and D.A. Arena[3] *1. Uppsala University, Uppsala, Sweden; 2. Univ. of Alabama, Tuscaloosa, AL, United States; 3. Univ. of South Florida, Tampa, FL, United States*

Thin films of spinel ferrites are oxide ferrimagnets with multiple technological uses including improved integrated microwave circuits, spin filters, and other spintronic applications. However, spinels have non-trivial crystal structures and thin films can exhibit a high degree of crystallographic defects such as antiphase boundaries (APBs). Symmetry matching and reducing lattice strain of Ni-ferrite [$NiFe_2O_4$ or NFO] spinel films on different single crystal substrates have been shown to be effective methods for controlling APBs and improving properties such as Gilbert damping and inhomogenous linewidth broadening [1]. NFO has an inverse spinel structure where Ni^{2+} cations reside on O_h coordinated sites surrounded by six O^{2-} ions while the Fe^{3+} cations are split between O_h and T_d sites. We have investigated the role of lattice strain on the ultrafast demagnetization and spin dynamics of NFO films grown on spinel substrates with different amounts of compressive lattice strain ranging from highly strained (~3%) to nearly-unstrained films. We use the HELIOS fs-scale EUV laser source coupled to a transverse MOKE (T-MOKE) apparatus [2] to examine both the static spin-asymmetry as well as the the spin dynamics of the Ni and Fe cations resolved to specific O_h and T_d sub-lattices in the inverse spinel structure. The T-MOKE static asymmetry spectra across the Fe and Ni $M_{2,3}$ core levels exhibit large variations in both amplitude and relative orientation as a function of lattice strain. The time-resolved spectra reveal the sub-ps demagnetization process of the

different NFO films as well as the long timescale magnetization recovery and resonance modes in the ferrimagnetic samples. We corroborate our experimental observations with detailed calculations of the static dielectric tensor and spin asymmetry, generated from first-principles methods, and time-resolved simulations of spectra based atomistic spin dynamics.

[1] A.V. Singh, A. Gupta *et al.*, Adv. Mater. 29, 1701222 (2017) [2] S. Jana, R. Knut, O. Karis *et al.*, Rev. Sci. Instrum. 88, 033113 (2017)

ER-05. Stacking Order Dependent Sign Change of Microwave Phase Due to Eddy Currents in Nanometer-Scale NiFe/Cu Heterostructures.
O. Gladii[1], R.L. Seeger[1], L. Frangou[1], G. Forestier[1], U. Ebels[1], S. Aufftet[1] and *V. Baltz*[1] *1. Univ. Grenoble Alpes / CNRS / CEA, SPINTEC, Grenoble, France*

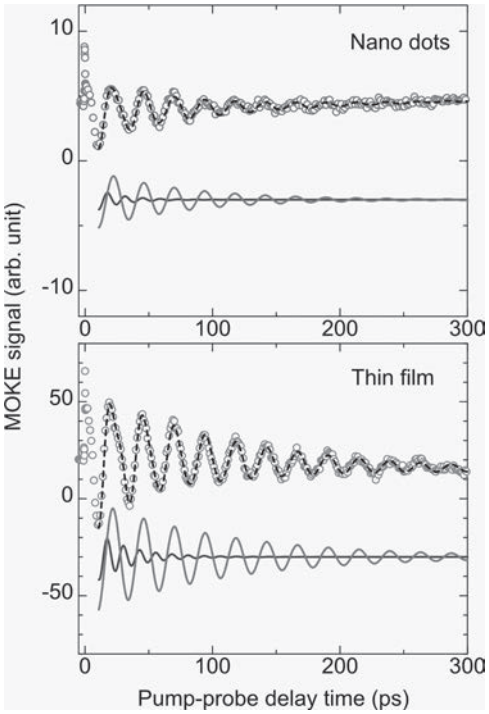
In ferromagnetic resonance (FMR) experiments, eddy currents need to be carefully considered to accurately determine damping and other related spintronic properties such as spin-mixing conductance and the spin-Hall angle in spin-pumping experiments, especially when characterizing low-damping materials. This type of effect has been thoroughly studied for film thicknesses above the skin-depth limit. In contrast, below this limit, the effects of eddy currents were most often neglected, except e.g. for a study on ac charge currents [1], and for series of comprehensive studies focused on microwave screening/shielding in ferromagnetic/non-magnetic(F/NM) metallic multilayers [2,4]. A recent experimental study revealed how the Oersted field - due to eddy currents in the NM layer - affects the dynamics of F magnetization, and more specifically, how it distorts the resonance lineshape [5]. Using a coplanar stripline transducer, we investigated experimentally the broadband FMR response of few nanometer-thick NiFe/Cu and Cu/NiFe bilayers [6]. The main contribution of our study is that it represents systematic experimental evidence of a stacking-order-dependent sign-change of the microwave phase. The effect could be ascribed to eddy currents generated in the Cu layer in the sub-skin-depth regime by the time varying magnetic fields in the experiment. Distinct sets of experimental data - layer thickness-, frequency- and size- dependences, were consistent with a simple quantitative analysis encompassing the main features of the phenomenon. Remarkably, the model could account for the difference in the thickness-dependence of Cu-resistivity due to the inversion of the growth order. These results contribute to our understanding of the impact of eddy currents below the microwave magnetic skin-depth and explain the contributions to lineshape asymmetry reported in stripline experiments. They also provide a straightforward way to detect the contributions of eddy currents from NM-adjacent conductors, as a caveat for the need in some cases to take these contributions into account.

[1] M. A. W. Schoen, J.M. Shaw, H.T. Nembach *et al*, Phys. Rev. B 92, 184417 (2015). [2] I.S. Maksymov and M. Kostylev, Phys. E 69, 253 (2015). [3] M. Bailleul, Appl. Phys. Lett. 103, 192405 (2013). [4] W.E. Bailey, C. Cheng, R. Knut *et al*, Nat.Com. 4, 2025 (2013). [5] V. Flovik, F. Macia, A.D. Kent, and E. Wahlstrom, J. Appl. Phys. 117, 143902 (2015). [6] O. Gladii, R. L. Seeger, L. Frangou *et al,* arXiv:1902.06501

ER-06. Optical detection of magnetization dynamics for synthetic ferrimagnetic thin film and nano dots.
S. Iihama[1,2] and S. Mizukami[1,2] *1. WPI Advanced Institute for Materials Research (AIMR), Tohoku university, Sendai, Japan; 2. Center for Spintronics Research Network (CSRN), Tohoku university, Sendai, Japan*

Recently, synthetic ferrimagnet (SyF) or antiferromagnet with perpendicular magnetic anisotropy has been attracted much attention for reference magnetic layer in magnetic memory devices. To measure magnetization dynamics in SyF are indispensable to understand the static and dynamic magnetic properties. Time-resolved magneto-optical Kerr effect (TRMOKE) using femtosecond laser pulse is a promising technique to measure ultrafast magnetization dynamics up to sub-terahertz frequency [1]. The detection of magnetization dynamics for nano dots where diameter down to 40 nm has been reported by using microwave [2], optical [3] as well as combined technique [4], however the measured frequency is limited up to ~ 20 GHz. Here, we studied high frequency dynamics for both blanket and patterned SyF films with large perpendicular magnetic anisotropy (PMA) using TRMOKE. The SyF stacking structures studied compose of a bottom Co/Pt multilayer and top CoFeB layer, which are antiferromagnetically coupled through Ir layer. The SyF thin film was patterned into 20-nm-diameter dot arrays. The wavelength, duration, repetition rate of the femtosecond laser pulse used for the pump-probe TRMOKE measurement were 800 nm, 120 fs, and 1 kHz, respectively. The probe laser was tightly focused onto the film. Figure shows TRMOKE results for SyF nano dot arrays and thin film where 1.8 T external magnetic field with the field angle 70 degree from film normal were applied. Magnetization precession for both thin film and nano dot arrays were clearly observed. Dotted curves show fitting results by using two sinusoidal decayed function. Evaluated two oscillation modes, corresponding to in-phase and out-of-phase modes, are shown as red and blue solid curves in the figure. The measured two frequency were ~ 40 and 75 GHz, respectively. The life-time of magnetization precession for nano dot arrays are found to be shorter than that for thin film. This work was partially supported by KAKENHI (Nos. 19K15430), and Sasakawa foundation.

[1] S. Mizukami *et al*. J. Appl. Phys. 120, 142102 (2016) [2] E. Hirayama *et al*. J. Appl. Phys. 117, 17B708 (2015) [3] B. Rana *et al*. ACS Nano 5, 9559 (2011) [4] H. T. Nembach *et al*. Phys. Rev. Lett. 110, 117201 (2013)



TRMOKE signal measured for SyF nano dot arrays and thin film. Red and blue solid curves represent two oscillation modes evaluated by fitting.

ER-07. Study of Static and Dynamic Properties of Planar Dumbell Shaped Structure of $Ni_{20}Fe_{80}$.
S. Khanal[1,2], P. Sherpa[2] and L. Spinu[2] *1. Physics and Mathematics, Charles University, Prague, Czechia; 2. AMRI, University of New Orleans, New Orleans, LA, United States*

Artificially patterned magnetic structures have drawn significant attention in the field of magnetism. Well-engineered structures allow accomplishing fine-tuning of both static and dynamic properties [1]. In this study, dumbbell-shaped structures of $Ni_{80}Fe_{20}$ were fabricated on the top of the signal line of the Coplanar Waveguide using electron beam lithography, sputtering and lift-off technique. Magneto-Optic Kerr Effect (MOKE) magnetometer was used to investigate the static properties. In addition, dynamic responses were probed through the Vector Network analyzer based ferromagnetic resonance (VNA-FMR) spectroscopy. Static and dynamic characterizations were

carried out along and perpendicular to the Dumbell. Nucleation, propagation, and annihilation of the vortexes in the system show unique configuration during the magnetizing process (figure 1). For dynamic characterization, microwave frequency was swept for each field step and the Scattering parameter of the microwave was tracked. The modulated response of spin waves from the components of the dumbbell was clearly noticed. The spatial variation of spin waves at the external magnetic field of 1000 Oe is presented in figure 2 when microwave frequency was scanned. The sizes of dots were varied to tune both static and dynamic response in a controlled manner. Magnetic hysteresis loops and ferromagnetic resonance spectra were reproduced with Micromagnetic simulation and corroborated with the experimental results. The spectral analyses of FMR spectra were performed at different field and frequency to better understand the experimental results.

1] Phys. Rev. B 95, 224426-L. L. Xiong, M. Kostylev, and A. O. Adeyeye

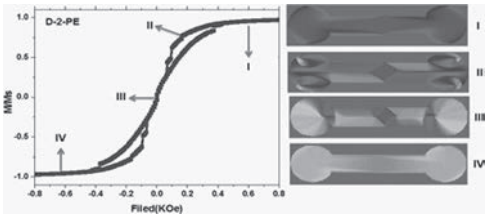


Figure 1- MHL at left and Spin configuration at the different magnetic field on right.

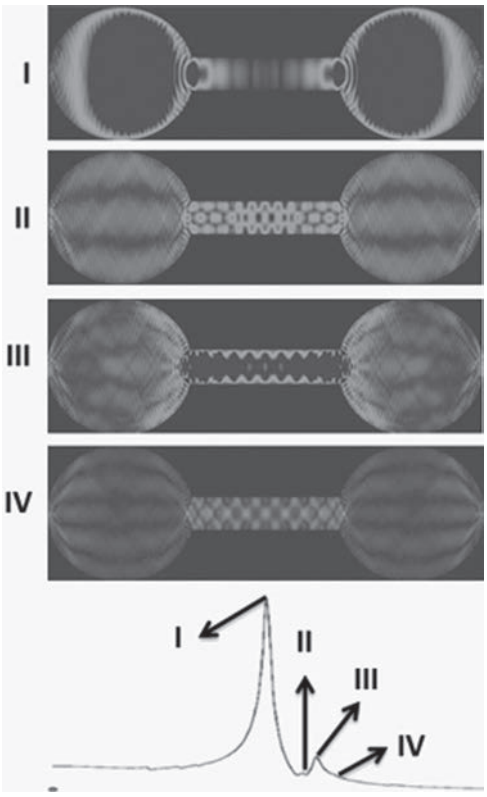


Figure 2 - Spatial variation of the spin wave at external field 1000 Oe during frequency sweeping.

ER-08. Chaotic Dynamics and Thermal Switching in AC-driven Nanomagnets. M. d'Aquino[1], *S. Perna*[2] and C. Serpico[2] *1. Department of Engineering, University of Naples "Parthenope", Naples, Italy; 2. DIETI, University of Naples Federico II, Naples, Italy*

The understanding of magnetization dynamics in nanoscale magnets subject to time-harmonic (AC) excitations and thermal fluctuations is of crucial importance both from fundamental and application points of view[1]. Magnetization dynamics of uniformly magnetized particles subject to AC fields has been traditionally studied in connection with ferromagnetic resonance[2], where magnetization oscillations are excited around a stable equilibrium. The amplitude of such oscillations follows the classical resonance curve peaked around the Kittel frequency[2]. At moderate AC powers, nonlinearity may lead to foldover[3]. At larger AC powers, for submicron particle dimensions, the spin-wave instabilities[4] are strongly inhibited by exchange interactions[1]. Thus, even at considerably large AC powers, nonlinear dynamics in nanomagnets exhibits mostly a spatially uniform mode of oscillations. In this work, we consider AC-driven magnetization dynamics for single-domain bistable nanomagnets in the presence of weak thermal noise. The presence of saddle points leads to enormous complexity in AC-excited dynamics where the chaotic behavior is often dominant. We study these phenomena with a special emphasis on the interplay between chaos and thermal excitations. A special perturbation technique based on Melnikov function[5] is developed in order to predict AC amplitude threshold values for the onset of deterministic chaos produced by microwave external fields or AC spin-torque. The reduction of the stability margin of magnetic nanoparticles' equilibria at finite temperature in the presence of AC-driven chaotic dynamics is then discussed in terms of basin erosion[6] (see fig. 1). In this respect, chaotic dynamics of the aforementioned type has been recently demonstrated by experimental observations on nanoscale magnetic tunnel junctions[7], which show that chaos can be the dominant mechanism which controls thermally-activated switching dynamics in AC-driven conditions.

[1] G. Bertotti, I. D. Mayergoyz, C. Serpico, Nonlinear Magnetization Dynamics in Nanosystems, Elsevier (2009). [2] C. Kittel, Phys. Rev. 73, 155 (1948). [3] D. J. Seagle et al., J. Appl. Phys. 57, 15, 3706 (1985). [4] H. Suhl, J. Phys. Chem. Solids 1, 209-227 (1957). [5] S. Wiggins, Introduction to applied nonlinear dynamical systems and chaos, Springer (2000). [6] J.M.T. Thompson, Proc. R. Soc. Lond. A 421, 195 (1989). [7] E. Montoya, S. Perna, Y-J. Chen, J.A. Katine, M. d'Aquino, C. Serpico, I.N. Krivorotov, Nature Communications 10, 543 (2019).

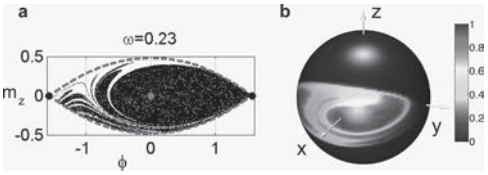
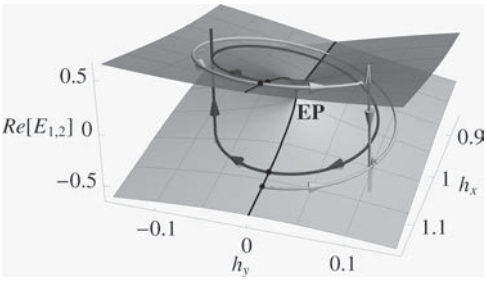


Fig 1. (a) Basin erosion in the (m_z, Φ) plane at zero temperature under microwave applied field (black dots are initial states not escaping the energy well in several periods of the AC field). (b) Probability of not switching under AC-driven chaos and room temperature.

ER-09. Non-reciprocal phenomena in non-equilibrium magnetization dynamics. *A. Galda*[1,2] and V. Vinokur[2] *1. James Franck Institute, University of Chicago, Chicago, IL, United States; 2. Materials Science Division, Argonne National Laboratory, Lemont, IL, United States*

The understanding of out-of-equilibrium spin transport, magnetization dynamics, and phase transitions is one of the major challenges of contemporary magnetics. In this work, we introduce the non-Hermitian spin Hamiltonian formalism that fully describes the time evolution of non-equilibrium magnetic systems in presence of Gilbert damping and angular-dependent spin-orbit-torques. The Hamiltonian approach to non-equilibrium spin dynamics provides a concise and illustrative representation of the underlying non-conservative fields and forces acting in driven dissipative magnetic systems. It offers a convenient way to determine exact system parameters necessary for minimizing the detrimental effects of noise and dissipation in the system, and explains the origin of non-linear spin-orbit terms in the corresponding Landau-Lifshitz-Gilbert equation. The Hamiltonian admits branch point singularities that appear as chiral exceptional points, where both eigenvalues and eigenstates coalesce. We will discuss the appearance of these exceptional spectral points in relation to parity-time symmetry, and how this provides access to a wealth of topological effects unique to non-Hermitian spin systems, e.g. asymmetric spin transport and spin filtering, and non-reciprocal magnetization dynamics.

[1] A.Galda *et al.*, Phys. Rev. B 94, 020408(R) (2016) [2] A.Galda, V.M. Vinokur, Phys. Rev. B 97, 201411(R) (2018) [3] A.Galda, V.M. Vinokur, arXiv:1903.09729 (2019)



Time evolution of a non-Hermitian magnetic system when encircling the exceptional point. The system's final state depends on the encircling direction, illustrating the non-reciprocity of non-Hermitian parametric driving.

ER-10. Experimental Detection of Dynamic Phase Transitions in $Co_{1-x}Ru_x$ Thin Films. *J.M. Marin*[1,2], P. Riego[1,3], E. Oblak[1], G.E. Campillo[4], J.A. Osorio[2], O.L. Arnache[2] and A. Berger[1] *1. CIC nanoGUNE, Donostia-San Sebastian, Spain; 2. Instituto de Física, Universidad de Antioquia, Medellin, Colombia; 3. IKERBASQUE, Fundación Vasca para la Ciencia, Bilbao, Spain; 4. Facultad de Ciencias Básicas, Universidad de Medellín, Medellin, Colombia*

In this work, $Co_{1-x}Ru_x$ (10$\underline{1}$0) ultrathin films (20 nm) were grown by co-sputter deposition at room temperature in Ar atmosphere at 3 mTorr for $0 \leq x \leq 26$ at.%, to experimentally study the presence of dynamic phase transitions (DPT) by using an ultrasensitive transversal magneto-optical Kerr effect (T-MOKE) set-up. A ferromagnetic system under the influence of a time-dependent external field H(t), can shift their time-magnetization M(t) response as function of H(t) period (P) and its amplitude (H_0). Therefore, as P gets closer to the system's relaxation time, M(t) is unable to follow H(t) anymore, leading to a symmetry breaking at a critical period (P_c) where the system undergoes a DPT [1,2]. So, for $P>P_c$, the mean time-dependent magnetization, i.e, the dynamic order parameter $\langle Q \rangle$ is zero and the system is at a dynamically disordered state, while for $P<P_c$ we have a dynamically ordered state ($\langle Q \rangle \neq 0$). Furthermore, an additional small time-independent bias field (H_b) is the conjugated field to $\langle Q \rangle$, and thus it can alter the systems dynamic response in both ordered and disordered regimes [2]. Hence, in our experimental set-up, dynamic and static magnetic fields where applied to the samples using an electromagnet with minimal coercivity and low latency. High field stability was reached by implementing an iterative routine to minimize field variations for H_0 and H_b closer to ±1 Oe, for frequencies up to 300 Hz. T-MOKE ultrasensitive configuration enable an enhanced signal-to-noise ratio 20 times higher than that for the conventional one [3]. Hence, N (> 250) independent real-time full hysteresis loops were recorded as function of the field period, H_b and H_0 field amplitudes to determine $\langle Q \rangle$ values under fast resolved conditions. These experimental settings enable the exploration of both $\langle Q \rangle(H_b,P)$ and $\langle Q \rangle(H_b,H_0)$ DPT's phase diagrams (Fig. 1), evidencing the presence of metamagnetic fluctuations (sidebands) in the disordered regime for our whole sample range.

[1] D. T. Robb, Y. Xu and P. A. Rikvold, Physical Review B, 78(13), 134422. (2008). [2] P. Riego, P. Vavassori and A. Berger, Physical Review Letters, 118(11), 117202 (2017). [3] E. Oblak, P. Riego and A. Berger, *Journal of Physics D: Applied Physics*, *50*(23), 23LT01, (2017).

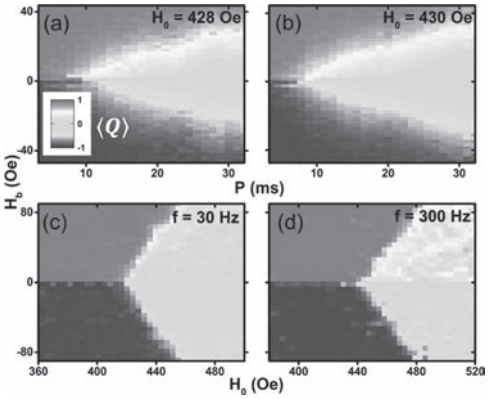


Fig. 1 (a) and (b) $Co_{76}Ru_{24}$ experimental $\langle Q \rangle(P, H_b)$ maps for H_0 = 428 Oe and H_0 = 430 Oe, respectively. (c) and (d) Experimental $\langle Q \rangle(H_0, H_b)$ maps for f = 30 Hz and f = 300 Hz. $\langle Q \rangle$ color scale bar is on the left-hand side of (a).

ER-11. Precession damping in $[Co_{60}Fe_{40}/Pt]_5$ multilayers with varying magnetic homogeneity investigated with femtosecond laser pulses. *M.A. B. Tavares*[1], L.H. F. Andrade[1], M.D. Martins[1], G.F. Moura Gomes[2,3], L.E. Fernandez-Outon[3,1] and F.M. Matinaga[3] *1. Nanotechnology, CDTN/CNEN, Belo Horizonte, Brazil; 2. PPGMCS, Unimontes, Montes Claros, Brazil; 3. 3 Depto de Fisica - UFMG, Belo Horizonte, Brazil*

Using femtosecond light pulses to study ultrafast magnetization dynamics has been a fruitful approach for investigating magnetic materials [1-3]. Here we report on the ultrafast magnetization dynamics of $[Co_{60}Fe_{40}/Pt]_5$ multilayers (MLs) which were synthesized with varying magnetic textures. The controlled growth rate of the Pt buffer layer modified the anisotropy fields and magnetic domain sizes of the MLs (S1-S4) as verified by VSM, MFM and simulations with MuMax3 software. Details of sample growth and characterization are presented in [4]. The time-resolved measurements were done with 100 fs laser pulses at a fluency ~0.2 $mJ.cm^{-2}$ in a degenerate pump and probe setup [1-3]. After photoexcitation by 100 fs pump pulses, we observed a ultrafast demagnetization of the ML's in hundreds of fs followed by a partial remagnetization, which occurs in ~1.5 ps. As displayed in Fig. 1a for the MLs with largest domain sizes a damped precession of the magnetization is observed to decay with a time constant of ~133 ps and its frequency varies from 5.8 GHz to 9.8 GHz as the magnetic field increases from 276 mT to 427 mT. We determined the efective damping (α) fitting the experimental data with the Landau-Lifshitz-Gilbert equation (Fig. 1b and Fig.1c) [1-3]. Expectedly, the decay time (η) increases for higher fields reaching a constant value of ~ 135 ps. For fitting the experimental data in Figure 1b we used the saturation magnetization and anisotropy field measured from VSM (± 5%) and a value of g=2.45 for Pt/Co/Pt layers as reported in ref. [5]. This large value of g may be related to additional orbital moment from the Co/Pt interface [5]. As shown in Fig. 2, α decreases from 0.18 to 0.04 for MLs with increasing magnetic domain sizes (S1-S4). These α values may be related to an enhanced scattering and spin pumping effects from Pt adjacent layers [3-5-6]. Finally, we note that the precession frequency (extracted fitting the data to LLG) increases from 2.04 GHz to 11.5 GHz as the anisotropy field of the MLs increases from 6.5 kOe to 13 kOe.

[1] A. Barman, J. Sinha, Spin Dynamics and Damping in Ferromagnetic Thin Films and Nanostructures, Springer (2017) [2] C. Papusoi, T. Le, C.C.H. Lo et al, J. Phys. D: Appl. Phys. 51 325002 (2018) [3] J. Walowski, M. Djordjevic Kaufmann, B. Lenk et al, J. Phys. D: Appl. Phys. 41 164016 (2008) [4] L. E. Fernandez-Outon, W. G. Schmidt, A. M. Fortini et. al, JMMM, 467, p. 139, (2018) [5] P. Neilinger, T. Scepka, M. Mruczkiewicz et al., Appl. Surface Science 461, 201 (2018) [6] E. Barati, M. Cinal, D. M. Edwards et al., Phys. Rev. B 90, 014420 (2014).

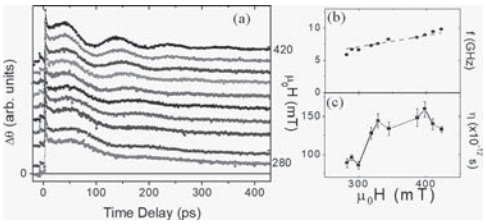


Fig. 1 (a) TRMOKE, (b) precession frequency and (c) decay time as a function of the external magnetic field for S4.

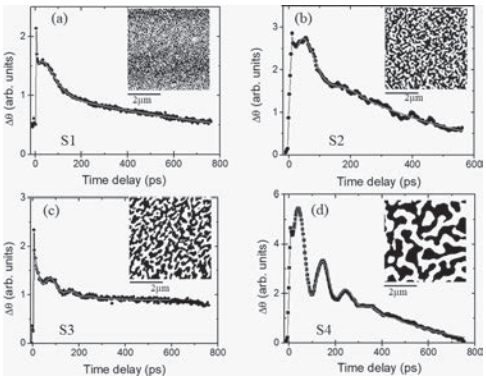


Fig. 2 Precession damping for MLs with increasing magnetic textures (S1-S4).

ER-12. Detection of torque effects in Co/Pt via ferromagnetic resonance. *Y. Weng*[1,2], C. Liang[1] and J.G. Lin[2,3] *1. Graduate Institute of Applied Physics, National Taiwan University, Taipei, Taiwan; 2. Center for Condensed Matter Sciences, National Taiwan University, Taipei, Taiwan; 3. Center for Atomic Initials for New Materials, National Taiwan University, Taipei, Taiwan*

Charge current-induced torque effect [Oersted (T_o) and spin-orbit torque (T_s)] on the magnetization dynamics of ferromagnet (FM)/metal bilayer is interesting from the aspect of fundamental physics as well as applications in spintronic devices. T_o is induced by charge current (J_c) gradient in a FM and T_s is due to spin action on magnetization. The behavior of T_o and T_s can be analogous to the field and damping torque, respectively. The torque-induced variation of damping constant ($\alpha \equiv \gamma W/4\pi f$) of magnetization can be determined from a change of the linewidth (W) of ferromagnetic resonance (FMR) spectrum. Thus, the current dependence of α provides a quantitative estimation for spin Hall angle (θ_{SHE}) which is defined as the conversion rate of charge current to spin current via spin-orbit coupling. However, the torque effect often was hindered due to heating-induced artifacts. In this work, we particularly pay attention to minimize the Joule heating effects in order to investigate the intrinsic torque effects in cobalt (Co)/platinum (Pt) bilayer with an applied J_c ranging from -60 to 60 mA. The way to distinguish T_o and T_s is by applying $\pm J_c$ on the plane of film along the two directions: transverse and parallel to the magnetic field. [1] This is because T_s can only occur in the transversal case and its direction depends on the direction of J_c. For transversal (parallel) case, the value of normalize linewidth $W^* \equiv [W(J_c)/W(0)]$ decreases from 1.000 to 0.945 (1.000 to 0.929) with J_c increases from 0 to 60 mA. The change of W* is mainly related to the T_o. For transversal case, the variation of α is not symmetric with respect to J_c=0. The $\Delta\alpha$, $\Delta\alpha \equiv [\alpha(+J_c)-\alpha(-J_c)] \propto \theta_{SHE} J_c$, increases from 0 to 0.376×10^{-4} with $|J_c|$ changing from 0 to 60 mA. Based on the asymmetrical part of α [red line in Fig. 2(b)], the θ_{SHE} of Pt is obtained as 0.20, which is higher than θ_{SHE} measured by ST-FMR for Co/Pt system (~0.11). [2]

[1] K. Ando, S. Takahashi, K.Harii et al. PRL 101 036602 (2008)
[2] Weifeng Zhang, Wei Han, Xin Jiang et al. Nature physics 11, 496 (2015)

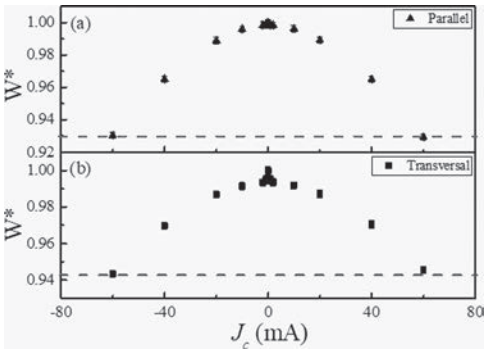


Fig. 1 The plot of W* versus J_c changing from -60 to 60 mA with J_c (a) transverse and (b) parallel to magnetic field

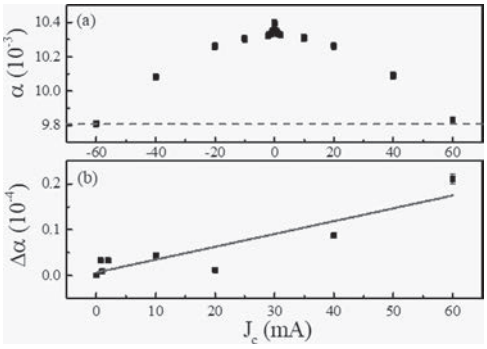


Fig. 2 For transversal case, (a) the variation of α with J_c ranging from -60 to 60 mA. (b) The variation of $\Delta\alpha$ with J_c ranging from 0 to 60 mA.

Session ES
EDUCATION, OUTREACH, & PUBLIC ENGAGEMENT IN MAGNETISM
(Poster Session)

Dafiné Ravelosona, Co-Chair
Center for Nanoscience and Nanotechnology, Palaiseau, France
Yukiko Takahashi, Co-Chair
NIMS, Tsukuba, Japan
Barry L Zink, Co-Chair
University of Denver, Denver, CO, United States

ES-01. Exploring magnetic resonance with a compass. *D. Nelson*[1], E. Cookson[1], M. Anderson[1], D. McKinney[2] and I. Barsukov[1] *1. Physics and Astronomy, UC Riverside, Riverside, CA, United States; 2. Santa Rosa Academy, Menifee, CA, United States*

Magnetic resonance plays an important role in today's science, engineering, and medical diagnostics. Learning and teaching magnetic resonance is challenging since it requires advanced knowledge of condensed matter physics and quantum mechanics. Driven by the need to popularize this technologically impactful phenomenon, we develop an inexpensive table-top demonstration experiment. It unveils the magnetic resonance of a hand-held compass in the magnetic fields of a permanent magnet. The setup provides an immediate visualization of the underlying physical concepts and allows for their translation to broad student audiences. This work was supported by the National Science Foundation under Grant No. ECCS-1810541.

ES-02. Magnetic Fields Web Series: Engaging Middle School Students in STEM. *P. Pena Martin*[1], J. Isberg[1], E. Ertekin[1,3], V. Lorenz[1,2] and N. Mason[1,2] *1. Materials Research Laboratory, University of Illinois at Urbana-Champaign, Urbana, IL, United States; 2. Department of Physics, University of Illinois at Urbana-Champaign, Urbana, IL, United States; 3. Department of Mechanical Science and Engineering, University of Illinois at Urbana-Champaign, Urbana, IL, United States*

Web based media can make scientific content accessible to audiences far beyond the scientific community. We created a web series called "Magnetic Fields" that aims to introduce materials science, particularly concepts related to magnetism, and promote themes more general to STEM fields, such as persistence and the scientific process, through use of characters and a story geared towards a middle school audience. The goal is to build and maintain interest in science at an age where this tends to drop off. The four-episode arc follows a group of high school characters as they encounter a strange new material during a class field trip to a laboratory. The series is directed by John Isberg, with professional actors making up most of the cast. The series was initiated by scientists in the Illinois MRSEC, and the storyline was developed in collaboration with MRSEC students and faculty. The episodes were released in May 2019 through Youtube. We report on the process of creating this series, response to it upon release, and discussion of its use as an educational tool. The authors acknowledge primary support of the NSF through the University of Illinois at Urbana-Champaign Materials Research Science and Engineering Center DMR-1720633.



Fig.1 Scene from an episode of "Magnetic Fields." Photo by John Isberg.

ES-03. In-class experiments with smart phones for teaching upper-level electricity and magnetism. A. Davidson[1], A. Ranjan[2] and *X. Fan*[1] *1. Physics and Astronomy, University of Denver, Denver, CO, United States; 2. Cherry Creek High School, Greenwood Village, CO, United States*

Interactive-engagement method such as studio physics [1, 2], has demonstrated higher learning gains than traditional lecturing in intro-level physics classes. However, there have been limited applications in upper-level classes, such as Electricity and Magnetism (E&M), possibly because experiments on E&M topics can be too costly and sophisticated to be carried out in the classroom. Smart phone, which is equipped with magnetic field sensors, radio signal detectors and light sensors, provides a convenient platform for carrying out E&M-related experiments. In this poster, we will present three examples of the implementation of smart-phone-based studio physics in an E&M class for Physics majors: (1) Detection of earth magnetic field inclination; (2) quantifying skin depth of aluminum foil with cellphone tower signals; and (3) Measurement of Brewster's angle. Besides sensitive sensors, smart phone also has computational power, which can be explored to further expand the breadth and depth of the smart-phone-based studio physics. Due to the wide accessibility of smart phones and the simplicity of experimental setup, we expect this teaching technique can be easily transferred to other institutes in the world.

[1] Gok, T., *Assessment of the effectiveness of the hybrid studio format in introductory undergraduate physics.* Energy Education Science and Technology Part B-Social and Educational Studies, 2012. 4(1): p. 117-130. [2] Sorensen, C.M., A.D. Churukian, S. Maleki, and D.A. Zollman, *The New Studio format for instruction of introductory physics.* American Journal of Physics, 2006. 74(12): p. 1077-1082.

ES-04. The Use of Virtue Modules in Physics Lab Teaching. *W. Zhang*[1], R. Bidthanapally[1], T. Sebastian[2], Y. Xiong[1,3], H. Qu[3] and J. Sklenar[4] *1. Physics Department, Oakland University, Rochester, MI, United States; 2. THATec Innovation GmbH, Mannheim, Germany; 3. Electronic and Computer Engineering, Oakland University, Rochester, MI, United States; 4. Physics Department, Wayne State University, Detroit, MI, United States*

Lab sessions in physics education connect the fundamental concepts to practical examples and are effective measures of the students' understanding and reasoning through ultimate real-world tests. Many topics in condensed

matter physics are known to be challenging to convey in both lectures and labs. In addition, these topics are usually resource demanding, which has been one of the challenging issues. Here, we introduce and demonstrate the use of virtue lab modules for teaching physics labs and for effectively integrating research and education. Experiments that are relevant to magnetism and spintronics include, but not limited to, spin current detecting, microwave energy harvesting, and spin-based thermoelectric effects. An important highlight of these modules is the highly-interactive laboratory learning platform. In the class, each piece of experimental hardware (e.g. electrometers, oscilloscopes, etc) will be paired with a computer-based virtual module. The individual modules mimic the hardware, which the students can use to become familiar with the hardware, acquire real-time feedback, and visualize the data acquisition dynamics, on-demand and risk-free. The virtual component is also helpful for demonstrating delicate, shared hardware in class, without risk of damaging the actual instrumentation. These individual components are connected to a central operating system and the experiment can be re-programmed by simple coding and user-interfaced commands [1]. Work at Oakland University is supported by NSF DMR-1808892.

[1] THATec Innovation GmbH: https://www.thatec-innovation.com/

Session ET
MICROMAGNETICS AND HYSTERESIS MODELING I (Poster Session)

Mario Carpentieri, Chair
Politecnico of Bari, Bari, Italy

ET-01. Quantitative Evaluation and Reduction of Error in Computation of the Demagnetization Tensor. *M.J. Donahue*[1] and D. Porter[1] *1. Applied and Computational Mathematics Division, National Institute of Standards and Technology, Gaithersburg, MD, United States*

Given two rectangular prisms (cells) with edge dimensions $h_x \times h_y \times h_z$ offset from one another by $\underline{r}$, the average field $\underline{H}$ in one prism arising from a uniform magnetization $\underline{M}$ in the other can be written as $\underline{H} = -N\,\underline{M}$, where N is the 3×3 symmetric demagnetization tensor. By computing N for all offsets across a 3D lattice, the self-magnetostatic field can be efficiently computed for arbitrary shapes and magnetization. Analytic closed-form expressions are known for N [1], but these suffer numerically from catastrophic cancellation at large offsets $R=|\underline{r}|$. We find the error using the analytic forms is $\approx \varepsilon R^3/(h_x h_y h_z)$, irrespective of the cell geometry, where ε is the floating point rounding error (10^{-16} for 8-byte double precision). It is better for large R to switch to asymptotic approximations. This method was used in [2], but only for cubic cells ($h_x=h_y=h_z$) and with a simple dipole asymptotic approximation. In this work asymptotic approximations are developed for general rectangular prisms with $O(1/R^{11})$ truncation error, as compared to $O(1/R^5)$ for the dipole approximation. However, the asymptotic error varies with cell geometry. This affects the optimal crossover point and maximal error, as seen in Fig. 1, where the scaled crossover offset and error grow as the cell geometry varies from 1×1×1 up through 10×1×1. The asymptotic error can be reduced by subdividing each prism into smaller subcells, but this is computationally costly in simulations with extended dimensions or periodic boundary conditions. The geometry effect can be accounted for by scaling by maximum cell edge length (Fig. 2), which allows for frugal application of prism subdivision while retaining high accuracy. This can provide a 100-fold speed-up in computation of N for plate-like cells common in micromagnetic modeling of thin films.

[1] A.J. Newell, W. Williams, and D.J. Dunlop, J. Geophysical Research - Solid Earth, 98, 9551-9555 (1993). [2] K.M. Lebecki, M.J. Donahue, and M.W. Gutowski, J. Phys. D - Appl. Phys., 41, 175005 (2008).

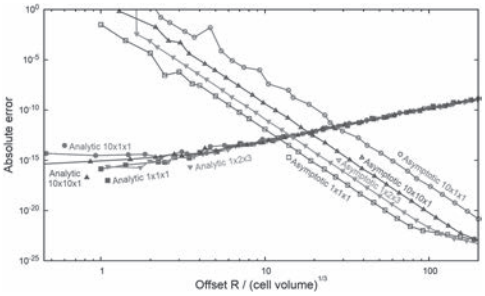


Fig.1 Absolute error in computation of the demagnetization tensor component N_{xx} using analytic formulae (filled symbols) and $O(1/R^{11})$ asymptotic approximation (open symbols) versus normalized cell offset R for four cell geometries. Optimal crossover offset and maximum error occur at the intersection of lines for the same cell geometry.

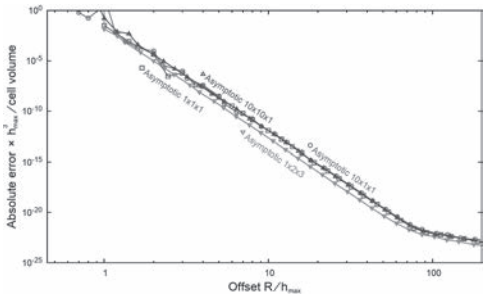


Fig.2 Absolute error in asymptotic approximation of N_{xx} scaled by longest cell edge instead of cell volume.

ET-02. Microresonator-integrated magnetic tunnel junctions allowing for thermal gradient sign reversal designed using COMSOL simulations. *H. Cansever*[1], J. Lindner[1], A. Niesen[2], T. Huebner[2], G. Reiss[2], J. Fassbender[1,3] and A.M. Deac[1] *1. Institute of Ion Beam Physics and Materials Research, HZDR, Dresden, Germany; 2. Center for Spinelectronic Materials and Devices, Bielefeld University, Bielefeld, Germany; 3. Institute of Solid State Physics, TU Dresden, Dresden, Germany*

In magnetic tunnel junctions (MTJs), it was theoretically predicted that magnetization dynamics can be induced by thermal gradients via thermal-spin transfer torques (T-STTs), similar to STTs induced by applied voltages[1]. We recently proposed an approach based on microresonators (μR) in order to detect T-STT terms acting on the free layer of an MTJ device by means of investigating the ferromagnetic response of an MTJ exposed to a cw laser in open-circuit conditions. The linewidth of the ferromagnetic signal is modified by the damping-like torque induced by thermal gradient, while the frequency is subject to changes induced by the field-like torque[2]. Here, we used COMSOL simulations to determine the temperature profile of Co2FeAl/MgO/CoFeB MTJs, when the MR structure is considered, see Fig 1. In this design, the structure is defined with laterally larger Co2FeAl (CFA) layer below CoFeB (CFB) layer. This allows for the laser beam to be focused on the CFA layer surface, in order to heat the bottom electrode of the MTJ rather than the top, as commonly investigated[3-6]. The temperature of both layers and temperature differences (ΔT) as a function of lateral width are shown in Fig 2. The temperature on the CFA layer decreases laterally about 25K towards to center of the structure and yields a ΔT over the barrier of about 680mK, if a gold pad is placed on the CFA layer, in the position where the laser is shined on (Fig 2). Without the gold pad and leaving the MgO on the CFA unpatterned, the ΔT over the barrier is reduced almost by factor of 2, and is estimated to be around 320mK and 270mK respectively. When both layers have gold contacts, ΔT drops to 20mK (Fig 2). Consequently, the magnitude and the sign of ΔT over the barrier can be engineered by appropriately designing the design of the device, which would allow for T-STTs induced by thermal gradients of different sign to be investigated experimentally in a single MTJ.

[1] Jia X, Xia K and Bauer G E W 2011 Phys. Rev. Lett.107 176603 [2] H. Cansever, R. Narkowicz, K. Lenz, C. Fowley, L. Ramasubramanian, O. Yildirim, A. Niesen, T. Huebner, G. Reiss, J. Lindner, J. Fassbender, A. M. Deac, 2018 J. Phys. D: Appl. Phys. 51 22400 [3] N. Liebing, S. Serrano-Guisan, K. Rott, G. Reiss, J. Langer, B. Ocker, H. W. Schumacher,

2011, Phys. Rev. Lett. 107, 177201. [4] J. C. Leutenantsmeyer, M. Walter, V. Zbarsky, M. Münzenberg, R. Gareev, K. Rott, A. Thomas, G. Reiss, P. Peretzki, H. Schuhmann, M. Seibt, M. Czerner, C. Heiliger, 2013, Spin3, 1350002. [5] A. Boehnke, M. Milnikel, M. Ehe, C. Franz, V. Zbarsky, M. Czerner, K. Rott, A. Thomas, C. Heiliger, G. Reiss, M. Münzenberg, 2015, Sci. Rep. 5, 8945. [6] H. Cansever, J. Lindner, T. Huebner, A. Niesen, G. Reiss, J. Fassbender, A. M. Deac, 2019, IEEE Trans.Magn. 51(17) Early Access

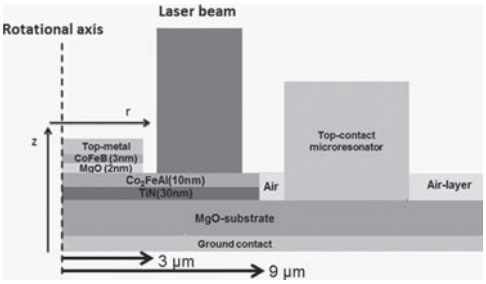


Fig.1 2D sketch of an MTJ structure considered for COMSOL modelling, where the loop of µR was taken into account and only the bottom layer is exposed to the laser.

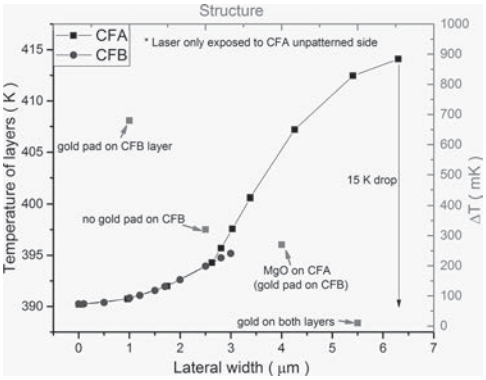


Fig.2 Temperature profile of the MTJ versus lateral size, ΔT dependence on designed structure.

ET-03. Topological states and skyrmions in thick spherical shells. *D.A. Rodríguez Cid*[1,2], F. Valencia[1,2], M. Kiwi[1,2] and F. Torres[1,2]
1. Departamento de Física, Universidad de Chile, Santiago, Chile; 2. Centro para el Desarrollo de la Nanociencia y la Nanotecnología, CEDENNA, Santiago, Chile

Magnetic topological structures have lately attracted much attention due to their potential technological applications such as information carriers and magnetic storage process [1, 2]. These states emerge naturally in low dimensional structures due to local curvature effects [3, 4] which induce effective magnetic interactions [5, 6, 7]. We studied the magnetization ground state, reversal modes and structural stability of nanoscopic hollow spherical shells numerically by micromagnetic simulation (with OOMMF) and by molecular dynamics simulation (with the Molecular Dynamics Simulator LAMMPS). We studied thick hollow nanospheres and their magnetic properties with several external radii R_e and thickness T. We performed simulations for the hysteresis loops and different reversal modes, such as as vortex, onion, whirligig, and skyrmion states were found, depending on the thickness T and the external radius R_e as shown in Fig. 1. While the onion, and whirligig states have already been observed [7], the skyrmion illustrated in Fig. 2 has not. In a two dimensional structure topological stable skyrmions have a topological charge Q = +1 or -1, while the ground state is topologically trivial Q = 0. In contrast, a planar skyrmion structure embedded in a spherical shell is topologically trivial Q=0, while the ground state is not trivial. We show that thick spherical shells display a non trivial topological skyrmion state.

[1] Yangqi Huang, Wang Kang, Xichao Zhang, Nanotechnology 28, 08LT02 (2017). [2] N S Kiselev, A N Bogdanov, R Schäfer, *Journal of Physics D: Applied Physics 44,* 392001 (2011). [3] V. P. Kravchuk, U. K. Roßler, O. M. Volkov, *Phys. Rev.* B 94, 144402 (2016). [4] D. Goll, A. E. Berkowitz, and H. N. Bertram, *Phys. Rev.* B 70, 184432 (2004). [5] D. D. Sheka, V. P. Kravchuk, and Y. Gaididei, *Journal of Physics A: Mathematical and Theoretical* 48, 125202 (2015). [6] R. Streubel, P.Fischer, F. Kronast, *Journal of Physics D: Applied Physics* 49, 363001 (2016). [7] M. I. Sloika, D. D. Sheka, V. O. Kravchuk, *Journal of Magnetism and Magnetic Materials* 443, 404-412 (2017).

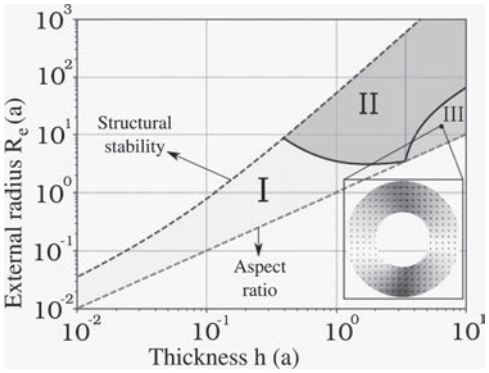


Fig.1: Spherical shell phase diagram. Dashed lines indicate the boundary of structural stability (blue) and the minimal aspect ratio condition (red). There are three magnetic phases: I) onion, II) whirligig, and III) skyrmions. In both axes "a" stands for the lattice parameter.

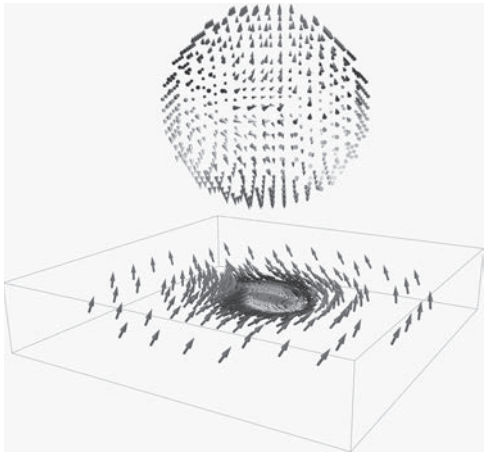


Fig. 2. Top: Micromagnetic simulation of a thick shell (R_e=100nm, T=60 nm). Bottom: Stereographic projection of a thin spherical layer of the thick shell (5nm). The reversal mode shows a skyrmion state oriented along the external field.

ET-04. On Hysterisis Based Random Number Generation. *C.E. Korman*[1] and I. Mayergoyz[2] *1. Electrical and Computer Engineering, George Washington University, Washington, DC, United States; 2. Electrical and Computer Engineering, University of Maryland, College Park, MD, United States*

Random number generation has many important applications, examples of which include cryptography, Monte Carlo simulations, statistical sampling and gambling. For these reasons, random number generation is a standard software (or hardware) component of modern computers. In the talk, we shall discuss a new hysteresis-based technique for random number generation which can be efficiently implemented by using modern spintronics based nano-technology. The central idea of this random number generation is the utilization of random switching of rectangular hysteresis loops (see Fig. 1). This approach naturally leads to the generation of random binary

numbers as the outputs of rectangular hysteresis loops (see Fig. 2). Mathematically, this random switching can be treated as a repeated sequence of two exit problems for stationary stochastic processes. These exit problems can be reduced to the solution of initial boundary value problems for the appropriate backward Kolmogorov equations. The analytical solution of these boundary value problems can be carried out for the Ornstein-Uhlenbeck process which is the only stationary Gaussian Markov process (see Ref. 1). The latter is relevant for the development of stationary techniques for random number generation. Another (alternative) approach to the analysis of the above random switching based on stochastic processes on graphs will be discussed in the talk, as well (see Ref. 2). In the discussion, special attention will be paid to the trade-offs between the strength of thermal noise which drives the random switching of rectangular hysteresis loops and the widths of these loops which is usually controlled by magnetic anisotropy of nano-magnetic hysteretic elements. Furthermore, the effect of the sampling rate on the stationary distribution of randomly generated binary numbers will be investigated as well. At the nano-scale, rectangular hysteresis loops can be realized by using standard nano-magnetic elements. For this reason, it is conceivable that hysteresis based random number generation may find many important applications in future spintronics based computer systems.

1. C. E. Korman and I. D. Mayergoyz, "Preisach model driven by stochastic inputs as a model for aftereffect," IEEE Transactions on Magnetics, Vol. 32 (5), pp. 4204-4209, 1996. 2. M. I. Freidlin, I. D. Mayergoyz and R. Pfeiffer, "Noise in hysteretic systems and stochastic processes on graphs," Physical Review E, Vol. 62, No. 2, pp. 1850-1855, 2000.

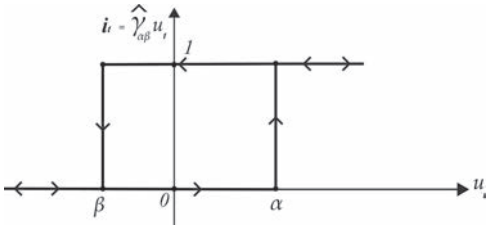


Fig. 1: Rectangular Hysteresis Loop

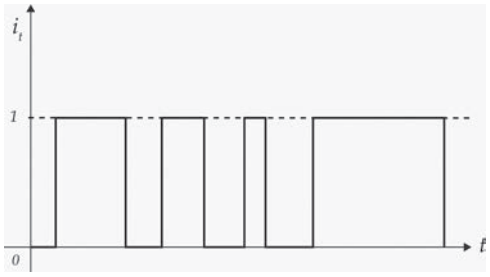


Fig. 2: Random Binary Output of the Hysteresis Loop

ET-05. General nature of the step-induced frustration at ferromagnetic/antiferromagnetic interfaces: Topological origin and quantitative understanding. X. Chen[1], T. Ji[1], L. Sun[1], B. Miao[1], Y. Millev[2] and *H. Ding*[1] *1. National Laboratory of Solid State Microstructures, Department of Physics and Collaborative Innovation Center of Advanced Microstructures, Nanjing University, Nanjing, China; 2. American Physical Society, New York, NY, United States*

We present a study of the magnetic configuration due to step-induced magnetic frustration at ferromagnetic/antiferromagnetic (FM/AFM) interfaces. At a substrate monatomic step edge, a 180° domain wall emerges. In the ultrathin limit of the capping layer, its width increases linearly with the thickness, whereby the initial slope of growth is found to depend only on the ratio of the inter-layer and intra-layer Heisenberg exchange constants, regardless of the presence the magneto-crystalline anisotropy in the system. These findings are in good agreement with previous experimental observations [1]. As the thickness grows beyond the ultrathin regime, the corresponding thickness dependence departs from linearity and tends to its bulk value. We propose a physically appealing form for the thickness dependence, which follows a universal behaviour in both cases of an AFM domain wall on top of the FM layer and a FM domain wall on top of an AFM substrate. The analytical insights are supported by conclusive, detailed micromagnetic simulations of two independent varieties: (i) the Monte Carlo method, and (ii) the object oriented micromagnetic framework. While the quantitative details of the study are naturally dependent on the specific material parameters of the complex magnetic system, the global features of the spin texture in the capping layer are dictated by the topological step-edge defect. The latter is quantifiable by a winding number of ±1/2 [2].

[1] U. Schlickum, N. Janke-Gilman, W. Wulfhekel, and J. Kirschner, Phys. Rev. Lett., 92, 107203 (2004). [2] O. Tchernyshyov and G.-W. Chern, Phys. Rev. Lett., 95, 197204 (2005).

ET-06. Massively parallel O(N) space-time hierarchical dipole-dipole method implemented in the VAMPIRE code for atomistic spin dynamics. *S. Jenkins*[1], R.W. Chantrell[1] and R.F. Evans[1] *1. Physics, University of York, York, United Kingdom*

Atomistic spin models[1] provide a natural bridge between electronic and micromagnetic length scales but are computationally expensive. In particular calculation of the long-range dipole-dipole interactions which causes complex magnetic structures, such as magnetic domains, vortices or Skyrmions. At the continuum level these interactions can be calculated assuming a uniform magnetization within a volume of but for atomistic simulations the continuum approximation does not accurately reflect the local dipole-dipole interactions and leads to systematic errors. A brute force atomistic dipole-dipole approach is infeasible for the timescales or lengthscales needed to extract useful data. The current approach in the code uses a dipole tensor [4] but the computational cost and memory usage scales with the square of the problem size. Here we present modifications to the VAMPIRE software package [1] to include accurate and scalable calculation of dipole-dipole interactions. We have developed a space-time hierarchical calculation of the dipole field calculation with order improved *O(N)* scalability with problem size. Our approach combines exact near-field computation of the dipole field with an *M*-Level hierarchical representation of the far-field dipole field [5], shown schematically in Fig. 1. The method is hierarchical in time and space, since the far-field time-evolution of the magnetization is much slower than the near-field which changes on the femtosecond timescale. Our improved algorithm enables the inclusion of accurate dipole-dipole interactions in atomistic simulation for large system sizes in the micrometre range for the first time. The massive improvement in scalability from the tensor calculation is shown in Fig.2. This major code improvement will allow large scale atomistic spin model simulations, bridging the gap between current simulation size ranges and those used in devices or investigated experimentally.

[1] R. F. L. Evans *et al,* J. Phys.: Condens. Matter 26, 103202 (2014) [2] S. Yuan and H. Bertram, IEEE Trans. Mag. 28, 2031 (1992) [3] G. Brown et al, IEEE Trans. Mag. 40 2146 (2004) [4] G.J. Bowden et al., J. Phys. Condens. Matter 28, 066001 (2016) [5] J.J. Miles and B.K. Middleton, J. Magn. Magn. Mater. 95, 99 (1991)

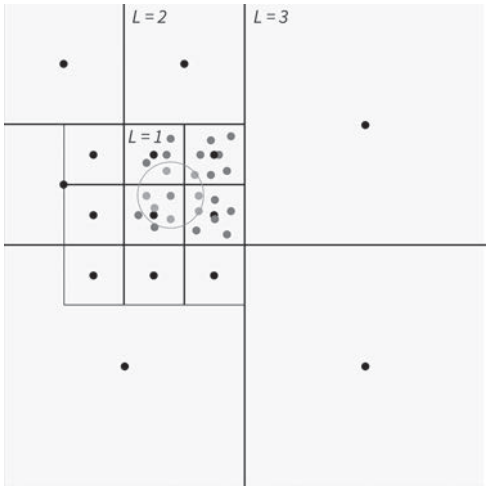


Fig. 1. Schematic implementation of the proposed hierarchical calculation of the dipole field. The method combines exact evaluation of short range dipole interactions with hierarchical calculation of far field sources.

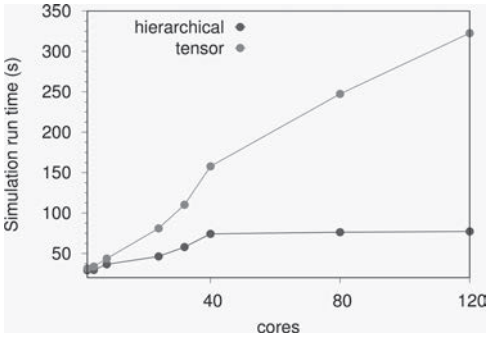


Fig. 2. Performance and weak scalability of the tensor vs the hierarchical methods.

ET-07. Micromagnetic Study of Soft Magnetic Nanowires. *F. Ahmadi*[1], M.J. Donahue[2], Y. Sozer[3] and I. Tsukerman[3] *1. Electrical and Computer Engineering, Youngstown State University, Youngstown, OH, United States; 2. Applied and Computational Mathematics Division, National Institute of Standards and Technology, Gaithersburg, MD, United States; 3. Electrical and Computer Engineering, University of Akron, Akron, OH, United States*

Magnetic nanowires (NWs) have vast applications in novel logic devices, data storage, permanent magnets, sensors, and biomedicine [1-5]. The higher shape anisotropy of NWs compared to their thin film and nanoparticle counterparts make them promising nanostructures for soft and hard magnetic materials. For instance, permanent magnets need to exhibit a high coercivity and energy product [3], while magnetic sensors require a low coercivity and hysteresis loss [6]. Such large-scale applications can be obtained by tuning the diameter, aspect ratio, and structure of the NWs. To control the magnetic properties of a densely packed array of NWs, one needs to understand the interwire and intrawire interactions, which is still challenging. In this paper, micromagnetic analysis of an array of long NWs embedded in a nonmagnetic matrix is studied. It is found that for NWs with diameters on the order of a hundred nanometers, the total energy is a sum of Zeeman and magnetostatic energies, while the anisotropy and exchange energies are negligible. Figure 1 shows the normalized Zeeman, magnetostatic, and total energies vs. an external magnetic field applied along the long axis of the NWs. The minimum magnetostatic energy corresponds to the maximum Zeeman energy, whereby half of the NWs are magnetized parallel to the external field, while the rest of the NWs are magnetized antiparallel to the external fields. The study shows a vortex behavior of the magnetic moments in the magnetization reversal process. Additionally, the average hysteresis loop area of the nanocomposite is inverse proportional to the NW diameter in the range from 20 to 200 nm. The results pave the way for designing of NW-based devices such as optimized magnetic sensors for biomedical applications with a trade-off between miniaturization and energy loss.

[1] D. A. Allwood, G. Xiong, C. C. Faulkner, *et al*., *Science* 309, 1688-1692 (2005) [2] S. S. P. Parkin, M. Hayashi, and L. Thomas, *Science* 320, 190-194 (2008) [3] K. Gandha, K. Elkins, N. Poudyal, *et al*., *Sci. Rep*. 4, 5345, 1-5 (2014) [4] D. Reyes, N. Biziere, B. Warot-Fonrose, *et al*., *Nano Lett*. 16, 1230-1236 (2016) [5] M. Safi, M. Yan, M. A. Guedeau-Boudeville, *et al*., *ACS Nano* 5, 5354-5364 (2011) [6] A. Remadevi, D. K. Sreedeviamma, and K. P. Surendran, *ACS Omega* 3, 10, 14245-14257 (2018)

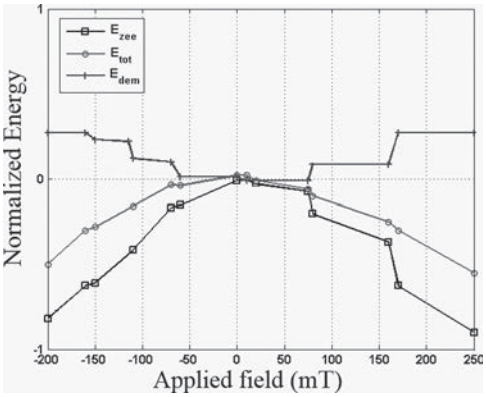


Fig. 1: Zeeman energy (black curve), demagnetization energy (blue curve), and total energy (green curve) in terms of an external magnetic field. In the simulation, the diameter, length, and center-to-center distance between each NW are 124 nm, 3200 nm, and 160 nm, respectively. Public domain micromagnetic software OOMMF is used for the simulation.

ET-08. Role of the shape anisotropy in curved magnetic slabs. *S. Castillo*[1], R. Corona[2,3], P. Landeros[4,3] and D. Altbir[2,3] *1. Departamento de Ingenieria, Universidad Autonoma de Chile, Santiago, Chile; 2. Física, Universidad de Santiago de Chile, Santiago, Chile; 3. CEDENNA, Santiago, Chile; 4. Física, Universidad Tecnica Federico Santa María, Valparaiso, Chile*

During the last decade, a strong interest has been focused on the properties of curved magnetic structures [1-3]. An important aspect in these systems is the possibility of controlling the magnetic behavior at the nanoscale by changing the curvature. One example of this behavior is magnetic nanotubes that exhibit chiral magnetic effects originated from the non-local dipolar interaction in the curved structure [4]. This interest has been reinforced by the development of a theory that allows calculating the exchange energy of nanomagnets with arbitrary shapes [5,6]. From the experimental side, curvature changes of magnetic properties in cylindrical magnetic segments with different radii of curvature were addressed by Streubel *et al.* [7], concluding that such geometric decrease magnetostatic interactions allowing higher areal density when used for racetrack memory devices. We develop a methodology that allows studying a magnetic slab that is progressively curved this study is done through modeling a truncated nanotube magnetic. Our results can be interpreted assuming that curvature generates an effective anisotropy in the structure and evidence that curvature contributes to strongly decrease the energy barriers. When we increase curvature, the magnetization tilts out of the surface, favoring the nucleation of transversal domain walls. Therefore, the use of curvature can be used to tailor energy barriers and the domain wall in the magnetic slab. Acknowledgments: The authors acknowledge financial support from Fondecyt 1160198 and 11170858, and Financiamiento Basal para Centros Científicos y Tecnológicos de Excelencia (CEDENNA), under project FB0807.

[1] A. Mehlin, B. Gross, M. Wyss, T. Schefer, G. Tütüncüoglu, F. Heimbach, A. Fontcuberta i Morral, D. Grundler, and M. Poggio, *Phys. Rev. B* 97,

134422 (2018). [2] P. S. C. Vilas-Boas, R. G. Elias, D. Altbir, J. M. Fonseca, and V. L. Carvalho-Santos, *Phys. Lett. A* 379, 47-53 (2015). [3] R. Streubel, D. J. Thurmer, D. Makarov, F. Kronast, T. Kosub, V. Kravchuk, D. D. Sheka, Y. Gaididei, R. Schafer, and O. G. Schmidt, *Nano Lett.* 12, 3961-3966 (2012). [4] P. Landeros and A. S. Núñez, *J. Appl. Phys.* 108, 033917 (2010). [5] Y. Gaididei, V. P. Kravchuk and D. D. Sheka, *Phys. Rev. Lett.* 112, 257203 (2014). [6] D. D. Sheka, V. P. Kravchuk, and Y. Gaididei, *J. Phys. A: Math. Theor.* 48, 125202 (2015). [7] R. Streubel, D. J. Thurmer, D. Makarov, F. Kronast, T. Kosub, V. Kravchuk, D. D. Sheka, Y. Gaididei, R. Schafer, and O. G. Schmidt, *Nano Lett.* 12, 3961-3966 (2012).

ET-09. Micromagnetics of thin films based on k-space fast convolution.

V. Scalera[1], *G. Tortora*[1], C. Serpico[1], S. Perna[1] and M. d'Aquino[2]
1. Department of Electrical Engineering and ICT, University of Naples Federico II, Naples, Italy; 2. Department of Engineering, University of Naples "Parthenope", Naples, Italy

The numerical studies of magnetization dynamics in micromagnetic systems with spatially distributed magnetization crucially rely on the computation of magnetostatic fields generated by the ferromagnet. The solution of the magnetostatic problem can be written as convolution of an appropriate Green's function with the magnetization vector field. Since the Green's function is long-range, after discretization of the problem in N cells, the direct numerical computation of the convolution integral has a computational cost scaling as N^2. In this work, we use, as it is often done in micromagnetics, the Fast Fourier Transform (FFT) method to reduce the computational cost to N log N. We consider micromagnetic systems with thin-film geometry where the magnetization can be considered costant across the thickness of the magnet. In this situations, only the field averaged across the thickness is relevant to the magnetostatic interations and both the magnetization and the averaged field inside the magnet depend only on two spatial variables. The usual approach to deal with this type of problem is to use FFT to compute the discretized version of the convolution integral relating the field and the magnetization [1]. Our algorithm, on the other hand, is based on the discretization of the integral relation between the field (averaged across the thickness) and the magnetization in the reciprocal space (k-space) [2]. The connection in the k-space is given by the Fourier transform of the Green function which, in the case of thin-films, can be written in a special form taking into account the thin-film geometry [3]. The advantage of this k-space method is that it can be used both for structure that are infinite or finite in one or both in-plane directions. In fact, this approach is the one usually preferred in the study of spin-waves dynamics in infinite structures. In the talk, the accuracy of the method is studied by comparing the results with analytical calculations (fig.1) and with those obtained by the usual approach by varying mesh size. In addition, we will study different techniques for the zero-padding used to eliminate the influence of periodic replica of the sources introduced by the FFT.

[1] R.D. McMichael, M.J. Donahue, D.G. Porter, J.Eicke, Journal of Applied Physics, Vol. 85, p.5816–5818 (1999) [2] F. Vico, L. Greengard, M. Ferrando, Journal of Computational Physics, Vol. 323, p. 191-203 (2016) [3] B.A. Kalinikos, A.N.Slavin, J. Phys. C: Solid State Phys. Vol. 19, p.7013-7033 (1986) [4] A.J. Newell, W. Williams, D.J. Dunlop, J. Geophysical Research, Vol. 98, pp. 9551-9555 (1993)

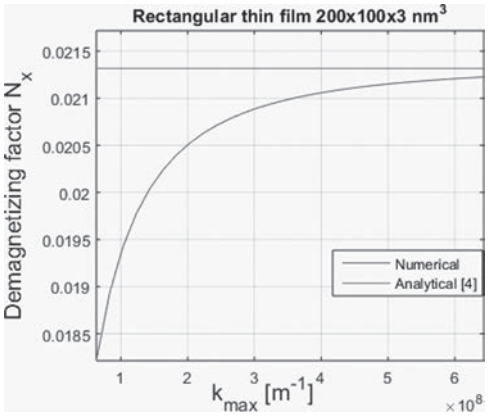


Fig.1 Example of the computed demagnetizing factor of a thin film

ET-10. Iron Loss Modeling and Analysis of Grain Oriented Silicon Steel Sheet under Harmonic Magnetization.

X. Zhao[1], R. Wang[1], L. Li[2] and R. Liu[2] *1. North China Electric Power University, Baoding, China; 2. North China Electric Power University, Beijing, China*

I. INTRODUCTION With the development of ultra-high voltage direct current (UHVDC) transmission system, application of nonlinear power electronic devices generates rich harmonics [1]. High order harmonics are superimposed on the fundamental component of 50Hz, which make it difficult to model the hysteresis and loss characteristics accurately [2]. II. METHODOLOGY AND MODEL The main experimental setup includes computer for displaying data, measuring system, and specimen silicon steel sheet. A single sheet tester (SST) made by BROCKHAUS is used to measure the magnetic and loss properties of GO silicon steel sheet (B27R095). The magnetic induction intensity are given in (1). Different harmonic excitations can be achieved by controlling the following three parameters, harmonic order k, amplitude ratio η and phase difference φ_k. $B(t)=-B_{1m}\cos(\omega t)-B_{km}\cos(k\omega t+\varphi k)$ (1) $\eta=B_{km}/B_{1m\ (2)}$ When the ferromagnetic materials are magnetized by harmonic voltage, iron loss will be dependent on the hysteresis and eddy current. Based on the theory of loss separation, the dynamic magnetic intensity can be divided into the following three parts, $H=H_h+H_{cl}+H_{ex}$ (3) where H_h refers to the static magnetic intensity, which can be fitted by Preisach model based on first order reversal curves (FORC) under harmonic excitation. An improved method is put forward to determine Hcl related to the eddy current loss. Considering the skin effect, the undetermined coefficients of time-varying functions can be obtained by the simulation of the measured dynamic hysteresis loop. Hex denotes the magnetic intensity corresponding to excess loss. III. RESULTS AND ANALYSIS The static and dynamic hysteresis loops under different harmonic parameters are simulated, and the total loss is calculated from the loop area (see Fig. 1). The results show that the hysteresis loop and loss under harmonic excitation determined by the proposed method is in practically good agreement with the simulated one. The total core loss will increase with harmonic order k and amplitude ratio η. Further results of the magnetic modeling and validation of the model will be presented in detail in the full paper.

[1] Z. Cheng, et al., "Eddy current and loss analysis of multisteel configuration and validation." *IEEE Trans. Magn.,* vol.43, no. 4, pp.1737-1740, 2007. [2] E. Dlala, Comparison of models for estimating magnetic core losses in electrical machines using the finite-element method, IEEE Trans. Magn., Vol. 45, No. 2, pp. 716–725, Feb. 2009.

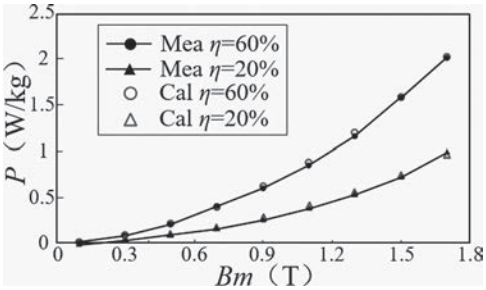


Fig. 1 Comparison between measured and modeled total loss

ET-11. The dynamic susceptibility tensor of nanostructured systems and the spectra of interface pinned walls. S.M. Martins Jr.[1], L.L. Oliveira[2], *A.L. Dantas*[2] and A.S. Carriço[1] *1. Department of Physics, Federal University of Rio Grande do Norte, Natal, Brazil; 2. Department of Science and Technology, State University of Rio Grande do Norte, Natal, Brazil*

We report a theoretical discussion of the spectra of domain walls (DW) sequences formed in Py stripes exchange coupled to two-sublattices vicinal antiferromagnetic substrates.(1,2) The DW are located at the edges of terraces holding magnetic moments from opposite substrate sublattices, and the terrace length sets the distance between consecutive DW. We have obtained a generalized dynamic susceptibility tensor, which may be applied to any nanostructured magnetic systems. These systems are likely to display inhomogeneous magnetization patterns. Apart from the anisotropy, Zeeman and dipolar energies, the exchange energy also contributes to the excitation spectra. A theoretical frame which gives both the equilibrium pattern and the excitation spectra is a valuable tool. Each polarized spectrum obtained from the diagonal elements (xx, yy and zz) of the susceptibility tensor, captures only the excitations which holds oscillations along the respective direction, allowing an association of spectral features with the domains (aligned in the x-direction) and the DW (with the center aligned in the y-direction). For large values of the terrace width, sequences of DW with the same chirality (SCHI) and those with alternate chirality (ACHI) have the same spectral densities. If the terrace length is below a threshold value, each domain wall is at the reach of the dipolar field of neighboring DW, and the stripe overall spectra are affected by the relative chirality of consecutive DW. For instance, a 240nm long, 50nm wide and 10nm thick Py stripe, with three 80nm long terraces and two DW, subjected to an interface exchange field of 15 kOe, has the same excitation spectra for SCHI and ACHI sequences of DW. However, a 300nm long Py stripe, holding five 60nm long terraces and four DW, has different spectral densities for SCHI and ACHI DW sequences. The DW modes have oscillations in the xz-plane. For the SCHI (ACHI) sequence the lowest DW mode frequency is f=3.7GHz (2.3GHz) and is localized at the DW region near the stripe boundaries, where the local field has the lowest value of 17kOe. The largest DW mode frequency is f=15.2GHz (11.7GHz), for oscillations at the DW centers, where the local field is largest, with a value of 27kOe.

[1] S. M. S. B. Martins, Jr., L. L. Oliveira, G. O. G. Rebouças, Ana L. Dantas, and A. S. Carriço, AIP Advanc. 8, 056004 (2018) [2] Ana L. Dantas, G. O. G. Rebouças, and A. S. Carriço, J. Appl. Phys. 105, 07C116 (2009)

ET-12. Withdrawn

ET-13. Magnetization Reversal Spin-Transfer-Torque Driven in Perpendicular Shape Anisotropy Magnetic Tunnel Junctions.
N. Caçoilo[1,2], S. Lequeux[1], N. Strelkov[1,3], B. Dieny[1], *I. Prejbeanu*[1], R. Sousa[1] and L. Buda-Prejbeanu[1] *1. Université Grenoble Alpes, CNRS, CEA, Grenoble INP, IRIG-SPINTEC, Grenoble, France; 2. Department of Physics & I3N, University of Aveiro, Aveiro, Portugal; 3. Department of Physics, Lomonosov Moscow State University, Moscow, Russian Federation*

The concept of Perpendicular Shape Anisotropy Spin-Transfer-Torque Magnetic Random Access Memory (PSA-STT-MRAM) consists in significantly increasing the thickness (L) of the storage layer of a conventional p-STT-MRAM to values close or above to the cell diameter to achieve shape anisotropy. The total anisotropy has thus a bulk contribution due to the shape anisotropy (SA) and an interfacial contribution (iPMA), provided by the FeCoB/MgO interface. The combination of these sources of anisotropy allows to extend the downsize scalability of STT-MRAM towards sub-10nm technological nodes [1, 2] thanks to a significant reinforcement of the thermal stability factor. It was also reported, using a string method, that upon increasing the thickness of the free layer, the most probable energy path between the two stable states of the memory evolves from a macrospin-like behaviour to a domain wall (DW) nucleation/propagation process [1]. The storage layer thickness is affecting the stability but also the writing operation of the cell. In this work, we have studied the magnetization reversal mechanism of the PSA-STT-MRAM induced by STT. Micromagnetic simulations have been carried out for various aspect ratios (diameter, thickness), the dependence of the switching time and the reversal behaviour have been analysed as a function of the applied voltage [Fig 1 and 2]. Above a threshold voltage, due to the spin-transfer-torque at the interface with the MgO, a transverse-DW motion [3] is nucleated and propagated towards the top surface. Upon increasing the thickness, the DW spends longer time in the middle of the pillar as seen in the inset of [Fig.1] and thus the switching time is considerably increased. Even though the nucleation of a DW is still present at the lowest thickness investigated (L=30nm, diameter=20nm), the magnetization switching is faster for shorter pillars, [Fig.2]. The simulations performed including stochastic thermal field indicate that this mechanism of reversal is robust against the thermal fluctuations.

[1] N. Perrisin *et al*, Nanoscale 10, 12187-12195 (2018). [2] K. Watanabe *et al*, Nat. Com. 9, 663 (2018). [3] A. Thiaville *et al*, EPS 69, 990 (2005)

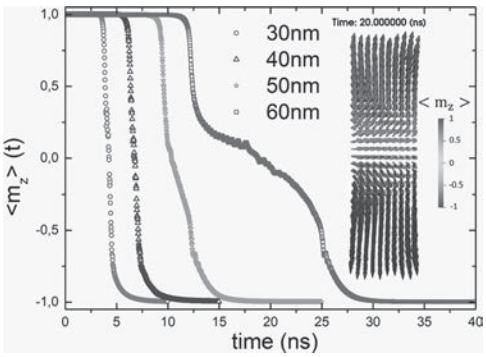


Fig.1. Magnetization time traces at a constant voltage of -2.5V. Inset: magnetization distribution at 20ns for L=60nm.

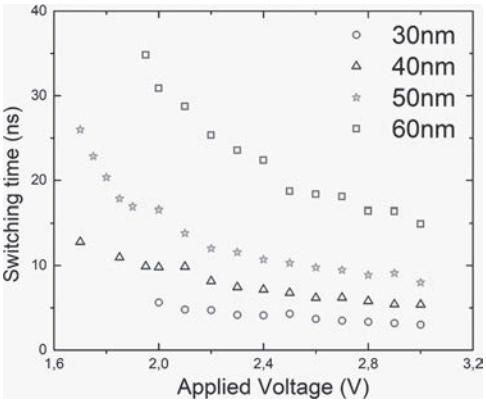


Fig.2. Switching time as a function of the applied voltage for different pillar thickness.

ET-14. Micromagnetic Simulations of First-Order Reversal Curves in Nanowire Arrays Using MuMax3. *R. Eimerl*[1], K. Muster[1] and R. Heindl[1] *1. Physics & Astronomy, San Jose State University, San Jose, CA, United States*

We used micromagnetic software MuMax3 [1] to model first-order reversal curves (FORC) in ordered arrays of magnetic nanowires. Our goal is to simulate the reversal processes in nanomagnet arrays and to map individual reversals to features in the FORC diagram. We simulated a set of reversal curves for a 3x3 array of nanowires, one μm in length and 80 nm in diameter. The nanowires are arranged in a square packing scheme, with a nearest neighbor distance of 200 nm. The average magnetization of each nanowire was recorded along with the total magnetization of the system at each field step. The reversal curves are transformed into the FORC distribution plotted in Fig. 1, showing that interacting nanowires create the so-called 'wishbone' FORC distribution. Two field distributions, one with constant coercive field and wide range of interaction fields (IFD) and one with constant interaction field varying coercive fields (CFD), are clearly visible [2]. Fig. 2 shows the relative FORC, indicating nine major changes in the magnetization of the system; these nine features are magnetization reversals of individual nanowires. By recording reversal process for all nine nanowires along the FORC curves, we are able to relate various switching processes to features in the FORC distribution. The location of the IFD along the coercive axis represents the nanowire's intrinsic coercivity, and the extent of the IFD along the interaction axis represents the upper and lower limits of the interaction field experienced by the system. We find that the CFD shows the real switching events, but the coercivity at which these reversals occur depends on the current state of the interaction field.

[1] A. Vansteenkiste, J. Leliaert, and M. Dvornik, AIP Adv., Vol. 4, p. 107133 (2014) [2] C. I. Dobrota and A. Stancu, J. Appl. Phys., Vol. 113, p. 043928 (2013)

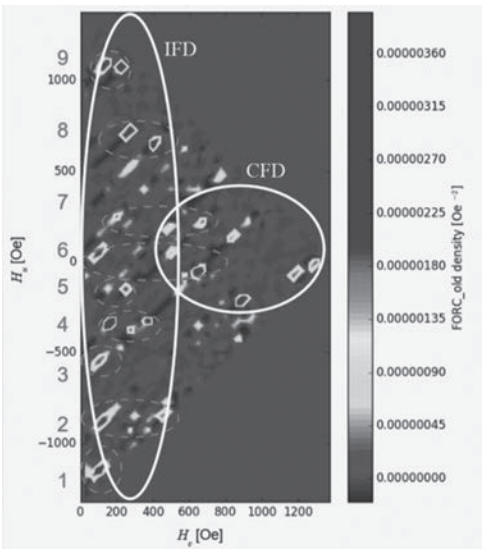


Fig.1 FORC distribution showing Interaction Field Distribution (IFD) and Coercive Field Distribution (CFD)

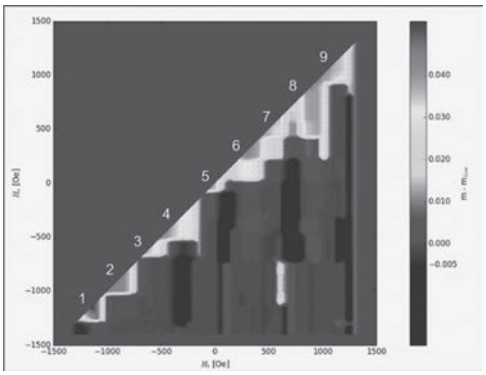


Fig.2 Relative FORC distribution

ET-15. Optimized Lateral Inhibition in Magnetic Domain Wall Tracks for Neuromorphic Computing. *C. Cui*[1], N. Hassan[2], C.H. Bennett[3], M.J. Marinella[3], J.S. Friedman[2] and J.C. Incorvia[1] *1. Electrical and Computer Engineering, The University of Texas at Austin, Austin, TX, United States; 2. Electrical and Computer Engineering, The University of Texas at Dallas, Dallas, TX, United States; 3. Sandia National Laboratory, Albuquerque, NM, United States*

Lateral inhibition is the neuron behavior that an active neuron cell prevents the firing of its less-active neighbors. It is a neural strategy commonly present in human brain[1]. So far, this important feature of neurons is either missing from devices or implemented through additional circuitry. Recently, an integrate-and-fire neuron based on magnetic domain wall (DW) racetracks has been demonstrated in modeling to be inherently inhibitory[2]. In Fig.1a, two adjacent magnetic nanowires have current-driven DW motion along +*y* via spin transfer torque. Neuron 1 (N1) with higher current density and DW velocity has a larger chance to "fire". Its stray field aligns Neuron 2 (N2) magnetization near DW2 in -*z*. DW2 motion is thus impeded, mimicking lateral inhibition. However, magnetic field has very limited control over average DW velocity in the precession regime of motion shown in this initial work. In this work, we show that significant lateral inhibition can be achieved with current- and field- induced DW motion below Walker breakdown[3] (WB). To this end, stray field must be controlled below Walker field for the inhibited neuron to operate in sub-WB regime. One way to realize such control is to vary the neuron spacing. We simulate in Mumax3 two side-by-side wires 32nm wide x 1.5nm thick x 3μm long using standard

material parameters for Co. In Fig.1, the wires are spaced apart 30nm. We see in Fig.1b simulation snapshot that when N1 has current density J_1 = 2 x 10^{12}A/m^2 and N2 J_2 = 1 x 10^{12}A/m^2, DW2 is inhibited compared to Fig.1c where when J_1 = 0 A/m^2 DW2 travels farther in the same amount of time. In Fig.2, we simulate DW2 velocity for wire spacings from 10 to 80 nm for both cases. The dip in inhibited velocity curve suggests an interaction strength for maximum lateral inhibition. We will further show optimized parameters for lateral inhibition implementation in magnetic DW neuron design via material and geometry engineering.

1. B.J. Baars and N.M. Gage, Cognition, Brain, and Consciousness: Introduction to Cognitive Neuroscience, Academic Press, (2010) 2. N. Hassan et al., Journal of Applied Physics, Vol.124, p.152127 (2018) 3. N.L. Schryer and L.R. Walker, Journal of Applied Physics, Vol.45, p.5406 (1974)

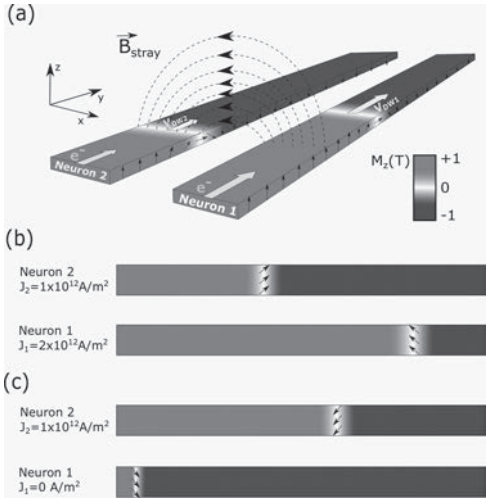


Fig. 1. Simulation setup. (a) Lateral inhibition condition: N1 stray field impedes DW2 motion. (b) Inhibited DW2 motion when DW1 is ahead. (c) Uninhibited DW2 motion when DW1 is behind.

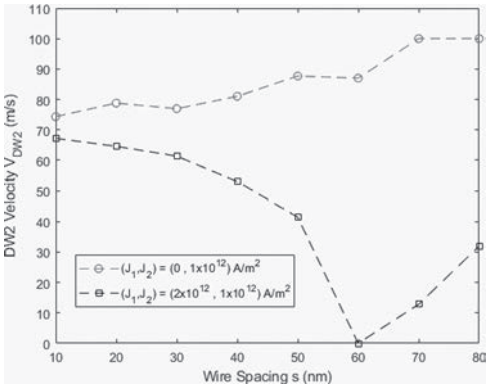


Fig. 2. Simulated DW2 velocity versus wire spacing, for non-inhibited (circles) and inhibited (squares) motion.

ET-16. A Hopfield Neural Network-Based Bouc-Wen Model for Magnetic Shape Memory Alloy Actuator. Y. Wang[1], C. Zhang[1], Z. Wu[1] and *M. Zhou*[1] *1. Department of Control Science and Engineering, Jilin University, Changchun, China*

With the development of modern science, the smart actuators are widely used in micro-nano positioning technology. As one of the smart actuators, magnetic shape memory alloy (MSMA) actuator, which is capable of positioning with the nanometer resolution, large energy density and small volume, has attracted much interest [1]. However, there are some difficulties in application of MSMA actuator, namely, 1) asymmetric loop between ascending and descending branches and 2) the output of MSMA actuator depends on the input frequency, which causes the deterioration of positioning accuracy in the system response. Therefore, precise modeling of MSMA actuator is the key to its applications. In this paper, a Bouc-Wen (BW) model is innovatively identified online by Hopfield neural network (HNN) to describe the hysteresis of MSMA actuator. BW model is a kind of differential equation hysteresis model. Compared with other models, such as Prandtl-Ishlinskii model, it has fewer parameters to be identified. Nevertheless, BW model is rate-independent. Identifying the applicable parameters is a significant part of modeling BW model. Neural network has the features of the nonlinear mapping property to be applied to adjust the model parameters online [2]. As a kind of fully interconnected recursive neural network, HNN has feedback connections from output to input and each neuron in HNN is connected to others. Hence, it has more computing power and better global searching capability. In this paper, HNN is innovatively used to identify the parameters of BW model online. Because it has ability of associative memory, it possesses the dynamic nonlinearity and can adjust the parameters of BW model adaptively. The identification results are shown in Fig. 1 and Fig. 2. The maximum modeling error rate at 1Hz and mixed frequency signal is 0.37% and 1.75%, respectively. The BW model identified in this paper can accurately describe the hysteresis of MSMA actuator at different input excitation. Therefore, the ability of precise modeling by HNN-based BW model is certified.

[1] B. Minorowicz, G. Leonetti, F. Stefanski, et al. Smart Mater. Struct., Vol. 25, art. no. 075005 (2016). [2] R. Xu and M. Zhou, IEEE Trans. Magn., Vol. 53, art. no. 2002004 (2017).

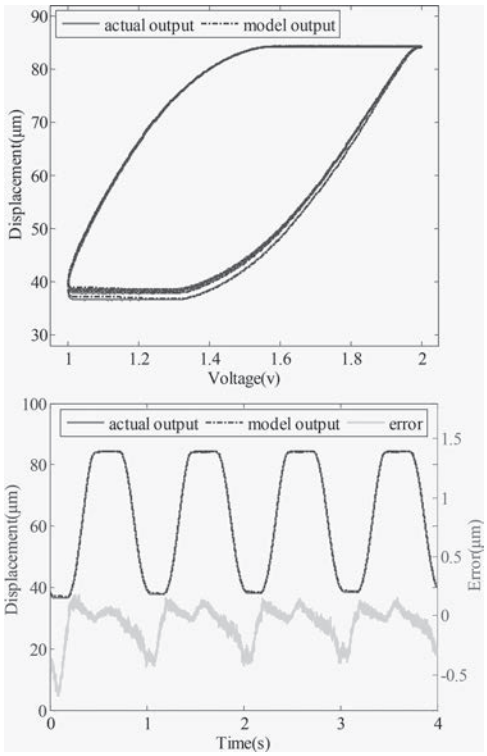


Fig. 1. Identification results of Bouc-Wen model in this paper at 1Hz.

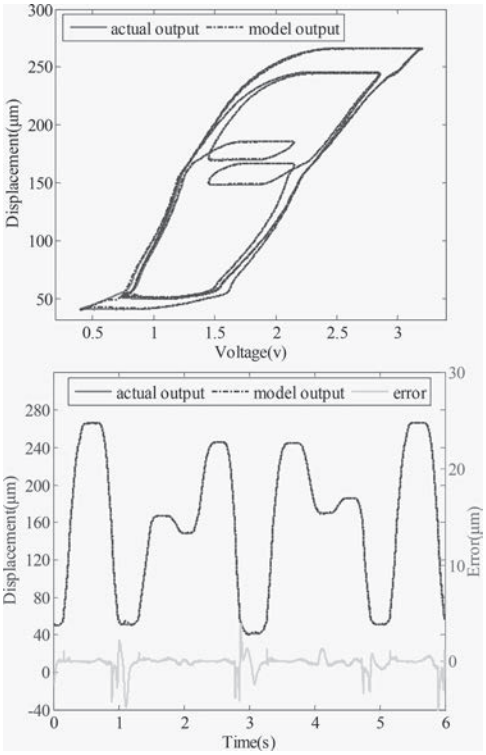


Fig. 2. Identification results of Bouc-Wen model in this paper at mixed frequency (0.6Hz and 1Hz) signal.

ET-17. Ferromagnetic Branch Design of Alnico for High Coercivity.

H. Won[1], Y. Hong[1,2], M. Choi[1], R. Wang[3,2] and F. Yan[2,3] *1. Department of Electrical and Computer Engineering and Center for Advanced Vehicle Technologies, The University of Alabama, Tuscaloosa, AL, United States; 2. Alabama Transportation Institute, Tuscaloosa, AL, United States; 3. Department of Metallurgical and Materials Engineering, The University of Alabama, Tuscaloosa, AL, United States*

A low coercivity (H_{ci}) of Alnico is attributed to the presence of a branch (B) between two ferromagnetic Fe-Co-rich rods (α_1-phase) that are embedded in a non-magnetic Al-Ni-rich matrix (α_2-phase) [1-3]. L. Ke observed the effects of B position on Z-axis on H_{ci} using micromagnetic simulation (MS) and concluded that the B connected in the bottom of the rod, namely U-shaped, showed low H_{ci} due to starts of magnetization reversal [4]. However, there is still a lack of studies on U-shaped structure for various B thickness ($T_{B\alpha1}$), width ($W_{B\alpha1}$), and position. Thus, this paper investigated the effects of various types of B on H_{ci} of U-shaped structure using MS. We used the following two conditions in the simulation: i) $T_{B\alpha1}$ for $W_{B\alpha1}$ of 40, 66, and 100% of the length of α_1-phase rod ($L_{\alpha1}$) while length of α_2-phase ($L_{\alpha2}$) is 10 nm and ii) B positions (middle- (MBC) and edge- (EBC) B -connected) while $W_{B\alpha1}$ and $L_{\alpha2}$ are 40% of $L_{\alpha1}$ and 10 nm, respectively. For $L_{\alpha1}$, 10 and 25 nm were chosen to represent coherent (ideal) and curling (real) rotations that occur in Alnico. Fig. 1 shows the structure of alnico used in the simulation. The element was divided into 1×1×2.5 nm^3 cell size and 2 Oe field steps with an aspect ratio (c/a) of 8 and simulated using LLG micromagnetic simulator v2.63b [5] for H_{ci}. Fig. 2 shows the change in H_{ci} with $T_{B\alpha1}$ under the above two conditions. The H_{ci} remains constant for all $L_{\alpha1}$ and $W_{B\alpha1}$ when $T_{B\alpha1}$ exceeds 30 nm. In Fig. 2(a), the H_{ci} increases as the $W_{B\alpha1}$ increases regardless of $L_{\alpha1}$, thereby, suggesting thicker $W_{B\alpha1}$ for higher H_{ci}. For the second condition shown in Fig. 2(b), for $L_{\alpha1}$ of 10 nm, MBC position shows 23% higher H_{ci} than EBC position, but for $L_{\alpha1}$ of 25 nm, EBC position shows 8-9% higher H_{ci} than MBC position. Thus, to obtain a higher H_{ci} than 5 and 2 kOe, design of Alnico with thicker $W_{B\alpha1}$ with MBC position for $L_{\alpha1}$ of 10 nm and EBC position for $L_{\alpha1}$ of 25 nm are recommended, respectively.

This work was supported in part by the NSF-I/UCRC for EV-STS under Grant No. 1650564.

[1] L. Zhou, M. K. Miller, Ping Lu, *Acta Materialia*, 74, 224 (2014). [2] S. Zhu, J. Zhao, W. Xia, *Journal of Alloys and Compounds*, 720, 401 (2017). [3] C. Zhang, Y. Li, X. Han, *Journal of Magnetism and Magnetic Materials*, 451, 200 (2018). [4] L. Ke, R. Skomski, T. Hoffmann, *Applied Physics Letter*, 111, 022403 (2017). [5] M. R. Scheinfein, LLG Micromagnetic Simulator™ [Online]. Available: http://llgmicro.home.mindspring.com

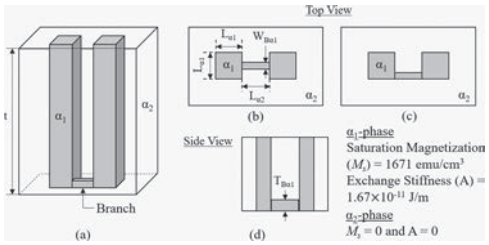


Fig. 1. Alnico structure: (a) Overall view; Top view of (b) MBC and (c) EBC; and (c) side view.

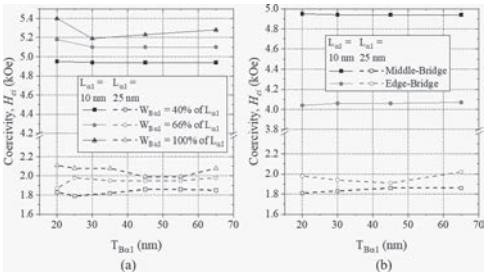


Fig. 2. H_{ci} as a function of $T_{B\alpha1}$ (a) for various $W_{B\alpha1}$ and (b) for MBC and EBC with $L_{\alpha1}$ of 10 and 25 nm and $L_{\alpha2}$ of 10 nm.

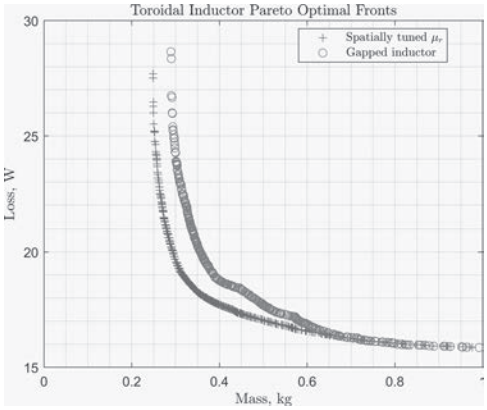
Session EU
POWER MAGNETICS - INDUCTORS AND TRANSFORMERS
(Poster Session)

Fumihiro Sato, Chair
Tohoku Gakuin University, Tagajo, Japan

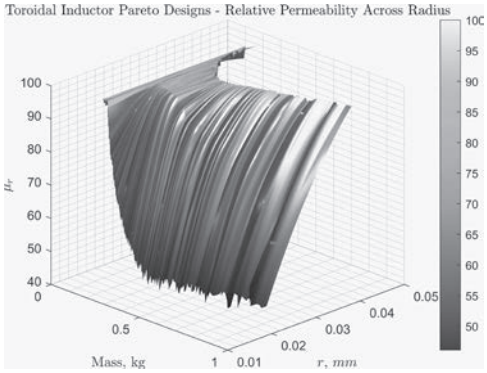
EU-01. A Multiphysics Assessment on Permeability Tuning Techniques in Power Inductors. *V. Cabral do Nascimento*[1], S. Moon[2], S. D. Sudhoff[1], K. Byerly[2], P. Ohodnicki[2] and R. Beddingfield[2] *1. Electrical and Computer Engineering, Purdue University, West Lafayette, IN, United States; 2. National Energy Technology Laboratory, Pittsburgh, PA, United States*

This paper investigates the benefits of spatial permeability optimization in the magnetic core in electromagnetic devices, using the achievable properties obtained through strain annealing treatment of Metal Amorphous Nanocomposite (MANC) alloys [1], [2]. This capacity introduces a new design element that can result in superior performance. However, the device characteristics result from a multitude of aspects besides the material properties, including its geometry and operational context (e.g. frequency, current waveform, and temperature constraints). A permeability profile can be heuristically selected to improve the performance of a device with a given geometry, but in order to fully leverage the capacity of spatial dependent permeability engineering, the geometry and permeability profile should be optimized simultaneously. The work herein presented compares viable solutions using permeability tuned ungapped inductors against traditional gapped devices, using multi-objective design optimization. This approach enables the determination of Pareto optimal fronts consisting of a set of optimal solutions against competing objectives (e.g. mass and loss) under imposed constraints. Pareto optimal fronts are a powerful tool to evaluate the true contributions of new technology in a certain application, since during the optimization the fundamental trade-off between competing objectives is identified. Also, in the inductor optimization, the device miniaturization and material savings are often limited not by the electromagnetic performance metrics, but rather thermal limits. This implies that a thorough optimization paradigm includes multi-physics aspects. The models used for the proposed assessment rely on coupling the electrodynamic behavior of the winding bundle, the magnetic solution of the inductor and the thermal model concerning the heat transfer between core, winding and ambient. The case studies included in this work evaluates AC and DC inductors with toroidal and racetrack parametrized geometries.

[1] R. Beddingfield *et al.*, "Thermal profile shaping and loss impacts of strain annealing on magnetic ribbon cores," *J. Mater. Res.*, vol. 33, no. 15, pp. 2189–2206, Aug. 2018. [2] K. Byerly *et al.*, "Metal Amorphous Nanocomposite (MANC) Alloy Cores with Spatially Tuned Permeability for Advanced Power Magnetics Applications," *JOM*, vol. 70, no. 6, pp. 879–891, Jun.



Toroidal inductor Pareto optimal fronts



Optimal relative permeability across the radius of the toroidal inductor Pareto optimal designs

EU-02. Study on the Performance of HCFCL Considering Different Magnetic Materials. J. Yuan[1], *Z. Zhang*[1], P. Gan[1] and H. Zhou[1] *1. School of Electrical Engineering and Automation, Wuhan University, Wuhan, China*

The saturated-core fault current limiter (SCFCL) is a promising way to suppress high fault current[1,2]. In order to increase DC bias capability and reduce core loss of SCFCL, our research team proposed a novel hybrid-type SCFCL (HSFCL)[3]. The topology of HSFCL is shown in Fig. 1(a). Its equivalent electric circuit and equivalent magnetic circuit are shown in Fig. 1 (b) and Fig. 1 (c). In order to make HSFCL have better sensitivity and current limiting performance, four different soft magnetic materials are selected to compare their effects on performance of HSFCL in this paper[4]. Fig.2(a) shows the B-H curves of four chosen soft magnetic materials (silicon steel 30Q130, ferrite H5B2, permalloy 1J50 and amorphous alloy NANO-amorphous). Ferrite and amorphous alloy have high sensitivity and rapid response speed because of their large slope of the magnetization curve μ_e and relatively small saturation magnetic flux density B_s. However, when a short-circuit fault occurs, if B_s is very small and the slope of the magnetization curve μ_e is large, soft magnetic materials will reverse saturation

the current-limiting inductance L_{fcl} will be small. In order to compare the current-limiting performance of four ferromagnetic materials, four types of HSFCL models are built in ANSYS. As is shown in Fig.2(b), HSFCL with all four materials has obvious current-limiting effect. Among the four materials, HSFCL with silicon steel has the best current-limiting effect, but as we discussed before, silicon steel has the slowest demagnetization speed. Different magnetization curves of four soft magnetic materials also lead to difference in core loss and permanent magnet stability of HSFCL. Detailed comparisons and experimental results will be shown in the full paper. The simulation shows that amorphous alloy with rapid demagnetization speed and relatively large B_s may be the best choice for HSFCL. And the material with large B_s like silicon steel and rapid demagnetization speed like amorphous alloy may be a future research direction of magnetic materials.

[1] J. W. Moscrop, "Experimental analysis of the magnetic flux characteristics of saturated core fault current limiters," IEEE Trans. Magn., vol. 49,no. 2, pp. 874–882, Feb. 2013. [2] A. Abramovitz, K. M. Smedley, F. de la Rosa, and F. Moriconi, "Prototyping and testing of a 15 kV/1.2 kA saturable core HTS fault current limiter," IEEE Trans. Power Del., vol. 28, no. 3, pp. 1271–1279, Jul. 2013 [3] J. Yuan, Y. Zhong, Y. Lei, C. Tian, W. Guan, Y. Gao, K. Muramatsu and B. Chen, "A novel hybrid saturated core fault current limiter topology considering permanent magnet stability and performance," *IEEE Trans. Magn*., vol. 53, no. 6, Jun. 2017, Art. no. 8400304. [4] Jiaxin, Y., Hang, Z., Yongheng, Z., Pengcheng, G., Yanhui, G., & Kazuhiro, M., et al. (2018). Performance investigation on dcsfcl considering different magnetic materials. AIP Advances,8(5), 056621-.

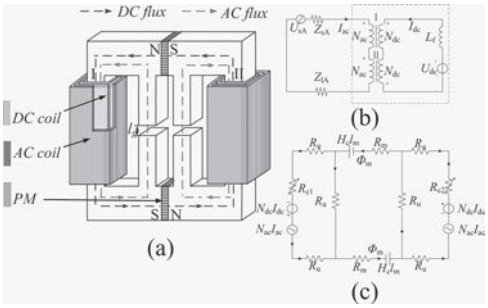


Fig.1 Configuration of HSFCL and its equivalent circuit

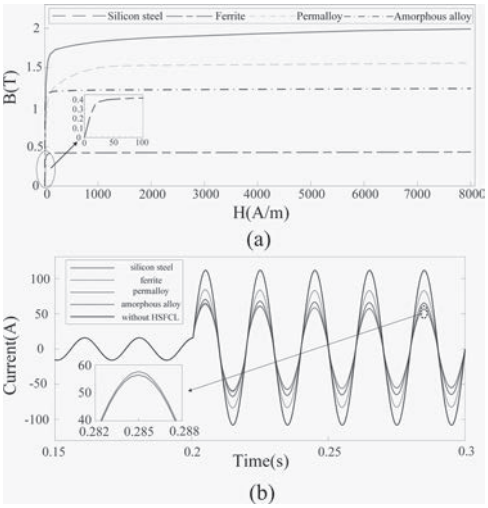


Fig.2 Different B-H curves of magnetic materials and current-limiting performances of HSFCL with four materials

EU-03. Study of thermal characteristics in variable inductor employing magnetic nanofluids driven by a high-frequency pulsed voltage source.
H. Lee[1] *1. Changshin University, Changwon-si, The Republic of Korea*

The characteristics of temperature rise were conducted experimentally and were tested numerically by adopting the multiphysics analyses technique in a variable inductor employing magnetic nanofluids(EFH series, Ferrotec Corporation). Recently, we presented a variable inductor which was developed by introducing the magnetic nanofluids resulting in the higher efficiency and the lower voltage shock in switching operation [1]-[2]. In a power inductor with high frequency, the temperature rise is critical issue and designers want to predict temperature rise while the circuit is operated. The core loss in this variable inductor is the main source of temperature rise in magnetic materials such as ferrite core and magnetic nanofluids for power electronics applications. The loss mechanism for ferrite is well known and relatively easily obtained the loss data from the manufacturer. However, for the magnetic nanofluid, such information is not readily available in the literature[3]-[4]. In order to evaluate the loss mechanism for the magnetic nanofluids, we first determined the electrical conductivity by use of our numerical results and measured the B-H curves with different temperatures. Finally, we measured and analyzed the inductance and temperature rise along with the average operating currents as shown in Fig. 1. The predicted temperature rise for a variable inductor showed good agreement with the experimental data and the developed magnetic-thermal-fluidic analysis technique can be employed to design a variable inductor with a high-frequency pulsed voltage source.

[1] D. W. Kim, H. N. Cha and D. H. Kim, IEEE Trans. on Magnetics, Vol. 49, p. 1901, (2013) [2] H. Y. Lee, I. M. Kang and S. H. Lee, J. Appl. Phys. Vol. 117, p. 17D508 (2015) [3] R. E. Rosensweig, J. Magn. Magn. Mater. Vol. 252, p. 370 (2002) [4] R. Hergt, S. Dutz, and M. Roder, J. Phys.: Condens. Matter. Vol. 20, p. 385214 (2008)

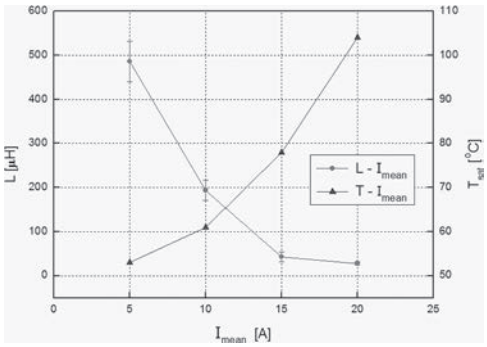


Fig. 1. The change of inductance and temperature along with the average operating currents in the variable inductor filled with magnetic nanofluids.

EU-04. Research on Hot-spot Temperature of Transformer with Nanopartical TiO_2.
X. Yang[1], G. Xu[1], Y. Zhang[3], L. Li[2], W. Fu[3], S. Ho[3] and Q. Yang[1] *1. Electircal Engineering, Hebei University of Technology, Tianjin, China; 2. Tianjin Polytechnic University, Tianjin, China; 3. The Hong Kong Polytechnic University, Hong Kong, Hong Kong*

With the increase of total economy, the power supply, which injects vigor into our society, has the more crucial position. Whereas the power transformer acts as the significant element of power systems, the hot-spot temperature inside the transformer tank should be calculated and measured accurately. Due to the hot-spot temperature has restricted the development of transformers, especially the oil-immersed transformer, so how to decrease the hot-spot temperature is a challenge for the researchers, engineers and manufacturers. Mineral transformer oil inside the transformer tank plays an essential role in transferring thermal, which produced by core loss, copper loss, stray loss and anomalous loss. Note, in 1995 Stephen had presented an innovative new class of heat transfer fluids, by suspending metallic nanoparticles to mineral transformer oil, exhibiting high thermal conductivities

compared to those of fluids without adding nanoparticles. Then the characteristics of cooling of transformer oil with nanoparticles can present excellent performance. Therefore, TiO_2 nanoparticles decorated with oleic acid to reduce agglomeration are added to mineral transformers oil as the coolant of a transformer. The transformer oil with different mass of fraction (0.005%, 0.01%, 0.02%, 0.05%, 0.1%, 0.2%, etc.) TiO_2 nanoparticle shows various performance through simulation and measurement. Through simulation and comparison finding the point of optimum operating temperature for each concentration. Then summarizing the optimum concentration from the results. During the measurement, the signal-phase transformer with power 500VA whose brand is DELIXI is adopted. The diameter of TiO_2 particles is under 100nm. Measuring the temperature of transformer oil adopts thermocouples on the different position inside the transformer tank. Then, to compare and analyze those results among each other, the best fraction is chosen as the ideal parameters, which can be as a reference for engineers or manufactures.

[1] D. Lin, P. Zhou, W. Fu, *IEEE Transactions on Magnetics,* vol. 40, p. 1318, (2004). [2] S. U. S. Choi, and J. A. Eastman, in Conference: 1995 International mechanical engineering congress and exhibition, San Francisco CA, United States,(1995). [3] F. X. Fang, W. M. Guan, H. Qian, *2016 Ieee International Conference on High Voltage Engineering and Application (Ichve)*, (2016).

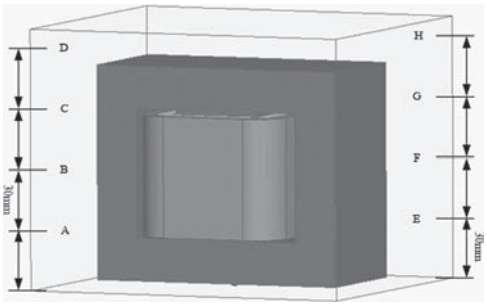


Fig.1 Simplified model of transformer

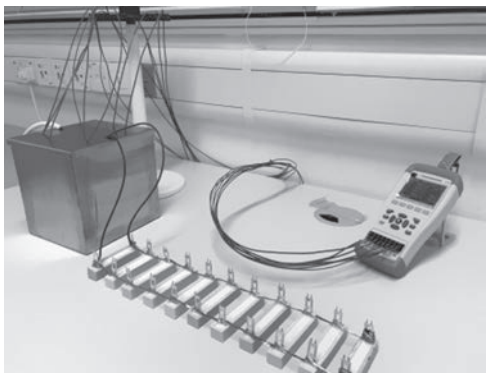


Fig.2 Transformer oil temperature test

EU-05. A Novel Iron Core Structure Design for Power Transformers Considering Magnetostriction and Joints. *J. Li*[1], B. Qu[2] and K. Yu[3]
1. State Key Laboratory of Control and Simulation of Power System and Generation Equipments, Tsinghua University, Beijing, China; 2. State Key Laboratory of Reliability and Intelligence of Electrical Equipment, Hebei University of Technology, Tianjin, China; 3. Global Information and Telecommunication Institute, Waseda University, Tokyo, Japan

The magnetic-force-deformation model due to magnetostriction (MS) and Maxwell stress model caused by joints are developed based on the major sources of vibration and acoustic noise in power transformer iron core in this paper. On the basis of forces created by the two sources, structure finite element method (SFEM) is used to calculate the iron core vibration, and then calculate the acoustic noise. Meanwhile, a three dimensional (3-D) structure model of power transformer is constructed, the natural frequencies and vibration modes of each order modal of the main system components are obtained according to the modal analysis, and sufficient experimental testing is used to verify all the steps of the study in detail. In the end, a novel structure design of iron core with the core and winding position interchange is put forward. The testing results of the prototype show that it is an effective means to reduce vibration and acoustic noise of power transformers. 1. The magnetic field force will be fed into SFEM with Maxwell stress produced on the interface between iron core and air to calculate the deformation of the magnetic materials when magnetostrictive modeling is performed. The simplest MS tests will be carried out by using a single closed circle or rectangular electrical steel sheet. 2. Then, a sheet with joint will be used to analyze the vibration and modeling calculation. Maxwell stress caused by joints and magnetostrictive force due to the sheet MS are all actually included in the model. Later, further complicated two or more pieces of sheets are designed up and down on the joint of the simple circle or rectangular sheet to simulate the joints forms in the iron cores of transformers with the magnetic flux transition circulation though the joints. 3. Compared to conventional power transformers, a novel structure design of iron core for power transformer is put forward, with the core and winding position interchange, and there are many design advantages. Comparisons between simulation and test data are used to verify the effect of vibration and noise reduction of the novel iron core structure design.

[1] Y. H. Chang, C. H. Hsu, H. L. Chu, et al, IEEE Transactions on Magnetics, Vol. 47, No. 10, pp. 2780-2783 (2011) [2] Y. L. Zhang, Q. Li, D. H. Zhang, et al, IEEE Transactions on Magnetics, Vol. 52, No. 3, p. 6100204 (2016) [3] Chang-Hung Hsu, Yi-Mei Huang, Min-Fu Hsieh, et al, AIP Advances, Vol. 7, p. 056681 (2017) [4] J. S. Li, Q. X. Yang, Y. J. Li, et al, IEEE Transactions on Magnetics, Vol. 53, No. 6, p. 6100404 (2017)

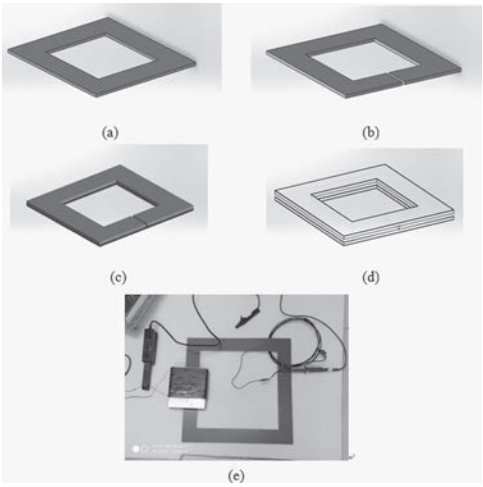


Fig. 1. Test verification models for MS and joints experiments.

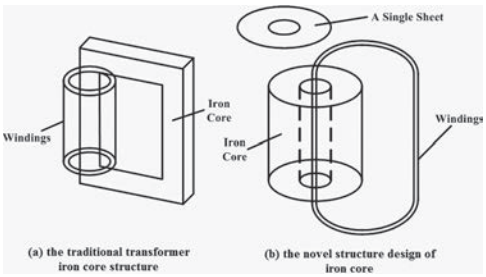


Fig. 2. Design comparisons of iron core structures.

EU-06. High frequency properties of Fe-1.5wt% Si powder cores.
J. Ahn[1], K. Lee[1], D. Lee[1] and J. Kim[1] *1. Hanyang University, Ansan, The Republic of Korea*

In order to improve the performance of electro-magnetic devices, these devices have been continuously required to increase the operation frequency and reduce the dimensions. Fe-Si alloys have been widely used in motors, inductors, etc., due to their high Bs and low magnetic anisotropy. However, the ductility and Bs of Fe-Si alloys decreased with increasing the Si content. It is, therefore, important to develop a new processing method for Fe-Si powder cores with high electrical resistance [1]. In this study, Fe-1.5wt%Si powders were coated of phosphate to minimize core losses. 2, 3 and 4wt% of phosphoric acid were added to acetone and 0.001wt% of sodium nitrite was added as a reaction accelerator. The FeP coating on Fe-Si powders with a size of 50~125μm were conducted in a thermostatic flask at 30°C for 30min. Before the FeP coating, the Fe-1.5wt% Si powders were heat treated at 1050°C in H_2 for 5hr to confirm a loss change due to crystal growth. The powders were compacted under a pressure of 1950MPa to form a toroidal shape. Then the compacts were annealed at 500°C for 30min under an Ar atmosphere. As shown in the Fig. 1, the FeP coating layer uniformly covers powders, and its thickness was less than 50nm. The density of the coated compacts reached a relative density of 97% despite the addition of Si and the FeP coating. Although the amount of phosphoric acid was changed, the density did not show any significant changes. This means that these powders have good ductility to form powder cores. As shown in the Fig. 2, there are not any significant differences between cores except the H_2 annealed core. The core loss of the cores is around 5.5W/kg at 50Hz, which is compatible to non-oriented commercial Fe-3.2wt%Si steel. The Eddy current loss was shown to be very low due to the high electrical resistivity of the compact. At 2kHz, the annealed core measured a core loss of 170W/kg while other cores measured around 230W/kg. These results clearly show that the Fe-1.5wt%Si powder cores coated with a FeP layer instead of Si electrical steels are applicable to devices working at a relatively high frequency.

[1] K. Lee, M. Choi, G. Lee, M. Kim, and J. Kim, IEEE TRANSACTIONS ON MAGNETICS, vol. 55, no. 2, 2000904, 2019.

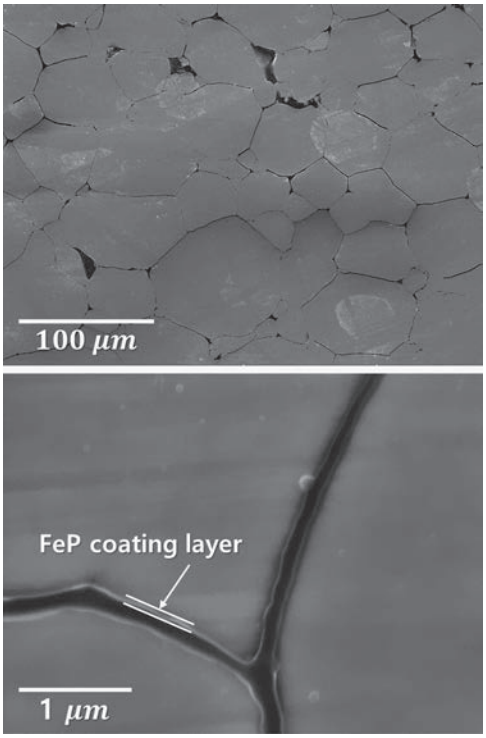


Fig.1 Cross-sectional images of a 3wt% phosphoric acid compact

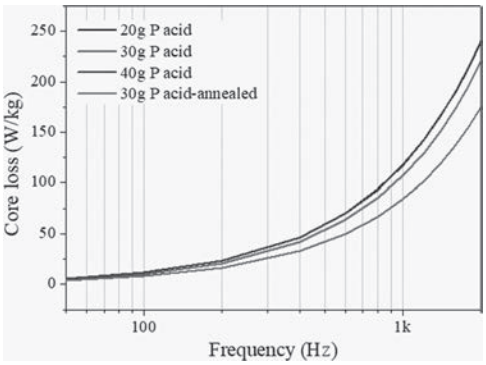


Fig.2 Core losses of coated Fe-1.5wt% Si powders

EU-07. Withdrawn

EU-08. Withdrawn

EU-09. Analytical Modeling of Multiple Segment Permanent Magnet Eddy Current Brake with Hybrid Secondary.
B. Kou[1], *W. Chen*[1,2] and L. Zhang[1] *1. Harbin Institute of Technology, Harbin, China; 2. Harbin University of Science and Technology, Harbin, China*

I. INTRODUCTION Compared with the electric excitation brake, permanent magnet eddy current brake has the advantages of compact structure, high efficiency and high reliability[1]-[4]. The secondary of non-magnetic reaction material with high conductivity is generally used for low-speed braking. The magnetic reaction secondary with high permeability is widely used in high-speed braking, such as high speed train braking systems. However, in the ejection experiment, it is necessary to brake the ejection object from high speed to low speed, in order to avoid the ejection object broken. The hybrid secondary eddy current brake is the combination of the non-magnetic reaction secondary and the magnetic reaction secondary eddy current brake, which can make the secondary have higher braking force in both high speed and low speed. In this paper, a multiple segment permanent magnet linear eddy current brake with hybrid secondary was presented as shown in Fig.1. First, the structure and working principle were introduced. Then, the nonlinear analytic model is derived using the Maxwell's equations. The iron secondary was split into thin sheets of constant permeability, determined by an iterative procedure. The analytic model takes into account higher harmonics and secondary saturation. Therefore, the accuracy is observably improved. Finally, the accuracy of the analytical model is verified by the finite element method. II. MODEL VALIDATION Fig. 2(a) is the iron secondary and the copper secondary braking force characteristic. The maximum braking force of the copper plate appears at a low speed range (about 5m/s). As the speed increases, the braking force decreases rapidly. Fig. 2(b) shows the resultant breaking force of the two conductor plates. The secondary braking force maintains a stationary value from high speed to low speed.

[1]Canova, B. Vusini,*IEEE Trans. Magn.*, vol. 41, no. 1, pp. 24-35, Jan. 2005. [2]S. Mohammadi, M. Mirsalim, S. Vaez-Zadeh, *IEEE Trans. Energy Convers.*, vol. 29, no. 1, pp. 224-231, Mar. 2014. [3]B. Kou, Y. Jin, H. Zhang, L. Zhang, H. Zhang,*IEEE Trans. Magn.*, vol. 50, no. 11, Nov. 2014. [4]S. M. Jang and S. H. Lee, IEEE Transactions on Magnetics, Vol. 39, no. 5, pp. 3004-3006, Sep. 2003.

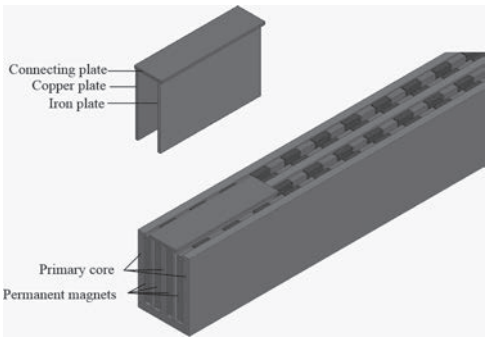


Fig. 1 3-D Structure of a multiple segment permanent magnet linear eddy current brake with hybrid eddy current

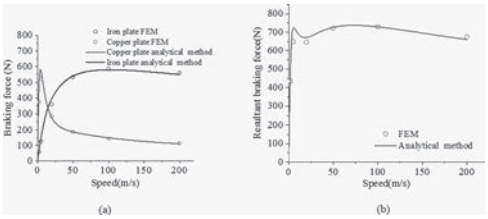


Fig.2 (a) Braking force of iron plate and copper plate respectively (b) Resultant breaking force of the multiple segment permanent magnet linear eddy current brake with hybrid eddy current brake.

EU-10. Numerical Study on Nanofluids Natural Convection Heat Transfer inside Power Transformer Windings. *Y. Zhang*[1], S. Ho[1], W. Fu[1], H. Wu[1] and X. Yang[2] *1. The Hong Kong Polytechnic University, Hong Kong, Hong Kong; 2. Hebei University of Technology, Tianjin, China*

I. Introduction Temperature rise is the major factor that limits the further advancement of power transformers in capacity and compactness. Although the thermal performance is improved through arranging the windings and cooling ducts reasonably, the inherent thermal conductivity of transformer oil is relatively small. Nanofluid is an innovative approach to improve the thermal conductivity of base fluid through dispersing nanoparticles of large thermal conductivity into it. The performance of nanofluid under natural convective mechanisms and in simple geometry has been studied numerically [1], which gives promising solutions when compared with the base fluid. In order to apply the nanofluid in transformer cooling, numerical method combined with the multiphase mixture model is employed to study the heat transfer inside nanofluid filled transformer windings in this paper. II. Numerical modeling The low-voltage windings of an ON transformer rated at 66 MVA are divided into four passes by the oil washers [2]. Except for the first pass, which has two more discs and an additional oil washer, each pass contains 19 discs. As is shown in Fig. 1, a 2-D axisymmetric model is built for the windings using the commercial software packages (Fluent) for fluid analysis. The coolant of the transformer is replaced by the SiC/oil nanofluid with the concentration of 1%, and the mixture model is introduced to the governing equations for the nanofluid. To determine the pattern of fluid motion, the nanofluid flow in the winding is treated as a conventional single-phase flow. The Reynolds number calculated for this problem is about 1000, which is much smaller than the critical value (2100) for laminar flow. Hence all the flows studied in this paper are laminar and no turbulence model is required. The second order upwind scheme is used for the spatial discretization of momentum and energy, and the problem is finally solved with the pressure-based solver in a coupled manner. The contours of the temperature of the winding cooled by nanofluid are shown in Fig. 2, and detailed results will be reported in the full paper.

[1] W. Rashmi, A. F. Ismail, M. Khalid, and Y. Faridah, Heat and Mass Transfer, vol. 47, p. 1301-1310 (2011) [2] A. Skillen, A. Revell, H. Iacovides, W. Wu, Applied Thermal Engineering, vol. 36, p. 96-105 (2012)

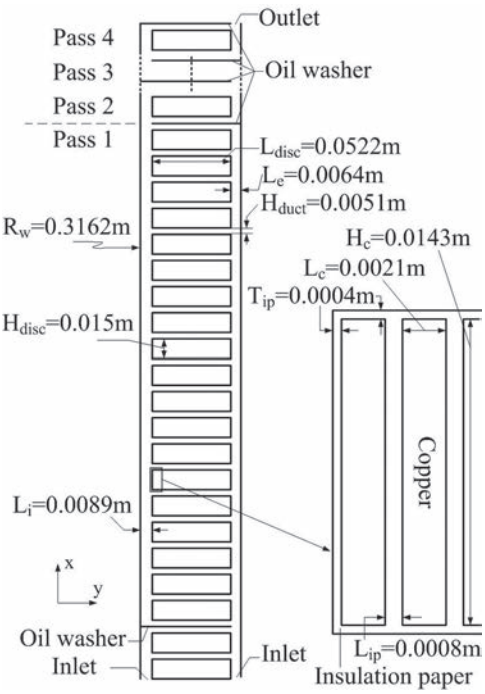


Fig. 1. The CFD model of the low-voltage winding.

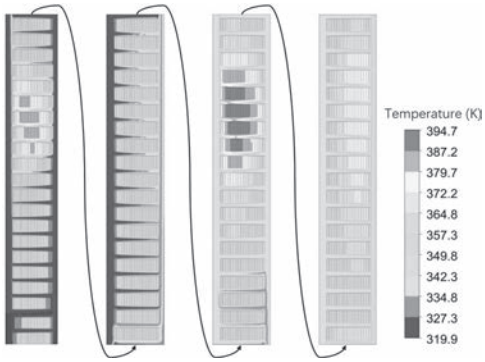


Fig. 2. The Contours of the temperature of the winding cooled by nanofluid.

EU-11. Modeling of Suspension Force on the Novel Integrated Five Degrees of Freedom DC Magnetic Levitated High-Speed Motor. *T. Zhang*[1], Z. Wang[1] and X. Ye[1] *1. Huaiyin Institute of Technology, Huai'an, China*

With the development of industrial technology, the speed of rotor is increasing, and the requirement of bearing performance is getting higher and higher. New types of bearings such as air bearing, liquid bearing and magnetic bearing have adopted. The magnetic bearings suspend the rotor by electromagnetic force, so that there is no mechanical contact between the rotor and the stator. Therefore, magnetic bearings have the advantages of no friction and wear, high rotor displacement accuracy, high supporting speed, no lubricants, and long service life [1]-[4]. Recently, magnetic bearings have been applied in flywheel energy storage, high-speed machine tools, turbo-molecular pumps and other equipment, and will replace traditional bearings in more fields, especially in vacuum, ultra-clean, ultra-high-speed, aerospace, nuclear energy, etc. In this paper, a three DOFs DC HMB is proposed, which is driven by three DC amplifiers in radial and axial direction, respectively. The characteristics of the three DOFs DC magnetic bearing are compactness, short axial length, simple control and automatic decoupling in the *x-y* direction. Firstly, the structure and suspension mechanism are introduced. Secondly, based on the equivalent magnetic circuit method, the

mathematic models are deduced. Finally, the simulation is carried out by the 3D finite element analysis. The theory analysis and simulation results have shown that the proposed hybrid magnetic bearing can achieve stable suspension, and the mathematic models are correct. A schematic diagram of the proposed five-DOF magnetic bearing is shown in Fig.1(a). The magnetic circuit of the proposed five-DOF magnetic bearing is schematically shown in Fig. 1(b). Fig. 2(a) shows the magnetic density. When the control winding currents are 0 to 5A, the variation curves of the suspension forces of the five-DOF DC magnetic bearing with respect to the control winding currents are shown in Fig. 2(b). The results of finite element simulation are basically in agreement with the theoretical values.

[1]S. Chen and F. Lin, "Robust Nonsingular Terminal Sliding-Mode Control for Nonlinear Magnetic Bearing System," *IEEE Trans. Control Syst. Technol.*, vol. 19, no. 3, pp. 636-643, May 2011. [2]C. R. Morrison, M. W. Siebert and E. J. Ho, "Electromagnetic Forces in a Hybrid Magnetic-Bearing Switched-Reluctance Motor," *IEEE Trans. Magn.,* vol. 44, no. 12, pp. 4626-4638, Dec. 2008. [3]Konrath M, Gorenflo J, Nils Hübner, et al. "Application of magnetic bearing technology in high-speed Centrifugation," *Chem. Eng. Sci.*, 2016, pp. 65-73. [4]B. Han, Q. Xu and S. Zheng, "Integrated radial/thrust magnetic bearing without thrust disk for a high-speed driving system," *IET Electric Power Appl.*, vol. 10, no. 4, pp. 276-283, Apr. 2016.

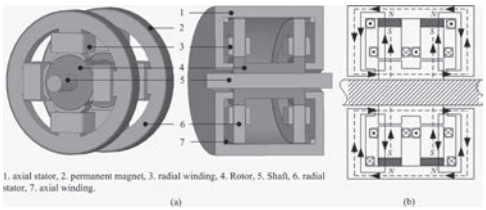


Fig. 1 3D model and magnetic circuit

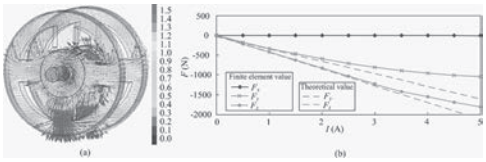


Fig. 2 Simulation results

EU-12. Analytical Calculation to Evaluate Influence of Structural Parameters on Performance in a Single-sided HTS Linear Induction Motor. *W. Qin*[1] *1. Electrical Engineer, Beijing Jiaotong university, BEIJING, China*

With the development of superconducting technology, high temperature superconducting (HTS) LIM has been developed successfully shown as in Fig.1(a). Duo to the low ac loss and the high current density, the HTS LIM has the advantages such as low volume, light weight, high efficiency and high power density, and so on [1]–[2]. However, the structure of HTS LIM is very different from conventional LIM, and the material properties as the electrical conductivity and the magnetic permeability are more complicated than the conventional materials. Fig.1(b) shows the relationship of the critical current and background feild in the HTS tapes. To evaluate the performance of the HTS LIM, the traditional analysis methods should be modified by considering the material properties of the HTS. Previously, the influence of structural parameters on performance was presented in which the HTS motor was modeled using numerical methods such as FEA[1]–[4]. Although numerical methods are capable of providing the accurate results, it is a serious problem when optimization is applied. In order to reduce the computation burden further, the HTS LIM has been analytically modeled with considering the slot parameters, critical current and slot leakage flux density and so all shown as in Fig.2. The flux density and force created by this analytical model are compared with FEM and experimental measurement shown as in Fig.2 and Tab.1, respectively. The implementation of analytical method and the influence of structural parameters on performance in the HTS LIM will also be discussed in the full paper.

[1] J. Zhao, T.Q. Zheng*, et al.*, "A Influence analysis of structual parameters on electromagnetic properties of HTS Linear induction motor," *Physica. C.,* vol. 471, no.21/22,pp. 1474-1478, 2011. [2] J. Fang, L. Sheng, D. Li, J. Zhao, S. Li, W, Qin, *et al,* "Influence analysis of structual parameters and operating parameters on electromagnetic properties of HTS Linear induction motor," in *Proc.24th Int.symp.supercond.*vol.27.Oct.2012,pp.408-411 [3] Dong Li, Weili Li, Jin Fang, *et al.*, "Investigation of a Low-Speed Single-Side HTS Linear Induction Motor With Different Primary Structures Used for Linear Metro," *IEEE Trans. Appl. Supercond,* vol. 24, no.5,pp. 3600710, 2014. [4] Bin Liu, Xiaoyue Zhang*, and Jin Fang et al.*, "A Novel Secondary Structure to Research on Dynamic Longitudinal Edge Effect of a Short-Primary HTS Linear Induction Motor for Subway Transportation," *IEEE Trans. Appl. Supercond,* vol. 26, no.7,pp. 5207305, 2016.

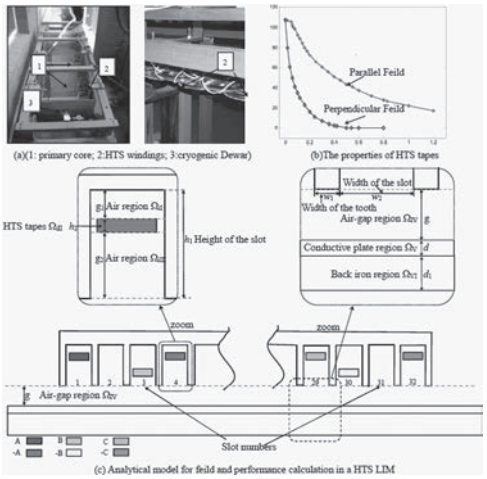


Fig. 1

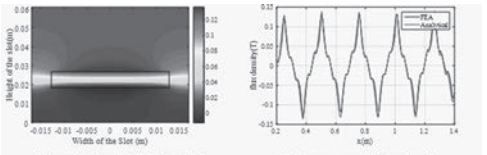


Fig.2 magnetic flux in slot and air gap

Table .1 The thrust force comparision between analttical, FEM and experimental measurement

Phase Current	frequency	speed	Analytical	FEA	Measurement
13.7A	10Hz	0.968m/s	272N	275N	208N
18.0A	10Hz	0.671m/s	533N	540N	410N
22.0A	8Hz	0.597m/s	627N	630N	493N
25.7A	6Hz	0.254m/s	1090N	1080N	786N
28.6A	5Hz	0.246m/s	1117N	1130N	839N
33.1A	4Hz	0.287m/s	1140N	1156N	861N

Fig. 2

Session EV
SENSOR, HIGH FREQUENCY, AND POWER DEVICES
(Poster Session)

Arkady Zhukov, Co-Chair
Basque Foundation for Science, San Sebastian, Spain
Conrad Rizal, Co-Chair
SeedNanoTech & Consulting, Brampton, ON, Canada

EV-01. Design and Fabrication of Miniature Magnetoelectric Antennas Using a Solidly Mounted Resonator Structure. *N. Sun*[2], Y. Gao[1], M. Sanghadasa[3] and N. Sun[2,1] *1. Winchester Technologies LLC, Burlington, MA, United States; 2. Electrical and Computer Engineering, Northeastern University, Boston, MA, United States; 3. U.S. Army Combat Capabilities Development Command Aviation & Missile Center, Redstone Arsenal, AL, United States*

One of the key challenges to state-of-the-art antennas lies in their size miniaturization. Conventional antennas rely on an EM wave resonance and require a size of more than one tenth of the EM wavelength λ_0. In this work, a new miniature magnetoelectric (ME) antenna is presented utilizing the multilayer Bragg reflector structure of a solidly mounted resonator (SMR) to enhance small scale antenna gain up to -16 dBi. The antenna radiates using a magnetoelectric heterostructure consisting of AlN and FeGaB, as the piezoelectric and magnetostrictive films respectively, with resonator diameters of 500 um and 1000 um. Different ME resonator shapes and sizes are designed, fabricated and compared along with varying anchor widths and lengths to provide better impedance matching. The acoustic resonance in the heterostructure films operates with an out-of-plane mode of vibration so that the thickness of each layer was optimized to produce a resonant frequency at 1.5 and 2.45 GHz to allow for seamless on-chip integration with WiFi, Bluetooth and GPS devices. The SMR structure replaces the freestanding membrane structure [1] with a Bragg acoustic reflector for concentrated energy confinement. The Bragg reflector was designed and fabricated with a quarter wavelength mode configuration to create maximum particle displacement in the AlN and FeGaB layers. Three periods of alternating low and high acoustic impedance films, using silicon dioxide and tungsten respectively, were deposited on top of a silicon substrate to provide greater acoustic resonance within the ME heterostructure. Antenna gain measurements were performed in an anechoic chamber using a GSG probe and a reference horn antenna linked to a vector network analyzer. The robust features of the SMR has more advantages compared to its FBAR freestanding membrane counterpart allowing for low cost monolithic integration, high operating frequency, better thermal dissipation and structural stability that will be vital for small-scale antennas and other wireless applications.

[1] T. Nan, H. Lin, Y. Gao, A. Matyushov, G. Yu, H. Chen*, et al.*, "Acoustically actuated ultra-compact NEMS magnetoelectric antennas," *Nature communications,* vol. 8, p. 296, 2017.

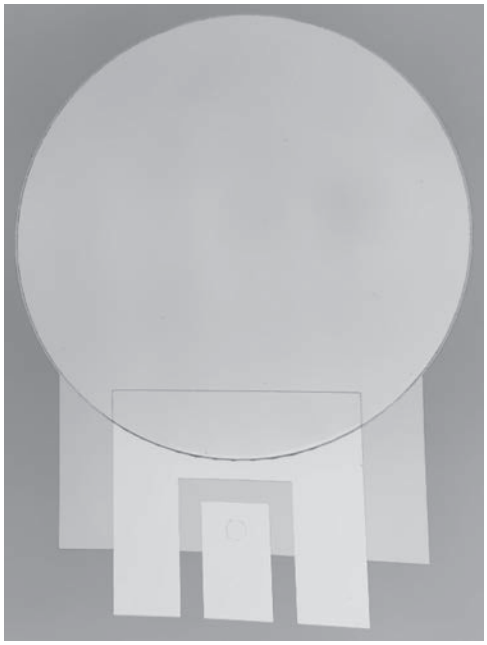


Figure 1. Microscopic picture of a fabricated SMR antenna.

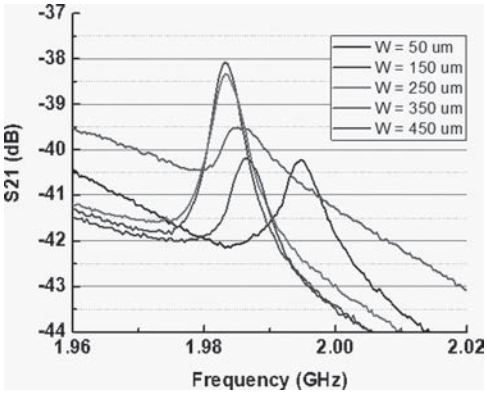


Figure 2. AUT demonstrating S-parameter (S21) with different anchor widths for impedance match optimization.

EV-02. Characteristics Analysis and Experimental Verification of a High-Speed Permanent Magnet Synchronous Generator with Magnetic Saturation Reactance Derived from Short Circuit Analysis. *H. Lee*[1], J. Lee[1], T. Bang[1], K. Shin[1], J. Nah[1] and J. Choi[1] *1. Electrical Engineering, Chungnam National University, Daejeon, The Republic of Korea*

In the initial design of a high speed permanent magnet synchronous generator (PMSG), the characteristics of voltage, current, and output can be calculated by using the equivalent circuit method (ECM). This is required to calculate

circuit constants in accurately, to obtain more precise output characteristics [1]. In general, when the ECM is applied to a PMSG, an equivalent circuit is constructed by using no-load reactance without considering magnetic saturation. However, this cannot predict the change in electromagnetic power characteristics because of the variation in magnetic saturation under load conditions. Therefore, in this paper, the magnetic saturation reactance is derived by using a short circuit analysis of a high speed PMSG. This is applied to the equivalent circuit to predict the output characteristics more accurately. PMSGs have a lower magnetic saturation under a load condition than under a no-load condition. Therefore, the inductance value changes. Fig. 1 shows the analysis model and the magnetic flux density distribution. Fig. 1(a) shows the analysis model. Fig. 1(c) shows the magnetic flux density under no-load analysis and that from a short-circuit analysis. Fig. 2 shows the results of the short-circuit analysis and load analysis. Fig. 2(a) shows a short-circuit current, and Fig. 2(b) shows the induced voltage and short-circuit current according to the rotation speed. Figs. 2(c) and 2(d) show the output characteristics obtained by applying the reactance derived from each result obtained from the rated speed. The results of the equivalent circuit composed of the derived circuit constants agree better with the finite element method than with the previous method. More detailed and experimental data will be presented in the full paper.

[1] Yeon-Ho Jeong, "The design and characteristics analysis of the 65kW High-speed permanent magnet synchronous generator", Doctoral thesis, Chung-Nam National University, 2007. [2] G. R Slemon, "On the design-performance surface mounted PM motor", IEEE Trans. Industry Applications, vol.30, pp.134-140, 1994. [3] J.R. Hendershot Jr. and T.J.E Miller, Design of brushless permanent-magnet motors, Magna Physics Publishing and Clarendon Press, Oxford, 1994.

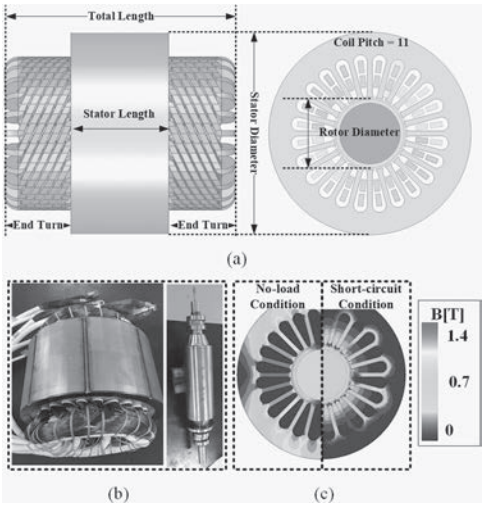


Fig. 1. (a) PMSG analysis model. (b) Manufactured model. (c) Magnetic flux density distribution under no-load and short-circuit conditions.

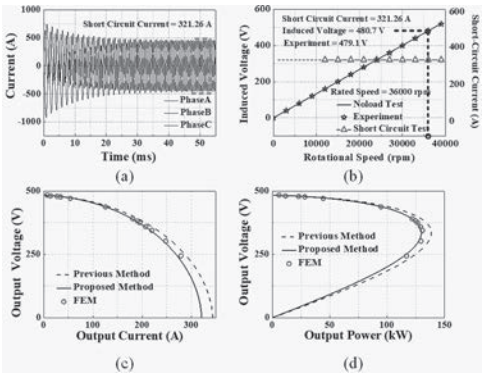


Fig. 2. Analysis results: (a) Current from short-circuit analysis. (b) Rotational speed versus induced voltage and short-circuit current. (c) Comparison of results of proposed method for output current and output voltage. (d) Comparison of results of proposed method for output power and output voltage.

EV-03. Experimental Verification and Electromagnetic Characteristics Analysis of Wound-Rotor Synchronous Generator Using Magnetic Equivalent Circuit Method. *D. Kwon*[1], C. Kim[1], T. Bang[1], I. Yoon[1] and J. Choi[1] *1. Electrical Engineering, Chung-Nam National University, Daejeon, The Republic of Korea*

Global energy consumption has increased rapidly in recent decades. Improving energy efficiency using distributed energy resources (DER) is a key area of study. Hydroelectric power generation usage in DER systems is increasing [1]. There are typically two types of hydropower generators, induction generators and synchronous generators. The Wound-Rotor Synchronous Generator (WRSG) can maintain the rated voltage according to the load fluctuation, and is optimal for hydropower generators, coping with the change of operation characteristics [2]. The finite element method (FEM) is used for electromagnetic characteristics analysis of a WRSG, but its analysis time increases with size. This paper analyzed the magnetic field characteristics of a synchronous generator with a salient pole structure using a simple magnetic equivalent circuit (MEC) method to reduce the analysis time while considering saturation region. In the MEC, the analysis accuracy is increased by considering the non-saturated rotor shoe. Additionally, the FEM and MEC results were validated against experimental data. Figure 1. (a) shows the rotor core structure model and the WRSG FEM analysis. Figure 1. (b) shows the magnetic flux density for a 270 A DC in the rotor windings, and rotor shoe and pole. The MEC is shown in Fig 2. (a). For a salient pole structure, the rotor shoe is not saturated and is shown as an unsaturated reluctance in the MEC. The magnitude change of the no-load flux density with varying field current was compared for the MEC and FEM as shown Fig 2. (b). The FEM analysis and experimental results were compared to verify the short-circuit ratio and the generator V-curve, as shown in Fig 2. (c). and (d). Detailed analysis and results for the MEC are presented in the full paper.

[1] O.A.C. Hoes, L.J.J. Meijer, R.J.van der Ent, PLoS ONE 12(2): e0171844 (2017). [2] C. Greacen, R. Engel, T. Quetchenbach, Published by Lawrence Berkeley National Laboratory in support of Global Lighting and Energy Access, pp.1-80, 2013

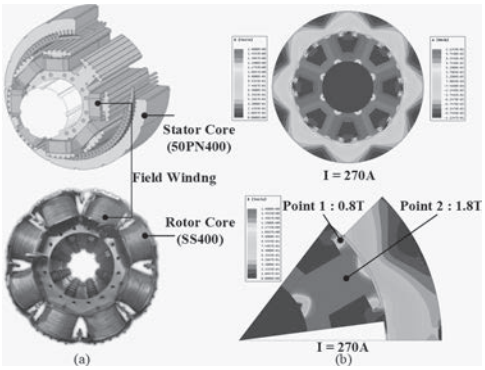


Fig 1. (a) Wound-rotor synchronous generator analysis model and rotor core experimental model; (b) Flux lines distribution and magnetic flux density.

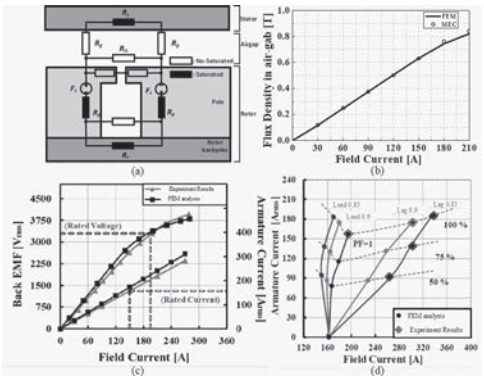


Fig 2. (a) MEC model; (b) Flux density in air-gab compared by FEM, MEC; Generator characteristic analysis: (c) Short-circuit ratio, (d) V-curve verification.

EV-04. Design Criteria and Experiments Considering the Mechanical Characteristics of High-Speed Permanent Magnet Synchronous Generators of 8kW and 40krpm Class. *J. Lee*[1], K. Shin[1], G. Jang[1], T. Bang[1], D. Ryu[1] and J. Choi[1] *1. Electrical Engineering, Chungnam National University, Daejeon, The Republic of Korea*

High-speed permanent magnet machines are being applied to various industrial fields due to their many advantages such as application of direct-drive system without gear system, high power density, high efficiency, and miniaturization [1]-[2]. High-speed permanent magnet machines mainly use rare-earth-based permanent magnets having high magnetic flux density and coercive force. However, due to high-speed operation, structures to prevent damage and scattering of permanent magnets are essential in the design of a rotor, and it is indispensable to determine the mechanical characteristics [3]. In this study, we analyze and test a synchronous generator considering the mechanical characteristics of a rotor and a stator of Unmanned Aerial Vehicle (UAV) system operating at a high speed of 40 krpm. The structure of the designed high-speed synchronous generator is shown in Fig. 1 (a), and the rotor size of the generator was derived using the TRV equation. A sleeve was used to prevent the magnet from damage during high-speed operation. Sleeves must be accompanied by a design that takes into account the mechanical characteristics that change with thickness and, therefore, the electromagnetic characteristics. Thus, the thickness of the sleeve and the permanent magnet, considering the mechanical characteristics at the rated speed rotation, are selected through the rotor structure analysis, as shown in Fig. 1 (b). Fig. 1 (c) shows the comparison of the line-to-line counter-electromotive force at no load of the designed generator, obtained through the FEM and test. Fig. 1 (d) is a graph comparing the generated voltage and current during the load, obtained through the test according to the speed of the FEM and generator. The performance of the designed generator was evaluated by constructing a back-to-back system using a high-speed motor as shown in Fig. 2. The design criteria, analysis results, and measurements of the high-speed PMSM will be presented in more detail in the final paper.

[1] Y. Zhang, S. McLoone, W. Cao, F. Qiu, and C. Gerada, IEEE Transactions on Energy Conversion, vol. 32, no. 4, p.1468-1478, (2017) [2] N. Uzhegov, E. Kurvinen, J. Nerg, J. Pyrhonen, J. T. Söpanen, S. Shirinskil, IEEE Transactions on Industrial Electronics, vol. 63, no. 2, p.784-795, (2016) [3] F. Zhang, G. Du, T. Wang, G. Liu, and W. Cao, IEEE Transaction son Industry Applications, vol. 51, no. 5, p.3675-3685, (2015).

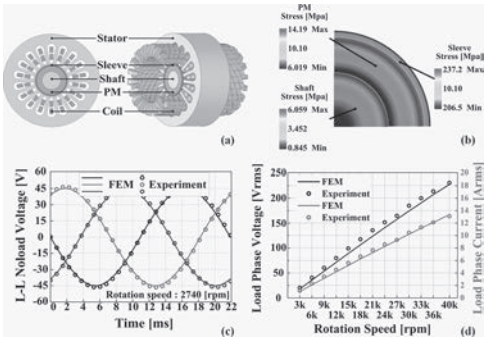


Fig. 1. (a) Structure of high-speed generator (b) analysis of rotor stress (c) Noload L-L Voltage (d) comparison of generating voltage and current characteristics by speed at the load

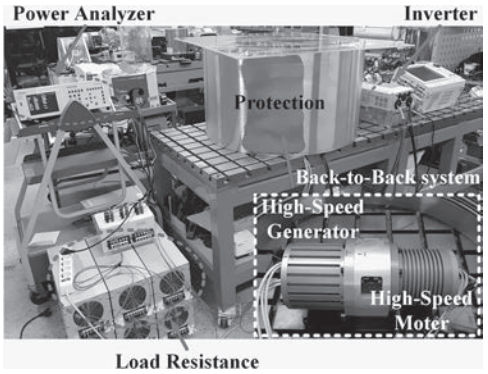


Fig. 2. Test bed of designed high-speed generator

EV-05. Experimental Verification and Analysis of Temperature Characteristics of Induction Generator Considering Stator Loss Distribution. *C. Kim*[1], G. Jang[1], D. You[2], C. Baek[1] and J. Choi[1] *1. Electrical engineering, Chungnam National University, Daejeon, The Republic of Korea; 2. Fire Safety Engineering, Chungnam State University, Chungnam, The Republic of Korea*

Induction generators are commonly used in hydropower installations owing to their numerous advantages such as reduced unit cost, ruggedness, ease of maintenance, and self-protection against severe overloads and short circuits. However, these advantages are a result of the cooling system and heat dissipation system of the induction generator. An accurate temperature analysis and verification of induction generators is therefore essential. In this study, the electro-magnetic characteristics and the temperature characteristics of the induction generator are analyzed, and the reliability of the analysis is verified experimentally. Electromagnetic loss in induction generators is mainly caused by eddy current losses, stator core losses, and copper losses. In this paper, the stator loss is analyzed, and the loss distribution is checked for each stator element. In the no-load operation, the copper losses and rotor eddy current losses can be neglected. Therefore, only the stator core loss is modeled as a heat source and the thermal analysis is performed. Fig. 1 (a) shows the analysis model of the induction generator. The rotor of the induction generator consists of a rotor bar and a rotor core, while the stator

consists of a stator winding and a stator core. Fig. 1. (b) and (c) show the rotor and stator fabrication models, respectively. Fig. 2 (a) shows the core loss per stator element. The stator consists of a shoe, tooth, yoke, etc., and it is possible to confirm that the loss distribution is different for each element. This is expressed as the amount of loss according to density, which can be seen in Fig. 2. (b). Model 1 is the heat source model for the total loss of the stator and Model 2 is the heat source model considering the loss distribution of each element. The result of the temperature analysis is shown in Fig. 2. (c). More detailed discussions, analysis results, and experimental results will be presented in the final paper.

[1] V. Rajagopal, B. Singh, and G.K. Kasal, "Electronic load controller with power quality improvement of isolated induction generator for small hydro power generation," *IET Renewable Power Generation*, vol. 5, no. 2, 2011. [2] Mahmud Ghasemi Bijan, Maher Al-Badri, Pragasen Pillay, and Pierre Angers, "Induction Machine Parameter Range Constraints in Genetic Algorithm Based Efficiency Estimation Techniques," *IEEE. Trans. Industry App*., vol. 54, no. 5, 2018. [3] Aldo Boglietti, Andrea Cavagnino, and David Staton, "Determination of Critical Parameters in Electrical Machine Thermal Models," *IEEE Trans. Industry App.*, vol. 44, no. 4, 2008.

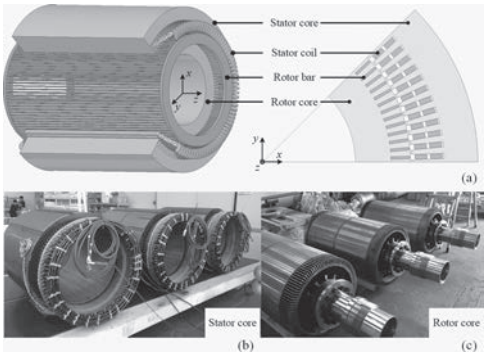


Fig.1. (a) Analysis model of induction generator, (b) manufactured model of stator core, (c) manufactured model of rotor core

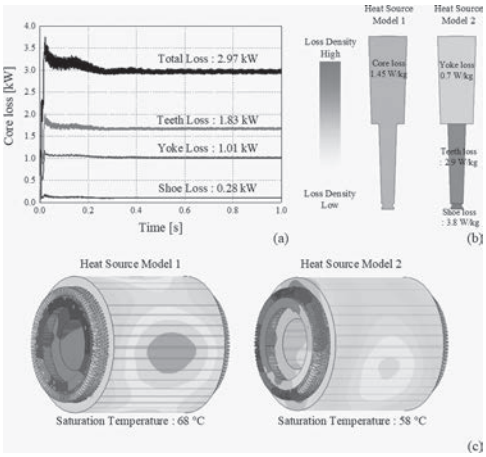


Fig.2. (a) Core loss distribution of each stator core element, (b) Heat source modeling, (c) Thermal analysis results

EV-06. Electromagnetic analysis of interior permanent magnet motor with dual and single layer magnet rotor. C. Baek[1,2], *C. Kim*[2] and J. Choi[2] *1. R&D, Hanon-systems, Daejeon, The Republic of Korea; 2. Electrical engineering, Chungnam National University, Daejeon, The Republic of Korea*

The permanent magnet synchronous motor (PMSM) is considered a promising candidate for several industrial applications owing to its high torque density and efficiency. These advantages make the PMSM suitable for several types of components of electric vehicle systems [1-2]. In general, the PMSM structure comprises a distributed winding type stator and a surface mounted permanent magnet type rotor. This structure exhibits a sinusoidal electric characteristic for the convenience and robustness of control; however, it also has the disadvantages of heavy weight and an inner wire cooling limitation. To overcome these disadvantages, i.e., to directly connect to the load, to improve the inner wire cooling, and to be light and compact, the concentrated winding type stator is a good proposal [3]. This study proposes an electric compressor target setup process and PMSM design process, and investigates the dual layer (delta-shape) of the interior permanent magnet type rotor design to reduce the number of magnets in the concentrated winding type. The dual magnet position parameters are calculated using ANSYS Maxwell's finite element method for the optimum torque ripple at the main operating point of the electric compressor. Additionally, the magnet volume and weight are compared with those of the existing distributed winding type single IPM motor of a vehicle refrigerant compressor application. Fig.1. (a) Proposed dual layer concentrated winding permanent magnet synchronous motor. Fig.1. (b) Magnetic flux density distribution at 6,500 rpm and 6.5 Nm. Fig.2. Proposed dual layer concentrated winding permanent magnet synchronous motor test result (000–6,400 rpm at 6.6 Nm). More detailed discussions, analysis results, and experimental results will be presented in the final paper.

[1] S. Vaez-Zadeh, "Variable flux control of permanent magnet synchronous motor drives for constant torque operation," IEEE Trans. Power Electron., vol. 16, no.4, pp. 52 7-534, 2001. [2] Edward C. Lovelace, Thomas M. Jahns, and Jeffrey H. Lang, "Impact of saturation and inverter cost on interior PM synchronous machine drive optimization," iEEE Tran. ind. Appl., vol. 36, no. 3, pp. 723 -729, June 2000. [3] D. Ishak, Z.Q. Zhu, D. Howe, "Permanent Magnet Brushless Machines with Unequal Tooth Widths and Similar Slot and Pole Numbers", Industry Applications Conference. Vol. 2, pp. 1055-1061, 3-7 Oct. 2004.

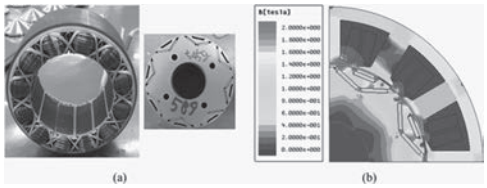


Fig.1. (a) Proposed dual layer concentrated winding permanent magnet synchronous motor (b) Magnetic flux density distribution

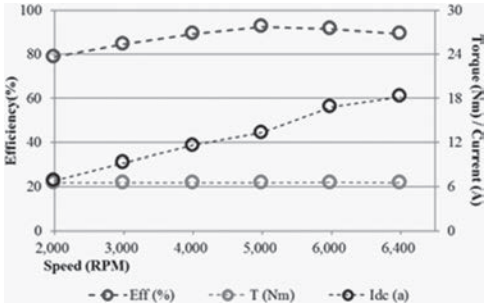


Fig.2. Proposed dual layer concentrated winding permanent magnet synchronous motor test result

EV-07. Core loss analysis of a permanent magnet synchronous motor of an electric vehicle refrigerant compressor. C. Baek[1,2], *C. Kim*[2] and J. Choi[2] *1. R&D, Hanon-systems, Daejeon, The Republic of Korea; 2. Electrical engineering, Chungnam National University, Daejeon, The Republic of Korea*

In this paper, the results of the core loss analyses of a permanent magnet synchronous motor in the refrigerant compressor of an eco-friendly automobile are analyzed and compared. Based on the results, the method for more accurate core loss calculation is presented. First, the iron loss is analyzed using the classical Steinmetz equation, which is based on frequency

decomposition. [1][2] However, the harmonics of core loss not considered in this approach. As the power-density of the permanent magnet synchronous motor is considerably high, it is necessary that the harmonics of core loss are considered during core loss calculation. Therefore, the results obtained using the classical Steinmetz equation are compared to those obtained using the improved generalized Steinmetz equation (IGSE), in which the minor loop hysteresis loss is taken into account.[3] To consider the changes in effective resistance that occurs due to the skin effect, the eddy current loss is also analyzed using the homogenization technique. Finally, the improved hysteresis loss also is performed the consideration of the DC bias, using a commercial finite element analysis software, and it will be compared. Figure 1(a) shows the stator and rotor of a concentrated winding permanent magnet synchronous motor used for operating the refrigerant compressor in an air-conditioner of an eco-friendly vehicle. Figure 1(b) is at 6500rpm & 6.5Nm, shows the magnetic flux density distribution. Figure 1 (c) shows the flowchart of calculating the eddy current loss using the classical Steinmetz equation, the hysteresis loss calculating also based on the minor loop. The results obtained are listed in table I, and those calculated under a DC bias using the modified method are listed in table I. More detailed discussions, analysis results, and experimental results will be presented in the final paper.

[1] C. P. Steinmetz, "On the law of hysteresis," Trans. Amer. Inst. Elect. Eng., vol. 9, no. 1, pp. 1–64, Jan. 1892. [2] G. Bertotti, "General properties of power losses in soft ferromagnetic materials", IEEE Trans. Magn., vol. 24, no. 1, pp.621-630, 1988 [3] T. Taitoda, Y. Takahashi, and K. Fujiwara, "Iron loss estimation method for a general hysteresis loop with minor loops," IEEE Trans. Magn., vol. 51, no. 11, Nov. 2015

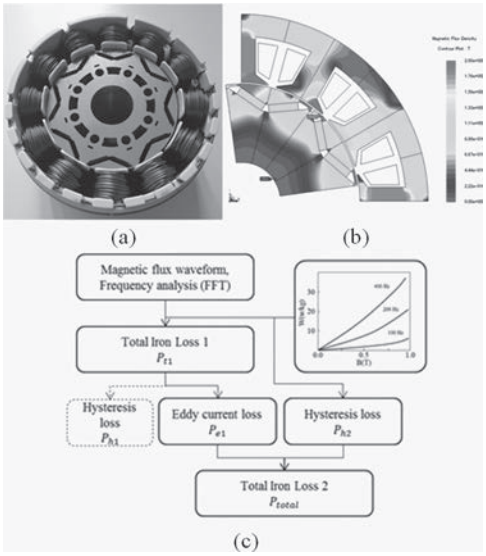


Fig.1. (a) Permanent magnet synchronous motor of the electric vehicle refrigerant compressor, (b) Magnetic flux density distribution, (c) coreloss calculation flowchart

Iron loss results considering minor loop and FFT		
	Rotor Core	Stator Core
Hysteresis Loss (W)	2.11	21.78
Eddy current Loss (W)	13.67	97.33
Total Loss (W)	15.78	119.11
Iron loss results considering DC bias and skin effect		
	Rotor Core	Stator Core
Hysteresis Loss (W)	3.73	22.58
Eddy current Loss (W)	11.78	86.79
Total Loss (W)	15.51	109.37

Table I. Iron loss analysis result with consideration of Minor Loop / FFT and DC bias / skin effect

EV-08. Quasi-3D Electromagnetic Analysis and Experimental Verification of Multi-pole Magnetization BLDC Motor. *H. Shin*[1], G. Jang[1], J. Lee[1], J. Nah[1] and J. Choi[1] *1. Chungnam National University, Daejeon, The Republic of Korea*

Brushless DC (BLDC) motors that use permanent magnets (PMs) have high power densities and incur low maintenance costs. Therefore, they are widely used in many applications. This paper presents a quasi-3D electromagnetic analysis of a multi-pole magnetization BLDC motor. The analysis model shown in Figure 1(a) has five permanent magnets (PMs) of multi-pole magnetization that makes two poles into one magnet. If the number of PMs are halved, the assembling time and manufacturing tolerance are also halved. In the multi-pole magnetization process, a polar separation section is generated by the structure of the magnetizer. To consider this section, a function of the magnetization pattern, which is shown in Figure 1(b), is applied to the analysis model. The function is assumed to decrease linearly in the polar separation section. As a result, the magnetic flux at the center of the PM is small as shown in Figure 1(c). This method will be verified by conducting an experiment on a manufactured multi-pole magnetization model in the final paper. Figure 2(a) shows a 3D configuration of the analysis model. These configurations require 3D analysis for accurate prediction of the electromagnetic characteristics. However, this consumes a considerable amount of time, making it inefficient in the design process. Therefore, in this paper, a quasi-3D electromagnetic analysis that corrects the 3D configuration to a 2D one is performed. The PM overhang is corrected by changing the operating point of the PM as shown in Figure 2(b) [1], and the housing-integrated rotor core is corrected by increasing the rotor core thickness. The validity of the quasi-3D electromagnetic analysis is verified by comparing the flux density at the air gap and the phase induced voltage at a no-load condition, as shown in Figure 2(c) and 2(d). Detailed explanations and experiment results will be presented in the final paper.

[1] K.-C. Kim, D.-H. Koo, and J. Lee, "The study on the overhang coefficient for permanent magnet machine by experimental design method", IEEE Trans, Magn., vol. 43, no. 6, pp. 2483-2485, Jun, 2007.

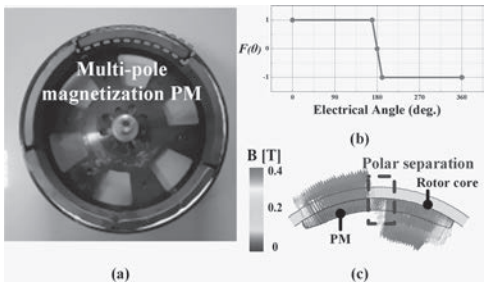


Fig. 1. (a) Multi-pole magnetization PM (b) A function of the magnetization pattern (c) The magnetic flux vector on multi-pole magnetization PM

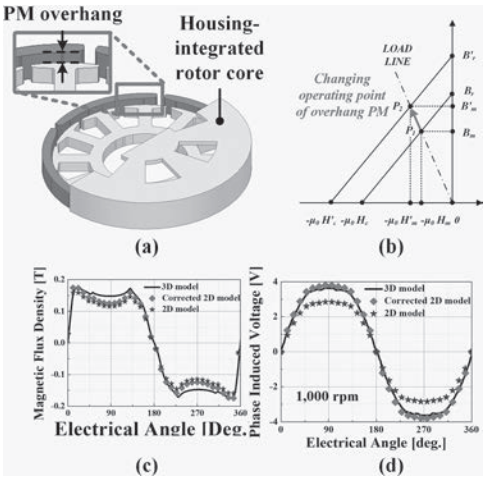


Fig. 2. (a) 3D configuration of the analysis model (b) B-H curve of PM (c) Comparison of magnetic flux density (d) Comparison of phase induced voltage

EV-09. Experimental and Comparative Study of Electromagnetic and Mechanical Aspects of a High-Speed Motor Using SmCo and Ferrite Permanent Magnets. *J. Woo*[1], T. Bang[1], C. Kim[1], I. Yoon[1] and J. Choi[1]
1. Electrical engineering, Chungnam National University, Daejeon, The Republic of Korea

A high-speed permanent magnet (PM) motor generally uses a rare-earth PM with a high coercive force and high residual magnetic flux density for the rotor structure. However, rare-earth PMs are expensive and are susceptible to price fluctuations based on the supply of rare-earth elements. Although it has low residual magnetic flux density, using a ferrite magnet instead of a rare-earth PM can ensure a more stable production of the rotor at a low cost. The diameter of the PM increases when using a ferrite magnet, and the sleeve thickness that withstands stress also changes. Additionally, the amount of interference between the sleeve and the PM should be set while considering the limit of the yield stress. In this paper, comparative study of a high-speed motor using smco and ferrite PMs at electromagnetic and mechanical aspects were performed through the analytical methods and the experiments, suggests that ferrite PM can replace rare-earth PM. An analytical method of stress analysis was performed to compare the stress due to the interference between the sleeve and the PM, for a set sleeve thickness based on the rotor diameter. Fig.2. (a) and (b) show the stress distribution caused by the interference. It shows that the stress generated by the selected interference does not reach the yield stress of the PM. In addition, circuit parameters including the air-gap magnetic flux density, back-EMF, and inductance of each model were derived using an analytical electromagnetic analysis. Fig.2. (c) shows the air gap magnetic flux densities according to the PM material in comparison with FEM and Analytical results, and Fig.2. (d) shows a comparison of the back-EMF of the rare-earth and ferrite PMs. A final comparison was carried out using the FEM and an experimental analysis. Further discussion and results are provided in the full paper.

[1] J. R. Hendershot Jt and T. J. E. Miler, "Design of Brushless Permanent-Magnet Motors," Magna Physics publising and Clarendon press-OXPOR, 1994. [2] I. Petrov and J. Pyrhonen, "Performance of low-cost permanent magnet material in PM synchronous machines," IEEE Trans. Magn., vol. 60, no. 6, pp. 2131–2138, Jun. 2013. [3] C. Zwyssig, S. D. Round, and J. W. Kolar, "An ultrahigh-speed, low power electrical drive system," IEEE Trans. Ind. Electron., vol. 55, no. 2, pp. 577– 585, Feb. 2008.

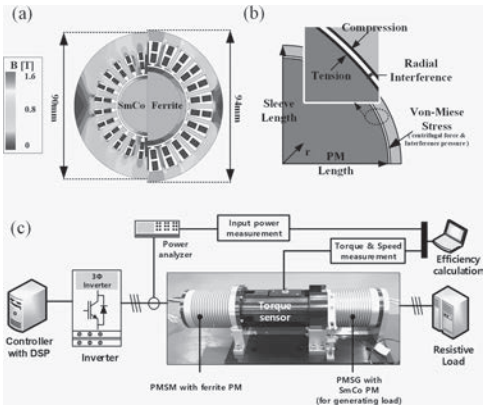


Fig.1. (a) No-load flux density (b) Concept for von-Mises stress (c) Experimental setup

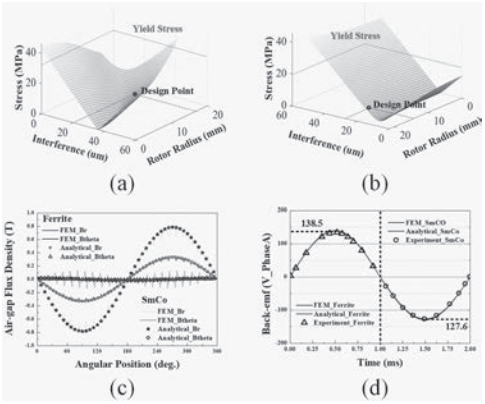


Fig.2. Stress distribution diagram of (a) SmCo PM (b) Ferrite PM Comparison graph of (c) Air-gap flux density (d) Back-emf

EV-10. Optimal Design of Reducing Cogging Torque in the V-shape Interior Permanent Magnet Synchronous Motor Using Random Walk Method. *J. O*[1], M. Shin[1], K. Shin[1], T. Bang[1], J. Choi[1] and H. Cho[1]
1. Chungnam National University, Daejeon, The Republic of Korea

Interior Permanent Magnet Synchronous Motors (IPMSMs) with V-shape permanent magnets have advantages of high torque and high output in comparison with a flat-type permanent magnet because the pole magnetic flux increases as the permanent magnet cross-sectional area increases [1][2]. However, not only IPMSMs with a flat-type permanent magnet but V-shape-IPMSM can also easily generates a cogging torque that causes vibration and noise due to change in magnetic circuit by the interaction between the permanent magnet rotor and the stator slots [1]. On the other hand, the random walk method is one of the useful optimization techniques for finding the minimum or maximum value of the objective function, and can be applied to cases where the objective function is discontinuous at some points or cannot be differentiated [3]. In this study, we proposed optimum design technique of the V-Shape IPMSMs for reducing cogging torque by using the random walk method. Fig. 1 shows the basic model and design variables of the V-shape IPMSM. The two design variables are the chamfering angle of the stator teeth and the angle between the V-shape permanent magnets. chamfering angle and V-shape angle set constraint as follows. 0 < chamfering angle < 6.5 (deg.), 45 < V-shape angle <160 (deg.). Fig. 2 shows a comparison of the cogging torque waveforms according to the rotation degree(mechanical) for the basic model versus the optimum model. It can be seen that the peak to peak cogging torque of the optimum model is reduced by 96.63 [%] of the cogging torque from the basic model. In the full paper, the optimal design model of V-shape IPMSM with improved operating characteristics regarding the magnetic flux density and back EMF-THD will be presented. In addition, optimum design technique in electro-magnetic machines by using random walk method will be confirmed.

[1] R. Dutta, L. Chong, and M. F. Rahman, IEEE Trans. Energy Convers., vol. 28, p.181 (2013) [2] W. Zhao, F. Zhao, T. A. Lipo, IEEE Trans. Magn., Vol. 50, Art. ID 8104504 (2014) [3] S. S. Rao, Engineering Optimization: Theory and Practice 4thed. John Wiley & Sons. Inc, (2009)

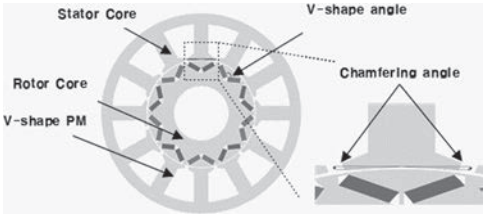


Fig. 1 V-shape IPMSM and optimization design variables

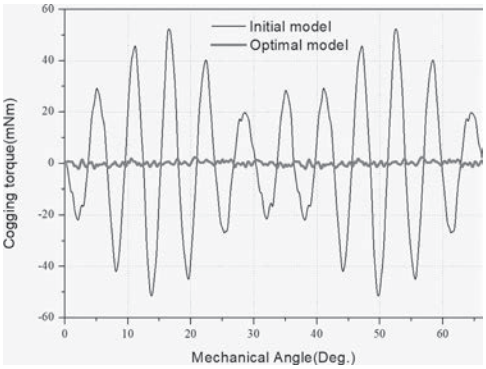
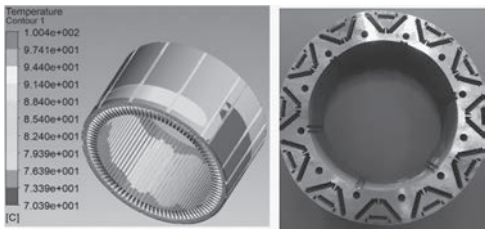


Fig. 2 Comparison of Cogging Torque Waveforms of Basic Model and Optimal Model

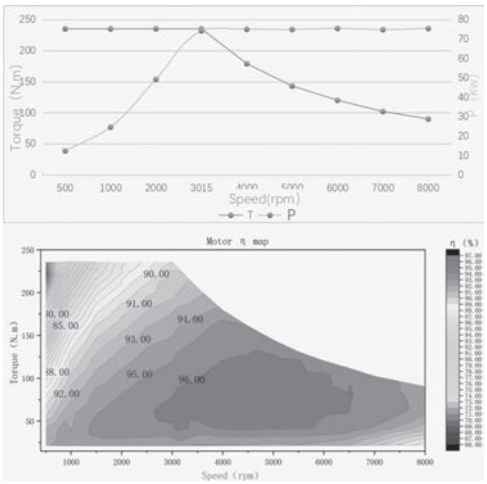
EV-11. Studies of Magnetic and Thermodynamic Characteristics Iron Core Under High Frequencies for Traction Motors. *R. Pei[1] 1. InnMag New Energy Ltd., Suzhou, China*

This paper mainly presents numerical modeling and experimental measurement of core loss and thermodynamic characteristics of an iron core in Permanent Magnet Synchronous Machine(PMSM) at various frequencies among 50Hz, 200Hz and 400Hz. Electrical Steel is of paramount importance as the EV traction motors. Thin-gage Non-Grain Oriented (NGO) silicon steel has been increasingly popular in high-speed and large-torque PMSM. A novel design strategy of PMSM will be described. The motor designed by authors is mounted on the vehicle and has 8 poles and 48 slots. The peak torque is 240 N.m. Three kinds of high-grade and thin NGO Silicon Steel sheets with 0.15mm, 0.30mm and 0.35mm are used in the stator and rotor, respectively. At first, the hysteric and eddy current loss of single electrical steel will be calculated, followed by measurement at different frequencies among 50Hz up to 400Hz. Then, the dynamic hysteresis loop and high-frequency harmonic losses will be accurately calculated with power loss and dimension of single sheet, which plays a key role in the total loss calculation, especially at high flux densities and high frequencies. The final section shows the numerical modeling and experimental results of (1) power losses of single sheet of non-grain oriented electrical steel, and (2) high-frequency iron core losses at 50Hz, 100Hz, 200Hz and 400Hz, which verify numerical algorithm. It is clarified that the numerical model and experimental iron core losses in each experiment are showed to be in good agreement. The numerical model for iron core losses and experimental results for single electrical steel sheet are especially useful to estimate power losses of electric machines running at higher frequency of 1000Hz~2000Hz. For different frequencies, the distribution of the thermodynamic model can be described by the iron core and the whole machine. Through the analysis and calculation, eddy-current loss is the main source that affects the thermodynamic characteristics of the motor. The speed-torque characteristic of electric motor made by these lamination electrical steels will be presented and discussed., which provides the direction for optimizing the cooling system of the motor.

[1] Takano Y, Takano M, Hoshi N, et al. Design and analysis of a switched reluctance motor for next generation hybrid vehicle without PM materials[C]// Proceedings of the 2010 International Power Electronics Conference. Sapporo:IEEE Press, 2010: pp. 1201-1206. [2] Abe S. Development of Toyata plug-in hybrid vehicle[J]. Journal of Asian Electric Vehicles, 2010, 8(2): 1399-1404. [3] Takano Y, TAKENO M, HOSHI N, et al. Design and analysis of a SRMe motor for next generation hybrid vehicle without PM materials[C]//Proceedings of the 2010 International Power Electronics Conference. Mexico: IEEE Press, 2010: 1801-1806.



The stator modeling and the rotor



EV-12. Withdrawn

EV-13. A Study on De-icing for Railway Turnouts Using 250kHz-200W-Class Induction Heating System. *H. Oh[1], C. Park[1], J. Lee[1], T. Kim[2], I. Jo[1], J. Lim[1], K. Seo[1] and H. Lee[1] 1. Korea National University of Transportation (KNUT), Uiwang-si, The Republic of Korea; 2. University of Michigan-Dearborn, Dearborn, MI, United States*

The railway turnout is one of the most important equipment in railway infrastructure [1]. Currently, an electric-heating wire is used as a heating device for a railway turnout. However, there are many drawbacks with the old technology, one of which is that the heating element requires a lot of power consumption [2]. Thus, the Induction Heating (IH) system is proposed that will replace the existing system. IH is a high-efficiency energy transfer system that transfers energy from the primary to the secondary without a medium [3]. In addition, since the use of high frequency reduces the skin depth of the secondary, a lot of heat can be generated on the surface of the secondary [4]. There are many limitations to be considered for the IH system in the turnouts. It should consume less power than the existing system and be designed to fit into the narrow space between the tongue rail and the main rail (see Fig. 1). Therefore, it is to design the heating system considering these limitations and introduced the Multi-physics method of the circuit, electromagnetic field, and thermal for the analysis of the IH system (see Fig. 2). The heating plate of the heating device needs to be heated only to the temperature at which the snow and ice melt. So, it was calculated by simulation that the heating plate requires about 200W loss to reach about 20°C.

The E-type core is reflected to shield the magnetic flux, and each inductance of the primary and secondary and the mutual inductance are calculated from the formula and designed to generate a loss of 200W on the heating plate. Also, IH devices should be installed within a narrow space, so the area is designed within 15×5 mm^2 size. To minimize the power, a resonant circuit was designed and analyzed in conjunction with an electromagnetic field model. In conclusion, the induction heating system which overcomes the limitation of the heating system for the railway turnout was designed, and the performance of the IH system was verified through introduced the Multi-physics method of the circuit, electromagnetic field, and thermal for the analysis.

[1] Omer Faruk Eker, IEEE Transactions on Industrial Electronics, Vol. 58, p. 1718-1726 (2011) [2] Dongwan Jang and Taehyun Jeon, Journal of the Korean Institute of Illuminating and Electrical Installation Engineers, Vol. 27, p. 61-67 (2013) [3] O. Lucia, P. Maussion, E. Dede and J. M. Burdio, IEEE Transactions on Industrial Electronics, Vol. 61, p. 2509-2520 (2015) [4] Hyoung-Gyun Woo and Dae-Chul Shin, Journal of the Korean Institute of Illuminating and Electrical Installation Engineers, Vol. 27, p. 6 (2013)

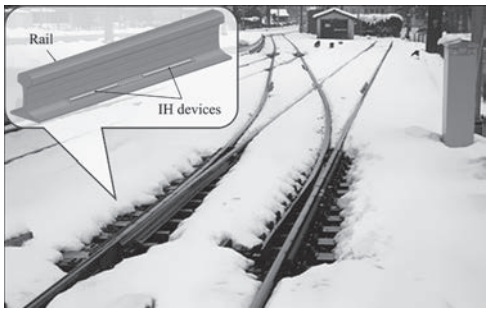


Fig. 1. Concept of applying IH system in the railway turnout

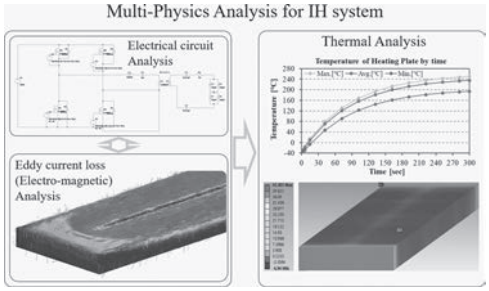
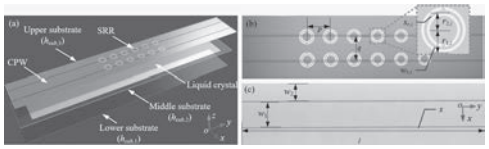


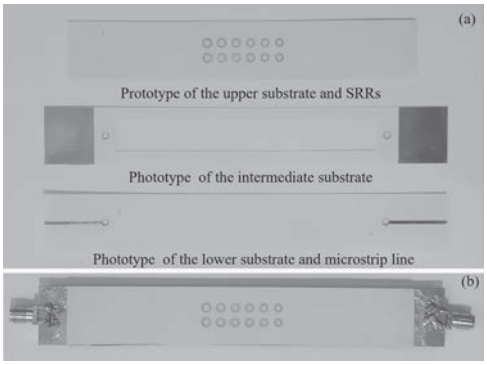
Fig. 2 Temperature distribution of the IH devices

EV-14. Design and application of the magnetic driven device in the microwave filtering tunable phase shifter. *F. Meng*[1], C. Ding[1] and S. Xu[2] *1. Harbin Institute of Technology, Harbin, China; 2. Emergency Department, First Hospital of Harbin City, Harbin, China*

In this paper, a novel magnetic driven device is designed and applied in the microwave filtering tunable phase shifter based on the liquid crystal (LC) technology. The proposed magnetic driven device composed of a pair of permanent magnets is utilized to generate the biased magnetic field which tunes the LC molecules of the filtering tunable liquid phase shifter (LCPS). This filtering tunable LCPS is based on the planar transmission line magnetically coupled with a series of split-ring resonators (SRRs). Under the action of the biased magnetic field induced by the magnetic driven device, the filtering tunable LCPS can simultaneously provide tunable phase shifts and self-embedded band-stop filtering function. Both the equivalent circuit model analysis and the transmission parameter characterization are afforded to comprehensively interpret the relationship between tunable phase shifts and stable filtering function. Then, the magnetic driven device and the filtering tunable LCPS are fabricated and tested, respectively. According to the measured results, the states of LC molecules are availably switched by the magnetic driven device. Thus, the filtering tunable LCPS not only achieves the stable stopband from 6.2 to 6.8 GHz but also realizes that the figure of merit (FoM) is more than 7.9 °/dB in the passband (from 4.0 to 6.1 GHz and from 6.9 to 10.0 GHz).



Schematics of the band-stop filtering tunable LCPS



Photographs of the fabricated band-stop filtering tunable LCPS (a) inner structures (b) packaged sample

EV-15. Withdrawn

EV-16. Very Broad Bandwidth Permeability Measurement of Thin Film Using a Flexible Microstrip Line-Type Probe up to 67 GHz. *K. Nozawa*[1], L.T. Ton[1], K. Okita[1], S. Yabukami[1], Y. Endo[1], Y. Shimada[2], S. Saito[1] and R. Utsumi[2] *1. Tohoku University, Sendai, Japan; 2. Toei Scientific Industrial co.,Ltd., Natori, Japan*

High frequency permeability measurement of magnetic thin film is important as sensors and spintronic devices are fabricated from very thin films of less than 10 nm in thickness. However, almost all permeameters [1-2] can only measure samples with a width of no more than several millimeters and a thickness of more than 0.1 μm, and exceedingly few permeameters can measure thin films over 30 GHz continuously. In this study, we developed a flexible microstrip line-type probe, and using the probe we measured permeability up to 67 GHz without restriction on sample size (also applicable to wafer-sized samples). As shown in in Fig. 1, the probe was composed of a straight microstrip conductor (10 mm in length, 0.36 mm in width) on a flexible substrate (130 μm in thickness, ε_r =2.3), a ground plane, lead lines, and two connectors. The microstrip line sloped to meet the lead line at either end, and had slopes to maintain a characteristic impedance of around 50 Ω and to allow close contact of a large samples with the probe. A thin film was in contact with the microstrip conductor via a 0.1 mm thick PET film. In permeability measurement, firstly, S_{21} is calibrated by applying of a strong dc field (around 20 kOe) in the direction of the easy axis to saturate the magnetic film. Secondly, S_{21} is measured, and then the complex permeability is optimized using the Newton–Raphson method to take the skin effect of the magnetic film into account [3]. Fig. 2 (a) shows the hard–axis permeability of CoFeB film (45 mm x 25 mm, 0.5 μm in thickness) when bias fields of 14 kOe was applied along the easy axis, and (b) shows the ferromagnetic resonance (FMR) frequency as a function of dc field. The symbols show measured value, and the dotted lines and solid lines show the theoretical value on the LLG equation and eddy current generation. A damping factor of 0.02 and a *g* factor of 2.12 were used to calculate the theoretical permeability. The Results show that the measured permeability and FMR frequency agreed well with the theoretical value up to 67 GHz.

[1] P. A. Calcagno et al., *Rev. Sci. Instrum.,* Vol. 46, p. 904 (1975) [2] H. B. Weir, *Proc IEEE.*, vol. 62, p. 33 (1975) [3] S. Yabukami et al., *J. Magn. Soc. Jpn.*, Vol. 41, p. 25-28 (2017)

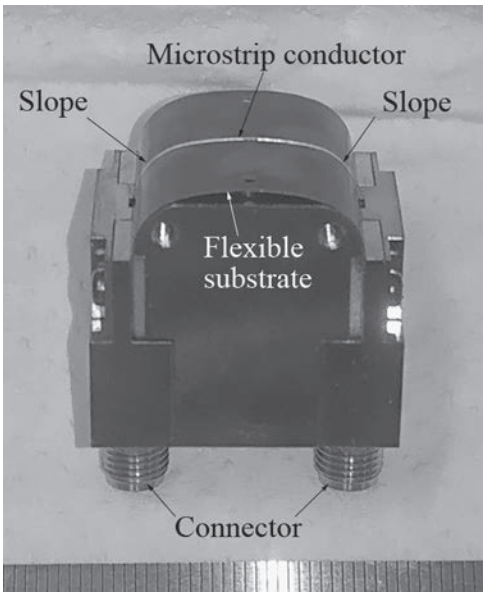


Fig. 1 Photograph of the probe.

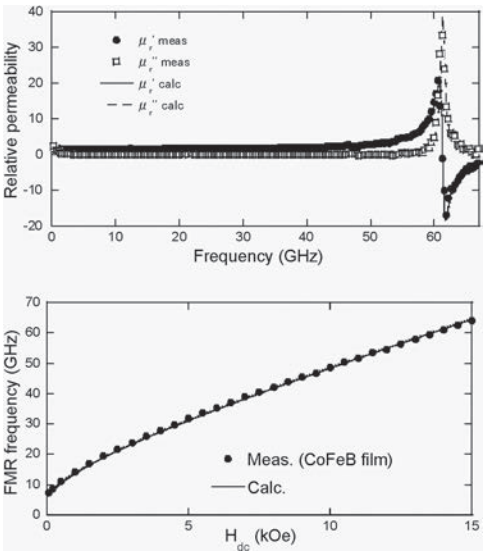


Fig. 2 (a) Relative permeability of CoFeB film (45 mm × 25 mm, 0.5 μm thick), (b) ferromagnetic resonance frequency as a function of dc field.

EV-17. Development of a spintronic vision system based on spin-torque diodes and its optimization for autonomous driving tasks. *G.D. Demin*[1,2], A. Buzdakov[2], N.A. Djuzhev[1], V.A. Bespalov[1] and K.A. Zvezdin[2] *1. R&D Center "MEMSEC", National Research University of Electronic Technology (MIET), Moscow, Russian Federation; 2. Laboratory of Physics of Magnetic Heterostructures and Spintronics for Energy-Efficient Information Technologies, Moscow Institute of Physics and Technology (MIPT), Dolgoprudny, Russian Federation*

Nowadays, development and searching for new solutions to the implementation of machine vision systems in vehicle control draw the attention of the scientific world. One of the crucial tasks is to ensure high accuracy in detecting road obstacles in the near vehicle zone in adverse conditions, such as bad weather, traffic overload, and poor lighting. One of the promising technologies capable of satisfying these requirements is the machine vision technology based on spin-torque diodes [1, 2]. A spin-torque diode is a magnetic tunnel junction, which demonstrates the effect of voltage rectification when microwave current flows through it. Spin-torque diodes have a sensitivity that substantially exceeds the sensitivity of semiconductor Schottky diodes [3]. Recently, it was shown that it is also possible to detect hidden objects located outside the line of sight by a microwave holography technique using spin-torque diode system [4]. Here we present a proposed spintronic machine vision system with a method of recording the amplitude of a reflected signal in the time domain by the array of spin-diode based microwave detectors. An experimental demonstration of this system was carried out using the setup consisting of the double-ridge horn antenna for transmission, several antipodal Vivaldi antenna elements for reception and a spin-diode based signal processing circuit (Fig. 1). Based on the experimental setup, we developed a finite-element model of microwave object detection system using an array of spin-torque diodes (CoFeB/MgO/CoFeB), the SPICE model of which was built by us earlier [5]. During the simulation, a frequency shift of the reflected signal on a spin-torque diode was detected when the object changed its position. The results show the effectiveness of using spintronic technologies to perform the tasks of near-field and far-field sensing of objects and can be used to improve the characteristics of the developed spintronic vision system for autonomous driving platforms. The work was performed using the equipment of R&D Center "MEMSEC" (MIET) and supported by the RF President Grant (No. 075-15-2019-1139).

[1] P.M. Holl and F. Reinhard, Phys. Rev. Lett., Vol. 118, p. 183901 (2017) [2] A.A. Khudorozhkov, P.N. Skirdkov and K.A. Zvezdin, Phys. Rev. B. Vol. 96, p. 214410 (2017) [3] L. Zhang, B. Fang and J. Cai, Appl. Phys. Lett, Vol. 113, p. 102401 (2018) [4] L. Fu, Y.S. Gui and L.H. Bai, J. Appl. Phys., Vol. 117, p. 213902 (2015) [5] G.D. Demin, E.E. Gusev and N.A. Djuzhev, Proceeding to SIBCON 2016 (2016)

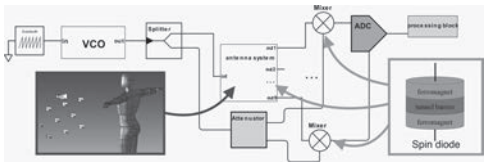


Figure 1. Circuit schematics of the spintronic machine vision system based on spin-torque diodes.

EV-18. Magnetoelectric control of the microwave sensitivity of a spin-torque diode based on the magnetic tunnel junction with a ferromagnetic/ferroelectric bilayer by short THz electromagnetic pulse. *G.D. Demin*[1,2], A.V. Popov[1] and N.A. Djuzhev[1] *1. R&D Center "MEMSEC", National Research University of Electronic Technology (MIET), Moscow, Russian Federation; 2. Laboratory of Physics of Magnetic Heterostructures and spintronics for energy-efficient information technologies, Moscow Institute of Physics and Technology (State University), Dolgoprudny, Russian Federation*

Over the past decade, significant progress has been made in the development of spintronic microwave detectors based on spin-torque diode effect in magnetic tunnel junctions (MTJs), which demonstrate a microwave sensitivity of the resonant type up to 200 kV/W and higher [1]. This effect is due to the voltage rectification in MTJ as a result of microwave modulation of its resistance by input microwave current. However, to obtain such high sensitivity of spin-torque diodes, the presence of additional dc bias current (about 0.1-0.3 mA) is still necessary, which reduces the energy efficiency of such devices. In this regard, today an important task is to find alternative ways to control the sensitivity of spin-torque diodes in the absence of a bias current, which is associated with the consideration of new mechanisms providing low-energy manipulation of magnetization [2-4]. The ultrafast polarization switching of a ferroelectric layer by a short THz electromagnetic pulse seems very promising to solve this issue [5]. This phenomenon makes it possible to effectively control the magnetization state of the ferromagnet/ferroelectric bilayer as a part of MTJ via magnetoelectric coupling (Fig. 1). Moreover, the Joule heating of the MTJ with a microwave current may

provide an additional increase in the microwave sensitivity [6]. We consider this concept as applied to tune the sensitivity in spintronic microwave detectors in the absence of a bias current. The dynamics of ferroelectric domains in the MTJ ferroelectric layer under the action of THz electromagnetic pulse was studied, and a numerical analysis of the diode sensitivity as a function of the ferroelectric polarization state was carried out. The results obtained can be used in the development of low-power spin-torque diodes operating on a new magnetoelectric detection principle. The work was performed using the equipment of MIET Core Facilities Center "MEMSEC" and supported by the RF President Grant (No. 075-15-2019-1139).

[1] L. Zhang, B. Fang and J. Cai, Appl. Phys. Lett., Vol. 113, p.102401 (2018) [2] P.K. Amiri and K.L. Wang, SPIN, Vol. 2, p.1240002 (2012) [3] M. Goto, Y. Wakatake and U.K. Oji, Nature Nanotech., Vol. 14, p.40 (2018) [4] S. Sayed, K.Y. Camsari and R. Faria, Phys. Rev. Appl., Vol. 11, p.054063 (2019) [5] E. Mishina and K.A. Grishunin, Russ. Technol. J., Vol. 5, p.41 (2017) [6] G.D. Demin, K.A. Zvezdin and A.F. Popkov, Adv. Cond. Mat. Phys., Vol. 2019, ArticleID 5109765 (2019)

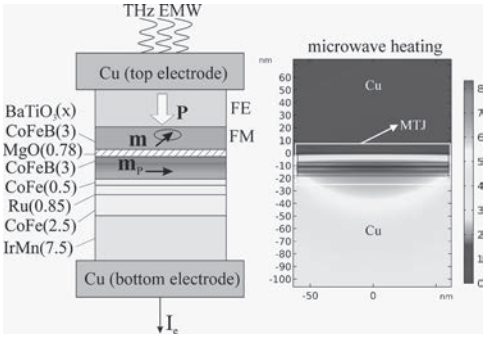


Figure 1. Sketch of the magnetoelectric control of the spin-torque diode based on MTJ with a ferromagnetic/ferroelectric bilayer by THz electromagnetic wave (EMW) irradiation and the temperature increment of MTJ due to its microwave heating (in mK).

EV-19. Theoretical Study on Lowering Loss of Skin Effect Suppressed Multi-layer Transmission Line with Positive/Negative (Cu/NiFe) Permeability Materials for High Data-Rate and Low Delay-Time I/O Interface Board. H. Nakayama[1], *Y. Aizawa*[2], K. Kubomura[2], R. Nakamura[1] and H. Tanaka[1] *1. Department of Electronics and Control Engineering, National Institute of Technology (KOSEN), Nagano College, Nagano, Japan; 2. Advanced Course of Production and Environment System, National Institute of Technology (KOSEN), Nagano College, Nagano, Japan*

INTRODUCTION - This paper proposes a new application of skin effect suppression technology [1]-[4] for long wiring on high-speed & low-delay I/O board. This proposal will overcome the difficulty of further reducing the transmission losses on the I/O board with >50 Gbps data rate. In previous research [5], it was demonstrated that suppression of the skin effect by electroplated conductor/magnetic multilayer, and estimated that the degree of transmission loss decrease at 16 GHz would be 5 %. A major challenge in this paper is to propose an electromagnetic field calculation theory for rectangular multilayer transmission line, verify it under the same conditions, clarify a lower loss structure by changing thickness of each layer. Also it is expanded to low loss design technology. *VERIFICATION* - Cu and NiFe were selected as metal conductor material and negative permeability magnetic material, respectively. The Cu and NiFe films are alternately stacked to form the multilayer, as shown in Fig. 1. The top and bottom surface layers are Cu layers. An electromagnetic field distribution, which considers of the skin effect in a rectangular multilayer transmission line, is derived based on Maxwell's equation. The current density of each layer and the total loss can be obtained by the equations (1) and (2) in Fig. 1. The loss suppression was compared under the following conditions. 1) Total number of layers is 33 and total thickness is 12.67 μm by a constant ratio, Cu t_N = 0.51 μm and NiFe t_F = 0.25 μm. 2) Optimal stacking determined by changing the thickness of each layer. *RESULTS AND DISCUSSION* - Fig. 2 shows the current density of multilayer transmission line. Compared to conventional thickness by a constant ratio, it was estimated that the loss is 90% in optimal thickness we proposed. By offsetting the phase change of current density, a lower loss structure could be determined. Compared with Cu conductor, the graph shows that the top and bottom surface current densities become low, and depth center current density becomes slightly high for the multilayer, showing the skin effect is suppressed.

[1] B. Rejaei and M. Vroubel, J. Appl. Phys., Vol. 96, p.6863 (2004) [2] Y. Zhuang, B. Rejaei and H. Schellevis, IEEE Electron Device Lett., Vol. 29, pp. 319–321 (2008) [3] M. Yamaguchi, N. Sato and Y. Endo, Proc. 40th Eur. Microw. Conf., pp. 1182-1185 (2010) [4] N. Sato, Y. Endo and M. Yamaguchi, J. Appl. Phys., Vol. 111, pp.07A501-1-07501-3 (2012) [5] M. Yamaguchi, T. Yanai and H. Nakayama, IEEE Trans. Magn., Vol. 54, pp.1-5 (2018)

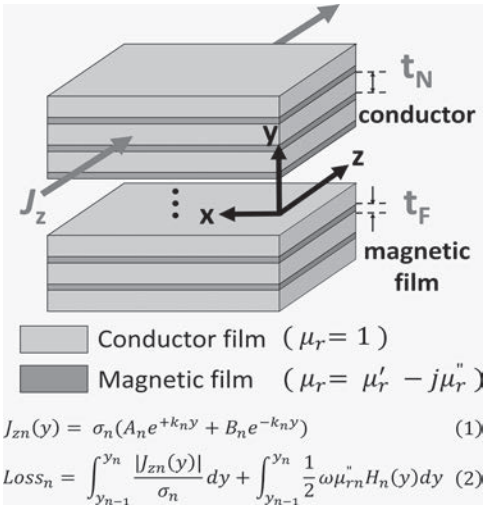


Fig. 1. Structure of conductor/magnetic film multilayer.

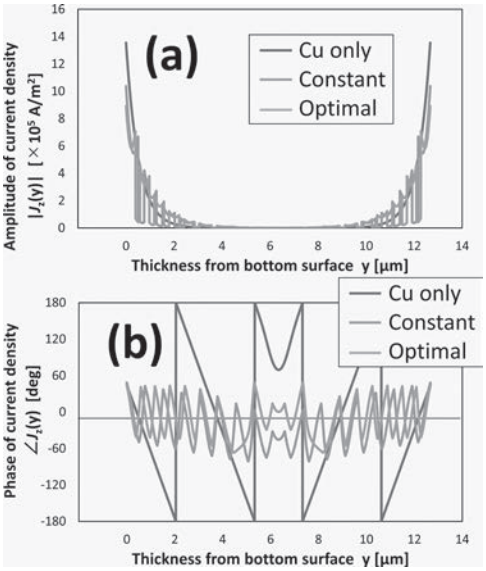


Fig. 2. Calculation result; (a) Current density (b) Current density phase.

EV-20. Frequency shift-based reader of magnetic lateral flow immunoassays for point of use bioanalysis. *M. Rivas*[1], J.C. Martínez García[1], M.C. Blanco-López[2], M. Salvador[1,3], A. Moyano[1,2], J.L. Marqués[1], P. Fernández-Miaja[4] and J. Sebastián[4] *1. Department of Physics, University of Oviedo, Gijón, Spain; 2. Department of Physical and Analytical Chemistry, University of Oviedo, Oviedo, Spain; 3. Institute of the Structure of Matter, Centre of National Research, Rome, Italy; 4. Department of Electrical Engineering, University of Oviedo, Gijón, Spain*

Bioanalysis of a many samples in short times and at low cost is a challenge of modern times. It applies to health issues, but also to food safety, drug control, or environmental monitoring. One of the desired features of this technology is frequently that it can be used *in situ*. These requirements are fulfilled by the Lateral Flow Immunoassays (LFIA.) These are chromatographic tests based on nitrocellulose strips [1] on which the molecule of interest is immobilized by an immunoreaction and labelled to make it visible. This provides a presence/absence response. However, for many applications quantification of the analyte is needed. This must be addressed without compromising the advantages of the method regarding costs, duration, and portability [2], what leads us to the use of magnetic nanoparticles as labels. Their large magnetic permeability in the megahertz range can make them detectable. The sensor built in this work is based on three elements: (i) A conductive micro-track that is printed or sputtered on an insulating substrate and constitutes the sensing element [3], (ii) a 3D-printed polymer automatic positioner that slides the nitrocellulose strip on the sensing track, and (iii) a Colpitts oscillator that integrates the sensing track as inductor (Fig. 1). The active device in the Colpitts oscillator is a silicon Junction Field Effect Transistor (JFET) J310, and the capacitors are ceramic NP0 type, in order to minimize the frequency drift due to the temperature variations. A buffer stage is connected in cascade with the oscillator to reduce the influence of the frequency counter over the oscillator operation. The system has been tested with a series of LFIAs to detect neutravidin concentration (Fig. 2). The results were cross-checked and validated by reflectance measurements obtained with a commercial optical reader. The magnetic sensor proved better limit of detection and independence of the colour of the paper. This work was supported by the Asturian and Spanish Governments (MAT2017-84959-C2-1-R, MAT2016-81955-REDT and FC-GRUPIN-IDI-2018-000185) and IUTA-Gijon Council (SV-19-GIJÓN-1-25).

[1] X. Huang, Z. P. Aguilar, H. Xu, W. Lai, Y. Xiong, Biosensors and Bioelectronics Vol. 75 p. 166 (2016) [2] W.C. Mak, V. Beni, A.P.F. Turner, TrAC Trends in Analytical Chemistry Vol. 79 p. 297 (2016) [3] D. Lago-Cachón, M. Oliveira-Rodríguez, M. Rivas, et al., IEEE Magnetics Letters Vol. 8 p. 1 (2017)

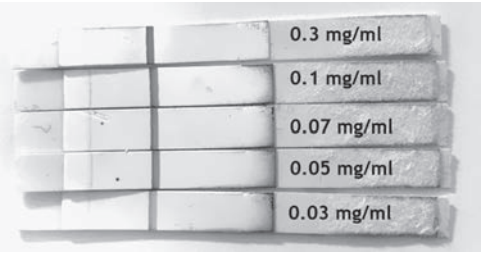


Fig.1 LFIAs for different concentrations of neutravidin.

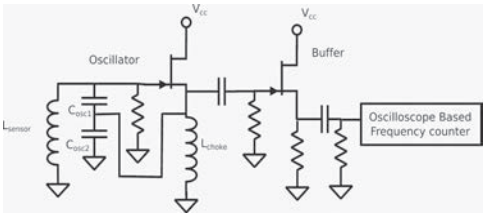


Fig.2 Scheme of the device electronics.

Session EW
SPIN WAVES: LOCALIZATION & MANIPULATION (Poster Session)

Oleksandr V. Dobrovolskiy, Chair
University of Vienna, Vienna, Austria

EW-01. Existence of left handed spin wave in ferrimagnet film studied by Brillouin light scattering. *K. Changsoo*[1], S. Lee[2,4], K. Moon[1], S. Kim[3], B. Park[4], K. Kim[2] and C. Hwang[1] *1. Quantum Technology Institute, Korea Research Institute of Standards and Science, Daejeon, The Republic of Korea; 2. Department of Physics, Korea Advanced Institute of Science and Technology, Daejeon, The Republic of Korea; 3. Department of Physics and Astronomy, University of Missouri, Columbia, MO, United States; 4. Department of Materials Science and Engineering, Korea Advanced Institute of Science and Technology, Daejeon, The Republic of Korea*

Ferrimagnet shows rich physics because two or more different sublattice spins interact with each other. In particular, if these two spins are coupled antiferromagnetically, not only the total magnetization but also the total angular momentum in ferrimagnet should be considered to explain the phenomena in dynamic properties. For ferrimagnet, which consists of transition metal and rare earth metal, the magnetization and angular momentum compensation points (T_M and T_A) are different because the g-factors of each spins are different[1]. Using Brillouin light scattering spectroscopy, we observed the inversion of Stokes-Antistokes intensities in surface spin wave mode at T_M and T_A, respectively, in Co_xGd_{1-x}(10)/Pt(5) system. This means that the mode in contact with the air and the mode in contact with the substrate is reversed at T_M and T_A, which leads to the conclusion that a left-handed spin wave exists between T_M and T_A. Moreover, we observed an increase of T_A in 0.83 Tesla magnetic field. Applying a magnetic field will change the total angular momentum of the system. To reach T_A, exchange fields should compensate the change of the total angular momentum. So, the interpretation of T_A in magnetic field supports the existence of left-handed spin wave. The reversal of the gyromagnetic ratio in $Ho_3Fe_5O_{12}$ at T_M and T_A, measured by macroscopic Barnett effect, also supports our experimental result[2].

[1] Y. Hirata, D. Kim, et al. Physical Review B 97, 220403 (2018) K. Kim, X. Marti, P. Wadley, et al. Nature Materials, 16, 1187 (2017) [2] M. Imai, Y. Ogata, et al. Applied Physics Letters 113, 052402 (2018) K. Kim, T. Li, S. Kim, et al, Applied Physics Express 12, 063001 (2019)

EW-02. Controlling the Dzyaloshinkskii-Moriya interaction by varying the thickness of an oxide layer. *M. Arora*[1,2], J.M. Shaw[1] and H. Nembach[1,3] *1. National Institute of Standards and Technology, Boulder, CO, United States; 2. Physics, University of Colorado, Boulder, CO, United States; 3. JILA, University of Colorado, Boulder, CO, United States*

We demonstrate that both the magnitude and sign of Dzyaloshinskii Moriya interaction (DMI) can be tuned by varying the oxide layer at an interface adjacent to a ferromagnet. We studied Ti(3)/Cu(5)/$Co_{90}Fe_{10}$(1.5)/Ta(d_{ta})/Oxide/Ta(3) structures. The deposition of 0 - 3 nm of Ta was followed by an exposure to oxygen (thicknesses in nm). Here, "Oxide" can stand for TaO_x or $CoFeO_x$. Brillouin light scattering (BLS) is used to directly determine the asymmetric spin wave dispersion caused by an interfacial DMI in the relevant samples [1]. Since significant DMI at the bottom interface of Cu/CoFe is not expected and the Cu seed layer structure is kept constant for all samples, the variation in the measured DMI can be attributed to changes of the top interface between CoFe and the oxide layer. The observed volumetric DMI due to the CoFe /Oxide/Ta interface increased by a factor of six, accompanied by a sign reversal after first oxidizing the CoFe surface. The DMI showed further variation in sign and strength, with an increase of Ta thickness, which implies a thicker TaO_x at the interface. We attribute this change in DMI to the charge transfer between CoFe and oxide layer and the associated hybridization between 3d (CoFe) - 5d (Ta) electronic bands, that changes the 3d density of states at the Fermi level and hence the DMI [2]. Moreover, the changes in the magnetic anisotropy and the damping with the thickness of the Ta layer are related to the degree of oxidation of the CoFe interface. The initial formation of an oxide at the CoFe/Ta interfaces reduces the total damping, because any spin-pumping into Ta is suppressed. This study shows that in systems grown for applications, which are typically capped by Ta, the DMI interactions can be tuned by varying the thickness of the oxide layer. An understanding of the tunability of DMI at the interface may facilitate the development of next generation magnetic memory based on chiral magnetic structures. This research was supported by DARPA award No. R18-687-0004 and DOE award No. DE-SC0017643

1. H. T. Nembach, J. M. Shaw, M. Weiler et al., Nature Physics Letters, 3418, (2015) 2. A. Belabbes, G. Bihlmayer, S. Bluegel et al., Sci. Rep. 6 (2016)

EW-03. Manipulation of parametric spin wave mode in a Permalloy nanowire using Oersted field. *S. Hwang*[1], S. Han[2] and B. Cho[1] *1. School of Materials Science and Engineering, Gwangju Institute of Science and Technology, Gwangju, The Republic of Korea; 2. Division of Navigation Science, Mokpo National Maritime University, Mokpo, The Republic of Korea*

Manipulation of the parametric spin wave property of the Permalloy nanowire, controlled by electric current, has been intensively studied by micro-Brillouin light scattering (μ-BLS). Parametric pumping is a nonlinear wave phenomena and a promising technique for spin wave excitation, which shows threshold characteristics and high excitation efficiency for spin wave with large wave vector. Recent studies have shown that one can generate selectively the parametric spin wave mode in the microscopic waveguide by applying the external magnetic field, which enhances the applicability of the parametric process to magnonic devices [1]. Here, we demonstrate clear parametric pumping of quantized spin wave modes at five frequencies with low microwave power in a nanowire, characterized with width of 800 nm and length of 20 μm. From the electric current dependency of parametric threshold power, we have obtained the butterfly-shaped threshold characteristics at each frequencies, as shown in Fig.1. This indicates that the parametric mode can be selectivity excited by electric current instead of magnetic field. We also provide the direct evidence that the efficiency of parametric process decreases under the certain low field range at specific frequency when the hybridization of fundamental mode with exchange-dominant higher-order mode occurs. So, mode transition from hybrid one to single discrete one is found to be an important mechanism in the change of overall threshold characteristics in a sub-micro sized magnetic system. Figure 2 shows the mode crossing between the fundamental mode and higher-order ones at a specific frequency, f_2, in (a) analytic calculation and (b) experimental observation by μ-BLS.

[1] T. Brächer, P. Pirro and B. Obry, Appl. Phys. Lett., Vol. 99, P.162501 (2011)

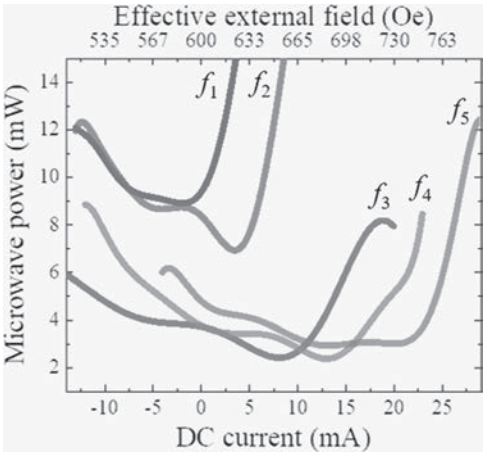


Fig.1 Integrated threshold power curves at several frequencies of f_1, f_2, f_3, f_4 and f_5 in terms of applied electric current.

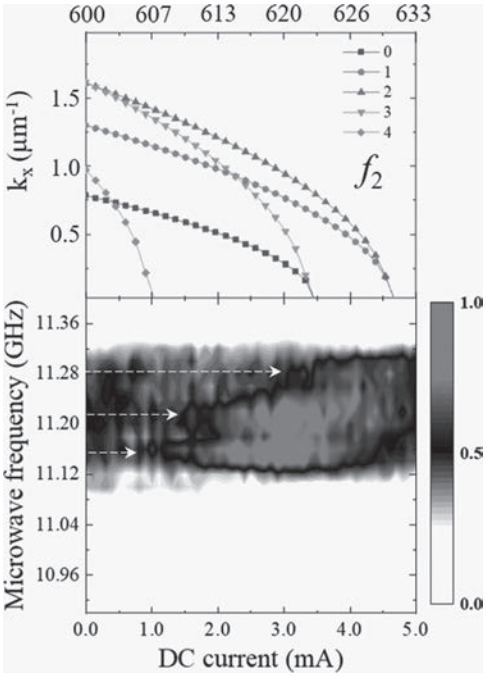


Fig. 2(a) The field-dependence of momentum vector k_x at a fixed frequency f_2, calculated by approximation analytic theory, (b) The parametric resonance spectrum in terms of applied electric current at frequency bands around the f_2.

EW-04. Manipulation of Quantized Spin Waves by Laterally Proximate Micromagnets. *Z. Zhang*[1,2], M. Vogel[1], J. Holanda[1], J. Ding[1], M. Jungfleisch[3], Y. Li[1,4], J. Pearson[1], R. Divan[5], W. Zhang[4], A. Hoffmann[1], Y. Nie[2] and V. Novosad[1] *1. Materials Science Division, Argonne National Laboratory, Lemont, IL, United States; 2. School of Optical and Electronic Information, Huazhong University of Science and Technology, Wuhan, China; 3. Department of Physics and Astronomy, University of Delaware, Newark, DE, United States; 4. Department of Physics, Oakland University, Rochester, MI, United States; 5. Center for Nanoscale Materials, Argonne National Laboratory, Lemont, IL, United States*

Spin waves (SWs) are promising for highly efficient information processing and transmission at the nanoscale. The manipulation of propagating SWs quantized in nanostructured waveguides is a critical step toward the novel functionality. In this work we study the manipulation of quantized SWs propagating in YIG stripes by lateral proximate micromagnets. The SWs in YIG stripes are classified into two categories: the edge localized SWs (E-SWs) and the waveguide SWs (W-SWs). We use micromagnetic modelling to demonstrate a lateral proximate permalloy (Py) stripe along the YIG stripe (Fig. 1a) induces inhomogeneous static dipolar magnetic field ($H_{dip\text{-}Py}$) in width direction. The properties (wavelength λ, decay length δ and group velocity v_g) of the E-SWs can be manipulated (Fig. 1b) through a control of the $H_{dip\text{-}Py}$. In addition, the W-SWs contain a set of modes with integral quantization numbers interfered in the middle of the YIG stripe. We use a combination of micro-focused Brillouin light scattering (μ-BLS) and micromagnetic modelling to demonstrate the paths of the W-SWs are determined by the phase difference (Δφ) between the even and odd modes. The Δφ can be changed by the relative position of a proximate Py dot to the SWs excitation (Fig. 2a) and the external magnetic field (H_{ext}) in this magnetic structure (Fig. 2b)[1]. These results not only open new perspectives for the design of magnonic devices, but also provide ideal models in the fundamental physics of wave propagation.

[1] Zhang Z., et al. *arXiv preprint* arXiv:1904.11613 (2019) *All work was performed at the Argonne National Laboratory and supported by the Department of Energy, Office of Science, Materials Science and Engineering Division. Use of the Center for Nanoscale Materials, an Office of Science user facility, was supported by the U.S. Department of Energy, Office of Science, Office of Basic Energy Sciences, under Contract No. DE-AC02-06CH11357. Z. Z. acknowledges financial support from the China Scholarship Council (no. 201706160146). J. H. acknowledges financial support from the Conselho Nacional de Desenvolvimento Científico e Tecnológico(CNPq)-Brasil. W. Z. acknowledges support from U.S. National Science Foundation under Grants No. DMR-1808892.*

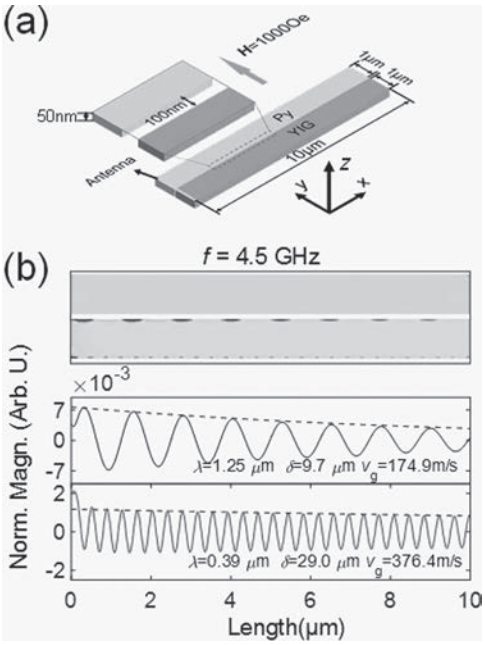


Fig. 1 (a) Schematic of E-SWs in YIG stripe manipulated by laterally proximate Py stripe. (b) The λ, δ and v_g of the 4.5GHz E-SWs close to Py stripe were modulated and different with those of the E-SWs far away from Py stripe.

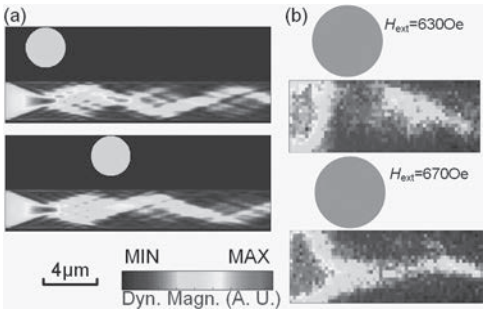


Fig. 2 The paths of 4 GHz W-SWs in YIG stripe manipulated by (a) the relative position of the laterally proximate Py dot (green); (b) the H_{ext}.

EW-05. Spin wave modes in Permalloy nanowires detected by spin orbit torque induced ferromagnetic resonance. *J. Xu*[1], Y. Quessab[1] and A.D. Kent[1] *1. physics department, New York University, New York, NY, United States*

Spin torque ferromagnetic resonance (ST-FMR) is a convenient method to determine the magnetization, magnetic anisotropy and Gilbert damping of nanostructures. It also provides a way to extract both the field-like and damping-like spin torque. Here we study spin-wave excitations in permalloy nanowires to examine finite size effects on the spin-wave spectra. The basic questions we seek to address are the selection rules for exciting and detecting higher order spin-wave modes in nanowires. We studied trilayer heavy metal (HM) – ferromagnet – heavy metal heterostructure nanowires. Permalloy (Py) is used as the ferromagnetic layer due to its large anisotropic magnetoresistance (AMR) and low damping. Platinum (Pt) and tantalum (Ta) are used as heavy metal layer because they have large but opposite spin Hall angles. We used magnetron sputtering to deposit the films, and then the films are patterned into nanowires of various widths, from 150 to 1000 nm. A GHz frequency current is injected into the wire to generate an oscillating spin torque that drives magnetization precession. Due to AMR the resistance oscillates at the same frequency, such that a DC voltage is induced and can be used to detect the spin-wave excitations. In our measurements, we fix the frequency and sweep the external magnetic field, including a small field modulation to increase the signal-to-noise ratio. Figure 1 shows the spectrum of ST-FMR signal at different frequencies for wires of two different wire widths. The small difference between these spectra indicates that we are exciting the lowest frequency mode, the most spatially uniform mode in the width of the nanowire. In figure 2, a fit to the Kittel relation gives the magnetization (mu0 Ms = 1.11 T) and gyromagnetic ratio (gamma/2pi = 27.2 GHz/T). In this presentation, we will describe the conditions for exciting higher spin-wave order modes by ST-FMR.

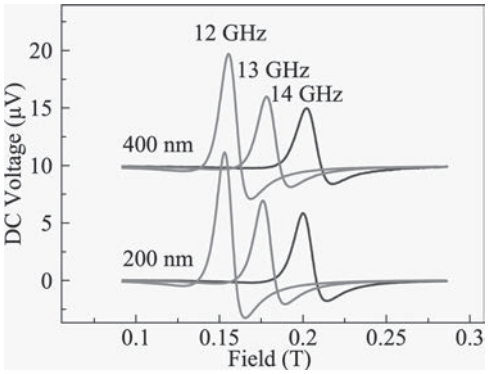


Fig 1. ST-FMR spectrum for nanowires with different width at different fixed rf frequency.

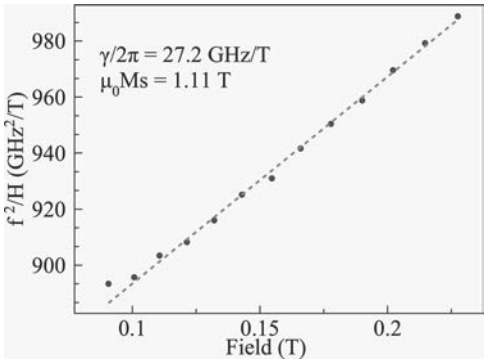


Fig 2. Fitting to in-plane Kittel relation for the 200 nm width nanowire.

EW-06. Spin-Wave Dynamics in Planar Connected Ferromagnetic Nanodot Arrays. S. Sahoo[1], S.N. Panda[1], *A. De*[1], Y. Otani[2] and A. Barman[1] *1. S. N. Bose National Centre for Basic Sciences, Kolkata, India; 2. University of Tokyo, Tokyo, Japan*

Two-dimensional (2D) nanodot arrays have long been interesting systems due to spin configuration, reversal properties, and spin dynamics as well as their potential applications in high density magnetic storage, memory, logic, transistor and communication devices. Several studies have reported the magnetization dynamics in 2D isolated nanodot arrays where the nanodots are magnetostatically coupled. Here, we investigate the spin-wave (SW) dynamics of square $Ni_{80}Fe_{20}$ nanodot arrays joined by rectangular nano-connectors of the same material which directly couple the dots via exchange interaction. The $Ni_{80}Fe_{20}$ nanodot arrays of thickness 20 nm are fabricated by using the combination of e-beam lithography and e-beam evaporation on Si (100) substrate. The nanodot width (connector length) varies as 900 (300), 600 (200) and 300 (100) nm, while the connector width is kept fixed at 300 nm. Custom build time-resolved magneto optical Kerr effect microscope is exploited to probe the precessional dynamics. The damped nonuniform oscillation shows multi-modal precession with high stability with bias magnetic field (H). The fast Fourier transform spectra of the time-resolved traces show the presence of four distinct SW modes for all three arrays. Further, the spatial profiles of the SW modes reveal that the lowest frequency mode forms an extended Damon-Eshbach(DE)-like mode. On the other hand, the two intermediate frequency modes from backward volume(B-V)-like standing wave modes whose quantization numbers increase with increasing frequency. Theses modes are coupled between the dots via the vertical connectors (VC), perpendicular to H. The highest frequency mode shows a mixed DE-BV-like behavior where the power of the mode is mainly concentrated inside the horizontal connector (HC) parallel to H. This mode is coupled between the dots via both HC and VC though the maximum power is concentrated inside HC. We have further numerically demonstrated the modulation of the highest frequency mode due to exchange coupling by varying the length of the connector. The observed modulation of SW dynamics in this new class of magnonic crystal opens the possibility of development of novel communication devices.

[1] B. Rana S. Pal, S. Barman, Y. Fukuma, Y. Otani and A. Barman, Appl. Phys. Express, 2011, 4, 113003. [2] A. Barman and A. Haldar, in Solid State Physics, ed. R. Stamps, R. Camley, Academic Press, 2014; Vol. 65, pp 1–108.

EW-07. Frequency Selective Spin-Wave Valve and Phase-Shifter in Damon-Eshbach Geometry. *K.G. Fripp*[1], F. Mushenok[1], V.D. Poimanov[2] and V.V. Kruglyak[1] *1. Physics and Astronomy, University of Exeter, Exeter, United Kingdom; 2. Donetsk National University, Donetsk, Ukraine*

The future of spin-wave logic devices requires us to excite spin waves with short wavelength and then to control their amplitude and / or phase at the nanoscale. Au et al demonstrated that a magnetic nano-element

formed above a longitudinally magnetised magnonic waveguide can act as an efficient spin-wave transducer, valve and phase shifter [1,2]. Here, we use micromagnetic simulations to extend this concept to the case of a an element magnetised orthogonal to the direction of spin-wave propagation, i.e. Damon-Eshbach geometry. This system is able to control the propagation of spin waves along the waveguide via magneto-dipolar coupling to the magnetic nano-element [1,2]. The direction of the magnetisation of the nano-element controls if spin waves are transmitted, reflected, or absorbed in the element. We explain our observations are explained in terms of the Fano resonance between the discrete spectrum of spin-wave modes of the nano-element and the spin-wave continuum in the waveguide, where a frequency dependent non-reciprocity in transmission is observed when the spin-wave wavelength becomes comparable to the width of the nano-element. Surprisingly, the switching of the confinement region of the magnetic field above or below the waveguide depending upon the direction of spin-wave propagation does not appear to explain the difference in coupling strength to the nano-element from the stray field. The research leading to these results has received funding from the EPSRC of the UK Project No. EP/L019876/1 and from the EU's Horizon 2020 research and innovation program under GA No. 644348 (MagIC).

[1] Y. Au, M. Dvornik, O. Dmytriiev, and V. V. Kruglyak, Appl. Phys. Lett. 100, 172408, (2012) [2] Y. Au, E. Ahmad, O. Dmytriiev, M. Dvornik, T. Davison, and V. V. Kruglyak, Appl. Phys. Lett. 100, 182404, (2012)

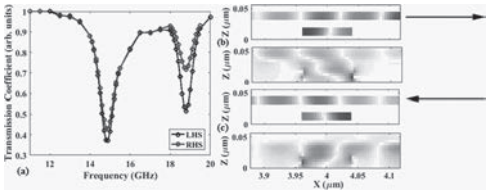


Fig.1 (a) Transmission coefficient obtained from micromagnetic simulations is shown for a waveguide – element separation of 12 nm. (b-c) The system's dynamics are shown for a spin wave at 18.8 GHz incident from the left (b) and right (c) hand sides. In each panel, the top and bottom images show the *x*-component of the magnetisation and the *z*-component of the magnetic field, respectively, at the same instance of time.

EW-08. Unique Spin Wave Eigenmodes of Magnetic Domain Walls.

I. Purnama[1] and C. You[1] *1. DGIST, Daegu, The Republic of Korea*

Magnon, also known as spinwave (SW), have been investigated as a novel mean to drive both magnetic domain walls (DWs) and skyrmions in a patterned magnetic nanowire [1,2]. The mechanism of these SW-driven motions were then attributed to the transfer of linear momentum or angular momentum from the SW to the DW or the skyrmion. In application point of view, this method is attractive because it practically eliminates the Joule heating that normally happens when the DWs or skyrmions were driven by electrical current instead. In this work, we show that by calculating the transmission matrix of the SW, the presence of the DW in the nanowire alters the SW eigenmodes of the system. In the case of nanowire with in-plane magnetization anisotropy (IMA), the presence of transverse DW creates an asymmetrical defect in the shape of the SW eigenmodes. This asymmetry is also found to be related to the chirality of the transverse DW, with right-handed and left-handed DW having opposite defect in the SW eigenmodes. In the case of nanowire with perpendicular magnetization anisotropy (PMA), the SW eigenmodes of the PMA DW is found to differ depending on whether the DW receives linear or angular momentum from the SW. In the case where there is a linear momentum transfer from the SW to the DW (frequency of SW = 41 GHz), the transmission matrix shows us that the system has three distinct eigenmodes; while in the case of angular momentum transfer (frequency of SW = 45 GHz), the transmission matrix shows us that the DW only has two SW eigenmodes. The result is unexpected because in the case where no DW was present, higher SW frequency typically would excite more SW eigenmodes instead of suppress them. The study of unique SW eigenmodes in both IMA and PMA systems shall then further our understanding of the relation between SWs and topological defects such as DWs and skyrmions.

[1] J. Ding, X. Yang, T. Zhu, IEEE Trans. MAG 51, 1500504 (2015). [2] H. Hata, T. Taniguchi, H-W. Lee, T. Moriyama, T. Ono, App. Phys. Exp. 7, 033001 (2014).

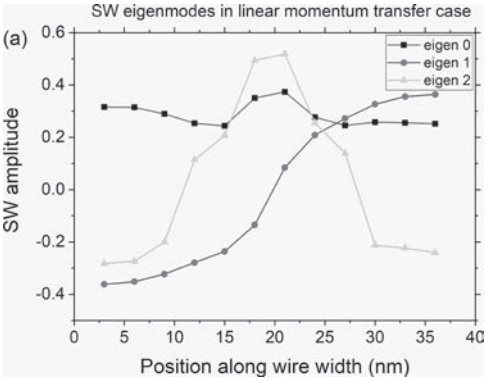
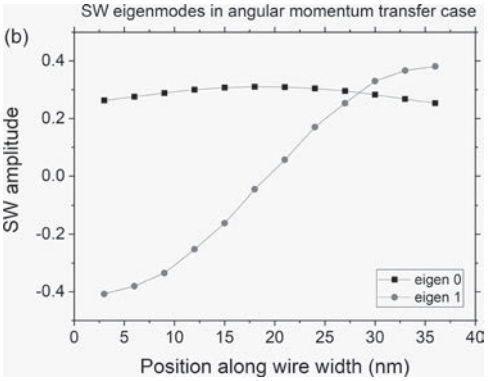


Fig. 1 Spinwave eigenmodes of PMA nanowire. (a) SW eigenmodes when the DW is driven in the same direction as the SW propagation direction (linear momentum transfer case). Here the wire width is 36 nm and the thickness is 1.4 nm.



(b) SW eigenmodes when the DW is driven in the opposite direction as the SW propagation direction (angular momentum transfer case).

EW-09. The Realization of Spin-Wave Frequency Division Multiplexer via Laterally and Inhomogeneously Magnetized Microstripe.

Z. Zhang[1,2], M. Vogel[1], J. Pearson[1], R. Divan[3], A. Hoffmann[1], Y. Nie[2] and V. Novosad[1] *1. Materials Science Division, Argonne National Laboratory, Lemont, IL, United States; 2. School of Optical and Electronic Information, Huazhong University of Science and Technology, Wuhan, China; 3. Center for Nanoscale Materials, Argonne National Laboratory, Lemont, IL, United States*

Modern computation requires parallel data processing and transmission at different frequencies simultaneously in a single line, where the frequency division multiplexer (FDM) play an important role in the separation of mixed signal. In microwave engineering, one traditional idea to realize the FDM function is the application of a set of resonators with different center frequencies. The corresponding signals then propagate in various channels with the highest efficiencies and consequently the hybridized signals are distinguished. In magnonics, it has been similarly reported that the specific frequency spin waves (SWs) in the waveguide could reach the highest intensity near the ferromagnetic resonant (FMR) field[1]. In this work, we use micro Brillouin light scattering (μ-BLS) to demonstrate that the spin-wave FDM function can be realized in 3-μm wide yttrium iron garnet (YIG) microstripe laterally and inhomogeneously magnetized by proximate 2-μm wide permalloy (Py) stripe (Fig. 1). The results show the YIG stripe

supports the simultaneous propagation of 4 GHz and 4.4 GHz SWs (Fig. 2a). Meanwhile, images of the BLS intensities integrated around the excitation frequencies indicate the lower (higher) frequency SWs propagates in the region far away from (close to) Py stripe (Fig. 2b) due to the weaker (stronger) effective field. These results show a new method to divide the SWs with different frequencies hybridized in a signal waveguide. This paves a way toward the parallel processing and transmission of the SWs encoded data.

[1] Zhang Z., et al. *arXiv preprint* arXiv:1904.11613 (2019) *All work was performed at the Argonne National Laboratory and supported by the Department of Energy, Office of Science, Materials Science and Engineering Division. Use of the Center for Nanoscale Materials, an Office of Science user facility, was supported by the U.S. Department of Energy, Office of Science, Office of Basic Energy Sciences, under Contract No. DE-AC02-06CH11357. Z. Z. acknowledges financial support from the China Scholarship Council (no. 201706160146).*

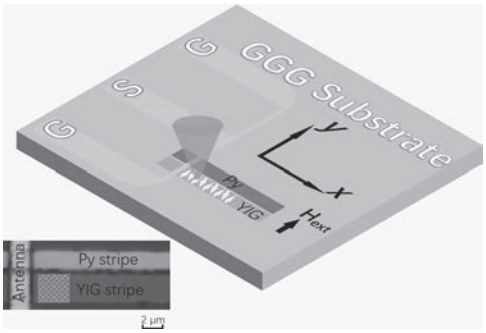


Fig. 1 Schematic illustration of the device layout. The inset shows an optical microscopy image of the device. The spin wave patterns were imaged in the grid region.

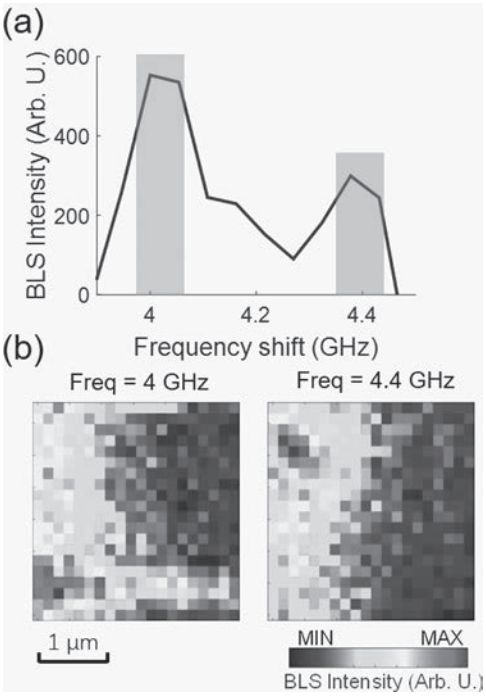


Fig. 2 (a) BLS spectrum recorded at an external field of 700 Oe and the excitations with 4 and 4.4 GHz simultaneously; (b) Images of the BLS intensities integrated around 4 GHz (4.4 GHz) as indicated in Green (Orange) region in (a).

EW-10. Spin dynamics driven by optical spin-orbit torque. *R. Mondal*[1], A. Donges[1] and U. Nowak[1] *1. Department of Physics, Universität Konstanz, Konstanz, Germany*

The manipulation of spins by using light has become an intense research area due to its potential applications in future technological devices [1]. Here, we discuss a direct interaction of spins with the light by using the spin angular momentum of a laser pulse, an effect which is different from the Zeeman effect. It exerts a torque on the spins that is named "optical spin-orbit torque" (OSOT) which originates from relativistic spin-orbit effect [2]. Starting from the Dirac Hamiltonian, we derive a general spin-orbit coupling Hamiltonian that accounts for both, the internal and external fields (laser). Such a spin-orbit coupling term, between electron spins and the light's angular momentum, leads to OSOT on the magnetization. Our preceding analytical calculations show that the OSOT depends on the intensity, helicity, and frequency of the light. Depending upon the absorption and intensity of the light, the equivalent opto-magnetic field which is induced by OSOT can range from several mT to T. Finally, we investigate spin dynamics that is triggered by OSOT for magnetic model systems.

[1] A. Kirilyuk, A. V. Kimel, and T. Rasing Rev. Mod. Phys. 82, 2731 (2010) [2] R. Mondal, M. Berritta, P. M. Oppeneer Phys. Rev. B 94, 144419 (2016)

EW-11. Terahertz Spectrum in SHNO Driven by the Pure Spin Current. *B. Jiang*[1], W. Zhang[1], H. Zhong[1], Y. Zhang[1], S. Yu[1], G. Han[1], G. Liu[1], S. Yan[1], S. Xiao[1] and S. Kang[1] *1. school of physics, Shandong university, Jinan, China*

We studied the auto-oscillation spectrum of spin Hall nano-oscillators (SHNO) based on synthetic antiferromagnets (SAFs) by micromagnetic simulations. In our model, Py/Ru/Py is used as the synthetic antiferromagnet (see the inset of Fig. 1), and the typical heavy metal Pt is used to generate the pure spin current via spin Hall effect (SHE). The pure spin current perpendicularly flows into SAF and drive the magnetizations in SAF to precession. We found that the oscillation frequency of the nano-gap SHNO driven by the pure spin current can reach terahertz once the Ruderman-Kittel-Kasuya-Yosida (RKKY) intensity of SAF and current density are reasonably strong. This terahertz spectrum can be excited even without any external magnetic field. The competition between RKKY interaction and SHE definitely boost up the dynamics of magnetization in SAF. As illustrated in Fig. 1, the terahertz spectrum can be tuned by DC current and/or RKKY intensity. Moreover, we studied the influence of the thickness of SAF on terahertz spectrum. It is found that the thickness of bottom magnetic layer in SAF should be relatively thinner than that of top magnetic layer in SAF in order to obtain the terahertz spectrum. Finally, the nonreciprocity of generated terahertz spectrum is demonstrated by introducing DMI between HM and SAF. Our results suggest a possible way to exploit terahertz spintronics devices.

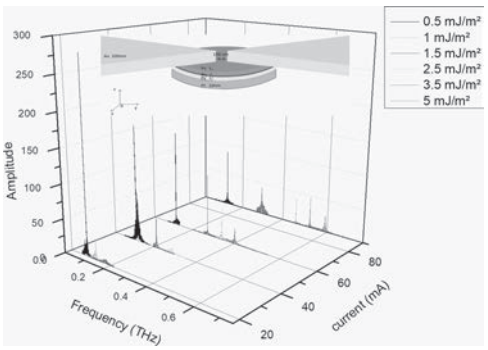


Fig.1: The FFT intensity of magnetization dynamics of the bottom magnetic layer in SAF for different RKKY intensity and DC current. The inset is the schematic drawing of SHNO.

EW-12. Spin Wave Spectra of 1D and 2D V[TCNE]$_{x\sim2}$ Magnonic Crystals. *K. Hu*[1] and M.E. Flatté[1,2] *1. Optical Science and Technology Center and Department of Physics, University of Iowa, Iowa city, IA, United States; 2. Pritzker School of Molecular Engineering, University of Chicago, Chicago, IL, United States*

The organic based ferrimagnet, vanadium tetracyanethylene (V[TCNE]$_{x\sim2}$) has received much attention recently as an attractive magnonic material. V[TCNE]$_{x\sim2}$ has ultra narrow ferromagnetic resonance, low Gilbert damping constant and high Q factor [1-3]. Furthermore, V[TCNE]$_{x\sim2}$ can be fabricated on various rigid and flexible substrates using low temperature chemical vapor deposition (CVD) [4]. These properties make V[TCNE]$_{x\sim2}$ a promising alternative to traditional magnonic crystals like yttrium iron garnet (YIG). Here, we present theoretical calculation of the band structures and linewidths of magnonic crystals of V[TCNE]$_{x\sim2}$. The calculation is based on Landau-Lifshitz-Gilbert (LLG) formalism [5]. We consider quasi one-dimensional and two-dimensional infinitely periodic heterostructures with other ferromagnets such as YIG and cobalt. First, we consier infinitely long cylinders of one magnetic material embedded in a second magnetic material forming a square lattice structure. Second, we study alternating finite slabs of magnetic materials as one-dimensional magnonic crystals. All calculations are done assuming an applied magnetic field of $\mu_0 H_0$=0.1T and a lattice constant of a=100nm. These results further the fundamental understanding of magnonic behavior in V[TCNE]$_{x\sim2}$ necessary for future application. We acknowledge support from NSF EFRI NewLAW under Award No. EFMA-1741666.

[1] H. Yu, M. Harberts, R. Adur, Y. Lu, P. C. Hammel, E. Johnston-Halperin, and A. J. Epstein, *Appl Phys. Lett.* 105, 012407 (2014) [2] N. Zhu, X. Zhang, I. H. Froning, M. E. Flatté, E. Johnston-Halperin and H. X. Tang, *Appl. Phys. Lett.* 109, 082402 (2016) [3] H. Liu et al. *Nat. Mater.* 17, 308-311 (2018) [4] K. I. Pokhodnya, A. J. Epstein, and J. S. Miller, *Adv. Mater.* 12, 410-413 (2000). [5] G Sietsema, T. Liu, M. E. Flatté, *SPIN.* 7, 1740012 (2017)

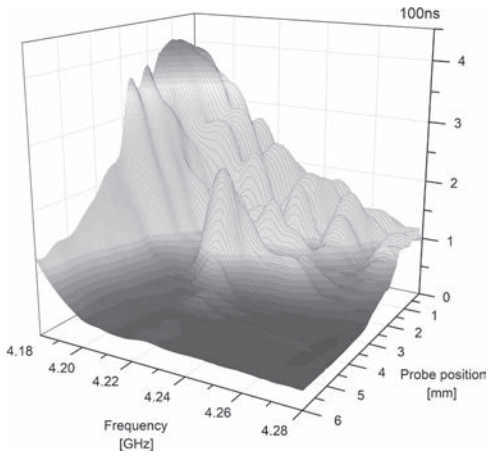
EW-13. Flat Bands, Indirect Gaps, and Unconventional Spin-Wave Behavior Induced by a Periodic Dayaloshinskii-Moriya Interaction. *R. Gallardo*[1], D. Cortés[2], T. Schneider[3], A. Roldán[4], F. Ma[5], K. Lenz[3], H. Fangohr[2,6], J. Lindner[3] and P. Landeros[1] *1. Universidad Técnica Federico Santa María, Valparaiso, Chile; 2. Faculty of Engineering and the Environment, University of Southampton, Southampton, United Kingdom; 3. Helmholtz-Zentrum Dresden–Rossendorf, Dresden, Germany; 4. Universidad de Aysén, Aysén, Chile; 5. Magnetoelectronic Lab, School of Physics and Technology, Nanjing, China; 6. European XFEL GmbH, Schenefeld, Germany*

Periodically patterned metamaterials are known for exhibiting wave properties similar to the ones observed in electronic band structures in crystal lattices. In particular, periodic ferromagnetic materials, also known as magnonic crystals, are characterized by the presence of bands and bandgaps in their spin-wave spectrum at tunable GHz frequencies. Recently, the fabrication of magnets hosting Dzyaloshinskii-Moriya interactions has been pursued with high interest since properties such as the stabilization of chiral spin textures and nonreciprocal spin- wave propagation emerge from the antisymmetric exchange interaction. In this context, to further engineer the magnonic band structure, we propose the implementation of magnonic crystals with periodic Dzyaloshinskii- Moriya interactions, which can be obtained, for instance, via patterning of periodic arrays of heavy metals wires on top of an ultrathin magnetic film. We demonstrate through theoretical calculations and micromagnetic simulations that such systems show a unique evolution of the standing spin waves around the gaps in areas of the film that are in contact with the heavy metal wires. We also predict the emergence of flat magnonic bands and indirect gaps, demonstrating that these effects depend on the strength of the Dzyaloshinskii- Moriya interaction. This study opens further pathways towards engineered magnonics for spin- wave-based devices.

EW-14. Spin wave localization in a magnonic crystal with defects. *C.L. Ordonez Romero*[2], Z. Lazcano-Ortiz[1], G. Pirruccio[2], M. Urbánek[3], T. Hrncir[4], N. Qureshi[5], O. Kolokoltsev[5] and G. Monsivais[2] *1. Physics, BUAP, Puebla, Mexico; 2. Instituto de Física, UNAM, Mexico City, Mexico; 3. CEITEC BUT, Brno University of Technology, Brno, Czechia; 4. TESCAN Brno s.r.o., Brno, Czechia; 5. ICAT, UNAM, Mexico City, Mexico*

A broken translational symmetry in a magnonic crystal via the introduction of tailored defects can beneficially enhance or modify its properties leading to scenarios with outstanding capabilities to connect fundamental physics with applications at microwave frequencies. Their characteristics have inspired multiple studies where detailed results on the behavior of the frequency-amplitude characteristic as a function of different structural parameters have been demonstrated [1]. However, up to now, all the scientific reports deal exclusively with the resulting spin wave spectrum for the complete structure and little has been said about the behavior of the spin wave inside the defects. Here, we present a detailed study of the propagation of surface spin waves (MSSW) through a MC with broken translational symmetry, the influence of the defect in the spin wave propagation, the evolution of frequency bandgaps inside the MC, and the spatial energy distribution as a function of frequency and position. A time and space resolved magneto inductive probing system has been used to map the spin wave propagation in a magnonic crystal with tailored defects. The results show that the spin wave modes get trapped by the defect and the energy is localized in the space for specific frequencies.

This work has been supported by UNAM-DGAPA grant 1N107318 [1] F. Filimonov, E. Pavlov, S. Vystostkii and S. Nikitov, Appl. Phys. Lett., 101, 242408, (2012)



Spin wave energy distribution as a function of frequency and probe position in a magnonic crystal with broken translational symmetry.

EW-15. Mesuring Spin Waves in Individual Magnetic Nanodots. O.V. Dobrovolskiy[1], S.A. Bunyaev[2], N. Vovk[3], D. Navas[2], P. Gruszecki[4], M. Krawczyk[4], R. Sachser[1], M. Huth[1], K. Guslienko[5,6] and *G.N. Kakazei*[2] *1. Physikalisches Institut, Goethe University, Frankfurt am Main, Germany; 2. IFIMUP-IN/Department of Physics and Astronomy, University of Porto, Porto, Portugal; 3. Department of Physics, V.N. Karazin Kharkiv National University, Kharkiv, Ukraine; 4. Nanomaterials Physics Division, Adam Mickiewicz University in Poznan, Poznan, Poland; 5. Departamento de Física de Materiales, Universidad del País Vasco, San Sebastian, Spain; 6. IKERBASQUE, the Basque Foundation for Science, Bilbao, Spain*

While micro- and nanosized magnetic elements are widely used in various microwave applications, the analytical description of spin waves that govern their magnetodynamic response is a complicated problem. This is because of the inhomogeneity of the internal demagnetizing field limiting finding exact eigenfrequencies to only few cases of simplest symmetry – circular disks and infinite stripes. Here, we employ a dipole-exchange spin-wave dispersion equation from Ref. [1] to deduce magnetization and exchange

constant for individual Co-Fe nanodisks. The disks were directly written by focused electron beam-induced deposition [2] and studied by broadband ferromagnetic resonance spectroscopy with external magnetic field applied along the normal to sample plane. The finite disk radius leads to the quantization of the in-plane spin-wave vector and gives rise to resonance drum modes with circular Bessel-function profiles (Fig. 1). We were able to record spin-wave spectra with high signal/noise ratio (shapes of at least 8 peaks can be analyzed) from the individual Co-Fe disk with thickness L = 40 nm and radius R = 200 nm, but even for the disk with R = 100 nm the positions of 3 peaks were detected (Fig. 2). The analytical theory has been generalized for large aspect ratios $L/R \leq 0.5$ and found to agree well with numerical simulations. The proposed approach is especially valuable for the characterization of magnetic materials that are unavailable in large arrays or in bulk form.

[1] G.N. Kakazei et al., Appl.Phys Lett. 85, 443 (2004). [2] M. Huth, F. Porrati, and O.V. Dobrovolskiy, Microelectr. Engin.185-186, 9 (2018).

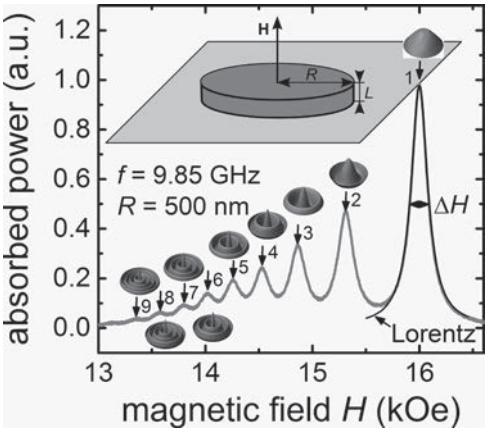


Fig. 1. Experimental spectrum of an individual Co-Fe disk with a radius of 500nm at 9.85 GHz. Arrows indicate resonance drum modes with the shown profiles of zero-order Bessel functions. Inset: Experimental geometry.

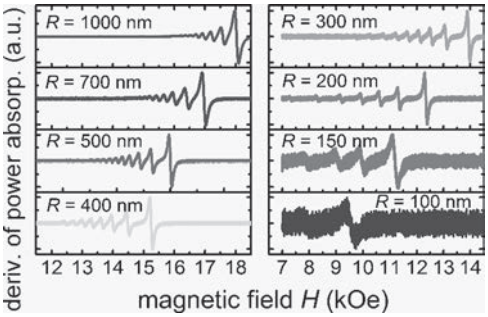


Fig. 2. Derivatives of the experimentally measured spin-wave resonance spectra at 9.85 GHz for a series of disk radii, as indicated.

Session FA
HYBRIDIZED MAGNONS

Axel Hoffmann, Chair
University of Illinois at Urbana-Champaign, Urbana, IL, United States

INVITED PAPERS

1:30

FA-01. Hybrid Magnon Modes: Strong Coupling with Phonons and Photons. *G. Bauer*[1] *1. Institute for Materials Research, Tohoku University, Sendai, Japan*

The strong coupling of the magnetic order with the phonons and photons opens the vista of coherent control of the magnetic order by the lattice and electromagnetic fields, respectively. The dynamics of the electrically insulating ferrimagnet yttrium iron garnet (YIG) [1] has superior magnetic, acoustic, and optical quality factors and is therefore the material of choice to achieve this goal. In this symposium I will report the progress of several collaborations on the "spin cavitronics" of YIG with microwaves [2], infrared light [3], and lattice vibrations [4] with emphasis on theoretical/conceptual aspects.

[1] M. Wu and A. Hoffmann, Solid State Physics 64, 1-392 (2013). [2] B.Z. Rameshti and G.E.W. Bauer, Phys. Rev. B 97, 014419 (2018); J. Chen et al., Phys. Rev. Lett. 120, 217202 (2018); T. Yu et al., Phys. Rev. B 99, 134424 (2019); J. Chen et al., arXiv:1903.00638. [3] J. A. Haigh et al., Phys. Rev. B 97, 214423 (2018); S. Sharma et al., Phys. Rev. Lett. 121, 087205 (2018); S. Sharma et al., arXiv:1903.01718. [4] S. Streib et al., Phys. Rev. Lett. 121, 027202 (2018); K. An et al., arXiv:1905.12523

2:06

FA-02. Strongly coupled magnon hybrid systems with permalloy thin films. *Y. Li*[1,2], T. Polakovic[3,4], Y. Wang[1,5], J. Xu[1,6], S. Lendinez[1], Z. Zhang[1,7], J. Ding[1], T. Khaire[1], H. Saglam[1], R. Divan[8], J. Pearson[1], W. Kwok[1], Z. Xiao[1,6], W. Cao[9], V. Amin[10,11], J. Gibbons[1,12], P. Haney[10], M.D. Stiles[10], W. Bailey[9], W. Zhang[2,1], A. Hoffmann[1] and V. Novosad[1] *1. Materials Science Division, Argonne National Laboratory, Lemont, IL, United States; 2. Physics, Oakland University, Rochester, MI, United States; 3. Physics Division, Argonne National Laboratory, Lemont, IL, United States; 4. Physics, Drexel University, Philadelphia, PA, United States; 5. School of Electronic Science and Engineering, Nanjing University, Nanjing, China; 6. Physics, North Illinois University, Dekalb, IL, United States; 7. Huazhong University of Science and Technology, School of Optical and Electronic Information, Wuhan, China; 8. Center for Nanoscale Materials, Argonne National Laboratory, Lemont, IL, United States; 9. Applied Physics and Applied Mathematics, Columbia University, New York, NY, United States; 10. Center for Nanoscale Science and Technology, NIST, Gaithersburg, MD, United States; 11. Maryland NanoCenter, University of Maryland, College Park, MD, United States; 12. Physics, UCSD, San Diego, CA, United States*

Recently, magnon-based hybrid systems have attracted increasing interests as a new branch in spintronics research [1-3]. Due to diverse coupling mechanisms, magnons can be coupled to a wide variety of excitations including microwave photons, optical photons, phonons, and other magnons. In addition, the excitation frequency of magnons can be easily tuned by an external magnetic field, which is highly desired for controllable hybrid systems. Magnon-based hybrid systems exhibit many physical phenomena, such as mode anti-crossing, Rabi oscillation, and level attraction. They are promising for coherent information transfer between distinct physical platforms, which may ultimately be useful for quantum information science where information can be carried by both the quanta and the phase of the excitation states. One requirement for coherent information transfer is to reach a coupling strength that is larger than the damping rate. Up to date, most studies are based on low-damping yttrium ion garnet (YIG) spheres or thick films, which are beneficial for strong coupling strength but unfavorable for scalable on-chip-integrated applications. In this talk, we will explore the use of permalloy ($Ni_{80}Fe_{20}$) thin films in hybrid magnon systems. Permalloy is a classical metallic ferromagnet with well-known magnetic dynamic properties and is easy to grow and integrate into complex devices. In the first part, we demonstrate strong coupling of magnons in a permalloy thin-film device to the microwave photons in a coplanar superconducting resonator [4]. The coupling is introduced by the magnetic dipolar interaction. Owing to the small mode volume and high-quality factor of the superconducting resonator, a large coupling strength of 0.152 GHz and a cooperativity of 68 can be achieved for a 30 nm thick permalloy device, along with a coupling efficiency of 26.7 Hz for a single Bohr magneton. In the second part, we show strong coupling of permalloy magnons to the spatially nonuniform magnon modes of a YIG film in a permalloy/YIG bilayer structure. The two layers are coupled by interfacial exchange coupling as a field-like torque. In addition, we show evidence that spin pumping creates a damping-like coupling torque. This torque leads to an increase in line width for the out-of-phase hybrid mode and a reduction for the in-phase hybrid mode. Our results provide new pathways for implementing on-chip magnonic devices with efficient and coherent information transducers. This work was supported by the U.S. DOE, Office of Science, Materials Sciences and Engineering Division and as part of Quantum Materials for Energy Efficient Neuromorphic Computing, an Energy Frontier Research Center funded by the U.S. DOE, Office of Science.

[1] H. Huebl, et al. High Cooperativity in Coupled Microwave Resonator Ferrimagnetic Insulator Hybrids, Phys. Rev. Lett. 111, 127003 (2013) [2] Y. Tabuchi, et al. Hybridizing Ferromagnetic Magnons and Microwave Photons in the Quantum Limit, Phys. Rev. Lett. 113, 083603 (2014) [3] X. Zhang, et al. Strongly Coupled Magnons and Cavity Microwave Photons, Phys. Rev. Lett. 113, 156401 (2014) [4] Y. Li, et al. Strong magnon-photon coupling in ferromagnet-superconducting resonator thin-film devices, arXiv: 1902.06795

2:42

FA-03. Strong Coupling between Microwave Photons and Nanomagnet Magnons. J.T. Hou[1] and *L. Liu*[1] *1. MIT, Cambridge, MA, United States*

Hybrid quantum systems have been extensively studied to harness advantages of distinct physical systems and realize functions that cannot be achieved with any individual sub-system alone. In particular, cavity and circuit quantum electrodynamics (Cavity/Circuit QED) provide promising platforms for realizing hybrid quantum systems using Josephson qubits, mechanical systems, atoms, quantum dots, as well as ensembles of spins. Recently, coupled microwave photon-magnon systems have received great attention as a potential approach to realize strong light-matter interactions. To overcome the weak coupling strength between a single spin and the

microwave field, millimeter size ferromagnetic metals or insulators with large spin numbers have been employed for reaching strong coupling. While great success has been demonstrated in achieving coherent sensing and control over the magnonic quantum state using this architecture, one important question remains unanswered: whether such a system is scalable for achieving integrable hybrid quantum systems. In this talk, we will show that by enhancing single spin coupling strength using lithographically defined superconducting resonators, we can reach high cooperativities between a resonator mode and a Kittel mode in nanometer thick Permalloy wires (Fig. 1), where the number of spins for reaching strong coupling is reduced by more than 3 orders of magnitude compared with previous studies [1]. Moreover, we confirm the scaling law of coupling strength by varying Py magnetic volume and extract the single spin coupling strength, which agrees well with the theoretical value derived from analytical model (Fig. 2). This highly engineerable device design and the large coupling strength with nanomagnets provides a direct avenue towards hybrid quantum systems which can benefit from various magnon physics, including nonlinearity, synchronized coupling, non-Hermitian physics, as well as current or voltage controlled magnetic dynamics.

[1] J. Hou and L. Liu, arXiv 1903.01887 (2019)

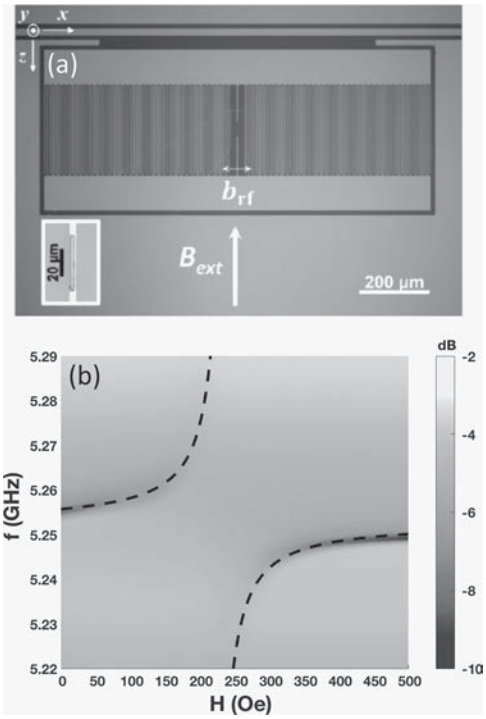


Fig.1 (a) Microscope photo of a typical superconducting resonator coupled with nanomagnets (b) Microwave transmission as a function of frequency and in-plane magnetic field

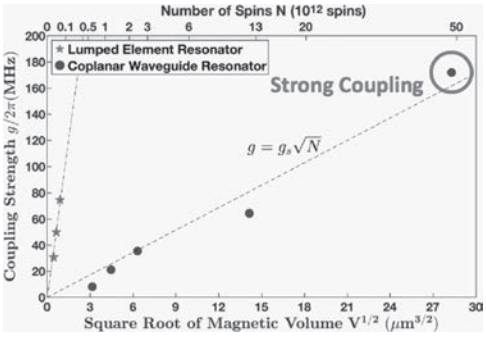


Fig.2 Magnon-photon coupling strength g as a function of magnetic volume and spin number.

3:18

FA-04. Cavity Optomagnonics: Lessons from Quantum Optics for Magnons. *S. Viola Kusminskiy*[1,2] *1. Max Planck Institute for the Science of Light, Erlangen, Germany; 2. Friedrich-Alexander University Erlangen-Nuremberg, Erlangen, Germany*

Optomagnonics studies the quantum-coherent coupling of light to collective magnetic excitations in solid state systems. The magnetic material hosting the magnetic excitations can be also used as an optical cavity if patterned appropriately. This not only enhances the magnon-photon coupling (making these systems promising for applications in quantum technologies) but also allows studying cavity-modified light-matter interaction in a novel platform. In my talk I will go over the basics of cavity optomagnonics and present results on recent theory developments in my group, including optomagnonics with magnetic textures, optical heralding of magnon Fock states, and antiferromagnetic cavity optomagnonics.

3:54

FA-05. Endowing Phonons with Spin via Coherent Coupling with Magnons. J. Holanda[1], D.S. Maior[1], *A. Azevedo*[1] and S. Rezende[1]
1. Department of Physics, Federal University of Pernambuco, Recife, Brazil

Spin waves (magnons) play a key role in many spintronics phenomena. For instance, they are responsible for the spin current flow in magnetic insulators and they can interact with other elementary excitations, such as phonons, photons, electrons, polarons, etc. In particular, magnons can strongly interact with phonons in materials with magnetostrictive interaction, creating hybrid magnon-phonon excitations (magnetoelastic waves). The interconversion between magnons and phonons was extensively investigated in the past in bulk samples of the ferrimagnetic insulator yttrium iron garnet (YIG) with the shape of rods and disks that have internal nonuniform magnetic fields. At that time, the research was mainly driven by applications in delay line technology. In this talk, we present an investigation of the conversion of magnons, generated by microwave fields, into phonons in a YIG film in the presence of a non-uniform magnetic field. We will present results obtained by means of two different experiments. First, we used pulsed microwave signals to launch spin-wave packets at one end of the YIG strip and use time resolved measurements to observe the delayed pulse at the other end of the film. Second, we used wave-vector resolved Brillouin light scattering (BLS) to measure the field dependence of the signal generated by continuous (CW) microwave driving, at various positions of the YIG film under a nonuniform field. Comparison of the measured time-delay vs field and wavevector vs field dependencies with calculations using the magnetoelastic wave dispersion shows that the magnon-phonon conversion occurs with constant energy and varying linear momentum. While it is well established that photons in circularly polarized light carry a spin, the spin of phonons has had little attention in the literature. With the BLS experiments we show that the light scattered by the phonons generated in the magnon-phonon conversion process is circularly polarized, thus demonstrating that the phonons carry angular moment [1].

[1] J. Holanda, D. S. Maior, A. Azevedo, and S. M. Rezende, Nat. Phys. 14, 500–506 (2018).

Session FB
SPINTRONICS IN 2D, TOPOLOGICAL MATERIALS, AND HETEROSTRUCTURES

Inhee Lee, Chair
The Ohio State University, Columbus, OH, United States

CONTRIBUTED PAPERS

1:30

FB-01. Spin States Protected from Intrinsic Electron-Phonon-Coupling Reaching 100 ns Lifetime at Room Temperature in $MoSe_2$. M. Ersfeld[1], F. Volmer[1], P. de Melo[2], R. de Winter[1], M. Heithoff[1], Z. Zanolli[3,4], C. Stampfer[1,5], M. Verstraete[2] and *B. Beschoten*[1] *1. 2nd Institute of Physics, RWTH Aachen University, Aachen, Germany; 2. nanomat/Q-mat/CESAM, Uniiversité de Liège, Liège, Belgium; 3. Catalan Institute of Nanoscience and Nanotechnology (ICN2), Barcelona, Spain; 4. Institute for Theoretical Solid State Physics, RWTH Aachen University, Aachen, Germany; 5. Peter Grünberg Institute (PGI-9), orschungszentrum Jülich, Jülich, Germany*

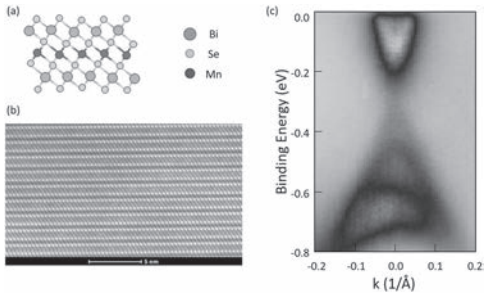
We present time-resolved Kerr rotation measurements in monolayer $MoSe_2$ showing spin lifetimes of over 100 ns at room temperature [1]. These long spin lifetimes are accompanied by an intriguing temperature dependence of the Kerr rotation amplitude, which increases with temperature up to 50 K and then abruptly switches sign. Using ab initio simulations we explain the latter behavior in terms of the intrinsic electron-phonon coupling and the activation of transitions to secondary valleys. The phonon-assisted scattering of the photo-excited electron-hole pairs prepares a valley spin polarization within the first few ps after laser excitation. The sign of the total valley magnetization, and thus the Kerr amplitude, switches as a function of temperature, as conduction and valence band states exhibit different phonon-mediated inter-valley scattering rates. However, the electron-phonon scattering on the ps time scale does not provide an explanation for the long spin lifetimes. Hence, we deduce that the initial spin polarization must be transferred into spin states which are protected from the intrinsic electron-phonon coupling, and are most likely resident charge carriers which are not part of the itinerant valence or conduction band states.

[1] M. Ersfeld, F. Volmer, P. M. M. C. de Melo et al., Nano Lett. 19, 4083 (2019).

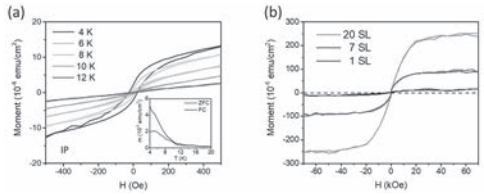
1:42

FB-02. Synthesis and Characterization of Intrinsic Magnetic Topological Insulator $MnBi_2Se_4$. *T. Zhu*[1], A. Bishop[1], D.J. O'Hara[2,3], A. Baker[3], M. Zhu[4,5], B. Noesges[1], S. Cheng[1], J. Freeland[6], M. Brenner[7], C. Jozwiak[8], E. Rotenberg[8], L. Brillson[7], J. Hwang[4,5] and R. Kawakami[1,2] *1. Department of Physics, The Ohio State University, Columbus, OH, United States; 2. Program in Materials Science and Engineering, University of California, Riverside, Riverside, CA, United States; 3. Materials Science Division, Lawrence Livermore National Laboratory, Livermore, CA, United States; 4. Center for Electron Microscopy and Analysis, The Ohio State University, Columbus, OH, United States; 5. Department of Materials Science and Engineering, The Ohio State University, Columbus, OH, United States; 6. Advanced Photon Source, Argonne National Laboratory, Lemont, IL, United States; 7. Department of Electrical & Computer Engineering, The Ohio State University, Columbus, OH, United States; 8. Advanced Light Source, Lawrence Berkeley National Laboratory, Berkeley, Berkeley, CA, United States*

Intrinsic magnetic topological insulators are stoichiometric materials with both magnetic ordering and topological electronic states. Due to its inherent magnetism, this class of materials provides a new route in achieving various novel topological quantum effects that require breaking time-reversal symmetry, while maintaining good crystallinity and high purity of the material. We report the synthesis and characterization of an intrinsic magnetic topological insulator $MnBi_2Se_4$. The $MnBi_2Se_4$ thin films are deposited with alternating layer growth of Bi_2Se_3 and a-MnSe. The high quality of the material is shown with cross-sectional TEM. Dirac surface state is demonstrated with angle-resolved photoemission spectroscopy above its magnetic ordering temperature. SQUID magnetometry measurement on films with different thicknesses shows layered-antiferromagnetic ordering in this material. Low-field SQUID measurement also shows a hysteresis loop, with magnetic moments preferred to stay within the lattice plane. The ferromagnetic signal is attributed to uncompensated magnetic moments at the surface. Its magnetic characterization is also confirmed with XMCD measurement. Furthermore, preliminary magnetometry measurement also shows that the magnetic ordering in $MnBi_2Se_4$ persists down to the monolayer limit.



(a) Schematics of the crystal structure of 1 septuple layer of $MnBi_2Se_4$. (b) The cross-sectional TEM image of $MnBi_2Se_4$ thin film grown with MBE. (c)ARPES data on a 7 SL $MnBi_2Se_4$ taken at 81K.



(a) Temperature-dependent magnetometry measurement on a 7 SL $MnBi_2Se_4$ sample. (b) Thickness-dependent magnetometry measurement on a few different $MnBi_2Se_4$ samples at 4K.

1:54

FB-03. Weak Antilocalization and Surface Quantum Oscillations in Topologically Nontrivial Half Heusler YPdBi Thin Films. *V. Bhardwaj*[1], A. Bhattacharya[2,1], L.K. Varga[3], A.K. Nigam[4] and R. Chatterjee[1]
1. Physics, IIT Delhi, New Delhi, India; 2. Mechanical Engineering, IIT Delhi, New Delhi, India; 3. Wigner research center for Physics Hungarian Academy of Sciences, Budapest, Hungary; 4. Tata Institute of Fundamental Research, Homi Bhabha Road, Mumbai, India

The topological insulator (TI) is a new quantum state of matter which carries metallic surface/edge states along with insulating bulk states[1]. Rare-earth(R) based RPdBi single and poly-crystalline Half-Heusler(HH) alloys are proposed to harbor topological nontrivial states based on first principle calculations[2-3]. In this work, we study the observation of topological non trivial properties in [110] oriented YPdBi(YPB) thin films grown on MgO (100) substrates. First, polycrystalline bulk sample of YPB is prepared in a specially designed RF induction melting set-up. XRD analysis reveal single phase with MgAgAs-type cubic crystal (lattice constant~ 6.68Å) structure. The thin films of YPB is prepared from the same target by pulsed laser deposition technique under the optimized conditions, which showed a textured structure with (110) planes parallel to the (100) plane of MgO[4]. The topological nontrivial properties of sample is studied using magnetotransport measurements. The longitudinal resistance R_{xx} vs temperature (T) data shows a typical semi metallic behavior from $4K \leq T \leq 350K$ but abrupt metallic transition is observed for $T \leq 4K$ (see Fig.1). Effect of external magnetic field (H=0 to 9T) is studied on this anomaly and it can be seen in the inset of Fig.1, that for $H \geq 5T$ this anomaly disappeared completely. This implies that the anomaly in R_{xx} data at 3.8K can be attributed to the dominance of metallic surface state below this temperature and degeneracy of surface states is lifted in presence of magnetic field due to breaking of time reversal symmetry. The low magnetic field magnetoresistance data follows the Hikami-Larkin-Nagaoka (HLN) model and confirms 2D WAL effect. The extracted values of phase coherence length (l_{Φ}) and α indicate the presence of the 2D surface states in YPB. The Dirac nature of the surface states is further confirmed by Landau level fan diagram analysis to extract finite Berry Phase from SdH oscillations data. Sheet Carrier density calculated from the SdH oscillations and Hall measurements agree well with each other. These findings show that thin films of the HH YPB can be used for studying the novel quantum transport properties of surface Dirac fermions

1. M. Z. Hasan, C. L. Kane, Colloquium: Topological insulators. *Rev. Mod. Phys*. 82, 3045–3067 (2010). 2. S. Chadov, X. Qi, J. Kübler, G.H. Fecher, C. Felser, and S.C. Zhang, *Nat. Mater*. 9, 541 (2010). 3. Y. Nakajima, R. Hu, J. Paglione, *et. al, Science Advances* 1, e1500242 (2015). 4. V. Bhardwaj, S. P. Pal, L. K. Varga, M. Tomar,V. Gupta, and R. Chatterjee, *Sci. Rep*. 8, 9931 (2018).

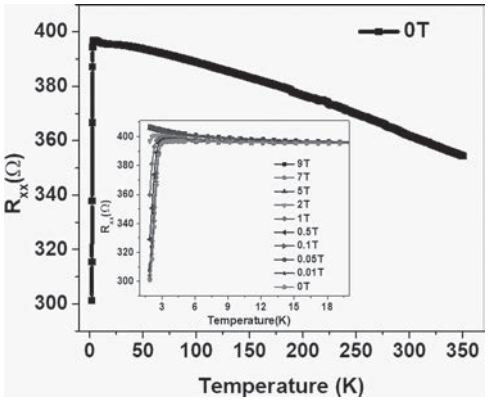


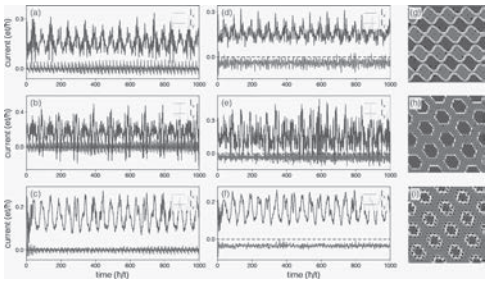
Fig. 1

2:06

FB-04. Dimension Transcendence and Anomalous Charge Transport in Magnets with Moving Multiple-Q Spin Textures. *Y. Su*[1], S. Hayami[2] and S. Lin[1] *1. Los Alamos National Lab, Los Alamos, NM, United States; 2. Hokkaido University, Sapporo, Japan*

Multiple-Q spin textures, such as magnetic bubble and skyrmion lattices, have been observed in a large family of magnets [1]. These spin textures can be driven into motion by external stimuli [2]. The motion of spin textures affects the electronic states. Here we show that to describe correctly the electronic dynamics, the momentum space needs to be transcended to higher dimensions by including the ancillary dimensions associated with phason modes of the translational motion of the spin textures [3]. The electronic states have non-trivial topology characterized by the first and second Chern numbers in the high dimensional hybrid momentum space [4]. This gives rise to an anomalous electric charge transport due to the motion of spin textures. By deforming the spin textures, a nonlinear response associated with the second Chern number can be induced. The charge transport is derived from the semi-classical equation of motion of electrons that depends on the Berry curvature in the hybrid momentum space. Our results suggest that the motion of multiple-Q spin textures has significant effects on the electronic dynamics and provides a new platform to explore high dimensional topological physics.

[1] S. Muhlbauer, B. Binz and F. Jonietz, Science, Vol. 323, p.915 (2009) [2] S.L. Zhang, W.W. Wang and D.M. Burn, Nature communications, Vol. 9, p.2115 (2018) [3] Y. Su and S.Z. Lin, Phys. Rev. B, Vol. 98, p.235116 (2018) [4] S.C. Zhang and J.P. Hu, Science, Vol. 294, p.823 (2001)



Currents along the x and y directions induced by the translational motion of spin textures. (a) Currents for the double-Q magnetic bubble lattice, (b) currents for the triple-Q magnetic bubble lattice, and (c) currents for the triple-Q skyrmion lattice. (d)-(f) Currents for the three spin textures under a shear deformation. (g)-(i) Sheared spin textures.

2:18

FB-05. Interaction of 2D materials and π-electron systems with magnetic surfaces. *N. Atodiresei*[1], V. Caciuc[1] and S. Bluegel[1]
1. Peter Grünberg Institut and Institute for Advanced Simulation, Forschungszentrum Jülich GmbH, Jülich, Germany

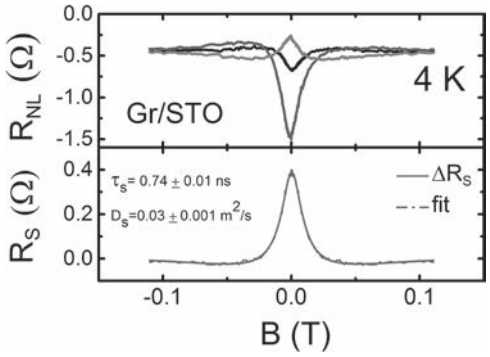
The density functional theory provides a framework with predictive power that can be used to describe hybrid systems incorporating 2D-materials, π-electron systems and metal substrates. In this respect, *ab initio* studies elucidate how the subtle interplay between the electrostatic, the weak van der Waals and the strong chemical interactions determine the geometric, electronic and magnetic structure of hybrid interfaces. More precisely, the interaction between 2D-materials and π-electron systems with the magnetic states of a metal influences the (i) spin-polarization, (ii) magnetic exchange coupling, (iii) magnetic moments and (iv) their orientation at such hybrid interfaces. In this talk I will briefly summarize how first-principles calculations (i) provide the basic insights needed to interpret surface-science experiments and (ii) are a key tool to design novel materials with tailored properties that can be integrated in 2D-materials and carbon-based spintronic devices.

[1] M. Callsen et al., *Phys. Rev. Lett.* 111, 106805 (2013). [2] K. V. Raman, et al., *Nature* 493, 509 (2013). [3] B. Warner, et al., *Nature Communications* 7, 12785 (2016). [4] F. Huttmann, et al., *J. Am. Chem. Soc.* 139, 9895 (2017). [5] M. Paβens, et al., *Nature Communications* 8, 15367 (2017). [6] V. Caciuc, et al., *Phys. Rev. Mat.* 2, 084001 (2018).

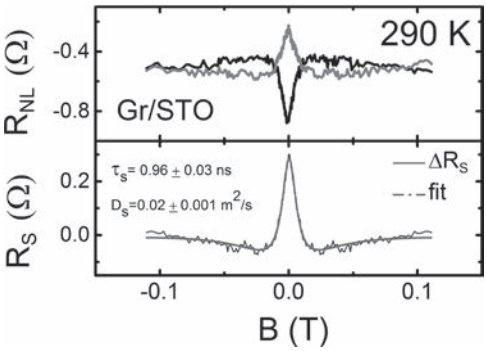
2:30

FB-06. Temperature and Electric Field Dependence of Spin Relaxation in Graphene due to Surface Electric Dipoles on $SrTiO_3$. *S. Chen*[1], R. Ruiter[1], V. Mathkar[1], B. van Wees[1] and T. Banerjee[1] *1. University of Groningen, Groningen, Netherlands*

The theoretically predicted intrinsic spin relaxation time of up to 1 μs in graphene along with extremely high mobility makes it a promising material in spintronics. Novel functionalities can be introduced in graphene via proximity effect with different underlying substrates. In this work, we use the electronically rich platform of $SrTiO_3$ (STO) with broken inversion symmetry and study spin transport in graphene in the presence of surface electric fields. We find spin relaxation time and length as large as 0.96 ± 0.03 ns and 4.1 ± 0.1 μm respectively at 290 K in graphene, using non-local spin valve studies and find a non-monotonous dependence with temperature, unlike that observed on other substrates. Analysis of the temperature dependence indicates the role of surface electric dipoles and electric field driven electronic and structural phase transitions, unique to STO, to spin transport and spin relaxation in graphene. We have further investigated the influence of breaking inversion symmetry at the surface of STO by introducing an 8 nm thick hBN layer. On the same STO substrate, we identically fabricate two different devices: graphene/STO and graphene/hBN/STO. Hanle measurements show a lower spin relaxation time in graphene/hBN/STO. Furthermore, we observe notable differences in the Hanle lineshapes for the graphene/hBN/STO device as compared to the graphene/STO device. A pronounced upturn in the Hanle lineshape, reminiscent of tunneling anisotropic magneto-resistance, is observed at high magnetic fields for the former device and that disappears at RT. Our study provides a new direction to understanding the role of spin-orbit interaction on spin transport in graphene.



Hanle measurements (top panel) and the calculated Hanle signal (blue, bottom panel) at 4 K after the background subtraction and fitting with the steady-state solution to the Bloch equation in the diffusive regime



Hanle measurements (top panel) and the calculated Hanle signal (blue, bottom panel) at 290 K after the background subtraction and fitting with the steady-state solution to the Bloch equation in the diffusive regime

2:42

FB-07. Magnetic properties of micrometer sized YIG/FGT heterostructure revealed by local ferromagnetic resonance. *B. Arkook*[1], M. Al ghamdi[1], V.H. Ortiz[1], J. Shi[1] and I. Barsukov[1] *1. Physics and Astronomy, UC Riverside, Riverside, CA, United States*

Multilayer heterostructures consisting of magnetic insulator and 2D spin system offer a versatile, promising platform for next-generation spintronics and quantum computation applications. Understanding interfacial spin coupling and transport in such heterostructures requires a local microwave spectroscopy technique, since the flakes of 2D materials obtained by exfoliation are limited to micrometers in size. Here, we fabricate disks of 20μm diameter from epitaxial ferrimagnetic insulator, yttrium iron garnet (YIG), thin film using pulsed laser deposition, e-beam lithography, and lift-off. We place few-nm thick flakes of van-der-Waals material Fe_3GeTe_2 (FGT) on the pre-patterned YIG disks and transfer them onto a planar microwave resonator. Employing angle-dependent ferromagnetic resonance, we observe low-energy spin wave modes in YIG at several microwave frequencies, allowing for evaluation of magnetic anisotropy and damping. Using cryogenic measurements, we find an anomalous temperature dependence of effective magnetic anisotropy. The results shed light on spin phenomena at YIG/FGT interfaces and present an experimental approach for studies of micro-scale magnetic insulator/2D heterostructures. This work was supported as part of SHINES, an Energy Frontier Research Center funded by the U.S. Department of Energy, Office of Science, Basic Energy Sciences under Award DE-SC0012670. Support by the National Science Foundation under Grant No. ECCS-1810541 is acknowledged.

INVITED PAPER

2:54

FB-08. Giant Spin Galvanic Effects in Topological Material Heterostructures. *S.P. Dash*[1] *1. Microtechnology and Nanoscience, Chalmers University of Technology, Gothenburg, Sweden*

Engineering 2D materials heterostructures by combining the best of different materials in one ultimate unit can offer a plethora of opportunities in condensed matter physics. Among the 2D materials, while large area CVD graphene is shown to be an excellent medium for long distance spin communication and fabrication of spin circuits [1,2], the insulating CVD h-BN has shown a very large tunnel spin polarization up to 65% at room temperature [3]. Furthermore, by inducing SOC and spin absorption effects, we demonstrated an electrical gate control of spin-polarization and spin lifetime in graphene/MoS_2 heterostructures at room temperature [4]. Recently,

we combined graphene with topological insulators in van der Waals heterostructures to demonstrate the emergence of a strong and tunable proximity-induced spin-orbit coupling in graphene [5], consequently giving rise to a giant spin galvanic effects at room temperature. Furthermore, using Weyl semimetals, we observed a giant spin to charge conversion [6] and efficient spin injection effects at room temperature. These findings demonstrate all-electrical spintronic devices at room temperature in van der Waals heterostructure, which can be key building blocks in future device architectures.

[1] Nature Commun., 6, 6766 (2015). [2] arXiv preprint arXiv:1905.04151 (2019). [3] Scientific Reports, 6, 21168 (2016). [4] Nature Commun. 8, 16093 (2017). [5] Science Advances, 4:eaat9349 (2018). [6] arXiv:1812.02113 (2018).

CONTRIBUTED PAPERS

3:30

FB-09. Fabrication and investigation of graphene/full Heusler alloy heterostructure for spintronics. *S. Li*[1], K. Larionov[2], Z. Popov[2], S. Entani[1], K. Amemiya[3], P. Avramov[4], Y. Sakuraba[5], H. Naramoto[1], P. Sorokin[2] and S. Sakai[1] *1. National Institutes for Quantum and Radiological Science and Technology, Chiba, Japan; 2. National University of Science and Technology MISiS, Moscow, Russian Federation; 3. High Energy Accelerator Research Organization, Tsukuba, Japan; 4. Kyungpook National University, Daegu, The Republic of Korea; 5. National Institute for Materials Science, Tsukuba, Japan*

For years graphene has been considered as the most potential material which paves the way to advanced high-performance spintronic devices due to its extraordinary electrical and physical properties. In those reported graphene-spintronic devices, conventional ferromagnets such as NiFe etc of low spin polarization have been often used due to the well-established synthesis method of graphene on them. However, the spin signal reported in those systems are far from being considered satisfactory for spintronic device applications [1,2]. Adopting highly spin-polarized material can be the most effective way to improve the performance of graphene spintronic devices, the experimental demonstration, however, is still lacking. Here we report the demonstration of a novel heterostructure consisting of graphene and full Heusler alloy $Co_2Fe(Ge_{0.5}Ga_{0.5})$ (CFGG), in which half-metallicity has been confirmed experimentally [3]. Single layer graphene was prepared by in situ chemical vapor deposition on a magnetron sputtered CFGG thin film grown on single crystalline MgO(001) substrate. As shown by the RHEED images in Fig. 1, the sharp streaky patterns from both graphene and CFGG indicate an atomic flatness of the SLG/CFGG interface. The high quality of graphene was further confirmed by Raman spectroscopy. A depth-resolved XMCD study reveals that the CFGG surface adjacent to graphene possesses a robust magnetic moment comparable to the bulk CFGG (Fig. 2) in association with the weak interfacial interaction. This finding is in sharp contrast to the large reduction of the magnetic moment reported in other graphene/ferromagnets heterostructures. DFT calculations show that the inherent properties such as half-metallicity of CFGG and the linear Dirac band of graphene are preserved at the interface. These findings are highly promising for realizing effective transport of highly spin-polarized electrons in graphene-based spintronic devices.

[1] W. Han et al, *Nat. Nanotechnol.* 9, 794 (2014) [2] E. D. Cobas, et al, *ACS Nano* 10, 10357 (2016) [3] S. Li et al, *Appl. Phys. Lett.* 103, 042405 (2013)

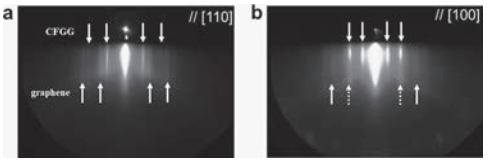


Fig. 1. RHEED images of graphene/CFGG heterostructure with the incident electron beam along (a) MgO[110] azimuth, and (b) MgO[100] azimuth.

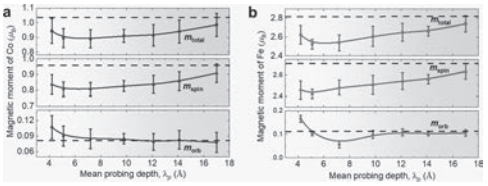


Fig. 2 Depth-resolved magnetic moment of (a) Co, and (b) Fe *vs.* mean probing depth in graphene/CFGG heterostrucutre. The dashed lines indicate the value for bulk CFGG.

3:42

FB-10. Extrinsic Spin-Orbit Coupling Induced Interfacial Dzyaloshinskii-Moriya Interaction in MoS_2/NiFe/Ta Heterostructures. *A. Kumar*[1], A. Chaurasiya[2], N. Chowdhury[1], A. Mondal[2], A. Barman[2] and P.K. Muduli[1] *1. Physics, Indian Institute of Technology Delhi, New Delhi, India; 2. S. N. Bose National Centre for Basic Sciences, Kolkata, India*

Dzyaloshinskii-Moriya interaction (DMI) leads to canted spins which gives an extra stability to skyrmions and other chiral structures [1, 2]. Investigation of 2D transition metal dichalcogenide (TMDs) materials have received increasing attention as they possess interesting properties like direct band gap, strong spin-orbit coupling [3], and lack of inversion centre in crystal structure [4] in their monolayer form. These properties of 2D TMDs with novel magnetic properties arising due to DMI may open up new avenues for spintronic devices. Therefore, in this work we explore the possibility of interfacial DMI (iDMI) in MoS_2/Py heterostructures. Two series of samples were prepared by varying the thickness of the Py layer from 0-10 nm on large area 2L and 3~4L MoS_2 layers. Photoluminescence (PL) and Raman mapping shows the presence of defects (Sulphur vacancies) at 3~4L MoS_2 [5]. DMI measurements were performed using Brillouin-light-scattering (BLS) spectroscopy in Damon-Eshbach (DE) geometry [6]. Fig. 1 (a) and (b) shows the asymmetry in the spin-wave frequency (Δf) in BLS measurements for 2L and 3-4L MoS_2/Py (5 nm), respectively. A linear increase in DMI constant (D) with inverse of Py thickness (t_{Py}) was observed for both 2L and 3-4L MoS_2/Py series. These observations indicate the presence of iDMI in these samples which arises due to MoS_2/Py interface. Interestingly our analysis shows ~58% enhancement of iDMI in 3-4L MoS_2/Py system as compared to 2L-MoS_2/Py. This observation is counterintuitive as strength DMI depends on spin-orbit coupling and hence should decrease with increase in number of MoS_2 layers. Therefore, we explain our results based on presence of higher defect density in 3-4L MoS_2 which leads to extrinsic spin-orbit coupling at 3-4L MoS_2/Py interface. This results in higher iDMI in 3-4L MoS_2/Py as compared to 2L-MoS_2/Py. Our results indicates the possibility of utilizing the defects at interface of 2D TMD/FM heterostructures for tailoring the chiral structures for spintronic devices.

1) T. Moriya, Phys. Rev. 120, 91 (1960). 2) I. E. Dzialoshinskii, Sov. Phys. JETP 5, 1259 (1957). 3) Z. Y. Zhu. *et al.,* Phys. Rev. B 84, 153402 (2011). 4) Di Xiao *et al.*, Phys. Rev. Lett. 108, 196802 (2012). 5) R. Bansal *et al.*, J. Magn. Magn. Mater 476, 337-341 (2019). 6) A. K. Chaurasiya *et al.,* Sci Rep. 6, 32592 (2016).

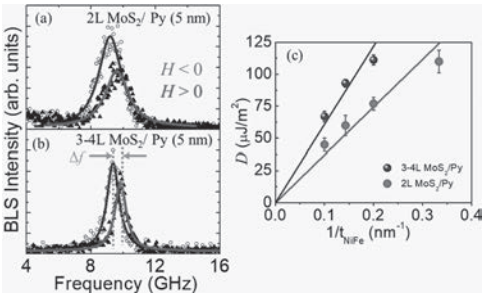


Fig1: (a) and (b) BLS spectra measured at wave vector (k) = 15.8 rad/μm for 2L and 3-4L MoS_2/Py (5 nm) for opposite orientation of magnetic field. (c) Variation of D vs. $1/t_{Py}$ for 2L and 3-4L MoS_2/Py samples.

3:54

FB-11. Chirality-induced Spin-Hall Magnetoresistance in 2D Chiral Hybrid Perovskites. E. Vetter[1], Y. Liang[2], Y. Xiong[3,4], S. Zhang[5], Z. Zhang[5,6], Y. Li[3,5], H. Qu[4], V. Novosad[5], A. Hoffmann[5], W. You[2], W. Zhang[3,5] and *D. Sun*[1] *1. Department of Physics, North Carolina State University, Raleigh, NC, United States; 2. Department of Chemistry, University of North Carolina at Chapel Hill, Chapel Hill, NC, United States; 3. Department of Physics, Oakland University, Rochester, MI, United States; 4. Department of Electronic and Computer Engineering, Oakland University, Rochester, MI, United States; 5. Materials Science Division, Argonne National Laboratory, Lemont, IL, United States; 6. School of Optical and Electronic Information, Huazhong University of Science and Technology, Wuhan, China*

2D ferromagnetism is an emerging field in spintronics applications. The use of generic 2D ferromagnetic materials, however, suffers of the so-called 'superparamagnetic limit', which imposes restrictions on the size and dimension of the ferromagnetic component used in spintronics devices. The recent discovery of the Chiral-Induced Spin Selectivity (CISS) effect offers a possibility to generate spin angular momentum by replacing the ferromagnetic component with chiral systems, e.g., chiral (left- or right-handed) molecules and their assemblies lacking inversion symmetry. As a result of the CISS effect, the chiral materials can produce an effective magnetic field at room temperature, whose direction is determined by the left or right chirality, circumventing the 'superparamagnetic limit'. Here, we report the observation of a large chiral-induced magnetic field in solution-processed, 2D-layered, organic-inorganic hybrid perovskites incorporating chiral molecule ligands. Such chiral-induced magnetic field is probed by measuring the resistance through an attached platinum layer, analogous with the spin-Hall magnetoresistance (SMR). We found a substantial angular dependent chirality-induced SMR that agrees well with theoretical models. By sweeping the magnetic field, the SMR reveals a clear hysteresis depending upon the chirality of 2D perovskites, which could be used to quantify the effective magnetic field strength produced via the CISS effect. Incorporating the chiral molecules into a 2D layered hybrid perovskite framework offers a versatile platform for designing 2D ferromagnetic materials at room temperature. Acknowledgment: E.V. and D.S. were thankful for the start-up support provided by North Carolina State University and NC State-Nagoya Collaboration Grant. Work at Oakland University was supported by AFOSR under no. FA9550-19-1-0254. Work at Argonne was supported by the Department of Energy, Office of Science, Materials Science and Engineering Division.

Session FC
MRAM THERMAL EFFECTS / SPIN CURRENTS

Xin Fan, Chair
University of Denver, Denver, CO, United States

INVITED PAPER

1:30

FC-01. Resistance-area product effects on spin torque switching in perpendicular STT-MRAM. *G. Mihajlovic*[1], N. Smith[1], T. Santos[1], J. Li[1], M. Tran[1], M. Carey[1], B. Terris[1] and J. Katine[1] *1. Western Digital Research Center, Western Digital Corporation, San Jose, CA, United States*

In a perpendicular STT-MRAM cell, the critical switching current density J_{c0} is not expected to depend on the resistance-area product RA. Experimentally, however, an RA dependence has been observed by several groups and attributed to an RA-dependent spin pumping contribution to the damping parameter of the free layer FL [1, 2]. In this talk we will present an experimental study of field and current-induced switching in perpendicular STT MRAM cells with variable RA = 5, 10, 15 and 20 Ωmm^2. We will show that the RA dependence of J_{c0} is influenced by phenomena other than spin pumping. Instead, the RA dependence is due to the current-induced self-heating of an MRAM cell (which reduces the effective H_k of the FL), and, to a smaller extent, the RA dependence is due to the voltage-controlled magnetic anisotropy effect (VCMA). As the temperature rise of the FL is proportional to the dissipated power density (RA)J^2, higher RA devices result in lower J_{c0}. In addition, as the VCMA effect is proportional to the bias voltage V_b across the MRAM cell, for a given J, VCMA effects are stronger with higher RA. We will present a simple quantitative model to include self-heating and VCMA contributions to the STT, which quantitatively explains all of our experimental findings, in particular the much stronger RA dependence of J_c for P→AP compared to AP→P switching. We will also show that the RA dependence of STT efficiency E_b/I_{c0} obtained from pulse width t_p dependent measurements of switching voltage V_c in the thermally assisted regime (E_b is the energy barrier for magnetization reversal of the FL and I_{c0} is the critical switching current) is due to an error when fitting the data assuming that only STT is responsible for switching, without including contributions from VCMA and self-heating effects. When the latter two contributions are properly included the RA dependence of STT efficiency disappears, as expected for STT switching.

1) J. Z. Sun, Phys. Rev. B 96, 064437 (2017). 2) Z. M. Zeng et al., App. Phys. Lett. 98, 072512 (2011). 3) G. Mihajlović et al., arXiv 1905.02673.

CONTRIBUTED PAPERS

2:06

FC-02. Importance of self-heating in perpendicular MRAM: modeling and experimental evidence. *D. Apalkov*[1], A. Khvalkovskiy[1,2], V. Voznyuk[1] and V. Nikitin[1] *1. New Memory Technology, Samsung Semiconductor Inc., San Jose, CA, United States; 2. Crocus Nanoelectronics LLC, Moscow, Russian Federation*

In the last few years, there were a number of breakthroughs in understanding the complex behavior of a free layer in perpendicular MRAM [1-4]. Despite that, there are still some experimental observations that cannot be adequately explained. One such example includes the dependence of switching current on the resistance-area product (RA)[5,6]. In this work, we present a comprehensive picture based on modeling and experimental measurements that demonstrates that a number of unsolved effects can be quantitatively explained by the presence of Joule heating during the current pulse application. Our 3D modeling of resistive (Joule) heating of a realistic perpendicular MRAM structure predicts large and very fast (1-3 ns) temperature increase with an applied voltage pulse of amplitude comparable to switching voltages of MRAM cells. Simulation results suggest that depending on the assumed thermal conductivity of the materials surrounding MTJ stack, temperature increase varies between ΔT_{min} and ΔT_{max} as shown in Fig. 1. For experimental verification, we have developed a novel technique [7] to directly measure temperature increase as a function of applied voltage (Fig. 1). This method relies on the temperature sensitivity of the switching field of the reference layer, and unlike a similar technique using the coercivity change of the free layer [8] avoids the unwanted contribution of the spin transfer effect. To understand the implications of the Joule heating on device behavior, we have included temperature increase and associated effects into a micromagnetic model and show that it can explain many phenomena that were previously observed experimentally. As an example, we compare the modeled dependence of switching current on RA with experimental measurements in Fig. 2. In conclusion, we will discuss some other important and not obvious implications of Joule heating on free layer behavior.

[1] L. Thomas, et al., "Solving the Paradox of the Inconsistent Size Dependence of Thermal Stability at Device and Chip-level in Perpendicular STT-MRAM," *IEDM*, 26.4.4, (2015). [2]. A. Khvalkovskiy, et al, " Characterization of the retention times and critical currents of STT-MRAM cells", *SPIE conference, 58th Magnetism and Magnetic Materials conference* (2013). [3] W. H. Butler, et al., "Switching Distributions for Perpendicular Spin-Torque Devices within the Macrospin Approximation," *IEEE Transactions on Magnetics*, 48(12), p. 4684-4700, (2012). [4] D. Apalkov, et al., "Thermal stability determination by current-driven switching: limitations of macrospin model", F1, *The 29th Magnetic Recording Conference (TMRC)* (2018). [5] Z. Zeng, et al., "Effect of resistance-area product on spin-transfer switching in MgO-based magnetic tunnel junction memory cells", *Appl. Phys. Lett.*, 98, 072512 (2011). [6] J. Z. Sun, "Resistance-area product and size dependence of spin-torque switching efficiency in CoFeB-MgO based magnetic tunnel junctions", *Phys. Rev. B* 96, 064437 (2017). [7] A. Khvalkovskiy, "Method of measuring temperature increase during STT switching using reference layer switching", internal report (2014); filed as *USPTO* #10,297,300 (2015). [8]. G. Mihajlovic et al., "Origin of the resistance-area product dependence of spin transfer torque switching in perpendicular magnetic random access memory cells", *arxiv 1905.02673v1 (2019)*.

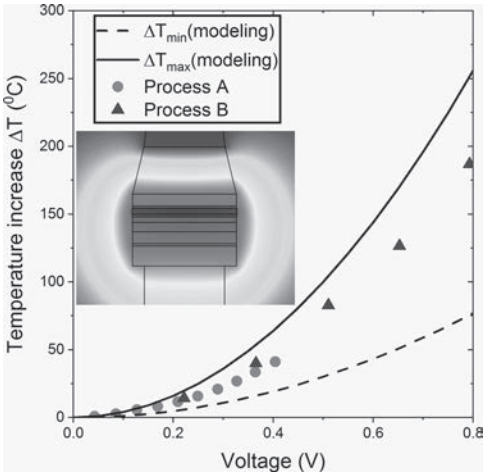


Fig. 1. Comparison of experimental data (symbols) on two different MTJ processes with 3D modeling of Joule heating (lines). The inset shows temperature profile of MTJ from Joule heating modeling.

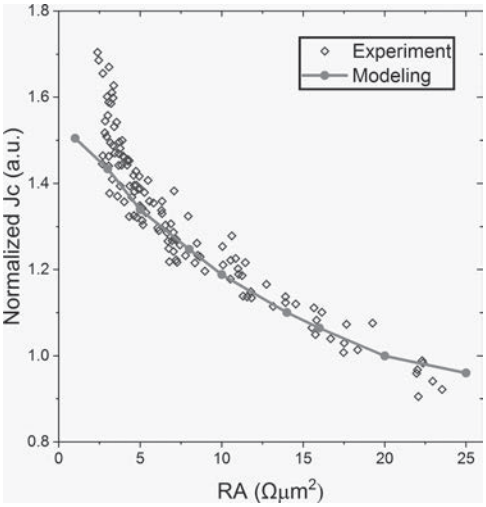


Fig. 2. Dependence of normalized switching current density for P->AP switching on the resistance-area product for 50 ns switching pulses.

2:18

FC-03. Enhancement of Thermal Spin Transfer Torque via Superlattice Design. *P. Priyadarshi*[1] and B. Muralidharan[1] *1. Electrical Engineering, Indian Institute of Technology Bombaay, Mumbai, India*

Apart from current induced spin transfer torque (STT), there is also a possibility to generate STT and consequently, magentization switching via thermal means [1]. In this work, we propose to harness the optical analog of anti-reflective (AR) coats [2,3] in a heterostructure MTJ device, as sketched in Fig. 1, as a means to improve the thermal spin transfer torque (TSTT). Using the spin-resolved non-equilibrium Green's function formalism, we propose the use of an energy bandpass filtering approach in the MTJ superlattice configurations that reports a large spin torque in the linear regime of temperature bias. The use of SL in the device leads to the formation of passbands and forbidden bands in energy for coherent electron transport. We note from Fig. 1(b, c), that the area under T(E) curve in the AR-SL configuration is maximum than the normal SL (NSL) configuration. The adjustment of passband with respect to the Fermi level enables to capture the full positive swing of current distribution due to the contacts. We plot the parallel component of the spin transfer torque due to temperature bias as a function of the number of barriers in the SL structures in Fig. 1(d) and note that the TSTT first increases up to 3 barriers and then almost saturates afterward in both the configurations. The thermally excited spin transfer torque is enhanced by almost five times more with our (AR-SL) device design. Although the thermally driven spin torque is much smaller than the potential driven torque, this technique provides an energy efficient way to switch the magnetization. This opens up a new viable area for spintronics applications. With the existing advanced thin-film growth technology, the optimized superlattice configurations can be achieved.

[1] M. Hatami, G. E. Bauer, Q. Zhang, and P. J. Kelly, "Thermal spin-transfer torque in magnetoelectronic devices, Physical Review Letters, vol. 99, no. 066603, pp. 1â□□4, 2007. [2] P. Priyadarshi, A. Sharma, S. Mukherjee, and B. Muralidharan, "Superlattice design for optimal thermoelectric generator performance," Journal of Physics D: Applied Physics, vol. 51, no. 18, p. 185301, 2018. [3] A. Sharma, A. A. Tulapurkar, and B. Muralidharan, "Band-pass Fabr Perot magnetic tunnel junctions, Applied Physics Letters, vol. 112, no. 19, p. 192404, 2018.

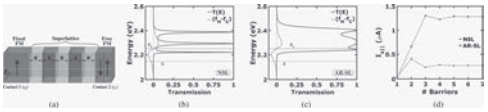


Figure 1 a) Device schematics: A typical MTJ with superlattice-like structure sandwiched between fixed and free ferromagnets. Transmission coefficient as a function of energy through a 4-barrier (a) NSL and (b) AR-SL (in solid blue curve) with the Fermi function difference (in red dash-dot line) created via the temperature gradient. (d) Thermal spin torque profile as a function of number of barriers in NSL and AR-SL.

2:30

FC-04. The magneto-optical Kerr effect for efficient characterization of thermal stability in dense arrays of pMTJs. *S. Van Beek*[1], R. Carpenter[1], S. Kundu[1], S. Couet[1], J. Swerts[1], S. Rao[1], W. Kim[1], Y. Wu[2,1], S.H. Sharifi[1], F. Yasin[1], B.F. Vermeulen[2,1] and G.S. Kar[1] *1. imec, Leuven, Belgium; 2. KU Leuven, Leuven, Belgium*

Magnetic Random Access Memory (MRAM) targets high density arrays of perpendicular Magnetic Tunnel Junctions (p-MTJs) [1]. MRAM is a non-volatile memory, therefore the MTJs require sufficient data retention, which is described by the thermal stability factor Δ, i.e. the ratio between the activation energy needed to switch states and the available thermal energy. We produced arrays with MTJs of 20 nm diameter and spaced at a dense pitch of only 50 nm, see Fig. 1. Evaluating the functionality of these arrays is time consuming and generally based on electric read out of the pillars. In this contribution, we show that magneto-optical Kerr effect (MOKE) measurements enable efficient and in-line characterization of both the magnetic properties and the data retention. We demonstrate this by studying the impact of engineering the stack and etch process. Furthermore, pillar-to-pillar variability is obtained by including various distributions of the Neel-Brown model parameters Δ and anisotropy field B_k. With MOKE, it is possible to distinguish the reversal of the free layer, reference layer and hard layer of the p-MTJ and gain insight in the magnetic properties of the MTJ stack. In this experiment, we use MOKE to characterize the thermal stability factor Δ by performing waiting time experiments [2]. After sweeping the magnetic field from negative saturation up to a positive waiting field, the magnetization is monitored as a function of time (see Fig. 2). The time-dependent switching of the magnetization during the sweep and at the waiting field contains a vast amount of information concerning the Neel-Brown model parameters. Finally, we compare the results with the thermal stability characterization based on electrical read out of the pillars.

[1] S. W. Chung, T. Kishi, J. W. Park, In Proc. IEDM, pp. 659, (2016). [2] P. J. Flanders and M. P. Sharrock, J. Appl. Phys., Vol. 62, 2918 (1987).

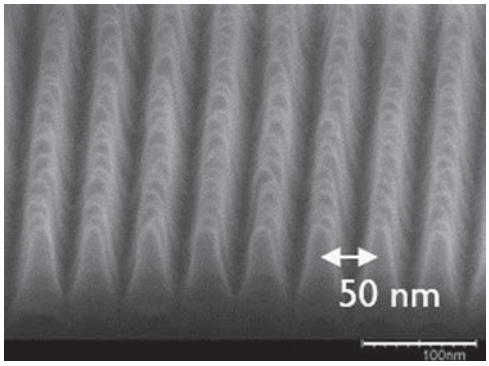


Fig. 1: SEM micrograph of p-MTJ pillars with 20 nm diameter and spaced with a distance of 50 nm.

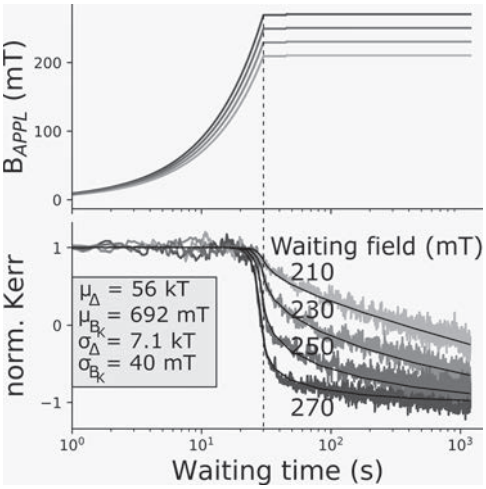


Fig. 2: MOKE measurements at different waiting fields. (Top) Magnetic field (B_{APPL}) ramp up to waiting field. (Bottom) Normalized Kerr signal with 1 and -1 being all pillars are in parallel and anti-parallel configuration, respectively. Black, solid lines represent the Neel-Brown switching model fit with a Gaussian distribution of Δ and B_K.

INVITED PAPER

2:42

FC-05. Giant Spin-Torque induced by Heat-Controlled Magnetic Anisotropy. *M. Goto*[1,2], Y. Wakatake[1], U.K. Oji[1], S. Miwa[1,2], N. Strelkov[3,4], B. Dieny[3], H. Kubota[5], K. Yakushiji[5], A. Fukushima[5] and Y. Suzuki[1,2] *1. Graduate School of Engineering Science, Osaka University, Toyonaka, Japan; 2. Center for Spintronics Research Network (CSRN), Osaka University, Toyonaka, Japan; 3. Univ. Grenoble Alpes, CEA, CNRS, Grenoble INP, INAC-SPINTEC, Grenoble, France; 4. Department of Physics, Moscow Lomonosov State University, Moscow, Russian Federation; 5. National Institute of Advanced Industrial Science and Technology, Tsukuba, Japan*

Heat controlled magnetic anisotropy in nano-magnet is efficient technology for spin control [1]. Generally, while a nano-scale heat engine is inefficient because of huge heat dissipation, the heat dissipation can be suppressed by interfacial thermal resistance at MgO|ferromagnetic metal interface even in the nano-scale [2]. In the MgO|FeB|MgO system, the temperature increase in FeB is enhanced, which provides the giant magnetic anisotropy change. Figure 1 shows the bias voltage dependence of perpendicular anisotropy constant in the CoFeB|MgO|FeB|MgO magnetic tunnel junctions (MTJs). The magnitude of magnetic anisotropy change characterized by the slope of the curve is corresponding to the voltage controlled magnetic anisotropy (VCMA) of 300 fJ/Vm. This value is close to the maximum value of conventional VCMA effect (320 fJ/Vm) which shows rapid anisotropy change [3]. The rapid and large anisotropy change exerts the spin torque on magnetization, which induce the large microwave property, microwave amplification effect. The microwave amplification effect had been studied using dc-biased MTJs [4-5]. However, the microwave was not amplified because the spin-torque was not efficient. We tried the microwave amplification using heat-induced spin torque and succeeded in observing amplification gain of more than 20% as shown in Fig. 2. This value is consistent with the theoretical result using macro-spin calculation. This result opens the way to develop new microwave devices. Also, the heat controlled magnetic anisotropy becomes the efficient spin control technology in nano-scale devices. This research was supported by Bilateral Programs (MEXT), MIC, ImPACT program of the Council for Science, Technology, and Innovation (Cabinet Office, Government of Japan), and JSPS KAKENHI (Grant No. JP16H03850).

[1] M. Goto *et al.*, Nat. Nanotechnol, Vol.14, p.40 (2019). [2] T. Böhnert *et al.*, Phys. Rev. B, Vol.95, p.104441 (2017). [3] T. Nozaki *et al.*, NPG. Asia. Mater, Vol.9, p.e451 (2017). [4] L. Xue, et al., Appl. Phys. Lett, Vol.99, p.022505 (2011), [5] K. Konishi, et al., Appl. Phys. Lett, Vol.102, p.162409 (2013)

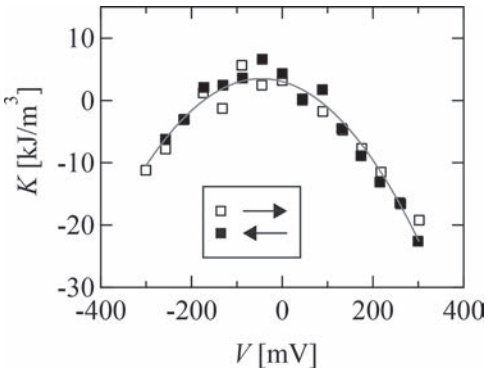


Fig. 1 Voltage dependence of perpendicular anisotropy. Filled and open squares show sweep direction. Solid line is polynomial fitting curve.

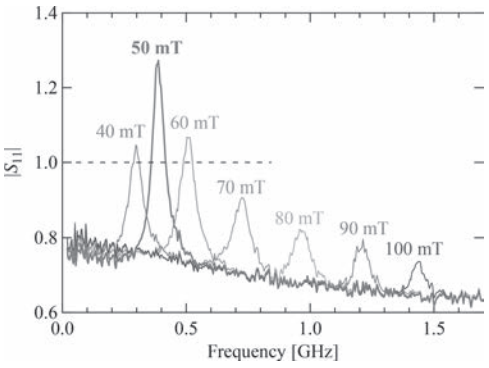


Fig. 2 Microwave reflectivity (S_{11}) spectra under the various magnetic field.

CONTRIBUTED PAPERS

3:18

FC-06. Magneto-Optical Control of Heat Current. *K. Uchida*[1], J. Wang[1] and Y. Takahashi[1] *1. National Institute for Materials Science, Tsukuba, Japan*

Active control of heat flow is crucial for the thermal management of increasingly complex electronic and spintronic devices. In addition to conventional phonon heat transport engineering, spin caloritronics has received extensive attention as a novel heat control principle owing to its high controllability and unique thermoelectric conversion symmetry [1,2]. Here, we demonstrate that the direction of heat currents generated by spin-caloritronic phenomena can be changed simply by illuminating magnetic materials with visible light [3]. The optical control of heat currents is realized through a combination of the spin-driven thermoelectric conversion called an anomalous Ettingshausen effect [4,5] and all-optical helicity-dependent switching of magnetization [6]. This approach enables not only pinpoint manipulation and flexible design of the heat current distribution by patterning the illuminating light but also on/off control of the resulting temperature modulation by tuning the light polarization. These versatile heat control functionalities will open up a new pathway for nanoscale thermal energy engineering.

[1] G. E. W. Bauer, E. Saitoh and B. J. van Wees, Nat. Mater., Vol. 11, p. 391 (2012) [2] S. R. Boona, R. C. Myers and J. P. Heremans, Energy Environ. Sci., Vol. 7, p. 885 (2014) [3] J. Wang, Y. K. Takahashi and K. Uchida (submitted) [4] T. Seki, R. Iguchi, K. Takanashi and K. Uchida, Appl. Phys. Lett., Vol. 122, p. 152403 (2018) [5] T. Seki, R. Iguchi, K. Takanashi and K. Uchida, J. Phys. D, Vol. 51, p. 254001 (2018) [6] C. D. Stanciu *et al*., Phys. Rev. Lett., Vol. 99, p. 047601 (2007)

3:30

FC-07. Effect of cap material on thermal tolerance in a structure with MgO/CoFeB-based free layer/MgO/cap layer. *H. Honjo*[1], M. Yasuhira[1], S. Ikeda[1,3], H. Sato[1,4] and T. Endoh[1,2] *1. Center for Inovative Integrated Electronic Systems, Tohoku University, Sendai, Japan; 2. Graduate School of Engineering, Tohoku University, Sendai, Japan; 3. Center for Spintronics Research Network, Tohoku University, Sendai, Japan; 4. Center for Science and Innovation in Spintronics, Tohoku University, Sendai, Japan*

STT-MRAMs have attracted a considerable attention because they offer the zero standby power required for low power consumption IoT and AI systems. Development of interface-perpendicular-anisotropy type CoFeB/MgO MTJs (p-MTJs) has led to mass production of STT-MRAMs [1-7]. The MgO cap layer (CL) on a free layer (FL) which enhances a perpendicular magnetic anisotropy (PMA) plays a crucial role in determining the performances of p-MTJs. Although we achieved high thermal tolerance in the MTJ with double CoFeB/MgO with MgO-CL by controlling boron composition in the FL [8,9], further improvement of deposition process with lower damage is required for further development of STT-MRAMs [10,11]. Because a CL on the MgO-CL also plays an important role for PMA [12], we investigated the effect of the CL on the MgO-CL on magnetic properties of the FL as well as underlying mechanism for it. First, we investigated the magnetic properties in the MTJ stacks with different CL materials on the MgO-CL. Fig. 1 shows the areal perpendicular anisotropy energy density $K_{\mathrm{eff}}t$ as a function of FL thickness t for MTJs with Ta, Ru and CoFeB CLs after annealing at 400°C. In the studied entire t range, the largest PMA is achieved for the MTJ stack with CoFeB CL. To gain insight into a reason for the behavior, we performed EDX line analysis of the MTJs after annealing at 400°C. In case of the Ta-CL, Ta penetrates the MgO-CL and the oxygen in MgO-CL diffuses into the Ta-CL (Fig.2(a)). Both of them are harmful for the interfacial anisotropy at CoFeB (FL)/MgO-CL, as the PMA of the structure originates from the Fe-O bond [1,13]. In contrast, in case of Ru and CoFeB CLs, oxygen stayed in around MgO-CL (Fig.2(b)-(c)), results in the higher PMA than that of Ta CL. However, in case of the Ru-CL, Ru diffuses into FL, which results in degradation of PMA, resulting in that the FL with CoFeB-CL shows highest PMA among the three structures. This work is supported by CIES's Industrial Affiliation on STT MRAM program, CIES Consortium, JST-OPERA, JST-ACCEL, and CSTI-SIP.

[1] S. Ikeda et al., Nature Mater. 9, 721 (2010). [2] H. Sato et al., Appl. Phys. Lett. 101, 022414 (2012). [3] H. Sato et al., Appl. Phys. Lett. 105, 062403 (2014). [4] Y. J. Song et al., IEDM 2018. [5] K. Lee et al., IEDM 2018. [6] Y- C. Shih et al., VLSI 2018. [7] L. Wei et al., ISSCC 2019. [8] H. Honjo et al., 2015 Symp. on VLSI Tech. Dig. of Tech. Papers, T161 (2015). [9] H. Honjo et al., IEEE. Trans. Magn., Vol. 52, No.7, 3401104 (2016). [10] H. Sato et al., IEDM 2018. [11] H. Honjo et al., IEEE. Trans. Magn., Vol. 53, No.11, 2501604 (2017). [12] M. Bersweiler et al., Appl. Phys. Lett. 113, 172401 (2018). [13] R. Shimabukuro et al., Physica E 42, 1014 (2010).

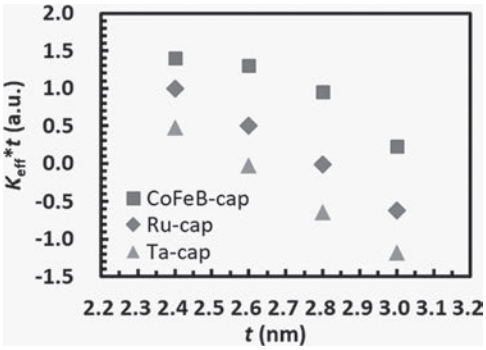


Fig. 1 K_{eff} t as a function of the free layer thickness for MTJs with different CL materials.

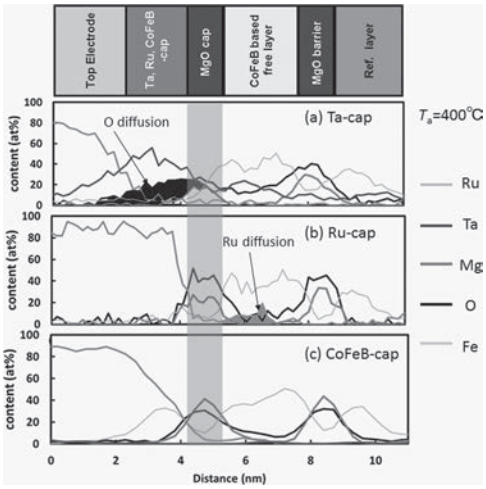


Fig.2 EDX line analysis of the MTJs with various CL annealed at 400°C.

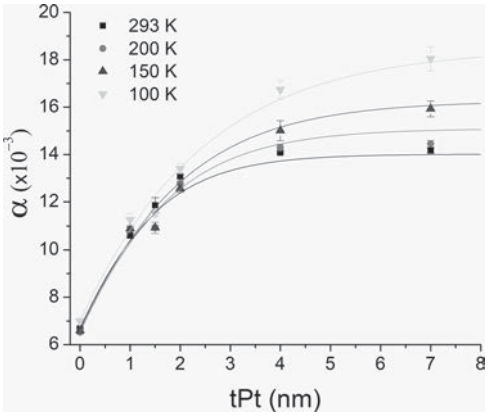
3:42

FC-08. Independence between spin and momentum relaxation characteristic times in Pt, revealed by spin pumping measurements. *C.A. Gonzalez-Fuentes*[1], R.K. Dumas[2], B. Bozzo[3], A. Pomar[3], M. Abellan[1] and C. Garcia[1] *1. Physics, UTFSM, Valparaiso, Chile; 2. Quantum Design, San Diego, CA, United States; 3. ICMAB, Bellaterra, Spain*

We present a broadband Ferromagnetic Resonance study of the Gilbert's damping (α) enhancement due to spin pumping in NiFe/Pt bilayers, with variable thickness of the Pt layer, performed at temperatures from 100 to 300 K. Our samples were fabricated with improved interfacial spin-current transparency by means of a post-annealing (500K) procedure. In the framework of diffusive spin pumping theory [1], we demonstrate that Dyakonov-Perel

(DP) or Elliot-Yaffet (EY) spin relaxation mechanisms acting by alone are incompatible with our observations. Instead, if we assume that the spin relaxation characteristic time (τ_{SF}) is independent of the momentum relaxation characteristic time (τ_p), the qualitative and quantitative agreement with our results is excellent. This is in conflict with the theoretically expected absence of DP mechanism in Pt [2], however, is in concordance with recent observations on similar systems in which was shown that τ_{SF} is nearly constant for the range of temperatures we work with, but interpreted as a compensation between DP and EY mechanisms [3].

[1] Y. Tserkovnyak, A. Brataas, and G. E. W. Bauer, Phys. Rev. B 66, 224403 (2002) [2] M. Dyakonov and V. Perel, Sov. Phys. Solid State 13, 3023 (1972) [3] R. Freeman, A. Zholud, Z. Dun, H. Zhou, and S. Urazhdin, Phys. Rev. Lett.120, 067204 (2018)



Gilbert' s damping dependence of a $Ni_{80}Fe_{20}$ 20nm thickness film capped with Pt layer of variable thickness (tPt) for different temperatures. Scatter points are experimental data and continuous lines are fits to the model of reference [1]

3:54

FC-09. Measurement of the Spin Relaxation Anisotropy in 3d Ferromagnets. *M. Cosset-Chéneau*[1,2], L. Vila[1], D. Gusakova[1], X. Waintal[1], A. Marty[1] and J. Attané[1] *1. Univ. Grenoble Alpes, CNRS, CEA, Grenoble INP, IRIG-SPINTEC, Grenoble, France; 2. Département de Physique, Ecole Normale Supérieure de Lyon, Lyon, France*

The relaxation of a spin current into a ferromagnetic material occurs through different processes depending on the spin currents' polarization orientation. For a polarization collinear with the material magnetization, the relaxation occurs through diffusive processes controlled by the spin diffusion length [1]. When the polarization is transverse with the magnetization, the relaxation is driven by ballistic processes due to band structure mismatch and non-coherent spin precession [2]. Despite being a key ingredient for the understanding of phenomena like Spin Transfer Torque, this anisotropy has never been directly observed so far. In this presentation, we report the observation of the spin relaxation anisotropy on a single device by using a spin absorption method in Lateral Spin Valves (LSVs) [3]. Using a magnetic field, we control the relative orientation between the spin current polarization and the magnetization of a nanodisk-shaped ferromagnetic absorber (fig. 1). We observed that the efficiency of the spin current absorption increases when this polarization and the absorber magnetization have transverse directions. We will present a device that allows the study of spin transport in a LSV with non-collinear ferromagnetic component. By demonstrating a good control over its magnetic states, we will show that we indeed observed the spin current relaxation anisotropy in a single device. We carried out an analysis by introducing bulk characteristic lengths of the transverse spin relaxation, and the spin mixing conductance describing transverse interfacial spin relaxation processes. This data analysis points out the role of both interfacial and bulk contribution in the non-collinear spin current relaxation.

[1] T. Valet and A. Fert, Phys. Rev. B 48, 7099 (1993) [2] C. Petitjean et al., Phys. Rev. Lett. 109, 117204 (2012) [3] G. Zahnd et al., Phys. Rev. B 98, 175514 (2018)

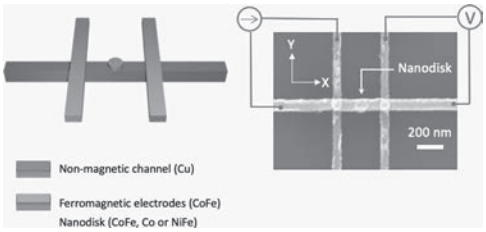


Fig. 1 : Drawing and SEM picture of the device used for the absorption anisotropy measurement. The nanodisk absorbs the spin current that flows between the ferromagnetic electrodes. Its isotropic shape allows to change its magnetization orientation by using a weak external magnetic field.

4:06

FC-10. Spin transport and conflicting values of spin diffusion length in FM/HM systems. *C. Swindells*[1], A. Hindmarch[1], A. Gallant[2] and D. Atkinson[1] *1. Department of Physics, Durham University, Durham, United Kingdom; 2. Department of Engineering, Durham University, Durham, United Kingdom*

Understanding interfacial spin transport is fundamental for modern spintronic devices. To fully exploit related interface phenomena, such as spin-orbit torques or spin-pumping, the dependence of the structure and properties of the interface on key transport parameters must be quantified. Our previous work has shown the enhancement in interfacial transport with improved structural matching between FM and NM materials [1], as well as the dependence of spin transport on the thickness of the NM layer [2]. The nature of the parameters governing this transport however remains a subject of debate with the reported values seemingly affected by the different experimental methods and analyses. In particular, experimental values for the spin-diffusion length of the NM layer are inconsistent; for Pt, spin diffusion lengths have been reported from 1 nm up to 10 nm [3,4] depending on the method used. The role of the interface structure and its influence on the effective spin-diffusion length are also unclear. Here we present results and new analysis of a recently published study (Swindells et al, Phys. Rev. B (2019)) [5] of spin transport in a variety of crystalline and amorphous HM/FM and FM/HM systems that fully quantifies spin transport across the interface. Building upon the proposed linkage of resistivity and the spin diffusion length [6] our new analysis of experimental FMR data takes into account the dependence of the damping on both the NM and FM thickness (see figure 1) and resolves the differences in previously reported values for the spin diffusion length of Pt, see table 1. This analysis demonstrates that larger values for the spin diffusion length are correct, and lower values obtained from dynamic spin-pumping studies are limited by an incomplete understanding of the role of the interface. This new understanding provides a more complete account of interfacial spin transport phenomena.

[1] M. Tokaç, S. et al., Phys. Rev. Lett. 115, 056601 (2015). [2] S. Azzawi, et al., Phys. Rev. B 93, 054402 (2016) [3] C. Stamm, et al., Phys. Rev. Lett. 119, 087203 (2017). [4] W. Zhang, et al., Appl. Phys. Lett. 103, 242414 (2013). [5] C Swindells, A Hindmarch, A Gallant and D Atkinson, Phys. Rev. B 99 064406 (2019) [6] M.-H. Nguyen, D. C. Ralph, and R. A. Buhrman, Phys. Rev. Lett. 116, 126601 (2016).

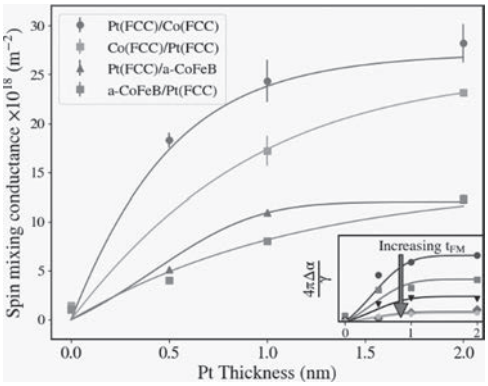


Fig 1: Increase in measured effective spin mixing conductance for various FM/NM interfaces as a function of Pt thickness. Inset is the associated interfacial in damping for one FM/NM case.

Sample	Spin-flip Probability ε	Constant λ_{sf}	Thickness Dependent λ_{sf}
Pt(fcc)/Co(fcc)	0.17	1.6 nm	9.4 nm
Co(fcc)/Pt(fcc)	0.26	1.6 nm	9.5 nm
Pt(fcc)/a-CoFeB	0.11	1.6 nm	6.6 nm
Co(hcp)/Ru(hcp)	0.004	-	22 nm
Co(fcc)/Ru(hcp)	0.003	-	22 nm

Table 1: Interfacial transport parameters for various FM/NM and NM/FM systems extracted from new analysis

4:18

FC-11. Reversible tuning of Cu spin relaxation length by ionic gating at room temperature. *X. Shen*[1], Y. Cai[1], Y. Wu[2] and Y. Ji[1] *1. Department of Physics and Astronomy, University of Delaware, Newark, DE, United States; 2. Department of Physics, State Key Laboratory of Surface Physics, Fudan University, Shanghai, China*

Electric control of spin current is long-sought-after, because of the prospect of enabling a spintronic version of the field effect transistors. [1] An injected spin current in a material decays over distance because of the ubiquitous process of spin relaxation, characterized by the spin relaxation length (λ_s). Therefore, one can control the spin current by tuning λ_s. In this work, we demonstrate electrical tuning of λ_s in mesoscopic Cu channels via ionic gating. Mesoscopic nonlocal spin valves (NLSV), each consisting of a Cu channel and a pair of Permalloy (Py) electrodes, are fabricated by using E-beam lithography. A gate electrode is placed 5 μm away from the Cu channel. A drop of electrolyte ($PEO/LiClO_4$) is applied onto the sample, covering the entire area including the NLSV and the gate. Cations (anions) accumulate on the surface of Cu channel when a positive (negative) gate voltage is applied while the channel is grounded. An intense electric field is generated at the Cu/electrolyte interface, due to the formation of an electric double layer. The measured nonlocal spin signals at 295 K show a clear dependence on the gate voltages. Figure 1 (a) and (b) show spin signals of 2.17 mΩ under +1.2 V and 0.98 mΩ under -1.5 V respectively, differing by 120%. Figure 1 (c) shows that the spin signals are tuned reversibly and reproducibly as the gate voltage cycles through +1.2 V, 0 V, and – 1.5 V. Figure 1 (d) demonstrates that the resistivity of the Cu channel is also tuned by the gate voltages with a tuning range of 5%. In a comparison experiment, we fabricate NLSVs with Al channels instead. No tuning is observed up to gate voltages of ± 3.0 V. This demonstrates that the tuning effects originate from the Cu channel rather than the Py electrodes. With the assumption of 10% injection and detection spin polarizations at 295 K, we estimate that the Cu spin relaxation length is tuned between 300 nm and 380 nm.

[1] S. Datta and B. Das, Appl. Phys. Lett. 56, 665 (1990)

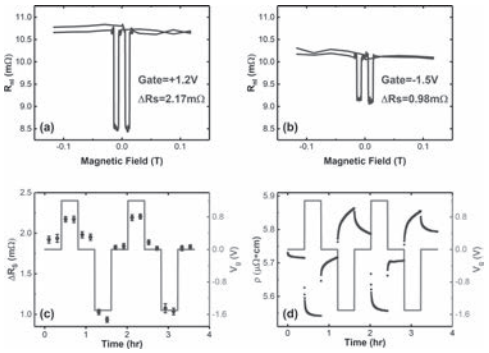


Fig. 1: (a) Spin signal under +1.2 V; (b) Spin signal under -1.5 V; (c) Spin signal (blue symbols) and gate voltage (red line) versus measurement time; (d) Resistivity (blue symbols) and gate voltage (red line) versus measurement time.

Session FD
MAGNETO-CALORIC AND MAGNETO-ELASTIC MATERIALS II

R Gopalan, Chair
International Advanced Research centre for Powder Metallurgy and Materials, Chennai, India

INVITED PAPER

1:30

FD-01. Exploiting Hysteresis in a Multicaloric Cooling Cycle.
T. Gottschall[1], A. Gràcia-Condal[2], A. Taubel[3], M. Fries[3], L. Pfeuffer[3], L. Mañosa[2], A. Planes[2], K. Skokov[3] and O. Gutfleisch[3] *1. Helmholtz-Zentrum Dresden-Rossendorf, Dresden, Germany; 2. University of Barcelona, Barcelona, Spain; 3. TU Darmstadt, Darmstadt, Germany*

Although there have been improvements in efficiency, the working principle for conventional cooling - vapor-compression - has remained largely unchanged for more than 100 years. However, with the world's increasingly affluent population demanding more comfortable living and working conditions, it is vital that we address the development of much more efficient cooling technologies as an urgent priority. Most research is focused on solid-state refrigeration and one of the caloric effects – electrocaloric, magnetocaloric, barocaloric or elastocaloric - where the material's entropy is forced to change under the application of an electrical, magnetic, or mechanical field [1]. The magnetocaloric effect, the most studied of the three, manifests itself as a change in the material's temperature as it is exposed to a magnetic field [2]. However, more than 20 years of research into materials exhibiting the giant magnetocaloric effect did not lead to the introduction of commercial products yet. In this work, we report on the novel approach that the thermal hysteresis, which is inherent in first-order magnetostructural transformations in magnetocaloric materials need not be the obstacle as it is always assumed. On the contrary, we demonstrate here that the thermal hysteresis of Heusler alloys is actually useful and can be exploited [3]. The hysteresis of the transition allows us to lock-in the ferromagnetic phase as the magnetizing field is removed and so the magnetic field is only required for a very short time. A second stimulus, uniaxial load, then causes the multicaloric material to transform back into its paramagnetic phase. This hysteresis-positive approach drastically reduces the costs of the magnetic field source made of expensive Nd–Fe–B permanent magnets because, in this case, the volume over which the magnetic field needs to be generated and maintained is very small. At the same time, focusing the magnetic field means we can double the magnetic field strength up to 2 T. In addition, the mass ratio between the magnetocaloric material and the permanent magnet can be increased, which allows scaling of the cooling power of a device simply by increasing the refrigerant body. The technical feasibility of this hysteresis-positive approach is demonstrated using Ni–Mn–In Heusler alloys. This novel solid-state refrigeration cycle could lead to an enhanced usage of the giant magnetocaloric effect in commercial applications.

[1] T. Gottschall, K. P. Skokov, O. Gutfleisch et al., Adv. Funct. Mater. 27, 1606735 (2017). [2] J. Liu, T. Gottschall, O. Gutfleisch et al., Nat. Mater. 11, 620 (2012). [3] T. Gottschall, Adrià Gràcia-Condal, Lluís Mañosa et al., Nat. Mater. 17, 929 (2018).

CONTRIBUTED PAPERS

2:06

FD-02. Tunable first order transition in La(Fe,Cr,Si)$_{13}$ compounds: retaining magnetocaloric response despite a magnetic moment reduction.
L.M. Moreno-Ramirez[1], C. Romero-Muñiz[2], J. Law[1], *V. Franco*[1], A. Conde[1], I.A. Radulov[3], F. Maccari[3], K. Skokov[3] and O. Gutfleisch[3] *1. Sevilla University, Sevilla, Spain; 2. Autonomous University of Madrid, Madrid, Spain; 3. TU Darmstadt, Darmstadt, Germany*

One usual method to seek for improved magnetocaloric effect in series of alloys and compounds is to increase their magnetic moment. In this work we demonstrate that even for doping elements that decrease the magnetic moment, the magnetocaloric response can be retained, in connection with the details of the phase transition that the material undergoes. To identify first order phase transition (FOPT), a recently proposed criterion based on the field dependence of magnetocaloric effect ($\Delta s_T(T,\Delta H)=a(T)\ \Delta H^{n(T,H)}$) has been used [1], whereby the field exponent n yields an overshoot above 2. In addition, n at transition temperature ($n(T_{trans})$) can further reveal the critical composition of the crossover of FOPT to second order phase transition (SOPT) as $n(T_{trans})<0.4$ indicates FOPT, $n(T_{trans})>0.4$ for SOPT and $n(T_{trans})=0.4$ as the crossover [2]. In this work, we report Cr-doped La(Fe,Si)$_{13}$ compounds (for $x \leq 0.6$ in $LaFe_{11.6-x}Cr_xSi_{1.4}$) can exhibit a maintained magnetocaloric response despite the dopant diluting the overall magnetic moment [3]. Unlike other transition metal dopants (e.g. Co or Mn), Cr occupies 8b sites and antiferromagnetically couples to Fe in the $NaZn_{13}$-type structure. Despite the reduction in overall magnetic moment, the magnetocaloric response is retained up to $x\approx0.3$ due to the increment of the FOPT-character (which is characterized by the reduction of $n(T_{trans})$ values). For higher Cr content, the series exhibit a crossover from FOPT to SOPT. These features are presented in Figure 1. Moreover, a direct relation between the first order character and thermal hysteresis is observed. Results from both experimental and first principle calculations are found in good agreement, indicating that they illustrate the importance of the nature of phase transition in both magnetocaloric response as well as its compositional dependence.

[1] J Y Law et al. Nat. Commun., 9,2680 (2018). [2] V Franco et al. J. Phys. D. Appl. Phys., 50, 414004 (2017). [3] L. M. Moreno-Ramírez et al. Acta Mater., doi:10.1016/j.actamat.2019.06.022 (2019).

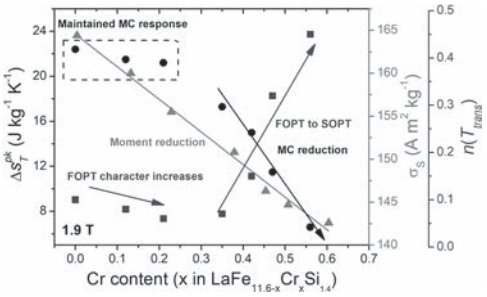


Fig. 1: Compositional dependence of maximum isothermal entropy change (Δs_T^{pk}), saturation magnetization (σ_s) and exponent *n* at the transition temperatures in $La(Fe,Cr,Si)_{13}$.

2:18

FD-03. Effect of martensite modulation on magnetocaloric properties of Ni-Mn-In, Ni-Mn-Sn and Ni-Fe-Ga melt-spun ribbons. *G. R*[1] and K. Srikanti[1] *1. International Advanced Research Centre for Powder Metallurgy and New Materials (ARCI), Chennai, India*

Ni-Mn-*X* (*X* = Ga, In, Sn) Heusler alloys have enormous potential for technological applications due to a rich variety of properties ranging from shape memory effect, magnetocaloric effect, magnetoresistance, exchange bias behavior [1-6]. These technologically important properties mainly arise due to the martensitic transition, which in many cases is coupled with the magnetic transition, giving rise to a first order magnetostructural transition from an ordered austenite (cubic) phase to a less ordered martensite (tetragonal or orthorhombic) phase on cooling. In this work we investigate the structure of the martensite twin boundaries in melt-spun samples through Transmission Electron Microscopy and discuss the microstructure in conjunction with the magnetocaloric properties. We have chosen three alloys *viz*. Ni Mn Sn, Ni Mn In and Ni Fe Ga for processing the ribbons by melt-spinning technique. Among several compositions investigated in the present study, $Ni_{50}Mn_{36.5}Sn_{13.5}$, $Ni_{50}Mn_{36.5}In_{13.5}$ and $Ni_{50}Fe_{44}Ga_6$ ribbons have shown the martensite and magneto structural transformations to occur close to 300 K. It is observed that among all the above-mentioned systems under study, Ni-Mn-In melt-spun ribbons exhibit huge magnetic entropy of 26 J/kg-K at 5 T. Figure 1 shows the Selected Area Electron Diffraction (SAED) pattern of Melt-spun (a) Ni-Mn-In, (b) Ni-Mn-Sn and (c) Ni-Fe-Ga. It is found that Ni-Mn-In sample has martensite structure with low modulation (< 5M) as compared to Ni-Mn-Sn (5M) and Ni-Fe-Ga (14M). A large positive magnetic entropy change at 2 T was obtained in Ni-Mn-In (7.5 J/kg-K) as compared to Ni-Mn-Sn (6 J/kg-K) and Ni-Fe-Ga (1.1 J/kg-K) (Fig. 1 (d-f)). The correlation between the order of modulation and magnetic entropy would be discussed in detail in terms of magnetic domains and twin planes. Apart from this we would be also presenting on the enhancement in magnetocaloric properties of Ni-Mn-Sn alloys with doping such as B.

1. T. Krenke, E. Duman, M. Acet, Nature 4, 450 (2005). 2. S.Kavita, V.V.Ramakrishna, P.Yadav, J.Alloys and Comp, 795, 519 (2019) 3. J. Du, Q. Zheng, W. J. Ren, J. Phys. D: Appl. Phys. 40, 5523 (2007). 4. S. Y. Yu, L. Ma, G. D. Liu, Appl. Phys. Lett. 90, 242501 (2007). 5. V. K. Sharma, M. K. Chattopadhyay, K. H. B. Shaeb, Appl. Phys. Lett. 89, 222509 (2006). 6. M. Khan, I. Dubenko, S. Stadler, Appl. Phys. Lett. 91, 072510(2007).

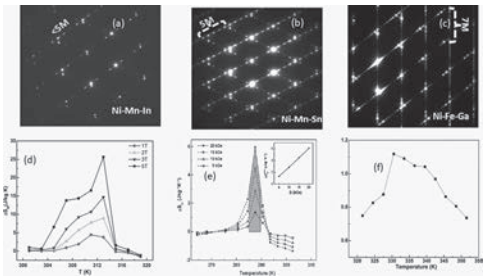


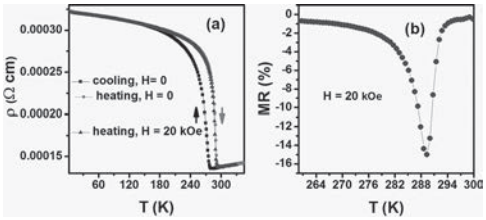
Fig.1 (a-c) SAED patterns of the Ni-Mn-In, Ni-Mn-Sn and Ni-Fe-Ga melt spun ribbons. Fig 1 (d-f) Magnetic entropy of the Ni-Mn-In, Ni-Mn-Sn and Ni-Fe-Ga melt spun ribbons.

2:30

FD-04. Magneto-transport and magnetocaloric properties of bulk and rapidly solidified nanostructured Ni-Co-Mn-Ti based shape memory alloys. *A.K. Pathak*[1], X. Liu[1], H. Bez[1], Y. Mudryk[1] and V.K. Pecharsky[1] *1. Materials Science and Enginering, Ames Laboratory, Ames, IA, United States*

Ferromagnetic shape memory alloys, which upon heating undergo magneto-structural transitions (MST) from antiferromagnetic/paramagnetic martensite to ferromagnetic austenite followed by second-order transformation to the paramagnetic austenite phase, are of considerable interest due to their potential applications in multi-calorics and sensors. Here we report the investigation of electrical and thermal conductivities in rapidly solidified nanostructured $Ni_{37.5}Co_{12.5}Mn_{35}Ti_{15}$ ribbons that exhibit giant magnetocaloric effect near room temperature [1]. We observed an anomaly in thermal conductivity in the vicinity of the MST, and the thermal conductivity was found to be 9.7 W m^{-1} K^{-1} at T = 300K. The magnetoresistance of the ribbons was found to be -15% at T = 289 K and H = 20 kOe. Thermomagnetic and electrical transport measurements indicate the Ni-Co-Mn-Ti bulk- and melt-spun-alloys show similar thermal hysteresis (~20 K). Temperature-dependent x-ray powder diffraction shows the sluggish MST from the high-temperature B2 (CsCl-type) phase to the low-temperature modulated M5 phase with thermal hysteresis of about 20-30 K, in agreement with the transport and magnetic measurement results. The effect of microstructure on hysteresis was studied as well. Our results indicate that the thermal hysteresis is not sensitive to microstructure of alloy, but is intimately related to the lattice misfit between the austenitic and martensitic phases. Work was funded through CaloriCool® – the Caloric Materials Consortium – which is a part of the Energy Materials Network. The Consortium is funded by the Advanced Manufacturing Office and is managed jointly by the Advanced Manufacturing Office and Building Technologies Office of the Office of Energy Efficiency and Renewable Energy of the United States Department of Energy. The research was performed at the Ames Laboratory. Ames Laboratory is operated for the U.S. Department of Energy by Iowa State University under contract No. DE-AC02-07CH11358.

[1] Bez et al., Acta Materialia 173, 225 (2019)



Electrical transport properties of $Ni_{37.5}Co_{12.5}Mn_{35}Ti_{15}$ ribbons. (a) Heating and cooling electrical resistivity curves as functions of temperature at H = 0 and 20 kOe and (b) corresponding magnetoresistance at H = 20 kOe.

2:42

FD-05. Impact of atomic disorder on the thermodynamic properties of ferromagnetic Fe_2MnSi – a computational study. H.G. Trigo[1], J.N. Gonçalves[1], B.M. Pimentel[2], D.L. Rocco[2], M.S. Reis[2] and *J.S. Amaral*[1] *1. Physics and CICECO, Universidade de Aveiro, Aveiro, Portugal; 2. Instituto de Física, Universidade Federal Fluminense, Rio de Janeiro, Brazil*

Heusler alloys are intermetallic compounds which exhibit many technologically relevant properties, including semi-metallic behavior, and strong magneto volume coupling [1]. The richness in the properties of this family of alloys lies in the wide range of possible doping compositions of magnetic and non-magnetic ions. In terms of applications in magnetic refrigeration, Heusler alloys (such as NiMnInCo) can show a giant magnetocaloric effect (MCE) [2], which demonstrates how tuning the thermodynamic properties of these alloys can lead to the discovery of new high-performance refrigerants. Fe2MnSi is a well-known ferromagnetic alloy, typically referred to as having a L21 structure. Still, in earlier works, a small degree (~12%) of DO3 disorder was observed via neutron scattering experiments [3]. This disorder corresponds to an exchange of atomic positions between Fe (A, C positions) and Mn (B position). Recently, it was shown through a combined Density Functional Theory (DFT) and Monte-Carlo (MC) approach that this 12% amount of DO3 disorder would lead to a remarkable increase of the Curie temperature (TC) from 160 K of the pure system to 200 K of the disordered one [4]. In this work, we computationally explore the impact of DO3 disorder on the magnetic and magnetocaloric properties of the Fe2MnSi alloy. Our detailed simulations show how the disorder at the atomic level strongly impacts the MCE properties of the alloy. To obtain an agreeable computational estimate of the MCE of this material compared to experimental results, the DO3 disorder needs to be considered not only as an average value, but as a distribution of disorder, which has a strong impact on the estimated MCE and Tc values, as shown in Fig. 1. The work here presented opens the way to explore the effects of atomic disorder on the magnetic and magnetocaloric properties of other Heusler alloys and of other families of materials where atomic disorder can easily occur.

[1] N. R. Checca, R. J. Caraballo-Vivas, A. A. Coelho et al., Materials & Design, Vol. 143, p. 268 (2018). [2] J. I. Pérez-Landazábal, V. Recarte, V. Sánchez-Alarcos et al., Scientific Reports Vol. 7, p. 13328 (2017). [3] K.A. R. Ziebeck, P. J. Webster, Phil. Mag., Vol. 34, p. 973 (1976). [4] M. Lezaic, P. Mavropoulos, S. Blügel et al., Phys. Rev. B Vol. 83, p. 094434 (2011)

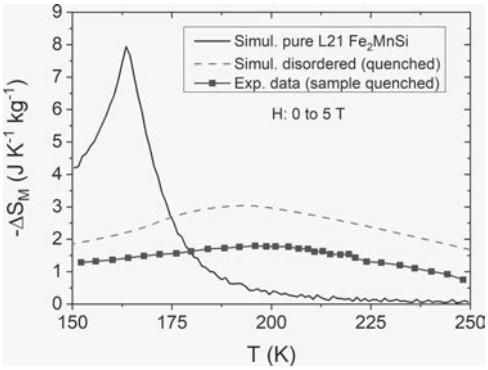


Fig. 1: Estimated MCE of Fe2MnSi for ΔH: 0 to 5 T. The solid line corresponds to the pure L21 structure, the dashed line to a disordered one, where the distribution of disorder comes from a system quenched at 1300K. The blue dotted lines show experimental data of a quenched sample.

2:54

FD-06. Tuning disorder in a first-order magnetoelastic transition. *M. Trassinelli*[1], S. Cervera[1], M. LoBue[2], E. Fontana[1,3], M. Eddrief[1], V.H. Etgens[2], E. Lamour[1], A. Lévy[1], S. Macé[1], M. Marangolo[1], S. Steydli[1] and D. Vernhet[1] *1. Institut des NanoSciences de Paris, CNRS, Sorbonne Université, Paris, France; 2. SATIE, CNRS, ENS Paris-Saclay, Université Paris-Saclay, Cachan, France; 3. Department of Applied Science and Technology, Politecnico di Torino, Torino, Italy*

Taming first order phase transitions and mastering the associated thermal hysteresis [1, 2] are the main objectives when studying the integration of caloric materials into energy conversion devices. The suppression of irreversible phenomena preserving the key properties of the phase transition (i.e their critical temperature T_c and the caloric effects) are the key issues in order to achieve energy efficient, high throughput devices. Hysteresis reduction has been achieved varying the material composition, the microstructure design, and tuning the phase change using an external control parameter [3–5]. We recently reported hysteresis suppression in manganese arsenide films (MnAs) after ion bombardment [6]; this result represents a potentially relevant tool to investigate the role of quenched disorder on phase transitions, a fundamental problem studied since four decades [7, 8]. Ion bombardment is often used to tailor material properties but the mechanism underlying their change is seldom understood. Here we show that in MnAs *150* nm thick films irradiated under different conditions (fluence, ion kinetic energy and mass), hysteresis reduction under weak fluence, and phase transition rounding after a stronger one, are both directly related to the number of atom-atom effective collisions, whereas they do not depend on the implanted ion density. This allows to tune defect density in order to study the interplay between pre-transition phenomena (i.e. precursors) and hysteresis reduction (i.e. metastable states decay). Our analysis suggests a weak T_c dependence on the average induced defect density, making local density fluctuations the leading mechanism responsible for the reduction of the critical nucleation barrier (i.e. hysteresis suppression), and of the transition rounding observed after a certain density threshold.

[1] F. Guillou, G. Porcari, H. Yibole et al., Adv. Mater., Vol. 26, pp. 2671 (2014) [2] O. Gutfleisch et al., Phil. Trans. R. Soc. A, Vol. 374, p. 20150308 (2016) [3] N. Trung, Z. Ou, T. Gortenmulder, et al., Appl. Phys. Lett., Vol. 94, p. 102513 (2009) [4] J. Lyubina, J. Appl. Phys., Vol. 109, p. 07A902 (2011) [5] J. Liu, T. Gottschall, K. P. Skokov,et al., Nature materials, Vol. 11, p. 620 (2012) [6] M. Trassinelli et al., Appl. Phys. Lett., Vol. 104, p. 81906 (2014) [7] A. Brooks Harris, J. Phys. C: Solid State Physics, Vol. 7, p.1671 (1974) [8] Y. Imry and M. Wortis, Phys. Rev. B, Vol. 19, p.3580 (1979)

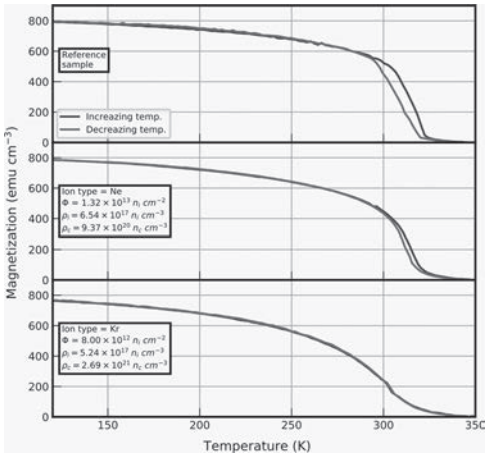


Fig. 1: Magnetization as a function of increasing or decreasing temperature (blue and red) for the reference sample and for the irradiated samples with different type of ions and fluences.

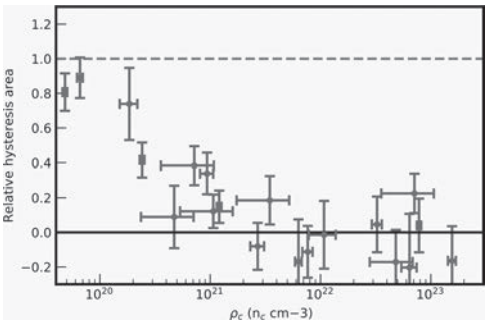


Fig. 2: Thermal hysteresis relative area with respect to the pristine sample as function of the induced collision density.

3:06

FD-07. Magnetofunctional response of FeRh nanoparticles obtained by novel processing routes. V. Sharmar[1], S. Gupta[2], A. Biswas[2], H. Fu[3], R.L. Hadimani[1], V.K. Pecharsky[2] and *R. Barua*[1] *1. Department of Mechanical & Nuclear Engineering, Virginia Commonwealth University, Richmond, VA, United States; 2. Division of Materials Sciences and Engineering, Ames Laboratory, Ames, IA, United States; 3. School of Physics, University of Electronic Science and Technology, Chengdu, China*

Materials that exhibit coupled magnetic and structural (magnetostructural) phase transitions can realize strong responses to perturbations in magnetic field, temperature, and strain. Nanostructuring of such materials offers a route to tailor both the transitions and functional responses by modifying the balance between surface and volume free energies of finite systems, potentially enabling emerging applications. To this end, near-equiatomic compositions of the B2 phase of FeRh is of interest in this study. Synthesis of FeRh nanoparticles (NPs) using traditional sol-gel wet-chemistry methods is fraught with challenges associated with phase purity, chemical inhomogeneity, and poor functional response [1,2]. Hence, here we focus on Fe_xRh_{1-x} NPs ($0.40 \leq x \leq 0.50$; dia = 40–100 nm) synthesized via two novel approaches - (i) Thermal decomposition method using precursor $FeCl_3$ and $RhCl_3$ solutions; (ii) Solvent-free mechanochemical co-reduction of $FeCl_2$ and $RhCl_3$. X-ray diffraction reveals that the as-made NPs exhibit an *fcc* structure, which can be converted into the ordered B2 structure upon annealing. Magnetothermal measurements indicate that depending upon particle size and composition, the magnetostructural transition temperatures (T_t) of the NPs can be tuned between 350 K and 415 K. The overall magnetization of the mechanochemically-processed NPs is significantly larger than the particles produced by thermal decomposition (see Fig 1). All samples show the presence of a secondary ferromagnetic phase below T_t – a feature attributed to chemical inhomogeneity due to presence of off-stoichiometric $Fe_{1-x}Rh_x$ ($x > 0.55$) phase. Last, the magnetocaloric response of promising nanoparticle compositions was evaluated and a maximum magnetic entropy change of ΔS_{mag} ~9 J/kgK at 2 T was noted (see inset). It is anticipated that the magnetocaloric FeRh NPs will be useful for biomedical aplications, mainly thermal magnetic resonance imaging and magnetic hyperthermia therapy. Acknowledgements: NSF (1726617) and U.S. Department of Energy (DE-AC02-07CH11358).

[1] Z. Jia et. al., *Appl. Phys. Lett.* 93.2, 022504, 2008 [2] H. Ko et. al., *J. Appl. Phys.* 103.7, 07D508, 2008

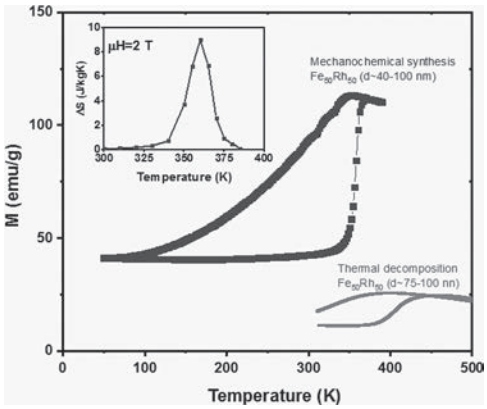


Fig 1. Magnetothermal properties of FeRh nanoparticles synthesized via different processing methods. Inset shows magnetocaloric response of mechanochemically processed nanoparticles.

3:18

FD-08. Investigation of the Magnetic Anisotropy in Sputtered Ga-rich Fe-Ga Thin Films. A. Muñoz-Noval[1], E. Salas-Colera[3,4], S. Fin[2], A. Begué[5], I. Hontecillas[1], D. Bisero[2], M. Ciria[5] and *R. Ranchal*[1] *1. Complutense University, Madrid, Spain; 2. Ferrara University, Ferrara, Italy; 3. BM25-Spline, ESRF., Grenoble, France; 4. Instituto de Ciencia de Materiales de Madrid-CSIC, Madrid, Spain; 5. ICMA-Universidad de Zaragoza, CSIC, Zaragoza, Spain*

Fe-Ga alloys are promising materials for magneto-elastic (ME) applications [1-2] since they are rare-earth free systems with large magnetostriction and low coercivity. The magnetostriction shows two maxima around 20 at.% and 28 at.%, respectively, being higher in the Ga-rich range. The reported strong influence of processing on the magnetostrictive properties of bulk alloys has pointed out the necessity of a precise control of the growth method when trying to develop FeGa nanosystems [2]. In our recent investigations about Ga-rich Fe-Ga thin films, we have explored how the flow regime of the sputtering technique can be used to tune the in-plane magnetic anisotropy [3]. Furthermore, we have also studied how anisotropy is also dependent on the layer thickness [4]. Our structural investigation combining x-ray diffractometry (XRD) and x-ray absorption near the edge spectroscopy (XANES) together with the magnetic characterization done by vibrating sample magnetometry (VSM) and magneto-optical Kerr effect (MOKE) indicate that both growth parameters and thickness have an influence on the structural phases present in the Fe-Ga films. The increase of B2 phase together with a preferential alignment of Ga-pairs that tetragonally distort the lattice seem to play a role on the enhancement of the magnetic anisotropy (fig. 1-2). When modifying the growth power for the sputtering deposition similar conclusions can be reached [5]. The effective ME coefficient is around -7.6 MPa for 250 nm films with both isotropic and preferential alignment of the Ga-pairs. This result suggests that the ME stress is barely affected by a non-homogeneous Ga pair distribution, although it is a fundamental parameter to explain de magnetic anisotropy in these films.

[1] A. E. Clark et al., IEEE Trans. Magn., Vol. 36, p. 3238 (2000). [2] Q. Xing et al., Acta Materialia, Vol.56, p. 4536 (2008). [3] A. Muñoz-Noval et al., Phys. Rev. B, Vol. 93, p. 214408 (2016). [4] A. Muñoz-Noval et al., J. Alloys Compnd., Vol. 745, p. 413 (2018). [5] A. Muñoz-Noval et al., J. Phys. Chem. C, Vol. 123, p. 13131 (2019).

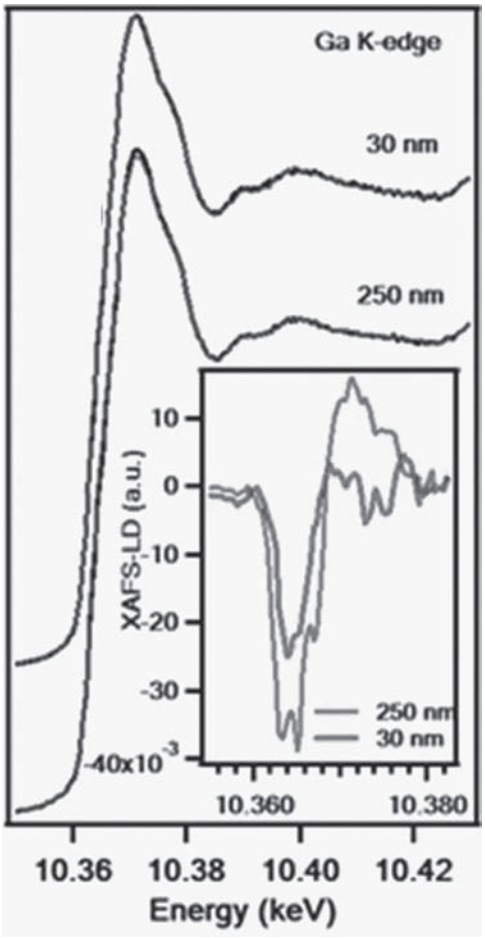


Fig. 1. XANES spectra in the Ga-K edge for FeGa layers with a thickness of 30 nm and 250 nm. The inset corresponds to the difference between the normal and the grazing incidence spectra for each sample.

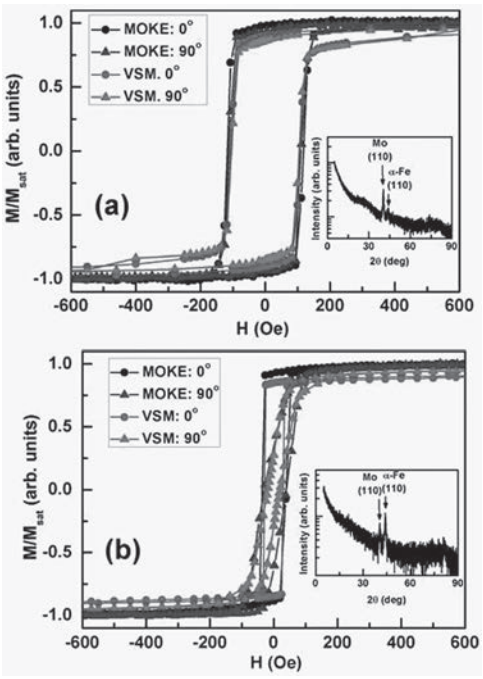


Fig. 2. Room temperature VSM and MOKE hysteresis loops measured with the applied magnetic field in the sample plane for FeGa layers with a thickness (a) 30 nm, and (b) 250 nm. Each inset corresponds to the XRD pattern for each sample.

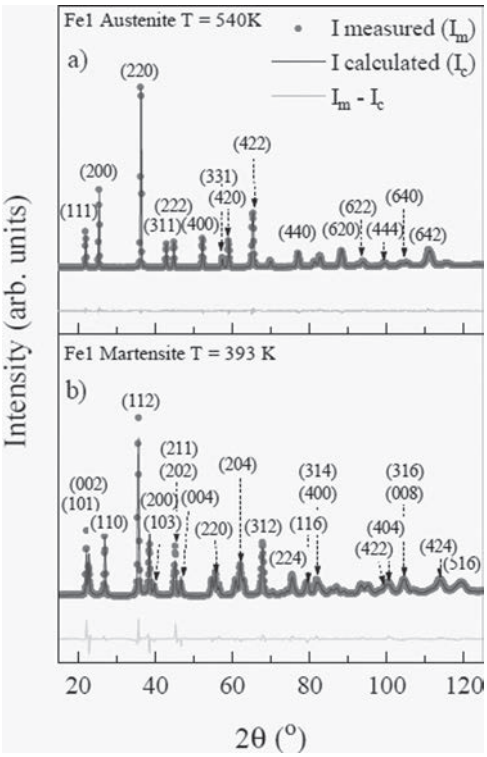
3:30

FD-09. Interplay between structure and magnetism in high temperature ferromagnetic shape memory alloys studied with neutron and x-ray scattering techniques. *J. Porro Azpiazu*[1,2], A. Pérez-Checa[1], P. Lázpita[3], J. Feuchtwanger[3], A. Stunault[4], J. Barandiaran[1,3], T. Nakamura[5], A. Sozinov[6], K. Ullakko[6] and V.A. Chernenko[1,2] *1. BCMaterials, Leioa, Spain; 2. Ikerbasque, the Basque Foundation for Science, Bilbao, Spain; 3. Electricity and Electronics Department, University of the Basque Country, Leioa, Spain; 4. Diffraction Group, Institut Laue-Langevin, Grenoble, France; 5. Japan Synchrotron Radiation Research Institute (JASRI), Sayo, Japan; 6. Material Physics Department, Lappeenranta University of Technology, Savonlinna, Finland*

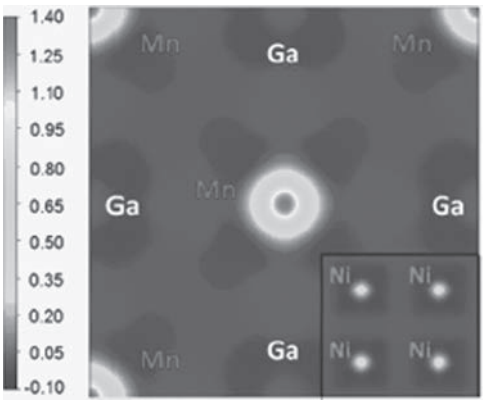
Ferromagnetic Shape Memory Alloys (FSMAs) are a group of active materials that undergo martensitic transformations induced by temperature, stress and/or magnetic fields, which result in large recoverable mechanical deformations [1]. Their fast response and high energy density make them ideal candidates for implementation in sensors and actuators. The magnetic properties of FSMAs depend on the interactions between the magnetic moments of atoms that, in turn, depend on the atomic positions within the lattice [2, 3]. Here we present a combination of powder neutron diffraction experiments in a series of polycrystalline samples of 6-element FSMAs with varied Fe content, where the alloys present actuation at temperatures around 370 K. Their atomic site occupancies, the ratio c/a and, therefore, the maximum achievable deformation ε, are calculated for each alloy [4]. Based on the atomic site occupancies and additional measurements of the saturation magnetization in each sample, the influence of the structure and atomic site occupancies on the magnetism in these samples is presented. This study is complemented by the single crystal polarized and non-polarized neutron diffraction experiments in one of the samples used for the powder neutron diffraction measurements, from which a single crystal was grown. Together with the atomic site occupancies in the single crystal, the analysis of the polarized neutron diffraction measurements provides us with information about the magnetic moment distribution in each atomic position present in the unit cell of the single crystal. Finally, the element-specific magnetic

moments contribution to the magnetism of the alloy are depicted via X-ray magnetic circular dichroism (XMCD) measurements. The combination of the polarized neutron diffraction and XMCD measurements allows us to unravel element and site-specific magnetic moment distributions in the alloy.

[1] R. C. O'Handley, J. Appl. Phys. 83, 3263 (1998) [2] J.M. Barandiaran et al., J. Phys.: Conf. Ser. 663, 012014 (2015) [3] P. Lázpita et al., New Journal of Physics 13, 033039 (2011) [4] A. Pérez-Checa et al., Scripta Materialia 134, 119 (2017)



Neutron powder diffraction patterns of the paramagnetic austenite (a) and ferromagnetic martensite (b) phases for one of the FSMA sample studied.



Magnetic moment distributions of the Fe5 single crystal at z=0 (main) and z=0.25 (inset) planes, where z is the unit vector along the c axis of the unit cell. The colour code units are $\mu_B/Å^3$.

3:42

FD-10. Magnetization Reversal of Ultra-soft PDMS-based Magnetorheological Elastomers. *A.T. Clark*[1], J. Li[2,1], T. Dang[1], E.A. Corbin[3,4], D.A. Gilbert[5], K. Buchanan[6], X. Jin[2] and X. Cheng[1]
1. Department of Physics, Bryn Mawr College, Bryn Mawr, PA, United States; 2. Department of Physics, Fudan University, Shanghai, China; 3. Department of Materials Science and Engineering, University of Delaware, Newark, DE, United States; 4. Department of Biomedical Engineering, University of Delaware, Newark, DE, United States; 5. Department of Materials Science and Engineering, University of Tennessee, Knoxville, TN, United States; 6. Department of Physics, Colorado State University, Fort Collins, CO, United States

Magnetorheological elastomers (MREs) are composite materials consisting of elastomer matrix with embedded micro- or nano- sized ferromagnetic entities. Ultra-soft polydimethylsiloxane (PDMS) based MREs are promising candidates for dynamic cell culture substrata [1-2]. The behavior of cells cultured on the surface of such MREs can be modified through tuning the mechanical and surface properties using an applied magnetic field. In this work, we report the fabrication and magnetic characterization of PDMS-based MREs. Sylgard 527 and carbonyl iron powder were mixed together at various ratios and cured at 60°C for 1 hour with applied magnetic fields ranging from 0 to 400 Oe. Magnetic hysteresis loops and first order reversal curves (FORC) [3-4] of the MREs were measured using a vibrating sample magnetometer. The MREs that were cured with no applied magnetic field show no angular dependence in the major hysteresis loop, consistent with the isotropic distribution of iron particles in the MREs. The hysteresis loops for MREs that were cured in a magnetic field, however, clearly display anisotropy. The applied field leads to alignment of the iron particles during the curing process and the alignment leads to the observed anisotropy. The difference in the FORC distribution characteristics of the isotropic and anisotropic MREs are also consistent with expectations based on the structural difference of these two types of MREs. Micromagnetic simulations give insight into the underlying mechanisms behind the magnetization reversal behavior. *This work is supported by the Center for Engineering MechanoBiology (CEMB), an NSF Science and Technology Center, under grant agreement CMMI: 15-48571. Work at Colorado State University is supported by NSF (DMR # 1709525)*

[1] Elise Corbin, et. al., ACS Appl. Mater. Interfaces, 11, 2320603-20614 (2019) [2] D.E. Discher, P. Janmey, Y-L Wang, Science, 310, 1139-1143 (2005) [3] D. A. Gilbert, et. al., Sci. Rep., 6, 32842 (2016) [4] L. Yu, et. al., IEEE Magnetic Letters, 8, 1-4 (2017)

3:54

FD-11. Frequency Dependence of Magnetic and Magnetoelastic Properties of Magnetostrictive Materials for Multiferroic Antennae. *P. Finkel*[1], M. Staruch[1] and N.J. Jones[2] *1. Naval Research Laboratory, Washington, DC, United States; 2. NSWC, Bethesda, MD, United States*

Magnetoelectric (ME) resonators are of significant interest for pure mechanically driven antennae targeting the ULF/VLF radio frequency range. Direct coupling of magnetostrictive and piezoelectric phases in the ME composites enables time variable magnetic field generation with exceptionally low operational power requirements. A dynamic stress loading of the magnetoelastic/magnetostrictive material by piezoelectric element results in a fluctuating magnetic field. In this work we fully characterize magnetostrictive materials $Fe_{81.6}Ga_{18.4}$ and Terfenol-D at high frequencies up to several kHz and studied the effect of eddy current losses that potentially curtail the magnetic response of the material. We evaluated the dynamic response of Galfenol rod up to 1000 Hz comparing both its sensing response (changing dynamic stresses) to its actuation response (changing dynamic magnetic fields) in both solid and laminated rods.

4:06

FD-12. Nonreciprocal Surface-Acoustic-Wave Phase Shifter Based on Magnetoelastic Coupling. *R.V. Verba*[1], V. Tiberkevich[2] and A.N. Slavin[2] *1. Institute of Magnetism, Kyiv, Ukraine; 2. Oakland University, Rochester, MI, United States*

Absence of nonreciprocity of pure linear acoustic waves is one of the major challenges in the surface acoustic wave (SAW) technology. This challenge can be met by using magnetoelastic coupling of SAWs with spin waves (SWs) propagating in ferromagnetic media, where wave nonreciprocity can be easily realized. Usually, for the development of magnetoelastic isolators the nonreciprocity of propagation losses is used [1,2], but other important nonreciprocal devices, such as circulators, use, instead, the nonreciprocity of phase accumulation [3]. This phase effect is hard to achieve in standard magnetoelastic devices, as in the ranges of effective magnetoelastic coupling damping of coupled waves becomes prohibitively large. In this work we propose a new method to realize nonreciprocal phase accumulation of SAW which is based on the coupling of SAW with a *strongly nonreciprocal* SW. It turns out, that in such a case magnetoelastic bandgaps for positive and negative propagation directions, which occur near the crossing of the dispersion lines, are situated at substantially different frequencies (Fig. 1). The strong magnetoelastic nonreciprocity can be achieved, e.g., by using ferromagnetic bilayers having antiparallel magnetization configuration, placed on a top of an acoustic crystal. In this case one can position the "working band"(see Fig.1) at the "tails"of the magnetoacoustic bandgaps, where the influences of magnetoelastic coupling on both the SAW dispersion and losses are weak, but still nonzero. The weak shift of dispersion leads to a nonreciprocal phase accumulation $\Delta\varphi=(|k_+|-|k_-|)L$, and the value of $\Delta\varphi=\pi$ required for applications can be achieved for the phase shifter length of L~100-300 μm, as shown in Fig. 2 for an example of a $LiNbO_3$/Co(16nm)/Ru(0.9)/Co(14) structure. Note also, that in the "working band"of 4.4-4.8 GHz the propagation losses remain small (3-4 dB) and, importantly, similar for both propagation directions.

[1] R. Sasaki, et al., Phys. Rev. B 95, 020407 (2017). [2] R. Verba, et al., Phys. Rev. Appl. 9, 064014 (2018). [3] A.G. Gurevich, G. A. Melkov, Magntization Oscillations and Waves (CRC Press, 1996).

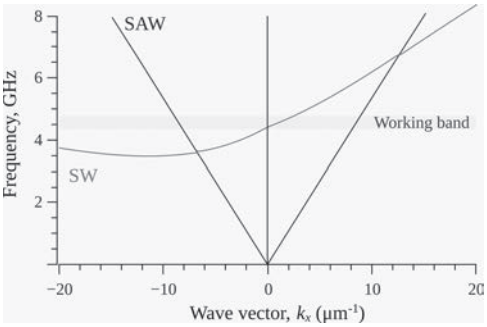


Fig.1. Spectra of SAW and SW.

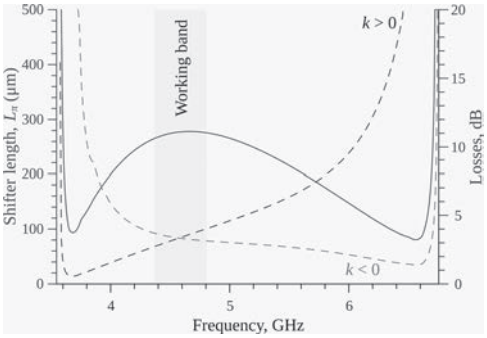


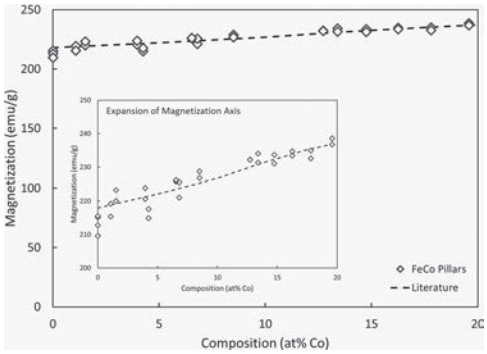
Fig. 2. Length *L* necessary to achieve the $\Delta\varphi=\pi$ nonreciprocal phase shift (left axis), and propagation losses of SAW in both propagation directions (right axis).

4:18

FD-13. Magnetic and Magnetostrictive Performance of $Fe_{1-x}Co_x$ Additively Manufactured Pillars. *N.J. Jones*[1], G. Petculescu[2], P.K. Lambert[1], J.M. Healy[1], R.T. Ott[3] and E. Simsek[3] *1. Physical Metallurgy and Fire Performance Branch, Naval Surface Warfare Center, Carderock Division, Bethesda, MD, United States; 2. Physics Department, University of Louisiana, Lafayette, LA, United States; 3. Division of Materials Science and Engineering, Ames Laboratory, Ames, IA, United States*

Traditional, slow crystal growth techniques can be very useful for fabricating highly textured magnetic and magnetostrictive materials. Additive manufacturing (AM) of metals, on the other hand, is composed of a large number of rapidly solidified regions that may provide textured growth, if configured correctly. If the growth parameters are not configured appropriately, however, poor crystal growth may result along with chemical inhomogeneity, which can also allow for multiple crystallographic phases. Therefore, if metal AM techniques are going to be used for magnetic materials and applications, their overall performance needs to be evaluated and linked to their crystallography, chemistry, and post-print material processing. Fifteen $Fe_{1-x}Co_x$ pillars (X = 0 – 20 at%) have been fabricated using the laser engineered net shaping (LENS^{TM}) technique, with various compositions of Co. Pillars were cut in half horizontally to evaluate variations in performance between the substrate and free ends. Magnetization and magnetostrictive strain has been measured as a function of composition and temperature. The room temperature magnetization values stay within 3% of the literature values, exhibiting 1 – 2% spread from sample to sample. The polycrystalline magnetostriction values ($3/2\ \lambda_s$) are isotropic in the plane, ranging from 3 – 50 ppm. Elastic constants have also been measured, along with crystal grain size, phase, orientation and composition.

[1] B. D. Cullity and C. D. Graham, Introduction to Magnetic Materials. John Wiley & Sons, Inc.: Hoboken, NJ, p. 142 (2009).



Saturation magnetization measured at 20 kOe as a function of cobalt composition for additively manufactured $Fe_{1-x}Co_x$ pillars. The dashed line is taken from reference [1].

Session FE
QUANTUM MAGNETIC PHASES

Denis R Candido, Chair
University of Iowa, Chicago, IL, United States

INVITED PAPER

1:30

FE-01. Quantum Criticality among Entangled Spin Chains. *A.P. Ramirez*[2], T. Siegrist[1], M. Mourigal[3], L. Balents[4], J. Trinh[2], L. Dong[4], A. Aczel[5] and X. Bai[3] *1. Florida State University, Tallahassee, FL, United States; 2. UCSC, Santa Cruz, CA, United States; 3. Georgia Tech, Atlanta, GA, United States; 4. UCSB, Santa Barbara, CA, United States; 5. ORNL, Oak Ridge, TN, United States*

In the quantum critical regime of a 3D Heisenberg antiferromagnet, the spins are nearly polarized, leading to a very small entropy change across the phase boundary. By contrast, an isolated 1D chain of such spins exhibits a large entropy change at its quantum critical point. Here we study an intermediate case, spin chains coupled to form a 3D ordered state, in the molecular salt $K_2PbCu(NO_2)_6$. We show that at the 3D quantum critical point, the system exhibits behavior characteristic of the constituent chains, with a specific heat comparable in magnitude to the spinon contribution[1]. We will also show that such behavior is generic to quasi-2D systems, opening up a new way to create highly fluctuating quantum magnetism.

1. N. Blanc, J. Trinh, L. Dong, X. Bai, A. A. Aczel, M. Mourigal, L. Balents, T. Siegrist, A. P. Ramirez, Nature Physics, 14, 273 (2018)

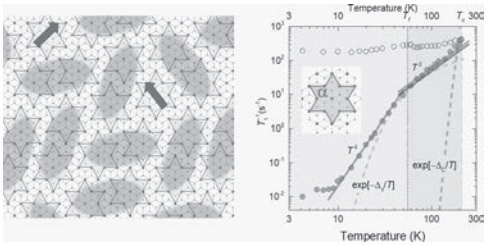
CONTRIBUTED PAPERS

2:06

FE-02. Quantum spin liquid in 1T-TaS_2. *D. Arcon*[2,1], M. Klanjšek[1], N. Jansa[1], I. Benedicic[1], D. Mihailovic[1] and P. Prelovsek[1] *1. Jozef Stefan Institute, Ljubljana, Slovenia; 2. University of Ljubljana, Faculty of Mathematics and Physics, Ljubljana, Slovenia*

The original Anderson's proposal of a resonating valence bond state [1] was put forward to account for the unusual magnetic properties of a triangular atomic lattice of Ta atoms in the layered transition metal dichalcogenide 1T-TaS_2. Compared to some recent candidates for quantum spin liquids (QSL) on triangular lattice, e.g., $YbMgGaO_4$ [2] or κ-$(ET)_2Cu_2(CN)_3$ [3], layered dichalcogenides have perfect triangular lattice geometry and a weaker effective spin-orbit coupling, offering a possibility for obtaining a unique insight into the competition between antagonistic QSL and Néel states. Here we report [4] on QSL that appears to be realized by atomic-cluster spins on the triangular lattice of a charge-density wave (CDW) state of 1T-TaS_2. In this system, nuclear magnetic quadrupole resonance and muon spin relaxation experiments reveal that the spins show gapless quantum spin liquid dynamics and no long range magnetic order down to 70 mK. Canonical T^2 power-law temperature dependence of the spin relaxation dynamics characteristic of a QSL is observed from 200 K to T_f = 55 K. Below this temperature we observe a new gapless state with reduced density of spin excitations and high degree of local disorder signifying new quantum spin order emerging from the QSL. The observed QSL is at first robust against applying chemical pressure in Se-doped samples before giving a way to superconducting state.

[1] P. W. Anderson, *Materials Research Bulletin* 8, 153 (1973). [2] Y. Shen, et al., *Nature* 540, 559 (2016). [3] T. Itou, A. Oyamada, and R. Kato, *Nature Physics* 6, 673 (2010). [4] M. Klanjšek, A. Zorko, R. Zitko, J. Mravlje, Z. Jagličić, P. K. Biswas, P. Prelovšek, D. Mihailovic, and D. Arčon, *Nature Physics* 13, 1130 (2017).



Left: the triangular lattice formed by Star of David Ta units hosts QSL. Right: Temperature dependence of ^{181}Ta spin-lattice relaxation rate for the alpha site (inset).

2:18

FE-03. Reestablishment of Spin-Density-Wave Magnetic Order in Epitaxial Chromium Films Following Photoexcitation. *S.K. Patel*[1,2], A. Singer[2], M. Chollet[3], J.M. Glownia[3], O.G. Shpyrko[2] and E. Fullerton[1] *1. Center for Memory and Recording Research, University of California, San Diego, La Jolla, CA, United States; 2. Physics Department, University of California, San Diego, La Jolla, CA, United States; 3. Linac Coherent Light Source, SLAC National Accelerator Laboratory, Stanford, CA, United States*

The emergence of order in complex systems such as itinerant antiferromagnets results in intriguing phenomena like spin density waves (SDW). Tuning material properties to extend magnetic control may offer new applications in spintronic devices. Here we discuss the response of the antiferromagnetic order of Cr films to photoexcitation. Epitaxial Cr (001) thin films exhibit a SDW and an associated charge density wave (CDW) normal to their surface. The number of periods of the SDW and CDW is quantized and changes hysteretically with temperature. The CDW can be measured in X-ray diffraction as satellite peaks centered on a specific Laue fringe around the (002) peak (see Fig. 1). Here, we study the CDW response in an X-ray pump probe experiment at the free electron laser LCLS where we excite a 28-nm Cr film with an optical pulse (800 nm, 40 fs) and probe with an X-ray pulse (8.9 keV, 50 fs). After photoexcitation, the static CDW is initially converted into a damped coherent dynamic phonon that is fully suppressed by 10 ps with sufficiently strong optical excitations. As the system cools, we measure how the magnetic order in the system is reestablished. The recovery to the initial ground state of the system is usually on the order of 1-10 ns, consistent with the cooling time for the lattice. However, near the hysteretic region where the number SDW and CDW periods discretely changes, the recovery of the lattice ordering stalls in a super-cooled metastable state which persists at least to the limit of measurement, 400 ns (see Fig. 2). Work at UCSD supported by the BES Award DE-SC0018237.

[1] A. Singer, et al., *Phys. Rev. Lett.*, 117, 056401 (2016).

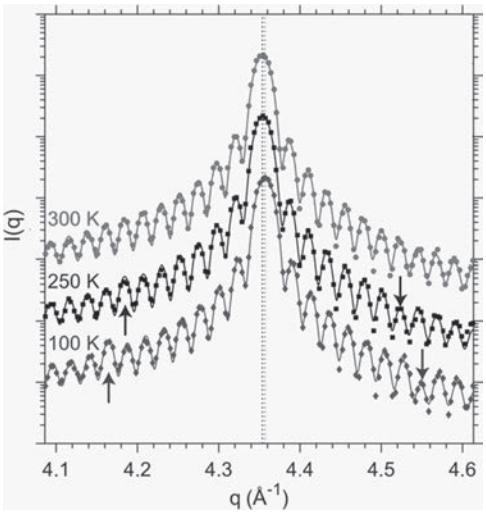


Fig. 1: X-ray diffraction of the (002) Bragg peak of a Cr thin film showing Laue fringes due to the finite sample thickness and satellite peaks due to the charge density wave ordering aligned on the seventh and eighth fringes at different temperatures.

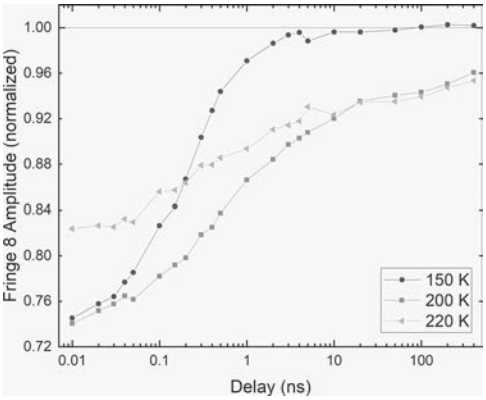


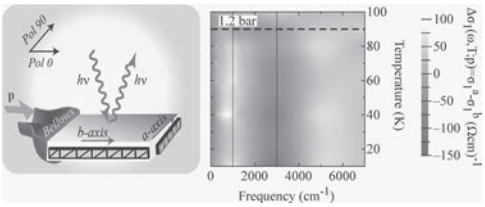
Fig. 2: Intensity of the eighth fringe after photoexcitation, demonstrating suppression and recovery of the charge density wave contribution. At an initial temperature of 150 K, the recovery tracks the cooling of the lattice. At an initial temperature near the hysteretic region where the CDW ordering changes, the system super-cools to a metastable state that persists to at least 400 ns.

2:30

FE-04. Optical evidence of an electronic nematic phase in FeSe driven by spin fluctuations. *L. Degiorgi*[1] *1. Physics, ETHZ, Zurich, Switzerland*

We have evinced, within one single experiment, all relevant ingredients determining the anisotropy in the charge dynamics as well as in the dc transport properties of FeSe, a prominent iron-based superconductor. It is established that the scattering by spin fluctuations turns out to be the most decisive effect with respect to the anisotropic nematic properties. FeSe lately acquired a prominent role within the panorama of superconducting materials, since it harbors a tetragonal-to-orthorhombic structural phase transition at T_s=90 K, where the lattice breaks a discrete rotational symmetry, in the absence of any subsequent, ambient pressure long-range magnetic order, prior the onset of superconductivity at 8 K. This is associated to an electronic nematic phase, the relevance of which in shaping the phase diagram of high temperature superconductors is certainly one of the most debated issues nowadays. This work describes novel results of reflectivity measurements from the far-infrared up to the ultraviolet that probe the optical response as a function of the tunable symmetry breaking field (stress) at any T < or > T_s. The data provide evidence that the low-energy excitation spectrum in the nematic phase is shaped by an important interplay of the anisotropic spectral (Drude) weight and scattering rate. In the zero-frequency limit though, the charge scattering rather than the Fermi surface parameters seems to determine the nematic anisotropy. In a broader context, these findings may support theoretical proposals advocating a close connection between spin fluctuations, nematicity (i.e., orbital order) and superconductivity [1,2].

[1] M. Chinotti et al., Phys. Rev. B, 96, 121112(R) (2017). [2] M. Chinotti et al., Phys. Rev. B, 98, 094506 (2018) (editors' suggestion).



2:42

FE-05. Dynamic, disordered ground state in the fluorite, $Dy_2Zr_2O_7$. *J.S. Gardner*[1], C. Wang[3], J. Ramon[2], L. Ishida[2], P.L. Bernardo[2], M.M. Leite[4], F.M. Vichi[4] and R.S. Freitas[2] *1. Songshan Lake Materials Laboratory, Dongguang, China; 2. Physics, Universidade de São Paulo, São Paulo, Brazil; 3. Neutron Group, National Synchrotron Radiation Research Center, Hsinchu, Taiwan; 4. Instituto de Química, Universidade de São Paulo, São Paulo, Brazil*

Neutron scattering, a.c. magnetic susceptibility and specific heat studies have been carried out on polycrystalline $Dy_2Zr_2O_7$ [1]. Unlike the pyrochlore spin ice $Dy_2Ti_2O_7$ [2,3], $Dy_2Zr_2O_7$ crystallizes into the fluorite structure and the magnetic Dy^{3+}moments randomly reside on the corner-sharing tetrahedral sublattice with non-magnetic Zr ions. Also unlike the Spin Ice compounds, antiferromagnetic spin correlations, not ferromagnetic ones, develop below 10 K. A.C. magnetic susceptibility suggests the magnetic Dy^{3+}moments remain dynamic down to 40 mK, with a significant amount of magnetic susceptibility. The spatial correlations extend over the length of two tetrahedra edges in zero magnetic field. We propose that the longer nearest neighbor distances promotes antiferromagnetic correlations and precludes the development of spin ice correlations. $Dy_2Zr_2O_7$ possesses fluctuating spins in a disordered, liquid-like state (albeit slow) and which do not freeze into a canonical spin glass state that one might intuitively expect. The application of a magnetic field to the polycrystalline sample results in extended correlations up to 6 nearest neighbors with the application of a 20 kOe magnetic field. Concomitantly, a subset of the spins enters a long-range ordered state, and resolution limited Bragg peaks are observed in neutron scattering experiments.

[1] J. G. A. Ramon, C. W. Wang, L. Ishida, P.L. Bernardo, M. M. Leite, F. M. Vichi, J. S. Gardner and R. S. Freitas, accepted in Physical Review B (2019) [2] A. P. Ramirez, A. Hayashi, R. J. Cava, R. Siddharthan, and B. S. Shastry, Nature (London) 399, 333 (1999). [3] T. Fennell, O. A. Petrenko, B. Fåk, J. S. Gardner, S. T. Bramwell, and B. Ouladdiaf, Phys. Rev. B 72, 224411 (2005).

2:54

FE-06. Probing the Antiferromagnetic-Ferromagnetic Transition in Artificial Spin Ice. *M. Massouras*[1], D. Lacour[1], M. Hehn[1] and F. Montaigne[1] *1. Institut Jean Lamour, Nancy, France*

Artificial spin ice, two-dimensional arrays of nanomagnets in close interaction, provide a playground to directly observe magnetic frustration [1–3]. By the use of shape anisotropy, mesoscopic Ising-like spins could be patterned with various spatial distributions. In this study, we experimentally examine

a tuned artificial spin ice system composed of nine tilted networks in which every bar is rotated around its central point. Rotating the elements of an angle ranging from 0° to 45° by 5° steps tunes the coupling strength inducing a transition from a antiferromagnetic phase for the square system to ferromagnetic phase for the 45°-tilted network or pinwheel system [3]. The as-grown state was observed [2] using Magnetic Force Microscopy (MFM) thus right after lift-off, the image obtained for the 35°-tilted network is shown in Fig.1. We characterize our system using vertex population, spin configurations, magnetic structure factor and dipolar energy to probe the phase exhibited by each array. We show that from the square up to the 25°-tilted array, the antiferromagnetic phase is clearly dominating although an increased number of excitations whereas the 40° and 45°-tilted networks exhibit a ferromagnetic phase arranged in domains. This transition is clearly demonstrated by their specific Bragg peaks on magnetic structure factor in Fig.2. This behavior is consistent with dipolar computations and Monte Carlo simulations for this tuned system. However in between, 30° and 35°-tilted arrays exhibit both phases on magnetic structure factor but their spin configurations show an arrangement in domains rather that a disorder state. Dipolar energy of our experimental system show deviations from the expected ground state that are described by an effective temperature determined by Monte Carlo simulations consistent with previous theoretical studies [3].

[1] R. F. Wang, C. Nisoli, R. S. Freitas, J. Li, W. McConville, B. J. Cooley, M. S. Lund, N. Samarth, C. Leighton, V. H. Crespi, and P. Schiffer, Nature 439, 303 (2006). [2] J. P. Morgan, A. Stein, S. Langridge, and C. H. Marrows, Nature Physics 7, 75 (2011). [3] R. Macêdo, G. M. Macauley, F. S. Nascimento, and R. L. Stamps, Physical Review B 98, (2018).

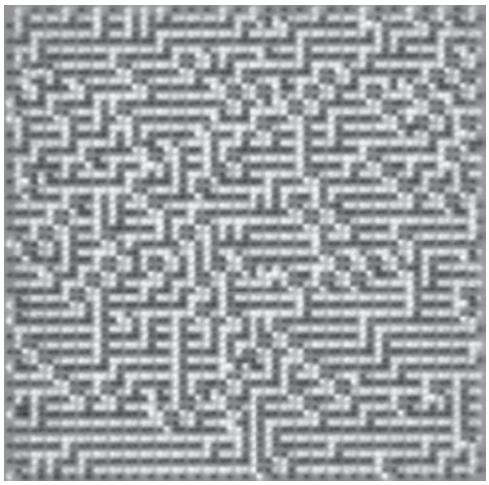


Fig.1: 35°-tilted network as-grown state imaged using MFM exhibiting domains both antiferromagnetic and ferromagnetic phases.

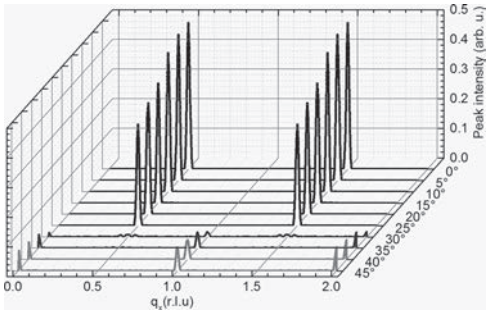


Fig.2: Cross-sections on magnetic structure factor. In black arrays exhibiting an antiferromagnetic phase, in red a ferromagnetic phase and in blue coexistence of both.

3:06

FE-07. Tunable Frustration in Antiferromagnetic Artificial Kagome Spin Ice. *Y. Li*[1], F.P. Barrows[2,1], A. Petford-Long[1,3] and C.M. Phatak[1]
1. Materials Science Division, Argonne National Laboratory, Lemont, IL, United States; 2. Northwestern University, Evanston, IL, United States; 3. Materials Science and Engineering, Northwestern University, Avanston, IL, United States

Artificial spin ices (ASI) are patterned nanomagnetic arrays in which the inter-play between the moment orientations of Ising-like elements and their coupling strength leads to the emergence of exotic phenomena such as magnetic frustration[1,2]. Here we report a novel ASI geometry – an antiferromagnetic (AFM) Kagome ASI, in which each element in the Kagome lattice is formed from a pair of islands. Such a geometry provides us with an additional degree of freedom to tune magnetic frustration by changing the inter-island distance, *s*, between the paired islands. Micromagnetic simulations were performed using Mumax[3] to predict the energies of all possible magnetic configurations for different lattice spacings, *a*, and inter-island spacing *s*, in the proposed antiferromagnetic Kagome ASI. With the distance between the paired islands being sufficiently small, the number of energy levels in the landscape is primarily determined by the number of possible combinations of the AFM- and ferromagnetic- (FM) aligned magnetization states between each pair at the vertices or the Kagome lattice. It is found that an increase in *s* decreases the energy difference between different magnetic configurations, leading to a more frustrated system. We also found that the degeneracy increases when the lattice constant *a* is reduced, thus leading to an increase in frustration. Guided by simulation results, we lithographically fabricated the antiferromagnetic Kagome ASI arrays from a Permalloy ($Ni_{80}Fe_{20}$) film, where each island has dimensions of 300 nm × 100 nm and approximately 3 nm thickness. The geometric parameters *a* and *s* of the lattice are varied from 350 to 550 nm and from 130 nm to 250 nm, respectively. Direct images of the magnetization configurations in the antiferromagnetic Kagome ASI arrays were obtained by use of the Lorentz transmission electron microscopy (LTEM). We will show how the magnetization state of the ASI sample is affected by the interaction strength determined by *a* and *s*.

[1] Farhan, A., Derlet, P. M., Kleibert, A., Balan, A., Chopdekar, R. V., Wyss, M., Anghinolfi, L., Nolting, F. and Heyderman, L. J., Nature Physics, 9, 375 (2013). [2] Gliga, S., Hrkac, G., Donnelly, C., Büchi, J., Kleibert, A., Cui, J., Farhan, A., Kirk, E., Chopdekar, R. V., Masaki, Y. and Bingham, N. S., Nature materials, 16 1106 (2017). [3] Vansteenkiste, A. and Van de Wiele, B., Journal of Magnetism and Magnetic Materials, 323 2585 (2011).
[4] This work was supported by the U.S. Department of Energy, Office of Science, Office of Basic Energy Science, Materials Sciences and Engineering Division.

INVITED PAPER

3:18

FE-08. Characterization of noncollinear spin textures in spin ice materials using capacitive torque magnetometry. *C. Beekman*[1,2]
1. Physics, Florida State University, Tallahassee, FL, United States; 2. National High Magnetic Field Laboratory, Tallahassee, FL, United States

Geometrically frustrated systems have received a lot of attention because incompatibility between the lattice geometry and the magnetic interactions results in macroscopically degenerate ground-state manifolds, and numerous unusual cooperative spin states [1]. In pyrochlore titanates ($A_2Ti_2O_7$ with A = Ho, Dy), large single ion anisotropy leads to a highly degenerate two-in/two-out spin ice state. Degeneracy is lifted when magnetic fields are applied, leading to magnetic transitions between various spin textures that depend on the direction of the field (see Fig. 1 [2,3]), and to emergent quasiparticle

excitations equivalent to magnetic monopoles. There is an enticing potential of harnessing these monopoles, as information carriers; to realize this thin films are required. The go-to tools for spin ice characterization, such as neutron scattering, are very challenging on thin films (due to the small amount of material present). We show that capacitive torque magnetometry can be used to perform magnetic crystallography on highly anisotropic systems such as spin ices, and more importantly, that the technique is sensitive enough to perform the same characterization on thin film samples. The technique involves a sample mounted on a flexible Cu-Be cantilever that serves as a top plate of a parallel plate capacitor. Changes in capacitance as a function of applied field strength, field direction, and temperature, are directly proportional to the torque, i.e., changes in the magnetic properties of the sample. Using capacitive torque magnetometry we can distinguish between the various noncollinear spin textures of the spin ice state shown in Fig. 1. Furthermore, transient states away from equilibrium, i.e., spin flips (monopoles), result in measurable changes in torque and can also be observed. We have performed torque measurements for a variety of rotation planes in a $Ho_2Ti_2O_7$ single crystal and we will show that a simple model suffices to explain the observed torque behavior. Hence, we can chart the respective phases of the spin ice state as a function of field strength and direction, and we can extract information on the transitions between them. This very sensitive technique is highly suitable for thin film characterization; hence, this paves the way to compilation of phase diagrams detailing spin ice physics in thin films as a function of temperature, film thickness, and strain. We will show data on thin films that indicate that spin ice physics in thin films grown on yttria-stabilized zirconia substrates [4] is modified compared to bulk spin ice behavior.

[1] C. Thompson, D. Reig-i-Plessis, L. Kish, A. A. Aczel, B. Zhang, E. Karapetrova, G. J. MacDougall, and C. Beekman, *Phys. Rev. Materials* 2, 104411 (2018) [2] J. P. Clancy, J. P. C. Ruff, S. R. Dunsiger, Y. Zhao, H. A. Dabkowska, J. S. Gardner, Y. Qiu, J. R. D. Copley, T. Jenkins, and B. D. Gaulin, *Phys. Rev. B* 79, 014408 (2009) [3] R.G. Melko, and M.J.P. Gingras," *J.Phys. Cond. Mat.* 16, R1277 (2004) [4] K. Barry, B. Zhang, N. Anand, Y. Xin, A. Vailionis, J. Neu, C. Heikes, C. Cochran, H. Zhou, Y. Qiu, W. Ratcliff, T. Siegrist and C. Beekman, arXiv:1805.06565 [cond-mat. str-el]

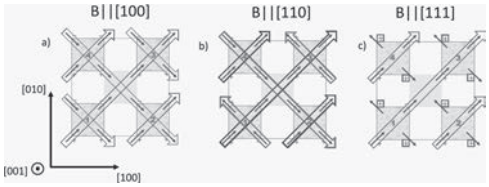


Fig. 1. $Ho_2Ti_2O_7$ unit cell projected down the [001] direction, the component parallel to the [001] is indicated with + and - signs. The axes indicate the crystallographic directions of the pyrochlore. The blue squares are tetrahedra, the gray square has diagonally opposite spins that inhabit the same lattice plane. Schematic of the a) $Q = 0$ state when B ||[100]; b) $Q = X$ state when B ||[110]; c) 3-out/1-in state when B ||[111]. The large open arrows are guides to the eye highlighting the alignment of the spin chains.

CONTRIBUTED PAPERS

3:54

FE-09. Emergent magnetic monopole dynamics in macroscopically degenerate artificial spin ice. A. Farhan[1,5], *M.D. Saccone*[2], C.F. Petersen[3], S. Dhuey[4], R.V. Chopdekar[5], A. Scholl[5] and S. van Dijken[1] *1. Department of Applied Physics, Aalto University, Espoo, Finland; 2. UC Santa Cruz, Santa Cruz, CA, United States; 3. University of Innsbruck, Innsbruck, Austria; 4. Molecular Foundry, Lawrence Berkeley National Laboratory, Berkeley, CA, United States; 5. Advanced Light Source, Lawrence Berkeley National Laboratory, Berkeley, CA, United States*

Magnetic monopoles, proposed as elementary particles that act as isolated magnetic south- and north poles as an explanation of the quantization of the electric charge [1] have long been the subject of intense research efforts. In solid state physics, a classical analogue to these elusive particles has been shown to emerge as topological excitations out of the ground state manifold of magnetic systems generally known as pyrochlore spin ices [2,3]. In our work, we introduce extensively degenerate artificial spin ice systems exhibiting thermally induced moment reorientations [4]. We not only directly visualize magnetic configurations achieved following thermal annealing, but also perform real-time observations and characterization of thermal fluctuations and motion of emergent magnetic monopole defects, allowing us to perform a first-time real-space characterization of emergent magnetic monopoles within the framework of the Debye-Hückel theory. Our work marks a starting point for a whole new line of research aiming at real-space investigations on the nature of macroscopic degeneracy, spin freezing phenomena and verification of magnetic analogues to electrolyte models [3,5].

[1] P. A. M. Dirac, Proc. R. Soc. A 133, 60 (1931) [2] C. Castelnovo et al., Nature 451, 42 (2008) [3] S. T. Bramwell et al., Nature 461, 956 (2009) [4] A. Farhan et al., Science Advances 5, eaav6380 (2019) [5] L. Onsager, J. Chem. Phys. 2, 599 (1934)

4:06

FE-10. Experimental and theoretical investigation of emergent excitations in artificial spin ice system with a magnetization reversal process. F. Martins[1], R. Gonçalves[1,2], T. Paiva[1], J. Rodrigues[2], L. Mól[2], A. Pereira[1] and *C.I. Levartoski de Araujo*[1] *1. Physics, Universidade Federal de Viçosa, Viçosa, Brazil; 2. Universidade de Federal de Minas Gerais, Belo Horizonte, Brazil*

Frustration refers to the inability of a system for simultaneously minimize its interactions, as a consequence, its ground state is degenerate. Geometric frustration in materials known as spin ices [1], which have magnetic moments in the net obeying the ice rule (a rule similar to that of water molecules), has attracted great attention of researchers in the last decade, due to emergence of quasi-particles like monopoles [2]. Studies of magnetic monopoles have also being directed to arrays of magnetic nanobars, known as artificial spin ices (ASI). In the ASI system magnetic monopoles can also be observed [3], with the advantage over natural spin ices of monopoles observation with magnetic microscopy techniques and manipulation of these monopoles at room temperature. In this work, we present a study on ASI emergent excitations for different lattice geometries and spacing during a magnetization reversal process through analysis of magnetic force microscopy images, as presented in Figure 1. Our results are well fitted by a theoretical model that describes the emergent excitations in the ASI with coulomb and dipolar interaction among monopoles and dipoles [4]. With our results we could investigate the density of monopoles and its response to the external magnetic field and map its highest mobility in function of lattice parameters. Acknowledgments: This work was realized with the support of the National Program of Academic Cooperation of Capes, process 88881.068506 / 2014-1. The authors would like to thank the CAPES oo1, CNPq and FAPEMIG (Brazilian agencies) for financial support.

1 - A. P. Ramirez, et al., Nature, v. 399, n. 6734, p. 333, (1999). 2 - C. Castelnovo, R. Moessner, S. L. Sondhi, Nature, v. 451, n. 7174, p. 42, (2008). 3 - L. A. S. Mól et al., Journal of Applied Physics, v. 106, n. 6, p. 063913, (2009). 4 - J. H. Rodrigues and L. A. S. Mól, Journal of Magnetism and Magnetic Materials, v. 458, p. 327-334, (2018).

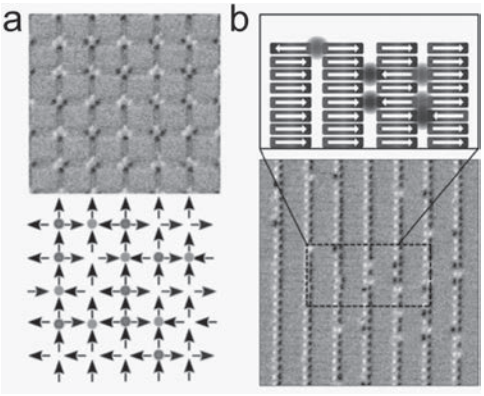


Fig. 1 - a) Magnetic force measurements and representation of magnetic monopoles performed in a) square artificial spin ice lattice and b) unidirectional artificial spin ice lattice.

4:18

FE-11. Domain Wall Propagation in Magnetic Galton Board.

M. Massouras[1], D. Lacour[1], M. Hehn[1] and F. Montaigne[1] *1. Institut Jean Lamour, Nancy, France*

A wide range of devices based on domain wall (DW) propagation has been proposed and investigated. Magnetic storage is obviously the key application either in the form of single bit or multi-level devices or in "racetrack" devices. But other applications are also targeted like magnetic logic devices, multiturn position sensors, memresistors… Many aspects are involved in this propagation: DW topology, pinning/depinning phenomena, temperature effects, driving force (magnetic field, charge currents, spin currents, light…), dynamic aspects and particularly Walker breakdown…. Reproducible and controllable domain wall propagation is therefore a challenge for most of the evocated devices that require a precise control of the DW propagation. On the other hand, other devices might benefit from random or pseudo-random propagation for random number generation[1], cryptography or neuromorphic structures. This aspect will be investigated in this presentation with the demonstration of the magnetic analog to the Galton board. We developed an artificial spin ice system arranged in honeycomb lattice to observe one-dimensional propagation of a DW[2]. The study of a classical design of a 3-output Galton board with connected nanomagnets demonstrated the successful injection of a DW with an ellipsoidal pad (Fig. 1) and its propagation throughout the structure by applying an in-plane field. Activated outputs show a stochastic behavior with a Gaussian distribution. The 8 outputs board highlighted the limitations of such a design: higher fields are needed to propagate the DW than to nucleate one at outter outputs as shown in Fig. 2. Thus, we elaborated a novel structure with smooth vertices in a funnel shape and sharp ends to decrease the pinning field increase the nucleation field at the outputs respectively as shown in Fig. 1. The corresponding activated outputs exhibit a better Gaussian distribution yet biased probably due to field misalignment but more acceptable number of activated outputs on the sides.

[1] K. Zeissler *et al.*, Sci Rep 3, (2013). [2] E. Mengotti *et al.*, Nature Physics 7, 68 (2011).

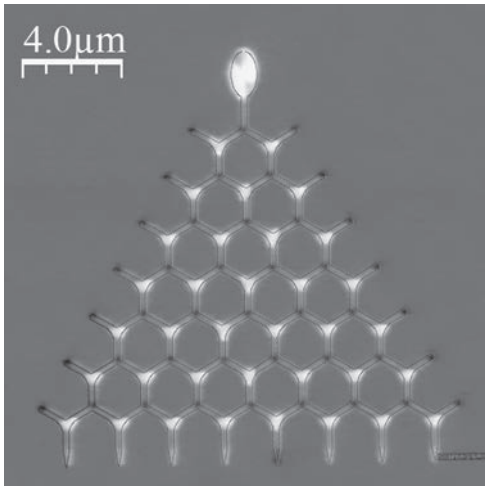


Fig. 1: MFM image of the optimized 8 outputs nanostructure showing the 1D-propagation of the DW injected from the pad to the fifth output from the left.

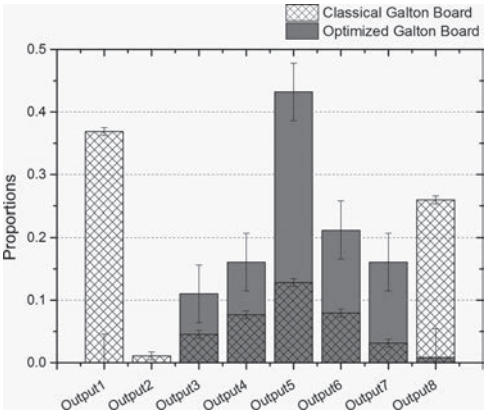


Fig. 2: Activated outputs of both classical and optimized Galton Boards.

Session FF
BIOMAGNETISM, BIOMEDICAL, AND MAGNETIC FLUIDS II

Akihiro Kuwahata, Chair
University of Tokyo, Bunkyo-ku, Japan

INVITED PAPER

1:30

FF-01. Magnetism, Hidden Order and Emergent Collective Behavior in a Bacterial Suspension. *R. Sooryakumar[1] 1. Department of Physics, The Ohio State University, Columbus, OH, United States*

One of the most fascinating aspects of living matter is their ability to form exotic structures emerging from large numbers of individual disordered components. Moreover, these structures span a staggering range of length scales ranging from, for example, bird flocks and ant colonies to microscopic cells that come together to form tissues. While bacteria are often thought of as solitary organisms, we have recently identified [1] a new form of collective behavior of bacteria in species which are not only abundant in nature but also *synthesize their own magnetic nanoparticle arrays.* In addition to their inherent magnetism, the species is motile where the chemically powered flagellum (a thin helical appendage responsible for cellular propulsion) provides the source of activity. When magnetically guided to orient near a surface, the hydrodynamic wake produced by these swimming bacteria draws in nearby cells, resulting in dense clusters and networks, reminiscent of large scale galactic structures. As these shapes grow larger, the process slows down, as the innate magnetic forces push the clusters apart leading to stable, long-lived cluster structures. To quantify the self-organization, a Lempel-Ziv compression algorithm [2] is applied to each recorded image. As recently demonstrated [3], this approach, which is widely used in file compression applications, yields the computable information density, which bounds the Shannon entropy. It also provides a generic measure of the order in the system without knowledge of the particular nature of the ordering and reveals the phase boundary defining the onset of self-organization. The high degree of experimental control offered through their magnetism and theoretical tractability offered by this bacterial system enables broad questions in active matter self-organization to be addressed. The ensuing mathematical description of order in a nonequilibrium living, many-body system provides a new framework to understand how microscopic active swimmers can be magnetically guided for diverse applications as in robotics and nano-medicine. The understanding gained from such complex, far-from-equilibrium systems are relevant to broader phenomena in biomagnetism, statistical mechanics and condensed matter physics.

[1] C. J. Pierce et. al., Physical Review Letters 121, 188001 (2018). [2] J. Ziv and A. Lempel, IEEE Trans. Inf. Theory 23, 337 (1977). [2] S. Matiniani, P. M. Chaikin and D. Levine, Physical Review X 9, 011031 (2019).

CONTRIBUTED PAPERS

2:06

FF-02. Mechanical resonator to measure magnetic susceptibility of structurally intact bone samples. L.R. Moore[1], M. Midura[1], R. Royer III[1], C. Androjna[1], E.I. Waldorff[2], N. Zhang[2], J.T. Ryaby[2], R.J. Midura[1] and *M. Zborowski[1] 1. Cleveland Clinic, Cleveland, OH, United States; 2. Orthofix Inc., Lewisville, TX, United States*

Low frequency, low field pulsed electromagnetic field (LF PEMF, below 10 kHz and 10 mT amplitude) is an FDA-approved treatment of fracture non-unions and an adjunct to cervical fusion surgery. LF PEMF exerts measurable magnetic force on bone [1] and the combined effect of the local B field vector and the bone susceptibility tensor determine the local force magnitude, a potentially important factor for treatment efficacy. We compared magnetic susceptibility measured by commercial susceptometer (MSB Auto, Sherwood Scientific) with that measured by a custom built mechanical resonator comprising a diametrically-polarized NeFeB permanent dipole magnet cylinder (25.4 x 25.4 mm, height by diameter) rotated about its axis by a stepper motor at even intervals from 53 – 63 RPM, acting on an intact bone sample (rat lumbar vertebrae) suspended 26.0 mm from magnet axis on a thin line of 71.0 mm effective length. The sample was exposed to a local oscillating mean field of 250 mT, gradient of 50 T/m, and its motion was captured by a video camera and resolved into 2D space coordinates versus time by ImagePro® and Excel® macros (Figure). The MSB Auto susceptometry required bone pulverization resulting in the loss of information about bone magnetic anisotropy, unlike that measured by mechanical resonator at three different spatial bone orientations. The amplitude of bone oscillations at twice the angular frequency of the rotating magnet yielded maximum displacement that agrees with the forced, damped simple pendulum model and the local diamagnetic Maxwell stress as the driving force. The mean volume magnetic susceptibility (SI) of -8.75 $x10^{-6}$ ± 2% (n=7 vertebrae) agreed with that calculated from the mechanical resonator traces showing the strongest field-tissue interaction for the vertebra axis orientation normal to the local field vector. The results point to site-specific aspect of LF PEMF therapy and provide novel, rational methods of designing next generation of effective LF PEMF therapies.

[1] Schwab S et al. IEEE TMAG 2016 DOI: 10.1109/TMAG.2016.2515069

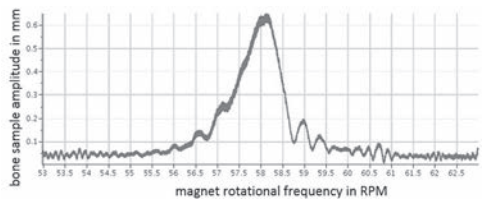


Figure. Magnetic bone oscillations envelope as a function of magnet rotational speed. Note resonance at 58.2 RPM, close to half that of the harmonic oscillator eigenfrequency, as expected.

2:18

FF-03. Reconfigurable ferromagnetic liquid droplet. *X. Liu*[1], N. Kent[3], A. Ceballos[2], R. Streubel[3], Y. Jiang[2], Y. Chai[3], P. Kim[3], J. Forth[3], F. Hellman[2], S. Shi[1], D. Wang[1], B. Helms[3], P. Ashby[3], P. Fischer[3] and T. Russell[4] *1. Beijing University of Chemical Technology, Beijing, China; 2. University of California, Berkeley, Berkeley, CA, United States; 3. Lawrence Berkeley National Lab, Berkeley, CA, United States; 4. University of Massachusetts, Amherst, Amherst, MA, United States*

Solid ferromagnetic materials are rigid in shape and cannot be reconfigured. Ferrofluids, while reconfigurable, are paramagnetic at room temperature and lose their magnetization when the applied magnetic field is removed. Here, we show a reversible paramagnetic to the ferromagnetic transformation of ferrofluid droplets by the jamming of a monolayer of magnetic nanoparticles assembled at the water-oil interface. These ferromagnetic liquid droplets exhibit a finite coercivity and remanent magnetization. The ferromagnetic response is striking since the separation distance between the dispersed nanoparticles is much larger than characteristic distances of ferromagnetic dipolar coupling. They can be easily reconfigured into different shapes while preserving the magnetic properties of solid ferromagnets with classic north-south dipole interactions. Their translational and rotational motions can be actuated remotely and precisely by an external magnetic field, inspiring studies on the active matter, energy-dissipative assemblies and programmable liquid constructs.

1. M. M. Cui, T. Emrick, T. P. Russell, *Science* 342, 460-463 (2013). 2. R. Streubel *et al.*, *Nano Lett* 18, 7428-7434 (2018). 3. X. Liu *et al., Angew Chem Int Edit* 56,12594-12598 (2017) 4. J. Forth *et al.*, *Adv Mater* 30, 1707603 (2018). 5. B. A. Grzybowski, H. A. Stone, G. M. Whitesides, *Nature* 405, 1033 (2000).

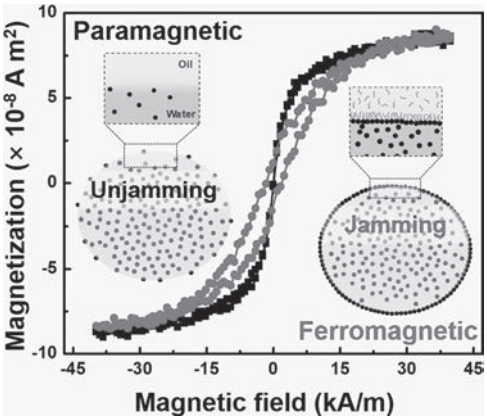


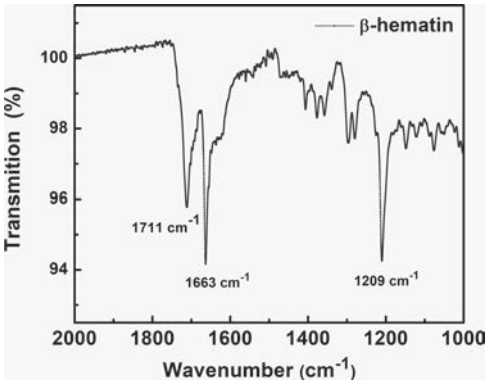
Fig. 1 Paramagnetic droplet transforms into a ferromagnetic liquid droplet at room temperature by interfacial jamming of magnetic nanoparticles at water-oil interface.

2:30

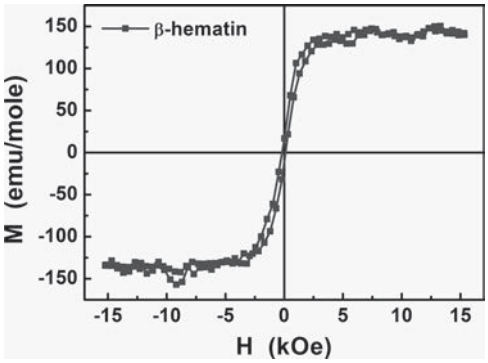
FF-04. Magnetism as an Efficient Tool for Malaria Detection. Y. Kumar[1], *A. Rathi*[1], A. Singh[1], G. Sumana[1], B. Gahtori[1], R. Pant[1] and G. Basheed[1] *1. AcSIR, CSIR-National Physical Laboratory (NPL) campus, New Delhi, India*

Malaria is an extremely devastating mosquito-borne blood disease caused by Plasmodium parasites (mainly falciparum, 99.7 %), resulting in approximately five million deaths every year around the world, according to world malaria report 2018 [1]. This situation is despite of malaria being easily preventable and curable. In this connection, the major challenge remains accurate and early stage (efficiency) detection of malaria on affordable prices. The present day moderate-cost rapid diagnostic tests (RDTs) are limited by sensitivity (detection only above 100-200 parasites/μl blood), and a more rapid, sensitive and affordable alternatives are need to be developed [2]. Here, we, in lab, chemically produced β-hematin, which is a synthetic analogous of malaria pigment hemozoin, resulted from hemoglobin detoxifcation by the Plasmodium parasite [3]. The analogy of β-hematin to hemozoin is confirmed by Fourier-transform infrared spectroscopy (FTIR) spectroscopy. The β-hematin is formed in shape of nano-sized needles with diameter of 50-100 nm, and length of 200-600 nm, as revealed by High-Resolution transmission electron microscopy (HRTEM) study. The X-ray diffraction and HRTEM study reveal a high crystalline nature of β-hematin (in similar to hemozoin). Importantly, Vibrating-sample magnetometer (VSM) shows that β-hematin nanoneedles are magnetic in nature with (technical) saturation field of 2 kOe. This highly sensitive magnetic and more importantly, highly anisotropic nature (due to needle shape) of β-hematin (hemozoin) enables us to develop an easy, cost-effective and highly efficient detection technique for malaria. We are in process to develop a compact magneto-optical setup using a set of diode red laser, polarizer, quartz cuvette (for sample mounting), NdFeB permanent magnets and highly sensitive photodiode (determining the efficiency for malaria detection) for highly efficient and cost-effective malaria detection.

1. World Health Organization. World Malaria Report 2018 (2018) 2. B. T. Grimberg and K. O. Grimberg, Expert Rev. Anti-Infect. Ther. 14, 879 (2016) 3. S. Pagola, P. Stephens, D. Bohle, Nature 16, 307 (2000).



The FTIR spectra of chemically synthesized β-hematin by pH-controlled incubation method, showng its analogy to malaria pigment, hemozoin.



The room temperature M-H loop of β-hematin, cofirming its magnetic nature.

2:42

FF-05. Interaction of Two Magnetic Micro-Chains in Rotating Field. *J. Cheng*[1], C. Lin[1] and C. Chen[1] *1. Mechanical Engineering, National Chiao Tung University, Hsinchu City, Taiwan*

Magneto-microfluidics have been popular research subjects because of their effective manipulability by an external magnetic field. One particular branch of these studies focuses on microchains consisted of magnetic

particles and driven by a rotating field. Under such a condition, the microchains are induced to perform two distinct modes of rotational motion: individual rotation and global revolution. Because of the magnetic torque induced by the phase lag between the external field and the individual microchain, the microchain rotates synchronously with the field. On the other hand, the magnetic attraction/repulsion between the microchains drives the microchains undergoing tangential motion similar to planetary revolution. To elucidate the dual rotational motion, experiments of two microchains, consisted of several 5-micrometer magnetic beads, are conducted. Two possible modes of the magnetic interactions between the chains are identified, referred to as chaining and lock-on, respectively. In more common situations, the two chains, subjected an overall magnetic attraction to each other while undergoing global revolution, would approach to connect, and form a longer rotating chain. Temporal evolution of the chaining mode is shown in Fig. 1. Nevertheless, an interesting mode of lock-on may occur, in which the two chain appear nearly parallel, and revolute along a certain origin, whose orbits mimic the system of binary stars as shown in Fig. 2. To understand the dynamics of these two distinct modes, the forces involves in the system, such as magnetic forces and hydrodynamic drags, are evaluated. The criterion forming the lock-on mode is analyzed based on the balance of these two forces.

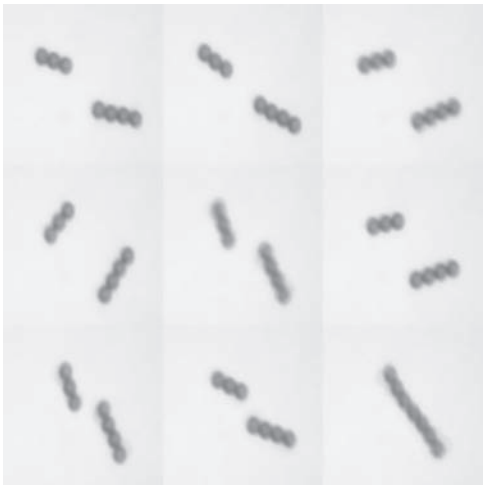


Fig. 1 Chaining mode: two rotating chains approach to form a longing chain

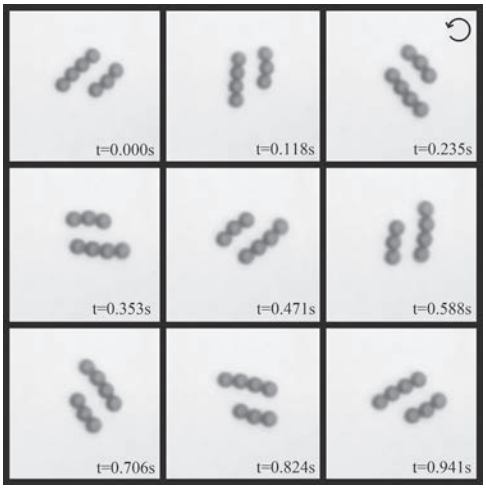


Fig. 2 Lock-on mode: two chains revolute mimicking the binary stars

2:54

FF-06. Auditory Evoked Fields (AEFs) Measurements via Peak to Peak Voltage Detector Type MI Gradiometer. *J. Ma*[1] and T. Uchiyama[1]
1. Department of Electrical Engineering, Graduate School of Engineering, Nagoya University, Nagoya, Japan

1. Introduction As one of the most prominent responses in AEF, N100 surfaces as a negative deflection with a latency of roughly 80 to 120 ms after the onset of a stimulus. In this study, we have developed a peak to peak voltage detector type MI sensor system for auditory evoked fields measurements. 2. Pk-pk VD-type MI sensor system For measuring extremely weak magnetic fields, we have developed Pk-pk VD-type MI sensor system based on the new MI magnetometer reported recently [1]. We have achieved a high sensitivity of 1.4×10^7 V/T with good linearity, which is 1.3 higher than that of previous MI sensor. The noise floor of new MI sensor system is lower than 1 pT/Hz$^{1/2}$ in the frequency range from 1 Hz to 100 Hz. It is 1/10 of noise level of previous MI gradiometer [2]. 3. N100 measurements We record MEG signals by Pk-pk VD-type MI sensor system, with a 1-20 Hz bandpass filter. Fig. 1 illustrates averaged N100 brain activity waveforms evoked by 1 kHz auditory stimuli, on the left and right sides of the temporal region. As shown in Fig. 1(a), there is a positive deflection with latency about 120 ms obviously elicited by auditory stimuli. In Fig. 1(b), there is a negative deflection. The polarity of deflections on the left and right temporal regions is opposite. The amplitudes of the N100 deflections are approximately 4 pT. We have also demonstrated N100 measurements in different stimuli conditions with different frequency of auditory stimuli. Fig. 2 illustrates the averaged N100 signals evoked by auditory stimuli with 1 kHz, 2 kHz, 4 kHz, 6 kHz and 8 kHz frequency. For all stimuli conditions, we have successfully observed positive deflections with a latency about 100 ms. Fig. 2(b) illustrates amplitudes and latency of N100 signals depending on frequency of stimuli. N100 amplitudes of all subjects have a tendency to decrease with frequency of auditory stimuli. According to the results, these characteristics coincides well with previous studies [3].

[1] J. Ma, and T. Uchiyama, IEEE TRANSACTIONS ON MAGNETICS, vol. 54, no. 11, pp. 1-5, Nov. 2018, Art no. 5000605. [2] T. Uchiyama, K. Mohri, Y. Honkura, and L. V. Panina, IEEE Transactions on Magnetics, vol. 48, no. 11, pp. 3833–3839, 2012. [3] M. Sereda, P. Adjamian, M. Edmondson-Jones, A. R. Palmer, and D. A. Hall, Hearing Res., vol. 302, pp. 50–59, Aug. 2013.

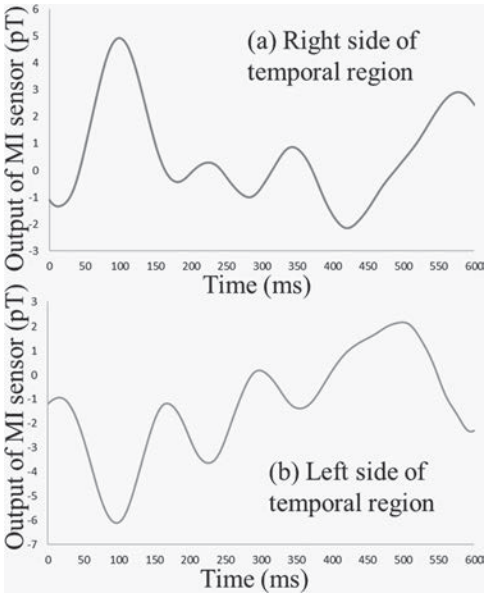


Fig. 1 Averaged N100 signals evoked by 1000 Hz auditory stimuli, on the left and right temporal regions.

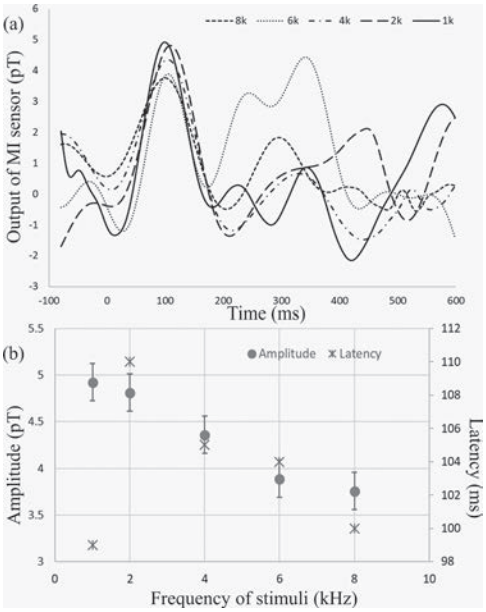


Fig. 2 (a): The averaged N100 signals evoked by auditory stimuli with 1 to 8 kHz frequency. (b): The amplitudes and latency of N100 signals depending on frequency of stimuli.

3:06

FF-07. Green Synthesis of Magnetic Nanoferrites (Fe, Co, Ni) from Aloe Vera Extract and Its Biomedical Potential. *G.C. Hermosa*[1], H. Wu[1], C. Liao[1], S. Wang[2], Y. Chen[1,3] and A. Sun[1] *1. Chemical Engineering and Materials Science, Yuan Ze University, Taoyuan, Taiwan; 2. Department of Materials and Mineral Resources Engineering, National Taipei of Technology, Taipei, Taiwan; 3. Surgery, Far Eastern Memorial Hospital, New Taipei, Taiwan*

The synthesis of magnetic nanoferrites is an active area of academic and, more importantly, "application research" in nanotechnology for potential biomedical use. A variety of chemical and physical procedures could be used for synthesis of nanoferrites. However, these methods are fraught with many problems with the use of toxic solvents, generation of hazardous by-products, and high energy consumption. Accordingly, there is a vital need to develop environmentally benign procedures for the synthesis of nanoferrites. A promising approach to achieve this objective is to exploit the array of biological resources in nature. Indeed, over the past several years, plants, have been used for production of low-cost, energy-efficient, and nontoxic metallic nanoferrites. Plant-mediated synthesis of nanoparticles is a green chemistry approach that connects nanotechnology with plants. This innovation is particularly compensating as far as decreasing the poisonous quality caused by the conventionally integrated NPs. Aloe Vera leaf extract is a medicinal agent with multiple properties including an antibacterial effect. Moreover, the constituents of Aloe Vera leaves include lignin, hemicellulose, and pectins which can be used in the reduction of nanoferrites. The magnetic nanoferrites (Fe, Co, Ni) were prepared by an eco-friendly hydrothermal method using an Aloe Vera plant extract solution as both a reducing and stabilizing agent. Magnetic nanoferrites were characterized using FTIR, XRD, VSM and SEM. Cytotoxicity were obtained using the MTT assay. X-ray diffraction analysis also demonstrated that the size range of the nanoferrites exhibited average diameters of 7- 19 nm. Results showed that all the metallic nanoparticles are magnetic with values Fe= 52 emu/g, Co= 33 emu/g and Ni=7.1 emu/g. The magnetic nanoferrites exhibited high cell viability rate at high concentrations signifying their non-toxic property. The magnetic nanoferrites produced in this study by green synthesis methodology from leaf extract of *Aloe Vera* needs to be further evaluated and could find greater biomedical application.

K. Schulze, A. Koch, B. Schopf and A. Petri, *Journal of Magnetism and Magnetic Materials*, Vol. 293, pp. 419-432, (2005). S. Das, C. Dickinson, F. Lafir and D. Brougham, *Green Chemistry*, Vol. 14, pp. 1322–1334, (2012). M. Ferrari, Nature Reviews Cancer, Vol. 5, pp.161-171, (2005). M. Venkatachalam, G. Parthasarathy and P. Gowthaman, *Imperial Journal of Interdisciplinary Research (IJIR)*, Vol. 2, pp. 1570-1575, (2016). T. Neuberger, B. Schopf and H. Hofmann, *Journal of Magnetism and Magnetic Materials,* Vol. 293, pp. 483–496, (2005).

3:18

FF-08. Magnetic Characteristics of Magnetic Markers for Localized Tumor Excision with a Handheld Magnetic Probe. *Y. Xiao*[1], O. Bhowmik Debnath[1], S. Chikaki[1], A. Kuwahata[1], M. Peek[1], I. Saito[2], S. Maeda[3], M. Kusakabe[4,1] and M. Sekino[1] *1. University of Tokyo, Tokyo, Japan; 2. iMed Japan Inc, Tokyo, Japan; 3. Kyoshin Co., Ltd, Nasu Shiobara, Japan; 4. Matrix Cell Research Institute Inc., Ushiku, Japan*

To excise the primary tumor on patient with a non-palpable breast cancer, surgeons estimate the excision margin by naked eyes subjectively with the help of a localization tool such as a hook wire(1). By introducing a magnetic detection system, location of the magnetic marker injected intratumorally can be identified with a handheld magnetic probe(2). Detection ranges of existing magnetic markers are up to 30 mm(3), limiting application in tumors located deeper down the skin. In this study, materials and designs of magnetic markers are evaluated to achieve an extended detection range. Todetermine the material that generates strong magnetic signal, magnetic properties of marker samples in selected materials including SUS (stainless steel) 304, SUS 316 and permalloy are analyzed. Samples are fabricated with wire with a diameter of 0.8 mm into the hook shape shown in Fig. 1(a). Measured magnetic signal strength is shown in Fig. 2(a). Amongst the three, SUS 304 generates the strongest signal, therefore is determined as the material for the marker. Three marker designs are evaluated. The first design is a hook shape, similar to the tip of a hook wire, as shown in Fig. 1(a). The second design is a 'Y' shape where one wire is folded and twisted as shown in Fig. 1(b). The third design is an 'X' shape where two wires are twisted together at the middle, as shown in Fig. 1(c). Three markers are made of SUS 304 wire with a diameter of 0.4 mm. Signals from these three markers are shown in Fig. 2(b). Results show that all three designs generate magnetic signals greater than 1μT, which can be detected by the magnetic probe, at distance of 42 mm, while the 'X' shape marker achieves the longest detection range of over 50 mm, which exceeds the detection range of 30 mm of existing magnetic markers. Application range of the marker is widened, including tumors at all depths and in all breast sizes. As a next step, magnetic properties of the marker in three dimensions will be evaluated.

(1)M. Ahmed, I. Rubio, J. Klaase, M, Douek: "Surgical treatment of nonpalpable primary invasive and *in situ*breast cancer" Nature Reviews Clinical Oncology 12,645-663, (2015) (2)M. Sekino, A. Kuwahata, T. Ookubo, M. Shiozawa, K. Ohashi, M. Kaneko, I. Saito, Y. Inoue, H. Ohsaki, H. Takei, M. Kusakabe: "Handheld magnetic probe with permanent magnet and Hall sensor for identifying sentinel lymph nodes in breast cancer patients"Scientific Reports,(2018) (3)J. Harvey, Y. Lim, J. Murphy, M. Howe, J. Morris, A. Goyal, A. Maxwell: 'Safety and feasibility of breast lesion localization using magnetic seeds (Magseed): a multi-center, open-label cohort study", Breast Cancer Research and Treatment (2018) 169:531-536

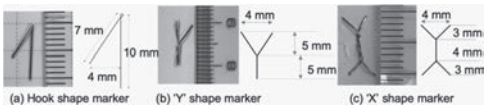


Fig. 1 Designs of the (a) Hook marker, (b) 'Y' shape marker and (c) 'X' shape marker.

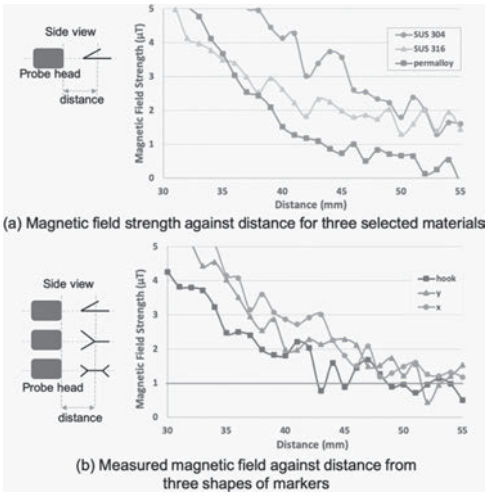


Fig. 2(a) Magnetic field strength against distance for SUS 304, SUS 316 and permalloy and (b)magnetic field strength from three shapes of markers

3:30

FF-09. Development of magnetometer with nitrogen-vacancy center in a bulk diamond for detecting magnetic nanoparticles in biomedical applications. *T. Kitaizumi*[1], A. Kuwahata[1], K. Saichi[1], T. Sato[1], R. Igarashi[2], T. Ohshima[2], Y. Masuyama[2,3], T. Iwasaki[3], M. Hatano[3], F. Jelezko[4], M. Kusakabe[1,5], T. Yatsui[1] and M. Sekino[1] *1. Graduate School of Engineering, The University of Tokyo, Tokyo, Japan; 2. National Institutes for Quantum and Radiological Science and Technology (QST), Chiba, Japan; 3. Department of Electrical and Electronic Engineering, Tokyo Institute of Technology, Tokyo, Japan; 4. Institute of Quantum Optics, Ulm University, Ulm, Germany; 5. Matrix Cell Research Institute Inc., Ibaraki, Japan*

Magnetic nanoparticles (MNPs) have been widely employed in biomedical applications, such as diagnosis and therapy of various diseases [1]. Advanced clinical studies have demonstrated the feasibility of the detection of MNPs using the magnetometer, as a promising technique alternative to harmful radioactive particles, to diagnose cancer metastasis in breast cancer patients [2,3]. To further expand the applicable clinical regime, there is a need to develop highly sensitive magnetic detection. The negatively charged nitrogen-vacancy (NV-) color center in a diamond provide immensely a remarkable quantum magnetic sensing, which enables us to detect sub-pico-Tesla at room temperature [4,5]. In this study, we have developed the novel magnetometer with NV- center in a bulk diamond for detecting MNPs (Fig. 1). The optical fiber-based system is employed to fabricate the compact probe system compared with a confocal-based optical system, and the alternating current (AC) magnetic fields (~1 mT) of the excitation coil system to magnetize MNPs yields the highly sensitive detection of MNPs. Figure 2(a) shows the magnetic sensitivity of the developed probe in the Lock-in detection system. The minimum detectable AC magnetic field is approximately 60 nT. The sensitivity of the MNPs detection with the developed probe strongly depends on the remnant excitation fields. We thus produced the magnetic null point at the NV- center location by using an additional cancellation coil for eliminating the remnant fields, and achieved the detectable distances with respect to MNPs of 40 and 5 mL are 9 and 5 mm, respectively, as shown in Fig. 2(b). These results indicate the developed probe can detect the tiny amount of MNPs. We will pursue the further highly sensitive detection by the enhancement of a light collecting efficiency and optimization of the excitation coil system.

[1]M. V. Yigit, A. Moore, and Z. Medarova, *Pharm Res.* 29, 1180 (2013). [2] M. Douek, J. Klaase, I. Monypenny *et al.*, *Ann. Surg. Oncol.*21, 1237 (2014). [3]M. Sekino, A. Kuwahata, T. Ookubo *et al*., *Scientific Reports*8, 1195 (2018). [4]J. M. Taylor, P. Cappellaro, L. Childress *et al*., *Nature Physics*4, 810 (2008). [5]T. Wolf, P. Neumann, K. Nakamura *et al*., *Phys. Rev. X*.5, 041001 (2015).

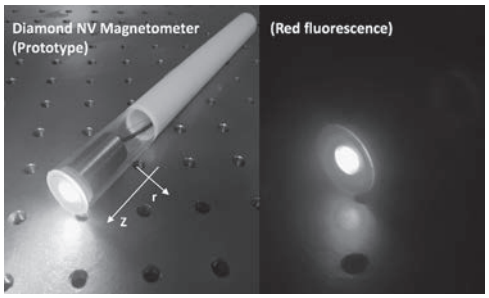


Fig.1 Developed magnetic probe with nitrogen-vacancy center in a bulk diamond. Green laser (532 nm) excites red fluorescence in a diamond NV. Longitudinal direction is *Z*-axis.

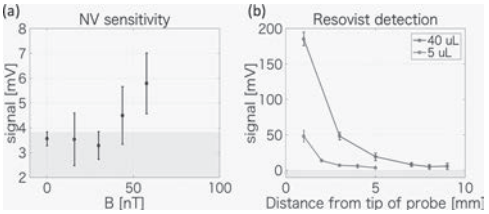


Fig.2 (a) Detectable magnetic field strength is approximately 60 nT for AC magnetic fields. (b) Longitudinal detectable distances with respect to MNPs (Resovist®) of 40 and 5 mL are 9 and 5 mm, respectively.

3:42

FF-10. Development of an automatic magnetic immunostaining system for rapid diagnosis of cancer metastasis. *M. Sekino*[1], A. Kuwahata[1], A. Yoshibe[1], K. Imai[1], M. Kaneko[1], S. Chikaki[1], I. Saito[1], A. Tsuruma[2], S. Sakamoto[2], H. Handa[3], S. Matsuda[4] and M. Kusakabe[5] *1. The University of Tokyo, Tokyo, Japan; 2. Tokyo Institute of Technology, Tokyo, Japan; 3. Tokyo Medical University, Tokyo, Japan; 4. Keio University School of Medicine, Tokyo, Japan; 5. Matrix Cell Research Institute Inc., Tokyo, Japan*

Magnetically-promoted rapid immunofluorescence staining – using the functionalized fluorescent ferrite beads (FF beads of ~200 nm with diameter) [1] and permanent magnets – is a novel technique providing us with the intraoperative diagnosis of cancer metastasis. The magnetic force of the magnets promotes the binding between the objects and FF beads, resulting in the reduction of the immunostaining time. Recent clinical studies have demonstrated the feasibility of this technique with experts' hand-operations [2]. There is a clinical need for the automation of this magnetic staining technique to diagnose without experts in medical institutions. In this paper, we established the specifications of an automatic system, such as the shape of a permanent magnet, the iron concentration of the FF beads, and the condition of immunoreaction, based on the hand-operated experimental results, and fabricated an automatic device. Figure 1(a) shows a magnetic immunostaining device to stain automatically five frozen sections of biomedical tissues, such as lymph nodes. The five sections are stained effectively by the reciprocating motion of the five magnets (the magnetic force: ~10^{-15} N for each nanoparticle). The automatic procedures are completed within 10 minutes, realizing the intraoperative diagnosis of cancer metastasis. Figure 1(b) shows five frozen sections of mouse xenograft samples stained simultaneously by the prototype device. While red fluorescence of cancer cells expressing EGFR (epidermal growth factor receptor) on the frozen section was clearly observed, there is no fluorescence on the section without EGFR.

The results indicate that we succeeded to demonstrate the feasibility of the automatic immunofluorescence staining. Further clinical studies with human lymph nodes are needed to develop as a medical device.

[1] S. Sakamoto, K. Omagari, Y. Kita *et al*., *Clinical Chemistry* 60, 610 (2014). [2] T. Ohnishi, S. Matsuda, Y. Nakamura *et al*., *Journal of Histochemistry & Cytochemistry* (2019).

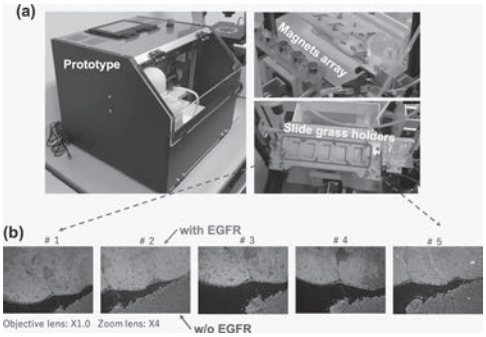


Fig.1 (a) Automatic magnetically-promoted rapid immunofluorescence staining device (prototype) with five permanent magnets and slide grass holders. (b) Five frozen sections of mouse xenograft samples simultaneously stained by the automatic staining device. Red and blue color represent the cancer cells expressing EGFR and the cell without EGFR, respectively.

3:54

FF-11. Development of an optimized dome-shaped magnet in magnetically-promoted rapid immunofluorescence staining for cancer diagnoses. *M. Sekino*[1], A. Kuwahata[1], S. Fujita[1], S. Matsuda[2], M. Kaneko[1], S. Chikaki[1], S. Sakamoto[3], I. Saito[4], H. Handa[5] and M. Kusakabe[6] *1. The University of Tokyo, Tokyo, Japan; 2. Keio University School of Medicine, Tokyo, Japan; 3. Tokyo Institute of Technology, Tokyo, Japan; 4. iMed Japan Inc., Tokyo, Japan; 5. Tokyo Medical University, Tokyo, Japan; 6. Matrix Cell Research Institute Inc., Ibaraki, Japan*

To accelerate the diagnosis speed of cancer cells, magnetically-promoted rapid immunofluorescence staining has been devised by the applications of the functionalized fluorescent ferrite beads (FF beads of ~200 nm with diameter) and the magnetic force generated by a permanent magnet [1,2]. This novel magnetic staining method enables us to diagnose cancer metastasis intraoperatively. To realize the spatial uniformity of magnetic immunostaining for enhancing the sensitivity of the diagnoses, the optimization of the magnetic shape that can generate the uniform/strong magnetic force is required. In this study, we developed the dome-shaped magnet optimized by numerical simulations and experimentally evaluated the uniformity of the immunostaining by using the optimized magnet. To promote the immunoreaction, the magnetic force (~10^{-13} N for each particle) is applied to the FF beads solution above the frozen section of cancer cells on the slide grass as shown in Fig. 1(a). Our numerical calculations show the magnetic force, particle trajectory of FF beads, and optimization of the magnet shape. Figure 1(b) shows the uniform distribution of the magnetic force and FF beads attracted on the frozen section compared with conventional column-shaped magnets. In Fig 2(a), red fluorescence color represents the cancer cell with EGFR (epidermal growth factor receptor) stained by the dome-shaped magnet. The spatial distribution of red fluorescence intensity of the dome-shaped magnet is uniform as same as numerical evaluations, as shown in Fig. 2(b). These results indicate the optimized dome-shaped magnet is effective for the uniform immunostaining. In the future, we will perform the clinical trial using human tissue, such as lymph nodes, to demonstrate the feasibility of this technique using the proposed magnet.

[1] S. Sakamoto, K. Omagari, Y. Kita *et al*., *Clinical Chemistry* 60, 610 (2014). [2] T. Ohnishi, S. Matsuda, Y. Nakamura *et al*., *Journal of Histochemistry & Cytochemistry* (2019).

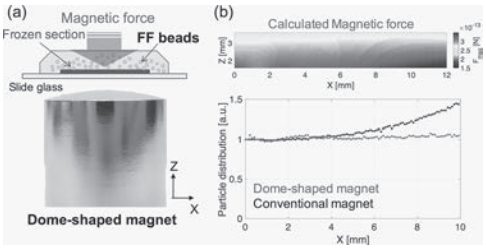


Fig.1 (a) Magnetically-promoted rapid immunofluorescence staining by using the optimized dome-shaped permanent magnet. (b) Distribution of the magnetic force applying to the FF beads (top) and spatial uniformity of the magnetic immunofluorescence staining (bottom) in numerical analyses.

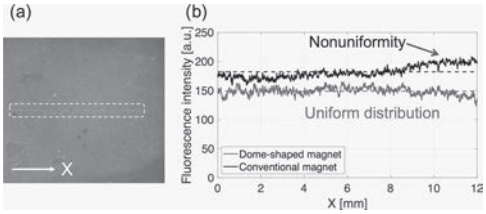


Fig.2 (a) Immunostaining of mouse xenograft samples using the proposed dome-shaped magnet and (b) the uniformity of the immunofluorescence staining.

4:06

FF-12. Capillary Hysteresis Effects in Magnetic Hyperthermia Cancer Treatment. *M. Pavel*[1], R. Tanasa[2], D. Constantinescu[1], C. Cianga[1], P. Cianga[1] and A. Stancu[1,2] *1. Department of Immunology, "Grigore T. Popa" University of Medicine and Pharmacy of Iasi, Iasi, Romania; 2. Department of Physics, Alexandru Ioan Cuza University of Iasi, Iasi, Romania*

As magnetic hyperthermia is gradually evolving towards an accepted technique for cancer treatment one observes the need for modeling the entire process with sufficient accuracy in order to avoid unnecessary destruction of healthy tissue during the treatment. The computation of the right doses of magnetic material for a concrete case includes not only the proper calculus of the heat produced by the magnetization a.c. process [1-3] but also the right distribution of the particles in the tissue with the proper consideration of the real physical properties of the tissue. This includes the initial process in which the magnetic fluid is inserted in the biological tissue by the means of a syringe. The most difficult part of this simulation is to take into account correctly how the fluid is flowing into the porous biological tissue. Recently, we have analyzed the case of homogenous porous media [4]. However the real media are non-homogenous and in order to correctly find the right distribution of particles in the porous material one should take into account the capillary hysteresis of the flow of the magnetic fluid. In this work we have simulated the flow of a magnetic fluid in a porous material with a known structure. We have evidenced a complex hysteretic behavior and identified the shape of a fundamental hysteron for the given structure (see Figs. 1-2). This type of hysteresis shows a number of similarities with the ferromagnetic hysteresis and potentially can be analyzed using the first-order reversal curves (FORC) technique, well known in magnetism. In the presentation we will show the properties of the hysteretic flow of the magnetic fluid in a real biological structure and evaluate the effect in the temperature field due to this fact.

[1] M. Pavel and A. Stancu, "Study of the Optimum Injection Sites for a Multiple Metastases Region in Cancer Therapy by Using MFH," Ieee Transactions on Magnetics, vol. 45, pp. 4825 (2009) [2] M. Pavel and A. Stancu, "Ferromagnetic Nanoparticles Dose Based on Tumor Size in Magnetic Fluid Hyperthermia Cancer Therapy," Ieee Transactions on Magnetics, vol. 45,

pp. 5251 (2009) [3] M. Pavel, G. Gradinariu, and A. Stancu, “Study of the Optimum Dose of Ferromagnetic Nanoparticles Suitable for Cancer Therapy Using MFH,” Ieee Transactions on Magnetics, vol. 44, pp. 3205 (2008) [4] I. Astefanoaei and A. Stancu, A computational study of the bioheat transfer in magnetic hyperthermia cancer therapy, J. Appl. Phys. 125, 194701 (2019)

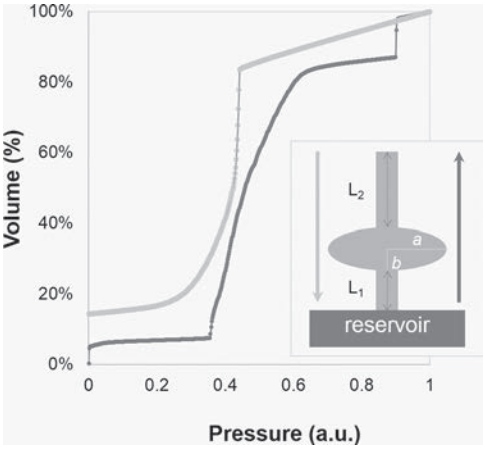


Fig.1. Typical hysteron for a system of one cavity and two necks (L1 and L2) presented in the inset.

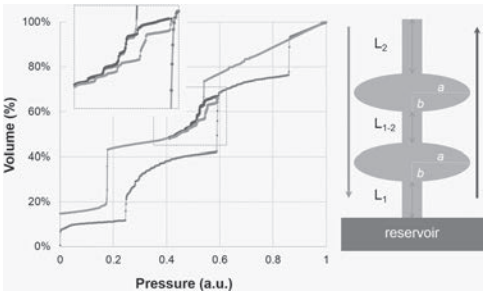


Fig. 2. The major hysteresis loop of two interacting hysterons. The inset shows a typical minor curve.

Session FG
THIN FILMS: EXCHANGE BIAS AND CHIRALITY

Jun Okabayashi, Chair
The University of Tokyo, Tokyo, Japan

CONTRIBUTED PAPERS

1:30

FG-01. The origin of the athermal training effect in exchange bias multilayers. *S. Jenkins*[1], R.W. Chantrell[1] and R.F. Evans[1] *1. Physics, University of York, York, United Kingdom*

The exchange bias effect occurs when a FM is coupled to an AFM, causing a shift of the magnetic hysteresis loop. The shift is caused by pinned interfacial spins, these cause a unidirectional field pinning the exchange coupling of atomic spins at the interface. The training effect causes a large drop in the measured exchange bias after the first measured hysteresis loop[1]. This has two main causes: thermal training and athermal training[1]. Thermal training is due to well understood thermal instabilities in the AFM\cite{training}. The origin of athermal training however is still a widely disputed problem due to the difficulty in experimentally probing the rearrangement of AFM spins at the interface. It has been proposed to be due to the degree of order of the AFM at the interface. Here we uncover the origin of training in a CoFe/$IrMn_3$ ferromagnet/antiferromagnet (FM/AFM) bilayer using an atomistic spin model. To model the properties of the CoFe/ $IrMn_3$ bilayer we have developed an atomistic spin model[2]. The properties of the disordered $IrMn_3$ AFM are modelled using the Heisenberg form of the exchange interaction and the anisotropy is calculated using the Neel pair anisotropy model. These reproduce key experimental results including the Neel temperature and magnetic ground state. It was found that for an atomically flat interface, after field cooling and equilibration, a simulated hysteresis loop gave an exchange bias field of less than 0.25T and the training effect was non existent. As the width of the interface mixing is increased the training effect becomes stronger as shown in Fig. 1. The exchange bias was observed to increase with interface mixing for the initial hysteresis loop but the training effect causes a much larger reduction for subsequent hysteresis loops when the interface is mixed. We will present further simulations of the temperature dependence of the exchange bias with thermal training and a statistical study of polygranular exchange biased systems.

[1] X. P. Qiu, et al. *Phys. Rev. Lett.*, 101: 147207, 2008. [2] Evans RFL et al. *Journal of Physics:Condensed Matter*, 26, 2014.

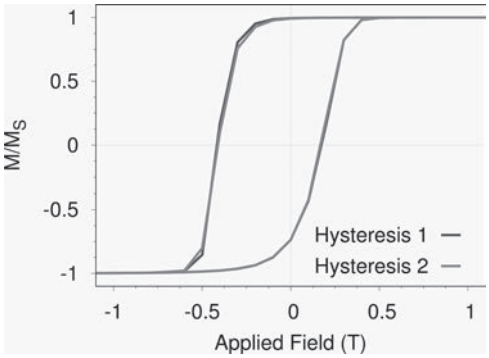


Fig. 1a. Simulated hysteresis loops showing the athermal training effect for an interface mixing of 0.4nm.

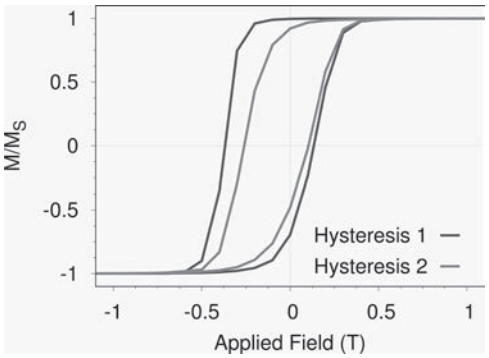


Fig. 1b. Simulated hysteresis loops showing the athermal training effect for an interface mixing of 0.8nm.

1:42

FG-02. Observation of a Chirality Created Exchange Bias Effect. *D. Lott*[3], K. Chen[1], A. Philippi-Kobs[2] and V. Lauter[4] *1. Helmholtz-Zentrum Berlin, Berlin, Germany; 2. Deutsches Elektronen-Synchrotron, Hamburg, Germany; 3. WPD, Helmholtz-Zentrum Geesthacht, Geesthacht, Germany; 4. Neutron Scattering Directorate, Oak Ridge National Laboratory, Oak Ridge, TN, United States*

The exchange bias effect refers to the unidirectional shift of the hysteresis loop of a magnetization curve, conventionally that of a ferromagnet in direct contact to an antiferromagnet. Chiral magnetism, on the other hand, that manifests in the existence of skyrmions or chiral domain walls, offers an alternative way for creating anisotropies in magnetic materials that might have large potential for being used in future spintronic devices. Alloys of rare-earth elements and 3d transition metals (RE-TM) became recently in the focus of attention due their rich variety of magnetic effects owed to the different anisotropies of both material classes [1-4]. Here we show experimental evidence for a new type of in-plane exchange bias effect present at room temperature that is created from a chiral 90 domain wall at the interface of a ferrimagnetic RE-TM (DyCo) layer in contact to a ferromagnetic (NiFe) layer. We found that the chiral interfacial domain wall is formed due to the presence of macroscopic Dzyaloshinskii-Moriya interaction in the ferrimagnetic layer and its orthogonal exchange coupling to the ferromagnetic layer at the interface. As a consequence of the fixed chirality of the interfacial domain wall, the sign of the shift of the hysteresis loop can be reversed by changing the direction of the out-of-plane magnetization of the ferrimagnetic layer (see Figure 1). The chirality created tunable exchange bias is very robust against high in-plane magnetic fields and does not show any damping effects after multiple reversal of the exchange bias direction, therefore, it overcomes the limitations of conventional exchange bias systems. Such chirality based EB systems may be of crucial importance for the development of future applications in the field of magnetic sensors and data storage devices.

[1] S. Mangin et.al, Phys. *Rev. B 80*, 2009, 224424; S. Mangin et.al, Phys. Rev. Lett. 82, 1999, 4336. [2] Chen, K., Lott, D. et al. *Phys. Rev. B* 91, 2015, 024409. [3] Chen, K., Lott, D. et al., *Sci. Rep.* 5, 2015, 18377. [4] F. Radu, R. Abrudan, I. Radu, D. schmitz H. Zabel, *Nat. Communications* 3, 2012, 715.

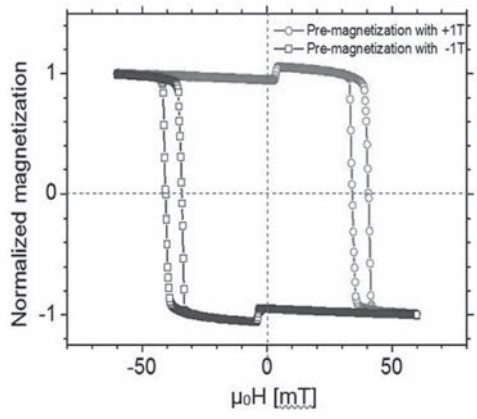


Fig. 1: Longitudinal Moke measurements showing the dual in-plane exchange bias effect: the red and blue curve after premagnetizing the bilayer along the positive or negative out-of-plane direction.

1:54

FG-03. Achiral in-plane Néel walls in interfacial Dzyaloshinskii-Moriya interaction systems. C.J. Agostino[1], *M. Robertson*[2], G. Chen[2], S. Kang[3], A. Mascaraque[4], E.G. Michel[5], C. Won[3], Y. Wu[6], A.K. Schmid[1] and K. Liu[2,7] *1. MSD, Lawrence Berkeley National Laboratory, Berkeley, CA, United States; 2. Department of Physics, University of California, Davis, Davis, CA, United States; 3. Department of Physics, Kyung Hee University, Seoul, The Republic of Korea; 4. Dpto. de Física de Materiales, Universidad Complutense de Madrid, Madrid, Spain; 5. Department of Condensed Matter Physics, Universidad Autonoma de Madrid, Madrid, Spain; 6. Department of Physics, Fudan University, Shanghai, China; 7. Department of Physics, Georgetown University, Washington, DC, United States*

The interfacial Dzyaloshinskii-Moriya interaction (DMI) is of great interest as it can stabilize chiral spin structures in thin film systems [1,2]. Usually in thin film systems with perpendicular magnetic anisotropy, the interfacial DMI vectors responsible for the type of magnetic chirality are expected to be parallel to the film plane [3], which has been experimentally demonstrated in many systems [4]. Measuring the rotation sense of in-plane Néel wall in in-plane magnetized systems may allow one to explore possible DMI vectors that are normal to the surface. In this work, we have measured the domain structures in magnetic films grown on fcc(001), fcc(110) and fcc(111) surfaces respectively. We find perpendicular magnetic anisotropy in Fe/Ni/Cu(001) and $[Co/Ni]_n$/Pt(111) systems where the interfacial DMI is sufficiently strong to stabilize chiral spin structures. By tailoring the effective anisotropy of the films, we observe achiral in-plane Néel walls in the in-plane magnetized regime in slightly thicker films with the same interfacial DMI interface. On the other hand, neither a perpendicularly magnetized regime nor in-plane Néel walls can be observed in Co/Pt(110) due to the presence of strong in-plane uniaxial magnetic anisotropy. These findings indicate that a substantial normal vector of the DMI is neither present in fcc(001) and fcc(111) oriented interfaces nor induced by atomic roughness. Supports by the NSF (DMR-1610060 and DMR- 1905468), UCOP (MRP-17-454963), and DOE (DE-AC02-05CH11231) are gratefully acknowledged.

[1] A. Fert, et al. Nat. Nanotech. 8, 152 (2013). [2] R. Wiesendanger, Nat. Rev. Mater. 1, 16044 (2016). [3] A. Crépieux, C. Lacroix, J. Magn. Magn. Mater. 182, 341 (1998). [4] W. Jiang, et al. Phys. Rep. 704, 1 (2017).

2:06

FG-04. Modulation vector dependence of a second helical phase pocket in FeGe. *D. Burn*[1], S. Zhang[2,3], S. Wang[4], H. Du[4], G. van der Laan[1] and T. Hesjedal[2] *1. Diamond Light Source, Oxford, United Kingdom; 2. Department of Physics, University of Oxford, Oxford, United Kingdom; 3. School of Physical Science and Technology, ShanghaiTech University, Shanghai, China; 4. High Magnetic Field Laboratory, Chinese Academy of Sciences, Hefei, China*

FeGe is a noncentrosymmetric helimagnet in which non-collinear spin textures result from a competition between the exchange interaction and the spin-orbit-induced Dzyaloshinskii-Moriya interaction. Below the ordering temperature, T_c, bulk FeGe has a well-established and rich magnetic phase diagram showing helical, conical, and skyrmion states [1]. The skyrmion pocket has a wide temperature-field window extending up to room temperature [2,3] which can be manipulated through changes to the sample thickness [2,4]. These features make FeGe of great interest due to the potential for novel room-temperature technological devices based on the manipulation of topological magnetic states. In this work, we characterize the magnetic states in a thin slab of FeGe with smallangle soft x-ray scattering on beamline I10 at the Diamond Light Source as a function of both temperature and magnetic field applied out-of-plane. In addition to the helical, conical, and skyrmion phases, we observe an additional helical phase which coexists beneath the skyrmion phase towards the higher field boundary of the helical phase. In contrast to the other phases this additional helical phase shows strong uniaxial preferential alignment of the modulation vector. We have also explored the variation in the magnitude of the modulation vector when traversing each of the magnetic phase pockets. For the helical and conical phases, this shows a field-dependent but temperature-independent variation, whereas for the skyrmion phase both a field and temperature variation is observed. Furthermore, the two helical phases show significantly different coefficients for the field-dependent modulation vector contraction. Our findings build on other work for FeGe, strengthening the case that the room-temperature topological magnetic properties are of great interest for the development of novel technological devices. Our work shows how multiple coexistent phases can be simultaneously and uniquely identified which will provide further opportunities for potential information processing and storage methodologies.

[1] A. Bauer and C. Pfleiderer, Springer Series in Materials Science 228, 1 (2016). [2] X. Z. Yu, N. Kanazawa, Y. Onose, K. Kimoto, W. Z. Zhang, S. Ishiwata, Y. Matsui, and Y. Tokura, Nat. Mater. 10, 106 (2011). [3] H. Wilhelm, M. Baenitz, M. Schmidt, C. Naylor, R. Lortz, U. K. Robler, A. A. Leonov, and A. N. Bogdanov, J. Phys.: Condens. Matter 24, 294204 (2012). [4] S. X. Huang and C. L. Chien, Phys. Rev. Lett. 108, 267201 (2012).

2:18

FG-05. Interlayer exchange coupling in Fe/MgO/$Co_xFe_{3-x}O_4$(001) trilayers. *H. Koizumi*[1], M. Hagihara[1], S. Kobayashi[1] and H. Yanagihara[1,2] *1. Department of Applied Physics, University of Tsukuba, Tsukuba, Japan; 2. Tsukuba Research Center for Energy Materials Science, Tsukuba, Japan*

Interlayer exchange coupling (IEC) is a phenomenon in which two ferromagnetic (FM) layers are magnetically coupled and is understood within the framework of the spin-dependent quantum well model [1]. IEC is often found in trilayer systems with various different metallic layers. Besides the metallic trilayer systems, IEC through an insulating layer has also been reported for Fe/MgO/Fe [2], Fe/MgO/γ-Fe_2O_3(001) [3] and so on. Since thin films of $(Co,Fe)_3O_4$(CFO)(001) grown on MgO(001) exhibit large perpendicular magnetic anisotropy [4], we can expect that the trilayer of Fe/ MgO(t_{MgO})/CFO(001) shows IEC between a perpendicular FM insulator and an in-plane FM metal films. The multilayered structure of Fe/MgO/CFO was deposited on a MgO(001) substrate by the RF magnetron sputtering method. The thickness of the MgO(t_{MgO}) layer was formed with a wedged shape by using a continuously moving mask. We used two alloy targets

of Co_xFe_{3-x} with the composition ratio of x=0.75 and 0.125. Since both MgO and CFO are good insulators, anomalous Hall effect (AHE) measurements of the trilayer system solely reflect the magnetization processes of the Fe layer, and therefore the change of the saturation field($\Delta\mu_0 H_A$) determined from the Hall curves indicates the variation of IEC as a function of t_{MgO}. Because of the low $\mu_0 H_A$ and positive remanence, the evaluated exchange coupling at the interface of the bilayer system of Fe/CFO with x=0.125 is ferromagnetic. While the bilayer with x=0.75 was antiferromagnetic because of negative remanence. The trilayer systems of Fe/MgO/CFO with t_{MgO} ranging from 0.5 to 1 nm showed antiferromagnetic coupling for both x=0.125 and x=0.75, as shown in Fig.1. The overall t_{MgO} dependent IEC can be understood as the combination of both the *direct* coupling component that simply decreases with t_{MgO} and the MgO-mediated *indirect* antiferromagnetic coupling that exhibits a maximum at 0.5 to 1 nm. This result suggests that the composition ratio of the ferromagnetic material can control the strength of the IEC.

[1] P. Bruno, Phys. Rev. B, 52 411(1995) [2] J. Faure Vincent, et al., Phys. Rev. Lett., 89 107206 (2002) [3] H. Yanagihara, et al., J. Appl. Phys., 101 09D101 (2007) [4] T.Niizeki, et al., Appl. Phys. Lett., 103 162407 (2013)

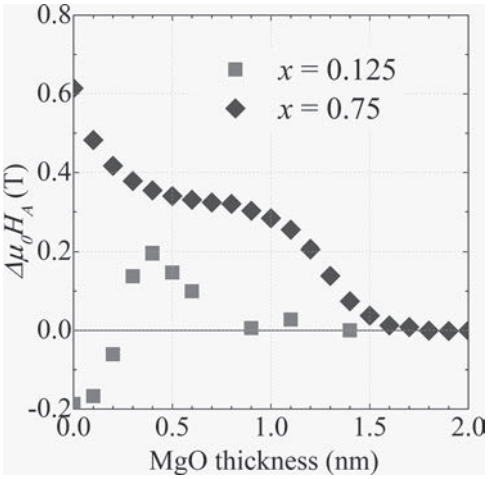


Fig.1 MgO film thickness dependence of $\Delta\mu_0 H_A$

2:30

FG-06. Ab initio calculation of interlayer exchange coupling in synthetic antiferromagnetic pinned layer. *R. Takashima*[1], T. Tsukagoshi[1], T. Ishihara[1] and T. Kai[1] *1. Institute of Memory Technology Research & Development, Toshiba Memory Corporation, Kawasaki, Japan*

Interlayer exchange coupling (IEC)[1,2], coupling between two magnetic layers separated by a non-magnetic spacer layer, plays a crucial role in MRAM. Antiferromagnetic IEC is commonly used in the pinned layer in magnetic tunneling junctions (MTJ); the stray field can be reduced with the use of synthetic antiferromagnets (SAF), where magnetic layers have anti-parallel spin configuration via IEC [3]. In previous works, Co/Ru/Co or Co/Ir/Co, which shows strong antiferromagnetic IEC, has been considered as a promising material for SAF pinned layers [4]. However, it is recently pointed out that even stronger IEC is required in SAF pinned layers to increase the reliability of the operation in high density MRAM [5]. Therefore, it is necessary to find materials that show stronger IEC. In this work, we theoretically investigate IEC in cobalt-based multilayers by first principles calculations based on density functional theory (DFT) (Fig. 1), and find that several alloy spacers exhibit much stronger IEC compared to previously known spacers such as Ru and Ir. We show that IEC in $Co/Ru_{1-x}Fe_x/Co$ ($0 \leqq x \leqq 0.5$) increases as x increases (left panel in Fig.2), which qualitatively agrees with a recent experiment [6]. Furthermore, we show that several binary alloy spacers composed of a group 8 element and a group 9 element have stronger IEC compared to a single element spacer. In particular, we find that IEC in $Co/Ru_{0.5}Ir_{0.5}/Co$ is 1.4 times as stronger as one in Co/Ru/Co (right panel in Fig. 2). We expect that our study opens up new perspectives for the development of high density MRAM.

[1] S. S. P. Parkin, N. More, and K. P. Roche, Phys. Rev. Lett. 64, 2304 (1990). [2] M. D. Stiles, J. Magn. Magn. Mater. 200, 322 (1999). [3] S. Bandiera et al., IEEE Magn. Lett., 1, 3000204 (2010). [4] K.Yakushiji et al., Appl. Phys. Lett. 110, 092406 (2017). [5] S. Itai et al., 2019 Joint MMM-Intermag Conference, AK-06 (2019). [6] Z. Nunn et al., 2019 Joint MMM-Intermag Conference, AD-12 (2019).

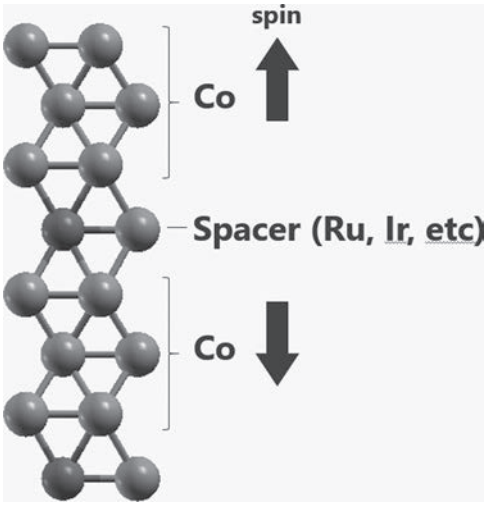


Fig.1 Superlattice structure used in DFT calculations. A magnetic layer is composed of 3 Co monolayers and a spacer layer is monolayer alloy.

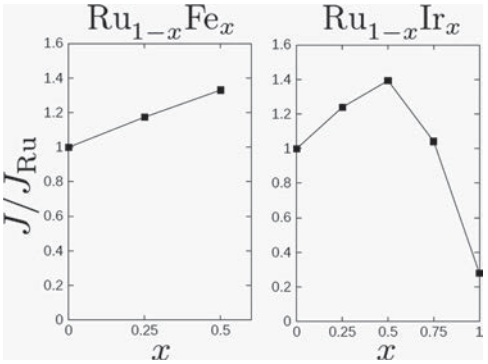


Fig.2 Interlayer exchange coupling (IEC) in $Co/Ru_{1-x}Fe_x/Co$ (left panel) and $Co/Ru_{1-x}Ir_x/Co$ (right panel). J denotes IEC in each system and J_{Ru} denotes IEC in Co/Ru/Co.

2:42

FG-07. Enhanced Exchange Interaction between Fe and FeO in Fe/FeO/CoO(NiO) due to the Antiferromagnetic Proximity Effect. *A. Koziol-Rachwal*[1], M. Slezak[1], P. Drozdz[1], W. Janus[1], K. Matlak[1], M. Szpytma[1], J. Korecki[1,2] and T. Slezak[1] *1. Solid State Physics, AGH University of Science and Technology, Krakow, Poland; 2. Jerzy Haber Institute of Catalysis and Surface Chemistry Polish Academy of Science, Krakow, Poland*

Antiferromagnets are promising candidates for future spintronic materials. However, due to the low ordering temperature a wide group of antiferromagnetic (AFM) materials seems to be useless for application. A new route towards formation of AFMs with a high ordering temperature and tunable spin configuration is to use magnetic proximity effect in AFM/AFM bi/multi-layered

structures.[1,2] In our study we examine the influence of proximity of antiferromagnetic layer with a higher ordering temperature on the magnetic properties of FeO in Fe/FeO/NiO(CoO). The layers were grown by molecular beam epitaxy on MgO(001) substrate. First, wedged shaped CoO(NiO) layers were prepared by reactive deposition of metal in an oxygen atmosphere on Cr buffer layer. After NiO(CoO) deposition FeO layer with a thickness of 1.9nm was prepared following the procedure described in [3]. Finally, 1-nm thick Fe layer was grown and capped with 3nm of MgO. The antiferromagnetic proximity effect was evaluated via examination of exchange interaction between Fe and FeO in Fe/FeO/NiO(CoO). Figure 1 presents temperature dependence of exchange bias field (H_{EB}) determined for Fe/FeO/NiO(CoO) systems from the hysteresis loops measured with longitudinal magnetooptic Kerr effect (LMOKE). While for Fe/FeO bilayer we noted H_{EB}=100Oe the exchange interaction between Fe and FeO was strongly enhanced when the Fe/FeO bilayer was grown on NiO(CoO). In particular for Fe/FeO/CoO(0.5nm) we noted a maximum of H_{EB} of about 600Oe. Moreover, with increasing CoO thickness significant enhancement of blocking temperature T_B was observed. For CoO thickness $t_{CoO} \geq$ 2nm T_B=290K can be estimated from MOKE data, which is much higher than a blocking temperature of Fe/FeO bilayer (140K). Similar enhancement of exchange interaction and increase of blocking temperature (T_B) was observed for Fe/FeO/NiO in comparison with Fe/FeO. In this case T_B was estimated to be 230K. Our study demonstrate the feasibility of tailoring the magnetic properties of AFM layer with a proximity of other AFM. Acknowledgment This work was supported by the "Antiferromagnetic proximity effect and development of epitaxial bimetallic antiferromagnets – two routes towards next-generation spintronics" project which is carried out within the Homing programme of the Foundation for Polish Science co-financed by the European Union under the European Regional Development Fund.

[1]J. Zhu, Q. Li, J. X. Li *et al.*, *Phys. Rev. B - Condens. Matter Mater. Phys.* 90, 1–7 (2014). [2]Q. Li, J. H. Liang, Y. M. Luo *et al.*, *Sci. Rep.* 6, 22355 (2016). [3]A. Koziol-Rachwal, T. Slezak, T. Nozaki *et al.*, *Appl. Phys. Lett.* 108, 041606 (2016).

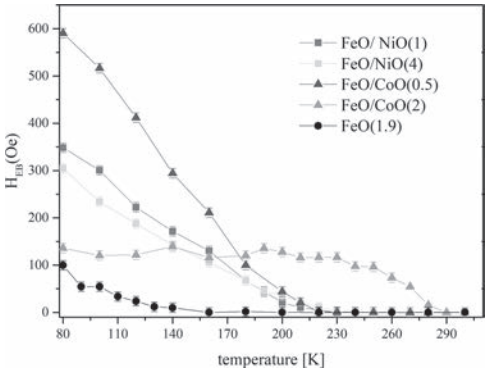


Fig. 1 Exchange bias field dependence on temperature obtained from LMOKE hysteresis loops for Fe/FeO and for Fe/FeO/NiO(CoO) for representative NiO(CoO) thicknesses.

2:54

FG-08. Fabrication and characterization of IrMn/PtMn/PtCr/PtMn antiferromagnets in terms of the role of each layer. *M. Saito*[1] and F. Koike[1] *1. Alps-Engineering Headquarters, Alps Alpine Co., Ltd., Nagaoka, Japan*

Antiferromagnet (AF) films of PtCr/Mn (0.5 nm), PtCr/FeMn (0.5 nm), and PtCr/PtMn (2 nm) exhibit a large unidirectional anisotropy constant (J_k) and high blocking temperature (T_b) [1], [2]. The $L1_0$ ordering temperature for PtCr (30 nm) was reduced by inserting PtMn (2 nm) at the CoFe/PtCr interface [2]. The AF layer structure was extended to $Ir_{80}Mn_{20}/Pt_{50}Mn_{50}/Pt_{50}Cr_{50}/Pt_{50}Mn_{50}$. Fig. 1 shows magnetization loops obtained for Si/alumina/NiFeCr/Cu/Ru/$Fe_{60}Co_{40}$(10 nm)/AF(30 nm)/Ru/Ta, where the AFs were PtMn(2 nm)/PtCr(28 nm) and IrMn(0.8 nm)/PtMn(1.2 nm)/PtCr(25 nm)/PtMn(3 nm), annealed at 350 °C for 20 h in a 10-kOe static field. Coercivity (H_c) was nearly halved while the exchange bias field (H_{ex}) remained almost unchanged, resulting in H_{ex}/H_c ratio > 1 for the later AF. Fig. 2 shows J_k plotted against total AF thickness, where the AFs were PtCr, PtMn, PtMn(2 nm)/PtCr, IrMn(0.8 nm)/PtMn(1.2 nm)/PtCr, and IrMn(0.8 nm)/PtMn(1.2 nm)/PtCr/PtMn(3 nm). The PtCr sandwiched by thin PtMn with ultrathin IrMn inserted at the FeCo layer interface showed J_k > 0.4 erg/cm^2, though total AF thickness was reduced to 18 nm. Effects of the PtMn layers are presumably the same as the reported effects of decreasing the $L1_0$ transformation temperature for FePt by AuCu [3] and PtMn [4] underlayers, and assisting PtMn ordering by the AuCu underlayer [5]. In other words, the typical annealing temperature to achieve ordered PtMn was much lower than that of PtCr, and the c/a ratio of bulk $L1_0$ PtMn was 0.92, lower than that of PtCr (0.99). The a-axis lattice constants of bulk $L1_0$ PtMn and PtCr were 0.400 nm and 0.382 nm, respectively. The larger lattice constants and lattice deformation during $L1_0$ transformation of PtMn may promote PtCr ordering, though the PtCr thickness was reduced to 11 nm. The dependence of each AF layer thickness on exchange bias properties and T_b will be shown at the conference to further discussed the role of each AF layer. GMR/TMR films utilizing the PtCr-based AF should achieve robust and thermally stable pin layers.

[1] B. Dai, Y. Lei, X. P. Shao, and J. Ni, J. Alloys Compd., Vol. 490, p. 427 (2010). [2] M. Saito and F. Koike, AIP Adv. Vol. 9, 035306 (2019) [3] Y. Zhu and J. W. Cai, Appl. Phys. Lett., Vol. 87, 032504 (2005). [4] C. C. Chiang, C. H. Lai, and Y. C. Wu, Appl. Phys. Lett., Vol. 88, 152508 (2006). [5] S. Soeya, Appl. Phys. Lett., Vol. 94, 242507 (2009).

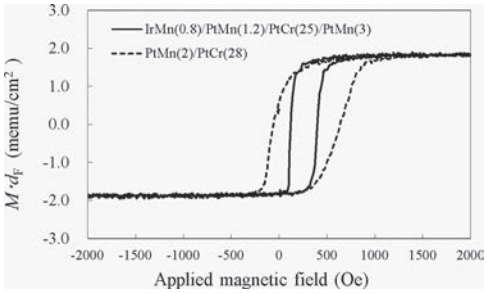


Fig. 1: Magnetization loops for Sub./NiFeCr/Cu/Ru/$Fe_{60}Co_{40}$(10 nm)/AF/Ru/Ta films.

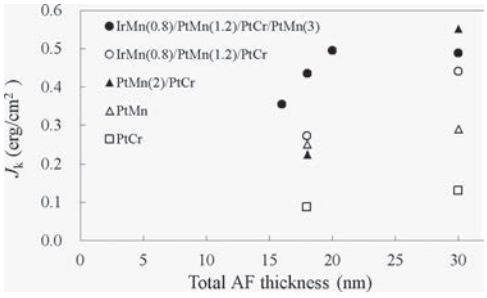


Fig. 2: J_k vs. total AF thickness for Sub./NiFeCr/Cu/Ru/$Fe_{60}Co_{40}$(10 nm)/AF/Ru/Ta films.

3:06

FG-09. Unidirectional and uniaxial anisotropies in the MnN/CoFeB exchange bias system. *A. Rai*[1,2], M. Dunz[3], A. Sapkota[1,2], P. Zilske[3], J.B. Mohammadi[4], M. Meinert[3], C.K. Mewes[1,2] and T. Mewes[1,2]
1. Department of Physics and Astronomy, The University of Alabama, Tuscaloosa, AL, United States; 2. Center for Materials for Information Technology, The University of Alabama, Tuscaloosa, AL, United States; 3. Center for Spinelectronic Materials and Devices, Department of Physics, Bielefeld University, Bielefeld, Germany; 4. Center for Quantum Phenomena, Department of Physics, New York University, New York, NY, United States

MnN as an antiferromagnet has a very large exchange bias and is known to have a large bulk Neel temperature of 600K [1] and is quite stable [2]. In this study we investigated Ta (10 nm)/MnN (30 nm)/CoFeB (t_{CoFeB})/Ta (0.5 nm)/Ta_2O_5 (2 nm) exchange bias system with CoFeB film thicknesses ranging from 5 to 20 nm. Using broadband and in-plane angle dependent ferromagnetic resonance measurements, we find a strong unidirectional anisotropy accompanied by a strong uniaxial in-plane anisotropy and a small interfacial perpendicular anisotropy $K_{\perp,i}$ = 0.043 ± 0.001 erg/cm^2. The strength of the interfacial exchange bias coupling in this system $\Delta\sigma_{eb}$ = 0.193 ± 0.005 erg/cm^2 is about 2.5 times larger than the interfacial uniaxial coupling strength $\Delta\sigma_u$= 0.076 ± 0.003 erg/cm^2 [3]. Exchange bias systems have shown a unidirectional contribution to relaxation [4,5]. For this system, we see a strong unidirectional and uniaxial in-plane anisotropy contribution to relaxation as shown in Fig 1 [3]. Our observations are consistent with the models of exchange bias that predict a square root dependence of the macroscopic coupling energies and on the corresponding local coupling energies [6]. In addition to that, the uniaxial anisotropy of the relaxation follows t_{CoFeB}^{-2} dependence (interfacial two-magnon scattering contribution). However, we find the uniaxial anisotropy of the relaxation does not strictly follow a t_{CoFeB}^{-2} dependence. Acknowledgements: MINT Center summer program & NSF-CAREER #1452670

1. M. Meinert, et al., Physical Review B., vol 92 (14), p. 144408 (2015) 2. A. Leineweber, et al., Journal of Materials Chemistry., vol 10 (12), p. 2827-2834 (2000) 3. A. Rai, et al., Journal of Magnetism and Magnetic Materials., vol 485, p. 374-380 (2019) 4. T. Mewes, et al., Magnetics Letters, IEEE., vol 1, p. 3500204-3500204 (2010) 5. J. B. Mohammadi, et al., Physical Review B., vol 95 (6), p. 064414 (2017) 6. F. Radu and H. Zabel, Springer Tracts in Modern Physics., vol 227, p. 97-184 (2008)

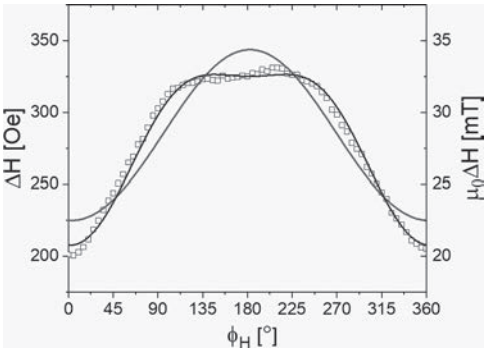


Fig 1: In-plane angle dependent ferromagnetic resonance measurement of sample (t_{CoFeB} = 9 nm). The red curve shows the least-square fit of the data assuming only a unidirectional contribution to the relaxation, whereas the blue fit curve includes a unidirectional and uniaxial contribution to the relaxation.

3:18

FG-10. Interface Engineering towards Enhanced Exchange Interaction between Fe and FeO in Fe/MgO/FeO Epitaxial Heterostructures. *A. Koziol-Rachwal*[1], W. Janus[1], M. Szpytma[1], P. Drozdz[1], M. Slezak[1], K. Matlak[1], T. Slezak[1] and J. Korecki[1,2] *1. Solid State Physics, AGH University of Science and Technology, Krakow, Poland; 2. Jerzy Haber Institute of Catalysis and Surface Chemistry Polish Academy of Science, Krakow, Poland*

Interface structure plays a decisive role in determining the properties of ultrathin multi- layer structures. For ferromagnetic(FM)/antiferromagnetic(AFM) bi-layers ability to grow controllable, well-defined interface is crucial for interface driven phenomena such as exchange coupling between FM and AFM. [1] Recently, we succeeded in stabilization of an epitaxial wüstite (FeO) film on MgO(001) by reactive deposition of Fe in oxygen atmosphere[2] and we showed that proximity of a metallic Fe layer deposited on FeO(001) modifies the chemical and magnetic properties of oxide in the Fe/FeO stack. In present study we examined chemical and magnetic properties of FeO in an epitaxial Fe/MgO(d_{MgO})/FeO trilayers for different MgO thicknesses, d_{MgO}. Analysis of the chemical structure revealed a stoichiometry improvement of the FeO layer in Fe/MgO/FeO in comparison with a Fe/FeO bilayer. Interestingly, in Fe/MgO/FeO system, despite the separation of Fe and FeO films, enhancement of the exchange bias was observed as compared with the Fe/FeO bilayers owing to the superior structural and magnetic structure quality of FeO. For d_{MgO}=1.4Å we noted a 200% enhancement of exchange bias in Fe/MgO/FeO as compared with Fe/FeO. Acknowledgment *This work was supported by the "Antiferromagnetic proximity effect and development of epitaxial bimetallic antiferromagnets – two routes towards next-generation spintronics" project which is carried out within the Homing programme of the Foundation for Polish Science co-financed by the European Union under the European Regional Development Fund.*

[1] W. Zhang and K.M. Krishnan, Mater. Sci. Eng. R 105, 1 (2016). [2] A. Koziol-Rachwal, T. Slezak, T. Nozaki *et al.,* Appl. Phys. Lett. 108, (2016).

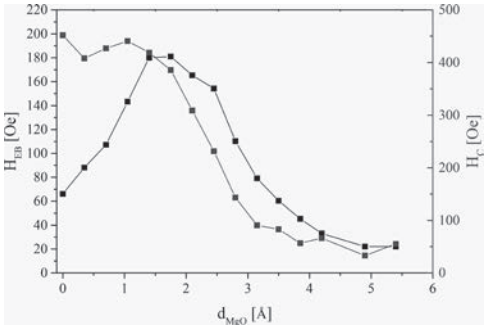


Fig. 1. Exchange bias field (black points) and coercive field (blue points) dependence on MgO thickness (d_{MgO}) in Fe/MgO(d_{MgO})/FeO determined from LMOKE measurements at 80 K.

3:30

FG-11. Magnetic Properties of Multilayers That Include GdFeCo Thin Films. *J. Bello*[1], M. Hehn[1] and S. Mangin[1] *1. Spintronics and Nanomagnetism group, Institut Jean Lamour, Nancy, France*

Amorphous rare-earth transition-metal (RE-TM) GdFeCo thin films are well-known to exhibit many interesting magnetic properties. Among those properties, perpendicular to film plane magnetization could be stabilized with weak anisotropies and total moment compensation depends on concentration and temperature. In addition to magnetic fields, its magnetic moment has been shown to be switched either by single femtosecond laser pulse [1] or spin orbit torque [2]. Since this material appears to be promising for future spintronics applications, we focused on the study of the magnetic

properties of multilayers that include this material. We first report the dependence of magnetic properties in $Gd_x(Fe_{90}Co_{10})_{1-x}$ ferrimagnetic alloys single layers on the composition and on the nature of the interfaces. 5nm thick $Gd_x(Fe_{90}Co_{10})_{1-x}$ layers were integrated in different multilayers, all grown by magnetron sputtering. For x between 22 and 33, we show that the composition at which the magnetic compensation occurs changes depending on the layers under and over the TE-RM layer. We studied different interfaces M/GdFeCo/N with M or N = Cu, Pt, Ta, Ir. We will detail which multilayer shows out of plane magnetization and for which compositions. Then, for GdFeCo layers having out of plane magnetization, more complex structures have been grown associating two GdFeCo layers. Especially, we grew GdFeCo/Ir/GdFeCo with varying Ir thickness. We show that it is possible to have an antiferromagnetic coupling (Fig. 1). As for ferromagnetic layers, the coupling depends on the thickness of the Ir layer and varies following the typical oscillation of the RKKY interaction. Those synthetic antiferromagnetics will be used in the future to extend the Walker breakdown limit for domain wall motion as predicted [3]. Domain wall motion at compensation of the SAF or of each layer will be measured. Furthermore, magnetization reversal using laser pulses or spin orbit torques will be tested in the near future on the same structures.

[1] C. D. Stanciu, et al., Phys. Rev. Lett. 99, 047601 (2007)
[2] N. Roschewsky, et al., Appl. Phys. Lett. 109, 112403 (2016)
[3] M. Kuteifan, et al., AIP Adv. 6, 045103 (2016)

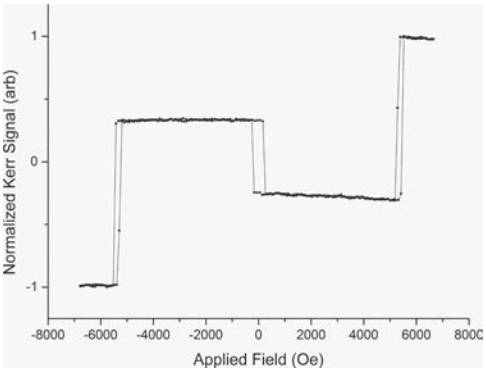


Fig. 1 Normalized Kerr signal of a GdFeCo(5)/Ir(0.5)/GdFeCo(5) sample

3:42

FG-12. Broad Tunability of Interfacial Magnetic Anisotropy by Rashba Spin-orbit Coupling in Metal/Ferrimagnetic-Insulator Bilayers. *A.J. Lee*[1], A.S. Ahmed[1], B. McCullian[1], S. Guo[1], M. Zhu[2], S. Yu[1], P. Balachandran[3], J. Hwang[2], P.C. Hammel[1] and F. Yang[1] *1. Physics, The Ohio State University, Columbus, OH, United States; 2. Center for Electron Microscopy and Analysis, The Ohio State University, Columbus, OH, United States; 3. Materials Science and Engineering, University of Virginia, Charlottesville, VA, United States*

It has been widely studied and accepted that the interface of a magnetic thin film can play a crucial role in the film's overall magnetism and therefore can be manipulated to alter magnetic properties. Specifically, interfacial magnetic anisotropy research has focused on metallic ferromagnets where specific seed and capping layers can be used to change the film's anisotropy. However, less attention has been dedicated to insulating ferrimagnets, which are advantageous for spintronic applications as they typically have low damping and are not susceptible to current shunting and Joule heating. In this work we studied how various capping layers can significantly change the interfacial magnetic anisotropy of high-quality, epitaxial thin films of $Tm_3Fe_5O_{12}$ (TmIG), an insulating ferrimagnet that is perpendicularly magnetized when under tensile strain. TmIG thin films were capped with a wide range of elemental metals spanning a significant portion of the periodic table to illuminate trends in interfacial magnetic anisotropy caused by Rashba spin-orbit coupling. The angular dependence of the ferromagnetic resonance fields (H_{res}) was utilized to extract the effective saturation magnetization ($4\pi M_{eff} = 4\pi M_s - H_\perp$) before and after the capping layers were grown. Figure 1a – h shows this angular dependence before and after capping TmIG as well as the extracted change in the effective saturation magnetization, $\Delta(4\pi M_{eff})$, for a subset of the capping layers tested. Depending on the capping material, $4\pi M_{eff}$ can vary from no change at all to as large as ~2000 G. Figure 2 shows $\Delta(4\pi M_{eff})$ for the fifteen capping layers that were tested as a function of the group number in the periodic table. This large survey of different capping layers in contact with a ferrimagnetic oxide will aid in the understanding of Rashba spin-orbit coupling that causes this large change in interfacial magnetism.

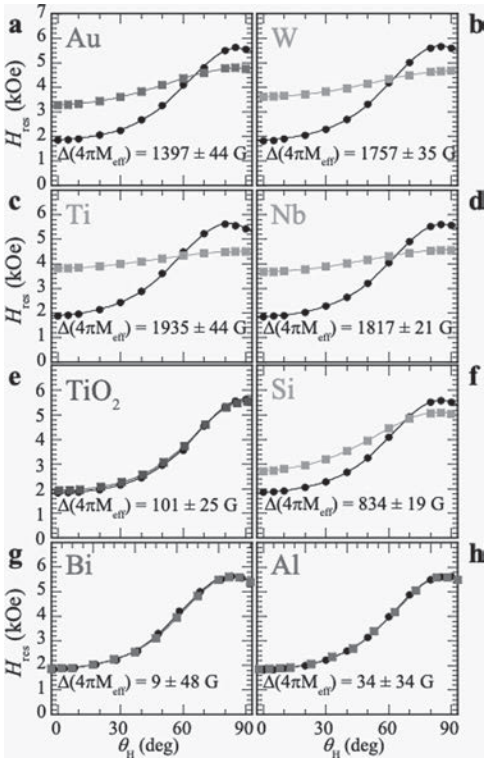


Fig.1 Angular dependence of the resonance fields before (circles) and after (squares) the TmIG(5 nm) films were capped with the material shown in the top left corner of each panel.

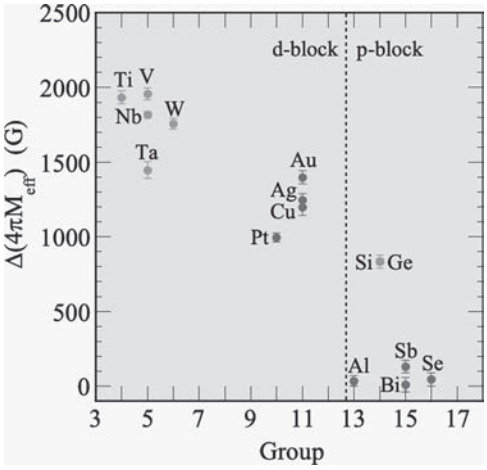


Fig.2 $\Delta(4\pi M_{eff})$ of TmIG(5 nm) as a function of the capping layer's group number in the periodic table.

3:54

FG-13. Epitaxial Ferrimagnetic Mn_4N Grown on MgO and GaN: A Comparative Study. *Z. Zhang*[1], J. Singhal[1], Y. Cho[1], P. Dang[1], H. Lee[1], Y. Tang[1], D. Ralph[1], H.G. Xing[1] and D. Jena[1] *1. Cornell University, Ithaca, NY, United States*

Epitaxial growth of ferromagnetic thin films on semiconductors is attracting much interest for devices that exploit spin-orbit torques, and aim to merge logic, memory and communication components. Among them, the rare-earth-free ferrimagnet Mn_4N (Fig.1(a)) is promising because of a high Neel temperature of 738K, perpendicular magnetic anisotropy, a large anomalous Hall resistance (AHR), as well as large domain size and high domain wall velocities [1-5]. Furthermore, GaN based RF and power electronics platforms can benefit tremendously if magnetic materials could be integrated seamlessly with the GaN material system [6]. However, properties of epitaxial Mn_4N films on GaN have not been reported. Here we report the successful growth of Mn_4N on both MgO substrates and GaN templates using plasma assisted molecular beam epitaxy (Fig.1(b)). Xray diffraction (XRD) on films grown on both substrates show no peaks from other manganese nitride phases (Fig.1(c)). The Mn_4N films on MgO are single crystal with roughness less than 8 Angstrom (Fig.1(d)). The films on GaN are polycrystalline with a rougher surface. For films on MgO, we observe negative AHR with rapid magnetization switching and full remanence at zero field, as shown in Fig.2(a). In sharp contrast, on GaN the AHR (Fig.2(b)) shows a positive sign with a much smaller Hall angle. In addition, we also observe humps in AHR especially at low temperatures for film on GaN. Both the coercive field and saturation moment are found to decrease much faster with temperature when grown on GaN (Fig.2(c)&(d)). The magnetic hysteresis loop of the Mn_4N film on GaN is more rounded with half remanence at zero field. Finally, a shift of the M vs H hysteresis loop as well as an increase in coercive field are observed when field cooling to 5K for Mn_4N on GaN. The underlying reason for these differences will be discussed in detail.

[1]. K. M. Ching et al., *J. Appl. Phys*. 76, 6582 (1994) [2]. S. Dhar et al., *Appl. Phys. Lett*. 86, 112504 (2005) [3]. Meng, M et al., *Appl. Phys. Lett*. 112, 132402 (2018) [4]. Toshiki Gushi et al., *Jpn. J. Appl. Phys*. 57, 120310 (2018) [5]. Yasutomi, Yoko et al., *J. Appl. Phys*. 115, 17A935 (2014) [6]. Debdeep Jena et al., *Jpn. J. Appl. Phys*. 58, SC0801 (2019)

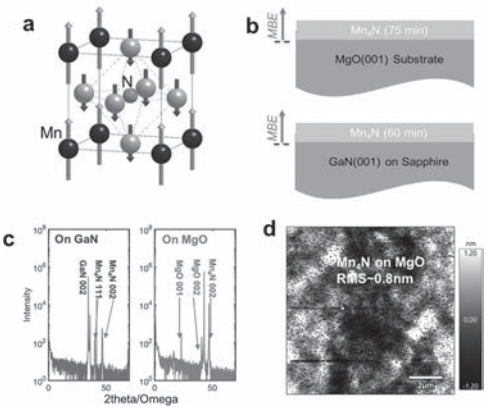


Fig.1 (a) Crystal structure of Mn_4N (b) Schematic of MBE growth of Mn_4N on MgO and GaN (c) XRD of Mn_4N on GaN (blue) and on MgO (red) (d) Atomic force microscopy image of Mn_4N on MgO

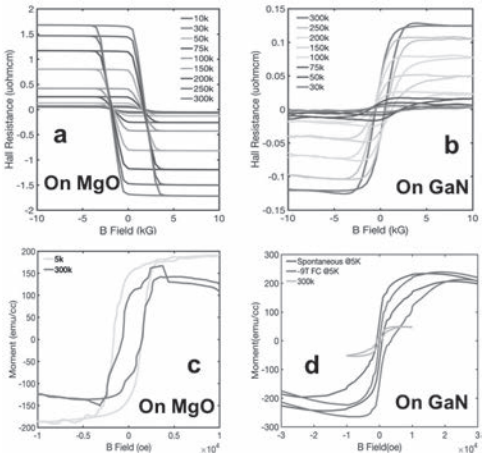


Fig.2 Anomalous Hall resistance of Mn_4N on (a) MgO and (b) GaN M vs H for Mn_4N on (c) MgO at RT and 5K under field cooling and (d) GaN under 0T and -9T cooling to 5K

4:06

FG-14. Impact of magnetic moment and anisotropy of $Co_{1-x}Fe_x$ thin films on the magnetic proximity effect of Pt. *T. Kuschel*[1] *1. Bielefeld University, Bielefeld, Germany*

We have investigated the magnetic proximity effect in Pt depending on the magnetic moment and anisotropy of adjacent metallic ferromagnetic films by x-ray resonant magnetic reflectivity (XRMR) at the Pt absorption edge (11565 eV) [1]. Thus, XRMR is element-selective and allows to obtain the spin depth profile of a chemical element, in our case Pt, by detecting x-ray reflectivity curves under opposite x-ray helicity and magnetic field directions, while varying the adjacent ferromagnetic support layers below from sample to sample. For Pt on ferromagnetic 3d metal alloys such as $Ni_{1-x}Fe_x$ [2] and $Co_{1-x}Fe_x$ [3], we observe a linear dependence between the Pt magnetic moment and the moment of the adjacent ferromagnet. The largest Pt magnetic moment of $(0.72\pm0.03)\ \mu_B$ per spin-polarized Pt atom has been detected in $Pt/Co_{0.33}Fe_{0.67}$ [3], while the number of affected Pt layers is independent from the magnetic moment of the ferromagnetic support. In addition, the Pt magnetic moment clearly follows the magnetic anisotropy of the ferromagnet below. This has been studied for Pt on Fe(001) and on $Co_{0.5}Fe_{0.5}$(001) with 45° rotated fourfold magnetocrystalline anisotropy as checked by magnetooptic Kerr effect [3], and substantiates the strong coupling between the moments of Pt and the ones of the ferromagnet. Our findings will support future investigations of the interplay of spin caloritronic and thermoelectric effects in these all-metallic bilayers.

[1] T. Kuschel et al., Phys. Rev. Lett. 115, 097401 (2015) [2] C. Klewe et al., Phys. Rev. B 93, 214440 (2016) [3] P. Bougiatioti et al., arXiv:1807.09032

4:18

FG-15. Large Perpendicular Magnetic Anisotropy in Single Crystalline Fe/MgO Heterostructures via Optimized Rf-Sputtering Processes. *Y. Iida*[1,2], J. Okabayashi[3], H. Sukegawa[2] and S. Mitani[2,1] *1. Graduate School of Pure and Applied Sciences, University of Tsukuba, Tsukuba, Japan; 2. Research Center for Magnetic and Spintronic Materials, National Institute for Materials Science, Tsukuba, Japan; 3. Research Center for Spectrochemistry, The University of Tokyo, Bunkyo, Japan*

Controlling interface perpendicular magnetic anisotropy (PMA) is important to develop high performance perpendicular magnetic tunnel junctions (p-MTJs). Many efforts have been made to obtain strong PMA, particularly in stacks with a CoFeB/MgO interface [1], which can be easily grown on a Si/SiO_2 substrate using sputtering. Recently epitaxial Fe/MgO grown by

molecular beam epitaxy (MBE) achieved larger PMA than CoFeB/MgO [2,3]. However, it is difficult to obtain sizable PMA in sputter-deposited boron-free Fe/MgO structures [4,5]. These PMA at polycrystalline Fe/MgO in Ref. [4,5] are smaller than that in CoFeB/MgO, although boron is not included. Therefore, Fe/MgO has been used only for basic researches in the PMA. It is also difficult to incorporate heavy metals, e.g. W and Ir, into the stack to enhance PMA. In this study, we aimed to achieve large PMA in sputter-deposited Fe/MgO on an MgO substrate. MgO(5 nm)/Cr(40 nm)/Fe(t_{Fe})/MgO(2 nm) stacks were grown by rf sputtering at room temperature. The MgO substrates and Cr layer were annealed at 500°C for 1 h, and post annealing was performed at T_{ann} = 300, 400, and 500°C. Fig. 1 shows *M-H* curves of the epitaxial Fe(0.7 nm)/MgO annealed at 300 and 500°C. When T_{ann} exceeds 400°C, Fe/MgO exhibited PMA. A large PMA energy K_{eff} of 0.77 MJ/m^3 was obtained at T_{ann} = 500°C, which is comparable to a value of an MBE grown Fe/MgO [3]. Also, the saturation magnetization drastically increases with increasing T_{ann}. Therefore, oxygen impurities remaining in the Fe layer may move to the MgO side during the high temperature annealing process, leading to large PMA. To evaluate an interface PMA energy K_i and areal PMA energy $K_{eff} \times t_{Fe}$ for T_{ann} = 500°C was plotted as a function of t_{Fe} in Fig. 2. Considering a 0.142 nm thick magnetic dead layer, K_i was deduced to be 1.55 mJ/m^2. These results suggest that a well-controlled sputter/annealing process can provide Fe/MgO stacks with sufficiently large PMA, which exceeds values in polycrystalline Fe/MgO and CoFeB/MgO.

[1] S. Ikeda, K. Miura, H. Yamamoto *et al*., Nat. Mater. 9, 721 (2010). [2] H. X. Yang, M. Chshiev, B. Dieny *et al*., Phys. Rev. B 84, 054401 (2011). [3] J. W. Koo, S. Mitani, T. T. Sasaki *et al*., Appl. Phys. Lett. 103, 192401 (2013). [4] J. Kil, Y. Choi, G. Bae *et al*., IEEE Trans. Magn. 51, 2004304 (2015). [5] Y. Iida, J. Okabayashi and S. Mitani, Appl. Phys. Lett. 113, 252401 (2018).

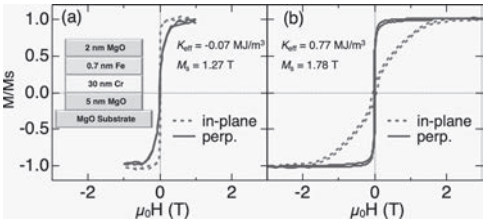


Fig. 1 *M-H* curves for epitaxial Fe/MgO at (a) T_{ann} = 300, and (b) 500°C. Inset shows a schematic of the stack.

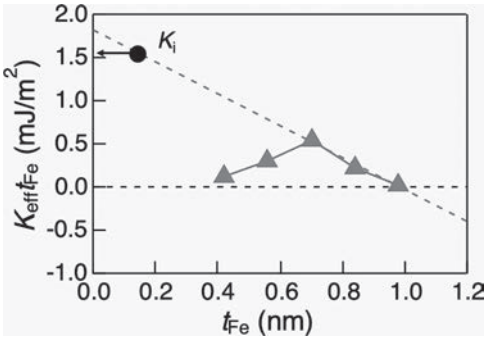


Fig. 2 Areal PMA energy $K_{eff}t_{Fe}$ as a function of Fe thickness in epitaxial Fe/MgO structures.

Session FH
RARE-EARTH PERMANENT MAGNETS

Ralph Skomski, Chair
University of Nebraska-Lincoln, Lincoln, NE, United States

CONTRIBUTED PAPERS

1:30

FH-01. Microscopic magnetic properties of Nd-Fe alloys.
V.P. Menushenkov[1], A.P. Menushenkov[2], F. Wilhelm[3], I.V. Shchetinin[1], I.A. Rudnev[2], A.A. Ivanov[2], D.G. Zhukov[1], A.G. Savchenko[1] and *A. Rogalev*[3] *1. National University of Science and Technology "MISIS", Moscow, Russian Federation; 2. National Research Nuclear University MEPhI, Grenoble, Russian Federation; 3. ESRF, Grenoble, France*

Magnetic properties of Nd-Fe alloys are subject of intense studies owing to an important role of the Nd-rich intergranular phases in the sintered Nd-Fe-B-based permanent magnets. Analysis of macroscopic magnetization curves is difficult due to the presence of several magnetic phases observed by electron microscopy studies: primary Nd crystals, Nd as part of metastable eutectic, primary Nd_2Fe_{17} and a poorly known so-called A_1 regions. These regions as identified by high resolution transmission electron microscopy are composed of nanocrystals embedded in an amorphous phase. To elucidate a relationship between local structural and magnetic properties of various magnetic phases we have exploited an element selective technique – x-ray magnetic circular dichroism (XMCD). We have studied XMCD spectra at the $L_{2,3}$-edges of Nd and at the K-edge of Fe in hypereutectic $Fe_{14}Nd_{86}$ alloy prepared by mold casting and melt spinning in temperature range from 5 to 300K and under a magnetic field of up to 17T. The spectra are compared with those measured on pure Nd metal and nanocrystalline $Nd_2Fe_{14}B$ samples. Analysis of XMCD spectra allowed to separate contributions from Nd and Fe-containing phases. To get a deeper insight into magnetic behavior of different phases we have recorded element-selective magnetization curves by monitoring intensity of Nd and Fe XMCD signals as a function of applied magnetic field. Analysis of Nd magnetization curve in as-cast sample revealed that it is a sum of three contributions: the primary pamagnetic Nd phase (*dhcp)*, a soft magnetic Nd-based phase (*fcc*) and a Fe-Nd phase with high coercivity contained in A_1 region, with chemical composition close to $NbFe_5$. In the rapidly quenched alloy, presence of only two magnetic phases paramagnetic Nd and a metastable hard magnetic Nd_2Fe phase has been evidenced. Obtained results are important for understanding microscopic origin of high-coercivity phase in Nd-rich Fe-Nd alloys.

1:42

FH-02. Unconventional Spin Textures and Domain Wall Pinning in Sm-Co Magnets.
L. Pierobon[1], A. Kovacs[2], R.E. Schäublin[1,3], S.S. Gerstl[1,3], U. Wyss[4], J. Caron[2], R.E. Dunin-Borkowski[2], J.F. Löffler[1] and M. Charilaou[1,5] *1. Laboratory of Metal Physics and Technology, ETH Zurich, Zurich, Switzerland; 2. Ernst Ruska-Centre for Microscopy and Spectroscopy with Electrons, Forschungszentrum Jülich, Jülich, Germany; 3. Scientific Center of Optical and Electron Microscopy, ETH Zurich, Zurich, Switzerland; 4. Arnold Magnetic Technologies, Lupfig, Switzerland; 5. Department of Phyiscs, University of Louisiana at Lafayette, Lafayette, Switzerland*

Sm-Co alloys are the best-performing high temperature permanent magnets as a result of their cellular microstructure, which comprises a Sm_2Co_{17} matrix and $SmCo_5$ cells, intersected by Zr-rich platelets [1]. A dense network of strongly-pinned domain walls forms in this microstructure, giving the material remarkable magnetic hardness. Despite extensive research on the connection between microstructure and magnetic properties [2], theoretical predictions and experimental results are still not in good agreement. Here, we combine high-resolution magnetic imaging by means of Lorentz transmission electron microscopy and off-axis electron holography with micromagnetic simulations to analyze how magnetic texture and magnetization reversal in this material are affected by its microstructure [3]. We find that magnetization reversal starts by the nucleation of domain walls at interfaces between Zr-rich platelets and the Sm_2Co_{17} matrix. Despite strong pinning at $SmCo_5$ cells, curling instabilities form at the intersections of all three phases and magnetization reversal propagates through the $SmCo_5$ cells *via* the Zr-rich platelets. Surprisingly, topologically non-trivial structures, such as 2π and 3π domain wall windings, are involved in domain wall pinning, significantly affecting the reversal mechanism. Our results demonstrate the important connection between microstructure and magnetic properties in Sm-Co alloys. Based on our observations, we propose a way to modify the microstructure of the alloy to increase its coercivity and remanence.

[1] J. F. Liu *et al*., *J. Appl. Phys*. 85, 2800 (1999) [2] M. Duerrschnabel *et al*., *Nat. Comm.* 8, 54 (2017) [3] L. Pierobon *et al*., arXiv:1901.01922 (2019)

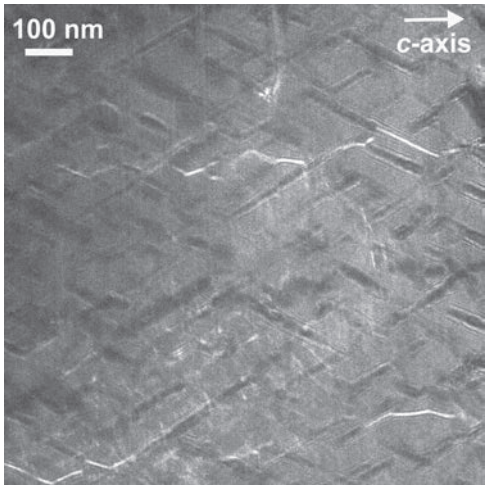


Fig. 1: Lorentz transmission electron microscopy of SmCo magnets reveals strongly pinned domain walls appearing as bright (convergent) and dark (divergent) contrast.

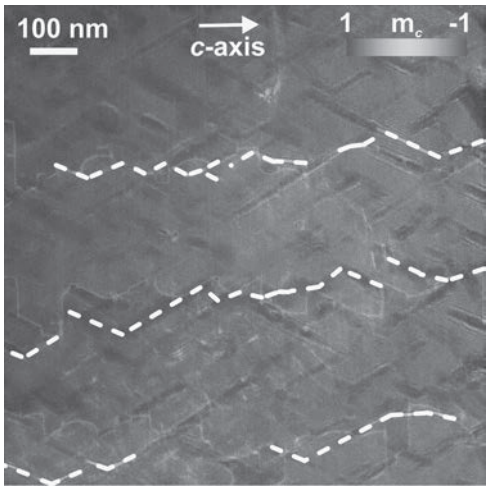


Fig. 2: Micromagnetic simulation of magnetization in area shown in Fig. 1 with experimental positions of domain walls (white dashed lines) superimposed shows good agreement between theory and experiment.

1:54

FH-03. The Effect of Zr in Progress toward the Development of High-Performance $SmFe_{12}$-based Magnet. *P. Tozman*[1], S. Hossein[1], Y. Takahashi[1], D. Ogawa[1], S. Hirosawa[1] and K. Hono[1] *1. National Institute for Materials Science, Tsukuba, Japan*

Permanent magnets are essential components for energy conversion and mobility applications where there is an increasing demand for new hard magnets, which has superior magnetic properties than that of $Nd_2Fe_{14}B$, at elevated temperatures over 140°C. $SmFe_{11}Ti_1$ has a large uniaxial anisotropy (K_1 = 4.87 MJ/m^3), high Curie temperature (T_c = 584 K) which are comparable those $Nd_2Fe_{14}B$ (K_1 = 4.9 MJ/m^3, T_c = 598 K) [1,2]. On the other hand, its saturation magnetization, ($\mu_0 M_s$ = 1.14 T) is lower than $Nd_2Fe_{14}B$ ($\mu_0 M_s$ = 1.14 T). Saturation magnetization can be increased with an optimum substitution of Co for Fe or by reducing non-magnetic Ti content. The latter can reduce the phase stability of $ThMn_{12}$ phase. This can be overcome by Zr substitution for Sm. Using this approaches, promising intrinsic hard magnetic properties have been reported; $\mu_0 H_a$, $\mu_0 M_s$ and T_c to be 10.9 T, 1.43 T, 800 K respectively for bulk $Sm(Fe_{0.8}Co_{0.2})_{11}Ti_1$ and 8.4 T, 1.53 T, 830 K, respectively for bulk $(Sm_{0.8}Zr_{0.2})(Fe_{0.8}Co_{0.2})_{11.5}Ti_{0.5}$ at 300 K [3]. However, the sole effect of Zr on the intrinsic magnetic properties cannot be investigated directly from bulk samples since $ThMn_{12}$-type structure without Ti cannot be stabilized in the absence of Zr. Hence, we developed highly textured $(Sm_{1-x}Zr_x)(Fe_{0.8}Co_{0.2})_{12}$ films for x = 0.18, 0.26 using an ultra-high vacuum co-sputtering system. The increment of Zr substitution from x = 0 to 0.26 for $(Sm_{1-x}Zr_x)(Fe_{0.8}Co_{0.2})_{12}$ increases $\mu_0 M_s$ from 1.78 T to 1.90 T, which is the *largest value* reported for hard magnetic compounds. The anisotropy field decreases by Zr substitution from 12 T for x = 0 to 9.8 T for x = 0.18 and 8.9 T for x = 0.26 at 300 K [4]. These values are still superior to those for $Nd_2Fe_{14}B$ ($\mu_0 H_a$ =6.2 T). Figure 1 compares $\mu_0 H_a$ and $\mu_0 M_s$ of $Nd_2Fe_{14}B$ with several compounds. This figure clearly shows the potential of $Sm(Fe_{0.8}Co_{0.2})_{12}$ compounds for practical applications as they have superior intrinsic magnetic properties at elevated temperature, 200°C where magnet application depends on. How to realize coercivity in the film by defect engineering will be discussed at the end of the talk.

[1] M. Sagawa, S. Fujimura, Y. Matsuura et al., J. Appl. Phys. 55, 2083 (1984). [2] B. P. Hu, H. S. Li, J. M. D. Coey et al., J. Phys.: Condens. Matter. 1, 755 (1989). [3] P. Tozman, H. Sepehri-Amin, K. Hono et al., Acta Mater. 153, 354 (2018). [4] Y. Hirayama, Y. K. Takahashi, K. Hono et al. Scripta Mater. 138, 62 (2017).

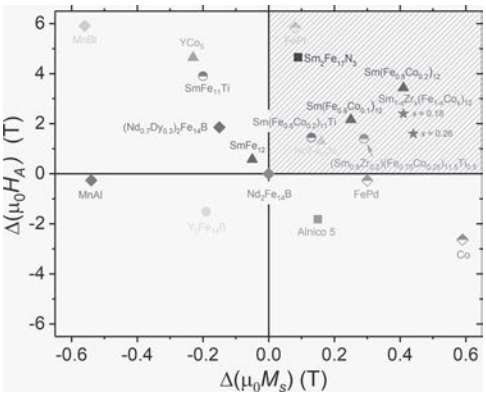


Fig.1 The difference between the anisotropy field of $Nd_2Fe_{14}B$ and the compounds versus the difference of magnetization at 200°C.

2:06

FH-04. Achievement of both high coercivity and maximum energy product for 2:17-type Sm-Co sintered magnets via microstructural adjustment. S. Wang[1], *Y. Fang*[1], K. Song[1], X. Zhu[1], L. Wang[1], W. Sun[2], W. Pan[1], M. Zhu[1,2] and W. Li[1,2] *1. Central Iron and Steel Research Institute, Beijing, China; 2. National Engineering Research Center for Magnetic Materials, Beijing, China*

2:17-type Sm-Co sintered magnet performs well for high temperature applications as its excellent magnetic properties and high Curie temperature [1-5]. To meet application at relatively high temperature for Sm-Co sintered magnet, high intrinsic coercivity (H_{cj}) is also prerequisite besides maximum energy product ($(BH)_{max}$), improving temperature stability. In this work, high $(BH)_{max}$ (>264 kJ/m^3) as well as high H_{cj} (>1800 kA/m) were simultaneously obtained in $Sm(Co_{bal}Cu_{0.062}Fe_{0.285}Zr_x)_{7.6}$ sintered magnets. More importantly, the magnet compacts were made from powders fabricated by jet milling process, not a traditional technique, i.e., ball milling. The optimal magnetic properties obtained is remanence B_r = 1.186 T, $(BH)_{max}$=264.8kJ/m^3, H_{cj}=1848 kA/m when x=0.021, and the magnet also shows good squareness of demagnetization curve, as shown in Fig.1. The comprehensive magnetic properties are impressive due to both high $(BH)_{max}$ and H_{cj}. The origin of the good magnetic performance and influence of Zr content on the microstructure and magnetic properties have been studied for the $Sm(Co_{bal}Cu_{0.062}Fe_{0.285}Zr_x)_{7.6}$ magnets (x=0.016, 0.019, 0.021, 0.023). With the decreasing of Zr content the B_r enhances from 1.174 T to 1.207 T, and H_{cj} decreases from 2314 kA/m to 131 kA/m. It is found that the average cell size and density of lamellar phase are strongly influenced by the Zr content. With the x decreasing from 0.023 to 0.016, the average cell size increase slightly from 100.4nm to 113nm, while the density of lamellar structure decrease dramatically from 0.043nm^{-1} to 0.008nm^{-1}. For high Zr content magnet (x=0.023), the Cu concentration average and peak values in the cell boundary are measured to be ~10.77at.% and ~21.58at.%, respectively. However, the two above values are only ~6 at.% and ~7.95 at.% for the lower Zr content magnet (x=0.016). It is experimentally confirmed that the relatively more Zr content results in the increase of the density of lamellar phase, promoting the segregation of Cu in the cell boundary, giving rise to the well comprehensive magnetic performance for 2:17-type Sm-Co sintered magnet.

[1] K. K. Song, W. Sun, H. S. Chen, et al, AIP Advances, 7, 056238 (2017). [2] N. J. Yu, M. G. Zhu, Y. K. Fang, L. W. Song, et al, Scripta Materialia, 132, 44 (2017). [3] O. Gutfleisch, M. A. Willard, E. Brück, et al, Adv. Mater. 23, 821 (2011). [4] N. J. Yu, M. G. Zhu, L. W. Song, et al, J. Magn. Magn. Mater. 452, 272 (2018). [5] K. K. Song, Y. K. Fang, S. Wang, et al, J. Magn. Magn. Mater. 465, 569 (2018).

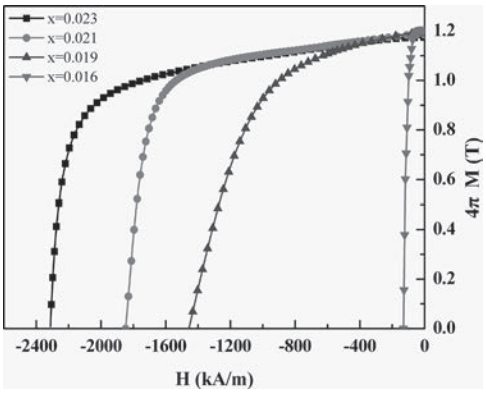
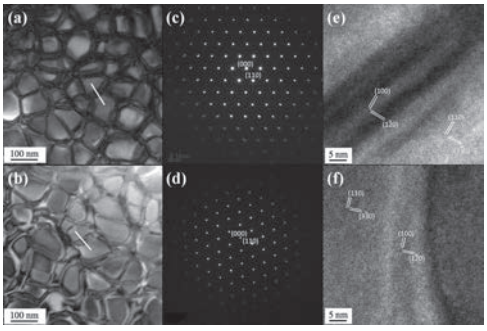


Fig 1. Demagnetization curves of the $Sm(Co_{bal}Cu_{0.062}Fe_{0.285}Zr_x)_{7.6}$ sintered magnets (x=0.016, 0.019, 0.021, 0.023)

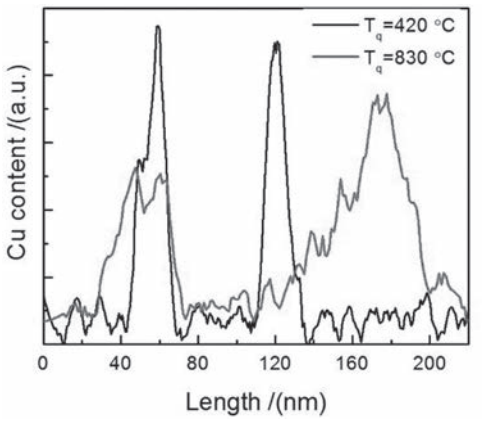
2:18

FH-05. High Temperature Properties Improvement and Microstructure Regulation of Sm_2Co_{17}-based Permanent Magnet.
C. Wang[1], M. Zhu[1], Y. Fang[1], S. Wang[1] and W. Li[1] *1. Central Iron and Steel Research Institute, Beijing, China*

In order to further improve the magnetic properties and the maximum operating temperatures of Sm_2Co_{17}-based permanent magnets, the effects of Sm content on the magnetic properties and microstructure of the $Sm(Co_{bal}Fe_{0.1}Cu_{0.09}Zr_{0.03})_z$(z=7-7.3) magnets were studied in this article. Then the solid solution process of $Sm(Co_{bal}Fe_{0.1}Cu_{0.09}Zr_{0.03})_{7.2}$ magnet was optimized from the perspective of high temperature magnetic properties. To acquire lower coercivity coefficient (β) for $Sm(Co_{bal}Fe_{0.1}Cu_{0.09}Zr_{0.03})_{7.2}$ magnet, the effects of the quenching temperature (T_q) on the magnetic properties and microstructure of the $Sm(Co_{bal}Fe_{0.1}Cu_{0.09}Zr_{0.03})_{7.2}$ magnet were also studied. The Sm content has no significant on phase composition, microstructure and cell size of magnets expect cell boundary. Higher Sm content will lead to wider cell boundary phase of magnet. The $Sm(Co_{bal}Fe_{0.1}Cu_{0.09}Zr_{0.03})_{7.2}$ magnet shows the optimal magnetic properties as: B_r=9.65kG, H_{cj}=28.3kOe, $(BH)_{max}$=22.5MGOe at room temperature (RT). After optimizing solution temperature and time, it is found that the $Sm(Co_{bal}Fe_{0.1}Cu_{0.09}Zr_{0.03})_{7.2}$ magnet solution-treated at 1195°C for 4h exhibits the best magnetic properties as B_r=7.22kG, H_{cj}=7.6kOe $(BH)_{max}$=11.6MGOe at 500°C. The variant T_q apparently affects the coercivity temperature dependent of $Sm(Co_{bal}Fe_{0.1}Cu_{0.09}Zr_{0.03})_{7.2}$ magnet. With T_q decreasing from 830°C to 420°C, the H_{cj} of the magnets increases from 1.406 kOe to 21.7kOe, while the β(RT-500°C) changes from +0.1113 %/°C of the T_q=830°C magnet to -0.134 %/°C of the T_q=420°C magnet. Analysis of the microstructure of the magnets with T_q=830°C and 420°C indicates that T_q has a great influence on the Cu distribution of the cell boundary phase. The difference of the Cu content and its distribution was ascribed to be the main reason for the different H_{cj} and its temperature dependence behavior of the T_q=830°C and 420°C magnets.



TEM, SEAD and HRTEM images of cellular structure of the $Sm(Co_{bal}Fe_{0.1}Cu_{0.09}Zr_{0.03})_z$ magnets with z=7.0(a, c, e) and 7.2(b, d, f)



Cu distribution of the cell boundary of the $Sm(Co_{bal}Fe_{0.1}Cu_{0.09}Zr_{0.03})_{7.2}$ magnets with T_q=420 °C and 830 °C

2:30

FH-06. Theoretical study on the electronic states and finite temperature magnetic properties of $Sm_2Fe_{17}N_x$.
S. Yamashita[1], D. Suzuki[1], T. Yoshioka[1,2], H. Tsuchiura[1,2] and P. Novak[3] *1. Department of Applied Physics, Tohoku University, Sendai, Japan; 2. Center for Spintronics Research Network, Tohoku University, Sendai, Japan; 3. Institute of Physics of ASCR, Prague, Czechia*

The $Sm_2Fe_{17}N_x$ nitrides have unusual anisotropic magnetic properties. It is well known that the system at x=3 exhibits strong uniaxial magnetocrystalline anisotropy, which is higher than that of $Nd_2Fe_{14}B$. On the other hand, the system at x=0, that is binary Sm_2Fe_{17}, has weak planar anisotropy. A first-principles study in early days showed that the Sm local anisotropy in Sm_2Fe_{17} is weak but strong enough to overcome that of the Fe sublattice when the Sm is treated as a trivalent ion in the calculations [1]. Another recent ab-initio study based on the KKR method has claimed that the Sm ions may have a divalent electronic configuration [2]. Motivated by these backgrounds, in this contribution, we examine the magnetocrystalline anisotropy of the $Sm_2Fe_{17}N_x$ systems assuming the Sm^{3+} or Sm^{2+} configuration based on first-principles calculations. Furthermore, we construct an effective spin model to describe the finite temperature magnetic properties of these systems based on the information such as crystal field parameters obtained in the first-principles way. First of all, we calculate the crystal field parameters, the leading term of which is $A_2^0\langle r^2\rangle$=-171 K (-8.85 K) and -554 K (-686 K) for Sm^{3+} (Sm^{2+}) ion in Sm_2Fe_{17} and $Sm_2Fe_{17}N_3$, respectively. These values are all negative, which indicates that the Sm ions has local uniaxial anisotropy. However, its amplitude is very small when we assume the divalent configuration for the Sm ions in Sm_2Fe_{17}. Fig. 1 and 2 show the temperature dependence of the magnetization curves along the c-axis and (100) direction of these systems obtained by using the effective spin model. We can see that the experimental result is well described for $Sm_2Fe_{17}N_3$ but not even qualitatively for Sm_2Fe_{17} when we assume the Sm^{3+} configuration for the Sm. Instead, we find that the spin model based on the Sm^{2+} ions can give a qualitatively consistent result with the experimental one. These results imply that the valency of the Sm ions in $Sm_2Fe_{17}N_x$ systems can be strongly affected by nitrogenation processes.

[1] L. Steinbeck, M. Richer, U. Nitzsche and H. Eschrig, Phys. Rev. Lett B 53, 7111 (1996). [2] M. Ogura, A. Mashiyama and H. Akai, J. Phys. Soc. Jpn. 84, 084702 (2015). [3] H. Kato, M. Yamada, G. Kido and Y.Nakagawa J. Appl. Phys. 73, 6931 (1993). [4] L. V. B. Diop, M. D. Kuz'min, K. P. Skokov, D. Yu. Karpenkov and O. Gutfleisch, Phys. Rev. B 94, 144413 (2016).

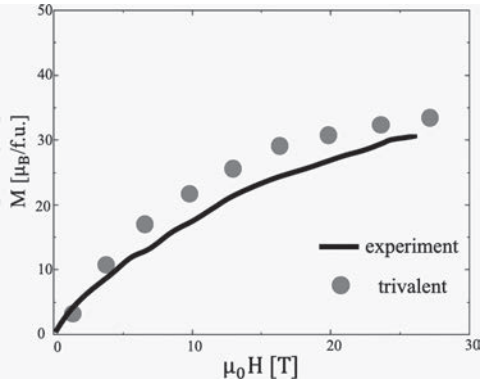


Fig. 1 Magnetization curves of trivalent $Sm_2Fe_{17}N_3$ and experimental result along with (100) direction.

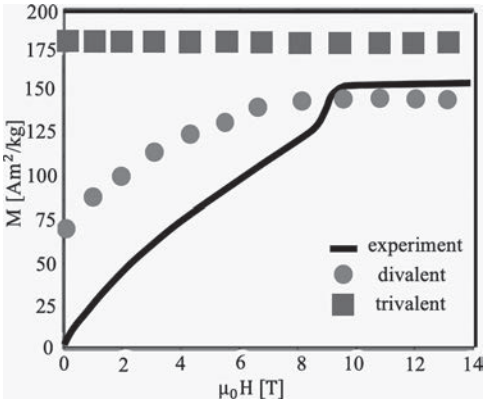


Fig. 2 Magnetization curves of trivalent and divalent Sm_2Fe_{17} and experimental result along with c-axis.

2:42

FH-07. Magnetic properties and microstructures of high heat-resistance Sm-Co magnets with high Fe and low Zr content.
H. Machida[1], T. Fujiwara[1], C. Fujimoto[1], Y. Kanamori[1], K. Sakakura[2] and M. Takezawa[2] *1. TOKIN Corporation, Sendai, Japan; 2. Kyushu Institute of Technology, Kitakyushu, Japan*

Sm-Co magnets have high Curie temperature and appropriate to devices working under high temperature. As a way of enhancing magnetic properties, increasing Fe content has been conducted. However, this leads to poor squareness and deterioration of heat resistance due to decrease of Co content [1]. We tackled these problems by decreasing Zr content to maintain Co content as much as possible and employing slow cooling between sintering and solid solution treatment to homogenize microstructure. Although Zr is known as making Fe magnetically stable, there seems to be no reports discussing magnetic properties and heat resistance with increasing Fe and decreasing Zr content [2]. Magnetic properties were evaluated with a B-H tracer, then $(BH)_m$ of 34.5 MGOe were obtained at 25°C and 30.5 MGOe at 150°C. Temperature coefficients of B_r and H_{cj} were 0.034 %/K and 0.28 %/K respectively, which were almost as same as conventional Sm-Co magnets. Moreover, B-H loop at 150°C was linear, which means irreversible demagnetization doesn't occur at 150°C (Fig. 1). Cell structure observation and its composition analysis were conducted with TEM-EDX. Cell size was 200~500 nm with Fe and Cu separated and concentrated to 2-17 and 1-5 phase respectively. This size was larger than conventional Sm-Co magnets and Fe and Cu concentration led to high squareness [3]. Degree of orientation was examined with EBSD, then *c*-axis orientation which is preferable for Sm-Co was obtained. From XRD results, *a*-axis was increased but *c*-axis was decreased with increasing Zr content. Considering atomic radius, it was suggested that Zr was incorporated in Co dumbbell site. This means Zr was preferentially substituted by Co dumbbell. Therefore, interaction between Co stronger, this led to high heat resistance. We have been observing magnetic domain structures with a Kerr effect microscope with a magnetic field applied. From our past studies, magnetic domains are expected to be generated evenly from grain boundaries and propagated to inside grains. Result details of magnetic domain structures will be given a presentation.

[1] Y. Horiuchi, et al, IEEE Trans. Magn. 55, 482 (2014) [2] W. Tang, et al, Proceedings of the Sixteenth International workshop on Rare-Earth Magnets and Their Applications, 1, 179 (2000) [3] H. Machida, et al, AIP Adv. 7, 056223 (2017)

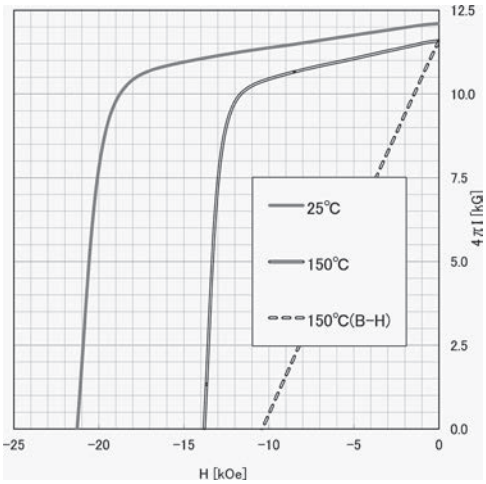


Fig. 1 Demagnetization curves at 25°C and 150°C.

2:54

FH-08. Magnetic properties of $Sm(Fe,Ti,V)_{12}$ magnets.
T. Saito[1], F. Watanabe[1] and D. Nishio-Hamane[2] *1. Chiba Institute of Technology, Narashino, Japan; 2. Institute for Solid State Physics, The University of Tokyo, Kashiwa, Japan*

RFe_{12} (R = rare earth) intermetallic compounds with a $ThMn_{12}$ structure have long been of interest in the production of high-performance permanent magnets [1]. Because binary RFe_{12} compounds are metastable, production of the RFe_{12} phase is difficult. However, it has been found that the small substitution of T (T = Cr, Mo, V, Ti) for Fe in the RFe_{12} compound results in the formation of the $R(Fe,T)_{12}$ compound [2–6]. In this study, $Sm(Fe,Ti,V)_{12}$ magnets were produced by the spark plasma sintering (SPS) method from $Sm(Fe,Ti,V)_{12}$ melt-spun ribbons. The structures and magnetic properties of the $Sm(Fe,Ti,V)_{12}$ magnets are discussed here. $Sm(Fe,Ti,V)_{12}$ alloy ingots were prepared by induction melting in an argon atmosphere. The alloy ingots were induction melted and then ejected through an orifice with argon onto a copper wheel rotating at a surface velocity of 50 ms^{-1}. The melt-spun ribbons were comminuted into powders and then hot-pressed in a vacuum at 873–1073 K for 300 s under a pressure of 100 MPa by the SPS method. The $Sm(Fe,Ti,V)_{12}$ melt-spun ribbons were successfully consolidated into bulk $Sm(Fe,Ti,V)_{12}$ magnets. The resultant $Sm(Fe,Ti,V)_{12}$ magnets consisted of the $Sm(Fe, Ti,V)_{12}$ phase. It was found that the magnetic properties of the $Sm(Fe,Ti,V)_{12}$ magnets were deeply dependent on the composition and consolidating temperature. Figure 1 shows the hysteresis loop of the $SmFe_{10}Ti_{0.5}V_{1.5}$ magnets consolidated at 973 K by the SPS method. This magnet achieved a coercivity of 9.2 kOe, the highest among all of the magnets produced.

[1] F. R. De. Boer, et al. J. Less-Common Met. 135, 199 (1987). [2] L. X. Liao, et al. J. Appl. Phys. 70, 6006 (1991). [3] L. Shultz and J. Wecker, J. Appl. Phys. 64, 5711 (1988). [4] Y. Wang, et al. J. Appl. Phys. 67, 4954 (1990). [5] Y. Otani, et al. IEEE Trans. Magn. 26,2658 (1990). [5] J. Yang, et al. J. Appl. Phys. 88, 988 (2000). [6] E. Tomey, et al. J. Alloys Compd. 231, 195 (1995).

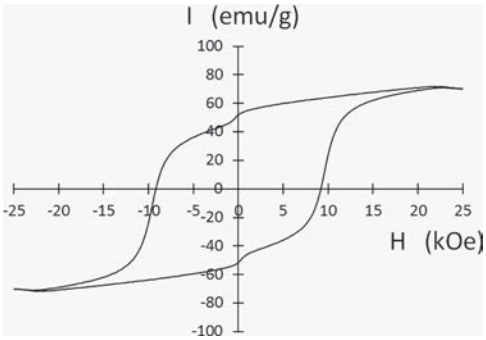


Figure 1 Hysteresis loop of the $SmFe_{10}Ti_{0.5}V_{1.5}$ magnets consolidated at 973 K by the SPS method.

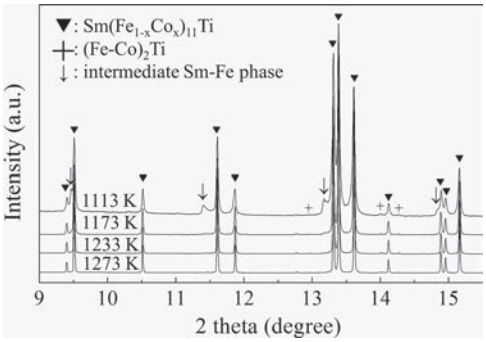


Fig. 1 Synchrotron X-ray diffraction (λ = 0.49623Å) patterns of $Sm(Fe_{1-x}Co_x)_{11}Ti$ particles obtained by the different RD temperatures.

Temperature (K) for 2h	H_c (kA/m)	Time (h) at 1233 K	H_c (kA/m)
1113	204.0	1/6	305.0
1133	228.8	1/2	270.2
1173	237.1	1	258.1
1273	236.3	2	225.6

Table 1 Coercivities of $Sm(Fe_{1-x}Co_x)_{11}Ti$ particles depending on various temperatures for 2 h and various times at 1233 K for the RD process.

3:06

FH-09. Nanoparticle-based synthesis and magnetic properties of $Sm(Fe_{1-x}Co_x)_{11}Ti$ ($0 \le x \le 0.3$) particle. *J. Kim*[1], T. Trinh[1], R. Sato[1] and T. Teranishi[1] *1. Advanced Inorganic Synthesis, Division of Synthetic Chemistry, Institute for Chemical Research Kyoto University, Uji-shi, Japan*

Recently, the $Sm(Fe_{1-x}Co_x)_{12}$ films with excellent intrinsic hard magnetic properties (M_s: 1.78 T, H_A: 12 T, T_C: 859 K) were successfully synthesized [1]. On the other hand, in case of the RFe_{12} isolated particles, we need a nonmagnetic stabilizer, *i.e.*, $R(Fe,M)_{12}$ (M: Ti, V, Cr, Mn, Mo, etc.), to maintain the $ThMn_{12}$ structure due to the thermodynamic instability. Element Ti can stabilize the $ThMn_{12}$ structure with the smallest amount [2] and can minimize the decrease of saturation magnetization by substitution with Fe sites. A reduction-diffusion (RD) process, which is one of the synthesis methods for $Sm_2Fe_{17}N_3$ particles [3-5], was used because this process can produce the equiaxed-shape particles with the lower temperature than metal melting method. In this study, we focus on the synthesis of a single-phase $Sm(Fe_{1-x}Co_x)_{11}Ti$ particles and the investigation on the magnetic properties depending on RD conditions. First, the mixture of Sm, Fe, and Co acetates and Ti isopropoxide was reacted in the organic solvent and calcined to remove organic ligands. Then, the H_2 and Ca reductions (RD process) were conducted for reducing the metal ions. Finally, the products were washed with N_2-purged mQH_2O to remove CaO. Figure 1 shows the XRD patterns of $Sm(Fe_{1-x}Co_x)_{11}Ti$ particles with different RD temperatures. The intermediate Sm-Fe-(Ti) phase can be observed at 1113 K (indicated by arrows in Fig.1) because the RD reaction did not finish due to the lower temperature than the Ca melting point (~1115 K). Nearly single-phase $Sm(Fe_{1-x}Co_x)_{11}Ti$ with <1wt% $(Fe\text{-}Co)_2Ti$ subphase was produced at above 1173 K. Table 1 shows the H_c of $Sm(Fe_{1-x}Co_x)_{11}Ti$ particles depending on the conditions of the RD process. The $Sm(Fe_{1-x}Co_x)_{11}Ti$ particles synthesized at above 1173 K for 2 h shows the H_c of around 237 kA/m. Meanwhile, the H_c increased with shorter RD time because the particle size and agglomeration were suppressed to maintain the equiaxed-shape of particles.

[1] Y. Hirayama, Y. K. Takahashi and S. Hirosawa, Scripta Materialia, Vol. 138, p.62–65 (2017). [2] K. H. J. Buschow, Report on Progress in Physics, Vol. 54, p.1123 (1991). [3] Y. Hirayama, A. K. Panda and T. Ohkubo, Scripta Materialia, Vol. 120, p.27–30 (2016). [4] S. Okada, K. Suzuki and E. Node, AIP Advances Vol. 7, p.056219 (2017). [5] J. Kim, H.-L. Wu and S. Hsu, Chemistry Letters, in press.

3:18

FH-10. Evolution of microstructure and magnetic properties in annealed high energy ball milled $Sm(Fe, Co, Ti)_{12}$ compounds doped with Zr. *M. Gjoka*[1,2], C. Sarafidis[3], D. Niarchos[1] and G.C. Hadjipanayis[2] *1. Department of Materials Science, INN, NCSR Demokritos, Athens, Greece; 2. Department of Physics and Astronomy, University of Delaware, Newark, DE, United States; 3. Department of Physics, Aristotle University of Thessaloniki, Thessaloniki, Greece*

The tetragonal $R_{1-x}Zr_x$ $(FeCo)_{11}Ti$ alloys, where R is a rare earth and T is a transition metal, are promising candidates for permanent magnets [1, 2]. $Sm_{1-x}Zr_x(Fe_{0.8}Co_{0.2})_{11-y}Ti_y$ (x=0 and 0.25; y=1 and 0.7)) master alloys were prepared by arc-melting under argon atmosphere. According to the Rietveld analysis, all as-cast samples were almost single-phase 1:12 compounds with a small amount of a-Fe. The as-cast ingots were milled using high-energy ball milling (HEBM) for different times (4 and 8 hours) in an argon atmosphere keeping a weight ratio of balls to powder 10:1. All samples after milling exhibit an amorphous/disordered phase. After annealing at 700 °C-900 °C at different interval times (15-90 min), the amorphous powders were re-crystallized into a majority 1:12 phase. However the SEM images show that the grain size of annealed sample depends strongly on the milling time of precursor material. The powder milled for 4 h after annealing contains a large variation of grain size from 2-4 μ to 20 μ or larger. While the respective sample milled for 8 h exhibits a grain size mainly in the range of 2-6 μ after annealing. This is reflected in the fact that the coercivity is higher in the last case reaching a maximum value of 5.5 kOe for $SmFe_9Co_2Ti$ annealed at 850 °C for 15 min. Representative demagnetization curves of $Sm_{0.75}Zr_{0.25}Fe_{9.04}Co_{2.26}Ti_{0.7}$ annealed for 15 and 30 min are shown in figure 1 and the respective SEM image of the annealed sample at 850 °C is shown in figure 2. The $SmFe_9Co_2Ti$ samples annealed at 900 °C exhibit a higher amount of a-Fe than when annealed at 800 °C, and this can explain the moderate value of coercivity, reaching the maximum value of 4.04 kOe (annealing for 30 min). Samples annealed at 700 °C for 15, 30 ad 60 min, exhibit a relatively low coercivity ~1.5 kOe. The microstructure evolution with emphasis on the particles size during annealing and their correlation with coercivity will be discussed. Acknowledgements: This project was partially supported by the H2020–MSCA-RISE-*2015 INAPEM* and H2020-NMP23-2015 NOVAMAG.

[1] P. Tozman, H. Sepehri-Amin, Y.K. Takahashi and al., Acta Materialia, Vol. 153, p. 354-363 (2018). [2] K. Kobayashi, S. Suzuki, T. Kuno and al., J.Alloys Compd., vol. 694, p. 914-920 (2017).

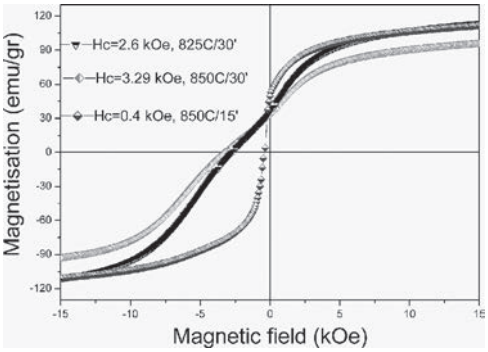


Fig. 1 Coercivity versus annealing time of $Sm_{0.75}Zr_{0.25}Fe_{9.04}Co_{2.26}Ti_{0.7}$ powder milled 8 h.

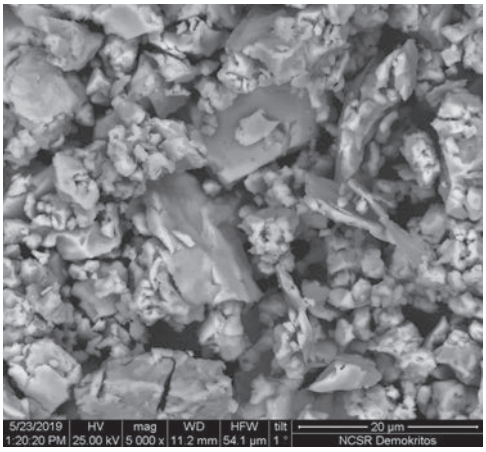


Fig. 2 SEM image of $Sm_{0.75}Zr_{0.25}Fe_{9.04}Co_{2.26}Ti_{0.7}$ powder annealed 30 min at 850 °C.

3:30

FH-11. Effect of Ingot Cooling Rate on Cu Distribution and Magnetic Properties of $Sm(Co_{bal}Fe_{0.28}Cu_{0.07}Zr_{0.03})_{7.6}$ Magnet. *Z. Shang*[1], D. Zhang[1], Y. Li[1], Z. Ma[1], X. Xu[1], H. Zhang[1], W. Liu[1], Q. Lu[1], Q. Wu[1] and M. Yue[1]
1. College of Materials Science and Engineering, Beijing University of Technology, Beijing, China

Cast process has obvious effect on magnetic properties of Sm_2Co_{17}-type magnets[1]. By changing the shape of metal mold, ingots with different cooling rates can be obtained. In this work, cast alloys with a nominal composition of $Sm(Co_{bal}Fe_{0.28}Cu_{0.07}Zr_{0.03})_{7.6}$ were prepared by induction melting. The alloy solution was casted into bullet type of copper mold (BM) and plate type of copper mold (PM) with water-cooling. The microstructure and corresponding Cu distributions of the magnets are shown in Fig. 1. A small amount of black phase in the BM magnet are observed and shown in Fig. 1 (a), while the content of the black phase in the PM magnet is very low, shown in Fig. 1 (d). According to the corresponding of Zr mapping in Fig. 1 (c) and (f), the Zr element enriches in the black phase, and it might be $Zr_6(Co, Fe)_{23}$ phase. The results are in agreement with the XRD results. Fig. 1 (a) and (b) show that for the BM magnet, the Cu element enriches in the regions near to Sm_2O_3 phase and grain boundaries. For the PM magnet, the Cu element distributes homogeneously in the magnet, as shown in Fig. 1 (e). The demagnetization curves of the magnets indicate that the coercivity and squareness of the PM magnet are significantly higher than that of the BM magnet. The faster cooling rate is helpful for the uniformity of the Cu element distribution in the ingots and magnets. The uneven Cu distribution leads to the loss of cell boundary phase, and the coercivity and squareness of the BM magnet is poor. For the PM sample, the Cu element diffuse evenly during homogenization and the cellular structure is well developed, therefore the PM magnet has more excellent magnetic properties.

[1] L. Liu, Z. Liu and R. J. Chen, IEEE Trans. Magn. Vol. 50 p.2101704 (2014).

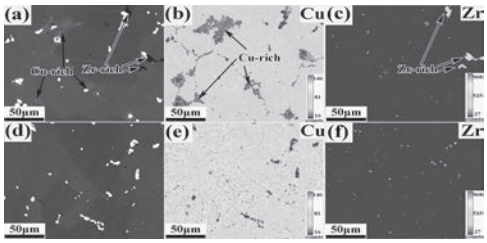


Fig. 1 The microstructure and corresponding Cu and Zr elements mapping of the BM and PM magnets. (a-c) BM magnet, (d-f)PM magnet.

3:42

FH-12. Strain-Induced Magnetic Properties in RCo_5 (R=rare earth) Magnets. *R. Choudhary*[1] and D. Paudyal[1] *1. U.S. Department of Energy, ISU, Ames Laboratory, Ames, IA, United States*

RCo_5 (R= rare earth metals) magnets have attracted the attention of researchers because of their large magnetocrystalline anisotropies [1-3]. RCo_5 with space group P6/mmm form with the three non-equivalent sites: R (1a), Co (2c), and Co (3g). R atom lies in the middle of the hexagonal layer of Co (2c) atoms, shown in Fig. 1(a). This layer is sandwiched by the hexagonal layers of Co (3g) atoms. This unique structural environment creates a crystal field that splits localized 4f states and partially quenches the R 4f orbital moment giving rise to the large part of the magnetic anisotropy and net 4f moment especially, in $SmCo_5$. First-principles calculations are performed to study the effect of strain on RCo_5 (R = La, Ce, Sm) magnets. R-Co exchange field is different for different rare earth R-atoms which affects the rare earth contribution to the magnetic anisotropy in RCo_5[4, 5] Therefore, the response of all three magnets here, RCo_5 for R = La, Ce, and Sm, to the strain will be different because of R-atoms. $LaCo_5$ and $SmCo_5$ have a borderline lattice constants ratio (c/a) to separate the planar and the uniaxial anisotropy. In contrast, magnetic anisotropy remains uniaxial in a wide range of c/a-ratio in $CeCo_5$ in which the 4f mixed valence states play a key role. Anisotropy variation of CeCo5 as a function of c/a ratio is shown in Fig. 1(b). Our calculations pinpoint $CeCo_5$ as a potential candidate model material for manipulating the uniaxial anisotropy. The underlying electronic structure of RCo_5 for different R-atoms plays an important role in optimizing and tailoring the uniaxial magnetic anisotropy. The projected outlook provides a path forward for the synthesis and characterization of the predicted materials with optimal strain and uniaxial magnetic anisotropy. This research is supported by the Critical Materials Institute, an Energy Innovation Hub funded by the U.S. Department of Energy, Office of Energy Efficiency and Renewable Energy, Advanced Manufacturing Office.

[1] T. Zhao et al., J. Appl. Phys., vol. 70, pp. 6134 (1991). [2] G. H. O. Daalderop et al., Phys. Rev. B, vol. 53, pp. 14415 (1996). [3] M. C. Nguyen et al., J. Phys.: Condens. Matter., vol. 30, pp. 195801 (2018). [4] Z. Tie-song et al., Phys. Rev. B vol. 43 pp. 8593 (1991). [5] H. Xiu-Feng et al., Acta Physica Sinica vol. 6, pp. 697 (1997).

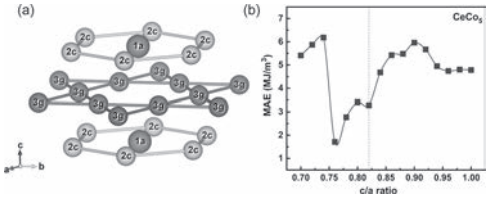


Fig.1 (a) Crystal structure of hexagonal RCo_5 magnet where R-1a (pink), Co-2c (cyan) and Co-3g (violet) are three different sites and (b) a variation in anisotropy of $CeCo_5$ as a function of c/a ratio.

3:54

FH-13. Torque Magnetometry Study of Magnetocrystalline Anisotropy in the Permanent Magnet $NdCo_5$. *S. Kumar*[1], C.E. Patrick[1], R.S. Edwards[1], G. Balakrishnan[1], M.R. Lees[1] and J.B. Staunton[1]
1. Department of Physics, University of Warwick, Coventry, United Kingdom

The permanent magnet $NdCo_5$ has attracted considerable attention owing to the observation of a giant rotating magnetocaloric effect close to room temperature [1] associated with a spin reorientation transition (SRT) [2]. To study the magnetic anisotropy and the SRT in this compound, we have carried out detailed torque and magnetization measurements on a single crystal of $NdCo_5$ grown using the optical floating zone technique. The SRT is reflected in a change in the polarity of the torque curves, $\tau(\gamma)$, measured as the direction of the applied field is varied in the *ac* plane. We compared our experimental results with the calculated torque data and found a good agreement above the transition (see Fig. 1). Torque measurements in magnetic fields as high as 6 T have allowed us to extract the temperature dependence of the anisotropy constants, K_1 and K_2, for $NdCo_5$. The observed behaviour has been compared with previous reports [2-4]. We have also calculated the finite temperature magnetocrystalline anisotropy of $NdCo_5$ from first principles using a recently developed framework, which combines density-functional theory based on the disordered local moment picture with crystal field theory. The calculations provide a good account of the temperature dependence of the spin reorientation and give a microscopic insight into the SRT, which occurs due to the competing perpendicular and uniaxial anisotropies of the Nd and Co sublattices. The current work is a part of the PRETAMAG project www.warwick.ac.uk/pretamag funded by the UK Engineering and Physical Sciences Research Council, Grant no. EP/M028941/1 and EP/M028771/1.

1. S. A. Nikitin *et al.,* Phys. Rev. Lett. 105, 137205 (2010). 2. M. Ohkoshi *et al.,* AIP Conf. Proc. 29, 616 (1976). 3. H. Bartholin *et al.,* J. Phys. Chem. Solids 27, 1287 (1966). 4. M. Seifert *et al.,* New J. Phys. 15, 013019 (2013).

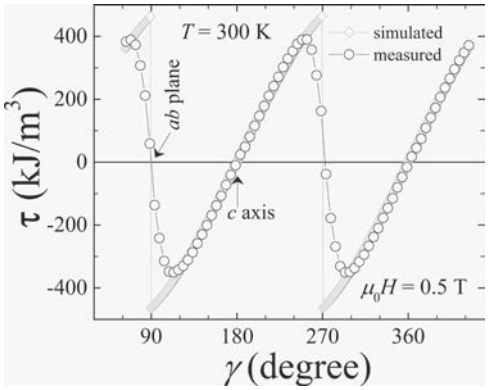


Fig. 1 Torque, τ, measured and calculated at T = 300 K versus the direction, γ, of the applied magnetic field in the *ac* plane.

4:06

FH-14. Magnetization Enhancement and Phase Stability of Mn Doped $SmCo_5$ System. *B. Song*[1], H. Zhang[1], Q. Lu[1], W. Liu[1], Y. Li[1], Z. Altounian[2] and M. Yue[1] *1. College of Materials Science and Engineering, Beijing University of Technology, Beijing, China; 2. Center for the Physics of Materials, Department of Physics, McGill University, Montreal, QC, Canada*

$SmCo_5$ permanent magnet has many advantages such as promising high temperature magnetic properties and easy preparation, comparing with Nd-Fe-B and other Sm-Co systems.[1] However, its permanent-magnet performance is limited by low saturation magnetization (M_S). In this work, we successively enhanced the M_S by introducing Mn on Co sites in $SmCo_5$. The method to get pure $Sm(Co, Mn)_5$ phase and the mechanism of phase stability in this system were also addressed. The BSE images in Fig.(a) show the coexistence of $SmCo_5$, Sm_2Co_7 and Sm_2Co_{17} in the annealed $Sm(Co, Mn)_5$ ingots, indicating the deterioration of phase stability with Mn doping. This is attributed to the increase of system energy based on the theoretical calculation. We thus adopted rapid solidification and subsequent annealing to obtain pure $SmCo_5$ phase, as shown in Fig.(b). With the increase of Mn content, the cell volume and c/a ratio increase monotonously, while the grain size increases from 1 to 60 mm after annealing. More importantly, M_S is enhanced for 13% by Mn doping, which is comparable with that of the Pr doping. Theoretical calculation also indicates that Mn doping has greater potential in the enhancement of M_S than Fe doping, which makes $Sm(Co, Mn)_5$ system a promising candidate for the application of permanent magnet.

[1]Kumar. K. Journal of Applied Physics, 1988, 63(6):R13-R57.

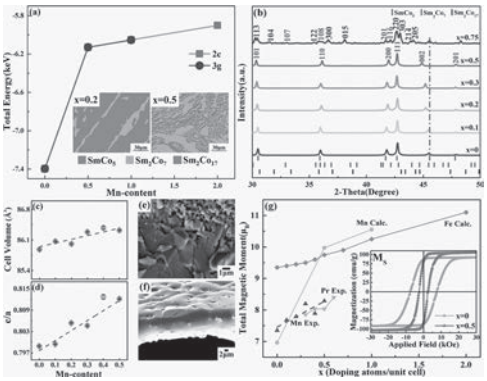


Fig. (a) Total energy of $Sm(Co, Mn)_5$ system based on first-principles calculation, the insets are the BSE images of the annealed ingots; (b) XRD patterns of the annealed $Sm(Co, Mn)_5$ ribbons; (c~d) Lattice parameters as functions of Mn content; (e~f) SEM images of $Sm(Co, Mn)_5$ ribbons before and after annealing; (g) Theoretical and experimental moment per molecular of Mn, Fe and Pr doping systems, the inset is the MH loops of the annealed $Sm(Co, Mn)_5$ ribbons.

4:18

FH-15. Optimizing the microtructure and magnetic properties of $SmCo_5$/α-Fe nanocomposite magnets by adjusting the morphology of Fe. *X. Xu*[1], Y. Li[1], Z. Shang[1], M. Yue[1], D. Zhang[1], Q. Lu[1], H. Zhang[1], W. Liu[1], Q. Wu[1] and Z. Altounian[2] *1. Beijing University of Technology, Beijing, China; 2. McGill University, Montreal, QC, Canada*

In recent years, nanocomposite magnets based on exchange coupling have become a research hotspot in the permanent magnetic material field. Compared with traditional single-phase coarse-grained permanent magnets, nanocomposite magnets have higher theoretical magnetic energy product, and become a powerful competitor for the new generation of permanent magnets [1]. Moreover, the addition of soft phase greatly reduces the content and rare earth and raw material cost of products. In this work, Fe nanoflakes

and Fe nanopowders were mixed with $SmCo_5$ ribbons, respectively. Subsequently, amorphous $SmCo_5$/Fe powders were obtained by high energy ball milling. Then the isotropic $SmCo_5$/Fe magnets were obtained by the same hot pressing process. The addition amount of Fe is 10wt.%, 15wt.%, 20wt.% and 25wt.%. Fig. 1 shows the hysteresis loops of $SmCo_5$/Fe HP magnets added with different Fe nanoflakes and Fe nanopowders. For Fe nanoflake-doped magnets, the magnetic properties show that the saturation magnetization and remanence increase gradually, and the coercivity decreases gradually with the increase of Fe content. The hp magnet with 15 wt.% has the best magnetic energy product. The product of magnetic energy is 13.8 MGOe. Moreover, all the remanence ratios of the magnets are above 0.75 indicating significant remanence enhancement effect. By contrast, Fe nanopowder-doped magnets show lower coercivity, remanence and squareness than those of the Fe nanoflake-doped magnets with the same Fe addition. The microstructure observation reveals that the soft phase Fe grains distributed more dispersed in the magnets with the addition of Fe nanoflakes. Moreover, based on experimental observations, micromagnetism model is established and the micromagnetic simulation is carried out to analyze the relation between microstructure and magnetization reversal.

[1] E. F. Kneller, R. Hawig, IEEE Trans. Magn. 1991, 27(4):3588-3560.

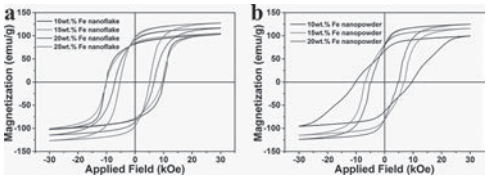


Fig. 1 Magnetic hysteresis loops of $SmCo_5$/Fe HP magnets added with different Fe nanoflakes (a) and Fe nanopowders (b).

Session FI
MICROMAGNETICS AND HYSTERESIS MODELING II
Riccardo Tomasello, Chair
Foundation for Research and Technology - Hellas, Heraklion, Greece

CONTRIBUTED PAPERS

1:30

FI-01. Learning Magnetization Dynamics. *T. Schrefl*[1], A. Kovacs[1], J. Fischbacher[1], H. Oezelt[1] and M. Gusenbauer[1] *1. Danube University Krems, Wiener Neustadt, Austria*

A deep neural network is trained to predict the magnetization dynamics of thin film elements. The model is tested by solving the micromagnetic standard problem 4 [1]. Neural network models for magnetization dynamics can be useful for applications where computing time is important. The basic idea is to learn the magnetic state at time $t+\Delta t$ from the magnetic state at time t. A model trained for such updates in time will then be able to predict the time evolution of the magnetization. However, the high total number of unknowns to describe the magnetic state of the thin film element makes learning expensive and data intensive. A successful neural network model would require a very large set of training data. Therefore, we first compress the magnetization and then learn time stepping in a low-dimensional latent space. We train a convolutional autoencoder to learn a low-dimensional representation whereby we achieve a compression of 1024:1. Learning the updates in time now involves magnetic states that are represented only with 16 variables. We use a dense seven-layer feed-forward network to learn magnetization dynamics in low-dimensional space. The application of the decoder to the predicted compressed states gives the magnetic states along the trajectory. We train the neural networks with the magnetic states of 200 trajectories computed for different applied fields using a finite difference solver [2]. We find that the predictions of the neural network model agree well with the solution of the Landau-Lifshitz-Gilbert equation obtained with the micromagnetic solver. Figure 1 shows the time evolution of the averaged magnetization components. Figure 2 shows the ground truth and the predicted magnetic states at different times. Please note that the external field used here was not part of the training data which was used to learn the low-dimensional representation and to learn time stepping.

[1] R. D. McMichael, M. J. Donahue, D. G. Porter et al., J. Appl. Phys. 89 7603 (2001) [2] M.-A. Bisotti, D. Cortes-Ortuno, R. Pepper et al., Journal of Open Research Software 6 (2018).

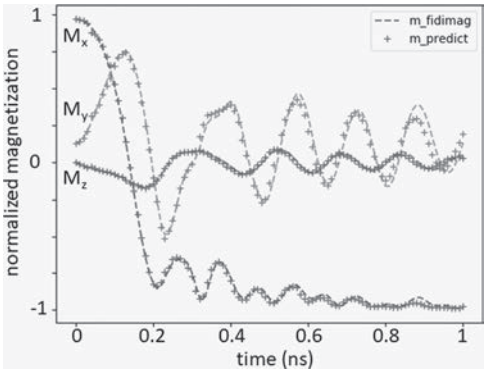


Fig.1 Magnetization components as function of time for the micromagnetic standard problem 4. Lines: Micromagnetic solver, symbols: Neural network prediction.

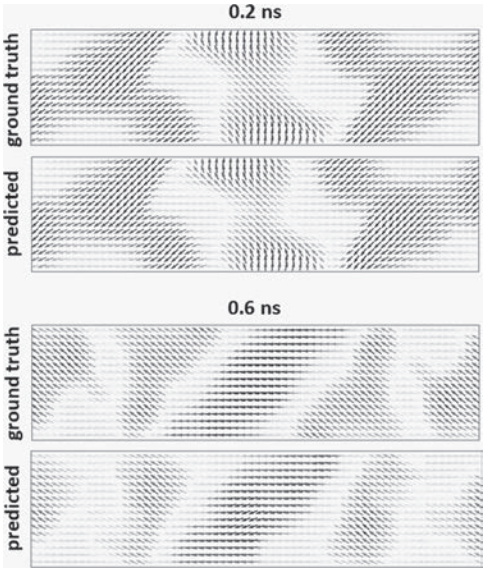


Fig.2 Ground truth and prediction for the magnetic states at 0.2 ns and 0.6 ns for the micromagnetic standard problem 4.

1:42

FI-02. Stochastic thermodynamics of noise-driven Landau-Lifshitz equation. *C. Serpico*[1], M. LoBue[2], M. Hoang-Ngoc[2], M. d'Aquino[3] and I. Mayergoyz[4] *1. University of Napoli "Federico II", Napoli, Italy; 2. SATIE, CNRS, ENS Paris-Saclay, Universit é Paris-Saclay, Paris, France; 3. University of Napoli "Parthenope", Napoli, Italy; 4. University of Maryland, College Park, College Park, MD, United States*

Micromagnetics is extensively used today in the area of magnetic nanotechnology and it has been demonstrated to be reasonably accurate in the analysis of magnetic systems up to the submicron spatial scale. In such systems, fluctuations cannot be neglected and micromagnetic theory has to be formulated in terms of a suitable statistical approach. In this work, we investigate and discuss the application of Stochastic Thermodynamics [1] to micromagnetics of small magnetic systems. Stochastic thermodynamics is an emergent field in statistical mechanics in which state variables of the system are assumed to be stochastic. The theory is formulated in terms of quantities, such as free energy, entropy, average magnetization, etc., associated with the ensemble of all possible realizations of the stochastic processes due to the noise mechanisms in the system. Stochastic thermodynamics is applied to a nanomagnet by using stochastic Landau Lifshitz equation to generate the realizations of the stochastic process. In this respect, we consider that the various heat/particle reservoirs in contact with the system, can be modeled in terms of a jump-noise stochastic process [2]. This enables to analyze the statistical properties of the system in terms of a Boltzmann equation. In the first part of the talk, we introduce and discuss the assumptions at the basis of the used formalism. The effect of each reservoir is included by an appropriate term in the kernel of the collision integral of the Boltzmann equation.

The form of these terms is specialized by imposing a generalized version of the detailed balance condition [3]. The stochastic termodynamics approach is then applied in the case when the magnetic nanoparticle under investigation is in contact with heat reservoirs and particle reservoirs. In this situation, it is possible to derive a suitable fluctuation theorem governing the statistics of the entropy production associated with the realizations of the stochastic magnetization dynamics [4]. In addition, the formalism enables to derive reciprocity (Onsager-type) relations associated to the presence of heat and particle fluxes [3]-[4].

[1] C. Van den Broeck, Shin-ichi Sasa, and U. Seifert, New J. Phys., Vol.18, p. 020401 (2016) [2] I. Mayergoyz, G. Bertotti, C. Serpico, Phys. Rev. B, Vol. 83, p. 20402 (2011) [3] P.G. Bergmann, J.L. Lebowtiz, Phys. Rev., Vol.99, 578 (1955) [4] J.L Lebowitz, H. Spohn, Journal of Statistical Physics, Vol. 95, p.333 (1999)

1:54

FI-03. Models of Advanced Recording Systems (MARS) - a multi-timescale micromagnetic code for granular film simulations.

S.E. Rannala[1], A. Meo[2], S. Ruta[1], R.W. Chantrell[1], P. Chureemart[2] and J. Chureemart[2] *1. Physics, University of York, York, United Kingdom; 2. Physics, Mahasrakham University, Mahasarakham, Thailand*

Micromagnetic modelling provides the ability to simulate large magnetic systems accurately without the computational cost limitation of atomistic modelling. Through this modelling it is possible to simulate thousands of grains over a time range of nanoseconds to years. Here we present an open-source multi-timescale micromagnetic code, called MARS, consisting of the key solvers: Landau-Lifshitz-Gilbert, Landau-Lifshitz-Bloch and Kinetic Monte Carlo. Extensive tests of the solvers has been performed and are included with the code to allow for quick verification after user desired changes have been made. Fig.1 shows a comparison between simulated data and analytical solutions for the magnetisation distribution at temperatures below and above the Curie point. MARS has been developed to allow for the simple addition of custom simulations, which can utilise any of the solvers separately or in a combined multi-timescale manner. MARS generates Voronoi films comprising of different layers, which can be specified separately. Input parameters such as Curie temperature and temperature dependent magnetisation and anisotropy are required and can be obtained via atomistic simulation [1,2]. MARS is capable of simulating the writing process of HAMR (heat assisted magnetic recording) for multiple tracks and bits with user configurable laser and field profiles. The writing process occurs in the short timescale and requires description of magnetisation at temperatures near the Curie temperature, this is done using the LLB solver. Fig.2 is a snapshot of the writing process for a single track consisting of five bits. These simulated bits are then read back at any time, ranging from nanoseconds to years after the writing process, via the KMC. This read back of the written data enables investigations into the success rate of HAMR writing and also the data longevity obtained by the recording medium.

[1] R. Evans, W. Fan and P. Chureemart, et al. Journal of Physics: Condensed Matter, Vol. 26, p 103202 (2014) [2] H. Callen, E. Callen, Journal of Physics and Chemistry of Solids, Vol. 27, p 1271-1285 (1966)

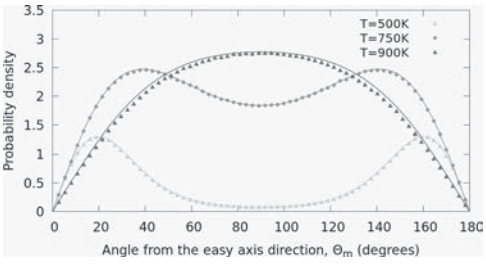


Fig.1 Comparison of angular probability distributions for an ensemble of grains between simulated data (points) and analytical solutions (lines).

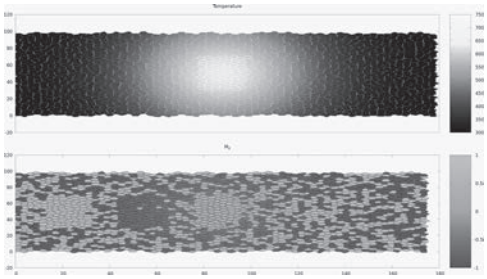


Fig.2 Snapshot of simulated HAMR writing process. Upper part shows the temperature profile and the lower part shows the magnetisation.

2:06

FI-04. Macroscopic effects due to atomistic colored noise in magnetization dynamics.

O. Chubykalo-Fesenko[1] and U. Atxitia[2] *1. Instituto de Ciencia de Materiales de Madrid, Madrid, Spain; 2. Freie Universitat Berlin, Berlin, Germany*

The atomistic spin dynamics has recommended itself as a valuable tool for modeling magnetization dynamics in the ultrafast timescale of exchange interactions in the presence of high excitations which lead to electronic temperatures higher than the Curie temperature [1]. This approach is based on the Langevin dynamics simulations with the assumption of a white (uncorrelated) noise [2]. However, the time and length scales in ultrafast magnetization dynamics are approaching limits where the memory effects in the spin-bath dynamics will play an important role. The correct atomistic spin dynamics with colored noise has been shown to be based on the Landau-Lifshitz-Miyasaki-Seki (LL-MS) approach [3]. Here we investigate the macroscopic effects arising from the assumption that at the atomic level the noise is colored. By using the same derivation as for the Landau-Lifshitz-Bloch (LLB) equation [4], we arrive at the modified LLB equation in the presence of colored noise. This allows us to discuss its macrosopic manifestations, namely that it (i) introduces a red shift in the precessional frequency which is temperature and correlation time dependent (ii) changes the susceptibility of an ensemble of non-interacting particles which may become negative at large exciting frequencies due to the memory effects [5] (iii) slows down both transverse and longitudinal relaxation times. To prove the viability of the macroscopic equation we compare the results with direct atomistic Langevin dynamics simulations using the LL-MS colored noise approach, see Fig.1. For the transverse dynamics the effect of the colored noise becomes significant for the correlation times larger than 1ps while for the longitudinal relaxation - for correlation times of the order of several femtoseconds (timescale of the precession in the exchange field). The new LLB equation constitutes a novel micromagnetic approach where the atomistic correlation times are already incorporates into the macroscopic equation and it may be useful for large-scale modeling at ultrafast timescales.

[1] T.Ostler et al at Nature Commun 3, 666 (2012) [2] R.F.Evans et al J.Phys.: Cond. Matt 26, 103202 (2014) [3] U.Atxitia et al Phys Rev.Lett. 102 057203 (2009). [4] D.Garanin Phys.Rev. B 55, 3050 (1997) [5] I Klik et al Sci. Rep. 8, 3271 (2018)

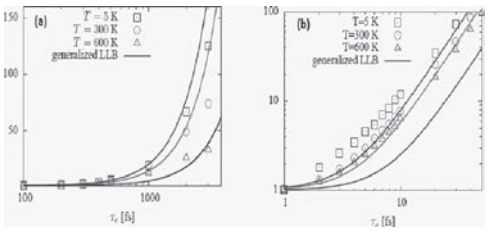


Fig.1 Comparison between atomistic LL-MS simulation and the macrosopic LLB predictions for (a) Transverse (b) Longitudinal relaxation times as a function of noise correlation time.

2:18

FI-05. Thermal fluctiations in the Landau-Lifshitz-Bloch equation.
M. Menarini[1] and V. Lomakin[1] *1. Electrical and Computer Engineering, University of California San Diego, La Jolla, CA, United States*

The Landau-Lifshitz-Bloch (LLB) equation allows micromagnetic simulations of the magnetization dynamics at low and high temperatures, including near Curie temperature. The LLB model is derived via thermal averaging of exchange-coupled spins and the magnetization length is a dynamic variable of the system, representing the thermal average obtained from atomistic models [1]. For high temperature application, such as heat assisted magnetic recording or laser induced demagnetization, having a correct description of the thermal fluctuations is essential to describe phenomena of interest, including signal to noise ratio, jitter, and optical reversal. Several stochastic LLB formulations have been proposed to incorporate the fluctuations into the deterministic formulation. However, these models either produce an average magnetization that differs from the expected value [2,3], making the formulation unsuited for multiscale atomistic-micromagnetic modeling techniques, or they ignore the fluctuations of the magnetization length [4]. In this paper, we introduced a formulation of the thermal fluctuations based on the Fokker-Plank (FP) equation following a procedure similar to the one used in Ref. [5] and [6] for the Landau-Lifshitz-Gilbert model. The thermal fields are introduced as 3 fluctuators applied to the precessional, longitudinal and perpendicular damping part of the LLB equation. The thermal fields are assumed to be (i) stationary, (ii) Gaussian stochastic processes with zero mean, and (iii) uncorrelated in time. No assumption is made on the probability distribution of the FP equation. We support out derivation with numerical results. We show that our formulation reproduces the Gaussian distribution at low temperature, while maintaining the value of the average magnetization at high temperatures (Fig.1).

[1] D. A. Garanin, Physical Review B 55, 3050 (1997) [2] R. F. L. Evans, D. Hinzke, U. Atxitia, U. Nowak, R. W. Chantrell, and O. Chubykalo-Fesenko, Physical Review B 85, 014433 (2012). [3] D. A. Garanin and O. Chubykalo-Fesenko, Physical Review B 70, 212409 (2004). [4] L. Xu and S. Zhang, Journal of Applied Physics 113, 163911 (2013). [5] W. F. Brown Jr, Physical Review 130, 1677 (1963). [6] J. L. García-Palacios and F. J. Lázaro, Physical Review B 58, 14937 (1998).

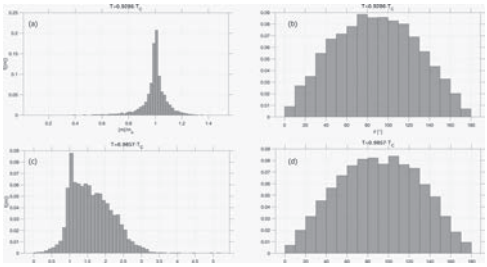


Fig.1 Distribution of angular and magnitude distribution of the magnetization using our model for an isotropic particle. The magnetization is normalized to the value of the equilibrium magnetization. (a) shows the length of the magnetization distribution for T=0.928 Tc and (b) shows the angular distribution of the magnetization for the same temperature. (c-d) show the magnetization and angular distribution for T=0.98Tc

2:30

FI-06. Pseudospectral method for the solution of the Fokker-Planck equation associated to stochastic magnetization dynamics.
V. Scalera[1], M. d'Aquino[2], S. Perna[1], M. Hoang-Ngoc[3] and C. Serpico[1] *1. Department of Electrical Engineering and ICT, University of Naples Federico II, Naples, Italy; 2. Engineering Department, University of Naples "Parthenope", Naples, Italy; 3. Physics, Université Paris-Saclay, Orsay, France*

In magnetic memories high density of data is obtained by reducing the size of the single bit cell. For a sufficiently small particle, in the submicrometer scale, the effect of thermal agitation is not negligible anymore and the magnetization dynamics is not deterministic [1]. One possible approach to study this situation consists in adding to the Landau-Lifshitz-Gilbert (LLG) equation a stochastic term in the effective field which models thermal fluctuations. In order to determine the statistics of thermal switching, LLG equation has to be numerically integrated for a large number of realization of the stochastic process. Alternatively, one can describe the stochastic magnetization dynamics by analyzing the probability density function (p.d.f.) of the magnetization. Assuming a spatially uniform magnetization for the specimen, the p.d.f. time evolution is described by the Fokker-Planck (FP) equation on the unit sphere. In the general case, it is not possible to derive an analytical solution for the FP equation and numerical methods must be employed. In this work, we present a numerical scheme to efficiently solve FP equation on the unit sphere based on the pseudospectral method. This method consist in choosing a grid of points and expanding the solution using a set of basis function, which are smooth, defined in the whole domain and equal to zero in all the grid points except one. The grid on the unit sphere is constructed by using as coordinates the component of magnetization along a given axis z and the azimuthal angle associated to rotation around axis z. Grid points are equispaced in the azimuth angle and are distributed as Chebyshev nodes in the z variable. The basis function are given by the product of Lagrange polynomials in the variable z and periodic sinc functions in the azimuth angle. We check the method accuracy by comparing the slowest thermal relaxation time constant numerically evaluated from the FP equation, Langevin dynamics of an ensemble of magnetic particles [2] and the approximated analytical expression given by Brown in [1], as shown in fig. 1.

[1] W.F. Brown, Physical Review, vol. 130, pp 1677-1686 (1963) [2] D.B. Reeves, J.B. Weaver, Appl. Phys. Lett., Vol. 107, 223106 (2015)

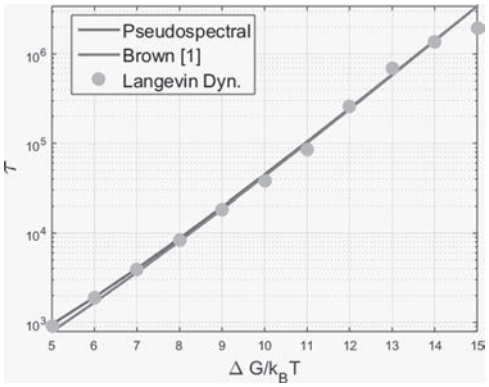


Figure 1

2:42

FI-07. Large-scale computation of magnetization eigenmodes in complex micromagnetic systems. *M. d'Aquino*[1], S. Perna[2] and C. Serpico[2] *1. Department of Engineering, University of Naples "Parthenope", Naples, Italy; 2. DIETI, University of Naples Federico II, Naples, Italy*

The study of normal oscillation modes of magnetic nanosystems is fundamental for analyzing magnetization dynamics under microwave applied fields[1,2], thermal fluctuations[3] and magnonic structures[4]. The normal oscillation problem was originally tackled with analytical techniques[1,5] limited to spherical/ellipsoidal particles for saturated equilibria. Recently, considerable research has been focused on normal modes for structures with generic shapes[4,6] and spatially non uniform magnetization equilibria such as vortices[3] or skyrmions[7]. In this work, normal modes around generic equilibria in arbitrarily-shaped micromagnetic systems are evaluated in the frequency domain by using a special formulation[8] of the linearized Landau-Lifshitz-Gilbert equation, which is recast as generalized eigenvalue problem for self-adjoint operators related to the micromagnetic effective field. This formulation has several advantages over time-domain or dynamical matrix approaches: 1) it naturally preserves the physical properties implied by magnetization amplitude conservation. 2) The discrete eigenvalue problem obtained by either finite difference or finite element methods preserves relevant properties of the continuum formulation. 3) This approach leads to a matrix-free eigenmode solver, in that it does not require assembling the effective field operator, which would result in unpractical $O(N^2)$ storage and computational cost (N is the number of cells), but rather it exploits classical exchange and magnetostatic field computational routines implemented within micromagnetic codes. This allows to perform large-scale computations of magnetization eigenmodes in systems composed of hundred thousand cells in reasonably short time (e.g. 200 modes for a system of $N=4\times10^5$ cells computed in 17 hours on single CPU, equivalent matrix eigenvalue problem size would be $(8\times10^5)^2$). Figure 1 reports examples of normal modes for complexly shaped structures with several microns size.

[1] W.F. Brown Jr, Micromagnetics, Interscience Publishers (1963). [2] H. Suhl, Proc. IRE 44, 1270 (1956); H. Suhl, J. Phys. Chem. Solids 1, 209 (1957). [3] K. Perzlmeier, M.Buess, C.H. Back, V.E. Demidov, B. Hillebrands, S.O. Demokritov, Phys. Rev. Lett. 94, 057202 (2005). [4] V.V. Kruglyak, S.O. Demokritov, D. Grundler. Journal of Physics D: Applied Physics. 43 (26): 264001 (2010) [5] A. Aharoni, Introduction to the theory of ferromagnetism, Oxford Press, New York (1996). [6] R.D. McMichael, M.D. Stiles, Journal of Applied Physics 97, 10J901 (2005). [7] K.Y. Guslienko, Z.V. Gareeva, Journal of Magnetism and Magnetic Materials, 442, 176 (2017). [8] M. d'Aquino, C. Serpico, G. Miano, C. Forestiere, Journal of Computational Physics 228, 6130-6149 (2009).

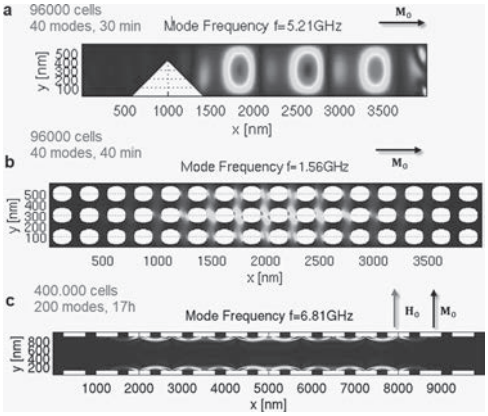


Fig 1. Examples of computed normal modes: (a) backward volume mode in notched strip line; (b) clustered oscillations in anti-dot lattice; (c) edge mode in strip line with periodical width modulation. Mode frequency, number of cells and computation time are reported.

2:54

FI-08. Computing resonant modes and excitation states in micromagnetic systems with finite element based solvers. *Z. Lin*[1,2] and V. Lomakin[1] *1. Electrical and Computer Engineering, University of California, San Diego, La Jolla, CA, United States; 2. Materials Science and Engineering, University of California, San Diego, La Jolla, CA, United States*

Solvers for excitation states and resonant modes serve as a powerful tool applicable to various micromagnetic systems. Linearized time domain Landau-Lifshitz-Gilbert (LLG) equation can be used to study situations with weak excitations but has limitations when the solution at a particular frequency is of interest. We present a finite element method (FEM) based eigen-value solver for computing normal oscillation frequencies and modes in micromagnetic systems. The solver can find resonant modes for both conservative (zero-damping) and non-conservative (non-zero damping) cases. This is achieved by directly using an eigen-value solver on a transformed linearized LLG. This approach does not use any perturbation theory [1] and allows handling zero-, small-, and large-damping cases, and can be accelerated by preconditioner. We also address the orthogonality properties between different resonant modes. Such a solver is useful for a set of applications, e.g. calculating noise in magnetic devices, such as magnetic sensors, or studying spin wave excitations. We also develop an FEM-based linear solver in frequency domain. The solver can compute excitation states with an iterative procedure and is accelerated by preconditioners. Specifically, we use a preconditioner based on keeping only exchange related terms, which itself is preconditioned with ILU preconditioner and a special block inverse precondioner. This approach can be used for modeling linear phenomena, such as spin waves. The solvers are integrated with the FastMag simulator framework and are accelerated by Graphics Processing Unit (GPU) and multi-core CPU computing. We carried out numerical experiments to study various systems.

[1] Massimiliano d'Aquino, Claudio Serpico, Giovanni Mianob, Carlo Forestiere, Journal of Computational Physics Vol 228, p. 6130–6149 (2009).

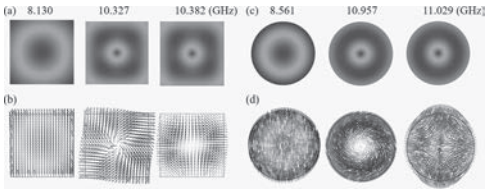


Figure 1. Resonant states of a 100 nm side permalloy film (a)-(b) and 100nm permalloy diameter disc (c)-(d) with a thickness of 3nm without anisotropy. (a) and (c) show the RMS value, (b) and (d) show the vector field.

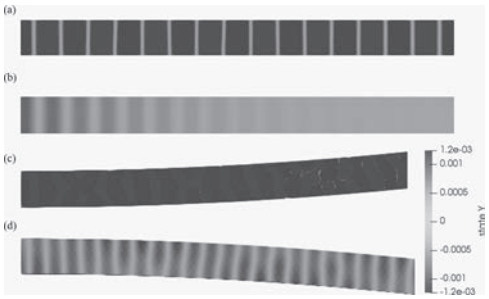


Figure 2. Simulation results of week excitation of a 100 μm×30 nm×5 nm straight (a)-(b) and semicircle (c)-(d) wave guide with large damping term. Spin wave propagation pattern observed. (a) and (c) show the parts near excitation source, (b) and (d) show the side far away the excitation, spin waves decay due to the damping term.

3:06

FI-09. Implementation of high-performance effective-field-calculation algorithm for ultra-large-scale micromagnetic simulation on multi-GPUs. *H. Tsukahara*[1] and K. Ono[1] *1. High Energy Accelerator Research Organization, Tsukuba, Japan*

Micromagnetic simulations have been revealing magnetization dynamics for various magnetic materials. A supercomputing system is indispensable to perform ultra-large-scale simulation over 0.1 billion calculation cells. In principle, a graphics processing unit (GPU) can execute massively parallel computing at high speed with low energy consumption. However, due to the slow data transfer between GPUs and between GPUs and CPUs, using GPUs for large-scale simulations tends to be difficult. We implement the high-performance demagnetization-field-calculation algorithm on our simulator for an ultra-large-scale micromagnetic simulation on multi-GPUs. Our simulator solves Landau–Lifshitz–Gilbert equation and with MPI and SMP parallelization. Figure 1(a) shows the algorithm of an effective field calculation. Basically, the calculations are performed on GPU, except for the data transfer. The most serious problem in demagnetization field calculation is MPI communications. We employ the heterogeneous computing algorithm to overlap data transfer and computing. We use three streams in which the computing is performed asynchronously. We performed calculations of other magnetic fields, such as the exchange field, during the MPI communication with CPU. Additionally, we can calculate three components of magnetic field vectors simultaneously. Figure 1(b) shows the elapsed time of one step with 2563 and 5123 cells. In these calculations, we use Cray XC50-LC and Cray CS-Storm 500GT supercomputer at Tohoku University in Japan. The elapsed times using multi-GPU and 512 CPU cores are almost the same, even we use only 4 GPUs (Tesla-V100). The calculation speed reaches 84.0 times faster compared to that with 32 CPU cores (Xeon E5-2699v3). This study shows the world largest simulation of about 0.1 billion cells can be performed single work-station with a few GPUs.

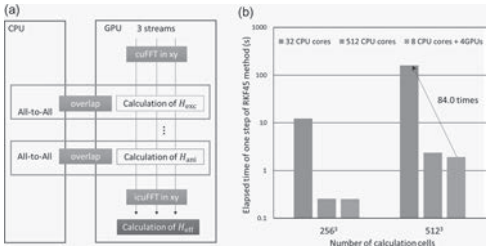


Fig. 1: (a) Schematic of the implemented algorithm. (b) Elapsed times of one step of RKF45 method. Blue, orange and gray colors represent the elapsed times using 32 CPU cores, 512 CPU cores, and 8 CPU cores + 4GPUs, respectively.

3:18

FI-10. Advancement in high-performance FEM-based micromagnetic codes on GPUs. X. Wang[1], S. Fu[1], R. Chang[1], M. Kuteifan[1], I. Volvach[1] and *V. Lomakin*[1] *1. CMRR, University of California, San Diego, La Jolla, CA, United States*

We present recent advancements in the development of high-performance finite element method (FEM) based micromagnetic framework FastMag. FastMag solves the Landau Lifshitz Gilbert (LLG) equation for modeling the magnetization dynamics and can handle multiscale problems, such as coupling the LLG equation with Maxwell's equations. It also implements the Nudged Elastic Band method for computing the energy barriers in complex systems. The simulator derives its high performance from efficient methods for evaluating the effective field and from implementations on massively parallel graphics processing unit (GPU) architectures and on multi-core CPU systems. FastMag uses tetrahedral geometrical discretization and thus it is highly flexible for general problems. For the magnetostatic fields, FastMag uses superposition principle for both volume and surface parts of the computational domain and uses a fast method for computing the related integrals in O(N log N) operations for N mesh elements. The time integration is accomplished via implicit time integrator, which is automatically adaptive in choosing the time step and order. We discuss various aspects of the implementation on GPUs and multi-core CPUs of all the code components, including all effective field computations, time integration, linear (GMRES) solver with preconditioners, and Jacobian operations. All these components are implemented in house and we show that it is important to make each one of them of high-performance to allow for high efficiency robust modeling of complex magnetic materials and devices. Table 1 shows computational time scaling versus the problem size. We chose to model the dynamics on standard micromagnetic problem 4, where we discretized the structure into a mesh with the edge length from 1nm to 7 nm for a dynamic simulation for 1 ns. Table 1 shows the performance statistics for the computations on CPU and nVidia RTX2080 GPU. It is evident that both CPU and GPU computation times exhibit a nearly linear scaling with the respect to the problem size, the time stepping is robust. Both CPU and GPU code components operate efficiently, and the GPU-CPU speed ups are around 30-fold for larger problems.

Mesh size, [nm]	# of nodes	#of elements	# of steps	# of linear iterations	Time on CPU	Time on GPU
1.0	358,249	1,716,795	776	22276	2712.9	98.0
1.5	128,039	570,175	620	20916	516.8	34.6
2.0	55,648	220,001	584	12349	161.7	12.9
2.5	36,594	145,005	543	12446	60.7	8.8
3.0	17,795	56,280	511	8790	29.9	4.5
4.0	9,311	27,014	609	3860	7.0	2.2
5.0	6,073	17,543	529	5233	5.4	2.8
6.0	4,209	12,023	535	2294	2.4	2.0
7.0	3,049	8,625	576	2192	2.4	1.6

Table 1: Computational time versus problem size.

3:30

FI-11. A fast algorithm to reconstruct 3D object in CXDI based on massively parallel processing. *F. Ai*[1], A. Shabalin[3], O.G. Shpyrko[3] and V. Lomakin[1,2] *1. ECE, UCSD, La Jolla, CA, United States; 2. CMRR, UCSD, La Jolla, CA, United States; 3. Physics, UCSD, La Jolla, CA, United States*

Coherent X-ray Diffraction Imaging (CXDI) is a computational method used for the reconstruction of images at nanoscale resolution. CXDI allows reconstructing magnetization states, such as magnetic domains, based on a series of images taken from synchrotron experiments. CXDI relies on an iterative procedure based on forward and backward FFTs allowing extracting the phase information from intensity measurements, which leads to a high-resolution reconstruction. CXDI for reconstructing 3D objects becomes computationally expensive and the computations can take significant time, which does not allow using it in real time while performing measurements. The long computational time is due to the need to do many 3D FFTs, which, for large systems, become slow and occupy large memory. We present a new algorithm to reconstruct 3D object using CXDI. This algorithm is based on the Fourier slice theorem and shrinkwrap iterative algorithm. Instead of performing phase reconstructions iterations using 3D FFTs we reconstruct a set of 2D images, each for a slice taking for a specific measured angle. Once this set of 2D reconstructed images is accomplished, we perform a 3D reconstruction step, which is rapidly converging since the 2D images already contain both intensity and phase information. In order to allow for efficient reconstruction of the 2D images, we developed an approach, allowing using a reconstruction for one of the images as a guess of the close in angle images. The benefits of the proposed algorithm include the reduction of the iterations needed for convergence, the ability to process a large number of images in parallel, a large reduction of the memory consumption, increased accuracy, and improved robustness of the reconstruction. Due to the reductions of the memory consumption and the ability to process sets of images independently, the proposed algorithm is well-suited for implementations on massively parallel graphics processing units (GPUs) with major speed

improvements. Figure 1 shows an example of running CXDI on a simulated particle. This result as an average of 60 independent reconstructions shows high quality while only taking 1 hour.

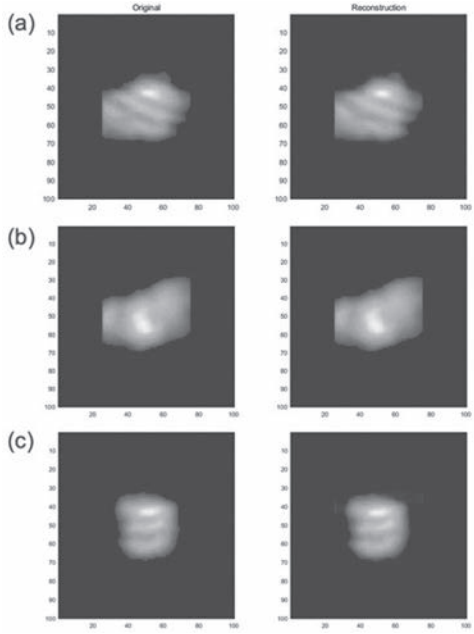


Fig.1: Center slices on (a)x-y plane (b) y-z plane and (z) x-z plane.

3:42

FI-12. Atomistic spin model simulations of magnetic properties of ferromagnetic (Ga,Mn)N. *D. Sztenkiel*[1], K. Gas[1,2], N. Gonzalez Szwacki[3], T. Dietl[4,5] and M. Sawicki[1] *1. Polish Academy of Sciences, Institute of Physics, Warszawa, Poland; 2. Institute of Experimental Physics, University of Wroclaw, Wroclaw, Poland; 3. Institute of Theoretical Physics, University of Warsaw, Warszawa, Poland; 4. International Research Centre MagTop, Polish Academy of Sciences, Warszawa, Poland; 5. WPI-Advanced Institute for Materials Research, Tohoku University, Sendai, Japan*

The interplay between magnetic and electric properties of magnetic layers is of considerable interest owing to the perspective of exploiting the underlying mechanisms for the next generation of devices for information storage and processing. Recently we observed an electric field-induced decrease of coercivity, and a non-reversible magnetization switching at $T \geq 2$ K for magnetic fields close to the coercive field in molecular beam epitaxy grown (Ga,Mn)N layers. The data are interpreted within the theory of the precessional magnetization switching adapted to (Ga,Mn)N by allowing for the control of the magnitude of trigonal deformation along the wurtzite *c* axis by the applied electric field [1]. Here we show that experimental data can be reproduced by theoretical results obtained from the Landau-Lifshitz-Gilbert (LLG) equation that describes how the magnetization direction evolves towards its new equilibrium orientation after a change of an effective magnetic field. We use atomistic spin model simulations [2], applied for ensembles of near ten thousands Mn spins randomly distributed on GaN lattice, with ferromagnetic superexchange included up to 14th neighbour. In general, the parallelization of the code has been applied. As shown in the Fig. 1 an experimentally established magnetization curve can be adequately reproduced within our approach. Elaboration of such numerical tool allows to theoretically investigate these factors which determine the probability of the precessional magnetization switching induced by electric field. The calculations are supplemented by density functional theory simulations.

The work is supported by the National Science Centre, Poland, through projects DEC-2018/31/B/ST3/03438, DEC-2011/02/A/ST3/00125, DEC-2016/23/B/ST3/03575 and DEC-2014/12/S/ST3/00549. We also acknowledge the access to the computing facilities of the Interdisciplinary Centre for Mathematical and Computational Modelling at the University of Warsaw.

[1] D. Sztenkiel *et al.*, Nature Comm., Vol 7, p. 13232 (2016) [2] R. F. L. Evans *et al.*, J. Phys.: Condens. Matter, Vol. 26, p. 103202 (2014).

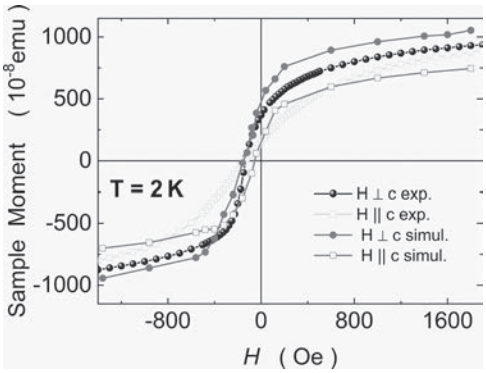


Fig. 1. Blue points: magnetic field H dependence of $Ga_{0.94}Mn_{0.06}N$ magnetic moment at $T = 2$ K measured along the magnetic easy (H ⊥ c) and hard (H ∥ c) axis. Red points: magnetization curve calculated using atomistic spin approach and LLG equation.

3:54

FI-13. Modelling of heating efficiency in magnetic hyperthermia: effect of non-harmonic driving field. *P. Tiberto*[1], P. Allia[2,1] and G. Barrera[1] *1. Advanced materials and life sciences, INRIM, Torino, Italy; 2. DISAT, Politecnico di Torino, Torino, Italy*

Rate equations are a useful tool to study high-frequency hysteresis loops of magnetic nanoparticles (MNPs) in the weak interaction limit and in the uniaxial anisotropy approximation [1]. The response of superparamagnetic nanoparticles described as double-well systems with randomly distributed easy axes is studied by a rate-equation approach in the typical range of frequencies and temperature adopted in magnetic hyperthermia. Hysteresis loops obtained applying non-harmonic driving field waveforms with various frequencies and vertex fields show that sawtooth (AT) and square (SQ) field waveforms substantially enhance the Specific Loss Power (SLP) with respect to a harmonic excitation (ST) of same frequency and amplitude. This improvement is related to the presence of fast, quasi-adiabatic transformations where the occupancy numbers in the two potential wells are virtually frozen, resulting in largely off-equilibrium magnetization states and in hysteresis loops with a greater area. In addition, the square driving field waveform is particularly promising for magnetic hyperthermia because the range of nanoparticle sizes useful to produce an optimal SLP becomes much wider respect to sawtooth harmonic waveform (Figure 1a). The observed temperature dependence of hysteresis power losses during hyperthermia can be taken into account considering the variation of MNP saturation magnetization and anisotropy in the studied temperature range. The calculated power loss evolution is included in a numerical model describing the Fourier's law of heat conduction to obtain the steady state and transient temperature profile in cancer tissue containing MNPs with selected size and concentrations excited by a radiofrequency field (frequency = 100 kHz, amplitude = 7.96 kA/m) (Figure 1b). The heat conduction model includes also terms describing the heat exchange between cancer tissues and blood flow.

[1] P. Allia, G. Barrera, P. Tiberto, Phys. Rev. B 98, 134423, (2018).

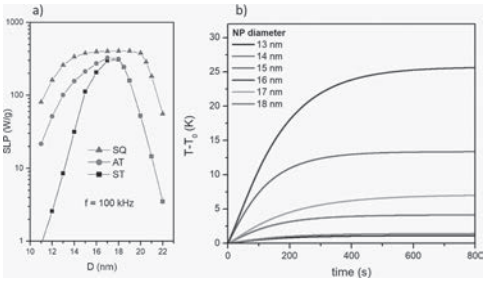


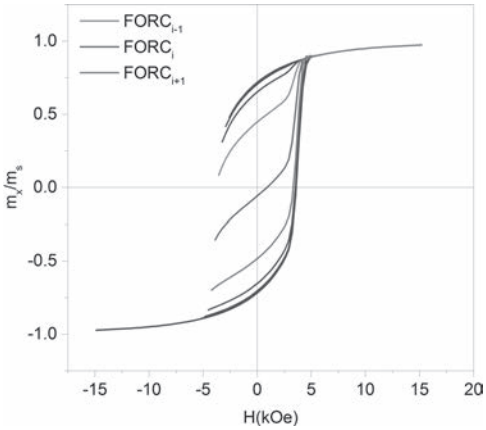
Figure 1: a) SLP released by a random assembly of monodisperse magnetite nanoparticles as a function of particle size D for three applied-field waveforms with same frequency and amplitude: ST, AT and SQ; b) transient temperature profile (T_0: initial temperature) in cancer tissue containing MNPs (volume fraction = 0.0025) as a function of D.

4:06

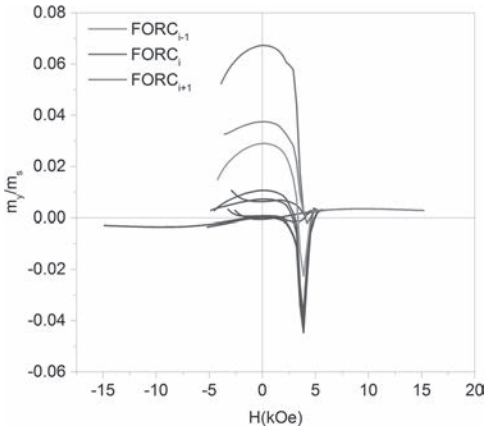
FI-14. Model for xyFORC vectorial characterization technique of multi-phase magnetic systems. *A. Stancu*[1] and L. Stoleriu[1] *1. Department of Physics, Alexandru Ioan Cuza University of Iasi, Iasi, Romania*

The most notable development in the use of magnetic characterization of materials is to use the second set of detection coils which many modern VSMs already have [1]. The classical measurement of first-order reversal curves (FORC) is giving the value of the magnetic moment of the sample along the direction of the applied field. If we call this set xFORC, the measurement made by the other set of detection coils could be named yFORC. We have named this type of measurement xyFORC and the main idea of this vectorial technique is to use the two sets of data to add information concerning the magnetic sample measured. This method has the clear advantage that it uses existent equipment in many laboratories and it is not significantly more complicated compared to the classical scalar one in which one uses only the xFORC data. The xyFORC technique could be a more attractive version of vectorial FORC characterization compared to the ones already used, which are more difficult to implement [2]. It could also provide the opportunity to clarify the problem of the reversible component in the FORC experiment [3]. In the figures we show typical xyFORCs for a system with two magnetic phases with perpendicular easy axes. One can observe in this example the typical problems in the understanding the yFORCs compared with the better known xFORCs. We see, for example, that the yFORCs show a non-monotonic behavior as a function of the reversal field. In the presentation we shall show how this property can be explained and how the yFORC diagram can provide supplementary information about the mixture of phases.

[1] A. Markou et al, J. Magn. Magn. Mater., 445, 95-102 (2018). [2] L. Stoleriu et al, J Appl. Phys., 103(7), 07D923 (2008). [3] I. Bodale et al, IEEE Trans. Magn., 47(1), 192-197 (2011).



xFORC



yFORC

4:18

FI-15. A Vector Hysteresis Model of Silicon Steel Based on Rotational Magnetization. *C. Zhang*[1,2], Y. Chen[1], Z. Zhang[2], Y. Li[1] and Q. Yang[3,1] *1. Hebei university of technology, Tianjin, China; 2. Ohio state university, Columbus, OH, United States; 3. Tianjin university of technology, Tianjin, China*

In the core of rotating machines, the trajectory of magnetic flux density can be very complex, including high order harmonics and rotational magnetization, especially in the tip region of stator teeth and slots. Due to strong magnetic anisotropy of the oriented silicon steel, it can be found that the core loss caused by rotational flux far exceeds that caused by alternating flux at low magnetic induction [1]. Among the research topics related to the analysis of rotational core loss, there are two types of calculation methods: Empirical loss model based on Steinmetz formula and vector hysteresis model [2]. The scalar hysteresis model such as Preisach model is more accurate and effective to estimate the core losses with several minor hysteresis loops, but relies on measurement results to identify the model and consume much more calculation resources [3]. This paper presents a novel core loss of silicon steel sheet based on rotational magnetization. The vectorial hysteresis loss is decomposed into the tangential and radial components which are defined based on rotational and alternating loss. Then, based on the pattern of rotational magnetization loci, the different regions in the stator core of induction motor are defined and classified. Rotational magnetization region produces much more core loss than the alternating core loss at low magnetic induction, but less core loss at high magnetic induction. The spatial angle difference α between vector H and vector B varies with the direction and magnitude of B. To simplify the loss model, the integral average of α is taken as the characteristic parameters as shown Fig. 1 based on rotational magnetization at different frequency. Fig. 2 illustrates the B-P curve of B35A210 specimen at 50 Hz with alternating and circular rotational excitation. Finally, the core loss of silicon steel calculated by the traditional Steinmetz formula and the modified hysteresis model are compared. It shows that the proposed model gives more precise result prediction than the traditional Steinmetz method.

[1] Y. Li, Q. Yang, C. and Zhang, *IEEE Trans. on Magn*, vol. 20, pp. 1-6(2011) [2] S. K. Chang, S. Y. Hahn, and G. S. Park, *IEEE Trans. on Magn*, vol. 36, no. 4, pp. 1254-1257 (2000) [3] O. Bottauscio, M. Chiampi, and M. Zucca, *IEEE Trans. on Magn* , vol. 38, no. 5, pp. 3294–3296 (2002)

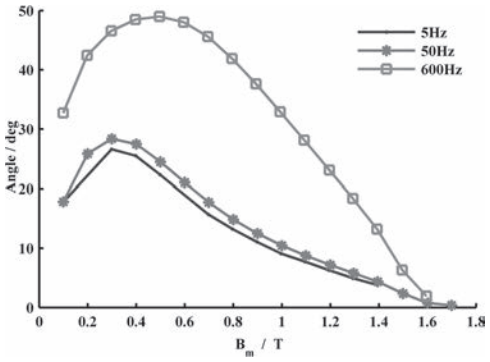


Fig.1 Relationship between amplitude and space angle of the rotation magnetization

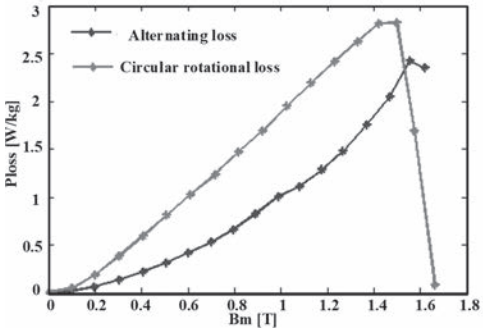


Fig.2 *B-P* curve of B35A210 specimen at 50Hz

Session FP
MAGNETICS FOR KINETIC MANIPULATION AND TRANSPORTATION (Poster Session)

Hellen Jiang, Chair
PNNL, Richland, WA, United States

FP-01. Optical Control of Diamagnetically Levitated Pyrolytic Graphite.

J. Young[1], S. Yee[1] and H. ElBidweihy[1] *1. Electrical and Computer Engineering, United States Naval Academy, Annapolis, MD, United States*

Pyrolytic graphite (PyG), when levitated above an array of alternating-pole permanent magnets, can be displaced by a localized increase in temperature due to the temperature dependence of its magnetic susceptibility. The increase in local temperature decreases the local diamagnetic forces, inducing a tilt and displacing the PyG sample in the plane of the permanent magnet array. Previous work has verified and demonstrated the optomechanical actuation of PyG using experiments and simulations [1]. Small-scale assembly methods can be extraordinarily complex processes because of the mediums in which they operate [2, 3]. This work proposes a milli-scale assembly system based on optical control of levitating diamagnetic milli-robots in air that minimizes undesirable effects such as stiction prevalent in systems with denser mediums [4]. Additionally, optical control allows accurate addressable control of multiple milli-robots able to move in close proximity to each other throughout the working surface with no work surface segmentation, a limitation of other diamagnetic control schemes [5]. A laser diode mounted on a 2-axis motorized translational stage and coupled to a controller accurately irradiates and actuates the PyG sample, which acts as a milli-robot with variable speed and acceleration. An infrared camera provides vision feedback to a MATLAB-based controller and user interface, permitting open loop or closed loop control. Figure 1 shows overlaid images providing an overview of an example trajectory of a PyG milli-robot levitating and actuated on top of an array of 6.35mm-diameter cylindrical NdFeB permanent magnets. The *x* and *y* pixel coordinates and yellow outline shown are MATLAB-generated computations of the milli-robot centroid and boundary, respectively. Figure 2 tracks the displacement of the PyG sample according to the same open loop input trajectory over a 23-second period.

[1] Miriam Ewall-Wice et al., IEEE Trans. Magn., 2019. [2] P Chen et al., Adv. Mater. 26, 2014. [3] F Xu et al., Adv. Mater. 37, 2011. [4] Z Zhakypov et al., IEEE T. Robot. 34, 2018. [5] A Hsu et al., J. Micro-Bio Robots, 2018.

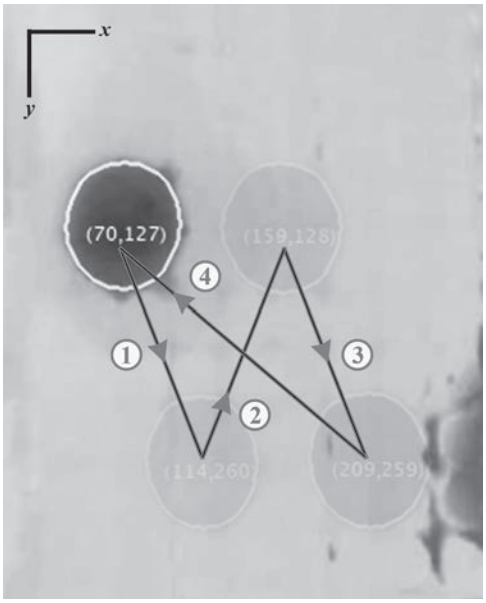


Fig. 1. Overlaid MATLAB-processed IR camera images depict an example overall trajectory of a 14mm diameter 25um thick PyG milli-robot actuated by laser irradiation.

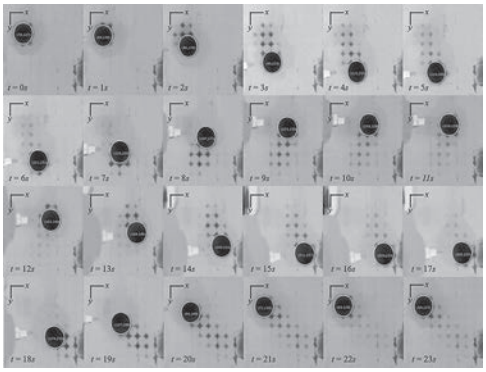


Fig. 2. IR camera images taken at one second intervals indicate the path of travel for the motion summarized by Figure 1.

FP-02. Magnetic Levitation of a Ferrofluid Droplet in Mid-Air.

T. Ohji[1], *S. Yamaguchi*[1], K. Amei[1] and K. Kiyota[1] *1. University of Toyama, Toyama, Japan*

This paper reports that the levitation of a ferrofluid droplet in the air at room temperature was realized using our magnetic levitation (maglev) device fabricated for non-contacting gripping and transport of ferrofluid droplets. The ferrofluid in a DC magnetic field theoretically deforms into an elongated spheroid in the direction of the magnetic field, as long as the surface tension of the droplet is higher than the tensile stress due to the magnetic field [1, 2]. Magnetic levitation system is suitable for experimentally verifying the

droplet deformation. Rhee et al. have reported on active magnetic levitation experiments of encapsulated ferrofluid in silicone oil [3]. The ferrofluid in the capsule floated at the steady position, but the viscous drag and buoyancy from the immiscible silicone oil slowed the capsule movement. Besides, the capsule filled with ferrofluid itself did not allow the deformation of the ferrofluid. We fabricated a new maglev system to observe the deformation and behavior of ferrofluid in an external DC magnetic field in mid-air. The maglev setup consists of an I-shaped electromagnet with a tapered magnetic pole tip, a laser displacement sensor, AD/DA, DSP, and power amplifier. The apex of a ferrofluid droplet (Base liquid: poly-alpha-olefin, viscosity: 5,000 mPa.sec, mass: 15 mg) placed on an oil-repellent film (Toyo Aluminium Inc., Toyal Ultra Lotus) was detected using the displacement sensor and actively stabilized by a PID controller. Figure 1 is a photograph of a magnetically levitated ferrofluid droplet. Figure 2 shows continuous shooting immediately before and after the levitation start with a high-speed camera (Photron Ltd., FASTCAM mini AX-50). The droplet extended upward just before leaving the oil-repellent film. After levitation, the droplet's apex fluctuated up and down for 2.5 seconds with deformation of the droplet. Finally, after 2.5 seconds, the droplet was stably levitated while keeping an oval shape of 3.4 mm height and 2.1 mm symmetrical axis length. Details of this research will appear at the conference.

[1] J. C. Bacri, et al., "Instability of ferrofluid magnetic drops under magnetic field," *J. Physique Lettres*, 43, (1982) 649-654. [2] L. D. Sherwood, "Breakup of fluid droplets in electric and magnetic fields," *J. Fluid Mech.* 188, (1988) 133-146. [3] E.J. Rhee, et al., "The position control of a capsule filled with magnetic fluid," *J. MMM*, 252, (2002) 350–352.

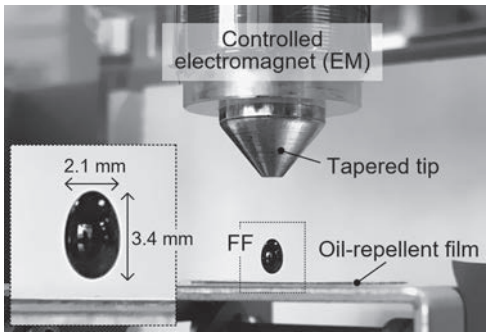


Fig. 1 Magnetically levitated ferrofluid droplet in mid-air.

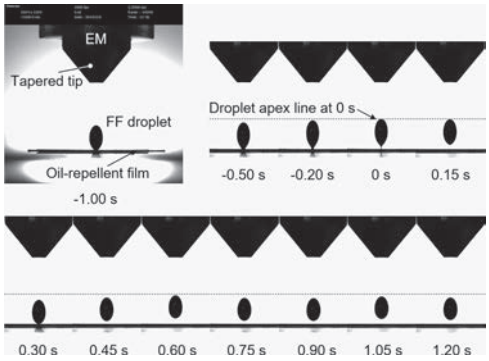


Fig. 2 Continuous shooting before and after levitation start.

FP-03. The Interaction between Two Permanent Magnets with Significantly Different Permeance Coefficients. *H. Meng*[1], Q. Wei[1], G. Tang[2], L. Cheng[3], G. Mizzell[4] and C.H. Chen[5] *1. Hangzhou Foresee Group Holding Co., LTD., Hangzhou, China; 2. Hangzhou Quadrant Technology Co. LTD, Hangzhou, China; 3. Hangzhou Magmax Technology Co., LTD., Hangzhou, China; 4. SuperMagnetMan, Pelham, AL, United States; 5. Quadrant Solutions, Louisville, KY, United States*

Even though Gauss' law for magnetic flux density (B-field) indicates there is no free magnetic charge, we can still define the effective bound magnetic charges from the magnetization of magnetic material [1]. The positive magnetic charge is what we usually called the "north pole", and correspondingly, the negative magnetic charge is what we usually called the "south pole". The interaction between the magnetic charges is governed by Coulomb's law so that like poles repel and unlike poles attract [2]. However, experiment shows that when two permanent magnets with significantly different permeance coefficients Pc (say, a small one with dimension of D4mm*4mm and Pc of 3.46, and a big one with dimension of D24mm*2mm and Pc of 0.18) were put together, with their directions of magnetization (DOM) pointing against each other, instead of repelling, they will attract to each other, especially when the coercivity of the big magnet is relatively low. This phenomenon may lead people to think that Coulomb's law for magnetic charges is not always right, and in some cases, like poles attract. In this work, we show that the above bizarre phenomenon is caused by the partial demagnetization in the low Pc magnet, rather than violation of Coulomb's law. When the experiment is carried out using sintered NdFeB magnet of N50 grade, the working point for the stand-alone low Pc magnet is very near to the knee of its demagnetizing curve, so it's very vulnerable to the external and its self-demagnetizing field. Finite Element Analysis (FEA) shows that demagnetization happens obviously in the central region of the magnet with low Pc, but the magnetization remains in the same direction all over the magnet. FEA also gives an attractive force when the above low Pc and high Pc magnets are close to each other and with opposite DOMs. Based on the magnetic charge model and Coulomb's law, the numerical integration of Coulomb's force is carried out, which gives almost the same attractive force as FEA.

[1] J. M. D. Coey, Magnetism and Magnetic Materials, 2010, Cambridge University Press, p.45. [2] Soshin Chikazumi, Physics of Ferromagnetism, second edition, 1997, Oxford University Press, p.3.

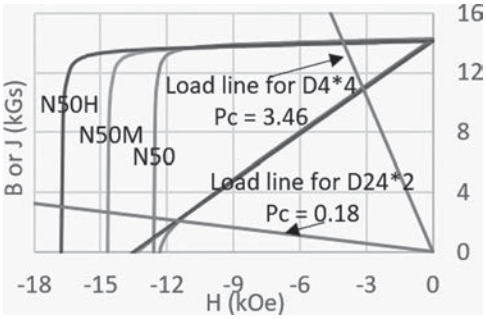


Fig.1 working point for the small and big magnets of different NdFeB grades.

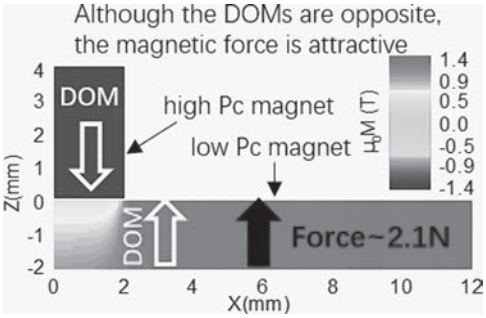


Fig.2 FEA results of magnetization distribution and magnetic force for the case of N50 NdFeB magnets. (only half of the model is shown)

FP-04. Reprogrammable Nanomagnets for Shape-morphing Micromachines. *J. Cui*[1,3], T. Huang[2], Z. Luo[1,3], P. Testa[1,3], H. Gu[2], X. Chen[2], B. Nelson[2] and L. Heyderman[1,3] *1. Laboratory for Mesoscopic Systems, ETH Zurich, Zurich, Switzerland; 2. Institute of Robotics and Intelligent Systems, ETH Zurich, Zurich, Switzerland; 3. Laboratory for Multiscale Materials Experiments, Paul Scherrer Institute, Villigen, Switzerland*

Shape-morphing micromachines have demonstrated significant potential in drug delivery, minimally invasive surgery, cell manipulation, and stenting applications [1]. With current fabrication methods, most micromachines are limited to a single type of transformation determined by their geometric design, which cannot be altered once fabricated [2]. In this work, we have developed a strategy to encode multiple shape-morphing information into transformable micromachines making use of the magnetic configurations of single-domain nanomagnet arrays. Inspired by origami, our micromachines consist of rigid panels carrying the arrays of nanomagnets separated by structured soft creases. The nanomagnets have tailored magnetic switching fields and, by applying a sequence of magnetizing fields, the arrays can be set into a particular magnetic configuration. By customizing the micromachine designs, we can obtain micromachines that perform specific shape transformations in an applied magnetic field (see Figure 1). Based on this strategy, we have built a simple four-pad micromachine with 2^4 possible magnetic configurations, demonstrating four distinct conformations when actuated by a magnetic field. Further, multicomponent micromachines were constructed by assembling modular units and, by customizing each individual unit, we have engineered a micromachine that can transform between two alphabet letters. We have also created complex folding behaviors, such as bending and twisting, and have implemented these folding modes in a microscale 'origami bird' capable of several different flapping modes. This work paves the way for the development of future intelligent microsystems that are reconfigurable and reprogrammable, which is required for biomedical applications and is also of interest for 3D magnetic and optical metamaterials. [3]

[1] B. J. Nelson, I. K. Kaliakatsos, J. J. Abbott, Microrobots for Minimally Invasive Medicine. *Annu. Rev. Biomed. Eng.* 12, 55–85 (2010). [2] M. Z. Miskin, K. J. Dorsey, B. Bircan, Y. Han, D. A. Muller, P. L. McEuen, I. Cohen, Graphene-based bimorphs for micron-sized, autonomous origami machines, *Proc. Natl. Acad. Sci.* 115, 466–470 (2018). [3] J. Cui, T.-Y. Huang, Z. Luo, P. Testa, H. Gu, X.-Z. Chen, B. J. Nelson, L. J. Heyderman, manuscript under review

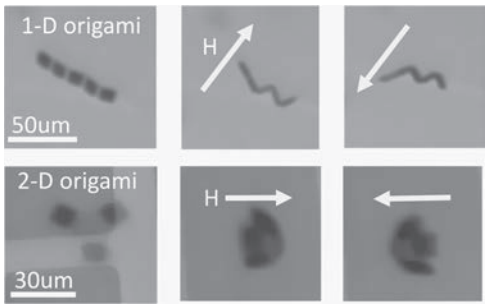


Figure 1. 1-D origami and 2-D origami micromachines demonstrate shape transformation in an applied magnetic field.

FP-05. Magnetic Control of Flexible Thermoelectric Devices Based on Macroscopic 3D Interconnected Nanowire Networks. *N. Marchal*[1], T. da Câmara Santa Clara Gomes[1], F. Abreu Araujo[1] and L. Piraux[1] *1. IMCN, Université catholique de Louvain, Louvain-la-Neuve, Belgium*

The emerging field of spin-caloritronics combines heat-driven transport with spintronics[1] and allows promising applications, such as magnetic heat valves or magnetically switchable cooling. However, dimensions in magnetic nanostructures lead to major experimental issues such as insufficient power generation capability and lack of reliable methods to obtain key spin-caloritronic parameters[2-3]. In contrast, more efficient macroscopic spin-caloritronics devices built from 3D interconnected multilayered nanowire (NW) networks (see Fig. 1) allow direct extraction of accurate key spin-caloritronics parameters[4]. They are fabricated by pulsed electrodeposition into 3D nanoporous polymer host membranes with no sample size limitation[5-7]. The branched structure of the network provides an excellent electrical connectivity, good mechanical robustness, while the pore-filled membranes show flexibility. The local removal of the gold layer serving as a cathode in the electrodeposition process yields a two-probe design suitable for magneto-transport measurements (see Fig. 2a). We studied Permalloy/copper (Py/Cu) multilayered NW networks showing giant magneto-transport (electrical, thermal and thermoelectric) properties (see Fig 2b-c), with room-temperature (RT) CPP-GMR up to 20%, and power factors comparable to that of bismuth telluride and that are magnetically modulated with magneto-power factor ratios up to 90% at RT. We observed large RT spin-dependent Seebeck coefficients of -12 μV/K. Those observations hold promise for magnetically modulated energy conversion using light and flexible thermoelectric generators and could lead to advances in future spin-caloritronic devices.

[1] G. E. W. Bauer, E. Saitoh and B. J. van Wees, *Nature Materials* 11, 391 (2012). [2] N. Liebing, *et al.*, *Phys. Rev. Lett.* 107, 177-201 (2011). [3] M. Walter, *et al.*, *Nature Materials* 10, 742 (2011). [4] T. da Câmara Santa Clara Gomes, F. Abreu Araujo and L. Piraux, *Science Advances* 5, eaav2782 (2019). [5] F. Abreu Araujo et al., *Advanced Electronic Materials* (in press). [6] T. da Câmara Santa Clara Gomes, L. Piraux, *et al.*, *Journal of Applied Physics* 120, 043904 (2016). [7] T. da Câmara Santa Clara Gomes, L. Piraux, *et al.*, *Nanoscale Research Letters* 11, 466 (2016).

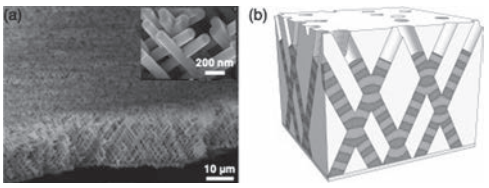


Fig. 1: (a) SEM image of a self-supported interconnected NW network film. The inset highlights the NW branched structure. (b) Schematic of the interconnected NW network with alternating magnetic and non-magnetic layers embedded within the 3D nanoporous polycarbonate template.

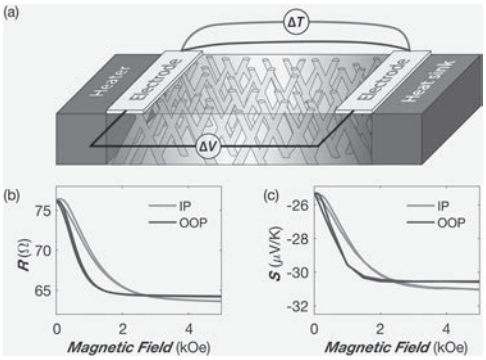


Fig. 2: (a) Device configuration for magneto-Seebeck measurements: a temperature difference Δ*T* between the metallic electrodes generates a thermoelectric voltage Δ*V*. Magnetoresistance (b) and magneto-Seebeck (c) curves for an interconnected Py/Cu NW network.

FP-06. Magnetic navigation system with a triangularly positioned triple coil set for the 2D manipulation of biomedical magnetic robots. *H. Lee*[1] and S. Jeon[1] *1. Mechanical and Automotive Engineering, Kongju National University, Cheonan, The Republic of Korea*

For 2D manipulation of biomedical small-scale magnetic robots such as in a fluid surface or a horizontal plane, conventional magnetic navigation systems (MNSs) were generally constructed with multiple numbers of 1D electromagnetic coils (Helmholtz coil, Maxwell coil, etc). However, conventional MNSs suffered from the ineffectively large overall structure, power consumption, asymmetric frequency response effect, etc [3, 4]. We propose a novel MNS simply composed of three circular coils (triple coil set, TCS), as shown in Fig.1a. Since it can be constructed with triangularly positioned identical coils, the MNS occupies minimal space to obtain a robot's working space within the system. Therefore, the corresponding power consumption and frequency response effect of the MNS can be effectively minimized during manipulation. We derived a general expression of a magnetic field generated by multiple numbers of arbitrarily positioned circular coils by using Jacobian and transformation matrices. From this expression, we could establish several constraint equations by which the proposed MNS with the TCS can selectively generate a uniform field or a gradient field near the geometric center of the coil set. Figs. 1c and 2 show several examples of the TCS's ability to generate a uniform magnetic field. Fig. 1c shows the variations of the field's uniformity and states that a TCS with a sufficiently large value of the aspect ratio can generate a more uniform field. Fig. 2 shows several cases of the uniform field generated along with the directions of 0, 45, and 90 degrees from x-axis, respectively (R/d = 1.3). We then constructed the proposed MNS, a magnetic robot, and a 2D robot manipulation environment and showed the validity of the proposed structure and manipulation method.

[1] E. Diller and M. Sitti, Found. Trends Robot., vol. 2, no. 3, pp. 143-259, 2011 [2] B. J. Nelson, I. K. Kaliakatsos, and J. J. Abbott, Annu. Rev. Biomed. Eng. 12, vol. 15, pp. 55-85, 2010 [3] S. Jeon, G. Jang, H. Choi, and S. Park, IEEE Trans. Magn., vol. 46, no. 6, pp. 1943-1946, 2010 [4] J. Nam, W. Lee, B. Jang, and G. Jang, IEEE Trans. Ind. Electron., vol. 64, no. 6, 2017

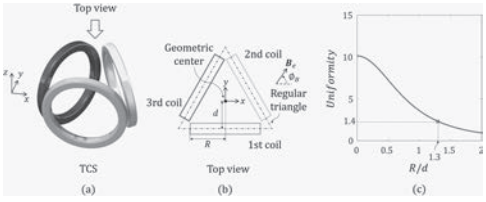


Fig. 1 (a) Schematic view of the TCS. (b) Geometric configuration of the TCS in xy-plane. (c) Variation of the field's uniformity (least square value of the Jacobian matrix) with respect to the coil's aspect ratio (R/d).

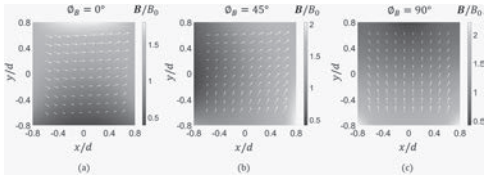


Fig. 2 Distribution of the uniform magnetic fields generated along with the directions of 0, 45, and 90 degrees from the x-axis, respectively, expressed with dimensionless values of the magnetic field and coordinate (R/d = 1.3).

FP-07. Separation of Diamagnetic and Weak Paramagnetic Solid Particles Realized by a Small Nd-Fe-B Magnetic Circuit. *C. Ueda*[1] *1. Science, Earth and Space Science, Osaka, Japan*

Most solid particles that are studied in industrial and/or basic researches are composed of diamagnetic or weak paramagnetic materials; possibilities of field-induced dynamical motions were not expected in these materials unless an ultra-strong field were applied to these particles. We were able to separate a mixture of heterogeous particles into groups of different materials for the first time using a pair of Nb-Fe-B magnetic plates, and the materials of the separated groups were immediately determined from their translating velocities; this was realized by comparing the value experimental susceptibility obtained from velocity with a list of published values [1][2]. The separation is based on a recent finding that acceleration *a* of particle induced by a magnetic volume force is independent to its mass [3]; it is deduced from an energy conservation law that *a* is uniquely determined by intrinsic susceptibility of the material. In performing a refined analysis on a mixture of heterogeneous particles, it is desirable to thoroughly separate the particles into groups of different materials before putting them to the analyses. In future, the proposed technique can realize the above task of pre-treatment, and then it may play a role of a chromatography technique, a conventional technique of pre-treatment. Extraction of rare-metal(i.e. Au, In, Ag) from the heterogeneous mixture is also possible because the susceptibilities of these materials are considerably small compared to other materials [2], A methodo separate mixture of weak magnetic particles by its concentration of paramagnetic Fe ion is newly proposed [4].

[1] Sci. Rep.6, 38431 (2016). [2] Sci. Rep.9, 3971 (2019). [3] J.PS.J. 79, 064709 (2010). [4] Adv. Mater. 1154, (2019) in print

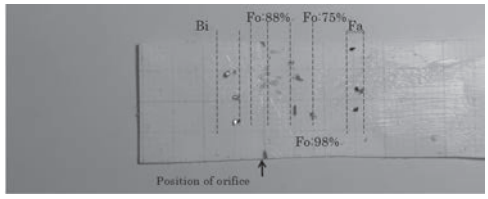


Image of a collecting sheet (cross sectional paper) observed after the experiment of magnetic separation performed in normal gravity. Sequence of the positions of the silicate samples are in the order of Fe concentrations [4].

FP-08. Optimal Design and Experimental Verification of a Linear Magnetic Gear. *S. Seo*[1], K. Shin[1], G. Jang[1], S. Kim[1] and J. Choi[1] *1. Dept. of Electrical Engineering, Chungnam National University, Daejeon, The Republic of Korea*

Electrical equipment typically cannot be driven without power transmission. For this reason, gears are used in a variety of mechanical systems [1–2]. However, mechanical gears cause mechanical losses when transmitting power. This problem has motivated various studies on magnetic gears, which can effectively compensate for the disadvantages of conventional gears [3–4]. In particular, in linear motion systems such as those used for wave power generation, utilizing a linear gear is inevitable. Thus, research on magnetic gears with tubular structures has recently been conducted.

Major limitations identified for this type of gear are manufacturing difficulties and high costs. Similar results are obtained when simplifying the tubular structure to a linear structure [5]. However, few studies related to linear magnetic gears have been conducted thus far. Therefore, this is a very relevant topic. In this study, we present an optimal design and verification of a linear magnetic gear (LMG). First, we choose a basic model that considers limitation specifications and then select an optimal model through parametric analysis. Next, an optimal model is presented considering mechanical characteristics through stress analysis. Finally, the reliability of the analysis is verified through experiments on an actual manufactured model. Fig. 1 present the structure and experimental system of the LMG. More specifically, Fig. 1(a)–(c) show the basic and two optimal shapes, respectively, of the flux-modulation poles (FMPs). Fig. 2(a) and (b) present comparisons of analytical and experimental results, and Fig. 2(c) shows stress analysis results of the optimal FMP shape. All results reveal the superiority of the optimal model design process. The final manuscript will provide more details on the design method and verification.

[1] B. Drew, A. R. Plummer, and M. N. Sahinkaya, "A review of wave energy converter technology," *in Proc. IMechE*, Part A: J. Power Energy, vol. 223, Jun. 2009, pp. 887–902. [2] I. Martins, J. Esteves, G. D. Marques, and F. P. Silva, "Permanentmagnets linear actuators applicability in automobile active suspensions," *IEEE Trans. Veh. Technol*., vol. 55, no. 1, pp. 86–94, Jan. 2006. [3] N. W. Frank and H. A. Toliyat, "Analysis of the concentric planetary magnetic gear with strengthened stator and interior permanent magnet inner rotor," *IEEE Trans. Ind. Appl*., vol. 47, no. 4, pp. 1652–1660, Jul.–Aug. 2011. [4] K. Atallah and D. Howe, "A novel high-performance magnetic gear," *IEEE Trans. Magn*., vol. 37, no. 4, pp. 2844–2846, Jul. 2001. [5] S. T. Boroujeni, J. Milimonfared, and M. Ashabani, "Design, prototyping, and analysis of a novel tubular permanent-magnet linear machine," *IEEE Trans. Magn*., vol. 45, no. 12, pp. 5405–5413, Dec. 2009.

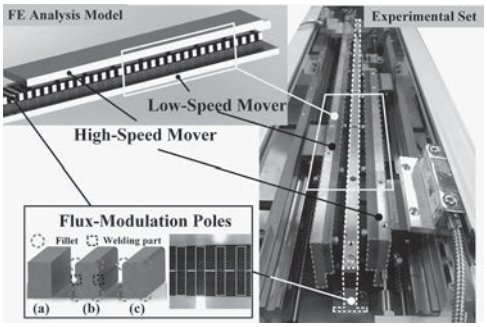


Fig. 1 Structure and experimental system of a linear magnetic gear : (a) basic model, (b) optimal model 1, (c) optimal model 2.

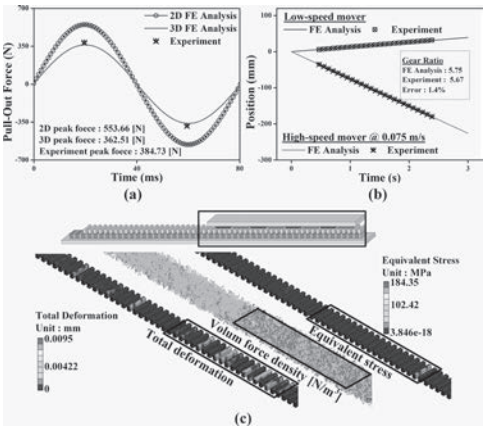


Fig. 2. Analytical results of a linear magnetic gear: (a) pull-out force comparison of optimal model 2, (b) position comparison of optimal model 2, (c) stress analysis results of flux-modulation pole of the optimal model 2.

FP-09. A Novel Five-Degree-of-Freedom AC-DC Hybrid Magnetic Bearing. *W. Zhu*[1] and Q. Le[1] *1. Huaiyin Institute of Technology, Huai'an, China*

High-speed motors have the advantages of high efficiency and power density. The high-speed motor directly drives the load, which eliminates the transmission mechanism, reduces the volume and weight of the drive system, and has no transmission loss and noise. It has broad application prospects in many fields such as aerospace, flywheel energy storage and high-speed CNC machine tools. HMB is a high-performance bearing which uses electromagnetic force to support high-speed rotor. The high-speed motor supported by HMB has many excellent qualities, such as no friction, no wear, no lubrication and sealing, no oil pollution, high speed, high precision, low noise, long life and adjustable dynamic characteristics [1]-[2]. The HMB realizes the development of the motor towards higher speed and power, and provides a new solution for the high-speed transmission system. A novel five degrees of freedom (DOFs) AC-DC HMB is proposed in this paper, whose structure is compact. Stable suspension performance can be implemented in one unit. The radial four DOFs are completely controlled by two three-phase power inverters. The axial one DOF is driven by a DC amplifier.Firstly, the structure and suspension force production mechanism are introduced. The magnetic circuits are calculated by equivalent magnetic circuit method. The mathematical models of suspension force are deduced. The main parameters of the five DOFs HMB is designed. The magnetic circuits are analyzed by the three-dimensional finite element method, and the suspension mechanism of the five DOFs is verified. The relationships between suspension forces and currents are calculated. The research results have shown that the structure of five DOFs AC-DC HMB is reasonable, and the suspension mechanism and mathematical models are correct. The 3D structure of the five-DOF AC-DC HMB is shown in Fig. 1(a). Fig. 1(b) shows the operating principle of the proposed HMB.Fig.2(a) shows the magnetic density distribution. The curve of the suspension force in the x, y and z- direction are calculated by the parametric method as shown in Fig. 2(b). The results of FEA are agree with the theoretical values.

[1] S. Chen and F. Lin, "Robust Nonsingular Terminal Sliding-Mode Control for Nonlinear Magnetic Bearing System," *IEEE Trans. Control Syst. Technol.*, vol. 19, no. 3, pp. 636-643, May 2011. [2] C. R. Morrison, M. W. Siebert and E. J. Ho, "Electromagnetic Forces in a Hybrid Magnetic-Bearing Switched-Reluctance Motor," *IEEE Trans. Magn.,* vol. 44, no. 12, pp. 4626-4638, Dec. 2008.

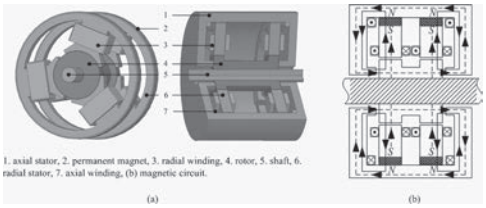


Fig. 1. 3D model and magnetic circuit

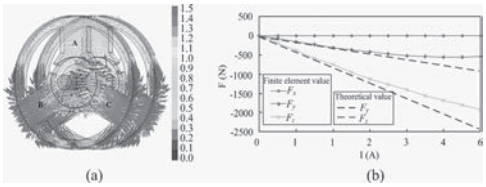


Fig. 2. Magnetic density diagram.

FP-10. Eddy Current Braking Force Analysis of an Ironless Linear Synchronous Motor with Cooling System. *L. Zhang*[1] *1. Harbin Institute of Technology, Harbin, China*

As the permanent magnet linear synchronous motor (LSM) have many advantages such as high force density, rapid dynamic response, low thermal losses, and simple structure, the linear motor drive technology is used

more and more widely in ultra-precision positioning and processing areas. However, the thrust ripple, which is the main disadvantage of permanent magnet linear synchronous motor, results in a periodic force oscillation with respect to the mover position. For the linear synchronous motor with cooling system, the eddy current braking force introduced in the cooling system is a main reason for thrust ripple. In this paper, analysis and calculation of the eddy current braking force of an ironless LSM is investigated. Fig. 1 shows the side-view of the ironless LSM which is investigated in this paper. This LSM consisting of a mover with ironless winding and a yoke with double layer Halbach magnet array mounted on it. The primary winding is divided into two layers, and the cooling system is located between the two layers. Water flowing through the cooling system and carrying the heat away. The vector magnetic potential is used to solve the magnetic system, and the differential equations are solved by the separation of variables method according to the boundary conditions. By solving the equations of the vector magnetic potential, the flux density distribution can be obtained and the expression of the eddy current density can be got furtherly. Then, the eddy current braking force introduced in the cooling system can be drived. The finite element model of the ironless LSM with cooling system is established by using Ansoft. The eddy current braking force introduced in the cooling system is calculated and compared with the analytical results. Based on the above investigation, an ironless LSM with cooling system is designed and established in laboratory as shown in Fig.2. Performance of the ironless LSM such as the detent force, eddy current braking force are measured with the prototype. And the experiment results are validated by finite element analyzed results.

[1] Ender Kazan, Ahmet Onat, "Modeling of air core permanent-magnet linear motors with a simplified nonlinear magnetic analysis," *IEEE Transactions on Magnetics*, Vol. 47, No. 6, pp. 1753-1762, Jun. 2011. [2] Changsoo Jang, Jong Young Kim, Yung Joon Kim, Jae Ok Kim, "Heat transfer analysis and simplified thermal resistance modeling of linear motor driven stages for SMT applications," *IEEE Transactions on Components and packaging TechnoloGies*, Vol. 26, No. 3, pp. 532-540, Sep. 2003.

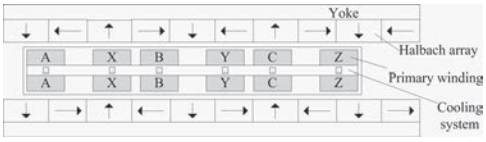


Fig. 1. The side-view of the ironless linear synchronous motor with cooling system.

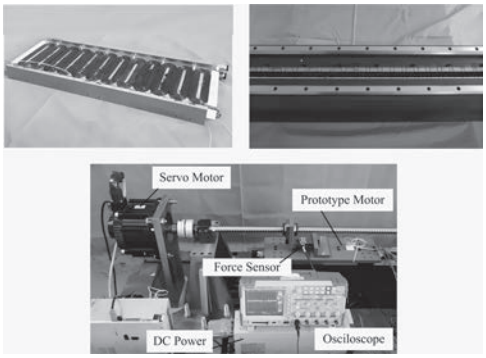


Fig. 2. The prototype motor.

FP-11. A New HTS Traveling Magnetic Electromagnetic Halbach Array for Electromagnetic Launch System. *W. Qin*[1] *1. School of Electrical Engineering, Beijing Jiaotong University, Beijing, China*

Electromagnetic launch (EML) systems need the driving sources featuring great thrust, high speed [1]. High Temperature Superconducting (HTS) has a bright future in the electromagnetic aircraft launch system for its high performance [2]–[3]. HTS windings with slotted iron core primary is the popular choices of LIM for the applications of EML[4]. The motor with slotted has a high efficiency, but its thrust ripple is high too and the core becomes saturated easily for large current carrying capacity of HTS. In this paper, a novel HTS Traveling Magnetic Electromagnetic Halbach Array (TMEHA) shown as in Fig.1 was proposed as the primary windings of the motor, of which are self-shielding, have ability for creating magnetic flux enhanced on one side (strong side) of the array while the flux cancelled on the other side (weak side) as Fig.1. The primary section for installing and fixing HTS coils is made of non-magnetic and non-conductive material, which is different from conventional iron core. HTS TMEHA successfully alleviates the saturation of the iron core and take full use of the advantages of the superconductors. The structure and the operation principle of the proposed array are described, and the major design parameters are optimized for maximum thrust force. Moreover, electromagnetic performances of different type array are compared by 3-D analytical and finite-element method. Theoretical and simulation analysis shows that the proposed array has a higher thrust and eliminates the cogging effect for heavy load EML. Finally, a 3-D modeling LIM with Electromagnetic Halbach array is built for a global observation of motor structure and further verification of the 3-D analysis. The results prove that the proposed motors can effectively satisfy the requirements of EML.

[1] M. R. Doyle, D. J. Samuel, T. Conway, and R. R. Klimowski, "Electromagnetic aircraft launch system-EMALS," IEEE Trans. Magn., vol. 31, no. 1, pp. 528–533, Jan. 1995. [2] K. Yoshida and H. Matsumoto, "Design and simulation of HTS bulk linear synchronous motor," Physica C, vol. 378-381, pp. 833–837, Oct. 2002. [3] K. Yoshida and H. Matsumoto, "Propulsion and guidance simulation of HTS bulk linear synchronous motor taking into account E–J characteristic," Phys. C, vol. 392-396, pp. 690–695, 2003. [4] J. Zhao, T. Q. Zheng, W. Zhang, J. Fang, and Y. M. Liu, "Influence analysis of structural parameters on electromagnetic properties of HTS linear induction motor," Phys. C, vol. 471, no. 21/22, pp. 1474–1478, Nov. 2011.

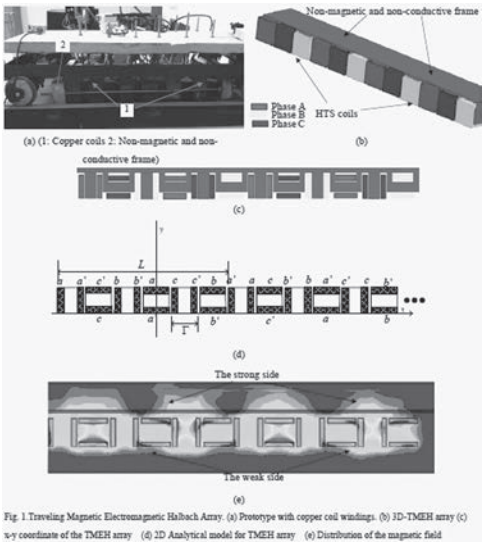


Fig. 1.Traveling Magnetic Electromagnetic Halbach Array. (a) Prototype with copper coil windings. (b) 3D-TMEH array (c) x-y coordinate of the TMEH array (d) 2D Analytical model for TMEH array (e) Distribution of the magnetic field

FP-12. A study on design feasibility through optimal design and performance test of All-In-One system using NSDLIM(Non-Symmetry Double-sided Linear Induction Motor). *K. Seo*[1], C. Park[1], J. Lee[1], T. Kim[2], H. Oh[1], J. Lim[1], w. Ji[3] and H. Lee[1] *1. Korea National University of Transportation (KNUT), Uiwang-si, The Republic of Korea; 2. University of Michigan-Dearborn, Dearborn, MI, United States; 3. Hanyang University, Seoul, The Republic of Korea*

The conventional railway uses the adhesive driving system and generates noise, vibration, dust, and abrasion due to mechanical contact, and because it travels in the air, the maximum speed is limited due to air resistance. To solve these problems, magnetic levitation trains such as hyperloop have been developed[1]. Because the Hyperloop is no mechanical friction, there requires propulsion, levitation, and guiding force for driving, and a device for generating each force is necessary. For these reasons, several countries

have used more than two devices to generate propulsion, levitation, and guidance forces of Hyperloop. However, if there are too many such devices, there is a disadvantage that maintenance and manufacturing costs increase and control is difficult. To solve these problems, recently, research of All-In-One system using NSDLIM (Non-Symmetry Double-sided Linear Induction Motor), which generates a force of propulsion, levitation, guidance in one interface has been carried out. In the study, the initial NSDLIM which travels at 1000km/h speed was designed and FEM analysis was carried out, and detailed design was carried out to achieve the required performance. In addition, the analysis of the change in the conductivity of the secondary material was carried out[2]. However, 1% conductivity of Aluminum model selected as the final performance improvement model is impossible in actual manufacturing and since the performance characteristics of the motor can not be predicted due to the repulsive magnetic field of the secondary material in high speed, Therefore, research on optimal design considering these problems is necessary and is being studied in many countries[3]. This paper is a follow-up study of the All-In-One system. The optimal design parameters of primary and secondary were selected through the FEM analysis using the reaction surface method (RSM) and the final performance improvement model was proposed. In addition, the design feasibility for the proposed final performance improvement model was verified through the performance test after manufacturing the small-scale rotary type test machine.

[1]. H. W. Lee, K. C. Kim, and J. Lee, "Review of maglev train technologies," IEEE Trans. Magn, Vol. 42, p.1917-1925 (2006) [2]. Woo-Young Ji (2018) A Study of Non-Symmetric Double-Sided Linear Induction Motor for Hyperloop All-In-One System(Propulsion, Levitation, and Guidance), IEEE Trans on Magnetics, Vol 54 (2019) [3.] G. Lv, T. Zhou, D. Zeng, Z. Liu, "Design of Ladder-Slit Secondaries and Performance Improvement of Linear Induction Motors for Urban Rail Transit", IEEE Trans. Ind. Electron, Vol. 65, p.1187-1195 (2018)

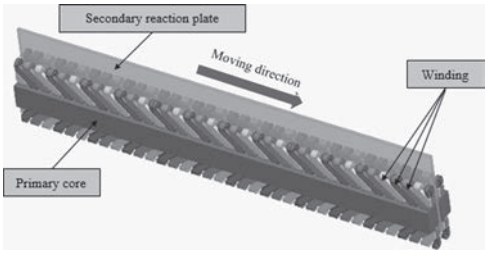


Fig. 1 Structure of NSDLIM

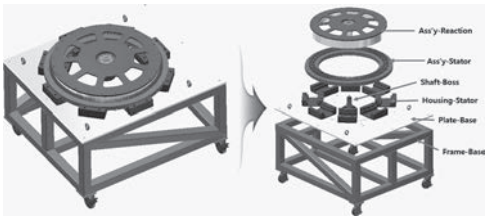
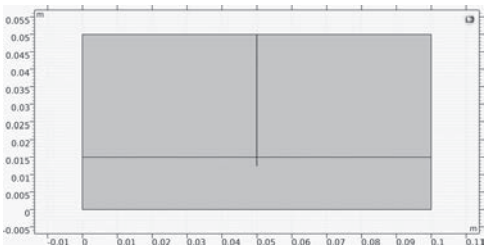


Fig. 2 Structure of small-scale rotary type test machine

FP-13. Feasibility Study on Combined Piezoelectric (Solid) and Ferrofluid (Liquid) Vibration Energy Harvester. *N. Anand*[1] and R. Gould[1] *1. Mechanical & Aerospace Engineering, North Carolina State University, Raleigh, NC, United States*

In this paper we have introduced and studied the feasibility of a hybrid solid-liquid vibration energy harvester. The energy harvester consists of a ferrofluid partially filled in a tank and a piezoelectric beam fixed at one of the tank walls. External to tank lies two powerful electromagnets which magnetize the ferrofluid non-uniformly in space, and hence creates a potential for energy harvesting due to changing magnetic field when subject to external oscillations. We used different piezoelectric beam configurations along with different oscillation loads to study and characterize this 2-D multi-scale, multiphysics and multiphase fluid structure interaction. The tank is subjected to an external oscillatory motion, which sloshes the ferrofluid and oscillates the beam by means of two modes, one due to beam's inertia and second due to the impact of the ferrofluid on the beam. An external circuit is also modelled which has a load resistor to measure the voltage generated from the piezo and from the ferrofluid sloshing. The parameters varied are the piezo beam length, beam thickness, piezo materials, ferrofluid fill height, oscillation frequency and the oscillation amplitude. The natural frequency modes for the piezoelectric beam are very important, since at those modes the beam harvests the highest power. We have observed that when the fluid motion vibrates the beam such that it is near its first natural frequency, the power harvested naturally increases. Finally, we have proposed design rules for such a system to obtain the highest performance.

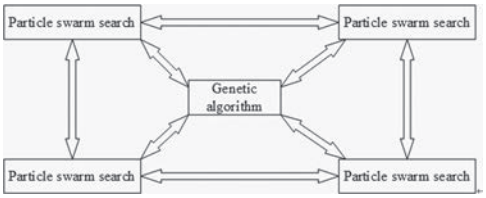


System Configuration

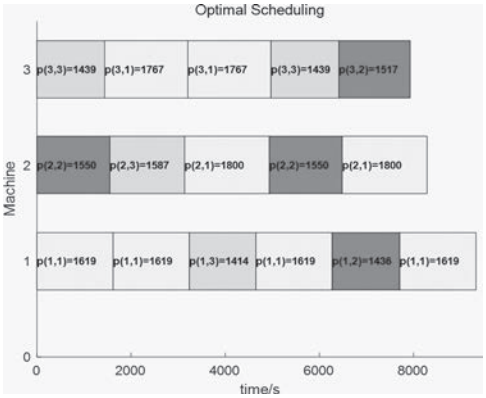
FP-14. Research on Multi-objective Task Scheduling Algorithm for Electromagnetic Cloud Computing. *L. Jin*[1], J. Wang[1], X. Liu[1] and W. Feng[1] *1. Tianjin Polytechnic University, Tianjin, Tianjin, China*

With the development of cloud computing in the field of high-performance computing, large-scale electromagnetic finite element and multi-sample computing are gradually completed by cloud computing. Therefore, cloud platform task scheduling has become an important issue to be solved. In this paper, a cloud resource scheduling model is constructed. Aiming at the indivisibility of electromagnetic finite element single sample computation, a multi-group hybrid genetic algorithm with particle swarm search is proposed. The approach is tested on instances taken from the literature and practical data. The computation results validate the effectiveness of the proposed algorithm. The finite element efficient calculation and the full utilization of resources are realized on the cloud platform. I. INTRODUCTION How to allocate cloud computing resources to the users of electromagnetic finite element computation under constrained conditions and achieve efficient scheduling to reduce the computing time of tasks and improve the efficient utilization of cloud computing resources has become a practical problem in the field of cloud computing[1,2]. II.Scheduling in cloud In the environment of cloud computing, different types of virtual machines with different performance characteristics are abstracted from a large number of physical resources by virtualization technology, and tasks are calculated by scheduling virtual machine resources. III.Cloud Platform Scheduling Algorithms A hybrid multi-population algorithm based on cloud platform is proposed by combining particle swarm optimization and genetic algorithm, as shown in Fig.1. IV.Conclusion Three-dimensional motors, three-dimensional inductors and TEAM Problem 7 were tested on cloud platform, and the optimal CPU core number and memory allocation in computing time and resource consumption were obtained. The sample numbers of three finite element calculation cases were 8, 4 and 4, respectively. The most satisfactory task scheduling scheme was obtained, as shown in Fig.2.

[1]Y. Zhao, and L. Chen, "Efficient task scheduling for many task computing with resource attribute selection," *China Communications*, Vol. 11, No. 12, PP. 125-140, 2014. [2]M. Mezmaz, N. Melab and D. Tuyttens, "A parallel bi-objective hybrid metaheuristic for energy-aware scheduling for cloud computing systems," *Journal of Parallel and Distributed Computing*, Vol. 71, No. 11, PP. 1497-1508, 2011.



Multi-population hybrid algorithm structure diagram

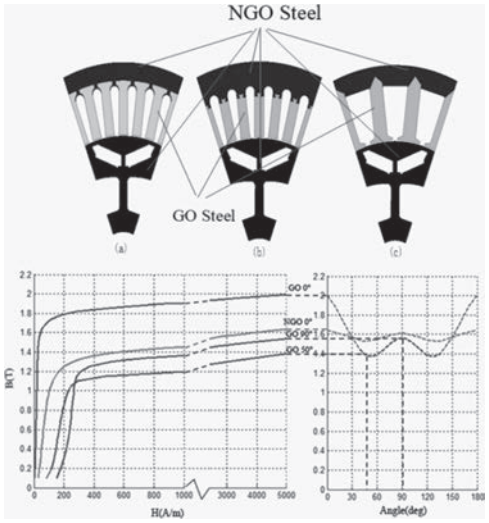


the most satisfactory scheduling scheme

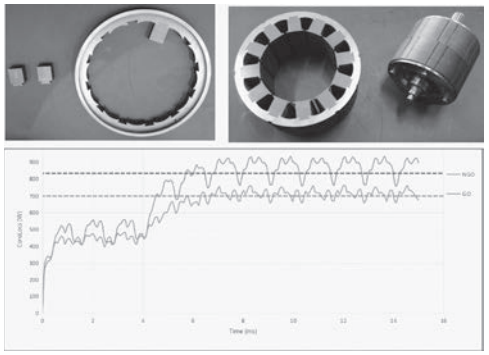
FP-15. Application of Grain-Oriented Electrical Steel Used in Super-High Speed Electric Machines. *R. Pei*[1] and L. Zeng[1] *1. InnMag New Energy Ltd., Suzhou, China*

Abstract — Electrical steel is one of the core magnetic materials in Electrical Vehicle(EV) traction motor. In terms of high power density and torque density for the EV traction motors. Traditional Non Grain-Oriented (NGO) silicon steel is difficult to satisfy these requirements because of limited saturation flux density and magnetic permeability. This paper mainly presents that a novel thin anisotropic Grain-Oriented (GO) silicon steel is used in high-speed (up to 14000rpm)traction motors after deeply analysing magnetic saturation, power loss, thermal conductivity and mechanical property of a traction motor with high-frequency (50Hz-400Hz) and high-torque running status. It applies a combination design between NGO and GO steel in order to avoid the low magnetic permeability in the transverse direction. The noise and magnetostriction of the electric machine can be reduced by applying a self-stick punching technique between GO steel sheets in a stator. The research on numerical modeling and experimental results has been done. The new prototype is being fabricated and it can be produced in mass production in next few years. The measured B-H curve states the difference between NGO and GO silicon steel in the direction of magnetization can be shown in Figures. The novel prototype of high-speed traction motor has been designed with 12 slots and 8 poles. The rating/peak power is 15/30kW. According to the relationship of flux density, iron loss and offset angle of the rolling direction for GO and NGO steel, we should use the magnetic property of GO steel in the range of 0^o and 30^o of the rolling direction to design a stator. The new design can be shown in the Figures. The new design shows the power loss of the stator remarkably decrease by using GO steel. Moreover, the saturation flux density and magnetic permeability will rise. After the motor teeth adopt the grain-oriented silicon steel sheet, the efficiency of the motor rated condition increases from 96.6% to 97.8%, an increase of 1.2%.

[1]Taghavi S, Pillay P. A Novel Grain-Oriented Lamination Rotor Core Assembly for a Synchronous Reluctance Traction Motor With a Reduced Torque Ripple Algorithm[J]. IEEE Transactions on Industry Applications, 2016, 52(5):3729-3738. [2]Taghavi S, Pillay P. An innovative rotor core assembly for high performance 4-pole synchronous reluctance traction motor using grain oriented lamination[C]// Electric Machines & Drives Conference. IEEE, 2016:90-95. [3]Enomoto Y, Ito M, Koharagi H, et al. Evaluation of experimental permanent-magnet brushless motor utilizing new magnetic material for stator core teeth[J]. IEEE Transactions on Magnetics, 2005, 41(11):4304-4308.



Different NGO and GO joint structures; The B-H curves between GO and NGO Silicon Steel



The iron core fabricated by GO and NGO; Results.

Session FQ
MAGNETOCALORIC MATERIALS II
(Poster Session)

Martino LoBue, Co-Chair
SATIE - CNRS, Cachan, France
Durga Paudyal, Co-Chair
Ames Laboratory, US DOE, Iowa State University, Ames, IA, United States

FQ-01. Differential Effect of Magnetic Alignment on Magnetocaloric Effect during Additive Manufacturing of Magnetocaloric Particles.
K. Al Milaji[1], S. Gupta[2], V.K. Pecharsky[2,3], H. Zhao[1], R. Barua[1] and *R.L. Hadimani*[1,4] *1. Mechanical and Nuclear Engineering, Virginia Commonwealth University, Richmond, VA, United States; 2. Materials Science and Engineering, Ames Laboratory, Ames, IA, United States; 3. Materials Science and Engineering, Iowa State University, Ames, IA, United States; 4. Biomedical Engineering, Virginia Commonwealth University, Richmond, VA, United States*

Thin films of ball-milled Gd_5Si_4 particles [2] were deposited using inkjet printing process in the presence of an external magnetic field. During the printing, NdFeB permanent magnet arrays were used to align the particles along the axis of the printing plane, normal to the printing plane and without the alignment. The external magnetic field aligns the magnetic particles along their magnetic easy axis. The combined effect of all the particles enhances the magnetization of the film by aligning the particle's magnetocrystalline easy axis with the direction of the magnetic field of the permanent magnet. We demonstrate the ability to print thin magnetic films with a defined anisotropy in any chosen direction which could lead to the enhancement of magnetic properties approaching those of single crystal materials. Fig.1 (a) shows hysteresis graphs measured at 300K along long axis of films printed with no applied field (random), field applied in parallel orientation to the plane and along long axis (parallel), field applied in parallel orientation to the plane and along short axis (random 90 deg.), field applied normal to the plane (normal) and photo paper without the Gd_5Si_4 particles. It can be seen that the when films are printed with a field applied parallel to the long axis the magnetization is highest and the lowest magnetization is seen for particles printed with field applied normal to the paper. Fig. 1 (b) shows SEM images of random and parallel films. Entropy change was calculated from Maxwell's equations for random, parallel and normal films. The entropy change for an applied field of 3T at 310K showed an increase of 440% for parallel films compared to normal films (2.3 J/kgK, 3.4 J/kgK and 10.2 J/kgK for normal, random and parallel films respectively). ACKNOWLEDGEMENTS The Ames Laboratory is operated for the U.S. DOE by Iowa State University of Science and Technology under contract No. DE-AC02-07CH11358. Work at VCU was partially funded by National Science Foundation, Award Numbers: 1357565 and 1726617

References [1] R. Hadimani, S. Gupta, S. Harstad, V. Pecharsky, and D. Jiles, "Investigation of room temperature ferromagnetic nanoparticles of Gd5Si4," *IEEE Trans. Magn.*, vol. 51, no. 11, p. 2504104, 2015.

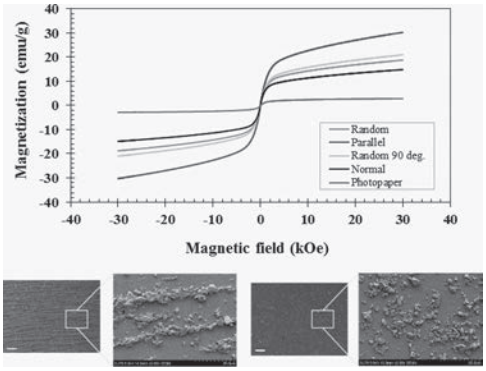


Fig.1 (a) Hysteresis at 300K of random film, parallel film, random 90 deg. film, normal film and photo paper without the Gd_5Si_4 particles. (b) SEM images of random and parallel films.

FQ-02. Magnetocaloric effect in rare-earth based oxynitrides.
Y. Jin[1], *A. Biswas*[1], A.K. Pathak[1], Y. Mudryk[1], S. Gupta[1] and V.K. Pecharsky[1] *1. Division of Materials Science and enigineerig, Ames Laboratory, Ames, IA, United States*

The magnetocaloric effect (MCE) is extensively studied in rare-earth (RE) based compounds, including alloys, intermetallics, and salts. Among these materials, RE-oxides, and other oxide-based salts such as carbonates, oxalates etc, are the most stable compounds and are easily obtained. However, their magnetic transition temperatures, if any, are often too low. There is hardly any study regarding MCE of rare-earth based oxynitride compounds of the type $RE^{2+}RE^{3+}ON$. In this work, we focus on the study of magnetic and magnetocaloric properties of a fully stoichiometric compound, GdEuON that crystallizes in the NaCl-type structure. Polycrystalline samples of GdEuON were prepared via mechanochemical reaction of EuO and GdN. As-reacted powders were annealed at 600 °C under Ar. The study of the temperature dependence of magnetization reveals that the sample exhibits a second order magnetic transition between paramagnetic and ferromagnetic state at $T_C \sim 60$ K. It also shows glassy behavior at low temperature, which may be due to the interplay between the magnetic Gd^{3+} and Eu^{2+} ions. Consistent with magnetization study, electrical resistivity measurement shows a clear phase transition near T_C for the sample and it exhibits semiconducting behavior above T_C The magnetic entropy change (DS_M), one of the important parameters characterizing magnetocaloric properties of materials, was estimated from the magnetization data. A large DS_M (-9 J/Kg K near T_C for a 2 T magnetic field change) has been observed over a broad temperature range (full width at half maximum of DS_M vs. T is ~80 K). The broad peak of large $-DS_M(T)$ is beneficial for application in magnetic refrigeration as it can provide high refrigeration capacity. Fig.1 The MCE of GdEuON as the magnetic entropy change from magnetization data. The Ames Laboratory is operated for the U. S. Department of Energy by Iowa State University of Science and Technology under contract No. DE-AC02-07CH11358. This work was supported by the Department of Energy, Office of Basic Energy Sciences, Materials Sciences Division.

1. Etourneau, J.; Chevalier, B.; Hagenmuller, P.; Georges, R., New magnetic semiconducting compounds: the rare earth oxynitrides Eu1-x2+Lnx-3+O1-xNx (Ln3+=Nd3+,Eu3+,Gd3+). *J. Phys., Colloq. (Orsay, Fr.)* 1980, (C5), C5-193-C5-204. 2. Chevalier, B.; Etourneau, J.; Hagenmuller, P., New ferromagnetic semiconductors: europium gadolinium oxide nitrides (Eu1-x2+Gdx3+O1-xNx). *Mater. Res. Bull.* 1977, *12* (5), 473-9.

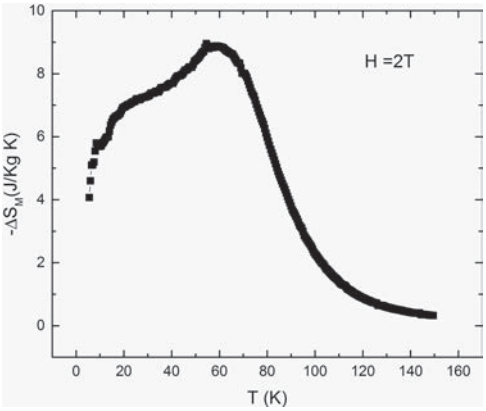


Figure 1

FQ-03. 3D checker board pattern formation of martensite/austenite domains in NiCoMnAl magnetic shape memory alloys. *A. Becker*[1], D. Ramerman[1], M. Gottschalk[1], I. Ennen[1], T. Matalla-Wagner[1], G. Reiss[1] and A. Hütten[1] *1. Physics, Bielefeld University, Bielefeld, Germany*

NiMnX (X=Al,Ga,Sn,In) magnetic shape memory Heusler alloys are considered as promising materials for magnetocaloric cooling applications due to their magnetoelastic coupling near room temperature [1]. However, most of them show a very large thermal hysteresis, which can span over several hundreds of Kelvin, limiting their potential in future applications. Therefore, efficient mechanisms to change the martensitic transformation behavior have to be identified. Our research showed that rigid substrates increase hysteresis width due to residual austenite at the interface in NiCoMnAl thin films [2],[3]. We conclude that thin martensite intercalations in those films should be beneficial for transforming films, because the formation energy during martensite nucleation is reduced. Our aim is to decrease the thermal hysteresis in off-stoichiometric NiCoMnAl thin films, grown by sputter deposition, by preparing multilayer systems, which consist of alternatively grown martensite intercalations and active transforming austenitic layers. The stoichiometry of these two layers is chosen in such a way that their individual thermal hysteresis do not overlap. In these intercalated multilayer systems we find from temperature dependent magnetization measurements that the thermal hysteresis of the active layer is decreased in comparison to the non-intercalated system. Furthermore, if the thickness of the active and fixed layer becomes comparable, the strain in these systems induces a long range order of martensite and austenite regions, which resembles a 3d checker board pattern in TEM cross-section images. However, the formation process of this system is still under investigation. High resolution XRD measurements, in combination with TEM analysis, allow us to visualize the microstructure and micro strain in this multilayer system. The results can be directly compared to molecular dynamics [4] and phase field model simulations [5]. This would enable us to refine martensitic intercalations in terms of crystallographic growth direction, thicknesses and transition temperatures to achieve a multilayer system with very low thermal hysteresis.

[1] Liu et al., Nature Materials 11, 7 (2012) [2] M. Wodniok et al., AIP Advances 7, 056428 (2017) [3] A. Waske et al., Energy Technology 6(8), pp. 1429-1447 (2018) [4] O. Kastner, Continuum Mechanics and Thermodynamics 15 (5), pp. 487-502 (2003) [5] V. I. Levitas et al., Int. J. Plast., Vol. 26 (3), pp. 395-422 (2010)

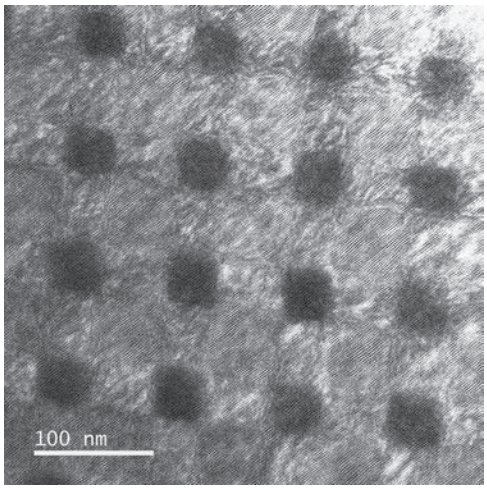


Fig 1: TEM cross section of the checker board pattern

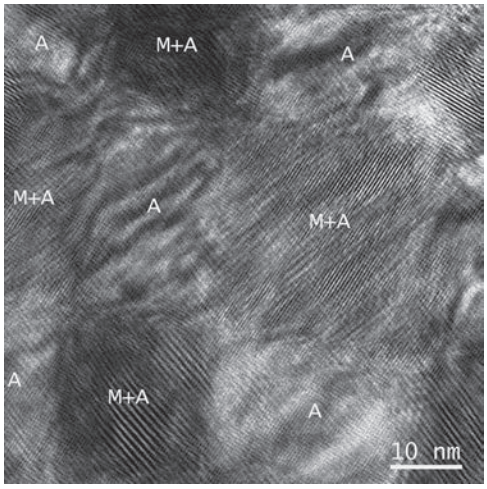


Fig: Close-up of the crystallographic domains

FQ-04. Controllable magnetic transitions and magnetocaloric effect of $Ho_{1-x}Tm_xNi$ ($0 \le x \le 0.8$) compounds. *J. Xu*[1], X. Zheng[1], S. Shao[1], S. Yang[1], J. Zhang[1], S. Wang[1], J. Liu[2], Y. Zhang[2], Y. Liu[2], Z. Xu[3], L. Wang[4] and B. Shen[2] *1. School of Materials Science and Engineering, University of Science and Technology Beijing, Beijing, China; 2. State key laboratory for Magnetism, Institute of Physics, Chinese Academy of Sciences & University of Chinese Academy of Sciences, Beijing, China; 3. National Institute of Metrology, Beijing, China; 4. Department of Physics, Capital Normal University, Beijing, China*

As a potential alternative technology for traditional refrigeration, magnetic refrigeration has received extensive attention. In the past few decades, some materials with large/giant magnetocaloric effect (MCE) have been reported near room temperature, such as La-Fe-Si[1] and Gd-Si-Ge. [2] Low-temperature MCE materials used for liquefaction of gas have also become a research hotspot recently. Rare earth based RNi compounds (R=Gd-Tm) have orthorhombic crystal structure and the basic magnetic properties and heat transport properties have been studied. [3-7] In this work, the magnetic transitions of HoNi compound were adjusted by introducing Tm with small spin quantum number to replace Ho atoms. The magnetic properties and MCEs of $Ho_{1-x}Tm_xNi$ ($0 \le x \le 0.8$) compounds have been investigated in detail. Both ZFC (zero-filed-cooling) and FCC (field-cooled-cooling) curves were measured for $Ho_{1-x}Tm_xNi$ ($0 \le x \le 0.8$) compounds and magnetic phase diagram is shown in Fig.1 (a). As Tm content increases, the transition temperature for spin reorientation (T_{SR}) changes little around 10 K and Curie temperature (T_C) decreases monotonously from 35.5 K to 9.3 K. When x=0.8, T_{SR} and T_C get

closer and only one phase transition can be observed. On basis of magnetic measurements, magnetic entropy change ($-\Delta S_M$) was calculated and the temperature dependences of $-\Delta S_M$ curves for field change of 0-5 T were shown in Fig. 1 (b). The maximum value of $-\Delta S_M$ is 16.6, 15.8, 17.4 and 22.4 J/kg K for x=0, 0.3, 0.5 and 0.8 respectively. It is worth noting that a platform was observed on ΔS_M curves for $Ho_{0.7}Tm_{0.3}Ni$ compound. The value of $-\Delta S_M$ is relatively stable over a temperature range as wide as 35.0 K, which is beneficial to practical applications. In summary, $Ho_{1-x}Tm_xNi$ ($0 \le x \le 0.8$) compounds has potential applications for low temperature magnetic refrigeration.

1. F. X. Hu, B. G. Shen, J. R. Sun, Z. H. Cheng, G. H. Rao and X. X. Zhang, Appl. Phys. Lett. 78, 3675 (2001). 2. V. K. Pecharsky and K. A. Gschneidner, Phys. Rev. Lett. 78, 4494 (1997). 3. R. Rajivgandhi, J. A. Chelvane, S. Quezado, S. K. Malik, and R. Nirmala, J. Magn. Magn. Mater. 433, 169 (2017). 4. Y. L. Yaropolov, A. S. Andreenko, S. A. Nikitin, S. S. Agafonov, V. P. Glazkov, and V. N. Verbetsky, J. Alloys Compd. 509, S830 (2011). 5. P. Kumar, K. G. Suresh, A. K. Nigam and O. Gutfleisch, J. Phys. D: Appl. Phys. 41, 245006 (2008). 6. X. Q. Zheng and B. G. Shen, Chin. Phys. B 26, 027501 (2017). 7. N. Kinami, K. Wakiya, M. Uehara, J. Gouchi, Y. Uwatoko, and I. Umehara, Jpn. J. Appl. Phys. 57, 103001 (2018).

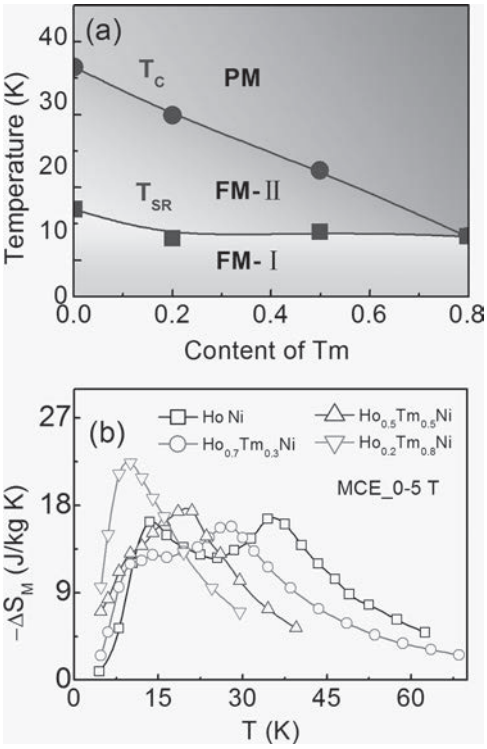


Fig. 1 (a) Magnetic phase diagram of $Ho_{1-x}Tm_xNi$ ($0 \le x \le 0.8$) compounds. (b) Temperature dependences of $-\Delta S_M$ for a field change of 0-5 T for $Ho_{1-x}Tm_xNi$ ($0 \le x \le 0.8$) compounds.

FQ-05. The Use of Magnetically Hard Materials in Thermomagnetic Power Generation Cycles. *A.N. Tantillo*[1,2], N. Dempsey[3], L. Ranno[3] and K.G. Sandeman[2,1] *1. Physics, CUNY Graduate Center, Brooklyn, NY, United States; 2. Physics, Brooklyn College, Brooklyn, NY, United States; 3. Universite Grenoble Alpes, CNRS, Institut Neel, Grenoble, France*

Thermomagnetic power generation (TMG) is the process by which magnetic flux, which comes from a temperature-driven change of magnetization, is converted into usable energy. Generally, TMG functional materials are magnetically soft, meaning they have little to no remnant magnetization and magnetize in the direction of the applied field, limiting TMG loops to the first quadrant of the *M-H* plane. This work investigates the ways in which magnetically hard materials, which have strong magnetic anisotropy and non-zero magnetic remanence, can be incorporated into TMG cycles in order to expand the area of *M-H* plane available for energy conversion. Three cases are considered: (i) hard ferrite magnets as the functional material for a two-quadrant TMG cycle; (ii) a hard magnet applying a bias field to a soft functional material, thus opening the second quadrant of the *M-H* plane; and (iii) spin-reorientation transition (SRT) TMG, in which a change of the direction of the magnetization vector (instead of a decrease in the magnitude of the magnetization) drives the observed magnetic flux. The literature shows that SRT TMG yields work outputs an order of magnitude greater than pyromagnetic TMG, with roughly equal relative efficiencies, without driving a Curie-point transition [1]. Experiments on commercially available hard ferrites reveal that these materials are not yet good TMG candidates, but hard magnets with higher thermal conductivity and a greater change of magnetization with temperature could outperform existing TMG materials. Computational results using *RADIA* [2] indicate that biasing a soft magnet with a hard magnet is essentially equivalent to shifting the *M-H* loop by an amount proportional to the field of the biasing magnet. In the case of polycrystalline gadolinium, the work output increases from 13.6 J/kg [3] without a bias field to 33.6 J/kg with a bias field for the same temperature range, but experimental verification is needed. Concerning the case of SRT TMG, the literature describes promising avenues of future investigation in single-material embodiments using $NdCo_5$ [1] as well as artificial spin-reorientation composites [4].

[1] K.P. Wetzlar, S.M. Keller, M.R. Phillips, and G.P. Carman, J. Appl. Phys. 120, 244101 (2016) [2] P. Elleaume, O. Chubar, J. Chavanne, proc. of the PAC97 Conference May 1997, p.3509-3511 [3] C.-J. Hsu, S.M. Sandoval, K.P. Wetzlar and G.P. Carman, J. Appl. Phys. 110, 123923 (2011) [4] V. Basso, C. Sasso, M. LoBue, and K. Sandeman, Solid State Energy Efficient Cooling Report, (2010)

FQ-06. Magnetocaloric Gadolinium thick films for energy harvesting applications. *D. Nguyen Ba*[1,2], L. Becerra[2], N. Casaretto[2], J. Duvauchelle[2], M. Marangolo[2] and M. LoBue[1] *1. SATIE, CNRS, ENS Paris-Saclay, Université Paris-Saclay, Cachan, France; 2. Sorbonne Université, CNRS, Institut des NanoSciences de Paris, UMR7588, Paris, France*

Improving energy efficiency and cutting greenhouse emissions have been the main motivation of the last two decades intense research activity in the field of caloric materials [1]. The research of new solid state cooling devices have been focused on bulk magnetocalorics (MC) with a particular emphasis on efficiency [2]. Recently a growing interest in energy harvesting applications with some emphasis on the micro and nano scales has triggered a paradigm shift towards the research of higher power output [3,4]. Gadolinium has been the benchmark material for bulk cooling devices and its study will be extremely relevant as well for development of micro-scale harvesting devices where the comparison between first and second order MC performance is still an open issue [5]. Unfortunately the use and characterization of Gd films are still rather preliminary with some controversial results concerning substrate role in modifying magnetic moment, and Curie temperature [6]. High thoroughput thermo-generation at the microscale requires relatively thick films (between 5 and 10 μm) and a reduced thermal influence from the substrate. Therefore, a detailed characterization of magnetic and MC properties as a function of thickness and substrate is in order. Here we study Gd films deposited with thicknesses ranging from nanometer to micrometer using a sputtering machine deposited on (i) different silicon substrates: with and without SiO_2, (ii) various buffer layers such as tungsten, tantalum, (iii) various growth conditions. Magnetic properties including magnetization as a function of temperature and magnetic field, and entropy change are investigated using a SQUID or VSM-PPMS. Crystal structure has been characterized using a high precision XRD machine. Results show a change of crystal structure as a function of both growth temperature and thickness. We observed that the magnetic phase transtion depends on thickness, growth condition, substrate and buffer layer. Growth at high temperature also sharpens the transition.

[1] X. Moya, S. Kar-Narayan, N. Mathur, *Nat. Mater.*, Vol. 13, p. 439 (2014) [2] K. G. Sandeman, *Scr. Mater.*, vol. 67, p. 566 (2012) [3] S. Pandya, J. Wilbur, J. Kim, et al., *Nat. Mater.*, vol. 17, p. 432 (2018) [4] M. Gueltig,

et al., *Adv. Energy Mater.*, vol. 7, p. 1601879 (2017) [5] M. Almanza, A. Pasko, et al*., IEEE Trans. Magn.*, vol. 53, p. 1 (2017) [6] G. Scheunert, O. Heinonen, et al., *Appl. Phys. Rev.*, vol. 3, p. 11301 (2016)

FQ-07. Enhanced Magnetocaloric Effect via Halide Substitution in the Tunable Molecular Magnet, $Cu_9Br_2(cpa)_6$. *S.F. Skinner*[1] and L.W. Ter Haar[1] *1. Chemistry, University of West Florida, Pensacola, FL, United States*

The magnetothermodynamic properties [1-4] of the low-dimensional 2-D metal organic framework (MOF) halide series, $Cu_9X_2(cpa)_6$ (X = F, Cl, Br; cpa = anion of 2-carboxypentonic acid), abbreviated as CPA, has been the subject of experimental studies suggesting the tunability of magnetic properties via halide and guest-host chemistry [1,3]. CPA is best described as a topologically spin frustrated triangles-in-triangles or triangulated-Kagome-lattice on a layered MOF. CPA consists of microporous channels (oriented transverse to the layers) available for chemical manipulation, which support tunability of properties and further expansion of this class of materials. While the spin frustrated topology of $Cu_9Cl_2(cpa)_6$ has been shown to exhibit a magnetocaloric effect at temperatures less than 10 K [5], we report here new temperature- and field-dependent magnetization data for the bromine derivative of CPA, $Cu_9Br_2(cpa)_6$. As shown in earlier studies [1], exchanging the halide in this material can enhance the magnetic properties of this system. In this study, we estimate the effect of halide interchangeability on the magnetocaloric effect produced by this system in low field and at cryogenic temperatures. Magnetic entropy change (ΔS_{mag}), relative cooling power (RCP), and refrigerant capacity (RC) are calculated for this material and the effects of halide interchangeability on the MCE are discussed. CPA, as a tunable molecular magnet that may also serve as a candidate for quantum spin liquid (QSL) studies [5], invites numerous opportunities for manipulations of its chemistry, and therefore variations in the magnetic properties, including the magnetocaloric effect. The limits of chemical variability in the molecular structure and the extent of channel guest host chemistry is the focus of future studies to support the need for application-specific, tunable, magnetic refrigerants. Supported by the National Aeronautics & Space Administration (NASA) through the University of Central Florida's administration of the NASA Florida Space Grant Consortium through grant #NASA-FSGC-11-NNX15-005 and -007. *Author of correspondence, lterhaar@uwf.edu

[1] S. Ateca, S. Maruti, and L. W. ter Haar, J. Magn. Magn. Mater. 147, 398 (1995). [2] M. Mekata, M. Abdulla, T. Asano, H. Kikuchi, T. Goto, T. Morshita, and H. Hori, J. Magn. Magn. Mater. 177, 731 (1998). [3] H.S.C. Hamilton, W.M. Farmer, S.F. Skinner and L.W. ter Haar, AIP Advances 8, 055802 (2018). [4] W.M. Farmer, S.F. Skinner and L.W. ter Haar, AIP Advances 8, 101404 (2018). [5] S.F. Skinner, R.A. Coro, W.M. Farmer, J.H. Lovett, J.C. Lupton, J.A. Moses, B.M. Ortolano, L.R. Reid, S.D. Richardson, J.D. Taylor, L.W. ter Haar, AIP Advances 9, 035112 (2019).

FQ-08. The first-order magnetoelastic transition in Eu_2In: A ^{151}Eu Mössbauer study. *D. Ryan*[1], D. Paudyal[2], F. Guillou[2], A.K. Pathak[2], Y. Mudryk[2] and V.K. Pecharsky[2] *1. Physics, McGill University, Montreal, QC, Canada; 2. Ames Laboratory, Ames, IA, United States*

First-order magnetic transitions (FOMTs) with large differences in magnetization are important in the development of advanced functional magnetic materials, *e.g.* magnetocalorics. Eu_2In exhibits a particularly sharp, isosymmetric ferromagnetic (FM) to paramagnetic (PM) transition at T_C = 55K (FWHM<1K) with a remarkable combination of large latent heat and magnetocaloric response, small volume discontinuity, and negligible hysteresis[1]. By contrast, the isostructural Eu_2Sn is a conventional second-order antiferromagnet with T_N = 31K. Here we study the difference in magnetic behaviour between Eu_2In and Eu_2Sn using ^{151}Eu Mössbauer spectroscopy and band structure calculations. The Mössbauer data in Fig. 1 shows the remarkable differences between these two materials. Eu_2Sn has a single Eu component with a rather small (13 T) hyperfine field (B_{hf}) at 5K that evolves normally as it is warmed through T_N (Fig. 2). By contrast, Eu_2In shows two, distinct, equal-area components with much larger hyperfine fields (17 T and 27 T) that decline by about 25% on warming towards the FOMT at T_C where both vanish abruptly. The very different, and larger, hyperfine fields observed at the two Eu sites in Eu_2In are particularly surprising given that the two sites in the isostructural Eu_2Sn are indistinguishable, and that DFT calculations indicate that the Eu moments at the two sites are essentially the same[1]. Calculations indicate that the Eu-5d states hybridize with the In-5p states, resulting in a large exchange splitting. While the Mössbauer behavior of each compound taken in isolation may appear as conventional examples of first-order (Eu_2In) and second-order (Eu_2Sn) transitions, the striking differences between the physical properties of these two structurally similar compounds demand an in-depth investigation of their underlying magnetism by neutron diffraction. Work at Ames Laboratory is supported by the Office of Basic Energy Sciences of the U.S. Department of Energy, Division of Materials Sciences and Engineering under contract No. DE-AC02-07CH11358 with Iowa State University.

[1] F. Guillou, A.K. Pathak, D. Paudyal, Y. Mudryk, F. Wilhelm, A. Rogalev, and V.K. Pecharsky, *Nature Comm.* 9 (2018) 2925.

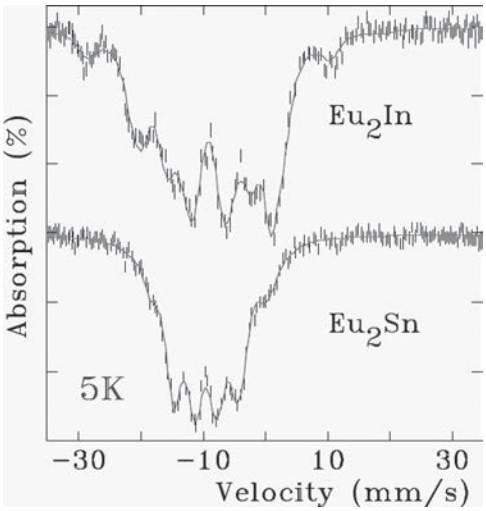


Fig.1 ^{151}Eu Mössbauer spectra of Eu_2In and Eu_2Sn at 5K

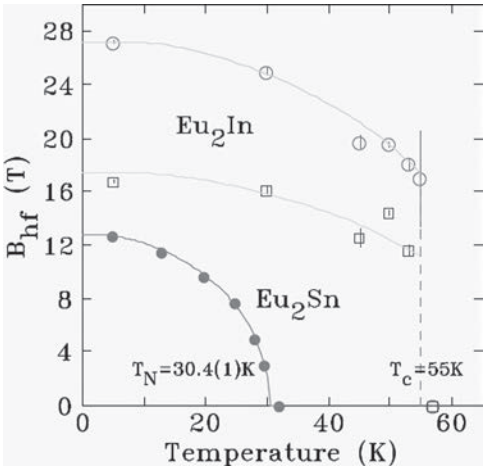


Fig.2 Hyperfine field (B_{hf}) *vs.* temperature for Eu_2In (open symbols) and Eu_2Sn (solid symbols)

FQ-09. Magnetic field dependence of the martensitic transition and magnetocaloric effects in $Ni_{49}BiMn_{35}In_{15}$. *A. Aryal*[1], I. Dubenko[1], S. Talapatra[1], S. Stadler[2] and N. Ali[1] *1. Physics, Southern Illinois University, Carbondale, IL, United States; 2. Physics and Astronomy, Louisiana State University, Baton Rouge, LA, United States*

The structural, magnetic, and magnetocaloric properties of Bi doped Heusler alloy $Ni_{49}BiMn_{35}In_{15}$ have been investigated using room temperature X-ray diffraction (XRD) and magnetization measurements in a temperature interval of 5-400 K and for magnetic field changes ($\mu_o\Delta H$) up to 5T. The magnetization measurements were carried out during heating and after the samples were cooled from 400 K to 10 K at zero magnetic field (ZFC), and in the presence of a magnetic field (FC). The alloy at room temperature was found to be in a mixture of a high temperature austenite phase (AP) and a low temperature martensite phase (MP). Two ground states characterized by different magnetization values of (40 and 110 emu/g) were found to stabilize at 5 K and $\mu_o\Delta H$ = 5T depending on the cooling protocol. Based on the magnetization data, the states were identified as ferromagnetic AP (110 emu/g, FC) and MP (40 emu/g, ZFC), respectively. A shift in the martensitic transition temperature (T_M) from 195 K to lower temperatures with applied magnetic field at the rate of 15 K/T was observed in the ZFC $M(T)$ curves. Metamagnetic behavior characterized by a jump in magnetization in the isothermal $M(H)$ curves near T_M was observed in the ZFC measurement. Maximum value of the magnetic entropy change and refrigerant capacity in the vicinity of the magnetostructural transition temperature was found to be 5.0 $Jkg^{-1}K^{-1}$ and 225 Jkg^{-1} for $\mu_o\Delta H$ = 5T. Acknowledgment: This work was supported by the U.S. Department of Energy (DOE), Office of Science, Basic Energy Sciences (BES) under Award No. DE-FG02-06ER46291 (SIU) and DE-FG02-13ER46946 (LSU).

FQ-10. Coupled Phase Transitions and Associated Magnetocaloric Effects in $Ni_2Mn_{0.70}Cu_{0.30}Ga$. *S.A. Agbo*[1], S. Bhatt[1] and M. Khan[1] *1. Physics, Miami University, Oxford, OH, United States*

In the last few decades, the Ni-Mn-Ga based Heusler alloys have been extensively studied for their multifunctional properties that are primarily associated with the first order martensitic phase transformation. It has been shown that the first and second order phase transitions in these materials can be precisely controlled by varying their stoichiometry and by atomic doping. For example, when Mn is partially replaced by Cu in $Ni_2Mn_{1-x}Cu_xGa$, the martensitic transition shifts from ~220 K to higher temperatures while the second order ferromagnetic transition shifts from ~380 K towards lower temperatures [1, 2]. For x = 0.25, the two transitions occur nearly at the same temperature resulting in a coupled first order phase transition. The structural and magnetic properties of $Ni_2Mn_{1-x}Cu_xGa$ with x > 0.25 have not yet been reported. Since a first order phase transition exhibits a thermal hysteresis while a second order phase transition does not, it is interesting to study the phase transitions in $Ni_2Mn_{1-x}Cu_xGa$ with x slightly larger than 0.25. Exciting coupling and decoupling effects may be expected in such a material. Keeping this discussion in mind, we have investigated the structural, electronic, magnetic, and magnetocaloric properties of $Ni_2Mn_{0.70}Cu_{0.30}Ga$. Upon heating, a first order coupled magnetostructural phase transformation was observed in the material near 345 K. A partial decoupling of the phase transitions occurred during cooling. The decoupling effect resulted in a large variation in the magnetocaloric properties of the material when the measurements were done while heating and cooling. For a field change of 5 T, the peak magnetic entropy change obtained while heating was -17 J $kg^{-1}K^{-1}$. Interestingly, the peak value was -33 $Jkg^{-1}K^{-1}$ when the measurements were done while cooling from 400 K to lower temperatures. The electrical resistivity data also exhibit interesting behavior. The results of this experimental study will be presented and discussed.

1. M. Khan, I. Dubenko, S. Stadler and N. Ali, J. Phys., Vol. 97, 10M304 (2005) 2. S. Stadler, M. Khan, J. Mitchell, and N. Ali, Appl. Phys. Lett., Vol. 88, 192511 (2006)

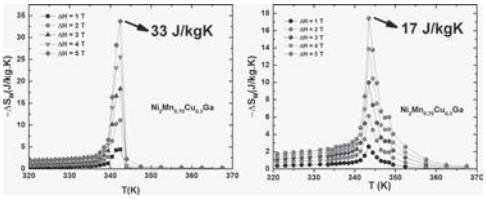


Fig. 1. The temperature dependence of the magnetic entropy change for $Ni_2Mn_{0.70}Cu_{0.30}Ga$ measured while (a) heating and (b) cooling.

FQ-11. An investigation of the dependence of the magnetocaloric properties of $AlFe_2B_2$ on compositional parameters using total scattering and PDF analysis. *S. Vallone*[1], B.A. Frandsen[2], R. Barua[3,4], B. Lejeune[4], L. Lewis[4,5] and K.G. Sandeman[1,6] *1. Physics, The Graduate Center at the City University of New York, New York, NY, United States; 2. Physics and Astronomy, Brigham Young University, Provo, UT, United States; 3. Mechanical and Nuclear Engineering, Virginia Commonwealth University, Richmond, VA, United States; 4. Chemical Engineering, Northeastern University, Boston, MA, United States; 5. Mechanical and Industrial Engineering, Northeastern University, Boston, MA, United States; 6. Physics, Brooklyn College, Brooklyn, NY, United States*

We present Pair Distribution Function (PDF) analysis of x-ray diffraction measurements of $AlFe_2B_2$ in order to quantify local disorder. $AlFe_2B_2$ is a second-order magnetocaloric material that has considerable promise for potential magnetic refrigeration applications, as it exhibits moderate room-temperature magnetocaloric effect (MCE) in the vicinity of a highly tunable Curie temperature near room temperature. Previous thermodynamic studies have shown a substantial dependence of both its Tc and MCE properties (magnetic entropy change and adiabatic temperature change) on compositional parameters such as stoichiometric ratio of the constituent elements and elemental substitution (Fig. 1, Ref. [1]) With this in mind, total scattering measurements with hard x-rays were made on a selection of different compositional variants of $AlFe_2B_2$, including both polycrystalline samples and crushed single crystals (see Fig. 2 for example). In doing so, we aim to provide a template for next-generation characterization of caloric materials, by obtaining a real space map of local (e.g. anti-site) disorder that can used in *ab initio* materials models to predict the thermomagnetic properties of materials with phase transitions at finite temperature.

1. R. Barua *et al.*, *J. Alloys and Compounds* 777, 1030-1038 (2019), and references therein

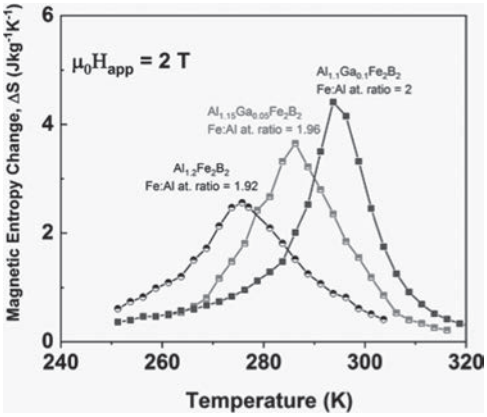


Fig. 1: The isothermal entropy change, observed in a 2 Tesla field, for three compositions of the $Al_{1.2-x}Ga_xFe_2B_2$ system (x=0, 0.05 and 0.1). The Fe:Al atomic ratio within the $AlFe_2B_2$ phase in this set of samples increases from 1.96 to 2.04 as the atomic % of Ga increases from 0 to 0.1. Up to a two fold increase in ΔS is observed upon addition of Ga. A similar increase in the adiabatic temperature change is observed, as determined from heat capacity measurements (taken from Ref. 1).

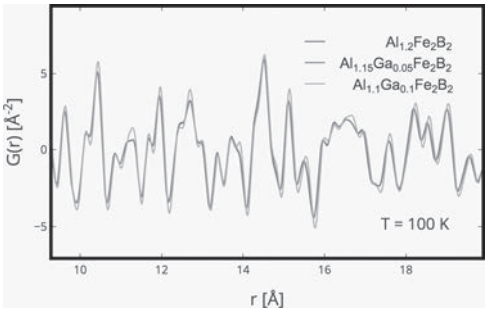


Fig. 2: A comparison of the pair distribution functions for polycrystalline samples of the same three compositions of the $Al_{1.2-x}Ga_xFe_2B_2$ system (x=0, 0.05 and 0.1) taken from x-ray diffraction measurements at 100 K.

FQ-12. Magnetocaloric effect in a cluster-glass system $Ho_5Pd_{2-x}Ag_x$ for hydrogen liquefaction. *H. Kitazawa*[1], S. Toyoizumi[2], K. Kujirai[2], H. Mamiya[3], R. Tamura[4], K. Morita[5] and A. Tamaki[2] *1. Center for Green Research on Energy and Environmental Materials, National Institute for Materials Science (NIMS), Tsukuba, Japan; 2. Graduate School of Advanced Science and Technology, Tokyo Denki University, Adachi-ku, Japan; 3. Research Center for Advanced Measurement and Characterization, National Institute for Materials Science (NIMS), Tsukuba, Japan; 4. International Center for Materials Nanoarchitectonics, National Institute for Materials Science (NIMS), Tsukuba, Japan; 5. School of Engineering, Tokyo Denki University, Adachi-ku, Japan*

The magnetic refrigeration based on magnetocaloric effect (MCE) of magnetic materials has attracted attention due to its potential application in energy-efficient environment-friendly refrigeration technology. T. Samanta *et al*. discovered that the rare-earth compound Ho_5Pd_2 which crystallizes in the cubic Dy_5Pd_2 structure has a large relative cooling power 6.32 J/cm^3 at around 30 K [1]. This material is expected to be a good candidate for hydrogen liquefaction by magnetic refrigeration because the boiling temperature 20 K of hydrogen gas is near the maximum temperature 30 K. Our neutron experiments clarified that Ho_5Pd_2 belongs to a cluster-glass specified by a short-range ordering with a long wavelength [2]. A. F. Gubkin *et al*. reported their spin-glass behaviors by DC and AC magnetization measurements with results of neutron experiments [3]. These glass-like behaviors should be originated from partial occupancies at Ho and Pd sites. In order to investigate of the relationship between large MCE and the cluster glass, we have shown the magnetic entropy change depends on number of vacancies at Ho sites [4] and substitution amount of Ni for Pd [5]. In this study, we examined magnetic and thermal properties of a solid solution system $Ho_5Pd_{2-x}Ag_x$ ($0 \leqq x \leqq 0.4$) by the measurements of magnetization and heat capacity to investigate substitutional effect of Ho_5Pd_2. We have obtained polycrystalline samples with a single phase for $Ho_5Pd_{2-x}Ag_x$ from $x = 0$ to $x = 0.2$. However, the volume fraction of a foreign phase Ho_2O_3 starts to increase with increase of x above $x = 0.4$. The lattice parameter a lineally increases with increase of x. The paramagnetic Curie-Weiss temperature θ_p gradually decreases with increase of x. However, the magnetic entropy change $-\Delta S_m$ for $Ho_5Pd_{2-x}Ag_x$ in a magnetic field of 5 T demonstrates anomalous x-dependence as shown in Figure 1. The maximum value of $-\Delta S_m$ suddenly drops from $x = 0$ to $x = 0.03$, gradually decreases from $x = 0.03$ to $x = 0.2$ and drops again from 0.2 to 0.4. We will discuss the vacancy and Ni substitutional effects of Ho_5Pd_2 with other magnetic and thermal properties.

[1] T. Samanta *et al*., Appl. Phys. Lett. 91, 082551 (2007). [2] H. Kitazawa *et al*., 19th Int. Conf. on Magnetism (Busan, July 2012) p 106 (Book of Abstracts). [3] A. F. Gubkin *et al*., J. Phys.: Cond. Mat. 25, 236003 (2013). [4] S. Toyoizumi *et al*., J. Appl. Phys. 117, 17D101 (2015). [5] S. Toyoizumi *et. al*., J. Physics: Conference Series 683, 012036 (2016).

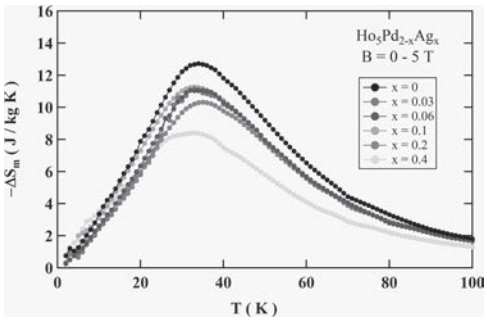


Fig. 1 Magnetic entropy change $-\Delta S_m$ of $Ho_5Pd_{2-x}Ag_x$ (B = 0 to 5 T).

FQ-13. Interstitial effects on the magnetic phase transition and magnetocaloric effects in (Hf, Ta)Fe_2 kagome phase. S. Li[1], T. Chen[2], *J. Chen*[3], X. Zhou[1], P. Jia[1], W. Cui[1,2] and Q. Wang[1] *1. Northeastern Unversity, Shenyang, China; 2. Lanzhou University of Technology, Lanzhou, China; 3. Institute Of Electronics, CAS, Beijing, China*

(Hf,Ta)Fe_2 phase crystallizes in the hexagonal Laves Kagome-like lattice in the whole Ta concentration [1]. With increasing temperature, the system abnormally undergoes a first-order magnetic phase transition from FM ground state to AFM state and then PM state without change in the crystal symmetry. Its interesting magnetic and electronic properties have caused lots of research attentions. The $Hf_{1-x}Ta_xFe_2C_y$(x=0.15, 0.165, 0.18, y=0, 0.015) ingots were prepared by arc-melting and annealed at 1273 K for 10 days. The phase constituent and magnetic properties have been examined by X-ray powder diffraction (XRD) and cryogenic VSM. The XRD patterns shows that the single-phase has been obtained in the $Hf_{1-x}Ta_xFe_2$(x=0.15, 0.165, 0.18, y=0, 0.015) alloys. More Ta substitution leads into the increased lattice parameter *a* but decreased *c*. Due to C addition, a is decreased but c is increased compared with C-free benchmark alloy. The first-order FM-AFM phase transition is confirmed with thermal hysteresis as shown in Fig.1. More Ta substitution reduces the Tc from 222 K at x = 0.15 to 153 K at x = 0.18 without widening the thermal hysteresis. By C addition, transition temperature is not affected in $Hf_{0.85}Ta_{0.15}Fe_2$ alloy. But the influence of C addition becomes obvious with more Ta additions not only in the reduced transition temperature but also the widened thermal hysteresis. Near their respective transition temperature, the typical step-like metamagnetic curves are observed, indicating the field-induced phase transition from AFM to FM state. The magnetic entropy changes are calculated by Maxwell relationship. For a field change of 7 T, the maximum of entropy change, delta S^{max}(7T), is 3.7 Jkg^{-1}K^{-1} in $Hf_{0.85}Ta_{0.15}Fe_2$ alloy and slightly increased to 4 Jkg^{-1}K^{-1} in $Hf_{0.835}Ta_{0.165}Fe_2$ alloy. While, the delta S^{max} is not influenced by C addition.

1. Y. Nishihara, J Phys Soc Japan 51 (1982) 1333.

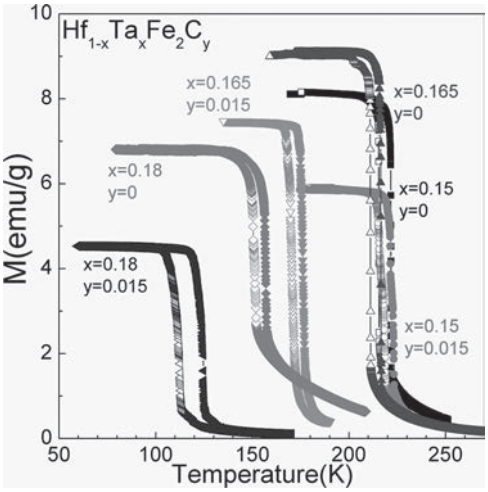


Fig.1 The M-T curves of $Hf_{1-x}Ta_xFe_2$(x=0.15, 0.165, 0.18, y=0, 0.015) alloys measured under 0.05 T.

FQ-14. Electric field controlled magnetocaloric effect in FeRh/PMN-PT heterostructure. *K. Qiao*[1], J. Li[1], C. Zhang[1], F. Hu[1], J. Wang[1], J. Sun[1] and B. Shen[1] *1. Institute of Physics, Chinese Academy of Scienes, Beijing, China*

With the increasing of high energy consumption and environmental problems in conventional cooling technology, magnetic refrigeration technology stands out as an alternative due to its energy-saving and environment-friendly characteristics. As typical magnetic refrigeration materials, first-order phase transition materials are limited by the narrow cooling temperature region. To solve this problem, FeRh films were successfully grown onto (011)-PMN-PT substrates with typical AFM-FM first order phase transition, as indicated by the *M-T* curves in Fig. 1a. Interestingly, two peaks occurs in d*M*/d*T-T* curves as shown inset of Fig.1a, indicating the AFM-FM phase transition of FeRh film was split in two successive parts. The reason is ascribed to the different strains of FeRh film grown on different ferroelectric domains in rhombohedral(R) phase PMN-PT substrates induced by lattice mismatch. However, two peaks merge into one peak at 6kV/cm and the peak position move to a higher temperature, which is attribute to electric field induced phase transition from multi-domain R phase to single domain orthorhombic(O) phase in PMN-PT[1]. There are also two peaks in Δ*S-T* curves at 0kV/cm in Fig.1b and one peak at 6kV/cm, coinciding with d*M*/d*T-T* curves. Actually, with electric field applied, not only the peak value of Δ*S-T* curves at 5T increased from 142 mJ/cm^{3}K to 153 mJ/cm^{3}K, but also the cooling temperature region expands from 25K to 33K as shown in shadow area in Fig.1b. With the help of electric field, the operating temperature region extends remarkably from 25K to 43K as shown in shadow area in Fig.1b and the value of Δ*S* at different temperature region is adjustable. This study lays a foundation for realizing a tunable magnetic entropy change by electric field in a broad cooling temperature region of first-order phase transition materials and promoting the application of magnetic refrigeration.

[1] Qiao K. M., Hu F. X., Liu Y., et al, Nano Energy 59, 285-294(2019).

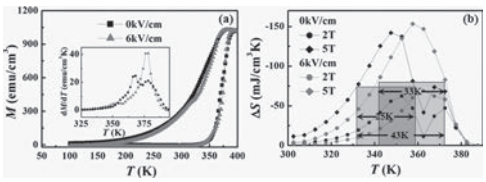


Fig.1(a) *M-T* curves and the corresponding d*M*/d*T-T* curves is shown in the inset; (b) Δ*S-T* curves at 2T and 5T at 0kV/cm and 6kV/cm, the shadow area indicates the cooling temperature region.

FQ-15. Influence of a magnetic field in $[Fe(pzt)_6](PF_6)_2$ (pzt=1-propyltetrazole), a spin-crossover material. *B.d. Alho*[1], P.d. Alho[1], R.M. Ribas[1], V.R. de Sousa[1], E.P. Nóbrega[1] and P. von Ranke[1] *1. Rio de Janeiro State University, Rio de Janeiro, Brazil*

Nowadays, there is a strong necessity of saving energy consumption in cooling processes as well as finding new environmental friendly materials to act as refrigerant, in the so called solid-state refrigeration. Those materials are used as an alternative to the actual gas-compression refrigeration systems, which have low efficiency and negative environmental effects. The caloric effects are described by two thermodynamic quantities: isothermal entropy change (ΔS_T) and adiabatic temperature change (ΔT_{ad}). The spin-crossover (SCO) phenomena is a switching between a high spin (HS) and low spin (LS) state when the system is submitted to an external parameter variation such as pressure and temperature [1-4]. Recently, SCO materials have been pointed as good candidates for caloric refrigeration due to their giant barocaloric potentials. However, other caloric effects are yet to be investigated in those compounds. In this work we studied the magnetic and magnetocaloric effects on the $[Fe(pzt)_6](PF_6)_2$ (pzt=1-propyltetrazole) spin-crossover compound [4]. Our theoretical microscopic model results in a total entropy with includes the magnetic, lattice, electronic and configurational contributions. We obtained, as expected, a small magnetocaloric effect in comparison with the giant barocaloric effect on the same compound. However, this results points out that a larger magnetocaloric effect may be obtained in SCO compounds which includes a ferromagnetic phase.

[1] K. G. Sandeman, APL Mater., v. 4, p. 111102 (2016). [2] P. J. von Ranke, Appl. Phys. Lett., v. 110, p. 181909 (2017) [3] P. J. von Ranke, B. P. Alho and P. O. Ribeiro, JAC, v. 749, p. 556 (2018). [4] P. J. von Ranke et. al. Phys. Rev. B., v. 98, p. 224408 (2018) [5] P. O. Ribeiro et. al., JMMM, v. 489, p. 165340 (2019)

FQ-16. Computational Discovery of Novel Iron-Based Amorphous Magnetocaloric Alloys. *A.M. Krajewski*[1,2], B. Dong[1], P. Wang[1] and M.A. Willard[1] *1. Department of Materials Science and Engineering, Case Western Reserve Univeristy, Cleveland, OH, United States; 2. Department of Materials Science and Engineering, The Pennsylvania State University, University Park, PA, United States*

In this study, we created a framework of machine learning and search algorithms to design novel high-performance magnetocaloric alloys. The framework operates by maximizing the magnitude of peak magnetic entropy change $|-\Delta S_M^{peak}|$ and tuning the Curie temperature T_C to the desired value (i.e. 320±10 K), while keeping the composition relatively close to known alloys. We have first collected data (e.g. $|-\Delta S_M^{peak}|$ and T_C) on magnetocaloric effect in 194 distinct alloys reported in 41 publications. These alloys lay in the 18-dimensional composition space: $Fe_{100-\Sigma}$ $Ni_{0–38}$ $Co_{0–40}$ Cu_{0-1} Zr_{0-11} $B_{0–29}$ $Cr_{0–10}$ $Nb_{0–10}$ $Gd_{0–4}$ $Y_{0–22}$ $Mo_{0–10}$ $Si_{0–10}$ $Nd_{0–15}$ $Ce_{0–13}$ $Sm_{0–3}$ $Mn_{0–24}$ $Ti_{0–8}$ $V_{0–14}$. All essential properties were normalized to their values at an applied induction of 1.5 T, using V. Franco's universal curve method.[1] Using our tool, we have selected known high-performing alloys, then predicted modifications to these alloys with varying degrees of deviation (with larger deviations deemed riskier but resulting in larger predicted magnetic entropy). Starting with a known alloy with $Fe_{80}Zr_{10}B_{10}$ composition, reported to have $|-\Delta S_M^{peak}|$ of 1.47 J/(kg K) at H=1 T (1.95 J/(kg K) at H=1.5 T) and T_C of 365K,[3] our tool predicted three new alloys based on it: $Fe_{79}Zr_{10}B_{10}Ce_1$, $Fe_{76}Cu_1Zr_{10}B_{10}Ce_2Ti_1$ and $Fe_{74}Cu_1Zr_{10}B_{10}Nd_1Ce_2Ti_2$. Each step was predicted to increase $|-\Delta S_M^{peak}|$ by roughly 0.05 J/(kg K) at H=1.5 T relative to each other, and lower T_C by 15, 25, 25 K relative to the base alloy. We measured that $Fe_{80}Zr_{10}B_{10}$ had $|-\Delta S_M^{peak}|$ of 0.91 J/(kg K) at H=0.9T (1.31 J/(kg K) at H=1.5T) and T_C of 343K. The first new alloy with composition $Fe_{79}Zr_{10}B_{10}Ce_{1,}$ was found to increase the $|-\Delta S_M^{peak}|$ by 0.09 J/(kg K) at H=1.5 T and lower T_C by 10 K. In this contribution, we will discuss details of the model methodology, further validation experiments, and availability of this tool to other researchers.

[1] V. Franco, J. Blázquez, and A. Conde, Applied Physics Letters 89 (2006) 222512. [2]X. Li, Y. Pan and T. Lu, *Journal of Non-Crystalline Solids* 487 (2018) 7-11, 2018. [3]Y. Fang et al., *Journal of Applied Physics* 105 (2009) 07A910.

FQ-17. Structural and Magnetic Phase Transition Coupling in Magnetocaloric LaFeCoSi Thin Films. *D. Read*[1], A. Evans[1], C. Kinane[2], A. Caruana[2], M. Pendharkar[3], S. Chatterjee[3], M. Gao[4] and C. Palmstrøm[3]
1. Physics & Astronomy, Cardiff University, Cardiff, United Kingdom; 2. ISIS Neutron and Muon Source, Didcot, United Kingdom; 3. Electrical & Computer Engineering, University of California Santa Barbara, Santa Barbara, CA, United States; 4. Engineering, Cardiff University, Cardiff, United Kingdom

A long-standing barrier to using magnetocalorics (MCs) in industrial applications is the requirement of high magnetic fields[1]. Recently intense research efforts have been undertaken to try to optimize MCs response to magnetic field and to increase the cooling power achievable close to room temperature. To further these goals various doping schemes of bulk materials have been extensively studied, however recently focus has shifted to optimizing synthesis techniques and structural engineering[2]. In order to develop advanced nano-structured MC materials, a fundamental understanding of how to produce high quality MC thin films will be required. We have used pulsed laser deposition to grow thin films, between 50nm and 150nm thick, on thermally oxidised Si substrates from a single LaFeCoSi target. Samples have been studied using SQUID magnetometry, AFM, XRR and PNR. Figure 1 presents XRR data for a 140nm thick film grown with a substrate temperature of 250°C and a laser pulse power of 200mJ with 18Hz repetition rate in a 20mTorr Ar atmosphere. The data clearly show the presence of Kiessig fringes out to a 2Θ angle of 6°, indicating low surface and interface roughness. Fits to the data indicate roughness of 3.52Å and 1.35Å at the surface and interface respectfully. Measurements of the magnetization as a function of temperature show a distinct change in gradient, characteristic of a magnetocaloric material near its Curie temperature. The change in gradient is close to 285K expected from previous measurements of bulk materials and corresponds to the structural phase transition. Hysteresis loops show a transition from ferromagnetic to paramagnetic behaviour as the temperature increases and approaches the gradient change seen in magnetization data. From these measurements the entropy change has been calculated (see figure 2) and shows a large negative magnetocaloric effect with a peak close to that expected for the bulk. A maximum peak of 20J/K in a 3T field is calculated for our LaFeCoSi thin films. For comparison we have also grown the more commonly studied material GdSiGe as thin films and have measured a peak entropy change of 4J/K at 3T[3, 4].

[1] V. Franco, J.Blazquez, B. Ingale, Annu. Rev. Mater. Res., Vol. 42, p.305-342 (2012) [2] J. Lyubina, J. Phys. D, Vol.50, p.053002 (2017) [3] R. Hadimani, I. Nlebedim, Y. Melikhov, J. Appl. Phys., Vol. 113, p.17A935 (2013) [4] R. Hadimani, J. Silva, A.Pereira, Appl. Phys. Lett., Vol.106, p. 032402 (2015)

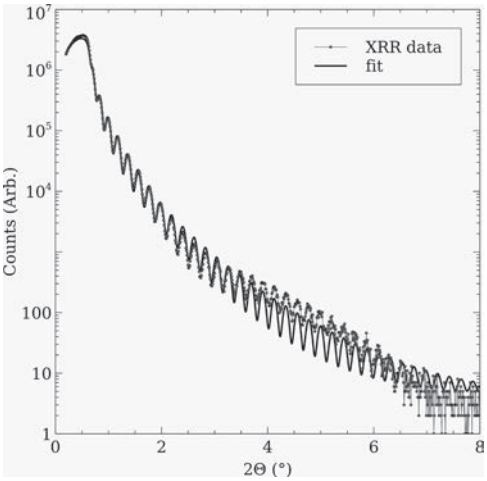


Figure 1 - XRR data for LaFeCoSi

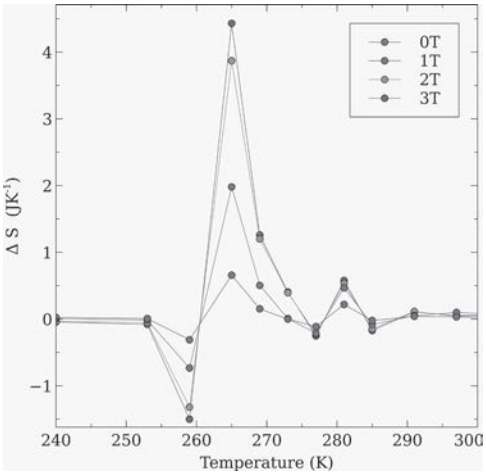


Figure 2 - Entropy change for LaFeCoSi

FQ-18. Synthesis and Magnetic Performance of Gadolinium Powder Produced with Rotating Disk Atomization. *S. Wolf*[2,1], T.M. Riedemann[2], J. Barclay[3], J. Holladay[4], I.E. Anderson[2,1] and J. Cui[2,1] *1. Department of Materials Science and Engineering, Iowa State University, Ames, IA, United States; 2. Materials Science and Engineering Division, Ames Laboratory, Ames, IA, United States; 3. Emerald Energy NW, Bothell, WA, United States; 4. Energy and Environment Directorate, Pacific Northwest National Laboratory, Richland, WA, United States*

Spherical powder is key for achieving good heat transfer and maintaining low pressure drop for heat transfer fluid in magnetocaloric regenerator. Obtaining relatively large spherical powder of rare earth metals that are extremely sensitive to oxygen is challenging. Comparing to gas atomization and plasma rotating electrode methods, rotating disk atomization (RDA) method is more robust for obtaining a small amount of powder with a short turn-around time, thereby, more suitable for research and development of new magnetocaloric materials. In this work, commercially bulk gadolinium was successfully atomized to produce spherical powder in the targeted 150-250 μm range. The obtained powder exhibited the expected magnetocaloric performance with a maximum change of magnetic entropy of 12.1 J/kg K and a maximum adiabatic temperature change of 12.8 K with an applied magnetic field of 7 T.

S. Wolf, T. Riedemann and J. Barclay, Manuscript Submitted for publication. (2019)



FQ-19. Enlarging the magnetocaloric operating window of the Dy_2NiMnO_6 double perovskite. *M. Balli*[1,2], S. Mansouri[2], P. Fournier[2,5], S. Jandl[2], K. Truong[2], P. de Rango[3], D. Fruchart[3] and A. Lebouc[4] *1. International University of Rabat, Rabat, Morocco; 2. Institut Quantique, University of Sherbrooke, Sherbrooke, QC, Canada; 3. Néel Institute, CNRS, Grenoble, France; 4. G2Elab, Grenoble Institute Of Technology, Grenoble, France; 5. Canadian Institute for Advanced Research, Toronto, ON, Canada*

In this paper, we mainly focus on the magnetic and magnetocaloric features of $La_{2-x}Dy_xNiMnO_6$ double perovskites. Their magnetocaloric properties are investigated in terms of both entropy and adiabatic temperature changes. In contrast to early works, it was found that the Dy_2NiMnO_6 compound unveils

dominant antiferromagnetic interactions under very low magnetic fields. The ordering of its Dy^{3+} magnetic moments is associated with a giant magnetocaloric effect at very low temperatures, while the established ferromagnetic Ni-O-Mn super-exchange interactions close to 100 K give rise to moderate magnetocaloric levels. On the other hand, the doping of Dy_2NiMnO_6 with high amounts of large-size rare earth elements such as La would enable us to cover an unusually wide magnetocaloric temperature range going from the liquid helium temperature up to room-temperature. More interestingly, the presence of both ordered and disordered ferromagnetic phases in $La_{1.5}Dy_{0.5}NiMnO_6$ maintains constant its magnetocaloric effect over a temperature span of about 200 K (Fig.1), being a favorable situation from a practical point of view [1, 2]. However, the $La_{2-x}Dy_xNiMnO_6$ family cannot be directly implemented in functional devices because of its moderate thermal effects. The latter can be markedly enhanced by increasing the grains size of its polycrystalline forms using optimum annealing conditions. Additionally, the entropy change exhibited by $La_{1.5}Dy_{0.5}NiMnO_6$ under 7 T (for example) in the temperature range between 50 and 255 K is only 2.5 % of the theoretical limit. This opens the way to further fundamental and experimental investigations of R_2NiMnO_6 double perovskites (R = rare earth element) with the aim to fully taking advantage of their magnetocaloric potential. Also, some of the R_2NiMnO_6 double perovskites exhibit additional degrees of freedom such as electrical polarization enabling potential supplemental caloric effects under electric fields.

[1] M. Balli, S. Jandl, P. Fournier, *Appl. Phys. Rev.* 4, 021305 (2017). [2] D. Matte, M. de Lafontaine, A. Ouellet, M. Balli, and P. Fournier, Phys. Rev. Applied 9, 054042 (2018).

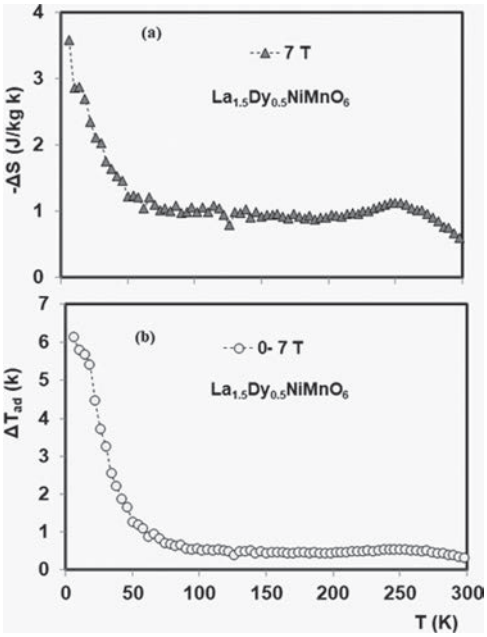


Fig.1: (a) Isothermal entropy change of $La_{1.5}Dy_{0.5}NiMnO_6$ as a function of temperature under a magnetic field change of 7 T. (b) Associated adiabatic temperature change.

Session FR
POWER MAGNETICS - MOTORS AND ACTUATORS
(Poster Session)

Marco Trapanese, Chair
Palermo University, Palermo, Italy

FR-01. Influence of Current Harmonics and Rotor Structure on Electromagnetic Losses of High Speed Permanent Magnet Synchronous Motor. *K. Shin*[1], J. Lee[1], G. Jang[1] and J. Choi[1] *1. Chungnam National University, Daejeon, The Republic of Korea*

High-speed permanent magnet synchronous motors (HPMSMs) are developed in direct-drive applications such as centrifugal compressor and vacuum pump because of the advantages of compact size and high efficiency [1]. However, due to the small size, it has a high loss density and a limited heat dissipation surface, which causes difficulties in cooling [2]. Therefore, the accurate prediction of electromagnetic losses is very important in the design stage of HPMSM. In this study, electromagnetic analysis considering pulse width modulation (PWM) inverter and effective three-dimensional (3D) electromagnetic structure is proposed for predicting accurate electromagnetic losses of stator and rotor of HPMSM. Fig. 1 shows the 3D structure and side view of the HPMSM and the evaluation system of the prototype. In order to improve the analysis time, an effective 3D analysis model has been defined based on physical properties. In addition, the phase current with carrier harmonics from PWM inverter was estimated by dynamic simulation model, and it was used for electromagnetic losses analysis. Figs. 2(a) and (b) show the predicted and measured current waveforms and FFT analysis results of currents. From the comparison of the analysis results with experiments, it can be confirmed that the modeling of the control system is valid. As shown in Fig.2(c), mechanical loss were measured from finite element analysis and open circuit test of prototype. Using effective 3D model and current harmonics, electromagnetic analysis deals with calculation of copper loss, core loss, and rotor loss, respectively. When the mechanical loss is added to the electromagnetic loss analysis result, the error between the proposed electromagnetic loss analysis and the experiment is within 3% according to the operating condition as shown in Fig. 2 (d). The analysis, discussions and measurements of HPMSM will be explained in more detail in the full paper.

[1] D. Gerada, A. Mebarki, and A. Boglietti, IEEE Trans. Ind. Electron., Vol. 61, pp. 2946–2959 (2014). [2] D.-K. Hong, B.-C. Woo, and D.-H. Koo, IEEE Trans. Magn., Vol. 48, pp. 871–874, (2012).

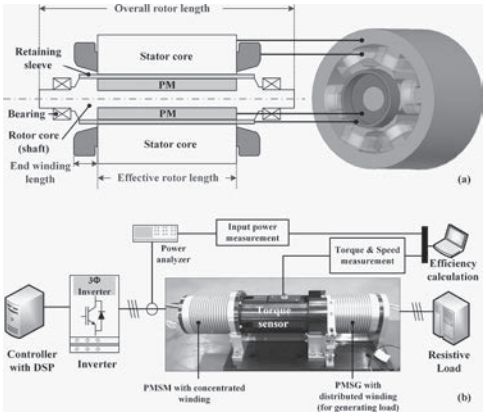


Fig. 1. (a) Structure of high-speed PMSM with concentrated winding and (b) performance evaluation system.

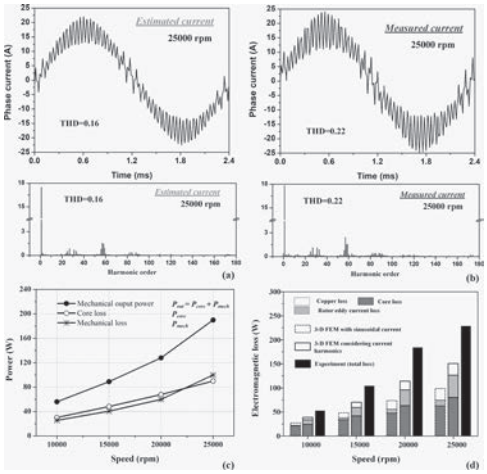


Fig. 2. Comparison with analysis and experimental results: (a) estimated, (b) measured phase current, (c) measured mechanical loss, and (d) electromagnetic losses.

FR-02. Magnet Selection in Permanent Magnet Synchronous Traction Motor for Electric Vehicles. *H. Won*[1], Y. Hong[1] and M. Choi[1] *1. Department of Electrical and Computer Engineering and Center for Advanced Vehicle Technologies, The University of Alabama, Tuscaloosa, AL, United States*

This paper has investigated the coercivity (H_c) and remanent flux density (B_r) of permanent magnet (PM), that meet the traction motor specifications set by US Department of Energy for electric vehicle (EV) application [1]. To identify the required values of H_c and B_r, five PM traction motors, which are fractional-slot concentrated wounded surface PM motor (FSCW-SPM), FSCW flux-switching PM motor (FSCW-FSPM), FSCW spoke interior PM motor (FSCW-SIPM), integer-slot distributed wounded SIPM (ISDW-SIPM), and ISDW V-shape interior PM motor (ISDW-VIPM) [1-5], were considered and simulated for motor performance using ANSYS Maxwell 2D under rated and peak conditions. Table I shows the motor specifications and performance of five optimized motors. The B_r and H_c of PM are swept from 0.6 to 1 T in steps of 0.1 T and 600 to 900 kA/m in steps of 100 kA/m, respectively. Fig. 1 shows the maximum torque in solid line and demagnetization rate (D_{rate}) in dashed line of the five motors. The D_{rate} is calculated by dividing the area where flux density of PM is lower than 0.1 T and/or magnetization direction (M_{dir}) is opposite to the initial M_{dir} to the space occupied by the whole magnet when the input current is 2.5x of rated current. To meet the DOE requirements with PM demanding low H_c and D_{rate} below 2 %, the required B_r needs to be 0.9, 0.7, 0.8, 0.7, and 0.9 T with H_c of 700, 900, 750, 600, and 700 kA/m for FSCW-SPM, FSCW-FSPM, FSCW-SIPM, ISDW-SIPM, and ISDW-VIPM, respectively. For PM requiring low B_r and D_{rate} below 2 %, the B_r of 0.85, 0.72, 0.75, 0.6, and 0.7 T for listed motors with H_c of 900, 900, 900, 700, and 900 kA/m, respectively, are required. The motors employing PM with low H_c are investigated further for rated and maximum speed using ANSYS motor toolkit. It was found that all motors meet the DOE requirements, as listed in Table I. Our results provide the

motor designers with some guidelines for PM selection for EV application. This work was supported in part by the NSF-I/UCRC for EV-STS under Grant number 1650564.

[1] P. Reddy, T. Jahns, and P. McCleer, 2010 IEEE Energy Conversion Congress and Exposition, pp. 1074 (2010) [2] R. Cao, C. Mi, and M. Cheng, *IEEE Transactions on Magnetics*, Vol. 48, no. 8, pp. 2374 (2012) [3] A. El-Refaie, J. Alexander, S. Galioto, *IEEE Transactions on Industry Applications*, vol. 50, no. 5, pp. 3235 (2014) [4] M. Kimiabeigi, J. Widmer, and R. Long, *IEEE Transactions on Industrial Electronics,* vol. 63, no. 1, pp. 113 (2016) [5] M. Olszewski, *FY2011 Oak Ridge National Laboratory,* pp. 1 (2011)

	DOE Target					
Stator Winding	-	Fractional-slot Concentrated	Fractional-slot Concentrated	Fractional-slot Concentrated	Integer-slot Distributed	Integer-slot Distributed
Rotor Topology	-	Surface-mounted	Flux-switching	Interior-mounted (Spoke)	Interior-mounted (Spoke)	Interior-mounted (V-shape used in Toyota Prius 2010)
Machine Diameter (mm)	≤ 210	210	210	210	210	210
Machine Length (mm)	≤100 for concentrated ≤ 90 for distributed	100	100	100	90	90
# of Winding Turns	-	10	11	8	6	9
Rated/Peak Current (A_{rms})	160/400	122/245	69/137	147/294	90.5/181	70/140.6
Rated/Peak Torque (Nm)	> 100/186	106/186	107/186	115/186	108/186	100/190
Rated/Peak Power (kW)	> 30/55	44/77	31/55	48/77	30/55	27/49.7
Rated/Maximum Speed (rpm)	> 2,800/14,000	4,000/15,000	2,800/14,000	4,000/15,000	2,800/14,000	2,500/13,500
B_r/H_c (T or kA/m)	-	0.9/700	0.7/900	0.8/750	0.7/600	0.9/700
Reference	[1]	[2]	[3]	[4]	[5]	[6]

Table 1. Motor Specifications and Performances

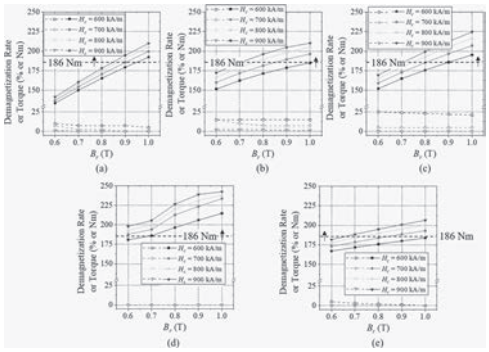


Fig. 1. Maximum torque and demagnetization rate of (a) FSCW-SPM, (b) FSCW-FSPM, (c) FSCW-SIPM, (d) ISDW-SIPM, and (e) ISDW-VIPM.

FR-03. Sensorless PMSM Drive Based on Modified MRAS Parameter Estimation with GWO Algorithm. J. Cao[1], *X. Sun*[1], G. Lei[2], J. Zhu[3] and Y. Guo[2] *1. Automotive Engineering Research Institute, Jiangsu University, Zhenjiang, China; 2. School of Electrical, Mechanical, and Mechatronic Systems, University of Technology Sydney, Sydney, NSW, Australia; 3. School of Electrical and Information Engineering, University of Sydney, Sydney, NSW, Australia*

Abstract-This paper proposes a modified model reference adaptive system (MRAS) method for sensorless control of permanent magnet synchronous motor (PMSM). To reduce the adverse effect of parameters variation, the stator resistance and magnet flux linkage are estimated and continuously updated. Besides, controller parameters of adaptive law are optimized by grey wolf optimization (GWO) algorithm. 1.Introduction Conventional MRAS takes rotor speed as adjustable parameter to obtain speed adaptive law [1], and ignores the adverse effect caused by parameters variation [2]. While the modified MRAS can improve control performance by estimating the parameters. Augmented with GWO algorithm, the performance of the control system can be improved greatly. 2.The proposed method The dynamic model of SPMSM in *dq*-axis reference frame can be described as $d(i_d+\Psi_f/L_s)/dt=-R/L_s(i_d+\Psi_f/L_s)+\omega_e i_q+(u_d+R\Psi_f/L_s)$ $d(i_q)/dt=-Ri_q/L_s-\omega_e(i_d+\Psi_f/L_s)+u_q/L_s$ where u_d, u_q, i_d, and i_q are stator voltages and currents. R, L_s, Ψ_f and ω_e are stator resistance, inductance, magnetic flux linkage, and electrical angular velocity, respectively. The currents are taken as variables to obtain adjustable model. According to Popov's inequality criteria, the adaptive law can be obtained as $\omega_e=-(k_p+k_i/s)(i_d\hat{i}_q-i_q\hat{i}_d-\Psi_f(i_q-\hat{i}_q)/L_s)$ The estimated parameters are substituted to obtain the modified model. Adaptation laws for R_s and Ψ_f are given respectively as $R'=-(k_{pres}+k_{ires}/s)(i_d\hat{i}_d+i_q\hat{i}_q-i_di_d-i_qi_q+\Psi_f(i_d-\hat{i}_d)/L_s)+R(0)$ $\Psi'f=-(k_{pflux}+k_{iflux}/s)(i_q-\hat{i}_q)\omega_e/L_s+\Psi_f(0)$ To reduce speed error and suppress overshoot, GWO is used to optimize controller parameters and cost function is given as $f=T_s/N\sum(k|\omega(k)-\omega^*|+k|i_d(k)-i^*\ d|+k\lambda(\omega(k)-\omega^*))$ whereT_s is the sampling period, λ is penalty factor, k is sample time index. 3.Results In this section, experiments are used to verify the performance of the modified MRAS and GWO is used to optimize the controller parameters. The experimental setup and results are shown in Fig.1 and Fig.2, respectively. 4.Conclusion In this paper, a sensorless PMSM drive scheme based on modified MRAS with GWO algorithm is proposed and verified by simulations and experiments.

[1] A. T. Nguyen, M. S. Rafaq, H. H. Choi and J. Jung, "A model reference adaptive control based speed controller for a surface-mounted permanent magnet synchronous motor drive," *IEEE Trans. Ind. Electron.*, vol. 65, no. 12, pp. 9399-9409, 2018. [2] H. Wang, W. Wu, H. S. Chung and F. Blaabjerg, "Coupled-inductor-based aalborg inverter with input DC energy regulation," *IEEE Trans. Ind. Electron*., vol. 65, no. 5, pp. 3826-3836, 2018.

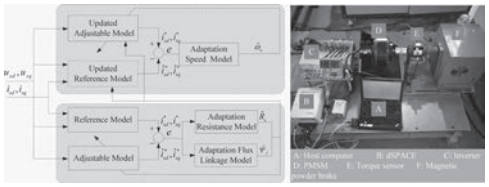


Fig.1.Block diagram of the modified method and experimental setup.

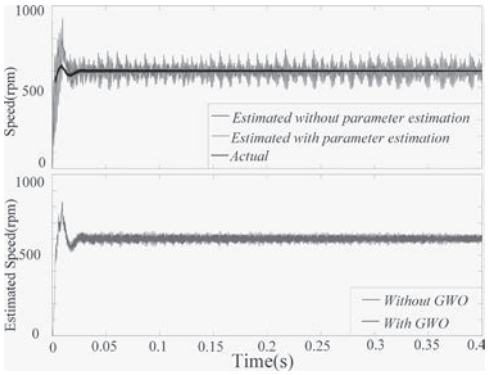


Fig.2.Simulation results of the proposed method.

FR-04. Dynamic Characteristic Analysis and Experimental Verification of IPMSM according to Operating Range. *G. Jang*[1], C. Kim[1], H. Lee[1], H. Shin[1], J. Gu[1] and J. Choi[1] *1. Chungnam National University, Daejeon, The Republic of Korea*

The interior permanent magnet synchronous motor (IPMSM) is a structure resistant to scattering due to centrifugal force by embedding a permanent magnet in a barrier inside a rotor core. The rotor core has a salient pole, and in addition to magnetic torque, reluctance torque can be generated. Therefore, when the flux weakening control is properly performed, high-speed operation and wide constant output operation can be achieved due to the influence of the reluctance torque. In particular, there is little impact on price, high performance, high output, and high reliability [1]. Many studies have focused on the design and performance evaluation of such an IPMSM. However, there is little detailed performance analysis considering the pulse width modulation (PWM) controller of the motor. In general, the FEM cannot accurately depict the torque ripple and loss because the PWM current harmonics cannot be considered. Therefore, when the motor is actually driven, the result of the experiment is different from that of the analysis [2]. In this paper, we propose a dynamic characteristics analysis method of

IPMSM to provide high-accuracy analysis of the motor controller. Fig. 1 (a) shows the shape of the IPMSM described in this paper. It comprises six poles and nine slots, and the magnet is embedded in a V shape. Fig. 1(b) shows the comparison of torque analysis results using the finite element method (FEM), the calculated value and the experiment according to the current magnitude and phase angle. Fig. 1 (c) is a block diagram describing the dynamic characteristics analysis of the IPMSM. Fig. 2 (a) and (b) show the d-axis and q-axis inductance values according to the current magnitude and phase angle of IPMSM. Fig. 2 (c) shows a comparison of the performance of the motor analyzed using the FEM and the dynamic characteristics. Detailed analysis methods, experimental methods and results are presented in the full paper.

[1] S. K. Cho, K. H. Jung, and J. Y. Choi, IEEE Transactions on Magnetics., Vol. 54, no. 11, 8204705, (2018) [2] S. Mukundan, H. Dhulipati, C. Lai, IEEE Transactions on Conversion., Vol. 33, no. 4, pp. 2060-2069, (2018)

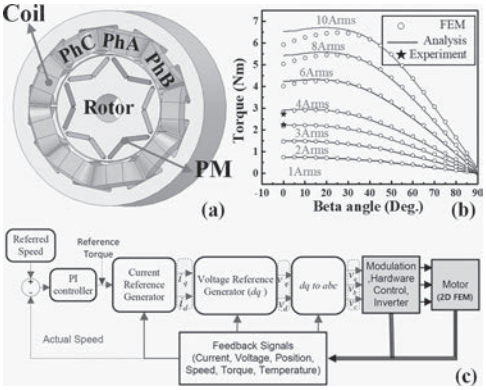
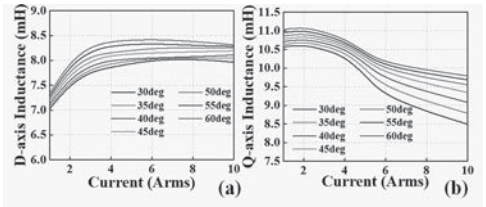


Fig. 1. (a) IPMSM analysis model, (b) comparison of torque analysis results, (c) dynamic analysis block diagram.



Parameter	Power (W)	Torque ripple (%)	Copper loss (W)	PM Loss(W)	Core loss (W)	Efficiency (%)
2D FEM	308	11.4	54.7	0.18	2.7	84.2%
Dynamic Analysis	290	65.3	54.7	14.6	32.3	74.0%

(c)

Fig. 2. Inductance of IPMSM: (a) d-axis, (b) q-axis, and (c) comparison of the performance of the motor according to analysis method.

FR-05. A Study of the Number of Axial Segments of Permanent Magnet in SPMSM for Ultra-High Speed Applications. *H. Lee*[1] *1. Electrical Engineering, Busan Institute of Science & Technology, Busan, The Republic of Korea*

This paper describes the analysis on the Number of Axial Segments of Permanent Magnet in SPMSM for Ultra-High-Speed Application; Electric-Turbo Compound System(E-TCS) for Construction Equipment. E-TCS is a device that combines a turbocharger, which is a regenerative device through exhaust gas, and a compressor to improve the turbo lag. As a result, E-TCS must be able to drive at least 80,000 rpm and require a large torque at low speeds. And because of scattering problem of permanent magnets, so limit to increase the rotor size and shaft length is realatively long. To increase performace of motor, difficulties of permanent magnetization and reduce permanent magnet loss, the segment must be applied in the axial direction on permanent magnet. Design criteria and power loss analysis of the ultra-high-speed motor are described by analytical method, and the results are validated by 3D-finite element method. And then, the prototype motor has been fabricated 3 cases and tested. The experimental results confrimed the validity of the proposed design and alalysis scheme of the ultra-high-speed SPMSM(Surfaced Permanent Magnet Synchronous Motor).

1. D.-K. Hong, B. C.Woo, J. Y. Lee, and D. H. Koo, “Ultra high speed motorsupported by air foil bearings for air blower cooling fuel cells,” IEEE Trans.Magn., vol. 48, no. 2, pp. 871–874, Feb. 2012. 2. Jorma Luomi, C. Zwyssig, A. Looser, and J. W. Kolar, “Efficiency optimizationof a 100-W 500 000-r/min permanent-magnet machine including air-friction losses,” IEEE Trans. Ind., vol. 45, no. 4, pp. 1368–1377, Jul./Aug. 2009. 3. D. H. Jung, J. K. Lee, J. Y. Kim, I. S. Jang, and H. J. Lee, “Design Method of an Ultrahigh Speed PM Motor/Generator for Electric-Turbo Compounding System”, *IEEE Trans. on Applied Superconductivity,* vol. 28., no. 3., Apr. 2018., 5202804

FR-06. Hybrid membrane computing and evolutionary algorithm for permanent magnet synchronous motor parameter design. X. Liu[1] and *W. Fu*[2] *1. Chongqing University, Chongqing, China; 2. The Hong Kong Polytechnic University, Hong Kong, Hong Kong*

I. Introduction To overcome the parameter design problem of a motor, optimization tools have been considered [1]. Genetic algorithm (GA) is a search algorithm simulates the natural selection mechanism. It has the ability of self-organization, self-adaptation and self-learning. Gheorghe Paun proposed the concept of membrane computing (MC) systems which are also known as P systems. In this paper, the optimization problem of a permanent magnet synchronous motor (PMSM) is solved by the proposed novel hybrid MC based GA (HMCGA). The HMCGA takes advantage of the MC model and GA, which can obtain satisfying searching efficiency and a good balance between exploration and exploitation. The simulations are conducted and comparative results are given in this work and show that the HMCGA is feasible. II. Hybrid MC based GA In order to fully use the advantages of GA, the HMCGA model is formulated in this section. The procedure can be described as follows: 1. Initialize parameters of HMCGA. 2. Initialize positions and velocities randomly. Evaluate their fitness values and generate the best individuals. 3. Implement the *R* operator and the landmark operator for membranes as Fig. 2(c). 4. Calculate the fitness value. 5. Go to 3 for the next iteration if needed and output the optimal solution. III. HMCGA To test and validate the proposed algorithm, functions in Fig. 2(a) are examined [2]. Then a dual-PM-excited synchronous motor, as shown in Fig. 1(b), is optimized. The main specification and the design variables of the motor are listed in Fig. 1(c). The Convergence curves conducted by proposed algorithm, GA and PSO are shown as Fig. 2(b). IV. Conclusion In this paper, a novel HMCGA is proposed for optimization problem of a PMSM. The MC model has the advantages of simplicity and efficiency and the GA is introduced into the framework of MC model. Finally, the performance of HMCGA for optimization of PMSM is evaluated. Comparative results show that the proposed HMCGA is more efficient than the basic GA and PSO algorithms.

[1] Qiu H X, Duan H B., Multi-objective pigeon-inspired optimization for brushless direct current motor parameter design. *Sci China Tech Sci.* Vol. 58. pp. 1915–1923. 2015. [2] Xiaoyu Liu, W. N. Fu. A Dynamic Dual-Response-Surface Methodology for Optimal Design of a Permanent-Magnet Motor Using Finite-Element Method. *IEEE Trans. on Mag.*, Vol. 52, no. 3: pp. 7204304. 2016.

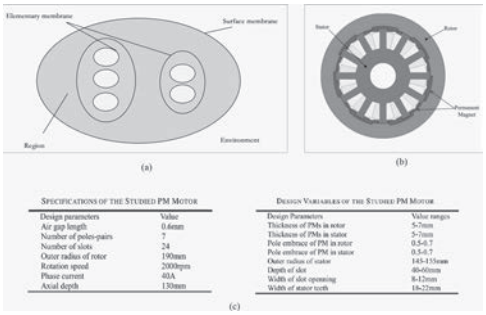


Fig. 1 (a) Membrane structure (b) Model of the PMSM. (c) Main specification and the design variables.

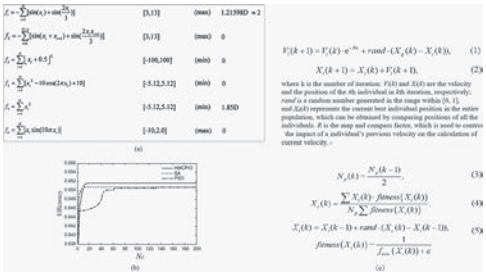


Fig. 2 (a)Test functions (b)Convergence curves (c)The procedure of HMCGA.

FR-07. Study on the Process for Improving the Design Precision of Working Bar of Double Cage Induction Motor. *D. Kim*[1], K. Kim[2], I. Yang[1], S. Song[1], S. Lee[1] and W. Kim[1] *1. Energy IT, Gachon University, Seungnam-si, The Republic of Korea; 2. Mechatronics Engineering, Halla University, Wonju-Si, The Republic of Korea*

Induction motors are the most commonly used energy consuming equipment and are highly effective in high efficiency design. Therefore, in order to satisfy both high efficiency and starting torque, an induction motor uses a double cage type rotor. In the case of the working bar of the double cage bar, most of the cases use an experience constant. However, these cases are applied to high voltage and large capacity induction motors (over 100kW), In case of medium and low capacity induction motors, errors are generated, resulting in lower results than the actual efficiency. This is because the resistance and impedance of the rotor at the time of design can not be accurately predicted. In this paper, we proposed a novel design process for improving precision on performance prediction in the design of rotor working bar of high efficiency double cage induction motor. The proposed process includes the process of determining the area of the rotor working bar and the process of determining the shape. The process for calculating the area of the rotor working bar sets the target value of current density and teeth flux density. The current density by obtaining the current and area of the working bar is calculated using the resistance. Regression of the efficiency constant until the target is collected, and find the optimal area of the working bar. This allows accurate rotor resistance to be predicted. Once the area is determined, a working bar shape determination process is performed that involves changing the shape of the working bar and calculating the rotor tooth flux density. The working bar is assumed to be rectangular, divide the height by dividing the width by the top, middle, and bottom. Change the width and repeatedly calculate the rotor tooth flux density until it converges to the target value using a magnetic equivalent circuit. Based on a model of 15 kw-class induction motor, the finite element analysis results of the design model using the existing experience constant and the proposed design process were compared. Finally, the validity of the process is verified by prototype performance test.

Shenoy, T.P, Nirody, J.S., PEDES'06. International Conference, pp. 1-5, (2006) Shu Yamamoto, Hideaki Hirahara, Akira Tanaka, Takahiro Ara, 2017 IEEE Energy Conversion Congress and Exposition(ECCE), (2017) Kersting, W.H., IEEE Transactions on Industry Applications, vol. 41, pp. 1499-1505 (2005) I. Boldea and S. A. Nasar, The induction machine handbook, CRC press, 2001

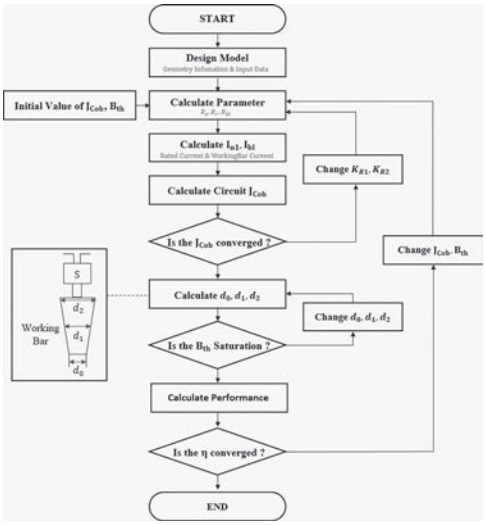


Fig.1 Performance calculation process of double cage induction motor

FR-08. Analyzing Position Detection by the Frozen Permeability of a Single-Phase BLDC Motor for Cordless Vacuum Applications. *H. Hwang*[1], Y. Choo[1], J. Cho[1], C. Kim[1], J. Choi[2], S. Hwang[3] and C. Lee[1] *1. Pusan National University, Busan, The Republic of Korea; 2. Kyungsung University, Busan, The Republic of Korea; 3. Kyungnam University, Changwon, The Republic of Korea*

This paper discusses the detection of rotor position in a single-phase blushless DC motor (BLDCM) without a sensor. Fig. 1(a) shows the direction of flux generated by permanent magnets (PMs) and coils, respectively. By injecting high-frequency voltage, relative permeability is changed in the core according to the interaction of PMs with coils. As a result, this permeability causes current offset by which the sensorless detection of rotor position has been implemented. To analyze permeability swing, it is mandatory to set the relative permeability of silicon steel in case of considering both coil and PM flux at the same time, and then total flux has to be decomposed into each flux. This is called frozen permeability method (FPM) and Fig. 1(b) shows B-H curve for explanation of the method. It is seen that a summation of flux densities of coil and PM is not the same as total flux density because of nonlinear permeability. The FPM should be used to avoid problem of the nonlinear permeability. Fig. 2(a) shows current offset and each flux linkage from coil and PM by the FPM. A direction of flux by coil and PM when negative current flows is the same as Fig. 1(a), and magnetic saturation occurs at this point. The magnetic saturation makes flux linkage from PM reduce and current offset as shown in Fig. 2(a). Fig. 2(b) shows experimental results on prototype of a single-phase BLDCM, and it is seen that negative current offset is occurred at the point of magnetic saturation. By detecting this current offset, rotor position of a single-phase BLDCM can be estimated without a sensor. In the final paper, we will discuss the experiment verification with detailed explanation through equations using FPM.

[1] H. Hwang, S. Bae and C. Lee. "Analysis and Design of a Hybrid Rare-Earth-Free Permanent Magnet Reluctance Machine by Frozen Permeability Method," IEEE Transactions on Magnetics, vol. 52, no. 7, pp. 1-4, July 2016. [2] D. Shuto, Y. Takahashi and K. Fujiwara, "Frozen Permeability Method for Magnetic Field Analysis of Permanent Magnet Motors Considering Hysteretic Property," in IEEE Transactions on Magnetics, vol. 55, no. 6, pp. 1-4, June 2019. [3] J. A. Walker, D. G. Dorrell and C. Cossar, "Flux-linkage calculation in permanent-magnet motors using the frozen permeabilities method," in IEEE Transactions on Magnetics, vol. 41, no. 10, pp. 3946-3948, Oct. 2005. [4] D. Kim, H. Hwang, S. Bae and C. Lee, "Analysis and Design of a Double-Stator Flux-Switching Permanent

Magnet Machine Using Ferrite Magnet in Hybrid Electric Vehicles," IEEE Transactions on Magnetics, vol. 52, no. 7, pp. 1-4, July 2016. [5] Y. Choo et al., "Investigation of Systematic Efficiency in a High-Speed Single-Phase Brushless DC Motor Using Multi-Physics Analysis for a Vacuum Cleaner," IEEE Transactions on Magnetics, vol. 55, no. 7, pp. 1-6, July 2019.

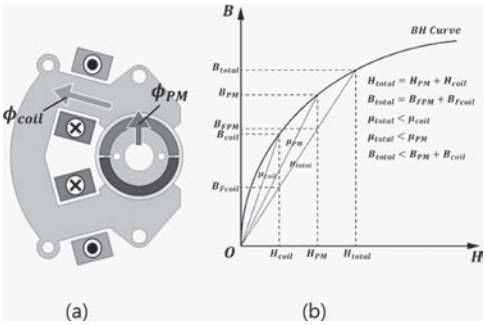


Fig 1. Single-Phase BLDC motor, (a) cross-sectional view, (b) B-H curve for FPM concept.

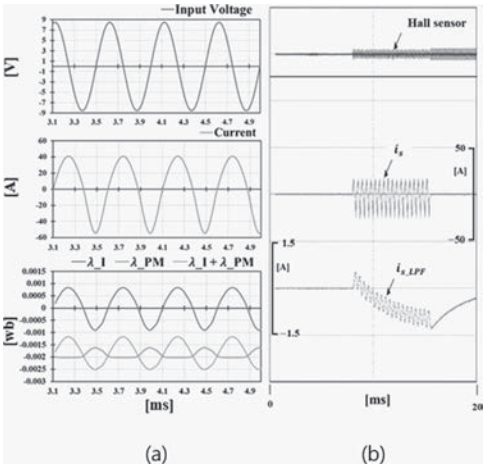


Fig 2. Verification of offset current and flux linkage, (a) simulation, (b) experiment

FR-09. Analytical and Experimental Verification for Electromagnetic Performances of Permanent Magnet Linear Synchronous Machines with Horizontally Magnetized Permanent Magnets. *K. Shin*[1], S. Seo[1], J. Woo[1] and J. Choi[1] *1. Chungnam National University, Daejeon, The Republic of Korea*

Permanent magnet linear synchronous machines (PMLSMs) are able to provide thrust force directly to the load without mechanical gears and transmission; therefore, they have significant advantages over rotary machines, such as simplicity and high efficiency [1]. A study on the performance comparison of PMLSM with magnet arrays showed that horizontal magnetization is better than vertical magnetization in terms of efficiency and weight in PMLSMs [2]. To develop design techniques for PMLSM with horizontal magnetization, this paper deals with the analytical modeling and experimental study for electromagnetic analysis of PMLSMs with horizontally magnetized permanent magnets (PMs) as shown in Fig. 1(a). The subdomains are divided into six regions: air gap (I, III), mover end (II), PMs (i), stator slots (j), and stator end (IV) as shown in Fig. 1 (b). The analytical solutions in all subdomains can be obtained by applying the boundary conditions to the interfaces between the subdomains. The validity of the proposed boundary condition was verified by comparing the air gap flux density as shown in Fig.1 (c) and (d). The analytical solutions allow for the prediction of the back-EMF, inductance, and generating characteristic in closed forms. The magnetic field and electromagnetic performances obtained by the analytical method were compared with those obtained by the finite element (FE) and experimental results. Fig. 2 (a) is a prototype and experiment set for verifying the reliability of the analytical results of the proposed analytical model. The generating characteristic analysis according to the load resistance connected to each phase are shown in Fig. 2 (b) and (c), and the results of the analytical method agreed well with the FE and experimental results. The analytical modeling, analysis results, and measurements will be presented in more detail in the full paper.

[1] W. X. Zhao, J. Q. Zheng, and Z. Y. Fang, IEEE Trans. Ind. Electron., Vol. 63, p. 2072–2082, (2016). [2] S.-W. Seo, M.-M Koo, and J.-Y. Choi, AIP Advances, Vol. 7, Art. no. 056674 (2017).

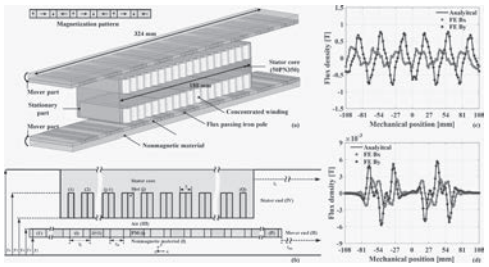


Fig. 1. (a) Structure of PMLSMs, (b) simplified analytical model, and flux density produced by (c) PMs and (d) stator coils.

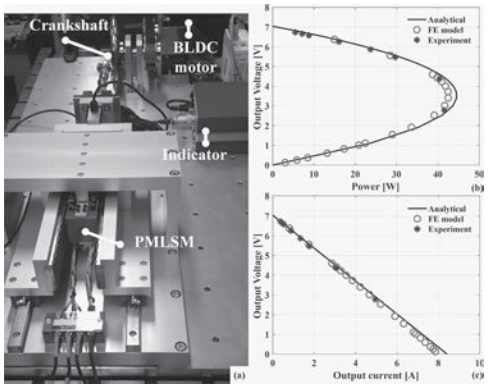


Fig. 2. (a) Experimental set and comparison with analytical, FE, and experimental results: (b) power-voltage and (c) current-voltage curve.

FR-10. Performance Verification of DR-PMSM for Traction System according to Permanent Magnet Shape. *C. Park*[1], H. Lee[1], G. Jeong[2], I. Jo[1], J. Lee[1] and T. Kim[3] *1. Korea National University of Transportation, Uiwang-si, The Republic of Korea; 2. Hanyang University, Seoul, The Republic of Korea; 3. University of Michigan-Dearbon, Dearbon, MI, United States*

Conventional driving systems of railway vehicle are composed of traction motor, mechanical reduction gear, and wheel sets, so that the structure of the driving systems is complicated and there is a limit in reducing the size and weight of them. In addition, the conventional driving systems have large maintenance cost problem due to transmission oil leakage and tooth wear of the ruction gear, and low efficiency problem due to additional power loss by the mechanical gear. Therefore, it is necessary to develop a new technology that can increase the output power density and maintainability of the conventional topology in driving system. Dual rotor permanent magnet synchronous motor (DR-PMSM) can be a good alternative to the conventional driving systems. DR-PMSM is structurally integrated with magnetic gear and PMSM, and it is directly mounted on the wheel without mechanical reduction gear. Currently, research on magnetic gears to replace mechanical reduction gears is being carried out variously all over the world [1]-[3]. However, the researches of DR-PMSM as a driving system for rail vehicle traction is now the beginning [4]. In this paper, the design study of the inner rotor including the permanent magnet is carried out in the application of the DR-PMSM. In designing the DR-PMSM models, Surface permanent

magnet (SPM) type and interior permanent magnet (IPM) type are considered according to the permanent magnet type of rotor, and IPM type is designed by dividing into bar type and V type. A comparative analysis of the three 1kW-class DR-PMSM models, in terms of electromagnetic properties, is performed to assess their general performance. The overall electromagnetic properties of the three designed models are similarly derived. But, the cogging torque and the rated torque characteristics of the IPM (V) type model are the best in comparison with the other models. In addition, the 1kW-class DR-PMSM prototype with V type magnet is fabricated to verify the validity of the analytical model and performance verification is performed.

[1] L. Sun, M. Cheng, H. Jia, "Analysis of a novel magnetic-geared dual-rotor motor with complementary structure," *IEEE Transaction on Industrial Electronics*, vol.62, no.11, pp.6737-6747, 2015. [2] K. T. Chau, D. Zhang, J. Z. Jiang, C. Liu, Y. Zhang, "Design of a magnetic-geared outer-rotor permanent-magnet brushless motor for electric vehicles," *IEEE Transaction on Magnetics*, vol.43, no.6, pp.2504-2506, 2007. [3] K. Atallah, S. D. Calverley, D. Howe, "Design, analysis and realization of a high-performance magnetic gear, IEE Proceedings- Electric Power Applications, vol. 151, no. 2, pp.135-143, 2004. [4] I. H. Jo, H. W. Lee, G. Jeong, W. Y. Ji, and C. B. Park, "A study on the reduction of cogging torque for the skew of a magnetic geared synchronous motor," *IEEE Transaction on Magnetics*, vol.55, no.2, asn.8100505, 2019.

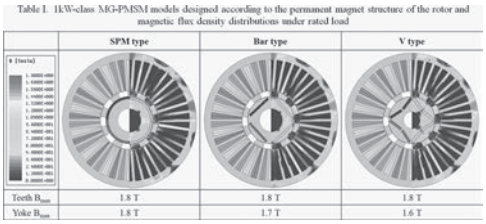


Table I. 1kW-class MG-PMSM models designed according to the permanent magnet structure of the rotor and magnetic flux density distributions under rated load

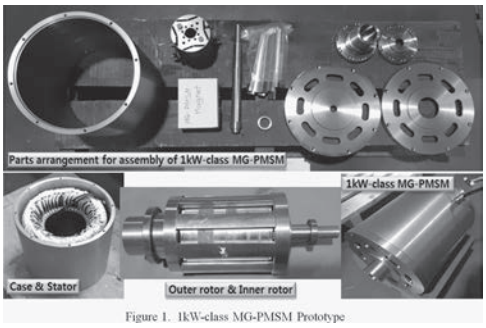


Fig. 1. 1kW-class MG-PMSM Prototype

FR-11. A Study on Position Control of Electro-mechanical Fin Actuator Using a New Position/Velocity Measurement Method Based Linear Type Hall-effect Sensor of BLDC Motor. J. Gu[2,1], *C. Kim*[1] and J. Choi[1]
1. Electrical engineering, Chungnam National University, Daejeon, The Republic of Korea; 2. Agency for Defense Development, Daejeion, The Republic of Korea

Electro-mechanical fin actuator system consists of a servo controller and an actuator. The electro-mechanical fin actuator for guided weapons requires robust controllers with position control algorithms to ensure robustness against uncertain disturbances such as aerodynamic loads and parameter variations. In order to design such robust controller, position and velocity of actuator are required. In general, position sensor(Potentiometer) and velocity sensor(Tachometer) are used shown in Fig.1(a). However, the use of such a sensor causes problems such as an increase in cost, an additional space for mounting, and a decrease in system reliability due to a sensor failure. To overcome this problem, we tried to implement the position and velocity signals by replacing the conventional latch type Hall-effect sensor of the BLDC motor with the linear type Hall-effect sensor as shown in Fig.1(b). The conventional position sensor and the velocity sensor were removed through a position and velocity implementation algorithm using the analog output of the linear type Hall-effect sensor while generating a commutation signal for driving the BLDC motor through a comparator having a hysteresis characteristic. Fig.2(a) shows the results of the 3/5deg step response test performed by applying the existing position/velocity sensor to the robust position controller, MFSMC(MFSMC : Model Following Sliding Mode Controller). Fig.2(b) shows the result of applying the newly proposed position/velocity signal by the linear type Hall-effect sensor to the robust position controller, MFSMC. As a result of the test, it is experimentally confirmed that the proposed method in this paper enables the position control through the robust position controller design without using the existing position/velocity sensor. In conclusion, it is confirmed that the proposed system can contribute to the miniaturization, cost reduction and system reliability improvement of the electro-mechanical fin actuator.

[1] J. H. Gu, C. Y. Song, and S. Y. Lee, "A new velocity measurement method using linear Hall-effect sensor for an electro-mechanical fin actuator", SICE Annual Conference 2007, pp.2179-2183. 2007 [2] C. Y. Song, J. H. Gu, " BRUSHLESS DC MOTOR USING LINEAR HALL-EFFECT SENSOR AND REALIZATION METHOD OF SPEED SIGNAL THEREOF" U.S. Patent, 7,800,325 B2(2010) [3]Park, J. H., Lee, Y. C., Lee, S. Y., and Lee, H. H., "An Application of Observer based Sliding Mode Control to an Electro-Mechanical Fin Actuator", *ICEMS,* session.LS2D, pp. 7-12, 2006

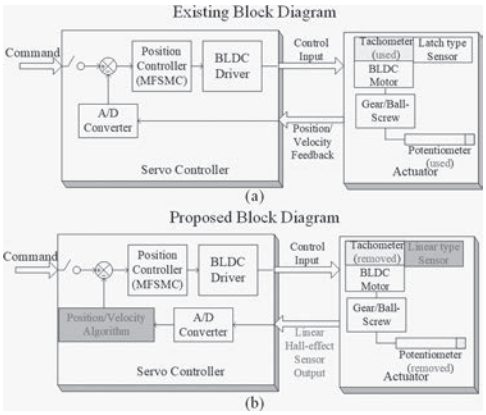


Fig. 1.(a) Existing block diagram of electro-mechanical fin actuator (b) The proposed block diagram of electro-mechanical fin actuator

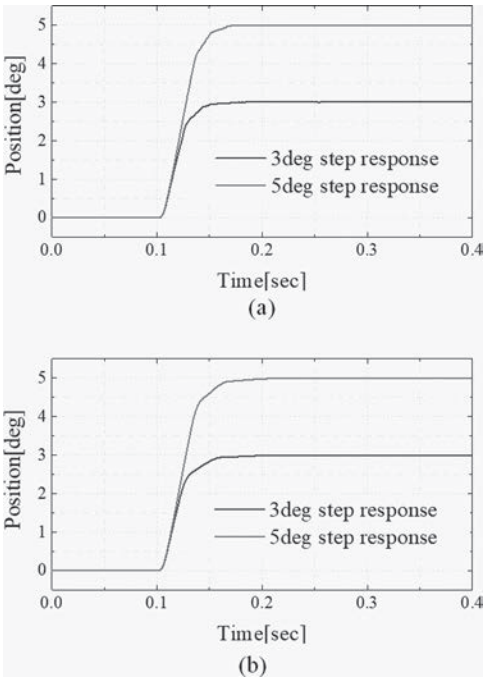


Fig. 2.(a) Test results using the position/velocity sensor. (b) Test results using the proposed position/velocity signal.

Session FS
EDUCATION, OUTREACH, & PUBLIC ENGAGEMENT IN MAGNETISM
(Poster Session)

Dafiné Ravelosona, Co-Chair
Center for Nanoscience and Nanotechnology, Palaiseau, France
Yukiko Takahashi, Co-Chair
NIMS, Tsukuba, Japan
Barry L Zink, Co-Chair
University of Denver, Denver, CO, United States

FS-01. Exploring magnetic resonance with a compass. *D. Nelson*[1], E. Cookson[1], M. Anderson[1], D. McKinney[2] and I. Barsukov[1] *1. Physics and Astronomy, UC Riverside, Riverside, CA, United States; 2. Santa Rosa Academy, Menifee, CA, United States*

Magnetic resonance plays an important role in today's science, engineering, and medical diagnostics. Learning and teaching magnetic resonance is challenging since it requires advanced knowledge of condensed matter physics and quantum mechanics. Driven by the need to popularize this technologically impactful phenomenon, we develop an inexpensive table-top demonstration experiment. It unveils the magnetic resonance of a hand-held compass in the magnetic fields of a permanent magnet. The setup provides an immediate visualization of the underlying physical concepts and allows for their translation to broad student audiences. This work was supported by the National Science Foundation under Grant No. ECCS-1810541.

FS-02. Magnetic Fields Web Series: Engaging Middle School Students in STEM. *P. Pena Martin*[1], J. Isberg[1], E. Ertekin[1,3], V. Lorenz[1,2] and N. Mason[1,2] *1. Materials Research Laboratory, University of Illinois at Urbana-Champaign, Urbana, IL, United States; 2. Department of Physics, University of Illinois at Urbana-Champaign, Urbana, IL, United States; 3. Department of Mechanical Science and Engineering, University of Illinois at Urbana-Champaign, Urbana, IL, United States*

Web based media can make scientific content accessible to audiences far beyond the scientific community. We created a web series called "Magnetic Fields" that aims to introduce materials science, particularly concepts related to magnetism, and promote themes more general to STEM fields, such as persistence and the scientific process, through use of characters and a story geared towards a middle school audience. The goal is to build and maintain interest in science at an age where this tends to drop off. The four-episode arc follows a group of high school characters as they encounter a strange new material during a class field trip to a laboratory. The series is directed by John Isberg, with professional actors making up most of the cast. The series was initiated by scientists in the Illinois MRSEC, and the storyline was developed in collaboration with MRSEC students and faculty. The episodes were released in May 2019 through Youtube. We report on the process of creating this series, response to it upon release, and discussion of its use as an educational tool. The authors acknowledge primary support of the NSF through the University of Illinois at Urbana-Champaign Materials Research Science and Engineering Center DMR-1720633.



Fig.1 Scene from an episode of "Magnetic Fields." Photo by John Isberg.

FS-03. In-class experiments with smart phones for teaching upper-level electricity and magnetism. A. Davidson[1], A. Ranjan[2] and *X. Fan*[1] *1. Physics and Astronomy, University of Denver, Denver, CO, United States; 2. Cherry Creek High School, Greenwood Village, CO, United States*

Interactive-engagement method such as studio physics [1, 2], has demonstrated higher learning gains than traditional lecturing in intro-level physics classes. However, there have been limited applications in upper-level classes, such as Electricity and Magnetism (E&M), possibly because experiments on E&M topics can be too costly and sophisticated to be carried out in the classroom. Smart phone, which is equipped with magnetic field sensors, radio signal detectors and light sensors, provides a convenient platform for carrying out E&M-related experiments. In this poster, we will present three examples of the implementation of smart-phone-based studio physics in an E&M class for Physics majors: (1) Detection of earth magnetic field inclination; (2) quantifying skin depth of aluminum foil with cellphone tower signals; and (3) Measurement of Brewster's angle. Besides sensitive sensors, smart phone also has computational power, which can be explored to further expand the breadth and depth of the smart-phone-based studio physics. Due to the wide accessibility of smart phones and the simplicity of experimental setup, we expect this teaching technique can be easily transferred to other institutes in the world.

[1] Gok, T., *Assessment of the effectiveness of the hybrid studio format in introductory undergraduate physics.* Energy Education Science and Technology Part B-Social and Educational Studies, 2012. 4(1): p. 117-130. [2] Sorensen, C.M., A.D. Churukian, S. Maleki, and D.A. Zollman, *The New Studio format for instruction of introductory physics.* American Journal of Physics, 2006. 74(12): p. 1077-1082.

FS-04. The Use of Virtue Modules in Physics Lab Teaching. *W. Zhang*[1], R. Bidthanapally[1], T. Sebastian[2], Y. Xiong[1,3], H. Qu[3] and J. Sklenar[4] *1. Physics Department, Oakland University, Rochester, MI, United States; 2. THATec Innovation GmbH, Mannheim, Germany; 3. Electronic and Computer Engineering, Oakland University, Rochester, MI, United States; 4. Physics Department, Wayne State University, Detroit, MI, United States*

Lab sessions in physics education connect the fundamental concepts to practical examples and are effective measures of the students' understanding and reasoning through ultimate real-world tests. Many topics in condensed

matter physics are known to be challenging to convey in both lectures and labs. In addition, these topics are usually resource demanding, which has been one of the challenging issues. Here, we introduce and demonstrate the use of virtue lab modules for teaching physics labs and for effectively integrating research and education. Experiments that are relevant to magnetism and spintronics include, but not limited to, spin current detecting, microwave energy harvesting, and spin-based thermoelectric effects. An important highlight of these modules is the highly-interactive laboratory learning platform. In the class, each piece of experimental hardware (e.g. electrometers, oscilloscopes, etc) will be paired with a computer-based virtual module. The individual modules mimic the hardware, which the students can use to become familiar with the hardware, acquire real-time feedback, and visualize the data acquisition dynamics, on-demand and risk-free. The virtual component is also helpful for demonstrating delicate, shared hardware in class, without risk of damaging the actual instrumentation. These individual components are connected to a central operating system and the experiment can be re-programmed by simple coding and user-interfaced commands [1]. Work at Oakland University is supported by NSF DMR-1808892.

[1] THATec Innovation GmbH: https://www.thatec-innovation.com/

Session FT
PATTERNED FILMS, PERPENDICULAR ANISOTROPY, AND DMI (Poster Session)

Hideto Yanagihara, Chair
University of Tsukuba, Tsukuba, Japan

FT-01. The Co thickness dependence of the Dzyaloshinskii-Moriya interaction and magnetic anisotropy in Pt/Co/W trilayers. *Y. Park*[1,2], J. Kim[1], Y. Nam[1], S. Jeon[1], J. Park[1], K. Kim[2], H. Lee[3], B. Min[2] and S. Choe[1] *1. Seoul National University, Seoul, The Republic of Korea; 2. Korea Institute of Science and Technology, Seoul, The Republic of Korea; 3. Pohang University of Science and Technology, Pohang, The Republic of Korea*

In nanostructures, physical properties are heavily influenced by the interface condition, requiring more comprehensive understanding of interfaces. The Dzyaloshinskii-Moriya interaction (DMI), one of interesting interfacial phenomena, has been extensively studied due to academic interests and technological opportunity for generating chiral spin structures in systems with broken inversion symmetry [1]. Here, we show the Co thickness tendency of the DMI. We fabricate 3-nm Pt/Co/5-nm W trilayers with different Co thickness t_{Co} and measure the DMI, D, and effective magnetic anisotropy, K_U^{eff}. The K_U^{eff} is known to have volume contribution K_V^{eff} and surface contribution K_S phenomenologically, with the relation $K_U^{eff}t_{Co}=K_U^{eff}t_{Co}+K_S$ [2]. Both contributions have structural dependence [2]. Since the DMI is sensitive to the interface condition, the D may be linked to the structural condition. In that point, we compare the tendency of K_U^{eff} and D with respect to the $t_{Co}^{eff}(\equiv t_{Co}\text{-}t^{d})$, where t^{d} is the dead layer. Like K_U^{eff}, the D may also be presented by the relation $Dt_{Co}^{eff}=D_V t_{Co}^{eff}+D_S$, to decompose the volume contribution D_V and surface contribution D_S. In fig.1(a), the deviate from the linear dependence when the t_{Co}^{eff} is thinner than ~ 1 nm, indicating interface condition begin to change. The Dt_{Co}^{eff} have saturated value in relatively thick t_{Co}^{eff} in fig.1(b), indicating $D_V\approx 0$ and the surface contribution is mostly responsible. Since the tendency of K_U^{eff} and D are not coincident, there may be another magnetic factors affecting the DMI as well as structural factor. Moreover, it is remarkable that the D deviate from the inverse proportionality to the t_{Co}^{eff} in relatively thin t_{Co}^{eff}. This peculiar behaviour of D will be discussed. The t_{Co}^{eff} tendencies of the DMI and SOT, and change of magnetic properties when very thin Cu layer is inserted at Co/W interface will also be discussed. The present observations provide physical understanding for the DMI and a guideline to maximize the DMI for spintronic applications. Figure 1. The $K_U^{eff}t_{Co}^{eff}$ and Dt_{Co}^{eff} with respect to t_{Co}^{eff}. The blue line in (a) is the linear fitting line. The blue horizontal line in (b) shows the average value over the relatively thick t_{Co}^{eff}.

[1] A. Soumyanarayanan, N. Reyren, A. Fert, and C. Panagopoulos, *Nature*, 539, 509–517 (2016). [2] R. Jungblut, M.T. Johnson, J. Stegge, A. Reinders. and F.J.A. Broeder, *J. Appl. Phys*. 75, 6424 (1994).

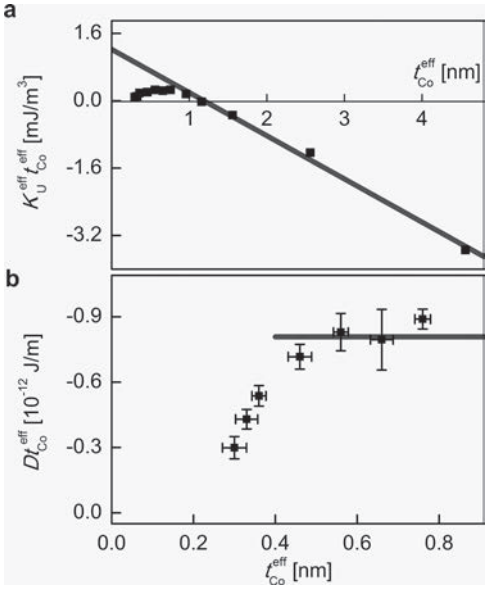


Figure 1

FT-02. The influence of MoC top layer on magnetic and microstructure of FePt(Ag, C) granular film. *J. Tsai*[1], C. Dai[1], J. Chen[1] and T. Hsu[1] *1. Department of Materials Science and Engineering, National Chung Hsing University, Taichung, Taiwan*

$L1_0$ ordered FePt thin film with (001) texture is the promising material for future heat-assisted magnetic recording (HAMR) media due to high uniaxial magnetocrystalline anisotropy and tunable Curie temperature (650-750K). To achieve high areal density (~2 Tb/in^2) for HAMR media, FePt granular film with uniformity columnar- and well-separated grains are necessary conditions. In this work, the (MoC, Ag, C) multiple segregants with different grains separation ability was doped in a different way to obtain columnar-like and granular FePt grains. The FePt(Ag, C) films were deposited on glass substrates by using magnetron sputtering under a working pressure of 10^{-3} Torr. The CrRu (002) seed-layer was grown on the glass substrate to induce the formation of a (002) textured MgTiON intermediate-layer, which promotes the epitaxial growth of (001) $L1_0$-FePt films. The FePt film was deposited at 470°C and thinner MoC layer with thickness ranged from 0.5 nm to 2 nm was toped on FePt at deposition temperature and post-annealed for 5 to 20 minutes. The FePt(MoC, Ag, C) granular film was formed after top layer segregants diffusion. The CrRu seed-layer and MgTiON intermediate-layer illustrate (002) reflection peak and the $L1_0$ FePt presents superlattice (001) and fundamental (002) reflection peaks in XRD pattern. The (002) oriented underlayer was promoted the formation of FePt hard phase with (001) orientation which is perpendicular to the film surface. From magnetic hysteresis loops, all the FePt(MoC, Ag, C) films show perpendicular magnetic anisotropy and the highest out of plane coercivity was 2.2T (8kOe for FePt single layer). The FePt(MoC, Ag, C) granular film show uniform and columnar-like grains evidenced in TEM images (Fig. 1 right). (Fig. 1(left) FePt single layer). The MoC is a suitable segregant to promote the columnar-like FePt grains from the top layer.

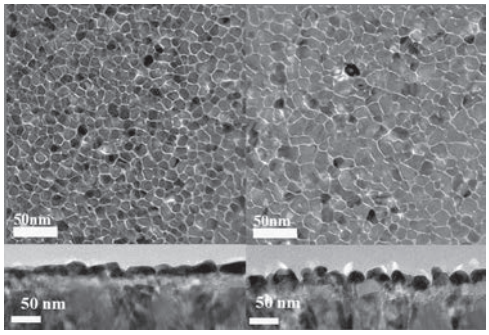
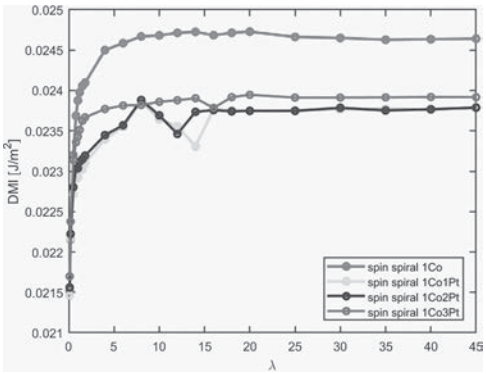


Fig. 1 Plane view and cross-sectional TEM images, (left) FePt single layer, (right), FePt(MoC, Ag, C) granular layer

FT-03. Determination of Dzyaloshinskii-Moriya Interaction in Ultrathin Films and Multilayer Structures Using First Principles. *A. Pokhrel*[1], M. Weber[2], A. Sapkota[1], A. Rai[1], D.K. Lau[3], V. Sokalski[3], T. Mewes[1] and C.K. Mewes[1] *1. Physics and Astronomy, University of Alabama, Tuscaloosa, AL, United States; 2. Physics and Astronomy, University of Kaiserslautern, Kaiserlautern, Germany; 3. Material Science & Engineering, Carnegie Mellon University, Pittsburgh, PA, United States*

Magnetic Skyrmions are topologically protected spin textures which are promising candidates for spintronic and spinlogic devices [1]. Their stability and dynamics depend strongly on their topological properties. They can be realized in bulk systems with broken inversion symmetry or in ultra-thin multilayers structures which utilizes the broken symmetry at the interfaces. Two key parameters in those thin film structures are the perpendicular anisotropy and the Dzyaloshinskii-Moriya interaction (DMI). Both effects rely on a strong spin-orbit coupling at the interface between the ferromagnetic and non-magnetic layers. In those hetero-structures there arises a phenomenon called spontaneous magnetic polarization in the interface region [2]. This effect commonly known as proximity effect influence the DMI in the heterostructure. Our aim in this project is to understand the microscopic origin of DMI, the surface anisotropy at different interfaces and proximity effect in DMI using first principles simulations based on density functional theory. In those simulations we consider different constrained spin spiral configurations to extract DMI vector at the interface [3,4]. Further, we probe isotropic and anisotropic nature of DMI in those heterostructure mainly in Pt/Co interface.

1. N. Nagoasoa and Y. Tokura, Nature Nanotechnology., Vol. 8, p.12 (2013) 2. Geissler, J., et al. *P*hysical Review B 65 020405. (2001) 3. Xiang, H., et al. Physical Review B 84, 224429 (2011) 4. Yang, H., et al. Physical Review Letters 115,267210 (2015)



Variation of DMI with penalty parameter (λ) for spin spirals in different layers

FT-04. Field Cooling Direction Dependent Asymmetric Magnetization Reversal in Perpendicular Exchange Biased CoPt/FeMn Bilayers. *C. Pan*[1,3], T. Gao[2], T. Harumoto[3], Z. Zhang[1], y. Nakamura[3] and J. Shi[3] *1. School of Materials Science and Engineering, Tsinghua University, Beijing, China; 2. Department of Applied Physics and Physico-Informatics, Keio University, Yokohama, Japan; 3. School of Materials and Chemical Technology, Tokyo Institute of Technology, Tokyo, Japan*

Magnetic anisotropy and magnetization reversal process in ferromagnet (FM) /antiferromagnet (AFM) exchange bias (EB) system are crucial from the view of both fundamental physics and practical application [1]. Recently, asymmetric reversal process has been observed in many EB systems. In IrMn/CoFe and CoO/Fe EB structures [2-3], the field cooling (FC) direction has been set as the variable and shows a strong influence on the asymmetric reversal process. Reviewing present reports, the effect of FC treatment has been investigated almost in longitudinal EB structures, while rarely in perpendicular EB system, and the mechanism of asymmetric reversal in EB system is still unclear. So more effects on perpendicular EB system are highly required. In this work, we investigated magnetization reversal process of CoPt/FeMn bilayers with perpendicular EB by analyzing the evolution of magnetic domains. External field H_{FC} was applied in FC treatment with tunable angle θ (θ= 0°, 30° and 90°) relative to the film normal direction. As shown in Fig. 1, after FC, hysteresis loops show obvious different EB values and magnetic anisotropies. Meanwhile, asymmetry in domain nucleation densities of descending and ascending branches shown in Fig. 2 suggests the corresponding asymmetric reversal process in two branches of the hysteresis loops. Moreover, distinct domain evolution modes varying with the direction of H_{FC} indicates that FC treatment plays an important role in magnetization reversal process. Magnetization reversal mechanism deduced by the evolution of domain pattern and density are found to depend on the strength of magnetic anisotropy of FM layer and direction of uncompensated AFM spins caused by the relative angle between H_{FC} and easy axis of FM layer. The study of the magnetic anisotropy and magnetization reversal process described by domain theory provides useful information to quantitatively investigating the complex interactions present in EB systems.

[1] B.Y. Wang, N.Y. Jih, W.C. Lin, etc., Phys. Rev.B 83, 104417 (2011). [2] A. Ehrmann and T Blachowicz. AIP Advan. 7,115223 (2017). [3] N. Akdogan, S. Kazan,B. Aktas, etc., J. Magn. Magn. Mater. 323, 346 (2011).

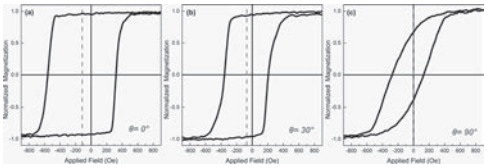


Fig. 1 Hysteresis loops measured in the perpendicular direction after FC treatment (a) perpendicular FC, θ= 0°, (b) θ= 30°, (c) in-plane FC, θ= 90°.

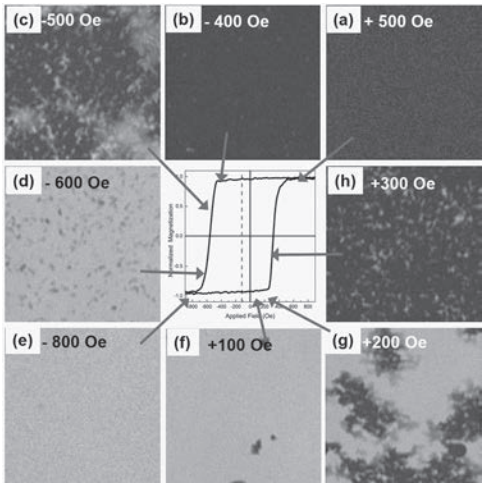


Fig. 2 Domain images obtained under various external fields along the hysteresis loop after perpendicular FC (θ= 0°).

FT-05. A comparative study: Role of Ta and Pt spacer layer on the domain structures in perpendicular exchange-biased CoPt/spacer layer/FeMn heterostructures. *C. Pan*[1,2], T. Gao[3], T. Harumoto[2], Z. Zhang[1], Y. Nakamura[2] and J. Shi[2] *1. School of Materials science and Engineering, Tsinghua University, Beijing, China; 2. School of Materials and Chemical Technology, Tokyo Institute of Technology, Tokyo, Japan; 3. Department of Applied Physics and Physico-Informatics, Keio University, Yokohama, Japan*

Perpendicular Exchange bias (PEB) effect has always been an attractive topic in information storage technology for long time. The concept of inserting non-magnetic (NM) spacer (V, W, Ru and Au) between ferromagnetic (FM) and antiferromagnetic (AFM) layers were previously demonstrated [1-2], which indicates that the spacer layers play a crucial role at the interfacial coupling. However, the specific mechanisms are still under debate. In this work, we investigates magnetic anisotropy and magnetization reversal process of CoPt/FeMn heterostructure spaced by Ta and Pt layers by observing the magnetic domains. The non-magnetic layer Ta and Pt spacer layers with varying thickness (t_{Ta}, t_{Pt}) from 0 ~ 1 nm were inserted to modify the exchange coupling between CoPt and FeMn, and their effects are shown as Fig. 1. Direct observation of magnetic domain configuration shown in Fig. 2 reveals the evolution of domain pattern and domain size with increasing thickness of spacer layer. For CoPt/Ta/FeMn, the average domain size and the contrast of upward domain show mono-trend descent with the thickness of Ta. While for CoPt/Pt/FeMn, the domain size and contrast show maxima at t_{Pt} =0.25 nm, which is in accordance with the magnetic properties measured by hysteresis loops. Therefore, different functions of spacer layer and interfacial spin configuration may be responsible for the dissimilar domain behaviors in these two hetero-structures. On the other hand, canting alignment of FeMn spins was verified and the effect of anisotropy induced by AFM layer to the FM domains can be manipulated by inserting spacer layer before and after field cooling. This study indicates inserting NM layer is an alternative to manipulate the coupling strength between FM and AFM layers and offers deeper understanding of EB systems.

[1] R Hara, K Hayakawa, K Ebata, etc., AIP Advances 6, 056117 (2016).
[2] T Gao, T Harumoto, S Zhang, etc., Physic Rev. B 95, 134406 (2017).

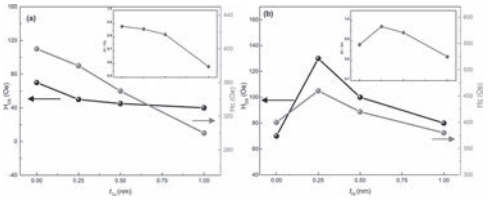


Fig. 1 Dependence of the exchange bias field, H_{EB} and the coercivity Hc on the (a) Ta spacer thickness and (b) Pt spacer thickness, inset is dependence of the romance ratio on spacer layer thickness, respectively.

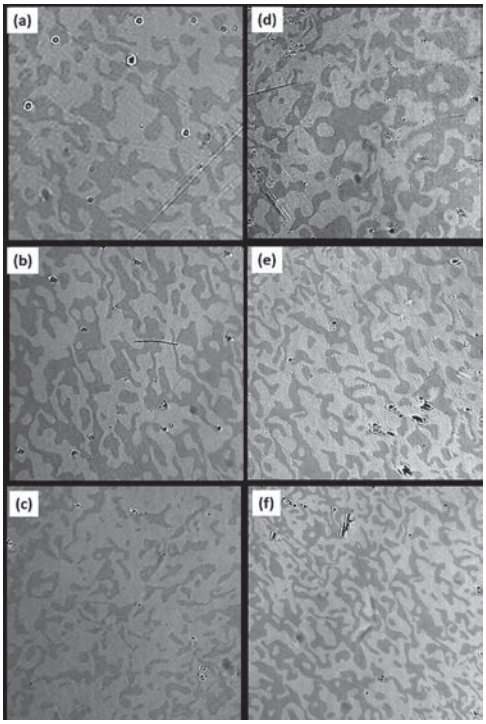


Fig. 2 Magnetic domain structure for samples of CoPt/Ta (*t* nm)/FeMn, (a-c) 0.25 nm, 0.5 nm and 1 nm respectively, CoPt/Pt(*t* nm)/FeMn, (d-f) are 0.25 nm, 0.5 nm and 1 nm respectively.

FT-06. XPS Analysis on $ZnFe_2O_4$ Thin Films Growth and its Influence in the Magnetic Behavior. *J. Gil Monsalve*[1], C. Ostos[1], J. Ramírez[2], E. Ramos[2], J. Uribe[1], J.A. Osorio[1] and O.L. Arnache[1] *1. Universidad de Antioquia, Medellín, Colombia; 2. Universidad de los Andes, Bogotá, Colombia*

Surface analysis of zinc ferrites and its correlation with magnetic measurement, can provide further information to understand effects like the spin Seebeck effect in magnetic insulators [1-2]. For this purpose, $ZnFe_2O_4$ (ZFO) thin films of approximately 90 nm thick were grown on Si (111) substrates by RF magnetron sputtering at 500 °C. Sputtering gas pressure was kept at 28 mTorr using a mixture Ar/O_2 at a ratio 2:1, 1:2 as well as pure Ar. The ZFO films were characterized by perfilometry, X-ray diffraction, X-ray photoelectron spectroscopy (XPS) and vibrating sample magnetometry (VSM). Comparing all the samples obtained at different atmospheres, the samples deposited under Ar/O_2 ratio of 1:2 exhibited a highly crystallographic orientation and the closest stoichiometric composition between Fe/Zn with a value of 1.97. XPS results showed that the Zn 2p spectra exhibits binding energies at 1021 eV and 1044 eV, which corresponds to Zn $2p_{3/2}$ and Zn $2p_{1/2}$ electrons in the Zn^{2+} oxidation state. Also, Zn $2p_{3/2}$ signal in all samples consisted of a single sharp peak corresponding to tetrahedrally coordinated zinc. Unlike the bulk sample where only Fe^{3+} ions in B sites were observed by Mössbauer spectra, for the thin films, XPS spectra indicated the presence of Fe^{2+} and Fe^{3+} species in the films; additionally, only for the films

deposited in pure Ar atmosphere, the appearance of a single low-intensity peak at the low binding energy side, indicates the formation of Fe ions (Fe^0) reduced by Ar ion sputtering. The O 1s spectrum presented oxygen ions different on the surface. It is known that the ZFO in bulk is governed by a weak superexchange interaction among Fe^{3+} ions (J_{BB}) with magnetization saturation (M_s) of about 1.2 emu/g [3-5]; however, with the enhancing of the M_s for the ZFO in our films, we hypothesize that Fe ions migrate to A sites and the interaction J_{AB} dominates the magnetic properties over the J_{BB} interaction. At room temperature, the number of μ_B per unit cell obtained was 8.03, whereas the ferromagnetic component is more notorious at 77 K with 14.27 μ_B/unit cell. Finally, we conclude that the best growth conditions were those obtained on samples prepared under 1:2 Ar/O_2 ratio.

[1] K. Uchida, J. Xiao and H. Adachi, Nature materials, Vol. 9, no 11, p. 894 (2010) [2] YoshiChika Otani, Masashi Shiraishi and Akira Oiwa, Nature Physics, Vol. 13, no 9, p. 829 (2017) [3] JD Arboleda, O Arnache and MH Aguirre, Solid State Communications, Vol. 270, p. 140-146 (2018) [4] C. E. Rodríguez Torres, G. A. Pasquevich and P. Mendoza Zélis, Physical Review B, Vol. 89, no 10, p. 104411 (2014) [5] JD Arboleda, O Arnache and MH Aguirre, Applied Physics Letters, Vol. 108, no 23, p. 232401 (2016)

FT-07. Effect of Co on the Magnetic Properties and Magnetic Domain Structure for FePt/ (Fe, FeCo) Nano-composites. *T. Sato*[1], K. Ohwada[1], F. Nakagawa[1], M. Doi[1] and T. Shima[1] *1. Graduate school of Engineering, Tohoku Gakuin University, Tagajo, Japan*

Rare earth permanent magnets have been widely used in various applications such as motors for hybrid vehicles and micro devices and hard disk drives. Especially, Nd-Fe-B sintered magnets exhibit high $(BH)_{max}$. However, these magnets contain environmental and geographical issues. Therefore, the development of high performance magnet is urgently required. Recently, nano-composite magnet has expected to increase hard magnetic properties through the exchange–coupling between the soft and the hard magnetic phases [1, 2]. However, there is no report that high-performance magnet has been obtained. In this study, an assembly of FePt/ (Fe, FeCo) nano-composites have been fabricated by electron beam lithography (EBL), and their magnetic properties and magnetic domain structure have been also investigated. FePt films were prepared using ultra-high vacuum magnetron sputtering system. On MgO (100) single crystal substrate, the Fe seed layer of 1 nm and Au buffer layer of 40 nm were first deposited at room temperature (RT). Then, it was annealed at T_a= 300 °C. After that FePt layer of 10 nm was deposited at 300 °C, and then it was annealed at 500 °C. $L1_0$ ordered FePt/ (Fe, FeCo) nano-composites were microfabricated the EBL. The outer diameter (D_{od}) of the FePt rings was fixed at 2.0 μm, while the inner diameter (D_{id}) was changed from 0.8 to 1.8 μm. The film structure was evaluted X-ray diffraction (XRD), the magnetic properties were measured by a superconducting quantum interference device (SQUID) magneto meter. Magnetic properties of microfabricated FePt/ (Fe, FeCo) nano-composites were measured by magneto-optical Kerr effect (MOKE), shapes and magnetic domain structure were observed by using atomic force microscope (AFM) and magnetic force microscopy (MFM). From XRD patterns, the FePt (002) fundamental peak, FePt (001) and (003) super lattice peaks were clearly observed. The coercivity of FePt/ Fe nano-composites was increased from 4.5 kOe for D_{id}= 1.8 to 6.0kOe for D_{id}= 0.8 μm. In addition, remarkable "Bull's eye contrast" in the magnetic domain patterns has been clearly observed for both D_{id}= 1.2 and 1.4 μm. Magnetic properties for FePt/ FeCo nano-composites with changing Co content will be discussed at the conference.

1. Skomski. R, Coey, J.M.D, Phys. Rev. B, vol. 48, pp. 15812-15816. (1993) 2. R. Kurosu, Aya Sugawara and T. Shima, IEEE Magn. Lett., vol. 8, No. 5502804. (2017)

FT-08. Toward fabrication of $L1_0$-FeCo thin films assisted by the nitrogen surfactant effect. *Y. Takahashi*[1,2], T. Miyamachi[2], T. Iimori[2], T. Hattori[2], T. Koitaya[3], K. Yamamoto[3], T. Yokoyama[3], F. Komori[2] and M. Kotsugi[1] *1. Tokyo University of science, Katsushika, Japan; 2. The Institute for Solid State Physics, The University of Tokyo, Kashiwa, Japan; 3. Institute for Molecular Science, Myodaiji, Japan*

An $L1_0$-type ordered FeCo alloy is theoretically predicted to have large perpendicular magnetic anisotropy among transition metal alloys [1], attracting great attention as a rare earth-free permanent magnet. The precisely controlled thin film growth of alternating Fe and Co layers using pulsed laser deposition have been used for the preparation of $L1_0$-FeCo thin films [2]. However, the degree of order of the $L1_0$ structure is considerably low due to atomic-scale structural and magnetic disorder at the Fe/Co interface and resultingly the perpendicular magnetization has not yet been achieved. Toward realizing high quality FeCo alloy thin films, we here focus on the fabrication method utilizing the nitrogen surfactant effect of a monatomic layer iron nitride (Fe_2N). High lateral lattice stability of Fe_2N[3], and surfactant nitrogen during the deposition of Fe and Co layers can effectively suppress the interdiffusion at the Fe/Co interface, leading to atomically flat and homogeneous surface and interface in FeCo alloy thin films. In this study, we investigated structural and magnetic properties of 1 monolayer (ML) Co on Fe_2N/Cu (001), the initial step for the fabrication of FeCo alloy thin films by means of the nitrogen surfactant effect, using scanning tunneling microscopy (STM) combined with x-ray magnetic circular dichroism (XMCD). We first confirmed from XMCD measurements the strong in-plane magnetic anisotropy of bare Fe_2N as previously reported [4]. STM measurements revealed that adding Co 1 ML on Fe_2N results in the formation of Co_2N/Fe/Cu (001) via nitrogen surfactant effect. Accordingly, relative increase in the out-of-plane magnetization of Fe to the in-plane magnetization was observed. We found that the out-of-plane magnetization of Fe was further increased by additional alternative deposition of Fe and Co (Co_2N/Fe/Co/Fe). The results indicate that the nitrogen surfactant effect is efficiently suppress the interdiffusion at the Fe/Co interface and keep atomically flat surface/interface in FeCo atomic layers, possibly reflecting the intrinsic out-of-plane magnetization of $L1_0$-FeCo.

[1] T. Burkert et. al., Phys. Rev. Lett. 93, 027203, (2004). [2] H. Ito et al., AIP Advances 9, 045307 (2019) [3] Y. Takahashi et al., Phys. Rev. Lett. 116, 056802 (2016). [4] Y. Takahashi et al., Phys. Rev. B 95, 224417(2017).

FT-09. Magnetic properties of CoPt/TiN films tuned by nitrogen. *H. An*[1], C. Pan[2] and J. Shi[3] *1. College of New Materials and New Energies, Shenzhen Technology University, Shenzhen, China; 2. School of Materials science and Engineering, Tsinghua University, Beijing, China; 3. School of Materials and Chemical Technology, Tokyo Institute of Technology, Tokyo, Japan*

Heat-assisted magnetic recording (HAMR) media, which can drastically increase the areal recording density, is expected to be the most promising recording media for the next generation of the high-density hard disk drives. As primary candidates for the HAMR materials, $L1_0$ FePt and CoPt structure have attracted researchers' interests due to their high magnetocrystalline anisotropy and large coercivity. Much effort has been devoted on enlarging the perpendicular coercivity, reducing the grain size, averaging the grain distribution, etc. To realize such objectives, (100) oriented MgO seed layer is widely used on amorphous substrates to promote the $L1_0$ ordering for FePt/ CoPt. However, the small surface energy of MgO (1.1 J/m^2) can result in a large contact angle between FePt/CoPt and MgO, which is not favorable for the epitaxial growth. Furthermore, it promotes the formation of in-plane variants and lead to a large in-plane coercivity. In this work, we use TiN instead of MgO on glass substrates as seed layer for the deposition of $L1_0$ CoPt. TiN has similar structure with MgO, but owns a larger surface energy (1.28 J/m^2), which is more suitable for the epitaxial growth of $L1_0$ CoPt. TiN was deposited from a Ti target by magnetron sputtering in a mixture of N_2 and Ar gases. By optimizing the flow rate ratio between N_2 and Ar, we successfully deposited highly (100) oriented TiN films on glass substrates. Then we deposited a 4 nm-thick CoPt layer on the TiN layer by varying the

thickness of TiN layer from 10 to 100 nm, respectively. Largest perpendicular magnetic anisotropy energy was obtained in the CoPt/TiN bilayer film with a 30 nm-thick TiN layer. Furthermore, we introduced N_2 into Ar atmosphere for the CoPt deposition to investigate the effect of N_2 incorporation on the magnetic properties of CoPt. As shown in Fig. 1, the magnetic properties of CoPt can be efficiently tuned by changing the N_2 flow rate ratio. Our work may provide a piece of information for other studies on the HAMR media.

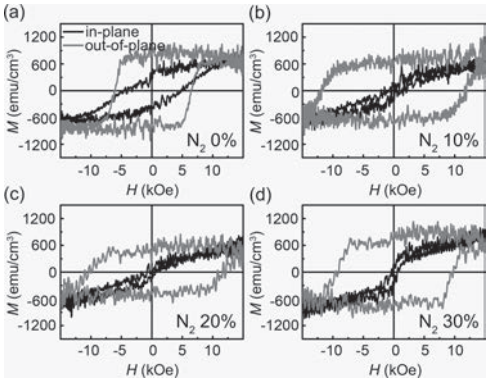


Fig. 1. *M-H* curves of the CoPt/TiN films by changing the flow rate ratio between N_2 and the mixture of N_2 and Ar for the CoPt deposition. (a) 0%, (b) 10%, (c) 20% and (d) 30%. All the films were annealed at 700 °C.

FT-10. Magnetic Anisotropy of CoV_2O_4 Thin Films Investigated through Torque Magnetometry. *C.J. Thompson*[1,2] and C. Beekman[1,3]
1. National High Magnetic Field Lab, Tallahassee, FL, United States; 2. Materials Science and Engineering, Florida State University, Tallahassee, FL, United States; 3. Physics, Florida State University, Tallahassee, FL, United States

We have grown thin films of the spinel vanadate CoV_2O_4 (CVO), a geometrically frustrated spin system, on $SrTiO_3$ substrates, resulting in an orthorhombic structure rather than the cubic structure of bulk [1]. The bulk structure has a collinear ferrimagnetic transition at T_N = 150 K, and a magnetic transition at T* = 90 K that has been suggested as a transition to a non-collinear state showing spin canting, accompanied by orbital ordering and a weak first order structural phase transition [2,3]; the orthorhombic thin film form strengthens the 90 K transition [1]. We have performed torque magnetometry measurements to investigate the magnetic structure and anisotropy of the system in two magnetic phases: below T*, and in the ferrimagnetic state. By investigating the torque response as we rotate films in various applied fields, we identify easy axes for each state, as well as find unusual hysteretic behavior in the low temperature regime (Fig. 1). Work at Florida State University is supported the National Research Foundation, under grant NSF DMR-1847887 Use of National High Magnetic Field Laboratory user facilities was supported by NSF Cooperative Agreement No. DMR-1157490 and DMR-1644779, and the state of Florida.

[1] C. J. Thompson, D. Reig-i- Plessis, L. Kish, A. A. Aczel, B. Zhang, E. Karapetrova, G. J. MacDougall, and C. Beekman, Phys. Rev. Mat. 2 104411 (2018) [2] R. Koborinai, S. E. Dissanayake, M. Reehuis, M. Matsuda, T. Kajita, H. Kuwahara, S.-H. Lee, and T. Katsufuji, Phys. Rev. Lett. 116 037201 (2016) [3] D. Reig-i-Plessis, D. Casavant, V. O. Garlea, A. A. Aczel, M. Feygenson, J. Neuefeind, H. D. Zhou, S. E. Nagler, and G. J. Macdougall, Phys. Rev. B 93 014437 (2016)

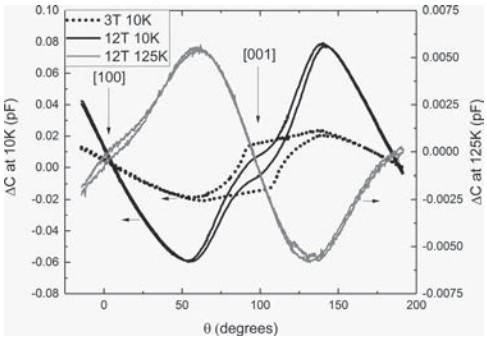


Fig. 1: Torque magnetometry measurement on a 280 nm thin film of CVO. Rotation is from the planar [100] axis at ~10° to the out of plane [001] direction at ~100°. A comparison of the ferrimagnetic regime measured at 12 T (grey, right axis) to the hysteretic behavior in the low temperature regime, at 3 T (dotted black, left axis) and 12 T (solid black, left axis).

FT-11. Controlling the angle between magnetic moments of adjacent magnetic layers. Z. Nunn[1] and *E. Girt*[1] *1. Physics, Simon Fraser University, Burnaby, BC, Canada*

The rapid increase in magnetic memory storage density and the design of new magnetic devices over the last three decades has been made possible by the discovery of interface-induced phenomena in ferromagnetic/non-magnetic multilayers. The interlayer exchange coupling is one of the interface effects, which plays a crucial role in many magnetic based applications. It has been intensively studied since its discovery, for over 30 years. However, this phenomenon has not been used to its full potential, since traditional non-magnetic coupling layers only allow for controlling collinear orientation (antiferromagnetic or ferromagnetic) of magnetic moments of the ferromagnetic layers. Recently, we discovered a new class of magnetic coupling layers [1], which can be inserted between two ferromagnetic layers to control the relative orientation of the magnetic moments of ferromagnetic layers from 180 to 0 degrees. Here we present a systematic study of non-collinear coupling of two Co layers separated by one of these discovered coupling layers, the magnetic RuFe (Fig.1). By varying the concentration of Fe in RuFe coupling layer, the angle between Co magnetic moments can be precisely controlled. Fig.2 shows how the coupling angle between Co magnetic moments, θ, varies as a function of Fe concentration in RuFe and RuFe thickness, *d*. Additionally, the biquadratic coupling strength in Co/RuFe/Co is isotropic and several times larger than ever observed, approaching 4 mJ/m^2. These unique properties allow for the study and fabrication of new magnetic structures that have potential for improving current state-of-the-art spintronic devices.

1) Nunn, Z. R., and Girt, E. Applications of non-collinearly coupled magnetic layers. U.S. 10,204,671, issued on Feb. 12, 2019.

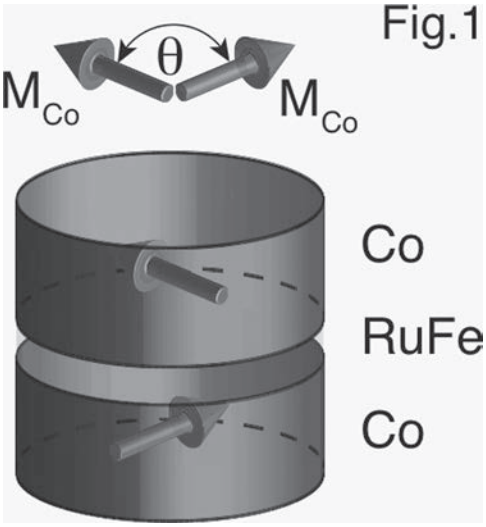


Figure 1

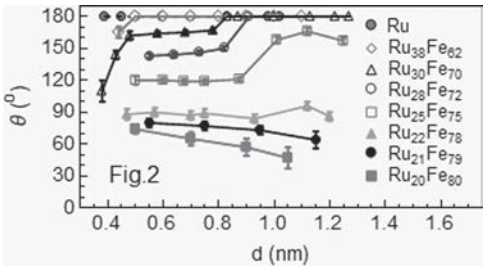


Figure 2

FT-12. Seed- and buffer layer control in the perpendicular magnetic anisotropy of sputter-deposited $L1_0$ FePd thin films. *X. Wang*[1,2], D. Zhang[1], J. Wang[1] and D.B. Gopman[2] *1. University of Minnesota, Twin Cities, MN, United States; 2. National Institute of Standards and Technology, Gaithersburg, MD, United States*

Thin ferromagnetic films with perpendicular magnetic anisotropy (PMA) show great potential for ultrahigh density spintronic devices due to their superior thermal stability and scalability. Materials possessing bulk PMA, such as manganese-based Heusler alloys and $L1_0$ Fe-based alloys, could deliver superior scaling compared to their interfacial anisotropy counterparts. $L1_0$ FePd in particular has been shown to have desirable properties, including large magnetic anisotropy energy ($K_u > 10^6$ J/m^3), low Gilbert damping ($\alpha<0.01$) and good annealing stability.[1] However, incorporating this material into a spintronic device remains challenging.[2] We grew a series of seed (SL) and buffer (BL) layers of the form SL(15 nm)/BL(4 nm) grown on a (001)-cut MgO substrate to explore possible alternatives for growing $L1_0$ FePd with the *c*-axis oriented perpendicular to the plane. Structures of Mo/(Pt, Ru, Ir)/FePd, Cr/(Pt, Ru, Ir)/FePd and Ir/FePd were deposited onto MgO (001) substrates at 350 °C with 2.0×10^{-9} Torr base pressure. X-ray diffractometry demonstrates that the Mo-buffered samples undergo a 45 degree rotation of the BL/FePd bilayer relative to the seed layer (e.g. Mo(100)||BL(110)||FePd(110)), which does not permit PMA. On the other hand, the Cr-seeded samples and the Ir-buffered sample with no seed layer all had the following relationship (MgO(100)||SL(100)||FePd(100)) and correspondingly showed PMA, with saturation magnetization M_s exceeding 1000 kA/m, $\mu_0 H_K^{eff}$ as high as 0.7 T and $\alpha < 0.01$. X-ray diffractometry and transmission electron microscopy will be presented in conjunction with results of ferromagnetic resonance spectroscopy (Fig. 2), Kerr magnetometry (Fig. 1(a)) and domain imaging (Fig. 1(b)), as well as vibrating sample magnetometry, to correlate the alternative microstructure introduced to the FePd layer by each seed/buffer combination.

1. S. Iihama, A. Sakuma, H. Naganuma, et al., Phys. Rev. B 94, 174425 (2016) 2. D.L. Zhang, K.B. Schliep, R. J. Wu, et al., Appl. Phys. Lett. 112, 152401 (2018)

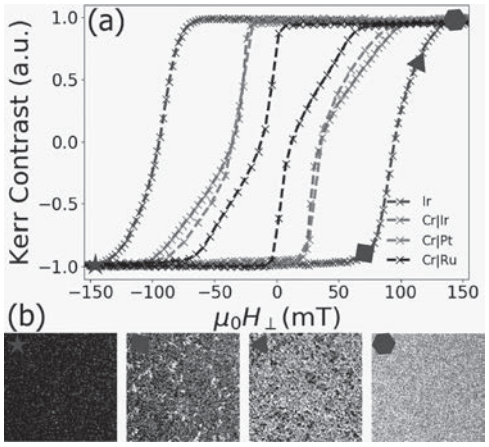


Fig.1 (a) Kerr hysteresis loops of structures Cr/(Pt, Ru, Ir)/FePd and Ir/FePd and (b) Magnetic domain images of Ir/FePd bilayer on MgO.

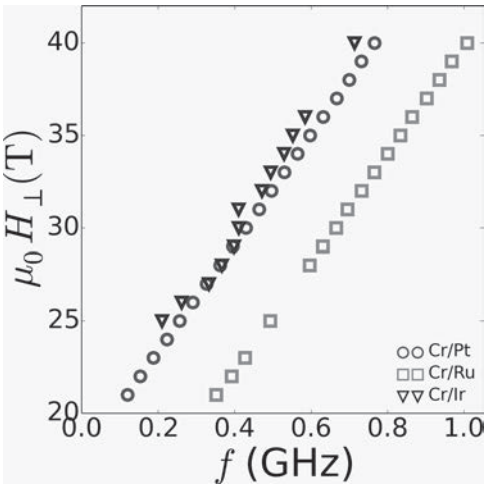
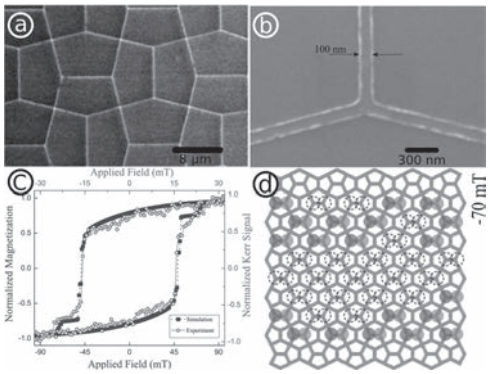


Fig.2 Out-of-plane ferromagnetic resonance field versus frequency for structures Cr/(Pt,Ru,Ir)/FePd.

FT-13. Pinning of Ferromagnetic Domains in Interconnected Pentagonal Spin Ice Lattices. E. Saavedra[1], J. Escrig[1,2] and *J.L. Palma*[3,2] *1. Fisica, Universidad de Santiago, Santiago, Chile; 2. Center for the Development of Nanoscience and Nanotechnology CEDENNA, Santiago, Chile; 3. Basic Science - Eng. School, Universidad Central de Chile, Santiago, Chile*

The magnetization reversal process of interconnected pentagonal spin ice systems was investigated using micromagnetic simulations and experimental measurements. Five different systems were investigated, beginning with the interconnected Shakti lattice [1] and introducing deformations with the idea of obtaining pentagonal tiling [2] (belonging to the P4 group) until reaching an interconnected square lattice. In all pentagonal lattices, ferromagnetic domains are pinned, acting as isolated domains in an antiferromagnetic lattice, with Cairo tiling being the lattice that allows pinning more domains. Experimental measurements on a Cairo lattice of larger dimensions show that the shape of the hysteresis curve is invariant to the size of the bars that make up the interconnected pentagonal spin ice systems.

1. I. Gilbert1, G-W. Chern, S. Zhang, Nature Physics, Vol. 10, p. 670 (2014) 2. V. Urumov, J. Phys. A: Math. Gen., Vol. 35, p. 7317 (2002)



(a) SEM image of pentagonal tiling, (b) with a line width of 100 nm and 10 nm Py thickness. Figure (c) shows the comparison between MOKE measurements (red dots) and micromagnetic simulations (blue squares) please note different scales in the applied field for the two loops, but the same shape of the hysteresis loop. Figure (d) shows the pinned domains for the plateau at -70 mT showed in (c) for the micromagnetic simulation hysteresis loop (blue squares).

FT-14. Control of an Asymmetric Bloch Wall in a Ferromagnetic Rectangular Disk. *S. Lee*[1], H. Han[1], M. Kang[1], H. Ok[1], M. Im[2] and K. Lee[1] *1. School of Materials Science and Engineering, Ulsan National Institute of Science and Technology (UNIST), Ulsan, The Republic of Korea; 2. Center for X-ray Optics, Lawrence Berkeley National Laboratory, Berkeley, CA, United States*

In a patterned ferromagnetic nanodisk, a flux-closure domain structure such as a Landau pattern is formed to reduce a magnetostatic energy [1]. For a relatively thicker patterned film with a few tens of nm, a flux-closure domain structure accompanying with in-plane Landau pattern should be formed along the thickness direction, resulting in a three-dimensional (3D) flux-closure domain structure [2-3]. In a rectangular shaped ferromagnetic disk, the 3D flux-closure structure, the asymmetric Bloch wall (ABW) is formed [4]. The ABW structure can be classified into two types of rotation sense (i.e. clockwise (CW) or counter-clockwise (CCW)) (shown in Fig.1.). Since those states have exactly the same energy, they are degenerate states and they appear at the same probability. To control those states, it is required to break the symmetry of two states. For example, asymmetric geometry was utilized for control the ABW states [5]. In this presentation, we propose an efficient way to control the rotating sense of ABW through the external magnetic field based on micromagnetic simulation. From magnetic transmission soft x-ray microscopy (MTXM) at the Advanced Light Source [6], this method were verified experimentally.

[1] A. Hubert and R, Schäfer. Magnetic Domains. (Springer, Berlin, 1999) [2] F. Cheynis et al., Phys. Rev. Lett. 102, 107201 (2009) [3] A. Masseboeuf et al., Phys. Rev. Lett. 104, 127204 (2010) [4] Hertel, R & Kronmüller, H, Phys. Rev. B. 60, 7366-7378 (1999) [5] Cheynis, F. et al. Phys. Rev. Lett. 102, 107201 (2009). [6] Fischer, P. et al. Mater. Today 9, 26–33 (2006).

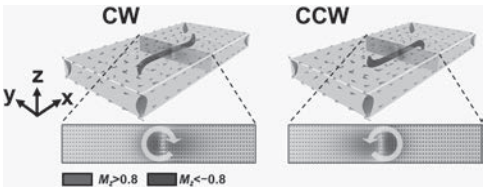


Fig.1 The simulated images for two degenerate states of the asymmetry Bloch wall (ABW) (top) and their magnetization configuration on the cross section area of the center region (bottom). The red and blue surface indicates the volume where Mz/Ms > 0.8 and Mz/Ms > –0.8 respectively.

FT-15. Gettering templates for nanoscale patterning of magnetic materials. W. Qiu[1], L.V. Chang[1] and *D. Litvinov*[1] *1. University of Houston, Houston, TX, United States*

We have explored low-temperature local reduction of non-magnetic CoO and $[CoO/Pd]_N$ multilayers using Ta and Ti gettering layers, effectively achieving patterning of magnetic nanostructures without the physical removal of magnetic materials. Local conversion of magnetic oxides is based on reduction of thin film magnetic oxides, e.g. CoO or $[CoO/Pd]_N$, sandwiched between gettering layers (Ta or Ti). The exothermic reduction/oxidation reaction (e.g. 5CoO + 2Ta = 5Co + Ta2O5 - 1.15 kJ/g) is promoted by annealing at 200-300 °C. The effect is similar to the ones exhibited by thermite nanocomposites. CoO thin films and $[CoO/Pd]_N$ multilayers were deposited using UHV DC magnetron sputtering with a base pressure of 5×10^{-8} Torr. The process pressure for all films is 5m Torr. CoO films are deposited by reactive magnetron sputtering in argon and oxygen; all other materials (Co, Pd, Ta, Ti) are deposited by magnetron sputtering in argon. The results of 5-minute annealing of a CoO thin films sandwiched between Ti seed (15 nm) and capping (30 nm) layers are illustrated in Figures 1 and 2. Initial saturation magnetization, M_S, of CoO is negligible and increases to approximately 1300 emu/cc as the temperature reaches 200-300 °C. The highest M_S of annealed CoO approaches the M_S of pure Co thin film. This presentation will detail the results of our study of applying Ti and Ta gettering layers for the conversion of magnetic oxide and magnetic oxide multilayers into magnetic thin films. The application of the technology for magnetic film patterning using structured gettering templates will also be presented.

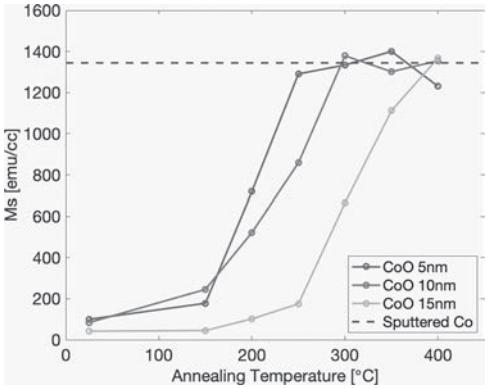


Figure 1. The saturation magnetization of annealed CoO thin film sandwiched between Ti seed and capping layers as a function of annealing temperature. An emergence of magnetization is observed for annealing at 150 °C and a full conversion is achieved for temperatures above 200 °C. The saturation magnetization of the annealed CoO is comparable to the saturation magnetization of sputtered Co.

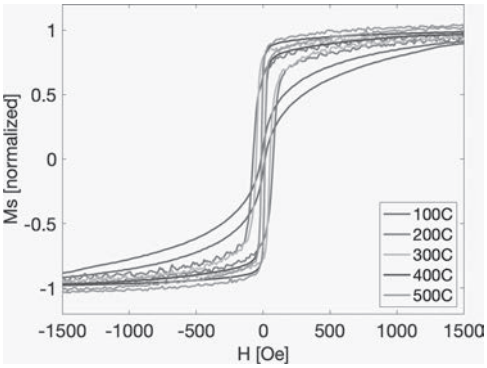


Figure 2. M-H loops of Ti (15 nm) / CoO (5 nm) / Ti (30 nm) films annealed at different temperatures.

FT-16. Sputtered high perpendicular magnetic anisotropy CoPt thin film on flexible substrate at low temperature. *A. Sun*[1] and G.C. Hermosa[1]
1. Department of Chemical Engineering and Materials Science, Yuan Ze University, Taoyuan, Taiwan

In order to prepare magnetic biosensor on flexible substrate, high magnetocrystalline anisotropy constant (K_u) material with high perpendicular magnetic anisotropy (PMA) and good chemical corrosion resistance must be deposited at lower temperature. A CoPt film with a rhombohedral $L1_1$ structure has similar magnetic properties to $L1_0$ FePt film and could be prepared at 300°C, which is regarded as a potential candidate for biosensor. According to the $L1_1$-CoPt unit cell, Co and Pt atoms stack layer-by-layer along the easy axis [111] direction. Hence, alternative sputtering Co and Pt layer-by-layer structure might be easily obtained $L1_1$-CoPt(111) during the annealing process, due to the relatively shorter diffusion length. Furthermore, the film would present high PMA because the easy axis is vertical to the substrate plane. Therefore, CoPt films were prepared by alternative sputtering of Co and Pt layers on glass and flexible PI substrates at low temperature in this study. The effects of different repetitions (n) as well as annealing temperatures of the magnetic layer and underlayer on magnetic properties of $[Co/Pt]_n$ films are compared. Results showed that $[Co/Pt]_n$ films annealed at 100°C had a high PMA ($S_\perp$>0.98) and a high K_u (~1.12×10^7 erg/cm^3), which were close to the properties of $L1_1$-CoPt film prepared at higher temperatures (~300°C) as seen in previous works. In addition, the maximum PMA and K_u were obtained at n = 4. Increasing repetition also increased residual stress and further reduced perpendicular magnetic properties. Thus, better magnetic properties would be obtained in the thinner case. Furthermore, it was proven that coercivity (H_c) was strongly affected by the grain size of the magnetic layer, which was strongly related to the grain size in the Pt underlayer. Thus, H_c became tunable by controlling the grain size of the Pt underlayer due to the epitaxial growth at the CoPt/Pt interface. In this work, $L1_1$-CoPt, with outstanding magnetic properties, could be prepared at lower temperatures (~100°C). It strongly enhanced low temperature applications of hard magnetic alloy thin films, such as magnetic electronic components with high K_u and PMA on flexible substrate.

T. Shima, K. Takanashi, Y.K. Takahashi, K. Hono, Preparation and magnetic properties of highly coercive FePt films, Appl. Phys. Lett. 81 (2002) 1050-1052. L.W. Wang, W.C. Shih, Y.C. Wu, C.H. Lai, Promotion of [001]-oriented $L1_0$-FePt by rapid thermal annealing with light absorption layer, Appl. Phys. Lett. 101 (2012) 252403. S. Iwata, S. Yamashita, S. Tsunashima, Perpendicular Magnetic Anisotropy and Magneto-Optical Kerr Spectra of MBE-Grown PtCo Alloy Films, IEEE Trans. Magn. 33 (1997) 3670-3672. A.C. Sun, F.T. Yuan, J.H. Hsu, H.Y. Lee, Evolution of structure and magnetic properties of sputter-deposited CoPt thin films on MgO(111) substrates: Formation of the $L1_1$ phase, Scri. Mater. 61 (2009) 713-716. F.T. Yuan, A.C. Sun, J.H. Hsu, Effect of underlayer (Pt, Ru, Au, Ag) on $L1_1$ ordering in sputtered CoPt thin films, Scri. Mater. 62 (2010) 762-765.

Session FU
MULTIFERROIC MATERIALS AND PHENOMENA
(Poster Session)

Dirk Fuchs, Chair
Karlsruhe Institute of Technology, Eggenstein-Leopoldshafen, Germany

FU-01. First-principles Prediction of Switchable Metallic Ferroelectricity in Multiferroic Tunnel Junctions. L. Jiang[1], W. Chen[1], B. Yang[1], X. Zhang[2], Y. Wang[3] and *X. Han*[1] *1. Institute of Physics, Chinese Academy of Sciences, Beijing, China; 2. Department of Physics and the Quantum Theory Project, University of Florida, Gainesville, FL, United States; 3. Department of Physics and Astronomy, Vanderbilt University, Nashville, TN, United States*

Coexistence of metallicity and ferroelectricity has been a curiosity without a practical application, both because free-electron screening due to metallicity prevents the polarization from being switched by an electric field, diminishing the value of ferroelectricity, and because metallicity is usually achieved by doping, which leads to disorder and is often detrimental to other electronic properties. Here, we predict via first-principles calculation a switchable metallic ferroelectric barrier in $(Co_2)_9$-TiO_2-$(BaO\text{-}TiO_2)_m$-CoO-Co (m = 4, 5, 6, 7, 8, 9) multiferroic tunnel junction without doping. Due to the uncompensated charge layer at the $BaTiO_3$ (BTO) interface in this system, the BTO barrier has a tendency to acquire electrons. When two metal electrodes are very close to BTO but not bonded with BTO, charge transfer still occurs from the electrodes to the barrier through tunneling. Such an electrode proximity effect moves the Fermi energy close to the barrier conduction band. When the polarization orientation points from the electrode with a CoO layer to the other electrode (upward polarization), this effect is accentuated by the large polarization of the CoO layer relatively to that of BTO, leading to a larger electrostatic potential drop on the interface containing CoO, thus further causing the entire BTO barrier region to become metallic. Increasing the polarization of BTO by applying strain turns off the metallic ferroelectric, so that the polarization can be reversed by an electric field. When the polarization is reversed (downward polarization), the Fermi level remains in the band gap almost everywhere in the BTO barrier, maintaining an insulating state. This metallic-insulating BTO difference between two polarization configurations leads to a large tunneling electroresistance.

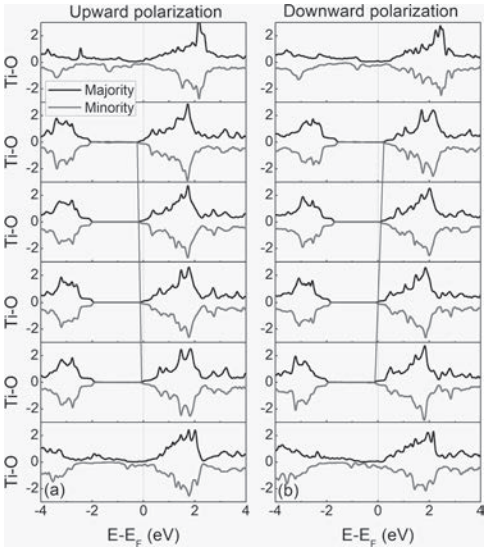


Fig. 1. Layer-resolved DOS of TiO_2 layers in the $(Co_2)_9$-TiO_2-$(BaO\text{-}TiO_2)_5$-CoO structure as a function of energy. From top to bottom, the DOS figures correspond to the TiO_2 layer in the Co_2-TiO_2 interface to the TiO_2 layer in the TiO_2-CoO interface. (a) and (b) are the DOS for polarization pointing up and down, respectively. The blue solid line connects the CBM of each TiO_2 layer. The black (red) line is the DOS of majority (minority).

FU-02. The Magnetic Properties of Multiferroic $Sr_3Fe_2F_{12}$. *Y. Yu*[1], W. Mi[1], L. Sun[2], S. Zhou[3], Q. Li[1], J. Du[2] and Q. Xu[1] *1. School of Physics, Southeast University, Nanjing, China; 2. School of Physics, Nanjing University, Nanjing, China; 3. Institute of Ion Beam Physics and Materials Research, Helmholtz-Zentrum Dresden-Rossendorf, Dresden, Germany*

The strong ionic bonding between the 3d transition metal (TM) ions and F^- ions in fluorides may break the contradicting requirement of the out shell electronic filling of 3d TM ions due to the covalent bonding with O^{2-} ions in oxide perovskites [1]. It has been reported that $Sr_3Fe_2F_{12}$ is ferroelectric with high Curie temperature of 922 K [2]. The partial contribution of the displacement of Fe^{3+} ions for the ferroelectric reversal indicates the possible multiferroicity and magnetoelectric coupling in $Sr_3Fe_2F_{12}$ [2]. However, till now, the reports on magnetic properties of $Sr_3Fe_2F_{12}$ are still lacking [3]. In this work, pure phase $Sr_3Fe_2F_{12}$ powders were prepared by solid state reaction using SrF_2 and FeF_3 powders as raw materials with molar ratio of 3.4:3, which has been confirmed by X-ray diffraction patterns. The morphology was studied by scanning electron microscope which shows the layered growth, and the Fe ions are in +3 valence state from X-ray photoelectron spectroscopy. The zero field cooled (ZFC) and field cooled (FC) temperature dependent magnetization (M-T) curves are shown in Fig. 1(a). Two kinks can be observed at 47 K an 29 K, respectively, suggesting two antiferromagnetic transitions [4]. A bifurcation between FC and ZFC M-T curves happens at T_{N1} of 47 K, suggesting a magnetic relax system. The field dependent magnetization (M-H) curves show that clear hysteresis can be observed below T_{N1}, indicating the occurrence of weak ferromagnetism. Similar

phenomena have been observed in $K_{0.6}FeF_3$ [4]. This might be related to the spin canting due to the Dzyaloshinskii-Moriya (DM) interaction. The two antiferromagnetic transitions with magnetic relaxation below T_{N1} might be related to the complicated arrangements of FeF_6 octahedra, leading to the complicated exchange interaction between Fe^{+3} ions [2].

[1] C. Drathen, T. Nakagawa, W. A. Crichton, et al., J. Mater. Chem. C 3, 4321 (2015) [2] S. C. Abrahams, J. Ravez, S. Canouet, et al., J. Appl. Phys. 55, 3056 (1984). [3] J. F. Scott and R. Blinc, J. Phys.: Condens. Matter 23, 113202 (2011). [4] A. Potočnik, A. Zorko, D. Arčon, er al., Phys. Rev. B 81, 214420 (2010).

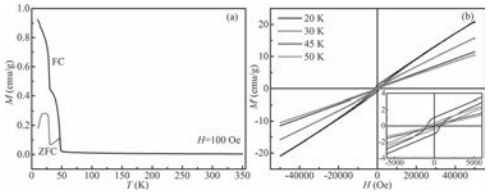


Fig. 1 (a) FC and ZFC *M-T* curves of $Sr_3Fe_2F_{12}$ measured under field of 100 Oe. The cooling field for FC process is 100 Oe. (b) *M-H* loops of $Sr_3Fe_2F_{12}$ measured at 20 K, 30 K, 45 K, and 50 K after cooling with a field of 1 T with the enlarged view in right bottom inset.

FU-03. Structural and Multiferroic Properties of Fe/Ni Co-doped $Bi_{3.15}Nd_{0.85}Ti_3O_{12}$ Ceramics. *S. Bhardwaj*[1], R.K. Mahajan[1] and S. Kumar[2] *1. Department of Materials and Metallurgical Engineering, Punjab Engineering College (Deemed to be University), Chandigarh, Chandigarh, India; 2. Department of Applied Sciences, Punjab Engineering College (Deemed to be University), Chandigarh, Chandigarh, India*

Polycrystalline Lead free samples of $Bi_{3.15}Nd_{0.85}(Ti_{3-x}Fe_{x/2}Ni_{x/2})O_{12}$ ($0.0 \le x \le 0.5$) were synthesized by conventional solid state reaction method. X-ray diffraction analysis confirms the formation of single phase with orthorhombic unit cell upto x=0.3 content matched with JCPDS No. 89-7500 shown in Figure 1. For x > 0.3, weak impurity peak encircle in figure 1 belong to bismuth iron oxide ($Bi_2Fe_4O_9$), which is attributed to non-stoichiometry induced by higher substitution. Raman spectroscopy was carried out to further investigate the effect of substitution on lattice structure. The broadening and reduction in the intensity with substitution in Raman modes confirms the local distortions in the lattice [1]. The ceramic with x=0.3 holds the best properties including pure phase, large remanant polarization and magnetic properties among all the synthesized compositions. The ME coupling coefficient (α) is calculated to observe the extent of coupling between the two ferroic orders [2]. The values of α has shown a linear behaviour with the applied magnetic field for all the synthesized samples as shown in Figure 2. The maximum value of α was observed for x=0.3 composition which is 0.67 mV $cm^{-1}Oe^{-1}$ The possible mechanism for M.E. coupling is considered to be interaction between electric and magnetic sub-lattices through the stress or strain transmitting from one sub-lattice to another [3]. The present work gives the existence of Fe/Ni co-doped $Bi_{3.15}Nd_{0.85}Ti_3O_{12}$ ceramic as room temperature multiferroic material.

[1] Ruixia Ti, Xiaomei Lu, Ju He, J. Mater. Chem. C, Vol. 3, p. 11868 (2015). [2] A Singh, A Gupta, R Chatterjee, Appl Phys Lett., Vol. 93, p. 022902 (2008). [3] A Srinivas, DW Kim, KS Hong, Appl Phys Lett., Vol. 83, p. 2217 (2003).

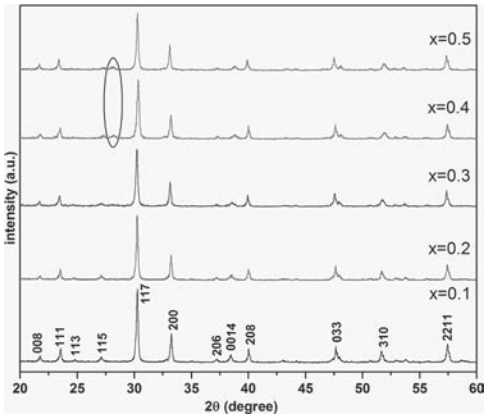


Fig.1 X-ray diffraction patterns of sintered $Bi_{3.15}Nd_{0.85}(Ti_{3-x}Fe_{x/2}Ni_{x/2})O_{12}$ samples with x = 0.1, 0.2, 0.3, 0.4 and 0.5.

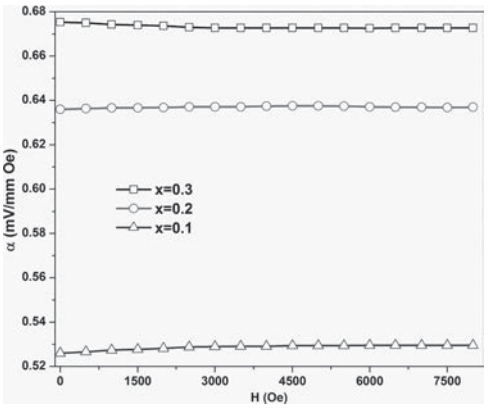


Fig.2 Magneto-electric coupling coefficient (α) for x=0.1, 0.2, 0.3.

FU-04. Analysis of Phase Segregation Using Rietveld Refinementand and Magnetic Properties of Mn Doped BCT Solid Solutions. *A. Chawla*[1], M. Singh[1] and A. Singh[1] *1. Physics, Guru Nanak Dev University, Amritsar, India*

Multiferroics are the materials which exhibit more than one ferroic properties like ferroelectricity and ferromagnetism simultaneously. This simultaneous presence of magnetic and electric ordering in materials is useful for many applications such as multistate memory devices, transducers, sensors, and microwave phase shifters etc. Transition metal ions (like Fe^{3+}, Mn^{3+}, Co^{2+} etc.) can be used for inducing magnetic character in otherwise strong ferroelectric materials [1–2]. In present work, Mn ions were incorporated in to lead free ferroelectric barium calcium titante (BCT). The polycrystalline samples of $Ba_{0.96}Ca_{0.04}Ti_{(1-x)}Mn_xO_3$ for $0.01 \le x \le 0.15$ were synthesized using conventional solid state reaction route. The XRD analysis shows that the samples crystallize in pure tetragonal structure (space group – P4mm) for $x \le 0.02$ while an additional phase (hexagonal, space group – P63/mmc) was detected in all other samples. The percentage of segregated phase was calculated using Rietveld refinement and was found to increase with increasing x. The P-E measurements revealed that all the samples exhibit ferroelectric behaviour. However, the remnant polarisation was found to decrease with increasing concentration of Mn ions. The samples started to exhibit magnetic character with Mn concentration as low as 3 mol %. However, the magnetic behaviour remains paramagnetic even with Mn concentration as high as 15 mol %. The oxidation state of the Mn ions in the samples was determined via fitting of virgin magnetic hysteresis curves using Brillouin function.

[1] C. Ederer, N.A. Spaldin, Phys. Rev. B - Condens. Matter Mater. Phys. 71 (2005) 1–4. [2] W.-M. Zhu, H.-Y. Guo, Z.-G. Ye, Phys. Rev. B. 78 (2008) 014401.

FU-05. Enhancement of multiferroic properties in (1-x)$GaFeO_3$-(x) $CoFe_2O_4$ nanocomposites. *T. Han*[1], Y. Wang[1] and B. Chen[1] *1. Department of Applied Physics, National University of Kaohsiung, Kaohsiung, Taiwan*

Multiferroic materials have rendered a revival of intensive research due to their application potential as next generation devices. However, there remains considerable scope for improvement of multiferroic behavior at room-temperature (RT). During the past several years, some elegant strategies such as particle size reduction, doping and ferroelectric-magnetic composite architecture have been employed to develop the RT multiferroic materials. Among various multiferroic materials, gallium ferrite, $GaFeO_3$ (GFO), is the most promising candidate which exhibits ferrimagnetism, piezoelectricity and magnetoelectric effects [1, 2]. Although the magnetization has been enhanced by substitution of various divalent or trivalent ion-doped GFO [3,4], but few attempt has been made to enhance the magnetization of the multiferroic system like GFO by using some other strong magnetic host of ferrite family in the nanocomposite state. In this work, therefore, we report on the characterization of (1-x)$GaFeO_3$-(x)$CoFe_2O_4$ (denoted as GFO-CFO) nanocomposites with x = 0, 0.17, 0.375, 0.5 and 1. The main objective of this work is to enhance the multiferroic properties of GFO in GFO-CFO nanocomposite at RT. The X-ray diffraction patterns confirmed that the nanocomposites consisted of orthorhombic GFO and cubic spinel CFO phases. It is also confirmed that there is no inter-diffusion between both phases. In addition, the magnetic characterization indicates that the magnetization of GFO-CFO nanocomposite was drastically enhanced compared to that of the pristine GFO. The value of RT saturation magnetization and coercive field increased to 53.8 emu/g and 1262.8 Oe, respectively. Furthermore, the inclusion of CFO enhanced magnetization and dielectric constant, as well as improved the ferroelectric properties of GFO. We conclude that magnetization, permittivity, and ferroelectricity of GFO have been significantly modulated by a spinel magnetic host of CFO probably due to the interfacial strain effect on GFO. The results will be also interesting for applications of the multiferroic nanocomposite in magnetoelectric devices.

[1] M. B. Mohamed, A. Senyshyn, H. Ehrenberg, and H. Fuess, J. Alloys Compd. 492 (2010) L20. [2] S. Mukherjee, V. Ranjan, R. Gupta, and A. Garg, Solid State Commum. 152 (2012) 1181. [3] A. Thomasson, S. Cherifi, C. Lefevre, F. Roulland, B. Gautier, D. Albertini, C. Many, and N. Viart, J. Appl. Phys. 113 (2013) 214101. [4] T. C. Han, Y. C. Lee, and Y. T. Chu, Appl. Phys. Lett. 105 (2014) 212407.

FU-06. Multiferroic properties of $Bi_{1-x}R_xFeO_3$ polycrystalline films on the glass substrates (R = La, Pr, Nd, Sm and Ho; x = 0.05-0.15). T. Lin[1], *H.W. Chang*[2], C.R. Wang[3], D. Wei[1] and C. Tu[4] *1. Institute of Manufacturing Technology and Department of Mechanical Engineering, National Taipei University of Technology, Taipei, Taiwan; 2. Department of Physics, National Chung Cheng University, ChiaYi, Taiwan; 3. Department of Applied Physics, Tunghai University, Taichung, Taiwan; 4. Department of Physics, Fu Jen Catholic University, Taipei, Taiwan*

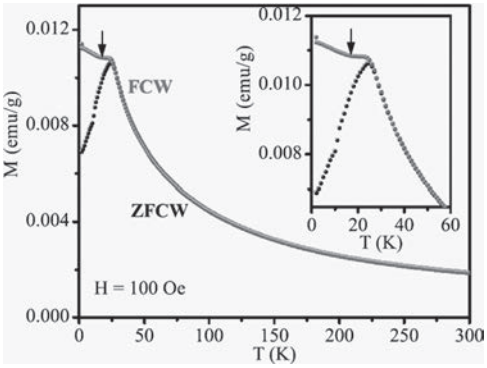
Perovskite $BiFeO_3$ (BFO) with ferroelectric and magnetic orderings at room temperature (RT) has attracted much attention for potential applications in advanced spintronic and memory devices based on the electric-magnetic couplings. However, the major problem in BFO is a large leakage current and needs to be overcome. The ion modification using rare-earth (R) cations was reported as an effective method to reduce leakage and thus enhance ferroelectric properties [1-2], but the effect of doping R element on magnetism properties is still unclear. In this study, $Bi_{1-x}R_xFeO_3$ (BRFO) (R = La, Pr, Nd, Sm and Ho; x = 0.05-0.15) polycrystalline films (x = 0.05-0.15) were deposited on optimized 20-nm-thick Pt bottom electrode on glass substrates at 450°C via pulsed laser deposition (PLD). XRD result shows that perovskite single phase is confirmed in all studied BRFO films. With increasing x, the microstructure refinement and the flattened surface are observed. The studied BAFO polycrystalline films exhibit coexistence of good ferroelectric and ferromagnetic properties. Remanent polarization ($2P_r$) of 60-120 μC/cm^2 and electrical coercive field of 180-300 kV/cm are obtained, while the saturation magnetization of 4.91-17.8 emu/cm^3 and coercivity of 400-600 Oe are attained for the substitution of La, Pr, Nd, Sm and Ho. BHFO exhibit the highest saturation magnetization (M) of 17.8 emu/cm^3 related to the highest magnetic moment of 10.6 μ_B of Ho among R. Besides, M is also affected by the result of suppressed spiral spin configuration from the distortion degree of the structure with different ionic radius of R. As the result, the magnetic properties are mainly dominated by the radius and the magnetic moment of R ion. The multiferroic properties with R substitution and as a function of its content x are also discussed in this presentation.

[1] A. R. Makhdoom et al., AIP Adv. 4 (2014) 037113 [2] Wenyu Xing et al., Smart Mater. Struct. 23 (2014) 085030

FU-07. A comparative study of spin-glass transition in $Ca(Fe_{1/2}Nb_{1/2})O_3$ and $Ba(Fe_{1/2}Nb_{1/2})O_3$. *A. Kumar*[1], A. Chaudhary[1] and D. Pandey[1] *1. School of Materials Science and Technology, Indian Institute of Technology (Banaras Hindu University), Varanasi, India*

The origin of the spin-glass (SG) phase in the well-known multiferroic $Pb(Fe_{1/2}Nb_{1/2})O_3$ compound remains controversial due to the complications introduced by the coexistence of SG and long-range ordered (LRO) antiferromagnetic (AFM) phases [1-2]. We have addressed this controversy through a comprehensive study on a Pb-free systems like $Ba(Fe_{1/2}Nb_{1/2})O_3$ (BFN), $Sr(Fe_{1/2}Nb_{1/2})O_3$ (SFN), and $Ca(Fe_{1/2}Nb_{1/2})O_3$ (CFN), which does not exhibit LRO AFM transition [3-5]. The SG transition is confirmed by the appearance of a cusp in the temperature dependence of dc magnetization M(T) with a SG freezing temperature T_f ~25K, and bifurcation of the zero-field cooled and field-cooled magnetization M(T) below the irreversibility temperature (T_{irr}). Using ac susceptibility measurements, we show that the spin dynamics follows power law / Vogel-Fulcher law type critical dynamics which diverges at T_{SG}~ 24K with an attempt time τ_o ~10^{-6}s suggesting cluster spin-glass (CSG) behaviour. The field dependence of T_f(H) and T_{irr}(H) is shown to follow de Almeida-Thouless (A-T) line which separates the ergodic and non-ergodic phases in the H-T plane. The existence of the glassy phase below T_{SG} is further confirmed by the observation of slow non-exponential decay of thermoremanent magnetization (TRM) with time, memory and rejuvenation effects and unidirectional exchange bias effect in the M-H hysteresis loop of field-cooled samples. The neutron powder diffraction patterns reveal the absence of any magnetic peak due to LRO AFM phase but show a broad diffuse peak due to the presence of ~2nm size AFM spin-clusters which are responsible for the CSG freezing in Pb-free systems.

1. W. Kleemann, V. V. Shvartsman, and A. Kania, Phys. Rev. Lett 105, 257202 (2010). 2. S. Chillal, M. Thede, and A. Zheludev, Phys. Rev. B 87, 220403 (R) (2013). 3. M. Maryško, V. V. Laguta, and S. P. Kubrin, AIP ADVANCES 7, 056409 (2017). 4. P. D. Battle, T. C. Gibb, and P. H. Munns, J. Mater. Chem. 5, 865 (1995). 5. A. Kumar, A. Senyshyn and D. Pandey, Phys. Rev. B 99, 214425 (2019).



Temperature dependence of dc magnetization of $Ca(Fe_{1/2}Nb_{1/2})O_3$ measured at 100 Oe field in warming cycle for both zero-field cooled (ZFC) and field cooled (FC) conditions.

FU-08. Strain modulated structure distortion and magnetic properties of orthorhombic $LuMnO_3$ thin films. H. Cao[1], *A. Zhang*[1], Y. Tang[1], J. Cui[1], L. Yang[2] and X. Wu[2] *1. Hohai University, Nanjing, China; 2. Nanjing University, Nanjing, China*

Epitaxial orthorhombic $LuMnO_3$ films were prepared on (001)-$LaAlO_3$ substrates by pulsed laser deposition (PLD). The results of structural investigation reveal that the out-of-plane parameter c slowly increases with decreasing thickness of films because of the tensile strain in the films. The lengths of in-plane Mn-O bonds expand with the enhancement of strain, which is proved by Raman scatting. The temperature dependence on magnetization M(T) curves proves that the magnetic transition temperatures T_N obviously increases with decreasing thickness of the films. The variation of in-plane Mn-O bonds under strain is discussed. The increasing of magnetic transition temperatures T_N is ascribed to evolution of the magnetic structure by strain. These results show that the magnetic transition temperature of LuMnO3 films can be sensitively manipulated by the strain of the films.

FU-09. Electric field induced magnetic anisotropy in [Co/Ni]/PMN-PT multiferroic heterostructures. *S. Ishikawa*[1] and T. Taniyama[1] *1. Department of Physics, Nagoya University, Nagoya, Japan*

Electric field control of magnetic anisotropy is currently being investigated extensively due to their potential for use in low energy dissipative spintronic devices. In particular, interfacial multiferroics composed of a ferromagnetic layer and a ferroelectric layer have attracted tremendous interest, since strong magnetoelectric coupling at the interface provides electric field controllability of magnetism [1][2]. In this study, we demonstrate electric field induced perpendicular magnetic anisotropy (PMA) in [Co/Ni] multilayer/PMN-PT interfacial multiferroic heterostructures. Au(2)/Pt(3)/[Co(t)/Ni(0.5)]$_8$/Pt(5)PMN-PT(111) heterostructures (thickness in nm) were fabricated by using molecular beam epitaxy in ultrahigh vacuum under a base pressure of ~10^{-10} Torr. X-ray diffraction measurement ensures the epitaxial growth of the multilayers. Magnetization of the heterostructures with a different Co layer thickness reveals switching of the magnetic anisotropy between the in-plane and the perpendicular magnetization orientation at a critical Co layer thickness (t=0.8 nm). Magnetooptical Kerr measurements were done in in-plane magnetic fields for [Co(0.8)/Ni(0.5)]$_8$ multilayers close to the critical layer thickness under electric fields across the PMN-PT at room temperature. The remanent in-plane magnetization is found to show a monotonic decrease by a factor of 13% with increasing electric field up to 6 kV/cm. The results clearly demonstrate that electric field induced PMA evolves in the multilayer. We consider that the modulation in PMA by an electric field arises primarily from the magnetoelastic effect in the [Co(0.8)/Ni(0.5)]$_8$ multilayer; compressive strain is transferred to the [Co(0.8)/Ni(0.5)]$_8$ multilayer via inverse piezoelectric effect of PMN-PT, enhancing the PMA due to a change in the orbital angular momentum. A possible modulation of the electronic structures due to charge accumulation is not likely since the polarization charges at the Pt/PMN-PT interface are effectively screened by the thick Pt layer. This work was supported in part by JST CREST Grant Number JPMJCR18J1, JSPS KAKENHI Grant Numbers JP17H03377, JP18F18353, the Asahi Glass Foundation, and the Kato foundation for Promotion of Science.

[1] Y. Shirahata et al., NPG Asia Mater. 7, e198 (2015). [2] J. Okabayashi et al., npj Quantum Mater. 4, 21 (2019).

FU-10. Magnetization reversal of [Co/Pd] perpendicular magnetic film fabricated onto (Bi,La)(Fe,Co)O_3 multiferroic film by applying electric field to multiferroic / magnetic laminated film. *S. Yoshimura*[1], N. Oshita[1] and M. Kuppan[1] *1. Graduate School of Engineering Science, Akita University, Akita, Japan*

Multiferroic materials with magneto-electric effect have been receiving greater attention because of their promising applications in the design of multifunctional devices with low power consumption. In these days, we succeeded to fabricate the highly-qualified $BiFeO_3$-based thin films with ferromagnetism and ferroelectricity by using reactive pulsed DC sputtering method and also demonstrated the inducement of magnetic domain by applying the local electric filed [1]. However, the magnetic properties of the films were not sufficient for device application. If the multiferroic film can control the magnetization direction of high functional magnetic film fabricated onto the multiferroic film by applying electric field to the laminated film, the multifunctional devices will be realized easily. In this study, we fabricated laminated film with (Bi,La)(Fe,Co)O_3 (BLFCO) multiferroic film / [Co/Pd] perpendicular magnetic film with dotted structure, and also demonstrated the magnetization switching of [Co/Pd] dot by applying the electric field. Figure 1 shows the schematic images of application of local electric field to BLFCO/[Co/Pd] laminated film and MFM images of laminated film (A) before and (B) after application of local electric field. Before application of local electric field (A), both of [Co/Pd] dots show de-magnetized domain structure. However, after application of local electric field (B), the magnetic contrast of dot (left) which was applied electric field became small. Figure 2 (a) and (b) show the line profiles of [Co/Pd] dots at line a and b of figure 1(B). The line profile (b) indicates de-magnetized domain structure, but the line profile (a) indicates 86%-upward magnetized domain structure. These results indicate that downward magnetic moment of 75% was reversed to upward by applying electric field. Therefore, we can say, the demonstration of magnetization switching of [Co/Pd] dot by applying the electric field was succeeded.

[1] S. Yoshimura and M. Kuppan, Japanese Journal of Applied Physics, Selected Topics in Applied Physics, 57, 0902B7 (2018).

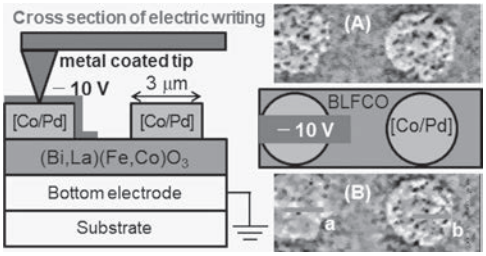


Fig.1 Schematic images of application of local electric field to BLFCO/[Co/Pd] laminated film and its MFM images (A) before and (B) after application of local electric field.

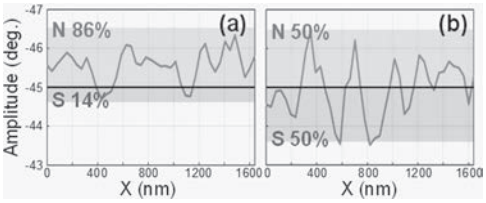


Fig.2 Line profiles of MFM images of [Co/Pd] dots in figure 1(B). Profile (a) and (b) corresponds to line a and b.

FU-11. Studies of Fe^{3+} Doped Barium Zirconate Titanate Nano Films for Energy Storage Applications. *M.K. Bhattarai*[1], S. Dugu[1], K.K. Mishra[1], A. Instan[1] and R. Katiyar[1] *1. Physics, University of Puerto Rico, Rio Piedras, San Juan, PR, United States*

Nature-friendly ABO_3 type multiferroic perovskite nano films were fabricated on $La_{0.67}Sr_{0.33}MnO_3$ (LSMO) buffer layer deposited on MgO (100) single crystal substrates by using a pulse laser deposition technique. The tetragonal multiferroic heterostructure thin films were found to be oriented along (100) direction consisting of alternate $Ba[(Zr_{0.30}Ti_{0.70})_{0.99}Fe_{0.01}]O_3$ (BZTF) and $Ba(Zr_{0.30}Ti_{0.70})O_3$ (BZT) layers with total thickness ~ 300 nm. Homogeneous distribution of grains with roughness of ~ 3- 5 nm were observed from surface topography studies using atomic force microscopy(AFM). Dielectric measurements on Au/BZT/BZTF/LSMO and Au/BZTF/BZT/LSMO metal-insulator-metal capacitors using an impedance analyzer in the temperature range 100-650 K at several frequencies ranges 0.1-100 kHz suggests their relaxor behavior concomitant with the slim hysteresis P-E loop feature. The distribution of magnetic nano clusters was

observed from the temperature dependent magnetization studies using a physical properties measurement system (PPMS). The charge-discharge energy storage performance was estimated from P-E loops at room temperature. The high dielectric constant, larger breakdown strength and, better energy storage density values suggest that the grown heterostructure thin films are suitable multiferroic for high energy storage and memory applications.

FU-12. Voltage Control of Magnetism in $Fe_{75}Al_{25}$/PMN-32 PT Multiferroic Heterostructures. *V. Sireus*[1], E. Menéndez[1], A. Quintana[1,2], I. Fina[3], B. Casals[3], R. Cichelero[3], m. kataja[3], M. Stengel[3,4], G. Herranz[3], G. Catalan[4,5], D. Baró[1], S. Suriñach[1] and J. Sort[1,4] *1. Physics, Universitat Autonoma de Barcelona, Cerdanyola del Valles, Spain; 2. Department of Physics, Georgetown University, Washington, WA, United States; 3. Institut de Ciencia de Materials de Barcelona, ICMAB-CSIC, Cerdanyola del Valles, Spain; 4. Institucio Catalana de Recerca i Estudis Avancats, ICREA, Barcelona, Spain; 5. Catalan Institute of Nanoscience and Nanotechnology, ICN2, CSIC and The Barcelona Institute of Science and Technology, Cerdanyola del Valles, Spain*

One of the main strategies to control magnetism by voltage is the use of magnetostrictive-piezoelectric hybrid materials, such as ferromagnetic/ferroelectric heterostructures. However, when such heterostructures are subjected to an electric field, piezostrain-mediated effects, electronic charging and voltage-driven oxygen migration may simultaneously occur, complicating the interpretation of the magnetoelectric effects and often leading to misinterpretations. We engineer a ferromagnetic/ferroelectric hybrid consisting of a magnetically soft and isotropic 50 nm-thick $Fe_{75}Al_{25}$ (at. %) thin film on top of a <110>-oriented PMN-32PT ferroelectric crystal which allows us to disentangle magnetoelectric effects. The large thickness of the FeAl layer allows us to dismiss any possible effect arising from charge accumulation, the high resistance to oxidation of FeAl ensures virtually no voltage-driven oxygen migration processes, leaving strain as the only mechanism to modulate the magnetoelectric response. Along the in-plane [001] direction of the ferroelectric crystal, the remanence of the hysteresis loops follows a butterfly-like dependence with the applied electric field, while, along the [1–10] direction, a non-volatile loop-like behavior is observed. This behavior arises from the asymmetry of the polarization reversal for this crystallographic orientation of the ferroelectric substrate. The results clearly evidence the need for controlled systems and systematic characterization to understand and optimize magnetoelectric effects in artificial multiferroic heterostructures.

FU-13. Room Temperature Multiferroicity in Fe and Mn-enriched Gallium Ferrite Thin Films. *S. Dugu*[1], S. Kumari[2], M.K. Bhattarai[1], A. Instan[1], D.K. Pradhan[3] and R. Katiyar[1] *1. Department of Physics, University of Puerto-Rico, San Juan, PR, United States; 2. Department of Physics, Pennsylvania State University, University Park, PA, United States; 3. Geophysical Laboratory, Carnegie Institute for Science, Washington, DC, United States*

Multiferroic materials showing the magnetically driven ferroelectricity have interesting properties that can be used for novel technologies, such as fast writing, power saving, and non-destructive data storage. Multiferroicity is typically observed at low temperatures. However, the materials with room temperature multiferroic are highly desirable for device applications. In pure gallium ferrite (GFO), Magnetic transition temperature (T_C) is observed at 220 K. However, T_C can be tuned to above RT by increasing Fe contents. Herein, we report the dielectric, morphological, piezoresponse force microscopic (PFM) and magnetic properties of ~ 200nm of $Ga_{0.6}Fe_{1.4}O_3$ and $Ga_{0.6}(Fe_{0.98}Mn_{0.02})_{1.4}O_3$ thin films deposited by pulsed laser deposition (PLD) method. Temperature-dependent magnetization behavior studied from 10-395 K with both field-cooled and zero-field-cooled conditions identify T_C at around 370 K and 350 K respectively for the above materials. The AFM studies revealed that the surfaces of thin films are smooth and homogeneous, free of microcracks, pores or holes with an average surface roughness of around 2-3 nm. The existence of ferroelectricity at the nanoscale has been confirmed by PFM measurement. The contrast observed within upward polarization, and downward polarization in the PFM phase and amplitude images of both films indicates re-orientation of the ferroelectric polarization in these compounds. On doping Mn in GFO, dielectric loss is significantly reduced that enhances the applicability of the material. The observed RT multiferroic (ferrimagnetic and ferroelectric) behavior with reduced leakage current in these compounds makes them suitable for nanoscale multifunctional device applications such as spintronics and sensors.

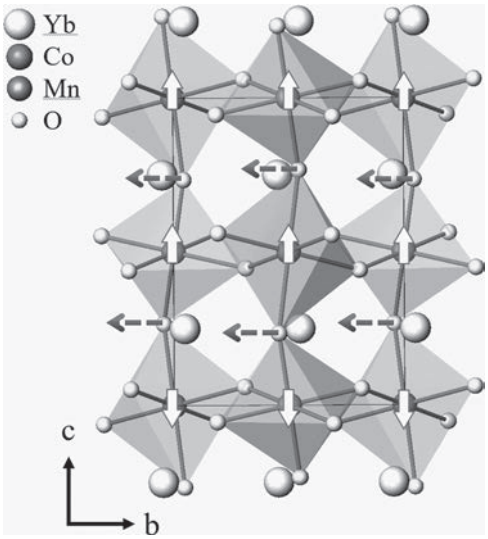
FU-14. Room temperature lead-iron-tungsten/lead-zirconate-titanate nanoscale multiferroic thin films. *K.K. Mishra*[1], M.K. Bhattarai[1] and R. Katiyar[1] *1. physics, University of Puerto Rico, San Juan, PR, United States*

The discovery of single-phase magnetoelectric multiferroic materials are of great scientific interest because of their fascinating coupling mechanisms between spin and polarization order parameters. Herein, we report fabrication, dielectric, ferroelectric and magnetic measurement of a room-temperature magnetoelectric multiferroic $0.6Pb(Zr_{0.53}Ti_{0.47})O_3$-$0.4Pb(Fe_{0.67}W_{0.33})O_3$ (0.6PZT-0.4PFT) thin film. Highly oriented 0.6PZT-0.4PFT thin films of thickness ~300 nm was deposited on $(LaAlO_3)_{0.3}(Sr_2AlTaO_6)_{0.7}$ substrates by following laser ablation processes in oxygen atmosphere using pulsed laser deposition technique. Diffraction studies revealed that the film had pseudocubic phase with (100) orientation. Surface topography studies via atomic force microscopy suggest a smooth and homogeneous distribution of grains on the film surface with surface roughness ~2 - 4 nm. The dielectric measurements as a function of temperature (100-700 K) were carried out in Pt/0.6PZT-0.4PFT /LSMO metal-dielectric-metal capacitors, fabricated using D.C. sputtering technique, exhibited a high dielectric constant of ~2200 at room temperature and showed a diffused behavior at several frequencies around 515 K. The measured polarization hysteresis loop is well saturated at room temperature with P_r = 23.4 μC/cm^2, P_s= 70.31 μC/cm^2 and coercive field E_c = 127 Oe, attributed to its ferroelectric behavior. To understand the magnetic ordering in the thin film, we employed magnetization studies as a function of magnetic field using PPMS down to 4 K. An irreversible magnetic ordering is evident from the ZFC and FC magnetization curves. A saturated magnetization *M-H* loop with remanent magnetization of 82.4 emu/cm^3 was observed at room temperature. These results suggest that our thin films are multiferroic (ferroelectric-ferromagnetic) at room temperature. The presentation will discuss the results in details.

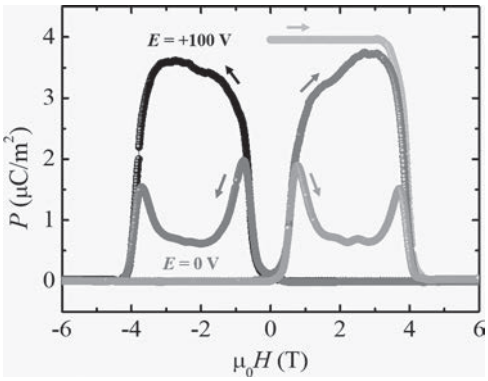
FU-15. Multiferroic behavior in double-perovskite Yb_2CoMnO_6. *J. Kim*[1], Y. Choi[1] and N. Lee[1] *1. Physics, Yonsei university, Seoul, The Republic of Korea*

We investigated the magnetic and magnetoelectric properties of single-crystalline double perovskite Yb_2CoMnO_6, which crystallizes in a monoclinic $P2_1/n$ structure. The crystals of Yb_2CoMnO_6 were grown by a conventional flux method with Bi_2O_3 flux. The size of a large crystal was 1x3x6 mm^3.[1] The up-up-down-down spin ordering of the Co^{2+} and Mn^{4+} moments emerges along the *c*-axis at T_N = 52 K, and the additional order of Yb^{3+} moments arises at T_{Yb} = 20 K. Below T_N, the ferroelectricity develops along the *b*-axis because of cooperative oxygen displacements via the symmetric exchange striction of up-up-down-down spin structure.[2] We observed magnetically-controlled ferroelectric polarization with strong hysteretic behavior, strongly correlated with the variation of isothermal magnetization. Interestingly, the magnetic-field dependence of ferroelectric polarization appears to be quite different relying on the presence of electric fields during magnetoelectric current measurement. This result suggests that ferroelectric domains are substantially affected by both of electric and magnetic fields. Our observations based on strong magnetoelectric coupling in Yb_2CoMnO_6 enrich fundamental and applied research on magnetic materials through the scope of distinct characteristics in double perovskites.

[1] H. Y. Choi et al., *Crystals* 7, 67 (2017) [2] J. Blasco, *Physical Review B* 96, 024409 (2017)



In Yb_2CoMnO_6, the direction of polarization is along the b-axis. Displacements of O^{2-} ions are induced by the exchange striction in the up-up-down-down spin structure.



The magnetic-field dependence of ferroelectric polarization was quite different relying on the presence of electric fields during magnetoelectric current measurement. (Red) under 0 V/cm (Black) under 2300 kV/cm

FU-16. Experimental and Computational Studies of Changes in Phonon Frequencies with Fe Concentration in $CuAl_{1-x}Fe_xO_2$ Delafossites.
M. Aziziha[1], S. Akbarshahi[1], S. Ghosh[2], P. Pramanik[2], G. Panapitiya[1], J.P. Lewis[1], S. Thota[2], A. Romero[1], M.S. Seehra[1] and M.B. Johnson[1]
1. Physics and Astronomy, West Virginia University, Morgantown, WV, United States; 2. Physics, Indian Institute of Technology, Guwahati, India

Delafossite (A1+M3+O2-2) are a less-studied family of complex oxides. In particular, CuAlO2 is p-type complex oxide semiconductor with a fundamental indirect bandgap with possible applications in opto-electric, photo-catalysis, and spintronic devices when doped with a magnetic ion. Previously, we reported on the magnetic properties of CuAl1-xFexO2 (x = 0, 0.01, 0.05, and 0.1) powders, prepared by a solid-state reaction at 1,100 °C. These samples show Curie-Weiss variation of magnetic susceptibility and antiferromagnetic exchange interaction between Fe3+ ions [1]. Long-range magnetic order expected based on some computational predictions was not found, [2] although our high-resolution hysteresis measurements demonstrated a small ferromagnetic component due to hematite impurities [3]. New results reported here include: Rietveld refinement of x-ray diffraction data for phase analysis and the calculation of the Goldschmidt tolerance factor for CuAlO2 and CuFeO2 to confirm their R-3m space group; room-temperature electron spin resonance (ESR) data confirm the presence of Fe3+ ions; and Raman and Fourier- transform infrared (FTIR) spectra to investigate changes in the phonon frequencies with Fe doping. Regarding the latter results, the Raman active modes at Eg = 419 cm-1 and Alg = 767 cm-1 for x = 0 [4] undergo red-shifts for x > 0, so that for x = 0.10 Eg = 412 cm-1 and Alg = 754 cm-1. Also, with increase in x, both modes broaden significantly and the intensity ratio of Eg to Alg modes decreases. In FTIR spectroscopy, six modes are observed; these modes also red shift vs. x. These red shifts are consistent with the expansion of the lattice with increased Fe content, which weakens the M–O bonds. Observed line broadening results from the red shifts and heterogeneity introduced by Fe-doping. Finally, we report density functional theory (DFT) calculations on CuAl1-xFexO2 to understand the influence of Fe-doping on the structure and vibrational modes. All plane-wave DFT calculations were performed using VASP. PBE+U method and spin-polarized Fe are considered. Using the finite displacement method, the variations of the phonon modes with x are calculated and compared to the experimentally observed variations.

[1] M. Aziziha, R. Beesley, J.R. Magers, N. Mottaghi, M.B. Holcomb, J.P. Lewis, M.S. Seehra, M.B. Johnson, Electronic state and concentration of Fe3+ in CuAl1−xFexO2 determined by magnetic measurements, Journal of Magnetism and Magnetic Materials. 471 (2019) 495–500. doi:10.1016/j.jmmm.2018.08.067. [2] H. Kizaki, K. Sato, H. Katayama-Yoshida, Materials Design of $CuAlO_2$ -Based Dilute Magnetic Semiconductors by First-Principles Calculations and Monte Carlo Simulations, Japanese Journal of Applied Physics. 47 (2008) 6488–6495. doi:10.1143/JJAP.47.6488. [3] M. Aziziha, S.A. Byard, R. Beesely, J.P. Lewis, M.S. Seehra, M.B. Johnson, Magnetic properties of Fe-doped $CuAlO_2$ and role of impurities, AIP Advances. 9 (2019) 035030. doi:10.1063/1.5080099. [4] J. Pellicer-Porres, D. Martínez-García, A. Segura, P. Rodríguez-Hernández, A. Muñoz, J.C. Chervin, N. Garro, D. Kim, Pressure and temperature dependence of the lattice dynamics of Cu Al O 2 investigated by Raman scattering experiments and *ab initio* calculations, Physical Review B. 74 (2006). doi:10.1103/PhysRevB.74.184301.

FU-17. Large Porosity-Dependent Magnetoelectric Coupling in Mesoporous BFO-in-CFO Composites.
C.T. Karaba[1], J. Chang[2], S.K. Patel[1], A. Acosta[2], K. Fitzell[2], J.P. Chang[2] and S. Tolbert[1]
1. Chemistry and Biochemistry, UCLA, Los Angeles, CA, United States; 2. Chemical Engineering, UCLA, Los Angeles, CA, United States

In multiferroic composites, nanoscale structure plays an important role in the control of strain transfer between the two materials. Traditional planar stack structures are substrate-clamped and have limited interface, but three-dimensional porous composites allow for a high interfacial surface area between the magnetostrictive and piezoelectric components, as well as allowing for higher strains because of the greater flexion of a mesoporous material. Here, we synthesized mesoporous cobalt ferrite (CFO) via a sol-gel evaporation induced self-assembly technique utilizing block copolymer templating. The pores were then conformally coated via atomic layer deposition with bismuth ferrite (BFO) at varying thicknesses to allow for differing residual porosities of the resultant composite. Using *ex situ* electrically poled SQUID magnetometry measurements, we determined that these composites indeed decrease in out-of-plane saturation magnetization with application of an electric field under 1MV/m. We have found that the strength of this magnetoelectric coupling increases with an increased residual porosity, up to a decrease in saturation magnetization to half the unpoled value in the composites with the thinnest BFO layer. High-resolution X-ray diffraction confirms that more residual porosity allows for greater strains in the magnetic material. Thus, despite having a lower overall volume of ferroelectric material, the magnetoelectric coupling is enhanced by the greater film flexion because of increased porosity.

FU-18. Theory of electro active magnetic excitation in frustrated Heisenberg models.
S. Miyahara[1] *1. Fukuoka University, Fukuoka, Japan*

In magnetoelectric mulitferroics, a strong coupling between magnetization and electric polarization induces an electro active spin wave excitation (so called electromagnon excitation) [1], where electric component of light can excite a spin wave excitation through the magnetoelectric couplings.

A typical example of the electromagnon is an electro active spin wave excitation in helical magnets. The spin wave can be simultaneously excited by both magnetic and electric components of light and the cross correlation effects of them can be observed as nonreciprocal direction dichroism in absorption under external magnetic fields [2]. We investigate the dynamics of spin-wave spin current in the J_1-J_2 classical Heisenberg model under external magnetic fields and clarify that the spin-wave spin current in the conical magnets can be excited by both magnetic and electric component of light and show the non-reciprocal property, i.e., the way of the propagation of the spin wave depends on the direction of the propagation. Such nonreciprocal properties can be tuned not only by the external magnetic fields but also the external electric fields due to the magnetoelectric coupling. The coupling between magnetization and electric polarization induces electro active excitation even in spin gap systems. In the Heisenberg system, the spin gap excitation from the singlet ground state to the triplet excitation cannot be excited by magnetic components of light. However, such a spin gap excitation can be excited by electric component of light. As a typical example, we show that the spin gap excitation in the orthogonal dimer models, which explanin the magentic propeties of $SrCu_2(BO_3)_2$ [3], can by excited by the electric components of light.

[1] H. Katsura, A.V. Balatsky, and N. Nagaosa, Phys. Rev. Lett. 98, 027203 (2007). [2] S. Miyahara and N. Furukawa, Phys. Rev. B 89, 195145 (2014). [3] S. Miyahara and K. Ueda, J. Phys.:Condens. Matter 15, R327 (2003).

FU-19. Non collinear magnetic textures at strained interfaces of $La_{0.67}Sr_{0.33}MnO_3$ on $LaAlO_3$. *A. Burema*[1], J. van Rijn[1] and T. Banerjee[1]
1. University of Groningen, Groningen, Netherlands

Strain engineering at interfaces of ultrathin films in strongly correlated oxides has triggered the study of new non-collinear magnetic textures such as conical, cycloidal, and skyrmions. Most studies require heterostructures that couples a metal with large spin-orbit coupling and a thin magnetic film and uses surface sensitive techniques such as STM [1], MOKE [2] or MFM [3] to study the engineered textures. In our work [4] we have observed magnetic textures in thin films of ferromagnetic $La_{0.67}Sr_{0.33}MnO_3$ (LSMO) on $LaAlO_3$ substrates without any additional heavy metal layer. We study this utilizing a Hall bar geometry and analyze the different components of charge and spin transport to establish this. We find strain to be a critical parameter governing the observed magnetotransport characteristics in LSMO. A systematic study of strain-dependent magnetic behavior reveals a magnetic phase transition from an antiferromagnetic insulating to a ferromagnetic metallic state with an applied magnetic field, figure 1 [4]. We will discuss in particular, the angular dependence of magneto transport with respect to the applied current with varying temperature and magnetic field strength. We show that this leads to an interplay between competing magnetic phases that exhibit non-collinear magnetic textures at different phase transition boundaries and is brought about by temperature induced changes in the anisotropy energy. This is also corroborated by our anisotropic magnetoresistance studies performed at similar interfaces. Such magnetic textures at oxide interfaces have rich potential to be used in new magnetic memory devices and their manipulation by electric fields.

[1] N. Romming, C. Hanneken, and M. Menzel, Science, Vol. 341, p. 636 (2013) [2] G. Yu, P. Upadhyaya and X. Li, Nano Letters, Vol. 16, p. 1981 (2016) [3] L. Wang, Q Feng, and Y. Kim, Nature Materials, Vol. 17, p. 1087 (2018). [4] A.A. Burema, J. J. L. van Rijn and T. Banerjee, J. Vac. Sci. Technol. A, Vol. 37, p. 021103 (2019).

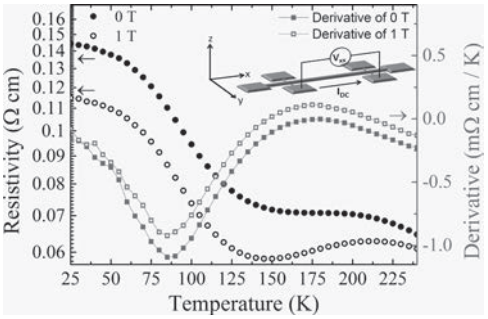


Fig 1 resistivity versus temperature, The solid dots are the resistivity without any magnetic field applied. The open black dots represent the resistivity under the application of 1 T out-of-plane. The application of a magnetic field causes the resistivity slope to change from negative to positive in the temperature region 150 to 225 K, indicating a change from insulating to metallic behavior [4].

FU-20. Electrically detected magnetic resonances in CMR oxides revealed by broadband magnetotransport. *R. Mahendiran*[1] *1. Physics Department, National University of Singapore, Singapore*

Although magnetoresistance of colossal magnetoresistive oxides with direct current passing through samples has been widely reported, little is known about magnetoresistive property of these oxides in response to alternating electrical current [1,2,3]. I discuss the room temperature magnetoimpedance in bulk samples of $La_{0.7}Sr_{0.3-x}Ca_xMnO_3$ ($0 \le x \le 1$) subjected to ac current excitation of frequency f = 1 MHz to 3 GHz and dc magnetic fields (-5 kOe < H < 5 kOe). The ground state changes from ferromagnetic (FM) for $x < 0.20$ to paramagnetic (PM) for $x \ge 0.24$ at 300K. It is shown that ac magnetoresistance is not only higher in magnitude than dc magnetoresistance but shows interesting features: It is negative and shows a single peak at $H_{dc} = 0$ below certain frequencies in FM samples but transforms into positive double peaks at $H_{dc} = \pm H_p$ and the double peak feature shift towards higher magnetic fields with increasing frequency of the ac current. Surprisingly, the ac magnetoresistance in PM samples is also negative and displays a single peak at 500 MHz, which transmutes into an abrupt increase at a critical field value for $f > 700$ MHz. A plot of H_{dc} corresponding to the double peak/ critical field versus frequency suggest that the curves are linear for PM samples and non-linear for FM samples [4]. These observed anomalies in the ac magnetoresistance are attributed to electron paramagnetic resonance for $x \ge 0.24$ and ferromagnetic resonance for $x < 0.20$. Thus, we are able to electrically detect paramagnetic and ferromagnetic resonances in these conducting magnetic oxides through a simple magnetoimpedance measurement. I will show that this technique can be also extended to insulating oxides by illustrating results on YIG and La_2NiMnO_6. Our results are important from view the viewpoints of current interest in electrical detection of magnetization dynamics in magnetic nanostructures.

[1] A. Schwartz, M. Scheffler and S. M. Anlage Phys. Rev. B 61, R870 (2000). [2] A. Rebello and R. Mahendiran, Euro. Phys. Lett. 86, 27004(2009). [3] P. Kumar, U. Chaudhuri, and R. Mahendiran, IEEE Trans. on Magn. 54, 2200105 (2018). [4] U. Chaudhuri and R. Mahendiran, submitted for publication

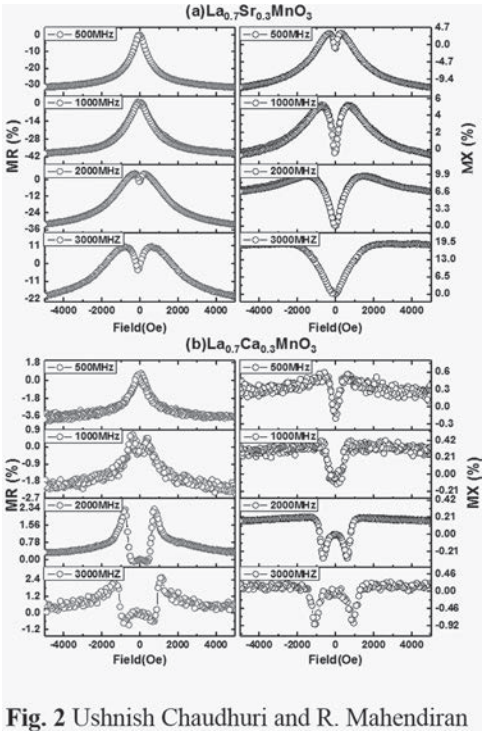


Fig. 2 Ushnish Chaudhuri and R. Mahendiran

(a) Field dependence of Magnetoresistance (MR) (left column) and Magnetoreactance (MX) (right column) for ferromagnetic $La_{0.7}Sr_{0.3}MnO_3$ under current excitation of different frequencies at room temperaure. (b) same as in (a) but for paramagnetic $La_{0.7}Ca_{0.3}MnO_3$ under current excitation of different frequencies.

Session FV
SPIN CURRENTS AND RESULTING SPIN TORQUES II (Poster Session)

Takashi Kimura, Chair
Kyushu University, Fukuoka, Japan

FV-01. Magnon Valves Based on YIG/NiO/YIG All-Insulating Magnon Junctions. C. Guo[1], C. Wan[1] and *X. Han*[1] *1. Institute of Physics, Chinese Academy of Sciences, Beijing, China*

Besides of electron spins, other quasi-particles such as magnons can also behave as carriers of angular moment. Recently, magnonics dealing with magnon-based spin current or magnon accumulation has become an emerging hot topic and attracted wide attentions. Instead of regulating transport of spin-polarized electrons, a magnon valve regulates flow of magnons, a low-energy collective excitation state of magnetic insulators such as $Y_3Fe_5O_{12}$ (YIG). In magnetic insulators, when a temperature gradient is applied, a nonuniform spatial distribution of magnons would contribute to a magnon current, i.e., spin Seebeck effect. Analogous to a spin valve based on giant magnetoresistance (GMR) effect [1,2] or tunneling magnetoresistance (TMR) effect [3,4], we show that an all-insulating magnon junction composed of a magnetic insulator (MI1)/antiferromagnetic insulator (AFI)/magnetic insulator (MI2) sandwich ($Y_3Fe_5O_{12}$/NiO/$Y_3Fe_5O_{12}$) can completely turn a thermogradient-induced magnon current on or off as the two $Y_3Fe_5O_{12}$ layers are aligned parallel or antiparallel[5]. When the temperature gradient is applied, the magnon current with spin would flow from one FMI to the other FMI through the AFMI. Then setting a heavy metal Pt on the top FMI, one could detect an electrical signal via Inverse Spin Hall Effect, which reflects the magnetizations of both FMI layers, similar to TMR effect in MTJ. Furthermore on-off ratio of the so-call magnon junction can be increased to 100%. This magnon junction may play an important role in the future magnonic device [5,6].

[1] M. N. Baibich, J. M. Broto, and A. Fert, et al., *Phys. Rev. Lett.* 61, 2472 (1988). [2] G. Binasch, P. Grunberg, F. Saurenbach, and W. Zinn, *Phys. Rev. B* 39, 4828 (1989). [3] T. Miyazaki and N. Tezuka, *J. Magn. Magn. Mater.* 139, L231 (1995). [4] J. S. Moodera, L. R. Kinder, T. M. Wong, and R. Meservey, *Phys. Rev. Lett.* 74, 3273 (1995). 5] [5] C. Y. Guo, C. H. Wan, and X. F. Han* et al., *Phys. Rev. B* 98, 134426 (2018). [6] H. Wu, and X. F. Han*et al., *Phys. Rev. Lett.*120(9),097205(2018).

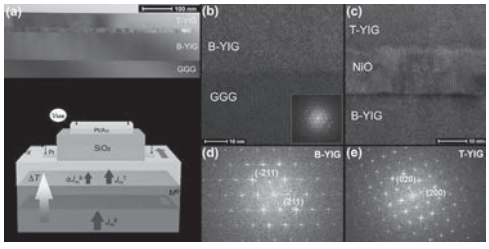


Fig. 1: Microstructure of the GGG//YIG(100)/NiO(15)/YIG(60) IMJ. (a) The cross-sectional TEM image of the sample. HRTEM images of (b) the GGG//YIG(100) and (c) YIG(100)/NiO(15)/YIG(60) interfaces, respectively. Fourier transformation of HRTEM for (d) the bottom YIG and (e) the top YIG only. (f) Schematic diagram of spin Seebeck effect and its measurement setup for an IMJ. During measurement, a field in the x-axis is applied.

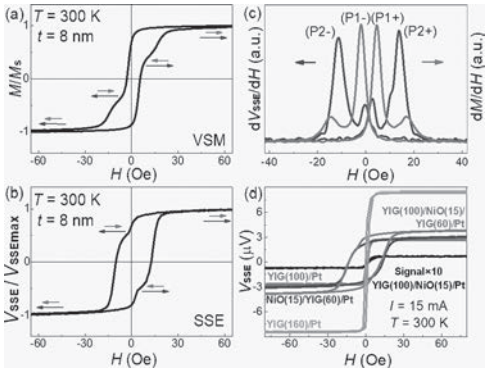
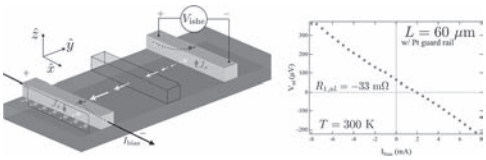


Fig. 2: (a) Hysteresis loop and (b) field dependence of V_{SSE} for an IMJ with t = 8 at room temperature. (c) Corresponding field dependences of dV_{SSE}/dH and dM/dH. (d) V_{SSE} of the control samples.

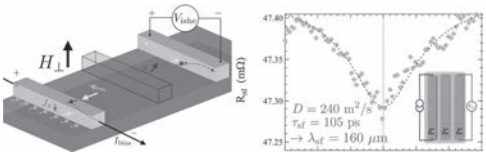
FV-02. Spin Transport in Disordered Semiconductors Probed via the Spin Hall Effect. *S.M. Bleser*[1], D.J. Wesenberg[1], R.K. Bennet[1], M. Roos[1] and B.L. Zink[1] *1. Physics & Astronomy, University of Denver, Denver, CO, United States*

Progress in spintronics requires continued study of spin injection and transport in a wide range of materials. Amorphous semiconductors are one class of materials not yet explored in detail despite theoretical predictions of long spin lifetimes. [1] This is due in part to the challenge of injecting spin into high charge resistivity materials using magnetic tunnel junctions and non-local or lateral spin valves. Here we describe an experimental demonstration of a method to measure spin transport in these systems using spins injected and detected via the spin Hall effect. [2] The method is a modification of experiments used to study spin currents in magnetic insulators. Here we have studied thin film samples of amorphous germanium (a-Ge) with and without a "guard-rail," an additional Pt strip that protects the spin detector from charge leakage effects. We electrically generate a spin signal by injecting a current density in one platinum strip to generate a transverse spin current via the Spin Hall Effect (SHE) and detected on a second platinum strip that generates a non-local voltage signal via the Inverse Spin Hall Effect (ISHE) between temperatures of 200 – 370 K. With an unguarded detector strip and a separation distance of 10 μm we see a positive non-local voltage signal throughout the entire temperature range and with a guarded detector strip at a separation distance of 60 μm we see a negative non-local voltage signal. This suggests that the inclusion of a "guard-rail" between the injector and detector blocks a significant portion of the electrical signal and allows the spin signal to pass relatively unaffected. We provide further confirmation of spin transport using non-local resistance measurements in applied out-of-plane magnetic field, which show the characteristic response of the Hanle effect. This implementation of a "guard-rail" could shed light on spin transport mechanisms in a wide range of high-resistivity semiconductor systems by eliminating charge transport signals.

[1] Harmon and Flatte, PRB 90 115203 (2014) [2] D. Wesenberg et al., (submitted) PRMats 2019



SHE-driven non-local resistance in *a*-Ge. Addition of a "guard rail" eliminates charge contributions and shows the expected negative slope for spin effects.



Hanle effect measurement in *a*-Ge confirms spin transport over long distances.

FV-03. Ferromagnetic Resonance and Inverse Spin Hall Effect in Permalloy/Pt bilayers. S. Martin-Rio[1], A. Pomar[1], L. Balcells[1], C. Frontera[1] and *B. Martinez*[1] *1. Magnetic Materials and Complex Oxides, ICMAB-CSIC, Bellaterra, Spain*

The temperature dependence of magnetodynamical physical effects such as Spin Pumping and Inverse Spin Hall effect (ISHE) has been measured in a set of Py/Pt bilayers as a function of the Pt thickness. Additionally, important physical parameters such as Gilbert damping, saturation magnetization and anisotropy field has been determined as well. It is found that the Gilbert damping follows a non-monotonic behaviour with temperature (Fig. 1a), as reported in other systems [1]. Previous measurements on the temperature dependence of Spin Pumping and ISHE [2] in this system have the serious drawback of requiring the use of complex fabrication process to prepare the samples. In this work we present an easy-to-implement FMR setup for measuring all of those effects and parameters straightforwardly. It is found that the amplitude of the FMR absorption curves is constant from room temperature to approximately 100K and then it starts to decrease. Because of this reduction, it is of major relevance to normalise the measured ISHE voltage with the FMR absorption amplitude in order to obtain physically coherent results. The resulting normalised ISHE voltage, depicted in Fig. 1b, follows a inverse linear relation with temperature.

1.- Lu, Guangduo, et al., Journal of Alloys and Compounds, 753 (2018) 475-482 2.- Obstbaum, M., et al., Physical Review B, 89.6 (2014), 060407

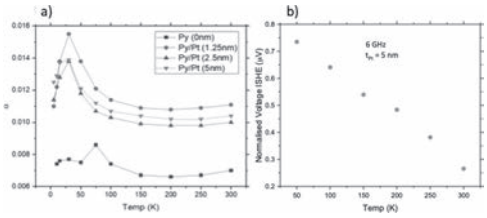


Fig.1 a) Temperature dependence of the Gilbert damping of the Py/Pt system as a function of the Pt layer thickness. b) Temperature dependence of the normalized ISHE in a Py (20nm)/Pt (5nm) bilayer at 6 GHz.

FV-04. Probing Phase Transition and Anisotropy Using the Spin Hall Magnetoresistance in EuO_{1-x} and La_2NiMnO_6. *K. Mallick*[1], A.A. Wagh[1], A. Ionescu[2], C.H. Barnes[2] and A.P. Kumar[1] *1. Physics, Indian Institute of Science, Bangalore, India; 2. Physics, University of Cambridge, Cambridge, United Kingdom*

Spin Hall magnetoresistance (SMR) has attracted a lot of attention recently as a tool for studying magnetic phases and associated phase transitions. In this regard, we investigate two ferromagnetic materials La_2NiMnO_6 (LNMO) and EuO_{1-X}, both predicted to be promising candidates for spintronics. LNMO is among the few ferromagnetic insulators which has a Curie temperature close to room temperature (T_C =280K). Thin films of this material allow tunability of its crystallographic and magnetic properties by varying deposition conditions, thickness and lattice strain. Interestingly, SMR measurements on bilayers of epitaxial LNMO films and Pt, exhibit features distinctly different from polycrystalline LNMO/Pt. While the temperature dependence of SMR seems to follow the bulk magnetization in polycrystalline films, the observed behavior in epitaxial films appears to be dominated by the interface magnetic anisotropy. The isotropic nature of the bulk of the film became evident from spin Seebeck and SQUID magnetometry experiments. We could track the evolution of this surface anisotropy as a function of temperature employing systematic magnetic field orientation dependent SMR measurements in out-of-plane and in-plane geometries. In addition, we observe SMR and anisotropic magnetoresistance (AMR) in bilayers of Pt/EuO_{1-X} thin films. The presence of oxygen vacancies manifested in a metal-insulator transition as well as an enhanced curie temperature. The AMR persisted up to room temperature, exhibiting two sign crossovers. On the other hand, the onset of SMR occurred only below Curie temperature and did not undergo any sign change. We deduce possible explanations for such behavior based on the temperature dependence of EuO_{1-X} bandstructure and spin mixing conductance of the Pt/EuO_{1-X} interface.

FV-05. Optimized 3d/5d heavy metals interfaces: Spin-Hall effect and THz emission. *H. Dang*[1], J. Hawecker[3], Q. Barbedienne[1], J. George[1], S. Collin[1], P. Bortolotti[2], J. Tignon[3], S. Dhillon[3] and H. Jaffres[1] *1. Unité Mixte de Physique CNRS-Thales, Palaiseau, France; 2. Thales Research and Technology, Palaiseau, France; 3. LPA, ENS, Paris, France*

Recently, the THz emission may be realized in heterostructures either in heavy metallic (HM) [1] or in Rashba system [2]. The heterostructures are composed of ferromagnetic (FM) and spin-orbital active materials via Inverse Spin Hall effect (ISHE) in picosecond scale using time-dependent spectroscopy (TDS) techniques. The experiments consist in exciting their magnetization and spin-currents within the FM layer via a femtosecond laser and in measuring the relaxation of the correlated spin and charge currents responsible for the THz dipolar emission. Some experimental works have been done to optimize the THz emission by using different materials, geometries of structures, techniques to fabricate the samples, etc. In parallel, some theoretical models were proposed to explain the dynamic of the spin current in ultrafast range [3]. However, the physics of the THz emission in those structures has not been well understood. Hence, we are working to optimize the THz emissions of 3d/5d transition-metal based multilayers such as Co/Pt, NiFe/Au:Ta and NiFe/Au:W. The first idea is to reduce the Spin Memory Loss (SML) at the interface between Co and Pt by including Au or Ti monolayers (MLs). Then, those samples are analyzed using experiments combining Radio frequency-spin-pumping-ISHE measurements and TDS –THZ spectroscopy. We obtain that the insertion of Au or Ti MLs based materials in Co/Pt structures may enhance either the THz or the ISHE signals depending on the layer sequences. In particular, the Co/Au (Ti) MLs/Pt systems evidence an increase of the ISHE signal by a decrease of the SML, conjugated to a decrease of the FMR-linewidth and the THz emission. From that, we propose a strict correlation between the THz signals and related Spin-Mixing conductances (SMC), then discuss a connection between THz and spin loss phenomena. The second idea is to optimize the spin current in HM by a spin-sink layer such as Au:W. We show that the THz emission of Co/Pt/spin-sink layer is slightly higher than the emission of Co/Pt. This system also follows the strict correlation between THz signal and SMC.

[1] T. Seifert et al., Nature photonics 10:483488, (2016) ; D. Yang et al., Adv. Opt. Mat.(2016) ; Y. Wu et al., Adv. Materials 29, 1603031 (2017) [2] M. B. Jungfleisch et al., Phys. Rev. Lett. 120, 207207 (2018) [3] M. Battiatoet al., Phys. Rev. Lett. 105, 027203 (2010); T. Kampfrath et al., Nature Nanotechnology8, 256–260 (2013)

FV-06. Direct optical detection of charge to spin conversion in heavy metals using modulation. *O. Van't Erve*[1], C.H. Li[1] and B. Jonker[1]
1. Naval Research Laboratorium, Washington, DC, United States

MOKE is often used to detect changes in magnetization caused by spin orbit torque in heavy metal (HM)/ ferromagnetic metal (FM) heterostructures, where the spin current created by spin Hall effect (SHE) in the HM creates the torque on the magnetization in the FM. A disadvantage of using heterostructures to measure the SHE is the ambiguous role of interface transparency. Methods that do not rely on the transparency of the interface with a FM are thus preferential in determining the real SHE angle of the HM. One such method is to use the direct optical detection of the charge to spin conversion by magneto optical Kerr effect (MOKE).[1] However, In ref [2] and [3], the authors conclude that it is impossible to measure a current-induced MOKE signal, due to heating effects. Nonetheless many groups have since shown convincing results on the optical detection of current induced spin polarization using magnetization-induced second harmonic generation. [4] While heating effects can contribute to the measured MOKE signal, Marui et. al. [5] have used a double modulation technique to separate the current induced heating effects caused by changes in the refractive index of the film from that in magnetization caused by spin orbit torque in a FM/HM heterostructure. Here we show that by applying a similar modulation technique to separate out the heating effect from the spin Hall effect of a single layer HM, we can unambiguously demonstrate that spin Hall effect can indeed be measured using a commercially available MOKE system.

[1] Van't Erve, O. M. J., Hanbicki, A. T., McCreary, K. M., Li, C. H. & Jonker, B. T. Optical detection of spin Hall effect in metals. *Applied Physics Letters* 104, 172402 (2014). [2] Riego, P. *et al.* Absence of detectable current-induced magneto-optical Kerr effects in Pt, Ta, and W. *Applied Physics Letters* 109, 172402 (2016). [3] Su, Y. *et al.* Absence of detectable MOKE signals from spin Hall effect in metals. *Applied Physics Letters* 110, 042401 (2017). [4] A. Pattabi, et al *Applied Physics Letters* 107 (15), 152404 (2015). [5] Marui, Y., Kawaguchi, M. & Hayashi, M. Optical detection of spin–orbit torque and current-induced heating. *Applied Physics Express* 11, 093001 (2018).

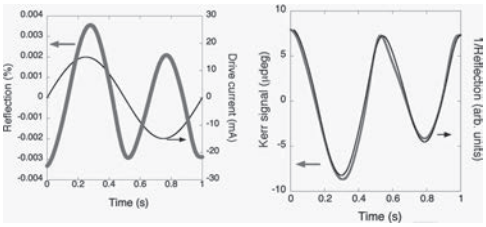


Figure 1, a) Reflectivity of beta-W (left axis) and drive current (right axis) plotted on the same time scale. Note reflectivity shows both first and second harmonic signals b) Kerr rotation signal (left axis) and scaled 1/reflectivity (right axis) as a function of time. Note, the reflectivity signal is $I_x + I_y$, independent of polarization and the Kerr rotation is proportional to $(I_x - I_y)/(I_x + I_y)$ for $I_x \sim= I_y$.

FV-07. Spin-transport properties of $IrMn_3$. J. Holanda[1], H. Saglam[1,2], V. Karakas[3], *M. Vogel*[1], J. Gibbons[1], S. Siddiqui[1], Z. Zhang[1,5], Y. Li[4], R. Divan[4], B. Fisher[4], Y. Liu[4], V. Novosad[1], O. Ozatay[3], J. Pearson[1] and A. Hoffmann[1] *1. MDS, Argonne National Laboratory, Lemont, IL, United States; 2. Illinois Institute of Technology, Chicago, IL, United States; 3. Physics Department, Bogazici University, Istanul, Turkey; 4. Center for Nanoscale Materials, Argonne National Laboratory, Lemont, IL, United States; 5. School of Optical and Electronic Information, Huazhong University of Science and Technology, Wuhan, China*

A current trend in spintronics is an increased focus on antiferromagnetic materials, as active spin-transport components, which is also known as antiferromagnetic spintronics. Especially non-collinear antiferromagnetic materials, such as $IrMn_3$, are of special interest. These non-collinear antiferromagnets have due to the net chirality of their spin structures additional spin Hall properties that are not available in ordinary non-magnetic materials. Here we studied films of $IrMn_3$, which were grown with magnetron sputtering system on (100)MgO substrates. We investigated MgO/$IrMn_3$/ferro(para)magnetic/Ti heterostructures. The Ti(2 nm) layer is used to protect the surface properties of $IrMn_3$, permalloy (Py) or platinum (Pt). The $IrMn_3$ was characterized by superconducting quantum interference device (SQUID) magnetometry, magnetotransport measurements, transmission electron microscopy and X-ray diffraction. We studied systematically the transport properties of the $IrMn_3$/ferro(para)magnetic material samples as a function of temperature. The results show that is possible manipulates the surface states of this type of antiferromagnet via electrical means. This work was supported by the U.S. Department of Energy, Office of Science, Materials Science and Engineering Division and CNPq, Conselho Nacional de Desenvolvimento Científico e Tecnológico - Brasil (Scholarship).

FV-08. Two spin-channel model for spin Hall effect in 3D micromagnetic simulations. *X. Wang*[1], A. Goncharov[2], P. Van Der Heijden[2] and V. Lomakin[1] *1. Electrical Computer Engineering, University of California, San Diego, La Jolla, CA, United States; 2. Western Digital, San Jose, CA, United States*

Spin Hall effect (SHE) leads to spin accumulation occurring at normal metal – ferromagnetic interface, which can lead to spin torque. Numerical simulations of spin Hall effect are typically done via a simplified model Slonczewski's-like models, which do not account for size and shape effects related to the structure composition. There exist more advanced models for perpendicular currents [1-3]. The two spin-channel model (TSCM) [3] is particularly attractive as the parameters it uses can be directly obtained from experiments. Here, we extend the TSCM to account for SHE and the related spin accumulation and spin torque at interfaces between ferromagnetic and normal material. For such an interface, torques are generated due to spin accumulation at non-magnetic layer, with charge current flowing parallel to the interface. In TSCM, two currents are defined: charge current and spin current. The charge current is represented as the sum of the gradient of charge chemical potential and the curl of the spin chemical potential. The spin current is represented as a combination of the gradient of spin chemical potential and certain components of the charge chemical potential. The charge and spin chemical potentials are coupled between each other inside nonmagnetic layer via the interface. Once the spin and charge chemical potentials and the resulting spin and charge currents are found, the spin torque at the interface can be directly obtained. Such calculations account for size, shape, and material related effects of both normal and ferromagnetic layers. We validated the model with respect to analytical solutions for specific two-layer geometry [4] and studied a set of additional more complicated structures. Figure 1 shows the magnetization dynamics for a SHO oscillator in a cylinder of both radius and height to be 5 nm made of a material with CoFe put on top of a normal layer. The dynamics shows that the simplified model results in inconsistent precession, whereas TSCM results in robust precession. The differences are due to size dependent effects and non-uniform magnetization dynamics.

1, S. Zhang, Z. Li, Roles of nonequilibrium conduction electrons on the magnetization dynamics of ferromagnets, Phys Rev Lett. 93(12), 127204 2, S. Zhang, P. M. Levy, and A. Fert, Mechanisms of Spin-Polarized Current-Driven Magnetization Switching, Phys. Rev. Lett. 88, 236601 3, T. Valet and A. Fert, Theory of the perpendicular magnetoresistance in magnetic multilayers, Phys. Rev. B 48, 7099 4, Paul M. Haney, Hyun-Woo Lee, Kyung-Jin Lee, Aurélien Manchon, and M. D. Stiles, Current induced torques and interfacial spin-orbit coupling: Semiclassical modeling, Phys. Rev. B 87, 174411

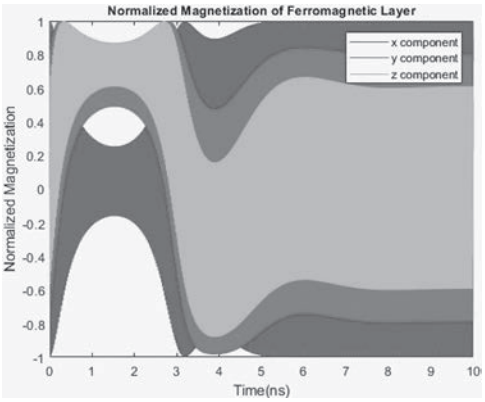


Fig.1 Magnetization dynamics of the spin hall oscillator.

FV-09. Spin currents in all-oxide heterostructures. S. T S[1], S. Kanikrishnan[1] and *M. Rao*[1] *1. Physics, IIT Madras, Chennai, India*

Generation, transportation and detection of spin in a controlled manner are very important in spintronic devices for efficient switching mechanisms in a magnetic tunnel junction (MTJ). The conversion of charge current to spin current is known as spin Hall effect (SHE) and the inverse phenomenon is inverse SHE (ISHE). The detection of spin is usually realized by the ISHE. Spin Hall magnetoresistance (SMR) arises due to the simultaneous effect of SHE and ISHE in a bilayer heterostructures consisting of a ferromagnetic (or ferrimagnetic) insulator (FMI) and a normal metal (NM). [1,2,3] Magnetic Proximity Effect (MPE) observed in YIG/Pt complicates the spin transport scenario with additional effects such as Anomalous Hall effect (AHE) which attenuate SMR signal.[4,5]. Our group has successfully studied Ga: ZnO insertion on Bi: YIG/Pt and observed SMR signals, but the increase in spurious paramagnetic signal hampered the SMR signals with increasing Ga: ZnO thickness[6]. A solution for this is to employ antiferromagnetic moments, which are quite stable to stray fields and MPE. Recent studies in this direction have proved successful in generating spin current using antiferromagnets NiO/Pt, Cr_2O_3/W, CuIr and $SrMnO_3$/Pt layers[7]. Also, groups have reported that spin current can be used as a detection method to probe interface magnetism[8]. We have fabricated Antiferromagnetic oxide and metal oxide heterostructures through pulsed laser deposition and demonstrated the generation of spin current through angle-dependent magnetoresistance measurements (ADMR). We have varied the deposition conditions such that the magnetic interactions changes from antiferromagnetic to ferromagnetic order and we could identify the magnetic behaviour through spin transport studies carried out in this bilayer samples. The spin current generated in $SrIrO_3$ has other higher order magnetoresistance components along with spin Hall magnetoresistance. We would be presenting our experimental observations on spin transport studies carried out in these bilayers.

1. Matthias Althammer *et. al.,* Phys. Rev. B 87, 224401 (2013). 2. T. Kikkawa *et. al.,* Phys. Rev. Lett. 110, 067207 (2013). 3. E. Saitoh *et. al.,* Appl. Phys. Lett. 88, 182509 (2006). 4. H. Nakayama *et al.,* Phys. Rev. Lett. 110, 206601 (2013). 5. V. Castel *et al.,* Appl. Phys. Lett. 101, 132414 (2012). 6. Matthias Althammer *et.al*.Appl. Phys. Lett. 110, 052403 (2017). 7. Y.Ji. *et.al* Appl. Phys. Lett. 110, 262401 (2017). 8. Qiu, Z. *et al*. *Nat. Commun.* 7,12670 (2016).

FV-10. Cross-shaped nanostructures for the study of spin to charge inter-conversion using spinorbit coupling in non-magnetic materials. V. Pham[1], *S. Ghosh*[1], L. Vila[1], G. Zahnd[2], M. Cosset-Cheneau[1], P. Noel[1], A. Brenac[1], A. Marty[1] and J. Attané[1] *1. University of Grenoble Alpes, CEA, CNRS, INP-G, IRIG-Spintec, Grenoble, France; 2. Hprobe, 4 Rue Irène Joliot-Curie, Eybens, France*

Spin current manipulation is at the core of spintronics. The spin–orbit interaction (SOI) in nonmagnetic materials is now used to create and detect spin currents. For instance, the spin Hall effect (SHE) and its inverse[1] allow performing the interconversion between charge and spin currents in bulk materials[2]. Edelstein Rashba effects, at interfaces or on the surfaces of topological insulators, can also ensure these conversions and are becoming highly competitive[3]. In this context, nanostructures that allow detecting the SHE electrically are of prime interest in view of SO-based logic devices[4] and nonvolatile magnetic random access memories (MRAMs), altogether with applications for spin–orbit torque experiments. Here, we focus on how these interconversions can be made electrically, using three different cross-shaped nanostructures. We apply the measurement configurations to the case of the spin Hall effect in Pt using CoFe electrodes to detect or inject spins. Both the direct and inverse spin Hall effects can be detected, with spin Hall signals up to two orders of magnitude higher than that of nonlocal measurements in metallic lateral spin valves, and with a much simpler fabrication protocol (the obtained spin signals are in the 10 mΩ range). We compare the respective signal amplitudes of the three proposed geometries. Finally, we show that finite element method calculations allow extracting from these measurements the spin Hall angle and the spin diffusion length of Pt. These results are also a step toward the development of computational magnetic devices, such as a nonvolatile memory with a single nanomagnet or spin–orbit based logic circuits[4]. Finally, we emphasize that these device geometries, can also be used to study the spin-charge interconversion at Rashba interfaces or surfaces of topological insulators.

1. E. Hirsch, Phys. Rev. Lett. 83, 1834 (1999). 2. A. Hoffmann, IEEE Trans. Magn. 49, 5172–5193 (2013). 3. A. Soumyanarayanan, N. Reyren, A. Fert, and C. Panagopoulos, Nature 539, 509 (2016). 4. S. Manipatruni, D. E. Nikonov, C. C. Lin, T. A. Gosavi, H. Liu, B. Prasad, Y. L. Huang, E. Bonturim, R. Ramesh, and I. A. Young, Nature 565, 35 (2019).

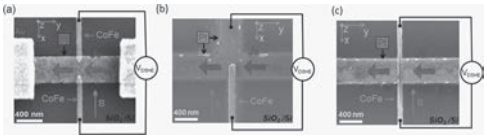


Fig.1. Colored SEM images of the studied devices, with the electrical set-ups corresponding to SHE measurements. The CoFe ferromagnetic electrodes appears in gray and the Pt ones in purple.

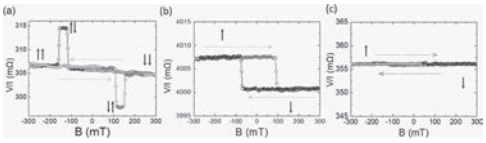


Fig. 2. Spin signals obtained for DSHE and ISHE experiments, corresponding to the measurement schemes of Fig. 1.

FV-11. Ferromagnet Structural Tuning of Interfacial Symmetry Breaking and Spin Hall Angle in Ferromagnet/Heavy Metal Bilayers. *M. Tang*[1], R. Ramaswamy[2], H. Yang[2], H. Yang[1], W. Fan[1], Z. Shi[1], S. Zhou[1] and X. Qiu[1] *1. School of Physics Science and Engineering, Tongji University, Shanghai, China; 2. Department of Electrical and Computer Engineering, National University of Singapore, Sigapore, Singapore*

The spin Hall angle (SHA) is one of the most important quantities in controlling the conversion efficiency between charge and spin currents. It has been reported there exists a correlation between the SHA and the structure of nonmagnetic metals (NM) in ferromagnet (FM)/NM heterojunctions [1]. In this study, we present our investigation on the influence of the FM structure on SHA in Py/Ta bilayers. The FM structure is modified by reversing stacking order of the bilayers and characterized by transmission electron microscopy (TEM) and X-ray diffraction (XRD). The SHA, θ_{SH}, is obtained firstly by the conventional method in spin-torque ferromagnetic resonance(ST-FMR) technique as described in Ref. [2], where only in-plane (IP) spin-orbit torque (SOT) is considered. Since a significant out-of-plane (OP) SOT has been observed in Ta/FM bilayers [3,4], we then extracted IP and OP SOTs and re-evaluate their corresponding SHAs, $\theta_{\parallel}$ and $\theta_{\perp}$, by employing the method in Refs. [5,6]. As shown in Fig. 1(a), fast Fourier transforms (FFTs) for the TEM images show a Py (111) texture is observed in sub./Ta/Py [7], while no such texture is detected in sub./Py/Ta. This modification of the FM structure

is also confirmed by XRD patterns in Fig. 1(b). The SHAs extracted from ST-FMR results are shown in Fig. 1(c). Without considering the OP SOT, the θ_{SH} is nearly one times larger in magnitude in sub./Ta/Py (-0.083) than that in sub./Py/Ta (-0.044). After considering the OP SOT, the $\theta_{\parallel}$ is not distinctly affected by the FM structure but the $\theta_{\perp}$ of sub./Ta/Py is around twice as large as that for sub./Py/Ta. We ascribe the FM structure dependent SHA to the interfacial symmetry breaking between FM and NM, which is tuned by the work functions due to different crystalline structure of FM. The emergence of the Py (111) structure enlarges the interfacial symmetry breaking and thus enhances the Rashba effect at the FM/HM interface. Our results highlight the importance of out-of-plane SOT in Py/Ta bilayers and demonstrate a simple and feasible way to manipulate SHA as well as SOTs via tuning FM structure.

[1] J. Liu, T. Ohkubo, S. Mitani et al., Appl. Phys. Lett., Vol. 107, p.232408 (2015). [2] L. Liu, T. Moriyama, D. C. Ralph et al., Phys. Rev. Lett., Vol. 106, p.036601 (2011). [3] X. Qiu, P. Deorani, K. Narayanapillai et al., Sci. Rep., Vol. 4, p.4491 (2013). [4] G. Allen, S. Manipatruni, D. E. Nikonov et al., Phys. Rev. B., Vol. 91, p.144412 (2015). [5] A. R. Mellnik, J. S. Lee, A. Richardella et al., Nature, Vol. 511, p.449 (2014). [6] Y. Wang, P. Deorani, K. Banerjee et al., Phys. Rev. Lett., Vol. 114, p.257202 (2015). [7] A. V. Svalov, B. G. Asensio, A. A. Chlenova et al., Vacuum, Vol. 119, p.245-249 (2015).

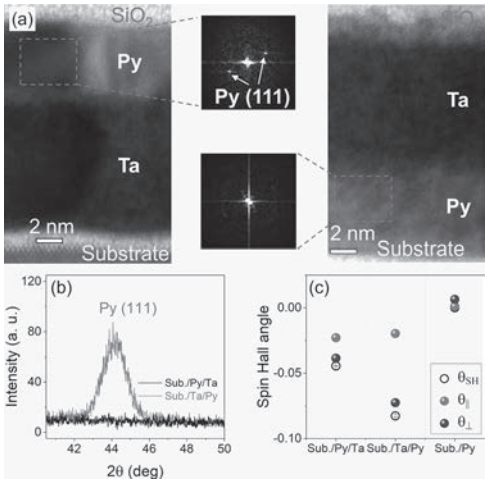


FIG.1. TEM images (a) and XRD patterns (b) of sub./Py/Ta and sub./Ta/Py. (c) The extracted θ_{SH}, $\theta_{\parallel}$ and $\theta_{\perp}$ of three samples.

FV-12. Spin Hall Angle and Spin Diffusion Length of Permalloy.
Y. Huang[1,2], Y. Weng[1,3], C. Liang[2,3] and J.G. Lin[1,4] *1. Center for Condensed Matter Sciences, National Taiwan University, Taipei, Taiwan; 2. Department of Physics, National Taiwan University, Taipei, Taiwan; 3. Graduate Institute of Applied Physics, National Taiwan University, Taipei, Taiwan; 4. Center for Atomic Initials for New Materials, National Taiwan University, Taipei, Taiwan*

The inverse spin Hall effect (ISHE) in a ferromagnetic material (FM) has been attracting much attention due to its importance in spintronic applications [1,2]. The ISHE, which converts spin currents into charge currents, is an effective method to detect spin currents. In this work, we report the observation of ISHE on permalloy (Py) thin films under ferromagnetic resonance (FMR) conditions. Experimentally, a series of Py thin films of thicknesses (t_{Py}) ranging from 5 to 40 nm were fabricated on rectangular silicon substrates. The dimensions were 1.5 mm × 3.0 mm for all samples. The FMR measurement was performed with a Bruker EMX electron spin resonance system. The samples were put in the center of a TE_{102} cavity, while a nanovoltmeter (Keithley 2181A) was connected to the samples to measure the electrical voltage. An electrical charge current (I_c) is recorded around the resonance field (H_r) for each sample. I_c as a function of t_{Py} is shown in Fig. 1. The electrical currents are attributed to ISHE and magnonic charge pumping (MCP) in Py [3]. The spin Hall angle (θ_{SHE}) and spin diffusion length (λ_{Py}) for Py are determined to be 0.034 % and 7.0 nm, respectively. The anomalous Hall effect (AHE) of Py is measured, and the anomalous Hall angle (θ_{AHE}) for Py is estimated as 0.005 %. The spin Hall angle of a FM is related to its anomalous Hall angle as $\theta_{SHE} = (1/p)\theta_{AHE}$ [1,2,4], where p is the spin polarization of the material. In our study, the value of p is estimated to be 0.14 for Py, comparable to the values reported in previous works [5]. The contribution from skew scattering to the θ_{SHE} of Py cancels out the intrinsic/side-jump contributions [4,6], hence yielding a small value of θ_{SHE}.

[1] A. Tsukahara, Y. Ando and Y. Kitamura, Phys. Rev. B 89, 236317 (2014). [2] Y. Omori, E. Sagasta and Y. Niimi, Phys. Rev. B 99, 014403 (2019). [3] A. Azevedo, R. O. Cunha and F. Estrada, Phys. Rev. B 92, 024402 (2015). [4] J, Sinova, S. O. Valenzuela and J. Wunderlich, Rev. Mod. Phys. 87(4), 1213 (2015). [5] E. Sagasta, Y. Omori and M. Isasa, Appl. Phys. Lett. 111, 082407 (2017). [6] N. Nagaosa, J. Sinova and S. Onoda, Rev. Mod. Phys. 82(2), 1539 (2010).

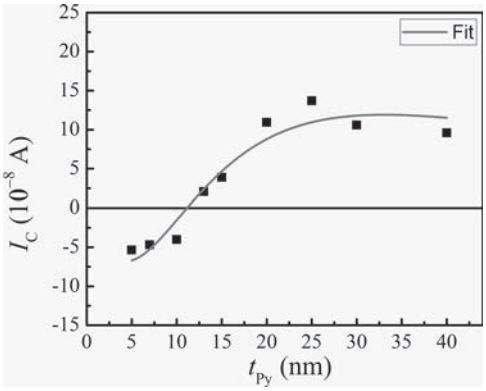


Fig. 1. The electrical current I_c as a function of the thickness t_{Py} of the Py thin films. The contributions to I_c from ISHE and MCP are separated, and the values of θ_{SHE} and λ_{Py} for Py are obtained through the fit (red curve) to the experimental data.

FV-13. Composition dependent spintronic THz emission of rare earth transition metal alloys combined with Pt.
M. Fix[1], R. Schneider[2], R. Heming[2], S. Michaelis de Vasconcellos[2], R. Bratschitsch[2] and M. Albrecht[1] *1. Institute of Physics, University of Augsburg, Augsburg, Germany; 2. Institute of Physics and Center for Nanotechnology, University of Münster, Münster, Germany*

Bilayers of ferro-/ferrimagnetic (FM/FIM) thin films and nonmagnetic metal (NM) layers have shown to be THz emitters when excited by femtosecond laser pulses [1,2]. Amplitude and frequency of the emitted THz radiation can be tuned by varying the film thickness, the electrical conductivity, the magnetic properties of the FM layer, and the spin-Hall conductivity of the NM layer [3]. However, the microscopic processes leading to the THz radiation and the role of the magnetic states especially for more complex magnetic layers are not fully understood, yet. Here we report on systematic studies on the THz emission of magnetron sputter deposited 20 nm thick ferrimagnetic Tb_xFe_{1-x} [4] and Gd_xFe_{1-x} ($0 \le x \le 1$) alloys combined with 5 nm thick Pt layers. The FIM layers show a great variety of different magnetic states depending on the composition, temperature, and applied magnetic field [5]. Thus, they are ideal candidates to investigate the role of different magnetic states on the emitted THz radiation. The samples were characterized by SQUID magnetometry and THz emission spectroscopy. Figure 1a shows the measured THz intensity with respect to the Tb content x for the Tb_xFe_{1-x}/Pt sample series. The measured THz radiation is mainly caused by the Fe electrons [2,4,6]. The high THz signals for $0.03 \le x \le 0.15$ derive from the reduced electrical conductivity compared to Fe/Pt. The decreased signal for higher x and the local maximum for $x = 0.5$ are attributed to the reduced Fe content and the in-plane magnetic moment of the Fe sublattice, which is schematically drawn in figure 1b. An inversion of the THz signal for $0.45 \le x \le 0.55$ (figure 1c) can be explained by the inverted alignment of the Fe magnetic moments. The small signals for high x are caused by

induced paramagnetic moments. Our study provides deeper insights into the role of complex magnetic materials used in spintronic THz emitters and will contribute to future optimized emitter designs.

[1] T. Kampfrath, M. Battiato, P. Maldonado, *et al.*, Nature Nanotechnology 8, 256-260 (2013). [2] T. J. Huisman, C. Ciccarelli, A. Tsukamoto, *et al.*, Applied Physics Letters 110, 072402 (2017). [3] T. Seifert, S. Jaiswal, U. Martens, *et al.*, Nature Photonics 10, 483-488 (2016). [4] R. Schneider, M. Fix, R. Heming, *et al.*, ACS Photonics 5, 3936-3942 (2018). [5] B. Hebler, A. Hassdenteufel, P. Reinhardt, *et al.*, Front. Mater. 3, 162408 (2016). [6] M. Chen, R. Mishra, Y. Wu, *et al.*, Advanced Optical Materials 6, 1800430 (2018).

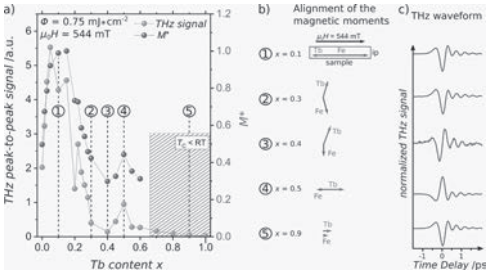


Fig. 1 a) Composition dependent THz amplitude of Tb_xFe_{1-x}/Pt bilayers measured at an applied in-plane magnetic field of 544 mT and results of a model function *M. b) Expected alignments of the magnetic moments of the Tb and Fe sublattices and c) corresponding THz waveforms.**

FV-14. Extrinsic Spin Hall Effect in Inhomogeneous Systems.
T. Funato[1] and H. Kohno[1] *1. Science, Nagoya University, Nagoya, Japan*

In spintronics, the spin Hall effect (SHE) plays a key role in the realization of spin-to-charge conversion[1]. Recently, several experimental studies suggested that the spin Hall angle of copper with weak spin-orbit interaction (SOI) are augmented by natural oxidation treatment, and attracted intense research attention[2,3]. As a related phenomenon, Okano et al. reported an experimental result that suggests the vorticity of electron flow arising from the gradient of oxidation induced spin accumulation (spin-vorticity coupling) and generated a spin current[4]. However, the mechanism of the enhancement of spin Hall angle by natural oxidation treatment is still incompletely understood. As one of the solution, our theoretical study focuses on the extrinsic SHE due to impurities with distribution gradient. We consider nearly free electrons subject to impurities with SOI. Assuming a spatially linear distribution of impurities, we treat the average of the distribution non-perturbatively and the fluctuation perturbatively. We analyze the spin accumulation and spin current in linear response to an electric field. In this presentation, we report spin accumulation and spin current calculated by including ladder vertex corrections due to impurity scattering with SOI. On the basis of the results, we discuss the relation between the induced spin accumulation and spin current, and estimate the order of magnitude of the effect.

[1] J. Sinova, S. O. Valenzuela, and J. Wunderlich et al., Rev. Mod. Phys. Vol. 87, p.1213 (2015). [2] H. An, Y. Kageyama, and Y. Kanno et al., Nat. Commun. Vol. 7, p.13069 (2016). [3] R. Enoki, H. Gamou, and M. Kohda et al., Appl. Phys. Express Vol. 11, p.033001 (2018). [4] G. Okano, M. Matsuo, and Y. Ohnuma et al., Phys. Rev. Lett. Vol. 122. p.217701 (2019).

FV-15. Spin pumping and large field-like torque at room temperature in sputtered amorphous W_xTe_{2-x} film.
Y. Fan[1], H. Li[3], D. Mahendra[2], J. Held[3], A. Mkhoyan[3] and J. Wang[1] *1. Electrical Engineering, University of Minnesota, Minneapolis, MN, United States; 2. Physics, University of Minnesota, Minneapolis, MN, United States; 3. Materials Science & Engineering, University of Minnesota, Minneapolis, MN, United States*

To improve the efficiency of spin orbit torque, materials with large charge spin conversion efficiency has become a research hotspot. Among these materials, WTe_2 has attracted a significant attention due to its potential type II Weyl semimetal properties, which leads to large conduction and strong spin orbit coupling at Weyl points existing in bulk. [1] However, molecular beam epitaxy[2] or mechanical exfloliation[3] is still the most common preparation method for tungsten dichalcogenide thin films, which is impractical for industrialization. In this work, we prepared W_xTe_{2-x} (x=0.85) film by magnetic sputtering method and studied the spin to charge and charge to spin conversion at room temperature in sputtered MgO/W_xTe_{2-x} (x=0.85)/CoFeB/MgO/Ta heterostructures. Spin pumping measurements at different frequencies is used to characterize the spin to charge efficiency as shown in Fig (a). The resulted spin to charge conversion ratio is J_C/J_S~0.05. Second harmonic measurement is carried out for the charge to spin conversion ratio. The resulted value for damping like torque and field like torque at different W_xTe_{2-x} thickness is shown in Fig (b). We found the system exhibits a large field like torque (~0.1) compared to heavy metals[4] while the damping like torque is small (~0.0005). The damping like torque value will change sign when changing thickness, which indicates a competition between the interfacial and bulk scheme. High resolution transmission electron microscopy images show that the W_xTe_{2-x} layer is amorphous, which may increase resistivity and induce large interface scattering[5], thus contribute to the large field like torque. This work broadens the methods to prepare materials with large spin-orbit coupling and pave the way to application.

[1] Wu, Yun, et al. Physical Review B 94.12 (2016): 121113. [2] Tang, Shujie, et al. Nature Physics 13.7 (2017): 683. [3] MacNeill, D., et al. Nature Physics 13.3 (2017): 300. [4] Avci, Can Onur, et al. Physical Review B 89.21 (2014): 214419. [5] Liu, Jun, et al. Applied Physics Letters 107.23 (2015): 232408.

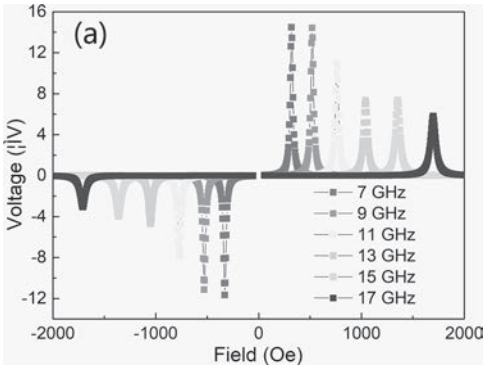
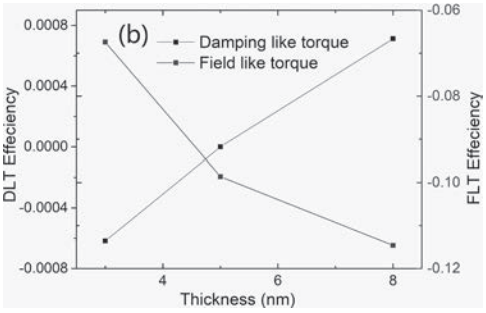


Fig (a). Spin pumping signal of the MgO(2)/ WxTe2-x (3)/CoFeB(6)/ MgO(2)/Ta(2) heterostructure at different frequencies.



(b). The field like torque and damping like torque efficiency at different thickness.

Session FW
SPIN MATERIALS AND DEVICES
(Poster Session)

Chi Zhang, Chair
Cornell University, Ithaca, NY, United States

FW-01. Nonlinear Dynamics of Two Spin-Transfer-Torque Nano-Oscillators Coupled via Magnetostatic Fields. *D. Mancilla*[1], A.O. Leon[2], R. Arias[3], S. Allende[1] and D. Altbir[1] *1. Universidad de Santiago de Chile, Santiago, Chile; 2. Pontificia Universidad Católica de Valparaíso, Valparaíso, Chile; 3. Universidad de Chile, Santiago, Chile*

A great deal of attention has been focused on the study of spin- transfer-torque nano-oscillators (STNOs) during the past years. This is due to their several potential applications in the implementation of magnetic field sensors, in telecommunications, and recently in neuromorphic computing [1]. While the dynamics of a single oscillator has been well characterized by the experimental, analytic, and numerical points of view, the behavior of several coupled elements is not fully understood yet. In this work, an analytical and numerical study of the nonlinear dynamics of two magnetostatically coupled spin valves driven by spin-transfer-torques [2] is presented considering uniform magnetization in each oscillator, i.e., under the macrospin approximation. In particular, we study the role that the position of the oscillators plays in the synchronization phenomenon. We observe that for most values of the current density, the system exhibits a synchronized motion of the magnetizations. In this regime, the difference between the oscillation phases of the free layers remains nearly zero for an *in-phase* mode and π for an *antiphase* mode. The transition between the two modes, when the current density is increased, is characterized by a *mixed-mode* state in which both the antiphase and in-phase modes participate with a finite amplitude of oscillation [3]. These results can be used as one step in the quest for the design and control of arrays of STNOs. We acknowledge financial support in Chile from FONDECYT 1161018, 1160198, and 1170781, and Financiamiento Basal para Centros Científicos y Tecnológicos de Excelencia FB 0807. This material is based upon work supported by the Air Force Office of Scientific Research under Grant No. FA9550-18-1-0438. D.M.-A. acknowledges Postdoctorado FONDECYT 2018 3180416.

[1] N. Locatelli, V. Cros, and J. Grollier, Nat. Mater. 13, 11 (2013). [2] D. C. Ralph and M. D. Stiles, J. Magn. Magn. Mater 320, 1190 (2008). [3] D. Mancilla-Almonacid, R. E. Arias, Alejandro. O. Leon, D. Altbir, and S. Allende, Phys. Rev E 99, 032210 (2019).

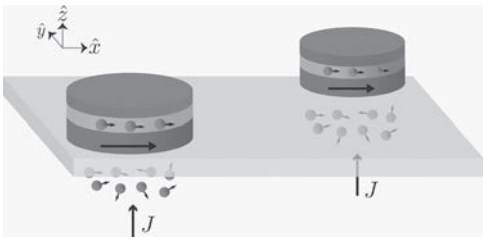


Fig 1. Two nano-oscillators driven by a spin-polarized current density *J* and coupled via magnetostatic fields.

FW-02. Investigation of Electrical Spin Injection into GaAs Using $Co_2Fe_{0.4}Mn_{0.6}Si$ Heusler Alloy. *J. Wang*[1], T. Koike[1], M. Oogane[1], M. Tsunoda[2] and Y. Ando[1] *1. Department of Applied Physics, Tohoku University, Sendai, Japan; 2. Department of Electronic Engineering, Tohoku University, Sendai, Japan*

1.Introduction The spin-MOSFET is expected to show a high performance in integrated circuits [1]. Highly efficient spin injection into semiconductors from ferromagnet is important for the realization of spin-MOSFET. However, it is difficult to realize efficient spin injection due to the conduction mismatch problem [2]. In order to enhance the efficiency of spin injection, it was proposed to use a half-metal theoretically having a spin polarization of 100% [2]. Co-based full Heusler alloys are expected to be a source of spin injection into semiconductors because of its high Curie temperature, small lattice mismatch with GaAs and high spin polarization. In this study, we focused on $Co_2Fe_{0.4}Mn_{0.6}Si$ (CFMS) and aimed to fabricate high quality thin films on GaAs substrates for the realization of high efficiency of spin injection. 2.Experiment procedure A structure of CFMS (30nm)/Ta (5nm) was deposited by magnetron sputtering on undoped GaAs (100) substrates. The annealing temperature (T_a) of CFMS layer was between 200 and 600°C. The magnetic properties of CFMS thin film were analyzed by vibrating samples magnetometer (VSM). The films with same structure were also deposited on GaAs (undoped)/n-GaAs (100μm) substrates at T_a= 400°C, which has the maximum saturation magnetization of CFMS films. The Si-doped densities in n-GaAs layer were $1\times10^{19}cm^{-3}$. For detecting spin injection signal, we performed 3- terminal Hanle measurement. 3.Experiment result Fig. 1 shows the annealing temperature dependence of saturation magnetization of CFMS thin films deposited on the undoped GaAs substrate. The saturation magnetization increased with increasing annealing temperature, and the maximum M_S~ 925 emu/cc was obtained at T_a= 400°C. The obtained high M_s indicates high B2 ordering in the CFMS films. Fig. 2 shows the Hanle signal using n-GaAs substrate under different bias current at 10K. The spin relaxation time calculated from narrow Hanle signals is about 7 ns, which is comparable to theoretical value [3] and previous report [4]. The result indicates that the spin-injection into GaAs was successfully demonstrated using highly ordered CFMS films.

[1] S. Datta *et al*., Appl.Phys.Lett. 56, 665 (1998) [2] G. Schmidt *et al*., Phy. Rev.B 62, R4790 (2000) [3] Pil Hun Song *et al.*, Phy.Rev.B 66, 035207 (2002) [4] P. A. Peterson*et al*., Phy.Rev.B 94, 235309 (2016)

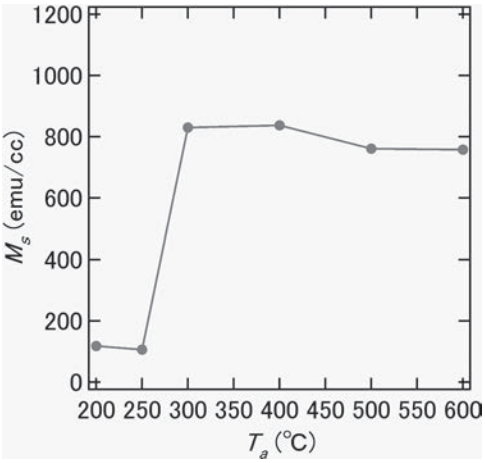


Fig.1 T_a dependence of M_s

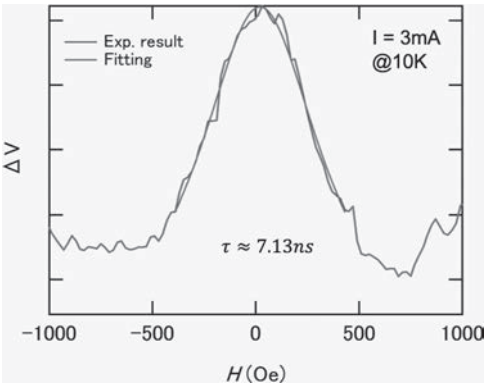


Fig.2 narrow Hanle signal

FW-03. Room-temperature spin-dependent transport through Sb-doped Ge in vertical spin-valve devices. *T. Shiihara*[1], M. Yamada[1], M. Honda[1], S. Yamada[1,2] and K. Hamaya[1,2] *1. Graduate School of Engineering Science, Osaka University, Toyonaka, Japan; 2. Center for Spintronics Research Network, Graduate School of Engineering Science, Osaka University, Toyonaka, Japan*

For germanium (Ge)-based spintronic devices on a silicon (Si) platform [1], it is important to clarify the influence of dopant species on spin transport in Ge channel layers. Up to now, room-temperature (RT) spin transport in phosphorus (P) doped n-type Ge has been demonstrated by using lateral spin valves [1,2]. For P-doped n-Ge, the spin relaxation mechanism was dominated by the short-range spin scattering due to the spin–orbit coupling of impurities rather than the spin–orbit interaction in the host materials [1,3]. Because the strength of the spin–orbit coupling in arsenic (As) and antimony (Sb) is generally larger than that of P, we can speculate that the observation of the spin transport in Sb-doped n-Ge is difficult at RT. Here we report on spin transport in Sb-doped n-Ge at RT by using vertically stacked spin-valve structures and discuss the influence of Sb. By combining solid phase epitaxy and molecular beam epitaxy with Sb doping, we fabricated a CoFe/Sb-doped Ge (15~ 20 nm)/Fe_3Si structures on Si(111) [4,5]. Flat interfaces without forming reaction layers can be confirmed [Fig. 1(a)], similar to our previous work [1]. Figure 1(b) shows a representative magnetoresistance curve of a vertical spin-valve device at RT. A hysteretic feature depending on the magnetization states between parallel and anti-parallel can be observed. The observed spin signal (ΔRs) is one order of magnitude larger than that in p-Ge [1,5]. From the experimental conditions and electrical properties of the device, we can assume that the carrier concentration in the Sb-doped Ge layer is $n \sim 1 \times 10^{19}$ cm^{-3}, leading to the resistivity of ~ 0.6 mΩcm and other parameters [5,6]. If the theory by Fert and Jaffrès [7] is used, we can roughly estimate the spin diffusion length (λ) of Sb-doped n-Ge to be ~ 150 nm at RT, smaller than that of P-doped n-Ge (~ 440 nm) at RT [2]. Therefore, this study experimentally clarifies that the dopant species in Ge channel layers can affect the spin transport in group-IV semiconductors. This work was partly supported by JSPS KAKENHI (16H02333 and 17H06120).

[1] K. Hamaya *et al*., J. Phys. D: Appl. Phys. 51, 393001 (2018). [2] M. Yamada *et al*., Appl. Phys. Express. 10, 093001 (2017). [3] Y. Song *et al*., Phys. Rev. Lett. 113, 167201 (2014). [4] T. Shiihara *et al*., Semicond. Sci. Technol. 33, 104008 (2018). [5] M. Kawano *et al*., Phys. Rev. Mater. 1, 034604 (2017). [6] J. Jeon *et al*., Jpn. J. Appl. Phys. 55, 04EB13 (2016). [7] A. Fert and H. Jaffrès, Phys. Rev. B 64, 184420 (2001).

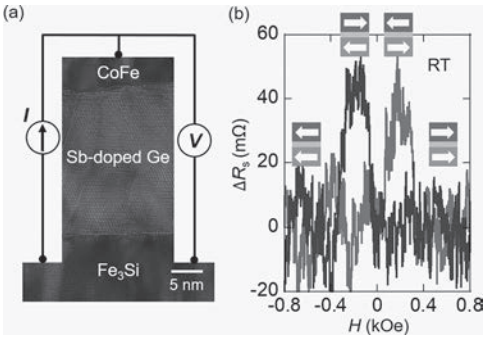


Fig. 1: (a) Cross-sectional TEM image of a CoFe/Sb-doped Ge/Fe_3Si interface. (b) Magnetoresistance curve of a vertical spin-valve device at RT.

FW-04. Experimental demonstration of spin xor logical operation in Si spin device. *R. Ishihara*[1], S. Lee[1], Y. Ando[1], R. Ohshima[1], Y. Suzuki[2], H. Koike[3] and M. Shiraishi[1] *1. Department of Electronic Science and Engineering, Kyoto Univ., Kyoto, Japan; 2. Graduate School of Engineering Science, Osaka Univ., Toyonaka, Japan; 3. Advance Products Development Center, TDK, Ichikawa, Japan*

Magnetologic gate (MLG) using spin accumulation and spin transport in the semiconductor was proposed as an path way to realize a reconfigurable and energy saving circuit [1,2]. MLG is composed of two spin xor device consisting three ferromagnetic (FM) electrodes contacting semiconductor spin channel. Si is one of the candidate for the spin channel because it has a good spin coherence and large spin drift effect which is required for the spin xor operation was demonstrated [3]. In this study, we demonstrate the spin xor operation with Si spin channel at room temperature. The device geometry and measurement circuit of the spin xor operation are schematically shown in Fig. 1. Nondegenerate n-Si channel was contacted by Co/Fe electrodes through MgO tunnel barriers (labeled as A, B, and M in Fig. 1). The spin xor device outputs three values by changing magnetization directions of two input electrodes A and B. Here, each input, i.e. 0 or 1, is defined by the magnetization of the FM electrode as shown in Fig. 1. The magnetization of the electrode M was kept 1. Spin polarized electrons were accumulated by a source current (I_s) under the FM electrodes A and B, and three different output states were measured on the electrode M depending on the relative configuration of the input magnetization. I_s was set to be 1.2 mA. Then, electrochemical potentials under electrode B for (0,0) and (1,1) of input states are modified to the equal each other by spin drift effect, resulting in three different output signals in electrode M. Fig. 2 shows the experimental demonstration of the spin xor operation with Si spin channel. Clear three outputs were obtained from the electrode M as requested for the MLG-operation. Detailed discussion is given in the presentation.

[1] H. Dery *et al*., Nature 447, 573 (2007). [2] H. Wen *et al*., Phys. Rev. Applied 5, 044003 (2016). [3] T. Tahara *et al.,*Phys. Rev. B 93, 214406 (2016).

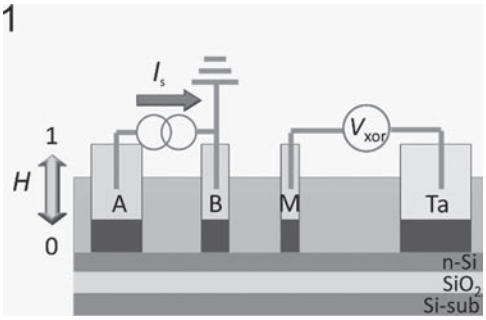


Figure 1. A schematic of the xor device. V_{xor} means voltage between electrode M and Ta.

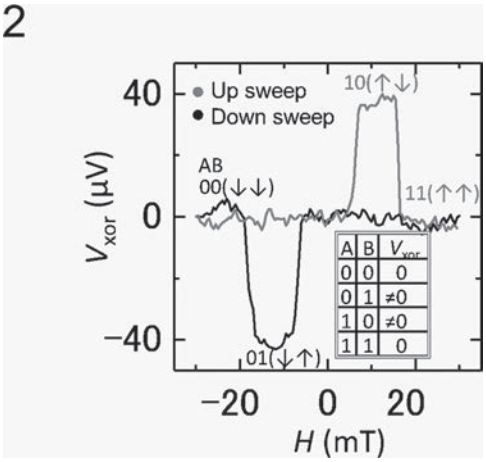


Figure 2. V_{xor} measured as a function of H. Black (red) curve indicates H sweeps upwards (downwards). Vertical arrowsindicate the magnetizationstates of A and B. Bottom-right inset: truth table of xor logic operation.

FW-05. Non linear spin dynamics induced in magnetically coupled CoFeB/Pt/NiFe trilayer. *M. Yafuso*[1] and T. Kimura[1,2] *1. Department of Physics, Kyusyu University, Fukuoka, Japan; 2. Research Center for Quantum Nano-Spin SCiences, Fukuoka, Japan*

In magnetic multilayers, the magnetic property is known to be modified by the interlayer coupling in magnetic multilayers. In addition, a ferromagnetic resonance (FMR) in one ferromagnetic layer produces the non-equilibrium spin currents injection into another ferromagnetic layer, leading to the modulation of the magnetization dynamics through the spin-transfer torque. Therefore, if the resonant frequencies for two ferromagnetic layers are close to each other, un-conventional magnetic features such as coherent resonance may be realized. For this purpose, here, we investigate the resonant magnetic property in a CoFeB/Pt/NiFe trilayer. The CoFeB/Pt/NiFe trilayer has been prepared by the magnetron sputtering under the base pressure of 10-8 Pa. The crystal and static magnetic properties have been evaluated by X-ray diffraction and vibrating-sample magnetometer, respectively. The resonant property was investigated by differential FMR measurement. Figure 1 shows the representative FMR spectra for the trilayer under GHz microwave irradiation. The FMR peaks for two ferromagnetic layers were clearly observed. For a comparison, the FMR spectra for the CoFeB/Pt and NiFe/Pt were plotted together with the trilayer's spectrum. We emphasize that the difference of the FMR field between two ferromagnetic layer becomes smaller than that for the monolayer case. More interestingly, as seen in Fig 2, the damping constant for the CoFeB layer is found to increase with increasing the microwave power. We analyze these unconventional features can be explained by taking into account the thermal spin injection due to the FMR heating.

K.Yamanoi,Y.Yokotani and T.Kimura, Dynamical Spin Injection Based on Heating Effect due to Ferromagnetic Resonance. (2017)

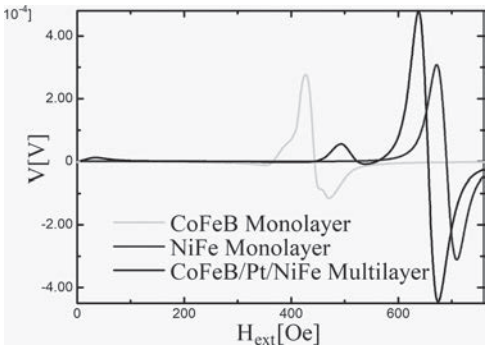


Fig. 1 : FMR spectra for CoFeB/Pt/NiFe trilayer film under 9.2 GHz microwave irradiation together with CoFeB/Pt and NiFe/Pt film

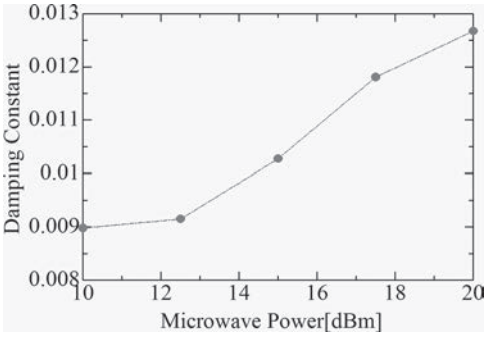
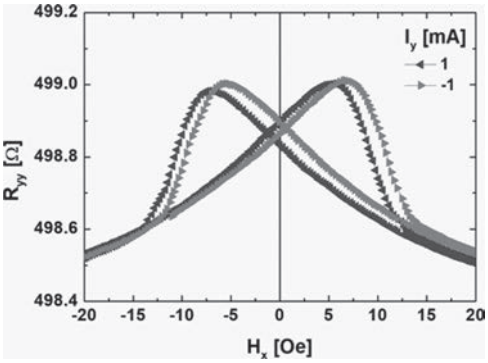


Fig. 2 : Estimated damping constant for various microwave power

FW-06. SMR based spin Hall measurement technique for in-plane magnetization. D. Kim[1], *J. Kim*[2], C. Yun[2], S. Joo[1], B. Lee[3] and K. Rhie[2] *1. Center for Nanometrology, Korea Research Institute of Standards and Science, Daejeon, The Republic of Korea; 2. Department of Display and Semiconductor Physics, Korea University, Sejong, The Republic of Korea; 3. Department of Physics, Inha University, Incheon, The Republic of Korea*

Spin Hall angle measurement technique is well developed at heavy metal/ferromagnet which has perpendicular magnetic anisotropy (PMA). However, a DC current based spin Hall angle measurement for in-plane anisotropy (IPA) has not been yet developed. We present a simple spin hall magnetoresistance (SMR) technique that measures spin Hall angle without any worry of artifacts which could be introduced in RF based spin Hall measurement. SMR signal is measured with applied field transverse to current. SMR peak shifts its maximum as applied current is increased, since spin Hall torque is added to the torque induced by transverse field. This shift yields spin Hall angle of heavy metal layer. For a Pt/CoFeB bilayer, we obtained $\theta_{SH}^{eff} = 0.045$, $l_s = 2.49$ nm, which is a reasonable value.



The R-H curve measured with two direct current flow in the Pt/CoFeB bilayer.

FW-07. Multi-State Magnetic Tunnel Junction with Inhomogeneous Magnetic Anisotropy for Neuromorphic Computing. *Z. Zhang*[1,2], G. Xu[1], Y. Zhang[1], K. Zhang[1], J. Nan[1], Z. Zheng[1], J. Wang[1], G. Wang[1], Y. Zhang[1,2] and W. Zhao[1] *1. Fert Beijing Research Institute, BDBC, School of Microelectronics, Beihang University, Beijing, China; 2. School of Electronics and Information Engineering, Beihang University, Beijing, China*

In this work, we propose a magnetic tunnel junction (MTJ) with inhomogeneous magnetic anisotropy (IMA) to conduct the multi-state magnetoresistance (MR) and spike-timing-dependent plasticity (STDP) function. In this MTJ, a series of regions with weaker perpendicular magnetic anisotropy (PMA) can be formed through treating the surface of the free layer, for example, irradiation [5]. As shown in Fig. 1, the PMA constant of the free layer is $6.5x10^5$ J/m^3 and the PMA constants of the inhomogeneous regions are from $3.0x10^5$ J/m^3 to $4.8x10^5$ J/m^3. By applying the COMSOL and Mumax[3] micromagnetic simulation platforms, the MR variation and magnetic dynamics induced by the current are investigated. When the working voltage is applied on the two terminals of the MTJ, the spin-polarization current will be injected into the free layer. The region with weaker PMA can be easier to be switched, which implies that these regions could be switched more quickly than the other regions with strong PMA. When the working voltage is removed, the partial switching state can be maintained due to the nucleation of domain walls and skyrmions, which leads to the multi-states of the MR. As illustrated in Fig. 2a, the resistance will increase with the augmentation of the working current. For example, eight stable resistance states are achieved by increasing the current density from $0.9x10^{10}$ A/m^2 to $6.5x10^{10}$ A/m^2. Moreover, we study the potentiation and depression process of the device. Fig. 2b shows that the relative resistance will increase with the duration time of the applied working current at the potentiation process, while the depression process can be implemented by switching the direction of the current. This time-dependent relative resistance implies that the proposed MTJ can emulate the STDP function [2-3]. This work provides a promising alternative for high-density memory and neuromorphic computing [4-7].

[1] P. Nongjai et al., Journal of Magnetism and Magnetic Materials, Vol. 394, p. 432 (2015) [2] S. H. Jo et al., Nano Letters, Vol. 10, p. 1297 (2010) [3] T. Serrano-Gotarredona et al., Frontiers in Neuroscience, Vol. 18, p. 1 (2013) [4] J. Wang, and F. Zhuge, Advanced Materials Technologies, Vol. 4, p. 1800544 (2019) [5] S. Yu, and P. Chen, IEEE Solid-State Circuits Magazine, Vol. 8, p. 43 (2016) [6] Irem Boybat et al., Nature Communications, Vol. 9, p. 2514 (2018) [7] Z. Wang et al., Nature Materials, Vol. 16, p. 101 (2017)

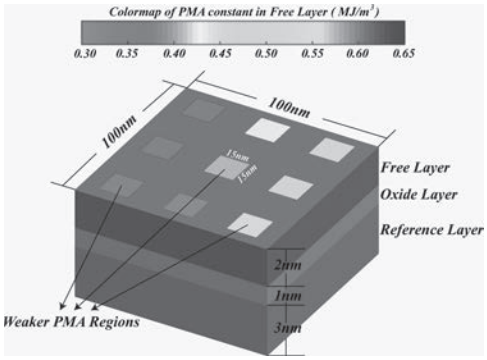


Fig. 1 Schematic of the MTJ with IMA.

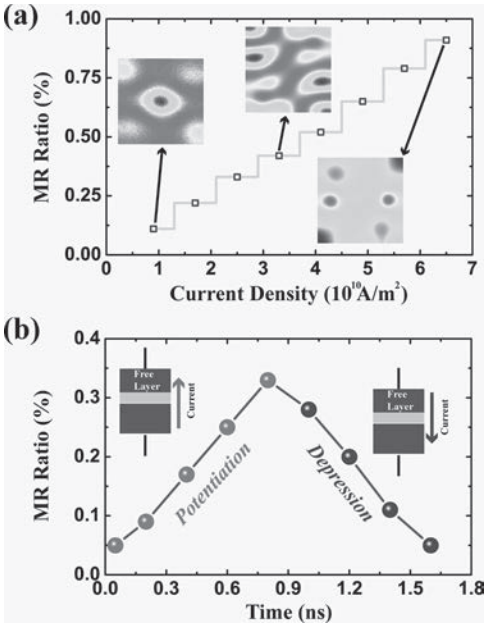


Fig. 2 (a) Multi-state MR with different applied current densities. (b) Potentiation and depression processes of the proposed MTJ by applying positive and negative currents.

FW-08. Field-Free Control of Exchange Bias by Spin Polarized Currents. *H. Kim*[1], S. Je[2], D. Jung[3], K. Lee[3] and J. Hong[1] *1. Department of Emerging Materials Science, DGIST, Daegu, The Republic of Korea; 2. Center for X-ray Optics, LBNL, Berkeley, CA, United States; 3. School of Materials Science and Engineering, UNIST, Ulsan, The Republic of Korea*

In the trilayers structure consisting of ferromagnetic (FM) alloy CoFeB/antiferromagnetic (AFM) IrMn/heavy metal (HM) Pt layers, we show that the spin polarized current of HM layer can control the spin alignment state in the neighboring antiferromagnetic material as well as the corresponding exchange bias effect in the ferromagnet coupled to the antiferromagnet. To directly inject the spin current into AFM layer, the CoFeB (5 nm)/IrMn (8 nm) bilayers were deposited at room temperature by magnetron sputtering on a wire-patterned Pt(8 nm)/Ta(4 nm) without an external magnetic field. Initial development of the exchange bias effect in the as-deposited film was measured as the in-plane current was increased progressively. AFM domains of the as-deposited film are expected to be randomly oriented, which is reflected in the measured hysteresis loop measured by Magneto-Optical Kerr Effect magnetometer system as shown in Fig. 1(a) (1st hysteresis loop). Upon increasing the in-plane currents of 10 and 20 mA, hysteresis loops exhibit increased exchange bias and squareness representing the increased degree of spin axes alignment. After the injection of 30 mA current, the well-defined square hysteresis could be measured with H_E of -250 Oe. To confirm the exchange bias setting with the polarized spins, the pulse current of

opposite polarity (-I) was applied and the switching in the exchange bias was measured. Figure 1(b) and 1(c) display hysteresis loops for two exchange biased states after injecting the positive and negative pulse currents of ±30 mA in sequence resulting in H_E's, of -250 and +250 Oe, respectively as well as repeatedly switching the exchange bias. It was demonstrated that the spin currents from the SHE in the Pt layer could be injected into AFM layer and that the injected spins work to align the magnetic moments in the AFM. Use of spin current to control the magnetization of AFM is expected to enhance the applications of AFM in spintronics technology.

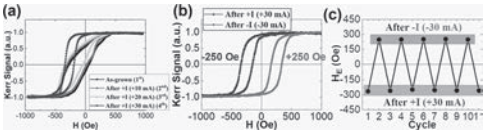


FIG. 1. (a) Change of magnetic hysteresis loops after injecting various magnitude of in-plane current. (b) Exchange bias reversal after the injection of pulse current in two opposite directions (±I), respectively. (c) Repeatable switching of the exchange bias

FW-09. Shape Anisotropy Effects on Spin-Torque Oscillators.

X. Chao[1], M. Jamali[1], *B.R. Zink*[1] and J. Wang[1] *1. University of Minnesota, Minneapolis, MN, United States*

Spin-torque oscillators are promising candidates for hard disk drive read head sensors, neuromorphic computing, and telecommunicationsdue to their frequency tunabilityby a direct current or a magnetic field [1-3]. A narrow linewidth and a large quality factor are of great importance for these applications. Previous studies have indicated that the spin-torque oscillation linewidth depends on the temperature, current, and in-plane field angle [4-6]. Here, we have investigated the spin-torque oscillations in MgO-based magnetic tunnel junctions (MTJs) and demonstrated the impact of the MTJ shape anisotropy on the oscillation linewidth as a function of current. Our experimental results might be significant for the device optimization.

[1] P. M. Braganca, B. A. Gurney, B. A. Wilson et al., Nanotechnology 21, 235202 (2010). [2] J. Torrejon, M. Riou, F. A. Araujo et al., Nature 547, 428 (2017). [3] H. S. Choi, S. Y. Kang, S. J. Cho et al., Sci. Rep. 4, 5486 (2014). [4] M. L. Schneider, W. H. Rippard, M. R. Pufall et al., Phys. Rev. B 80, 144412 (2009). [5] B. Georges, J. Grollier, V. Cros et al., Phys. Rev. B 80, 060404(R) (2009). [6] K. V. Thadani, G. Finocchio, Z.-P. Li et al., Phys. Rev. B 78, 024409 (2008).

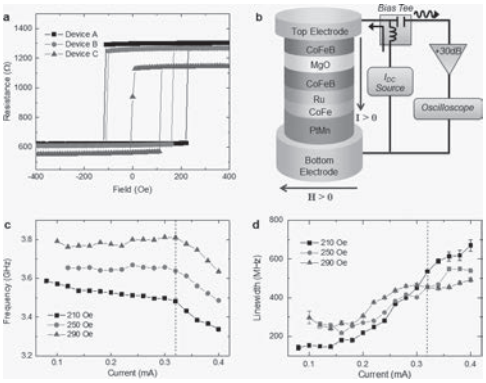


Fig 1. (a) The magnetoresistance minor loops of MTJs with different aspect ratios. (b) Schematic of the sample structure and the STO measurement setup with the sign convention for the current and magnetic field. A positive current corresponds to electrons flowing from the fixed layer to the free layer and favors the parallel state. The magnetic field is applied along the easy axis of the ellipse, and a positive field favors the antiparallel state. (c) The frequency variation of device B as a function of current at 210, 250, and 290 Oe. The lateral size is 50 x 150 nm^2. (d) The corresponding linewidth of device B as a function of current. The error bars are from Lorentzian fits to the spectra.

Session GA
MAGNETIC CONTROL AND SENSING IN BIOMEDICINE

Gary Zabow, Chair
National Institute of Standards and Technology (NIST), Boulder, CO, United States

INVITED PAPERS

8:30

GA-01. Biomedical Applications of Magnetic Nanoparticles: Remote Control of Cells. *J. Dobson*[1] *1. Biomedical Engineering, University of Florida, Gainesville, FL, United States*

The use of magnetic micro and nanoparticles for biomedical applications was first proposed in the 1920s as a way to measure the rheological properties of the cytoplasm. Since that time, particle synthesis techniques and functionality have advanced significantly. Magnetic micro and nanoparticles are now used in a variety of biomedical applications such as targeted drug delivery, MRI contrast enhancement, gene transfection, immunoassay and cell sorting. More recently, magnetic micro and nanoparticles have been used to investigate and manipulate cellular processes both *in vitro* and *in vivo*. This talk will focus on our work developing Magnetically Activated Receptor Signaling (MARS) – a magnetic nanoparticle–based technique for activating cell surface receptors and controlling the activity of biomolecules such as growth factors. The basic principles involve surface functionalization of magnetic nanoparticles (MNPs) with molecules targeting specific cell surface receptors. We have investigated antibodies targeting specific ion channels (e.g. TREK-1), surface receptors (e.g. PDGFRα & β) and peptides (e.g. RGD) targeting integrins. The particles bind to the receptors and, upon the application of a high-gradient external magnetic field, energy is transferred to the particles. The energy delivery induces a conformation change in the receptor, activating the specific biochemical signaling pathway associated with that receptor. By targeting specific receptors, we have been able to control ion channel activity, activate bone and cartilage matrix formation, and control the differentiation of human mesenchymal stem cells both *in vitro* and *in vivo*. We have developed this technology for applications in cell engineering/regenerative medicine and stem cell therapy The MARS technology has applications in regenerative medicine, drug screening and cell engineering.

9:06

GA-02. GMR Biosensing – A Versatile Biosensor Platform for Noninvasive Cancer Diagnostics. *S. Wang*[1,2] *1. Materials Science and Engineering, Stanford University, Stanford, CA, United States; 2. Electrical Engineering, Stanford University, Stanford, CA, United States*

Blood borne biomarkers, such as secreted proteins, circulating tumor DNA (ctDNA) and circulating tumor cell (CTC), have garnered much attention as minimally invasive cancer biomarkers for the "liquid biopsy" of tumors over the past decade. In this talk, we will describe three magnetic-nanoparticle-based diagnostic tools that have been used to assess cancer in peripheral blood successfully: 1) Stanford spin-off MagArray Inc. has launched REVEAL, a cancer-specific blood test that may aid clinicians in characterizing indeterminate pulmonary nodules (4-30mm) in current smokers aged 25-85. The REVEAL Score (Figure 1) is calculated using an algorithm based on the measurement of 3 clinical factors and 3 blood proteins associated with the presence of lung cancer. The GMR biosensor assay is optimized to rule out lung cancer with a negative predictive value (NPV) of ≥ 94%. 2) We have developed sequence-specific capture of hypermethylated or mutated genes of interest from cfDNA for early detection of colorectal cancer (CRC). With downstream analysis of polymerase chain reaction (PCR) products on giant magnetoresistive (GMR) biosensors and high-resolution melt analysis for a highly multiplexable assay, we have achieved a sensitivity of 0.01% mutant/methylated allele fractions. Our optimized assay has the ability to detect down to 16 pg (~4 genome equivalents) of hypermethylated DNA spiked-in to 3.5 mL of plasma. 3) We have utilized the MagSifter and immunocytochemistry combined with automated image analysis and machine learning techniques (random forest, transfer learning) for the enumeration and diagnosis/prognosis of non-small cell lung cancer (NSCLC) derived CTCs in patient samples, which are well suited for therapy selection and monitoring.

1. R. S. Gaster, D. A. Hall et al., "Matrix-insensitive protein assays push the limits of biosensors in medicine," *Nature Medicine*, 15, 1327-1332, 2009. 2. V.S. Nair, H. Yu, A. Juang, A. Hattori, M. Ito, G. Horng, W. Kuschner, S.M. Hanash, M. Beggs, L. Carbonell, S.X. Wang, "Plasma TIMP-1 Identifies Lung Cancer in Smokers," the 2016 ATS International Conference in San Francisco, California, MAY 18, 2016. 3. N. N. Trivedi et al., "Analytical validation of a novel multi-analyte plasma test for lung nodule characterization," *Biomed Res Rev*, 2(3): 1-10, 2018. 4. G. Rizzi, J.-R. Lee et al., "Simultaneous Profiling of DNA Mutation and Methylation by Melting Analysis Using Magnetoresistive Biosensor Array," *ACS Nano* 11, 8864-8870, 2017. 5. S. Park, D. J. Wong, C. C. Ooi et al., "Molecular profiling of single circulating tumor cells from lung cancer patients," *Proc. Natl. Acad. Sci.* (*PNAS)*, 113(52): E8379–E8386, 2016.

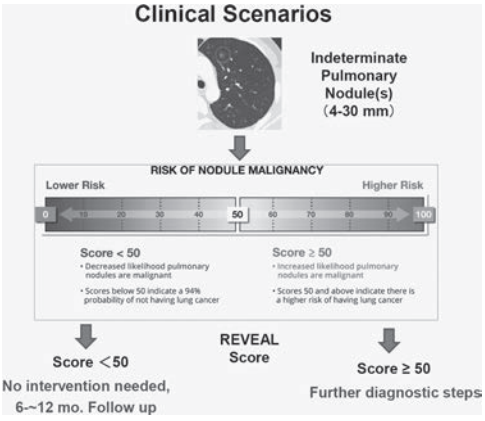


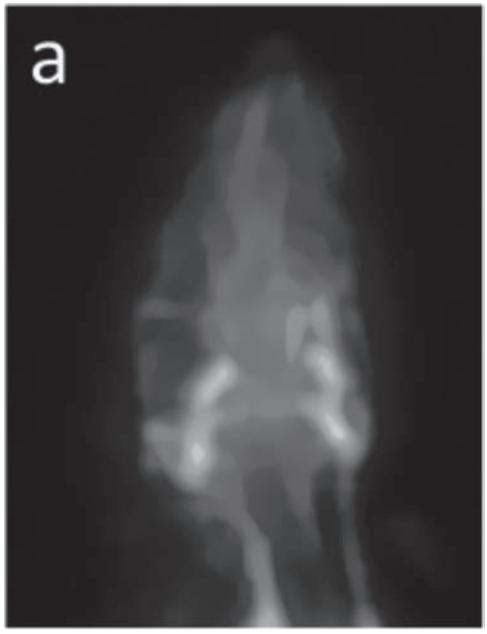
Figure 1: REVEAL Score to assess the probability of malignancy of inderminate lung nodules found in CT scans in human patients. The score is calculated with an algorithm from protein biomarker concentrations (measured by GMR biosensors) and clinical factors.

9:42

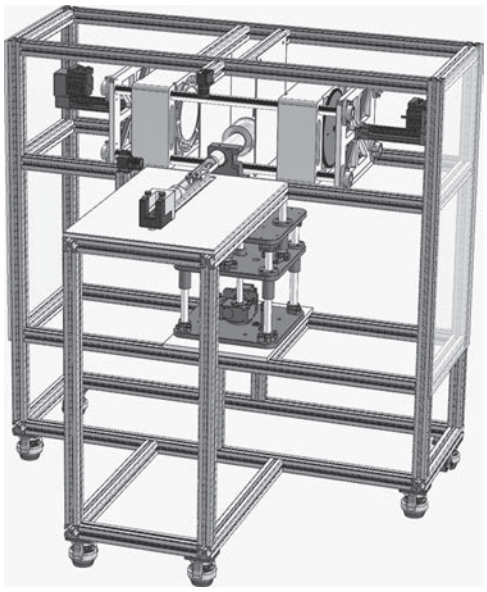
GA-03. Magnetic Particle Imaging and Guided Magnetic Hyperthermia. *P. Goodwill*[1], D. Hensley[1], Z. Tay[2], E. Yu[1], B. Kettlewell[1], R. Orendorff[1], M. Weber[1], K. Fields[1] and S. Conolly[2] *1. Magnetic Insight, Inc., Alameda, CA, United States; 2. Bioengineering, University of California, Berkeley, Berkeley, CA, United States*

Magnetic Particle Imaging (MPI) is an emerging tracer imaging technique that directly detects superparamagnetic iron oxide (SPIO) nanoparticles with exceptional contrast and high sensitivity at millimeter-scale resolutions[1]. MPI's contrast is similar to nuclear medicine, but without the complex workflow, safety, and half-life limitations of a radioactive tracer. These capabilities help fill in some of the gaps of current technologies and position MPI as complementary to anatomical imaging techniques such as MRI and X-ray/CT. The magnetic properties of the nanoparticle tracers seen by MPI define the technique's image resolution and sensitivity. This is because the MPI signal arises from the interaction between a magnetic nanoparticle, a strong magnetic field gradient, and a time varying magnetic drive field.[2,3]. Our group and others have begun testing MPI on animal models. We have used long circulating PEG coated nanoparticles to image the brain, detect cancers,[5] detect gut bleeds,[6] and visualize traumatic brain injury.[7] MPI's high sensitivity also makes it well suited for cell tracking [8-10]. For example, we have tracked therapeutic neural stem cells for three months[8] and the biodistribution of mesenchymal stem cells post administration.[9] In the future, we see opportunities for MPI tracking of immune therapies or immune cells to sites of inflammation such as cancer. Magnetic Fluid Hyperthermia (MFH) is a promising magnetic nanoparticle (MNP)-based therapy for diseases such as cancer [11,12]. Currently, MFH largely relies on nanoparticle localization (e.g., via direct injection of MNPs) for therapy localization. Here we describe how MPI and MFH can be combined into new instrumentation that incorporates strong field gradients to enable a second form of spatial localization, magnetic localization. Based on creation of a "field-free region" (FFR) using spatial gradient fields, this approach allows us to have flexible control over which MNPs are actuated (heated) anywhere within a subject to millimeter-scale accuracy [13-15]. We recently constructed prototype hardware for combined MPI-MFH (FIG 2), which uses gradient fields to spatially locate MNPs to be heated. MNPs coincident with the FFR are free to rotate and can be heated or actuated more generally, while MNPs away from the FFR are locked in place, unable to rotate. We are then able to target regions of interest (ROIs) located anywhere in the body while avoiding regions containing MNPs, such as the liver. A user's workflow would be comprised of determining ROIs using a first imaging modality, such as MPI, that this then co-registered to the MPI-MFH system. ROIs include target regions and regions that must be avoided in therapy. Using this information, a therapeutic trajectory is then generated and applied. A therapeutic trajectory generally consists of serially heating target regions. Beyond treatment of diseases using direct injection of MNPs into an ROI, we are also interested in enabling new RF actuation applications using systemic injection of MNPs followed by local targeting. For example, we can locally release drug [16] (break thermally labile bonds/nanocarriers) without requiring active chemical targeting. MPI combined with MFH enables targeted heating with tailored therapies while avoiding regions of MNP accumulation in healthy tissue, potentially opening the door to applications that do not require direct injection. Further, combining MPI image-guided MFH could one day be used in workflows similar to image-guided radiation therapy or image-guided high intensity focused ultrasound.

1. Gleich, B. & Weizenecker, J. *Nature* 435,1214–1217 (2005). 2. Goodwill, P. W. & Conolly, S. M. *IEEE Trans Med Imaging*29,1851–1859 (2010). 3. Rahmer, J., Weizenecker, J., Gleich, B. & Borgert, J. *BMC Med Imaging*9,4 (2009). 4. Kemp, S. J., Matthew Ferguson, R., Khandhar, A. P. & Krishnan, K. M. *RSC Adv*6,77452–77464 (2016). 5. Yu, E. Y. *et al. Nano Lett*17,1648–1654 (2017). 6. Yu, E. Y. *et al.ACS Nano*11,12067–12076 (2017). 7. Orendorff, R. *et al.Phys Med Biol*62,3501–3509 (2017). 8. Zheng, B. *et al.Sci Rep*5,14055 (2015). 9. Zheng, B. *et al*. *Theranostics*(2015). 10. Wang, P. *et al*. *Quant. Imaging Med. Surg.*8,114–122 (2018). 11. Jordan, A. et al. *Journal of Magnetism and Magnetic materials*, (1999). 12. Latorre, M. *Puerto Rico health sciences journal*, *28*(3) (2009). 13. Murase, K. *Physica Medica*, *29*(6), 624-630 (2013). 14. Hensley, D. *Physics in Medicine & Biology*, *62*(9), 3483 (2017). 15. Tay, Z. *ACS nano*, *12*(4), 3699-3713 (2018). 16. Liu, J. F., *Small*, *14*(44), 1802563 (2018).



MPI blood pool image of a live rat using a PEG coated MPI tracer.



Prototype MPI-MFH hardware capable of targeted actuation (heating) in mice and rats.

10:18

GA-04. Wireless Stress Sensor Based on Magnetoelastic Microwires for Biomedical Applications. *P. Marin*[1], D. Archilla[1], E. Navarro[1], J. López[1] and m. Vélez[2] *1. Instituto de Magnetismo Aplicado, Universidad Complutense de Madrid, Madrid, Spain; 2. Instituto de Catálisis, Consejo Superior de Investigaciones Científicas, Madrid, Spain*

In recent years, much interest and effort have been devoted to develop soft magnetic materials due to their technological potential [1]. Amorphous microwires are one of the most widely studied soft materials. They are

fabricated by means of extracting melt-spinning Taylor technique [2]. Those microwires are composed by a metallic core and a Pyrex cover both in the micrometer range. The ratio between the total diameter and the magnetic core, often called aspect ratio, is one of the key parameters of such microwires, since magnetic properties depend dramatically on it. Many properties of these materials have been deeply studied both from the point of view of the basic physics and the applications. This is the case of the giant magnetoimpedance effect [3], bistability, ferromagnetic resonance [4], and magnetoelastic resonance [5]. It is easy, also, to find much literature regarding microwave-related applications of microwires or microwire-based materials [6]. In the frequency range of GHz, some experimental and theoretical studies of the effect of the magnetization on the scattering properties of a single microwire have been developed [7]. This kind of work gives experimental evidence showing that the microwave scattering by a single microwire depends on the magnetic permeability with sufficient strength to be experimentally detected as an effect of the GMI. This dependence was used to show the potential of such microwire as a wireless field and/or stress sensor. Experimental results are followed by a theoretical approach where the influence of the microwire magnetic state in its microwave reflection features is taken into account. Besides these investigations on magnetic microwires, it should be stated that technological development has spurred the growing interest in the investigation of new biosensors aimed at simplifying present-day diagnostic methods and thereby improving medical care, so that it improves the quality of life of the patients and allows for outpatient treatment for a number of pathologies, avoiding unnecessary hospital admissions. Magnetic sensors are at the helm of technological development seen in this field over the last decades, offering numerous advantages attributed to their elevated sensitivity, reduced size, systems without the need for an external source of energy, and wireless connections. The use of wireless sensor network (WSN) technologies offers the possibility of developing implantable biomedical sensors allowing for the monitorization and follow-up of certain physiological parameters with precise and, up until now, unthinkable measurements. The aim of the present work is to show the physical fundamentals and the particular biomedical applications of magnetic microwires as wireless stress sensors. Two main applications will be described. On one side we proposed a flexible magnetic element able to be integrated both in artery and prosthesis suitable for wireless localized blood pressure monitoring. The sensor made of a ring of glass-covered magnetic microwire is simple and inexpensive and could be detected by means of a simple exciting and detecting set up able of emitting and detecting microwaves simultaneously applying a low-frequency magnetic field. The reflectivity of the microwire is determined by mechanical changes. In the experimental study, a piece of a cardiovascular prosthesis and a piece of an artery both sensed with a ring of magnetic microwire have been situated in a hydraulic setup simulating cardiovascular human circuit. Reflectivity changes of the sensor show its capability of measuring pressure variations in the circuit. The same kind of material and based also in the same kind of experiment has been used to wirels determine colagen density and stress distribution to determine stress distribution on bioreactors.

[1] P. Marín, M. López, P. Agudo, M. Vázquez, A. Hernando. Sensors and Actuators A: Physical. Vol.91(1-2), p.218 (2001) [2] G.F. Taylor Physical Review B. Vol.23, p.4655 (1924) [3] R.S. Beach, A.E. Berkowitz. Applied Physics Letters. Vol (64), p.3652 (1994) [4] L. Kraus, G. Infante, Z. Frait, M. Vázquez. Physical Review B Vol.83, p. 174438 (2011) [5] P. Marín, M. Marcos, A. Hernando. Applied Physics Letters. Vol. 96, p.262512(1) (2010) [6] C. Herrero-Gómez, P: Marín, A: Hernando. Applied Physics Letters. Vol.103, p.142414(1) (2013) [7] C. Herrero-Gómez C, A.M. Aragón, M. Hernando-Rydings, P. Marín, A. Hernando. Applied Physics Letters. Vol.105, p.092405(1) (2014)-

10:54

GA-05. Rotating magnetic fields in particle manipulation: Applications in attacking microbes, transport through tissues, and drug delivery.

L. Mair[1] and I. Weinberg[1] *1. Weinberg Medical Physics, Inc, North Bethesda, MD, United States*

Magnetic particles in the presence of rotating magnetic fields have the ability to impart mechanical shear to biological systems. Such shear can be used to induce separation of microbes from biofilms, enhance the transport of particles undergoing magnetophoretic transport through viscoelastic media, or enable directed transport via surface-mediated particle tumbling. In this talk we will review some of the most promising particles which rely on rotating magnetic fields for their application in medicine, and discuss three ways in which we are using rotating magnetic fields to enhance particle functions in future medical settings. Specifically, we will discuss using rotating magnetic particles to treat microbial biofilms, to enhance the transport of particles through brain tissue, and to deliver drugs to the targeted regions of the cortex and spinal cord *in vitro*. We will discuss the manipulation of hard magnetic particles in the frequency range of 1 Hz to 1000 Hz, and lay out paths forwards for further improving the application of magnetic particles in medicine, as well as how these manipulation schemes may interface with medical imaging modalities such as MRI and ultrasound.

Session GB
GENERATING AND ENHANCING SPIN CURRENTS
Ken-ichi Uchida, Chair
National Institute for Materials Science, Tsukuba, Japan

CONTRIBUTED PAPERS

8:30

GB-01. Spin Coherence Length in Ferrimagnetic CoGd. *Y. Lim*[1], B. Khodadadi[1], J. Li[2], D. Viehland[2] and S. Emori[1] *1. Physics, Virginia Tech, Blacksburg, VA, United States; 2. Materials Science and Engineering, Virginia Tech, Blacksburg, VA, United States*

Ferrimagnets consisting of transition metal and rare-earth metal sublattices are promising materials exhibiting efficient spin torque switching and ultra-fast magnetization dynamics [1,2]. Recently, a long transverse spin coherence length of >10 nm for the ferrimagnetic CoTb has been reported, despite the strong spin-orbit coupling of Tb [3]. Here, we determine the spin coherence length in CoGd which has weaker spin-orbit coupling than CoTb by using broadband ferromagnetic resonance (FMR) spin pumping on NiFe(7 nm)/Cu(4 nm)/CoGd(t nm) [4]. A coherent spin current is pumped from the resonantly excited NiFe layer and decoheres in the CoGd spin sink. Gilbert damping in the NiFe spin source is enhanced with spin decoherence in CoGd, such that the relationship between the measured damping and CoGd thickness provides direct insight into the spin coherence length in CoGd. Such a measurement shows that the CoGd layer actually acts as a good spin sink layer, as evidenced by a significant increase of damping (Fig 1). We also find that the enhanced damping saturates at the CoGd thickness of ~2 nm or less, comparable to the trend observed for ferromagnetic Co spin sink structures (Fig. 2). This suggests that the spin coherence length in ferrimagnetic CoGd layer is short, similar to that in ferromagnetic metals. Our results point to the need for further studies on the spin coherence length in ferrimagnets.

[1] K. Kim, S. Kim, Y. Hirata et al., Nature Materials., Vol. 16, p.1187–1192 (2017) [2] M. Hennecke, I. Radu, R. Abrudan et al., Phys. Rev. Lett., Vol. 122, p.157202 (2019) [3] J. Yu, D. Bang, R. Mishra et al., Nature Materials., Vol. 18, p.29-34 (2019) [4] A. Ghosh, S. Auffret, U. Ebels et al., Phys. Rev. Lett., Vol. 109, p.127202 (2012)

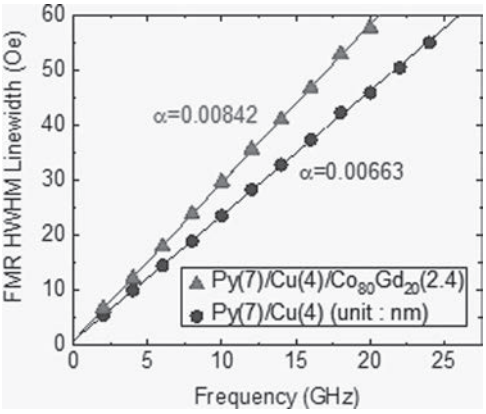


Fig. 1 : Frequency dependence of FMR linewidth for samples with and without a CoGd spin sink. For each sample, the Gilbert damping parameter α is extracted from the linear fit.

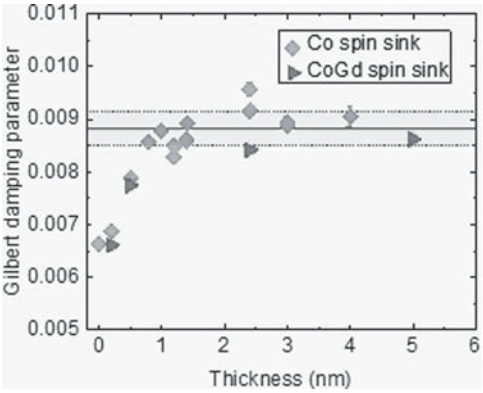


Fig. 2 : Gilbert damping parameter plotted against the thickness of the spin sink layer (Co or CoGd).

8:42

GB-02. Coherent AC spin current transmission through antiferromagnetic CoO probed by X-ray ferromagnetic resonance. Q. Li[1], M. Yang[1], *C. Klewe*[2], P. Shafer[2], A.T. N'Diaye[2], D. Hou[3], T. Wang[1], N. Gao[1], E. Saitoh[3], C. Hwang[4], R. Hicken[5], J. Li[6], E. Arenholz[2,7] and Z.Q. Qiu[1] *1. Department of Physics, University of California, Berkeley, CA, United States; 2. Advanced Light Source, Lawrence Berkeley National Laboratory, Berkeley, CA, United States; 3. WPI Advanced Institute for Materials Research, Tohoku University, Sendai, Japan; 4. Korea Research Institute of Standards and Science, Daejeon, The Republic of Korea; 5. Department of Physics and Astronomy, University of Exeter, Exeter, United Kingdom; 6. International Center for Quantum Materials, Peking University, Beijing, China; 7. Cornell High Energy Synchrotron Source, Cornell University, Ithaca, NY, United States*

For decades, ferromagnetic materials have dominated the field of information technology. Recently, however, there has been a boost of new research in antiferromagnetic (AFM) materials. While these materials to-date have primarily been used to manipulate the magnetization reversal in adjacent ferromagnets through exchange bias, researchers today strive to harness the potential applications of antiferromagnetic materials for low power spintronics devices. In particular, new studies have proven AFM insulators to be excellent conductors of DC spin currents with intriguing temperature dependent transmission properties [1-4], however it is unclear to what extent coherent AC spin currents can be transmitted through an AFM material. We used X-ray detected ferromagnetic resonance (XFMR) [5-7] to study spin dynamics in $Ni_{80}Fe_{20}$/Ag/CoO/Ag/$Co_{75}Fe_{25}$ multilayers [8]. We were able to excite and observe AC spin current propagation from the $Ni_{80}Fe_{20}$ source to the $Co_{75}Fe_{25}$ sink layer at different temperatures around the CoO antiferromagnetic transition. By utilizing the element resolved phase information, we can unambiguously distinguish between different contributions to the magnetic excitation and identify the spin current signal. Our findings show that a coherent AC spin current is transmitted through antiferromagnetic CoO, and that transmission is strongly enhanced around its Neel temperature

(see Fig.1). Additionally, in order to investigate the mechanisms behind the AC spin current transmission through antiferromagnetic CoO in detail, we utilized linearly polarized x-rays for the dynamic XFMR measurements, enabling sensitivity to the spin axis rather than only the spin direction and allowing to observe spin excitations even in the absence of a net magnetic moment.

[1] C. Hahn *et al.*, EPL 108, 57005 (2014). [2] H. Wang *et al.*, Phys. Rev. Lett. 113, 097202 (2014). [3] W. Lin *et al.*, Phys. Rev. Lett. 116, 186601 (2016). [4] Z. Qiu *et al.*, Nat. Commun. 7, 12670 (2016). [5] M. K. Marcham *et al.*, J. Appl. Phys. 109, 07D353 (2011) [6] A. Baker *et al.*, Phys. Rev. Lett. 116, 047201 (2016). [7] J. Li *et al.*, Phys. Rev. Lett. 117, 076602 (2016). [8] Q. Li *et al.*, submitted for publication (2019).

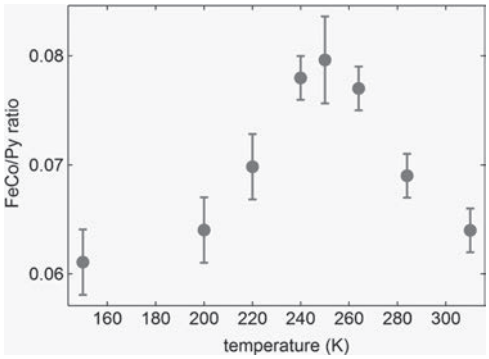


Fig. 1: Ratio between $Co_{75}Fe_{25}$ and Py XFMR amplitude. The AC spin current induced $Co_{75}Fe_{25}$ excitation shows a pronounced enhancement around the CoO Neel temperature.

8:54

GB-03. Spin Polarization Characterization by Spin Hall Magnetoresistance in Ferrimagnetic Pt/$Co_{1-x}Tb_x$ bilayers. Y. Xu[1,2], J. Zhao[1,2] and *D. Wei*[1,2] *1. State Key Laboratory of Superlattices and Microstructures, Institute of Semiconductors, Chinese Academy of Sciences, Beijing, China; 2. Center of Materials Science and Optoelectronics Engineering, University of Academy of Science, Beijing, China*

Rare earth-transition metal (RE-TM) ferrimagnets have compensation of magnetic properties duo to the competition between antiferomagnetically coupled sublattices. They have received great attentions and are utilized in varies of spintronics devices. For example, the high efficiency of SOT has been realized in Pt/CoTb near the compensation point of magnetization for the small magnetic moments [1], while the fast domain wall motion is achieved in FeCo/Gd near the compensation point of angular momentum for fast dynamic behaviors [2]. The spin polarization (*P*), which is directly related to all spin related transport phenomena, could also exhibit the compensation. The possible degrade of *P* due to the compensation must be considered for any practical application of ferrimagnetic materials for spintronics devices. However it is barely mentioned probably due to the difficulty in probe the *P*. Here we provid a convenient way to characterizing the spin polarization of the RE-TM ferrimagnets via the spin Hall magnetoresistance (SMR). We study the spin transport behavior in Pt/$Co_{1-x}Tb_x$ bilayers by varying x and temperature, and an anomalous behavior of SMR near the temperature compensation point of magnetization (T_M) was observed. As the shown by Fig.1, the R_{AH} has a sharp sign change at T_M =238 K, where the AMR also vanishes. In contrast, the SMR has a minimum below T_M. As shown by Fig. 2, we attribute this phenomenon to the compensation and dramatical change of *P* of $Co_{1-x}Tb_x$ alloy, which modulate the degree of the absorption for the longitudinal spin current flowing from Pt layer. The spin polarization was extracted from the SMR and plotted in Fig.2 (b), and the temperature compensation point of spin polarization (T_P) was determined to be at T_P =220 K.

[1] R. Mishra, *et. al*., Phys. Rev. Lett. 118, 167201 (2017). [2] K.-J. Kim, *et al*., Nat. Mater. 16, 1187 (2017).

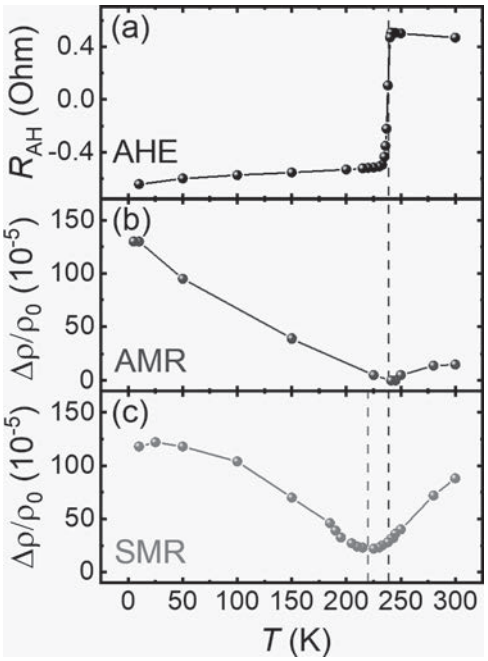


Fig.1 Temperature dependence of the anomalous Hall resistance (a), AMR (b), and SMR (b) respectively, the blue dash line shows the T_M.

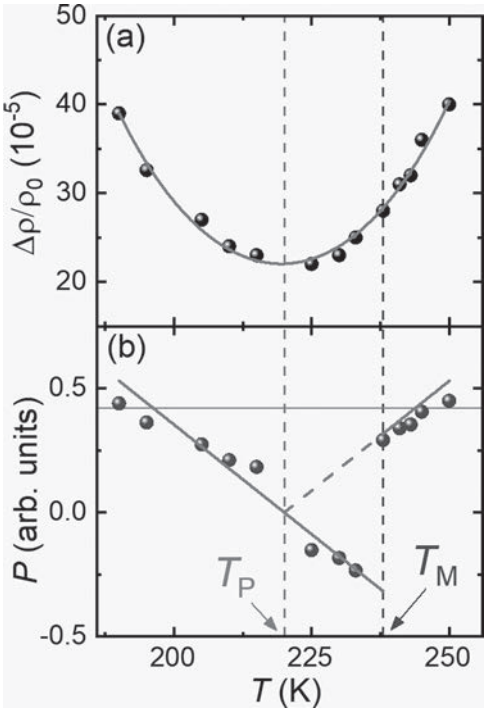


Fig.2 (a) SMR measured as the function of temperature in the neighborhood of SMR minimum, (b) The deduced spin polarization, red curves are the fitting outcome.

INVITED PAPER

9:06

GB-04. The ferroelectric Rashba semiconductor GeTe for spin-orbit logic. S. Varotto[1], L. Nessi[1], S. Cecchi[2], P. Noel[3], S. Petrò[1], I. Vobornik[4], G. Panaccione[4], R.J. Cava[5], R. Calarco[2], M. Cantoni[1], L. Vila[3], R. Bertacco[1] and *C. Rinaldi*[1] *1. Physics, Politecnico di Milano, Milano, Italy; 2. Epitaxy, Paul-Drude-Institut für Festkörperelektronik, Berlin, Germany; 3. Univ. Grenoble Alpes, CNRS, CEA, Grenoble INP, IRIG-SPINTEC, Grenoble, France; 4. Istituto Officina dei Materiali CNR Laboratorio TASC, Basovizza, Italy; 5. Department of Chemistry, Princeton University, Princeton, NJ, United States*

Scalable and energy efficient spin-orbit logic has been very recently pointed out by Intel as technologically suitable computing alternative to CMOS devices [1]. It comprises an electrically driven memory element, with a spin-orbit-based detection of the state performed by spin-to-charge conversion. In this talk, we show that the *ferroelectric Rashba semiconductor Germanium Telluride* [2] offers memory as well as both electric and spin-orbit readout in a silicon-compatible semiconductor. Indeed, GeTe possesses giant bulk *Rashba-like spin texture*, which can be reversed by its non-volatile *ferroelectricity*, paving the way to the electric control of *spin-to-charge conversion*. We have already proved the existence of two opposite spin textures in GeTe thin films, corresponding to opposite ferroelectric states [3]. Here, we first demonstrate the *switchability of the ferroelectric polarization* in films of GeTe *through gate electrodes,* enabling the *electric control of charge transport and spin-to-charge conversion*. The switching is obtained through voltage pulses and measured as resistance variation of metal/GeTe heterojunctions. The modulation of resistance is due to the different local band bending induced at the metal/semiconductor interface by the screening of the polarization charge. Piezoresponse Force Microscopy correlated the microscopic distribution of ferroelectric domains with the electrical resistivity of the junction. The low-voltage control is provided by the coercive voltage (3-7 V), with *modulation of resistivity up to 800%.* The switching is robust, with *endurance up to 10^5 cycles*. The number of subsequent voltage pulses, their amplitude and duration, as well as ferroelectric minor loops, enable a continuous distribution of intermediate resistive states. The control over ferroelectricity enables the electric control of spin-to-charge interconversion. The latter is studied by spin Hall magnetoresistance [4] and spin pumping [5] in Fe/GeTe heterostructures [6], where the magnetic layer serves as detector or injector of spins, respectively. Finally, we show how to obtain *carrier compensation* of the intrinsic and degenerate *p*-doping of GeTe, keeping alive Rashba effect and ferroelectricity, towards the realization of single-compound spin-orbit logic devices.

[1] S. Manipatruni *et al.*, Nature, Vol. 565, p. 35 (2019) [2] D. Di Sante *et al.*, Adv. Mater., Vol. 25, p. 509 (2013) [3] C. Rinaldi *et al.*, Nano Letters, Vol. 18, p. 2751 (2018) [4] S. Varotto *et al.*, Proc. SPIE Vol. 10732, Spintronics XI, p. 10732 (2018) [5] C. Rinaldi *et al.*, APL Mater., Vol. 4, p. 032501 (2016) [6] J. Slawinska *et al.*, Phys. Rev. B, Vol. 99, p. 075306 (2019)

CONTRIBUTED PAPERS

9:42

GB-05. Effects of a Molecular C_{60} Interface on the Spin-dependent scattering of YIG/Pt. *S. Alotibi*[1], M. Ali[1], B. Hickey[1] and O. Céspedes[1] *1. University of Leeds, Leeds, United Kingdom*

We have studied the Spin Hall magnetoresistance (SHMR) in YIG/Pt interfaces with and without a C_{60} overlayer. The SHMR is generated by a current flow in thin (~nm) heavy metal layers with a large spin orbit coupling (SOC) deposited on a magnetic insulators. A spin current (Js) is generated in the metallic layer, perpendicular (⊥) to the electronic current. When the direction of the magnetisation (M) in the ferrimagnet is parallel to Js, the spin current is reflected from the interface and back into the metal due to the inverse spin Hall Effect. However, if the direction of the M and spin polarisation are ⊥, the Js propagates into the insulator as spin waves. Thus, the SHMR can be observed by rotating the M vector. This effect has generated large interest and it is critical in the study of spin orbit scattering and its applications, e.g. for devices such as spin torque MRAM [1, 2]. At metallo-molecular interfaces, the electronic properties of both materials are changed due to charge transfer and hybridisation. Previously, it has been shown that this can lead to the emergence of spin ordering.[3]. This interfacial effect is also critical in spin filtering and spin transport effects.[4]. Here, we have studied the effect of C_{60} interfaces on the SHMR and low field, anisotropic magnetoresistance (AMR) generated in YIG/Pt. We find that conducting interface formed between C_{60} and Pt layers results in lower resistance%. The SHMR of Pt layers between 1.5 and 5 nm is enhanced by up to a factor 6 with C_{60} see Fig.1. Thus, the spin Hall angle Θ_{SH} is bigger for Pt/C60 than Pt, which we attribute to an enhancement of the SOC by the C_{60}. The AMR at fields ≤10 mT can be correlated with the M of the YIG surface. This low field AMR is also enhanced by the C_{60}, in particular when the field is applied out of plane see Fig.2. This is all consistence with an enhanced spin orbit scattering in Pt induced by a C_{60} overlayer, and molecules could then be used to improve the performance of spin orbit torque devices.

1. H. Nakayama, *et al*., Phys. Rev. Lett. 110, 206601 (2013) 2. S. Marmion, *et al*., Phys. Rev. B. 89, 220404 (2014) 3. F. Al ma'mari, *et al*., Nature. 524, 69—73 (2015) 4. M. Cinchetti, *et al*., Nature materials. 16, 507 (2017)

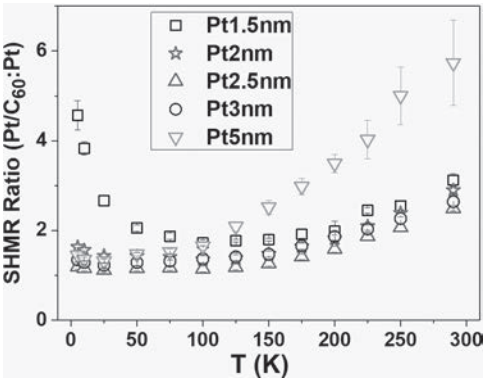


Fig.1. Ratio of the SHMR of Pt on YIG with and without a C_{60} layer.

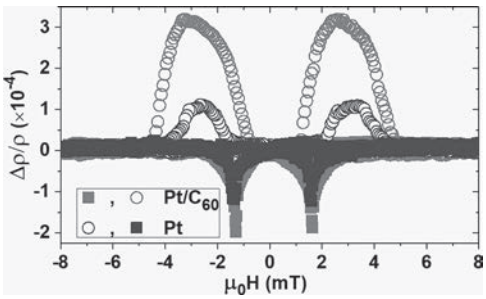


Fig.2.AMR peaks at 200 K for YIG(170 nm)/ Pt(1.5 nm) with (red) and without C_{60} (blue) for out-of-plane (open symbols) and in-plane longitudinal fields (closed).

9:54

GB-06. Large Anomalous Hall Effect in Amorphous $Fe_{1-y}Co_ySi$ Thin Films. *J. Karel*[1,2], D. Bouma[3,4], S. Bennett[1], A. Nguyen[1] and F. Hellman[3,4]
1. Materials Science and Engineering, Monash University, Melbourne, VIC, Australia; 2. ARC Centre of Excellence in Future Low-Energy Electronics Technologies, Monash University, Melbourne, VIC, Australia; 3. Materials Science Division, Lawrence Berkeley National Lab, Berkeley, CA, United States; 4. Physics Department, University of California Berkeley, Berkeley, CA, United States

Magnetoresistive random access memory (MRAM) utilizing spin orbit torque (SOT) based switching has emerged as a promising non-volatile memory candidate, and amorphous materials offer a unique prospect with respect to this technology. They lack long range order, and theory has predicted that disorder may lead to an enhancement in spin orbit torques.[1,2] Moreover, amorphous materials are extremely tolerant to defects, meaning less stringent manufacturing requirements and thus lower costs. This work will present a study of the anomalous Hall effect (AHE) in a series of amorphous $Fe_{1-y}Co_ySi$ ($0<y<1$) thin films. The mechanisms used to describe the spin Hall effect (SHE) borrow directly from the physics of the AHE; therefore, a large AHE may point to a large SHE and a potential application in SOT-MRAM. A large AHE was found in amorphous $Fe_{1-y}Co_ySi$ thin films with y = 0-0.3 (representative plot Figure 1a). The magnitude of the Hall resistivity is larger than previously reported in the bulk crystalline analog (e.g. $Fe_{0.9}Co_{0.1}Si$ ~2μΩcm at 5K).[3] This large effect persists up to room temperature. Figure 1b shows that the magnetic moment is also larger than previously reported in bulk crystalline $Fe_{1-y}Co_ySi$ (e.g. y=0.1 M_s~50 emu/cm^3).[3] Similar enhancements in magnetization have been reported in amorphous Fe_xSi_{1-x}($0.45<x<0.65$) thin films in comparison to the crystalline analogue.[4] The origins of this large AHE will be discussed. Specifically, we will show that the results suggest the intrinsic mechanism (e.g. non-zero Berry curvature) may play an important role. In these amorphous materials, the possible dependence of the AHE on the intrinsic mechanism is remarkable because it indicates a local atomic level description of a Berry phase in a system that lacks lattice periodicity.

[1] I. A. Ado, O. A. Tretiakov, *et al.*, *Phys. Rev B* 95, 094401 (2017) [2] O. A. Tretiakov, *et al.,* Phys. Rev Lett 119, 077203 (2017) [3] N. Manyala, *et al., Nature Materials*3255 (2004) [4] J. Karel, *et al.,Europhysics Letters* 11457004 (2016)

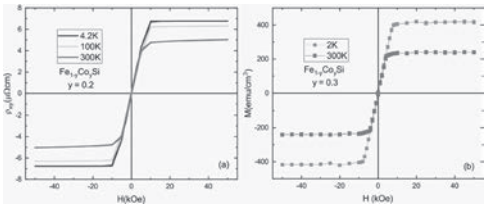


Figure 1. (a) Hall resistivity (ρ_{xy}) versus applied magnetic field (*H*) at various temperatures for a $Fe_{1-y}Co_ySi$ thin film with y = 0.2. (b) Magnetization (*M*) versus applied magnetic field (*H*) measured at various temperatures for y = 0.3. The applied magnetic field is oriented out of the plane of the film. Samples with y = 0-0.3 exhibit similar curves with a magnetic moment of ~400 emu/cm^3.

10:06

GB-07. A first-principles study on the spin anomalous Hall effect of $L1_0$-type alloys. *Y. Miura*[1], K. Nawa[1] and K. Masuda[1] *1. Research Center for Magnetic and Spintronic Materials(CMSM), National Institute for Materials Science(NIMS), Tsukuba, Japan*

Recently, spin anomalous Hall effect (SAHE) which is spin Hall effect (SHE) in ferromagnetic metals has attractive much attention [1,2]. SAHE can generate spin orbit torque (SOT) to magnetization of another ferromagnetic layer through the non-magnetic spacer in magnetic junctions. SOT magnetization switching by the SAHE has an advantage compared with SOT switching by SHE of nonmagnetic metals, because the direction of spin quantum axis of injected electrons related to direction of torque can be controlled by the magnetization direction of the ferromagnetic layers. According to the previous theoretical study[1], the most important parameter to realize large SOT in ferromagnetic layers is a ratio of spin anomalous Hall conductivity (SAHC) σ_{xy}^{spin} to anomalous Hall conductivity (AHC) σ_{xy}, i.e., $\zeta=\sigma_{xy}^{spin}/\sigma_{xy}$. In this work, we investigate and discuss the intrinsic SAHC and AHC on the basis of the firs-principles calculations and the linear response theory. We focused on the $L1_0$-type FePt and FeAu alloys. We assumed that the magnetization is directed parallel to the [001] direction (c-axis), the electric field is applied along [110] direction of fcc lattice, and Hall current flows perpendicular to them. Fig. 1 shows the spin-resolved AHC of $L1_0$-FePt and FeAu. We found that FePt has large AHC σ_{xy}=761[Ω^{-1}cm^{-1}], and SAHC of FePt is σ_{xy}^{spin}=498[Ω^{-1}cm^{-1}]. The SAHC is smaller than that of the AHC, resulting in the small ζ less than 1. This is attributed to relatively large spin-flip AHC $\sigma_{xy}^{\downarrow\uparrow}$ due to strong spin-orbit interaction of Pt. On the other hand, SAHC of FeAu is σ_{xy}^{spin}=472[Ω^{-1}cm^{-1}], which is much larger than that of the AHC σ_{xy}=79[Ω^{-1}cm^{-1}], resulting in the large ζ=5.9. The large ζ in FeAu is originated in the small spin-flip AHC $\sigma_{xy}^{\downarrow\uparrow}$ due to the absence of majority-spin local density of states of Au *d* orbitals of FeAu. This work was supported by Grant-in-Aids for Scientific Research (S) (JP16H06332) from the JSPS.

[1] Taniguchi, *et al*., Phys. Rev. Appl., Vol. 3, P. 044001 (2015). [2] S. Iihama, *et al*., Nature electronics, Vol. 1, P. 120-123 (2018).

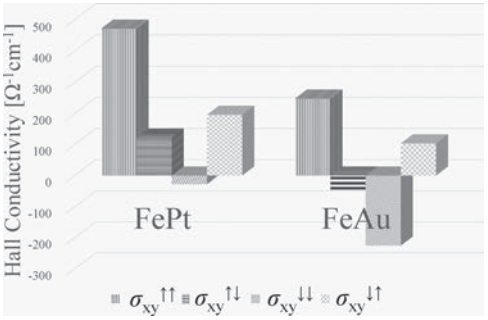


Fig. 1: Spin-resolved anomalous Hall conductivity (AHC) of $L1_0$-FePt and FeAu.

10:18

GB-08. Nonlinear planar Hall effect. P. He[1], *S. Zhang*[2], D. Zhu[1], S. Shi[1], O. Heinonen[2], G. Vignale[3] and H. Yang[1] *1. Department of Electrical and Computer Engineering, and NUSNNI, National University of Singapore, Singapore; 2. Materials Science Division, Argonne National Laboratory, Lemont, IL, United States; 3. Department of Physics and Astronomy, University of Missouri, Columbia, MO, United States*

An intriguing property of a three-dimensional (3D) topological insulator (TI) is the existence of surface states with spin-momentum locking, which offers a new frontier of exploration in spintronics. Here, we report the observation of a new type of Hall effect in a 3D TI Bi_2Se_3 film [1]. The Hall resistance scales linearly with both the applied electric and magnetic fields and exhibits a π/2 angle offset with respect to its longitudinal counterpart, in contrast to the usual angle offset of π/4 between the linear planar Hall effect and the anisotropic magnetoresistance. This novel nonlinear planar Hall effect originates from the conversion of a nonlinear transverse spin current to a charge current due to the concerted actions of spin-momentum locking and time-reversal symmetry breaking, which also exists in a wide class of noncentrosymmetric materials [e.g., WTe_2 and the 2DEG on the $SrTiO_3$(001) surface] with a large span of magnitude. It provides a new way to characterize and utilize the nonlinear spin-to-charge conversion in a variety of topological quantum materials. We will also reveal the correlation

between nonlinear planar Hall and the novel bilinear magneto-electric resistance (BMER) previously discovered in 3D topological insulators [2,3] and at the $SrTiO_3$(111) surface [4]. The work by P. H, D. Z, S. S, and H. Y. was partially supported by the A*STAR's Pharos Programme on Topological Insulators; the work by S.S.-L.Z. and G.V. at the University of Missouri on initial development of the theoretical framework was supported by National Science Foundation (NSF) grant DMR-1406568, and work by S.S.-L.Z. and O. G. H. at Argonne National Laboratory on further theoretical development, data analysis and manuscript writing was supported by Department of Energy, Office of Science, Basic Energy Sciences, Materials Sciences and Engineering Division.

[1] P. He, S. S.-L. Zhang, D. Zhu, et al., Phys. Rev. Lett. (In Press). [2] P. He, S. S.-L. Zhang, D. Zhu, et al., Nat. Phys. Vol. 14, p. 495 (2018). [3] S. S.-L. Zhang and G. Vignale, Proc. SPIE. Vol. 10732, p. 1073215 (2018). [4] P. He, S. M. Walker, S. S.-L. Zhang et al., Phys. Rev. Lett. Vol. 120, p. 266802 (2018).

10:30

GB-09. Interface Magnetic Property Impact on Spin Injection and Pumping in YIG/Ultrathin Magnetic layer/Pt Systems. *H. Yuasa*[1], T. Niimura[1], Y. Kurokawa[1], R. Weber[2] and A. Berger[2] *1. Kyushu University, Fukuoka, Japan; 2. nanoGUNE, San Sebastian, Spain*

The ultrathin magnetic layers were inserted into the interface between YIG and Pt so as to control spin pumping and injection. Although we reported that the spin Seebeck effect (SSE) voltage was increased by the ultrathin magnetic layer insertion between YIG and Pt [1], the reasonable explanation has not been given yet. In this report, we additionally measured spin Hall magnetoresistance (SMR) which are originated from spin pumping, having reciprocal relationship with spin injection generating SSE voltage. The sample structure is SiO_2 wafer/YIG 50 nm/M 0.3 or 0.6 nm/Pt 5 nm where M denotes Cr, $Ni_{80}Fe_{20}$, $Co_{90}Fe_{10}$, $Fe_{50}Co_{50}$ and Fe. As shown in Fig. 1, spin Seebeck coefficient S and ΔR of SMR have the strong correlation as expected, indicating the spin pumping and spin injection were equally controlled by the inserted layers. In order to reveal the reason of SSE and SMR improvement, it is necessary to study magnetic properties of the inserted layers. Figure 2(a) shows the ΔR as a function of bulk-M_s of inserted layers in literature. Although the higher Ms leads the higher ΔR as expected from [2], the M_s is not an actual magnetization here. Unfortunately, the inserted layers are too thin to measure the actual magnetization by macroscopic M-H loop. Therefore, we applied Generalized Magneto-Optical Ellipsometry (GME) to investigated the magnetic properties of ultrathin inserted layers, since GME is sensitive to the surface and the ultrathin inserted layers and YIG possess the different optical constants [3]. Figure 2(b) is ΔR dependence on |α|, where |α| is the off-diagonal element of the reflection matrix due to the longitudinal Kerr effect and denotes a magnetization near the surface. ΔR was obviously decreased as increasing |α|, which is opposite to the relationship of ΔR and bulk-Ms in Fig. 2 (a). Taking into account YIG effect, it is important to extract the original magnetization of inserted layer from |α|. It is the important step to discuss the interface magnetic property impact on spin injection and pumping.

[1] H. Yuasa et al. AIP Advances 7, 055928 (2017). [2] X. Jia et al., Europhys. Lett. 96 17005 (2011). [3] A. Berger et al., Appl, Phys. Lett. 71, 965 (1997).

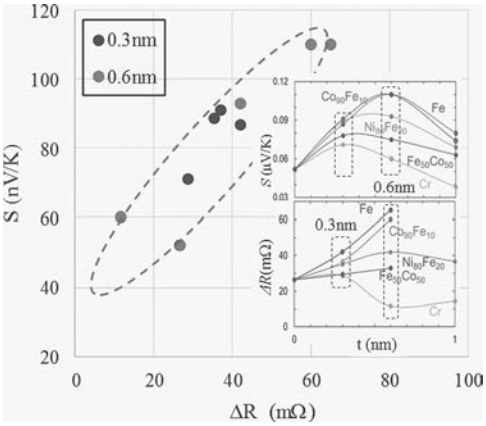


Fig. 1 Relationship between spin Seebeck coefficient S and ΔR of SMR.

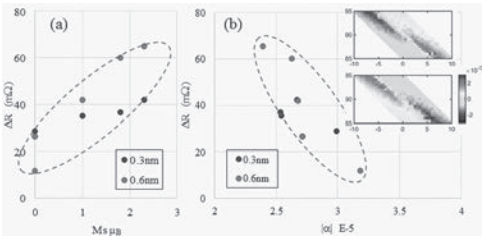


Fig. 2 ΔR as a function of bulk-M_s in literature (a) and |α| obtained by GME. Insets are GME data of YIG 50nm/$Fe_{50}Co_{50}$ 0.3nm/Pt 1nm.

10:42

GB-10. Spin transport in a magnetic insulator with charge current induced zero effective damping. *M. Althammer*[1,2], T. Wimmer[1,2], L. Liensberger[1,2], S. Geprägs[1], M. Weiler[1,2], R. Gross[1,2] and H. Huebl[1,2] *1. Walther-Meißner-Institut, Bayerische Akademie der Wissenschaften, Garching, Germany; 2. Physik-Department, Technische Universität München, Garching, Germany*

Pure spin currents, i.e. the flow of angular momentum without an accompanying charge current represents a new paradigm in the field of spintronics. Most importantly, pure spin currents can be transported by fermions, i.e. by electrons, in electrical conductors as well as by bosons, i.e. by quantized magnetic excitations, in magnetically ordered insulators. Interestingly, heterostructures consisting of spin-orbit coupled metals with magnetically ordered insulators allow to investigate pure spin current transport in both regimes and their interconversion at the interface. We here present our recent experiments [1] on the control of magnon spin transport via a DC charge current injected pure spin current. To this end, we utilize three electrically isolated platinum (Pt) electrodes deposited on an ultrathin yttrium iron garnet (YIG) film. Employing all-electrical injection and detection mechanisms, we provide evidence for efficient spin transport manipulation by a DC charge current in these devices. At large charge current densities we can compensate the effective magnetic damping in the YIG layer underneath the central Pt strip. We then investigate the magnon spin transport through this volume by electrical magnon transport experiments utilizing the remaining two Pt strips to the left and right of the central Pt strip. From these measurements we extract a zero resistance spin transport in the regime of magnetic damping compensation. We discuss the origin of the observed non-linear effects and threshold behavior in the frame work of magnon Bose-Einstein condensation [2] induced by a DC charge current. Above a critical DC current, the magnon density is sufficient to form a magnon condensate and eventually trigger auto-oscillations of the magnetization. We compare these different phases to our diffusive magnon transport experiments to explain the observed a zero-resistance state below the injector strip.

[1] T. Wimmer *et al.*, arXiv:1812.01334 (2018). [2] S. Demokritov *et al.*, Nature 443, 430 (2006).

10:54

GB-11. Mutual spin-pumping in the antiferromagnetically exchange coupled Py/Ru/Py trilayers - dependence on the external magnetic field. *S. Sorokin*[1,2], R. Gallardo[3], K. Lenz[1], C. Fowley[1], G. Atcheson[4], J. Fassbender[1], J. Lindner[1] and A.M. Deac[1] *1. Institute of Ion Beam Physics and Materials Research, Helmholtz-Zentrum Dresden-Rossendorf, Dresden, Germany; 2. Institute for Physics of Solids, Technische Universität Dresden, Dresden, Germany; 3. Universidad Tecnica Federico Santa Maria, Valparaíso, Chile; 4. School of Physics, Trinity College Dublin, Dublin, Ireland*

We investigate magnetization dynamics in asymmetric interlayer exchange coupled Py/Ru/Py trilayers using vector network analyzer-based ferromagnetic resonance (VNA-FMR) and electrically-detected ferromagnetic resonance (ED-FMR). Two different FMR modes are observed, as expected for coupled systems, and the two above mentioned approaches are compared. We show, that, unlike in the spin-flop and saturated regimes, which are fairly well understood, in the field range where the two layers remain antiferromagnetically (AF) oriented in static measurements, the changes exhibited in the frequency-field dependence connected only with the changes in the dynamical terms in the coupled Landau-Lifshitz-Gilbert (LLG) equations. On the other hand, it was predicted that the two modes have different linewidth, due to mutual spin-pumping between the layers [1, 2]. This was to-date experimentally confirmed for symmetric Py/Ru/Py synthetic antiferromagnets, in the saturated regime, where the linewidth difference between the modes was practically field-independent [3]. Here, we show, that by changing magnetic field in the AF regime, one can tune the linewidth difference between the modes in case of asymmetric layers. Moreover, a connection between the non-monotonic frequency-field dependence and the variation of the linewidth difference in the AF regime is established, which to our knowledge, was not previously reported in the literature.

1. S. Takanashi, Appl. Phys. Lett. Vol. 104, p. 052407 (2014). 2. H. Skarsvag, G. E. W. Bauer A. Brataas, Physical Review B, vol. 90, p. 054401 (2014). 3. H. Yang, Y. Li, W. E. Bailey, Appl. Phys. Lett., Vol. 108, p. 242404 (2016).

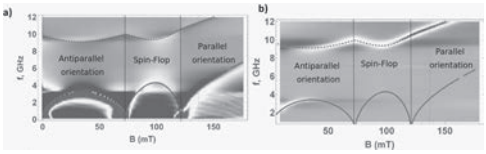


Fig. 1. ED-FMR a) and VNA-FMR b) measurements for Py(9nm)/Ru/Py(3nm). Solid and dashed lines represent modeling according to the LLG equation in the thin film approximation. Main parameters for the modeling: $J_1 = 120$ μJ/m², $M_{eff1} = 577$ kA/m, $M_{eff2} = 420$ kA/m; were estimated from the modeling of the magnetometry data (not shown). Colors represent relative amplitudes of the resonances.

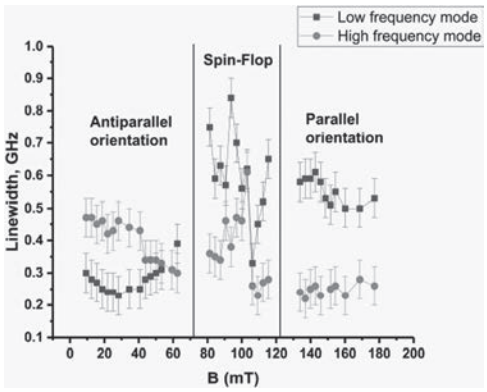


Fig. 2. Dependence of the linewidth of the Py(9nm)/Ru/Py(3nm) sample for low frequency (in black) and high frequency (in red) modes for different magnetic fields. Vertical lines correspond to the different static regimes, namely: antiparallel for the low fields, spin-flop for the intermediate fields, and parallel for high fields (above 120 mT).

11:06

GB-12. Effect of Interface Roughness Spin Scattering on Spin-current Transport in YIG/NiO/Pt Heterostructures. *L. Jin*[1], H. Zhang[1], Z. Zhong[1] and K. Jia[1] *1. University of Electronic Science and Technology of China, Chengdu, China*

In this work, the spin current transport in YIG/NiO/Pt heterostructures were investigated by spin Hall magnetoresistance and inverse spin Hall effect (ISHE) measurements. By inserting antiferromagnetic insulator NiO, the magnetic proximity effect on Pt atoms induced by YIG and anomalous spin Hall voltage can be efficiently blocked. The ferromagnetic resonance and ISHE measurements verify that the ferromagnetic/antiferromagnetic exchange coupling inhibits the transmission of the spin current at the YIG/NiO interface when the NiO layer is thick. Atomic force microscopy and Spherical aberration corrected transmission electron microscopy prove that the strong interface roughness spin scattering between NiO and Pt can largely improve the inverse spin Hall voltage and spin Hall magnetoresistance when the NiO layer is thin or even discontinuous. This interface roughness related spin scattering mechanism based on antiferromagnetic materials is a new discovery and have great potential in the construction of high-speed spintronic devices.

[1] Du C, Wang H, Yang F, et al. Physical Review Applied, 1(4): 044004 (2014). [2] Tao X, Liu Q, Miao B, et al. Science Advances, 4(6): 1670 (2018).

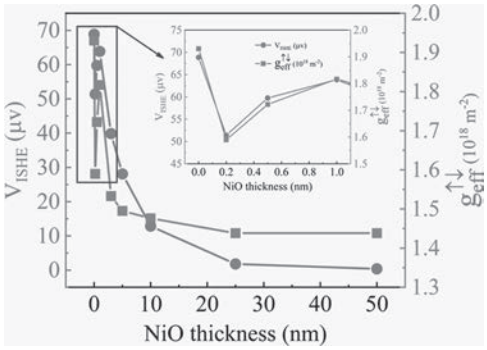


Fig.1

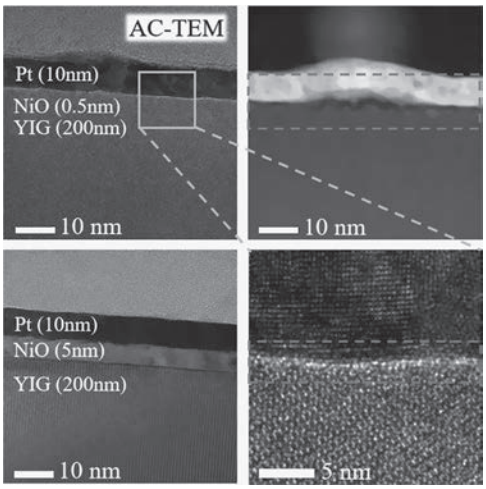


Fig.2

11:18

GB-13. Anisotropic Enhancement of Spin current in Epitaxial Co based Co/Pt/Co trilayer. *J. Ryu*[1], R. Thompson[2], J. Park[1], M. Kohda[2,3], J. Yuk[1], J. Nitta[2,3] and B. Park[1] *1. Materials Science and Engineering, Korea Advanced Institute of Science and Technology, Daejeon, The Republic of Korea; 2. Materials Science, Tohoku University, Sendai, Japan; 3. Spintronics Research Network, Tohoku University, Sendai, Japan*

Spin currents generated by strong spin-orbit coupling in ferromagnet(FM) and heavy metal(HM) provide intriguing physical phenomena. For conventional spin orbit toques(SOTs) in FM/HM systems, the generated spin current is polarized along an in-plane direction[1,2]. In FM/HM/FM trilayers, however, SOTs induced by out-of-plane polarized spin currents are reported, enabling field-free magnetization switching[3,4]. Here, the spin currents in epitaxial Co based Co/Pt/Co trilayers are investigated. We find spin currents present anisotropic enhancements depending on the magnetization of the epitaxial Co. In-plane magnetized Co(4.0nm) is epitaxially grown on an MgO(110) substrate, as the bottom Co has its *c*-axis aligned with MgO[001] (Fig.1(a)) [5]. Therefore, epitaxial Co shows strong magnetocrystalline anisotropy in-plane, where the easy axis and the hard axis correspond to [001] and [-110], respectively (Fig.1(b)). Ta(0.5nm)/Pt(1.5nm)/Co(0.6nm) is subsequently deposited, leading to the perpendicular anisotropy of the top Co layer. Harmonic Hall measurements are performed to investigate spin currents for injected current J_c directions along the easy and hard axes. At an azimuthal field angle of φ_B=0° and 90°, a conventional 2nd harmonic voltage V_{2f} for damping-like and field-like SOT appears for J_c along the easy axis. Strikingly, however, the amplitude of V_{2f} is drastically increased when the external field is applied at φ_B=120°(300°)(Fig.2(a)). Moreover, for J_c along the hard axis, the enhanced is observed at φ_B=30°(210°). The peak of V_{2f} as a function of φ_B in Fig.2(b) clearly suggests that the spin currents generated in epitaxial Co/Pt show an anisotropic enhancement of SOT depending on the bottom Co magnetization state rather than by conventional SOTs in the Pt/Co top layer. Furthermore, field-free switching is achieved for devices aligned with the angle of maximum enhancement of the spin current.

[1] I. M. Miron *et al*., Nature (London) Vol.476, p.189 (2011). [2] L. Liu *et al*., Science Vol.336, p.555 (2012). [3] S-h. C. Baek *et al.*, Nat. Mater. Vol.17, p.509 (2018). [4] V. P. Amin, J. Zemen, M. D. Stiles, Vol.121, p.125805 (2018). [5] Y. Nukaga *et al.*, IEEE Trans. Magn. Vol.45, p.2519 (2009)

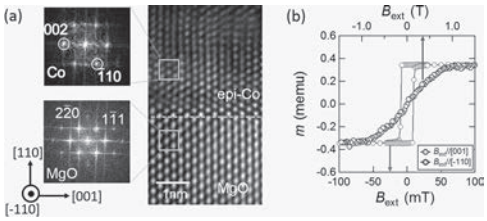


Fig.1(a)Cross sectional transmission electron micrographs in epitaxial Co/MgO. Left panels show Fourier transforms. (b)Magnetic property of epitaxial Co.

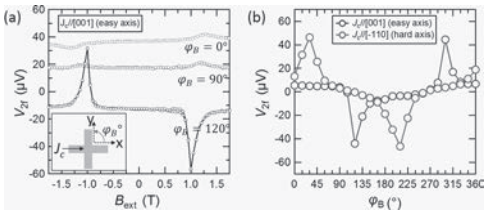


Fig.2(a)V_{2f} depending on external field applied at φ_B=0,90 and 120° for *J*c along the easy axis. Inset indicates experiment schematic. (b)φ_B dependence of the peak of V_{2f}

Session GC
MRAM AND RELATED DEVICES

Damien Querlioz, Chair
Centre de Nanosciences et de Nanotechnologies, Palaiseau, France

CONTRIBUTED PAPERS

8:30

GC-01. High Speed and Low Energy Spin-Transfer Switching of Perpendicular Magnetic Tunnel Junction Nanopillars at Low Temperature. *L. Rehm*[1], G. Wolf[2], B. Kardasz[2], M. Pinarbasi[2] and A.D. Kent[1] *1. Center for Quantum Phenomena, Department of Physics, New York University, New York, NY, United States; 2. Spin Memory Inc., Fremont, CA, United States*

Thermal fluctuations play a central role in the understanding of spin-transfer induced magnetization switching, both the switching time scale and probability. However, systematic spin-transfer switching experiments as a function of temperature have not been conducted on perpendicularly magnetized magnetic tunnel junctions (pMTJs). Here we investigate switching characteristics of 40, 50, and 60nm diameter circular pMTJ nanopillars with CoFeB free layers over a broad range of time scales τ from ms to ns. Figure 1 shows the switching characteristics of a 40nm pMTJ at several temperaturesfor a slow continuous voltage ramp. The resistance in the antiparallel state (R_{AP}) increases significantly as the temperature decreases from room temperature to 4K, resulting in a factor of two increase in TMR (to 214%), while the P state resistance is nearly independent of temperature. Also, the switching voltages increase at low temperatures and R_{AP} decreases with read bias voltage, consistent with the voltage bias opening conduction channels by creating magnetic excitations. We demonstrate pulsed switching from 295 down to 4K with pulse durations below 5ns, thereby probing the ballistic spin-torque switching regime. Figure 2 shows switching phase diagrams of the same device at 4K. We observe reliable sub-ns switching for both switching directions with characteristic time scales of 0.94 and 1.03ns for AP→P and P→AP direction, respectively. This results in low write energies of 66 (AP→P) and 270 fJ (P→AP), comparable to write energies found in metallic spin-valves with a Py free layer [1]. Surprisingly, we observe a speed-up of the reversal in both switching directions at 4K compared to the 295K data at the same overdrive V/V_c. We will also present measurements in the thermally assisted regime ($\tau \geq 10\mu s$), extracting the thermal stability factor and characteristic switching voltage for several temperatures.

[1] L. Rehm *et al.*, Appl. Phys. Lett. 114, 212402 (2019).

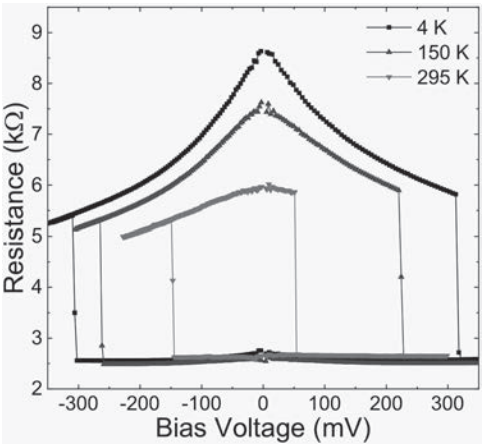


Fig. 1: Quasi-static voltage switching of a 40nm pMTJ at several temperatures.

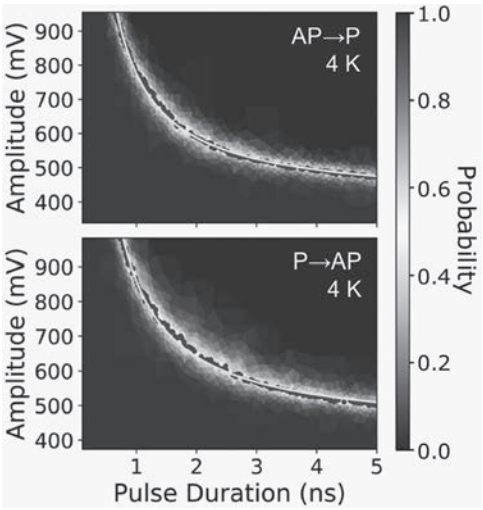


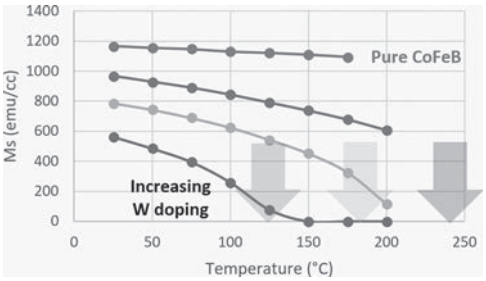
Fig. 2: Pulsed switching phase diagramsof a 40nm pMTJ at 4K. The color bar represents the switching probability. The blue points represent the 50% switching probability and the solid cyan line shows the fit of the macrospin model: $V_{50\%}=V_c(1+t_0/\tau)$.

8:42

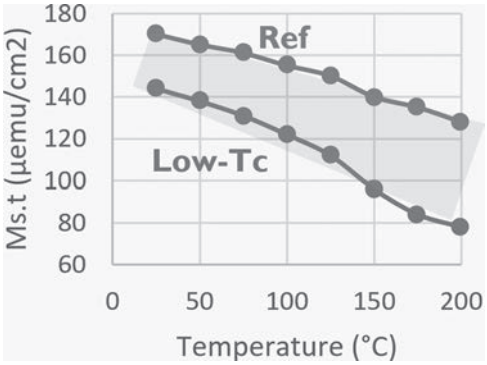
GC-02. Low Tc, low Ms CoFeBX alloy free layers for perpendicular STT-MRAM. *S. Couet*[1], S. Rao[1], J. Swerts[1], S. Van Beek[1], K. Sankaran[1], R. Carpenter[1], S. Mertens[1], W. Kim[1] and G.S. Kar[1] *1. IMEC, Leuven, Belgium*

Current STT-MRAM technology relies on MgO/CoFeB based magnetic tunnel junctions (MTJs) for high TMR, high (interfacial) PMA and low switching current [1,2]. CoFeB as a magnetic material has however limited room to modify its properties such as saturation magnetization Ms, damping α or Curie temperature Tc. We have doped the CoFeB alloy with variable quantity of heavy metals such as Ta & W. This enables to reduce and control the Ms and Tc of thick (~20nm) CoFeBX films, as shown in Fig. 1. The low heavy metal content ensures that damping remains low for efficient spin transfer torque. 2-3nm thin CoFeBX alloys have been integrated as free layer material in a state-of-the-art 400C compatible bottom pinned STT-MRAM stack. These CoFeBX alloys retain similar junction interface properties (TMR, RA, PMA) as CoFeB, indicating the new alloys mostly behave like CoFeB, albeit with lower Ms and Tc. Indeed the alloy is showing a faster moment reduction with temperature, as shown in Fig. 2. Comparing the standalone thick (20nm) vs MTJ integrated thin film (2-3nm), a shift of the Tc to slightly higher value (for the thin integrated film) is visible. This possibly is being induced by the different interfaces and reduced thickness. The lower Ms enables to stabilize PMA in relatively thick films of about 3-4nm using a double MgO free layer structure. The electrical performance (retention & switching dynamics) of scaled 40nm diameter devices will be presented, highlighting the potential benefits of these alloys for STT-based MRAM.

[1] S. Ikeda, H. Sato, H. Honjo, et al., IEDM Tech Dig. 796 (2014) [2] H. Almasi, M. Xu, Y. Xu et al., Appl. Phys. Lett. 109, 032401 (2016)



Magnetization Ms vs temperature of 20nm films on SiO_2. The (lower) Ms of WCoFeB alloy can be controlled by adjusting the W doping level. Tc as low as 120°C can be reached for the higher W content.



VSM measurements on a pMTJ integrated double MgO free layer based on CoFeB (Ref) or WCoFeB (Low-Tc). The magnetic moment of the low Tc free layer decreases faster than the reference.

8:54

GC-03. Superlattice MTJ for Energy Efficient STT-MRAM. A. Sharma[1], A. Tulapurkar[1] and *B. Muralidharan*[1] *1. Electrical Engineering, Indian Institute of Technology Bombay, Mumbai, India*

Superlattice structures offer tremendous possibilities to utilize non-trivial resonant tunnelling physics for device applications[1]. In the recent work [2], in the context of spintronic devices, superlattice structures designed to exhibits anti-reflective resonant physics has been proposed to enhance the performance magnetic tunnel junctions (MTJ). Here, we present an energy efficient spin transfer torque-magnetic random access memory (STT-MRAM) device based on anti-reflective superlattice magnetic tunnel junctions(AR-SLMTJ). Utilizing the non-equilibrium Green's function spin transport formalism self-consistently coupled with stochastic magnetization dynamics, we predict that cells comprising of AR-SLMTJ structures, as shown in Fig. 1(a), are capable of exhibiting an ultra-high peak tunnel magnetoresistance (TMR»5 * 10^4 %) and a large spin transfer torque in comparison with a traditional trilayer MTJ cell. Owing to the large spin current injection efficiency in the AR-SLMTJ, the switching bias voltage reduces significantly in these devices. It can be seen clearly from Fig. 1(b) and (c) that for nearly same switching time the AR-SLMTJ based STT-MRAM cell is nearly 1200% more energy efficient than a traditional trilayer MTJ based STT-MRAM cell. The reason for this energy efficient switching lies in band pass spin filtering physics accompanied in the AR-SLMTJ devices.

[1] C. Pacher, C. Rauch, G. Strasser, E. Gornik, F. Elsholz, A. Wacker, G. Kießlich, and E. Scholl, Appl. Phys. Lett. 79, 1486 (2001). [2] A. Sharma, A. A. Tulapurkar and B. Muralidharan, Appl. Phys. Lett., 112, 192404 (2018)

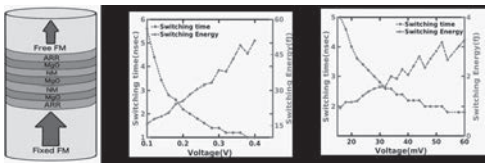


Fig. 1. (a) AR-SLMTJ-based device comprises of an anti-reflective region (ARR) along with superlattice structure of MgO-Normal metal(NM) sandwiched between the free and the fixed ferromagnetic (FM) layers. (b) Switching time and energy consumed during switching of free FM in the MTJ and (c) AR-SLMTJ based MRAM cell.

9:06

GC-04. Perpendicular Magnetic Tunnel Junctions with Low M_s Free Layer for Reduction of STT Switching Current. *K. Nakamura*[1], H. Maehara[2,3], H. Tomita[1,3], K. Nagasaka[1,3], S. Bosu[1,3], Y. Tanaka[1], A. Gomi[1] and N. Watanabe[1] *1. Tokyo Electron Technology Solutions Limited, Nirasaki, Japan; 2. Tokyo Electron Limited, Akasaka, Japan; 3. Spintronics Research Center, National Institute of Advanced Industrial Science and Technology (AIST), Tsukuba, Japan*

MgO based perpendicular magnetic tunnel junctions (p-MTJs) have been developed for spin-transfer torque magnetic random access memory (STT-MRAM) applications [1-3]. Recently, STT-MRAM is expected to be adopted to last level cache (LLC) as a replacement for SRAM because of the feature such as non-volatility and excellent scalability. However, one major challenge of STT-MRAM to overcome for LLC application is to reduce the write current in terms of low power consumption. Reduction of saturation magnetization (M_s) and damping constant of free layer of the p-MTJ is generally effective for reduction of the write current [4,5]. Moreover, realization of an efficient free layer is requisite for low write current without sacrificing other MTJ properties (e.g. MR ratio and annealing stability). In this study, we demonstrated p-MTJs with low M_s free layer having high annealing stability for reduction of STT switching current. The p-MTJs were prepared on thermally oxidized Si wafers using high vacuum magnetron sputtering system (Tokyo Electron EXIM™). All metallic layers were deposited using

dc sputtering and MgO tunnel barrier layer was fabricated by natural oxidation process after metallic Mg layer deposition. Fig. 1 (a) and (b) show MR ratio and STT switching properties of p-MTJs annealed at 400°C for 1h, respectively. Areal moment ($M_s t$) of the low M_s free layer is 142 μemu/cm^2, whereas that of conventional composite free layer comprising CoFeB and metallic spacer layer is 224 μemu/cm^2. Critical current (I_{c0}) of p-MTJ with the low M_s free layer is about 50% lower than that of p-MTJ with the composite free layer, while there is no significant difference in MR ratio between them. MR ratio of 174% and I_{c0} of 41 μA were obtained at resistance area product (RA) of 5.1 Ωμm^2 in sub-40 nm sized p-MTJ with the low M_s free layer. Low write current can be achieved without sacrificing MR ratio by employing the low M_s free layer. More detailed results will be discussed in the presentation.

[1] L. Thomas et. al., J. Appl. Phys. 115, 172615 (2014) [2] K. Yakushiji et. al., Appl. Phys. Lett. 110, 092406 (2017) [3] S. Couet et. al., Appl. Phys. Lett. 111, 152406 (2017) [4] H. Tomita et. al., Appl. Phys. Lett. 102, 042409 (2013) [5] K. Yamada et. al., Appl. Phys. Lett. 106, 042402 (2015)

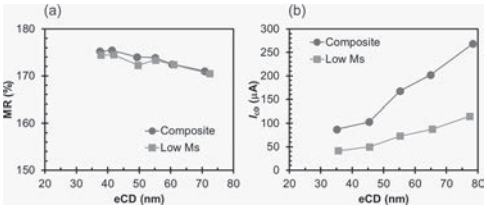


Fig. 1. MR ratio and STT switching properties of p-MTJs annealed at 400°C for 1h. (a) MR ratio and (b) critical current (I_{c0}) as a function of electrical size (eCD).

9:18

GC-05. How to tilt magnetic moments in STT-MRAM devices. *Z. Nunn*[1] and E. Girt[1] *1. Simon Fraser University, Burnaby, BC, Canada*

In spin transfer torque magnetic random access memory (STT-MRAM) devices, memory writing is most efficient when there is a non-collinear alignment between the free and fixed layer [1]. All perpendicular STT-MRAM structures require it's collinear symmetry to be broken with thermal fluctuations, leading to probabilistic switching, large current densities and/or switching times [2]. We discovered a new form of interlayer coupling that can reliably control the relative angle of adjacent magnetic moments [3]. This coupling provides stable tilted magnetic moments at any angle out of the plane of the device which allows for the creation of novel STT-MRAM structures that have superior operational performance in comparison to all perpendicular STT-MRAM structures [4]. The design shown in Fig.1 has all the benefits of perpendicular STT-MRAM with the advantage of an initial offset of magnetizations adjacent to the tunneling magnetoresistance (TMR) layer, giving an instant STT when current is applied. Our results show that this new from of interlayer coupling can be fully integrated into MRAM devices as the coupling materials can be annealed at high temperatures, are fully conductive, and can be scaled to nanometer size devices. Non-collinear coupling is a when the relative angle of adjacent magnetizations is controlled using interlayer exchange coupling as shown in Fig. 1. Due to the isotropic nature of interlayer coupling, non-collinear coupling can be combined with ferromagnetic layers that have perpendicular anisotropy to create stable tilted magnetizations. Ferromagnetic layers of Co, Fe, Ni and their alloys can be directly non-collinear coupled using a RuFe interlayer. Fig. 2 shows the measured coupling angle in a Co|RuFe|Co structure as a function of RuFe thickness and composition. For thicknesses between 0.5-0.8 nm the coupling angle was found to be constant, which from a fabrication point of view is very important in order to utilize non-collinear coupling in applications as small thickness errors do not contribute to large changes in coupling angle.

[1] Slonczewski, J. C. Current-driven excitation of magnetic multilayers, J. Mag. Mag. Mat. 159, L1 (1996). [2] Bedau, D., Liu, H., Sun, J. Z., Spin-transfer pulse switching: From the dynamic to the thermally activated regime. *Applied Physics Letters*, *97*(26), 262502. (2010). [3] Nunn, Z. R., & Girt, E. Non-collinear coupling across RuCo and RuFe alloys. *arXiv preprint arXiv:1901.07055*. (2019). [4] Nunn, Z. R., & Girt, E. *U.S. Patent Application No. 10/204,671*. (2019).

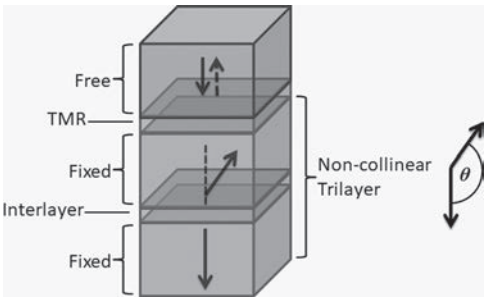


Fig. 1 Non-collinear STT-MRAM with tilted fixed layer due to non-collinear coupling

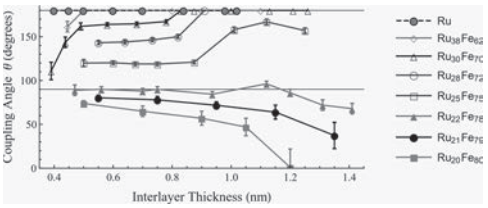


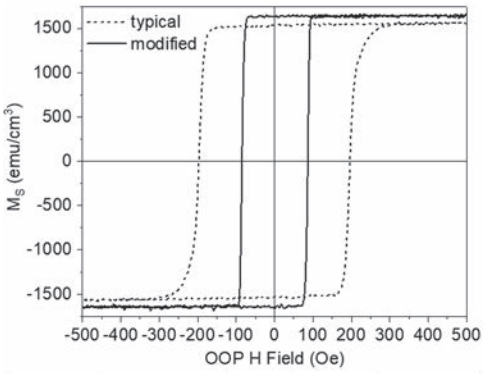
Fig. 2 Coupling angle of Co|RuFe|Co as a function of RuFe thickness and composition

9:30

GC-06. Ultrathin Perpendicular Free Layers for Lowering the Switching Current in STT-MRAM. *T. Santos*[1], N. Smith[1], G. Mihajlovic[1], J. Li[1], M. Carey[1], J. Katine[1] and B. Terris[1] *1. NVM Research, Western Digital, San Jose, CA, United States*

A primary challenge in the creation of a commercial spin-transfer torque magnetic random access memory (STT-MRAM) technology is lowering of the switching current needed to switch the magnetization of the free layer when writing a bit in the MRAM cell, while maintaining high thermal stability for data retention. Because the switching current is directly proportional to the thickness of the free layer, reducing the free layer thickness is a route toward lowering the switching current. The typical free layer stack consists of double MgO-CoFeB interfaces and a non-magnetic, metallic layer inserted within the free layer [1]. Reducing the free layer thickness is challenging, as the magnetic properties, such as M_S, degrade for very thin perpendicular free layers, which will lower thermal stability, and the damping parameter α often increases [2], which is expected to increase the switching current. In addition, tunnel magnetoresistance decreases for very thin CoFeB [3]. We have modified the free layer design such that we can reduce the free layer thickness well below 1.4nm while minimizing the magnetic dead layer, so that high $M_S > 1500$ emu/cm^3, and thus high thermal stability, is maintained. Our ferromagnetic resonance (FMR) measurements (see Fig. 1) show that in comparison to a free layer of equivalent thickness using the typical stack design, our modified stack has higher effective perpendicular anisotropy field $H_{K\perp}$, damping α as low as 0.004, and a 3-fold reduction in the inhomogeneous broadening ΔH (which is due to anisotropy non-uniformity), as low as ~ 0.1 kOe. We will discuss these improvements to the free layer properties. Such high-quality, ultrathin free layers are promising for lowering the switching current.

[1] H. Sato, M. Yamanouchi, S. Ikeda et al, Appl. Phys. Lett. 101, 022414 (2012). [2] E. C. I. Enobio, H. Sato, S. Fukami et al, IEEE Mag. Lett. 6, 5700303 (2015). [3] H. Sato, M. Yamanouchi, K. Miura et al, IEEE Mag. Lett. 3, 3000204 (2012).



	Ms (emu/cm³)	$H_{K\perp}$ (kOe)	α	$\Delta H\|_{f\to 0}$ (Oe)
typical	1560	3.02	0.0040	420
modified	1645	4.07	0.0037	125

Fig. 1) Out-of-plane M(H) loops for a typical free layer and our modified free layer, both 1.2nm thick blanket films. Film properties $H_{K\perp}$, α and ΔH were determined by FMR measurement.

INVITED PAPER

9:42

GC-07. Spin-transfer torque MRAM with reliable 5 ns writing. *G. Hu*[1], J. Nowak[1], M. Gottwald[1], J. Sun[1], d. Houssameddine[1], J. Bak[1], S. Brown[1], P. Hashemi[1], Q. He[1], J. Kim[1], C. Kothandaraman[1], G. Lauer[1], H. Lee[1], T. Suwannasiri[1], P. Trouilloud[1] and D. Worledge[1] *1. IBM T J Watson Research Center, Yorktown Heights, NY, United States*

Spin-transfer torque magneto-resistive random access memory (STT-MRAM) is an emerging non-volatile memory with a unique combination of high speed, and high endurance due to its unique switching mechanism. Significant investment and progress have been made in recent years with product demonstration from all major semiconductor manufacturing companies [1-5]. Despite its potential for high speed applications, there has been no demonstration of reliable switching of STT-MRAM devices below 10 ns pulse-width and the first generation embedded STT-MRAM products are limited to applications with write pulses longer than 50 ns. We report reliable 5 ns switching of STT-MRAM devices by demonstrating 100% write-error-rate (WER) yield at 1e-6 write-error floor of 256 devices at a nominal device size of 43 nm and a resistance area product (RA) = 11 Ω-μm^2. These devices show steep WER slope (20 mV/decade) tight distributions (1 sigma of 3.6% and 4.5% for write 0 and write 1 respectively at WER = 1e-6) and clean WER curves with no free layer related anomalies. A single device was demonstrated to have less than 1e-10 write-error rate with 5 ns write pulse. Promising 3 ns switching performance, with 94% WER yield at 1e-6 write-error floor of 64 devices was demonstrated in 50 nm devices with RA = 6.6 Ω-μm^2. In this talk, we will also discuss reference layer related WER anomalies and the results from the improved reference layers to address the issue.

[1] Y. K. Lee, et al., "Embedded STT-MRAM in 28-nm FDSOI Logic Process for Industrial MCU/IoT Application", *VLSI Symposium, Tech. Dig.*, 181-182 (2018). [2] K. Lee, et al., "22 nm FD-SOI Embedded MRAM with Full Solder Reflow Compatibility and Enhanced Magnetic Immunity", *VLSI Symposium, Tech. Dig.* 183-184 (2018). [3] O. Golonzka et al., "MRAM as Embedded Non-Volatile Solution for 22FFL FinFET Technology", *IEDM, Tech. Dig.* 412-415 (2018). [4] Y. J. Song et al., "Demonstration of Highly Manufacturable STT-MRAM Embedded in 28nm Logic", *IEDM Tech. Dig.*, 416-419 (2018). [5] K. Lee et al., "22-nm FD-SOI Embedded MRAM Technology for Low-Power Automotive-Grade-1 MCU Applications", *IEDM, Tech. Dig.* 604-607 (2018).

CONTRIBUTED PAPERS

10:18

GC-08. Reference layer engineering for back-hopping control in scaled perpendicular magnetic tunnel junctions (MTJs). *S. Rao*[1], S. Couet[1], R. Carpenter[1], W. Kim[1], K. Garello[1] and G.S. Kar[1] *1. IMEC, Leuven, Belgium*

Over the past decade, significant advances in the state-of-the art of STT-MRAM technology have been achieved by engineering the ferromagnet/insulator interface in MTJs [1,2]. Perpendicular magnetic anisotropy (PMA) arising at this interface is critical to obtain a high TMR and efficient switching. Therefore, to enable full commercialization, a high switching probability or low write error rate (WER), is required, a large PMA is critical. Past reports have indicated that weak free (FL) or reference (RL) layers can result in increased error rates due to unintentional switching, otherwise known as back-hopping [3, 4]. In this study, we investigate in-depth the occurrence of this back-hopping in 400 °C-compatible pMTJs as a function of the RL thickness. STT-mediated switching studies show consistent back-hopping in the P-AP switching direction, while the AP-P switching direction is not impacted, as seen in Fig. 1. For a fixed diameter, we also demonstrate that the window between full switching and back-hopping is maximized for the thickest RL. This observation is attributed to RL magnetization flipping as can be deduced from the electron flow direction. We find that TMR increases with RL thickness, due to an increased spin filtering efficiency, which is at a cost of RL pinning field (Fig. 2). Temperature-dependent switching studies also show that back-hopping is inversely proportional to the RL PMA, thus highlighting the importance of engineering the RL PMA over pinning field. To address the challenges of back-hopping in scaled devices, we will also discuss the switching behaviour for diameters from 150 nm down to 50 nm, in the context of voltage bias and pulse-widths. We will also discuss the dynamical nature of back-hopping, and the inverse dependence on applied pulse-widths.

[1] S Ikeda *et al*., Nat. Mater. 9, 721-724 (2010) [2] A V Khvalkovskiy *et al*., J. Phys. D: Appl. Phys. 46, 074001 (2013) [3] W Kim et al., IEEE Trans. Magn. 52, 3401004 (2016) [4] C Abert et al., Phys. Rev. Applied 9, 054010 (2018)

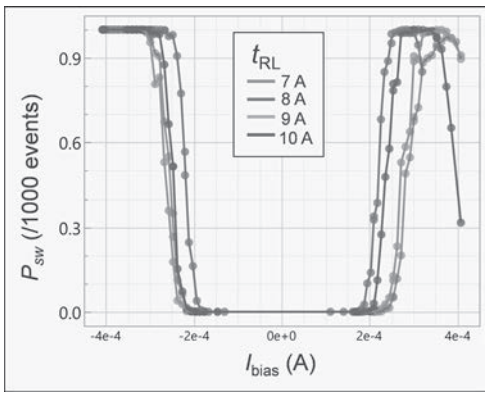


Fig. 1: Switching probability as a function of reference layer (RL) thickness. Positive currents result in AP-to-P switching, while negative currents result in P-to-AP switching. Backhopping is evident for all RL flavours in the AP-to-P switching direction.

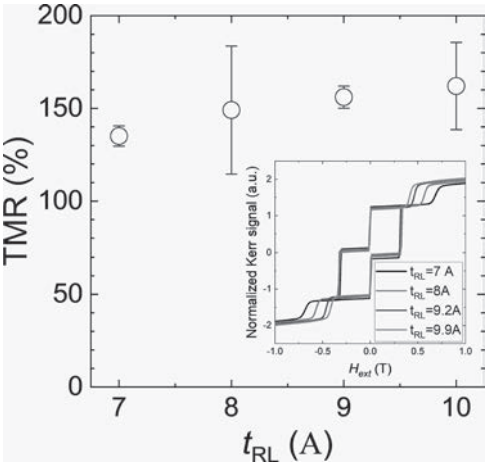


Fig. 2: TMR trends as a function of RL thickness, with TMR gain evident. (Inset) Normalized Kerr loops highlight the loss of RL pinning field and gain in RL PMA, with increasing RL thickness.

10:30

GC-09. Asymmetric Reliability Performance of Mg-inserted MTJ. *K. Chen*[1], C. Cheng[1], J. Wei[2], Y. Wu[3] and Y. Tseng[1] *1. National Chiao Tung University, Hsinchu, Taiwan; 2. Industrial Technology Research Institute, Hsinchu, Taiwan; 3. Taiwan Semiconductor Research Institute, Hsinchu, Taiwan*

Inserting Mg between CoFeB and MgO is a common strategy to reduce damping [1] and interface traps [2] in STT-MRAM. This work demonstrates notable asymmetric reliability performance in Mg-inserted MTJ for low (parallel) and high (antiparallel) resistance states. In a SAF-layer/CoFeB(3Å)/Ta(2Å)/CoFeB(12Å)/MgO(7Å)/Mg(3Å)/CoFeB(12Å)/Ta(3 Å)/CoFeB(8Å)/Capping-layer MTJ, we obtain a lower switching voltage, a greater breakdown voltage and a longer endurance in the high resistance state (HRS) than those of the low resistance state (LRS). Upon breakdown the LRS exhibited a two-step reversal characteristic, suggesting that a reversal pinning-effect arose as breakdown approached. Nevertheless, this was absent to the case of HRS. Such LRS/HRS performance asymmetry was reduced with the removal of Mg insertion. We observe the phenomenon in 80-, 130- and 180-nm MTJs, indicating it as a universal concern in MTJ scaling. The real-time breakdown effect was explored by in-situ synchrotron x-ray for MTJ with/without Mg insertion. Upon breakdwon, the CoFeB/MgO interface appeared to reconstruct differently for the cases of with/without Mg. We conclude that the interfacial reconstruction during MTJ operation is critical to the asymmetric performance.

[1]: Q. L. Ma et al., *Appl. Phys. Lett.* 101, 122414 (2012) [2]: C. M. Choi et al., *Semicond. Sci. Technol.* 32, 105007 (2017)

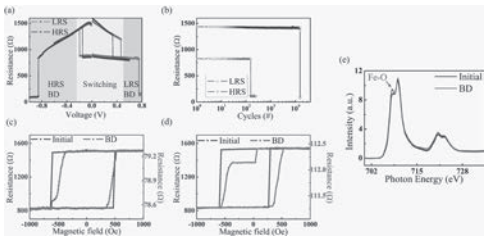


Fig.1 (a) Ramping voltage stress measurements for LRS (red) and HRS (blue), with breakdown (denoted BD in figure) occurring at positive and negative regime, respectively. Switching voltages for LRS and HRS are +0.38 V and -0.18 V, respectively. (b) Unipolar-stress (+/- 0.8 V) endurance test for LRS and HRS. The applied stress exceeded LRS/HRS switching voltages in order to achieve early breakdown. Initial and after-breakdown R-H loops for (c) HRS and (d) LRS. (e) In-situ x-ray spectra (taken at Fe L_2/L_3 absorption edge) showing emergence of Fe-O hybridization after breakdown.

10:42

GC-10. Electric-Field Control of Interlayer Exchange Coupling for Efficient Magnetization Switching. *S. Sayed*[1], N. Roschewsky[2], C. Hsu[1] and S. Salahuddin[1] *1. EECS, University of California, Berkeley, CA, United States; 2. Physics, University of California, Berkeley, CA, United States*

Electrical switching of nano-magnets is of great current interest for efficient non-volatile memory applications. Technological advancements in the state-of-the-art current controlled spin-torque (ST) based mechanisms are limited by the large switching current density requirement and exhibit a trade-off between the switching energy and the speed. In this talk, we will discuss that magnetization switching solely by the interlayer exchange coupling (IEC) between the fixed and the free magnets, may exhibit several benefits over the ST-switching. Specifically, the switching energy and the speed becomes decoupled and the speed can be independently tuned by the dynamic parameters like Gilbert damping and the magnetic anisotropy. We argue that the IEC can be controlled with an electric-field via resonant tunneling phenomena within a double-barrier magnetic tunnel junction structure, if the two oxide barriers are separated by a metal that is well-known for exhibiting a large IEC. Using non-equilibrium Green's function (NEGF) method, we show that the proposed structure exhibits a bias-dependent oscillatory IEC with sizable magnitude that may switch the free magnet to have either a parallel or an antiparallel configuration with respect to the fixed magnet, depending on the sign of the IEC. The new configuration will retain when the electric-field is removed because the equilibrium IEC is negligible due to the presence of the oxide barriers. We further argue that the current in the two-terminal structure can be significantly lowered with proper design and material choices, which could lead to significant lowering in the energy-delay product for magnetic memory applications. This work was supported by ASCENT, one of six centers in JUMP, a SRC program sponsored by DARPA.

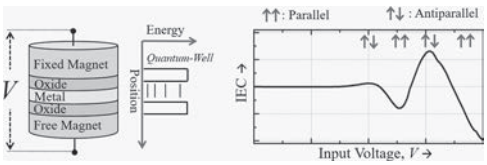


Fig.1 Proposed structure to control interlayer exchange coupling (IEC) between the fixed and the free magnets using an electric-field or a voltage. A quantum-well is formed between the oxide barriers, which are separated by a metallic spacer that exhibits a large IEC.

10:54

GC-11. Integration of Tb/Co Multilayers within Ultrafast Optically Switchable p-MTJ. *L. Avilés Félix*[1], C. Davies[2,3], G. Li[3], L. Álvaro Gómez[1], M. Rubio-Roy[1], S. Aufftet[1], A. Kirilyuk[2,3], T. Rasing[3], L. Buda-Prejbeanu[1], B. Dieny[1], R. Sousa[1] and I. Prejbeanu[1] *1. Université Grenoble Alpes, CNRS, CEA, Grenoble INP, IRIG-SPINTEC, Grenoble, France; 2. FELIX Laboratory, Radboud University, Nijmegen, Netherlands; 3. Radboud University Nijmegen, Institute for Molecules and Materials, Nijmegen, Netherlands*

Rare earth/transition metal (RE/TM) systems have been used to achieve perpendicular anisotropy in RE/TM multilayers. The discovery of all-optical switching of the magnetization, achieved on ultrafast timescales using femtosecond laser pulses have generated a renewed interest in these type of systems for data-recording applications. In particular, the ultrafast speed of the switching process permits a significant improvement in the writing speeds associated with magnetic memory devices. This work reports the development of perpendicular magnetic tunnel junction, incorporating a multilayered stack of Tb/Co that can be all-optical addressed via helicity-independent single-shot switching of the magnetization. Toggling of the magnetization in the Tb/Co multilayered stack was observed using both 40 femtosecond- and 3 picosecond-long laser pulses with fluences below 5mJ/cm^2. As illustrated in Fig. 1, these results could be achieved for Co-rich compositions of the multilayer, either alone or embedded in a tunnel junction stack coupled to a CoFeB electrode on an MgO barrier. This result is maintained even after annealing at 250°C. After annealing, a TMR signal of 30% and RxA value of 19Ωμm^2 was obtained. The stability of the multilayer degrades for higher annealing temperatures. This is due to a loss of the interface sharpness that could be compensated by the increase of the number of bilayer repetitions. The annealing stability of the multilayer was improved using a Ta insertion layer, at the cost of reducing the strength of the perpendicular anisotropy and magnetic coercivity. These results open the way to the development of hybrid spintronic photonic systems with unique features of THz MTJ switching speeds and fJ switching energies. The authors acknowledge the funding support from project SPICE (EU ITC 2020 grant agreement No. 713481)

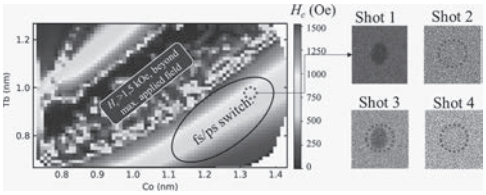


Fig.1 Left: Coercive field mapping of half-MTJ structure for different values of Co and Tb thickness. Right: Magneto-optical switching experiments performed for a FeCoB/Ta/[Tb(1 nm)/Co(1.3 nm)] half-MTJ stack annealed at 250°C after 4 shots of the 3 ps-laser pulse with fluence ~ 4.7 mJ/cm^2.

11:06

GC-12. Reduced Exchange Interactions in Perpendicular Magnetic Tunnel Junction Free Layers with Insertion Layers. *J. Beik Mohammadi*[1], Y. Chen[1], B. Kardasz[2], G. Wolf[2], M. Pinarbasi[2] and A.D. Kent[1] *1. Center for Quantum Phenomena, Physics, New York University, New York, NY, United States; 2. Spin Memory Inc, Fremont, CA, United States*

Perpendicular magnetic tunnel junctions are widely used in spintronic devices such as in magnetic random-access memories. The free layer is typically formed by CoFeB layers with a thin non-magnetic insertion layer to enhance the perpendicular magnetic anisotropy (PMA) to achieve long-time thermal stability of the memory device. However, the exchange constant of the layer is equally important as it sets the length scales for micromagnetic structure, the energy barrier for thermally activated switching and the spin torque switching efficiency [1]. We present a systematic study of the exchange constant of on a full pMTJ layer stack that allows for the optimization of its magnetic properties. We study a series of samples with CoFeB/W(t_W=0 to 0.7 nm)/CoFeB free layers (FL) while the reference and synthetic antiferromagnetic layers (SAF) layers of the pMTJ stack remain unchanged. Magnetization measurements were taken as a function of temperature, from 5 to 400 K. The well-separated switching field of individual layers enables characterization of their magnetic moments. The exchange constant of individual layers is then determined by fitting $m(T)=M_s(T)/M_s(0\ K)$ vs. T data to Bloch's $T^{3/2}$ law [3]. Figure 1(a) shows m(T) for a single CoFeB layer (brown symbols) and pMTJ free layers with 0.1 to 0.3 nm W thickness (triangular symbols). We observe a significant reduction of the exchange constant of the free layer as W is introduced (Fig. 1(b)). Further, we determined the effective magnetization of the free layer from ferromagnetic resonance measurements at room temperature (Fig. 1(c)). The sign of changes from negative to positive, indicating perpendicular anisotropy, for 0.2 nm W. Therefore, W insertion enhances the PMA, while it leads to a dramatic reduction in the exchange constant. We will discuss the implications that the reduced exchange constant has on thermal stability and switching dynamics of pMTJ devices [3]. This project is supported by Spin Memory Inc.

[1] G. D. Chaves-O'Flynn, G. Wolf, J. Z. Sun and A. D. Kent, Physical Review Applied 4, 024010 (2015). [2] H. T. Nembach, J. M. Shaw, M. Weiler, E. Jué and T. J. Silva, Nature Physics 11, 825 (2015). [3] J. Beik Mohammadi, Y. Chen, B. Kardasz, G. Wolf, M.Pinarbasi and A. D. Kent, arXiv:1905.09329v1

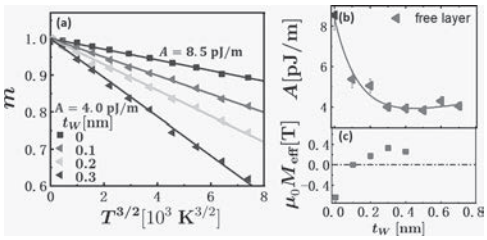


Figure 1: (a) $m(T)=M_s(T)/M_s(0\ K)$ for a single CoFeB layer (brown squares), pMTJ free layers with t_W=0.1-0.3 nm (triangular symbols). (b) Exchange constant of the free layer (red), and (c) effective magnetization of the free layer vs. t_W.

11:18

GC-13. Resonant surface acoustic wave (r-SAW) assisted spin-transfer-torque switching of a perpendicular magnetic tunnel junction (p-MTJ). *A.R. Roe*[1], D. Bhattacharya[1] and J. Atulasimha[1] *1. Mechanical and Nuclear Engineering, Virginia Commonwealth University, Richmond, VA, United States*

As the technology of spin transfer torque random access memory (STTRAM) matures, devices with lateral dimensions ~11 nm with extremely low switching error rates, ~7×10^{-10} [1], have been demonstrated. However, the energy dissipation remains high at ~100 fJ/bit. This motivates research that allows aggressive scaling of STTRAM, while drastically reducing energy dissipation in the write process. We numerically study the use of a resonant dynamic stress created by surface acoustic waves (SAW) used in conjunction with spin-transfer-torque (STT) to significantly reduce the write energy. While SAW alone has been experimentally shown to manipulate the magnetization state of larger nanomagnets [2], and prior work has shown that low frequency SAW can be used in conjunction with STT to switch in-plane magnetization in nanomagnets of lateral dimensions ~100 nm [3], competitive scaling to 50 nm and below is infeasible with this approach in p-MTJs where thickness of the soft magnetic layer is typically limited to ~1 nm. We will present Landau-Lifshitz-Gilbert (LLG) simulations with a dynamic stress of 100 MPa applied to a circular nanomagnet with moderate magnetostriction (~350 micro-strain) and 50 nm diameter and 1.5 nm thickness with

thermal noise. We show that the small anisotropy changes due to low amplitude SAWs, which are resonant with the magnetization dynamics of the nanomagnet (soft layer of p-MTJ), are sufficient to deflect the magnetization significantly (precess with a conical angle of ~45° as shown in Fig 1). Thus, the STT write current to reverse the magnetization is reduced by ~2 times, leading to a ~4 fold decrease in write energy compared to the case without SAW at the same switching error rate. This shows a path for scaling p-MTJ lateral dimensions while reducing write energies. Further optimization and lower damping could result in more competitive scaling and lower write energy. Authors acknowledge NSF grant CCF-1815033.

[1] J. J. Nowak, R. P. Robertazzi, J. Z. Sun, G. Hu, J.-H. Park, J. Lee, A. J. Annunziata, G. P. Lauer, R. Kothandaraman, E. J. O'Sullivan, P. L. Trouilloud, Y. Kim, and D. C. Worledge, IEEE Magn. Lett. 7, 1 (2016). [2] V. Sampath, N. D'Souza, D. Bhattacharya, G. M. Atkinson, S. Bandyopadhyay, and J. Atulasimha, Nano Lett. 16, 5681 (2016). [3] A. K. Biswas, S. Bandyopadhyay, and J. Atulasimha, Appl. Phys. Lett. 103, 232401 (2013).

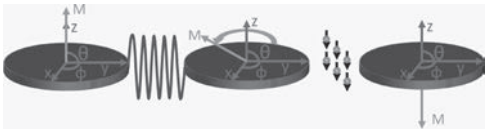


Fig.1 Illustration of the application of resonant SAW causing the magnetization to first rotate about the out-of-plane axis then application of STT causing magnetization reversal.

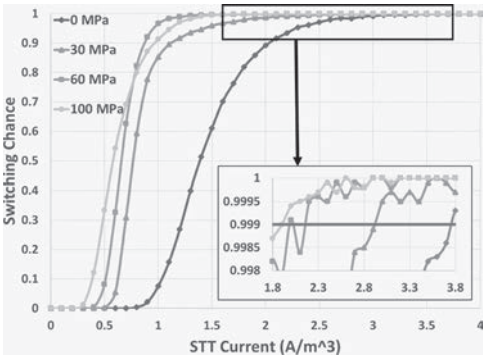


Fig.2 Switching probability vs. STT current at different amplitudes of applied SAW.

Session GD
SPIN ORBIT COUPLING AND TOPOLOGY

Rolando Valdes Aguilar, Chair
The Ohio State University, Columbus, OH, United States

INVITED PAPER

8:30

GD-01. A Family of Intrinsic Magnetic Topological Insulators $(MnBi_2Te_4)(Bi_2Te_3)_n$, $n = 0, 1, 2$. *A. Isaeva*[1,2], A. Zeugner[1], A. Wolter[2], J. Facio[2] and H. Bentmann[3] *1. Technische Universität Dresden, Dresden, Germany; 2. Leibniz IFW Dresden, Dresden, Germany; 3. University of Würzburg, Würzburg, Germany*

Topological quantum materials constitute one of the most vibrant contemporary directions of condensed matter research and material science. Presently one of the central challenges in the field is to understand how topologically non-trivial electronic states evolve in the presence of strong electronic correlations and magnetism. In turn, this interplay is believed to unleash a plethora of novel topological phenomena as well as pathways to exploit them for spintronic device concepts. Following theoretical advances material candidates are emerging. For a long while, the magnetic doping approach was one of the central routes to explore the interplay with magnetism in the paradigmatic TIs like Bi_2Te_3. Recent advances have provided access to long-sought Bi_2Te_3-derivatives with a periodic Mn sublattice, the layered van der Waals compounds $(MnBi_2Te_4)(Bi_2Te_3)_n$, n = 0,1,2 [1-3]. These natural heterostructures are built by varying sequences of septuple and quintuple layers and represent the first intrinsically magnetic topological insulators. I will present our structural, magnetic, transport and angle-resolved photoemission spectroscopy measurements of $MnBi_2Te_4$ ($n = 0$) and $MnBi_4Te_7$ ($n = 1$) that corroborate a combination of the non-trivial band topology and a long-range magnetic order in this class of materials [4-7]. Our team highly values the careful optimization of crystal-growth techniques and accurate determination of chemical purity and crystal structure. To obtain high-quality single crystals, the synthetic conditions have been thoroughly optimized with respect to temperature profiles and starting materials. We establish ubiquitous off-stoichiometry of the materials, $Mn_{1-x}Bi_{2+2x/3}Te_4$ (x = 0.15) and $Mn_{1-x}Bi_{4+2x/3}Te_7$ ($0.15 \le x \le 0.25$) by single-crystal X-ray diffraction [3, 5, 7]. Furthermore, all of $(MnBi_2Te_4)(Bi_2Te_3)_n$ are thermodynamically stable only in narrow high-temperature ranges at around 873 K that strongly challenges their crystal-growth [3, 5]. For $MnBi_2Te_4$, temperature- and field-dependent magnetization measurements establish a 3D AFM order below $T_N = 24$ K. It originates from an antiferromagnetic coupling between the septuple layers, which exhibit ferromagnetic intralayer coupling. Competing AFM and FM couplings are indicated as well by the small and positive value of the Curie-Weiss temperature. This magnetic ground state and a centrosymmetric space group entail the $Z_2 = 1$ topological classification and render $MnBi_2Te_4$ as the first antiferromagnetic topological insulator [4]. The expected Mn(II) out-of-plane magnetic state is confirmed by the magnetization, X-ray photoemission, X-ray absorption and linear dichroism data. Angle-resolved photoemission experiments provide evidence for a surface state forming a gapped Dirac cone [4,6]. For $MnBi_4Te_7$, which is diluted by the insertion of (Bi_2Te_3) layers between the septuple $(MnBi_2Te_4)$ ones, we find several competing magnetic states below $T_N = 13$ K by a variety of experimental techniques and uncover the complexity of the paramagnetic state. We use angle-resolved photoemission measurements in broad temperature and photon-energy ranges to directly confirm the topological surface states on the (0001) surface of both possible surface terminations. These observations are complemented with first-principle density-functional calculations that corroborate the proximity in energy of different magnetic states, confirm the inverted character of the electronic band structure and show how the band topology is affected by the different magnetic orders. Based on that, a preliminary phase diagram of possible topological states in $MnBi_4Te_7$ dependent on the magnetic structure can be sketched. $MnBi_4Te_7$ is the first realization of a band-inverted material with intrinsic net magnetization [7]. We envision that their versatile magnetic and electronic properties will establish $(MnBi_2Te_4)(Bi_2Te_3)_n$ as a unique material platform for the realization of tunable topological quantum phenomena.

[1] D.-S. Lee, T.-H. Kim, C.-H. Park et al., Cryst. Eng. Comm., Vol. 15, p. 5532 (2013) [2] Z. S. Aliev, I. R. Amiraslanov, D. I. Nasonova et al., J. Alloys Cmpd., Vol. 789, p. 443 (2019) [3] D. Souchay, M. Nentwig, D. Günther et al. Accepted to J. Mater. Chem. C., available on 10.26434/chemrxiv.8244719 (2019) [4] M. M. Otrokov, I. I. Klimovskikh, H. Bentmann et al. Available on arXiv.org: 1809.07389 (2018) [5] A. Zeugner, F. Nietschke, A. U. B. Wolter et al., Chem. Mater., Vol. 31, 2795 (2019) [6] R. C. Vidal, H. Bentmann, T. R. F. Peixoto et al. Available on arXiv.org: 1903.11826 (2019) [7] R. C. Vidal, A. Zeugner, J. I. Facio et al. Available on arXiv.org: 1906.08394 (2019)

CONTRIBUTED PAPERS

9:06

GD-02. Incommensurate Magnetic Order from 1-D Correlated Topological Bulk States. *J.L. Lussier*[1] *1. Physics, Kent State University, Kent, OH, United States*

The onset of incommensurate magnetic order (IC) in a periodic crystalline lattice has many different origin including next-nearest-neighbor interaction in insulators, coupling to lattice displacements or electron band filling in a metal. In the latter, IC order is often explained by the onset of spin/charge density waves. However, it is possible to calculate the reciprocal space position of incommensurate magnetic satellites seen in diffraction experiments of systems with metallic characters using a one-dimensional topological Dirac equation. In such an approach, the IC magnetic order originates from the onset of fluctuating correlated topological bulk states and is characterized by an average wave vector from crystallographic Bragg planes defining the moving center of mass of the magnetic electrons. This novel approach works particularly well with f-electron systems with itinerant characters, like in Ce-compounds, but also also in the High-Tc BSSCO and in the skyrmion-lattice system with no inversion symmetry MnSi. The phenomenological algorithm for the calculation of the IC satellites is given in details.

9:18

GD-03. RIXS With In-Situ Magnetic Field: Towards Understanding The Complex Magnetism Of Li_2IrO_3. *A. Ruiz*[1], A. Allen[1], V. Nagarajan[2], N. Breznay[3], J. Analytis[2] and A. Frano[1] *1. University of California San Diego, La Jolla, CA, United States; 2. University of California, Berkeley, CA, United States; 3. Harvey Mudd College, Claremont, CA, United States*

Unconventional magnetism appears in correlated electron systems with strong spin-orbit coupling. 5d iridate compounds coordinated in a honeycomb lattice like Li_2IrO_3 are a promising avenue to realize the peculiar

anisotropic, frustrated magnetism scenario of Kitaev's Hamiltonian [1, 2] which could host a quantum spin liquid ground state. Experimentally, the material displays a degeneracy of magnetic ground states upon the application of a magnetic field [3]: one incommensurate spiral and a commensurate 'zigzag' phase. The mechanism by which the magnetic order and the associated low-energy excitations vary with magnetic field is unknown. Measuring the excitation spectrum associated with each of the two magnetic phases is challenging for two reasons: the energy scale of said excitations is low and thus at the limit of experimental resolution of RIXS spectrometers, and the application of in-situ magnetic fields within RIXS chambers is highly challenging. Using the state-of-the-art RIXS spectrometer at Sector 27 of the Advanced Photon Source, we have overcome both challenges to measure the spin excitations of both spiral and commensurate phases by tracking low-energy excitations near their respective q-vectors in an applied magnetic field of 2 Tesla (as well as 0 Tesla). We have identified magnon branches near each q-vector. Surprisingly, the magnon velocity near the spiral q-vector is much higher than the expected *sin(qa/2)* behavior, possibly suggesting a larger magnetic coupling strength than previously thought. This data may provide insight into the interactions between pseudo-spins in this fascinating material. Finally, we will discuss how the application of modest magnetic fields within modern high-resolution RIXS setups is now possible and will open up interesting new avenues of research in exotic 5d-magnetism.

[1] G. Jackeli and G. Khalliulin, *Phys. Rev. Lett.* 102, 017205 (2009) [2] J. Chaloupka et al., *Phys. Rev. Lett.* 105, 027204 (2010) [3] A. Ruiz, A. Frano, N. Breznay et al., *Nat. Comm.* 8:961 (2017)

9:30

GD-04. Topological Classification of Magnetic Plateaux and Haldane Phases in Quantum Spin Chains. *I. Maruyama*[1] and S. Miyahara[2]
1. Department of Information and Systems Engineering, Fukuoka Institute of Technology, Fukuoka, Japan; 2. Department of Applied Physics, Fukuoka University, Fukuoka, Japan

Topological phases cannot be characterized by local order parameters and require non-local or new quantities for phase characterization. One of historical examples is the Haldane phase, which is one of the symmetry protected topological(SPT) phases. As a phase characterization method for these phases, a fractionally quantized Berry phase has been proposed [1]. Recently, the fractionally quantized Berry phase has successfully classified the SU(N) AKLT chains [2]. To demonstrate its ability for coupled molecular magnets, we have studied spin-1/2 Heisenberg multimer (N-mer) chains, i.e., highly frustrated N-leg ladders. The models have been studied as a generalization of an orthogonal dimer chain [3]. In the case of symmetric frustration it has been known that there are magnetization plateau phases which have exact ground states written as direct product states, except for the Haldane phase. The definition of the Berry phase requires a spin-twisted ground state and it is not a direct product state. We calculated the Berry phase numerically with using the spin-twisted ground state obtained by the Lanczos method. As a result, we obtained exact fractional quantization $2\pi/N$ of the Berry phase in dimer (N=2) and tetramer (N=4) chains [4]. For example, in the coupled tetramer case, six magnetic plateaux existing in the phase diagram are classified by four kinds of Berry phases, 0, $\pi/4$, $\pi/2$, and $3\pi/4$. We have found that the exact quantization of the Berry phase arises from translational symmetry of local multimer, including S=2 Haldane phase. In addition, we discuss nonzero Berry phase of S=2 Haldane phase when the model has XXZ and on-site anisotropies, in order to study new internal symmerty of the even S Haldane phases, which have no SPT order. This work is supported in part by JPSJ KAKENHI Grant Number JP17H02926. The computation is partially carried out using the computer facilities at Research Institute for Information Technology, Kyushu University.

[1] Y. Hatsugai, and I. Maruyama, Eur. Phys. Lett., Vol. 95, p.20003 (2011) [2] T. Kariyado, T. Morimoto, and Y. Hatsugai, Phys. Rev. Lett. Vol. 120, p.247202 (2018) [3] A. Honecker, F. Mila, and M. Troyer, Eur. Phys. J. B., Vol. 15, p.227 (2000) [4] I. Maruyama, and S. Miyahara, J. Phys. Soc. Jpn, Vol. 87, p.123703 (2018)

9:42

GD-05. Magnon excitations in the three dimensional Kitaev spin liquid candidate β -Li_2IrO_3. *Y. Wang*[1], A. Ruiz[2], J. Analytis[2] and K. Burch[1]
1. Physics, Boston College, Boston, MA, United States; 2. Physics, UC Berkeley, Berkeley, CA, United States

Kitaev quantum spin liquid (QSL) is a highly frustrated state in topological magnets with excitations from fractional particles[1,2,3]. Via time reversal symmetry breaking (e.g. ordered state below T_c), fractional particles can show non-Abelian exchange statistics, which offers topological quantum computing immune to de-coherence[4]. An open question is how the spin liquid like fraction excitations emerge from the magnons of the ordered state. Here, we report the Raman scattering result on three-dimensional magnet β-Li_2IrO_3. We identified the temperature dependence of the magnons for the first time and demonstrated how they melt into the fractional excitations expected from the QSL state.

[1] Kitaev, A. Annals of Physics 321, 2–111 (2006) [2] Sandilands, L. J., Tian, Burch, K. S. etc. Physical Review Letters 114 (2015). [3] Wang, Y., Osterhoudt, Burch, K. S. etc. arXiv preprint arXiv:1809.07782 (2018). [4] Banerjee, A. etc. npj Quantum Materials 3, 8 (2018).

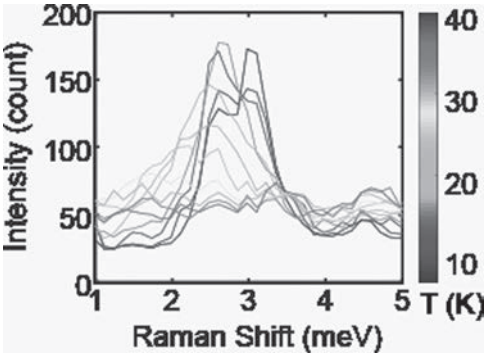


Fig.1 Temperature dependence of magnon excitation.

9:54

GD-06. Magneto-Raman study of the proximate quantum spin liquid α-$RuCl_3$. *T.T. Mai*[1], A. McCreary[1], J.R. Simpson[2,1], P. Lampen-Kelley[5], N. Butch[7,8], S. Nagler[4], D. Mandrus[5,6], R. Valdes Aguilar[3] and A.R. Hight Walker[1] *1. Physical Measurement Laboratory, National Institute of Standards and Technology, Gaithersburg, MD, United States; 2. Physics, Astronomy, and Geosciences, Towson University, Towson, MD, United States; 3. Physics, Ohio State University, Columbus, OH, United States; 4. Neutron Scattering Division, Oak Ridge National Laboratory, Oak Ridge, TN, United States; 5. Materials Science and Technology Division, Oak Ridge National Laboratory, Oak Ridge, TN, United States; 6. Materials Science and Engineering, University of Tennessee, Knoxville, TN, United States; 7. NIST Center for Neutron Research, National Institute of Standards and Technology, Gaithersburg, MD, United States; 8. Physics, University of Maryland, College Park, MD, United States*

The honeycomb lattice of α-$RuCl_3$ is a potential candidate to study the Kitaev model. The predicted ground state for such a model is a Quantum Spin Liquid (QSL). There is significant interest in studying the Kitaev interaction in α-$RuCl_3$, which orders antiferromagnetically below 6 K. In the magnetic phase, the Kitaev exchange energy is in the order of the antiferromagnetic (AFM) energy [1,2]. Interestingly, above an applied magnetic field of approximately 8 T, long-range magnetic order is suppressed and the QSL phase is recovered [3,4]. Inelastic light scattering, such as Raman spectroscopy, has been theoretically shown to be a direct probe of the itinerant Majorana fermions excitation [5,6]. Subtle hints of this fractionalized spin excitation had been experimentally observed in the broad scattering continuum in α-$RuCl_3$, where the typical bosonic thermal behavior of the

quasiparticles that typically make up these scattering continua was found to be fermionic [7,8,9]. Initially we identified two distinct A_g and B_g Raman responses of this scattering continuum in bulk α-$RuCl_3$ using angle-resolved Raman spectroscopy [10]. It was shown that the Fano resonances resulted from these responses come from the interaction of two different Raman phonons and a 2-Dimensional continuum. We extend this work to measure the temperature dependence of the scattering continuum down to 4 K, and in magnetic field up to 9 T. Implications on the anisotropic Kitaev exchange energies are discussed based on previously calculated Raman response, where $J_x = J_y \neq J_z$ (where x, y, z label the 3 different Ru-Ru directions in the 2D honeycomb lattice) [6].

[1] A. Banerjee, et al., Nature Materials 15, 733 EP (2016). [2] A. Banerjee, et al., Science 356, 1055 (2017). [3] R. Yadav, et al., Scientific Reports volume 6, Article number: 37925 (2016). [4] A. Banerjee, et al., npj Quantum Materials 3, 8 (2018). [5] J. Knolle, et al., Phys. Rev. Lett. 113, 187201 (2014). [6] B. Perreault, et al., Phys. Rev. B 92, 094439 (2015). [7] L. J. Sandilands, et al., Phys. Rev. Lett. 114,147201 (2015). [8] A. Glamazda, et al., Phys. Rev. B 95, 174429 (2017). [9] J. Nasu, J. Knolle, et al., Nature Physics 12, 912 (2016). [10] Manuscript in review

10:06

GD-07. Impact of spin-canting in the electrodynamic response of Dirac material $Ca_{1-x}Na_xMnBi_2$. *M. Chinotti*[1] *1. Physics, ETHZ, Zurich, Switzerland*

The quasi-two-dimensional bismuth layer-like $AMnBi_2$ (A = alkaline as well as rare earth atom) lately advanced as an arena for the investigation of low-energy quasiparticle excitations in topological materials. We describe optical reflectivity measurements from the far-infrared up to the ultraviolet range and as a function of temperature of $Ca_{1-x}Na_xMnBi_2$, also discussed in connection with their dc transport properties. This is the prerequisite for reliable Kramers-Kronig transformation, giving access to the optical conductivity. Besides observing a vestigial linear frequency dependent behaviour of the optical conductivity, which is ascribed to electronic interband transitions involving Dirac bands, the asset of our work consists in experimentally revealing an incipient Fermi surface (FS) gapping, which strengthens with Na doping and turns out to pair with the anomaly in the dc transport properties, generally ascribed to the onset of a spin reorientation. We conjecture that this latter (spin-canting) transition could be associated with a density-wave order directly affecting the electronic structure at the Dirac cones. Our findings may generally underline the proneness towards FS instabilities in topological materials, driven by an incipient symmetry breaking magnetic ordering.

INVITED PAPER

10:18

GD-08. Interlayer Dzyaloshinskii-Moriya Interactions. *E.Y. Vedmedenko*[1] *1. Physics, University of Hamburg, Hamburg, Germany*

The magnetic interfacial Dzyaloshinskii-Moriya interaction (DMI) in multi-layered thin films can lead to exotic chiral spin states, of paramount importance for future spintronic technologies [1]. Interfacial DMI is normally manifested as an intralayer interaction defining a rotational sense for the magnetization within two-dimensional films. Recently, we have shown theoretically that in addition to the interfacial DMI, magnetic layers can interact by means of a so-far neglected interlayer DM coupling across a spacer [2]. In contrast to the interfacial DMI, this interaction leads to the formation of three-dimensional spin spirals with unique rotational sense within as well as between the interfaces and, hence, combines intra- and inter-plane chiralities. Direct evidence of the interlayer-DMI at room temperature has recently been observed in synthetic magnetic heterostructures resulting in chiral exchange-biased hysteretic loops [3]. Schematics of the interlayer-DMI in synthetic magnetic heterostructures is shown in Fig.1. The realization of systems integrating interlayer magnetic chiral interactions paves the way for the creation of unprecedented magnetic effects in the emerging field of three-dimensional nanomagnetism and spintronics.

[1] J. Hagemeister, N. Romming, K. von Bergmann, E. Y. Vedmedenko, R. Wiesendanger, *Stability of single skyrmionic bits*, Nature Commun. 6, 8455 (2015). [2] E. Y. Vedmedenko, P. Arregi, J. Anders, A. Berger, *Interlayer Dzyaloshinskii-Moriya Interactions*, Phys. Rev. Lett. (2019), https://journals.aps.org/prl/accepted/04074Y36E301db5e778088d1a53f-825b2ecaea097. [3] A. Fernandez-Pacheco, E. Y. Vedmedenko, F. Ummelen, R. Mansell, D. Petit, R. P. Cowburn, *Symmetry-Breaking Interlayer Dzyaloshinskii-Moriya Interactions in Synthetic Antiferromagnets*, Nature Mater. https://doi.org/10.1038/s41563-019-0386-4 (2019).

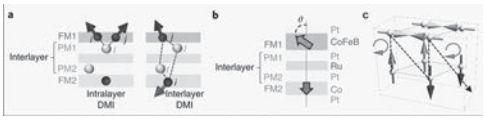


Fig.1 ***(a) The presence of standard intralayer DMI (left) in ultra-thin ferromagnetic ferromagnetic layers results in interactiion between spins within the same ferromagnetic layer via a paramagnetic layer leading to chiral coupling and noncollinear spin configurations within the layer. Analogously, an interlayer DMI effect (right) results in a chiral coupling between spins of two neighbouring layers separated by a spacer. (b) Schematics of the magnetic state in strongly ferromagnetic multilayers with interlayer DMI. (c) Unit cell of a low-energy three-dimensional spin structure due to the interlayer DMI between two very weakly ferromagnetic layers. This magnetic state shows clockwise chirality across the layers in two different directions.***

CONTRIBUTED PAPERS

10:54

GD-09. Majorana States in Atomic-Scale Magnet-Superconductor Hybrid Systems. H. Kim[1], A. Palacio-Morales[1] and *R. Wiesendanger*[1] *1. Dept. of Physics, University of Hamburg, Hamburg, Germany*

Majorana states in atomic-scale magnet-superconductor hybrid systems have recently become of great interest because they can encode topological qubits and ultimately provide a new direction in topological quantum computation [1,2]. First, it will be demonstrated how well defined 1D atomic chains of magnetic adatoms on superconducting substrates with high spin-orbit coupling can be artificially fabricated using STM-based atom-manipulation techniques. Spin-polarized STM measurements [3] allow revealing the presence of non-collinear spin textures, i.e. spin spiral ground states, stabilized by interfacial Dzyaloshinskii-Moriya interactions [4,5]. Simultaneously performed scanning tunneling spectroscopy on the magnetic atom chains on the superconductor substrate reveal the evolution of the spatially and energetically resolved local density of states as well as the emergence of zero-energy bound states at the chain ends above a critical chain length. Based on the exact knowledge of the geometrical, electronic, and spin structure of the magnetic chain – superconductor hybrid system, the experimental results can be compared rigorously with ab-initio and model-type tight-binding calculations supporting the interpretation of the spectroscopic signatures at the ends of the chains as Majorana bound states [6]. More recently, the atomic-scale design of more complex network structures for Majorana state manipulation, including braiding operations, has been in the focus of our research. In a second part, experimental and theoretical studies of monolayer topological superconductivity and chiral Majorana edge modes in model-type 2D magnetic islands on elemental superconductors will be presented [7]. In particular, it will be demonstrated that interface engineering by an atomically thin oxide layer is crucial for driving the studied hybrid system

into a topologically non-trivial state as confirmed by theoretical calculations of the topological invariant, the Chern number. Finally, the prospects for studies of Majorana states in skyrmion – superconductor hybrid systems [8] will be discussed.

[1] J. Alicea et al., Nature Phys. 7, 412 (2011). [2] S. Nadj-Perge et al., PRB 88, 20407 (2013). [3] R. Wiesendanger, Rev. Mod. Phys. 81, 1495 (2009). [4] A. A. Khajetoorians et al., Nature Commun. 7, 10620 (2016). [5] M. Steinbrecher et al., Nature Commun. 9, 2853 (2018). [6] H. Kim et al., Science Advances 4, eaar5251 (2018). [7] A. Palacio-Morales et al., Science Advances (2019), accepted for publication. See also: arXiv:1809.04503. [8] N. Romming et al., Science 341, 6146 (2013).

11:06

GD-10. Spin-orbit coupling-driven superconducting spintronics.
N. Banerjee[1], M. Blamire[2], J. Linder[3] and A.T. N'Diaye[4] *1. Physics, Loughborough University, Loughborough, United Kingdom; 2. University of Cambridge, Cambridge, United Kingdom; 3. Physics, Norwegian University of Science and Technology, Trondheim, Norway; 4. Lawrence Berkeley National Laboratories, Berkeley, CA, United States*

Recently, we have demonstrated the crucial role spin-orbit coupling plays in generating and controlling triplet Cooper pairs [1] confirming theoretical predictions of this phenomenon [2,3]. This provides a radically novel way to generate and control triplet Cooper pairs which is significantly simpler than the traditional conversion of singlet Cooper pairs into triplet Cooper pairs in the presence of inhomogeneous magnetic fields [4-6]. In this talk, I will discuss our results on proximity-coupling Pt/Co/Pt trilayer to a Nb thin-film superconductor to generate and control triplet Cooper pairs. The results demonstrate the generation and control of triplets using a single homogeneous ferromagnet instead of complex magnetic inhomogeneties. I will highlight our recent progress in this direction to better understand the origin of spin-orbit coupling in these heavy-metal/ferromagnet heterostructures using x-ray magnetic circular dichrosism and also briefly focus on some recent theoretical progress we have made in understanding the effect of superconductivity on magnetism in spin-orbit coupled structures [7]. Our experiments combine superconductivity, ferromagnetism and spin-orbit coupling into a new platform for spin-orbit coupling-driven superconducting spintronics.

1. N. Banerjee et al. Phys. Rev. B. 97, 184521 (2018). 2. F. S. Bergeret and I. V. Tokatly, Phys. Rev. Lett. 110, 117003 (2013). 3. S. H. Jacobsen, J. A. Ouassou, and J. Linder, Phys. Rev. B. Phys. 92, 024510 (2015). 4. J. W. A. Robinson, J. D. S. Witt, and M. G. Blamire, Science 329, 59 (2010). 5. N. Banerjee, et al, Nature Communications 5, 3048 (2014). 6. N. Banerjee, J. W. A. Robinson, and M. G. Blamire, Nature Communications 5, 4771 (2014). 7. Lina G Johnsen, Niladri Banerjee, Jacob Linder, Phys. Rev. B. 99, 134516 (2019).

11:18

GD-11. Superchiral spin waves.
F. Torres[1,2] *1. Departamento de Física, Universidad de Chile, Santiago, Chile; 2. Centro para el desarrollo de la Nanociencia y Nanotecnología Cedenna, Santiago, Chile*

The interference of two electromagnetic waves of opposite chirality leads to a locally enhanced chiral asymmetry (or superchiral fields) [1-3], due to the suppression of the electric dipole transitions [2]. This, in turn, produces an asymmetry in the absorption rate of chiral molecules [2, 3]. We demonstrate that an analogous field configuration arises from the superposition of two spin waves with opposite chirality, see Fig.[1]. We consider a ferromagnetic spin chain with an effective magnetic anisotropy at ends induced by the symmetry breaking and the Dzyaloshinskii-Moriya interaction. The magnetic moments located at the ends of the chain experience an additional torque, because of the boundary conditions, tilting away from the rest of the magnetic moments of the chain in the opposite directions. This model describes the dynamics and magnetic properties of superchiral spin waves, and shown an enhanced chiral asymmetry along the chain, that can be used, for instance, to manipulate the chiral magnetic coupling at the atomic scale. Further potential applications for spintronics also are discussed.

[1] A. Vázquez-Guardado, and D. Chanda, *Phys. Rev. Lett.* 120, 137601 (2018). [2] Y. Tang, and A. E. Cohen, *Phys. Rev. Lett.* 104, 163901 (2010). [3] Y. Tang, and A. E. Cohen, *Science* 332, 333 (2011).

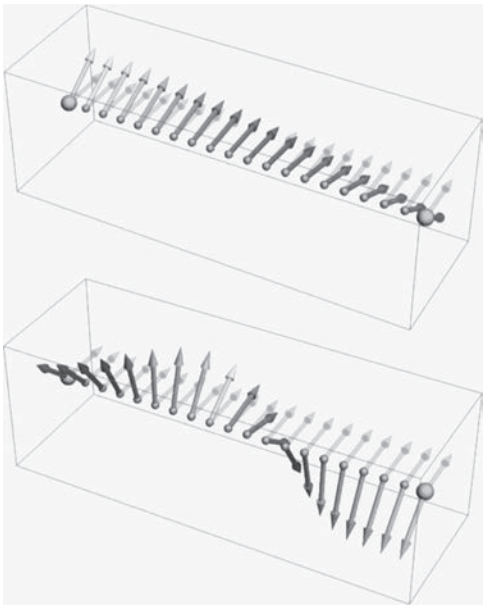


Fig.1. Superchiral spin wave simulation obtained from the interference between two spin waves with opposite chirality. Reversal mode of a ferromagnetic spin chain with boundary conditions induced by Dzyaloshinskii-Moriya interaction.

Session GE
SPIN WAVES: PROPAGATION & DETECTION

Satoshi Iihama, Chair
Tohoku University, Sendai, Japan

CONTRIBUTED PAPERS

8:30

GE-01. Generation of Propagating Spin Waves by YIG-based Spin-Orbit Torque Oscillators. *V.E. Demidov*[1], M. Evelt[1], L. Soumah[2], S.O. Demokritov[1], V. Cros[2], J. Ben-Youssef[3], G. de Loubens[4], O. Klein[5], P. Bortolotti[2] and A. Anane[2] *1. University of Muenster, Muenster, Germany; 2. Université Paris-Sud, Palaiseau, France; 3. Université de Bretagne Occidentale, Brest, France; 4. CEA-Saclay, Gif-sur-Yvette, France; 5. Université Grenoble Alpes, Grenoble, France*

Recent advances in the studies of the spin-orbit torque (SOT) opened novel perspectives for nano-spintronics and magnonics by enabling utilization in spintronic devices of insulating magnetic materials such as Yttrium Iron Garnet (YIG), which is famous for its unprecedented small magnetic damping. In particular, SOT was shown to enable highly efficient compensation of the decay of propagating spin waves and excitation of localized coherent magnetization auto-oscillations in YIG. However, for a long time, it was not possible to achieve generation of propagating spin waves by insulator-based SOT oscillators, which is of particular importance for implementation of efficient magnonic nano-devices and circuits. Here, by using the space- and time-resolved micro-focus Brillouin light scattering (BLS) spectroscopy, we experimentally demonstrate an approach, which allows one to achieve an efficient emission of SOT-excited coherent spin waves into an extended magnetic-insulator film. We show that this can be accomplished by utilizing nanometer-thick Bi-substituted YIG films exhibiting large perpendicular magnetic anisotropy (PMA). The effects of PMA result in a compensation of the in-plane shape anisotropy of the film. Due to this compensation, the nonlinear frequency shift vanishes leading to the current-independent frequency of the auto-oscillations. As the result, the auto-oscillations do not experience nonlinear self-localization and can emit propagating spin waves with the wavelength of about 300 nm. We emphasize that, in our devices, the excitation of microwave-frequency spin waves requires dc current only, i.e. they incorporate an internal microwave source. Since microwave generation is performed directly in the device, the proposed approach is free from difficulties associated with the coupling and transmission of microwave-frequency electric currents in nano-scale circuits.

M. Evelt et al., Appl. Phys. Lett. 108, 172406 (2016) M. Collet et al., Nature Commun. 7, 10377 (2016) V. E. Demidov et al., Phys. Rep. 673, 1 (2017) L. Soumah et al., Nat. Commun. 9, 3355 (2018) B. Divinskiy et al., Adv. Mater. 30, 1802837 (2018) M. Evelt et al., Phys. Rev. Appl. 10, 041002 (2018)

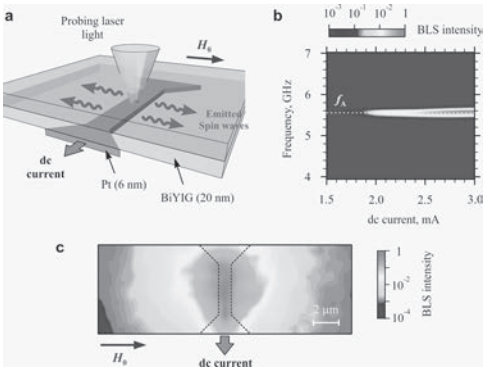


Fig.1 (a) Experimental layout. (b) Current-dependent spectra of SOT-induced auto-oscillations. (c) Color-coded spatial map of the spin-wave intensity.

8:42

GE-02. Anisotropic transport of spontaneously accumulated magneto-elastic bosons in Yttrium Iron Garnet films. *P. Frey*[1], D.A. Bozhko[1,2], V. Vasyuchka[1], A.A. Serga[1] and B. Hillebrands[1] *1. Fachbereich Physik and Landesforschungszentrum OPTIMAS, Technische Universität Kaiserslautern, Kaiserslautern, Germany; 2. School of Engineering, University of Glasgow, Glasgow, United Kingdom*

Macroscopic quantum states---Bose-Einstein condensates (BECs) can be created in overpopulated gases of bosonic quasiparticles as excitons, polaritons or magnons [1]. However, interactions between quasiparticles of a different nature, for example, between magnons and phonons in a magnetic medium, can significantly alter the properties of these gases and thus modify the condensation scenarios. Recently, we reported on the discovery of a novel condensation phenomenon mediated by the magnon-phonon interaction: an accumulation of hybrid magneto-elastic bosons [2]. Unlike a BEC, the accumulated magneto-elastic bosons possess a nonzero group velocity, making them promising data carriers in prospective magnon spintronic circuits. Here, we present the results of two-dimensional transport measurements of magneto-elastic bosons in a single-crystal Yttrium Iron Garnet film. Due to the strong magnetically induced anisotropy the curvature of the magnon-phonon spectrum is changed in the hybridization area (see Fig. 1) and therefore we observe several spatially localized beams with different group velocities for the magnon-phonon hybrid states. The observed behavior can be explained trough precise modeling of the avoided crossing region in wavevector space. This work is supported by the European Research Council within the ERC Advanced Grant “Supercurrents of Magnon Condensates for Advanced Magnonics”.

1. S.O. Demokritov *et al*., *Bose-Einstein condensation of quasi-equilibrium magnons at room temperature under pumping*, Nature 443, 430 (2006). 2. D.A. Bozhko *et al*., *Bottleneck accumulation of hybrid magneto-elastic bosons*, Phys. Rev.Lett. 118, 237201 (2017).

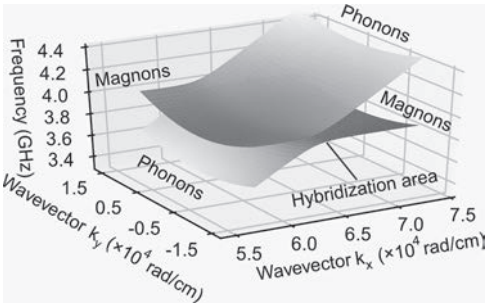


Fig.1 This graph shows a simulation of the interaction region between magnon and phonons. Depending on the wavevector the particle is a pure phonon, a pure magnon or a hybridized particle.

8:54

GE-03. Spin Wave Propagation in Individual Nano-Sized Yttrium Iron Garnet Magnonic Conduits. B. Heinz[1], T. Brächer[1], M. Schneider[1], Q. Wang[1], P. Pirro[1], B. Lägel[1], D. Breitbach[1], A.M. Friedel[1], C. Dubs[3] and *A. Chumak*[2,1] *1. University of Kaiserslautern, Kaiserslautern, Germany; 2. Nanomagnetism and Magnonics, University of Vienna, Vienna, Austria; 3. INNOVENT e.V. Technologieentwicklung, Jena, Germany*

Yttrium iron garnet (YIG) is a unique material with the lowest known spin wave damping. It is therefore well suited for the investigation of fundamental spin wave dynamics and a promising candidate for the application in spin wave based circuits and logic devices [1, 2]. In this work, we study the impact of nanostructuring by means of electron beam lithography and successive ion milling on the spin wave propagation in individual spin wave waveguides. These structures are fabricated from a 44 nm thin high-quality YIG film grown by liquid phase epitaxy (LPE) [3] and their width varies from a few microns down to 40 nm (Fig. 1.a) [4]. By exciting the magnetization dynamics with a coplanar waveguide antenna and performing spatially resolved Brillouin Light Scattering (BLS) microscopy measurements, the propagation of spin waves in such nanostructures could be measured directly. In addition, the decay length of the spin waves in these conduits was investigated as a function of the conduit width. It is shown that for the smallest conduit width of 40 nm, the decay length decreases from 15.5 μm to 1.8 μm (Fig. 1.b). However, this decrease is mainly due to a change in the dispersion resulting in a significant decrease in the spin wave group velocity. This was confirmed by the measurement of the group velocity of the spin waves generated by pulse excitation and the temporal tracking of the spin wave packet using BLS microscopy. In addition, the spin wave mode spectra were extracted using thermal BLS measurements from which the effective exchange constant was derived. No significant dependence on the conduit width is found, which allows the conclusion that the impact of the nanostructuring process on the quality of YIG is minor. These findings pave the way for magnon-based data processing in nanoscale magnonic circuits. This research has been supported by ERC Starting Grant 678309 MagnonCircuits, DFG Grant DU 1427/2-1 and the Graduate School Material Science in Mainz (MAINZ).

[1] A. A. Serga *et al.*, J. Phys. D: Appl. Phys. 43, 264002 (2010). [2] Q. Wang, B. Heinz, R. Verba, *et al.*, Phys. Rev. Lett. 122, 247202 (2019). [3] C. Dubs *et. al.*, J. Phys. D: Appl. Phys. 50 204005 (2017). [4] Q. Wang, M. Kewenig, M. Schneider, *et al.*, arXiv:1905.12353 (2019).

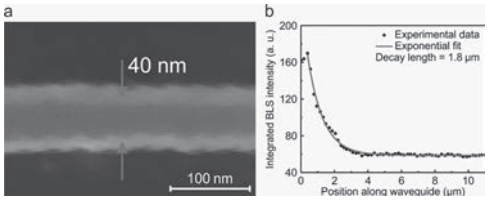


Figure 1: a) SEM micrograph of a 40 nm wide YIG waveguide. b) Exponential decay of the spin wave intensity measured in Backward-Volume-Geometry in the structure shown in a), for an excitation frequency of 3.78 GHz and an external magnetic field of 55 mT.

9:06

GE-04. Reconfigurable Magnonic Crystals Based on YIG thin films and Co/Pt Bar-Magnets with Perpendicular Magnetic Anisotropy. *M. Kiechle*[1], A. Papp[1,2], M. Golibrzuch[1], S. Mendisch[1], V. Ahrens[1] and M. Becherer[1] *1. Department of Electrical and Computer Engineering, Technical University of Munich, Munich, Germany; 2. Pazmany Peter Catholic University, Budapest, Hungary*

This work presents an experimental demonstration of reconfigurable magnonic crystals (MC) based on periodic magnetic field profiles applied on YIG by nano-imprinted Co/Pt bar-magnets. The dipole fields of the hard-magnetic Co/Pt bars fabricated on top of YIG influence the propagation of spin waves (SWs) locally. In contrast to previously demonstrated MCs [1-3], reconfigurability is hereby achieved through the reversible magnetization of the Co/Pt stripes, resulting in the formation of magnonic bandgaps dependent on their magnetization direction. This concept promises additional degrees of freedom for bandgap engineering by simply switching nanomagnets in a global field and furthermore provides significant advantages in fabrication, since nano-patterning of Co/Pt is by far less challenging compared to that of YIG itself. The Co/Pt nanomagnets have perpendicular magnetic anisotropy (PMA), hence their magnetization is switchable from up to down and vice versa. Their coercivity is significantly higher than the required out-of-plane bias field for YIG, thus keeping their magnetization state in the experiment. An established method of engineering the coercivity in PMA magnets is inducing local defects via focused ion beam (FIB) irradiation. Switching the magnetization in FIB manipulated Co/Pt requires lower bias fields, facilitating altering dipole field directions by inverting selected magnets only; e.g. an antiferromagnetic field map by switching every second bar-magnet. The magnonic crystal is characterized by all-electrical metrology, i.e. measuring the transmission between two short-circuited coplanar waveguides (Fig. 1), as well as by means of trMOKE microscopy. Until now, we are able to excite wavelengths down to 2 μm and visualize the dispersion in the first Brillouin zone. Complementary, the SW dispersion in the MC is modelled in micromagnetic simulations in Mumax3. With varying field configurations of the bar-magnets, magnonic band gaps of variable size can be obtained. (Fig. 2).

[1]: Chumak, A. V., A. A. Serga, and B. Hillebrands, *Journal of Physics D: Applied Physics* 50.24 (2017): 244001. [2]: Qin, Huajun, et al., *Nature communications* 9.1 (2018): 5445. [3]: Goto, Taichi, et al., *Physical Review Applied* 11.1 (2019): 014033.

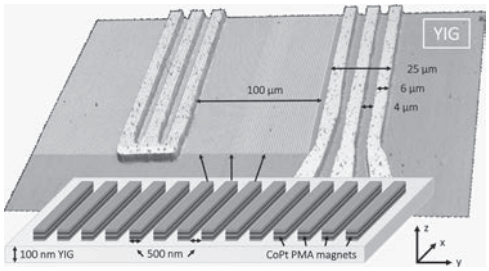


Fig.1 Microscopy image of the fabricated YIG film with the Co/Pt nanomagnets between two CPWs. The geometrical dimensions are illustrated schematically.

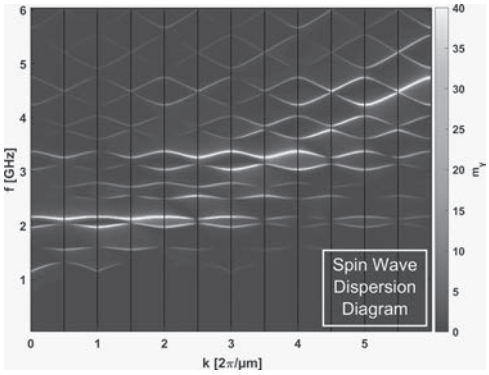


Fig.2 Dispersion curve simulation of the MC based on the experimental parameters in Fig 1.

9:18

GE-05. Withdrawn

9:30

GE-06. Experimental Demonstration of a Spin-Wave-Based Spectrum Analyzer Using FIB Patterning of YIG. A. Papp[1,2], *M. Kiechle*[1], S. Mendisch[1], V. Ahrens[1], G. Csaba[2], W. Porod[3] and M. Becherer[1] *1. TU Munich, München, Germany; 2. Pazmany Peter Catholic University, Budapest, Hungary; 3. University of Notre Dame, Notre Dame, IN, United States*

We present a new method for locally altering the magnetization of YIG (yttrium iron garnet), and using this technique we demonstrate a spin-wave-based spectrum analyzer proposed in [1]. YIG is an attractive candidate for magnonic applications due to its very low damping, but precise nanoscale patterning of YIG is challenging. We demonstrate the use of FIB (focused ion beam) irradiation to achieve magnetically inactive regions in YIG with nanoscale precision. This way, instead of patterning YIG by removing material, we only 'switch off' its magnetization in the irradiated regions, which results in similar behavior for guiding spin waves. We used a high-dose irradiation (10^{15} ions/cm^2) to achieve a binary magnetization landscape, however, we are also investigating the use of lower doses for smooth changes in magnetization, which could be useful for gradient index spin-wave optics or phase-shifter plates for magnonic computing. Film level ion irradiation of YIG was recently investigated in [2]. To demonstrate the utility of this technique, we present an experimental demonstration of the spin-wave-based microwave spectrum analyzer proposed in [1]. This device requires a concave grating, which can act as a source of spin waves driven by a nearby microwave antenna. In the original design, this was achieved by patterning YIG by removing material. Here, we demonstrate that this is also possible using FIB irradiation in the required pattern. Fig. 1 shows a proof-of-concept experimental result, where the resulting diffraction peaks are clearly visible (zero order and first order peaks). The irradiated region does not allow the propagation of spin waves, and the edge of the irradiated region acts as the source of new spin waves, which are excited by the magnetic field of the neighboring CPW (coplanar waveguide), at the same frequencies as the microwave signal in the CPW.

[1] Papp, A. et al. "Nanoscale spectrum analyzer based on spin-wave interference." *Scientific Reports 7* (2017): 9245. [2] Ruane, W. T. et al. "Controlling and patterning the effective magnetization in Y3Fe5O12 thin films using ion irradiation." AIP Advances 8.5 (2018): 056007

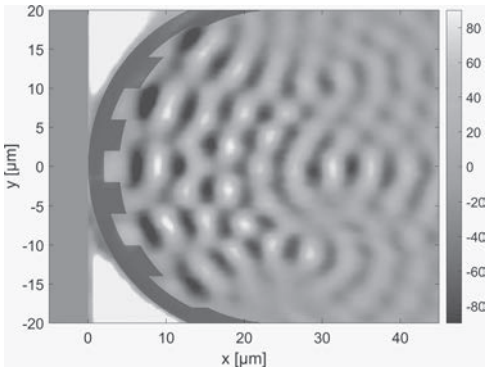


Fig. 1 Time-resolved MOKE measurements of the spin-wave interference pattern created by a concave grating. The gray stripe indicates the location of the GND line of the CPW obtained for wave excitation. The semi-transparent red pattern is where FIB irradiation was performed (grating). The film was magnetized out-of-plane (isotropic wave propagation).

9:42

GE-07. Brillouin Light Scattering (BLS) Measurements of Spin Waves Excited by Surface Acoustic Waves (SAWs). *K.E. Nygren*[1], J.D. Schneider[2], Q. Wang[2], D. Labanowski[3], S. Salahuddin[3], G. Carman[2] and K. Buchanan[1] *1. Department of Physics, Colorado State University, Fort Collins, CO, United States; 2. Department of Mechanical and Aerospace Engineering, University of California Los Angeles, Los Angeles, CA, United States; 3. Deparment of Electrical Engineering and Computer Science, University of California Berkeley, Berkeley, CA, United States*

Propagation distances for surface acoustic waves (SAWs) are much longer than most spin waves in metals. However, spin waves may travel farther with propagation distances similar to that of SAWs if they can be coupled to these SAWs. Acoustic waves have recently garnered interest as an efficient means to drive magnetic oscillations. Indirect measurements have shown acoustic power absorption by magnetic materials attributed to the creation of spin waves, but few measurements have been done to directly measure coupled spin waves [1-3]. Here, we have used an interdigital transducer (IDT) on a piezoelectric substrate to convert an electrical signal into surface acoustic waves that can then propagate along the substrate surface. When a thin magnetic film is deposited on top of the substrate, the mechanical ripple of the SAW strains the thin magnetic layer [4]. We have made Brillouin light scattering (BLS) measurements on a 25 nm thick nickel pad, while driving the IDT at 1.8 GHz (a sample schematic is shown in Fig. 1a). For higher external magnetic fields, a BLS signal at the 1.8 GHz driving frequency is detected. At lower fields where the driving frequency overlaps the spin wave manifold, we see a BLS signal at 1.8 GHz (Fig. 1b) as well as at 3.6 GHz (Fig. 1c), twice the driving frequency, attributed to a non-linear magnetic process. Measurements at multiple locations across the 300 x 300 µm^2 square nickel pad provide a means to determine how the coupled spin waves decay with distance. We will also discuss the power dependence of the non-linear magnetic signal. This work is supported by NSF EFMA 1741666, NSF DEEC 1160504, and NSF EFRI NewLaw Award no. 1641128.

[1] P. G. Gowtham, T. Moriyama, D. C. Ralph, and R. A. Buhrman, Jour. of App. Phys., 118, 233910 (2015) [2] D. Labanowski, V. P. Bhallamudi, Q. Guo, et. al., Sci. Adv., 4, eaat6574 (2018) [3] M. Foerster, F. Macia, H. Statuto, et. al., Nat. Comm., 8, 407 (2017) [4] M. Weiler, L. Dreher, C. Heeg, et. al., Phys. Rev. Lett., 106, 117601 (2011)

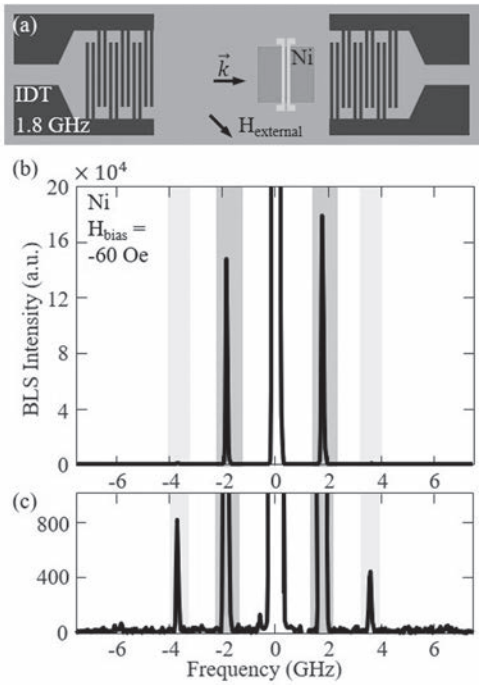


Fig. 1 a) Diagram showing double-finger IDT used to launch 1.8 GHz SAWs that travel towards a nickel pad. A BLS spectra measured over the nickel film with an external magnetic field $H_{external}$ of -60 Oe, shows resonances at 1.8 GHz (b) and at 3.6 GHz on a much smaller scale (c).

9:54

GE-08. Real Space Observation of Scattering on Magnonic Space-Time Crystals. *N. Träger*[3], P. Gruszecki[1], F. Lisiecki[2], J. Förster[3], F. Gross[3], M. Weigand[3,4], P. Kuswik[2,5], J. Dubowik[2], G. Schütz[3], M. Krawczyk[1] and J. Gräfe[3] *1. Faculty of Physics, Adam Mickiewicz University, Poznan, Poland; 2. Institute of Molecular Physics, Polish Academy of Science, Poznan, Poland; 3. Max Planck Institute for Intelligent Systems, Stuttgart, Germany; 4. Helmholtz-Zentrum, Berlin, Germany; 5. Centre for Advanced Technology, Adam Mickiewicz University, Poznan, Poland*

In analogy to conventional space crystals in condensed matter and atomic physics, Wilczek proposed the theory of spontaneous breaking of time symmetry and the emergence of Time Crystals [1]. Furthermore, a simultaneous crystalline formation in space permits the emergence of discrete space-time crystals (STC). Experiments confirmed the existence in abstract quantum systems [2, 3]. Here, we directly observe lattice scattering on a driven STC within a magnonic Py waveguide. Due to the generated periodicity in space and time, a band structure is formed and mode folding at the first Brillouin has to be taken into account. Therefore, magnons can scatter at the driven STC into higher spatial frequencies, which are forbidden in the conventional dispersion relation theory for the same structure (*cf.* Fig. 2). These scattering processes are observed and imaged in real space by scanning transmission x-ray microscopy (STXM) with magnetic contrast that features the necessary spatial (< 20 nm) and temporal (< 40 ps) resolution. The initial formation of the driven STC is caused by a continuous wave (CW) global radio frequency field, which leads to spin wave emission from the left and right edge of the waveguide [4]. Consequently, a standing spin wave pattern arises revealing oscillation in space and time (*cf.* Fig. 1). With the realization of a driven space-time crystal in magnonic waveguides, we take the abstract idea of space-time crystalline structures to the next level and reveal new phenomena in the field of non-linear wave physics. These fundamental findings could pave the way for reconfigurable magnonic crystals without nanoscale patterning and for a new generation of spin wave emitter at ultra short length scales.

1. Wilczek, F., *Quantum Time Crystals.* PRL., Vol. 109(16), p. 160401 (2012) 2. Smits, J. et al., *Observation of a Space-Time Crystal in a Superfluid Quantum Gas.* PRL., Vol. 121(18), p. 185301 (2018) 3. Kreil, A. et al., *Tunable space-time crystal in room-temperature magnetodielectrics.* arXiv preprint arXiv:1811.05801 (2018) 4. Mushenok, F. B. et al., *Broadband conversion of microwaves into propagating spin waves in patterned magnetic structures.* APL., Vol. 111(4), p. 042404 (2017)

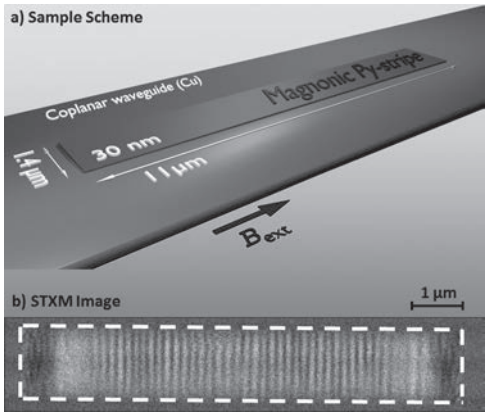


Fig. 1: (a) Sketch of the Magnonic Py waveguide (blue) with the coplanar waveguide (gray). (b) STXM image during continuous wave RF excitation. The grayscale represents the m_z component.

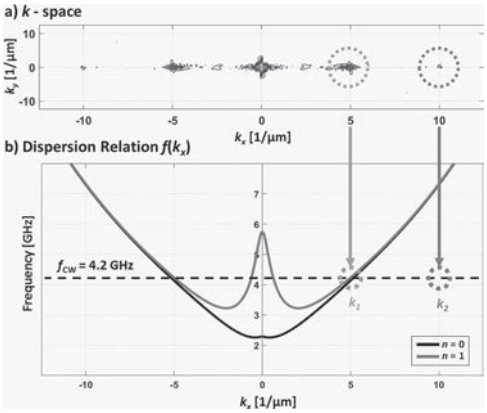


Fig. 2: (a) *k*-space image of the excited standing spin wave pattern. (b) The dispersion relation $f(k_x)$ shows the CW excitation f_{CW}. The mode numbers $n = 0$ and $n = 1$ are depicted in black and red, respectively. Folding of bands due the formation of a space-time crystalline structure explains the double spatial frequency of k_2.

10:06

GE-09. Direct observation of short-wave magnons emitted from periodic and aperiodic grating couplers. *K. Baumgaertl*[1], J. Gräfe[2], P. Che[1], A. Mucchietto[1], J. Förster[2], N. Träger[2], M. Bechtel[2], M. Weigand[2,3], G. Schütz[2] and D. Grundler[1,4] *1. Laboratory of Nanoscale Magnetic Materials and Magnonics, Institute of Materials, Ecole Polytechnique Fédérale de Lausanne (EPFL), Lausanne, Switzerland; 2. Max-Planck-Institute for Intelligent Systems, Stuttgart, Germany; 3. Helmholtz-Zentrum Berlin für Materialien und Energie, Berlin, Germany; 4. Institute of Microengineering, Ecole Polytechnique Fédérale de Lausanne (EPFL), Lausanne, Switzerland*

Coherent emission and phase-resolved detection of exchange-dominated magnons with wavelengths of λ = 100 nm and below is one of the biggest challenges of the emerging field of nanomagnonics. A promising approach is the magnonic grating coupler (GC) effect [1], in which a periodic lattice of nanomagnets (periodicity *p*) is integrated on a magnetic thin film to modulate the electromagnetic near field of a conventional coplanar waveguide (CPW). In Ref. [2] GC-excited SWs were consistent with a wavelength of λ = 50 nm [2]. However, λ was not measured directly, but estimated from theoretically predicted dispersion relations assuming a reciprocal lattice vector $G = 2\pi/p$ of the GC. Using time resolved scanning transmission x-ray microscopy (TR-STXM) we investigated the GC effect in real space. We prepared periodic gratings with p = 200 nm (p = 400 nm) consisting of 100 nm (200 nm) wide and 20 nm thick Permalloy (Py) stripes underneath a CPW on a 100 nm thick Yttrium iron garnet (YIG) film. We imaged the first and second GC mode of the p = 200 nm grating by TR-STXM. In the latter case, plane-wave SWs with λ = 100 nm were induced underneath the GC and emitted into the bare YIG, where the wavelength amounted to λ = 104 nm. The emitted plane-wave SWs were still detected 10 µm away from the CPW. Preferential emission of SWs to one side of the antenna was observed. Also the p = 400 nm GC showed emission of SWs with λ = 100 nm. Their wave vector corresponded to 4G. At 8.7 GHz and fields around 24 mT, the so-called resonant grating coupler effect was apparent in that magnetization oscillations with the periodicity of the Py lattice were superimposed on 100 nm SWs in the YIG film underneath the GC. When arranging 100-nm-wide Py stripes in an aperiodic 1D Fibonacci sequence [3] we observed additional high frequency SW branches compared to the periodic lattices reports above. From broadband spectroscopy based on a vector network analyzer we estimated wavelengths down to below 100 nm for the additional branches. The aperiodic Fibonacci sequence hence allowed us to excite more wave vectors compared to a periodic grating. The work is funded by SNF 163016. We thank HZB, Germany for the allocation of synchrotron radiation beamtime.

[1] H. Yu, et al., Nature communications 4, 2702 (2013) [2] C. Liu, et al., Nature communications 9, 738 (2018) [3] J. Rychly, et al., Phys. Rev. B 92, 054414 (2015)

10:18

GE-10. Wavelength-Selective Optical Detection of Spin Waves Beyond the Diffraction Limit. *M. Peeters*[1], J. Lucassen[1], C. Schippers[1], R. Duine[1,2], H. Swagten[1], B. Koopmans[1] and R. Lavrijsen[1] *1. Applied Physics, Eindhoven University of Technology, Eindhoven, Netherlands; 2. Institute for Theoretical Physics, Utrecht University, Utrecht, Netherlands*

The introduction of spin waves in next-generation computing devices is expected to lead to several advantages, such as the ability for wave computing or chargeless information transport [1]. However, its introduction is hampered by an inability to efficiently excite and detect these spin waves. One of the more interesting ways to do this is optically, although here we run into the limitation of accessible length scales (wavelength of the spin-waves) set by the optical diffraction limit. In this work, we demonstrate optical detection of spin waves beyond the diffraction limit by nanostructuring light reflecting elements (a grating) on top of a magnetic strip (Fig. 1). We electrically excite spin waves in this strip using a spin wave antenna, and detect them by focusing a pulsed fs-laser onto the grating. The grating will modify the spatial intensity profile of the laser spot, leading to a non-vanishing magneto-optical Kerr effect if the grating matches the spin wave wavelength. Experimentally, we demonstrate that the grating allows us to detect spin waves with a wavelength of 700 nm using a spot with a full width at half maximum (FWHM) of 12 µm (Fig. 2). Additionally, we see that the spatial filtering of the grating makes these measurements extremely wavelength selective. Our current efforts are aimed at unravelling the measured spectra, which is done using an analytical model that describes the excited spin waves based on Fourier analysis. The resulting behavior is qualitatively similar to the measurements (such as the one in Fig. 2). We expect that this technique can provide a new non-invasive and artefact free way of measuring spin waves as a function of position and help integrate the field of optics with nanoscale magnetism.

[1] A. V. Chumak, V. I. Vasyuchka and B. Hillebrands, Nat. Phys. Vol. 11, p.453 (2015)

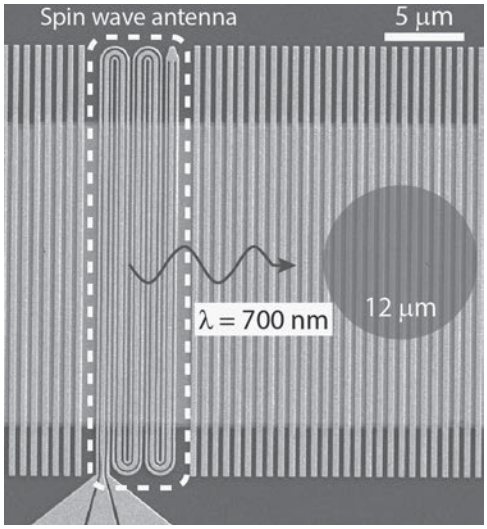


Fig. 1: Fabricated device. The electrical spin wave antenna generates spin waves with a wavelength of 700 nm. We can detect this spin wave away from the antenna using a grating and a laser spot with a FWHM of 12 µm.

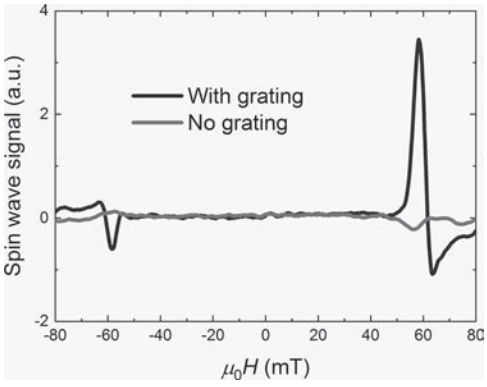


Fig. 2: Optical spin wave measurements with and without grating. The resonances at ±60 mT correspond to a spin wave with a wavelength of 700 nm measured with a spot size of 12 µm. This resonance is no longer present if the grating is not used.

10:30

GE-11. Exploration of modified density of states and multi-directional emission of spin-waves in artificial magnetic quasicrystals.
S. Watanabe[1], V.S. Bhat[1], K. Baumgaertl[1] and D. Grundler[1,2] *1. Institute of Materials, Ecole Polytechnique Fédérale de Lausanne (EPFL), Lausanne, Switzerland; 2. Institute of Microengineering, Ecole Polytechnique Fédérale de Lausanne (EPFL), Lausanne, Switzerland*

A quasicrystal possesses a long range order but no translational invariance. Penrose tiling [1] is known as a 2D analogue of a natural quasicrystal. Photonic artificial quasicrystals based on Penrose tiling, i.e., nanostructures engineered to create quasicrystalline properties, exhibit a complete band gap for light due to their manifold rotational symmetry [2]. Artificial magnetic quasicrystals (AMQs) provide further interesting features in that collective spin excitations (spin waves) exhibit anisotropic dispersion relations and depend on the inhomogeneity of the internal field and rotational symmetry [3, 4]. We fabricated AMQs based on 100 nm thick yttrium iron garnet (YIG) thin films. Nanotroughs with a depth of 18 nm and a diameter of 330 nm were structured at the vertices of a Penrose P3 tiling whose characteristic length amounted to 900 nm. The AMQs covered 52.8 x 50.2 μm^2. Two coplanar waveguides were integrated on top of the samples to excite spin waves (SWs). Here we report SW properties explored by broadband SW spectroscopy and Brillouin light scattering (BLS). Angular-dependent SW spectroscopy showed broad frequency bands of excited spin waves which contained narrow regime of forbidden frequency gaps. We attribute this observation to the formation of a pseudo Brilloun zone (p-BZ) [2] and modified density of state for SW in the AMQ. SW transmission spectra indicated that the wave vector of the SW was modified by the basic reciprocal vector of the AMQ [5]. SW imaging via BLS technique with phase and time resolution evidenced irregular SW phase fronts, which are not observed in periodic structures. Our experimental results suggest that aperiodically arranged nanogratings [5] allow one to emit spin waves with a manifold of propagation directions and wavelengths. This work was supported by Swiss National Science Foundation via Grant No. 163016.

[1] M. Gardner. Penrose Tiles to Trapdoor Ciphers: And the Return of Dr. Matrix (Cambridge University Press, 1997). [2] M.A. Kaliteevski, et al. Nanotechnology, Vol.11, No.4, p.274 (2000) [3] V. S. Bhat, and D. Grundler, Physical Review B, Vol.98, p.174408 (2018) [4] J. Rychly et al., J. Magn. Magn. Mater., Vol.450, p.18 (2018) [5] H. Yu, et al. Nature communications, Vol.7, p.11255 (2016)

10:42

GE-12. Magnons in a Quasicrystal: Propagation, Extinction and Localization of Spin Waves in Fibonacci Structures.
F. Lisiecki[3], J. Rychly[2], P. Kuswik[2], H. Glowinski[3], J. Klos[2], F. Gross[1], N. Träger[1], I. Bykova[1], M. Weigand[5], M. Zelent[2], E. Goering[1], G. Schütz[1], G. Gubbiotti[4], M. Krawczyk[2], F. Stobiecki[3], J. Dubowik[3] and *J. Gräfe*[1] *1. Max Planck Institute for Intelligent Systems, Stuttgart, Germany; 2. Adam Mickiewicz University, Poznan, Poland; 3. Institute of Physics, Polish Academy of Sciences, Poznan, Poland; 4. Istituto Officina dei Materiali del Consiglio Nazionale delle Ricerche, Perugia, Italy; 5. Helmholtz-Zentrum Berlin, Berlin, Germany*

Magnonic quasicrystals exceed the possibilities of spin wave (SW) manipulation offered by regular magnonic crystals, because of their more complex SW spectra with fractal characteristics. Here, we report a combined X-ray microscopic and Brillouin Light Scattering observation of propagating SWs in a magnonic quasicrystal, consisting of dipolar coupled permalloy nanowires arranged in a one-dimensional Fibonacci sequence. SWs from the first and second band as well as evanescent waves from the band gap between them are imaged (cf. Figure). Moreover, additional mini-band gaps in the spectrum are demonstrated, directly indicating an influence of the quasiperiodicity of the system. Finally, the localization of SW modes within the Fibonacci crystal is shown. The experimental results are interpreted using numerical calculations and we deduce a simple model to estimate the frequency position of the magnonic gaps in quasiperiodic structures. The demonstrated features of SW spectra in one-dimensional magnonic quasicrystals allows utilizing this class of metamaterials for magnonics and makes them an ideal basis for future applications. We confirm the existence of collective spin waves propagating through the structure as well as dispersionless modes; the reprogammability of the resonance frequencies, dependent on the magnetization order; and dynamic spin wave interactions. With the fundamental understanding of these properties, we lay a foundation for the scalable and advanced design of spin wave band structures for spintronic, microwave and magnonic applications.

F. Lisiecki, J. Rychly, P. Kuswik, H. Glowinski, J. W. Klos, F. Groß, Iu. Bykova, M. Weigand, M. Zelent, E. Goering, G. Schütz, M. Krawczyk, F. Stobiecki, J. Dubowik, J. Gräfe: Magnons in a Quasicrystal: Propagation, Localization and Extinction of Spin Waves in Fibonacci Structures. In: *Physical Review Applied* 11 (2019), 054061. F. Lisiecki, J. Rychly, P. Kuswik, H. Glowinski, J. W. Klos, F. Groß, Iu. Bykova, M. Weigand, M. Zelent, E. Goering, G. Schütz, G. Gubbiotti, M. Krawczyk, F. Stobiecki, J. Dubowik, J. Gräfe: Reprogrammability and scalability of Fibonacci magnonic quasicrystals. In: *Phyiscal Review Applied* 11 (2019), 054003.

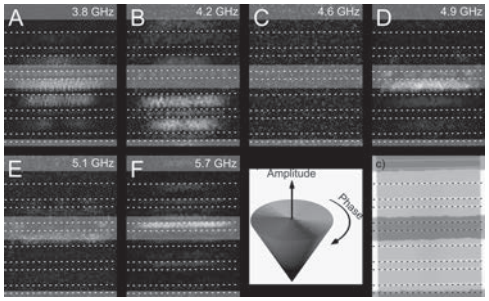


Fig.1 ***(a)*** **SW amplitude and phase for different excitation frequencies at 5 mT. The transparent gray rectangles mark the position of the CPW and the dashed white lines mark the gaps between the stripes.** ***(b)*** **Color code for SW amplitude (brightness) and phase (color).** ***(c)*** **Static image of the Fibonacci structure (light gray) with the signal line (dark gray) near the center of the image, and the ground lines at the top and bottom edges of the image (dark gray).**

10:54

GE-13. Long range coupling of magnetic bilayers by coherent phonons.
K. An[1], A. Litvinenko[1], A. Fuad[1], V. Naletov[1,2], L. Vila[1], U. Ebels[1], G. de Loubens[3], H. Hurdequint[3], N. Beaulieu[4], J. Ben-Youssef[4], N. Vukadinovic[5], G. Bauer[6], A.N. Slavin[7], V. Tiberkevich[7] and O. Klein[1] *1. Univ. Grenoble Alpes, CNRS, Grenoble INP, INAC-Spintec, Grenoble, France; 2. Institute of Physics, Kazan Federal University, Kazan, Russian Federation; 3. SPEC, CEA-Saclay, CNRS, Université Paris-Saclay, Gif-sur-Yvette, France; 4. LabSTICC, CNRS, Université de Bretagne Occidentale, Brest, France; 5. Dassault Aviation, Saint-Cloud, France; 6. Institute for Materials Research and WPI-AIMR and CSRN, Tohoku University, Sendai, Japan; 7. Department of Physics, Oakland University, Rochester, MI, United States*

We demonstrate that the spin waves can be strongly coupled to coherent shear waves that have very long characteristic decay length and propagate ballistically over millimetric distances. In our spin valve structure, which consists of two insulating magnetic layers (YIG) deposited on both sides of a dielectric GGG substrate, the standing acoustic waves couple to the magnetization oscillations in both layers. The coupling signifies a change of sign between the acoustic modes with even or odd indices, which results in a contrast between two tones separated by half a wavelength. We measure the contrast at different polar angles via inverse spin Hall effect using a thin Pt wire deposited on one side of the YIG layer. In our sample the two YIG layers resonate at slightly different frequencies. The change in

the polar angle allows to detune their resonances and make them cross, which leads to a peak of the contrast at the crossing point. We show that the observed behavior is in agreement with theoretical prediction. This long range coherent coupling by phononic angular momentum currents adds new functionalities to insulator spintronic circuits and devices.

R. L. Comstock and R. C. LeCraw, Journal of Applied Physics 34, 3022 (1963) M. Ye, A. Brockmeyer, H. Dötsch, Le Journal de Physique Colloques 49, C8 (1988) X. Zhang, C.-L. Zou, L. Jiang, and H. X. Tang, Science Advances 2, e1501286 (2016) K. An, A. N. Litvinenko, O. Klein., arXiv:1905.12523 (2019)

11:06

GE-14. Coupling between acoustic and optic magnons in synthetic antiferromagnets. *Y. Shiota*[1], T. Taniguchi[2], M. Ishibashi[1], T. Moriyama[1] and T. Ono[1] *1. Institute for Chemical Research, Kyoto University, Uji, Japan; 2. Spintronics Research Center, National Institute of Advanced Industrial Science and Technology (AIST), Tsukuba, Japan*

Synthetic antiferromagnets consist of two or more ferromagnetic layers separated by nonmagnetic layers. When the magnetizations are coupled antiferromagnetically through the interlayer exchange coupling, this enables us to investigate the antiferromagnetic resonance modes; an acoustic mode (in-phase precession) and an optic mode (out-of-phase precession). Recently, an anti-crossing gap of ferromagnetic resonance (k = 0 μm^{-1}) between acoustic and optic modes, so-called magnon-magnon coupling, was reported in the layered antiferromagnet of $CrCl_3$[1]. In this study, we observed the anti-crossing gap of spin wave resonance ($k \neq 0$ μm^{-1}) between acoustic and optic modes in synthetic antiferromagnet of FeCoB/Ru/FeCoB. The films were prepared by sputter deposition on a thermally oxidized Si wafer: Ta(3)/Ru(3)/$Fe_{60}Co_{20}B_{20}$(15)/Ru(0.6)/$Fe_{60}Co_{20}B_{20}$(15)/Ru(3) (thickness in nm). The two in-plane magnetized FeCoB layers separated by a Ru layer with a thickness of 0.6 nm were antiferromagnetically coupled through the interlayer exchange coupling. The films were micro-fabricated to spin wave devices, as shown in inset of Fig. 1. The efficiently excited spin wave wavenumber k was determined by the design of coplanar waveguides (CPWs). The scattering parameter S_{11} for reflection was measured by a vector network analyzer connected to the CPWs. The external magnetic field was applied at an angle φ_H with respect to the spin wave propagation direction. Figure 1 shows the Re[S_{11}] spectra as a function of magnetic field. When φ_H = 0, 90 deg. (Fig. 1(a)(c)), spin wave resonance frequencies of acoustic and optic modes are degeneracy at their crossing point and there is no anti-crossing gap. On the other hand, when φ_H = 45 deg. (Fig. 1(b)), two resonant modes are hybridized and the anti-crossing gap is generated. This is due to the interaction between two ferromagnetic layers through the magnetostatic dipole fields generated by spin waves. In the presentation, we will discuss more detail about φ_H and k dependence of anti-crossing gap, and provide a quantitative description of coupling strength.

[1] D. MacNeill et al., arXiv: 1902.05669 (2019)

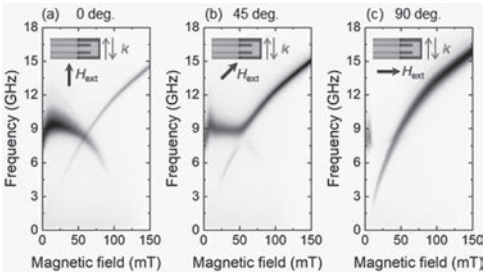


Fig. 1 Two-dimensional map of Re[S_{11}] spectra as a function of magnetic field with k = 1.2 μm^{-1} for φ_H of (a) 0 deg. (b) 45 deg. and (c) 90 deg.

11:18

GE-15. Nonlinear magnon scattering mechanism for microwave pumping in magnetic films. *T. Qu*[1,2], A. Venugopal[1], J.M. Etheridge[2], W. Peria[2], P.A. Crowell[2] and R. Victora[1] *1. Department of Electrical and Computer Engineering, University of Minnesota, Minneapolis, MN, United States; 2. School of Physics and Astronomy, University of Minnesota, Minneapolis, MN, United States*

The nonlinear properties of magnons have been a focus both as a prototypical nonlinear system [1,2] and for their potential applications. Nonlinear microwave devices, such as Signal to Noise Enhancers and Frequency Selective Limiters are known to provide useful manipulation of microwave signals without the need for power-hungry (and fragile) electronic circuitry, exploiting nonlinear magnon properties. However, the underlying physical processes are poorly understood, making efficient device design impossible. Here we examine this nonlinearity from the perspectives of micromagnetic simulation and experiment, for the perpendicular-pumping configuration, a common device arrangement. Parallel computing on graphical processing (GPUs) is used to overcome the barriers of long time and length scales, and thus predict steady state phenomena. We use a 2D simulation model to quantitatively identify magnon scattering regimes, in the light of magnon-band structure. The experimental nonlinearity is measured as a function of microwave power using heterodyne ferromagnetic resonance. A strong agreement is shown between the two approaches (shown in Fig. 1), with a clear theoretical demonstration that the complex experimentally observed phenomena are caused by magnon scattering, consistent with the predicted magnon dispersion curve (in Fig. 2). For the same sample, the power threshold indicating the nonlinear region, increases for higher microwave frequency. For fixed microwave frequency, the power threshold is very sensitive to the film thickness in varying samples. These results yield fundamental insights, as well as direct application to the design of microwave devices. This work was supported by the DARPA M3IC program, the Center for Micromagnetics and Information Technologies (MINT), and SMART a SRC NCore center sponsored by NIST.

[1] J. W. Fleischer, M. Segev, N. K. Efremidis, and D. N. Christodoulides, Nature 422, 147 (2003). [2] H. Suhl, Journal of Physics and Chemistry of Solids 1, 209 (1957).

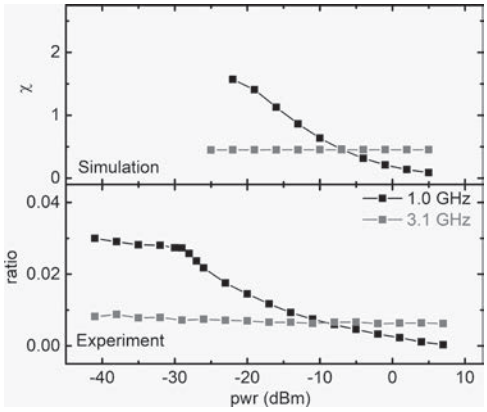


Fig.1 Simulated susceptibility (top panel) and experimental absorption ratio (bottom panel) versus microwave powers at the FMR resonance peak.

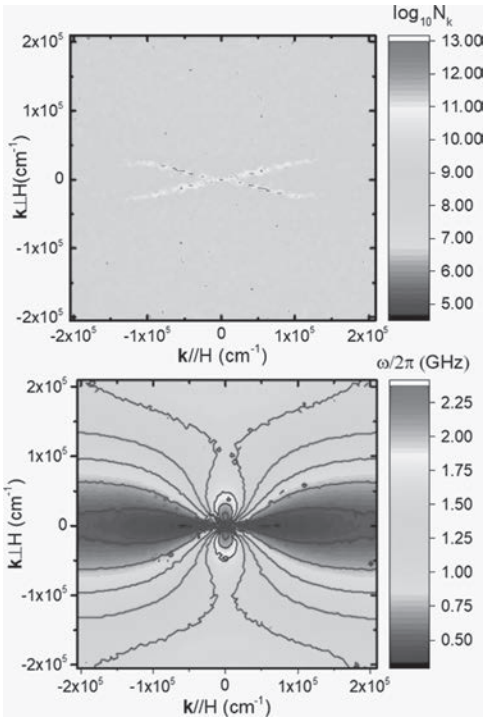


Fig.2 The magnon number (top panel) and magnon dispersion (bottom panel) at a microwave frequency of 1.0 GHz.

Session GF
SKYRMIONS IN B20 MATERIALS AND SKYRMION DEVICES

Hans Nembach, Chair
NIST, Boulder, CO, United States

CONTRIBUTED PAPERS

8:30

GF-01. Increased Lifetime of Metastable Skyrmions by Controlled Doping. *M.T. Birch*[1,2], R. Takagi[3], S. Seki[3,4], M. Wilson[1], F. Kagawa[3], A. Štefančič[5], G. Balakrishnan[5], R. Fan[2], P. Steadman[2], C. Ottley[1], M. Crisanti[5,6], R. Cubitt[6], T. Lancaster[1], Y. Tokura[3,4] and P.D. Hatton[1]
1. Durham University, Durham, United Kingdom; 2. Diamond Light Source, Didcot, United Kingdom; 3. RIKEN Centre for Emergent Matter Science, Wako, Japan; 4. University of Tokyo, Tokyo, Japan; 5. University of Warwick, Coventry, United Kingdom; 6. Institut Laue-Langevin, Grenoble, France

The magnetic skyrmion lattice (SkL) is an example of a state protected by a topological energy barrier [1]. This barrier arises from the inability to continuously transform between spin structures with different topological charge; it can only be overcome by large discontinuous deformations, such as those caused by thermal fluctuations. In bulk materials, skyrmions typically exist in a narrow range of magnetic field and temperature, just below the Curie temperature, T_c [2,3]. However, metastable skyrmions have recently been observed, achieved by cooling the sample under an applied field, allowing the skyrmions to survive to low temperatures [4]. Fig. 1. displays a magnetic phase diagram showing the metastable SkL region as measured in Cu_2OSeO_3, a multiferroic skyrmion material [5], and the subject of the current work. These metastable skyrmions decay to the competing conical phase with a finite lifetime which is temperature dependent [6]. Close to T_c, the metastable SkL state therefore has a short lifetime, necessitating a rapid cooling rate to ensure a significant population of metastable skyrmions survives to low temperature [7]. In our study, we demonstrate that the introduction of non magnetic Zn ions into the underlying crystal lattice of Cu_2OSeO_3 dramatically increases the lifetime of the metastable SkL state – by a factor of 50 at just 2.5% Zn doping, as shown in Fig. 2. In turn, this reduces the required cooling rate to produce a substantial metastable SkL population. Our time-resolved AC susceptibility measurements suggest that this is not due to a change in the energy barrier protecting the metastable skyrmion state, but due to an increased pinning site density because of the included Zn ions. We expect that this effect can be exploited to engineer and control the metastable skyrmion lifetime in other doped skyrmion-hosting systems.

[1] N. Nagaosa and Y. Tokura, Nature Nanotechnology 8, 899 (2013). [2] S. Mühlbauer, B. Binz, F. Jonietz, et al, Science 323, 915 (2009). [3] A. Chacon, L. Heinen, M. Halder, et al, Nature Physics 14, 936–941 (2018). [4] K. Karube, J. S. White, N. Reynolds, et al, Nature Materials 15, 1237 (2016). [5] S. Seki, X. Z. Yu, S. Ishiwata and Y. Tokura, Science 336, 198 (2012). [6] K. Karube, J. S. White, D. Morikawa, et al, Phys. Rev. Mat. 1, 074405 (2017). [7] M. Birch, R. Takagi, S. Seki, et al, arXiv: 1809.02590v2 [cond-mat.str-el] (2018).

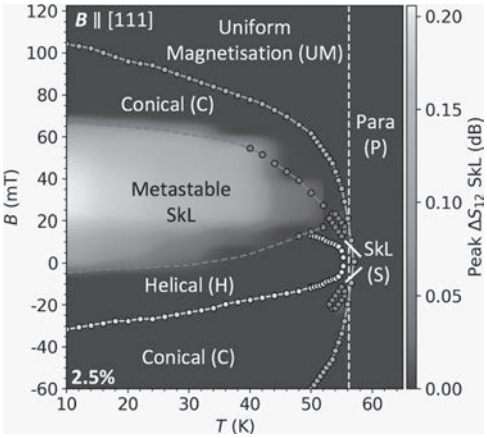


Fig.1 Magnetic phase diagram of 2.5% Zn-doped Cu_2OSeO_2 as measured by magnetic resonance (colourmap) and AC magnetometry (dots).

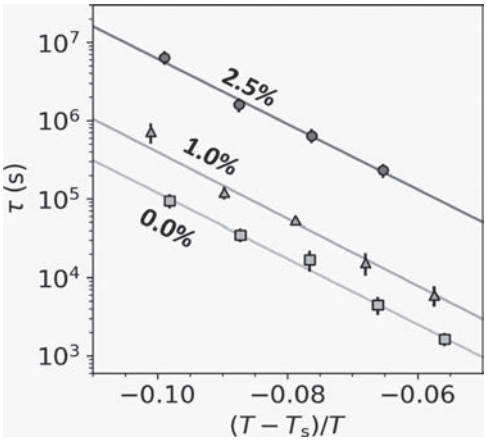


Fig.2 Lifetime of the metastable skyrmion state measured as a function of temperature below the lowest extent of the skyrmion state, Ts, for 0.0%, 1.0% and 2.5% Zn-doped Cu_2OSeO_3.

8:42

GF-02. Room temperature skyrmions in B20 Fe-rich $Fe_{1.2}Ge$ films. *T. Liu*[1], R. Bennett[1], S. Cheng[1], A. Ahmed[1] and R. Kawakami[1]
1. Department of Physics, The Ohio State University, Columbus, OH, United States

The topological stability, small size, and the ability to be very energy efficiently written, read and manipulated, put magnetic Skyrmions at the forefront of candidates for next-generation storage technology. Current skyrmion research is focused on metallic multilayers and B20 crystals. However, none of them can achieve skyrmions at room temperature with size smaller than

10 nm, which has already become a major bottleneck of their development. For metallic multilayers, they have small Dzyaloshinskii-Moriya interaction (DMI) arising from surface inversion symmetry breaking and consequently large skyrmions. On the contrary, B20 crystals have a large bulk DMI and nanoscale skyrmions with sizes down to 3 nm but have not achieved room temperature operation. The closest B20 material is FeGe which has a Curie temperature of ~280 K. In this work, we successfully synthesized Fe-rich $Fe_{1.2}Ge$ films by non-equilibrium alternating layer molecular beam epitaxy at room temperature to incorporate additional Fe atoms within the B20 FeGe structure. The cross-sectional TEM indicates that the $Fe_{1.2}Ge$ film maintains the B20 structure. XRD exhibits a peak corresponding to the B20 FeGe structure but with a shift in peak position to a lower angle indicating an expanded lattice constant. This peak shift and the absence of additional XRD peaks as well as the lack of visible clusters in the TEM images suggests the absence of phase separation and macroscopic secondary phases. Rather, the structural characterization is more consistent with the incorporation of Fe into interstitial sites with possible formation of atom-scale Fe aggregates (e.g. dimers, trimers, etc.). Magnetic characterization result shows that the Curie temperature of the $Fe_{1.2}Ge$ film is above room temperature (RT). More interestingly, we observe topological Hall resistance above room temperature with a maximum value around H ~1.5 kOe, which provides strong evidence for the skyrmion formation above room temperature.

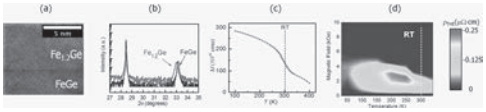


Fig. 1. (a)Cross section TEM; (b) XRD; (c) temperature dependence magnetization; (d) Topological Hall resistance of 54 nm $Fe_{1.2}Ge$ on 5 nm FeGe buffer

8:54

GF-03. Quantum Phase Transition and Room-Temperature Skyrmions in B20-Ordered Co-Si. *B. Balasubramanian*[1,2], P. Manchanda[3], R. Pahari[1,2], Z. Chen[4], W. Zhang[1,2], S. R. Valloppilly[1], X. Li[1], A. Sarella[1], L. Yue[1], A. Ullah[1,2], P. Dev[3], D. Muller[4], R. Skomski[1,2], G.C. Hadjipanayis[5] and D.J. Sellmyer[1] *1. Nebraska Center for Materials and Nanoscience, University of Nebraska, Lincoln, NE, United States; 2. Department of Physics and Astronomy, University of Nebraska, Lincoln, NE, United States; 3. Department of Physics and Astronomy, Howard University, Washington, DC, United States; 4. School of Applied and Engineering Physics, Cornell University, Ithaca, NY, United States; 5. Department of Physics and Astronomy, University of Delaware, Newark, DE, United States*

Magnetic compounds with the noncentrosymmetric cubic B20 structure such as MnSi are potential spin-electronics materials due to skyrmion spin structures associated with non-zero Dzyaloshinskii-Moriya (DM) interactions [1, 2]. However, a disadvantage of existing B20 compounds is their low magnetic-ordering temperatures T_c < 300 K and some are not even ordered at zero temperature, including CoSi and FeSi. Furthermore, T_c improvements in these compounds are normally accompanied by unfavorable increase in helical periodicity and skyrmion size [1]. This study reports a non-equilibrium fabrication of B20-ordered $Co_{1+x}Si_{1-x}$ with $0 \le x \le 0.043$ (Figs. 1a and 1b), which exhibit a T_c = 328 K for x = 0.043, the highest among all B20-type magnets. DFT calculations show a transition from Pauli paramagnetism to a magnetically ordered state above a critical excess Co concentration x_c = 0.028 (Fig. 1c) and explain that the onset of magnetism has the character of a quantum phase transition (QPT), similar to that observed in disordered alloys [3]. The chirality of the crystals supports spin spirals caused by DM interactions, and we estimate a helical periodicity λ of about 17 nm from magnetic measurements, which also reveal skyrmionic spin structures around room temperature as depicted in a temperature-field magnetic phase diagram (Fig. 1d). A unique combination of high T_c and relatively small λ achieved in $Co_{1+x}Si_{1-x}$ will be explained in terms of QPT, where spin-polarized excess-Co atoms are coupled through the host matrix. This research is primarily supported by NSF-DMREF: SusChEM (award no. 1729288, fabrication and characterization) and the U.S. DOE (award no. DE-FG02-04ER46152, theory).

[1] N. Nagaosa and Y. Tokura, Nature Nanotech. Vol 8, p. 899 (2013) [2] B. Das, B. Balasubramanian and D.J. Sellmyer *et al*. Nanoscale, Vol 10, p.9504 (2018) [3] R. Pahari, B. Balasubramanian and D.J. Sellmyer *et al*. Phys. Rev. B, Vol. 99, p.184438 (2019).

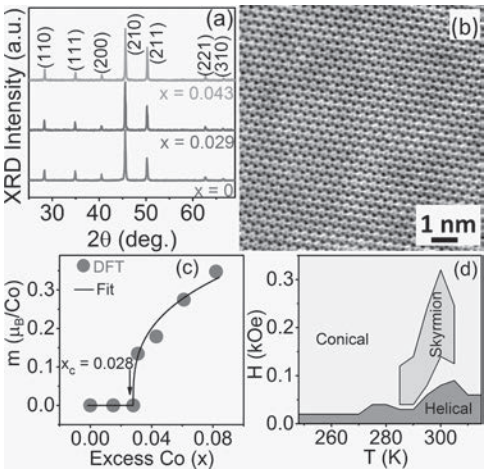


Fig. 1 Strucure and magnetism of $Co_{1+x}Si_{1-x}$: (a) experimental XRD patterns indexed to the B20 structure, (b) annular bright-field STEM image showing atomic columns of Si (gray) and Co (black) for x = 0.043, (c) the DFT moments fitted using $m \sim (x\text{-}x_c)^{\beta'}$, where the quantum critical exponent β' = 0.33 and critical excess Co content x_c = 0.028, and (d) a *H-T* phase diagram showing various spin structures for x = 0.43.

INVITED PAPER

9:06

GF-04. Novel low temperature spiral and skyrmionic states. *C. Pappas*[1], L.J. Bannenberg[1], F. Qian[1], H. Wilhelm[2], R. Cubitt[3], L. DeBeer-Schmitt[6], E. Lelièvre-Berna[3], A. Labh[1], M.P. Schmidt[4], A. Aqeel[5], M. Mostovoy[5] and A.O. Leonov[7] *1. Delft University of Technology, Delft, Netherlands; 2. Diamond Light Source, Didcot, United Kingdom; 3. Institut Laue- Langevin, Grenoble, France; 4. Max Planck Institute for Chemical Physics of Solids, Dresden, Germany; 5. University of Groningen, Groningen, Netherlands; 6. Oak Ridge National Laboratory, Oak Ridge, TN, United States; 7. Hiroshima University, Hiroshima, Japan*

Skyrmion-hosting materials, and in particular the archetype cubic chiral magnets, show the same generic behaviour, which was so far assumed to be universal. Recent experiments on the insulator Cu_2OSeO_3, however, show remarkable deviations from this universal behavior, with far-reaching implications. A new phase occurs when it is the least expected, at low temperatures and high magnetic fields, but only when the field is applied along the [001] easy crystallographic axis [1]. Furthermore, extremely robust skyrmionic states, can be produced in large areas of the magnetic phase diagram [2, 3]. Nascent and disappearing spiral states near critical lines catalyze topological charge changing processes, leading to the formation and destruction of skyrmionic states at low temperatures, which are thermodynamically stable or metastable depending on the orientation and strength of the magnetic field. The metastable low temperature skyrmions are surprisingly resilient to high magnetic fields and their memory persists in the field polarized state, even when the skyrmion lattice signal has disappeared [3]. These results hint to novel routes for skyrmion nucleation [4] and highlight the paramount role of magnetic anisotropies in stabilizing exotic chiral magnetic states.

[1] F. Qian et al. Sci. Adv. 4, eaat7323 (2018). [2] A. Chacon, et al. Nat. Phys. 14, 936 (2018). [3] L. J. Bannenberg, et al., NPJ Quantum Mater. 4, 11 (2019). [4] A.O. Leonov, C. Pappas; Phys.Rev.B. 99, 144410 (2019)

CONTRIBUTED PAPERS

9:42

GF-05. Search for skyrmionic structures in nanoparticles of Cu_2OSeO_3. *S.J. Holt*[1], A. Štefančič[1], M.R. Lees[1], J.C. Loudon[2] and G. Balakrishnan[1] *1. Department of Physics, University of Warwick, Coventry, United Kingdom; 2. Department of Materials Science and Metallurgy, University of Cambridge, Cambridge, United Kingdom*

Recently, there has been appreciable interest in the physics of magnetic skyrmions due to their potential use in spintronic devices [1]. Magnetic skyrmions are topological magnetic spin structures originally identified in the B20 class of materials, but have more recently been found in other non-centrosymmetric materials [2]. Bulk Cu_2OSeO_3 is a multiferroic insulator that crystallises in the $P2_13$ space group and has been shown to host a Bloch-type skyrmion lattice. The magnetoelectric coupling in Cu_2OSeO_3 means that skyrmions can be manipulated by electric fields, a useful property for spintronic devices. The skyrmion lattice in Cu_2OSeO_3 has a magnetic modulation period of ~ 62 nm in the skyrmion phase, situated just below the T_c of ~ 59 K [3]. The understanding of confinement and isolation of single skyrmions is vital for applications [4]. Previously a large increase in the temperature and magnetic field stability region of skyrmions has been observed in thinned bulk crystal samples of Cu_2OSeO_3 using Lorentz TEM, showing that confinement of one spatial dimension plays an important role in the stabilisation of skyrmions. We have produced Cu_2OSeO_3 nanoparticles with sizes ranging from 20 to 250 nm using a modified hydrothermal method (Fig. 1). This has enabled us to investigate the effect of confinement on the formation of skyrmions and probe the magnetism within these nanoparticles, with close attention being paid to studying the effects when the size of the nanoparticles is made comparable to the size of the skyrmions expected in this system (Fig. 2). Here, we present the results of our investigation of the dependence of their magnetic properties on the particle size by using x-ray diffraction, *dc* and *ac* magnetic susceptibility measurements, and microscopy techniques.

[1] A. Fert, *et al.*, Nat. Nanotechnol. 8, 152 (2013). [2] S. Mühlbauer, *et al.*, Science 323, 915 (2009). [3] J. S. White, *et al.,* J. Phys. Condens. Matter 24, 432201 (2012). [4] M. M. Devi, *et al*., J. Mater. Chem. C 7, 1337 (2019).

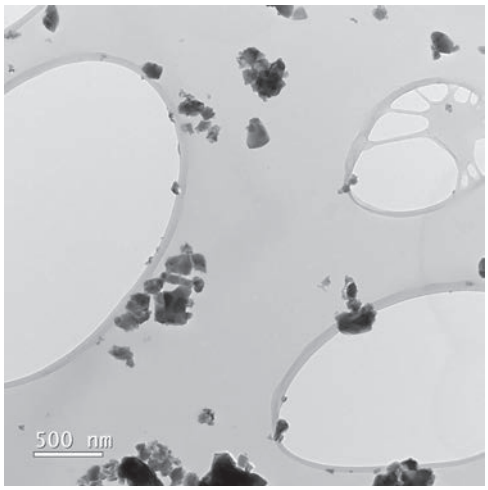


Fig.1 TEM image of Cu_2OSeO_3 nanoparticles at room temperature showing the range of particle sizes obtained.

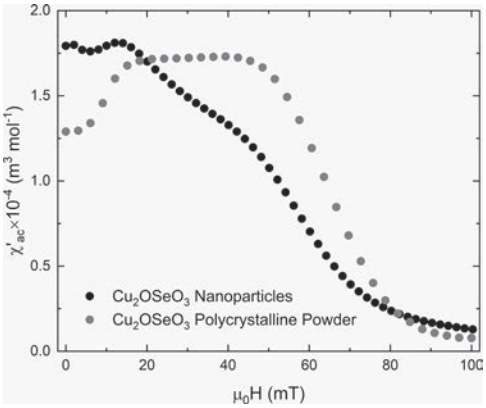


Fig.2 Comparison of the ac susceptibility of Cu_2OSeO_3 nanoparticles with particle sizes ranging from 20 to 250 nm, and polycrystalline powder at T = 53 K. The differences in the shape of the curves highlight the effect of particle size.

9:54

GF-06. Magnetic and Structural Properties of Cobalt-Zinc Alloy Thin Films. *M. Dearg*[1], G. Burnell[1], S. Langridge[2] and C.H. Marrows[1] *1. School of Physics and Astronomy, University of Leeds, Leeds, United Kingdom; 2. Science and Technology Facilities Council, Rutherford Appleton Laboratory, Oxon, United Kingdom*

Skyrmions, topologically protected particle-like vortices in the magnetization, hold potential as an energy efficient, high-density magnetic storage media due to their nanometric size and the low driving current densities [1]. The widely-studied B20 skyrmion materials (chiral cubic $P2_13$ space group) present a bottleneck to technological applications due to their below room-temperature transition [2]. However, CoZn alloys are known to host a β-Mn phase [3], creating a structurally chiral cubic magnet which breaks spatial inversion symmetry. Such alloys can host Dzyaloshinkii-Moriya interaction (DMI) stabilised skyrmions at and above room temperature [4], making them a candidate for developing skyrmion technologies. To date these materials have primarily been studied as bulk crystals, but to realise technological applications it is necessary to produce thin films on planar substrates from which devices can be fabricated. We present the results of work to address this gap by growing thin films by co-sputtering of CoZn alloys from elemental targets. The films were grown on Si/SiO_2 substrates at room-temperature. In their as-deposited form they are amorphous or nanocrystalline, lacking Bragg peaks in XRD or showing weak contributions from constituents' crystalline phases. After annealing at 400 °C for 48 hours, crystallites with the β-Mn structure form, as shown by the presence of Bragg reflections in XRD and further confirmed by TEM imaging (Fig. 1b). Typical lateral crystallite sizes are of the order of 40-50 nm, with exceptional cases of around 100 nm. Annealed samples also show an above room-temperature transition around 380 K (Fig. 1a), with as-grown samples showing an emergent transition in the M(T) down-sweep. These thin film alloys present with the β-Mn phase ($P4_132/P4_332$ space group), and thus possess an appropriate point group symmetry to give rise to a bulk DMI and are potential candidates for an above room-temperature thin film skyrmion material. This work was supported in part by the STFC ISIS Neutron and Muon Source.

[1] A. Fert, V. Cros & J. Sampiao, Nat. Nanotechnol. 8, 152-156 (2013) [2] N. Kanazawa, S. Seki & Y. Tokura, Adv. Mater. 29, 1603227 (2017). [3] K. H. J. Buschow et al., J. Magn. Magn. Mater. 38, 1 (1983). [4] Y. Tokunaga et al., Nature Commun. 6, 7638 (2015).

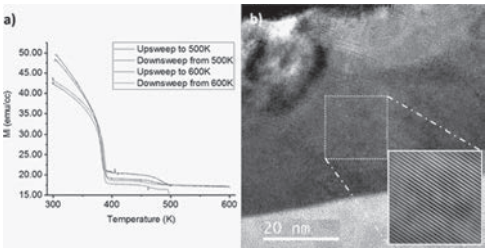


Fig. 1. a) M(T) for a CoZn alloy of 25:35 W growth ratio, annealed at 500 °C for 12 hrs; b) TEM image of crystalline order in a sample of 24:25 W growth ratio, annealed at 400 °C for 48 hrs.

10:06

GF-07. Manipulation of skyrmion motion by magnetic field gradients.
D. Burn[1], S. Zhang[2,3], T. Hesjedal[2] and G. van der Laan[1] *1. Diamond Light Source, Oxford, United Kingdom; 2. Department of Physics, University of Oxford, Oxford, United Kingdom; 3. School of Physical Science and Technology, Shanghai Tech University, Shanghai, China*

Magnetic skyrmions are nanoscale, particle-like entities made up of a swirling, topologically protected spin texture which exist in chiral magnetic systems. These skyrmions are promising candidates for novel memory technologies and spintronic devices due to the potential to encode information as the presence or absence of skyrmions, allowing for a racetrack memory system [1]. Techniques to manipulate the skyrmions in such a system are key to development of such devices. Here we present a novel method to manipulate skyrmion motion using magnetic field gradients (Fig. 1) [2]. Cu_2OSeO_3 is a well-established skyrmion system in which individual skyrmions assemble into a closed-packed hexagonally ordered magnetic lattice [3,4]. The magnetic lattice constant is relatively large ~(60 nm), allowing for the observation of skyrmions using resonant elastic x-ray scattering (REXS). This technique is ideally suited to studying slow dynamics in situ and uses polarized soft x-rays only available at synchrotrons. Our REXS experiments on beamline I10 at the Diamond Light Source show that the skyrmion lattice structures in single-crystal Cu_2OSeO_3 are highly mobile in a radial field gradient. The skyrmions rotate collectively in a shell-like structure following a given velocity-radius relationship. The direction of the field can be used to control the sense of rotation of the lattice. These results show that field gradients provide an effective mechanism for fine control of skyrmion motion. In this scheme, no local electric currents are needed, thus providing an alternative, lower energy approach to shift-register-type operations based on spin-transfer torque. Our findings open the door to a new way to manipulate and engineer the skyrmion state which will enable applications in the future.

[1] A. Fert, V. Cros and J. Sampaio, Nature Nano. 8, 152 (2013). [2] S.L. Zhang, W.W. Wang, D.M. Burn, *et al.*, Nature Comms. 9, 2115 (2018). [3] S. Seki, X.Z. Yu, S. Ishiwata and Y. Tokura, Science 336, 198 (2012). [4] S.L. Zhang, A. Bauer, D.M. Burn, *et al*., Nano. Lett. 16, 3285 (2016).

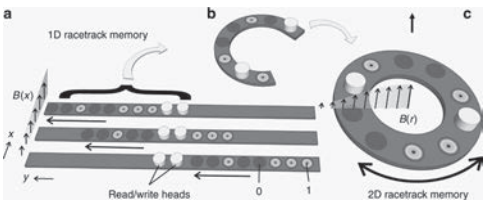


Fig. 1. Manipulation of skyrmions along a linear racetrack and the application to a circular racetrack memory concept. (a) In a 1D linear racetrack scheme, skyrmions are moved past read/write heads collectively in a shift register fashion. (b) Morphing half of the 1D strip into a circular structure is the basis for the 2D racetrack memory element shown in (c). The required linear motion/rotation is controlled via a magnetic field gradient.

10:18

GF-08. Skyrmion ratchet for single-electrode skyrmion transport.
W. Gan[1], C.C. Ang[1], X. Wang[2] and W. Lew[1] *1. Nanyang Technological University, Singapore; 2. Lanzhou University of Technology, Lanzhou City, China*

The use of voltage-controlled magnetic anisotropy gradients to drive skyrmions promises highly efficient skyrmion transport.[1] However, their complicated designs thus far have eluded experimental realization.[2] In this work, we demonstrate a new type of skyrmion transport mechanism, the skyrmion ratchet, which uses a single gate electrode to drive any number of skyrmions. To achieve the feat, a transverse driving force was used instead of a longitudinal type previously proposed. The driving mechanism relies on the skyrmion Hall effect for the forward propagation force. In doing so, the speed limit is no longer limited by skyrmion annihilation by the skyrmion Hall effect. As the transverse driving scheme is a self-restoring, an array of engineered potential wells was constructed to serve as a ratchet for unidirectional skyrmion motion. A succinct advantage of the skyrmion ratchet lies in its ability to move the skyrmion very closely to the centerline of the nanowire, thus allowing for predictable behavior and high transport velocities. Finally, we demonstrate that, despite the unidirectional operation, the skyrmion ratchet can recirculate the skyrmions in a closed loop and achieving high data densities

1. C. Ma, X. Zhang, J. Xia, M. Ezawa, W. Jiang, T. Ono, S. N. Piramanayagam, A. Morisako, Y. Zhou and X. Liu, *Nano Letters*, 2019, 19, 353-361. 2. X. Wang, W. L. Gan, J. C. Martinez, F. N. Tan, M. B. A. Jalil and W. S. Lew, *Nanoscale*, 2018, 10, 733-740.

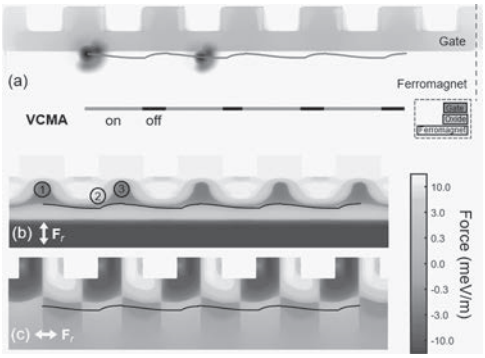


Fig.1 (a) Image of a 192 nm long skyrmion ratchet device. The red line represents the skyrmion's trajectory across the device. To shift the skyrmion, a series of four voltage pulses were applied and the on/off state of the gate electrode is represented by the green/black bars underneath the image. On the bottom right, the inset shows the cross-section of the nanowire. (b-c) Force map of nanowire edge repulsion force F_r acting on the skyrmion where (b) and (c) shows the *y* and *x* magnitude, respectively.



Fig.2 Image of a closed-loop skyrmion ratchet where the red line represents the skyrmion trajectory. To shift the skyrmion by a step, a voltage pulse of 0.8 ns was applied followed by a 1 ns interval for the skyrmion to relax into the potential well.

10:30

GF-09. Beyond Skyrmions - Utilizing alternative magnetic quasiparticles for spintronics devices. *B. Göbel*[1], A.F. Schäffer[2], A. Mook[2], J. Henk[2], J. Berakdar[2], O. Tretiakov[3,4], S.S.P. Parkin[1] and I. Mertig[2,1] *1. Max Planck Institute of Microstructure Physics, Halle (Saale), Germany; 2. Martin Luther University Halle Wittenberg, Halle (Saale), Germany; 3. School of Physics, The University of New South Wales, Sydney, NSW, Australia; 4. Institute for Materials Research and Center for Science and Innovation in Spintronics, Tohoku University, Sendai, Japan*

Over the last 10 years the field of skyrmionics has attracted an enormous research interest, as skyrmions (small, whirl-like spin textures) possess strong stability, characterized by an integer topological invariant $N_{Sk} = \pm 1$. Due to their non-trivial real-space topology, skyrmions offer a topological contribution to the Hall effect, commonly measured in skyrmion crystals, and can be stabilized as individual quasiparticles in collinear ferromagnets. They can be driven by currents in thin films allowing for spintronics applicability for example as carriers of information in racetrack storage devices. However, one issue which is hindering the utilization of skyrmions in applications is the skyrmion Hall effect: A skyrmion does not move parallel to an applied spin-polarized current but is pushed towards the edge of the sample [1]. In this talk, I discuss magnetic quasiparticles that are related to skyrmions and exhibit either effects that are interesting from a fundamental point of view, or are attractive application-wise. After giving a general overview over different observed or proposed quasiparticles, I focus on the antiferromagnetic skyrmion (topological charge $N_{Sk} = 0$), the skyrmionium ($N_{Sk} = 0$), the biskyrmion ($N_{Sk} = 2$), and the bimeron ($N_{Sk} = 1$); cf. Fig. 1. All of these objects can be understood as the combination of two smaller topologically non-trivial quasiparticles, what brings about different properties compared to conventional skyrmions. The most remarkable results are that antiferromagnetic skyrmions [2,3] and skyrmioniums [4] do not exhibit a skyrmion Hall effect when driven by currents, that the bimeron [5,6] (the topological equivalent of a skyrmion in in-plane magnetized samples) exhibits a pure version of the topological Hall effect, and that biskyrmions [7,8] can be generated in centrosymmetric materials without the chiral Dzyaloshinskii-Moriya interaction.

[1] J. Sampaio, V. Cros, S. Rohart et al., Nature Nanotechnol., 8, 839 (2013) [2] J. Barker, O. Tretiakov, Phys. Rev. Lett., 116, 147203 (2016) [3] B. Göbel, A. Mook, J. Henk et al., Phys. Rev. B, 96, 060406(R) (2017) [4] B. Göbel, A. Schäffer, J. Berakdar et al., arXiv: 1902.06295 (2019) [5] Y. Kharkov, O. Sushkov, M. Mostovoy, Phys. Rev. Lett., 119, 207201 (2017) [6] B. Göbel, A. Mook, J. Henk et al., Phys. Rev. B, 99, 060407(R) (2019) [7] X. Yu, Y. Tokunaga, Y. Kaneko, Nature Communications, 5, 3198 (2014) [8] B. Göbel, J. Henk, I. Mertig, arXiv: 1902.10491 (2019)

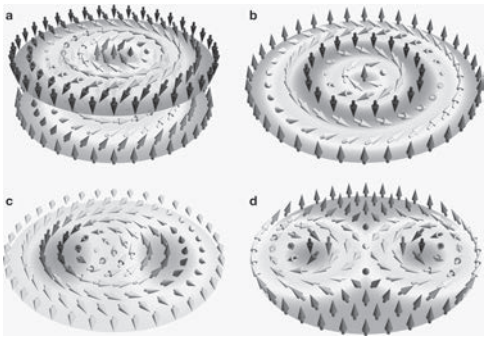


Fig.1 Considered quasiparticles. (a) Antiferromagnetic skyrmion, (b) skyrmionium, (c) bimeron, and (d) biskyrmion. The arrows correspond to magnetic moments whose color represents the out-of-plane component (red: positive and blue: negative).

10:42

GF-10. Control of The Skyrmion Hall Effect via External Magnetic Fields and its Skyrmion Multiplexer Applications. *S. Yang*[1], D. Kim[2], K. Moon[1], S. Kim[3], B. Chun[1], C. Kim[1], J. Cho[1], J. Shin[4], J. Hong[4] and C. Hwang[1] *1. Quantum Technology Institute, Korea Research Institute of Standards and Science, Daejeon, The Republic of Korea; 2. Institute for Chemical Research, Kyoto University, Kyoto, Japan; 3. Department of Physics and Astronomy, University of Missouri, Columbia, MO, United States; 4. Nanoscale Semiconductor Engineering, Hanyang University, Seoul, The Republic of Korea*

The skyrmions which are the topological chiral spin textures, have drawn significant interests because of their novel topological phenomena including emergent electromagnetism, the topological Hall effect and the skyrmion Hall effect (SkHE) [1]. In addition, magnetic skyrmions have become one of the most promising candidates as robust information carriers in the next-generation spintronic devices. However, the current-driven motion of skyrmions is deflected from the direction of the current by SkHE [2,3]. Therefore, it is essential to understand and manipulate SkHE not for only unveiling the underlying physics but also for making the best use of skyrmions in spintronics applications. Here, we address a novel method to control the skyrmion Hall angle (SkHA), the angle between the skyrmion motion and the current direction, using both out-of-plane and in-plane external magnetic fields, and an efficient way to achieve the straight motion of magnetic skyrmions by completely suppressing the SkHE. Manipulation of the SkHA via the external magnetic fields is experimentally confirmed by studying chiral stripe shooting with the half-skyrmion end as shown in Fig.1. The observed field dependence of the SkHA is explained by generalizing the existing theory for the elongated chiral bubbles [4] to the cases with the simultaneous presence of external magnetic fields and spin-orbit torques. Finally, based on the demonstrated precise control of the SkHA, skyrmion multiplexer (S-MUX) devices are fabricated where the direction of the current-induced elongation of skyrmions is determined by the external magnetic field.

1. N. Nagaosa & Y. Tokura. *Nature Nanotechnology*. Vol. 8, p. 899 (2013). 2. W. Jiang, X. Zhang, G. Yu *et al. Nature Physics*. Vol. 13, p. 162 (2016). 3. K. Litzius, I. Lemesh, B. Krüger *et al. Nature Physics*. Vol. 13, p. 170 (2016). 4. Y. Hirata, D.-H. Kim, S. K. Kim *et al. Nature Nanotechnology*. Vol. 14, p. 232 (2019).

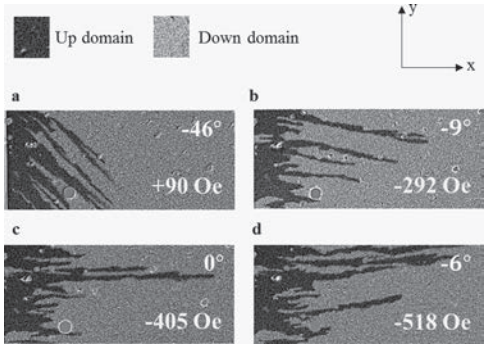


Fig.1 The current-induced stripe shooting angle as a function of the y-axis external magnetic field (H_y). Current-driven stripe shooting under 1.78 Oe of H_z and a, +90 Oe, b, -292 Oe, c, -405 Oe, d, -518 Oe of H_y with 6 MA/cm^2 of current along the x-axis. The white numbers indicate the stripe shooting angle, that is, the skyrmion Hall angle (SHA). The angle is defined as positive counter clockwise from the x-axis.

10:54

GF-11. Thermodynamic concept for current-induced skyrmion dynamics at Pt/Co interfaces. *S. Sugimoto*[1], S. Kasai[1] and Y. Takahashi[1]
1. Research Center for Magnetic and Spintronic Materials, National Institute for Materials Science, Tsukuba, Japan

Magnetic skyrmions are topological defects in magnetization mostly induced by the chiral interaction [1,2]. Interfacial skyrmions hosted at heterostructures of ferromagnets and heavy metals can be stabilized at room-temperature [3], and attract great interest for device applications [3]. One of the excellent characteristics of skyrmions is the ultralow threshold current density for driving [4], and their current-induced dynamics are usually described by the Thiele equation [5] as kinds of steady particle motions. We here report observations of different types of current-induced dynamics between (i) CoFeB/MgO and (ii) Pt/Co interfaces, where the latter can be described with the thermodynamic concept beyond the scope of particle nature. Figure 1 shows responses to current injections at (i) W/CoFeB/MgO and (ii) Pt/Co/Ir interfaces, respectively. For (i) W/CoFeB/MgO interfaces (Fig. 1(a)), skyrmion's trajectories can be described by the Thiele equation with spin-orbit torque terms [5]: skyrmions are driven along the charge flow with finite skyrmion Hall angle (SkHA), and increase in current leads to increase in SkHA [6,7]. On the contrary, dynamics at (ii) Pt/Co/Ir interfaces in Fig. 1(b) appear different from Thiele's descriptions: skyrmions show accumulation phenomena along the Hall (y) direction prior to threshold current for longitudinal driving (~4.0×10^{10} A/m^2) [6]. The distribution of skyrmion shows linear profiles along the direction, which can be described by a phenomenological diffusion model with assumption of macroscopic intensive property, i.e., chemical potential. Such thermodynamic concept can be applicable over ten of micrometers even where current is absent. We've demonstrated large scale of skyrmion pumping by tuning the chemical at nonlocal devices designed as analogies of "canal gates" of water control, where skyrmions are transferred between different canals though narrow junctions following profile of the chemical potential. This work provides a new methodologies of handling distributions of skyrmions over several tens of micrometers only by switching local currents.

1) N. Nagaosa and Y. Tokura, Nat. Nanotech., Vol. 8, p.899 (2013) 2) A. Fert, V. Cros and J. Sampaio, Nat. Nanotech., Vol. 8, p.152 (2013) 3) W. Jiang, P. Upadhyaya and A. Hoffmann, Science, Vol. 349, p.283 (2015) 4) F. Jonietz, S. Mühlbauer and A. Rosch, A. Science, Vol. 330, p.1648 (2010) 5) R. Tomasello, E. Martinez and G. Finocchio, Sci. Rep., Vol. 4, p.6784 (2014) 6) W. Jiang, X. Zhang and S. G. E. te Velthuis, Nat. Phys., Vol. 13, p.162 (2017) 7) K. Litzius, I. Lemesh and M. Kläui, Nat. Phys., Vol. 13, p.170 (2017)

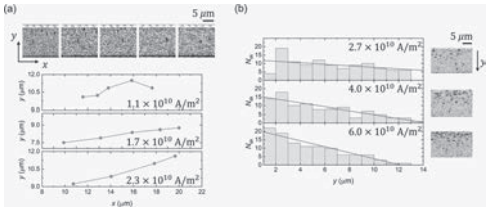


Figure 1: (a) Skyrmion driving at W/CoFeB/MgO interfaces. (b) Nonequilibrium skyrmion accumulation at Pt/Co/Ir interface.

11:06

GF-12. Voltage-driven high speed skyrmion motion in Skyrmion shift device. *N. Lei*[1] *1. Beihang University, Beijing, China*

Magnetic skyrmions are topological protected chiral spin textures, which are promising for memory and logic applications. Low energy cost of skyrmion manipulation is crucial, especially for skyrmion motion. Large driving current is required to achieve high-speed skyrmion motion, which results in significant Joule heating and instability of devices. Here, we propose a voltage-driven skyrmion motion approach in a skyrmion shift device made of magnetic nanowires. As the figure shown below, a simple structure with equidistant identical electrodes on a uniform-thickness nanowire, which allows voltage-driven high-speed skyrmion motion with low power. To demonstrate its feasibility, numerical calculations have been done by standard micromagnetic simulator. This work provides a new scope to fill in the gap of studies on skyrmion nanodevices [1].

[1] Y. Liu, N. Lei*, C. Wang, X. C. Zhang, W. Kang, D. Q. Zhu, Y. Zhou, X. X. Liu, Y. Zhang, W. Zhao*, *Phys. Rev. Appl.* 1, 111 (2019).

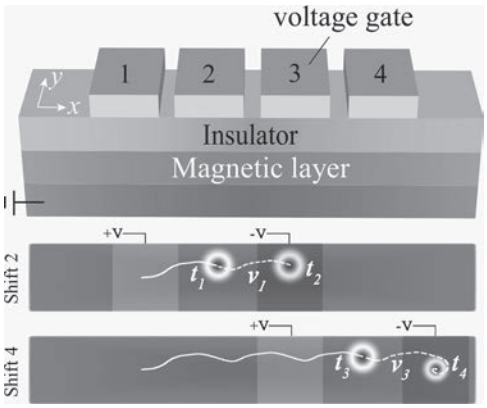


Fig.1 Schematic structure of the device, and the skyrmion trajectory.

11:18

GF-13. Thermal skyrmion diffusion used in a reshuffler device. J. Zázvorka[1,5], F. Jakobs[3], D. Heinze[1], N. Keil[1], S. Kromin[1], S. Jaiswal[1,6], K. Litzius[1,2], G. Jakob[1,2], P. Virnau[1], D. Pinna[1], K. Everschor-Sitte[1,2], *B. Seng*[1,2], L. Rózsa[4], A. Donges[3], U. Nowak[3] and M. Kläui[1,2] *1. Institute of Physics, Johannes Gutenberg-Universität, Mainz, Germany; 2. Graduate School of Excellence MAINZ, Mainz, Germany; 3. Fachbereich Physik, Universität Konstanz, Konstanz, Germany; 4. Fachbereich Physik, Universität Hamburg, Hamburg, Germany; 5. Institute of Physics, Charles University, Prague, Czechia; 6. Singulus Technologies AG, Kahl, Germany*

A key problem for probabilistic computing is that cascading gates propagate undesired correlations and thus vitiate the functionality of the logic device. Therefore, in order to implement probabilistic computing, one needs to reshuffle the signals to keep them uncorrelated. While for many non-conventional computing approaches non-magnetic implementations have been identified as promising, for building a reshuffler device, skyrmions [1,2] might be ideally suited due to the low footprint and low power compared to e.g. CMOS implementations [3]. We develop a low pinning material, where we can stabilize skyrmions and controllably nucleate and displace them by current injection due to spin-orbit torques [4]. We find topologically non-trivial N=1 skyrmions that exhibit strong motion also at zero applied current, which we ascribe to thermally activated skyrmion dynamics [4]. By tracking the trajectories of skyrmions, we can identify motion by pure diffusion and obtain the diffusion constant that shows a surprisingly strong temperature dependence [4]. We then employ thermal skyrmion motion in a reshuffler device. We evaluate its performance for the decorrelation of the input signal and find an uncorrelated output signal while keeping the stream's mean value with high fidelity showing the applicability of skyrmions for information processing in stochastic computing approaches. Finally by lowing the temperature, we can crystallize skyrmions into a lattice. We measure the time-resolved crystallization dynamics and from the pair correlation function quantify the interaction potential.

[1] W. Jiang, Phys. Rep. 704, 1 (2017) [2] G. Finocchio et al., J. Phys. D: Appl. Phys. 49, 423001 (2016) [3] D. Pinna et al., Phys. Rev. Applied 9, 064018 (2018) [4] J. Zazvorka et al., Nat. Nanotechnol., in print (2019)

Session GG
MAGNETIC INTERACTIONS AND STRUCTURES

Jean-Yves Chauleau, Chair
CEA, Gif-sur-Yvette, France

INVITED PAPER

8:30

GG-01. Engineering Magnetic Interactions in Complex Oxide Heterostructures. A.M. Kane[1], B. Li[1], N. Ahlm[1], J. Byers[1], R.V. Chopdekar[1,2], P. Shafer[2], A.T. N'Diaye[2], A. Scholl[2], N. Browning[3], V. Lauter[4], E. Arenholz[5,2] and *Y. Takamura*[1] *1. Materials Science and Engineering, University of California, Davis, Davis, CA, United States; 2. Advanced Light Source, Lawrence Berkeley National Laboratory, Berkeley, CA, United States; 3. Imaging Centre at Liverpool, University of Liverpool, Liverpool, United Kingdom; 4. Neutron Sciences Directorate, Oak Ridge National Laboratory, Oak Ridge, TN, United States; 5. Cornell High Energy Synchrotron Source, Cornell University, Ithaca, NY, United States*

Complex oxides possess a wide range of technologically relevant functional properties including ferromagnetism, ferroelectricity, and superconductivity. Furthermore, their interfaces exhibit unexpected functional properties not found in the constituent materials due to structural and chemical changes as well as electronic and magnetic interactions occurring over nanometer length scales. These unique interfacial effects lead to fundamental differences compared to analogous metallic systems. For example, spin-flop coupling is observed at ferromagnetic (FM) $La_{0.7}Sr_{0.3}MnO_3$ / antiferromagnetic (AF) $La_{0.7}Sr_{0.3}FeO_3$ interfaces where the AF spin are oriented perpendicular to the magnetization of the FM layer.[1] Moreover, FM/FM interfaces consisting of magnetically hard $La_{0.7}Sr_{0.3}CoO_3$ and soft $La_{0.7}Sr_{0.3}MnO_3$ display exchange-spring behavior where the magnetically hard layer pins the FM moments of the soft layer, however, the hard/soft magnetic interface does not coincide with the chemical interface.[2] Rather, an interfacial $La_{0.7}Sr_{0.3}CoO_3$ layer forms that is characterized by magnetically active Co^{2+} ions which couple to the soft $La_{0.7}Sr_{0.3}MnO_3$ layer. The full characterization of the magnetic and structural properties of this $La_{0.7}Sr_{0.3}CoO_3$/$La_{0.7}Sr_{0.3}MnO_3$ bilayer system required the combined results of synchrotron-radiation and neutron-scattering based techniques as well as high resolution electron microscopy. We found that the proportion of the Co^{2+} ion-rich $La_{0.7}Sr_{0.3}CoO_3$ layer and the magnitude of the exchange bias shift of the hysteresis loops depended sensitively on parameters such as the individual layer thicknesses, the BO_6 octahedral tilt pattern of the underlying substrate, and the stacking order of the layers.[3] These results demonstrate how the competing interactions in complex oxides enable intriguing opportunities to tailor functional properties for new, versatile, and energy efficient spintronic devices. We are grateful to the support by NSF (DMR 1411250 and 1745450), SRC (No. 2309.001), UC MRPI (No. MR-15-328528), and the DOE SCGSR program. This research utilized DOE user facilities including ALS at LBNL, SSRL at SLAC, SNS at ORNL, and EMSL at PNNL.

[1]E. Arenholz, Y. Takamura *et al., APL* 94, 072503 (2009) [2] B. Li, Y. Takamura *et al., APL,* 105, 202401 (2014) [3]B. Li, Y. Takamura *et al., APL* 109, 152401 (2016); A.M. Kane, Y. Takamura *et al., PRM* 3, 014413 (2019); J.P. Byers *et al.*, *JAP*, 125, 082518 (2019).

CONTRIBUTED PAPERS

9:06

GG-02. Determining Reversal Mechanisms in Amorphous Tb-Fe Exchange Coupled to NiFe. *M.E. Jamer*[1], T. Lee[2], A. Barra[4], K. Fitzell[5], J. Borchers[3], J.P. Chang[6] and G. Carman[7] *1. Physics, United States Naval Academy, Annapolis, MD, United States; 2. Materials Science and Engineering, University of California, Los Angeles, CA, United States; 3. NCNR, NIST, Gaithersburg, MD, United States; 4. Mechanical Engineering, University of California, Los Angeles, Los Angeles, CA, United States; 5. Chemical & Biomolecular Engineering, University of California, Los Angeles, Los Angeles, CA, United States; 6. Chemical & Biomolecular Engineering, University of California, Los Angeles, CA, United States; 7. Mechanical and Aerospace Engineering, University of California, Los Angeles, CA, United States*

Multiferroic materials have been proposed for an array of applications due to their binary or ternary co-existing magnetic spin, electric dipole, and ferroelastic properties. While many researchers are interested in optimizing these single-phase compounds, creating a strain-coupled multiferroic to mimic two or three types of ordering is a more tunable and less expensive option for device components. In strain-coupled multiferroics, a magnetostrictive/magnetoelastic thin film is grown on a piezoelectric substrate to control the desirable multiferroic ordering. Previous work on magnetostrictive Galfenol (400 ppm) coupled with permalloy (NiFe) to reduce the energy required to flip the magnetization, indicated that the magnetization rotates coherently in-plane with magnetic field and with an applied voltage.[1] In this work, the reversal mechanisms of amorphous Tb_xFe_{1-x} ($0.1<x<0.45$) was studied when exchange-coupled with NiFe to create a system with a unique switching mechanism during magnetic reversal.[3] Amorphous Tb_xFe_{1-x} has a large magnetostriction close to 1000 ppm,[2] perpendicular magnetic anisotropy[3] and a lower magnetic coercivity than its crystalline counterparts. It was coupled to soft NiFe which will switch its magnetization faster than TbFe. This work reports on the magnetic and structural profiles that were studied at multiple field conditions to characterize the depth profile of the vector magnetization through the Tb_xFe_{1-x}/NiFe layers by using polarized neutron reflectometry (PNR) at several fields. Fig. 1(a) illustrates the saturation PNR fits for the compound system on a silicon substrate with respect to the applied magnetic field in-plane. The resulting nuclear and magnetic scattering profile can be seen in Fig. 1(b). After magnetic reversal, the spin flip scattering, shown in Fig. 1(b) reveals a unique reversal state where the NiFe magnetization is canted away from the in-plane field direction at intermediate fields. A full analysis for several field states to uncover the unique reversal mechanisms and MOKE microscopy will be discussed in this presentation. The reversal mechanisms of exchange coupled Tb_xFe_{1-x}/NiFe provide insight on how to best utilize this compound system in future devices.

[1] Jamer, Rementer, Barra, et al, Phys. Rev. Appl. 10, 044045 (2018). [2] J. Huang, C. Prados, J. E. Evetts, Phys. Rev. B 51, 297 (1995). [3] T. Lee, Novel Magnetoelastic Materials for Multiferroic Applications (2019).

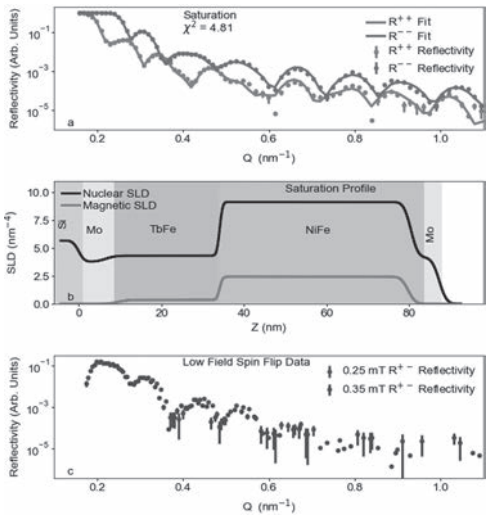


Figure 1

9:18

GG-03. Unveiling the high temperature properties of ε-Fe_2O_3.
A. Romaguera[1], Z. Ma[1], J. Garcia-Muñoz[1], F. Fauth[2], J. Nogués[3,4] and *M. Gich*[1] *1. ICMAB-CSIC, Bellaterra, Spain; 2. ALBA Synchrotron Light Source, Cerdanyola del Vallès, Spain; 3. Catalan Institute of Nanoscience and Nanotechnology, Bellaterra, Spain; 4. The Barcelona Institute of Science and Technology, Barcelona, Spain*

ε-Fe_2O_3 displays remarkable properties such as huge coercivity (20 kOe at room temperature)[1], magnetoelectric coupling, multiferroicity at room temperature in film form.[2] The difficulties related to its complex preparation make ε-Fe_2O_3 the less studied of all the iron (III) oxide polymorphs. Indeed, obtaining extremely pure sample has been a challenge necessary to achieve a thorough structural study using synchrotron diffraction of the fine structural evolution above ambient temperature and across the transition associated to the disappearance of the hard ferrimagnetic phase. This system presents a complex non-centrosymmetric *Pna2₁* frustrated structure isomorphous to the multiferroic $GaFeO_3$ with four non-equivalent Fe^{3+} sites, three octahedral and one tetrahedral environments, from which a rich physics arise, in part associated to the existence of a substantial spin-orbit coupling.[3] Our studies have been extended to a series of Cr doped ε-Fe_2O_3, in which the *Pna2₁* structure is rather robust against the substitution of Fe by Cr., being so a way of modifying the spin-lattice coupling. Upon heating from room temperature, the saturation magnetization of ε-Fe_2O_3 nanoparticles undergoes a monotonic decrease while the coercivity and remanence sharply drop, virtually vanishing around ~500 K. However, above that temperature the hysteresis loops present a non-linear response with finite coercivity, evidencing signs of ferrimagnetic order up to temperatures as high as 850 K (T_{N1}).[4] Interestingly, this transition from superhard to soft ferrimagnetism involves changes in the magnetic state and magnetostructural effects that are relevant for a better understanding of the origin of spin-lattice coupling in ε-Fe_2O_3. With the aim of refuting previous belief that the magnetic ordering temperature of ε-Fe_2O_3 is well below that of other iron oxides such as hematite, magnetite or maghemite, and to shed light on the structural evolution across the hard-soft transition and the physical origin of the high temperature properties, we present temperature-dependent studies combining magnetic, x-ray and neutron diffraction measurements to understand different anomalies present in the interval 300K-900K.

1 B. Jin, S. Ohkoshi and K.Hashimoto, Advanced Materials., vol. 16, p. 48 (2004) 2 M. Gich, I. Fina, A. Morelli, F. Sanchez, M. Alexe, J. Gàzquez, J. Fontcuberta and A. Roig, Advanced Materials., vol. 26, p. 4645 (2014) 3 Y. C. Tseng, N. Souza-Neto, D. Haskel, M. Gich, C. Frontera, A. Roig, M. van Veenendaal and J. Nogués, Physical Review B., vol. 79, p.094404 (2009) 4 J.L. García-Muñoz, A. Romaguera, F. Fauth, J. Nogués and M. Gich, Chemistry of Materials., vol. 29, p. 9705 (2017)

9:30

GG-04. Metamagnetism and kinetic arrest in a long-range ferromagnetically ordered multicaloric double perovskite Y_2CoMnO_6.
R. Pokharel Madhogaria[1], E. Clements[1], V. Kalappattil[1], N. Dang[2], R. Das[1,3], N. Bingham[4], D. Kozlenko[5], M. Phan[1] and H. Srikanth[1] *1. University of South Florida, Tampa, FL, United States; 2. Duy Tan University, Da Nang, Vietnam; 3. Phenika University, Hanoi, Vietnam; 4. Yale University, New Haven, CT, United States; 5. Joint Institute of Nuclear Research, Dubna, Russian Federation*

Among double perovskite oxides ($A_2BB'O_6$), Y_2CoMnO_6 (YCMO) emerges as a multifunctional system for device applications, as it has shown multiferroicity and a multicaloric effect [1]. However, the exact nature of the magnetic ground state and its association with the magnetocaloric, magnetoelectric and electrocaloric effect remains to be investigated [2]. To address this important issue, we have performed a systematic magnetic study of the monoclinic $P2_1/n$ phase of YCMO, synthesized using a *sol-gel* method. Neutron diffraction (ND) measurements evidence the onset of long-range ferromagnetic (FM) ordering at T_C = 76 K, which persists down to 4 K. The absence of any E-type structure peaks in the ND data indicates that YCMO is a centrosymmetric system in nature. The presence of 25% antisite disorder, estimated from the ND data, leads to the appearance of short-range antiferromagnetic interactions, giving rise to an exchange bias effect at temperatures below 10 K. The pinning of magnetic domains at the antiphase boundaries resulted in a metamagnetic-like behavior. The kinetic arrest of the high temperature FM state at low temperature (< 35 K) in YCMO is also evident from magnetization versus magnetic field/temperature measurements. In full agreement with the ND data, a detailed analysis of critical exponents near the paramagnetic-FM phase transition also confirms YCMO as a long-range interacting mean-field system. A careful examination of temperature- and field-dependent magnetic entropy change yields a better understanding of coexisting ordered and disordered phases in the system from high to low temperature. The occurrence of the different magnetic phases in the system causes the exotic effects observed in this class of double perovskites.

1. G. Sharma, J. Saha, S.D. Kaushik, V. Sirguri, and S. Patnaik, *Appl. Phys. Lett*., 103,012903(2013) 2. J. Blasco, J. García, G. Subías, J. Stankiewicz, J. A. Rodríguez-Velamazán, C. Ritter, J. L. García- Muñoz, and F. Fauth, *Phys. Rev. B*, 93, 214401 (2016)

INVITED PAPER

9:42

GG-05. Microscopic origin of high temperature magnetism in multiferroic superlattices $(LuFeO_3)_m$:$(LuFe_2O_4)_n$. *J. Musfeldt*[2,1], S. Fan[1], K. Smith[2], H. Das[3], A. Rebola[3], J. Mundy[4], C. Brooks[5], M. Holtz[3], D. Muller[3], R. Ramesh[4], D. Schlom[5], C. Fennie[3] and S. McGill[6] *1. Physics, University of Tennessee, Knoxville, TN, United States; 2. Chemistry, University of Tennessee, Knoxville, TN, United States; 3. Physics, Cornell University, Ithaca, NY, United States; 4. Materials Science, University of California at Berkeley, Berkeley, CA, United States; 5. Materials Science, Cornell University, Ithaca, NY, United States; 6. National High Magnetic Field Laboratory, Florida State University, Tallahassee, FL, United States*

Multiferroics are fascinating materials in which ferroelectric and magnetic orders coexist and spatial-inversion and time-reversal symmetries are simultaneously broken. Outstanding challenges that currently prevent widespread application in memory and logic devices as well as neuromorphic computing

include requirements for (i) a large coupling coefficient and (ii) room temperature operation. The development of a homologous series of superlattices with formula $(LuFeO_3)_m$:$(LuFe_2O_4)_n$ offers a path forward, although questions still exist about the microscopic origin of the high temperature magnetism and the nature of the charge ordering pattern. In order to resolve these issues and provide additional insight into how external stimuli like high magnetic fields can control behavior, we combined optical spectroscopy, magnetic circular dichroism, and first principles calculations to reveal the response of the $(LuFeO_3)_3$:$(LuFe_2O_4)_1$ superlattice. Importantly, the dichroic response is proportional to magnetization in a chemically-specific, site-selective manner. Analysis of the optical hysteresis loops demonstrates that the unique magnetic behavior of the (3, 1) material emanates primarily from the $Fe^{2+} \rightarrow Fe^{3+}$ charge transfer excitations the $LuFe_2O_4$ layer. In addition to illustrating how control of composition and local strain (which is modulated by Lu ion positions) enables high-temperature properties to emerge, we discuss how the two-component nature of these superlattices (in the form of $LuFeO_3$ and $LuFe_2O_4$ end members) interact at the interface. These techniques open the door to the microscopic analysis of engineered materials with multiple metal centers and strong charge, spin, orbital, and lattice entanglement.

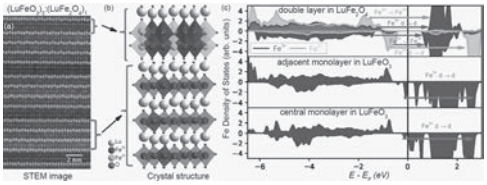


Figure 1

CONTRIBUTED PAPERS

10:18

GG-06. Creating Long Range Magnetic Order in a Configurationally Disordered Single Crystal Perovskite. *T.Z. Ward*[1], Y. Sharma[1], E. Skoropata[1] and A.R. Mazza[1] *1. Oak Ridge National Laboratory, Oak Ridge, TN, United States*

The ABO_3 perovskite and its derivatives are broadly important to a range of fundamental and applied magnetic interests. Modification of the A and B sites through substitutional doping allows for a wide variety of distortions and charge states to be tuned. Local distortions arising from cation size variance are balanced by internal changes to Jahn-Teller distortions and octahedral tilts and rotations which are often used to design functionality. In strongly correlated systems, these shifts to local environment are often central to the emergence of important macroscopic functionalities such as complex magnetic textures and phases. We will describe our recent work using entropy stabilization [1] to synthesize single crystal ABO_3 perovskite films possessing 6 or more cations to understand how microscopic disorder might be used to generate unexpected long range and highly tunable ordering responses. We will discuss how the element specific magnetic and charge states of the cations in $La(Cr_{0.2}Mn_{0.2}Fe_{0.2}Co_{0.2}Ni_{0.2})O_3$ films are impacted by the presence of site-to-site disorder. Experimental results from STEM-EELs, XRD, XMCD, neutron diffraction, and SQUID magnetometry demonstrate that the extreme cation disorder present in $La(5B)O_3$ films generates long range magnetic order. Epitaxy driven strain studies on these single crystal films also point to an acute sensitivity to lattice anisotropy. Both strain and cation radii may be used to finely tune metastability and functionality.

[1] Y. Sharma, et al, *Single-crystal high entropy perovskite oxide epitaxial films*, Physical Review Materials 2, 060404(R) (2018).

10:30

GG-07. Role of rare-earth size on the structural, electronic, and magnetic properties of doubly ordered R_2NiMnO_6 perovskites. *M. Nasir*[1], M. Khan[2] and S. Sen[1] *1. Physics, IIT Indore, Indore, India; 2. Physics, Miami University, Oxford, OH, United States*

The R_2NiMnO_6 (R = La, Pr, Nd, Sm, Gd, Tb, Dy, Y, and Ho) double perovskites, prepared by sol-gel assisted combustion route, have been systematically investigated using powder x-ray diffraction, Raman spectroscopy, ultraviolet–visible spectroscopy, magnetization, and synchrotron based x-ray absorption spectroscopy measurements. All compounds in the family crystallize in the monoclinic structure ($P2_1/n$ space group) and the monoclinic distortion enhances with decreasing R^{3+} radii. The magnetic ordering temperature (T_C) decreases from 270 K for La_2NiMnO_6 to 80 K for Ho_2NiMnO_6 as the R^{3+} radii ($r_R{}^{3+}$) decrease from 1.16 Å (La^{3+}) to 1.02 Å (Ho^{3+}). An additional anomaly is observed in Nd_2NiMnO_6, Sm_2NiMnO_6, Tb_2NiMnO_6, and Dy_2NiMnO_6 at lower temperatures, which originates from the 3*d*-4*f* coupling between Mn-Ni and $Nd^{3+}/Sm^{3+}/Tb^{3+}/Dy^{3+}$ magnetic moments. Further, high saturation magnetization is achieved for all samples indicating that they are atomically ordered and have less antisite disorders. Upon decreasing the size of R^{3+}, the local structure shows an expansion of NiO_6 octahedra and almost unchanged MnO_6 octahedra. X-ray-absorption near-edge spectroscopy reveals that majority of Ni and Mn ions are in +2 and +4 valence states in all the samples. Raman spectra of RNMO show a softening of phonon modes resulting in the elongation of Ni/Mn-O bond length. Finally, a correlation between lattice parameters, structural distortion, octahedral tilting, superexchange angle, and electronic band gap, Curie temperature, and the rare-earth ionic radius is established.

1. H. J. Zhao, X. Q. Liu, X. M. Chen and L. Bellaiche, *Physical Review B*, 90, 195147 (2014) 2. M. Retuerto, Á. Muñoz, and J. Sánchez-Benítez, *Inorganic Chemistry*, 54, 10890 (2015) 3. D. Choudhury, P. Mandal, and D. D. Sarma, *Physical Review Letters*, 108, 127201 (2012) 4. R. I. Dass, J. Q. Yan and J. B. Goodenough, *Physical Review B*, 68, 064415 (2003) 5. J. Blasco, J. L. García-Muñoz and C. Ritter, *Physical Review B*, 96, 024409 (2017)

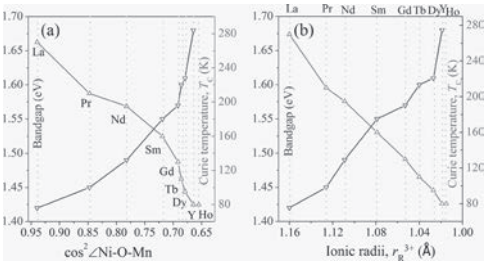


Fig. 1. Electronic band gap and Curie temperature, T_C of R_2NiMnO_6 as a function of (a) superexchange angle, ∠Ni-O-Mn and (b) ionic radii $r_R{}^{3+}$.

10:42

GG-08. Magnetic and thermoelectric properties of Bi, Cu double-substituted $La_{1-x}Sr_xCoO_3$ at room temperature. *D.P. Dubey*[1] and R. Chatterjee[1] *1. Physics Department, Indian Institute of Technology- Delhi, New Delhi, India*

Recycling of waste heat and the search for renewable energy sources is a contemporary issue of the interest for the world in general *[1-3]*. Oxides thermoelectric materials (TEs) have an advantage over other well-known alloy based TEs, due to their chemical and thermal robustness, high thermal stability and excellent oxidation resistance *[4]*. Among all oxides, the perovskite transition metal oxides like cobaltite, exhibit rich physical properties for a good thermoelectric figure of merit. In this work, a detailed magnetic and thermoelectric properties are investigated for Bi, Cu co-doped cobaltite sample. The polycrystalline samples of $La_{0.95-x}Bi_xSr_{0.05}Co_{0.5}Cu_{0.5}O_3$,

have been synthesized through Solid State Reaction route. The X-ray diffraction (XRD) data shows a distorted rhombohedral phase (space group) with lattice parameters $a=b=$ 5.46Å, c= 13.160Å and 90^0, 120^0. A monotonic decrease of lattice constants was noted with increasing x for all samples. The scanning electron microscopy (SEM) data on bulk shows optimal grain growth with grain size ~1-3μm. The electron dispersive analysis of X-ray (EDAX) with elemental mapping, confirms the existence of stoichiometric and homogeneous compositions for all prepared samples. The ZFC-FC and (M-H) plots show the spin glass behavior at low (~10K) and paramagnetic nature of the system at room temperature. The specific heat capacity C_p measurement was carried out on PPMS, where an anomaly observed around room temperature. The data of specific heat used to calculate the thermal conductivity from the values of thermal diffusivity by Discovery DXF-900. The electrical conductivity and Seebeck measurement performed by ZEM-3 Advanced Riko Inc. It was found that, with increasing the Bi-substitution for samples, the thermal conductivity (κ) decreases, while the Seebeck voltage (S) increases. The decrease of κ and increase of S, is desirable for good thermoelectric properties. The power factor (PF) and ZT values were extracted from the derived parameters and the results (ZT~ 0.016, PF~ 80μW/mK²) shows the co-doping system of $La_{0.95-x}Bi_xSr_{0.05}Co_{0.5}Cu_{0.5}O_3$ have enough potential for efficient thermoelectric performance.

[1] Jian He and Terry M. Tritt, Science 357, eaak9997 (2017). [2] Christopher J. Vineis, Ali Shakouri, Arun Majumdar, and Mercouri G. Kanatzidis Adv. Mater. 22, 3970–3980 (2010). [3] J. Ravichandran J. Mater. Res. 32(1), 183-203 (2017). [4] J. Androulakis, P. Migiakis, J. Giapintzakis, Appl. Phys. Lett. 84, 1099–1101 (2004).

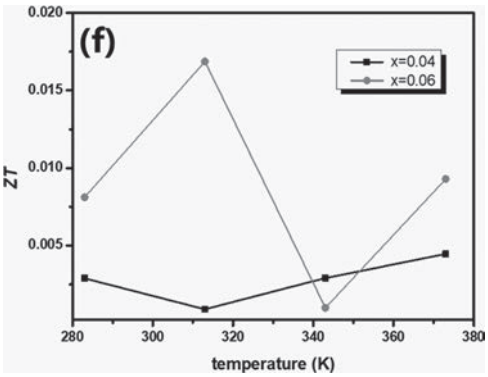


Fig.1 *ZT* vs temperature

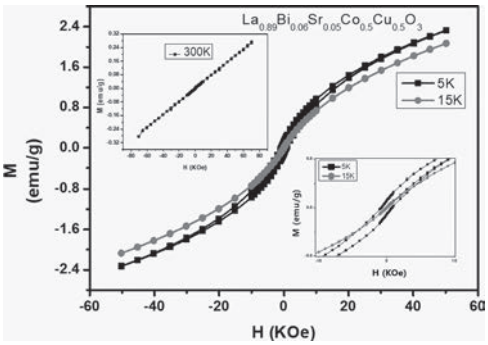


Fig.2 M-H plot at 5K, 15K and 300K

10:54

GG-09. Spin and Dipole Ordering in Flexoelectrical Coupled Strain Gradient Garnet Ferrite Thin Films. *H. Tabata*[1] *1. School of Engineering, The University of Tokyo, Tokyo, Japan*

Rare-earth iron garnets (RIGs) are ferrimagnetic insulators whose chemical formula is $Re_3Fe_5O_{12}$ (R : rare-earth elements). They have been industrially available for optical devices such as optical isolators since they show large magneto-optical effects. On the other hand, they are unlikely to show remnant po-larization character in bulk phase, due to their centrosymmetric crystal structure. If remnant magnetiza-tion and dielectric polarization co-exist in RIGs, multiferroic behaviors and magneto-electric correlation (ME-effect) are expected, which is promising materials design for the future application on spintronics devices. In this research, $Re_3Fe_5O_{12}$ (Re=Sm,Lu,Y; SmIG, LuIG, YIG) films are formed on $Gd_3Ga_5O_{12}$ (GGG) substrates by a pulsed laser deposition. The lattice mismatch between SmIG and GGG is −1.2%, so that the critical thickness where misfit dislocation occurs is estimated to be around 60 nm [1]. TEM observations suggest that SmIG films grown on GGG show three regions of tetragonal, strain-gradient, and cubic structure from the interface to the surface caused by the epitaxial strain and the lattice relaxation as shown in Figure 1. Especially, in the strain-gradient region, the inhomogeneous strain can generate flexoelectric polarization, P(flexoelectricity) = μ(∂u/∂x), where μ and (∂u/∂x) are flexoelectric tensor and strain-gradient, respectively. The inhomogeneous atomic displacement and the presence of dielectric polarization in the strain-gradient region are confirmed by a scanning nonlinear dielectric microscopy (SNDM) [2]. Moreover, as shown in Fig. 2, coercive magnetic fields are dramatically enhanced (from 0.08T to 0.4T) in the strain gradient region. Simultaneous ordering of spin and dielectric polarization is observed in these strain-gradient SmIG films. The strain gradient (flexoelectric) engineering is one of the promising techniques to create novel multi-functional materials.

[1] H. Yamahara, M. Mikami, M. Seki, H. Tabata, J. Magn. Mag. Mat., 323, 3143 (2011). [2] Y. Cho, A. Kirihara, T. Saeki, Rev. Sci. Inst. 67, 2297 (1996).

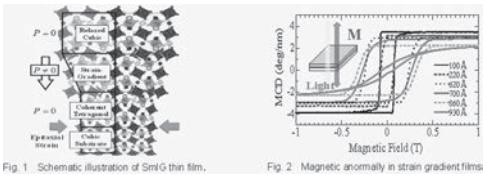


Fig. 1 Schematic illustration of SmIG thin film. Fig. 2 Magnetic anormally in strain gradient films

11:06

GG-10. Tuning the Perpendicular Magnetic Anisotropy and the Dzyaloshinskii-Moriya Interaction by Ferroelectric Polarization at BeO/Co Interfaces. *F. Ibrahim*[1], A. Hallal[1] and M. Chshiev[1] *1. Univ. Grenoble Alpes, CEA, CNRS, Grenoble INP, IRIG-SPINTEC, Grenoble, France*

Spin-orbit coupling (SOC) at material interfaces leads to the emergence of a wealth of phenomena such as perpendicular magnetic anisotropy (PMA) and Dzyaloshinskii–Moriya interaction (DMI). Interestingly, PMA and DMI were reported even at interfaces with weak SOC such as Co/graphene [1,2]. However, the efficient control of these phenomena by low-consumption means, e.g. electric fields, is a key gradient towards potential applications in memory and logic devices [3,4,5]. We demonstrate by first-principles calculations the possibility of tuning both PMA and DMI by the ferroelectric polarization (P) in wurtzite w-BeO at the w-BeO/Co interface. The calculated potential shows a typical double well between two polar states (P_+ and P_-) with an estimated P switching barrier of 0.1 eV/atom. The magnetic anisotropy energy MAE per Co layer shows a favorable PMA for ferroelectric (P_- and P_+) and paraelectric states [Fig. 1]. The remarkable PMA value (~ 3 erg/cm²) is highly dependent on the BeO polar state and

changes by 70% upon *P* switching. The total DMI coefficient calculated for polar w-BeO/Co heterostructure, comprising both P_+ and P_- interfaces, is d^{tot} = -0.62 meV whereas it vanishes in paraelectric case. This is due to the breaking of inversion symmetry by *P* while the inversion geometry of the stacking in the paraelectric case is preserved. The layer resolved SOC energy difference ΔE_{soc} associated with DMI between clockwise and anticlockwise spin spirals reveals the asymmetry imposed by *P*; an effect that extends beyond the interface [Fig. 2]. We also note opposite DMI chiralites for P_+ and P_- interfaces which provides the ability of controlling the DMI of Co by switching *P* in the adjacent w-BeO layers.

[1] H. X. Yang et al., Nano Lett. 16, 145 (2016) [2] H. X. Yang et al., Nature Mater. 17, 605 (2018) [3] S. S. P. Parkin et al., Science 320, 190 (2008) [4] M. Schott et al., Nano Lett. 17, 3006 (2017) [5] T. Srivastava et al., Nano Lett. 18, 4871 (2018)

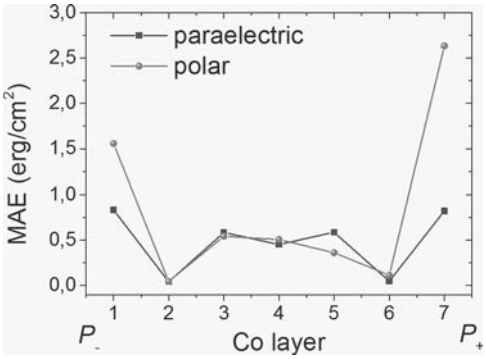


Fig.1 Layer resolved magnetic anisotropy energy of Co in paraelectric (squares) and polar (circles) w-BeO/Co heterostructures. P_+ (P_-) denote the ferroelectric polarization towards (away from) the Co interface.

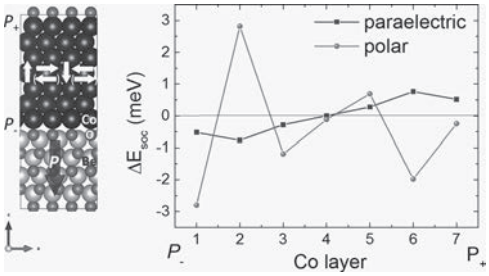


Fig.2 (Left) Crystal and spin configurations of the w-BeO/Co structure used for DMI calculations. Clockwise (anti-clockwise) configurations are shown by arrows. (Right) Layer resolved SOC energy difference ΔE_{soc} associated with DMI between clockwise and anticlockwise spin spirals in paraelectric and polar cases.

11:18

GG-11. Correlation of Hyperfine Field Distribution and Isomer Shifts with Magnetoelectric Properties in Mo-substituted Z-type Barium Hexaferrites. *M. Przybylski*[1], J. Zukrowski[1], K. Latka[2], Z. Su[3,4], P. Kukil[3], Z. Celinski[5] and V. Harris[3] *1. Academic Centre for Materials and Nanotechnology, AGH University of Science and Technology, Kraków, Poland; 2. Department of Physics, Jagiellonian University, Kraków, Poland; 3. Electrical and Computer Engineering, Northeastern University, Boston, MA, United States; 4. EE, Princeton University, New York, NY, United States; 5. Physics, University of Colorado, Colorado Springs, CO, United States*

Barium hexaferrites are important for technological applications, in particular, in data storage and microwave communications [1]. Among them, Z-type barium hexaferrites can exhibit magnetoelectric properties. The electrical polarization partly stems from transverse conical spin configurations and strongly depends upon an external magnetic field and temperature. Moreover, since the Fe atoms are ferro- or antiferromagnetically coupled to the Fe atoms occupying other sublattices, a preferential substitution of iron in one of them can result in a drastic change of the magnetization. Mössbauer spectroscopy is the optimal tool for such studies since the spectra of barium hexaferrites consist of several well-separated components corresponding to the sublattices occupied by Fe atoms. We prepared series of single phase $Ba_3Co_{2+x}Mo_xFe2_{4-2x}O_{41}$ samples. We measured magnetic properties using VSM, and the Mössbauer spectra (MS) of these samples as functions of their composition, temperature (4.2 – 700 K), and external magnetic field. Such measurements, in combination with analysis of MS reveal presents of collinear ferrimagnetic between 500 K and Curie temperatures. For temperatures smaller than 500 K the transverse conical spin structure is present in measured samples. Despite the fact that there are ten inequivalent crystallographic sites of Fe, the spectra were almost perfectly fitted with three components which correspond to the groups of the crystallographic sites showing similar hyperfine parameters [2]. Two of these are spin-up and the other one spin-down sites. However, only by applying magnetic field the components of different spin can be separated and therefore their relative contributions to the total spectrum can be deducted. Figure 1 shows examples of Mössbauer spectra for x=2 measured at 4.2 K with and without external magnetic field. We conclude that the competition between the uniaxial and planar magnetic anisotropies may produce either an easy magnetization axis, cone, or plane. This eventually depends on the types and amounts of the substitutional cations in the unit cell.

[1] V. G. Harris, IEEE Transactions on Magnetics, Vol.48 (3), p.1075 (2012); A. Geiler et al., Journal of Magnetism and Magnetic Materials, Vol. 324, p.3393 (2012) [2] Z. W. Li et al., Phys. Rev. B, Vol.72, p.104420 (2005)

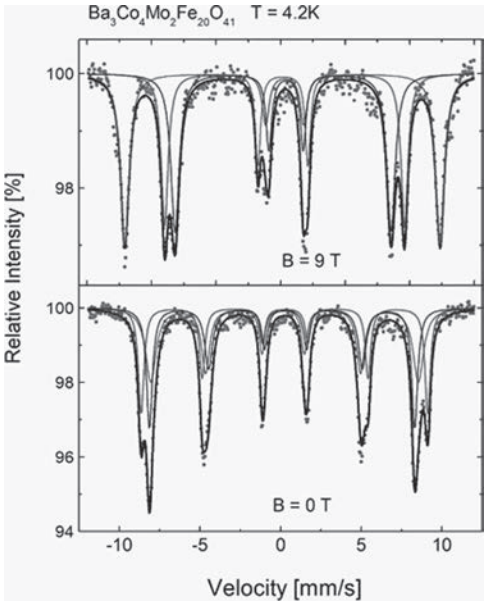


Fig.1 Mössbauer spectra of $Ba_3Co_4Mo_2Fe_{20}O_{41}$ measured at 4.2 K with and without external magnetic field.

Session GH
SOFT MAGNETIC MATERIALS - METALLIC

Xinjun Wang, Chair
Northeastern University, Boston, MA, United States

CONTRIBUTED PAPERS

8:30

GH-01. Synthesis and Electromagnetic Properties of Fe-based Nanocrystalline Powders with High M_s. *Y. Li*[1], C. Zhang[1] and W. Zhang[1]
1. Dalian University of Technology, Dalian, China

With the rise of the new generation of wireless communication technology, plenty of electronic devices have been applied in GHz frequency range, and the ensuing electromagnetic (EM) interference and EM pollution are also increasing seriously. Therefore, it is of great significance to explore and develop new EM wave absorbing/shielding materials for the GHz frequency range. Ferrites have been widely used as EM wave absorbers in the frequency below 1 GHz but not suitable for higher frequency applications due to the Snoek's limit. Compared with ferrites and other traditional magnetic materials, Fe-based soft magnetic nanocrystalline alloys with a composite structure of bcc-Fe nano grains homogeneously dispersing in amorphous matrix exhibit superior soft magnetic properties, especially high saturation magnetization (M_s) and permeability at higher frequency. Combined with their high resistivity, the Fe-based nanocrystalline alloys might be good candidates for EM wave absorption materials. Considering that non-magnetic elements would lower the M_s, nanocrystalline alloys containing higher Fe contents may exhibit superior absorption performance. Accordingly, a FeSiBCu alloy with Fe content of over 80 at.% has been designed for developing new nanocrystalline EM wave absorbers in this work. We investigated the evolutions of structure and morphology of the alloy powders by ball-milling for different milling time, and studied the effects of structure and morphology on the magnetic and EM properties as well as EM wave absorption performance. The as-milled powders can form a bcc-Fe/amorphous composite structure with the bcc-Fe grain size of around 10 nm, and exhibit large M_s, high permeability, and matchable permittivity in the GHz range. The absorption samples with a thickness of around 2 mm exhibit large reflection loss (RL) of -39.1−-50.5 dB with effective absorption bandwidth (RL < -10 dB) of 4.5−5.0 GHz covering the X-band (8−12 GHz).

8:42

GH-02. FeBNbP Nanocrystalline Alloy Powder with High Amorphous Forming Ability and High B_s for Magnetic Core. *A. Hasegawa*[1], H. Kumaoka[1], K. Yoshiki[1], M. Hosono[1], K. Yoshidome[1], S. Mori[1], K. Horino[1] and H. Matsumoto[1] *1. Material Development Center, TDK Corporation, Narita, Japan*

The effect of additional P with Fe-B-Nb type nanocrystalline alloy already researched to improve amorphous forming ability using a thin film method [1]. The influence of P content on amorphous forming ability and the magnetic properties were investigated in the Fe-B-Nb-P nanocrystalline alloys using a metallic ribbon. The $Fe_{84-x}B_9Nb_7P_x$(x=0-3) nanocrystalline alloy metallic ribbons prepared by a single-roller melt-spinning method. The $Fe_{84-x}B_9Nb_7P_x$(x=0-3) nanocrystalline alloys annealed at 873-923 K consist of stable α-Fe grain formed in a residual amorphous phase, and the average α-Fe grain diameter showed nanocrystal of 6.3 to 7.7 nm. Critical thickness of ribbon indicating amorphous forming ability was increased from 20 μm (x=0) to maximum 68.7 μm with $Fe_{81}B_9Nb_7P_3$ by increasing P content. Especially, $Fe_{81}B_9Nb_7P_3$ alloy also exhibited high saturation magnetic flux density (B_s) of 1.51 T. In addition, $Fe_{81}B_9Nb_7P_3$ alloy indicated a good magnetic softness of low coercivity (H_c) of 4.8 A/m and high permeability of approximately 33000 at 1kHz-20A/m. From the above results, the possibility of producing a powder up to 60 μm was explained in Fe-B-Nb-P alloys. Although FeBNb type alloys has not been realized as powders due to difficulty of obtaining high amorphous formation ability for producing powder, $Fe_{80}B_{10}Nb_7P_3$ alloy increasing B content succeeded to obtain the powder with precursor of a single amorphous phase by rapid quenching gas atomization method. $Fe_{80}B_{10}Nb_7P_3$ annealed alloy powder at 873 K exhibited nanocrystalline structure withα-Fe grain of average diameter 8.1 nm and high B_s of 1.46 T. Therefore, the $Fe_{80}B_{10}Nb_7P_3$ nanocrystalline alloy powder can acquire a large advantage due to miniaturization of magnetic core for power device by 20 % higher B_s compared with commercialized composition of $Fe_{73.5}Si_{13.5}B_9Nb_3Cu_1$ (B_s=1.24 T) [2].

[1] H. Amano, A. Hasegawa, H. Matsumoto, AIP Advance, Vol. 9, 035027 (2019) [2] Y. Yoshizawa, S. Oguma, K. Yamauchi, J Appl Phys.,Vol. 64, 6044 (1988)

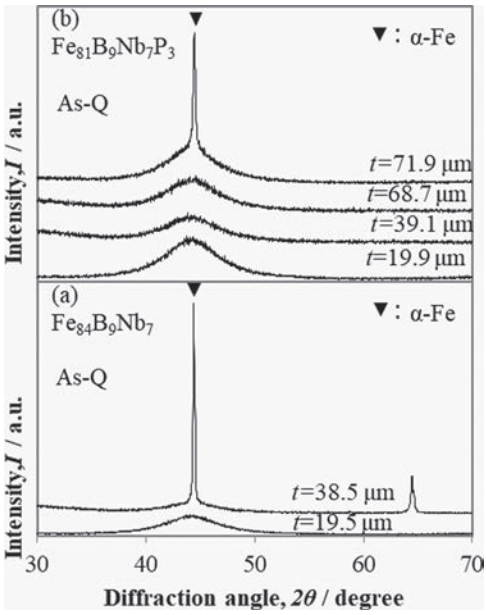


Fig1 XRD pattern of the different thickness as-quenched ribbons, (a) $Fe_{84}B_9Nb_7$ and (b) $Fe_{81}B_9Nb_7P_3$.

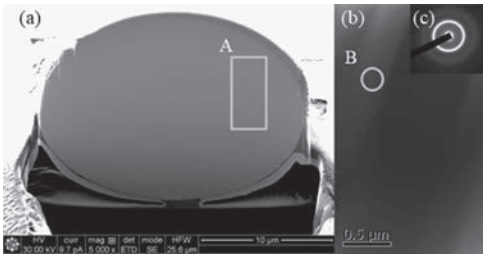


Fig. 2 Particle internal structure with composition of $Fe_{80}B_{10}Nb_7P_3$, (a) Cross sectional SEM image, (b) TEM bright field image of region of A, (c) SAED pattern of region of B.

8:54

GH-03. Magnetic and structural properties of $(Fe,Ni)_{86}B_{14}$ nanocrystalline soft magnetic alloys prepared by ultra-rapid annealing.
Z. Li[2], R. Parsons[2], B. Zang[2], J. Karel[2], H. Kishimoto[1], T. Shoji[1], A. Kato[1] and K. Suzuki[2] *1. Toyota Motor Corporation, Susono, Japan; 2. Material Science and Engineering, Monash University - Engineering Faculty, Melbourne, VIC, Australia*

Nanocrystalline soft magnetic materials consist of nano-sized grains embedded within an amorphous matrix. The nanocrystalline structure in early reports [1] was achieved through the use of non-magnetic additives such as Cu and Nb. However, the recently developed rapid annealing technique has allowed for the production of nano-scale grains even in an Fe-B binary system without addition of these non-magnetic elements. With a low concentration of non-magnetic elements, a higher saturation magnetization (J_s) up to 1.92 T has been obtained for the ultra-rapidly annealed (URA) $Fe_{87}B_{13}$ [2]. Although, an addition of 2 at.% Ni to this binary alloy resulted in a reduction of the coercivity from 6.4 to 3.8 A/m [2], the effect of larger amount of Ni in the URA Fe-B alloys remains unknown. In this study, the magnetic and structural properties of nanocrystalline $(Fe_{1-x}Ni_x)_{86}B_{14}$ (x = 0, 0.1, 0.2 and 0.3) were investigated. A low coercivity of 2.6 A/m was obtained for $(Fe_{0.9}Ni_{0.1})_{86}B_{14}$, while maintaining a high J_s of 1.7 T. This low coercivity is suggested to be the result of a reduction in the magnetocrystalline anisotropy brought about by the addition of Ni. Furthermore, apart from bcc nanocrystallites as normally observed in most Fe-rich nanocrystalline systems, the formation of fcc phase was also found with extremely small grain size of < 5 nm for x > 0.2.

[1] For example, Y. Yoshizawa, S. Oguma, and K. Yamauchi, *J. Appl. Phys.* 64, 6044 (1988). [2] K. Suzuki, R. Parsons, B. Zang, K. Onodera, H. Kishimoto, T. Shoji, and A. Kato, *AIP Adv.* 9, 035311 (2019).

9:06

GH-04. Iron loss characteristics of a high-temperature amorphous ring under PWM inverter excitation.
A. Yao[1] and T. Hatakeyama[1] *1. Department of Electrical and Computer Engineering, Toyama Prefectural University, Imizu, Japan*

Several researchers have recently focused on high-temperature (HT) and high speed (HS) motor drive systems in HT environments[1~5]. In these HT and HS motor systems, pulse width modulation (PWM) inverters are generally used to control the rotational speed[4~8]. The iron loss of magnetic cores under PWM inverter excitation increases compared to case of sinusoidal input[4~8]. To realize low loss HT and HS motor systems, it is important to understand iron loss characteristics of amorphous magnetic materials (AMM) at HT fed by PWM inverter. However, there has been no report on AMM properties at HT under PWM inverter excitation. In this study, the iron losses of AMM as a function of carrier frequency under inverter excitation are experimentally and numerically examined at RT and HT (300°C). Fig. 1 shows a schematic of the ring test at RT and HT under PWM inverter excitation. The ring specimen is made of AMM and is exposed to HT variations in the oven. Here, the iron loss W is calculated by $W = \int H dB/T\rho$, where T is the period, ρ is the density, H is the magnetic field intensity, and B is the magnetic flux density. The fundamental frequency and the maximum magnetic flux density of the ring are set to 50 Hz and 0.8 T, respectively. See Refs. 4,5) for details of the measurements and numerical methods. Figs. 2 (a) and (b) show experimental and numerical B-H curves at RT and HT under PWM inverter excitation. The area of the minor loop at RT is larger than that at 300°C. Here, it is found that the temperature dependency of iron loss properties depends not only on major loop but also on minor loops. Fig. 2(c) and (d) show the iron and eddy current losses with respect to carrier frequency under inverter excitation at RT and 300°C. The iron loss under PWM inverter excitations decreases with an increase in temperature. In addition, we for the first time found that the ratio of the eddy current losses under PWM inverter excitation depended strongly on the temperature. These results open the way to further research in HT and HS motor system based on studies of magnetic properties.

[1] L. Burdet, Active magnetic bearing design and characterization for high temperature applications, PhD thesis, (Citeseer, 2006). [2] T. D. Kefalas and A. G. Kladas, Thermal investigation of permanent-magnet synchronous motor for aerospace applications., IEEE Transactions on Industrial Electronics, 61 (8), 4404{4411 (2014). [3] A. Yao, A. Adachi, and K. Fujisaki, Iron loss characteristics of electric motor in high-temperature environment, 2017 IEEE International Electric Machines and Drives Conference (IEMDC), 1{7 (2017). [4] A. Yao, S. Odawara, and K. Fujisaki, Iron loss and hysteretic properties under pwm inverter excitation at high ambient temperatures, IEEJ Journal of Industry Applications, 7 (4), 298{304 (2018). [5] A. Yao and T. Hatakeyama, Iron loss and hysteresis properties under high-temperature inverter excitatio, Journal of the Magnetics Society of Japan, (2019). [6] K. Fujisaki and S. Liu, Magnetic hysteresis curve in uenced by power-semiconductor characteristics in pulse-width- modulation inverter, Journal of Applied Physics, 115 (17), 17A321 (2014). [7] A. Yao, K. Tsukada, S. Odawara, K. Fujisaki, Y. Shindo, N. Yoshikawa, and T. Yoshitake, PWM inverter-excited iron loss characteristics of a reactor core, AIP Advances, 7 (5), 056618 (2017). [8] A. Yao, K. Tsukada, and K. Fujisaki, Investigating iron loss properties in an amorphous ring excited by inverters based on silicon and gallium nitride, IEEJ Journal of Industry Applications, 7 (4), 321{328 (2018).

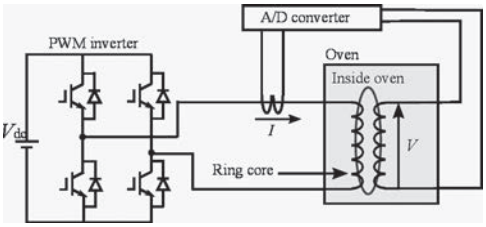


Fig.1 Schematic of a ring test at HT under PWM inverter excitation

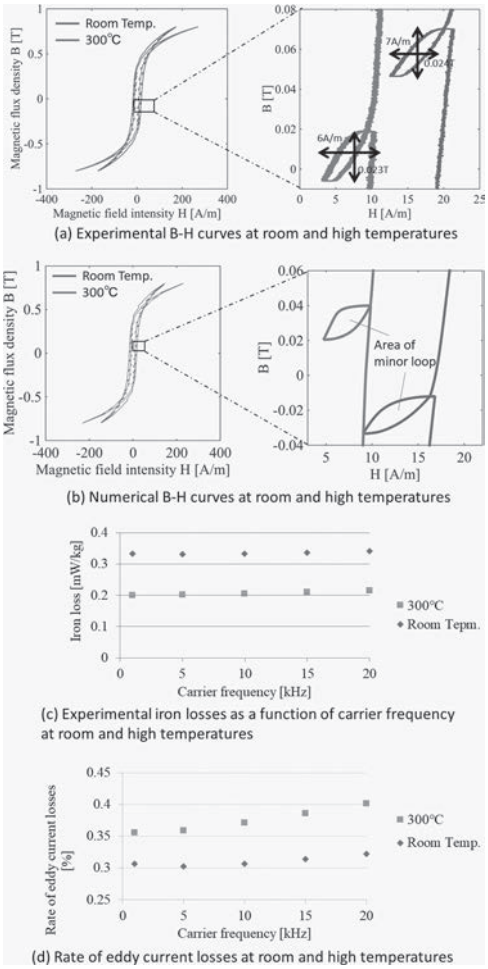


Fig.2 Loss characteristics at RT and 300°C

9:18

GH-05. Influence of Circular Magnetic Field and Combined Mechanical Stress on Spiral Domain Structures in Magnetic Microwires. *A. Chizhik*[1], J. Gonzalez[1], A. Zhukov[1,2], P. Corte-Leon[1], V. Zhukova[1], P. Gawronski[4] and A. Stupakiewicz[3] *1. Departamento de Fisica de Materiales, Universidad del Pais Vasco, UPV/EHU, San Sebastian, Spain; 2. Ikerbasque, Basque Foundation for Science, San Sebastian, Spain; 3. University of Bialystok, Bialystok, Poland; 4. AGH University of Science and Technology, Krakow, Poland*

The experimental observation of the spiral domain structure has opened a new possibility of the fine control of the domain structure with different magnetization states in magnetic microwires which are the base elements of the magnetic sensors [1]. Here we demonstrate that the tuning of magnetic domain structures in Fe-rich amorphous microwires can be engineered by the circular magnetic field and the combination of tension and torsion mechanical stresses. The application of the circular field rotates the domain structure towards the axial direction (Fig.1). The axial direction could not be reached in the present experiments because of the limit of the circular field. It is determined in turn by the limit value of the electric current producing the circular field, related to the heating limit. Here we also present the results of the micromagnetic simulations of the influence of the circular magnetic field created by the electric current passing through the microwire on the modification of a spiral domain structure during the magnetization reversal process (Fig.2). In the presence of the tension stress only rotation of the magnetization takes place. Torsion stress stabilized the helical structure – helical bistability becomes more pronounced with the torsion increase. The addition of tension to the torsion does not cause the extinction of the helical bistability. The effect of the stress combination increases the switching field and decreases the value of the remanent magnetization. The main reason of the observed transformation is the induced change of the helical outer shell. Competing action of torsion and tension permits found the structure with predictable angle of magnetic helicity which is important for GMI effect and establishes the switching in wide range of the magnetic field which is important for bistability based sensors.

[1] A. Chizhik, A. Zhukov, J. Gonzalez, P. Gawronski, K. Kulakowski and A. Stupakiewicz, Sci Rep. 8, 15090 (2018)



Figure 1. Images of domain structures under circular magnetic field: a) 0, b) 7A/m.

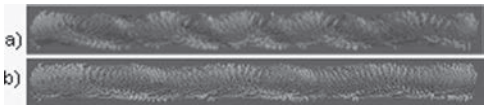


Figure 2. Images of simulated magnetic structures for different amplitudes of the circular magnetic field created by the electric current passing through the microwire: a) I = 1 mA, b) I = 5 mA.

9:30

GH-06. Prediction of Good Glass Forming Ability in Amorphous Soft Magnetic Alloys by Thermocalc Simulation and Experimental Validation. *Y. Krimer*[1], N. Aronhime[2], P. Ohodnicki[3] and M. McHenry[1] *1. Materials Science, Carnegie Mellon University, Pittsburgh, PA, United States; 2. Research and Development, Carpenter Technologies, Reading, PA, United States; 3. National Energy Technology Laboratory, Pittsburgh, PA, United States*

Advances in Metal Amorphous Nanocomposite (MANC) alloys where the amorphous phase has excellent glass forming ability (GFA) may impact formability in hot stamping motor laminates. [1-2]. Thermocalc software was used to simulate liquidus temperatures and solidification ranges of $(Fe_{70}Ni_{30})_{80}$(B-Si-Nb)$_{20}$ alloys, with varying proportions of glass forming elements, to identify regions with good GFA. A region with excellent GFA was identified at 14-18% B and 0-7% Si with the balance Nb, showing minima in both liquidus and solidification range. GFA was ranked using differential scanning calorimetry (DSC), using the GFA parameters T_{rg}, ΔT_{xg}, and γ_m. DSC data showed liquidus results to be in good agreement with simulation, and that GFA correlates well with predictions. DSC was used to determine Curie temperatures, T_c's, of the alloys, and these results were confirmed by PPMS magnetometry measurements. It was found that T_c decreases with increasing Nb content and increases with increasing B. Si content has little effect on Curie temperature. T_c's are plotted vs. B/Nb, where B and Nb are the atomic fractions of these glass forming elements. T_c's increase with increasing B/Nb, from 294 to 422 °C at B/Nb=10, and then saturate. The role of B in increasing T_c in Fe-based amorphous alloys is known [3]. Nb virtual bound states (VBS) decrease induction and T_c and increase resistivity [2]

J.M. Silveyra, P. Xu, V. Keylin, J. Electron. Mater. 45 219–225 (2015) N. Aronhime, P. R. Ohodnicki and M. E. McHenry; Scripta Materiala 169, 9-13, (2019) R. C. O'Handley, J. Appl. Phys. 62(10), R15-R49, (1987)

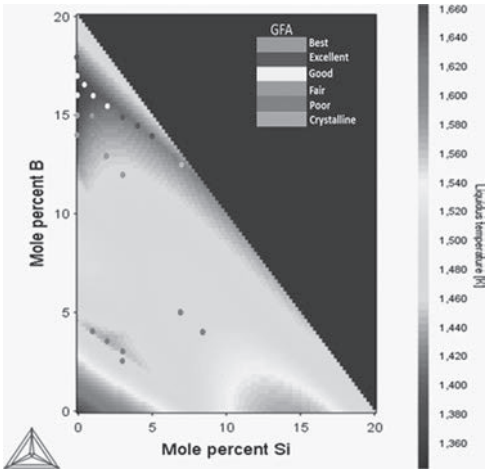


Fig. 1. Simulated plot of liquidus temeperature, showing ranking of compositions by measured GFA.

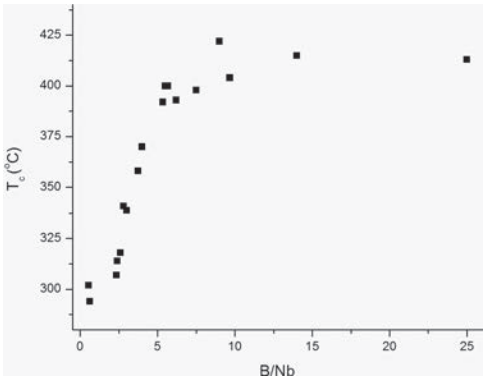


Fig. 2. Curie temperature vs. B/Nb ratio, where B and Nb are atomic fractions of B and Nb, respectively.

9:42

GH-07. Engineering of magnetic properties and domain wall dynamics in Fe-Ni-based amorphous microwires by annealing. V. Zhukova[1,2], A. Talaat[1], P. Corte-Leon[1,2], J. Blanco[2], M. Ipatov[1,2] and *A. Zhukov*[1,3]
1. Dept. Phys. Mater., Univ. Basque Country, UPV/EHU, San Sebastian, Spain; 2. Dpto. Física Aplicada, EIG, Univ. Basque Country, UPV/EHU, San Sebastian, Spain; 3. Basque Foundation for Science, Ikerbasque, Bilbao, Spain

Thin magnetically soft wires exhibiting Giant magnetoimpedance (GMI) effect and fast domain wall (DW) dynamics attracted growing attention owing to promising industrial applications [1,2]. It was demonstrated that properly prepared and processed glass-coated microwires prepared using Taylor-Ulitovsky technique can exhibit excellent magnetic softness, GMI effect and fast DW dynamics [1]. DW propagation observed in thin (mostly planar) magnetic wires has been proposed for applications in data storage devices (magnetic random memory devices, logic devices)[3]. Most of studies have been reported for Fe-Ni-rich permalloy-like nanowires [3]. Generally cast glass-coated microwires present one order higher DW velocities, however most of results have been obtained in Fe-Co- based materials. Fe-Ni-rich permalloy-like microwires have been studied in only a few papers [1,4]. Consequently, we present our last experimental results on effect of annealing on magnetic properties and DW dynamics of Fe-Ni based glass-coated microwires. We studied the effect of annealing on hysteresis loops and DW dynamics of $Fe_{62}Ni_{15.5}Si_{7.5}B_{15}$ and $Fe_{49.6}Ni_{27.9}Si_{7.5}B_{15}$ microwires with metallic nucleus diameters of about 14 μm. We found that as-prepared and annealed (at 410 °C) microwires present perfectly rectangular hysteresis loops. Generally as-prepared samples present soft properties with switching field of about 100 A/m (see Fig). After annealing we observed increase of the switching field up to about 200 A/m. In both samples we observed linear dependence of domain wall velocity, v, on applied magnetic field, H, and maximum v-values up to 1000 m/s. Upon annealing we achieved quite fast domain wall propagation in $Fe_{62}Ni_{15.5}Si_{7.5}B_{15}$ sample where maximum v-values up to 2500 m/s have been observed. In $Fe_{49.6}Ni_{27.9}Si_{7.5}B_{15}$ microwire we observed moderate increase of v-values up to 1200 m/s. We attributed these changes to the stress relaxation after annealing. Consequently, appropriate annealing is the effective method for engineering of the DW dynamics in Fe-Ni-based glass-coated microwires.

1. M. Vazquez et.al., Phys. Status Solidi A, 208 493 (2011) 2. H. Chiriac et.al. J. Appl. Phys., 107 (2010) 09A301 (2010) 3. D.A. Allwood et.al. Science 309 1688 (2005) 4. A. Zhukov et.al. J. Alloys Compound, 707, 15, 35–40 (2017)

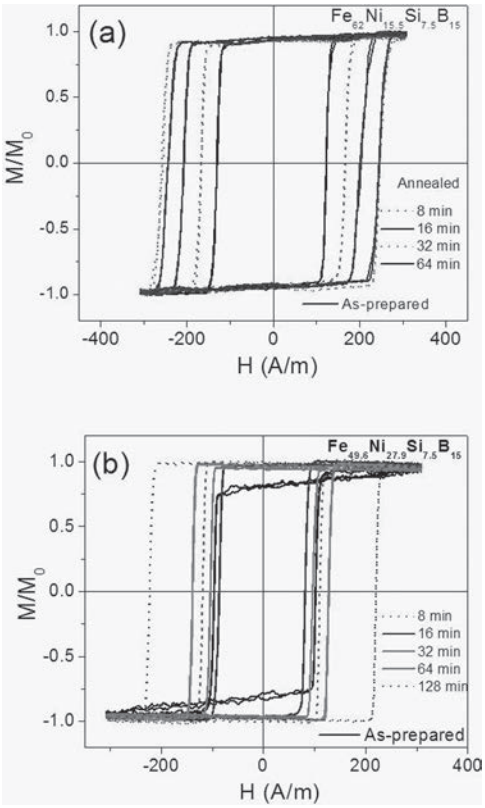


Fig.1 Hysteresis loops of $Fe_{62}Ni_{15.5}Si_{7.5}B_{15}$ (a) and $Fe_{49.6}Ni_{27.9}Si_{7.5}B_{15}$ (b) microwires

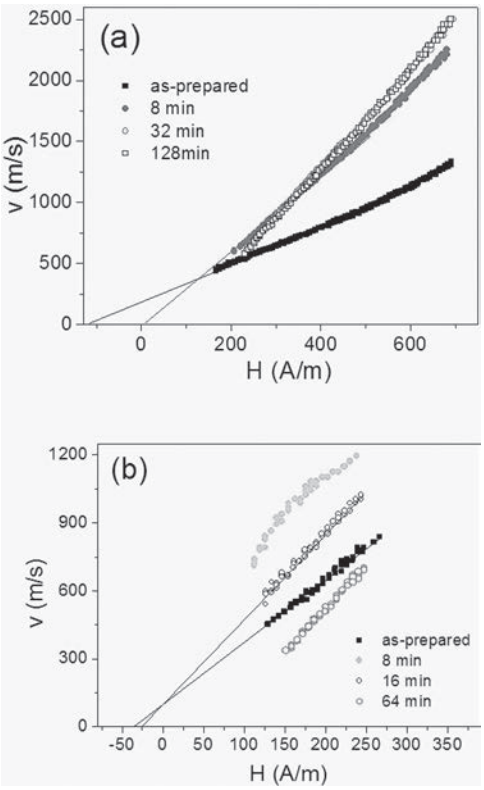


Fig.2 DW dynamics of $Fe_{62}Ni_{15.5}Si_{7.5}B_{15}$ (a) and $Fe_{49.6}Ni_{27.9}Si_{7.5}B_{15}$ (b) microwires

9:54

GH-08. Effect of latent heat during primary crystallization on nanostructural formation process in nanocrystalline soft magnetic materials. R. Parsons[1], H. Kishimoto[2], T. Shoji[2], A. Kato[2] and *K. Suzuki*[1] *1. Monash University, Clayton, VIC, Australia; 2. Toyota Motor Corp., Mishuku, Japan*

Nanocrystalline soft magnetic materials are known to be prepared by primary crystallization of Fe-based amorphous precursors. Since the crystallization reaction is exothermic, the amorphous precursor may experience a temporary rise in its temperature relative to its surroundings during the process of nanocrystallization. Given the typical latent heat of crystallization (~ 10 kJ/mol), this temperature rise may exceed hundreds of degrees if not adequately controlled and thus, lead to the formation of unwanted magnetically hard compounds. Recently, an ultra-rapid annealing (URA) process realized by a pair of preheated Cu blocks (heating rate of ~10^4 K/s, annealing time of 0.5 s) has been shown to be effective for grain refinement [1] and in the production of nanocrystalline soft magnetic materials with a saturation magnetisation greater than 2 T [2]. However, despite the use of very high heating rates, the resultant microstructures are free of magnetically hard compounds. In this study, the effect of latent heat during crystallization on nanostructural formation process is investigated at a range of heating rates by in-situ observation of temperature with a fine 20-mm thick thermocouple and also by finite element analysis. Figure 1 shows the change in sample temperature of an amorphous $Fe_{86}B_{14}$ precursor which was rapidly annealed by a pair of preheated Cu blocks both with and without a single layer of polyimide tape. Indications of an overheating effect are only observed in the sample annealed with the insulating polyimide tape layer. It is found that the high thermal conductivity of the junction between the sample and the Cu block allows for the heat produced during crystallisation to be effectively removed. This limits any significant overheating effect during crystallisation and allows for the use of high heating rates without the formation of magnetically hard phases. As a result, a small coercivity < 8 A/m is realized for URA $Fe_{86}B_{14}$. Contrarily, a significant overheating effect (> 100 K) was seen when a conventional infrared lamp furnace is used even at a moderate heating rate of ~ 10 K/s. Annealing by preheated Cu blocks is ideal for preventing the detrimental effect of latent heat.

[1] K. Suzuki, R. Parsons, B. Zang, K. Onodera, H. Kishimoto, A. Kato, Copper-free nanocrystalline soft magnetic materials with high saturation magnetization comparable to that of Si steel, Appl. Phys. Lett. 110 (2017) 012407. [2] R. Parsons, Z. Li, K. Suzuki, Nanocrystalline soft magnetic materials with a saturation magnetization greater than 2 tesla, J. Magn. Magn. Mater. (2019).

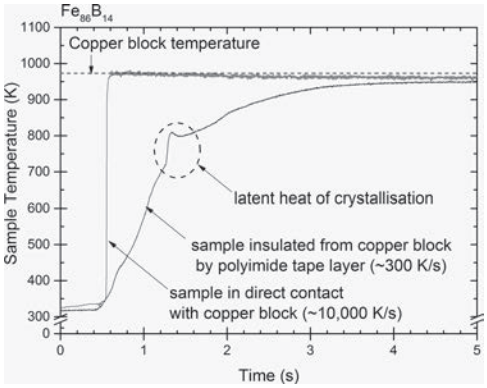


Figure 1.

10:06

GH-09. Role of heavy metal interface in controlling the structural and magnetic properties of amorphous FeCoB film. *J. Dwivedi*[1], M. Gupta[2], V. Reddy[2], D. Mishra[1], P. Pandit[3] and A. Gupta[4] *1. School of Physics, Devi Ahilya University, Indore, India; 2. UGC DAE Consortium for Scientific Research, Indore, India; 3. Deutsches Elektronen-Synchrotron (DESY), Hamburg, Germany; 4. Amity Center for Spintronic Materials, Amity University, Noida, India*

Thin films of FeCoB are the best candidates for magnetic electrodes in MgO based magnetic tunnel junctions. Buffer layer of heavy metals like Mo, has been used to tailor magnetic anisotropy in this system. Post deposition annealing results in crystallization of amorphous FeCoB film into bcc-FeCo phase and plays an important role in enhancing tunnel magnetoresistance. Film having structure; substrate/Mo(30nm)/ FeCoB(70nm)/Mo(2nm) was deposited using dc-magnetron sputtering (dc-MS). The hysteresis loops were taken by magneto-optical Kerr microscope, in UGC-DAE CSR, Indore. The transition from amorphous to crystalline phase of FeCoB was confirmed by wide angle x-ray scattering (WAXS) at P03 Beamline, PETRA III, DESY, Hamburg, Germany. Anomalous behaviour of magnetic anisotropy in FeCoB film (70nm) sandwiched between Mo layers using has been studied as a function of thermal annealing at different temperatures. In general assumption, the anisotropy should vanish after crystallization of FeCoB. In contrast, MOKE measurement reveals that magnetic anisotropy remained in the film after appearance of bcc-FeCo phase. We find an anomalous magnetization reversal behaviour that occurs for partially disordered, but still anisotropic samples in the vicinity of the HA, at 350°C and 400°C annealed sample. The anomaly of the occurrence of non-uniform magnetization near hard axis can be explained by two-grain Stoner-Wohlfarth model [1].

1. O. Idigoras et al., Phy. Rev. B 84, (2011) 132403.

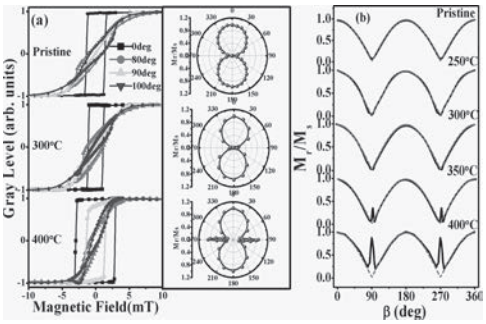


Figure 1. (a) Hysteresis loop Mo/CoFeB/Mo multilayer at pristine, 300°C and 400°C with corresponding azimuthal angle dependence of remanence magnetization, (b) angular dependence of M_r/M_s for samples with thermal annealing. The solid line represent the M_r/M_s data, while dashed line shows the fitting data using SW formula.

10:18

GH-10. Magnetic domains in Pt/Co(Fe)B/Ir multilayers grown on ferroelectric substrates. *K.N. Alshammari*[1], L. Benito[1], R.C. Temple[1], M. Alyami[1], M. Ali[1], T.R. Forrest[2], F. Maccherozzi[2], S.S. Dhesi[2], S. Cavill[3] and T. Moore[1] *1. University of Leeds, Leeds, United Kingdom; 2. Diamond Light Source, Harwell, United Kingdom; 3. University of York, York, United Kingdom*

At the interface of a 5d metal and a thin film 3d ferromagnet such as Pt/Co, the interfacial Dzyaloshinskii-Moriya interaction (DMI) leads to domain walls with a defined chirality and skyrmion bubbles in the ferromagnet that are promising for low power magnetic memory devices [1]. Furthermore, the strain control of thin film magnetism promises power-reduction in nanomagnetic devices [2]. Recently we have measured the effect of out-of-plane strain on DMI and domain walls in Pt/Co thin films [3,4]. In this work we study the effect of strain on magnetic properties by depositing Pt/Co(Fe)B/Ir thin films directly onto ferroelectric substrates. In the first study, Ta(5)/[Pt(2.3)/$Co_{68}B_{32}$(0.8)/Ir(0.5)]$_n$/Pt(2.3) multilayers (nominal thicknesses in nm) were deposited by dc magnetron sputtering onto a $BaTiO_3$ (BTO) substrate. X-ray magnetic circular dichroism - photoemission electron microscopy (XMCD-PEEM) was used to obtain high resolution magnetic images in the remanent state. Strain was generated by varying the temperature from -150 to 35 C° to change the BTO crystal structure. It was found that the domain period increases as the temperature increases as shown in Fig.1.(a). In the second study, Ta(5)/[Pt(2.3)/$Co_{68}Fe_{22}B_{10}$(0.7)/Ir(0.5)]$_n$/Pt(2.3) multilayers (nominal thicknesses in nm) were deposited by dc magnetron sputtering onto polished PMN-PT(011) substrates. Local changes of the position and shape of the domains were evident in XMCD-PEEM images as the voltage was varied from 0-250-0V, as shown in Fig.1.(b). This can be attributed to the movement of ferroelectric grain boundaries and the strain. As the voltage is varied from 0-180 V, a U-shaped domain in the middle of the image has moved by ~1um^2 and slightly elongated. While there are other localised changes in the domain pattern, when averaging over a larger number of domains, the characteristic domain size does not change (520±3 nm) as a function of the strain.

[1] A. Fert et al., *Nat. Nanotechnol.* 8, 152 (2013). [2] K. L. Wang et al., *IEEE Proc.* 104, 1974 (2016). [3] P.M. Shepley et al., *Sci. Rep.* 5, 7921 (2015). [4] P.M. Shepley et al., *J. Phys.: Condens. Matter* 30, 344002 (2018).

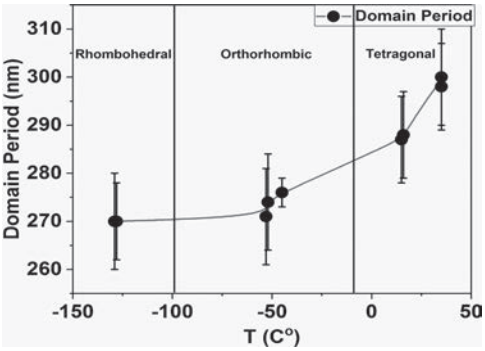


Fig. 1. (a) Temperature dependence of the magnetic domain period for the multilayer Pt/CoB/Ir n=10 grown onto (100)- oriented BTO substrate.

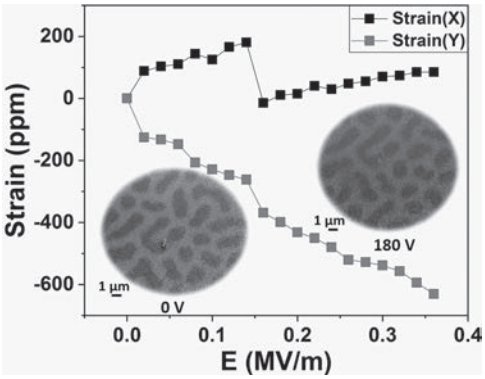


Fig. 1. (b) Electric-field dependence of the in-plane strain developed in the multilayer Pt/CoFeB/Ir n=2 grown onto (011)-oriented PMN-PT substrate.

10:30

GH-11. Tuning of magnetic and structural properties of Fe-rich ferromagnetic microwires. *I. Baraban*[1], V. Kolesnikova[1], A. Bazlov[2], N. Andreev[2], S. Evstigneeva[2], A. Morchenko[2], L. Panina[2,1] and V. Rodionova[1,2] *1. Laboratory of Novel Magnetic Materials, Immanuel Kant Baltic Federal University, Kaliningrad, Russian Federation; 2. National University of Science and Technology (MISIS), Moscow, Russian Federation*

Amorphous ferromagnetic microwires with Fe-rich nucleus present outstanding magnetic properties, such as magnetic bistability [1] and high velocity of the domain wall propagation [2]. Magnetization reversal process occurs through the fast propagation of the domain wall. Therefore, these properties can be used for the creation of modern high-speed mass storage devices with a high recording density and logic elements [3]. In this work, we have demonstrated that the change in critical parameters of microwire fabrication, namely, the drawing velocity, offers the opportunity to optimize the structural and magnetic properties of FeCo-based glass-coated microwires. During the fabrication process of microwires by the Ulitovsky Taylor method, one can control magnetic properties by varying the geometric parameters of the microwires: d, a diameter of the nucleus, and the diameter ratio of the microwire, d/D. In its turn, d is associated with solidification stress, d/D – with stress arising due to the difference of thermal expansion coefficient for metal and glass during the manufacturing process. The decreasing of these stresses will dramatically change the magnetic properties of microwires. Changing the manufacturing conditions as a slower drawing velocity and air cooling make it possible to produce microwires in a complex state (amorphous/nanocrystalline). For different compositions and manufacturing conditions, the structural features were studied by Mossbauer and XRD spectroscopy and HRTEM imaging. In Fe-based microwires, the

amorphous state prevails but for very low velocities crystalline microregions were observed. In FeCo- microwires the centers of crystallization appeared in an amorphous matrix and the size of crystalline grains increases with reducing the drawing velocity. The possibilities of phase transformations were studied by DSC technique. Two stages of the crystallization processes were detected and the activation energy of crystallization was calculated. Identifying the inflection point on the DSC curve, the Curie temperature was also deduced.

[1] M. Vazquez et al, Phys. Status Solidi A 207 (2010). [2] M. Hayashiet al, Science 320 (2008)209–211. [3] V. Vega et al, J. Appl. Phys. 112 (2012) 033905.

10:42

GH-12. Improvement of Soft Magnetic Properties in $Fe_{81}Sn_7B_{12}$ Nanocrystalline Alloys Upon Rapid Annealing. *I. Skorvanek*[1], B. Kunca[1], I. Janotova[2], J. Skoviera[2], J. Marcin[1] and P. Svec[2] *1. Institute of Experimental Physics SAS, Kosice, Slovakia; 2. Institute of Physics SAS, Bratislava, Slovakia*

The continuing interest in Fe-based nanocrystalline alloys is motivated mainly due to their high saturation magnetic flux density combined with relatively low coercivity. An improvement of magnetic performance in these alloys is possible by using a compositional tuning as well as by employing special processing techniques resulting in optimal phase content and reduced grain sizes. Ternary Fe-M-B type alloys (M = Zr, Nb, Hf, …) belong to the most frequently investigated compositions of this material family [1]. On the other hand, only few reports are available in scientific literature on rapidly quenched Fe–Sn–B ribbons [2,3]. In this work, formation of amorphous and nanocrystalline phases has been investigated in $Fe_{81}Sn_7B_{12}$ alloy system. Short ribbon-shaped samples were prepared by planar flow casting and subsequently annealed in the regions of phase transformation determined by differential scanning calorimetry. Structure analysis has been performed on as-quenched and annealed samples using X-ray diffraction and transmission electron microscopy. The results show a dependence of lattice parameter of primary bcc-Fe phase with proceeding nanocrystallization and indicate supersaturation of this phase with Sn. The size evolution of nanocrystalline grains is correlated with observed magnetic behavior. We show that a significant improvement of the soft magnetic properties can be achieved by employing of rapid annealing technique that utilizes a pair of pre-heated Cu blocks [4]. A high heating rate and much lower processing time (10 seconds at 480°C) as compared to conventional annealing (30 minutes at 400°C) results in formation of markedly smaller nanocrystalline grains. An observed grain refinement induced by rapid annealing is accompanied by a strong reduction of the coercivity to 7.3 A/m, which is superior value for Fe–Sn–B alloys. This work was supported by the projects APVV-15-0621, VEGA 2/0171/19 and JRP SAS-TUBITAK MAGSAT.

[1] K. Suzuki A.Makino, A. Inoue, T. Masumoto, J. Appl. Phys. 70, 6232 (1991) [2] E. Illeková, I. Matko, P. Švec et al., J. Alloys. Comp. 509S, S46 (2011) [3] I. Matko, E. Illeková, P. Švec et al., J. Alloys. Comp. 615, S462 (2014) [4] K. Suzuki, R. Parsons, B. Zang et al., Appl. Phys. Lett. 110, no. 012407 (2016)

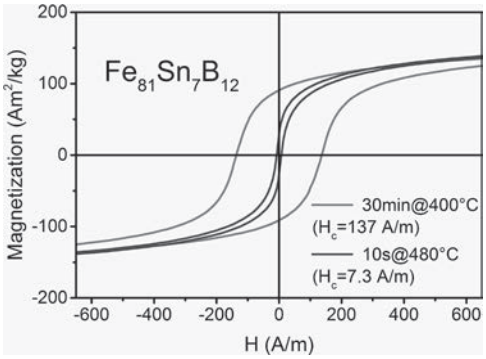


Figure 1

10:54

GH-13. Withdrawn

11:06

GH-14. Nanoclusters formation and their influence on the superferromagnetic behavior of glassy Fe-Cr-Nb-B magnetic particles. H. Chiriac[1], M. Lostun[1], M. Grigoras[1], G. Ababei[1], G. Stoian[1], T.A. Ovari[1] and *N. Lupu*[1] *1. Magnetic Materials and Devices, National Institute of Research and Development for Technical Physics, Iasi, Romania*

Magnetite particles (MPs), magnetic-vortex NiFe microdiscs, ultrathin perpendicularly magnetized MPs, synthetic antiferromagnetic and ferrimagnetic microdiscs with no magnetic remanence, nanowires with various compositions obtained by electrodeposition in aluminum membranes were studied at large for use in different cancer treatment applications. In this work we present our recent results on the microstructure, nanoclusters formation and specific magnetic behavior of $Fe_{79.7-x}Cr_xNb_{0.3}B_{20}$ (x = 11.5÷13 at.%) magnetic particles (MPs) obtained by high-energy ball milling the superferromagnetic rapidly solidified melt-spun ribbons precursors. By controlling the process, we can downsize the particles to 10-200 nm. The MPs have non-zero coercivity at room temperature, exhibit large magnetization, large magnetic susceptibility and low Curie temperature of about 47°C. High resolution imaging and electron diffraction confirm that in the as-milled state the structure is completely amorphous, independent of the Cr content. Clear indications have been found of Fe and Cr clusters varying from approximately 1-2 nm to 7-8 nm in size with the increase of Cr content from 11.5 to 13 at.%. The Fe and Cr atoms clearly segregate the atomic scale to form nanometer sized clusters, influencing strongly the macroscopic magnetic behavior. The magnetization curves were analyzed with a model based on superferromagnetism. The Curie transition temperature of the system, T_C^{system}, confirmed by the plot of inverse susceptibility versus temperature, gives the strength of the magnetic interactions between clusters. The inter-cluster interactions are much stronger for lower contents of Cr, the microstructure is less uniform and T_C^{system} increases from 290 K for 13% at. Cr to 330 K for 11.5 at.% Cr. The whole system transforms to a ferromagnetic state through interactions between the clusters. Zero-field cooling and field cooling curves confirm the cluster behavior. Work supported by the Nucleu Programme (Project PN 19 28 01 01) and Contract No. 11PFE/16.10.2018 financed by the Romanian Ministry of Research and Innovation (MCI).

11:18

GH-15. Stress- induced Magnetic Anisotropy Enabling Engineering of Magnetic Softness and GMI effect of Fe-rich Amorphous Microwires.
P. Corte-Leon[1,2], V. Zhukova[1,2], M. Ipatov[1,2], J. Blanco[2], J. Gonzalez[1] and *A. Zhukov*[1,3] *1. Dept. Phys. Mater., Univ. Basque Country, UPV/EHU, San Sebastian, Spain; 2. Dpto. Física Aplicada, EIG, Univ. Basque Country, UPV/EHU, San Sebastian, Spain; 3. Basque Foundation for Science, Ikerbasque, Bilbao, Spain*

Giant magnetoimpedance (GMI) effect exhibited by soft magnetic materials allows achievement of extremely high sensitivity (up to 10 %/A/m) to applied magnetic field, *H,* reported for magnetic wires [1]. Therefore, GMI effect is considered as one of the most promising phenomena for creation of magnetic sensors and magnetometers. The value of GMI effect and the magnetic field dependence are determined by the type of magnetic anisotropy: for achievement of high GMI ratio the high circumferential magnetic permeability is essentially important [1]. Studies on GMI effect have been focused mainly to develop extremely soft magnetic materials opening a new branch of research in soft magnets. Obviously, the different geometry leads to some differences in the GMI response like the frequency range or the magnetic field dependence of the impedance with single or double-peaks behavior etc. Modifications of the circular magnetic permeability can be reached by stress annealing of amorphous microwires allowing development of the magnetic anisotropy with the magnetization easy axis circumferentially oriented to the longitudinal direction of the microwire [2]. In this work we report a study on the GMI response in a stress-annealed Fe-rich glass-coated microwire (metallic diameter of about 15 μm). Stress-annealing of $Fe_{75}B_9Si_{12}C_4$ glass-coated microwire (300 ^oC, 1 hour) allows induction of macroscopic transverse magnetic anisotropy with the anisotropy field of around 750 A/m. The magnetization curve of the stress-annealed sample shows almost unhysteretic behavior. This anisotropy very significantly improves the GMI effect with respect to the observed in the as-prepared microwire. A resolved double-peaks behavior (symmetrical with respect to *H*) emerges as increasing the frequency. The values of anisotropy field obtained from frequency dependence of GMI effect are very different to those obtained from the hysteresis loops The analysis of the GMI response as a function of the frequency (10 – 1000 MHz) opens new lights to understand the distribution of the magnetic anisotropy inside the glass-coated microwire.

[1] N. A. Usov, et.al, *J. Magn. Magn. Mater.*, vol. 185, 159-173 (1998).
[2] V. Zhukova, et.al., Sci. Reports 8 3202 (2018)

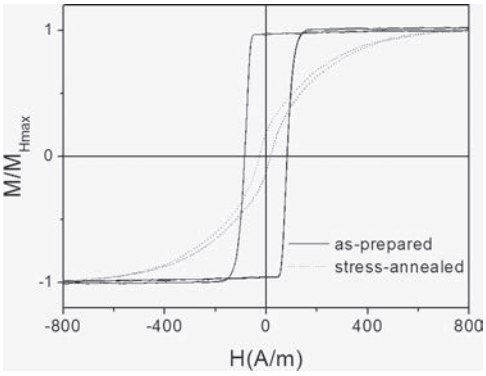


Fig.1 Hysteresis loops of as-prepared and stress-annealed microwires

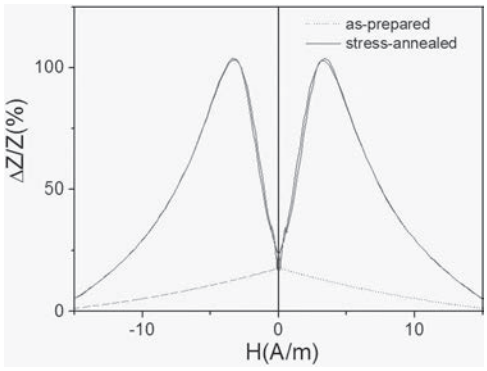


Fig.2 GMI ratio of as-prepared and stress-annealed microwires

FRIDAY MORNING, 8 NOVEMBER 2019 MIRANDA 5, 8:30 TO 11:30

Session GI
SENSORS AND HIGH FREQUENCY DEVICES

Rair Macedo, Chair
University of Glasgow, Glasgow, United Kingdom

CONTRIBUTED PAPERS

8:30

GI-01. Magneto-structural characterization and micromagnetic modeling of Co nanowire arrays for microwave applications up to 30 GHz. *M. Pasquale*[1], D. Gonzales Trabada[2], E.S. Olivetti[1], C.P. Sasso[1], M. Coisson[1], A. Magni[1], F. Garcia-Sanchez[1,3] and M. Vázquez[2] *1. INRIM, Torino, Italy; 2. Instituto de Ciencia de Materiales, CSIC, Madrid, Spain; 3. Applied Physics, Universidad de Salamanca, Salamanca, Spain*

In order to develop novel microwave circuits operating above 10 GHz [1], metallic magnetic systems possessing a combination of high permeability, high saturation magnetization, and high electrical resistivity are desirable. At these frequencies, eddy currents reduce the effective permeability and the simplest method to limit their presence goes through the reduction of the sample cross-section. Unfortunately, a generalized approach to producing tunable high-frequency magnetic materials of sub-micron size with a high density, and a high magnetic anisotropy has yet to be found [2,3]. To this end, ten Co nanowire array samples were grown by electrochemical route in solutions with a pH ranging from 2 to 6.5 using anodic alumina membranes with ~50 nm nanowire diameter and ~100 nm interwire distance (hexagonal lattice) and with a wire length ranging from 1 to 15 um [4]. The samples were analyzed by X-ray diffraction, Scanning Electron Microscopy, vector Vibrating Sample Magnetometry and field swept Ferromagnetic Resonance absorption. The analysis of the frequency vs. applied magnetic field behavior of the arrays was performed using a microwave source with an amplitude-modulated signal (100 kHz-40 GHz), a microwave detector (0.01-50 GHz) and a lock-in amplifier. Each sample was set on a wideband coplanar waveguide positioned in the gap of an electromagnet, and the DC bias field was swept from -1 T to + 1 T along the wire axis, while measuring the microwave absorption at each frequency value in the 1 GHz-40 GHz range. Using the magneto-structural data obtained by XRD and vector VSM as input parameters of the Mumax3 micromagnetic simulation program [5] we were able to successfully reproduce both the static magnetic behavior parallel/perpendicular to the wire axis and the respective microwave absorption spectra. This work shows that by a proper selection of the preparation conditions of Co nanowire arrays (e.g.,pH electroplating), the direction of the anisotropy can be engineered from perpendicular to given angles to the wire axis so that the tuning of the ferromagnetic resonance absorption frequency at zero applied field can be achieved in the 1-30 GHz range, allowing for the development of novel microwave applications.

[1] A. Saib, D. Vanhoenacker-Janvier, *and* I. Huynen Appl. Phys. Lett. 83, 2378 (2003) [2] Mohammad Almasi-Kashi, Mohammad Hossein Mokarian, Sima Alikhanzadeh-Arani J of Alloys and Compounds 742, 25, 413-420 (2018) [3] Shaoli Guo, Liuding Wang, Hongjing Wu Advanced Powder Technology 26, 4, 1250-1255 (2015) [4] Yu P Ivanov, D G Trabada, A Chuvilin, J Kosel, O Chubykalo-Fesenko and M Vázquez Nanotechnology 25 475702 (2014) [5] Arne Vansteenkiste, Jonathan Leliaert, Mykola Dvornik *et al.* AIP Advances 4, 107133 (2014)

8:42

GI-02. Superparamagnetic, Partially-Inverted Ni-ferrite and NiZn-ferrite Thin Film: Promising Material for On-chip RF Inductor Core. *R. Sai*[1], R. Kahmei[1], S. Arackal[1], N. Bhat[1], M. Yamaguchi[2] and S.A. Shivashankar[1] *1. Centre for Nano Science and Engineering, Indian Institute of Science, Bengaluru, India; 2. Dept. of Electrical Engineering, Tohoku University, Sendai, Japan*

The advent of 5G cellular communication escalates the demand for on-chip RF inductor with self-resonating frequency >10 GHz [1]. Continued miniaturization of such passive devices necessitates a magnetic-film core having ferromagnetic resonance (FMR) frequency > 10 GHz. Very few on-chip magnetic-core inductors in and around C-band (6-8 GHz) have been realized and published, excepting those with the core made of thin (t≈500 nm) zinc ferrite (ZF) and manganese-zinc ferrite (MZF) films with FMR at ~26 GHz and ~12 GHz respectively [2, 3]. However, owing to their low μ_r', inductance enhancement only up to 13% could be achieved. Thus, a superior magnetic material and a thicker (>1 μm) film is needed. In this paper, we explore nanocrystalline and superparamagnetic nickel ferrite (NF) and nickel-zinc ferrite (NZF) thick films, expecting superior high-frequency performance to ZF and MZF. Nanocrystalline NF and NZF films with various thicknesses (0.2~1.2 μm) were deposited on Si (100) and Si-CMOS foundry-fabricated inductors by a solution-based, low-temperature (<200 °C), microwave-assisted solvothermal (MAS) process [2]. The deposition rate was high – about 30 nm/min for both compositions. The structure and composition of the films were characterized by XRD, SEM, AFM, XPS, and Raman spectroscopy. The magnetic hysteresis loop was traced by SQUID magnetometry, whereas the frequency dispersion of complex permeability up to 22 GHz was measured by the all-shielded and shorted microstrip line-based technique [4]. Partial inversion in the crystal structure of both NF and NZF was evidenced by Raman spectroscopy (Fig. 1), unlike in bulk NF and NZF. The NF film surface is smooth and uniform (Fig. 1 inset). Both films are in-plane isotropic, with NF showing lower coercivity (25 Oe) than NZF (35 Oe). The μ_r' at C-band is larger in NF than in NZF (Fig. 2) and is 1.4 times more than our reported [3] value in MZF. The FMR frequency in both NF and NZF nanocrystalline thin films is beyond the upper limit of the measurement (22 GHz) - the highest ever reported.

[1] B. Bertenyi et al., J. ICT Stand., vol. 6, no. 1, pp. 31–58, (2018). [2] R. Sai et al., IEEE Magnetics Letters, vol. 8, pp. 3703904, (2017). [3] R. Sai et al., IEEE Transaction on Magnetics (accepted), (2019). [4] S. Takeda et al., J. Jap. Soc. of Powder Metal., vol. 61, pp. 303-307, (2014)

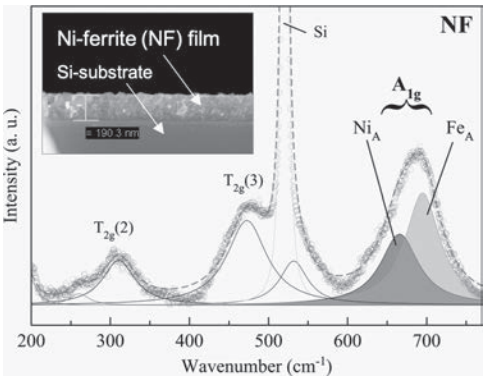


Fig.1 NF film: Raman modes evidencing partial inversion; (inset) SEM image

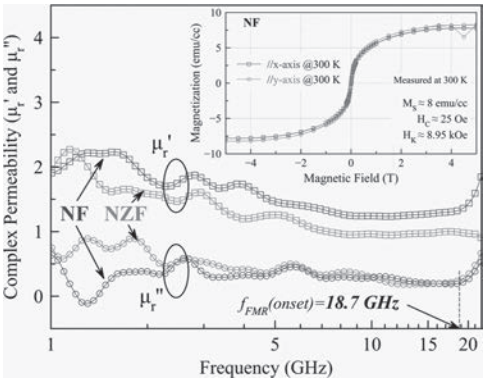


Fig.2 The μ-f plot of NF and NZF exhibiting FMR frequency >20 GHz; (inset) M-H plot of NF film

8:54

GI-03. Giant Magnetoimpedance effect at GHz frequencies in amorphous microwires. V. Zhukova[1,2], M. Ipatov[1,2], P. Corte-Leon[1,2], J. Blanco[2] and *A. Zhukov*[1,3] *1. Dept. Phys. Mater., Univ. Basque Country, UPV/EHU, San Sebastian, Spain; 2. Dpto. Física Aplicada, EIG, Univ. Basque Country, UPV/EHU, San Sebastian, Spain; 3. Basque Foundation for Science, Ikerbasque, Bilbao, Spain*

Studies of Giant Magnetoimpedance (GMI) effect have attracted considerable attention considering various technological applications [1,2]. One of the main tasks in this field is the achievement of the highest GMI effect that will allow improvement of the sensitivity of the magnetic sensors and devices utilizing GMI effect. Additionally, small size and high magnetic field resolution are the features of magnetic field sensors made from magnetically soft microwires [1]. Furthermore, high frequency GMI effect is suitable for development of smart composites with tunable magnetic permittivity [2,3] It must be underlined that the diameter reduction must be associated with the increasing of the optimal GMI frequency range: a tradeoff between dimension and frequency is required in order to obtain a maximum effect [2, 4]. Additionally the GMI effect at microwave frequencies has been described considering analogy between the GMI and the ferromagnetic resonance [4]. Consequently development of thin soft magnetic materials required for miniaturization of the sensors and devices requires an extension of the frequency range for the impedance toward the higher frequencies (GHz range). Accordingly, the purpose of this paper is to study the GMI effect in thin amorphous magnetically soft microwires extending the frequency range up to GHz band. Studies of magnetic properties and GMI effect of amorphous Co-Fe rich microwires reveals that they present GMI effect at GHz frequencies. Magnetic field dependences of GMI effect are affected by the microwires composition, post-processing conditions and geometry. In particularly stress-annealing at certain conditions (time and temperature) allows achievement of better magnetic softness and higher GMI ratio. We observed that in both Co-rich and Fe-rich microwires maximum value of the GMI ratio, $\Delta Z/Z_m$, and the optimal frequency for GMI effect observation have been improved by stress annealing (see Fig.). We discussed observed experimental dependences considering both different magnetic structure and the anisotropy in the bulk and near the surface and close analogy between giant magnetoimpedance and ferromagnetic resonance.

[1] T. Uchiyama, K. Mohri, and Sh. Nakayama, IEEE Trans. Magn., 47, No 10 (2011) pp. 3070-3073 [2] A. Zhukov et.al, J. Alloys Compd., 727 (2017) pp. 887-901. [3] F.Qin, H.-X. Peng, Prog.Mater. Sci,58 (2013) 183–259 [4] D. Ménard et.al J. Appl. Phys. 84, (1998) pp. 2805–2814.

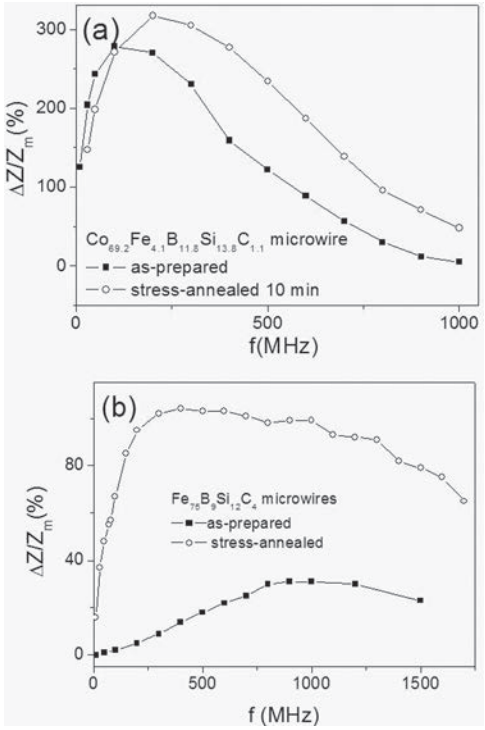


Fig.1 $\Delta Z/Z_m$ (f) for as-prepared and stress-annealed Co and Fe-rich microwires

9:06

GI-04. Ferromagnetic FeCo and Co nanowired substrates based integrated tunable microwave isolator with ultra-wideband application. S. Aslam[2,1], M. Khanna[2] and *B.K. Kuanr*[1] *1. Special Centre for Nanoscience, Jawaharlal Nehru University, New Delhi, India; 2. Department of Electronic Science, University of Delhi, New Delhi, India*

Rapid growth in wireless technology seen a fast evolution in communication systems from 1G to futuristic 5G, which is expected in 2020s. However, it is quite challenging to move to millimeter-wave based 5G technology from the existing devices[1]. Keeping this in mind, we have synthesized 1-D metamaterial in the form of magnetic nanowires(NWs) of FeCo and Co in alumina matrix and designed coplanar waveguide (CPW) based microwave isolators. Prior to isolator design, NWs were characterized by vibrating sample magnetometry:Fig(A). For an ideal isolator, the circularly polarized EM wave should have full transmission in forward direction and full attenuation in reverse direction. The basic principle of the isolator is its *asymmetrical loading* in the CPW:Fig.(B). The present scheme of experiment exhibit non-reciprocal behavior of EM-wave both experimentally and theoretically. In a CPW with NWs (length=30μm) in alumina matrix placed in one-side gap between signal and ground generate circular polarization of RF magnetic field[2]. With a dc magnetic bias (H) parallel to the NWs and perpendicular to propagation direction, the transmission direction of left-hand circular

polarization (LHCP) and right-hand circular polarization (RHCP) are opposite. In this investigation, non-reciprocity was found where $(M_i h_{rf}) \perp k$, as whole magnetic volume of the sample interacts with h_{rf}. We have observed maximum isolation of 9.0 dB with an insertion loss of ~2.0 dB at 27.0 GHz at H=6.0 kOe. Further, we tune the frequency of the device from 21.0 GHz to 37.0 GHz with H from 3 to 10 kOe. Isolation has been demonstrated in a broad frequency range. Using a micromagnetics [3] approach the simulated h_{rf} distribution for forward (+k) and reverse (-k) wave propagation exhibit non-reciprocity. We have model an NWs-alumina matrix of thickness 30 μm, and length and breadth of 3 mm each in one side of the CPW. The matrix is partitioned into a grid with μm size cells through the thickness, length and breadth. While these are large cells, this is sufficient for looking at the transmission parameters (S_{21}, S_{12}). The proposed schemes are potentially helpful to identify the essential requirements of a planar two-port isolator useful for 5G frequency.

References: [1] P. Gupta, "Evolvement of mobile generations: 1G to 5G," Int. J. Tech. Res. Eng., vol. 1, p. 152-157, (2013) [2] Rongdi Guo, Hwaider Lin, Wei Shi, Yuan Gao, Zhiguang Wang, Nian Xiang Sun, Zhong Yu, and Zhongwen Lan; AIP ADVANCES Vol.8, p.056620 (2018) [3] Bijoy K. Kuanr, V. Veerakumar, Ryan Marson, Sanjay R. Mishra, R. E. Camley, and Z. Celinski; APPLIED HYSICS LETTERS Vol.94, p.202505 (2009).

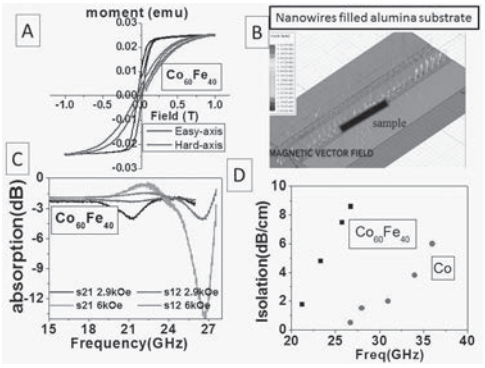


Fig.1 NWs isolator

9:18

GI-05. 400MHz MEMS Antenna Based on Magnetoelectric Coupling Effect. *H. Chen*[1], X. Liang[1], N. Sun[1], H. Lin[2], Y. Gao[2] and N.X. Sun[1,2] *1. Northeastern University, Boston, MA, United States; 2. Winchester Technologies, LLC, Burlington, MA, United States*

Abstract – 400MHz frequency band is the most commonly used band for Medical Implant Communications Service (MICS). However, most of recent antenna researches for this application are based on electromagnetic wave resonance, which lead to a comparable size to the wavelength [1, 2]. To solve this problem, a new antenna design based on the magnetoelectric coupling is introduced by our group [3], which is a thin-film bulk acoustic resonance (FBAR) antenna for 2.5GHz applications, based on the AlN resonator and magnetoelectric coupling. Since acoustic wave has smaller wavelength than electromagnetic wave, the antenna size can be easily scaled down by more than 100 times. However, for most AlN resonator designs, impedance matching is a problem because of the high electric impedance. Hence, a parallel antenna array structure is applied to reduce the impedance and increase the antenna gain [4]. In this work, nano-plate resonance (NPR) antenna arrays for 400MHz application are designed, fabricated and tested. This antenna is based on the magnetoelectric coupling between AlN thin film and FeGaB/SiO_2 multilayer. The antenna array structure is shown in Fig. 1 (a) with 8um width and array numbers of 1,4, 8 and 16. This strip structure resonates at in-plane mode, and this resonance is limited in width direction by the strip. The measured S-parameters are shown in Fig. 1 (b), with operating frequency of 371MHz, and 10dB-bandwidth of 3.875MHz. A radiation peak of S_{21} is observed clearly at the resonant frequency, and a peak antenna gain of -54.82dBi is achieved. This radiation peak is from the vibration and domain rotation of magnetic film. The measured S_{11} and calculated Z_{11} are shown in Fig. 2. For fewer array numbers, the impedance is higher, and the related return loss is also higher, so the radiation peak is cover by the baseline. For this reason, array structure with more than 16 strips is necessary for impedance matching and high antenna gain.

[1] C. Liu, Y.-X. Guo, and S. Xiao, "Compact dual-band antenna for implantable devices," *IEEE Antennas and Wireless Propagation Letters,* vol. 11, pp. 1508-1511, 2012. [2] N. Cho, T. Roh, J. Bae, and H.-J. Yoo, "A planar MICS band antenna combined with a body channel communication electrode for body sensor network," *IEEE Transactions on Microwave Theory and Techniques,* vol. 57, no. 10, pp. 2515-2522, 2009. [3] T. Nan *et al.*, "Acoustically actuated ultra-compact NEMS magnetoelectric antennas," *Nature communications,* vol. 8, no. 1, p. 296, 2017. [4] R. Gardelli, M. Albani, and F. Capolino, "Array thinning by using antennas in a Fabry–Perot cavity for gain enhancement," *IEEE Transactions on Antennas and Propagation,* vol. 54, no. 7, pp. 1979-1990, 2006.

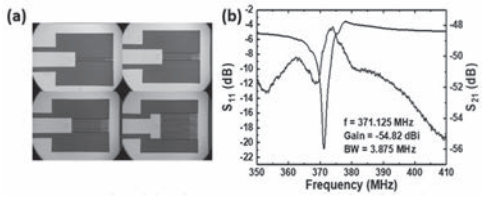


Fig.1. (a) Optical top view of NPR antenna with different array numbers; (b) measured S_{11} and S_{21} of 16-array antenna

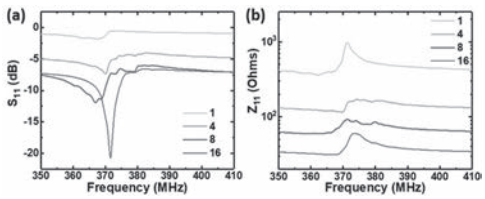


Fig.2. (a) Measured S_{11} and (b) calculated Z_{11} of NPR antenna with 1, 4, 8, 16 arrays

9:30

GI-06. Design and Fabrication of ZnO-Based SMR Magnetoelectric Antennas for High-Gain Applications. *X. Liang*[1], H. Chen[1], N. Sun[1], Y. Gao[2], H. Lin[2] and N. Sun[1] *1. Northeastern University, Boston, MA, United States; 2. Winchester Technologies, LLC, Burlington, MA, United States*

Magnetoelectric (ME) antennas based on the suspended ME circular disk consisting of FeGaB/AlN thin-film have been demonstrated recently [1]. However, the FBAR devices are very fragile and delicate due to the releasing structure, although the complicated packaging process [2]is able to solve this problem. From the device point of view, the solid mounted resonator (SMR) with Bragg reflector has attracted much attention as a promising technology for the film bulk acoustic wave resonator (FBAR) devices [3]. Typically, the SMR devices are formed of a piezoelectric film, such as ZnO that is sandwiched between top and bottom metal electrodes, on top of a Bragg reflector. A resonance is created when a radio frequency (RF) signal is applied across the FBAR device. There are a variety of products such as filters [4], duplexers [4], and voltage controlled oscillators (VCOs) [5] based on SMR designs have been developed in past years. In this work, we designed, fabricated and tested ZnO-based SMR ME antennas that operate at GHz with high gain performance. As shown in Fig. 1, the Bragg reflector consisting of three pairs of SiO_2/W layers was sputter deposited in one run with RF reactive magnetron sputtering for $SiO_2$and DC sputtering for W. The piezoelectric ZnO layer was sputter deposited by RF reactive sputtering with Zn target and high-purity Oxygen gas. The XRD curves and rocking

curves for ZnO films under different temperature were measured and exhibited in Fig. 2. In order to grow high quality ZnO films, it is vital to have sufficient ion bombardment during deposition. Therefore, high temperature of 450 degrees Celsius is preferred here with rocking curve FWHM of 2.25 degrees. After optimizing the performance of Bragg reflector and piezoelectric ZnO films, we fabricated and tested the SMR ME antennas. A gain enhancement of 12 dB was achieved in this novel design for robust ME antennas. Therefore, it is very promising in practical applications.

[1] T. Nan, H. Lin, Y. Gao, A. Matyushov, G. Yu, H. Chen*, et al.*, "Acoustically actuated ultra-compact NEMS magnetoelectric antennas," *Nature communications,* vol. 8, p. 296, 2017. [2] J. D. Larson III, S. Ellis, and Y. Oshmyansky, "Film bulk acoustic resonator (fbar) devices with simplified packaging," ed: Google Patents, 2008. [3] R. Ruby, "11E-2 Review and comparison of bulk acoustic wave FBAR, SMR Technology," in *2007 IEEE Ultrasonics Symposium Proceedings*, 2007, pp. 1029-1040. [4] R. Ruby, P. Bradley, D. Clark, D. Feld, T. Jamneala, and K. Wang, "Acoustic FBAR for filters, duplexers and front end modules," in *2004 IEEE MTT-S International Microwave Symposium Digest (IEEE Cat. No. 04CH37535)*, 2004, pp. 931-934. [5] R. Boudot, M. Li, V. Giordano, N. Rolland, P. Rolland, and P. Vincent, "A solid-mounted resonator-oscillator-based 4.596 GHz frequency synthesis," *Review of Scientific Instruments,* vol. 82, p. 034706, 2011.

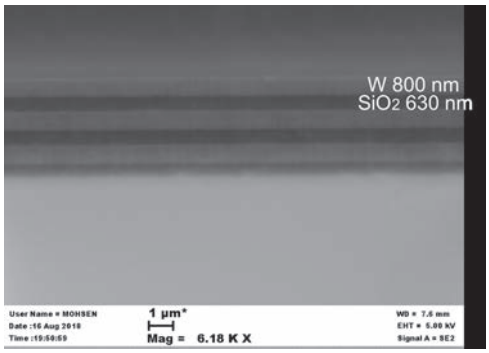


Fig. 1 SEM cross-section image of Bragg reflector.

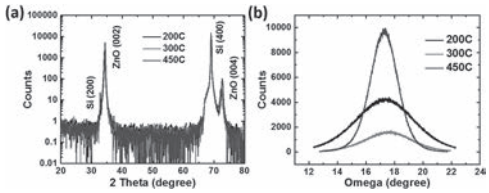


Fig. 2 (a) XRD curves of ZnO films deposited with increasing temperature.(b) Rocking curves of ZnO films deposited with increasing temperature.

9:42

GI-07. Electrically Small Multiferroic Antenna Enhanced by Energy Reelecting Components. *J. Hu*[1,2], W. Yan[1], G. Carman[1] and A. Sepulveda[1,2] *1. Mechanical & Aerospace Engineering Department, UCLA, Los Angeles, CA, United States; 2. Vilya Nanotechnologies, Inc, Los Angeles, CA, United States*

Conventionally, antennas such as dipoles and loops rely on an electromagnetic (EM) wave resonance, therefore the sizes of such antennas are within the same order of free space wavelength. Electrically small antennas (i.e. size < λ/10) at ultra-high frequency hold promises for reducing the antenna system's size, weight and volume, yet state-of-the-art electrically small antennas confront a daunting challenge. So far, electrically small antennas radiate poorly when placed near a conducting surface because of platform effects. Recently, induced strain-mediated multiferroic composites interconvert between alternating magnetization and mechanical strain wave with ultra-high energy efficiency due to negligible current and Ohmic loss. Several reports of such devices, modified from thin-film bulk acoustic resonator (FBAR), have demonstrated a new concept on electrically small antenna[1-4]. However, until now, fabrication challenges hindered attempts at forming large scale antenna arrays to improve the signal strength. This work demonstrates a new strain-mediated multiferroic antenna that relies on lamb wave resonance of piezoelectrical substrate such as Aluminum Nitride (AlN). Oscillation of Ni micro elements excited by free space EM wave is detected by comb-shaped arrays of metallic electrodes through out-of-plane electrical field. Surrounding the Ni micro elements and comb-shaped electrodes there are acoustic gratings and Bragg acoustic mirror to reflect the acoustic energy to form a standing wave and prevent energy dissipation[5]. At least -40dBm radiation power is expected according for a 10dBm's energy be input to a 2cm*2cm antenna in the numerical finite element model. Based on the model and Monte-Carlo optimization on the structure, we designed the system and we plan to fabricate a device and made preliminary tests on it. This work demonstrates the feasibility of shear mode strain-mediated multiferroic antenna, which shows promising potential for the next-generation electrically small antenna at ultra-high frequency.

[1] Z. Yao and Y. Ethan Wang, "Dynamic analysis of acoustic wave mediated multiferroic radiation via FDTD methods," *IEEE Antennas Propag. Soc. AP-S Int. Symp.*, pp. 731–732, 2014. [2] Z. Yao, Y. E. Wang, S. Keller, and G. P. Carman, "Bulk Acoustic Wave-Mediated Multiferroic Antennas: Architecture and Performance Bound," *IEEE Trans. Antennas Propag.*, vol. 63, no. 8, pp. 3335–3344, 2015. [3] S. Tiwari, P. Nordeen, Q. Xu, Z. Yao, Y. E. Wang, G. P. Carman, and R. N. Candler, "Ferromagnetic Resonance in Bulk-Acoustic Wave Multiferroic Devices," vol. 1, no. 1, pp. 420–423, 2016. [4] J. P. Domann and G. P. Carman, "Strain powered antennas," *J. Appl. Phys.*, vol. 121, no. 4, 2017. [5] Arapan L., Katardjiev I., Yantchev V. (2012) An intermode- coupled thin-film micro-acoustic resonator J. Micromech. Mi- croeng. 22(8): 085004

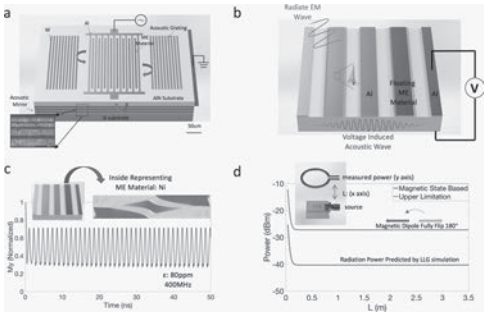


Fig.1 (a) Structure of lamb wave multiferroic antenna. (b) Working principle of multiferroic antenna. (c) Magnetic state in Nickel element. (d) Radiation power predicted by dipole-dipole assumption.

9:54

GI-08. Tunable Properties of Microwave Absorber and FMR Relaxation for GO Doped $MnFe_2O_4$ Nanoparticles. *A. Mishra*[1] and B.K. Kuanr[2] *1. School of Physical Sciences, Jawaharlal Nehru University, New Delhi, India; 2. Special Center for Nanoscience, Jawaharlal Nehru University, New Delhi, India*

In the present investigation, the reduced manganese ferrite/ graphene oxide ($MnFe_2O_4$/rGO) nanocomposites with different weight amounts of GO sheets have been synthesized using a simple and efficient one-step hydrothermal method. The crystallinity, morphology and magnetic studies were conducted using X-ray diffraction (XRD), confocal Raman imaging and vibrating sample magnetometry (VSM). The electromagnetic and microwave power absorption properties were examined in a broad frequency range of 5-30 GHz using a Keysight vector network analyzer. The largest ferromagnetic resonance (FMR) absorption of 27.5 dB of electromagnetic power was observed when the weight of GO sheets in maximum in the nanocomposites at the 22GHz frequency. The FMR relaxation and damping

parameters can be tuned by adding of GO sheets in $MnFe_2O_4$/rGO nanocomposites at specific frequency. It is observed that the damping parameters decreases if the weight amount of GO sheets increases in the nanocomposites. The micromagnetic model was used to calculate FMR linewidth as well as both intrinsic and extrinsic damping parameters of the $MnFe_2O_4$/rGO nanocomposites. Therefore, due to above properties $MnFe_2O_4$/rGO nanocomposites have various applications in the field of microwave absorber as well as in high speed microwave monolithic devices and amount circuits.

10:06

GI-09. High-gain Wideband Miniature Axial-mode Helical Antenna with Multi-layer Ferrite and Dielectric Structure. *H. Won*[1], Y. Hong[1,3], W. Lee[1,2] and M. Choi[1] *1. Department of Electrical and Computer Engineering and Center for Advanced Vehicle Technologies, The University of Alabama, Tuscaloosa, AL, United States; 2. RF Product Development Group, Samsung Electro-Mechanics, Suwon-si, The Republic of Korea; 3. Alabama Transportation Institute, Tuscaloosa, AL, United States*

For many advantages, the axial-mode helical antenna (AM-HA) received much attention for satellite communications. For the conventional AM-HA, either air (AC) or dielectric-core is employed but results in large antenna volume (*V*). A lossy ferrite-core/dielectric-shell (FD) structure was used for AM-HA to reduce the *V* without sacrificing gain, but with the expense of 400 MHz of axial ratio at boresight below 3 dB (AR_{3dB}), compared to that of air-core [1]. To address this issue, we propose high-gain wideband miniaturized N-layer FD-AM-HA (N-FD-AM-HA), where N is equal to 1, 2, and 3. All antennas were simulated for antenna performance using ANSYS HFSS. The specifications and designs of AC- and N-FD-AM-HAs are summarized in Fig. 1. To realize the *V* reduction by N-FD loading, the AC-AM-HA of 55 cm^3 was designed and compared with the N-FD-AM-HAs of 40 cm^3 for antenna performance. For accurate comparison between N-FD-AM-HAs, same ferrite-core (permeability (μ_r)=2, permittivity (ε_r)=7, dielectric/magnetic loss tangent ($\tan\delta_e/\tan\delta_u$)=0.01/0.1, and *V*=10.6 cm^3) and dielectric-shell (μ_r=1, ε_r=2.3, $\tan\delta_e/\tan\delta_u$=0.01/0, and *V*=15.6 cm^3) are used [1]. Fig. 2 shows the simulated antenna performances. From Fig. 2, all antennas resonate at 2.25 GHz, show 8.85 dBic of the peak realized gain (RG), and start AR_{3dB} at 2.83 GHz, indicating 27% *V* reduction without sacrificing RG from lossy FD loading. However, as Fig. 2 (b) and (c) show, low RG of 4.7 - 6.5 dBic above 3.2 GHz and narrow AR_{3dB} of 1.18 GHz were observed for the 1-FD-AM-HA. These issues were solved by adopting a multi-layer structure. The 2- and 3-FD-AM-HA show not only 0.8 - 0.9 dBic and 1.1 - 1.5 dBic higher RG but also 270 and 310 MHz higher AR_{3dB}, respectively, than those of the 1-FD-AM-HA. Further, the 2- and 3-FD-AM-HA show similar RG and AR_{3dB} compared to that of AC-AM-HA. Thus, multi-layer FD loading not only can effectively miniaturize antenna but also improve antenna performance. This work was supported in part by the NSF-I/UCRC for EV-STS under Grant number 1650564.

[1] W. Lee, Y. Hong, and H. Won, *IEEE Ant. Wirel. Propag. Lett.* vol. 18, p. 951 (2019).

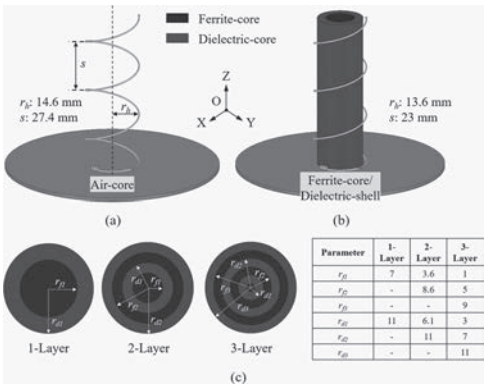


Fig. 1. Design and specifications of (a) AC- and (b-c) N-layer FD-AM-HA.

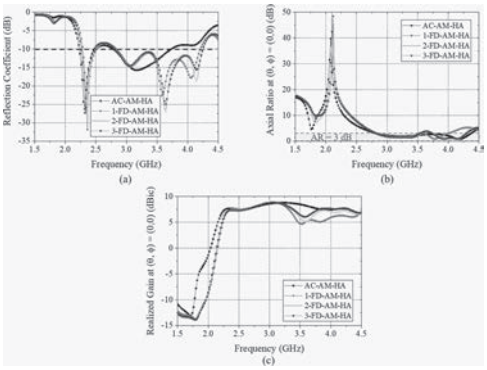


Fig. 2. Simulated AC and N-FD-AM-HA antenna performances: (a) reflection coefficient, and (b) RG and (c) axial ratio at bore-sight.

10:18

GI-10. Efficient Adjustment of Finite Graphene Scattering Properties via Magnetic-bias Control for Advanced Beam Manipulation. S. Amanatiadis[1], T. Ohtani[2], *Y. Kanai*[3] and N. Kantartzis[1] *1. Electrical and Computer Engineering, Aristotle University of Thessaloniki, Thessaloniki, Greece; 2. 1-17-134 Omachi, Asahikawa, Japan; 3. Niigata Institute of Technology, Kashiwazaki, Japan*

In the present work, the scattering of an incident plane wave due to magnetically-biased graphene patches is thoroughly investigated at millimeter-wave and THz bands. Graphene is placed perpendicular to the propagation of the incident wave, as depicted in Fig. 1 along with the 3D radar cross-section and static bias fields are applied to control its surface conductivity. Especially, magnetostatic bias is activating anisotropic effects due to the Lorentz forces on electrons, thus revealing various interesting phenomena, such as gyrotropy, non-reciprocity and magnetoplasmon propagation [1]. It is evident that bias control is able to tune the scattering properties and this is confirmed in Fig. 2, where the radar cross-section at a plane normal to graphene is illustrated. Specifically, as the strength of bias decreases, the transmitted wave is lower at the direction of propagation, namely 0^o, compared to a slight angle of approximately $\pm 10^o$. This effect is justified due to the magnetoplasmon surface wave that is propagating on graphene. The excitation of magnetostatic bias is implemented effectively via circular loops since the dimensions of graphene patches are in the micrometric order and relatively strong fields can be induced using coils of small radius. Moreover, the efficient adjustment of the bias field is achieved utilizing high-speed electronics that activate the desired number of active loops. It is worth to mention, that this kind of excitation is considered in the full-wave simulations to investigate the possible influence of the loops on the plane wave propagation. Finally, the extracted results from the previous analysis are

evaluated appropriately to design an array of graphene patches, of different magnetic-bias fields, to investigate the potential of advanced beam manipulation. All numerical results are extracted via an accurate modification of the popular Finite-Difference Time-Domain scheme [2].

[1] D. Sounas and Christophe Caloz, "Gyrotropy and nonreciprocity of graphene for microwave applications." IEEE Transactions on Microwave Theory and Techniques, Vol. 60, No. 4, p.901-914 (2012). [2] S. Amanatiadis, N. Kantartzis, T. Ohtani and Y. Kanai, "Precise Modeling of Magnetically Biased Graphene Through a Recursive Convolutional FDTD Method." IEEE Transactions on Magnetics, Vol. 54, No. 3, p.1-4 (2017).

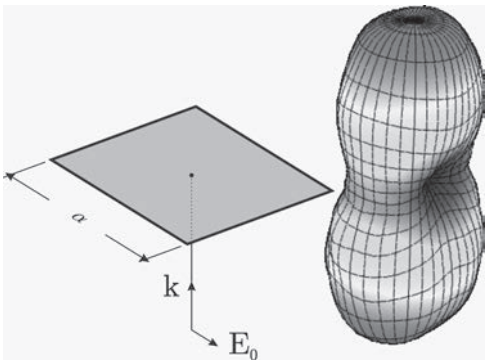


Fig.1 Plane wave propagation towards magnetically-biased graphene patch and the calculated radar cross-section.

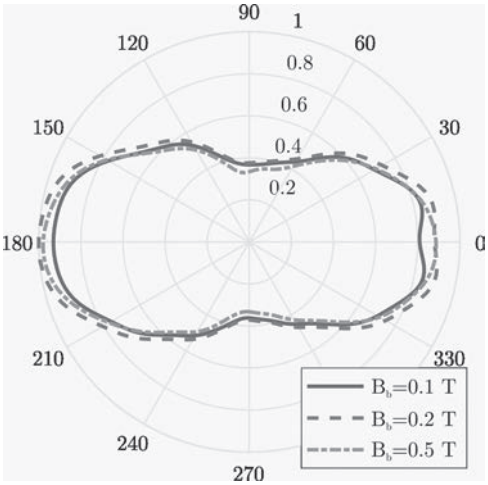


Fig.2 Radar cross-section of the plane that is perpendicular to graphene surface and the polarization of the incident wave at 1 THz.

10:30

GI-11. Near-Field Probing of the Effective Electromagnetic Shielding Using CoZrTaB Thin Films. *P. Miller*[1], Y. Wu[1] and H. Yu[1] *1. Arizona State University, Tempe, AZ, United States*

With rapidly decreasing electronic size and increasing multi-functionality that oftentimes mixing RF and digital circuit close to each other, it is critical to provide sufficient electromagnetic shielding between functional circuits to prevent electromagnetic noise interference. The unique resistivity and magnetic properties documented for the material indicate that it may well-suited to provide effective shielding, and is particularly applicable for Internet-of-Things (IoT) devices and others operating in the 5G spectrum. This work focuses on analyzing the variance in shielding effectiveness and electromagnetic field effects of a thin film of Cobalt-Zirconium-Tantalum-Boron (CoZrTaB) in the band of frequencies most likely to require innovative solutions to long-standing problems of noise and interference [1,2]. The CoZrTaB films were sputter-deposited onto silicon or polyimide substrate, with film thickness varying in the range of several hundreds nanometer to demonstrate the thickness effect, as well as multi-layered structure magnetic film and compared with Cu film of thickness on the order of a few micrometers. The measurements were performed using a commercial probing system that include Near H-Field attenuation and field effects, Far Field shielding, and Backscatter, with sample placed on microwave stripline (Fig.1) Minor variances in the thickness and layering of sputter deposition can have significant changes electromagnetic signature of devices which radiate energy through the material, as shown in Fig. 2. The material properties presented in this research are H-Field attenuation, H-Field Flux Orientation, Far-Field Approximation, E Field Vector Directivity, H Field Vector Directivity, and Backscatter Magnitude. The results demonstrated the effective shielding of thin CoZrTaB magnetic film compared to much thicker Cu film, across broad frequency range between 1.25-5.75 GHz, with average shielding effectiveness across all samples and frequencies over 13.9 dBm.

1. J. Choi, X. Cao, and D. Maslyk, "Component Level EMI Shielding for Semiconductor Packages," (2017). Henkel and Associates. 2. M. Yamaguchi, S. Tanaka, Y. Endo, S. Muroga, and M. Nagata, "On-chip integrated magnetic thin-film solution to countermeasure digital noise on RF IC," in *Proc. IEEE Asia–Pacific Symp. Electromagn. Compat. (APEMC)*, May 2015, pp. 536–539.

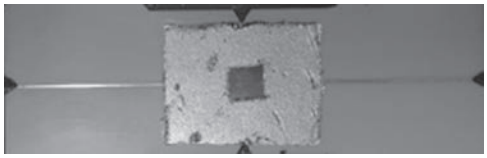


Fig. 1 Microwave stripline with magnetic film under test.

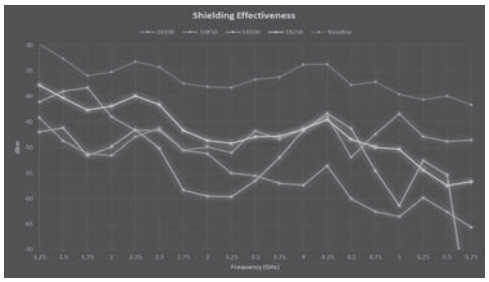


Fig. 2 Shielding effectiveness using magnetic thin films.

10:42

GI-12. Tunable Band-Stop Frequency Selective Surface by Permeability Control of Ferromagnetic Material. *J. Ge*[1] and G. Wang[1] *1. Electrical Engineering, University of South Carolina, Columbia, SC, United States*

Tunable frequency-selective surfaces (FSSs) attracted great interest in recent years as tunable filters for reconfigurable antenna systems, for tunable radar absorbers, or to provide a varying transmission window in radomes [1]. Traditional magnetically tunable FSSs are implemented by using a ferrite substrate with controllable permeability. This type of FSSs suffers from several disadvantages, i.e., low tuning speed and small tuning range [2]. To overcome these problems, in this paper, a ferromagnetic layer controlled by the biasing circuit is employed to cover the metal layer of FSS. The ferromagnetic layer can change the effective permeability of FSS by different inputs of the biasing circuit, leading to the variable resonant frequencies. A simple FSS using the square loop as a unit cell is employed in this paper to verify the proposed concept [3]. This FSS shows a band-stop filtering response since it strongly reflects an incident plane wave at the resonant frequency. The equivalent circuit of this FSS is given as a series LC network, which means the equivalent inductance is critical to the resonant frequency.

Meanwhile, the inductance can be changed by variable effective permeability caused by the ferromagnetic layer. In addition, permalloy ($Ni_{80}Fe_{20}$) is employed to form the ferromagnetic layer. Then, a tunable FSS can be achieved by permeability control of the ferromagnetic layer with the biasing circuit. Fig 1 shows the simulated results of the proposed FSS with different effective permeability. The results exhibit a frequency tuning range from 4.8GHz to 6.4GHz with peak attenuation greater than -41dB. Compared with traditional magnetically tunable FSSs, the proposed design shows a wider tuning range and a higher tuning speed.

[1] L. Boccia, I. Russo, G. Amendola, et al., "Tunable frequency-selective surfaces for beam-steering applications," Electron. Lett., vol. 45, no. 24, pp. 1213–1214, Nov. 2009. [2] T. K. Chang, R. J. Langley, and E. A. Parker, "Frequency selective surfaces on biased ferrite substrate," IEE Electron. Lett., vol. 30, no. 15, pp. 1193–1194, Jul. 1994. [3] Rashid A. K, Li B, Shen Z. "An overview of three-dimensional frequency-selective structures". IEEE Antennas and Propagation Magazine, vol. 56, no. 3, pp. 43-67, 2014.

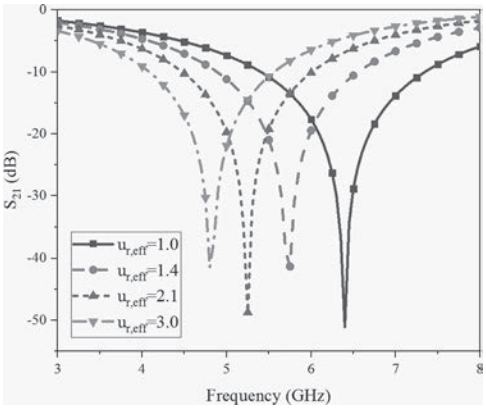


Fig.1 Full-wave simulated results of the proposed FSS with different effective permeability.

10:54

GI-13. Hexagonal Nano-ferrites used on a V-band Self-bias On-chip Circulator for CMOS. *M.N. Afsar*[1], V. Koomson[1] and W. Quam[1] *1. ECE, Tufts University, Medford, MA, United States*

Hexagonal ferrite materials such as BaFe12O19 and SrFe12O19 have strong anisotropic magnetic field and strong remnant magnetism. These properties enable the working frequency of devices such as phase shifter, isolator and circulator, move up to tens of GHz without a strong external bias field and even achieve self-biasing. The advantage of ferrite devices such as passive circulators are their low insertion loss, high isolation, broad bandwidth and high power handling ability compared to their active counterparts. Ferrite circulators consume no power and are more suitable for lower-power applications because these are passive, unlike active quasi circulator, In this work, thin film ferrite material was deposited by employing spin-casting method [Liu 2013] and patterned with the help of Chemical-Mechanical Polishing (CMP). The spin-casting is a low-temperature process: the nano-sized barium ferrite materials can be processed into composite and spin-casted into thin film layer. This method requires only 120°C baking under external biasing filed. This is advantageous when future integration with CMOS is taken into consideration. In this paper, we present the design, simulation, fabrication and measured results of a self-bias micro-strip line Barium hexagonal Nano-ferrite (BaM) circulator on silicon wafer. This planar Y-junction circulator is 2mm by 2mm by 0.5mm in size, which is capable of future integration with the top three layers of 180nm CMOS technology. Ferrite thin film is deposited and patterned employing composite spin-casting method. Typical characterization techniques are employed together with free-space quasi-optical spectrometry to study complex permittivity and permeability of deposited film up to 120GHz. S parameters of fabricated circulators are characterized by a set of on wafer probes up to 67GHz. We observed over 15dB non-reciprocal phenomenon at 55GHz. The probes setting is shown in Fig. 1. The measured S-parameter are shown in Fig. 2.

L. Chao, H. Oukacha, E. Fu, V. J. Koomson, and M. N. Afsar, "Millimeter wave complementary metal–oxide–semiconductor on-chip hexagonal nano-ferrite circulator", *Journal of Applied Physics*, vol. 117, pp. 17C123 (2015) L. Chao, H. Oukacha, E. Fu, V.J. Koomson, M.N. Afsar, "Millimeter wave hexagonal nano-ferrite circulator on CMOS substrate," *IEEE International Microwave Symposium*, pp. 1 – 4, 2014. L. Chao, E. Fu, V. J. Koomson, M.N. Afsar, "Millimeter Wave Complementary Metal-Oxide-Semiconductor on-chip Hexagonal Ferrite Circulator", *Journal of Applied Physics*, vol. 115, no. 17, pp. 17E511-17E511-3, 2014.

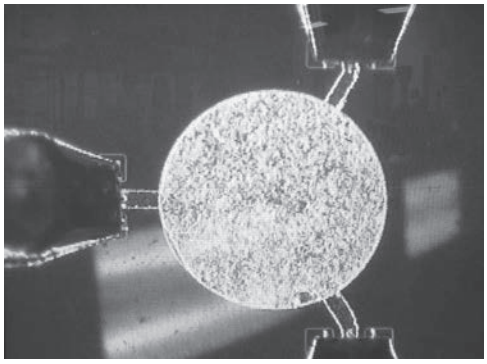


Fig.1 Three ports probing of fabricated circulator

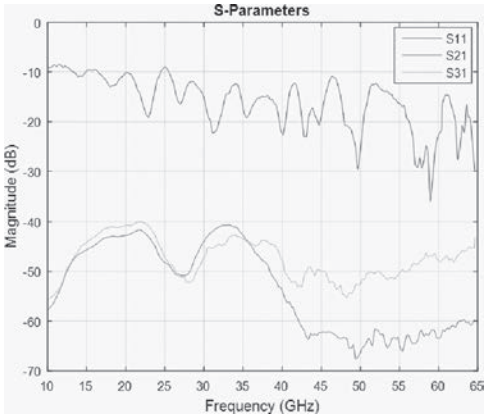


Fig.2 Measured S-parameter of fabricated ferrite circulator

11:06

GI-14. Structural and magnetic properties of La^{3+} substituted Co_2Z hexaferrites for tele-communicational antennas and EMI shielding applications. *A. Singh*[1] and P. Sharma[1] *1. School of Physics and Materials Science, Thapar Institute of Engineering and Technology, Punjab, Patiala, India*

Co_2Z hexaferrite ($Ba_{3-x}La_xCo_2Fe_{24}O_{41}$ with x = 0.0-0.2 and 0.6) were synthesized using solid state reaction method. X-ray diffraction confirmed the single Z-type phase formation with x = 0.0 to 0.2 and for x = 0.6, Z-type coexist with W-type. The lattice parameters were found to increase with La doping. The magnetic measurements were carried out using the Vibrating Sample Magnetometer (VSM). The saturation magnetization (M_s), magnetic coercive force (H_c) and retentivity (M_r) were increased with La content in the samples. The microstructure morphology showed that the hexagonal plate like grains appeared in pure and hexagonality and grain growth increased with La substitution. The increasing M_s indirectly played an important role between antenna operating and cutoff frequencies on the basis of its

increasing resonance frequency [1-3]. The bandwidths increased and the length of antennas decreased with the magneto-dielectric materials [4,5]. The big hexagonal grains materials are suitable for radar absorbing and EMI shielding technology because its dielectric losses increased. Therefore, La substituted Co_2Z hexaferrite can be used in miniaturized antenna fabrication and radar absorption materials.

1.J. Lee, Y. K. Hong, W. Lee, G.S. Abo, J. Park, W.M. Seong and S. Bae, IEEE Magn. Lett. 4, 5000104 (2013). 2. L. Zhang, A. Puri, K. Sertel, J. L. Volakis and H. Verweij, IEEE Trans. Magn. 47, 2149-2152 (2011). 3. H. Aoyama, M. Gonda, S. Fujii and S. Tankano, US Patent: 7821468B2 (2010). 4. M. Gonda and H. Aoyama, EP Patent: 1798210A1 (2007). 5. S. Bae, Y. K. Hong, J. J. Lee, J. Jalli, G. S. Abo, W.M. Sung, G. H. Kim, S.H. Park, J. S. Kum and H. M. Kwon, IEEE Trans. Magn. 45, 4199-4202 (2009).

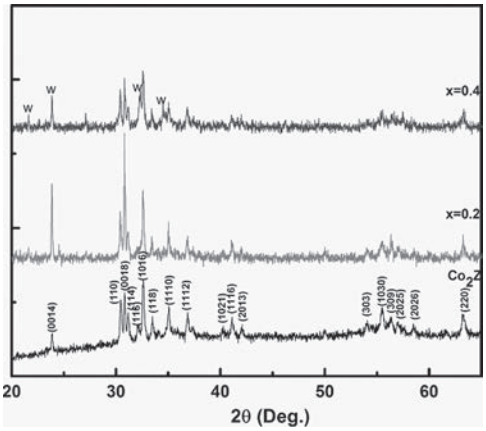


Fig.1 X-ray diffraction patterns of $Ba_{3-x}Co_2Fe_{24}O_{41}$ (with x = 0.0, 0.2 and 0.6) sintered samples at 1250^0C for 1h.

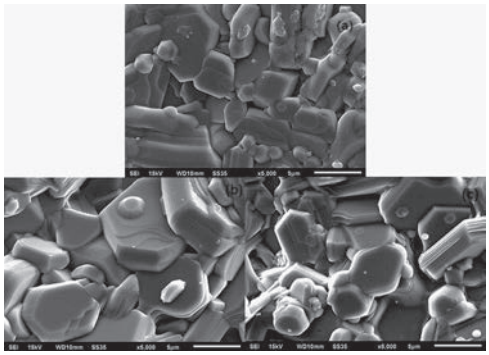


Fig.2 SEM microgaphs of $Ba_{3-x}Co_2Fe_{24}O_{41}$ (with x = 0.0, 0.2 and 0.6) sintered samples at 1250^0C for 1h.

Session GP
DOMAIN WALLS AND SPIN-ORBIT TORQUE (Poster Session)

Eduardo Martinez, Co-Chair
Universidad de Salamanca, Salamanca, Spain
Helmut Schultheiss, Co-Chair
Helmholtz-Zentrum Dresden-Rossendorf, Dresden, Germany

GP-01. Domain wall motion-based spin synapsis-neuron functions manipulated by spin orbit torque in heavy metal / CoFeB/ MgO stacks.
J. Shin[1], J. Choi[2], Y. Ji[2], S. Yang[3], J. Yang[4] and J. Hong[1,2] *1. Nanoscale Semiconductor Engineering, Hanyang University, Seoul, The Republic of Korea; 2. Physics, Hanyang University, Seoul, The Republic of Korea; 3. Kriss, Daejeon, The Republic of Korea; 4. Physics, Kunsan University, Kunsan, The Republic of Korea*

Neuromorphic computing architectures basically aims to mimic brain-like behaviors through the combination of neurons strongly inter-connected by huge synapses [1, 2]. There are two key devices: artificial neuron and synapsis devices that should be carefully designed to achieve extremely low power operation and highly integrated density in a compact size. Here, we address the performance of domain wall motion (DWM), driven by spin orbit torque (SOT) -based neuron and synapsis functionality in heavy metal / CoFeB/ MgO frames under continuously repeated electrical stimulus.[3] Firstly, an in-plane direct current (DC) measurement approach was employed to identify spin orbit torque-driven effective fields without adopting the commonly used harmonic analyses, as seen in Fig. 1.[4] Proper manipulation of SOT-driven domain wall motion (DWM) under various positive/negative current pulses led to gradual variation in temporal synaptic weight: in particular, demonstration of long-term potentiation functionalities. In addition, artificial spiking neuron functions ensuring an integrate-fire (IF) behaviors in an asymmetric hall bar were detected by utilizing the input current pulses that were similar to the DC analysis current used for magnetization switching. Typical IF behaviors were shown in Fig. 2, along with the DWM along the hall bar under consecutively applied current pulses. The MOKE images clearly indicated that the neuron functions in our Heavy metal / CoFeB / Mgo frame came from SOT-driven DWM. More parameter details of the devices will be presented in the conference.

[1] Shuai Zhang, Shijiang Luo, Nuo Xu., ADVANCED ELECTRONIC MATERIALS., Vol. 5, p. 1800782 (2019) [2] Steven Lequeux, Joao Sampaio, Vincent Cros., SCIENTIFIC REPORTS., Vol. 6 p. 31510 (2016) [3] Abhronil Sengupta, Sri Harsha Choday, Yusung Kim., Applied physics letters., Vol. 106 p. 143801 (2015) [4] Seungmo Yang, Jinhyung Choi, Junghun Shin., SCIENTIFIC REPORTS., Vol. 8 p. 11065 (2018)

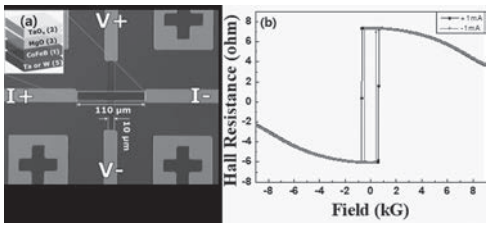


Fig 1. Magnetic features under a DC source for two measurement schemes. (a) Optical image of Hall bar device. (b) Hall resistance versus H field parallel to the positive (black line) and negative (red line) current with a magnitude of 1 mA.

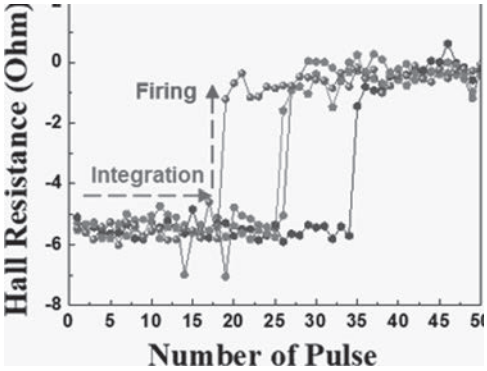


Fig 2. Resistance and Domain wall dynamics. SOT-based neuron function, in which the neuron functions were stimulated by the square waveforms of the current pulse.

GP-02. Ion-Beam Controlled Switching Field Distributions in the Low Coercivity Regime.
S. Mendisch[1], M. Kiechle[1], V. Ahrens[1], A. Papp[1] and M. Becherer[1] *1. Department of Electrical and Computer Engineering, Technical University of Munich (TUM), München, Germany*

Perpendicular Nanomagnetic logic (pNML) is a form of domain-wall (DW) logic utilizing the anti-parallel stray fields of next-neighbor nanomagnetic islands with perpendicular magnetic anisotropy (PMA) to process information [1]. In the past, we published a comprehensive family of fully functional Boolean and non-Boolean logic devices and projected a possible power dissipation of low, single-digit Atto-Joules per equivalent NAND/NOR operation, achieved via monolithic 3D integration and global on-chip clocking [2]. However, this is only possible via tailored coercivities (H_c < 20 mT) and narrow switching-field-distributions (SFD), that are significantly smaller than the clocking window ($\sigma_c < \Delta H_{clk}$). The design goals of pNML are therefore contradictory to those of bit-patterned media, on which earlier investigations put their focus on [3]. This work opens the door to a better understanding of how partial Ga^+ and He^+ ion irradiation effects and limits coercivity and SFD in magnets with low PMA. The irradiation spots create artificial nucleation centers (ANC) by locally decreasing the PMA leading to reduced nucleation fields. This is essential for the non-reciprocal coupling in pNML. The experiments are based on the statistics of thousands of circular nanomagnets ($Pt_1\backslash Co_{0.25}[Ni_{0.7}\backslash Co_{0.15}]_{xN}$), grouped in multiple dot arrays. The arrays are irradiated with varying ion types and doses and are subsequently compared to their as-grown states. The samples are characterized via wide-field MOKE, utilizing automated image recognition and pattern matching software, which enables to track the H_c change of every magnet ($0.5 < r_{dot} <$ 1 μm). Additionally to the overall statistical analysis, this approach reveals the irradiation impact-noise ($\sigma_{\Delta Hc}$) with respect to the applied ion-type and irradiation parameter. Fig. 1 and 2 depict the SFDs and impact-noise data of a 5 ML stack before and after irradiation. While the SFDs validate the effectiveness in reducing $H_{c,mean}$ even in the low coercivity regime, the ΔH_c distribution reveals a linear dependency on the as-grown H_c.

[1] Breitkreutz et al., IEEE Transactions on Magnetics., Vol. 49.7, p.4464 - 4467 (2013) [2] Becherer et al., Solid-State Electronics., Vol. 115, p.74-80 (2016) [3] T. Thomson, G. Hu, and B. D. Terris, Physical Review Letters., Vol. 96.25, p. 257204 (2006)

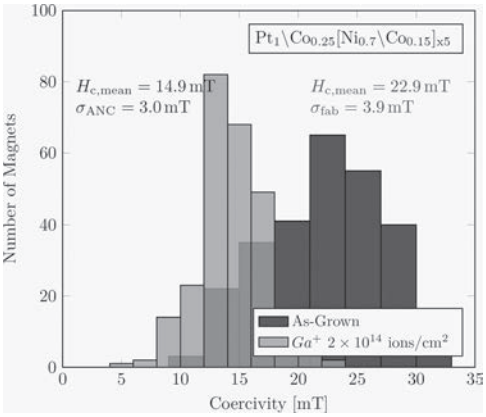


Fig.1 SFD histogram illustrating the effects of local Ga+ ion irradiation on the coercivity of low PMA nano-dots.

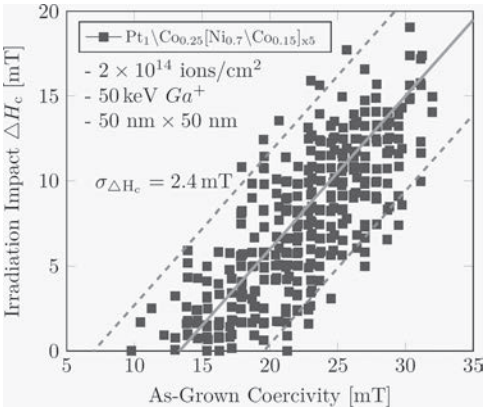


Fig.2 Distribution of the absolute H_c reduction depending on the as-grown coercivity

GP-03. Current-induced or field-induced domain wall depinning of a domain wall in a circular cross-section wire with modulated diameter. A. De Riz[1], B. Trapp[2], J. Fernandez-Roldan[3], C. Thirion[2], J. Toussaint[2], O. Fruchart[1] and *D. Gusakova*[1] *1. Univ. Grenoble Alpes, CNRS, CEA, Grenoble INP, IRIG-Spintec, Grenoble, France; 2. Univ. Grenoble Alpes, CNRS, Institut NEEL, Grenoble, France; 3. Institute of Materials Science of Madrid, CSIC, Madrid, Spain*

Domain wall propagation in cylindrical nanowires with modulations of diameter is a key phenomenon to design physics-oriented devices, or a disruptive three-dimensional magnetic memory. The information stored in this type of solid-state device would be encoded by magnetic domains separated by magnetic domain walls, whose position may be controlled by introducing geometrical modulations. A smaller cross-section reduces the internal domain wall energy, and thus plays the role of the energy well. This implies that a threshold driving force must be applied to overcome the barrier. In this context, our work presents a combination of analytical modelling and micromagnetic simulations [1,2], with the aim to draw a comprehensive panorama of the physics of domain wall pinning at geometrical modulations, when moved under the stimulus of a magnetic field or a spin-polarized current. For the sake of considering simple physics, we focus on diameters of a few tens of nanometers at most, and accordingly on domain walls of transverse type. We compare the domain wall behavior subjected to the magnetic field and subjected to the spin-polarized current. Modeling with suitable approximations provides in each case simple scaling laws, which relate the critical driving force needed to unpin the domain wall to the geometry parameters. We find major difference of efficiency of the driving force between both cases: while pinning increases with the relative change of diameter between two wire segments, the pinning efficiency is much larger upon considering current rather than field, due to the drastic decrease of the current density in larger cross-section. The quantitative investigation of experimental domain-wall pinning in modulations of diameter is still in its infancy. It has been carried-out under magnetic field so far, with scattered results, however pointing at the moderate strength of pinning compared with extrinsic pinning on material defects, when considering smoothly-varying modulations. The drastically higher efficiency of pinning under current, raises hope that modulations of diameter can be designed efficiently for spin-torque fundamental or applied devices.

[1] J. A. Fernandez-Roldan *et al*., Sci. Rep. 9, 5130 (2019). [2] A De Riz *et al*. in preparation.

GP-04. Structure of domain walls in synthetic antiferromagnets with an inverted Dzyaloshinskii-Moriya interaction. *N. Pandey*[1], A. Prudnikov[1], M.P. Li[1], C.K. Mewes[2], T. Mewes[2], M. De Graef[1] and V. Sokalski[1] *1. Materials Science and Engineering, Carnegie Mellon University, Pittsburgh, PA, United States; 2. Physics and Astronomy, University of Alabama, Tuscaloosa, AL, United States*

Synthetic antiferromagnets (SAFs) are ubiquitous in magnetic storage and memory technology due to the strength of the antiferromagnetic coupling and their suppression of unwanted stray fields. More recently, SAFs have been considered for use in racetrack memory in the form of domain walls (DWs) or skyrmions where the velocities are reportedly much larger than their ferromagnetic counterparts. [1] The work presented here features a new kind of chiral DW where the top and bottom layer of the SAF have parallel internal DW magnetization directions despite AF interlayer coupling (See Fig 1). This occurs due to an inversion of the DMI sign and, consequently, the DW chirality between the layers. [2] Here we present semi-analytical calculations combined with micromagnetic modeling, using the M^3 software package, to describe the ground state of DWs in SAFs.[3] Experimental results on SAFs with tunable coupling strength and DMI are presented along with Lorentz TEM images of SAF DWs. Each layer of the SAF is based on a HM/FM/HM multi-layer where the HM is either Pt or Ir and the FM is either Co or a Co/Ni multi-layer. AF coupling strength was measured between these layers using Ru and/or Ir as the coupling layer. Peaks in AF coupling are observed consistent with an RKKY interlayer exchange mechanism. Initial Lorentz TEM (See Fig 2) using a Pt/$[Co/Ni]_6$/Co/Ir/Co/$[Co/Ni]_6$/Pt SAF show domain walls that adopt a tiger-tail pattern and a clear separation of the top and bottom domain walls with application of a perpendicular field. The possible forms of topological defects in SAF domain walls and a proposed strategy for their detection is also presented. [4]

1. S. Yang, K. Ryu and S. Parkin, Nature Nanotechnology., Vol. 10 no. 3, p. 221–226. (2015) 2. A. Prudnikov et al., IEEE Magnetics Letters., Vol. 10, p. 1-4. (2019) 3. "Micromagnetics code M^3" http://magneticslab.ua.edu/micromagnetics-code.html. 4. This research is supported by the Defense Advanced Research Project Agency (DARPA) program on Topological Excitations in Electronics (TEE) under grant number D18AP00011. The authors also acknowledge use of the Materials Characterization Facility at Carnegie Mellon University supported by grant MCF-677785.

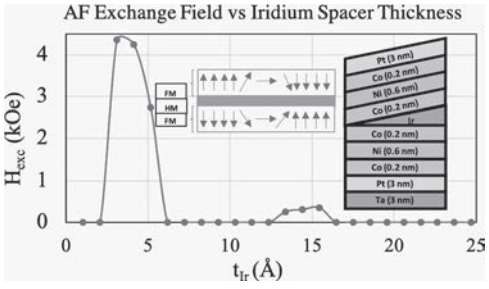


Fig 1. AF Exchange coupling strength (H_{exc}) vs Ir thickness (t_{Ir}) along with the sample stack and expected SAF domain structure.

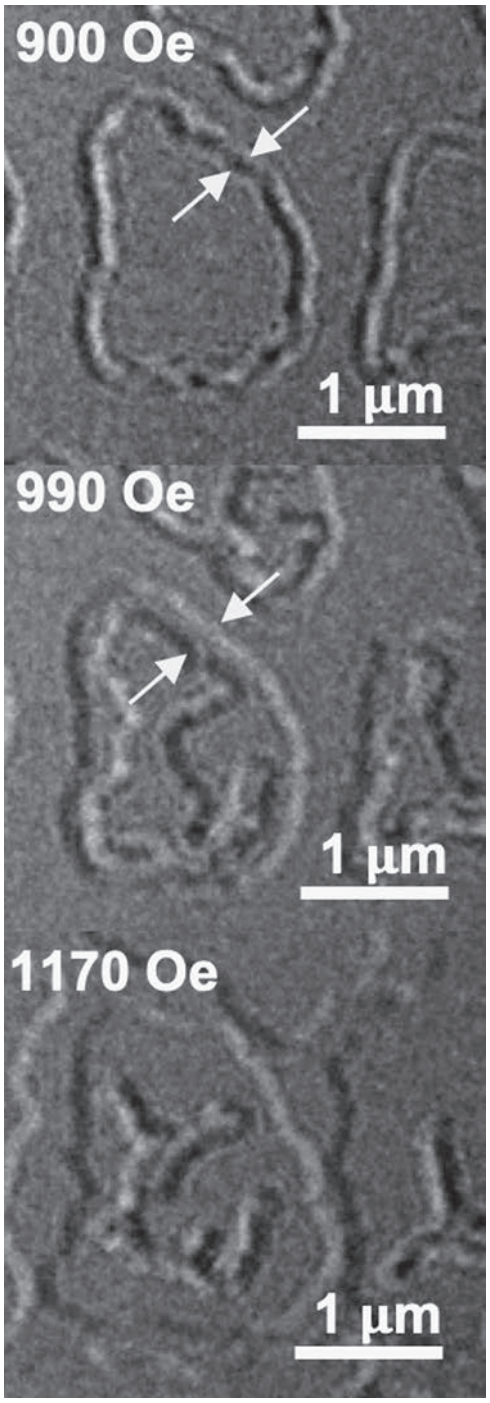


Fig 2. LTEM image showing separation of top and bottom layer DWs with perpendicular field applied in situ. Yellow arrows point to a section where DWs in top and bottom layers have separated

GP-05. Systematic Characterisation of DMI in Co/Pt, Co/Ir Systems.
E. Darwin[1], C.H. Marrows[1] and B. Hickey[1] *1. Condensed Matter, University of Leeds, Leeds, United Kingdom*

Skyrmions are chiral, topologically non-trivial, spin textures which have a unique set of topological properties which lead them to be highly stable. Skyrmions which have diameters in the nanometer range, can now be stabilized at room temperature without a magnetic field and can also be manipulated using an electric current; all of which makes them suited for applications such as data storage and logic technology.[1][2][3] Skyrmions occur due to the Dzyaloshinskii-Moryia interaction (DMI), which is an additional anti-symmetric term in the exchange energy shown by Equation 1. HDMI = d12. (S1 x S2) (1) Where d12 is the DMI characteristic vector and S1 and S2 are two neighbouring spins.[4] The more recent room temperature Néel skyrmions have been observed in heavy metal/ferromagnet/heavy metal multilayers. Materials were used such as cobalt for the ferromagnet and Ir and Pt for the heavy metals. Part of the process to attain reliable and stable skyrmions is to study these materials and their properties. The DMI constant directly affects the shape, size and stability of skyrmions, so to be able to nucleate an appropriate skyrmion, it should be known how different material parameters affect the DMI. Throughout this study, measurements were made of numerous samples of materials which should invoke various DMI whilst varying only one factor in order to understand how that factor affects the DMI. The further goal was to obtain a set of material configurations with known DMI constants to aid with reliable methods for skyrmion nucleation. Figure 1a shows the set of effective DMI constants, these were attained using the bubble expansion method (Figure 1b) to find the DMI field, and SQUID measurements. Further measurements were also made to test how a different number of magnetic multilayer repeats would affect the magnetic properties of skyrmion materials to find the highest possible sample thickness. This is in order to create successful on-chip coplanar waveguides with the ability to host skyrmions with the aim of performing THz time domain spectroscopy measurements to observe possible skyrmion resonances at THz frequencies.
Funded by EMPIR TOPS

[1] A.Fert et al. *Nature Reviews Materials* 2, 7: 17031 (2017). [2] S.Finizio et al. *arXiv preprint arXiv:1902.10435* (2019). [3] K.Zeissler et al. *Nature nanotechnology* 13,12: 1161 (2018). [4] O.Boulle et al. *Nature nanotechnology* 11,5: 449 (2016).

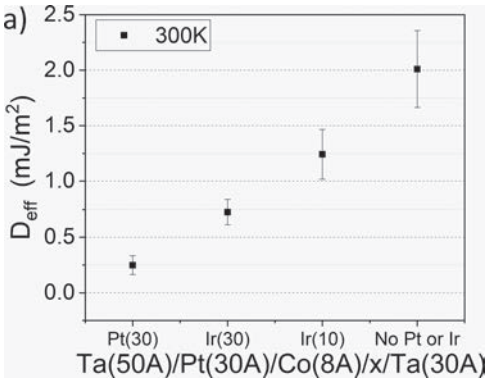


Figure 1

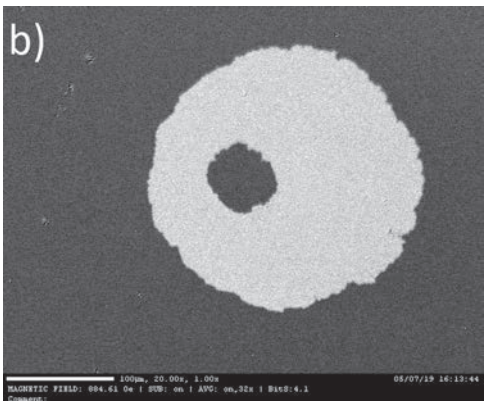


Figure 2

GP-06. Analysis of self-heating effects on current-driven ferrimagnetic domain wall motion. *G. Wang*[1], Y. Zhang[1], Z. Zhang[1,2], Z. Huang[1], J. Wang[1], K. Zhang[1], J. Nan[1], Z. Zheng[1,2], Y. Zhang[1,2] and W. Zhao[1] *1. Fert Beijing Research Institute, BDBC, School of Microelectronics, Beihang University, Beijing, China; 2. School of Electronic and Information Engineering, Beihang University, Beijing, China*

Recent progresses have demonstrated that spin-orbit torque (SOT) driven ferrimagnetic (FIM) domain wall (DW) motions near the angular momentum compensation point T_A possess extremely high velocity [1-4]. However, as FIM materials are thermally sensitive [5-6], the behavior of the current-induced FIM DW motions will be significantly influenced by self-heating. Here we analyze the impact of self-heating on the velocity of SOT driven FIM DW motions by synthetizing Joule heating effect, temperature-dependent FIM compensation effect and SOT effect [See Fig. 1]. Firstly, we investigate the dependence of DW motion velocity (v_{DW}) on temperature with different current densities in heavy metal (j_{HM}), as shown in Fig. 2(a). Fig. 2(b) shows the Joule heating effect on the temperature. The significant influence of the temperature variation on FIM DW motion is then demonstrated in Fig. 2(c). We can find that v_{DW}-t curves of small j_{HM} are steady during 1ns of self-heating. In contrast, large j_{HM} can induce high v_{DW} at the beginning of the current application. Then the v_{DW} will drop even lower than that of small j_{HM}, owing to the self-heating effect that makes the temperature away from T_A. Moreover, appropriately increasing T_A is an effective approach to increase the average speed. As shown in Fig. 2(d), when T_A=312K, the v_{DW} is kept above 1.5km/s within 1ns, resulting in the maximum propagation length. From this analysis, we summarize that suitable j_{HM} should be provided according to specific demands: large current can boost the speed for the application with short DW propagation length, such as three-terminal DW device; in the cases requiring long DW propagation length, such as racetrack memory, small current can generate stable speed and minimize the impact of self-heating. This work is conducive to the future application of FIM materials in spintronic devices.

[1] K.-J. Kim, et. al., Nature Material, Vol. 16, p. 1187. (2017) [2] M. Binder, et. al., Physical Review, Vol. 74, p. 134404 (2006) [3] L. Caretta, et. al., Nature Nanotechnology, Vol. 13, p. 1154 (2018) [4] S. A. Siddiqui, et. al., Physical Review Letters, Vol.121, p. 057701 (2018) [5] K.-J. Kim, et. al., Applied Physics Letters, Vol. 92, p.192509 (2008) [6] H. Fangohr, et. al., Physical Review B, vol. 84, p. 054437, (2011)

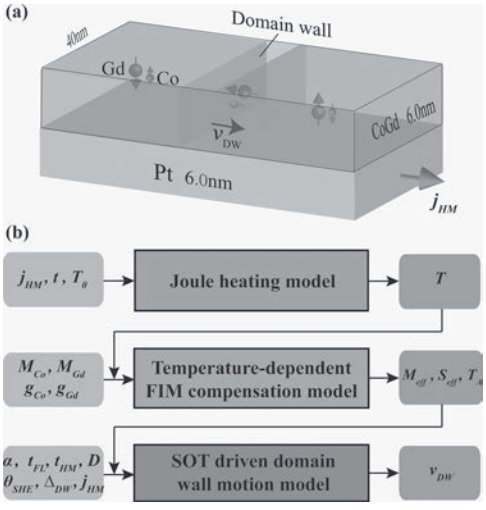


Fig.1 (a) FIM DW motions driven by SOT effect. (b) Theoretical models involved in the analysis of self-heating effect.

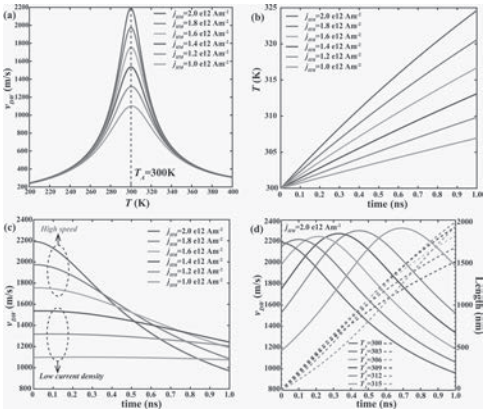


Fig.2 Analysis of self-heating effect: (a) DW velocity as a function of temperature. (b) temperature and (c) DW velocity as functions of duration time of applied current density. (d) DW velocity and propagation length as functions of T_A.

GP-07. Current Induced Domain Wall Motion with a Ta/Gd-Fe/Si-N Magnetic Nanowire for a Magneto-optical Light Modulator. *K. Aoshima*[1], N. Funabashi[1], R. Higashida[1] and K. Machida[1] *1. NHK Japan Broadcasting Corp., Tokyo, Japan*

Magneto-optical light modulator driven by current-induced domain wall motion (CIDWM) has been developed for holography display application [1-3]. Driving speed of the device, which is proportional to domain wall (DW) velocity, has to be fast enough to refresh pixel data over large scale such as 10K × 10K or larger. Fast CIDWM has been found in a magnetic layer sandwiched by a heavy metal and an insulator, which is attributed to chiral Néel DW driven by spin orbit toque (SOT) [4-6]. However, there is not much research about how initial domains nucleated on the SOT driven nanowire and its CIDWM for a light modulator. In this article we investigate a Ta/Gd-Fe nanowire with a hard magnet(HM), and show a domain nucleation and CIDWM as fast as 180 m/s. Fig.1(a) shows a fabricated device, which comprises a Ta(3 nm)/$Gd_{22.6}$-$Fe_{77.4}$(10 nm)/Si-N(5 nm) nanowire with 500 nm width, a HM of $[Co(0.3\text{ nm})/Pd(0.6\text{ nm})]_{25}$ with 0.5 × 3 μm^2, and electrodes for current injection. As shown in Fig. 1(b) and (c), an initial domain was observed as a dark spot on the left (right) side of the HM, which was nucleated by the positive (negative) current pulse without external magnetic field after uniformly magnetized along +z-direction. This is attributed to the SOT with local in-plane component (x-direction) of fringe magnetic field induced by the HM [Fig.1(d)], which is known for the SOT switching [7, 8]. Two initial domains have been observed on both side of the HM for the nanowire without Ta [1]. As shown in Fig.2, positive (negative) DW velocity increased with an increasing positive (negative) current, indicating DW moves along the current flow which was opposite to the nanowire without Ta underlayer [1]. The velocity significantly increased as fast as 180m/s with an application of external in-plane magnetic field (H_x), which was more than an order of magnitude faster than that without Ta [1]. The fast DW motion is attributed to the chiral Néel wall promoted by the H_x and SOT induced by Ta [4-6].

[1] K. Aoshima, R. Ebisawa, N. Funabashi, et al., Jpn. J. Appl. Phys., Vol. 57, p. 09TC03 (2018) [2] R. Higashida, N. Funabashi, K. Aoshima, et al., MMM-Intermag conference. 2019, paper GN-02 [3] K. Aoshima, H. Kinjo, K. Machida, et al., J. Disp. Technol., Vol. 12, p. 1212 (2016). [4] S. Emori, U. Bauer, S. Ahn, et al., Nat. Mater., Vol. 12, p. 611 (2013) [5] K. Ryu, L. Thomas, S. Yang, et al., Nat. Nanotech, Vol. 8, p. 527 (2013) [6] B. Do and H. Awano, IEEE Tans. Magn. Vol. 50, p. 1401704 (2014) [7] L. Liu, C. Pai, Y. Li, et al., SCIENCE Vol. 336, p. 555 (2012), [8] Z. Zhao, M. Jamali, A. Smith, et, al., Appl. Phys. Lett. Vol. 106, p. 132404 (2015)

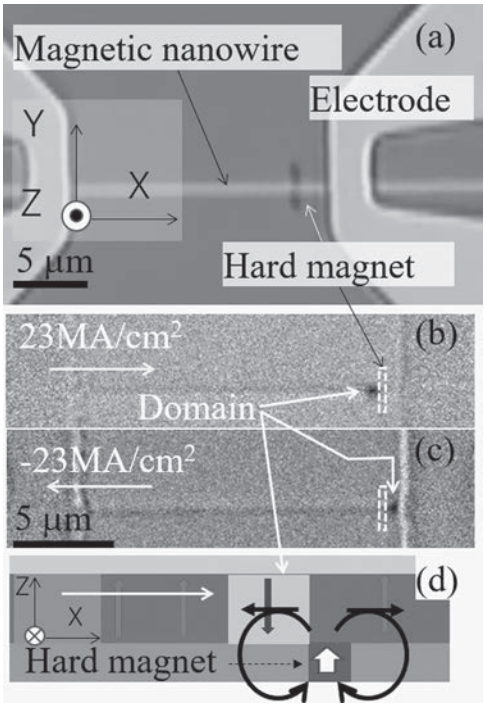


Fig.1 (a) A micrograph of a fabricated nanowire with HM, (b), (c) Magneto-optical micrographs after pulse current injection (50ns) for an initial domain nucleation, (d)Cross-sectional nanowire illustration

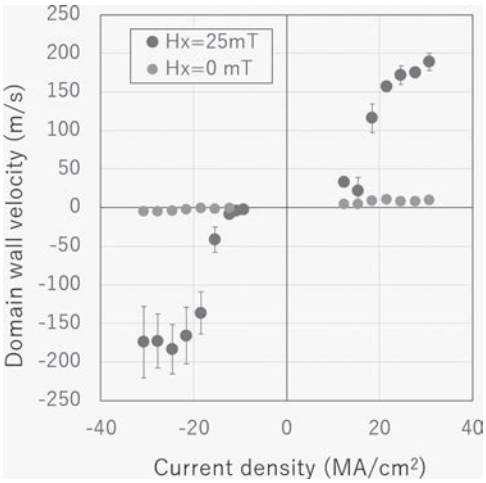


Fig.2 DW velocity versus current amplitude

GP-08. 2D magnetic domain wall ratchet: the limit of submicrometric holes. J. Herrero-Albillos[6], C. Castan-Guerrero[1], F. Valdes-Bango[1], J. Bartolomé[1], F. Kronast[5], A. Hierro-Rodriguez[4], L.M. Alvarez-Prado[3], J. Martín[3], M. Velez[3], J. Alameda[3], J. Sesé[2], L. Garcia[1] and *F. Bartolome*[1]
1. CSIC - Universidad de Zaragoza, Zaragoza, Spain; 2. Universidad de Zaragoza, Zaragoza, Spain; 3. CSIC - Universidad de Oviedo, Oviedo, Spain; 4. Universidade do Porto, Porto, Portugal; 5. Helmholtz - Zentrum Berlin fur Materialien und Energie, Berlin, Germany; 6. Centro Universitario de la Defensa, Academia General Militar, Zaragoza, Spain

In the last decade, magnetic ratchet effect of domain walls has been proposed by several groups as a working principle for spintronic devices like magnetic diodes or shift registers. Indeed, some of the proposed strategies are promising candidates to be seen in the near future in working devices. As an alternative route, we have succeeded in producing and observing magnetic ratchet effects, as well as crossed-ratchet effects, in a ferromagnetic thin film where we have nanopatterned 2D arrays of asymmetric holes in the submicrometric limit for hole sizes. The combination of Kerr microscopy, X-Ray PhotoEmission Electron Microscopy and micromagnetic simulations has allowed a full magnetic characterisation of the domain wall (DW) propagation processes over the whole array and the local DW morphology and pinning at the holes. It is found that the DW dynamics in the submicrometric size limit are governed by the interplay between DW elasticity and half vortex propagation along hole edges: as hole size becomes comparable to DW width, flat DW propagation modes are favoured over kinked DW propagation due to an enhancement of DW stiffness, and pinned DW segments adopt asymmetric configurations related with Nèel DW chirality. Both ratchet and crossed-ratchet effects have been experimentally found, and we propose a new ratchet/inverted-ratchet effect in the submicrometric range driven by magnetic fields and electrical currents [1].

[1] J. Herrero-Albillos et. Al. Accepted Manuscript. Materials & Design 138, 111-118(2018)

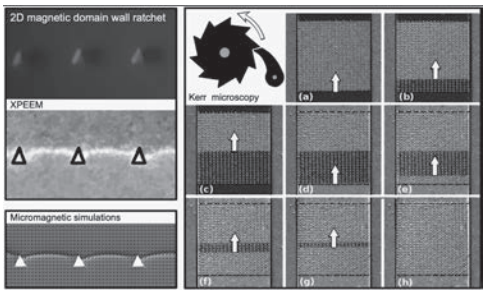


Fig.1 XPEEM, Kerr microscopy and micromagnetic simulations on arrays of asymmetric holes (see text and Ref. [1]).

GP-09. Geometrically tuned Spin-orbit torque based memristor. *R. Singh*[1] and X. Zhang[1] *1. School of Materials Science & Engineering, Tsinghua University, Beijing, China*

Spin orbit torques (SOT) based memristors have drawn much attention due to their potential application in magnetic memory and logic devices.[1] The spin-based memristors offered significant endurance and high energy efficiency as compared with other types of memristors.[2] Here, we proposed geometrically tunable Hall bar based magnetic memristors in which the gradual switching of magnetic domains in magnetic material (CoFeB) resembles memristor *R-I* curves. We modified the geometry of the conventional Hall bar in such a way that the current density (*J*) will be different in different part of the device. The current density is given by ($J=I/A$), where I is the applied current and A is the cross-sectional area of the device. Due to different current density, the magnetic domain switching in CoFeB will occur gradually. This gradual switching of magnetization gives *R-I* curve that resembles memristor behavior. The Ta(3)/CoFeB(0.7)/MgO(1.3) (the number shows film thickness in nanometers) multilayers were deposited by sputtering. To achieve good perpendicular magnetic anisotropy (PMA) property, the film stack was annealed at 220°C for 1hr. Later, lithography and etching were performed to fabricate devices. Figure 1 shows Hall resistance variation of the fabricated devices. It can be seen that the conventional Hall bar geometry (10 μm device) has only two stages (Low resistance state and High resistance state). However, other devices (30 and 50 μm devices) shows multistate resistance switching. The larger curvature device (50 μm) shows large number of switching stats (5 steps in *R-I* curve). If we varied the write current then different states of resistance can be achieved (figure 2, measured for 30 μm device). This shows multistate *R-I* curve, that resembles the memristor kind of behavior. To understand the mechanism of our device simulation and MOKE microscopy has been performed.

1. Jiangwei Cao, Yifei Chen, Tianli Jin *et al.*, Sci. Rep., Vol. 8, P. 1355 (2018). 2. Shuai Zhang, Shijiang Luo, Nuo Xu *et al*., Adv. Electron. Mater., Vol. 5, P. 1800782 (2019).

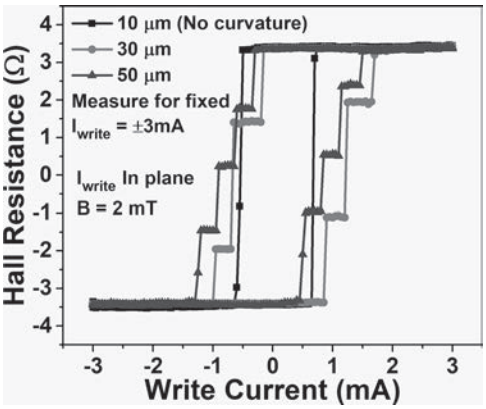


Fig.1 Hall resistance variation for different curvature devices, measured at ±3 mA current

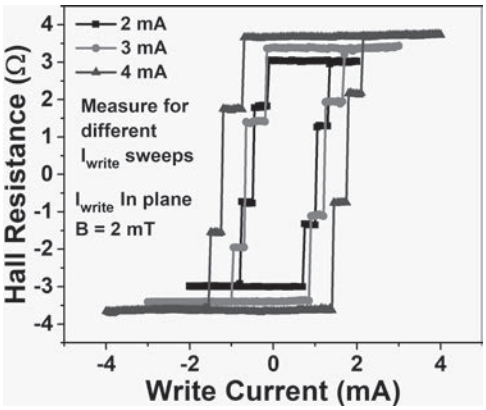


Fig.2 Multistate *R-I* curve of the device, for different write current sweeps

GP-10. Introducing multiple stable states in an antiferromagnet-free spin-orbit torque device. *P. Chen*[1], C. Yang[1] and C. Lai[1] *1. Materials Science and Engineering, National Tsing Hua University, Hsing Chu, Taiwan*

Neuromorphic computing arouses extensive interests in its associated artificial intelligence and machine learning application, which has been currently accomplished by MRAM-based analogous memory technologies [1,2]. In this work, we are going to demonstrate a Pd(6)/Co/Ta(2), numbers representing thickness in nm, trilayer device featuring the multiple stable states upon driving the spin-orbit torque (SOT) effect through, and each intermediate state was electrically determined by the amplitude of pulse voltage with a tailorable range of approximately 6 volts and was strongly dependent on the size of device. As we patterned the devices into 100-nm in linewidth, the multi-level switching behavior becomes extinct, indicating that the phenomenon might be similar with the result from others' work [3]. Absence of the multi-level nature in Pt/Co/Ta and Pd/Co/Ta(<2) trilayer suggests the uniqueness of the combined Pd/Co and Co/Ta interfaces in giving rise to the peculiar multi-level. Also the behavior was still distinct in the as-deposit Pd/Co/Ta samples, meaning the diffusion of Ta has the lowest influence. At last, we function a whole structure integrating Pd/Co/Ta with a magnetic tunnel junction for the potential MRAM-based memory application. To summarize, the new structure design sheds a new light on future analog memory application. Other reports indicate that using anti-ferromagnetic as spin current source would result in this kind of slope when switching. However, in our structure design, we achieve analog switching while at the same time did not possess any anti-ferromagnetic layers, and can be potentially well-integrated into common MTJ design.

1.J. Grollier et. al, Proceeding of the IEEE, 104, No.10(2016) 2.S. Fukami et. al, Nature Materials, 15, p.535(2016) 3.A. Kurenkov et. al, Applied Physics Letters, 110, p.092410(2017)

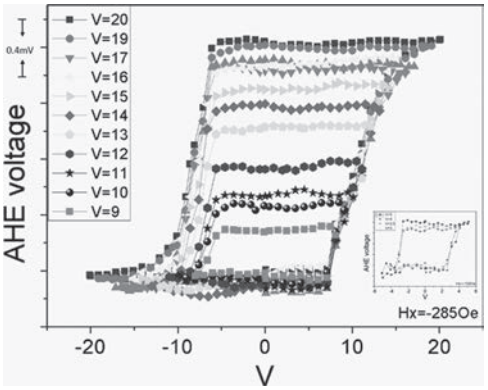


Fig.1 Switching curves of Pd(6)/Co/Ta(2) trilayer device with 5 um width, thickness in nanometer. Inset shows a comparison of the switching curves acquired by the device with reduced dimension to 100 nm width.

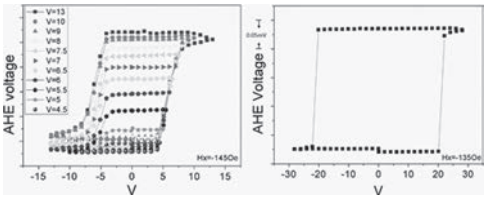


Fig. 2 Switching curves of as-deposited Pd/Co/Ta (left) and Pt/Co/Ta (right) in the 5 um width device. This set is for a comparison to show Pd/Co is necessary to give rise to the multiple stable states in Co layer upon driving SOT.

GP-11. Enhancement of spin Hall effects inducing damping-like torque in spin-orbit torque using partially A15-phase intermetallic compound W_3Ta film. *B. Chun*[1], S. Yang[1], C. Kim[1], K. Moon[1] and C. Hwang[1] *1. KRISS, Daejeon, The Republic of Korea*

In heavy metal (HM)/ferromagnet (FM) heterostructure, a spin current generated from HM with large spin-orbit coupling exerts a torque on the FM magnetization via spin Hall effects (SHE), so that for efficient magnetization switching the spin-orbit torque must be large especially for large damping-like torque is indispensable. Here, we demonstrate that the intermetallic compound W_3Ta layer with partially A15-phase can be more efficiently switch the magnetization of a FM by enhancing the damping-like torque [1]. In partially A15-phase W_3Ta/CoFeB/MgO/Ta systems, by considering the spin pumping effect, we obtained an SHE-induced damping-like torque of -0.678 (± 0.093), which was higher than that of the β-phase W/CoFeB/MgO/Ta structure of -0.477 (± 0.005). Recent theoretical report based on the Berry phase contribution to this large spin Hall effect supports our experimental verification.[1] We also studied the dependence of effective spin mixing conductance (on magnetic materials to evaluate the interface modification effect between HM/FM. Because of the larger in the W_3Ta/Co/MgO/Ta system, we obtained smaller damping-like torque of -0.541 (± 0.032) than W_3Ta/CoFeB/MgO/Ta system.

[1] E. Derunova, Y. Sun, C. Felser, S. S. P. Parkin, B. Yan, and M. N. Ali1, Giant intrinsic spin Hall effect in W_3Ta and other A15 superconductors, Sci. Adv. 5 (2019) 8575.

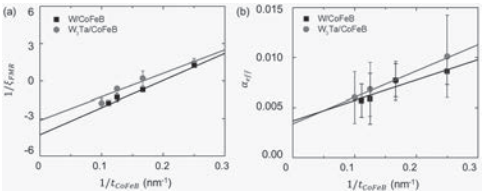


Fig. 1. (a) The damping-like torque is obtained from the intercept of the linear fit of versus $1/t_{CoFeB}$ curve and the values of W_3Ta/CoFeB/MgO/Ta and W/CoFeB/MgO/Ta system are -0.318 (± 0.048) and -0.233 (± 0.013), respectively. (b) Illustrates the CoFeB layer thickness dependence of. In this case, was found to be 0.0034 and 0.0037 for W_3Ta/CoFeB/MgO/Ta and W/CoFeB/MgO/Ta system, respectively, as obtained from the x-intercept in the linear fit of the versus $1/t_{CoFeB}$ graph.

GP-12. Magneto-optical Line Light Modulator Consisted of Single [Co/Tb] Magnetic Nanowire utilizing Current-driven Domain Wall Motion. *Y. Miyamoto*[1], Y. Hori[1], M. Endo[1] and N. Ishii[1] *1. Science & Technology Research Labs., NHK (Japan Broadcasting Corp.), Setagaya, Japan*

Spatial light modulator (SLM) [1] and magnetic nanowire (NW) memories [2, 3] that utilize current-driven domain wall motion have been proposed, in which precise control of the "bit shift" of magnetic domains is essential. SLMs are considered as future three-dimensional displays for holography. In this study, we fabricated a prototype of magneto-optical line light modulator (LLM), which was consisted of a single NW equipped with a pixel writer for forming magnetic domains in NW as shown in Fig. 1. The operation of LLM is as follows: (1) the pixel writer generates current magnetic field in one direction corresponding to the first bit datum and forms a domain in NW, *i.e.* act as the first pixel. (2) by application of driving current along NW, the written pixel is shifted to the right along NW. (3) by repeating pixel formation and shift one by one, the given serial data are stored along NW length direction as the domains with up or down magnetic moments. (4) the incident light may be modulated in polarization according to the stored pixel queue in NW, and the light modulation may be achieved by magneto-optical Kerr effect (MOKE). Fig.2(a) shows the microscopy image of fabricated LLM. The NW was consisted of Pt(3nm)/[Co(0.3)/Tb(0.6)]$_5$ film with perpendicular anisotropy on SiO_x/Si substrate, while the pixel writer was consisted of Ta(5)/Au(100)/Ta(5) with a separation layer of 18nm-thick Si_3N_4 insulator. The width and length of the NW was 3μm and 40μm, respectively. The stored pixels were observed by MOKE microscopy at wave length λ=408nm in real-time. Fig. 2(b) shows the MOKE image for post-operation of LLM. Here, the 500ns-width one pulse currents for driving and pixel writer were applied at 2.5×10^7A/cm^2 and 2.6×10^7A/cm^2 for each operation. The speed of domain shift is about 2.1m/s without existence of applied field. We have succeeded in observing bright and dark pattern referred to the stored pixels, although [Co/Tb] film showed maximum Kerr rotation angle of 0.28° at λ=650nm. A precise control of multiple domain shift can be achieved along the NW without intentional trap sites.

[1] K. Aoshima *et al*., Journal of Display Technology, Vol. 12, p. 1212 (2016) [2] S. S. P. Parkin *et al*., Science, Vol. 320, p.190 (2008) [3] M. Okuda *et al*., IEEE Transactions on Magnetics, Vol. 52, p. 3401204 (2016)

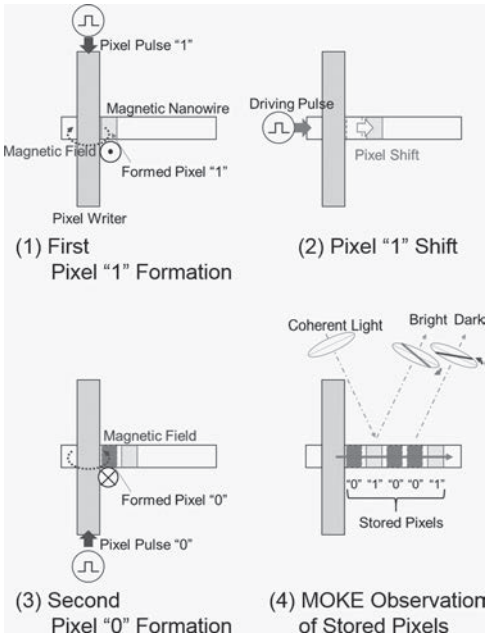


Fig.1 Operation of proposed LLM.

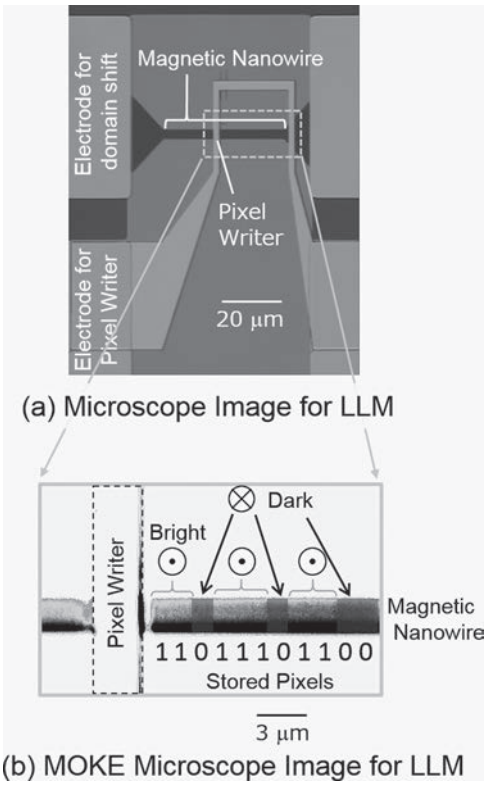


Fig.2 Typical images of (a) microscope and (b) MOKE microscope for fabricated LLM with 3μm-width NW.

GP-13. Synaptic Element For Neuromorphic Computing Using Magnetic Domain Wall Device With Synthetic Pinning Sites. *T. Jin*[1], N. Sernicola[1], W. Gan[1], F. Tan[1], W. Lew[1] and S. Piramanayagam[1] *1. Nanyang Technological University, Singapore*

The ability to make devices that mimic the human brain has been a subject of great interest in scientific research. Current artificial intelligence algorithms, which are primarily based on the von Neumann architecture, are not energy

efficient[1]. Neuromorphic computing (NC), which consists of a network of synthetic neurons interconnected through synaptic devices, is expected to perform complex information processing at low power. In an NC system, synapses can be considered as the memory element of a neuromorphic device[2]. We have investigated magnetic wires made of Co/Pd multilayers with synthetic pinning sites as a potential candidate for a synaptic element. B^+ ions-implantation was utilised to locally modify the magnetic properties, which was carried out with an energy of 10 keV. A sample without implantation was also investigated as reference sample (Ref). The implantation depth was controlled by varying the thickness of an additional Ta overcoat to achieve deep-implantation (DI), medium- implantation (MI) and shallow-implantation (SI). Polar-MOKE and Kerr microscope measurements were performed to measure hysteresis switching loops and monitor DW propagation in the presence of a perpendicular magnetic field. The reference sample showed a sharp hysteresis switching curve, indicating that the magnetization reverses with a swift DW motion. Such a sample cannot be used in an NC system as synapse requires multiple states. For samples implanted with B^+, the magnetization reversal showed multiple states, indicating that the DW propagation is hindered by the pinning sites. The loops become wider for the samples with deeper implantation of B^+, indicating a stronger DW pinning, as shown in Fig. 1. The electrical measurements indicated that multiple resistive states can be achieved in samples implanted with B^+, as shown in Fig. 2. These results show that the DW device can be used as a neuromorphic synaptic element.

1. C. Krittanawong, H. J. Zhang, Z. Wang, M. Aydar, and T. Kitai, J. Am. Coll. Cardiol. 69, 2657 (2017). 2. W. A. Borders, H. Akima, S. Fukami, S. Moriya, S. Kurihara, Y. Horio, S. Sato, and H. Ohno, Appl. Phys. Express 10, 013007 (2017).

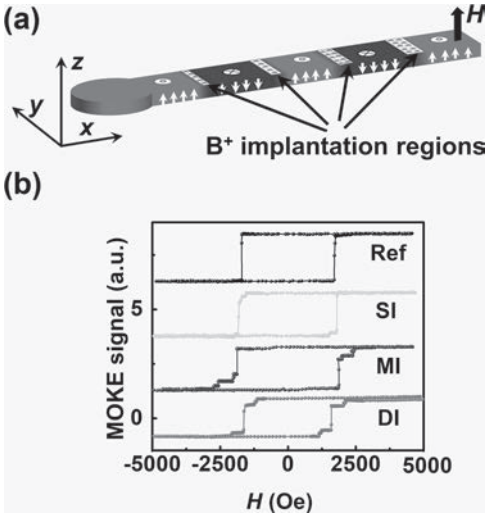


Figure 1. (a) Schematic view of the DW microwire. (b) Hysteresis loops of the device with different depth of B^+ implantation.

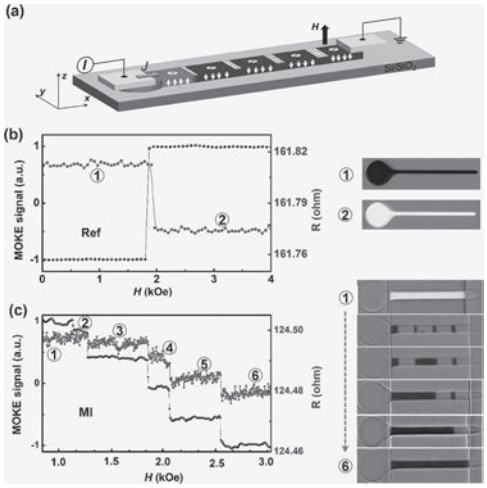


Figure 2. (a) Schematic of the setup used for magnetoresistance measurement for devices. The resistance changes, as well as the MOKE signal change for (b) Ref sample and (c) MI sample.

GP-14. Unusual phenomenon in which domain walls move in the current direction by STT in thick GdFeCo wire w/o heavy metal interface. *H. Awano[1] 1. Graduate School, Toyota Technological Institute, Nagoya, Japan*

Unusual phenomenon in which domain walls move in the current direction by STT in thick GdFeCo wire w/o heavy metal interface A. Takahashi[1], S. Sumi[1], P. V. Thack[1], K. Tanabe[1], Y. Kurokawa[2] and *H, Awano[1] 1 Toyota Technological Institute, JAPAN 2 Kyushu University, Fukuoka, JAPAN E-mail; *awano@toyota-ti.ac.jp Current-driven magnetic domain walls (DWs) in magnetic wires will be one of the attractive candidates for next generation low energy consumption memory devices. The critical current density for driving DW in RE-TM (Rare Earth Transition Metal) ferrimagnetic wire is one digit smaller than that of Co/Ni ferromagnetic wire [1]. As shown in Fig. 1 (a), when there is no Pt heavy metal layer on one side of the magnetic layer, the DW moves in the opposite direction to the current by Spin Transfer Torque (STT). On the other hand, as shown in Fig. 1 (b), when there is a hetero interface with the Pt layer, the DW moves in the current direction by the spin orbit torque (SOT). Since the SOT is just interface effect, it does not work when the thickness of the ferromagnetic layer exceeds several nm. However, we found that in the case of RE-TM wire, the SOT continues to work even if the layer thickness exceeds 10 nm [2-3]. This is considered to be the bulk SOT [4]. Therefore, the current density dependence of DW speed is investigated when the thickness of the GdFeCo wire was increased to 500 nm. The result is shown in fig. 2. In the GdFeCo wire having the hetero interface with Pt layer, the DW moves to the current direction even if the layer thickness is increased to 500 nm. However, it is hard to think that bulk SOT reaches to 500 nm. Therefore, we prepared GdFeCo wire without Pt hetero interface of the same thickness. This result is also shown in Fig. 2, but the DW moves to the current direction. In this case, SOT does not work because there is no Pt layer. Therefore, it is considered that the DW driving force is only STT. However, the DW moves opposite direction to the STT. We would like to discuss the unusual phenomenon of this current driven DW motion. This work was supported by JSPS Grant-in-Aids for Scientific Research (17H03240, 18K14128) and Research Center for smart energy technology of TTI.

[1] D. Ngo, K. Ikeda, and A. Hiroyuki, *Applied Physics Express*, Vol. 4, No. 9, 093002(2011). [2] Do Bang et. al., *Phys. Rev. B* 93, 174424 (2016) [3] Yuichiro Kurokawa et. al., *Jpn. J. of Applied Physics* 55, 07MC02 (2016) [4] Jiawei Yu, et. al., *Nature Materials* 18, 29-34 (2019)

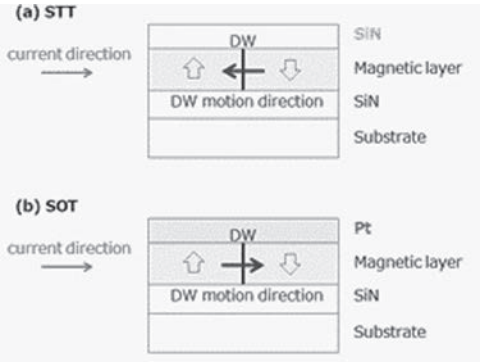


Fig. 1 Current driven DW motion image by (a) STT, (b) SOT

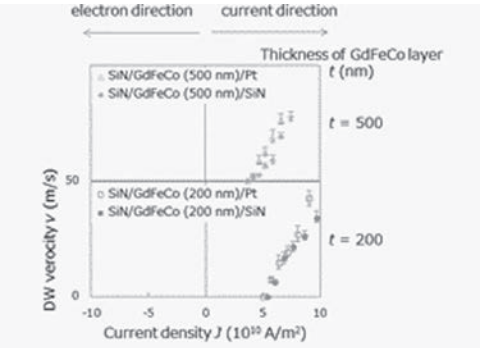


Fig. 2 Domain Wall (DW) motion observation results by current in thick GdFeCo wire with and without (w/o) Pt layer

GP-15. Complex Current-driven Spin-Orbit Torque Switching Behaviors In Co/Pt Multilayer-based Synthetic Antiferromagnets. *L. Zhu*[1], X. Xu[1], K. Meng[1], Y. Wu[1], J. Miao[1] and Y. Jiang[1] *1. University of Science and Technology Beijing, School of Materials Science and Engineering, Beijing, China*

Spin-orbit torques (SOTs) switching have been observed in Co/Pt multilayers with strong perpendicular magnetic anisotropy (PMA).[1] In bilayers system made of heavy-nonmagnetic metals (HMs) and ferromagnets (FMs), SOTs are derived from spin Hall effect (SHE) and interfacial Rashba spin-orbit coupling. However, in multilayers, SOTs arise from the global imbalance of the spin currents from the top and bottom interfaces for each Co layer.[1] Moreover, synthetic antiferromagnets (SyAFs) can be switched by SOTs, and the switching mechanism does not obey the usual SOTs switching rule[2] of the macrospin model[3]. Therefore, it is important to clarify the mechanism of SyAFs based SOTs switching. In this work, the film was fabricated by magnetron sputtering and patterned into a Hall bar using electron beam lithography (EBL) and an Ar ion milling technique. Then, the magnetism test and electrical measurement were taken to analyze the properties. Figure 1 presents the normalized magnetization curve (M/Ms) and the Hall resistance curve (RAHE) as a function of the out-of-plane magnetic field. It is obvious that both of the M-H and R-H loops indicate an antiferromagnetic (AFM) interlayer coupling as well as a strong PMA in the multilayer structure. As shown in Fig. 2, the magnetization can be switched with a pulse current and the orientation depends on the direction of the external field. Moreover, the anomalous switching behavior is also shown in Fig. 2. The switching orientation changes again with a larger in-plane external field. The anomalous switching behavior indicates the different switching mechanism in SyAFs. The total thickness of magnetic layer Co in our film is up to 3.2 nm, which is much thicker than previous reports, which is meaningful for real application in spintronics devices.

[1] Huang, K. F., Wang, D. S. & Lai, C. H, Applied Physics Letters, 107(23), 232407(2015). [2] Bi, C., Almasi, H. & Wang, W, Physical Review B, 95(10), 104434(2017). [3] Liu, L., Lee, O. J. & Buhrman, R. A, Physical review letters, 109(9), 096602(2012).

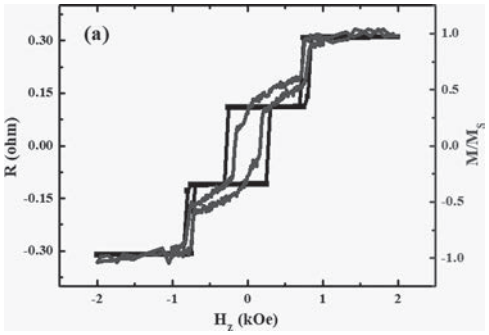


Fig.1 The Hall resistance curve (black) and the normalized magnetization curve (blue).

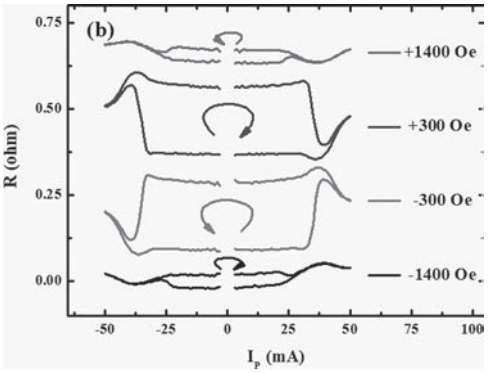


Fig.2 The current-driven magnetization switching under different in-plane external field.

GP-16. Orbital Anisotropic Magnetoresistance. *H. Ko*[1], H. Park[1], G. Go[2], J. Oh[2], K. Kim[3] and K. Lee[1,2] *1. KU-KIST Graduate School of Converging Science and Technology, Korea University, Seoul, The Republic of Korea; 2. Department of Materials Science and Engineering, Korea University, Seoul, The Republic of Korea; 3. Center for Spintronics, Korea Institute of Science and Technology, Seoul, The Republic of Korea*

The spin-orbit interaction has enriched the field of spintronics through various phenomena such as the interconversion between charge and spin currents, the dependence of electrical resistance on the direction of magnetization, and so forth. Among these effects, recent studies[1,2] clarified the origin of intrinsic spin Hall effect as the orbital Hall effect which describes the electric-field-induced generation of transverse orbital current. These studies suggest that some features in the spin system are concomitant results of analogous features in the orbital system, demanding thorough research on the orbital origin of spin-related phenomena. In this work, we investigate the longitudinal orbital currents in ferromagnets (FMs) based on first-principles calculation. The longitudinal orbital currents depend on the direction of magnetization due to the effective correlation between the orbital and magnetization via concerted action of spin-orbit interaction and exchange interaction. This anisotropic behavior of orbital currents contributes to the anisotropic magnetoresistance (AMR), which we call the *orbital anisotropic magnetoresistance* (OAMR). The OAMR arises from two universal characteristics of the multi-orbital systems, the orbital hybridization and the anisotropic orbital splitting where the latter was previously unveiled as the origin of ballistic AMR[3]. We illustrate the significance of orbital

hybridization as the newly found origin of AMR and also as the common origin of OAMR and orbital Hall effect[1,2], implying the correlation between AMR and intrinsic spin Hall effect. We also predict that the OAMR appears even in non-magnetic metals through the Zeeman coupling.

1. H. Kontani, T. Tanaka, D. S. Hirashima, K. Yamada, and J. Inoue, Phys. Rev. Lett. 102, 016601 (2009). 2. D. Go, D. Jo, C. Kim, and H. –W. Lee, Phys. Rev. Lett. 121, 086602 (2018). 3. J. Velev, R. F. Sabirianov, S. S. Jaswal, and E. Y. Tsymbal, Phys. Rev. Lett. 94, 127203 (2005).

GP-17. ANE and SOT effective fields in (Fe_4N, Mn_4N)/NM bilayers characterized by using harmonic Hall voltage measurements. *S. Isogami*[1] *1. Research Center for Magnetic and Spintronic Materials, National Institute for Materials Science, Tsukuba, Japan*

Spin-orbit torque (SOT) based magnetization switching is attracting great interest owing to its potential highly efficient magnetic random access memories. The SOT, originating from angular momentum transfer process from nonmagnetic (NM) to ferromagnetic (FM) layers in NM/FM bilayer systems, are strongly dependent not only on the NM but also the adjacent FM layers [1,2]. In this study, we have studied current induced SOT effective fields for the bilayer systems with nitrides such as (Fe_4N : ferromagnet, Mn_4N : ferrimagnet)/NM, where the NM = Pt and/or W. Note that the sign of spin polarization of density of state for the present Fe_4N is negative with minority-spin conduction [3], and the possible spin structure of the present Mn_4N is non-colinear order [4]. Using the harmonic-Hall voltage measurements [5], the anomalous Nernst effect (ANE) of the Fe_4N [6] and the SOT effective fields of the Fe_4N and Mn_4N were estimated as functions of measurement temperature (T) and applied fields. The inset of Fig. 1(a) shows one of the present stacking structures and the measurement configuration. Figures 1(a) and 1(b) show the 1st ($V_{1\omega}$) and 2nd ($V_{2\omega}$) harmonic Hall voltage while rotating the angle of magnetization in the film plane, respectively. When the temperature decreased from 300 K to 4 K, signs for both the $V_{1\omega}$ and $V_{2\omega}$ reversed, as shown in Figs. 1(c) and 1(d). The sign reversal can be explained by the additional ANE [6] that decreased with decreasing T, and the resultant damping-like and field-like torque efficiency at 300 K were estimated to be $\xi_{DL} \approx 0.098$ and $\xi_{FL} \approx 0.10$, respectively. The magnitude of ξ_{DL} was comparable to that of Ta/CoFeB systems [7], whereas high ξ_{FL} emerged for the Fe_4N/W system. The results of Mn_4N/Pt and Fe_4N/Pt will be shown and the specific SOT features for the bilayers with nitrides will be discussed.

[1] I. M. Miron, et al., *Nature* 476, 189 (2011). [2] N. Roschewsky, et al., *Appl. Phys. Lett.* 109, 112403 (2016). [3] S. Kokado, et al., *Phys. Rev.* B 73, 172410 (2006). [4] M. Uhl, et al., *Phys. Rev*. B 55, 2995 (1996). [5] M. Hayashi, et al., *Phys*. *Rev*. B, 89, 144425 (2014). [6] S. Isogami, et al., *Appl. Phys. Express* 10, 073005 (2017). [7] Y. C. Lau, et al., *Jpn. J. Appl. Phys*.56, 0802B5 (2017).

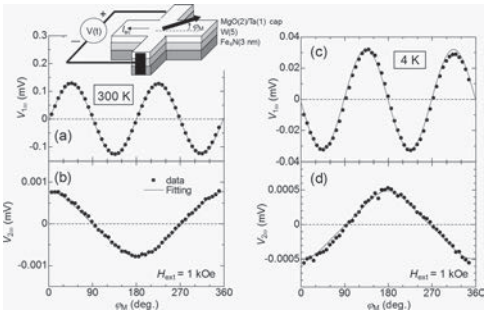


Fig. 1 (a,b) 1st-harmonic (a) and 2nd-harmonic (b) Hall voltage as a function of in-plane magnetization angle (ψ_M) for MgO substrate/ Fe_4N(3)/W(5)/MgO(2)/Ta(1) (thickness in nm) at 300 K. Solid symbols and line correspond to the experimental data and fitting result, respectively. The inset of Fig. 1(a) represents the measurement configuration. (c, d) Same as Figs. 1(a) and 1(b) but for 4 K.

GP-18. Improvement of the spin-orbit torque efficiency by thermal treatment during the Pt deposition. *W. Kwak*[1], J. Kwon[1], S. Hwang[1] and B. Cho[1] *1. School of Materials Science and Engineering (SMSE), Gwangju Institute of Science and Technology (GIST), Gwangju, The Republic of Korea*

The transfer efficiency of spin-orbit torque (SOT) to a magnetic moment in a ferromagnetic layer is determined by both the interface transparency between ferromagnetic and heavy metal layers and the bulk properties of heavy metal itself. In addition, the conversion efficiency of charge current to spin current is expected to increase as the amount of current, flowing through the interface area, increases, which is observed in the materials of Pt, Ta, and W [1]. Therefore, the SOT efficiency is supposed to be enhanced by using the highly resistive heavy metal as a spin current source. Here, we perform thermal treatment of the Pt layer to induce resistivity change (equivalently, the SOT efficiency). First, a Pt layer is deposited at 500 °C in a vacuum chamber after the buffer layer (Ta) deposition, and then cooled under the vacuum, followed by deposition of Co/Cu/Ta layers on the top surface of Pt. For comparison, the same thermal treatment is also performed after full-stack deposition. The films are patterned to the Hall bar with a width of 10 mm to estimate the transferred SOT by the harmonic measurement. Figure 1 shows the second harmonic voltage as a function of azimuthal angle with a field of 3000 Oe being applied along the Hall bar for the film of thermal annealing during Pt-deposition. From the data analysis, the resistivity of Pt is found to increase from 28.8 μΩcm to 81.81 μΩcm and the Slonczewski-like effective field to increase from 4.3 Oe/10^{11} Am^{-2} to 14.56 Oe/10^{11} Am^{-2}, indicating the enhancement of SOT efficiency. On the other hand, no significant change is observed for the film of full-stack annealing. We believe that our results provide an efficient way to improve the effective spin-Hall angle for current-driven spintronic devices.

[1] L. Wang et al., Phys. Rev. Lett. 116, 196602 (2016)

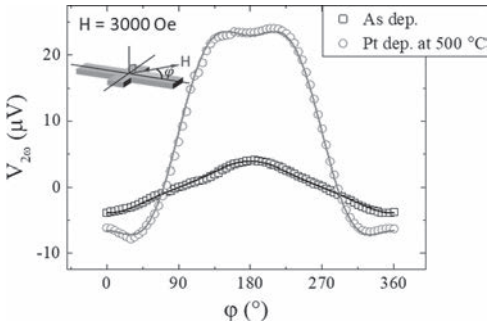


Fig. 1 The second harmonic voltage as a function of azimuthal angle for the film of thermal annealing during the Pt-deposition.

Session GQ
INTERFACES: SURFACE EFFECTS AND EXCHANGE BIAS
(Poster Session)

H.W. Chang, Chair
National Chung Cheng University, Chiayi, Taiwan

GQ-01. Superconducting Proximity Effects Near A Domain Wall In Magnetic Heterostructures. R.L. Seeger[1], G. Forestier[1], M. Akthar[2], A. Haykal[2], O. Gladii[1], S. Aufftet[1], I. Joumard[1], C. Gomez[3], M. Rubio-Roy[1], D. Gusakova[1], A.I. Buzdin[5], V. Jacques[2], M. Houzet[4] and *V. Baltz*[1] *1. Univ. Grenoble Alpes / CNRS / CEA, SPINTEC, Grenoble, France; 2. Univ. Montpellier / CNRS, L2C, Montpellier, France; 3. Grenoble INP, CIME Nanotech, Grenoble, France; 4. Univ. Grenoble Alpes / CEA, Pheliqs, Grenoble, France; 5. Univ. Bordeaux / CNRS, LOMA, Bordeaux, France*

In ferromagnet/(non-magnet)/superconductor (F/(N)/S) heterostructures, suppression of superconductivity can be partially lifted when different directions of the short-range exchange field are sampled simultaneously by a Cooper pair. Partial recovery of superconducting critical temperature (DTc/Tc) is therefore expected for a multi-domain state [1]. Observation of the effect requires adjustment of a broad set of parameters: the superconducting coherence length (XsiS) vs. the layers' thicknesses (tS, tN, tF) vs. the domain and domain wall sizes (D, d). Long-range dipolar interactions further alter the recovery. For multilayers with out-of-plane anisotropy, (Pt/Co)/Nb, maximum recovery of DTc/Tc ~1% have been reported [2], preventing investigation of the influence of the magnetic configuration. In this work, we present series of experimental results for F/S (Pt/Co)/NbN and F/antiferromagnetic-metal(AF)/S (Pt/Co)/IrMn/NbN heterostructures. We created domains in the F and in the AF [3] and varied the configurations from multi- to single-domain, controlling the density of domain walls. Nitrogen-vacancy single spin magnetometry was used in search for revealing the AF configuration [4]. Electrical measurements (resistance versus temperature) across the normal-superconductor transition were performed. The AF was found fully transparent. By tuning the various parameters into play (XsiS, tS, tAF, tF, D, and d), we obtained up to a tenfold improvement of DTc/Tc (~10%), opening the pathway for novel investigations. In particular, a gradual enhancement of DTc/Tc with the density of F domain walls could be observed. Experimental data were compared to numerical calculations based on the Usadel formalism, and encompassing the main features of the phenomenon [5].

[1] M. Houzet and A. I. Buzdin, Phys. Rev. B 74, 214507 (2006). [2] L. Y. Zhu, T. Y. Chen, and C. L. Chien, Phys. Rev. Lett. 101, 017004 (2008). [3] V. Baltz, A. Manchon *et al*, Rev. Mod. Phys. 90, 015005 (2018). [4] I. Gross, W. Akhtar *et al*, Nature 549, 252 (2017). [5] R. L. Seeger, G. Forestier *et al*, to be published.

GQ-02. Exchange Bias Effects in $Mn_2Ni_{1+x}Ga_{1-x}$ Alloys. *S. Biswas*[1], T. Schaeffer[1] and M. Khan[1] *1. Physics, Miami University, Oxford, OH, United States*

A group of Mn-rich Heusler alloys exhibit the exchange bias (EB) effect, [i], [ii], [iii] a phenomenon discovered in 1956 by Meiklejohn and Bean and is signified by a shift of the magnetic hysteresis loop along the magnetic field axis. [iv], [v] The effect is of great interest both due to its fundamental aspects[vi] and its application in technologies including spin valves, magnetic recording read heads, and giant magnetoresistive sensors.[vii], [viii] The EB effect in Heusler alloys are attributed to the coexisting ferromagnetic (FM) and antiferromagnetic (AFM) interactions in the materials. Mn_2NiGa is a Heusler alloy where the Mn moments show both parallel and anti-parallel alignments. However, the material does not exhibit any EB effect. It is interesting to manipulate the magnetic interactions in this material and explore if EB can be induced in the system by stoichiometry variation. Therefore, we have systematically investigated the magnetic and EB properties of $Mn_2Ni_{1+x}Ga_{1-x}$ ($0 \leqq x \leqq 0.65$). The samples were fabricated by arc melting and annealing techniques. For $x \leqq 0.20$ no EB was observed in the $Mn_2Ni_{1+x}Ga_{1-x}$ materials (Fig. 1). As x exceeded 0.20, EB started appearing in the materials. An EB field of as large as 4000 Oe and coercive field of more than 10 kOe were observed in the materials (Fig. 2). For selected compositions, the effect of annealing temperatures on the EB properties were also investigated. The structural and magnetic properties of all the $Mn_2Ni_{1+x}Ga_{1-x}$ materials will be presented and discussed.

[i] M. Khan, I. Dubenko, S. Stadler, and N. Ali, Appl. Phys. Lett., Vol. 91, p.072510 (2007) [ii] B. M. Wang, Y. Liu, P. Ren, B. Xia, K. B. Ruan, J. B. Yi, J. Ding, X. G. Li, and L. Wang, Phys. Rev. Lett., Vol. 106, p.077203 (2011) [iii] Z. D. Han, B. Qian, D. H. Wang, P. Zhang, X. F. Jiang, C. L. Zhang, and Y. W. Du, Appl. Phys. Lett., Vol. 103, p.172403 (2013) [iv] W. H. Meiklejohn and C. P. Bean, Phys. Rev., Vol. 102, p.1413 (1956) [v] J. Nogués, J. Sort, V. Langlais, V. Skumryev, S. Suriñach, J.S. Muñoz, and M.D. Baró, Phys. Rep., Vol. 422, p.65 (2005) [vi] J. Nogués and I. K. Schuller, J. Magn. Magn. Mater., Vol. 192, p.203 (1999) [vii] Manuel Bibes, Javier E. Villegas, and AgnèsBarthélémy, Adv. Phys., Vol. 60, p.5 (2011) [viii] B. Dieny, V. S. Speriosu, S. S. P. Parkin, B. A. Gurney, D. R. Wilhoit, and D. Mauri, Phys. Rev. B Vol. 43, p.1297 (1991)

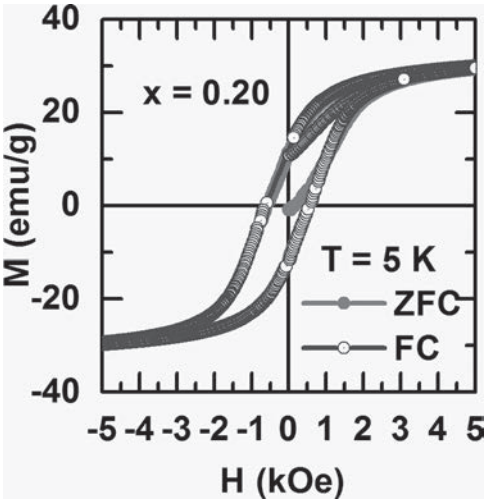


Fig. 1. Field dependence of magnetization of $Mn_2Ni_{1+x}Ga_{1-x}$ (x = 0.20) measured at 5 K.

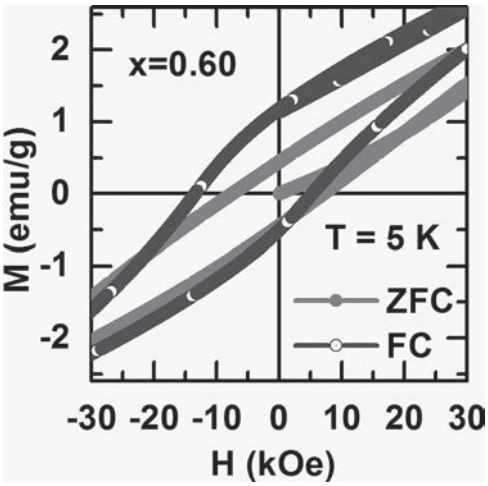


Fig. 2. Field dependence of magnetization of $Mn_2Ni_{1+x}Ga_{1-x}$ (x = 0.60) measured at 5 K.

GQ-03. X-ray resonant magnetic reflectometry (XRMR) study of the interface between ferromagnetic transition metals and MgO. *S.E. Ilse*[1], D.B. Boltje[1,2], G. Schütz[1] and E. Goering[1] *1. Modern Magnetic Systems, Max Planck Institute for Intelligent Systems, Stuttgart, Germany; 2. Delmic BV, Delft, Netherlands*

Multilayer systems of ferromagnetic transition metals and MgO attract a lot of attention in the last years because of their application in STT-MRAMs. Especially the interface between the magnetic transition metal and MgO is of interest since the chemical and magnetic properties at this interface are important for the performance of STT-MRAM cells. Because those properties determine for example the strength of the interfacial perpendicular magnetic anisotropy and the thickness of possible magnetic dead layers [1]. With our own reflectometer dedicated to (soft-) x-ray resonant magnetic reflectometry (XRMR) we are able to study such multilayer systems and determine the chemical and magnetic properties at the interfaces [2]. With XRMR we combine the advantages of reflectometry and X-ray magnetic circular dichroism (XMCD). Thus, we are able to determine element specific chemical and magnetic depth profiles. And since, XRMR is particular sensitive to interfaces the element specific roughness of each layer can be determined as well [3,4]. To determine those depth profiles we simulate XRMR measurements using ReMagX [3-5] and fit the simulations to match actual measurements. We performed X-ray absorption spectroscopy (XAS), XMCD and XRMR measurements on Ta|CoFeB|MgO|Al2O3|Au stacks. With off-resonant reflectometry measurements at different energies, we determined the chemical depth profile, which revealed a pronounced roughness at the Ta|CoFeB interface and that especially Fe intermixes largely with other species at the interfaces. Resonant magnetic reflectometry measurements at the Cobalt and Iron L3 edge enabled us to determine the magnetic depth profile, which revealed a 10 Å and a 4 Å thick magnetic dead layer for Fe and Co, respectively, at the CoFeB|MgO interface.

[1] B. Dieny and M. Chshiev, *Rev. Mod. Phys., 89.2, 025008 (2017).* [2] S. Brück, et al., Rev. Sci. Instrum., 79, 083109, (2008); [3] S. Macke and E. Goering, J. Phys.: Condens. Matter, 26.36, 363201 (2014). [4] S. Macke, et al., Adv. Mater., 26.38, 6554-6559 (2014) [5] S. Macke, www.remagx.org

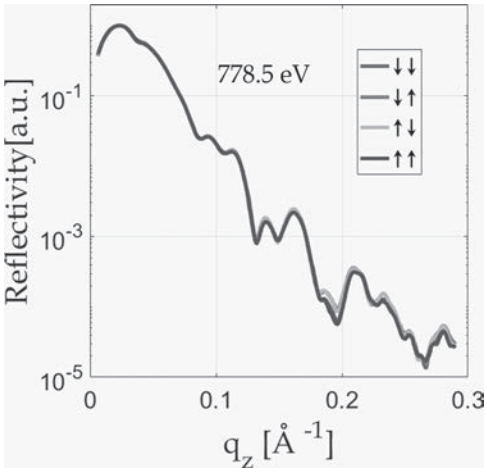


Fig.1 Resonant reflectivity curves measured at 778.5 eV (Co L3 edge) with parallel (blue and purple) and antiparallel (orange and yellow) alignment of x-ray polarization and magnetization.

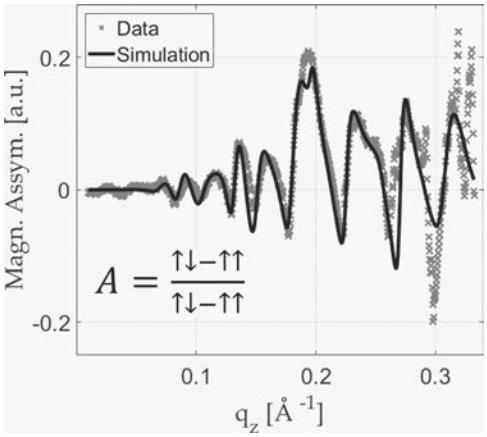


Fig.2 Measured and with ReMagX [3-5] simulated magnetic asymmetry *A* at 778.5 eV (Co L3 edge).

GQ-04. Investigation of the interlayer thickness dependent variation of saturation magnetization in Co/RuFe/Co multilayer systems using XMCD. *F. Schulz*[1], Z. Nunn[2], E. Girt[1] and E. Goering[2] *1. Modern Magnetic Systems, Max-Planck-Institute for Intelligent Systems, Stuttgart, Germany; 2. Department of Physics, Simon Fraser University, Burnaby, BC, Canada*

The effect of interlayer exchange coupling in magnetic thin films has proven to be of great technological use, enabling the development of hard drives with very high storage densities [1-3]. And yet, there are aspects of this effect that are still not fully understood. Recent studies have found that the interlayer thickness of Co/RuFe/Co sandwiches does not only affect the type of interlayer coupling and its strength, but also causes a non-monotonous variation of the saturation magnetization of these systems [4]. In order to investigate this effect, X-ray absorption spectra have been measured in total electron yield, mainly at the L_2 and L_3 edges of Fe and Co respectively. Making use of the X-ray magnetic circular dichroism (XMCD) effect, this gives an element specific method of measuring the magnetic properties of the samples. By applying the sum rules [5-7], it was possible to determine the magnetic moment per atom coming from Co and Fe respectively. Additionally, magnetometric measurements have been performed using a superconducting quantum interference device (SQUID), which were combined with simulations using an enhanced Stoner-Wohlfarth model. With these methods, it could be shown that the change in saturation magnetization does not stem from the magnetic contribution of the Fe in the interlayer, but instead can be attributed to a non-magnetic dead layer of Co near the

interface of Co and RuFe. The thickness of this dead layer was estimated using a model that incorporates electron damping, as well as self absorption effects, to be approximately 0.1 nm. In this model, an effective electron mean free path is used to calculate the damping of electrons from buried layers.

[1] P. Grünberg, R. Schreiber and H. Sowers, Physical Review Letters, Vol. 57, p. 2442 (1986) [2] G. Binasch, P. Grünberg and W. Zinn, Physical Review B, Vol. 39, p. 4828 (1989) [3] M.N. Baibich, J.M. Broto, A. Fert and J. Chazelas, Physical Review Letters, Vol. 61, 2472 (1988) [4] Z. Nunn, F. Schulz, E. Goering and E. Girt, Unpublished (2019) [5] B. T. Thole, P. Carra and G. van der Laan, Physical Review Letters, Vol. 68, p. 1943 (1992) [6] P. Carra, B.T. Thole and X. Wang, Physical Review Letters, Vol. 70, p. 694 (1993) [7] C.T. Chen, Y. U. Idzerda and F. Sette, Physical Review Letters, Vol. 75, p 152 (1995)

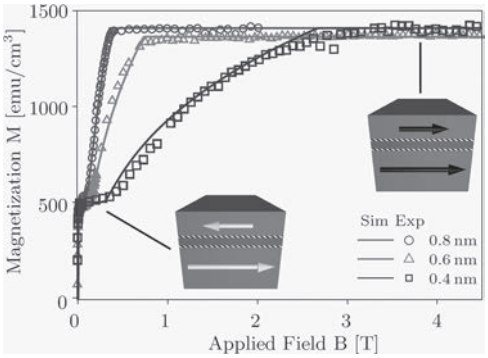


Fig. 1 Measured (markers) and simulated (solid lines) magnetization curves for the three samples with different interlayer thickness. The two sketches illustrate how the magnetization (black and white arrows) of the two Co layers (orange) is aligned at different field strengths.

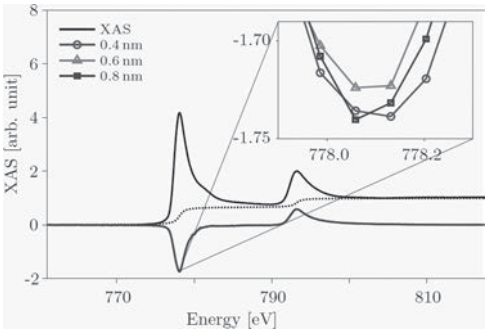


Fig. 2 Edge-normalized XAS and XMCD spectra near the Co $L_{2;3}$ edges for samples with different interlayer thicknesses (indicated by color). The dotted line is the function used for subtracting the edge jumps, and the inset shows a zoom into the L_3 peak.

GQ-05. Comparison on phase component and exchange bias in sputtered CoFe/MnN and MnN/CoFe polycrystalline films. *H.W. Chang*[1], Y. Chien[2], F. Yuan[3], Y. Lai[2], C.R. Wang[2], L. Horng[4] and C. Ouyang[5] *1. Department of Physics, National Chung Cheng University, Chia-Yi, Taiwan; 2. Department of Applied Physics, Tunghai University, Taichung, Taiwan; 3. iSentek Inc. Advanced Sensor Laboratory, Taipei, Taiwan; 4. Department of Physics, National Changhua University of Education, Changhua, Taiwan; 5. National Tsing Hua University, Hsinchu, Taiwan*

Exchange bias (EB), characterized by a shift of hysteresis loop originated from the interaction between the ferromagnetic (FM) and antiferromagnetic (AF) layers, could be a foundation for spin-valve (SV) and applied at various advanced spintronic devices. For practical EB system, the main requirements for AF layer include large magnetocrystalline anisotropy (K_{AF}), high Neel temperature, good corrosion resistance, environmental safety and low cost [1]. Recently, MnN is reported to be an excellent antiferromagnetic material to meet the above requirements [1-2]. In this work, CoFe/MnN and MnN/CoFe films with 5-nm-thick CoFe layer and 20-nm-thick MnN layer are prepared on 10-nm-thick Ta underlayer buffered SiO_2/Si(100) substrates at RT by magnetron sputtering at the external magnetic field of 350 Oe induced by the NdFeB sintered magnet. Magnetic properties and phase constitution of both MnN/CoFe (MnN at top of bilayer) and CoFe/MnN films (MnN at bottom of bilayer) bilayers with various annealing temperatures (T = 300-450 °C) during the external magnetic field of 1.5 kOe are compared. The experimental results show that EB field (H_E) of the studied films is highly related to phase constitution of AF layer. The increase of H_E with T possibly results from the improvement of magnetocrystalline anisotropy of AF related to the promoted crystallinity and stress release of θ-MnN phase with T. The reduction of H_E is due to the decreased volume fraction or disappearance of θ-MnN phase and the formation of impurity phases, such as Mn_4N and Mn. The induction of impurity phases is possibly related to the diffusion of part of N out of MnN phase at higher T. Higher H_E for CoFe/MnN than MnN/CoFe at T = 300-375 °C might be attributed to larger amount and higher degree of stress release for θ-MnN phase. In this study, the highest H_E=560 Oe is attained for CoFe/MnN film annealed at T = 350 °C. Finally, high interfacial exchange energy of 0.47 mJ/m² attained for CoFe/MnN films in this study is comparable to the literature (0.41 mJ/m²)[1]. Microstructure and interfacial morphology of the above films with T are also discussed. This study provides useful information to fabricate EB system with θ-MnN as an AF layer.

[1] M. Meinert et al., Phys. Rev. B 92, 144408 (2015). [2] P. Zilske et al., Appl. Phys. Lett. 110, 192402 (2017).

GQ-06. Magnetic Domain Wall Pinning at a Ferromagnet-Antiferromagnet Interface. *R.A. Khan*[1], T.R. Forrest[2], S.S. Dhesi[2], M. Ali[1], B. Hickey[1], C.H. Marrows[1] and T. Moore[1] *1. School of Physics and Astronomy, University of Leeds, Leeds, United Kingdom; 2. Diamond Light Source, Didcot, United Kingdom*

We sputter-deposited polycrystalline multilayers of Pt(2 nm)/Co(1 nm)/IrMn(t_{IrMn}) and Pt(2 nm)/Co(0.6 nm)/FeMn(t_{FeMn}) exhibiting perpendicular exchange bias (EB) [1]. These multilayers are of interest because of the coincidence of the Dzyaloshinskii-Moriya interaction [2, 3] with a vertical exchange field that could remove the need for an externally applied field to stabilise skyrmions [4]. We measured the EB as a function of the layer thickness of the antiferromagnetic (AFM) layers, IrMn and FeMn. Utilising Kerr microscopy and XMCD-PEEM imaging, the domain morphology of the ferromagnetic (FM) Co layer was studied when crossing over the paramagnetic to AFM phase transition of the neighbouring AFM layer. The domain texture is influenced by the FM-AFM exchange coupling. In the presence of EB, an initially smooth domain wall (DW) becomes rough when displaced by a field (Fig. 1). In the absence of EB, the DW remains smooth after displacement by a field (not shown). Meanwhile, a DW in a sample cooled from the paramagnetic phase (no EB) to the AFM phase (EB) maintains its smooth appearance if not displaced (Fig. 2). The different phases of the AFM layer were confirmed by identifying [5] the Néel and the blocking temperatures by performing temperature dependent magnetometry. These results indicate that the pinning experienced by a DW passing through the Co layer originates predominantly from the microstructure and magnetism at the interface with the AFM.

[1] R Khan et al. Phys. Rev. B 98, 064413 (2018). [2] S Emori et al. Nature Materials 9, 611-616 (2013). [3] R Khan et al. App. Phys. Lett. B 109, 132404 (2016). [4] A Fert et al. Nat. Nano. 8, 152 (2013). [5] M Ali et al. Phys. Rev. B 68, 214420 (2003). This work has been funded by EPSRC.

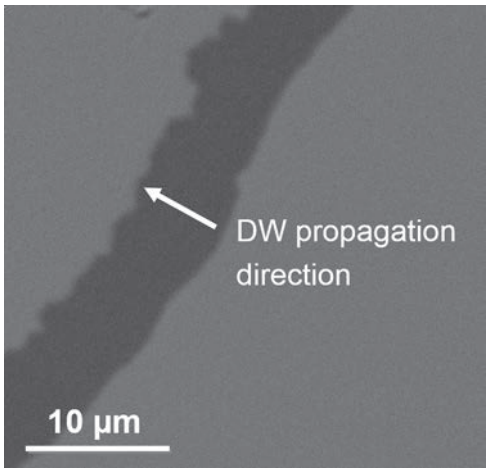


Fig. 1: Kerr microscope image showing a domain wall displaced by an applied field in the presence of exchange bias.

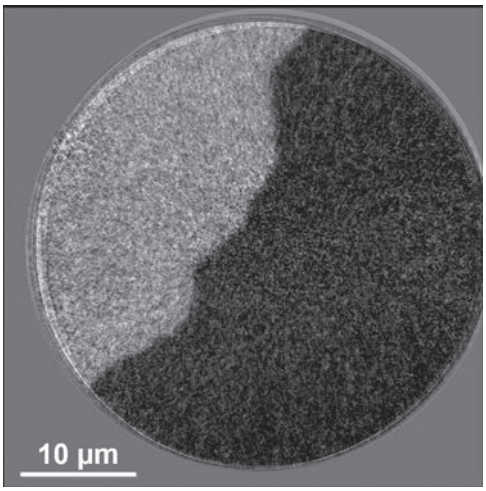


Fig. 2: XMCD-PEEM image showing a domain wall (not displaced) in the presence of exchange bias.

GQ-07. The effect of x-ray illumination on magnetic domain memory in [Co/Pd] / IrMn multilayers. *C.S. Walker*[1], M. Parkes[1], D. Keavney[2], E. Fullerton[3] and K. Chesnel[1] *1. Department of Physics & Astronomy, Brigham Young University, Provo, UT, United States; 2. Advanced Photon Source, Argonne National Laboratory, Lemont, IL, United States; 3. Center for Memory and Recording Research, UCSD, San Diego, CA, United States*

We are studying the effect that illumination by coherent x-rays may have on magnetic domain memory (MDM) in a [Co / Pd] / IrMn multilayers [1-3]. MDM is the ability of the magnetic domains to retain their exact same domain topology upon field cycling. Earlier studies have suggested that under higher dose of x-ray illumination, the material may lose its existing MDM. To investigate this potential effect we have used both x-ray resonant magnetic scattering (XRMS) along with magneto-transport measurements [4,5] to track the exchange bias while the sample is illuminated with x-rays, as illustrated in Figure 1. Magneto-transport is here used to measure the hysteresis loop of our multilayers material from which we can measure the exchange bias and its possible alteration. A loss of exchange bias would indicate that the x-rays illumination dose may alter the strength of the exchange couplings and ultimately the amount of MDM. Knowing if a loss of exchange bias has occurred requires collecting magneto-transport data as well as XRMS data and correlating the observed changes under various dose of x-ray illumination.

[1] K. Chesnel, A. Safsten, M. Rytting, and E.E. Fullerton, Nature Communications 7, (2016). [2] K. Chesnel, B. Wilcken, M. Rytting, S.D. Kevan, and E.E. Fullerton, New Journal of Physics 15, 023016 (2013). [3] K. Chesnel, J. Nelson, B. Wilcken, and S.D. Kevan, Journal of Synchrotron Radiation 19, 293 (2012). [4] C. Hurd, *Hall Effect in Metals and Alloys* (Springer, 2012). [5] L.J. van der Pauw, A Method of Measuring Specific Resistivity and Hall Effect of Discs of Arbitrary Shape (1958).

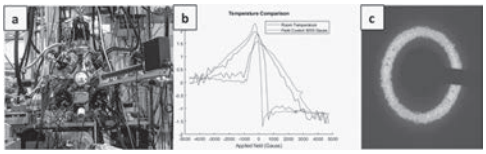


Fig.1 a) Instrument used for our x-ray resonant magnetic scattering (XRMS) experiment at the APS, showing the vacuum scattering chamber and the octupolar magnet to apply a field in any direction. b) Magneto-transport measurement taken while [Co/Pd] / IrMn multilayers was illuminated with x-rays. c) XRMS speckle pattern from the [Co/Pd] / IrMn film, measured at the Co L_3 edge.

GQ-08. Influence of the magnetic properties of the Ni films through applications of electric field on the ZnO under layer. *C. Yu*[1] and Z. Lin[1] *1. Department of Applied Physics, National University of Kaohsiung, Kaohsiung, Taiwan*

For the bilayers system consisted of a [FM/Oxide] structure, the strain effect imposed on the FM layer induced by the inverse piezoelectric effect of the oxide film was expected. In addition, the heating effect resulted from the leakage current in the oxide film also play an important role. In this study, the magnetic properties of the Ni/ZnO bilayers under the applications of the electric fields were studied. In the virgin state, the Ni/ZnO displayed a unidirectional exchange anisotropy with a $H_c \approx$ 45 Oe and an $H_{ex} \approx$ -70 Oe. The formation of the antiferromagnetically ultrathin NiO between Ni and ZnO was expected. Moreover, in our study, the I-V curve of the ZnO film displayed a diode behaviour. Same as other reports, we observed a leakage current passed through the ZnO layer as applying a reverse bias across the bilayers. Consequently, the coercivity of the Ni films was then decreased due to the heating effect as the leakage current density > 5.1×10^4 A/m^2. In the experiments of the reverse bias modulation, the MOKE intensity can be modulated under the application of a high voltage (-8V). And the variation of the MOKE intensity directly correlated to the current flowed through the bilayers structure. On the other hand, in the case of the froward bias with a lower leakage current < 1.25×10^4 A/m^2, instead of the coercivity, the decreasing of the exchange field, H_{ex} was observed as shown in Fig. 1. The H_{ex} correlated to the spin structure of the NiO layer. We concluded that the reductions of the H_{ex} was due to the strain effect applied by the ZnO under layer. For the intermediate leakage current, 1.25×10^4 A/m^2< J< 5.1×10^4 A/m^2, the Hc and Hex were decreased as applyng the reverse and forward bias, respectively, as shown in Fig. 2. In the ZnO/Ni bilayers, the current heating and interfacial strain were two factors that influence the H_c and H_{ex} of the system.

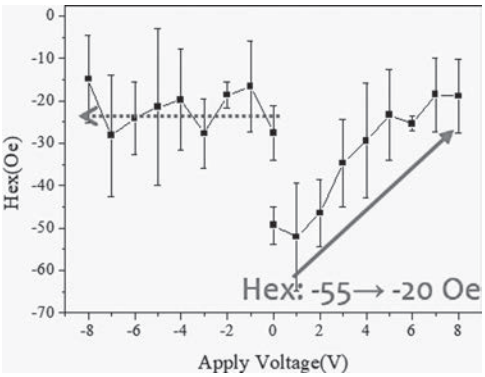


Fig.1 The H_{ex} distribution of the ZnO/NiO bilayer under applying bias voltages with a low leakage current.

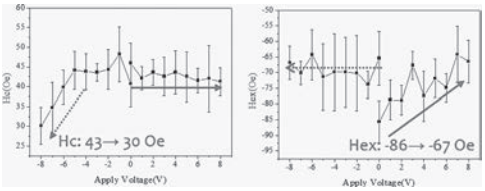


Fig.2 The H_c and H_{ex} distribution of the ZnO/NiO bilayer under applying bias voltages with a intermediate leakage current.

GQ-09. Tuning of the coercivity and Kerr Signal of NiFe films by a ZnO(0001) layer. *C. Yu*[1] and H. Ko[1] *1. Department of Applied Physcis, National University of Kaohsiung, Kaohsiung, Taiwan*

The magnetic states of traditional spin electronic devices usually controlled by magnetic fields or small currents. In such devices, the thermal stability must be well controlled. To overcome the thermal disaster, voltage-control magnetic devices composed of a ferroelectric/ferromagnetic bilayer have been developed. In this study, permalloy films with 80 at% of Ni with different thickness (t) were fabricated on ZnO(0001)/highly doped N-type Si(001). The MOKE signals and hysteresis loops of NiFe were measured while the ZnO(0001) layer was subject to an electrical voltage. The piezoelectric constant d_{33} and coercivity of the ZnO(0001) film was characterized by a PFM and has values of 5.0 pm/V and 3.4V, respectively. The lattice constant of ZnO crystal, while application of 10V, changed +/-9.6% and -/+5.2% along c- and a- axes, respectively, in the case of constant volume. The threshold voltage for the reduction of coercivity (Hc) is 2.2V, 2.7 and 5.1V for t= 10, 30 and 50nm, respectively, as shown in Fig.1. And a monotonic reduction of the Hc and Kerr signal of the NiFe films was observed no matter what polarity of the electric field was. While applying 10V across the ZnO layer, the reduction ratios of the Hc (/ Kerr signal) were 64%, 12% and43% (/ 0.5mV, mV and 0.4mV) for t=10nm, 30nm and 50nm, respectively. It is clear that the strain field stored in the NiFe layer fade away as t getting larger. Fig. 2(a) showed the variation of the Kerr signal of the 30-nm-thick NiFe under a 0-10V voltage modulation. Fig. 2(b) is the variation of the peak-to-peak MOKE intensity under different voltages and periods. These phenomena can be attributed to the lattice stress of the ZnO imposed on the NiFe layer and reversed in a range of ±10V. Therefore, modulations of the values of Kerr signal and Hc of the NiFe films through application of voltage were successfully demonstrated.

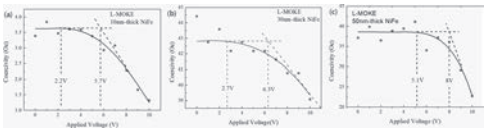


Fig.1 The coercivity distributions of the NiFe films with thickness (a) 10nm, (b) 30nm and (c) 50nm under bias voltages.

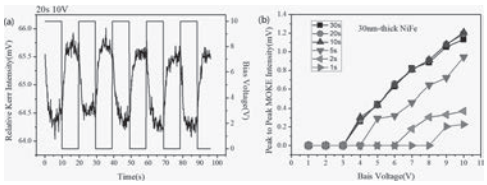


Fig.2 (a) The variation of the Kerr signal under a voltage modulation (0-10V, period=20s) of the 30-nm-thick NiFe film. (b) The variations of the peak-to-peak MOKE intensity under different periods and bias voltages.

GQ-10. The Role of Boron on Exchange Coupling in NiFe/$Ru_{1-x}B_x$/FeCo Trilayer Structures. *T.J. McKinnon*[1] and E. Girt[1] *1. Physics, Simon Fraser University, Burnaby, BC, Canada*

In our previous work, we found that coupling in FeCoB/Ru/FeCoB changes from antiferromagnetic to ferromagnetic after annealing above 200 ^{0}C for Ru spacer layer thicknesses below 0.5 nm. [1] This strong effect of annealing on the interlayer exchange coupling was not observed in structures having ferromagnetic layers without B coupled across a spacer layer. To understand the role of B on the interlayer exchange coupling, we studied the coupling in (111) textured NiFe(6 nm)/$Ru_{1-x}B_x$(*d*)/FeCo(4 nm) as a function of B concentration in Ru, x, and spacer layer thickness, *d*. These films were deposited at room temperature and ferromagnetic resonance and vibrating sample measurements were used to measure the coupling in as-deposited and annealed samples. It was found that in as deposited samples the sign and strength of coupling is not affected significantly for up to 15 at. % of B in Ru as shown in Fig.1. This indicates that the presence of only B in Ru is not responsible for the change in coupling in FeCoB/Ru/FeCoB after annealing [1]. Next, we annealed the samples at 250 C. For samples with boron in the spacer layer, this resulted in a strong ferromagnetic coupling for spacer layers thinner than approximately 0.5 nm, which is the same that was observed in annealed samples. These measurements are shown in Fig.2. By measuring the samples with high resolution energy-dispersive x-ray spectroscopy (EDX) and x-ray diffraction (XRD), we have determined that the presence of B within the Ru spacer layer enhances the diffusion of Fe into the Ru spacer layer. This is likely the cause of the change in coupling from antiferromagnetic to ferromagnetic that we observed.

[1] T. McKinnon, and E. Girt, *Applied Physics Letters* 113, 19 (2018)

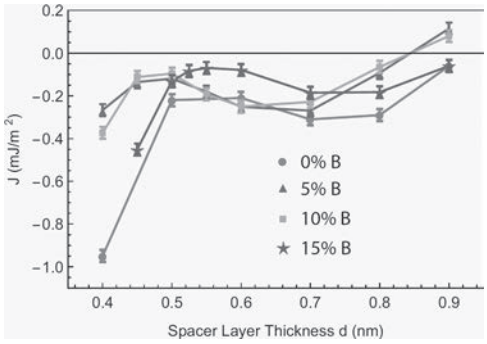


Fig. 1: Magnetic coupling constant of a NiFe layer coupled to a FeCo layer across a ruthenium boron alloy, with 0, 5, 10, and 15% boron. Samples are as-deposited. Negative J corresponds to antiferromagnetic coupling, and positive J is ferromagnetic coupling.

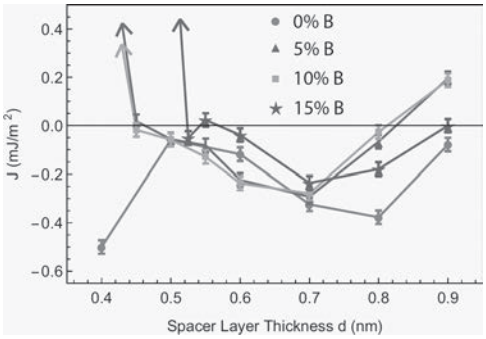


Fig. 2: Magnetic coupling constant of a NiFe layer coupled to a FeCo layer across a ruthenium boron alloy, with 0, 5, 10, and 15% boron, after annealing at 250C. Negative J corresponds to antiferromagnetic coupling, and positive J is ferromagnetic coupling.

GQ-11. New magnetic phases of thin terbium (Tb) films. *F.H. Sales*[1], A.S. Carriço[2] and A.L. Dantas[3] *1. Department of Physics, Federal Institute of Maranhão (IFMA), São Luís, Brazil; 2. Department of Physics, Federal University of Rio Grande do Norte, Natal, Brazil; 3. Departament of Physics, University of State of Rio Grande do Norte, Natal, Brazil*

In recent years a considerable research effort has been dedicated to investigate the impact of confinement and surface effects on the equilibrium phases and excitations of magnetic systems with size comparable to fundamental magnetic lengths [1-3]. Confinement effects are particularly interesting in magnetic systems in which the leading bulk magnetic phases consist of patterns made of a periodical repetition of units containing a finite number of spins. This is the case of the helical structure of rare earth metals, and the helix period might be a valuable length scale to predict the impact of finite size effects [4-6]. We report model calculations of the magnetic phases of thin terbium (Tb) films in the temperature (T) interval between 220K and 280K, and external magnetic field (H) strength up to 300Oe. We show that size and surface effects may produce relevant changes in the magnetic phases such as the presence of phases of alternate double helix (Figure 1) and deformed helix (Figure 2). Surface effects originate in the break of the exchange energy balance near the surface, and confinement effects are stronger for film thicknesses of the order of the period of the helix.

[1] E. Weschke, H. Ott, E. Schierle, C. Schüßler-Langeheine, D. V. Vyalikh, G. Kaindl, V. Leiner, M. Ay,T. Schmitte, H. Zabel, and P. J. Jensen, Phys. Rev. Lett. 93, 157204 (2004) [2] Ana L. Dantas, R. E. Camley and A. S. Carrio, IEEE Trans. Magn. 42, 2942 (2006) [3] A. L. Dantas, R. E. Camley, and A. S. Carriço, Phys. Rev. B 75, 094436 (2007) [4] F. H. S. Sales, A. L. Dantas, V. D. Mello, and A. S. Carriço, Journal of Materials Science 45, 5036 (2011) [5] F. H. S. Sales, A. L. Dantas, V. D. Mello, and A. S. Carriço, AIP Advances 2, 032158 (2012) [6] V.D.Mello, D.H.A.L.Anselmo, M.S.Vasconcelos, and N.S.Almeida, Solid State Communications, 268, 56-60, (2017)

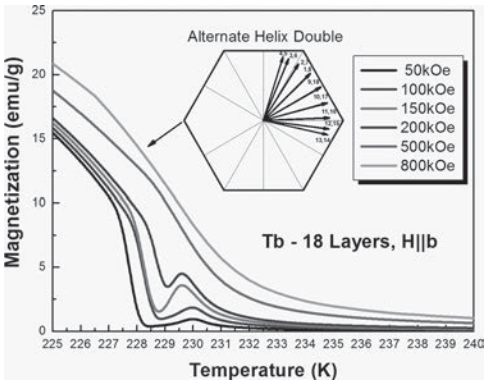


Fig.1 Magnetization for 18 layers terbium thin film for an external field of 50 to 800kOe along the b-axis. The spin panels are schematic representations of the magnetic phases at selected temperatures

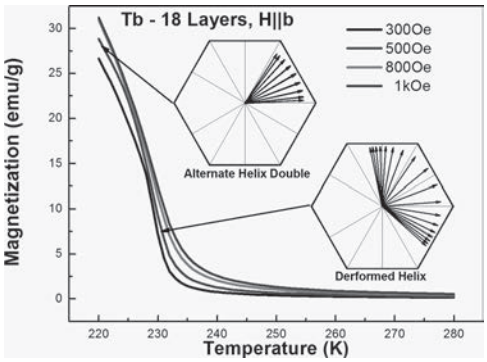


Fig 2. Magnetization for 18 layers terbium thin film for an external field of 300Oe to 1kOe along the b-axis. The spin panels are schematic representations of the magnetic phases at selected temperatures

GQ-12. Structural and Magnetic Properties of Thermally Annealed *Nd–Fe–B /Fe* Multilayer Thin Fims. *S. Yazdani*[1], A. Mosey[1], J. Soruco[1], T. Bsaibes[1], J. G. Giuliani[2], C. Monton[2], R. Decca[1] and R. Cheng[1] *1. Physics, Indiana University Purdue University Indianapolis, Indianapolis, IN, United States; 2. Physics, University of Texas at San Antonio, San Antonio, TX, United States*

In this investigation, we are working toward creating a heterogeneous structure with zero total magnetization while possessing a net spin by developing a multilayer structure composed of Fe and NdFeB thin films on silicon substrate. Samples were prepared by DC magnetron sputtering in a high vacuum chamber. To improve the quality of multilayer thin films, nanocrystalline growth of metal compound NdFeB was achieved using a house-made vacuum compatible heater made by paralleled filaments covered with ceramic materials. Samples were heated in situ at different temperatures. It is shown that a suitable thickness of the wetting layer can reduce the roughness of the films and also prevent NdFeB from oxidization. Characterizations of samples were done with X-ray diffraction (XRD) and Vibrating Sample Magnetometer (VSM) and results indicate that the crystal structure shows dependence upon in situ heater temperature. Ferromagnetic thin films of rare earth NdFeB and transition metal Fe were separated by a non-magnetic layer (Ti). We fabricated a series of samples with different spacer layer thickness in order to study the exchange coupling between NdFeB and Fe layers. Experiments indicating that as the thickness of spacer layer changes, the magnetic coupling switches from ferromagnetic coupling to antiferromagnetic coupling.

1. *Magnetic Properties and Magnetic Domains of Nd-Fe-B Thin Films.* S. L. Chen, W. Liu, Z.D. Zhang, and G. H. Gunaratne, Journal of Applied Physics (2008) 2. Effect of wetting layer and substrate temperature on the surface morphology, the domain structure and magnetic properties of X-axis-oriented

NdFeB-S.L.Chen, W.Liu, C.L.Chen and Z.D. Zhang, Journal App Phys (2005) 3. W.B. Cui, W. Liu, J. Li, Y. Fang, Q. Zheng, X.G. Liu, et al, J. Phys. D Appl. Phys. 41, 245007. (2008) 4. M. Amato, M.G. Pini, A. Rettori, Phys. Rev. B 60 3414 (1999) 5. J.M.D. Coey, Magnetism and Magnetic Materials, Cambridge University Press, Cambridge, pp. 242. (2010) 6. H. Sepehri-Amin, T. Ohkubo, T. Shima, K. Hono, Acta Mater. 60 819 (2012) 7. Y. Murakami, T. Tanigaki, T.T. Sasaki, Y. Takeno, H.S. Park, T. Matsuda, et al., Acta Mater. 71 370 (2014)

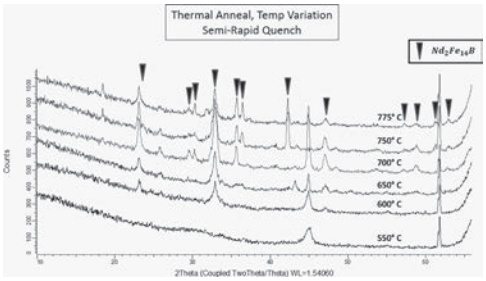


Fig.1 XRD spectra of successive samples made at different temperatures. Intensity is relative

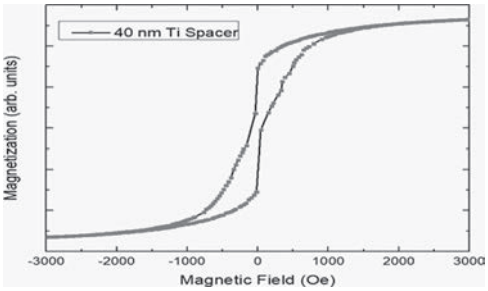


Fig.2 Hysteresis loop of sample [Si/Ti(20 nm)/NdFeB(300 nm)/Ti(40 nm)/Fe(270 nm)/Ti (20 nm)] layer annealed at 700 °C

GQ-13. Improving Exchange Bias via Oblique Incidence Deposition.
T. Gurieva[1], K. Schlage[1], L. Bocklage[1,2], S. Willing[1], M. Ramin Moayed[1] and R. Röhlsberger[1,2] *1. Photon Science, Deutsche Elektronen-Synchrotron (DESY), Hamburg, Germany; 2. The Hamburg Center for Ultrafast Imaging, Hamburg, Germany*

Exchange bias (EB) layer structures consisting of an antiferromagnetic (AFM) and a ferromagnetic (FM) material have been in the focus of intense research for decades due to their high technical relevance for the realization of thin film reference magnetizations, e.g. in magnetoresistive sensor systems of type TMR or GMR. The pressing requirement for these sensors to be increasingly robust against external magnetic stray fields, for example in automotive applications, causes the need for continuous improvement of this unidirectional AFM/FM interface pinning. Various approaches are tested to improve EB, most of them are based on a chemical or crystalline modification of the layer structure. Here we show that a small variation in the thin film deposition process without a change of chemical composition can lead to a significant improvement of the EB pinning. Deposition of the AFM layer at an oblique incidence at an optimized polar angle θ can lead to higher induced anisotropy energy into the FM layer that enlarges the sensor's possible working regime. The effect, which could be reproduced in different material systems (Fig. 1) will be investigated addressing the EB dependence on the deposition angle θ and the layer thickness of the AFM. Influences on the crystalline layer structure and thermal stability of the EB pinning will be shown. The presented approach to improve EB in polycrystalline layer systems is interesting for both, scientific investigations to identify its origin and limits as well as a convenient approach to significantly improve the stability of a reference magnetization in magnetoresistive sensor systems [1].

1. K. Schlage, T. Gurieva, S. Willing, L. Bocklage and R. Röhlsberger, European patent application EP18179692.1 (2018, pending)

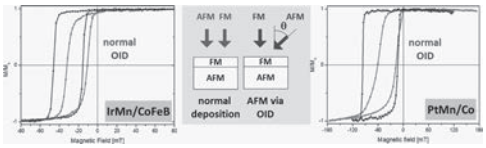


Fig. 1. Effect of oblique incidence deposition on the magnetic pinning in polycrystalline IrMn/CoFeB and PtMn/Co EB layer structures. Red curves show the magnetic behavior of the sample systems deposited at normal incidence, blue curves show the magnetic behavior when the AFM layers are deposited in oblique incidence. The strength of the EB pinning of the FM layers is significantly increased in both cases, quantitatively and qualitatively.

GQ-14. Dehydration Behavior of Hydrated MgO Thin Film Barrier-MTJs.
S. Tigunta[1], N. Valanoor[3], D. Sando[3], Q. Zhang[3] and S. Pojprapai[2] *1. School of Materials Engineering, Suranaree Univerisy of Technology, Muang, Thailand; 2. School of Ceramics Engineering, Suranaree University of Technology, Muang, Thailand; 3. School of Materials Science and Engineering, University of New South Wales, Sydney, NSW, Australia*

Magnesium oxide (MgO) thin film has been used as an insulating thin film layer of magnetic tunneling junctions (MTJs) in hard disk drives (HDDs) read head sensor [1-2]. Since the tunneling magnetoresistance (TMR) value of the MTJs can be enhanced to 600% at room temperature, the sensitivity of the read head sensor of HDDs increases [3-4]. Researchers point out that the crystallographic symmetry, electronic state and the thickness of the barrier are the crucial factors of the extremely high TMR ratio [5-6]. They attempt to control these factors. However, the hygroscopic nature of MgO is a considerate problem. Under normal atmosphere condition, the humidity from the environmental generate surface hydroxyls on their surface [7-8]. This can result in the change of structure, chemical compositions and thickness of the film. Moreover, it could lead to the degradation of MTJs and the performance of HDDs. Therefore, a better understanding of the dehydration reaction of the film is necessary for the further development of the applications of the MgO thin film. In this work, we focused on the investigation of the dehydration behavior under different atmospheres of the hydrated MgO thin film. The MgO thin films with 20 nm thickness were exposed to the humid environment for 24 h. Then, the hydrated films were annealed at various temperatures under either air atmosphere or nitrogen gas atmosphere. The roughness, the thickness and the chemical composition of the films were carried out by using the Atomic Force Microscopy (AFM), X-ray reflectivity (XRR) and X-ray photoelectron spectroscopy (XPS), respectively. The XPS results demonstrate that the MgO thin film forms the hydroxide layer over their surface after being exposed to a humid environment. The AFM results also show that the roughness of the film increases after being exposed to a humid environment. After the annealing process, the roughness of the films decreases with an increasing of annealing temperature. In addition, the XRR results also reveal that the thickness of the MgO thin film after being annealed can be recovered back to be similar to the fresh sample while the most prominent recovery is observed in the sample annealed under argon gas atmosphere.

1. S. K. Mahadeva, J. Fan, A. Biswas, Nanomater., 3(3), 486-497 (2013). 2. C.Y. Chou, Y. D. Yao, P. C. Kuo, J. Magn. Magn. Mater., 304, 103-105 (2006). 3. H. Yang, S. H. Yang, S. Parkin, AIP Adv., 2, 012150 (2012). 4. P. Wisniowski, M. Dabek, S. Cardoso, Sens Actuators A Phys., 202, 64-68 (2013). 5. Y. Z. Wu, Z. Q. Qiu, A. K. Schmid, J. Magn. Magn. Mater., 310, 1629-1631 (2007). 6. S. Yuasa, D. D. Djayaprawira, J. Phys. D: Appl. Phys., 40, 337-354 (2007). 7. J. H. Lee, J. H. Eun, S. Y. Park, Thin Solid Films., 435, 95-101 (2003). 8. B. B. Singh, V. Agrawal, A. G. Joshi, Thin Solid Films., 520, 6734-6739 (2012).

GQ-15. Magnetization reversal mechanisms of ferromagnetic layers in NiFe/IrMn/NiFe exchange bias thin film structures. *C. Gritsenko*[1], V. Rodionova[1,2] and M. Rivas[3] *1. Institute of Physics, Mathematics and Information Technology, Immanuel Kant Baltic Federal University, Kaliningrad, Russian Federation; 2. National University of Science and Technology MISIS, Moscow, Russian Federation; 3. Departamento de Fisica, Campus de Viesques, Universidad de Oviedo, Gijon, Spain*

The exchange bias thin film structures NiFe/IrMn/NiFe based either on $Ni_{40}Fe_{60}$ or $Ni_{75}Fe_{25}$ alloy, and with different antiferromagnetic layer thickness from 2 to 10 nm were studied. Magnetization reversal mechanisms, exchange bias and coercivity fields were examined in the temperature range from room down do 80K. The ferromagnetic-antiferromagnetic interface morphology was examined by the transmission electron microscopy. Magnetic properties of the samples were studied by vibrating sample magnetometry. The magnetization reversal sequence of the two ferromagnetic layers was found to depend only on the type of NiFe alloy. In the samples with 75% relative content of Ni, the bottom ferromagnetic layers reverse prior to the top one. On the contrary, in the samples with 40% of Ni, the top ferromagnetic layers reverse prior to the bottom one. The obtained results were analyzed in terms of the switching field distribution theory. The magnetization reversal process was simulated using Matlab software. The obtained diversity in magnetization reversal sequence of the ferromagnetic layers was explained to be caused by the morphological difference of the bottom interfaces in the samples of the different types.

Martínez-García, José Carlos, et al. “First-order reversal curves analysis in nanocrystalline ribbons.” *Journal of Physics D: Applied Physics* Vol. 47.1, p. 015001 (2013)

GQ-16. Non-collinear coupling materials and mechanism. *Z. Nunn*[1] and E. Girt[1] *1. Simon Fraser University, Burnaby, BC, Canada*

Non-collinear coupling is the relative angle control of two ferromagnetic layers separated by an interlayer. Non-collinear coupling is demonstrated experimentally by mixing a non-magnetic material which provides antiferromagnetic alignment (180°) with a ferromagnetic material which causes ferromagnetic alignment (0°). The coupling angle was found to change from 180° to 0° alignment dependent on the non-magnetic/magnetic ratio of the alloy [1]. For specific interlayer materials such as RuCo and RuFe this 180-0° transition was found to be over a wide concentration range. Fig. 1 shows the concentration, x, range for which a $Co|Ru_{100-x}\ Fe_x$ (0.75 nm)|Co structure has non-collinear alignment. The data was collected by SQUID and room temperature (298 K) as described in the methods of reference [2]. In addition to Co ferromagnetic layers, a variety of materials were found to achieve non-collinear coupling including CoFe, CoFeB, CoNi, Py and Ni. Magnetic polarization of the interlayer plays an important role in non-collinear as the interlayer of RuCo and RuFe were found to have magnetic properties. Additionally, high amounts of magnetically polarisable materials such as Pt and Pd can replace Co or Fe in RuCo or RuFe without drastically affecting the coupling properties. The interlayer mechanism which causes the non-collinear alignment of ferromagnetic layers is a complicated and frustrated system, consisting of multiple known sources leading to a non-collinear alignment of ferromagnetic layers [3][4][5]. Fig.2 shows an atomistic simulation demonstrating non-collinear coupling of ferromagnetic layers across an interlayer. This interlayer has random atom placement of magnetic and non-magnetic materials which creates sub 2 nm spatial fluctuations of ferromagnetic and antiferromagnetic coupling across the films surface. These fluctuations are the leading cause of non-collinear coupling in our structures. In addition of spatial fluctuations, the direct exchange coupling of the randomly placed atoms were also found to contribute to non-collinear coupling of the surrounding feromagnetic layers.

[1] Nunn, Z. R., & Girt, E. *U.S. Patent Application No. 10/204,671*. (2019). [2] Nunn, Z. R., & Girt, E. Non-collinear coupling across RuCo and RuFe alloys. *arXiv preprint arXiv:1901.07055*. (2019). [3] Stiles, M. D. Ultrathin Magnetic Structures III-Fundamentals of Nanomagnetism. (2005). [4] Slonczewski, J. C. Origin of biquadratic exchange in magnetic multilayers. *Journal of Applied Physics*, *73*(10), 5957-5962. (1993). [5] Slonczewski, J. C. Fluctuation mechanism for biquadratic exchange coupling in magnetic multilayers. *Physical review letters*, *67*(22), 3172. (1991).

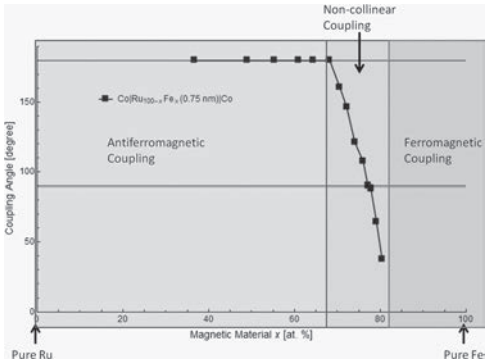


Fig. 1 180-0° coupling transition of the structure $Co|Ru_{100-x}\ Fe_x$ (0.75 nm)|Co

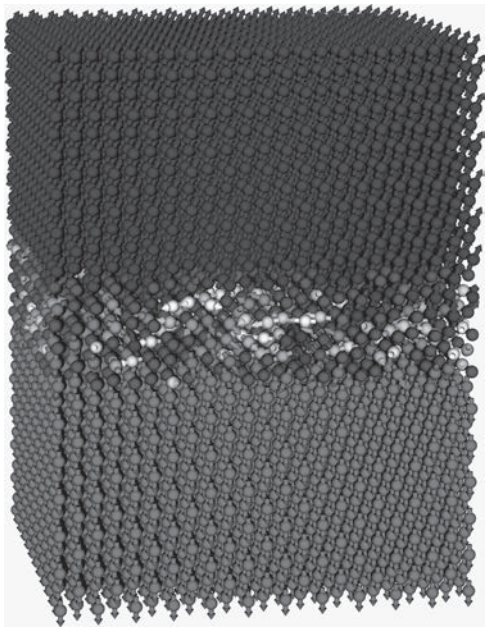


Fig. 2 Atomistic simulation of non-collinear coupling

Session GR
MAGNETIC RECORDING I
(Poster Session)

Joseph E. Davies, Chair
NVE Corporation, Eden Prairie, MN, United States

GR-01. Interlayer Coupling of Nano Circular $L1_0$-MnGa/ Cr/ $D0_{22}$-Mn_3Ga Tri-layered Dots Array. *Y. Kikuchi*[1], T. Shima[1] and M. Doi[1] *1. Graduate School of Engineering, Tohoku Gakuin University, Tagajo, Japan*

A lot of studies of Mn-Ga thin films have been performed, however, there are few reports about the Mn-Ga thin film in submicron scale. In this study, Mn_xGa circular dot arrays have been microfabricated and a relation between the magnetic properties and the diameter of the dots have been investigated in order to obtain the design guide line of new high-performance magnetic thin film material for multilevel ultra high-density magnetic recording[1)-3)]. The Mn_xGa thin films were prepared by alternate deposition method. The single layer thin films and multilayered thin films were grown on an MgO (100) single crystal substrate using by the ultrahigh vacuum multiple sputtering system. A Cr buffer layer was deposited, and then, Mn and MnGa layers were stacked alternately. The number n was fixed as 10 and 20, whereas the magnetic layer thickness was fixed at 20 nm. Substrate temperature during deposition of this magnetic layer was 150 and 200 °C. The MnGa circular dots were microfabricated from the continuous films through the electron beam lithography and an Ar ion milling. The diameter of the circular dots (D) was varied from 0.1 to 2.0 μm$^{\Phi}$. The crystalline structure of the films was characterized by the X-ray diffraction (XRD). The magnetic properties of the films and the dots were characterized by the super conducting quantum interference device magnetometer (SQUID), and the polar magneto optical Kerr effect (μ-MOKE). Surface roughness of the thin films and shape of the dots was confirmed by the atomic force microscope (AFM). The K_u was approximately 14 Merg/ ccfor the multilayered thin film with t_{Cr}= 5 to 20 nm, and15Merg/ ccfor t_{Cr}= 10 nm. A remarkable step was clearly observed in the third quadrant of the magnetization curve with the out-of-plane field for the film with t_{Cr}= 10 to 20 nm, which indicates the individual magnetization reversal of the top and bottom MnGa layers. It was confirmed that the values of coercivity were comparable between $L1_0$-MnGa and $D0_{22}$-Mn_3Ga at D= 0.2 μm$^{\Phi}$. Coercivity with smaller particle size less than D= 0.1μm$^{\Phi}$ will be discussed at the conference.

[1] H. Makuta, H. Iwama and M. Doi Jpn. *J. Appl. Phys*. 56, 055504 (2017) [2] D. Oshima, T. Kato and S. Tsunashima: *IEEE Trans. Magn*., 49, 3608 (2013) [3] N.Kikuchi, S. Okamoto and K. Fukamichi, *Appl. Phys. Lett*. 82, 4313 (2003)

GR-02. (001)-textured MnGa ultrathin films grown on thermally oxidized Si substrate using CoGa buffer layer. Y. Miwa[1], *D. Oshima*[2], T. Kato[1] and S. Iwata[2] *1. Department of Electronics, Nagoya University, Nagoya, Japan; 2. Institute of Materials and Systems for Sustainability, Nagoya University, Nagoya, Japan*

Ion irradiation technique is quite useful to realize low-cost bit patterned media (BPM) with an extremely flat surface. We have previously reported that (001)-textured MnGa films were fabricated by optimizing the growth condition of the buffer layer of Cr(20 nm) / MgO(20 nm) / CrB(5 nm) / NiTa(25 nm) on thermally oxidized Si substrates, achieving low-cost fabrication of the ion-irradiation BPM [1]. Recently, it was reported that CoGa buffer layers were effective to grow (001)-textured MnGa films even with the thickness < 5 nm [2]. Since thinner MnGa films are better for realizing high-density BPM [3], we investigated the growth of (001)-textured ultrathin MnGa films by depositing the CoGa layer on the optimized buffer layer. The stack was Cr(2 nm) / MnGa(5 nm) / CoGa(30 nm) / Cr(20 nm) / MgO(20 nm) / CrB(5 nm) / NiTa(25 nm) / SiO_2(500 nm) / Si substrate. The MgO layer was deposited by e-beam evaporation and others by RF magnetron sputtering. After the deposition of Cr buffer layer, the sample was annealed at 800 °C for 1 h. Then, the CoGa layer was deposited at T_s and post-annealed at T_a for 30 min. The MnGa layer was grown on the buffer layer at 200 °C and annealed at 400 °C for 1 h. Since T_s dependence of the saturation magnetization M_s of MnGa films showed that M_s took a maximum when the CoGa layer was grown on T_s = 400 °C, T_s was fixed to be 400 °C. Fig. 1 shows out-of-plane and in-plane M-H curves of MnGa films grown on CoGa annealed at T_a = (a) 600 °C and (b) 700 °C, and the M-H curves of the films grown on an MgO substrate are also shown in Fig. 1 (c) as a reference. M_s of 290 emu/cc was obtained when T_a = 700 °C, which was almost the same value as that grown on the MgO substrate. In addition, the slope of the out-of-plane curve became steep for T_a = 700 °C, which implies the improvement of the film quality and the smooth propagation of domain walls inside the film. Thus, it is concluded that high-quality ultrathin MnGa films are obtained by using CoGa buffer layers.

[1] T. Ishikawa et. al., IEEE Trans. Magn., DOI: 10.1109/TMAG.2018.2889499. [2] A. Ono et. al., Appl. Phys. Exp., vol. 10, 023005 (2017). [3] Y. Horie et. al., Intermag 2018 conf., BQ-12 (2018).

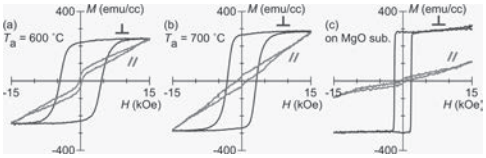


Fig. 1 Out-of-plane and in-plane M-H curves of MnGa films grown on SiO_2/Si sub. using CoGa buffer layers annealed at T_a = (a) 600 and (b) 700 °C. M-H curves of the film grown on an MgO substrate are also shown in Fig. (c) as a reference.

GR-03. Analysis of the Relationship between Error Rate Performances and Grain Size Distributions for Recording Media in Heat Assisted Magnetic Recoding. *H. Saito*[2], S. Uesugi[3] and F. Akagi[1] *1. School of Advanced Engineering, Kogakuin University, Tokyo, Japan; 2. School of Advanced Engineering, Kogakuin University, Tokyo, Japan; 3. Graduate School of Engineering, Kogakuin University, Tokyo, Japan*

In this research, it analyzes reproducing signal waveforms which correspond to any binary recorded data patterns are obtained from the superposing calculation of isolated playback pulses in heat assisted magnetic recording [1]-[3]. Each isolated playback pulse which corresponds to a recorded symbol 1 or 0 is obtained from the average value of several playback signal amplitudes with respect to a normalized recording interval T_b. In evaluating approximate expression for an isolated playback pulse, it considers a given grain size distribution of the recording medium. The head/medium conditions to achieve an areal recording density of 2.5Tb/in^2 using micro-magnetic simulation is assumed. It assumes to present the modeling result by using FePt granular magnetic media. In the recording process, magnetization is calculated by use of the Landau-Lifshitz-Gilbert equation. In calculating this equation, the saturation magnetization, the anisotropic magnetic field and variance of the anisotropy constant are set to 820emu/cm^3, 43.6kOe and 5%,

respectively. The average grain size of the medium and the width of a grain boundary are 4.5nm and 1nm, respectively. The effective recorded magnetic field intensity under the optical spot emitting device is set to about 11kOe in a central axis of a thickness direction of the medium. The reproducing track width is 20.0nm and the standard deviation of a grain size distribution of 15% or below is assumed. Under these conditions, we get the reproducing signal waveform corresponding to the recording pattern which has the repetition period 8 of the symbol 1 or 0 alternately. Fig.1 shows an example of the reproducing signal waveforms. From the given reproducing signal waveform, we derive the approximate formula for the signal waveform corresponding to the symbol 1. Finally, using partial response maximum likelihood equalization for the reproducing signal waveforms, it evaluates the BER performances of the recorded binary data in Fig.2. From Fig.2, it is found that the improvement of the BER performance of the recording scheme is obtained if the grain size distribution of the recording medium sets about 10%.

[1] H. Saga, H. Nemoto, H. Sukeda, M. Takahashi, "New recording method combining thermo-magnetic writing and flux detection," *Jpn. J. Appl. Phys.*, vol.38, no.3B, pp.839–1840. Mar. 1999. [2] F. Akagi, T. Matsumoto, and K. Nakamura, "Effect of switching field gradient for thermally assisted magnetic recording," *Journal of Applied Physics*, 101, 09H501-1, April 2007. [3] F. Akagi, et al., "Thermally assisted magnetic recording with bit-patterned media to achieve areal recording density beyond 5Tb/in^2," *Journal of Magnetism and Magnetic Materials*, 324, pp.309-313, 2012.

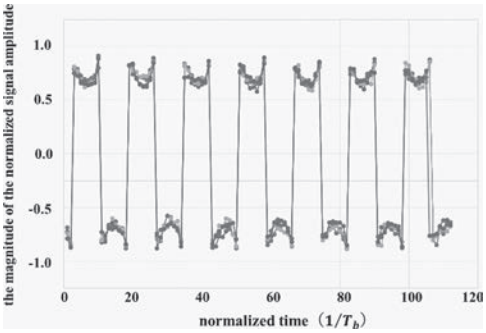


Fig.1 An example of reproducing signal waveforms.

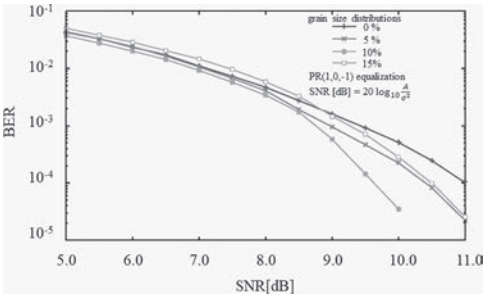


Fig.2 BER performances.

GR-04. A Study of Detection Scheme for MR Reading of Double Granular Recording Layer. *Y. Nakamura*[1], M. Nishikawa[1], Y. Kanai[2], H. Osawa[1] and Y. Okamoto[1] *1. Ehime University, Matsuyama, Japan; 2. Niigata Institute of Technology, Kashiwazaki, Japan*

In this research, we propose a detection scheme to read double granular recording layer using the magnetoresistive (MR) read-sensor. The granular medium has the grain size fluctuation and it results in the jitter-like medium noise and so on [1]. Essentially, the writing process must be assisted by the microwave magnetic field from the spin torque oscillator (STO) [2]. However, we applied the slope model [1] for each layer for simplification of the writing process in this research. In the reading process, the MR read sensor detects the magnetic stray fields from both recording layers at a time, and the reproducing waveform includes the signals from the both layers, which we call the inter-layer interference (ILI). We define the magnetic spacing between the bottom of reader and the top of upper recording layer as Δ_1 and that of the lower layer as Δ_2. In our previous research shown in [3], we found out that it is difficult to equalize the mixed waveform from the layers to the partial response (PR) signal due to the different magnetic spacing loss. Therefore, in order to compensate the influences of the spread distribution at the equalizer output, we try to increase the number of states in the sequence decoder to estimate the levels due to the ILI in the lump decoding for the first and second layers [3], and evaluate the bit-error rate (BER) performance of the system under the specification of an areal recording density of 4 Tbits/inch^2 per layer. Figure 1 shows the bit-error rate (BER) performances for SNR_S for the system noise [4]. In this figure, the square and triangle symbols show the BER performances by the Viterbi detector [5] for single layer (4 Tbits/inch^2) in the respective cases of Δ_1 = 2.0 nm and Δ_2 = 5.0 nm with the number of decoder states N_s = 2. Furthermore, the circle symbol shows that for double layers (8 Tbits/inch^2) with $N_s = 4^7$. As can be seen from the figure, the lump decoding for the double layer shows the almost same performance as that of single layer for Δ_1 = 2.0 nm. The results show that the lump decoding was effective for the double granular recording layer.

[1] M. Yamashita, et al., IEICE Trans. Electronics, vol.E96-C. no.12, pp.1504–1507, Dec. 2013. [2] S. Greaves, et al., IEEE Trans. Magn., vol.53, no.2, 3000510, Feb. 2017. [3] Y. Nakamura, et al., IEEE Digest of TMRC 2019, P1-05, July, 2019. [4] R. Suzutou, et al., IEEE Trans. Magn., vol.51, no.11, 3002004, Nov. 2015. [5] A. Viterbi, IEEE Trans. Info. Theory, vol.13, no.2, pp.260–269, April 1967.

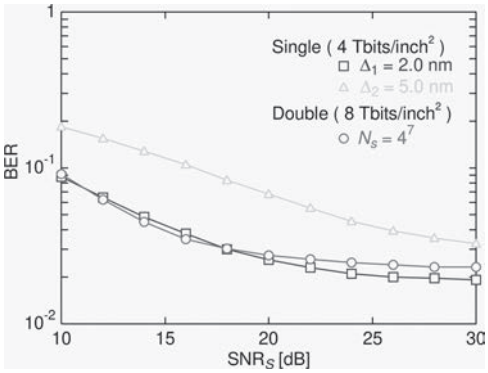


Fig.1 BER performance for SNR_S.

GR-05. Extremely flat surface full granular media with cap layer consists of high-K_u CoPt grains and ferromagnetic oxide grain boundaries. *K. Tham*[1,2], R. Kushibiki[1], T. Kamada[1] and S. Saito[2] *1. Tanaka Kikinzoku Kogyo, Tsukuba, Japan; 2. Electronic Engineering, Tohoku University, Sendai, Japan*

Perpendicular recording media with a granular recording layer (GRL) and a cap layer (CL) have been adopted in the HDD industry. GRL consists of CoPt alloy grains and non-ferromagnetic oxide boundaries. To control intergranular exchange coupling[1)] and switching field[2)] in GRL, various low magnetic anisotropy (K_u) continuous layers such as, Co/Pd multilayers[3)], rare earth (RE) metal alloy layer[4,5)], and CoPtCrB layer[6)] have been proposed for the CLs. However, it is quite challenging to obtain a homogeneous structure in the thickness direction with a continuous CL deposited on the GRL[7)] which leads to inhomogeneous intergranular exchange coupling. To address the issue, we propose a granular CL consists of high K_u CoPt grains and ferromagnetic oxide boundaries. In this study, RE oxides such as Gd_2O_3, Nd_2O_3, Sm_2O_3 and CeO_2 are utilized for the ferromagnetic oxide boundaries materials. Fig. 1 shows M/M_s-H loops of media with (a) CoPt-Gd_2O_3 and (b) (CoPtCr)-10B CLs (9 nm) deposited on CoPt-B_2O_3 GRL (16 nm). M/M_s-H loop of GRL (16 nm) without CL is shown in broken line. Both media show comparable nucleation field and saturation field of 0.9 and 12.5 kOe, respectively, which are better than those of medium without CL. Evaluation of switching field ($\Delta H_c/H_c$)[8)] for media with CL thickness from 9 to 4 nm also shows comparable value from 0.08 to 0.12. This indicates that CoPt-Gd_2O_3

CL is effective to control intergranular exchange coupling and switching field in the GRL. Fig. 2 shows cross section TEM images of media with (a) CoPt-Gd_2O_3 and (b) (CoPtCr)-10B CLs. Focusing on media top surface, the medium with CoPt-Gd_2O_3 CL is extremely flat as compared to that of the medium with (CoPtCr)-10B CL. According to the EDX element analysis, homogeneous structure of magnetic grains and grain boundaries from the GRL to CL can be observed. These results suggest that CoPt- RE oxide CL is promising to realize media with flat surface and comparable magnetic properties with current CL.

1) Y. Sonobe et al., *J. Appl. Phys*., 91, 8055 (2002). 2) Y. Sonobe et al., *J. Magn. Magn. Mater.,* 303, 292 (2006). 3) K. K. Tham et al., *IEEE Trans. Magn.*, 43, 671 (2007) 4) T. Shimatsu et al., *J. Appl. Phys*., 91, 8061 (2002). 5) G. Choe et al., *IEEE Trans. Magn.*, 41, 3172 (2005). 6) G. A. Bertero et al., *IEEE Trans. Magn.*, 38, 1627 (2002). 7) K. K. Tham et al., *J. Appl. Phys*., 112, 093917 (2012). 8) I. Tagawa et al., *IEEE Trans. Magn*. 27, 4975(1991).

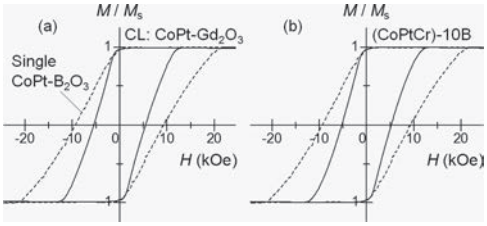


Fig. 1 M/M_s-H loops of media with (a) CoPt-30vol%Gd_2O_3 and (b) (CoPtCr)-10B CLs (9 nm) deposited on GRL (16 nm). M/M_s-H loop of GRL (16 nm) without CL is shown in broken line.



Fig. 2 Cross section TEM images of media with (a) CoPt-Gd_2O_3 and (b) (CoPtCr)-10B CLs.

GR-06. Dual-structure microwave-assisted magnetic recording using only a STO. *S. Greaves*[1] and W. Saito[1] *1. Tohoku University, Sendai, Japan*

Microwave-assisted magnetic recording is a candidate technology for use in future hard disk drives. Usually the spin torque oscillator (STO) that generates the high frequency (HF) magnetic field that assists magnetisation switching is integrated into a write head. However, it is also possible to switch the magnetisation of a grain deterministically using only the field from the STO [1,2]. In this work we examine switching of a dual structure magnetic dot using only the field from a STO. The dual structure dot consisted of two, discrete recording layers, RL1 and RL2. The 30 nm diameter STO was located above a 20 nm dual structure dot with RL2 closest to the STO. RL1 had an exchange coupled composite structure with a 3 nm hard layer and 2 nm soft layer, whilst RL2 was a 3 nm thick hard layer. A 2 ns field pulse from the STO was applied to the dot and the switching probabilities of RL1 and RL2 were calculated. Fig. 1 shows the switching probabilities of RL1 and RL2 as a function of the STO frequency. The thin lines are the switching probabilities calculated without magnetostatic interactions between RL1 and RL2 whilst the points were calculated with magnetostatic interactions between the two structures. Selective switching of RL1 and RL2 was achieved with switching probabilities greater than 0.9, although it was clear that the magnetostatic interaction was detrimental. Several approaches were examined to improve the performance, such as increasing the pulse length, reducing M_s and tuning the magnetic properties of the structures. Antiferromagnetic exchange coupling can partially compensate for the magnetostatic interaction. In practice, AFC coupling increased the switching probability for some STO frequencies, but decreased it for others. Fig. 2 shows examples of the switching of RL1 and RL2 at different STO frequencies. The magnetisation of the non-target structure was largely unaffected by magnetisation reversal of the target structure.

[1] T. Taniguchi, Appl. Phys. Expr. 8, 083004-1-4, (2015). [2] S. Greaves, IEEE Trans. Magn. 54, 3001705-1-5, (2018).

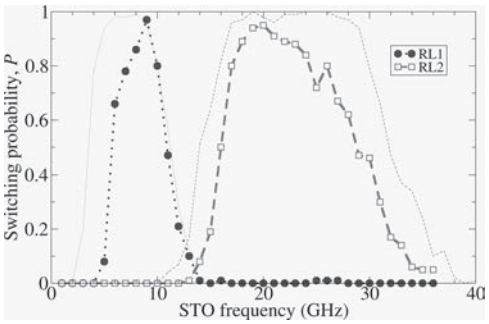


Fig. 1 Switching probabilities of RL1 and RL2 with and without magnetostatic interactions between structures. Thin lines = no magnetostatic interactions. Points and thick lines = magnetostatic interactions.

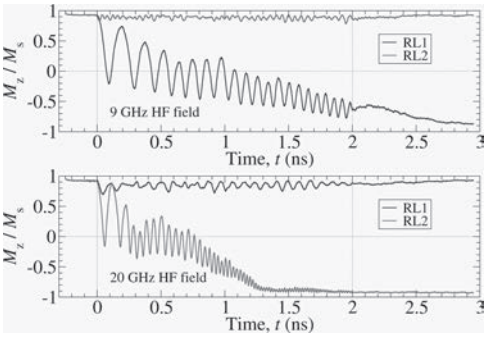


Fig. 2 Switching of RL1 (top) and RL2 (bottom) at different STO frequencies.

GR-07. Soft-Information Flipping Scheme Based on a Priori LLRs Summation for Ultra-High Density Magnetic Recording. *W. Busyatras*[2] and C. Warisarn[1] *1. College of Advanced Manufacturing Innovation, King Mongkut's Institute of Technology Ladkrabang, Bankok, Thailand; 2. Rajamangala University of Technology Thanyaburi, Pathum Thani, Thailand*

An inter-track interference (ITI) effect can degade the performance of bit-patterned media recording (BPMR) system [1-2]. Even though the two-dimensional (2D) modulation code can protect the severe ITI [3] which can efficiently improve the overall system performance, it cannot offer performance gain over the conventional system when recording system must encounter with ITI from its sidetracks. Then, the flipping technique [4] is proposed to deal with that ITI sidetrack effect using the normalized soft-information values which can improve the system performance. However, those normalized values are difficult to confirm an optimal threshold value in bit-flipping process. Therefore, this paper proposes a novel of soft-information flipping scheme to deal with mentioned shortcoming which leads to improve the bit-error rate (BER) performance. The relationship between data encoding condition and a priori log-likelihood ratios (LLRs), $\lambda_{k,l}$ obtained from SOVA detectors is utilized to be a criterion for flipping the ambiguous data bits. Here, we first calculate the normalized LLRs, $\lambda'_{k,l}$ of the k^{th} data bit and l^{th} track from $\lambda'_{k,l} = \lambda_{k,l} / \sum\lambda_{k,l}$, where $l \in \{-1,0,1\}$ represents the upper, middle and lower tracks, respectively. These normalized LLRs are compared with the threshold value for

deciding which soft-information bits should be flipped as shown in Fig. 1. Here, the optimal threshold value, α_T is obtained from our investigation which is depended on areal density (AD). For bit-flipping process, we consider only two soft-information patterns that have the sign according with [+ + +] and [- - -] in across track direction. If we found that the normalized LLRs value is less than the optimal threshold value, $\lambda'_{k,l} < \alpha_T$, then the RLL will be flipped in another directions. Simulation results indicate that, at the same user density, the proposed system provides BER performance gain over the conventional uncoded and systems as shown in Fig. 2. Moreover, the BER performance can be more improved especially when the AD is increase and high media fluctuation effect.

References [1] Y. Shiroishi et al., "Future options for HDD storage," IEEE Trans. Magn., vol. 45, no. 10, pp. 3816-3822, Oct. 2009. [2] C. Warisarn, W. Busyatras, and L. M. M. Myint, "Soft-information flipping approach in multi-head multi-track BPMR systems," AIP ADVANCES., vol. 8, pp. 056509 (1-5), Dec. 2018. [3] C. Warisarn, A. Arrayangkool, and P. Kovintavewat, "An iti-mitigating 5/6 modulation code for bit-patterned media recording," IEICE Trans. Electron. vol. E98-C, no.6, pp. 528-533, Jun. 2015. [4] W. Busyatras, N. Jongsawat, L.M. Myint, and C. Warisarn, "A bit-flipping technique based on 2D modulation constraint in BPMR systems," in Proceeding of Intermag 2018, Apr. 2018.

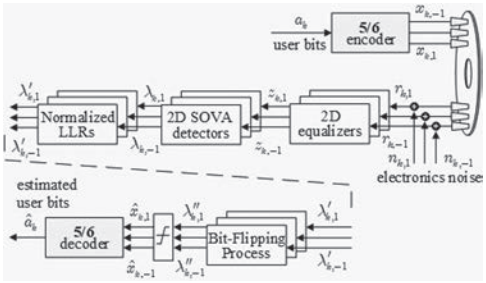


Fig. 1. A BPMR channel model with the proposed bit-flipping technique.

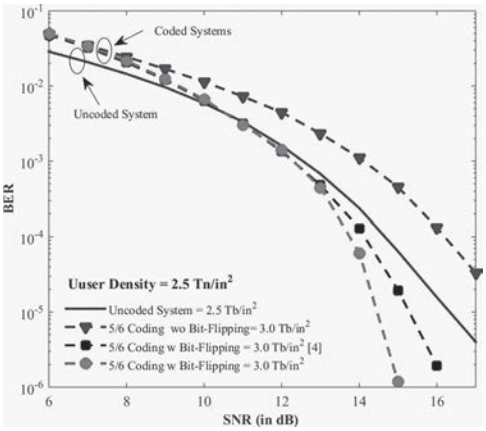


Fig. 2. BER performance of various systems under different ADs (same UD = 2.5 Tb/in^2).

GR-08. Stable Oscillation of Spin-Torque Oscillator with Reduced Injected Current Density for Microwave-Assisted Magnetic Recording.

Y. Kanai[1], R. Itagaki[1] and S. Greaves[2] *1. Engineering Dept., Niigata Institute of Technology, Kashiwazaki, Japan; 2. RIEC, Tohoku University, Sendai, Japan*

The spin torque oscillator (STO) is the most important component in a microwave-assisted magnetic recording (MAMR) system [1]. Obtaining stable STO oscillation when the STO is inserted into a write head main pole (MP) – trailing shield (TS) gap is the key to realizing a MAMR system. We have reported that a tilted STO inserted into a non-parallel gap is one solution [2], however, the structure is hard to fabricate. Also, reducing the injected current density, J, in the STO is the key for long-term reliability. In this paper, a micromagnetic model analysis of a STO is performed to realize stable STO oscillation with small J. Fig. 1 shows the arrangement of the STO, write head and double-layered recording medium. The write head had a parallel MP – TS gap. We used a relatively large Gilbert damping factor $\alpha = 0.2$ in the write head, except for the MP – TS gap region ($\alpha = 0.02$), because eddy currents were not explicitly included in the model. The recording layer was assumed to be air. The MP – TS gap = 20 nm to obtain a large head field gradient. The width of the MP trailing edge = 40 nm. The STO should fit into the 20 nm MP – TS gap, therefore, we utilized transmission spin torque [3] as thin soft magnetic layers are relatively easy to fabricate. STO area = 20 nm × 20 nm at MP side. The thickness of the field generation layer (FGL) and spin injection layer (SIL) were 10 nm and 2 nm, respectively. There was a 2 nm thick non-magnetic interlayer (IL) in between the FGL and SIL. $4\pi M_s$ of FGL and SIL was 20 kG and 10 kG, respectively. α of FGL and SIL was 0.02. Anisotropy field H_k of FGL and SIL was 31.4 Oe. In the model we varied the exchange A, H_k and α of FGL and SIL. The results showed that there were optimum values for these parameters, however, they were not relatively critical to reduce J. Next, we varied θ of the write head, as shown in Fig. 1. There was a notable difference for relatively small J (3.0×10^8 A/cm^2) [2] when comparing $\theta = 0°$and 15°as shown in Fig. 2. Varying α in the vicinity of the MP gave significant changes in the FGL rotation at small J.

[1] J.-G. Zhu, X. Zhu, and Y. Tang, *IEEE Trans. on Magn*., vol. 44, p. 125 (2008). [2] Y. Kanai, R. Itagaki, S. J. Greaves, and H. Muraoka, *IEEE Trans. on Magn.*, vol. 55, p. 3000613 (2019). [3] J.-G. Zhu, *MMM Conf*., AC-13 (2014).

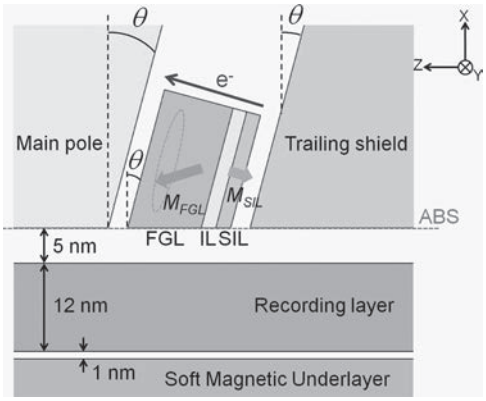


Fig.1 Schematic model used for calculations.

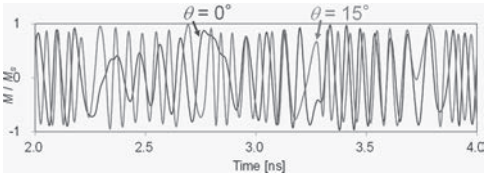


Fig.2 In-plane component of FGL magnetization rotation for θ=0° and 15°.

Session GS
EDUCATION, OUTREACH, & PUBLIC ENGAGEMENT IN MAGNETISM
(Poster Session)

Barry L Zink, Co-Chair
University of Denver, Denver, CO, United States
Dafiné Ravelosona, Co-Chair
Center for Nanoscience and Nanotechnology, Palaiseau, France
Yukiko Takahashi, Co-Chair
NIMS, Tsukuba, Japan

GS-01. Exploring magnetic resonance with a compass. *D. Nelson*[1], E. Cookson[1], M. Anderson[1], D. McKinney[2] and I. Barsukov[1] *1. Physics and Astronomy, UC Riverside, Riverside, CA, United States; 2. Santa Rosa Academy, Menifee, CA, United States*

Magnetic resonance plays an important role in today's science, engineering, and medical diagnostics. Learning and teaching magnetic resonance is challenging since it requires advanced knowledge of condensed matter physics and quantum mechanics. Driven by the need to popularize this technologically impactful phenomenon, we develop an inexpensive table-top demonstration experiment. It unveils the magnetic resonance of a hand-held compass in the magnetic fields of a permanent magnet. The setup provides an immediate visualization of the underlying physical concepts and allows for their translation to broad student audiences. This work was supported by the National Science Foundation under Grant No. ECCS-1810541.

GS-02. Magnetic Fields Web Series: Engaging Middle School Students in STEM. *P. Pena Martin*[1], J. Isberg[1], E. Ertekin[1,3], V. Lorenz[1,2] and N. Mason[1,2] *1. Materials Research Laboratory, University of Illinois at Urbana-Champaign, Urbana, IL, United States; 2. Department of Physics, University of Illinois at Urbana-Champaign, Urbana, IL, United States; 3. Department of Mechanical Science and Engineering, University of Illinois at Urbana-Champaign, Urbana, IL, United States*

Web based media can make scientific content accessible to audiences far beyond the scientific community. We created a web series called "Magnetic Fields" that aims to introduce materials science, particularly concepts related to magnetism, and promote themes more general to STEM fields, such as persistence and the scientific process, through use of characters and a story geared towards a middle school audience. The goal is to build and maintain interest in science at an age where this tends to drop off. The four-episode arc follows a group of high school characters as they encounter a strange new material during a class field trip to a laboratory. The series is directed by John Isberg, with professional actors making up most of the cast. The series was initiated by scientists in the Illinois MRSEC, and the storyline was developed in collaboration with MRSEC students and faculty. The episodes were released in May 2019 through Youtube. We report on the process of creating this series, response to it upon release, and discussion of its use as an educational tool. The authors acknowledge primary support of the NSF through the University of Illinois at Urbana-Champaign Materials Research Science and Engineering Center DMR-1720633.



Fig.1 Scene from an episode of "Magnetic Fields." Photo by John Isberg.

GS-03. In-class experiments with smart phones for teaching upper-level electricity and magnetism. A. Davidson[1], A. Ranjan[2] and *X. Fan*[1] *1. Physics and Astronomy, University of Denver, Denver, CO, United States; 2. Cherry Creek High School, Greenwood Village, CO, United States*

Interactive-engagement method such as studio physics [1, 2], has demonstrated higher learning gains than traditional lecturing in intro-level physics classes. However, there have been limited applications in upper-level classes, such as Electricity and Magnetism (E&M), possibly because experiments on E&M topics can be too costly and sophisticated to be carried out in the classroom. Smart phone, which is equipped with magnetic field sensors, radio signal detectors and light sensors, provides a convenient platform for carrying out E&M-related experiments. In this poster, we will present three examples of the implementation of smart-phone-based studio physics in an E&M class for Physics majors: (1) Detection of earth magnetic field inclination; (2) quantifying skin depth of aluminum foil with cellphone tower signals; and (3) Measurement of Brewster's angle. Besides sensitive sensors, smart phone also has computational power, which can be explored to further expand the breadth and depth of the smart-phone-based studio physics. Due to the wide accessibility of smart phones and the simplicity of experimental setup, we expect this teaching technique can be easily transferred to other institutes in the world.

[1] Gok, T., *Assessment of the effectiveness of the hybrid studio format in introductory undergraduate physics.* Energy Education Science and Technology Part B-Social and Educational Studies, 2012. 4(1): p. 117-130. [2] Sorensen, C.M., A.D. Churukian, S. Maleki, and D.A. Zollman, *The New Studio format for instruction of introductory physics.* American Journal of Physics, 2006. 74(12): p. 1077-1082.

GS-04. The Use of Virtue Modules in Physics Lab Teaching. *W. Zhang*[1], R. Bidthanapally[1], T. Sebastian[2], Y. Xiong[1,3], H. Qu[3] and J. Sklenar[4]
1. Physics Department, Oakland University, Rochester, MI, United States; 2. THATec Innovation GmbH, Mannheim, Germany; 3. Electronic and Computer Engineering, Oakland University, Rochester, MI, United States; 4. Physics Department, Wayne State University, Detroit, MI, United States

Lab sessions in physics education connect the fundamental concepts to practical examples and are effective measures of the students' understanding and reasoning through ultimate real-world tests. Many topics in condensed matter physics are known to be challenging to convey in both lectures and labs. In addition, these topics are usually resource demanding, which has been one of the challenging issues. Here, we introduce and demonstrate the use of virtue lab modules for teaching physics labs and for effectively integrating research and education. Experiments that are relevant to magnetism and spintronics include, but not limited to, spin current detecting, microwave energy harvesting, and spin-based thermoelectric effects. An important highlight of these modules is the highly-interactive laboratory learning platform. In the class, each piece of experimental hardware (e.g. electrometers, oscilloscopes, etc) will be paired with a computer-based virtual module. The individual modules mimic the hardware, which the students can use to become familiar with the hardware, acquire real-time feedback, and visualize the data acquisition dynamics, on-demand and risk-free. The virtual component is also helpful for demonstrating delicate, shared hardware in class, without risk of damaging the actual instrumentation. These individual components are connected to a central operating system and the experiment can be re-programmed by simple coding and user-interfaced commands [1]. Work at Oakland University is supported by NSF DMR-1808892.

[1] THATec Innovation GmbH: https://www.thatec-innovation.com/

Session GT
ORIGINS OF MAGNETIC ORDER II
(Poster Session)

Amal El-Ghazaly, Chair
Cornell University, Ithaca, NY, United States

GT-01. Structural stability and magnetic properties of the Mn-doped WS_2 thin films in *ab initio* calculations. *M. Kim*[1] and J. Hyun[1] *1. Sookmyung Womens University, Seoul, The Republic of Korea*

Two-dimensional (2D) transition-metal dichacogenides (TMDs) materials possess very interesting semiconducting, metallic, superconducting, and magnetic properties, which have been spurred lots of research in both experiment and theory to realize their advantageous features in, for example, the flexible and transparent electronics device applications. Among these TMDs, the nonmagnetic semiconductor WS_2 is one of the most exciting family of which the magnetic properties by transition metal doping exhibits exotic phenomena [1-4]. In this presentation, we report density functional theory (DFT) calculations on the Mn-doped WS_2 thin films, that is, monolayer and double layers. The spin magnetic moment of Mn-doped WS_2 monolayer is calculated to be 1.00 μ_B, respectively, at 4% impurity concentration in a 5×5 supercell. Upon the extension of the unit cell up to 7×7, we calculated the two Mn doped films to find the energy stability in accordance with the distance, which revealed that the nearest neighboring position on Mn atoms is most stable. Each total magnetic moment and Mn moments are 2.00 and 1.27 μ_B, respectively. We have examined the single as well as the double dopants of Mn in various probable interlayer doping positions using the structural stability and magnetic properties optimization and the formation energy calculations to decide the preferred doping sites as shown in Fig. 1. It was found that the single Mn dopant prefers the direct on-top positions (i) between the W atoms for the AA configuration (as shown in Fig 1(b)) and (ii) between the S and W atoms for the AB configuration (as in Fig 1(d)), to the hollow sites. The magnetic properties are also found to vary depending the configurations. *kimmy@sm.ac.kr **This work was supported by the Basic Science Research Program (No. 2017R1A2B4012972) through the National Research Foundation of Korea(NRF).

1. Q. Wang *et al*., Nat. Nanotechnol 7, 699 (2012). 2. S. Kim *et al*., Nat. Commun. 3, 1011 (2012). 3. D. Lembke *et al*., ACS Nano 6, 10070 (2012). 4. D. Braga *et al*., Nano Lett. 12, 5218 (2012).

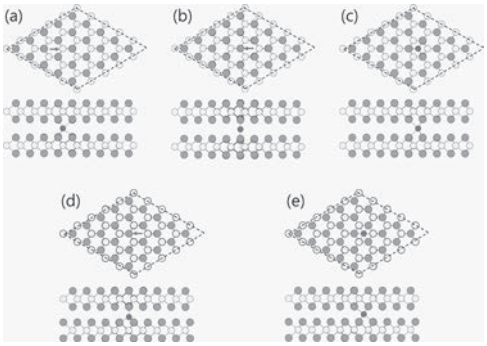


Fig. 1. Atomic models of a single Mn dopant in bilayer WS_2 with the (a) AA-W, (b) AA-S, (c) AA-H, (d) AB-WS, and (e) AB-H configurations. W, S, and Mn atoms are indicated by the yellow, gray, and red circles.

GT-02. Electronic and Magnetic Properties of Stoichiometric $CeAuBi_2$. M. Moda Piva[1,2], G. Silva Freitas[1], S.M. Thomas[2], J. Leao[3], *C. Adriano*[1], R.R. Urbano[1], J.W. Lynn[3], J. Thompson[2], P. Ferrari Silveira Rosa[2] and P. Pagliuso[1] *1. Instituto de Física "Gleb Wataghin" - UNICAMP, Campinas, Brazil; 2. Los Alamos National Laboratory, Los Alamos, NM, United States; 3. NIST Center for Neutron Research, Gaithersburg, MD, United States*

Rare-earth-based compounds have attracted attention of the scientific community as they are paradigms of multiple, often competing, interactions, such as the Ruderman-Kittel-Kasuya-Yoshida (RKKY) magnetic interactions, crystalline electrical field (CEF) effects, Kondo effect and Fermi surface effects. The interplay among these effects are complex and can lead to novel ground states. $CeAuBi_2$ is an example. It belongs to the $REMBi_2$ (RE = rare-earth, M = Cu, Au) family of antiferromagnets with competing magnetic interactions and, for RE = Ce, moderately heavy electrons [1-4]. Moreover, a breakdown of the de Gennes scaling for $CeMBi_2$ and $PrMBi_2$ implicates CEF enhancement of T_N [3, 4]. Furthermore, Au vacancies in some $CeAuBi_2$ materials indicate that disorder may also play an important role in this system [2]. Here we report the electronic and magnetic properties of stoichiometric $CeAuBi_2$ single crystals. $CeAuBi_2$ crystallizes in the tetragonal *P4/nmm* structure and orders antiferromagnetically below T_N = 19 K, the highest value reported for this compound [2, 4, 5]. At low temperatures (2 K) and ambient pressure, the application of magnetic fields parallel to the *c*-axis results in two transitions at 7.2 T and 7.7 T in the magnetoresistance, similar to $CeAuSb_2$ [6]. AC calorimetry and electrical resistivity experiments under pressure reveal that the application of external pressure favors antiferromagnetic order, which reaches a maximum T_N of 21 K at 23 kbar. Finally, neutron magnetic diffraction measurements find a commensurate antiferromagnetic structure with a propagation vector (0 0 1/2) with the magnetic moments aligned along the *c*-axis, similar to $CeCuBi_2$ [1].

[1] C. Adriano, P. F. S. Rosa, C. B. R. Jesus *et al.*, Phys. Rev. B, Vol. 90, p. 235120 (2014); [2] C. Adriano, P. F. S. Rosa, C. B. R. Jesus *et al.*, J. Appl. Phys., Vol. 117, p. 17C103 (2015); [3] C. B. R. Jesus, M. M. Piva, P. F. S. Rosa *et al.*, J. Appl. Phys., Vol. 115, p. 17E115 (2014); [4] C. B. R. Jesus, M. M. Piva, P. F. S. Rosa *et al.*, Phys. Procedia, Vol. 75, p. 618-624 (2015); [5] E. M. Seibel, W. Xie, Q. D. Gibson and R. J. Cava, J. Solid State Chem., Vol. 230, p. 318-324 (2015); [6] G. G. Marcus, D.-J. Kim, J. A. Tutmaher *et al.*, Phys. Rev. Lett., Vol. 120, p. 097201 (2018).

GT-03. The Effect of Manganese Substituted Sodium Iron Phosphate Maricite-$NaFe_{1-x}Mn_xPO_4$. *J. Seo*[1], H. Choi[1] and C. Kim[1] *1. Department of Physics, Kookmin University, Seoul, The Republic of Korea*

Transition metal ion substitution in sodium phosphate is effective in enhancing the performance of cathode material. [1] The Mn-doped maricite-$NaFe_{1-x}Mn_xPO_4$ (x = 0.1, 0.2, 0.3, 0.4, 0.5) samples were synthesized by solid-state route. The crystallographic and magnetic properties of the effect Mn substitution were investigated by x-ray diffraction (XRD) measurement, vibrating sample magnetometer (VSM), and Mössbauer spectroscopy. The XRD patterns of $NaFe_{1-x}Mn_xPO_4$ ($0.1 < x < 0.5$) revealed that the structure had orthorhombic structure with space group of *Pmnb*. The lattice parameters and the volume of the $NaFe_{1-x}Mn_xPO_4$ increased from for a_0 = 6.866, b_0 = 8.999, c_0 = 5.047 Å and V = 311.544 Å^3 for x = 0.1, a_0 = 6.881, b_0 = 9.037, c_0 = 5.075 Å and V = 315.418 Å^3 for x = 0.5. The temperature

dependence of the magnetization curves exhibits Néel temperature (T_N) of $NaFe_{1-x}Mn_xPO_4$ decreased with the increasing Mn concentrations from 14 K for x = 0.1 and 10 K for x = 0.5, indicating in weakened antiferromagnetic interaction. The Mössbauer spectra exhibited to have asymmetrical line-shapes below T_N and were fitted with eight Lorentzian lines, due to the strong crystalline field in the distorted $Fe(Mn)O_6$ octahedral site. At room temperature, exhibits a doublet absorption line. The decrease in antiferromagnetic order can be explained by the fact that the Fe-O-Mn interaction is weaker than the interaction of the paramagnetic region.

[1] T. Boyadzhieva, V. Koleva and R. Stoyanova, Phys.Chem.Chem.Phys., Vol. 19, p.12730 (2017)

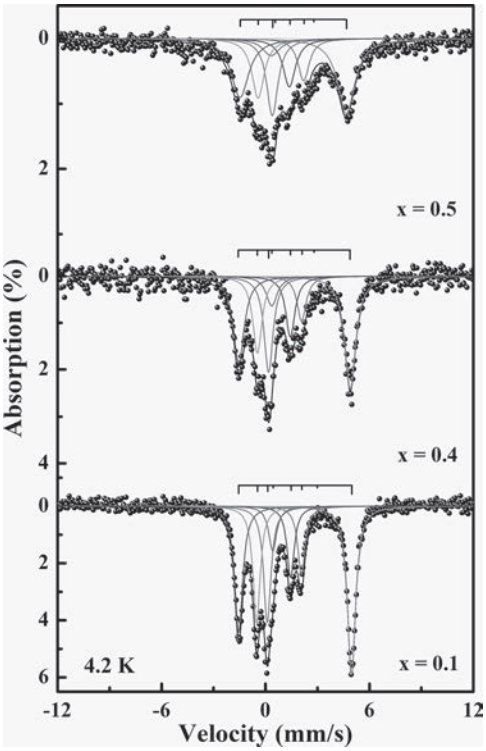


Fig 1. Mössbauer spectra of $NaFe_{1-x}Mn_xPO_4$ (x = 0.1, 0.4, 0.5) at 4.2 K.

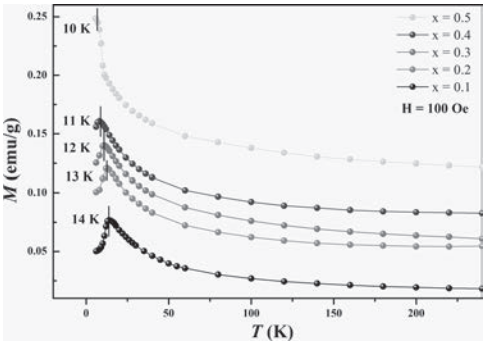


Fig 2. Temperature-dependent magnetization curve of the $NaFe_{1-x}Mn_xPO_4$ at various temperatures.

GT-04. Atomic-layer stacking dependence of the magnetocrystalline anisotropy and Dzyaloshinskii-Moriya interaction in Fe-Co multilayers on MgO. *Y. Kato*[1], A.M. Pradipto[1], T. Akiyama[1], T. Ito[1], T. Oguchi[2], M. Weinert[3] and K. Nakamura[1] *1. Engineering, Mie University, Tsu, Japan; 2. Scientific and Industrial Research, Osaka University, Suita, Japan; 3. Physics, University of Wisconsin-Milwaukee, Milwaukee, WI, United States*

For the next generation of magnetic tunnel junctions, control of the magnetocrystalline anisotropy (MCA) and the Dzyaloshinskii-Moriya interaction (DMI) in thin ferromagnetic films has attracted much attention. A promising approach to deal with such magnetic properties is by tuning the atomic-layer stacking sequences in multilayer thin films [1]. Here, we theoretically investigated the atomic-layer stacking dependence of the MCA and DMI in prototypical Fe-Co multilayer thin films on MgO(001). The generalized gradient approximation calculations were carried out using the film full-potential linearized augmented plane-wave method [2] employing single slabs with six-atomic layers of Co-Fe on MgO(001). The MCA energy is determined as difference in total energy for magnetizations oriented along the in-plane and perpendicular directions with respect to the film plane, and the DMI parameter of the multilayers is estimated from the total energy difference with respect to the spin-spiral wavevectors. The results predict that both MCA and DMI depend significantly on the atomic-layer stacking sequences. MCA energies, ranging from 1.4 [meV/unit-area] (perpendicular magnetization) to -1.5 [eV/unit-area] (in-plane magnetization), depending on the atomic-layer stacking sequences are observed. Similarly, complicated behavior of the DMI parameters versus the atomic-layer stacking sequences is observed, where the magnitude of the DMI parameter interestingly increases by one order of magnitude compared to that of pure Fe films even though the spin-orbit coupling is quite weak. We further analyze these magnetic properties by using cluster expansion and neural network methods in order to elucidated the underlying trends. We find that the MCA is very sensitive to the short-range order in the atomic-layer stacking sequences, whereas an asymmetry in the whole film along the stacking direction may play a role in determining the DMI.

[1] Hotta *et.al.,* Phys. Rev. Lett. 110, 267206 (2013) [2] Wimmer *et.al.*, Phys. Rev. B 24, 864 (1981), Weinert *et.al.*, Phys. Rev. B 26, 4571 (1982); Nakamura *et al.*, Phys. Rev. B 67, 014420 (2003).

GT-05. Effects of Simultaneous Cd and Ir Doping in Ce_2RhIn_8 Antiferromagnet. *D.S. Christovam*[1], G. Silva Freitas[1], M.M. Piva[1], J.C. Souza[1], J. Leao[2], W.D. Ratcliff[2], J.W. Lynn[2], P. Pagliuso[1] and C. Adriano[1] *1. DEQ, Instituto de Física Gleb Wataghin - Unicamp, Campinas, Brazil; 2. NIST Center for Neutron Research, NIST, Gaithersburg, MD, United States*

Ce_2RhIn_8 is an antiferromagnet (T_N = 2.8 K) that belongs to the family of Ce-based heavy fermion (HF) compounds Ce_mMIn_{3m+2} (*M* = Co, Rh, Ir). This family has been heavily investigated due to its intricate phase diagrams, which display complex magnetism, disordered phases and superconducting states [1,2]. These phase diagrams result from the competition between long-range Ruderman–Kittel–Kasuya–Yosida interaction, local on-site Kondo effect and crystalline electric field (CEF) effects, which have an important role in determining the ground state (GS) and physical properties of the compound [3]. The determination of the magnetic structure of these compounds is very helpful when studying the spin anisotropy of the CEF GS, since the moment direction can relate to its symmetry properties and magnetic anisotropy. The evolution of the physical properties of the $Ce_2Rh_{1-x}Ir_xIn_8$ series and the role of Cd doping in the Ce_2MIn_8 (*M* = Rh, Ir) site have been previously investigated [2,4]. It has been shown that Ir substitution seems to suppress the antiferromagnetism (AFM) and induce a coexisting superconducting phase, as well as a disordered spin-glass phase in the Ir-rich compounds. This evolution is accompanied by an enhancement of the Kondo effect and likely changes in the CEF scheme. On the contrary, Cd doping in Ce_2MIn_8 increases T_N favoring AFM for *M* = Rh and suppresses the superconductivity for *M* = Ir, suggesting that the main role of Cd in these systems is the electronic tuning of the GS, such as for the $CeMIn_5$

compounds [5,6,7]. However, the magnetic structure of these alloys and their CEF scheme remain to be explored in greater detail. In this work, we discuss the magnetic structures of the Cd doped $Ce_2Rh_{0.5}Ir_{0.5}In_8$ antiferromagnetic alloys (T_N = 2.0 K, x = 0 and T_N = 4.2 K, x = 0.21) by neutron magnetic diffraction measurements. The evolution of these magnetic structures will be connected to preliminary studies of the CEF effects using a mean field model with tetragonal CEF and exchange interactions.

[1] J. D. Thompson, *et al.*, J. Magn. Magn. Mater. 226–230 (2001) 5. [2] E. N. Hering *et al*, Phys. Rev. B,82, 184517 (2010). [3] P. G. Pagliuso *et al*, J. Appl. Phys.99, 08P703 (2006). [4] C. Adriano *et al*, Phys. Rev. B 81, 245115 (2010). [5] R. R. Urbano *et al*, Phys. Rev. Lett., 99(14) 146402 (2007). [6] S. Seo *et al.*, Nat. Phys. 10, 120–125 (2014). [7] K. Chen *et al*, Phys. Rev. B,97,045134 (2018).

GT-06. Inelastic Neutron Scattering Studies on the $CeCuBi_{2-x}Sb_x$ Antiferromagnetic Compounds. *G. Silva Freitas*[1], M. Moda Piva[1], J.C. Souza[1], C.B. Ramos de Jesus[2], C. Adriano[1], J. Leao[3], J.W. Lynn[3] and P. Pagliuso[1] *1. Departamento de Eletrônica Quântica, Instituto de Física "Gleb Wataghin", Campinas, Brazil; 2. Departamento de Física, Universidade Federal de Sergipe - Campus de Itabaiana, Itabaiana, Brazil; 3. NIST Center for Neutron Research, National Institute of Standards and Technology, Gaithersburg, MD, United States*

Rare earth intermetallic compounds present an intriguing interplay between the Crystalline Electrical Field (CEF), the Kondo effect and the Ruderman-Kittel-Kasuya-Yoshida (RKKY) magnetic interaction. These competing effects provide an interesting playground for the scientific community, often resulting in non-trivial ground states. In particular, the $CeCuBi_{2-x}Sb_x$ series presents antiferromagnetic ordering (3.7 K T_N 16.0 K) with an interesting evolution of the Ce^{3+} (J = 5/2) magnetic anisotropy along the series. The compound with x = 0 [1] presents a large magnetic anisotropy with the easy magnetization axis along the *c*-axis with is strongly suppressed along with T_N by Sb-substitution up to x = 0.25. At higher Sb-concentration, for x = 0.6, the magnetization easy direction rotates towards the *ab*-plane and T_N and the magnetic anisotropy starts to slightly increase as a function of Sb-concentration (x = 1 and 2). This evolution is governed by CEF effects and their changes as a function of Sb-substitution. Inelastic neutron scattering (INS) experiments were performed on single crystals of $CeCuBi_{2-x}Sb_x$ grown by the metallic self-flux technique to directly probe the CEF levels and their evolution as a function of Sb-substitution. These results will be presented and analyzed along with the macroscopic magnetic properties of these compounds to shed light on the interesting evolution of the magnetic properties of these compounds along the series.

[1] C. Adriano, et al, Physical Review B 90, 235120 (2014).

GT-07. Interconfigurational fluctuation valence in putative topological Kondo Lattice Gd^{3+}-doped SmB_6. *J.C. Souza*[1,2], M. Carlone[3], P. Venegas[3], P. Ferrari Silveira Rosa[4], J. Sichelschmidt[2], P.E. Menegasso[1], R.R. Urbano[1], Z. Fisk[5], P. Pagliuso[1] and C. Rettori[1,6] *1. Institute of Physics Gleb Wataghin, Unicamp, Campinas, Brazil; 2. Max Planck Institute for Chemical Physics of Solids, Dresden, Germany; 3. Faculdade de Ciências, UNESP, Bauru, Brazil; 4. Los Alamos National Laboratory, Los Alamos, NM, United States; 5. University of California Irvine, Irvine, CA, United States; 6. UFABC, Santo Andre, Brazil*

SmB_6 is an intermediate valence (IV) 4*f* Kondo lattice insulator with an estimated indirect semiconducting gap of $\Delta \approx 50$ K [1] which has been predicted to host nontrivial topological surface states [2]. Coherent hybridization between the Sm *4f* states and the *5d* conduction band is presumable responsible for the opening of this small gap at low temperatures [3]. Previous electron spin resonance (ESR) measurements attributed the ESR spectra in $Sm_{1-x}Gd_xB_6$ at $T \leq 10$ K to Gd^{2+} ions [4]. In this work we show that, for $T \leq$ 4 K and low enough Gd concentrations ($Sm_{1-x}Gd_xB_6$; $x \leq 0.0005$), the fine structure observed in the Gd^{3+} ESR spectra can be unambiguously simulated by a cubic crystal field and, therefore, attributed to Gd^{3+} ions located at insulating cubic sites, i.e., substituting Sm IV ions. Nevertheless, as T increases above ~ 4 K, the resonances of the Gd^{3+} ESR spectra broadens and above $T \approx 10$ K show a single resonance with an exponential line broadening, leading to an activation energy of the order of the hybridization gap, i.e., $\Delta \approx 50$ K. Based on the Interconfigurational Fluctuation model [5], the fluctuation between the $4f^n$ and $4f^{n+1}$ configurations of Sm ions provokes a fluctuating field at the Gd^{3+} site. Thus, the exchange interaction between the localized magnetic moment of Gd^{3+} and the IV Sm ions leads to a relaxation with an exponential dependence on the excitation energy of the IV ions, E_{ex} which is, notably, of the order of the hybridization gap Δ [6].

[1] J. C. Cooley, M. C. Aronson, Z. Fisk, and P. C. Canfield, Phys. Rev. Lett. 74, 1629 (1995). [2] S. Wolgast, C. Kurdak, K. Sun, J. W. Allen, D. J. Kim, and Z. Fisk, Phys. Rev. B 88, 180405(R) (2013); D. J. Kim, S. Thomas, T. Grant, J. Botimer, Z. Fisk, and J. Xia, Scientific Reports 3, 3150 (2013) [3] K. Flachbart, S. Gabani, K. Neumaier, Y. Paderno, V. Pavlik, E. Schuberth, and N. Shitsevalova, Physica B 378–380, 610–611 (2006). [4] G. Wiese, H. Schaffer, and B. Elschner. Europhy. Lett.,11, 791 (1990). [5] L.L. Hirst, Phys. Kondens. Mater., 11, 255(1970). [6] P. A. Venegas and G. E. Barberis, Phys. Rev. B 46, 911(1992); P. A. Venegas, F. A. Garcia, D. J. Garcia, G. G. Cabrera, M. A. Avila, and C. Rettori. Phys Rev. B 94, 235143 (2016).

GT-08. Electron spin resonance in the non-symmorphic antiferromagnetic $Eu_5In_2Sb_6$. *J.C. Souza*[1], S.M. Thomas[2], E. Bauer[2], J. Thompson[2], F. Ronning[2], P. Pagliuso[1] and P. Ferrari Silveira Rosa[2] *1. Institute of Physics Gleb Wataghin, Unicamp, Campinas, Brazil; 2. Los Alamos National Laboratory, Los Alamos, NM, United States*

The search for topological phases protected by crystal symmetries has brought attention to non-symmorphic materials, which could host topologically nontrivial surface fermions displaying hourglass dispersion [1]. $Eu_5In_2Sb_6$ crystallizes in the non-symmorphic space group *Pbam* [2] and exhibits a colossal magnetoresistance, which might be caused by magnetic polarons. In this work, we perform electron spin resonance in the non-symmorphic antiferromagnet $Eu_5In_2Sb_6$ in the temperature range of 15 K < T < 300 K for different microwave frequencies (ν = 9.4 and 33 GHz). We observe a systematic decrease of the Eu^{2+} ESR line-width as a function of microwave frequency, which indicates a field-dependent relaxation mechanism driven by magnetic polarons, similar to previous reports in EuB_6 [3]. In addition, the Eu^{2+} g-value and ESR line-width show two distinct anisotropies when the applied magnetic field is rotated in the *ac* plane. We will discuss these anisotropies in light of a possible anisotropy in the resistivity and/or in the internal field at the Eu^{2+} site due to the magnetic structure of the compound.

[1] Z. Wang, A. Alexandradinata, R. J. Cava, and B. A. Bernevig, Nature 532, 190 (2016); [2] Wieder et al., Science 361, 246 (2018); [3] R. Urbano et al., Phys. Rev. B 70, 140401(R) (2004).

GT-09. Magnetic and structural transitions in $EuAg_4As_2$ studied using ^{151}Eu Mössbauer spectroscopy. *D. Ryan*[1], S. Bud'ko[2], N. Ni[3] and C. Hu[3] *1. Physics, McGill University, Montreal, QC, Canada; 2. Department of Physics and Astronomy, Ames Laboratory and Iowa State University, Ames, IA, United States; 3. Department of Physics and Astronomy, University of California, Los Angeles, CA, United States*

Trigonal $CaCu_4P_2$–type (R-3m #166) $EuAg_4As_2$ is part of a wider family of 1-4-2 pnictides[1]. Preliminary magnetic characterization suggested antiferromagnetic (AF) ordering below T_N=15K[2] and that the Eu was divalent. The isostructural $SrAg_4As_2$ compound hosts non-magnetic, formally divalent Sr in place of Eu and serves as a well-defined reference. It is a diamagnetic semimetal with a structural transition around 110K[3] that may be electron or phonon driven. A transport and neutron diffraction study of single crystal $EuAg_4As_2$ found a similar structural event at 120K and two magnetic events at 15K and 9K[4] and suggested that short-ranged AF correlations develop at 15K followed by incommensurate long-ranged AF order at 9K with a reduced moment of 3.7μ_B[4]. Here we present the results of an extensive ^{151}Eu Mössbauer study of $EuAg_4As_2$ using crystals from the previous

work[4]. The 5K spectrum consists of a single, sharp magnetic pattern with B_{hf}=27.1(1) T and an isomer shift of –11.04(3) mm/s consistent with fully divalent Eu in a single magnetic environment with a full 7μ_B ordered moment. No trivalent Eu (<1%) was detected. The thermal evolution of the average B_{hf} (Fig.1) appears conventional, yielding T_N=14.4(1)K. However, above 8K the fitted linewidth increased significantly and a model invoking an incommensurate sine-modulated structure gave a more consistent fit. On the Mössbauer timescale (10-100ns) the ordering appears to proceed via an initial sine-modulated phase starting at 15K that squares up below 9K. We also looked for the structural transition at 120K. If the transition involved a significant change in electron density around the Eu, or a softening of a phonon associated with the Eu atoms, we might expect changes in the isomer shift or spectral area[5] respectively. No changes in linewidth, isomer shift or spectral area were detected (Fig.2). The temperature dependence of the area gave a Debye temperature (θ_D) of 184(3)K, somewhat higher than the 140K reported for $SrAg_4As_2$[3], but it should be noted that the Mössbauer value is locally weighted to the Eu site rather than representing a global average.

[1] S.S. Stoyko et al., *J. Solid State Chem.* 192 (2012) 325 [2] B. Gerke et al., *Solid State Sci.* 20 (2013) 65 [3] B. Shen et al., *Phys.Rev.B* 98 (2018) 235130 [4] B. Shen et al., *arXiv* 1809.07317 [5] W.N. Rowan-Weetaluktuk et al., *Hyp. Int.* 198 (2010) 1

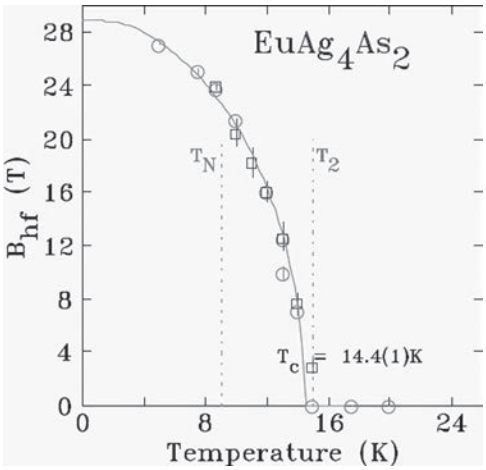


Fig.1 Average B_{hf} vs. temperature showing the primary transition at 14.4K

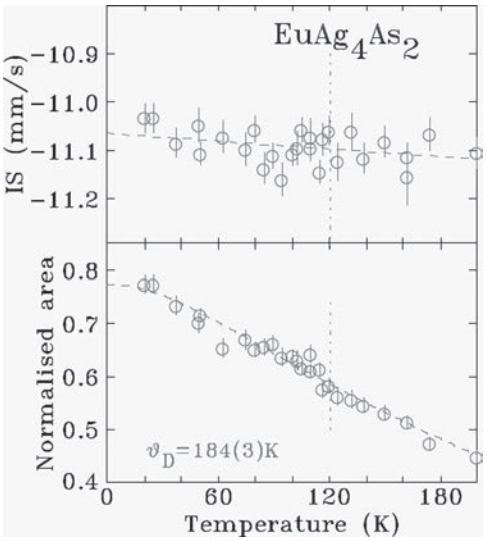


Fig.2 Isomer shift and spectral area vs. T

GT-10. Withdrawn

GT-11. Magnetic properties, Magnetic entropy and Adiabatic temperature change in antiferromagnetic NdCuGa compounds.
M.B. Tchoula Tchokonte[1], M.H. Mbulunge[1], J.J. Mboukam[2], A.K. Bashir[1,4], B. Sahu[2], A.M. Strydom[3] and D. Kaczorowski[3] *1. Physics & Astronomy, University of the Western Cape, Bellville, South Africa; 2. Physics, University ofJohannesburg, Johanneburg, South Africa; 3. Magnetic, Institute of Low Temperature and Structure Research, Polish Academy of Sciences, Wroclaw, Poland; 4. Materials Research Group, iThemba LABS, Fourie, South Africa*

Magnetic properties, magnetic entropy change ($-\Delta S_M$) and adiabatic temperature change (ΔT_{ad}) in NdCuGa has been investigated by means of magnetic susceptibility, $\chi(T)$, heat capacity, $C_p(T)$ and isothermal magnetization, $M(\mu_0 H, T)$ measurements. The compound was found to order antiferromagnetically at T_N = 7 K with a second – order phase transition as observed from $\chi(T)$, $C_p(T)$ data and the Arrott – plots. The low temperature $C_p(T)$ data just above T_N can be fitted to the Debye relationship given a Sommerfeld coefficient and Debye temperature values of Y = 0.210(1) J/mole.K and θ_D = 99(8) K. At higher temperatures, $\chi(T)$ data follows the paramagnetic Curie – Weiss behavior with an effective magnetic moment, μ_{eff} = 3.495(1) μ_B and a paramagnetic Weiss temperature θ_p = -3.8(2) K. The value obtained for μ_{eff}, is fairly close to the theoretical value of 3.62 μ_B expected for the free Nd^{3+} – ion. The magnitude of the magnetic entropy change ($-\Delta S_M$) and the adiabatic temperature change (ΔT_{ad}) was estimated from the isothermal magnetization data to be 8.59 J/kg.K and 7.1 K, respectively with the corresponding relative cooling power (*RCP*) value of 150 J/kg.K

GT-12. Magnetic Anisotropy of Rare Earth Systems.
M. Henderson[1,2], B. Ensign[1], R. Choudhary[1] and D. Paudyal[1] *1. Critical Materials Institute, US DOE, Ames Laboratory, Iowa State University, Ames, IA, United States; 2. West Chester University of Pennsylvania, West Chester, PA, United States*

Magnetic anisotropy is critical parameter in rare earth magnetism. In the presence of magnetic anisotropy, a material becomes more easily magnetized in a certain direction, and less susceptible to removal of the dipole alignment due to external magnetic fields. Many models exist for magnetic anisotropic energy density, each of which depend on the symmetry of the material. In this study, several of the symmetry dependent mathematical models, including uniaxial, cubic, hexagonal, and other configurations, have been analyzed. As for example, the simplest model used for the uniaxial anisotropic energy density uses even powers of sinusoidal functions. The models are then tested on praseodymium-based compounds with varying symmetries and structures. The compounds include Pr, $PrCo_2$, $PrCo_3$, and $PrCo_5$. The compounds also have their electronic structure examined using density functional theory based calculations. The linearized augmented plane wave method (LAPW) is used along with the local spin density approximation (LSDA), corrections for spin-orbit coupling (SOC) as well as the Hubbard model (U). Additionally, the density of states (DOS) and charge densities (Fig.1) [1] for each compound is calculated, and based on the DOS, magnetic behavior is derived through the exchange splitting of electrons near the Fermi-level. This work is supported by the Critical Materials Institute, an Energy Innovation Hub funded by the U.S. Department of Energy, Office of Energy Efficiency and Renewable Energy, Advanced Manufacturing Office. M.H. is grateful to the DOE for the assistantship and opportunity to participate in the Science Undergraduate Laboratory Internship (SULI) program.

[1] A. K. Pathak, D. Paudyal, W. T. Jayasekara, S. Calder, A. Kreyssig, A. I. Goldman, K. A. Gschneidner, Jr., and V. K. Pecharsky; "Unexpected magnetism, Griffiths phase, and exchange bias in the mixed lanthanide $Pr_{0.6}Er_{0.4}Al_2$"; Phys. Rev. B 89, 224411 (2014)

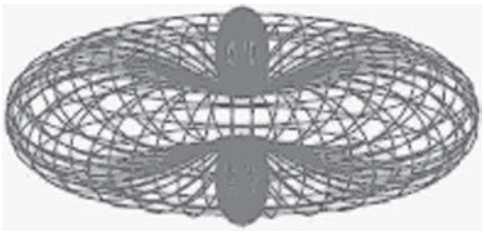


Fig.1 The 4f charge densities of Pr from point charge model calculations including quadrupolar (Q_2/a_0^2) and octupolar (Q_4/a_0^4) moments [1].

GT-13. Peculiarity of a magnetic structure in a quasi-one-dimensional columbite $Co_{0.4}Ni_{0.6}Nb_2O_6$. *P.W. Sarvezuk*[1], M.A. Gusmao[2], J.B. Marimon da Cunha[2] and O. Isnard[3] *1. Universidade Tecnológica Federal do Paraná, Campo Mourão, Brazil; 2. Universidade Federal do do Rio Grande do Sul, Porto Alegre, Brazil; 3. Institute Néel, Grenoble, France*

Quasi-one-dimensional (Q1D) spin chain systems have a great potential applications in high-density information storage devices, quantum: information and computers, given their quantum magnetic properties. The low-dimensional magnetic behavior have been investigated in ANb_2O_6, (A = Mn, Fe, Co or Ni) compounds, they structural and magnetic properties are very interesting because the system presents weakly interacting Ising chains, which leads to his quasi-one-dimensional magnetic order. Our investigation combines specific heat and magnetic measurements; x-ray and neutron diffraction (ND). In this work, we present a Co/Ni orthorhombic structure, called columbite, which crystallize with *Pbcn* space group, whose formula is $Co_{0.4}Ni_{0.6}Nb_2O_6$. Co for Ni substitution induces a continuous lattice volume decrease, preserving the orthorhombic crystal structure. Magnetic susceptibility and specific heat measurements reveals that antiferromagnetic order occurs at 3.4 K, as consequence of a weak interchain interactions. Partial substitution of the magnetic ion tends to change the magnetic ordering observed in the $CoNb_2O_6$ and $NiNb_2O_6$. Lastly, we present this magnetic structure changes with the Ni-Co substitution.

GT-14. Multiple Antiferromagnetic structures in $HoCoGa_5$ studied by X-ray resonant magnetic scattering. *C. Adriano*[1], R.M. Grossi[1], K.R. Pakuszewski[1], P. Pagliuso[1] and C. Giles[2] *1. DEQ, University of Campinas, Campinas, Brazil; 2. DFMC, University of Campinas, Campinas, Brazil*

The relationship between magnetism and superconductivity (SC) in strongly correlated electron systems is still a subject of investigation since the existence of series of structurally related compounds is a good opportunity to explore how the evolution of the physical properties along the series can affect the ground state of each compound. In this context, the isostructural family of intermetallic compounds R_nMX_{3n+2} (R = rare earth or actinides, M = transition metal, X = In, Ga and n = 1, 2) has allowed a remarkable opportunity to further explore the relationship between magnetism, SC, crystalline electrical field effects and crystal structure. Among this isostructural family the most important members are the heavy fermions superconductors $CeCoIn_5$ [1] and $PuCoGa_5$ [2] and their related compounds. The interesting properties arise from the interaction between the 4*f* and 5*f*, respectively, with the conduction electrons. In low temperatures the *f*-electrons start to interact with the conduction electrons and the ground state is mainly determined by an intricate balance between the RKKY (Ruderman-Kittel-Kasuya-Yosida) interactions and the Kondo Effect [3]. As the SC in these materials is believed to be magnetic mediated [4] the systematic study of the non-Kondo compounds within the R_nMX_{3n+2} family is very elucidative to investigate the evolution of the magnetism of the 4*f* electrons. In this work we add new results to the Ga-based series, for which the trends observed in the magnetic properties along these series can be further explored. We report the solution of the magnetic structure of the intermetallic antiferromagnet $HoCoGa_5$ by means of the X-ray magnetic resonant technique. We found a magnetic structure consistent with a commensurate antiferromagnetic phase below 7.4 K with a magnetic propagation vector (1/2 0 1/2) and an incommensurate antiferromagnetic ordering phase between 7.4 K and 9.7 K where the spins align in the ab-plane an rotate with an angle of around 65 degrees along the c direction and with a propagation vector (1/2 0 0.359). The spin reorientation found for this compound and existing in related 5*f* compounds like $NpMGa_5$ with (M = Rh,Co) is further discussed in this work.

[1] R. Movshovich, M. Jaime, J. D. Thompson, C. Petrovic, Z. Fisk, P. G. Pagliuso, and J. L. Sarrao, Phys. Rev. Lett. 86, 5152 (2001). [2] J. L.Sarrao, L. A. Morales, J. D. Thompson, B. L. Scott, G. R. Stewart, F.Wastin, J. Rebizant, P. Boulet, E. Colineau, and G. H. Lander, Nature (London) 420, 297 (2002). [3] A. C. Hewson, The Kondo Problem to Heavy Fermions, (Cambridge University Press, Cambrige, 1993). [4] T. Park, F. Ronning, H. Q. Yuan, M. B. Salamon, R. preMovshovich, J. L. Sarrao and J. D. Thompson, Nature 440, 65 (2006).

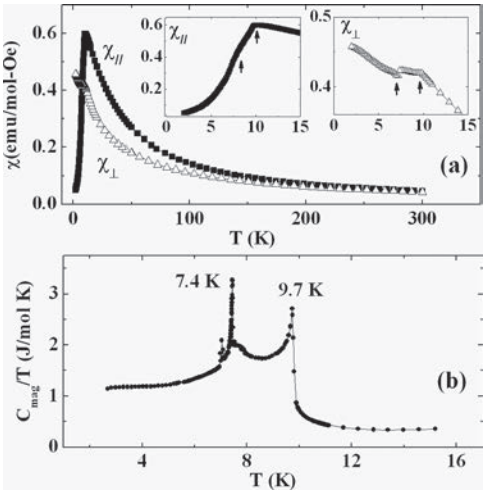


Fig.1 HoCoGa5 magnetic properties.

GT-15. Investigation of Local Magnetic Properties of CeCd as a Function of the Unit Cell Volume by means of First Principles Calculations. L.F. Pereira[1], L.M. Scalise[1], J. Mestnik-Filho[1], W.L. Ferreira[1], V.C. Gonçalves[1] and *A.W. Carbonari*[1] *1. Research Reactor Center, Nuclear and Energy Research Institute, São Paulo, Brazil*

In the work here reported magnetic hyperfine field (B_{hf}) at Cd site as well as the cerium magnetic moment (*m*-Ce) were calculated from simulation of the CeCd compound in many different unit cell volumes. Results are compared with the experimental values of B_{hf} (5.10 T) obtained with Perturbed Angular Correlation spectroscopy measurements [1] and *m*-Ce from magnetization measurements. The electronic structure calculations of the CeCd cubic cells (under normal conditions the space group is Pm-3m) were performed using density functional theory implemented on ELK and WIEN2k codes with "full-potential linearized augmented plane wave" method and the local density or generalized gradient approximations to estimate exchange-correlation energy. Three methodologies were carried out in our simulations: just spin polarized (SP); spin-orbit coupling (SO); and, SO plus *ad hoc U* parameter to treat the strong correlation in the cerium *4f* shell. The cell energy (CE), *m*-Ce and Fermi-contact contribution (B_{Fc}) of Cd-B_{hf} from electrons (labelled core and valence) inside the atomic spheres and others quantities were calculated for volume fractions varying from -14% to 5% of the experimental unit cell volume, in steps of 1%. The smallest energy and bestest Cd-B_{hf} agreement were reached when the volume is compressed by 12%. Results are discussed in terms of Ce-*4f* electron (de)localization and its strong correlation as well as hybridization effects between Cd and Ce observed through density of states plots to understand the dependence of Cd-B_{Fc} with the compression and relaxation of the cell. A brief comparison of Cd-B_{Fc} for 3 the methodologies and *m*-Ce and Cd-B_{Fc} versus volume (SP calculation) from WIEN2k are presented.

[1] F.H.M. Cavalcante, M. Forker and L.F.D. Pereira, PRB, Vol. 96, p. 064417-1 (2016)

Contact Magnetic Hyperfine Field at Cadmium site (Tesla)						
	Experimental Volume (0 %)			Reduced Volume		
	SP	SP+SO	SP+SO+U	SP (-12%)	SP+SO (-10%)	SP+SO+U (-10%)
B_c core	-0.2255	-8.5098	-9.211	-0.1389	-0.1165	-0.0717
B_c valence	-9.462	-0.1945	-0.1504	-5.6056	-4.9785	-3.3734
B_c total	-9.6875	-8.7043	-9.3614	-5.7445	-5.095	-3.4451

Fig. 1. Fermi contact hyperfine field at Cd site from different methodologies.

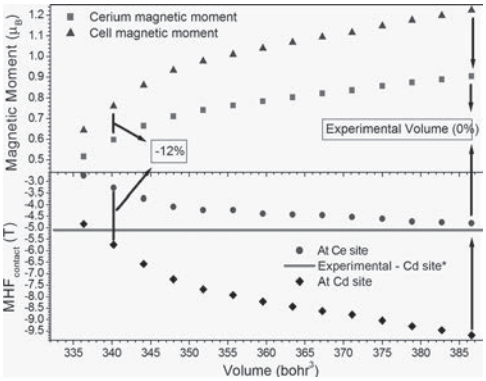


Fig. 2. Cerium and unit cell magnetic moment and Fermi contact hyperfine field at Cd site versus volume variation

GT-16. Magnetic-Field Driven Pr-Valence Change in $(Pr_{1-y}Sm_y)_{1-x}Ca_xCoO_3$. *T. Naito[1] 1. Iwate University, Morioka, Japan*

A metal-insulator transition (MIT) and spin-state transition (SST) is known to take place simultaneously in $(Pr_{1-y}RE_y)_{1-x}Ca_xCoO_3$ (RE=rare earth elements) system. This MI-SST originates from the fact that the spin-state of Co^{3+} changes between the intermediate (or high) and low spin states. Recently, several works revealed that the valence shift of a part of Pr ions from trivalent to tetravalent played an important role in the MI-SST by the X-ray absorption spectroscopy (XAS) at the Pr L_3 edge [1]. On the other hand, we have studied a magnetic-field effect on the MI-SST to control the SST, because the magnetic-field stabilizes the higher spin states and should influence the transition temperature. As a result, we found that the MI-SST temperature decreases with increasing magnetic-field, and finally the MI-SST is fully suppressed. For instance, the magnetic-field of 9 T wiped out the MI-SST in $(Pr_{0.9375}Y_{0.0625})_{0.7}Ca_{0.3}CoO_3$ sample with the transition temperature of 41 K at zero field [2]. In this paper, we have studied the XAS at the Pr L_3 edge in magnetic-field up to 10 T for $(Pr_{1-y}Sm_y)_{1-x}Ca_xCoO_3$ system to examine the relationship between the magnetic-field effect and the valence of Pr ions. For $(Pr_{0.8}Sm_{0.2})_{0.7}Ca_{0.3}CoO_3$ with the transition temperature of about 50 K, a $4f^2$ peak due to Pr^{3+} increases with increasing magnetic-field at 50 K, and returns to the starting spectrum at 0 T by removing the magnetic-field. The valence of Pr estimated from the XAS spectra changes from approximately 3.14 at 0T to 3.09 at 10 T. The decrease in Pr-valence by applying magnetic-field is consistent with the suppression of the MI-SST. We discuss the mechanism of the change in Pr-valence induced by the magnetic-field.

[1] H. Fujishiro et al., J. Phys. Soc. Jpn., Vol. 81, 064709 (2012) [2] T. Naito et al., J. Appl. Phys., Vol. 115, 233914 (2014)

GT-17. Co-site Substitution Effects on the Simultaneous Metal-Insulator and Spin-State Transition in $(Pr_{1-y}Gd_y)_{1-x}Ca_xCoO_3$. *T. Naito[1] 1. Iwate University, Morioka, Japan*

A metal-insulator transition (MIT) and spin-state transition (SST) is known to take place simultaneously in $(Pr_{1-y}RE_y)_{1-x}Ca_xCoO_3$ (RE=rare earth elements) system. This MI-SST originates from the fact that the spin-state of Co^{3+} changes between the intermediate (or high) and low spin states. Several works revealed that the valence shift of a part of Pr ions from trivalent to tetravalent played an important role in the MI-SST by the identification of the Pr^{4+}-related Schottky peak in heat capacity measurements [1] and by X-ray absorption spectroscopy (XAS) at the Pr L_3 edge [2]. The increase of the fraction of Co^{3+} by the valence change of Pr ions induced the MI-SST. In this paper, we have studied that a Co-site substitution effect by various metal elements (M=Mn, Fe, Ni, Ga, etc.) on the MI-SST in $(Pr_{1-y}Gd_y)_{1-x}Ca_x(Co_{1-z}M_z)O_3$, to clarify the relationship between the fraction of Co^{3+} and the MI-SST. For M=Mn, the transition temperature increased with increasing the amount of Mn. The introduction of Mn^{4+}, revealed by the XAS, increases the fraction of Co^{3+}, and resulted in the increase of the transition temperature. On the other hand, for M=Ni, the transition temperature decreased with the amount of Ni, and finally the MI-SST was fully suppressed at z=0.05. The results of the Ni-substitution is quite similar to the magnetic-field effect, in which the MI-SST disappeared above a strong magnetic field [3]. Although the valence of Ni was not determined by the XAS, we found that the ferromagnetic element also suppress this transition.

[1] J. Hejtmanek et al., Eur. Phys. J. B, Vol.86, 305 (2013). [2] H. Fujishiro et al., J. Phys. Soc. Jpn., Vol.81, 064709 (2012). [3] T. Naito et al., J. Appl. Phys., Vol. 115, 233914 (2014).

GT-18. Withdrawn

GT-19. Withdrawn

Session GU
POWER MAGNETICS - ADVANCED MACHINES
(Poster Session)

Yang-Ki Hong, Chair
The University of Alabama, Tuscaloosa, AL, United States

GU-01. Study on construction of leakage magnetic field reduction coil system for contactless power supply during EV driving. *T. Abe*[1], S. Oba[1], T. Sawa[1], S. Miyahara[1], F. Sato[1], K. Ishikawa[1], H. Mastuki[2] and S. Sasaki[3] *1. Tohoku Gakuin University, Tagajyo, Japan; 2. Tohoku University, Sendai, Japan; 3. Hikaridenshi Co.,Ltd, Osaki, Japan*

EVs are rapidly developing as a solution to the recent energy saving problems and environmental pollution, but it is difficult to say that they are still widely accepted. With the policy of becoming an all-vehicle EV by 2040 in Europe, EV shifts have spread throughout the world. However, in order to further promote EV, it is necessary to solve the issues regarding battery capacity and power supply system. As a system to solve these problems at once, a contactless power transfer system while traveling is being considered. Various proposals have been made for this system at present, but there is no system with a significant function to reduce the leakage magnetic field, and none of them has reached the practical stage. Therefore, we propose a non-contact power supply system during traveling with a function to reduce the leakage magnetic field. By this proposal, the infrastructure implementation of the contactless power supply system while driving becomes more realistic. In this study, we constructed a feed system with an extended transmission coil length using an 8-figure-coil and LC booster system. A schematic diagram of the leakage magnetic field of the 8-figure-coil is shown in Fig. 1. We compare this system with a system in which the transmitting coil proposed in the previous research[1] is rectangular and the receiving coil is in the form of spiral, and confirm that the leakage magnetic field is actually reduced. In this experiment, several sizes of feed systems were created, and the leakage magnetic field under multiple conditions was compared. A comparison of the leakage magnetic field at constant output is shown in Fig. 2. From these results, it was confirmed that the leakage magnetic field was actually reduced in the feed system using an 8-figure-coil. In this study, we constructed a system to reduce the leakage magnetic field. It was confirmed that the leakage magnetic field can be reduced by actually comparing the 8-figure-coil and the conventional spiral-shaped feeding system. In the future, we will further study the construction of coil shapes more suitable for infrastructure mounting.

[1] Aoki Shuta et al., "Study on the shape of the power transmission side coil for reduction of ambient leakage electromagnetic field in contactless power supply while driving" IEICE Technical Report WPT 2015 - 28 (2015)

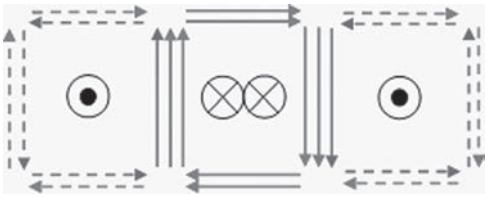


Fig. 1 8-figure-Coil magnetic field schematic

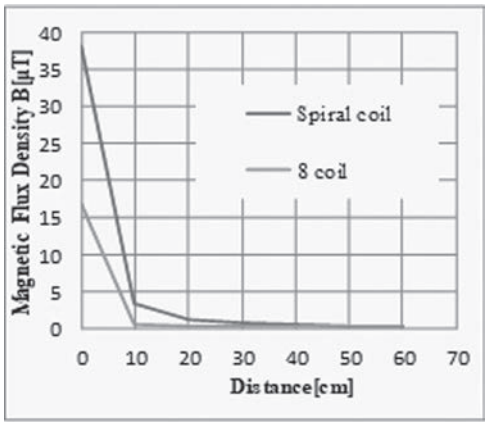


Fig. 2 Leakage magnetic field comparison diagram with constant output power

GU-02. Design of Stable Feeding System Using Repeater Coils for Contactless Power Transmission System During EV Driving. *S. Oba*[1], T. Abe[1], F. Sato[1], S. Miyahara[1], T. Sawa[1], K. Ishikawa[1], S. Sasaki[2] and H. Mastuki[3] *1. Tohoku Gakuin University, Tagajo, Japan; 2. Hikaridenshi Co.,Ltd, Osaki, Japan; 3. Tohoku University, Sendai, Japan*

Many research institutes are researching the technology of contactless power transmission system during EV driving as a method to extend the cruising distance of Electric Vehicle (EV). In order to realize the system in full scale, it is necessary to extend the feeding section per power source and to form an enough power feeding section with a small number of power sources as a whole[1]. Therefore, an extension method has been proposed using a repeater coil. This method is combined with the power feeding coil that is connected to the power source to extend the feeding section. However, it is known that there is a coil configuration in which the power transmission efficiency to the load is significantly reduced. It has different characteristics depending on the number of repeater coils and the position of the load. Furthermore, the repeater method corresponding to the rectangular coil which is a coil shape that can be stably fed in the traveling direction has not been studied so far. In addition, when making a power feeding section with the same distance, using a rectangular coil requires less wire than using a spiral coil on the power feeding side. Therefore, the repeater method corresponding to the rectangular coil is required in the contactless power transmission system during EV driving. Fig. 1 shows a schematic diagram of the repeater method using the spiral coil, which has been mainly studied so far. Therefore, in this study, we examined the new repeater method that can supply EV stably on a rectangular coil. A cross coil and a rectangular coil were combined on the feeding side, and a spiral coil was used on the receiving side. Fig. 2 shows the new repeater method we propose in this study. In this new repeater method, the features of the cross coil, rectangular coil, and spiral coil are used. As a result, it was confirmed by experiments that stable power feeding to the load is possible on the rectangular coil without a place where the feeding efficiency drops significantly. Furthermore, we have also proposed a repeater method for a rectangular coil suitable for contactless power transmission to EV.

[1]T. Misawa, T. Takura, F. Sato, T. Sato, and H. Matsuki, "Relationship between Feeding Coil Size and Transmission Efficiency of Contactless Power Transmission for Moving Electric Vehicle." IEICE Technical Report, pp.13-18, (2012) [2]K. E. Koh, T. Imura, and Y. Hori, "Impedance Inverter based Analysis of Wireless Power Transfer Consists of Repeaters via Magnetic Resonant Coupling," IEICE Technical Report, pp.35-40, (2012)

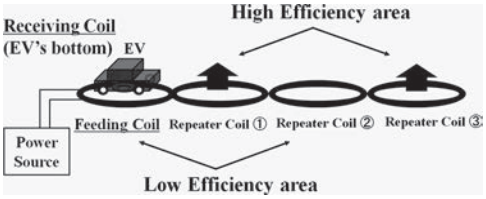


Fig. 1 Schematic of relay system using spiral coil

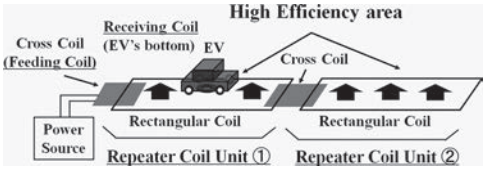


Fig. 2 Schematic of the new repeater system we propose

GU-03. Effect of Physical Contact on the Evolution of Cube-on-Face Texture in Fe-1%Si Steel during the Phase Transformation from γ to α. *S. Kwon*[1] *1. POSCO, Pohang, The Republic of Korea*

Recently, electrical vehicles are becoming increasingly popular and will replace the vehicles using an internal combustion engine in near future. Therefore, there is a strong demand for the development of high efficiency electrical steel for motors and generators. It is well known that the ideal texture of silicon steel for motors and generators is a cube-on-face texture, {100}<uv0>, where each grain has two <100> directions in the plane of the sheet to give excellent magnetic properties. When any sample is heat treated, it is in physical contact with the supporting material. Normally, such physical contact is not expected to affect the microstructure evolution of the sample. However, the physical contact between Fe-1%Si sheet and the Al2O3 plate was found to have a strong effect on the evolution of a cube-on-face texture during heat treatment, producing as much as 76.0% when determined by the orientation within {100} ±15'. The similar result was obtained for the tungsten and quartz plates. The results provide a promising new method to produce the high efficiency non-oriented electrical steel of a cube-on-face texture.

GU-04. Investigation of Variable Flux Characteristics in Parallel Hybrid Permanent Magnets. *Y. Jie*[1], H. Yang[1], X. Guo[1], J. Li[1] and M. Wang[1] *1. School of Electrical Engineering, Southeast University, Nanjing, China*

I. INTRODUCTION Variable flux permanent magnet (VFPM) machines [1] [2] equipped with both low coercive force (LCF) AlNiCo magnet and high coercive force (HCF) NdFeB magnet can achieve both acceptable torque capability and excellent flux adjustment range. However, the nonlinear magnetization characteristics of AlNiCo PM make precise online MS manipulation relatively complicated [2]. Thus, a C-core magnetizer device with a parallel hybrid (PH) PM arrangement is designed to provide an in-depth insightful understanding for variable flux property, as well as a utility design guideline of PH PMs [3]. In addition, an experiment-based methodology with both continuous and transient current pulse tests is proposed. II. MAGNETIZER DESIGN The finite element (FE) model of the device is illustrated in Fig. 1(a). The relationship between the proportion of NdFeB PM and the peak air-gap flux density is shown in Fig. 1(b). In order to maximize flux adjustment range when ensuring the maximum air-gap flux density reach 0.65T, an appropriate proportion of NdFeB PM is selected as 58% for the prototype manufacturing. III. EXPERIMENTAL RESULTS The prototype is shown in Fig. 2(a). The experimental results of one-way magnetization and demagnetization with continuous current are shown in Figs. 2(b) and (c), respectively. The blue line represents the major hysteresis loop, of which the left branch shows high nonlinearity that is mainly due to the nonlinear hysteresis property of the AlNiCo PM. Meanwhile, the linearity of right branch suggests that the NdFeB PM dominates the air-gap flux density. Nevertheless, the recoil line results are measured by the continuous low current tests, which reflects the linear movement trajectories of the LCF PMs during the magnetization. In full paper, the analysis of the magnetization characteristics and an equivalent hysteresis model of the PH PMs will be presented.

[1] H. Yang, H. Lin, and Z. Q. Zhu, "Recent advance in variable flux memory machines for traction applications: a review," in CES Trans. Electr. Machin. and Syst., vol. 2, no. 1, pp. 34-50, March 2018. [2] H. Yang, S. Lyu, and H. Lin, "Stepwise magnetization control strategy for DC-Magnetized memory machine", IEEE Trans. Ind. Electron., vol. 66, no. 6, pp. 4273-4285, Jun. 2019. [3] D. Fernandez, D. Reigosa, and J. M. Guerrero, "Influence of PM coating on PM magnetization state estimation methods based on magnetoresistive effect", IEEE Trans Ind. Appl. vol. 54, no. 3, pp. 2141-2150, Jan. 2018.

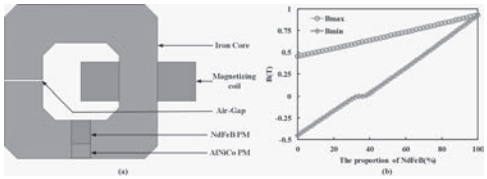


Fig. 1. (a) The FE model. (b) The influence of the NdFeB PM proportion on the maximum and minimum air gap flux densities under different MSs of AlNiCo PMs.

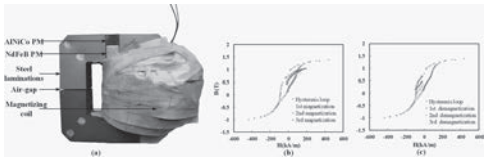


Fig. 2. Magnetization and demagnetization experiments. (a) The C-core device prototype. (b) Magnetization with continuous current. (c) Demagnetization with continuous current.

GU-05. On-Load Demagnetization Effect of High-Coercive-Force PMs in Switched Flux Hybrid Magnet Memory Machine. *H. Yang*[1], H. Lin[1], Z. Zhu[2] and S. Lyu[1] *1. Electrical Engineering, Southeast University, Nanjing, China; 2. Electrical and Electronics Engineering, The University of Sheffield, Sheffield, United Kingdom*

I. INTRODUCTION Hybrid magnet memory machines (HMMMs) [1] [2] equipped with both high-coercive-force (HCF) and low-coercive-force (LCF) magnets is able to achieve high-efficiency operation within a wide speed range, since the magnetization state (MS) of the LCF PMs can be conveniently magnetized/demagnetized with a current pulse. Due to the high-level current pulse, the accidental irreversible demagnetization of NdFeB PMs should be discussed. Therefore, this paper aims to establish an in-depth investigation into the on-load unintentional demagnetization (UD) behavior of NdFeB magnets in a newly developed switched flux HMMM (SF-HMMM) [3]. II. UD EFFECT IN HCF PMS Fig. 1(a) shows the structure of the proposed SF-HMMM. The NdFeB PM serves as a dominant contributor for air-gap flux, while the LCF PM acts as a flux adjustor due to its changeable MS. When the temperature is set as 120 °C, the armature and magnetizing windings are fed with 40A *q*-axis current and 50A DC current, respectively. By using the frozen permeability method (FPM) [4], Fig. 1(b) shows the field contours produced by either the resultant armature/magnetizing or individual fields. It shows that the magnetizing MMFs possibly penetrate the NdFeB PMs, and hence posing the potential demagnetization risk, as evidenced in the working point variations in Fig. 2(a).

III. EXPERIMENTAL VERIFICATION When LCF PM of the SF-HMMM prototype (see Fig. 2(b)) is with the full MS, the back-EMF is measured in advance. Afterward, the prototype machine is fed by various magnitudes of *q*-currents, and then the resultant back-EMFs are tested after withdrawing the load currents. The FE and measured peak EMFs are shown in Fig. 2(b). It shows that the back-EMF rarely varies with increasing load currents, which suggests that the HCF PMs in the proposed SF-HMMM well resist the UD effect. The detailed UD characteristics, mechanism, and dynamic test results will be given in the full paper.

[1] V. Ostovic, "Memory motors," *IEEE Ind. Appl. Mag*., vol. 9, no. 1, pp. 52-61, Jan./Feb. 2003. [2] C. Yu, K. T. Chau, J. Z. Jiang, "A flux-mnemonic permanent magnet brushless machine for wind power generation," *Jour. of Appl. Phys.*, vol. 105, no. 7, pp: 07F114, 2009. [3] H. Yang, Z. Q. Zhu, H. Lin, K. Guo, Y. Guo, S. Fang, and Y. Huang, "Analysis of on-load magnetization characteristics in a novel partitioned stator hybrid magnet memory machine," *IEEE Trans Magn.*, vol. 53, no. 6, 8103404, Jun. 2017. [4] W. Q. Chu and Z. Q. Zhu, "Average torque separation in permanent magnet synchronous machines using frozen permeability," *IEEE Trans. Magn*., vol. 49, no. 3, pp. 1202-1210, Mar. 2013.

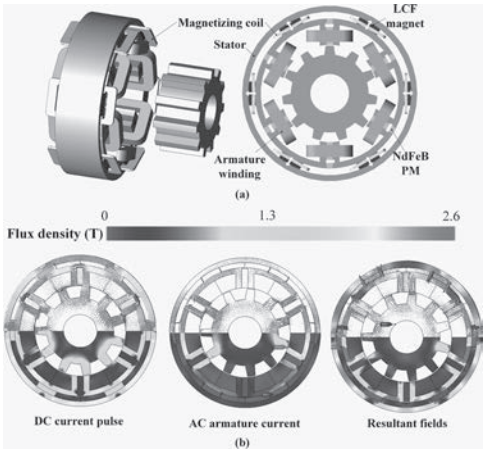


Fig. 1. (a) SF-HMMM configuration. (b) Field contours produced by either the resultant armature/magnetizing or individual fields.

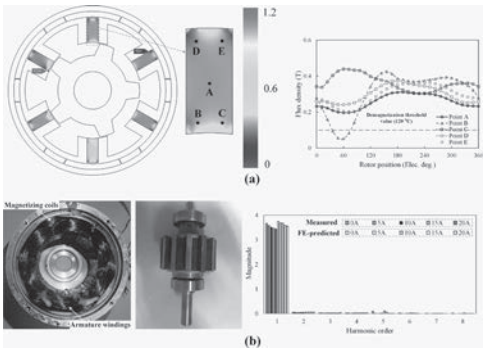


Fig. 2. (a) Field contours of the HCF magnets subject to the synthetic armature and magnetizing fields. (b) Prototype and FE/measured Back-EMF magnitudes.

GU-06. Balanced Bidirectional-Magnetization Effect of a Novel Hybrid-Magnet-Circuit Variable Flux Memory Machine. *H. Yang*[1], H. Lin[1], Z. Zhu[2] and S. Lyu[1] *1. Electrical Engineering, Southeast University, Nanjing, China; 2. Electrical and Electronics Engineering, The University of Sheffield, Sheffield, United Kingdom*

I. INTRODUCTION Variable flux memory machine (VFMM) [1]-[6] can achieve high efficiency over a wide operation range by applying a current pulse to magnetize the low coercive force (LCF) magnets. This paper combines the design concepts of parallel and series VFMMs, proposing a new hybrid-magnetic-circuit VFMM (HMC-VFMM). The HMC design can achieve wide flux adjustment range in parallel type [5] and beneficial on-load demagnetization withstand capability in series type [6]. This paper attempts to reveal and investigate a balanced bidirectional-magnetization effect of the proposed HMC-VFMM, i.e., the required demagnetizing and remagnetizing current levels are basically similar, which will benefit the inverter rating reduction and online flux control. II. CONFIGURATION AND BIDIRECTIONAL-MAGNETIZATION BALANCED EFFECT The proposed HMC-VFMM structure is illustrated in Fig. 1(a). For the parallel branch, the "U"-shaped hybrid magnets are employed. For the series branch, the HCF PMs feature a spoke-type configuration. The underlying mechanism of the balanced bidirectional-magnetization effect can be physically characterized by hysteresis curves of the LCF PM in Fig. 1(b). The load line of the HMC design is placed between those of the parallel and series cases, which allows a better balance between the magnetizing and demagnetizing currents. Meanwhile, the oversized inverter rating issue for either parallel or series VFMMs can be well avoided by appropriately reducing maximum magnetizing currents. III. EXPERIMENTAL VERIFICATION As shown in Fig. 2(a), an HMC-VFMM prototype is manufactured and tested. The FE and measured open-circuit phase back-EMF magnitudes versus various peak current pulse curves are shown in Fig 2(b). It shows that the experiments agree well with FE results. Besides, the proposed HMC-VFMM shows comparable peak demagnetization and remagnetization currents, which confirms the balanced bidirectional-magnetization effect. The detailed mechanism, characteristics analyses, and test results will be given in the full paper.

[1] V. Ostovic, "Memory motors," *IEEE Ind. Appl. Mag*., vol. 9, no. 1, pp. 52-61, Jan./Feb. 2003. [2] C. Yu and K. T. Chau, "Design, analysis, and control of dc-excited memory motors," *IEEE Trans. Energy Convers.*, vol. 26, no. 2, pp. 479-489, Jun. 2011. [3] H. Yang, S. Lyu, H. Lin, and Z. Q. Zhu, "A variable-mode stator consequent pole memory machine," *AIP Advances*, vol. 8, no. 5, Article No. 056612, 2018. [4] H. Yang, H. Lin, Z. Q. Zhu, and S Lyu, "Influence of magnet eddy current on magnetization characteristics of variable flux memory machine," *AIP Advance*, vol. 8, no. 5, Article No. 056602, 2018. [5] K. Sakai, K. Yuki, Y. Hashiba, N. Takahashi, and K. Yasui, "Principle of the variable-magnetic-force memory motor," in *Proc. Int. Conf. Electr. Mach. Syst.*, Tokyo, Japan, 2009, pp. 1-6. [6] A. Athavale, K. Sasaki, B. S. Gagas, T. Kato, and R. D. Lorenz, "Variable flux permanent magnet synchronous machine (VF-PMSM) design methodologies to meet electric vehicle traction requirements with reduced losses", *IEEE Trans. Ind. Appl*., vol. 53, no. 5, pp. 4318-4326, Sep./Oct. 2017.

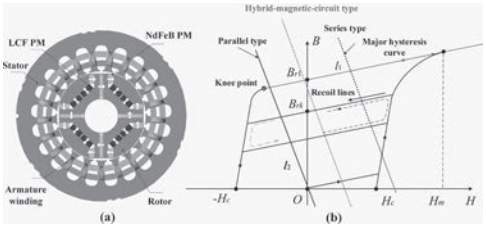


Fig. 1. (a) Topology and (b) balanced bi-directional magnetization effect of the proposed HMC-VFMM.

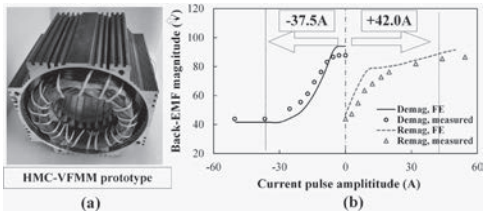


Fig. 2. (a) Prototype. (b) FE and measured back-EMF magnitudes versus the current pulses.

GU-07. Comparative Study of Hybrid-PM Variable-Flux Machines with Different Series PM Configurations. *F. Liu*[1], L. Cheng[1], M. Wang[1], G. Qiao[1] and P. Zheng[1] *1. School of Electrical Engineering & Automation, Harbin Institute of Technology, Harbin, China*

Variable flux PM synchronous machine (VF-PMSM) is considered as a promising candidate for adjustable-speed drive applications [1]. Since low coercivity (H_c) magnets are used, the magnetization state of low-H_c magnet in VF-PMSM can be changed through *d*-axis current pulse. It is obviously that the rotor scheme and stator winding configuration have crucial influences on the magnetization characteristic and electromagnetic performance of VF-PMSMs. In this paper, a comparison study of three proposed hybrid-PM variable-flux machines (HPM-VFMs) with both low- and high-H_c magnets is conducted, which could give an insight into the influence of the arrangement of magnets on the performance of the machines, as shown in Fig. 1. The red and the yellow blocks are the low- and high-H_c magnets, and the arrows demonstrate the magnetization directions. In order to obtain reverse salient characteristics, the optimal *q*-axis flux barrier is determined by calculating L_d and L_q under light and heavy load conditions for each rotor scheme. The contributions of high-H_c magnets to the magnetization state and no-load air-gap flux density are evaluated, and the simulation results shows that the rotor scheme II and III are much better. The influence of the width and thickness of low-H_c magnet on electromagnetic performance of HPM-VFMs is investigated. A general rule of the arrangement and usage proportion of low- and high-H_c magnets of the machine is given. 8 stator winding configurations of rotor scheme III, including integral- and fractional-slot windings, are studied and compared. It reveals that the required magnetization current is decreased as the number of slots is increased. Torque and torque ripple of rotor scheme III after being magnetized by different stator winding configurations with the same MMF are illustrated in Fig.2. Apart from 9-slot winding configuration, the torque ripple of fractional-slot configuration is much lower than that of integral-slot configuration. However, an uneven demagnetization among different pieces of low-H_c magnets is observed in fractional-slot configurations. More information and discussion will be included in the full paper.

[1] V. Ostovic, IEEE Ind. Appl. Mag., Vol. 9, p. 52 (2003)

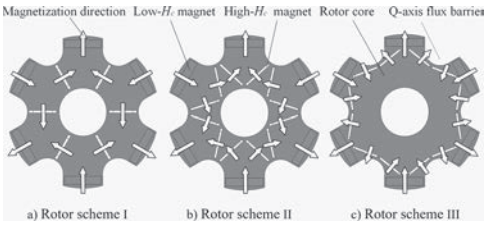


Fig. 1 Three rotor schemes

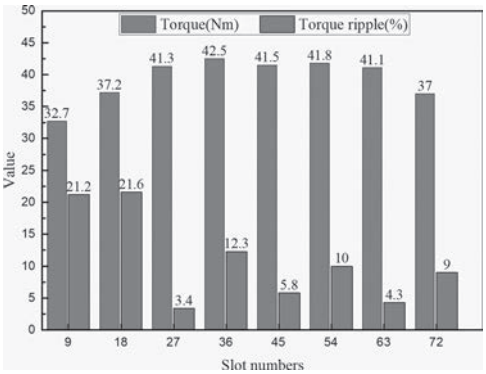


Fig. 2 Torque characteristics of rotor scheme III

GU-08. Study on communication element design for communication magnetic field stabilization in implanted FES. *Y. Hongo*[1], F. Sato[1], T. Abe[1] and S. Miyahara[1] *1. Tohoku Gakuin University, Tagajo, Japan*

FES (Functional Electrical Stimulation) rebuilds motor function by applying electrical stimulation to the Residual function of peripheral nerves of the limbs in Spinal cord injury. Method of FES is suggesting fully embedded element by direct power feeding [1]. A small stimulation element is embedded in the object to be stimulated, internal element receives power and communication at the same time by near electromagnetic field generated from the external feeding coil and communication coil (Fig. 1). However, the communication unit is wrapped on the feeding unit, and is magnetic couple strong. In this study, to solve for this problem, suggested low magnetic coupled model that wrapped rectangle spiral coil to feeding power solenoid coil for induced voltage cancel. Those wrapped coils are divided into three. One of those is additional coil unit that connected inverter and modulator, other units is inner coil and outer coil (Fig. 2). Additional coil generated magnetic field is reflect by those units. In drive alone this communication coil shape, a region where the magnetic field is canceled occurs inside the coil. By using two coils and giving them a phase difference, the area where the magnetic field is always canceled gradually disappears. Previous studies have shown that the region where the magnetic field disappears is minimized when the current phase difference flowing through the two coils is $\pi/2$ [2]. But, in the state of magnetic interference in a plurality of resonant circuits, it is difficult to calculate the optimum value of the phase difference by calculation. Therefore, we performed simulation by electromagnetic wave analysis using numerical analysis and parameters calculated from it. In numerical analysis, calculation is performed with the parameters of the coil actually created, and the current value and phase information obtained from it was adapt to the coil model of magnetic field analysis. The result is a significant improvement over the single low coupling communication coil model.

[1] F. Sato, T. Nomoto, G. Kano, H. Matsuki, T. Sato, A New Contactless Power-Signal Transmission Device for Implanted Functional Electrical Stimulation (FES), IEEE Transactions on Magnetics, Vol. 40,No. 4(2004)
[2] K. Kato, F. Sato and H. Matsuki, Bidirectional communication system for magnetic direct feeding FES, IEEE Transactions on Magnetics, Vol. 47, No.10, (2011)

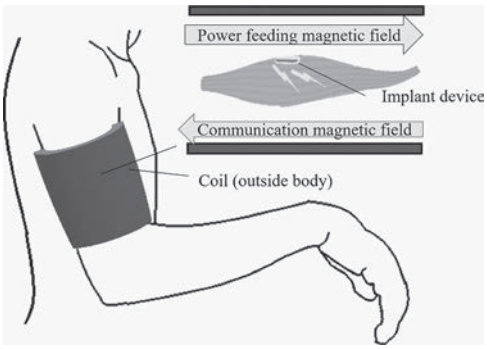


Fig.1 FES system

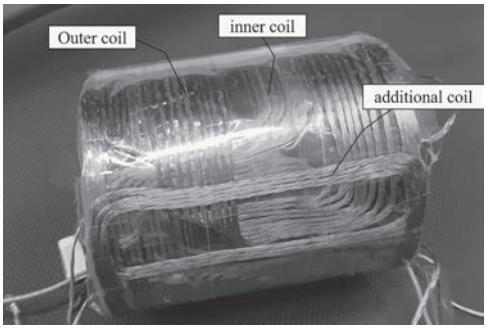


Fig.2 Communication Coil

GU-09. Optimal Design of Induction Machines Based on an Improved Fast Steady-state Reaching Method and Finite Element Method.
H. Wu[1], S. Wang[1], Y. Zhang[1] and W. Fu[1] *1. The Hong Kong Polytechnic University, Hong Kong, Hong Kong*

I. Introduction Pareto-front based multi-objective optimization algorithms have been widely employed in the optimal design of induction machines [1,2]. The number of objectives in most optimal designs is, however, limited to two, which does not satisfy the industrial requirements. In addition, the reaching steady state process in simulation is time-consuming. In this paper, a fast reaching steady-state method, in combination with a load-balanced multi-objective evolutionary algorithm, is proposed for solving the induction machine design problem with three or more objectives and improving the speed of optimization. II. The Fast Reaching Steady State Method Currently, the greatest challenge for evaluating the performance of induction machines is that it takes a long time to reach steady state in simulation. Compared with conventional methodologies, improved rotor conductivity referring method and alternating flux linkage method (AFM) [3] proposed an equivalent model in simulation, which can make the induction machine reach the steady state in a few cycles. The simulated torques using the proposed method and the conventional method are plotted alongside time, as shown in Fig.1(a). The reaching steady-state time of conventional model is more than 80ms, while it only takes roughly 8ms for the equivalent model with AFM to reach the steady-state. III. Design Example The optimal design problem of a squirrel cage induction machine, which has four objectives, is employed to verify the proposed method. A set of Pareto-front based solution is derived from the optimization algorithm, as shown in Fig. 1(b). It should be noted that the solution set shown in three-dimension is the projection of four objective vectors, which is not a smooth surface. In addition, the finite element analysis time of equivalent model could be saved by 90%, as is shown in Fig. 2. Finally, a prototype of the optimized model will be manufactured and tested to verify the method proposed in this paper.

[1] L. A. Pereira, S. Haffner, G. Nicol and T. F. Dias, "Multi-objective Optimization of Five-Phase Induction Machines Based on NSGA-II," in IEEE Transactions on Industrial Electronics, vol. 64, no. 12, pp. 9844-9853, Dec. 2017. [2] Y. Duan and D. M. Ionel, "A review of recent developments in electrical machine design optimization methods with a permanent magnet synchronous motor benchmark study," 2011 IEEE Energy Conversion Congress and Exposition, Phoenix, AZ,2011, pp. 3694-3701 [3] D. Lin and P. Zhou and N. Chen and C. Lu and M. Christini "Fast methods for reaching AC steady state in FE transient analysis," 2017 IEEE International Electric Machines and Drives Conference (IEMDC), Miami, FL, 2017, pp. 1-6.

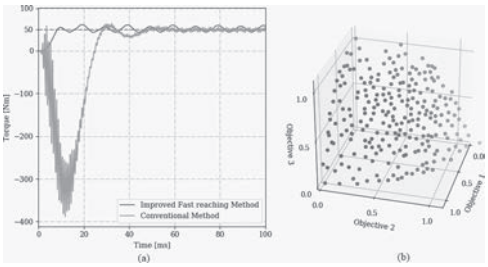


Fig1.(a) Simulated Torque of Induction Machine (b)Solution set of Optimal Design

Model Type	Simulation Time (Seconds)
Equivalent Model	110
Conventional Model	959

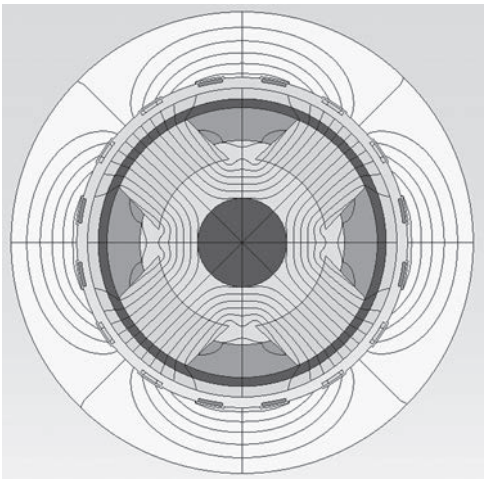
Fig.2 Computing Time of Equivalent and original Model

GU-10. Design and Simulation Mini Size Fully Passive Iron-core Compensated Pulsed Alternator. *Y. Yang*[2], S. Wang[2], C.P. Chao[1], S.B. Nguyen[1] and W. Yen[1] *1. Institut of Electrical and Control Engineering, National Chiao Tung University, Hsinchu, Taiwan; 2. Department of Mechanical Engineering, National United University, Miaoli, Taiwan*

There are a lot of paper discuss CPA in military application which was in mega joule order until now [1-6]. Although these is a CPA designed for powder spraying [7], there is no CPA designed in general purpose and only few paper present in kilo joule level CPA [8]. A 0.220 x 0.132 m^2 and 10 kJ power level compensated pulsed alternator (CPA) was designed in this paper. The rotation speed of CPA was designed in 10000 rpm, the voltage of CPA was lower than 110V and two phase system each phase including six pole was implement in this CPA. The CPA system block diagram is present in figure 1. CPA was carried by an industrial motor driven by three phase inverter to rated speed. When the fire signal bottom was turn on, thyristor based full bridge rectifier was turned to short the output circuit to the load. The electromagnetic simulation of CPA is illustrated in figure 2. The magnetic flux was compressed completely inside the CPA and conserve flux throughout the rotation. The induce current density is 3.4386 x 108 A/m2 due to the variation of the flux. Thus, each phase was induced 2.063 kA. The CPA is discharged in 4.5 ms with output circuit and load. Both A and B phase output voltage, open circuit voltage, was 90 V in rotation speed 10000 rpm. The maximum current tested with output load is 3.450 kA and average current is 15 kA in 4.5ms. The angular velocity of CPA was slow down from 10000 rpm to 9775 rpm during 4.5 ms discharge. In the simulation, the open circuit output voltage was 102V at 10260 rpm and 1050 A current was induced by CPA with load at 5500 rpm.

Wu, S., Zhao, W., Wang, S., etc. *IEEE Transactions on Plasma Science*, *45*(7), 1078-1085.(2017) Driga, M. D., Pratap, S. B., & Weldon, W. F., *IEEE Transactions on Magnetics*, *25*(1), 142-146.(1989) Kitzmiller, J. R., Faidley, R. W., Fuller, R. L., etc. *IEEE Transactions on Magnetics*, *27*(1), 50-55. (1991) Zhang, Q., Wu, S., Yu, C., etc. *IEEE Transactions on Plasma science*, *39*(1), 346-353. (2010) Wu, S., Cui, S., & Song, L., In *2012 16th International Symposium on Electromagnetic Launch Technology* (pp. 1-5). IEEE. (2012, May) Wang, H., Liu, K., Zhu, B., etc. *IEEE Transactions on Magnetics*, *51*(8), 1-9. (2015) Driga, M. D., & Ozdemir, M. In *Digest of Technical Papers. 11th IEEE International Pulsed Power Conference (Cat. No. 97CH36127)* (Vol. 2, pp. 1066-1071). IEEE. (1997, June) Cui, S., Wu, S., & Cheng, S. *IEEE Transactions on Magnetics*, *45*(1), 261-265. (2009)





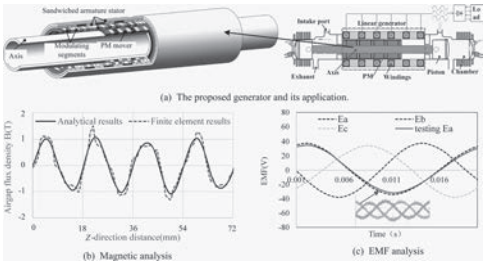


Fig. 1 The proposed generator and analysis results.

GU-11. Performance Evaluation of a Tubular Flux-modulated PM Linear Generator with Sandwiched Armature. *M. Ma*[1] *1. College of Electrical Engineering and Automation, Hefei University of Technology, Hefei, China*

Abstract—A novel flux-modulated permanent magnet (PM) linear generator with sandwiched armature is used for free-piston energy converter system. It shows significant advantages in terms of thrust force density, efficiency and response capability. This paper discusses issues that are pertinent to the design of the proposed linear generator. First, a two-dimensional magnetic field analytical model is developed. And then the influence of key dimensional ratios of sandwiched armature (flux-modulated layer and air-cored layer) on electromagnetic performances are discussed. Finally the effectiveness of analysis results is verified by experiment on the prototype. I. Introduction Free piston energy converter is an integrated combination of a free piston engine and a linear electrical machine. The linear generator is the key part in free-piston energy system. This paper presents a novel tubular linear PM generator with sandwiched structure, aiming to realize high power density and fast response, as shown in Fig. 1(a). The topology has the novel sandwiched armature. The sandwiched armature consists of three layers: modulated segments and windings deployed inside it, air-cored windings, and iron core. The flux-modulated layer and air-cored layer windings are series connection. The arrangement of modulated segments is based on magnetic-gear effects, which has the capability of realize high thrust density. II.analytical model A comprehensive analysis of the novel topology has been presented. The magnetic field distribution of the subdomains are solved by using boundary and interface conditions as shown in Fig. 1(b). And then some design criteria have been found. III. Performance evaluation The influence of design parameters on electromagnetic performance are analyzed. The characteristics of output voltage, efficiency, and inductance parameter are investigated. Accordingly the generator can be optimized by the match of parameters in sandwiched armature. And then the preliminary test of the proposed generator has been completed as shown in Fig. 1(c). The output performance are compared with the existing different types of tubular linear ones for the same application [1].

[1] Jiabin Wang, M. West, David Howe, etc. IEEE Transaction Energy Conversion, Vol. 22(2), p. 299(2007).

Session GV
SENSORS II
(Poster Session)

Denys Makarov, Chair
HZDR, Dresden, Germany

GV-01. Fabrication of the magnetoresistive sensor with enhanced sensitivity by the application of repetitive bending stress. *J. Kwon*[1], W. Kwak[1], S. Hwang[1] and B. Cho[1] *1. School of Materials Science and Engineering, Gwangju Institute of Science and Technology, Gwangju, The Republic of Korea*

Magnetoresistive (MR) sensors, such as spin-valves (SVs), have been widely used for magnetic field and beads sensing.[1-3] However, complicated patterning and post-annealing processes are required to fabricate SV sensors.[4] In this study, we describe the fabrication of the MR sensor by the application of bending stress, which controls the magnetization by magnetostriction effect. The structure of Ta (3)/$Ni_{79}Fe_{21}$ (4)/$Co_{70}Fe_{30}$ (1)/Cu (2.8)/$Co_{70}Fe_{30}$ (1)/Ni (3)/$Ir_{20}Mn_{80}$ (15)/Ta (1) is deposited on a flexible polyimide film where the numbers are in nm unit. The free (NiFe) and pinned (Ni) layers have positive and negative magnetostriction, respectively. The CoFe sub-layers adjacent to the Cu spacer prevent the formation of dead layers to improve the initial MR ratio value.[5] As shown in Fig. 1, after the repetitive downward bending is applied along the easy axis, the magnetic anisotropy of the free layer is weakened so that the magnetic direction is relatively easy to rotate, while the anisotropy of the pinned layer is strengthened at the flat state. Figure 2 shows minor MR loops. The MR ratio increases as the number of bending increases and the effective anisotropy field ($2H_k$) also increases as shown in the inset (pink diamond symbols). The sensitivity, defined as MR/$2H_k$, increases from 0.142 %/Oe to 0.159 %/Oe since the increase rate of the MR ratio is larger than that of $2H_k$. A notable feature is the reduction of minimum resistance (R_{min}), as shown in the inset (purple pentagon symbols). The strong correlation between R_{min} and MR ratio is inferred. A new approach in this study demonstrates the enhancement of both MR ratio and sensitivity at the same time as well as the simplicity of sensor fabrication.

[1] Graham, D.L., Ferreira, H.A., Freitas, P.P., and Cabral, J.M.S. *Bio-sens. Bioelectron.* 18, 483 (2003). [2] Li, G. et al. *Sens. Actuators A: Phys.* 126, 98 (2006). [3] Wang, S.X. and Li, G. *IEEE Trans. Magn.* 44, 1687 (2008). [4] Rijks, Th. G. S. M. et al. *Appl. Phys. Lett.* 65, 916 (1994). [5] Kwon, J.-H., Kwak, W.-Y., and Cho, B. K. *Sci. Rep.* 8, 15765 (2018).

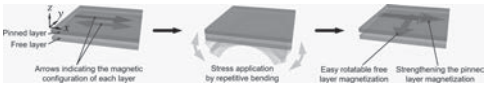


Figure 1. Schematic illustration for the change of magnetic configuration by repetitive bending stress along the magnetic easy axis.

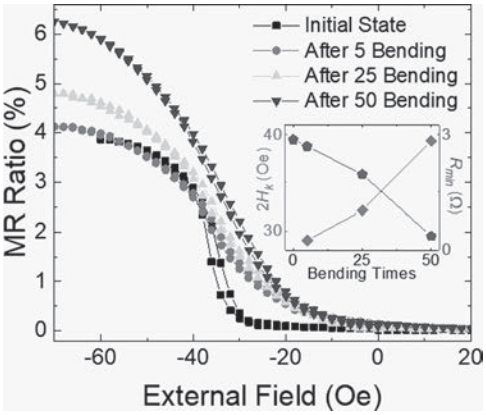


Figure 2. Minor MR loops in flat states after 5, 25, and 50-times repetitive bending, as shown in Fig.1. Inset shows the change of anisotropic field, $2H_k$, and minimum resistance, R_{min}.

GV-02. Detection of Printed Magnetic Ink Strips by High-Tc Superconductivity SQUID Magnetometer. *S. Tanaka*[1], H. Chiba[1], K. Hayashi[1], T. Ohtani[1], A. Varfolomeev[3] and I. Volkov[2] *1. Toyohashi University of Technology, Toyohashi, Japan; 2. Moscow Institute of Physics and Technology, Moscow, Russian Federation; 3. NRC Kurchatov Institute, Moscow, Russian Federation*

Composites based on single-walled carbon nanotubes (single-walled CNTs or SWCNTs) combined with iron nanoparticles are interesting materials, which can be used for a fingerprint to identify a genuine document or a bank bill for example. We prepared some samples with CNT-based inks on four different surfaces printed by Dimatix Materials Printer DMP-2831 [1]. The composition of carbon nanomaterial was SWCNTs (76 wt. %), iron nanoparticles (11 wt. %) and other carbon phases (13 wt. %). The four different surfaces were as follows: Type 1- MF-Millipore membrane (mixed cellulose esters, 0.45 μm pore size), Type 2 - MF-Millipore membrane (mixed cellulose esters, 0.8 μm pore size), Type 3 - Office paper A4 (160 g/m^2), Type 4 – Photo paper A4 (220 g/m^2). They were cut out into L4 mm x W1 mm and three stripes were placed in a row (Fig.1 (a)). A high-Tc superconductivity SQUID (Superconducting Quantum Interference Device) was designed and fabricated using a $YBa_2Cu_3O7_{-y}$ (YBCO) thin film. The SQUID was installed in a specially designed liquid nitrogen (LN_2) cryostat, which nabled the SQUID to approach the sample as close as 1 mm [2] (Fig.1 (b)). A dc magnetic field of 2.81 mT was applied in the direction parallel to the SQUID surface to magnetize the ink sample [3]. The stripe sample was drawn above the SQUID surface with 25 mm/s. A large signal peak was detected from the ink stripes on each Millipore membrane, Type 1 and Type 2 but not on Type 3; a small peak could be seen on Type 4 (Fig.2). The signal peak was proportional to magnetization of the sample. The measurements of conductance of the samples showed that the value of conductance increased exponentially in dependence on the magnetization. The iron nanoparticles were superparamagnetic due to their small size. Therefore the increase in magnetization was due to an increase in the exchange interaction between nanoparticles when the conductance increased. We suppose that this effect

can be explained by spin-dependent tunneling between CNTs, doped by iron nanoparticles, below percolation threshold. We are planning a further not only a magnetic but a magnetoresistance measurement.

[1] Varfolomeev, V. Solovey, Ivan Volkov and T. Maeder, Oriental Journal of Chemistry, Vol. 34, p.24 (2018). [2] S. Tanaka, T. Matsuo, and S. Ariyoshi, IEEE Trans. Appl. Supercond., 2792405_1-6 (2018). [3] Saburo Tanaka, Takeyoshi Ohtani, and M. Kikuchi, Journal of Magnetism and Magnetic Materials Vol. 459 p.171 (2018).

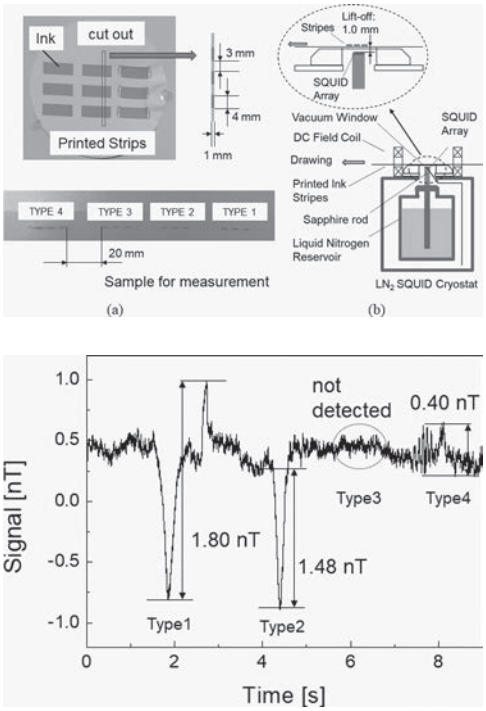


Fig 2. Detected signals.

GV-03. Ultra-high Sensitivity Magnetic Impedance Sensor by Applying GHz Pulse Current. *F. Akagi*[1] and H. Ohta[1] *1. Kogakuin University, Tokyo, Japan*

Magnet-impedance (MI) sensor is highly sensitive magnetic sensor based on a magnet-impedance effect in an amorphous wire [1]. Recently, the development of a high-sensitivity MI sensor of micro size for integration into systems-on-chip has attracted attention, which is used in biological and medical fields [2, 3]. However, for detecting weak magnetic fields of several pico-tesla, as in applications such as magnetoencephalography and magnetocardiography, the MI sensor needs to be more sensitive. Honkura et al. reported that GHz-spin-rotation sensor (GSR sensor) has a largest sensitivity by using GHz pulse current [4]. In this study, the effects of frequency and damping constant on output voltage and magnetization-reversal process for the magnetic impedance sensor by applying GHz pulse current was investigated by using the Landau-Lifshitz-Gilbert equation with eddy current field. Fig. 1 shows the schematic picture of magnetic sensor. The wire, which has a diameter and a length were 10 μm and 500 μm, respectively, was discretized by rectangular prism cells of 0.2×0.2×50 μm. The resistivity was 130 μΩcm. When the high frequency pulse current rises, magnetization turns from the sensor axis direction to the circumference direction. The pickup coil detects a time change of magnetic flux in the sensor. Fig.2 shows the dependence of the output voltage on the frequency with different damping constant α. The output voltage increases with increasing frequency, however, it is steady over 3 GHz. This result coincides with the experimental result [4]. Also the smaller damping constant is, the larger the output voltage is and the stronger the dependency of the output voltage on frequency is.

[1] K. Mohri, F. B. Humphrey, L. V. Panina, et al., *Phys. Status Solidi A,* 206, p. 601 (2009). [2] T. Uchiyama, S. Nakayama, K. Mohri, et al., *Phys. Status Solidi A,* 206, p. 639 (2009). [3] S. Corodeanu, H. Chiriac, L. Radulescu, et al., *J. Appl. Phys.* 115, 17A301, doi: 10.1063/1.4855976 (2014). [4]Y. Honkura, S. Honkura, The Ninth International Conference on Sensor Device Technologies and Applications, SENSORDEVICES 2018, SENSORDEVICES1 (2018).

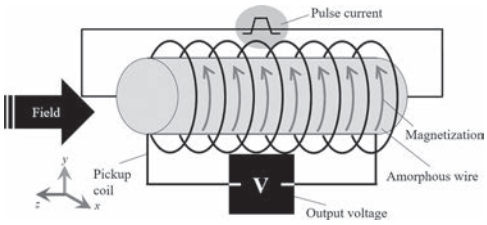


Fig. 1 Schematic picture of magnetic inpedance sensor.

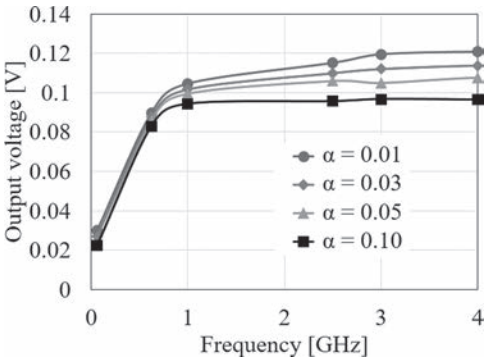


Fig. 2 Dependence of output voltage on frequency with different damping constant α.

GV-04. Effects of parallel and meander configuration on thin-film magnetoimpedance element. *H. Kikuchi*[1], M. Tanii[1] and T. Umezaki[1] *1. Iwate University, Morioka, Japan*

Thin-film magnetoimpedance (MI) sensor has advantages of compatibility with integrated electronic circuits and of miniaturization aiming at field detection with high spatial resolution. To enhance sensitivity, a multilayer system has been examined [1, 2]. Meanwhile, we developed MI simple monolayer elements and a contrivance of element shape such as ellipsoid, triangular, then performed sensing action with miniaturized elements less than 100-μm length [3]. Since thin-film can be patterned by a lithography, we can easily alter a configuration of sensor elements, which contributes to extensive design of sensor geometry considering active sensor area, adjusting bias field and impedance value at bias point, etc. Thus, we made parallel line type or meander type thin-film MI element, then the effects of geometry or configuration on impedance profiles were systematically investigated. Fig. 1 show concepts of the element design. In parallel line type, the total width is fixed. For example, in case of 40-μm width, each line widths of 1, 2 and 4 lines were 40, 20 and 10 μm, respectively. The total length of meander type was unified in 2 mm. Therefore the length of each vicinity for 1 and 2 turns was 1 and 0.5 mm, respectively. Fig. 2 shows the field dependence of impedance for parallel and meander type. The width of elements were 40 and 20 μm respectively. As to parallel type, the results of 1 and 2 lines show the same tendency, however, the element with 4 lines decreases impedance change. Note that the field intensity where impedance has a peak shifts to lower field compared with a case of 1 and 2 lines. The width of each line becomes narrower with increasing number of lines, which reduces a demagnetizing effect. As the amount of turn increases for meander, the impedance changes decreases. When the number of turn increases, the length per one side becomes shorter, which induces a larger demagnetizing effect.

Therefore, the magnetic field strength at which impedance peak appears shifts to higher field. The results indicate a potential of broad strategy for sensor element design.

[1] L. Chen, Y. Zhou, C. Lei, Z.M. Zhou, W. Ding, *J. Magn. Magn. Mate*r., Vol. 322, pp. 2834-2839 (2010). [2] A. García-Arribasa, E. Fernández, A. Svalov, G.V. Kurlyandskaya, *J. Magn. Magn. Mate*r., Vol. 400, pp. 321-326 (2016). [3] H. Kikuchi, T. Shima, H. Uetake, S. Yabukami, *IEEE Magn. Lett*., Vol. 7, #6508105 (2016).

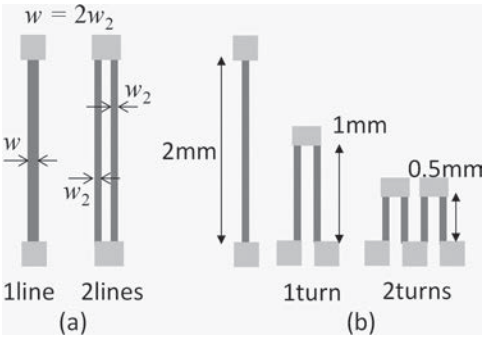


Fig. 1 Design concept of parallel (a) and meander (b) type.

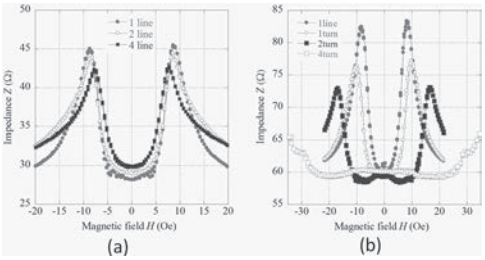


Fig. 2 Field dependence of impedance for (a) parallel line type and (b) meander type.

GV-05. Localization of Rotating Magnetic Marker from the Fourier components of its Magnetic Flux Density. *A. Chiba*[1] and T. Nara[1] *1. The University of Tokyo, Tokyo, Japan*

1. Introduction Indoor localization and navigation of humans and robots have various applications. In contrast to conventional electromagnetic wave-based methods, which have accuracies of approximately 1 m owing to the multi-path effects, the use of quasi-static magnetic field has great potential for better localization accuracy because the reflection of metals does not have a considerable influence on it. Several studies have proposed using a rotating magnetic dipole for localization: rotating electrically[1] or mechanically[2]. However, to use these methods the phase of the rotating source, i.e., the direction of the dipole when the magnetic field is measured, must be known. Moreover, the maximum and minimum magnetic flux densities should be detected, which are considerably affected by noise. In this paper, we derive a reconstruction formula for the three-dimensional position of a rotating magnetic dipole in terms of the Fourier components of the magnetic flux density to improve robustness to the noise. This method does not require the knowledge of the phase of the rotating source. This is an extension of our previous study[3] in which only the azimuth angle was determined. 2. Theory and method Our reconstruction formulae are given in Equations (1), (2), and (3) in Fig. 1: the azimuth angle, $0 \leqq \varphi < \pi$, and zenith angles, $0 \leqq \psi \leqq \pi/2$, as well as the distance, r, of the rotating source from the sensor are explicitly expressed in terms of the Fourier components of the measured magnetic flux density, where ω is the angular frequency of the rotation. We rotated four serially connected neodymium magnets (length: 828 mm and diameter: 23 mm) with a motor (KM-1); the rotating speed was 240 rpm (4 Hz). Three orthogonal magnetic impedance sensors (MI-CB-1DH) were used to measure the magnetic flux density. 3. Result As shown in Fig. 2, the three-dimensional position of the source was estimated with mean absolute errors of 92.0 mm in a 4000 mm by 2000 mm domain, where z = 423 mm. This method can be used in a various situation for indoor localization, for example, of a robot with a rotating dipole. Removal of the assumptions of φ and ψ will be discussed in the paper.

[1] E. Paperno, I. Sasada, and E. Leonovich, IEEE Transactions on Magnetics, Vol. 37, No. 4, pp. 1938-1940 (2001) [2] K. Watanabe, K. Hiroi, T. Kamiyama, H. Sano, M. Tsukamoto, M. Katagiri, and N. Kawaguchi. In 2017 Tenth International Conference on Mobile Computing and Ubiquitous Network (ICMU), pp. 1-7 (2017) [3] A. Chiba and T. Nara, Intermag 2018 (2018)

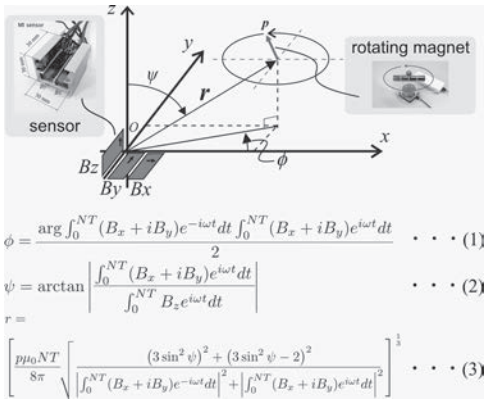


Fig. 1 Localization formula

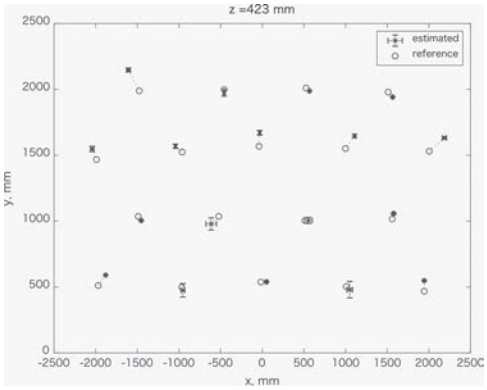


Fig. 2 Localization results

GV-06. Orientation and Position of a Vector-MagnetometerOptically Referenced to an External Coordinate System. *N. Rott*[1] *1. PTB, Braunschweig, Germany*

Vector magnetometers are widely used. To calibrate them, their readings need to be orthogonalized. This is because they are composed of three sensors with individual sensitive axes, whose relative orientation to each other is not known. Furthermore, for applications such as field mapping devices, where the measurement of the magnetic flux density vector should be conducted spatially resolved, the sensor positions also need to be determined. This means, one needs to find the orientation and position of every directional sensor with respect to an external coordinate system. From the determination of sensor orientations and positions one can find the parameters to calculate the field vector in the desired coordinate system. This work presents methods to determine the sensors orientations and positions from the sensor readings under relative motion in defined magnetic fields, enabling measurements that are traceable to the angle and length scale. Our vector magnetometer is attached to mutual orthogonal faces of a mirror cube. The cube itself can be used as an optical reference and can be aligned to any external coordinate system. On the other hand, the orientation and position of every sensor can be determined relative to this cube by performing a scheme of coil and sensor rotations. By rotation about two axes the orientation of the

sensors can be referenced to the coordinate system of the mirror cube and thus transitively to the external coordinate system. The setup for angle determination reaches an uncertainty better 130 μrad. It consists of an autocollimator, two rotation stages and a well-defined homogeneous field coil with its own optical reference mirror. We will present ongoing work which addresses the determination of the translational degrees of freedom. A three-axial coil system will be introduced that can generate different gradient configurations. In combination with translation stages and optical references the position of the sensor will be determined.

GV-07. Piezoelectric strain tuned magnetic field sensor. *Z. Wang*[1] and M. Liu[1] *1. ECE, Xi'an Jiaotong University, Xi'an, China*

Anisotropic magnetoresistive sensors with high sensitivity and stability have been widely used in various industrial applications, including navigation, current sensing, position and rotation sensing, and biosensing. Traditional linear anisotropic magnetoresistive sensors used barber-pole electrodes to rotate the current direction by 45 degree in order to obtain a linear electrical output as a function of external magnetic field. However, the adoption of barber-pole electrodes greatly reduced the working area of the sensor, i.e., the part of strip beneath the barber-pole electrodes could not contribute to the magnetoresistive signal[1]. Here we report an anisotropic magnetoresistive sensor with antiferromagnetic layer to regulate the magnetization-current angle instead of barber pole electrodes. The proposed sensor design, thereby, could fully use the magnetostrictive area, and the stabilized magnetization could help suppressing magnetic noise, enhancing stability and improving linearity[2]. Moreover, we have fabricated AMR sensors on piezoelectric PMN-PT single crystals to investigate the strain effect on the magnetoresistance of the sensor. With strain tunable magnetic permeability and therefore the sensitivity of the magnetic sensor, we have demonstrated a novel magnetic sensor with tunable measurement range and tunable sensitive direction.

[1] Z. Wang, X. Wang, M. Li, *et al.*, *Advanced Materials,* Vol. 28, p. 9370(2016). [2] W. Su, Z. Wang, Z. Hu, *et al.*, *IEEE Electron Device Letters,* Vol. 40, p. 969(2019).

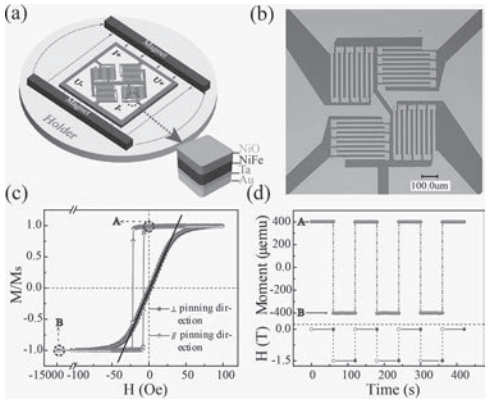


Fig.1 (a) Setup for depositing AMR sensors with bias magnetic field. (b) Microscope image of the AMR Wheatstone bridge. (c) M-H loops along magnetic easy/hard axes. (d) Magnetization measurement before and after applying –1.5 T disturbing magnetic field.

GV-08. Simulation of DC SQUID Output Voltage Characteristics in Time Domain. *Z. Zou*[1] *1. Space Environment Simulation Research Infrastructure, Harbin Institute of Technology, Harbin, China*

The Superconducting QUantum Interference Device (SQUID) has the highest sensitivity in the area of detecting and measuring magnetic fields so far. The flux contained in the closed superconducting loop of the SQUID is quantized in units of the flux quantum $\Phi_0 = h/(2e) = 2.07\times10^{-15}$ Wb, where h and e are Planck's constant and elementary electronic charge, respectively. When a direct current (DC) is applied to the loop, the magnitude order of the output voltage frequency may be as large as GHz due to the junction capacity of the loop is approximately in the order of pF. This paper focuses on the time-domain characteristics of the DC SQUID's output voltage. The loop is composed of two identical Josephson junctions connected in parallel. The phase differences of the junctions are governed by Josephson's equation [1]. The resistively- and capacitively-shunted junction (RCSJ) model [1-2] are utilized to calculate the output voltage numerically. The critical currents I_0, capacity (C_1, C_2), and resistance (R_1, R_2) of each junction are taken as 20 μA, 1 pF, and 3 Ω, respectively. The bias direct current applied to the loop is equal to 41 μA. Calculation results of output voltages in time domain with various values of flux (0.0~0.5 Φ_0) through the SQUID loop are demonstrated in Fig. 1. The output voltage frequency increases with the flux, which is from 7.72 GHz under 0.00 Φ_0 to 29.8 GHz under 0.48 Φ_0; the output voltage is nearly a DC voltage under 0.50 Φ_0. The average output voltage vs. flux curves are illustrated in Fig. 2. The output voltage reaches the maximum value when Φ equals $(n+1/2)\Phi_0$ (n = 0, 1, 2, ...). The impact of the flux through the loop on I_0 is also considered [3-4]. When the flux is several tens of times the quantum Φ_0, the output voltage becomes stable, and hence the device sensitivity decreases seriously. Moreover, when the ratio of the junction resistance R_2/R_1 equals 1.0, the sensitivity or the voltage-flux transfer coefficient is the largest (90.8 μV/Φ_0). Thus it is necessary to maintain the symmetry of the configuration and parameters of the junctions. The simulator device for SQUID and the noise analysis are discussed in detail in the full manuscript.

[1] J. Clarke, A. I. Braginski, The SQUID Handbook, p. 30-37 (2004) [2] L. Ponta, A. Carbone, M. Gilli, et al, Canadian Conf. Electr. Comput. Eng. (2011) [3] Department of Geophysics of PKU and USTC, Geomagnetism Tutorial, p. 374-382 (1986) [4] H. Wang, X. Xie, Rare Metal Materials Eng., Vol. 37, p. 377-380 (2008)

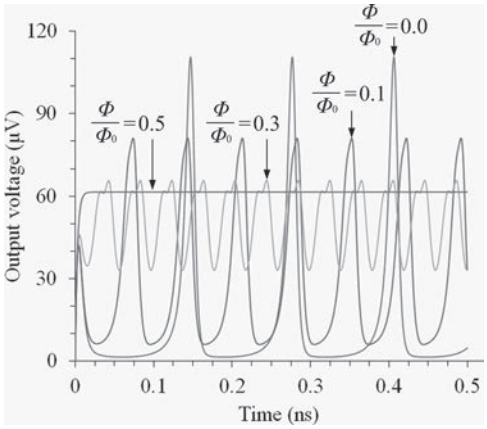


Fig. 1 Voltages vs. time

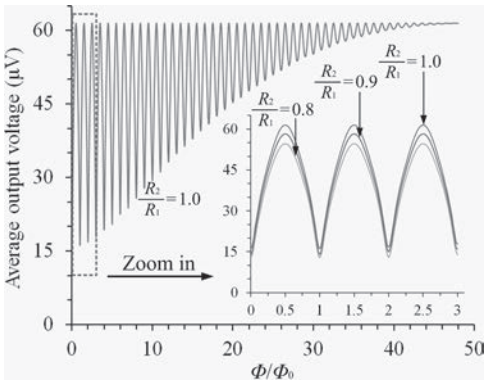


Fig. 2 Voltages vs. Φ/Φ_0

GV-09. Large-Area Granular GMR Sensors for Ultra-Sensitive Bioassays. *D. Su*[1], K. Wu[2] and J. Wang[2] *1. Chemical Engineering and Materials Science, University of Minnesota, Minneapolis, MN, United States; 2. Electrical and Computer Engineering, University of Minnesota, Minneapolis, MN, United States*

Over the past few years, giant magnetoresistance (GMR) sensors have been widely employed in the detection of biomarkers. In the presence of a bias field, the stray field from the magnetic nanoparticles (MNPs) bound to the sensor surface can be detected by the GMR sensors, which is proportional to the number of captured biomarkers (Figure 1(a)). To achieve a linear response, stripe-shaped GMR biosensors with large aspect ratio have been widely used. However, the effective sensing area is significantly limited by the width of the sensor stripes. Furthermore, the GMR sensor signal was found to be highly dependent on the position of the MNPs[1], which limits both the sensitivity and repeatability of the bioassay. To increase the effective sensing area, large-area GMR biosensors based on a reverse nucleation mechanism were proposed and demonstrated[2-4]. As the MNPs bind to the sensor surface, localized magnetization reversal sites occur in the free layer of the GMR sensor (Figure 1(b) and Figure 2(a)). Our simulation results showed that by transforming a stripe into a square, the sensor signal increased by over 20 times under the same amount of MNPs. The large-area sensor signal also exhibits a linear response to the number of MNPs regardless of the position of the MNPs. Here we further propose and simulate a CoFe-Cu or NiFe-Cu granular structure as the free layer of the large-area GMR. This granular structure results in a superparamagnetic behavior, which facilitates real-time biomarker detection due to the negligible hysteresis in the MH curve. Since the ferromagnetic granules are separated by Cu, the localized reverse nucleation in the granules onsets under a lower MNP stray field compared to uniform ferromagnetic films, which further improves the sensitivity in biomarker detection (Figure 2(b)).

[1] T. Klein, Y. Wang, and J. P. Wang, Sensors and Actuators A-Physical, Vol. 216, p. 349 (2014). [2] B. Srinivasan, Y. P. Li, and J. P. Wang, Angewandte Chemie-International Edition, Vol. 48, p. 2764 (2009). [3] D. Q. Su, K. Wu, and J. P. Wang, Journal of Magnetism and Magnetic Materials, Vol. 473, p. 484 (2019). [4] Y. L. Feng, J. M. Liu, and J. P. Wang, Journal of Applied Physics, Vol. 122, p. 123901 (2017).

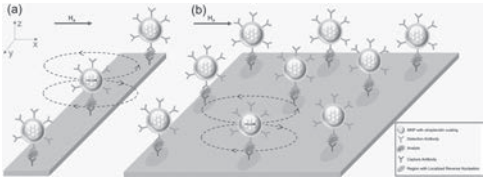


Fig.1 Schematic illustration of the detection process of (a) Stripe-shaped GMR sensors and (b) Large-area GMR sensors with localized reverse nucleation sites.

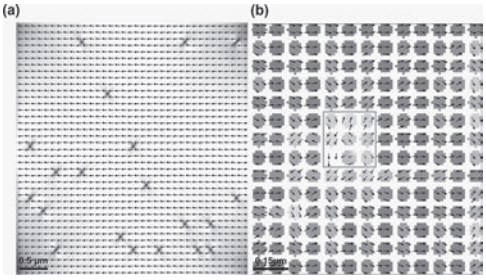


Fig.2 OOMMF simulation results of reverse nucleation sites in (a) A large-area GMR sensor with continuous free layer and (b) A large-area GMR sensor with granular free layer. Black arrows indicate the magnetization directions.

GV-10. Simultaneous enhancement of spin-torque diode sensitivity and detection frequency by using voltage controlled magnetic anisotropy. *N. Sisodia*[1] and P.K. Muduli[1] *1. Department of Physics, Indian Institute of Technology Delhi, New Delhi, India*

Magnetic Tunnel Junctions (MTJs) can be used for Radio Frequency (RF) detection by using the spin-torque diode effect, which was first reported by Tulapurkar *el al*.[1] in an MTJ nanopillar with in-plane magnetized magnetic electrodes (ip-MTJ). In the spin-torque diode effect, an MTJ nanopillar generates a rectified d.c. voltage (V_{mix}) when an alternating current of frequency close to the eigen frequency of the free magnetic layer of the MTJ is applied. An important parameter desirable for efficient RF detection is the high RF sensitivity, which is defined as $S=V_{pp}/P_{rf}$, where V_{pp} is the observed peak-to-peak voltage for an external RF power of P_{rf}. With recent advancements[2-6], the sensitivity of the MTJ based RF detectors has already surpassed that of the currently used semi-conductor detectors which have typical sensitivities of 4000 mV/mW. However, the detection frequency remains low <2 GHz compared to commercial RF detectors. In this work, we introduce a novel method of achieving very high sensitivity while also simultaneously enhancing the detection frequency by utilizing a combination of two different phenomena namely, (i) Voltage Controlled Magnetic Anisotropy (VCMA) [7], and (ii) parametric synchronization [8]. We show the simulated spectra with and without VCMA in Fig. 1 (a) and (b), respectively. We achieve a giant sensitivity of $>10^5$ mV/mW at a high detection frequency of around 4--6 GHz. In the insets, we also show the magnetization trajectory for both cases at the extremum points from which V_{pp} is calculated. The magnetization follows a Clamshell orbit and shows a large shift for the maximum and minimum of V_{mix} in the presence of VCMA. We will discuss the detailed d.c. bias, RF power and field dependence of the phenomenon and show that the simultaneous enhancement of sensitivity and the detection frequency is due to a large coupling of external RF signal to MTJ assisted by the VCMA effect. The results will be useful for realizing highly sensitive RF detectors with high detection frequency working at ultra-low input powers.

1.) A. A. Tulapurkar, Y. Suzuki, A. Fukushima, et al., Nature 438, 339 (2005) 2.) S. Miwa, S. Ishibashi, H. Tomita, et al., Nat. Mater. 13, 50 (2014) 3.) B. Fang, M. Carpentieri, X. Hao, et al., Nat. Commun. 7 (2016) 4.) L. Zhang, B. Fang, J. Cai, et al., Phys. Lett. 113, 102401 (2018) 5.) A. S. Jenkins, R. Lebrun, E. Grimaldi, et al., Nat. Nanotechnol. 11, 360 (2016) 6.) S. Tsunegi, T. Taniguchi, K. Yakushiji, et al., Appl. Phys. Express 11, 053001 (2018) 7.) T. Nozaki, Y. Shiota, M. Shiraishi, et al., Appl. Phys. Lett. 96, 022506 (2010) 8.) S. Urazhdin, V. Tiberkevich, and A. Slavin, Phys. Rev. Lett. 105, 237204 (2010)

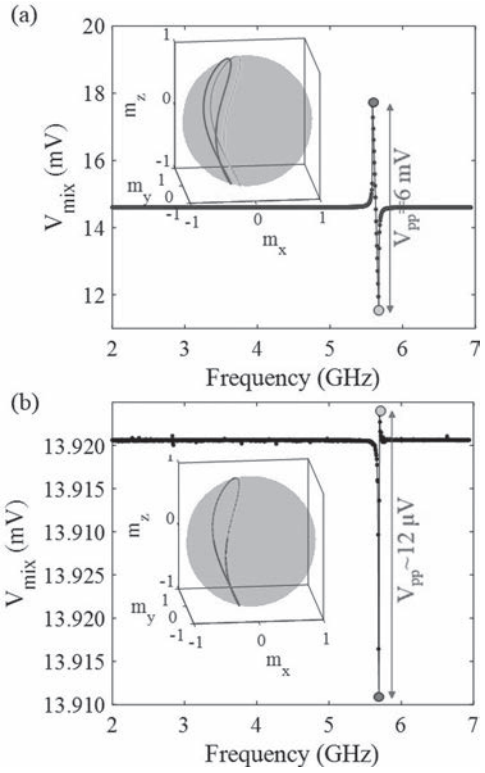


Fig. 1 : V_{mix} as a function of driving frequency in (a) presence and (b) absence of VCMA. Insets show the magnetization trajectories at extremum values (red and green dots) of V_{mix}

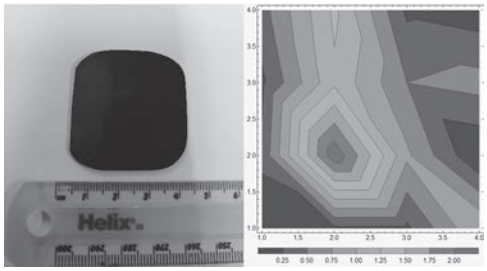
GV-11. Effect of Magnetic Domain Structures on Magnetic Sensing Properties of Magnetic Tunnel Junctions. *G. He*[1], Y. Zhang[1] and G. Xiao[1] *1. Physics, Brown University, Providence, RI, United States*

High performance magnetic tunneling junction (MTJ) sensors is exploited to be an ultra-sensitive solid-state magnetic sensors needed in many applications. By incorporating MTJ with magnetic flux concentrator (MFC) we can achieve picoTesla detectability, but further improvement relies on more detailed understanding of the domain structures in its magnetic layers which determines its sensing performance. Stabilized domain structures could lead to big coercivity and small sensitivity, while relaxed ones could have increased noise due to domain fluctuation. We have fabricated MTJs of multiple shapes and sizes, so we can study domain structures under various shape anisotropy and external magnetic fields, by doing transport measurement, micromagnetic simulation, magnetic force microscopy and Kerr microscopy. The domain structures and sample morphology are related to their transport properties such as sensitivity, coercivity and noise also, as we will explain in detail. Such correlation can be used as guidance for designing MTJs that integrate with MFC most effectively, to make the best magnetic sensor. This study unveils the microscopic domain states at different external fields, which also provides insights for the dynamics of different domain shapes or vortex states.

GV-12. Ferrite Impregnated Epoxy Actuators for Composite Impact Damage. J. Surakarnkha[1], *Z. Leong*[1], W. Holmes[1], P. Desai[2], J. Foreman[1] and N. Morley[1] *1. University of Sheffield, Sheffield, United Kingdom; 2. Perlemax Limited, Sheffield, United Kingdom*

Carbon fibre reinforced polymers composites (CFRCs) possess properties that outstrip their component parts, so are seeing increased adoption in sectors such as the aerospace industry. The complex structure of CFRCs, which contributes to their unique properties are also prone to an increased variety of damages such as fibre breakage, debonding, transverse-ply cracking, and delamination. This means that their failure modes are more complex, hence there are many more routes to potential failure [1]. Previous work has shown the efficacy of magnetostrictive materials as damage detection actuators; issues such as their spatial sensitivity require improvement to progress their applicability in structural health monitoring [2]. One solution is to embed magnetostrictive micron-sized particles within a suitable flexible matrix. Early simulations have shown that the strain experienced by a magnetostrictive particle embedded in a softer material will be enhanced. In this paper we demonstrate a step-by-step approach to the fabrication and optimisation of an impregnated magnetostrictive epoxy matrix that aims to satisfy these requirements. Such that the fabrication of ferrite impregnated epoxy can function as a replacement for composite surface mounted magnetostrictive ribbons as damage actuators. A ferrite impregnated epoxy actuator was fabricated from Epikote 828 and ferrite microparticles, and other polymerising additives. Their strain response was characterised with a bending rig. They were then subjected to impact damage followed by a magnetic scan using a HMC5883L sensor to visualise the damage induced (Fig. 1). Figure 1. Fabricated actuator and visualised location of damage. The results found that 1) Increased ferrite additions to the system do not change the magnetostrictive sensitivity, possibly due to interaction effects at the small scale. Thus, better magnetostrictive materials were studied to optimise the actuator behaviour and sensitivity. 2) Despite the low sensitivity of the ferrite particles, damage induced via impact testing is shown to be detectable. A contour map of the results show clearly the region of impact damage, and its effect on subsequent impacts.

[1] V. Giurgiutiu, Structural health monitoring of aerospace composites (2016) [2] Z. Leung, A. Al-Taher, L. Chan, 2017 IEEE International Magnetics Conference (INTERMAG), pp. 1–1. (2017)



GV-13. Low-Frequency Noise of Full Wheatstone Bridge Based GMR Angular Sensors. *Z. Zhou*[1], Q. An[1], S. Yan[2], W. Zhao[1,2], Q. Leng[1,3] and Z. Cao[1] *1. Beihang-Goertek Joint Microelectronics Institute, Qingdao Research Institute, Beihang University, Qingdao, China; 2. Fert Beijing Institute, BDBC, School of Electronic and Information Engineering, Beihang University, Beijing, China; 3. Goertek Inc, Weifang, China*

Giant magnetoresistance(GMR) sensor is developing towards miniaturization and better performance, especially for weak field detection. However, the low-frequency noise limits the sensitivity of the sensors for their applications. Noise analysis is an essential way to reduce sensor noise and explore the electrical and magnetic characteristics. In this paper, we test and analyze the low-frequency noise of a full Wheatstone-bridge-based GMR angular sensor, in order to improve its performance. The GMR sensor is fabricated by a concise microelectronic process[1]. As illustrated in Fig.1a the device has a full Wheatstone-bridge structure and anneals with a magnetic field along the y-axis. Its sensing direction is in x-axis. Fig.1b shows the output of the GMR sensor in two axes. It shows kinks near zero field in both axes, which will be improved with optimized process to fabricate relatively ideal bridge arms in the patterned GMR elements. The field linear range is from -50 to 50Oe while eliminating the kinks and the sensitivity is 0.16mV/V/Oe. Fig.2a shows the power spectral density (PSD) of the sensor with fitting. The 1/f noise is the main source in the frequency bands below 10kHz[2]. Fig. 2b shows the Hooge parameter α of the sensor utilized to parameterize the noise level of 1/f noise. Increase of α value indicates a higher level of the sensor noise[3]. The α value in this research is about 2*10^(-3) that indicates in

low noise level since it is generally between 10^(-2) and 10^(-3)[2] in GMR devices. It's clearly seen that the α shows a maximum without external field. This could be pure magnetic noise attributed to none single domain of the free layer in the transducer. Of course, the magnetic noise decreases when the applied field reaches the effective anisotropic field to saturate moment of the free layer because its domain is fully oriented along magnetic field direction[2]. We obtain the sensitivity of 0.16mV/V/Oe in the GMR sensor and its noise level of 10^(-8) V/√Hz. This is suitable for high accuracy angular sensing application such as geomagnetic devices and biosensors. More comparisons and analysis of low-frequency noise for our GMR sensors with improved film process will present in this paper.

[1] W. Yan, Shaohua.Cao, Zhiqiang.Guo, Zongxia.Zheng, Zhenyi.Cao, Anni.Qi, Yue.Leng, Qunwen.Zhao, "Design and Fabrication of Full Wheatstone-Bridge-Based Angular GMR Sensors," *Sensors*, vol. 18, no. 6, p. 1832, 2018. [2] R. J. M. Van De Veerdonk *et al.*, "1/F Noise in Anisotropic and Giant Magnetoresistive Elements," *J. Appl. Phys.*, vol. 82, no. 12, pp. 6152–6164, 1997. [3] P. W. T. Lei, Z. Q.Li, G. J.Egelhoff, William F.Lai, P. T.Pong, "Review of noise sources in magnetic tunnel junction sensors," *IEEE Trans. Magn.*, vol. 47, no. 3, pp. 602–612, 2011.

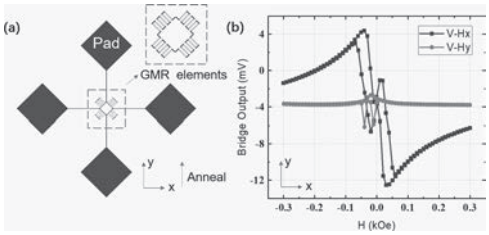


Fig.1

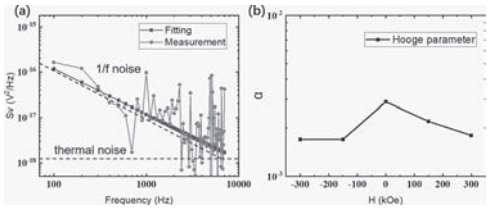


Fig.2

Session HA
NOVEL SPIN TEXTURES: SKYRMIONS 2.0 AND BEYOND

Peter Fischer, Chair
Lawrence Berkeley National Laboratory, Berkeley, CA, United States

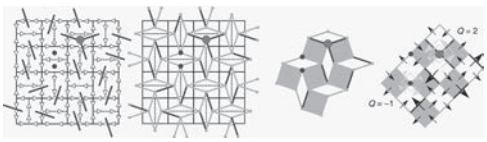
INVITED PAPERS

1:30

HA-01. Emergent States in Artificial Spin Ice. *C. Nisoli*[2], X. Zhang[1], N.S. Bingham[1], A. Duzgun[2], J. Sklenar[3], Y. Lao[3], F. Caravelli[2] and P. Schiffer[1] *1. Physics, Yale, New Haven, CT, United States; 2. Theoretical Division, Los Alamos National Laboratory, Los Alamos, NM, United States; 3. Physics, University of Illinois, Urbana, IL, United States*

Intriguing new phenomena generally emerge from the collective behavior of numerous simple interacting degrees of freedom. Indeed, physicists typically first discover new systems and then proceed to describe them via higher level models that often deliberately neglect the detail of the building blocks. Instead, they concentrate on the relevant symmetries and interactions of an emergent description [1]. Today, advances in nano and micro fabrication, characterization, and control, can invert that approach. We can realize artificial systems whose interacting, elementary degrees of freedom can be tailor-designed for exotic behaviors in their collective, low-energy kinetics. That is the case of artificial spin ice materials [2], which can now be variously manufactured in arrays of magnetic nano-islands [3], trapped colloids [4], vortices in nano-patterned superconductors [5], or possibly with skyrmions in liquid crystals. They can produce new phenomena often non seen in natural materials, such as complex kinetics of magnetic charges and magnetic monopoles [6], new forms of frustration [7], classical forms of topological order [8], dimensionality reduction [9], or ergodicity breaking in absence of quenched disorder, while phase transitions can be engineered [10]. We will briefly summarize the fiend and then report on the more recent results in the Yale-LANL collaboration [5-10].

[1] Anderson, Philip W. Science 177.4047 (1972): 393. [2] Wang, 1. RF, et al. Nature 439.7074 (2006): 303. [3] Nisoli, Cristiano, et al. Reviews of Modern Physics 85.4 (2013): 1473. [4] Ortiz-Ambriz, Antonio, and Pietro Tierno. Nature communications 7 (2016): 10575. [5] Latimer, M. L., et al. Physical review letters 111.6 (2013): 067001. [6] Zhang, Sheng, et al. Nature 500.7464 (2013): 553. [7] Nisoli, Cristiano, et al. Nature Physics 13.3 (2017): 200. [8] Lao, Yuyang, et al. Nature Physics 14 (2018): 723. [9] Gilbert, Ian, et al. Nature Physics 12.2 (2016): 162. [10] J Sklenar et al. Nature Physics 15, no. 2 (2019): 191.



2:06

HA-02. Propagating spin excitations along skyrmion strings. *S. Seki*[1] *1. Department of Applied Physics and Institute of Enginnering Innovation, University of Tokyo, Tokyo, Japan*

Magnetic skyrmion, a topological soliton characterized by swirling spin texture appearing in two-dimensional system, has recently attracted attention as a stable particle-like object. In the three-dimensional system, skyrmion forms a string structure in analogy with the vortex-line in superconductors / superfluids and cosmic string in the universe, whose unique topology and symmetry may also host nontrivial response functions. In this talk, we discuss the propagation character of spin excitations on skyrmion strings. We find that this propagation is directionally non-reciprocal, and the degree of non-reciprocity, as well as the associated group velocity and decay length, are strongly dependent on the character of the excitation modes. Our theoretical calculation establishes the corresponding dispersion relationship, which well reproduces the experimentally observed features. Notably, these spin excitations can propagate over a distance exceeding 10^3 times the skyrmion diameter, demonstrating the excellent long-range nature of the excitation propagation on the skyrmion strings. The present results offer a comprehensive picture of the propagation dynamics of skyrmion string excitations, and suggest the possibility of unidirectional information transfer along such topologically-protected strings.

[1] S. Seki *et al.*, Science 336, 198 (2012). [2] S. Seki *et al*., arXiv:1902.10302

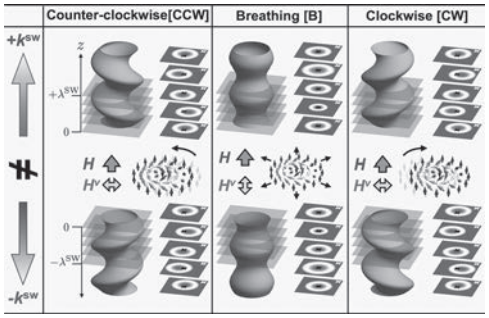


Fig 1. Schematic illustration of spin excitation propagating along skyrmion strings.

2:42

HA-03. Magnetization textures beyond skyrmions: bobbers, quanco balls and hopfions. *S. Bluegel*[1] *1. Peter Grünberg Institute and Institute for Advanced Simulation, Forschungszentrum Jülich and JARA, Jülich, Germany*

Magnetic textures called skyrmions are two-dimensional (2D) topological magnetization solitons localized in space with particle like properties, which are currently under intense scrutiny as a new entity for information storage and processing. The unforeseen stability comes from a chiral symmetry breaking facilated by the Dzyaloshinskii-Moriya interaction (DMI). The skyrmion and the antiskyrmion are global minimizer of the micromagntic energy functional in topological subsectors characterized by a topological invariant, the topological charge with the values Q=-1, Q=1, respectively [1]. In difference to skyrmions in ultra-thin films, in films of finite thickness and bulk crystals, skyrmions take the form of skyrmion tubes, as illustrated in Fig.1. Since skyrmion tubes are not intrinsically confined in 3D, they are considered 2D particles. This raises the fundamental and fully unexplored questions whether it is possible to localize skyrmions tubes in 3D on a nanometer scale (e.g. 50 nm or below) such that the so-formed objects are

stable, maybe even topologically protected. In this presentation we follow two approaches to localize the skyrmion tube in 3D space: (i) to cut the tube to finite length, leading to the formation of singular points at each end. Examples are the chiral bobber (ChB) and the quanco ball (QB) (see Fig.1) or (ii) connect the ends of the tupe to form a closed vortex tube, of which the hopfions present topologically protected versions (see Fig.1). Recently, we were able to extend the scope of skyrmions in cubic chiral magnets to a second class of particles: (a) ChB, first through theoretical analysis [2, 3] and then veryfied experimentally by the direct observation in thin films of B20-type FeGe by means of quantitative off-axis electron holography [4]. The interaction of electrons with such hybrid-objects [5], e.g. to understand how to move ChB by spin currents is subject to ongoing investigations. (b) Quanco ball, we show that a pair of coupled Bloch points may appear as a truely 3D localized stable state in cubic chiral magnets. Detailed analysis is presented of the stability of such objects in the interior of crystals and in geometrically confined systems [6]. We noticed that the magnetic structure of the cubic chiral magnets MnGe and FeGe in their B20 phases are quantitatively and qualitatively totally different. We introduce a novel class of magnetic exchange interactions – the topological-chiral interactions (TCI) – that can potentially dominate over the DMI in selecting the chiral ground state. The novel interactions are rooted in the so-called topological orbital moment, which manifests as a result of finite scalar spin chirality in non-coplanar magnets. The long-wave length limit of the interactions relates to the highly acclaimed Faddeev model demonstrating that the TCI are an origin of 3D magnetization textures all the way down to hopfions. -- Independent, in our search of replacing the DMI as skyrmion stabilizer we found that competing Heisenberg exchange provides a completely new mechanism model to stabilize magnetic Hopfions [8]. *Acknowledgment:* I acknowledge discussions and collaborations with G. Bihlmayer, A. Borisov, J. Bouaziz, R. E. Dunin-Borkowski, O. V. Gomonay, S. Grytsyuk, J.-P. Hanke, M. Hoffmann, N. S. Kiselev, A. Kovác, S. Lounis, C. Melcher, G. P. Müller, Y. Mokrousov, F. N. Rybakov, B. Zimmermann, F. Zheng. We acknowledge funding from DFG through SPP 2137 "Skyrmionics" (Project BL444/16-1), SFB 1238 (project C01) and SFB/TRR 173 (project MO 1731/5-1), DARPA TEE program, through grant MIPR# HR0011831554 from DOI, and ERC-consolidator grant 681405 – DYNASORE.

[1] M. Hoffmann *et al*., Nat. Commun. 8, 308 (2017). [2] F. N. Rybakov *et al.,* Phys. Rev. Lett. 115, 117201 (2015). [3] F. N. Rybakov *et al*., New J. Phys. 18, 045002 (2016). [4] F. Zheng et al., Nature Nanotech. 13, 451 (2018). [5] M. Redis *et al*., Phys. Rev. B. 99, 140407 (2019). [6] G. P. Müller *et al.,* arXiv:1903.12446 (2019). [7] S. Grytsiuk *et al.,* arXiv:1904.02369 (2019). [8] F. N. Rybakov *et al.,* arXiv:1904.00250 (2019).

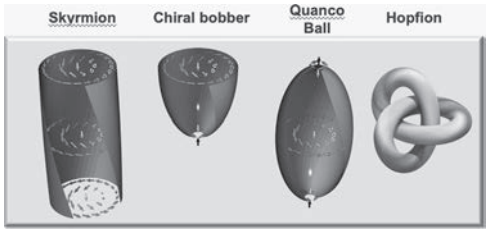


Fig 1. Typical magnetization fields for a skyrmion string, a bobber consisting of a smooth magnetization field and a Blochpoint, a quanco ball of "two bobbers attached" with two blochpoints, and for a hopfion with trefoil knot-like shape with hopf-index H=7. The color presents isosurfaces of the magnetization texture with constant m_z.

3:18

HA-04. Magnetic Skyrmions and Hopfions in Three-dimensional Chiral Magnets. *J. Zang*[1] *1. Physics and Astronomy, University of New Hampshire, Durham, NH, United States*

In this talk, various three-dimensional (3D) topological spin textures in magnets without inversion symmetry will be introduced. The first part of the talk features the recent observation of target skyrmions in chiral magnet nanodisks through theory-experiment collaborations. Two types of zero-field target skyrmions are confirmed, and Bloch points are identified during topological transition between different types of target skyrmions. The spectrum of collective spin wave modes in target skyrmions also reveal the 3D nature of spin excitations. Second part of the talk introduces a very recent work on hopfions in chiral magnetic nanodisk. This is one of the first experimentally feasible prediction on magnetic hopfions. The hopfion in this setup is confirmed by analyzing the linking between any two equal-spin loops and calculating the Hopf invariant. Another topological configuration, the pairing between monopole and anti-monopole, is also identified in the same system. Transition from this state to hopfion, being identical to sphere-torus topological deformation, can be achieved by an external magnetic field. Dynamics of hopfions will also be discussed.

1. H. Du, et. al., Nat. Comm. 6, 7637 (2015). 2. X. Zhao, et. al., Proc. Natl. Acad. Sci. 113, 4918 (2016). 3. F. Zheng, et. al., Phys. Rev. Lett. 119, 197205 (2017). 4. A. Booth, Y. Liu, and J. Zang, Special Edition in J. Magn. Magn. Mater. (2019) 5. Y. Liu, R. K. Lake, and J. Zang, Phys. Rev. B 98, 174437 (2018).

3:54

HA-05. Antiferromagnetic Textures: Eigen Modes and Spin Current Induced Dynamics. *O. Gomonay*[1], V. Kravchuk[2] and K. Everschor-Sitte[1] *1. Institute of Physics, JGU Mainz, Mainz, Germany; 2. IFW Dresden, Dresden, Germany*

Searching for new functionalities of antiferromagnetic (AF) systems, controlled by spin and/or electric current, we focus on the (spin) current-induced magnetic dynamics of AF domain walls and skyrmions [1]. First, we review different types of forces acting on the domain walls in presence of spin-orbit torques and discuss underlying switching mechanisms together with interpretation of the recent experiments [2-4]. We demonstrate that spin-orbit torques which originate from the effective staggered field at the magnetic sublattices can effectively split degeneracy of non-180 AF domains and induce fast domain wall motion toward unfavourable domain. We also predict the "Walker-breakdown effect" which sets the velocity limit for the spin-current induced motion of AF domain walls. This effect originates from simultaneous excitation of spin-waves translational domain wall motion by spin-orbit torques. Second, we discuss free and forced magnetic dynamics of an isolated AF skyrmion [5] focusing mainly on the features which have no direct ferromagnetic counterpart. In particular, AF skyrmion shows two branches of localised eigen-modes with substantially different dynamics, which can be mapped on the dynamics of the closed domain wall, see Fig.1. The low-frequency branch can be viewed as a local translations of skyrmion boundary in the direction of the domain wall normal (Fig.1a). Corresponding frequency vanishes in the limit of large skyrmion radius. The high-frequency branch is associated with the rotations of the Neel vectors respective to skyrmion boundary (Fig.1b). This type of motion is governed by competition of Dzyaloshinskii-Moria interactions and strong exchange coupling leading to a nonzero frequencies of the modes. Basing on classification of localised modes according to their spin, angular mometum and frequency we also show how the localised modes can be selectively excited by ac magnetic field or spin current. DC magnetic field which removes degeneracy of clock-and couterclockwise modes is an additional tool for manipulation of AF skyrmion dynamics. Aiming to develop an effective

formalism for description of (spin)-current induced dynamics of AF textures we extend the collective coordinate approach for the closed AF domain walls and suggest the so-called domain wall string model. This model is based on the reduced number of the dynamic variables such as domain wall position and width. In application to the localised eigen modes the model gives the correct asymptotics in a limit of large skyrmion radius. We believe that our results open a way for manipulation, control and detection of the dynamical states of AF textures.

1. O. Gomonay, V. Baltz, A. Brataas, and Y. Tserkovnyak, Nature Physics, Vol.14, p. 213 (2018) 2. T. Moriyama, K. Oda, and T. Ono, Sci. Rep., Vol. 8, p.14167 (2018) 3. X. Z. Chen, R. Zarzuela, J. Zhang et al, Phys. Rev. Lett., Vol. 120, p. 207204 (2018) 4. L. Baldrati, O. Gomonay, A. Ross et al., arXiv:1810.11326 (2018) 5. V. Kravchuk, O, Gomonay, D. Sheka et al., Phys. Rev. B, Vol. 99, p.1 (2019)

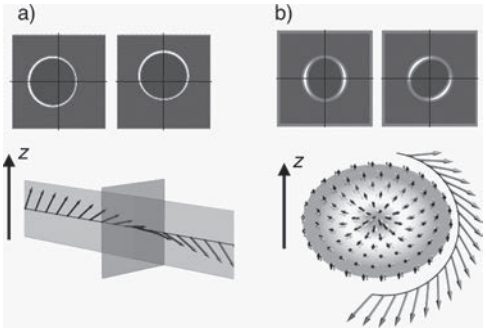


Fig 1. Cartoons of two branches of localised skyrmion modes. The colour code corresponds to the out-of-plane component of the Neel vector. (a) Low-frequency branch correspond to local translations of the skyrmion boundary. (b) High-frequency branch involves oscillations of the domain wall width.

Session HB
SPIN-ORBIT TORQUES IV
Roberto Lo Conte, Chair
University of California, Berkeley, Berkeley, CA, United States

INVITED PAPER

1:30

HB-01. Nonreciprocal spin-current generation using conductance gradient in surface-oxidized copper films. *Y. Nozaki*[1,2], G. Okano[1], M. Matsuo[3], Y. Ohnuma[3] and S. Maekawa[4,3] *1. Department of Physics, Keio University, Yokohama, Japan; 2. Center for Spintronics Research Network, Keio University, Yokohama, Japan; 3. Kavli Institute for Theoretical Sciences, University of Chinese Academy of Sciences, Beijing, China; 4. Center for Emergent Matter Science (CEMS), RIKEN, Wako, Japan*

A mutual conversion between charge current and spin current (SC), *i.e.* a flow of electric charge and spin angular momentum, respectively, has been widely used to control a variety of spintronics devices. Most of traditional spin current generation based on a spin-orbit interaction (SOI) shows a reciprocity. Here, we report a strongly nonreciprocal spin current generation, where the charge-to-spin conversion has an efficiency 320 times larger than the spin-to-charge conversion in 10-nm-thick surface-oxidized Cu film (Cu*) where an oxidization level is rapidly varied within 6 nm from the surface [1]. Our experimental result suggests that the spin current is generated via novel mechanism other than the traditional SOI. The nonreciprocity has been demonstrated from the careful comparison between the unidirectional spin Hall magnetoresistance (USMR) in Cu* (charge to spin conversion) and the spin current injection into Cu* using a spin pumping technique (spin to charge conversion). The USMR is the magnetoresistance arising from the spin accumulation generated via the spin Hall effect (SHE) at the interface of a bilayer consisting of a ferromagnetic and a non-magnetic metallic thin film [2-4]. The USMR exhibits a non-linear dependence of the electrical resistance on the current amplitude, which leads to unique unidirectional properties. Owing to the USMR property that the electrical resistance exhibits a first-order variation with respect to the conversion efficiency, we can evaluate the conversion efficiency from the slope of the USMR as a function of the current. We also confirmed that similar value of the conversion efficiency could be obtained from a conventional spin torque-ferromagentic resonance (ST-FMR) experiment. As schematically shown in Fig. 1, the origin of the nonreciprocity is attributable to a nonuniform spin scattering along the thickness direction in Cu*. Unlike the ordinary SOI, the spin scattering in the Cu* is anisotropic so that the inverse conversion is no longer occurred. Moreover, we confirm that the magnitude of spin current generated in Cu* is quite similar to an estimation using our numerical model where a gradual distribution of spin scattering along the thickness is considered. Similar spin current generation using the vorticity have been observed in liquid Hg [5] and surface-acoustic-wave injected Cu film [6]. These phenomena are based on spin-vorticity coupling [7, 8] which utilizes a conversion of spin angular momentum indirectly from the macroscopic rotation of the Hg and Cu atoms, respectively. On the contrary, our experimental result is regarded as the experimental demonstration of the coupling of electron vorticity and spin current. The non-reciprocal spin current generation will greatly increases the variety of materials usable for spintronics devices because large SOI materials are not necessary.

[1] G. Okano, YN et al., Phys. Rev. Lett. 122, 217701 (2019). [2] C. O. Avci et al., Nat. Phys. 11, 570-575 (2015). [3] S. S. L. Zhang and G. Vignale, Phys. Rev. B 94, 140411 (2016). [4] Y. Lv et al., Nat. Commun. 9, 111 (2016). [5] R. Takahasi et al., Nature Phys. 12, 3526 (2015). [6] D. Kobayashi, YN et al., PRL 119, 077202 (2017). [7] M. Matsuo et al., Phys. Rev. B 87, 180402(R) (2013). [8] M. Matsuo et al., Phys. Rev. B 96, 020401(R) (2017).

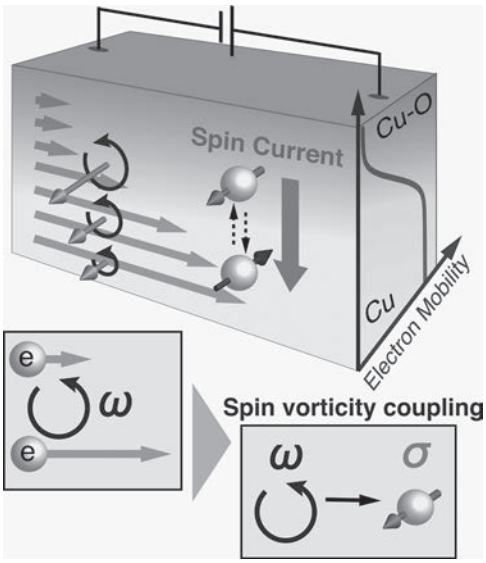


Fig. 1 Schematic origin of non-reciprical generation of spin current in surface-oxidized copper film where a vorticity of electric current is produced by a gradient of electric conductance.

CONTRIBUTED PAPERS

2:06

HB-02. Spin-Orbit Torque and Dzyaloshinskii-Moriya Interaction effects in perpendicularly magnetized trilayers. *A. Gudín*[1], A. Anadón[1], R. Guerrero[1], J. Díez-Toledano[1], P. Olleros[1], F. Ajejas[1], J. Camarero[1], R. Miranda[1] and P. Perna[1] *1. Nanomagnetism, IMDEA Nanoscience, Madrid, Spain*

In magnetic multilayers, the interplay between the perpendicular magnetic anisotropy, the interfacial Dzyaloshinskii-Moriya interaction (DMI) and the dipolar coupling may result in the appearance of a variety of chiral magnetic textures, such as skyrmions, even at room temperature [1–3]. A strong DMI [4,5] usually allows the stabilization of such topological textures which can be nucleated and manipulated via spin-orbit torque (SOT) by applying external current pulses [1]. We have studied a Ta(5nm)/Co(0.8nm)/Pt(5nm)/Ta(5nm)//SiO_2(300nm)/Si patterned by optical lithography and Ar milling in 10 μm wide Hall bars. The interest of this structure lies in: i) the different spin Hall angle signs in Ta and Pt enhances the SOT, ii) large DMI has demonstrated in reference [2,5] of the order of 1.3 mJm^{-2} iii) and the possibility to neglect the interlayer coupling contribution (potentially large in systems with several repetition) that may be play a fundamental role on the effect of SOT on the magnetic behavior. We have investigated

the anomalous Hall effect (AHE) that is, generally, proportional to the out of plane component of the magnetization, as function of the magnetic field applied along the z direction. We have disclosed the effect of the SOT by detecting simultaneously the Hall resistance curve and the polar Kerr hysteresis. We observe discrepancies between both behaviors at current densities as low as $6x10^8 Am^{-2}$. We have moreover investigated these features as function as the current density and in-plane magnetic fields in order to discriminate the role of the antidamping and field like torques.

[1] W. Legrand, D. Maccariello, N. Reyre, Nano Letter., Vol. 17, p.2703-2712 (2017) [2] S. Woo, K. Litzius, B. Krüger, Nature materials., Vol. 15, p.501 (2016) [3] C. Moreau-Luchaire, C. Moutafis, N. Reyren, Nature Nanotechnology., Vol. 11, p.444 (2016) [4] F. Ajejas, V. Krizaková, D. de Souza Chaves, Applied Physics Letters., Vol. 111, p.202402 (2017) [5] J. Torrejon, J.Kim, J. Sinha, Nature communications., Vol. 5, p.4655 (2014)

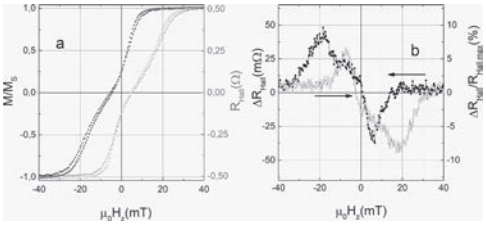


Figure 1. Part depicts the comparison of the polar Kerr magnetometry (black curve) and AHE acquired simultaneously. The b part shows the difference between both measurements.

2:18

HB-03. Current-Induced Domain Wall Motion in Pd-based Multilayered Structures with Different Ferromagnetic Layer Composition. M. Kado[1], N. Umetsu[1], S. Hashimoto[1], M. Quinsat[1], S. Nakamura[1] and *T. Kondo*[1] *1. Institute of Memory Technology R&D, Toshiba Memory Corporation, Kawasaki, Japan*

We have investigated characteristics of current-induced domain wall motion (CIDWM) in the perpendicularly magnetized 3nm-Ta/3nm-Pd/[0.16nm-TM/0.22nm-Pd]*4.5/3nm-Pd/5nm-Ta multilayered structures (TM = Co, CoFe, and CoNi), as examples of the situation in which domain wall (DW) is driven, by applying current, with both spin-transfer torque (STT) and spin-orbit torques (SOT's). The systematic experiments on TM-composition dependence of CIDWM characteristics for the samples reveal that higher Fe-content gives rise to smaller threshold current density J_c, and higher Ni-content results in larger J_c to the contrary. The values J_{c_MODEL} estimated using a conventional STT-based CIDWM model [1-3] with obtained magnetic properties for the samples show almost opposite dependence in respect to the TM-composition [Fig. 1]. Although direction of the CIDWM for the Pd-based samples in this study is parallel to electron-flow, these results strongly suggest that SOT's contribute to CIDWM in the samples. Considering the contribution of SOT's is not enough to express the observed CIDWM characteristics of the samples. Fig. 2(a) shows TM-composition dependence of current-induced effective fields being associated with damping-like (H_{DL}) and field-like (H_{FL}) SOTs determined by harmonic response measurements [4]. Even though the observed H_{DL} is varied by changing TM-composition significantly, its trend doesn't match that of the J_c. To understand the characteristics, we believe that not only SOT's, but also quantitative information on Dzyaloshinskii-Moriya interaction and extrinsic DW pinning, induced with inhomogeneity of magnetic properties in the structures, should be taken into the account.

[1] S. V. Tarasenko *et al.*, J. Magn. Magn. Mater. Vol. 189, p.19 (1998). [2] A. Moujin *et al*., Lett. J. Expl. Vol. 78, p.57007 (2007). [3] E. Martinez, J. Phys. Cond Matt. Vol. 24, p. 024206 (2012). [4] M. Hayashi *et al*., Phys. Rev. B Vol. 89, p. 144425 (2014).

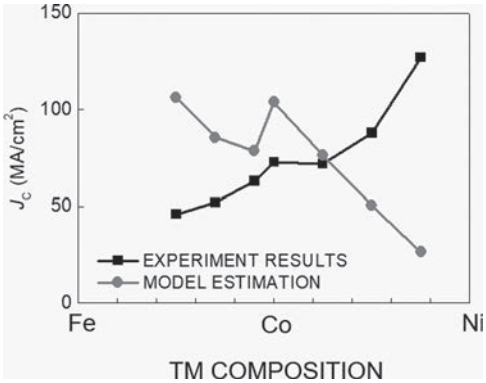


FIG.1. TM composition dependence of estimated and experimentally obtained J_C for Pd-based samples.

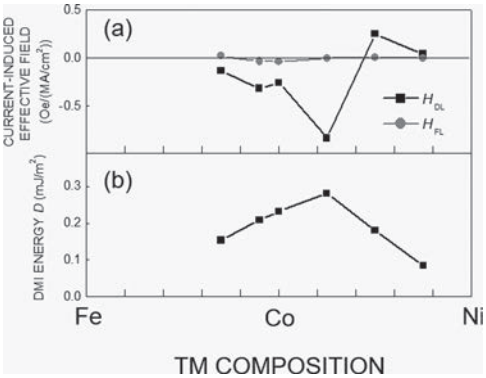


FIG.2. TM composition dependence of (a) current-induced effective fields (H_{DL} and H_{FL}), and (b) DMI energy D for the Pd-based samples.

2:30

HB-04. Bulk Spin Torque Driven Perpendicular Magnetization Switching in $L1_0$ FePt. *M. Tang*[1], K. Shen[2], S. Xu[1], H. Yang[1], S. Hu[1], W. Lü[3,4], C. Li[5], M. Li[5], Z. Yuan[2], S. Pennycook[5], K. Xia[2], A. Manchon[6], S. Zhou[1] and X. Qiu[1] *1. School of Physics Science and Engineering, Tongji University, Shanghai, China; 2. Department of Physics, Beijing Normal University, Beijing, China; 3. Spintronics Institute, University of Jinan, Jinan, China; 4. Condensed Matter Science and Technology Institute, School of Science, Harbin Institute of Technology, Harbin, China; 5. Department of Materials Science and Engineering, National University of Singapore, Singapore; 6. Division of Physical Science and Engineering, King Abdullah University of Science and Technology, Thuwal, Saudi Arabia*

Manipulating magnetization by a charge current lays the most important foundation for modern spintronics devices. However, recent emerging spin orbit torque (SOT) in the ferromagnet (FM)/heavy metal (HM) bilayer has restricted its application in a 3 terminal device which is not favored in circuit design[1]. Moreover, the interface nature of the SOT in FM/NM bilayers hinders the thermal stability and nonvolatility[2, 3]. Here, we show these obstacles can be overcome by exploring current induced effective magnetic fields and magnetization switching in a single $L1_0$ FePt layer. Fig. 1(a) illustrates the $L1_0$ FePt crystal structure, and our films are identified to be monocrystallines of this structure by TEM and XRD. Fig. 1(b) shows anomalous Hall effect (AHE) loops associated with the strong perpendicular magnetic anisotropy of FePt. A clear current driven magnetization switching in the FePt is detected by AHE signal [Fig. 1(c)]. The current induced effective fields H_L and H_T have been quantified with a harmonic voltage method[3].As shown in Fig. 1(d), the H_L and H_T increase with t_{FePt} indicating a bulk characteristic of the SOT in $L1_0$ FePt. Moreover, the H_L and H_T are also revealed to increase with chemical ordering and therefore

their correlation with spin orbit coupling is identified. The emergence of SOT and current driven magnetization switching in FePt of centrosymmetric $L1_0$ structure is counter-intuitive from the established framework of SOT[4]. Nevertheless, several forms of symmetry breaking, such as variants, anti-phase boundaries, and gradient of lattice constant have been probed by TEM and XRD and a possible origin of the observed SOT will be discussed in the conference. By ascribing the current induced effective fields to a new form of SOT in $L1_0$ FePt, our results not only push forward the frontier of the material systems for generating spin torque, but also bring a transformative impact to the magnetic storage and spin memory applications with simple architecture, ultra-high density and readily application.

[1] M. Cubukcu, O. Boulle, M. Drouard et al., Appl. Phys. Lett., Vol. 104, p.042406 (2014). [2] X. P. Qiu, K. Narayanapillai, Y. Wu et al., Nat. Nanotechnol., Vol. 10, p.333 (2015). [3] J. Kim, J. Sinha, M. Hayashi et al., Nat. Mater., Vol 12, p.240 (2013). [4] A. Manchon, I. Miron, T. Jungwirth et al., arXiv preprint arXiv:1801.09636 DOI (2018).

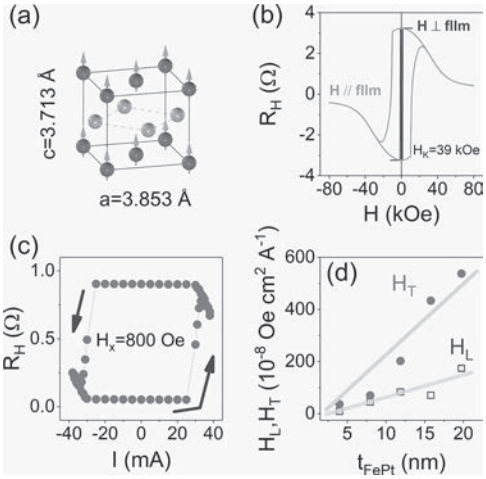


Fig.1. (a)$L1_0$ crystal structure. (b)AHE loops and (c)Hall signal for current induced magnetization switching of an 8 nm FePt device. (d)Thickness dependence of current induced effective fields.

2:42

HB-05. Surfactant-aided Growth for Enhancement of Spin Orbit Torques in Platinum. *C. Garg*[1], S. Yang[1], L. Thompson[1], T. Topuria[1], A. Capua[2], B. Hughes[1], T. Phung[1], P. Filippou[1] and S.S.P. Parkin[1] *1. IBM Almaden Research Center, San Jose, CA, United States; 2. The Hebrew University of Jerusalem, Jerusalem, Israel*

Spin-orbit torques (SOT) are an effective means for controlling magnetization switching behavior in racetracks[1] and three-terminal memory devices. Typically, highly efficient SOT generators are formed from heavy elements like Pt[2], Ta and W. Increasing the magnitude of SOT by discovering new materials or modifying existing ones is an area of vigorous research. Here we show that Pt films can be successfully grown by using surfactants resulting in an altered growth. By growing perpendicularly magnetized ferrimagnetic layers on top of this altered Pt layer, we demonstrate fast domain wall motion (~300 m/s) at significantly lower current densities when compared to our earlier work[1]. SOT measurements on this sample reveal a ~52% enhancement in the damping-like component of SOT as well. We attribute this change to growth of a mixture of (111) and (100) oriented Pt grains as opposed to exclusively (111) grains in the absence of surfactant use. Our findings show a novel pathway to engineering materials for higher SOT.

1) K-S. Ryu et al. Nature Nanotechnology volume8, pages 527–533 (2013)
2) J. Sinova, et al. Rev. Mod. Phys. 87, 1213 (2015)

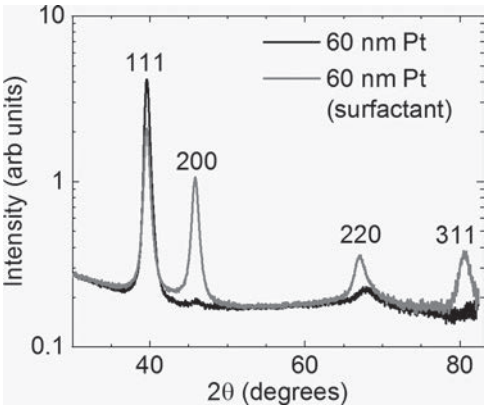


Fig.1 : X-ray diffraction patterns of 60 nm thick films of Pt grown with (red) and without (black) the aid of a surfactant.

2:54

HB-06. Spin orbit torque in Pt/[Co/Tb]$_2$ multilayers with non-collinear spin states. *H. Chen*[1], R. Mishra[2], H. Yang[2], S. Zhou[1] and X. Qiu[1]
1. School of Physics Science and Engineering, Tongji University, Shanghai, China; 2. Department of Electrical and Computer Engineering, National University of Singapore, Singapore

In recent years, ferrimagnetic spintronic has attracted great attention with revelations of many intriguing properties: large spin orbit torque (SOT) [1], long spin-dephasing length[2], ultra-small skyrmion, fast domain wall motion[3] *etc.* However, the studies of SOT in ferrimagnet have been still controversial, and the non-collinear spin state[4] between magnetic sub-lattices has not been considered. In this study, SOT is investigated in the Pt/[Co/Tb]$_2$ multilayers with temperature-evolving spin configurations associating with the spin flip and spin canting transitions. By modulating the net magnetization and exchange coupling of ferrimagnet through temperature, the SOT exhibits intriguing features in response to the Co magnetization. (1) It is found the non-collinear magnetic state (spin-canted state) emerges when temperature is near the magnetization compensation temperature (T_M), as shown in Fig. 1(b). (2) The longitudinal effective field (H_L) changes sign at T_M and at a lower temperature, as shown in Fig. 2(a), which is related to the transition from spin-canted state to linear spin state. The temperature dependence of transversal effective field (H_T) can be also explained by the spin state transition. (3) Both H_L and H_T shows maximum at T~T_M, which is the result of the vanishing net magnetization. (4) The effective spin Hall angle of the Pt/[Co/Tb]$_2$ multilayers is higher than that of Pt[5], indicating that ferrimagnetic nature can lead an enhancement of the SOT efficiency in this system. Our results not only demonstrate ferrimagnet as a promising candidate for spin-orbitronic application with high thermal stability, but also provide important insight into spin orbit torque in magnet with non-collinear spin structure such as ferrimagnet, synthetic antiferromagnet and spin glass *etc*.

[1] R. Mishra, J. Yu, X. Qiu, et al., Phys. Rev. Lett. 118(16): 167201, (2017). [2] J. Yu, D. Bang, R. Mishra, et al., Nature Mat. 18(1): 29, (2019). [3] L. Caretta, M. Mann, F. Büttner, et al., Nature Nanotech. 13(12): 1154, (2018). [4] K. Ganzhorn, J. Barker, R. Schlitz, et al., Phys. Rev. B 94(9): 094401, (2016). [5] P. Sethi, S. Krishnia, S. Li, et al., J. Mag. Mag. Mater. 426: 497-503, (2017).

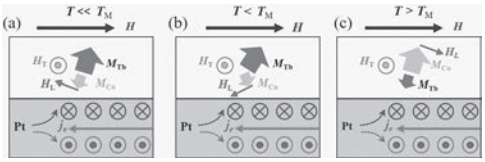


Fig 1. Illustrations of the flow of electrons, accumulated spins, the anti-damping like and filed-like effective field at different temperature for Pt/[Co/Tb]$_2$ multilayers.

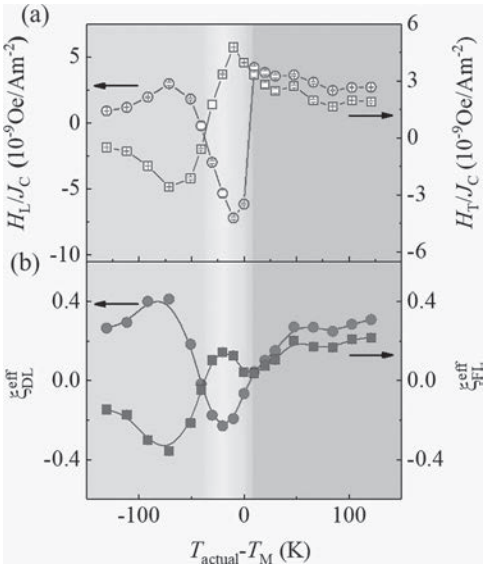


Fig. 2. Temperature dependence of (a) anti-damping like and field like effective fields (H_L and H_T, respectively) per unit current density (b) effective spin Hall angle of anti-damping like and torque field like for Pt/[Co/Tb]$_2$ multilayers.

3:06

HB-07. Effects of spin–orbit torque on domain wall motion in a Ta/MnGa/NiAl structure. *M. Yamanouchi*[1], N.V. Bao[2], M. Inoue[2] and T. Uemura[2] *1. Research Institute for Electronic Science, Hokkaido University, Sapporo, Japan; 2. Division of Electronics for Informatics, Graduate School of Information Science and Technology, Hokkaido University, Sapporo, Japan*

Spintronics devices using spin–orbit torques (SOTs) are expected to be the building blocks for next-generation electronics. Perpendicularly magnetized MnGa is a candidate for the ferromagnetic layer of such spintronics devices owing to a relatively large perpendicular magnetic anisotropy, low magnetization, and relatively high spin polarization. Although SOTs and SOT-induced magnetization switching have been reported in magnetic heterostructure based on MnGa [1,2], effects of SOT on domain walls (DWs) has not been clarified. Here, we investigated interaction between SOT and DWs created during magnetization reversal by out-of-plane magnetic field H_z under various in-plane magnetic fields H_xs along the current I direction in perpendicularly magnetized ultrathin MnGa sandwiched between Ta and NiAl. A MgO(2 nm)/Ta(5 nm)/MnGa(1 nm)/NiAl (3 nm) stack was deposited on a (001) MgO single-crystal substrate. The stack was processed into Hall devices with a 10-mm-wide channel and a pair of Hall probes. We measured transverse resistance, which reflects perpendicular component of magnetization, by sweeping H_z under various Is and H_xs. The centers of hysteresis loops under H_x are shifted along H_z axis and the shift amount is almost proportional to I, which indicates that I acts as an effective perpendicular magnetic field H_{eff} on magnetization under H_x. The slope of H_{eff} versus I varies proportionally to H_x and becomes saturated above ~0.15 T, which is consistent with the model based on the modulation of the coercive field through SOT-assisted chiral DW motion [3]. The saturated slope is well described by the interaction between the chiral DWs and the Slonczewski-like SOT originating from the spin Hall effect in the Ta layer. The saturation of H_{eff} is caused by realignment of the internal magnetization in the chiral DWs rather than that in the Bloch DWs because the saturation threshold H_x is smaller than the hard-axis anisotropy field for the Bloch DW. These results suggest that the magnetization is reversed through SOT-assisted chiral DW motion [3] This work was supported in part by Japan Society for the Promotion of Science KAKENHI Grant No. 17H03225 and the Center for Spintronics Research Network.

[1] R. Ranjbar *et al*., Jpn. J. Appl. Phys. 55, 120302 (2016) [2] K. Meng *et al.*, Sci. Rep. 6, 38375 (2016). [3] C. - F. Pai *et al*., Phys. Rev. B 93, 144409 (2016).

3:18

HB-08. Spin-orbit torques in Pt/Co based structures with inserted Tb layers. *Y. Wu*[1], K. Meng[1], J. Chen[1], Z. Li[1], J. Miao[1] and Y. Jiang[1] *1. University of Science and Technology Beijing, Beijing, China*

Spin-orbit torque (SOT) devices, which exhibit high energy efficiency, low Joule heating and small size, has attracted many attentions for its potential in industrial application [1-4]. Recent works indicated that there're two sources of SOT, spin currents from the spin Hall effect (SHE) and the spin accumulation originated from the Rashba-Edelstein effect. To enhance the SHE or Rashba-Edelstein effect is the immediate approach to realize the high efficiency of SOT. In this work, we use Tb as inserted layer to enhance the SOT in Pt/Co/Pt structures, and investigate the current-induced magnetization switching at low temperature. The schematic of the SOT device is shown in Fig. 1(a). Fig. 1(b) shows the anomalous Hall effect of the Pt/Co/Tb(0~3 nm)/Pt structures, which reveal good perpendicular magnetic anisotropy. The SOT signals are shown in Fig. 1(c). The critical switching current is significantly reduced after inserting the Tb layer, indicates that the Tb layer has enhanced the SOT efficiency. To exclude that the enhancement of the SOT may come from the insulation of the spin current from the top Pt layer, we replaced the top Pt layer by AlO_x layer. The SOT signals at 50-300K are shown in Fig. 2(a). The critical switching current density is smaller than the Pt/Co/Tb/Pt structure, as shown in Fig. 2(a) and (b), reveals that the absent of the spin current from the top Pt layer may contribute to the enhancement of SOT, but not the mainly factor. We consider that the Tb layer can increase the effectivity spin Hall angle, thus increase the spin currents, and enhance SOT efficiency. At low temperature, the Pt/Co/Tb/Pt and Pt/Co/Tb/AlO_x samples also reveal obvious SOT signal. On the other hand, the SMR measurements of the structures in Fig. 2(c) and (d) proved that the inserted Tb layer can significantly increase the effective spin Hall angle.

[1] I. M. Miron, K. Garello, G. Gaudin, P. J. Zermatten, M. V. Costache, S. Auffret, S. Bandiera, B. Rodmacq, A. Schuhl, P. Gambardella, Nature 476 (2011) 189. [2] K. Garello, I. M. Miron, C. O. Avci, F. Freimuth, Y. Mokrousov, S. Blugel, S. Auffret, O. Boulle, G. Gaudin, P. Gambardella, Nat. Nanotechnol. 8 (2013) 587. [3] K. K. Meng, J. Miao, X. G. Xu, J. X. Xiao, J. H. Zhao, Y. Jiang, Phys. Rev. B 93 (2016) 060406(R). [4] K. Cai, M. Yang, H. Ju, S. Wang, Y. Ji, B. Li, K. W. Edmonds, Y. Sheng, B. Zhang, N. Zhang, S. Liu, H. Zheng, K. Wang, Nat. Mater. 16 (2017) 712.

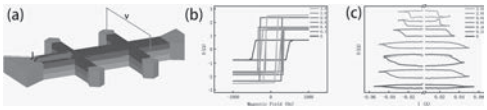


Figure 1. (a) The schematic of the Hall bars. (b) The out-of-plan magnetic field dependence of the Hall resistance. (c) The SOT signals of the Pt/Co/Tb (0~3 nm)/Pt samples.

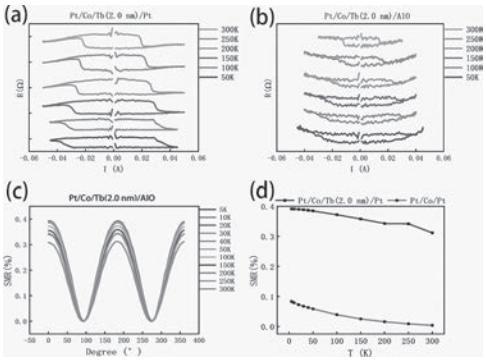


Figure 2. The SOT signals of (a)Pt/Co/Tb/Pt and (b)Pt/Co/Tb/AlO_x samples. (c) the SMR measurements of Pt/Co/Tb/AlO_x sample. (d) the temperature dependence of SMR in Pt/Co/Tb/Pt and Pt/Co/Tb/AlO_x samples.

Session HC
MAGNETOELECTRIC PHENOMENA IN FILMS, HETEROSTRUCTURES, AND COMPOSITES

Ignasi Fina, Chair
Institut de Ciència de Materials de Barcelona (ICMAB-CSIC), Bellaterra, Spain

INVITED PAPER

1:30

HC-01. Interfacial magnetoelectricity at multiferroic interfaces.
J. Santamaria[1] *1. Universidad Complutense, Madrid, Spain*

The electronic reconstruction occurring at oxide interfaces may be the source of interesting device concepts for future oxide electronics. Among oxide devices, multiferroic tunnel junctions are being actively investigated as they offer the possibility to modulate the junction current by independently controlling the switching of the magnetization of the electrodes and of the ferroelectric polarization of the barrier. In this talk I will discuss the interplay between ferroelectric polarization and the ionization of oxygen vacancies, a ubiquitous defect in perovskite oxides. Oxygen vacancies carry doping and a strain fields which can induce deep modifications of the conducting properties of tunnel barriers and may drastically change the electronic properties at their interfaces. I will discuss that coupled oxygen vacancy and ferroelectric switching is the source of novel magnetoelectric effects. In particular, I will show that the spin reconstruction at the interfaces of a La Sr MnO /BaTiO / La Sr MnO multiferroic tunnel junction is the origin of a spin filtering functionality which can be turned on and off by reversing the ferroelectric polarization. The ferroelectrically controlled interface spin filter enables a giant electrical modulation of the tunneling magnetoresistance between values of 10% and 1000%, that could inspire device concepts in oxides based low dissipation spintronics.

Work done in collaboration with F. Gallego[1], J. Tornos[1], D. Hernandez-Martin[1], G. Sanchez-Santolino[2], M. Cabero[1], J. I. Beltran[1], C. Munuera[2], A. Rivera-Calzada[1], Z. Sefrioui[1], F. Mompean[2], M. Garcia-Hernandez[2], S. J. Pennycook[3], M. Varela[1], M. C. Muñoz[2], S. Valencia[4], Y. H. Liu[5,6], V. Lauter[5], R. Abrudan[4], C. Luo[4], R. Hanjo[4], F. Radu[4]Q. Wang[6], S. G. E. te Velthuis[6], C. Leon[1], [2]*Instituto de Ciencia de Materiales de Madrid ICMM-CSIC* [3]Department of Mat. Sci.& Engineering, Natnl. Univ.of Singapore, Singapore 117575. [4]Hemholtz-Zentrum Berlin für Materialen und Energie, Albert-Einstein-Str.15, Berlin [5]Quantum Condensed Matter Division., Oak Ridge National Laboratory, Oak Ridge, TN37831, USA [6]Materials Science Division, Argonne Natnl. Lab. Argonne, Illinois 60439, USA.

CONTRIBUTED PAPERS

2:06

HC-02. Changing the Magnetic States of a Fe/$BaTiO_3$ interface through Crystal field effects controlled by Strain.
C. Amorim[1], J.N. Gonçalves[1], J.S. Amaral[1] and V. Amaral[1] *1. Physics Department and CICECO, University of Aveiro, Aveiro, Portugal*

The search for better and inexpensive magnetoelectric materials is now commonplace in solid state physics. The desired intense coupling between electric and magnetic properties, embedded in a single material, is still the main motivation of this line of research [1-3]. A magnetoelectric material that successfully manages to couple the strong, above room-temperature ferroelectricity of $BaTiO_3$ with the also strong and above room-temperature ferromagnetism of Fe would naturally be a strong candidate for applications. Using DFT, the study of a specific interface between the TiO_2 layer of $BaTiO_3$ and a monolayer of Fe atoms is presented, probing different uniaxial strain effects of the considered supercell. Several different metastable magnetic states are predicted: a perfectly balanced antiferromagnetic state, an unbalanced ferrimagnetic state, a ferromagnetic state, and a non-magnetic state where each atom has its total magnetic moment quenched. These multiple magnetic behaviors are influenced by different possible hybridizations between the Fe and Ti atoms, as well as through O's crystal field effects, which collectively change the local charge and spin density surrounding each atom (Fig. 1-2) [4]. Interestingly, these multiple magnetic states can be reversibly controlled by strain. Under optimized conditions, the interface can switch from the ferromagnetic state to the non-magnetic state, with enticing prospects for applications.

[1] Fiebig, M.; Lottermoser, T.; Meier, D.; Trassin, M. The evolution of multiferroics. *Nature Reviews Materials* 2016, *1*, 16046. [2] Spaldin, N.; Ramesh, R. Advances in magnetoelectric multiferroics. *Nature materials* 2019, *18*, 203. [3] Scott, J. Data storage: Multiferroic memories. *Nature materials* 2007, *6*, 256–257. [4] Amorim, Carlos O., et al. "Electric Field Induced Room Temperature Null to High Spin State Switching: A Computational Prediction." *Advanced Theory and Simulations*: 1900005.

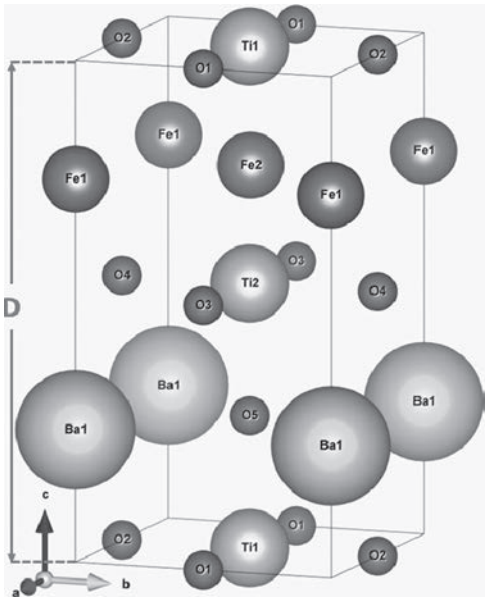


Fig 1. The considered supercell of the BTO/Fe interface considered in this study.

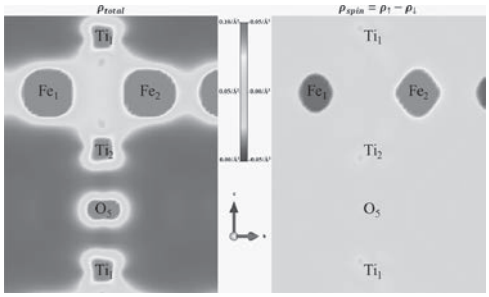


Fig 2. Total charge and polarized charge difference of the Ferrimagnetic State, one of the possible magnetic states of the Fe monolayer of the BTO/Fe interface.

2:18

HC-03. Electric-field controlled, exchange-coupled bilayer microstructures with tunable magnetoelastic effect. *Z. Xiao*[1,3], R. Lo Conte[2], M. Goiriena-Goikoetxea[2], R.V. Chopdekar[3], X. Li[1], C. Lambert[2], S. Tiwari[1], A.T. N'Diaye[3], P. Shafer[3], A. Chavez[1], A. Barra[1], G. Carman[1], S. Salahuddin[2], K. Wang[1], E. Arenholz[3], J. Bokor[2] and R. Candler[1,4] *1. Electrical and Computer Engineering, University of California Los Angeles, Los Angeles, CA, United States; 2. Electrical Engineering and Computer Sciences, University of California Berkeley, Berkeley, CA, United States; 3. Advanced Light Source, Lawrence Berkeley National Lab, Berkeley, CA, United States; 4. California NanoSystems Institute, Los Angeles, CA, United States*

Multiferroic systems hold great promise for energy-efficient control of magnetization [1-3]. Previously, electrically-induced magnetization reorientation in negatively magnetostrictive Ni microstructues on PMN-PT has been demonstrated [4]. Positively magnetostrictive CoFeB has also drawn substantial interest for its significant tunneling magnetoresistance in magnetic tunnel junctions for strain-mediated multiferroic random access memory. In order to combine the ease of reorienting magnetization in Ni microstructures with the potential for memory applications in CoFeB, we engineered a novel strain-mediated multiferroic system, composed of bilayer Ni/CoFeB magnetostrictive microstructures on a ferroelectric $Pb(Mg_{1/3}Nb_{2/3})_{0.69}Ti_{0.31}O_3$ (PMN-PT) single crystal. This work examines the influence of the exchange coupling on the magneto-elastic behavior through electrically driven magnetization reorientation in bilayer microstructures. Arrays of 2x2 μm^2 magnetic squares of Ni/CoFeB films with various thickness combinations are imaged by X-ray magnetic circular dichroism-photoemission electron microscopy (XMCD-PEEM) to obtain element-specific magnetic contrast. The correlations between the magnetization of individual layers highlights the strong exchange coupling behavior (Fig. 1). In an electric field across the PMN-PT, a compressive strain is generated along the [100], tensile strain along [01-1] of the PMN-PT. The piezostrain tunes the magnetic anisotropy in the patterned microstructures. For pure CoFeB, the magnetic moments realign to the tensile strain direction, whereas in pure Ni the moment aligns toward the compressive strain direction. However, when both CoFeB and Ni are present in equal volume, the magnetic anisotropy tends to favor magnetization reorientation in the tensile strain direction. Quantitative analysis of PEEM images and micromagnetic simulations provides insight into the tunable magnetoelastic effect of such bilayer systems. This work highlights the potential for hybrid ferromagnetism in composite multiferroics with tunable magnetoelasticity for next-generation memory applications.

[1] M. Bibes & A. Barthélémy Agnès, Nature 7, 425 (2008). [2] J. Cui *et al.*, Applied Physics Letters 103, 232905 (2013). [3] Y. H. Chu, *et al.*, Nat Mater 7, 478 (2008). [4] R. Lo Conte, *et al.*, Nano Lett 18, 1952 (2018).

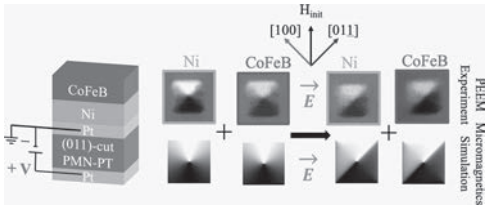


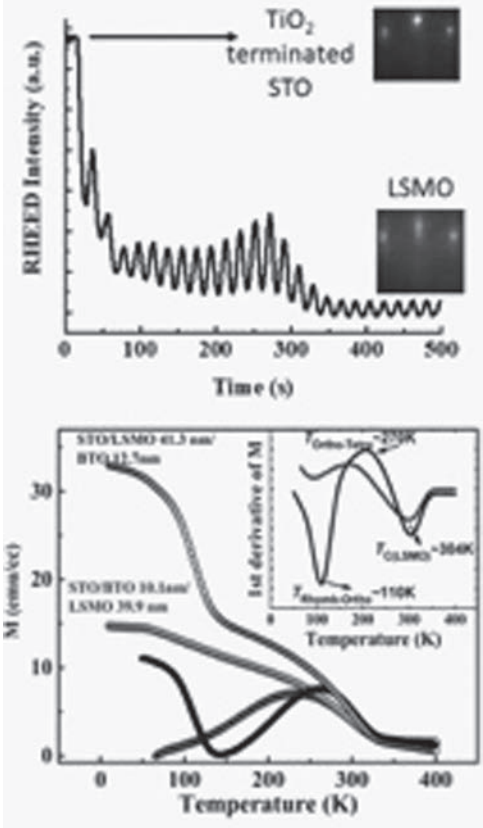
Fig. 1: Electric-field induced magnetic domain reorientation in CoFeB/Ni bilayer.

2:30

HC-04. Investigations of the magneto-strictive coupling at the interface of $SrTiO_3$ (001) /$La_{0.6}Sr_{0.4}MnO_3$/$BaTiO_3$ system. S.G. Bhat[1] and *A.P. Kumar*[1] *1. Department of Physics, Indian Institute of Science, Bangalore, India*

The quest for the search of scarcely available multiferroic/magnetoelectric materials for technological application is active since 2-3 decades. But, the artificial synthesis of the same using ferromagnet (FM)/ferroelectric (FE) heterostructure stack is an alternative [1,2]. However, growing ferromagnetic film on a single crystal of ferroelectric substrate is common for demonstrating the strain dependent magnetoelectric coupling (also known as magnetostriction coupling in the ferromagnet). The strain induced modification of FE thin films reflecting in the magnetization of adjacent FMs are not so obvious; even with the poled FE such as $BaTiO_3$ [3,4]. In this regard, we have grown high quality epitaxial 2D bi-layer of $La_{0.6}Sr_{0.4}MnO_3$(LSMO)/ $BaTiO_3$(BTO) on $SrTiO_3$(STO) with good indication of magnetization coupling to the BTO. We have grown RHEED assisted pulsed laser deposited heterostructures of LSMO/BTO on STO which exhibit a fine control on crystallographic domains of BTO. The sequence of growth clearly indicates the control of single/multi-crystallographic domains in the BTO layer along with the evident quality of the growth. We further observe a very evident modulation of magnetization across the expected structural transitions of BTO even without any electric poling, similar to single crystal study [5,6] which is rare to find in ultra-low thickness of BTO. The systematic slope change corresponding to the structural transitions of BTO can be one-to-one mapped to the lattice parameter variation of BTO and hence the magnetostriction in LSMO. Despite reports of magnetostriction studies at LSMO films on BTO single crystal, our preliminary study shows epitaxial ultrathin BTO can also exhibit an equally good magnetic coupling with LSMO. The control over the single crystallographic domains of the BTO thin films provides a unique opportunity to study the pinning of magnetic domains of LSMO in a simpler way unlike the existing studies [2,5,7] with mixed domains of BTO.

[1] Nature Materials, 7, 478 (2008) [2] Sci. Rep., 2, 258 (2012) [3] Appl. Phys. Lett. 100, 232904 (2012) [4] J. Appl. Phys. 116, 224104 (2014) [5] App. Phys. Lett. 101, 262405 (2012) [6] Appl. Phys. Lett. 94, 022504 (2009) [7] Phys. Rev. B, 92, 054406 (2015)



2:42

HC-05. Strain engineered multiferroic phase diagram of orthorhombic RMnO$_3$ (R = Gd - Lu) epitaxial thin films. *S. Mukherjee*[2], C. Schneider[1] and C. Niedermayer[1] *1. Paul Scherrer Institute, Villigen, Switzerland; 2. University of Oxford, Oxford, United Kingdom*

Magnetoelectric multiferroics demonstrate simultaneous coexistence of magnetic and electric order paramerters. In addition, they show unique ability of cross-coupling between order parameters. These unique properties make them exciting both for technological development and fundamental studies. Rare-earth manganites (RMnO$_3$) in orthorhombic phase is one such archetypical candidate showing magneto-electric behavior. Depending upon R-ion radii they show a wide range of multiferroic phase governed by competing magnetic interactions as shown in the multiferroic phase diagram for bulk (Fig. 1) [1, 2, 3, 4]. Interestingly, on application of epitaxial strain the multiferroic phase diagram shows a dramatic change [5, 6] (Fig. 2). The most prominent effect observed is that the ground state gets independent of the R-ion radii and is forced to demonstrate a homogenous magnetic and electric property. Under epitaxial strain the films stabilize into an E-type order with ferroelectric ordering along a-axis. This suggested that the competing interactions are tuned to favor a symmetric exchange striction mechanism for the multiferroicity. In our work, we employed neutron and x-diffraction to study the magnetic phase in detail. In addition, in-house capacitance and ferroelectric loop measurements were conducted to confirm the electric ground states. These studies also highlight the development of instrumentation which provided the unique oppurtunity to study the magnetic order of thin films (thickness~10 -40 nm) with neutron diffraction. We plan to discuss in further details and reveal the variation in the microscopic mechanism induced by epitaxial strain to tailor the multiferroic phase diagram. This presentation will help in providing the audience a better outlook on using strain to engineer physical properties of materials.

[1] K. Shimamoto, S. Mukherjee, et. *al,* Phys. Rev. B 95, 184105 (2017). [2] S. Ishiwata, Y. Kaneko, et. *al,* Phys. Rev. B 81, 100411 (2010). [3] T. Kimura, T. Goto, et. *al,* Nature 426, 55 (2003). [4] M. Mochizuki, N. Furukawa, and N. Nagaosa, Phys. Rev. B 84, 144409 (2011). [5] K. Shimamoto, S. Mukherjee, et. *al,* Sci. Rep. 7, 44753 (2017). [6] S. Mukherjee, K. Shimamoto, et. *al,* Phys. Rev. B 98, 174416 (2018).

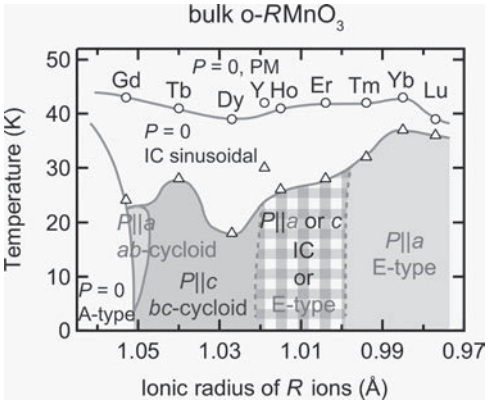


Fig. 1 : Multiferroic phase diagram for bulk RMnO$_3$ (Raken from Ref. [1]).

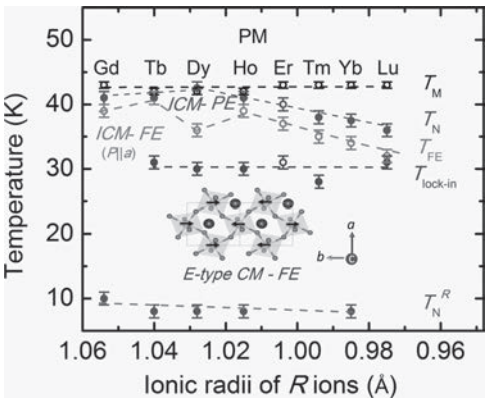


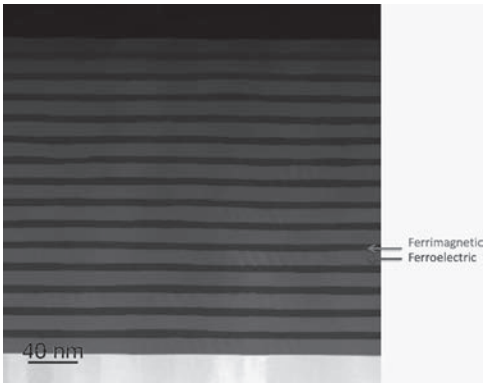
Fig. 2 : Multiferroic phase diagram for epitaxial strained RMnO$_3$ thin films (Taken from Ref. [6]).

2:54

HC-06. Epitaxial Room Temperature Multiferroic Superlattices Combining Hexagonal and Cubic Ferrites. *R. Steinhardt*[1], M. Holtz[1], P. Barrozo da Silva[2], J. Mundy[3], R. Ramesh[2] and D. Schlom[1] *1. Cornell University, Ithaca, NY, United States; 2. Berkeley University of California, Berkeley, CA, United States; 3. Harvard, Boston, MA, United States*

Hexagonal rare earth ferrites offer a promising and relatively unexplored area for multiferroic materials design. An exciting new method for creating multiferroic materials by combining rare earth ferrites into epitaxial superlattices has previously been developed using $LuFeO_3$ for it's ferroelectric properties and $LuFe_2O_4$ for it's ferrimagnetism [1]. While these lutetium ferrite superlattices demonstrated magnetoelectric coupling near room temperature, for device applications we seek materials that have stronger magnetism at higher temperatures. We use molecular beam epitaxy to combine ferroelectric hexagonal $LuFeO_3$ and ferrimagnetic cubic spinel ferrite into a superlattice. Depending on growth conditions, the spinel can form as surface polycrystalline precipitates [2], ordered 3D epitaxial structures, or well-ordered superlattices. The resulting superlattices show both strong magnetism and ferroelectricity above room temperature, which is promising for device applications. Multiferroic properties such as magnetoelectric coupling are currently being investigated.

1. Mundy, Julia A., et al. "Atomically engineered ferroic layers yield a room-temperature magnetoelectric multiferroic." *Nature*537.7621 (2016): 523-527. 2.Moyer, J. A., et al. "Intrinsic magnetic properties of hexagonal LuFeO3 and the effects of nonstoichiometry." *APL Materials*, *2*.1 (2014): 012106



3:06

HC-07. Room Temperature Strong Magnetoelectricity in Single Phase Multiferroic Materials. *S. Kumari*[4,1], D.K. Pradhan[2], S. Liu[3], M.M. Rahaman[2], A. Kumar[5], Q. Li[1] and R.S. Katiyar[4] *1. Department of Physics, The Pennsylvania State University, University Park, PA, United States; 2. Geophysical Laboratory, Carnegie Institution for Science, Washington, DC, United States; 3. Army Research Laboratory, Adelphi, MD, United States; 4. Department of Physics and Institute for Functional Nanomaterials, University of Puerto Rico, San Juan, PR, United States; 5. CSIR-National Physical Laboratory, New Delhi, India*

Magnetoelectric - Multiferroic (MF) materials have drawn enormous interest because of their fascinating physics and great potential for memory, spintronics, and multifunctional applications. Obtaining single-phase ME materials with strong ME coupling, understanding its origin, and manipulating the processing and composition to realize large ME coefficients at room temperature constitute the holy grail of multiferroic research and remain difficult to achieve until now. Recently Intel research group have designed magnetoelectric spin–orbit logic device utilizing a single-phase material (La doped $BiFeO_3$) which has higher switching energy (10 to 30 times), lower switching voltage (5 times) and higher logic density (by a factor of 5) than the present CMOS devices. But La doped $BiFeO_3$ still not optimal, due to its high leakage current and small ME coupling coefficient. In continuation of our search for better ME materials for device applications, we have investigated the multiferroic and ME properties of Ni-doped $Pb(Zr_{0.20}Ti_{0.80})O_3$ ($Pb(Zr_{0.20}Ti_{0.80})_{0.70}Ni_{0.30}O_{3-\delta}$). We find that the ferroelectric (T_c ~ 700K) and weak ferromagnetic (~ 602 K) phase transitions of Ni-doped PZT are well above room temperature, leading to a strong ME coupling coefficient ($a_{E,31}$) of 11.7 mV/cm. Oe (H_{ac} = 1 Oe and f = 1 kHz). We further demonstrate that Ni-doped PZT exhibits low loss tangent, low leakage current, large saturation polarization and weak ferromagnetism. Our first-principles investigations suggest the defect is likely to be responsible for the experimental ME coupling in Ni-doped PZT. The requirement of for magnetization also explains the magnetization observed experimentally as majority of Ni dopants tend to replace *B*-site cations. Ultimately, our work demonstrates Ni-doped PZT is a cost-effective room-temperature single-phase multiferroic with strong ME coupling. The strong ME coupling above room-temperature makes it a possible future alternative of other single phase multiferroics with a strong possibility for device applications.

3:18

HC-08. Room temperature multiferroicity and magnetodielectric coupling in 0-3 composite thin films. *D.K. Pradhan*[1], S. Kumari[2], P.T. Das[5], R. Vasudevan[4] and R. Katiyar[3] *1. Geophysical Laboratory, Washington, DC, United States; 2. Department of Physics, The Pennsylvania State University, University Park, PA, United States; 3. Department of Physics, University of Puerto Rico, San Juan, PR, United States; 4. Center for Nanophase Materials Sciences, Oak Ridge National Laboratory, Oak Ridge, TN, United States; 5. Department of Physics, Bar-Ilan University, Ramat-Gan, Israel*

With the development of devices miniaturization beyond Moore's exploration, there is increasing activities in combining magnetic and electronic properties in a material for potential applications in novel multifunctional devices. Magnetoelectric (ME) composite thin films have the potential for applications in novel spintronics and multifunctional devices as they exhibit much higher ME coupling and operational temperatures compared to single phase materials. Due to the shortcomings of (2-2) layered and (1-3) vertically composite nanostructures, the ME coupling is comparatively smaller which restrict them for applications. Here we have studied the structural, dielectric, ferroelectric, magnetic and magnetodielectric properties of pulsed laser deposited 0-3 (magnetic quasiparticles (0) embedded in a ferroelectric film matrix (3)) multiferroic composite thin films. We have synthesized the (1-*x*) $Pb(Fe_{0.5}Nb_{0.5})O_3$-*x*$Ni_{0.65}Zn_{0.35}Fe_2O_4$ (*x* = 0 (PFN), 0.10 (PN1), 0.20(PN2), 0.30(PN3)) composite thin films by optimized pulsed laser deposition. The θ-2θ large angle XRD patterns (20° to 80°) showed only the diffraction peaks from the substrate and (00*l*) pseudocubic reflections from PFN and NZFO confirms that these films are highly c- axis oriented in nature, and that the secondary phases are absent. We observed the ferroelectric T_c of ~ 430, 440, 460 (+/- 5) and magnetic T_c of ~435, 526, 555 (±10) K with broad transitions for PN1, PN2 and PN3 respectively. These composite thin films exhibit ferroelectric and magnetic phase transitions above room temperature. All these nanostructures possess saturated large polarization, soft magnetization, low loss tangent and magnetodielctric coupling (observed in PN1) at room temperature which might be useful for next generation nanoscale electronic and spintronic devices. The detailed studies on structural, morphological, dielectric, ferroelectric, piezoresponse force microscopic and magnetic properties of the composite thin films will be presented in the meeting.

3:30

HC-09. Influence of the $BaTiO_3$ Crystallinity on the Electric-field Induced Switching of Perpendicular Magnetization. *M. Goiriena-Goikoetxea*[1,2], Z. Xiao[3], A. El-Ghazaly[1], C. Stan[4,5], J. Chatterjee[1], A. Ceballos[6], A. Pattabi[1], R. Lo Conte[7], F. Hellman[6], R. Candler[3] and J. Bokor[1] *1. Department of Electrical Engineering and Computer Sciences, University of California Berkeley, Berkeley, CA, United States; 2. Department of Electricity and Electronics, University of the Basque Country, Leioa, Spain; 3. Department of Electrical and Computer Engineering, University of California, Los Angeles, Los Angeles, CA, United States; 4. Advanced Light Source, Lawrence Berkeley National Laboratory, Berkeley, CA, United States; 5. NIF and Photon Science, Lawrence Livermore National Laboratory, Livermore, CA, United States; 6. Department of Physics, University of California Berkeley, Berkeley, CA, United States; 7. The Molecular Foundry, Lawrence Berkeley National Laboratory, Berkeley, CA, United States*

We report on the influence of the $BaTiO_3$ crystal microstructure on its ferroelectric response and the direct effect on the modulation of the perpendicular magnetic anisotropy (PMA) of the top Co/Ni multilayers. The presence of multiple grains in the $BaTiO_3$ significantly reduces its ferroelectric response by hindering the reorientation of the ferroelectric domains with an applied electric field, which results in a a small reduction of the PMA (Fig. 1(a)). On the other hand, the ferroelectric reorientation is complete in $BaTiO_3$ with larger crystallinity, inducing an in-plane compressive strain of 11 ppt. A large fraction of this uniaxial strain is transferred to the magnetoelastically coupled ferromagnetic layers whose magnetization switches to in-plane (Fig. 1(b)) via the inverse

magnetostriction effect. This 90° switching is featured by a giant converse magnetoelectric coefficient, close the highest values reported so far,[1,2] highlighting the outstanding magnetoelectric properties of the system composed of single-crystal $BaTiO_3$ and Co/Ni multilayers with PMA. It is also worth emphasizing the difficulty of achieving a full switching of the perpendicular magnetization to an in-plane orientation by pure voltage-driven magnetoelectric effect, which has been reported in a very scarce number of works only[3,4] and is a key feature in the applicability of such a material system in a memory device, where each magnetic orientation would represent the digital *1* and *0* states. This work reveals the critical role of the crystal microstructure within a ferroelectric substrate in the performance of multiferroic heterostructures and provides insight into the development of high energy efficient devices.

[1]T. H. E. Lahtinen, K. J. A. Franke and S. van Dijken, Sci. Rep., Vol. 2, p. 258 (2012) [2]R. Lo Conte, J. Gorchon and A. Mougin, Phys. Rev. Mater., Vol. 2, p. 091402 (2018) [3]Y. Shirahata, R. Shiina and D. López González, NPG Asia Mater., Vol. 7, p. e198 (2015) [4]B. Peng, Z. Zhou and T. Nan, ACS Nano, Vol. 11, p. 4337 (2017)

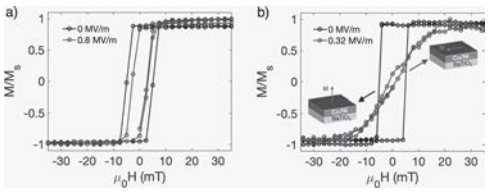


Fig. 1. Electric-field induced PMA modulation in Co/Ni multilayers coupled with (a) polycrystalline $BaTiO_3$ and (b) single-crystal $BaTiO_3$.

3:42

HC-10. Large magnetoelectric effects in nanoscale Ni-PZT composites measured by Anisotropic Magnetoresistance. *H. Ahmad*[1], M. Kouwenhoven[2], F. Vanderveken[1], D. Tierno[3], I. Radu[4], F. Ciubotaru[1] and C. Adelmann[5] *1. Exploratory Device, IMEC, Leuven, Belgium; 2. TU Delft, Delft, Netherlands; 3. Interconnect and Packaging Reliability, IMEC, Leuven, Belgium; 4. Compute Technologies and Enablement, IMEC, Leuven, Belgium; 5. BEOL and Spintronics, IMEC, Leuven, Belgium*

Manipulating nanomagnets by the magnetoelectric (ME) effect is highly promising for low-power spintronic applications. A ME effect can be observed in composite materials combining piezoelectric with magnetostrictive thin films. To date, the ME effect has been mainly studied in thin magnetostrictive films on bulk piezoelectric substrates. At the nanoscale, ME devices promise much larger voltage coupling coefficients due to large electric fields at low voltages. Here, we investigate nanoscale devices based on Ni-PZT thin film composites (Fig. 1) using anisotropic magnetoresistance (AMR). The devices consisted of a 1-μm-wide Ni stripe on a 500-nm-thick PZT mesa on SiO_2/Si (100) substrate. Two electrodes with 750-nm-wide gaps with respect to the Ni stripe were used to generate piezoelectric strain in the PZT. Additional contacts allowed for an AMR measurement of the Ni stripe *vs.* an applied bias voltage. Applying a DC voltage to the electrodes generates electric fringing fields in the PZT mesa, inducing strain in the PZT and the Ni stripe. The strain modifies the magnetoelastic anisotropy field in Ni by the Villari effect. The anisotropy field depends on both the strain tensor and the magnetization direction, leading to a modulation of the AMR. A COMSOL study allowed for the optimization of the magnitude of different strain components for different voltage biasing schemes. Using the most uniform and largest strain configuration, AMR was then used to extract the magnetoelastic coupling in the Ni/PZT devices. The observed variation of the AMR (Fig. 2) with the applied magnetic field and DC bias voltage led to a value of 5200 (A/m)/V, considerably larger than previously reported values for macroscopic devices [1]. This shows the great potential of scaled ME devices for low-voltage spintronic applications. Funding by the European Union's Horizon 2020 research and innovation programme under the Marie Sklodowska-Curie grant No. 794354 and the FET-OPEN project CHIRON under grant No. 801055 is acknowledged.

[1] M. Liu and N.X. Sun, Phil. Trans. R. Soc. A 372, 20120439 (2014).

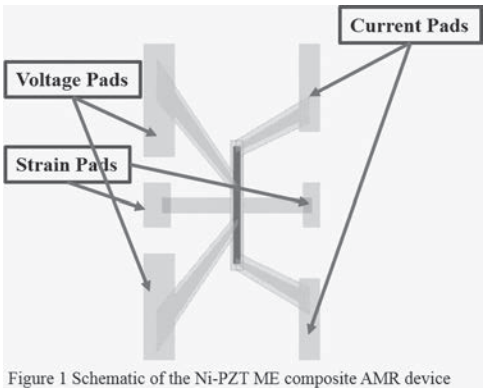


Figure 1 Schematic of the Ni-PZT ME composite AMR device

Fig. 1

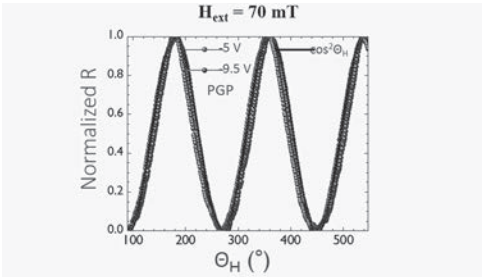


Figure 2 Perpendicular AMR measurements vs the angle of the external magnetic field at different bias voltages

Fig. 2

3:54

HC-11. Strain mediated magnetoelectric coupling in Ni-Mn-In/PLZT multiferroic heterostructure for MEMS device applications. *A. Kumar*[1], S. Pawar[1] and D. Kaur[1] *1. Department of Physics, Indian Institute of Technology Roorkee, Roorkee, India*

Recently, multiferroic heterostructures are gaining popularity for magnetic field sensing applications. The fabrications of rarely studied ferromagnetic shape memory alloys (FSMAs) based multiferroic heterostructures are more fruitful because FSMAs possesses large magnetostriction compared to reported ferromagnetic oxides, terfenol-D and metglas in literature. In this report, the Ni-Mn-In/(Pb,La)(Zr,Ti)O_3 thin film based multiferroic heterostructures have been fabricated with upper (Pb,La)(Zr,Ti)O_3 layer deposited at varying temperature (550 to 650 ^oC) using magnetron sputtering. The structural, ferroelectric, ferromagnetic and magnetoelectric coupling characteristics of the fabricated heterostructures have been studied. The polarization vs electric field and magnetization vs magnetic field measurements reveal the co-existence of ferromagnetic and ferroelectric orders in all the fabricated heterostructures. The highest magnetoelectric coupling coefficient of 1.28 V/cm Oe has been observed at 420 Oe DC magnetic field, 2 Oe AC magnetic field of frequency 1 kHz for PLZT layer deposited at 600 ^oC. Such Ni-Mn-In/(Pb,La)(Zr,Ti)O_3 all thin film based multiferroic heterostructures are appropriate candidate for magnetic field sensing and microelectromechanical systems (MEMS) based devices applications.

1. N.A. Spaldin, S.W. Cheong, and R. Ramesh, Physics Today 63, 38 (2010). 2. J.M. Hu, L.Q. Chen, and C.W. Nan, *Advance Material 28*, 15 (2016) 3. S. Tiwari and S. Vitta, Scientific Report 8, 1 (2018). 4. C. S. Park, A. Khachaturyan, and S. Priya, Applied Physics Letter 100, 192904 (2012) 5. W. Eerenstein, N.D. Mathur, J.F. Scott, Nature, 442(7104), 759 (2006) 6. N.A. Spaldin, R. Ramesh, Nature materials, 18(3), 203 (2019). 7. A. Kumar, S. Pawar, S. Sharma, and D. Kaur, Appl. Phys. Lett. 112, 262106 (2018).

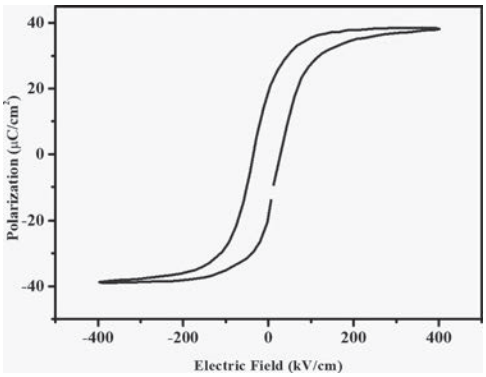


Fig 1. P-E loop for Ni-Mn-In/PLZT heterostructure with PLZT layer deposited at 600 °C sputtering temperature.

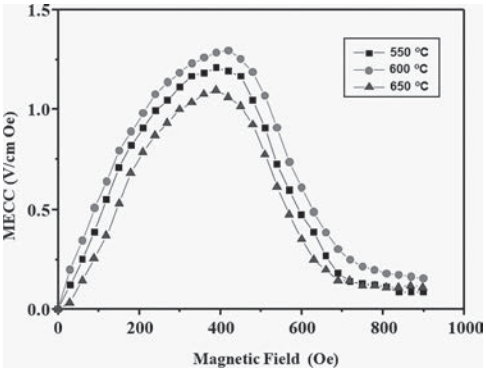


Fig 2. Magnetoelectric Coupling coefficient for Ni-Mn-In/PLZT heterostructures with PLZT layer deposited at 550 °C, 600 °C and 650 °C sputtering temperatures.

4:06

HC-12. Room temperature magnetoelectric response in 2-2 bilayer PNNZT/CTFO thin film deposited by pulsed laser deposition.
A.H. Pandey[1], K. Miriyala[1], N. Kumar[1], N. Sowmya[1], A.R. Kulkarni[1] and N. Venkataramani[1] *1. Department of Metallurgical Engineering and Materials Science, Indian Institute of Technology Bombay, Mumbai, India*

Multiferroic (MF) materials with coexisting ferroelectricity and magnetism provided an avenue to produce large magnetoelectric (ME) response (desired ME response ~1 V/cm.Oe) with effective voltage control of magnetism and power-efficient electric-field-tunable devices [1]. The ME response is realized by a parameter called magnetoelectric voltage coefficient (MEVC), where t is the thickness of the sample and δV is the induced voltage across the piezoelectric phase [1]. With motivation to achieve high MEVC, a 2-2 bilayer composite thin film of multiferroic 0.5Pb(Ni1/3Nb2/3O3-0.35PbTiO3-15PbZrO3 (PNNZT)/Co1.2Ti0.2Fe1.6O4 (CTFO) has been deposited on Pt/Ti/SiO2/Si(100) substrate using pulsed laser deposition technique. The structural investigation by XRD and Raman spectroscopy confirms the formation of pure phase PNNZT/CTFO 2-2 bilayer laminate structure. The piezoresponse force microscopic studies confirm the ferroelectric nature of PNNZT thin films and the nano scale piezo coefficient is ~150 pm/V which is 25% higher than well known PZT thin films. The reported value of magnetization for bulk CTFO is Ms ~60 emu/g and Hc ~130 Oe and we have obtained, Ms ~30 emu/g and Hc ~1.4 kOe for CTFO in bilayer thin film. The PNNZT/CTFO 2-2 bilayer thin film gives a maximum MEVC, ~1.05 V/cm. Oe at a frequency of 1 kHz, implying that the modified composite thin film is a potential candidate for application. Our prior PNNZT/CTFO bilayer thin film yielded MEVC ~0.5 V/cm. Oe at 1 kHz [2], by substituting 0.2 Ti4+ in CoFe2O4, the magnetic properties could be enhanced to provide a higher MEVC of 1.05 V/cm.Oe. The systematic details of this bilayer development will be discussed in this paper.

1. G. Srinivasan, S. Priya and N. X. Sun, Composite Magnetoelectrics: Materials, Structure and Applications, Woodhead Publishing Series (2015). 2. R. Ade, T. Karthik, J. Kolte, V. Sambasiva, A R. Kulkarni and N. Venkataramani, Scripta Mat. 150, 125–129 (2018).

4:18

HC-13. Strong Magnetoelectric Coupling in Mixed Ferrimagnetic-Multiferroic Phases of a Double Perovskite.
D. Oh[1], M. Kim[2,3], Y. Choi[1] and N. Lee[1] *1. Department of Physics, Yonsei University, Seoul, The Republic of Korea; 2. Department of Physics, Seoul National University, Seoul, The Republic of Korea; 3. Center for Correlated Electron Systems, Institute for Basic Science, Seoul, The Republic of Korea*

Exploring new magnetic materials is essential for finding advantageous functional properties such as magnetoresistance, magnetocaloric effect, spintronic functionality, and multiferroicity. Versatile classes of double perovskite compounds have been recently investigated because of intriguing physical properties arising from the proper combination of several magnetic ions. In this study, it is observed that the dominant ferrimagnetic phase is coexisted with a minor multiferroic phase in single-crystalline double-perovskite Er_2CoMnO_6. The majority portion of the ferrimagnetic order is activated by the long-range order of Er^{3+} moments below T_{Er} = 10 K in addition to the ferromagnetic order of Co^{2+} and Mn^{4+} moments arising at T_C = 67 K, characterized by compensated magnetization at T_{Comp} = 3.15 K. The inverted magnetic hysteresis loop observed below TComp can be described by an extended Stoner–Wohlfarth model. The additional multiferroic phase is identified by the ferroelectric polarization of ~0.9 μC/m^2 at 2 K. The coexisting ferrimagnetic and multiferroic phases appear to be strongly correlated in that metamagnetic and ferroelectric transitions occur simultaneously. The results based on intricate magnetic correlations and phases in Er_2CoMnO_6 enrich fundamental and applied research on magnetic materials through the scope of distinct magnetic characteristics in double perovskites.

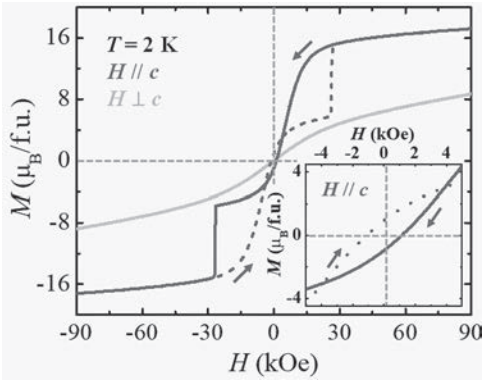


Fig 1. Isothermal magnetization (*M*) of the Er_2CoMnO_6 crystal in H//c and H⊥c, measured at T = 2 K up to 90 kOe after ZFC. The inset shows the magnified view in the range of H = ±10 kOe of the hysteresis loop in H//c.

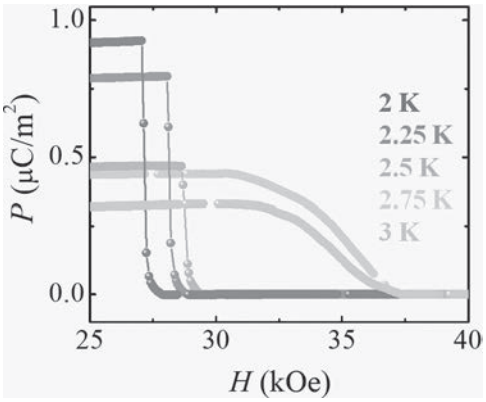


Fig 2. Temperature evolution of ferroelectric polarization at T = 2, 2.25, 2.5, 2.75 and 3 K shown in the range of 25–40 kOe.

Session HD
MAGNETIC RECORDING II
Eric Fullerton, Chair
University of California San Diego, La Jolla, CA, United States

CONTRIBUTED PAPERS

1:30

HD-01. The Role of Inverse Faraday Effect and Magnetic Circular Dichroism in All Optical Switching. R. Guedas-Garcia[1], F. Garcia-Sanchez[1], *E. Martinez*[1] and V. Raposo[1] *1. Fisica Aplicada, Universidad de Salamanca, Salamanca, Spain*

Ultrafast control of magnetic state by circular polarized femtosecond laser pulses has been experimentally demonstrated by the nucleation of inverted regions [1], domain wall displacement [2] or the generation of an inverted domain along the path of a moving laser [3]. However, the underlying physics governing these processes still remain unclear. The most adopted hypothesis are the induction of a transient magneto-optical field due to the inverse Faraday Effect (IFE) and/or the Magnetic Circular Dichroism (MCD). Here we present micromagnetic simulations based on the Landau-Lifshitz-Bloch equation [4] that describes the magnetization dynamics in the ultrashort time scale coupled to the two temperatures model, which describes the temporal evolution of the electron and phonon subsystems of the material. The IFE is included as a magneto-optical field, whereas the MCD is taken into account by considering the different energy absorption rates depending on the magnetic state and the helicity of the laser pulses. With adequate combinations of laser fluence and the IFE-induced magneto-optic field, our modeling reproduces the magnetic states observed experimentally (see Fig. 1a). However, the MCD is not able to reproduce clearly all the domain patterns (see Fig. 1b), neither the domain wall displacement as the ones obtained in [2]. Our modeling allows to elucidate the physical mechanisms responsible for experimental observations, and it will be useful for further research of optical control of the magnetization.

[1] K. Vahaplar *et al.*, "All-optical magnetization reversal by circularly polarized laser pulses: Experiment and multiscale modeling," *Phys. Rev. B*, vol. 85, no. 10, p. 104402, 2012. [2] Y. Quessab *et al.*, "Helicity-dependent all-optical domain wall motion in ferromagnetic thin films," *Phys. Rev. B*, vol. 97, no. 5, pp. 1–8, 2018. [3] R. Medapalli *et al.*, "Mechanism of all-optical control of ferromagnetic multilayers with circularly polarized light," *arXiv*, pp. 2–6, 2016. [4] V. Raposo, *et al.*, "Micromagnetic Modeling of All-Optical Switching," *IEEE Trans. Magn.*, pp. 1–6, 2019.

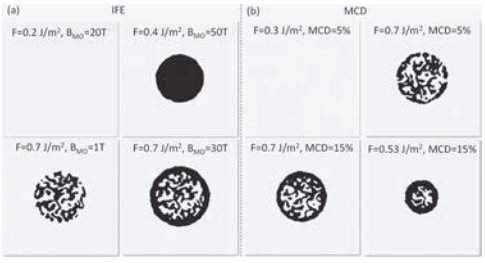


Fig. 1. Final magnetic states after 25 pulses of 200fs of duration for different combinations of the fluence (F) and B_{MO} for the IFE (a) and percentage of circular dichroism for the MCD (b).

1:42

HD-02. Improving all-optical switching efficiency by tuning the femtosecond pulses into the infrared wavelength range. R. John[1], *J. Walowski*[1], C. Müller[2], M. Berritta[3], D. Hintzke[4], O. Chubykalo-Fesenko[5], T. Santos[6], H. Ulrichs[7], R. Mondal[4], P.M. Oppeneer[3], U. Nowak[4], J. McCord[2] and M. Münzenberg[1] *1. Greifswald University, Greifswald, Germany; 2. Kiel University, Kiel, Germany; 3. Uppsala University, Uppsala, Sweden; 4. Konstanz University, Konstanz, Germany; 5. CSIC, Madrid, Spain; 6. Western Digital, San Jose, CA, United States; 7. Göttingen University, Göttingen, Germany*

In basic research as well as application development, magnetization manipulation remains an indispensable tool [1]. The energy transfer from the electrons to the spins is the basis for the response dynamics to optical laser excitation and thus, it determines the speed of ultrafast magnetization. The material FePt gained a special interest in magnetic storage development for heat-assisted magnetic recording [2]. However, in a seminal experiment, all-optical writing has been demonstrated for FePt nanoparticles of a magnetic hard disc media, by Lambert et al. in Science 2014 [3]. Despite a thorough investigation, the involved processes have not been disentangled entirely yet, leaving the mechanism unclear, and opening many questions about the extension of possibilities for all-optical writing as a general mechanism. In the meantime, writing experiments by single laser spots point to an asymmetric writing per each shot. As was consistently observed in different groups [4,5,6]. In the current understanding of the interaction of ultrafast excitation and heating, the influence of magnetic dichroism and the presence of the inverse Faraday effect jointly work as forces causing magnetization reversal. We calculate the switching rates of the individual FePt nanoparticles in ab-initio calculations of the optical effects (inverse Faraday effect and magnetic dichroism induced heating) included in thermal modelling. The latter then provides switching rates for the ensembles. We can trace the different processes from the beginning of the laser pulse impact [4]. In addition, this theoretical description allows us to optimize the required number of shots to write the magnetization of FePt nanoparticles and to pinpoint how to optimize the all-optical writing by tuning the laser fluence and wavelength. We review these recent developments that may lead to address an individual nanosized magnetic element in the future all-optically, for writing magnetic memory.

[1] J. Walowski and M. Münzenberg, J. Appl. Phys., 120, 140901 (2016). [2] J. Mendil et al., Sci. Rep., 4, 3980 (2014). [3] C.-H. Lambert et al., Science, 345,1337-1340, (2014). [4] R. John et al., Scientific Reports, 7, 4114 (2017). [5] M.S. El Hadri et al., Appl. Phys. Lett., 108, 092405 (2016). [6] Y.K. Takahashi et al., Phys. Rev. Applied, 6, 054004 (2016).

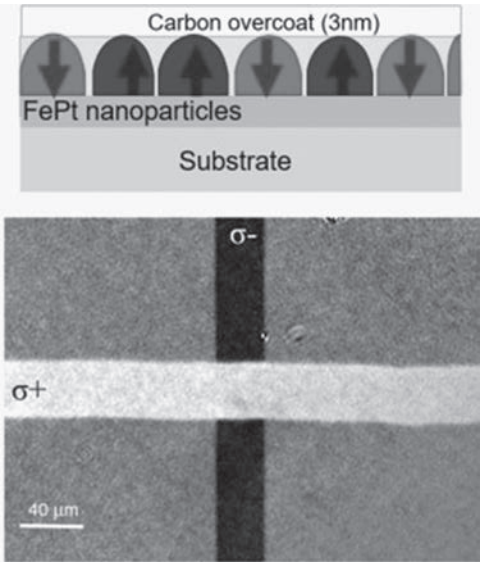


Fig 1. Top: Schematics of FePt grains showing the up or down magnetization entering our rate model. Below: Writing and overwriting the magnetization in a FePt granular medium, starting in the demagnetized state (50% of grains with down, 50% with up magnetization).

1:54

HD-03. Plasmonic layer-selective all-optical switching of magnetization with nanometer resolution. *C. Davies*[1,2], D. Ignatyeva[3,4], D. Sylgacheva[3,4], A. Tsukamoto[5], H. Yoshikawa[5], P. Kapralov[4], A. Kirilyuk[2], V. Belotelov[3,4] and A. Kimel[1,6] *1. Institute for Molecules and Materials, Radboud University, Nijmegen, Netherlands; 2. FELIX Laboratory, Radboud University, Nijmegen, Netherlands; 3. Faculty of Physics, Lomonosov Moscow State University, Moscow, Russian Federation; 4. Russian Quantum Center, Moscow, Russian Federation; 5. Nihon University, Tokyo, Japan; 6. Moscow Technological University, Moscow, Russian Federation*

All-optical magnetization reversal with femtosecond laser pulses facilitates the fastest and least dissipative magnetic recording[1], but writing magnetic bits with spatial resolution better than the wavelength of light has so far been seen as a major challenge, making the application of optical techniques in recording technically challenging or even impossible. Here, inspired by electromagnetic simulations, we experimentally demonstrate that using light with the wavelength of 800 nm and without any magnetic fields, it is possible to obtain full control over two magnetic bits separated by just 80 nm. In our experiment, two bits are represented by two 10-nm thick GdFeCo layers, separated by a 80-nm thick layer of Si_3N_4, and mounted on a glass prism (Fig. 1 (a)). Upon focusing a single femtosecond laser pulse through the glass prism on to a surface of the magnetic bilayer, we toggle the magnetization exclusively within a single magnetic nanolayer without affecting the other one (Fig. 1 (b)). The choice of the toggled layer is enabled by the excitation of a plasmon-polariton[2] at a targeted interface of the nanostructure, and realized merely by rotating the polarization-axis of the linearly-polarized ultrashort optical pulse by 90°. The underlying mechanism is robust, well reproducible and relies on the polarization-dependent excitation of plasmon-polaritons in the magnetic nanostructure. Our results unveil a new tool that can be deployed to switch magnetization in targeted nanolayers of heterostructures, and paves the way to increase the density of opto-magnetic recording by a factor of at least 2.

[1] T. A. Ostler *et al.*, Nature Comms. 3, 666 (2012). [2] S. A. Maier, "Plasmonics: fundamentals and applications." Springer Science & Business Media. (2007).

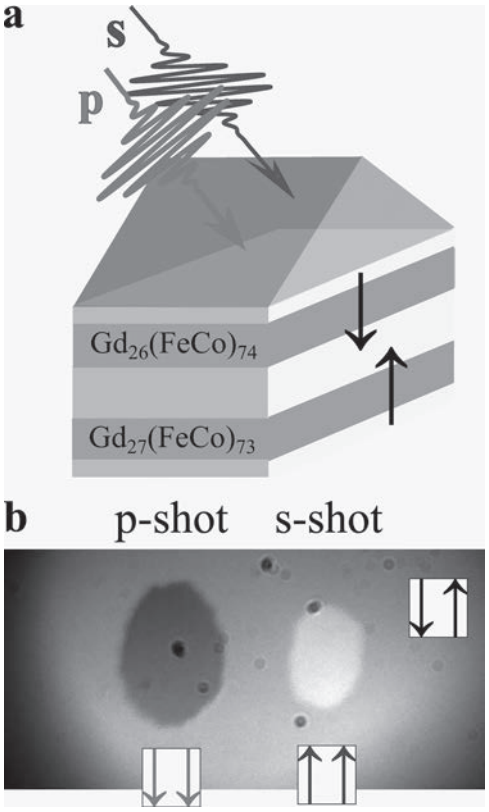


Fig. 1 (a) Physical scheme and sample design. The arrows indicate the polarity of the Gd magnetization in the indicated layer, before exposure to any optical pulses. (b) Raw magneto-optical image, of width 100 μm, taken after exposing the multi-layered structure to a p-polarized (left spot) and s-polarized (right spot) optical pule. The left and right arrow in the boxes indicate the orientation of the magnetization of Gd within the top $Gd_{26}(FeCo)_{74}$ and bottom $Gd_{27}(FeCo)_{73}$ layer respectively.

2:06

HD-04. Optimisation of magnetisation reversal in granular HAMR media. *A. Meo*[1], S.E. Rannala[2], S. Ruta[2], R.W. Chantrell[2], P. Chureemart[1] and J. Chureemart[1] *1. Department of Physics, Mahasarakham University, Mahasarakham, Thailand; 2. Department of Physics, University of York, York, United Kingdom*

Perpendicular magnetic recording cannot provide the required increase in storage density due to the recording trilemma, and a technology that relies on the aid of heat during the writing, called heat assisted magnetic recording (HAMR), was proposed[1,2]. However, HAMRs require optimisation to become a real alternative. Therefore, we aim to investigate the writing process of HAMR granular media using a multiscale approach combining atomistic simulations and micromagnetic calculations based on Landau-Lifshitz-Bloch (LLB) formalism. Atomistic approaches can provide temperature dependent equilibrium quantities, required by the micromagnetic model, and details on the magnetisation dynamics, while micromagnetic simulations allow to simulate large systems for long times and span over a large set of parameters. We simulate HAMR magnetisation dynamics for a system of 400 identical FePt grains with a 10% distribution of Curie temperature Tc (σ_{Tc}) for different heat pulse peak temperatures by LLB calculations and we compare it with atomistic results. Fig 1(a) shows that LLB dynamics, atomistically parametrised, reproduces well the atomistic magnetisation reversal, proving its reliability. We then use it to obtain the switching probability of such grains as function of laser pulse peak temperature and length, as shown in Fig 1(b), due to the small computational cost. The switching probability is not abrupt and does not reach the maximum due to the nature of reversing

dynamics at elevated temperature (close to Tc). These findings agree with the results presented in [3], especially considering that we have simulated an isolated grain. Our initial results show the potential of such a multi-scale approach to simulate realistic systems accounting for distributions of size and magnetic properties, and emphasise the importance of optimising HAMR properties. Based on these results we plan to simulate extended systems investigating the effect of different parameters, such as the effect of the heat profile.

1) Robert E. Rottmayer, Sharat Batra, *et al,* Heat-Assisted magnetic recording, IEEE, Transactions on Magnetics, 42(10):2417–2421, 2006 2) D. Weller, G. Parker, *et al*, J. Vac. Sci. Technol. B, Nanotechnol. Microelectron. Mater. Process. Meas. Phenom. 34, 060801 (2016). 3) Z. Liu, P.-W. Huang, G. Ju, and R.H. Victora, Appl. Phys. Lett. 110, 182405 (2017).

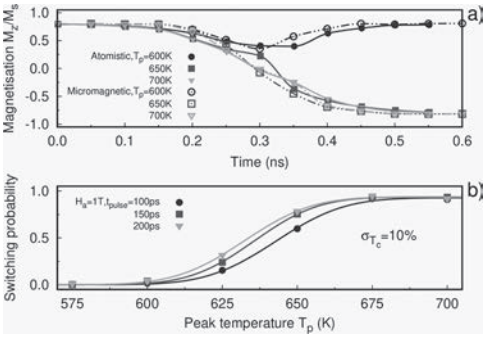


Fig 1. a) Comparison of atomistic and micromagnetic HAMR magnetisation dynamic of a FePt grain for different peak temperatures (Tp), b) micromagnetic switching probability as function of Tp and pulse length for 10% σ_{Tc}.

2:18

HD-05. A new method for fabricating granular FePt-$L1_0$ HAMR media with well-controlled nucleation and growth. *B. Zhou*[3,1], C. Xu[3,1], Y. Yan[3,1], B. Varaprasad[2,1], D.E. Laughlin[3,1] and J. Zhu[2,1] *1. The Data Storage Systems Center, CMU, Pittsburgh, PA, United States; 2. Department of Electrical and Computer Engineering, CMU, Pittsburgh, PA, United States; 3. Department of Materials Science and Engineering, CMU, Pittsburgh, PA, United States*

In HAMR, the recording happens at elevated temperatures, just below the media Curie temperature (T_c), because of the limitation of the write-head field. Thus, increasing the FePt grain height is crucial to counter the thermally induced transition jitter, especially at small grain size.[1] Therefore, it is desirable to have small, isolated and columnar shapes of FePt grains with narrow size distributions. Amorphous C is a common choice as part of the grain boundaries in order to obtain small isolated FePt grains in the nucleation stage, but it also presents many challenges, such as the formation of a double layer, the lateral growth and the bimodal distribution, all of which limit the columnar growth of FePt grains.[2-4] Thus, the C needs to be replaced in the nucleation stage. These challenges could potentially be overcome by developing pre-defined and robust matrix boundaries, which define the nucleation sites and force the FePt grains to grow columnarly with the boundaries together in the later stage of the film growth. As shown in Fig. 1 (a), such matrix template layer, which consists of a sacrificial material (Au) embedded in a matrix of another material (SiO_2), can be fabricated by co-sputtering on top of the MgO underlayer. After forming the desired microstructure, Au can be selectively etched from the SiO_2 matrix and MgO underlayer by a commercially available Au etchant (Transene Au etchant TFA). The results shown in Fig. 1 (b) to (c), which correspond to the samples in step 1 and 2, demonstrate that the SiO_2 matrix can be formed by the above-mentioned methodology. Fig. 1 (d), which corresponds to the sample in step 3, demonstrates that the FePt grains can be forced to nucleate in the trenches of the matrix where the MgO surface is exposed, with their c-axes perpendicular to the film plane. The details of the effects of the template layer on the nucleation and growth of FePt grains will be presented.

[1] Y. Qin and J. Zhu, IEEE Magnetics Letters, Vol. 10, 6502305 (2019) [2] B. S. D. Ch. S. Varaprasad, M. Chen, Y. K. Takahashi *et al*., IEEE Transactions on Magnetics, Vol. 49, p. 718 (2013) [3] D. Weller, O. Mosendz, G. Parker *et al.*, Physica Status Solidi A, Vol. 21, p. 1245 (2013) [4] B. Zhou, B. S. D. C. S. Varaprasad, E. Zhang *et al.*, IEEE Transactions on Magnetics, Vol. 54, 3201104 (2018)

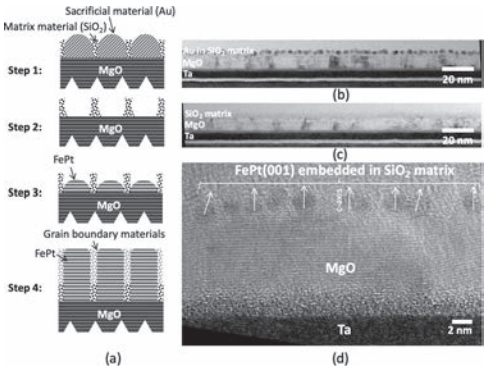


Fig. 1 (a) Schematic of various fabrication steps involved, formation of the template layer, selective etch of the sacrificial material, FePt nucleation and growth; the cross-section TEM images corresponding to step 1 (b), step 2 (c) and step 3 (d). White arrows indicate the c-axis of FePt grains.

2:30

HD-06. Utilizing Boron-nitride and carbon as the hybrid grain boundary materials for controlling the grain size distribution in HAMR media. *B. Zhou*[1,2], Y. Yan[1,2], C. Xu[1,2], B. Varaprasad[3,2], D.E. Laughlin[1,2] and J. Zhu[3,2] *1. Department of Materials Science and Engineering, CMU, Pittsburgh, PA, United States; 2. The Data Storage Systems Center, CMU, Pittsburgh, PA, United States; 3. Department of Electrical and Computer Engineering, CMU, Pittsburgh, PA, United States*

Grain-to-grain Curie temperature variation (σT_c) in heat-assisted magnetic recording (HAMR) media can be reduced by controlling FePt grains size distribution. [1] However, the elevated processing temperature required for obtaining the highly ordered $L1_0$-FePt makes it challenging to obtain a microstructure with narrow grain size distribution. Although the commonly adopted FePt-C media produces well-separated FePt grains, the amorphous carbon grain boundaries appear to actually allow the continuous nucleation of new FePt grains on the MgO underlayer even at late stage of the thin film growth process. [2] As a result, this continuous nucleation of new FePt grains during film growth often lead to a broad and bimodal distribution of FePt grain size. One way to suppress the continuous nucleation of FePt grains and to gain control the grain size distributions in HAMR media is to use different grain boundary materials other than just carbon. In this study, we present a study utilizing boron-nitride (BN) and carbon(C) together as the hybrid grain boundary materials to control the microstructure of FePt grains. The thin film stack of Ta(5)|MgO(9)|FePt-$C_{35vol.\%}$ or FePt-$C_{30vol.\%}$-$BN_{5vol.\%}$(3 nm) were sputtered on a-SiO_2 substrate using an AJA Orion-8 system with base pressure better than 1 x 10^{-8} torr. All layers up to MgO were deposited at room temperature, while FePt-C or FePt-C-BN layer was deposited at 650°C. The results shown in Fig. 1 (a) and (b) are the in-plane microstructure corresponding to the samples of FePt-C and FePt-C-BN, whose grain size distributions are shown in Fig. 1(c) and (d). It can be clearly observed that the formation of the small particles is suppressed by utilizing C-BN hybrid grain boundaries. The study shows that the grain size distribution of FePt can be significantly improved.

[1] Y. Kubota, Y. Peng, Y. Ding et al., IEEE Transactions on Magnetics, Vol. 54, 3201206 (2018) [2] B. Zhou, B. S. D. C. S. Varaprasad, E. Zhang et al., IEEE Transactions on Magnetics, Vol. 54, 3201104 (2018)

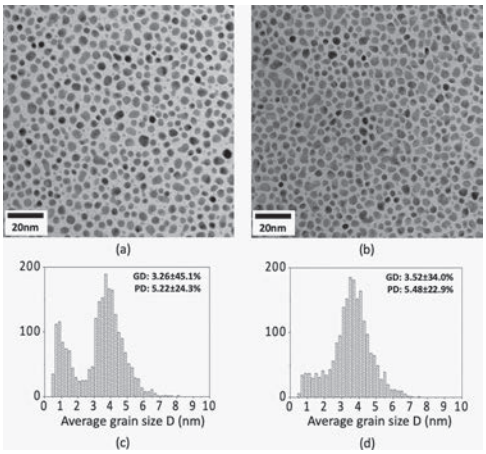


Fig. 1 The in-plane microstructures and grain size distributions of 3nm-thick FePt-C (a), (c) and FePt-C-BN (b), (d).

2:42

HD-07. Temperature-Dependent Studies of Coupled $Fe_{55}Pt_{45}/Fe_{49}Rh_{51}$ Thin Films and Patterned elements. R.A. Griffiths[1], J.L. Warren[1], C. Barton[1,2], J.J. Miles[1], P.W. Nutter[1] and *T. Thomson[1] 1. School of Computer Science, University of Manchester, Manchester, United Kingdom; 2. National Physical Laboratory, Teddington, United Kingdom*

Equiatomic $Fe_{49}Rh_{51}$, with its highly unusual antiferromagnetic to ferromagnetic phase transition at approximately 370 K [1], provides the ability to create artificial multifunctional materials when combine with high-anisotropy magnetic thin films in an exchange-mediated structure [2]. We investigate the temperature dependence of switching in $L1_0$ $Fe_{55}Pt_{45}/Fe_{49}Rh_{51}$ bilayer thin films, where the $Fe_{49}Rh_{51}$ assists the switching of the $Fe_{55}Pt_{45}$ at modestly increased temperatures [3]. A simple layered macrospin model is able to capture the switching characteristics of these films and shows good agreement with experimental results, fig. 1. Patterned $L1_0$ $Fe_{55}Pt_{45}/Fe_{49}Rh_{51}$ structures measured using the anomalous Hall effect, fig.2, show a similar temperature-dependent switching behavior, paving the way for reduced switching fields in future applications including heat-assisted bit-patterned-media recording and spintronic devices.

[1] J.S. Kouvel and C. C. Hartelius, "Anomalous magnetic moments and transformations in ordered alloy FeRh", J. Appl. Phys. 33 (1962) 1343-1344. [2] J.U. Thiele et al. "FeRh/FePt exchange spring films for thermally assisted magnetic recording media", Appl. Phys. Lett. 82 (2003) 2859-2861. [3] R.A. Griffiths, T. Thomson et al. "Temperature-Dependent Studies of Coupled Fe55Pt45/Fe49Rh51 Thin Films" Phys. Rev. Appl. 10 (2018) 054015.

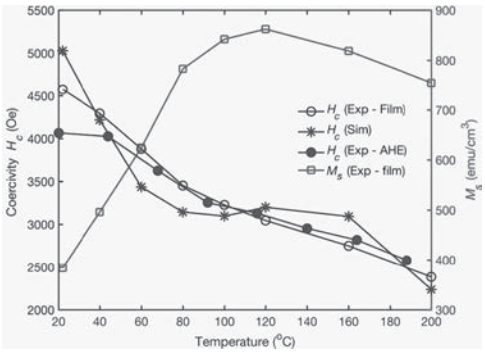


Fig.1: Temperature dependence of coercivity, Hc (experimental - open blue circles), macrospin model (blue stars) and patterned island (closed blue circles), and saturation moment, Ms, (open red squares) for the Fe55Pt45/Fe49Rh51 bilayer.

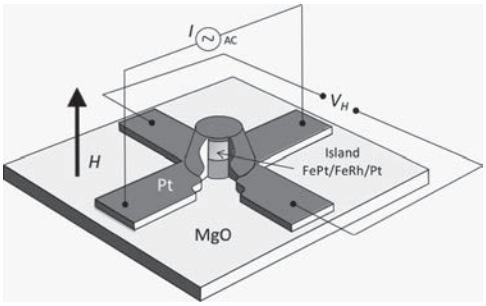


Fig. 2: Pt Hall cross and AHE measurement geometry. The FePt/FeRh island is located under the centre Pt Hall cross, where the width of the Hall cross arms is 2.5 µm. AHE measurements are taken by applying an AC current, I, down one arm of the cross and the resulting Hall voltage, V_H, is measured across the adjacent arm as the applied magnetic field (H) is varied.

2:54

HD-08. Using magneto-structural phase transitions to enhance the coercivity of ferromagnetic films. *R. Need*[1], J. Lauzier[2], L. Sutton[2], B.J. Kirby[1] and J. de la Venta[2] *1. NIST Center for Neutron Research, Gaithersburg, MD, United States; 2. Physics, Colorado State University, Fort Collins, CO, United States*

Storing information in magnetic recording technologies requires careful optimization of the recording media's magnetic properties. For example, heat-assisted magnetic recording (HAMR) relies on a pre-recording heating step that momentarily lowers the coercivity of the ferromagnetic recording media, and thereby decreases the energy required for each writing operation. However, reducing the coercivity of common storage media can require local temperature increases of several hundred Kelvin, which in turn can cause lateral heat spreading and limit recording rates. Here, we describe a mechanism for creating dramatic changes in the coercivity of ferromagnetic films over small temperature ranges, by coupling them to an adjacent layer that undergoes a structural phase transition with large volume change. The method is demonstrated in Ni/FeRh bilayers where the Ni layer was deposited at 300 K and 523 K, above and below the FeRh metamagnetic transition at ~370 K. When the Ni layer is grown at high temperatures and then cooled, the ~1% FeRh lattice contraction strains the overlying Ni and promotes domain wall pinning that increases the coercivity by 500% over a 50 K temperature window. This ability to thermally tune the coercivity of ferromagnetic materials, if as general as our model suggests, may open up new materials to HAMR and new avenues to magnetic information storage.

3:06

HD-09. Impact of Straightened Thermal Profiles Generated by Gapped Near Field Transducers on Recording SNR. M. Yin[1], *C. Chow*[1], Y. Qin[1], J.A. Bain[1] and J. Zhu[1] *1. Data Storage Systems Center, Carnegie Mellon University, Pittsburgh, PA, United States*

Transition curvature is a limiting factor for areal density (AD) gain in heat assisted magnetic recording (HAMR) [1]. It arises from the curved thermal profile generated by a near field transducer (NFT). In the NFT gap device presented in [2], bringing the plasmonic underlayer closer to the NFT results in a two lobed temperature T profile. We quantitatively assess the relative impact on recording signal-to-noise ratio (SNR) using thermal profiles with reduced curvature generated by the split pole-gapped NFT recording head described in [3]. The hotspot shape is changed by reducing the interlayer (IL) thickness t_{IL} in the media stack so the plasmonic heatsink is closer to the gapped NFT. Fig. 1 shows the normalized change in T from ambient (ΔT) in the storage layer for (a) t_{IL} = 5 nm and (b) t_{IL} = 10 nm. The thinner IL results in a straighter thermal profile in the cross track direction but a larger cross track size. (Thermal management is not considered, but reduction of the IL thermal resistance and a wider hotspot will both lower ΔT_{max} for a given incident power.) The effect on SNR from the tradeoff between reduced curvatures versus adjacent track interference (ATI) from wider spot size is assessed by micromagnetic modelling. A center track is recorded on media with Curie temperature T_C = 750K ± 2%, center-to-center grain spacing of 6 nm ± 2%, and room temperature anisotropy field H_k = 80 kOe. Two side tracks are written to measure ATI on the center track. Recording is performed at T_{max} of 800K, 850K, and 900K by combining a uniform write field and the thermal profiles in Fig. 1. A reader with a Gaussian sensing function is used to read the center track. Fig. 2 shows the resulting contours of constant SNR at optimum T_{max} vs. bit and track density. The straighter, wider thermal profile in Fig. 1 does not offer significant AD gain. At 10 dB, the more curved profile has a maximum AD of 1.65 Tb/in^2 at 1100 kTPI. The straighter profile has a maximum AD of 1.5 Tb/in^2 at 840 kTPI. Detailed discussion on how track density suffers more than bit density improves in this scenario will be presented.

[1] Rea, Chris et al. "Areal-Density Limits for Heat-Assisted Magnetic Recording and Perpendicular Magnetic Recording," IEEE Transactions on Magnetics, vol. 52, no. 7, pp. 1–4, Jul. 2016. [2] Rea, Chris et al. "Heat Assisted Magnetic Recording Performance and Integration Challenges." Proc. SPIE. Vol 9201, Optical Data Storage 2014, 92010K, Sep. 2014. [3] Chow, Cheng-Ming, and James A. Bain. "A Split-Pole-Gapped NFT Write Head Design for Transition Curvature Reduction in Heat-Assisted Magnetic Recording." IEEE Transactions on Magnetics, 2018, 1–4.

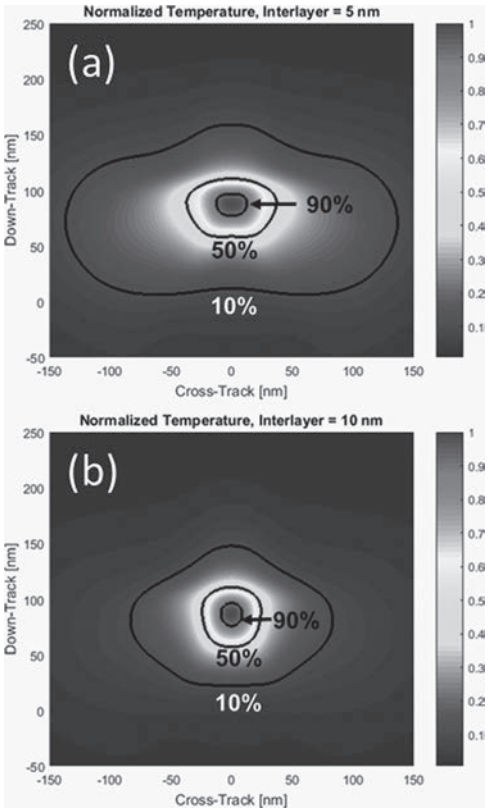


Figure 1. Normalized ΔT for (a) t_{IL} = 5 nm and (b) t_{IL} = 10 nm.

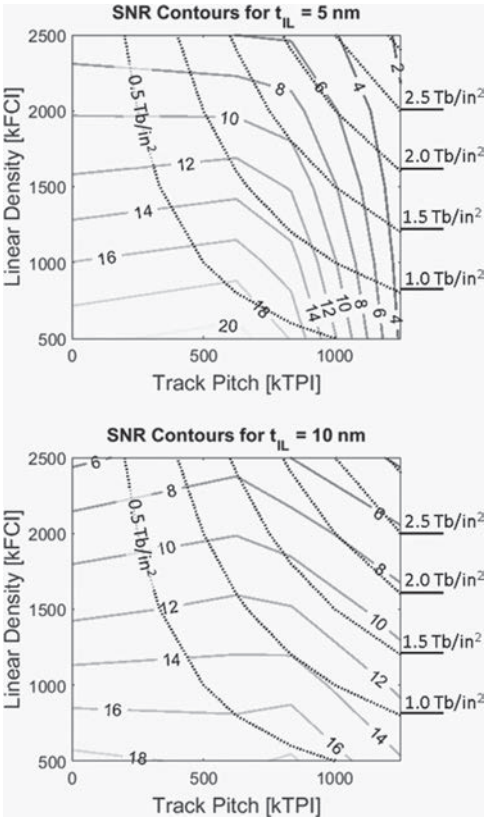


Figure 2. SNR plots for (a) t_{IL} = 5 nm and (b) t_{IL} = 10 nm.

3:18

HD-10. Magnetic in-plane components of FePt nanogranular film on polycrystalline MgO underlayer for heat-assisted magnetic recording media. *Y. Takahashi*[2], J. Wang[1,2], S. Hossein[2], T. Ohkubo[2] and K. Hono[2] *1. International Center for Young Scientists (ICYS), National Institute for Materials Science (NIMS), Tsukuba, Japan; 2. Research Center for Magnetic and Spintronic Materials, National Institute for Materials Science (NIMS), Tsukuba, Japan*

A systematic study is conducted on the effect of MgO substrate/underlayer in terms of the surface roughness, grain boundary, and crystallographic texture on the magnetic in-plane components of the FePt-based heat-assisted magnetic recording (HAMR) media (Fig.1). Cross-sectional transmission electron microscope observations revealed that good (001) texture can be developed in FePt granular films even when they are grown on a rough surface of a single crystal-MgO (001) substrate or across the grain boundaries of a (001)-textured polycrystalline-MgO underlayer. The misoriented FePt grains with magnetic easy axes (c-axes) tilted away from the film normal direction mainly originate from their epitaxial growth on an initially misoriented MgO underlayer grains. Micromagnetic simulation results revealed that the FePt grains with misorientation angles larger than ~20° are attributed to the detected magnetic in-plane components (medium noise). Based on these experimental results, we discuss how to improve the (001) texture of the polycrystalline underlayer as well as to develop FePt-based HAMR media with the enhanced signal-to-noise ratio.

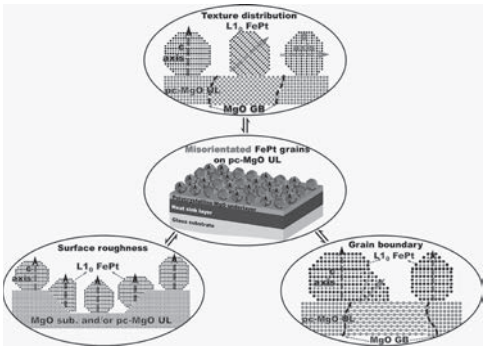


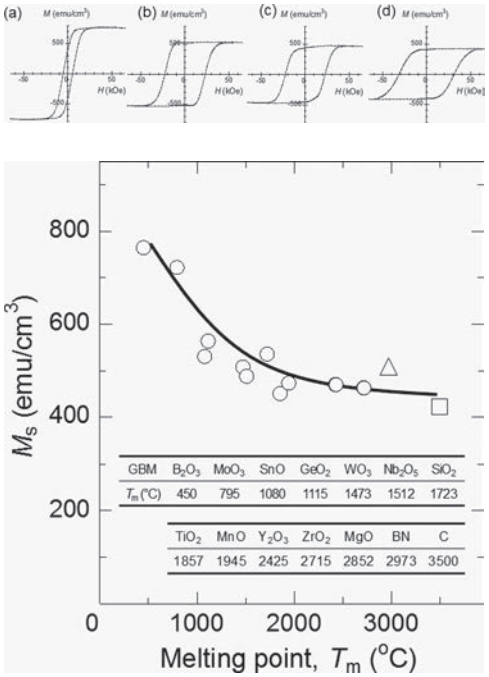
Fig.1 The effect of MgO substrate/underlayer in terms of the surface roughness, grain boundary, and crystallographic texture on the magnetic in-plane components of the FePt-based HAMR media

3:30

HD-11. Effect of melting point of grain boundary material on nanostructure and magnetic properties for $L1_0$ typed FePt granular media. *T. Saito*[1], K. Tham[2], R. Kushibiki[2] and S. Saito[1] *1. Department of Electronic Engineering, Graduate School of Engineering, Tohoku University, Sendai, Japan; 2. Tanaka Kikinzoku Kogyo KK, Tsukuba, Japan*

For granular typed perpendicular media with high areal recording density, it is necessary to realize columnar structure, high *c*-axis orientation, well magnetically isolation, and high magnetocrystalline anisotropy (K_u). In the case of conventional CoPt based granular media deposited at room temperature, the critical thickness of columnar growth (d_{cri}) and the amount of stacking faults (P_{fcc}) strongly depend on melting point (T_m) of grain boundary material (GBM). The GBM with low T_m results in well phase separation from magnetic grains in granular media, which leads to increasing d_{cri} and decreasing P_{fcc}[1,2]. On the other hand, for heat assisted magnetic recording as next generation technology, FePt based granular media on flat MgO underlayer deposited at high substrate temperature is a promising candidate. Although researches about GBM focused on electronegativity[3], surface energy[4] and cohesive energy[5] has already reported, T_m of GBM has not been focused. Therefore, we have evaluated the effect of T_m of GBM on phase separation, nanostructure, and intergranular exchange coupling for $L1_0$ typed FePt granular media with various GBMs. Figs. 1 show typical *M–H* loops of $L1_0$ typed ($Fe_{50}Pt_{50}$)–30 vol% (a) B_2O_3 (T_m (°C): 450), (b) SnO (T_m: 1080), (c) MnO (T_m: 1945), and (d) C (T_m: 3500) media with the thickness of 10 nm. Although volume ratio of non-magnetic GBM to FePt is the same amount as 30 vol%, magnetic properties such as M_s, H_c, and α are totally different among these media. Increasing H_c and decreasing α with raising T_m suggest suppression of intergranular exchange coupling. Fig. 2 shows M_s for FePt granular media plotted against T_m of the GBMs. When T_m increases from 450 °C to 3500 °C, M_s decreases from 760 to 420 emu/cm^3 monotonously. M_s for granular media reflects degree of phase separation mentioned above. These results suggest that there is trade-off relationship between promoting phase separation and suppressing intergranular exchange coupling for T_m of the GBM on the condition of a flat MgO underlayer. In the presentation, sheet texture, degree of order obtained from in-plane XRD, and K_u measured by high field torque magnetometer with 9 T will be also discussed.

[1] R. Kushibiki et al., IEEE Trans. Magn., vol. 53, p. 3200604 (2017) [2] K. K. Tham et al., Jpn. J. Appl. Phys., vol. 55, p. 07MC06 (2016) [3] T. Ono et al., The 13th Joint MMM-Intermag Conference, CV-08, January, San Diego (2016) [4] S. D. Granzet et al., Eur. Phys. J. B, vol. 86, p. 81 (2013) [5] T. Shiroyama et al., IEEE Trans. Magn., vol. 49, pp. 3616 (2013)



3:42

HD-12. Observation of Out-of-Plane Precession in All-in-Plane Spin-Torque Oscillator for Microwave-Assisted Magnetic Recording. W. Zhou[1], S. Hossein[1], T. Taniguchi[2], S. Tamaru[2], *Y. Sakuraba*[1], S. Kasai[1], H. Kubota[2] and K. Hono[1] *1. National Insititute for Materials Science (NIMS), Tsukuba, Japan; 2. National Institute of Advanced Industrial Science and Technology (AIST), Tsukuba, Japan*

The main challenge for realizing MAMR is to develop a spin-torque oscillator (STO) that can generate strong ac magnetic field. A new design of STO has been recently proposed, where only a soft magnetic layer is exploited as the polarizer. [1] It was predicted by both macro-spin and micromagnetic simulations that the magnetization of both polarizer and FGL oscillate together in out-of-plane precession (OPP) mode during operation under perpendicular field of about 1T from the writing pole. [2,3] However, the oscillation dynamics has not been clarified experimentally so far because

of the complex dynamics excited by the interaction between oscillating FGL and polarizer. In this study, we fabricated all-in-plane type STO and investigate its oscillating behavior. A 7-nm-thick $Fe_{67}Co_{33}$(FeCo) layer was used as the FGL while a 7-nm-thick $Ni_{80}Fe_{20}$(NiFe) layer was used as the polarizer, which were separated by 5-nm-thick Ag spacer. The thin film was microfabricated into circular shape nano-pillar device having the diameter of 28 nm. For characterization of the STO, the resistance (R), dV/dI, and the power spectral density of the device were measured with increasing bias DC voltage (U) under a constant H. Fig. 1 shows the MR curve measured under low U. Both magnetizations are aligned to the perpendicular direction over ~ 0.8 T. With Uincreased to ~ 20 mV under 0.81T, the magnetization of NiFe was reversed to the direction opposite to H by STT as indicated by the peak in dV/dI(Fig. 2(a)). As shown in the PSD mapping (Fig. 2(b)), further increase of U led to the emergence of multiple microwave signals. Here the strong microwave signal showing red shift is the result of both the FGL and the polarizer in OPP mode oscillation with different f. The microwave signals marked f_{NiFe} and f_{FeCo} in Fig. 2(b) reflect OPP mode oscillation of the NiFe and FeCo.[4] Such dynamics were well reproduced by micromagnetic simulation, as shown in Fig. 2(c). This result indicates that all-in-plane STO works to realize OPP mode oscillation in FGL and generate ac magnetic field.

[1] J.-G. Zhu, Joint MMM-Intermag Conference (2016), AB11. [2]T. Taniguchi, J. Magn. Magn. Mater. 452, 464 (2018). [3] H. Sepehri-Amin *et al.*, J. Magn. Magn. Mater. 476, 361 (2019). [4] W. Zhou *et al.*, Appl. Phys. Lett. 114, 172403 (2019).

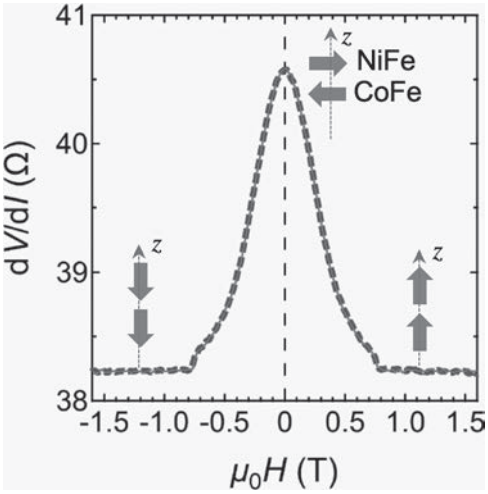


Fig 1. dV/dI-Hcurve measured at low U.

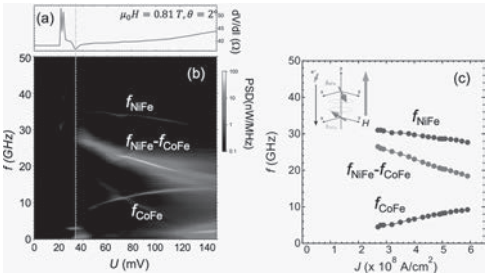


Fig 2. (a) (b) The dV/dI and mapping of PSD under $\mu_0 H$= 0.81 T. (c) f of OPP mode oscillation of NiFe and FeCo obtained from micromagnetic simulation.

3:54

HD-13. Asymmetric Far Track Erasure by Domain Walls in Recording Heads. *A. Goncharov*[1], A. Bashir[1] and P. Van Der Heijden[1] *1. Western Digital, San Jose, CA, United States*

Modern recording heads use magnetic shields around the magnetic write pole to control stray fields in the recording media. Although the primary purpose of the shield is to improve recording performance it has an undesirable side effect. This effect is known as Far Track Erasure (FTE) and is a result of erasure by the shield's stray fields on the recording media. The mechanism of erasure is governed by a sharp increase of the magnetic stray field locally underneath the domain wall during switching of the writer's polarity. The magnitude of this field in the media plane can reach several kOe within 100-150 picoseconds. It is found that these stray fields depend drastically on the orientation of the magnetization in the adjacent domains and not on the polarity of the magnetization in the domain wall or on the direction of the flux in the main pole. Micromagnetic simulations confirm this phenomenon both for the pulsed external field applied transverse to the domain wall plane in the thin film and for the recording head during main pole switching. Images of the domain wall in the shield obtained using micromagnetic simulations are shown in Fig.1. In the top image, the domain wall width is reduced at the surface of the shield, resulting in large stray fields at Air Bearing Surface (ABS). The bottom image shows the domain wall which is not affected by the main pole switching process. The difference between two cases is the relative direction of the magnetization in adjacent domains. The domain wall induced erasure has an asymmetric nature resulting in the preferred direction of the magnetization in the shield.

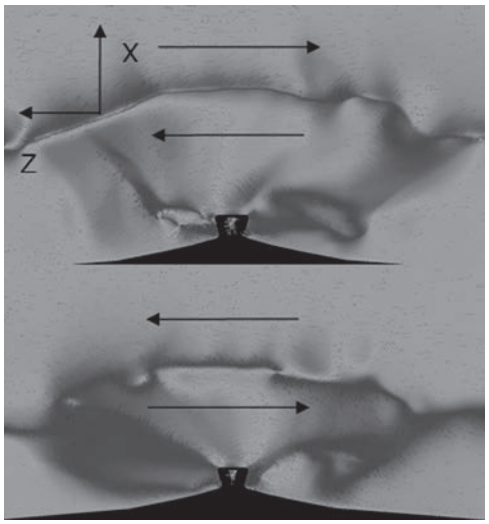


Fig. 1 Simulated domains walls in the shield during main pole magnetization switching. Top: potentially erasing domain wall, right – not erasing domain wall. Arrows show directions of the magnetization in adjacent domains. Color represents magnetization component along the X axis: red – positive, blue – negative.

4:06

HD-14. Analytical estimation of transition jitter using switching probability calculations. *N.A. Natekar*[1] and R. Victora[1] *1. Electrical Engineering, University of Minnesota, Twin Cities, Minneapolis, MN, United States*

Micromagnetic simulations are used to calculate the transition jitter, which is an indicator of the HAMR recording performance. To ensure accurate jitter values with low error bars, a high number of transitions are needed. These calculations are long (~ 300 ns) and computationally demanding. Here, we derive analytical equations that estimate the transition jitter via the switching

probability calculations for the single layer FePt media. These calculations are faster since they do not involve demag calculations. To calculate the switching probability distribution (SPD), the media is cooled from a peak temperature down to the room temperature (300K) at a constant cooling rate and the applied field is reversed at a certain temperature. Two factors mainly affect the jitter: grain size (GS) and the heat spot geometry. The GS effect on jitter is derived based on the fact that the desired transition center can lie anywhere within the grain, but the written transition must lie in a grain boundary. This effect was described in [1] and argues that the square of the jitter equals the grain size cubed divided by (12*Read Width). To model the effect of the heat spot, we use the chain rule to relate the switching probability as a function of position to the SPD. An additional factor affecting the total jitter is the size variation for Voronoi grains of the media. Essentially this is a correlation term because larger grains are expected to have smaller switching probability distributions. The resulting jitter is found to be proportional to the square of the Grain Size Distribution (GSD)*Grain Size (GS). The theoretical jitter is estimated as a sum of the jitter due to these three effects. This theoretical estimate is compared to the jitter obtained via micromagnetic simulations for different GS (Fig. 1). The close agreement of the theoretical estimate of jitter obtained using the analytical equations with the jitter values from the micromagnetic simulations shows the accuracy of the analytical equations for estimating the jitter for different grain sizes.

[1] B. Valcu and N.-H. Yeh, IEEE Trans. Magn. 46(6), 2160 (2010)

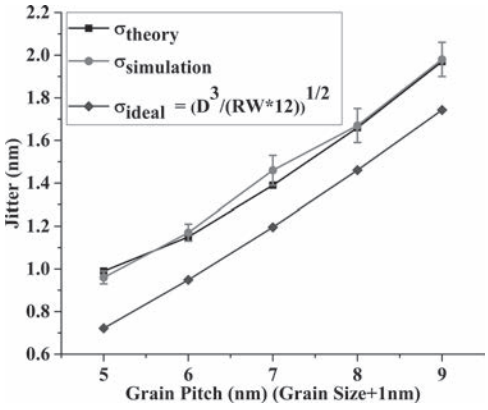


Fig.1 Comparison of jitter (σ_{theory} & $\sigma_{simulation}$) for different Grain Size/ Grain Pitch. (T_{peak} = 850K; Heat spot FWHM =40nm; Read Width RW=20nm)

4:18

HD-15. Deep Neural Network: Data Detection Channel for Hard Disk Drives with High Degrees of Freedom. *Y. Qin*[1] and J. Zhu[1] *1. Data Storage Systems Center, Electrical and Computer Engineering, Carnegie Mellon University, Pittsburgh, PA, United States*

In this work, we explore the possible performance gain and underlying mechanisms of using a deep neural network (DNN, Fig.1 inset)[1,2], a machine learning (ML) method, as data recovery channel in hard disk drives to replace the conventional data detection channel. Simulated perpendicular recording with both additive white Gaussian noise (AWGN) and transition jitter noise are used for bit-error rate (BER) performance evaluation. The DNN channel is constructed with n-consecutive sampling inputs (green) and 1-bit output (red) with sequential detection. The most renowned property for DNN as data recovery channel is to adaptively optimize the detection performance by directly learning the un-equalized signals without prior knowledge of the recording channel. In this light, DNN can automatically adapt to inter-symbol interference (ISI) at any user bit density. Fig. 1 compares the detection BER as a function of signal-to-noise ratio (SNR) for DNN (solid) and conventional read channel consisting the equalizer and BCJR detector[3] (dashed) at two user bit densities. Only AWGN is included in this experiment. At same BER, it is found that the DNN channel tolerates signals of lower SNR, and the SNR gain grows at higher user bit density. This advantage is mainly because DNN can adaptively extract features/low-level signal representations that naturally embody signal characteristics. Therefore, minimal noise will be boosted by DNN during detection. Another appealing characteristic for DNN channel is the strong resilience for data-dependent noise. Fig. 2 compares the detection performance for both channels as the magnetic transition jitter noise becomes more dominant given constant total noise power. This time, the learned features uniquely show position shifts to cater for the jittering, hence enables DNN to learn the right classification boundary accurately. As a result, the DNN channel maintains similar BER with increasing jitter noise while the conventional channel detection performance severely degrades.

[1] Hinton G, Deng L, Yu D, et al. Deep neural networks for acoustic modeling in speech recognition. IEEE Signal processing magazine, 2012, 29. [2] Sutskever I, Vinyals O, Le Q V. Sequence to sequence learning with neural networks//Advances in neural information processing systems. 2014: 3104-3112. [3] Nabavi S, Kumar B V K V. Two-dimensional generalized partial response equalizer for bit-patterned media//2007 IEEE International Conference on Communications. IEEE, 2007: 6249-6254.

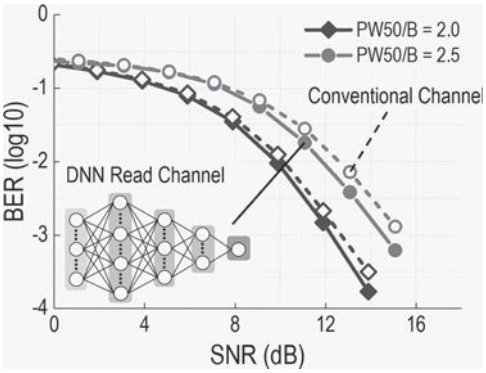


Figure 1. Detection BER vs. SNR at two user bit densities described by PW50/B, where B is the physical bit length.

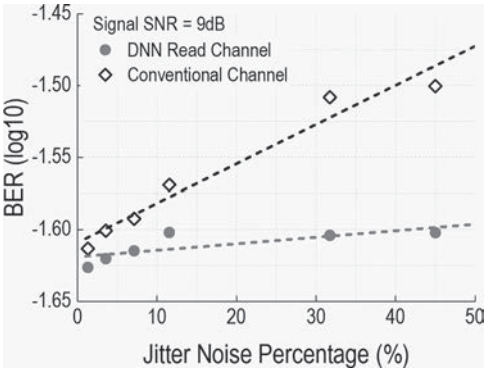


Figure 2. Detection BER vs. jitter noise power percentage for conventional channel (black) and DNN (red).

Session HE
MOLECULAR AND NANOPARTICLE MAGNETISM

Ezekiel Johnston-Halperin, Chair
The Ohio State University, Columbus, OH, United States

INVITED PAPER

1:30

HE-01. Creating Chemical Qubits. J. Zadrozny[2,1], M. Graham[1], M. Fataftah[1] and *D. Freedman[1] 1. Northwestern University, Evanston, IL, United States; 2. Colorado State University, Ft Collins, CO, United States*

Harnessing synthetic chemistry we can design candidate qubits with angstrom scale precision. Within this space we can ask fundamental scientific questions and make synthetic modifications to answer those questions. For example, we can probe the impact of nuclear spin distance on electronic spin coherence. In another approach, we can link candidate qubits into arrays. These results and others will be presented.

Zadrozny, J. M.; Niklas, J.; Poluektov, O. G.; Freedman, D. E. Millisecond Coherence Time in a Tunable Molecular Electronic Spin Qubit *ACS Cent. Sci.* 2015*, 1,* 488–492 Graham, M. J.; Zadrozny, J. M.; Fataftah, M. S.; Freedman, D. E. Forging Solid-State Qubit Design Principles in a Molecular Furnace *Chem. Mater.* 2017, *29,* 1885–1897. Graham, M. J.; Yu, C.; Krzyaniak, M.; Wasielewski, M.; Freedman, D. E. Synthetic Approach to Determine the Effect of Nuclear Spin Distance on Electronic Spin Decoherence *J. Am. Chem. Soc.* 2017, *139*, 3196–3201. Zadrozny, J. M.; Gallagher, A. T.; Harris, T. D.; Freedman, D. E. A Porous Array Of Clock Qubits *J. Am. Chem. Soc.* 2017, 39, 7089–7094. Fataftah, M.S.; Freedman, D. E. Progress towards creating optically addressable qubits *Chem. Commun.* 2018, *54*, 13773–13781.

CONTRIBUTED PAPERS

2:06

HE-02. Control of Spin Relaxation Times via The Spin Bath and its Edge. C. Jackson[1], I. Moseley[1], C. Lin[1], S. Johnson[1] and *J. Zadrozny[1] 1. Chemistry, Colorado State University, Fort Collins, CO, United States*

Magnetic molecules are critical components in current and next generation applications in magnetic resonance imaging and quantum information processing.[1] Toward functionality in these applications, long spin-lattice relaxation (T1) and spin-spin relaxation (T2) times are desired. However, there is a fundamental challenge here – most magnetic molecules display short T1 and T2 values when in the presence of a magnetic environment (the spin bath). Bioimaging environments and information storage environments are spin-rich, and expected to induce fast relaxation (and small T1 and T2). Hence, to move toward actually using magnetic molecules for these applications, we need to understand how to design long relaxation times in highly magnetic environments. This presentation will detail previous [2] and ongoing [3,4] efforts to understand the spin-bath to molecule interaction via molecular chemistry and spin resonance spectroscopy. Specifically, we will discuss the response of the relaxation times in magnetic complexes of vanadium(IV) and cobalt(II) to specific magnetic environments, wherein we tune the magnetic species within and beyond the immediate shell of the metal ion. In both cases, we demonstrate how this tuning is an efficient means to (counterintuitively) slow down magnetic relaxation. Importantly, these results provide previously inaccessible mechanistic insight into processes governing magnetic relaxation in molecular species. In the long term, this fundamental knowledge will lead to molecules with long relaxation times in chaotically magnetic environments.

[1] D. Gatteschi, R. Sessoli and J. Villain, *Molecular Nanomagnets.* Oxford (2006). [2] C.-Y. Lin, T. Ngendahimana, S. S. Eaton, et al., Chem. Sci., Vol. 10, p.548 (2019). [3] C. E. Jackson, C.-Y. Lin, S. H. Johnson, et al., Submitted Manuscript (2019). [4] I. P. Moseley and J. M. Zadrozny Submitted Manuscript (2019).

2:18

HE-03. Giant Barocaloric Effect at the Spin Crossover Transition of a Molecular Crystal. *S. Vallone[1,2]*, A.N. Tantillo[1,2], A.M. dos Santos[3], J.J. Molaison[3], R. Kulmaczewski[4], A. Chapoy[5], P. Ahmadi[5], M.A. Halcrow[4] and K.G. Sandeman[1,2] *1. Department of Physics, Brooklyn College, City University of New York, Brooklyn, NY, United States; 2. Physics Program, The Graduate Center, City University of New York, New York, NY, United States; 3. Neutron Sciences Directorate, Oak Ridge National Laboratory, Oak Ridge, TN, United States; 4. School of Chemistry, University of Leeds, Leeds, United Kingdom; 5. Institute of Petroleum Engineering, Heriot-Watt University, Edinburgh, United Kingdom*

Spin crossover occurs in compounds where the crystal field splitting of d-orbitals associated with a magnetic moment is of the order of k_BT. As a result, a change of state from low spin (LS) to high spin (HS) can occur at the so-called spin crossover temperature, T_{SCO} [1]. Crucially for caloric applications, the change of state from LS to HS can be either continuous or first order, and it can occur at temperatures up to and beyond room temperature. This makes SCO transitions of interest for caloric cooling applications. Since SCO compounds are paramagnets or diamagnets, the largest caloric effects will be barocaloric rather than magnetocaloric. The caloric potential of SCO compounds has been proposed from a thermodynamic perspective [2] and by use of a microscopic, Ising-like model [3]. In this presentation, we combine neutron scattering at pressures up to 1.2 kbar on a deuterated sample with calorimetry data and SQUID magnetometry under pressures of up to 4.5 kbar to examine the evolution of the structure and transition hysteresis of a first order SCO compound [4]. We provide the first direct experimental demonstration of a giant, low pressure barocaloric effect (BCE) and outline future research directions for the development and optimization of the BCE associated with spin crossover.

[1] K.S. Murray, in Spin-Crossover Materials: Properties and Applications, edited by M.A. Halcrow, 1st ed. (John Wiley & Sons Ltd, 2013). [2] K.G. Sandeman, APL Materials 4, 111 (2016). [3] P.J. von Ranke, Appl. Phys. Lett. 110, 181909 (2017). [4] S. Vallone et al., Advanced Materials 31, 1807334 (2019).

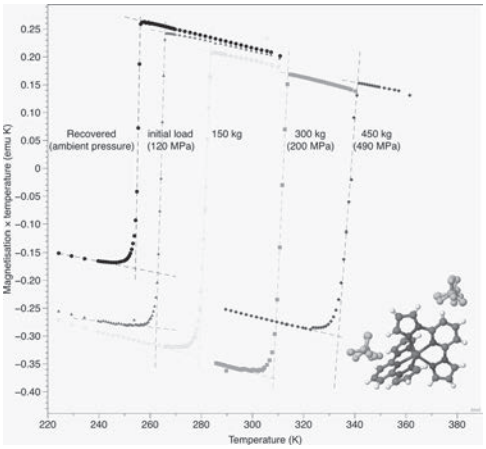


Fig. 1: SQUID magnetometry for protonated $[FeL_2][BF_4]_2$ [L = 2,6-di(pyrazol-1-yl)pyridine] at pressures up to 490 MPa. Load levels in kilograms correspond to applied pressures of 120 MPa (initial load), 200 MPa (300 kgs) and 490 MPa (450 kgs) respectively.

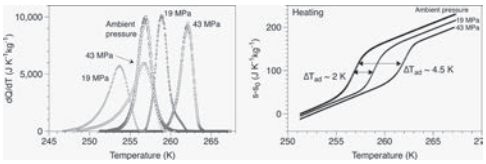


Fig. 2: (Left) Calorimetry data on partially deuterated $[FeL_2][BF_4]_2$, showing how the spin crossover transition shifts in 19 MPa and 43 MPa on heating (red) and cooling (blue). Data in ambient conditions are shown in heating only. (Right) Calculated entropy vs temperature showing that the maximum irreversible adiabatic temperature change in 19 MPa is 2 K and in 43 MPa is about 4.5 K. Entropy is plotted as s-s_0, where s_0 is the entropy at ambient pressure and 251 K, away from the phase transition.

2:30

HE-04. Magnetism of a Cr_{10} molecular wheel with unexpected ground-state. *F. Bartolome*[1], A. Arauzo[1], E. Bartolomé[2], F. Sedona[3], J. Rubin[4], L. Ferrari[3], J. Herrero-Albillos[5], M. Panighel[6], A. Mugarza[6,7], M. Rancan[3], M. Sambi[3] and J. Bartolomé[1] *1. Instituto de Ciencia de Materiales de Aragn and Dept. de Fisica de la Materia Condensada, CSIC - Universidad de Zaragoza, Zaragoza, Spain; 2. Escola Universitaria Salesiana de Sarria, Barcelona, Spain; 3. Dipartimento di Scienze Chimiche, Universita di Padova, Padova, Italy; 4. Instituto de Ciencia de Materiales de Aragon and Dept. de Ciencia y Tecnologia de Materiales y Fluidos, CSIC - Universidad de Zaragoza, Zaragoza, Spain; 5. Centro Universitario de la Defensa, Academia General Militar, Zaragoza, Spain; 6. Catalan Institute of Nanoscience and Nanotechnology (ICN2), CSIC and Barcelona Institute of Science and Technology, Barcelona, Spain; 7. Institucio Catalana de Recerca i Estudis Avancats, Barcelona, Spain*

Molecular nanomagnets formed by clusters of ions with large number of unpaired electrons have attracted intense study since the discovery that molecular aggregates stabilizing high ground spin states can display Single-Molecule Magnetism (SMM). Cyclic complexes are of particular interest because of their planar high symmetry. We have studied wheel molecules of formula $\{Cr_{10}(OMe)_{20}(O_2CCMe_3)_{10}\}$, ($\{Cr_{10}\}$ from now-on, see Fig. 1a), both in bulk and evaporated by direct sublimation in UHV on metallic single-crystal surfaces [1]. When the molecules are deposited onto the Cu(111) or Au(111) surfaces, a monolayer of $\{Cr_{10}\}$ molecules, self-organized in a quasi-hexagonal 2D network is formed. The magnetic characterization of monolayer, multilayer and bulk (powder) samples of $\{Cr_{10}\}$ has revealed that this cluster exhibits an unusually high S-ground state. The magnetic characterization of grafted $\{Cr_{10}\}$ were studied byXMCD at the Cr $L_{2,3}$ edge at T=2 K and magnetic fields up to B=6T. Magnetization and susceptibility were measured by SQUID on the multilayer and the powder sample up to B=14 T. Static $M(H)$ and dc c(T) measurements resemble the curves previously reported earlier [2], where the $\{Cr_{10}\}$ wheels were described in terms of a total molecule spin S=9 ground state, with overall ferromagnetic coupling. $M(H)$ curves are shown in Fig. 1b). Although Monte Carlo simulations considering the Cr(III) as a Heisenberg S=3/2 spin entity are able to describe the $M(H)$ curves qualitatively, a static Hamiltonian based on nearest-neighbour interactions leading to a S=9 needs a particular combination of ferro- and antiferromagnetic interactions, which is hard to reconcile with the underlying five-fold symmetry of Cr_{10}. Therefore, both experimental results and theoretical considerations suggest complex ground-state properties.

[1] F. Sedona, M. Di Marino, D. Forrer, A. Vittadini, M. Casarin, A. Cossaro, L. Floreano, A. Verdini, M. Sambi, *Nat. Mater.* 2012, *11*, 970. [2] J. Bartolomé, F. Bartolomé, N. Brookes, F. Sedona, A. Basagni, D. Forrer, M. Sambi, *J. Phys. Chem. C* 2015,*119*, 12488.

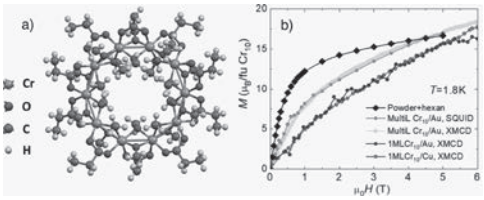


Fig. 1 (a) Structure of the {Cr10} molecule. (b) Magnetization at T=1.8 K in bulk (powder), thin film (MultiL), and monolayer (1ML).

2:42

HE-05. Donor Bound Magnetic Polaron in Semimagnetic Quantum Ring. *P. Kalpana*[1] and K. Jayakumar[1] *1. Nanostructure Lab, Department of Physics, The Gandhigram Rural Institute - Deemed to be University, Gandhigram, India*

The experimental realization of Quantum Rings (QR)[1] has paved the way for the theoretical physicists to give attention towards developing theoretical model for Semiconducting QR with magnetic impurity[2, 3]. In the present work, the binding energy of the donor impurity confined inside a semimagnetic QR made up of CdTe / $Cd_{1-x}Mn_xTe$ (Fig. 1) in the presence of perpendicular magnetic field (γ, a dimensionless parameter) applied externally has been focused for various Ring parameters like inner radius R_1, outer radius R_2, Ring width ΔR (= R_2 - R_1) and height of the Ring 'd' of the QR using variational principle in the effective mass approximation. The effect of Bound Magnetic Polaron (BMP)[4] on the donor states due to the presence of magnetic impurity in semimagnetic QR is considered through the calculation of Spin Polaronic Shift (SPS) using mean field theory including modified Brillouin function. The observed results of the binding energy as a function of Ring width ΔR for various 'd' by placing the impurity at the centre of the radial direction ($\rho_i = (R_1+R_2)$ / 2) and the axial direction ($Z_i = 0$) of QR shows that the binding energy increases as 'R_2' decreases from the bulk limit towards the narrower size of the Ring. The donor states are strongly affected by the applied magnetic field which can be ascertained from the rapid fall of binding energy when the strength of γ increases from γ = 0.05 (1.5Tesla) to γ = 0.1 (3Tesla). In the absence of magnetic field, the enhancement in the exchange interaction between the spin of the carrier and the spin of the Mn^{2+} ion is promising only for the Ring parameter d ~ 40Å and R ~ 80Å. But the same is not true when the system is subjected to strong γ as the height of the Ring gets lowered because of the reduction in potential barrier height, $Cd_{1-x}Mn_xTe$. Moreover, the applied field aids the strong exchange interaction which leads to the larger polaronic shift for γ = 0.1 (Fig. 2). The results are presented and discussed.

1. T. W. Kim, E. H. Lee, K. H. Lee, J. S. Kim and H. L. Park, Appl. Phys. Lett., 84, 595 – 597 (2004) 2. J S Sheng and Kai Chang, J. Phys.: Condens. Matter, 20, 025222 (2008) 3. AregGhazaryan, Aram Mabaselya, Tapash Chakraborty, Physica E, 66,157 – 161 (2015) 4. P. Kalpana and K. Jayakumar, Physica E, 93, 252-256 (2017)

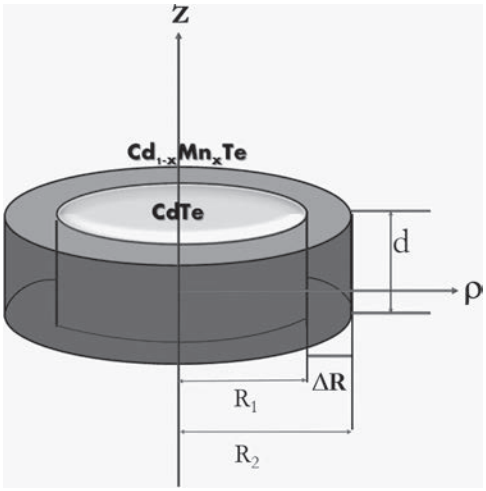


Fig 1. Schematic Diagram of CdTe / $Cd_{1-x}Mn_xTe$ Quantum Ring

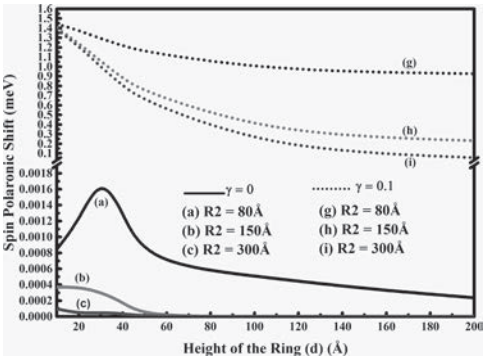


Fig 2. Variation of SPS as a function of 'd' for various γ with different outer radius of the QR.

2:54

HE-06. Tuning the Magnetic Moment of high density FePc/Ag(110) phases by oxygen dosing. E. Bartolomé[1], J. Bartolomé[2], F. Sedona[3], J. Herrero-Albillos[4], J. Lobo[2], M. Piantek[5], L. Garcia[2], M. Panighel[6], A. Mugarza[6,7], M. Sambi[3] and *F. Bartolome[2] 1. Escola Universitaria Salesiana de Sarria (EUSS), Barcelona, Spain; 2. Instituto de Ciencia de Materiales de Aragon, CSIC - Universidad de Zaragoza, Zaragoza, Spain; 3. Dipartimento di Scienze Chimiche, Universita di Padova, Padova, Spain; 4. Centro Universitario de la Defensa, Academia General Militar, Zaragoza, Spain; 5. Instituto de Nanociencia de Aragon, Universidad de Zaragoza, Zaragoza, Spain; 6. Catalan Institute of Nanoscience and Nanotechnology (ICN2), CSIC and Barcelona Institute of Science and Technology, Barcelona, Spain; 7. ICREA - Institucio Catalana de Recerca i Estudis Avancats, Barcelona, Spain*

Molecular overlayers on substrates have a broad field of application in catalysis, sensing, molecular electronics, light-to-energy conversion, etc. In particular, iron-phtalocyanines (FePc) are being investigated as viable substitutes for precious metals in catalysis of the Oxygen Reduction. Recent studies of FePc on Ag(110) have shown that sub-monolayer phases are catalitically active [1]; remarkably, in oxygen-dosed phases O2 intercalates between the molecules and the surface, thereby substantially changing the Fe magnetic moment. Reversible switching of the Fe magnetic moment in some low-density (LD-R1/R2) FePc phases upon an oxygenation-annealing cycle has been demonstrated [2]. In this contribution, we report on the oxygenation capabilities and associated magneto-structural changes of higher-density FePc/Ag(110) phases, the oblique (OB) and square (SQ)/quasi-squared (R3) high-density phases, investigated by combining high-resolution Scanning Tunneling Microscopy (STM), Scanning Tunneling Spectroscopy (STS), Density Functional Theory (DFT) simulations and x-ray magnetic circular dichroism (XMCD) at the Fe L2,3, edge. The STM images reveal the steric impediments of high-density phases to allocate O2 between the FePc and the substrate, which result in less efficient oxygenation / deoxydation processes compared to previously reported LD phases. In the SQ/R3 squared phases, only a fraction of the molecules are able to oxygenate, rotating and suffering a displacement. For the OB oblique phase, the oxygenation efficiency is smaller; and among the oxygenated molecules, only a minor fraction do rotate, while the majority allocate O2 without rotation. The XMCD spectra of the oxygenated phases reflect the different distribution of non- oxygenated, oxygenated-rotated and non-rotated species in the samples (Fig. 1).

[1] F. Sedona et al., Nat. Mater. 2012, 11, 970. [2] J. Bartolome et al., J. Phys. Chem. C 2015, 119, 12488.

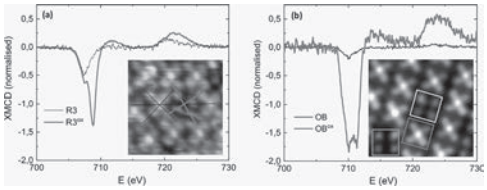


Fig. 1 XMCD of as deposited and oxygenated (a) R3 and (b) OB phases, and STM images of the O2 dosed samples.

3:06

HE-07. Strain Effects in Atomic Spin Model. *Y. Hsiao*[1], O.G. Udalov[2], I.S. Beloborodov[2], C.S. Lynch[3] and G. Carman[1] *1. Mechanical and Aerospace Engineering, UCLA, Los Angeles, CA, United States; 2. Physics, California State University, Northridge, Northridge, CA, United States; 3. University of California, Riverside, Riverside, CA, United States*

Recent demands for high-density magnetic storage have resulted in the need for atomistic scale magnetic devices. Strain control of magnetic devices have been demonstrated to be the most energetically viable solution for high-density magnetic storage [1]. For successful implementation of these devices, magnetic modeling techniques are used to better understand magnetization behavior. Atomistic discrete simulation methods have been developed to bridge the gap between micromagnetics and electronic structure [2][3]. However, currently developed atomic spin codes do not incorporate elastodynamics effects. These effects are necessary for determining magnetic states of strain-mediated devices and other strain-related magnetic properties. Here, we introduce coupling between mechanical (phonons) and magnetic (magnons) degrees of freedom into the atomic spin approach. A simple system of two atoms incorporating magnetoelastic effects was tested. Coupled Landau-Lifshitz-Gilbert (LLG) equation, governing the magnetization dynamics, and Newton's equation of motion to govern the mechanical behavior are studied to demonstrate mutual influence of magnetic and mechanical degrees of freedom. Strain effects are introduced as a correction term to both the exchange and anisotropy constants. Magnetoelastic coupling in two-atom system leads to essential modification of magnetic ground state from canted antiferromagnetic to ferromagnetic configuration.

[1] J. L. Hockel, P. K. Nordeen, D. M. Pisani, C. Liang, G. P. Carman, and C. S. Lynch, "A method to control magnetism in individual strain-mediated magnetoelectric islands," *Appl. Phys. Lett.*, vol. 103, no. 23, p. 232905, Dec. 2013. [2] J. Eriksson, O., Bergman, A., Bergqvist, L., & Hellsvik,

Atomistic Spin Dynamics: Foundations and Applications. Oxford university press., 2017. [3] A. Kirilyuk, A. V Kimel, and T. Rasing, "Atomistic spin model simulations of magnetic nanomaterials Related content Fundamentals and applications of the Landau-Lifshitz-Bloch equation U Atxitia, D Hinzke and U Nowak-Laser-induced magnetization dynamics and reversal in ferrimagnetic alloys," *J. Phys. Condens. Matter Top. Rev.*

3:18

HE-08. Fractional Skyrmions in Ensembles of Exchange-Coupled Nanoparticles. *R. Skomski*[1], A. Ullah[1], B. Balasubramanian[1], W. Zhang[1] and D.J. Sellmyer[1] *1. Physics and Astronomy & NCMN, University of Nebraska, Lincoln, NE, United States*

Conduction electrons exchange-interacting with noncollinear spin structures accumulate a Berry phase that translates into an emergent magnetic field and yields a topological Hall effect (THE) [1]. We investigate the THE in magnetic nanoparticles containing partially developed (fractional) skyrmions, which is a new research direction. The particles are conducting through compaction or embedding in a conductive matrix, and the THE depends on crystal structure, particle size, grain orientation, and grain-boundary morphology. Point-group analysis yields a canonical division into centrosymmetric crystals, noncentrosymmetric crystals (NCSC) without Dzyaloshinski-Moriya (DM) interactions, NCSC with DM interactions but no spin spirals, and NCSC supporting both DM interactions and helical spin structures [2]. However, inversion symmetry, polarity, and chirality, which lead to this four-fold distinction, are not the only consideration. For example, our experiments show that compacted Co nanoparticles do not exhibit a measurable THE, in contrast to the crystallographically very similar NiMnGa (point group D_{6h}). The emergent field includes both radial and angular contributions, both depending on the real-structure morphology. The angular integration shows that the THE decreases with particle size, which agrees with our recent magnetization measurements on MnSi [3] and Co nanoparticles. Second, the THE may be zero for nanoparticles that directly touch each other, due to the involvement of Erdmann-Weierstrass boundary conditions. This mechanism, Fig. 1, strongly reduces the THE but is not fully operative in the case of weakly magnetic grain boundaries and in the presence of a nonmagnetic matrix. Furthermore, strong magnetization gradients near the particle's surface violate Berry's adiabacity condition [4], a consideration much more important in nanoparticulate systems than in ordinary skyrmionic thin films. — This research is supported by DOE BES (DE-FG02-04ER46152).

[1] Sh. Seki and M. Mochizuki, *Skyrmions in Magnetic Materials*, Springer International, Cham 2016. [2] A. Ullah, B. Balamurugan, W. Zhang, S. S. Valloppilly, X.-Zh. Li, R. Pahari, L.-P. Yue, A. Sokolov, D. J. Sellmyer, and R. Skomski, IEEE Trans. Magn., in press (2019). [3] B. Das, B. Balasubramanian, R. Skomski, P. Mukherjee, S. R. Valloppilly, G. C. Hadjipanayis, and D. J. Sellmyer, Nanoscale, Vol. 10, p. 9504 (2018). [4] M. V. Berry, Proc. R. Soc. Lond., Vol. A 392, p. 45 (1984).

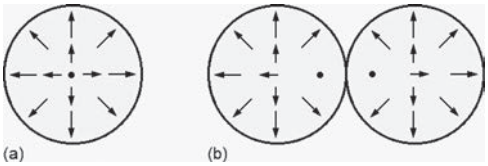


Fig. 1. Schematic spin structure in nanoparticles with centrosymmetric crystal structure: (a) isolated particle and (b) effect of Erdmann-Weierstrass boundary conditions. The spin arrows are top views parallel to the particles' uniaxial symmetry axis.

3:30

HE-09. Slow magnetic relaxation in well crystallized, monodispersed, octahedral and spherical magnetite nanoparticles. E. Navarro[1], Y. Luengo[2], S. Veintemillas[2], M. Morales[2], F. Palomares[1], U. Urdiroz[1], F. Cebollada[3] and *J.M. González*[1] *1. Nanostructures and Surfaces, Instituto de Ciencia de Materiales de Madrid, Madrid, Spain; 2. Energy, Environment and Health, Instituto de Ciencia de Materiales de Madrid, Madrid, Spain; 3. POEMMA-CEMDATIC, Universidad Politécnica de Madrid, Madrid, Spain*

Thermally activated relaxation over energy barriers concurrently related to local properties and interparticle interactions constitutes a major contribution to both the coercivity and the applied field frequency dependence of that quantity [1]. We have measured the slow magnetic relaxation of magnetite nanoparticles (NPs), synthetized by using the oxidative precipitation technique, having spherical (S) and octahedral (O) shapes and monodispersed size distributions with average diameters (S NPs) and major diagonals (O NPs) of 21 nm as determined by transmission electron microscopy (TEM). The characterization of the slow relaxation behavior of our NPs was completed at temperatures in the range from 5 K up to 290 K by measuring the time dependence of the magnetization at constant temperature and applied field (the measurements were taken at different fields having magnitudes of the order of the dc coercivity, measured by cycling the field at a rate of 3.2 x $10^2 Am^{-1}s^{-1}$). From our data we evaluated the temperature dependencies of a) the irreversible demagnetization susceptibility, b) the fluctuation field (associated to the thermally induced demagnetization occurring during the measuring time range) and c) the activation volume (corresponding to the demagnetization produced by the fluctuation field). From our results we conclude that i) the irreversible susceptibility peaks in both samples at ca. 135 K (Verwey transition temperature [2]) and ii) the temperature variation of the activation volume shows (Fig. 1) similar values in both samples for temperatures below ca. 135 K and, in the whole considered temperature range, corresponds to an increase of the activation volume by a factor of 10 (S NPs) and 30 (O NPs) with respect to the average NPs volume measured by TEM. Those large increases of the activation volume are compatible with a transition of the thermal activation processes from local to collective.

[1] J.B. Weaver, X. Zhang, E. Kuehlert *et al,* Nanotechnology 24 (32), 325502, (2013) [2] A. Kosterov in D. Gubbins, et al (eds.) "Encyclopedia of geomagnetism and paleomagnetism" (Springer, Dordrecht, 2007) pp. 515–525

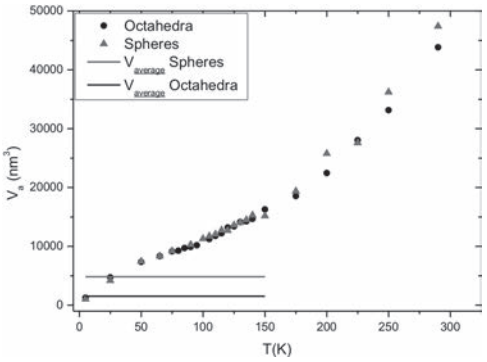


Fig.1. Temperature dependence of the activation volume of O and S NPs compared to the average volume of both types or NPs

3:42

HE-10. Probing Superparamagnetism in Fe_3O_4 Nanoparticles with Muon Spin Relaxation. *B.A. Frandsen*[1], C. Read[1], J. Stevens[1], M. Christianson[1], C.S. Walker[1] and K. Chesnel[1] *1. Physics and Astronomy, Brigham Young University, Provo, UT, United States*

The transition from the superparamagnetic state to the blocked state in assemblies of single-domain magnetic nanoparticles remains a topic of sustained experimental and theoretical study in the field of nanomagnetism. Historically, most experimental work on superparamagnetism has relied on magnetometry techniques that are sensitive to the macroscopic magnetization of the nanoparticle assemblies. However, local probes of magnetism such as muon spin relaxation (μSR) can provide valuable complementary information to aid our understanding of superparmagnetic dynamics and the blocking transition mechanism. Here, we present a μSR characterization of the transition from the superparamagnetic state to the blocked state in monodisperse Fe_3O_4 nanoparticle samples ranging in size from 5 nm to 20 nm. Analysis of the thermal evolution of the μSR asymmetry spectra (see Fig. 1) allows us to extract relevant physical quantities from the data, including the blocking temperature, characteristic spin fluctuation rates, and the relative phase fractions of the superparamagnetic and blocked states. We discuss systematic trends as a function of temperature and particle size. In addition to providing valuable information about the superparamagnetic behavior of Fe_3O_4 nanoparticles, this work demonstrates the utility of the μSR technique for investigations of magnetic nanoparticles, motivating future studies of related systems.

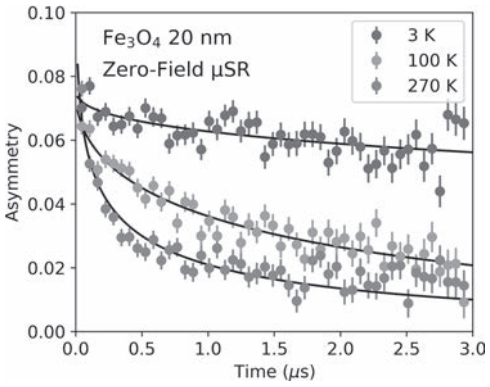


Fig. 1. Muon spin relaxation asymmetry spectra collected from an assembly of 20-nm Fe_3O_4 nanoparticles at various temperatures above and below the blocking transition.

3:54

HE-11. Withdrawn

4:06

HE-12. Tuning the Properties of Colloidal Magnetic Particles for Thermometry on the Nanoscale. *A.J. Biacchi*[1], E. De Lima Correa[1], F. Zhang[1], T. Moffat[1], W. Tew[1], M.J. Donahue[1], S. Woods[1], C. Dennis[1] and A.R. Hight Walker[1] *1. National Institute of Standards and Technology (NIST), Gaithersburg, MD, United States*

Accurate, local, remote, and real-time temperature measurements are essential for many technological applications. While conventional thermometry can accurately measure the temperature of a microscale spot on a surface, magnetic nanothermometry is being explored as a method to measure temperature at comparable spatial resolution throughout a volume. Although progress has been made in the development of magnetic nanothermometry,[1] current methods still lack the sensitivity necessary for widespread application. Specifically, the nanomaterials display only modest changes in magnetization with temperature; this response must be strengthened to improve the signal-to-noise ratio as a prerequisite to practical volumetric nanothermometry. Recent theory has predicted sharp temperature features in magnetization can be induced in bilayer nanoparticles, where each layer is composed of a different magnetically coupled material.[2] Here, we engineer solution-synthesized nanoparticles and measure their magnetization dependence on the temperature of their local environment. Prudent selection of the material composition, morphology, and layer thickness provides a means to control the magnetic interaction arising from the coupled layers. This modulation of interfacial properties allows for different magnetic transition temperature regimes and sensitivities, thus providing an opportunity to engineer these nanothermometers' performance as a function of their constituent magnetic coupling. Over the range 100 K to 350 K, under an applied magnetic field of 0.01 T, these structurally complex samples show considerable temperature-dependent change in magnetization. To better understand the underlying causes of the magnetic response, extensive structural characterization was performed. Results collected from X-ray scattering and diffraction, Raman spectroscopy, and high-resolution electron microscopies provide correlations between the nanoscale structure of these particles with their magnetic thermosensistivity. These improved systems of heterostructured, magnetic nanoparticle thermometers will subsequently form the basis of a metrological program for spatially resolved, 3D, high-sensitivity measurements of temperature.

[1] J. Zhong, J. Dieckhoff, M. Schilling and F. Ludwig, Journal of Applied Physics, 120, 143902 (2016). [2] N. Anderson and R. Camley, Physical Review B, 94, 134432 (2016).

4:18

HE-13. Structural and Magnetic Properties of Co_3V Nanoparticles. *O. Tosun*[1], B. Balasubramanian[2,3], R. Skomski[2,3], D.J. Sellmyer[2,3] and G.C. Hadjipanayis[1] *1. Physics & Astronomy, University of Delaware, Newark, DE, United States; 2. Physics & Astronomy, University of Nebraska, Lincoln, NE, United States; 3. Nebraska Center for Materials and Nanoscience, University of Nebraska, Lincoln, NE, United States*

We have investigated the structural and magnetic properties of Co_3V nanoparticles prepared by the cluster-beam deposition (CBD) technique. The composition, structure and magnetic properties of the nanoparticles have been characterized by energy-dispersive X-ray spectroscopy (EDS), X-ray diffraction (XRD), high-resolution transmission electron microscopy (HR-TEM), and magnetometry, respectively. Bulk Co_3V exists in two phases: An ordered hexagonal (Al_3Pu-type) low-temperature phase (LTP) and a cubic $L1_2$ (Cu_3Au)-type high-temperature phase (HTP) [1, 2]. Both the LTP and HTP are paramagnetic at room temperature. As-made Co_3V nanoparticles with an average size of 6 nm exhibit a mixture of the LTP and HTP. Thermomagnetic measurements performed showed that the as-made nanoparticles are ferromagnetic with Curie temperature (T_C) of 380 K. Hysteresis-loop measurements revealed that the as-made nanoparticles have saturation magnetization (M_s) values of 65 and 75 emu/cm^3 and coercivity (H_c) values of 0 and 0.30 kOe at 300 and 50 K, respectively. When the particles are annealed at 573 K for 4 hours, their size is increased to 20 nm and the particles show predominantly the HTP structure. Their magnetic properties drastically change; their M_s values increased to 300 and 325 emu/cm^3 and H_c values to 0.10 and 0.50 kOe at 300 and 50 K, respectively. The dramatic increase in the magnetic properties of the Co_3V nanoparticles could be attributed to segregation of excess Co on the particles surface which can lead to polarization of the neighboring Co atoms on the surface.

[1] Y. Aoki, Y. Obi, and H. Komatsu, Z. Metallk. 70, 436 (1979) [2] E. T. Peters and L. E. Tanner, Trans. Met. Soc. AIME 233, 2126 (1965)

Session HF
HEUSLER ALLOYS AND MAGNETIC SEMICONDUCTORS II

Xinyu Liu, Chair
University of Notre Dame, Notre Dame, IN, United States

CONTRIBUTED PAPERS

1:30

HF-01. Electronic, magnetic and structural properties of epitaxial Co_2MnZ (Z=Al, Si, Ga, Ge, Sn, Sb) Heusler alloys. *C. Guillemard*[1,2], S. Petit-Watelot[1], J. Rojas-Sanchez[1], P. Le Fevre[2], F. Bertran[2] and S. Andrieu[1] *1. Nanomagnetism and Spintronics Team, Institut Jean Lamour, Nancy, France; 2. Cassiopée Beamline, Synchrotron SOLEIL, Saint-Aubin, France*

Although giant magneto-resistance was discovered more than 25 years ago, the development of spintronics is still very active due to a continuous flow of discoveries. In most spintronics studies, standard transition metals like Fe, Ni, Co (and alloys thereof) are conveniently used. However, alternative materials with superior electronic properties are desirable. In particular, a class of materials called Half Metal Magnets (HMM) in theory satisfies such properties [1]. HMM compounds are metallic for majority spins and insulator for minority spins which leads to exciting properties for spintronic and magnonic devices. For instance, 100 % of spin polarization was obtained in Co_2MnSi(001) epitaxial layers grown by Molecular Beam Epitaxy (MBE) [2], confirming its HMM behavior and explaining the huge TMR observed in Co_2MnSi-based magnetic tunnel junctions [3]. Moreover, extremely low Gilbert damping values (down to 7 $x10^{-4}$) were measured, confirming the reduction of the magnetic damping [2]. We propose here a study of MBE grown Co_2MnZ (Z=Al, Si, Ga, Ge, Sn, Sb) epitaxial layers. In a first step, a structural investigation of the chemical ordering in the series is presented through high resolution scanning electron microscopy (Fig.1), confirming the $L2_1$ chemical ordering in our Heusler layers (except for Z=Al). Additionally, the spin polarization of each layer is measured using spin-resolved photoemission spectroscopy and is compared with *ab initio* calculations. Then, ultra-low effective damping values are confirmed for the whole series (down to 4.6 $x10^{-4}$) using broadband ferromagnetic resonance and finally, the interplay between spin polarization and magnetic damping is analyzed [4].

[1] R. A. De Groot, F. M. Mueller, P. G. van Engen *et al.*, *Phys. Rev. Lett* 50, 2024 (1983) [2] S. Andrieu, A. Neggache, T. Hauet *et al.*, *Phys. Rev. B* 93, 094417 (2016) [3] H. Liu, Y. Honda, T. Taira *et al.*, *Appl. Phys. lett.* 101, 132418 (2012) [4] C. Guillemard, F. Bertran, S. Andrieu *et al.*, *Phys. Rev. Appl.* 11, 064009 (2019)

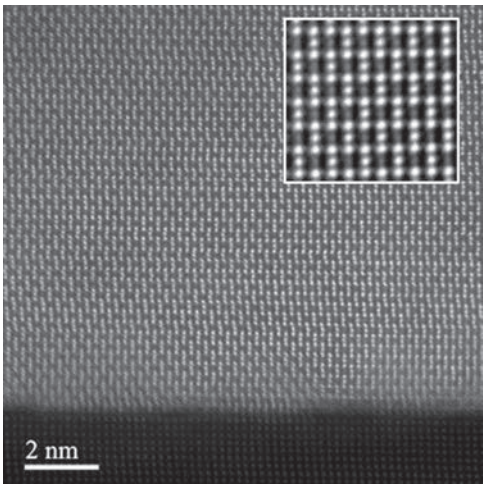


Fig 1. STEM-HAADF image of Co_2MnSi single crystal along the [110] zone axis. According to the electronic contrast, Mn and Co atoms are bright (indistinguishable with the eye) and Si atoms are dark. The inset is a magnified inverse Fourier transform of the same image (*i. e.* filtered)

1:42

HF-02. Structural characterization and magneto-transport properties of magnetron co-sputtered ferromagnetic Weyl semimetal Co2TiGe. *D. Dyck*[1], A. Becker[1], T. Matalla-Wagner[1], J. Koo[1], I. Ennen[1], K. Rott[1] and G. Reiss[1] *1. Physics Department, Center for Spinelectronic Materials & Devices, Bielefeld, Germany*

Weyl semimetals theoretically promise exotic transport properties and are also interesting for spintronic devices. Thus, the research is pursued with high effort in the recent years [1, 2]. Implementation in real life applications requires a scalable and energy efficient approach. As a highly tunable material class, Heusler compounds are particularly interesting in this respect [3, 4]. Here, we investigate the ferromagnetic Weyl semimetal candidate and transition metal based Full Heusler compound Co2TiGe [5, 6, 7]. X-ray diffraction (XRD) analysis and φ-scans of the magnetron co-sputtered thin films show a highly textured $L2_1$ structure of the 225 (Fm-3m) space group with a lattice constant of 5.81 Å at room temperature which is close to the literature value [5]. Transmission electron microscopy (TEM) confirms the high crystallographic quality and smooth growth. The magnetic properties have been examined by magneto-optical Kerr effect (MOKE) and vibrating sample magnetometry (VSM). The results (Fig. 1) show a magnetic moment of 1.4 Bohr magneton per formula unit at room temperature and 1.9 μ_B / f.u. at 5 K. The extrapolated saturation magnetization and Curie temperature are 1.92 μ_B / f.u. and 379.3 K, respectively, which is in accordance to the theoretical predictions and recent results for bulk samples [5]. In addition, magneto-transport measurements have been carried out. The resistivity shows the expected metallic behavior and the residual resistance ratio of approximately 1.5 is in good agreement with the literature values [8]. The residual resistivity is around 50 μΩcm. The temperature dependent anomalous Hall effect

(AHE) shows a decreasing Hall resistivity and increasing perpendicular saturation magnetization for decreasing temperatures. Figure 2 shows, that the anomalous Hall conductivity is only weakly dependent on the longitudinal conductivity, which is considered as an indication for Weyl halfmetallicity as their chiral anomaly contributes to a dominant intrinsic mechanism. Additionally, FMR and TMR measurements have been performed on the samples.

[1] Weyl, H., Proc. Natl. Acad. Sci. U.S.A., (1929) [2] Liu, H. et al., APL, 101, p.132418 (2012) [3] Heusler, F., Verh. Dtsch. Phys. Ges., 5, p.219 (1903) [4] Webster, P.J., J. Phys. Chem. Solids, 34, p.1647 (1973) [5] Barth, J. et al., Phys. Rev. B, 81, p.064404 (2010) [6] Chang, G. et al., Scient. Rep., 6:38839 (2016) [7] Logan, J. A. et al., J. Appl. Phys., 121, p.213903 (2017) [8] Prathiba, G. et al., J. Magn. and Magn. Materials, 323, p.22 (2011)

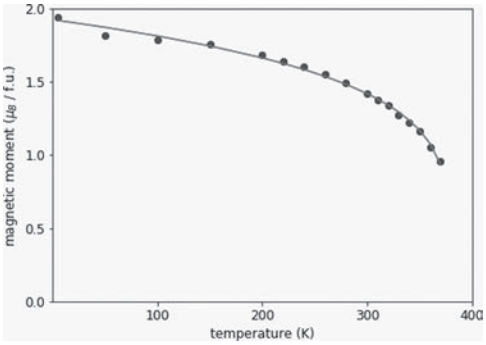


Fig 1. Magnetic moment in Bohr magneton per formula unit in dependence on the temperature.

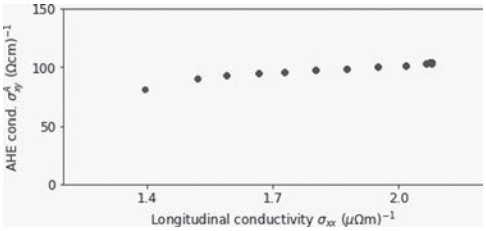


Fig 2. Anomalous Hall conductivity in dependence on the longitudinal conductivity.

1:54

HF-03. Large anomalous Hall angle in topological semimetal Co2MnGa thin films. *Y. Zhang*[1,2], G. Dubuis[1,2] and S. Granville[1,2]
1. Robinson Research Institute, Victoria University of Wellington, Wellington, New Zealand; 2. MacDiarmid Institute for Advanced Materials and Nanotechnology, Wellington, New Zealand

Full Heusler ferromagnet Co2MnGa is predicted to be a magnetic Weyl semimetal. having a large net Berry curvature near the Fermi energy associated with nodal lines and Weyl points[1, 2]. Moreover, Tung *et al*.[3] and Manna *et al*.[4] found the anomalous Hall current would be nearly fully spin-polarized, even though Co2MnGa is not a half-metallic ferromagnet for charge current. These exotic transport properties, along with the large Curie temperature $T_c \approx 694$ K, make Co2MnGa an ideal candidate for studying the interplay of topology and magnetism and realizing room temperature spintronics applications. Recently, bulk Co2MnGa crystals have shown large anomalous Hall and giant anomalous Nernst effects, which support the predicted Weyl behaviour, however so far there is little evidence from thin films. We have systematically investigated the transport properties of epitaxial Co2MnGa thin films with thicknesses from 5 nm to 50 nm. For the 50 nm film, both anomalous Hall conductivity (σ_{xy}) and longitudinal conductivity (σ_{xx}) increase monotonically on cooling and approach a constant 812 Ω^{-1} cm^{-1} and 7250 Ω^{-1} cm^{-1}, respectively, at low temperature, as shown in Figure 1. Figure 2 shows the thickness dependence of the anomalous Hall angle, measured from 300 K to 3 K. The thick films show a new room temperature record for anomalous Hall angle 9.7%. For films with thicknesses below 20 nm, the anomalous Hall angle becomes much smaller and is temperature independent due to a significantly lower anomalous Hall conductivity. The magnetotransport properties of the thick films (above 20 nm) resemble those of bulk Co2MnGa, but for films thinner than 15 nm the sudden decrease in indicates size-dependent changes to the electronic properties near the Fermi level.

1 A. Sakai *et al.*, Nature Physics, Vol. 14, p 1119–1124 (2018) 2 S. N. Guin *et al*., NPG Asia Materials, Vol. 11, 16 (2019) 3 J. Tung *et al*. New Journal of Physics, Vol. 15, 033014 (2013) 4 K. Manna *et al*. Physical Review X, Vol. 8, 041045 (2018)

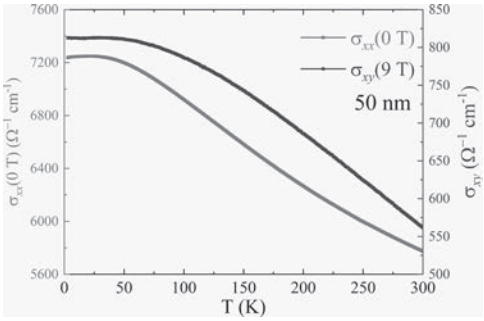


Figure1. Anomalous Hall conductivity σ_{xy} and longitudinal conductivity σ_{xx} as a function of temperature from 300 K to 3 K for thin film with 50 nm.

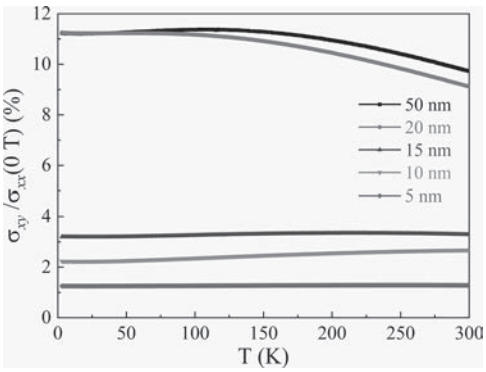


Figure 2. Thickness dependence of anomalous Hall angle as a function of temperature from 300 K to 3 K.

2:06

HF-04. Spin-gapless Semiconducting Nature of Co-rich $Co_{1+x}Fe_{1-x}CrGa$. *D. Rani*[1], E. Enamullah[1], L. Bainsla[2], K. Suresh[1] and A. Alam[1] *1. Physics, IIT BOMBAY, Mumbai, India; 2. WPI Advanced Institute for Materials Research, Tohuku university, Sendai, Japan*

Spin gapless semiconductors (SGSs) are an interesting class of materials which bridge the gap between semiconductors and half-metallic ferromagnets. This class of materials shows band gap in one of the spin channels and a zero band gap in the other [1]. The structural, electronic, magnetic, and transport properties of Co-rich SGS $Co_{1+x}Fe_{1-x}CrGa$ are investigated using both theoretical and experimental techniques. The key advantage of Co-rich samples $Co_{1+x}Fe_{1-x}CrGa$ is the high Curie temperature (T_C) and magnetization, without compromising the SGS nature (up to $x = 0.4$), and hence our choice. The quaternary Heusler alloys $Co_{1+x}Fe_{1-x}CrGa$ ($x = 0.1$ to 0.5) are found to crystallize in LiMgPdSn-type structures. The measured Curie temperature increases from 690 K ($x = 0$) to 870 K ($x = 0.5$). The obtained T_C for $x = 0.3$ (790 K) is found to be the highest among all previously reported SGS materials. Observed magnetization values follow the Slater-Pauling

rule[2, 3]. Measured electrical resistivity, in the temperature range of 5–350 K, suggests that the alloys retain the SGS behavior up to x = 0.4, beyond which it reflects metallic character. Unlike conventional semiconductors, the conductivity value (σ_{xx}) at 300 K lies in the range of 2289 S cm−1 to 3294 S cm−1, which is close to that of other reported SGS materials [4, 5]. The anomalous Hall effect is comparatively low. The intrinsic contribution to the anomalous Hall conductivity increases with x, which can be correlated with the enhancement in chemical order [6]. The anomalous Hall coefficient is found to increase from 38 S/cm for x = 0.1 to 43 S/cm for 0.3. Seebeck coefficients turn out to be vanishingly small below 300 K, another signature for being SGS [5]. Ab-initio calculations indicates that the spin-gapless behavior is retained in the system for x < 0.375 and the alloy becomes HM for x ≥0.375. As such, Co-rich CoFeCrGa is a promising candidate for room temperature spintronic applications, with enhanced T_C, magnetic properties, and SGS nature [7].

o I. M. Tsidilkovski, *Electron Spectrum of Gapless Semiconductors*, edited by K. von Klitzing, Springer Series in Solid-State Sciences, Vol. 116 (Springer, New York, 1997). o J. C. Slater, Phys. Rev. 49, 931 (1936). o L. Pauling, Phys. Rev. 54, 899 (1938). o L. Bainsla, A. Alam, and K. G. Suresh, Phys. Rev.B 92, 045201 (2015). o S. Ouardi, G. H. Fecher, C. Felser, and J. Kübler, Phys. Rev. Lett. 110,100401 (2013). o L. J. Zhu, D. Pan, and J. H. Zhao, Phys. Rev. B 89, 220406(R) (2014). o Deepika Rani, K. G. Suresh, and Aftab Alam, Phys. Rev. B 99, 104429 (2019).

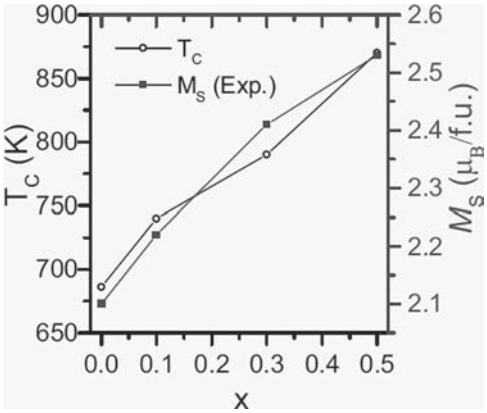


Fig.1 Variation of Curie temperature (T_C) and experimental saturation magnetization with x for $Co_{1+x}Fe_{1-x}CrGa$ alloys.

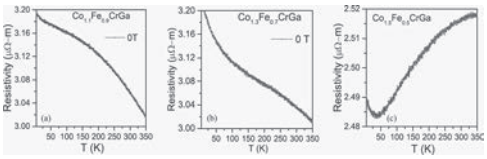


Fig.2 Temperature dependence of electrical resistivity (ρ) for $Co_{1+x}Fe_{1-x}CrGa$ alloys in zero field.

2:18

HF-05. Observation of positive linear magnetoresistance in epitaxial Mn_2CoAl films. *K. Kudo*[1], S. Yamada[2,1], A.N. Hattori[3], H. Tanaka[3,2] and K. Hamaya[2,1] *1. Department of Systems Innovation, Graduate School of Engineering Science, Osaka University, Toyonaka, Japan; 2. Center for Spintronics Research Network, Graduate School of Engineering Science, Osaka University, Toyonaka, Japan; 3. Institute of Scientific and Industrial Research, Osaka University, Ibaraki, Japan*

Spin-gapless semiconductors (SGSs) have been widely explored in the field of spintronics [1,2]. Recently, one of the ferromagnetic Heusler alloys, Mn_2CoAl (MCA), was theoretically and experimentally regarded as an SGS because positive and linear magnetoresistance (MR) due to the quantum linear MR effect [3] was observed despite a ferromagnetic material. However, the previous work was demonstrated in bulk samples [2], which could not be applied to electronics device structures. Although there are lots of studies of MCA films [4-7] for device applications, the positive linear MR effect has not been observed yet in the films. Here we demonstrate high-quality epitaxial MCA films showing the positive linear MR effect for the first time. Epitaxial MCA films were grown on $MgAl_2O_4$(100) substrates at 100 °C by using molecular beam epitaxy. From HAADF-STEM image and EDX line profiles (Fig. 1), we can confirm stoichiometric and uniform MCA layers on $MgAl_2O_4$(100). We also observed XA- or $L2_1$-ordered structures from XRD measurements. Figure 2 shows field-dependent MR curves for a representative MCA film at low temperatures. In addition to the small anisotropic MR (AMR) effect in low magnetic-field region, clear positive and linear MR curves, similar to bulk-MCA [2], are observed even for the film. For the MCA films, we also observed nearly temperature-independent electrical resistivity [2] and gate-tunable resistivity by using electric-double-layer field effect transistors [5] (not shown here). Although the estimated carrier concentration was ~10^{22} cm^{-3}, relatively large compared to bulk-MCA (~10^{20} cm^{-3}) [2], we consider that the observed positive linear MR effect due to the quantum linear MR effect originates from the gapless-like electronic band structure near the Fermi level in MCA [2]. This work was partly supported by JSPS KAKENHI (No. 16H02333, 18KK0111) and JST-CREST (No. JPMJCR18J1).

[1] X. L. Wang, Phys. Rev. Lett. 100, 156404 (2008). [2] S. Ouardi *et al.*, Phys. Rev. Lett. 110, 100401 (2013). [3] A. A. Abrikosov, Phys. Rev. B 58, 2788 (1998). [4] G. Z. Xu *et al.*, Appl. Phys. Lett. 104, 242408 (2014). [5] K. Ueda *et al.*, Appl. Phys. Lett. 110, 202405 (2017). [6] K. Arima *et al.*, Phys. Rev. B 97, 054427 (2018). [7] P. Chen *et al.*, Appl. Phys. Lett. 113, 122402 (2018).

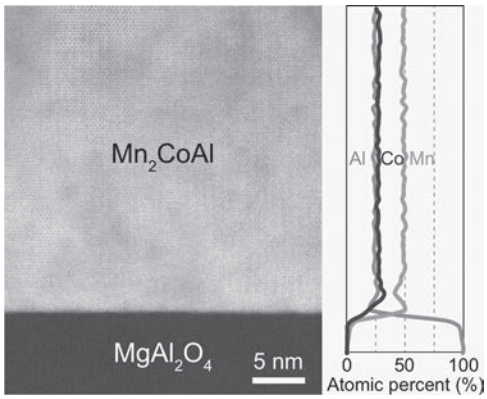


Fig. 1: HAADF-STEM image and EDX line profiles of an epitaxial Mn_2CoAl film.

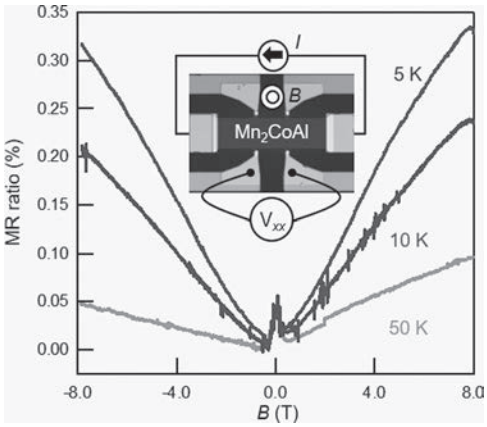


Fig. 2: Field-dependent MR curves at low temperatures for an epitaxial Mn_2CoAl film.

2:30

HF-06. The atomic ordering dependence of valence electronic structure in half-metallic $Co_2Fe(Ga_{0.5}Ge_{0.5})$ Heusler alloy observed by hard X-ray photoemission spectroscopy. *K. Goto*[1,2], Y. Sakuraba[2], Y. Miura[2], I. Kurniawan[2,1], A. Yasui[3], K.R. Loku Singgappulige[3], Z. Chen[2,1], H. Tajiri[3], A. Kimura[4] and K. Hono[2,1] *1. University of Tsukuba, Tsukuba, Japan; 2. Research Center for Magnetic and Spintronic Materials, National Institute for Materials Science, Tsukuba, Japan; 3. Japan Synchrotron Radiation Research Institute, Sayo, Japan; 4. Hiroshima University, Higashi-hiroshima, Japan*

Recently, large MR ratio over 50% at room temperature have been demonstrated in CPP-GMR devices using half-metallic Heusler alloy, $Co_2FeGa_{0.5}Ge_{0.5}$ (CFGG),[1] which is promising for future applications such as a next generation read head for HDD. However, it is still an open question how much intrinsic spin-polarization in the bulk region (β) and how β changes with temperature. To find an answer to this question, it is crucial to see the bulk electronic structure of the Heusler alloy and investigate its correlation with bulk sensitive spin-dependent transport. In this study, first, anomalous XRD was performed for CFGG thin films annealed at different temperature at BL13XU SPring-8 to quantitatively evaluate the degree of atomic ordering including the order between Co and Fe. Then, hard X-ray photoemission spectroscopy (HAXPES) was performed at BL09XU SPring-8 to observe how half-metallic valence band (VB) structure forms with atomic ordering. Fig 1 shows the X-ray energy dependence of $I_{(002)}/I_{(004)}$ intensity ratio of different ordered CFGG measured by AXRD. The enlargement of the peak at Co *K* absorption edge indicates the improvement of Co-Fe ordering with increasing annealing temperature. Fig. 2(a) shows VB HAXPES spectra. The observed variation of VB structure agrees well with the spin integrated DOS calculated by the *ab initio* calculation results for different atomic ordering evaluated by AXRD (Fig 2(b)). Structures A-E corresponded to structures a-e in Fig. 2(b) are enhanced with the atomic ordering. In contrast, the structure Z around $E_B = 0.3$ eV is suppressed with the atomic ordering. This result suggests HAXPES directly observed the existence of in-gap state by Co-Fe disordering and the formation of half-metallic gap by improving Co-Fe ordering. The spin-dependent transport property of CFGG will be discussed from viewpoint of the electronic structure in bulk region based on our HAXPES study.

1. J. W. Jung *et al*., Appl. Phys. Lett. 108, 102408 (2016)

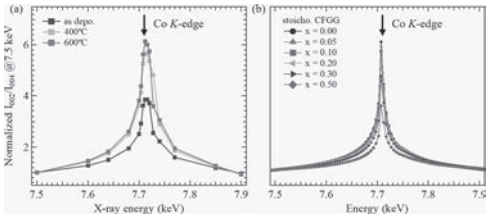


Fig. 1. (a) The $I_{(002)}/I_{(004)}$ intensity ratio and (b) simulation of different ordered CFGG.

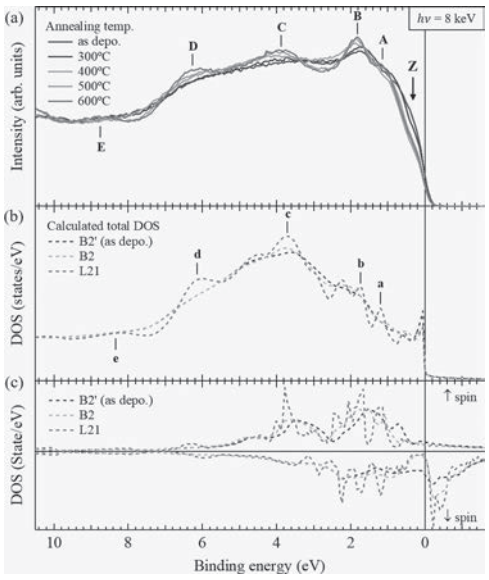


Fig. 2. (a) Valence band HAXPES spectra of CFGG annealed at different temperature. (b) Spin integrated (considering photoionized cross section) and (c) spin separated total DOS of different ordering CFGG calculated by KKR method.

2:42

HF-07. Nanoscale Magnetic Phase Competition Across the $Ni_{50-x}Co_xMn_{40}Sn_{10}$ Phase Diagram: Insights from Small-Angle Neutron Scattering. *S. El-Khatib*[1,2], K. Bhatti[2], V. Srivastava[3], R. James[3] and C. Leighton[2] *1. Physics, American University of Sharjah, Sharjah, United Arab Emirates; 2. Chemical Engineering and Materials Science, University of Minnesotta, Minneapolis, MN, United States; 3. Department of Aerospace Engineering and Mechanics, University of Minnesota, Minneapolis, MN, United States*

Ni_2MnSn-derived $Ni_{50-x}Co_xMn_{25+y}Sn_{25-y}$ alloys are prime examples of off-stoichiometric Heusler alloys recently discovered to exhibit attractive magnetic properties and extraordinarily reversible martensitic phase transformations. Multiferroicity, magnetic phase competition/separation, magnetic shape memory, and magneto-, elasto-, and baro-caloric effects result, generating great interest and application potential [1]. Here, we use small-angle neutron scattering (SANS) (previously applied only at a single *x* [2]) to explore all three regions of the $Ni_{50-x}Co_xMn_{40}Sn_{10}$ phase diagram (Fig. 1) [1]. Wide temperature and scattering vector range (20 – 500 K, 0.004 – 0.2 $Å^{-1}$) SANS on $x = 2$, 6, and 14 polycrystals (e.g., Fig. 2) provides a detailed picture of the evolution in magnetic order and inhomogeneity. Phase separation into short-range coexisting ferromagnetic and antiferromagnetic regions is deduced below the martensitic transformation at $x = 2$ and 6, with ~13 nm ferromagnetic cluster spacing. Remarkably, at $x = 14$, where the martenstic transformation is suppressed and ferromagnetic austenite is stabilized to low temperatures, nanoscopic magnetic inhomogeneity nevertheless persists. Distinct ferromagnetic clusters (~36 nm spacing) in a ferromagnetic matrix are observed at intermediate temperatures, homogenizing into uniform ferromagnetism only at low temperatures. This unusual ferromagnet cluster/ferromagnet matrix inhomogeneity, as well as subtleties of magnetic cluster freezing, are discussed in light of nuclear magnetic resonance data [3,4], and the recent observation of annealing-induced core/shell nanoprecipitates. Implications for origins of magnetic inhomogeneity in such alloys will be discussed.

Work supported by DOE Center for Quantum Materials [1] Bhatti, Srivastava, Phelan, El-Khatib, James and Leighton, in *Heusler Alloys*, eds. A. Hirohata and C. Felser, Springer (2015). [2] Bhatti, El-Khatib, Srivastava, James and Leighton, Phys. Rev. B. 85, 134450 (2012). [3] Yuan,

Kuhns, Reyes, Brooks, Hoch, Srivastava, El-Khatib, James and Leighton, Phys. Rev. B. 91, 214421 (2015). [4] Yuan, Kuhns, Reyes, Brooks, Hoch, Srivastava, James and Leighton, Phys. Rev. B. 93, 094425 (2016).

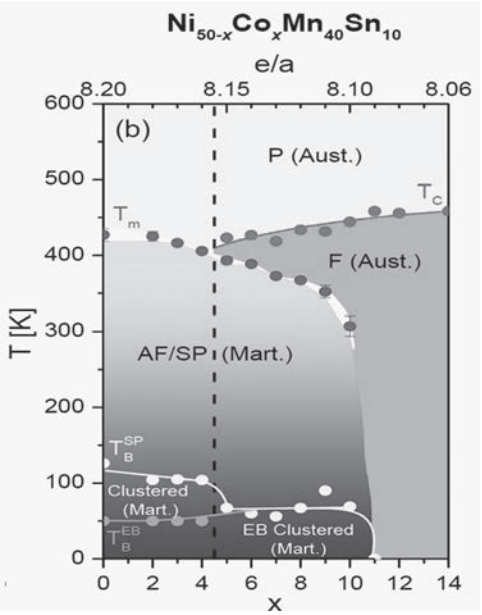


Fig. 1: Magnetic phase diagram of $Ni_{50-x}Co_xMn_{40}Sn_{10}$. T_M and T_C are the martensitic transformation and Curie temperature; T_B^{SP} and T_B^{EB} are the superparmagnetic and exchange bias blocking temperatures. "Aust." and "Mart." are austenite and martensite. P, F, AF, and SP are paramagnetic, ferromagnetic, antiferromagnetic, and superparamagnetic.

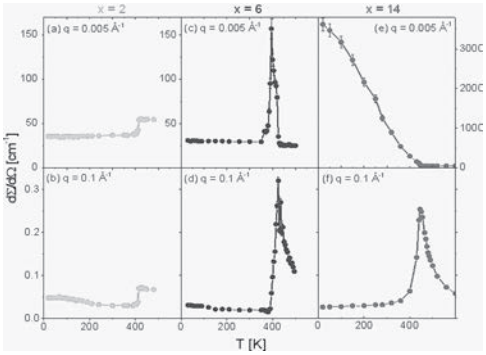


Fig. 2: Temperature (T) dependence of the SANS cross section ($d\Sigma/d\Omega$) for x = 2 (a,b), 6 (c,d), and 14 (e,f), at low (0.005 Å^{-1}) and high (0.1 Å^{-1}) scattering vector (q).

2:54

HF-08. Giant current-orientation effect of the anisotropic magnetoresistance in Co_xFe_{1-x} single crystal films. *F. Zeng*[1], Z. Ren[2,4], Y. Li[3], J. Zeng[1], J. Miao[2], W. Zhang[3], Z. Yuan[4] and Y. Wu[1] *1. Department of Physics, Fudan University, Shanghai, China; 2. School of Materials Science and Engineering, University of Science and Technology Beijing, Beijing, China; 3. Department of Physics, Oakland University, Rochester, MI, United States; 4. Department of Physics, Beijing Normal University, Beijing, China*

Anisotropic magnetoresistance (AMR) is one of the most fundamental magneto-transport properties. Although in polycrystalline system AMR is independent of the current orientation, in single crystalline system the current orientation with respect to the crystal axis could influence AMR owing to the crystal symmetry breaking. So far, the reported current orientation effects on AMR have been restricted to 100 % ~ 200 % in semiconducting ferromagnetic alloys [1]. Understanding the current-orientation effect on AMR in metallic crystalline alloys could be crucial for further revealing the intrinsic mechanism of the spin-dependent transport properties in magnetic materials. In this work, we systematically studied the current-orientation effect of AMR in single-crystal Co_xFe_{1-x} alloys, which have recently aroused tremendous interests due to the ultralow Gilbert damping exhibited [2]. For Co concentrations x between 0.2 and 0.65, we found a significantly large current-orientation effect of the AMR. At x=0.65, for example, the difference in the relative magnitudes of the AMR ratio reaches over 4000 % for current along <100> an <110> directions. But the planar Hall effect shows a clear reciprocal relationship for this two current directions. In addition, the current-orientation effect of the AMR also strongly influences the spin rectification effect at gigahertz frequencies. The experimental AMR observations are consistently described by a symmetry-based phenomenological model and first-principles calculations. The band structure calculation explains the giant anisotropic AMR effect in Co_xFe_{1-x} alloys, which reveals that AMR is related to the nodal ring points in the electronic band structure. This large current-orientation AMR effect is expected to have significant potential to be implemented in future dc and high-frequency spintronics devices, e.g., as a signal readout technique.

[1] A. W. Rushforth, et al. Phys. Rev. Lett. 99, 147207 (2007) [2] M. A. W. Schoen, et al. Nature Phys. 12, 839 (2016)

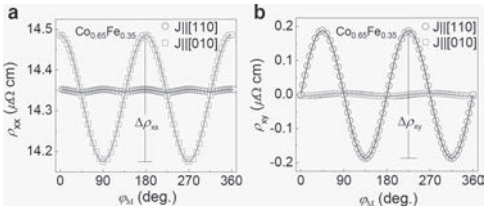


Figure 1 (a) The longitudinal resistivity ρ_{xx} and (b) transverse resistivity ρ_{xy} as a function of φ_M with the current along [110] and [010] for a 10-nm-thick single crystalline $Co_{0.65}Fe_{0.35}$ sample.

3:06

HF-09. Low-Symmetry Transverse Magnetoresistance in Permalloy. *J. Gibbons*[1,2], J. Pearson[2], R. Winkler[3,2] and A. Hoffmann[2] *1. Physics, University of California, San Diego, La Jolla, CA, United States; 2. Materials Science Division, Argonne National Laboratory, Lemont, IL, United States; 3. Department of Physics, Northern Illinois University, DeKalb, IL, United States*

Magnetic ordering, interfacial effects, and spin-orbit coupling can effectively break symmetries in crystal structures, and thus have been observed to generate magnetoresistances with anisotropic properties. Spin Hall magnetoresistance was detected in YIG/Pt systems in 2013 [1-2], while more recently, uniaxial magnetoresistance [3-5] and anomalous Hall magnetoresistance [6-7] have been discovered. In addition to direct applications for resistance control or magnetic direction detection, these effects can probe the strength and nature of the underlying mechanism by which the symmetry is broken. Spin Hall magnetoresistance and anomalous Hall magnetoresistance have been used to understand spin accumulations generated by spin-orbit coupling, and it is possible that other spintronics effects, including potential spin-induced planar Hall magnetoresistances, may be probed through magnetoresistance effects. While longitudinal magnetoresistance effects have been studied in some depth for simple ferromagnets, transverse magnetoresistance (Hall voltage) effects have received less attention. We have conducted an investigation of transverse and longitudinal magnetoresistance in sputtered permalloy ($Ni_{80}Fe_{20}$) and permalloy/heavy metal bilayers as the permalloy's magnetization is manipulated with external magnetic fields up to 14 T. We have particularly focused on the transverse magnetoresistance generated as the magnetization of the permalloy is rotated into the out-of-plane direction.

We report magnetoresistance signals indicative of novel symmetry-breaking mechanisms in ferromagnetic systems and discuss the implications of these findings. This work was supported as part of Quantum Materials for Energy Efficient Neuromorphic Computing, an Energy Frontier Research Center funded by the U.S. DOE, Office of Science.

[1] H. Nakayama et al., Phys. Rev. Lett. 110, 206601 (2013) [2] Yan-Ting Chen et al., Phys. Rev. B 87, 144411 (2013) [3] K. Olejník, V. Novák, J. Wunderlich, and T. Jungwirth, Phys. Rev. B 91, 180402(R) (2015) [4] Can Onur Avci et al., Nat. Phys. 11, 570-575 (2015) [5] Can Onur Avci et al., Appl. Phys. Lett. 107, 192405 (2015) [6] Yumeng Yang et al., Nat. Commun. 9, 2255 (2018) [7] Masashi Kawaguchi et al., Appl. Phys. Lett. 112, 202405 (2018)

3:18

HF-10. Origin of Perpendicular Magnetic Anisotropy of the Ferromagnetic Semiconductor (Ba,Zn)(Zn,Mn)$_2$As$_2$: Angle-dependent XMCD Study. *S. Sakamoto*[1,2], G. Zhao[3], G. Shibata[1], Z. Deng[3], K. Zhao[3], B. Chen[3], Y. Nonaka[1], K. Ikeda[1], Z. Chi[1], Y. Wan[1], M. Suzuki[1], T. Koide[4], S. Maekawa[5], Y. Uemura[6], C. Jin[3] and A. Fujimori[1] *1. Physics, The University of Tokyo, Bunkyo-ku, Japan; 2. SIMES, SLAC National Accelerator Laboratory, Menlo Park, CA, United States; 3. Chinese Academy of Sciences, Beijing, China; 4. KEK, Tsukuba, Japan; 5. JAEA, Tokai, Japan; 6. Columbia University, New York, NY, United States*

(Ba,K)(Zn,Mn)$_2$As$_2$ is a new *p*-type diluted ferromagnetic semiconductor, which crystallizes in the tetragonal $ThCr_2Si_2$ structure (*I*4/*mmm*) [1]. The host compound $BaZn_2As_2$ is a narrow-gap semiconductor with a band gap of 0.2 eV [2]. Since Mn^{2+} substitution for Zn^{2+} does not introduce carriers to the system, it is possible to control the number of holes independently by substituting K^+ for Ba^{2+}. The Curie temperature (T_C) reaches 230 K exceeding the highest T_C = 200 K of (Ga,Mn)As. Owing to the layered crystal structure, this material has a perpendicular magnetic anisotropy [3]. In this study, to reveal the origin of the uniaxial magnetic anisotropy, we have measured K 9.6%- and Mn 19.5%-doped single crystals using the angle-dependent x-ray magnetic circular dichroism (AD-XMCD) method. AD-XMCD is a unique method by which one can directly measure the anisotropy of spin and orbital magnetic moments. In addition, by aligning the spin magnetic moment perpendicular to the incident x ray (transverse geometry), one can probe the anisotropic distribution of the 3*d* spin density [4]. The obtained x-ray absorption spectra (XAS) and XMCD spectra were similar to those of (Ga,Mn)As [5] as shown in Fig. 1. This indicates that the ferromagnetism is carrier-induced as in the case of (Ga,Mn)As. Figure 2 shows the XMCD spectra taken with the transverse geometry (TXMCD). The observed finite dichroic signals originate from the aspherical distribution of 3*d* electrons, and indeed the TXMCD spectra were well reproduced by the configuration-interaction cluster-model calculation incorporating the D_{4h} crystal-field splitting. Since hole carriers were found to reside in the d_{xz} and d_{yz} orbitals in the calculation, we propose that lifting the degeneracy of p-$d_{xz,yz}$ hybridized orbitals at the Fermi level caused by spin-orbit interaction is responsible for the perpendicular magnetic anisotropy of this compound.

[1] K. Zhao, Z. Deng, X. C. Wang *et al*., Nature Communications, Vol. 4, p.1442 (2013) [2] Z. Xiao, F.-Y. Ran, H. Hiramatsu *et al*., Thin Solid Films, Vol. 559, p.100 (2014) [3] G. Q. Zhao, C. J. Lin, Z. Deng *et al*., Scientific Reports, Vol 7, p.14473 (2017) [4] G. Shibata, M. Kitamura, M. Minohara *et al*., npj Quantum Materials, Vol. 3, p. 3 (2018) [5] Y. Takeda, M. Kobayashi, T. Okane *et al*., Physical Review Letters, Vol.100, p. 24702 (2008)

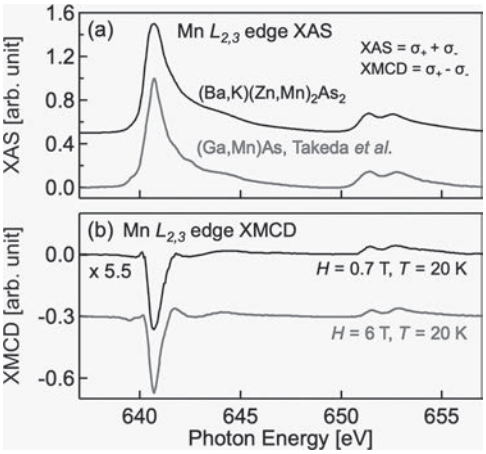


Fig. 1 (a) XAS and (b) XMCD spectra of (Ba,K)(Zn,Mn)$_2$As$_2$ and (Ga,Mn)As [5].

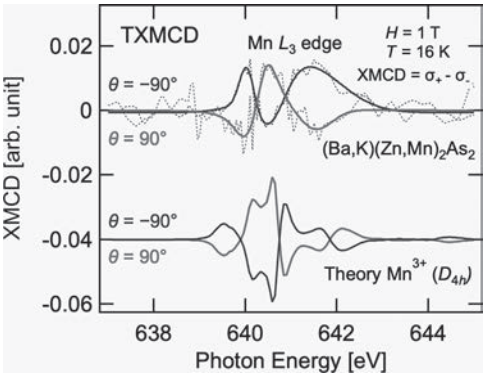


Fig. 2 Transverse XMCD spectra. Calculated spectra are also shown at the bottom. Here, θ represents the angle between the magnetic moment and x rays.

3:30

HF-11. Ferromagnetism and Anisotropic Spinodal Phase Separation in (In,Fe)As. *Y. Yuan*[1], R. Hübner[1], M. Birowska[2], M. Helm[1], M. Sawicki[3], T. Dietl[4,5] and S. Zhou[1] *1. Institute of Ion Beam Physics and Materials Research, Helmholtz-Zentrum Dresden-Rossendorf, Dresden, Germany; 2. Institute of Theoretical Physics, University of Warsaw, Warsaw, Poland; 3. Institute of Physics, Polish Academy of Sciences, Warsaw, Poland; 4. International Research Centre MagTop, Institute of Physics, Warsaw, Poland; 5. WPI-Advanced Institute for Materials Research, Tohoku University, Sendai, Japan*

We report on the experimental observation and theoretical studies of a self-assembled Fe-rich (In,Fe)As nano-lamellar structure that is driven by anisotropic spinodal decomposition at the growth front during laser heating-induced recrystallization of Fe-implanted InAs [1]. Pseudomorphically embedded in the InAs lattice, those Fe-rich nano-lamellae are perpendicular to the (001) surface and parallel to the in-plane [1-10] crystallographic direction. The Fe atoms are substitutionally incorporated at the indium sites. Magnetic measurements indicate a typical blocked superparamagnetic behavior suggesting strong ferromagnetic orderings inside the Fe-rich nanostructures, but weak coupling between the nano-lamellae. Our findings explain the surprisingly high apparent Curie temperatures and unexpected two- and eight-fold symmetry of crystalline anisotropic magnetoresistance found previously in Be-doped n-type (In,Fe)As grown by molecular beam epitaxy [2]. Prompted by these results we discuss how a different d-level electronic configuration of Fe in InAs and Mn in GaAs [3] affects the magnetic ion incorporation and spatial distribution and, thus, magnetism

and anisotropy. Our results also indicate that the directional distribution of impurities or alloy components setting in during the growth may account for the observed nematicity in other classes of correlated systems.

[1] Y. Yuan, R. Hübner, M. Birowska etc., Phys. Rev. Materials 2, 114601(2018). [2] P. N. Hai, D. Sasaki, L. Anh etc., Appl. Phys. Lett. 100, 262409(2012). [3] M. Birowska, C. Sliwa, J. A. Majewski etc., Phys. Rev. Lett. 108, 237203(2012).

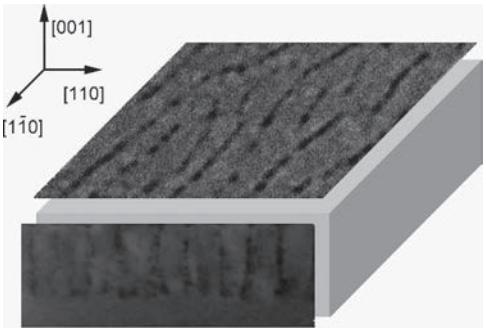


Fig 1. The plain- and cross-sectional view of Fe-rich nano-sheets embedded in InAs: They are aligned along one crystalline direction.

3:42

HF-12. <100>/<110> In Plane Cubic Anisotropy Switching in (Ga,Mn)As. *M. Sawicki*[1], O. Proselkov[1], C. Sliwa[1], P. Aleshkevych[1], J.Z. Domagala[1], J. Sadowski[1,2] and T. Dietl[3,4] *1. Institute of Physics, Polish Academy of Sciences, Warszawa, Poland; 2. Department of Physics and Electrical Engineering, Linnaeus University, Kalmar, Sweden; 3. International Research Centre MagTop, Institute of Physics, Polish Academy of Sciences, Warszawa, Poland; 4. WPI-Advanced Institute for Materials Research, Tohoku University, Sendai, Japan*

Historically, comprehensive studies of dilute ferromagnetic semiconductors, e.g., *p*-type (Cd,Mn)Te and (Ga,Mn)As, paved the way for a quantitative theoretical description of effects associated with spin-orbit interactions in solids, such as crystalline magnetic anisotropy. In particular, the theory was successful in explaining *uniaxial* magnetic anisotropies associated with biaxial strain and non-random formation of magnetic dimers in epitaxial (Ga,Mn)As layers. However, the situation appears much less settled in the case of the *cubic* term: the theory [1] predicts switchings of the easy axis between in-plane <100> and <110> directions as a function of the hole concentration, whereas only the <100> orientation has been found experimentally. Here, we report on the experimental observation of such switchings by magnetization and ferromagnetic resonance studies on a series of high-crystalline quality (Ga,Mn)As films [2]. Our findings are described by the mean-field *p-d* Zener model [1] augmented with three new ingredients [2]. The first one is a scattering broadening of the hole density of states, which reduces significantly the amplitude of the alternating carrier-induced contribution. This opens the way for the two other ingredients, namely the so-far disregarded single-ion magnetic anisotropy and disorder-driven non-uniformities of the carrier density, both favoring the <100> direction of the apparent easy axis. Accordingly, when the disorder gets reduced a switching to the <110> orientation is possible in a certain temperature (as presented in Fig. 1) and hole concentration range. The work has been supported by the National Science Centre, Poland through UMO - 2011/02/A/ST3/00125 grant.

[1] T. Dietl, H. Ohno, and F. Matsukura, *Hole-mediated ferromagnetism in tetrahedrally coordinated semiconductors*, Phys. Rev. B Vol 63, 195205 (2001). [2] M. Sawicki O. Proselkov, C. Sliwa, P. Aleshkevych, J. Z. Domagala, J. Sadowski and T. Dietl, *Cubic anisotropy in (Ga,Mn)As layers: Experiment and theory,* Phys. Rev. B Vol 97, 184403 (2018).

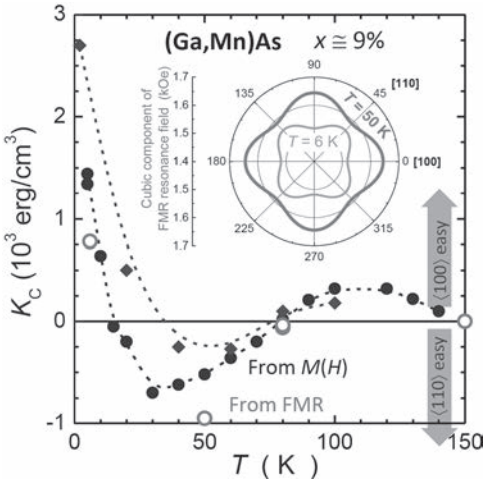


Fig.1. Temperature dependence of cubic anisotropy constants, K_C. Solid points are obtained from analysis of uniaxial hard axis magnetization curves, open ones are obtained from analysis of in-plane angular dependence of FRM resonance positions (their cubic component is shown in the inset). Dashed lines are guides for the eye only. In the notion adopted here the positive/negative sign of K_C indicates that the cubic easy axes are aligned along <100> / <110> directions, respectively.

3:54

HF-13. Transition Metal Doped MoS_2 with Controllable Doping Concentration. *M. Bian*[1,3], J. Wang[2], K. Yao[2], Y. Li[2,1], S. Yang[2], Y. Hou[3] and H. Zeng[1] *1. Department of Physics, University at Buffalo, SUNY, Buffalo, NY, United States; 2. Xi'an Jiaotong University, Xi'an, China; 3. Peking University, Beijing, China*

Two-dimensional (2D) transition metal dichalcogenides (TMDs) have attracted enormous attention due to their unique spin-locked valley properties. Breaking valley degeneracy is an approach to manipulate the valley degree of freedom for classical and quantum information applications. Based on the idea of realizing diluted magnetic semiconductor, introducing magnetic transition metal ions into TMDs may provide a convenient route to introduce magnetic order, and break the time reversal symmetry. In situ doped manganese (Mn) in monolayer molybdenum disulfide (MoS_2) via vapor phase deposition techniques was reported earlier. However, the doping concentration was low and there was no direct demonstration by magnetic measurements. In this work, we developed an effective approach to dope MoS_2 monolayer with controllable concentration of Mn ions. In this approach, a single phase Mn-doped MoO_3 compound precursor was used to synthesize Mn-doped MoS_2. The magnetic properties of monolayer Mn doped MoS_2 and undoped MoS_2 were measured with Quantum Design Magnetic Property Measurement System (MPMS), which indicated that the ferromagnetism of monolayer MoS_2 was enhanced dramatically (as shown in Figure 1). Furthermore, we use magneto-optical measurements to investigate the valley properties.

K. Zhang et al., *Nano Letters* 2015, *15*, 6586-6591.

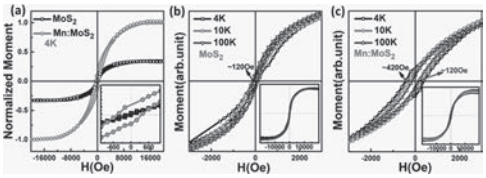


Figure 1 (a) The M-H curves of un-doped MoS_2 monolayer and Mn: MoS_2 monolayer at 4K; inset is the M-H curves in the field range of -1000 to 1000 Oe. The M-H curves of (b) MoS_2 monolayer, (c) Mn: MoS_2 monolayer at 4K, 10K and 100K, plotted in the field range of -3000 to 3000 Oe in order to demonstrate the change in coercivity; inset are the M-H curves in the range of -20000 to 20000 Oe.

4:06

HF-14. Magnon-contributed Unidirectional Magnetoresistance in Ferrimagnet/heavy-metal Bilayers. *S. Lee*[1,2], J. Kang[1], J. Lee[2], J. Kim[2], S. Kim[3], N. Lee[3], K. Changsoo[5], K. Moon[5], C. Hwang[5], S. Park[4], B. Park[2] and K. Kim[1] *1. Department of Physics, Korea Advanced Institute of Science and Technology (KAIST), Daejeon, The Republic of Korea; 2. Department of Materials Science and Engineering, Korea Advanced Institute of Science and Technology (KAIST), Daejeon, The Republic of Korea; 3. Department of Physics, University of Ulsan, Ulsan, The Republic of Korea; 4. Division of Scientific Instrumentation, Korea Basic Science Institute (KBSI), Daejeon, The Republic of Korea; 5. Quantum Technology Institute, Korea Research Institute of Standards and Science (KRISS), Daejeon, The Republic of Korea*

Ferrimagnet (FIM) is an excellent platform to explore the antiferromagnetic spintronics because it shows antiferromagnetic spin dynamics at the magnetization or angular momentum compensation points. For example, the ultrafast domain wall motion was indeed realized in angular-momentum-compensated GdFeCo-FIM [1]. However, at the compensation points, the effect of spin dynamics on the electrical transport have received less attention, despite the exotic electrical transport in magnetic materials (e.g. various magnetoresistance effects) lies at the heart of spintronic applications. Moreover, the recently discovered unidirectional magnetoresistance (UMR) in ferromagnet/heavy-metal bilayers is a good probe to study on the interaction between spin dynamics and the electrical transport because the UMR is possibly induced by the spin-current-driven magnon excitation [2-4]. In this study, we investigated the magnon-induced UMR in CoGd 10/Pt 5 (nm) bilayers with composition variation and compared it with Brillouin light scattering (BLS) spectra in order to clarify the effect of the spin dynamics on the spin transport across the compensation point. Figure 1(a) shows that the UMR is obtained from bilayers with different compositions. We found that two peaks near zero field, representing magnon-induced UMR, are clearly enhanced in the magnetization-compensated $Co_{65}Gd_{35}$/Pt bilayer. Figure 1(b) presents the center frequencies of BLS spectra under different in-plane fields as a function of Gd concentration, demonstrating that the lowest value appears at 35% of Gd. This indicates that CoGd has the smallest magnon gap at the magnetization compensation point. Thus, we can conclude that the magnon-induced UMR is effectively generated by the strong magnon excitation due to a small magnon gap. These results suggest that the dynamics of FIM is strongly correlated to the magnetoelectrical transport.

[1] K. Kim, Se Kwon Kim, and Yuushou Hirata, et al. Nature Materials, 16, 1187 (2017) [2] K. Kim, T. Li, and S. Kim, et al, Applied Physics Express 12, 063001 (2019) [3] K. Yasuda, A. Tsukazaki, and R. Yoshimi, et al, Physical Review Letters, 117, 127202 (2016) [4] C. O. Avci, J. Mendill, and G. S. D. Beach, et al, Physical Review Letters, 121, 087207 (2018)

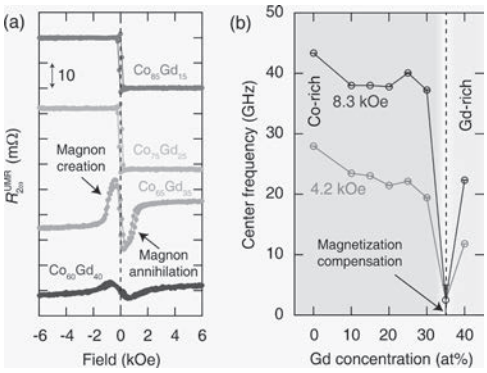


Fig. 1 (a) The current density dependent UMR in the CoGd 10/Pt 5 (nm) bilayers with composition variation of CoGd. (b) CoGd composition dependent center frequencies of BLS spectra.

4:18

HF-15. Magnetic Field Driven Electrical Diodes using InAs Nanowire. *J. Jeon*[1,2], T. Kim[1,2], S. Joo[3], J. Shin[4], H. Koo[1,5] and J. Hong[2] *1. Center of Spintronics, Korea Institute of Science and Technology, Seoul, The Republic of Korea; 2. Department of Applied Physics, Korea University, Sejong, The Republic of Korea; 3. Center of Electricity and Magnetism, Korea Research Institute of Standards and Science, Daejeon, The Republic of Korea; 4. Department of Physics, Yeungnam University, Gyeongsan, The Republic of Korea; 5. KU-KIST Graduate School of Converging Science and Technology, Korea University, Seoul, The Republic of Korea*

Large magneto-conductance effect has received considerable attention for reconfigurable logic applications[1,2]. However, practical efforts to develop this new device suffer from low signal-to-noise ratio and scale down issues. Here we investigate magneto-conductance in InAs nanowires which have high mobility and narrow band-gap in comparison with silicon-based nano-channelones, leading to highly sensitive to the magnetic field. Due to impact ionization mechanism, this material exhibits a considerable change of conductance in response to a bias voltage[3] (see Fig.1). We demonstrate that this impact ionization is controlled effectively by the magnetic field as well. This feature comes from the magnetic field dependent carrier generation and recombination. The correlation between impact ionization and magnetic field results in the four-order-change of magneto-conductance. Thus, our devices can be used as an electrical switch whose ON/OFF state is determined by the magnetic field. Moreover, this ON/OFF state is dependent on the polarity of magnetic field: for a given field strength, the device shows ON state for a certainsome field direction, while it becomes OFF state for the opposite direction (see Fig.2). Through photoconductivity measurement, we experimentally verify this diode characteristics is caused by the recombination at the nanowire surfaces. We believe that this work shows the possibility of application for reconfigurable logic devices[1,2].

1. S. Joo, T. Kim, S. Shin, Nature, 494, 72-76 (2013) 2. S. Manipatruni, D. Nikonov, C. Lin, Nature, 565, 7737 (2019) 3. S. Li, W. Luo, J. Gu, Nano Lett, 15(12), 8026-8031 (2015)

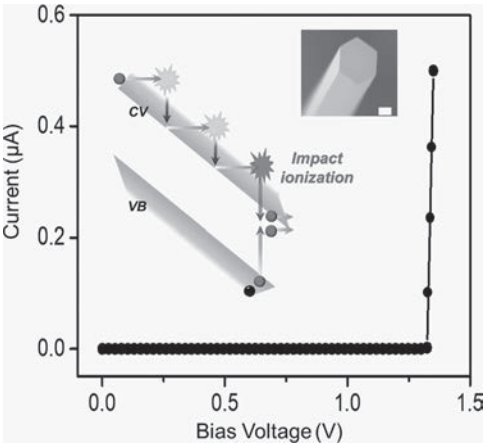


Fig.1 Plots of current versus bias voltage in the absence of magnetic field. Electric current dramatically increases at a threshold voltage of near 1.3V. Impact ionization is illustrated in the middle inset. The right-top inset is a scanning electron microscopySEM image of InAs nanowire.

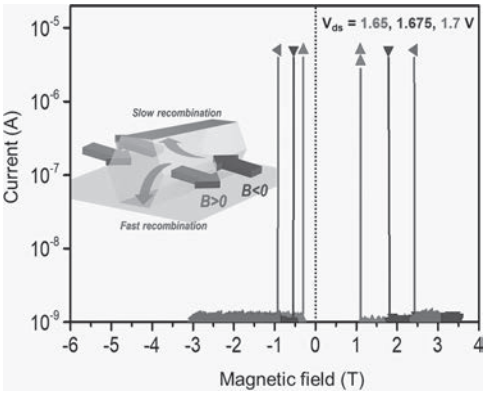


Fig.2 Plot of current versus magnetic field for various external voltage ranging between 1.65 V and 1.9 V. The threshold magnetic field dependent on bias voltage. The impact ionization is suppressed for the negative magnetic field and is strengthen for the positive one, which leads to diode character of the present device.

Session HG
DOMAIN WALLS AND DOMAIN WALL DEVICES

Anjan Soumyanarayanan, Chair
Agency for Science, Technology & Research, Singapore

INVITED PAPER

1:30

HG-01. Chiral Exchange Drag. *S. Yang*[1] *1. IBM Research - Almaden, San Jose, CA, United States*

Long-range interactions between quasiparticles give rise to a 'drag' that affects the fundamental properties in condensed matter physics like Coulomb drag [1]. Drag typically involves the exchange of linear momentum between quasiparticles affecting transport properties. We recently discovered a new form of drag, "Chiral Exchange Drag", that involves the exchange of angular momentum between two current-driven magnetic domain walls (DWs) [2]. We found that the DWs motions are correlated and determined by the strength of the drag. For example, when the drag is below a threshold value, the DWs move together at a constant intermediate velocity with a steady leakage of angular momentum from the faster to the slower wall. On the other hand, we showed that when the drag exceeds a threshold value, an entirely different dynamic can take place in which the faster DW's magnetization oscillates synchronously with a precessional motion of the slower DW's magnetization, and angular momentum is continuously transferred between them: "Chiral Exchange Drag Anomaly". Our findings demonstrate a method for delivering spin angular momentum remotely to magnetic entities showing analogues with Dirac fermions.

[1] B. N. Narozhny, and A. Levchenko, "Coulomb drag", Rev. Mod. Phys. 88, 025003 (2016). [2] S.-H. Yang, C. Garg, and S. S. P. Parkin, "Chiral Exchange Drag and Chirality Oscillations in Synthetic Antiferromagnets", Nat. Phys. DOI: 10.1038/s41567-019-0438-3 (2019).

CONTRIBUTED PAPERS

2:06

HG-02. Ultrafast Current-Driven Domain Wall Motion in Magnetic Insulting Garnets. *L.M. Caretta*[1], S. Oh[2], T. Fakhrul[1], D. Lee[2], S. Kim[3], C. Ross[1], K. Lee[2,4] and G. Beach[1] *1. MIT, Cambridge, MA, United States; 2. Korea University, Seoul, The Republic of Korea; 3. University of Missouri, Columbia, MO, United States; 4. KU-KIST, Seoul, The Republic of Korea*

The study of the dynamics of magnetic quasiparticles, such as chiral skyrmions and domain walls (DW), has attracted much attention, not only for its underlying physics, but also for its potential technological applications in next-generation memory and logic operations. As such, the urge to push the boundaries of quasiparticle velocities to their fundamental limits has been of strong interest. Research of quasi particle dynamics has focused on chiral spin textures in metallic ferromagnet systems, where a heavy metal underlayer, such as Pt, provides both a large spin-orbit torque and an interfacial DMI[1–3]. However, damping in metals is generally high, which limits the spin texture mobility. Furthermore, ferromagnets have fundamental limits for spin texture speed[4]. A broader, ubiquitous class of materials, magnetic insulating garnets, have been extensively studied for their technologically desired spintronic properties[5]. Their low damping and ferrimagnetic dynamics make them ripe candidates for ultrafast spin textures. Moreover, the Dzyaloshinskii-Moriya interaction (DMI) has recently been observed in these materials, and spin-orbit effects from adjacent heavy metal layers have been used to manipulate the magnetisation in these materials[6,7]. Here, we use a pure spin current from an adjacent Pt overlayer to characterise chiral DW motion in epitaxial iron garnet films with perpendicular magnetic anisotropy. By studying both the rare-earth dependence and thickness dependence of the DMI, we find that the DMI is a general feature of rare-earht iron garnet films, and that DMI manifests from the substrate oxide – magnetic oxide interface. We use the significant interfacial DMI and a large spin-orbit torque to drive chiral DWs in GGG/TmIG/Pt to over 2000 m/s. Moreover, we characterize the dynamics in this system as a function of both TmIG thickness and temperature. Finally, we demonstrate current-driven DW motion in low-damping GSGG/BiYIG/Pt to record velocities of over 4000 m/s, approaching the magnon group velocity in the system.

1 Emori, S. *et al. Nat. Mater.* 12, 611–6 (2013) 2 Ryu, K.-S. *et al. Nat. Nanotechnol.* 8, 527–533 (2013) 3 Woo, S. *et al. Nat. Mater.* 15, 501–506 (2016) 4 Caretta, L. *et al. Nat. Nanotechnol.* 13, 1154–1160 (2018) 5 Bibes, M. *et al. IEEE Trans. Electron. Dev.* 54, 1003–1023 (2007) 6 Avci, C. O. *et al. Nat. Mater.* 16, 309–314 (2017) 7 Avci, C. O. *et al. Nat. Nanotechnol.* 14, 561–566 (2019)

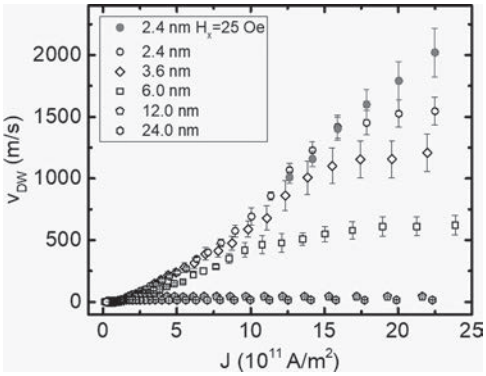


Fig 1. Thickness-dependent DW velocity in TmIG/Pt

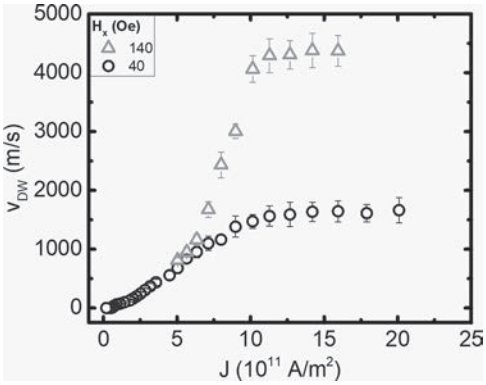


Fig 2. Ultrafast, current-driven DW motion in BiYIG

2:18

HG-03. Ultrafast current induced domain wall motion in Mn_4N ferrimagnetic thin films for sustainable spintronics. *S. Ghosh*[1], T. Gushi[2,1], M.J. Klug[3], J.P. Garcia[3], J. Attané[1], O. Fruchart[1], J. Vogel[3], T. Suemasu[2], S. Pizzini[3] and L. Vila[1] *1. University of Grenoble-Alpes, CEA, CNRS, Grenoble INP, IRIG, SPINTEC, Grenoble, France; 2. Institute of Applied Physics, Graduate School of Pure and Applied Sciences, University of Tsukuba, Ibaraki, Japan; 3. University of Grenoble Alpes, CNRS, Institut Néel, Grenoble, France*

Spintronics, which is the basis of a low-power, beyond-CMOS technology for computational and memory devices, remains up to now entirely based on critical materials such as Co, heavy metals and rare-earths. Here, we show that Mn_4N, a rare-earth free ferrimagnet made of abundant elements [1], is an exciting candidate for the development of sustainable spintronics devices. Mn_4N thin films grown epitaxially on $SrTiO_3$ substrates possess remarkable properties, such as a perpendicular magnetisation, a very high extraordinary Hall angle (2%) and smooth domain walls, at the millimeter scale [2]. Moreover, domain walls can be moved at record speeds by spin polarised currents, in absence of spin-orbit torques. This can be explained by the large efficiency of the adiabatic spin transfer torque, due to the conjunction of a reduced magnetisation and a large spin polarisation [3]. The domain wall velocity can reach over 900m/s at $1.4e^{12}$ A/m^2. This result is close to that obtained for chiral Néel walls driven by spin orbit torques in ferrimagnetic films with Dzyaloshinskii-Moriya interaction. Finally, we show that the coercivity of Mn_4N films can be tuned by a gate voltage, this ability constituting a tool for DW manipulation. Through the application of gate voltages through the $SrTiO_3$ substrates, the Mn_4N (4 nm) coercive field can be modulated with a large efficiency, reaching -15pJ/m^2, a value larger than those obtained for sub-nm thick layers.

[1] J.M.D. Coey and P.A.I. Smith. "Magnetic nitrides". J. Magn. Magn. Mat. 200, 405 (1999) [2] T. Gushi, L. Vila, O. Fruchart, A. Marty, S. Pizzini, J. Vogel, F. Takata, A. Anzai, K. Toko, T. Suemasu, and J.P. Attane, "Millimeter-sized magnetic domains in perpendicularly magnetized ferrimagnetic Mn_4N thin film grown on $SrTiO_3$," Jpn. J. Appl. Phys. 57, (2018): 120310. [3] T. Gushi, M. Jovičević Klug, J. Peña Garcia, J. Vogel, J.P. Attané, T. Suemasu, S. Pizzini, L. Vila. Arxiv 1901.06868 (2019)

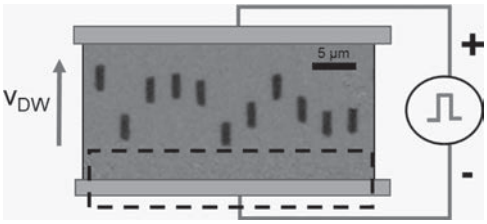


Figure 1: Differential MOKE image showing the displacement of domain walls in 2µm wide strips after eight current pulse injection of 1.2 A/m^2 and 1 ns. The area through which the DW propagated appears in black. The DW motion direction is opposite to the current, and thus follows the electrons flow.

2:30

HG-04. Domain wall dynamics in ferrimagnetic strips explained by means of a two interacting sublattices model. *E. Martinez*[1], V. Raposo[1] and O. Alejos[2] *1. Universidad de Salamanca, Salamanca, Spain; 2. Universidad de Valladolid, Valladolid, Spain*

The development of racetrack memories is attracting much interest in the recent times. [1] Many efforts have been addressed in that way, particularly, the finding of optimal systems allowing fast displacement of domain walls (DWs). Recent experimental evidence shows that DW velocities in the order of 1km/s can be achieved along ferrimagnetic (FiM) strips. [2-3]. Additionally, it has been found a linear relationship between DW velocity and the magnitude of the applied current. [2-4]. Based on these promising experimental results, here we provide a full micromagnetic (mM) study dealing with FiM strips. Our mM simulations treat them as constituted by two ferromagnetic sublattices, coupled by means of an additional inter-lattice exchange interaction. Such micromagnetic simulations are also backed up with an extended one-dimensional model, [5] that, differently from other approaches based on effective parameters, also considers the FiM as formed by two coupled sublattices with experimentally definite parameters. Such approach permits to infer results not achievable from the mentioned effective models. The model has been applied to two different structures. In the first case, a FiM strip on top of a heavy metal is considered. The interface in this case promotes the existence of an interfacial asymmetric exchange, that allows current driven domain wall motion (CDDWM) due to spin orbit torques. The CDDWM involves rigid DWs with stationary magnetic moment orientation, that at the angular momentum compensation temperature (TA) keeps aligned with the current, leading to linear increases of DW velocities with current magnitudes. DW velocities are then maximized at TA. Secondly, the FiM strip is not considered to lie on a heavy metal, and then interfacial asymmetric exchange is absent. CDDWM is dominated by the spin transfer torque, and DW precessional regimes result due to reduced magnetostatic interactions. As long as this situation holds, DW velocities are also proportional to current magnitude, and they are again maximized at TA, when precession freezes, leading to a CDDWM characterized by rigid DWs. Briefly, our methods allow to explain experimental observations of relevance for the future development of DW based devices.

[1] S. S. P. Parkin, M. Hayashi, T. Thomas, T. Science 320, 90 (2008) [2] D.-H. Kim, T. Okuno, S. K. Kim, S.-H. Oh, T. Nishimura, Y. Hirata, Y. Futakawa, H. Yoshikawa, A. Tsukamoto, Y. Tserkovnyak, Y. Shiota, T. Moriyama, K.-J. Kim, K.-J. Lee, and T. Ono, Phys. Rev. Lett. 122, 127203 (2019) [3] L. Caretta, M. Mann, F. Büttner, K. Ueda, B. Pfau, C. M. Günther, P. Hessing, A. Churikova, C. Klose, M. Schneider, D. Engel, C. Marcus, D. Bono, K. Bagschik, S. Eisebitt, and G. S. D. Beach, Nature Nanotechnology, 3, 2018. [4] S. A. Siddiqui. Phys. Rev. Lett. 121, 057701 (2018). [5] O. Alejos et al. Journal of Applied Physics 123, 013901 (2018)

2:42

HG-05. Domain wall-based spin-Hall nano-oscillators. N. Sato[1], K. Schultheiss[1], L. Korber[1], N. Puwenberg[2], T. Mühl[2], A.A. Awad[3], S. Arekapudi[4], O. Hellwig[1,4], J. Fassbender[1] and *H. Schultheiss*[1] *1. Institute for Ion Beam Physics and Materials Research, Helmholtz-Center Dresden-Rossendorf, Dresden, Germany; 2. Leibniz Institute for Solid State and Materials Research, Dresden, Germany; 3. Department of Physics, University of Gothenburg, Gothenburg, Sweden; 4. Technische Universität Chemnitz, Chemnitz, Germany*

In the last decade, two revolutionary concepts in nano magnetism emerged from research for storage technologies and advanced information processing. The first suggests the use of magnetic domain walls in ferromagnetic nanowires to permanently store information in domain-wall racetrack memories. The second proposes a hardware realization of neuromorphic computing in nanomagnets using nonlinear magnetic oscillations in the GHz range. Both ideas originate from the transfer of angular momentum from conduction electrons to localized spins in ferromagnets, either to push data encoded in domain walls along nanowires or to sustain magnetic oscillations in artificial neurones. Even though both concepts share a common ground, they live on very different time scales which rendered them incompatible so far. Here, we bridge both ideas by demonstrating the excitation of magnetic auto-oscillations inside nanoscale domain walls using pure spin currents. This presentation will shed light on the current characteristic and spatial distribution of the excited auto-oscillations.

Domain wall-based spin-Hall nano-oscillators N. Sato, K. Schultheiss, L. Körber, N. Puwenberg, T. Mühl, A.A. Awad, S.S.P.K. Arekapudi, O. Hellwig, J. Fassbender, and H. Schultheiss under review with Physical Review Letters, arXiv:1812.06702

2:54

HG-06. Tuning magnetic chirality by dipolar interactions. *J. Lucassen*[1], M.J. Meijer[1], F. Kloodt-Twesten[2], R. Frömter[2], O. Kurnosikov[1], R. Duine[1,3], H. Swagten[1], B. Koopmans[1] and R. Lavrijsen[1] *1. Applied Physics, Eindhoven University of Technology, Eindhoven, Netherlands; 2. Center of Hybrid Nanostructures, Universität Hamburg, Hamburg, Germany; 3. Institute for Theoretical Physics, Utrecht University, Utrecht, Netherlands*

Chiral magnetism has gained enormous interest in recent years because of the anticipated wealth of applications in nanoelectronics. The demonstrated stabilization of chiral magnetic domain walls and skyrmions has been attributed to the actively investigated interfacial Dzyaloshinskii-Moriya interaction (iDMI). Recently, however, predictions were made that suggest dipolar interactions can also stabilize chiral domain walls and skyrmions, but direct experimental evidence has been lacking. Because the net chirality determines, for example, the interaction of magnetic textures with spin-orbit torques, it is vital that we understand the interplay between the iDMI and dipolar fields. [1] Here, we show that dipolar interactions can indeed stabilize chiral domain walls by directly imaging magnetic domain walls in archetype Pt/CoB/Ir multilayer stacks using scanning electron microscopy with polarization analysis (SEMPA) as shown in fig. 1. [2] The strength of the iDMI and dipolar interactions are systematically tuned by varying the thickness of magnetic Co layer. We find that the competition between the iDMI and dipolar interactions can reverse the domain-wall chirality and verify our interpretation with an analytical model and micromagnetic simulations. Finally, we suggest that this competition can be tailored by an interlayer Ruderman-Kittel-Kasuya-Yosida interaction and provide the first experimental data in this direction. This experimental and modeling work unambiguously confirms that dipolar interactions play a key role in the stabilization of chiral spin textures. This insight will open up new routes towards balancing interactions for the stabilization of chiral magnets.

[1] Legrand, W., Chauleau, J. Y., Maccariello, D., et al. Science advances, 4(7) (2018) [2] Lucassen, J., Meijer M.J., Kloodt-Twesten F., et al. arXiv:1904.01898 (2019)

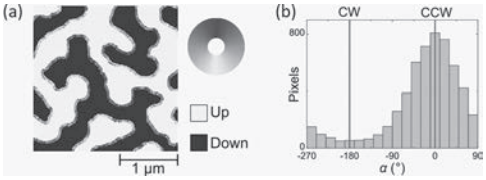


Fig. 1 (a) SEMPA image of the multidomain state in $[Pt/CoB(0.7nm)/Ir]_{x6}$ Pt/CoB(1.0nm). The out-of-plane domains are indicated in black and white. The in-plane magnetization in the domain wall is indicated by the colorwheel. The magnetization in the domain wall systematically points from a down domain towards an up domain revealing the presence of counterclockwise Néel walls. (b) Histogram of the domain-wall angle α for all pixels in the domain walls where α = 0, 180° indicates a counter-clockwise (CCW) and clockwise (CW) Néel wall respectively.

INVITED PAPER

3:06

HG-07. Magnetic domain wall devices for artificial neural network. *S. Siddiqui*[2], S. Dutta[1], A. Tang[1], L. Liu[1], C. Ross[1] and M. Baldo[1] *1. Massachusetts Institute of Technology, Cambridge, MA, United States; 2. Argonne National Laboratory, Lemont, IL, United States*

Spintronics promises intriguing device paradigms where electron spin is used as the information token instead of its charge counterpart. In the future cognitive era, nonvolatile magnetic memories hold the key to solve the bottleneck in the computational performance due to data shuttling between the processing and the memory units. The application of spintronic devices for these purposes requires versatile, scalable device design that is adaptable to emerging material physics. We design, model and experimentally demonstrate spin orbit torque induced magnetic domain wall devices as the building blocks (i.e. linear synaptic weight generator and the nonlinear activation function generator) for in-memory computing, in particular for artificial neural networks. Spin orbit torque driven magnetic tunnel junctions show great promise as energy efficient emerging nonvolatile logic and memory devices. In addition to its energy efficiency, we take advantage of the spin orbit torque induced domain wall motion in magnetic nanowires to demonstrate the linear change in resistance of the synaptic devices. Modifying the spin-orbit torque from a heavy metal or utilizing the size dependent magnetoresistance of tunnel junctions, we also demonstrate a nonlinear activation function for thresholding signals (analog or digitized) between layers for deep learning. The analog modulation of resistances in these devices requires characterizing the resolution of the resistance. Since domain wall in magnetic wires is the nonvolatile data token for these devices, we study the spatial resolution of discrete magnetic domain wall positions in nanowires. A complete neuromorphic hardware accelerator using embedded nonvolatile magnetic domain wall devices can also revolutionize computer architectures by embedding memory into logic circuits in a fine grained fashion.

CONTRIBUTED PAPERS

3:42

HG-08. Magnetic Domain Wall Neurons with Intrinsic Leaking. *W.H. Brigner*[1], N. Hassan[1], X. Hu[1], L. Jiang-Wei[1], D. Saha[1], C.H. Bennett[2], M.J. Marinella[2], F. Garcia-Sanchez[4,5], J.C. Incorvia[3] and J.S. Friedman[1] *1. Electrical and Computer Engineering, University of Texas at Dallas, Richardson, TX, United States; 2. Sandia National Laboratories, Albuquerque, NM, United States; 3. Electrical and Computer Engineering, University of Texas at Austin, Austin, TX, United States; 4. Istituto Nazionale di Ricerca Metrologica, Turin, Italy; 5. Department of Applied Physics, University of Salamanca, Salamanca, Spain*

The challenge of developing an efficient artificial neuron for machine learning is impeded by the use of external CMOS circuits to perform both leaking and lateral inhibition. To resolve this issue, we previously proposed a spintronic leaky integrate-and-fire (LIF) neuron with no external circuitry. This was achieved with a three-terminal magnetic tunnel junction (3T-MTJ) device with an externally applied magnetic field that provides a constant leaking force. We also demonstrated that the neurons recognize handwritten digits with an accuracy of 94% when used as the output layer of a neural network [1],[2]. Here, we propose the two alternate LIF neurons shown in Fig. 1, where the leaking capability is implemented by shifting the neurons' DWs in the direction opposite of integration using a non-uniform energy landscape resulting from either shape or magnetic anisotropy variation. First, for anisotropy-gradient-induced leaking, the DW shifts in a standard rectangular DW track, from regions of higher anisotropy to regions of lower anisotropy [3]. Second, for shape-based leaking, we developed a trapezoidal DW track that induces an energy landscape more favorable to the DW existing in the narrower region of the track than the wider region, causing the DW to shift from the wide region to the narrow region in the absence of external stimuli [4]. Fig. 2 demonstrates the combined integrating and leaking functionalities of an LIF neuron using shape-based DW drift. By combining our proposed neurons with 3T-MTJ synapses [5], we aim to develop a monolithic neural network system using only 3T-MTJ devices.

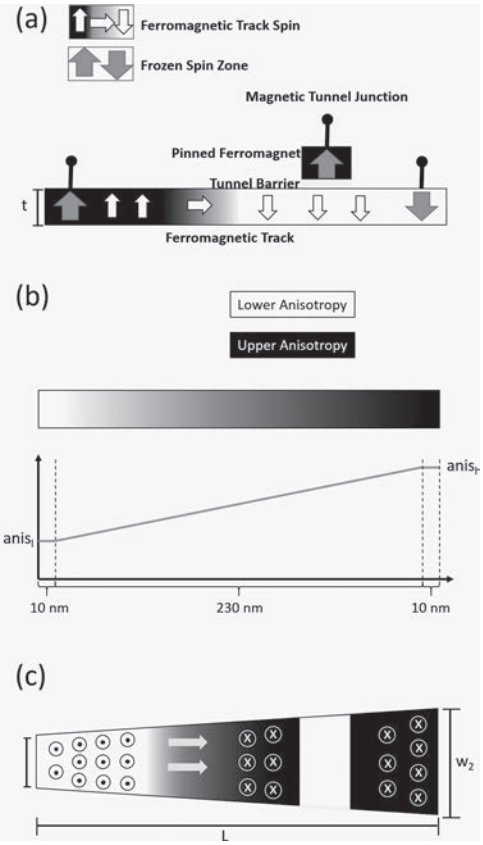


Figure 1. (a) Side view of a 3T-MTJ LIF neuron. (b) Side view of a 3T-MTJ neuron implemented using a magneto-crystalline anisotropy gradient. The DW shifts from right to left in the absence of external stimuli. (c) Top view of a 3T-MTJ neuron implemented using shape variations of the DW track. Again, the DW shifts from right to left in the absence of external stimuli.

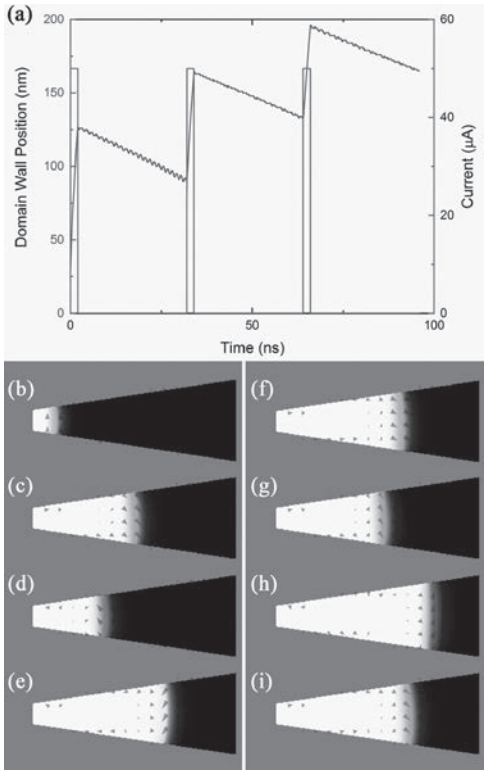


Figure 2. (a) DW position and current versus time. Snapshots during micromagnetic simulations shown for (b) t = 0 ns, (c) t = 17 ns, (d) t = 17 ns, (e) = 32 ns, (f) t = 34 ns, (g) t = 64 ns, (h) t = 66 ns, (i) t = 96 ns.

3:54

HG-09. Fast Domain Walls Governed by Œrsted Fields in Cylindrical Magnetic Nanowires. *M. Schöbitz*[1,2], A. De Riz[1], S. Martin[1,3], S. Bochmann[2], C. Thirion[3], J. Vogel[3], M. Foerster[4], L. Aballe[4], A. Locatelli[5], T. Mentes[5], F. Genuzio[5], L. Cagnon[3], S. Le-Denmat[3], J. Toussaint[3], D. Gusakova[1], J. Bachmann[2,6] and O. Fruchart[1] *1. Univ. Grenoble Alpes / CNRS / CEA, SPINTEC, Grenoble, France; 2. Friedrich-Alexander Univ. Erlangen-Nürnberg, CTFM, Erlangen, Germany; 3. Univ. Grenoble Alpes / CNRS, Institut Néel, Grenoble, France; 4. CELLS, Alba Synchrotron Light Facility, Barcelona, Spain; 5. Elettra-Sincrotrone Trieste, S.C.p.A., Trieste, Italy; 6. Institute of Chemistry, Saint-Petersburg State Univ., Saint-Petersburg, Russian Federation*

Current-induced magnetic domain wall (DW) motion has attracted immense interest, not only in the context of shift registers for futuristic non-volatile 3D data storage concepts, but also from a fundamental point of view. Experimental efforts focused on flat nanostrips which, however, suffer from intrinsic DW instabilities, greatly limiting DW speed and their reliable use in potential applications. In contrast, simulations and theory state that cylindrical nanowires (NWs) should not experience the same fundamental issue and simultaneously give rise to fascinating new physics [1,2]. Key to these predictions is the novel Bloch-point wall (BPW), which is unique to NWs [3]. It has a distinct topology and exhibits azimuthal curling of magnetic moments around a Bloch-point [4], a local vanishing of magnetisation, at the DW core. This feature and its rotational symmetry are at the origin of the steady state dynamics of this DW type, allowing theoretical speeds of over 1000 m/s and the controlled emission of spin waves (spin-Cherenkov effect) [5]. So far, experiments for DW dynamics in NWs are missing. Here we report unprecedented experimental results on current-induced DW motion in NWs [6]. We use magnetic force microscopy and shadow X-Ray Magnetic Circular Dichroism coupled to PhotoEmission Electron Microscopy (XMCD PEEM) to image DWs in 90 nm diameter $Co_{30}Ni_{70}$ NWs before and after the

application of nanosecond current pulses. We evidence that although previously disregarded, the Œrsted field induced by the current plays a crucial and valuable role: above a well-defined threshold current, it stabilises exclusively BPWs with a unique circulation (Fig. 1). This allows BPWs to reach velocities > 600 m/s (Fig. 2), quantitatively consistent with predictions, thereby also approaching the conditions where the spin-Cherenkov effect are expected.

[1] A. Fernandez-Pacheco, R. Streubel and R. P. Cowburn, Nat. Commun., Vol. 8, p.15756 (2017) [2] A. Thiaville and Y. Nakatani, Spin dynamics in confined magnetic structures III., Vol. 101, p. 161–205 (2006) [3] S. Da Col, S. Jamet and O. Fruchart, Phys. Rev. B., Vol. 89, p. 180405 (2014) [4] R. Feldtkeller, Z. Angew. Physik., Vol. 19, p. 530 (1965) [5] R. Hertel, J. Phys.: Condens. Matter., Vol. 28, p. 483002 (2016) [6] M. Schöbitz, A. De Riz and O. Fruchart, arXiv: 1903.08377 (2019)

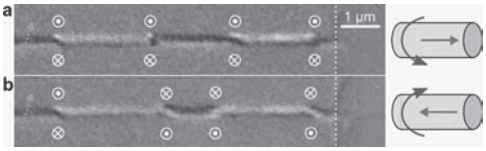


Fig 1. BPW circulation (white arrows into/out-of plane) switching under the stimulus of the Œrsted field (blue arrow in right hand schematic) produced by a current pulse (red arrow), observed in consecutive XMCD PEEM images.

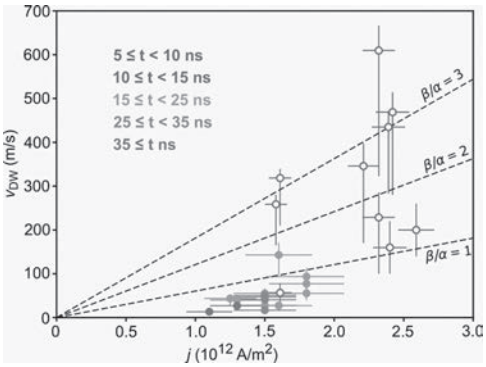


Fig 2. BPW speed as a function of applied current density recorded with MFM (open circles) and XMCD PEEM (full circles).

4:06

HG-10. Dynamics of domain wall transport in a magnetic nanotrack shared by multiple magnetic tunnel junctions. *E. Raymenants*[1,3], V. Nguyen[1], D. Wan[1], S. Couet[1], O. Bultynck[1,3], I. Radu[1], M. Heyns[1,3] and T. Devolder[2] *1. imec, Leuven, Belgium; 2. CNRS, C2N, Palaiseau - Paris, France; 3. KU Leuven, Leuven, Belgium*

Domain-wall (DW) based device concepts are explored for racetrack memory [1] and spin-logic applications [2]. So far, research was mainly focused on the study of DW transport in a single magnetic nanotrack, lacking the read/write elements for a practical DW-based device implementation. Here, we present dynamics of DW transport along a nanotrack in a fully integrated DW device with CoFeB/MgO-based perpendicular magnetic tunnel junctions (pMTJs) as read/write elements. Our device is scalable and compatible with MRAM technology. DW nucleation by spin transfer torque (STT), transport and detection by tunneling magnetoresistance (TMR) were demonstrated by time-resolved measurements in a track shared by three MTJs [3]. DW velocity between neighboring pillars was extracted as function of applied field (Fig. 1). Similar DW velocities were found in CoFeB blanket films [4]. This confirms that nor the challenging fabrication process [5], nor the fact that the track is highly scaled (i.e. 150 nm wide), are detrimental for DW transport in our devices. Time-resolved measurements at three neighboring MTJs, show that the DW dynamics in the parallel to anti-parallel (P2AP) transition are not simply symmetric to the AP2P transition, Fig. 2. This asymmetry can be attributed to fringing fields induced by the pinning layer in the pMTJs [6]. Additionally, it was found by VNA-FMR that the anisotropy is non-uniform along the track, leading to DW pinning [7]. The impact of the fringing fields and the non-uniform anisotropy on the dynamics of DW transport along the nanotrack are validated by micromagnetic simulations using OOMMF (inset of Fig. 2) These devices provide insightful information on domain wall dynamics in fully integrated device structures.

[1] Parkin, Stuart SP, Masamitsu Hayashi, and Luc Thomas. Science 320.5873 (2008): 190-194. [2] Currivan, Jean Anne, et al. IEEE Magnetics Letters 3 (2012): 3000104-3000104. [3] Raymenants, E., et al. 2018 IEEE International Electron Devices Meeting (IEDM). IEEE, 2018. [4] Burrowes, C., et al. Applied Physics Letters 103.18 (2013): 182401. [5] Wan, Danny, et al. Japanese Journal of Applied Physics 57.4S (2018): 04FN01. [6] Lavanant, M., et al. Physical Review Applied 11.3 (2019): 034058. [7] Franken, Jeroen H., et al. Journal of Physics: Condensed Matter 24.2 (2011): 024216. [8] Donahue, Michael J. OOMMF user's guide, version 1.0. No. 6376. 1999.

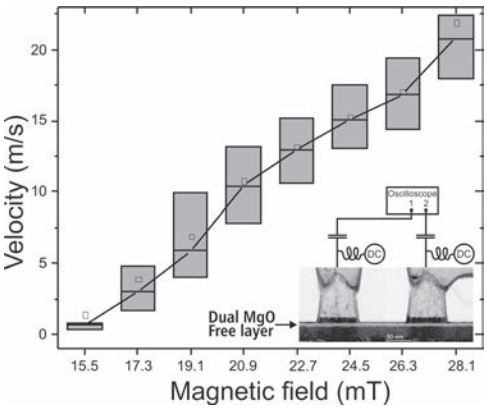


Fig 1. DW velocity in magnetic nanotrack measured between two neighboring pillars. TEM image of 2 pillars and measurement setup to extract DW velocity (inset).

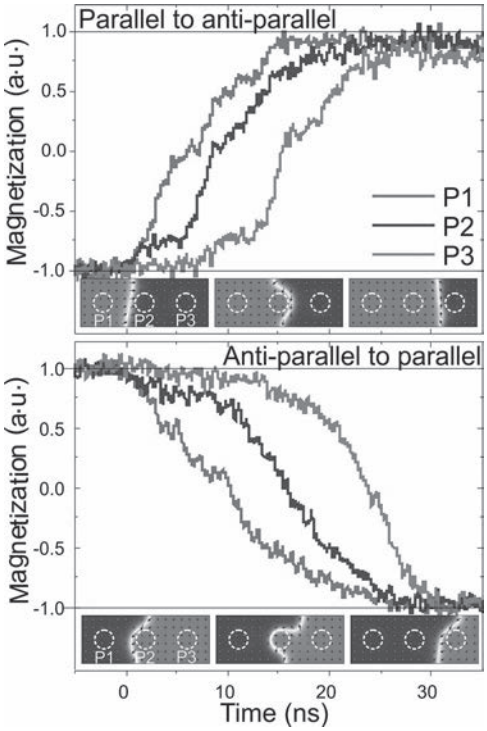


Fig 2. Time-resolved DW propagation measured in three neighboring MTJs sharing their free layer. Snapshots of micromagnetic simulations of such DW transport from left to right (inset). The fringing fields are positive inside the pillars and negative outside of the pillars, evidently influencing DW transport.

4:18

HG-11. Modelling of the Spin Transfer Torque Induced Domain Wall Motion in a Perpendicularly Magnetized Thin Disk. *P. Bouquin*[1,2], T. Devolder[1], S. Rao[2], G.S. Kar[2] and J. Kim[1] *1. Centre de Nanosciences et Nanotechnologies, Palaiseau, France; 2. IMEC, Leuven, Belgium*

In spin transfer torque magnetic random access memories the magnetization of a perpendicularly-magnetized thin disk is reversed by a polarized spin current. Knowing the intermediate states that the magnetization undergoes during the reversal is of paramount importance since it determines device performances. It has been shown previously that domain walls (DW) are expected to be involved in the reversal of disks measured [1] or simulated [2]. It is therefore necessary to develop a model for DW dynamics within a perpendicularly-magnetized disk under spin transfer torque. We present such a model, using as a starting point the *(q,φ)* model (DW position and tilt angle) that was already developed for DW dynamics within an infinite stripe [3]. We include the exact geometry of the system, which introduces new effective fields acting on the DW such as demagnetizing fields or a DW position dependent stretch field. The geometry has an important impact on the DW dynamics as seen in the figure. The DW moves at a constant drift velocity with in addition correlated oscillations of its position and tilt angle. The frequency and amplitude of the oscillations vary along the DW displacement. The manner in which the DW crosses the disk center depends on initial conditions: in some cases it is done in a linear fashion, while in other cases the wall can get stuck and position oscillations of strong amplitudes are expected near the center (Fig. 1). Therefore, if we assume that the initial conditions in which the DW is nucleated are not fully deterministic, the reversal through DW motion presents an intrinsic stochasticity. Our result is compared with micromagnetic simulations yielding a good qualitative match, which corroborates our model assumptions. Then we discuss the impact of the external field or external voltage applied to the system. In certain conditions DW annihilation through the stretch field are predicted near the disk edges, which is consistent with the impossibility to nucleate a DW from the edges of a disk that was previously reported in micromagnetic simulations [4].

[1] T. Devolder et al, Phys. Rev. B, 93, 024420 (2016) [2] P. Bouquin et al, Appl. Phys. Lett., 113, 222408 (2018) [3] A. Thiaville et al, Europhys. Lett., 69 (6), pp. 990-996 (2005) [4] P.B Visscher, K. Munira, and R.J. Rosati, arXiv:1604.03992 (2016)

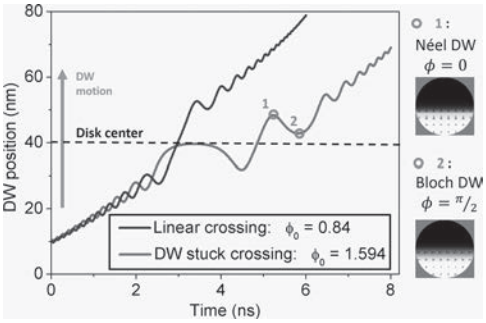


Fig. 1: dynamics of the DW position predicted by the model during the reversal of a 80 nm diameter disk, for two different initial tilt angles.

Session HH
FERRITES AND SOFT MAGNETIC ALLOYS

Guohan Hu, Co-Chair
IBM TJ Watson Research Center, Yorktown Heights, NY, United States
Zhongqiang Hu, Co-Chair
Xi'an Jiaotong University, Xi'an, China

CONTRIBUTED PAPERS

1:30

HH-01. Dysprosium Iron Garnet Films on Si with Large Grains and Perpendicular Magnetic Anisotropy. *J. Bauer*[1], E.R. Rosenberg[1] and C. Ross[1] *1. Materials Science and Engineering, Massachusetts Institute of Technology, Cambridge, MA, United States*

Rare earth iron garnets (REIGs) are magnetic insulators that can be grown in nanometer scale films with perpendicular magnetic anisotropy (PMA), making them attractive for studies of spin orbit torques (SOT) and chiral spin textures. PMA has been achieved in epitaxial films of several REIG systems on garnet substrates due to magnetoelastic anisotropy from epitaxial lattice mismatch strain[1-2] and in polycrystalline REIG films due to the thermal expansion mismatch between the film and substrate following a high temperature anneal[3]. However, it is of interest to develop PMA garnet films on silicon for practical spintronic devices using SOT from an adjacent heavy metal layer. Here we report the growth and properties of polycrystalline dysprosium iron garnet (DyIG) films on Si (100) substrates. Films were grown by pulsed laser deposition and were crystallized by a rapid thermal anneal (850 °C/5 min.). After the anneal, films were in tensile strain, which combined with the negative magnetostriction coefficients overcomes the shape anisotropy and results in PMA. X-ray diffraction shows phase-pure garnet, and atomic force microscopy (AFM) of the films indicates sub-nanometer surface roughness with large grain sizes on the order of 10 μm in a 41 nm thick film. Vibrating sample magnetometry (VSM) measurements of a 41 nm DyIG/Si film showed PMA with a saturation magnetization of 20 emu cm^{-3}, slightly lower than bulk, and a coercivity of ~4.5 kOe. The film coercivity can be tuned from 2.5-6 kOe by varying the annealing temperature, and the anisotropy field is in excess of 10 kOe. The magnetic compensation temperature of the films is ~190 K, about 30 K below the bulk compensation temperature. Spin Hall magnetoresistance (SMR) measurements on a Pt (4 nm)/DyIG (22nm)/Si Hall cross demonstrated out of plane Hall resistivity of $11*10^{-4}$ μΩ*cm and imaginary spin mixing conductance G_i of $1.0*10^{13}$ $\Omega^{-1}m^{-2}$, comparable to other REIG materials, indicating high interfacial spin transparency.

1. A. Quindeau, C. Avci, W. Liu, Adv. Elec. Mater., Vol. 3, 1600376 (2017). 2. E. Rosenberg, L. Beran, C. Avci, Phys. Rev. Mater., Vol. 2, 094405 (2018). 3. J. Bauer, E. Rosenberg, C. Ross, APL, Vol. 114, 052403 (2019).

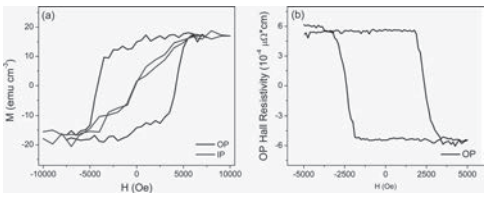


Fig 1. (a) In plane and out of plane VSM hysteresis loop for a 41 nm DyIG/Si film. (b) Out of plane SMR loop on a 22 nm DyIG/Si film.

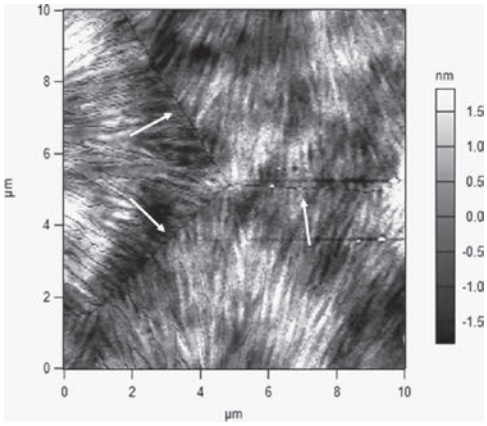


Fig 2. AFM image of large grains in a 41 nm DyIG/Si film. Grain boundaries are indicated by the arrows.

1:42

HH-02. Sol-Gel Synthesized YIG Nanoparticles with Low Magnon Damping. *J. Silva*[1], R. Vilarinho[1], S.A. Bunyaev[1], J.A. Moreira[1], G.N. Kakazei[1] and A.M. Pereira[1] *1. IFIMUP, Porto, Portugal*

Epitaxial Yttrium Iron Garnet (YIG) films are actively used in magnonics and spin caloritronics since YIG is an excellent electrical insulator with the lowest known Gilbert damping parameter α_G below 10^{-4}. However, polycrystalline YIG nanoparticles, prepared by different methods, so far demonstrated rather high values of α_G. To improve this issue, we varied different sol-gel fabrication parameters, namely the drying temperature, drying time, and calcining time. The morphological analysis at room conditions evidenced that YIG has a cubic structure, such that the particles aggregate in the form of prisms. The phase formation and the crystallographic structure were ascertained by XRD and Raman scattering at room temperature. The cubic symmetry of all the as-prepared samples was confirmed, and the lattice parameter was found to be 1.24 nm. We estimate the crystallite sizes to range from 63 nm to 111 nm. The Raman spectra confirm the garnet structure of the synthesized YIG [1,2]. No bands assigned to magnon excitations were observed, suggesting these are not Raman-active in YIG due to symmetry constraints. The isothermal magnetic hysteresis cycles were measured at room temperature and the saturation magnetization M_{sat} and coercive field H_c were determined. M_{sat} varied from 20.0 emu/g to 25.4 emu/g when H_c had similar values (around 80 Oe) for all the samples. Finally, the broadband ferromagnetic resonance (FMR) in the frequency range 0-20 GHz was measured on a sample with the highest value of M_{sat}. Using Kittel formulas, we were able to fit the experimental resonance frequency vs magnetic field dependence using typical parameters for epitaxial YIG films. α_G was obtained using the procedure described in Ref. [3], based on the fact that

the apparent damping α_{app} converges at high fields, as seen in Fig. 1 and the obtained value $\alpha_G = 0.075$ is about two times lower than $\alpha_G = 0.12$, reported previously for sol-gel synthesized polycrystalline YIG nanoparticles [4]. This result is particularly relevant because it paves the way for the use of polycrystalline YIG in microwave, magneto-optical and spincaloritronics applications.

1. Peña-Garcia, R. *et al., Mater. Res. Express*, Vol. 4, 016103 (2017). 2. Paiva, D. V. M. *et al., J. Alloys Compd.*, Vol. 644, 763–769 (2015). 4. Kalarickal, S.S. *et al.*, *J. Appl. Phys.*, Vol. 99, 093909 (2006). 3. Sharma, V. *et al.*, *AIP Adv.*, Vol. 7, 056405 (2017).

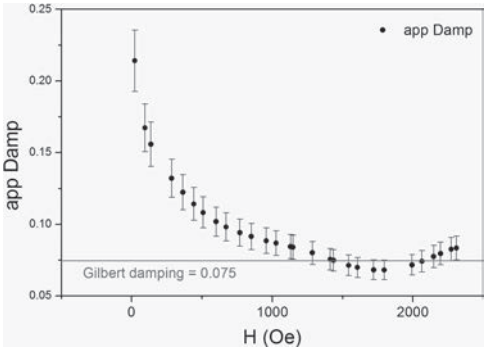


Fig. 1. Extraction of Gilbert damping parameter α_G using the procedure described in Ref. 4.

1:54

HH-03. In vivo doping and morphology modification of magnetosomes synthesized by *M. gryphiswaldense*. *L. Marcano*[1,2], L. Gandarias[3], D. Gandia[4], I. Orue[5], A. García Prieto[6,4], S. Valencia[1], R. Abrudan[1], A. Serrano[7,8], A. Muela[3,4] and M. Fdez-Gubieda[2,4] *1. Helmholtz-Zentrum Berlin für Materialen und Energie, Berlin, Germany; 2. Electricidad y Electrónica, Universidad del País Vasco, Leioa, Spain; 3. Inmunología, Microbiología y Parasitología, Universidad del País Vasco, Leioa, Spain; 4. BCMaterials, Leioa, Spain; 5. SGIker, Leioa, Spain; 6. Física Aplicada I, Universidad del País Vasco, Leioa, Spain; 7. SpLine, ESRF, Grenoble, France; 8. Instituto de Ciencia de Materiales de Madrid, CSIC, Madrid, Spain*

M. gryphiswaldense synthesizes cubo-octahedral shaped magnetite nanoparticles, called magnetosomes, with a mean diameter of 40 nm [1]. The high quality of the biosynthesized nanoparticles makes them suitable for numerous applications [2,3]. Aiming to further increase their potential applications, different authors have focused on modifying the main properties of magnetosomes by doping them with transition elements [4,5]. In this work, we present a complete and novel characterization of magnetosomes synthesized in Mn or Zn-rich medium. X-ray absorption spectroscopies at Fe and Mn/Zn *K* and $L_{2,3}$-edge evidence the incorporation of Mn and Zn into the magnetite structure concomitant with drastic changes in their magnetic properties (Fig.1). The low incorporation of these elements, below 1%, is however not sufficient on its own to explain the decrease on the coercive field and remanence. Our experimental and theoretical findings suggest an additional change of the morphology of the magnetosomes synthesized in the supplemented mediums. Thus, we have accurately reproduced the magnetization dynamics by using a magnetic model that considers the competition between the magnetocrystalline and shape anisotropies.

[1] M. L. Fdez-Gubieda, A. Muela, J. Alonso, et al., ACS Nano, 7 (4), 3297-3305 (2013). [2] A. Muela, D. Muñoz, R. Martín-Rodríguez, et al., J. Phys. Chem. C 120, 24437 (2016) [3] A. M. Huízar-Félix, D. Muñoz, I. Orue, et al., Appl. Phys. Lett. 108, 063109 (2016). [4] S. Staniland, W. Williams, N. Telling, et al., Nat. Nanotechnol. 3, 158 (2008). [5] L. Marcano, D. Muñoz, R. Martín-Rodríguez, et al., J. Phys. Chem. C, 122, 7541-7550 (2018)

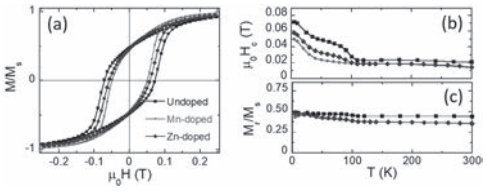


Fig 1. (a) 5 K hysteresis loops and temperature dependence of (b) coercivity and (c) remanence magnetization of undoped, Mn and Zn-doped magnetosomes.

2:06

HH-04. Separation of sublattice magnetism in $Tb_3Fe_5O_{12}$ using magneto-optical spectroscopy. *L. Beran*[1], E.R. Rosenberg[2], J. Setina[1], A.U. Quindeau[2], J. Zázvorka[1], C. Ross[2] and M. Veis[1] *1. Charles University, Prague, Czechia; 2. Massachusetts Institute of Technology, Cambridge, MA, United States*

Ferrimagnetic garnets with perpendicular magnetic anisotropy have drawn a considerable attention in recent years due to the possibility to control their magnetism via spin orbit torque [1]. These materials exhibit three magnetic sublattices where magnetic ions are surrounded tetrahedrally, octahedrally and dodecahedrally by oxygen atoms. The net magnetic properties are tunable with temperatureand changing of growth parameters. Compensation temperature near the room temperature is important for utilization of these materials in novel spintronic concepts. However, physical mechanisms responsible for the changes in this temperature remain still not well understood. Separation of the sublattice magnetism can give in important information and insight into compensation mechanism of these materials. Here we present temperature and field dependent magneto-optical spectroscopy of $Tb_3Fe_5O_{12}$ (TbIG) in the vicinity of the compensation temperature. The spectral dependence of magneto-optical Faraday and Kerr effect allowed us to disentangle the contributions from all three sublattices in TbIG thin films. Investigated samples were grown by pulsed laser deposition onto GGG (111) substrates. The Kerr and Faraday magneto-optical spectroscopies were measured in the spectral range from 1.2 to 5 eV using rotating analyzer method [2]. The spectra were fitted using the framework of paramagnetic and diamagnetic lines derived from microscopic theory of magneto-optical effects. These lines origin in electronic transitions of magnetic ions in various sublattices. Figure 1 shows the room temperature Faraday rotation spectrum of 38 nm thick TbIG layer decomposed into the contributions of different sublattices. Field dependent measurements showed the inverse magnetic behavior of tetrahedral and octahedral sublattices, while the dodecahedral sublattice followed the octahedral one. Presented separation approach can be used on wide variety of ferrimagnetic garnets.

[1] C. Avci et al., Nat. Nanotechnol., 16, p. 309 (2017) [2] E. Jesenska et al., Optical Materials Express, 6, p.1986 (2016)

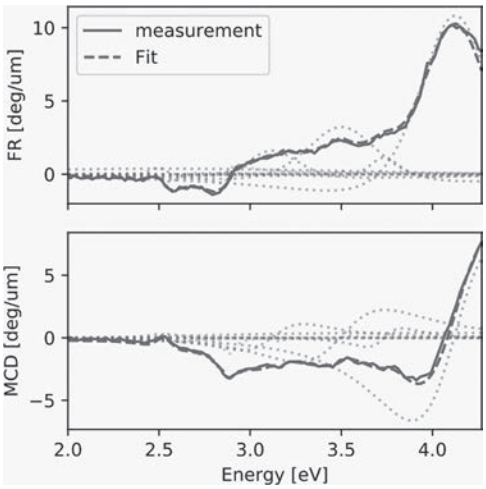


Fig 1. Room temperature Faraday spectrum of 38 nm thick TbIG with disantangeled contribution of thee magnetic sublattices.

2:18

HH-05. Improved Magnetorheological Response in $Zn_{0.2}Fe_{2.8}O_4$ nano-hollow spheres. *P. Saha*[1] and K. Mandal[1] *1. Department of Condensed Matter Physics and Material Science, S. N. Bose National Centre for Basic Sciences, Kolkata, India*

Potential applications of Fe_3O_4 nanostructures can be enhanced by preparing nano-hollow spheres (NHSs) instead of nanoparticles. We prepared $Zn_xFe_{3-x}O_4$ (x=0.0, 0.1, 0.2, 0.3, 0.4, 1.0) NHSs with different Zn doping concentration. Temperature dependent magnetic studies indicate their increase in saturation magnetization (M_S) with Zn doping, attaining a maximum for x=0.2 and then fall off with increasing Zn content [Fig. 2], due to replacement of antiferromagnetically coupled Fe_A^{3+} ions on the A site by non-magnetic Zn^{2+} ions and transformation of Fe_B^{2+} to Fe_B^{3+} at B site for maintaining charge neutrality. The dynamic magnetic properties studied by analysing ac susceptibility revealed spin cluster interaction in our systems. Magnetorheological (MR) effect is a reversible phenomenon which arises due to the chain formation [Fig 2] of suspended magnetic particles in a carrier fluid under external magnetic field and in turn increasing the effective viscosity. Micron or nano-sized particles with low-density and high saturation magnetization are desirable for magnetorheological applications. As saturation magnetism is an important parameter for magnetorheology, $Zn_{0.2}Fe_{2.8}O_4$ NHSs can be an interesting candidate. We have prepared silicon oil based MR fluids by dispersing $Zn_{0.2}Fe_{2.8}O_4$ and Fe_3O_4 NHSs of diameter 700 nm, each with 50 wt. % and studied their magnetorheological response in flow mode. $Zn_{0.2}Fe_{2.8}O_4$ shows much better MR response than Fe_3O_4. The hollow interior makes the sub-micron sized spheres stable in carrier fluid due to reduced density. The curve of shear stress vs shear rate under externally applied magnetic field is fitted with various established model such as Herschel-Bulkley (HB) fluid model and Bingham Plastic (BP) model to understand the MR mechanism. The viscoelastic modulus is studied under oscillatory shear rate at different applied magnetic field to comprehend the viscous and elastic properties under the deformation. We have simulated theoretical model using dipolar interaction and it matches well with the experimental behaviour.

[1] P. Saha, R. Rakshit, K. Mandal, Physical Review Applied, 11, 024059 (2019).

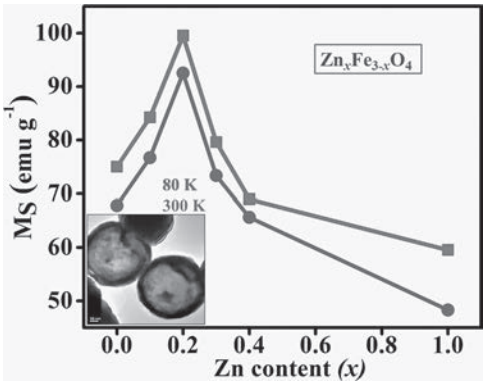


Fig 1. Variation of Magnetization with Zn doping Content (x) of $Zn_xFe_{3-x}O_4$ NHSs

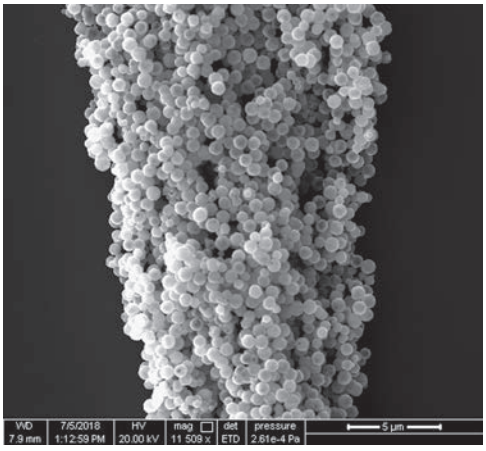


Fig 2. FESEM image of chain formation of $Zn_{0.2}Fe_{2.8}O_4$ NHSs under applied magnetic field

2:30

HH-06. Structural, magnetic and electrochemical activity of $Ti_{0.5}Ni_{0.5}Fe_2O_4$ nanoparticles synthesized by high energy ball milling. *N.S. Osman*[1,2], N. Thapliyal[3], T. Moyo[2] and R. Karpoormath[3] *1. Medical and Biological Applications, Institute of Laser, Sudan University of Science and Technology, Khartoum, Sudan; 2. School of Chemistry and Physics, University of KwaZulu-Natal, Durban, South Africa; 3. Department of Pharmaceutical Chemistry, Discipline of Pharmaceutical Sciences, College of Health Sciences, University of KwaZulu-Natal, Durban, South Africa*

High energy ball milling technique was used to synthesize $Ti_{0.5}Ni_{0.5}Fe_2O_4$ nanoparticles. The spinel phase structure was formed after short milling time of 1.5 hours. The phase formation was confirmed by X-ray diffraction measurements. William-son plot shows homogenous strain in the sample. The elemental composition was confirmed by energy dispersive X-ray and further by inductively coupled plasma optical emission spectrometry. The morphology was studied by high-resolution transmission electron microscope and high-resolution scanning electron microscope. The results show mono-dispersive character of the synthesized sample. The magnetic properties were investigated by vibrating sample magnetometer and Mössbauer spectroscopy. The values of the saturation magnetization and coercive field are 71.5±0.1 emu/g and 216±16 Oe respectively. The electrochemical sensing characteristic of the synthesized nanoparticles was investigated using cyclic voltammetry. The $Ti_{0.5}Ni_{0.5}Fe_2O_4$ nanoparticles modified glassy carbon electrode ($Ti_{0.5}Ni_{0.5}Fe_2O_4$/GCE) displayed excellent electrocatalytic behaviour towards potassium ferricyanide, a typical redox species as evidenced by a

decrease in peak potential and a substantial increase in peak current. The $Ti_{0.5}Ni_{0.5}Fe_2O_4$ nanoparticles are thus envisaged to be novel and promising candidates for constructing electrochemical sensors with high performances.

2:42

HH-07. Mössbauer and Magnetometry Studies of Ferrite Particles for Magnetic Resonance Imaging Thermometry. *M. Przybylski*[1], J. Zukrowski[1], N. Alghamdi[2], J. Stroud[2], J.H. Hankiewicz[2,3] and Z. Celinski[2,3] *1. Academic Centre for Materials and Nanotechnology, AGH University of Science and Technology, Kraków, Poland; 2. BioFrontiers, University of Colorado BioFrontiers (BioFrontiers - UCCS), Colorado Springs, CO, United States; 3. MRX Analytics, PBC, Colorado Springs, CO, United States*

Designing ferrites' composition to achieve the best possible particles for magnetic resonance-imaging thermometry (tMRI) requires that one understand the distribution of the magnetic ions in a crystal structure. To do this we carried out Mossbauer and magnetometry studies of MgZn and CuZn ferrites. However, not all Mössbauer measurements allowed us to determine Fe ion distributions due to relaxation nature of the collected spectra. Figure 1 shows such a case of the Mössbauer spectra (MS) acquired in MgZn ferrite. Even at 80 K, the spectrum has a relaxation character possibly due to an oscillation of domain walls in ferrites [1] or due to oscillations of the magnetic moments in nanometer-size domains. Figure 2 shows that MS of some CuZn ferrites at 80 K exhibit relaxation character even though for all studied compositions the Curie temperature is well above 80 K [2]. Our spectra were fitted using method described by Rancourt [3], within the Blume-Tjon model [4]. The only way to "switch off" magnetization relaxations was by reducing the temperature down to ~ 4K. The results of fitting MS at 6K for the same samples confirm the tendency observed by XRD [5]: with increasing Zn concentration, Fe cations are displaced by the Zn cations from the tetrahedral to octahedral sites. Analysis of MS allowed us also determine values of hyperfine fields and isomer shifts. To select the best ferrites' composition for tMRI, MS studies were augmented by SQUID measurements of magnetization vs. temperature.

[1] C. M. Srivastava, S. N. Shringi, and R. G. Srivastava, Phys. Rev. B, Vol.14, p.204 (1976) [2] N.A. Alghamdi, J.H. Hankiewicz, N.R. Anderson, K.F. Stupic, R.E. Camley, M. Przybylski, J. Zukrowski, and Z. Celinski, Phys. Rev. Appl., Vol.9, p.054030 (2018) [3] D.G. Rancourt and J.M. Daniels, Phys. Rev. B, Vol.29, p.2410 (1984) [4] M. Blume and J.A. Tjon, Phys. Rev., Vol.165, p.446 (1968) [5] N. Alghamdi, J. Stroud, M. Przybylski, J. Zukrowski, A. Cruz Hernandez, J. Brown, J. Hankiewicz and Z. Celinski, submitted to JMMM

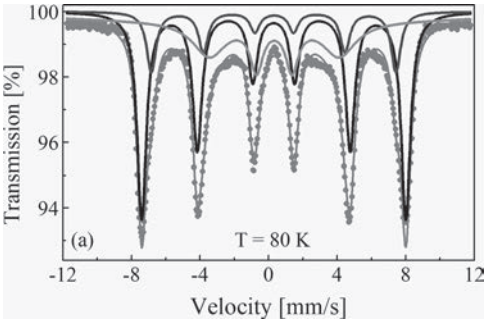


Fig 1. Mossbauer spectrum of $(Mg_{0.36}Zn_{0.64})_{0.8}Fe_{2.2}O_4$ ferrite measured at 80 K.

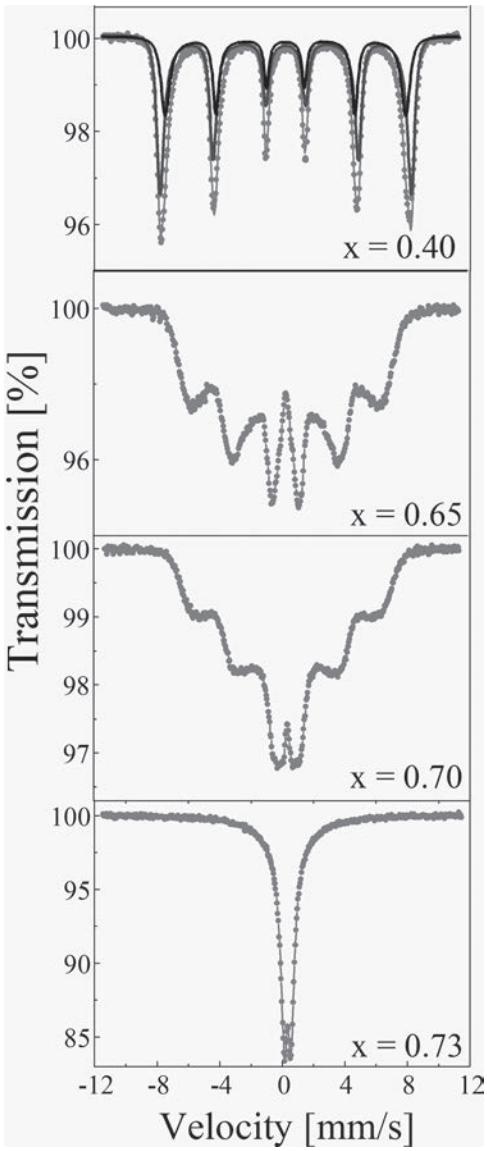


Fig 2. Mössbauer spectra of $Cu_{1-x}Zn_xFe_2O_4$ ferrites measured at 80 K.

2:54

HH-08. Crystallographic inversion-mediated superparamagnetic relaxation in Zn ferrite and Mn-Zn ferrite nanocrystals. *R. Sai*[1], R. Kahmei[1], S. Arackal[1], N. Bhat[1], M. Yamaguchi[2] and S.A. Shivashankar[1] *1. Centre for Nano Science and Engineering, Indian Institute of Science, Bengaluru, India; 2. Dept. of Electrical Engineering, Tohoku University, Sendai, Japan*

Magnetic nanoparticles are excellent microwave absorbers owing to their large ferromagnetic resonance (FMR) loss [1]. The natural FMR frequency, which originates from magnetocrystalline anisotropy of the material and is observed near or below 1 GHz in spinel ferrites, can be exceeded in nanoparticles via superparamagnetic relaxation (SR) [1, 2]. The characteristics of SR are generally tuned by employing magnetic core-shell nanostructure and thus, by altering dipolar interactions between particles [2, 3]. However, adding a non-magnetic shell causes loss in effective permeability. In this paper, we explore dipolar interactions in superparamagnetic zinc ferrite ($ZnFe_2O_4$) nanocrystalline (ZF-NC) and manganese-zinc ferrite ($Mn_{0.5}Zn_{0.5}Fe_2O_4$) (MZF-NC) with various degree of crystallographic

inversion. Various ZF-NC and MZF-NC samples were synthesized by a solution-based, low-temperature (<200 °C), microwave-assisted solvothermal (MAS) process [4]. Owing to the far-from-equilibrium process, the resultant as-synthesized nanocrystals possess a very high degree of crystallographic inversion. The samples were then subjected to rapid thermal annealing (2 min at 300 °C and 500 °C, with a heating rate of 200 °C/min) to alter the degree of inversion without a noticeable change in crystallite size. The crystal structures, particle shapes, and compositions of the nanocrystalline sample were characterized by XRD, SEM, and electron probe micro-analysis. The samples are phase-pure, with particle size in the range 4.5 to 8.4 nm and their compositions are stoichiometrically correct. Partial inversion in the crystal structure of both ZF-NC and MZF-NC was evidenced by Raman spectroscopy and confirmed by XPS. The dipolar interaction study was performed in a SQUID magnetometer by measuring the FC-ZFC magnetization at two different dc bias fields – 50 Oe and 500 Oe, on the temperature range 5 K to 350 K (Fig. 1). The dipolar interaction is present in both as-prepared ZF-NC and MZF-NC, but the interaction is stronger in MZF-NC. The role of crystallographic inversion-mediated superparamagnetic relaxation on the FMR characteristics is being discussed for the first time.

[1] V. G. Harris, IEEE Transaction on Magnetics, vol. 48, pp. 1075–1104, (2012). [2] N. Song et al., Scientific Reports, vol. 3, pp. 3161, (2013). [3] H. Yun et al., ACS Nano, vol. 8, No. 12, pp. 12323 (2014). [4] R. Sai et al., J. Mater. Chem., vol. 22, No. 5, pp. 2149, (2012)

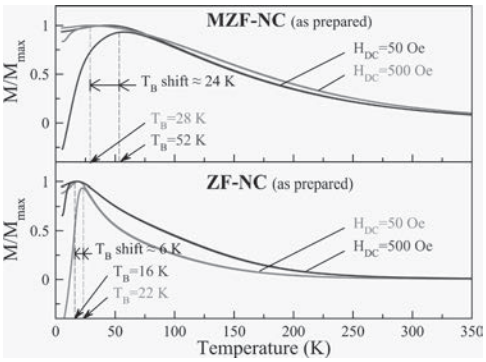


Fig 1. FC-ZFC measurement of as-prepared ZF-NC and MZF-NC samples

3:06

HH-09. Soft Magnetic and Structural Properties of $(Fe_{75}Co_{25})_{75}(Al_{50}Si_{50})_{25}$ Alloy Thin Films. *T. Nakano*[1,2], B. Nepal[2], Y. Tanaka[1], S. Wu[2], K. Abe[1,2], G.J. Mankey[2], T. Mewes[2], C.K. Mewes[2] and T. Suzuki[2] *1. Materials Development Center, TDK Corporation, Narita, Japan; 2. Center for Materials for Information Technology, The University of Alabama, Tuscaloosa, AL, United States*

Improvements in soft magnetic properties such as low coercivity (H_C) and low effective damping parameter (α_{eff}) are indispensable and previous works on FeCoAl [1] and FeCoSi [2, 3] thin films reported the soft magnetic properties attractive for future high frequency device applications. However, few studies about FeCoAlSi alloy thin films have been found in literature [4]. This work presents a systematic study of the soft magnetic properties of $(Fe_{75}Co_{25})_{75}(Al_{50}Si_{50})_{25}$ alloy thin films. Multilayers of [$Fe_{75}Co_{25}$ (0.7 nm)/ $Al_{50}Si_{50}$ (0.4 nm)]×N, where N is the number of repetitions, were sputter-deposited onto MgO (100) single crystal substrates using DC magnetron sputtering in Ar atmosphere of 4mTorr. The substrate deposition temperature (T_S) was varied from ambient to approximately 400 deg.C. The thickness was varied from 10 to 300 nm. Structural analyses were performed by XRD and TEM. Measurements of magnetic properties were carried out by VSM and longitudinal MOKE. The magnetization dynamics were evaluated by ferromagnetic resonance at room temperature over a frequency range from 12 to 66 GHz. As shown in the XRD pattern in Fig.1, the DO_3 phase is found in the sample fabricated at T_S = 410 deg.C, while an amorphous phase is produced with T_S = 40 deg.C and a bcc phase is present for T_S = 100 to 300 deg.C. The dependences of (a) saturation magnetization (M_S), (b) Hc and (c) α_{eff} on T_S are shown in Fig.2. The values of M_S and Hc are approximately 700 emu/cm^3 and 4 Oe, respectively, and remain nearly constant throughout the entire range of Ts. The α_{eff} decreases and then slightly increases with T_S. The minimum value of α_{eff} is 2.2×10^{-3}. Further optimization of fabrication condition is in progress aimed at further improving soft magnetic and dynamic properties. The thickness dependence of the soft magnetic properties will also be reported. This work is in part supported by the MINT-TDK collaboration program.

[1] Y. Ariake et al. AIP Advances 8, 056119 (2018). [2] K. Abe et al. AIP Advances 9, 035139 (2019). [3] S. Wu et al., Phys. Rev. B, 99, 144416 (2019) [4] M. Hayakawa et al., IEEE Trans. Magn., 23, 5 (1987).

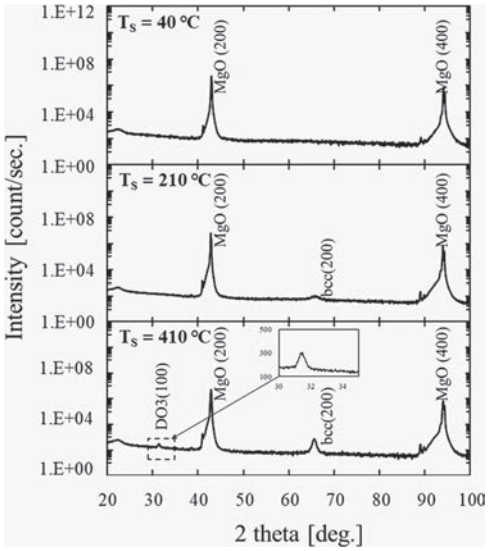


Fig.1 XRD spectra of $(Fe_{75}Co_{25})_{75}(Al_{50}Si_{50})_{25}$ thin films onto MgO(100) substrate with the various T_S

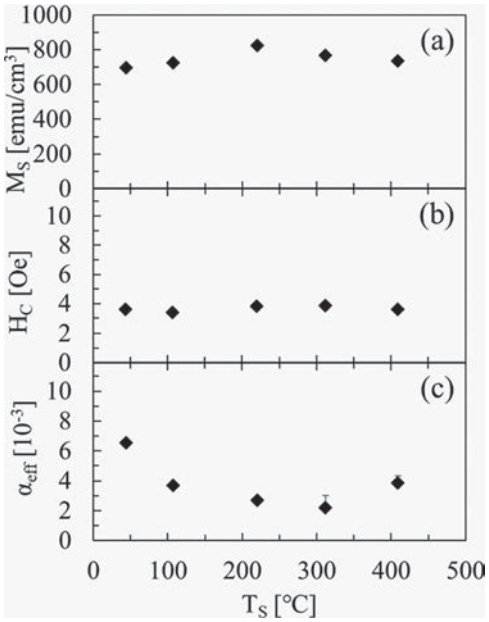


Fig.2 The dependences of (a) M_S, (b) Hc and (c) α_{eff} on T_S of $(Fe_{75}Co_{25})_{75}(Al_{50}Si_{50})_{25}$ thin films

3:18

HH-10. Microstructure of novel Fe-Mn soft magnetic powders produced by hydrogen reduction of nanoferrites. *N. Imaoka*[1], Y. Kawakami[1] and K. Ozaki[1] *1. Magnetic Powder Metallurgy Research Center, National Institute of Advanced Industrial Science and Technology (AIST), Nagoya, Japan*

The global market for electric vehicles is expected to reach 15 million units by 2020. Currently, soft magnetic stators for electric motors in automotive applications are typically assembled by stacking several hundreds of rolled electrical steel sheets with surface insulating layers. Herein, we have attempted to develop novel high-performance soft magnetic powders using a simple and low-cost fabrication process for solidification of powders. In our previous paper [1], we reported on high-magnetization Fe-Mn powders that can be easily solidified by conventional powder metallurgy processes. Fe-Mn powders doped with 0.1 at% manganese (hereafter denoted as Mn0.1) were prepared by the reduction of $(Fe,Mn)_3O_4$ nanopowders using hydrogen gas. The starting nanopowders with a particle size of 5–50 nm were prepared by our aqueous process [2, 3]. The saturation magnetization of the Mn0.1 sample was about 219 emu/g, and the sample exhibited a coercivity of 0.1–1 Oe, as measured using a vibrating sample magnetometer. An example of this domain structure observed using Lorentz transmission electron microscopy (TEM) is shown for the Mn0.1 TEM specimen in Fig. 1 [1]. The different domains divided the sample into rectangular strips across its thickness. The magnetization direction of these domains alternated, leading to a closure domain, formed by large magnetic walls. However, such domain structures are not normally observed. We further investigated the microstructure of the Mn0.1 powders by TEM and electron diffraction (ED). The satellite spots of the {110} main diffraction in the ED patterns were observed near the forbidden reflections due to extinction rules, such as 100 and 111 reflections, as shown in Fig. 2. Furthermore, layers of thickness of a few tens of nanometers were observed by dark-field TEM images obtained from satellite reflections. These layers are suggested to have a long period structure in Fe-Mn powders. On the basis of these results, we discuss the mechanism of magnetization reversal in Mn0.1 powders.

[1] N. Imaoka, S. Yamamoto and K. Ozaki, 2018 IEEE International Magnetic Conference (INTERMAG), pp.1–7 (2018). [2] N. Imaoka and K. Ozaki, US patent application 2019/105708 (2019). [3] N. Imaoka et al., J. Magn. Magn. Mater., Vol. 476, p.613 (2019).

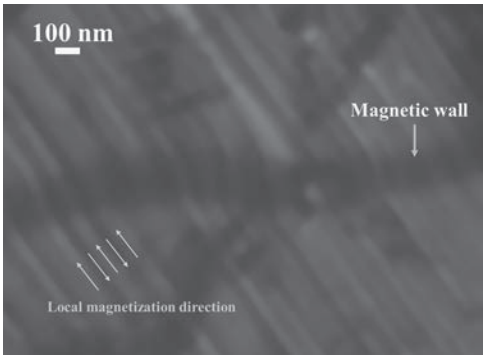


Fig. 1. Lorentz TEM image of Mn0.1 powder with a cross-section of approximately 100 nm thickness [1].

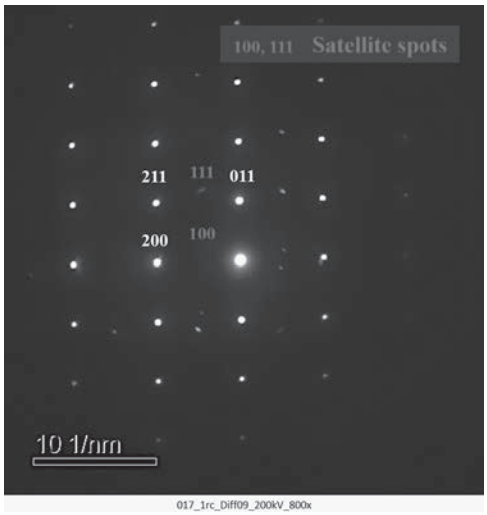


Fig. 2. Electron diffraction image of Mn0.1 powder with a cross-section of approximately 100 nm thickness.

3:30

HH-11. Magnetic properties of FeCoMnCrSi multi-principal element alloy. *R. Jangid*[1], K. Ainslie[1] and R. Kukreja[1] *1. Materials Science and Engineering, University of California, Davis, CA, United States*

High entropy alloys (HEA) or multi-principal element alloys (MPEAs) have recently gained interest due to their unique properties such as high-temperature strength, exceptional ductility, and potential applications in permanent magnets.[1, 2] However, the magnetic behavior of MPEA thin films as a function of temperature is still not well understood as most of the studies have focused on bulk magnetic properties and thus have not been able to identify the behavior of individual elements in this complex multi-dimensional compositional space.[3-6] In this study, we focus on one such system, FeCoMnCrSi, which contains 95 at% of magnetic elements including both ferromagnetic (Fe, Co) and antiferromagnetic ions (Mn, Cr). Thin films with different thicknesses were deposited on a silicon (001) substrate using magnetron sputtering. The X-Ray diffraction measurements show coexisting FCC and HCP phases while energy dispersive x-ray analysis shows that both phases have the same composition. Hysteresis loops show two orders of magnitude enhancement in magnetization for thin film samples when compared to bulk sample. Magnetization as a function of temperature shows a spin glass phase transition near room temperature and ferromagnetic transition near 150 K, which increases to 250 K for films with lower thickness. Consequently, the film thickness can be used to tailor the ferromagnetic transition and the magnetization of MPEAs. These studies provide detailed characterization of magnetic and structural properties of FeCoMnCrSi HEA which is critically needed to guide the design and development of MPEA based soft magnetic systems.

[1] Zhiming Li, Konda Gokuldoss Pradeep, Yun Deng et al., Nature, 534(7606):227–230, 2016. ISSN 14764687. doi: 10.1038/nature17981. [2] Yong Zhang, Ting Ting Zuo, Zhi Tang et al., Progress in Materials Science, 61(October 2013):1–93, 2014. ISSN 00796425. doi: 10.1016/j.pmatsci.2013.10.001. [3] Oldich Schneeweiss, Martin Friak, Marie Dudova et al., Physical Review B, 96(1):1–13, 2017. ISSN 24699969. doi: 10.1103/PhysRevB.96.014437. [4] M. S. Lucas, L. Mauger, J. A. Muoz, et al., Journal of Applied Physics, 109(7):107–110, 2011. ISSN 00218979. doi: 10.1063/1.3538936. [5] Shuo Huang, Erik Holmstrom, Olle Eriksson, et al., Intermetallics, 95(February):80–84, 2018. ISSN 09669795. doi: 10.1016/j.intermet.2018.01.016. [6] Ming Hung Tsai. Entropy, 15(12):5338–5345, 2013. ISSN 10994300. doi: 10.3390/e15125338.

3:42

HH-12. Impact of Post-Annealing Temperatures and Durations on the Composition of Iron Nitride. *L. Jiang*[1] and Y. Jiang[2] *1. Chemical Engineering, UC Berkeley, Berkeley, CA, United States; 2. Jiangnan University, Wuxi, China*

In this paper, we investigated the effect of different post-annealing temperature and duration on the extent of transformation from α-Fe(bcc) into γ'-Fe_4N (fcc). After iron and nitrogen were mixed during ball-miling, post-annealing activated the diffusion of nitrogen atoms inside the amorphous phase. As a result, γ'-Fe_4N was formed. In our experiment, all the samples were obtained from the same batch of ball-milled iron nitrite, and they were post-annealed at three different temperatures of 150, 200 and 300 Celsius for 24, 48, 72 and 96 hours. X-ray diffraction was used to characterize the compositions of the post-annealed samples. With the help of the XRD spectra, the relative proportions of the two phases, γ'-Fe_4N (fcc) and a-Fe(bcc), could be determined qualitatively. Diffraction peaks at 2θ=42.5° and 44.5° had the best resolution and the highest intensities. 44.5° corresponds to (110) plane of bcc α-Fe, and 42.5° reflects (111) plane of fcc γ'-Fe_4N. By comparing the relative intensities between the two peaks, a general, qualitative evaluation of the extent of phase transformation could be obtained. In general, a growing intensity of the 42.5° peak relative to the 44.5° peak indicated a greater degree of transformation from α-Fe(bcc) into γ'-Fe_4N (fcc). Under lower post-annealing temperatures of 200 °C and 150 °C, γ'-Fe_4N showed significant presence, but the proportion of the two phases α and γ' tend to fluctuate dramatically as the duration of post-annealing increased. Steady growth of γ'-Fe_4N was not observed. At certain instances, the proportion of γ'-Fe_4N was even shown to derease, possibly converting back to a-Fe. Thus, it became uncertain whether post-annealing at low temperatures of 200 °C and 150 °C helped to propel the transformation at all. At 300 Celsius, the desired γ'-Fe_4N phase was formed very gradually. The γ'-Fe_4N phase grew at a very steady rate. No fluctuation of phase proportion took place as observed at 150 and 200 Celsius. In conclusion, 300 °C was found to be a very suitable post-annealing temperature for the purpose of furthering the phase transformation from α-Fe to γ'-Fe_4N after balling milling, due to the observed steady growth rate and high extent of phase transformation.

1. Jiang,Y., &Jiang, L. (2019). Synthesis of γ'-Fe_4N powder in liquid nitrogen. *AIP Advances, 9*(3), [035215]. 2. Jiang,Y., &Jiang, L. (2019). Synthesis of γ'-Fe_4N soft magnetic material by high-pressure nitriding approach. *IEEE Transaction on Magnetics, 55(2),* [8458231].

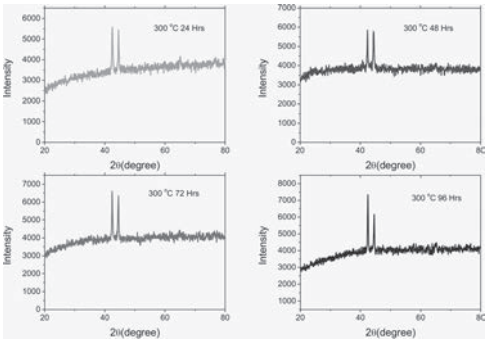


Fig. 1

3:54

HH-13. $M_xFe_{3-x}O_4$ (M = Li, Zn, Al, Zr, Ce or Hf) nanoparticles: possible *in-vivo* switch during magnetic hyperthermia. *N.K. Prasad*[1], M. Srivastava[1], S.K. Alla[1,2], A. Gangwar[1], S.K. Shaw[1], S. Singh Meena[3] and R.K. Mandal[1] *1. Metallurgical Engineering, Indian Institute of Technology (Banaras Hindu University), Varanasi, India; 2. Basic Science and Humanities, Vignan's Institute of Information Technology, VishakhaPatnam, India; 3. Solid State Division, Bhabha Atomic Research Center, Mumbai, India*

The iron oxide based nanoparticles (MNPs) (e.g. $M_xFe_{3-x}O_4$ or γ-$M_xFe_{2-x}O_3$) have suitable magnetic properties as well as biocompatibility and hence are used for cellular therapy, tissue repair, targeted drug delivery, magnetic resonance imaging, magnetic hyperthermia treatment (MHT) of cancer, etc. [1]. However, to avoid damage to the surrounding tissues the essential requirement is that temperature during MHT should not go beyond 48 °C. Such controlled heating is possible for MNPs with Curie temperature (T_C) which is less likely for such biocompatible oxides. In our recent studies, we observed that the substituted $M_xFe_{3-x}O_4$ (M = Li, Zn, Al, Zr, Ce or Hf and $0 \le x \le 1$) nanoparticles display stabilization of temperature (T_S) near 42 °C during MHT experiments which are shown in table 1 [2-7]. Nevertheless, the values of T_S were varying for the same material with applied external fields. In contrast, the unsubstituted Fe_3O_4 or γ-Fe_2O_3 did not show such T_S values at any fields. The structural, microstructural and magnetic characterizations for all the materials were carried to analyze the variation in the properties after doping.

N. K. Prasad, D. Bahadur, S. Vasseur and E. Duguet, John Wiley & Sons, Ltd. UK, 2008, 15-30. N. K. Prasad et al. *RSC Adv.*, 6, 41268–41274, (2016). M. Srivastava et al., *J. Alloys and Comp.* 688, 219-227, (2016). S. K. Shaw et al., *J. Magn. Magn. Mater.* 434, 181–186, (2017). M. Srivastava et al. *New J. Chem.*, 42, 7144, (2018). Patent Application# 201811002355, (19.01.2018) on Trivalent Al^{+3} doped magnetite and a method of preparation there of. M. Srivastava et al. *Cera. Inter.* 45, 12028-12034, (2019).

x	9 mT & 640 kHz	11 mT & 478 kHz	17 mT & 170 kHz	17 mT & 337 kHz	17 mT & 733 kHz	23 mT & 173 kHz	23 mT & 260 kHz	24 mT & 521 kHz	25 mT & 112 kHz
$Zr_xFe_{3-x}O_4$									
0.01	>60	>60	Experiment not performed	>60	Experiment not performed	57	Experiment not performed	Experiment not performed	>60
0.02	>60	>60		>60		>60			43
0.04	40	31		53		29			47
0.05	>60	>60		>60		>60			55
0.06	>60	>60		36		33			37
0.07	>60	40		>60		>60			43
0.1	48	>60		>60		31			>60
0.2	>60	>60		>60		>60			>60
0.4	>60	>60		>60		>60			>60
0.5	>60	>60		>60		39			>60
0.6	43	36		>60		>60			>60
0.7	>60	58		>60		>60			>60
0.9	>60	32		>60		>60			>60
1	47	>60		>60		40			>60
$Hf_xFe_{3-x}O_4$									
0.05	35	38	Experiment not performed	50	49	37	Experiment not performed	Experiment not performed	38
0.08	49	49		>60	33	33			>60
0.2	45	38		>60	52	50			>60
0.4	36	34		>60	42	39			>60
0.8	>60	>60		>60	41	>60			>60
$Zn_xFe_{3-x}O_4$									
0.01	60	46	45	>60	Experiment not performed	>60	>60	Experiment not performed	>60
0.07	50	42	29	>60		>60	>60		>60
0.2	52	>60	40	>60		>60	>60		>60
0.4	56	36	36	>60		>60	>60		>60
0.8	30	34	>60	30		30	30		30
$Li_xFe_{3-x}O_4$									
0.06	Experiment not performed	>60	Experiment not performed	>60	>60	Experiment not performed	>60	>60	>60
0.1		40		50	36		25	26	25
0.3		20		26	29		25	26	18
$Ce_xFe_{3-x}O_4$									
0.01	32	Experiment not performed	Experiment not performed	35	Experiment not performed	33	Experiment not performed	31	35
0.05	33			36		32		36	34
0.1	34			39		36		>60	37
0.3	>60			>60		>60		>60	>60
0.5	>60			>60		>60		>60	>60

Fig 1. The temperature achieved during magnetic hyperthermia by $M_xFe_{3-x}O_4$ (M = Li, Zn, Zr, Ce or Fe) nanoparticles at various AC magnetic fields. The values more than 60 °C indicate continuous rise during hyperthermia.

4:06

HH-14. Withdrawn

4:18

HH-15. Bi and Ce-substituted Terbium Iron Garnet thin films for integrated photonics. *T. Fakhrul*[2], S. Tazlaru[1], L. Beran[1], E. Tsotsos[2], E.R. Rosenberg[2], M. Veis[1] and C. Ross[2] *1. Charles University, Prague, Czechia; 2. Materials Science and Engineering, MIT, Cambridge, MA, United States*

Cerium and Bismuth doped yttrium iron garnet (YIG) films have excellent magneto-optical (MO) figure of merit (ratio of Faraday rotation to optical absorption) in the near-IR and have been incorporated into on-chip optical isolators. Recently, rare earth garnets have also been developed for MO applications that have the advantage of not requiring garnet seed-layers to crystallize on Si. Here we examine the structure and the optical and magnetic properties of polycrystalline thin films of terbium iron garnet ($Tb_3Fe_5O_{12}$, TbIG) and Ce and Bi substituted TbIG grown on Si substrates using pulsed laser deposition (PLD). TbIG and $Ce_xTb_{3-x}Fe_5O_{12}$ crystallize on Si without a seed layer. However, increasing Ce content, for example in $Ce_{1.5}Tb_{1.5}Fe_5O_{12}$, made crystallization without a seed layer difficult. The growth conditions that produced polycrystalline single-phase TbIG films were at temperatures of 750^{o}C and at oxygen pressures of 2-10 mTorr, with a rapid thermal anneal at 900^{o}C/3 min. The magnetic moment of TbIG, Ce_1Tb_2IG and Bi_1Tb_2IG were 40, 60 and 10 kA/m respectively. This is lower than that of YIG due to the proximity to the compensation temperature of TbIG films, 330 K. TbIG and $Ce_{0.25}$TbIG films on Si were polycrystalline without any secondary phases. Faraday rotation of TbIG/Si, Ce_1TbIG/Si and Bi_1TbIG/Si films measured at a wavelength of 1550 nm was +600^{o}cm^{-1}, -800 ^{o}cm^{-1} and -400^{o}cm^{-1} respectively. The figure of merit of the TbIG was found to be 900 ^{o}dB^{-1} and the effect of Ce and Bi substitutions in TbIG on the figure-of-merit is studied in detail. Temperature and spectral dependence of the Faraday rotation, optical absorption and refractive index is also characterized in this work.

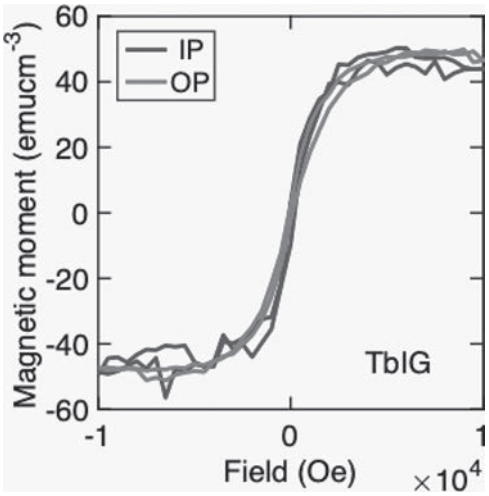


Fig. 1 In-plane (IP) and out-of-plane (OP) hysteresis loops for TbIG/Si.

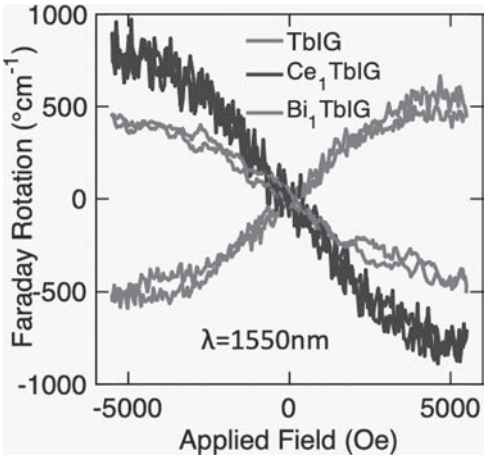


Fig. 2 Faraday Rotation of TbIG/Si, Ce_1TbIG/Si and Bi_1TbIG/Si films at 1550nm.

Session HI
SENSORS AND MAGNETIC RECORDING
Stéphane Mangin, Chair
Université de Lorraine, Vandoeuvre-lès-Nancy, France

INVITED PAPER

1:30

HI-01. Tape in the Cloud -- Technology Developments and Roadmaps Supporting 80 TB Cartridge Capacities. *R. Fontana*[1], R. Biskeborn[1], M. Lantz[2] and G. Decad[1] *1. Systems, IBM, San Jose, CA, United States; 2. Research, IBM, Zurich, Switzerland*

Tape provides critical storage needs for the Cloud as evidenced by continued growth in exabyte (EB) shipments of tape media. This paper outlines the present storage landscape environment for tape, HDD, and NAND flash, describes the tape roadmap for capacity improvements, and presents recording data on narrow track, 32 channel, TMR tape heads spanning read sensor widths from 1.0 um to 0.20 um to show the potential for 80 TB cartridge operation. This paper details the following points. First, the storage landscape for tape and HDD shows annual increases in manufactured EB of 15% to 20%. For the last 6 years the ratio of HDD EB to tape EB has remained constant, ~ 6%. Specifically, tape technology has demonstrated sustained importance in data storage. In 2017 manufactured EB data for tape and HDD were 44 EB and 745 EB respectively. Figure 1 shows these data. Second, the 2015 INSIC tape roadmap projects an annual areal density growth rate of 31% and annual cartridge capacity growth rate of 41%. Enterprise drive characteristics (TS1160) achieved these projections in 2017 (~ 12 Gbit/in^2) with 20 TB cartridge capacities, implying that cartridge capacities of ~ 80 TB in the next 4 years will likely be achieved via evolutionary developments in head/media technology and not from revolutionary developments required for HAMR and MAMR. Third, to demonstrate the extendibility of tape technology, recording data (particularly channel SNR) are presented for sensor widths from 1.0 um widths (20 TB cartridge capacity) down to 0.20 um sensor widths (potentially 80 TB cartridge capacity). The data, shown in Figure 2, were obtained using multi track (32 channel) read/write modules, which are compatible with Linear Tape Open (LTO) operation, on media that presently supports 20 TB cartridge capacities. Channel SNR improvements for the lower trackwidth data will improve with optimized media (smaller particle size) and reduced sensor recession. In summary, near term tape strategies to achieve 80 TB tape cartridge capacities exist and demonstrate that tape technology will remain a critical storage component for the cloud.

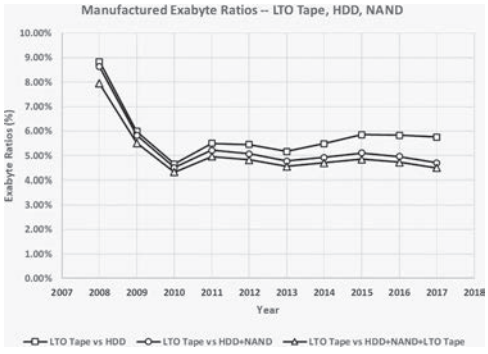


Fig. 1. Manufacured exabytes (EB) ratios for LTO Tape, HDD, NAND

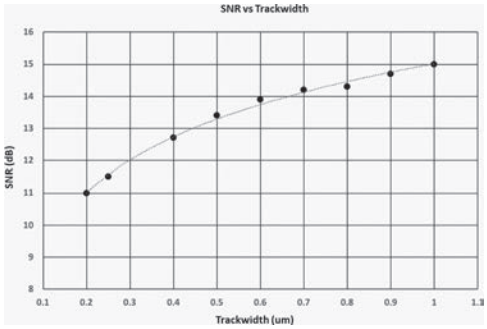


Fig. 2. Channel SNR vs trackwidth from drive data with 32 channel TMR tape heads

CONTRIBUTED PAPERS

2:06

HI-02. Pico-Tesla Sensitive Magnetoelectric Magnetometer Based on Delta-E Effect. *C. Dong*[1], Y. He[1] and N. Sun[1] *1. Northeastern University, Boston, MA, United States*

Ultra-sensitive, compact size, and low cost magnetometers for DC and low frequency magnetic field measurement are significant in bio-magnetic sensing and magnetic anomaly detection. We present a resonant magnetoelectric (ME) magnetometer, which utilizes the magnetic field induced elastic modulus change, i.e. the ΔE effect in the magnetostrictive layers. The sensor is based on a magnetostrictive/piezoelectric heterostructure, and the magnetic field induced elastic modulus change will result in electromechanical resonant frequency shift in the ME heterostructure, which can be read out through the impedance of the piezoelectric layers. By integrating four of such ME sensors into a Wheatstone Bridge circuit structure, the impedance change in each sensor unit will induce a voltage output between the two branches of the circuit, which can accurately reflect the change of magnetic field. The maximum frequency shift of the ME sensor unit due to magnetization has been characterized as 12.7%, and with 0.3 mT bias magnetic field, the sensor has the highest frequency sensitivity of 8.2 kHz/mT. By driving all the sensor units at frequency between the resonance and anti-resonance, where the slope of the impedance curve over frequency gives the highest impedance sensitivity of 318 Ohm/Hz, the magnetometer has an overall sensitivity of 6.65×10^4 V/T, and an extremely low limit of detection of 90 pT for DC magnetic field.

M. Staruch, M.-T. Yang, and P. Finkel, Applied Physics Letters., Vol. 111, p.2905 (2017) S. Zabel, C. Kirchhof, and F. Faupel, Applied Physics Letters., Vol. 107, p.2402 (2015) R. Jahns, S. Zabel, and F. Faupel, Applied Physics Letters., Vol. 105, p.2414 (2014) B. Gojdka, R. Jahns, and F. Faupel, Applied Physics Letters., Vol. 99, p.3502 (2011)

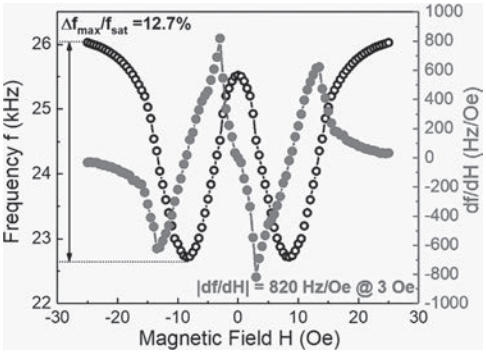


Fig. 1. Frequency shift and frequency sensitifity over bias magnetic field of a single ME sensor unit.

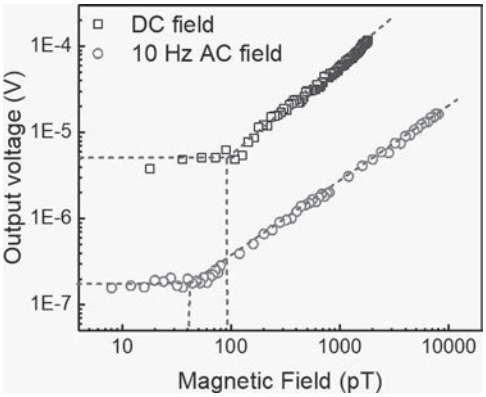


Fig. 2. Limit of Detection of the Wheatstone bridge ME sensor system at DC and 10 Hz AC magnetic field.

2:18

HI-03. Four-level Dual-track Readback Scheme for Synchronized Interlaced Magnetic Recording. S. Yoon[1] and *E. Hwang*[1] *1. Gwangju Institute of Science and Technology, Gwangju, The Republic of Korea*

In this study, multi-level joint-track readback scheme is proposed for interlaced magnetic recording (IMR) with synchronized tracks. IMR provides an areal density capability (ADC) gain by pre-fixing the recording orders as interlaced and customizing the write configurations for neighboring tracks [1]. Heat-assisted IMR is introduced to achieve extra ADC gain by jointly modulating the optical spot over the high coercivity media [2]. In addition, inter-track interference (ITI) cancellation [3] and array-reader schemes [4] are introduced for IMR to reliably retrieve recorded data. Dual-track readback IMR with an array reader jointly covering neighboring tracks is also investigated for doubling the read data rate but with complicated skew effects by multiple readers [5]. This study focuses on the feasibility of the dual-track readback by a single wide reader, by taking advantage of interlaced feature of the IMR. By synchronized writing of neighboring tracks in an interlaced manner, a single wide reader covering two-tracks jointly is capable of capturing four-level (4L) signals. The single-reader based dual-track read (DTR) IMR relaxes the skew issues and processing overheads in the array reader based IMR. The 4L-DTR IMR channel is illustrated in Fig. 1. The wide reader captures two neighboring tracks jointly but with different weights by differentiated relative track widths of the written tracks. For example, when bottom tracks are initially written widely and later trimmed by the top tracks as in Fig. 1, the raw waveform, $\underline{r}$, is processed by analog front-end (AFE) and loops to get ADC sample sequence, $\underline{x}_{4L}$, which has four levels. Fig. 2 illustrates the raw waveforms and histograms of ADC samples of the 4L-DTR IMR conditioned on the input data. Due to the inevitable read offsets, the relative weights of the target signal are varying and the joint 4L equalizer $\underline{h}(\delta)$ need to be adaptively adjusted by accounting the read-offset δ for equalized output $\underline{y}_{4L}$. Then, the equalized samples are later processed by multi-level detector as two-bit sequence, $\underline{z}_{2b}$.

1) E. Hwang, J. Park, R. Rauschmayer, *IEEE Transactions on Magnetics,* 53(4) a#3101407 (2017) 2) S. Granz, W. Zhu, E. Gage, *IEEE Transactions on Magnetics,* 54(2) a#3100504 (2018) 3) E. Hwang, *IEEE Global Telecommunication Conference* (*Globecom'17*), a# 8255007, (2017) 4) E. Hwang, W. Chang, S. Yoon, *IEEE Transactions on Magnetics*, 55(3) a#3100107 (2019) 5) E. Hwang, S. Yoon, *IEEE Transactions on Magnetics*, accepted, a#2794723 (2019)

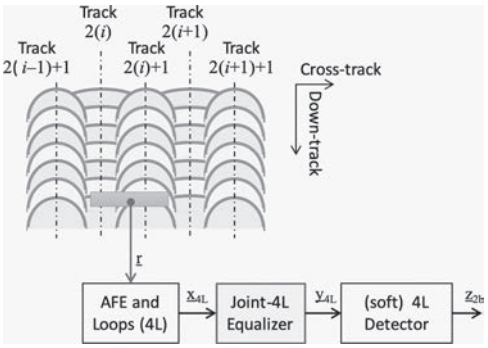


Fig. 1. Block diagram of the four-level (4L) dual-track read (DTR) IMR.

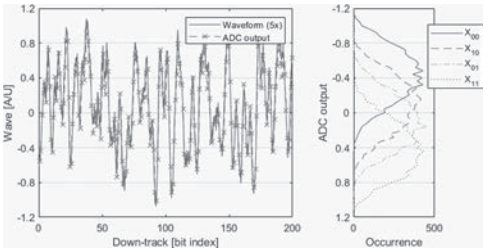


Fig. 2. Illustration of the waveforms (left) and ADC samples (right) of the 4L-DTR IMR.

2:30

HI-04. Statistical Analysis of Read-back Signals in Magnetic Recording on Granular Media. *F. Slanovc*[1], C. Vogler[1], O. Muthsam[1] and D. Suess[1] *1. Faculty of Physics, University of Vienna, Vienna, Austria*

The simulation of magnetic writing and read-back processes on granular media becomes computationally expensive for individually computed switching probability of each single grain within the writing process (see [1,2]). The a priori calculation of switching probability phase diagrams (as in [3]) allows an arbitrary amount of writing processes afterwards. For a conventional writing method, the magnetization of each grain (up or down) is chosen according to the extracted switching probabilities from the diagram (see Fig. 1). It requires $m>1$ repetitions to investigate the mean signal as well as the noise (see [4,5]). In addition, the different grain alignment in various media must also be taken into account for further $n>1$ repetitions in order to obtain correct statistics for the final read-back signal. In this work we present two different methods that improve the statistical evaluation of the read-back. In the first approach we avoid setting the magnetization to up respectively down. Instead, we just assign each grain its magnetization probability. In the read-back process, we combine the probabilities to calculate a mean signal and its variance. Afterwards n repetitions on different media lead to the final read-back signal. The second approach does not even require a certain granular medium and directly correlates the switching probabilities in certain areas of the magnetic medium according to the mean grain diameter of the medium. In this case no statistical repetitions are necessary, both signal and noise can be determined directly from the magnetization

probabilities. Finally, we conclude that the different methods show good agreement and that the statistical behaviour of the evaluated signal-to-noise ratio is improved. (see Fig. 2). Nevertheless, we also find that fewer repetitions do not automatically mean faster computation time, since determining the right correlation between the switching probabilities is also computationally complex.

[1] CA Ross, Annual Review of Materials Research 31, 203-235 (2001) [2] P.-W. Huang and R.H. Victora, Journal of Applied Physics 115, 17B710 (2014) [3] C. Vogler et al., Applied Physics Letters 108, 102406 (2016) [4] J.-G. Zhu and H. Li, IEEE Transactions on Magnetics 49, 765-772 (2013) [5] S. Hernández et al., IEEE Transactions on Magnetics 53, 3000406 (2017) [6] J.-G. Zhu and H. Li, IEEE Transactions on Magnetics 53, 3100507 (2017)

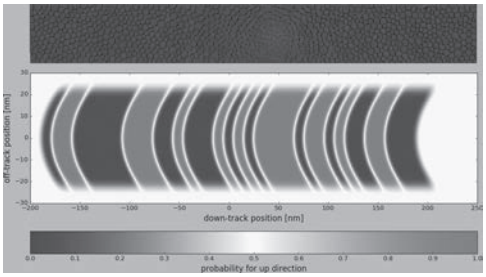


Fig 1. Top: Conventional bit pattern with magnetization in up (red) respectively down (blue) direction. Bottom: Magnetization probability map of the medium.

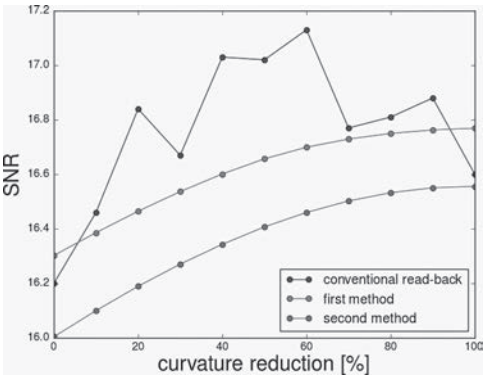


Fig 2. SNR values for various bit curvatures (see [6]). Chosen number of repeats: *m=1 and n=50*

2:42

HI-05. Development of High Resolution Programable Oversampling MI Sensor System with 32-bit ADC for Multi-Channel Bio-Magnetic Measurements. *J. Ma*[1] and T. Uchiyama[1] *1. Department of Electrical Engineering, Graduate School of Engineering, Nagoya University, Nagoya, Japan*

1. Introduction Recently, we have reported a high performance Pk-pk VD-type MI magnetometer [1]. In order to further improving noise performance and achieving higher spatial resolution for bio-magnetic sensing, there is a tendency to develop a multi-channel integrated system for micro magnetic sensors. In this study, we have developed a high resolution programable oversampling MI sensor system, as a unit module for multi-channel integrated bio-sensor system, based on Pk-pk VD-type MI sensor system. 2. Programable Oversampling MI sensor system The new developed MI sensor system is combined with Pk-pk VD-type MI sensor system and programable oversampling ADC & digital filter system. As illustrated in Fig. 1(a), we program the ADC configuration, sampling frequency, down sampling factor, and Filter configuration by Python; and communicate to FPGA with these programed ADC & Filter systems. After receiving the configuration programs from PC, the FPGA will setup ADC & Filter systems and control the ADC by supplying controlling and configuration signals. As illustrated in Fig. 1(b), we measure output noises in time domain of new MI sensor system with 30 Hz lowpass filter. The output RMS noise is about 10 pT with a 30 Hz lowpass filter. Fig. 2(a) illustrates magnetic noise spectral density of programable oversampling MI sensor system. The noise floor is lower than 1 pT/Hz$^{1/2}$ in the frequency range from 1 Hz to 100 Hz. It is 1/10 of noise level of previous MI gradiometer [2]. Furthermore, we have investigated high frequency noise components via new MI sensor system. Fig. 2(b) illustrates magnetic noise spectral density of new MI sensor system with 0.5 MHz sampling frequency. The noise peak at 800 Hz and the reduction of noise floor after 800 Hz are because of 800 Hz lowpass filter in analog circuit. Meanwhile, the noise peaks at high frequency component marked with red circle in Fig. 2(b) are oscillation noises.

[1] J. Ma, and T. Uchiyama, IEEE TRANSACTIONS ON MAGNETICS, VOL. 53, NO. 11, 4003404, NOVEMBER 2017. [2] T. Uchiyama and T. Takiya, AIP Adv., vol. 7, no. 5, p. 056644, 2017.

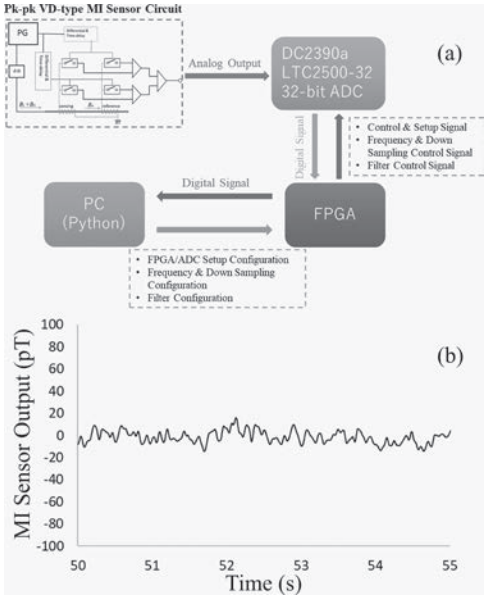


Fig. 1 (a) Block diagram of programable oversampling MI sensor system. (b) The output noises in time domain of new MI sensor system with 30 Hz lowpass filter.

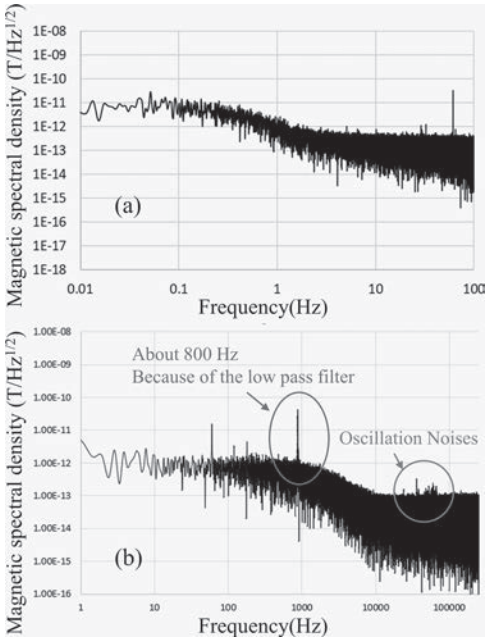


Fig. 2 (a) The magnetic noise spectral density of new MI sensor system. (b) Investigation of high frequency noise components for new MI sensor system.

2:54

HI-06. Radio-frequency magnetic noise of magnetic vortex states in magnetic tunnel junctions. *R. Okuno*[1], M. Goto[1,2], S. Tsunegi[3], K. Yakushiji[3], H. Kubota[3], A. Fukushima[3], S. Yuasa[3], H. Nomura[1,2] and Y. Suzuki[1,2] *1. Graduate School of Engineering Science, Osaka University, Toyonaka, Japan; 2. Center for Spintronics Research Network, Osaka University, Toyonaka, Japan; 3. National Institute of Advanced Industrial Science and Technology, Tsukuba, Japan*

Understanding the magnetic noise is important for realizing highly sensitive magnetic field sensors. Currently, the magnetic noise such as magnoise [1], nonlinear magnoise [2], and 1/f noise [3] has been investigated in magnetic tunnel junctions (MTJs) with single domain states. Moreover, the low frequency noise has been studied in a MTJ with the magnetic vortex state. It is the candidate for a highly sensitive sensor with wide dynamic range because of its negligible hysteresis and high saturation field [4]. However, the magnetic noise of the magnetic vortex state is not studied in wide frequency range. In this study, we investigate the magnetic noise in the MTJ with a magnetic vortex state in the free layer (FL) in radio-frequency (RF) range. Figure 1 shows the noise measurement circuit. The film stack structure is Buffer/ IrMn(6)/ CoFe(2.5)/ Ru(0.85)/ CoFeB(2.1) and CoFe(0.4) pinned layer/ MgO(1.1)/ FeB(5) magnetic vortex FL/ MgO(1.1)/ Ta(5)/ Ru(5) (nm in thickness). The external magnetic field is applied in an antiparallel direction to the pinned layer. Figure 2 shows the magnetic field dependence of the magnoise spectrum. From the magnetoresistance curve (MR curve), the FL is the magnetic vortex state in 0 mT, and the single domain state in 40 and 80 mT. The magnoise peak is caused by a rotation of a vortex-core in the magnetic vortex or a precession of the magnetization in the single domain by the heat at room temperature. From Fig. 2, the magnoise peak of the magnetic vortex appears in lower frequency than the single domain state. Furthermore, we observed 1/f magnetic noise of the magnetic vortex in the MHz frequency range. Our results provide the fundamental knowledge for the magnetic field sensor using magnetic vortex. This research was supported by Bilateral Programs (MEXT) and JSPS KAKENHI (Grant No. JP16H03850).

[1] N. Stutzke *et al*., Appl. Phys. Lett. 82, 1 (2003), [2] S. Miwa *et al.,* Nat. mater. 13, 50 (2014), [3] S. Ingvarsson *et al*., Phys. Rev. Lett. 85, 3289 (2000), [4] D. Suess *et al*., Nat. Elec. 1, 362 (2018)

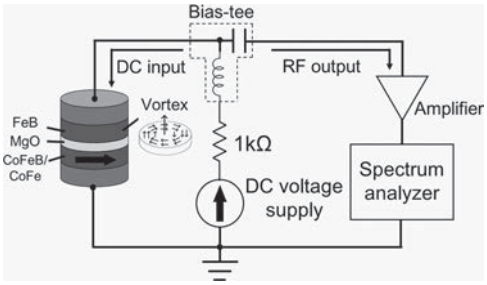


Fig. 1. Noise measurement circuit

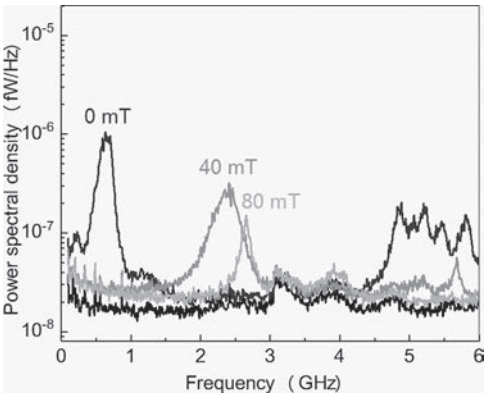


Fig. 2. Magnoise spectrum

3:06

HI-07. Optimization of thin film magnetoimpedance structures for low field sensing applications. *E. Fernandez-Martin*[2], N. Lete-Segura[1], J. Beato[3], C. Gomez-Polo[3] and A. Garcia-Arribas[1,2] *1. Electricidad y Electronica, Universidad del Pais Vasco (UPV/EHU), Leioa, Spain; 2. BCMaterials, Basque Center on Materials, Applications and Nanostructures, Leioa, Spain; 3. Departamento de Ciencias, Universidad Publica de Navarra, Pamplona, Spain*

The magneto-impedance (MI) is the great change of the electrical impedance that soft ferromagnetic materials exhibit when an external magnetic field is applied. The impedance change with magnetic field is related to the reduction of the effective cross section available for the ac current to flow due to the skin effect. In previous studies, we have systematically optimized the preparation conditions, structure and combination of shape and induced anisotropies to enhance the MI ratios and sensitivities on $Ni_{80}Fe_{20}$ multilayers [1-3]. In this work, $[FeNi(50nm)/Ti(6nm)]_8$ /Cu(400nm)/ $[Ti(6nm)FeNi(50nm)/Ti(6nm)]_8$ 12x0.5 mm samples were sputtered onto silicon. During the deposition, a 250 Oe magnetic field is applied parallel to the film plane in order to induce a uniaxial magnetic anisotropy perpendicular to the long side of the sample. Cooper electrical contacts are deposited at both ends of the samples and to connect the elements of the meanders. We aim to determine the best strategy to increase the field sensitivity of the MI samples by impedance matching to 50 Ω. There are mainly two options: one is to adapt the impedance of the prepared sample by a combination of passive elements. The matching is then done for a certain field and frequency (Fig. 1). The matched sample maintains the original relative MI ratio (240 %) and sensitivity (170 %/Oe - derivative of the MI ratio), but the impedance sensitivity is increased by an order of magnitude, from 4 Ω/Oe to 40 Ω/Oe. The second option is to increase the length of the MI element, by forming a meander structure. This option needs a more detailed study due to the role played by the increased self-inductance of the structure. For this reason, we have

simulated different meander configurations. The simulations show an increase of MI ratio as the distance between the meander elements is reduced and a substantial increase of the MI ratio with the number of meander elements (Fig. 2), that seems to saturate with 9 elements.

[1] A. V. Svalov et al., "Structure and magnetic properties of thin permalloy films near the "transcritical" state", IEEE Trans. on Mag., 46(2), 333–336, (2010). [2] E. Fernández et al., "GMI in nanostructured FeNi/Ti multilayers with different thicknesses of the magnetic layers" IEEE Trans. on Mag., 49(1), 18–21, (2013). [3] A. García-Arribas et al.,"Thin-film magneto-impedance structures with very large sensitivity", J. Magn. Magn. Mater., Vol. 400, pp. 321-326, (2016).

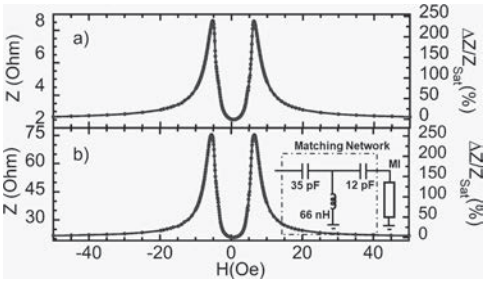


Fig1. MI dependence with magnetic field and its ratio at 90 MHz, before a) and b) after matching.

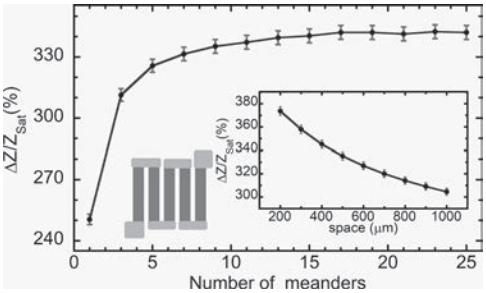


Fig2. MI ratios vs. of the number of meanders with a 500 μm spacing. Inset: the dependence with the spacing for a meander with 9 elements.

3:18

HI-08. Detection of Strain Direction Using a Flexible Exchange-Biased Spin Valve. *H. Matsumoto*[1,2], S. Ota[1,2], A. Ando[3] and D. Chiba[2,4]
1. Department of Applied Physics, The University of Tokyo, Bunkyo, Tokyo, Japan; 2. Institute of Scientific and Industrial Research, Osaka University, Ibaraki, Osaka, Japan; 3. Murata Manufacturing Co., Ltd., Nagaokakyo, Kyoto, Japan; 4. Center for Spintronics Research Network, Osaka University, Toyonaka, Osaka, Japan

Magnetization direction of ferromagnetic metal thin films can be controlled by applying a tensile strain [1, 2]. Based on this, we have recently developed a strain direction sensor formed on a flexible substrate [3], which is a giant magnetoresistive pseudo spin valve (SV) with a strain-sensitive Co free layer and a strain-insensitive NiFe pinned layer [3]. Only the magnetization of the Co layer rotates to the strain direction, while the magnetization of the NiFe layer always points toward an assisting magnetic field H_a direction. Thus, a resistance R of the SV changes depending on the strain direction. Here we show H_a-free strain direction sensing [4]. To realize this, a flexible exchange-biased SV (EBSV) is formed. In this case, the magnetization of the free layer can more freely rotate by strain application without being disturbed by H_a because the exchange bias (EB) only pins the NiFe layer. As a result, the sensitivity is improved. We also demonstrate a human body motion detection using this sensor [4]. We prepared a Co/Cu/NiFe/FeMn EBSV on a flexible substrate. Fig. 1 shows the dependence of the R change on tensile strain ε measured for the EBSV without H_a (top panel) and for the pseudo SV measured under $\mu_0 H_a$ =20 mT (bottom panel) [3]. θ is the angle between the EB or H_a direction and ε axis. As seen in the curve for θ = 90°, R of the EBSV increases more sharply by ε application and saturates at smaller ε compared with the pseudo SV case, meaning that the strain direction can be identified more sensitively. We fabricated a finger motion sensor using the flexible EBSV. As shown in Fig. 2, the sensor can identify which finger is bent. The authors thank T. Sekitani and T. Koyama for their useful discussion and technical help. This work was partly supported by Murata Manufacturing Co., Ltd., JSPS KAKENHI (Grant Nos. 25220604 and 17J03125) from JSPS, and Spintronics Research Network of Japan.

[1] S. Ota and D. Chiba *et al*., *Appl. Phys. Express*, Vol. 9, p.043004(1)-(4) (2016) [2] R. Asai, S. Ota and D. Chiba *et al*., *J. Appl. Phys.*, Vol. 120, p.083906(1)-(4) (2016) [3] S. Ota, A. Ando and D. Chiba, *Nat. Electron.*, Vol. 1, p.124-129 (2018) [4] H. Matsumoto, S. Ota, A. Ando and D. Chiba, *Appl. Phys. Lett.*, Vol.114, p. 132401(1)-(5) (2019)

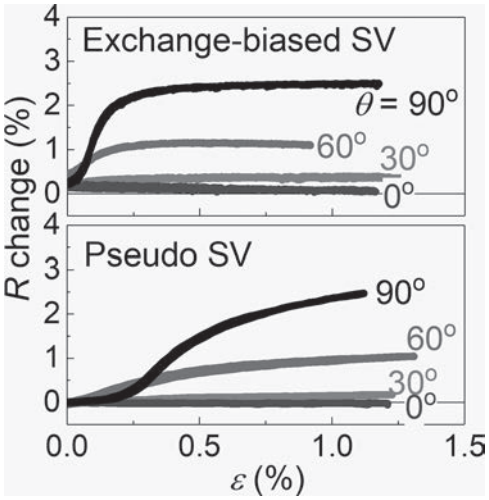


Fig. 1. ε dependence of R changes for the EBSV without H_a (top panel) and for the pseudo SV under H_a (bottom panel) [3].

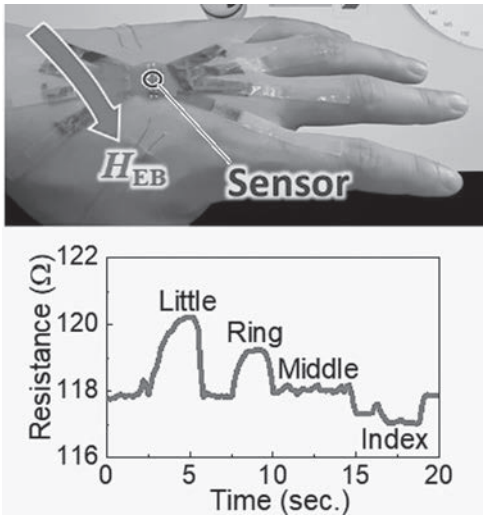


Fig. 2. Photograph of the finger motion sensor (top panel) and the resistance log when the fingers were bent in turn (bottom panel).

3:30

HI-09. Flexible magnetoelectronics for interactive wearables. G. Canon Bermudez[1] and *D. Makarov[1] 1. Helmholtz-Zentrum Dresden-Rossendorf, Dresden, Germany*

The recent rapid advance and eagerness of portable consumer electronics stimulate the development of functional elements towards being lightweight, flexible, and wearable. Next generation flexible appliances aim to become fully autonomous and will require ultra-thin and flexible navigation modules, body tracking and relative position monitoring systems. Key building blocks of navigation and position tracking devices are magnetic field sensors. Although there is a remarkable progress in the field of shapeable magnetoelectronics [1], there is no technology available that can enable sensitivities to geomagnetic fields of 50 μT and, ultimately, magnetic fields of smaller than 1 μT in a mechanically compliant form factor. If available, these devices would contribute greatly to the realization of high-performance on-skin interactive electronics [2-5] and point of care applications [6,7]. Here, we will present technological platforms allowing to realize not only mechanically imperceptible electronic skins, which enable perception of the geomagnetic field (e-skin compasses) [8], but also enable sensitivities down to ultra-small fields of sub-50 nT [9]. We demonstrate that e-skin compasses allow humans to orient with respect to earth's magnetic field ubiquitously. Furthermore, biomagnetic orientation enables novel interactive devices for virtual and augmented reality applications. We showcase this by realizing touchless control of virtual units in a game engine using omnidirectional magnetosensitive skins.

[1] D. Makarov et al., Applied Physics Reviews 3, 011101 (2016). [2] G. S. Canon Bermudez et al., Science Advances 4, eaao2623 (2018). [3] M. Melzer et al., Nature Communications 6, 6080 (2015). [4] M. Melzer et al., Advanced Materials 27, 1274 (2015). [5] N. Münzenrieder et al., Advanced Electronic Materials 2, 1600188 (2016). [6] G. Lin et al., Lab Chip 14, 4050 (2014). [7] G. Lin et al., Lab Chip 17, 1884 (2017). [8] G. S. Canon Bermudez et al., Nature Electronics 1, 589 (2018). [9] P. N. Granell et al., npj Flexible Electronics 3, 3 (2019).

3:42

HI-10. Variable Temperature Study of Noise and Field Detectability in Magnetic Tunnel Junctions with Superparamagnetic Free Layers. *Y. Zhang*[1], G. He[1], X. Zhang[2] and G. Xiao[1] *1. Department of Physics, Brown University, Providence, RI, United States; 2. Division of Physical Science and Engineering, King Abdullah University of Science and Technology, Thuwal, Saudi Arabia*

Magnetic tunnel junctions (MTJs) with a superparamagnetic free layer have attracted attention due to its linear and hysteresis-free behavior, as well as possible reduction of low-frequency *1/f* noise. A comprehensive study on superparamagnetic MTJs under various conditions is currently lacking. In this work, we have performed a systematic study on transport and noise properties of superparamagnetic MTJs over a broad range of frequency, magnetic field, and temperature. From the magneto-transport properties, we have found a size variation of nanoclusters composing the free layer. Such size distribution is important in understanding the smooth change of noise and sensitivity near the blocking temperature of superparamagnetic transition. Particularly, relationship between *1/f* noise and sensitivity is closely examined. Different scaling relations between *1/f* noise and sensitivity have been found in ferromagnetic and superparamagnetic states. The change of scaling law implies that magnetic nanoclusters in ferromagnetic and superparamagnetic states are under different thermodynamic conditions. An explanation based on fluctuation-dissipation theorem is given. This result shows that noise measurement is an efficient tool in understanding thermodynamics of nanostructures. Finally, significance of scaling law to MTJ performance and approaches to further optimize superparamagnetic MTJs will be discussed.

3:54

HI-11. MTJ Based Magnetic Sensor for Current Measurement in Grid. *K. Gao*[1], X. Yin[3], Y. Yang[2], D. Ewing[4], P.J. De Rego[5] and S. Liou[2] *1. Research and Development, International Business and Technology Service Corporation, North Oaks, MN, United States; 2. University of Nebraska, Lincoln, Lincoln, NE, United States; 3. Western Digital Corporation, Fremont, CA, United States; 4. Department of Energy's Kansas City National Security Campus, Kansas City, KS, United States; 5. New Mexico Operations, Department of Energy's Kansas City National Security Campus, Albuquerque, NM, United States*

Here we review the status and the challenges utilizing MTJ based magnetic sensor for Grid sensing [1-4]. We show that with both modeling and experiment measurement optimized MTJ based magnetic (RemG) sensor can be utilized to monitor Grid current, particular for each individual transmission line measurement. Unlike the traditional approach where the sensing element needs to be either integrated, in contact with or near the transmission line, this measurement can be based on a contactless or a "remote" sensing setup, where the sensor is placed away from the Grid line. We have demonstrated that, utilizing special designed and optimized MTJ based magnetic sensor, we are able to conduct remote real time measurement of the magnetic field generated from the Grid current [5]. From sensor perspective, the sensitivity, the signal to noise ratio and the linearity can all meet the target device requirement. Combined with finite difference time domain microcurrent model, one can back calculate current waveform in each line when complex Grid topology is present [6]. This approach enables a system to detect the situation of the Grid. MTJ based sensing technology with high sensitivity, small size, light weight and low power consumption and potential low cost have been shown [5]. We do see that as the complexity of the Grid topology increases, the system complexity increases significantly. From sensing perspective, MTJ based sensor is ideal to conduct a "remote" sensing, in a way it can be placed meters away from the Grid line. One of the challenges is that the complex topology and multiple Grid lines may exists with different current levels. The other challenge is that with an improved sensing capability provided by MTJ sensors, significant more data can be collected, the system bottle neck has been shifted to transfer of data instead of sensing.

1. Zheng C., Zhu K., ... and Pong P.W.T., Magnetoresistive Sensor Development Roadmap (Non-Recording Applications), IEEE Trans. Magn., Vol. 55, No. 4, 0800130, April, 2019. 2. Huang Q., ... Pong P.W., IEEE Trans. Magn., Vol. 50, Is 7, 0900107, July 2014. 3. Ouyang Y., He J, Wang S.X., IEEE Trans. Magn., Vol. 51, Is 11, 4004904, Nov. 2015. 4. Sun X., Liu K.S.,Pong P.W.T., IEEE Trans. Magn., Vol 47, Is. 10, 2608, Sept. 2011. 5. K. Z. Gao and S. H. Liou, to be published in IEEE Magn. Lett, 2019. 6. WEILAND T., International Journal of Numerical Modelling, Vol. 9, Is.4, p. 295-319, July 1996.

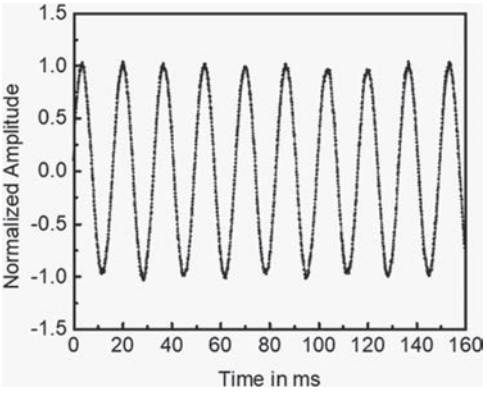


Fig 1. Modeled (red) and measurement (blue) of the magnetic field from the Grid line in operation.

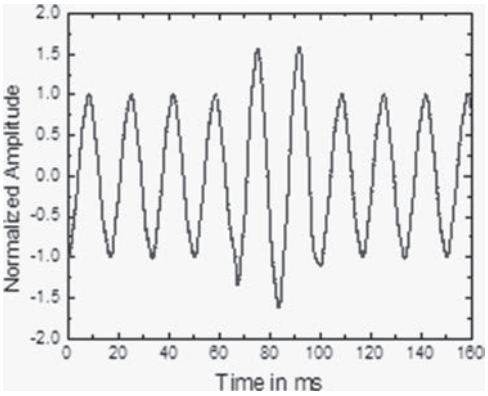


Fig 2. Measured waveform change when anomaly in the Grid current exists.

4:06

HI-12. Noise Optimization in Magnetic Tunnel Junctions. *J.E. Davies*[1], J. Watts[1], J. Novotny[1], D. Huang[1] and P.G. Eames[1] *1. Advanced Technology, NVE Corporation, Eden Prairie, MN, United States*

MgO-based tunneling magnetoresistive (TMR) sensors are blossoming into a large and dynamic application space [1]. One of the key goals in sensor development is minimization of the noise; which is dominated by a magnetic *1/f* component at low frequencies and Johnson noise at high frequencies [2]. While noise minimization by itself is a noble goal, and has become somewhat of a technology marketing point, there are significant trade-offs when looking at the TMR sensor's best application space. We have evaluated the noise parameters of a number of sensor configurations and found that the sensors with the lowest measured noise floor in (μV/V/ÖHz) did not have the lowest detectivity (nT/ÖHz). This is on account of the sensitivity playing the dominant role in determining the detectivity and comes at the expense of the sensor's size and linear range. These other parameters set the ultimate bounds for sensor performance. One clear path forward is to maximize the TMR. Egelhoff, *et al.* showed that there are diminishing returns on improving the overall noise when the TMR is much higher than 100%. However, TMR maximization is bountiful when it comes to increasing sensor range, minimizing size and hysteresis. Additionally, improvements to the traditional Wheatstone bridge design with shielded MTJ resistors by moving to a push-pull bridge configuration yields a nearly 100% increase in the sensitivity; adding to the design space. This is challenging to achieve monolithically due to having to pin MTJ reference layers in opposing directions. TMR and sensor configuration thus become the two biggest areas for sensor performance gains. We demonstrate these improvements in recently fabricated sensors and are able to achieve <10 pT/√Hz@ 1 kHz and <1 nT/√Hz @ 1 Hz while maintaining a linear range greater than 0.1 mT.

[1] C. Zheng *et al.*, "Magnetoresistive Sensor Development Roadmap (Non-Recording Applications)," *IEEE Trans. Magn.*, vol. 55, no. 4, pp. 1–30, 2019. [2] W. F. Egelhoff *et al.*, "Critical challenges for picoTesla magnetic-tunnel-junction sensors," *Sensors Actuators A Phys.*, vol. 155, no. 2, pp. 217–225, Oct. 2009.

4:18

HI-13. A Full Sample-Type MI Magnetometer with Programable Circuit for High Compatibility. *K. Shi*[1] and T. Uchiyama[1] *1. Graduate School of Engineering, Nagoya University, Nagoya, Japan*

The MI sensor which is based on magneto-impedance effect in an amorphous wire used for numerous applications[1], such as electronic compass, foreign matter detection, healthcare[2]. However, the conventional circuit are still working with sample-hold(S/H) circuit that are not suitable for all type of MI sensor.in this work, we propose a novel circuit design for MI sensor system that consists of analogue integration circuit and a field-programmable gate array (FPGA)to sample the whole waveform of sensor's output. The external magnetic field was generated by a Helmholtz coil. And the whole system is put in Permalloy shield box (50dB@2Hz). The controllable integration of the two parts of the MI sensor output can be achieved by the FPGA controlled circuit. Figure.1 (a)shows The output waveform of the MI sensor is divided into two areas by the rising and falling edges of the excitation pulse. which have opposite conversion rates of the external magnetic field. In order to maximize the sensitivity of the system, we integrate the two parts separately.Figure.1 (b)shows the two parts of the MI sensor output have the same sensitivity to the external magnetic field, which has different sensitivity ratio than S/H mode circuit [3]. Figure.2 shows the external magnetic field is set to a 10 Hz sine wave with an amplitude of 300 pT. The decibel value near 10 Hz in the previous system is -25 dB, in the proposed system, the decibel value near 10 Hz is -35 dB. By adjusting the integral distribution ratio of the two parts, we can reduce the noise and improve the SNR. We have demonstrated a new MI sensor system based on FPGA-based programmable circuits. Compared with the conventional S/H circuit system, the proposed system has better compatibility to the MI sensor, and it is not necessary to adjust the switch opening time for better performance. The results show that the proposed system has high resolution and high signal to noise ratio.

[1]T. Uchiyama, K. Mohri, Y. Honkura, and L. V. Panina, "Recent advances of pico-Tesla resolution magneto-impedance sensor based on amorphous wire CMOS IC MI sensor" IEEE Trans. Magn., Vol. 48, NO. 11,pp. 3833–3839, Nov. 2012. [2] K. Mohri, T. Uchiyama, and L. V. Panina, "Recent advances of micro magnetic sensors and sensing application" Sens. Actuators A, Phys.vol. 59, pp. 1–8, Apr. 1997. [3] Tsuyoshi Uchiyama, Norihiko Hamada, and Changmei Cai "Highly Sensitive CMOS Magnetoimpedance Sensor Using Miniature Multi-Core Head Based on Amorphous Wire" IEEE TRANSACTIONS ON MAGNETICS, Vol. 50, NO. 11, Nov 2014

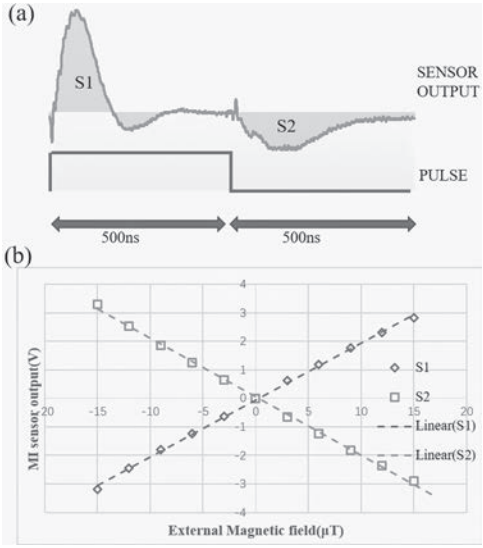


Figure.1 (a)Schematics of the MI sensor's output waveform. (b) Sensitivity of S1 and S2 to external magnetic fields.

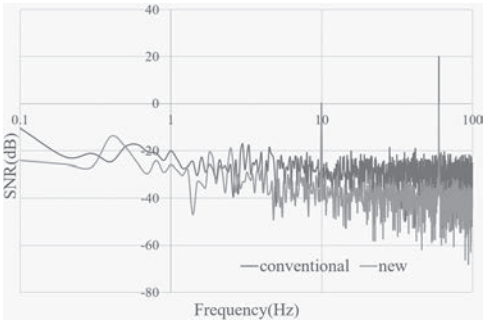


Figure.2 The S/N ratio of the system.

- A -

A., S.M. (AT-03) . . . 81
Ababei, G. (GH-14) . . . 714
Aballe, L. (ED-04) . . . 469
Aballe, L. (HG-09) . . . 807
Abe, K. (HH-09) . . . 814
Abe, T. (GU-01) . . . 754
Abe, T. (GU-02) . . . 754
Abe, T. (GU-08) . . . 757
Abellan, M. (FC-08) . . . 569
Abreu Araujo, F. (BT-17) . . . 206
Abreu Araujo, F. (EF-01) . . . 478
Abreu Araujo, F. (EQ-04) . . . 513
Abreu Araujo, F. (FP-05) . . . 617
Abrudan, R. (HH-03) . . . 811
Abugri, J.B. (EP-17) . . . 511
Acet, M. (BI-03) . . . 167
Acet, M. (EH-09) . . . 495
Acosta, A. (DW-09) . . . 446
Acosta, A. (FU-17) . . . 654
Acosta, V.M. (DT-01) . . . 423
Aczel, A. (FE-01) . . . 579
Adams, J. (BR-05) . . . 190
Adelmann, C. (CE-08) . . . 258
Adelmann, C. (CE-12) . . . 260
Adelmann, C. (HC-10) . . . 779
Adhikari, A. (CC-10) . . . 246
Adhikari, A. (EQ-02) . . . 512
Adhikari, K. (EQ-03) . . . 513
Adolff, C.F. (CE-02) . . . 255
Adriano, C. (CT-13) . . . 322
Adriano, C. (GT-02) . . . 748
Adriano, C. (GT-05) . . . 749
Adriano, C. (GT-06) . . . 750
Adriano, C. (GT-14) . . . 752
Aeschlimann, M. (ER-03) . . . 519
Afsar, M.N. (GI-13) . . . 722
Agarwal, N. (DD-02) . . . 361
Agbo, S.A. (FQ-10) . . . 627
Agostino, C.J. (FG-03) . . . 592
Ahlberg, M. (BD-06) . . . 134
Ahlm, N. (GG-01) . . . 703
Ahmad, H. (HC-10) . . . 779
Ahmadi, F. (ET-07) . . . 529
Ahmadi, P. (HE-03) . . . 790
Ahmadpour, G. (BP-05) . . . 174
Ahmed, A. (GF-02) . . . 697
Ahmed, A.S. (BB-04) . . . 116
Ahmed, A.S. (CR-02) . . . 306
Ahmed, A.S. (DC-03) . . . 357
Ahmed, A.S. (DH-06) . . . 387
Ahmed, A.S. (FG-12) . . . 596
Ahn, J. (AR-09) . . . 73
Ahn, J. (CT-04) . . . 318
Ahn, J. (EU-06) . . . 538
Ahrens, A. (CF-12) . . . 268
Ahrens, V. (GE-04) . . . 690
Ahrens, V. (GE-06) . . . 691
Ahrens, V. (GP-02) . . . 724
Ai, F. (FI-11) . . . 611
Ain, Q. (BT-18) . . . 207
Ainslie, K. (HH-11) . . . 815
Aires, A. (DG-04) . . . 380
Aizawa, Y. (EV-19) . . . 550
Ajaz-un-Nabi, M. (BI-15) . . . 171
Ajejas, F. (AF-07) . . . 32
Ajejas, F. (BG-10) . . . 156
Ajejas, F. (CD-01) . . . 249
Ajejas, F. (DE-01) . . . 368
Ajejas, F. (ED-05) . . . 469
Ajejas, F. (HB-02) . . . 770
Akagi, F. (GR-03) . . . 742
Akagi, F. (GV-03) . . . 761
Akagi, K. (DT-05) . . . 424
Akamatsu, S. (DW-04) . . . 443
Akansel, S. (AP-05) . . . 60
Akashi, N. (CI-11) . . . 289
Akbar, S. (DR-02) . . . 414
Akbarshahi, S. (FU-16) . . . 654
Akdogan, O. (BP-14) . . . 177
Åkerman, J. (AD-04) . . . 17
Åkerman, J. (AP-05) . . . 60
Åkerman, J. (CB-11) . . . 241
Åkerman, J. (CC-11) . . . 247
Åkerman, J. (DF-08) . . . 378
Åkerman, J. (EG-02) . . . 485
Akhtar, W. (EE-02) . . . 473
Akhtar, W. (EE-06) . . . 475
Akiyama, T. (AV-17) . . . 99
Akiyama, T. (GT-04) . . . 749
Akthar, M. (GQ-01) . . . 734
Al ghamdi, M. (DB-09) . . . 353
Al ghamdi, M. (FB-07) . . . 563
Al Mamoori, M. (BF-02) . . . 146
Al Milaji, K. (FQ-01) . . . 623
Al-Mahdawi, M. (DV-04) . . . 437
Ala, G. (BW-15) . . . 231
Alam, A. (DR-12) . . . 418
Alam, A. (HF-04) . . . 796
Alameda, J. (AF-09) . . . 33
Alameda, J. (GP-08) . . . 728
Alawein, M. (BC-11) . . . 128
Alawein, M. (DV-11) . . . 440
Alawein, M. (EP-04) . . . 504
Albrecht, M. (AW-04) . . . 102
Albrecht, M. (CR-06) . . . 308
Albrecht, M. (FV-13) . . . 661
Alejos, O. (HG-04) . . . 805
Aleman, A. (CC-11) . . . 247
Aleshkevych, P. (CU-05) . . . 326
Aleshkevych, P. (HF-12) . . . 801
Alghamdi, N. (DG-11) . . . 384
Alghamdi, N. (HH-07) . . . 813
Alho, B.d. (FQ-15) . . . 629
Alho, P.d. (FQ-15) . . . 629
Ali, A. (BI-15) . . . 171
Ali, M. (BE-09) . . . 143
Ali, M. (GB-05) . . . 673
Ali, M. (GH-10) . . . 713
Ali, M. (GQ-06) . . . 736
Ali, N. (AQ-17) . . . 69
Ali, N. (DQ-01) . . . 405
Ali, N. (DR-01) . . . 414
Ali, N. (DR-15) . . . 420
Ali, N. (FQ-09) . . . 627
Aliev, F.G. (CF-03) . . . 263
Alla, S.K. (HH-13) . . . 816
Allen, A. (GD-03) . . . 685
Allen, S.R. (AD-05) . . . 18
Allende, S. (FW-01) . . . 663
Allenspach, R. (BE-09) . . . 143
Allia, P. (FI-13) . . . 612
Almasi, H. (BB-14) . . . 120
Almasy, L. (DW-03) . . . 443
Almeida, T. (AB-06) . . . 6
Almeida, T. (BB-11) . . . 119
Alnahari, E.G. (DQ-08) . . . 407
Alonso Masa, J. (DG-05) . . . 381
Alonso, M. (BH-02) . . . 158
Alonso, M. (BH-11) . . . 163
Alotibi, S. (GB-05) . . . 673
Alpern, H. (BG-09) . . . 155
Alshammari, K.N. (GH-10) . . . 713
Altbir, D. (AU-05) . . . 86
Altbir, D. (AU-12) . . . 89
Altbir, D. (AW-15) . . . 108
Altbir, D. (BQ-06) . . . 182
Altbir, D. (ET-08) . . . 529
Altbir, D. (FW-01) . . . 663
Althammer, M. (GB-10) . . . 675
Altounian, Z. (DI-07) . . . 393
Altounian, Z. (DQ-09) . . . 408
Altounian, Z. (FH-14) . . . 605
Altounian, Z. (FH-15) . . . 605
Alvarez Lucio, G. (BT-15) . . . 205
Alvarez-Prado, L. (AF-09) . . . 33
Alvarez-Prado, L.M. (GP-08) . . . 728
Álvaro Gómez, L. (GC-11) . . . 683
Alyami, M. (GH-10) . . . 713
Alyousef, Z. (AQ-06) . . . 64
Alyousef, Z. (AR-16) . . . 76
Amanatiadis, S. (GI-10) . . . 720
Amara, S. (BC-11) . . . 128
Amara, S. (DV-11) . . . 440
Amara, S. (EP-04) . . . 504
Amaral, J.S. (AF-03) . . . 31
Amaral, J.S. (EH-05) . . . 494
Amaral, J.S. (FD-05) . . . 574
Amaral, J.S. (HC-02) . . . 775
Amaral, V. (AF-03) . . . 31
Amaral, V. (HC-02) . . . 775
Ambaye, H. (BA-01) . . . 111
Ambaye, H. (EE-07) . . . 475
Amei, K. (FP-02) . . . 615
Amemiya, K. (FB-09) . . . 564
Amin, N. (BI-15) . . . 171
Amin, V. (AD-05) . . . 18
Amin, V. (DA-01) . . . 347
Amin, V. (EC-03) . . . 462
Amin, V. (FA-02) . . . 559
Amirov, A. (DQ-18) . . . 412
Amorim, C. (AF-03) . . . 31

*Best student presentation award finalist

Amorim, C. (HC-02) . . . 775
An, H. (FT-09) . . . 644
An, K. (GE-13) . . . 694
An, Q. (GV-13) . . . 765
An, S. (CI-07) . . . 287
Anadón, A. (BE-08) . . . 143
Anadón, A. (CD-01) . . . 249
Anadón, A. (HB-02) . . . 770
Analytis, J. (GD-03) . . . 685
Analytis, J. (GD-05) . . . 686
Anami, R. (EG-10) . . . 490
Anand, K. (EH-03) . . . 493
Anand, N. (FP-13) . . . 621
Anane, A. (BD-03) . . . 132
Anane, A. (BD-12) . . . 136
Anane, A. (GE-01) . . . 689
Anderson, A. (DG-11) . . . 384
Anderson, I.E. (FQ-18) . . . 630
Anderson, M. (AS-01) . . . 78
Anderson, M. (BS-01) . . . 197
Anderson, M. (CS-01) . . . 315
Anderson, M. (DS-01) . . . 421
Anderson, M. (ES-01) . . . 524
Anderson, M. (FS-01) . . . 639
Anderson, M. (GS-01) . . . 746
Anderson, N.R. (AU-10) . . . 89
Andersson, G. (DQ-06) . . . 407
Ando, A. (HI-08) . . . 822
Ando, F. (AV-06) . . . 94
Ando, K. (DA-04) . . . 348
Ando, Y. (BU-09) . . . 213
Ando, Y. (BU-11) . . . 214
Ando, Y. (CP-16) . . . 298
Ando, Y. (DP-04) . . . 397
Ando, Y. (DV-04) . . . 437
Ando, Y. (DV-13) . . . 441
Ando, Y. (DW-04) . . . 443
Ando, Y. (EB-11) . . . 459
Ando, Y. (EF-10) . . . 482
Ando, Y. (EP-05) . . . 505
Ando, Y. (FW-02) . . . 663
Ando, Y. (FW-04) . . . 664
André-Filho, J. (CU-01) . . . 324
Andreev, A. (BI-05) . . . 167
Andreev, N. (GH-11) . . . 713
Andrejka, F. (DW-11) . . . 447
Andrew, J. (AT-10) . . . 83
Andrew, J. (CH-01) . . . 276
Andrieu, S. (DH-04) . . . 387
Andrieu, S. (HF-01) . . . 795
Androjna, C. (FF-02) . . . 584
Androvitsaneas, P. (CD-05) . . . 250
Ang, C.C. (GF-08) . . . 700
Angara, R.C. (CH-09) . . . 281
Angel González Barrio, M. (AG-02) . . . 38
Antonio, P. (BE-08) . . . 143
Aoki, S. (CI-12) . . . 289
Aoshima, K. (GP-07) . . . 727
Apalkov, D. (FC-02) . . . 566
Aqeel, A. (GF-04) . . . 698
Arackal, S. (GI-02) . . . 716
Arackal, S. (HH-08) . . . 813
Arai, H. (DF-06) . . . 377
Arai, K. (DV-02) . . . 435
Arakawa, T. (AE-09) . . . 27
Arakawa, T. (EB-02) . . . 455
Arakawa, T. (EC-05) . . . 463
Araki, Y. (EB-06) . . . 457
Arauzo, A. (HE-04) . . . 791
Archilla, D. (GA-04) . . . 669
Arcon, D. (FE-02) . . . 579
Arekapudi, S. (BD-01) . . . 131
Arekapudi, S. (BH-01) . . . 158
Arekapudi, S. (HG-05) . . . 805
Arena, D.A. (AP-05) . . . 60
Arena, D.A. (ER-04) . . . 519
Arenholz, E. (BA-04) . . . 112
Arenholz, E. (CB-10) . . . 240
Arenholz, E. (GB-02) . . . 671
Arenholz, E. (GG-01) . . . 703
Arenholz, E. (HC-03) . . . 776
Argüello, E. (DP-02) . . . 396
Arias, R. (FW-01) . . . 663
Arkkio, A. (DW-01) . . . 442
Arkook, B. (AI-11) . . . 55
Arkook, B. (CB-09) . . . 240
Arkook, B. (FB-07) . . . 563
Arnache, O.L. (ER-10) . . . 522
Arnache, O.L. (FT-06) . . . 643
Arnalds, U.B. (BH-04) . . . 159
Arnalds, U.B. (BH-10) . . . 162
Arnau, A. (EB-07) . . . 457
Arnold, D.P. (AT-10) . . . 83
Arnold, D.P. (CH-01) . . . 276
Aronhime, N. (GH-06) . . . 710
Arora, M. (ER-03) . . . 519
Arora, M. (EW-02) . . . 552
Arras, R. (DH-01) . . . 386
Arshad, M.I. (BI-15) . . . 171
Artemchuk, P. (AB-08) . . . 7
Aryal, A. (AQ-17) . . . 69
Aryal, A. (DQ-01) . . . 405
Aryal, A. (DR-01) . . . 414
Aryal, A. (DR-15) . . . 420
Aryal, A. (FQ-09) . . . 627
Asada, H. (BW-09) . . . 228
Asada, H. (BW-11) . . . 229
Asahara, H. (BC-08) . . . 126
Asano, H. (CP-12) . . . 296
Ashby, P. (FF-03) . . . 585
Ashida, T. (AC-07) . . . 14
Aslam, S. (GI-04) . . . 717
Aslani, A. (AQ-18) . . . 69
Assaf, B. (DT-06) . . . 424
Ataca, C. (BI-11) . . . 169
Ataka, T. (EP-11) . . . 507
Atcheson, G. (GB-11) . . . 676
Atkinson, D. (CG-12) . . . 274
Atkinson, D. (EC-12) . . . 466
Atkinson, D. (FC-10) . . . 570
Atodiresei, N. (FB-05) . . . 562
Attané, J. (AP-03) . . . 59
Attané, J. (DP-08) . . . 399
Attané, J. (DP-12) . . . 400
Attané, J. (FC-09) . . . 570
Attané, J. (FV-10) . . . 660
Attané, J. (HG-03) . . . 805
Atulasimha, J. (DE-07) . . . 371
Atulasimha, J. (GC-13) . . . 683
Atxitia, U. (FI-04) . . . 608
Audry, M. (DU-01) . . . 428
Aufftet, S. (AH-13) . . . 49
Aufftet, S. (BC-13) . . . 129
Aufftet, S. (EC-09) . . . 464
Aufftet, S. (ED-04) . . . 469
Aufftet, S. (ER-05) . . . 520
Aufftet, S. (GC-11) . . . 683
Aufftet, S. (GQ-01) . . . 734
Auslaender, O.M. (DE-09) . . . 372
Avci, C. (AG-08) . . . 40
Avci, C. (DA-03) . . . 348
Avilés Félix, L. (AE-13) . . . 29
Avilés Félix, L. (GC-11) . . . 683
Avramov, P. (FB-09) . . . 564
Awad, A.A. (CC-04) . . . 244
Awad, A.A. (CC-11) . . . 247
Awad, A.A. (HG-05) . . . 805
Awano, H. (BT-09) . . . 202
Awano, H. (CF-13) . . . 268
Awano, H. (GP-14) . . . 731
Awari, N. (BD-01) . . . 131
Awasthi, A. (DH-10) . . . 389
Ayala, P. (AT-09) . . . 83
Aydin, U. (CH-07) . . . 280
Aydin, U. (DW-01) . . . 442
Azevedo, A. (FA-05) . . . 560
Azhar, M. (AG-09) . . . 41
Azinfar, A. (CF-12) . . . 268
Aziziha, M. (FU-16) . . . 654
Azzerboni, B. (BB-06) . . . 117

- B -

B. Tavares, M.A. (ER-11) . . . 522
Babcock, E. (DT-03) . . . 423
Babu, P. (DH-10) . . . 389
Bac, S. (DR-04) . . . 415
Bac, S. (DR-05) . . . 415
Bachmaier, A. (BF-09) . . . 149
Bachmann, J. (HG-09) . . . 807
Back, C. (AW-02) . . . 101
Bae, J. (DR-07) . . . 416
Baek, C. (EV-05) . . . 543
Baek, C. (EV-06) . . . 544
Baek, C. (EV-07) . . . 544
Baek, E. (CG-05) . . . 272
Bagchi, M. (CC-02) . . . 243
Bagués, N. (DC-03) . . . 357
Bai, X. (FE-01) . . . 579
Bailey, J. (ED-01) . . . 467
Bailey, W. (FA-02) . . . 559
Bain, J.A. (HD-09) . . . 786

*Best student presentation award finalist

Bainsla, L. (DR-12) . . . 418
Bainsla, L. (HF-04) . . . 796
Bajpai, U. (AE-05) . . . 26
Bajpai, U. (AI-05) . . . 52
Bak, J. (GC-07) . . . 681
Baker, A. (DB-12) . . . 354
Baker, A. (EI-04) . . . 499
Baker, A. (EI-05) . . . 499
Baker, A. (FB-02) . . . 561
Balachandran, P. (AI-06) . . . 53
Balachandran, P. (FG-12) . . . 596
Balakrishnan, G. (AW-11) . . . 106
Balakrishnan, G. (AW-17) . . . 109
Balakrishnan, G. (BT-04) . . . 200
Balakrishnan, G. (FH-13) . . . 605
Balakrishnan, G. (GF-01) . . . 697
Balakrishnan, G. (GF-05) . . . 699
Balasubramanian, B. (AW-16) . . . 108
Balasubramanian, B. (EH-13) . . . 497
Balasubramanian, B. (GF-03) . . . 698
Balasubramanian, B. (HE-08) . . . 793
Balasubramanian, B. (HE-13) . . . 794
Balcells, L. (BH-02) . . . 158
Balcells, L. (BT-16) . . . 206
Balcells, L. (FV-03) . . . 658
Baldo, M. (HG-07) . . . 806
Baldrati, L. (BB-01) . . . 114
Baldrati, L. (CB-04) . . . 237
Baldrati, L. (EC-07) . . . 464
Balema, V. (AQ-19) . . . 69
Balents, L. (FE-01) . . . 579
Ballet, P. (DP-12) . . . 400
Balli, M. (FQ-19) . . . 630
Baltz, V. (AH-13) . . . 49
Baltz, V. (EC-09) . . . 464
Baltz, V. (ER-05) . . . 520
Baltz, V. (GQ-01) . . . 734
Balzar, D. (AD-05) . . . 18
Banerjee, A. (DG-08) . . . 382
Banerjee, C. (EQ-02) . . . 512
Banerjee, N. (GD-10) . . . 688
Banerjee, S. (CF-09) . . . 266
Banerjee, T. (AG-09) . . . 41
Banerjee, T. (CB-05) . . . 238
Banerjee, T. (FB-06) . . . 563
Banerjee, T. (FU-19) . . . 655
Bang, H. (CP-17) . . . 298
Bang, H. (DR-14) . . . 419
Bang, T. (EV-02) . . . 541
Bang, T. (EV-03) . . . 542
Bang, T. (EV-04) . . . 543
Bang, T. (EV-09) . . . 546
Bang, T. (EV-10) . . . 546
Bannenberg, L.J. (GF-04) . . . 698
Bao, N.V. (HB-07) . . . 773
Baraban, I. (DQ-18) . . . 412
Baraban, I. (GH-11) . . . 713
Barandiaran, J. (FD-09) . . . 576
Barbedienne, Q. (AE-08) . . . 26
Barbedienne, Q. (FV-05) . . . 658
Barbosa, J. (CE-04) . . . 256
Barclay, J. (FQ-18) . . . 630
Bargheer, M. (BD-12) . . . 136
Barker, J.A. (AW-11) . . . 106
Barman, A. (BQ-14) . . . 186
Barman, A. (CC-10) . . . 246
Barman, A. (EQ-01) . . . 512
Barman, A. (EQ-02) . . . 512
Barman, A. (EQ-03) . . . 513
Barman, A. (ER-01) . . . 518
Barman, A. (EW-06) . . . 554
Barman, A. (FB-10) . . . 564
Barnas, J. (AD-11) . . . 20
Barnes, C.H. (FV-04) . . . 658
Barnsley, L. (BF-07) . . . 149
Barnsley, L. (DT-03) . . . 423
Baró, D. (BA-02) . . . 112
Baró, D. (FU-12) . . . 653
Baron, M.S. (BW-12) . . . 230
Barone, P. (EE-08) . . . 475
Barra, A. (GG-02) . . . 703
Barra, A. (HC-03) . . . 776
Barrera, G. (DG-09) . . . 383
Barrera, G. (FI-13) . . . 612
Barri, R. (BV-07) . . . 220
Barriocanal, J.G. (AI-08) . . . 54
Barron III, E.J. (AQ-04) . . . 63
Barrows, F.P. (FE-07) . . . 581
Barrozo da Silva, P. (HC-06) . . . 777
Barsoum, M.W. (BI-04) . . . 167
Barsukov, I. (AI-11) . . . 55
Barsukov, I. (AS-01) . . . 78
Barsukov, I. (BS-01) . . . 197
Barsukov, I. (CB-09) . . . 240
Barsukov, I. (CS-01) . . . 315
Barsukov, I. (DS-01) . . . 421
Barsukov, I. (ES-01) . . . 524
Barsukov, I. (FB-07) . . . 563
Barsukov, I. (FS-01) . . . 639
Barsukov, I. (GS-01) . . . 746
Bartell, J. (BG-11) . . . 156
Bartell, J. (EG-06) . . . 488
Barthelemy, A. (DP-08) . . . 399
Bartlett, M.D. (AQ-04) . . . 63
Bartolomé, E. (HE-04) . . . 791
Bartolomé, E. (HE-06) . . . 792
Bartolome, F. (GP-08) . . . 728
Bartolome, F. (HE-04) . . . 791
Bartolome, F. (HE-06) . . . 792
Bartolomé, J. (GP-08) . . . 728
Bartolomé, J. (HE-04) . . . 791
Bartolomé, J. (HE-06) . . . 792
Barton, C. (DE-01) . . . 368
Barton, C. (DE-05) . . . 369
Barton, C. (HD-07) . . . 785
Barts, E. (AG-09) . . . 41
Barua, R. (DQ-03) . . . 405
Barua, R. (DQ-13) . . . 409
Barua, R. (FD-07) . . . 575
Barua, R. (FQ-01) . . . 623
Barua, R. (FQ-11) . . . 627
Barwal, V. (CR-12) . . . 311
Basha, A. (CG-08) . . . 273
Basheed, G. (BR-11) . . . 193
Basheed, G. (DH-10) . . . 389
Basheed, G. (DR-16) . . . 420
Basheed, G. (FF-04) . . . 585
Bashir, A. (HD-13) . . . 788
Bashir, A.K. (GT-11) . . . 751
Batista, C. (EI-08) . . . 501
Batley, J.T. (BH-06) . . . 160
Batley, J.T. (BH-07) . . . 161
Battiato, M. (BD-06) . . . 134
Bauer, E. (GT-08) . . . 750
Bauer, G. (FA-01) . . . 559
Bauer, G. (GE-13) . . . 694
Bauer, J. (DA-03) . . . 348
Bauer, J. (HH-01) . . . 810
Baumberger, F. (DP-08) . . . 399
Baumgaertl, K. (GE-09) . . . 693
Baumgaertl, K. (GE-11) . . . 694
Baumgartner, M. (CG-04) . . . 271
Bazlov, A. (GH-11) . . . 713
Beach, G. (AG-08) . . . 40
Beach, G. (BA-03) . . . 112
Beach, G. (DA-03) . . . 348
Beach, G. (DC-04) . . . 358
Beach, G. (EG-06) . . . 488
Beach, G. (EG-07) . . . 488
Beach, G. (HG-02) . . . 804
Beato, J. (HI-07) . . . 821
Beatty, J. (AT-05) . . . 81
Beatty, J. (AT-06) . . . 82
Beatty, J. (BH-13) . . . 164
Beaulieu, N. (GE-13) . . . 694
Becerra, L. (FQ-06) . . . 625
Becherer, M. (GE-04) . . . 690
Becherer, M. (GE-06) . . . 691
Becherer, M. (GP-02) . . . 724
Bechtel, M. (GE-09) . . . 693
Becker, A. (FQ-03) . . . 624
Becker, A. (HF-02) . . . 795
Becker, S. (AG-05) . . . 39
Becker, S. (CB-04) . . . 237
Beddingfield, R. (EU-01) . . . 535
Beekman, C. (FE-08) . . . 581
Beekman, C. (FT-10) . . . 645
Beens, M. (DD-07) . . . 364
Beens, M. (DD-10) . . . 366
Beg, M. (DD-02) . . . 361
Begué, A. (FD-08) . . . 575
Behera, N. (CR-12) . . . 311
Beigang, R. (EC-06) . . . 463
Beigné, C. (DP-14) . . . 401
Beik Mohammadi, J. (GC-12) . . . 683
Belahcen, A. (CH-07) . . . 280
Belahcen, A. (DW-01) . . . 442
Belashchenko, K. (AB-14) . . . 10
Belashchenko, K. (AD-14) . . . 23
Belkhou, R. (ED-04) . . . 469
Bello, J. (AW-09) . . . 105
Bello, J. (FG-11) . . . 595
Belmeguenai, M. (CG-01) . . . 270

*Best student presentation award finalist

Beloborodov, I.S. (HE-07) . . . 792
Belotelov, V. (HD-03) . . . 783
Ben Ammar, S. (CI-14) . . . 290
Ben-Youssef, J. (GE-01) . . . 689
Ben-Youssef, J. (GE-13) . . . 694
Bencok, P. (AF-11) . . . 34
Bender, S. (CB-04) . . . 237
Benedicic, I. (FE-02) . . . 579
Benítez, L.A. (DB-01) . . . 350
Benito, L. (GH-10) . . . 713
Bennet, R.K. (BE-01) . . . 140
Bennet, R.K. (FV-02) . . . 657
Bennett, C.H. (ET-15) . . . 532
Bennett, C.H. (HG-08) . . . 806
Bennett, L.H. (AQ-18) . . . 69
Bennett, R. (GF-02) . . . 697
Bennett, S. (GB-06) . . . 674
Bennett, S.P. (CT-09) . . . 320
Bentmann, H. (GD-01) . . . 685
Berakdar, J. (GF-09) . . . 701
Beran, L. (AB-13) . . . 9
Beran, L. (AQ-07) . . . 64
Beran, L. (CP-09) . . . 295
Beran, L. (DT-10) . . . 425
Beran, L. (HH-04) . . . 811
Beran, L. (HH-15) . . . 817
Bereciartua-Perez, P. (AF-12) . . . 35
Bergeal, N. (DP-08) . . . 399
Bergemann, M. (DD-02) . . . 361
Berger, A. (ER-10) . . . 522
Berger, A. (GB-09) . . . 675
Berges, L. (AI-12) . . . 56
Bernardo, P.L. (FE-05) . . . 580
Berritta, M. (HD-02) . . . 782
Bertacco, R. (GB-04) . . . 673
Bertran, F. (HF-01) . . . 795
Beschoten, B. (EB-11) . . . 459
Beschoten, B. (FB-01) . . . 561
Bespalov, V.A. (EV-17) . . . 549
Bessarab, P. (BD-07) . . . 134
Bez, H. (FD-04) . . . 573
Bhallamudi, V.P. (CR-02) . . . 306
Bhardwaj, S. (FU-03) . . . 650
Bhardwaj, V. (FB-03) . . . 562
Bhat, N. (GI-02) . . . 716
Bhat, N. (HH-08) . . . 813
Bhat, S.G. (BE-13) . . . 145
Bhat, S.G. (HC-04) . . . 776
Bhat, V.S. (GE-11) . . . 694
Bhatt, M. (BF-08) . . . 149
Bhatt, R.C. (BU-02) . . . 209
Bhatt, R.C. (BV-01) . . . 217
Bhatt, R.C. (CV-03) . . . 333
Bhatt, R.C. (CV-07) . . . 335
Bhatt, S. (FQ-10) . . . 627
Bhattacharjee, N. (AE-03) . . . 24
Bhattacharya, A. (CB-13) . . . 242
Bhattacharya, A. (FB-03) . . . 562
Bhattacharya, D. (DE-07) . . . 371
Bhattacharya, D. (GC-13) . . . 683
Bhattarai, M.K. (FU-11) . . . 652
Bhattarai, M.K. (FU-13) . . . 653
Bhattarai, M.K. (FU-14) . . . 653
Bhattarai, S. (EI-06) . . . 500
Bhatti, K. (HF-07) . . . 798
Bhatti, S. (AG-10) . . . 42
Bhoi, B. (BD-11) . . . 136
Bhoi, B. (CR-09) . . . 310
Bhoi, D. (EI-07) . . . 500
Bhowmik Debnath, O. (FF-08) . . . 587
Bhowmik, D. (DF-04) . . . 376
Bhowmik, D. (DF-07) . . . 377
Bi, C. (CB-01) . . . 236
Biacchi, A.J. (HE-12) . . . 794
Bian, M. (CV-06) . . . 335
Bian, M. (HF-13) . . . 801
Bibes, M. (DP-08) . . . 399
Bibes, M. (EE-02) . . . 473
Bibes, M. (EE-06) . . . 475
Bidthanapally, R. (AS-04) . . . 79
Bidthanapally, R. (BS-04) . . . 197
Bidthanapally, R. (CS-04) . . . 315
Bidthanapally, R. (DS-04) . . . 421
Bidthanapally, R. (ES-04) . . . 524
Bidthanapally, R. (FS-04) . . . 639
Bidthanapally, R. (GS-04) . . . 747
Bikondoa, O. (BF-11) . . . 150
Bilardello, D. (DU-09) . . . 432
Billington, D. (BP-08) . . . 174
Billington, D. (CI-04) . . . 285
Billoni, O. (BI-01) . . . 166
Binder, R.H. (EC-06) . . . 463
Bingham, N. (GG-04) . . . 704
Bingham, N.S. (BH-06) . . . 160
Bingham, N.S. (BH-07) . . . 161
Bingham, N.S. (HA-01) . . . 767
Bini, R. (AT-01) . . . 80
Birch, M.T. (BT-04) . . . 200
Birch, M.T. (GF-01) . . . 697
Birge, N. (DI-04) . . . 392
Birol, T. (BA-01) . . . 111
Birol, T. (DH-07) . . . 388
Birowska, M. (HF-11) . . . 800
Bischof, J.C. (DG-01) . . . 379
Bisero, D. (FD-08) . . . 575
Bishop, A. (FB-02) . . . 561
Biskeborn, R. (HI-01) . . . 818
Biswas, A. (AQ-19) . . . 69
Biswas, A. (FD-07) . . . 575
Biswas, A. (FQ-02) . . . 623
Biswas, S. (GQ-02) . . . 734
Blamire, M. (AE-06) . . . 26
Blamire, M. (GD-10) . . . 688
Blanco-López, M.C. (EV-20) . . . 551
Blanco-Rey, M. (EB-07) . . . 457
Blanco, J. (GH-07) . . . 711
Blanco, J. (GH-15) . . . 715
Blanco, J. (GI-03) . . . 717
Blaz, N.V. (DV-10) . . . 439
Blazer, D.S. (BT-07) . . . 201
Blazer, D.S. (CT-07) . . . 320
Bleser, S.M. (FV-02) . . . 657
Blinov, M. (DR-01) . . . 414
Blinov, M. (DR-15) . . . 420
Blonsky, A. (ER-03) . . . 519
Bloom, R. (EP-10) . . . 507
Bluegel, S. (CC-02) . . . 243
Bluegel, S. (FB-05) . . . 562
Bluegel, S. (HA-03) . . . 767
Blundell, S. (AV-01) . . . 92
Blundell, S. (AW-11) . . . 106
Bobo, J. (AF-04) . . . 31
Bochmann, S. (HG-09) . . . 807
Bocklage, L. (BD-15) . . . 138
Bocklage, L. (CE-02) . . . 255
Bocklage, L. (CF-06) . . . 264
Bocklage, L. (GQ-13) . . . 740
Boehler, R. (EE-07) . . . 475
Boekema, C. (BR-13) . . . 194
Böhm, B. (CG-07) . . . 272
Böhm, B. (CG-13) . . . 275
Bokor, J. (AQ-05) . . . 63
Bokor, J. (DD-08) . . . 365
Bokor, J. (DD-09) . . . 366
Bokor, J. (DG-02) . . . 379
Bokor, J. (HC-03) . . . 776
Bokor, J. (HC-09) . . . 778
Boldrey, J. (DU-04) . . . 429
Boldrin, D. (AB-13) . . . 9
Boldrin, D. (CP-09) . . . 295
Boltje, D.B. (GQ-03) . . . 735
Bonetti, S. (BD-01) . . . 131
Bonetti, S. (BD-03) . . . 132
Bonetti, S. (BD-05) . . . 133
Bonetti, S. (BD-08) . . . 134
Bonetti, S. (DD-02) . . . 361
Böni, P. (AW-04) . . . 102
Borchers, J. (AW-16) . . . 108
Borchers, J. (BA-01) . . . 111
Borchers, J. (BA-04) . . . 112
Borchers, J. (CC-07) . . . 245
Borchers, J. (DE-02) . . . 368
Borchers, J. (DH-07) . . . 388
Borchers, J. (DI-04) . . . 392
Borchers, J. (ED-08) . . . 470
Borchers, J. (GG-02) . . . 703
Bormio-Nunes, C. (DW-02) . . . 442
Bortolotti, P. (AC-01) . . . 11
Bortolotti, P. (EQ-04) . . . 513
Bortolotti, P. (EQ-05) . . . 513
Bortolotti, P. (FV-05) . . . 658
Bortolotti, P. (GE-01) . . . 689
Bosch-Santos, B. (AU-14) . . . 90
Bosch-Santos, B. (BT-19) . . . 207
Bosch-Santos, B. (CU-10) . . . 329
Bosu, S. (BU-07) . . . 212
Bosu, S. (BU-08) . . . 212
Bosu, S. (GC-04) . . . 679
Böttcher, T. (CE-07) . . . 257
Bottegoni, F. (DP-07) . . . 398
Bottegoni, F. (EB-01) . . . 455
Bouchenoire, L. (EC-12) . . . 466
Boulle, O. (ED-04) . . . 469

*Best student presentation award finalist

Bouma, D. (GB-06) 674
Bouquin, P. (EP-13) 508
Bouquin, P. (HG-11) 809
Bourhill, J. (CI-14) 290
Bourhill, J. (CI-15) 291
Bouzehouane, K. (AF-07) 32
Bouzehouane, K. (BG-10) 156
Bouzehouane, K. (CC-01) 243
Bouzehouane, K. (ED-05) 469
Boventer, I. (AG-05) 39
Boventer, I. (CE-03) 255
Bowen, D. (EB-03) 456
Bozhko, D.A. (BD-09) 135
Bozhko, D.A. (BE-11) 144
Bozhko, D.A. (CE-04) 256
Bozhko, D.A. (CE-13) 260
Bozhko, D.A. (GE-02) 689
Bozzo, B. (FC-08) 569
Brächer, T. (CE-07) 257
Brächer, T. (CE-08) 258
Brächer, T. (GE-03) 690
Brahlek, M. (DH-09) 389
Brataas, A. (CB-04) 237
Bratschitsch, R. (FV-13) 661
Brede, J. (CC-02) 243
Breese, M. (DB-08) 353
Breitbach, D. (GE-03) 690
Brenac, A. (AP-03) 59
Brenac, A. (FV-10) 660
Brenner, M. (FB-02) 561
Breznay, N. (GD-03) 685
Brigner, W.H. (HG-08) 806
Brillson, L. (FB-02) 561
Briones-Leon, A. (AT-09) 83
Brock, J.A. (DE-08) 371
Brodyanski, A. (EC-06) 463
Brooks, C. (GG-05) 704
Brown, J. (DG-11) 384
Brown, S. (GC-07) 681
Browning, N. (GG-01) 703
Brubaker, Z.E. (BA-04) 112
Brubaker, Z.E. (DB-12) 354
Brückel, T. (BF-07) 149
Bruneel, P. (DP-08) 399
Bruno, F. (DP-08) 399
Bsaibes, T. (GQ-12) 739
Buchanan, K. (DC-06) 359
Buchanan, K. (EQ-11) 516
Buchanan, K. (FD-10) 577
Buchanan, K. (GE-07) 691
Buckley, R.G. (DR-10) 417
Bud'ko, S. (EH-10) 496
Bud'ko, S. (GT-09) 750
Buda-Prejbeanu, L. (EF-07) 481
Buda-Prejbeanu, L. (ET-13) 531
Buda-Prejbeanu, L. (GC-11) 683
Budhathoki, S. (AI-06) 53
Buergler, D. (CD-03) 250
Buettner, F. (AG-08) 40
Buettner, F. (DC-04) 358
Buhrman, R. (BE-07) 142
Buhrman, R. (BV-04) 218
Buhrman, R. (DA-05) 348
Bultynck, O. (EP-16) 510
Bultynck, O. (HG-10) 808
Bunyaev, S.A. (BD-09) 135
Bunyaev, S.A. (CE-13) 260
Bunyaev, S.A. (EW-15) 557
Bunyaev, S.A. (HH-02) 810
Burch, K. (GD-05) 686
Burema, A. (CB-05) 238
Burema, A. (FU-19) 655
Burgos Parra, E.O. (AF-07) 32
Burimova, A. (BT-19) 207
Burkhanov, G.S. (BP-11) 176
Burkhanov, G.S. (BP-15) 178
Burkov, A. (AE-01) 24
Burn, D. (CB-10) 240
Burn, D. (FG-04) 592
Burn, D. (GF-07) 700
Burnell, G. (BE-09) 143
Burnell, G. (DE-05) 369
Burnell, G. (ED-01) 467
Burnell, G. (GF-06) 699
Burton, T. (DW-13) 448
Bussmann, E. (BG-05) 153
Busyatras, W. (GR-07) 744
Butch, N. (GD-06) 686
Butera, A. (AE-13) 29
Butera, R.E. (EB-03) 456
Butler, T. (DR-10) 417
Butorin, S.M. (DI-10) 394
Butta, M. (DV-09) 439
Buzdakov, A. (EV-17) 549
Buzdin, A.I. (GQ-01) 734
Byerly, K. (EU-01) 535
Byers, J. (GG-01) 703
Bykova, I. (DE-03) 369
Bykova, I. (GE-12) 694

- C -

Cabral do Nascimento, V. (EU-01) 535
Cabrera-Pasca, G. (AU-14) 90
Cabrera-Pasca, G. (AU-15) 91
Cabrera-Pasca, G. (BT-19) 207
Cabrera-Pasca, G. (CU-10) 329
Caciuc, V. (FB-05) 562
Çaçoilo, N. (ET-13) 531
Cagnon, L. (HG-09) 807
Cahaya, A. (BQ-06) 182
Cai, J. (CI-13) 290
Cai, K. (BC-03) 123
Cai, K. (CD-08) 252
Cai, K. (DB-04) 351
Cai, X. (EA-05) 454
Cai, Y. (FC-11) 571
Cai, Z. (BA-05) 113
Cailing, H. (CU-14) 331
Cakir, A. (BI-03) 167
Cakir, A. (EH-09) 495
Calarco, R. (GB-04) 673
Calle, E. (DV-09) 439
Calvano, L.J. (CV-04) 334
Calvano, L.J. (CV-09) 336
Camarero, J. (BE-08) 143
Camarero, J. (CD-01) 249
Camarero, J. (HB-02) 770
Camley, R. (BI-12) 170
Camley, R. (CE-09) 258
Camley, R. (CI-09) 287
Camley, R. (CI-10) 288
Camley, R. (ED-10) 471
Campillo, G.E. (ER-10) 522
Campion, R. (AB-06) 6
Camsari, K.Y. (EG-03) 486
Candido, D.R. (EQ-13) 517
Candler, R. (DG-02) 379
Candler, R. (HC-03) 776
Candler, R. (HC-09) 778
Caneiro, A. (EI-11) 502
Canfield, P. (EH-10) 496
Canon Bermudez, G. (HI-09) 823
Cansever, H. (ET-02) 526
Cantoni, M. (GB-04) 673
Cao, H. (FU-08) 652
Cao, J. (FR-03) 633
Cao, K. (AC-03) 12
Cao, L. (CR-16) 314
Cao, W. (FA-02) 559
Cao, Y. (DB-02) 350
Cao, Z. (GV-13) 765
Capic, D. (AW-20) 110
Capua, A. (HB-05) 772
Caravelli, F. (HA-01) 767
Carbonari, A.W. (AU-14) 90
Carbonari, A.W. (AU-15) 91
Carbonari, A.W. (BT-19) 207
Carbonari, A.W. (CU-10) 329
Carbonari, A.W. (GT-15) 752
Carbonio, R.E. (BI-01) 166
Carbonio, R.E. (CT-11) 321
Caretta, L.M. (AG-08) 40
Caretta, L.M. (DA-03) 348
Caretta, L.M. (DC-04) 358
Caretta, L.M. (EG-06) 488
Caretta, L.M. (HG-02) 804
Carey, M. (FC-01) 566
Carey, M. (GC-06) 680
Carleschi, E. (DW-14) 448
Carley, R. (DD-02) 361
Carlone, M. (GT-07) 750
Carman, G. (BT-14) 205
Carman, G. (CQ-05) 301
Carman, G. (DG-02) 379
Carman, G. (DW-09) 446
Carman, G. (GE-07) 691
Carman, G. (GG-02) 703
Carman, G. (GI-07) 719
Carman, G. (HC-03) 776
Carman, G. (HE-07) 792
Carmona, I.C. (BW-12) 230

*Best student presentation award finalist

Carnahan, C. (EA-05) . . . 454
Caron, J. (FH-02) . . . 599
Carpenter, E. (DQ-03) . . . 405
Carpenter, R. (FC-04) . . . 567
Carpenter, R. (GC-02) . . . 679
Carpenter, R. (GC-08) . . . 681
Carpentieri, M. (AB-03) . . . 5
Carpentieri, M. (AC-08) . . . 15
Carpentieri, M. (AW-10) . . . 105
Carpentieri, M. (AW-13) . . . 107
Carpentieri, M. (BB-06) . . . 117
Carpentieri, M. (DE-03) . . . 369
Carrétéro, C. (EE-02) . . . 473
Carrey, J. (AF-04) . . . 31
Carriço, A.S. (AT-02) . . . 80
Carriço, A.S. (AU-03) . . . 86
Carriço, A.S. (ET-11) . . . 531
Carriço, A.S. (GQ-11) . . . 739
Caruana, A. (DT-11) . . . 426
Caruana, A. (FQ-17) . . . 630
Carvajal, D. (EQ-08) . . . 515
Carvalho Jr, R.N. (AU-15) . . . 91
Casals, B. (FU-12) . . . 653
Casamento, J. (AC-04) . . . 12
Casamento, J. (AH-01) . . . 44
Casamento, J. (AH-05) . . . 45
Casanova, F. (EC-04) . . . 462
Casaretto, N. (FQ-06) . . . 625
Cash, S. (AH-06) . . . 46
Casola, F. (BG-04) . . . 153
Castan-Guerrero, C. (GP-08) . . . 728
Castel, V.M. (CI-14) . . . 290
Castel, V.M. (CI-15) . . . 291
Castellano, C. (DG-12) . . . 384
Castilla, D. (BE-10) . . . 144
Castillo, S. (AU-05) . . . 86
Castillo, S. (ET-08) . . . 529
Castro, G. (DG-12) . . . 384
Catalan, G. (FU-12) . . . 653
Catapano, E. (AW-04) . . . 102
Cava, R.J. (GB-04) . . . 673
Cavill, S. (GH-10) . . . 713
Ceballos, A. (DD-08) . . . 365
Ceballos, A. (FF-03) . . . 585
Ceballos, A. (HC-09) . . . 778
Cebollada, F. (BH-02) . . . 158
Cebollada, F. (BH-11) . . . 163
Cebollada, F. (CR-14) . . . 312
Cebollada, F. (HE-09) . . . 793
Cecchi, S. (GB-04) . . . 673
Cegan, T. (BP-11) . . . 176
Cegan, T. (BP-15) . . . 178
Cejpek, P. (CW-16) . . . 345
Celegato, F. (DG-09) . . . 383
Celinski, Z. (CI-10) . . . 288
Celinski, Z. (DG-06) . . . 381
Celinski, Z. (DG-11) . . . 384
Celinski, Z. (GG-11) . . . 707
Celinski, Z. (HH-07) . . . 813
Cervera, S. (FD-06) . . . 574
Céspedes, O. (GB-05) . . . 673
Cha, I. (DE-06) . . . 370
Cha, I. (EC-08) . . . 464
Chai, J. (DB-08) . . . 353
Chai, Y. (FF-03) . . . 585
Chaix-Pluchery, O. (BI-04) . . . 167
Chalifour, C.R. (AU-10) . . . 89
Champagne, A. (BI-04) . . . 167
Chan, M. (DH-01) . . . 386
Chanda, A. (CR-13) . . . 311
Chandran, K. (DH-11) . . . 390
Chang, C. (BU-12) . . . 214
Chang, C. (BV-14) . . . 223
Chang, C. (CG-09) . . . 273
Chang, C. (CT-15) . . . 323
Chang, C. (EE-10) . . . 476
Chang, H. (CW-10) . . . 343
Chang, H.W. (AQ-01) . . . 62
Chang, H.W. (AR-01) . . . 70
Chang, H.W. (BP-12) . . . 177
Chang, H.W. (FU-06) . . . 651
Chang, H.W. (GQ-05) . . . 736
Chang, J. (CR-11) . . . 311
Chang, J. (EG-07) . . . 488
Chang, J. (FU-17) . . . 654
Chang, J.P. (DW-09) . . . 446
Chang, J.P. (FU-17) . . . 654
Chang, J.P. (GG-02) . . . 703
Chang, K. (CQ-02) . . . 300
Chang, L.V. (CQ-04) . . . 301
Chang, L.V. (FT-15) . . . 647
Chang, P. (AB-14) . . . 10
Chang, R. (FI-10) . . . 611
Chang, S. (AH-02) . . . 44
Chang, S. (CV-03) . . . 333
Chang, W. (AQ-01) . . . 62
Chang, W. (AR-01) . . . 70
Chang, W. (BP-12) . . . 177
Changsoo, K. (EW-01) . . . 552
Changsoo, K. (HF-14) . . . 802
Chantrell, R.W. (AB-11) . . . 8
Chantrell, R.W. (AR-08) . . . 73
Chantrell, R.W. (BH-12) . . . 163
Chantrell, R.W. (ET-06) . . . 528
Chantrell, R.W. (FG-01) . . . 591
Chantrell, R.W. (FI-03) . . . 608
Chantrell, R.W. (HD-04) . . . 783
Chao, C.P. (GU-10) . . . 758
Chao, W. (CC-03) . . . 244
Chao, W. (CC-08) . . . 245
Chao, X. (FW-09) . . . 667
Chapoy, A. (HE-03) . . . 790
Charilaou, M. (FH-02) . . . 599
Charlier, J. (BI-04) . . . 167
Charlton, T.R. (BA-01) . . . 111
Charlton, T.R. (EE-07) . . . 475
Chatterjee, J. (BC-13) . . . 129
Chatterjee, J. (DD-09) . . . 366
Chatterjee, J. (HC-09) . . . 778
Chatterjee, R. (FB-03) . . . 562
Chatterjee, R. (GG-08) . . . 705
Chatterjee, S. (FQ-17) . . . 630
Chaturvedi, V. (DH-07) . . . 388
Chatzimpaloglou, K.O. (CD-05) . . . 250
Chaudhary, A. (FU-07) . . . 651
Chaudhary, S. (BV-10) . . . 221
Chaudhary, S. (CR-12) . . . 311
Chaudhuri, U. (CR-13) . . . 311
Chauhan, N. (BH-08) . . . 161
Chauleau, J. (AF-07) . . . 32
Chauleau, J. (EE-02) . . . 473
Chauleau, J. (EE-05) . . . 474
Chauleau, J. (EE-06) . . . 475
Chaurasiya, A. (FB-10) . . . 564
Chaurasiya, A.K. (EQ-02) . . . 512
Chaurasiya, R. (DR-03) . . . 414
Chavant, A. (BC-13) . . . 129
Chavent, A. (EF-07) . . . 481
Chavent, A. (EP-08) . . . 506
Chavez, A. (HC-03) . . . 776
Chawla, A. (FU-04) . . . 650
Che, P. (AW-04) . . . 102
Che, P. (GE-09) . . . 693
Che, X. (BB-02) . . . 114
Chelvane, A. (AR-15) . . . 76
Chelvane, J. (ER-01) . . . 518
Chen, B. (FU-05) . . . 651
Chen, B. (HF-10) . . . 800
Chen, C. (FF-05) . . . 585
Chen, C.H. (FP-03) . . . 616
Chen, D. (EE-10) . . . 476
Chen, F. (BF-04) . . . 147
Chen, F. (CW-13) . . . 344
Chen, G. (AG-02) . . . 38
Chen, G. (AG-03) . . . 38
Chen, G. (AV-15) . . . 98
Chen, G. (BB-10) . . . 118
Chen, G. (CG-11) . . . 274
Chen, G. (FG-03) . . . 592
Chen, H. (AH-06) . . . 46
Chen, H. (AW-12) . . . 106
Chen, H. (BB-10) . . . 118
Chen, H. (BV-07) . . . 220
Chen, H. (CF-11) . . . 267
Chen, H. (CP-12) . . . 296
Chen, H. (GI-05) . . . 718
Chen, H. (GI-06) . . . 718
Chen, H. (HB-06) . . . 772
Chen, J. (AQ-14) . . . 68
Chen, J. (BQ-09) . . . 183
Chen, J. (BQ-11) . . . 184
Chen, J. (BQ-13) . . . 185
Chen, J. (CD-02) . . . 249
Chen, J. (CD-08) . . . 252
Chen, J. (CT-06) . . . 319
Chen, J. (CV-10) . . . 336
Chen, J. (DB-08) . . . 353
Chen, J. (DP-11) . . . 400
Chen, J. (DQ-05) . . . 406
Chen, J. (DR-08) . . . 416
Chen, J. (EE-08) . . . 475
Chen, J. (FQ-13) . . . 628
Chen, J. (FT-02) . . . 641

*Best student presentation award finalist

Chen, J. (HB-08) . . . 773
Chen, K. (AH-02) . . . 44
Chen, K. (DG-07) . . . 382
Chen, K. (FG-02) . . . 591
Chen, K. (GC-09) . . . 682
Chen, L. (AC-03) . . . 12
Chen, L. (BQ-08) . . . 183
Chen, P. (GP-10) . . . 729
Chen, Q. (CR-16) . . . 314
Chen, S. (BQ-08) . . . 183
Chen, S. (BW-03) . . . 226
Chen, S. (DB-08) . . . 353
Chen, S. (DU-02) . . . 428
Chen, S. (FB-06) . . . 563
Chen, T. (AQ-14) . . . 68
Chen, T. (AU-04) . . . 86
Chen, T. (BV-04) . . . 218
Chen, T. (BW-13) . . . 230
Chen, T. (CT-06) . . . 319
Chen, T. (DU-13) . . . 433
Chen, T. (EC-01) . . . 461
Chen, T. (FQ-13) . . . 628
Chen, W. (BQ-01) . . . 179
Chen, W. (CQ-07) . . . 302
Chen, W. (EU-09) . . . 538
Chen, W. (FU-01) . . . 649
Chen, X. (ED-02) . . . 467
Chen, X. (ED-09) . . . 471
Chen, X. (ET-05) . . . 528
Chen, X. (FP-04) . . . 617
Chen, X.M. (BH-03) . . . 159
Chen, Y. (AI-01) . . . 50
Chen, Y. (BE-04) . . . 141
Chen, Y. (BR-04) . . . 190
Chen, Y. (BT-03) . . . 199
Chen, Y. (CQ-07) . . . 302
Chen, Y. (DG-07) . . . 382
Chen, Y. (DP-16) . . . 402
Chen, Y. (FF-07) . . . 587
Chen, Y. (FI-15) . . . 613
Chen, Y. (GC-12) . . . 683
Chen, Y.P. (EB-12) . . . 459
Chen, Z. (BH-05) . . . 160
Chen, Z. (EQ-12) . . . 516
Chen, Z. (GF-03) . . . 698
Chen, Z. (HF-06) . . . 798
Cheng, C. (CQ-02) . . . 300
Cheng, C. (GC-09) . . . 682
Cheng, J. (FF-05) . . . 585
Cheng, L. (FP-03) . . . 616
Cheng, L. (GU-07) . . . 757
Cheng, R. (CB-12) . . . 241
Cheng, R. (ED-03) . . . 468
Cheng, R. (GQ-12) . . . 739
Cheng, S. (FB-02) . . . 561
Cheng, S. (GF-02) . . . 697
Cheng, W. (AQ-01) . . . 62
Cheng, W. (CT-15) . . . 323
Cheng, X. (DC-05) . . . 358
Cheng, X. (DC-06) . . . 359
Cheng, X. (FD-10) . . . 577
Cheng, Y. (BB-03) . . . 115
Cheng, Y. (BB-04) . . . 116
Cheng, Y. (CB-03) . . . 237
Chernenko, V.A. (FD-09) . . . 576
Chesnel, K. (BF-05) . . . 148
Chesnel, K. (BF-06) . . . 148
Chesnel, K. (GQ-07) . . . 737
Chesnel, K. (HE-10) . . . 794
Chi, C. (CW-10) . . . 343
Chi, Z. (EB-08) . . . 458
Chi, Z. (HF-10) . . . 800
Chiappini, S. (AC-08) . . . 15
Chiappini, S. (DE-09) . . . 372
Chiba, A. (GV-05) . . . 762
Chiba, D. (AD-07) . . . 18
Chiba, D. (AQ-02) . . . 62
Chiba, D. (BQ-05) . . . 181
Chiba, D. (HI-08) . . . 822
Chiba, H. (GV-02) . . . 760
Chien, Y. (GQ-05) . . . 736
Chikaki, S. (DU-11) . . . 432
Chikaki, S. (FF-08) . . . 587
Chikaki, S. (FF-10) . . . 588
Chikaki, S. (FF-11) . . . 589
Chimata, R. (BD-06) . . . 134
Chimborazo, J. (AT-09) . . . 83
Chinotti, M. (GD-07) . . . 687
Chioar, I. (BH-04) . . . 159
Chioar, I. (BH-10) . . . 162
Chiou, J. (CW-10) . . . 343
Chirac, T. (EE-06) . . . 475
Chiriac, H. (GH-14) . . . 714
Chisholm, M. (DH-08) . . . 388
Chiu, C. (BP-12) . . . 177
Chiu, I. (AF-08) . . . 33
Chizhik, A. (GH-05) . . . 710
Chlan, V. (DR-01) . . . 414
Cho, B. (CP-01) . . . 292
Cho, B. (DQ-10) . . . 408
Cho, B. (EW-03) . . . 552
Cho, B. (GP-18) . . . 733
Cho, B. (GV-01) . . . 760
Cho, H. (EV-10) . . . 546
Cho, J. (FR-08) . . . 635
Cho, J. (GF-10) . . . 701
Cho, K. (DQ-10) . . . 408
Cho, Y. (FG-13) . . . 597
Choa, Y. (CW-07) . . . 342
Choe, S. (CR-11) . . . 311
Choe, S. (DC-09) . . . 360
Choe, S. (FT-01) . . . 641
Choi, C. (EH-02) . . . 492
Choi, C. (EH-04) . . . 493
Choi, H. (AV-18) . . . 100
Choi, H. (BR-10) . . . 193
Choi, H. (GT-03) . . . 748
Choi, J. (BP-10) . . . 175
Choi, J. (EV-02) . . . 541
Choi, J. (EV-03) . . . 542
Choi, J. (EV-04) . . . 543
Choi, J. (EV-05) . . . 543
Choi, J. (EV-06) . . . 544
Choi, J. (EV-07) . . . 544
Choi, J. (EV-08) . . . 545
Choi, J. (EV-09) . . . 546
Choi, J. (EV-10) . . . 546
Choi, J. (FP-08) . . . 618
Choi, J. (FR-01) . . . 632
Choi, J. (FR-04) . . . 633
Choi, J. (FR-08) . . . 635
Choi, J. (FR-09) . . . 636
Choi, J. (FR-11) . . . 637
Choi, J. (GP-01) . . . 724
Choi, K. (AV-05) . . . 94
Choi, M. (CH-10) . . . 281
Choi, M. (EH-06) . . . 494
Choi, M. (ET-17) . . . 534
Choi, M. (FR-02) . . . 632
Choi, M. (GI-09) . . . 720
Choi, Y. (AR-09) . . . 73
Choi, Y. (CT-01) . . . 317
Choi, Y. (CT-04) . . . 318
Choi, Y. (DH-09) . . . 389
Choi, Y. (DR-07) . . . 416
Choi, Y. (FU-15) . . . 653
Choi, Y. (HC-13) . . . 780
Chollet, M. (FE-03) . . . 579
Choo, Y. (FR-08) . . . 635
Chopdekar, R.V. (BA-04) . . . 112
Chopdekar, R.V. (BA-05) . . . 113
Chopdekar, R.V. (BH-05) . . . 160
Chopdekar, R.V. (BH-07) . . . 161
Chopdekar, R.V. (DC-06) . . . 359
Chopdekar, R.V. (DG-02) . . . 379
Chopdekar, R.V. (DH-09) . . . 389
Chopdekar, R.V. (EE-03) . . . 473
Chopdekar, R.V. (FE-09) . . . 582
Chopdekar, R.V. (GG-01) . . . 703
Chopdekar, R.V. (HC-03) . . . 776
Chou, F. (DR-13) . . . 419
Chouaieb, S. (BG-10) . . . 156
Chouaieb, S. (ED-05) . . . 469
Choudhary, R. (DI-06) . . . 393
Choudhary, R. (EH-11) . . . 496
Choudhary, R. (FH-12) . . . 604
Choudhary, R. (GT-12) . . . 751
Choudhury, S. (BQ-14) . . . 186
Choudhury, S. (EQ-02) . . . 512
Chow, C. (HD-09) . . . 786
Chow, Y. (CG-09) . . . 273
Chowdhury, N. (BV-02) . . . 217
Chowdhury, N. (FB-10) . . . 564
Christiansen-Salameh, J. (BA-05) . . . 113
Christianson, M. (HE-10) . . . 794
Christopher, N. (EH-03) . . . 493
Christovam, D.S. (GT-05) . . . 749
Chshiev, M. (CG-02) . . . 270
Chshiev, M. (EC-09) . . . 464
Chshiev, M. (GG-10) . . . 706
Chu, Y. (EE-10) . . . 476
Chua, D. (AC-05) . . . 13
Chuang, T. (AD-06) . . . 18

*Best student presentation award finalist

Chubykalo-Fesenko, O. (FI-04) 608
Chubykalo-Fesenko, O. (HD-02) 782
Chudnovsky, E. (AW-20) 110
Chulkov, E.V. (EB-07) 457
Chumak, A. (CE-07) 257
Chumak, A. (CE-08) 258
Chumak, A. (CE-13) 260
Chumak, A. (GE-03) 690
Chun, B. (GF-10) 701
Chun, B. (GP-11) 729
Chureemart, J. (FI-03) 608
Chureemart, J. (HD-04) 783
Chureemart, P. (FI-03) 608
Chureemart, P. (HD-04) 783
Cialone, M. (DG-09) 383
Cianga, C. (FF-12) 589
Cianga, P. (FF-12) 589
Ciccarelli, C. (AE-06) 26
Cichelero, R. (FU-12) 653
Cinal, M. (DI-11) 395
Ciomaga Hatnean, M. (AW-11) 106
Ciomaga Hatnean, M. (BT-04) 200
Ciou, S. (BV-01) 217
Ciria, M. (FD-08) 575
Ciubotariu, O. (CR-06) 308
Ciubotaru, F. (CE-08) 258
Ciubotaru, F. (CE-12) 260
Ciubotaru, F. (CE-13) 260
Ciubotaru, F. (HC-10) 779
Clark, A.T. (DC-06) 359
Clark, A.T. (FD-10) 577
Clark, B.D. (EP-17) 511
Clark, S.J. (AW-11) 106
Clavel, M. (AI-02) 51
Clements, E. (BT-12) 204
Clements, E. (GG-04) 704
Cobden, D. (EA-05) 454
Cochet, G. (CI-14) 290
Cogulu, E. (BB-08) 117
Cogulu, E. (CB-02) 237
Cohen, L. (AB-13) 9
Cohen, L. (AE-06) 26
Cohen, L. (CP-09) 295
Coisson, M. (DG-09) 383
Coisson, M. (GI-01) 716
Colás, L. (DG-04) 380
Cole-Piepke, K. (DW-13) 448
Coll, M. (AH-11) 48
Collin, S. (AF-07) 32
Collin, S. (BG-10) 156
Collin, S. (BV-03) 218
Collin, S. (ED-05) 469
Collin, S. (FV-05) 658
Colman, R. (BB-07) 117
Conde, A. (FD-02) 572
Cong, J. (BT-05) 200
Cong, K. (BT-02) 199
Conolly, S. (GA-03) 669
Constantinescu, D. (FF-12) 589
Cookson, E. (AS-01) 78
Cookson, E. (BS-01) 197
Cookson, E. (CS-01) 315
Cookson, E. (DS-01) 421
Cookson, E. (ES-01) 524
Cookson, E. (FS-01) 639
Cookson, E. (GS-01) 746
Copie, O. (DH-04) 387
Copus, M. (CE-09) 258
Corbin, E.A. (FD-10) 577
Corona, R. (AU-05) 86
Corona, R. (ET-08) 529
Corrêa, B.S. (AU-14) 90
Corrêa, B.S. (AU-15) 91
Correa, E. (AU-14) 90
Correa, E. (AU-15) 91
Correa, E. (BT-19) 207
Correa, E. (CU-10) 329
Correia, D.M. (AH-12) 48
Cortajarena, A.L. (DG-04) 380
Corte-León, H. (DE-01) 368
Corte-Leon, P. (AQ-13) 67
Corte-Leon, P. (GH-05) 710
Corte-Leon, P. (GH-07) 711
Corte-Leon, P. (GH-15) 715
Corte-Leon, P. (GI-03) 717
Cortés, D. (EW-13) 557
Cosset-Cheneau, M. (AP-03) 59
Cosset-Chéneau, M. (DP-08) 399
Cosset-Chéneau, M. (DP-12) 400
Cosset-Chéneau, M. (FC-09) 570
Cosset-Cheneau, M. (FV-10) 660
Costa, M.S. (AU-15) 91
Costache, M. (DB-01) 350
Cótica, L.F. (AT-01) 80
Cotofana, S. (CE-08) 258
Couet, S. (BC-05) 124
Couet, S. (EG-09) 489
Couet, S. (EG-11) 490
Couet, S. (EP-13) 508
Couet, S. (EP-16) 510
Couet, S. (FC-04) 567
Couet, S. (GC-02) 679
Couet, S. (GC-08) 681
Couet, S. (HG-10) 808
Couture, P. (CI-10) 288
Covas, T.R. (CU-01) 324
Cowburn, R. (EA-04) 454
Cramer, J. (EC-07) 464
Crawford, T.M. (AU-10) 89
Cress, C.D. (CT-09) 320
Crisanti, M. (AW-11) 106
Crisanti, M. (GF-01) 697
Cros, V. (AC-01) 11
Cros, V. (AF-07) 32
Cros, V. (BG-10) 156
Cros, V. (CC-01) 243
Cros, V. (DE-01) 368
Cros, V. (ED-05) 469
Cros, V. (EQ-04) 513
Cros, V. (EQ-05) 513
Cros, V. (GE-01) 689
Crotti, D. (EG-11) 490
Crotti, D. (EP-13) 508
Crowell, P.A. (AI-08) 54
Crowell, P.A. (BD-02) 131
Crowell, P.A. (GE-15) 695
Crupi, F. (AC-08) 15
Cruz Hernandez, A. (DG-11) 384
Csaba, G. (CB-01) 236
Csaba, G. (EP-12) 508
Csaba, G. (GE-06) 691
Cubitt, R. (GF-01) 697
Cubitt, R. (GF-04) 698
Cui, C. (ET-15) 532
Cui, J. (AW-08) 105
Cui, J. (CG-04) 271
Cui, J. (EH-01) 492
Cui, J. (FP-04) 617
Cui, J. (FQ-18) 630
Cui, J. (FU-08) 652
Cui, Q. (CG-02) 270
Cui, W. (AQ-14) 68
Cui, W. (CT-06) 319
Cui, W. (FQ-13) 628
Cui, X. (DV-01) 435
Curcio, A. (DG-12) 384
Currie, M. (CT-09) 320
Czubak, D. (DB-10) 354

- D -

D. Sudhoff, S. (EU-01) 535
d'Albuquerque e Castro, J. (BQ-06) 182
d'Aquino, M. (AI-01) 50
d'Aquino, M. (ER-08) 521
d'Aquino, M. (ET-09) 530
d'Aquino, M. (FI-02) 607
d'Aquino, M. (FI-06) 609
d'Aquino, M. (FI-07) 610
da Câmara Santa Clara Gomes, T. (BT-17) 206
da Câmara Santa Clara Gomes, T. (FP-05) 617
Dabrowski, M. (CB-10) 240
Dabrowski, M. (DI-11) 395
Dahal, B.R. (CW-17) 346
Dahal, B.R. (DQ-12) 409
Dahnovsky, Y. (BI-08) 168
Dahnovsky, Y. (DP-03) 396
Dai, B. (DE-07) 371
Dai, C. (FT-02) 641
Dai, Y. (DD-05) 363
Dai, Z. (BC-02) 122
Damnjanovic, M.S. (DV-10) 439
Dang, H. (FV-05) 658
Dang, N. (GG-04) 704
Dang, P. (AC-04) 12
Dang, P. (AH-01) 44
Dang, P. (AH-05) 45
Dang, P. (FG-13) 597
Dang, T. (FD-10) 577
Daniel, L. (DW-01) 442
Dankert, A. (DR-13) 419
Dantas, A.L. (AT-02) 80

*Best student presentation award finalist

Dantas, A.L. (AU-03) . . . 86
Dantas, A.L. (ET-11) . . . 531
Dantas, A.L. (GQ-11) . . . 739
Dao, T. (CG-04) . . . 271
Darwin, E. (GP-05) . . . 726
Das, A. (AG-09) . . . 41
Das, A. (AT-04) . . . 81
Das, A. (CB-05) . . . 238
Das, D. (AR-15) . . . 76
Das, H. (GG-05) . . . 704
Das, P. (BH-08) . . . 161
Das, P.T. (HC-08) . . . 778
Das, R. (AU-06) . . . 87
Das, R. (BE-13) . . . 145
Das, R. (BT-12) . . . 204
Das, R. (CV-05) . . . 334
Das, R. (DU-12) . . . 433
Das, R. (GG-04) . . . 704
Das, S. (AG-05) . . . 39
Dash, S.P. (DR-13) . . . 419
Dash, S.P. (FB-08) . . . 563
Datta, S. (EG-03) . . . 486
Dau, M. (DP-14) . . . 401
Davidson, A. (AD-05) . . . 18
Davidson, A. (AS-03) . . . 78
Davidson, A. (BS-03) . . . 197
Davidson, A. (CS-03) . . . 315
Davidson, A. (DS-03) . . . 421
Davidson, A. (ES-03) . . . 524
Davidson, A. (FS-03) . . . 639
Davidson, A. (GS-03) . . . 746
Davies, C. (DD-04) . . . 362
Davies, C. (GC-11) . . . 683
Davies, C. (HD-03) . . . 783
Davies, J.E. (HI-12) . . . 824
Davino, D. (BG-07) . . . 154
DC, M. (BC-10) . . . 127
De Boeck, J. (BC-05) . . . 124
De Graef, M. (AQ-09) . . . 65
De Graef, M. (AW-05) . . . 103
De Graef, M. (CR-03) . . . 307
De Graef, M. (DE-10) . . . 372
De Graef, M. (ED-03) . . . 468
De Graef, M. (GP-04) . . . 725
de la Venta, J. (AI-07) . . . 53
de la Venta, J. (HD-08) . . . 785
De Lima Correa, E. (HE-12) . . . 794
de Loubens, G. (GE-01) . . . 689
de Loubens, G. (GE-13) . . . 694
de Melo, P. (FB-01) . . . 561
de Rango, P. (FQ-19) . . . 630
De Rego, P.J. (HI-11) . . . 823
De Riz, A. (GP-03) . . . 725
De Riz, A. (HG-09) . . . 807
De Rose, R. (AC-08) . . . 15
de Sousa, V.R. (FQ-15) . . . 629
de Vaulchier, L. (DT-06) . . . 424
de Winter, R. (FB-01) . . . 561
De, A. (BQ-14) . . . 186
De, A. (CC-10) . . . 246
De, A. (EQ-01) . . . 512
De, A. (EQ-02) . . . 512
De, A. (EQ-03) . . . 513
De, A. (ER-01) . . . 518
De, A. (EW-06) . . . 554
Deac, A.M. (ET-02) . . . 526
Deac, A.M. (GB-11) . . . 676
Dean, M.P. (EI-08) . . . 501
Dean, P.R. (BT-04) . . . 200
Dearg, M. (GF-06) . . . 699
Deb, M. (DD-01) . . . 361
DeBeer-Schmitt, L. (CC-07) . . . 245
DeBeer-Schmitt, L. (DE-02) . . . 368
DeBeer-Schmitt, L. (ED-08) . . . 470
DeBeer-Schmitt, L. (GF-04) . . . 698
Decad, G. (HI-01) . . . 818
Decca, R. (GQ-12) . . . 739
Deenen, A. (DD-07) . . . 364
Degawa, N. (CI-12) . . . 289
Degiorgi, L. (FE-04) . . . 580
Deka, A. (EG-10) . . . 490
Delczeg-Czirjak, E.K. (ER-03) . . . 519
DeLong, L.E. (BH-03) . . . 159
Deman, A. (DU-01) . . . 428
DeMann, A. (CB-01) . . . 236
Demidov, V.E. (GE-01) . . . 689
Demin, G.D. (EV-17) . . . 549
Demin, G.D. (EV-18) . . . 549
Demokritov, S.O. (GE-01) . . . 689
Dempsey, N. (FQ-05) . . . 625
Demura, S. (AV-08) . . . 95
Denardin, J. (AU-12) . . . 89
Deng, J. (CH-06) . . . 279
Deng, P. (EB-10) . . . 458
Deng, Z. (HF-10) . . . 800
Denker, C. (CF-12) . . . 268
Denker, C. (ED-11) . . . 472
Dennis, C. (AU-14) . . . 90
Dennis, C. (HE-12) . . . 794
Desai, P. (GV-12) . . . 765
Desautels, R. (ED-08) . . . 470
Desautels, R. (EE-07) . . . 475
Desautels, R.D. (DH-09) . . . 389
Descamps, L. (DU-01) . . . 428
Dev, P. (GF-03) . . . 698
Devlin, E. (AR-02) . . . 70
Devolder, T. (CC-01) . . . 243
Devolder, T. (EP-13) . . . 508
Devolder, T. (EP-16) . . . 510
Devolder, T. (HG-10) . . . 808
Devolder, T. (HG-11) . . . 809
Dhagat, P. (CE-05) . . . 256
Dhagat, P. (CE-06) . . . 257
Dhagat, P. (CU-07) . . . 327
Dhar, S.K. (BI-06) . . . 168
Dhesi, S.S. (BB-12) . . . 119
Dhesi, S.S. (GH-10) . . . 713
Dhesi, S.S. (GQ-06) . . . 736
Dhillon, S. (FV-05) . . . 658
Dhuey, S. (BH-03) . . . 159
Dhuey, S. (BH-05) . . . 160
Dhuey, S. (FE-09) . . . 582
Di Carlo, D. (DG-02) . . . 379
Di Marco, I. (BD-06) . . . 134
Dieny, B. (AC-01) . . . 11
Dieny, B. (BC-13) . . . 129
Dieny, B. (EF-07) . . . 481
Dieny, B. (EP-08) . . . 506
Dieny, B. (ET-13) . . . 531
Dieny, B. (FC-05) . . . 568
Dieny, B. (GC-11) . . . 683
Dietl, T. (BQ-17) . . . 187
Dietl, T. (EB-13) . . . 460
Dietl, T. (FI-12) . . . 612
Dietl, T. (HF-11) . . . 800
Dietl, T. (HF-12) . . . 801
Díez-Toledano, J. (BE-08) . . . 143
Díez-Toledano, J. (CD-01) . . . 249
Díez-Toledano, J. (HB-02) . . . 770
Difini Accioly, A. (EF-06) . . . 480
Ding, B. (AW-08) . . . 105
Ding, B. (CV-10) . . . 336
Ding, B. (DR-08) . . . 416
Ding, C. (EV-14) . . . 548
Ding, H. (AG-02) . . . 38
Ding, H. (BV-06) . . . 219
Ding, H. (ET-05) . . . 528
Ding, J. (BR-17) . . . 195
Ding, J. (BV-06) . . . 219
Ding, J. (CB-01) . . . 236
Ding, J. (CB-02) . . . 237
Ding, J. (EW-04) . . . 553
Ding, J. (FA-02) . . . 559
Ding, S. (AG-05) . . . 39
Dinulovic, D. (CH-03) . . . 277
Divan, R. (DC-05) . . . 358
Divan, R. (EW-04) . . . 553
Divan, R. (EW-09) . . . 555
Divan, R. (FA-02) . . . 559
Divan, R. (FV-07) . . . 659
Dixit, A. (DR-03) . . . 414
Djuzhev, N.A. (EV-17) . . . 549
Djuzhev, N.A. (EV-18) . . . 549
Do, S. (AV-05) . . . 94
Dobak, S. (DW-05) . . . 444
Dobrovolskiy, O.V. (CE-07) . . . 257
Dobrovolskiy, O.V. (EW-15) . . . 557
Dobrowolska, M. (DR-04) . . . 415
Dobrowolska, M. (DR-05) . . . 415
Dobson, J. (GA-01) . . . 668
Doi, M. (AR-03) . . . 71
Doi, M. (CW-15) . . . 345
Doi, M. (FT-07) . . . 644
Doi, M. (GR-01) . . . 742
Dolezal, P. (CW-16) . . . 345
Dolui, K. (AE-05) . . . 26
Domagala, J.Z. (EB-13) . . . 460
Domagala, J.Z. (HF-12) . . . 801
Domann, J.P. (AQ-10) . . . 66
Domanov, O. (AT-09) . . . 83

*Best student presentation award finalist

Domíguez-Cañizares, G. (BH-11) 163
Donahue, M.J. (ET-01) 526
Donahue, M.J. (ET-07) 529
Donahue, M.J. (HE-12) 794
Dong, B. (FQ-16) 629
Dong, C. (HI-02) 818
Dong, F. (BW-13) 230
Dong, L. (FE-01) 579
Dong, S. (EE-08) 475
Donges, A. (EW-10) 556
Donges, A. (GF-13) 702
Donnelly, C.A. (EF-03) 479
Dopita, M. (CW-16) 345
Dormidontov, N. (BP-11) 176
Dormidontov, N. (BP-15) 178
dos Santos, A.M. (HE-03) 790
Doty, M. (BV-07) 220
Dou, Y. (CU-15) 331
Doyle, B. (DW-14) 448
Dragos, O. (DG-01) 379
Dreyer, M. (EB-03) 456
Drozdz, P. (CP-05) 293
Drozdz, P. (FG-07) 593
Drozdz, P. (FG-10) 595
Drube, W. (DT-15) 427
Du, C. (BG-04) 153
Du, H. (FG-04) 592
Du, J. (AV-03) 93
Du, J. (BQ-07) 182
Du, J. (BU-15) 216
Du, J. (CR-16) 314
Du, J. (EH-04) 493
Du, J. (FU-02) 649
Du, Y. (AD-13) 22
Dubenko, I. (AQ-17) 69
Dubenko, I. (DQ-01) 405
Dubenko, I. (DR-01) 414
Dubenko, I. (DR-15) 420
Dubenko, I. (FQ-09) 627
Dubey, D.P. (GG-08) 705
Dubowik, J. (GE-08) 692
Dubowik, J. (GE-12) 694
Dubs, C. (CE-08) 258
Dubs, C. (GE-03) 690
Dubuis, G. (HF-03) 796
Ducos, P. (DP-02) 396
Ducruet, C. (BC-13) 129
Dugu, S. (FU-11) 652
Dugu, S. (FU-13) 653
Duine, R. (CB-04) 237
Duine, R. (CE-11) 259
Duine, R. (DD-07) 364
Duine, R. (EA-03) 454
Duine, R. (GE-10) 693
Duine, R. (HG-06) 806
Dumas, R.K. (FC-08) 569
Dumesnil, K. (BD-12) 136
Dumesnil, K. (DH-04) 387
Dunin-Borkowski, R.E. (FH-02) 599
Dunz, M. (BB-05) 116
Dunz, M. (FG-09) 595
Dupe, B. (CV-01) 333
Dupe, B. (ED-10) 471
Dupuis, V. (EH-08) 495
Dupuy, J. (AF-01) 30
Dushenko, S. (BC-04) 123
Dutta, K. (CC-10) 246
Dutta, S. (HG-07) 806
DuttaGupta, S. (BB-12) 119
DuttaGupta, S. (DF-05) 376
Duvauchelle, J. (FQ-06) 625
Duverger-Nédellec, E. (BB-07) 117
Duzgun, A. (HA-01) 767
Dvornik, M. (EG-02) 485
Dwivedi, J. (GH-09) 712
Dybko, K. (EB-13) 460
Dyck, D. (HF-02) 795

- E -

Eames, P.G. (HI-12) 824
Ebels, U. (AC-01) 11
Ebels, U. (EF-07) 481
Ebels, U. (EP-08) 506
Ebels, U. (EQ-05) 513
Ebels, U. (ER-05) 520
Ebels, U. (GE-13) 694
Echenique, P.M. (EB-07) 457
Eckert, J.C. (CV-04) 334
Eckert, J.C. (CV-09) 336
Eda, G. (DB-04) 351
Eddrief, M. (FD-06) 574
Ederer, K. (DT-15) 427
Edwards, E. (AV-16) 99
Edwards, E. (CR-04) 307
Edwards, R.S. (FH-13) 605
Ehresmann, A. (AH-10) 47
Eimerl, R. (ET-14) 532
Eisebitt, S. (DC-04) 358
Eisebitt, S. (DD-02) 361
El Baggari, I. (DA-05) 348
El Hadri, M. (EC-10) 465
El-Gendy, A.A. (CQ-06) 302
El-Gendy, A.A. (CQ-10) 304
El-Gendy, A.A. (CQ-11) 304
El-Gendy, A.A. (DQ-08) 407
El-Ghazaly, A. (AQ-05) 63
El-Ghazaly, A. (DD-08) 365
El-Ghazaly, A. (HC-09) 778
El-Khatib, S. (HF-07) 798
ElBidweihy, H. (FP-01) 615
Elkins, J. (AT-05) 81
Elkins, J. (AT-06) 82
Elkins, J. (BH-13) 164
Ellis, D. (CB-04) 237
Elphick, K. (AV-02) 92
Elphick, K. (BU-01) 209
Elphick, K. (BU-05) 211
Elphick, K. (BU-06) 211
Elphick, K. (CP-04) 293
Elphick, K. (CP-07) 294
Emori, S. (AI-02) 51
Emori, S. (AI-06) 53
Emori, S. (GB-01) 671
Enamullah, E. (HF-04) 796
Endo, M. (EG-04) 486
Endo, M. (GP-12) 730
Endo, T. (DP-04) 397
Endo, Y. (AI-10) 55
Endo, Y. (AQ-08) 65
Endo, Y. (CR-01) 306
Endo, Y. (EV-16) 548
Endoh, T. (AI-10) 55
Endoh, T. (CR-01) 306
Endoh, T. (EC-11) 465
Endoh, T. (FC-07) 569
Ennen, I. (FQ-03) 624
Ennen, I. (HF-02) 795
Ensign, B. (GT-12) 751
Entani, S. (FB-09) 564
Eom, N. (BP-07) 174
Epicier, T. (EH-08) 495
Eremeev, S.V. (EB-07) 457
Erhart, P. (DR-13) 419
Eriksson, O. (AI-07) 53
Eriksson, O. (AP-05) 60
Eriksson, O. (BD-06) 134
Eriksson, O. (BD-07) 134
Eriksson, O. (ER-03) 519
Eriksson, O. (ER-04) 519
Ernst, A. (EB-07) 457
Ersan, F. (BI-11) 169
Ersfeld, M. (FB-01) 561
Ertekin, E. (AS-02) 78
Ertekin, E. (BS-02) 197
Ertekin, E. (CS-02) 315
Ertekin, E. (DS-02) 421
Ertekin, E. (ES-02) 524
Ertekin, E. (FS-02) 639
Ertekin, E. (GS-02) 746
Erugu, U. (BV-06) 219
Esawa, M. (AW-19) 110
Escrig, J. (AU-05) 86
Escrig, J. (AW-15) 108
Escrig, J. (EQ-08) 515
Escrig, J. (FT-13) 646
Espinosa, A. (DG-12) 384
Estevez, D. (AQ-12) 66
Estevez, D. (CV-02) 333
Estrada, V.M. (CQ-05) 301
Etgens, V.H. (FD-06) 574
Etheridge, J.M. (GE-15) 695
Eun Sang, C. (DH-09) 389
Evans, A. (DQ-19) 413
Evans, A. (FQ-17) 630
Evans, R.F. (AB-11) 8
Evans, R.F. (AR-08) 73
Evans, R.F. (BH-12) 163
Evans, R.F. (ET-06) 528

*Best student presentation award finalist

Evans, R.F. (FG-01) 591
Evelt, M. (GE-01) 689
Everschor-Sitte, K. (GF-13) 702
Everschor-Sitte, K. (HA-05) 768
Evstigneeva, S. (GH-11) 713
Ewing, D. (HI-11) 823
Exl, L. (CA-03) 233

- F -

F. Andrade, L.H. (ER-11) 522
Facio, J. (GD-01) 685
Fahl, A. (CT-13) 322
Fakhrul, T. (AG-08) 40
Fakhrul, T. (DA-03) 348
Fakhrul, T. (HG-02) 804
Fakhrul, T. (HH-15) 817
Fallarino, L. (CG-07) 272
Fallon, K. (BB-11) 119
Fan, R. (AB-06) 6
Fan, R. (AF-11) 34
Fan, R. (BF-11) 150
Fan, R. (GF-01) 697
Fan, S. (GG-05) 704
Fan, W. (FV-11) 660
Fan, X. (AD-05) 18
Fan, X. (AS-03) 78
Fan, X. (BS-03) 197
Fan, X. (CS-03) 315
Fan, X. (DS-03) 421
Fan, X. (ES-03) 524
Fan, X. (FS-03) 639
Fan, X. (GS-03) 746
Fan, Y. (FV-15) 662
Fang, B. (CI-13) 290
Fang, C. (AD-09) 19
Fang, C. (BV-15) 223
Fang, W. (AB-14) 10
Fang, Y. (FH-04) 600
Fang, Y. (FH-05) 601
Fangohr, H. (DD-02) 361
Fangohr, H. (EW-13) 557
Farhan, A. (BH-05) 160
Farhan, A. (FE-09) 582
Farheen, A. (BT-13) 204
Fariborzi, H. (BC-11) 128
Fariborzi, H. (DV-11) 440
Fariborzi, H. (EP-04) 504
Farle, M. (BD-04) 133
Farmer, B.W. (BH-03) 159
Farmer, T. (DH-09) 389
Farrar, A. (AI-03) 51
Fassbender, J. (CC-04) 244
Fassbender, J. (CD-03) 250
Fassbender, J. (EE-11) 477
Fassbender, J. (ET-02) 526
Fassbender, J. (GB-11) 676
Fassbender, J. (HG-05) 805
Fataftah, M. (HE-01) 790
Faure, S. (AF-04) 31
Fauth, F. (GG-03) 704
Fdez-Gubieda, M. (DG-05) 381
Fdez-Gubieda, M. (HH-03) 811
Fecher, G. (DT-15) 427
Feggeler, T. (BD-04) 133
Fei, Z. (EA-05) 454
Fekete, L. (AQ-09) 65
Felfer, P. (BF-09) 149
Felser, C. (AB-12) 9
Felser, C. (AE-04) 25
Feng, H. (CR-10) 310
Feng, J. (BR-01) 189
Feng, Q. (BR-08) 192
Feng, W. (FP-14) 621
Feng, X. (BV-13) 223
Feng, X. (CH-06) 279
Fennie, C. (DA-05) 348
Fennie, C. (GG-05) 704
Feoktystov, A. (BF-07) 149
Feoktystov, A. (DT-03) 423
Feoktystov, A. (DW-03) 443
Fernandes Cauduro, A. (AG-03) 38
Fernandes Cauduro, A. (CG-11) 274
Fernandes, L. (AH-12) 48
Fernandes, R. (BA-01) 111
Fernández Scarioni, A. (DE-01) 368
Fernandez-Martin, E. (AH-12) 48
Fernandez-Martin, E. (HI-07) 821
Fernández-Miaja, P. (EV-20) 551
Fernandez-Outon, L.E. (ER-11) 522
Fernandez-Roldan, J. (GP-03) 725
Fernandez, P.M. (AH-13) 49
Ferrante, Y. (EC-01) 461
Ferrari Silveira Rosa, P. (GT-02) 748
Ferrari Silveira Rosa, P. (GT-07) 750
Ferrari Silveira Rosa, P. (GT-08) 750
Ferrari, L. (HE-04) 791
Ferreira, R. (AC-01) 11
Ferreira, R. (EQ-05) 513
Ferreira, W.L. (GT-15) 752
Ferrer, S. (AF-09) 33
Fert, A. (AE-08) 26
Fert, A. (AF-07) 32
Fert, A. (BG-10) 156
Fert, A. (DP-08) 399
Fert, A. (ED-05) 469
Fettar, F. (BC-13) 129
Feuchtwanger, J. (FD-09) 576
Feygenson, M. (BF-07) 149
Fiagbenu, A. (DC-06) 359
Field, S. (CB-01) 236
Fields, K. (GA-03) 669
Figueiredo-Prestes, N. (BV-03) 218
Filianina, M. (BB-01) 114
Filippou, P. (HB-05) 772
Fin, S. (FD-08) 575
Fina, I. (EE-04) 474
Fina, I. (FU-12) 653
Finco, A. (BG-10) 156
Finco, A. (ED-05) 469
Finco, A. (EE-02) 473
Finco, A. (EE-06) 475
Finizio, S. (DE-05) 369
Finizio, S. (ED-01) 467
Finkel, P. (FD-11) 577
Finocchio, G. (AB-03) 5
Finocchio, G. (AC-08) 15
Finocchio, G. (AW-10) 105
Finocchio, G. (AW-13) 107
Finocchio, G. (BB-06) 117
Finocchio, G. (BB-14) 120
Finocchio, G. (CI-13) 290
Finocchio, G. (DE-03) 369
Finocchio, G. (DE-09) 372
Fischbacher, J. (AR-08) 73
Fischbacher, J. (CA-03) 233
Fischbacher, J. (FI-01) 607
Fischer, J. (EE-02) 473
Fischer, J.A. (CC-02) 243
Fischer, P. (CC-03) 244
Fischer, P. (FF-03) 585
Fisher, B. (FV-07) 659
Fisk, Z. (GT-07) 750
Fitzell, K. (BT-14) 205
Fitzell, K. (DW-09) 446
Fitzell, K. (FU-17) 654
Fitzell, K. (GG-02) 703
Fitzsimmons, M. (BA-01) 111
Fitzsimmons, M. (CC-07) 245
Fitzsimmons, M. (DE-02) 368
Fitzsimmons, M. (ED-08) 470
Fitzsimmons, M. (EE-07) 475
Fix, M. (FV-13) 661
Flatté, M.E. (EB-12) 459
Flatté, M.E. (EQ-13) 517
Flatté, M.E. (EW-12) 557
Flores, J. (DH-06) 387
Foerster, M. (ED-04) 469
Foerster, M. (HG-09) 807
Foltyn, M. (BQ-17) 187
Fontana, E. (FD-06) 574
Fontana, R. (HI-01) 818
Foreman, J. (GV-12) 765
Forestier, G. (EC-09) 464
Forestier, G. (ER-05) 520
Forestier, G. (GQ-01) 734
Forrest, T.R. (BB-01) 114
Forrest, T.R. (GH-10) 713
Forrest, T.R. (GQ-06) 736
Förster, J. (GE-08) 692
Förster, J. (GE-09) 693
Forth, J. (FF-03) 585
Fournier, P. (FQ-19) 630
Fowley, C. (GB-11) 676
Franco, V. (FD-02) 572
Francoual, S. (AE-07) 26
Francoual, S. (AF-12) 35
Frandsen, B.A. (FQ-11) 627
Frandsen, B.A. (HE-10) 794

*Best student presentation award finalist

Frangou, L. (EC-09) 464
Frangou, L. (ER-05) 520
Franke, K.J. (AW-11) 106
Franke, K.J. (BT-04) 200
Franklin, J. (BG-07) 154
Franklin, R. (DG-05) 381
Frano, A. (GD-03) 685
Frazitta, V. (CH-11) 282
Freedman, D. (HE-01) 790
Freeland, J. (FB-02) 561
Freire, R. (AU-12) 89
Freitas, R.S. (AU-15) 91
Freitas, R.S. (FE-05) 580
Frey, P. (BE-11) 144
Frey, P. (CE-13) 260
Frey, P. (GE-02) 689
Fried, N. (DT-07) 425
Friedel, A.M. (GE-03) 690
Friedlein, J. (EF-13) 483
Friedman, A.L. (EB-03) 456
Friedman, J.S. (BC-09) 126
Friedman, J.S. (ET-15) 532
Friedman, J.S. (HG-08) 806
Frielinghaus, H. (DT-03) 423
Fries, M. (FD-01) 572
Friesen, C. (EF-13) 483
Fripp, K.G. (EW-07) 554
Frisbie, D. (BA-01) 111
Frisk, A. (CB-10) 240
Fritz, K. (EC-02) 461
Frömter, R. (HG-06) 806
Frontera, C. (DH-08) 388
Frontera, C. (FV-03) 658
Frost, W.J. (CF-08) 266
Fruchart, D. (FQ-19) 630
Fruchart, O. (GP-03) 725
Fruchart, O. (HG-03) 805
Fruchart, O. (HG-09) 807
Fu, H. (CG-08) 273
Fu, H. (FD-07) 575
Fu, S. (FI-10) 611
Fu, W. (BW-01) 225
Fu, W. (DP-17) 403
Fu, W. (EU-04) 536
Fu, W. (EU-10) 539
Fu, W. (FR-06) 634
Fu, W. (GU-09) 758
Fuad, A. (GE-13) 694
Fuchs, D. (BT-01) 199
Fuchs, G. (AF-13) 35
Fuchs, G. (BG-11) 156
Fuentes, G. (BE-10) 144
Fuentes, V. (BT-16) 206
Fuh, H. (CT-15) 323
Fuhrmann, F. (EC-07) 464
Fujii, H. (DR-09) 417
Fujimori, A. (HF-10) 800
Fujimoto, C. (FH-07) 602
Fujimoto, J. (BQ-02) 179
Fujimoto, K. (CQ-09) 303
Fujimoto, K. (DG-10) 383
Fujita, S. (FF-11) 589
Fujita, Y. (EF-09) 482
Fujiwara, H. (DR-09) 417
Fujiwara, H. (EQ-07) 514
Fujiwara, T. (FH-07) 602
Fukami, S. (BB-12) 119
Fukami, S. (DD-01) 361
Fukami, S. (DF-05) 376
Fukami, S. (EG-02) 485
Fukatani, N. (CV-14) 337
Fukuma, Y. (EG-10) 490
Fukunaga, H. (BP-13) 177
Fukunaga, H. (CW-11) 343
Fukunaga, H. (CW-12) 344
Fukunaga, H. (DW-08) 445
Fukunaga, H. (DW-16) 449
Fukushima, A. (BU-07) 212
Fukushima, A. (BU-08) 212
Fukushima, A. (CF-01) 262
Fukushima, A. (CF-04) 263
Fukushima, A. (DF-01) 374
Fukushima, A. (EF-01) 478
Fukushima, A. (EG-01) 485
Fukushima, A. (EG-04) 486
Fukushima, A. (EG-05) 487
Fukushima, A. (EG-12) 491
Fukushima, A. (EP-02) 503
Fukushima, A. (EQ-04) 513
Fukushima, A. (FC-05) 568
Fukushima, A. (HI-06) 821
Fukushima, Y. (AV-04) 93
Fulara, H. (EG-02) 485
Fuller, E. (DU-12) 433
Fullerton, E. (BC-07) 125
Fullerton, E. (BD-05) 133
Fullerton, E. (CC-07) 245
Fullerton, E. (CC-08) 245
Fullerton, E. (CV-04) 334
Fullerton, E. (CV-09) 336
Fullerton, E. (DD-01) 361
Fullerton, E. (DE-02) 368
Fullerton, E. (DE-08) 371
Fullerton, E. (EA-01) 453
Fullerton, E. (EC-10) 465
Fullerton, E. (EC-13) 466
Fullerton, E. (ED-08) 470
Fullerton, E. (EF-12) 483
Fullerton, E. (FE-03) 579
Fullerton, E. (GQ-07) 737
Funabashi, N. (GP-07) 727
Funato, T. (BE-06) 142
Funato, T. (FV-14) 662
Furdyna, J.K. (DR-04) 415
Furdyna, J.K. (DR-05) 415
Furutani, S. (CW-11) 343
Furutani, S. (CW-12) 344
Furuya, A. (EP-11) 507
Furuya, M. (CQ-08) 303
Fusil, S. (EE-02) 473
Fusil, S. (EE-06) 475
Futakawa, Y. (DC-09) 360
Fuzer, J. (DW-05) 444

- G -

G. Giuliani, J. (GQ-12) 739
Gabay, A. (EH-01) 492
Gahtori, B. (DR-16) 420
Gahtori, B. (FF-04) 585
Galazka, Z. (BR-09) 192
Galda, A. (ER-09) 521
Galia, M. (BW-15) 231
Galindo, A. (AT-07) 82
Gallant, A. (FC-10) 570
Gallardo, R. (EW-13) 557
Gallardo, R. (GB-11) 676
Gambardella, P. (BB-12) 119
Gambardella, P. (CG-04) 271
Gambarelli, S. (DP-14) 401
Gambarelli, S. (EC-09) 464
Gamou, H. (AD-13) 22
Gan, P. (EU-02) 535
Gan, W. (AC-05) 13
Gan, W. (AD-10) 20
Gan, W. (DC-08) 359
Gan, W. (GF-08) 700
Gan, W. (GP-13) 730
Gandarias, L. (DG-05) 381
Gandarias, L. (HH-03) 811
Gandha, K. (BT-07) 201
Gandha, K. (CT-07) 320
Gandhi, A.C. (AU-09) 88
Gandia, D. (DG-05) 381
Gandia, D. (HH-03) 811
Ganesh, R. (EE-10) 476
Gangwar, A. (DW-15) 449
Gangwar, A. (HH-13) 816
Gao, K. (HI-11) 823
Gao, M. (AI-06) 53
Gao, M. (DQ-19) 413
Gao, M. (FQ-17) 630
Gao, N. (GB-02) 671
Gao, S. (DV-03) 436
Gao, T. (BI-07) 168
Gao, T. (FT-04) 642
Gao, T. (FT-05) 643
Gao, X. (DH-09) 389
Gao, Y. (EV-01) 541
Gao, Y. (GI-05) 718
Gao, Y. (GI-06) 718
Gao, Z. (DG-01) 379
Gao, Z. (DP-02) 396
Garanin, D. (AW-20) 110
Garbovskiy, Y. (DG-06) 381
García Prieto, A. (HH-03) 811
Garcia-Arribas, A. (HI-07) 821
Garcia-Muñoz, J. (GG-03) 704
Garcia-Sanchez, F. (BC-09) 126

*Best student presentation award finalist

Garcia-Sanchez, F. (GI-01) 716
Garcia-Sanchez, F. (HD-01) 782
Garcia-Sanchez, F. (HG-08) 806
Garcia, C. (AD-15) 23
Garcia, C. (AQ-13) 67
Garcia, C. (CU-16) 332
Garcia, C. (FC-08) 569
Garcia, J. (DU-01) 428
Garcia, J.H. (DB-01) 350
Garcia, J.P. (HG-03) 805
Garcia, L. (GP-08) 728
Garcia, L. (HE-06) 792
García, M. (DG-12) 384
Garcia, V. (EE-02) 473
Garcia, V. (EE-06) 475
Gardner, J.S. (FE-05) 580
Garello, K. (BC-05) 124
Garello, K. (EG-11) 490
Garello, K. (GC-08) 681
Garesci, F. (AB-03) 5
Garesci, F. (AW-10) 105
Garesci, F. (BB-14) 120
Garg, C. (BC-01) 122
Garg, C. (HB-05) 772
Gargiani, P. (AG-08) 40
Garitaine, B. (EQ-04) 513
Gas, K. (BG-12) 156
Gas, K. (BQ-17) 187
Gas, K. (DR-06) 416
Gas, K. (FI-12) 612
Gaucher, S. (DB-10) 354
Gaudin, G. (ED-04) 469
Gaur, A. (BR-07) 191
Gautam, N. (BW-04) 226
Gawronski, P. (GH-05) 710
Gazquez, J. (DH-08) 388
Ge, H. (BW-10) 229
Ge, H. (EH-04) 493
Ge, J. (GI-12) 721
Gebretsadik, A. (EI-06) 500
Gegenwart, P. (CP-12) 296
Geilen, M. (CE-08) 258
Gemming, S. (EE-10) 476
Gensch, M. (BD-01) 131
Gentry, C. (DT-02) 423
Gentry, C. (ER-03) 519
Genuzio, F. (HG-09) 807
George, J. (AE-08) 26
George, J. (BV-03) 218
George, J. (FV-05) 658
Geprägs, S. (GB-10) 675
Ger, T. (BW-13) 230
Ger, T. (DU-13) 433
Gerken, M. (BG-08) 154
Gerrity, M. (ER-03) 519
Gerstl, S.S. (FH-02) 599
Ghahremani, M. (AQ-18) 69
Ghanbaja, J. (DH-04) 387
Ghemes, A. (DG-01) 379
Ghimire, N. (AB-01) 4
Ghoreyshi, A. (DU-09) 432
Ghose, S. (EE-09) 476
Ghosh, R.K. (BQ-12) 185
Ghosh, S. (AP-03) 59
Ghosh, S. (DQ-11) 408
Ghosh, S. (FU-16) 654
Ghosh, S. (FV-10) 660
Ghosh, S. (HG-03) 805
Gibbons, J. (EC-10) 465
Gibbons, J. (FA-02) 559
Gibbons, J. (FV-07) 659
Gibbons, J. (HF-09) 799
Gich, M. (GG-03) 704
Gil Monsalve, J. (FT-06) 643
Gilbert, D.A. (BA-04) 112
Gilbert, D.A. (BA-05) 113
Gilbert, D.A. (CC-07) 245
Gilbert, D.A. (DE-02) 368
Gilbert, D.A. (ED-08) 470
Gilbert, D.A. (FD-10) 577
Gilbert, M. (AB-09) 7
Gilbert, M. (EB-04) 456
Giles, C. (GT-14) 752
Gillemot, F. (DW-03) 443
Ginzburg, B. (BP-15) 178
Giordano, A. (AW-10) 105
Giordano, A. (AW-13) 107
Girt, E. (FT-11) 645
Girt, E. (GC-05) 680
Girt, E. (GQ-04) 735
Girt, E. (GQ-10) 738
Girt, E. (GQ-16) 741
Gitzel, W. (BI-09) 169
Giuliani, J.G. (AT-07) 82
Gjoka, M. (AR-02) 70
Gjoka, M. (FH-10) 603
Gladii, O. (EC-09) 464
Gladii, O. (ER-05) 520
Gladii, O. (GQ-01) 734
Gloskovskii, A. (DT-15) 427
Glowinski, H. (GE-12) 694
Glownia, J.M. (FE-03) 579
Go, G. (GP-16) 732
Göbel, B. (AW-14) 107
Göbel, B. (DP-08) 399
Göbel, B. (GF-09) 701
Goering, E. (CU-02) 324
Goering, E. (GE-12) 694
Goering, E. (GQ-03) 735
Goering, E. (GQ-04) 735
Goforth, M.E. (AQ-10) 66
Goiriena-Goikoetxea, M. (DG-02) 379
Goiriena-Goikoetxea, M. (HC-03) 776
Goiriena-Goikoetxea, M. (HC-09) 778
Goldberger, J.E. (AA-01) 2
Goldberger, J.E. (DB-12) 354
Golibrzuch, M. (GE-04) 690
Gollwitzer, J. (BD-15) 138
Gollwitzer, J. (CE-02) 255
Gomez-Polo, C. (HI-07) 821
Gomez, C. (GQ-01) 734
Gómez, J.E. (AE-13) 29
Gomi, A. (BU-07) 212
Gomi, A. (BU-08) 212
Gomi, A. (GC-04) 679
Gomonay, O. (BB-01) 114
Gomonay, O. (CB-04) 237
Gomonay, O. (HA-05) 768
Gonçalves, J.N. (FD-05) 574
Gonçalves, J.N. (HC-02) 775
Gonçalves, R. (FE-10) 582
Gonçalves, V.C. (GT-15) 752
Goncharov, A. (FV-08) 659
Goncharov, A. (HD-13) 788
Gong, C. (EI-01) 498
Gong, J. (EP-17) 511
Gong, X. (AE-09) 27
Gonzales Trabada, D. (GI-01) 716
González Chávez, D. (AE-13) 29
Gonzalez Hernandez, R.J. (CV-01) 333
Gonzalez Szwacki, N. (BQ-17) 187
Gonzalez Szwacki, N. (FI-12) 612
Gonzalez-Fuentes, C.A. (AD-15) 23
Gonzalez-Fuentes, C.A. (CU-16) 332
Gonzalez-Fuentes, C.A. (FC-08) 569
Gonzalez-Ruano, C. (CF-03) 263
Gonzalez, J. (GH-05) 710
Gonzalez, J. (GH-15) 715
González, J.M. (BH-02) 158
González, J.M. (BH-11) 163
Gonzalez, J.M. (CR-14) 312
González, J.M. (HE-09) 793
Goodwill, P. (GA-03) 669
Gopman, D.B. (CF-02) 263
Gopman, D.B. (FT-12) 646
Gorchon, J. (DD-01) 361
Gordon, E.E. (DP-13) 401
Gorny, K. (DG-11) 384
Gorobets, O. (AQ-03) 63
Gort, R. (DD-02) 361
Goryachev, M. (CI-15) 291
Gospodaric, P. (CD-03) 250
Goswami, P. (DH-03) 386
Goswami, R. (BI-10) 169
Goto, K. (HF-06) 798
Goto, M. (BQ-02) 179
Goto, M. (CI-12) 289
Goto, M. (EP-02) 503
Goto, M. (FC-05) 568
Goto, M. (HI-06) 821
Goto, Y. (BE-03) 141
Goto, Y. (CV-12) 337
Gotsmann, B. (BE-09) 143
Gottschalk, M. (FQ-03) 624
Gottschall, T. (FD-01) 572
Gottwald, M. (GC-07) 681
Gould, R. (FP-13) 621
Goumri-Said, S. (DP-01) 396
Goyal, K. (DF-07) 377
Gràcia-Condal, A. (FD-01) 572

*Best student presentation award finalist

Gräfe, J. (CU-02) . . . 324
Gräfe, J. (DE-03) . . . 369
Gräfe, J. (ED-04) . . . 469
Gräfe, J. (GE-08) . . . 692
Gräfe, J. (GE-09) . . . 693
Gräfe, J. (GE-12) . . . 694
Graham, M. (HE-01) . . . 790
Granovsky, A. (DR-01) . . . 414
Granovsky, A. (DR-15) . . . 420
Granville, S. (DR-10) . . . 417
Granville, S. (HF-03) . . . 796
Graulich, D. (AE-07) . . . 26
Grave, D. (CB-04) . . . 237
Gray, B.A. (CR-02) . . . 306
Gray, I. (AF-13) . . . 35
Gray, I. (BG-11) . . . 156
Grayson, M. (BB-14) . . . 120
Greaves, S. (GR-06) . . . 744
Greaves, S. (GR-08) . . . 745
Green, B. (BD-01) . . . 131
Greenberg, A. (BG-06) . . . 153
Greene, R.l. (DI-02) . . . 391
Greven, M. (BA-01) . . . 111
Greven, M. (DH-07) . . . 388
Greving, D. (BH-04) . . . 159
Griffiths, R.A. (HD-07) . . . 785
Grigoras, M. (GH-14) . . . 714
Griner, D. (BF-05) . . . 148
Griner, D. (BF-06) . . . 148
Gritsenko, C. (GQ-15) . . . 741
Grochot, K. (AD-11) . . . 20
Groeseneken, G. (EG-09) . . . 489
Groeseneken, G. (EG-11) . . . 490
Grollier, J. (EF-01) . . . 478
Grollier, J. (EQ-04) . . . 513
Gross, F. (CU-02) . . . 324
Gross, F. (GE-08) . . . 692
Gross, F. (GE-12) . . . 694
Gross, I. (EE-06) . . . 475
Gross, R. (GB-10) . . . 675
Grossi, R.M. (CT-13) . . . 322
Grossi, R.M. (GT-14) . . . 752
Grübel, G. (DD-02) . . . 361
Grundler, D. (AW-04) . . . 102
Grundler, D. (GE-09) . . . 693
Grundler, D. (GE-11) . . . 694
Gruszecki, P. (EW-15) . . . 557
Gruszecki, P. (GE-08) . . . 692
Grutter, A.J. (BA-01) . . . 111
Grutter, A.J. (BA-04) . . . 112
Grutter, A.J. (BA-05) . . . 113
Grutter, A.J. (CC-07) . . . 245
Grutter, A.J. (DE-02) . . . 368
Grutter, A.J. (DH-07) . . . 388
Gu, B. (EC-05) . . . 463
Gu, H. (FP-04) . . . 617
Gu, J. (DR-14) . . . 419
Gu, J. (FR-04) . . . 633
Gu, J. (FR-11) . . . 637
Gu, Q. (CU-09) . . . 329
Guang, Y. (DE-03) . . . 369
Gubbiotti, G. (GE-12) . . . 694
Gudín, A. (BE-08) . . . 143
Gudín, A. (CD-01) . . . 249
Gudín, A. (HB-02) . . . 770
Guedas-Garcia, R. (HD-01) . . . 782
Guerrero, R. (BE-08) . . . 143
Guerrero, R. (CD-01) . . . 249
Guerrero, R. (HB-02) . . . 770
Guevara, M. (BT-14) . . . 205
Guillemard, C. (HF-01) . . . 795
Guillet, T. (AE-08) . . . 26
Guillet, T. (DP-07) . . . 398
Guillet, T. (DP-14) . . . 401
Guillet, T. (EB-01) . . . 455
Guillou, F. (FQ-08) . . . 626
Guimarães, M. (AB-02) . . . 4
Guimaraes, M. (DA-05) . . . 348
Guitarra, S. (EI-11) . . . 502
Gunduz Akdogan, N. (BP-14) . . . 177
Günther, C. (DD-02) . . . 361
Guo, C. (FV-01) . . . 657
Guo, E. (EE-07) . . . 475
Guo, G. (CW-06) . . . 341
Guo, J. (AW-12) . . . 106
Guo, J. (BW-10) . . . 229
Guo, L. (EH-06) . . . 494
Guo, M. (BU-02) . . . 209
Guo, R. (AR-11) . . . 74
Guo, S. (FG-12) . . . 596
Guo, X. (GU-04) . . . 755
Guo, Y. (AR-01) . . . 70
Guo, Y. (FR-03) . . . 633
Guodong, W. (BQ-04) . . . 180
Gupta, A. (BI-11) . . . 169
Gupta, A. (BR-09) . . . 192
Gupta, A. (ER-04) . . . 519
Gupta, A. (GH-09) . . . 712
Gupta, D. (BV-02) . . . 217
Gupta, M. (GH-09) . . . 712
Gupta, P. (BV-02) . . . 217
Gupta, S. (DP-04) . . . 397
Gupta, S. (EP-17) . . . 511
Gupta, S. (FD-07) . . . 575
Gupta, S. (FQ-01) . . . 623
Gupta, S. (FQ-02) . . . 623
Gupta, V. (DA-05) . . . 348
Guragain, D. (AR-13) . . . 75
Guragain, D. (BR-02) . . . 189
Guragain, D. (BR-15) . . . 195
Gürbüz, I. (CH-07) . . . 280
Gurieva, T. (BU-13) . . . 215
Gurieva, T. (CF-06) . . . 264
Gurieva, T. (GQ-13) . . . 740
Gurung, G. (AD-03) . . . 17
Gurung, G. (CP-03) . . . 292
Gusakova, D. (FC-09) . . . 570
Gusakova, D. (GP-03) . . . 725
Gusakova, D. (GQ-01) . . . 734
Gusakova, D. (HG-09) . . . 807
Gusenbauer, M. (FI-01) . . . 607
Gushi, T. (HG-03) . . . 805
Gusieva, Y. (AQ-03) . . . 63
Guslienko, K. (EW-15) . . . 557
Gusmao, M.A. (GT-13) . . . 752
Gutfleisch, O. (FD-01) . . . 572
Gutfleisch, O. (FD-02) . . . 572
Gutierrez, A. (BH-11) . . . 163
Gutmann, M.J. (AW-17) . . . 109

- H -

Haase, C. (AT-03) . . . 81
Hache, T. (CC-04) . . . 244
Hadimani, R.L. (BW-12) . . . 230
Hadimani, R.L. (DU-04) . . . 429
Hadimani, R.L. (DU-08) . . . 431
Hadimani, R.L. (FD-07) . . . 575
Hadimani, R.L. (FQ-01) . . . 623
Hadjipanayis, G.C. (CQ-06) . . . 302
Hadjipanayis, G.C. (CQ-10) . . . 304
Hadjipanayis, G.C. (CQ-11) . . . 304
Hadjipanayis, G.C. (EH-01) . . . 492
Hadjipanayis, G.C. (FH-10) . . . 603
Hadjipanayis, G.C. (GF-03) . . . 698
Hadjipanayis, G.C. (HE-13) . . . 794
Haghighirad, A. (DI-09) . . . 394
Hagihara, M. (FG-05) . . . 592
Hahn, C. (EQ-10) . . . 516
Haider, S. (BP-06) . . . 174
Hajiri, T. (CP-12) . . . 296
Halcrow, M.A. (HE-03) . . . 790
Halevy, I. (BI-05) . . . 167
Hallal, A. (CG-02) . . . 270
Hallal, A. (EC-09) . . . 464
Hallal, A. (GG-10) . . . 706
Haltz, E. (AI-12)* . . . 56
Haltz, E. (CR-07) . . . 309
Ham, W. (CD-06) . . . 251
Hamad, M.K. (DQ-08) . . . 407
Hamad, R. (DQ-08) . . . 407
Hamaya, K. (EF-09) . . . 482
Hamaya, K. (FW-03) . . . 664
Hamaya, K. (HF-05) . . . 797
Hamilton, G. (AB-09) . . . 7
Hammel, P.C. (AA-01) . . . 2
Hammel, P.C. (CR-02) . . . 306
Hammel, P.C. (DC-03) . . . 357
Hammel, P.C. (FG-12) . . . 596
Han, D. (AB-07) . . . 6
Han, G. (EW-11) . . . 556
Han, H. (AT-08) . . . 83
Han, H. (AW-18) . . . 109
Han, H. (CC-03) . . . 244
Han, H. (CC-08) . . . 245
Han, H. (FT-14) . . . 647
Han, S. (CP-01) . . . 292
Han, S. (DU-10) . . . 432
Han, S. (EW-03) . . . 552

*Best student presentation award finalist

Han, T. (AU-04) . . . 86
Han, T. (BR-03) . . . 189
Han, T. (FU-05) . . . 651
Han, W. (DI-08) . . . 394
Han, X. (AD-09) . . . 19
Han, X. (BQ-01) . . . 179
Han, X. (BR-01) . . . 189
Han, X. (BV-15) . . . 223
Han, X. (DB-07) . . . 352
Han, X. (DB-08) . . . 353
Han, X. (DB-11) . . . 354
Han, X. (DE-03) . . . 369
Han, X. (EH-06) . . . 494
Han, X. (FU-01) . . . 649
Han, X. (FV-01) . . . 657
Han, Z. (DB-11) . . . 354
Hanashima, T. (AF-10) . . . 34
Handa, H. (FF-10) . . . 588
Handa, H. (FF-11) . . . 589
Haney, P. (AD-02) . . . 16
Haney, P. (AD-05) . . . 18
Haney, P. (DA-01) . . . 347
Haney, P. (EC-03) . . . 462
Haney, P. (FA-02) . . . 559
Hang, X. (CW-08) . . . 342
Hanke, J. (AB-07) . . . 6
Hankiewicz, J.H. (DG-06) . . . 381
Hankiewicz, J.H. (DG-11) . . . 384
Hankiewicz, J.H. (HH-07) . . . 813
Hansen, M. (CE-06) . . . 257
Hanstorp, D. (CC-11) . . . 247
Hao, J. (AQ-15) . . . 68
Hao, J. (DQ-05) . . . 406
Hao, J. (DQ-17) . . . 412
Hao, L. (EI-08) . . . 501
Hara, S. (CI-12) . . . 289
Hara, T. (CH-02) . . . 277
Hara, Y. (AV-01) . . . 92
Harada, Y. (DR-09) . . . 417
Haravifard, S. (DI-01) . . . 391
Hardy, F. (DI-09) . . . 394
Harris, V. (BR-04) . . . 190
Harris, V. (BR-05) . . . 190
Harris, V. (GG-11) . . . 707
Harrison, R. (BF-05) . . . 148
Harrison, R. (BF-06) . . . 148
Harumoto, T. (FT-04) . . . 642
Harumoto, T. (FT-05) . . . 643
Hasama, R. (CW-12) . . . 344
Hasanain, S. (DR-02) . . . 414
Hase, T.P. (BF-11) . . . 150
Hase, T.P. (BH-04) . . . 159
Hasegawa, A. (GH-02) . . . 708
Hasegawa, K. (AD-07) . . . 18
Hasegawa, T. (CW-01) . . . 340
Hashemi, P. (GC-07) . . . 681
Hashimoto, S. (HB-03) . . . 771
Haskel, D. (DH-09) . . . 389
Hassan, M. (AQ-06) . . . 64
Hassan, M. (AR-16) . . . 76
Hassan, N. (AB-01) . . . 4
Hassan, N. (BC-09) . . . 126
Hassan, N. (ET-15) . . . 532
Hassan, N. (HG-08) . . . 806
Hassan, O. (EG-03) . . . 486
Hastings, J.T. (BH-03) . . . 159
Hatakeyama, T. (CH-04) . . . 278
Hatakeyama, T. (GH-04) . . . 709
Hatano, M. (FF-09) . . . 588
Hatton, P.D. (BT-04) . . . 200
Hatton, P.D. (GF-01) . . . 697
Hattori, A. (CI-02) . . . 284
Hattori, A.N. (HF-05) . . . 797
Hattori, T. (FT-08) . . . 644
Haug, M. (CH-03) . . . 277
Haughey, K. (BV-07) . . . 220
Hauser, A.J. (AI-06) . . . 53
Havela, L. (BI-05) . . . 167
Hawai, T. (CI-05) . . . 286
Hawai, T. (EH-12) . . . 497
Hawecker, J. (FV-05) . . . 658
Hayakawa, J. (CV-14) . . . 337
Hayami, S. (FB-04) . . . 562
Hayasaka, J. (DV-02) . . . 435
Hayashi, K. (GV-02) . . . 760
Hayashi, M. (AE-02) . . . 24
Hayashi, M. (BC-12) . . . 128
Hayashi, M. (BE-06) . . . 142
Hayashi, M. (EB-08) . . . 458
Haydon, A. (DG-13) . . . 385
Haygood, I.W. (AV-16) . . . 99
Haygood, I.W. (EF-03) . . . 479
Haykal, A. (BG-10) . . . 156
Haykal, A. (ED-05) . . . 469
Haykal, A. (EE-02) . . . 473
Haykal, A. (GQ-01) . . . 734
He, G. (GV-11) . . . 765
He, G. (HI-10) . . . 823
He, J. (AQ-15) . . . 68
He, L. (DQ-05) . . . 406
He, P. (BC-03) . . . 123
He, P. (DB-04) . . . 351
He, P. (GB-08) . . . 674
He, Q. (GC-07) . . . 681
He, S. (CH-06) . . . 279
He, W. (BP-02) . . . 172
He, Y. (HI-02) . . . 818
Healy, J.M. (FD-13) . . . 578
Heczko, O. (AB-13) . . . 9
Heczko, O. (AQ-07) . . . 64
Heczko, O. (AQ-09) . . . 65
Hehn, M. (AW-09) . . . 105
Hehn, M. (DD-01) . . . 361
Hehn, M. (FE-06) . . . 580
Hehn, M. (FE-11) . . . 583
Hehn, M. (FG-11) . . . 595
Heid, R. (DI-09) . . . 394
Heidenreich, M. (BI-09) . . . 169
Heigl, M. (AW-04) . . . 102
Heindl, R. (BF-03) . . . 147
Heindl, R. (ET-14) . . . 532
Heinonen, O. (AE-01) . . . 24
Heinonen, O. (CB-01) . . . 236
Heinonen, O. (GB-08) . . . 674
Heinz, B. (BE-11) . . . 144
Heinz, B. (CE-08) . . . 258
Heinz, B. (GE-03) . . . 690
Heinze, D. (GF-13) . . . 702
Heithoff, M. (FB-01) . . . 561
Hejazi, A. (BF-01) . . . 146
Held, J. (FV-15) . . . 662
Held, K. (AG-09) . . . 41
Hellbruck, L. (ER-03) . . . 519
Hellman, F. (DD-08) . . . 365
Hellman, F. (DD-09) . . . 366
Hellman, F. (FF-03) . . . 585
Hellman, F. (GB-06) . . . 674
Hellman, F. (HC-09) . . . 778
Hellwig, O. (BD-01) . . . 131
Hellwig, O. (BH-01) . . . 158
Hellwig, O. (CG-07) . . . 272
Hellwig, O. (CG-13) . . . 275
Hellwig, O. (HG-05) . . . 805
Helm, C.A. (CF-12) . . . 268
Helm, M. (EE-10) . . . 476
Helm, M. (HF-11) . . . 800
Helms, B. (FF-03) . . . 585
Heming, R. (FV-13) . . . 661
Henderson, M. (GT-12) . . . 751
Hendriks, A. (AF-06) . . . 32
Henk, J. (AW-14) . . . 107
Henk, J. (GF-09) . . . 701
Hensley, D. (GA-03) . . . 669
Heremans, J.J. (AI-06) . . . 53
Herfort, J. (DB-10) . . . 354
Herklotz, A. (EE-07) . . . 475
Hermosa, G.C. (BW-07) . . . 227
Hermosa, G.C. (CQ-07) . . . 302
Hermosa, G.C. (DG-07) . . . 382
Hermosa, G.C. (FF-07) . . . 587
Hermosa, G.C. (FT-16) . . . 648
Hernàndez Ferras, J. (EQ-10) . . . 516
Hernandez-Maldonado, D. (BA-04) . . . 112
Hernandez, L.A. (AP-06) . . . 60
Heron, J. (AF-13) . . . 35
Herranz, G. (FU-12) . . . 653
Herrero-Albillos, J. (GP-08) . . . 728
Herrero-Albillos, J. (HE-04) . . . 791
Herrero-Albillos, J. (HE-06) . . . 792
Herzog, M. (BD-12) . . . 136
Hesjedal, T. (DE-03) . . . 369
Hesjedal, T. (FG-04) . . . 592
Hesjedal, T. (GF-07) . . . 700
Hester, J.R. (CI-05) . . . 286
Heyderman, L. (CG-04) . . . 271
Heyderman, L. (FP-04) . . . 617
Heyen, H. (ED-11) . . . 472
Heyns, M. (EP-16) . . . 510
Heyns, M. (HG-10) . . . 808
Hicken, R. (CB-10) . . . 240

*Best student presentation award finalist

Hicken, R. (CD-05) . . . 250
Hicken, R. (DT-14) . . . 427
Hicken, R. (GB-02) . . . 671
Hicken, T.J. (AW-11) . . . 106
Hickey, B. (BE-09) . . . 143
Hickey, B. (EC-12) . . . 466
Hickey, B. (GB-05) . . . 673
Hickey, B. (GP-05) . . . 726
Hickey, B. (GQ-06) . . . 736
Hierro-Rodriguez, A. (AF-09) . . . 33
Hierro-Rodriguez, A. (GP-08) . . . 728
Higashida, R. (GP-07) . . . 727
Hight Walker, A.R. (AB-01) . . . 4
Hight Walker, A.R. (DB-03) . . . 351
Hight Walker, A.R. (DB-13) . . . 355
Hight Walker, A.R. (GD-06) . . . 686
Hight Walker, A.R. (HE-12) . . . 794
Higo, T. (AB-15) . . . 10
Higo, T. (CF-01) . . . 262
Higo, Y. (EG-04) . . . 486
Hill, M.R. (DG-13) . . . 385
Hillebrands, B. (BD-09) . . . 135
Hillebrands, B. (BE-11) . . . 144
Hillebrands, B. (CE-07) . . . 257
Hillebrands, B. (CE-13) . . . 260
Hillebrands, B. (GE-02) . . . 689
Hiller, S. (EI-11) . . . 502
Hillion, A. (BD-12) . . . 136
Hindmarch, A. (CG-01) . . . 270
Hindmarch, A. (EC-12) . . . 466
Hindmarch, A. (FC-10) . . . 570
Hinkel, D. (EB-03) . . . 456
Hintzke, D. (HD-02) . . . 782
Hioki, K. (CI-02) . . . 284
Hirai, T. (AQ-02) . . . 62
Hirai, T. (BQ-05) . . . 181
Hiramatsu, B. (CQ-09) . . . 303
Hiramatsu, B. (DG-10) . . . 383
Hiramatsu, R. (CR-05) . . . 308
Hiraoka, Y. (DT-05) . . . 424
Hirata, Y. (CR-08) . . . 309
Hirata, Y. (DC-09) . . . 360
Hirohata, A. (AV-02) . . . 92
Hirohata, A. (BU-01) . . . 209
Hirohata, A. (BU-05) . . . 211
Hirohata, A. (BU-06) . . . 211
Hirohata, A. (CF-08) . . . 266
Hirohata, A. (CP-04) . . . 293
Hirohata, A. (CP-07) . . . 294
Hirosawa, S. (CI-03) . . . 285
Hirosawa, S. (CI-04) . . . 285
Hirosawa, S. (FH-03) . . . 600
Hirose, H. (AE-02) . . . 24
Hirotoshi, F. (DW-18) . . . 450
Hjörvarsson, B. (BF-11) . . . 150
Hjörvarsson, B. (BH-04) . . . 159
Hjörvarsson, B. (BH-10) . . . 162
Hlawacek, G. (BH-01) . . . 158
Ho, S. (BW-01) . . . 225
Ho, S. (EU-04) . . . 536
Ho, S. (EU-10) . . . 539
Hoang-Ngoc, M. (FI-02) . . . 607
Hoang-Ngoc, M. (FI-06) . . . 609
Hoffmann, A. (AB-09) . . . 7
Hoffmann, A. (AF-06) . . . 32
Hoffmann, A. (BT-02) . . . 199
Hoffmann, A. (CB-01) . . . 236
Hoffmann, A. (DC-05) . . . 358
Hoffmann, A. (DC-06) . . . 359
Hoffmann, A. (EC-10) . . . 465
Hoffmann, A. (ER-02) . . . 518
Hoffmann, A. (EW-04) . . . 553
Hoffmann, A. (EW-09) . . . 555
Hoffmann, A. (FA-02) . . . 559
Hoffmann, A. (FB-11) . . . 565
Hoffmann, A. (FV-07) . . . 659
Hoffmann, A. (HF-09) . . . 799
Hoffmann, M. (CC-02) . . . 243
Hoffmann, M. (EB-07) . . . 457
Hofherr, M. (ER-03) . . . 519
Hofhuis, K. (BH-05) . . . 160
Hojem, A. (BE-01) . . . 140
Holanda, J. (ER-02) . . . 518
Holanda, J. (EW-04) . . . 553
Holanda, J. (FA-05) . . . 560
Holanda, J. (FV-07) . . . 659
Holcomb, M. (CR-15) . . . 313
Holladay, J. (FQ-18) . . . 630
Holland, R. (CE-04) . . . 256
Holmes, W. (GV-12) . . . 765
Holt, M. (BA-05) . . . 113
Holt, S.J. (AW-17) . . . 109
Holt, S.J. (GF-05) . . . 699
Holtz, M. (GG-05) . . . 704
Holtz, M. (HC-06) . . . 777
Holzinger, D. (AH-10) . . . 47
Hommel, D. (BQ-17) . . . 187
Honda, M. (FW-03) . . . 664
Hong, D. (CB-13) . . . 242
Hong, I. (AW-06) . . . 104
Hong, I. (CC-08) . . . 245
Hong, J. (CC-03) . . . 244
Hong, J. (CC-08) . . . 245
Hong, J. (CF-03) . . . 263
Hong, J. (CV-15) . . . 338
Hong, J. (FW-08) . . . 666
Hong, J. (GF-10) . . . 701
Hong, J. (GP-01) . . . 724
Hong, J. (HF-15) . . . 802
Hong, S.C. (BT-18) . . . 207
Hong, Y. (CH-10) . . . 281
Hong, Y. (EH-06) . . . 494
Hong, Y. (ET-17) . . . 534
Hong, Y. (FR-02) . . . 632
Hong, Y. (GI-09) . . . 720
Hongo, Y. (GU-08) . . . 757
Honjo, H. (FC-07) . . . 569
Hono, K. (BP-08) . . . 174
Hono, K. (CF-07) . . . 265
Hono, K. (CI-02) . . . 284
Hono, K. (FH-03) . . . 600
Hono, K. (HD-10) . . . 787
Hono, K. (HD-12) . . . 787
Hono, K. (HF-06) . . . 798
Hontecillas, I. (FD-08) . . . 575
Hopkins, P. (EF-03) . . . 479
Hori, Y. (GP-12) . . . 730
Horie, A. (AV-14) . . . 98
Horiike, S. (AF-10) . . . 34
Horino, K. (GH-02) . . . 708
Horio, Y. (DF-05) . . . 376
Horita, T. (AR-04) . . . 71
Horng, L. (BV-14) . . . 223
Horng, L. (GQ-05) . . . 736
Horvath, A. (DW-03) . . . 443
Hosomi, M. (EG-04) . . . 486
Hosono, M. (GH-02) . . . 708
Hossein, S. (CI-02) . . . 284
Hossein, S. (FH-03) . . . 600
Hossein, S. (HD-10) . . . 787
Hossein, S. (HD-12) . . . 787
Hosseinnia, M. (AQ-18) . . . 69
Hou, D. (EC-07) . . . 464
Hou, D. (GB-02) . . . 671
Hou, J.T. (BD-13) . . . 137
Hou, J.T. (FA-03) . . . 559
Hou, Y. (CV-06) . . . 335
Hou, Y. (HF-13) . . . 801
Hou, Z. (DR-08) . . . 416
Houshmand Sharifi, S. (EG-11) . . . 490
Houssameddine, d. (GC-07) . . . 681
Houzet, M. (GQ-01) . . . 734
Hrabec, A. (CG-04) . . . 271
Hrkac, G. (AR-08) . . . 73
Hrncir, T. (EW-14) . . . 557
Hsiao, C. (CW-10) . . . 343
Hsiao, Y. (HE-07) . . . 792
Hsieh, C. (CG-09) . . . 273
Hsu, C. (GC-10) . . . 682
Hsu, K.W. (CH-09) . . . 281
Hsu, T. (BT-11) . . . 203
Hsu, T. (FT-02) . . . 641
Hu, C. (GT-09) . . . 750
Hu, F. (AH-03) . . . 45
Hu, F. (AQ-15) . . . 68
Hu, F. (BT-08) . . . 202
Hu, F. (DQ-05) . . . 406
Hu, F. (DQ-15) . . . 410
Hu, F. (DQ-17) . . . 412
Hu, F. (DT-13) . . . 426
Hu, F. (FQ-14) . . . 629
Hu, G. (GC-07) . . . 681
Hu, J. (DW-09) . . . 446
Hu, J. (GI-07) . . . 719
Hu, K. (EW-12) . . . 557
Hu, S. (BI-07) . . . 168
Hu, S. (CD-09) . . . 252
Hu, S. (CP-08) . . . 294
Hu, S. (HB-04) . . . 771
Hu, W. (BH-03) . . . 159

*Best student presentation award finalist

Hu, X. (HG-08) . . . 806
Hu, Z. (DV-12) . . . 440
Huaman, N.R. (AT-01) . . . 80
Huang, C. (DU-13) . . . 433
Huang, D. (BD-02) . . . 131
Huang, D. (CH-06) . . . 279
Huang, D. (HI-12) . . . 824
Huang, H. (BT-10) . . . 203
Huang, L. (CV-15) . . . 338
Huang, M. (EG-06) . . . 488
Huang, S. (AD-06) . . . 18
Huang, S. (BE-04) . . . 141
Huang, S. (BE-05) . . . 142
Huang, T. (FP-04) . . . 617
Huang, W. (DV-01) . . . 435
Huang, W. (DV-03) . . . 436
Huang, Y. (AH-02) . . . 44
Huang, Y. (BB-02) . . . 114
Huang, Y. (BH-05) . . . 160
Huang, Y. (BR-03) . . . 189
Huang, Y. (BW-13) . . . 230
Huang, Y. (FV-12) . . . 661
Huang, Z. (GP-06) . . . 727
Hübner, R. (HF-11) . . . 800
Hudait, M. (AI-02) . . . 51
Huddart, B. (AW-11) . . . 106
Huebl, H. (GB-10) . . . 675
Huebner, T. (BU-12) . . . 214
Huebner, T. (ET-02) . . . 526
Hughes, B. (BC-01) . . . 122
Hughes, B. (HB-05) . . . 772
Huh, Y. (CW-17) . . . 346
Huh, Y. (DQ-12) . . . 409
Huhnstock, R. (AH-10) . . . 47
Hula, T. (CC-04) . . . 244
Hultman, L. (BI-04) . . . 167
Humbert, V. (EB-09) . . . 458
Hung, C. (CF-03) . . . 263
Hung, C. (DQ-04) . . . 406
Hunt, C.S. (DQ-03) . . . 405
Hunt, M. (BF-01) . . . 146
Hurdequint, H. (GE-13) . . . 694
Husain, S. (CR-12) . . . 311
Huth, M. (BF-02) . . . 146
Huth, M. (CE-07) . . . 257
Huth, M. (EW-15) . . . 557
Hütten, A. (FQ-03) . . . 624
Huxtable, A. (DE-05) . . . 369
Huxtable, A. (ED-01) . . . 467
Hwang, C. (EW-01) . . . 552
Hwang, C. (GB-02) . . . 671
Hwang, C. (GF-10) . . . 701
Hwang, C. (GP-11) . . . 729
Hwang, C. (HF-14) . . . 802
Hwang, E. (HI-03) . . . 819
Hwang, H. (FR-08) . . . 635
Hwang, J. (BB-03) . . . 115
Hwang, J. (BB-04) . . . 116
Hwang, J. (FB-02) . . . 561
Hwang, J. (FG-12) . . . 596
Hwang, K. (AA-01) . . . 2
Hwang, S. (EW-03) . . . 552
Hwang, S. (FR-08) . . . 635
Hwang, S. (GP-18) . . . 733
Hwang, S. (GV-01) . . . 760
Hyun, J. (GT-01) . . . 748

- I -

Ibarra, M. (BE-08) . . . 143
Ibe, T. (EB-02) . . . 455
Ibrahim, F. (GG-10) . . . 706
Ichimura, M. (CV-14) . . . 337
Ichinose, T. (BU-01) . . . 209
Ichinose, T. (BU-05) . . . 211
Ichinose, T. (BU-06) . . . 211
Ichinose, T. (CP-07) . . . 294
Igarashi, J. (DD-01) . . . 361
Igarashi, R. (FF-09) . . . 588
Ignatyeva, D. (HD-03) . . . 783
Iguchi, R. (AP-01) . . . 58
Iida, Y. (BU-10) . . . 213
Iida, Y. (FG-15) . . . 597
Iihama, S. (AI-13) . . . 56
Iihama, S. (DD-01) . . . 361
Iihama, S. (ER-06) . . . 520
Iimori, T. (FT-08) . . . 644
Ikebuchi, T. (CP-13) . . . 296
Ikebuchi, T. (CP-14) . . . 297
Ikebuchi, T. (CR-08) . . . 309
Ikeda, K. (HF-10) . . . 800
Ikeda, S. (AI-10) . . . 55
Ikeda, S. (CR-01) . . . 306
Ikeda, S. (EC-11) . . . 465
Ikeda, S. (FC-07) . . . 569
Ikeda, T. (CP-16) . . . 298
Ilse, S.E. (CU-02) . . . 324
Ilse, S.E. (GQ-03) . . . 735
Im, M. (CC-03) . . . 244
Im, M. (CC-08) . . . 245
Im, M. (DE-08) . . . 371
Im, M. (FT-14) . . . 647
Imai, K. (FF-10) . . . 588
Imai, Y. (BV-12) . . . 222
Imam, H. (DQ-02) . . . 405
Imam, H. (DQ-09) . . . 408
Imamura, H. (BQ-16) . . . 187
Imamura, H. (DF-06) . . . 377
Imamura, H. (EG-01) . . . 485
Imamura, H. (EG-04) . . . 486
Imamura, H. (EG-05) . . . 487
Imamura, H. (EG-08) . . . 489
Imaoka, N. (HH-10) . . . 815
Ina, T. (AQ-02) . . . 62
Incorvia, J.C. (ET-15) . . . 532
Incorvia, J.C. (HG-08) . . . 806
Indla, S. (AR-15) . . . 76
Inoue, K. (BP-13) . . . 177
Inoue, M. (CP-04) . . . 293
Inoue, M. (HB-07) . . . 773
Instan, A. (FU-11) . . . 652
Instan, A. (FU-13) . . . 653
Inyang, O.A. (CG-12) . . . 274
Inyang, O.A. (EC-12) . . . 466
Ionescu, A. (FV-04) . . . 658
Ionin, A. (BA-05) . . . 113
Ipatov, M. (AQ-13) . . . 67
Ipatov, M. (GH-07) . . . 711
Ipatov, M. (GH-15) . . . 715
Ipatov, M. (GI-03) . . . 717
Iramina, K. (CQ-01) . . . 300
Isaeva, A. (GD-01) . . . 685
Isarain Chávez, E. (AH-11) . . . 48
Isberg, J. (AS-02) . . . 78
Isberg, J. (BS-02) . . . 197
Isberg, J. (CS-02) . . . 315
Isberg, J. (DS-02) . . . 421
Isberg, J. (ES-02) . . . 524
Isberg, J. (FS-02) . . . 639
Isberg, J. (GS-02) . . . 746
Isella, G. (AE-08) . . . 26
Ishibashi, M. (GE-14) . . . 695
Ishida, L. (FE-05) . . . 580
Ishida, Y. (DC-02) . . . 357
Ishigami, K. (BP-09) . . . 175
Ishihara, R. (FW-04) . . . 664
Ishihara, T. (FG-06) . . . 593
Ishii, F. (CV-08) . . . 335
Ishii, N. (GP-12) . . . 730
Ishii, T. (CC-09) . . . 246
Ishikawa, K. (GU-01) . . . 754
Ishikawa, K. (GU-02) . . . 754
Ishikawa, S. (FU-09) . . . 652
Ishizuka, H. (EB-02) . . . 455
Isnard, O. (GT-13) . . . 752
Isogami, S. (BC-12) . . . 128
Isogami, S. (GP-17) . . . 733
Issac, F. (AF-04) . . . 31
Itagaki, R. (GR-08) . . . 745
Ito, D. (AE-10) . . . 27
Ito, D. (AP-02) . . . 58
Ito, D. (AP-04) . . . 60
Ito, H. (CG-10) . . . 274
Ito, K. (CG-06) . . . 272
Ito, K. (CW-14) . . . 345
Ito, M. (AR-08) . . . 73
Ito, M. (CA-03) . . . 233
Ito, T. (AV-17) . . . 99
Ito, T. (GT-04) . . . 749
Itoh, K. (TU-02) . . . 1
Iturriaga, H. (BT-07) . . . 201
Iturriaga, H. (CT-07) . . . 320
Iurchuk, V. (AC-01) . . . 11
Iurchuk, V. (EP-08) . . . 506
Ivanov, A.A. (FH-01) . . . 599
Ivanov, B.A. (AD-04) . . . 17
Ivanov, B.A. (CB-11) . . . 241
Iwahashi, M. (CQ-01) . . . 300
Iwaki, H. (CP-13) . . . 296
Iwaki, H. (CP-14) . . . 297
Iwasaka, M. (BW-09) . . . 228
Iwasaka, M. (BW-11) . . . 229

*Best student presentation award finalist

Iwasaki, T. (FF-09) . . . 588
Iwashita, K. (AE-09) . . . 27
Iwata, S. (CW-02) . . . 340
Iwata, S. (EP-14) . . . 509
Iwata, S. (GR-02) . . . 742

- J -

J. Quigley, L. (CC-07) . . . 245
Jackson, C. (HE-02) . . . 790
Jacob, A. (BI-09) . . . 169
Jacques, V. (BG-10) . . . 156
Jacques, V. (ED-05) . . . 469
Jacques, V. (EE-02) . . . 473
Jacques, V. (EE-06) . . . 475
Jacques, V. (GQ-01) . . . 734
Jafarpisheh, S. (EB-11) . . . 459
Jaffres, H. (FV-05) . . . 658
Jaffri, G. (DR-02) . . . 414
Jaiswal, A. (BT-01) . . . 199
Jaiswal, S. (GF-13) . . . 702
Jakob, G. (AG-05) . . . 39
Jakob, G. (GF-13) . . . 702
Jakobs, F. (GF-13) . . . 702
Jal, E. (DD-02) . . . 361
Jalali, M. (CR-16) . . . 314
Jalil, M.B. (AV-11) . . . 97
Jalil, M.B. (DP-15) . . . 402
Jamali, M. (FW-09) . . . 667
Jamer, M.E. (GG-02) . . . 703
James, R. (HF-07) . . . 798
Jamet, M. (AE-08) . . . 26
Jamet, M. (DP-07) . . . 398
Jamet, M. (DP-14) . . . 401
Jamet, M. (EB-01) . . . 455
Jamil, M. (DR-02) . . . 414
Jana, S. (AP-05) . . . 60
Jana, S. (BD-06) . . . 134
Jana, S. (DI-10) . . . 394
Jander, A. (CE-05) . . . 256
Jander, A. (CE-06) . . . 257
Jander, A. (CU-07) . . . 327
Jandl, S. (FQ-19) . . . 630
Jang, G. (DU-05) . . . 430
Jang, G. (DU-14) . . . 434
Jang, G. (DU-15) . . . 434
Jang, G. (EV-04) . . . 543
Jang, G. (EV-05) . . . 543
Jang, G. (EV-08) . . . 545
Jang, G. (FP-08) . . . 618
Jang, G. (FR-01) . . . 632
Jang, G. (FR-04) . . . 633
Jang, W. (CT-02) . . . 317
Jang, Y. (CP-17) . . . 298
Jangid, R. (DD-02) . . . 361
Jangid, R. (HH-11) . . . 815
Janotova, I. (GH-12) . . . 714
Jansa, N. (FE-02) . . . 579
Jansen, R. (EF-08) . . . 481
Jansen, R. (EF-09) . . . 482
Janssen, M.H. (CC-12) . . . 247
Janssen, T. (DD-04) . . . 362
Janus, W. (CP-05) . . . 293
Janus, W. (FG-07) . . . 593
Janus, W. (FG-10) . . . 595
Jaouen, N. (AF-07) . . . 32
Jaouen, N. (DD-02) . . . 361
Jaouen, N. (EE-02) . . . 473
Jaouen, N. (EE-06) . . . 475
Jara, A. (BR-06) . . . 191
Jara, A. (DI-05) . . . 392
Jaris, M. (BD-14) . . . 138
Jayakumar, K. (HE-05) . . . 791
Jayaraman, T.V. (AR-15) . . . 76
Jayaraman, T.V. (BI-10) . . . 169
Je, S. (CC-08) . . . 245
Je, S. (FW-08) . . . 666
Jeffries, J.R. (BA-04) . . . 112
Jeffries, J.R. (DB-12) . . . 354
Jelezko, F. (FF-09) . . . 588
Jen, S.U. (AQ-01) . . . 62
Jena, D. (AC-04) . . . 12
Jena, D. (AH-01) . . . 44
Jena, D. (AH-05) . . . 45
Jena, D. (FG-13) . . . 597
Jenichen, B. (DB-10) . . . 354
Jenkins, A. (AC-01) . . . 11
Jenkins, S. (AB-11) . . . 8
Jenkins, S. (ET-06) . . . 528
Jenkins, S. (FG-01) . . . 591
Jensen, B.A. (DQ-13) . . . 409
Jensen, C.J. (AH-09) . . . 47
Jensen, C.J. (BA-04) . . . 112
Jeon, J. (HF-15) . . . 802
Jeon, K. (AE-06) . . . 26
Jeon, S. (FP-06) . . . 618
Jeon, S. (FT-01) . . . 641
Jeong, G. (CH-12) . . . 282
Jeong, G. (FR-10) . . . 636
Jeong, J. (DH-07) . . . 388
Jeong, J. (EP-03) . . . 504
Jeong, W. (AD-12) . . . 21
Jeong, W. (BV-08) . . . 220
Jha, G. (AH-06) . . . 46
Jha, N. (CF-12) . . . 268
Ji, B. (AW-02) . . . 101
Ji, S. (AV-05) . . . 94
Ji, T. (ET-05) . . . 528
Ji, w. (FP-12) . . . 620
Ji, Y. (FC-11) . . . 571
Ji, Y. (GP-01) . . . 724
Jia, K. (GB-12) . . . 676
Jia, M. (AV-15) . . . 98
Jia, M. (BB-10) . . . 118
Jia, P. (AQ-14) . . . 68
Jia, P. (CT-06) . . . 319
Jia, P. (FQ-13) . . . 628
Jia, Y. (AU-02) . . . 85
Jia, Y. (EE-03) . . . 473
Jiang-Wei, L. (HG-08) . . . 806
Jiang, B. (EW-11) . . . 556
Jiang, J. (CB-01) . . . 236
Jiang, L. (EP-07) . . . 506
Jiang, L. (FU-01) . . . 649
Jiang, L. (HH-12) . . . 816
Jiang, M. (BC-08) . . . 126
Jiang, P. (CG-09) . . . 273
Jiang, X. (AR-11) . . . 74
Jiang, Y. (BC-01) . . . 122
Jiang, Y. (BQ-03) . . . 180
Jiang, Y. (BQ-09) . . . 183
Jiang, Y. (BQ-11) . . . 184
Jiang, Y. (BQ-13) . . . 185
Jiang, Y. (CD-02) . . . 249
Jiang, Y. (DP-20) . . . 404
Jiang, Y. (DU-03) . . . 429
Jiang, Y. (EP-06) . . . 505
Jiang, Y. (EP-07) . . . 506
Jiang, Y. (EP-09) . . . 506
Jiang, Y. (FF-03) . . . 585
Jiang, Y. (GP-15) . . . 732
Jiang, Y. (HB-08) . . . 773
Jiang, Y. (HH-12) . . . 816
Jiang, Z. (AI-06) . . . 53
Jiao, J. (BF-10) . . . 150
Jibiki, Y. (BQ-02) . . . 179
Jie, Y. (GU-04) . . . 755
Jiles, D.C. (AQ-04) . . . 63
Jiles, D.C. (CQ-12) . . . 304
Jiles, D.C. (DT-08) . . . 425
Jiles, D.C. (DU-04) . . . 429
Jiménez-Cavero, P. (BE-08) . . . 143
Jin, C. (AA-02) . . . 2
Jin, C. (HF-10) . . . 800
Jin, L. (FP-14) . . . 621
Jin, L. (GB-12) . . . 676
Jin, T. (EF-02) . . . 478
Jin, T. (GP-13) . . . 730
Jin, X. (AE-09) . . . 27
Jin, X. (FD-10) . . . 577
Jin, Y. (FQ-02) . . . 623
Jin, Z. (DV-13) . . . 441
Jindal, S. (AU-13) . . . 90
Jinno, K. (CQ-09) . . . 303
Jinno, K. (DG-10) . . . 383
Jo, I. (EV-13) . . . 547
Jo, I. (FR-10) . . . 636
Jo, S. (EG-07) . . . 488
Johansson, A. (DP-08) . . . 399
John, R. (HD-02) . . . 782
Johnsen, P.C. (DT-02) . . . 423
Johnson, A.T. (DP-02) . . . 396
Johnson, F. (AB-13) . . . 9
Johnson, F. (CP-09) . . . 295
Johnson, M.B. (FU-16) . . . 654
Johnson, S. (HE-02) . . . 790
Jones, N.J. (BI-02) . . . 166
Jones, N.J. (FD-11) . . . 577
Jones, N.J. (FD-13) . . . 578
Jonker, B. (DP-05) . . . 397
Jonker, B. (FV-06) . . . 659
Joo, S. (FW-06) . . . 665

*Best student presentation award finalist

Joo, S. (HF-15) . . . 802
Jotta Garcia, M. (EQ-05) . . . 513
Jouffret, L. (BI-04) . . . 167
Joumard, I. (BC-13) . . . 129
Joumard, I. (GQ-01) . . . 734
Jozwiak, C. (FB-02) . . . 561
Ju, B. (AD-12) . . . 21
Jué, E. (EP-12) . . . 508
Juge, R. (ED-04) . . . 469
Jung, B. (CT-14) . . . 322
Jung, D. (AW-18) . . . 109
Jung, D. (FW-08) . . . 666
Jung, E. (DU-05) . . . 430
Jung, E. (DU-14) . . . 434
Jung, E. (DU-15) . . . 434
Jung, M. (AB-07) . . . 6
Jung, M. (CC-03) . . . 244
Jung, M. (CP-17) . . . 298
Jung, M. (DR-14) . . . 419
Jungfleisch, M. (EW-04) . . . 553
Junk, Y.L. (ED-11) . . . 472
Jurga, S. (DG-06) . . . 381
Jurica, J. (BP-11) . . . 176

- K -

Kabeya, N. (AE-09) . . . 27
Kaczorowski, D. (GT-11) . . . 751
Kado, M. (HB-03) . . . 771
Kagawa, F. (GF-01) . . . 697
Kahmei, R. (GI-02) . . . 716
Kahmei, R. (HH-08) . . . 813
Kai, T. (FG-06) . . . 593
Kaji, J. (DW-08) . . . 445
Kaji, J. (DW-16) . . . 449
Kaji, J. (DW-18) . . . 450
Kajiwara, K. (BP-09) . . . 175
Kakay, A. (CC-04) . . . 244
Kakay, A. (CD-03) . . . 250
Kakazei, G.N. (BD-09) . . . 135
Kakazei, G.N. (CE-13) . . . 260
Kakazei, G.N. (EW-15) . . . 557
Kakazei, G.N. (HH-02) . . . 810
Kalappattil, V. (AU-06) . . . 87
Kalappattil, V. (BE-13) . . . 145
Kalappattil, V. (CV-05) . . . 334
Kalappattil, V. (DP-19) . . . 404
Kalappattil, V. (GG-04) . . . 704
Kalinikos, B.A. (CE-13) . . . 260
Kally, J. (CB-01) . . . 236
Kalpana, P. (HE-05) . . . 791
Kamada, T. (GR-05) . . . 743
Kamantsev, A. (DQ-18) . . . 412
Kambayashi, M. (AR-03) . . . 71
Kambe, S. (AV-10) . . . 96
Kamil, E. (DD-02) . . . 361
Kamimaki, A. (AI-13) . . . 56
Kaminskaya, T.P. (BP-15) . . . 178
Kammerbauer, F. (AW-09) . . . 105
Kan, D. (AV-06) . . . 94
Kan, D. (DH-05) . . . 387
Kanai, S. (EG-02) . . . 485
Kanai, Y. (GI-10) . . . 720
Kanai, Y. (GR-04) . . . 743
Kanai, Y. (GR-08) . . . 745
Kanak, J. (AD-11) . . . 20
Kanaki, T. (CC-09) . . . 246
Kanamori, Y. (FH-07) . . . 602
Kane, A.M. (BA-05) . . . 113
Kane, A.M. (GG-01) . . . 703
Kaneko, M. (FF-10) . . . 588
Kaneko, M. (FF-11) . . . 589
Kaneko, Y. (BP-08) . . . 174
Kanetaka, H. (CQ-08) . . . 303
Kang, D. (BV-08) . . . 220
Kang, J. (HF-14) . . . 802
Kang, M. (CW-04) . . . 341
Kang, M. (CW-07) . . . 342
Kang, M. (FT-14) . . . 647
Kang, S. (EW-11) . . . 556
Kang, S. (FG-03) . . . 592
Kang, W. (ED-09) . . . 471
Kang, W. (EP-15) . . . 509
Kanikrishnan, S. (FV-09) . . . 660
Kannan, H. (BV-07) . . . 220
Kanoun, M.B. (DP-01) . . . 396
Kantartzis, N. (GI-10) . . . 720
Kao, C. (BT-11) . . . 203
Kao, I. (AW-01) . . . 101
Kao, S. (CQ-02) . . . 300
Kapaklis, V. (BF-11) . . . 150
Kapaklis, V. (BH-04) . . . 159
Kapaklis, V. (BH-10) . . . 162
Kapralov, P. (HD-03) . . . 783
Kapteyn, H. (DT-02) . . . 423
Kapteyn, H. (ER-03) . . . 519
Kar, G.S. (BC-05) . . . 124
Kar, G.S. (EG-09) . . . 489
Kar, G.S. (EG-11) . . . 490
Kar, G.S. (EP-13) . . . 508
Kar, G.S. (FC-04) . . . 567
Kar, G.S. (GC-02) . . . 679
Kar, G.S. (GC-08) . . . 681
Kar, G.S. (HG-11) . . . 809
Karaba, C.T. (BT-06) . . . 201
Karaba, C.T. (FU-17) . . . 654
Karakas, V. (FV-07) . . . 659
Kardasz, B. (GC-01) . . . 678
Kardasz, B. (GC-12) . . . 683
Karel, J. (GB-06) . . . 674
Karel, J. (GH-03) . . . 709
Karimeddiny, S. (DA-05) . . . 348
Karis, O. (AP-05) . . . 60
Karis, O. (BD-06) . . . 134
Karis, O. (DI-10) . . . 394
Karis, O. (ER-04) . . . 519
Karki, U. (BI-11) . . . 169
Karl, R. (DT-02) . . . 423
Karonovich, A. (BI-08) . . . 168
Karpiak, B. (DR-13) . . . 419
Karpoormath, R. (HH-06) . . . 812
Karsch, J. (BG-11) . . . 156
Karube, S. (AD-13) . . . 22
Karwacki, L. (AD-11) . . . 20
Kasahara, Y. (AV-06) . . . 94
Kasai, S. (GF-11) . . . 702
Kasai, S. (HD-12) . . . 787
kataja, m. (FU-12) . . . 653
Katine, J. (AI-01) . . . 50
Katine, J. (CD-05) . . . 250
Katine, J. (FC-01) . . . 566
Katine, J. (GC-06) . . . 680
Katiyar, R. (FU-11) . . . 652
Katiyar, R. (FU-13) . . . 653
Katiyar, R. (FU-14) . . . 653
Katiyar, R. (HC-08) . . . 778
Katiyar, R.S. (HC-07) . . . 778
Kato, A. (AR-08) . . . 73
Kato, A. (BP-08) . . . 174
Kato, A. (CA-03) . . . 233
Kato, A. (GH-03) . . . 709
Kato, A. (GH-08) . . . 712
Kato, T. (CW-02) . . . 340
Kato, T. (EP-14) . . . 509
Kato, T. (GR-02) . . . 742
Kato, Y. (AC-06) . . . 13
Kato, Y. (GT-04) . . . 749
Kaur, D. (HC-11) . . . 779
Kaur, H. (BQ-12) . . . 185
Kaushik, D. (DF-04) . . . 376
Kawabe, Y. (AQ-08) . . . 65
Kawada, T. (BE-06)* . . . 142
Kawaguchi, M. (AE-02) . . . 24
Kawaguchi, M. (BE-06) . . . 142
Kawakami, R. (AA-04) . . . 3
Kawakami, R. (DB-12) . . . 354
Kawakami, R. (DE-02) . . . 368
Kawakami, R. (FB-02) . . . 561
Kawakami, R. (GF-02) . . . 697
Kawakami, Y. (HH-10) . . . 815
Kay, A. (CB-04) . . . 237
Kazachkova, N. (DR-15) . . . 420
Kazakov, A. (EB-13) . . . 460
Kazakova, O. (DE-01) . . . 368
Kazakova, O. (DE-05) . . . 369
KC, S. (BI-11) . . . 169
KC, S. (BR-09) . . . 192
Ke, L. (DB-06) . . . 352
Ke, L. (DP-13) . . . 401
Ke, L. (EI-02) . . . 498
Keatley, P.S. (CD-05) . . . 250
Keavney, D. (EE-07) . . . 475
Keavney, D. (GQ-07) . . . 737
Kehayias, P. (BG-05) . . . 153
Kehayias, P. (DT-01) . . . 423
Keil, N. (GF-13) . . . 702
Keller, L. (BF-02) . . . 146
Kempka, M. (DG-06) . . . 381
Kenawy, A. (AH-04) . . . 45
Kennan, K.E. (DG-03) . . . 380
Kent, A.D. (AG-06) . . . 39
Kent, A.D. (BB-08) . . . 117

*Best student presentation award finalist

Kent, A.D. (BT-03) . . . 199
Kent, A.D. (CB-02) . . . 237
Kent, A.D. (EQ-10) . . . 516
Kent, A.D. (EW-05) . . . 554
Kent, A.D. (GC-01) . . . 678
Kent, A.D. (GC-12) . . . 683
Kent, N. (FF-03) . . . 585
Kerber, N. (AW-09) . . . 105
Kerber, N. (DD-02) . . . 361
Keswani, N. (BH-08) . . . 161
Kettlewell, B. (GA-03) . . . 669
Kewenig, M. (CE-08) . . . 258
Khaire, T. (FA-02) . . . 559
Khalifa, A. (AH-06) . . . 46
Khalili Amiri, P. (AB-03) . . . 5
Khalili Amiri, P. (BB-14) . . . 120
Khalyavin, D. (BT-04) . . . 200
Khan, A. (CA-05) . . . 234
Khan, A. (CE-01) . . . 254
Khan, K. (AW-03) . . . 102
Khan, M. (FQ-10) . . . 627
Khan, M. (GG-07) . . . 705
Khan, M. (GQ-02) . . . 734
Khan, R.A. (GQ-06) . . . 736
Khanal, S. (ER-07) . . . 520
Khanna, M. (GI-04) . . . 717
Kharel, P.R. (CW-17) . . . 346
Kharel, P.R. (DQ-12) . . . 409
Khim, S. (EI-07) . . . 500
Khodadadi, B. (AI-06) . . . 53
Khodadadi, B. (GB-01) . . . 671
Khodadadi, M. (CQ-04) . . . 301
Khojah, R. (BT-14) . . . 205
Khojah, R. (DG-02) . . . 379
Khoo, K. (ED-02) . . . 467
Khurana, B. (DA-03) . . . 348
Khvalkovskiy, A. (FC-02) . . . 566
Khymyn, R. (AD-04) . . . 17
Khymyn, R. (CB-11) . . . 241
Khymyn, R. (CC-11) . . . 247
Khymyn, R. (EG-02) . . . 485
Kiarie, W.M. (AQ-04) . . . 63
Kida, N. (CC-09) . . . 246
Kiechle, M. (GE-04) . . . 690
Kiechle, M. (GE-06) . . . 691
Kiechle, M. (GP-02) . . . 724
Kikuchi, H. (GV-04) . . . 761
Kikuchi, N. (BP-08) . . . 174
Kikuchi, N. (CI-02) . . . 284
Kikuchi, N. (CU-04) . . . 326
Kikuchi, Y. (GR-01) . . . 742
Kim, B. (AR-14) . . . 76
Kim, B. (BD-11) . . . 136
Kim, B. (BP-07) . . . 174
Kim, B. (BP-10) . . . 175
Kim, B. (CR-09) . . . 310
Kim, C. (AR-14) . . . 76
Kim, C. (AV-18) . . . 100
Kim, C. (BR-10) . . . 193
Kim, C. (CP-17) . . . 298
Kim, C. (DR-14) . . . 419
Kim, C. (EV-03) . . . 542
Kim, C. (EV-05) . . . 543
Kim, C. (EV-06) . . . 544
Kim, C. (EV-07) . . . 544
Kim, C. (EV-09) . . . 546
Kim, C. (FR-04) . . . 633
Kim, C. (FR-08) . . . 635
Kim, C. (FR-11) . . . 637
Kim, C. (GF-10) . . . 701
Kim, C. (GP-11) . . . 729
Kim, C. (GT-03) . . . 748
Kim, D. (BP-06) . . . 174
Kim, D. (CI-01) . . . 284
Kim, D. (CR-08) . . . 309
Kim, D. (CR-11) . . . 311
Kim, D. (CT-16) . . . 323
Kim, D. (CV-15) . . . 338
Kim, D. (DC-09) . . . 360
Kim, D. (FR-07) . . . 635
Kim, D. (FW-06) . . . 665
Kim, D. (GF-10) . . . 701
Kim, G. (CU-11) . . . 330
Kim, G. (EC-08) . . . 464
Kim, H. (CV-15) . . . 338
Kim, H. (DR-07) . . . 416
Kim, H. (FW-08) . . . 666
Kim, H. (GD-09) . . . 687
Kim, J. (AR-10) . . . 74
Kim, J. (AR-12) . . . 75
Kim, J. (AV-18) . . . 100
Kim, J. (BR-10) . . . 193
Kim, J. (CC-01) . . . 243
Kim, J. (CG-05) . . . 272
Kim, J. (CI-01) . . . 284
Kim, J. (CW-04) . . . 341
Kim, J. (CW-07) . . . 342
Kim, J. (CW-09) . . . 343
Kim, J. (DR-07) . . . 416
Kim, J. (DU-05) . . . 430
Kim, J. (DU-14) . . . 434
Kim, J. (DU-15) . . . 434
Kim, J. (ED-10) . . . 471
Kim, J. (EF-06) . . . 480
Kim, J. (EH-02) . . . 492
Kim, J. (EP-03) . . . 504
Kim, J. (EU-06) . . . 538
Kim, J. (FH-09) . . . 603
Kim, J. (FT-01) . . . 641
Kim, J. (FU-15) . . . 653
Kim, J. (FW-06) . . . 665
Kim, J. (GC-07) . . . 681
Kim, J. (HF-14) . . . 802
Kim, J. (HG-11) . . . 809
Kim, K. (AB-07) . . . 6
Kim, K. (CR-08) . . . 309
Kim, K. (CT-02) . . . 317
Kim, K. (CT-14) . . . 322
Kim, K. (CT-16) . . . 323
Kim, K. (EI-07) . . . 500
Kim, K. (EW-01) . . . 552
Kim, K. (FR-07) . . . 635
Kim, K. (FT-01) . . . 641
Kim, K. (GP-16) . . . 732
Kim, K. (HF-14) . . . 802
Kim, M. (AR-12) . . . 75
Kim, M. (GT-01) . . . 748
Kim, M. (HC-13) . . . 780
Kim, N. (AT-08) . . . 83
Kim, N. (AW-18) . . . 109
Kim, N. (CG-05) . . . 272
Kim, N. (DU-05) . . . 430
Kim, N. (DU-14) . . . 434
Kim, N. (DU-15) . . . 434
Kim, P. (FF-03) . . . 585
Kim, S. (BD-11) . . . 136
Kim, S. (CC-08) . . . 245
Kim, S. (CD-06) . . . 251
Kim, S. (CI-01) . . . 284
Kim, S. (CR-08) . . . 309
Kim, S. (CR-09) . . . 310
Kim, S. (CV-15) . . . 338
Kim, S. (DC-09) . . . 360
Kim, S. (EQ-06) . . . 514
Kim, S. (EW-01) . . . 552
Kim, S. (FP-08) . . . 618
Kim, S. (GF-10) . . . 701
Kim, S. (HF-14) . . . 802
Kim, S. (HG-02) . . . 804
Kim, T. (AB-07) . . . 6
Kim, T. (CH-12) . . . 282
Kim, T. (CP-01) . . . 292
Kim, T. (CT-14) . . . 322
Kim, T. (EC-08) . . . 464
Kim, T. (EV-13) . . . 547
Kim, T. (FP-12) . . . 620
Kim, T. (FR-10) . . . 636
Kim, T. (HF-15) . . . 802
Kim, W. (CT-16) . . . 323
Kim, W. (EG-09) . . . 489
Kim, W. (EG-11) . . . 490
Kim, W. (FC-04) . . . 567
Kim, W. (FR-07) . . . 635
Kim, W. (GC-02) . . . 679
Kim, W. (GC-08) . . . 681
Kim, Y. (CR-09) . . . 310
Kim, Y. (DE-06) . . . 370
Kim, Y. (DU-06) . . . 430
Kim, Y. (EC-08) . . . 464
Kimel, A. (DD-04) . . . 362
Kimel, A. (HD-03) . . . 783
Kimura, A. (HF-06) . . . 798
Kimura, T. (AE-10) . . . 27
Kimura, T. (AP-02) . . . 58
Kimura, T. (AP-04) . . . 60
Kimura, T. (AV-02) . . . 92
Kimura, T. (BW-09) . . . 228
Kimura, T. (FW-05) . . . 665
Kinane, C. (DT-11) . . . 426
Kinane, C. (EC-12) . . . 466
Kinane, C. (FQ-17) . . . 630
Kinoshita, A. (CA-03) . . . 233
Kinoshita, K. (AU-08) . . . 88

*Best student presentation award finalist

Kinoshita, T. (EQ-07) . . . 514
Kioussis, N. (AD-08) . . . 19
Kioussis, N. (EG-13) . . . 491
Kirby, B.J. (AG-11) . . . 42
Kirby, B.J. (BA-01) . . . 111
Kirby, B.J. (BA-04) . . . 112
Kirby, B.J. (BH-15) . . . 164
Kirby, B.J. (BR-17) . . . 195
Kirby, B.J. (DH-07) . . . 388
Kirby, B.J. (DI-04) . . . 392
Kirby, B.J. (HD-08) . . . 785
Kirilyuk, A. (DD-04) . . . 362
Kirilyuk, A. (GC-11) . . . 683
Kirilyuk, A. (HD-03) . . . 783
Kirk, E. (CG-04) . . . 271
Kirschner, F. (AV-01) . . . 92
Kiselev, N.S. (CG-07) . . . 272
Kiselev, N.S. (EA-02) . . . 453
Kishimoto, H. (GH-03) . . . 709
Kishimoto, H. (GH-08) . . . 712
Kishimoto, K. (BW-11) . . . 229
Kisic, M.G. (DV-10) . . . 439
Kitaizumi, T. (FF-09) . . . 588
Kitakami, O. (BP-08) . . . 174
Kitakami, O. (CI-02) . . . 284
Kitazawa, H. (FQ-12) . . . 628
Kitcher, M.D. (AW-05) . . . 103
Kittaka, S. (AV-13) . . . 98
Kiwa, T. (CQ-09) . . . 303
Kiwa, T. (DG-10) . . . 383
Kiwi, M. (EI-04) . . . 499
Kiwi, M. (EI-05) . . . 499
Kiwi, M. (ET-03) . . . 527
Kiyota, K. (FP-02) . . . 615
Klanjšek, M. (FE-02) . . . 579
Kläui, M. (AB-07) . . . 6
Kläui, M. (AF-10) . . . 34
Kläui, M. (AG-05) . . . 39
Kläui, M. (AW-09) . . . 105
Kläui, M. (BB-01) . . . 114
Kläui, M. (CB-04) . . . 237
Kläui, M. (CE-03) . . . 255
Kläui, M. (DD-02) . . . 361
Kläui, M. (EC-07) . . . 464
Kläui, M. (GF-13) . . . 702
Kleibert, A. (CG-04) . . . 271
Klein, D. (BD-13) . . . 137
Klein, O. (GE-01) . . . 689
Klein, O. (GE-13) . . . 694
Kletečka, V. (DT-10) . . . 425
Klewe, C. (CB-10) . . . 240
Klewe, C. (GB-02) . . . 671
Klimczyk, P. (AF-01) . . . 30
Kloodt-Twesten, F. (HG-06) . . . 806
Klos, J. (GE-12) . . . 694
Klug, M.J. (AF-05) . . . 31
Klug, M.J. (HG-03) . . . 805
Kluyver, T. (DD-02) . . . 361
Knispel, T. (CC-02) . . . 243
Knobloch, J. (DT-02) . . . 423
Knut, R. (BD-06) . . . 134
Knut, R. (ER-04) . . . 519
Ko, H. (GP-16) . . . 732
Ko, H. (GQ-09) . . . 738
Ko, M. (DU-06) . . . 430
Kobayashi, A. (AB-15) . . . 10
Kobayashi, K. (AE-09) . . . 27
Kobayashi, K. (EB-02) . . . 455
Kobayashi, K. (EC-05) . . . 463
Kobayashi, S. (CI-03) . . . 285
Kobayashi, S. (CI-04) . . . 285
Kobayashi, S. (DW-03) . . . 443
Kobayashi, S. (FG-05) . . . 592
Koch, L. (BH-01) . . . 158
Koch, L. (CG-07) . . . 272
Koch, L. (CG-13) . . . 275
Koenig, A. (DW-13) . . . 448
Koga, Y. (AV-07) . . . 94
Koganezawa, T. (CG-10) . . . 274
Koh, C. (CQ-07) . . . 302
Koh, C. (DG-07) . . . 382
Koh, Y. (AR-10) . . . 74
Kohda, M. (AD-13) . . . 22
Kohda, M. (GB-13) . . . 677
Köhler, T. (BF-07) . . . 149
Kohn, A. (CG-08) . . . 273
Kohno, H. (AB-10) . . . 8
Kohno, H. (BE-06) . . . 142
Kohno, H. (BV-12) . . . 222
Kohno, H. (FV-14) . . . 662
Koide, T. (HF-10) . . . 800
Koike, F. (FG-08) . . . 594
Koike, H. (EF-10) . . . 482
Koike, H. (FW-04) . . . 664
Koike, T. (FW-02) . . . 663
Koitaya, T. (FT-08) . . . 644
Koizumi, H. (FG-05) . . . 592
Kolchugina, N. (BP-15) . . . 178
Kolchugina, N.B. (BP-11) . . . 176
Kolesnikov, A. (DE-06) . . . 370
Kolesnikova, V. (GH-11) . . . 713
Kollar, P. (DW-05) . . . 444
Kolokoltsev, O. (EW-14) . . . 557
Kolomiets, A. (BI-05) . . . 167
Komaee, A. (BW-14) . . . 231
Komaee, A. (DU-07) . . . 430
Komninou, P. (EP-17) . . . 511
Komori, F. (CG-10) . . . 274
Komori, F. (FT-08) . . . 644
Komori, S. (DP-09) . . . 399
Kon, S. (CF-05) . . . 264
Kondo, K. (DC-02) . . . 357
Kondo, K. (DP-09) . . . 399
Kondo, T. (HB-03) . . . 771
Kong, J. (ED-02) . . . 467
Kong, W. (BV-15) . . . 223
Kono, T. (AE-12) . . . 28
Konopelnyk, Y. (DQ-07) . . . 407
Konoto, M. (EG-04) . . . 486
Konstantinovic, Z. (BT-16) . . . 206
Koo, H. (AD-12) . . . 21
Koo, H. (HF-15) . . . 802
Koo, J. (AB-04) . . . 5
Koo, J. (HF-02) . . . 795
Koo, M. (EP-12) . . . 508
Koomson, V. (GI-13) . . . 722
Koopmans, B. (AB-02) . . . 4
Koopmans, B. (CC-12) . . . 247
Koopmans, B. (CE-11) . . . 259
Koopmans, B. (DD-03) . . . 362
Koopmans, B. (DD-06) . . . 364
Koopmans, B. (DD-07) . . . 364
Koopmans, B. (DD-10) . . . 366
Koopmans, B. (DE-04) . . . 369
Koopmans, B. (GE-10) . . . 693
Koopmans, B. (HG-06) . . . 806
Kopecky, V. (AQ-07) . . . 64
Kopietz, P. (BE-11) . . . 144
Kopyt, P. (BG-02) . . . 152
Kopyt, P. (CU-05) . . . 326
Korber, L. (CC-04) . . . 244
Korber, L. (CC-05) . . . 244
Korber, L. (HG-05) . . . 805
Korczak, J. (EB-13) . . . 460
Korecki, J. (CP-05) . . . 293
Korecki, J. (FG-07) . . . 593
Korecki, J. (FG-10) . . . 595
Korman, C.E. (ET-04) . . . 527
Koroteev, Y.M. (EB-07) . . . 457
Kosaka, T. (CH-05) . . . 278
Kosel, J. (DG-04) . . . 380
Koshkid'ko, Y. (BP-15) . . . 178
Kostylev, M.P. (BD-09) . . . 135
Kosub, T. (CP-06) . . . 294
Kota, Y. (CG-06) . . . 272
Kotani, T. (DB-06) . . . 352
Kotani, Y. (BP-08) . . . 174
Kotani, Y. (CD-06) . . . 251
Kotani, Y. (CI-04) . . . 285
Kotani, Y. (EE-01) . . . 473
Kothandaraman, C. (GC-07) . . . 681
Kotsugi, M. (CG-10) . . . 274
Kotsugi, M. (DT-05) . . . 424
Kotsugi, M. (FT-08) . . . 644
Kotter, S. (BF-06) . . . 148
Kou, B. (EU-09) . . . 538
Kou, Z. (CR-16) . . . 314
Kouhia, R. (DW-01) . . . 442
Koumpouras, K. (ER-03) . . . 519
Kourentzi, K. (CQ-04) . . . 301
Kourkoutis, L. (DA-05) . . . 348
Kouwenhoven, M. (HC-10) . . . 779
Kovac, F. (DW-05) . . . 444
Kovacs, A. (CA-03) . . . 233
Kovacs, A. (CG-08) . . . 273
Kovacs, A. (FH-02) . . . 599
Kovacs, A. (FI-01) . . . 607
Kovalev, A. (AB-14) . . . 10
Kovalev, A. (AD-14) . . . 23
Kovalev, A. (EB-05) . . . 457
Kovalev, S. (BD-01) . . . 131
Koyama, T. (AD-07) . . . 18
Koyama, T. (AQ-02) . . . 62

*Best student presentation award finalist

Koyama, T. (BQ-05) . . . 181
Koyanagi, T. (BW-11) . . . 229
Koziol-Rachwal, A. (CP-05) . . . 293
Koziol-Rachwal, A. (FG-07) . . . 593
Koziol-Rachwal, A. (FG-10) . . . 595
Kozlenko, D. (GG-04) . . . 704
Krafft, C. (EB-03) . . . 456
Krajewski, A.M. (FQ-16) . . . 629
Kral, D. (AQ-07) . . . 64
Kramer, M. (AT-03) . . . 81
Kramer, M. (DQ-13) . . . 409
Kratochvilova, M. (EI-03) . . . 498
Krause, S. (EF-13) . . . 483
Krautscheid, P. (AF-10) . . . 34
Kravchuk, V. (HA-05) . . . 768
Krawczyk, M. (EW-15) . . . 557
Krawczyk, M. (GE-08) . . . 692
Krawczyk, M. (GE-12) . . . 694
Kreil, A. (BD-09) . . . 135
Krenn, H. (BF-09) . . . 149
Kret, S. (EB-13) . . . 460
Krieft, J. (AE-07) . . . 26
Krimer, Y. (GH-06) . . . 710
Krishnan, K. (BH-09) . . . 162
Krishnaswamy, G. (BB-12) . . . 119
Krishnaswamy, G. (CG-04) . . . 271
Krishnia, S. (AI-12) . . . 56
Krivorotov, I. (AI-01) . . . 50
Krivorotov, I. (BR-06) . . . 191
Krivorotov, I. (CE-01) . . . 254
Krivorotov, I. (DA-02) . . . 347
Krivorotov, I. (DI-05) . . . 392
Krizakova, V. (BB-12) . . . 119
Krizanova, K. (CP-09) . . . 295
Krizman, G. (DT-06) . . . 424
Kromin, S. (GF-13) . . . 702
Kronast, F. (BB-01) . . . 114
Kronast, F. (CB-04) . . . 237
Kronast, F. (GP-08) . . . 728
Kruglyak, V.V. (AQ-03) . . . 63
Kruglyak, V.V. (CE-07) . . . 257
Kruglyak, V.V. (EW-07) . . . 554
Krupka, J. (BG-02) . . . 152
Krupka, J. (CU-05) . . . 326
Krycka, K.L. (AW-16) . . . 108
Krycka, K.L. (EI-06) . . . 500
Kuanr, B.K. (AT-04) . . . 81
Kuanr, B.K. (BQ-12) . . . 185
Kuanr, B.K. (GI-04) . . . 717
Kuanr, B.K. (GI-08) . . . 719
Kubomura, K. (EV-19) . . . 550
Kubota, H. (BU-07) . . . 212
Kubota, H. (BU-08) . . . 212
Kubota, H. (CI-11) . . . 289
Kubota, H. (CU-04) . . . 326
Kubota, H. (DF-01) . . . 374
Kubota, H. (EF-01) . . . 478
Kubota, H. (EG-01) . . . 485
Kubota, H. (EG-04) . . . 486
Kubota, H. (EG-05) . . . 487
Kubota, H. (EG-12) . . . 491
Kubota, H. (EP-02) . . . 503
Kubota, H. (EQ-04) . . . 513
Kubota, H. (FC-05) . . . 568
Kubota, H. (HD-12) . . . 787
Kubota, H. (HI-06) . . . 821
Kubota, T. (AI-04) . . . 52
Kubota, T. (CF-08) . . . 266
Kubota, T. (CG-06) . . . 272
Kubota, T. (CW-14) . . . 345
Kuchi, R. (BP-06) . . . 174
Kudo, H. (DV-02) . . . 435
Kudo, K. (HF-05) . . . 797
Kudo, N. (BU-11) . . . 214
Kuepper, K. (AF-11) . . . 34
Kuhns, P. (AV-10) . . . 96
Kujirai, K. (FQ-12) . . . 628
Kukil, P. (GG-11) . . . 707
Kukreja, R. (BA-05) . . . 113
Kukreja, R. (DD-02) . . . 361
Kukreja, R. (HH-11) . . . 815
Kulik, P. (BR-05) . . . 190
Kulkarni, A.R. (HC-12) . . . 780
Kulmaczewski, R. (HE-03) . . . 790
Kumagai, T. (CG-10) . . . 274
Kumah, D.P. (BT-07) . . . 201
Kumaoka, H. (GH-02) . . . 708
Kumar, A. (AP-05) . . . 60
Kumar, A. (BV-02) . . . 217
Kumar, A. (BV-10) . . . 221
Kumar, A. (CR-12) . . . 311
Kumar, A. (FB-10) . . . 564
Kumar, A. (FU-07) . . . 651
Kumar, A. (HC-07) . . . 778
Kumar, A. (HC-11) . . . 779
Kumar, A.P. (BE-13) . . . 145
Kumar, A.P. (FV-04) . . . 658
Kumar, A.P. (HC-04) . . . 776
Kumar, D. (DE-11) . . . 373
Kumar, D. (DF-02) . . . 374
Kumar, D. (EF-02) . . . 478
Kumar, N. (DR-03) . . . 414
Kumar, N. (HC-12) . . . 780
Kumar, P. (BR-11) . . . 193
Kumar, R. (DI-03) . . . 391
Kumar, S. (BH-08) . . . 161
Kumar, S. (DW-15) . . . 449
Kumar, S. (FH-13) . . . 605
Kumar, S. (FU-03) . . . 650
Kumar, Y. (FF-04) . . . 585
Kumari, S. (CR-15) . . . 313
Kumari, S. (FU-13) . . . 653
Kumari, S. (HC-07) . . . 778
Kumari, S. (HC-08) . . . 778
Kumbhare, D. (BW-12) . . . 230
Kunca, B. (GH-12) . . . 714
Kundu, S. (EG-11) . . . 490
Kundu, S. (EP-13) . . . 508
Kundu, S. (FC-04) . . . 567
Kunimatsu, K. (BU-05) . . . 211
Kuo, C. (DP-16) . . . 402
Kuppan, M. (FU-10) . . . 652
Kurahashi, M. (BW-11) . . . 229
Kurdi, S. (AB-04) . . . 5
Kurebayashi, H. (AE-06) . . . 26
Kurenkov, A. (BB-12) . . . 119
Kurenkov, A. (DF-05) . . . 376
Kurniawan, I. (HF-06) . . . 798
Kurnosikov, O. (HG-06) . . . 806
Kuroda, F. (DR-09) . . . 417
Kurokawa, Y. (AF-10) . . . 34
Kurokawa, Y. (GB-09) . . . 675
Kursa, M. (BP-11) . . . 176
Kursa, M. (BP-15) . . . 178
Kusakabe, M. (DU-11) . . . 432
Kusakabe, M. (FF-08) . . . 587
Kusakabe, M. (FF-09) . . . 588
Kusakabe, M. (FF-10) . . . 588
Kusakabe, M. (FF-11) . . . 589
Kuschel, T. (AE-07) . . . 26
Kuschel, T. (BE-12) . . . 145
Kuschel, T. (BU-12) . . . 214
Kuschel, T. (FG-14) . . . 597
Kushibiki, R. (GR-05) . . . 743
Kushibiki, R. (HD-11) . . . 787
Kuswik, P. (AD-11) . . . 20
Kuswik, P. (GE-08) . . . 692
Kuswik, P. (GE-12) . . . 694
Kuteifan, M. (FI-10) . . . 611
Kuwahata, A. (DU-11) . . . 432
Kuwahata, A. (FF-08) . . . 587
Kuwahata, A. (FF-09) . . . 588
Kuwahata, A. (FF-10) . . . 588
Kuwahata, A. (FF-11) . . . 589
kuwata, h. (DW-10) . . . 446
Kvashnin, Y. (BD-06) . . . 134
Kvashnin, Y. (ER-03) . . . 519
Kvashnin, Y. (ER-04) . . . 519
Kwak, W. (GP-18) . . . 733
Kwak, W. (GV-01) . . . 760
Kwok, W. (FA-02) . . . 559
Kwon, D. (EV-03) . . . 542
Kwon, H. (BP-10) . . . 175
Kwon, J. (GP-18) . . . 733
Kwon, J. (GV-01) . . . 760
Kwon, S. (EG-13) . . . 491
Kwon, S. (EI-07) . . . 500
Kwon, S. (GU-03) . . . 755

- L -

Laakso, S. (DW-01) . . . 442
Labanowski, D. (GE-07) . . . 691
Labh, A. (GF-04) . . . 698
Lacour, D. (FE-06) . . . 580
Lacour, D. (FE-11) . . . 583
Laczkowski, P. (AP-03) . . . 59
Ladak, S. (BF-01) . . . 146
Lage, E. (ED-11) . . . 472
Lägel, B. (CE-08) . . . 258
Lägel, B. (GE-03) . . . 690
Lähderanta, E. (DR-01) . . . 414

*Best student presentation award finalist

Lähderanta, E. (DR-15) 420
Lai, C. (BB-02) 114
Lai, C. (BB-13) 120
Lai, C. (BU-03) 210
Lai, C. (BV-11) 222
Lai, C. (CD-04) 250
Lai, C. (CP-10) 295
Lai, C. (CP-15) 297
Lai, C. (GP-10) 729
Lai, K. (BV-14) 223
Lai, Y. (GQ-05) 736
Lainez-Garcia, S.P. (BC-09) 126
Lalieu, M. (DD-07) 364
Lamard, N. (EP-08) 506
Lamb, R. (AB-06) 6
Lambert, C. (DD-08) 365
Lambert, C. (HC-03) 776
Lambert, P.K. (BI-02) 166
Lambert, P.K. (FD-13) 578
Lamichhane, T.N. (EH-10) 496
Lamour, E. (FD-06) 574
Lampen-Kelley, P. (GD-06) 686
Lancaster, T. (AW-11) 106
Lancaster, T. (GF-01) 697
Lanceros, S. (AH-12) 48
Landeros, P. (ET-08) 529
Landeros, P. (EW-13) 557
Langer, J. (EP-08) 506
Langer, M. (ED-01) 467
Langridge, S. (GF-06) 699
Lantz, M. (HI-01) 818
Lanuzza, M. (AC-08) 15
Lao, Y. (BH-06) 160
Lao, Y. (BH-07) 161
Lao, Y. (HA-01) 767
Lapa, P.N. (AB-05) 5
Lapa, P.N. (BT-03) 199
Lapa, P.N. (DC-05) 358
Lapa, P.N. (DC-06) 359
Laref, S. (DP-10) 399
Larionov, K. (FB-09) 564
Latcham, O. (AQ-03) 63
Lathiya, P. (BR-12) 194
Latka, K. (GG-11) 707
Lattery, D.M. (BD-02) 131
Lattery, D.M. (CF-02) 263
Lau, D.K. (FT-03) 642
Lau, Y. (EB-08) 458
Lauer, G. (GC-07) 681
Laughlin, D.E. (EI-10) 502
Laughlin, D.E. (HD-05) 784
Laughlin, D.E. (HD-06) 784
Laurenceau, E. (DU-01) 428
Lauter, V. (FG-02) 591
Lauter, V. (GG-01) 703
Lauzier, J. (AI-07) 53
Lauzier, J. (HD-08) 785
Lavrijsen, R. (AB-07) 6
Lavrijsen, R. (CC-12) 247
Lavrijsen, R. (CE-11) 259
Lavrijsen, R. (DD-03) 362
Lavrijsen, R. (DD-06) 364
Lavrijsen, R. (DD-10) 366
Lavrijsen, R. (GE-10) 693
Lavrijsen, R. (HG-06) 806
Law, J. (FD-02) 572
Law, W. (AD-10) 20
Lazarski, S. (AD-11) 20
Lazcano-Ortiz, Z. (EW-14) 557
Lázpita, P. (FD-09) 576
Le Fevre, P. (HF-01) 795
Le Gallou, J. (CU-06) 327
Le Guyader, L. (DD-02) 361
Le Roy, D. (DU-01) 428
Le Roy, D. (EH-08) 495
Le Tacon, M. (DI-09) 394
Le-Denmat, S. (HG-09) 807
Le, Q. (FP-09) 619
Leao, J. (GT-02) 748
Leao, J. (GT-05) 749
Leao, J. (GT-06) 750
Leary, A. (DW-13) 448
Lebouc, A. (FQ-19) 630
Lebrun, R. (AG-05) 39
Lebrun, R. (BB-01) 114
Lebrun, R. (CB-04) 237
Lebrun, R. (EC-07) 464
LeClair, P. (BI-11) 169
Lee, A.J. (DC-03) 357
Lee, A.J. (FG-12) 596
Lee, B. (AR-09) 73
Lee, B. (CT-01) 317
Lee, B. (CT-04) 318
Lee, B. (FW-06) 665
Lee, C. (CV-03) 333
Lee, C. (CV-07) 335
Lee, C. (FR-08) 635
Lee, D. (AD-12) 21
Lee, D. (DC-09) 360
Lee, D. (DR-07) 416
Lee, D. (EE-07) 475
Lee, D. (EU-06) 538
Lee, D. (HG-02) 804
Lee, E. (DT-12) 426
Lee, G. (CW-04) 341
Lee, G. (CW-07) 342
Lee, H. (AH-01) 44
Lee, H. (AH-05) 45
Lee, H. (AR-12) 75
Lee, H. (CD-06) 251
Lee, H. (CH-12) 282
Lee, H. (CI-01) 284
Lee, H. (CW-04) 341
Lee, H. (DH-09) 389
Lee, H. (DR-07) 416
Lee, H. (DU-10) 432
Lee, H. (EE-07) 475
Lee, H. (EU-03) 536
Lee, H. (EV-02) 541
Lee, H. (EV-13) 547
Lee, H. (FG-13) 597
Lee, H. (FP-06) 618
Lee, H. (FP-12) 620
Lee, H. (FR-04) 633
Lee, H. (FR-05) 634
Lee, H. (FR-10) 636
Lee, H. (FT-01) 641
Lee, H. (GC-07) 681
Lee, I. (AA-01) 2
Lee, J. (BP-10) 175
Lee, J. (BV-08) 220
Lee, J. (CH-12) 282
Lee, J. (CW-07) 342
Lee, J. (DQ-10) 408
Lee, J. (EI-05) 499
Lee, J. (EQ-06) 514
Lee, J. (EV-02) 541
Lee, J. (EV-04) 543
Lee, J. (EV-08) 545
Lee, J. (EV-13) 547
Lee, J. (FP-12) 620
Lee, J. (FR-01) 632
Lee, J. (FR-10) 636
Lee, J. (HF-14) 802
Lee, J.M. (BC-03) 123
Lee, K. (AB-07) 6
Lee, K. (AD-12) 21
Lee, K. (AG-05) 39
Lee, K. (AT-08) 83
Lee, K. (AW-06) 104
Lee, K. (AW-18) 109
Lee, K. (CC-03) 244
Lee, K. (CC-08) 245
Lee, K. (CD-06) 251
Lee, K. (CP-17) 298
Lee, K. (CR-08) 309
Lee, K. (CT-14) 322
Lee, K. (DC-09) 360
Lee, K. (DR-05) 415
Lee, K. (DR-14) 419
Lee, K. (EG-07) 488
Lee, K. (EU-06) 538
Lee, K. (FT-14) 647
Lee, K. (FW-08) 666
Lee, K. (GP-16) 732
Lee, K. (HG-02) 804
Lee, M. (AF-08) 33
Lee, M. (AR-09) 73
Lee, M. (BA-05) 113
Lee, M. (CT-01) 317
Lee, M. (EC-08) 464
Lee, M. (EE-03) 473
Lee, N. (FU-15) 653
Lee, N. (HC-13) 780
Lee, N. (HF-14) 802
Lee, O. (AD-12) 21
Lee, P. (CP-15) 297
Lee, S. (AI-08) 54
Lee, S. (AT-08) 83
Lee, S. (BE-05) 142
Lee, S. (CC-03) 244
Lee, S. (CT-02) 317
Lee, S. (CT-14) 322

*Best student presentation award finalist

Lee, S. (CT-16) . . . 323
Lee, S. (CV-15) . . . 338
Lee, S. (DR-04) . . . 415
Lee, S. (DR-05) . . . 415
Lee, S. (DR-14) . . . 419
Lee, S. (DT-09) . . . 425
Lee, S. (EF-10) . . . 482
Lee, S. (EI-07) . . . 500
Lee, S. (EI-09) . . . 501
Lee, S. (EW-01) . . . 552
Lee, S. (FR-07) . . . 635
Lee, S. (FT-14) . . . 647
Lee, S. (FW-04) . . . 664
Lee, S. (HF-14) . . . 802
Lee, T. (GG-02) . . . 703
Lee, W. (CH-10) . . . 281
Lee, W. (CI-01) . . . 284
Lee, W. (DU-05) . . . 430
Lee, W. (DU-14) . . . 434
Lee, W. (DU-15) . . . 434
Lee, W. (GI-09) . . . 720
Lee, Y. (BP-12) . . . 177
Lee, Y. (CP-17) . . . 298
Lee, Y. (DB-06) . . . 352
Lees, M.R. (AW-17) . . . 109
Lees, M.R. (FH-13) . . . 605
Lees, M.R. (GF-05) . . . 699
Legrand, W. (AF-07) . . . 32
Legrand, W. (BG-10) . . . 156
Legrand, W. (DE-01) . . . 368
Legrand, W. (ED-05) . . . 469
Lehikoinen, A. (CH-07) . . . 280
Lehmann, Z. (DQ-12) . . . 409
Lei, G. (FR-03) . . . 633
Lei, N. (AW-02) . . . 101
Lei, N. (BV-13) . . . 223
Lei, N. (GF-12) . . . 702
Leighton, C. (BA-01) . . . 111
Leighton, C. (BH-06) . . . 160
Leighton, C. (BH-07) . . . 161
Leighton, C. (DH-07) . . . 388
Leighton, C. (HF-07) . . . 798
Leistner, K. (AH-10) . . . 47
Leite, M.M. (FE-05) . . . 580
Leitus, G. (CG-08) . . . 273
Lejeune, B. (DQ-13) . . . 409
Lejeune, B. (FQ-11) . . . 627
Lekshmi, P. (DH-11) . . . 390
Lelièvre-Berna, E. (GF-04) . . . 698
Lendinez, S. (FA-02) . . . 559
Leng, Q. (GV-13) . . . 765
Lenz, K. (CR-06) . . . 308
Lenz, K. (EW-13) . . . 557
Lenz, K. (GB-11) . . . 676
Lenz, M. (BH-01) . . . 158
Leon, A.O. (BQ-06) . . . 182
Leon, A.O. (FW-01) . . . 663
Leong, Z. (GV-12) . . . 765
Leonov, A.O. (GF-04) . . . 698
Lequeux, S. (ET-13) . . . 531
Lesne, E. (AB-12) . . . 9
Lesseux, G. (AV-10) . . . 96
Létang, J. (CC-01) . . . 243
Lete-Segura, N. (HI-07) . . . 821
Leulmi Pichot, S. (EA-04) . . . 454
Leupold, O. (CE-02) . . . 255
Levartoski de Araujo, C.I. (AW-19) . . . 110
Levartoski de Araujo, C.I. (FE-10) . . . 582
Leveille, C. (BB-01) . . . 114
Levi, G. (CG-08) . . . 273
Lévy, A. (FD-06) . . . 574
Lew, W. (AC-05) . . . 13
Lew, W. (AD-10) . . . 20
Lew, W. (DC-08) . . . 359
Lew, W. (EF-02) . . . 478
Lew, W. (GF-08) . . . 700
Lew, W. (GP-13) . . . 730
Lewis, J.P. (FU-16) . . . 654
Lewis, L. (DQ-13) . . . 409
Lewis, L. (FQ-11) . . . 627
Li, B. (GG-01) . . . 703
Li, C. (CW-13) . . . 344
Li, C. (DP-20) . . . 404
Li, C. (HB-04) . . . 771
Li, C.H. (DP-05) . . . 397
Li, C.H. (FV-06) . . . 659
Li, D. (BW-03) . . . 226
Li, G. (GC-11) . . . 683
Li, H. (AW-08) . . . 105
Li, H. (CV-10) . . . 336
Li, H. (DR-08) . . . 416
Li, H. (FV-15) . . . 662
Li, J. (AD-02) . . . 16
Li, J. (AI-06) . . . 53
Li, J. (AI-11) . . . 55
Li, J. (BB-09) . . . 118
Li, J. (BB-10) . . . 118
Li, J. (BT-08) . . . 202
Li, J. (CB-08) . . . 239
Li, J. (CB-09) . . . 240
Li, J. (CH-06) . . . 279
Li, J. (CU-03) . . . 325
Li, J. (DB-09) . . . 353
Li, J. (DQ-17) . . . 412
Li, J. (EU-05) . . . 537
Li, J. (FC-01) . . . 566
Li, J. (FD-10) . . . 577
Li, J. (FQ-14) . . . 629
Li, J. (GB-01) . . . 671
Li, J. (GB-02) . . . 671
Li, J. (GC-06) . . . 680
Li, J. (GU-04) . . . 755
Li, L. (DP-05) . . . 397
Li, L. (DW-07) . . . 445
Li, L. (EH-06) . . . 494
Li, L. (ET-10) . . . 530
Li, L. (EU-04) . . . 536
Li, M. (HB-04) . . . 771
Li, M.P. (CR-03) . . . 307
Li, M.P. (DE-10) . . . 372
Li, M.P. (ED-03) . . . 468
Li, M.P. (GP-04) . . . 725
Li, P. (CB-01) . . . 236
Li, P. (DV-05) . . . 437
Li, Q. (AV-03) . . . 93
Li, Q. (AV-15) . . . 98
Li, Q. (BR-04) . . . 190
Li, Q. (BU-15) . . . 216
Li, Q. (CB-10) . . . 240
Li, Q. (FU-02) . . . 649
Li, Q. (GB-02) . . . 671
Li, Q. (HC-07) . . . 778
Li, R. (CT-08) . . . 320
Li, S. (FB-09) . . . 564
Li, S. (FQ-13) . . . 628
Li, W. (BF-10) . . . 150
Li, W. (CI-07) . . . 287
Li, W. (DE-03) . . . 369
Li, W. (FH-04) . . . 600
Li, W. (FH-05) . . . 601
Li, W.J. (DT-07) . . . 425
Li, X. (AC-04) . . . 12
Li, X. (AH-01) . . . 44
Li, X. (AH-05) . . . 45
Li, X. (BC-10) . . . 127
Li, X. (GF-03) . . . 698
Li, X. (HC-03) . . . 776
Li, Y. (AB-09) . . . 7
Li, Y. (AR-07) . . . 72
Li, Y. (BP-02) . . . 172
Li, Y. (BP-04) . . . 173
Li, Y. (BT-02) . . . 199
Li, Y. (CH-08) . . . 280
Li, Y. (CU-12) . . . 330
Li, Y. (CU-15) . . . 331
Li, Y. (CV-06) . . . 335
Li, Y. (DQ-09) . . . 408
Li, Y. (DU-02) . . . 428
Li, Y. (DW-17) . . . 450
Li, Y. (EH-07) . . . 495
Li, Y. (ER-02) . . . 518
Li, Y. (EW-04) . . . 553
Li, Y. (FA-02) . . . 559
Li, Y. (FB-11) . . . 565
Li, Y. (FE-07) . . . 581
Li, Y. (FH-11) . . . 604
Li, Y. (FH-14) . . . 605
Li, Y. (FH-15) . . . 605
Li, Y. (FI-15) . . . 613
Li, Y. (FV-07) . . . 659
Li, Y. (GH-01) . . . 708
Li, Y. (HF-08) . . . 799
Li, Y. (HF-13) . . . 801
Li, Z. (BC-06) . . . 125
Li, Z. (BQ-09) . . . 183
Li, Z. (BQ-11) . . . 184
Li, Z. (BR-09) . . . 192
Li, Z. (CD-02) . . . 249
Li, Z. (DP-18) . . . 403
Li, Z. (DR-08) . . . 416
Li, Z. (GH-03) . . . 709
Li, Z. (HB-08) . . . 773
Liang, C. (ER-12) . . . 523

*Best student presentation award finalist

Liang, C. (FV-12) . . . 661
Liang, F. (DQ-05) . . . 406
Liang, F. (DQ-17) . . . 412
Liang, G. (BC-03) . . . 123
Liang, G. (DB-04) . . . 351
Liang, J. (CG-02) . . . 270
Liang, T. (DQ-05) . . . 406
Liang, W. (AH-03) . . . 45
Liang, W. (DQ-15) . . . 410
Liang, X. (AH-06) . . . 46
Liang, X. (AH-07) . . . 46
Liang, X. (GI-05) . . . 718
Liang, X. (GI-06) . . . 718
Liang, Y. (BB-10) . . . 118
Liang, Y. (BT-02) . . . 199
Liang, Y. (FB-11) . . . 565
Liao, C. (BW-07) . . . 227
Liao, C. (CQ-07) . . . 302
Liao, C. (DG-07) . . . 382
Liao, C. (FF-07) . . . 587
Liao, W. (EC-01) . . . 461
Liao, Z. (EE-07) . . . 475
Lichtenberg, T. (CC-12) . . . 247
Lichtenberg, T. (DE-04) . . . 369
Lickliter, J. (DG-13) . . . 385
Liensberger, L. (GB-10) . . . 675
Lim, G.J. (AC-05) . . . 13
Lim, G.J. (AD-10) . . . 20
Lim, J. (CH-12) . . . 282
Lim, J. (EV-13) . . . 547
Lim, J. (FP-12) . . . 620
Lim, S. (EI-09) . . . 501
Lim, W. (AP-03) . . . 59
Lim, Y. (AI-02) . . . 51
Lim, Y. (AI-06) . . . 53
Lim, Y. (GB-01) . . . 671
Lin, C. (FF-05) . . . 585
Lin, C. (HE-02) . . . 790
Lin, H. (AH-07) . . . 46
Lin, H. (CD-04) . . . 250
Lin, H. (GI-05) . . . 718
Lin, H. (GI-06) . . . 718
Lin, H. (GU-05) . . . 755
Lin, H. (GU-06) . . . 756
Lin, J.G. (DP-16) . . . 402
Lin, J.G. (ER-12) . . . 523
Lin, J.G. (FV-12) . . . 661
Lin, K. (BT-11) . . . 203
Lin, M. (CF-03) . . . 263
Lin, M. (ED-02) . . . 467
Lin, P. (BV-11) . . . 222
Lin, P. (CD-04) . . . 250
Lin, P. (CP-15) . . . 297
Lin, S. (BC-10) . . . 127
Lin, S. (FB-04) . . . 562
Lin, T. (AW-02) . . . 101
Lin, T. (FU-06) . . . 651
Lin, W. (DB-08) . . . 353
Lin, X. (BQ-04) . . . 180
Lin, X. (CF-10) . . . 267
Lin, X. (DB-02) . . . 350
Lin, X. (DP-17) . . . 403
Lin, Z. (FI-08) . . . 610
Lin, Z. (GQ-08) . . . 737
Linder, J. (GD-10) . . . 688
Linderalv, C. (DR-13) . . . 419
Lindner, J. (ET-02) . . . 526
Lindner, J. (EW-13) . . . 557
Lindner, J. (GB-11) . . . 676
Linfield, E. (BB-11) . . . 119
Linfield, E. (DE-05) . . . 369
Ling, D. (CF-03) . . . 263
Liou, S. (HI-11) . . . 823
Lisenkov, I. (AD-04) . . . 17
Lisenkov, I. (AE-03) . . . 24
Lisenkov, I. (BB-06) . . . 117
Lisenkov, I. (CE-06) . . . 257
Lisfi, A. (AQ-06) . . . 64
Lisfi, A. (AR-16) . . . 76
Lisiecki, F. (GE-08) . . . 692
Lisiecki, F. (GE-12) . . . 694
Litvinenko, A. (AC-01) . . . 11
Litvinenko, A. (GE-13) . . . 694
Litvinov, D. (CQ-04) . . . 301
Litvinov, D. (FT-15) . . . 647
Litzius, K. (GF-13) . . . 702
Liu, C. (AU-02) . . . 85
Liu, C. (BB-10) . . . 118
Liu, C. (BV-06) . . . 219
Liu, C. (CB-13) . . . 242
Liu, E. (AW-08) . . . 105
Liu, E. (CV-10) . . . 336
Liu, E. (DR-08) . . . 416
Liu, F. (BP-03) . . . 172
Liu, F. (BP-04) . . . 173
Liu, F. (GU-07) . . . 757
Liu, G. (EW-11) . . . 556
Liu, H. (AW-02) . . . 101
Liu, H. (CE-06) . . . 257
Liu, J. (AH-03) . . . 45
Liu, J. (AR-13) . . . 75
Liu, J. (AT-05) . . . 81
Liu, J. (AT-06) . . . 82
Liu, J. (BH-13) . . . 164
Liu, J. (CF-02) . . . 263
Liu, J. (CQ-14) . . . 305
Liu, J. (CW-06) . . . 341
Liu, J. (DQ-15) . . . 410
Liu, J. (DQ-16) . . . 411
Liu, J. (DT-13) . . . 426
Liu, J. (EI-08) . . . 501
Liu, J. (FQ-04) . . . 624
Liu, K. (AG-02) . . . 38
Liu, K. (AG-03) . . . 38
Liu, K. (AH-09) . . . 47
Liu, K. (BA-04) . . . 112
Liu, K. (BA-05) . . . 113
Liu, K. (CG-11) . . . 274
Liu, K. (FG-03) . . . 592
Liu, L. (AE-11) . . . 28
Liu, L. (BB-15) . . . 121
Liu, L. (BD-13) . . . 137
Liu, L. (CD-08) . . . 252
Liu, L. (DB-08) . . . 353
Liu, L. (FA-03) . . . 559
Liu, L. (HG-07) . . . 806
Liu, M. (DV-12) . . . 440
Liu, M. (GV-07) . . . 763
Liu, P. (BQ-09) . . . 183
Liu, P. (BQ-13) . . . 185
Liu, Q. (CD-02) . . . 249
Liu, Q. (CR-10) . . . 310
Liu, Q. (ER-02) . . . 518
Liu, R. (AV-03) . . . 93
Liu, R. (BQ-07) . . . 182
Liu, R. (ET-10) . . . 530
Liu, S. (DV-03) . . . 436
Liu, S. (HC-07) . . . 778
Liu, T. (CE-01) . . . 254
Liu, T. (DE-02) . . . 368
Liu, T. (GF-02) . . . 697
Liu, W. (AR-07) . . . 72
Liu, W. (DQ-09) . . . 408
Liu, W. (FH-11) . . . 604
Liu, W. (FH-14) . . . 605
Liu, W. (FH-15) . . . 605
Liu, X. (AR-11) . . . 74
Liu, X. (BQ-08) . . . 183
Liu, X. (DI-07) . . . 393
Liu, X. (DR-04) . . . 415
Liu, X. (DR-05) . . . 415
Liu, X. (DT-06) . . . 424
Liu, X. (FD-04) . . . 573
Liu, X. (FF-03) . . . 585
Liu, X. (FP-14) . . . 621
Liu, X. (FR-06) . . . 634
Liu, Y. (BC-02) . . . 122
Liu, Y. (BP-03) . . . 172
Liu, Y. (BP-04) . . . 173
Liu, Y. (CB-01) . . . 236
Liu, Y. (CD-08) . . . 252
Liu, Y. (CT-07) . . . 320
Liu, Y. (DB-11) . . . 354
Liu, Y. (DE-03) . . . 369
Liu, Y. (DQ-16) . . . 411
Liu, Y. (FQ-04) . . . 624
Liu, Y. (FV-07) . . . 659
Liu, Z. (EH-06) . . . 494
Livesey, K. (AU-10) . . . 89
Livesey, K. (BI-12) . . . 170
Livesey, K. (CI-09) . . . 287
Livesey, K. (CI-10) . . . 288
Livesey, K. (EQ-11) . . . 516
Liyanage, W. (BA-04) . . . 112
Liyanage, W. (DE-02) . . . 368
Lo Conte, R. (AG-02) . . . 38
Lo Conte, R. (AG-03) . . . 38
Lo Conte, R. (CG-11) . . . 274
Lo Conte, R. (HC-03) . . . 776
Lo Conte, R. (HC-09) . . . 778
Lo, S. (BR-14) . . . 194
Lobo, J. (HE-06) . . . 792
LoBue, M. (FD-06) . . . 574

*Best student presentation award finalist

LoBue, M. (FI-02) 607
LoBue, M. (FQ-06) 625
Locatelli, A. (HG-09) 807
Locht, I.L. (BD-06) 134
Lockwood, O. (BV-06) 219
Löffler, J.F. (FH-02) 599
Lograsso, T. (AT-03) 81
Lohmann, M. (BB-09) 118
Lohmann, M. (DB-09) 353
Loku Singgappulige, K.R. (HF-06) 798
Loloee, R. (DI-04) 392
Lomakin, V. (FI-05) 609
Lomakin, V. (FI-08) 610
Lomakin, V. (FI-10) 611
Lomakin, V. (FI-11) 611
Lomakin, V. (FV-08) 659
Lopez Moreno, E. (BT-15) 205
Lopez-Diaz, L. (CB-07) 239
López, J. (GA-04) 669
Lopez, V. (AB-03) 5
Lopez, V. (BB-14) 120
Lorenz, V. (AD-05) 18
Lorenz, V. (AS-02) 78
Lorenz, V. (BS-02) 197
Lorenz, V. (CS-02) 315
Lorenz, V. (DS-02) 421
Lorenz, V. (ES-02) 524
Lorenz, V. (FS-02) 639
Lorenz, V. (GS-02) 746
Loreto, R. (AW-19) 110
Lostun, M. (GH-14) 714
Lott, D. (FG-02) 591
Loudon, J.C. (GF-05) 699
Louis, S. (AB-08) 7
Louis, S. (AC-01) 11
Lowther, D. (CA-05) 234
Lu, J. (BI-04) 167
Lu, Q. (AR-07) 72
Lu, Q. (DQ-09) 408
Lu, Q. (FH-11) 604
Lu, Q. (FH-14) 605
Lu, Q. (FH-15) 605
Lu, T. (BG-05) 153
Lü, W. (HB-04) 771
Lu, Z. (EP-01) 503
Lucas, I. (BE-08) 143
Lucassen, J. (CE-11) 259
Lucassen, J. (GE-10) 693
Lucassen, J. (HG-06) 806
Lue, C. (DP-16) 402
Luengo, Y. (HE-09) 793
Lukashev, P. (CW-17) 346
Lukin, A. (BP-11) 176
Lukin, A. (BP-15) 178
Luo, B. (BA-01) 111
Luo, W. (BQ-08) 183
Luo, Z. (CG-04) 271
Luo, Z. (FP-04) 617
Lupu, N. (GH-14) 714
Lurgo, F.E. (BI-01) 166
Lurgo, F.E. (CT-11) 321
Lusakowska, E. (EB-13) 460
Lussier, J.L. (EI-06) 500
Lussier, J.L. (GD-02) 685
Lv, Y. (CU-13) 330
Lv, Y. (EP-10) 507
Lynch, C.S. (BT-14) 205
Lynch, C.S. (HE-07) 792
Lynn, J.W. (GT-02) 748
Lynn, J.W. (GT-05) 749
Lynn, J.W. (GT-06) 750
Lyu, S. (GU-05) 755
Lyu, S. (GU-06) 756

- M -

M. (BR-07) 191
Ma, B. (CW-06) 341
Ma, C.T. (AG-06) 39
Ma, C.T. (AG-11) 42
Ma, D. (EH-07) 495
Ma, F. (EW-13) 557
Ma, J. (FF-06) 586
Ma, J. (HI-05) 820
Ma, M. (GU-11) 759
Ma, Q. (BP-03) 172
Ma, Q. (BP-04) 173
Ma, Y. (BT-05) 200
Ma, Y. (DU-03) 429
Ma, Z. (AR-07) 72
Ma, Z. (CI-07) 287
Ma, Z. (FH-11) 604
Ma, Z. (GG-03) 704
Maccari, F. (FD-02) 572
Maccariello, D. (AF-07) 32
Maccariello, D. (BG-10) 156
Maccariello, D. (ED-05) 469
Maccherozzi, F. (BB-01) 114
Maccherozzi, F. (BB-12) 119
Maccherozzi, F. (GH-10) 713
Macé, S. (FD-06) 574
Macedo, R. (BD-10) 136
Macedo, R. (CE-03) 255
Macedo, R. (CE-04) 256
Macedo, R. (CI-09) 287
Macedo, R. (CI-10) 288
Machida, H. (FH-07) 602
Machida, K. (GP-07) 727
Macià, F. (EQ-10) 516
MacNeill, D. (BD-13) 137
MacNeill, D. (DA-05) 348
Madsen, M. (CG-11) 274
Maeda, S. (FF-08) 587
Maehara, H. (BU-07) 212
Maehara, H. (BU-08) 212
Maehara, H. (GC-04) 679
Maekawa, S. (EC-05) 463
Maekawa, S. (HB-01) 770
Maekawa, S. (HF-10) 800
Maekawa, S. (XA-02) 452
Maeno, A. (BE-03) 141
Maeno, A. (CV-12) 337
Magen, C. (BH-02) 158
Magni, A. (GI-01) 716
Magnus Gomes Carvalho, A. (DQ-14) 410
Magnus, W. (AH-04) 45
Magsood, H. (DU-08) 431
Mahadevan, S. (CT-05) 319
Mahajan, R.K. (FU-03) 650
Mahat, R. (BI-11) 169
Mahat, R. (BR-09) 192
Mahato, R.N. (BR-07) 191
Mahendiran, R. (CR-13) 311
Mahendiran, R. (FU-20) 655
Mahendra, D. (FV-15) 662
Mahfouzi, F. (AD-08) 19
Mahmood, K. (BI-15) 171
Mai, T. (DB-03) 351
Mai, T. (DB-13) 355
Mai, T.T. (GD-06) 686
Maior, D.S. (FA-05) 560
Mair, L. (GA-05) 670
Majetich, S. (AW-01) 101
Majetich, S. (CF-11) 267
Majetich, S. (DF-03) 375
Mak, K.F. (AA-02) 2
Makarov, D. (CP-06) 294
Makarov, D. (EE-11) 477
Makarov, D. (HI-09) 823
Makhnovskiy, D. (CV-02) 333
Maleček, T. (DT-10) 425
Malik, R. (BD-06) 134
Malik, R. (ER-04) 519
Malinowski, G. (DD-01) 361
Malkinski, L. (BF-08) 149
Mallesh, S. (CT-02) 317
Mallick, K. (FV-04) 658
Maloberti, O. (AF-01) 30
Mamiya, H. (FQ-12) 628
Manago, T. (CD-05) 250
Manchanda, P. (GF-03) 698
Manchec, A. (CI-14) 290
Manchon, A. (AD-01) 16
Manchon, A. (CP-02) 292
Manchon, A. (DP-10) 399
Manchon, A. (HB-04) 771
Mancilla, D. (FW-01) 663
Mandal, D. (CT-03) 318
Mandal, K. (CT-03) 318
Mandal, K. (DQ-11) 408
Mandal, K. (EE-09) 476
Mandal, K. (HH-05) 812
Mandal, P. (DI-02) 391
Mandal, R. (AI-04) 52
Mandal, R.K. (HH-13) 816
Mandal, S. (CF-12) 268
Mandrus, D. (BT-12) 204
Mandrus, D. (GD-06) 686
Manfrinetti, P. (BI-06) 168
Manfrinetti, P. (BI-13) 170
Mangin, S. (AW-09) 105
Mangin, S. (DD-01) 361

*Best student presentation award finalist

Mangin, S. (EB-10) . . . 458
Mangin, S. (FG-11) . . . 595
Mankey, G.J. (HH-09) . . . 814
Manna, K. (AE-04) . . . 25
Mañosa, L. (FD-01) . . . 572
Mansouri, S. (FQ-19) . . . 630
Mansueto, M. (EF-07) . . . 481
Manuel, P. (BT-04) . . . 200
Marangolo, M. (FD-06) . . . 574
Marangolo, M. (FQ-06) . . . 625
Maranloo, Z.I. (AW-04) . . . 102
Maranville, B.B. (DE-02) . . . 368
Marcano, L. (HH-03) . . . 811
Marchal, N. (BT-17) . . . 206
Marchal, N. (FP-05) . . . 617
Marchionni, A. (DP-07) . . . 398
Marchionni, A. (EB-01) . . . 455
Marcin, J. (DW-11) . . . 447
Marcin, J. (GH-12) . . . 714
Mardegan, J. (AF-12) . . . 35
Marimon da Cunha, J.B. (GT-13) . . . 752
Marin, J.M. (ER-10) . . . 522
Marin, P. (GA-04) . . . 669
Marinella, M.J. (ET-15) . . . 532
Marinella, M.J. (HG-08) . . . 806
Markou, A. (AB-12) . . . 9
Marqués, J.L. (EV-20) . . . 551
Marrows, C.H. (AB-06) . . . 6
Marrows, C.H. (BB-11) . . . 119
Marrows, C.H. (DE-05) . . . 369
Marrows, C.H. (ED-01) . . . 467
Marrows, C.H. (GF-06) . . . 699
Marrows, C.H. (GP-05) . . . 726
Marrows, C.H. (GQ-06) . . . 736
Martens, K.M. (EG-09) . . . 489
Martens, U. (BU-12) . . . 214
Martín-Cid, A. (CI-03) . . . 285
Martín-Cid, A. (CI-04) . . . 285
Martin-Rio, S. (FV-03) . . . 658
Martin, C. (BI-01) . . . 166
Martin, C. (CT-11) . . . 321
Martin, F. (DW-01) . . . 442
Martin, I. (AE-01) . . . 24
Martín, J. (AF-09) . . . 33
Martín, J. (GP-08) . . . 728
Martin, S. (HG-09) . . . 807
Martínez Banderas, A.I. (DG-04) . . . 380
Martínez García, J.C. (CU-02) . . . 324
Martínez García, J.C. (EV-20) . . . 551
Martinez-Teran, E. (DQ-08) . . . 407
Martínez, B. (BH-02) . . . 158
Martinez, B. (BT-16) . . . 206
Martinez, B. (DH-08) . . . 388
Martinez, B. (FV-03) . . . 658
Martinez, E. (HD-01) . . . 782
Martinez, E. (HG-04) . . . 805
Martinez, I. (CF-03) . . . 263
Martinez, J.C. (DC-08) . . . 359
Martinez, L.M. (CT-07) . . . 320
Martins Cardoso, F. (DW-02) . . . 442
Martins Jr., S.M. (ET-11) . . . 531
Martins, F. (FE-10) . . . 582
Martins, M.D. (ER-11) . . . 522
Martos-Repath, I. (AH-06) . . . 46
Marty, A. (AE-08) . . . 26
Marty, A. (AP-03) . . . 59
Marty, A. (DP-07) . . . 398
Marty, A. (DP-14) . . . 401
Marty, A. (EB-01) . . . 455
Marty, A. (FC-09) . . . 570
Marty, A. (FV-10) . . . 660
Maruf, A. (CW-17) . . . 346
Maruyama, I. (GD-04) . . . 686
Mascaraque, A. (AG-02) . . . 38
Mascaraque, A. (FG-03) . . . 592
Mašková, S. (BI-05) . . . 167
Mason, N. (AB-09) . . . 7
Mason, N. (AS-02) . . . 78
Mason, N. (BS-02) . . . 197
Mason, N. (CS-02) . . . 315
Mason, N. (DS-02) . . . 421
Mason, N. (EB-04) . . . 456
Mason, N. (EB-09) . . . 458
Mason, N. (ES-02) . . . 524
Mason, N. (FS-02) . . . 639
Mason, N. (GS-02) . . . 746
Masood, K.I. (CU-07) . . . 327
Masset, G. (DH-04) . . . 387
Massey, J. (AB-06) . . . 6
Massey, J. (BB-11) . . . 119
Massey, J. (DE-05) . . . 369
Massouras, M. (FE-06) . . . 580
Massouras, M. (FE-11) . . . 583
Mastuki, H. (GU-01) . . . 754
Mastuki, H. (GU-02) . . . 754
Masuda, K. (GB-07) . . . 674
Masuyama, Y. (FF-09) . . . 588
Maswadeh, Y. (DQ-08) . . . 407
Matalla-Wagner, T. (BB-05) . . . 116
Matalla-Wagner, T. (FQ-03) . . . 624
Matalla-Wagner, T. (HF-02) . . . 795
Mathias, S. (ER-03) . . . 519
Mathkar, V. (FB-06) . . . 563
Matinaga, F.M. (ER-11) . . . 522
Matlak, K. (CP-05) . . . 293
Matlak, K. (FG-07) . . . 593
Matlak, K. (FG-10) . . . 595
Matsuda, R. (AP-02) . . . 58
Matsuda, R. (AP-04) . . . 60
Matsuda, S. (FF-10) . . . 588
Matsuda, S. (FF-11) . . . 589
Matsuda, Y. (AV-06) . . . 94
Matsui, N. (CH-05) . . . 278
Matsumori, H. (CH-05) . . . 278
Matsumoto, H. (GH-02) . . . 708
Matsumoto, H. (HI-08) . . . 822
Matsumoto, M. (EH-12) . . . 497
Matsumoto, R. (BQ-16) . . . 187
Matsumoto, R. (EG-08) . . . 489
Matsuo, M. (HB-01) . . . 770
Matsuura, Y. (BP-09) . . . 175
Matte, K.V. (DW-15) . . . 449
Matveev, V. (DR-01) . . . 414
Maurel, V. (DP-14) . . . 401
Maurya, K.K. (BR-11) . . . 193
May, A. (AA-05) . . . 3
May, A. (BF-01) . . . 146
Mayergoyz, I. (EB-03) . . . 456
Mayergoyz, I. (ET-04) . . . 527
Mayergoyz, I. (FI-02) . . . 607
Mayoral, A. (CR-14) . . . 312
Mayr, S. (ED-01) . . . 467
Mazin, I. (CT-09) . . . 320
Mazumdar, D. (DQ-01) . . . 405
Mazur, G.P. (EB-13) . . . 460
Mazza, A.R. (GG-06) . . . 705
Mazzoli, C. (BH-03) . . . 159
Mboukam, J.J. (GT-11) . . . 751
Mbulunge, M.H. (GT-11) . . . 751
McCall, S.K. (DB-12) . . . 354
McCall, S.K. (EI-10) . . . 502
McCann, S.M. (AF-02) . . . 30
McComb, D.W. (DC-03) . . . 357
McCord, J. (AF-05) . . . 31
McCord, J. (ED-11) . . . 472
McCord, J. (HD-02) . . . 782
McCreary, A. (AB-01) . . . 4
McCreary, A. (DB-03) . . . 351
McCreary, A. (DB-13) . . . 355
McCreary, A. (GD-06) . . . 686
McCullian, B. (CR-02) . . . 306
McCullian, B. (DC-03) . . . 357
McCullian, B. (FG-12) . . . 596
McElfresh, M. (EI-10) . . . 502
McGill, S. (GG-05) . . . 704
McGrath, B.R. (BI-12) . . . 170
McGrouther, D. (AB-06) . . . 6
McGrouther, D. (BB-11) . . . 119
McGuire, M. (EA-05) . . . 454
McHenry, M. (EI-10) . . . 502
McHenry, M. (GH-06) . . . 710
McKeown, S. (DP-08) . . . 399
McKinney, D. (AS-01) . . . 78
McKinney, D. (BS-01) . . . 197
McKinney, D. (CS-01) . . . 315
McKinney, D. (DS-01) . . . 421
McKinney, D. (ES-01) . . . 524
McKinney, D. (FS-01) . . . 639
McKinney, D. (GS-01) . . . 746
McKinnon, T.J. (GQ-10) . . . 738
McMichael, R.D. (AF-14) . . . 36
McMorran, B.J. (BG-06) . . . 153
McVitie, S. (AF-09) . . . 33
McVitie, S. (BB-11) . . . 119
Meagher, L. (DG-13) . . . 385
Meckenstock, R. (BD-04) . . . 133
Medapalli, R. (BD-05) . . . 133
Medlej, I. (BB-06) . . . 117
Mehta, A. (AF-08) . . . 33
Mei, A. (AC-04) . . . 12
Mei, A. (AF-13) . . . 35
Meier, G. (BD-15) . . . 138
Meier, G. (CE-02) . . . 255

*Best student presentation award finalist

Meijer, M.J. (HG-06) . . . 806
Meinert, M. (BB-05) . . . 116
Meinert, M. (EC-02) . . . 461
Meinert, M. (FG-09) . . . 595
Mekkaoui, S. (DU-01) . . . 428
Melkov, G.A. (BE-11) . . . 144
Menarini, M. (FI-05) . . . 609
Mendisch, S. (GE-04) . . . 690
Mendisch, S. (GE-06) . . . 691
Mendisch, S. (GP-02) . . . 724
Menegasso, P.E. (GT-07) . . . 750
Menéndez, E. (AH-11) . . . 48
Menéndez, E. (AH-13) . . . 49
Menéndez, E. (BA-02) . . . 112
Menéndez, E. (FU-12) . . . 653
Meneses Brassea, B. (CQ-06) . . . 302
Meneses Brassea, B. (CQ-10) . . . 304
Meneses Brassea, B. (CQ-11) . . . 304
Meng, F. (EV-14) . . . 548
Meng, H. (FP-03) . . . 616
Meng, K. (BQ-09) . . . 183
Meng, K. (BQ-11) . . . 184
Meng, K. (BQ-13) . . . 185
Meng, K. (CD-02) . . . 249
Meng, K. (DH-06) . . . 387
Meng, K. (DP-20) . . . 404
Meng, K. (GP-15) . . . 732
Meng, K. (HB-08) . . . 773
Meng, L. (BI-07) . . . 168
Menges, F. (BE-09) . . . 143
Menshawy, S. (EQ-05) . . . 513
Mentes, T. (HG-09) . . . 807
Mentink, J. (DD-04) . . . 362
Menushenkov, A.P. (FH-01) . . . 599
Menushenkov, V.P. (FH-01) . . . 599
Meo, A. (BH-12) . . . 163
Meo, A. (FI-03) . . . 608
Meo, A. (HD-04) . . . 783
Mercadier, L. (DD-02) . . . 361
Mercer, T. (AF-02) . . . 30
Mercurio, G. (DD-02) . . . 361
Mertens, S. (GC-02) . . . 679
Mertig, I. (AW-14) . . . 107
Mertig, I. (DP-08) . . . 399
Mertig, I. (GF-09) . . . 701
Merz, M. (DI-09) . . . 394
Merzaban, J.S. (DG-04) . . . 380
Mestnik-Filho, J. (GT-15) . . . 752
Mestres, N. (DH-08) . . . 388
Meunier, T. (DP-12) . . . 400
Mewes, C.K. (AI-03) . . . 51
Mewes, C.K. (AI-06) . . . 53
Mewes, C.K. (AW-05) . . . 103
Mewes, C.K. (CR-03) . . . 307
Mewes, C.K. (DW-13) . . . 448
Mewes, C.K. (ED-03) . . . 468
Mewes, C.K. (FG-09) . . . 595
Mewes, C.K. (FT-03) . . . 642
Mewes, C.K. (GP-04) . . . 725
Mewes, C.K. (HH-09) . . . 814
Mewes, T. (AI-03) . . . 51
Mewes, T. (AI-06) . . . 53
Mewes, T. (AW-05) . . . 103
Mewes, T. (BR-09) . . . 192
Mewes, T. (CR-03) . . . 307
Mewes, T. (DW-13) . . . 448
Mewes, T. (ED-03) . . . 468
Mewes, T. (FG-09) . . . 595
Mewes, T. (FT-03) . . . 642
Mewes, T. (GP-04) . . . 725
Mewes, T. (HH-09) . . . 814
Meyer, T. (CF-12) . . . 268
Meyers, D. (EI-08) . . . 501
Mi, W. (FU-02) . . . 649
Miao, B. (ET-05) . . . 528
Miao, J. (BQ-03) . . . 180
Miao, J. (BQ-09) . . . 183
Miao, J. (BQ-11) . . . 184
Miao, J. (BQ-13) . . . 185
Miao, J. (CD-02) . . . 249
Miao, J. (DP-20) . . . 404
Miao, J. (GP-15) . . . 732
Miao, J. (HB-08) . . . 773
Miao, J. (HF-08) . . . 799
Michaelis de Vasconcellos, S. (FV-13) . . . 661
Michea, S. (AU-12) . . . 89
Michel, E.G. (AG-02) . . . 38
Michel, E.G. (FG-03) . . . 592
Michely, T. (CC-02) . . . 243
Midiri, M. (BW-15) . . . 231
Midura, M. (FF-02) . . . 584
Midura, R.J. (FF-02) . . . 584
Mieda, K. (DW-08) . . . 445
Mieda, K. (DW-16) . . . 449
Mieda, K. (DW-18) . . . 450
Mihai, A. (AB-13) . . . 9
Mihai, A. (CP-09) . . . 295
Mihailovic, D. (FE-02) . . . 579
Mihajlovic, G. (CD-05) . . . 250
Mihajlovic, G. (FC-01) . . . 566
Mihajlovic, G. (GC-06) . . . 680
Miki, R. (CP-12) . . . 296
Miles, J.J. (HD-07) . . . 785
Miller, C.W. (BH-15) . . . 164
Miller, P. (GI-11) . . . 721
Millev, Y. (ET-05) . . . 528
Mills, S.C. (AT-10) . . . 83
Mills, S.C. (CH-01) . . . 276
Milosevic, M. (AH-04) . . . 45
Min, B. (AD-12) . . . 21
Min, B. (CR-11) . . . 311
Min, B. (FT-01) . . . 641
Mina, M. (CQ-03) . . . 300
Minami, S. (CV-08) . . . 335
Miotkowski, I. (EB-12) . . . 459
Miranda, R. (BE-08) . . . 143
Miranda, R. (CD-01) . . . 249
Miranda, R. (HB-02) . . . 770
Mirchandani, N. (AH-06) . . . 46
Miriyala, K. (HC-12) . . . 780
Misawa, T. (EB-06) . . . 457
Mishner, M. (BR-06) . . . 191
Mishra, A. (GI-08) . . . 719
Mishra, D. (GH-09) . . . 712
Mishra, K.K. (FU-11) . . . 652
Mishra, K.K. (FU-14) . . . 653
Mishra, R. (BC-03) . . . 123
Mishra, R. (DF-02) . . . 374
Mishra, R. (HB-06) . . . 772
Mishra, S.R. (AR-13) . . . 75
Mishra, S.R. (BR-02) . . . 189
Mishra, S.R. (BR-15) . . . 195
Misisrlioglu, B. (BP-14) . . . 177
Mitani, S. (BC-12) . . . 128
Mitani, S. (BU-10) . . . 213
Mitani, S. (FG-15) . . . 597
Mitra, D. (DI-03) . . . 391
Mitsumata, C. (DT-05) . . . 424
Mittal, A. (AH-06) . . . 46
Mittelstaedt, J. (DA-05) . . . 348
Miura, D. (BQ-10) . . . 184
Miura, D. (CR-05) . . . 308
Miura, K. (AV-07) . . . 94
Miura, K. (BQ-14) . . . 186
Miura, K. (EG-10) . . . 490
Miura, Y. (AG-07) . . . 40
Miura, Y. (CQ-08) . . . 303
Miura, Y. (GB-07) . . . 674
Miura, Y. (HF-06) . . . 798
Miwa, S. (BQ-02) . . . 179
Miwa, S. (CF-01) . . . 262
Miwa, S. (CI-12) . . . 289
Miwa, S. (DF-01) . . . 374
Miwa, S. (FC-05) . . . 568
Miwa, Y. (GR-02) . . . 742
Miyahara, S. (FU-18) . . . 654
Miyahara, S. (GD-04) . . . 686
Miyahara, S. (GU-01) . . . 754
Miyahara, S. (GU-02) . . . 754
Miyahara, S. (GU-08) . . . 757
Miyamachi, T. (CG-10) . . . 274
Miyamachi, T. (FT-08) . . . 644
Miyamoto, T. (CC-09) . . . 246
Miyamoto, Y. (GP-12) . . . 730
Miyashita, T. (CG-10) . . . 274
Miyata, Y. (DP-04) . . . 397
Miyawaki, J. (DR-09) . . . 417
Miyazaki, T. (AQ-08) . . . 65
Miyazawa, K. (BP-08) . . . 174
Mizuguchi, M. (BE-02) . . . 140
Mizuguchi, M. (BE-03) . . . 141
Mizuguchi, M. (CG-06) . . . 272
Mizukami, S. (AI-13) . . . 56
Mizukami, S. (BU-01) . . . 209
Mizukami, S. (BU-05) . . . 211
Mizukami, S. (BU-06) . . . 211
Mizukami, S. (CP-07) . . . 294
Mizukami, S. (DD-01) . . . 361
Mizukami, S. (DR-11) . . . 418
Mizukami, S. (ER-06) . . . 520

*Best student presentation award finalist

Mizuno, H. (CR-08) . . . 309
Mizzell, G. (FP-03) . . . 616
Mkhoyan, A. (CF-02) . . . 263
Mkhoyan, A. (DH-07) . . . 388
Mkhoyan, A. (FV-15) . . . 662
Mlynczak, E. (CD-03) . . . 250
Mo, C. (BP-12) . . . 177
Mo, S. (BV-06) . . . 219
Moda Piva, M. (GT-02) . . . 748
Moda Piva, M. (GT-06) . . . 750
Modiano, J. (DG-05) . . . 381
Moen, E. (DI-05) . . . 392
Moffat, T. (HE-12) . . . 794
Mohamad, H.S. (CF-12) . . . 268
Mohammadi, J.B. (FG-09) . . . 595
Mohanty, J. (DE-06) . . . 370
Mohanty, J. (ER-01) . . . 518
Mohanty, P. (DW-14) . . . 448
Mohapatra, J. (AR-13) . . . 75
Mohapatra, J. (AT-05) . . . 81
Mohapatra, J. (AT-06) . . . 82
Mohapatra, J. (BH-13) . . . 164
Mohapatra, S. (BQ-12) . . . 185
Moharana, G. (CT-10) . . . 321
Mohseni, F. (AF-03) . . . 31
Mohseni, F. (EH-05) . . . 494
Mohseni, M. (CE-08) . . . 258
Mok, J. (DU-10) . . . 432
Mokrousov, Y. (AB-07) . . . 6
Mól, L. (FE-10) . . . 582
Molaison, J.J. (EE-07) . . . 475
Molaison, J.J. (HE-03) . . . 790
Momeni Pakdehi, D. (BG-08) . . . 154
Monarch, J. (DT-07) . . . 425
Mondal, A. (FB-10) . . . 564
Mondal, A.K. (EQ-02) . . . 512
Mondal, A.K. (EQ-03) . . . 513
Mondal, R. (EW-10) . . . 556
Mondal, R. (HD-02) . . . 782
Mondal, S. (CC-10) . . . 246
Mondal, S. (ER-01) . . . 518
Monsivais, G. (EW-14) . . . 557
Montaigne, F. (FE-06) . . . 580
Montaigne, F. (FE-11) . . . 583
Montiel, H. (BT-15) . . . 205
Montiel, X. (AE-06) . . . 26
Monton, C. (EI-04) . . . 499
Monton, C. (EI-05) . . . 499
Monton, C. (GQ-12) . . . 739
Montoya, E.A. (AI-01) . . . 50
Montoya, E.A. (DA-02) . . . 347
Montoya, S. (CC-07) . . . 245
Montoya, S. (CC-08) . . . 245
Montoya, S. (DE-02) . . . 368
Montoya, S. (DE-08) . . . 371
Montoya, S. (ED-08) . . . 470
Mook, A. (AW-14) . . . 107
Mook, A. (GF-09) . . . 701
Moon, K. (EW-01) . . . 552
Moon, K. (GF-10) . . . 701
Moon, K. (GP-11) . . . 729
Moon, K. (HF-14) . . . 802
Moon, S. (EU-01) . . . 535
Moore, L.R. (FF-02) . . . 584
Moore, T. (BB-11) . . . 119
Moore, T. (DE-05) . . . 369
Moore, T. (GH-10) . . . 713
Moore, T. (GQ-06) . . . 736
Mora Hernandez, A. (CG-01) . . . 270
Morais, P.C. (CU-01) . . . 324
Morales, M. (HE-09) . . . 793
Moran, K. (BE-09) . . . 143
Moran, K. (EC-12) . . . 466
Morante, C. (BR-13) . . . 194
Morchenko, A. (GH-11) . . . 713
Moreira, J.A. (HH-02) . . . 810
Morellón, L. (BE-08) . . . 143
Moreno-Ramirez, L.M. (FD-02) . . . 572
Moreno, J.A. (DG-04) . . . 380
Morgan, W. (AQ-06) . . . 64
Morgan, W. (AR-16) . . . 76
Mori, S. (GH-02) . . . 708
Morimura, T. (DW-16) . . . 449
Morita, K. (FQ-12) . . . 628
Morita, T. (CP-16) . . . 298
Moriyama, T. (AC-08) . . . 15
Moriyama, T. (AI-09) . . . 54
Moriyama, T. (AV-06) . . . 94
Moriyama, T. (CP-13) . . . 296
Moriyama, T. (CP-14) . . . 297
Moriyama, T. (CR-08) . . . 309
Moriyama, T. (DC-09) . . . 360
Moriyama, T. (GE-14) . . . 695
Morley, N. (GV-12) . . . 765
Mosavian, N. (DT-01) . . . 423
Mosca, D.H. (BV-03) . . . 218
Moseley, I. (HE-02) . . . 790
Mosey, A. (GQ-12) . . . 739
Moskaltsova, A. (AE-07) . . . 26
Mostovoy, M. (AG-09) . . . 41
Mostovoy, M. (GF-04) . . . 698
Mottaghi, N. (CR-15) . . . 313
Mougin, A. (AI-12) . . . 56
Mougin, A. (CR-07) . . . 309
Moulin, J. (EQ-05) . . . 513
Mounce, A. (BG-05) . . . 153
Moura Gomes, G.F. (ER-11) . . . 522
Mourigal, M. (FE-01) . . . 579
Moyano, A. (EV-20) . . . 551
Moyo, T. (HH-06) . . . 812
Mu, Y. (DV-05) . . . 437
Mucchietto, A. (GE-09) . . . 693
Mudryk, Y. (AQ-19) . . . 69
Mudryk, Y. (BI-13) . . . 170
Mudryk, Y. (DQ-13) . . . 409
Mudryk, Y. (FD-04) . . . 573
Mudryk, Y. (FQ-02) . . . 623
Mudryk, Y. (FQ-08) . . . 626
Muduli, P.K. (AW-03) . . . 102
Muduli, P.K. (BV-02) . . . 217
Muduli, P.K. (BV-10) . . . 221
Muduli, P.K. (FB-10) . . . 564
Muduli, P.K. (GV-10) . . . 764
Muela, A. (DG-05) . . . 381
Muela, A. (HH-03) . . . 811
Mugarza, A. (HE-04) . . . 791
Mugarza, A. (HE-06) . . . 792
Mühl, T. (HG-05) . . . 805
Mukherjee, S. (DI-10) . . . 394
Mukherjee, S. (HC-05) . . . 777
Müller, C. (HD-02) . . . 782
Muller, D. (GF-03) . . . 698
Muller, D. (GG-05) . . . 704
Müller, J. (BF-02) . . . 146
Müller, L. (DD-02) . . . 361
Mundy, J. (GG-05) . . . 704
Mundy, J. (HC-06) . . . 777
Muneyama, E. (BW-09) . . . 228
Muñoz-Noval, A. (DG-12) . . . 384
Muñoz-Noval, A. (FD-08) . . . 575
Muñoz, M. (BE-10) . . . 144
Muñoz, M. (CD-01) . . . 249
Münzenberg, M. (BU-12) . . . 214
Münzenberg, M. (CF-12) . . . 268
Münzenberg, M. (DD-11) . . . 367
Münzenberg, M. (ED-11) . . . 472
Münzenberg, M. (HD-02) . . . 782
Murakami, H. (DW-03) . . . 443
Muralidhar, S. (CC-11)* . . . 247
Muralidharan, B. (FC-03) . . . 567
Muralidharan, B. (GC-03) . . . 679
Murapaka, C. (AC-01) . . . 11
Murapaka, C. (AC-05) . . . 13
Murapaka, C. (AD-10) . . . 20
Murnane, M. (DT-02) . . . 423
Murnane, M. (ER-03) . . . 519
Murphy, J.R. (CV-18) . . . 339
Murphy, K. (BR-05) . . . 190
Murray, P. (AH-09) . . . 47
Murray, P. (BA-04) . . . 112
Murray, P. (BA-05) . . . 113
Musfeldt, J. (GG-05) . . . 704
Mushenok, F. (EW-07) . . . 554
Muster, K. (BF-03) . . . 147
Muster, K. (ET-14) . . . 532
Muthsam, O. (HI-04) . . . 819
Muthu, M.S. (DW-15) . . . 449
Myrzakhan, U. (EP-04) . . . 504

- N -

N'Diaye, A.T. (GB-02) . . . 671
N'Diaye, A.T. (GD-10) . . . 688
N'Diaye, A.T. (GG-01) . . . 703
N'Diaye, A.T. (HC-03) . . . 776
Na, S. (BI-02) . . . 166
Nadeem, S. (BI-15) . . . 171
Nagae, M. (BP-09) . . . 175
Nagahama, T. (BE-03) . . . 141

*Best student presentation award finalist

Nagahama, T. (BU-14) . . . 215
Nagahama, T. (CV-12) . . . 337
Nagai, R. (BW-09) . . . 228
Nagai, R. (BW-11) . . . 229
Nagano, H. (AP-01) . . . 58
Nagarajan, V. (GD-03) . . . 685
Nagasaka, K. (BU-07) . . . 212
Nagasaka, K. (BU-08) . . . 212
Nagasaka, K. (GC-04) . . . 679
Nagashima, G. (AF-10) . . . 34
Nagaya, A. (AV-14) . . . 98
Nagler, S. (GD-06) . . . 686
Nah, J. (EV-02) . . . 541
Nah, J. (EV-08) . . . 545
Naito, T. (GT-16) . . . 753
Naito, T. (GT-17) . . . 753
Nakagawa, F. (CW-15) . . . 345
Nakagawa, F. (FT-07) . . . 644
Nakagawa, H. (BW-02) . . . 225
Nakagawa, H. (BW-05) . . . 227
Nakagawa, H. (BW-06) . . . 227
Nakagawa, H. (BW-08) . . . 228
Nakagawa, S. (AQ-11) . . . 66
Nakajima, K. (CI-11) . . . 289
Nakajima, K. (DF-01) . . . 374
Nakajima, Y. (BH-08) . . . 161
Nakamura, K. (AV-17) . . . 99
Nakamura, K. (BU-07) . . . 212
Nakamura, K. (BU-08) . . . 212
Nakamura, K. (GC-04) . . . 679
Nakamura, K. (GT-04) . . . 749
Nakamura, R. (EV-19) . . . 550
Nakamura, S. (AV-06) . . . 94
Nakamura, S. (HB-03) . . . 771
Nakamura, T. (BP-08) . . . 174
Nakamura, T. (BP-09) . . . 175
Nakamura, T. (CD-06) . . . 251
Nakamura, T. (CI-03) . . . 285
Nakamura, T. (CI-04) . . . 285
Nakamura, T. (EE-01) . . . 473
Nakamura, T. (FD-09) . . . 576
Nakamura, y. (FT-04) . . . 642
Nakamura, Y. (FT-05) . . . 643
Nakamura, Y. (GR-04) . . . 743
Nakane, J.J. (AB-10) . . . 8
Nakano, M. (BP-13) . . . 177
Nakano, M. (CW-11) . . . 343
Nakano, M. (CW-12) . . . 344
Nakano, M. (DW-08) . . . 445
Nakano, M. (DW-16) . . . 449
Nakano, M. (DW-18) . . . 450
Nakano, T. (CB-10) . . . 240
Nakano, T. (CF-01) . . . 262
Nakano, T. (CF-04) . . . 263
Nakano, T. (HH-09) . . . 814
Nakashima, H. (AV-17) . . . 99
Nakatani, R. (EE-01) . . . 473
Nakatani, T. (CF-07) . . . 265
Nakatsuji, S. (AB-15) . . . 10
Nakatsuji, S. (CF-01) . . . 262
Nakayama, H. (EV-19) . . . 550
Nakazawa, K. (AB-10) . . . 8
Naletov, V. (GE-13) . . . 694
Nam, Y. (FT-01) . . . 641
Nan, J. (AC-03) . . . 12
Nan, J. (AW-07) . . . 104
Nan, J. (BV-13) . . . 223
Nan, J. (CV-16) . . . 338
Nan, J. (FW-07) . . . 666
Nan, J. (GP-06) . . . 727
Nandakumaran, N. (BF-07) . . . 149
Nandy, A.K. (AG-03) . . . 38
Nara, T. (GV-05) . . . 762
Naramoto, H. (FB-09) . . . 564
Narayanan, H. (CT-10) . . . 321
Narducci, D. (CE-12) . . . 260
Naritsuka, M. (AV-06) . . . 94
Nash, K. (AT-07) . . . 82
Nasir, M. (GG-07) . . . 705
Nasirpouri, F. (BP-05) . . . 174
Nasrollahpour, M. (AH-06) . . . 46
Natale, M.R. (CR-04) . . . 307
Natekar, N.A. (HD-14) . . . 788
Navarro Senent, C. (AH-11) . . . 48
Navarro, C. (BA-02) . . . 112
Navarro, E. (BH-02) . . . 158
Navarro, E. (BH-11) . . . 163
Navarro, E. (GA-04) . . . 669
Navarro, E. (HE-09) . . . 793
Navas, D. (EW-15) . . . 557
Nawa, K. (GB-07) . . . 674
Nazari, H. (BE-13) . . . 145
Need, R. (HD-08) . . . 785
Neeraj, K. (BD-01) . . . 131
Neeraj, K. (BD-08) . . . 134
Neeraj, K. (DD-02) . . . 361
Nelson, B. (FP-04) . . . 617
Nelson, D. (AS-01) . . . 78
Nelson, D. (BS-01) . . . 197
Nelson, D. (CS-01) . . . 315
Nelson, D. (DS-01) . . . 421
Nelson, D. (ES-01) . . . 524
Nelson, D. (FS-01) . . . 639
Nelson, D. (GS-01) . . . 746
Nemati Porshokouh, Z. (DG-05) . . . 381
Nembach, H. (AG-01) . . . 37
Nembach, H. (AG-06) . . . 39
Nembach, H. (AI-07) . . . 53
Nembach, H. (ER-03) . . . 519
Nembach, H. (EW-02) . . . 552
Nenno, D. (EC-06) . . . 463
Neogi, K. (DW-15) . . . 449
Nepal, B. (AI-06) . . . 53
Nepal, B. (HH-09) . . . 814
Nesser, M. (AF-01) . . . 30
Nessi, L. (GB-04) . . . 673
Neto, O.F. (AU-14) . . . 90
Neumann, L. (EC-02) . . . 461
Neupane, D. (AR-13) . . . 75
Neupane, D. (BR-02) . . . 189
Newbold, B. (BF-05) . . . 148
Newbold, B. (BF-06) . . . 148
Newman, D. (CB-10) . . . 240
Newman, G.A. (CV-04) . . . 334
Newman, G.A. (CV-09) . . . 336
Ney, A. (BD-04) . . . 133
Nguyen Ba, D. (FQ-06) . . . 625
Nguyen, A. (GB-06) . . . 674
Nguyen, H. (CT-01) . . . 317
Nguyen, H. (CT-04) . . . 318
Nguyen, S.B. (GU-10) . . . 758
Nguyen, T. (AI-10) . . . 55
Nguyen, T. (CR-01) . . . 306
Nguyen, V. (EP-16) . . . 510
Nguyen, V. (HG-10) . . . 808
Ni, N. (GT-09) . . . 750
Niarchos, D. (AR-02) . . . 70
Niarchos, D. (FH-10) . . . 603
Nichols, J. (DH-09) . . . 389
Nicholson, B. (CG-12) . . . 274
Nicolenco, A. (AH-13) . . . 49
Nicolenco, A. (BA-02) . . . 112
Nie, Y. (EW-04) . . . 553
Nie, Y. (EW-09) . . . 555
Niebieskikwiat, D. (AT-09) . . . 83
Niebieskikwiat, D. (DP-02) . . . 396
Niebieskikwiat, D. (EI-11) . . . 502
Niedermayer, C. (HC-05) . . . 777
Nielsch, K. (AH-10) . . . 47
Nielsch, K. (CG-07) . . . 272
Nielsen, R.D. (BI-08) . . . 168
Nielsen, S. (ED-11) . . . 472
Niesen, A. (ET-02) . . . 526
Nieto, W. (AT-09) . . . 83
Nigam, A.K. (FB-03) . . . 562
Niimi, Y. (AE-09) . . . 27
Niimi, Y. (EB-02) . . . 455
Niimi, Y. (EC-05) . . . 463
Niimura, T. (GB-09) . . . 675
Niizeki, T. (EC-07) . . . 464
Nikitin, A.A. (CE-13) . . . 260
Nikitin, V. (FC-02) . . . 566
Nikitov, S. (DE-05) . . . 369
Nikitov, S. (DE-06) . . . 370
Nikolić, B.K. (AE-05) . . . 26
Nikolić, B.K. (AI-05) . . . 52
Ning, S. (AH-08) . . . 47
Nishikawa, M. (GR-04) . . . 743
Nishimoto, K. (DT-04) . . . 423
Nishimura, T. (DC-09) . . . 360
Nishio-Hamane, D. (AR-05) . . . 71
Nishio-Hamane, D. (AR-06) . . . 72
Nishio-Hamane, D. (FH-08) . . . 602
Nisoli, C. (BH-06) . . . 160
Nisoli, C. (BH-07) . . . 161
Nisoli, C. (HA-01) . . . 767
Nitta, J. (AD-13) . . . 22
Nitta, J. (GB-13) . . . 677
Nlebedim, C.I. (BT-07) . . . 201
Nlebedim, C.I. (CT-07) . . . 320
Nlebedim, C.I. (DI-07) . . . 393
Nlebedim, I.C. (AT-03) . . . 81
Noack, T.B. (BE-11) . . . 144

*Best student presentation award finalist

Nóbrega, E.P. (FQ-15) 629
Noebe, R. (DW-13) 448
Noel, P. (DP-12) 400
Noel, P. (EC-09) 464
Noel, P. (FV-10) 660
Noel, P. (GB-04) 673
Noesges, B. (FB-02) 561
Nogués, J. (BA-02) 112
Nogués, J. (GG-03) 704
Noh, S. (BP-07) 174
Nomura, H. (EP-02) 503
Nomura, H. (HI-06) 821
Nomura, K. (EB-06) 457
Nonaka, Y. (HF-10) 800
Novak, P. (FH-06) 601
Novosad, V. (CB-01) 236
Novosad, V. (ER-02) 518
Novosad, V. (EW-04) 553
Novosad, V. (EW-09) 555
Novosad, V. (FA-02) 559
Novosad, V. (FB-11) 565
Novosad, V. (FV-07) 659
Novotny, J. (HI-12) 824
Nowak, J. (GC-07) 681
Nowak, L. (DT-10) 425
Nowak, U. (AG-04) 38
Nowak, U. (ED-07) 470
Nowak, U. (EW-10) 556
Nowak, U. (GF-13) 702
Nowak, U. (HD-02) 782
Nozaki, T. (BQ-15) 186
Nozaki, T. (EG-01) 485
Nozaki, T. (EG-04) 486
Nozaki, T. (EG-05) 487
Nozaki, T. (EG-12) 491
Nozaki, T. (EP-02) 503
Nozaki, Y. (HB-01) 770
Nozawa, K. (EV-16) 548
Nujhat, N. (CE-05) 256
Nunes, M.S. (AU-03) 86
Nunn, Z. (FT-11) 645
Nunn, Z. (GC-05) 680
Nunn, Z. (GQ-04) 735
Nunn, Z. (GQ-16) 741
Nutter, P.W. (HD-07) 785
Nygren, K.E. (GE-07) 691

- O -

O, J. (EV-10) 546
O'Bannon, E. (DB-12) 354
O'Hara, D.J. (DB-12) 354
O'Hara, D.J. (FB-02) 561
O'Mahoney, D.A. (AQ-05) 63
Oba, S. (GU-01) 754
Oba, S. (GU-02) 754
Obayashi, I. (DT-05) 424
Oberdick, S. (DG-03) 380
Obi, O. (BR-05) 190
Oblak, E. (ER-10) 522
Oda, K. (AI-09) 54
Oda, K. (CP-13) 296
Oda, K. (CP-14) 297
Odkhuu, D. (BT-18) 207
Odkhuu, D. (CP-11) 296
Oezelt, H. (FI-01) 607
Ogasawara, T. (BU-09) 213
Ogawa, D. (FH-03) 600
Ogawa, Y. (AR-04) 71
Ogawa, Y. (AR-05) 71
Ognev, A. (BP-05) 174
Ognev, A. (DE-06) 370
Oguchi, T. (DR-09) 417
Oguchi, T. (GT-04) 749
Oh, D. (HC-13) 780
Oh, H. (EV-13) 547
Oh, H. (FP-12) 620
Oh, J. (AB-09) 7
Oh, J. (EB-04) 456
Oh, J. (EB-09) 458
Oh, J. (GP-16) 732
Oh, S. (CP-16) 298
Oh, S. (DC-09) 360
Oh, S. (HG-02) 804
Oh, Y. (BV-05) 219
Oh, Y. (CD-06) 251
Ohgane, K. (BQ-10) 184
Ohji, T. (FP-02) 615
Ohkochi, T. (EQ-07) 514
Ohkubo, T. (AP-01) 58
Ohkubo, T. (BP-08) 174
Ohkubo, T. (CI-02) 284
Ohkubo, T. (HD-10) 787
Ohldag, H. (AD-05) 18
Ohldag, H. (BD-04) 133
Ohldag, H. (CB-02) 237
Ohmori, H. (EG-04) 486
Ohno, H. (BB-12) 119
Ohno, H. (DF-05) 376
Ohno, H. (EG-02) 485
Ohnuma, Y. (HB-01) 770
Ohodnicki, P. (EU-01) 535
Ohodnicki, P. (GH-06) 710
Ohsawa, Y. (AC-06) 13
Ohshima, R. (DP-04) 397
Ohshima, R. (EF-10) 482
Ohshima, R. (FW-04) 664
Ohshima, T. (FF-09) 588
Ohta, H. (DH-02) 386
Ohta, H. (GV-03) 761
Ohta, M. (AC-07) 14
Ohtani, T. (GI-10) 720
Ohtani, T. (GV-02) 760
Ohwada, K. (FT-07) 644
Ohya, S. (BC-08) 126
Ohya, S. (CC-09) 246
Oikonomou, I.M. (EP-17) 511
Oji, U.K. (FC-05) 568
Ok, H. (FT-14) 647
Ok, J. (DH-09) 389
Okabayashi, J. (AG-07) 40
Okabayashi, J. (BU-10) 213
Okabayashi, J. (BU-14) 215
Okabayashi, J. (FG-15) 597
Okada, H. (CT-12) 321
Okamoto, H. (CC-09) 246
Okamoto, S. (BP-08) 174
Okamoto, S. (CI-02) 284
Okamoto, S. (CU-04) 326
Okamoto, S. (DH-09) 389
Okamoto, Y. (GR-04) 743
Okano, G. (HB-01) 770
Okazaki, H. (CI-03) 285
Okazaki, H. (CI-04) 285
Okita, K. (CQ-08) 303
Okita, K. (EV-16) 548
Okubo, Y. (AV-13) 98
Okuno, H. (DP-08) 399
Okuno, H. (DP-14) 401
Okuno, R. (HI-06) 821
Okuno, T. (CR-08) 309
Okuno, T. (DC-09) 360
Oleshko, V. (AU-14) 90
Oliveira, L.L. (AT-02) 80
Oliveira, L.L. (AU-03) 86
Oliveira, L.L. (ET-11) 531
Olivetti, E.S. (GI-01) 716
Ollefs, K. (BD-04) 133
Olleros, P. (BE-08) 143
Olleros, P. (CD-01) 249
Olleros, P. (HB-02) 770
Olmos, R. (BT-07) 201
Olmos, R. (CT-07) 320
Omagari, Y. (CW-11) 343
Omagari, Y. (CW-12) 344
Omoumi, A. (DI-09) 394
Onabajo, M. (AH-06) 46
Onal, N.E. (CH-09) 281
Onbasli, M. (BG-04) 153
Ono, K. (CA-02) 233
Ono, K. (CI-05) 286
Ono, K. (EH-12) 497
Ono, K. (FI-09) 611
Ono, T. (AC-08) 15
Ono, T. (AI-09) 54
Ono, T. (AV-06) 94
Ono, T. (CD-06) 251
Ono, T. (CP-13) 296
Ono, T. (CP-14) 297
Ono, T. (CR-08) 309
Ono, T. (DC-09) 360
Ono, T. (GE-14) 695
Onodera, H. (CQ-08) 303
Onodera, H. (DV-02) 435
Onozawa, H. (AQ-11) 66
Oogane, M. (BU-09) 213
Oogane, M. (BU-11) 214
Oogane, M. (CP-16) 298
Oogane, M. (DV-04) 437

*Best student presentation award finalist

Oogane, M. (DV-13) . . . 441
Oogane, M. (DW-04) . . . 443
Oogane, M. (EP-05) . . . 505
Oogane, M. (FW-02) . . . 663
Opagiste, C. (BI-04) . . . 167
Ophus, C. (AG-03) . . . 38
Opletal, P. (CW-16) . . . 345
Oppeneer, P.M. (HD-02) . . . 782
Ordonez Romero, C.L. (EW-14) . . . 557
Orellana, C. (CU-16) . . . 332
Orendorff, R. (GA-03) . . . 669
Ortega, M. (CQ-11) . . . 304
Orth, P. (BA-01) . . . 111
Ortiz-Jimenez, V. (DP-19) . . . 404
Ortiz, V.H. (AI-11) . . . 55
Ortiz, V.H. (CB-08) . . . 239
Ortiz, V.H. (CB-09) . . . 240
Ortiz, V.H. (FB-07) . . . 563
Orue, I. (HH-03) . . . 811
Osamura, K. (BP-09) . . . 175
Osawa, H. (EQ-07) . . . 514
Osawa, H. (GR-04) . . . 743
Oshima, D. (CW-02) . . . 340
Oshima, D. (EP-14) . . . 509
Oshima, D. (GR-02) . . . 742
Oshita, N. (FU-10) . . . 652
Osman, N.S. (HH-06) . . . 812
Osofsky, M. (BT-12) . . . 204
Osorio, J.A. (ER-10) . . . 522
Osorio, J.A. (FT-06) . . . 643
Osterhage, H. (EF-13) . . . 483
Ostler, T. (AR-08) . . . 73
Östman, E. (BH-04) . . . 159
Östman, E. (BH-10) . . . 162
Ostos, C. (FT-06) . . . 643
Oswald, S. (AH-10) . . . 47
Ota, S. (AQ-02) . . . 62
Ota, S. (DT-04) . . . 423
Ota, S. (HI-08) . . . 822
Otani, Y. (AB-15) . . . 10
Otani, Y. (BQ-14) . . . 186
Otani, Y. (CC-10) . . . 246
Otani, Y. (EG-10) . . . 490
Otani, Y. (EQ-03) . . . 513
Otani, Y. (EW-06) . . . 554
Otrokov, M.M. (EB-07) . . . 457
Ott, R.T. (FD-13) . . . 578
Ottley, C. (GF-01) . . . 697
Ou-Yang, J. (BQ-08) . . . 183
Ou, Y. (BV-04) . . . 218
Ou, Y. (BV-07) . . . 220
Ouisse, T. (BI-04) . . . 167
Oura, M. (EQ-07) . . . 514
Ouyang, C. (AQ-01) . . . 62
Ouyang, C. (GQ-05) . . . 736
Ovari, T.A. (GH-14) . . . 714
Ovcharov, R. (CB-11) . . . 241
Oyamada, T. (DH-02) . . . 386
Ozaki, K. (HH-10) . . . 815
Ozatay, O. (FV-07) . . . 659

- P -

P N, s. (DH-11) . . . 390
P, R. (DQ-06) . . . 407
Pablo, J. (BD-13) . . . 137
Pacewicz, A. (BG-02) . . . 152
Pacewicz, A. (CU-05) . . . 326
Padhan, P. (BI-11) . . . 169
Page, M.R. (CR-02) . . . 306
Pagliuso, P. (AV-10) . . . 96
Pagliuso, P. (CT-13) . . . 322
Pagliuso, P. (GT-02) . . . 748
Pagliuso, P. (GT-05) . . . 749
Pagliuso, P. (GT-06) . . . 750
Pagliuso, P. (GT-07) . . . 750
Pagliuso, P. (GT-08) . . . 750
Pagliuso, P. (GT-14) . . . 752
Pahari, R. (GF-03) . . . 698
Pahwa, C. (AR-17) . . . 77
Pai, C. (AD-06) . . . 18
Pai, C. (BV-04) . . . 218
Pai, C. (EC-01) . . . 461
Paik, H. (TU-03) . . . 1
Paiva, T. (FE-10) . . . 582
Pakuszewski, K.R. (CT-13) . . . 322
Pakuszewski, K.R. (GT-14) . . . 752
Palacio-Morales, A. (GD-09) . . . 687
Palasyuk, A. (EH-10) . . . 496
Palasyuk, O. (EH-10) . . . 496
Paléo, C. (EH-08) . . . 495
Palma, J. (AU-12) . . . 89
Palma, J.L. (FT-13) . . . 646
Palmstrøm, C. (FQ-17) . . . 630
Palomares, F. (BH-02) . . . 158
Palomares, F. (BH-11) . . . 163
Palomares, F. (CR-14) . . . 312
Palomares, F. (HE-09) . . . 793
Paltiel, Y. (BG-09) . . . 155
Pan, C. (FT-04) . . . 642
Pan, C. (FT-05) . . . 643
Pan, C. (FT-09) . . . 644
Pan, S. (EQ-01) . . . 512
Pan, W. (FH-04) . . . 600
Panaccione, G. (GB-04) . . . 673
Panagopoulos, C. (AW-10) . . . 105
Panagopoulos, C. (DE-09) . . . 372
Panapitiya, G. (FU-16) . . . 654
Pancaldi, M. (DD-02) . . . 361
Panda, S.N. (EW-06) . . . 554
Pandey, A. (DF-07) . . . 377
Pandey, A.H. (HC-12) . . . 780
Pandey, D. (FU-07) . . . 651
Pandey, N. (GP-04) . . . 725
Pandey, P. (EE-10) . . . 476
Pandey, S. (DR-01) . . . 414
Pandey, S. (DR-15) . . . 420
Pandit, P. (GH-09) . . . 712
Panduranga, M.K. (DG-02) . . . 379
Panier, S. (AF-01) . . . 30
Panighel, M. (HE-04) . . . 791
Panighel, M. (HE-06) . . . 792
Panina, L. (GH-11) . . . 713
Pant, R. (BR-11) . . . 193
Pant, R. (DH-10) . . . 389
Pant, R. (FF-04) . . . 585
Papackova, A. (DT-10) . . . 425
Papaioannou, E.T. (EC-06) . . . 463
Papp, A. (GE-04) . . . 690
Papp, A. (GE-06) . . . 691
Papp, A. (GP-02) . . . 724
Pappas, C. (GF-04) . . . 698
Papynov, E. (BP-05) . . . 174
Parajuli, S. (BR-01) . . . 189
Parakkat, V. (BH-09) . . . 162
Paranthaman, M. (AT-03) . . . 81
Pariyar, A. (CF-12) . . . 268
Park, B. (BV-05) . . . 219
Park, B. (CD-06) . . . 251
Park, B. (DU-06) . . . 430
Park, B. (EP-03) . . . 504
Park, B. (EW-01) . . . 552
Park, B. (GB-13) . . . 677
Park, B. (HF-14) . . . 802
Park, C. (CH-12) . . . 282
Park, C. (DB-12) . . . 354
Park, C. (EI-07) . . . 500
Park, C. (EV-13) . . . 547
Park, C. (FP-12) . . . 620
Park, C. (FR-10) . . . 636
Park, H. (EQ-06) . . . 514
Park, H. (GP-16) . . . 732
Park, J. (BI-02) . . . 166
Park, J. (CD-06) . . . 251
Park, J. (CR-11) . . . 311
Park, J. (CV-15) . . . 338
Park, J. (DU-05) . . . 430
Park, J. (DU-14) . . . 434
Park, J. (DU-15) . . . 434
Park, J. (EG-07) . . . 488
Park, J. (EH-02) . . . 492
Park, J. (EI-03) . . . 498
Park, J. (EI-09) . . . 501
Park, J. (EP-03) . . . 504
Park, J. (FT-01) . . . 641
Park, J. (GB-13) . . . 677
Park, K. (EI-09) . . . 501
Park, S. (AD-12) . . . 21
Park, S. (CD-06) . . . 251
Park, S. (DR-07) . . . 416
Park, S. (EI-07) . . . 500
Park, S. (HF-14) . . . 802
Park, Y. (CR-11) . . . 311
Park, Y. (DR-14) . . . 419
Park, Y. (FT-01) . . . 641
Parkes, M. (GQ-07) . . . 737
Parkin, S.S.P. (AB-12) . . . 9
Parkin, S.S.P. (BC-01) . . . 122
Parkin, S.S.P. (EC-01) . . . 461
Parkin, S.S.P. (GF-09) . . . 701
Parkin, S.S.P. (HB-05) . . . 772

*Best student presentation award finalist

Parks, B. (AW-01) . . . 101
Parks, B. (DF-03) . . . 375
Parpiiev, T. (BD-12) . . . 136
Parsons, R. (GH-03) . . . 709
Parsons, R. (GH-08) . . . 712
Parthasarathy, A. (BB-08) . . . 117
Pasquale, M. (GI-01) . . . 716
Patel, A.K. (DR-12) . . . 418
Patel, R. (DR-13) . . . 419
Patel, S.K. (BT-06) . . . 201
Patel, S.K. (CC-07) . . . 245
Patel, S.K. (CV-04) . . . 334
Patel, S.K. (CV-09) . . . 336
Patel, S.K. (ED-08) . . . 470
Patel, S.K. (FE-03) . . . 579
Patel, S.K. (FU-17) . . . 654
Pathak, A.K. (AQ-19) . . . 69
Pathak, A.K. (BI-06) . . . 168
Pathak, A.K. (BI-13) . . . 170
Pathak, A.K. (FD-04) . . . 573
Pathak, A.K. (FQ-02) . . . 623
Pathak, A.K. (FQ-08) . . . 626
Pati, S. (BT-20) . . . 207
Patrick, C.E. (FH-13) . . . 605
Pattabi, A. (DD-08) . . . 365
Pattabi, A. (DD-09) . . . 366
Pattabi, A. (HC-09) . . . 778
Paudel, T.R. (DB-05) . . . 352
Paudyal, D. (DI-06) . . . 393
Paudyal, D. (EH-11) . . . 496
Paudyal, D. (FH-12) . . . 604
Paudyal, D. (FQ-08) . . . 626
Paudyal, D. (GT-12) . . . 751
Paul, A. (DH-07) . . . 388
Pavel, M. (FF-12) . . . 589
Pawar, S. (HC-11) . . . 779
Payen, L. (DU-01) . . . 428
Pearson, J. (AF-06) . . . 32
Pearson, J. (CB-13) . . . 242
Pearson, J. (DC-05) . . . 358
Pearson, J. (DC-06) . . . 359
Pearson, J. (ER-02) . . . 518
Pearson, J. (EW-04) . . . 553
Pearson, J. (EW-09) . . . 555
Pearson, J. (FA-02) . . . 559
Pearson, J. (FV-07) . . . 659
Pearson, J. (HF-09) . . . 799
Pecharsky, V.K. (AQ-19) . . . 69
Pecharsky, V.K. (BI-13) . . . 170
Pecharsky, V.K. (DQ-13) . . . 409
Pecharsky, V.K. (FD-04) . . . 573
Pecharsky, V.K. (FD-07) . . . 575
Pecharsky, V.K. (FQ-01) . . . 623
Pecharsky, V.K. (FQ-02) . . . 623
Pecharsky, V.K. (FQ-08) . . . 626
Peek, M. (FF-08) . . . 587
Peeters, M. (DD-10) . . . 366
Peeters, M. (GE-10) . . . 693
Pei, R. (EV-11) . . . 547
Pei, R. (FP-15) . . . 622
Pelekhov, D.V. (CR-02) . . . 306
Pellicer, E. (AH-11) . . . 48
Pellicer, E. (AH-13) . . . 49
Pellicer, E. (BA-02) . . . 112
Pena Martin, P. (AS-02) . . . 78
Pena Martin, P. (BS-02) . . . 197
Pena Martin, P. (CS-02) . . . 315
Pena Martin, P. (DS-02) . . . 421
Pena Martin, P. (ES-02) . . . 524
Pena Martin, P. (FS-02) . . . 639
Pena Martin, P. (GS-02) . . . 746
Pendharkar, M. (FQ-17) . . . 630
Peng, C. (BU-04) . . . 210
Peng, H. (AQ-12) . . . 66
Peng, H. (CV-02) . . . 333
Peng, R. (BF-04) . . . 147
Peng, R. (CW-13) . . . 344
Peng, Y. (BQ-08) . . . 183
Pennycook, S. (HB-04) . . . 771
Pentcheva, R. (DH-01) . . . 386
Pereira, A. (FE-10) . . . 582
Pereira, A.M. (HH-02) . . . 810
Pereira, L.F. (GT-15) . . . 752
Pereira, P. (DW-02) . . . 442
Pereiro, E. (AF-09) . . . 33
Pereiro, M. (AP-05) . . . 60
Pereiro, M. (BD-07) . . . 134
Pérez Alcázar, G.A. (CW-03) . . . 341
Pérez del Real, R. (DV-09) . . . 439
Pérez-Checa, A. (FD-09) . . . 576
Peria, W. (AI-08) . . . 54
Peria, W. (GE-15) . . . 695
Perna, P. (BE-08) . . . 143
Perna, P. (CD-01) . . . 249
Perna, P. (HB-02) . . . 770
Perna, S. (AI-01) . . . 50
Perna, S. (ER-08) . . . 521
Perna, S. (ET-09) . . . 530
Perna, S. (FI-06) . . . 609
Perna, S. (FI-07) . . . 610
Perrin, A.E. (EI-10) . . . 502
Perrine, A. (DC-03) . . . 357
Perween, S. (DR-16) . . . 420
Petculescu, G. (FD-13) . . . 578
Peters, N. (AB-06) . . . 6
Petersen, C.F. (FE-09) . . . 582
Petford-Long, A. (FE-07) . . . 581
Petit-Watelot, S. (CC-01) . . . 243
Petit-Watelot, S. (HF-01) . . . 795
Petit, D. (EA-04) . . . 454
Petracic, O. (BF-07) . . . 149
Petrò, S. (GB-04) . . . 673
Petrovic, C. (CT-07) . . . 320
Petryshynets, I. (DW-05) . . . 444
Pezeril, T. (BD-12) . . . 136
Pfau, B. (DC-04) . . . 358
Pfeuffer, L. (FD-01) . . . 572
Pham, V. (AP-03) . . . 59
Pham, V. (FV-10) . . . 660
Phan, M. (AU-06) . . . 87
Phan, M. (BE-13) . . . 145
Phan, M. (BT-12) . . . 204
Phan, M. (CV-05) . . . 334
Phan, M. (DP-19) . . . 404
Phan, M. (DQ-04) . . . 406
Phan, M. (DU-12) . . . 433
Phan, M. (GG-04) . . . 704
Phan, T. (CT-01) . . . 317
Phan, T. (CT-04) . . . 318
Phatak, C.M. (FE-07) . . . 581
Philippi-Kobs, A. (DD-02) . . . 361
Philippi-Kobs, A. (FG-02) . . . 591
Phung, T. (BC-01) . . . 122
Phung, T. (HB-05) . . . 772
Phuyal, D. (DI-10) . . . 394
Piantek, M. (HE-06) . . . 792
Pichler, T. (AT-09) . . . 83
Picozzi, S. (EE-08) . . . 475
Pieper, J. (BF-02) . . . 146
Pierobon, L. (FH-02) . . . 599
Pierz, K. (BG-08) . . . 154
Pillsbury, T. (CB-01) . . . 236
Pimachev, A. (BI-08) . . . 168
Pimentel, B.M. (FD-05) . . . 574
Pinarbasi, M. (GC-01) . . . 678
Pinarbasi, M. (GC-12) . . . 683
Pinek, D. (BI-04) . . . 167
Pinna, D. (GF-13) . . . 702
Pinto, R.H. (AU-15) . . . 91
Pippan, R. (BF-09) . . . 149
Piramanayagam, S. (AG-10) . . . 42
Piramanayagam, S. (DE-11) . . . 373
Piramanayagam, S. (EF-02) . . . 478
Piramanayagam, S. (GP-13) . . . 730
Piraux, L. (BT-17) . . . 206
Piraux, L. (FP-05) . . . 617
Pirro, P. (CE-08) . . . 258
Pirro, P. (GE-03) . . . 690
Pirruccio, G. (EW-14) . . . 557
Piva, M.M. (GT-05) . . . 749
Pizzini, S. (HG-03) . . . 805
Planes, A. (FD-01) . . . 572
Plaza-García, S. (DG-04) . . . 380
Plucinski, L. (CD-03) . . . 250
Poellath, S. (AW-02) . . . 101
Pogoryelov, Y. (AP-05) . . . 60
Pohl, D. (CG-07) . . . 272
Pohlmann, T. (AE-07) . . . 26
Pohlmann, T. (AF-11) . . . 34
Poimanov, V.D. (EW-07) . . . 554
Pojprapai, S. (GQ-14) . . . 740
Pokharel Madhogaria, R. (GG-04) . . . 704
Pokharel, G. (BT-12) . . . 204
Pokharel, S. (AQ-06) . . . 64
Pokharel, S. (AR-16) . . . 76
Pokhrel, A. (CR-03) . . . 307
Pokhrel, A. (ED-03) . . . 468
Pokhrel, A. (FT-03) . . . 642
Polakovic, T. (FA-02) . . . 559
Pollard, S.D. (DB-04) . . . 351
Polley, D. (BD-01) . . . 131
Polley, D. (BD-03) . . . 132
Polley, D. (BD-08) . . . 134

*Best student presentation award finalist

Polley, D. (DD-02) 361
Pomar, A. (BT-16) 206
Pomar, A. (DH-08) 388
Pomar, A. (FC-08) 569
Pomar, A. (FV-03) 658
Pong, P. (AW-12) 106
Poniatowski, N.R. (DI-02) 391
Poon, J. (AG-06) 39
Poon, J. (AG-11) 42
Poorman, M.E. (DG-03) 380
Popescu, H. (AF-07) 32
Popov, A.V. (EV-18) 549
Popov, Z. (FB-09) 564
Popovici, M.I. (EG-09) 489
Porod, W. (EP-12) 508
Porod, W. (GE-06) 691
Porro Azpiazu, J. (FD-09) 576
Porter, D. (ET-01) 526
Portnyagin, A. (BP-05) 174
Pot, C. (DR-10) 417
Poudel, T.P. (AR-13) 75
Poudel, T.P. (BR-02) 189
Poudel, T.P. (BR-15) 195
Pourmiri, S. (CQ-06) 302
Pourmiri, S. (CQ-10) 304
Pourmiri, S. (CQ-11) 304
Prabhakaran, D. (AV-01) 92
Prabhu Gaunkar, G. (DT-08) 425
Prabhu Gaunkar, N. (CQ-03) 300
Prabhu Gaunkar, N. (DT-08) 425
Pradhan, D.K. (FU-13) 653
Pradhan, D.K. (HC-07) 778
Pradhan, D.K. (HC-08) 778
Pradipto, A.M. (AV-17) 99
Pradipto, A.M. (GT-04) 749
Pramanik, P. (FU-16) 654
Prasad, N. (CF-09)* 266
Prasad, N.K. (DW-15) 449
Prasad, N.K. (HH-13) 816
Pratt, F.L. (AW-11) 106
Prchal, J. (BI-05) 167
Prchal, J. (EI-03) 498
Prejbeanu, I. (BC-13) 129
Prejbeanu, I. (EF-07) 481
Prejbeanu, I. (EP-08) 506
Prejbeanu, I. (ET-13) 531
Prejbeanu, I. (GC-11) 683
Prelovsek, P. (FE-02) 579
Prestigiacomo, J. (CT-09) 320
Prieto, J.L. (BE-10) 144
Primetzhofer, D. (AP-05) 60
Prinsloo, A. (DW-14) 448
Priyadarshi, P. (FC-03) 567
Prokofev, P. (BP-11) 176
Prokofev, P. (BP-15) 178
Prokopenko, O. (AB-08) 7
Prokopenko, O. (BE-11) 144
Prokscha, T. (DR-06) 416
Prophet, S. (CW-17) 346
Proschek, P. (EI-03) 498
Proselkov, O. (HF-12) 801
Proskurin, I. (BD-10) 136
Proskurin, I. (CB-06) 238
Proskurin, I. (EF-04) 479
Prost, D. (AF-04) 31
Provino, A. (BI-06) 168
Provino, A. (BI-13) 170
Prudnikov, A. (GP-04) 725
Prudnikov, V. (DR-01) 414
Prudnikov, V. (DR-15) 420
Przybylski, M. (DI-11) 395
Przybylski, M. (GG-11) 707
Przybylski, M. (HH-07) 813
Psycharis, V. (AR-02) 70
Pudell, J. (BD-12) 136
Pufall, M. (AV-16) 99
Pufall, M. (EF-03) 479
Pufall, M. (EP-12) 508
Puliafito, V. (AC-08) 15
Puliafito, V. (BB-06) 117
Pullar, R.C. (EH-05) 494
Purnama, I. (DC-08) 359
Purnama, I. (EW-08) 555
Puwenberg, N. (HG-05) 805

- Q -

Qaiumzadeh, A. (CB-04) 237
Qian, F. (GF-04) 698
Qiao, G. (GU-07) 757
Qiao, K. (BT-08) 202
Qiao, K. (DQ-17) 412
Qiao, K. (DT-13) 426
Qiao, K. (FQ-14) 629
Qin, F. (AQ-12) 66
Qin, F. (CV-02) 333
Qin, W. (EU-12) 540
Qin, W. (FP-11) 620
Qin, Y. (HD-09) 786
Qin, Y. (HD-15) 789
Qiu, W. (FT-15) 647
Qiu, X. (BV-09) 221
Qiu, X. (CD-09) 252
Qiu, X. (CP-08) 294
Qiu, X. (DP-06) 398
Qiu, X. (FV-11) 660
Qiu, X. (HB-04) 771
Qiu, X. (HB-06) 772
Qiu, Z. (EC-07) 464
Qiu, Z.Q. (CB-10) 240
Qiu, Z.Q. (GB-02) 671
Qu, B. (CU-03) 325
Qu, B. (EU-05) 537
Qu, D. (AB-15) 10
Qu, D. (BE-05) 142
Qu, H. (AS-04) 79
Qu, H. (BS-04) 197
Qu, H. (BT-02) 199
Qu, H. (CS-04) 315
Qu, H. (DS-04) 421
Qu, H. (ES-04) 524
Qu, H. (FB-11) 565
Qu, H. (FS-04) 639
Qu, H. (GS-04) 747
Qu, T. (EQ-14) 517
Qu, T. (GE-15) 695
Quam, W. (GI-13) 722
Quan, Z. (BV-06) 219
Quarterman, P. (BR-17) 195
Quarterman, P. (DI-04) 392
Que, L. (DU-04) 429
Querlioz, D. (EF-01) 478
Querlioz, D. (EQ-04) 513
Querlioz, D. (TU-01) 1
Quessab, Y. (AG-06) 39
Quessab, Y. (EW-05) 554
Quigley, L.J. (DE-02) 368
Quindeau, A.U. (HH-04) 811
Quinsat, M. (HB-03) 771
Quintana Puebla, A. (BA-02) 112
Quintana, A. (AH-09) 47
Quintana, A. (AH-11) 48
Quintana, A. (BA-04) 112
Quintana, A. (FU-12) 653
Quiros, C. (AF-09) 33
Quispe Flores, C.M. (DC-06) 359
Quispe Flores, C.M. (EQ-11) 516
Qureshi, N. (EW-14) 557

- R -

R, G. (FD-03) 573
R. Valloppilly, S. (GF-03) 698
Raabe, J. (DE-05) 369
Raabe, J. (ED-01) 467
Rackham, J. (BF-05) 148
Rackham, J. (BF-06) 148
Radelytskyi, I. (DQ-07) 407
Radhakrishnan, A. (AD-05) 18
Radu, I. (CE-12) 260
Radu, I. (EP-16) 510
Radu, I. (HC-10) 779
Radu, I. (HG-10) 808
Radulov, I.A. (FD-02) 572
Raeliarijaona, A.S. (AB-14) 10
Rafi-Ul-Islam, S. (AV-11) 97
Ragazzo, H. (AF-04) 31
Raghav, D. (AU-07) 87
Rahaman, M.M. (HC-07) 778
Rai, A. (AI-06) 53
Rai, A. (CR-03) 307
Rai, A. (ED-03) 468
Rai, A. (FG-09) 595
Rai, A. (FT-03) 642
Rai, B.K. (BR-02) 189
Rai, B.K. (BR-15) 195
Rai, S. (BF-08) 149
Raimer, O. (BU-12) 214
Raju, M. (AW-10) 105
Raju, M. (DE-09) 372
Rakheja, S. (BB-08) 117

*Best student presentation award finalist

Ralph, D. (AC-04) . . . 12
Ralph, D. (AF-13) . . . 35
Ralph, D. (AH-05) . . . 45
Ralph, D. (BE-07) . . . 142
Ralph, D. (DA-05) . . . 348
Ralph, D. (FG-13) . . . 597
Ramanathan, S. (AF-08) . . . 33
Ramaswamy, R. (FV-11) . . . 660
Ramerman, D. (FQ-03) . . . 624
Ramesh, R. (AF-13) . . . 35
Ramesh, R. (GG-05) . . . 704
Ramesh, R. (HC-06) . . . 777
Ramin Moayed, M. (BU-13) . . . 215
Ramin Moayed, M. (CF-06) . . . 264
Ramin Moayed, M. (GQ-13) . . . 740
Ramirez, A.P. (FE-01) . . . 579
Ramírez, J. (FT-06) . . . 643
Ramon, J. (FE-05) . . . 580
Ramos de Jesus, C.B. (GT-06) . . . 750
Ramos-Cabrer, P. (DG-04) . . . 380
Ramos, E. (FT-06) . . . 643
Ramos, R. (BB-01) . . . 114
Ramos, R. (CF-08) . . . 266
Ramos, R. (EC-07) . . . 464
Ramshaw, B. (DH-01) . . . 386
Ramsteiner, M. (DB-10) . . . 354
Rana, B. (BQ-14) . . . 186
Rana, B. (EG-10) . . . 490
Rana, K. (ED-04) . . . 469
Rancan, M. (HE-04) . . . 791
Ranchal, R. (FD-08) . . . 575
Randeria, M. (DC-03) . . . 357
Rani, D. (HF-04) . . . 796
Ranjan, A. (AS-03) . . . 78
Ranjan, A. (BS-03) . . . 197
Ranjan, A. (CS-03) . . . 315
Ranjan, A. (CW-10) . . . 343
Ranjan, A. (DS-03) . . . 421
Ranjan, A. (ES-03) . . . 524
Ranjan, A. (FS-03) . . . 639
Ranjan, A. (GS-03) . . . 746
Ranjan, P. (AU-01) . . . 85
Ranjbar, M. (AP-05) . . . 60
Ranjbar, S. (DV-04) . . . 437
Rannala, S.E. (FI-03) . . . 608
Rannala, S.E. (HD-04) . . . 783
Ranno, L. (FQ-05) . . . 625
Rao, M. (FV-09) . . . 660
Rao, S. (EG-11) . . . 490
Rao, S. (EP-13) . . . 508
Rao, S. (FC-04) . . . 567
Rao, S. (GC-02) . . . 679
Rao, S. (GC-08) . . . 681
Rao, S. (HG-11) . . . 809
Raposo, V. (HD-01) . . . 782
Raposo, V. (HG-04) . . . 805
Rasilo, P. (CH-07) . . . 280
Rasilo, P. (DW-01) . . . 442
Rasing, T. (GC-11) . . . 683
Rastogi, A. (BR-09) . . . 192
Rastogi, A. (DH-09) . . . 389
Rastogi, P. (CQ-12) . . . 304
Ratcliff, W.D. (GT-05) . . . 749
Rathi, A. (BR-11) . . . 193
Rathi, A. (DH-10) . . . 389
Rathi, A. (DR-16) . . . 420
Rathi, A. (FF-04) . . . 585
Ravasi, T. (DG-04) . . . 380
Raymenants, E. (EP-16) . . . 510
Raymenants, E. (HG-10) . . . 808
Razavi, A. (AD-09) . . . 19
Razavi, S. (DE-07) . . . 371
Razavi, S. (EB-10) . . . 458
Read, C. (HE-10) . . . 794
Read, D. (DQ-19) . . . 413
Read, D. (FQ-17) . . . 630
Rebola, A. (GG-05) . . . 704
Reches, M. (BG-09) . . . 155
Reddy, P. (AG-08) . . . 40
Reddy, V. (GH-09) . . . 712
Reeve, R.M. (AF-10) . . . 34
Register, L. (CF-09) . . . 266
Regmi, S. (BI-11) . . . 169
Regmi, S. (BR-09) . . . 192
Reguera, J. (DG-12) . . . 384
Rehm, L. (GC-01) . . . 678
Reid, A. (BF-06) . . . 148
Reis, M.S. (FD-05) . . . 574
Reiss, G. (AB-04) . . . 5
Reiss, G. (AE-07) . . . 26
Reiss, G. (ET-02) . . . 526
Reiss, G. (FQ-03) . . . 624
Reiss, G. (HF-02) . . . 795
Rellinghaus, B. (CG-07) . . . 272
Rementer, C. (DW-09) . . . 446
Ren, H. (BC-07) . . . 125
Ren, H. (EC-10) . . . 465
Ren, L. (BC-03) . . . 123
Ren, L. (CD-08) . . . 252
Ren, Z. (BQ-13) . . . 185
Ren, Z. (HF-08) . . . 799
Rensmo, H. (DI-10) . . . 394
Repa, K. (BH-15) . . . 164
Retamal, J. (BQ-06) . . . 182
Retana, M. (BF-08) . . . 149
Rettner, C. (BC-01) . . . 122
Rettori, C. (GT-07) . . . 750
Reyes, A. (AV-10) . . . 96
Reyes, J. (AT-07) . . . 82
Reynolds, N. (DA-05) . . . 348
Reyren, N. (AE-08) . . . 26
Reyren, N. (AF-07) . . . 32
Reyren, N. (BG-10) . . . 156
Reyren, N. (BV-03) . . . 218
Reyren, N. (DE-01) . . . 368
Reyren, N. (ED-05) . . . 469
Rezende, S. (FA-05) . . . 560
Reznikov, M. (DE-09) . . . 372
Rhie, K. (FW-06) . . . 665
Rhim, S.H. (BT-18) . . . 207
Rhyne, J.J. (AW-16) . . . 108
Riahi, N. (BW-14) . . . 231
Riahi, N. (DU-07) . . . 430
Ribas, R.M. (FQ-15) . . . 629
Ribeiro, A. (CT-13) . . . 322
Rice, W.D. (CV-18) . . . 339
Richards, B.A. (DT-01) . . . 423
Riedemann, T.M. (FQ-18) . . . 630
Riego, P. (ER-10) . . . 522
Riepp, M. (DD-02) . . . 361
Riley, G.A. (AG-06) . . . 39
Riley, G.A. (AI-07) . . . 53
Rimal, G. (CB-01) . . . 236
Rinaldi, C. (CH-01) . . . 276
Rinaldi, C. (GB-04) . . . 673
Riney, L. (DT-06) . . . 424
Riou, M. (EF-01) . . . 478
Riou, M. (EQ-04) . . . 513
Rippard, W.H. (AV-16) . . . 99
Rippard, W.H. (EF-03) . . . 479
Rippard, W.H. (EP-12) . . . 508
Rippy, G. (BA-05) . . . 113
Ritter, C. (AW-17) . . . 109
Ritter, C. (BI-06) . . . 168
Ritzmann, U. (ED-10) . . . 471
Rivas, M. (CU-02) . . . 324
Rivas, M. (EV-20) . . . 551
Rivas, M. (GQ-15) . . . 741
Riveros, A. (AW-15) . . . 108
Riveros, A. (EQ-08) . . . 515
Rizal, C. (BI-14) . . . 171
Rizzo, G. (BW-15) . . . 231
Robbennolt, S. (AH-13) . . . 49
Robbennolt, S. (BA-02) . . . 112
Roberto Pirota, K. (DQ-14) . . . 410
Robertson, M. (AG-02) . . . 38
Robertson, M. (CG-11) . . . 274
Robertson, M. (FG-03) . . . 592
Robinson, I.K. (BH-03) . . . 159
Robinson, J. (AE-06) . . . 26
Robles-Garcia, J. (DU-12) . . . 433
Rocco, D.L. (AT-01) . . . 80
Rocco, D.L. (FD-05) . . . 574
Roche, S. (DB-01) . . . 350
Rodionov, V. (DQ-18) . . . 412
Rodionova, V. (GH-11) . . . 713
Rodionova, V. (GQ-15) . . . 741
Rodrigues, J. (FE-10) . . . 582
Rodrigues, R.d. (DQ-14) . . . 410
Rodríguez Cid, D.A. (ET-03) . . . 527
Roe, A.R. (GC-13) . . . 683
Roessler, U. (EE-11) . . . 477
Rogalev, A. (BI-04) . . . 167
Rogalev, A. (FH-01) . . . 599
Roh, J. (CI-01) . . . 284
Röhlsberger, R. (BD-15) . . . 138
Röhlsberger, R. (BU-13) . . . 215
Röhlsberger, R. (CE-02) . . . 255
Röhlsberger, R. (CF-06) . . . 264
Röhlsberger, R. (GQ-13) . . . 740
Rojas-Sanchez, J. (HF-01) . . . 795
Roldán, A. (EW-13) . . . 557
Roldan, M. (EE-07) . . . 475

*Best student presentation award finalist

Romaguera, A. (GG-03) 704
Romano, A. (AH-06) 46
Romano, P. (BW-15) 231
Romanque, C. (CU-16) 332
Romero-Muñiz, C. (FD-02) 572
Romero, A. (FU-16) 654
Ronning, F. (GT-08) 750
Rontani, D. (CC-01) 243
Rontani, D. (EF-06) 480
Roos, M. (AP-06) 60
Roos, M. (BR-17) 195
Roos, M. (FV-02) 657
Rortais, F. (DP-04) 397
Rortais, F. (EF-10) 482
Rosamond, M. (BB-11) 119
Rosamond, M. (BE-09) 143
Rosamond, M. (DE-05) 369
Rosca, R. (DD-02) 361
Roschewsky, N. (GC-10) 682
Roseker, W. (DD-02) 361
Rosen, J. (BI-04) 167
Rosenberg, E.R. (AG-08) 40
Rosenberg, E.R. (DA-03) 348
Rosenberg, E.R. (HH-01) 810
Rosenberg, E.R. (HH-04) 811
Rosenberg, E.R. (HH-15) 817
Roshchin, I.V. (AB-05) 5
Ross, A. (AG-05) 39
Ross, A. (BB-01) 114
Ross, A. (CB-04) 237
Ross, A. (EC-07) 464
Ross, C. (AG-08) 40
Ross, C. (AH-08) 47
Ross, C. (BG-04) 153
Ross, C. (DA-03) 348
Ross, C. (HG-02) 804
Ross, C. (HG-07) 806
Ross, C. (HH-01) 810
Ross, C. (HH-04) 811
Ross, C. (HH-15) 817
Rossle, M. (BD-12) 136
Rotenberg, E. (FB-02) 561
Rothschild, A. (CB-04) 237
Rott, K. (HF-02) 795
Rott, N. (GV-06) 762
Roussel, P.J. (EG-09) 489
Roussigné, Y. (CG-01) 270
Rout, P. (DH-10) 389
Rowan-Robinson, R. (BF-11) 150
Rowland, J.R. (DC-03) 357
Roy, D. (CB-02) 237
Roy, k. (EP-12) 508
Roy, S. (BH-03) 159
Royer III, R. (FF-02) 584
Rózsa, L. (GF-13) 702
Rubin, J. (HE-04) 791
Rubio-Roy, M. (EC-09) 464
Rubio-Roy, M. (GC-11) 683
Rubio-Roy, M. (GQ-01) 734
Rudnev, I.A. (FH-01) 599
Rudolf, P. (DR-02) 414
Ruiter, R. (FB-06) 563
Ruiz, A. (BH-02) 158
Ruiz, A. (BH-11) 163
Ruiz, A. (GD-03) 685
Ruiz, A. (GD-05) 686
Ruiz, M. (DD-09) 366
Rusinov, I.P. (EB-07) 457
Russek, S.E. (BG-01) 152
Russek, S.E. (DG-03) 380
Russek, S.E. (DG-06) 381
Russek, S.E. (EF-03) 479
Russell, T. (FF-03) 585
Ruta, S. (FI-03) 608
Ruta, S. (HD-04) 783
Ryaby, J.T. (FF-02) 584
Ryan, D. (FQ-08) 626
Ryan, D. (GT-09) 750
Rychly, J. (GE-12) 694
Ryu, D. (EV-04) 543
Ryu, J. (BV-05) 219
Ryu, J. (EP-03) 504
Ryu, J. (GB-13) 677

- S -

Saari, M. (DG-10) 383
Saavedra, E. (FT-13) 646
Saccone, M.D. (BH-05) 160
Saccone, M.D. (FE-09) 582
Sachser, R. (CE-07) 257
Sachser, R. (EW-15) 557
Sadiq, M.M. (DG-13) 385
Sadovnikov, A.V. (DE-05) 369
Sadovnikov, A.V. (DE-06) 370
Sadowski, J. (HF-12) 801
Safi, T.S. (AE-11) 28
Safranski, C. (DA-02) 347
Saglam, H. (AB-09) 7
Saglam, H. (FA-02) 559
Saglam, H. (FV-07) 659
Saha, A. (BG-09) 155
Saha, D. (HG-08) 806
Saha, P. (HH-05) 812
Saha, R. (CQ-13) 304
Saha, R. (CQ-14) 305
Sahin, C. (EB-12) 459
Sahoo, S. (CC-10) 246
Sahoo, S. (EQ-03) 513
Sahoo, S. (ER-01) 518
Sahoo, S. (EW-06) 554
Sahu, B. (GT-11) 751
Sahu, P. (DP-11) 400
Sahu, U. (DF-04) 376
Sahu, U. (DF-07) 377
Sai, R. (GI-02) 716
Sai, R. (HH-08) 813
Saichi, K. (FF-09) 588
Saiki, M. (AU-15) 91
Saito, G. (AR-03) 71
Saito, H. (CF-05) 264
Saito, H. (EF-08) 481
Saito, H. (EF-09) 482
Saito, H. (GR-03) 742
Saito, I. (DU-11) 432
Saito, I. (FF-08) 587
Saito, I. (FF-10) 588
Saito, I. (FF-11) 589
Saito, M. (FG-08) 594
Saito, S. (EV-16) 548
Saito, S. (GR-05) 743
Saito, S. (HD-11) 787
Saito, T. (AR-04) 71
Saito, T. (AR-05) 71
Saito, T. (AR-06) 72
Saito, T. (FH-08) 602
Saito, T. (HD-11) 787
Saito, W. (GR-06) 744
Saito, Y. (EC-11) 465
Saitoh, E. (BB-01) 114
Saitoh, E. (CF-08) 266
Saitoh, E. (EC-07) 464
Saitoh, E. (GB-02) 671
Sakai, H. (AV-10) 96
Sakai, K. (CQ-09) 303
Sakai, K. (DG-10) 383
Sakai, S. (FB-09) 564
Sakakibara, T. (AV-13) 98
Sakakura, K. (FH-07) 602
Sakamoto, S. (FF-10) 588
Sakamoto, S. (FF-11) 589
Sakamoto, S. (HF-10) 800
Sakuma, A. (BQ-10) 184
Sakuma, A. (CR-05) 308
Sakuma, N. (CA-03) 233
Sakuraba, Y. (CF-07) 265
Sakuraba, Y. (FB-09) 564
Sakuraba, Y. (HD-12) 787
Sakuraba, Y. (HF-06) 798
Sala, G. (BB-12) 119
Salahuddin, S. (DD-08) 365
Salahuddin, S. (DD-09) 366
Salahuddin, S. (GC-10) 682
Salahuddin, S. (GE-07) 691
Salahuddin, S. (HC-03) 776
Salamon, M. (EI-11) 502
Salas-Colera, E. (FD-08) 575
Salazar Mejia, C. (DQ-14) 410
Salerno, S. (BW-15) 231
Sales, F.H. (GQ-11) 739
Sales, T. (AU-14) 90
Salev, P. (BT-03) 199
Salhi, Z. (DT-03) 423
Salikhov, R. (CG-13) 275
Salloum, E. (AF-01) 30
Salski, B. (BG-02) 152
Salski, B. (CU-05) 326
Salvador, M. (EV-20) 551
Samad, F. (BH-01) 158
Samad, F. (CG-13) 275
Samardak, A. (BP-05) 174
Samardak, A.S. (BP-05) 174

*Best student presentation award finalist

Samardak, A.S. (DE-06) . . . 370
Samarth, N. (CB-01) . . . 236
Sambi, M. (HE-04) . . . 791
Sambi, M. (HE-06) . . . 792
Samiepour, M. (CP-04) . . . 293
Sampaio, J. (AI-12) . . . 56
Sampaio, J. (CR-07) . . . 309
Sanad, M. (CQ-10) . . . 304
Sanad, M. (CQ-11) . . . 304
Sanchez Hanke, C. (DD-02) . . . 361
Sánchez Llamazares, J. (DQ-01) . . . 405
Sánchez-Agudo, M. (BH-11) . . . 163
Sanchez-Valdes, C. (DQ-01) . . . 405
Sandeman, K.G. (DG-13) . . . 385
Sandeman, K.G. (FQ-05) . . . 625
Sandeman, K.G. (FQ-11) . . . 627
Sandeman, K.G. (HE-03) . . . 790
Sanders, A. (DP-08) . . . 399
Sandhoefner, S. (EB-05) . . . 457
Sando, D. (GQ-14) . . . 740
Sanghadasa, M. (EV-01) . . . 541
Sankar, R. (DR-13) . . . 419
Sankaran, K. (GC-02) . . . 679
Santamaria, J. (HC-01) . . . 775
Santos, M.d. (AT-01) . . . 80
Santos, T. (FC-01) . . . 566
Santos, T. (GC-06) . . . 680
Santos, T. (HD-02) . . . 782
Santos, Y.S. (AU-03) . . . 86
Sanvito, S. (CA-01) . . . 233
Sapkota, A. (AI-03) . . . 51
Sapkota, A. (AI-06) . . . 53
Sapkota, A. (CR-03) . . . 307
Sapkota, A. (ED-03) . . . 468
Sapkota, A. (FG-09) . . . 595
Sapkota, A. (FT-03) . . . 642
Sarafidis, C. (FH-10) . . . 603
Sarathi, R. (AU-01) . . . 85
Sarella, A. (GF-03) . . . 698
Sarkar, A. (AT-03) . . . 81
Sarkar, T. (DI-02) . . . 391
Sarpi, B. (ED-04) . . . 469
Sarvezuk, P.W. (GT-13) . . . 752
Sasaki, S. (GU-01) . . . 754
Sasaki, S. (GU-02) . . . 754
Sasaki, T. (AC-07) . . . 14
Sasaki, T. (BC-12) . . . 128
Sasaki, T. (BP-08) . . . 174
Sasaki, T. (CF-07) . . . 265
Sassi, Y. (BG-10) . . . 156
Sassi, Y. (ED-05) . . . 469
Sasso, C.P. (GI-01) . . . 716
Satchell, N. (DI-04) . . . 392
Sato, A. (CQ-01) . . . 300
Sato, F. (GU-01) . . . 754
Sato, F. (GU-02) . . . 754
Sato, F. (GU-08) . . . 757
Sato, H. (AI-10) . . . 55
Sato, H. (CR-01) . . . 306
Sato, H. (EC-11) . . . 465
Sato, H. (FC-07) . . . 569
Sato, N. (HG-05) . . . 805
Sato, R. (FH-09) . . . 603
Sato, S. (BC-08) . . . 126
Sato, T. (BP-08) . . . 174
Sato, T. (BQ-16) . . . 187
Sato, T. (FF-09) . . . 588
Sato, T. (FT-07) . . . 644
Savchenko, A.G. (FH-01) . . . 599
Savchenko, T. (CG-04) . . . 271
Savero Torres, W.F. (DB-01) . . . 350
Savliwala, S. (CH-01) . . . 276
Sawa, T. (BT-09) . . . 202
Sawa, T. (GU-01) . . . 754
Sawa, T. (GU-02) . . . 754
Sawahata, H. (CV-08) . . . 335
Sawicki, M. (BG-12) . . . 156
Sawicki, M. (BQ-17) . . . 187
Sawicki, M. (DR-06) . . . 416
Sawicki, M. (EB-13) . . . 460
Sawicki, M. (FI-12) . . . 612
Sawicki, M. (HF-11) . . . 800
Sawicki, M. (HF-12) . . . 801
Saxena, R.N. (CU-10) . . . 329
Sayed, S. (GC-10) . . . 682
Sbiaa, R. (DE-11) . . . 373
Sbiaa, R. (EF-02) . . . 478
Scalera, V. (BD-01) . . . 131
Scalera, V. (ET-09) . . . 530
Scalera, V. (FI-06) . . . 609
Scalise, L.M. (GT-15) . . . 752
Schaeffer, T. (GQ-02) . . . 734
Schäfer, R. (AH-10) . . . 47
Schäfer, R. (CD-03) . . . 250
Schäffer, A.F. (GF-09) . . . 701
Schaller, R. (BT-02) . . . 199
Schäublin, R.E. (FH-02) . . . 599
Scherz, A. (DD-02) . . . 361
Scheuer, L. (EC-06) . . . 463
Schiffer, P. (BH-06) . . . 160
Schiffer, P. (BH-07) . . . 161
Schiffer, P. (HA-01) . . . 767
Schippers, C. (AB-02) . . . 4
Schippers, C. (CE-11) . . . 259
Schippers, C. (GE-10) . . . 693
Schlage, K. (BU-13) . . . 215
Schlage, K. (CE-02) . . . 255
Schlage, K. (CF-06) . . . 264
Schlage, K. (GQ-13) . . . 740
Schlenhoff, A. (EF-13) . . . 483
Schlom, D. (AC-04) . . . 12
Schlom, D. (AF-13) . . . 35
Schlom, D. (AH-01) . . . 44
Schlom, D. (AH-05) . . . 45
Schlom, D. (GG-05) . . . 704
Schlom, D. (HC-06) . . . 777
Schlueter, C. (DT-15) . . . 427
Schmalhorst, J. (AE-07) . . . 26
Schmid, A.K. (AG-02) . . . 38
Schmid, A.K. (AG-03) . . . 38
Schmid, A.K. (AV-15) . . . 98
Schmid, A.K. (CG-11) . . . 274
Schmid, A.K. (FG-03) . . . 592
Schmidt, H. (BD-14) . . . 138
Schmidt, M.P. (GF-04) . . . 698
Schneider, A. (CE-03) . . . 255
Schneider, C. (HC-05) . . . 777
Schneider, C.M. (CD-03) . . . 250
Schneider, H.C. (EC-06) . . . 463
Schneider, I. (DU-04) . . . 429
Schneider, J.D. (DW-09) . . . 446
Schneider, J.D. (GE-07) . . . 691
Schneider, M. (CE-08) . . . 258
Schneider, M. (DD-02) . . . 361
Schneider, M. (GE-03) . . . 690
Schneider, M.L. (AI-07) . . . 53
Schneider, M.L. (EF-03) . . . 479
Schneider, R. (BT-01) . . . 199
Schneider, R. (FV-13) . . . 661
Schneider, S. (AH-10) . . . 47
Schneider, T. (EW-13) . . . 557
Schöbitz, M. (HG-09) . . . 807
Scholl, A. (BH-05) . . . 160
Scholl, A. (FE-09) . . . 582
Scholl, A. (GG-01) . . . 703
Schönhense, G. (DT-15) . . . 427
Schönke, D. (AF-10) . . . 34
Schönke, D. (AW-09) . . . 105
Schrefl, T. (AR-08) . . . 73
Schrefl, T. (CA-03) . . . 233
Schrefl, T. (FI-01) . . . 607
Schröder, C. (BF-02) . . . 146
Schroeder, A. (EI-06) . . . 500
Schuller, I. (BT-03) . . . 199
Schuller, I. (EI-04) . . . 499
Schuller, I. (EI-05) . . . 499
Schuller, I.K. (AB-05) . . . 5
Schuller, I.K. (AF-08) . . . 33
Schultheiss, H. (CC-04) . . . 244
Schultheiss, H. (CC-05) . . . 244
Schultheiss, H. (HG-05) . . . 805
Schultheiss, K. (CC-04) . . . 244
Schultheiss, K. (CC-05) . . . 244
Schultheiss, K. (HG-05) . . . 805
Schulz, F. (GQ-04) . . . 735
Schumacher, H. (BG-08) . . . 154
Schumacher, H. (DE-01) . . . 368
Schütz, G. (CU-02) . . . 324
Schütz, G. (DE-03) . . . 369
Schütz, G. (GE-08) . . . 692
Schütz, G. (GE-09) . . . 693
Schütz, G. (GE-12) . . . 694
Schütz, G. (GQ-03) . . . 735
Schwingenschlögl, u. (AD-01) . . . 16
Sciamanna, M. (CC-01) . . . 243
Sciamanna, M. (EF-06) . . . 480
Sears, J. (AF-12) . . . 35
Sebastián, J. (EV-20) . . . 551
Sebastian, T. (AS-04) . . . 79
Sebastian, T. (BS-04) . . . 197
Sebastian, T. (CS-04) . . . 315
Sebastian, T. (DS-04) . . . 421
Sebastian, T. (ES-04) . . . 524

*Best student presentation award finalist

Sebastian, T. (FS-04) 639
Sebastian, T. (GS-04) 747
Sechovsky, V. (EI-03) 498
Sedona, F. (HE-04) 791
Sedona, F. (HE-06) 792
Seeger, R.L. (EC-09) 464
Seeger, R.L. (ER-05) 520
Seeger, R.L. (GQ-01) 734
Seehra, M.S. (CR-15) 313
Seehra, M.S. (FU-16) 654
Segre, C.U. (DI-10) 394
Seibt, M. (CF-12) 268
Seki, S. (GF-01) 697
Seki, S. (HA-02) 767
Seki, T. (EQ-01) 512
Sekino, M. (DU-11) 432
Sekino, M. (FF-08) 587
Sekino, M. (FF-09) 588
Sekino, M. (FF-10) 588
Sekino, M. (FF-11) 589
Sekiyama, A. (DR-09) 417
Sekiyama, A. (EQ-07) 514
Sellmyer, D.J. (AW-16) 108
Sellmyer, D.J. (EH-13) 497
Sellmyer, D.J. (GF-03) 698
Sellmyer, D.J. (HE-08) 793
Sellmyer, D.J. (HE-13) 794
Semisalova, A. (BD-01) 131
Semisalova, A. (CR-06) 308
Sen, K. (DI-09) 394
Sen, P. (DQ-11) 408
Sen, S. (GG-07) 705
Sena, C. (AU-15) 91
Seng, B. (AW-09) 105
Seng, B. (GF-13) 702
Sengupta, P. (DE-11) 373
Seo, J. (GT-03) 748
Seo, K. (CH-12) 282
Seo, K. (EV-13) 547
Seo, K. (FP-12) 620
Seo, S. (FP-08) 618
Seo, S. (FR-09) 636
Sepulveda, A. (CQ-05) 301
Sepulveda, A. (DW-09) 446
Sepulveda, A. (GI-07) 719
Serga, A.A. (BD-09) 135
Serga, A.A. (BE-11) 144
Serga, A.A. (CE-13) 260
Serga, A.A. (GE-02) 689
Sergeev, I. (CE-02) 255
Serha, R.O. (BD-09) 135
Sernicola, N. (EF-02) 478
Sernicola, N. (GP-13) 730
Serpico, C. (AI-01) 50
Serpico, C. (CA-04) 234
Serpico, C. (ER-08) 521
Serpico, C. (ET-09) 530
Serpico, C. (FI-02) 607
Serpico, C. (FI-06) 609
Serpico, C. (FI-07) 610
Serrano, A. (HH-03) 811
Sesé, J. (GP-08) 728
Sethi, P. (AC-01) 11
Setina, J. (HH-04) 811
Shabalin, A. (FI-11) 611
Shafer, P. (AF-08) 33
Shafer, P. (CB-10) 240
Shafer, P. (GB-02) 671
Shafer, P. (GG-01) 703
Shafer, P. (HC-03) 776
Shah, S. (DR-02) 414
Shan, J. (AA-02) 2
Shang, Z. (FH-11) 604
Shang, Z. (FH-15) 605
Shao, D. (AD-03) 17
Shao, D. (CP-03) 292
Shao, L. (CT-07) 320
Shao, Q. (AD-09) 19
Shao, Q. (DG-01) 379
Shao, S. (DQ-16) 411
Shao, S. (FQ-04) 624
Sharif, M. (BI-15) 171
Sharifabad, M.E. (DT-14) 427
Sharifi, S.H. (FC-04) 567
Sharma, A. (DG-01) 379
Sharma, A. (DW-15) 449
Sharma, A. (GC-03) 679
Sharma, H. (BE-02) 140
Sharma, H. (BE-03) 141
Sharma, M. (AT-04) 81
Sharma, M. (BQ-12) 185
Sharma, P. (AR-17) 77
Sharma, P. (AU-13) 90
Sharma, P. (CT-05) 319
Sharma, P. (EH-07) 495
Sharma, P. (GI-14) 722
Sharma, R. (BV-10) 221
Sharma, Y. (GG-06) 705
Sharmar, V. (FD-07) 575
Shaw, C. (AR-01) 70
Shaw, J.M. (AG-06) 39
Shaw, J.M. (AI-07) 53
Shaw, J.M. (CR-04) 307
Shaw, J.M. (DD-02) 361
Shaw, J.M. (ER-03) 519
Shaw, J.M. (EW-02) 552
Shaw, S.K. (HH-13) 816
Shchetinin, I.V. (FH-01) 599
Shen, B. (AH-03) 45
Shen, B. (AQ-15) 68
Shen, B. (BT-08) 202
Shen, B. (BT-10) 203
Shen, B. (DQ-05) 406
Shen, B. (DQ-15) 410
Shen, B. (DQ-16) 411
Shen, B. (DQ-17) 412
Shen, B. (DT-13) 426
Shen, B. (FQ-04) 624
Shen, B. (FQ-14) 629
Shen, F. (DQ-05) 406
Shen, F. (DQ-17) 412
Shen, J. (AW-02) 101
Shen, K. (HB-04) 771
Shen, L. (DD-05) 363
Shen, M. (BQ-08) 183
Shen, T. (AR-11) 74
Shen, X. (FC-11) 571
Sheppard, C. (DW-14) 448
Sherpa, P. (ER-07) 520
Sheth, N.K. (CH-09) 281
Shevyrtalov, S. (AQ-13) 67
Shi, D. (BB-10) 118
Shi, J. (AI-11) 55
Shi, J. (BB-09) 118
Shi, J. (BB-14) 120
Shi, J. (CB-08) 239
Shi, J. (CB-09) 240
Shi, J. (DB-09) 353
Shi, J. (DD-05) 363
Shi, J. (FB-07) 563
Shi, J. (FT-04) 642
Shi, J. (FT-05) 643
Shi, J. (FT-09) 644
Shi, K. (HI-13) 824
Shi, S. (DB-04)* 351
Shi, S. (FF-03) 585
Shi, S. (GB-08) 674
Shi, Z. (FV-11) 660
Shibata, G. (HF-10) 800
Shibata, T. (AC-07) 14
Shiihara, T. (FW-03) 664
Shikoh, E. (AE-12) 28
Shim, Y. (EP-12) 508
Shima, T. (AR-03) 71
Shima, T. (CW-15) 345
Shima, T. (FT-07) 644
Shima, T. (GR-01) 742
Shimada, T. (BU-14) 215
Shimada, T. (CV-12) 337
Shimada, Y. (EV-16) 548
Shimakawa, Y. (AV-06) 94
Shimizu, T. (CH-05) 278
Shimura, A. (CI-12) 289
Shin, H. (CV-15) 338
Shin, H. (EV-08) 545
Shin, H. (FR-04) 633
Shin, J. (GF-10) 701
Shin, J. (GP-01) 724
Shin, J. (HF-15) 802
Shin, K. (EV-02) 541
Shin, K. (EV-04) 543
Shin, K. (EV-10) 546
Shin, K. (FP-08) 618
Shin, K. (FR-01) 632
Shin, K. (FR-09) 636
Shin, M. (BV-08) 220
Shin, M. (EV-10) 546
Shinohara, T. (AC-07) 14
Shiokawa, Y. (BC-12) 128
Shiota, Y. (AV-06) 94
Shiota, Y. (CP-13) 296
Shiota, Y. (CR-08) 309
Shiota, Y. (DC-09) 360

*Best student presentation award finalist

Shiota, Y. (GE-14) 695
Shiozawa, H. (AT-09) 83
Shirai, C. (CW-01) 340
Shirai, M. (BE-03) 141
Shirai, M. (CV-12) 337
Shiraishi, M. (DP-04) 397
Shiraishi, M. (EF-10) 482
Shiraishi, M. (FW-04) 664
Shirakihara, S. (CR-05) 308
Shiratsuchi, Y. (CR-01) 306
Shiratsuchi, Y. (EE-01) 473
Shiu, D. (BV-14) 223
Shivashankar, S.A. (GI-02) 716
Shivashankar, S.A. (HH-08) 813
Shklovskii, B. (BA-01) 111
Shklovskij, V. (CE-07) 257
Shoji, T. (AR-08) 73
Shoji, T. (CA-03) 233
Shoji, T. (CI-05) 286
Shoji, T. (GH-03) 709
Shoji, T. (GH-08) 712
Shore, D. (DG-01) 379
Shousha, M. (CH-03) 277
Shpyrko, O.G. (FE-03) 579
Shpyrko, O.G. (FI-11) 611
Shrestha, N. (CV-18) 339
Shrivastava, A. (AH-06) 46
Shu, X. (DB-08) 353
Shytov, A. (AQ-03) 63
Si, L. (AG-09) 41
Si, P. (BW-10) 229
Si, P. (EH-04) 493
Si, Z. (BQ-04) 180
Si, Z. (DP-17) 403
Sichelschmidt, J. (GT-07) 750
Siddiqui, S. (FV-07) 659
Siddiqui, S. (HG-07) 806
Sidi El Valli, A. (EP-08) 506
Siegrist, T. (FE-01) 579
Sierra, J.F. (DB-01) 350
Sievers, S. (BG-08) 154
Sievers, S. (DE-01) 368
Silva Freitas, G. (GT-02) 748
Silva Freitas, G. (GT-05) 749
Silva Freitas, G. (GT-06) 750
Silva, J. (HH-02) 810
Silva, T.J. (AD-05) 18
Silva, T.J. (DD-02) 361
Silva, T.J. (ER-03) 519
Sim, H. (EI-09) 501
Simonelli, L. (DI-10) 394
Simpson, J.R. (DB-03) 351
Simpson, J.R. (DB-13) 355
Simpson, J.R. (GD-06) 686
Simsek, E. (FD-13) 578
Sinclair, R. (CB-01) 236
Singamaneni, S. (BT-07) 201
Singamaneni, S. (CT-07) 320
Singer, A. (FE-03) 579
Singh Meena, S. (DW-15) 449
Singh Meena, S. (HH-13) 816
Singh, A. (BR-11) 193
Singh, A. (FF-04) 585
Singh, A. (FU-04) 650
Singh, A. (GI-14) 722
Singh, G. (DP-08) 399
Singh, H.K. (AB-13) 9
Singh, H.K. (AU-07) 87
Singh, M. (FU-04) 650
Singh, N. (EH-03) 493
Singh, R. (BH-08) 161
Singh, R. (BT-01) 199
Singh, R. (BT-13) 204
Singh, R. (BW-04) 226
Singh, R. (GP-09) 728
Singh, S. (CT-10) 321
Singh, S.K. (DR-13) 419
Singh, U. (DF-04) 376
Singhal, J. (AH-05) 45
Singhal, J. (FG-13) 597
Sinha, J. (EQ-02) 512
Sinha, S.q. (DE-02) 368
Sinova, J. (BB-01) 114
Sinova, J. (CV-01) 333
Sinusía, M. (BE-10) 144
Siracusano, G. (AC-08) 15
Siracusano, G. (AW-10) 105
Sireus, V. (BA-02) 112
Sireus, V. (FU-12) 653
Sisodia, N. (AW-03) 102
Sisodia, N. (GV-10) 764
Siu, Z. (AV-11) 97
Siu, Z. (DP-15) 402
Sivadas, N. (DA-05) 348
Skelland, C. (AR-08) 73
Skinner, S.F. (FQ-07) 626
Sklenar, J. (AB-09) 7
Sklenar, J. (AS-04) 79
Sklenar, J. (BH-06) 160
Sklenar, J. (BH-07) 161
Sklenar, J. (BS-04) 197
Sklenar, J. (CS-04) 315
Sklenar, J. (DS-04) 421
Sklenar, J. (EB-04) 456
Sklenar, J. (EB-09) 458
Sklenar, J. (ES-04) 524
Sklenar, J. (FS-04) 639
Sklenar, J. (GS-04) 747
Sklenar, J. (HA-01) 767
Skokov, K. (FD-01) 572
Skokov, K. (FD-02) 572
Skomski, R. (DI-06) 393
Skomski, R. (EH-13) 497
Skomski, R. (GF-03) 698
Skomski, R. (HE-08) 793
Skomski, R. (HE-13) 794
Skoropata, E. (DH-09) 389
Skoropata, E. (GG-06) 705
Skorvanek, I. (DW-11) 447
Skorvanek, I. (GH-12) 714
Skotnicova, K. (BP-11) 176
Skotnicova, K. (BP-15) 178
Skoviera, J. (GH-12) 714
Skowronski, W. (AD-11) 20
Slanovc, F. (HI-04) 819
Slavin, A.N. (AB-08) 7
Slavin, A.N. (AC-01) 11
Slavin, A.N. (BB-06) 117
Slavin, A.N. (CC-04) 244
Slavin, A.N. (CC-05) 244
Slavin, A.N. (FD-12) 578
Slavin, A.N. (GE-13) 694
Slezak, M. (CP-05) 293
Slezak, M. (FG-07) 593
Slezak, M. (FG-10) 595
Slezak, T. (CP-05) 293
Slezak, T. (FG-07) 593
Slezak, T. (FG-10) 595
Sliwa, C. (HF-12) 801
Slobodianiuk, D.V. (BE-11) 144
Smetana, B. (BP-11) 176
Smith, C.S. (AT-10) 83
Smith, C.S. (CH-01) 276
Smith, D. (BF-05) 148
Smith, D. (BF-06) 148
Smith, D.A. (AI-02) 51
Smith, D.A. (AI-06) 53
Smith, K. (GG-05) 704
Smith, N. (FC-01) 566
Smith, N. (GC-06) 680
Soares de Oliveira Paixão, L. (DQ-14) 410
Sobolev, N. (CR-14) 312
Sochnikov, I. (BG-07) 154
Soderstrom, J. (BD-06) 134
Sohn, C. (DH-09) 389
Sokalski, V. (AW-05) 103
Sokalski, V. (CR-03) 307
Sokalski, V. (DE-10) 372
Sokalski, V. (ED-03) 468
Sokalski, V. (FT-03) 642
Sokalski, V. (GP-04) 725
Soldatov, I. (AH-10) 47
Soldatov, I. (CD-03) 250
Soldatov, I. (DE-06) 370
Solignac, A. (BG-08) 154
Solignac, A. (EQ-05) 513
Som, T. (BH-08) 161
Sommer, R. (AE-13) 29
Son, J. (DT-12) 426
Son, J. (EG-07) 488
Son, S. (EI-03) 498
Song, B. (DQ-02) 405
Song, B. (DQ-09) 408
Song, B. (FH-14) 605
Song, K. (AD-01) 16
Song, K. (FH-04) 600
Song, M. (DQ-10) 408
Song, S. (CT-16) 323
Song, S. (DR-07) 416
Song, S. (FR-07) 635
Song, T. (EA-05) 454
Sonobe, Y. (CW-14) 345
Sonobe, Y. (EP-14) 509

*Best student presentation award finalist

Sooryakumar, R. (FF-01) 584
Soree, B. (AH-04) 45
Soree, B. (BC-05) 124
Soree, B. (EP-16) 510
Soriano, L. (BH-11) 163
Sorokin, P. (FB-09) 564
Sorokin, S. (GB-11) 676
Sorrentino, A. (AF-09) 33
Sort, J. (AH-11) 48
Sort, J. (AH-13) 49
Sort, J. (BA-02) 112
Sort, J. (FU-12) 653
Soruco, J. (GQ-12) 739
Soucaille, R. (DT-14) 427
Soumah, L. (BD-03) 132
Soumah, L. (GE-01) 689
Soumyanarayanan, A. (ED-02) 467
Sousa, R. (BC-13) 129
Sousa, R. (EF-07) 481
Sousa, R. (EP-08) 506
Sousa, R. (ET-13) 531
Sousa, R. (GC-11) 683
Souza, C.M. (AT-02) 80
Souza, J.C. (CT-13) 322
Souza, J.C. (GT-05) 749
Souza, J.C. (GT-06) 750
Souza, J.C. (GT-07) 750
Souza, J.C. (GT-08) 750
Souza, R.M. (AU-03) 86
Sowmya, N. (HC-12) 780
Sozer, Y. (ET-07) 529
Sozinov, A. (FD-09) 576
Sparks, P.D. (CV-04) 334
Sparks, P.D. (CV-09) 336
Spiesser, A.M. (CF-05) 264
Spiesser, A.M. (EF-08) 481
Spiesser, A.M. (EF-09) 482
Spinu, L. (ER-07) 520
Spoddig, D. (BD-04) 133
Srikanth, H. (AU-06) 87
Srikanth, H. (BE-13) 145
Srikanth, H. (BT-12) 204
Srikanth, H. (CV-05) 334
Srikanth, H. (DQ-04) 406
Srikanth, H. (DU-12) 433
Srikanth, H. (GG-04) 704
Srikanti, K. (FD-03) 573
Srivastava, A. (AI-06) 53
Srivastava, A. (BR-09) 192
Srivastava, A. (DW-13) 448
Srivastava, M. (HH-13) 816
Srivastava, V. (HF-07) 798
Stadler, B. (DG-01) 379
Stadler, B. (DG-05) 381
Stadler, B. (DU-09) 432
Stadler, S. (AQ-17) 69
Stadler, S. (DQ-01) 405
Stadler, S. (DR-01) 414
Stadler, S. (DR-15) 420
Stadler, S. (FQ-09) 627
Stadtmuller, B. (ER-03) 519
Stampfer, C. (EB-11) 459
Stampfer, C. (FB-01) 561
Stamps, R.L. (BD-10) 136
Stamps, R.L. (CB-06) 238
Stamps, R.L. (EF-04) 479
Stan, C. (HC-09) 778
Stancu, A. (FF-12) 589
Stancu, A. (FI-14) 613
Stanescu, S. (ED-04) 469
Stanton, M. (EA-04) 454
Staruch, M. (FD-11) 577
Stashkevich, A. (CG-01) 270
Statuto, N. (EQ-10) 516
Staunton, J.B. (FH-13) 605
Steadman, P. (AB-06) 6
Steadman, P. (AF-11) 34
Steadman, P. (BF-11) 150
Steadman, P. (GF-01) 697
Štefančič, A. (AW-11) 106
Štefančič, A. (AW-17) 109
Štefančič, A. (GF-01) 697
Štefančič, A. (GF-05) 699
Stefanou, G. (BE-09) 143
Stefanuik, R. (BD-06) 134
Stefanuik, R. (ER-04) 519
Stehli, A. (CE-03) 255
Stein, A. (BH-04) 159
Stein, A. (BH-10) 162
Stein, C.R. (CU-01) 324
Steinbach, F. (DC-04) 358
Steinhardt, R. (HC-06) 777
Stengel, M. (FU-12) 653
Stepankova, H. (DR-01) 414
Stevens, J. (HE-10) 794
Steydli, S. (FD-06) 574
Stiehl, G. (AF-13) 35
Stiehl, G. (DA-05) 348
Stiles, M.D. (DA-01) 347
Stiles, M.D. (EC-03) 462
Stiles, M.D. (EF-01) 478
Stiles, M.D. (EQ-04) 513
Stiles, M.D. (FA-02) 559
Stillwell, R. (DB-12) 354
Stobiecki, F. (AD-11) 20
Stobiecki, F. (GE-12) 694
Stobiecki, T. (AD-11) 20
Stoffes Júnior, M.J. (CU-01) 324
Stoian, G. (GH-14) 714
Stoleriu, L. (FI-14) 613
Stoll, J. (DG-06) 381
Stopfel, H. (BH-04) 159
Stopfel, H. (BH-10) 162
Story, T. (EB-13) 460
Straka, L. (AQ-09) 65
Strandqvist, N. (BF-11) 150
Strelkov, N. (ET-13) 531
Strelkov, N. (FC-05) 568
Streubel, R. (FF-03) 585
Strickland, N.M. (DR-10) 417
Strohm, C. (CE-02) 255
Stroud, J. (DG-06) 381
Stroud, J. (HH-07) 813
Strydom, A.M. (GT-11) 751
Stückler, M. (BF-09) 149
Stunault, A. (FD-09) 576
Stupakiewicz, A. (DD-04) 362
Stupakiewicz, A. (GH-05) 710
Su, C. (BW-13) 230
Su, D. (CQ-13) 304
Su, D. (CQ-14) 305
Su, D. (GV-09) 764
Su, T. (DB-09) 353
Su, Y. (FB-04) 562
Su, Z. (GG-11) 707
Suemasu, T. (HG-03) 805
Suess, D. (HI-04) 819
Suga, S. (DR-09) 417
Sugai, M. (BW-02) 225
Sugaya, Y. (AV-07) 94
Sugihara, A. (CF-04) 263
Sugihara, A. (EG-01) 485
Sugihara, A. (EP-02) 503
Sugimoto, S. (GF-11) 702
Sukegawa, H. (BU-10) 213
Sukegawa, H. (FG-15) 597
Sukenik, N. (BG-09) 155
Suko, R. (AP-02) 58
Suko, R. (AP-04) 60
Sumana, G. (FF-04) 585
Sumi, S. (BT-09) 202
Sumi, S. (CF-13) 268
Sumitani, K. (BP-09) 175
Sun, A. (BW-07) 227
Sun, A. (CQ-07) 302
Sun, A. (DG-07) 382
Sun, A. (FF-07) 587
Sun, A. (FT-16) 648
Sun, D. (BT-02) 199
Sun, D. (FB-11) 565
Sun, F. (CV-06) 335
Sun, H. (CU-12) 330
Sun, H. (DW-17) 450
Sun, J. (AH-03) 45
Sun, J. (AQ-15) 68
Sun, J. (BC-07) 125
Sun, J. (BT-08) 202
Sun, J. (BT-10) 203
Sun, J. (DQ-05) 406
Sun, J. (DQ-15) 410
Sun, J. (DQ-17) 412
Sun, J. (DT-13) 426
Sun, J. (FQ-14) 629
Sun, J. (GC-07) 681
Sun, J. (XA-01) 452
Sun, K. (AR-11) 74
Sun, L. (AV-03) 93
Sun, L. (BQ-07) 182
Sun, L. (BU-15) 216
Sun, L. (ET-05) 528
Sun, L. (FU-02) 649
Sun, M. (CG-06) 272
Sun, M. (CW-14) 345

*Best student presentation award finalist

Sun, N. (AD-04) . . . 17
Sun, N. (AE-03) . . . 24
Sun, N. (AH-07) . . . 46
Sun, N. (EV-01) . . . 541
Sun, N. (GI-05) . . . 718
Sun, N. (GI-06) . . . 718
Sun, N. (HI-02) . . . 818
Sun, N.X. (AH-06) . . . 46
Sun, N.X. (GI-05) . . . 718
Sun, Q. (EG-13) . . . 491
Sun, W. (FH-04) . . . 600
Sun, X. (FR-03) . . . 633
Sun, Y. (AW-02) . . . 101
Sun, Y. (BT-05) . . . 200
Surakarnkha, J. (GV-12) . . . 765
Suresh, K. (DR-12) . . . 418
Suresh, K. (HF-04) . . . 796
Suri, D. (DR-13) . . . 419
Suriñach, S. (FU-12) . . . 653
Sussmuth, M. (AF-11) . . . 34
Sutton, L. (HD-08) . . . 785
Suwa, H. (EI-08) . . . 501
Suwannasiri, T. (GC-07) . . . 681
Suzuki, D. (DC-04) . . . 358
Suzuki, D. (FH-06) . . . 601
Suzuki, K. (BU-05) . . . 211
Suzuki, K. (DG-13) . . . 385
Suzuki, K. (GH-03) . . . 709
Suzuki, K. (GH-08) . . . 712
Suzuki, M. (CD-06) . . . 251
Suzuki, M. (HF-10) . . . 800
Suzuki, S. (EB-02) . . . 455
Suzuki, T. (AV-04) . . . 93
Suzuki, T. (CI-12) . . . 289
Suzuki, T. (HH-09) . . . 814
Suzuki, Y. (BQ-02) . . . 179
Suzuki, Y. (CI-12) . . . 289
Suzuki, Y. (DH-01) . . . 386
Suzuki, Y. (EF-10) . . . 482
Suzuki, Y. (EG-04) . . . 486
Suzuki, Y. (EG-05) . . . 487
Suzuki, Y. (EP-02) . . . 503
Suzuki, Y. (FC-05) . . . 568
Suzuki, Y. (FW-04) . . . 664
Suzuki, Y. (HI-06) . . . 821
Svec, P. (DW-11) . . . 447
Svec, P. (GH-12) . . . 714
Svedlindh, P. (AP-05) . . . 60
Svedlindh, P. (CR-12) . . . 311
Svedlindh, P. (DQ-06) . . . 407
Swagten, H. (AB-02) . . . 4
Swagten, H. (AB-07) . . . 6
Swagten, H. (CE-11) . . . 259
Swagten, H. (DE-04) . . . 369
Swagten, H. (GE-10) . . . 693
Swagten, H. (HG-06) . . . 806
Swerts, J. (BC-05) . . . 124
Swerts, J. (EG-09) . . . 489
Swerts, J. (EG-11) . . . 490
Swerts, J. (EP-13) . . . 508
Swerts, J. (FC-04) . . . 567
Swerts, J. (GC-02) . . . 679
Swindells, C. (FC-10) . . . 570
Syariati, R. (CV-08) . . . 335
Syed, M. (DT-07) . . . 425
Sylgacheva, D. (HD-03) . . . 783
Syoji, Y. (CT-12) . . . 321
Szczerbakow, A. (EB-13) . . . 460
Szpytma, M. (CP-05) . . . 293
Szpytma, M. (FG-07) . . . 593
Szpytma, M. (FG-10) . . . 595
Sztenkiel, D. (BQ-17) . . . 187
Sztenkiel, D. (FI-12) . . . 612

- T -

T S, S. (FV-09) . . . 660
Tabakovic, I. (DG-01) . . . 379
Tabares, J.A. (CW-03) . . . 341
Tabata, H. (CC-13) . . . 248
Tabata, H. (CI-06) . . . 286
Tabata, H. (GG-09) . . . 706
Tadokoro, T. (BW-08) . . . 228
Tajiri, H. (HF-06) . . . 798
Takada, Y. (BP-08) . . . 174
Takagi, R. (GF-01) . . . 697
Takahashi, H. (BQ-14) . . . 186
Takahashi, H. (CQ-08) . . . 303
Takahashi, H. (EG-10) . . . 490
Takahashi, K. (EP-02) . . . 503
Takahashi, S. (AD-13) . . . 22
Takahashi, S. (CQ-08) . . . 303
Takahashi, S. (CW-14) . . . 345
Takahashi, S. (EP-14) . . . 509
Takahashi, T. (DW-10) . . . 446
Takahashi, Y. (AI-04) . . . 52
Takahashi, Y. (FC-06) . . . 569
Takahashi, Y. (FH-03) . . . 600
Takahashi, Y. (FT-08) . . . 644
Takahashi, Y. (GF-11) . . . 702
Takahashi, Y. (HD-10) . . . 787
Takala, E. (CH-07) . . . 280
Takamura, Y. (AF-08) . . . 33
Takamura, Y. (AQ-11) . . . 66
Takamura, Y. (BA-04) . . . 112
Takamura, Y. (BA-05) . . . 113
Takamura, Y. (EE-03) . . . 473
Takamura, Y. (GG-01) . . . 703
Takanashi, K. (AI-04) . . . 52
Takanashi, K. (BE-02) . . . 140
Takanashi, K. (CF-08) . . . 266
Takanashi, K. (CG-06) . . . 272
Takanashi, K. (CW-14) . . . 345
Takanashi, K. (EQ-01) . . . 512
Takano, Y. (AV-08) . . . 95
Takashima, K. (BP-13) . . . 177
Takashima, R. (FG-06) . . . 593
Takayanagi, K. (AV-01) . . . 92
Takei, Y. (AV-04) . . . 93
Takeichi, S. (BP-13) . . . 177
Takemasa, Y. (CW-01) . . . 340
Takemura, Y. (DT-04) . . . 423
Takenaka, H. (EB-05) . . . 457
Takeuchi, I. (AI-08) . . . 54
Takezawa, M. (FH-07) . . . 602
Talaat, A. (GH-07) . . . 711
Talapatra, A. (DE-06) . . . 370
Talapatra, A. (ER-01) . . . 518
Talapatra, S. (AQ-17) . . . 69
Talapatra, S. (DQ-01) . . . 405
Talapatra, S. (DR-01) . . . 414
Talapatra, S. (FQ-09) . . . 627
Talmelli, G. (CE-12) . . . 260
Tamaki, A. (FQ-12) . . . 628
Tamaru, S. (BQ-15) . . . 186
Tamaru, S. (CU-04) . . . 326
Tamaru, S. (EG-05) . . . 487
Tamaru, S. (EP-02) . . . 503
Tamaru, S. (HD-12) . . . 787
Tamazawa, Y. (AR-03) . . . 71
Tamming, R. (BU-12) . . . 214
Tamura, R. (BP-09) . . . 175
Tamura, R. (FQ-12) . . . 628
Tan Kok Cheng, A. (ED-02) . . . 467
Tan, A. (EG-07) . . . 488
Tan, F. (GP-13) . . . 730
Tan, H. (ED-02) . . . 467
Tanabe, K. (BT-09) . . . 202
Tanaka, H. (AI-10) . . . 55
Tanaka, H. (EV-19) . . . 550
Tanaka, H. (HF-05) . . . 797
Tanaka, M. (BC-08) . . . 126
Tanaka, M. (CC-09) . . . 246
Tanaka, R. (DW-08) . . . 445
Tanaka, R. (DW-16) . . . 449
Tanaka, R. (DW-18) . . . 450
Tanaka, S. (GV-02) . . . 760
Tanaka, T. (EP-11) . . . 507
Tanaka, Y. (AE-12) . . . 28
Tanaka, Y. (BU-08) . . . 212
Tanaka, Y. (GC-04) . . . 679
Tanaka, Y. (HH-09) . . . 814
Tanasa, R. (FF-12) . . . 589
Tang, A. (HG-07) . . . 806
Tang, G. (FP-03) . . . 616
Tang, J. (BV-06) . . . 219
Tang, J. (CB-01) . . . 236
Tang, J. (CV-18) . . . 339
Tang, J. (DB-11) . . . 354
Tang, M. (FV-11) . . . 660
Tang, M. (HB-04) . . . 771
Tang, N. (CC-07) . . . 245
Tang, N. (DE-02) . . . 368
Tang, N. (ED-08) . . . 470
Tang, P. (DB-07) . . . 352
Tang, Y. (AH-05) . . . 45
Tang, Y. (CQ-12) . . . 304
Tang, Y. (FG-13) . . . 597
Tang, Y. (FU-08) . . . 652
Taniguchi, H. (AE-09) . . . 27
Taniguchi, H. (EB-02) . . . 455
Taniguchi, H. (EC-05) . . . 463

*Best student presentation award finalist

Taniguchi, T. (AI-13) . . . 56
Taniguchi, T. (BC-12) . . . 128
Taniguchi, T. (CI-11) . . . 289
Taniguchi, T. (DB-09) . . . 353
Taniguchi, T. (DF-01) . . . 374
Taniguchi, T. (EC-05) . . . 463
Taniguchi, T. (EF-05) . . . 480
Taniguchi, T. (EP-02) . . . 503
Taniguchi, T. (GE-14) . . . 695
Taniguchi, T. (HD-12) . . . 787
Tanii, M. (GV-04) . . . 761
Taniyama, T. (AG-07) . . . 40
Taniyama, T. (BT-20) . . . 207
Taniyama, T. (FU-09) . . . 652
Tantillo, A.N. (FQ-05) . . . 625
Tantillo, A.N. (HE-03) . . . 790
Tao, Q. (BI-04) . . . 167
Tao, Z. (AA-02) . . . 2
Taubel, A. (FD-01) . . . 572
Taufour, V. (BA-04) . . . 112
Taufour, V. (EH-10) . . . 496
Tay, Z. (GA-03) . . . 669
Taylor, C.S. (CV-04) . . . 334
Taylor, C.S. (CV-09) . . . 336
Taylor, J.M. (AB-12) . . . 9
Taylor, P. (EB-03) . . . 456
Tazlaru, S. (HH-15) . . . 817
Tchoula Tchokonte, M.B. (GT-11) . . . 751
te Velthuis, S.G. (AF-06) . . . 32
te Velthuis, S.G. (DC-05) . . . 358
te Velthuis, S.G. (DC-06) . . . 359
Teixeira, B.M. (CR-14) . . . 312
Tejo, F. (AW-15) . . . 108
Teki, Y. (AE-12) . . . 28
Telling, N. (DT-14) . . . 427
Temple, R.C. (AB-06) . . . 6
Temple, R.C. (BB-11) . . . 119
Temple, R.C. (GH-10) . . . 713
Temst, K. (EG-09) . . . 489
Tengdin, P. (ER-03) . . . 519
Teo, K. (CD-08) . . . 252
Teo, K.L. (BC-03) . . . 123
Ter Haar, L.W. (FQ-07) . . . 626
Teranishi, T. (FH-09) . . . 603
Terasaki, I. (AV-14) . . . 98
Terasaki, Y. (AC-07) . . . 14
Terris, B. (FC-01) . . . 566
Terris, B. (GC-06) . . . 680
Testa, P. (FP-04) . . . 617
Tew, W. (HE-12) . . . 794
Tezuka, N. (EC-11) . . . 465
Thabt, A. (CR-02) . . . 306
Thabt, A. (DC-03) . . . 357
Tham, K. (GR-05) . . . 743
Tham, K. (HD-11) . . . 787
Thapliyal, N. (HH-06) . . . 812
Theh, W. (CQ-03) . . . 300
Thibaudeau, p. (EE-06) . . . 475
Thirion, C. (GP-03) . . . 725
Thirion, C. (HG-09) . . . 807
Thomas, A. (BU-12) . . . 214
Thomas, C. (DP-12) . . . 400
Thomas, S.M. (GT-02) . . . 748
Thomas, S.M. (GT-08) . . . 750
Thompson, C.J. (FT-10) . . . 645
Thompson, G. (DW-13) . . . 448
Thompson, J. (AV-10) . . . 96
Thompson, J. (GT-02) . . . 748
Thompson, J. (GT-08) . . . 750
Thompson, L. (HB-05) . . . 772
Thompson, R. (GB-13) . . . 677
Thomson, T. (HD-07) . . . 785
Thonig, D. (AP-05) . . . 60
Thonig, D. (BD-07) . . . 134
Thonig, D. (ER-03) . . . 519
Thonig, D. (ER-04) . . . 519
Thota, S. (FU-16) . . . 654
Thotakura, G. (AR-15) . . . 76
Thotakura, G. (BI-10) . . . 169
Thurston, J. (DT-02) . . . 423
Tian, J. (EB-12) . . . 459
Tian, M. (CR-16) . . . 314
Tiberkevich, V. (AB-08) . . . 7
Tiberkevich, V. (AC-01) . . . 11
Tiberkevich, V. (CC-04) . . . 244
Tiberkevich, V. (CC-05) . . . 244
Tiberkevich, V. (CE-10) . . . 259
Tiberkevich, V. (CE-13) . . . 260
Tiberkevich, V. (FD-12) . . . 578
Tiberkevich, V. (GE-13) . . . 694
Tiberto, P. (DG-09) . . . 383
Tiberto, P. (FI-13) . . . 612
Tierno, D. (HC-10) . . . 779
Tignon, J. (FV-05) . . . 658
Tigunta, S. (GQ-14) . . . 740
Timmermans, M. (DB-01) . . . 350
Tippey, K.E. (EP-17) . . . 511
Tiwari, S. (HC-03) . . . 776
Tobar, M. (CI-15) . . . 291
Tobey, R. (BU-12) . . . 214
Tokuda, M. (AE-09) . . . 27
Tokuda, M. (EB-02) . . . 455
Tokuda, M. (EC-05) . . . 463
Tokunaga, Y. (AV-10) . . . 96
Tokura, Y. (GF-01) . . . 697
Tol, J.v. (AA-01) . . . 2
Tolbert, S. (BT-06) . . . 201
Tolbert, S. (FU-17) . . . 654
Toma, R. (AV-12) . . . 97
Tomanek, B. (DG-08) . . . 382
Tomasello, R. (AB-03) . . . 5
Tomasello, R. (AW-10) . . . 105
Tomasello, R. (AW-13) . . . 107
Tomasello, R. (DE-03) . . . 369
Tomasello, R. (DE-09) . . . 372
Tomasz Baczewski, L. (BG-09) . . . 155
Tomita, H. (BU-07) . . . 212
Tomita, H. (BU-08) . . . 212
Tomita, H. (GC-04) . . . 679
Tomita, M. (AQ-11) . . . 66
Tomita, T. (DW-10) . . . 446
Ton That, L. (CQ-08) . . . 303
Ton That, L. (DV-02) . . . 435
Ton, L.T. (EV-16) . . . 548
Töpfer, J. (BI-09) . . . 169
Topuria, T. (HB-05) . . . 772
Torii, T. (CQ-01) . . . 300
Torosyan, G. (EC-06) . . . 463
Torrejon, J. (EF-01) . . . 478
Torrejon, J. (EQ-04) . . . 513
Torres, F. (EI-04) . . . 499
Torres, F. (EI-05) . . . 499
Torres, F. (ET-03) . . . 527
Torres, F. (GD-11) . . . 688
Torres, W.S. (AT-01) . . . 80
Tortora, G. (ET-09) . . . 530
Tosun, O. (HE-13) . . . 794
Totsuka, S. (AV-08) . . . 95
Toussaint, J. (GP-03) . . . 725
Toussaint, J. (HG-09) . . . 807
Toyoizumi, S. (FQ-12) . . . 628
Toyoki, K. (BP-08) . . . 174
Toyoki, K. (CI-03) . . . 285
Toyoki, K. (CI-04) . . . 285
Toyoki, K. (EE-01) . . . 473
Tozman, P. (FH-03) . . . 600
Trabuco, J. (CQ-04) . . . 301
Träger, N. (GE-08) . . . 692
Träger, N. (GE-09) . . . 693
Träger, N. (GE-12) . . . 694
Tran, B. (DD-08) . . . 365
Tran, M. (FC-01) . . . 566
Tran, N. (AR-09) . . . 73
Tran, N. (CT-01) . . . 317
Tran, N. (CT-04) . . . 318
Tranchida, J. (EE-06) . . . 475
Transtrum, M. (BF-05) . . . 148
Transtrum, M. (BF-06) . . . 148
Trapanese, M. (BW-15) . . . 231
Trapanese, M. (CH-11) . . . 282
Trapp, B. (GP-03) . . . 725
Trassinelli, M. (FD-06) . . . 574
Tretiakov, O. (BB-12) . . . 119
Tretiakov, O. (GF-09) . . . 701
Trevillian, C.A. (CE-10) . . . 259
Trier, F. (DP-08) . . . 399
Trigo, H.G. (FD-05) . . . 574
Trinh, J. (FE-01) . . . 579
Trinh, L. (BA-05) . . . 113
Trinh, T. (FH-09) . . . 603
Trivedi, N. (AA-01) . . . 2
Trivedi, N. (DB-03) . . . 351
Trouilloud, P. (GC-07) . . . 681
Trudel, S. (DG-08) . . . 382
Trujillo Hernandez, J.S. (CW-03) . . . 341
Truong, K. (FQ-19) . . . 630
Tsai, J. (FT-02) . . . 641
Tsai, W. (BC-10) . . . 127
Tsay, J. (CG-09) . . . 273
Tseng, D. (AQ-01) . . . 62
Tseng, Y. (AH-02) . . . 44
Tseng, Y. (BB-02) . . . 114
Tseng, Y. (CQ-02) . . . 300

*Best student presentation award finalist

Tseng, Y. (GC-09) 682
Tseplyaev, V. (CC-02) 243
Tserkovnyak, Y. (BG-04) 153
Tserkovnyak, Y. (DC-09) 360
Tsotsos, E. (HH-15) 817
Tsou, C. (BW-13) 230
Tsou, C. (DU-13) 433
Tsuchiura, H. (CI-06) 286
Tsuchiura, H. (FH-06) 601
Tsuchiya, T. (BU-05) 211
Tsuchiya, T. (DR-11) 418
Tsujikawa, M. (BE-03) 141
Tsujikawa, M. (CV-12) 337
Tsujimoto, H. (AE-12) 28
Tsujimura, F. (AV-09) 96
Tsukada, K. (CQ-09) 303
Tsukada, K. (DG-10) 383
Tsukagoshi, T. (FG-06) 593
Tsukahara, H. (FI-09) 611
Tsukamoto, A. (CR-08) 309
Tsukamoto, A. (DC-09) 360
Tsukamoto, A. (DD-04) 362
Tsukamoto, A. (HD-03) 783
Tsukerman, I. (ET-07) 529
Tsumita, A. (BC-12) 128
Tsunashima, K. (CQ-09) 303
Tsunashima, K. (DG-10) 383
Tsunegi, S. (CI-11) 289
Tsunegi, S. (DF-01) 374
Tsunegi, S. (EF-01) 478
Tsunegi, S. (EP-02) 503
Tsunegi, S. (EQ-04) 513
Tsunegi, S. (HI-06) 821
Tsunoda, M. (BU-09) 213
Tsunoda, M. (BU-11) 214
Tsunoda, M. (CP-16) 298
Tsunoda, M. (DW-04) 443
Tsunoda, M. (EP-05) 505
Tsunoda, M. (FW-02) 663
Tsuruma, A. (FF-10) 588
Tsymbal, E.Y. (AD-03) 17
Tsymbal, E.Y. (CP-03) 292
Tsymbal, E.Y. (DB-05) 352
Tsymbal, E.Y. (EB-05) 457
Tu, C. (FU-06) 651
Tu, M. (EA-05) 454
Tu, Y. (BE-05) 142
Tu, Z. (BR-03) 189
Tulapurkar, A. (GC-03) 679
Tung, Y. (BT-11) 203
Tyagi, S. (EB-03) 456
Tzitzios, V. (CQ-06) 302

- U -

Ucar, H. (EH-11) 496
Uchida, H. (CP-04) 293
Uchida, K. (AP-01) 58
Uchida, K. (FC-06) 569
Uchiyama, T. (FF-06) 586
Uchiyama, T. (HI-05) 820
Uchiyama, T. (HI-13) 824
Udalov, O.G. (HE-07) 792
Ueda, C. (FP-07) 618
Uemura, T. (HB-07) 773
Uemura, Y. (HF-10) 800
Ueno, R. (DW-08) 445
Ueno, S. (BW-02) 225
Ueno, T. (DT-05) 424
Uesugi, S. (GR-03) 742
Uetake, H. (DV-02) 435
Ugochukwu, K.C. (DG-13) 385
Uhlirova, K. (BB-07) 117
Uhlirova, K. (EI-03) 498
Uji, K. (DW-10) 446
Ullah, A. (GF-03) 698
Ullah, A. (HE-08) 793
Ullakko, K. (FD-09) 576
Ulloa, C. (CB-04) 237
Ulrichs, H. (BU-12) 214
Ulrichs, H. (HD-02) 782
Um, J. (DG-01) 379
Um, J. (DG-05) 381
Umetsu, N. (HB-03) 771
Umetsu, R.Y. (CG-06) 272
Umetsu, R.Y. (DR-09) 417
Umetsu, R.Y. (EH-07) 495
Umezaki, T. (GV-04) 761
Ummelen, F.C. (DE-04) 369
Unikandanunni, V. (BD-03) 132
Unikandanunni, V. (BD-05) 133
Unikandanunni, V. (BD-08) 134
Upadhyaya, P. (BG-04) 153
Urabe, J. (CI-12) 289
Urashita, S. (AQ-11) 66
Urazhdin, S. (BD-08) 134
Urbánek, M. (AW-04) 102
Urbánek, M. (EW-14) 557
Urbano, R.R. (AV-10) 96
Urbano, R.R. (GT-02) 748
Urbano, R.R. (GT-07) 750
Urdiroz, U. (BH-02) 158
Urdiroz, U. (BH-11) 163
Urdiroz, U. (CR-14) 312
Urdiroz, U. (HE-09) 793
Uribe, J. (FT-06) 643
Usami, T. (BT-20) 207
Ustinov, A.V. (CE-03) 255
Ustinov, A.V. (CE-13) 260
Usuda, É. (DQ-14) 410
Utermohlen, F.G. (AA-01) 2
Utermohlen, F.G. (DB-03) 351
Utsumi, R. (EV-16) 548

- V -

Valanoor, N. (GQ-14) 740
Valdes Aguilar, R. (DB-03) 351
Valdes Aguilar, R. (DB-13) 355
Valdes Aguilar, R. (GD-06) 686
Valdes-Bango, F. (GP-08) 728
Valencia, F. (ET-03) 527
Valencia, S. (BB-01) 114
Valencia, S. (HH-03) 811
Valenta, J. (EI-03) 498
Valenzuela, S.O. (DB-01) 350
Vallone, S. (FQ-11) 627
Vallone, S. (HE-03) 790
Valls, O. (DI-05) 392
Valvidares, M. (AG-08) 40
Van't Erve, O. (CT-09) 320
Van't Erve, O. (FV-06) 659
van Ballegooie, Y. (DD-10) 366
Van Beek, S. (EG-11) 490
Van Beek, S. (FC-04) 567
Van Beek, S. (GC-02) 679
van de Meugheuvel, P. (DD-06) 364
Van Den Berg, A. (BF-01) 146
Van Der Heijden, P. (FV-08) 659
Van Der Heijden, P. (HD-13) 788
van der Laan, G. (CB-10) 240
van der Laan, G. (FG-04) 592
van der Laan, G. (GF-07) 700
van der Meer, L. (DD-04) 362
Van der Sar, T. (BG-04) 153
van Dijken, S. (FE-09) 582
van Hees, Y. (AB-07) 6
van Hees, Y. (DD-03) 362
van Hees, Y. (DD-06) 364
Van Houdt, J. (EG-11) 490
van Rijn, J. (FU-19) 655
van Schilfgaarde, M. (AD-14) 23
Van Thach, P. (BT-09) 202
Van Thach, P. (CF-13) 268
van Wees, B. (FB-06) 563
Van't Erve, O. (DP-05) 397
Vanatka, M. (AW-04) 102
Vande Vondel, J. (EG-09) 489
Vanderveken, F. (HC-10) 779
Varaprasad, B. (HD-05) 784
Varaprasad, B. (HD-06) 784
Vardhanapu, P.K. (CF-12) 268
Varela, M. (BA-04) 112
Varfolomeev, A. (GV-02) 760
Varga, L.K. (FB-03) 562
Vargas, N. (BT-03) 199
Vargas, N. (EI-04) 499
Vargas, N. (EI-05) 499
Varma, G.D. (AU-07) 87
Varma, G.D. (DI-03) 391
Varotto, S. (GB-04) 673
Vasam, S. (DW-06) 444
Vasic, B. (BT-16) 206
Vasudevan, R. (HC-08) 778
Vasyuchka, V. (GE-02) 689
Vasyuchka, V.I. (BD-09) 135
Vasyuchka, V.I. (BE-11) 144
Vaz, D.C. (DP-08) 399
Vázquez, M. (DV-09) 439
Vázquez, M. (GI-01) 716
Vechiola, A. (BG-10) 156

*Best student presentation award finalist

Vechiola, A. (ED-05) 469
Vedmedenko, E.Y. (GD-08) 687
Veeturi, S. (AU-01) 85
Veeturi, S. (DW-06) 444
Veintemillas, S. (HE-09) 793
Veis, M. (AB-13) 9
Veis, M. (AQ-07) 64
Veis, M. (CP-09) 295
Veis, M. (DT-10) 425
Veis, M. (HH-04) 811
Veis, M. (HH-15) 817
Veit, M. (DH-01) 386
Velez, M. (AF-09) 33
Vélez, m. (GA-04) 669
Velez, M. (GP-08) 728
Velten, S. (BH-05) 160
Vemulkar, T. (EA-04) 454
Venegas, P. (GT-07) 750
Venkataramani, N. (HC-12) 780
Venugopal, A. (EQ-14) 517
Venugopal, A. (GE-15) 695
Verba, R.V. (BD-09) 135
Verba, R.V. (CC-04) 244
Verba, R.V. (CC-05) 244
Verba, R.V. (CE-08) 258
Verba, R.V. (FD-12) 578
Vergnaud, C. (AE-08) 26
Vergnaud, C. (DP-14) 401
Verheijen, M. (CE-11) 259
Verheyen, J. (EA-04) 454
Vermeulen, B.F. (EG-09) 489
Vermeulen, B.F. (EG-11) 490
Vermeulen, B.F. (FC-04) 567
Vernhet, D. (FD-06) 574
Verstraete, M. (FB-01) 561
Vetter, E. (BT-02) 199
Vetter, E. (FB-11) 565
Vichi, F.M. (FE-05) 580
Victora, R. (EQ-14) 517
Victora, R. (GE-15) 695
Victora, R. (HD-14) 788
Vidal-Silva, N. (AW-15) 108
Viehland, D. (AI-06) 53
Viehland, D. (GB-01) 671
Vieira, J.M. (EH-05) 494
Vignale, G. (GB-08) 674
Vijayakumar, J. (CG-04) 271
Vila, L. (AP-03) 59
Vila, L. (BC-13) 129
Vila, L. (BV-03) 218
Vila, L. (DP-08) 399
Vila, L. (DP-12) 400
Vila, L. (EC-09) 464
Vila, L. (EP-08) 506
Vila, L. (FC-09) 570
Vila, L. (FV-10) 660
Vila, L. (GB-04) 673
Vila, L. (GE-13) 694
Vila, L. (HG-03) 805
Vilarinho, R. (HH-02) 810
Villar, P. (CH-09) 281
Vinokur, V. (ER-09) 521
Viola Kusminskiy, S. (FA-04) 560
Viola, F. (BW-15) 231
Viret, M. (EE-02) 473
Viret, M. (EE-06) 475
Virnau, P. (GF-13) 702
Vishvakarma, S. (AU-01) 85
Visscher, P.B. (CU-08) 328
Visscher, P.B. (DU-09) 432
Visscher, P.B. (EP-17) 511
Vivek, M. (DP-08) 399
Vlaskova, K. (CW-16) 345
Vobornik, I. (GB-04) 673
Vogel, J. (ED-04) 469
Vogel, J. (HG-03) 805
Vogel, J. (HG-09) 807
Vogel, M. (AF-06) 32
Vogel, M. (DC-05) 358
Vogel, M. (DC-06) 359
Vogel, M. (ER-02) 518
Vogel, M. (EW-04) 553
Vogel, M. (EW-09) 555
Vogel, M. (FV-07) 659
Vogler, C. (HI-04) 819
Volkov, I. (GV-02) 760
Volkov, O. (EE-11) 477
Volmer, F. (EB-11) 459
Volmer, F. (FB-01) 561
Volny, J. (BB-07) 117
Volvach, I. (FI-10) 611
von Korff Schmising, C. (DC-04) 358
von Ranke, P. (FQ-15) 629
von Reppert, A. (BD-12) 136
Voneshen, D. (AV-05) 94
Vovk, N. (EW-15) 557
Vovk, R. (CE-07) 257
Voznyuk, V. (FC-02) 566
Vronka, M. (AQ-09) 65
Vudya Sethu, K. (BC-05) 124
Vukadinovic, N. (GE-13) 694
Vyazovskaya, A.Y. (EB-07) 457
Vyborny, K. (BB-07) 117

- W -

W.L.N.C., L. (CC-07) 245
W.L.N.C., L. (ED-08) 470
Wagenknecht, D. (BB-07) 117
Wagh, A.A. (FV-04) 658
Wagner, K. (CC-04) 244
Waintal, X. (FC-09) 570
Wakatake, Y. (FC-05) 568
Waldorff, E.I. (FF-02) 584
Walker, C.S. (GQ-07) 737
Walker, C.S. (HE-10) 794
Walowski, J. (BU-12) 214
Walowski, J. (CF-12) 268
Walowski, J. (ED-11) 472
Walowski, J. (HD-02) 782
Walsworth, R. (BG-04) 153
Walter, J. (BA-01) 111
Walter, J. (DH-07) 388
Wan, C. (BV-15) 223
Wan, C. (FV-01) 657
Wan, D. (EP-16) 510
Wan, D. (HG-10) 808
Wan, L. (CD-05) 250
Wan, L. (DV-07) 438
Wan, L. (DV-08) 438
Wan, Y. (HF-10) 800
Wang, B. (AV-03) 93
Wang, B. (CT-08) 320
Wang, B. (DV-01) 435
Wang, B. (DV-03) 436
Wang, B. (DV-07) 438
Wang, B. (DV-08) 438
Wang, C. (BB-14) 120
Wang, C. (BC-06) 125
Wang, C. (EE-10) 476
Wang, C. (FE-05) 580
Wang, C. (FH-05) 601
Wang, C.R. (FU-06) 651
Wang, C.R. (GQ-05) 736
Wang, D. (FF-03) 585
Wang, G. (AW-07) 104
Wang, G. (BU-15) 216
Wang, G. (BV-13) 223
Wang, G. (CV-16) 338
Wang, G. (FW-07) 666
Wang, G. (GI-12) 721
Wang, G. (GP-06) 727
Wang, H. (AV-03) 93
Wang, H. (BA-01) 111
Wang, H. (DH-08) 388
Wang, H. (EC-10) 465
Wang, H. (EC-13) 466
Wang, H. (EF-12) 483
Wang, J. (AC-02) 11
Wang, J. (AE-03) 24
Wang, J. (AH-03) 45
Wang, J. (AQ-15) 68
Wang, J. (AW-07) 104
Wang, J. (BD-02) 131
Wang, J. (BQ-07) 182
Wang, J. (BR-12) 194
Wang, J. (BT-08) 202
Wang, J. (BV-13) 223
Wang, J. (CF-02) 263
Wang, J. (CH-08) 280
Wang, J. (CQ-13) 304
Wang, J. (CQ-14) 305
Wang, J. (CR-10) 310
Wang, J. (CR-16) 314
Wang, J. (CU-13) 330
Wang, J. (CW-06) 341
Wang, J. (CW-08) 342
Wang, J. (DB-04) 351
Wang, J. (DP-11) 400
Wang, J. (DQ-05) 406
Wang, J. (DQ-17) 412
Wang, J. (DT-06) 424

*Best student presentation award finalist

Wang, J. (EP-10) . . . 507
Wang, J. (ER-02) . . . 518
Wang, J. (FC-06) . . . 569
Wang, J. (FP-14) . . . 621
Wang, J. (FQ-14) . . . 629
Wang, J. (FT-12) . . . 646
Wang, J. (FV-15) . . . 662
Wang, J. (FW-02) . . . 663
Wang, J. (FW-07) . . . 666
Wang, J. (FW-09) . . . 667
Wang, J. (GP-06) . . . 727
Wang, J. (GV-09) . . . 764
Wang, J. (HD-10) . . . 787
Wang, J. (HF-13) . . . 801
Wang, K. (AD-09) . . . 19
Wang, K. (BB-02) . . . 114
Wang, K. (DE-07) . . . 371
Wang, K. (EB-10) . . . 458
Wang, K. (EQ-09) . . . 515
Wang, K. (HC-03) . . . 776
Wang, L. (DQ-15) . . . 410
Wang, L. (DQ-16) . . . 411
Wang, L. (EQ-12) . . . 516
Wang, L. (FH-04) . . . 600
Wang, L. (FQ-04) . . . 624
Wang, M. (BF-04) . . . 147
Wang, M. (BQ-03) . . . 180
Wang, M. (CW-13) . . . 344
Wang, M. (GU-04) . . . 755
Wang, M. (GU-07) . . . 757
Wang, P. (FQ-16) . . . 629
Wang, Q. (AQ-14) . . . 68
Wang, Q. (CE-08) . . . 258
Wang, Q. (CE-13) . . . 260
Wang, Q. (CT-06) . . . 319
Wang, Q. (CT-07) . . . 320
Wang, Q. (FQ-13) . . . 628
Wang, Q. (GE-03) . . . 690
Wang, Q. (GE-07) . . . 691
Wang, R. (EH-06) . . . 494
Wang, R. (ET-10) . . . 530
Wang, R. (ET-17) . . . 534
Wang, S. (BC-10) . . . 127
Wang, S. (BW-07) . . . 227
Wang, S. (CQ-07) . . . 302
Wang, S. (DB-08) . . . 353
Wang, S. (DG-07) . . . 382
Wang, S. (DQ-16) . . . 411
Wang, S. (FF-07) . . . 587
Wang, S. (FG-04) . . . 592
Wang, S. (FH-04) . . . 600
Wang, S. (FH-05) . . . 601
Wang, S. (FQ-04) . . . 624
Wang, S. (GA-02) . . . 668
Wang, S. (GU-09) . . . 758
Wang, S. (GU-10) . . . 758
Wang, T. (AD-05) . . . 18
Wang, T. (GB-02) . . . 671
Wang, W. (AD-05) . . . 18
Wang, W. (AW-08) . . . 105
Wang, W. (BW-13) . . . 230
Wang, W. (CB-01) . . . 236
Wang, W. (CV-10) . . . 336
Wang, W. (DP-18) . . . 403
Wang, W. (DR-08) . . . 416
Wang, X. (BD-02) . . . 131
Wang, X. (BP-03) . . . 172
Wang, X. (BP-04) . . . 173
Wang, X. (CF-02) . . . 263
Wang, X. (CF-10) . . . 267
Wang, X. (DB-02) . . . 350
Wang, X. (DB-11) . . . 354
Wang, X. (DC-05) . . . 358
Wang, X. (DC-06) . . . 359
Wang, X. (DP-17) . . . 403
Wang, X. (FI-10) . . . 611
Wang, X. (FT-12) . . . 646
Wang, X. (FV-08) . . . 659
Wang, X. (GF-08) . . . 700
Wang, Y. (AD-05) . . . 18
Wang, Y. (BT-05) . . . 200
Wang, Y. (CH-06) . . . 279
Wang, Y. (CV-02) . . . 333
Wang, Y. (DV-13) . . . 441
Wang, Y. (EH-07) . . . 495
Wang, Y. (ET-16) . . . 533
Wang, Y. (FA-02) . . . 559
Wang, Y. (FU-01) . . . 649
Wang, Y. (FU-05) . . . 651
Wang, Y. (GD-05) . . . 686
Wang, Z. (AW-02) . . . 101
Wang, Z. (BC-06) . . . 125
Wang, Z. (DV-12) . . . 440
Wang, Z. (EB-11) . . . 459
Wang, Z. (EU-11) . . . 539
Wang, Z. (GV-07) . . . 763
Ward, T.Z. (EE-07) . . . 475
Ward, T.Z. (GG-06) . . . 705
Warin, P. (EC-09) . . . 464
Warisarn, C. (GR-07) . . . 744
Warren, J.L. (HD-07) . . . 785
Wasef, S. (BC-11) . . . 128
Wasef, S. (EP-04) . . . 504
Watanabe, F. (FH-08) . . . 602
Watanabe, K. (BE-03) . . . 141
Watanabe, K. (DB-09) . . . 353
Watanabe, M. (EB-02) . . . 455
Watanabe, N. (BU-07) . . . 212
Watanabe, N. (BU-08) . . . 212
Watanabe, N. (GC-04) . . . 679
Watanabe, S. (EE-01) . . . 473
Watanabe, S. (GE-11) . . . 694
Watanabe, T. (AV-01) . . . 92
Watanabe, T. (AV-04) . . . 93
Watanabe, T. (AV-07) . . . 94
Watanabe, T. (AV-09) . . . 96
Watson, A. (CB-05) . . . 238
Watts, J. (HI-12) . . . 824
Weber, D. (AA-01) . . . 2
Weber, D. (DB-12) . . . 354
Weber, M. (FT-03) . . . 642
Weber, M. (GA-03) . . . 669
Weber, R. (GB-09) . . . 675
Wegrowe, J. (BD-01) . . . 131
Wehrmann, F. (CC-04) . . . 244
Wei, D. (FU-06) . . . 651
Wei, D. (GB-03) . . . 672
Wei, G. (DP-17) . . . 403
Wei, J. (GC-09) . . . 682
Wei, L. (BQ-07) . . . 182
Wei, Q. (FP-03) . . . 616
Weides, M. (CE-03) . . . 255
Weides, M. (CE-04) . . . 256
Weigand, M. (DE-03) . . . 369
Weigand, M. (ED-04) . . . 469
Weigand, M. (GE-08) . . . 692
Weigand, M. (GE-09) . . . 693
Weigand, M. (GE-12) . . . 694
Weil, R. (AI-12) . . . 56
Weiler, M. (GB-10) . . . 675
Weimann, T. (BG-08) . . . 154
Weinberg, I. (GA-05) . . . 670
Weinert, M. (GT-04) . . . 749
Weissenhofer, M. (AG-04) . . . 38
Weissitsch, L. (BF-09) . . . 149
Welbourne, E. (EA-04) . . . 454
Wen, H. (BT-02) . . . 199
Wen, Y. (CP-02) . . . 292
Wen, Y. (DV-05) . . . 437
Wen, Z. (AI-04) . . . 52
Wen, Z. (BE-02) . . . 140
Wende, H. (BD-04) . . . 133
Weng, L. (DV-01) . . . 435
Weng, L. (DV-03) . . . 436
Weng, Y. (ER-12) . . . 523
Weng, Y. (FV-12) . . . 661
Weschke, E. (AH-11) . . . 48
Wesenberg, D.J. (AP-06) . . . 60
Wesenberg, D.J. (CR-04) . . . 307
Wesenberg, D.J. (FV-02) . . . 657
Westmoreland, S.C. (AR-08) . . . 73
White, R. (BI-11) . . . 169
Wiesendanger, R. (AG-02) . . . 38
Wiesendanger, R. (AG-03) . . . 38
Wiesendanger, R. (EF-13) . . . 483
Wiesendanger, R. (GD-09) . . . 687
Wilhelm, C. (DG-12) . . . 384
Wilhelm, F. (BI-04) . . . 167
Wilhelm, F. (EH-08) . . . 495
Wilhelm, F. (FH-01) . . . 599
Wilhelm, H. (GF-04) . . . 698
Wilkins, S.B. (BH-03) . . . 159
Willa, K. (DI-09) . . . 394
Willard, M.A. (FQ-16) . . . 629
Wille, H. (CE-02) . . . 255
Willey, T. (EI-04) . . . 499
Willey, T. (EI-05) . . . 499
Williame, J. (EF-06) . . . 480
Willig, L. (BD-12) . . . 136
Willing, S. (BU-13) . . . 215
Willing, S. (CF-06) . . . 264
Willing, S. (GQ-13) . . . 740
Willson, R. (CQ-04) . . . 301

*Best student presentation award finalist

Wilson, M. (GF-01) . . . 697
Wimmer, T. (GB-10) . . . 675
Wines, D. (BI-11) . . . 169
Winkler, R. (HF-09) . . . 799
Winklhofer, M. (AR-08) . . . 73
Winklhofer, M. (BD-04) . . . 133
Winter, G. (BR-05) . . . 190
Wintz, S. (ED-01) . . . 467
Wittrock, S. (EQ-05) . . . 513
Wolf, G. (GC-01) . . . 678
Wolf, G. (GC-12) . . . 683
Wolf, M.S. (CR-02) . . . 306
Wolf, S. (FQ-18) . . . 630
Wollschlager, J. (AF-11) . . . 34
Wolter, A. (GD-01) . . . 685
Wolz, T. (CE-03) . . . 255
Won, C. (FG-03) . . . 592
Won, H. (CH-10) . . . 281
Won, H. (EH-06) . . . 494
Won, H. (ET-17) . . . 534
Won, H. (FR-02) . . . 632
Won, H. (GI-09) . . . 720
Wong, K. (AD-09) . . . 19
Wong, Q. (AD-10) . . . 20
Wong, Y. (AR-01) . . . 70
Wong, Y. (BP-12) . . . 177
Woo, J. (EV-09) . . . 546
Woo, J. (FR-09) . . . 636
Woo, S. (DC-01) . . . 356
Woo, S. (EG-07) . . . 488
Woodrum, D. (DG-11) . . . 384
Woods, J.S. (BH-03) . . . 159
Woods, S. (HE-12) . . . 794
Worledge, D. (GC-07) . . . 681
Wrona, J. (EP-08) . . . 506
Wu, B. (BC-06) . . . 125
Wu, C. (AR-11) . . . 74
Wu, D. (DD-05) . . . 363
Wu, G. (AW-08) . . . 105
Wu, G. (CV-10) . . . 336
Wu, G. (DR-08) . . . 416
Wu, H. (AD-09) . . . 19
Wu, H. (BB-02) . . . 114
Wu, H. (BW-01) . . . 225
Wu, H. (CQ-07) . . . 302
Wu, H. (DE-07) . . . 371
Wu, H. (EB-10) . . . 458
Wu, H. (EU-10) . . . 539
Wu, H. (FF-07) . . . 587
Wu, H. (GU-09) . . . 758
Wu, J. (BV-01) . . . 217
Wu, J. (CP-10) . . . 295
Wu, J. (CV-03) . . . 333
Wu, J. (DV-12) . . . 440
Wu, K. (CQ-13) . . . 304
Wu, K. (CQ-14) . . . 305
Wu, K. (GV-09) . . . 764
Wu, M. (BR-17) . . . 195
Wu, M. (BV-06) . . . 219
Wu, M. (CB-01) . . . 236
Wu, M. (CB-02) . . . 237
Wu, M. (CE-01) . . . 254
Wu, P. (BE-05) . . . 142
Wu, P. (DC-03) . . . 357
Wu, Q. (AR-07) . . . 72
Wu, Q. (FH-11) . . . 604
Wu, Q. (FH-15) . . . 605
Wu, R. (CF-02) . . . 263
Wu, S. (BC-07) . . . 125
Wu, S. (HH-09) . . . 814
Wu, S.Y. (AU-09) . . . 88
Wu, T. (BU-02) . . . 209
Wu, T. (BV-01) . . . 217
Wu, T. (CV-03) . . . 333
Wu, T. (CV-07) . . . 335
Wu, W. (BT-11) . . . 203
Wu, X. (BR-08) . . . 192
Wu, X. (FU-08) . . . 652
Wu, Y. (AV-15) . . . 98
Wu, Y. (AW-02) . . . 101
Wu, Y. (AW-12) . . . 106
Wu, Y. (BB-10) . . . 118
Wu, Y. (BQ-11) . . . 184
Wu, Y. (CD-02) . . . 249
Wu, Y. (DP-20) . . . 404
Wu, Y. (EG-09) . . . 489
Wu, Y. (EG-11) . . . 490
Wu, Y. (FC-04) . . . 567
Wu, Y. (FC-11) . . . 571
Wu, Y. (FG-03) . . . 592
Wu, Y. (GC-09) . . . 682
Wu, Y. (GI-11) . . . 721
Wu, Y. (GP-15) . . . 732
Wu, Y. (HB-08) . . . 773
Wu, Y. (HF-08) . . . 799
Wu, Z. (ET-16) . . . 533
Wurster, S. (BF-09) . . . 149
Wuth, C. (BH-05) . . . 160
Wuttig, M. (AQ-06) . . . 64
Wuttig, M. (AR-16) . . . 76
Wynn, A. (EF-03) . . . 479
Wyss, U. (FH-02) . . . 599

- X -

Xi, X. (CV-10) . . . 336
Xi, X. (DP-18) . . . 403
Xi, X. (DR-08) . . . 416
Xia, H. (DD-05) . . . 363
Xia, K. (HB-04) . . . 771
Xia, X. (DB-11) . . . 354
Xiang, Q. (BU-10) . . . 213
Xiao, D. (EA-05) . . . 454
Xiao, D. (ED-03) . . . 468
Xiao, F. (AW-11) . . . 106
Xiao, G. (EQ-09) . . . 515
Xiao, G. (GV-11) . . . 765
Xiao, G. (HI-10) . . . 823
Xiao, J. (AD-05) . . . 18
Xiao, J. (BV-07) . . . 220
Xiao, S. (EW-11) . . . 556
Xiao, Y. (EC-10) . . . 465
Xiao, Y. (EC-13) . . . 466
Xiao, Y. (EF-12) . . . 483
Xiao, Y. (FF-08) . . . 587
Xiao, Z. (DC-06) . . . 359
Xiao, Z. (DG-02) . . . 379
Xiao, Z. (FA-02) . . . 559
Xiao, Z. (HC-03) . . . 776
Xiao, Z. (HC-09) . . . 778
Xie, Q. (DB-08) . . . 353
Xie, Y. (CT-08) . . . 320
Xie, Z. (AR-07) . . . 72
Xing, H.G. (AC-04) . . . 12
Xing, H.G. (AH-01) . . . 44
Xing, H.G. (AH-05) . . . 45
Xing, H.G. (FG-13) . . . 597
Xing, M. (AT-05) . . . 81
Xing, M. (AT-06) . . . 82
Xing, M. (BH-13) . . . 164
Xing, T. (AW-02) . . . 101
Xing, W. (AA-03) . . . 3
Xiong, C. (DW-12) . . . 447
Xiong, Y. (AS-04) . . . 79
Xiong, Y. (BS-04) . . . 197
Xiong, Y. (BT-02) . . . 199
Xiong, Y. (CS-04) . . . 315
Xiong, Y. (DS-04) . . . 421
Xiong, Y. (ES-04) . . . 524
Xiong, Y. (FB-11) . . . 565
Xiong, Y. (FS-04) . . . 639
Xiong, Y. (GS-04) . . . 747
Xiong, Z. (BR-08) . . . 192
Xu, C. (HD-05) . . . 784
Xu, C. (HD-06) . . . 784
Xu, G. (EU-04) . . . 536
Xu, G. (FW-07) . . . 666
Xu, H. (EI-08) . . . 501
Xu, J. (AG-06) . . . 39
Xu, J. (AV-15) . . . 98
Xu, J. (BB-10) . . . 118
Xu, J. (DQ-15) . . . 410
Xu, J. (DQ-16) . . . 411
Xu, J. (EW-05) . . . 554
Xu, J. (FA-02) . . . 559
Xu, J. (FQ-04) . . . 624
Xu, Q. (AV-03) . . . 93
Xu, Q. (BQ-07) . . . 182
Xu, Q. (BU-15) . . . 216
Xu, Q. (FU-02) . . . 649
Xu, S. (EV-14) . . . 548
Xu, S. (HB-04) . . . 771
Xu, X. (BQ-03) . . . 180
Xu, X. (BQ-11) . . . 184
Xu, X. (BQ-13) . . . 185
Xu, X. (BV-06) . . . 219
Xu, X. (CD-02) . . . 249
Xu, X. (DP-20) . . . 404
Xu, X. (DU-03) . . . 429
Xu, X. (EA-05) . . . 454
Xu, X. (FH-11) . . . 604
Xu, X. (FH-15) . . . 605

*Best student presentation award finalist

Xu, X. (GP-15) 732
Xu, Y. (DD-01) 361
Xu, Y. (EB-10) 458
Xu, Y. (GB-03) 672
Xu, Z. (AH-06) 46
Xu, Z. (DQ-16) 411
Xu, Z. (FQ-04) 624
Xue, F. (AD-02) 16

- Y -

Yabukami, S. (CQ-08) 303
Yabukami, S. (DV-02) 435
Yabukami, S. (EV-16) 548
Yacoby, A. (BG-04) 153
Yafuso, M. (FW-05) 665
Yagil, A. (DE-09) 372
Yahagi, Y. (BQ-10) 184
Yakushiji, K. (BU-07) 212
Yakushiji, K. (BU-08) 212
Yakushiji, K. (CF-01) 262
Yakushiji, K. (CF-04) 263
Yakushiji, K. (DF-01) 374
Yakushiji, K. (EF-01) 478
Yakushiji, K. (EG-01) 485
Yakushiji, K. (EG-05) 487
Yakushiji, K. (EG-12) 491
Yakushiji, K. (EP-02) 503
Yakushiji, K. (EQ-04) 513
Yakushiji, K. (FC-05) 568
Yakushiji, K. (HI-06) 821
Yamada, K. (AV-02) 92
Yamada, M. (FW-03) 664
Yamada, S. (AC-07) 14
Yamada, S. (EF-09) 482
Yamada, S. (FW-03) 664
Yamada, S. (HF-05) 797
Yamada, T. (DT-04) 423
Yamada, T. (DT-05) 424
Yamada, Y. (CI-12) 289
Yamaguchi, A. (EQ-07) 514
Yamaguchi, M. (CH-02) 277
Yamaguchi, M. (GI-02) 716
Yamaguchi, M. (HH-08) 813
Yamaguchi, S. (FP-02) 615
Yamaguchi, T. (BV-12) 222
Yamaguchi, T. (CI-11) 289
Yamakage, A. (BV-12) 222
Yamakawa, H. (CC-09) 246
Yamamoto, K. (FT-08) 644
Yamamoto, M. (AE-12) 28
Yamamoto, T. (BQ-15) 186
Yamamoto, T. (EG-04) 486
Yamamoto, T. (EG-05) 487
Yamamoto, T. (EG-12) 491
Yamamoto, T. (EP-02) 503
Yamamoto, T.D. (AV-14) 98
Yamane, T. (CI-12) 289
Yamanouchi, M. (DH-02) 386
Yamanouchi, M. (HB-07) 773
Yamashita, A. (BP-13) 177
Yamashita, A. (CW-11) 343
Yamashita, A. (CW-12) 344
Yamashita, A. (DW-08) 445
Yamashita, A. (DW-16) 449
Yamashita, A. (DW-18) 450
Yamashita, S. (FH-06) 601
Yamauchi, K. (EE-08) 475
Yamazaki, T. (AP-01) 58
Yan, C. (DP-05) 397
Yan, F. (EH-06) 494
Yan, F. (ET-17) 534
Yan, S. (BF-08) 149
Yan, S. (CV-16) 338
Yan, S. (EW-11) 556
Yan, S. (GV-13) 765
Yan, W. (GI-07) 719
Yan, Y. (AQ-14) 68
Yan, Y. (HD-05) 784
Yan, Y. (HD-06) 784
Yanagihara, H. (FG-05) 592
Yanai, T. (BP-13) 177
Yanai, T. (CW-11) 343
Yanai, T. (CW-12) 344
Yanai, T. (DW-08) 445
Yanai, T. (DW-16) 449
Yanai, T. (DW-18) 450
Yanase, T. (BU-14) 215
Yanase, T. (CV-12) 337
Yanes, R. (CB-07) 239
Yang, B. (BQ-01) 179
Yang, B. (CG-02) 270
Yang, B. (CP-15) 297
Yang, B. (DB-08) 353
Yang, B. (FU-01) 649
Yang, C. (BB-02) 114
Yang, C. (BB-13) 120
Yang, C. (BT-11) 203
Yang, C. (BU-03) 210
Yang, C. (CP-10) 295
Yang, C. (GP-10) 729
Yang, F. (BB-03) 115
Yang, F. (BB-04) 116
Yang, F. (DC-03) 357
Yang, F. (DH-06) 387
Yang, F. (FG-12) 596
Yang, H. (BC-03) 123
Yang, H. (BV-09) 221
Yang, H. (CD-08) 252
Yang, H. (CG-02) 270
Yang, H. (CT-08) 320
Yang, H. (DB-04) 351
Yang, H. (DB-08) 353
Yang, H. (DF-02) 374
Yang, H. (DP-06) 398
Yang, H. (FV-11) 660
Yang, H. (GB-08) 674
Yang, H. (GU-04) 755
Yang, H. (GU-05) 755
Yang, H. (GU-06) 756
Yang, H. (HB-04) 771
Yang, H. (HB-06) 772
Yang, I. (CT-16) 323
Yang, I. (FR-07) 635
Yang, J. (AG-05) 39
Yang, J. (BR-14) 194
Yang, J. (EI-08) 501
Yang, J. (EQ-06) 514
Yang, J. (GP-01) 724
Yang, L. (FU-08) 652
Yang, M. (CB-10) 240
Yang, M. (CU-12) 330
Yang, M. (DB-08) 353
Yang, M. (DW-17) 450
Yang, M. (GB-02) 671
Yang, Q. (CH-08) 280
Yang, Q. (CU-12) 330
Yang, Q. (EU-04) 536
Yang, Q. (FI-15) 613
Yang, R. (BR-14) 194
Yang, S. (BC-01) 122
Yang, S. (BV-06) 219
Yang, S. (CV-06) 335
Yang, S. (DQ-16) 411
Yang, S. (FQ-04) 624
Yang, S. (GF-10) 701
Yang, S. (GP-01) 724
Yang, S. (GP-11) 729
Yang, S. (HB-05) 772
Yang, S. (HF-13) 801
Yang, S. (HG-01) 804
Yang, W. (BD-14) 138
Yang, W. (CF-10) 267
Yang, X. (BQ-08) 183
Yang, X. (BV-06) 219
Yang, X. (BW-01) 225
Yang, X. (EU-04) 536
Yang, X. (EU-10) 539
Yang, Y. (AQ-14) 68
Yang, Y. (BW-10) 229
Yang, Y. (EH-02) 492
Yang, Y. (GU-10) 758
Yang, Y. (HI-11) 823
Yano, M. (AR-08) 73
Yano, M. (CI-05) 286
Yao, A. (CH-04) 278
Yao, A. (GH-04) 709
Yao, C. (BC-10) 127
Yao, K. (HF-13) 801
Yao, W. (EA-05) 454
Yao, Y. (AW-08) 105
Yao, Y. (DI-09) 394
Yao, Y. (ED-09) 471
Yarbrough, P.M. (CI-09) 287
Yaresko, A. (BD-06) 134
Yaroslavtsev, A. (DD-02) 361
Yasin, F. (BG-06) 153
Yasin, F. (EG-11) 490
Yasin, F. (FC-04) 567
Yasuhira, M. (FC-07) 569
Yasui, A. (HF-06) 798
Yasui, S. (BU-14) 215

*Best student presentation award finalist

Yasui, Y. (AV-12) . . . 97
Yasui, Y. (AV-13) . . . 98
Yasui, Y. (AV-14) . . . 98
Yasukawa, Y. (CF-05) . . . 264
Yatsui, T. (FF-09) . . . 588
Yazdani, S. (GQ-12) . . . 739
Ye, L. (BU-02) . . . 209
Ye, L. (BV-01) . . . 217
Ye, L. (CV-03) . . . 333
Ye, L. (CV-07) . . . 335
Ye, X. (CU-09) . . . 329
Ye, X. (EU-11) . . . 539
Yee, S. (FP-01) . . . 615
Yen, F. (BI-07) . . . 168
Yen, W. (GU-10) . . . 758
Yen, Y. (BV-11) . . . 222
Yenugonda, V. (DR-12) . . . 418
Yi, D. (DH-01) . . . 386
Yim, H. (CW-09) . . . 343
Yin, M. (HD-09) . . . 786
Yin, T. (CI-07) . . . 287
Yin, X. (HI-11) . . . 823
Ying, S. (EQ-09) . . . 515
Yochelis, S. (BG-09) . . . 155
Yoda, H. (AC-06) . . . 13
Yokota, K. (CQ-08) . . . 303
Yokoyama, T. (FT-08) . . . 644
Yomogita, T. (BP-08) . . . 174
Yomogita, T. (CI-02) . . . 284
Yoo, M. (CC-01) . . . 243
Yoo, W. (AB-07) . . . 6
Yoo, W. (CP-17) . . . 298
Yoo, W. (DR-14) . . . 419
Yoon, I. (EV-03) . . . 542
Yoon, I. (EV-09) . . . 546
Yoon, S. (AR-13) . . . 75
Yoon, S. (AR-14) . . . 76
Yoon, S. (BR-02) . . . 189
Yoon, S. (BR-15) . . . 195
Yoon, S. (CC-03) . . . 244
Yoon, S. (HI-03) . . . 819
Yoshibe, A. (FF-10) . . . 588
Yoshida, C. (EP-11) . . . 507
Yoshida, H. (EB-02) . . . 455
Yoshida, H. (EE-01) . . . 473
Yoshida, K. (DW-10) . . . 446
Yoshidome, K. (GH-02) . . . 708
Yoshihara, Y. (CP-04) . . . 293
Yoshikawa, H. (CR-08) . . . 309
Yoshikawa, H. (DC-09) . . . 360
Yoshikawa, H. (HD-03) . . . 783
Yoshiki, K. (GH-02) . . . 708
Yoshimura, S. (FU-10) . . . 652
Yoshioka, T. (CI-06) . . . 286
Yoshioka, T. (FH-06) . . . 601
You, B. (BQ-07) . . . 182
You, B. (CR-16) . . . 314
You, C. (AB-07) . . . 6
You, C. (CG-05) . . . 272
You, C. (CG-08) . . . 273
You, C. (EW-08) . . . 555
You, D. (EV-05) . . . 543
You, L. (BQ-08) . . . 183
You, W. (BT-02) . . . 199
You, W. (FB-11) . . . 565
Young, J. (FP-01) . . . 615
Yu, B. (BA-01) . . . 111
Yu, B. (DH-07) . . . 388
Yu, C. (GQ-08) . . . 737
Yu, C. (GQ-09) . . . 738
Yu, E. (GA-03) . . . 669
Yu, G. (AD-09) . . . 19
Yu, G. (AW-13) . . . 107
Yu, G. (BA-01) . . . 111
Yu, G. (BR-01) . . . 189
Yu, G. (DB-11) . . . 354
Yu, G. (DE-03) . . . 369
Yu, H. (AI-08) . . . 54
Yu, H. (GI-11) . . . 721
Yu, J. (CR-11) . . . 311
Yu, K. (CU-03) . . . 325
Yu, K. (EU-05) . . . 537
Yu, L. (EP-05) . . . 505
Yu, P. (AH-11) . . . 48
Yu, R. (BV-06) . . . 219
Yu, S. (BB-03) . . . 115
Yu, S. (BB-04) . . . 116
Yu, S. (EW-11) . . . 556
Yu, S. (FG-12) . . . 596
Yu, T. (BQ-01) . . . 179
Yu, X. (DB-08) . . . 353
Yu, Y. (CC-03) . . . 244
Yu, Y. (FU-02) . . . 649
Yu, Z. (AQ-15) . . . 68
Yu, Z. (AR-11) . . . 74
Yu, Z. (DQ-17) . . . 412
Yuan, F. (GQ-05) . . . 736
Yuan, J. (EU-02) . . . 535
Yuan, W. (AI-11) . . . 55
Yuan, W. (BB-09) . . . 118
Yuan, W. (CB-08) . . . 239
Yuan, W. (CB-09) . . . 240
Yuan, X. (DW-07) . . . 445
Yuan, Y. (BQ-07) . . . 182
Yuan, Y. (HF-11) . . . 800
Yuan, Z. (HB-04) . . . 771
Yuan, Z. (HF-08) . . . 799
Yuasa, H. (AF-10) . . . 34
Yuasa, H. (GB-09) . . . 675
Yuasa, S. (BQ-15) . . . 186
Yuasa, S. (BU-07) . . . 212
Yuasa, S. (BU-08) . . . 212
Yuasa, S. (CF-01) . . . 262
Yuasa, S. (CF-04) . . . 263
Yuasa, S. (CF-05) . . . 264
Yuasa, S. (EF-01) . . . 478
Yuasa, S. (EF-08) . . . 481
Yuasa, S. (EF-09) . . . 482
Yuasa, S. (EG-01) . . . 485
Yuasa, S. (EG-05) . . . 487
Yuasa, S. (EG-12) . . . 491
Yuasa, S. (EP-02) . . . 503
Yuasa, S. (EQ-04) . . . 513
Yuasa, S. (HI-06) . . . 821
Yubuta, K. (EH-07) . . . 495
Yue, D. (AE-09) . . . 27
Yue, L. (GF-03) . . . 698
Yue, M. (AR-07) . . . 72
Yue, M. (DQ-09) . . . 408
Yue, M. (FH-11) . . . 604
Yue, M. (FH-14) . . . 605
Yue, M. (FH-15) . . . 605
Yue, S. (CU-12) . . . 330
Yue, S. (DW-17) . . . 450
Yuk, J. (GB-13) . . . 677
Yun, C. (FW-06) . . . 665
Yun, D. (AD-12) . . . 21

- Z -

Zabow, G. (DG-03) . . . 380
Zadorozhniy, A. (DP-03) . . . 396
Zadrozny, J. (HE-01) . . . 790
Zadrozny, J. (HE-02) . . . 790
Zaeimbashi, M. (AH-06) . . . 46
Zaeimbashi, M. (AH-07) . . . 46
Zahedinejad, M. (EG-02) . . . 485
Zahnd, G. (AP-03) . . . 59
Zahnd, G. (FV-10) . . . 660
Zaitsev, A. (BT-01) . . . 199
Zajac, M. (CP-05) . . . 293
Zalewski, T. (DG-06) . . . 381
Zamani Kouhpanji, M. (DG-05) . . . 381
Zamani Kouhpanji, M. (DU-09) . . . 432
Zamora, J. (DQ-01) . . . 405
Zang, B. (GH-03) . . . 709
Zang, J. (HA-04) . . . 768
Zanolli, Z. (FB-01) . . . 561
Zarpellon, J. (BV-03) . . . 218
Zázvorka, J. (AB-13) . . . 9
Zázvorka, J. (CP-09) . . . 295
Zázvorka, J. (DT-10) . . . 425
Zázvorka, J. (GF-13) . . . 702
Zázvorka, J. (HH-04) . . . 811
Zborowski, M. (FF-02) . . . 584
Zehner, J. (AH-10) . . . 47
Zeissler, K. (DE-05) . . . 369
Zeissler, K. (ED-01) . . . 467
Zelent, M. (GE-12) . . . 694
Zemen, J. (AB-13) . . . 9
Zemen, J. (AQ-07) . . . 64
Zemen, J. (CP-09) . . . 295
Zeng, F. (HF-08) . . . 799
Zeng, H. (CV-06) . . . 335
Zeng, H. (HF-13) . . . 801
Zeng, J. (HF-08) . . . 799
Zeng, L. (FP-15) . . . 622
Zeng, Z. (AC-08) . . . 15
Zeng, Z. (AW-10) . . . 105
Zeng, Z. (CI-13) . . . 290
Zeugner, A. (GD-01) . . . 685
Zeuschner, S. (BD-12) . . . 136

*Best student presentation award finalist

Zgirski, M. (EB-13) 460
Zhai, Y. (CR-16) 314
Zhan, X. (CD-07) 251
Zhang, A. (FU-08) 652
Zhang, B. (DV-03) 436
Zhang, C. (AA-01) 2
Zhang, C. (BG-11) 156
Zhang, C. (BT-08) 202
Zhang, C. (CH-08) 280
Zhang, C. (CU-12) 330
Zhang, C. (CU-15) 331
Zhang, C. (DF-05) 376
Zhang, C. (ET-16) 533
Zhang, C. (FI-15) 613
Zhang, C. (FQ-14) 629
Zhang, C. (GH-01) 708
Zhang, D. (AR-07) 72
Zhang, D. (AV-03) 93
Zhang, D. (BD-02) 131
Zhang, D. (BU-04) 210
Zhang, D. (CF-02) 263
Zhang, D. (FH-11) 604
Zhang, D. (FH-15) 605
Zhang, D. (FT-12) 646
Zhang, E. (BC-02) 122
Zhang, F. (CW-06) 341
Zhang, F. (HE-12) 794
Zhang, G. (BB-10) 118
Zhang, G. (DB-11) 354
Zhang, G. (EP-09) 506
Zhang, H. (AB-13) 9
Zhang, H. (AR-07) 72
Zhang, H. (BG-04) 153
Zhang, H. (CI-07) 287
Zhang, H. (CV-10) 336
Zhang, H. (DQ-02) 405
Zhang, H. (DQ-09) 408
Zhang, H. (DR-08) 416
Zhang, H. (EE-08) 475
Zhang, H. (EP-15) 509
Zhang, H. (FH-11) 604
Zhang, H. (FH-14) 605
Zhang, H. (FH-15) 605
Zhang, H. (GB-12) 676
Zhang, J. (AH-03) 45
Zhang, J. (AH-09) 47
Zhang, J. (BA-04) 112
Zhang, J. (BC-01) 122
Zhang, J. (BQ-01) 179
Zhang, J. (BT-10) 203
Zhang, J. (DQ-16) 411
Zhang, J. (FQ-04) 624
Zhang, K. (AC-03) 12
Zhang, K. (AW-07) 104
Zhang, K. (BV-13) 223
Zhang, K. (CV-16) 338
Zhang, K. (FW-07) 666
Zhang, K. (GP-06) 727
Zhang, L. (CI-13) 290
Zhang, L. (EU-09) 538
Zhang, L. (FP-10) 619
Zhang, M. (BP-02) 172
Zhang, N. (FF-02) 584
Zhang, P. (AG-09) 41
Zhang, P. (BB-15) 121
Zhang, P. (BD-13) 137
Zhang, P. (CB-05) 238
Zhang, P. (DQ-02) 405
Zhang, P. (EB-10) 458
Zhang, Q. (BT-02) 199
Zhang, Q. (ED-04) 469
Zhang, Q. (GQ-14) 740
Zhang, S. (AB-09) 7
Zhang, S. (AE-01) 24
Zhang, S. (AW-20) 110
Zhang, S. (CB-01) 236
Zhang, S. (CB-03) 237
Zhang, S. (CP-03) 292
Zhang, S. (DB-07) 352
Zhang, S. (DE-03) 369
Zhang, S. (FB-11) 565
Zhang, S. (FG-04) 592
Zhang, S. (GB-08) 674
Zhang, S. (GF-07) 700
Zhang, T. (CU-09) 329
Zhang, T. (EU-11) 539
Zhang, W. (AB-09) 7
Zhang, W. (AS-04) 79
Zhang, W. (BB-10) 118
Zhang, W. (BQ-07) 182
Zhang, W. (BS-04) 197
Zhang, W. (BT-02) 199
Zhang, W. (CB-01) 236
Zhang, W. (CS-04) 315
Zhang, W. (DS-04) 421
Zhang, W. (EH-07) 495
Zhang, W. (ER-02) 518
Zhang, W. (ES-04) 524
Zhang, W. (EW-04) 553
Zhang, W. (EW-11) 556
Zhang, W. (FA-02) 559
Zhang, W. (FB-11) 565
Zhang, W. (FS-04) 639
Zhang, W. (GF-03) 698
Zhang, W. (GH-01) 708
Zhang, W. (GS-04) 747
Zhang, W. (HE-08) 793
Zhang, W. (HF-08) 799
Zhang, X. (AH-09) 47
Zhang, X. (AW-12) 106
Zhang, X. (AW-19) 110
Zhang, X. (AW-20) 110
Zhang, X. (BA-04) 112
Zhang, X. (BH-06) 160
Zhang, X. (BH-07) 161
Zhang, X. (BP-02) 172
Zhang, X. (BP-03) 172
Zhang, X. (BP-04) 173
Zhang, X. (BR-01) 189
Zhang, X. (CP-02) 292
Zhang, X. (DW-12) 447
Zhang, X. (EA-05) 454
Zhang, X. (EP-01) 503
Zhang, X. (EP-06) 505
Zhang, X. (FU-01) 649
Zhang, X. (GP-09) 728
Zhang, X. (HA-01) 767
Zhang, X. (HI-10) 823
Zhang, Y. (AC-03) 12
Zhang, Y. (AQ-12) 66
Zhang, Y. (AW-07) 104
Zhang, Y. (BQ-08) 183
Zhang, Y. (BV-06) 219
Zhang, Y. (BV-13) 223
Zhang, Y. (BW-01) 225
Zhang, Y. (CV-16) 338
Zhang, Y. (DQ-16) 411
Zhang, Y. (EB-04) 456
Zhang, Y. (EP-15) 509
Zhang, Y. (EU-04) 536
Zhang, Y. (EU-10) 539
Zhang, Y. (EW-11) 556
Zhang, Y. (FQ-04) 624
Zhang, Y. (FW-07) 666
Zhang, Y. (GP-06) 727
Zhang, Y. (GU-09) 758
Zhang, Y. (GV-11) 765
Zhang, Y. (HF-03) 796
Zhang, Y. (HI-10) 823
Zhang, Z. (AC-04) 12
Zhang, Z. (AF-08) 33
Zhang, Z. (AH-05) 45
Zhang, Z. (AW-07) 104
Zhang, Z. (BA-01) 111
Zhang, Z. (BQ-11) 184
Zhang, Z. (BV-13) 223
Zhang, Z. (CV-16) 338
Zhang, Z. (DB-08) 353
Zhang, Z. (DH-07) 388
Zhang, Z. (ER-02) 518
Zhang, Z. (EU-02) 535
Zhang, Z. (EW-04) 553
Zhang, Z. (EW-09) 555
Zhang, Z. (FA-02) 559
Zhang, Z. (FB-11) 565
Zhang, Z. (FG-13) 597
Zhang, Z. (FI-15) 613
Zhang, Z. (FT-04) 642
Zhang, Z. (FT-05) 643
Zhang, Z. (FV-07) 659
Zhang, Z. (FW-07) 666
Zhang, Z. (GP-06) 727
Zhao, C. (ER-02) 518
Zhao, G. (HF-10) 800
Zhao, H. (AV-03) 93
Zhao, H. (DD-05) 363
Zhao, H. (FQ-01) 623
Zhao, J. (GB-03) 672
Zhao, K. (CP-12) 296
Zhao, K. (HF-10) 800
Zhao, N. (CT-06) 319
Zhao, S. (BF-10) 150
Zhao, T. (DQ-15) 410

*Best student presentation award finalist

Zhao, T. (DT-13) . . . 426
Zhao, W. (AC-03) . . . 12
Zhao, W. (AW-07) . . . 104
Zhao, W. (AW-12) . . . 106
Zhao, W. (BC-06) . . . 125
Zhao, W. (BQ-04) . . . 180
Zhao, W. (BV-13) . . . 223
Zhao, W. (CF-10) . . . 267
Zhao, W. (CV-16) . . . 338
Zhao, W. (DB-02) . . . 350
Zhao, W. (DP-17) . . . 403
Zhao, W. (ED-09) . . . 471
Zhao, W. (EP-14) . . . 509
Zhao, W. (EP-15) . . . 509
Zhao, W. (FW-07) . . . 666
Zhao, W. (GP-06) . . . 727
Zhao, W. (GV-13) . . . 765
Zhao, X. (ET-10) . . . 530
Zhao, Y. (CV-02) . . . 333
Zhao, Y. (CV-15) . . . 338
Zheng, H. (BF-10) . . . 150
Zheng, L. (BF-10) . . . 150
Zheng, P. (GU-07) . . . 757
Zheng, R. (CQ-05) . . . 301
Zheng, X. (DQ-15) . . . 410
Zheng, X. (DQ-16) . . . 411
Zheng, X. (FQ-04) . . . 624
Zheng, Z. (AC-03) . . . 12
Zheng, Z. (AW-07) . . . 104
Zheng, Z. (BF-08) . . . 149
Zheng, Z. (BR-08) . . . 192
Zheng, Z. (BV-13) . . . 223
Zheng, Z. (CV-16) . . . 338
Zheng, Z. (FW-07) . . . 666
Zheng, Z. (GP-06) . . . 727
Zhong, H. (EW-11) . . . 556
Zhong, X. (CQ-12) . . . 304
Zhong, Y. (AF-10) . . . 34
Zhong, Z. (GB-12) . . . 676
Zhou Hagström, N. (BD-01) . . . 131
Zhou Hagström, N. (DD-02) . . . 361
Zhou, B. (BC-02) . . . 122
Zhou, B. (HD-05) . . . 784
Zhou, B. (HD-06) . . . 784
Zhou, C. (AV-15) . . . 98
Zhou, C. (BB-10) . . . 118
Zhou, D. (BF-10) . . . 150
Zhou, H. (BA-01) . . . 111
Zhou, H. (BC-06) . . . 125
Zhou, H. (DH-07) . . . 388
Zhou, H. (EU-02) . . . 535
Zhou, L. (DD-05) . . . 363
Zhou, M. (ET-16) . . . 533
Zhou, S. (AV-03) . . . 93
Zhou, S. (BU-15) . . . 216
Zhou, S. (DD-05) . . . 363
Zhou, S. (EE-10) . . . 476
Zhou, S. (FU-02) . . . 649
Zhou, S. (FV-11) . . . 660
Zhou, S. (HB-04) . . . 771
Zhou, S. (HB-06) . . . 772
Zhou, S. (HF-11) . . . 800
Zhou, T. (BG-04) . . . 153
Zhou, T. (DB-08) . . . 353
Zhou, W. (AG-06) . . . 39
Zhou, W. (AG-11) . . . 42
Zhou, W. (BF-08) . . . 149
Zhou, W. (HD-12) . . . 787
Zhou, X. (DV-05) . . . 437
Zhou, X. (FQ-13) . . . 628
Zhou, Y. (AW-12) . . . 106
Zhou, Y. (AW-19) . . . 110
Zhou, Y. (DC-07) . . . 359
Zhou, Y. (DR-04) . . . 415
Zhou, Z. (DV-12) . . . 440
Zhou, Z. (GV-13) . . . 765
Zhu, B. (BQ-08) . . . 183
Zhu, D. (GB-08) . . . 674
Zhu, J. (BC-02) . . . 122
Zhu, J. (CU-15) . . . 331
Zhu, J. (DD-02) . . . 361
Zhu, J. (FR-03) . . . 633
Zhu, J. (HD-05) . . . 784
Zhu, J. (HD-06) . . . 784
Zhu, J. (HD-09) . . . 786
Zhu, J. (HD-15) . . . 789
Zhu, L. (BE-07) . . . 142
Zhu, L. (GP-15) . . . 732
Zhu, M. (BB-03) . . . 115
Zhu, M. (BB-04) . . . 116
Zhu, M. (BF-10) . . . 150
Zhu, M. (BP-02) . . . 172
Zhu, M. (FB-02) . . . 561
Zhu, M. (FG-12) . . . 596
Zhu, M. (FH-04) . . . 600
Zhu, M. (FH-05) . . . 601
Zhu, T. (CD-07) . . . 251
Zhu, T. (FB-02) . . . 561
Zhu, W. (FP-09) . . . 619
Zhu, X. (FH-04) . . . 600
Zhu, Y. (AW-07) . . . 104
Zhu, Z. (BC-03) . . . 123
Zhu, Z. (CR-10) . . . 310
Zhu, Z. (DB-04) . . . 351
Zhu, Z. (GU-05) . . . 755
Zhu, Z. (GU-06) . . . 756
Zhukov, A. (AQ-13) . . . 67
Zhukov, A. (GH-05) . . . 710
Zhukov, A. (GH-07) . . . 711
Zhukov, A. (GH-15) . . . 715
Zhukov, A. (GI-03) . . . 717
Zhukov, D.G. (FH-01) . . . 599
Zhukova, V. (AQ-13) . . . 67
Zhukova, V. (GH-05) . . . 710
Zhukova, V. (GH-07) . . . 711
Zhukova, V. (GH-15) . . . 715
Zhukova, V. (GI-03) . . . 717
Zhuo, F. (CP-02) . . . 292
Zietek, S. (AD-11) . . . 20
Zieve, R.J. (BA-04) . . . 112
Zilske, P. (AB-04) . . . 5
Zilske, P. (FG-09) . . . 595
Ziman, T. (EC-05) . . . 463
Zimanyi, G. (AR-08) . . . 73
Zingsem, B.W. (BD-04) . . . 133
Zink, B.L. (AD-05) . . . 18
Zink, B.L. (AP-06) . . . 60
Zink, B.L. (BE-01) . . . 140
Zink, B.L. (BR-17) . . . 195
Zink, B.L. (CR-04) . . . 307
Zink, B.L. (FV-02) . . . 657
Zink, B.R. (CU-13) . . . 330
Zink, B.R. (EP-10) . . . 507
Zink, B.R. (FW-09) . . . 667
Ziq, K.A. (DQ-08) . . . 407
Ziv, A. (BG-09) . . . 155
Zivanov, L.D. (DV-10) . . . 439
Zivotsky, O. (BP-11) . . . 176
Zivotsky, O. (BP-15) . . . 178
Zou, B. (AB-13) . . . 9
Zou, B. (CP-09) . . . 295
Zou, Y. (BV-01) . . . 217
Zou, Z. (GV-08) . . . 763
Zucchetti, C. (AE-08) . . . 26
Zucchetti, C. (DP-07) . . . 398
Zucchetti, C. (EB-01) . . . 455
Zukrowski, J. (GG-11) . . . 707
Zukrowski, J. (HH-07) . . . 813
Zuo, J. (BP-02) . . . 172
Zuo, S. (DT-13) . . . 426
Zusin, D. (ER-03) . . . 519
Zvezdin, K.A. (EV-17) . . . 549

*Best student presentation award finalist